CODEN: JASMAN 4966

THE JOURNAL of the Acoustical Society of America

Vol. 106, No. 5 November 1999

SOUNDINGS SECTION

GENERAL LINEAR ACOUSTICS [20]

NONLINEAR ACOUSTICS [25]

AEROACOUSTICS, ATMOSPHERIC SOUND [28]

UNDERWATER SOUND [30]

(Continued)

CONTENTS—*Continued from preceding page*

(Continued)

CONTENTS—*Continued from preceding page*

PHYSIOLOGICAL ACOUSTICS [64]

PSYCHOLOGICAL ACOUSTICS [66]

SPEECH PRODUCTION [70]

SPEECH PERCEPTION [71]

(Continued)

CONTENTS—*Continued from preceding page*

Time delay spectrometry for hydrophone calibrations below 1 MHz

Paul M. Gammell and Gerald R. Harris

Center for Devices and Radiological Health, Food and Drug Administration, Rockville, MD 20850, USA
pmg@cdrh.fda.gov grh@cdrh.fda.gov

Abstract: Knowing the response of miniature ultrasonic hydrophones at frequencies below 1 MHz is important for assessing the accuracy of acoustic pressure pulse measurements in medical ultrasound applications. Therefore, a time delay spectrometry (TDS) system was developed as an efficient means to measure hydrophone sensitivity in this frequency range. In TDS a swept-frequency signal is transmitted. A tracking receiver distinguishes arrivals with different propagation delays by their frequency offset relative to the signal being transmitted, thus eliminating spurious signals such as those reflected from the water surface or tank walls. Two piezoelectric ceramic source transducers were used: a standard planar disk and a disk with varying thickness to broaden the thickness-resonance. This latter design was preferred for its more uniform response without significant sensitivity loss. TDS is not an absolute method, but it was demonstrated to provide efficient, accurate calibrations via comparison with a reference hydrophone using a substitution technique.

PACS numbers: 43.38.Fx, 43.58.Vb

Introduction

Miniature ultrasonic hydrophones are the primary measurement devices used to characterize the acoustic pressure fields produced by medical diagnostic ultrasound transducers. Because of the broadband nature of the pressure pulses, particularly when distorted by nonlinear propagation effects in water as commonly observed, it is important that the hydrophone's response be known over a wide range of frequencies extending down to approximately 100 kHz.[1] However, at present, hydrophone sensitivities below 1 MHz are rarely reported because of the lack of suitable calibration techniques. In this regard, three-transducer reciprocity and laser interferometry have been used in this frequency range, but these are time-consuming single-frequency techniques.[2,3] A method employing broadband, plane-wave pulses of known spectral content also has been used successfully, but the sensitivity of this method is low because of the unfocused, nonresonant operation of the source transducer.[4]

A calibration procedure that overcomes both of these deficiencies involves the swept-frequency technique known as time delay spectrometry or TDS. [5-7] However, in the past TDS has been used for hydrophone calibrations only at frequencies above 1-2 MHz. Therefore, a calibration system based on TDS, but designed to operate at frequencies from approximately 100 kHz to 2 MHz, was successfully developed and tested, and the results are presented herein. In this approach, the digitized TDS response of a "reference" hydrophone, i.e., one having a known frequency response, was subtracted (on a dB scale) from the response of a "test" hydrophone to be calibrated. This procedure results in an efficient method of producing sensitivity plots over the entire frequency range.

In the following sections, a description is given of the TDS swept-frequency generation system, the source transducers used to create the broadband calibration field, and the reference

and test hydrophones. Then calibration plots are presented, including a comparison with single-frequency sensitivity measurements performed at a national measurement laboratory using the methods of Refs. 2 and 3.

TDS system

The basics of TDS, including its signal-to-noise enhancement (compared to a broadband pulse) and immunity to multipath interference effects, have been described elsewhere (see Refs. 5-7 and references therein). In the implementation used here, the source transducer is excited with a sine wave signal whose frequency is swept linearly with time. At any instant, signals from paths with different propagation times or time delays will have different frequencies when they arrive at the receiving transducer. The frequency difference between any two signals is equal to the difference in their propagation times or time delays multiplied by the sweep rate (in frequency per unit time). A narrow-band tracking filter passes only those signals that fall within the time-delay window around the desired time delay. The width of this time delay window is equal to the bandwidth of the tracking filter divided by the sweep rate. Because the frequency is swept linearly with time, the tracking filter follows the transmitted signal with a constant frequency offset. Because of this constant frequency offset, the tracking filter can be implemented by heterodyning the received signal with the transmitted signal frequency and using a fixed-frequency filter.

A tracking receiver with a -3 dB bandwidth of 300 Hz was used. For the frequency sweep rate of 20 MHz/s, this bandwidth provides a 3-dB temporal resolution of 15 μs, which yields a measured -3 dB full-width frequency resolution of 32 kHz. Although the source was swept from 0–2 MHz, only the portion between 100 kHz and 1.9 MHz was used for data. This is due to limitations of this particular implementation: at the end of the sweep the transmitted and received signals were not simultaneously available to heterodyne, and there were start-up transients at the beginning of the sweep.

For all measurements, the source transducers were driven with a swept frequency source of 50 ohms impedance, which was specified to provide an output of 200 mW into a 50-ohm load. This level, which could have been increased by at least an order of magnitude, was found to be sufficient for these experiments. The voltage sensitivity of the TDS system was measured by connecting the tracking receiver to a calibrated CW source instead of the hydrophone output.

Measurements were made in a 40x40x62-cm tank filled with distilled, degassed, room-temperature water. The direction of the ultrasound beam was along the 62-cm tank dimension, and the back of the tank was lined with an acoustically absorbing rubber sheet.

Source transducers and hydrophones

The main factor that determines the usable frequency range for calibration is the bandwidth of the source transducer. In this study, two different transducers were used: a 3.8 cm diameter, plane ceramic disk with a thickness-resonance frequency of 500 kHz (Model V389, Panametrics, Waltham, MA) and a 2.5 cm diameter, plano-concave, broadband ceramic disk fabricated by Gerald Posakony of the Battelle Pacific Northwest National Laboratory. Posakony used the design of Vopilkin et al.,[8] a design that also has been used in a medical imager based on TDS.[7] The nonuniform thickness of the plano-concave transducer acted to broaden the usual thickness-resonance behavior. The plane surface was in contact with the water; the concave surface was spherical and the thickest and thinnest dimensions were 1.37 mm and 0.25 mm, respectively. (This transducer was a split disk originally designed for transmit-receive use, but in the present work the two halves were connected electrically in parallel for transmit-only operation.) The back surfaces of both transducers were acoustically damped.

Two commercial hydrophones having piezoelectric polyvinylidene fluoride as the active element were used: a bilaminar spot-poled membrane hydrophone for the reference device (Model 804, Perceptron, Hatboro, PA) and a needle-type for the test hydrophone (Model HPM1/1, Precision Acoustics, Dorchester, England).[4] The geometrical diameters of the piezoelectrically active regions were 0.4 mm and 1.0 mm for the membrane and needle, respectively. The needle hydrophone included an integral preamplifier. An external broadband amplifier having 40 dB gain was used with the membrane hydrophone (Model 5676, Panametrics).

TDS calibration via substitution

For the substitution calibration procedure, both hydrophones were placed at the same location in the ultrasound field, and their responses were measured. The test hydrophone sensitivity, $M_t(f)$, at frequency f, is

$$M_t(f) = M_r(f) \bullet S_t(f,z)/S_r(f,z) \quad \text{V/Pa}, \tag{1}$$

where $M_r(f)$ is the reference hydrophone sensitivity, and $S_t(f,z)$ and $S_r(f,z)$ are the measured test and reference hydrophone responses at point z on the source transducer axis.

Equation (1) was evaluated (in dB) using the needle and membrane hydrophones as the test and reference hydrophones, respectively. The membrane hydrophone was chosen as the reference because membrane hydrophones have been shown to have a flat, uniform response (within the measurement uncertainty of approximately ±1 dB) over the frequency range of interest.[3,4] Therefore, $M_r(f)$ can be treated as a constant whose value was determined as follows: An independent calibration of the needle hydrophone used had been performed previously at discrete frequencies from 100 kHz to 1 MHz in 100 kHz steps (National Physical Laboratory, UK), so a separate comparison of the two hydrophone outputs was made at 1 MHz, from which M_r(1 MHz) was found to be 1.4 V/MPa (at amplifier output). This value was taken as the membrane (reference) sensitivity $M_r(f)$ in Eq. (1) over the measured frequency range. In addition, errors introduced by spatial averaging over the hydrophone's active surfaces were negligible, because the measured -6 dB beamwidths for the planar transducer at 1.5 MHz and the plano-concave transducer at 1.9 MHz were both 1 cm or greater.

Selection of distance z entails a trade-off, in that z should be chosen large enough to avoid significant near-field effects at the highest frequency of interest, but small enough to maintain useful pressure amplitudes at the lower frequencies. Regarding the latter, a decrease in frequency places a given axial position farther beyond the last axial maximum, causing a corresponding drop in the pressure amplitude. For the planar transducer, a measurement distance of 25 cm was chosen, which, based on planar piston behavior, is at the last axial maximum at 1 MHz. For the plano-concave transducer, measurements were made at four source-to-hydrophone distances to investigate potential near/far-field effects: z = 11, 17, 21, and 25 cm. At 1 MHz the 11-cm distance is at the last axial maximum for an ideal planar piston transducer having the same diameter as the plano-concave transducer.

Results and discussion

As stated previously, the usable frequency range for calibration is determined primarily by the bandwidth of the source transducer. Therefore, first the TDS system was used with the membrane hydrophone to measure the transmit spectrum T(f,z) = Sr(f,z)/Mr(f). The results for both source transducers when driven by the 200 mW, 50-ohm source described above are plotted in Fig. 1 from 100 kHz to 1.9 MHz. The peak pressures were between 30 kPa and 100 kPa, levels at which nonlinear effects are negligible for these calibration measurements. The acoustic output of the 500 kHz planar transducer shows a transmit spectrum that peaks at the fundamental

(approximately 500 kHz) and third harmonic. It has a sharp minimum at the second harmonic, as expected for a simple thickness-mode resonance. The responses of the plano-concave transducer at all four distances are similar but decrease with increasing distance.

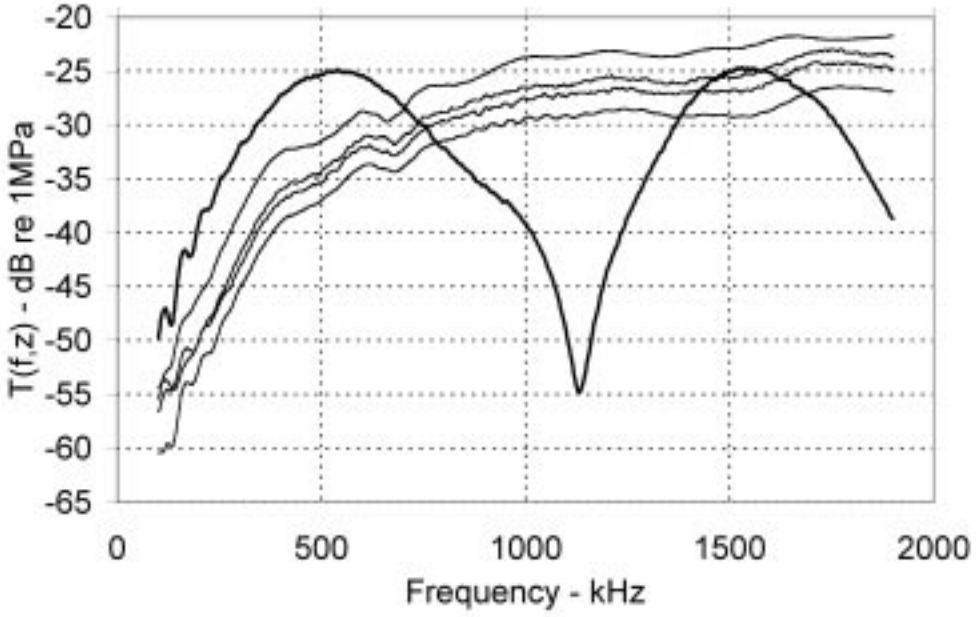

Fig.1. Pressure response, T(f,z), vs frequency for the 500 kHz planar source transducer at z = 25 cm (heavy line), and for the plano-concave source transducer at, top to bottom, z = 11, 17, 21, and 25 cm.

Figure 2 shows the results of using the plano-concave transducer to calibrate the needle hydrophone via substitution. As described above, for each of the four calibrations, the acoustic pressure was measured with the membrane hydrophone, as shown in Fig. 1. Then the needle hydrophone was substituted at the same location, and its response was recorded and divided (subtracted on a dB scale) by the acoustic pressure to produce the absolute response of the needle hydrophone. The measurements from z = 17 cm to 25 cm are within 1 dB of each other for all frequencies above 300 kHz and within 2 dB down to 100 kHz. For frequencies below 1 MHz, the measurements at all four distances agree within 3 dB. At frequencies above 1 MHz only the response at the 11 cm distance, which is in the near field, differs significantly from the others. The data at 17 cm show no appreciable deviation from 21 cm and 25 cm even though this distance is at the edge of the far field at 2 MHz. It should be remembered that this transducer is considerably apodized compared to the true planar transducer.

Figure 3 compares the substitution calibrations of the needle hydrophone using both the planar and plano-concave transducers at 25 cm. At most frequencies these two calibrations agree within 1 dB. The anomalous peak in the calibration using the planar transducer occurs at the second harmonic of the source transducer, where its response is a minimum. The 2 dB difference of the planar transducer at 1.9 MHz probably is due to the proximity of the measurement point to the last axial minimum in the near field. Also plotted in Fig. 3 are the individual calibration

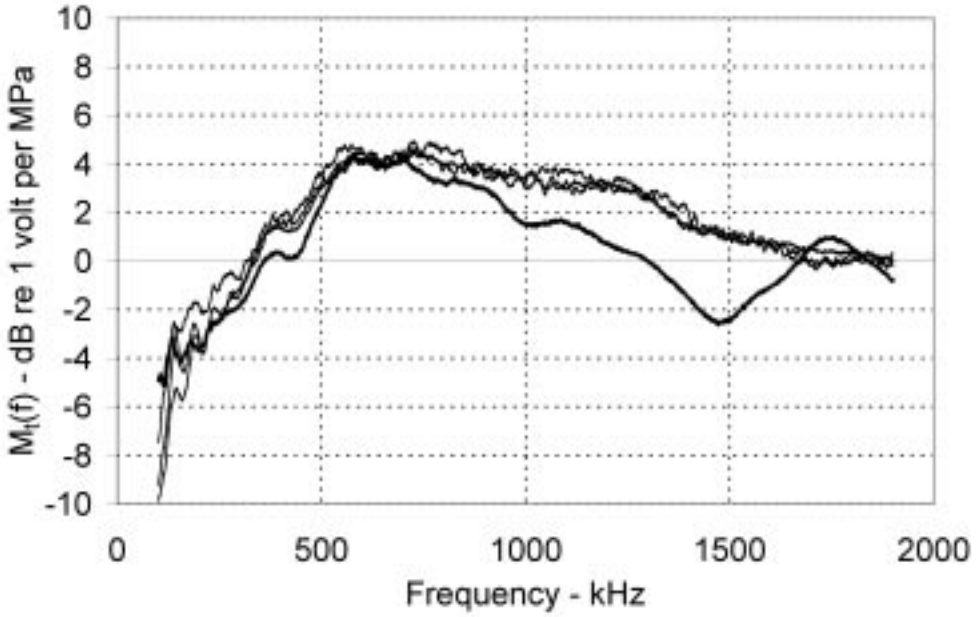

Fig. 2. Substitution calibration plots for needle hydrophone at z = 11, 17, 21, and 25 cm. The response at 11 cm (heavy line) differs significantly from the others.

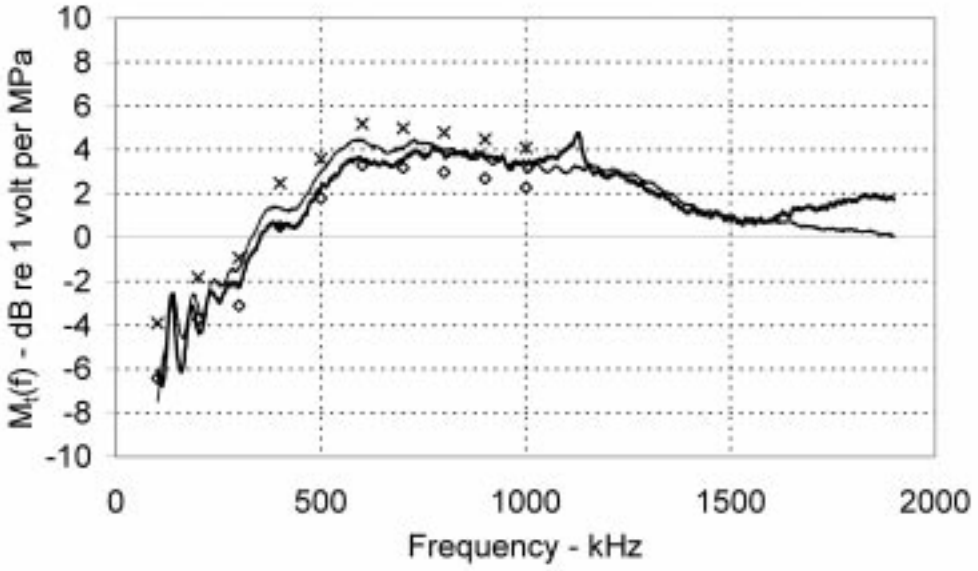

Fig. 3. Substitution calibration plots for needle hydrophone at z = 25 cm using both source transducers and upper and lower 95% confidence limit pairs for ten independent, single-frequency calibration measurements. Heavy line: planar transducer; light line: plano-concave transducer.

points for the needle. These ten data pairs represent the upper and lower 95% confidence limits for the independent, single-frequency sensitivity measurements described previously. The TDS calibration plots generally fall within these limits. The oscillations below 300 kHz were present in the membrane but not the needle response. This effect does not appear to be the case with all membrane hydrophones and is being investigated.

Conclusions

The TDS system described was shown to be a useful tool for substitution calibration methods in the 100 kHz to 2 MHz frequency range. It gives, in a single, rapid swept-frequency measurement, the data over the entire range, while excluding spurious signals and providing an improved signal-to-noise ratio compared to broadband pulse calibration techniques. To utilize the ability of TDS to furnish a calibration over a wide frequency range in one measurement for each source-receiver combination, it is desirable to have a broadband source transducer. In this regard, the plano-concave transducer was demonstrated to be a useful source because its response does not have the minimum at twice the fundamental frequency that is characteristic of a constant-thickness transducer.

References

[1] G.R. Harris, "Are current hydrophone low frequency response standards acceptable for measuring mechanical/cavitation indices?," Ultrasonics **34**, 649-654 (1996).

[2] S.P. Robinson and G.R. Dore', "Uncertainties in the calibration of hydrophones at NPL by the three-transducer spherical-wave reciprocity method in the frequency range 10 kHz to 500 kHz," NPL Report RSA(EXT)0054, National Physical Laboratory, Teddington, Middlesex, UK (November 1994).

[3] S.P. Robinson, "A comparison of the frequency response of membrane and needle probe PVDF hydrophones," in D. Evans and K. Martin, eds., *Physics in Medical Ultrasound II* (York, UK: Institute of Physical Sciences in Medicine, 1988) pp. 79-86.

[4] G.R. Harris and P.M. Gammell, "Sensitivity measurements of piezoelectric polymer hydrophones from 0.2-2 MHz using a broadband pulse technique," J. Acoust. Soc. Am. **105**, 725-731 (1999).

[5] R.C. Heyser, "Acoustical measurements by time delay spectrometry," J. Audio Eng. Soc., **15**, 370-382 (1967).

[6] P. Pedersen, P.A. Lewin, and L. Bjorno, "Application of time delay spectrometry for calibration of ultrasonic transducers," IEEE Trans. Ultrason. Ferroelec. Freq. Contr. **35**, 185-205 (1988).

[7] R.C. Heyser, J.D. Hestenes, J.A. Rooney, P.M. Gammell, and D.H. Le Croissette, "Medical ultrasound imager based on time delay spectrometry," Ultrasonics **27**, 31-39 (1989).

[8] W. Sachse and N.N. Hsu, "Ultrasonic transducers for materials testing and their characterization," in Physical Acoustics, Vol. XIV, edited by W.P. Mason and R.N. Thurston (Academic Press, New York, 1979) pp. 304-305.

Note: This paper was presented at the 43rd Annual Convention of the American Institute of Ultrasound in Medicine, San Antonio, Texas, March 1999. The mention of commercial products in this paper should not be construed as an actual or implied endorsement by the U.S. Department of Health and Human Services.

Intelligibility of 1/3-octave speech: Greater contribution of frequencies outside than inside the nominal passband

Richard M. Warren and James A. Bashford, Jr.

Department of Psychology, University of Wisconsin-Milwaukee, Milwaukee, Wisconsin 53201-0413
rmwarren@csd.uwm.edu bashford@csd.uwm.edu

Abstract: We reported previously that "everyday" sentences were highly intelligible when limited to a 1/3-octave passband centered at 1,500 Hz and having transition-band slopes of approximately 100 dB/octave. The present study determined the relative contributions to intelligibility made by the passband (PB) and the transition bands (TBs) by partitioning the same bandpass sentences using 2,000-order FIR filtering. Intelligibility scores were: PB with both TBs, 92%; deletion of both TBs (leaving only the 1/3-octave PB with nearly vertical slopes), 24%; deletion of the PB (leaving both TBs separated by a 1/3-octave gap), 83%. These and other results indicate a remarkable ability to compensate for severe spectral tilt and the consequent importance of considering frequencies outside the nominal passband in interpreting studies using filtered speech.

PACS numbers: 43.71.Es, 43.71.An

1. Introduction

The bandwidth of a filtered signal is normally defined as the frequency span of the passband bounded by the 3-dB downpoints along the slopes of the flanking transition bands. The present study was undertaken to determine the extent to which transition bands can contribute to the high intelligibility reported earlier for sentences with a nominal bandwidth of 1/3-octave.

It has been reported by Warren, Riener, Bashford, and Brubaker (1995) that the 100 Central Institute for the Deaf (CID) sentences representing "everyday American speech" [Silverman and Hirsh, 1955] have an intelligibility score for keywords of approximately 95% when stimuli are spectrally limited to 1/3-octave bands having a center frequency of 1,500 Hz and transition bands with slopes of about 100 dB/octave (conventionally considered as very steep). These sentences were used in the present study to examine the relative contributions to intelligibility made by the passband and transition bands. The broadband versions of these sentences were filtered digitally to produce 1/3-octave bandpass stimuli with a center frequency of 1,500 Hz and transition bands having slopes of approximately 100 dB/octave. (The 1995 study by Warren et al. had used analog filtering to produce equivalent slopes.) Subsequent FIR filtering (2,000 order) yielding slopes averaging approximately 1,000 dB/octave was used for: (1) deletion of both the upper and lower transition bands, leaving a nearly rectangular 1/3-octave passband; (2) deletion of the 1/3-octave passband, leaving the transition bands separated by a 1/3-octave notch; (3) deletion of only the higher frequency transition band, leaving the passband and the lower transition band; and (4) deletion of only the lower frequency transition band, leaving the passband and higher transition band.

2. Method

2.1 Subjects

The 20 listeners were undergraduate student volunteers from the University of Wisconsin who were paid for their participation. They were native speakers of English and had no known hearing deficits.

2.2 Stimuli

The 100 (10 lists of 10) CID "everyday" sentences that contain 500 keywords used for scoring [Silverman and Hirsh, 1955] served as experimental stimuli in this study. An additional 25 sentences, drawn from the high-predictability subset of the revised SPIN (Speech Perception in Noise) test [Kalikow et al., 1977; Bilger et al., 1984] served as practice stimuli for familiarizing listeners with the different filtering conditions. The CID and SPIN sentence stimuli were derived from broadband digital recordings (44.1 kHz sampling, 16-bit quantization) used earlier by Warren et al. (1995). All sentences were produced by a male speaker with no evident regional accent and an average voicing frequency of approximately 100 Hz.

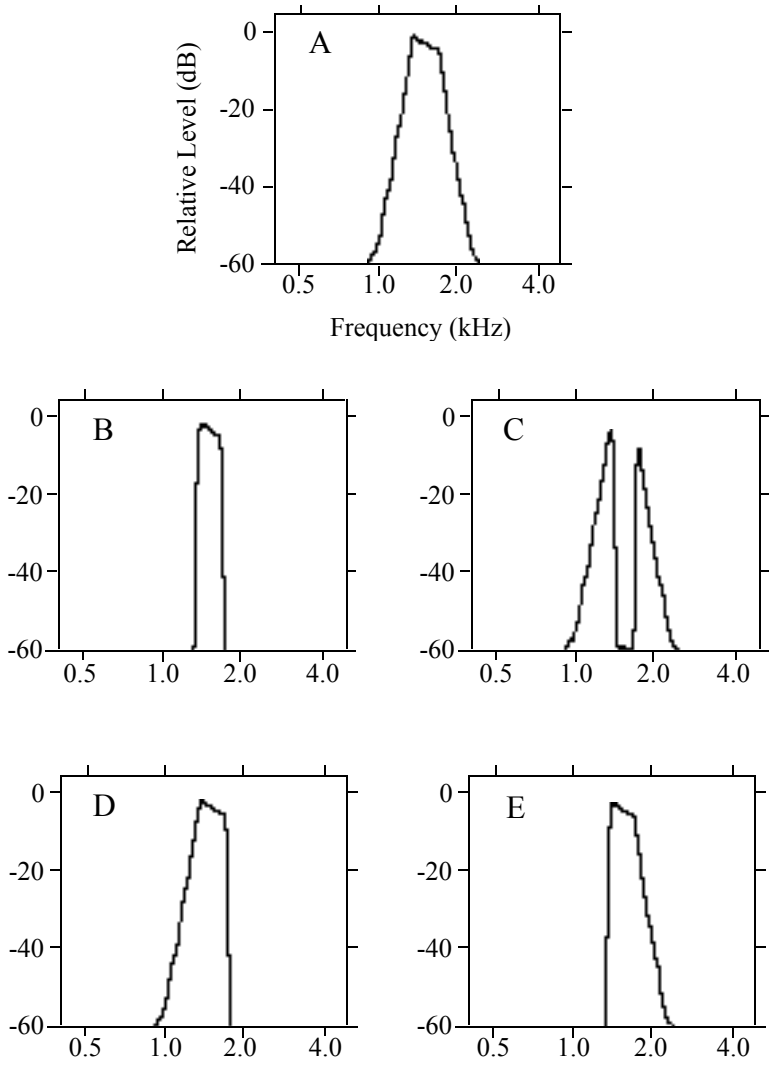

Fig. 1. Long-term averaged spectra based upon the 100 1/3-octave CID sentences: (A) passband with flanking transition bands; (B) passband alone; (C) transition bands alone; (D) passband and lower transition band; and (E) passband and higher transition band. The plots were generated offline via discrete Fourier transform (DFT) with linear averaging of spectra obtained using a 8192-point (186 ms, 5 Hz resolution) Blackman window across the entire set of digitally recorded sentences. DFT software was produced by the Metric Halo Laboratories, Inc.

Fig. 1 shows the long-term averaged spectra of the five filtered versions of the 100 sentences used in this study. Low-pass followed by high-pass filtering using the function *ellip* in MATLAB with order n = 7 was used to produce the intact or "standard" 1/3-octave band geometrically centered at 1,500 Hz with transition bands having steep slopes of approximately 100 dB/octave (the bandpass function in MATLAB could not be used because it can only produce even numbered orders for n). Four reduced versions of the 1/3-octave band were then produced using the function *fir1* in MATLAB with order n = 2,000, resulting in slopes with values ranging from 924 to 1,130 dB/octave as determined by discrete Fourier transforms (see Fig. 1 caption for details) calculated for the entire sentence set. The reduced versions of the bandpass speech consisted of: (1) the standard band subjected to 1/3-octave bandpass FIR filtering from 1,336 to 1,684 Hz that removed both transition bands; (2) the standard band subjected to FIR notch filtering between 1,336 and 1,684 Hz that removed the passband; (3) the standard band subjected to lowpass FIR filtering at 1,684 Hz, removing the upper transition band; and (4) the standard band subjected to highpass FIR filtering at 1,336 Hz, removing the lower transition band.

Before FIR filtering, the standard 1/3-octave sentences (Fig. 1A) were transduced by a Sennheiser HD 250 Linear II headphone. The slow peak level of each sentence was matched to within ± 0.2 dBA using an artificial ear coupler in conjunction with a Brüel and Kjaer Model 2,230 sound-level meter. Following the FIR filtering described above, the four reduced versions shown in Fig. 1 along with the intact 1/3-octave sentences were recorded on an audio compact disk. The five sets of recorded sentences were presented to listeners using a Marantz Model PMD CD player, amplified by a Mackie Microseries 1202-VLZ audio mixer and delivered diotically through the Sennheiser headphones. The slow peak level for each of the standard (intact) 1/3-octave sentences was 75 ± 0.2 dBA. For the partitioning conditions (Figs. 1B through 1E), all frequencies of the recorded sentences (except those removed by FIR filtering) were played back at the same level that they had in the standard sentences. This resulted in slow peak levels (averages for all sentences in each condition) as follows: passband alone (Fig. 1B) = 73.1 dBA; transition bands alone (Fig. 1C) = 68.7 dBA; passband plus lower transition band (Fig. 1D) = 74.5 dBA; passband plus upper transition band (Fig. 1E) = 73.6 dB.

2.3 Procedure

A repeated measures design was employed in this experiment. Listeners heard the 10 CID lists in a balanced order: The five filtering conditions were assigned pseudorandomly to successive pairs of lists (e.g., lists 1 & 2, 3 & 4,…, 9 & 10), with the restriction that, across subjects, each filtering condition was applied an equal number of times (4) to each of the list pairs. Half the listeners received the odd numbered list in the pair first, and the others received the even numbered list first (this produced a balanced arrangement that permitted examination of block-order effects). Prior to receiving the 20 test sentences in a given filtering condition, listeners were presented with a set of 5 SPIN sentences for familiarization. Each of these practice sentences was first heard broadband, and then, following a 1-s delay, heard filtered in the same manner as the test sentences that followed.

Listeners were tested individually while seated in an audiometric chamber with the experimenter. They were instructed to repeat the sentences as accurately as possible and encouraged to guess if unsure. The experimenter noted which keywords were repeated correctly and recorded the percentage of correct responses (out of 100 keywords) that occurred for each of the five 20-sentence sets. Testing occurred in a single session lasting about 30 minutes.

3. Results

Fig. 2 shows the intelligibility scores for each of the five experimental conditions expressed as the percentage of keywords identified correctly. It can be seen that the standard, intact 1/3-octave band (Fig. 2A) produced the highest intelligibility (92%), and the passband presented without the two transition bands (Fig. 2B) yielded the lowest intelligibility (24%). The stimulus produced by deleting only the passband, leaving the two transition bands separated by a 1/3-octave gap (Fig. 2C) had the second highest intelligibility score (83%). When only

the upper transition band was deleted from the standard band (Fig. 2D), intelligibility was reduced to 72%, whereas removal of only the lower transition band (Fig. 2E) had a much greater effect, reducing intelligibility to just 55%.

These results are supported by statistical analyses. The scores were subjected to a two-way (filtering condition x blocks) analysis of variance (ANOVA) for repeated measures, which yielded a significant main effect of filtering [$F(4,76) = 130.8$, $p < .0001$], a nonsignificant main effect for blocks [$F(1,19) = 2.90$, $p > .10$], and a nonsignificant interaction of filtering condition x blocks [$F(4,76) = 2.44$, $p > .05$]. Tukey HSD tests conducted to examine the main effect of filtering indicated that all pairwise comparisons across filtering conditions were statistically significant ($p < .05$ or better) except the comparison between the intact 1/3-octave band (Fig. 2A) and the reduced stimulus lacking only the passband (Fig. 2C).

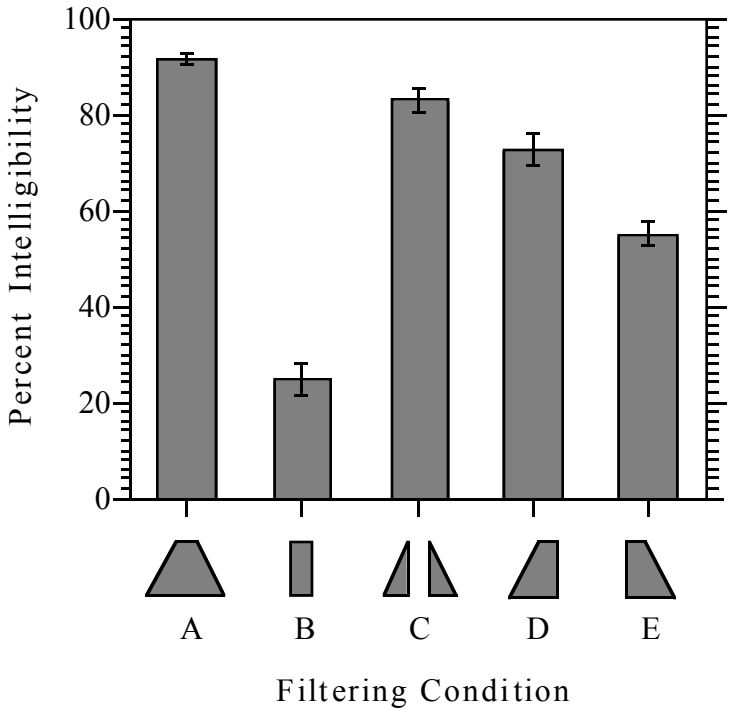

Fig. 2. Mean intelligibility scores along with standard error confidence limits (N=20) for the intact 1/3-octave sentences and their derivatives produced by excising one or both of the 100 dB/octave transition bands, or by excising the 1/3-octave passband, as indicated by the icons: (A) passband with flanking transition bands; (B) passband alone; (C) transition bands alone; (D) passband and lower transition band; and (E) passband and higher transition band.

Audio samples of the CID sentences having average intelligibility for the particular filtering condition indicated can be heard by clicking on the appropriate loudspeaker icon below.

Mm. 1. Audio demo file no. 1 (1 Mb)
Sample of three bandpass filtered CID sentences (1.5 kHz center frequency) having a spectrum consisting of a 1/3-octave passband plus 100-dB/octave transition bands, as illustrated in Fig. 1A.

Mm. 2. Audio demo file no. 2 (752 Kb)
Sample of three filtered CID sentences having a spectrum consisting of the 1/3-octave passband alone, as illustrated in Fig. 1B.

Mm. 3. Audio demo file no. 3 (996 Kb)
Sample of three filtered CID sentences having a spectrum consisting of the transition bands alone, separated by a 1/3-octave notch, as illustrated in Fig. 1C.

4. Discussion

The high intelligibility of narrowband sentences reported by Warren et al. (1995) was verified by Stickney and Assmann (1997). They also reported that the intelligibility of keywords in sentences dropped appreciably when these words had low contextual probability. There was a further large drop when the narrowband speech consisted of isolated words. It seems clear that supralexical linguistic skills can permit listeners to identify words in narrowband speech when they are used for communication in everyday sentential format, even though they lack the spectral information spanning several octaves that is needed for accurate identification of words produced in isolation.

In the present study, it was found that the pair of transition bands of the 1/3-octave sentences had an intelligibility score more than three times higher than the passband (83% vs. 24%), despite the notch and the fact that the spectral profiles of components within the transition bands were subject to a severe spectral tilt of 100 dB/octave. The relatively high intelligibility of the transition bands appears to be due to the presence of speech information over a range considerably greater than 1/3-octave. Work in our laboratory has indicated that the intelligibility of the nominal 1/3-octave band shown in Fig. 1A is equivalent to that obtained by expanding the rectangular band shown in Fig. 1B to approximately one octave in width while keeping the center frequency at 1,500 Hz. This indicates that the nominal 1/3-octave band shown in Fig. 1A has information spanning at least one-octave contributing to intelligibility. It is possible to determine directly how far down the slopes information can be utilized by truncating the slopes of narrowband speech at any desired downpoint with the aid of high-order FIR filtering: It was found that transition-band information can be utilized more than 40 dB below the passband level.

It is suggested that the fixed transfer function of a particular set of filtering conditions permits listeners to calibrate its characteristics, and partially compensate for the spectral distortion over a considerable range of frequencies within the sloped bands. On the basis of experiments employing other types of spectral-envelope distortion, Watkins and Makin (1996) suggested that stored knowledge concerning undistorted speech could enable mechanisms to compensate for the changes through a process "that is like applying an inverse form of the carrier's filter to the test sound." However, it should be kept in mind that such inverse filtering can restore neither the reduced signal-to-noise ratio nor the dynamic range of the attenuated frequencies in the transition bands.

The low amplitude levels in the transition bands make them especially vulnerable to the effects of extraneous noise. Broadband noise is customarily added to high-pass and low-pass filtered speech to avoid ceiling effects in studies designed to determine the relative importance functions for both 1/3-octave and one-octave bands of speech [see ANSI, 1969, R1986; ANSI, 1997; Studebaker et al., 1987; Pavlovic, 1994]. In calculating the signal-to-noise ratio, it is customary to consider that the signal consists solely of the passband. However, the present study has demonstrated that transition bands can contribute significantly to intelligibility. Hence, the addition of broadband noise not only decreases the signal-to-noise ratio of passbands, but also masks lower amplitude regions of transition bands, resulting in a decrease in the range of frequencies responsible for intelligibility. It should be possible to

avoid this confound by employing nearly vertical filter slopes when determining frequency importance functions for speech intelligibility.

Acknowledgments

This work was supported in part by NIH through Grant DC 00208. The authors thank Peter W. Lenz for his technical assistance.

References

ANSI (**1969, R1986**). ANSI S3.5-1969. "American National Standard Methods for the Calculation of the Articulation Index," New York: American National Standards Institute.

ANSI (**1997**). ANSI S3.5-1997. "American National Standard Methods for the Calculation of the Speech Intelligibility Index," New York: American National Standards Institute.

Bilger, R.C., Nuetzel, J.M., Rabinowitz, W.M., and Rzeczkowski, C. (**1984**). "Standardization of a test of speech perception in noise," J. of Speech and Hearing Res., **27**, 32-48.

Kalikow, D.N., Stevens, K.N., and Elliott, L.L. (**1977**). "Development of a test of speech intelligibility in noise using sentence materials with controlled word predictability," J. Acoust. Soc. Am., **61**, 1337-1351.

Pavlovic, C.V. (**1994**). "Band importance functions for audiological applications," Ear & Hearing, **15**, 100-104.

Silverman, S.R., and Hirsh, I.J. (**1955**). "Problems related to the use of speech in clinical audiometry," Annals of Otology, Rhinology, and Laryngology, **64**, 1234-1245.

Stickney, G.S. and Assmann, P.F. (**1997**). "Intelligibility of bandpass-filtered speech," J. Acoust. Soc. Am., **102**, 3134A.

Studebaker, G.A., Pavlovic, C.V., and Sherbecoe, R.L. (**1987**). "A frequency importance function for continuous discourse," J. Acoust. Soc. Am., **81**, 1130-1138.

Warren, R.M., Riener, K.R., Bashford, J.A., Jr., and Brubaker, B.S. (**1995**). "Spectral redundancy: Intelligibility of sentences heard through narrow spectral slits," Perception & Psychophysics, **57**, 175-182.

Watkins, A.J., and Makin, S.J. (**1996**). "Effects of spectral contrast on perceptual compensation for spectral-envelope distortion," J. Acoust. Soc. Am., **99**, 3749-3757.

SOUNDINGS

Section Editor: Richard Stern

This front section of the *Journal* includes acoustical news, views, reviews, and general tutorial or selected research articles chosen for wide acoustical interest and written for broad acoustical readership.

ACOUSTICAL NEWS—USA

Elaine Moran
Acoustical Society of America, Suite 1NO1, 2 Huntington Quadrangle, Melville, NY 11747-4502

Editor's Note: *Readers of this Journal are asked to submit news items on awards, appointments, and other activities about themselves or their colleagues. Deadline dates for news items and notices are 2 months prior to publication.*

James West and Gerhard Sessler elected to National Inventors Hall of Fame

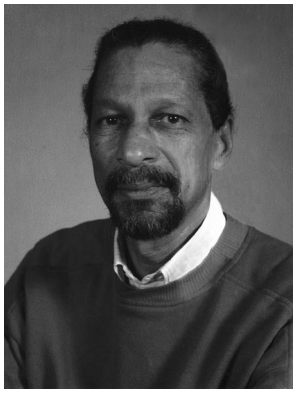

James West

Gehard Sessler

On September 18, 1999, ASA Fellows James E. West and Gerhard M. Sessler were inducted into the National Inventors Hall of Fame at a ceremony at Inventure Place in Akron, Ohio, in recognition of their invention of the ''Foil Electret Microphone.'' Nearly 90% of all microphones used today are based on the foil electret principle.

Jim West is Past President of ASA (1998–1999) and received the ASA Silver Medal in Engineering Acoustics in 1995. He is a member of the National Academy of Engineering and a Fellow of the Institute of Electrical and Electronics Engineers. He is also the recent recipient of the George R. Stibitz Trophy, sponsored by the third annual AT&T Patent Award (1993), the MH Black History Recognition Award (1993), the New Jersey Inventor of the Year (1995), an honorary Doctor of Science degree from New Jersey Institute of Technology (1997), the Golden Torch Award (1998) sponsored by the National Society of Black Engineers, and the Industrial Research Institutes 1998 Achievement Award.

Gerhard M. Sessler, past president of the German Acoustics Association (DAGA) (1984–1990), received the ASA Helmholtz–Rayleigh Interdisciplinary Silver Medal in Acoustics in 1997. He has earned many awards throughout his distinguished career including the Thomas W. Dakin Award (1986) by the Dielectrics and Electrical Insulation Society, the George R. Stibitz Trophy (1993) at the Third Annual AT&T Patent Awards Ceremony, and the Helmholtz Medal (1993), highest award of the German Acoustical Society.

James West and Gerhard Sessler join other members of the ASA who have been inducted into the National Inventors Hall of Fame including Marvin Camras for his patent on ''Method and Means of Magnetic Recording,'' Lee Deforest for his patent on ''Space Telegraphy,'' and Thomas Alva Edison for his invention of the ''Electric Lamp.''

The National Inventors Hall of Fame highlights the lives and inventions of its 141 inductees. The Hall of Fame was founded in the early 1970s by the United States Patent and Trademark Office and National Council of Intellectual Property Law Associations. To learn more about the National Inventors Hall of Fame and its inductees visit the website at www.invent.org.

USA Meetings Calendar

Listed below is a summary of meetings related to acoustics to be held in the U.S. in the near future. The month/year notation refers to the issue in which a complete meeting announcement appeared.

1999

1–5 Nov.	138th meeting of the Acoustical Society of America, Columbus, OH [Acoustical Society of America, Suite 1NO1, 2 Huntington Quadrangle, Melville, NY 11747-4502; Tel.: 516-576-2360; Fax: 516-576-2377; E-mail: asa@aip.org; WWW: asa.aip.org].
14–19 Nov.	1999 International Mechanical Engineering Congress and Exposition, Winter Annual Meeting of the ASME, Nashville, TN [ASME Headquarters, Three Park Ave., New York, NY 10016-5990; Tel.: 212-591-7722; Fax: 212-591-7674; E-mail: infocentral@asme.org].
2–4 Dec.	ACTIVE 99, Fort Lauderdale, FL [Institute of Noise Control Engineering, P.O. Box 3206 Arlington Branch, Poughkeepsie, NY 12603; Tel.: 914-462-4006; Fax: 914-463-0201; E-mail: INCEUSA@aol.com;/users.aol.com/inceusa/ince.html].
6–8 Dec.	INTER-NOISE 99, Fort Lauderdale, FL [Institute of Noise Control Engineering, P.O. Box 3206 Arlington Branch, Poughkeepsie, NY 12603; Tel.: 914-462-4006; Fax: 914-463-0201; E-mail: INCEUSA@aol.com;/users.aol.com/inceusa/ince.html].

2000

1–13 Jan.	38th AIAA Aerospace Sciences Meeting & Exhibit, Reno, NV [American Institute of Aeronautics and Astronautics, 1801 Alexander Bell Drive, Suite 500, Reston, VA 2019X; Tel.: 703-264-7500 or 800-639-2422; E-mail: custserv@aiaa.org].
17–19 Feb.	National Hearing Conservation Association (NHCA) 25th Annual Conference, Denver, CO [NHCA, 9101 E. Kenyon Ave., Suite 3000, Denver, CO 80237; Tel.: 303-224-9022; Fax: 303-770-1812; E-mail: nhca@gwami.com; WWW: www.hearingconservation-.org].
6–9 Mar.	Society of Automotive Engineers Congress, Detroit, MI [SAE Headquarters, 400 Commonwealth Dr., Warrendale, PA 15096-0001; Fax: 724-776-1830; E-mail: congress2000@sae.org].
17–19 May	ASNE Day 2000, Arlington, VA [Andrea Zari, Meetings Department, American Society of Naval Engineers, 1452 Duke St., Alexandria, VA 22314-3458; Tel.: 703-836-6727; Fax: 703-836-7491; E-mail: azari@navalengineers.org].
30 May–3 June	139th meeting of the Acoustical Society of America, Atlanta, GA [Acoustical Society of America, Suite 1NO1, 2 Huntington Quadrangle, Melville, NY 11747-4502; Tel.: 516-576-2360; Fax: 516-576-2377; E-mail: asa@aip.org; WWW: asa.aip.org].

 0001-4966/99/106(5)/2321/2/$15.00

13–16 July ClarinetFest 2000, Norman, OK [Dr. Keith Koons, Music Dept., Univ. of Central Florida, P.O. Box 161354, Orlando, FL 32816-1354; Tel.: 407-823-5116; E-mail: kkoons@pegasus.cc.ucf.edu]. Abstract deadline: 15 January 2000.

4–8 Dec. 140th meeting of the Acoustical Society of America, Newport Beach, CA [Acoustical Society of America, Suite 1NO1, 2 Huntington Quadrangle, Melville, NY 11747-4502; Tel.: 516-576-2360; Fax: 516-576-2377; E-mail: asa@aip.org; WWW: asa.aip.org].

2001

30 April–3 May 2001 SAE Noise & Vibration Conference & Exposition, Traverse City, MI [Patti Kreh, SAE Int'l., 755 W. Big Beaver Rd., Suite 1600, Troy, MI 48084; Tel.: 248-273-2474; Fax: 248-273-2494; E-mail: pkreh@sae.org]. Deadline for submitting abstracts, 14 July 2000.

BOOK REVIEWS

P. L. Marston
Physics Department, Washington State University, Pullman, Washington 99164

These reviews of books and other forms of information express the opinions of the individual reviewers and are not necessarily endorsed by the Editorial Board of this Journal.

Editorial Policy: *If there is a negative review, the author of the book will be given a chance to respond to the review in this section of the Journal and the reviewer will be allowed to respond to the author's comments. [See ''Book Reviews Editor's Note,'' J. Acoust. Soc. Am.* ***81****, 1651 (May 1987).]*

The Loudspeaker Design Cookbook, 5th Edition

Vance Dickason

Audio Amateur Press, 1997, Peterborough, NH 03458.
xii+216 pp. (including 51 pp. advertising section). Price: $34.95.

The first edition of the *Loudspeaker Design Cookbook* was released 22 years ago. According to the author, each successive edition reflects the current engineering trends in the ever-shifting field of loudspeaker design. The first two editions were published by the author himself, and then Audio Amateur Press took over the publication of subsequent editions.

It is not hard to see why Dickason's text enjoys brisk sales (over 60 000 copies of the latest edition have been printed). He writes clearly, thoroughly, and provides much data necessary for speaker design. The target audience can range from amateurs who are beginning to learn the ropes to well-established designers who like to keep a reference manual on hand. The back of the text contains 51 pages of advertisements by suppliers of drivers, parts for making drivers, electrical/electronic components, test equipment, computer programs to assist and evaluate design, various publications, and even complete speaker kits and assembled speaker systems.

The format of the text follows a rather logical path, although the chapter numbering is slightly quirky. There are twelve chapters in all, but the first chapter is titled ''Chapter 0,'' effectively causing the last (twelfth) chapter to be christened ''Chapter 11.'' Technical terms are carefully defined so that there should be no doubt in the mind of a novice as to what they mean. Dickason did not stint on providing tables and parametric curves that are used in designing speaker systems and predicting the performance capabilities of components acting individually and in unison; and a fairly thorough, potentially valuable reference listing is given at the end of each chapter.

Chapter 0 describes how electrodynamic loudspeakers work, the effect of gap/coil geometries, the real-world behavior of loudspeaker cones with their resonance modes, the necessity for dust caps, dome shapes in higher frequency drivers, suspension of the cone that is attached to the voice coil which, in turn, interacts with the speaker magnet, modeling of loudspeaker impedance, and speaker input power required on the basis of loudspeaker efficiency and room size.

The simplest loudspeaker design is that of a closed box, which is the topic of Chap. 1. The closed box system, more suitable for low-frequency response, subdivides into two categories: the infinite baffle and the air suspension, the latter made popular in the 1950s by Acoustic Research cofounded by Edgar Villchur and Henry Kloss. It remained for Richard Small to publish in the *Journal of Audio Engineering Society* in June 1972 the most definitive study of closed-box design. The Q-factor of the driver represents the interaction of the electrical, mechanical, and pneumatic factors of the woofer/enclosure combination in determining the system resonance and response curves. Computer simulation through the use of LEAP 4.0®, arguably the most sophisticated speaker design program available at the time, is used by the author to model a series of closed boxes with different values of Q. Performance characteristics such as group delay, cone excursions, impedance curves, etc. are shown to depend on physical parameters such as box size, woofer cone mass, free-air resonance, voice coil overhang, effective driver radiating area, reference efficiency, etc.

Vented boxes constitute the subject of Chap. 2. Vented boxes carry the advantage of lower cone excursions near the box resonance frequency, thus providing higher power-handling capacity and lower modulation distortion, and they operate more efficiently. However, vented systems are considerably more sensitive than closed boxes to inappropriately chosen values of parameters. Manipulation of the total speaker-box Q can be achieved by changing the volume of a closed box; vented enclosures are dealt with in terms of specific alignments, entailing adjustments of a number of specific parameters to achieve a more or less flat response. There are at least 15 well-established alignment categories, such as SSB_4 (Super Fourth-Order Boom Box), SC_4 (Fourth Order Sub-Chebychev), QB_3 (Quasi Third-Order alignment), and discrete alignments such as the Fourth-Order Butterworth (B_4), Fourth-Order Bessel (BE_4), and Butterworth Inter-Order (IB_4). The rather involved procedure of selecting a box size and relevant parameters is described with a discussion of box losses, use of accompanying design tables, calculation of vent dimensions, box tuning, and other parameters. Two drivers serve as examples of suitability for use in vented boxes, accompanied by a description of measurement parameters. Other topics in the chapter include box damping, the dual-woofer format, resistive and distributed vents, and electronically assisted vented designs, and vented rear chamber bandpass enclosures.

Passive-radiator low-frequency systems, covered in Chap. 3, contain ''drone cones'' that substitute for vents. While they closely follow the vented loudspeaker design methodology, the passive-radiator systems carry the advantage of lacking vent pipe coloration and can be used in small enclosures where the required vent lengths would exceed the box dimensions. The procedure of selecting a woofer is the same as that described in Chap. 2, and alignments are generally restricted to QB_3, B_4, and C_4 types. The determination of box size and relevant parameters are generally dealt with in the same manner as with vented enclosures. An additional factor is the so-called delta, the compliance ratio of the passive radiator. A section in this chapter also treats passive radiator bandpass enclosures, which can be best designed through computer simulation by the use of a speaker design program such as Speak® (by DLC) or LEAP 4.0 (by Audio Technology). The augmented passive-radiator (APR), a double-cavity version of the customary drone cone design, is capable of most of the vented and passive-radiator systems alignment variations. While it requires more volume in the way of enclosure size, the APR yields higher power output and a 15%–25% lower cutoff (corresponding up to $\frac{1}{2}$-octave extension). The layout for the APR consists of two unequal area passive radiators, connected back-to-back, with the front baffles joined to the inner dividing baffle. A special table (Table 3.4) provides the requisite data for designing an APR system.

In Chap. 4, the transmission line (TL) low-frequency system is described as a means of obtaining low cabinet resonance and strong deep bass. The design situation is somewhat murkier here, as there seems to be little agreement among TL enthusiasts as to what is the optimal system parameter *Q*. One computer program described in the text was specifically developed for TL design by Juha Backman, but it is not currently available. However, curves based on the use of LEAP, a program that does not model TL designs, yielded results that show similarity to the performance curves developed by Backman. The line length and damping material, tuning of a TL, the TL enclosure configuration, and the selection of the woofer are discussed. An exhaustive listing of articles on construction of the TL enclosure is also given.

Chapter 5 covers the topics of cabinet construction. The sphere is the best possible shape to provide the flattest frequency response, but obviously it is the most impractical to build and manufacture. However, the rectangular box, which is considerably less than optimum radiator, is the enclosure type most easily built. Standing wave modes depend on the enclosure shape and can be minimized by choosing appropriate dimensional ratios for the box. Nonparallel shapes can also attenuate standing waves. Box damping is

 0001-4966/99/106(5)/2329/2/$15.00

needed in order to eliminate as much as possible the coloration that is retransmitted by most wood enclosures. Internal cabinet bracing, driving mounting techniques, enclosure floor coupling, and selection of wall materials are factors to be considered in damping an enclosure. In this chapter the emphasis is on enclosure features rather than cabinet construction ''tips.''

Chapter 6 shows how to determine the proper crossover frequencies on the basis of driver bandwidth and boundary orientation and to establish baffle locations for mid- and high-frequency drivers. Among the topics are two-way versus three-way loudspeaker formats (neither one is inherently superior to the other), the effect of boundaries (room walls and ceilings) on the loudspeaker power response, boundary-induced interference patterns, driver separation and horizontal dispersion, midrange enclosures, and midrange and high-frequency baffle configuration.

Attention is paid to attendant factors such as driver placement, radiation pattern of separate drivers, and zero delay plane (ZDP). Other topics include crossover network power response. Two-way crossover characteristics are described, including those of first- through fourth-order Butterworth filters, second- and fourth-order Linkwitz–Riley filters, second- and fourth-order Bessel filters, second-order Chebychev filters, fourth-order Legendre filters, fourth-order Gaussian filters, and fourth-order linear phase filters. Design formulas are given for two-way and three-way crossovers. Examples are given for the low-pass filter, high-pass filter, and high-pass/low-pass summation. Driver load compensating circuitry, series notch filter, impedance equalization, driver attenuation circuits, response-shaping circuits, and inductors and capacitors in crossover circuits are also discussed.

Passive crossover networks constitute the main thrust of Chap. 7. An excellent history of the development of crossover networks is rendered here, followed by a primer on the fundamental principles of crossover design. Rather than delving into the esoteric aspects of this rather complex subject, the author chose to maintain a cookbook format by treating examples of accepted methods commonly used in the loudspeaker industry. Active networks do not lie in the scope of this chapter, but a number of references on construction details of active filter circuits are given.

Chapter 8 is an important one, since it describes loudspeaker testing. While it is not as comprehensive as Joseph D'Appolito's *Testing Loudspeakers* (Audio Amateur Press, Peterborough, NH, 1998), it contains enough information to conduct loudspeaker performance tests. Break-in of loudspeakers is recommended, and the procedures described are those for measuring driver resonance, impedance (AC resistance), complex impedance, driver mass (delta mass and delta compliance methods), driver suspension compliance, driver motor strength BL, and voice coil impedance. Formulas are included for calculating driver voice coil impedance, amplifier source resistance, and volume of air equal to driver compliance. Measurement procedures are given for driver Q, frequency response, phase, and enclosure vibration. Equipment for determining frequency response is discussed, and microphone types are examined. An important facet of testing, too often given short shrift, is that of measuring voice coil temperature over time—the description of measuring this parameter concludes the chapter.

Chapter 9 is essentially a compilation of the software intended for loudspeaker design. While this is a useful listing, it was done in mid-1991 and much new hardware and later versions of software have been developed.

While Chap. 9 is somewhat remiss with respect to its modernity, Chap. 10 deals with an area that is growing more popular—the home theater system that is intended to reproduce movie soundtracks rather than conventional stereo programs. It is pointed out that soundtrack recording techniques for conventional home listening and motion picture theatre listening differ considerably, with the result of less than optimal reproduction in the home. Because film soundtracks are not remixed for home playback, Tom Holman developed the THX (Tomlinson Holman eXperiment) home specification, essentially an equalization fix-up. Controlled directivity led to the specification of THX speakers, which call for additional channels.

An overview is rendered of the home theater loudspeaker system, including as subtopics the placement of left/right front speakers, magnetic shielding of drivers (which may need to be placed close to a video monitor), center channel speakers (possibly the most important speaker in a home theater system), controlled vertical directivity, rear channel surround sound speakers, and subwoofers.

Chapter 11 devotes itself to the special requirements of designing a loudspeaker system for automobiles. The automobile passenger compartment is essentially a closed-field environment. Sections of the car body tend to flex, so the acoustic situation becomes one of a ''lossy'' pressure field. Also, the relatively cramped dimensions of the passenger compartment tend to limit the wavelength response. Because the Thiel–Small predictions are based on free-field performance of the speakers, adjustments need to be made by establishing the impedance, cone excursion, and frequency response in a small ''lossy'' field by actual measurements. Computer simulation can also be achieved by using commercially available programs. Both predictions and actual performance are shown to correlate rather well for a couple of actual speakers and automotive interiors. A somewhat tongue-in-cheek discussion of the desirability of including center channel imaging is included with a set of generic installation rules for those who absolutely must have this feature. It was wise of Dickason to point out the most overlooked method of improving automotive sound quality, namely cutting down on the ambient background noise levels generated by engine operation and car motion.

In summary, *The Loudspeaker Design Cookbook* merits a place on the bookshelf of every serious speaker designer, whether he/she be a professional or a hobbyist. All of its chapters are well done, although Chap. 9 lacks immediacy in its compilation of computer programs but the reader can easily update himself or herself by checking out the Internet or consulting advertisements in current issues of *The Speaker Builder*. Loudspeakers other than the conventional electromagnetic type, e.g., electrostatic and planar systems, are not treated in *The Loudspeaker Cookbook.* There is no index to facilitate easy location of particular subjects in the text, but the table of contents is sufficiently detailed to help in finding the subject of interest.

DANIEL R. RAICHEL
CUNY Graduate School
Mechanical and Aerospace Engineering Department
and the School of Architecture and Environmental Studies
The City College of the City University of New York
New York, New York 10031

An analytic secondary source model of edge diffraction impulse responses

U. Peter Svensson[a] and Roger I. Fred[b]
Department of Applied Acoustics, Chalmers University of Technology, SE-412 96 Göteborg, Sweden

John Vanderkooy
Audio Research Group, Department of Physics, University of Waterloo, Waterloo, Ontario N2L 3G1, Canada

(Received 14 July 1997; revised 18 June 1999; accepted 19 July 1999)

A new impulse-response model for the edge diffraction from finite rigid or soft wedges is presented which is based on the exact Biot–Tolstoy solution. The new model is an extension of the work by Medwin *et al.* [H. Medwin *et al.*, J. Acoust. Soc. Am. **72**, 1005–1013 (1982)], in that the concept of secondary edge sources is used. It is shown that analytical directivity functions for such edge sources can be derived and that they give the correct solution for the infinite wedge. These functions support the assumption for the first-order diffraction model suggested by Medwin *et al.* that the contributions to the impulse response from the two sides around the apex point are exactly identical. The analytical functions also indicate that Medwin's second-order diffraction model contains approximations which, however, might be of minor importance for most geometries. Access to analytical directivity functions makes it possible to derive explicit expressions for the first- and even second-order diffraction for certain geometries. An example of this is axisymmetric scattering from a thin circular rigid or soft disc, for which the new model gives first-order diffraction results within 0.20 dB of published reference frequency-domain results, and the second-order diffraction results also agree well with the reference results. Scattering from a rectangular plate is studied as well, and comparisons with published numerical results show that the new model gives accurate results. It is shown that the directivity functions can lead to efficient and accurate numerical implementations for first- and second-order diffraction.
[S0001-4966(99)02111-6]

PACS numbers: 43.20.Bi, 43.20.Fn, 43.20.Px [DEC]

INTRODUCTION

The classic problem of edge diffraction from an infinite wedge irradiated by a point source has explicit impulse-response (IR) solutions for the cases of a rigid wedge and a pressure-release wedge. These were presented by Biot and Tolstoy in 1957,[1] but few studies employed these solutions until Medwin applied them to underwater and noise-barrier cases.[2] Comparisons of his model with measurements show good accuracy for geometries with infinite edges[2–4] and Ouis has applied Biot–Tolstoy's model in room acoustics to studies of a room with balconies, a case which can be modeled with infinite edges.[5]

An earlier alternative to the Biot–Tolstoy solution has been the Kirchhoff diffraction approximation, which can be used for both frequency- and time-domain methods. In seismics,[6,7] as well as in room acoustics,[8] the Kirchhoff diffraction approximation has commonly been employed in time-domain methods for edge diffraction. However, as has been shown using the Biot–Tolstoy expressions,[9] and other accurate methods,[10] the Kirchhoff diffraction approximation leads to large errors, not only for low frequencies but also for high frequencies in certain directions. Consequently, the Biot–Tolstoy is the preferred method for impulse response models of edge diffraction.

The Biot–Tolstoy expressions, explicit as they are, do not immediately suggest how the infinite wedge expressions can be interpreted to lead to expressions for finite wedges or for multiple diffraction. Medwin, Childs, and Jebsen suggest an interpretation, ''a discrete Huygens interpretation,'' which can be used for finite wedges and also be extended to handle multiple diffraction.[3] This is the basis for numerical methods such as the wedge assemblage (WA) method.[11] Measurements of noise barriers with a finite thickness and comparisons with other calculation methods seem to support that model. Whereas Medwin's interpretation leads to numerical calculation methods, the current paper proposes an approach in which directivity functions for the secondary edge sources *á la* Medwin are derived analytically from the IR solution for the infinite wedge. The expressions for analytical directivities are directly applicable to nonstraight edges and multiple diffraction. It will be shown that these analytical expressions support Medwin's assumption for modeling first-order diffraction, namely that the contributions from the two sides of the edge around the apex point are exactly identical. On the other hand, the analytical functions indicate approximations in Medwin's assumptions for second- and higher-order diffraction. These approximations, however, seem to be of minor importance for geometries

[a]Present address: Department of Telecommunications, Norwegian University of Science and Technology, N-7491 Trondheim, Norway.
[b]Present address: Akustik Forum AB, Stampgatan 15, SE-416 64 Göteborg, Sweden.

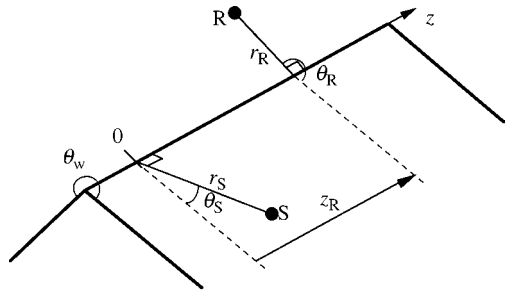

FIG. 1. The geometry of an infinite wedge irradiated by a point source *S*. Cylindrical coordinates are used with the *z*-axis along the edge of the wedge. The source has coordinates r_S and θ_S and is placed at $z_S=0$. The receiver has the coordinates r_R, θ_R, and z_R and the wedge has an open angle of θ_w.

where the second-order sound paths pass edges with small angle deviations, as in most noise-barrier cases.

Section I of this paper reviews the Biot–Tolstoy solution and Medwin's extension to this. A new derivation using analytical directivity functions is presented, and its extension to second-order diffraction is described. In Sec. II the numerical calculation of edge diffraction impulse responses is discussed. Section III presents numerical calculations for finite edges and analytical derivations for a thin circular disc. The wealth of exact and asymptotic frequency-domain solutions (see Pierce[12] for a review) is addressed here only for comparisons with calculations where the uniform theory of diffraction (UTD) by Kouyoumjian and Pathak is used.[13]

I. THEORY

The problem to be considered here is that of a point source irradiating a rigid or soft, (i.e., pressure-release) object, a special case of which is the infinite wedge. Impulse responses will be used throughout as descriptors of the sound fields, with the sound pressure $p(t)$ as output signal and a source signal $q(t)=\rho_0 A(t)/(4\pi)$, where ρ_0 is the density of the air and $A(t)$ the volume acceleration of the point source. Free-field radiation is then described by the IR, $h_{\mathrm{FF}}(\tau)=\delta(\tau-R/c)/R$, where R is the source-to-receiver distance. The IR for plane-surfaced objects can be written as a sum of the geometrical acoustics IR, h_{GA}, and diffraction components h_{diffr}. The direct sound and specular reflections of first and higher orders will be contained in h_{GA}, as long as their respective validity criteria are fulfilled. In the case of an object with an entirely convex geometry (i.e., no indents), h_{diffr} will consist of only first- and higher-order edge diffraction, whereas other geometries might cause combinations of specular reflections and edge diffraction. In this study, only convex geometries will be considered, in particular infinite and finite wedges, and circular and rectangular plates.

As a starting point, consider an infinite rigid wedge with a geometry as indicated in Fig. 1 where the cylindrical coordinates r_S, θ_S, 0 are used for the source and r_R, θ_R, z_R for the receiver. The edge diffraction IR can be written in a form which is a combination of the forms given in Refs. 3 and 14, and based on the solution presented in Ref. 1,

$$h_{\mathrm{diffr}}(\tau)=-\frac{cv}{2\pi}\frac{\beta(\tau)}{r_S r_R \sinh\eta(\tau)}H(\tau-\tau_0), \tag{1}$$

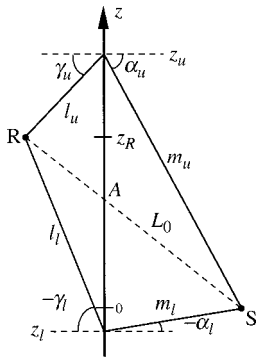

FIG. 2. A plane view of the edge constructed from the two half-planes containing the edge and the source *S*, and the edge and the receiver *R*, respectively. Two *z*-coordinates, z_l and z_u, are indicated for which the two sound paths $S-z_l-R$ and $S-z_u-R$ have identical path lengths. Also indicated is the shortest distance, L_0, via the apex point, denoted *A*, of the edge. Angles are defined with signs so that $\sin\alpha=z/m$ and $\sin\gamma=(z-z_R)/l$.

where

$$\beta(\tau)=\beta_{++}(\tau)+\beta_{+-}(\tau)+\beta_{-+}(\tau)+\beta_{--}(\tau), \tag{2}$$

$$\beta_{\pm\pm}(\tau)=\frac{\sin[v(\pi\pm\theta_S\pm\theta_R)]}{\cosh[v\,\eta(\tau)]-\cos[v(\pi\pm\theta_S\pm\theta_R)]}, \tag{3}$$

$$\eta(\tau)=\cosh^{-1}\frac{c^2\tau^2-(r_S^2+r_R^2+z_R^2)}{2r_S r_R}, \tag{4}$$

where c is the speed of sound, the wedge index v equals π/θ_w, $H(\tau-\tau_0)$ in Eq. (1) is Heaviside's unit step function, and the time τ_0 equals L_0/c. The distance $L_0=[(r_S+r_R)^2+z_R^2]^{1/2}$ is the shortest path from the source to the receiver via the edge of the wedge, passing through the so-called apex point of the edge, indicated as A in Fig. 2. For an infinite wedge with soft (pressure-release) surfaces, the IR is given by using a modified version of the β-expression[15]

$$\beta_{\mathrm{soft}}(\tau)=-\beta_{++}(\tau)+\beta_{+-}(\tau)+\beta_{-+}(\tau)-\beta_{--}(\tau). \tag{5}$$

Wedges with a combination of rigid and soft surfaces could be studied using variants of the β-expressions in Eqs. (2) or (5); however, in the following discussion, rigid surfaces will always be assumed except for the example of a circular soft disc, studied in Sec. III B.

A. Models of finite wedge diffraction

Although the analytical solution in Eq. (1) describes explicitly the IR of an infinite wedge, it does not indicate what a solution for a finite wedge might look like. Medwin *et al.* suggest a ''discrete Huygens interpretation,''[3] placing a number of small secondary sources along the edge and adjusting their strengths so that together they give the known exact solution. According to this model, these secondary sources emit pulses when they are hit by the incident, impulsive, sound wave. Thus, the reaction at the edge is assumed to be instantaneous. This leads to the conclusion that the value of the IR h_{diffr} at time τ is caused by the reradiation from the two parts of the edge indicated in Fig. 2, a lower

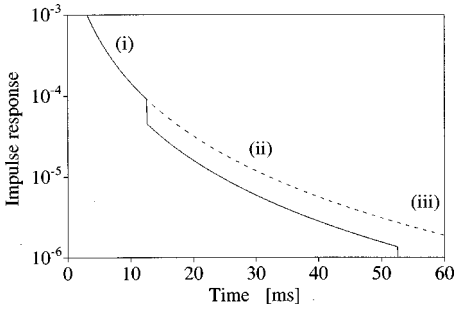

FIG. 3. Illustration of a diffraction impulse response for a finite wedge, h_{finite} (solid line) and the corresponding infinite wedge, h_{infinite} (dotted line), indicating the three parts where [i] $h_{\text{finite}}=h_{\text{infinite}}$, [ii] h_{finite} is a scaled version of h_{infinite}, and [iii] where $h_{\text{finite}}=0$. The initial part of the impulse responses has been truncated.

branch indicated by the subscript l, and an upper branch indicated by a subscript u. The two branches must obey the condition

$$m_l + l_l = m_u + l_u = c\tau. \tag{6}$$

The two edge portions at positions z_l and z_u will cause two radiated sound-field components, h_l and h_u, which summed together equal the known amplitude h_{diffr},

$$h_l(\tau) + h_u(\tau) = h_{\text{diffr}}(\tau). \tag{7}$$

As indicated in Fig. 3, an IR for a single finite wedge will then have three parts. In the initial part, [i], the IR is identical to the infinite wedge response. In the final part, [iii], the IR is zero, after the sound wave has reached the furthest end of the edge. The intermediate part, [ii], where only h_l or h_u in Eq. (7) is present, is then a scaled version of the infinite wedge IR. The scaling for the intermediate part was suggested in Ref. 2, and is based on the finite wedge IR having half the amplitude of the infinite wedge IR, i.e., $h_l = h_u$. In a later paper,[3] it was instead suggested that this factor should be

$$\frac{h_{\text{finite}}(\tau)}{h_{\text{infinite}}(\tau)} = \frac{h_l(\tau)}{h_l(\tau)+h_u(\tau)} = \frac{m_u l_u}{m_u l_u + m_l l_l}, \tag{8}$$

where it is assumed that the lower branch of the edge has the longest extension. It will be shown below that a theoretical derivation supports the relation $h_l = h_u$.

For multiple scattering, Medwin's model and the WA method assume that the secondary edge sources radiate as point sources, with source strength modifications based on Eq. (8). Second-order diffraction is then calculated by having all these secondary edge sources along the first edge generate individual diffraction contributions via the second edge.

Medwin *et al.* present comparisons between measurements and calculations for noise barriers of finite widths where second-order diffraction must be taken into account, and the agreement seems to be quite good.[3] The agreement is also good for the scattering from a circular disc.[11] As will be shown in Sec. I C, however, the derived analytical directivity functions indicate that having the secondary sources along the first edge use the ordinary diffraction expression to generate second-order diffraction via the second edge, as in Eq. (1), is only an approximation as far as we can determine. However, the errors in Medwin's model do not appear to show up for geometries with symmetrical situations, such as for noise barriers with parallel edges. The second-order diffraction paths which will be of highest amplitude are those passing the apex points, that is, with as little angular deviation as possible during the passage of the edge. The methods in Refs. 2, 3, and 11 correctly predict these high-amplitude parts, and thus predict the second-order diffraction quite well, as long as the geometry is such that sound paths with little angular deviation are possible. A critical benchmark case would then be one where all sound paths across edges experience large angular deviation. For such cases, an accurate secondary source model would be important.

B. Derivation of analytical directivity functions for the secondary edge source

A derivation of analytical directivity function for the secondary edge sources starts by assuming the existence of a directivity function for the secondary edge sources which depends only on the angles of the incident sound path, α and θ_s, and of the reradiated sound path, γ and θ_r in Figs. 1 and 2. This directivity function must be independent of the distances m and l, and must be symmetric so that the source and receiver positions can be interchanged with identical results. Thus, the reciprocity principle is always fulfilled. A consequence of such directivity functions is that the incident wavefront is split up when it hits a point of the edge, and the reradiated wavefront spreads in all directions with different amplitudes. To derive such a directivity function, the method of retarded potentials is employed as in Ref. 7, and a prototype solution can be formulated for the edge diffraction. The prototype solution is then matched to the known solution for the infinite wedge. Thus, the diffracted pressure $p_{\text{diffr}}(t)$ could be written as an integral over contributions from the entire wedge

$$P_{\text{diffr}}(t) = \int_{-\infty}^{\infty} q\left[t - \frac{m(z)+l(z)}{c}\right] \frac{D[\alpha(z),\gamma(z),\theta_S,\theta_R]}{m(z)l(z)}\,dz, \tag{9}$$

where $D[\alpha(z),\gamma(z),\theta_S,\theta_R]$ is the unknown directivity function. The position along the wedge is given by the z-coordinate, and this causes a retardation of the source signal $q(t)$, an amplitude attenuation caused by the ray paths m and l, and a further amplitude attenuation by the directivity function D. The variable z can be substituted for a variable $\tau=(m+l)/c$, the time delay. There will, however, be two values of z giving the same value of τ, corresponding to the upper and lower branches of the edge. Thus, the integral in Eq. (9) is first rewritten as a sum of the upper and lower branch integrals, as

$$p_{\text{diffr}}(t) = \int_{-\infty}^{z_{\text{apex}}} q\left[t - \frac{m(z)+l(z)}{c}\right] \frac{D[\alpha(z),\gamma(z),\theta_S,\theta_R]}{m(z)l(z)}\,dz + \int_{z_{\text{apex}}}^{\infty} q\left[t - \frac{m(z)+l(z)}{c}\right] \frac{D[\alpha(z),\gamma(z),\theta_S,\theta_R]}{m(z)l(z)}\,dz, \tag{10}$$

where z_{apex} corresponds to the apex point on the edge, which is given by $z_{\text{apex}}=z_R r_S/(r_S+r_R)$. Now, a variable substitution is carried out so that

$$p_{\text{diffr}}(t)=\int_{\infty}^{\tau_0} q(t-\tau)\frac{D_l(\tau)}{m_l(\tau)l_l(\tau)}\frac{dz_l}{d\tau}d\tau + \int_{\tau_0}^{\infty} q(t-\tau)\frac{D_u(\tau)}{m_u(\tau)l_u(\tau)}\frac{dz_u}{d\tau}d\tau = \int_{\tau_0}^{\infty} q(t-\tau)\left\{-\frac{D_l(\tau)}{m_l(\tau)l_l(\tau)}\frac{dz_l}{d\tau} + \frac{D_u(\tau)}{m_u(\tau)l_u(\tau)}\frac{dz_u}{d\tau}\right\}d\tau, \tag{11}$$

where the subscripts l and u, respectively, indicate that for each value of τ, the solution of $D(\tau)$, $m(\tau)$, $l(\tau)$, and $z(\tau)$ is chosen to correspond to the lower and upper branches, respectively. Also, in Eq. (11) the directivity function is written as $D_l(\tau)$ rather than $D[\alpha_l(\tau),\gamma_l(\tau),\theta_S,\theta_R]$. The quantities $dz/d\tau$ can then be defined as being zero before $\tau=\tau_0$, the first arrival time of the diffracted sound-field component, so that the lower integration limit can be expanded to $-\infty$. From this it becomes clear that the integral in Eq. (11) is a convolution integral of the source signal $q(t)$ with an IR which must be the diffraction IR, since

$$p_{\text{diffr}}(t)=\int_{-\infty}^{\infty} q(t-\tau)h_{\text{diffr}}(\tau)d\tau, \tag{12}$$

and $h_{\text{diffr}}(\tau)$ can be identified as

$$h_{\text{diffr}}(\tau)=-\frac{D_l(\tau)}{m_l(\tau)l_l(\tau)}\frac{dz_l}{d\tau}+\frac{D_u(\tau)}{m_u(\tau)l_u(\tau)}\frac{dz_u}{d\tau}. \tag{13}$$

To find a directivity function D which satisfies Eq. (13), the observations

$$-\frac{1}{m_l(\tau)l_l(\tau)}\frac{dz_l}{d\tau}=\frac{1}{m_u(\tau)l_u(\tau)}\frac{dz_u}{d\tau}=\frac{cH(\tau-\tau_0)}{r_S r_R\sinh\eta(\tau)}, \tag{14}$$

which are proven in Appendix A, will be used. The relations in Eq. (14) can be inserted into Eq. (13), which leads to

$$-\frac{\nu\beta(\tau)}{2\pi}=D[\alpha_l(\tau),\gamma_l(\tau),\theta_S,\theta_R] + D[\alpha_u(\tau),\gamma_u(\tau),\theta_S,\theta_R]. \tag{15}$$

Furthermore, it is possible to express β as function of the angles α and γ. To do this, another relation shown in Appendix B,

$$\eta(\tau)=\cosh^{-1}\frac{1+\sin\alpha(\tau)\sin\gamma(\tau)}{\cos\alpha(\tau)\cos\gamma(\tau)}, \tag{16}$$

can be used. It should be noted that α and γ can be exchanged without affecting the result, and thus reciprocity is assured. This relation is valid regardless of whether one chooses the lower or upper branch combination of the α and γ angles, an observation which could be formulated as $\eta[\alpha_l(\tau),\gamma_l(\tau),\theta_S,\theta_R]=\eta[\alpha_u(\tau),\gamma_u(\tau),\theta_S,\theta_R]$ and consequently, $\beta[\alpha_l(\tau),\gamma_l(\tau),\theta_S,\theta_R]=\beta[\alpha_u(\tau),\gamma_u(\tau),\theta_S,\theta_R]$, so it can be stated that

$$\beta(\tau)=\tfrac{1}{2}\{\beta[\alpha_l(\tau),\gamma_l(\tau),\theta_S,\theta_R] + \beta[\alpha_u(\tau),\gamma_u(\tau),\theta_S,\theta_R]\}. \tag{17}$$

This expression can finally be inserted into Eq. (15), and the unknown directivity function D can be identified as

$$D[\alpha(\tau),\gamma(\tau),\theta_S,\theta_R]=-\frac{\nu\beta[\alpha(\tau),\gamma(\tau),\theta_S,\theta_R]}{4\pi}, \tag{18}$$

where either $\alpha_l(\tau)$ and $\gamma_l(\tau)$, or $\alpha_u(\tau)$ and $\gamma_u(\tau)$, could be chosen as solutions for $\alpha(\tau)$ and $\gamma(\tau)$. These derivations lead to the conclusion that the branches of the edge on each side of the apex point contribute with exactly equal amounts to the diffraction IR $h_{\text{diffr}}(\tau)$. This has two consequences. First, one could choose either the upper or lower branch solutions for $\alpha(\tau)$, $\gamma(\tau)$, $z(\tau)$, $m(\tau)$, and $l(\tau)$ to formulate the total diffraction IR in this new form,

$$h_{\text{diffr}}(\tau)=-\frac{\nu}{4\pi}\frac{\beta[\alpha(\tau),\gamma(\tau),\theta_S,\theta_R]}{m(\tau)l(\tau)}\frac{dz}{d\tau}, \tag{19}$$

where β is as in Eqs. (2) and (3), and uses $\eta(\tau)$ from Eq. (16). Second, for a finite wedge, $h_l(t)=h_u(t)$ in Eq. (7), i.e., the part of the IR which is a scaled version of the infinite wedge IR, illustrated as part [ii] in Fig. 3, has the simple scaling factor 1/2,

$$\frac{h_{\text{finite}}(\tau)}{h_{\text{infinite}}(\tau)}=\frac{1}{2}. \tag{20}$$

This scaling factor supports the suggestion by Medwin in Ref. 2, but contradicts the suggested relationship in Ref. 3, as discussed in Sec. I A.

Decomposition of the infinite wedge diffraction into local edge contributions also makes it possible to derive diffraction from nonstraight edges. As is shown below among the examples in Sec. III, the first- and second-order diffraction components of a circular thin disc can be derived analytically. Such derivations can employ a rewritten version of the original expression in Eq. (9), using the β function, as

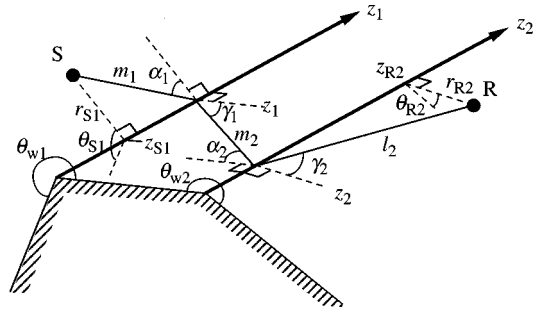

FIG. 4. The geometry of a truncated infinite wedge, with two parallel infinite edges, a point source S and a receiver R. One sound path, via the two points z_1 and z_2 on the two edges, is marked. For the first edge with the open wedge angle θ_{w1}, the source S has the cylindrical coordinates r_{S1}, θ_{S1}, z_{S1}, and the point at z_2 along edge 2, which acts as a receiver, has the coordinates w,θ_{w1},z_2. Relative to the second edge with the open wedge angle θ_{w2}, the point z_1 along edge 1 acts as a source and has the coordinates w, $\theta_{S2}=0$, z_1, and the receiver R has the coordinates r_{R2}, $\theta_{w2}-\theta_{R2}$, z_{R2}. It is assumed that the two z-axes are aligned with respect to each other. The angles α and γ are as defined in Fig. 2.

$$p_{\text{diffr}}(t) = -\frac{v}{4\pi}\int_{z_1}^{z_2} q\left[t - \frac{m(z)+l(z)}{c}\right] \times \frac{\beta[\alpha(z),\gamma(z),\theta_S,\theta_R]}{m(z)l(z)}\,dz, \tag{21}$$

where z_1 and z_2 are the two endpoints of the finite or infinite wedge.

C. Second-order edge diffraction

To derive expressions for second-order diffraction, the case of a truncated infinite wedge with two parallel, infinitely long edges as in Fig. 4 is studied. Expanding the formulation in Eq. (21), and using the sound-path designations in Fig. 4, the second-order diffracted pressure can be written

$$p_{\text{diffr}}(t) = \frac{v_1 v_2}{(4\pi)^2}\int\int_{-\infty}^{\infty} q\left[t - \frac{m_1(z_1)+m_2(z_1,z_2)+l_2(z_2)}{c}\right] \frac{\beta[\alpha_1(z_1),\gamma_1(z_1,z_2),\theta_{S1},0]\beta[\alpha_2(z_1,z_2),\gamma_2(z_2),0,\theta_{R2}]}{2m_1(z_1)m_2(z_1,z_2)l_2(z_2)}\,dz_1 dz_2, \tag{22}$$

where it has been assumed that the path from edge 1 to edge 2 runs along a plane connecting the two edges. This is indicated by the values $\theta_{R1}=0$ and $\theta_{S2}=0$ in the two β factors and the factor of 2 in the denominator of the integral. This factor of 2 compensates for the doubling in pressure generated by an acoustic source when it is mounted on a baffle. It should have the value of 1 if the ray from edge 1 to edge 2 does not run along a plane. In the double integral in Eq. (22), the factor m_1 and the delay corresponding to m_1 can be moved out from the integral over dz_2, so that

$$p_{\text{diffr}}(t) = \frac{v_1}{4\pi}\int_{-\infty}^{\infty}\left[\frac{\delta(t-m_1(z_1)/c)}{m_1(z_1)} * I_2\right] dz_1, \tag{23}$$

where* indicates a convolution and

$$I_2 = \frac{1}{2}\frac{v_2}{4\pi}\int_{-\infty}^{\infty} q\left[t - \frac{m_2(z_1,z_2)+l_2(z_2)}{c}\right] \frac{\beta[\alpha_1(z_1),\gamma_1(z_1,z_2),\theta_{S1},0]\beta[\alpha_2(z_1,z_2),\gamma_2(z_2),0,\theta_{R2}]}{m_2(z_1,z_2)l_2(z_2)}\,dz_2. \tag{24}$$

For each value of z_1, there is a $z_{2,\text{apex}}$ around which the integral I_2 can be split into the upper and lower branches, as was described before. Then, a variable substitution is possible with $(m_2+l_2)/c=\tau$, and the factors $dz_2/d\tau$ can be defined as being zero before $\tau=\tau_{02}$. Here, $\tau_{02}=L_{02}/c$ where $L_{02}=[(w+r_{R2})^2+(z_{R2}-z_1)^2]^{1/2}$. Since the geometry is basically the same as for the diffraction for a single wedge, the left-hand relation in Eq. (14) holds here, too. The integral I_2 can then be written

$$I_2 = \frac{1}{2}\frac{v_2}{4\pi}\int_{-\infty}^{\infty} q(t-\tau)\frac{(\beta_{1l}\beta_{2l}+\beta_{1u}\beta_{2u})}{m_2 l_2}\frac{dz_2}{d\tau}\,d\tau = q(t) * h_{\text{diffr},z_1\to R}(\tau), \tag{25}$$

where the values of m_2, l_2, and $dz_2/d\tau$ can be chosen as the upper or lower branch solutions for a certain value of τ. If one studies the impulse response $h_{\text{diffr},z_1\to R}(\tau)$ further,

$$h_{\text{diffr},z_1\to R}(\tau) = \frac{1}{2}\frac{v_2}{4\pi}\frac{1}{m_2 l_2}\frac{dz_2}{d\tau}\{\beta[\alpha_1,\gamma_{1l},\theta_{S1},0] \times \beta[\alpha_{2l},\gamma_{2l},0,\theta_{R2}] + \beta[\alpha_1,\gamma_{1u},\theta_{S1},0]\beta[\alpha_{2u},\gamma_{2u},0,\theta_{R2}]\}. \tag{26}$$

Equation (17) can be applied, implying that $\beta[\alpha_{2l},\gamma_{2l},0,\theta_{R2}]=\beta[\alpha_{2u},\gamma_{2u},0,\theta_{R2}]$ and

$$h_{\text{diffr},z_1\to R}(\tau) = \frac{1}{2}\frac{v_2}{4\pi}\frac{\beta(\alpha_{2u},\gamma_{2u},0,\theta_{R2})}{m_2 l_2}\frac{dz_2}{d\tau} \times \{\beta[\alpha_1,\gamma_{1l},\theta_{S1},0]+\beta[\alpha_1,\gamma_{1u},\beta_{S1},0]\} = h_{\text{diffr,1st,edge2}}(\tau)\{\beta[\alpha_1,\gamma_{1l},\theta_{S1},0] + \beta[\alpha_1,\gamma_{1u},\theta_{S1},0]\}/2. \tag{27}$$

This means that the IR $h_{\text{diffr},z_1\to R}(\tau)$ is a first-order edge-diffraction IR from the position z_1 on edge 1 to the receiver position R via edge 2, scaled by 1/2, and multiplied with a weighting function which is the sum of the two β functions in Eq. (27). The approach for second-order diffraction in Ref. 3 is to place discrete edge sources along edge 1, and to use an ordinary first-order diffraction IR to calculate their contributions at the receiver point. However, the factor with two β functions in Eq. (27) will modify the first-order diffraction IR $h_{\text{diffr,1st,edge2}}$, which in principle makes it impossible to let the edge sources on edge 1 irradiate edge 2 via ordinary first-order diffraction IRs. The method used in Ref. 3 probably does calculate the onset of $h_{\text{diffr},z_1\to R}(\tau)$ correctly and, since the high-frequency properties are determined to a large degree by the transient onset, the overall second-order edge diffraction is predicted rather well. Employing the IR $h_{\text{diffr},z_1\to R}$, the second-order diffracted pressure becomes

$$p_{\mathrm{diffr}}(t)$$
$$= \frac{v_1}{4\pi}\int_{-\infty}^{\infty}\left\{\frac{\delta[t-m_1(z_1)/c]}{m_1(z_1)} * [q(t) * h_{\mathrm{diffr},z_1\to R}(z_1,t)]\right\} \times dz_1$$
$$= q(t) * \left\{\frac{v_1}{4\pi}\int_{-\infty}^{\infty}\left[\frac{\delta[t-m_1(z_1)/c]}{m_1(z_1)} * h_{\mathrm{diffr},z_1\to R}(z_1,t)\right] \times dz_1\right\}. \quad (28)$$

This expression means that the second-order diffraction IR, $h_{\mathrm{diffr,2nd}}(\tau)$, can be found from a single integral,

$$h_{\mathrm{diffr,2nd}}(\tau)$$
$$= \frac{v_1}{4\pi}\int_{-\infty}^{\infty}\left[\frac{\delta[\tau-m_1(z_1)/c]}{m_1(z_1)} * h_{\mathrm{diffr},z_1\to R}(z_1,\tau)\right] dz_1$$
$$= \frac{v_1}{4\pi}\int_{-\infty}^{\infty}\frac{h_{\mathrm{diffr},z_1\to R}[\tau-m_1(z_1)/c]}{m_1(z_1)}\,dz_1. \quad (29)$$

However, since the IR $h_{\mathrm{diffr},z_1\to R}(\tau)$ is zero for $\tau<\tau_{02}$, the infinite integration limits in Eq. (29) can be replaced by the values $z_{1,1}$ and $z_{1,2}$, which both satisfy $\tau=\tau_{02}+m_1/c$. Explicit solutions to Eq. (29) might be possible for certain geometries, for instance the axisymmetric reflection from a circular disc, as shown in Sec. III B.

II. NUMERICAL IMPLEMENTATION—DISCRETE-TIME IMPULSE RESPONSES

The default solution for numerical calculations is to use a discrete-time IR which, for instance, can be given by area sampling of the continuous-time expression in Eqs. (1) or (19). A value of the discrete-time diffraction IR $h_{\mathrm{diffr}}(n)$ at a certain discrete time $\tau=n/f_s$, where f_s is the sampling frequency and n is a sample number, is thus given by

$$h_{\mathrm{diffr}}(n)=\int_{(n-1/2)/f_s}^{(n+1/2)/f_s} h_{\mathrm{diffr}}(\tau)\,d\tau, \quad (30)$$

where $h_{\mathrm{diffr}}(\tau)$ is the continuous-time diffraction IR, such as in Eq. (1). The singularity at $\tau=\tau_0$ in Eq. (1) deserves special attention, and the original function can be approximated by an analytically integrable function for values of τ close to τ_0.[14] The integration in Eq. (30) corresponds to filtering the continuous-time signal $h_{\mathrm{diffr}}(\tau)$ prior to sampling, employing a low-pass filter with an IR in the form of a rectangular pulse of width $1/f_s$. This is quite a crude low-pass filter, and Clay and Kinney suggest the use of a wider pulse of width $4/f_s$.[14] The sampling frequency can, however, always be raised high enough to give a low enough aliasing error at the highest frequency of interest. In the numerical examples in this study, numerical integration as in Eq. (30) has been used throughout with rather high sampling frequencies (20 to 40 times the highest frequency of interest) to get accurate results.

Formulating the diffraction as a sum of contributions from along the edge, as in Eq. (19), it can be seen that the integration of $h_{\mathrm{diffr}}(\tau)$ in Eq. (30) over a time segment $d\tau$ is equivalent to the integration over a segment of the edge which corresponds to this particular $d\tau$. To do this, another variable substitution can be done so that

$$h(n)=\int_{(n-0.5)/f_s}^{(n+0.5)/f_s} h_{\mathrm{diffr}}(\tau)\,d\tau=\int_{z_{n1}}^{z_{n2}} h_{\mathrm{diffr}}(z)\frac{d\tau}{dz}\,dz, \quad (31)$$

where z_{n1} and z_{n2} are the z-coordinates that correspond to $\tau=(n\pm1)/(2f_s)$, respectively. As discussed in conjunction with Eq. (19), one could choose either the lower or upper branch z-coordinates that correspond to τ. Since Eq. (19) can be used to find that

$$h_{\mathrm{diffr}}(z)\frac{d\tau}{dz}=-\frac{v}{4\pi}\frac{\beta[\alpha(z),\gamma(z),\theta_S,\theta_R]}{m(z)l(z)}, \quad (32)$$

the integration in Eq. (31) can be written

$$h(n)=-\frac{v}{4\pi}\int_{z_{n1}}^{z_{n2}}\frac{\beta[\alpha(z),\gamma(z),\theta_S,\theta_R]}{m(z)l(z)}\,dz. \quad (33)$$

This integration can be approximated by the midpoint value so that

$$h(n)\approx-\frac{v}{4\pi}\frac{\beta[\alpha(z_n),\gamma(z_n),\theta_S,\theta_R]}{m(z_n)l(z_n)}\Delta z_n, \quad (34)$$

where z_n is the midpoint between z_{n1} and z_{n2}. If, for a simplified numerical implementation, one chooses to divide the edge into equally sized elements of size Δz, then an element i placed at z_i will give a contribution Δh_i to the IR

$$\Delta h_i\approx-\frac{v}{4\pi}\frac{\beta[\alpha(z_i),\gamma(z_i),\theta_S,\theta_R]}{m(z_i)l(z_i)}\Delta z. \quad (35)$$

This should be added to a single time sample $n=f_s(m+l)/c$ or divided among two or more consecutive time samples. This division is determined by the edge element's position and size relative to the time positions for sample n. The contribution Δh_i should be viewed as a rectangular pulse with a width Δt as given by the element size Δz and its position z_i. If the edge element size is chosen so that $\Delta z<c/f_s$, the contribution from each element will never spread out over more than two time samples.

For efficient numerical implementations, the β function can be written in a much more compact form than in Eqs. (2), (3), and (16) if one uses the relation

$$\cosh(v\eta)=(A^v+A^{-v})/2, \quad (36)$$

where $A=(y^2-1)^{1/2}+y$ and $y=[ml+z(z-z_r)]/(r_s r_r)$, which is taken from Eq. (A7), with the same variables as before. With this formulation, only basic mathematical computations need to be recalculated for each edge element and very efficient implementations are possible.

Second-order diffraction is straightforward to implement using a formulation which is based on Eq. (22). If two finite edges are divided into equally sized edge elements Δz_1 and Δz_2, the second-order contribution Δh_{ij} to the IR $h_{\mathrm{diffr,2nd}}$, of edge element i at z_i of edge 1 and edge element j at z_j of edge 2, can be written

$$\Delta h_{ij}=\frac{v_1 v_2}{32\pi^2}\frac{\beta[\alpha_1(z_1),\gamma_1(z_1,z_2),\theta_{S1},\theta_{R1}]\beta[\alpha_2(z_1,z_2),\gamma_2(z_2),\theta_{S2},\theta_{R2}]}{m_1(z_1)m_2(z_1,z_2)l_2(z_2)}\Delta z_1,\Delta z_2. \tag{37}$$

This expression is valid for both parallel and nonparallel edges, as long as the appropriate expressions for the involved α, γ, and θ angles, and m and l distances, are used. Note that a second-order contribution via two edge elements should be viewed as a triangular pulse, and a third-order contribution appears as a pulse with second-order polynomial shape, etc. This affects how each contribution should be divided among time samples. A simplified implementation, giving the correct low-frequency response, was used by Vanderkooy.[16] The contribution Δh can be distributed over the two time samples adjacent to the arrival time of the edge element center, with a linear weighting that depends on the center arrival time's position relative to the two sample times.

Other models have used time-domain formulations for edge diffraction, the most common ones being based on the Kirchhoff diffraction approximation, as mentioned in the Introduction. Another model, suggested by Vanderkooy, has an interesting equivalence to the new model suggested here.[16] Vanderkooy's model started from a frequency-domain high-frequency asymptotic expression for the infinite wedge.[17] The model uses discrete edge sources, each of which gives a contribution

$$\Delta h=-\frac{v}{4\pi}\frac{\kappa(\theta_S,\theta_R)}{ml}\Delta z, \tag{38}$$

which is delayed by the time $\tau=(m+l)/c$. Vanderkooy used a parameter v_{Vand} which is the reciprocal of the wedge index v used here, but for clarity the parameter v_{Vand} was replaced by v in Eq. (38) so that the similarity with Eq. (35) is clear. The directivity function κ is

$$\kappa(\theta_S,\theta_R)=\sin v\pi\left\{\frac{1}{\cos v\pi-\cos[v(\theta_R-\theta_S)]}+\frac{1}{\cos v_\pi+\cos[v(2\pi-\theta_R-\theta_S)]}\right\}, \tag{39}$$

which can be rewritten into the form

$$\kappa(\theta_S,\theta_R)=\beta_{++}^{\mathrm{Vand}}+\beta_{+-}^{\mathrm{Vand}}+\beta_{-+}^{\mathrm{Vand}}+\beta_{--}^{\mathrm{Vand}}, \tag{40}$$

where

$$\beta_{\pm\pm}^{\mathrm{Vand}}=\frac{\sin[v(\pi\pm\theta_S\pm\theta_R)]}{1-\cos[v(\pi\pm\theta_S\pm\theta_R)]}. \tag{41}$$

If $\cosh(v\eta)=1$, which happens for the time $\tau=\tau_0$ (i.e., at the onset of the diffraction), these β terms are identical with the analytical ones in Eqs. (2) and (3). Since rapid variations in the IR always occur at the onset, the high-frequency part of the response is determined entirely by this initial part of the diffracted signal. Thus, it is not surprising that Vanderkooy's model correctly reproduces the initial part of the IR and consequently the high-frequency response. The model does, however, give large errors at low frequencies, which is clearly due to using the constant value 1 in Eq. (41) instead of the monotonically increasing function $\cosh v\eta$.

III. EXAMPLES

In this section, the new model employing analytical directivity function for the secondary edge sources is compared with other methods. Only IRs have been discussed so far, but results are often more interesting when presented as transfer functions. These are calculated from the IRs using a discrete Fourier transform (DFT), and it is then possible to check if a sufficiently high sampling frequency has been used. The sampling frequency should be increased until the results at the highest frequencies of interest have stabilized. In all calculations, unless otherwise stated, a value of 344 m/s has been used for the speed of sound.

A. Infinite wedges

Two different infinite and rigid wedges were studied as illustrated in Fig. 5. Figure 5(a) shows a thin plate edge, with one fixed source position S (with cylindrical coordinates $r_S=25\,\mathrm{cm}$, $\theta_S=15°$, and $z_S=0$) and with two different receiver positions, R1 and R2 (at $r_R=25\,\mathrm{cm}$, $z_R=0$, and $\theta_R=300°$ for R1, and $\theta_R=196°$ for R2). The position R2 is 1° into the shadow zone, which is critical from a numerical point of view due to the singularity of the diffraction IR at the boundary of shadow zones. In Fig. 5(b), another case is shown with a plate of thickness w, an example which is duplicated from Ref. 3. In this case, the source is at cylindrical coordinates $r_S=25\,\mathrm{cm}$, $\theta_S=15°$, and the receiver is at $r_R=25\,\mathrm{cm}$, $\theta_R=300°$, $z_R=0$. It should be noted that because of the width w of the plate, the receiver coordinates are relative to the second edge, closest to the receiver.

Calculations of IRs were made with the new model using the discrete edge decomposition described by Eq. (35) for the single edge, and by Eq. (37) for the double edge. IRs

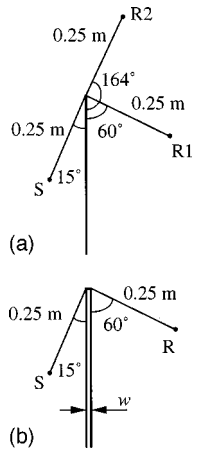

FIG. 5. The two infinite wedge situations that have been studied. (a) shows a thin plate edge. (b) shows a plate of thickness w, where the values $w=5$, 22, and 35 mm have been studied.

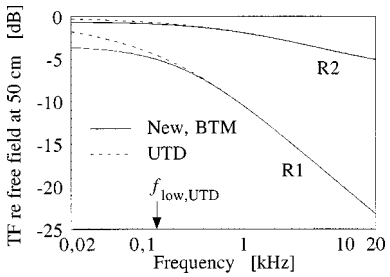

FIG. 6. Transfer function (relative to free-field propagation) at 50 cm distance for the two receiver points at the infinite wedge in Fig. 5(a). The frequency marked, $f_{low,UTD}$, is the frequency above which the UTD method should give less than 0.5 dB error according to Ref. 16.

were also calculated with the Biot–Tolstoy model from Ref. 3, here denoted BTM, and transfer functions were calculated for the single edge with the uniform theory of diffraction (UTD) by Kouyoumjian and Pathak.[13] The lowest frequency for which the UTD method gives accurate results—that is, within 0.5 dB of exact solutions—was found to be $f_{low,UTD} \approx 140$ Hz based on Fig. 4 in Ref. 18. Sampling frequencies of 800 kHz were used for the IRs since, compared with a sampling frequency of 400 kHz, the difference was less than 0.1 dB at 20 kHz. The edge element sizes were 0.43 mm for all cases, and the wedge had an extension of ± 5 m relative to the source.

Results for the wedge in Fig. 5(a) are presented in Fig. 6, where the results for the new model and the BTM model come within 0.001 dB. It can also be seen that the UTD method is indeed accurate down to $f_{low,UTD} \approx 140$ Hz. Figure 7 shows results for the double-edge wedge in Fig. 5(b), together with single-edge diffraction for the corresponding infinitely thin wedge. Comparing these results with Fig. 9 in Ref. 3, it can be seen that the results with the new method and the BTM results are very close to each other. As is also observable for the double-edge plates in Ref. 3, the differences between the thin plate limit and the low-frequency results decrease with decreasing thicknesses, yet a small but significant difference always remains. This remaining difference is probably caused by the lack of higher-order diffraction components in these calculations. It can also be noted

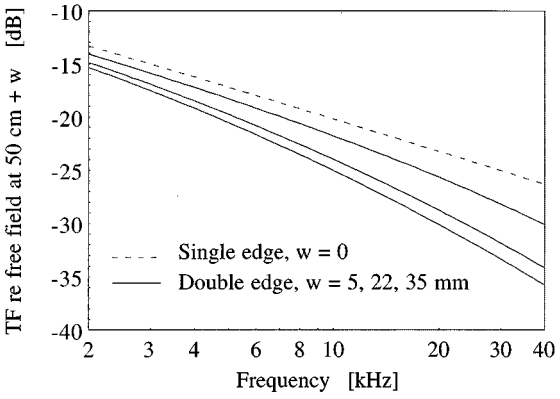

FIG. 7. Transfer function (relative to free-field propagation) at 50 cm$+w$ for the infinite plate in Fig. 5(b), calculated with the new method. The dashed line indicates the single-edge case, that is, the thin plate limit. Solid lines give results for a double wedge with $w=5$, 22, and 35 mm (from the top).

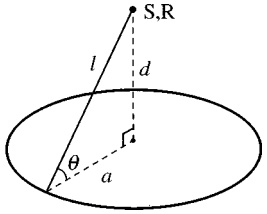

FIG. 8. The geometry for the axisymmetric scattering from a thin, rigid circular disc of radius a, with colocated source and receiver at height d.

that this new model and the BTM model give very similar results for double-edge diffraction for a geometry with parallel long edges, a happenstance that does not display well the significant differences in the two theories.

B. On-axis scattering from a rigid circular disc

The cases of on-axis scattering from rigid and soft circular discs was studied in Ref. 11, employing both an accurate, frequency-domain T-matrix formalism, and time-domain expressions using the WA method. The accurate frequency-domain expressions were transformed into IRs using the inverse discrete Fourier transform, and adjusting the sampling frequencies to the geometry so that delays corresponded to exact integer sample numbers, which should ensure that accurate time-domain expressions were retrieved. Thus, these could be seen as accurate reference cases against which the present method can be compared. Nevertheless, although the possible effects of windowing on the time signal were mentioned in Ref. 11, no estimate was given. The first-order diffraction is a single pulse, for which it should in principle be possible to accurately find the amplitude. Since second- and higher-order diffraction components are continuous-time signals with onsets exactly at the arrival of the first-order impulse, these higher-order components will inevitably influence the sample in which the impulse arrives. This effect is small since the onset amplitude of the higher-order diffraction is very small, but the accumulated effect is not clear.

To derive analytical expressions for the diffraction IR, the formulation in Eq. (21) is used. The β function must be found for the case with the source and receiver colocated, as illustrated in Fig. 8. In this case, the angles θ_S and θ_R are equal and consequently, both will be referred to as θ. The β function can be derived using the form of $\cosh(\nu\eta)$ which is valid for the wedge index $\nu=0.5$, as shown in Appendix C,

$$\cosh\frac{\eta}{2}=\frac{\cos[(\alpha-\gamma)/2]}{(\cos\alpha\cos\gamma)^{1/2}}, \tag{42}$$

which, as is also shown in Appendix C, leads to

$$\beta=2\cosh\frac{\eta}{2}\left\{\frac{\cos[(\theta_S+\theta_R)/2]}{\cosh^2(\eta/2)-\sin^2[(\theta_S+\theta_R)/2]}+\frac{\cos[(\theta_S-\theta_R)/2]}{\cosh^2(\eta/2)-\sin^2[(\theta_S-\theta_R)/2]}\right\}. \tag{43}$$

When θ_S equals θ_R and both are denoted θ, β can be written

TABLE I. Amplitude of the first-order diffraction component for axisymmetric scattering from a circular rigid disc of radius 1 m, normalized to the specular reflection. Results are either calculated using the new method, Eq. (47), or taken from Ref. 11. The errors are relative to the T-matrix solution which is considered as the reference result.

Height [m]	T matrix (Ref. 11)	WA (Ref. 11)	Rel. error [%]	Eq. (47)	Rel. error [%]
1.1	−1.221	−1.223	(−0.16)	1.238	(−1.4)
1.5	−1.273	1.247	(2.0)	−1.294	(−1.6)
3.0	−1.243	−1.252	(−0.7)	−1.249	(−0.5)
5.0	−1.163	−1.118	(3.9)	−1.173	(−0.9)
10.0	−1.093	−1.099	(−0.5)	−1.094	(−0.1)

$$\beta=\frac{2}{\cosh(\eta/2)}+\cos\theta\left[\frac{1}{\cosh(\eta/2)+\sin\theta}+\frac{1}{\cosh(\eta/2)-\sin\theta}\right]. \tag{44}$$

Furthermore, the $\cosh(\eta/2)$ factor is simplified for the axisymmetric case that is studied here. For the entire circular edge, the incident ray angles α and the reradiated ray angles γ will have the value 0, and then the quantity $\cosh(\eta/2)=1$, as is clear from Eq. (42). The β function in Eq. (44) can consequently be further simplified as

$$\beta=2+\cos\theta\left(\frac{1}{1+\sin\theta}+\frac{1}{1-\sin\theta}\right)=2\left(1+\frac{1}{\cos\theta}\right)=2\frac{a+l}{a}, \tag{45}$$

where a is the radius of the disc and $l=(a^2+d^2)^{1/2}$, d being the height of the source and receiver above the disc. Inserting this constant value of the β term into Eq. (21), together with the constant values of m and l, it is found that if the z-coordinate runs along the disc perimeter,

$$p_{\mathrm{diffr}}(t)=-\frac{a+l}{4\pi a l^2}\int_0^{2\pi a} q\left(t-\frac{2l}{c}\right)dz=-\frac{a+l}{2l^2}q\left(t-\frac{2l}{c}\right), \tag{46}$$

where it can be noted that $p_{\mathrm{diffr}}(t)$ is nothing but a scaled and delayed version of the source signal. In other words,

$$h_{\mathrm{diffr}}(\tau)=-\frac{a+l}{2l^2}\delta\left(\tau-\frac{2l}{c}\right). \tag{47}$$

The first-order diffraction for a soft disc can be found by employing the expression in Eq. (5) and repeating the derivations above, which yields

$$h_{\mathrm{diffr,soft}}(\tau)=-\frac{a-l}{2l^2}\delta\left(\tau-\frac{2l}{c}\right). \tag{48}$$

With Eqs. (47) and (48), the value of the first-order diffraction component can be calculated directly as a Dirac impulse amplitude. In Tables I and II, the values given by Eqs. (47) and (48) are, respectively, compared with corresponding values from Ref. 11, when normalized to the specular reflection for the disc, $1/(2d)$. The results, while not identical, differ at most by 2.3%, or 0.20 dB, from the reference T-matrix results. The sign of the error is always negative for the rigid disc and positive for the soft disc so that, if the second-order diffraction component contributes within the same sample as the first-order component, the error would decrease, if just marginally. The results with the WA method, as reproduced from Ref. 11, give errors of the same magnitude as those given by Eqs. (47) and (48) but with a larger spread, because of varying signs of the errors.

An explicit expression for second-order diffraction can be derived as well, and it is done here for the rigid disc only. The expression in Eq. (22) can be used if the two z-coordinates run along the disc perimeter, from $z=0$ to $z=2\pi a$, so that

$$p_{\mathrm{diffr}}(t)=2\frac{1}{(8\pi)^2}\int\int_0^{2\pi a} q\left[t-\frac{m_1+m_2(z_1,z_2)+l_2}{c}\right]\times\frac{\beta[\alpha_1,\gamma_1(z_1,z_2),\theta_{S1},0]\beta[\alpha_2(z_1,z_2),\gamma_2,0,\theta_{R2}]}{2m_1m_2(z_1,z_2)l_2}\times dz_1dz_2. \tag{49}$$

Here, the parameters m_1 and l_2 are constant and will be denoted l; θ_{S1} and θ_{R2} are identical and will be denoted θ; and α_1 and γ_2 are both equal to zero. The initial factor 2 reflects the fact that for a thin plate, there will always be identical diffraction components via the rear side of the plate which contribute to double the second-order diffraction amplitude. Furthermore, because of rotational symmetry, one of the integrations can be replaced by a factor $2\pi a$, and any fixed value of z_1 can be used in evaluating the z_2-integration. Then, with $z_1=0$,

TABLE II. Amplitude of the first-order diffraction component for axisymmetric scattering from a circular soft disc of radius 1 m, normalized to the specular reflection. Results are either calculated using the new method, Eq. (48), or taken from Ref. 11. The errors are relative to the T-matrix solution which is considered as the reference result.

Height [m]	T matrix (Ref. 11)	WA (Ref. 11)	Rel. error [%]	Eq. (48)	Rel. error [%]
1.1	0.239	0.236	(−1.3)	0.242	(1.3)
1.5	0.364	0.366	(0.5)	0.371	(1.8)
3.0	0.634	0.642	(1.3)	0.649	(2.3)
5.0	0.777	0.782	(0.6)	0.789	(1.5)
10.0	0.890	0.880	(−1.1)	0.896	(0.7)

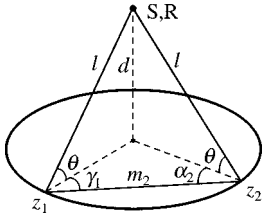

FIG. 9. Sound paths for second-order diffraction for the circular disc, indicating that the incident sound path to the first edge has a constant length l and a constant incidence angle $\alpha_1=0$. Also, the reradiated sound path from the second edge point has a constant length l and a constant angle $\gamma_2=0$. The intermediate sound path has the length m_2, and the two angles γ_1 and α_2 have the same value.

$$p_{\text{diffr}}(t)=\frac{a}{32\pi l^2}\int_0^{2\pi a} q\left[t-\frac{m_2(0,z_2)+2l}{c}\right] \times\frac{\beta[0,\gamma_1(0,z_2),\theta,0]\beta[\alpha_2(0,z_2),0,0,\theta]}{m_2(0,z_2)}dz_2. \tag{50}$$

Because of symmetry around $z_2=\pi a$, the upper integration limit can be halved, and the result doubled instead. Furthermore, a variable substitution with $(m_2+2l)/c=\tau$ leads to

$$p_{\text{diffr}}(t)=\frac{a}{16\pi l^2}\int_0^{\pi a} q(t-\tau) \times\frac{\beta[0,\gamma_1(\tau),\theta,0]\beta[\alpha_2(\tau),0,0,\theta]}{m_2(\tau)}\frac{dz_2}{d\tau}d\tau, \tag{51}$$

and, as before, the factor $dz_2/d\tau$ can be defined as being zero before $\tau=2l/c$ and after $\tau=2(l+a)/c$, so that the integration limits can be expanded to $\pm\infty$, and a convolution integral can be identified. The impulse response is then

$$h_{\text{diffr,2nd}}(\tau)=\frac{a}{16\pi l^2}\frac{\beta[0,\gamma_1(\tau),\theta,0]\beta[\alpha_2(\tau),0,0,\theta]}{m_2(\tau)}\frac{dz_2}{d\tau}. \tag{52}$$

The values of m_2, the angles γ_1 and α_2, and $dz_2/d\tau$ can be found by inspecting Fig. 9. Thus,

$$m_2=c\tau-2l, \tag{53}$$

$$\cos\gamma_1=\cos\alpha_2=\frac{m_2}{2a}, \tag{54}$$

$$z_2=a(\pi-2\gamma_1)=a\left(\pi-2\cos^{-1}\frac{m_2}{2a}\right)\Rightarrow\frac{dz_2}{d\tau}=\frac{c}{\sin\gamma_1}. \tag{55}$$

By employing the expression in Eq. (43), the product of the β functions in Eq. (52) can be molded into the form

$$\beta[0,\gamma_1(\tau),\theta,0]\beta[\alpha_2(\tau),0,0,\theta] =16\cos^2\frac{\theta}{2}\cosh^2\frac{\eta}{2}\left(\cosh^2\frac{\eta}{2}-\sin^2\frac{\theta}{2}\right)^{-2}, \tag{56}$$

where the fact that $\cosh(\eta/2)$ is identical for the two edges has been used. Using Eq. (42) and the fact that $\alpha_1=\gamma_2=0$, the function $\cosh^2(\eta/2)$ can be simplified to

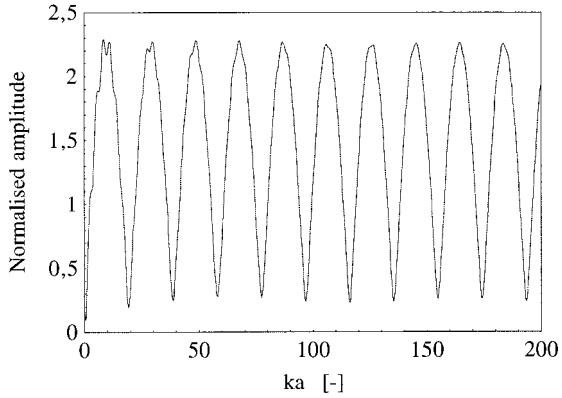

FIG. 10. Transfer function for the case in Fig. 8, with $a=1$ m and $d=3$ m, calculated with the new method. The specular reflection plus first- and second-order diffraction is included, and the amplitude is normalized to the specular reflection. The fine structure in this graph agrees with the details in Fig. 6 of Ref. 7.

$$\cosh^2\frac{\eta}{2}=\frac{1+\cos\gamma_1}{2\cos\gamma_1}, \tag{57}$$

which is valid for both the first and second edges, as $\gamma_1=\alpha_2$. If the expression in Eq. (57), together with expressions for $\sin^2(\theta/2)$ and $\cos^2(\theta/2)$, are inserted into Eq. (56), which is then used in Eq. (52), an expression for $h_{\text{diffr,2nd}}(\tau)$ results

$$h_{\text{diffr,2nd}}(\tau)=\frac{c[1+\cos\gamma_1(\tau)](1+\cos\theta)}{2\pi l^2\sin\gamma_1[1+\cos\theta\cos\gamma_1(\tau)]^2}w(\tau) =\frac{c(1+\cos\theta)}{2\pi l^2[1+\cos\theta\cos\gamma_1(\tau)]^2}\left[\frac{1+\cos\gamma_1(\tau)}{1-\cos\gamma_1(\tau)}\right]^{1/2} \times w(\tau), \tag{58}$$

where $\cos\gamma_1(\tau)$ can be found from Eqs. (53) and (54), $\cos\theta=a/l$, and $w(\tau)=H(\tau-2l/c)-H(\tau-2(a+l)/c)$. Including the first-order diffraction, Eq. (47), and second-order diffraction, Eq. (58), IRs were calculated and transformed into transfer functions. Figure 10 presents the resulting transfer function for the case with $a=1$ m and $d=3$ m. Calculation parameters were $f_s=78\,569$ Hz and a DFT size of 2048 was used. These results are very similar to those in Fig. 6 in Ref. 7. Figure 11(a) shows the second-order diffraction IR when normalized to the specular reflection amplitude $1/(2d)$.

In Ref. 11, the amplitude of the second-order diffraction was presented in terms of the peak value of the function illustrated in Fig. 11(a). This peak value is critically dependent on the sampling frequency and the low-pass filtering technique used. For purposes of comparison, the process in Ref. 11 was reproduced as closely as possible. The sampling frequency was chosen so that the delay between the specular reflection and the first-order diffraction pulse was an integer number of steps, using a speed of sound of 1500 m/s. Furthermore, an oversampling by a factor of 8 was used here and, after transforming the IR into a transfer function using a DFT size of 16 384, only the first 1024 frequencies were kept before transforming back to an IR using a DFT size of 2048.

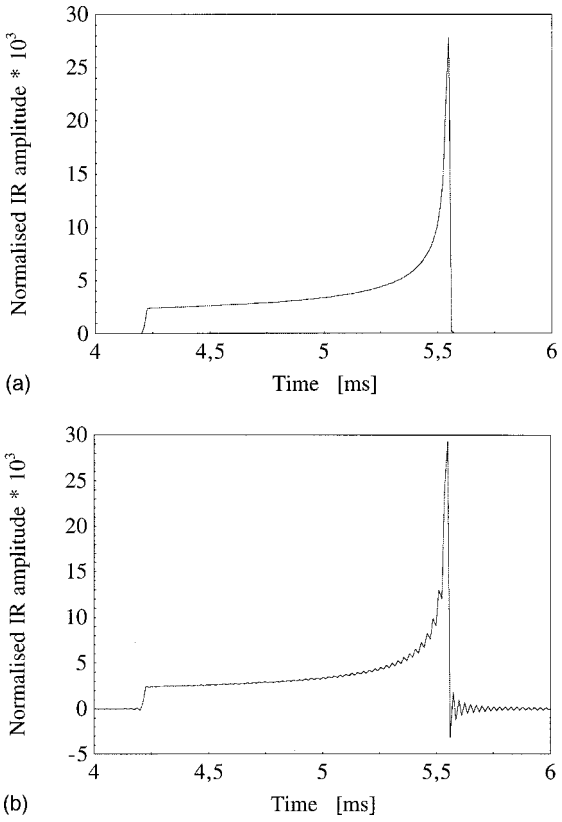

FIG. 11. Second-order diffraction impulse response for the case in Fig. 8, with $a=1$ m and $d=3$ m, calculated with the new method. The amplitude has been normalized to the specular reflection. (a) A sampling frequency of 78 569 Hz was used. (b) An oversampling by a factor of 8, relative to (a), was used and a frequency-domain low-pass filtering as described in the text gave the same final sampling frequency as in (a).

This frequency-domain low-pass filtering should be equivalent to the technique used in Ref. 11. Figure 11(b) shows an example of one such second-order diffraction IR, where the small ripple indicates the filtering effects.

Table III gives the results for the peak amplitude of the second-order diffraction IR, both when calculated using edge sources as in Eq. (50), and after the oversampling/frequency-domain filtering described above. Although the results from Ref. 11 are reproduced here, it should be noted that it is stated in Ref. 11 that the values in their Table IV are normalized to the first-order diffraction pulse rather than to the specular reflection, which is used elsewhere in that paper. We believe that this is a mistake for three reasons. First, the values in Table IV of Ref. 11 are positive rather than negative. Second, it is stated earlier in Ref. 11 that the specular reflection was used for normalization for all the results presented, even for off-axis geometries. The third argument is that our results are very close to the reference results when the specular normalization is assumed, and especially after the frequency-domain low-pass filtering was used.

The results with our new method are close enough to the reference results for the circular disc to generally support the relations derived here, but more comparisons with reference calculations should be made. Comparisons of the frequency-domain values might then be easier to carry out, avoiding ambiguities involving filtering effects as discussed above.

C. Scattering from a rectangular plate

The last example is scattering from a rectangular plate. Cox and Lam present an example of a rectangular plate of size $0.302\times1.92\times0.010$ m and with calculated directivity plots at two single frequencies, 2012 and 3995 Hz.[19] The source was positioned at a height of $d=3.96$ m, right above the center point of the plate. The receiver was moved along an arc at a constant radius of $R=1.178$ m, from the center points of the plate. The arc was in the direction of the short length of the plate. The total reflection strength was calculated using the boundary element method both for a three-dimensional model and for a thin plate limit model of the plate. It was normalized to the direct sound amplitude. Figure 12 shows results using Eqs. (35) and (37) to calculate the first- and second-order diffraction IRs for an infinitely thin model of the plate. A sampling frequency of 257 536 Hz was used, corresponding to 128 times oversampling with respect to the target frequency of 2012 Hz. The four edges were divided into 0.67-mm elements for the first-order diffraction, and twice that size for the second-order diffraction. The receiver was moved along the arc in steps of 1 deg. A DFT size of 8192 was used, to get the transfer function values exactly at 2012 Hz. The sound speed $c=346$ m/s was used in Ref. 19 and here, too.

If one compares the level of the total field in Fig. 12 with the results for the thin plate limit in Fig. 4 of Ref. 19, one can see good agreement for angles between 0 and ca. 80 deg. The larger deviations above 80 deg are probably due to the need for higher-order diffraction components. This is

TABLE III. Peak amplitude of the second-order diffraction component for axisymmetric scattering from a circular rigid disc of radius 1 m, normalized to the specular reflection. Results are either calculated using the new method [based on Eq. (50)] or taken from Ref. 11. The results denoted LPF have been low-pass filtered as described in the text. The errors are relative to the T-matrix solution which is considered as the reference results. The T matrix and WA results were specified in Ref. 11 as being relative to the first-order diffraction strength, but it has been assumed here that the specular reflection was used for the normalization as discussed in the text.

Height [m]	T matrix (Ref. 11)	WA (Ref. 11)	Rel. error [%]	Eq. (50)	Rel. error [%]	Eq. (50) (LPF)	Rel. error [%]
1.1	0.043	0.039	(−9)	0.0415	(−3)	0.0469	(+9)
1.5	0.043	0.031	(−28)	0.0374	(−13)	0.0427	(−1)
3.0	0.031	0.023	(−26)	0.0278	(−10)	0.0293	(−5)
5.0	0.024	0.016	(−33)	0.0205	(−15)	0.0234	(−3)
10.0	0.014	0.009	(−36)	0.0114	(−19)	0.0126	(−10)

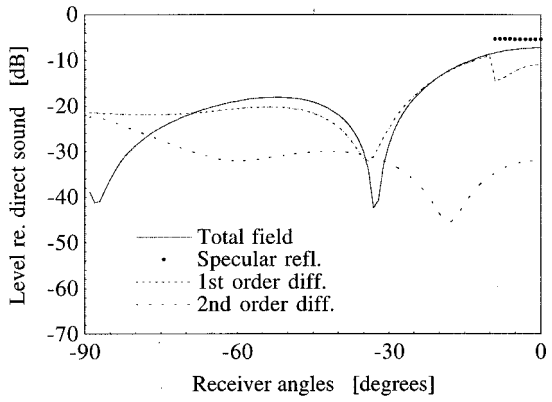

FIG. 12. Scattering from a thin rectangular plate, described in the text, calculated with the new method. Shown are levels of the total field, of the specular reflection only, of the first-order diffraction only, and of the second-order diffraction only. The frequency was 2012 Hz; the source was fixed symmetrically above the plate and the receiver position was varied along an arc.

also indicated in Fig. 12 by the large amplitude of the second-order diffraction component for large receiver angles. The deviation at the dip around 30 deg might be caused by a less dense sampling in Ref. 19, or small differences in the speed of sound. Furthermore, the smoothness of the total field around 10–12 deg, where the specular reflection disappears, indicates that the numerical method used, Eq. (35), is accurate enough up to within half a deg from the transition zone where the specular reflection disappears. This is compensated by the corresponding jump in value for the first-order diffraction. Very high oversampling was used, together with a very fine division of the edge into elements. This is needed only for the positions close to the transition zone and for the largest receiver angles. For the larger receiver angles, higher-order diffraction is needed anyway, so the total field might be calculated more accurately by using fewer edge elements but higher orders of diffraction.

A three-dimensional model of the plate was tested as well, but it was then clear that it was necessary to include higher-order diffraction since the results differed significantly from the thin plate limit model, when second-order edge diffraction was included. In conclusion, the results with the new model and the results in Ref. 19 seem to agree well enough to support the new model as long as it is realized that it may be necessary to include higher-order diffraction components for some situations.

IV. DISCUSSION AND CONCLUSIONS

The interpretation of the exact Biot–Tolstoy solution for the infinite wedge diffraction that was presented here has not been proven to be true *per se*. It has, however, been shown that if the existence of analytical directivity functions for the secondary edge sources is assumed, such functions can indeed be derived and yield the exact solution for an infinite wedge. Since this also leads to a possible application to non-straight edges, and the comparison with the result for the circular rigid disc was accurate within 0.20 dB, it is concluded that the suggested interpretation is generally valid. It should then, in principle, be possible to show that the total field, specular reflections plus diffraction components, satisfies the wave equation. The complexity of the higher-order diffraction components might, however, prevent this possibility for cases other than the infinite wedge.

The proposed model gives results that, for first-order diffraction, should be identical to those by the WA model.[11] For second-order diffraction, the results by the proposed model are very similar to results by methods which are based on Medwin's model.[3,11] Conceptually, however, the difference between Medwin's model and the proposed model is significant since the proposed model gives a complete motivation and mathematical proof for the directivity functions of the secondary edge sources.

As for the numerical implementation, very high sampling frequencies are often needed. This is because the crude low-pass ''antialiasing'' filter, which is equivalent to the single time sample integration, has a gentle roll-off characteristic. Refined integration techniques could be tested, and the directivity functions might lead to somewhat simpler functions to handle, compared to the original Biot–Tolstoy solution in Eqs. (1)–(4). Also, since each higher order of diffraction causes a response that basically falls 3 dB/octave more quickly than the previous order, lower and lower sampling frequencies could be used for each new order. This decrease occurs, however, above a cutoff frequency which is given by the size of the individual planes of the object, and the proximity to the various shadow zones. Below those frequencies, the response decreases in a way which is more difficult to predict.

Higher-order diffraction IRs should tend towards Gaussian-shaped pulses, according to the central limit theorem in statistics, since it is equivalent to convolving any function with itself many times, resulting essentially in a Gaussian function. Thus, properly time-aligned Gaussian pulses with the right areas, widths, and polarities could serve as replacement functions for higher-order diffraction.

It was shown that the case of axisymmetric backscattering from a circular disc could yield explicit expressions for the first- and second-order diffractions. It is probably possible to find such explicit expressions for several other geometries too. Further developments could lead to solutions which satisfy more general boundary conditions.

The proposed model is relevant for all cases where scattering/diffraction from idealized, rigid, or soft objects is studied, such as when the WA is applied to underwater acoustics cases, noise barriers, etc. In architectural acoustics, most IR prediction models are based on geometrical acoustics, possibly handling surface scattering, but without the possibility to handle edge diffraction accurately.[20] The Kirchhoff diffraction approximation has been tested before, but this new model should be much more accurate since it is valid at all frequencies and for all source and receiver positions.[10] In electroacoustics, edge diffraction has important applications such as the effect of the loudspeaker enclosure on the radiated sound; many simpler edge diffraction models have been tested,[16] but the proposed model should, here too, prove to be more accurate.

In conclusion, deriving analytical directivity functions for the edge sources both supports, and takes a step beyond,

previous models such as those based on Medwin's work, and gives new possibilities to solving diffraction problems in the time domain. These directivity functions support some previous first-order diffraction models, but also demonstrate that previous second-order diffraction models contain approximations, reflecting the greater accuracy of the proposed model. Derivation of explicit diffraction expressions for certain geometries, and for efficient and accurate numerical calculations, become possible using the proposed model.

ACKNOWLEDGMENTS

This project was financed in part by grants from the Swedish Institute and the Adlerbert Research Foundation, which supported the first author's research visit to the University of Waterloo. Parts of the project were also financed by the Johnson Foundation. The third author has research support from the Natural Sciences and Engineering Research Council of Canada. The authors have appreciated the comments offered by an anonymous reviewer.

APPENDIX A: PROOF OF EQ. (14)

The factor $c(r_S r_R \sinh\eta)^{-1} H(\tau-\tau_0)$ in Eq. (1) can be rewritten, introducing an auxiliary variable y,

$$\eta=\cosh^{-1} y=\log[y+(y^2-1)^{1/2}], \tag{A1}$$

so that $\sinh\eta$ can be written

$$\sinh\eta=(y^2-1)^{1/2}. \tag{A2}$$

The auxiliary variable y introduced above is [see Eq. (4)]

$$y=\frac{c^2\tau^2-(r_S^2+r_R^2+z_R^2)}{2r_S r_R}, \tag{A3}$$

and with the relation $c\tau=m+l$, y can be written

$$y=\frac{(m+l)^2-(r_S^2+r_R^2+z_R^2)}{2r_S r_R}. \tag{A4}$$

By further using the relations for m and l (see Figs. 1 and 2)

$$m=(r_S^2+z^2)^{1/2}, \tag{A5}$$

and

$$l=[r_R^2+(z-z_R)^2]^{1/2}, \tag{A6}$$

it is possible to write y as

$$y=\frac{ml+z(z-z_R)}{r_S r_R}. \tag{A7}$$

Now, using Eqs. (A2) and (A7), it can be found that

$$\begin{aligned} r_S r_R \sinh\eta &= \{[ml+z(z-z_R)]^2-r_S^2 r_R^2\}^{1/2} \\ &= [m^2l^2+z^2(z-z_R)^2+2mlz(z-z_R)-r_S^2 r_R^2]^{1/2}. \end{aligned} \tag{A8}$$

By further employing Eqs. (A5) and (A6) to get rid of r_S and r_R, it is found that

$$\begin{aligned} r_R r_R \sinh\eta &= [z^2l^2+2mlz(z-z_R)+(z-z_R)^2m^2]^{1/2} \\ &= |zl+(z-z_R)m|. \end{aligned} \tag{A9}$$

All expressions so far have been valid for both the upper and lower branch solutions of m and l. Moving temporarily to the expressions for $dz/d\tau$, this quantity can be found by studying the total path length $L=m+l$. A small increase in path length ΔL corresponds to a small increase, Δz, along the edge, and the relation between these is found by the derivative of $L(z)$

$$\frac{dL}{dz}=\frac{z}{m}+\frac{z-z_R}{l}=\frac{zl+(z-z_R)m}{ml}, \tag{A10}$$

which, using $\Delta L=c\Delta\tau$, leads to

$$\frac{1}{ml}\frac{dz}{d\tau}=\frac{c}{zl+(z-z_R)m}, \tag{A11}$$

for both the upper and lower branches of the edge, which is the left-hand relation in Eq. (14). Since $dz_u/d\tau$ is always positive, Eq. (A11) implies that $z_u l_u+(z_u-z_R)m_u$ also must always be positive. Then, Eqs. (A9) and (A11) show that the right-hand relation in Eq. (14) holds true.

APPENDIX B: PROOF OF EQ. (16)

The relation in Eq. (16) is shown using the definitions of the angles α and γ.

$$\sin\alpha=z/m, \quad \cos\alpha=r_S/m, \tag{B1}$$

$$\sin\gamma=(z-z_R)/l, \quad \cos\gamma=r_R/l. \tag{B2}$$

If these are inserted into Eq. (A7),

$$y=\frac{ml+z(z-z_R)}{r_S r_R}=\frac{1+\dfrac{z(z-z_R)}{ml}}{\dfrac{r_S r_R}{ml}}=\frac{1+\sin\alpha\sin\gamma}{\cos\alpha\cos\gamma}, \tag{B3}$$

which is the relation in Eq. (16).

APPENDIX C: PROOFS OF EQS. (42) AND (43)

For the thin plate case, the wedge index ν equals 0.5, and then the β term in Eq. (1) can be simplified. The quantity $\cosh(\nu\eta)$ is, for the wedge index $\nu=0.5$,

$$\cosh\frac{\eta}{2}=\frac{1}{2}\left(\exp\frac{\eta}{2}+\exp\frac{-\eta}{2}\right)=\frac{1}{2}\frac{\exp(\eta)+1}{[\exp(\eta)]^{1/2}}. \tag{C1}$$

Squaring this expression gives

$$\cosh^2\frac{\eta}{2}=\frac{1}{4}\frac{\exp(2\eta)+2\exp(\eta)+1}{\exp(\eta)}. \tag{C2}$$

The expression for η in Eq. (A1) can be employed, which readily leads to the simplification

$$\cosh^2\frac{\eta}{2}=\frac{y+1}{2}. \tag{C3}$$

The auxiliary quantity y can then be written as in Eq. (B3), which yields

$$\cosh^2\frac{\eta}{2}=\frac{1+\sin\alpha\sin\gamma+\cos\alpha\cos\gamma}{2\cos\alpha\cos\gamma}=\frac{1+\cos(\alpha-\gamma)}{2\cos\alpha\cos\gamma}$$

$$=\frac{\cos^2[(\alpha-\gamma)/2]}{\cos\alpha\cos\gamma}. \tag{C4}$$

Then, $\cosh(\eta/2)$ can finally be expressed as

$$\cosh\frac{\eta}{2}=\frac{\cos[(\alpha-\gamma)/2]}{(\cos\alpha\cos\gamma)^{1/2}}, \tag{C5}$$

which is the form in Eq. (42). Taking the square root of the right-hand term in Eq. (C4) is safe, as α and γ are always within the range $-\pi/2$ to $\pi/2$. Furthermore, the sine and cosine terms in the expression for β in Eq. (1) can be simplified, since

$$\sin[\nu(\pi\pm\theta_S\pm\theta_R)]=\sin\{[\pi\pm(\theta_S\pm\theta_R)]/2\}$$
$$=\cos[(\theta_S\pm\theta_R)/2], \tag{C6}$$

$$\cos[\nu(\pi\pm\theta_S\pm\theta_R)]=\cos\{[\pi\pm(\theta_S\pm\theta_R)]/2\}$$
$$=\pm\sin[(\theta_S\pm\theta_R)/2], \tag{C7}$$

and allows the β term to be written as

$$\beta(\alpha,\gamma,\theta_S,\theta_R)=\frac{\cos[(\theta_S+\theta_R)/2]}{\cosh(\eta/2)+\sin[(\theta_S+\theta_R)/2]}$$
$$+\frac{\cos[(\theta_S-\theta_R)/2]}{\cosh(\eta/2)+\sin[(\theta_S-\theta_R)/2]}$$
$$+\frac{\cos[(\theta_S-\theta_R)/2]}{\cosh(\eta/2)-\sin[(\theta_S-\theta_R)/2]}$$
$$+\frac{\cos[(\theta_S+\theta_R)/2]}{\cosh(\eta/2)-\sin[(\theta_S+\theta_R)/2]}$$
$$=2\cosh(\eta/2)$$
$$\times\left\{\frac{\cos[(\theta_S+\theta_R)/2]}{\cosh^2(\eta/2)-\sin^2[(\theta_S+\theta_R)/2]}\right.$$
$$\left.+\frac{\cos[(\theta_S-\theta_R)/2]}{\cosh^2(\eta/2)-\sin^2[(\theta_S-\theta_R)/2]}\right\}, \tag{C8}$$

where $\cosh(\eta/2)$ is given in Eq. (C5), and this is the form in Eq. (43).

[1] M. A. Biot and I. Tolstoy, ''Formulation of wave propagation in infinite media by normal coordinates with an application to diffraction,'' J. Acoust. Soc. Am. **29**, 381–391 (1957).

[2] H. Medwin, ''Shadowing by finite noise barriers,'' J. Acoust. Soc. Am. **69**, 1060–64 (1981).

[3] H. Medwin, E. Childs, and G. M. Jebsen, ''Impulse studies of double diffraction: A discrete Huygens interpretation,'' J. Acoust. Soc. Am. **72**, 1005–1013 (1982).

[4] J. P. Chambers and Y. H. Berthelot, ''Time-domain experiments on the diffraction of sound by a step discontinuity,'' J. Acoust. Soc. Am. **96**, 1887–1892 (1994).

[5] D. Ouis, ''Scattering by thin strip-like elements and applications in room acoustics,'' Dissertation, Report TVBA-1005, Lund University of Technology, Lund, Sweden (1995).

[6] A. W. Trorey, ''Diffractions for arbitrary source–receiver locations,'' Geophysics **42**, 1177–1182 (1977).

[7] J. R. Berryhill, ''Diffraction response for nonzero separation of source and receiver,'' Geophysics **42**, 1158–1176 (1977).

[8] Y. Sakurai and K. Nagata, ''Sound reflections of a rigid plane and of the live end composed by those panels,'' J. Acoust. Soc. Jpn. (E) **2**, 5–14 (1981).

[9] G. M. Jebsen and H. Medwin, ''On the failure of the Kirchhoff assumption in backscatter,'' J. Acoust. Soc. Am. **72**, 1607–11 (1982).

[10] G. V. Norton, J. C. Novarini, and R. S. Keiffer, ''An evaluation of the Kirchhoff approximation in predicting the axial impulse response of hard and soft disks,'' J. Acoust. Soc. Am. **93**, 3049–3056 (1993).

[11] R. S. Keiffer, J. C. Novarini, and G. V. Norton, ''The impulse response of an aperture: Numerical calculations within the framework of the wedge assemblage method,'' J. Acoust. Soc. Am. **95**, 3–12 (1994).

[12] A. D. Pierce, ''Diffraction of sound around corners and over wide barriers,'' J. Acoust. Soc. Am. **55**, 941–955 (1974).

[13] R. G. Kouyoumjian and P. H. Pathak, ''A uniform geometrical theory of diffraction for an edge in a perfectly conducting surface,'' Proc. IEEE **62**, 1448–1461 (1974).

[14] C. S. Clay and W. A. Kinney, ''Numerical computations of time-domain diffractions from wedges and reflections from facets,'' J. Acoust. Soc. Am. **83**, 2126–2133 (1988).

[15] W. A. Kinney, C. S. Clay, and G. A. Sandness, ''Scattering from a corrugated surface: Comparison between experiment, Helmholtz–Kirchhoff theory, and the facet ensemble method,'' J. Acoust. Soc. Am. **73**, 183–194 (1983).

[16] J. Vanderkooy, ''A simple theory of cabinet edge diffraction,'' J. Aud. Eng. Soc. **39**, 923–933 (1991).

[17] J. J. Bowman and T. B. A. Senior, *Electromagnetic and Acoustic Scattering by Simple Shapes*, edited by J. J. Bowman, T. B. A. Senior, and P. L. E. Uslenghi (North-Holland, Amsterdam, 1969), Chap. 6.

[18] T. Kawai, ''Sound diffraction by a many sided barrier or pillar,'' J. Sound Vib. **79**, 229–242 (1981).

[19] T. J. Cox and Y. W. Lam, ''Evaluation of methods for predicting the scattering from simple rigid panels,'' Appl. Acoust. **40**, 123–140 (1993).

[20] B.-I. Dalenbäck, ''Room acoustic prediction based on a unified treatment of diffuse and specular reflection,'' J. Acoust. Soc. Am. **100**, 899–909 (1996).

Surface waves over a convex impedance surface

Qiang Wang
Department of Environmental and Mechanical Engineering, Faculty of Technology, The Open University, Milton Keynes MK 7 6AA, United Kingdom

Kai Ming Li[a)]
Department of Mechanical Engineering, Hong Kong Polytechnic University, Hung Hom, Kowloon, Hong Kong

(Received 17 February 1998; revised 13 July 1999; accepted 26 July 1999)

The existence of the surface wave in an upward refracting medium has been predicted by Raspet *et al.* [J. Acoust. Soc. Am. **89**, 107–114 (1991)]. Making use of an acoustic analogy, one is able to study the surface waves above a convex cylinder and, hence, to simulate the propagation of sound over an impedance ground in an upward refracting medium. A suitable comblike surface may be used to facilitate the generation of surface waves above the convex ground. This paper describes laboratory experiments for the observation of surface waves over a convex impedance ground. [S0001-4966(99)05311-4]

PACS numbers: 43.20.Fn, 43.28.Fp [LCS]

INTRODUCTION

Many of the essential features associated with surface wave propagation near a flat impedance plane have been clarified by a number of theoretical and experimental studies.[1–5] By analyzing the classic data of Parkin and Scholes,[6] Piercy *et al.*[7] have confirmed the presence of surface waves in sound propagation outdoors. Furthermore, surface wave propagation has been demonstrated by Albert[8] for his outdoor experiment with impulse sounds propagated over snow. The existence of the surface wave above an impedance plane in a homogeneous atmosphere is now generally accepted.[9]

Theoretical studies[1,2,10,11] have revealed that surface waves propagate horizontally above porous ground, decaying exponentially with height, at a phase velocity less than the sound speed in the air. Laboratory measurements have detected these surface waves using both continuous and pulse sources[1,5,11–15] above lighting diffuser lattices mounted on flat rigid boards. It has been verified[4,16] that a true surface wave exists independently in spherical wave propagation above such an impedance ground. Daigle *et al.*[5] and Howorth and Attenborough[15,17] have demonstrated that a surface wave may be identified, in pulse experiments, as a separate arrival from that of a body wave arriving earlier.

Raspet *et al.*[18] have pointed out that the surface wave pole identified in the analytical solution for sound propagation in a homogeneous atmosphere is present also in the solution for the sound field in an upward refracting medium provided that the phase of the complex impedance, φ_z, is greater than $\pi/3$. They stated that this surface wave pole arises from the residue series that contains an independent contribution from the surface wave. Surface waves propagating outdoors have been observed and reported by several authors.[7,8] However, there is little experimental evidence as to whether and how the surface wave exists over a curved porous surface.

Furthermore, the technique of pole searching in an upward refracting medium suggested by Pierce[19] works well for $\varphi_z < \pi/3$, but Raspet *et al.* indicated that this technique would not work for if $\varphi_z > \pi/3$. Instead, they have developed a numerical scheme of pole searching that can effectively track the surface wave pole for $\varphi_z > \pi/3$. However, the scheme of Raspet *et al.* has not yet been confirmed by experimental evidence although it is beyond doubt in their theoretical analysis.

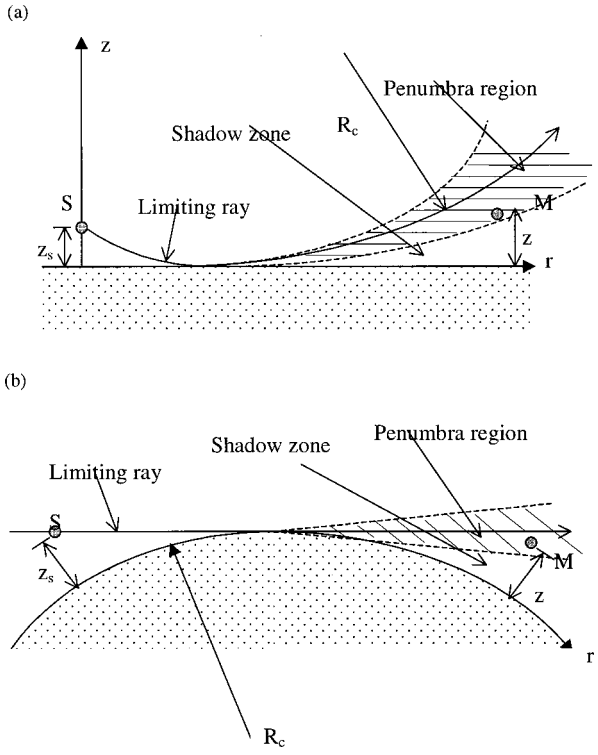

FIG. 1. Sketch showing the analogy between propagation along a curved ray path above a plane boundary and straight line propagation above a convex surface.

a)Electronic mail: mmkmli@polyu.edu.hk

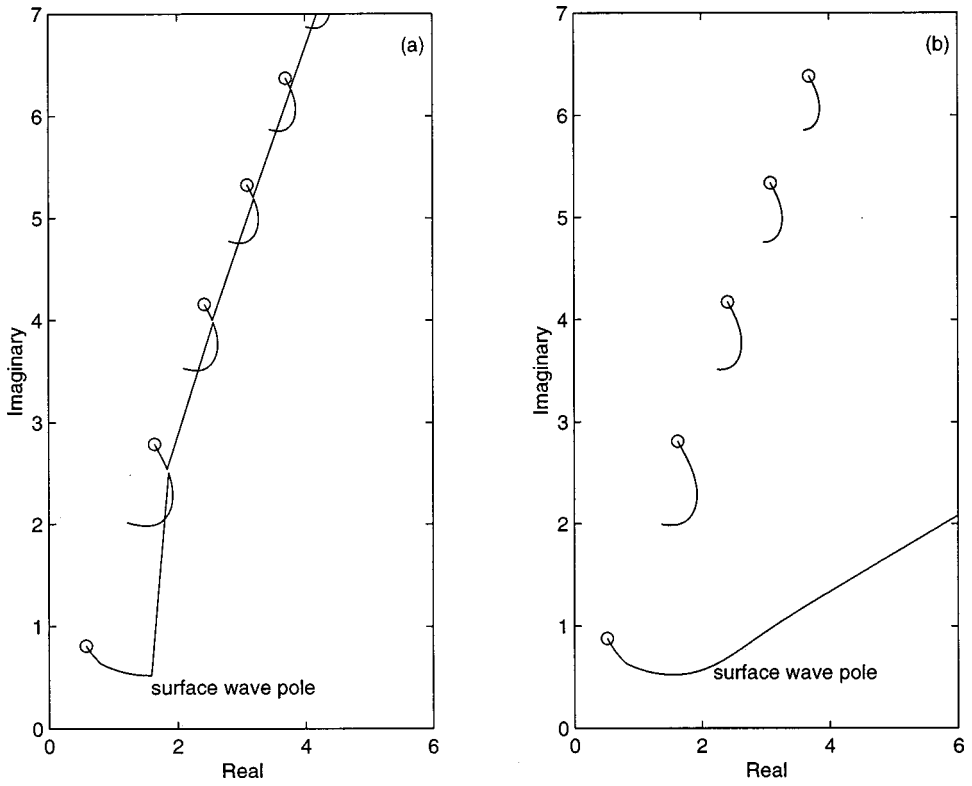

FIG. 2. Behavior of the $(-\xi_0)$ as $|q|$ varies from 0 to 20 with $\varphi=10$ degrees. Circles: the zeros of the Airy function; lines: imaginary part of $(-\xi_0)$ plotted as a function of real part of $(-\xi_0)$. (a) Calculation obtained from Pierce's technique, (b) calculation obtained from the Raspet *et al.* scheme. [Note that τ_n is used in Ref. 18 and $\tau_n \equiv (-\xi_0)$.]

Previous studies suggest that the nature of the surface waves can be investigated from controlled experiments above appropriate model surfaces. It should be possible to study the surface waves that would occur over an impedance plane in an upward refracting medium by making measurements above a convex porous surface. In this paper, we shall examine the surface wave pole locations and the sound fields above convex impedance ground with significant contributions from the surface wave pole. In addition, we shall present experimental evidence for the existence of the surface waves above a convex cylindrical surface.

I. THEORY

In a companion paper,[20] we have developed residue series solutions for the propagation of sound over convex impedance surfaces. In particular, we have shown that the sound field behind a large cylinder of radius R_c in an otherwise homogeneous medium corresponds to the sound field above a flat surface in an upward refracting medium where the adiabatic sound speed, $c(z)$, is given in an exponential form as

$$c(z)=c_0 \exp(-z/R_c). \tag{1}$$

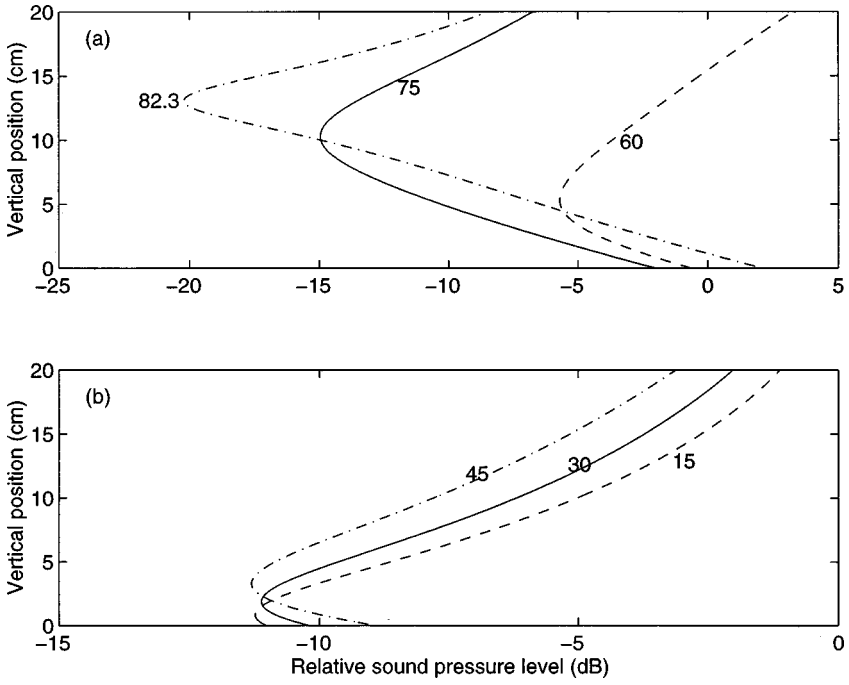

FIG. 3. Vertical sound pressure level profiles for 4 kHz at a distance of 1 m from the source with various receiver positions above an impedance ground. The normalized impedance is $|Z|=3.24$ with phase angles of (a) 82.3, 75, and 60 degrees and (b) 45, 30, and 15 degrees.

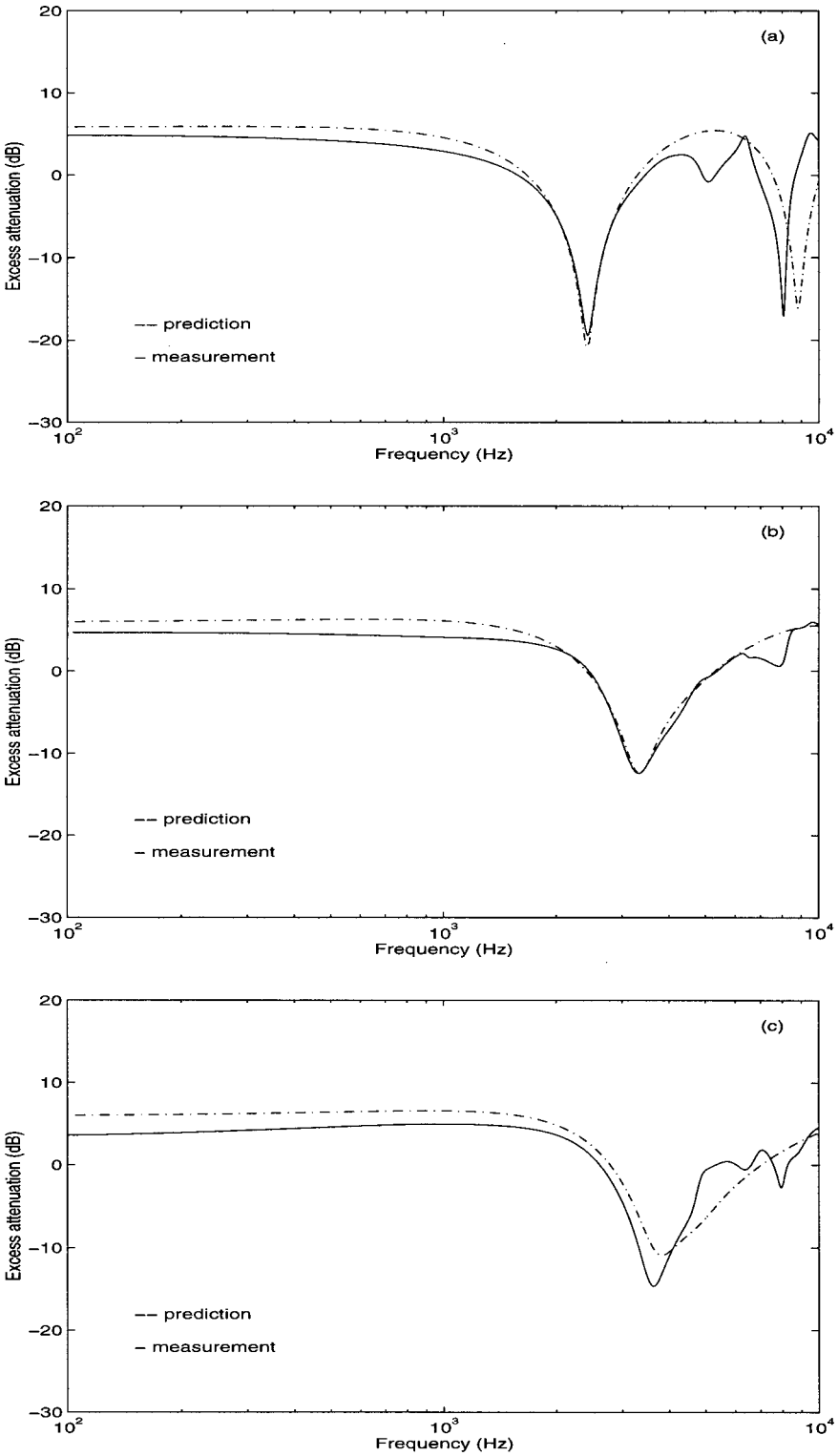

FIG. 4. Excess attenuation obtained above a flat mat-on-masonite surface, with $\sigma_e = 4$ kPa s m^{-2}, $\alpha_e = 570$ m^{-1}, $r = 1.0$ m and $z_s = z = (a)$ 0.08 m, (b) 0.10 m, and (c) 0.15 m.

In the above equation, $c_0 \equiv c(0)$ is the reference sound speed, $z(z \ll R_c)$ is the height above the impedance ground, and $1/R_c$ may be regarded as the normalized sound speed gradient, $|(dc/dz)/c_0|$, which has unit of m^{-1}. For a homogeneous medium, z may be interpreted as the distance measured normal to the curved surface and R_c as the radius of the cylinder. The geometrical configurations are shown in Fig. 1. The sound field in both situations may be computed by a residue series solution although a fast field formulation has been used recently[21] to predict the sound field behind a curved surface. In the present investigation, we are mainly concerned with the propagation of surface waves above a convex impedance surface. Both source and receiver are necessarily close to the ground for the detection of the surface wave because it decays exponentially with height. This requirement allows one to use a more convenient approximation,[21] by replacing Eq. (1) with the bilinear sound speed profile,

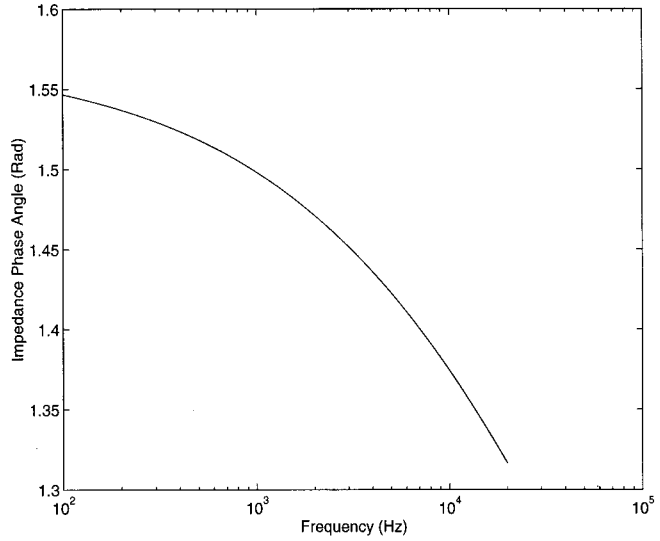

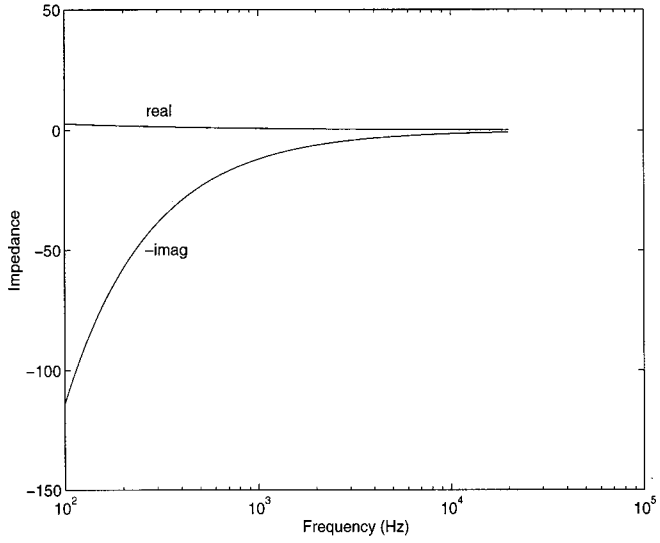

FIG. 5. (a) Predicted impedance phase angle, φ_z, of a mat-on-masonite surface versus frequency showing $\varphi_z > \pi/3$. (b) Predicted imaginary part and real part of the impedance of the mat-on-masonite surface versus frequency.

$$c(z) = \frac{c_0}{\sqrt{1+2z/R_c}}. \tag{2}$$

The solution for the acoustic pressure can then be expressed as[20,22]

$$p(r,z) = -\int_{-\infty}^{\infty} H_0^{(1)}(k,r) P(z,k_r) k_r \, dk_r, \tag{3}$$

where r is the horizontal distance from the source, k_r is the horizontal wave number, and the height-dependent Green's function, $P(z,k_r)$, is given by

$$P(z,k_r) = -2\pi l e^{i\pi/6} \mathrm{Ai}(-\xi_> e^{i2\pi/3}) \times [\mathrm{Ai}(-\xi_<) - \Gamma \mathrm{Ai}(-\xi_< e^{i2\pi/3})], \tag{4}$$

where $\mathrm{Ai}(\vartheta)$ is the Airy function with a complex argument ϑ. Notations used in the height-dependent Green's function are

$$l = (R_c/2k_0^2)^{1/3}, \tag{5}$$

$$\xi(z) = (k_0^2 - k_r^2) l^2 - \frac{z}{l}, \tag{6}$$

$$q = ik_0 \beta l, \tag{7}$$

$$\Gamma = \frac{\mathrm{Ai}'(-\xi_0) - q\,\mathrm{Ai}(-\xi_0)}{e^{i2\pi/3}\mathrm{Ai}'(-\xi_0 e^{i2\pi/3}) - q\,\mathrm{Ai}(-\xi_0 e^{i2\pi/3})}, \tag{8}$$

β is the specific normalized admittance of the ground, $\xi_> \equiv \xi(z_>)$, $\xi_< \equiv \xi(z_<)$, $z_<$ is the lesser of z and z_s, and $z_>$ is the greater of z and z_s, where z is the receiver height and z_s is the source height. The primes in Eq. (8) denote the derivatives of the Airy functions with respect to their arguments. The physical interpretation of l, q, and Γ are the thickness of the creeping wave layer, the nondimensional scaled admittance, and the reflection factor, respectively. The residue for the integrand of Eq. (3) can be evaluated at each pole of Eq. (8), and the results summed to form the total solution for the acoustic pressure. The condition for a pole is

$$e^{i2\pi/3}\mathrm{Ai}'(-\xi_0 e^{i2\pi/3}) - q\,\mathrm{Ai}(-\xi_0 e^{i2\pi/3}) = 0. \tag{9}$$

Equation (9), which is also known as the dispersion equation, has to be solved numerically for k_r. Suppose that the poles can be determined with

$$k_r = K_n, \quad \text{where } n = 1,2,3,\ldots. \tag{10}$$

Evaluating the residue at each pole K_n and summing all contributions gives the residue series representation for the acoustic pressure as

$$p(r,z) = \frac{\pi e^{i\pi/6}}{l} \sum_n H_0^{(1)}(K_n r) \times \frac{\mathrm{Ai}(-\overline{\xi}_s e^{i2\pi/3})\mathrm{Ai}(-\overline{\xi} e^{i2\pi/3})}{[\mathrm{Ai}'(-\overline{\xi}_0 e^{i2\pi/3})]^2 + \overline{\xi}_0 e^{i2\pi/3}[\mathrm{Ai}(-\overline{\xi}_0 e^{i2\pi/3})]^2}. \tag{11}$$

Raspet *et al.* investigated the behavior of the residue series solution in an upward refracting medium as the radius of curvature becomes large.[18] In this limit, they showed that the height-dependent Green's function, Eq. (4), can be reduced to

$$P(z,k_r) = \frac{\exp(\sqrt{k_0^2 - k_r^2})(z_> - z_<) + R_p \exp(\sqrt{k_0^2 - k_r^2})(z_> + z_<)}{2i\sqrt{k_0^2 - k_r^2}}, \tag{12}$$

where

$$R_p = \frac{\cos\theta_0 - \beta}{\cos\theta_0 + \beta} \tag{13}$$

is the plane wave reflection coefficient, and θ_0 the incidence angle of a wave with wave number k_0 and horizontal wave number k_r. They also identified that the surface wave pole is also present in an upward refracting medium for sufficiently large q and phase angle of the impedance greater than $\pi/3$.

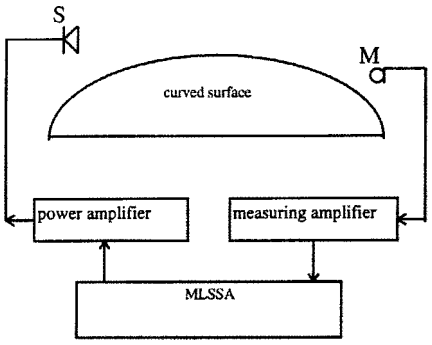

FIG. 6. Schematic diagram of the experiments.

This condition is somewhat different from the case of a homogeneous medium in which there is a surface wave pole as long as the phase of the complex surface impedance is greater than $\pi/4$. They also improved Pierce's numerical scheme[19] in locating the surface wave pole for large q.

Figure 2(a) and (b) shows, using both numerical schemes, the behavior of $(-\xi_0)$ as $|q|$ increases from 0 to 20 with a phase angle of impedance of 80 degrees. In this particular example, the first term of the residue series is the contribution due to the surface wave. The circles are the zeros of $Ai'(-\xi_0 e^{i2\pi/3})$ which are, incidentally, the locations of poles when $q=0$. Comparing these two methods, it is noted that if $|q|$ is small,[18] the corresponding locations of all the poles are the same; if $|q|$ is large,[18] the corresponding locations of all terms except the first are the same. They originate from the nth zero of the Airy function derivative to the $(n-1)$th zeros of the Airy function, as $|q|$ increases from 0 to 20. A more detailed description of the variation of the pole locations with q is given in Ref. 18. We note that the relative magnitudes of $|q|$ for each pole depend on the frequency, the radius of curvature, and the impedance of the ground. Nevertheless, Pierce's numerical scheme is invalid for the successful tracking of the surface wave pole [cf. Fig. 2(a) and (b)] if $|q|$ is approximately greater than 1 for this particular case. In this situation, it is necessary to use the Raspet *et al.* scheme.[18]

The above analysis may be used to suggest criteria for the observation of the surface wave above convex impedance

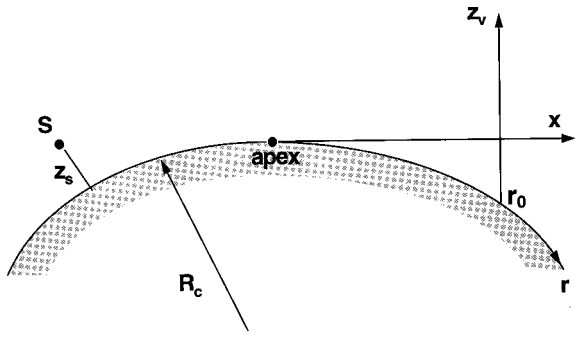

FIG. 7. A sketch of the experimental configurations (cf. Fig. 1). r represents *distance from source*, that is the arc length measured from source. x represents *distance from apex*, that is the length measured from the apex along the line of sight. z_v represents *vertical distance*, that is the length coordinate vertically above the surface with an initial position at an arc distance $r=r_0$ from the source.

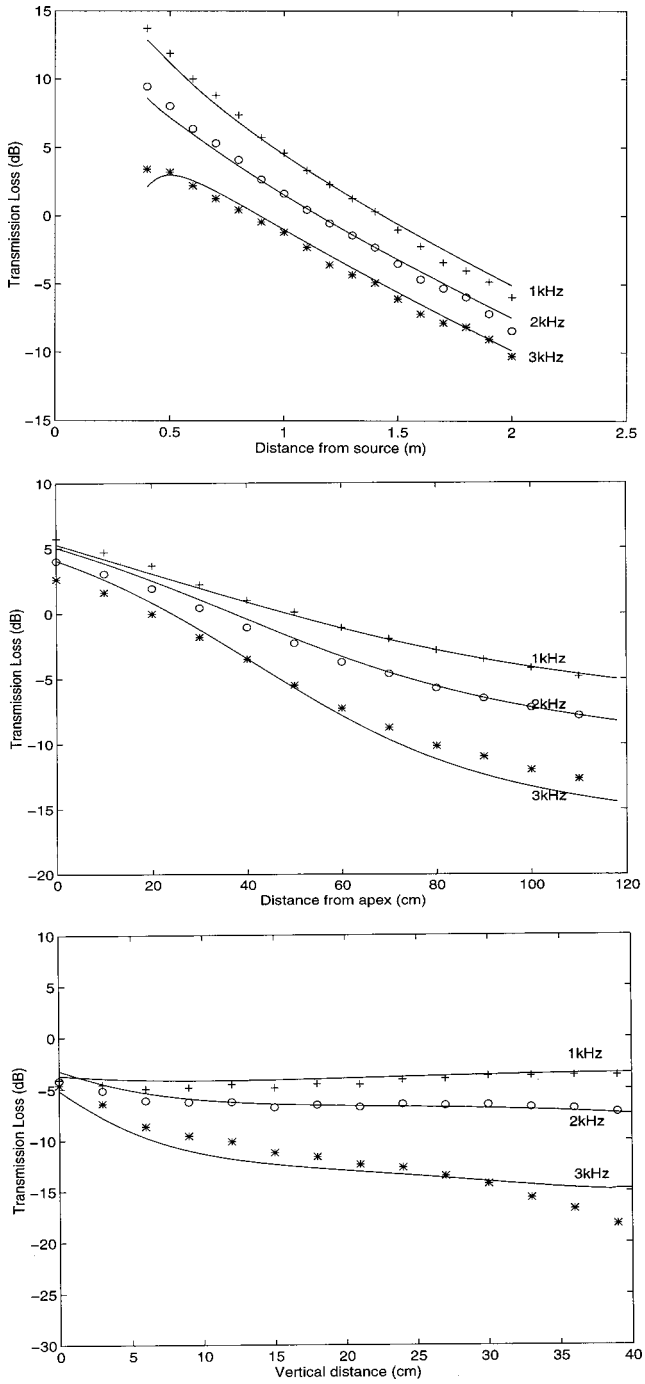

FIG. 8. Transmission loss from a monopole source measured above a convex mat-on-masonite surface: (a) along the surface; (b) along the line of sight and $z_s=0.21$ m; and (c) along a vertical distance z_v starting at $r_0=1.90$ m (cf. Fig. 7). The plus signs: 1.0 kHz, circles: 2.0 kHz, and stars: 3.0 kHz. $\sigma_e=4$ kPa s m^{-2}, $\alpha_e=570$ m^{-1}, $z_s=0.1$ m and $z=0.06$ m. Solid curves: predictions.

ground. First, the phase angle of impedance must be between $\pi/3$ and $\pi/2$. Second, the scaled admittance q should be sufficiently large (e.g., $|q|$ is approximately greater than 1) so that the sound field is dominated by the surface wave in the penumbra region (see Fig. 5 of Ref. 18). Since the surface wave and creeping wave[19] are travelling at different speeds, it should be possible to detect their separate arrivals in the pulse experiments described in the following sections. It is of interest to point out that the criterion used by Stinson and

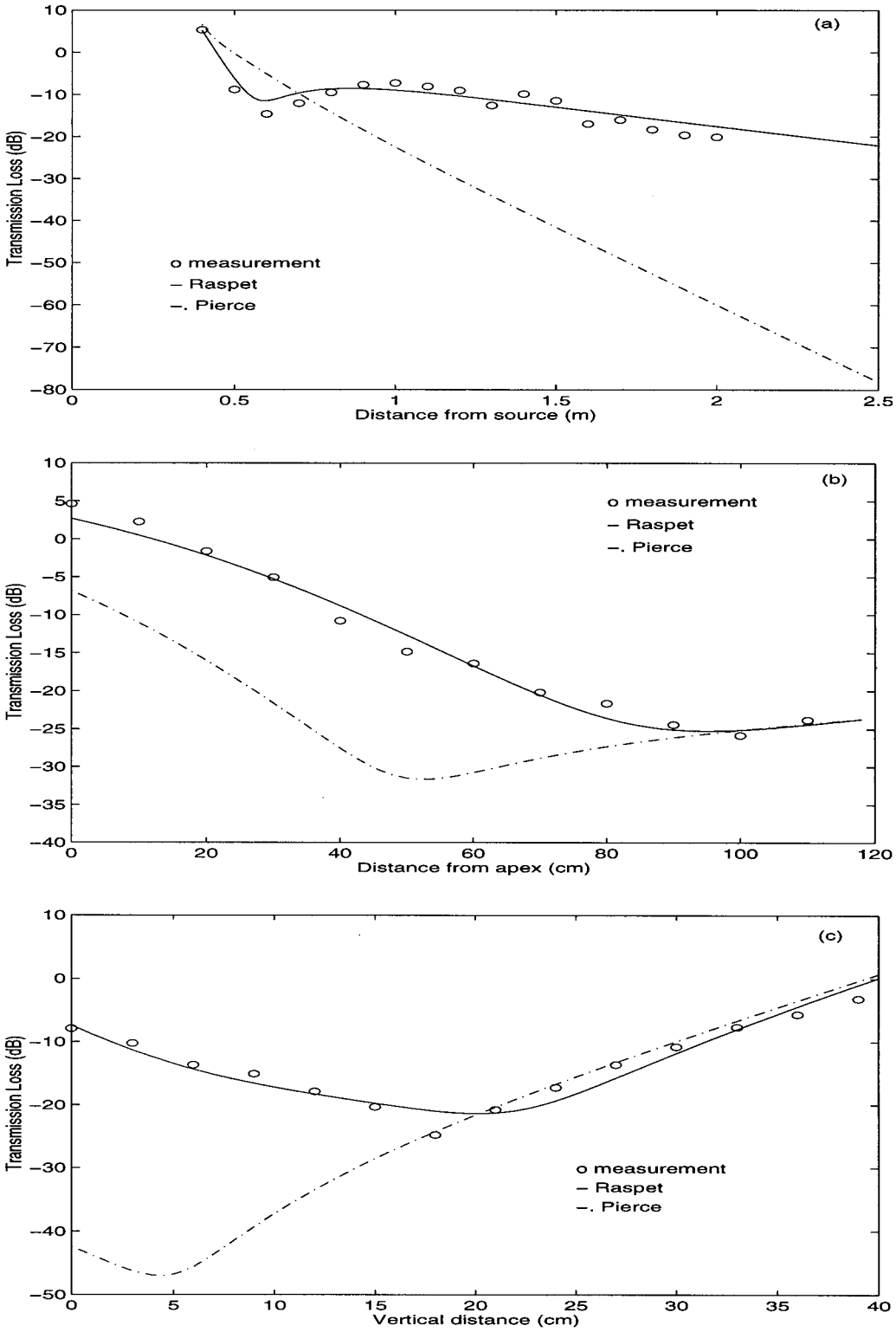

FIG. 9. Transmission loss obtained above the convex mat-on-masonite surface for (a) along the surface, $f=3.9$ kHz, $z_s=0.10$ m and $z=0.08$ m; (b) along the line of sight $f=3.9$ kHz and $z_s=0.21$ m; and (c) along the vertical distance, $f=3.7$ kHz, $z_s=0.21$ m, z_v starting at $r_0=1.90$ m (cf. Fig. 8).

Daigle[23] for the observation of surface wave is not applicable here. They suggest that the surface wave is localized near the surface and it can be detected as an additional component to the total field [see the interference pattern shown in Fig. 2(b) of Ref. 23]. However, this will not be the case for the propagation over convex cylindrical surfaces because creeping waves are always present in the shadow zone and, like the surface wave, it decays exponentially with height.[19] It is not possible to discriminate the individual contribution from the creeping wave and surface wave in the total sound field. To demonstrate this point, we plot the relative sound pressure level versus the vertical position above the impedance ground in Fig. 3(a) and (b). In general, the relative sound pressure level always shows interference patterns that are

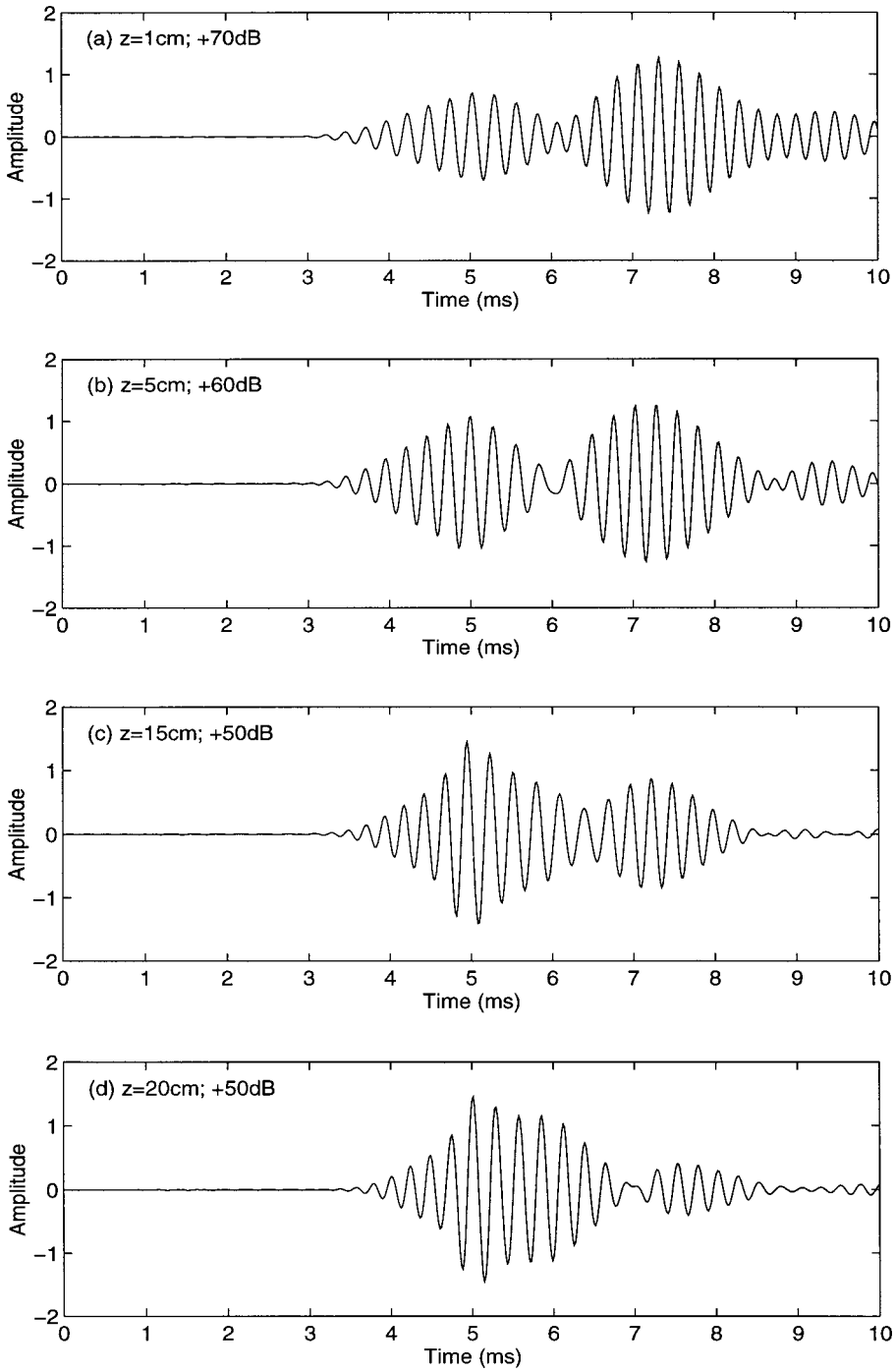

FIG. 10. Pulses measured above a mat-on-masonite convex surface at a frequency of 4 kHz for $z_s=4$ cm, $z=1$, 5, 15, and 20 cm, and $r=1.5$ m.

localized near the ground. Figure 3(a) shows the plot for the ground with impedance phase angles, $\varphi_z \geqslant \pi/3$, that has the surface wave pole. There is a clear interference pattern near the ground. Figure 3(b) shows the theoretical predictions above the ground with impedance phase angles less than $\pi/3$ and the frequency of 4 kHz. Hence, no surface wave pole will be expected in this type of ground. However, interference patterns of the relative sound pressure levels are evinced in Fig. 3(b). Clearly, these interference patterns are due to the contributions of creeping waves instead. For the dash-dotted curve in Fig. 3(a), the scale admittance q and the phase angle of impedance φ_z are chosen to be identical to those parameter values that are used to characterize the convex ground surface employed in our experimental studies.

II. EXPERIMENTAL PROCEDURES

A. Curved surface

The experiments were conducted in an anechoic chamber has an approximate dimension of $3\times3\times3$ m^3. Convex surfaces were constructed to behave as a rigid surface and as a surface of finite impedance, respectively. The rigid convex surface was constructed by attaching sheets of masonite to a curved wooden frame. Due to the space limitation in the anechoic chamber, a long convex cylinder was constructed with a radius of curvature of 2.5 m, a span of 1.8 m, and a maximum height of 0.45 m. It was built by overlying sheets of masonite attached to a wooden frame. Particular care was taken when fastening the sheets to the frame in order to

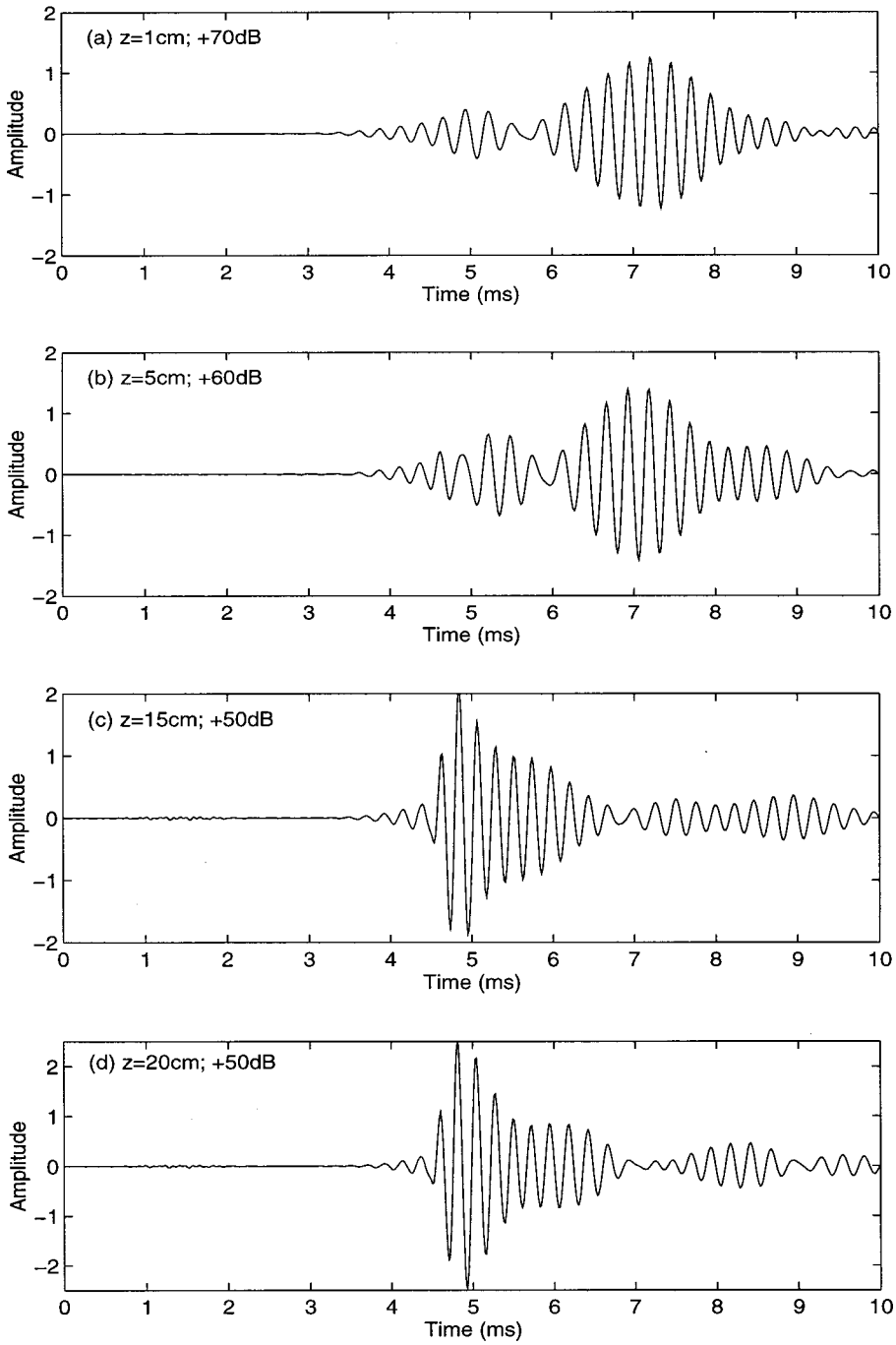

FIG. 11. Same as Fig. 10, but above a mat-on-masonite flat surface.

ensure that the model surface behaved as a rigid reflector. To obtain the surface of finite impedance, the masonite surface was covered by a rubber mat with a thickness of 12 mm and a mesh size of 22 mm^2. The rubber mat was secured to the rigid cylinder by means of double-sided tape. Note that the hard ground was used to conduct control experiments as it can be used to demonstrate that no observable surface waves were generated on this type of surface. On the other hand, the rubber mat was designed to allow the generation of the surface waves over the convex cylindrical surface.

The lighting diffuser lattice that has been used as the model surface to produce a surface wave by previous researchers[12,15,23] cannot be attached to a curved surface because it is inflexible. To obtain a surface with impedance in which the imaginary part is larger than the real part and $\varphi_z > \pi/3$, a suitable comblike structure has to be found to cover the curved surface. The material must be sufficiently flexible to follow the contour of the surface uniformly and behave as a locally reacting medium. A commercial mat was found to be the most suited for this purpose. The mat is open meshed with a hole size of 22 mm^2 and a depth of 12 mm.[24] In an earlier study, Li *et al.*[25] have investigated the sound field due to a dipole source above a flat impedance surface. In the present study, we have used the rubber mat as the impedance surface instead. A two-parameter impedance model[26] is used to calculate the specific normalized impedance, Z, by

$$Z = 1/\beta = 0.436(\sigma_e/f)^{1/2} + i[0.436(\sigma_e/f)^{1/2} + 19.48(\alpha_e/f)], \tag{14}$$

where σ_e is the effective flow resistivity and α_e is the effec-

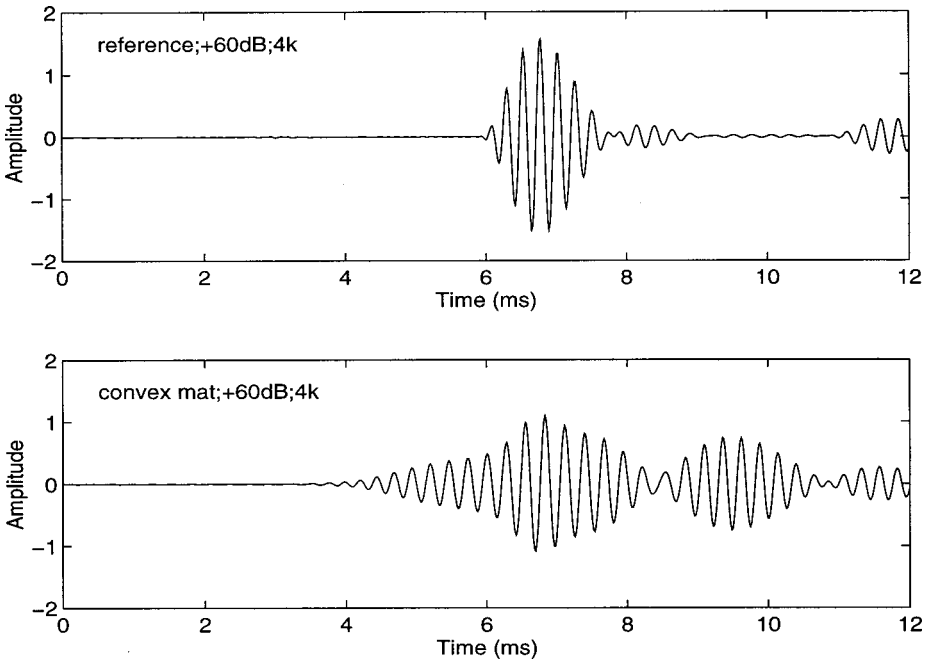

FIG. 12. The reference pulse measured in a free field and pulses measured above the convex mat-on-masonite surface at a frequency of 4 kHz, for $z_s=4$ cm, $z=5$ cm, and $r=2.0$ m.

tive (exponential) rate of change of porosity with depth. Preliminary experiments were conducted for the measurements of sound above a flat ground covered with the rubber mat. Figure 4 shows the excess attenuation measured above a flat mat-on-masonite surface with a point source and a receiver 1.0 m apart at heights of (a) 0.15 m, (b) 0.10 m, and (c) 0.08 m. The solid curves were calculated from the classical Weyl–van der Pol formula.[27] The impedance was evaluated by using Eq. (14). The best agreement between the predictions and the measurements was found with $\sigma_e=4$ kPa s m^{-2} and $\alpha_e=570\,\mathrm{m}^{-1}$. In these figures, the angles of incidence are 81.0, 78.7, and 73.3 degrees, respectively. The measurements are in accord with predictions assuming local reaction and using the two-parameter impedance model. Figure 5(a) shows the impedance phase angle of the mat-on-masonite surface as a function of frequency. The imaginary part and the real part of the impedance versus frequency are plotted in Fig. 5(b). It is seen that the impedance of the mat-on-masonite surface satisfies $\varphi_z>\pi/3$. The imaginary component produces a decreasing amplitude above the surface with absolute values larger than those of the real component. The chosen mat-on-masonite should therefore allow the generation of a surface wave component in both a flat and a convex ground.

B. Measurement system and data analysis

A Tannoy type PD-30T loudspeaker fitted with a tube 90 cm long and 3 cm internal diameter has been used as a point monopole source. A B&K 4311 $\frac{1}{4}$-in. condenser microphone was used for making the sound pressure measurements. The microphone was connected to a B&K 2608 measuring amplifier via the preamplifier. A PC-based maximum length sequence system analyzer (MLSSA) was used both as the signal generator for the speaker and as the analyzer for subsequent signal processing. The signal was analyzed using a half Blackman-Harris window and Fourier transformed.[28] Figure 6 is a schematic diagram of the experiments. An initial measurement in the absence of the boundary serves as the direct field, i.e., reference field and subsequent measurements were divided by the reference field to obtain the transmission loss (TL). Alternatively, the excess attenuation (EA) may be used where appropriate. The transmission loss and excess attenuation are defined as follows:

$$\mathrm{TL}=20\lg(p/p_1) \quad \text{and} \quad EA=20\lg(p/p_0), \tag{15}$$

where p_1 and p_0 are, respectively, the sound pressure at a distance of 1 m from the source and the sound pressure at an identical field point. Both p_1 and p_0 are computed in the absence of the reflected wave.

Experiments were conducted with both the source and receiver in the plane transverse to the centerline of the cylinder. Figure 7 shows a detailed sketch of the experimental configurations. In this figure, r represents the distance from source measured from source to receiver along the surfaces, x represents the distance from apex measured along the line of sight starting from the apex of a curved surface, and z_v represents the vertical distance above the surface starting at an arc distance $r=r_0$ from the source. Data were taken along the surface, along a vertical distance across the illuminated region and shadow zone, along the line of sight, and above the limiting ray.

III. MEASURED SOUND FIELDS ABOVE A CONVEX IMPEDANCE GROUND

The experimental results for a point source above the hard ground are very similar to those results reported by others, for example, in Ref. 22. Consequently, these experimental measurements and theoretical comparisons are not shown in this paper. Rather, the results are shown in the time domain as control experiments in order to demonstrate that no surface waves are generated on this type of surface, see Sec. III B below.

A. The sound field above a convex mat-on-masonite surface

To investigate the surface wave contribution for $\varphi_z > \pi/3$, we performed a series of laboratory measurements above the mat-on-masonite convex surface ($dc/dz \sim -137.2\,\mathrm{s}^{-1}$) in an anechoic chamber. The corresponding sound speed gradient is an approximation for the bilinear profile given in Eq. (2). Three experimental configurations (cf. Fig. 7), i.e., along the surface, along the line of sight, and along a vertical distance across the bright and shadow zones in the frequency domain, are used. The measurement results are presented as functions of r, x, or z_v in this section.

First, we present experimental and theoretical results for numerical schemes discussed earlier. The residue series calculations evaluated at the poles searched by the two techniques (based, respectively, on Pierce[19] and Raspet *et al.*[18]) are compared with the measurement results. At lower frequencies where the magnitude of nondimensional scaled admittance $|q|$ is small,[18] these two techniques give similar results which are shown as the solid curves in Fig. 8(a)–(c) for the receiver placed along the surface, along the line of sight and along a vertical distance across the bright and shadow zones, respectively. In each figure, the results were plotted at frequencies of 1.0, 2.0, and 3.0 kHz, corresponding to $|q| = 0.24$, 0.58, and 0.97. The calculations agree with the measurements in each region.

As $|q|$ increases, however, the sum of the poles calculated by Pierce's technique, which failed to trace the pole related to the surface wave, diverges significantly from the experimental measurements as shown in Fig. 9. The circles represent measurement results, the solid curves represent predictions from the residue series solution according to the Raspet *et al.* technique, and the dash–dotted lines represent predictions from the solution evaluated at the poles calculated by Pierce's technique. Figure 9(a) shows the results along the convex mat-on-masonite surface for a frequency of 3.9 kHz ($|q| = 1.34$, $\varphi_z = 82$degrees), with a source height of 0.1 m and a receiver height of 0.08 m. The transmission loss shows a dip in the transition area and high levels in the shadow zone resulting from the contributions of the surface wave and the creeping wave in the shadow zone. The sound field, see Eq. (11), is dominated by the contributions of the first pole, which includes the surface wave.

Figure 9(b) shows the results along the line of sight for the same frequency as Fig. 9(a), with a source height of 0.21 m above the surface. The first term, which contains the surface wave contribution, dominates out to a distance of 0.8 m from the apex along the limiting ray. As the height of the receiver increased, the surface wave contribution becomes weaker and the second term of the residue series contributes most significantly to the total field.

Figure 9(c) displays the results along a vertical distance starting with an arc length 1.90 m from the source for a frequency of 3.7 kHz ($|q| = 1.29$, $\varphi_z = 82.5$ degrees). The source height is 0.21 m. The term with contribution from the surface wave only dominates at short ranges where the receiver is close to the surface. As the receiver height is increased, the surface wave contribution becomes smaller than other residue series terms. At a vertical distance of 0.4 m, the surface wave contribution has decayed such that it is weaker than even the fourth term of the residue series [cf. Eq. (11)].

It should be noted that the good agreement between experimental data and predictions in Figs. 8 and 9 has been obtained with a somewhat simpler model for the surface impedance than was found necessary by Daigle and co-workers.[5,23]

B. Observations of surface waves in the time domain

In pulse experiments above a lighting diffuser lattice mounted on a flat rigid surface, the surface wave has been observed as a separate arrival from the body wave.[5,17] So far, there have been no reports of similar experiments for propagation over a curved surface of finite impedance. Maximum-length-sequence (MLS) signals were generated from the MLSSA system. The pulses were conditioned by a B&K 5612 Spectrum Shaper to optimize the observation of separation between creeping wave and surface wave.[5] The signals were detected in a $\frac{1}{3}$-octave band centered at 4 kHz and tapered by a 3 dB per octave filter on each side. At this frequency, there was a sufficient arrival time difference between the surface wave and the remainder of the field beyond a horizontal range of 1.5 m. That surface wave appears as a separate arrival above both the flat and the convex surfaces. The velocity of the surface wave is, as expected, less than the velocity of that of the remaining field, which in the case of a convex surface may be identified as the creeping wave.[19]

Figures 10 and 11 show the results of measurements obtained above the convex mat-on-masonite surface. In Fig. 10, the source height was approximately 4.0 cm and the receiver heights were 1.0, 5.0, 15.0, and 20.0 cm above the surface at a constant range of 1.5 m. All receiver positions were below the line of sight in these configurations. For the purpose of comparison, the measurement results obtained above a flat mat-on-masonite surface, where the source and receiver were located at the same heights as those above the convex surface, are also shown in Fig. 11. As the receiver was moved closer to the surface, the amplitude of the surface wave was much larger than that of the creeping wave. However, the surface wave component of the pulse decayed quickly with increasing receiver height. At a height of 20.0 cm above the convex surface, the surface wave amplitude was much smaller than the creeping wave amplitude. This satisfies a standard property of a true surface wave.[1] Similar results can be observed over the flat mat-on-masonite surface.

Note that the recorded signals were contaminated by some unwanted reflections in the anechoic chamber as they manifested themselves as extra ''spikes'' towards the end of the recording period. The use of MLSSA technique allows one to remove these artifacts in the subsequent signal processing. To exemplify this point, we compare the measured pulse with a reference pulse in a $\frac{1}{3}$-octave band centered at a frequency of 4 kHz measured over the convex surface in Fig. 12. The source and receiver were 2.0 m apart and at heights of 4.0 and 5.0 cm, respectively. The reference pulse was generated by the same point source (Tannoy speaker) and measured in a free field at an identical distance between the source and the receiver to the measured pulse. The second

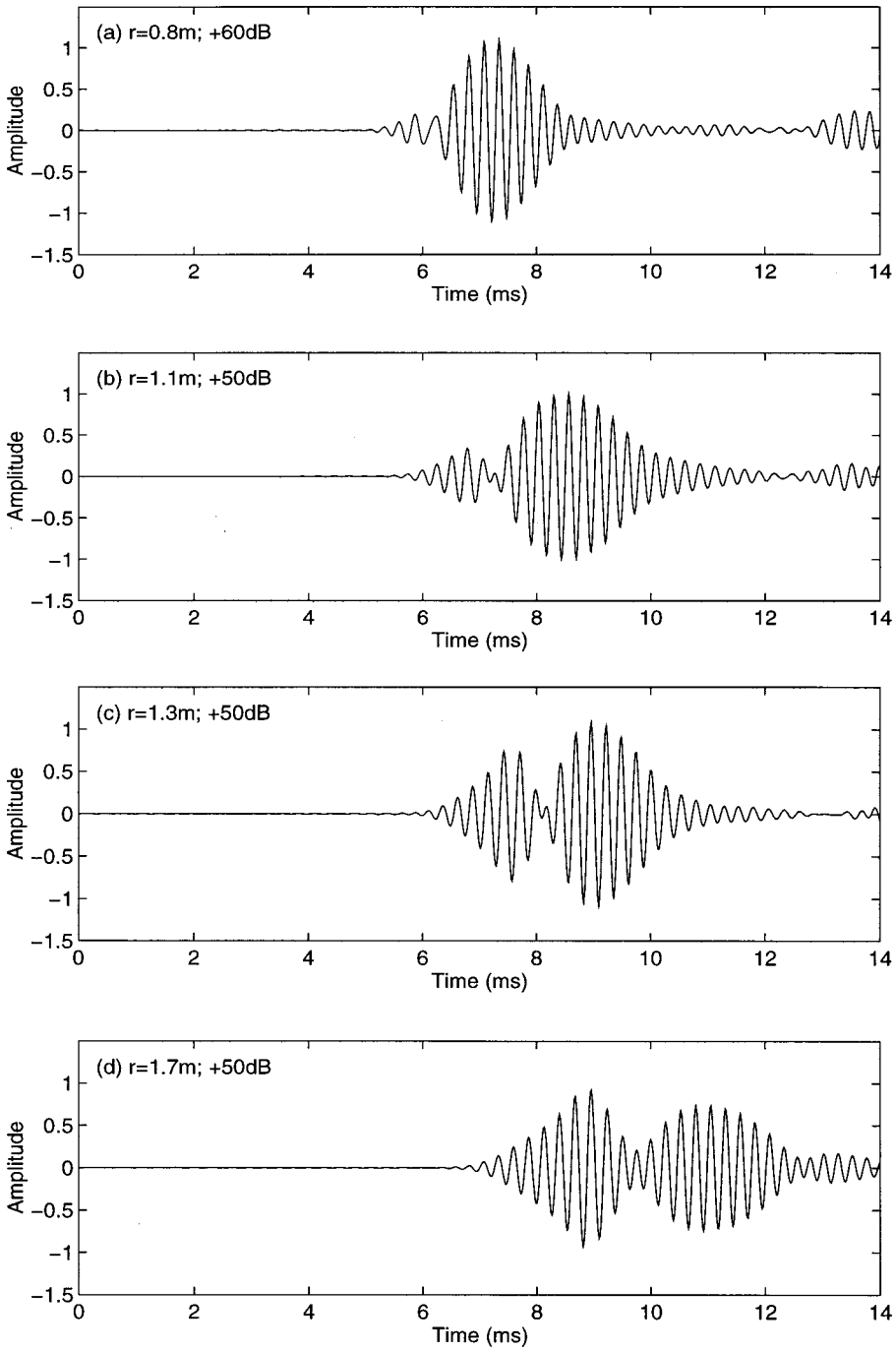

FIG. 13. Pulses measured above a mat-on-masonite convex surface at a frequency of 4 kHz for $z_s = 4$ cm, $z = 2$ cm, and various ranges.

arrival, which has a time delay of approximately 5.3 ms, indicates an unwanted reflection caused by the Tannoy speaker. However, this unwanted reflection can be filtered out by appropriate signal processing techniques so that it does not affect the measurements of sound pressure levels.

Figure 13 shows that the measured pulses deform with increasing range. The pulse was measured at a carrier frequency of 4 kHz. At shorter ranges (<1.0 m), the creeping wave and surface wave overlap in time, with the surface wave arrival delayed with respect to that of the creeping wave. As the range was increased, beyond a horizontal range of 1.0 m, for source and receiver heights of 4.0 and 2.0 cm, respectively, the two waves started to separate. Again, the unwanted reflections are present toward the end of the measuring period.

Finally, we wish to confirm the arrival of the surface wave pulse (the second pulse) is linked with the property of the impedance surface. We have conducted a control experiment by measuring the sound field above a hard convex surface in time domain. Figure 14 displays a typical result where measured pulses above a mat-on-masonite surface and above a rigid surface are shown for comparison. The same carrier frequency, 4 kHz, was used with source height of 4 cm, receiver height of 2 cm, and range of 2.0 m. It is obvious that the surface wave pulse is not present in the rigid surface and it is an apparent feature for the mat-on-masonite surface.

IV. CONCLUDING REMARKS

A series of laboratory experiments has been conducted to study the sound field above a convex mat-on-masonite

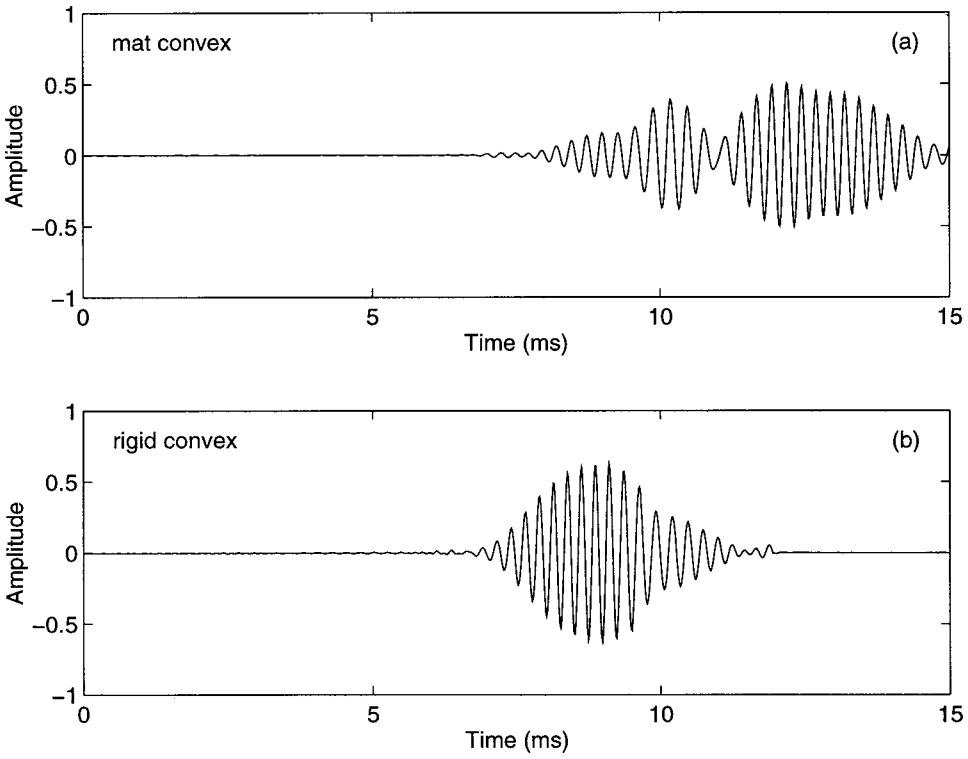

FIG. 14. Pulses measured at a frequency of 4 kHz for $z_s = 4$ cm, $z = 2$ cm, and $r = 1.5$ m above (a) a mat-on-masonite convex surface and (b) a rigid convex surface.

surface with the phase angles of the impedance greater than $\pi/3$. There is generally good agreement between the measurements and the residue series predictions from poles evaluated by using Raspet *et al.*'s technique rather than by using Pierce's technique. Surface waves have been observed in the experiments over a convex mat-on-masonite surface, which may be considered to simulate propagation over an impedance plane under an upward refracting atmosphere.

ACKNOWLEDGMENTS

One of the authors (QW) was supported by an Open University Research Studentship. The authors benefited from many useful discussions with Keith Attenborough. The work was supported in part by EPSRC through Grant Ref. GR/L 15236. In the preparation of the revised manuscript, KML was supported by a Hong Kong Polytechnic University Research Grant (Project No. A-PB33).

[1] A. R. Wenzel, ''Propagation of waves along an impedance boundary,'' J. Acoust. Soc. Am. **55**, 956–963 (1974).
[2] R. J. Donato, ''Propagation of a spherical wave near a plane boundary with a complex impedance,'' J. Acoust. Soc. Am. **60**, 34–39 (1976).
[3] R. J. Donato, ''Model experiments on surface waves,'' J. Acoust. Soc. Am. **63**, 700–703 (1978).
[4] R. Raspet and G. E. Baird, ''The acoustic surface wave above a complex impedance ground surface,'' J. Acoust. Soc. Am. **85**, 638–640 (1989).
[5] G. A. Daigle, M. R. Stinson, and D. I. Havelock, ''Experiments on surface waves over a model impedance plane using acoustical pulses,'' J. Acoust. Soc. Am. **99**, 1993–2005 (1996).
[6] P. H. Parkin and W. E. Scholes, ''The Horizontal propagation of sound from a jet engine close to the ground at Hatfield'' J. Sound Vib. **2**, 353–374 (1965).
[7] J. E. Piercy, T. F. W. Embleton, and L. C. Sutherland, ''Review of sound propagation in the atmosphere,'' J. Acoust. Soc. Am. **61**, 1403–1418 (1997).
[8] D. G. Albert, ''Observations of acoustic surface waves propagating above a snow cover,'' Proc. Fifth Symposium on Long Range Sound Propagation, pp. 10–16 (1992).
[9] L. C. Sutherland and G. A. Daigle, ''Atmospheric sound propagation,'' in *Handbook of Acoustics*, edited by M. J. Crocker (Wiley, New York, 1998), pp. 305–329.
[10] L. M. Brekhovskikh, ''Surface wave in acoustics,'' Sov. Phys. Acoust. **5**(1), 3–12 (1959).
[11] S. I. Thomasson, ''Sound propagation above a layer with a large refraction index,'' J. Acoust. Soc. Am. **61**, 659–674 (1977).
[12] M. R. Stinson, G. A. Daigle, and D. I. Havelock, ''The formation of surface waves over a model surface,'' in *Proceedings of the 5th International Symposium on Long Range Sound Propagation* (Milton Keynes, UK, 1992), pp. 17–28.
[13] G. A. Daigle, ''Surface waves above porous ground surfaces,'' J. Acoust. Soc. Am. Suppl. 1 **85**, S82 (1989).
[14] G. A. Daigle and T. F. W. Embleton, ''Surface waves and surface wave devices in atmospheric acoustics,'' J. Acoust. Soc. Am. Suppl. 1 **88**, S190 (1990).
[15] C. H. Howorth and K. Attenborough, ''Model experiments on air-coupled surface waves,'' J. Acoust. Soc. Am. **92**, 2431(A) (1992).
[16] I. Tolstoy, *Wave Propagation* (McGraw-Hill, New York, 1973).
[17] C. H. Howorth, ''Sound propagation over rigid porous layers,'' Ph.D. Thesis, The Open University, 1991.
[18] R. Raspet, G. E. Baird, and W. Wu, ''The relationship between upward refraction above a complex impedance plane and the spherical wave evaluation for a homogeneous medium,'' J. Acoust. Soc. Am. **89**, 107–114 (1991); [also see R. Raspet, G. E. Baird, and W. Wu, ''Normal mode solution for low-frequency sound propagation in a downward refracting atmosphere above a complex impedance plane,'' J. Acoust. Soc. Am. **91**, 1341–1352 (1992)].
[19] A. D. Pierce, *Acoustics: An Introduction to Its Physical Principles and Applications* (Acoustical Society of America, New York, 1989), pp. 469–478.
[20] K. M. Li, Q. Wang, and K. Attenborough, ''Sound propagation over convex impedance surfaces,'' J. Acoust. Soc. Am. **104**, 2683–2691 (1998).
[21] J. P. Chambers, R. Raspet, Y. H. Berthelot, and M. J. White, ''Use of the fast field program for predicting diffraction of sound by curved surfaces,'' J. Acoust. Soc. Am. **102**, 642–649 (1997).
[22] A. Berry and G. A. Daigle, ''Controlled experiments of the diffraction of sound by a curved surface,'' J. Acoust. Soc. Am. **83**, 2047–2058 (1988).
[23] M. R. Stinson and G. A. Daigle, ''Surface wave formation at an impedance discontinuity,'' J. Acoust. Soc. Am. **102**, 3269–3275 (1997).
[24] Q. Wang, ''Atmospheric refraction and propagation over curved surfaces,'' Ph.D. thesis, The Open University, UK, 1997.

[25] K. M. Li, S. Taherzadeh, and K. Attenborough, ''Sound propagation from a dipole source near an impedance plane,'' J. Acoust. Soc. Am. **101**, 3343–3352 (1997).
[26] K. Attenborough, ''Ground parameter information for propagation models,'' J. Acoust. Soc. Am. **92**, 418–427 (1992).
[27] K. Attenborough, ''Review of ground effects on outdoor sound propagation from continuous broadband sources,'' Appl. Acoust. **24**, 289–319 (1988).
[28] D. D. Rife and J. Vanderkooy, ''Transfer-function measurement with Maximum-Length Sequences,'' J. Audio Eng. Soc. **37**, 419 (1989).

Sound propagation over concave surfaces

Qiang Wang
Department of Environmental & Mechanical Engineering, Faculty of Technology, The Open University, Milton Keynes MK 7 6AA, United Kingdom

Kai Ming Li[a)]
Department of Mechanical Engineering, Hong Kong Polytechnic University, Hung Hom, Kowloon, Hong Kong

(Received 11 December 1997; revised 1 July 1999; accepted 26 July 1999)

Diffraction of sound by concave surfaces is investigated theoretically and experimentally. In an earlier study [J. Acoust. Soc. Am. **104**, 2683–2691 (1998)], it has been demonstrated that a rigorous analogy exists for the sound field above a convex circular cylinder in an otherwise homogeneous medium. The predicted sound field corresponds to the situation where the sound speed of the medium decreases exponentially with height. Extending the previous work, this paper investigates of the sound field above a concave surface and explores the corresponding analogy. Normal mode solutions have been developed for a downward refracting medium with an exponential sound speed profile. The solutions are used to predict the sound fields diffracted by a cylindrical concave surface. A series of laboratory experiments is conducted using point monopole, horizontal dipole, and vertical dipole sources over cylindrical concave surfaces. The experimental measurements are compared with the normal mode predictions. For monopole and horizontal dipole sources, good agreement has been found between measurements and the normal mode predictions using an exponential profile. However, the agreement is less satisfactory where the sound field was due to vertical dipole sources. © *1999 Acoustical Society of America.* [S0001-4966(99)05411-9]

PACS numbers: 43.20.Fn, 43.28.Fp [LCS]

INTRODUCTION

Diffraction of waves by convex surfaces is of interest in many fields. It has been studied in great detail since the initial work of Fock[1] for the propagation of electromagnetic waves and subsequent work in acoustics by Pierce[2] and others.[3–5] In more recent studies, Chambers *et al.*[6] have used the fast field formulation to reexamine the sound field above a convex circular cylinder. On the other hand, Li *et al.*[7] have used the residue series approach to explore the 3-D sound fields above convex impedance surfaces. However, there is relatively little attention focused on the diffraction of sound by concave surfaces and most of these earlier studies have been concerned with monopole sources. Two notable exceptions are, first, a study by Almgren[8] where he measured the sound field above a rigid concave curved surface. He reported that the measurements agreed reasonably well with the sound fields calculated by using the theories of Pridmore-Brown,[9,10] Pierce,[3] and Rasmussen[11] for propagation over a flat rigid ground in a downward refracting medium. He suggested that further work could be extended to a finite impedance surface. Second, Gabillet *et al.*[12] conducted analogous indoor experiments over rigid and finite impedance concave surfaces with the radius of curvature of 20 m. Satisfactory agreements were obtained for a receiver locating at a few wavelengths above the curved surface. We remark that these two previous studies were aimed to simulate the propagation of sound in a downward refracting medium.

In this paper, we report a continuation of our previous study[7] by examining the sound field above a concave surface both theoretically and experimentally. We consider not only monopole but also dipole sources. A normal mode solution is developed that is based on a recent study by Li and Wang.[13] Essentially, the residue series solution[7] for sound field above a convex cylindrical surface is extended to enable calculation of the sound field scattered by a concave cylindrical surface. Measurement results using point monopole and horizontal dipole and vertical dipole sources over cylindrical concave surfaces are reported and compared with theoretical predictions.

I. THE NORMAL MODE SOLUTION

It has been suggested[3] that an acoustic analogy exists between downwardly curving ray paths over flat ground and propagation over a concave surface in a neutral atmosphere. The analogy is illustrated in Fig. 1. Almgren[8] has shown that it is valid to use a concave surface to simulate the propagation of sound in the downward refracting atmosphere. The corresponding sound speed profile is modeled in a bilinear form where the speed of sound, $c(z)$, is expressed in terms of the vertical height, z ($z \ll R_c$), as

$$c(z) = \frac{c_0}{\sqrt{1-2z/R_c}} \approx c_0\left(1+\frac{z}{R_c}-\frac{2z^2}{3R_c^2}+\cdots\right). \tag{1}$$

In Eq. (1), $c_0 \equiv c(0)$, and R_c is the radius of the curved surface. We note that, to first approximation, $1/R_c \approx (dc/dz)/c_0$ may be interpreted as the normalized sound speed gradient for the downward refracting atmosphere. Given the bilinear sound speed profile, the normal mode so-

a)Electronic mail: mmkmli@polyu.edu.hk

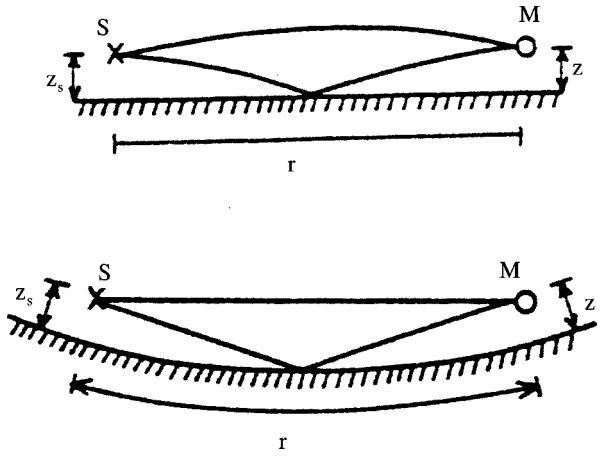

FIG. 1. Sketch showing the analogy between curved ray path above a plane boundary and straight-line propagation above a concave surface.

lution for the sound field, $p(r,z)$, can be expressed in terms of Airy functions Ai and their derivatives Ai′ as[13,14]

$$p^{(b)}(r,z) = \frac{i\pi e^{-i\pi/4}}{l}\sum_n \sqrt{\frac{2}{\pi K_n r}}\,\frac{\mathrm{Ai}(\tau_n+z_s/l)\mathrm{Ai}(\tau_n+z/l)e^{iK_n r}}{\{\tau_n[\mathrm{Ai}(\tau_n)]^2-[\mathrm{Ai}'(\tau_n)]^2\}}, \tag{2}$$

where

$$\tau_n=(K_n^2-k_0^2)l^2 \quad \text{for } n=0,1,2,3,\ldots. \tag{3}$$

The variables τ_n (for $n=0,1,2,3,...$) are the zeros of the dispersion equation:

$$\mathrm{Ai}'(\tau_n)+q_n\mathrm{Ai}(\tau_n)=0, \tag{4}$$

with

$$q_n=ik_0\beta l_n, \tag{5a}$$

$$l_n=(R_c/2k_0^2)^{1/3}=l, \tag{5b}$$

say, $k_0(\equiv 2\pi f/c_0)$ is the reference wave number, r is the distance from the source along the curved surface, z_s and z are, respectively, the source and receiver heights, and K_n is the horizontal wave number of the nth mode. In Eq. (2), the superscript (b) denotes the sound field in a medium with the bilinear sound speed profile. Here, in Eqs. (4) and (5a), q_n may be regarded as the nondimensional scaled admittance,[15] l_n as the wave layer thickness,[14] and β as the specific normalized admittance of the ground. It is evident from Eqs. (5a) and (5b) that the wave layer thickness and the nondimensional scaled admittance are the same for all modes for the case of the bilinear profile.

With the acoustic analogy suggested by Refs. 3 and 8, it is possible to use Eq. (2) to approximate the sound field above a concave cylindrical surface in an otherwise homogeneous medium. However, Di and Gilbert[16] suggest a stricter acoustic analogy by using a conformal transformation. They show that an exponential sound speed profile should be used instead of the bilinear profile in predicting the sound field. In this paper, we wish to investigate the validity of approximating the sound field above a concave cylindrical surface in a homogeneous medium by using the bilinear sound speed profile over a flat surface.

Using the same approach, Li *et al.*[7] extend the conformal transformation to three dimensions and they derive a residue series solution for the sound field behind a long convex cylinder. In the light of these earlier studies, it is possible to show that the sound field scattered by a concave cylindrical surface in a homogenous medium is identical to the sound field above an impedance flat ground surface in the presence of an exponential sound speed profile.[17] In the downward refracting medium, the speed of sound is determined according to

$$c(z)=c_0\exp(z/R_c)\approx c_0\left(1+\frac{z}{R_c}+\frac{z^2}{2R_c^2}+\cdots\right), \tag{6}$$

where $z\ll R_c$. Making use of our previous analyses,[7,13] we can show that the sound field above a concave cylinder is given by

$$p^{(c)}(r,\psi_r,z)=e^{i\pi/4}\sqrt{\frac{8\pi}{r}}\sum_n\left[\frac{\overline{\xi}_s\overline{\xi}}{\overline{k}_z^2(z_s)\overline{k}_z^2(z)}\right]^{1/4}\frac{\sqrt{K_n}\mathrm{Ai}(-\overline{\xi}_s)\mathrm{Ai}(-\overline{\xi})e^{iK_n r}}{(\partial\tau_n/\partial K_n)\{\tau_n[\mathrm{Ai}(\tau_n)]^2-[\mathrm{Ai}'(\tau_n)]^2\}+(\partial q_n/\partial K_n)[\mathrm{Ai}(\tau_n)]^2}, \tag{7}$$

where

$$\overline{\xi}(z)=\begin{cases}\left\{\frac{3}{2}K_nR_c\cos\psi_r\left[\frac{\overline{k}_z(z)}{K_n\cos\psi_r}-\tan^{-1}\left(\frac{\overline{k}_z(z)}{K_n\cos\psi_r}\right)\right]\right\}^{2/3} & \text{if } z\leqslant \mathrm{Re}(z_t),\\ -\left\{\frac{3}{2}K_nR_c\cos\psi_r\left[-\frac{\sqrt{-\overline{k}_z^2(z)}}{K_n\cos\psi_r}+\tanh^{-1}\left(\frac{\sqrt{-\overline{k}_z^2(z)}}{K_n\cos\psi_r}\right)\right]\right\}^{2/3} & \text{if } z>\mathrm{Re}(z_t),\end{cases} \tag{8}$$

$$z_t=R_c\ln\left(\frac{\sqrt{k_0^2-K_n^2\sin^2\psi_r}}{K_n\cos\psi_r}\right), \tag{9}$$

$$\overline{k}_z(z)=+\sqrt{(k_0^2-K_n^2\sin^2\psi_r)\exp(-2z/R_c)-K_n^2\cos^2\psi_r}, \tag{10}$$

ψ_r is the azimuthal angle of the receiver in the plane of constant z, the superscript (c) denotes the sound field above a cylindrical concave surface, and z_t is known as the turning point[13] in the terminology of ray acoustics. Again, the variable τ_n represents the zeros of Eq. (4) but it is expressed, in terms of K_n, differently as follows:

$$\tau_n = -\xi(0) = -\left\{\frac{3}{2}K_n R_c \cos\psi_r \times\left[\frac{\sqrt{k_0^2-K_n^2}}{K_n\cos\psi_r}-\tan^{-1}\left(\frac{\sqrt{k_0^2-K_n^2}}{K_n\cos\psi_r}\right)\right]\right\}^{2/3}. \tag{11}$$

In Eq. (5) the variable $\partial\tau_n/\partial K_n$ can be evaluated to give

$$\frac{\partial\tau_n}{\partial K_n} = \frac{R_c}{\sqrt{-\tau_n}}\sec\psi_r \tan^{-1}\left(\frac{\sqrt{k_0^2-K_n^2}}{K_n\cos\psi_r}\right). \tag{12}$$

The numerical values of τ_n, q_n, and K_n can be determined by using the method described in Refs. 7 and 13. Substituting these numerical values into Eq. (7), we can compute the sound field above a cylindrical curved surface. The numerical results for the bilinear and exponential sound speed profiles will be shown in Sec. II.

Noting that the horizontal range and the vertical-height-dependent factors are not coupled in the residue series solution for a monopole source, the dipole field p_d can be derived from the monopole field p by noting[18]

$$p_d = 2\Delta_d S_0\left[\sin\gamma_d\cos(\psi_d-\psi_r)\frac{\partial}{\partial r}p+\cos\gamma_d\frac{\partial}{\partial z_s}p\right], \tag{13}$$

where $2\Delta_d$ is the separation of the components of two out-of-phase monopole components and γ_d and ψ_d are the polar and azimuthal angles of the dipole moment vector.[6] The normal mode solution for a bilinear profile can be extended for an arbitrarily oriented dipole source over a concave surface, i.e.,

$$p_d^{(b)} = p_h^{(b)} + p_v^{(b)}, \tag{14}$$

where $p_h^{(b)}$ and $p_v^{(b)}$ are, respectively, the horizontal component and the vertical component of a dipole. They are determined according to[24]

$$p_h^{(b)}(r,\psi_r,z) \approx \frac{e^{i\pi/4}}{l}\sqrt{\frac{\pi}{2r^3}}S_d\sin\gamma_d\cos(\psi_d-\psi_r) \times\sum_n \frac{(2iK_n-1)\mathrm{Ai}(\tau_n+z_s/l)\mathrm{Ai}(\tau_n+z/l)e^{ik_n r}}{\sqrt{K_n}\{\tau_n[\mathrm{Ai}(\tau_n)]^2-[\mathrm{Ai}'(\tau_n)]^2\}}, \tag{15}$$

and

$$p_v^{(b)}(r,\psi_r,z) \approx \frac{\pi e^{i\pi/4}}{l^2}S_d\cos\gamma_d \times\sum_n \sqrt{\frac{2}{\pi K_n r}}\frac{\mathrm{Ai}'(\tau_n+z_s/l)\mathrm{Ai}(\tau_n+z/l)e^{iK_n r}}{\{\tau_n[\mathrm{Ai}(\tau_n)]^2-[\mathrm{Ai}'(\tau_n)]^2\}}. \tag{16}$$

The normal mode solution for an exponential profile for an arbitrarily oriented dipole source may be expressed by

$$p_d^{(c)} = p_h^{(c)} + p_v^{(c)}, \tag{17}$$

where

$$p_h^{(c)} \approx e^{i\pi/4}S_d\sin\gamma_d\cos(\psi_d-\psi_r) \times\sqrt{\frac{2\pi}{r^3}}\sum_n\left[\frac{\bar{\xi}_s\bar{\xi}}{\bar{k}_z^2(z_s)\bar{k}_z^2(z)}\right]^{1/4}\frac{(2iK_n-1)\sqrt{K_n}\mathrm{Ai}(-\bar{\xi}_s)\mathrm{Ai}(-\bar{\xi})e^{iK_n r}}{(\partial\tau_n/\partial K_n)\{\tau_n[\mathrm{Ai}(\tau_n)]^2-[\mathrm{Ai}'(\tau_n)]^2\}+(\partial q_n/\partial K_n)[\mathrm{Ai}(\tau_n)]^2}, \tag{18}$$

and

$$p_v^{(c)} \approx e^{i\pi/4}S_d\cos\gamma_d\sqrt{\frac{8\pi}{r}}\sum_n\left[\frac{\bar{k}_z^2(z_s)\bar{\xi}}{\bar{k}_z^2(z)\bar{\xi}_s}\right]^{1/4}\frac{\sqrt{K_n}\mathrm{Ai}'(-\bar{\xi}_s)\mathrm{Ai}(-\bar{\xi})e^{iK_n r}}{(\partial\tau_n/\partial K_n)\{\tau_n[\mathrm{Ai}(\tau_n)]^2-[\mathrm{Ai}'(\tau_n)]^2\}+(\partial q_n/\partial K_n)[\mathrm{Ai}(\tau_n)]^2}. \tag{19}$$

Locations of poles for dipole sources are the same as those for a monopole source and they are determined by solving the dispersion equation [see Eq. (4)].

II. THEORETICAL COMPARISONS

The normal mode solution for an exponential profile, Eq. (7), can be examined by means of numerical comparisons. A frequency of 2915 Hz corresponding to a wavelength of 0.12 m in atmosphere, at which some experiments have been conducted, is presented for these numerical comparisons.

A. Comparison of the normal mode solution to the fast field program results

The normal mode solution for an exponential profile should agree with the fast field program (FFP)[19] solution for

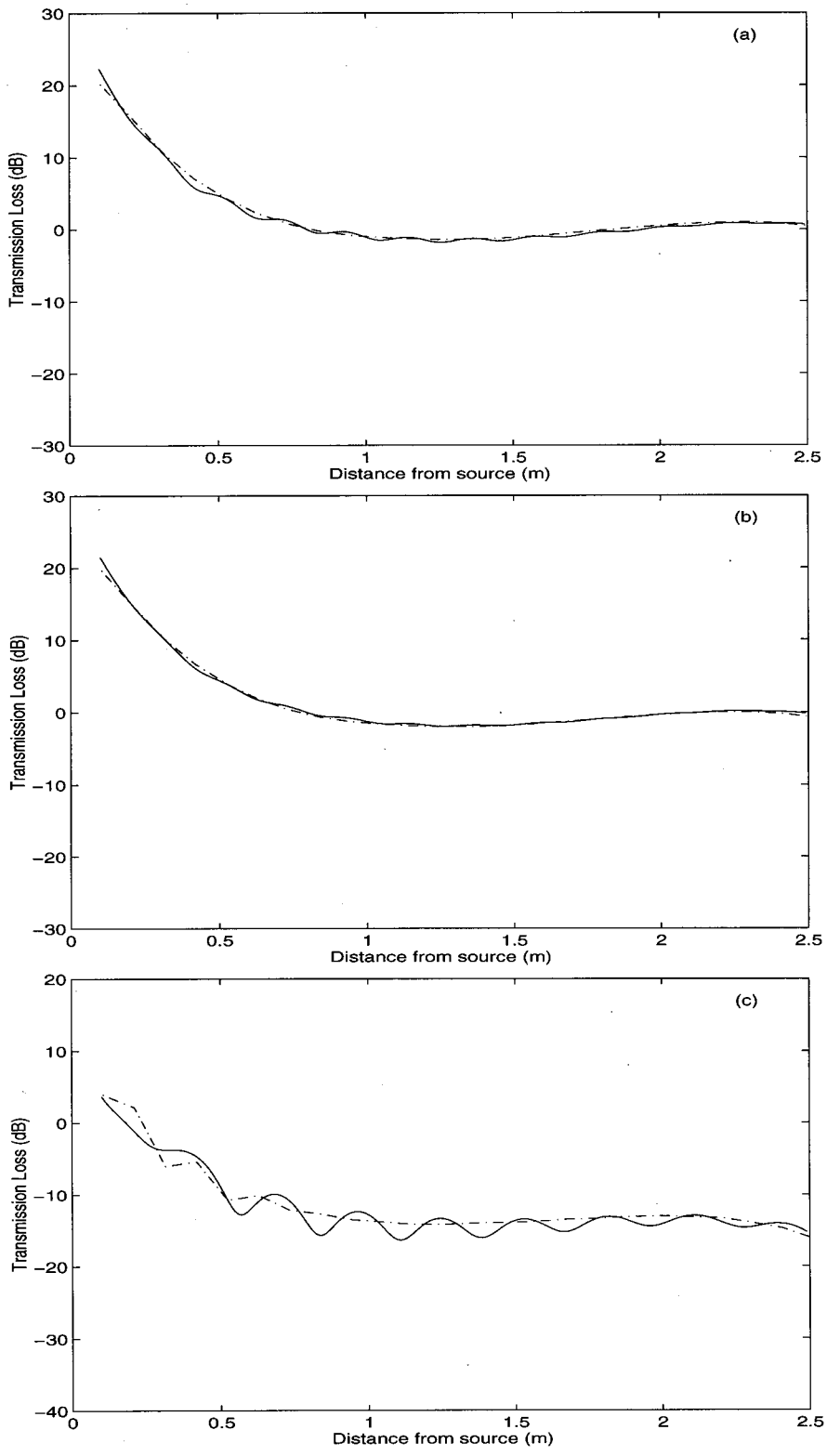

FIG. 2. Transmission loss predicted over a felt-covered concave surface with $R_c = 2.5$ m and $z_s = z = 0.10$ m at a frequency of 2915 Hz. Dash-dotted curves: FFP calculations, solid curves: the normal mode calculations with exponential profiles for (a) monopole, (b) horizontal dipole, and (c) vertical dipole.

the same sound speed gradient. To validate the numerical solutions, we compare the transmission loss (TL) versus the distance from source where

$$\mathrm{TL} = 20 \lg (p/p_1) \tag{20}$$

and p_1 is the free field acoustic pressure at a distance of 1 m from the source.

Figure 2 shows the results of the normal mode calculation (solid lines) compared with the FFP calculation (dash-dotted lines) for the sound speed profile varying exponentially with height. In Fig. 2(a), the sound propagation due to a monopole source above a felt-covered concave surface was predicted at a frequency of 2915 Hz with $R_c = 2.5$ m and the gradient was truncated at 1.24 m altitude. A good approxi-

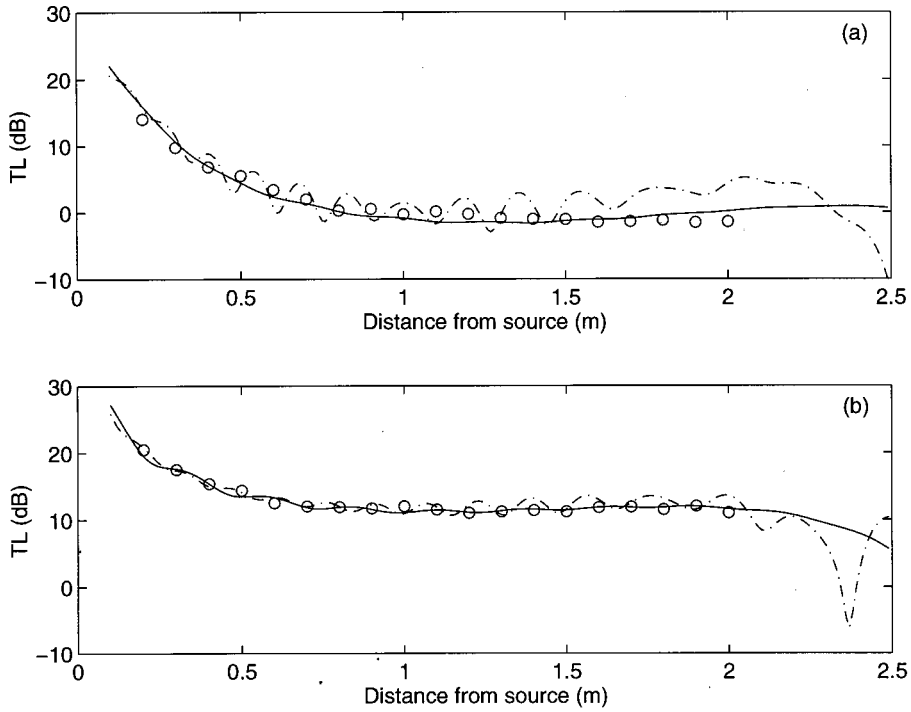

FIG. 3. Transmission loss due to a monopole source obtained at a frequency of 2915 Hz in a gradient with $R_c = 2.5$ m, over (a) a felt-covered concave surface with $z_s = z = 0.10$ m and (b) a rigid surface with $z_s = 0.02$ m and $z \sim 0.00$ m. Circles: measurements, solid curves: the normal mode calculations for exponential profiles, and dash-dotted curves: for bilinear profiles.

mation for the truncated gradient may be obtained by using 14 modes. This number of modes is the so-called full solution.[14] The complex impedance of the surface is calculated by using a two-parameter model[20] with $\sigma_e = 38\,\mathrm{kPa\,s\,m^{-2}}$ and $\alpha_e = 15\,\mathrm{m^{-1}}$. The chosen parameters (R_c, σ_e, and α_e) reflect the radius and the impedance of the curved surfaces used in our subsequent laboratory measurements. The source and receiver heights are 0.1 m. Figure 2(b) and (c) shows the comparisons for the propagation due to a horizontal dipole source and a vertical dipole source, respectively. The agreement between the two numerical schemes for monopole and horizontal dipole sources is excellent. However, for the vertical dipole source, the agreement between the FFP and the normal mode predictions is less satisfactory. There are considerable oscillations in the magnitudes of TL for the normal mode predictions. This is largely due to the fact that the contribution due to a branch-line integral has been ignored in the normal mode solution.[21] The inadequacy of the approximation is only apparent for the case of a vertical dipole because the solution involves the spatial differentiation with respect to the vertical height. In view of the acoustic analogy, the normal mode solution may be used to predict the sound field above a curved surface in an otherwise homogeneous medium. Its predictions will be compared with laboratory measurements in Sec. III.

B. Comparison of the normal mode solutions for two profiles

Typical comparisons of the normal mode predictions between bilinear and exponential profiles are displayed. Figure 3(a) shows the predictions above the felt-covered concave surface in a gradient with $R_c = 2.5$ m, at frequencies of 2915 Hz, for both profiles. The solid curves are calculated from Eq. (7) for the exponential sound speed profile and the dotted curves are calculated from Eq. (2) for the bilinear sound speed profile. The source height is 0.02 m and the receiver is on the surface. For the present situation, the wave layer thickness, l_n, and the wave number, k_0, can be determined as about 0.075 m and 54 $\mathrm{m^{-1}}$, respectively.

It is noteworthy that the predicted sound fields for the exponential and bilinear sound speed profiles are comparable only at ranges less than about 20 l_n. This feature is somewhat different from the case of upward refracting medium in which the predicted sound fields for both profiles are comparable in most practical situations.[7] However, this is not the case for the downward refracting medium. The difference becomes more significant when the receiver is located at a few wavelengths from the source. To illustrate the case, we consider the following example. A noise source of frequency 100 Hz is situated in a stratified medium with a normalized sound speed gradient of $1 \times 10^{-4}\,\mathrm{m^{-1}}$ (i.e., $R_c = 10\,000$ m). The wave layer thickness l_n can be determined as about 10 m. Hence, there should be notable discrepancies in the sound fields when the range extends beyond 200 m.

Over a rigid concave surface, the trends are similar to those over the felt-covered concave surface. The solid and dashed lines in Fig. 4(b) show the normal mode predictions for both profiles over a rigid surface with the source height of 0.02 m and the receiver on the surface.

C. Comparison with the boundary element method

To examine the calculations for both profiles over a cylindrical concave surface, the normal mode solutions are compared to the predictions due to the boundary element method (BEM). The BEM predictions serve an important purpose of ''benchmarking'' the normal mode solution because the numerical scheme of the BEM is based on an exact formulation of sound reflected by arbitrary surfaces. The numerical implementation of the BEM is well known and the details are described elsewhere.[22,23] In the BEM predictions,

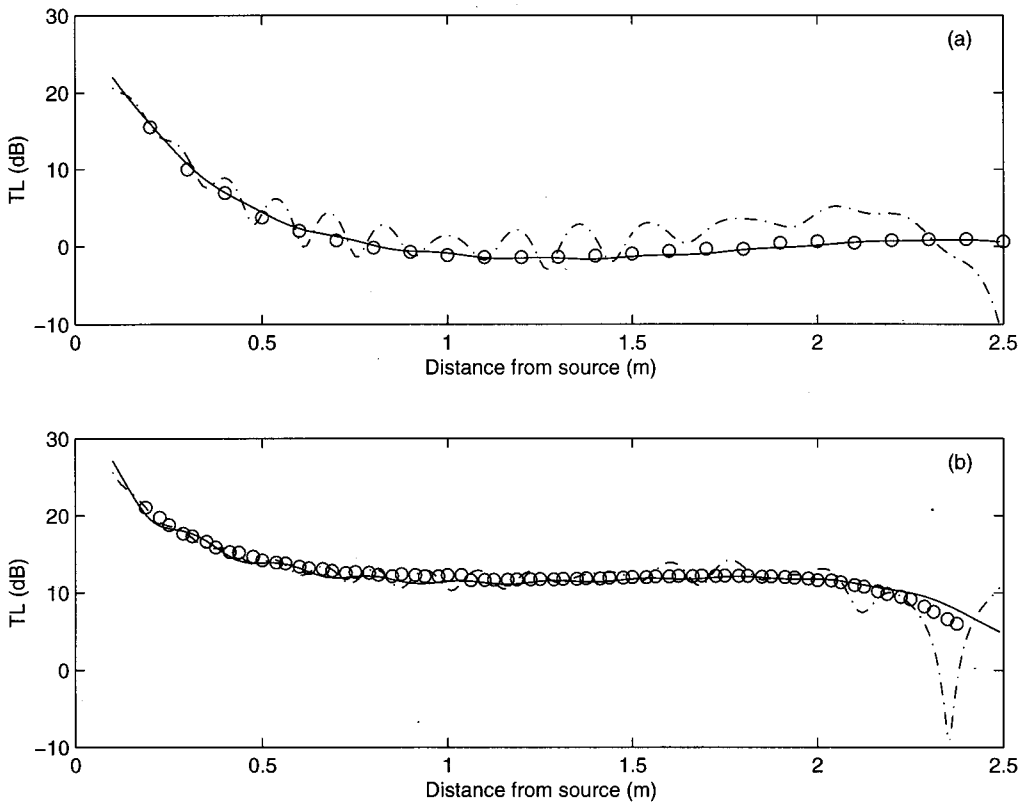

FIG. 4. Transmission loss predicted at a frequency of 2915 Hz in a gradient with $R_c = 2.5$ m, over (a) a felt-covered concave surface with $z_s = z = 0.10$ m and (b) a rigid surface with $z_s = 0.02$ m and $z \sim 0.00$ m. Circles: BEM calculations, solid curves: the normal mode calculations for exponential profiles, and dash-dotted curves: the normal mode calculations for bilinear profiles.

the cross section of the cylindrical concave surface is modeled as a series of adjacent elements with impedance surfaces.

Figure 4 shows two typical examples of prediction over concave surfaces, in a gradient with $R_c = 2.5$ m [(a) the felt-covered surface and (b) the rigid surface]. The solid lines represent the predictions for the exponential profile and the dotted lines represent those for the bilinear profile. The circles represent the calculations from the BEM.

There are considerable discrepancies between the normal mode predictions for the bilinear profile and predictions calculated from the BEM, especially at longer ranges. At short ranges, the discrepancies are small except that the normal mode solution shows considerable oscillations in magnitude. As the receiver is moved away from the source, the differences become greater.

Contrary to the bilinear sound speed profile, the normal mode predictions for the exponential profile accord generally with the BEM calculations over the concave surfaces. This implies that the equivalent sound speed increases exponentially rather than bilinearly with height over a cylindrical concave surface. This implication is in agreement with the conclusion obtained in the case of a cylindrical convex surface.[7] In the following section, the data obtained from measurements over cylindrical concave surfaces will be compared with the normal mode predictions for both sound speed profiles to test the performance of the theoretical models.

III. EXPERIMENTAL INVESTIGATIONS

A series of laboratory experiments was performed, using a point monopole source and horizontal and vertical dipole sources, above both felt-covered and rigid concave surfaces, to investigate sound propagation over concave surfaces. The experimental data is analyzed and compared to predictions of the normal mode solutions for both the exponential [Eq. (7)] and the bilinear [Eq. (2)] profiles.

A. Measurement techniques

The concave surfaces were constructed to behave either as rigid surfaces or as surfaces of finite impedance. The rigid concave surface was constructed by attaching sheets of masonite to a series of curved ribbed structures. The resulting surface was that of a long cylinder with a radius of curvature 2.5 m. It was built to have a transverse length of 2.5 m (subtended angle of about 60 degrees), a span of 1.8 m and a depth of 0.45 m. To ensure that the surface acted as a rigid reflector, particular care was paid in fastening the masonite sheets to the structures. To obtain a surface of finite impedance, felt was secured to the rigid surface using double-sided tape to eliminate the possible transmission path between the sheets and the felt. The impedance of the felt was characterized by measurements over a flat surface.[17] A two-parameter impedance model[20] with an effective flow resistivity of 38

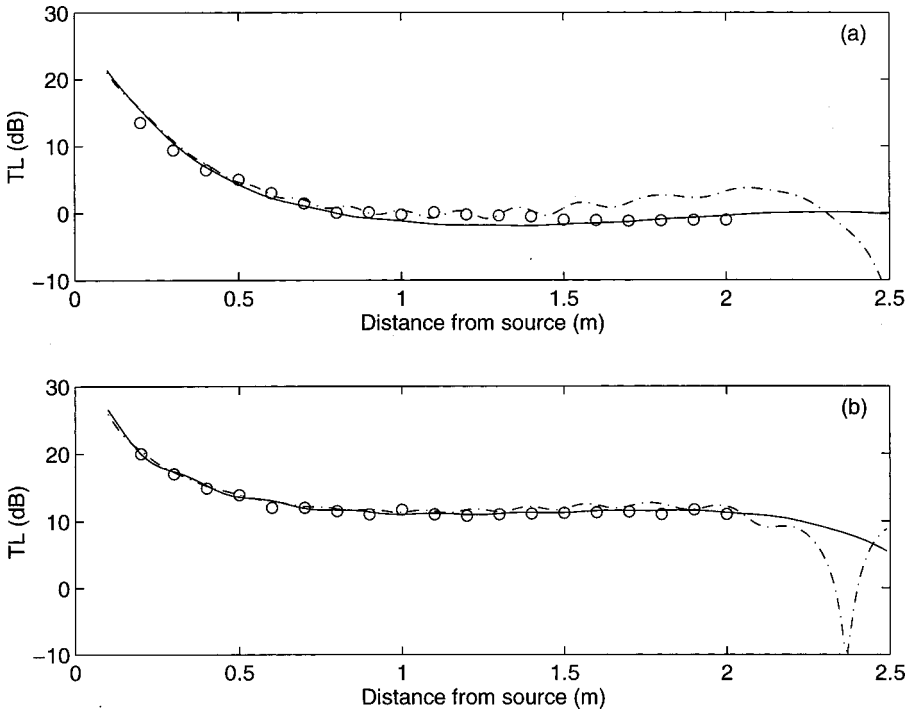

FIG. 5. Transmission loss due to a horizontal dipole source obtained at a frequency of 2915 Hz in a gradient with $R_c = 2.5$ m, over (a) a felt-covered concave surface with $z_s = z = 0.10$ m and (b) a rigid surface with $z_s = 0.02$ m and $z \sim 0.00$ m. Circles: measurements, solid curves: normal mode predictions for exponential profiles, dash-dotted curves: predictions for bilinear profiles.

kPa s m^{-2} and a rate of change of porosity with depth of 15 m^{-1} was found to be adequate in modeling the impedance of the felt-covered surface.

The hard and felt-covered surfaces allow sound propagation distances of up to 2.5 m in the direction perpendicular to the axis of the long cylinder. Propagation above the concave surface simulates propagation in the presence of a positive sound speed gradient with $R_c = 2.5$ m. The model was placed in an anechoic chamber which has an effective volume of $3 \times 3 \times 3$ m^3. A B&K 4311 1/4-in. condenser microphone was used to measure the sound pressure measurements. A Tannoy speaker type PD-30T, fitted with a tube of 3-cm internal diameter and 90 cm long, was used as the point monopole source. Two piezoceramic transducer discs with resonance frequencies of 2915 and 4350 Hz were found to be adequate as the dipole sources.[24] When the disc plane is vertical, it acts as a horizontal dipole source and, when it is horizontal, it acts as a vertical dipole source.

A PC-based maximum length sequence system analyzer (MLSSA) was used both as the signal generator for the sources and as the analyzer for subsequent signal processing. The impulse signal was analyzed using a half Blackman-Harris window and Fourier transformed.[25]

B. The sound field due to a monopole source over concave surfaces

The circles in Fig. 3(a) represent measurements for a frequency of 2915 Hz over the felt-covered concave surface. Both the source and receiver are at heights of 0.10 m. The solid curves represent predictions of the normal mode solution for the exponential profile and the dash-dotted curves represent predictions for the bilinear profile. The agreement between the measured data and the two curves is excellent out to 2.0 m (about 25 times the wave layer thickness, l_n) from the source. Beyond this distance, no reliable experimental data were obtained because the receiver is too close to the edge of the curved surface.

The circles in Fig. 3(b) represent measurements at 2915 Hz, with the receiver moved along the rigid surface ($z \sim 0.00$ m) and the source at a height of 0.02 m. Good agreement is found between measurements and predictions for the exponential profile (solid curves). However, there are considerable discrepancies between the measured data and the calculations for the bilinear profile (dash-dotted curves).

It is found that the predictions given by Eq. (7) for the exponential profiles agree with the experimental results obtained over the cylindrical concave surfaces. The agreement is better than that with the predictions given by Eq. (2) for the bilinear profiles. This accords with the general conclusion as with the propagation over cylindrical convex surfaces: the exponential sound speed profile is the most appropriate profile for the acoustic analogy.[3]

C. The sound field due to a horizontal dipole source over concave surfaces

The circles in Fig. 5(a) represent measurements at 2915 Hz over the felt-covered concave surface with both the source and receiver at heights of 0.10 m. The solid curves represent predictions for the normal mode solution from Eq. (18) for the exponential profile and the dash-dotted curves denote predictions for the normal mode solution from Eq. (15) for the bilinear profile. The agreement between the experimental data and the calculations for both profiles is very good out to 2.0 m (about 25 l_n) from the source.

In Fig. 5(b), we show experimental measurements (circles) at 2915 Hz, with the receiver moved along the rigid surface ($z \sim 0.00$ m) and the source height of 0.02 m. The calculations for the exponential profile are in excellent agreement with experimental data. However, there are consider-

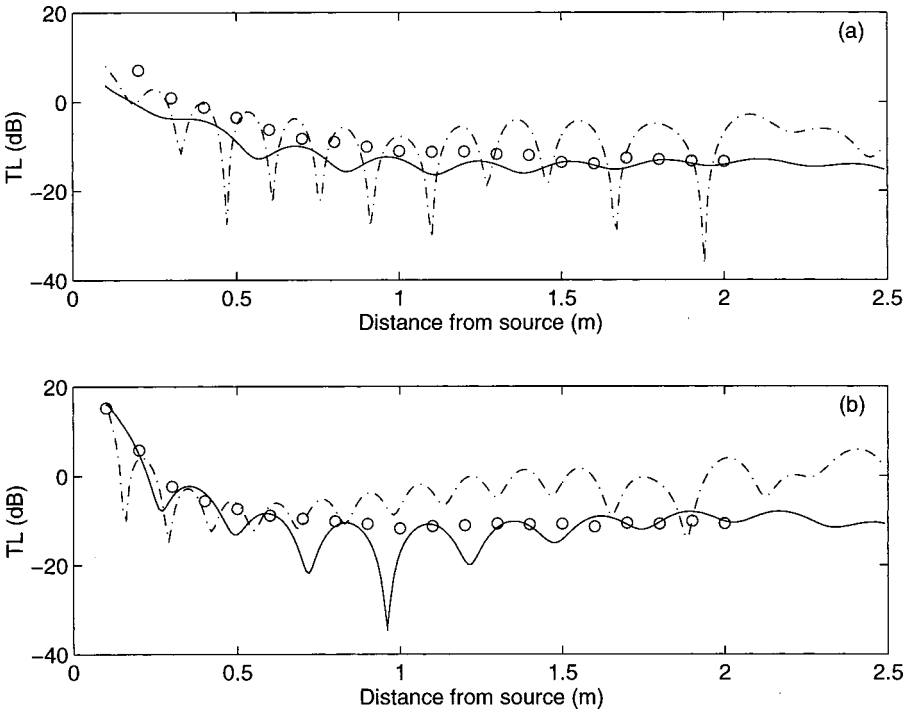

FIG. 6. Transmission loss due to a vertical dipole source at a frequency of 2915 Hz obtained in a gradient with $R_c = 2.5$ m, over (a) a felt-covered concave surface with $z_s = z = 0.10$ m and (b) a rigid surface with $z_s = 0.02$ m and $z \sim 0.00$ m. Circles: measurements, solid curves: normal mode predictions for exponential profiles, and dash-dotted curves: predictions for bilinear profiles.

able discrepancies between the measurements and the predictions for the bilinear profile (dash-dotted curves) at distances longer than 1.0 m from the source.

Comparing Figs. 3 and 5, it is noted that over concave surfaces, the sound field due to a horizontal dipole source is very similar to that due to a monopole source. This is consistent with what has been found in the case of convex surfaces.[7] Moreover, as was the case with a monopole source, the experimental measurements agree better with the predictions based on the exponential sound speed profile than those predicted according to the bilinear profile. Indeed, this should be the case because our mathematical analyses suggest that the conformal transformation of a cylindrical curve surface leads to the exponential rather than the bilinear sound speed profile.

D. The sound field due to a vertical dipole source over concave surfaces

The circles in Fig. 6(a) represent measurements at 2915 Hz over the felt-covered concave surface with both the source and receiver at heights of 0.10 m. The solid curves represent predictions from Eq. (19) for the exponential profile and the dash-dotted curves represent predictions from Eq. (16) for the bilinear profile. In contrast to the theoretical predictions, the experimental results lie on smooth curves (the dashed curves), which show similar trends to predictions of the monopole sound fields (cf. Fig. 3). Note that the scale in Fig. 6 is different from Figs. 3–5 in order to allow a better presentation of data.

Similar results have been obtained over the felt-covered concave surface. The circles in Fig. 6(b) represent data at 2915 Hz with the receiver moved along the rigid surface ($z \sim 0.00$ m) and the source at a height of 0.02 m.

It would appear that, for a vertical dipole source over a cylindrical concave surface, the agreement between the measurements and the normal mode predictions for both profiles is relatively poor. As mentioned earlier, the inaccuracy is due to the fact that the branch line contributions have been ignored in the normal mode solution. Nevertheless, relatively speaking, there is better agreement with the predictions based on the exponential profile than those based on the bilinear profile. It is of interest to note that, for the dipole source, use of the FFP predictions agrees reasonably well with experimental measurements (results are not shown for brevity).

IV. CONCLUSIONS

A normal mode solution has been developed for propagation in an exponential sound speed profile and used to predict the sound field diffracted by a cylindrical concave surface. Analytical expressions for dipole sources have been deduced directly from those for a monopole source.

A series of laboratory measurements of transmission loss have been conducted using a monopole source and horizontal or vertical dipole sources over cylindrical concave surfaces. The measurement results have been compared with normal mode predictions for both the exponential profile and the bilinear profile. For a monopole and a horizontal dipole, good agreement has been found between measurements and normal mode predictions using an exponential profile. However, the agreement is less satisfactory where the sound field was due to vertical dipole sources. The solution for a bilinear profile showed considerable disagreement with measurements in both monopole and horizontal dipole sound fields, and significant discrepancies from measurements in vertical dipole sound fields.

The predicted and measured transmission loss due to a horizontal dipole source, as a function of range, have been found to be close to those predicted for a monopole source.

However, the predicted transmission loss due to a vertical dipole source shows significant oscillations according to the normal mode solution.

ACKNOWLEDGMENTS

We thank the Open University Research Committee for financial support, Keith Attenborough for many useful discussions, and Shahram Taherzadeh for his latest version of the FFP. This work was supported in part by EPSRC Grant No. GR/L 15236. In the preparation of the revised manuscript, KML was partially supported by a Hong Kong Polytechnic University Research Grant, Project No. A-PB33.

[1] V. A. Fock, *Electromagnetic Diffraction and Propagation Problems* (Pergamon, Oxford, 1965).
[2] A. D. Pierce, *Acoustics: An Introduction to Its Physical Principles and Applications* (Acoustical Society of America, New York, 1989).
[3] A. Berry and G. A. Daigle, ''Controlled experiments of the diffraction of sound by a curved surface,'' J. Acoust. Soc. Am. **83**, 2047–2058 (1988) [see also A. Berry, ''Propagation of sound above a curved surface,'' J. Acoust. Soc. Am. Suppl. 1 **81**, S8 (1987)].
[4] Y. H. Berthelot and J. X. Zhou, ''Scale model experiments on the validity of the matched asymptotic expansions theory for sound diffraction by curved surfaces of finite impedance,'' J. Acoust. Soc. Am. **93**, 605–608 (1993).
[5] Y. H. Berthelot, ''A note on the acoustic penumbra behind a curved surface,'' J. Acoust. Soc. Am. **99**, 2428–2429 (1996).
[6] J. P. Chambers, R. Raspet, Y. H. Berthelot, and M. J. White, ''Use of the fast field program for predicting diffraction of sound by curved surfaces,'' J. Acoust. Soc. Am. **102**, 646–649 (1997).
[7] K. M. Li, Q. Wang, and K. Attenborough, ''Sound propagation over convex impedance surfaces,'' J. Acoust. Soc. Am. **104**, 2683–2691 (1998).
[8] M. Almgren, ''Simulation by using a curved ground scale model of outdoor sound propagation under the influence of a constant sound speed gradient,'' J. Sound Vib. **118**, 353–370 (1987).
[9] D. C. Pridmore-Brown and U. Ingard, ''Sound propagation into the shadow zone in a temperature-stratified atmosphere above a plane boundary,'' J. Acoust. Soc. Am. **27**, 36–42 (1955).
[10] D. C. Pridmore-Brown, ''Sound propagation in a temperature- and wind-stratified medium,'' J. Acoust. Soc. Am. **34**, 438–443 (1962).
[11] K. B. Rasmussen, ''Outdoor sound propagation under the influence of wind and temperature gradients,'' J. Sound Vib. **104**, 321–336 (1986).
[12] Y. Gabillet, H. Schroeder, G. A. Daigle, and A. L'Esperance, ''Application of the Gaussian beam approach to sound propagation in the atmosphere: Theory and experiments,'' J. Acoust. Soc. Am. **93**, 3105–3116 (1993).
[13] K. M. Li and Q. Wang, ''Analytical solutions for outdoor sound propagation in the presence of wind,'' J. Acoust. Soc. Am. **102**, 2040–2049 (1997).
[14] R. Raspet, G. Baird, and W. Wu, ''Normal mode solution for low-frequency sound propagation in a downward refracting atmosphere above a complex impedance plane,'' J. Acoust. Soc. Am. **91**, 1341–1352 (1992).
[15] A. D. Pierce and G. L. Main, in *Advances in Computer Methods for Partial Differential Equations 6*, edited by R. Vichnevetsky and R. Stepleman (IMACS, Rutgers Univ., New Brunswick, NJ, 1987), pp. 187–194.
[16] X. Di and K. E. Gilbert, ''The effect of turbulence and irregular terrain on outdoor sound propagation,'' in *Proceedings of 6th International Symposium on Long Range Sound Propagation* (1994), pp. 315–333.
[17] Q. Wang, ''Atmospheric refraction and propagation over curved surfaces,'' Ph.D. thesis, The Open University, UK, 1997.
[18] A. P. Dowling and J. E. Ffowcs Williams, *Sound and Sources of Sound* (Ellis Horwood, Chichester, 1983), p. 152.
[19] K. Attenborough, S. Taherzadeh, H. E. Bass, X. Di, R. Raspet, G. R. Becker, A. Gudesen, A. Chrestman, G. A. Daigle, A. L'Esperance, Y. Gabillet, K. E. Gilbert, Y. L. Li, M. J. White, P. Naz, J. M. Noble, and H. A. J. M. van Hoof, ''Benchmark cases for outdoor sound propagation models,'' J. Acoust. Soc. Am. **97**, 173–191 (1995).
[20] K. Attenborough, ''Ground parameter information for propagation modeling,'' J. Acoust. Soc. Am. **92**, 418–427 (1992).
[21] D. C. Strickler, ''Normal mode program with both discrete and branch line contributions,'' J. Acoust. Soc. Am. **61**, 856–861 (1974).
[22] S. N. Chandler-Wilde and D. C. Hothersall, ''Sound propagation above an inhomogeneous impedance plane,'' J. Sound Vib. **98**, 475–491 (1985).
[23] K. M. Li and Q. Wang, ''A BEM Approach to assess the acoustic performance of noise barriers in a refracting atmosphere,'' J. Sound Vib. **211**, 663–681 (1998).
[24] K. M. Li, S. Taherzadeh, and K. Attenborough, ''Sound propagation from a dipole source near an impedance plane,'' J. Acoust. Soc. Am. **101**, 3343–3352 (1997).
[25] D. D. Rife and J. Vanderkooy, ''Transfer-function measurement with Maximum-Length Sequences,'' J. Audio Eng. Soc. **37**, 419 (1989).

Shear-speed gradients and ocean seismo-acoustic noise resonances

Oleg A. Godin[a)]
School of Earth and Ocean Sciences, University of Victoria, P.O. Box 3055, Victoria, British Columbia V8W 3P6, Canada

David M. F. Chapman
Defence Research Establishment Atlantic, P.O. Box 1012, Dartmouth, Nova Scotia B2Y 3Z7, Canada

(Received 10 September 1998; revised 10 June 1999; accepted 16 June 1999)

Measurements of infrasonic seismo-acoustic ambient noise using an ocean bottom seismometer in shallow water have uncovered an unusual phenomenon: the noise spectrum of the horizontal component of seabed velocity shows several prominent peaks in the frequency range 0–8 Hz, whereas the noise spectra of both the acoustic pressure and the vertical component of seabed velocity show very weak or nonexistent features at the same frequencies. This structure is interpreted theoretically as resonances of shear waves of vertical polarization in the upper sediment layer, excited by the diffuse infrasonic sound field in the water. Independent interface wave dispersion studies at the site have revealed an approximate power-law profile of shear speed versus depth, having the form $c(z)=c_0 z^{\nu}$, with $c_0=21.5$ and $\nu=0.60$ (SI units). The theoretical development concentrates on exact analytic solutions for the resonance frequencies and wave field for power-law profiles and on the WKB and more advanced asymptotic solutions in the more general case of smooth shear-speed profiles with a power-law singularity. The experimental observations are interpreted in light of these analytic results, and are consistent with the previously determined power-law shear speed-profile. © *1999 Acoustical Society of America.*
[S0001-4966(99)04110-7]

PACS numbers: 43.20.Gp, 43.25.Gf, 43.28.Dm, 43.30.Ma [DLB]

INTRODUCTION

Shear waves in marine sediments have proved to be a significant factor in bottom-interacting ocean acoustics in some environments.[1] Specifically, Hughes *et al.*[2] have shown that shear wave resonances in a thin sediment layer over a rock substrate have a profound effect on acoustic reflection loss and shallow water acoustic transmission loss. In that study, it was adequate to model the thin sediment layer as a single homogeneous layer with average properties; however, others have argued that gradients in material properties cannot be ignored.[3–5] This paper presents experimental evidence of a seabed resonance phenomenon involving shear waves in surficial sediments for which the theoretical explanation depends critically on the shear-speed gradient; the paper also proposes a wave-theoretical model for the phenomenon. The experiment consisted simply of measuring the seismo-acoustic ambient noise field at the seabed using an ocean bottom seismometer (OBS). The OBS was equipped with geophones for measuring the particle velocity at the top of the sediment layer and a hydrophone for measuring the pressure in the water layer just above. Interestingly, we observed large resonance effects on the horizontal geophone, but these resonances were absent on the hydrophone. In this paper, we are not so concerned with the seismo-acoustic noise field itself, its source mechanisms, or modeling its spectrum; these topics are covered in a good review by Orcutt *et al.*[6] and a recent monograph by Kibblewhite and Wu.[7] We are more interested in how the noise field interacts with the seabed, and the insight this provides into the seismo-acoustics of the seafloor.

A preliminary computational investigation[8] of this phenomenon using a stacked-layer geoacoustic model approximating a continuous power-law shear-speed profile of the form $c(z)=c_0 z^{\nu}$ provided encouraging results. However, we found that results converged slowly as the number of layers increased. It appears that prohibitively large numbers of layers would be necessary to adequately model the physics of such a profile using this method. Accordingly, in this paper we abandon the stacked-layer approach in favor of analytic treatment, returning to the fundamental equations of motion of acoustic waves in a continuously stratified elastic medium. These equations are difficult to solve exactly, but the low shear speeds present in the upper sediment layer of the experimental site admit a simplifying assumption that opens an avenue for an approximate analytical solution of the equations of motion. The analytic results provide characteristic equations for the expected resonance frequencies. Numerical solution of the resonance conditions is straightforward, and provides much insight into the observed ambient noise structure.

In Sec. I we present the experimental data showing the seafloor noise resonances and a description of the environment. In Sec. II we relate the noise resonances to normal modes of *P-SV* waves and indicate the small parameters of the problem that allow its analytical consideration. It is es-

[a)]Also affiliated to: Acoustic Wave Propagation Laboratory, P. P. Shirshov Oceanography Institute of the Russian Academy of Sciences, Moscow 117851, Russia.

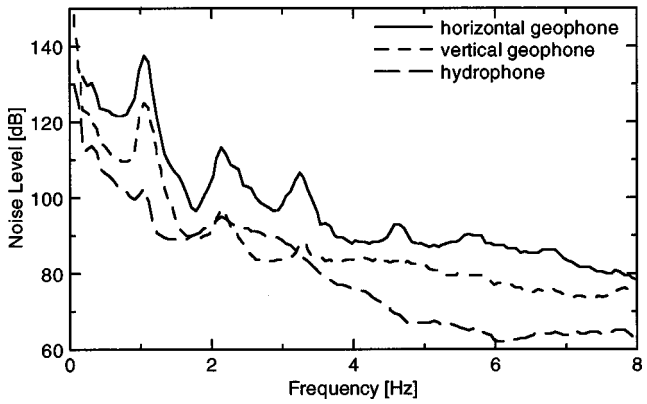

FIG. 1. Seismo-acoustic ambient noise resonances measured using an ocean bottom seismometer in a shallow-water site on the Scotian shelf. (Noise level units are dB *re*: 1 $(\text{nm/s})^2$/Hz for the geophones and dB *re*: 1 μPa^2/Hz for the hydrophone.)

tablished in Sec. III that analysis of the normal modes at normal incidence provides sufficient accuracy to determine resonance frequencies. An exact solution for shear wave normal modes in a layer with power-law profile of rigidity is obtained and analyzed in Sec. IV. Effects of deviations from the power law are addressed in Sec. V. We provide some computational results in Sec. VI, to illustrate some of the analytically derived conclusions. Finally, in Sec. VII, we examine the interplay of the various model parameters, the most significant being the profile of shear speed versus depth in the sediment.

I. EXPERIMENT: RESONANCES IN SEISMO-ACOUSTIC AMBIENT NOISE

In 1993, the Defence Research Establishment Atlantic (DREA) built and tested an OBS to investigate the geophone as a sensor for ocean acoustics experiments.[9–11] Many experimental sites were visited on several cruises, including a site on the Scotian Shelf not far from the Eastern Shore coastal region of Nova Scotia. Seismo-acoustic propagation, ambient noise, and interface wave experiments were conducted at this site. The interface wave dispersion data (i.e., group speed versus frequency) were inverted to produce a shear speed versus depth profile in the seabed.[12] The site is located in a basin whose water depth is about twice as deep as the surrounding sand banks, and whose surficial sediment is composed of ponded layers of clay and silt over a harder material, probably glacial till.[12,13] Shear velocity in the hard sediment is estimated to be 900–1000 m/s. The water depth is 156 m and the clay/silt layer is about 25.5 m thick. The shear-speed profile was modeled as a stack of homogeneous sub-layers, but the resulting staircase could be viewed as an approximation to a continuous power-law profile of the form $c(z)=c_0 z^{\nu}$, with $c_0=21.5$ and $\nu=0.60$ (SI units), the shear speed varying from 21.5 m/s at 1 m depth to 150 m/s at the top of the till layer at 25.5 m depth.

Of particular interest in this paper are the resonance features in the seismo-acoustic ambient noise measured by the OBS on the seabed, shown in Fig. 1. We observed these features with the DREA OBS on two visits, but we initially saw them with a borrowed OBS of different design; this is persuasive evidence that the phenomenon is not an instrument effect. The resonances in the noise on the horizontal geophone are quite noticeable: the first five peaks are at 1.06, 2.16, 3.24, 4.64, and 5.70 Hz, the sequence closely approximating a harmonic progression with a fundamental frequency of 1.11 ± 0.04 Hz. (Later we show that the nonharmonic progression $1.18n-0.21$ is a better fit to this sequence.) Only one horizontal geophone channel is shown; the others are similar. The vertical geophone channel displays similar features, but they are much weaker, showing only the first three peaks. On the hydrophone channel, there is only a suggestion of a resonance at the fundamental frequency. We have not observed such resonances at other sites we visited with the DREA OBS; however, Dorman *et al.*[14] published OBS noise spectra from an entirely different location showing noticeable peaks on the horizontal geophone in the same frequency band (with a smoother and quieter noise spectrum on the vertical geophone), but they did not remark on the features.

The cause of these noise resonances was not immediately evident. At first, we suspected them to be instrument related, but their appearance at the same site at different times with different instruments convinced us that they are environmental features. We now believe that these peaks in the horizontal motion are caused by vertically polarized shear waves resonating in the clay/silt layers. At this time, we do not have a complete model of the phenomenon, but the following sections will examine seismo-acoustic propagation in this environment and the role of the shear-speed profile in placing the modeled resonances at the appropriate frequencies.

II. QUALITATIVE CONSIDERATIONS AND APPROACH

Our hypothesis to explain the observed features of the seismo-acoustic noise field assumes that the water column supports a diffuse infrasonic noise field that is horizontally isotropic, but which may have some vertical directionality. This noise field interacts with the elastic seabed, generating vertically polarized shear waves (*SV* waves). Previous analysis of similar problems suggests that the strongest generation of shear waves would occur at the large impedance contrast at the sediment/substrate boundary.[15] Subsequent multiple transits of the sediment layer by the shear waves give rise to resonances at frequencies that favor constructive interference. (Note that the lower boundary is necessary both to generate the shear waves and to provide a distinct layer thickness to form the resonances.) According to Snell's law, for very slow shear speeds the sediment-borne *SV* waves excited by water-borne sources would travel in an almost vertical direction, insensitive to the incidence angle of the wave in the water. Also, for very low shear speeds, there would be a negligible effect on the bottom reflection coefficient, hence we would not expect the hydrophone to register large resonance effects. However, the geophones of an OBS are capable of sensing the underlying seabed motion associated with shear waves, so resonances would be seen in the

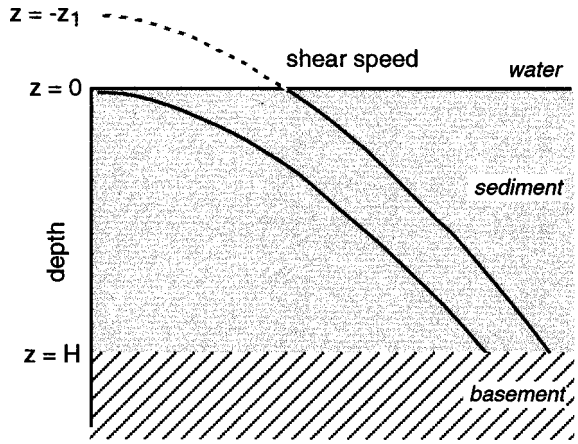

FIG. 2. Simple and truncated power-law shear-speed profiles in the sediment layer.

geophone ambient noise, although they should be more noticeable on the horizontal geophone signals than on the vertical geophones, as we explain below.

It is the low shear-wave velocities that are responsible for predominantly horizontal particle motion in vertically polarized shear waves. According to the Snell's law, sound waves incident from the water column give rise to shear waves that propagate almost vertically. Being transverse waves, these create almost-horizontal particle displacement. In addition, the shear-wave particle motion at the water/sediment boundary is the sum of an upward-traveling incident shear wave and a downward-traveling reflected shear wave. For low shear speeds, the shear wave is almost perfectly reflected with a phase inversion. This gives rise to a net displacement that is large in the horizontal direction and further reduced in the vertical direction.

Conventionally, numerical simulations of acoustic propagation in a stratified elastic medium are performed by subdividing the inhomogeneous layer into a number of homogeneous sub-layers. Although layer-stack models are remarkably versatile, they ultimately need a large number of sub-layers to model a depth interval where the shear velocity is small but its gradient is large, which is a characteristic feature of the environment at hand. Moreover, as noted in Ref. 5, ''the layer-stack method presents no expression that yields insight into the effects being studied.'' In this paper, we abandon the assumption of piecewise constant medium parameters and consider the upper portion of the sediment to be a *continuously stratified* solid. The shear modulus of marine sediments is small in the vicinity of the water-sediment interface and may vanish at the interface. Then it is natural to assume a power-law dependence

$$\mu=\rho_0 c_0^2 (z+z_1)^{2\nu}, \quad \nu>0, \quad z_1 \geqslant 0 \tag{1}$$

of shear modulus on depth in the upper portion of the sediment column. Here ρ_0 is a constant with the dimensions of density ρ and $c_0=\text{const}$. There is both theoretical and empirical evidence in support of this assumption.[5,12,16–18] At the experimental site, a strong case for the power-law geoacoustic profile is made by Osler and Chapman[12] and by Chapman.[8] Figure 2 illustrates the model, and depicts the simple power-law profile ($z_1=0$) as well as a truncated power-law profile ($z_1>0$) formed by offsetting the singularity of the profile. For the simple power-law profile, note that when $\nu<1/2$, $\nabla\mu$ tends to infinity when μ tends to zero. This makes the approach of Robins,[4,19] who assumes slow variation of μ and discards terms with μ derivatives, inapplicable to the problem at hand.

Mathematically, an analytic treatment of the problem on noise resonances is made possible by the existence of two small parameters. The first one, Δ_1, is the ratio of Lame constants μ and λ in the soft sediment. At the experimental site it does not exceed 0.007. The second small parameter, Δ_2, is the ratio of the horizontal component of wave vector to the shear-wave wave number in the soft sediment. It follows from the Snell's law that, if the ambient noise sources are in the water column or at the ocean surface, Δ_2 is limited from above by the ratio of shear-wave velocity in the soft sediment to the sound speed in the water. If the ambient noise sources are situated deep in the bottom, Δ_2 does not exceed the ratio of shear-wave velocities in soft and hard sediments. At the site considered, for the second small parameter we have, respectively, upper bounds of 0.09 and 0.14. Related to Δ_2 is another small parameter, T, defined as the product of density and shear velocity ratios in soft and hard sediments at their interface. In this case, it is on the order of $T=0.1$.

At normal incidence ($\Delta_2=0$) and with $T=0$, the interfaces with the water and the hard sediment act like a free and a rigid boundary for shear waves in soft sediment, and there exist normal modes of shear waves with real frequencies f_n. At oblique incidence and/or when T is finite, the eigenfrequencies take on complex values because of radiation losses into the water and the hard sediment. However, variations in the eigenfrequencies compared to the ideal case $\Delta_2=T=0$ are small, including their imaginary parts, as long as Δ_2 and T are small. In the problem of broadband wave reflection from the sediment layer, the existence of complex eigenfrequencies near the real axis leads to frequency resonances. This can be demonstrated in several ways. First, compare the reflection problem for the continuous wave and the eigenvalue problem. In terms of the amplitudes of the four linearly independent *P-SV* waves in the layer, each problem reduces to a linear algebraic system. The only difference is, the algebraic system is homogeneous in the eigenvalue problem (free vibrations) but has a nonzero right hand side due to the incident wave in the reflection problem (forced vibrations). When the frequency f of the incident wave approaches an eigenfrequency, the determinant of the linear system tends to zero and, hence, solutions of the inhomogeneous system generally tend to infinity. Of course, with CW excitation, the amplitudes of the resonance peaks remain bounded because the eigenfrequencies are slightly complex.

For a more graphic explanation, consider a continuous plane sound wave incident on the layer $0<z<H$ of soft sediment from a fluid half-space $z<0$. Let $z=H$ be a rigid boundary. If the horizontal displacement in the incident wave is $U^{(in)}(z)$, then the horizontal displacement in P waves at $z=H$ is proportional to $U^{(in)}(H)$. (The coefficient of proportionality is 2 when P wave reflection above the boundary $z=H$ is negligible.) Let $u(z,f)$ stand for the horizontal dis-

placement in S waves as a function of depth and frequency. From the boundary condition of no horizontal displacement at $z=H$ it follows that $u(H,f)=\text{const}\,U^{(in)}(H)$. (The constant equals -2 when P wave reflection above the boundary $z=H$ is negligible.) On the other hand, $u(z,f)$ is proportional to one of the two linear-independent solutions for shear waves, say, $U^{(s)}(z,f)$ that obeys the boundary condition of no horizontal traction at $z=0$. Therefore, $u(z,f)=u(H,f)U^{(s)}(z,f)/U^{(s)}(H,f)=\text{const}\,U^{(in)}(H)U^{(s)}(z,f)/U^{(s)}(H,f)$. At an eigenfrequency $f=f_n$, the shear wave obeys the boundary conditions at *both* interfaces $z=0$ and $z=H$. Hence, $U^{(s)}(H,f_n)=0$. We now see that $u(0,f)$ tends to infinity when f tends to f_n and that resonant peaks in horizontal displacement are related to normal modes of shear waves. In reality, the height of the resonance peaks is large but limited because of the small shift of the eigenfrequency away from the real axis.

Consequently, although no normal mode is actually excited at plane-wave reflection, to determine the frequencies of noise resonances it is sufficient to study the eigenfrequencies of P-SV waves in the soft sediment layer. Prediction of the heights of the peaks is a more subtle issue as the heights depend on both imaginary parts of the eigenfrequencies and the noise power spectrum and directionality. In this paper, we will concentrate on the resonance condition, which determines positions of the resonance frequencies, leaving analysis of the heights of the peaks for further research.

III. THE EFFECT OF THE ANGLE OF INCIDENCE ON THE RESONANCE FREQUENCIES

Consider elastic P-SV waves in a stratified fluid/solid medium. The medium is infinite or has horizontal ideal (free or rigid) horizontal boundaries. The solid is assumed to be locally isotropic. Let $\mathbf{u}^{(\alpha)}$, $\sigma_{jk}^{(\alpha)}$, $\mathbf{q}^{(\alpha)}=(q_1^{(\alpha)},q_1^{(\alpha)},0)$, and ω_α be the displacement, stress tensor, horizontal wave vector, and frequency corresponding to two normal modes; $\alpha=1,2$; $j,k=1,2,3$. The fields of the normal modes are orthogonal in fluid/solid media. We express the orthogonality relation in the form[20]

$$\int dz[(\omega_1^2-\omega_2^2)\rho u_j^{(1)}u_j^{(2)} + i(q_\alpha^{(1)}-q_\alpha^{(2)})(\sigma_{j\alpha}^{(1)}u_j^{(2)}-\sigma_{j\alpha}^{(2)}u_j^{(1)})]=0. \quad (2)$$

Here the integration is performed throughout the vertical extent of the medium; summation over repeated indices is implied.

The orthogonality relation enables us to relate eigenfrequencies corresponding to two different values of the wave vector. At normal incidence, shear and compression waves are known to be uncoupled in layered solids (Ref. 21, Sec. 1.3). Let $\mathbf{q}^{(1)}=0$ (normal incidence), $\mathbf{q}^{(2)}=(q,0,0)$. Assume that the normal mode considered is a shear wave at $\mathbf{q}=0$. (It may have a P component at $\mathbf{q}\neq 0$.) Hence, $\mathbf{u}^{(1)}=(u_1^{(1)},0,0)$. According to the Hooke's law $\sigma_{jk}=\lambda\delta_{jk}\partial u_s/\partial x_s+\mu(\partial u_j/\partial x_k+\partial u_k/\partial x_j)$, where $j,k,s=1,2,3$; $\sigma_{j1}^{(1)}$ is nonzero only when $j=3$. Then one obtains from Eq. (2)

$$\omega^2(q)-\omega^2(q=0)=-iq\frac{\int dz[\sigma_{13}^{(1)}u_3^{(2)}-\sigma_{11}^{(2)}u_1^{(1)}]}{\int dz\rho u_1^{(1)}u_1^{(2)}}. \quad (3)$$

Of course, both eigenfrequencies in the left side are real in the absence of dissipative processes for normal modes in a solid layer with ideal boundaries and for proper normal modes in an unbounded medium. When the depth dependence of horizontal displacement is chosen to be real-valued, the integral in numerator on the right side of Eq. (3) is pure imaginary. As $u_3^{(2)}$ and $\sigma_{11}^{(2)}$ tend to $u_3^{(1)}$ and $\sigma_{11}^{(1)}$ and, hence, vanish at $q\to 0$, it follows from Eq. (3) that the eigenfrequency increment is proportional to q^2 for small q.

For comparison, consider the analogous expressions for shear waves of horizontal polarization (*SH* waves). These waves are not coupled to P-SV waves in layered solids and have zero vertical displacement at all angles of incidence. The horizontal component of displacement obeys the wave equation (Ref. 21, Sec. 1.3)

$$\frac{\partial^2 u}{\partial z^2}+\frac{1}{\mu}\frac{\partial\mu}{\partial z}\frac{\partial u}{\partial z}+(k^2-q^2)u=0,\quad k=\frac{\omega}{c},\quad c=\sqrt{\frac{\mu}{\rho}}, \quad (4)$$

where k is the shear-wave wave number. From Eq. (4) it follows [cf. Eq. (3)]

$$\omega^2(q)-\omega^2(q=0)=q^2\frac{\int dz\mu(z)u(q,z)u(0,z)}{\int dz\rho(z)u(q,z)u(0,z)}. \quad (5)$$

Expressing the integrals on the right side through depth-averaged values of shear modulus and density, one has

$$\omega^2(q)/\omega^2(q=0)=1+q^2\langle\mu\rangle/\omega^2(q=0)\langle\rho\rangle=1+O(q^2/K^2) \quad (6)$$

when $q\ll K$. Here K is a representative value of shear-wave wave number. Thus the relative change of the eigenfrequency of *SH* waves due to the variation of the horizontal wave number is of the order q^2/K^2 when q is small compared to the shear-wave wave number.

The same conclusion is valid for waves of vertical polarization as well. It can be demonstrated in two different ways. First, one can merely note that shearlike waves are supported even by an incompressible solid. Therefore, there exist elastic waves for which all the stress tensor components remain finite at $\lambda\to\infty$. In other words, all the stress tensor components are proportional to μ in these shearlike waves. Then $\sigma_{11}^{(2)}$ is on the order of $\mu q u_1^{(1)}$. Noting also that $\sigma_{13}^{(1)}$ and $u_3^{(1)}$ are on the order of $\mu k u_1^{(1)}$ and $q u_1^{(1)}/k$, respectively, one obtains the estimate Eq. (6) for *vertically* polarized waves from Eq. (3).

Alternatively, for a more formal derivation, one can apply the method of multi-scale expansions. Formally substituting $\epsilon^{-2}\lambda$ for λ and ϵq for q in the vector wave equation for P-SV waves (Ref. 21, Sec. 1.3.3) and developing the displacement vector into a power series in the formal small parameter ϵ, after equating coefficients at similar powers of ϵ, one arrives at a system of equations for zero, first, and higher order contributions to the displacement. For the sake of brevity, we omit details of the analysis and present the relevant findings only. It turns out that when $\epsilon\ll 1$, that is, in solids with $\mu\ll\lambda$, there are two types of elastic waves.

Waves of different type are uncoupled to leading order in ϵ. When $\mathrm{div}\,\mathbf{u}$ is not small, the waves are essentially compressional, and shear rigidity results in small corrections only. For the other wave type, $\mathrm{div}\,\mathbf{u}=O(\epsilon^2)$, that is, the displacement is almost purely rotational, as in a shear wave. Then, according to Hooke's law, $\sigma_{13}^{(1)}u_3^{(2)}$ and $\sigma_{11}^{(2)}u_1^{(1)}$ are on the order of $\mu q u_1^{(1)}$, and the estimate Eq. (6) follows from Eq. (3).

An important corollary of this result is that the relative variation in the frequency of the eigenmode due to variation of the angle of incidence is of the order of the square of the small parameter Δ_2. Therefore, under the environmental conditions at the experimental site, the spread of eigenfrequencies of a given normal mode due to various possible (real) incidence angles results in broadening of the respective spectral line in the power spectrum by a few percent at most. This is much less than width of spectral lines observed in the seismo-acoustic ambient noise. Hence, to determine eigenfrequencies it is sufficient to consider the case of the normal incidence only. At normal incidence *SV* and *SH* waves become indistinguishable.

IV. EXACT SOLUTIONS FOR THE POWER-LAW PROFILE

A. General solution

Consider elastic waves in a continuously stratified solid with constant density and a power-law profile Eq. (1) of the shear modulus with $z_1=0$. Written in terms of $\psi=\mu^{1/2}u$, the wave equation (4) for waves *SH* becomes the Helmholtz equation

$$\frac{d^2\psi}{dz^2}+K^2\psi=0,$$
$$K^2=\frac{\rho\omega^2}{\mu}-q^2+\left(\frac{1}{2\mu}\frac{d\mu}{dz}\right)^2-\frac{1}{2\mu}\frac{d^2\mu}{dz^2} \tag{7}$$

with effective wave number K. We are interested in the case $q=0$, when the same wave equation applies to *SV* waves.

In connection with reflection of acoustic and electromagnetic waves, exact solutions to the Helmholtz equation with effective wave number squared

$$K^2(z)=\tfrac{1}{4}b^2(z+z_1)^2[b^{-2}-4m^2+4lQ(z+z_1)^b - Q^2(z+z_1)^{2b}] \tag{8}$$

have been studied in Ref. 21, Sec. 3.3, and Ref. 22. Such an equation is solvable in terms of confluent hypergeometric functions (Ref. 23, Chap. 13), the general solution being

$$\psi(z)=\eta^{(1-b)/2b}[A_1M_{l,m}(\eta)+A_2W_{l,m}(\eta)],$$
$$\eta=Q(z+z_1)^b, \tag{9}$$

where $M_{l,m}$ and $W_{l,m}$ are Whittaker functions and $A_{1,2}$ are arbitrary constants. Note that if $l=0$ the Whittaker functions reduce to the simpler and more frequently used cylindrical functions.

At $q=0$, the effective wave number in Eq. (7) for shear waves is the same as in Eq. (8) if parameters in Eq. (8) are chosen in the following way:

$$l=0,\quad m=\pm(1/2-\nu)/(1-\nu),\quad b=1-\nu,$$
$$Q=2i\omega c_0^{-1}/(1-\nu),\quad z_1=0. \tag{10}$$

Hence, at normal incidence and $\nu\neq1$, the exact solution of the wave equation for shear waves is given by Eqs. (9) and (10). Taking into account the relations (Refs. 21, Sec. 3.3; 23, Chap. 13) between cylindrical functions and the Whittaker functions, it is convenient to re-write Eq. (9) as

$$u=z^{1/2-\nu}\left[B_1J_m\left(\frac{\omega}{c_0(1-\nu)}z^{1-\nu}\right)+B_2Y_m\left(\frac{\omega}{c_0(1-\nu)}z^{1-\nu}\right)\right],$$
$$m=\frac{2\nu-1}{2(1-\nu)}, \tag{11}$$

where J_m and Y_m are the Bessel functions of the first and the second kind. Note that m is a monotonically increasing function of ν, and it varies between $-\frac{1}{2}$ and plus infinity when ν increases from 0 to 1. By using the Bessel equation (Ref. 23, Chap. 9), to which J_m and Y_m are solutions, it is straightforward to check by direct substitution that $u(z)$ as defined in Eq. (11) is a solution of the wave equation (4). We note in passing that exact closed-form solutions of the wave equation (7) can be also obtained from Eqs. (8) and (9) in the case of *oblique* incidence $(q\neq0)$, but only for the particular values ($\nu=-1$, 0, $\frac{1}{2}$, and 1) of the parameter ν.

B. A layer with ideal boundaries

Consider a sediment layer $0<z<H$ with constant density, a power-law profile Eq. (1) for the shear modulus, $z_1=0$, and the following boundary conditions (BCs) imposed on the layer boundaries:

$$\sigma_{13}=0\quad(z=0), \tag{12}$$

$$u_1=0\quad(z=H). \tag{13}$$

Physically, the BC at $z=0$ corresponds to the boundary with the (inviscid) fluid; the BC at $z=H$ corresponds to a rigid boundary.

From Hooke's law and the limiting forms of the Bessel functions for small arguments

$$J_m(\eta)=\Gamma^{-1}(1+m)(\eta/2)^m[1+O(\eta^2)],$$
$$Y_0(\eta)=2\pi^{-1}\ln z+O(1),$$
$$Y_M(\eta)=-\pi^{-1}\Gamma(M)(\eta/2)^{-M}[1+O(\eta^2)]+o(1),\quad M>0, \tag{14}$$

it follows that one should put $B_2=0$ in (11) to satisfy BC Eq. (12). Hence, the particle displacement in a normal mode is given by

$$u=B_1z^{1/2-\nu}J_m\left(\frac{\omega}{c_0(1-\nu)}z^{1-\nu}\right), \tag{15}$$

where B_1 is an amplitude constant. The displacement is bounded throughout the layer and is nonzero at the interface

$z=0$. The BC Eq. (13) immediately gives the resonance condition

$$J_m\left(\frac{\omega}{c_0(1-\nu)}H^{1-\nu}\right)=0. \tag{16}$$

Using the common designation $j_{m,n}$ (Ref. 23, Sec. 9.5) for the nth positive zero of the function $J_m(x)$, one has from the dispersion relation Eq. (16) the explicit expression

$$f_n=(2\pi)^{-1}c_0(1-\nu)H^{\nu-1}j_{m,n} \tag{17}$$

for the nth resonance frequency, $n=1,2,...$ All the resonance frequencies are real. It follows from the properties of the Bessel function zeros (Ref. 23, Sec. 9.5) that for a given ν the sequence $\{f_n\}$ is not generally equally spaced: $f_{n+1}-f_n \neq f_n-f_{n-1}$, but rapidly becomes so as n increases. At $n \gg 1+m^2$

$$f_n=\frac{c_0(1-\nu)}{2\pi H^{1-\nu}}\beta\left[1-\frac{4m^2-1}{8\beta^2}+O\left(\frac{1}{\beta^4}\right)\right],$$
$$\beta=\pi\left(n+\frac{m}{2}-\frac{1}{4}\right). \tag{18}$$

For instance, at $m=1$, substituting 1 for the square brackets in Eq. (18) results in errors in f_n that are less than 2.5% for the fundamental (lowest) mode ($n=1$) and less than 1% at $n\geqslant 2$. According to Eq. (18), the sequence of the resonance frequencies can only be spaced equally if $m^2=1/4$. That is, among the power-law profiles (other than the trivial case of μ constant) only the one with $\nu=\frac{2}{3}$ can possibly result in an equi-spaced set of resonance frequencies. As will be shown in a moment, in the case $\nu=\frac{2}{3}$, the sequence of the resonance frequencies is indeed equi-spaced and, furthermore, harmonic.

The general expressions Eqs. (15) and (17) for the resonance frequencies and field of the normal mode can be further simplified when m takes the half-integer values $m=M+\frac{1}{2}$ and, hence, $\nu=1-(2M+1)^{-1}$, where $M=0,1,2,...$ The Bessel functions of half-integer order are proportional to the spherical Bessel functions (Ref. 23, Chap. 10), which are in turn a combination of elementary functions. In particular,

$$J_{1/2}(\eta)=(2/\pi\eta)^{1/2}\sin\eta,$$
$$J_{3/2}(\eta)=(2/\pi\eta)^{1/2}(\eta^{-1}\sin\eta-\cos\eta), \tag{19}$$
$$J_{-1/2}(\eta)=-Y_{1/2}(\eta)=(2/\pi\eta)^{1/2}\cos\eta.$$

According to Eq. (19), at $\nu\to 0$ Eq. (15) gives the solution $u=\text{const}\cos(\omega z/c_0)$ which was certainly anticipated for the homogeneous layer with the boundary condition Eq. (12). At $\nu=\frac{2}{3}$, one has from Eqs. (15) and (19)

$$u=B_1\sqrt{\frac{2c_0}{3\pi\omega}}z^{-1/3}\sin\left(\frac{3\omega}{c_0}z^{1/3}\right). \tag{20}$$

Note that in this case the mode phase (argument of the sine) becomes zero at $z=0$ and not $\pi/2$, as one might expect by assuming similarity to the case of homogeneous layer. From Eq. (18) and BC Eq. (13) it is clear that the resonance frequencies form the harmonic sequence $f_n=\text{const}\cdot n$ in this case.

At $\nu=4/5$ it follows from Eqs. (15) and (19) that

$$u=B_1(2/\pi)^{1/2}(5\omega/c_0)^{-3/10}\eta^{-3}(\sin\eta-\eta\cos\eta),$$
$$\eta=5\omega c_0^{-1}z^{1/5}. \tag{21}$$

Now the normal mode field contains both sine and cosine components, with comparable and nearly mutually annihilating values at $z\to 0$.

C. Truncated power-law profile

Consider now a somewhat more general geoacoustic model. We retain the assumptions made in Sec. IV B about the problem geometry, constant density, boundary conditions, and normal incidence, but take z_1 to be positive in Eq. (1). The model will be referred to as *the truncated power-law profile*. Of primary interest to us is the effect that small but nonzero $\mu(0)$ has on the resonance frequencies.

The general solution of the wave equation is still given by Eq. (11) if $z+z_1$ is substituted for z in the right side of that equation. Using the identities

$$mJ_m(\eta)\mp\eta\,dJ_m(\eta)/d\eta=\eta J_{m\pm1}(\eta),$$
$$mY_m(\eta)\mp\eta\,dY_m(\eta)/d\eta=\eta Y_{m+1}(\eta), \tag{22}$$

BCs Eqs. (12) and (13) can now be written as

$$B_1J_{m+1}(a)+B_2Y_{m+1}(a)=0,\quad a=\omega z_1^{1-\nu}/c_0(1-\nu), \tag{23a}$$

$$B_1J_m(b)+B_2Y_m(b)=0,\quad b=\omega(H+z_1)^{1-\nu}/c_0(1-\nu). \tag{23b}$$

By requiring that these simultaneous equations have a nontrivial solution with respect to amplitude constants $B_{1,2}$, one obtains the resonance condition

$$J_{m+1}(a)Y_m(b)-J_m(b)Y_{m+1}(a)=0 \tag{24}$$

for shear waves in the ''truncated'' layer. Note that in Eq. (24) $b>a$ and $b\gg a$ when $z_1\ll H$. Using the limiting forms Eq. (14) of the Bessel function for small arguments, it is easy to verify that in the limit $z_1\to 0$ Eq. (24) reduces to the dispersion relation Eq. (16) for a nontruncated layer.

Consider two special cases:

1. The case $a\ll 1$

According to Eq. (23a), this is the case when z_1 or, in other words, the shear-wave velocity near the upper boundary of the sediment layer is sufficiently small. (As will become clear soon, the exact meaning of ''sufficiently'' depends on the mode number.) The inequality $z_1\ll H$ is a necessary, but generally not a sufficient condition for a to be much smaller than unity at a resonance frequency.

Note that $1+m>0$ for all possible ν values. It follows from Eq. (14) that $J_{m+1}(a)/Y_{m+1}(a)$ tends to zero when a tends to zero. Therefore $J_m(b)$ in the dispersion relation Eq. (24) is small when $a\ll 1$. Hence, b is close to a zero $j_{m,n}$ of the Bessel function. Using small argument forms for $J_{m+1}(a)$ and $Y_{m+1}(a)$ and developing $J_m(b)$ and $Y_m(b)$ into Taylor series in the vicinity of $b=j_{m,n}$, after some algebra one obtains from Eq. (24)

$$f_n=\frac{c_0(1-\nu)j_{m,n}}{2\pi(z_1+H)^{1-\nu}}\left[1+d_{m,n}\frac{z_1}{z_1+H}+O\left(\left(\frac{z_1}{z_1+H}\right)^{\gamma}\right)\right], \tag{25}$$

where $\gamma=\min(2,3-2\nu)$,

$$d_{m,n}=-\frac{2^{-2(m+1)}\pi j_{m,n}^{2m+1}}{(m+1)\Gamma^2(m+1)}\frac{Y_m(j_{m,n})}{J_m^l(j_{m,n})}, \tag{26}$$

and prime denotes derivative of the function with respect to its argument. The expression for $d_{m,n}$ can be simplified in some cases. In particular, using Eq. (19) one finds $d_{1/2,n}=\pi^2n^2/3$ at $\nu=\frac{2}{3}$. At arbitrary m and large n the simple expression

$$d_{m,n}\approx\frac{\pi}{2(m+1)\Gamma^2(m+1)}\left[\frac{\pi}{2}\left(n+\frac{m}{2}-\frac{1}{4}\right)\right]^{2m+1} \tag{27}$$

is obtained by noting (Ref. 23, Sec. 9.2) $J_m'(j_{m,n})/Y_m(j_{m,n})=-1+O(n^{-2})$. Although Eq. (27) has been derived for large n, it turns out to be rather accurate even for $n=2$ when $m\lesssim 1$.

Written in terms of the ratio of shear-wave velocities at the top and bottom of the sediment layer, Eq. (25) becomes

$$f_n=\frac{c_0(1-\nu)j_{m,n}}{2\pi(z_1+H)^{1-\nu}}\left[1+d_{m,n}\left(\frac{c(0)}{c(H)}\right)^{1/\nu}+O\left(\left(\frac{c(0)}{c(H)}\right)^{\gamma/\nu}\right)\right]. \tag{28}$$

The expressions in the square brackets in Eqs. (25) and (28) represent a correction factor relating the resonance frequency for a truncated layer to that of the nontruncated layer *with the same shear-wave velocity at its bottom*. It should be emphasized that relative variation in the frequency is much less than the relative variation of wave travel time between the boundaries $z=0$ and $z=H$, the latter relative variation being $(1+H/z_1)^{\nu-1}$. If one compares resonance frequencies of the truncated and nontruncated layers *of the same thickness H*, then similar expressions hold. In particular,

$$f_n=\frac{c_0(1-\nu)j_{m,n}}{2\pi H^{1-\nu}}\left[1+(d_{m,n}-1+\nu)\left(\frac{c(0)}{c(H)}\right)^{1/\nu}+O\left(\left(\frac{c(0)}{c(H)}\right)^{\gamma/\nu}\right)\right]. \tag{29}$$

As the leading term in the correction factor in both cases is proportional to the (small) ratio $c(0)/c(H)$ of the shear-wave velocities to the power greater than unity, the resonance frequencies of the truncated layer are relatively insensitive to $c(0)$ for first normal modes. For instance, with $c(0)=7.5$ m/s, $c(H)=130$ m/s, from Eq. (28) one has 1.0456 and 1.182 for the ratio of resonance frequencies of truncated and nontruncated layers at $n=1$ and $n=2$ and $\nu=\frac{2}{3}$. At $\nu=\frac{1}{2}$, the ratios are 1.006 17, 1.0144, and 1.022 58 for $n=1$, $n=2$, and $n=3$, respectively. The smaller ν, the smaller are changes in the resonance frequencies and slower their increase with mode number. These properties of the resonance frequencies are illustrated in Sec. VI.

The coefficient $d_{m,n}$ increases with the normal mode order n as n^{2m+1} [see Eq. (27)] making Eqs. (28) and (30) inapplicable to high-order modes. An analysis shows that the restriction on mode number is determined by the inequality $a\ll 1$ which can be re-written with the help of Eq. (28) as $z_1/H\ll(\pi n)^{-1/(1-\nu)}$.

2. The case $a\gg 1+m^2$

When $z_1\ll H$, this case applies to high-order normal modes only. Using Hankel's asymptotic expansions (Ref. 23, Sec. 9.2)

$$\begin{aligned}&J_m(\eta)=(2/\pi\eta)^{1/2}[N(m,\eta)\cos\chi-M(m,\eta)\sin\chi],\\&\chi=\eta-\pi m/2-\pi/4,\\&Y_m(\eta)=(2/\pi\eta)^{1/2}[M(m,\eta)\cos\chi+N(m,\eta)\sin\chi],\\&N(m,\eta)\sim\sum_{k=0}^{\infty}(-)^k\frac{(m,2k)}{(2\eta)^{2k}},\\&M(m,\eta)\sim\sum_{k=0}^{\infty}(-)^k\frac{(m,2k+1)}{(2\eta)^{2k+1}}\end{aligned} \tag{30}$$

for the Bessel functions in Eq. (24), one finds, after some algebra,

$$\cos(b-a)+\sin(b-a)\left[\frac{4(m+1)^2-1}{8a}-\frac{4m^2-1}{8b}\right]+O(a^{-2}+b^{-2})=0. \tag{31}$$

The equation can be solved with respect to the frequency leading to

$$2\pi f_n\tau=\frac{\pi}{2}+\pi n+\frac{(H+z_1)^{1-\nu}-z_1^{1-\nu}}{8\pi(n+1/2)}\left[\frac{4(m+1)^2-1}{z_1^{1-\nu}}-\frac{4m^2-1}{(H+z_1)^{1-\nu}}\right]+O(n^{-2}), \tag{32}$$

where

$$\tau=\int_0^H\frac{dz}{c(z)}=\frac{(H+z_1)^{1-\nu}-z_1^{1-\nu}}{c_0(1-\nu)} \tag{33}$$

is wave travel time between the layer boundaries at normal incidence. Unlike the case in Sec. IV C 3, the relative variation in the resonance frequency due to truncation of the layer is approximately equal to the relative variation in wave travel time. One can recognize in terms $O(n)$ and $O(1)$ in Eq. (32) the WKB resonance condition (for the case of one free and one rigid boundary) whereas terms $O(1/n)$ represent leading-order corrections to the WKB approximation. The connection between Eq. (32) and the WKB resonance condition is not accidental; it will be shown in Sec. V that the inequality $a\gg 1+m^2$ ensures applicability of the WKB approximation throughout the truncated layer.

D. The effect of the boundary conditions

In the Secs. IV B and IV C above, ideal boundary conditions Eqs. (12), (13) have been assumed. While the first of these BCs is the correct BC for shear waves at normal incidence on a solid/fluid interface provided fluid viscosity and surface roughness are negligible, the second BC corresponds

to an absolutely rigid surface and is a strong idealization. Instead of imposing that BC at the boundary $z=H$, we now make a more realistic assumption that half-space $z>H$ is occupied by a homogeneous solid with density ρ_2 and shear-wave velocity c_2. At a solid/solid interface with a ''welded'' contact, shear waves at normal incidence are not coupled to compressional waves, and the physical requirements of displacement and traction continuity at the interface reduce to two boundary conditions, namely, continuity of the x-component of the displacement and of the σ_{13} component of the stress tensor. In the absence of waves coming from infinity, the displacement field in the half-space $z>H$ is given by

$$u_1 = A\exp(i\omega z/c_2), \quad z>H, \quad A=\text{const.} \tag{34}$$

Therefore, $\sigma_{13}/u_1 = i\omega\rho_2 c_2$ at the interface $z=H$. Continuity of u_1 and σ_{13} leads then to the following BC for waves within the sediment layer:

$$u_1 + i\omega^{-1} cT\,\partial u_1/\partial z = 0 \qquad (z=H), \quad \text{where} \quad T=\rho(H)c(H)/\rho_2 c_2 \tag{35}$$

and $\rho(H)$ and $c(H)$ are the density and shear-wave velocity in the layer just above the boundary with the solid halfspace. We will assume $T\ll 1$. This is the case when shear-wave velocity in the ''substrate'' $z>H$ is much greater than in the sediment layer. T is the only parameter characterizing the effect of the substrate on the normal modes of the shear waves. In the limit $T\to 0$ Eq. (35) turns into Eq. (13). That is why the presence of the substrate with finite impedance can be considered as a perturbation with respect to the idealized problem with a rigid boundary.

Let us derive the resonance condition for shear waves in a layer between fluid and solid halfspaces. Imposing BC Eq. (35) on the solution Eq. (15) that meets the boundary condition at $z=0$, for the nontruncated layer one immediately obtains

$$J_m(\omega\tau) = iTJ_{m+1}(\omega\tau), \quad \tau = H^{\nu-1}/c_0(1-\nu). \tag{36}$$

As long as $T\ll 1$, $\omega\tau$ in Eq. (36) is close to a zero $j_{m,n}$ of the Bessel function. Developing $\omega\tau - j_{m,n}$ into a power series in T and using the identities $J_{m+1}(j_{m,n}) = -J'_m(j_{m,n})$ and $J''_m(j_{m,n}) = -J'_m(j_{m,n})/j_{m,n}$ [see Eq. (22)], after simple transformations one finds

$$f_n = \frac{c_0(1-\nu)}{2\pi} H^{\nu-1}\left[j_{m,n} - iT + \frac{1+2m}{2j_{m,n}} T^2 + O(T^3)\right] \tag{37}$$

for the resonance frequencies. In the special cases $\nu=\frac{2}{3}$ ($m=\frac{1}{2}$) and $\nu\to 0$ ($m=-\frac{1}{2}$) the problem can easily be solved independently, without invoking cylindrical functions. Without presenting respective derivations, we note that the results obtained in the special cases agree with Eq. (37).

Comparison of Eq. (37) to Eq. (17) for the resonance frequencies in the case of a rigid lower boundary shows that penetrability of the boundary in the realistic model results in perturbations of both real and imaginary part of f_n. Because of the wave energy leakage through the boundary, the resonance frequencies cease to be real-valued. When $T\ll 1$, $\mathrm{Im}\, f_n$ is independent of mode number. With broadband excitation, the complexity of f_n manifests itself in the power spectrum as smearing of spectral lines, with the width of the lines (approximately) independent of their frequency. The term $O(T^2)$ in Eq. (37) is responsible for a shift of the spectral lines in the power spectrum. The shift is small, particularly if ν is small, and decreases as $1/n$ with mode number increasing. At $T<0.2$ and $m\sim 0.5$ the frequency shift does not exceed 0.41% even for the first normal mode and is practically negligible. Hence, the spectral line broadening is the only major effect of the finite impedance of the lower boundary of the nontruncated layer.

Consider now the truncated layer. Then the BC at the upper boundary leads to Eq. (23a), while the BC Eq. (35) becomes

$$[J_m(b) - iTJ_{m+1}(b)]B_1 + [Y_m(b) - iTY_{m+1}(b)]B_2 = 0, \qquad b = \frac{\omega}{c_0(1-\nu)}(H+z_1)^{1-\nu} \tag{38}$$

in terms of the unknown amplitude coefficients $B_{1,2}$. From the requirement that the linear simultaneous equations (23a) and (38) have a nontrivial solution with respect to $B_{1,2}$ one obtains the resonance condition

$$J_{m+1}(a)Y_m(b) - Y_{m+1}(a)J_m(b) = iT[J_{m+1}(a)Y_{m+1}(b) - Y_{m+1}(a)J_{m+1}(b)]. \tag{39}$$

It is a generalization of the dispersion equations (36) for the nontruncated layer with transparent lower boundary and Eq. (24) for the truncated layer with rigid lower boundary and reduces to those simpler relations in the limits $a\to 0$, $T\neq 0$ and $T\to 0$, $a\neq 0$, respectively.

Without delving into a detailed analysis of the dispersion relation Eq. (39), consider only one special case which is of primary practical interest. Namely, let $n=O(1)$, $a\ll 1$, $T\ll 1$. We will be interested in the leading-order corrections only with respect to the small parameters z_1 and T. Cast Eq. (39) as

$$J_m(b) = \frac{J_{m+1}(a)}{Y_{m+1}(a)} Y_m(b) + iT\left[J_{m+1}(b) - \frac{J_{m+1}(a)}{Y_{m+1}(a)} Y_{m+1}(b)\right]. \tag{40}$$

Developing the left side in powers of $b-j_{m,n}$ and the right side in powers of a and discarding terms $O(Tz_1)$, one finds

$$f_n \approx \frac{c_0(1-\nu)}{2\pi}(z_1+H)^{\nu-1} j_{m,n}\left[1 + d_{m,n}\frac{z_1}{z_1+H} - \frac{iT}{j_{m,n}}\right], \tag{41}$$

where $d_{m,n}$ is defined in Eq. (26). Equation (41) describes perturbations in the resonance frequencies due to (i) finite impedance of the lower boundary and (ii) small but nonzero shear-wave velocity near the upper boundary. From Eq. (41) we see that, to leading order, the perturbations are additive as it should have been expected. These two perturbations have been already discussed above.

V. ASYMPTOTIC SOLUTIONS OF THE SHEAR-WAVE WAVE EQUATION

In this section we consider WKB and more advanced asymptotic approximations to solutions of the shear-wave equation at normal incidence. The results of Sec. IV will be extended to geoacoustic models with variable density and shear modulus profiles deviating from the power-law depth dependence.

A. WKB approximation and its conditions of use

Formal high-frequency asymptotic representation of the solutions of the wave equation (4) (with $q=0$) is

$$u=(\mu k)^{-1/2}(C_1e^{i\phi}+C_2e^{-i\phi})$$
$$=(\rho c)^{-1/2}(B_1\sin\phi+B_2\cos\phi),\quad \phi(z)=\omega\int_0^z\frac{dz'}{c(z')}, \tag{42}$$

where $B_{1,2}$ and $C_{1,2}$ are arbitrary constants, and ϕ is the phase integral. Equation (42) is the first approximation of the WKB method (Ref. 21, Sec. 8.1). The amplitude factor $\mu^{-1/2}$ in Eq. (42) stems from the term with the first derivative of u in Eq. (4). As long as $\mu\to 0$ at $z\to 0$, this factor dramatically changes the amplitude behavior of the solutions near the upper boundary of the layer.

The WKB asymptotic solutions are commonly interpreted as local plane waves, in which the phase ϕ is a much more rapidly varying function of position that the amplitude, the latter being $(\rho c)^{-1/2}$ in our case. The interpretation is justified as long as

$$\omega/c\gg|c^{-1}\,dc/dz|+|\rho^{-1}\,d\rho/dz| \tag{43}$$

This condition is often viewed as the applicability condition of the WKB approximation. For the power-law profile of the velocity and constant or slowly varying density, the condition Eq. (43) becomes $\omega\gg dc/dz=\nu c_0z^{\nu-1}$. When $\nu\geqslant 1$, this condition is met throughout the layer if it is met at $z=H$. On the contrary, at $\nu<1$ the condition is violated in a vicinity of $z=0$ no matter how large the wave frequency is. This highly peculiar behavior is brought about by the infinite value of the wave speed gradient at $z=0$.

For acoustic waves in fluids it is known (Ref. 21, Sec. 8.2) that in some cases the WKB solution can be close to or coincide with the exact solution even when wave amplitude is not a slowly varying function compared to its phase. As it will be shown below, such a situation is possible for shear waves as well. It is of considerable interest because of the great simplification of the analysis and interpretation for respective ν values.

Strict estimates of the deviation of the WKB solution from the exact solution are available in the case of the Helmholtz equation (see Ref. 21, Sec. 8.1 and references therein). In particular, let $W(s)$ be an exact solution to the equation

$$d^2W/ds^2+N^2(s)W(s)=0,\quad N^2(s)>0, \tag{44}$$

and let

$$w_{1,2}(s)=N^{-1/2}(s)\exp\left(\pm i\int_0^s N(s_1)ds_1\right) \tag{45}$$

be its two WKB solutions. Then, if $W(s)$ and one of the functions $w_{1,2}$ have equal values and equal first derivatives at some point $s=s_0$, the relative error of the WKB solution obeys the inequality

$$|\delta(s)|\leqslant e^{F(s,s_0)}-1,\quad F(s,s_0)=2\left|\int_{s_0}^s\epsilon(s_1)N(s_1)ds_1\right|, \tag{46}$$

where

$$\epsilon(s)=0.5N^{-3/2}\,d^2N^{-1/2}/ds^2. \tag{47}$$

Remarkably, the exact solution and its WKB asymptotics coincide when $N^{-1/2}$ is a linear function of s.

According to Eq. (46), the smallness of ϵ (more precisely, validity of the inequality $|N\epsilon|\ll 1$ for all s considered) is a sufficient condition of the WKB approximation applicability. On the other hand, taking second and third WKB approximations into account, one obtains (Ref. 21, Sec. 8.1)

$$u=(\rho c)^{-1/2}\exp\left(-\frac{\epsilon}{2}\pm i\omega\int_0^z\frac{dz'}{c}(1+\epsilon)\right) \tag{48}$$

instead of Eq. (42). Therefore, smallness of ϵ is also a necessary condition for the use of Eq. (42).

To apply these results to shear waves, we transform the wave equation (4) into the Helmholtz equation by introducing instead of z a new independent variable $s(z)$ according to the equation[24,25] $ds/dz=\mu_0/\mu$, where μ_0 is a constant. In terms of the new vertical coordinate s, the wave equation (4) (with $q=0$) becomes the Helmholtz equation

$$d^2u/ds^2+\mu_0^{-2}\rho\omega^2\mu u=0. \tag{49}$$

It is the same as Eq. (44) with $W=u$ and $N^2=\mu_0^{-2}\rho\omega^2\mu$. Designate $\mu_0=\rho_0c_0^2H^{2\nu}$; ρ_0 is a constant which in the case of depth-independent density we are considering is conveniently chosen as equal to ρ; H stands for the layer thickness. Then one has the following explicit expressions for $s(z)$:

$$s(z)=(1-2\nu)^{-1}H^{2\nu}z^{1-2\nu},\quad \nu>0,\quad \nu\neq 1/2;$$
$$s(z)=H\ln(z/H),\quad \nu=1/2. \tag{50}$$

When z increases from 0 to plus infinity, s increases: from 0 to plus infinity, if $0<\nu<\frac{1}{2}$, from minus infinity to plus infinity, if $\nu=\frac{1}{2}$, or from minus infinity to 0, if $\nu>\frac{1}{2}$.

Calculation of the quantities ϵ and F for $\nu\neq 1$ using Eqs. (46), (47), and (50) gives simple expressions

$$\epsilon(s(z))=\frac{\nu(2-3\nu)c_0^2}{8\omega^2}z^{2\nu-2},$$
$$F(s(z),s(z_0))=\left|\frac{\nu(2-3\nu)c_0}{4(1-\nu)\omega}(z^{\nu-1}-z_0^{\nu-1})\right|. \tag{51}$$

We see that when $0<\nu<1$, $\epsilon\to\infty$ and the error of the WKB approximation increases indefinitely when $z\to 0$ making the approximation meaningless. The only exception, according to Eq. (51) occurs when $\nu=\frac{2}{3}$. Then ϵ is identically zero, and the WKB solution is not just a good approximation but is *precisely equal* to the exact solution. The finding can be verified directly by comparing the WKB solution as defined by Eq. (42) with $\nu=\frac{2}{3}$ to the exact solution Eq. (11) where

cylindrical functions of the order $m=\frac{1}{2}$ are given by Eq. (19). What cannot be verified by collating the two solutions but follows immediately from Eq. (47) is that the power-law profile with $\nu=\frac{2}{3}$ is *the only case* of continuously stratified, inhomogeneous solid of constant density when WKB solutions are exact for shear waves at normal incidence.

With ν, z_0, and wave frequency given, Eqs. (46) and (51) allow one to estimate the vicinity of the horizon $z=z_0$ in which one can use the WKB approximation. We will restrict ourselves to the case $\nu=\frac{2}{3}+\delta$, $|\delta|\ll 1$. It is of primary interest for two reasons. First, according to Eq. (51), it is a favorable case when applicability domain of the WKB approximation is larger than usual. (The other favorable case is that of small ν, $\nu\ll 1$, that is, of weakly inhomogeneous medium. It could be considered in a similar way but is of little interest in the problem of the ambient noise resonances.) Second, ν values in the geoacoustic model fitting available experimental data are close to $\frac{2}{3}$.[8,12]

In the problem of normal modes in the sediment layer it is natural to choose $z_0=H$. Then the contribution to F from the term with z_0 in Eq. (51) is much smaller than unity and can be neglected at the fundamental resonance and higher frequencies. The condition of the WKB approximation validity, $|F|\ll 1$, to within linear terms in δ becomes $\delta\omega c_0 z^{-1/3}\ll 1$. Using Eq. (17) for the resonance frequencies, we cast the condition as

$$z/H\gg \delta^3/n^3. \tag{52}$$

Hence, at the fundamental frequency ($n=1$) the WKB approximation is valid in the entire layer with the exception of a narrow range in the vicinity of the boundary $z=0$. The vertical extent of this range is of the order $10\delta^3 H$ and decreases rapidly, as n^{-3}, with increasing mode number. For instance, at $\delta=0.07$ the vertical extent is within 0.35% of the total layer thickness H for the fundamental mode. In terms of the shear wave velocity and the phase integral Eq. (42), the condition Eq. (52) becomes $c(z)/c(H)\gg\delta/n$ or $\phi(z)\gg\delta$. In the case of a truncated layer, the WKB approximation applies throughout the layer if $c(0)/c(H)\gg\delta/n$. For example, with $c(H)=130$ m/s, $n=2$, and $\delta=0.07$ this condition is met if $c(0)\gg 18$ m/s.

So far the WKB approximation has been analyzed in the case when an exact solution is available. The real value of the WKB approximation consists, of course, in its ability to treat efficiently a much wider class of environmental models than those admitting an exact analytic solution. To illustrate this point, we briefly consider three examples.

(1) Let the shear modulus be given by the power-law Eq. (1) with $z_1=0$ and $\nu=\frac{2}{3}$ in the layer with depth-dependent density $\rho(z)$. The layer is situated between homogeneous fluid ($z<0$) and solid ($z>H$) half-spaces. It is assumed that $\rho>0$, is a smooth function of z, and varies slowly with depth compared to the wave field, that is

$$|\rho^{-1}\,d\rho/dz|\ll\omega/c(H),\quad |\rho^{-1}\,d^2\rho/dz^2|\ll\omega^2/c^2(H). \tag{53}$$

The latter assumption is met for all the normal modes, if the representative space scale L of ρ variation is large compared to H or if $\rho(z)=\rho_0+\delta\cdot\rho_1(z)$, where ρ_0 and δ are constants, $\delta\ll 1$, and the representative space scale of ρ_1 variation is of the order of H. For any smooth $\rho(z)$, condition Eq. (53) holds for modes of order high enough, namely, with $n\gg H/L$. Note that because of the density depth-dependence shear wave velocity $c(z)$ does not follow a power law.

With arbitrary smooth $\mu(z)$ and $\rho(z)$, for ϵ one has from Eq. (47)

$$\epsilon=-\frac{\mu}{8\rho\omega^2}\left[\frac{d^2}{dz^2}\ln\rho-\frac{1}{4}\left(\frac{d}{dz}\ln\rho\right)^2+\frac{d^2}{dz^2}\ln\mu+\frac{3}{4}\left(\frac{d}{dz}\ln\mu\right)^2+\frac{1}{2}\left(\frac{d}{dz}\ln\rho\right)\left(\frac{d}{dz}\ln\mu\right)\right]. \tag{54}$$

For the power-law profile of $\mu(z)$ and $\nu=\frac{2}{3}$, the terms without ρ in the square brackets in Eq. (54) equal zero. Then $\epsilon\to 0$ at $z\to 0$, and, because of Eq. (53), $|\epsilon|\ll 1$ throughout the layer and $|F(s(z),s(H))|\ll 1$. Therefore, the WKB approximation is valid at $0<z<H$.

The general solution of the wave equation is given by Eq. (42). For the displacement to be finite at $z\to 0$ one has $B_2=0$ in Eq. (42). Imposing the BC Eq. (35) at the lower boundary, one obtains the resonance condition

$$\tan\phi(H)=-iT\left[1-\frac{iT}{2\omega}\left(c'(H)+c(H)\frac{\rho'(H)}{\rho(H)}\right)\right]^{-1}. \tag{55}$$

This equation is easily solved when $T\ll 1$:

$$f_n=\frac{n}{2\tau}\left[1-\frac{iT}{\pi n}+\frac{\tau T^2}{2\pi^2 n^2}\left(c'(H)+c(H)\frac{\rho'(H)}{\rho(H)}\right)+O(T^3)\right], \tag{56}$$

where τ is wave travel time between layer boundaries. Noting that $j_{1/2,n}=\pi n$, it is straightforward to check that Eq. (56) reduces to Eq. (37) in the particular case of the depth-independent density. Like its counterpart Eq. (37) derived from the exact solution, Eq. (56) describes both broadening of the spectral line due to energy leakage at the solid/solid interface and a small shift of the spectral line compared to the case of rigid boundary ($T=0$). Equation (56) shows that observations made in Sec. IV D hold for a more general geoacoustic model.

In the case of a rigid lower boundary Eq. (55) gives the harmonic sequence $f_n=n/2\tau$ of the resonance frequencies. For a *homogeneous* layer with the same value of travel time τ and the same boundary conditions one gets $f_n=(2n+1)/4\tau$, which is not harmonic. The difference occurs because the free surface BC at the upper boundary leads to the *different choice of solutions* when $c(0)=0$ and $c(0)\neq 0$. Indeed, when $c(0)\neq 0$, to meet the BC one has to choose the solution with $\cos\phi$ in Eq. (42) When $c(0)=0$, both sine and cosine solutions give $\sigma_{13}=0$ at $z=0$ but only the sine solution is bounded, leading to $B_2=0$ and $f_n=n/2\tau$.

Put differently, the harmonic sequence of the resonance frequencies results from the fact the wave equation (4) for the shear waves *is not* a Helmholtz equation. It is the amplitude factor $\mu^{-1/2}$ in the WKB solution Eq. (42) that is responsible for the distinction in the resonance frequencies of the inhomogeneous and homogeneous layers with the same τ. The amplitude factor, in its turn, originates from the term with the first derivative of u in the wave equation (4).

(2) Let us consider two elastic layers sandwiched between homogeneous fluid ($z<0$) and solid ($z>H+h$) halfspaces. In the layer $0<z<H$, $\mu(z)$ follows the power law with $\nu=\frac{2}{3}$. In the layer $H<z<H+h$, $\mu(z)$ is an arbitrary smooth function varying slowly compared to the wave field. Density is a smooth function of z at $0<z<H+h$, varying slowly compared to the wave field. Density and shear modulus are continuous at $z=H$ together with their first derivatives.

Then the WKB approximation is applicable at $0<z<H+h$, and one gets the same resonance condition for the shear waves, as in case (1) above, with τ being now travel time between the boundaries $z=0$ and $z=H+h$. We see, that elastic layers with the same τ and the same type of μ singularity at $z\to 0$ have very similar dispersion curves. (Additional examples of such a behavior are given in Sec. V B below.) In practice, therefore, no unique inversion of the resonance frequencies for the shear modulus depth dependence is possible, even within the class of monotonic $\mu(z)$ and with many resonance frequencies measured.

(3) Consider an elastic layer with the BCs Eqs. (12), (13) imposed on its boundaries. Let $\mu>0$ at $z=0$ and throughout the layer, μ and ρ be smooth functions of depth, and the wave frequency be high enough so that the WKB approximation is valid at $0<z<H$. Calculating the derivative of Eq. (42) with respect to z and neglecting terms $O(1/n)$ compared to 1, one obtains from the BCs Eqs. (12), (13) the resonance condition $\cos(\phi(H)-\phi(0))=0$, or $f_n=(2n+1)/4\tau$, where τ is the wave travel time between the boundaries $z=0$ and $z=H$. The dispersion relation, within its accuracy, agrees with the dispersion relation Eq. (32) derived from the exact solution and extends it to the case of arbitrary smooth variation of the medium parameters. Note that the shear-wave dispersion relation is no different from the dispersion relation for acoustic waves in a fluid layer with one free and the other rigid boundary *provided* the shear modulus does not turn to zero within the elastic layer or on its boundary.

B. Uniform asymptotics

The WKB method enables one to derive high-frequency asymptotics of solutions to the wave equation with an *arbitrary* smooth depth dependence of medium parameters, but, as discussed in Sec. V A, with a few exceptions is not applicable in a vicinity of the horizon where the shear modulus vanishes. The exact solutions considered in Sec. IV have no limitations on frequency or depth but refer to media with $\rho=$const and specific $\mu(z)$. In this section, we derive an asymptotic representation that possesses virtues of both the approaches mentioned.

As before, we assume normal incidence. Let $\mu=\rho(z)c^2$, $c=F(z)z^{\nu}$; ρ and F are smooth functions with L being the representative spatial scale of their variation: $F'/F=O(L^{-1})$, $\rho'/\rho=O(L^{-1})$. Neither F nor ρ vanishes within the layer. In this geoacoustic model, the shear modulus retains its power-law singularity at $z\to 0$, but can deviate from the power law considerably at $z\gtrsim L$.

To derive a wave field asymptotics applicable at $z\to 0$, we apply the *reference equation method* (see Ref. 21, Chap. 9 and references therein). The exactly solvable wave equation for the power-law $\mu(z)$ dependence will serve as the ''reference equation.'' Let $W(s)$ be a solution of Eq. (44) in the reference case. Then the function

$$U(s)=(d\eta/ds)^{-1/2}W(\eta(s)) \tag{57}$$

obeys the equation (Ref. 21, Sec. 9.1)

$$\begin{aligned} &d^2U/ds^2+[(d\eta/ds)^2N^2+P(s)]U=0,\\ &P(s)=0.5(\ln\eta')''-0.25[(\ln\eta')']^2, \end{aligned} \tag{58}$$

where prime denotes derivatives with respect to s. Generally, the variable substitution $\eta(s)$ is chosen from the following two conditions: (i) $(\eta')^2N^2$ equals to the coefficient $\mu_0^{-2}\rho\omega^2\mu$ in the Helmholtz equation (49) to be solved, and (ii) positions and types of ''critical points'' (i.e., zeros and singularities) in the coefficients of Eqs. (49) and (58) coincide. In the problem at hand, there is a single critical point, $z=0$, where coefficients of Eq. (49) and the reference equation have power-law singularities.

For brevity, only the case $\frac{1}{2}<\nu<1$ will be considered below. Then $s\to-\infty$ at $z\to+0$ [see Eq. (50)], and the appropriate variable substitution is

$$\int_{-\infty}^{\eta}N(\eta')d\eta'=\frac{\omega}{\mu_0}\int_{-\infty}^{s}[\rho(s')\mu(s')]^{1/2}ds'. \tag{59}$$

Calculating the integrals, one finds

$$\begin{aligned} &\eta(s)=\mathrm{sgn}(1-2\nu)\left|\frac{\phi}{2\alpha m}\right|^{-2m},\\ &\alpha=\frac{\omega}{c_0H^{2\nu}}\left|\frac{1-2\nu}{H^{2\nu}}\right|^{\nu/(1-2\nu)}, \end{aligned} \tag{60}$$

with ϕ defined in Eq. (42). Taking $W(s)$ as the general solution of the reference problem, after some algebra one obtains from Eqs. (11), (57), and (60) a concise expression

$$U=(\phi/\rho c)^{1/2}[B_1J_m(\phi)+B_2Y_m(\phi)], \tag{61}$$

where $B_{1,2}$ are arbitrary constants. Note that U, like the WKB solutions Eq. (42), is expressed in terms of the phase integral and ρ and c values at the point considered, but, unlike the WKB solutions, also depends on the exponent ν which determines m by Eq. (11). According to Eq. (61), with $c(z)$ given, the only effect of the density stratification on U is multiplication by the amplitude factor const$\cdot\rho^{-1/2}$. For comparison, the situation is similar with acoustic waves in fluids (Ref. 21, Sec. 9.1) but the factor is const$\cdot\rho^{1/2}$ in that case.

The function $U(s)$ Eq. (57) is an asymptotic solution to the wave equation, *if* the ratio

$$R=\frac{P(s)}{(d\eta/ds)^2N^2(s)} \tag{62}$$

is small with respect to the parameter L for all the coordinate s values considered (Ref. 21, Sec. 9.1). Using Eqs. (58) and (60) to calculate R, one finds

$$R=\frac{F^2(z)z^{2\nu}}{2\omega^2}\Bigg[(\ln\rho Fg)''+(\ln\rho Fg)'(\ln\rho F^2)''+\frac{2\nu}{z}(\ln\rho Fg)'-\frac{1}{2}((\ln\rho Fg)')^2\Bigg], \tag{63}$$

where $g(z)=z^{\nu}[\phi(z)]^{-\nu/(1-\nu)}$. It is a smooth function with the same spatial scale L as $F(z)$; in particular, $g'(0)/g(0)=\nu(2-\nu)^{-1}F'(0)/F(0)$. Therefore, one can cast Eq. (63) as

$$R=\frac{F^2}{\omega^2}[z^{2\nu}O(L^{-2})+\nu z^{2\nu-1}O(L^{-1})]=\frac{C_1(z/L)^{2\nu}+C_2(z/L)^{2\nu-1}}{k^2(L)L^2}, \tag{64}$$

where $C_{1,2}$ are dimensionless constants on the order of 1 and $k(z)$ is a wave number. Note that $R\to 0$ at $z\to 0$, $R\simeq(k(L)L)^{-2}$ at $z\gtrsim L$, and $R\ll(k(L)L)^{-2}$ at $z\ll L$. [We assume that the power-law increase of $c(z)$ ceases at some $z\gtrsim L$ and, therefore, do not consider the case $z\gg L$.] Hence, if

$$k(L)L\gg 1, \tag{65}$$

Eqs. (57) and (61) are applicable at any z and, then, Eq. (61) is a uniform asymptotics. As Eq. (65) is the condition of the WKB approximation applicability away from the singularity, the uniform asymptotics extends the WKB result up to the boundary $z=0$ *without any additional assumptions or additional restrictions on the wave frequency*. At the resonance frequency, according to Eq. (17), $k(H)H\simeq n$. Hence, with $L\lesssim H$ the uniform asymptotics Eq. (61) generally applies to high-order modes ($n\gg 1$) only. It applies to all normal modes if (i) $L\gg H$ or (ii) $\rho=\rho_0+\delta\cdot\rho_1(z)$ and $F=F_0+\delta\cdot F_1(z)$, where $\delta\ll 1$, ρ_0, and F_0 are constants and L is the spatial scale of ρ_1 and F_1 variation. In both cases the deviation of density from a constant and shear velocity from the power law are small within the layer. (That is not surprising, for one needs a small parameter to construct an approximation valid for all the modes.)

As expected, Eq. (61) reduces to the exact solution Eq. (11) when density is constant and $F=\text{const}$. It follows from Eq. (19) that the uniform asymptotics turns into the WKB solution Eq. (42) when $m=\frac{1}{2}$. Moreover, using the asymptotic expansions Eq. (30) of the Bessel functions it is easy to verify that for arbitrary m Eq. (61) reduces to the WKB solutions far away from the boundary $z=0$, namely, when $\phi\gg 1+m^2$.

A similar analysis can be carried out when $0<\nu<\frac{1}{2}$. However, it turns out that it that case R Eq. (62) tends to *infinity* at $z\to 0$, and Eq. (61) is generally not a uniform asymptotics. This fact is best understood by considering the wave equation in the form Eq. (7). The effective wave number in Eq. (7) contains $\rho'c'/\rho c$ and other terms $O(1/zL)$ which have a stronger singularity at $z\to 0$ than $\omega^2c_0^{-2}z^{-2\nu}$ when $\nu<\frac{1}{2}$. These terms change the asymptotic behavior of the solution at $z\to 0$ and call for a reference equation different from the one we used. If the first derivatives of both ρ and F become zero at $z=0$, then the indicated difficulty disappears, $R\to 0$ at $z\to 0$, and Eq. (61) turns out to be a uniform asymptotic in the case $0<\nu<\frac{1}{2}$ as well.

Now, let us use Eq. (61) to derive a resonance condition for shear waves in a layer $0<z<H$ between homogeneous fluid and solid half-spaces. For the displacement u to be finite at $z\to 0$, $B_2=0$ in Eq. (61). Imposing the BC Eq. (35) at $z=H$ and taking Eq. (65) into account, one obtains the resonance condition Eq. (36) where τ stands for the wave travel time between the boundaries $z=0$ and $z=H$. The only difference from the exactly solvable case involves the value of τ which now is not related to H and ν in as simple way as in Eq. (36). There is no need therefore to discuss anew the solution of the resonance condition. It is worth mentioning that the asymptotic derivation of the resonance condition extends conclusions made in Sec. IV D (without changing them) about effects of boundary conditions on the resonance frequencies to more general geoacoustic models.

Quite similarly one can derive from Eq. (61) a resonance condition in the case of truncated layer. We will not present the derivation here.

Consider the resonance condition Eq. (36) in the case $T=0$ (rigid lower boundary). Then the resonance frequencies are $\omega_n=j_{m,n}/\tau$. Using the asymptotic expansion for the Bessel function zeros (Ref. 23, Chap. 9) one has at $n\gg 1$ [cf. Eq. (18)]

$$\omega_n=\frac{\pi}{\tau}\left(n+\frac{m(\nu)}{2}-\frac{1}{4}\right)+O\left(\frac{1}{n}\right). \tag{66}$$

In the case $m=\frac{1}{2}$ Eq. (66) is exact for all $n=1,2,\ldots$. Compare Eq. (66) to the formal WKB resonance condition $\omega_n=\pi n/\tau$. At $m\neq\frac{1}{2}$ inapplicability of the WKB approximation in the vicinity of the boundary $z=0$ deletes the term $\pi(m/2-1/4)$ on the right side of the formal WKB result. The phase term $\pi(m/2-1/4)$ is analogous to the term $-\pi/4$ in the case of a turning point (Ref. 21, Sec. 9.2) but, because of its m dependence, is different for different media. Naturally, the phase term vanishes at $m=\frac{1}{2}$ when the WKB approximation is exact.

VI. DATA ANALYSIS AND COMPUTATIONAL EXAMPLES

The analysis so far provides valuable insight into the physics of the observed noise resonances. Here we reconsider the experimental noise data in light of the analytical results and we present some calculations based on the derived formulas to illustrate their applicability.

First we consider the simple power-law profile (i.e., nontruncated, with $z_1=0$) with a perfectly rigid lower boundary. The resonance frequencies for this case are expressed in terms of the zeros of Bessel functions in Eq. (17). For a shear wave at normal incidence, the two-way travel time through the upper sediment layer is $2H^{1-\nu}/c_0(1-\nu)$, so we normalize all frequencies by the reference frequency

$$F=(1-\nu)c_0/2H^{1-\nu}. \tag{67}$$

This is not the frequency of the fundamental resonance (except in the special case $\nu=\frac{2}{3}$), but in the limit of large mode order it is the frequency spacing of adjacent resonances, and

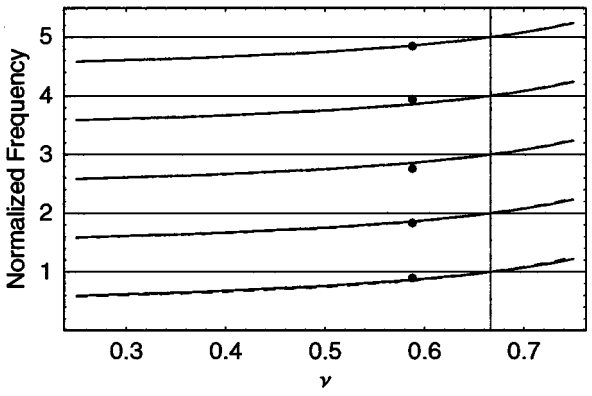

FIG. 3. Normalized resonance frequencies f_n/F vs exponent value ν in the shear-speed profile $c=c_0z^{\nu}$ with a rigid bottom boundary for shear resonances 1–5. The reference frequency F is defined by Eq. (67). Solid lines: exact solution; dashed lines: asymptotic approximation Eq. (66); thin horizontal lines: WKB approximation; solid circles: observed resonances, normalized by $F=1.18$ Hz.

we will show that it is a very good approximation even for low mode order.

Figure 3 shows the normalized shear resonance frequencies versus ν for the first five modes, calculated three different ways: (1) ignoring terms of $1/n$ and higher powers in Eq. (66) asymptotically valid for high-order modes; (2) by numerical solution of the exact normal mode resonance condition; and (3) by the WKB approximation $f_n=nF$. For method (2), the FindRoot function of Mathematica® is employed to solve Eq. (16) using f_n from method (1) as starting values. These two methods have nearly identical results, the only perceptible difference occurring at low mode order. The separation of adjacent normalized frequencies is very close to unity, but the offset of the sequence of resonances is clearly ν-dependent. Note that the resonance frequencies are exactly harmonic in the special case $\nu=\frac{2}{3}$. Note also that in the limit $\nu\rightarrow 0$, which corresponds to a homogeneous layer, the sequence of normalized frequencies approaches $n-\frac{1}{2}$. Method (3), the WKB approximation, was shown in Sec. V to apply only in the case $\nu=\frac{2}{3}$, in which case it is exact. In terms of normalized frequencies, the WKB resonance frequencies are simply the sequence of integers, n.

The precision of the asymptotic approximation Eq. (66) allows a straightforward reduction of the experimental data reported in Sec. I. To first order in $1/n$, Eqs. (66) and (17) can be written as $f_n=F(n+m/2-1/4)$, which is applied to the sequence of five noise resonances to determine the free parameters by linear regression. The resulting fit gives $F=1.18$ and $m=0.21$, which corresponds to the shear speed profile parameters $c_0=21.7\pm 1.5$ and $\nu=0.59\pm 0.06$. The experimental resonance frequencies, normalized by $F=1.18$, have been added to Fig. 3, plotted at the exponent value $\nu=0.59$. The good agreement between experimental and modeled resonances supports the hypothesis that the observed noise peaks are shear-wave resonances in a sediment layer having a power-law shear-speed profile. (It should be emphasized, however, that two shear-speed profiles having the same two-way travel time and power-law singularities of the shear speed at $z\rightarrow 0$ with the same ν cannot be distinguished by their resonance frequencies.) Owing to the natural uncertainties in the experimental data, no further improvement in the agreement is expected by introducing complicating factors, such as a truncated profile or a nonideal bottom boundary condition.

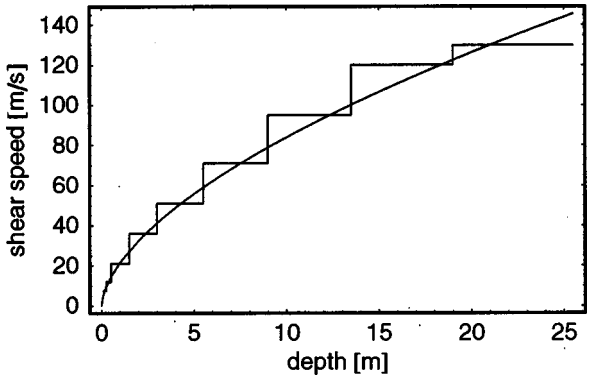

FIG. 4. The experimental shear-speed profile. The staircase is the stacked-layer profile previously derived from interface wave dispersion and the continuous line is the power-law profile $c(z)=21.7z^{0.59}$ (SI units) implied by the noise resonances. See text for more details.

The implied power-law shear-speed profile is nearly identical to that independently determined from analysis of interface wave dispersion at the same site, discussed in Ref. 12 and reported in Sec. I. The continuous profile inferred from the seismo-acoustic noise analysis is plotted in Fig. 4 along with the stacked-layer ''staircase'' of shear-speed values used in the interface wave study. (It must be emphasized that the noise resonances being examined in this paper are modes of vibration of the sediment layer that are distinct from the interface waves studied in Ref. 12, although they are related through the common shear-speed profile.) It is satisfying that the power-law profile implied by the noise resonances is consistent with the profile derived from the interface-wave studies.

Figure 5 shows three power-law profiles having different exponents ν but the same two-way travel time, that is, they all have the same reference frequency F. The exponent values are $\nu=\frac{1}{4}$, $\nu=\frac{1}{2}$, and $\nu=\frac{2}{3}$. For each profile, Fig. 6 shows the shapes of the first three resonances in this ideal environment, assuming a perfectly rigid boundary at the bottom. The functions describing horizontal displacement are given by

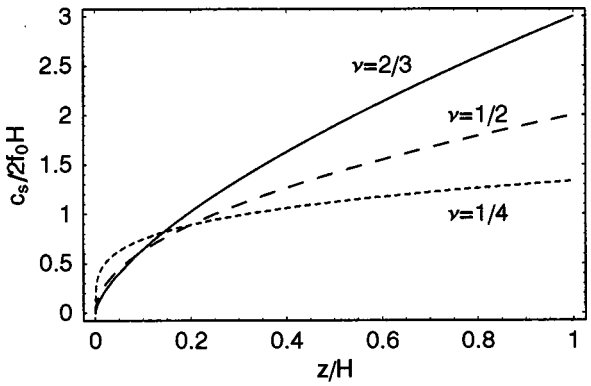

FIG. 5. Shear speed versus depth for power-law profiles having different exponential parameters, keeping fixed the two-way travel time through the layer.

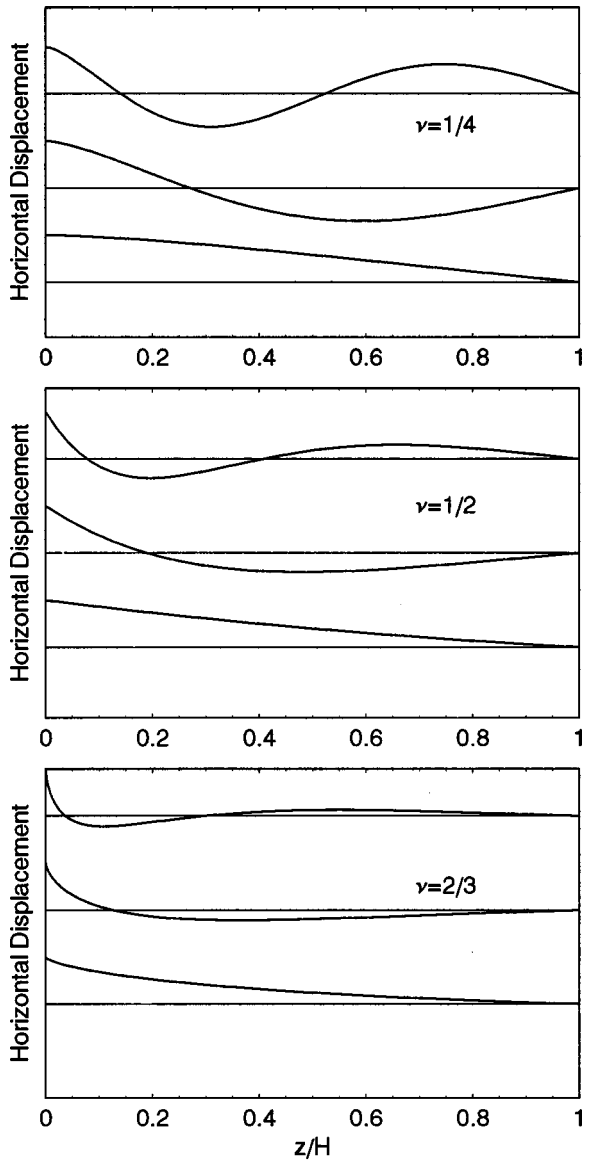

FIG. 6. Shapes of the first three shear-wave resonances associated with the profiles of Fig. 4. The zeros of the functions are offset by their normalized resonance frequencies.

Eq. (15), normalized to unity at the upper boundary, and are evaluated at the resonance frequencies given by Eq. (17). Note that at large values of the exponent the modes are trapped near the surface, while at small values of the exponent the modes span the sediment layer. In the limit $\nu \to 0$, the layer becomes isospeed and one would expect cosinusoidal mode shapes. The modes for the experimental case, having the exponent $\nu = 0.59$, are very similar to those for the case $\nu = \frac{2}{3}$.

Finally, we present an example of the resonance frequencies for the truncated power-law profile, whose resonance condition is Eq. (24). The numerical solutions of this equation were again found using the FindRoot function of Mathematica®, with starting values given by the corrected WKB approximation in Eq. (33). Computed for the case $z_1/H = 0.01$, the resonance frequencies given by these two methods are compared in Fig. 7 alongside the results from the simple (nontruncated) profile having the same parameters. Note that the truncated profile gives higher frequencies, owing to the reduced travel time through the sediment. The WKB approximation improves with mode order, as expected.

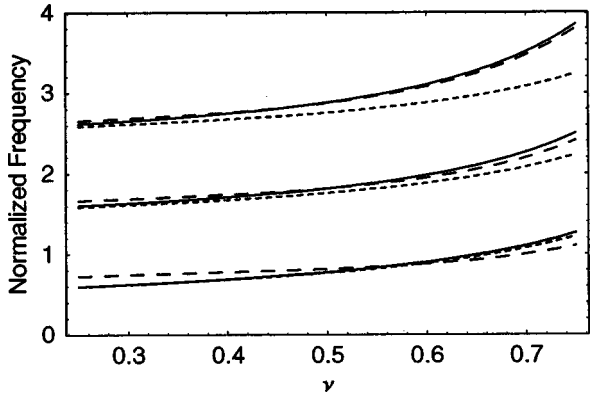

FIG. 7. Normalized resonance frequencies versus exponent value ν in the truncated shear-speed profile $c = c_0(z + z_1)^\nu$ with a rigid bottom boundary for shear resonances 1–3. The reference frequency is given by Eq. (67) and $z_1/H = 0.01$. Solid lines: exact solution; long dashed lines: the corrected WKB approximation, Eq. (33); short dashed lines: the nontruncated solution (as a reference).

VII. DISCUSSION AND CONCLUSIONS

Noise peaks in the spectra of seismo-acoustics signals observed on an ocean bottom seismometer have been interpreted as resonances of vertically polarized shear waves in a surficial layer of soft sediment overlaying a hard substrate, with the shear speed in the sediment layer increasing with depth according to a power law of the form $c(z) = c_0 z^\nu$ with $c_0 = 21.7 \pm 1.5$ (SI units) and $\nu = 0.59 \pm 0.06$. This profile agrees with that suggested by inversion of interface wave group speed data at the same experimental site. The noise resonances are related to quasi-modes of P-SV waves trapped in the sediment layer. Particle motion in these modes is dominated by the horizontal shear displacement. This is consistent with the absence of resonances in the observed noise spectra of the pressure sensor (the hydrophone) and with the resonances being much more pronounced on the horizontal geophone compared with the vertical geophone.

The shear-wave resonances are natural modes of vibration of this environment and their characteristics are independent of the level and origin of the noise. Rather, the mode frequencies and shapes are determined by seismo-acoustic propagation within the layered sediment. In our theoretical analysis, we have been able to circumvent the complicated problem of continuous P-S coupling in solids having inhomogeneous elastic properties. The very small shear speeds in the sediment layer permit the simplifying assumption that the modal frequencies are independent of the incidence angle of the exciting wave. Hence, although oblique incidence is necessary to couple the incident sound wave to shear waves in the sediment, one can determine the resonance frequencies by considering the normal-incidence case, reducing the problem to the solution of a well-known scalar wave equation. Furthermore, the insensitivity of the resonance frequencies to incidence angle is essential to our hypothesis if the noise

source is thought to be the diffuse infrasonic ambient noise field in the ocean overhead. Otherwise, the peaks would be smeared out in frequency and would not be observed.

Assuming normal incidence, constant density, and a power-law shear-speed profile, exact solutions have been obtained for eigenfrequencies and modes in terms of Bessel functions of real order between $-\frac{1}{2}$ and plus infinity. In general, the resonance frequencies are not harmonic, or even equally spaced, although they are precisely equally spaced for $\nu=0$ and $\nu=\frac{2}{3}$, and exactly harmonic for $\nu=\frac{2}{3}$. However, a uniform asymptotic approximation (that is, a corrected WKB approximation) predicts nearly equal spacing and provides a workable estimate of the exact resonance frequencies for all mode orders.

Theoretically, the continuous variation of the shear speed introduces into the wave equation a term involving the logarithmic derivative of the shear modulus, distinguishing our problem from the analogous acoustical problem. This is critically important for the correct description of the field behavior in the vicinity of the surface, where the shear speed vanishes in a singular manner. The combined effects of this term and the upper boundary conditions remain significant even away from the interface, where the critical term is locally small compared to other terms in the wave equation. The net effect of the singular profile is a ν-dependent frequency shift of the resonances. It would not be possible to explain the nearly harmonic sequence of the experimentally observed noise peaks without accounting for the effect of the logarithmic derivative term.

Strictly speaking, the existence of the shear-speed singularity at the sediment invalidates the WKB method for this problem, and it is no surprise that the resonance frequencies predicted by the WKB method are generally impractical. However, for the special case of $\nu=\frac{2}{3}$, the WKB method is exact! A uniform asymptotic approximation, obtained by the method of reference equation, proves to be a better approach. In effect, this provides a corrected WKB approximation that is surprisingly good. The uniform asymptotics possess advantages of both the exact solution and the WKB approximation: like the WKB approximation, it applies to rather general smooth variation of the medium parameters but, like the exact solution, it remains valid when the shear modulus vanishes according to the power law.

In the problem considered, the resonance frequencies are primarily determined by two characteristics, namely, the two-way travel time of shear waves in the sediment layer and the exponent ν, which governs the type of shear-speed singularity. In practice, if only resonance frequencies are measured, there is a little hope to distinguish between two distinct geoacoustic models sharing the same values of these parameters. Of some importance are also elastic parameters of the substrate and—in the case of the truncated power-law profile—the surface value of the shear modulus. Some of the broadening of the noise peaks is attributed to the finite contrast between the sediment and substrate properties. Further research would be required to theoretically explain the shapes of the resonance peaks in the noise spectrum measured as well as the relation between spectra of vertical and horizontal displacements and near-bottom pressure.

ACKNOWLEDGMENTS

The authors are grateful to Dave Heffler of the Atlantic Geoscience Center/Bedford Institute of Oceanography for the loan of the OBS used on the sea test that discovered the seismo-acoustic noise resonances and to N. Ross Chapman of School of Earth and Ocean Sciences/University of Victoria for stimulating discussions. The contribution of John Osler to the DREA OBS project was invaluable. The Department of National Defense and the Natural Sciences and Engineering Research Council of Canada have supported this work.

[1] J. M. Hovem, M. D. Richardson, and R. D. Stoll, Eds., *Shear Waves in Marine Sediments* (Kluwer, Dordrecht, 1991).

[2] S. J. Hughes, D. D. Ellis, D. M. F. Chapman, and P. R. Staal, ''Low-frequency acoustic propagation loss in shallow water over hard-rock seabeds covered by a thin layer of elastic-solid sediment,'' J. Acoust. Soc. Am. **88**, 283–297 (1990).

[3] F. B. Jensen, ''Excess attenuation in low-frequency shallow-water acoustics: A shear wave effect?,'' in *Shear Waves in Marine Sediments*, edited by J. M. Hovem, M. D. Richardson, and R. D. Stoll (Kluwer, Dordrecht, 1991), pp. 421–430.

[4] A. J. Robins, ''Generation of shear and compression waves in an inhomogeneous elastic medium,'' J. Acoust. Soc. Am. **96**, 1669–1676 (1994).

[5] M. V. Hall, ''Acoustic reflectivity of a sandy seabed: A semianalytic model of the effect of coupling due to shear modulus profile,'' J. Acoust. Soc. Am. **98**, 1075–1079 (1995).

[6] J. A. Orcutt, C. S. Cox, A. C. Kibblewhite, W. A. Kuperman, and H. Schmidt, ''Observations and causes of ocean and seafloor noise at ultra-low and very-low frequencies,'' in *Natural Physical Sources of Underwater Sound*, edited by B. R. Kerman (Kluwer, Dordrecht, 1993), pp. 203–232.

[7] A. C. Kibblewhite and C. Y. Wu, *Wave Interactions as a Seismo-acoustic Source* (Springer-Verlag, Berlin, 1996).

[8] D. M. F. Chapman, ''Shear speed gradients and resonances in ocean seismo-acoustic modelling,'' in *Theoretical and Computational Acoustics '97*, edited by Y. C. Teng *et al.* (World Scientific, Singapore, 1999), pp. 147–158.

[9] D. M. F. Chapman, J. C. Osler, W. C. Risley, and J. C. Dodds, ''Underwater acoustic measurements with a digital ocean bottom seismometer,'' J. Acoust. Soc. Am. **96**, 3330(A) (1994).

[10] D. J. Dodds, D. M. F. Chapman, J. C. Osler, and W. C. Risley, ''Minimizing instrument effects in an ocean bottom seismometer,'' Can. Acoust. **22**, 161–162 (1994).

[11] J. C. Osler, D. M. F. Chapman, W. C. Risley, and J. C. Dodds, ''*In situ* calibration of the coupling of an ocean bottom seismometer to sand and clay surficial sediments,'' EOS Trans. Am. Geophys. Union **75**, 419 (1994).

[12] J. C. Osler and D. M. F. Chapman, ''Seismo-acoustic determination of the shear-wave speed of surficial clay and silt sediments on the Scotian Shelf,'' Can. Acoust. **24**, 11–22 (1996).

[13] L. H. King, *Surficial Geology of the Halifax-Sable Island Map Area, Marine Science Paper 1* (Department of Energy, Mines and Resources, Ottawa, 1970).

[14] L. M. Dorman, A. E. Schreiner, L. D. Bibee, and J. A. Hildebrand, ''Deep-water sea-floor array observations of seismo-acoustic noise in the eastern Pacific and comparisons with wind and swell,'' in *Natural Physical Sources of Underwater Sound*, edited by B. R. Kerman (Kluwer, Dordrecht, 1993), pp. 165–174.

[15] N. R. Chapman and D. M. F. Chapman, ''A coherent ray model of plane-wave reflection from a thin sediment layer,'' J. Acoust. Soc. Am. **94**, 2731–2738 (1993).

[16] E. I. Hamilton, ''Attenuation of shear waves in marine sediments,'' J. Acoust. Soc. Am. **60**, 334–338 (1976).

[17] J. E. White, *Underground Sound Application of Seismic Waves* (Elsevier, Amsterdam, 1983), pp. 67–68.

[18] T. Iwasaki and F. Tatsuoka, ''Effects of grain size and grading on dynamic shear moduli of sands,'' Soils Found. **17**, 19–35 (1997).

[19] A. J. Robins, ''Plane-wave reflection from a solid layer with nonuniform density, sound speed, and shear speed,'' J. Acoust. Soc. Am. **103**, 1337–1345 (1998).
[20] O. A. Godin, ''Acoustic mode reciprocity in fluid/solid systems: Implications on environmental sensitivity and horizontal refraction,'' in *Theoretical and Computational Acoustics '97*, edited by Y. C. Teng *et al.* (World Scientific, Singapore, 1999), pp. 59–76.
[21] L. M. Brekhovskikh and O. A. Godin, *Acoustics of Layered Medium. I: Plane and Quasi-Plane Waves* (Springer-Verlag, Berlin, 1990 and 1998).
[22] O. A. Godin, ''On plane waves reflection by a stratified halfspace,'' Dokl. Akad. Nauk SSSR **255**, 1069–1072 (1980).
[23] M. Abramowitz and I. A. Stegun, Eds., *Handbook of Mathematical Functions with Formulas, Graphs, and Tables*, Appl. Math. Ser., Vol. 55 (National Bureau of Standards, Washington, 1964).
[24] S. O. Coen, ''On the elastic profiles of a layered medium from reflection data. Part 1. Plane-wave sources,'' J. Acoust. Soc. Am. **70**, 172–175 (1981).
[25] O. A. Godin, ''On a modification of the wave equation for a layered medium,'' Wave Motion **7**, 515–528 (1985).

Boundary conditions for the weak formulation of the mixed ($\underline{u},p$) poroelasticity problem

Patricia Debergue, Raymond Panneton, and Noureddine Atalla
G.A.U.S., Department of Mechanical Engineering, Université de Sherbrooke, Sherbrooke Québec J1K 2R1, Canada

(Received 10 May 1998; accepted for publication 21 July 1999)

This paper presents the boundary conditions that apply to the weak integral formulation of the Biot mixed ($\underline{u},p$) poroelasticity equations. These boundary conditions are derived from the classical boundary conditions of the Biot displacement ($\underline{u},\underline{U}$) poroelasticity equations. They are applied to the surface integrals of the associated weak form to account for exterior excitations, supports, and couplings with exterior elastic, acoustic, poroelastic media, and a septum. It will be shown that the derived boundary conditions for the ($\underline{u},p$) formulation lead to simpler finite element equations compared to those obtained from the ($\underline{u},\underline{U}$) formulation. Finally, two numerical examples are presented to validate the poroelastic-septum coupling condition, and to highlight the limitations of the free edge condition on a poroelastic medium. © *1999 Acoustical Society of America.* [S0001-4966(99)04911-5]

PACS numbers: 43.20.Gp, 43.50.Gf, 43.20.Tb, 43.40.Rj [CBB]

INTRODUCTION

Finite multilayer structures containing poroelastic materials are widely used in many engineering applications for their sound absorption, sound insulation, and vibration damping properties. To simulate the vibroacoustic behavior of such structures, finite element and boundary element methods have been used.[1–6] For the last decade, poroelastic finite element models have been developed to complement actual finite element libraries in vibroacoustics.[1–6] These finite element models are based on the Biot's poroelasticity equations,[6] and use the solid ($\underline{u}$) and fluid ($\underline{U}$) [or relative ($\underline{W}$)] displacements as field variables. Hence, in a three-dimensional application, six degrees-of-freedom per node are required: the three components of the solid phase vector and the three components of the fluid phase vector. To reduce the number of degrees-of-freedom to its minimum, a mixed displacement-pressure ($\underline{u},p$) formulation was developed by Bonnet[7] for harmonic motions, and by Gorog *et al.*[8] in the time domain for anisotropic poroelastic materials. In a three-dimensional application, only four degrees-of-freedom per node are now required: the three components of the solid phase vector and the pore fluid pressure. The ($\underline{u},p$) model was finally solved using the finite element method and applied to acoustic problems.[9,10]

Contrary to the displacement ($\underline{u},\underline{U}$) formulation, for which boundary conditions have been derived,[3,11,12] no boundary condition for the ($\underline{u},p$) formulation has been yet derived in terms of the associated set of variables. In the following, a recall of the weak integral form of the Biot ($\underline{u},p$) formulation is first given. Then, boundary conditions for the ($\underline{u},p$) formulation are derived based on the Biot ($\underline{u},\underline{U}$) formulation. They are applied to the surface integrals of the associated weak form to account for exterior excitations, supports, and couplings with exterior elastic, acoustic, poroelastic media, and a septum. Also, the advantages of a finite element implementation of such mixed boundary conditions over the classical boundary conditions of the displacement model will be highlighted. Finally, two numerical examples are presented to validate the poroelastic-septum coupling condition, and to highlight the limitations of the free edge condition on a poroelastic medium.

I. BOUNDARY INTEGRALS OF THE WEAK FORMULATION

In this section, the boundary integrals of the weak ($\underline{u},p$) poroelastic formulation are recalled and written in a more suitable form. The problem under consideration is depicted in Fig. 1. A primary poroelastic domain Ω is supported and excited on its boundary surface Γ. This primary poroelastic domain is surrounded by elastic, acoustic, and secondary poroelastic domains. It may also be covered by a septum. Consequently, the boundary conditions applied on the boundary surface Γ are of three types: excitation, support, and coupling.

The weak formulation of the mixed ($\underline{u},p$) poroelastic boundary value problem is given by Atalla *et al.*[9] In this formulation, the integral equations related to the solid and fluid phases are, respectively,

$$\int_\Omega \hat{\underline{\underline{\sigma}}}^s(\underline{u}):\underline{\underline{\varepsilon}}^s(\delta\underline{u})\,d\Omega-\omega^2\int_\Omega \tilde{\rho}\underline{u}\cdot\delta\underline{u}\,d\Omega-\int_\Omega \tilde{\gamma}\underline{\nabla}p\cdot\delta\underline{u}\,d\Omega-\int_\Gamma[\hat{\underline{\underline{\sigma}}}^s\cdot\underline{n}]\cdot\delta\underline{u}\,dS=0\quad\forall(\delta\underline{u}),\tag{1}$$

$$\int_\Omega\left[\frac{h^2}{\omega^2\tilde{\rho}_{22}}\underline{\nabla}p\cdot\underline{\nabla}\delta p-\frac{h^2}{\tilde{R}}p\,\delta p\right]d\Omega-\int_\Omega\tilde{\gamma}\underline{\nabla}\delta p\cdot\underline{u}\,d\Omega+\int_\Gamma\left[\tilde{\gamma}u_n-\frac{h^2}{\tilde{\rho}_{22}\omega^2}\frac{\partial p}{\partial n}\right]\delta p\,dS=0\quad\forall(\delta p).\tag{2}$$

Here, Ω and Γ refer to the poroelastic domain and its boundary surface. $\underline{u}$ and p are the solid phase displacement vector

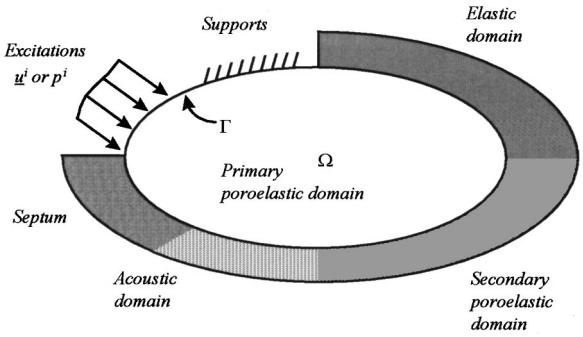

FIG. 1. Typical boundary conditions on a poroelastic domain.

and the interstitial fluid pressure of the poroelastic medium, respectively, while $\delta\underline{u}$ and δp refer to their admissible variation. $\underline{n}$ is the unit external normal vector of the boundary surface Γ, and subscript n denotes the normal component of a vector. The mass coefficients $\tilde{\rho}$, $\tilde{\rho}_{22}$ and the coupling coefficient $\tilde{\gamma}$ are given by Atalla *et al.*[9] h is the porosity of the porous material. $\underline{\underline{\varepsilon}}^s$ is the strain tensor of the solid phase and $\hat{\underline{\underline{\sigma}}}^s$ is the *in vacuo* stress tensor of the poroelastic aggregate. $\hat{\underline{\underline{\sigma}}}^s$ represents the stress tensor prevailing in the poroelastic material when the fluid is totally drained off. It is related to the total stress tensor $\underline{\underline{\sigma}}^t$ of the material by the following relation:

$$\hat{\underline{\underline{\sigma}}}^s(\underline{u}) = \underline{\underline{\sigma}}^t(\underline{u},\underline{U}) + h\left(1+\frac{\tilde{Q}}{\tilde{R}}\right)p\,\underline{\underline{1}}, \tag{3}$$

where $\underline{u}$ and $\underline{U}$ refer to the solid and fluid macroscopic displacement vectors,[6] $\tilde{Q}$ is an elastic coupling coefficient between the two phases, and $\tilde{R}$ may be interpreted as the bulk modulus of the air occupying a fraction h of a unit volume of aggregate.[13]

By substituting Eq. (3) into Eq. (1), the boundary integral of the solid phase rewrites

$$I_1 = -\int_\Gamma (\underline{\underline{\sigma}}^t\cdot\underline{n})\cdot\delta\underline{u}\,dS - \int_\Gamma h\left(1+\frac{\tilde{Q}}{\tilde{R}}\right)p\,\delta u_n\,dS, \tag{4}$$

where $\delta u_n = (\underline{\underline{1}}\cdot\underline{n})\cdot\delta\underline{u}$. This integral represents the work done by external forces on the solid phase. This writing of the boundary integral is a more suitable form for the application of the boundary conditions.

Similarly, to rewrite the boundary integral of the fluid phase weak form in a more suitable way, consider the relation between the fluid phase displacement vector $\underline{U}$ and the pressure gradient $\underline{\nabla} p$:[9]

$$\underline{U} = \frac{h}{\tilde{\rho}_{22}\omega^2}\underline{\nabla} p - \frac{\tilde{\rho}_{12}}{\tilde{\rho}_{22}}\underline{u}. \tag{5}$$

Using this relation and the expression of the coupling coefficient $\tilde{\gamma}$ given by[9]

$$\tilde{\gamma} = h\left(\frac{\tilde{\rho}_{12}}{\tilde{\rho}_{22}} - \frac{\tilde{Q}}{\tilde{R}}\right), \tag{6}$$

the boundary integral of Eq. (2) simplifies to

$$I_2 = -\int_\Gamma h\left(1+\frac{\tilde{Q}}{\tilde{R}}\right)u_n\,\delta p\,dS - \int_\Gamma h(U_n-u_n)\,\delta p\,dS, \tag{7}$$

where the second member is related to the flow through boundary Γ. This integral represents the work done by external forces on the fluid phase.

We can now use Eqs. (4) and (7) to express the different boundary conditions that apply on the boundary of a poroelastic domain modeled using the $(\underline{u},p)$ formulation.

II. EXCITATIONS

A. Case of an imposed pressure field

In the case of an imposed pressure field p^i applied on Γ, the boundary conditions that apply on Eqs. (4) and (7) are

$$\left.\begin{array}{l}\underline{\underline{\sigma}}^t\cdot\underline{n} = -p^i\underline{\underline{1}}\cdot\underline{n}\\ p = p^i\end{array}\right\}\ \text{on}\ \Gamma \tag{8}$$

which express the continuity of the total normal stress and the continuity of the pressure (i.e., no pressure drop) through the interface Γ. Since the pressure is imposed, the admissible variation δp in Eq. (7) will fall to zero. Consequently,

$$\begin{aligned} I_1 &= \int_\Gamma \left(1-h\left(1+\frac{\tilde{Q}}{\tilde{R}}\right)\right)p^i\,\delta u_n\,dS,\\ I_2 &= 0.\end{aligned} \tag{9}$$

For $h=0$, integral I_1 reduces to the weak form surface integral of an elastic domain loaded by a pressure field. However, for classical sound-absorbing materials, this term vanishes since $h(1+\tilde{Q}/\tilde{R})\cong 1$.[13]

In summary, for classical sound-absorbing materials excited by an imposed pressure field, only the kinematic relation $p=p^i$ applies on the pore pressure of the fluid phase at the boundary Γ. This boundary condition applies more simply on the $(\underline{u},p)$ finite element model than on the $(\underline{u},\underline{U})$ model, since, for the later model, nodal excitation vectors have to be computed for both phases.[3]

B. Case of an imposed displacement field

In the case of an imposed displacement field $\underline{u}^i$ applied on Γ, used in some cases to simulate a piston motion, the boundary conditions that apply on Eqs. (4) and (7) are

$$\left.\begin{array}{l}\underline{u} = \underline{u}^i\\ u_n^i = (1-h)u_n + hU_n \Rightarrow U_n - u_n = 0\end{array}\right\}\ \text{on}\ \Gamma. \tag{10}$$

The first condition expresses the continuity between the imposed displacement vector and the solid phase displacement vector. The second equation expresses the continuity of the normal displacements between the solid phase and the fluid phase. Since the displacement is imposed, the admissible variations $\delta\underline{u}$ and δu_n in Eq. (4) will fall to zero. Consequently,

$$\begin{aligned} I_1 &= 0,\\ I_2 &= -\int_\Gamma h\left(1+\frac{\tilde{Q}}{\tilde{R}}\right)u_n^i\,\delta p\,dS.\end{aligned} \tag{11}$$

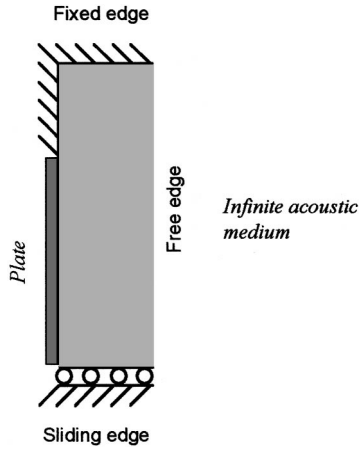

FIG. 2. Support conditions on a poroelastic material: fixed edge, sliding edge, and free edge.

Once again, for classical sound-absorbing materials, integral I_2 reduces to the classical boundary term of a fluid medium since $h(1+\tilde{Q}/\tilde{R}) \cong 1$.[13]

In the particular case of an imposed tangential displacement on Γ-shear excitation-the normal displacement u_n^i falls to zero and the boundary integral I_2 vanishes. In this case, only the kinematic relation $\underline{u} = \underline{u}^i$ is to be applied on the solid phase on Γ.

III. SUPPORTS

To account for the support conditions on a poroelastic medium, Dirichlet-type boundary conditions have to be applied on the boundary surface Γ. In general, three types of support conditions are commonly encountered: the free edge condition, the sliding edge condition, and the fixed edge condition. These three conditions are schematized in Fig. 2.

A. Free edge condition

When one part of the boundary surface is opened to an infinite acoustic medium, the free edge condition applies. This condition means that no support restrains the motion of the poroelastic frame. In reality, this is not exactly true. In fact, since the air surrounding the poroelastic material is of similar impedance as the air in the porous network, the loading of the surrounding air on the fluid phase at the free edge will not be negligible. Moreover, while this loading may be neglected for the solid phase of an elastic porous material, such as the plastic foam shown in Fig. 3(a), it has to be considered for a limp frame such as the limp white wool shown in Fig. 3(b). In a similar fashion to the fluid loading on an elastic plate, the loading of the surrounding fluid on the poroelastic material must be taken into account by a radiation impedance condition. The evaluation of the radiation impedance of a poroelastic material is a more complex problem than the boundary conditions presented in this paper. On-going works are currently being performed to develop such a radiation impedance condition for poroelastic media.[14]

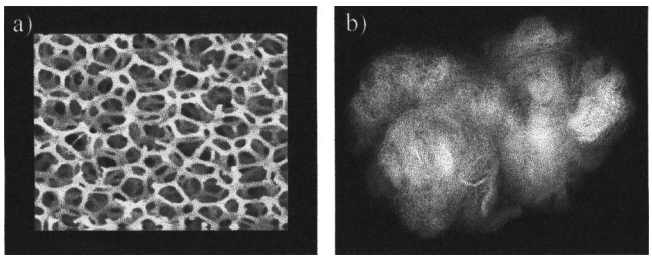

FIG. 3. Typical porous materials: elastic frame and limp frame.

In this paper, to simplify the free edge condition problem, only the case of a plate bonded to a poroelastic material and vibrating in an infinite acoustic medium is addressed. In this case, it is assumed that the impedance of the solid phase is much higher than the impedance of the surrounding acoustic medium, and that only the elastic behavior of the poroelastic material has a notable effect on the plate vibrations. Following these assumptions, one can consider the plate-porous system vibrating *in vacuo*. Hence, to simulate this particular case, the boundary conditions to apply on the $(\underline{u},p)$ formulation are

$$\left.\begin{array}{l} \underline{\underline{\sigma}}^t \cdot \underline{n} = 0 \\ p = 0 \end{array}\right\} \quad \text{on } \Gamma, \tag{12}$$

where Γ is the free surface in contact with the exterior medium. These conditions indicate that there is no loading on the free surface. Consequently, there is no external work on Γ, and integral I_1 and I_2 fall naturally to zero. The solid displacement is then free on Γ, and the pressure field has to be explicitly imposed to zero on Γ. A validation test of the previous assumptions is presented in Sec. V.

B. Fixed edge condition

To simulate the case of a poroelastic medium bonded onto a rigid impervious wall, the following boundary conditions apply on the corresponding rigid surface Γ:

$$\left.\begin{array}{l} \underline{u} = 0 \\ U_n - u_n = 0 \end{array}\right\} \quad \text{on } \Gamma. \tag{13}$$

Here, the solid phase displacement vector and the normal relative displacement vanish at the rigid wall. These conditions imply that there is no motion on Γ. Since the solid displacements are imposed, the admissible variations $\delta\underline{u}$ and δu_n in Eq. (4) will fall to zero. Consequently, there is no external work on Γ and integrals I_1 and I_2 fall naturally to zero. The interstitial pressure field p is then free on Γ, and the solid displacement vector has to be explicitly imposed to zero on Γ.

C. Sliding edge condition

The sliding edge condition signifies that the normal displacements on Γ—here an impervious rigid wall—are constrained and the tangential displacements are free. This is represented by the following boundary conditions:

$$\left.\begin{array}{l} \sigma_s^t = 0 \\ u_n = 0 \\ U_n - u_n = 0 \end{array}\right\} \quad \text{on } \Gamma. \tag{14}$$

The first condition expresses that no tangential stress (σ_s^t) acts on Γ. The second and third conditions indicate that the normal solid displacement and the relative displacement vanish at the rigid wall, respectively. Since the normal solid displacement is imposed, the admissible variation δu_n in Eq. (4) will fall to zero. Consequently, knowing that there is no work tangential to Γ, integrals I_1 and I_2 fall naturally to zero. The interstitial pressure field p and the tangential solid displacements are then free on Γ, and the normal solid displacement has to be explicitly imposed to zero.

In a finite element implementation, the fixed and the sliding support conditions apply, once again, more simply on the $(\underline{u},p)$ poroelastic model than on the $(\underline{u},\underline{U})$ model. In fact, in the later model, both the fixed and sliding conditions imply that a Dirichlet condition has to be applied simultaneously on the solid and fluid phases on Γ.

IV. COUPLINGS

In many practical situations, poroelastic materials are used in multilayer configurations. They increase the attenuation of the system in terms of absorption, transmission, and structural damping. These multilayers may be made up from several elastic, acoustic, poroelastic, and septum layers, e.g., the roof of a car or an aircraft panel. In the following, the different coupling conditions shown in Fig. 1 are presented and applied to the boundary integrals of the mixed $(\underline{u},p)$ poroelastic weak formulation, Eqs. (4) and (7).

A. Poroelastic-elastic coupling condition

The elastic medium is described in terms of its displacement vector $\underline{u}^e$. If the weak formulation of the poroelastic medium is combined with the one of the elastic medium,[3] the boundary integrals, Eqs. (4) and (7), of the assembly rewrite as

$$\begin{aligned} I_1 &= -\int_\Gamma (\underline{\underline{\sigma}}^t\cdot\underline{n})\cdot\delta\underline{u}\,dS - \int_\Gamma h\left(1+\frac{\tilde{Q}}{\tilde{R}}\right) p\,\delta u_n\,dS \\ &\quad + \int_\Gamma (\underline{\underline{\sigma}}^e\cdot\underline{n})\cdot\delta\underline{u}\,dS, \\ I_2 &= -\int_\Gamma h\left(1+\frac{\tilde{Q}}{\tilde{R}}\right) u_n\,\delta p\,dS - \int_\Gamma h(U_n-u_n)\,\delta p\,dS, \end{aligned} \tag{15}$$

where $\underline{\underline{\sigma}}^e$ represents the stress tensor of the elastic medium. The positive sign of the third term of I_1 is due to the direction of the normal vector $\underline{n}$, inward to the elastic medium. The coupling conditions at the interface Γ are given by Panneton *et al.*:[3]

$$\left.\begin{array}{l} \underline{\underline{\sigma}}^t\cdot\underline{n} = \underline{\underline{\sigma}}^e\cdot\underline{n} \\ U_n - u_n = 0 \\ \underline{u} = \underline{u}^e \end{array}\right\} \quad \text{on } \Gamma. \tag{16}$$

The first equation ensures the continuity of the total normal stresses at the interface. The second equation expresses the fact that there is no relative mass flux across the interface. The third equation ensures the continuity of the solid displacement vectors.

Substituting the two first relations of Eq. (16) into Eq. (15) leads to

$$\begin{aligned} I_1 &= -\int_\Gamma h\left(1+\frac{\tilde{Q}}{\tilde{R}}\right) p\,\delta u_n\,dS, \\ I_2 &= -\int_\Gamma h\left(1+\frac{\tilde{Q}}{\tilde{R}}\right) u_n\,\delta p\,dS. \end{aligned} \tag{17}$$

These equations show that the poroelastic medium will be coupled to the elastic medium through a symmetrical coupling term. This coupling occurs naturally between the normal displacement vector of the elastic medium and the interstitial fluid pressure of the poroelastic medium. In addition to this surface coupling term, the kinematic relation $\underline{u}=\underline{u}^e$ will have to be explicitly imposed on Γ.

For classical sound absorbing materials for which $h(1+\tilde{Q}/\tilde{R})\cong 1$, Eq. (17) reduces to the classical coupled fluid-structure problem, e.g., plate-cavity problem. This emphasizes the advantage of the $(\underline{u},p)$ formulation over the $(\underline{u},\underline{U})$ formulation.

B. Poroelastic-acoustic coupling condition

The acoustic medium is described in terms of its pressure field p^a. Combining both the weak formulations of the poroelastic and acoustic media,[3] the boundary integrals, Eqs. (4) and (7), rewrite as

$$\begin{aligned} I_1 &= -\int_\Gamma (\underline{\underline{\sigma}}^t\cdot\underline{n})\cdot\delta\underline{u}\,dS - \int_\Gamma h\left(1+\frac{\tilde{Q}}{\tilde{R}}\right) p\,\delta u_n\,dS, \\ I_2 &= -\int_\Gamma h\left(1+\frac{\tilde{Q}}{\tilde{R}}\right) u_n\,\delta p\,dS - \int_\Gamma h(U_n-u_n)\,\delta p\,dS \\ &\quad + \int_\Gamma \frac{1}{\rho_0\omega^2}\frac{\partial p^a}{\partial n}\,\delta p^a\,dS, \end{aligned} \tag{18}$$

where ρ_0 refers to the density of the acoustic medium. The positive sign of the last term of I_2 is due to the direction of the normal vector $\underline{n}$, inward to the acoustic medium. The coupling conditions at the interface Γ are given by Panneton *et al.*:[3]

$$\left.\begin{array}{l} \underline{\underline{\sigma}}^t\cdot\underline{n} = -p^a\underline{n} \\ \dfrac{1}{\rho_0\omega^2}\dfrac{\partial p^a}{\partial n} = (1-h)u_n + hU_n = u_n + h(U_n-u_n) \\ p = p^a \end{array}\right\} \quad \text{on } \Gamma. \tag{19}$$

The first equation ensures the continuity of the normal stresses on Γ. The second equation ensures the continuity of the relative mass flux across the boundary. The third equation refers to the continuity of the pressure across the boundary.

Substituting Eq. (19) into Eq. (18), the boundary integrals rewrite as

$$I_1 = \int_\Gamma \left(1-h-h\frac{\tilde{Q}}{\tilde{R}}\right) p^a\,\delta u_n\,dS, \tag{20}$$

$$I_2 = \int_\Gamma \left(1 - h - h\frac{\tilde{Q}}{\tilde{R}}\right) u_n \delta p^a \, dS.$$

These equations show that the poroelastic medium will be coupled to the acoustic medium through a symmetrical coupling term. This coupling occurs naturally between the solid phase normal displacement and the acoustic pressure on Γ. In addition to this surface coupling term, the kinematic relation $p = p^a$ will have to be explicitly imposed on Γ.

For classical sound absorbing materials for which $h(1 + \tilde{Q}/\tilde{R}) \cong 1$, integrals I_1 and I_2 in Eq. (19) fall to zero. Thus, the coupling term in Eq. (20) is eliminated and only the kinematic relation $p = p^a$ has to be applied. This simplified poroelastic-acoustic coupling condition makes the $(\underline{u}, p)$ model more interesting than the $(\underline{u}, \underline{U})$ model. In the later model, coupling terms appear between the acoustic medium and the solid and fluid phases of the poroelastic medium.

C. Poroelastic-poroelastic coupling condition

Let indices 1 and 2 denote the primary and secondary poroelastic media, respectively. Here, $\underline{n}$ is the normal vector outward to the primary poroelastic medium. Both media are described in terms of the solid phase displacement vector $\underline{u}$ and the fluid phase interstitial pressure p. Combining the weak integral formulations of both poroelastic media—Eqs. (4) and (7) for both media—the boundary integrals, rewrite

$$\begin{aligned} I_1 = &- \int_\Gamma (\underline{\underline{\sigma}}_1^t \cdot \underline{n}) \cdot \delta \underline{u}_1 \, dS - \int_\Gamma h_1 \left(1 + \frac{\tilde{Q}_1}{\tilde{R}_1}\right) p_1 \delta u_{1n} \, dS \\ &+ \int_\Gamma (\underline{\underline{\sigma}}_2^t \cdot \underline{n}) \cdot \delta \underline{u}_2 \, dS + \int_\Gamma h_2 \left(1 + \frac{\tilde{Q}_2}{\tilde{R}_2}\right) p_2 \delta u_{2n} \, dS, \end{aligned} \tag{21}$$

$$\begin{aligned} I_2 = &- \int_\Gamma h_1 \left(1 + \frac{\tilde{Q}_1}{\tilde{R}_1}\right) u_{1n} \delta p_1 \, dS - \int_\Gamma h_1 (U_{1n} - u_{1n}) \delta p_1 \, dS \\ &+ \int_\Gamma h_2 \left(1 + \frac{\tilde{Q}_2}{\tilde{R}_2}\right) u_{2n} \delta p_2 dS + \int_\Gamma h_2 (U_{2n} - u_{2n}) \delta p_2 \, dS. \end{aligned}$$

The opposite signs between the two first terms and the two last terms of both integrals I_1 and I_2 are due to the direction of the normal vector $\underline{n}$, outward to the primary poroelastic medium. The coupling equations at the interface Γ are given by Panneton *et al.*:[3]

$$\left.\begin{array}{l} \underline{\underline{\sigma}}_1^t \cdot \underline{n} = \underline{\underline{\sigma}}_2^t \cdot \underline{n} \\ h_1 (U_{1n} - u_{1n}) = h_2 (U_{2n} - u_{2n}) \\ \underline{u}_1 = \underline{u}_2 \\ p_1 = p_2 \end{array}\right\} \quad \text{on } \Gamma. \tag{22}$$

The first condition ensures the continuity of the total normal stresses. The second equation ensures the continuity of the relative mass flux across the boundary. The two last equations ensure the continuity of the solid phase displacement vector and the interstitial fluid pressure, respectively.

Substituting the first and third relations of Eq. (22) into Eq. (21), the boundary integral I_1 reduces to

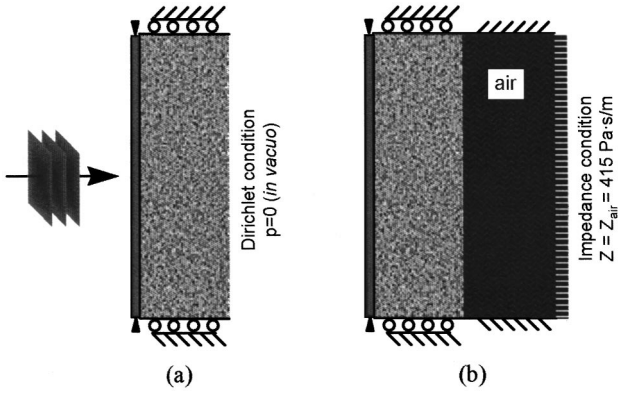

FIG. 4. Configurations for the validation of the free edge boundary condition on the foam.

$$\begin{aligned} I_1 = &- \int_\Gamma h_1 \left(1 + \frac{\tilde{Q}_1}{\tilde{R}_1}\right) p_1 \delta u_{1n} \, dS \\ &+ \int_\Gamma h_2 \left(1 + \frac{\tilde{Q}_2}{\tilde{R}_2}\right) p_2 \delta u_{2n} \, dS. \end{aligned} \tag{23}$$

Substituting the second and fourth relations of Eq. (22) into Eq. (21), the boundary integral I_2 reduces to

$$\begin{aligned} I_2 = &- \int_\Gamma h_1 \left(1 + \frac{\tilde{Q}_1}{\tilde{R}_1}\right) u_{1n} \delta p_1 \, dS \\ &+ \int_\Gamma h_2 \left(1 + \frac{\tilde{Q}_2}{\tilde{R}_2}\right) u_{2n} \delta p_2 \, dS. \end{aligned} \tag{24}$$

Equations (23) and (24) show that the primary poroelastic medium will be coupled to the secondary poroelastic medium through symmetrical coupling terms. This coupling occurs naturally between the solid phase normal displacement of one medium and the interstitial fluid pressure of the other medium. In addition to these surface coupling terms, the kinematic relation $\underline{u}_1 = \underline{u}_2$ and $p_1 = p_2$ will have to be explicitly applied on Γ.

For classical sound absorbing materials for which $h(1 + \tilde{Q}/\tilde{R}) \cong 1$, both integrals I_1 and I_2 fall to zero. In this case, only the kinematic relations have to be applied. These relations are naturally taken into account in the assembly process. This poroelastic-poroelastic coupling condition is simpler than the one required for the $(\underline{u}, \underline{U})$ model. In fact, for the later model, kinematic relations between u_1, U_1, u_2 and U_2—see Eq. (22)—have to be explicitly applied on Γ. In a finite element implementation, these relations cannot be simply taken into account during the assembly process since it is not a one-to-one kinematic relation as $u_1 = u_2$. Lagrange multipliers or matrix manipulations have to be used.

D. Poroelastic-septum coupling condition

Here, the septum is represented by the surface domain S. It is assumed to be a very limp and thin impervious layer having a surface density m. The septum is described in terms of its displacement vector $\underline{u}^s$. One side of the septum is in contact with the poroelastic domain (surface S^+ or Γ^-), and the other side supports the loading (surface S^-). The hypoth-

TABLE I. Physical properties and dimensions for the structures presented in Fig. 4.

Plate	
Width	$a=0.35$ m
Height	$b=0.22$ m
Thickness	$e=0.001$ m
Mass density	$\rho_s=2742$ kg/m^3
Young's modulus	$E_s=69$ GPa
Plane wave amplitude	$P_i=1$ N/m^2
Poisson's ratio	$\nu=0.33$
Loss factor	$\eta_s=0.007$
Foam	
Thickness	$e=0.05$ m
Flow resistivity	$\sigma=13.5$ kNs/m^4
Porosity	$h=0.98$
Tortuosity	$\alpha_\infty=1.7$
Viscous characteristic dimension	$\Lambda=80$ μm
Thermal characteristic dimension	$\Lambda'=160$ μm
Poisson's ratio	$\nu=0.35$
Bulk modulus	$E=540$ kPa
Loss factor	$\eta=0.1$
Solid mass density	$\rho_1=30$ kg/m^3
Air cavity	
Thickness	$e=0.01$ m
Fluid mass density	$\rho_0=1.213$ kg/m^3
Sound speed	$c_0=342.2$ m/s
Impedance surface	
Air impedance	$Z_0=415$ Pa.s/m

esis of a thin layer supposes that S and Γ are virtually the same. The virtual work principle applied to the septum leads to

$$\int_S \omega^2 m \underline{u}^s \cdot \delta \underline{u}^s \, dS + \int_{S^- \cup S^+} t \cdot \delta \underline{u}^s \, dS = 0. \tag{25}$$

The first term corresponds to the work of the inertial forces while the second term corresponds to the work of the exterior forces. The exterior forces acting on the septum are written as follows:

$$\begin{aligned} &\underline{t} = -\underline{\underline{\sigma}}^t \cdot \underline{n} \quad \text{on } S^+, \\ &\underline{t} = \underline{F} \quad \text{on } S^-, \end{aligned} \tag{26}$$

where $\underline{\underline{\sigma}}^t$ is the total stress tensor of the poroelastic medium, and $\underline{F}$ is the excitation force vector applied on the septum. By considering the hypothesis of a thin layer, S, S^-, S^+, and Γ are virtually the same. Substituting Eq. (26) into Eq. (25), the virtual work principle rewrites as

$$\int_\Gamma \omega^2 m \underline{u}^s \cdot \delta \underline{u}^s \, dS - \int_\Gamma (\underline{\underline{\sigma}}^t \cdot \underline{n}) \cdot \delta \underline{u}^s \, dS + \int_\Gamma \underline{F} \cdot \delta \underline{u}^s \, dS = 0. \tag{27}$$

Also, at the septum-poroelastic interface, the following conditions have to be verified:

$$\left.\begin{aligned} &h(U_n - u_n) = 0 \\ &\underline{u} = \underline{u}^s \end{aligned}\right\} \quad \text{on } \Gamma. \tag{28}$$

The first relation indicates that there is no mass flux across the boundary Γ, and the second relation expresses the continuity of the displacement vectors. Substituting the second Eq. (28) into Eq. (27) yields

$$-\int_\Gamma (\underline{\underline{\sigma}}^t \cdot \underline{n}) \cdot \delta \underline{u} \, dS = -\int_\Gamma \omega^2 m \underline{u} \cdot \delta \underline{u} \, dS - \int_\Gamma \underline{F} \cdot \delta \underline{u} \, dS. \tag{29}$$

Now, substituting Eqs. (29) and (27) into the boundary integral Eq. (4) and substituting the first Eq. (28) into the boundary integral Eq. (7) leads to

$$\begin{aligned} I_1 &= -\int_\Gamma \omega^2 m \underline{u} \cdot \delta \underline{u} \, dS \\ &\quad - \int_\Gamma \underline{F} \cdot \delta \underline{u} \, dS - \int_\Gamma h \left(1 + \frac{\tilde{Q}}{\tilde{R}}\right) p \, \delta u_n \, dS, \\ I_2 &= -\int_\Gamma h \left(1 + \frac{\tilde{Q}}{\tilde{R}}\right) u_n \delta p \, dS. \end{aligned} \tag{30}$$

Therefore, the effect of the impervious screen on the poroelastic medium consists of a classical symmetrical coupling term (common term to I_1 and I_2), an added mass term (first term of I_1), and an excitation term (second term of I_1).

V. VALIDATION

Validations of the different coupling and excitation conditions have been realized by comparing the $(\underline{u},p)()$ and $(\underline{u},\underline{U})$ formulations.[10] They are not presented here for conciseness. The section will concentrate mostly on the valida-

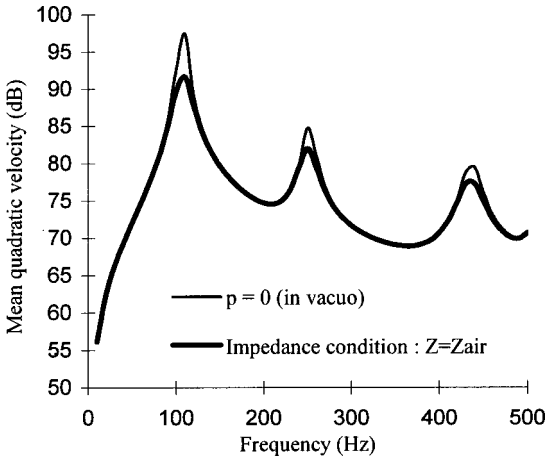

FIG. 5. Mean quadratic velocity of the plate for the plate-foam system shown in Fig. 4. Effects of the light fluid loading on the foam.

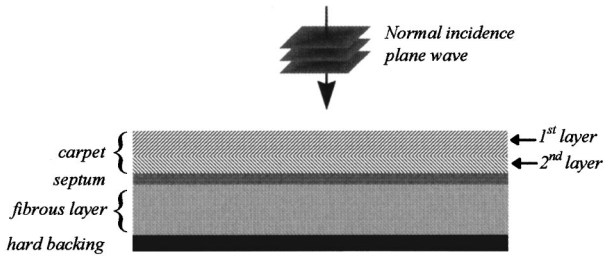

FIG. 6. Configuration of the multilayer acoustic material.

TABLE II. Physical properties and dimensions for the system depicted in Fig. 6.

Carpet—First layer	
Thickness	$e=0.0035$ m
Flow resistivity	$\sigma=20$ kNs/m^4
Porosity	$h=0.99$
Tortuosity	$\alpha_\infty=1$
Viscous characteristic dimension	$\Lambda=150$ μm
Thermal characteristic dimension	$\Lambda'=220$ μm
Poisson's ratio	$\nu=0$
Bulk modulus	$E=20$ kPa
Loss factor	$\eta=0.5$
Solid mass density	$\rho_1=60$ kg/m^3
Carpet—Second layer	
Thickness	$e=0.0035$ m
Flow resistivity	$\sigma=5$ kNs/m^4
Porosity	$h=0.99$
Tortuosity	$\alpha_\infty=1$
Viscous characteristic dimension	$\Lambda=230$ μm
Thermal characteristic dimension	$\Lambda'=280$ μm
Poisson's ratio	$\nu=0$
Bulk modulus	$E=20$ kPa
Loss factor	$\eta=0.5$
Solid mass density	$\rho_1=60$ kg/m^3
Septum	
Thickness	$e=0.003$ m
Mass density	$\rho_s=2000$ kg/m^3
Fibrous layer	
Thickness	$e=0.0125$ m
Flow resistivity	$\sigma=33$ kNs/m^4
Porosity	$h=0.98$
Tortuosity	$\alpha_\infty=1.1$
Viscous characteristic dimension	$\Lambda=50$ μm
Thermal characteristic dimension	$\Lambda'=100$ μm
Poisson's ratio	$\nu=0$
Bulk modulus	$E=100$ kPa
Loss factor	$\eta=0.88$
Solid mass density	$\rho_1=60$ kg/m^3

tions of the free edge condition and the coupling with a septum. In the first case, comparison is made between two numerical results using the finite element method to verify the assumptions of Sec. III A. Concerning the septum, a comparison is made between numerical results, analytical results and experimental results found in the literature.[15]

A. Validation of the free edge condition

The problem under consideration is shown in Fig. 4(a). A normal acoustic plane wave excites a plate-foam system vibrating in an infinite acoustic medium. The foam is bonded onto the plate. The plate is simply supported on its four edges, and sliding conditions are applied on the four lateral faces of the foam. Two different types of boundary conditions, applied at the rear face of the foam, are studied: first, the free edge condition of Eq. (12) [see Fig. 4(a)] second, the coupling condition with an acoustic cavity ended by an acoustic impedance surface [see Fig. 4(b)]. The speed of sound c and the acoustic impedance Z are set to the ambient air value to simulate a coupling with an infinite air medium. The material properties and dimensions of the studied configuration are listed in Table I. The frequency range of interest is 0–500 Hz.

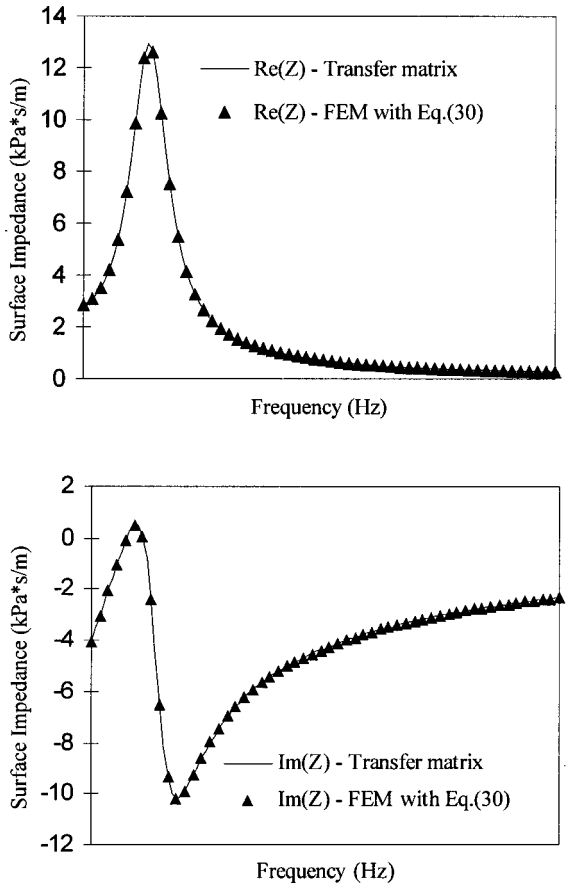

FIG. 7. Normal surface impedance of the multilayer system shown in Fig. 6. Comparison between numerical and analytical predictions.

To identify if the proposed free edge condition applies when the poroelastic medium is coupled to an infinite exterior light fluid, such as air, the configuration shown in Fig. 4(a) is compared with the configuration shown in Fig. 4(b). The mean quadratic velocities of the plate in these two configurations are presented in Fig. 5. The results are not strictly identical. The plate resonances and the off-resonance vibration levels are identical, but the vibration levels at the resonances are lower in the case where the foam is coupled to the infinite air medium; yet, it is noted that this difference in the level reduces with increasing frequencies. This may be explained by the fact that as the excitation frequency departs, toward higher frequencies, from the decoupling frequency between the fluid and solid phases of the poroelastic material, the coupling between both phases gets weaker[13] and, ultimately, the behavior of the system approaches the *in vacuo* behavior. For the foam described in Table I, the decoupling frequency is around 70 Hz.

B. Coupling with a septum

A septum is often used in practical applications to protect a porous layer and to increase its sound absorption at low frequencies. In the following, the use of Eq. (30) in a finite element implementation to account for the effect of the septum on a poroelastic material is validated. The studied

configuration is depicted in Fig. 6. It consists of a multilayer material excited by an normal acoustic plane wave. The multilayer material is made up of a carpet, a septum, and a fibrous layer. The carpet is modeled as a porous material made up of two layers. The material properties and dimensions of the multilayer material are listed in Table II. The frequency range of interest is 200–1300 Hz.

In view of comparing the normal surface impedance predicted by the finite element model, based on Eq. (30), with the one predicted by a transfer matrix method,[13] the assumption of infinite lateral dimensions is made. Figure 7 compares the results obtained by these two models. It is shown that both models predict identical results. Consequently, the use of Eq. (28) to account for the coupling between a poroelastic medium and a septum is validated.

VI. CONCLUSION

In this paper, boundary conditions on a poroelastic medium have been developed for the poroelastic mixed $(\underline{u},p)$ formulation. The developed boundary conditions account for exterior excitations, supports, and couplings with exterior elastic, acoustic, poroelastic, and septum media. The surface integrals of the weak form of the mixed $(\underline{u},p)$ formulation have been rewritten for each boundary condition. It was shown that these surface integrals for the $(\underline{u},p)$ formulation handle more directly and simply, in a finite element sense, the various boundary conditions on a poroelastic medium than does the $(\underline{u},\underline{U})$ formulation. Consequently, the $(\underline{u},p)$ formulation leads to simpler finite element equations.

Finally, validations against numerical and analytical results have shown the validity of the free edge condition and the poroelastic-septum coupling condition. However, when the foam is coupled to an infinite exterior air medium, it has been shown that the exterior fluid loading on the foam may be important. Consequently, the free edge condition has to be used with prudence.

ACKNOWLEDGMENTS

The authors wish to thank Bombardier Aerospace, the Natural Sciences and Engineering Research Council of Canada (N.S.E.R.C.), and the Fonds pour la formation de chercheurs et l'aide à la recherche du Québec (F.C.A.R.) for their financial support.

[1] R. Panneton, N. Atalla, and J.-F. Allard, ''A 3-D finite element model for sound transmission through a double-plate system with isotropic elastic porous materials,'' J. Acoust. Soc. Am. **96**, 3339 (1994).

[2] R. Panneton and N. Atalla, ''Numerical prediction of sound transmission through multilayer systems with isotropic poroelastic materials,'' J. Acoust. Soc. Am. **100**, 346–354 (1996).

[3] R. Panneton and N. Atalla, ''An efficient finite element scheme for solving the three-dimensional poroelasticity problem in acoustics,'' J. Acoust. Soc. Am. **101**, 3287–3298 (1997).

[4] V. Easwaran, W. Lauriks, and J. P. Coyette, ''Displacement-based finite element method for guided wave propagation problems: Application to poroelastic media,'' J. Acoust. Soc. Am. **100**, 2989–3002 (1996).

[5] Y. J. Kang and J. S. Bolton, ''A finite element model for sound transmission through foam-lined double-panel structures,'' J. Acoust. Soc. Am. **99**, 2755–2765 (1996).

[6] M. A. Biot, ''The theory of propagation of elastic waves in a fluid-saturated porous solid,'' J. Acoust. Soc. Am. **28**, 168–191 (1956).

[7] G. Bonnet, ''Basic singular solutions for a poroelastic medium in the dynamic range,'' J. Acoust. Soc. Am. **82**, 1758–1762 (1987).

[8] S. Gorog, R. Panneton, and N. Atalla, ''Mixed displacement-pressure formulation for acoustic anisotropic open porous media,'' J. Appl. Phys. **82**, 4192–4196 (1997).

[9] N. Atalla, R. Panneton, and P. Debergue, ''A mixed displacement pressure formulation for poroelastic materials,'' J. Acoust. Soc. Am. **104**, 1444–1452 (1998).

[10] P. Debergue, ''Développement d'une formulation mixte en déplacement-pression pour les matériaux poroélastiques,'' Master thesis, Univ. de Sherbrooke, Québec, Canada, 1998.

[11] H. Deresiewicz and R. Skalak, ''On uniqueness in dynamic poroelasticity,'' Bull. Seismol. Soc. Am. **53**, 783–788 (1963).

[12] O. M. Lovera, ''Boundary conditions for a fluid-saturated porous solid,'' Geophysics **52**, 174–178 (1987).

[13] J.-F. Allard, *Propagation of Sound in Porous Media: Modeling Sound Absorbing Materials* (Elsevier, New York, 1993).

[14] R. Panneton, ''Calculation of the sound radiation impedance of a poroelastic material,'' GAUS Report, Mech. Eng. Dept., Univ. of Sherbrooke (1998).

[15] B. Brouard, D. Lafarge, and J.-F. Allard, ''Measurement and prediction of the surface impedance of a resonant sound absorbing structure,'' Acta Acust. (China) **2**, 301–306 (1994).

Exact solution for sound propagation in ducts with an axial mean temperature gradient and particulate damping

B. Karthik, R. Krishna Mohanraj, Rajesh Ramakrishnan, and R. I. Sujith
Department of Aerospace Engineering, I. I. T. Madras, India 600036

(Received 12 December 1998; accepted for publication 19 July 1999)

An exact solution for one-dimensional sound propagation in ducts in the presence of axial mean temperature gradient and particulate damping is presented in this paper. The acoustic wave equation is derived starting from the one-dimensional momentum and energy equation. The application of appropriate transformations leads to an analytically solvable Whittaker's differential equation for the case of a linear mean temperature gradient and Bessel's differential equation for the case of an exponential mean temperature gradient. The derived analytical solutions are used to investigate the dependence of the acoustic field in a duct on temperature gradient and particulate damping. [S0001-4966(99)02211-0]

PACS numbers: 43.20.Mv, 43.20.Tb [DEC]

LIST OF SYMBOLS

c_1,c_2	coefficients of solutions in Eqs. (26) and (36)
i	$\sqrt{-1}$, imaginary number
J_n	Bessel function of nth order
K	damping coefficient (kg/m^{3}s)
M, W	Whittakers's functions
p	pressure
P	complex acoustic pressure amplitude (Pa)
R	specific gas constant (J/kg/K)
s	transformation variable in Eqs. (33) and (34)
t	time (s)
T	temperature (K)
u	velocity (m/s)
U	complex acoustic velocity amplitude (m/s)
x	distance (m)
z	transformation variable in Eqs. (14) and (15)
ρ	density (kg/m^3)
α,β	constants in Eqs. (20) and (28)
ω	angular frequency (rad/s)
τ	transformation constant in Eqs. (13) and (14)
κ	temperature gradient (K/m)
η,ν	constants in Eqs. (32) and (33)
μ,χ	constants in Eqs. (15) and (16)
Φ	confluent hypergeometric function

Superscripts

$'$	oscillating quantity
$\bar{}$	time-averaged quantity
*	complex conjugate

INTRODUCTION

The objective of this paper is to obtain exact analytical solutions for acoustic waves in ducts in the presence of factors such as mean temperature gradient and particulate damping. The behavior of one-dimensional acoustic fields in ducts is a problem of considerable scientific and practical interest. For instance, there is a need to develop an understanding of the manner in which a mean axial temperature gradient (caused, for example, by heat transfer to or from the walls) in the presence of mean flow affects the propagation of sound waves and the stability of small amplitude disturbances in a duct. Such understanding will improve existing capabilities for controling combustion instabilities in propulsion and power generating systems, designing pulse combustors and automotive mufflers, analyzing the behavior of resonating thermal systems, and measuring impedances of high-temperature systems (e.g., flames). These results can also be used to analyze the propagation of sound waves in catalytic converters.

In real life problems, some amount of damping is always present. Examples of this includes solid rocket motors with aluminized propellants, resonant driving of packed beds and spray dryers, and drying of slurries in pulse combustor tail pipe to accelerate drying. Therefore, it is desirable to obtain exact analytical solutions that describe one-dimensional wave systems in ducts with axial mean temperature gradients and damping.

Cummings[1] developed an approximate, semi-analytical solution for ducts with axial mean temperature gradients in the absence of mean flows which is valid at sufficiently high frequencies. Munjal and Prasad[2] and Peat[3] developed exact solutions for ducts with small temperature gradients, in the presence of mean flows. Kapur *et al.*[4] obtained numerical solutions for sound propagation in ducts with axial temperature gradients, in the absence of mean flows, by integrating the wave equation using a Runge–Kutta method. The same approach was followed by Zinn and co-workers[5–9] who developed the impedance tube technique for high-temperature systems, in the presence of mean flows. Sujith *et al.*[10–12] have found exact solutions for acoustic waves in ducts which are valid even in the presence of large temperature gradients. Cherng and Tsung-Yen[13] developed an analytical method for the determination of the required shape of a duct for a prescribed sound pressure level distribution in the presence of

an unsteady isentropic flow. Recently Peat[14,15] developed an approximate analytical solution for sound propagation through capillary ducts with very small temperature gradients in the presence of mean flow. Munjal and Doige[16] adapted the two-microphone method for sound propagation in the presence of mean flow and acoustic damping.

While the numerical solutions are accurate they often do not provide adequate insight and feel for the physics of the problem. Analytical solutions can also be used to benchmark numerical results. Hence it is desirable to obtain analytical solutions.

A derivation of the exact solution that describes the behavior of one-dimensional oscillations in a duct with a mean temperature gradient and particulate damping is outlined in this paper. First, the one-dimensional wave equation for a constant area duct with an arbitrary axial temperature gradient and particulate damping in the absence of mean flow is derived for a perfect, inviscid, and non-heat-conducting gas. Next, assuming periodic solutions, the derived wave equation is reduced to a second-order wave equation with variable coefficients. Using appropriate transformations, this second-order wave equation is then reduced to Whittaker's equation for the case of a linear mean temperature profile and Bessel's differential equation for an exponential mean temperature profile. The analysis is valid only for very small mean Mach numbers.

I. DERIVATION OF THE WAVE EQUATION

This section begins with the development of the wave equation for a constant area duct with a mean temperature gradient and damping. Assuming a perfect, inviscid, and non-heat-conducting gas, the one-dimensional acoustic momentum, energy[17] in the absence of mean flow, and the equation of state can be expressed in the following form.[5–8]
Momentum:

$$\overline{\rho}\frac{\partial u'}{\partial t}+\frac{\partial p'}{\partial x}+Ku'=0. \tag{1}$$

Energy:

$$\frac{\partial p'}{\partial t}+\gamma\overline{p}\frac{\partial u'}{\partial x}=0. \tag{2}$$

State:

$$p=\rho RT. \tag{3}$$

Assuming a harmonic solution of the form

$$u'=U(x)e^{i\omega t};\quad p'=P(x)e^{i\omega t}, \tag{4}$$

Eqs. (1) and (2) become

$$U(i\omega\overline{\rho}+K)+\frac{dP}{dx}=0, \tag{5}$$

$$Pi\omega+\gamma\overline{p}\frac{dU}{dx}=0. \tag{6}$$

Solving Eqs. (5) and (6) by eliminating P and its derivative yields

$$\frac{d^2U}{dx^2}+\left(\frac{\omega^2\overline{\rho}}{\gamma\overline{p}}-\frac{K\omega}{\gamma\overline{p}}i\right)U=0. \tag{7}$$

Using the equation of state, i.e., Eq. (3), the preceding equation becomes

$$\frac{d^2U}{dx^2}+\left(\frac{\omega^2}{\gamma R\overline{T}}-\frac{K\omega}{\gamma\overline{p}}i\right)U=0. \tag{8}$$

Transforming the above equation to mean temperature space, the preceding equation reduces to

$$\left(\frac{d\overline{T}}{dx}\right)^2\frac{d^2U}{d\overline{T}^2}+\frac{d^2\overline{T}}{dx^2}\frac{dU}{d\overline{T}}+\left(\frac{\omega^2}{\gamma R\overline{T}}-\frac{K\omega}{\gamma\overline{p}}i\right)U=0. \tag{9}$$

II. SOLUTION FOR A DUCT WITH A LINEAR TEMPERATURE PROFILE

In this section, solution is found for wave propagation in ducts with a linear mean temperature distribution, which is given by the expression

$$\overline{T}=T_0+\kappa x. \tag{10}$$

Transforming Eq. (8) from the x space to the mean temperature space using Eq. (10) yields

$$\frac{d^2U}{d\overline{T}^2}+\left(\frac{\omega^2}{\gamma R\kappa^2\overline{T}}-\frac{K\omega}{\gamma\overline{p}\kappa^2}i\right)U=0. \tag{11}$$

In order to simplify Eq. (11) to Whittaker's form of differential equation the following variables are introduced:

$$\overline{T}=\tau z, \tag{12}$$

where

$$\tau=\kappa\sqrt{\frac{\gamma\overline{p}}{K\omega i}}. \tag{13}$$

Substituting Eq. (12) in Eq. (11) yields the following equation:

$$\frac{d^2U}{dz^2}+\left(-\frac{1}{4}+\frac{\tau\omega^2/\gamma R\kappa^2}{z}\right)U=0. \tag{14}$$

The above equation is a special case of the Whittaker's form of differential equation whose general form is given as[18–20]

$$\frac{d^2U}{dz^2}+\left(-\frac{1}{4}+\frac{\chi}{z}+\frac{1/4-\mu^2}{z^2}\right)U=0, \tag{15}$$

where

$$\mu=\frac{1}{2}\quad\text{and}\quad\chi=\frac{\tau\omega^2}{\gamma R\kappa^2}. \tag{16}$$

Equation (15) is a second-order ordinary differential equation which has two linearly independent solutions. One of the solutions, U_1, is given by the Whittaker's first solution

$$U_1=M_{\mu,\chi}(z). \tag{17}$$

The function M is given by expression

$$M_{\mu,\chi}(z)=z^{\mu+1/2}e^{-z/2}\Phi(\tfrac{1}{2}-\chi+\mu,2\mu+1;z)$$
$$=ze^{-z/2}\Phi(1-\chi,2,z), \tag{18}$$

where

$$\Phi(a,c;z)=\sum_{k=0}^{k=\infty}\frac{(a)_k z^k}{(c)_k k!}, \tag{19a}$$

$$(a)_k=a(a+1)(a+2)\cdots(a+k-1), \tag{19b}$$

$$(c)_k=c(c+1)(c+2)\cdots(c+k-1). \tag{19c}$$

The second Whittaker's solution is not defined for the value of $\mu=\frac{1}{2}$. A solution to Eq. (14) is sought in the form of $W=ze^{-z/2}f$. Equation (14) then reduces to

$$zf''+(\gamma-z)f'-\alpha f=0, \tag{20}$$

where $\alpha=(1-\chi)$ and $\gamma=2$.

One of the solutions for f in Eq. (20) is Φ itself from Eq. (18). Seeking a linearly independent solution of the form $\Phi\log z+g$, Eq. (20) becomes

$$zg'+(2-z)g'-\alpha g+2\Phi'-\Phi+\frac{\Phi}{z}=0. \tag{21}$$

Series expansions for Φ and g of the form $\Phi=\Sigma_{n=0}^{n=\infty}a_n z^n$ and $g=\Sigma_{n=0}^{n=\infty}C_n z^{n+\rho}$ are introduced in Eq. (21). The roots of the resulting indicial equation for g are 0 and -1. Here $\rho=0$ does not give a nonzero solution. Equating the coefficients of $z^{n+\rho}$ on the lhs of Eq. (21) to 0, for $\rho=-1$, the following recurring relation is obtained:

$$n(n+1)C_{n+1}-C_n(n+\alpha-1)+(2n+1)a_n-a_{n-1}=0. \tag{22a}$$

When $n\neq -1,0$,

$$C_{n+1}=\frac{C_n(n+\alpha-1)-(2n+1)a_n+a_{n-1}}{n(n+1)}. \tag{22b}$$

Noting that $a_0=1$ and $a_{-1}=0$ from Eq. (19), the relations for $n=0$ and 1 lead to the following expressions:

$$n=0\Rightarrow C_0=\frac{1}{(\alpha-1)}; \tag{23}$$

$$n=1\Rightarrow 2C_2-\alpha C_1+3a_1-1=0. \tag{24}$$

Hence it can be noticed that C_0 and C_1 are not related. All the other C_n's can be obtained by (22b).

Hence the second solution of Eq. (15) is given by

$$U_2=ze^{-z/2}f, \tag{25}$$

where f is given by $\Phi\log z+\Sigma_{n=0}^{n=\infty}C_n z^{n+\rho}$ and the C_n's are obtained by Eqs. (22a) and (22b).

Any solution of Eq. (14) can now be expressed as a linear combination of U_1 and U_2 for a particular set of coefficients c_1 and c_2:

$$U=c_1U_1+c_2U_2. \tag{26}$$

Using Eq. (6) the expression for acoustic pressure can be derived as

$$p=-\frac{\gamma\kappa\overline{p}(du/dz)}{\tau\omega i}. \tag{27}$$

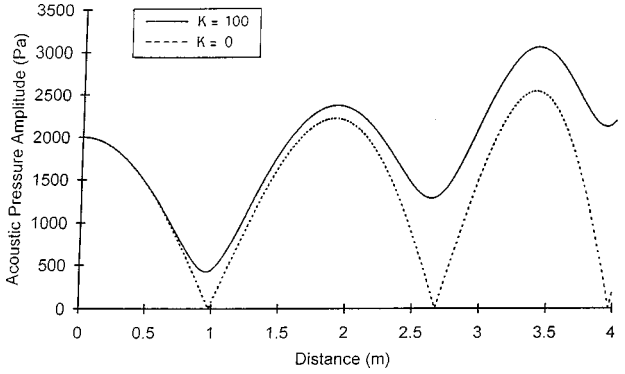

FIG. 1. The variation of the acoustic pressure amplitude distribution in a duct closed at one end for a temperature distribution of $\overline{T}=1100-200x$ and a circular frequency of $\omega=1000$ rad/s for different values of damping constants.

It should be noted that the mean pressure $\overline{p}$ is assumed to be a constant, unlike $\overline{\rho}$ and $\overline{T}$ which depend upon x.

The derived solution was used to evaluate the acoustic field in a duct in the presence of mean temperature gradient and particulate damping. The problem to be solved is a duct with an acoustically closed end in which a standing wave of a given frequency and amplitude is established using an acoustic driver. The constants were found by imposing the conditions that at $x=0$ the acoustic pressure was forced to P_0 and the acoustic velocity $U=0$. For the calculations presented here, P_0 was chosen as 2000 Pa. The specific heat ratio (γ) was chosen as 1.4, that of a diatomic gas.

The axial variation of acoustic pressure and velocity amplitudes ($|P|^2=PP^*$ and $|U|^2=UU^*$) for the case with no damping, and for a damping constant of $K=100$ kg/m^{3}s were calculated and are shown in Figs. 1 and 2, respectively. As expected, the amplitudes at the nodal locations go up with increasing values of damping constant. The effect of the mean temperature gradient is reflected in the unevenness in the spacing of the acoustic pressure and velocity nodes and antinodes. The selected value of K is typical for packed beds.[21]

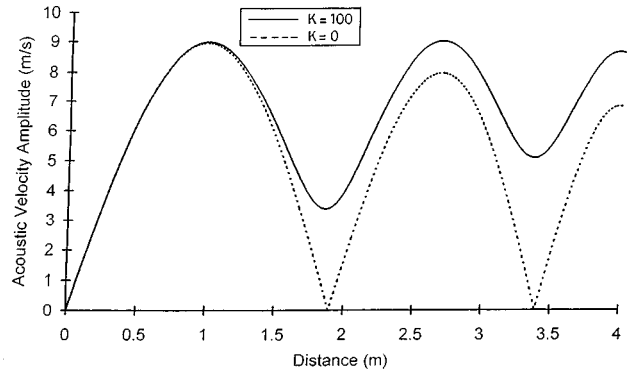

FIG. 2. The variation of the acoustic velocity amplitude distribution in a duct closed at one end for a temperature distribution of $\overline{T}=1100-200x$ and a circular frequency of $\omega=1000$ rad/s for different values of damping constants.

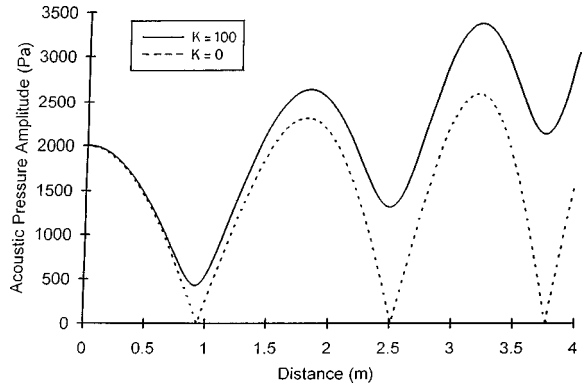

FIG. 3. The variation of the acoustic pressure amplitude distribution in a duct closed at one end for a temperature distribution of $\overline{T}=1100e^{-0.324x}$ and a circular frequency of $\omega=1000$ rad/s for different values of damping constants.

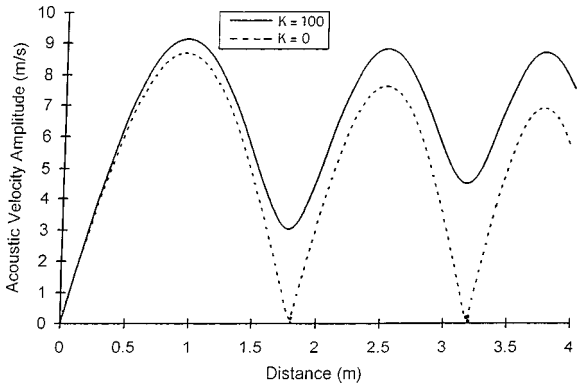

FIG. 4. The variation of the acoustic velocity amplitude distribution in a duct closed at one end for a temperature distribution of $\overline{T}=1100e^{-0.324x}$ and a circular frequency of $\omega=1000$ rad/s for different values of damping constants.

III. SOLUTION FOR A DUCT WITH AN EXPONENTIAL TEMPERATURE PROFILE

In this section, solution for wave propagation in ducts with an exponential mean temperature distribution given by the expression

$$\overline{T}=\alpha e^{-\beta x}, \tag{28}$$

where α and β are constants, is derived.

Using Eq. (28), Eq. (9) can be reduced to the following form:

$$\overline{T}^2\frac{d^2U}{d\overline{T}^2}+\overline{T}\frac{dU}{d\overline{T}}+\left(\frac{\omega^2}{\gamma R\beta^2\overline{T}}-\frac{K\omega}{\gamma\overline{p}\beta^2}i\right)U=0. \tag{29}$$

In order to simplify the above equation, the following transformation was used

$$z=\frac{1}{\sqrt{\overline{T}}}. \tag{30}$$

This reduces Eq. (29) to

$$\frac{d^2U}{dz^2}+\frac{1}{z}\frac{dU}{dz}+\left(\frac{4\omega^2}{\gamma R\beta^2}-\frac{4K\omega}{\gamma\overline{p}\beta^2z^2}i\right)U=0. \tag{31}$$

The preceding equation can be written as

$$\frac{d^2U}{dz^2}+\frac{1}{z}\frac{dU}{dz}+\left(\eta^2-\frac{\nu^2}{z^2}\right)U=0 \tag{32}$$

where

$$\eta^2=\frac{4\omega^2}{\gamma R\beta^2} \quad \text{and} \quad \nu^2=\frac{4\omega K}{\gamma\overline{p}\beta^2}i. \tag{33}$$

Making use of the following transformation for further simplification,

$$z=\frac{s}{\eta}, \tag{34}$$

Eq. (32) can be further reduced to

$$\frac{d^2U}{ds^2}+\frac{1}{s}\frac{dU}{ds}+\left(1-\frac{\nu^2}{s^2}\right)U=0. \tag{35}$$

The above equation is Bessel's differential equation of complex order, whose solution is given by[18–20]

$$U(s)=c_1J_\nu(s)+c_2J_{-\nu}(s). \tag{36}$$

Using Eq. (6) the expression for acoustic pressure can be derived as

$$P=-\frac{\beta\gamma\overline{p}}{2i\omega}s\frac{dU}{ds}. \tag{37}$$

Equations (36) and (37) were evaluated for a duct with an exponential mean temperature gradient and damping. The problem to be solved is a duct with an acoustically closed end in which a standing wave of a given frequency and amplitude is established using an acoustic driver. The constants were found by imposing the conditions that at $x=0$ the acoustic pressure was forced to P_0 and the acoustic velocity $U=0$.

The variation of acoustic pressure and acoustic velocity amplitudes calculated based on the derived solution for an exponential mean temperature profile were compared with that of the numerical solution. The acoustic pressure amplitude and the acoustic velocity amplitude matched very well with the numerical result indicating the correctness of the solution.

The axial variation of acoustic pressure and velocity amplitudes for different damping constants were calculated and are shown in Figs. 3 and 4, respectively. As expected, the amplitudes at the nodal locations go up with increasing values of damping constant. The effect of the mean temperature gradient is reflected in the unevenness in the spacing of the acoustic pressure and velocity nodes and antinodes.

IV. CONCLUSIONS

Exact solutions describing the behavior of one-dimensional acoustic waves in ducts in the presence of an axial mean temperature gradient and particulate damping were obtained by applying suitable transformations to the wave equation. Solutions were obtained for both linear and exponential mean temperature profiles. The solutions were applied to investigate the nature of acoustic fields in ducts in the presence of mean temperature gradient and damping.

The solutions obtained in this analysis are in terms of special functions (e.g., Bessel functions) and are easy to evaluate. These closed form expressions presented herein can be used also as benchmarks for checking the results obtained from computer programs that are intended for applications for systems with axial mean temperature gradients and damping.

ACKNOWLEDGMENTS

The authors wish to thank Manoj Kumar Bobba and Squadron Leader R. Ramesh with whom they had many interesting discussions.

[1] A. Cummings, ''Ducts With Axial Temperature Gradients: An Approximate Solution for Sound Transmission and Generation,'' J. Sound Vib. **51**, 55–67 (1977).
[2] M. L. Munjal and M. G. Prasad, ''On plane-wave propagation in a uniform pipe in the presence of a mean flow and a temperature gradient,'' J. Acoust. Soc. Am. **80**, 1501–1506 (1986).
[3] K. S. Peat, ''The Transfer Matrix of a Uniform Duct with a Linear Temperature Gradient,'' J. Sound Vib. **123**, 43–53 (1988).
[4] A. Kapur, A. Cummings, and P. Mungur, ''Sound Propagation in a Combustion Can with Axial Temperature and Density Gradients,'' J. Sound Vib. **25**, 129–138 (1972).
[5] M. Salikuddin and B. T. Zinn, ''Adaptation of Impedance Tube Technique for the Measurement of Combustion Process Admittances,'' J. Sound Vib. **68**, 119–132 (1980).
[6] J. D. Baum, B. R. Daniel, and B. T. Zinn, ''Determination of Solid Propellant Admittance by the Impedance Tube Technique,'' AIAA Paper No. 80-0281 (1980).
[7] L. Meyer, B. R. Daniel, and B. T. Zinn, ''Acoustic Radiation from Axisymmetric Ducts: A Comparison of Theory and Experiment,'' AIAA Paper No. 80-0097 (1981).
[8] B. T. Zinn and L. Narayanasami, ''Application of Impedance Tube Technique in the Measurement of Driving Provided by Solid Propellants during Combustion Instabilities,'' Acta Astron. **9**, 303–315 (1982).
[9] L. M. Matta and B. T. Zinn, ''Theoretical Study of Flow Turning Losses in the Presence of Temperature Gradients,'' AIAA Paper No. 94-0099 (1994).
[10] R. I. Sujith, G. A. Waldherr, and B. T. Zinn, ''An Exact Solution for One-dimensional Acoustic Fields in Ducts with an Axial Temperature Gradient,'' J. Sound Vib. **184**, 389–402 (1995).
[11] B. Manoj Kumar and R. I. Sujith, ''Exact solution for one-dimensional acoustic fields in ducts with a quadratic mean temperature profile,'' J. Acoust. Soc. Am. **101**, 3798–3799 (1997).
[12] B. Manoj Kumar and R. I. Sujith, ''Exact Solution for One-dimensional Acoustic Fields in Ducts with Polynomial Temperature Profiles,'' Trans. ASME, J. Vib. Acoust. **120**, 965–969 (1998).
[13] G. Cherng and N. Tsung-Yen, ''Unsteady Isentropic Flow through Ducts with Prescribed Sound Pressure Level Distribution,'' Trans. ASME, J. Vib. Acoust. **117**, 279–284 (1995).
[14] K. S. Peat, ''A First Approximation to the Effects of Mean Flow on Sound Propagation Through Cylindrical Capillary Tubes,'' J. Sound Vib. **175**, 475–489 (1994).
[15] K. S. Peat, ''Convected Acoustic Wave Motion Along a Capillary Duct with an Axial Temperature Gradient,'' J. Sound Vib. **203**, 855–866 (1997).
[16] M. L. Munjal and A. G. Doige, ''The Two Microphone Method Incorporating the Effects of Mean Flow and Acoustic Damping,'' J. Sound Vib. **137**, 135–138 (1990).
[17] F. E. C. Culick, ''Acoustic Oscillations in Solid Propellant Rocket Chambers,'' Acta Astronautica **12**, 113–126 (1966).
[18] M. Humi and W. Miller, *Second Course in Ordinary Differential Equations for Scientists and Engineers* (Springer-Verlag, New York, 1988).
[19] M. Abramowitz and I. A. Stegun, *Handbook of Mathematical Functions with Formulas, Graphs and Mathematical Tables* (Wiley, New York, 1972).
[20] N. Lebedev, *Special Functions and their Applications* (Dover, New York, 1972).
[21] R. I. Sujith, T. John, and B. T. Zinn, ''A Theoretical Investigation of the Possibility of Enhancement of Mass Transfer from a Packed Bed using Acoustic Oscillations,'' 3rd Technical Session of the Madras India Regional Chapter of the Acoustical Society of America, NIO, Donna Paula, GOA, 8–9 September 1997.

Analysis of transient wave scattering from rigid bodies using a Burton–Miller approach

A. A. Ergin,[a] Balasubramaniam Shanker, and Eric Michielssen
Center for Computational Electromagnetics, Department of Electrical and Computer Engineering, University of Illinois at Urbana-Champaign, 1406 West Green Street, Urbana, Illinois 61801

(Received 21 October 1998; accepted for publication 22 June 1999)

Transient scattering from closed rigid bodies can be analyzed using a variety of time domain integral equations, e.g., the Kirchhoff integral equation and its normal derivative. Unfortunately, when the spectrum of the incident field includes one or more of the resonance frequencies of the corresponding interior problem, the solutions to these time domain integral equations become corrupted with spurious interior modes. In this article, this phenomenon is demonstrated via numerical experiments, and a Burton–Miller-type time domain combined field integral equation is proposed as a remedy. To verify that the solutions to this Burton–Miller-type equation are not corrupted by interior modes, various numerical results are presented. It is anticipated that this equation, when used in conjunction with fast time domain integral equation solvers (e.g., plane wave time domain algorithms), will enable the accurate analysis of transient wave scattering from acoustically large bodies. © *1999 Acoustical Society of America.* [S0001-4966(99)02811-8]

PACS numbers: 43.20.Px, 02.60.Cb, 02.60.Nm, 02.70.Pt [ANN]

INTRODUCTION

Numerical schemes for studying acoustic wave scattering phenomena are based on either differential or integral equations. Differential equation-based techniques, e.g., the finite difference and finite element methods, offer unquestionable advantages over integral equation methods when studying volume scattering phenomena. However, with the recent advances in boundary element technology, the scale appears to tip in favor of integral equation-based methods when surface scattering problems are analyzed. Indeed, boundary integral equation methods require a discretization of the scatterer surface rather than some volume enclosing it, and their solutions automatically satisfy the radiation condition, thereby eliminating the need for imposing absorbing boundary conditions.

Unfortunately, while integral equation-based techniques are widely used for analyzing time harmonic surface scattering phenomena, their time domain counterparts—often referred to as marching-on-in-time (MOT) schemes—have received only scant attention from the computational acoustics community. Although MOT schemes for solving the Kirchhoff integral equation and its normal derivative date back to 1962,[1] two important deficiencies have prevented them from attaining popularity. First, explicit MOT implementations have often been found to be unstable unless they are supplemented by additional measures, e.g., time averaging.[2,3] However, recent research has shown that implicit MOT schemes that employ accurate surface representations and sophisticated numerical integration and differentiation rules produce stable results for all practical purposes.[4–7] Second, performing a scattering analysis using MOT schemes is computationally expensive.[6] However, recently it has been demonstrated that the computational cost of MOT methods can be considerably reduced when they are retrofitted with plane wave time domain algorithms.[8,9] In view of this recent progress, MOT schemes now offer a viable approach for analyzing transient scattering from objects whose dimensions span several wavelengths within the frequency range of interest.

As mentioned earlier, MOT schemes that rely on explicit time stepping for solving both the Kirchhoff integral equation and its normal derivative are typically unstable. In the past, considerable research effort has been directed towards improving our understanding of the source of these instabilities. In this regard, the contribution of interior cavity modes to instabilities has been investigated both theoretically and by numerical experimentation.[10,11] In these studies, the time domain integral equation is considered as a linear time invariant system that is characterized by the location of its transfer function poles—often referred to as the singularity expansion method (SEM) poles. The poles corresponding to the resonant modes of the associated interior problem reside on the imaginary axis and, theoretically, are never excited by an externally incident field.[12] However, in a numerical solution procedure, the coupling between the incident field and the internal resonance modes does not vanish exactly, and ''all the resonant solutions are likely to be excited to some extent by the incident field.'' [11] Rynne and Smith[11] also state that ''the inaccuracies induced by the numerical discretization of the integral equation causes some SEM poles, which theoretically should lie on the imaginary axis, to move into the right half plane.'' Then, the corresponding components of the solution grow exponentially due to the positive real part of the pole, giving rise to instabilities. The poles with larger imaginary parts have a better chance of drifting into the right half plane since the loss of accuracy is more pronounced at higher frequencies. To prevent the instabilities due to the shifting of these high-frequency poles, time averaging procedures have been suggested.[11,13] Indeed, in appli-

[a]Electronic mail: aergin@decwa.ece.uiuc.edu

cations where the scatterer's resonance frequencies were beyond the frequency range of interest, the averaging process that ''filtered out'' the unwanted frequency components proved useful in enforcing stability with negligible loss of accuracy.[13] Later, Bluck and Walker[6,7] observed that the highly oscillatory instabilities could be eliminated by using implicit MOT schemes that are characterized by larger time step sizes than those used in explicit methods. This observation is in line with Rynne and Smith's work since resonant solutions with frequencies exceeding $1/(2\Delta_t)$, where Δ_t is the time step size, cannot be represented at all by the temporal discretization. Hence, for sufficiently large Δ_t, only the low-frequency modes, which are less likely to result in instabilities, can be adequately represented by the discretization. Both of these approaches eliminate the highly oscillatory instabilities. However, if some poles of the system that fall within the frequency range of interest are excited, then the solution may still be corrupted by spurious oscillations. It should be noted that these poles are less likely to result in instabilities since they are not affected by numerical inaccuracies as much as the high-frequency poles. Clearly, the effect of these oscillations on the solution is highly dependent on the details of the implementation, as they are the by-product of numerical inaccuracies.

The corruption of solutions to boundary integral equations by resonant modes of the corresponding interior problem has been studied thoroughly in the frequency domain, where the presence of resonant modes near the frequency of interest results in an ill-conditioned matrix, whose inversion is problematic. This ill conditioning is a consequence of the fact that the frequency domain solutions to the Helmholtz integral equation and its normal derivative are nonunique at the resonance frequencies. Although the solutions to the time domain counterparts of these integral equations—namely the Kirchhoff integral equation and its normal derivative—are unique by virtue of the initial conditions, evidently the presence of resonant modes affects their numerical evaluation. Hence, it is instructive to study the approaches that have been employed to overcome the nonuniqueness difficulty in the frequency domain. A popular approach is the combined Helmholtz integral equation formulation—usually referred to as CHIEF—which forces the field to be zero at selected points inside the rigid scatterer.[14] The second approach, which was proposed by Burton and Miller,[15] is to supplement the Helmholtz integral equation with its normal derivative to arrive at a boundary integral equation that does not admit any interior resonance modes. Extensions to, and combinations of, both approaches have also been proposed.[16,17]

In this paper, the problems stemming from the presence of resonant modes in the solution of the time domain Kirchhoff integral equation and its normal derivative are studied when the spectrum of the incident field includes the resonance frequencies of the corresponding interior problem. It is shown through numerical experiments that spurious oscillations corrupt the solutions to these integral equations and may eventually lead to instabilities. Finally, a time domain Burton–Miller-type combined field integral equation is proposed, and it is demonstrated that the solutions to this integral equation are devoid of any interior resonance modes.

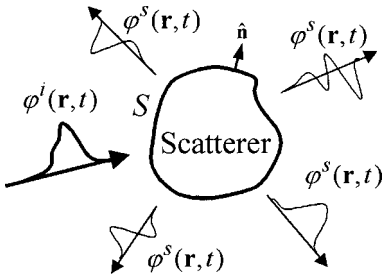

FIG. 1. Geometry of the surface scattering problem.

The remainder of this paper is organized as follows: In Sec. I we review the derivation of the Kirchhoff integral equation and its normal derivative, and introduce a Burton–Miller-type time domain integral equation. Energy arguments are invoked to determine whether these integral equations can sustain internal fields. In Sec. II we outline the formulation of the MOT method used in this study to solve the aforementioned integral equations. Numerical results and conclusions are presented in Secs. III and IV, respectively. Details regarding the numerical implementation of the MOT method are discussed in the Appendix.

I. TIME DOMAIN INTEGRAL EQUATIONS

Consider a rigid body residing in a homogeneous medium with wave speed c that is illuminated by an incident field with velocity potential $\varphi^i(\mathbf{r},t)$ (Fig. 1). Let S denote the surface of the body, and let $\hat{\mathbf{n}}$ be the position-dependent, outward pointing unit normal to S. Hypothetical surfaces conformal to S, but residing just inside and just outside S, are denoted by S_- and S_+, respectively. When $\varphi^i(\mathbf{r},t)$ interacts with S, a scattered field with potential $\varphi^s(\mathbf{r},t)$ is generated such that the total velocity potential $\varphi^t(\mathbf{r},t)=\varphi^i(\mathbf{r},t)+\varphi^s(\mathbf{r},t)$ satisfies the boundary condition $\hat{\mathbf{n}}\cdot\nabla\varphi^t(\mathbf{r},t)=0$ on S. It is assumed that no interaction between the incident field and the scatterer takes place prior to $t=0$; hence, $\varphi^t(\mathbf{r},t)=0$ on S for $t<0$. Using the Kirchhoff–Helmholtz integral theorem,[18] $\varphi^s(\mathbf{r},t)$ can be expressed as

$$\varphi^s(\mathbf{r},t)=\int_S d\mathbf{r}'\,\varphi^t(\mathbf{r}',t)*\hat{\mathbf{n}}'\cdot\nabla'\frac{\delta(t-R/c)}{4\pi R}, \tag{1}$$

where $*$ denotes temporal convolution, $\delta(\cdot)$ is the Dirac impulse, and $R=|\mathbf{r}-\mathbf{r}'|$. Next, three different integral equations that permit the reconstruction of $\varphi^t(\mathbf{r},t)$ on S—and hence the scattered field outside S—are considered.

A. Kirchhoff integral equation

The incident, scattered, and total pressure fields are related to their respective velocity potentials as

$$p^\xi(\mathbf{r},t)=-\rho_0\partial_t\varphi^\xi(\mathbf{r},t), \tag{2}$$

where $\xi\in\{t,i,s\}$ and ρ_0 is the fluid density of the ambient medium. The Kirchhoff integral equation[19] is obtained by setting the total pressure field on S_- to zero, i.e.,

$$p^i(\mathbf{r},t)=-p^s(\mathbf{r},t),\quad \mathbf{r}\in S_-. \tag{3}$$

Using Eqs. (1) and (2) in Eq. (3) and taking its limit as $\mathbf{r}$ approaches a smooth part of S yields an integral equation

that relates the unknown surface potential $\varphi^t(\mathbf{r},t)$ to the incident field as

$$-\partial_t\varphi^i(\mathbf{r},t)=-\frac{1}{2}\partial_t\varphi^t(\mathbf{r},t)+\partial_t\int_S d\mathbf{r}'\,\varphi^t(\mathbf{r}',t)*\hat{\mathbf{n}}'\cdot\nabla'\frac{\delta(t-R/c)}{4\pi R}$$
$$\doteq\mathcal{L}_p\{\varphi^t(\mathbf{r},t)\},\quad \mathbf{r}\in S, \tag{4}$$

where $\mathcal{L}_p$ is the pressure field operator and the integral is to be evaluated in the principal value sense. Note that, assuming that no initial conditions on $\varphi^t(\mathbf{r},t)$ are imposed, there exist many $\varphi^t(\mathbf{r},t)\neq 0$ that satisfy the homogeneous equation $\mathcal{L}_p\{\varphi^t(\mathbf{r},t)\}=0$. These fields are superpositions of the resonant modes of a soft cavity bounded by the surface S.[15] However, these solutions to Eq. (4) are ruled out since they do not satisfy the condition that $\varphi^t(\mathbf{r},t)=0$ on S for $t<0$.

B. Normal derivative of the Kirchhoff integral equation

The incident, scattered, and total velocity fields are related to their respective velocity potentials as

$$\mathbf{v}^\xi(\mathbf{r},t)=\nabla\varphi^\xi(\mathbf{r},t), \tag{5}$$

where $\xi\in\{t,i,s\}$. The normal derivative of the Kirchhoff integral equation[20] is obtained by setting the normal component of the velocity field on S to zero, i.e.,

$$\hat{\mathbf{n}}\cdot\mathbf{v}^i(\mathbf{r},t)=-\hat{\mathbf{n}}\cdot\mathbf{v}^s(\mathbf{r},t),\quad \mathbf{r}\in S. \tag{6}$$

Note that Eq. (6) is also valid on S_- and S_+ because the normal component of the velocity field is continuous across S. Using Eqs. (1) and (5) in Eq. (6) yields an integral equation which relates the unknown surface potential to the incident field as

$$\hat{\mathbf{n}}\cdot\nabla\varphi^i(\mathbf{r},t)=-\oint_S d\mathbf{r}'\,\varphi^t(\mathbf{r}',t)*\hat{\mathbf{n}}\cdot\nabla\hat{\mathbf{n}}'\cdot\nabla'\frac{\delta(t-R/c)}{4\pi R}$$
$$\doteq\mathcal{L}_v\{\varphi^t(\mathbf{r},t)\},\quad \mathbf{r}\in S, \tag{7}$$

where $\mathcal{L}_v$ is the velocity field operator and the integral is to be evaluated in the finite part sense.[21] Again, there exist many $\varphi^t(\mathbf{r},t)\neq 0$ that satisfy the homogeneous equation $\mathcal{L}_v\{\varphi^t(\mathbf{r},t)\}=0$; these fields are the superpositions of the resonant modes of a hard cavity bounded by S.[15] However, again, these solutions to Eq. (7) do not satisfy the initial conditions and therefore should be ruled out.

C. Burton–Miller-type time domain combined field integral equation

As mentioned in Secs. I A and B, although both Eqs. (4) and (7) permit internal resonances, the condition that $\varphi^t(\mathbf{r},t)=0$ on S for $t<0$ rules out any resonant components in the solutions to these equations. However, due to numerical inaccuracies introduced in the discretization of these integral equations, the resonant modes of the scatterer (or slightly perturbed versions thereof) are often excited, and the solutions to these equations are therefore corrupted by the presence of spurious oscillations. Numerical solutions to the frequency domain counterparts of Eqs. (4) and (7) (Helmholtz integral equation and its normal derivative) are also corrupted in the vicinity of the frequencies at which the scatterer's resonant modes render the solution nonunique. Burton and Miller have shown that a linear combination of the Helmholtz integral equation and its normal derivative does not support any internal cavity modes, thereby guaranteeing a unique solution.[15] Here, we introduce a similar time domain combined field integral equation (CFIE). The mechanism by which this approach eliminates the corruption of the solutions by internal modes will be discussed in the next subsection.

The Burton–Miller-type time domain CFIE is derived by imposing a linear combination of the conditions expressed by Eqs. (3) and (6) as

$$-\frac{(1-\alpha)}{c\rho_0}p^i(\mathbf{r},t)+\alpha\hat{\mathbf{n}}\cdot\mathbf{v}^i(\mathbf{r},t)$$
$$=\frac{(1-\alpha)}{c\rho_0}p^s(\mathbf{r},t)-\alpha\hat{\mathbf{n}}\cdot\mathbf{v}^s(\mathbf{r},t),\quad \mathbf{r}\in S_-, \tag{8}$$

where α is a real constant whose range is to be determined. Using Eqs. (1), (2), and (5) in Eq. (8), and letting $\mathbf{r}$ approach S, yields the integral equation

$$(1-\alpha)\partial_t\varphi^i(\mathbf{r},t)+\alpha c\hat{\mathbf{n}}\cdot\nabla\varphi^i(\mathbf{r},t)$$
$$=-(1-\alpha)\mathcal{L}_p\{\varphi^t(\mathbf{r},t)\}+\alpha c\mathcal{L}_v\{\varphi^t(\mathbf{r},t)\}$$
$$\doteq\mathcal{L}_c\{\varphi^t(\mathbf{r},t)\}\quad \mathbf{r}\in S. \tag{9}$$

Note that the combined field operator $\mathcal{L}_c$ is a linear combination of the pressure and velocity field operators $\mathcal{L}_p$ and $\mathcal{L}_v$, and that Eq. (9) reduces to Eqs. (4) and (7) for $\alpha=0$ and $\alpha=1$, respectively.

D. Corruption of numerical solutions to Eqs. (4), (7), and (9) by internal fields

The interpretation of time domain integral equations as linear time invariant systems and the relation of the resonant modes to the SEM poles of these systems were already alluded to in the Introduction. It was also mentioned that the internal modes of the scatterer are always excited to some extent due to numerical inaccuracies. Here, we present the same picture from a different perspective and invoke energy arguments to study whether the integral equations (4), (7), and (9) sustain internal fields.

Assume that at time $t=t_0$ a spurious source distribution that supports resonant modes exists on S because of the numerical excitation of (perturbed) resonance poles. Of course, this source distribution generates a field in the cavity bounded by S_-. The law of conservation of energy dictates that[18]

$$W(t)=W(t_0)-\int_{t_0}^{t}dt'\int_{S_-}d\mathbf{r}'\,\hat{\mathbf{n}}'\cdot[p^t(\mathbf{r}',t')\mathbf{v}^t(\mathbf{r}',t')], \tag{10}$$

where $W(t)=\frac{1}{2}\rho_0\int_{V_-}d\mathbf{r}'\{|\mathbf{v}^t(\mathbf{r}',t)|^2+[p^t(\mathbf{r}',t)/(c\rho_0)]^2\}$ is the energy stored in volume V_- enclosed by S_- at time t. If the Kirchhoff integral equation is used, $p^t(\mathbf{r},t)=0$ on S_- is automatically enforced by Eq. (3). On the other hand, if the normal derivative of the Kirchhoff integral equation is used, $\hat{\mathbf{n}}\cdot\mathbf{v}^t(\mathbf{r},t)=0$ on S_- by Eq. (6) and by the continuity of $\hat{\mathbf{n}}$

$\cdot \mathbf{v}^s(\mathbf{r},t)$ across S. In either case, the integral over S_- in Eq. (10) equals zero and the energy that has leaked into the cavity is trapped there as $W(t)=W(t_0)>0$ for all $t\geqslant t_0$. In other words, Eqs. (4) and (7) do not provide an *intrinsic* mechanism for reducing the energy inside the cavity. However, if the combined field formulation is used, Eqs. (8) and (10) imply that

$$W(t)=W(t_0)-\frac{(1-\alpha)}{\alpha}\frac{1}{c\rho_0}\int_{t_0}^{t}dt'\int_{S_-}d\mathbf{r}'[p^t(\mathbf{r}',t')]^2$$
$$=W(t_0)-\frac{\alpha}{(1-\alpha)}c\rho_0\int_{t_0}^{t}dt'\int_{S_-}d\mathbf{r}'[\hat{\mathbf{n}}'\cdot\mathbf{v}^t(\mathbf{r}',t')]^2. \tag{11}$$

For $W(t_0)>0$, $[p^t(\mathbf{r}',t')]^2=[\hat{\mathbf{n}}'\cdot\mathbf{v}^t(\mathbf{r}',t')c\rho_0\alpha/(1-\alpha)]^2$ on S_- cannot be zero for all $t'\geqslant t_0$ since the energy inside the cavity will at some point interact with the cavity walls. During this interaction, the integrands in Eq. (11) will be positive and the energy stored in the cavity will decrease if $0<\alpha<1$. This process will go on until $W(t)=0$. Hence, for $0<\alpha<1$, Eq. (9) provides an intrinsic mechanism for reducing the energy present inside the cavity. On the other hand, as α approaches 0 or 1, it is evident from Eq. (11) that the effect of this intrinsic mechanism diminishes. This is expected as Eq. (9) reduces to either Eq. (4) or (7) for these limiting cases.

While the above insights into the behavior of the introduced integral equations are heuristic in nature, much supporting evidence for the resonance-suppressing character of the CFIE comes from the numerical experiments reported in Sec. III. Our results indicate that the CFIE does indeed provide an intrinsic mechanism that suppresses all energy that (numerically) leaks into the cavity, and that the CFIE produces accurate solutions free from spurious oscillations.

II. THE MARCHING-ON-IN-TIME METHOD

To solve Eq. (9) numerically, $\varphi^t(\mathbf{r},t)$ on S is represented in terms of spatial and temporal basis functions $f_n(\mathbf{r})$, $n=1,\ldots,N_s$, and $T_i(t)$, $i=1,\ldots,N_t$, as

$$\varphi^t(\mathbf{r},t)=\sum_{i=1}^{N_t}\sum_{n=1}^{N_s}\varphi_{i,n}f_n(\mathbf{r})T_i(t), \tag{12}$$

where $\varphi_{i,n}$ are unknown expansion coefficients. Assuming that the spectral content of the incident field vanishes for $\omega>\omega_{\max}$, an accurate representation of $\varphi^t(\mathbf{r},t)$ can be obtained by choosing the number of basis functions as $N_s\propto S_A(\omega_{\max}/c)^2$ and $N_t\propto T\omega_{\max}$, where S_A denotes the surface area of the scatterer and T the duration of the analysis. In this study, S is modeled as a collection of N_s flat triangular facets S_n, $n=1,\ldots,N_s$, and the $f_n(\mathbf{r})$ are chosen to be unit pulse functions defined as

$$f_n(\mathbf{r})=\begin{cases}1; & \mathbf{r}\in S_n,\\ 0; & \text{elsewhere.}\end{cases} \tag{13}$$

These piecewise constant basis functions simplify the evaluation of the finite part integral associated with the operator $\mathcal{L}_v$ as detailed in the Appendix [see Eq. (A7)]. Numerical schemes employing more sophisticated spatial basis functions (e.g., isoparametric elements) are expected to behave similarly to the present scheme—although their results should be corrupted to a lesser extent—as whether an intrinsic loss mechanism is in effect or not is associated with the underlying integral equation regardless of how it is discretized. The temporal basis functions are chosen to be cubic interpolation functions defined as $T_i(t)=T(t-t_i)$, where $t_i=i\Delta_t$ and

$$T(t)=\begin{cases}1+\frac{11}{6}(t/\Delta_t)+(t/\Delta_t)^2+\frac{1}{6}(t/\Delta_t)^3; & -\Delta_t\leqslant t\leqslant 0,\\ 1+\frac{1}{2}(t/\Delta_t)-(t/\Delta_t)^2-\frac{1}{2}(t/\Delta_t)^3; & 0\leqslant t\leqslant\Delta_t,\\ 1-\frac{1}{2}(t/\Delta_t)-(t/\Delta_t)^2+\frac{1}{2}(t/\Delta_t)^3; & \Delta_t\leqslant t\leqslant 2\Delta_t,\\ 1-\frac{11}{6}(t/\Delta_t)+(t/\Delta_t)^2-\frac{1}{6}(t/\Delta_t)^3; & 2\Delta_t\leqslant t\leqslant 3\Delta_t,\\ 0; & \text{elsewhere.}\end{cases} \tag{14}$$

The function $T(t)$ is an extension of the quadratic basis function proposed by Manara *et al.*[22] ensuring that the temporal variation of all the quantities to be evaluated are piecewise polynomials [see Appendix Eqs. (A3)–(A6)]. Substituting Eq. (12) into Eq. (9) and testing the resulting equation at time $t=t_j$ with $\tilde{f}_m(\mathbf{r})=\delta(\mathbf{r}-\mathbf{r}_m^c)$, $m=1,\ldots,N_s$, where $\mathbf{r}_m^c$ denotes the centroid of the mth triangular facet, the following matrix equation is obtained:

$$\overline{\mathbf{Z}}_0\mathbf{\Phi}_j=\mathbf{F}_j-\sum_{l=1}^{j-1}\overline{\mathbf{Z}}_l\mathbf{\Phi}_{j-l}, \tag{15}$$

where the elements of the vectors $\mathbf{\Phi}_j$ and $\mathbf{F}_j$ and the interaction matrix $\overline{\mathbf{Z}}_l$ are given by

$$\mathbf{\Phi}_{j,n}=\varphi_{j,n}, \tag{16}$$

$$\mathbf{F}_{j,m}=\int_S d\mathbf{r}\tilde{f}_m(\mathbf{r})[(1-\alpha)\partial_t\varphi^i(\mathbf{r},t)+\alpha c\hat{\mathbf{n}}\cdot\nabla\varphi^i(\mathbf{r},t)]|_{t=t_j}, \tag{17}$$

$$\overline{\mathbf{Z}}_{l,mn}=\int_S d\mathbf{r}\tilde{f}_m(\mathbf{r})[\mathcal{L}_c\{f_n(\mathbf{r})T_{j-l}(t)\}]|_{t=t_j}. \tag{18}$$

The numerical evaluation of the integrals appearing in Eqs. (17) and (18) is detailed in the Appendix.

Equation (15) relates the velocity potential expansion coefficients at the jth time step to the incident field and the coefficients that model the potential at prior time steps. Hence, all the expansion coefficients $\varphi_{j,n}$ can be evaluated by starting at the first time step ($j=1$), forming the right-hand side, and recursively solving Eq. (15) for all time steps. This procedure is known as the MOT scheme.[23]

In the past, most MOT implementations relied on explicit time stepping, which not only considerably limited the allowed time step size but also often resulted in late time

instabilities. As mentioned above, it has been demonstrated that use of higher-order quadrature rules and/or larger time step sizes yields implicit schemes that are stable for all practical purposes.[6] In the present study, the surface integrals over triangular domains are evaluated as described in the Appendix, and the time step size is chosen—independent of the mesh size—as $\Delta_t = 2\pi/(\beta\omega_{\max})$. Developing guidelines for choosing the parameter β is still an area of active research and the interested reader is referred to Refs. 4 and 7. For all the examples that will be presented, $\beta=10$ yielded stable results.

III. NUMERICAL RESULTS

In order to study the quality of the solutions to the different time domain integral equations presented above, plane wave scattering from several rigid bodies is analyzed. The results obtained by solving Eq. (9), which reduces to Eq. (4) for $\alpha=0$ and to Eq. (7) for $\alpha=1$, are compared with solutions obtained either analytically or using a frequency domain boundary element method (FD-BEM) code, which has been validated independently. The FD-BEM employed uses the same spatial basis functions as the MOT scheme and circumvents the nonuniqueness problem by using the Burton–Miller approach. The wave speed of the medium is assumed to be $c=343$ m/s. In all MOT analyses that will be presented, the matrix equation in Eq. (15) is solved using a transpose-free quasi-minimal residual algorithm.[24] The initial guess vector for this solver is set equal to the $\mathbf{\Phi}$ vector of the previous time step. With this initial guess, a relative residual error of 10^{-6} was obtained in less than 15 iterations for all cases presented below. Such residual error guarantees that the solutions presented here would not be effected if an exact solver (e.g., a single sparse LU factorization of $\overline{\mathbf{Z}}_0$ with repeated back-substitution at each time step) had been used. In all MOT simulations, the excitation is a plane wave defined as

$$\varphi^i(\mathbf{r},t) = \cos[\omega_o(t-\mathbf{r}\cdot\hat{\mathbf{k}}^i/c)] \times \exp[-(t-\mathbf{r}\cdot\hat{\mathbf{k}}^i/c-6\sigma)^2/2\sigma^2], \tag{19}$$

where ω_o is the pulse's center frequency, σ is a measure of the pulse's temporal width, and $\hat{\mathbf{k}}^i$ is the propagation direction of the incident wave. This pulse can be assumed to be bandlimited to $\omega_{\max}=\omega_o+6/\sigma$ since at that frequency the spectral content of the pulse is down by 78 dB from its peak value at ω_o. It should be stressed that the MOT scheme used in generating the results in this section is not supplemented with any averaging or similar stabilization schemes.

As a first example, scattering from a sphere of radius 1 m centered at the origin and modeled by 2210 triangular facets is analyzed [see inset of Fig. 2(a)]. The incident pulse parameters are chosen as $\omega_o=2\pi\times200$ rad/s, $\sigma=7.639$ ms, and $\hat{\mathbf{k}}^i=-\hat{\mathbf{z}}$ so that the two soft cavity modes at 171.5 and 245.3 Hz and the rigid cavity modes at 182.4, 245.3, and 246.4 Hz could possibly be excited. The magnitude of the calculated velocity potential on the sphere at an arbitrary angle of $\theta=42.5$ degrees is shown in Fig. 2(a) as a function of time for $\alpha=0$, 0.5, and 1. Clearly, the solutions for both

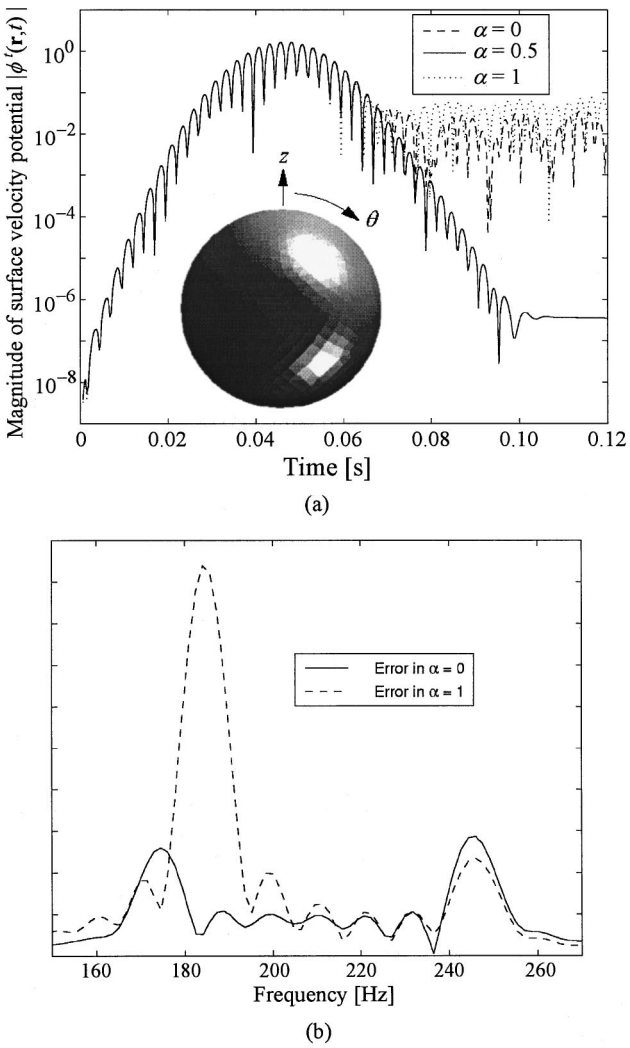

FIG. 2. (a) Magnitude of the total surface velocity potential $|\varphi^t(\mathbf{r},t)|$ at $\theta=42.5$ degrees for a rigid sphere modeled with 2210 triangular facets calculated using the Kirchhoff integral equation ($\alpha=0$), its normal derivative ($\alpha=1$), and the CFIE with $\alpha=0.5$. (b) Magnitude of the Fourier transform of the differences between the $\alpha=0,1$ solutions and the $\alpha=0.5$ solution plotted in part (a).

$\alpha=0$ and $\alpha=1$ are corrupted by oscillations whereas the solution obtained with $\alpha=0.5$ is free of any resonances. The spectra of the oscillations that corrupt the solutions to the $\alpha=0$ and $\alpha=1$ cases are obtained by Fourier transforming the difference of the these solutions from the $\alpha=0.5$ solution, and their magnitudes are plotted in Fig. 2(b). Clearly the frequencies of oscillations that corrupt the solutions coincide with those of the cavity modes.

The effects of the internal resonances on the scattered fields are studied by extracting the scattering cross section (SCS) of the scatterer at several frequencies from the time domain far fields computed via MOT and comparing them with analytical calculations using the Mie series. As seen in Fig. 3, the SCS data extracted from the MOT analysis with $\alpha=0.5$ shows perfect agreement with the analytical results, verifying that the potential all over the sphere has been calculated accurately for all time steps. Figure 3(c) shows that the SCS obtained by the normal derivative of the Kirchhoff integral equation ($\alpha=1$) agrees well with the analytical values, although the surface potential values were corrupted

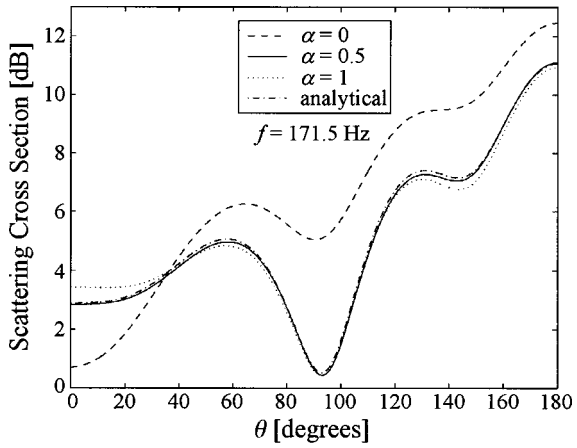

(a)

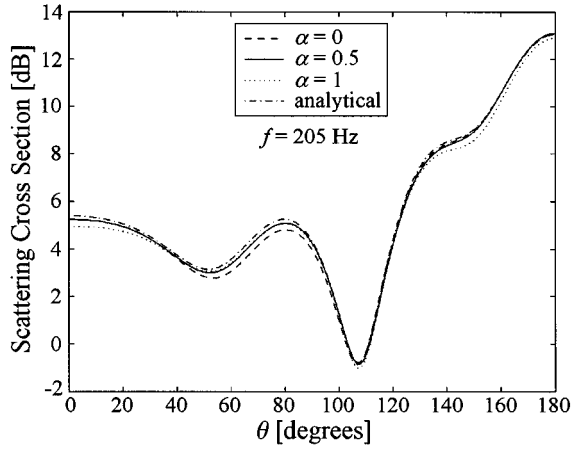

(b)

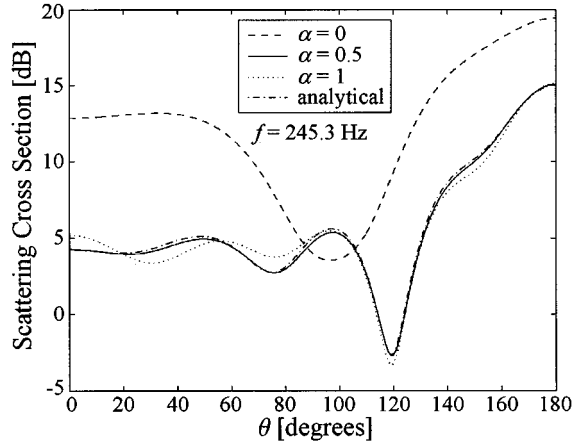

(c)

FIG. 3. Scattering cross section of a unit sphere extracted from the MOT simulations compared against the analytical values at (a) 171.5 Hz, (b) 205 Hz, and (c) 245.3 Hz.

with a cavity mode at 245.3 Hz. On the other hand, for $\alpha=0$, the resonances at 171.5 and 245.3 Hz dramatically affect the calculated scattered fields [Fig. 3(a) and (c)] and have almost no effect at other frequencies [Fig. 3(b)]. These results can be explained as follows. The resonant fields trapped inside the cavity have to be sustained by equivalent surface sources that reside on S, and the pressure field will be discontinuous across S by an amount proportional to the strength of these

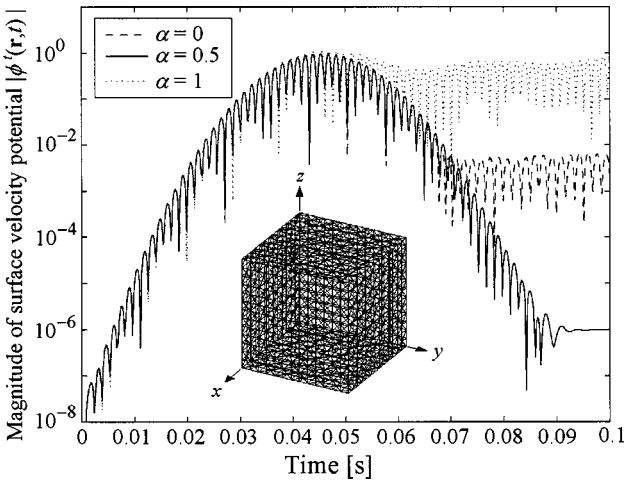

FIG. 4. Magnitude of the total surface velocity potential $|\varphi^t(\mathbf{r},t)|$ on the surface of a rigid cube modeled with 2028 triangular facets calculated using the Kirchhoff integral equation ($\alpha=0$), its normal derivative ($\alpha=1$), and the CFIE with $\alpha=0.5$.

sources. In the formulation of the Kirchhoff integral equation ($\alpha=0$), $p^s(\mathbf{r},t)=-p^i(\mathbf{r},t)$ is enforced on S_-; hence, the same condition will not hold true on S_+. Therefore, there will be a field induced external to S by the resonant component of the equivalent surface sources, and the scattered fields will also be corrupted. On the other hand, in the formulation of the normal derivative of the Kirchhoff integral equation, Eq. (6) enforces $\hat{\mathbf{n}}\cdot\mathbf{v}^s(\mathbf{r},t)=-\hat{\mathbf{n}}\cdot\mathbf{v}^i(\mathbf{r},t)$ on S_+ regardless of the discontinuity of the pressure field across S. Therefore, by the uniqueness of the solutions to the exterior problem, the corruption of the surface fields by resonant modes will not influence the scattered fields if Eq. (7) is used for the transient analysis. Although this final observation regarding the normal derivative of the Kirchhoff integral equation is justified by many numerical examples, there are cases when the corruption of the surface fields reflects itself on the radiated fields. However, in general, the scattered fields computed via the normal derivative of the Kirchhoff integral equation tend to be affected far less by the presence of resonant modes.

Analysis of scattering from a rigid cube with side length of 1 m constitutes the second example. The structure is modeled in terms of 2028 triangular facets, and it is positioned such that the cube's edges coincide with the coordinate axes as shown in the inset of Fig. 4. The incident pulse is defined as $\omega_o=2\pi\times350$ rad/s, $\sigma=7.639$ ms, and $\hat{\mathbf{k}}^i=-\hat{\mathbf{z}}$. As can be verified from Fig. 4, the surface fields oscillate at about 297 and 343 Hz for $\alpha=0$ and $\alpha=1$, respectively. Furthermore, for $\alpha=1$, the oscillations, which are distinctly different from the late time instabilities of the explicit MOT schemes, seem to grow exponentially with a slowly varying envelope. However, no spurious oscillations are present in the solution obtained by setting $\alpha=0.5$. The xz-plane SCS data extracted from the MOT simulation is compared against the SCS obtained by the FD-BEM solver. As seen in Fig. 5, the agreement between the $\alpha=0.5$ and FD-BEM results is excellent at both 297 and 343 Hz. As expected, the solution with $\alpha=0$ deviates considerably from the others at 297 Hz while the

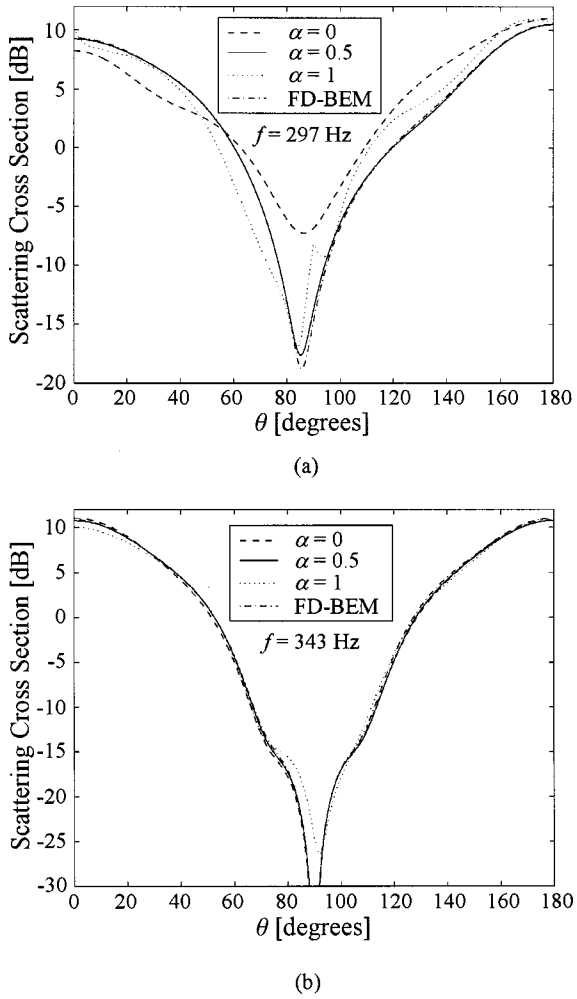

FIG. 5. Scattering cross section of a unit cube in the *xz* plane extracted from the MOT simulations compared against those obtained by the FD-BEM at (a) 297 Hz and (b) 343 Hz.

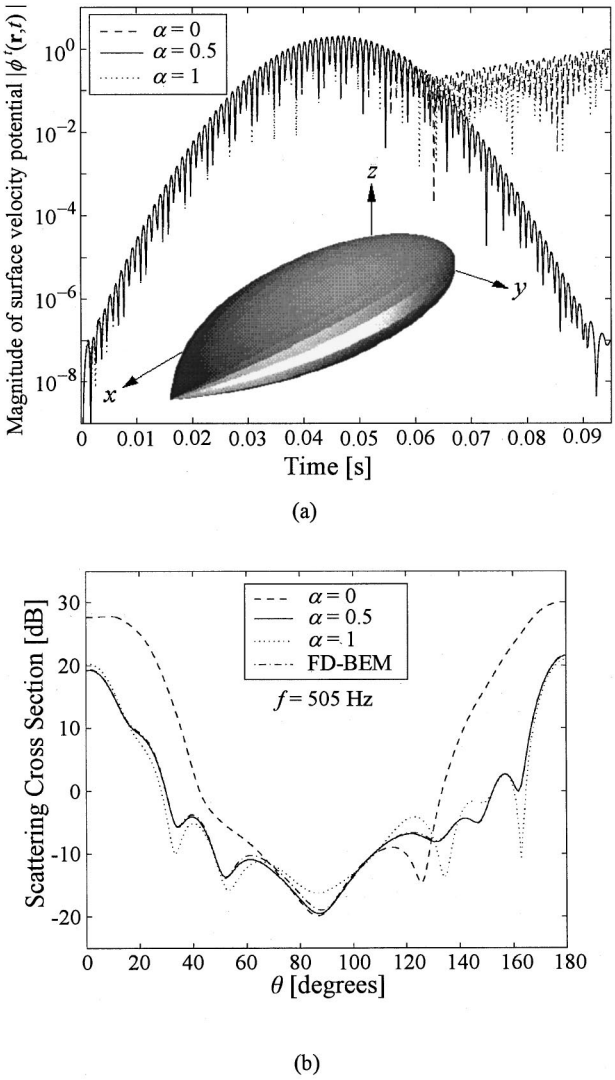

FIG. 6. (a) Magnitude of the total surface velocity potential $|\varphi^t(\mathbf{r},t)|$ on the surface of a rigid almond modeled with 2572 triangular facets using different α values. (b) The SCS data in the *xz* plane obtained from the MOT simulations and the FD-BEM at 505 Hz.

corruption of the surface fields has some effect on the radiated fields for $\alpha=1$ at 343 Hz.

As the last example, scattering from an almond modeled with 2572 triangular facets is studied. The scatterer, which is depicted in the inset of Fig. 6(a), fits into a box of dimensions $3\times1.15\times0.4\,\mathrm{m}^3$ and is a modified version of the almond described in Ref. 25. The parameters characterizing the incident pulse are $\omega_o=2\pi\times500$ rad/s, $\sigma=7.639$ ms, and $\hat{\mathbf{k}}^i=-\hat{\mathbf{z}}$. As seen in Fig. 6(a), spurious oscillations not only corrupt the surface fields for $\alpha=0$ and $\alpha=1$, but they also show an exponential increase in amplitude. Thorough experimentation has shown that this type of instability, unlike the high-frequency instabilities encountered with explicit MOT schemes, cannot be avoided by increasing the time step size. Furthermore, if only the Helmhotz integral equation or its derivative is used, the system matrix of the FD-BEM becomes ill conditioned at about 505 Hz, which corresponds to the frequency of the oscillations in the MOT solutions. Thus, it can be inferred that internal cavity modes exist in the vicinity of this frequency. As seen in Fig. 6(a), setting $\alpha=0.5$ yields a stable solution that is also free of sustained oscillations. In Fig. 6(b), the SCS of the scatterer in the *xz* plane extracted from the time domain simulation results at 505 Hz is again compared to that computed via the FD-BEM that employed the Burton–Miller approach. The perfect match between the $\alpha=0.5$ case and the FD-BEM result, together with the fact that the $\alpha=0$ case deviates considerably more than the $\alpha=1$ case, also supports the conclusion that the observed instabilities were due to the presence of resonant modes that were avoided by setting $\alpha=0.5$. Finally, although all the resonance-free results presented here were obtained by setting $\alpha=0.5$, tests with other values of α in the range $0<\alpha<1$ were conducted and, as expected (see Sec. I D), the results were observed to be stable and devoid of sustained oscillations except for $\alpha<0.1$ and $\alpha>0.9$.

IV. CONCLUSIONS

The resonance-suppressing properties of different time domain boundary integral equations for analyzing transient scattering from rigid bodies were investigated. It was shown that the solutions to both the Kirchhoff integral equation and its normal derivative are vulnerable to corruption by cavity

modes. It was also pointed out that the scattered fields calculated via the Kirchhoff integral equation are affected by the presence of interior modes, whereas those calculated through the normal derivative formulation are not. A time domain Burton–Miller-type CFIE was shown both theoretically and experimentally to effectively eradicate resonant components supported by the other time domain integral equations. It is anticipated that the proposed time domain CFIE will enable the accurate simulation of transient scattering from large structures, which possibly support cavity modes, using fast methods such as the plane wave time domain algorithm.[8,9,26]

ACKNOWLEDGMENTS

This work was supported in part by a grant from AFOSR via the MURI program under Contract No. F49620-96-1-0025, NSF grant No. ECS 95-02138, and the Gebze Institute of Technology, Turkey.

APPENDIX: Numerical evaluation of vector and matrix elements

In this appendix, the numerical evaluation of the vector and matrix elements given in Eqs. (17) and (18) is elucidated. The vector elements in Eq. (17) are evaluated as

$$\mathbf{F}_{j,m}=(1-\alpha)\partial_t\varphi^i(\mathbf{r}_m^c,t)|_{t=t_j}+\alpha c\hat{\mathbf{n}}\cdot\nabla\varphi^i(\mathbf{r}_m^c,t_j). \quad \text{(A1)}$$

The matrix elements $\overline{\mathbf{Z}}_{l,mn}$ are evaluated as follows. Using Eqs. (4), (7), and (9) in Eq. (18) yields

$$\overline{\mathbf{Z}}_{l,mn}=-(1-\alpha)\mathcal{L}_p\{f_n(\mathbf{r})T_{j-l}(t)\}|_{t=t_j;\mathbf{r}=\mathbf{r}_m^c} + \alpha c\mathcal{L}_v\{f_n(\mathbf{r})T_{j-l}(t)\}|_{t=t_j;\mathbf{r}=\mathbf{r}_m^c}, \quad \text{(A2)}$$

where

$$\mathcal{L}_p\{f_n(\mathbf{r})T_{j-l}(t)\}|_{t=t_j;\mathbf{r}=\mathbf{r}_m^c} = \begin{cases} -\frac{1}{2}\partial_t T_{j-l}(t)|_{t=t_j}; & m=n \\ \displaystyle\int_{S_n} d\mathbf{r}'\hat{\mathbf{n}}'\cdot\nabla'\frac{\partial_t T_{j-l}(t-R/c)}{4\pi R}\bigg|_{t=t_j;\mathbf{r}=\mathbf{r}_m^c}; & m\neq n \end{cases} \quad \text{(A3)}$$

$$\mathcal{L}_v\{f_n(\mathbf{r})T_{j-l}(t)\}|_{t=t_j;\mathbf{r}=\mathbf{r}_m^c} = -\int_{S_n} d\mathbf{r}'\hat{\mathbf{n}}\cdot\nabla\hat{\mathbf{n}}'\cdot\nabla'\frac{T_{j-l}(t-R/c)}{4\pi R}\bigg|_{t=t_j;\mathbf{r}=\mathbf{r}_m^c}. \quad \text{(A4)}$$

The integrands in Eqs. (A3) and (A4) can also be written as

$$\hat{\mathbf{n}}'\cdot\nabla'\frac{\partial_t T_{j-l}(\tau)}{4\pi R}=\hat{\mathbf{n}}'\cdot\hat{\mathbf{R}}\left[\frac{\partial_\tau^2 T_{j-l}(\tau)}{cR}+\frac{\partial_\tau T_{j-l}(\tau)}{R^2}\right], \quad \text{(A5)}$$

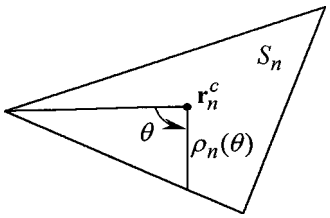

FIG. A1. Definition of the variables θ and $\rho_n(\theta)$ used in the evaluation of the contour integral in Eq. (A7).

$$\hat{\mathbf{n}}\cdot\nabla\hat{\mathbf{n}}'\cdot\nabla'\frac{T_{j-l}(\tau)}{4\pi R}=-(\hat{\mathbf{n}}\cdot\hat{\mathbf{R}})(\hat{\mathbf{n}}'\cdot\hat{\mathbf{R}})\left[\frac{\partial_\tau^2 T_{j-l}(\tau)}{c^2R}+3\frac{\partial_\tau T_{j-l}(\tau)}{cR^2}+3\frac{T_{j-l}(\tau)}{R^3}\right]+(\hat{\mathbf{n}}\cdot\hat{\mathbf{n}}')\times\left[\frac{\partial_\tau T_{j-l}(\tau)}{cR^2}+\frac{T_{j-l}(\tau)}{R^3}\right]. \quad \text{(A6)}$$

In the above equations, $\tau=t-R/c$, $\hat{\mathbf{R}}=(\mathbf{r}-\mathbf{r}')/R$, and analytical expressions for each term with time derivatives can be readily obtained via Eq. (14). When $m=n$ in Eq. (A4), the integrand becomes hypersingular. Using Eq. (A6) and applying a limiting procedure similar to that performed by Terai[27] in the frequency domain, the finite part of this hypersingular integral can be evaluated as

$$\int_{S_n} d\mathbf{r}\mathcal{L}_v\{f_n(\mathbf{r})T_{j-l}(t)\}\bigg|_{t=t_j} = A_n\int_0^{2\pi} d\theta\frac{T_{j-l}(t_j-\rho_n(\theta)/c)}{\rho_n(\theta)}+\frac{2\pi}{c}\partial_t T_{j-l}(t)\bigg|_{t=t_j}, \quad \text{(A7)}$$

where θ and $\rho_n(\theta)$ are depicted in Fig. A1. The contour integral in the first term can be evaluated analytically, although using a 17-point Gauss–Legendre quadrature rule on each edge of the triangular facet yields values of comparable accuracy.

The surface integrals over triangular domains which appear in Eqs. (A3) and (A4) for the nonself terms ($m\neq n$) are evaluated numerically. Different quadrature rules are used for adjacent and separated facet pairs. If the source and observation domains are not adjacent, i.e., if S_m and S_n do not have a common vertex, the integral over S_n is evaluated using a seven-point Gaussian quadrature rule (see Section 25.4.63 in Ref. 28). For the adjacent facet pairs, the integrals over S_n in Eqs. (A3) and (A4) are evaluated by first subdividing S_n into four triangles, by connecting the centers of the edges, and then applying the seven-point quadrature rule on each of these four triangles. While applying all the aforementioned quadrature rules, the retarded time between each source–observer quadrature point pair is calculated separately.

[1] M. B. Friedman and R. Shaw, ''Diffraction of pulses by cylindrical obstacles of arbitrary cross section,'' J. Appl. Mech. **29**, 40–46 (1962).
[2] B. P. Rynne, ''Stability and convergence of time marching methods in scattering problems,'' IMA J. Appl. Math. **35**, 297–310 (1985).
[3] P. J. Davies, ''Numerical stability and convergence of approximations of

retarded potential integral equations,'' SIAM (Soc. Ind. Appl. Math.) J. Numer. Anal. **31**(3), 856–875 (1994).
[4] S. J. Dodson, S. P. Walker, and M. J. Bluck, ''Implicitness and stability of time domain integral equation scattering analysis,'' Appl. Comput. Electromagn. Soc. J. **13**(3), 291–301 (1998).
[5] W. Pinello, A. Ruehli, and A. Cangellaris, ''Stabilization of time domain solutions of EFIE based on partial element equivalent circuit models,'' Proceedings of IEEE Antennas and Propagation Society International Symposium, Montreal, Canada (1997), Vol. 3, pp. 966–969.
[6] M. J. Bluck and S. P. Walker, ''Analysis of three-dimensional transient acoustic wave propagation using the boundary integral equation method,'' Int. J. Numer. Methods Eng. **39**, 1419–1431 (1996).
[7] M. J. Bluck and S. P. Walker, ''Time-domain BIE analysis of large three-dimensional electromagnetic scattering problems,'' IEEE Trans. Antennas Propag. **45**(5), 894–901 (1997).
[8] A. A. Ergin, B. Shanker, and E. Michielssen, ''Fast evaluation of three-dimensional transient wave fields using diagonal translation operators,'' J. Comput. Phys. **146**(1), 157–180 (1998).
[9] A. A. Ergin, B. Shanker, K. Aygun, and E. Michielssen, ''Transient analysis of acoustic scattering using marching-on-in-time with plane wave time domain algorithm,'' Proceedings of 14th Annual Review of Progress in Applied Computational Electromagnetics, Monterey, CA (1998), Vol. 2, pp. 866–872.
[10] P. D. Smith, ''Instabilities in time marching methods for scattering: Cause and rectification,'' Electromagnetics **10**, 439–451 (1990).
[11] B. P. Rynne and P. D. Smith, ''Stability of time marching algorithms for the electric field integral equation,'' J. Electromagn. Waves Appl. **4**(12), 1181–1205 (1990).
[12] D. S. Jones, *Methods in Electromagnetic Wave Propagation*, 2nd ed. (Oxford U.P., New York, 1994).
[13] A. Sadigh and E. Arvas, ''Treating the instabilities in marching-on-in-time method from a different perspective,'' IEEE Trans. Antennas Propag. **41**(12), 1695–1702 (1993).
[14] H. A. Schenck, ''Improved integral formulation for acoustic radiation problems,'' J. Acoust. Soc. Am. **44**, 41–58 (1967).
[15] A. J. Burton and G. F. Miller, ''The application of integral equation methods to the numerical solution of some exterior boundary-value problems,'' Proc. R. Soc. London, Ser. A **323**, 201–210 (1971).
[16] T. W. Wu and Z. H. Jia, ''A choice of practical approaches to overcome the nonuniqueness problem of the BEM in acoustic radiation and scattering,'' in *Boundary Element Technology VII*, edited by C. A. Brebbia and M. S. Ingber (Computational Mechanics Publications, Southampton, UK, 1992), pp. 501–510.
[17] S.-A. Yang, ''Acoustic scattering by a hard or soft body across a wide frequency range by the Helmholtz integral equation method,'' J. Acoust. Soc. Am. **102**, 2511–2520 (1997).
[18] A. D. Pierce, *Acoustics: An Introduction to its Physical Principles and Applications* (McGraw–Hill, New York, 1981).
[19] P. H. L. Groenenboom, ''Wave propagation phenomena,'' in *Progress in Boundary Element Methods*, edited by C. A. Brebbia (Pentech, London, 1983), Vol. 2, pp. 24–52.
[20] S. Hirose and J. D. Achenbach, ''BEM method to analyze the interaction of an acoustic pulse with a rigid circular disk,'' Wave Motion **10**, 267–275 (1988).
[21] G. Krishnasamy, L. W. Schmerr, T. J. Rudolphi, and F. J. Rizzo, ''Hypersingular boundary integral equations: Some applications in acoustic and elastic wave scattering,'' J. Appl. Mech. **57**, 404–414 (1990).
[22] G. Manara, A. Monorchio, and R. Reggiannini, ''A space-time discretization criterion for a stable time-marching solution of the electric field integral equation,'' IEEE Trans. Antennas Propag. **45**(3), 527–532 (1997).
[23] A. G. Tijhuis, *Electromagnetic Inverse Profiling: Theory and Numerical Implementation* (VNU Science, Utrecht, The Netherlands, 1987).
[24] R. W. Freund, ''A transpose-free quasi-minimal residual algorithm for non-hermitian linear systems,'' SIAM J. Sci. Comput. **14**(2), 470–482 (1993).
[25] A. C. Woo, H. T. G. Wang, M. J. Schuh, and M. L. Sanders, ''Benchmark radar targets for the validation of computational electromagnetics programs,'' IEEE Antennas Propag. Mag. **35**(1), 84–89 (1993).
[26] A. A. Ergin, B. Shanker, and E. Michielssen, ''Fast transient analysis of acoustic wave scattering from rigid bodies using two-level plane wave time domain algorithm,'' J. Acoust. Soc. Am. **106**, 2405–2416 (1999).
[27] T. Terai, ''On calculation of sound fields around three dimensional objects by integral equation methods,'' J. Sound Vib. **69**(1), 71–100 (1980).
[28] M. Abramowitz and I. A. Stegun, *Handbook of Mathematical Functions with Formulas, Graphs, and Mathematical Tables* (Dover, New York, 1972).

Fast transient analysis of acoustic wave scattering from rigid bodies using a two-level plane wave time domain algorithm

A. A. Ergin, Balasubramaniam Shanker, and Eric Michielssen
Center for Computational Electromagnetics, Department of Electrical and Computer Engineering, University of Illinois at Urbana-Champaign, 1406 West Green Street, Urbana, Illinois 61801

(Received 10 December 1998; accepted for publication 22 June 1999)

It is well known that the computational cost associated with the application of classical time domain integral equation methods to the analysis of scattering from acoustical targets scales unfavorably with problem size. Indeed, performing a three-dimensional scattering analysis using these methods requires $O(N_t N_s^2)$ operations, where N_s denotes the number of basis functions that model the spatial field distribution over the surface of the scatterer and N_t is the number of time steps in the analysis. Recently, novel plane wave time domain algorithms that augment these classical methods and thereby reduce their high computational cost have been introduced. This paper describes such a plane wave time domain algorithm within the context of the analysis of acoustic scattering from rigid bodies and outlines its incorporation into a time domain integral equation solver in a two-level setting. It is shown that the resulting scheme has a computational complexity of $O(N_t N_s^{1.5} \log N_s)$. Examples comparing the accuracy and computational efficiency of the conventional and accelerated methods are presented. The proposed two-level scheme renders feasible the broadband analysis of scattering from large and complex bodies. © *1999 Acoustical Society of America.* [S0001-4966(99)02911-2]

PACS numbers: 43.20.Px, 43.20.Fn, 02.70.Pt [ANN]

INTRODUCTION

Historically, boundary integral equation- (BIE) based methods have enjoyed widespread use in the study of *time harmonic* acoustic surface scattering phenomena.[1,2] The advantages of BIE techniques over differential equation-based methods are that (*i*) the number of unknowns scales as the surface area of the scatterer and (*ii*) the radiation condition is implicitly imposed by the formulation. Although time domain integral equation-based techniques, often referred to as the marching-on-in-time (MOT) schemes,[3–5] share the same advantages, they have received only scant attention from the computational acoustics society since they have long been conceived as unstable and computationally expensive. Recent research, however, has shown that the MOT schemes can be stabilized by using implicit time stepping along with more accurate numerical integration and differentiation rules.[5–7] On the other hand, literature on techniques for reducing its high computational complexity is scarce.

In classical MOT schemes,[4,5,8] the instantaneous spatial distribution of the wave field over the surface of a three-dimensional scatterer is represented in terms of N_s (spatial) basis functions. The field amplitudes associated with these basis functions at a given point in time are calculated from knowledge of the surface field values at all prior time steps via a retarded potential boundary integral and the incident field. Hence, at each time step in a MOT scheme, N_s field values are evaluated from N_s past field values, incurring a computational cost that scales as $O(N_t N_s^2)$ for an analysis that lasts N_t time step. It is this high computational complexity that renders the analysis of transient scattering from realistic structures intractable using MOT methods with the current computational resources. It should be noted that, until the advent of the fast multipole method (FMM),[9–11] the frequency domain BIE methods also suffered from similar unfavorable cost scalings. Recently, plane wave time domain (PWTD) algorithms[12,13] have been introduced that can be considered the time domain counterparts of the frequency domain FMM schemes. These algorithms permit evaluation of the field radiated by a remote cluster of sources at a set of observer locations by using a plane wave expansion. In Refs. 12 and 13, it has been *theoretically* shown that incorporation of the PWTD algorithm into a MOT scheme in a two-level setting reduces the computational complexity of a transient scattering analysis to $O(N_t N_s^{1.5} \log N_s)$. Here, the term ''two-level setting'' signifies that the scatterer is divided into subscatterers, and that the interactions between the subscatterers that are spatially close to one another are accounted for using the classical MOT method, while those between all other subscatterers are computed using the PWTD algorithm. Preliminary results obtained by applying such a two-level scheme in the analysis of acoustic scattering from rigid bodies were presented in Ref. 14.

In this paper, first, a detailed description is presented of a PWTD algorithm that relies on a Whittaker-type representation of fields in terms of propagating plane waves. Then, this algorithm is used in tandem with a MOT scheme to solve a time domain BIE that is used in the analysis of acoustic scattering from rigid bodies. As opposed to the finite-cone representations used in Ref. 14, the Whittaker-type complete spherical expansion of the far field used here renders the description of the PWTD algorithm more transparent and its implementation easier. Furthermore, this paper addresses issues that arise in the practical implementation of

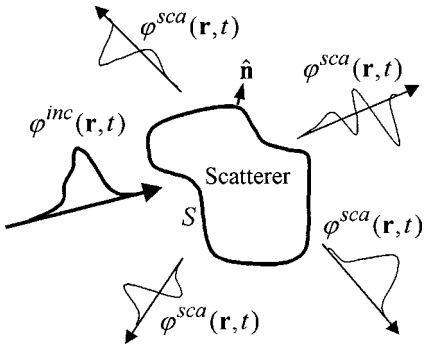

FIG. 1. Description of the scattering problem.

the PWTD algorithm and in its incorporation into the MOT scheme in a two-level setting.

The organization of the paper is as follows. In the next section, the classical MOT scheme for analyzing transient scattering from rigid bodies is presented. The PWTD algorithm is described and practical implementation issues are discussed in Sec. II. In Sec. III, the incorporation of the PWTD algorithm into the MOT method is elucidated and the computational complexity of the resulting scheme is derived. Numerical examples, which verify the applicability and computational complexity of the proposed two-level scheme, are presented in Sec. IV. The conclusions of this study are stated in Sec. V.

I. MARCHING-ON-IN-TIME FORMULATION FOR ACOUSTIC WAVE SCATTERING ANALYSIS

Consider a rigid body defined by a surface S that resides in a homogeneous medium with wave speed c (Fig. 1). The surface S may be open or closed, connected or disconnected, and has surface area S_A. Let this body be insonified by an incident field with a velocity potential $\varphi^{\text{inc}}(\mathbf{r},t)$, whose frequency content vanishes for frequencies above $\omega_{\max}$ radians per second. When the incident field interacts with S, a scattered field with potential $\varphi^{\text{sca}}(\mathbf{r},t)$ is generated such that the total velocity potential $\varphi(\mathbf{r},t)=\varphi^{\text{inc}}(\mathbf{r},t)+\varphi^{\text{sca}}(\mathbf{r},t)$ satisfies the boundary condition $\hat{\mathbf{n}}\cdot\nabla\varphi(\mathbf{r},t)=0$ on S, where $\hat{\mathbf{n}}$ is the position-dependent outward-pointing unit normal to S. It is assumed that no interaction takes place prior to time $t=0$; hence, $\varphi(\mathbf{r},t)=0$ on S for $t\leqslant 0$. It can be shown that $\varphi(\mathbf{r},t)$ on S satisfies both the (time derivative of the) Kirchhoff integral equation[15]

$$-\partial_t\varphi^{\text{inc}}(\mathbf{r},t)=-C(\mathbf{r})\partial_t\varphi(\mathbf{r},t)+\partial_t\int\!\!\!\!\!\!-_S d\mathbf{r}'\,\varphi(\mathbf{r}',t)*\hat{\mathbf{n}}'\cdot\nabla'\frac{\delta(t-R/c)}{4\pi R}\doteq\mathcal{L}_p\{\varphi(\mathbf{r},t)\},\quad \mathbf{r}\in S, \tag{1}$$

and the normal derivative of the Kirchhoff integral equation[16]

$$\hat{\mathbf{n}}\cdot\nabla\varphi^{\text{inc}}(\mathbf{r},t)=-\int\!\!\!\!\!\!=_S d\mathbf{r}'\,\varphi(\mathbf{r}',t)*\hat{\mathbf{n}}\cdot\nabla\hat{\mathbf{n}}'\cdot\nabla'\frac{\delta(t-R/c)}{4\pi R}\doteq\mathcal{L}_v\{\varphi(\mathbf{r},t)\},\quad \mathbf{r}\in S. \tag{2}$$

In the above equations, $*$ denotes a temporal convolution, $R=|\mathbf{r}-\mathbf{r}'|$, $\delta(\cdot)$ is the Dirac pulse, and single and double dashes on the integral signs denote, respectively, that the principal value and the finite part of the integrals are to be evaluated.[17] Also, the position-dependent coefficient $C(\mathbf{r})$ has the value 1 minus the solid angle subtended by the surface at point $\mathbf{r}$ divided by 4π, and reduces to 1/2 when $\mathbf{r}$ is on a smooth part of S. Both Eqs. (1) and (2) can be used to solve for $\varphi(\mathbf{r},t)$ on volume enclosing (closed) S. However, for analyzing scattering from thin structures characterized by open surfaces, Eq. (2) should be employed since use of Eq. (1) leads to the well-known thin-shape breakdown problem.[18,19]

It was recently shown that for closed S, the numerical solutions to both Eqs. (1) and (2) are susceptible to corruption by spurious oscillations when the spectrum of the incident field encompasses one or more of the scatterer's internal resonance frequencies.[20] The source of these oscillations was identified as the numerical excitation of internal resonance modes, and it was shown that such corrupt solutions are avoided by using a Burton–Miller-type time domain combined field integral equation (CFIE) given by[20]

$$\begin{aligned}(1-\alpha)\partial_t\varphi^{\text{inc}}(\mathbf{r},t)+\alpha c\hat{\mathbf{n}}\cdot\nabla\varphi^{\text{inc}}(\mathbf{r},t)&\\ =-(1-\alpha)\mathcal{L}_p\{\varphi(\mathbf{r},t)\}+\alpha c\mathcal{L}_v\{\varphi(\mathbf{r},t)\}&\\ \doteq\mathcal{L}_c\{\varphi(\mathbf{r},t)\},&\end{aligned} \tag{3}$$

which reduces to Eq. (1) for $\alpha=0$ and to Eq. (2) for $\alpha=1$. It was demonstrated in Ref. 20 that Eq. (3) does not support any internal fields for $0<\alpha<1$ and therefore yields accurate solutions devoid of resonant components. Once $\varphi(\mathbf{r},t)$ on S is computed by solving Eq. (3), $\varphi^{\text{sca}}(\mathbf{r},t)$ can be calculated using

$$\varphi^{\text{sca}}(\mathbf{r},t)=\int_S d\mathbf{r}'\,\varphi(\mathbf{r}',t)*\hat{\mathbf{n}}'\cdot\nabla'\frac{\delta(t-R/c)}{4\pi R}. \tag{4}$$

To solve Eq. (3), the unknown surface potential $\varphi(\mathbf{r},t)$ for $0\leqslant t\leqslant T$ is represented in terms of N_s spatial basis functions $f_n(\mathbf{r})$ and N_t temporal basis functions $T_i(t)$ as

$$\varphi(\mathbf{r},t)=\sum_{n=1}^{N_s}\sum_{i=1}^{N_t}\varphi_{i,n}f_n(\mathbf{r})T_i(t), \tag{5}$$

where $\varphi_{i,n}$ is the expansion coefficient associated with the space–time basis $f_n(\mathbf{r})T_i(t)$. To ensure an accurate representation of $\varphi(\mathbf{r},t)$, it is assumed that the number of spatial basis functions scales with the acoustical size of the scatterer as $N_s\propto S_A(\omega_{\max}/c)^2$ and the number of temporal samples scales with the maximum frequency of interest as $N_t\propto T\omega_{\max}$. In this study, S is modeled as a collection of N_s flat triangular facets S_n, $n=1,\ldots,N_s$, and the $f_n(\mathbf{r})$ are chosen to be unit pulse functions defined as

$$f_n(\mathbf{r})=\begin{cases}1; & \mathbf{r}\in S_n,\\ 0; & \text{elsewhere.}\end{cases} \tag{6}$$

The use of these simple piecewise constant basis functions facilitates the efficient evaluation of the finite part integrals that appear in Eq. (2) by using a method that is analogous to the limiting procedure employed by Terai[21] (see Ref. 20).

However, the acceleration technique presented in this paper does not depend on the choice of basis functions and also applies to more sophisticated basis functions such as those described by Bluck and Walker.[5] The temporal basis functions are chosen to be cubic interpolation functions defined as $T_i(t)=T(t-t_i)$, where $t_i=i\Delta_t$ for a time step size $\Delta_t=T/N_t$, and

$$T(t)=\begin{cases}1+\frac{11}{6}(t/\Delta_t)+(t/\Delta_t)^2+\frac{1}{6}(t/\Delta_t)^3; & -\Delta_t\leqslant t\leqslant 0,\\ 1+\frac{1}{2}(t/\Delta_t)-(t/\Delta_t)^2-\frac{1}{2}(t/\Delta_t)^3; & 0\leqslant t\leqslant\Delta_t,\\ 1-\frac{1}{2}(t/\Delta_t)-(t/\Delta_t)^2+\frac{1}{2}(t/\Delta_t)^3; & \Delta_t\leqslant t\leqslant 2\Delta_t,\\ 1-\frac{11}{6}(t/\Delta_t)+(t/\Delta_t)^2-\frac{1}{6}(t/\Delta_t)^3; & 2\Delta_t\leqslant t\leqslant 3\Delta_t,\\ 0; \quad \text{elsewhere.}\end{cases} \tag{7}$$

The function $T(t)$ is an extension of the quadratic basis function used by Manara *et al.*[22] ensuring that the temporal variation of all the quantities to be evaluated are approximated by piecewise polynomials (see Ref. 20). Substituting the expansion in Eq. (5) into Eq. (3) and testing the resulting equation with $\tilde{f}_m(\mathbf{r})=\delta(\mathbf{r}-\mathbf{r}_m^c)$, where $\mathbf{r}_m^c$ denotes the centroid of the mth triangular facet, at time $t=t_j$ yields a system of equations that can be expressed in matrix form as[8]

$$\overline{\mathbf{Z}}_0\mathbf{\Phi}_j=\mathbf{F}_j^{\text{inc}}-\sum_{k=1}^{j-1}\overline{\mathbf{Z}}_k\mathbf{\Phi}_{j-k}, \tag{8}$$

where the nth element of the vector $\mathbf{\Phi}_j$ and the mth element of the vector $\mathbf{F}_j^{\text{inc}}$ are given by

$$\mathbf{\Phi}_{j,n}=\varphi_{j,n}, \tag{9}$$

$$\mathbf{F}_{j,m}^{\text{inc}}=\int_S d\mathbf{r}\tilde{f}_m(\mathbf{r})[(1-\alpha)\partial_t\varphi^{\text{inc}}(\mathbf{r},t)+\alpha c\hat{\mathbf{n}}\cdot\nabla\varphi^{\text{inc}}(\mathbf{r},t)]\big|_{t=t_j}, \tag{10}$$

and an element of the $\overline{\mathbf{Z}}_k$ matrix is given by

$$\overline{\mathbf{Z}}_{k,mn}=\int_S d\mathbf{r}\tilde{f}_m(\mathbf{r})\mathcal{L}_c\{f_n(\mathbf{r})T_{j-k}(t)\}\big|_{t=t_j}. \tag{11}$$

A detailed explanation of how the vector and matrix elements in Eqs. (10) and (11) can be evaluated for the current choice of basis functions can be found in Ref. 20.

Equation (8) constitutes the basis of the MOT method. It relates the surface potential at time $t=t_j$ to the incident field at that time and to $\varphi(\mathbf{r},t)$ on S at earlier times. At each time step in the MOT scheme, the right-hand side of Eq. (8) is formed from the incident field and the $\mathbf{\Phi}$ vectors of the prior time steps ($\mathbf{\Phi}_i$, $i<j$). Then, the $\mathbf{\Phi}_j$ vector at the current time step is obtained by solving the resulting system of equations. Since the interaction matrix $\overline{\mathbf{Z}}_0$ is sparse, solution of the matrix equation is obtained in $O(\kappa N)$ operations with a nonstationary iterative solver, where κ denotes the number of iterations.

Evaluation of the summation on the right-hand side of Eq. (8) is the most expensive part of the MOT scheme. This operation is equivalent to evaluating $\mathcal{L}_c\{\varphi(\mathbf{r},t)\}$, which can be written as a sum over N_s basis functions, at N_s observation points and requires $O(N_s^2)$ operations per time step.[5,7,12,13] Hence, the complexity of a MOT analysis for N_t time steps scales as $O(N_tN_s^2)$. This cost renders the classical MOT method prohibitively expensive for large-scale scattering analysis.

Traditional implementations of the MOT scheme relied on explicit time stepping that suffered from late time instabilities. These instabilities were attributed to a variety of causes including the inaccurate evaluation of the integrals and time derivatives that appear in Eq. (3).[4,8,22,23] Recently, it has been experimentally demonstrated that stability can be achieved by employing implicit schemes that use higher-order quadrature rules and/or larger time step sizes.[5–7] In the present study, the integrals over triangular domains are numerically evaluated as outlined in Ref. 20, and the time step size is chosen—independent of the mesh size—as $\Delta_t=2\pi/(\beta\omega_{\max})$. Developing guidelines for choosing the parameter β is still an area of active research and the interested reader is referred to Refs. 7 and 24. For all the examples that will be presented, $\beta=10$ yielded stable results.

II. THE PLANE WAVE TIME DOMAIN ALGORITHM

It has been pointed out in the previous section that the most expensive part of the MOT method lies in the evaluation of the discrete analog of

$$u(\mathbf{r},t)=\mathcal{L}_c\{\varphi(\mathbf{r},t)\}, \tag{12}$$

which from hereon will be referred to as *the field radiated by a surface bound source distribution of strength* $\varphi(\mathbf{r},t)$. The computation of this radiated field at multiple observation points can be accelerated if it is represented in terms of a plane wave basis. In Sec. II A, a plane wave expansion for $u(\mathbf{r},t)$ is presented and an algorithm to compute this field is described. Details pertaining to the practical implementation of the algorithm are presented in Sec. II B.

A. Plane wave expansion

Consider two fictitious spheres whose centers are located at $\mathbf{r}_s$ and $\mathbf{r}_o$ [Fig. 2(a)]. The radius of each sphere is denoted by R_s and it is assumed that $|\mathbf{r}_o-\mathbf{r}_s|>2R_s$, i.e., the spheres do not overlap. Assume that a source distribution $\varphi(\mathbf{r},t)$ resides on a surface S' enclosed by the first sphere and that the field $u(\mathbf{r},t)$ due to this source distribution is observed on a surface S inside the second sphere. As the source and observation domains can never overlap, Eqs. (1)–(3) and (12) imply that $u(\mathbf{r},t)$ can be expressed as

$$u(\mathbf{r},t)=-[(1-\alpha)\partial_t+\alpha c\hat{\mathbf{n}}\cdot\nabla]\int_{S'}d\mathbf{r}'\,\varphi(\mathbf{r}',t)*\hat{\mathbf{n}}'\cdot\nabla'\frac{\delta(t-R/c)}{4\pi R}. \tag{13}$$

To make the discussion more tractable, the following notation is introduced. The points $\mathbf{r}$ and $\mathbf{r}'$ denote the observer and source locations in the observation and source spheres, respectively. Their positions relative to respective sphere

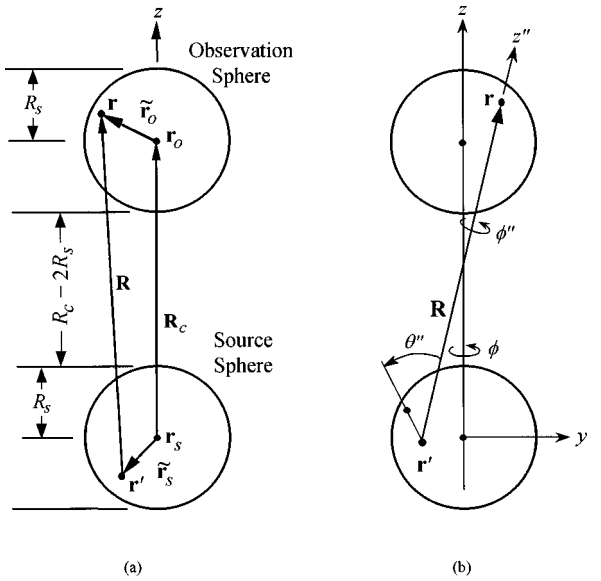

FIG. 2. Description of the geometry for the PWTD algorithm. (a) Definition of various vectors. (b) Coordinate transformation to double primed coordinates.

centers are denoted by $\tilde{\mathbf{r}}_o=\mathbf{r}-\mathbf{r}_o$ and $\tilde{\mathbf{r}}_s=\mathbf{r}'-\mathbf{r}_s$. Let $\mathbf{R}_c=\mathbf{r}_o-\mathbf{r}_s$ denote the vector connecting the source and observation sphere centers, and, without loss of generality, assume it to be aligned with the $\hat{\mathbf{z}}$ axis, i.e., $\mathbf{R}_c=R_c\hat{\mathbf{z}}$, where $R_c=|\mathbf{R}_c|$.

As will be evident in the forthcoming analysis, the plane wave representation to be derived is valid for sources of a finite duration T_s (the maximum of which depends on R_c and R_s). However, for signals longer than the maximum allowable T_s, this restriction can be circumvented using the linear nature of the representation. Hence, the first step towards representing the field $u(\mathbf{r},t)$ as a superposition of plane waves is to break up the source signal $\varphi(\mathbf{r}',t)$ of duration $T=N_t\Delta_t$ into L overlapping subsignals $\varphi_l(\mathbf{r}',t)$, $l=0,\ldots,L-1$, each of duration T_s, such that

$$\varphi(\mathbf{r}',t)=\sum_{l=0}^{L-1}\varphi_l(\mathbf{r}',t). \tag{14}$$

Let $t_l^{\min}$ and $t_l^{\max}$ denote the starting and ending times of the lth subsignal, i.e., $\varphi_l(\mathbf{r}',t)=0$ outside the interval $t_l^{\min}\leqslant t<t_l^{\max}$, and let $u_l(\mathbf{r},t)$ denote the field at $\mathbf{r}$ due to $\varphi_l(\mathbf{r}',t)$; hence, $u(\mathbf{r},t)=\Sigma_{l=0}^{L-1}u_l(\mathbf{r},t)$.

To arrive at a plane wave representation of $u_l(\mathbf{r},t)$, consider the field $\tilde{u}_l(\mathbf{r},t)$ given by

$$\tilde{u}_l(\mathbf{r},t)=[(1-\alpha)\partial_t+\alpha c\hat{\mathbf{n}}\cdot\nabla]\frac{\partial_t}{8\pi^2 c}\int_0^{2\pi}d\phi\int_0^{\pi}d\theta \times\sin\theta\,\delta(t-\hat{\mathbf{k}}\cdot\tilde{\mathbf{r}}_o/c)*\delta(t-\hat{\mathbf{k}}\cdot\mathbf{R}_c/c)*\tilde{\varphi}_l(\hat{\mathbf{k}},t), \tag{15}$$

where $\hat{\mathbf{k}}=\hat{\mathbf{x}}\sin\theta\cos\phi+\hat{\mathbf{y}}\sin\theta\sin\phi+\hat{\mathbf{z}}\cos\theta$ and $\tilde{\varphi}_l(\hat{\mathbf{k}},t)$ is the Slant Stack Transform (SST)[25–27] of the source distribution $\varphi_l(\mathbf{r}',t)$ defined as

$$\tilde{\varphi}_l(\hat{\mathbf{k}},t)=\int_{S'}d\mathbf{r}'\,\varphi_l(\mathbf{r}',t)*\hat{\mathbf{n}}'\cdot\nabla'\,\delta(t+\hat{\mathbf{k}}\cdot\tilde{\mathbf{r}}_s/c) =\frac{\partial_t}{c}\int_{S'}d\mathbf{r}'(\hat{\mathbf{n}}'\cdot\hat{\mathbf{k}})\,\delta(t+\hat{\mathbf{k}}\cdot\tilde{\mathbf{r}}_s/c)*\varphi_l(\mathbf{r}',t). \tag{16}$$

The SST maps the source distribution to a time-dependent plane wave emanating from the source sphere and propagating along direction $\hat{\mathbf{k}}$. Henceforth, plane waves obtained by a SST will be termed *outgoing rays*. Note that, since the outgoing rays are obtained by delaying the subsignal $\varphi_l(\mathbf{r}',t)$ by an amount $-\hat{\mathbf{k}}\cdot\tilde{\mathbf{r}}_s/c$, which can assume values between $-R_s/c$ and R_s/c within a source sphere, each outgoing ray can span a maximum duration of T_s+2R_s/c for a fixed observer.

Substituting Eq. (16) into (15), rearranging the order of integrations, and using the fact that $\mathbf{R}=\tilde{\mathbf{r}}_o+\mathbf{R}_c-\tilde{\mathbf{r}}_s$ yields

$$\tilde{u}_l(\mathbf{r},t)=-[(1-\alpha)\partial_t+\alpha c\hat{\mathbf{n}}\cdot\nabla]\int_{S'}d\mathbf{r}'\,\varphi_l(\mathbf{r}',t)*\hat{\mathbf{n}}' \cdot\nabla'\tilde{g}(\mathbf{r}',\mathbf{r},t), \tag{17}$$

where

$$\tilde{g}(\mathbf{r}',\mathbf{r},t)=-\frac{\partial_t}{8\pi^2 c}\int_0^{2\pi}d\phi\int_0^{\pi}d\theta\sin\theta\,\delta(t-\hat{\mathbf{k}}\cdot\mathbf{R}/c). \tag{18}$$

The first step in evaluating the spherical integral in Eq. (18) is to transform the integration variables (θ,ϕ) to a new set of angular coordinates (θ'',ϕ'') which are defined with respect to the $\hat{\mathbf{z}}''$ axis aligned with the vector $\mathbf{R}$ as shown in Fig. 2(b). In this new coordinate system, the $\hat{\mathbf{k}}\cdot\mathbf{R}$ term in Eq. (18) becomes $R\cos\theta''$, and setting $\tau=(R/c)\cos\theta''$ yields

$$\tilde{g}(\mathbf{r}',\mathbf{r},t)=-\frac{\partial_t}{8\pi^2 R}\int_0^{2\pi}d\phi''\int_{-R/c}^{R/c}d\tau\,\delta(t-\tau) =\frac{1}{8\pi^2 R}\int_0^{2\pi}d\phi''[\,\delta(t-R/c)-\delta(t+R/c)\,] =\frac{\delta(t-R/c)}{4\pi R}-\frac{\delta(t+R/c)}{4\pi R}. \tag{19}$$

Substituting Eq. (19) in (17) yields

$$\tilde{u}_l(\mathbf{r},t)=-[(1-\alpha)\partial_t+\alpha c\hat{\mathbf{n}}\cdot\nabla]\int_{S'}d\mathbf{r}'\,\varphi_l(\mathbf{r}',t)*\hat{\mathbf{n}}' \cdot\nabla'\frac{\delta(t-R/c)}{4\pi R}+[(1-\alpha)\partial_t+\alpha c\hat{\mathbf{n}}\cdot\nabla] \times\int_{S'}d\mathbf{r}'\,\varphi_l(\mathbf{r}',t)*\hat{\mathbf{n}}'\cdot\nabla'\frac{\delta(t+R/c)}{4\pi R}. \tag{20}$$

In Eq. (20), the first term on the right-hand side corresponds to the true observed field $u_l(\mathbf{r},t)$ given in Eq. (13). Note that, were it not for the second term, which will be referred to as the ghost signal, $\tilde{u}_l(\mathbf{r},t)$ would be identical to $u_l(\mathbf{r},t)$. This derivation is similar to those presented in Refs. 12, 26, and 28. If the ghost signal can somehow be removed from $\tilde{u}_l(\mathbf{r},t)$, then Eq. (15) implies that the true observed field can be constructed as a superposition of plane waves.

To derive a scheme that retains only the true observed field upon time gating $\tilde{u}_l(\mathbf{r},t)$, the following observations are in order. From Eq. (20), it follows that the ghost signal present in $\tilde{u}_l(\mathbf{r},t)$ vanishes after $t_l^{\text{ghost}}=-\min\{R\}/c+t_l^{\max}$ and that the observed field coincides with the true field for $t>t_l^{\text{ghost}}$. Also, the true field does not reach the observer before $t_l^{\text{trans}}=\min\{R\}/c+t_l^{\min}$. Therefore, provided that $t_l^{\text{trans}}>t_l^{\text{ghost}}$, the ghost field ceases to exist before the true signal arrives. In addition, if $t_l^{\text{trans}}\geqslant t_l^{\max}$, all source activity related to the lth time interval ends before the true signal reaches the observer. Hence, it is possible to obtain a ghost-free solution via Eq. (15) by choosing $T_s\leqslant\min\{R\}/c$, which satisfies both the conditions $t_l^{\text{trans}}>t_l^{\text{ghost}}$ and $t_l^{\text{trans}}\geqslant t_l^{\max}$. Consequently, since $(R_c-2R_s)\leqslant\min\{R\}$ for arbitrary $\mathbf{r}'$ and $\mathbf{r}$ in the source and observation spheres, respectively, the choice $T_s\leqslant(R_c-2R_s)/c$ guarantees that a ghost-free solution can be obtained inside the observation sphere via Eq. (15).

In summary, provided that $T_s\leqslant(R_c-2R_s)/c$, the field $u_l(\mathbf{r},t)$ inside the observation sphere can be expressed as

$$u_l(\mathbf{r},t)=\begin{cases}0; & t<t_l^{\text{trans}},\\ \tilde{u}_l(\mathbf{r},t); & t\geqslant t_l^{\text{trans}},\end{cases} \tag{21}$$

where, by Eqs. (15) and (16), and the identity $\nabla\delta(t\pm\hat{\mathbf{k}}\cdot\mathbf{r}/c)=\pm\hat{\mathbf{k}}\partial_t\delta(t\pm\hat{\mathbf{k}}\cdot\mathbf{r}/c)/c$, $\tilde{u}_l(\mathbf{r},t)$ is given by

$$\begin{aligned}\tilde{u}_l(\mathbf{r},t)=&\int_0^{2\pi}d\phi\int_0^{\pi}d\theta\sin\theta\,[(1-\alpha)-\alpha\hat{\mathbf{n}}\cdot\hat{\mathbf{k}}]\\&\times\delta\left(t-\frac{\hat{\mathbf{k}}\cdot\tilde{\mathbf{r}}_o}{c}\right)*\mathcal{T}(\hat{\mathbf{k}},\mathbf{R}_c,t)\\&*\int_{S'}d\mathbf{r}'\hat{\mathbf{n}}'\cdot\hat{\mathbf{k}}\delta\left(t+\frac{\hat{\mathbf{k}}\cdot\tilde{\mathbf{r}}_s}{c}\right)*\varphi_l(\mathbf{r}',t),\end{aligned} \tag{22}$$

and the translation function $\mathcal{T}(\hat{\mathbf{k}},\mathbf{R}_c,t)$ is defined as

$$\mathcal{T}(\hat{\mathbf{k}},\mathbf{R}_c,t)=\frac{\partial_t^3}{8\pi^2c^2}\delta(t-\hat{\mathbf{k}}\cdot\mathbf{R}_c/c). \tag{23}$$

Equations (21)–(23) constitute the crux of the PWTD algorithm, which is a three-stage process for evaluating $u_l(\mathbf{r},t)$. In the first stage, outgoing rays are formed by evaluating the SST of the source distribution $\varphi_l(\mathbf{r}',t)$. The second stage maps the outgoing rays from the source sphere to *incoming rays* that impinge upon the observation sphere. This is accomplished by convolving the outgoing rays with the translation function $\mathcal{T}(\hat{\mathbf{k}},\mathbf{R}_c,t)$ at $t=t_l^{\text{trans}}$. In the final stage, the incoming rays are projected onto the observer location yielding the true field $u_l(\mathbf{r},t)$.

B. Practical implementation issues

In practice, the spectral integration over the unit sphere in Eq. (22) cannot be performed over a continuum of directions. In this subsection, it is shown that $u_l(\mathbf{r},t)$ can be evaluated by using only a finite number of directions if (*i*) the subsignals $\varphi_l(\mathbf{r}',t)$ are temporally bandlimited and (*ii*) a spatially bandlimited version of the translation function is used.

For $t\geqslant t_l^{\text{trans}}$, Eq. (21) can be rewritten as

$$u_l(\mathbf{r},t)=\int_0^{2\pi}d\phi\int_0^{\pi}d\theta\sin\theta\,\mathcal{T}(\hat{\mathbf{k}},\mathbf{R}_c,t)*f_l(\hat{\mathbf{k}},t), \tag{24}$$

where

$$\begin{aligned}f_l(\hat{\mathbf{k}},t)=&\int_{S'}d\mathbf{r}'[(1-\alpha)-\alpha\hat{\mathbf{n}}\cdot\hat{\mathbf{k}}](\hat{\mathbf{k}}\cdot\hat{\mathbf{n}}')\\&\times\delta(t-\hat{\mathbf{k}}\cdot(\tilde{\mathbf{r}}_o-\tilde{\mathbf{r}}_s)/c)*\varphi_l(\mathbf{r}',t).\end{aligned} \tag{25}$$

The function $f_l(\hat{\mathbf{k}},t)$ can be interpreted as the time-dependent radiation pattern (or SST) of a source distribution enclosed in a sphere of radius $2R_s$. Therefore, assuming that $\varphi_l(\mathbf{r}',t)$ is temporally bandlimited to $\omega_s>\omega_{\max}$, $f_l(\hat{\mathbf{k}},t)$ is spatially quasi-bandlimited and can be expressed in terms of spherical harmonics as[29]

$$f_l(\hat{\mathbf{k}},t)=\sum_{n=0}^{K}\sum_{m=-n}^{n}f_{l,nm}(t)P_n^m(\cos\theta)e^{-jm\phi}, \tag{26}$$

where $K=\lceil 2\chi_1R_s\omega_s/c\rceil$, $\chi_1>1$ is an excess bandwidth factor, $\lceil\cdot\rceil$ means ''rounded to nearest larger integer,'' and $P_n^m(\cdot)$ is the associated Legendre function of degree n and order m. The error incurred by approximating $f_l(\hat{\mathbf{k}},t)$ with only K spherical harmonics decreases exponentially fast with increasing χ_1 (see Ref. 29 and references therein). Also, note that the translation function given in Eq. (23) has a directional dependence given by $\hat{\mathbf{k}}\cdot\mathbf{R}_c=R_c\cos\theta$, which is independent of ϕ. Making use of this fact in Eq. (23) and using

$$\begin{aligned}\delta(t-R_c\cos\theta/c)=&\frac{c}{2R_c}\sum_{k=0}^{\infty}(2k+1)P_k^0(ct/R_c)\\&\times P_k^0(\cos\theta)\quad\text{for }|t|\leqslant\frac{R_c}{c},\end{aligned} \tag{27}$$

the translation function can be written as

$$\begin{aligned}\mathcal{T}(\hat{\mathbf{k}},\mathbf{R}_c,t)=&\frac{\partial_t^3}{16\pi^2cR_c}\sum_{k=0}^{\infty}(2k+1)P_k^0(ct/R_c)\\&\times P_k^0(\cos\theta)\quad\text{for }|t|\leqslant\frac{R_c}{c}.\end{aligned} \tag{28}$$

Substituting (26) and (28) in Eq. (24) and evaluating the ϕ integral yields

$$\begin{aligned}u_l(\mathbf{r},t)=&\frac{\partial_t^3}{8\pi cR_c}\sum_{k=0}^{\infty}(2k+1)\sum_{n=0}^{K}f_{l,n0}(t)*P_k^0(ct/R_c)\\&\times\int_0^{\pi}d\theta\sin\theta P_n^0(\cos\theta)P_k^0(\cos\theta).\end{aligned} \tag{29}$$

Due to the orthogonality of the Legendre polynomials, the integral in Eq. (29) is nonzero only for $n=k$. Consequently, a spatially bandlimited version of the translation function obtained by truncating the infinite sum in Eq. (28) at $K'\geqslant K$ can be used. This also implies that the translation function is not unique since the time-dependent coefficients multiplying the $P_k^0(\cos\theta)$ terms for $k>K$ in Eq. (28) can be chosen arbitrarily. In the remainder of this paper it will be assumed that the translation function is given by

$$\overline{\mathcal{T}}(\hat{\mathbf{k}},\mathbf{R}_c,t) = \begin{cases} \dfrac{\partial_t^3}{16\pi^2 c R_c} \displaystyle\sum_{k=0}^{K} (2k+1) P_k^0\left(\frac{ct}{R_c}\right) P_k^0(\cos\theta); & |t| \leqslant \dfrac{R_c}{c}, \\ 0; \quad \text{elsewhere.} \end{cases} \tag{30}$$

This translation function ensures that the integrand in Eq. (24) can be written as a product of two functions, each of which can be expressed in terms of spherical harmonics with degree less than or equal to K. Such an integral can be evaluated exactly by using a $(2K+1)$-point trapezoidal rule in the ϕ direction and a $(K+1)$-point Gauss–Legendre quadrature in the θ direction.[9,10] Although this choice of sampling points seems to depend on the axis connecting the centers of the spheres, this is not true owing to the fact that under a coordinate system rotation a spherical harmonic of degree K is transformed into a linear combination of harmonics of the same degree. Hence, a given set of sampling points can be used in evaluating the spherical integral in Eq. (24) even if $\mathbf{R}_c$ is not aligned with the $\hat{\mathbf{z}}$ axis.

Finally, note that in the above discussion it was assumed that each subsignal $\varphi_l(\mathbf{r}',t)$ is temporally bandlimited to $\omega_s > \omega_{\max}$. This assumption contradicts the requirement that each subsignal should also be time limited to a duration of T_s. However, as the source distribution $\varphi(\mathbf{r}',t)$ is bandlimited to $\omega_{\max}$, it can be broken up into *approximately* time-limited subsignals that are bandlimited to $\omega_s = \chi_2 \omega_{\max}$, where $\chi_2 > 1$, by expanding $\varphi(\mathbf{r}',t)$ in terms of temporally bandlimited and approximately time limited interpolation functions $\psi(t)$. In this study, a variant of the approximate prolate spheroidal interpolation functions introduced by Knab[30] is used. These interpolation functions have the property that the error incurred by temporally truncating these functions for $|t| > p_t \Delta_t$ decreases exponentially fast as either p_t or χ_2 increase.[12,30] Using these interpolation functions, subsignals $\varphi_l(\mathbf{r}',t)$ can be expressed as

$$\varphi_l(\mathbf{r}',t) = \sum_{i=lM_t}^{(l+1)M_t-1} \varphi(\mathbf{r}',t_i)\,\psi(t-t_i). \tag{31}$$

Note that each subsignal is defined in terms of M_t samples of the signal $\varphi(\mathbf{r}',t)$ but spans M_t+2p_t time steps (Fig. 3). In other words, whereas each subsignal $\varphi_l(\mathbf{r}',t)$ is formed from samples of $\varphi(\mathbf{r}',t)$ in an interval of length $M_t\Delta_t$, the duration of each $\varphi_l(\mathbf{r}',t)$ is $T_s = (M_t+2p_t)\Delta_t$, and adjacent subsignals overlap by $2p_t$ samples. Furthermore, each $\varphi_l(\mathbf{r}',t)$ starts at time $t_l^{\min} = l(T_s - 2p_t\Delta_t) - p_t\Delta_t$ and vanishes after $t_l^{\max} = (l+1)(T_s - 2p_t\Delta_t) + p_t\Delta_t$. Since the interpolation function $\psi(t)$ is bandlimited to ω_s, so is each subsignal.

In conclusion, the error incurred in the numerical evaluation of the integration over the unit sphere in Eq. (22) depends solely on the choice of the parameters χ_1, χ_2, and p_t, and can be estimated beforehand. As demonstrated in Refs. 12 and 13, this error can be reduced to desired precision by varying these three parameters.

III. THE TWO-LEVEL FAST ALGORITHM AND ITS COMPUTATIONAL COMPLEXITY

The PWTD algorithm introduced in the previous section does not permit the evaluation of the scattered field observed everywhere on S since it assumes that the sources producing the field are separated from a spherical region enclosing the observers. However, the PWTD algorithm can be used in tandem with the classical MOT scheme to yield a reduced complexity algorithm, as outlined next and illustrated in Fig. 4. Note once again that the acceleration scheme below is independent of the particular discretization used in the MOT scheme because interactions between all sufficiently remote basis/testing functions can be described by pointwise interactions upon application of the proper quadrature rule.

The first step in arriving at a fast algorithm is to divide S into N_g subscatterers, each of which can be enclosed in a sphere of radius R_s (Fig. 5). It is assumed that each subscatterer, on average, is comprised of $M_s = N_s/N_g$ spatial basis functions. Let $R_{c,\gamma\gamma'}$ denote the distance between the centers of the spheres enclosing subscatterers γ and γ', $\gamma,\gamma' = 1,\ldots,N_g$. Then, a *fundamental subsignal duration* T_s of order R_s/c is chosen. The constraint $T_s \leqslant (R_{c,\gamma\gamma'} - 2R_s)/c$, derived for a two sphere setting in Sec. II A, dictates that the PWTD algorithm can be applied to all sphere pairs for which $R_{c,\gamma\gamma'} \geqslant 2R_s + cT_s$. Hence, two subscatterers γ and γ' are said to be in each other's *far field* if $R_{c,\gamma\gamma'}$ is larger than $2R_s + cT_s$. If this condition is not met, they are said to reside in each other's *near field.*

The subsignal duration $T_{s,\gamma\gamma'} \leqslant (R_{c,\gamma\gamma'} - 2R_s)/c$ for each far-field pair (γ,γ') is determined such that the outgoing rays associated with this pair can be easily formed by concatenating the rays associated with subsignals of fundamental duration T_s. Hence, in accordance with the choice $T_s = (M_t+2p_t)\Delta_t$, the subsignal duration is defined as $T_{s,\gamma\gamma'} = (M_{t,\gamma\gamma'} + 2p_t)\Delta_t$, where

$$M_{t,\gamma\gamma'} = M_t \left\lfloor \frac{R_{c,\gamma\gamma'} - 2R_s}{cT_s - 2p_t\Delta_t} \right\rfloor \tag{32}$$

is an integer multiple of M_t and $\lfloor\cdot\rfloor$ means ''rounded to nearest smaller integer.''

With this partitioning of the scatterer into subscatterers, the field distribution on S at the jth time step is calculated via the following scheme:

(1) Calculate the field on each subscatterer due to sources residing on near-field subscatterers using the interaction

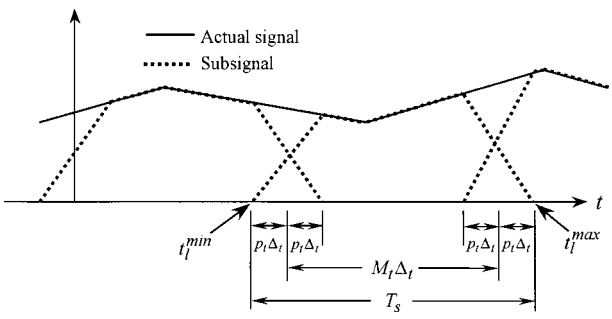

FIG. 3. Partitioning of the actual signal $\varphi(\mathbf{r}',t)$ into overlapping subsignals $\varphi_l(\mathbf{r}',t)$.

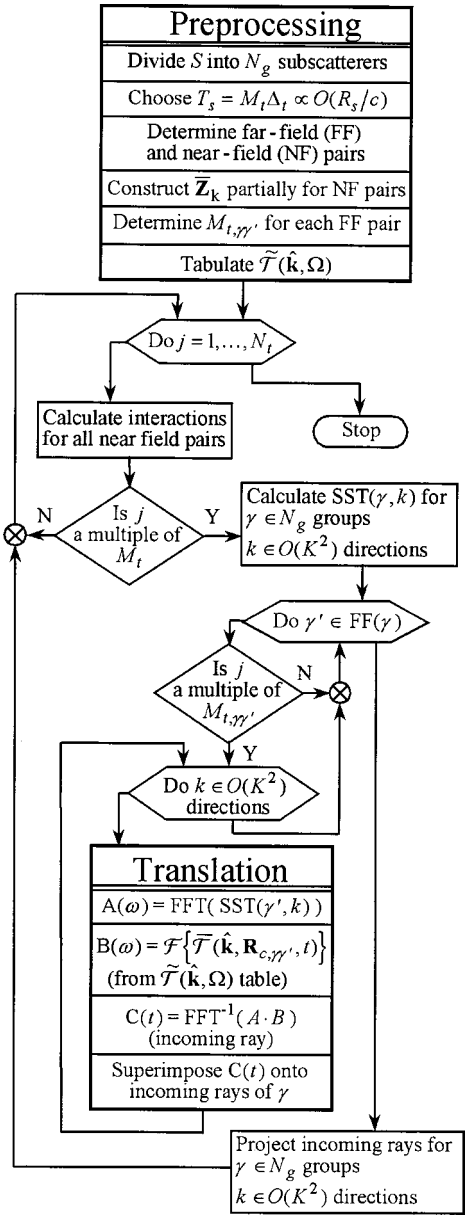

FIG. 4. Block diagram of the two-level PWTD enhanced MOT algorithm.

coefficients given in Eq. (11). Since only a few subscatterers are in the near field of a given subscatterer, this step requires $O(M_s^2)$ operations per subscatterer.

(2) If j is a multiple of M_t, form outgoing rays of duration T_s+2R_s/c for each subscatterer by evaluating the SST of the source distribution for $O(K^2)$ directions corresponding to the sampling points discussed in Sec. II B. Note that both the number of directions and the number of spatial basis functions per subscatterer scale as the surface area of the sphere. Hence this step can be accomplished in $O(M_tM_s^2)$ operations, and the average cost per time step is seen to scale as $O(M_s^2)$.

(3) Translate outgoing rays between subscatterer pairs (γ,γ') whenever j is a multiple of $M_{t,\gamma\gamma'}$. This is accomplished by first forming the outgoing rays of duration $T_{s,\gamma\gamma'}+2R_s/c$ by concatenating the rays of duration T_s+2R_s/c generated at step 2, and then convolving these rays with the translation function $\overline{\mathcal{T}}(\hat{\mathbf{k}},\mathbf{R}_{c,\gamma\gamma'},t)$ given in Eq. (30). As each outgoing ray spans a duration of $T_{s,\gamma\gamma'}+2R_s/c$ and $\overline{\mathcal{T}}(\hat{\mathbf{k}},\mathbf{R}_{c,\gamma\gamma'},t)$ is of duration $2R_{c,\gamma\gamma'}/c$, the duration of both these signals is proportional to $M_{t,\gamma\gamma'}$ time steps. Hence, it is possible to evaluate the convolution of these two signals in $O(M_{t,\gamma\gamma'}\log M_{t,\gamma\gamma'})$ operations using fast Fourier transforms. However, as the translation function $\overline{\mathcal{T}}(\hat{\mathbf{k}},\mathbf{R}_{c,\gamma\gamma'},t)$ is not bandlimited in time, its Fourier transform needs to be evaluated at $O(M_{t,\gamma\gamma'})$ frequencies analytically. To this end, note that the Fourier transform of $\overline{\mathcal{T}}(\hat{\mathbf{k}},\mathbf{R}_{c,\gamma\gamma'},t)$ is given by

$$\mathcal{F}\{\overline{\mathcal{T}}(\hat{\mathbf{k}},\mathbf{R}_{c,\gamma\gamma'},t)\} = \int_{-\infty}^{+\infty} dt\,\overline{\mathcal{T}}(\hat{\mathbf{k}},\mathbf{R}_{c,\gamma\gamma'},t)e^{-j\omega t}$$

$$= \frac{(j\omega)^3}{8\pi^2c^2}\sum_{k=0}^{K}(2k+1)$$

$$\times(-j)^k j_k(\omega R_{c,\gamma\gamma'}/c)P_k(\cos\theta)$$

$$= \frac{c}{R_{c,\gamma\gamma'}^3}\tilde{\mathcal{T}}(\hat{\mathbf{k}},\Omega), \tag{33}$$

where $\Omega = \omega R_{c,\gamma\gamma'}/c$ is the normalized frequency and $j_k(\cdot)$ denotes the spherical Bessel function of order k. Since $\tilde{\mathcal{T}}(\hat{\mathbf{k}},\Omega)$ is bandlimited both in θ and Ω, the Fourier transform of $\overline{\mathcal{T}}(\hat{\mathbf{k}},\mathbf{R}_{c,\gamma\gamma'},t)$ for any group pair can be evaluated from the samples of $\tilde{\mathcal{T}}(\hat{\mathbf{k}},\Omega)$ in $O(M_{t,\gamma\gamma'})$ operations for a given direction. After convolving the outgoing rays with the translation function, the resulting rays are superimposed onto the incoming rays of the observer group.

(4) Evaluate the field on each subscatterer due to far–field subscatterers by projecting the incoming rays onto observer locations. This is the reverse operation of the mapping described in step 2 above. Hence, it can be accomplished in $O(M_s^2)$ operations per time step.

Clearly, the last three steps implement the three-stage PWTD algorithm in a multiple sphere setting. Note that in this scheme important savings result from superimposing the

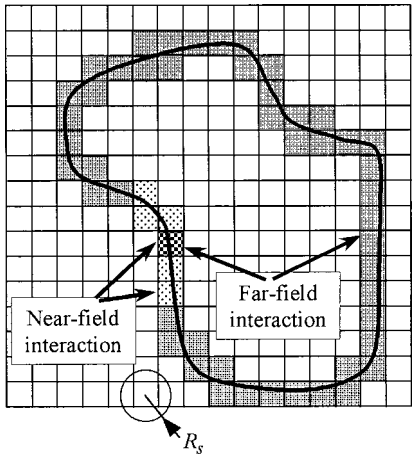

FIG. 5. Partitioning of S into subscatterers, each of which can be enclosed in a sphere of radius R_s, and identification of near-field and far-field interaction pairs.

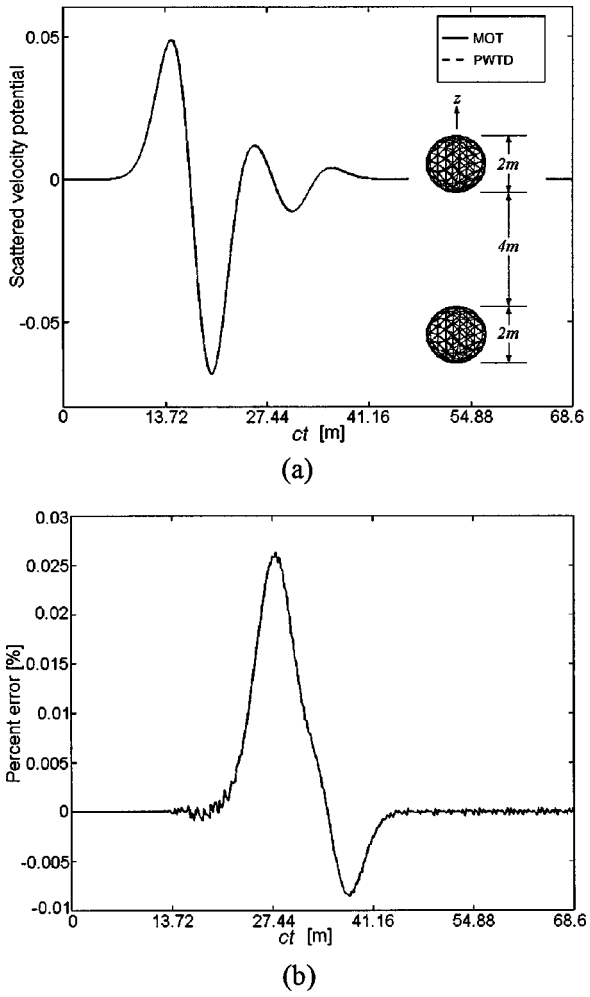

FIG. 6. Transient scattering of a Gaussian plane wave from two rigid spheres modeled by 524 triangular facets. (a) Velocity potential of the scattered field observed at the top sphere. (b) Percent difference between the classical and accelerated solutions normalized to maximum scattered velocity potential amplitude.

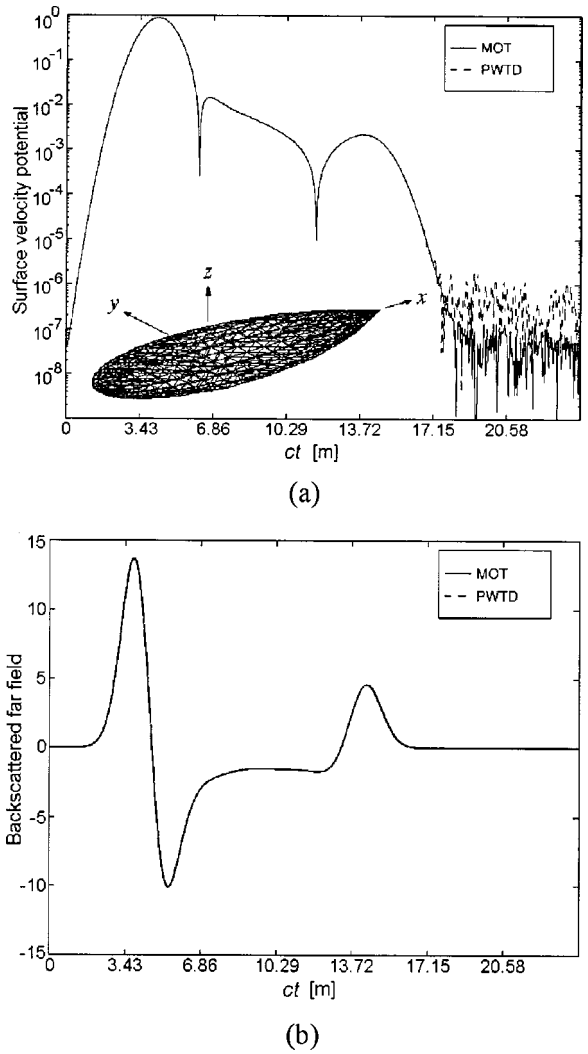

FIG. 7. Transient scattering of a Gaussian plane wave by a 3120 unknown almond. (a) Total velocity potential observed near the front end. (b) Backscattered far field.

incoming rays translated from different source spheres before they are projected onto observers.

To arrive at an estimate of the computational complexity of a surface scattering analysis using the above described algorithm, the cost of performing these four steps for N_t time steps is studied. The first, second, and fourth steps are carried out for $N_g = N_s/M_s$ subscatterers at an average cost of $O(M_s^2)$ for each of the $O(N_t)$ time steps. Hence, their computational costs scale as $O(N_t N_s M_s)$. In the third step, $N_t/M_{t,\gamma\gamma'}$ outgoing rays are translated between N_g^2 subscatterer pairs for $O(K^2) = O(M_s)$ directions. This yields a cost that scales as $O(N_t N_s^2 M_s^{-1} \log M_{t,\gamma\gamma'})$. Noting that $M_{t,\gamma\gamma'}$ is proportional to the longest linear dimension of the scatterer, which scales as $O(N_s^{1/2})$ for a surface scatterer, the cost of the third step is seen to scale as $O(N_t N_s^2 M_s^{-1} \log N_s)$. Hence, the total computational cost asymptotically scales as $c_1 N_t N_s M_s + c_2 N_t N_s^2 M_s^{-1} \log N_s$, where c_1 and c_2 are machine- and implementation-dependent constants. If M_s is chosen proportional to $N_s^{1/2}$, the optimal computational complexity is found to scale as $O(N_t N_s^{1.5} \log N_s)$.

IV. NUMERICAL RESULTS

In this section, the accuracy and efficiency of the proposed algorithm are demonstrated through the numerical analysis of plane wave scattering from several rigid bodies. Two sets of examples are used to validate the proposed two-level scheme. First, scattering from relatively small rigid bodies is analyzed using both the classical MOT scheme and the two-level algorithm, and the temporal variations of the velocity potential at a point on the surface of the scatterer calculated by the two methods are compared. Second, scattering from larger structures, whose analysis using the classical MOT scheme becomes unfeasible, is analyzed using the two-level scheme. Then, the far-field signature associated with the surface velocity potential $\varphi(\mathbf{r},t)$ along a direction $\hat{\mathbf{k}}^s$, given by

$$\varphi^{\text{far}}(\hat{\mathbf{k}}^s,t) = \lim_{r\to\infty} 2\sqrt{\pi} r \varphi^{\text{sca}}(r\hat{\mathbf{k}}^s, t+r/c)$$

$$\cong \frac{\partial_t}{2c\sqrt{\pi}} \int_S d\mathbf{r}' (\hat{\mathbf{n}}' \cdot \hat{\mathbf{k}}^s) \varphi(\mathbf{r}', t+\hat{\mathbf{k}}^s \cdot \mathbf{r}'/c), \tag{34}$$

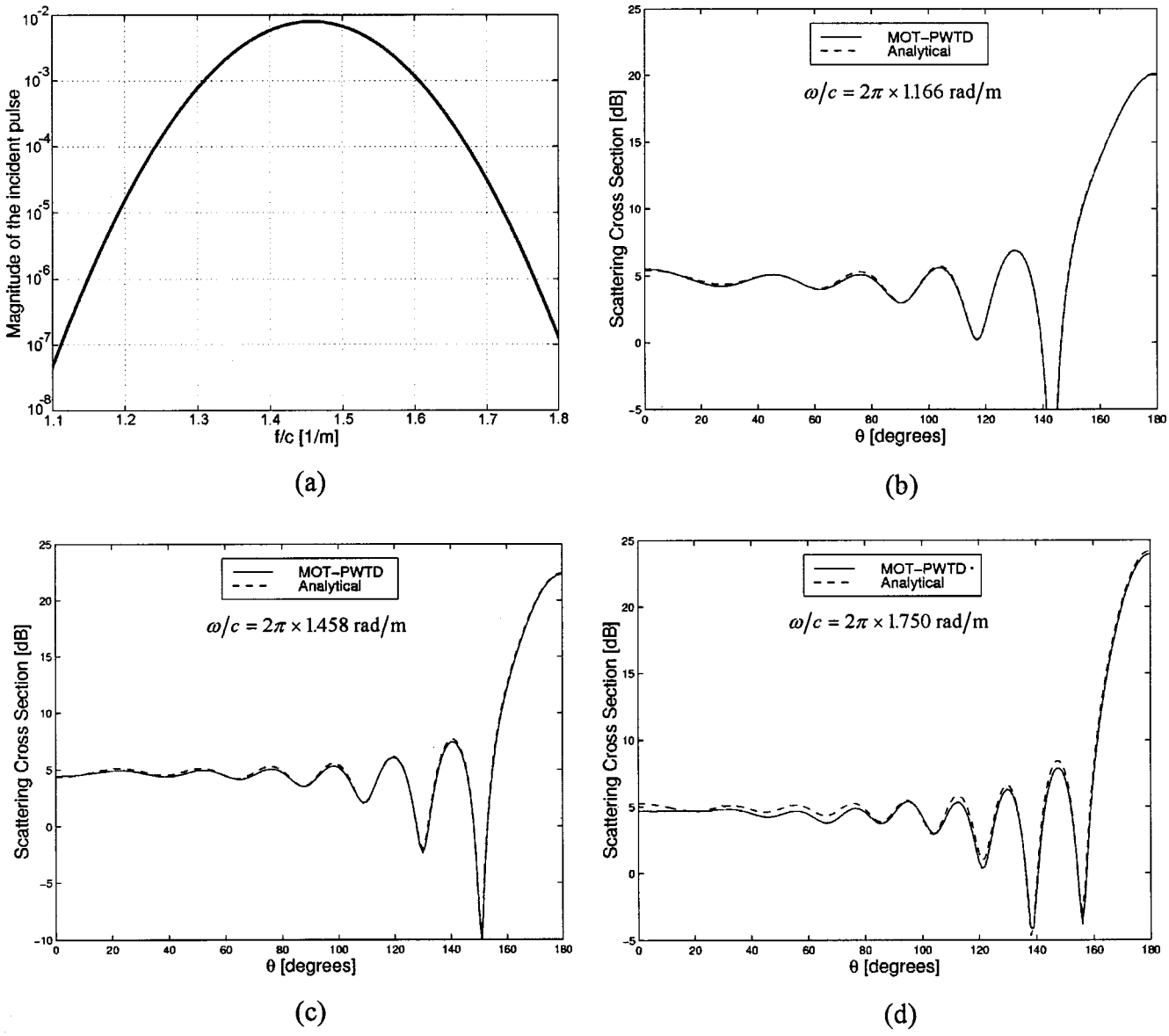

FIG. 8. Scattering cross sections of a unit radius sphere calculated through a single transient simulation. (a) Spectrum of the incident pulse. The SCS data at (b) $\omega/c=2\pi\times1.166$ rad/m, (c) $\omega/c=2\pi\times1.458$ rad/m, and (d) $\omega/c=2\pi\times1.750$ rad/m.

is calculated for several directions, and the scattering cross section (SCS) of the scatterer along these directions is extracted using a discrete time Fourier transform. Then, the obtained SCS results are compared against SCS data calculated either analytically or by a frequency domain two-level FMM-based boundary element method (FD-BEM). The FD-BEM code, which has been validated independently, uses the same spatial basis functions as the MOT code and circumvents the nonuniqueness difficulty using the Burton–Miller approach.[31]

In all the MOT analyses that will be presented, the CFIE in Eq. (3) with $\alpha=0.5$ (unless otherwise specified) is solved. The excitation is assumed to be a modulated Gaussian plane wave defined as

$$\varphi^{\mathrm{inc}}(\mathbf{r},t)=\cos[(ct-\mathbf{r}\cdot\hat{\mathbf{k}}^{\mathrm{inc}})\omega_o/c] \times\exp[-(ct-\mathbf{r}\cdot\hat{\mathbf{k}}^{\mathrm{inc}}-6\sigma)^2/2\sigma^2], \tag{35}$$

where ω_o/c is the center frequency of the pulse normalized to the wave speed in the medium, σ is a measure of the pulse's temporal width, and $\hat{\mathbf{k}}^{\mathrm{inc}}$ is the propagation direction of the incident wave. This pulse can be assumed to be band-limited to $\omega_{\max}=\omega_o+6c/\sigma$ since at that frequency the spectral content of the pulse is down by 78 dB from its peak value at ω_o. Finally, the matrix equation in Eq. (8) is solved using a transpose-free quasi-minimal residual algorithm.[32] The initial guess vector for this solver is set equal to the velocity potential vector of the previous time step. With this initial guess, a relative residual error of 10^{-6} was obtained in $\kappa<20$ iterations even when several thousand spatial basis functions were used.

As a first example, the velocity potential on two spheres illuminated by a Gaussian plane wave characterized by $\omega_o/c=0$, $\sigma=2.848$ m, and $\hat{\mathbf{k}}^{\mathrm{inc}}=-\hat{\mathbf{z}}$ is computed using both the classical and accelerated MOT methods. The scatterer geometry is shown in the inset of Fig. 6(a). Each sphere was modeled by 262 triangular patches. The parameters of the

PWTD algorithm are chosen such that all the interactions *between* the two spheres are accounted for by the PWTD algorithm. The velocity potential of the scattered field observed at a point on the top sphere is plotted in Fig. 6(a) for both solution schemes, and the agreement is observed to be excellent. Figure 6(b) shows the percent difference between the two solutions normalized to the peak amplitude of the scattered field velocity potential. This error is due to the temporal truncation of the interpolation functions $\psi(t)$ used in generating the subsignals. As shown in Refs. 12 and 13, this error can be reduced to the desired precision by properly choosing χ_1, χ_2, and p_t.

As a second example, scattering of a Gaussian plane wave from an almond modeled with 3120 spatial basis functions is analyzed. The almond fits in a box of dimensions $5\times 2\times 0.5\,\mathrm{m}^3$ and is a variant of the almond described in Ref. 33. The parameters of the incident plane wave are chosen to be $\omega_o/c=0$, $\sigma=0.7279$ m, and $\hat{\mathbf{k}}^{\mathrm{inc}}=\hat{\mathbf{x}}$. The analysis is performed both with the classical MOT method and the two-level PWTD augmented algorithm. Figure 7(a) and (b) compares the total surface velocity potential at a point near the front end of the almond and the normalized backscattered ($\hat{\mathbf{k}}^s=-\hat{\mathbf{k}}^{\mathrm{inc}}$) far-field signature, respectively. Both figures show perfect agreement between results obtained using the classical and fast methods. The error at the level of 10^{-5} incurred by the two-level method is again due to the choice of interpolation parameters and can be reduced if so desired. Note that the reflection from the front end and the diffraction from the sharp tip of the almond are accurately captured in the backscattered far-field response.

Next, the efficacy of the fast method for generating SCS data is tested. To this end, a rigid sphere of 1-m radius, modeled with 10 106 triangular facets, is illuminated by a Gaussian plane wave, characterized by $\omega_o/c=2\pi\times 1.458$ rad/m, $\sigma=2.1836$ m, and $\hat{\mathbf{k}}^{\mathrm{inc}}=-\hat{\mathbf{z}}$. The spectral content of the incident pulse is shown in Fig. 8(a). Comparisons of the SCS data calculated via the two-level algorithm with those obtained analytically using the Mie series are shown for three different frequencies in Fig. 8(b)–(d). Note that although the energy content of the incident pulse at $\omega/c=2\pi\times 1.166$ rad/m and $\omega/c=2\pi\times 1.750$ rad/m is 72 dB below the peak at $\omega/c=2\pi\times 1.458$ rad/m, the SCS is accurately extracted from the time domain response.

Next, scattering from a corner reflector with equal arms of $1\times 1\,\mathrm{m}^2$ is considered. As the scatterer is composed of thin surfaces, Eq. (3) with $\alpha=1$ was used for the analysis. The arms are aligned with the *xz* and the *yz* planes as depicted in the inset of Fig. 9(a). The scatterer is modeled using 1600 triangular facets, and it is excited by a pulse for which $\omega_o/c=2\pi\times 1.02$ rad/m, $\sigma=1.6378$ m, and $\hat{\mathbf{k}}^{\mathrm{inc}}=-\hat{\mathbf{x}}\cos 30^\circ-\hat{\mathbf{y}}\sin 30^\circ$. The temporal variation of the surface velocity potential at the center of the arm in the *xz* plane is plotted in Fig. 9(a). Clearly, the values obtained by the classical and fast methods are indistinguishable. As an independent check, the frequency domain solutions to the same problem were obtained at 50 different frequencies and the time domain surface velocity potential was obtained by an inverse Fourier transform. This result, also shown in Fig. 9(a), validates the MOT results, albeit with a lower precision. In Fig. 9(b), it is seen that the SCSs in the *xy* plane are accurately predicted by the MOT scheme at $\omega/c=2\pi\times 0.729$ rad/m and $\omega/c=2\pi\times 1.312$ rad/m.

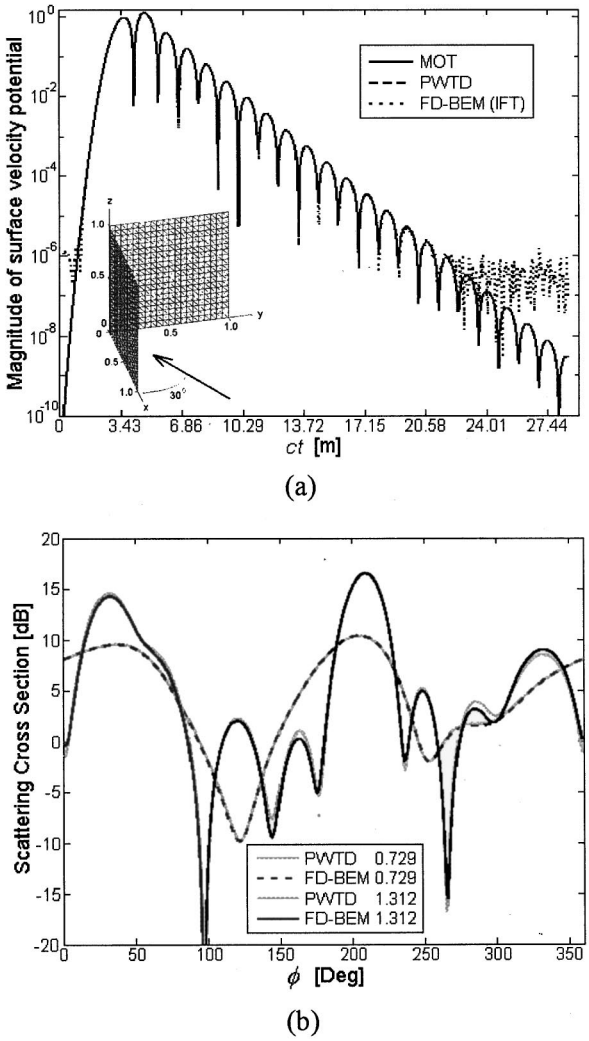

FIG. 9. Transient analysis of scattering from a corner reflector with $1\,\mathrm{m}\times 1\,\mathrm{m}^2$ arms. (a) Magnitude of surface velocity potential at the center of the arm on the *xz* plane. (b) Scattering cross section in the *xy* plane at $\omega/c=2\pi\times 0.729$ rad/m and $\omega/c=2\pi\times 1.312$ rad/m.

As a more realistic example, the SCS of a submarine modeled by 15 294 triangular facets [see inset of Fig. 10(a)] is extracted from a single time domain simulation and the results are compared with those obtained by FD-BEM at $\omega/c=2\pi\times 0.2915$ rad/m. The submarine is 35 m long, 3.5 m wide, and 6 m high. The parameters of the incident pulse are chosen as $\omega_o/c=2\pi\times 0.2915$ rad/m, $\sigma=4.367$ m, and $\hat{\mathbf{k}}^{\mathrm{inc}}=-(\hat{\mathbf{y}}+\sqrt{3}\hat{\mathbf{z}})/2$. As Fig. 10(a) and (b) illustrates, the SCSs in the *xz* and *xy* planes are in excellent agreement with those obtained using the frequency domain method.

Finally, the computational complexity of the two-level algorithm is verified by studying scattering from a rigid sphere of unit radius. The sphere was modeled with progressively larger numbers of triangular facets (N_s), and the maximum frequency component of the incident field was also scaled so that the average edge length of the triangular facets was $\frac{1}{10}$ of the wavelength at that frequency. The total

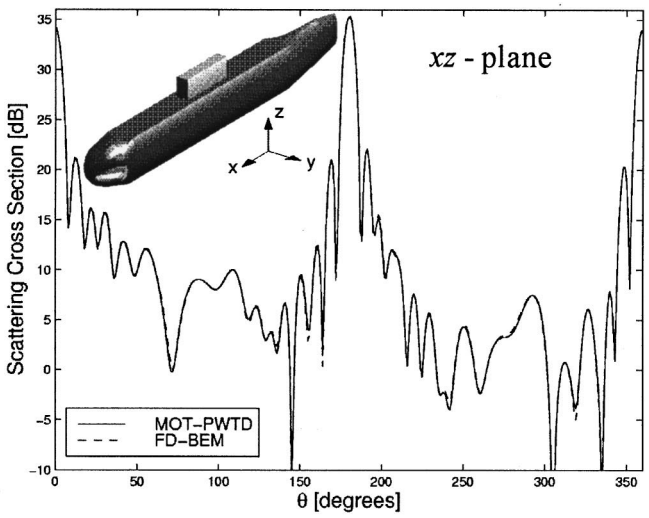

(a)

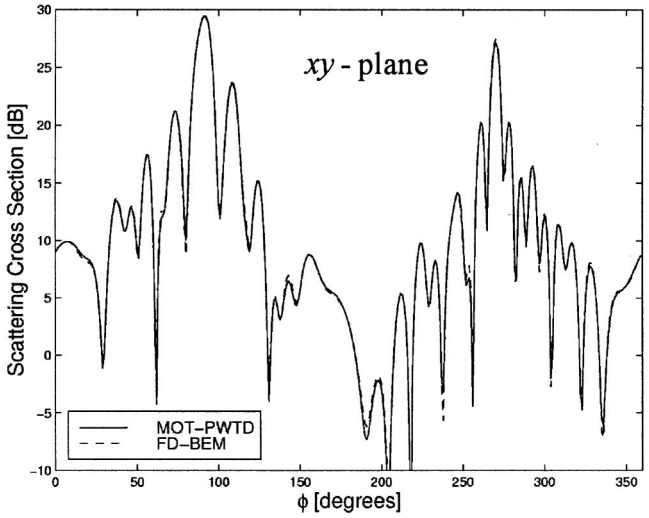

(b)

FIG. 10. Scattering cross-section of a submarine, modeled with 15 294 triangular facets, at $\omega/c = 2\pi \times 0.2915$ rad/m in the (a) *xz* plane and (b) *xy* plane.

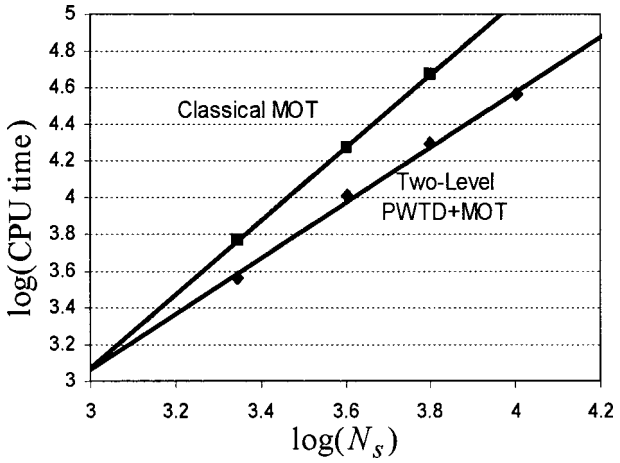

FIG. 11. Scaling of CPU time with respect to the number of spatial unknowns.

number of time steps in the analysis was fixed at $N_t = 500$. The CPU times required to compute the surface velocity potential via the classical method and the PWTD-enhanced MOT algorithm on a 360-Mflop Origin2000 computer are shown in Fig. 11. In this log–log graph, the slopes of the linear lines, which are the ''best fitting'' lines to the data points in the least squares sense, are 2.0 for the classical MOT method and 1.51 for the PWTD-enhanced MOT algorithm. Evidently, the two-level scheme achieves the predicted computational complexity and it becomes advantageous to use this scheme as opposed to the classical MOT scheme for scatterers modeled with more than approximately 1000 spatial unknowns.

V. CONCLUSIONS

This paper presented a two-level PWTD-enhanced MOT algorithm that permits the fast analysis of transient wave scattering from rigid bodies. The computational cost of performing a scattering analysis using the proposed two-level algorithm was shown to scale as $O(N_t N_s^{1.5} \log N_s)$, which is considerably lower than the $O(N_t N_s^2)$ complexity of the classical MOT methods. As verified by the numerical results, the PWTD-enhanced MOT scheme puts the accurate characterization of broadband scattering from large, realistic objects within the reach of current computing resources. A multilevel scheme with a computational complexity of $O(N_t N_s \log^2 N_s)$ has also been implemented and its description as well as relevant results will be reported elsewhere.

ACKNOWLEDGMENTS

This work was supported in part by a grant from AFOSR via the MURI program under Contract No. F49620-96-1-0025, the NSF Grant No. ECS 95-02138, and the Gebze Institute of Technology, Turkey. The authors would also like to acknowledge the National Center for Supercomputing Applications for granting access to its computational facilities.

[1] R. P. Shaw, ''Boundary integral equation methods applied to wave problems,'' in *Developments in Boundary Element Methods*, edited by P. K. Banerjee and R. Butterfield (Applied Science Publishers, London, 1979), Vol. 1.
[2] C. A. Brebbia and S. Walker, *Boundary Element Techniques in Engineering* (Newnes–Butterworth, 1979).
[3] M. B. Friedman and R. Shaw, ''Diffraction of pulses by cylindrical obstacles of arbitrary cross section,'' J. Appl. Mech. **29**, 40–46 (1962).
[4] A. G. Tijhuis, *Electromagnetic Inverse Profiling: Theory and Numerical Implementation* (VNU Science, Utrecht, The Netherlands, 1987).
[5] M. J. Bluck and S. P. Walker, ''Analysis of three-dimensional transient acoustic wave propagation using the boundary integral equation method,'' Int. J. Numer. Methods Eng. **39**, 1419–1431 (1996).
[6] W. Pinello, A. Ruehli, and A. Cangellaris, ''Stabilization of time domain solutions of EFIE based on partial element equivalent circuit models,'' Proceedings of IEEE Antennas and Propagation Society International Symposium, Montreal, Canada (1997), Vol. 3, pp. 966–969.
[7] M. J. Bluck and S. P. Walker, ''Time-domain BIE analysis of large three-dimensional electromagnetic scattering problems,'' IEEE Trans. Antennas Propag. **45**(5), 894–901 (1997).
[8] Y. Ding, A. Forestier, and T. H. Duong, ''A Galerkin scheme for the time domain integral equation of acoustic scattering from a hard surface,'' J. Acoust. Soc. Am. **86**, 1566–1572 (1989).
[9] R. Coifman, V. Rokhlin, and S. Wandzura, ''The fast multipole method

for the wave equation: a pedestrian prescription,'' IEEE Antennas Propag. Mag. **35**, 7–12 (1993).
[10] V. Rokhlin, ''Diagonal forms of translation operators for the Helmholtz equation in three dimensions,'' Appl. Comput. Harmon. Anal. **1**, 82–93 (1993).
[11] J. M. Song and W. C. Chew, ''Multilevel fast-multipole algorithm for solving combined field integral equations of electromagnetic scattering,'' Microwave Opt. Technol. Lett. **10**(1), 14–19 (1995).
[12] A. A. Ergin, B. Shanker, and E. Michielssen, ''Fast evaluation of three-dimensional transient wave fields using diagonal translation operators,'' J. Comput. Phys. **146**(1), 157–180 (1998).
[13] A. A. Ergin, B. Shanker, and E. Michielssen, ''The plane wave time domain algorithm for the fast analysis of transient wave phenomena,'' IEEE Antennas Propag. Mag. **41**(4), 39–52 (1999).
[14] A. A. Ergin, B. Shanker, K. Aygun, and E. Michielssen, ''Transient analysis of acoustic scattering using marching-on-in-time with plane wave time domain algorithm,'' Proceedings of 14th Annual Review of Progress in Applied Computational Electromagnetics, Monterey, CA (1998), Vol. 2, pp. 866–872.
[15] P. H. L. Groenenboom, ''Wave propagation phenomena,'' in *Progress in Boundary Element Methods*, edited by C. A. Brebbia (Pentech, London, 1983), Vol. 2, pp. 24–52.
[16] S. Hirose and J. D. Achenbach, ''BEM method to analyze the interaction of an acoustic pulse with a rigid circular disk,'' Wave Motion **10**, 267–275 (1988).
[17] G. Krishnasamy, L. W. Schmerr, T. J. Rudolphi, and F. J. Rizzo, ''Hypersingular boundary integral equations: Some applications in acoustic and elastic wave scattering,'' J. Appl. Mech. **57**, 404–414 (1990).
[18] R. Martinez, ''The thin-shape breakdown (TSB) of the Helmholtz integral equation,'' J. Acoust. Soc. Am. **90**, 2728–2738 (1991).
[19] T. W. Wu, ''A direct boundary element method for acoustic radiation and scattering from mixed regular and thin bodies,'' J. Acoust. Soc. Am. **97**, 84–91 (1995).
[20] A. A. Ergin, B. Shanker, and E. Michielssen, ''Analysis of transient wave scattering from rigid bodies using a Burton–Miller approach,'' J. Acoust. Soc. Am. **106**, 2396–2404 (1999).
[21] T. Terai, ''On calculation of sound fields around three dimensional objects by integral equation methods,'' J. Sound Vib. **69**(1), 71–100 (1980).
[22] G. Manara, A. Monorchio, and R. Reggiannini, ''A space-time discretization criterion for a stable time-marching solution of the electric field integral equation,'' IEEE Trans. Antennas Propag. **45**(3), 527–532 (1997).
[23] B. P. Rynne, ''Stability and convergence of time marching methods in scattering problems,'' IMA J. Appl. Math. **35**, 297–310 (1985).
[24] S. J. Dodson, S. P. Walker, and M. J. Bluck, ''Implicitness and stability of time domain integral equation scattering analysis,'' Appl. Comput. Electromagn. Soc. J. **13**(3), 291–301 (1998).
[25] C. H. Chapman, ''Generalized radon transforms and slant stacks,'' Geophys. J. R. Astron. Soc. **66**(2), 445–453 (1981).
[26] E. Heyman, ''Time-dependent plane-wave spectrum representations for radiation from volume source distributions,'' J. Math. Phys. **37**, 658–681 (1996).
[27] A. Shlivinski, E. Heyman, and R. Kastner, ''Antenna characterization in the time domain,'' IEEE Trans. Antennas Propag. **45**(7), 1140–1149 (1997).
[28] M. Tygel and P. Hubral, *Transient Waves in Layered Media* (Elsevier Science, Amsterdam, 1987).
[29] O. M. Bucci, C. Gennarelli, and C. Savarese, ''Optimal interpolation of radiated fields over a sphere,'' IEEE Trans. Antennas Propag. **39**(11), 1633–1643 (1991).
[30] J. J. Knab, ''Interpolation of band-limited functions using the approximate prolate series,'' IEEE Trans. Inf. Theory **25**(6), 717–720 (1979).
[31] A. J. Burton and G. F. Miller, ''The application of integral equation methods to the numerical solution of some exterior boundary-value problems,'' Proc. R. Soc. London, Ser. A **323**, 201–210 (1971).
[32] R. W. Freund, ''A transpose-free quasi-minimal residual algorithm for non-hermitian linear systems,'' SIAM J. Sci. Comput. (USA) **14**(2), 470–482 (1993).
[33] A. C. Woo, H. T. Wang, M. J. Schuh, and M. L. Sanders, ''Benchmark radar targets for the validation of computational electromagnetics programs,'' IEEE Antennas Propag. Mag. **35**(1), 84–89 (1993).

Elucidation of the relationship between complex acoustic power and radiation efficiency for vibrating bodies

Pei-Tai Chen[a)]
Department of Naval Architecture, National Taiwan Ocean University, Keelung, Taiwan, Republic of China

(Received 8 January 1999; revised 22 June 1999; accepted 29 July 1999)

This investigation examines the physical meaning of surface complex acoustic power and its relationship to acoustic radiation efficiency. It is shown that the radiated power is the power radiating out of a far-field surface where the plane wave relationship between pressure and particle velocity holds. Meanwhile, the reactive power pertains to the difference between kinetic energy and potential energy. A stationary condition of the ratio between the radiated power to the reactive power yields an eigenvalue problem, subsequently decomposing the surface acoustics into a modal representation. Doing so further allows the examination of the relationship between acoustic radiation efficiency and power factor of the complex power. According to the results, the radiation efficiency of the first radiation mode is nearly equal to the square of the first modal power factor. The modes beyond the first of the modal radiation efficiencies are relatively larger than the corresponding squared modal power factors. Numerical examples of elastic structures subjected to external forces illustrate the relationship between radiation efficiencies and power factors of complex powers. © *1999 Acoustical Society of America.* [S0001-4966(99)04211-3]

PACS numbers: 43.20.Tb [ANN]

INTRODUCTION

The power radiated from a radiator vibrating at harmonic monofrequencies can be computed by taking the real part of a surface complex power.[1] Complex power is defined as one half of the surface integral of the surface pressure product of the complex conjugate of normal velocity. The imaginary part is frequently referred to as reactive power. Reactive power has received considerably less attention than radiated power. For the case of a one-degree-of-freedom mass/spring/dashpot system under harmonic vibration, the responding velocity due to an applied force is determined by the system's impedance. The phase between velocity and force is derived on the basis of the phase of the complex impedance, which is also the phase of the complex power, where the complex power is computed as one half of the external force multiplying the complex conjugate of the velocity. Moreover, the phase or the power factor, which is defined as the cosine of the phase, can describe the efficiency of the external force sending power into the one-degree-of-freedom system. This raises a question of whether or not the complex power for a radiator correlates with the radiation efficiency of the radiator. Since it is a common practice to compute radiated powers by taking the real part of the surface complex powers, it would be practical and useful to identify the radiation efficiencies using the complex powers. A conventional means of describing the ability of radiators to radiate power is by radiation efficiency, i.e., the radiated power divided by the spatial sum of square normal velocity.[2] A factor of free-space impedance is in the denominator to make the efficiency dimensionless. This definition can be regarded as a comparison among radiated powers of the radiators under the same amount of spatial sum of square normal velocity. In view of the acoustic field as an infinite-degree-of-freedom mass/spring/dashpot system, the radiated power can be regarded as the power delivered into the infinite degree system by the vibrating surface. This work investigates the complex power in relation to the radiation efficiency and the physical meaning underlying the complex power.

[a)]Electronic mail: ptchen@mail.na.ntou.edu.tw

I. COMPLEX POWER FOR ACOUSTIC FIELD

Initially, a one-degree-of-freedom mass/spring/dashpot system is subjected to a monofrequency external force $fe^{i\omega t}$ in which the equation of motion is

$$mi\omega v+\frac{kv}{i\omega}+cv=f, \tag{1}$$

where v is the amplitude of the responded velocity, and m, k, and c are the mass, stiffness, and damping, respectively. The values of f and v are complex. The complex power caused by the force f is defined as

$$\frac{1}{2}fv^*=\frac{1}{2}\left(mi\omega+\frac{k}{i\omega}+c\right)vv^*, \tag{2}$$

and the force f delivering power into the system is

$$\text{Real}\left(\tfrac{1}{2}fv^*\right)=\frac{1}{2}\frac{ff^*}{\left|mi\omega+\frac{k}{i\omega}+c\right|}\cos\theta, \tag{3}$$

where ''Real'' represents the real part of complex value, ''*'' denotes the complex conjugate, ''||'' is the magnitude of complex value, and θ is the phase angle between the force f and velocity v. This phase is also related to the complex power of Eq. (2) by

$$\theta = \tan^{-1}\left(\frac{\text{Imag}(\frac{1}{2}fv^*)}{\text{Real}(\frac{1}{2}fv^*)}\right), \tag{4}$$

where ''Imag'' denotes the imaginary part of a complex value. The term of $\cos\theta$ in Eq. (3) is usually referred to as a power factor in which a zero degree of θ implies that the force and velocity are in phase. This is the most efficient way for the force to deliver power to the system. A 90° value of the θ implies that no net power flows into the system by the applied force. Consequently, Eqs. (3) and (4) imply that the power factor of complex power can be an indicator of the efficiency of the applied force delivering power to mass/spring/dashpot systems. In the following, we demonstrate the acoustic field generated by a vibrating radiator in which the radiated power is the power propagating to a far field. The pressure wave at the far field becomes a plane wave and the reactive power is related to the difference between acoustic potential energy and kinetic energy in a volume between the surface of the radiator and the far field. Herein, we consider the acoustic field equation under a vibration frequency ω

$$\nabla^2\phi + k^2\phi = 0, \tag{5}$$

where ϕ is a velocity potential, k is the wave number, $k = \omega/c$, and c is the sound speed. The velocity potential ϕ is related to pressure and particle velocity by

$$v = \nabla\phi, \quad p = -\rho_0 i\omega\phi. \tag{6}$$

A known velocity v_n is prescribed on the surface, in which

$$\frac{\partial\phi}{\partial n} = v_n. \tag{7}$$

Above Eqs. (6) and (7) is a Neumann problem, which can be recast into a variational formulation,

$$\delta I = 0, \tag{8}$$

where I is identified as

$$I = \frac{1}{2}\int\int\int_V (k^2\phi^2 - \nabla\phi\cdot\nabla\phi)dv - \int\int_S v_n\phi\, ds + \frac{1}{2}\int\int_{C_\infty} ik\phi^2\, ds, \tag{9}$$

where ''$\cdot$'' denotes vector inner product. According to Eq. (9), the volume integral is performed over a volume that is bounded by the radiator's surface S and a large spherical surface where the acoustic pressure waves become planar wave propagations. If one takes variational increments of I due to virtual increments $\delta\phi$, Eqs. (8) and (9) lead to

$$\delta I = \int\int\int_V (\nabla^2\phi + k^2\phi)\,\delta\phi\, dv + \int\int_S \left(\frac{\partial\phi}{\partial n} - v_n\right)\delta\phi\, ds - \int\int_{C_\infty}\left(\frac{\partial\phi}{\partial n_\infty} - ik\phi\right)\delta\phi\, ds = 0, \tag{10}$$

where $\partial\phi/\partial n$ is the normal derivative of ϕ on the surface, and $\partial\phi/\partial n_\infty$ is the normal derivative on the far field surface C_∞. The first two terms in Eq. (10) yield Eqs. (5) and (7), respectively, where the last term denotes the plane wave relationship,

$$\frac{\partial\phi}{\partial n_\infty} = ik\phi. \tag{11}$$

If one takes the virtual increment $\delta\phi$ to be $\varepsilon\phi^*$ so that ϕ satisfies Eqs. (5)–(7), where ε is an arbitrarily small value, then Eq. (10) becomes the following:

$$\delta I = \varepsilon\int\int\int_V (k^2\phi\phi^* - \nabla\phi\cdot\nabla\phi^*)dv - \varepsilon\int\int_S v_n\phi^*\, ds + \varepsilon\int\int_{C_\infty} ik\phi\phi^*\, ds = 0. \tag{12}$$

Taking the complex conjugate of the above equation and factoring out ε leads to

$$\int\int\int_V (k^2\phi\phi^* - \nabla\phi\cdot\nabla\phi^*)dv - \int\int_S v_n^*\phi\, ds + \int_{C_\infty} ik\phi\phi^*\, ds = 0. \tag{13}$$

The physical meaning of Eq. (13) becomes clear when one multiplies a factor $-\rho_0 i\omega/2$ and uses Eq. (6) so that

$$\frac{1}{2}\int\int_S pv_n^*\, ds = \frac{-i\omega}{2}\int\int\int_V \frac{pp^*}{\rho_0 c^2}dv + \frac{1}{2}i\omega\int\int\int_V \rho_0 vv^*\, dv + \frac{1}{2}\int\int_{C_\infty}\frac{pp^*}{\rho_0 c}ds. \tag{14}$$

Equation (14) depicts that the radiated power is the power radiated at the far-field sphere C_∞ as indicated in the third term on the right-hand side of the equation. The expressions $\frac{1}{2}pp^*/\rho_0 c^2$ and $\frac{1}{2}\rho_0 vv^*$ are twice that of averaged potential and kinetic density energies. Notably, Eq. (14) has the identical physical interpretation with Eq. (2) if Eq. (2) is rewritten as

$$\tfrac{1}{2}fv^* = i\omega(\tfrac{1}{2}mvv^* - \tfrac{1}{2}kxx^*) + \tfrac{1}{2}cvv^*, \tag{15}$$

where x is the displacement amplitude. The term $(1/2)cvv^*$ is the dissipated power, while the imaginary part of Eq. (15) corresponds to the difference of kinetic to potential energy. Correspondingly, the phase of the complex acoustic power can be computed by

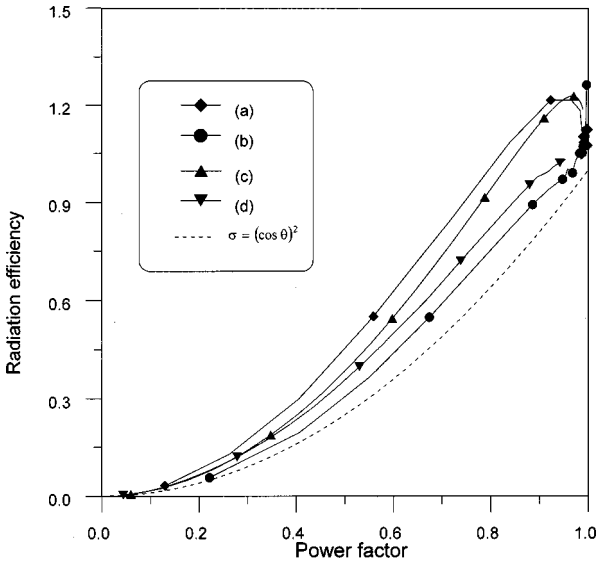

FIG. 1. Radiation efficiencies versus power factors for various radiators.

$$\theta=\tan^{-1}\left(\frac{\text{Real}(\int \frac{1}{2} p v_n^* \, ds)}{\text{Imag}(\int \frac{1}{2} p v_n^* \, ds)}\right), \tag{16}$$

and the corresponding power factor is defined as the cosine of the phase angle. As mentioned earlier, from Eqs. (2)–(4) for the one-degree-of-freedom system, we can infer that the phase angle of the complex power indicates the effectiveness of the power delivered to the system by the force. Of relevant concern is how the phase angle of surface complex power relates to radiation efficiency for radiators.

II. POWER FACTOR AND RADIATION EFFICIENCY

A commonly adopted definition of radiation efficiency σ is

$$\sigma=\frac{\text{Real}(\frac{1}{2}\int_S p v_n^* \, ds)}{\rho c(\frac{1}{2}\int_S v v_n^* \, ds)}, \tag{17}$$

where the factor ρc is to make σ dimensionless. The value of σ denotes the radiated power under a specified amount of squared normal velocity over the vibrating surface. To understand the correlation between radiation efficiency and power factor of complex acoustic power, this work chooses various radiators whose geometrical configurations differ from each other. The power factors are computed by Eq. (16). Figure 1 plots the radiation efficiencies versus power factors for cases: (a) a $3\times4\times5$-m box where a normal velocity, $\sin(\pi x/3)\sin(\pi y/4)$, vibrates at one 3×4-m surface, the coordinate (x,y) referring to a corner of the vibrating surface as the origin, (b) a spheroidal body whose major to minor axis a is 4 vibrating at the region around the equator with a strip width of $3.4a$, (c) 1×1-m baffled plate with a uniform velocity on the surface, (d) a sphere with radius 1 m vibrating at one cap around an apex subtending an angle of 72°. The data are computed by scanning frequencies from zero to 300 Hz so that the radiation efficiencies approach 1 when the scanning frequency becomes large. Figure 1 reveals that these correlations between radiation efficiencies and power factors have similar features, although they are derived from various radiators. Moreover, those plots are slightly above a parabola displayed by a dotted line whose equation is $\sigma=(\cos\theta)^2$. The radiation efficiencies are relatively larger than the square of the power factors. That is,

$$\sigma \geqslant (\cos\theta)^2. \tag{18}$$

This relationship is investigated as follows.

III. RADIATION EFFICIENCY VERSUS POWER FACTOR OF MODAL REPRESENTATIONS

Owing to the dependency of the phase angle θ on distributions of surface pressure and normal velocity, we consider the quotient λ of the radiated power to reactive power for a vibration body,

$$\lambda=\frac{1}{\tan\theta}=\frac{\text{Real}(\frac{1}{2}\int_S p v_n^* \, dS)}{\text{Imag}(\frac{1}{2}\int_S p v_n^* \, dS)}, \tag{19}$$

where θ is the phase angle of the complex power. The surface pressure and normal velocity can be related symbolically by

$$L_p(p)=L_v(v_n), \tag{20}$$

where L_p and L_v are complex linear operators with respect to p and v_n, respectively. The surface pressure p can be expressed in terms of v_n by multiplying the inverse operator L_p^{-1} on both sides of Eq. (20),

$$p=L_p^{-1}L_v(v_n). \tag{21}$$

Let the normal velocity v_n be discretized as

$$v_n=\sum_j v_j\phi_j, \tag{22}$$

where ϕ_j are basis functions which can be defined over the entire surface or locally such as shape functions on discretized nodal points, and v_j are the corresponding discretized coefficients. Substituting Eqs. (21) and (22) into (19) leads to

$$\lambda=\frac{\text{Real}(\frac{1}{2}\Sigma_j\Sigma_k h_{jk}v_j v_k^*)}{\text{Imag}(\frac{2}{2}\Sigma_j\Sigma_k h_{jk}v_j v_k^*)}, \tag{23}$$

where the coefficients h_{jk} are identified as

$$h_{jk}=\int_S L_p^{-1}L_v(\phi_j)\phi_k \, dS. \tag{24}$$

In our previous investigation,[3] the complex-valued coefficients h_{jk} were shown to be symmetric by using a surface acoustic reciprocal principle. Let $[h]$ denote the matrix formed by the coefficients h_{jk} and write the matrix $[h]$ into real and imaginary matrices,

$$[h]=[h_R]+i[h_I], \tag{25}$$

where the matrices $[h_R]$ and $[h_I]$ are symmetric. Correspondingly, Eq. (23) becomes

$$\lambda=\frac{\frac{1}{2}\{v\}^T[h_R]\{v^*\}}{\frac{1}{2}\{v\}^T[h_I]\{v^*\}}, \tag{26}$$

where $\{v\}$ is the vector formed by discretized coefficients of the velocity expansion in Eq. (22). The above equation is analogous to Rayleigh's quotient in structural dynamics for natural vibration analyses. Herein, we consider stationary conditions for every possible coefficient $\{v\}$, which yields an eigenvalue problem

$$[h_R]\{\alpha\}_j = \lambda_j [h_I]\{\alpha\}_j, \tag{27}$$

The eigenvalue λ_j is the stationary quotient value of Eq. (26) when $\{v\}$ becomes the eigenvector $\{\alpha\}_j$ of Eq. (27). The eigenvalue problem in Eq. (27) has been studied in a previous investigation[3] where the eigenvectors are normalized with respect to the matrix $[h_I]$. The normal velocity corresponding to the eigenvector $\{\alpha\}_j$ defines a velocity radiation mode Φ_j,

$$\Phi_j = \sum_k \alpha_{kj} \phi_k. \tag{28}$$

Consequently, an arbitrary normal velocity distribution can be superposed by the set of velocity radiation modes,

$$v_n = \sum_j V_j \Phi_j, \tag{29}$$

where the modal amplitude V_j is computed by

$$V_j = \frac{\int_S v_n P_j \, dS}{\int_S P_j \Phi_j \, dS} = \frac{1}{\lambda_j + i} \int_S v_n P_j \, dS, \tag{30}$$

where P_j is the responsive pressure due to the velocity mode Φ_j. Also, the surface complex acoustic power P has the modal summation, in which

$$P = \frac{1}{2} \int_S p v_n^* \, dS = \frac{1}{2} \sum_j |V_j|^2 (\lambda_j + i), \tag{31}$$

where the real part of P is the radiated power. In addition, Eq. (31) indicates that weak radiators modes, whose eigenvalues are nearly zero, do not radiate acoustic powers. Furthermore, the phase θ_j between the modal velocity mode Φ_j and the responsive pressure P_j is constant over the vibrating surface, which is determined by Eq. (16)

$$\theta_j = \tan^{-1} \frac{1}{\lambda_j}. \tag{32}$$

The modal power factor is defined as $\cos \theta_j$. Equations (29)–(31) present the feature that an arbitrary normal velocity can be decomposed into modal representation and the complex acoustic power is superposed by each modal power. Thus, investigating the power factor versus radiation efficiency involves examining modal power factor versus modal radiation efficiency.

IV. MODAL POWER FACTOR VERSUS MODAL RADIATION EFFICIENCY

The modal radiation efficiency for the radiation modes is defined as

$$\sigma_j = \frac{\text{Real}(\frac{1}{2}\lambda_j + \frac{1}{2}i)}{\rho c \, \frac{1}{2} \int_S \Phi_j^2 \, dS} = \frac{\lambda_j}{\rho c \int_S \Phi_j^2 \, dS}, \tag{33}$$

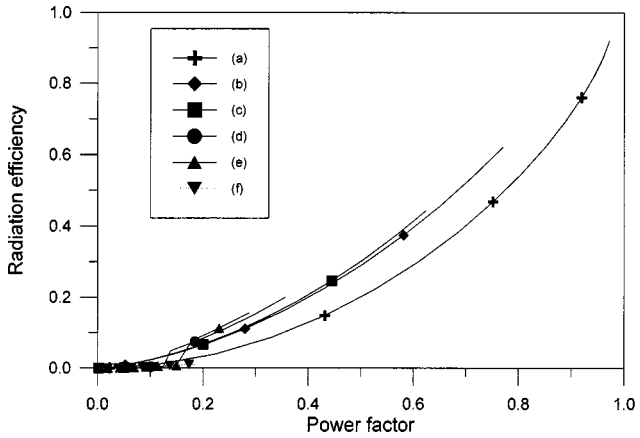

FIG. 2. Modal radiation efficiencies versus modal power factors for the baffled plate.

which is derived from Eq. (17) so that the normal velocity is taken as the velocity radiation mode Φ_j and the modal complex power is obtained from Eq. (31) by taking $V_j = 1$ for the jth modal amplitude, and zero for other modes. To understand the correlation between modal radiation efficiencies and modal power factors, we initially compute the modal efficiencies by Eq. (33) and modal power factor by Eq. (32) for a 3×4-m baffled plate. Figure 2 plots the radiation efficiency versus power factor for each mode. The nondimensionalized exciting frequency ka ($k = \omega/c$, $a = 3$ m) is scanned from zero to 4. Those radiation efficiencies versus power factors resemble each other. Such a resemblance implies that the radiation efficiency is roughly a function of power factor. This correlation between power factor and radiation efficiency is also roughly independent of exciting frequency, although both the radiation efficiencies and power factors depend on exciting frequency. To provide further insight into various radiators, we select, in addition to the previous demonstrated radiators in Fig. 1, a sphere and a spheroid of aspect ratio 4 vibrating at entire surfaces. Figure 3 plots modal radiation efficiencies versus modal power factors for the various radiators. Figure 3 denotes (a) the $3 \times 4 \times 5$-m box vibrating on one 3×4-m surface, (b) the spheroid of aspect ratio 4 vibrating on the region around the equator, (c) the 1×1-m baffled plate, (d) the sphere vibrating on the region around one cap, (e) the sphere vibrating on the entire surface, and (f) the spheroid vibrating on the entire surface. The resemblance of radiation efficiency versus power factor in Fig. 6 reveals that the power factors, which are determined by the phase of complex power, denote the efficiencies in which powers are radiated from the vibrating surfaces. The preceding figures allow us to infer that the phase of complex power, or its corresponding power factor, can be an indicator of the effectiveness of radiators to radiate acoustic power. Based on the close resemblance of Figs. 1, 2, and 3, Fig. 4 plots the radiation efficiency versus power factor for the first radiation mode for the radiators demonstrated. According to this figure, the relationship of efficiency versus power factor is nearly identical regardless of the various radiators. As mentioned earlier in Eq. (19), the normal velocity distribution of the first radiation mode provides the smallest phase angle, or the largest power factor for

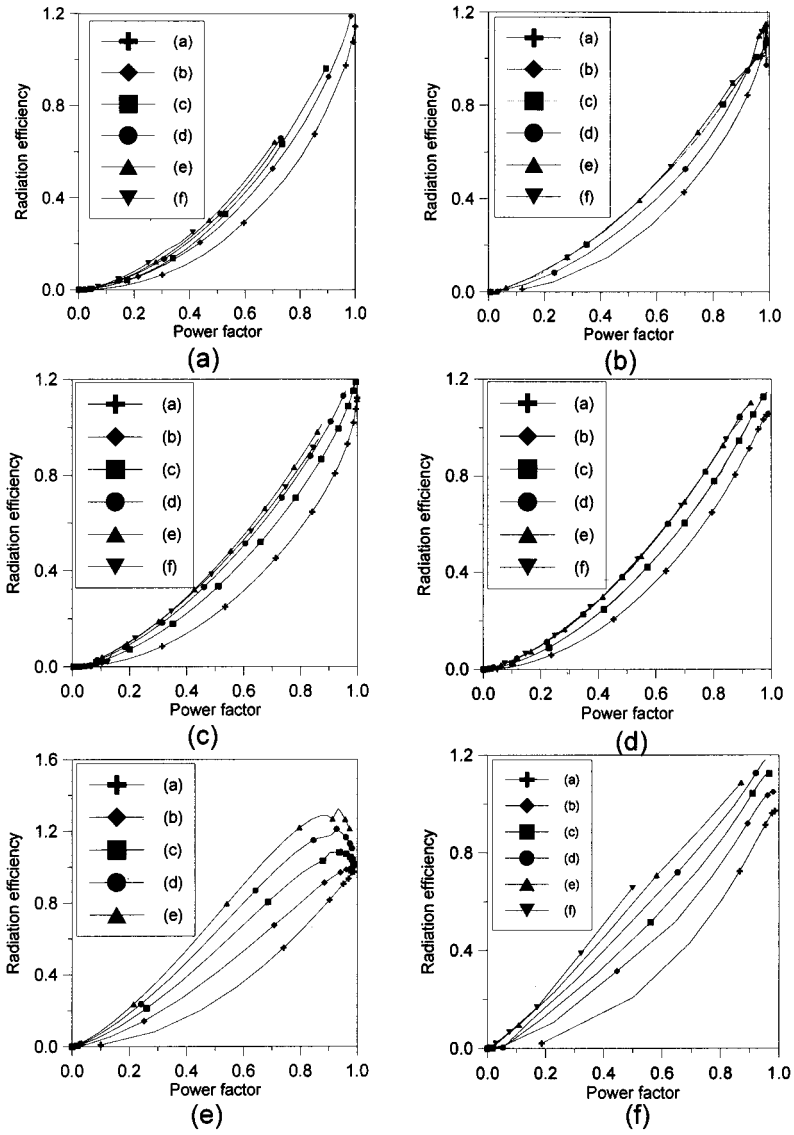

FIG. 3. Modal radiation efficiencies versus modal power factors for various radiators.

a radiator under a specified vibrating frequency. An equivalent statement delivered from Fig. 4 is that the radiation efficiency and power factor have a one-to-one correspondence regardless of the geometrical configuration of radiators for situations in which the normal velocity distribution is in such a manner to make the radiating power most efficient. Moreover, Fig. 3 reveals that, for a specified power factor of each radiation mode, the corresponding radiation efficiency for the first radiation mode has the smallest value, indicating the first mode radiating the least power. However, this observation does not imply greater efficiency for higher radiation modes. In contrast, the higher modes have substantially less power factors for a given vibration frequency, resulting in less effective radiation. The equation of radiation efficiency versus power factor for the first radiation mode can be easily written by considering the spherical radiator, because the normal velocity distribution of the first radiation mode for the sphere remains constant over the surface. Thus, the phase θ_s of the complex power and radiation efficiency σ_s are[1]

$$\theta_s = \tan^{-1}\left(\frac{1}{ka}\right), \tag{34}$$

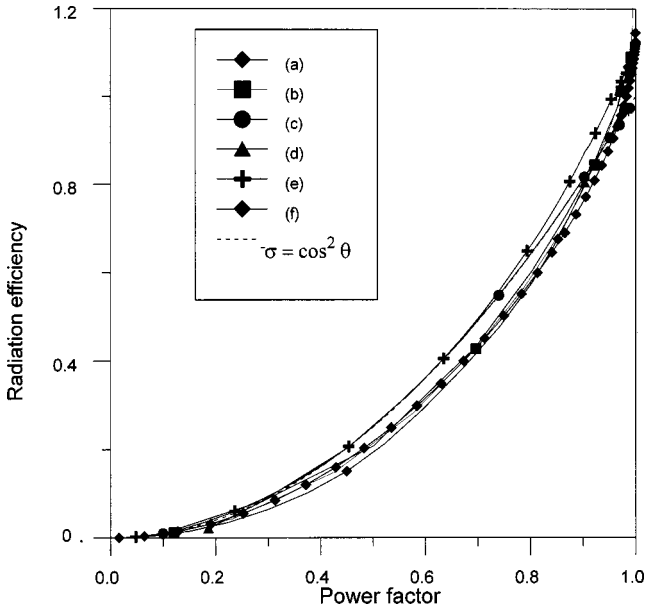

FIG. 4. Modal radiation efficiencies versus modal power factors for the first radiation mode of various radiators.

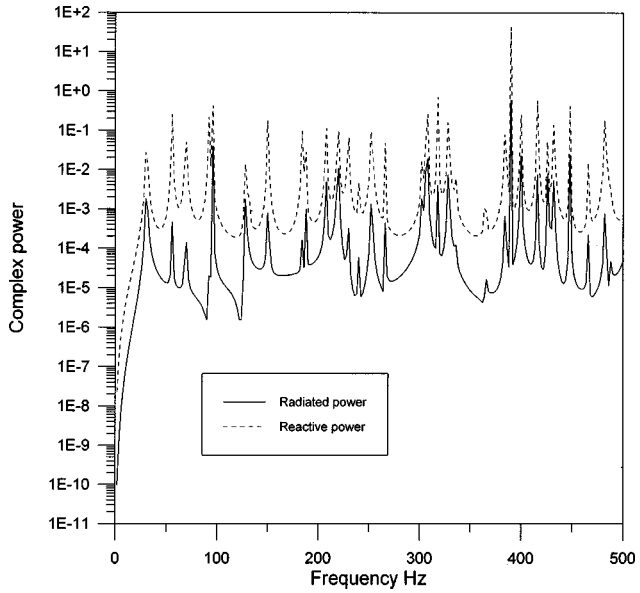

FIG. 5. Radiated and reactive powers for a baffled elastic plate subjected to a point force.

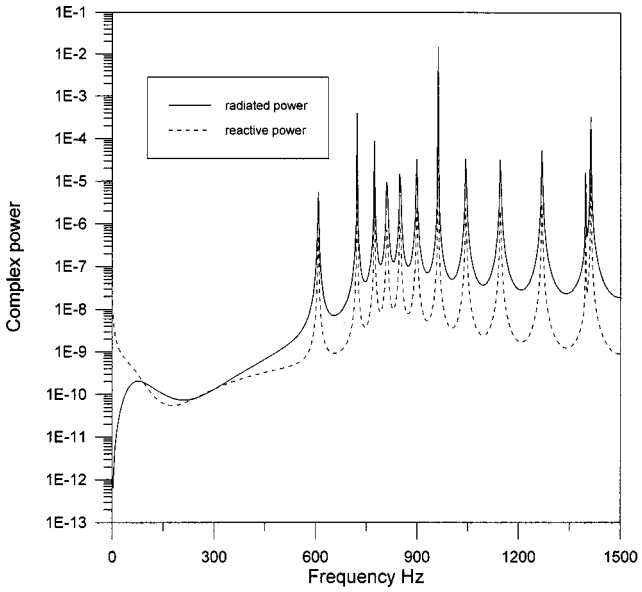

FIG. 7. Radiated and reactive power for a spherical thin shell subjected to a point force.

and

$$\sigma_s = \frac{-(ka)^2}{(ka)^2+1}, \tag{35}$$

for which the power factor and radiation efficiency are related by

$$\sigma_s = (\cos\theta_s)^2. \tag{36}$$

For modes other than the first mode, Fig. 3 indicates that the radiation efficiencies are relatively larger than the square of power factors. Correspondingly, the radiation efficiency for a normal velocity is relatively larger than the square of power factor because of the superposition principle of radiation modes.

Finally, two numerical examples of acoustic radiations for elastic structures subjected to monofrequency external forces are presented. Figure 5 depicts the complex power of a 0.5×0.6-m baffled plate subjected to an alternative point force exerted at the location $x=0.4$ m, $y=0.333$ m, where the origin of the coordinate is at one corner of the plate. The plate thickness is 1 millimeter. Figure 6 plots the radiation efficiency based on Eq. (17) and the square of power factor. These two curves approximately resemble each other with the squared power factors smaller than the radiation efficiency, as displayed by Eq. (18). The other numerical example is a spherical shell of 3-cm thickness, 1-m radius exerted by a point force.[4] Figure 7 illustrates the complex power versus exciting frequency. Figure 8 presents the radiation efficiency and the square of power factor, which again

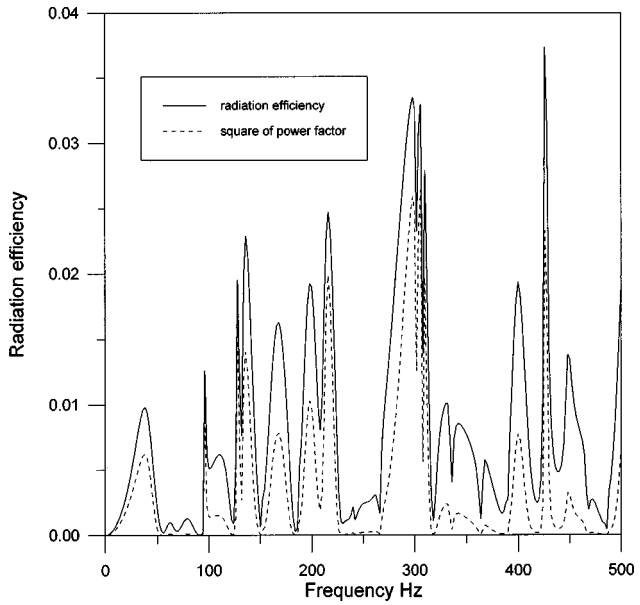

FIG. 6. Comparison of radiation efficiency and estimated radiation efficiency from complex power for the baffled elastic thin plate.

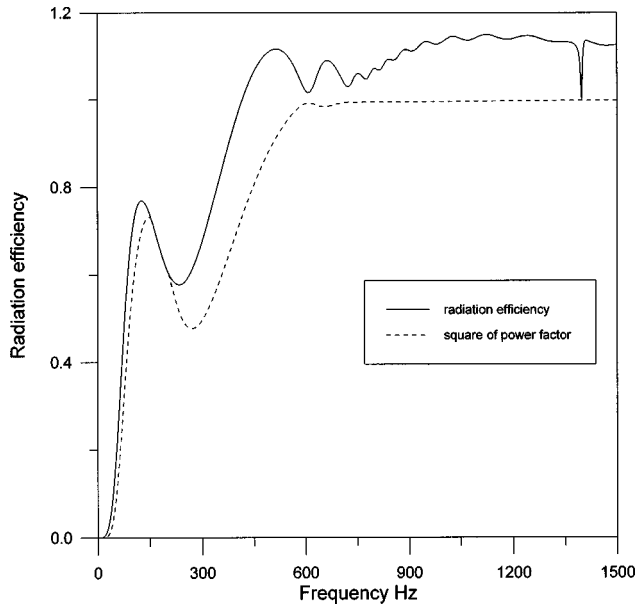

FIG. 8. Comparison of radiation efficiency and estimated radiation efficiency from complex power for the spherical shell.

shows the resemblance of those two quantities with respect to the radiation efficiency being larger than the square of power factor.

V. CONCLUSION

This work examines the physical meaning underlying surface complex acoustic power and its relationship to radiation efficiency. The analysis proceeds with a variational formulation of a radiator with the surface prescribed a normal velocity. The radiation condition at far fields is a planar wave situation where the pressure and particle velocity are in phase. The surface complex power is identified by the variational formulation that the reactive power pertains to the difference between kinetic and potential energies of the acoustic field enclosed by the vibrating surface and the far fields. The radiated power can be viewed as power dissipated by the in phase of pressure and particle velocity at the far fields. The acoustic field caused by the radiator is regarded as an infinite-degree-of-freedom mass/spring/dashpot system. This infinite-degrees-of-freedom system is decomposed into a modal representation when a consideration of stationary conditions is to be applied to the ratio of the radiated to reactive power. In addition, a set of velocity radiation modes is obtained by solving the corresponding eigenvalue problem. Owing to such modal decompositions, studying the correlation between radiation efficiency and power factors becomes an examination of those two quantities in terms of the radiation modes. To demonstrate this relationship, various radiators are presented. It follows that modal radiation efficiencies are roughly approximated as the square of modal power factors and the plots of radiation efficiencies versus power factors for the first modes are nearly the same feature. Also presented herein are a thin baffled plate and a thin elastic spherical shell with applied point forces to illustrate the correlation between radiation efficiency and power factor.

[1] M. C. Junger and D. Feit, *Sound, Structure, and Their Interaction* (Acoustical Society of America, Woodbury, NY, 1990), Chap. 2.
[2] F. Fahy, *Sound and Structural Vibration: Radiation, Transmission, and Response* (Academic, New York, 1985).
[3] P. T. Chen and J. H. Ginsberg, ''Complex power, reciprocity, and radiation modes for submerged bodies,'' J. Acoust. Soc. Am. **98**, 3343–3351 (1995).
[4] S. Hayek, ''Vibration of a spherical shell in an acoustic medium,'' J. Acoust. Soc. Am. **94**, 342–348 (1966).

Numerical simulation of pulse propagation in nonlinear 1-D media

M. Scalerandi and P. P. Delsanto
INFM, Dipartimento di Fisica, Politecnico di Torino, Torino, Italy

C. Chiroiu and V. Chiroiu
Institute of Solid Mechanics, Romanian Academy, 70701 Bucuresti, Romania

(Received 23 June 1998; accepted for publication 9 June 1999)

The problem of convergence of finite difference (FD) schemes for simulating the propagation of pulses in nonlinear media is analyzed. In order to establish the reliability of the numerical procedure, different FD schemes are considered and compared among themselves, with the results of a Von Neumann analysis and with the analytical solution (when available). Examples of application of the method are also provided: e.g., the propagation of semi-infinite waves and pulses in active media with periodic and exponentially decaying nonlinearities. © *1999 Acoustical Society of America.* [S0001-4966(99)00810-3]

PACS numbers: 43.25.Ts [MFH]

INTRODUCTION

The relevance of nonlinear effects has been repeatedly demonstrated by a variety of phenomena, such as solitons generation,[1,2] the photo- and acoustoelastic effect,[3–5] anharmonic properties of disordered and fractal structures,[6,7] chaotic behaviors, and many others. A further ground for the interest in the topic is the connection between the structural complexity of a material and its nonlinearity.[8] In fact, the observation of nonlinear vibro-acoustical effects can be used, in principle, for the determination of the structural and mechanical characteristics of the material under investigation.

In spite of the wealth of available experimental information, a satisfactory method for the treatment of nonlinear systems is still missing. Even in the lucky case of solitonic equations, where analytical solutions in the form of stable propagating waves have been found, the problem becomes too difficult to solve in the presence of inhomogeneities, nontrivial boundary conditions, etc. In general, a theoretical analysis leads at most to the formulation of a solution in nonclosed form, to the description of the asymptotic behavior of the system or to special solutions.

A numerical approach can be a valid alternative to an analytical solution. In fact, several simulation techniques[9,10] have been proposed and developed in the last decades. Among them, we mention here the local interaction simulation approach (LISA),[11,12] which aims to derive, by means of a discrete model, the iteration equations for the spatio-temporal evolution directly from physical principles, rather then from a partial differential equation (PDE). LISA has been successfully applied to the simulation of the propagation of pulses in linear 1-D, 2-D, and 3-D arbitrarily complex media.[13] Its extension to nonlinear problems is formally straightforward.

However, even in a numerical treatment several difficulties may arise, due to problems of stability and convergence.[14] In fact, the classical stability analysis (e.g., the Von Neumann approach[15]) is valid only for linear systems. Its application to nonlinear cases is only an approximation, not always sufficient to guarantee the convergence of the numerical solution.

In several instances instabilities arising at early stages of the procedure preclude the possibility of performing a numerical simulation. Usually, however, it is possible to ensure stability by properly choosing the discretization scheme[16] and defining an upper limit for the choice of the time step.[17] More problems arise for what concerns convergence. In fact, since nonlinear effects are usually small (e.g., in acoustoelasticity[18]), the choice of the discretization parameters (lattice and time steps) is fundamental in order to eliminate or reduce the numerical noise, which might otherwise jeopardize the interpretation of the effects of the nonlinearity. Therefore, a reliable simulation of the evolution of nonlinear systems is possible only when a satisfactory criterion for verifying convergence has been established.

In this contribution we have proposed a method for analyzing the convergence, based on the comparison of the results obtained from the simulation of the same nonlinear problem by means of two schemes with different accuracy order. The equivalence of the results may be a good empirical test of the correctness of the solution. Due to its operational simplicity, such a test may be very useful in practical cases, even though it is not conclusive.[19] Moreover, such a procedure may be validated through additional convergence tests, such as a comparison with known analytical solutions, when available (even if they are valid only in special cases or as an asymptotic limit), or a somewhat approximative Von Neumann stability analysis.

Although this contribution is restricted to a specific one-dimensional propagation problem, the methodology proposed may be applied to treat a large variety of nonlinear problems. In order to show the applicability of the method, we have focused our attention on the problem of determining the response of an active system to an external forcing. An active system is a body whose response depends on the intensity of the forcing. In our particular case, we have considered bodies with some internal degrees of freedom due to an internal structure (e.g., porous media). The nonlinearity is

introduced by assuming that the elastic constants increase with the applied strains. Other nonlinear problems have also been considered.[20]

In Sec. I, the problem to be studied and the corresponding physical model are discussed in detail. The nonlinear PDE describing the system is derived from a nonlinear constitutive law and some general properties of the system are presented. Some analytical solutions in special cases are also found. In Sec. II, the numerical method is described and preliminary results of the convergence analysis are reported. In Sec. IV, the numerical results are compared with the analytical solution. Finally, in Sec. V, the response of the system after the injection of a longitudinal pulse is studied numerically in detail.

I. ANALYTICAL RESULTS

The purpose of this contribution is to consider the nonlinear effects, which usually accompany the elastic wave propagation in an initially deformed and stressed homogeneous solid. The material constitutive law can be written as

$$\sigma_{ij}=\omega_{ijkl}\epsilon_{k,l}, \tag{1}$$

where σ_{ij} and $\epsilon_{kl}=1/2(u_{k,l}+u_{l,k})$ are the stress and strain components and u_k represent the displacement components. The tensor ω_{ijkl} defines the material elastic properties. If we assume the initial deformation of the body to be homogeneous and small, compared with the elastic deformations, ω_{ijkl} is defined as[3]

$$\omega_{ijkl}=S_{ijkl}+\Gamma^0_{ij}\delta_{kl}, \tag{2}$$

where S_{ijkl} is the unperturbed elastic constant tensor and Γ^0_{ij} is the Cauchy's stress tensor in the initially deformed equilibrium configuration. In order to consider an active system, we have assumed Γ^0_{ij} to be proportional, through an external perturbation $b(\mathbf{x})$, to the displacement induced by the wave propagation

$$\Gamma^0_{ij}=A_{ij}b(\mathbf{x})u(\mathbf{x},t). \tag{3}$$

From the constitutive law, it is possible to derive the law of motion. If the initial stress and deformation are induced by a small external perturbation, all the terms containing the derivatives of Γ^0_{ij} and/or the corresponding nonlinear contributions may be neglected.

Restricting the treatment to the one-dimensional case and assuming that the medium supports the propagation of waves in the x direction, we obtain

$$\rho\frac{\partial^2u(x,t)}{\partial t^2}=S\frac{\partial^2u(x,t)}{\partial x^2}(1+b(x)u(x,t)), \tag{4}$$

where ρ is the medium density.

Equation (4) is of engineering interest in the field of vibration theory, when the elastic constants depend on the displacements amplitudes. It usually must be solved for the set of boundary and initial conditions:

$$\begin{aligned} &u(0,t)=f(t),\\ &u(L,t)=F(t), \quad t\geqslant 0, \end{aligned} \tag{5}$$

$$\begin{aligned} &u(x,0)=g(x),\\ &\dot{u}(x,0)=h(x), \quad 0<x<L, \end{aligned} \tag{6}$$

where f, F, g, and h are considered arbitrary functions (assumed to be known) and L is the length of the 1-D specimen.

An exact solution of Eqs. (4)–(6), for an arbitrary choice of the nonlinear term $b(x)$ and/or of boundary and initial conditions, is very difficult (if at all possible). However, for the reasons mentioned in the Introduction, it is useful to look for particular cases in which explicit stationary solutions may be found. As examples, a couple of stationary solutions are derived in the Appendix for specific choices of $b(x)$.

II. NUMERICAL APPROACH

In order to simulate the propagation of a wave in a medium described by Eq. (4) under arbitrary initial conditions and/or external forcing, we discretize both space and time, with lattice and time steps ϵ and τ, respectively. Applying the usual FD formalism using centered schemes for all derivatives but up to different accuracy orders, the following two basic schemes may be obtained:

$$\tilde{w}_i^{t+1}=2\tilde{w}_i^{t}-\tilde{w}_i^{t-1}+\alpha(\tilde{w}_{i+1}^{t}-\tilde{w}_i^{t}+\tilde{w}_{i-1}^{t})(1+b_i\tilde{w}_i^{t}) +O(\varepsilon^4,\tau^4), \tag{7}$$

$$\tilde{w}_i^{t+1}=2\tilde{w}_i^{t}-\tilde{w}_i^{t-1}+\frac{\alpha}{12}(\tilde{w}_{i+2}^{t}-16\tilde{w}_{i+1}^{t}+30\tilde{w}_i^{t} -16\tilde{w}_{i-1}^{t}+\tilde{w}_{i-2}^{t})(1+b_i\tilde{w}_i^{t})+O(\varepsilon^6,\tau^4), \tag{8}$$

where $\tilde{w}_i^{t}=w(i\varepsilon,\tilde{t}\tau)=w(x,t)$, $b_i=b(i\varepsilon)$, and $\alpha=S\tau^2/(\rho\varepsilon^2)$. The two schemes are expected to be equivalent, if convergent, albeit with a different level of accuracy. The error in the discretization can be easily evaluated as

$$\begin{aligned} E(\tau,\varepsilon)&=\frac{\varepsilon^2\tau^2}{12}\left(\frac{S}{\rho}w^{IV}(1+bw)-\frac{\tau^2}{\varepsilon^2}\ddot{\ddot{w}}\right),\\ E(\tau,\varepsilon)&=\frac{\varepsilon^2\tau^2}{3}\left(\frac{2}{5}\frac{S}{\rho}w^{IV}(1+bw)\varepsilon^2-\frac{1}{4}\frac{\tau^2}{\varepsilon^2}\ddot{\ddot{w}}\right), \end{aligned} \tag{9}$$

for the two schemes of Eqs. (7) and (8), respectively.

As already mentioned, a proper choice of lattice and time steps is fundamental to guarantee stability. The Von Neumann analysis leads to the following stability conditions for the above-mentioned schemes [(7) and (8), respectively]:

$$\tau\leqslant\frac{\varepsilon}{\sqrt{S/\rho(1+bu)}} \tag{10}$$

and

$$\tau\leqslant\frac{\varepsilon\sqrt{12}}{4\sqrt{S/\rho(1+bu)}}, \tag{11}$$

where u is a local value of the wave amplitude w (i.e., its maximum to guarantee stability everywhere).

The same analysis yields an estimate of the convergence of the numerical solution. Considering the dispersion relations for both continuous and discrete equations, it is possible to write the ratio $Q(k)$ between the discrete and the

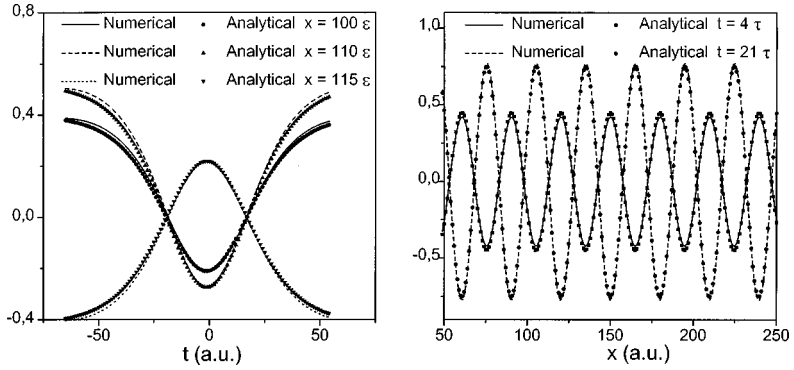

FIG. 1. Solution of Eq. (4) vs t (left plot) and vs x (right plot). Comparison of the numerical and analytical solutions of Eq. (4) for $b(x)=\exp(i\omega x)$, $S=1$, and $\rho=1$.

continuous phase velocities (v_D and v_C) of the wave as a function of the wave number k. Of course, maximal convergence is obtained when such a ratio approaches to 1. For the schemes (7) and (8) we obtain, respectively,

$$Q(k)=\frac{\arccos\left(1+\alpha(\cos k\varepsilon-1)(1+bu)\right)}{k\tau\sqrt{S/\rho(1+bu)}},$$

$$Q(k)=\frac{\arccos\left(1+\alpha(\cos 2k\varepsilon-16\cos k\varepsilon+15)(1+bu)\right)}{k\tau\sqrt{S/\rho(1+bu)}}.$$

Therefore, the choice

$$\tau=\frac{\varepsilon}{\sqrt{S/\rho(1+bu)}} \tag{12}$$

for scheme (7) leads to Q equal one, confirming the convergence of the method. Conversely, it is not possible to find an optimal value of τ for scheme (8). In this case, the shift between the velocities can only be minimized and some effects due to numerical dispersion are expected.

III. CONVERGENCE AND STABILITY

Several numerical tests have been performed in order to verify the stability and convergence of the two schemes presented in Eqs. (7) and (8). The stability of both schemes is very sensitive to the ratio between the time and lattice step [Eqs. (10) and (11)]. In fact, a strong instability appears already in the early stages of the simulation when τ is slightly above its maximum allowed value, while full stability (but not convergence) is obtained for values immediately below the threshold. These results have been discussed in more detail in Ref. 19 and are not reported here for brevity.

Also convergence depends, albeit weakly, on the τ/ε ratio. In fact, several computer experiments have shown that good convergence may be obtained for both schemes for a large interval of values of τ: $0.5\tau_{\max}\leqslant\tau\leqslant\tau_{\max}$, where $\tau_{\max}$ is defined as the upper limit in the choice of τ for stability. In the following we have chosen $\tau=0.5\varepsilon/\sqrt{S/\rho(1+bu)}$, which is valid for both schemes.

For both schemes we have compared the numerical solution of Eq. (4) with the analytical one. In Fig. 1, we show the comparison for scheme (7) in the case $b(x)=\exp(-\omega x)$, $S=1$ a.u. and $\rho=1$ a.u. The two initial conditions for the numerical solution are given by Eq. (A10) with $m=0.98$ at the time $t=-41\tau$ and $-40\ \tau$, respectively. The agreement between the two solutions is excellent. A similar agreement is found using scheme (8) for the numerical simulation and for other choices of m and of $b(x)$.

The results of the numerical simulations obtained by using the two discretization schemes are compared in Fig. 2 for $b(x)=0.1\cos(-0.1\pi x)$. In this case, we have considered a forcing $w(0,t)=\sin(\omega t)$ with $t\geqslant 0$ and $\omega=2\pi/100$ a.u. The agreement between the two solutions is again very good, confirming the convergence of both schemes also in the case of an external forcing. We must remark that small nonconvergence effects appear in the wavefront of the solution with scheme (8) (not shown in the figure), as expected from the convergence analysis reported at the end of the previous section.

IV. RESULTS AND DISCUSSION

We have applied the scheme (7) to study the propagation of different pulses in active media characterized by several kinds of nonlinearities. The results of the previous section have shown that the proposed numerical approach is stable and convergent for the adopted choice $\epsilon=1$ and $\tau=0.5\tau_{\max}$. Nevertheless, additional tests of convergence similar to the one performed in Fig. 2 have been carried out, confirming the convergence of the two schemes. To illustrate the application of our numerical method and some interesting effects arising from the nonlinearity, we show in the following a few examples of simulation of the propagation of a semi-infinite sinusoidal wave $u(0,t)=\sin\omega t$ and of a Gaussian pulse $u(0,t)=\exp(-(t-t_0)^2/\omega)$ injected from the left side of the specimen, both for periodical

$$b(x)=\gamma\sin\theta x \tag{13}$$

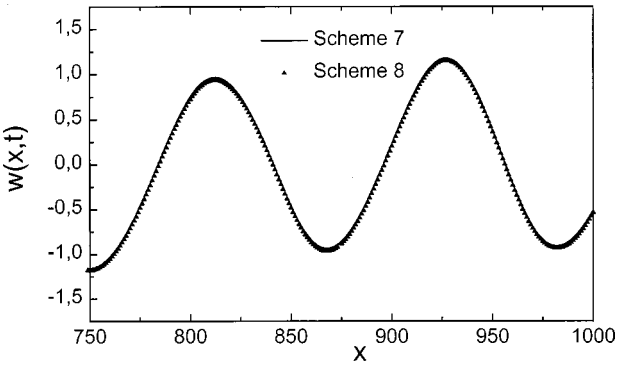

FIG. 2. Comparison of the numerical solutions of Eq. (4) using the two schemes.

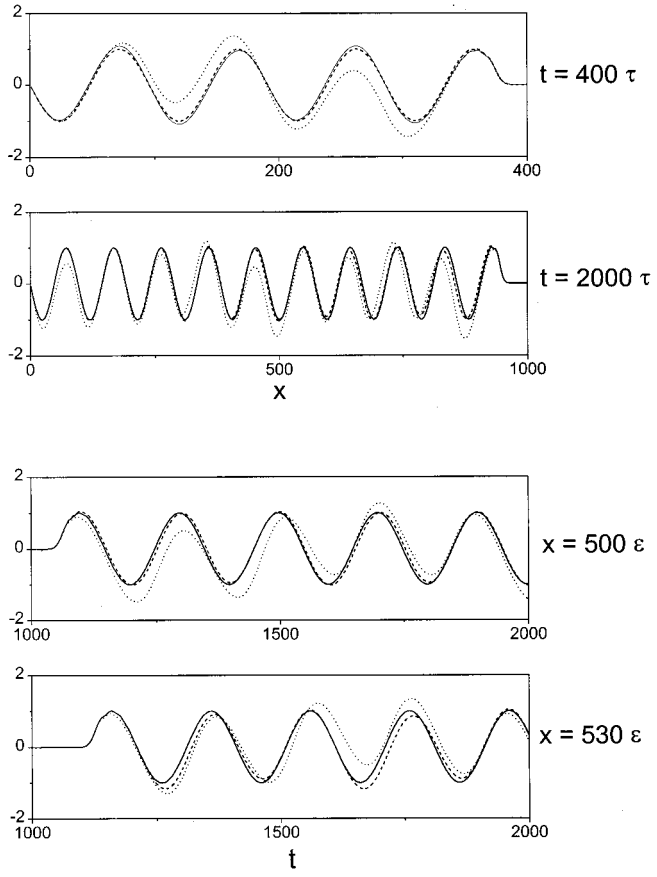

FIG. 3. Propagation of a semi-infinite sine wave in a medium with periodic nonlinearity [Eq. (13)]. Displacement vs x (top two plots) and vs t (bottom two plots). (a) $\gamma=0$ (solid line); (b) $\gamma=0.1$, $\theta=2\omega$ (dashed line); (c) $\gamma=0.1$, $\theta=\omega$ (dots).

and exponentially decaying

$$b(x)=\gamma\exp(-x/\theta) \tag{14}$$

nonlinearities.

First, we consider the effects of a periodic nonlinearity on a semi-infinite sine wave with $\omega=2\pi/200$. In Fig. 3, we plot the displacement $w(i,t)$ vs $x=i\varepsilon$ at $t=400\tau$ and $t=2000\tau$ and vs t at $x=500\varepsilon$ and $i=530\varepsilon$. In each plot we have reported the results of the simulation for three cases: (a) $\gamma=0$; (b) $\gamma=0.1$, $\theta=2\omega$, and (c) $\gamma=0.1$, $\theta=\omega$. The presence of the nonlinear term introduces a periodical variation of the group velocity v_g with respect to the linear case (a). We observe almost no dispersion for high-frequency waves [case (b)], i.e., the ones for which the period of the wave is much smaller than the one of the nonlinearity ($\omega\gg v_g\theta$). The amplification and phase shift effects appearing in case (c) reveal the presence of resonances when the wave and the nonlinear term frequencies are comparable. In this frequency domain the system is highly dispersive. Similar results have been recently obtained for the propagation of pulses in media with periodically varying elastic constants.[21]

Very detailed informations on the behavior of the system may be obtained from the analysis of the positions of the first, second, and third maximum of the wave: p_1, p_2, and p_3, respectively. In Fig. 4, the wave frequency modulation is analyzed by means of plots of (p_2-p_1) and (p_3-p_1).

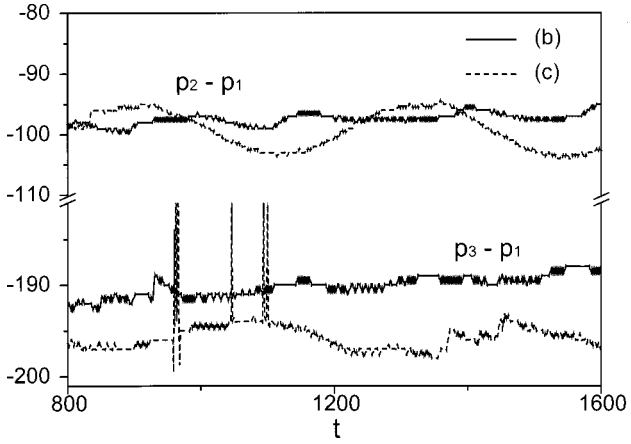

FIG. 4. Propagation of a semi-infinite sine wave in a medium with periodic nonlinearity. Distance between the first (p_1) and the second (p_2) or the third peak (p_3) vs time for cases (b) and (c) considered in Fig. 3.

While in the case (b) both (p_2-p_1) and (p_3-p_1) are almost constant and small, rather large and almost periodical fluctuations appear in the case (c), where strong distortions of the pulse are present.

The effects reported in Figs. 3 and 4 may be better analyzed by considering the Fourier spectrum of the wave at a given time: see Fig. 5. In the linear case (upper plot) the spectrum is almost monochromatic with leading frequency at $\nu=0.01$. The small distortions are due to numerical effects caused by the choice of the time step, which does not satisfy Courant's condition for the simulation of the wave propagation in linear homogeneous media. The distortion effects are stronger in case (b) and even more in case (c). We also

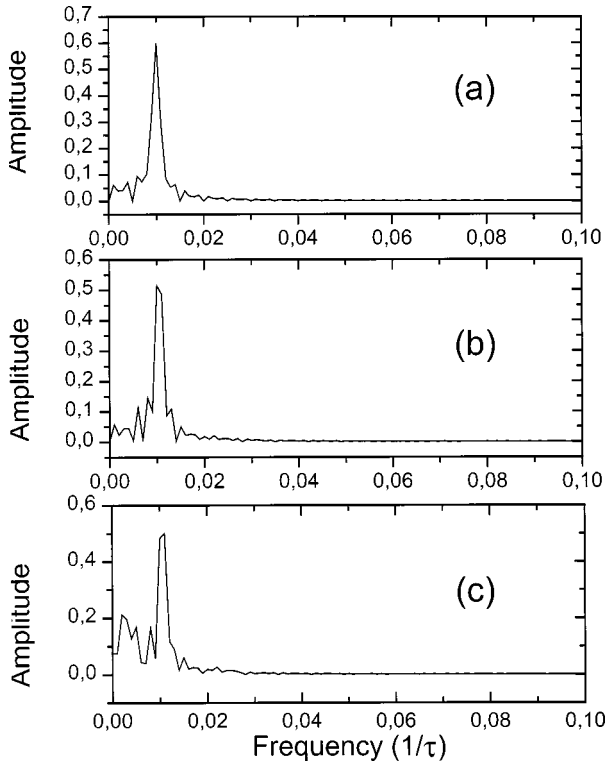

FIG. 5. Propagation of a semi-infinite sine wave in a medium with periodic nonlinearity. Fourier spectrum at $t=1200\tau$ for the three cases considered in Fig. 3.

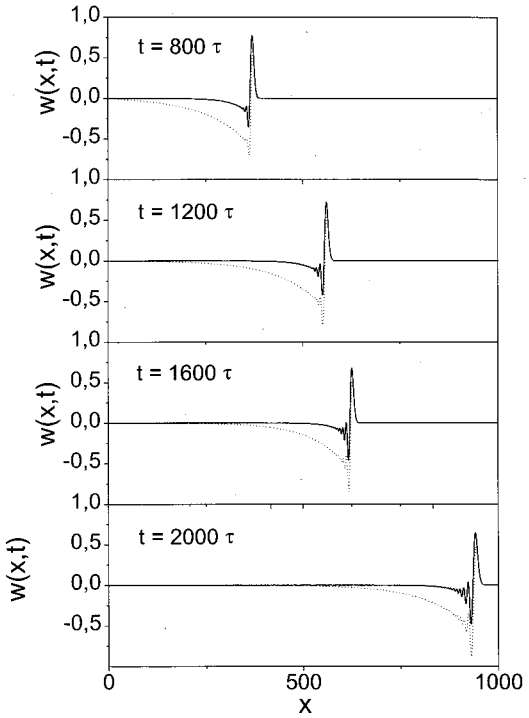

FIG. 6. Snapshots of the propagation of a Gaussian pulse in a 1-D medium with exponentially decaying nonlinearity [Eq. (14)]: $\theta=\omega$ (solid line); $\theta=2\omega$ (dashed line).

notice that, in the latter case, at least one large harmonic component, corresponding to the nonlinear term frequency, emerges for $\nu'=0.005$, leading to a large modulation of the pulse.

In Figs. 6 and 7 we have studied the effects of an exponentially decaying nonlinearity on a Gaussian pulse ($t_0=100\tau$) and on a sinusoidal wave, respectively. We have considered two cases: (a) $\theta=\omega$ (solid line) and (b) $\theta=2\omega$ (dotted line). In both cases, after some sizable distortion in the region where the nonlinearity is not negligible, the wave propagates undisturbed without any further shape modification.

In Fig. 6, snapshots of the propagation of a Gaussian pulse are reported at four given times: $t=800\tau$, 1200τ, 1600τ, and 2000τ. The amplitude of the pulse is reduced and a tail, caused by the retarded response of the active system, appears. We observe that the retarded response reaches very quickly an asymptotic configuration. In fact, snapshots at $t=1600\tau$ and $t=2000\tau$ differ only for the position of the pulse, while shape and amplitude are the same. The effect increases dramatically with the penetration depth parameter θ of the nonlinear contribution, but the time at which a stable asymptotic state is reached is the same for the two cases considered.

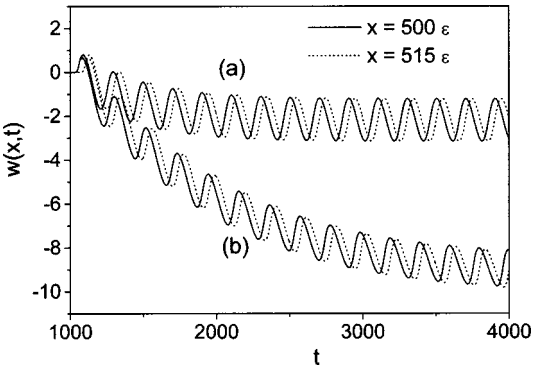

FIG. 7. Propagation of a semi-infinite sine wave in a 1-D medium with exponentially decaying nonlinearity: (a) $\theta=\omega$ and (b) $\theta=2\omega$. Wave amplitude time for $x=500\epsilon$ (solid line) and $x=515\epsilon$ (dashed line).

A similar effect is depicted in Fig. 7 for a semi-infinite sine wave. The wave amplitude is plotted versus t at $x=500\varepsilon$ (solid line) and 515ε (dashed line). Again, a retarded response of the system is superimposed to the continuous incoming of the wave, leading to the shapes reported in the plots. As in the previous case, the effect increases with θ. Likewise, the time at which the wave reaches stability depends strongly on θ: the asymptotic solution is already reached at $t\approx2000\tau$ for case (a), but much later ($t\approx4000\tau$) for case (b).

V. CONCLUSIONS

In this contribution we have presented a numerical method for the simulation of the propagation of acoustic pulses in nonlinear 1-D media. The results are assumed to be reliable, if simulations performed with two schemes of different accuracy order lead to sufficiently close results. Since this convergence test is not totally decisive, the availability of analytical solutions in particular cases and/or an approximate Von Neumann analysis may be used for a more conclusive analysis of the convergence of the solution.

In order to illustrate the method and its applicability, we have considered the propagation of acoustic waves in the presence of a specific nonlinear term which describes active systems with a retarded response proportional to the perturbation itself, i.e., to the wave amplitude. Also, we have considered specific nonlinear perturbations in the form of periodic and exponentially decaying functions. In fact, the proposed procedure may be applied to any kind of nonlinearity.[20]

In the specific case considered, some physical properties of the system have been discussed. In particular, it has been found that a periodic nonlinearity is effective only under resonance conditions, i.e., it affects only the propagation of the monochromatic components with wavelength comparable with the spatial period of the nonlinearity. Also, it has been shown that in the case of exponentially decaying nonlinearities, an asymptotic behavior is readily reached.

ACKNOWLEDGMENTS

This work was partly supported by the EC Program Copernicus No. ERBCIPACT940132.

APPENDIX: SOLUTION FOR $b(x)=\exp(-iwx)$

We wish to study here the analytical solution of Eq. (4) with $b(x)=\alpha\exp(-i\omega x)$ in the case of an infinite 1-D medium. A stationary solution can be written in the form

$$u(x,t)=v(x)w(t).$$

By substituting into Eq. (4), we obtain

$$v(x)=Ae^{i\omega x}, \tag{A1}$$

$$\rho\ddot{w}+k^2(w+\alpha w^2)=0, \tag{A2}$$

where $k^2=S\omega^2$.

By integrating once and introducing the change of variable

$$w(t)=-\frac{6\rho}{k^2\alpha}\left(z(t)+\frac{k^2}{12\rho}\right),$$

Eq. (A2) becomes the Weierstrass elliptic equation

$$w'^2=4z^3-g_2z-g_3, \tag{A3}$$

with

$$g_2=\frac{k^4}{12\rho^2}, \quad g_3=\left(\frac{k^2}{6\rho}\right)^3-\frac{2C}{\rho}, \tag{A4}$$

where C is an integration constant. A stable solution of Eq. (A3) is possible only if $g_2^3-27g_3^2>0$ and, therefore,

$$0<C<\frac{k^6}{216\rho^2}.$$

Drazin[1] has shown that the only stable and bounded solutions for Eq. (A3) are the cnoidal waves of order m:

$$cn_m\Phi=\cos\left(\int_0^{\phi}\frac{d\theta}{\sqrt{1-m\sin^2\theta}}\right). \tag{A5}$$

Cnoidal waves of order m are periodical functions with period $4K(m)$, where $K(m)$ is the complete elliptic integral of the first kind. The waveform depends on the nonlinear distortion factor m, and for $m=1$ it reduces to the classical sech^2 soliton. In the interaction between two cnoidal waves, the following superposition principle can be applied: if w_1 and w_2 are two solutions of Eq. (A3), then

$$w_3=-w_1-w_2+\frac{1}{4}\left(\frac{w_1'-w_2'}{w_1-w_2}\right)^2 \tag{A6}$$

is also a solution. The extension of this superposition principle to an N-cnoidal solution is straightforward.

Then, the solution of Eq. (A2) becomes

$$w(t)=\frac{3}{2\alpha m^2}\left(\frac{1+\sqrt{4m^4-3}}{2}cn_m^2\left(\frac{t^*}{m}\right)-\frac{\sqrt{4m^4-3}}{3}\right)-\frac{1}{2\alpha}, \tag{A7}$$

where

$$t^*=kt/(2\sqrt{\rho}),$$

$$\beta=\frac{1}{\sqrt{m^{*2}-m^*+1}},$$

$$m=(m^{*2}=m^*+1)^{1/4}.$$

The integration constant defined in Eq. (A4) becomes

$$C=\frac{\rho}{2}\left(\frac{k^2}{6\rho}\right)^2\left(1-\frac{9}{2}\beta^3m^*(m^*-1)(2m^*-2)\right), \tag{A8}$$

and the stability condition may be written as

$$\left(\tfrac{3}{4}\right)^{1/4}\leqslant m\leqslant 1.$$

The complete solution of Eq. (4) with $b(x)=\alpha e^{-i\omega x}$ and on an infinite line is

$$u(x,t)=Ae^{i\omega x}\left(\frac{3}{2\alpha m^2}\left(\frac{1+\sqrt{4m^4-3}}{2}cn_m^2\left(\frac{t^*}{m}\right)-\frac{\sqrt{4m^4-3}}{3}\right)-\frac{1}{2\alpha}\right), \tag{A9}$$

where m depends nontrivially on the initial conditions $g(x)$ and $h(x)$.

A similar solution can also be obtained by substituting ω with $i\omega$:

$$u(x,t)=Ae^{-\omega x}\left(\frac{3}{2\alpha m^2}\left(\frac{1+\sqrt{4m^4-3}}{2}cn_m^2\left(\frac{t^*}{m}\right)-\frac{\sqrt{4m^4-3}}{3}\right)-\frac{1}{2\alpha}\right). \tag{A10}$$

Finally, we consider a time-dependent nonlinear term of the form

$$b(x,t)=\frac{(1+Ae^{kx-\omega t})^2}{e^{kx-\omega t}}. \tag{A11}$$

It can be shown[22] that the solution can then be expressed as

$$u(x,t)=\frac{\partial^2}{\partial x^2}\ln(\Phi(x,t)), \tag{A12}$$

where

$$\Phi(x,t)=1+Ae^{kx-\beta t},$$

$$\beta^2\rho=k^2S(1+Ak^2). \tag{A13}$$

[1] P. G. Drazin and R. S. Johnson, *Solitons: an Introduction* (Cambridge U.P., Cambridge, 1989).

[2] D. J. Korteweg and G. de Vries, ''On the change of form of long waves in a rectangular canal,'' Philos. Mag. **39**, 422 (1895).

[3] R. A. Toupain and B. Bernstein, ''Sound waves in deformed perfectly elastical materials. Acoustoelastic effect,'' J. Acoust. Soc. Am. **33**, 216 (1961).

[4] V. Chiriou *et al.*, ''Determination from the natural frequencies of the second and third order elastic constants in Al,'' J. Acoust. Soc. Am. **102**, 193–198 (1997).

[5] M. Capanu and E. Soos, ''The three-dimensional theory of bucking of composite elastic bars. The influence of a lateral hydrostatic pressure,'' Rev. Roum. Sci. Techn. Mech. Appl. **41**, 132 (1996).

[6] A. Alippi, F. Craciun, and E. Molinari, ''Finite size effects in the frequency response of piezoelectric composite plates,'' J. Appl. Phys. **66**, 2828–2832 (1989).

[7] F. Craciun *et al.*, ''Direct experimental observation of fracton mode patterns in one-dimensional Cantor composites,'' Phys. Rev. Lett. **68**, 1555–1558 (1992).

[8] L. A. Ostrovsky, ''Wave processes in media with strong acoustic nonlinearity,'' J. Acoust. Soc. Am. **90**, 3332–3337 (1990).

[9] M. Fuyuki and Y. Matsumoto, ''Finite difference analysis of Rayleigh waves scattering at a trench,'' Bull. Seismol. Soc. Am. **70**, 2051–2069 (1980).

[10] N. R. S. Simons and A. A. Seebak, ''Spatially weighted numerical models for the two-dimensional wave equation: FD algorithm and synthesis of the equivalent TLM model,'' Int. J. Num. Modelling: Electr. Netw., Devices and Fields **6**, 47–65 (1993).

[11] P. P. Delsanto, R. B. Mignogna, S. Schechter, H. H. Chaskelis, and R. Kline, ''Connection machine simulation of ultrasonic wave propagation in materials II: the two-dimensional case,'' Wave Motion **20**, 295–314

(1994); ''Connection machine simulation of ultrasonic wave propagation in materials III: the three-dimensional case,'' *ibid.* **26**, 329–339 (1997).
[12] R. S. Schechter *et al.*, ''Real-time parallel computation and visualization of ultrasonic pulses in solids using the Connection Machine,'' Science **265**, 1188–1192 (1994).
[13] P. P. Delsanto *et al.*, ''Simulation of ultrasonic pulse propagation in complex media,'' in *New Perspectives on Problems in Classical and Quantum Physics*, edited by P. P. Delsanto and A. W. Saenz (Gordon & Breach, 1998), Vol. 2, pp. 51–74.
[14] D. Iordache, P. P. Delsanto, and M. Schalerandi, ''Pulse distortions in the FD simulation of elastic wave propagation,'' Math. Comp. Mod. **25**, 31–43 (1997).
[15] J. C. Strickwerda, *Finite Difference Schemes and Partial Differential Equations* (Wadsworth-Brooks, 1989).
[16] A. C. Vliegenthart, ''On finite-difference methods for the Korteweg-de Vries equation,'' J. Eng. Math. **5**, 137 (1971).
[17] M. Scalerandi *et al.*, ''A stable finite difference scheme for the Boussinesq equation,'' Nuovo Cimento D **20**, 1–13 (1998).
[18] P. P. Delsanto *et al.*, ''Rayleigh wave propagation in deformed orthotropic materials,'' J. Acoust. Soc. Am. **81**, 952–960 (1987).
[19] P. P. Delsanto and M. Scalerandi, ''Discretization schemes for the simulation of nonlinear propagation equations,'' in *Proceedings of the International Symposium on Hydroacoustics and Ultrasonics*, edited by A. Stepnowski and E. Kozaczka (1997), pp. 65–70.
[20] P. P. Delsanto *et al.*, ''Nonlinear propagation of Ultrasonic Waves in Multilayers,'' submitted to J. Comput. Acoustics (1999).
[21] N. Cretu, P. P. Delsanto, G. Nita, C. Rosca, M. Scalerandi, and I. Sturzu, ''Propagation of acoustic pulses in inhomogeneous media,'' J. Acoust. Soc. Am. **104**, 57–63 (1998).
[22] K. Konno and H. Ito, ''Nonlinear interaction between solitons in complex *t*-plane,'' J. Phys. Soc. Jpn. **56**, 897–904 (1987).

Nonlinear Doppler effect and its use for bubble flow velocity measurement

I. N. Didenkulov,[a] S. W. Yoon, A. M. Sutin,[b] and E. J. Kim
Acoustics Research Laboratory, Department of Physics, Sung Kyun Kwan University, Suwon 440-746, Republic of Korea

(Received 24 January 1998; revised 21 May 1999; accepted 27 May 1999)

The Doppler effect is a familiar phenomenon in linear acoustics. The nonlinear Doppler effect is also possible when a moving target exhibits nonlinear responses. In these cases Doppler frequency shifts arise at harmonics or combination frequencies in the scattered waves. For collinear geometry of primary beams, the nonlinear Doppler frequency shifts at the second harmonic and the combination frequencies are found to be the same as those for the linear scattering of those frequency components by the target. However, for highly, noncollinear primary beams, the difference frequency Doppler frequency shift can greatly exceed the linear one. This phenomenon is mainly studied in the present work. Experimental verification done with flowing bubbles in a tube shows good agreement with the theory. The suggested difference frequency Doppler technique can find applications in medical diagnostics of blood flow as well as in industries and in oceanology. [S0001-4966(99)03709-1]

PACS numbers: 43.25.Yw [MAB]

INTRODUCTION

The Doppler effect is currently applied to various fields in human life and industries. It is also a very powerful research tool in many sciences, from astronomy to microphysics.[1] In acoustics, the Doppler frequency shift is used to estimate velocities of moving objects such as ship, ocean current, fluid flow in pipelines, blood flow in human body, etc.[1–3] In such applications the Doppler effect is investigated for linear responses from moving scatterers or targets.

Since propagation media are not ideally linear, nonlinear responses also can be observed. Typical values of the nonlinear parameter are not high and therefore nonlinear responses from a small volume of the medium are detectable only in relatively strong acoustic fields.[4] However, nonlinear responses from gas bubbles in liquids can be observed even for relatively low-intensity incident waves.[5,6] Therefore, in bubbly media one may neglect nonlinear properties of the liquid itself compared to the nonlinear responses from bubbles. In this paper, we consider only nonlinear scattering from such highly nonlinear targets. Easily observed phenomena of nonlinear responses from bubbles are the harmonics and combination frequency generation. The second or higher harmonics can be detected in the scattered field. If two different frequency primary waves are incident on a bubble, then the sum and the difference frequencies, i.e., the combination frequencies of primary waves, appear in the scattered field. Such nonlinear responses become much stronger if the bubble resonance frequency coincides with either the primary or combination frequencies. Such coincidence makes possible nonlinear acoustic bubble counting and sizing.[7–12] For the last decade linear and nonlinear acoustic techniques based on the use of microbubbles—so-called contrast agents—find increasing applications in medical ultrasound diagnostics.[13–15]

If a nonlinear target moves, one may expect Doppler frequency shifts to appear not only in the linear scattered waves, but also in the harmonics or the combination frequency waves. Such phenomena can be called the nonlinear Doppler effect. The nonlinear Doppler effect was probably first introduced by Chapelon *et al.*[16,17] Later, application to blood velocity measurements with microbubble contrast agents was published in medical journals.[18–20] In those works two nonlinear Doppler techniques were investigated. The first one is the modulation method. The pump wave has a frequency equal to the bubble resonance frequency and interacts with the high-frequency probe wave. Their interaction results in a Doppler frequency shift at modulation-combination frequency components.[16,17] The second method is the second harmonic method. A Doppler frequency shift can be observed at the second harmonic of the incident wave when the incident wave is in resonance with the moving bubble.[18–20]

In the previous works only simple backscattering geometries of the nonlinear Doppler effect were considered. The results can be formulated as follows: the Doppler frequency shifts for higher harmonics or modulation frequency components are the same as such frequencies radiated directly from an emitting transducer to a bubble. However, no attention was paid to the possibility of an enhanced Doppler effect in the nonlinear scattering. This was first reported by the authors with emphasis on possible applications in underwater acoustics.[21–23] Since the frequency shift depends on the relative motion of the target and the transducer, the Doppler effect is a vector-type phenomenon. However, the nonlinear frequency transformation is a scalar sum or subtraction between the incoming wave frequencies. Both combined phenomena show very intriguing effects in the nonlinear scatter-

[a]On leave from Institute of Applied Physics, Russia. Present address: Institute of Applied Physics, 46 Ulyanov Str., Nizhny Novgorod, 603600, Russia. Electronic mail: din@appl.sci-nnov.ru
[b]On leave from Institute of Applied Physics, Russia. Present address: Davidson Laboratory, Stevens Institute of Technology, Castle Point on Hudson, Hoboken, NJ 07030.

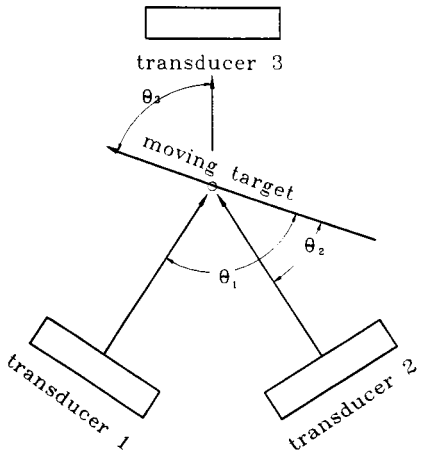

FIG. 1. Schematic diagram for the nonlinear Doppler effect.

ing of highly noncollinear incident waves by a moving target.

In this paper we analytically describe nonlinear Doppler effect for the general geometrical configuration. The main emphasis is on the new method—the difference frequency Doppler technique, which shows an enormous Doppler frequency shift compared to the linear one. The difference frequency Doppler technique is experimentally verified with bubbly water flow.

I. THEORY

A general configuration for nonlinear sound scattering is shown in Fig. 1. Monochromatic plane waves of frequencies ω_1 and ω_2 from transducers 1 and 2 are incident on a moving target. The angles between the wave vectors of two incident waves and the velocity vector of the target are θ_1 and θ_2, respectively. Scattered signals are received by transducer 3, whose beam axis is at angle θ_3 with the target velocity vector.

The target is a nonlinear scatterer. It converts the spectra of incident waves into scattered signal spectrum which consists not only of the primary frequency components but also of their second and higher harmonics and combination frequency components. We restrict our consideration by including only the quadratic nonlinearity of the target. For a static target, the scattered spectrum includes the frequency components of ω_1, ω_2, $2\omega_1$, $2\omega_2$, $\omega_1+\omega_2$, and $\omega_1-\omega_2$.

The Doppler effect for sound scattering by a moving target can be considered a two-stage process: the sound wave reaches a moving scatterer and is then emitted into the medium.[2] If a target moves with a constant velocity $\vec{v}$, then the frequencies of primary waves arriving at the target are

$$\omega_{1,2}^{(r)}=\omega_{1,2}\left(1-\frac{v}{c_0}\cos\theta_{1,2}\right). \tag{1}$$

The frequency of acoustic wave emitted from the moving target into the medium in the direction of transducer 3 is

$$\omega_{1,2}^{(l)}=\frac{\omega_{1,2}^{(r)}}{1-(v/c_0)\cos\theta_3}, \tag{2}$$

where the superscript (l) denotes the quantities for a linearly scattered wave.

The same procedure can be used to obtain the Doppler frequency shift for a nonlinear scattered wave. An intermediate stage must be added in this case. In this stage, the frequencies of waves arriving at the target are changed into the combination frequencies due to nonlinearity of the target. Note that the second harmonic can be considered as the sum frequency if $\omega_1=\omega_2$. Therefore, for the most general case the combination frequencies $\omega^{(r\pm)}$ generated at the target are as follows:

$$\omega^{(r\pm)}=\omega_1^{(r)}\pm\omega_2^{(r)}, \tag{3}$$

where the plus and the minus signs in the superscript denote the sum and the difference frequencies, respectively.

In the second stage of nonlinear scattering by the moving particle, we can use the same procedure as for the linear case. From Eq. (2) the frequencies of waves emitted from the target in the direction of transducer 3 are given as follows:

$$\omega_3^{(\pm)}=\frac{\omega^{(r\pm)}}{1-(v/c_0)\cos\theta_3}. \tag{4}$$

With Eqs. (1) and (2), Eq. (4) can be written as

$$\begin{aligned}\omega_3^{(\pm)}&=\frac{\omega_1[1-(v/c_0)\cos\theta_1]\pm\omega_2[1-(v/c_0)\cos\theta_2]}{1-(v/c_0)\cos\theta_3}\\&\simeq(\omega_1\pm\omega_2)\\&\quad-\frac{v}{c_0}[\omega_1\cos\theta_1\pm\omega_2\cos\theta_2-(\omega_1\pm\omega_2)\cos\theta_3].\end{aligned} \tag{5}$$

Equation (5) describes the Doppler frequency shifts which arise under the combination scattering of two primary waves by a nonlinear target. The plus sign corresponds to the sum frequency, and the minus sign corresponds to the difference frequency received by transducer 3.

One can see from this equation that the resulting Doppler frequency shift is derived from the Doppler frequency shifts at the primary frequencies and also from the shift at the combination frequency. For the important particular case of collinear primary beams ($\theta_1=\theta_2$), physical meaning for the nonlinear Doppler effect is as follows: Doppler frequency shifts at all nonlinear scattered frequencies (higher harmonics or combination frequencies) are the same as for linear scattering of those frequencies directly emitted by the transducer to the target. For example, Doppler shift for the second harmonic backscattering can be described if we use the plus sign in Eq. (5) and set $\omega_1=\omega_2=\omega$, and $\theta_1=\theta_2=\theta_3+\pi=\theta$:

$$\omega^{(2)}=2\omega\left(1-\frac{2v}{c_0}\cos\theta\right).$$

II. DOPPLER EFFECT FOR THE DIFFERENCE FREQUENCY SCATTERING

Consider the difference frequency scattering of two incident waves on a nonlinear target. Taking the minus sign in Eq. (5) we find

$$\omega_3^{(-)}=(\omega_1-\omega_2)$$

$$-\frac{v}{c_0}[\omega_1\cos\theta_1-\omega_2\cos\theta_2-(\omega_1-\omega_2)\cos\theta_3]. \tag{6}$$

One of the most interesting cases takes place if the angle between the beams of transducers 1 and 2 is not small. We call this geometry the highly noncollinear primary beams. In this case it can be seen that the Doppler frequency shifts for two primary waves are not subtracted from each other but are summed in the received wave at the difference frequency. Then Doppler frequency shift due to the scatterer movement relative to transducer 3 is small enough to be neglected if $|\omega_1-\omega_2|\ll\omega_{1,2}$. Thus the Doppler frequency shift for the difference frequency is the sum of frequency shifts produced by each incident wave. For oppositely directed primary beams with $\theta_1=\theta_2+\pi$, the Doppler shift is

$$\omega_3^{(-)}\simeq(\omega_1-\omega_2)-\frac{v}{c_0}(\omega_1+\omega_2)\cos\theta_1. \tag{7}$$

In this case the Doppler frequency shift at the difference frequency can be very large and even greater than the difference frequency between two primary waves.

It is worthwhile to compare the nonlinear Doppler frequency shift with the linear one for difference frequency scattering. The largest linear Doppler frequency effect occurs for the backscattering geometry if the difference frequency is directly emitted by transducer 1 to the target and received by the same transducer. Then, the Doppler frequency shift $\Delta\omega^{(l)}$ is given as:

$$\Delta\omega^{(l)}=-\frac{2v}{c_0}(\omega_1-\omega_2)\cos\theta_1. \tag{8}$$

Comparing Eq. (8) with Eq. (7) one may obtain

$$\frac{\Delta\omega_3^{(-)}}{\Delta\omega^{(l)}}=\frac{1}{2}\cdot\frac{\omega_1+\omega_2}{\omega_1-\omega_2}\gg 1. \tag{9}$$

Hence, the nonlinear Doppler effect at the difference frequency becomes enormous for highly noncollinear primary beams. This feature can be used in various applications.

III. BUBBLE FLOW MEASUREMENT WITH THE DIFFERENCE FREQUENCY DOPPLER TECHNIQUE

Difference frequency scattering from bubbles can be observed.[12] If there is a flow in the medium, bubbles also move with the flow. This allows nonlinear Doppler flow velocity measurements in such media. The measurements were carried out in a laboratory tank of size $91\times30\times45\,\mathrm{cm}^3$. The measurement setup is shown in Fig. 2. Two high-frequency primary beams were generated by two separate focused transducers with resonance frequencies around 2.25 MHz. Each transmitter of 2.54 cm diameter has a focal length of 10 cm and can produce acoustic pressure of 1.5×10^5 Pa in the focal area. One of the primary frequencies was kept constant at 2.25 MHz, and the other was varied from 2.18 to 2.05 MHz. Therefore, the difference frequency could be varied from 70 kHz to 200 kHz. This allowed us to measure the

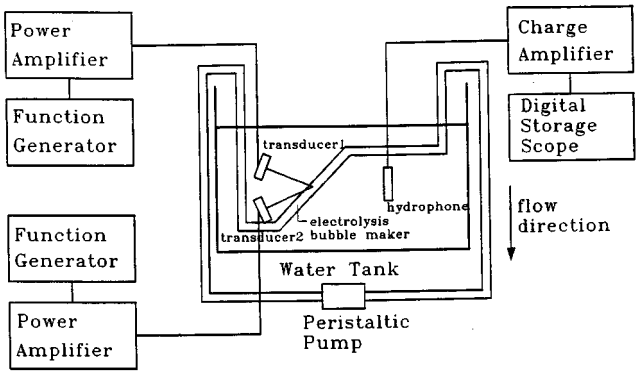

FIG. 2. A block diagram of the experimental setup for bubble flow measurements by a nonlinear ultrasound Doppler technique.

acoustic responses of bubbles with different resonance frequencies corresponding to bubble radii from 45 to 15 μm. The two primary beams interacted at their focal spots. The angle between two beams also could be varied. The tube radius R and the wall thickness were 5 mm and 0.5 mm, respectively. The tube was put into the water tank so that the intersection of primary beams was inside the tube. The bubbles were created by an electrolysis method. An electrolysis-type bubble maker consisting of several thin wires was placed inside the tube upstream to the water flow.[12] It produced many small bubbles whose concentration could be changed by changing the applied voltage. The water flow speed was varied by an electric pump. The flow speed was independently estimated by measuring the water flow rate. The flow rate Q is measured by water volume passing through the tube cross section in a unit time. The mean flow speed V_r over the tube cross section is described by

$$V_r=\frac{Q}{\pi R^2}. \tag{10}$$

When the resonant bubbles pass through the interaction region, they radiate acoustic waves at the difference frequency. This wave is detected by a hydrophone placed outside the tube at a distance of 5 cm from the interaction region. In our experiments, the signal from the hydrophone with a pre-amplifier was analyzed by a digital storage oscilloscope LeCroy 9310 M. Averaged spectra of the received signals were obtained over the period of time of about 60 s.

IV. RESULTS AND DISCUSSION

The experimental results are presented in Figs. 3–6. First, the response of pure water in the tube without bubbles was measured. The averaged spectrum of the received signal in the frequency range 119–122 kHz is plotted in Fig. 3 (curve ''a''). The difference between the frequencies of two tranducers was 120 kHz. No peak response due to bubbles was observed in this case.

When bubbles were affected by the input voltage of the electrolysis bubble maker another situation was observed. Bubbles are very adhesive to the plastic walls of the tube. Even though the bubble maker was turned on only once for a short period of time, many small bubbles were attached to

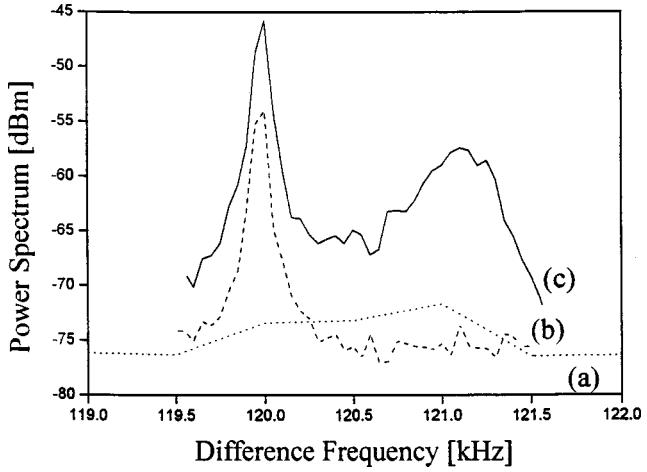

FIG. 3. Difference frequency spectra of signals received by a hydrophone from the interaction zone of two high-frequency beams. Difference frequency: 120 kHz, $\theta_1=95°$, $\theta_2=30°$. (a) No bubbles and no flow; (b) no flow but bubbles attached to the tube walls; and (c) flow with bubbles at the reference flow speed 65 cm/s.

the tube walls. Since the attached bubbles were not in motion, bubbles whose eigenfrequencies were in resonance with the difference frequency responded at the difference frequency. The corresponding spectrum for the case when the bubble maker is turned on and there is no water flow inside the tube is curve ''b'' in Fig. 3.

Figure 3(c) was observed when both bubble maker and water flow were turned on. It can be concluded from the comparison of curves in Fig. 3 that the nonlinear response at the difference frequency is due to the static resonant bubbles attached to the walls in the interaction region while the Doppler frequency shift is due to the resonant bubbles moving with flow velocity.

From the nonlinear response spectrum of moving bubbles the flow speed v can be calculated from Eq. (6), assuming $(\omega_1-\omega_2)\ll\omega_{1,2}$, as follows:

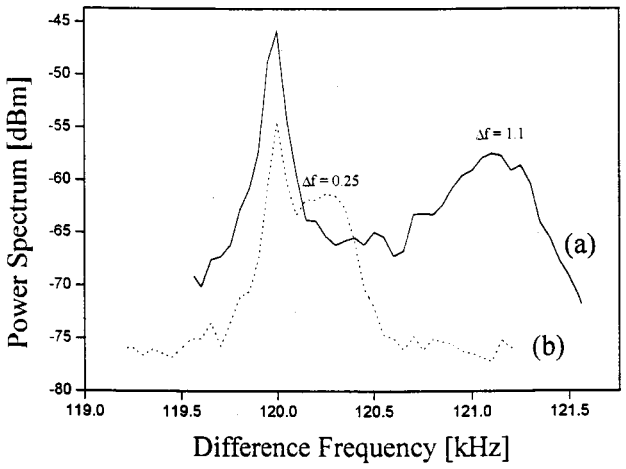

FIG. 4. Difference frequency spectra of signals received by a hydrophone from the interaction zone for different flow velocities. Difference frequency: 120 kHz, $\theta_1=95°$, $\theta_2=30°$. Reference flow velocities are (a) 65 cm/s, and (b) 17.5 cm/s, respectively.

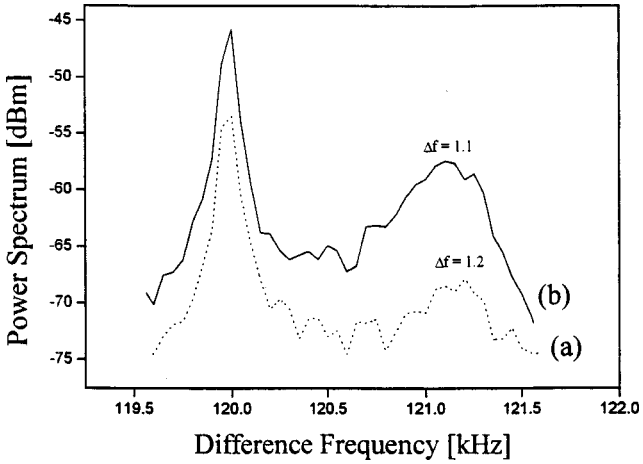

FIG. 5. Difference frequency spectra of signals received by a hydrophone from the interaction zone for different incident angles between high-frequency beams and flow direction in the tube. Reference flow velocity 65 cm/s. Angles: (a) $\theta_1=120°$, $\theta_2=40°$; (b) $\theta_1=95°$, $\theta_2=30°$.

$$v=c_0\frac{\omega_3^{(-)}-(\omega_1-\omega_2)}{[\omega_1\cos\theta_1-\omega_2\cos\theta_2]}\approx c_0\frac{\omega_3^{(-)}-(\omega_1-\omega_2)}{\omega_1(\cos\theta_1-\cos\theta_2)}. \tag{11}$$

The difference frequency spectra measured for the flow speeds of 65 cm/s and 17.5 cm/s are depicted in Fig. 4, respectively. In those cases the frequency differences between the waves radiated by two transducers were also 120 kHz. The nonlinear Doppler frequency shifts calculated from the independently measured flow rate are shown as the reference above the maxima of the frequency spectra. They are in good agreement with experimental observations.

The Doppler frequency spectra for two different incident angle setups are depicted in Fig. 5. The ratio between Doppler frequency shifts for these two cases can be found from Eq. (11):

$$\frac{\Delta f^{(1)}}{\Delta f^{(2)}}=\frac{\omega_1\cos\theta_1^{(1)}-\omega_2\cos\theta_2^{(1)}}{\omega_1\cos\theta_1^{(2)}-\omega_2\cos\theta_2^{(2)}}. \tag{12}$$

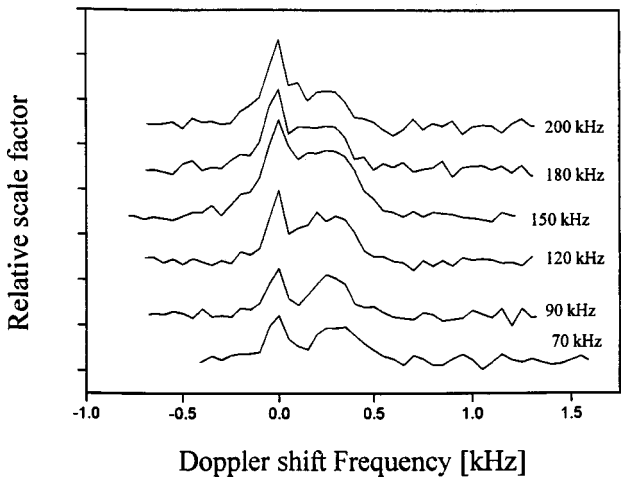

FIG. 6. Difference frequency spectra of signals received by a hydrophone from the interaction zone for six difference frequencies. Reference flow velocity 17.5 cm/s. The incident angles are $\theta_1=95°$ and $\theta_2=30°$, respectively. The zero value of the frequency axis corresponds to the difference frequency values.

For the case of $\theta_1^{(1)}=95°$, $\theta_2^{(1)}=30°$, $\theta_1^{(2)}=120°$, and $\theta_2^{(2)}=45°$ the frequency shift ratio is $\Delta f^{(1)}/\Delta f^{(2)}\approx 0.8$, which is close to the experimental value $1.1/1.2\approx 0.9$. This tends to confirm that the observed frequency shift is caused by the nonlinear Doppler effect.

The nonlinear Doppler frequency shift is almost independent of the difference frequencies as described in Eqs. (6) and (7). Such an effect is demonstrated in Fig. 6, where the Doppler shift spectra are presented for six difference frequencies, i.e., 70, 90, 120, 150, 170, and 200 kHz measured for the flow speed 17.5 cm/s and the angles $\theta_1=95°$ and $\theta_2=30°$. As shown in Fig. 6, the amplitude of bubble response depends on the difference frequency. This is due to bubble size distribution because only resonant bubbles respond at the difference frequency. Doppler frequency shifts in the measurements did not exceed 1% of bubble resonance frequencies, which is much less than the relative resonance curve width.[2] Therefore, the Doppler frequency shift did not influence the amplitude of bubble responses. It also demonstrates the possibility of independent measurements of bubble size distribution[12] and bubble flow velocities.

Comparison of the Doppler measured speed with the reference speed shows good agreement. However, one can see some systematic excess of the measured Doppler speed over the reference value. This excess seems to be reasonable. The reference speed was estimated by water flux measurements through the vessel, which gave an average flow velocity over the tube cross section. Thus the flow speed distribution across the vessel is related to the Doppler shift spectrum, and can be measured with this technique.

In this paper the general configuration of the nonlinear scattering of two acoustic waves of different frequencies by a moving target was studied. With nearly collinear primary beam geometry the nonlinear Doppler frequency shifts were shown to be the same as the linear ones. The difference frequency Doppler shift was found to be very large compared to that from the linear scattering if the angle between two primary beams is not small. Such an enormous Doppler shift at the difference frequency was experimentally observed with bubble flows. The difference frequency Doppler technique of bubble flow velocity measurements can find applications for pipelines or for blood vessels. Since it is based on resonance nonlinear scattering of ultrasound waves, this effect is very sensitive to bubble size. By sweeping the frequency of one of the primary waves, one can measure both the bubble size distribution and the bubble flow velocities.

ACKNOWLEDGMENTS

The authors appreciate the anonymous referees' suggestions improving the paper. This work was supported by the Korea-Russia collaboration program through the STEPI. One of the authors (S.W.Y.) was also supported in part by the Korea Science and Engineering Foundation and by the Sung Kyun 63 Research Foundation. Two authors (I.N.D.) and (A.M.S.) were supported in part by the Russian Foundation for Basic Research (98-02-17225, 97-05-64711, 96-15-96603).

[1] *Encyclopedia of Physics*, edited by R. G. Lerner and G. L. Trigg (VCH Publishers, New York, 1991).
[2] C. S. Clay and H. Medwin, *Acoustical Oceanography: Principles and Applications* (Wiley, New York, 1977).
[3] P. Atkinson and J. P. Woodcock, *Doppler Ultrasound and Its Use in Clinical Measurements* (Academic, New York, 1982).
[4] R. T. Beyer, *Nonlinear Acoustics* (Naval Sea System Command, Washington, D.C., 1974).
[5] E. A. Zabolotskaya and S. I. Soluyan, ''Emission of harmonics and combination frequency waves by air bubbles,'' Sov. Phys. Acoust. **18**, 396–398 (1972).
[6] L. A. Ostrovsky and A. M. Sutin, ''Nonlinear acoustic diagnostics of descrete inhomogeneities in liquid and solids,'' in Proc. 11th International Congress on Acoustics, Paris, 1983, Vol. 2, pp. 137–140.
[7] D. L. Miller, ''Ultrasonic detection of resonance cavitation bubbles in a flow tube by their second-harmonic emissions,'' Ultrasonics **19**, 217–224 (1981).
[8] L. A. Ostrovsky and A. M. Sutin, ''Nonlinear sound scattering from subsurface bubble layer,'' in *Natural Physical Sources of Underwater Sound*, edited by B. R. Kerman (Kluwer Academic, Dordrecht, 1993), pp. 363–370.
[9] B. M. Sandler, D. A. Selivanovsky, and A. Y. Sokolov, ''The measurements of gas bubble concentration in a subsurface sea layer,'' Dokl. Akad. Nauk SSSR **260**, 1474–1476 (1981).
[10] V. L. Newhouse and P. M. Shankar, ''Bubble size measurement using the nonlinear mixing of two frequencies,'' J. Acoust. Soc. Am. **75**, 1473–1477 (1984).
[11] T. G. Leighton, A. D. Phelps, D. G. Ramble, and D. A. Sharpe, ''Comparison of the abilities of eight acoustic techniques to detect and size a single bubble,'' Ultrasonics **34**, 661–667 (1996).
[12] A. M. Sutin, S. W. Yoon, E. J. Kim, and I. N. Didenkulov, ''Nonlinear acoustic method for bubble density measurements in water,'' J. Acoust. Soc. Am. **103**, 2377–2384 (1998).
[13] B. B. Goldberg, J. B. Liu, and F. Forsberg, ''Ultrasound contrast agents: A review,'' Ultrasound Med. Biol. **20**, 319–333 (1994).
[14] N. deJong, R. Cornet, and C. T. Lance, ''Higher harmonics of vibrating gas-filled microspheres. Part two: Measurements,'' Ultrasonics **32**, 455–459 (1994).
[15] B. A. Schrope and V. L. Newhouse, ''Second harmonic ultrasonic blood perfusion measurement,'' Ultrasound Med. Biol. **19**, 567–579 (1993).
[16] J. Y. Chapelon, D. Cathignol, V. L. Newhouse, and P. M. Shankar, ''A double frequency Doppler technique for bubble size measurement,'' in Proc. IEEE Ultrasonics Symposium, 1987, pp. 885–888.
[17] J. Y. Chapelon, V. L. Newhouse, D. Cathignol, and P. M. Shankar, ''Bubble detection and sizing with a double frequency Doppler system,'' Ultrasonics **26**, 148–154 (1988).
[18] P. N. Burns, J. E. Powers, and D. H. Simpson, ''Harmonic power mode Doppler using microbubble contrast agents: An improved method for small vessel flow imaging,'' in Proc. IEEE Ultrasonics Symposium, 1994, pp. 1547–1550.
[19] P. H. Chang, K. K. Shung, S. J. Wu, and H. B. Levene, ''Second harmonic imaging and harmonic Doppler measurements with Albunex,'' IEEE Trans. Ultrason. Ferroelectr. Freq. Control **42**, 1020–1027 (1995).
[20] P. H. Chang, K. K. Shung, and H. B. Levene, ''Quantitative measurements of second harmonic Doppler using ultrasound contrast agents,'' Ultrasound Med. Biol. **22**, 1205–1214 (1996).
[21] E. J. Kim, S. W. Yoon, I. N. Didenkulov, and A. M. Sutin, ''Feasibility of nonlinear Doppler velocity measurements,'' in Proc. 10th Underwater Acoustics Symposium, Acoust. Soc. Kor., Korea, 1995, pp. 33–38.
[22] I. N. Didenkulov, E. J. Kim, S. W. Yoon, and A. M. Sutin, ''Doppler effect in nonlinear acoustics of bubble flows,'' Preprint No. 381 of the Institute of Applied Physics of Russian Academy of Sciences, Nizhny Novgorod, 1995.
[23] I. N. Didenkulov, E. J. Kim, S. W. Yoon, and A. M. Sutin, ''Nonlinear acoustic Doppler effect in a bubble flow,'' J. Acoust. Soc. Am. **99**, 2514(A) (1996).

Experimental investigations of perforated liners with bias flow

Xiaodong Jing and Xiaofeng Sun
Department of Jet Propulsion, Beijing University of Aeronautics and Astronautics, Beijing 100083, People's Republic of China

(Received 29 July 1998; revised 15 June 1999; accepted 29 June 1999)

It has been found that the presence of a bias flow can enhance the low-frequency sound absorption of a perforated liner. Therefore it is important to understand the acoustic characteristics of a liner with bias flow for practical applications. This paper presents experimental investigations of the acoustic properties of a perforated liner with bias flow. First, the experimental results show that the presence of a bias flow markedly increases both the absorption coefficient and effective bandwidth of a perforated liner. Second, it is shown in the present experiment that plate thickness has a major influence on the acoustic properties of a liner with bias flow. A simple model is presented to consider this behavior; the model gives good agreement with the measured data. Considering that blowing and suction will have a different effect on the mean shear flow over the surface of a perforated liner, comparative experimental results between blowing and suction are also included in the present investigation. [S0001-4966(99)04410-0]

PACS numbers: 43.28.Py, 43.50.Gf [LCS]

LIST OF SYMBOLS

a	aperture radius
c	sound speed
C	complex Rayleigh conductivity
d	spacing between apertures
i	$=\sqrt{-1}$
$I_1(x)$	modified Bessel function of the first kind
k	$=2\pi/\lambda$, sound wave number
$K_1(x)$	modified Bessel function of the second kind
l	cavity depth
M	average bias flow Mach number through aperture
n	number of apertures per unit area
Q	resonance parameter
r	normalized specific acoustic resistance by ρc
R	reflection coefficient
S	effective area of liner
S_c	transverse area of cavity or cell
S_r	Strouhal number
t	plate thickness
U	average bias flow speed through aperture
V	cavity volume
x	normalized specific acoustic reactance by ρc
z	normalized specific acoustic impedance by ρc, $z=r+ix$.
α	absorption coefficient
δ	$=-\mathrm{Im}(C/2a)$
γ	$=\mathrm{Re}(C/2a)$
η	$=(\gamma-i\delta)^{-1}$
λ	wavelength
μ	S_c/S, cell wall thickness parameter
ν	kinematic viscosity
ρ	air density
σ	open area ratio
τ	plate thickness normalized by a
ω	angular frequency

INTRODUCTION

It is of interest that an aperture's low-frequency acoustic resistance will increase greatly when there is bias flow through it. This physical process has been evaluated previously by Ingard and Ising.[1] However, the mechanism of the energy conversion had not been understood clearly until Howe[2] and Bechert[3] explained it in detail in 1970s. They showed that the increase of the aperture's acoustic resistance is due to the energy conversion between sound and vortices. Based on this mechanism of the energy conversion, Howe[2] presented an analytical model for the Rayleigh conductivity of an aperture with a bias flow in an infinitely thin plate. The model was afterward validated in the experiment presented by Hughes and Dowling.[4] One of the encouraging results of Hughes and Dowling's work shows that all the sound incident on a perforated liner with bias flow can be absorbed if the flow speed and the geometry of the liner are chosen properly. Hughes and Dowling's work makes evident the potential benefit of perforated liners with bias flow. However, there are still some questions that need to be answered if we wish to realize practical applications of this potential. First, we believe that it is necessary to provide concrete experimental evidence to show to what extent the efficiency of a perforated liner can be increased by introducing a bias flow. Second, although the acoustic properties of a perforated liner with bias flow have fully been studied by Hughes and Dowling[4] on the hypothesis of infinitely thin perforated plate, there is need for incorporating the effect of finite plate thickness into a theoretical model since plate thickness is one characteristics of a real liner structure. Finally, if we suppose there is a mean shear flow over the surface of a liner, two ways of introducing the flow—blowing and suction will have a different influence on the mean flow boundary layer. Whether or not blowing and suction affect the liner's prop-

erties in different ways is also of interest. In order to answer these questions we carried out experimental investigations on a perforated liner with bias flow. First, the results of the comparison between a perforated liner without bias flow and the same liner with bias flow show, as expected, that the presence of a bias flow can increase greatly the efficiency of the liner. In general, a perforated liner with larger diameter apertures and a thinner plate tends to have a smaller absorption coefficient or effective bandwidth. It also creates manufacturing problems that considerably decrease the aperture diameter. In practice, in order to improve the efficiency of a perforated liner, porous materials are often used in the cavity of a perforated liner. So the means of introducing a bias flow through a liner provides an alternative of great potential to achieve the same goal. Second, a simple model is presented to describe the effect of plate thickness, which has a marked influence on the acoustic impedance of the liner as shown by experimental data. Furthermore, based on our experiment data, blowing and suction have the same influence on the acoustic behavior of a perforated liner when there is no shear flow over its surface.

I. BASIC MODELS

A. Acoustic properties of an aperture with bias flow

As illustrated in Fig. 1, a circular aperture of radius a is in an infinitely thin rigid plate, and there is a mean flow of high Reynolds number—low Mach number through the aperture. When a sinusoidal pressure variation appears on one side of the plate, the effect of viscosity leads to the production of unsteady vortices shedding from the rim of the aperture and the unsteady vortices are assumed to convect downstream at the average flow speed U through the aperture. In this process, the acoustic energy is converted into the energy of the vortex formation. This mechanism of the energy conversion accounts for the increase of the acoustic resistance of the aperture as the bias flow velocity increases. Howe[2] developed a model to solve the complex Rayleigh conductivity C of the aperture, which is expressed as below, according to Ref. 2,

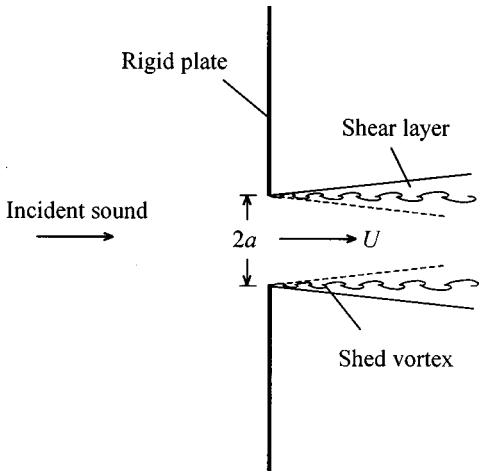

FIG. 1. An aperture with a bias flow in an infinitely thin plate. The shed vortices are assumed to convect at the average flow speed U through the aperture.

$$C=2a(\gamma-\delta i), \tag{1}$$

where γ, δ are functions of Strouhal number $S_r=\omega a/U$,

$$\gamma=\frac{I_1^2(S_r)(1+1/S_r)+(4/\pi^2)\exp(2S_r)\cosh(S_r)K_1^2(S_r)[\sinh(S_r)-\sinh(S_r)]/S_r}{I_1^2(S_r)+(4/\pi^2)\exp(2S_r)\cosh^2(S_4)K_1^2(S_r)},$$

$$\delta=\frac{(2/\pi S_r)I_1(S_r)K_1(S_r)\exp(2S_r)}{I_1^2(S_r)+(4/\pi^2)\exp(2S_r)\cosh^2(S_r)K_1(S_r)}.$$

The normalized specific acoustic impedance z_e of the aperture can be derived from the Rayleigh conductivity,

$$z_e=\frac{\pi ka\,\delta}{2(\gamma^2+\delta^2)}-i\frac{\pi ka\,\gamma}{2(\gamma^2+\delta^2)}. \tag{2}$$

On the condition that the rigid plate is of finite thickness, the total acoustic impedance of the aperture must include the effect of finite plate thickness. When there is no mean flow, the normalized specific acoustic impedance z_i for a single tube with radius $a(\mathrm{m})>0.01/\sqrt{f}$ is given by Beranek,[5]

$$z_i=\frac{\sqrt{2\nu\omega t}}{ca}-i\frac{\omega t}{c}, \tag{3}$$

where t is the length of the tube. When there is a bias flow, in order to take the effect of finite plate thickness into account, a hypothesis is made that the total acoustic impedance is the sum of the thickness term z_i and the end correction z_e. For most practical applications, the plate thickness t is small or not large compared to the aperture radius a. On such a condition, the viscous resistance term of z_i is insignificant compared to the resistance term of z_e resulting from the bias flow at low frequency. Then the total normalized specific acoustic impedance z_a of an aperture is approximately given by

$$z_a=\frac{\pi ka\,\delta}{2(\gamma^2+\delta^2)}-i\left[\frac{\pi ka\,\gamma}{2(\gamma^2+\delta^2)}+kt\right]. \tag{4}$$

B. Reflection coefficient of a perforated liner with bias flow

The geometrical arrangement of a perforated liner with bias flow is illustrated in Fig. 2. The apertures in the perforated plate are well separated. For a low-frequency incident

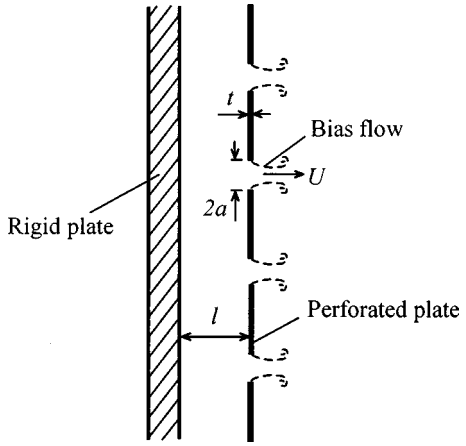

FIG. 2. The geometry of a perforated liner with bias flow. The apertures are in a square array or 60° stagger pattern, and the spacing between the apertures is d.

sound wave the wavelength greatly exceeds the cavity depth and the spacing between the apertures. So the following condition is satisfied:

$$a,\ t \ll d,\ l \ll \lambda. \tag{5}$$

Consider a small portion of the perforated liner which is tested on the present experimental setup, as illustrated in Fig. 3. The experimental setup will be introduced in detail in the next section. Under the condition of Eq. (5) we employ an electro-acoustic analogy method to calculate the liner's reflection coefficient. The liner can be regarded as nS parallel apertures of impedance z_a in series with the cavity volume V. Then, the normalized specific acoustic impedance z of the liner is

$$z = z_a/\sigma + i/\mu kl, \tag{6}$$

where $\sigma = n\pi a^2$ and $\mu = S_c/S$. For a normal-incident sound, the reflection coefficient R is related to the normalized specific acoustic impedance z through

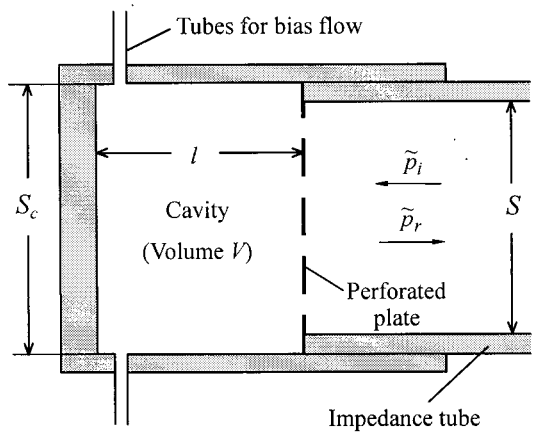

FIG. 3. The structure of the test liner at one end of the impedance tube. S_c is the cross area of the cavity, and S is the effective area of the liner. The total number of the apertures in the perforated plate is nS. $\tilde{p}_i$, $\tilde{p}_r$ indicate separately the incident sound and reflected sound.

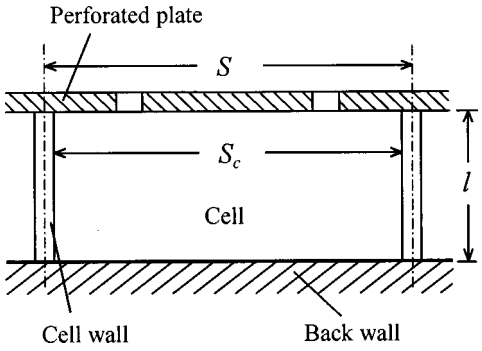

FIG. 4. The cellular structure of a perforated liner in practical use. The cross area S_c of the cell is less than the effective area S of the liner for one cell due to the effect of the cell wall thickness.

$$R = \frac{z-1}{z+1}. \tag{7}$$

On substituting Eq. (6) into Eq. (7), and rearranging the resulting expression, the reflection coefficient R is obtained,

$$R = \frac{Q\eta + (2/\pi)Q\tau - i\mu kl - 1}{Q\eta + (2/\pi)Q\tau + i\mu kl - 1}, \tag{8}$$

where $\eta = (\gamma - i\delta)^{-1}$, and Q is given by

$$Q = \frac{\pi}{2}(\mu kl)^2(a/\mu l\sigma). \tag{9}$$

Q is the ''resonance parameter'' defined by Hughes and Dowling.[4] The introduction of Q shows that the reflection coefficient R depends on a certain combination of the geometrical parameters, $\mu l\sigma/a$. Equation (8) shows that the reflection coefficient of the liner can be expressed as a function of four nondimensional parameters: the resonance parameter Q, the Helmholtz number μkl, the Strouhal number S_r, and the normalized thickness τ. It should be mentioned that, although parameter μ is introduced in consideration of the structure of the present experimental setup, it is useful in considering the cell wall thickness characteristic of a perforated liner in practice. As shown in Fig. 4, if the cell wall is of finite thickness, the cavity depth l has to be modified as μl where the parameter $\mu = S_c/S$ is referred to as the cell wall thickness parameter in this paper. When a perforated liner is infinitely extended and the cell wall thickness is ignored, μ is equal to unity.

II. EXPERIMENTAL SETUP

In the present experiment, we use a two-microphone method developed by Johnson and Schmidt[6] to test the properties of a perforated liner with bias flow. The experimental setup is illustrated in Fig. 5. The impedance tube is a rectangular pipe of 100 mm×100 mm cross-section. The first cutoff frequency of the tube is 1.7 kHz. Two microphones are mounted flush with the inner surface of the impedance tube. At one end of the impedance tube is the sound source, which consists of four loudspeakers; at the other end are the test liner and cavity. The cross section of the cavity is a 120 mm×120 mm square. It is connected to the end of the impedance tube and can be moved along the axis of the tube

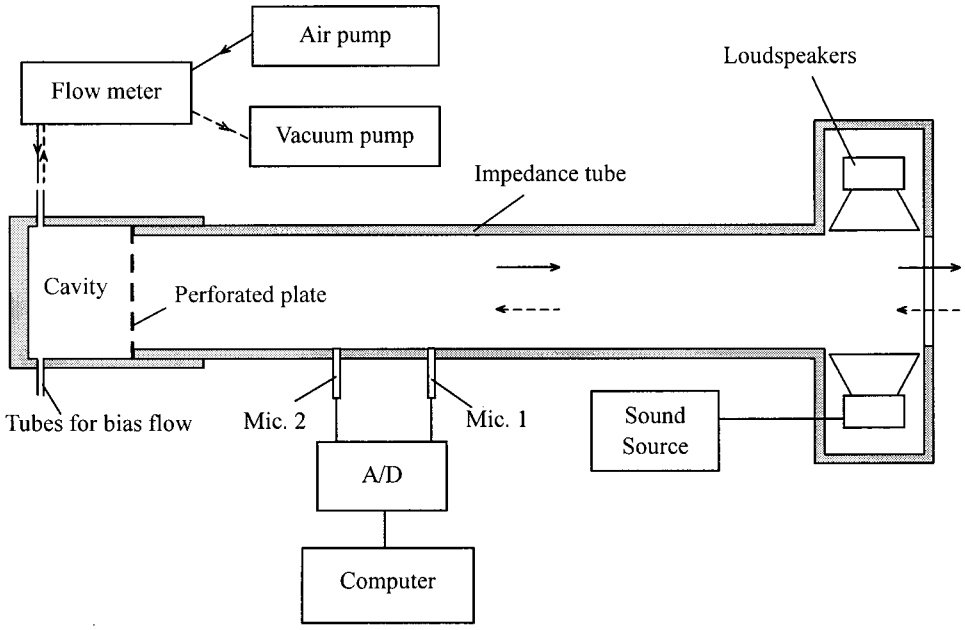

FIG. 5. Schematic of the present experimental setup. The solid lines and arrows indicate the path of the blowing air flow, and the dashed lines and arrows indicate the path of the suction air flow.

continuously. The reflection coefficient of the cavity bottom is unity. There are four inlet tubes of 4 mm inner diameter into the cavity through which steady, but adjustable airflow is introduced. As illustrated in Fig. 5, this airflow is introduced in two different ways—blowing and suction. In the blowing process, the airflow produced by an air pump goes through the perforated plate and the impedance tube, then flows into the air at the end of the loudspeakers. In the suction process, the airflow is sucked into the impedance tube, and goes through the perforated plate, then is expelled into the air by a vacuum pump. The airflow is metered by a flow meter. In the present experiment we select three different perforated plates to test the properties of the perforated liners with bias flow. For all the perforated plates the apertures are arranged in square arrays. The geometrical parameters of the test perforated plates are shown in Table I. The sound pressure level in the impedance tube is kept within the range 90–125 dB. Over this range it has been checked that the measured acoustic properties are independent of the SPL.

III. THE ANALYSIS OF THE EXPERIMENTAL RESULTS

A sound wave is normally incident on a perforated liner with bias flow in the impedance tube. The normalized specific acoustic impedance z of the liner is calculated from Eq. (7) and Eq. (8). The normalized specific acoustic impedance z has a real part, the normalized specific acoustic resistance r, and an imaginary part, the normalized acoustic reactance x. The absorption coefficient α can be expressed in terms of the reflection coefficient R,

TABLE I. The geometrical parameters of the test perforated plates.

	a (mm)	d (mm)	t (mm)	σ (%)
No. 1	1.5	17	0.2	2.54
No. 2	1.0	13	0.2	2.01
No. 3	1.5	17	2.0	2.54

$$\alpha = 1 - |R|^2. \tag{10}$$

In practice, we are concerned with how the acoustic properties of a liner vary with the bias flow speed, so the impedance z is calculated as a function of the bias flow Mach number instead of the Strouhal number. The Mach number M is related to the Strouhal number S_r as follows:

$$S_r = [(2/\pi)(\mu I \sigma/a)Q]^{1/2}(\mu l/a)^{-1}M^{-1}. \tag{11}$$

In this section, the experimental and theoretical results are presented using the resonance parameter Q, the Mach number M, and the combinations of the geometrical parameters: $\mu l\sigma/a$, $\mu l/a$, and τ.

A. Acoustic properties of a perforated liner with bias flow

In Fig. 6, the acoustic properties are plotted as functions of the Mach number M. It is shown that resistance r proportionally increases as the Mach number M is increased while reactance x remains almost unchanged. In Fig. 7, the acoustic properties are plotted as a function of the resonance parameter Q while keeping the Mach number equal to 0.0141. As shown in the figure, the maximum absorption coefficient nearly reaches unity. This result reconfirms the conclusion made by Hughes and Dowling[4] that all the incident sound can be absorbed for certain combinations of the geometrical parameters and the bias flow speed. As we know, a perforated liner with larger diameter apertures and smaller plate thickness tends to have a smaller absorption coefficient or effective bandwidth in the absence of a bias flow. In Fig. 8, the acoustic properties of a perforated liner without bias flow are compared with that of the same liner with bias flow. The comparative results show that the absorption coefficient of the perforated liner with bias flow is much higher than that of the same liner without bias flow over the range from $Q = 0.24$ to 5.16 (correspondingly from $f = 300$ Hz to 1400 Hz), and the absorption bandwidth of the former is also much greater than the latter. In Fig. 8(a), the maximum ab-

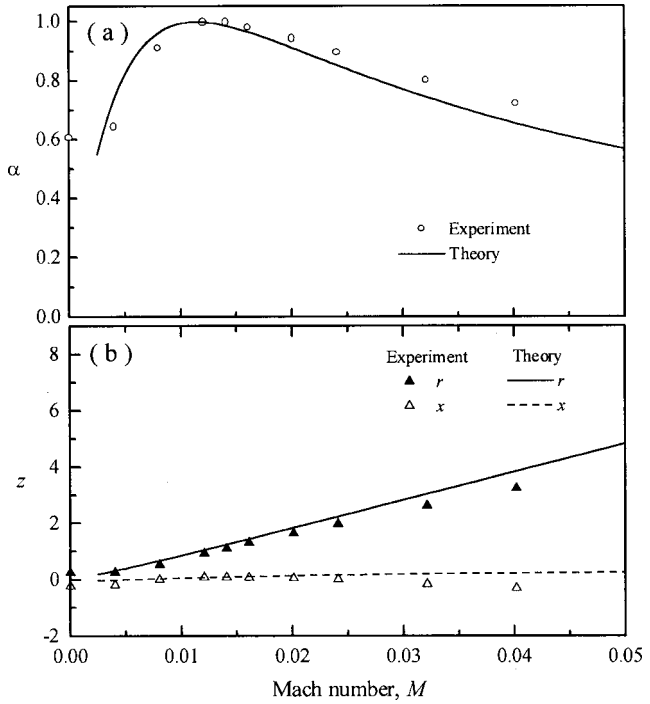

FIG. 6. The acoustic properties as a function of the Mach number M for perforated plate No. 2 with a cavity of $l=60$ mm. $\mu l\sigma/a=1.74$, $\mu l/a=84.0$, $\tau=0.2$; $Q=1.0$. In Figs. 6–10, α is the absorption coefficient and $z=r+ix$ is the normalized specific acoustic impedance.

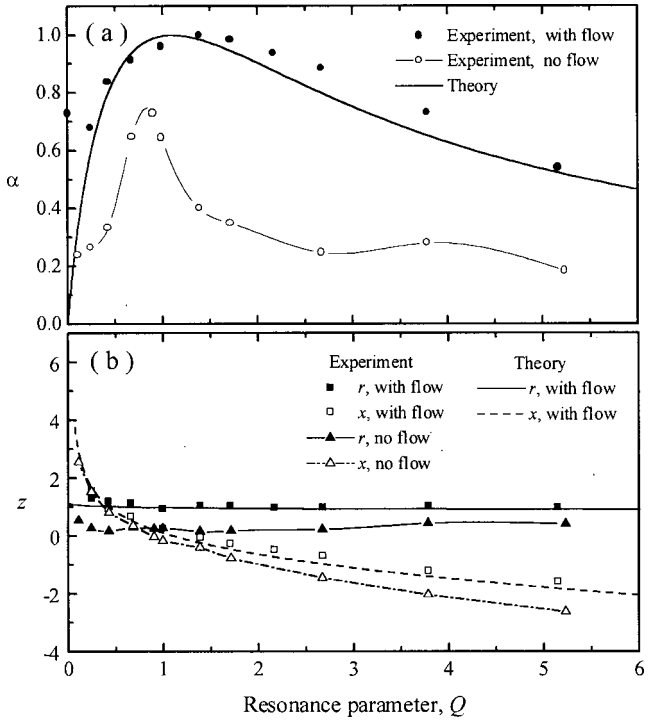

FIG. 8. The comparison between the perforated liner with and without bias flow. The acoustic properties are plotted as a function of the resonance parameter Q for perforated plate No. 1 with a cavity of $l=60$ mm. $\mu l\sigma/a=1.46$, $\mu l/a=56.0$; $M=0.0143$.

sorption coefficient increases from 0.71 to 1.0. The improvement of the acoustic performance of the liner results from the increase of its resistance; as shown in Fig. 8(b), the normalized specific acoustic resistance approaches a value of 1.0 in the presence of a bias flow. From the above analysis, we can see that the means of introducing a bias flow is of great potential to increase the efficiency of a perforated liner.

Figure 9 shows the comparative results between the acoustic properties of perforated plate No. 1 and No. 3 with

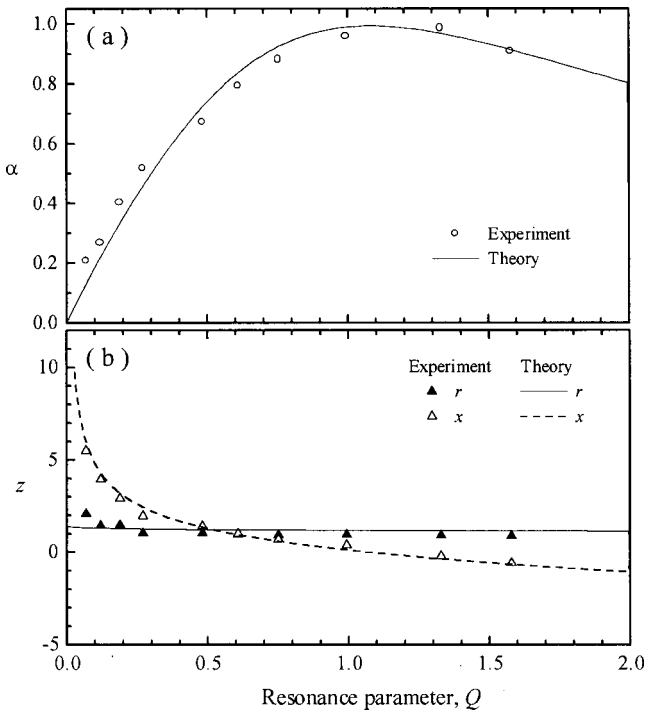

FIG. 7. The acoustic properties as a function of the resonance parameter Q for perforated plate No. 2 with a cavity of $l=20$ mm. $\mu l\sigma/a=0.579$, $\mu l/a=28.0$, $\tau=0.2$; $M=0.0141$.

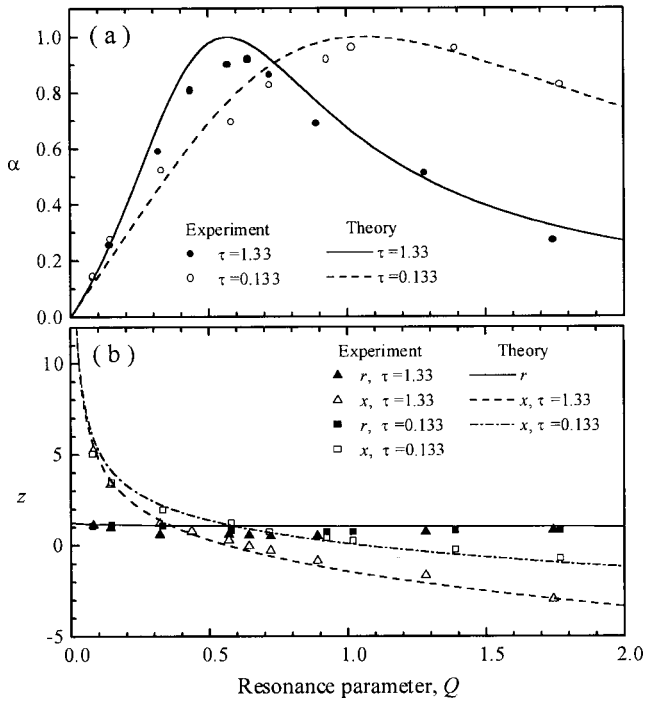

FIG. 9. The comparison between the perforated liners of two different plate thickness, $\tau=0.133$ and $\tau=1.33$. The acoustic properties are plotted as a function of the resonance parameter Q for perforated plate No. 1 or No. 3 with a cavity of $l=20$ mm. $\mu l\sigma/a=0.488$, $\mu l/a=18.7$; $M=0.0160$.

a cavity of $l=20$ mm. All the geometrical parameters of the two perforated plates are the same except the plate thickness. The normalized plate thickness of perforated plate No. 1 and No. 3 are separately 0.133 and 1.33. The bias flow Mach number is also the same for the two liners, that is $M=0.0160$. Figure 9(a) shows that plate thickness has a marked influence on the resonance frequency. The change of the resonant frequency results from the effect of plate thickness on the acoustic reactance, as shown by Fig. 9(b). Figure 9 also shows that Eq. (8) gives good prediction to the effect of the plate thickness on the acoustic properties of a perforated liner with bias flow.

In this section, experimental data are presented to compare with the theoretical predictions that include the effect of finite plate thickness on the acoustic properties of a liner with bias flow. Generally speaking, as shown in Figs. 6–9, the experimental results are in good agreement with the theoretical results.

B. Comparison between blowing and suction

The comparative results between blowing and suction for perforated plate No. 1 with a cavity of $l=60$ mm are given in Fig. 10. We can see that the data for the blowing experiment agree very well with that for the suction experiment. Therefore blowing and suction affect the acoustic properties of the liner in the same way when there is no mean shear flow over its surface; that is, the case in the present experiment. However, further investigation is needed to generalize the present conclusion to the situation where there is a shear flow over the liner surface.

IV. CONCLUSIONS

(1) The presence of a bias flow can markedly increase both the absorption coefficient and effective absorption bandwidth of a perforated liner. Its absorption coefficient can reach 1.0 provided the bias flow speed and the geometrical parameters are chosen properly. The increase of the absorption coefficient and effective bandwidth results from the increase of the acoustic resistance in the presence of a bias flow. When the bias flow speed increases, the acoustic resistance of the liner linearly goes up, while the change of the reactance is slight.

(2) The experimental results show that, as expected, plate thickness has a major influence on the acoustic properties of a perforated liner with bias flow. In practice, a finite plate thickness will change the acoustic reactance, thus the resonant frequency of the liner. A simple model is presented to predict this behavior, and it gives good agreement with the measured data.

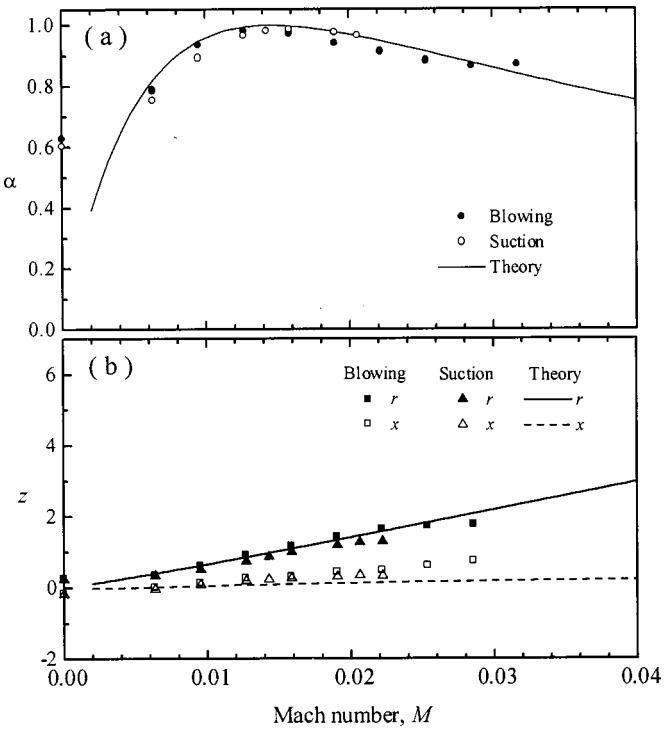

FIG. 10. The comparison between blowing and suction. The acoustic properties are plotted as a function of the Mach number M for perforated plate No. 1 with a cavity of $l=60$ mm. $\mu l\sigma/a=1.46$, $\mu l/a=56.0$; $Q=1.0$.

(3) For the condition where there is no mean shear flow over the surface of a liner, two ways of introducing air flow—blowing and suction will affect the properties of the liner in the same way.

ACKNOWLEDGMENT

This work was supported by the National Natural Science Foundation of China.

[1] U. Ingard and H. Ising, ''Acoustic nonlinearity of an orifice,'' J. Acoust. Soc. Am. **42**, 6–17 (1967).

[2] M. S. Howe, ''On the theory of unsteady high Reynolds number flow through a circular aperture,'' Proc. R. Soc. London, Ser. A **366**, 205–233 (1979).

[3] D. W. Bechert, ''Sound absorption caused by vorticity shedding demonstrated with a jet flow,'' J. Sound Vib. **70**, 389–405 (1980).

[4] I. J. Hughes and A. P. Dowling, ''The absorption of sound by perforated linings,'' J. Fluid Mech. **218**, 299–332 (1990).

[5] L. L. Beranek, *Acoustics* (McGraw-Hill, New York, 1954).

[6] J. P. Johnson and W. E. Schmidt, ''Measurement of acoustic reflection from an obstructions in a pipe with flow,'' J. Acoust. Soc. Am. **63**, 1455–1460 (1978).

Robustness of a ray travel-time inversion approach

I-Tai Lu[a)]
Polytechnic University, Route 110, Farmingdale, New York 11735

(Received 4 February 1998; revised 25 May 1999; accepted 12 July 1999)

The robustness of a ray travel-time approach is studied using simulated data in both shallow waters and Arctic oceans. Effects of travel-time measurement error, sound speed profile mismatch, and source/array parameters mismatch on the solution accuracy are quantified. The approach is then employed to analyze the data generated by the first two SUS shots in the ICESHELF-89 experiment. Source location, array depth, array tilting angle, sound speed profile, and bathymetry are characterized. © *1999 Acoustical Society of America.* [S0001-4966(99)01011-5]

PACS numbers: 43.30.Bp [SAC-B]

INTRODUCTION

Parameter inversion in oceans is a very difficult task due to three major challenges: the temporal and spatial varying features, the unavoidable model mismatch, and the enormous number of unknowns.[1–4] To remedy these difficulties, a ray travel-time inversion approach has been developed[5] to simultaneously localize the source, calibrate the array position, and characterize environmental parameters such as sound speed profiles (in both water column and sediment), bathymetry, etc. The inversion procedure of this powerful approach is briefly summarized below.

The first step is to choose nominal values of the important environment and system parameters. These values can be provided by other measurements, by previous inversion results, or by an educated guess. The second step is to sort out some ray arrivals and to determine their arrival times T_{ij} (which denotes the measured travel time of the ith ray arriving at the jth receiver). The ray travel times obtained in this step will serve as the reference for estimating the unknowns. For broadband data, early ray arrivals are separated in time already and, therefore, the travel times and arrival angles can be easily obtained by calculating the correlations between ray arrivals. In a narrow-band case, spectrum estimation approaches can be employed to find the direction and travel times of arrivals. The third step is to give an initial estimate of the source location. A good candidate to provide the initial source location is the back-propagating ray approach[6] which exploits both the temporal and spatial characteristics of ray arrivals to remove localization ambiguity. The fourth step is to compute travel times of the corresponding rays (denoted by τ_{ij}) by using a ray tracing approach. The fifth step is to compare the simulated travel times from step 4 with the observed travel times obtained from step 2 and, then, determine a new model using a parameter optimization scheme. The iteration between steps 4 and 5 stops when the cost function $\Delta = \Sigma_{ij} |T_{ij} - \tau_{ij}|$ (misfit between simulated and measured travel times) converges. When the number of unknowns is not small, the computation required by a brute force search for the global minimum becomes prohibitive, and some kinds of directed search are needed. If the initial starting point is fairly close to the optimum solution, the classical gradient search method would be a likely technique. It might be coupled with some repetitive randomization of the initialization in order to find all local minima in the vicinity of the global minimum. The global minimum could then be found by searching over the small set of resulting local minima. If the initial starting point is far away from the optimum, a genetic approach[7] is very promising because of its randomized update process which serves to effectively avoid many traps associated with local minima.

There are two key elements in the proposed inversion approach: travel times and ray propagators. The reasons for focusing only on travel times are; (1) noise tolerance may be enhanced and the sensitivity to the environment model mismatch may be reduced by neglecting amplitude information; (2) phase ambiguity is eliminated by employing the group delay of arriving wave packets; and (3) travel times are pseudo-linear functions of sound speed profiles of the medium. The reasons for using the ray model to interpret experimental data are listed as follows:

(1) Ray tracing is very simple and efficient.
(2) Rays are nondispersive in lossless media and their travel times can be obtained at a single frequency even for broadband signals.
(3) Full-wave matched field processing is not required.
(4) Ray approach is very flexible. It works in range-dependent environments. It can also adapt to various signal scenario (narrow-or broadband, deterministic or random, etc.).
(5) Rays characterize only local properties of the environment. The required knowledge about the global environment is therefore minimized.
(6) Ray travel times are linked directly to local unknowns. Thus, most unknowns can be searched for sequentially.
(7) Bad rays can be excluded from the inversion process. Thus noise tolerance can be improved by a proper selection of rays.

Using both simulation and experiment data, preliminary numerical studies[5] have shown that the algorithm is indeed extremely efficient. It is suitable for real time operation to adapt in the face of changing environments and changing system requirements. The algorithm seems to be insensitive to the model mismatch and to yield rather accurate results

a)Electronic mail: itailu@rama.poly.edu

when the number of unknowns is small. However, several important questions remain unanswered. When the number of unknowns is not small, different sound speed profile (SSP) or system models and different initial values of the unknown parameters may lead to different final results. If so, how can one know which result to be trusted? The cost functions (travel-time misfit Δ's) derived in these different situations are also different. It is unclear what contributes to larger Δ's for some cases. Is it due to the travel time detection errors in experiment, or due to the inaccurate SSP models used in inversion? Does a small cost Δ always correspond to a better (more accurate) estimated result? Can the cost Δ be further reduced by the inversion process in which SSP and system parameters are simultaneously searched? What is the practical parametrization of SSP? In this paper, we will address these issues by studying the robustness of the ray travel time inversion approach in details.

In Sec. I, the effects of travel time measurement error or sound speed profile (SSP) mismatch on the accuracy of the inversion scheme are discussed using a shallow water example. In Sec. II, the approach is employed to characterize the SSP and the source/array arrangement simultaneously. The resolution of SSP as a function of travel time measurement error is studied. Both a piecewise linear model and an empirical orthogonal functions (EOF) model are employed to describe the SSP of the shallow water. In Sec. III, the effects of mismatch of source location or array arrangement on the accuracy of the inversion scheme are discussed using the same shallow water example. To further test the robustness of this approach, the approach is employed to analyze the Arctic ocean data. Simulated data are first analyzed in Sec. IV and the first and second SUS shots of ICESHELF-89 data are then studied in Sec. V. Conclusions are made in Sec. VI.

The ICESHELF-89 experiment took place in the Lincoln Sea North of Ellesmere Island. The first SUS shot data has been employed to estimate the location of the source and the position of array.[5,8] In Ref. 8, a modal approach was employed and range independency is assumed. However, using the estimated values derived from Ref. 8, the cost Δ was found to be as high as 7.87 ms.[5] Thus, the ray travel-time inversion approach was employed in Ref. 5 to reduce the cost Δ. Based on several (different) SSP models, the cost Δ was reduced to be around 1.3 ms in Ref. 5. However, we did not know which set of the estimated results should be used. In Sec. V, the first shot data will be analyzed again based on the new lessons learned from the robustness study in Secs. I–IV. Here, SSP and system parameters will be simultaneously adjusted to further reduce the cost Δ. We will also analyze the second shot data where the environment is no longer range independent.

I. SSP MISMATCH AND TRAVEL-TIME MEASUREMENT ERROR

In this section, effects of measurement errors of ray travel times and sound speed profiles on accuracy of the proposed ray inversion approach are studied. Consider an impulse source and a receiving array of 11 elements in shallow water. The arrangement of the source and the receiver array is shown in Fig. 1(a). In numerical simulation, the water depth z_b is chosen to be 155 m. The true SSPs in water column and in sediment are shown by the thick-dashed lines in Fig. 1(b) and (c), respectively. The array depth d is 5 m, the array tilt α is 0.6 degrees, and the separation L between adjacent array elements is 15 m. The source depth z_s is 51 m, and the distance x_s between source and the receiving array is 650 m. During the parameter inversion process, the SSP in water column is assumed known (although inaccurately). In addition, there also exist some randomly generated measurement errors of travel times. The inaccurate SSP and the measured travel times will be used to search for the source location (x_s, z_s), the array parameters (α, d), the bottom depth z_b, and the sediment SSP. The characterization of SSP in water column will be discussed in the next section.

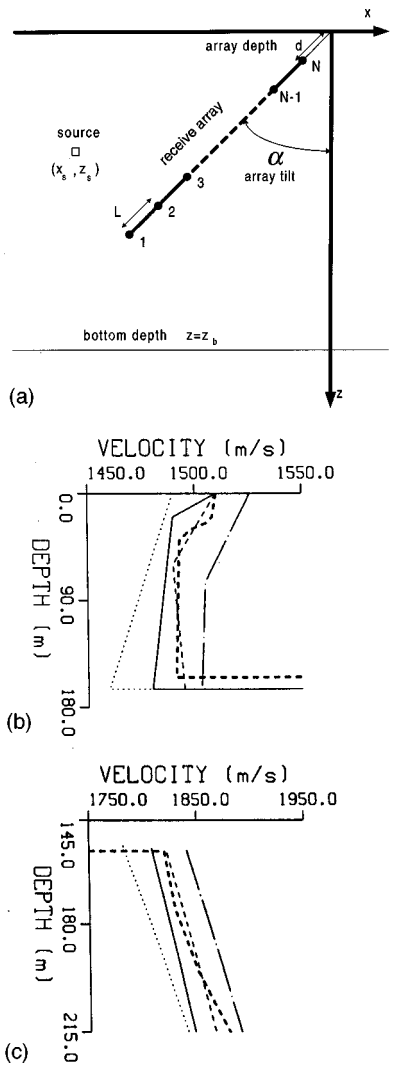

FIG. 1. (a) The arrangement of source and receiver array. The array has N hydrophones at L meters spacing. The array tilt is denoted by α, and the distance between the top hydrophone and the water surface along the array tilting direction is denoted by d. The source depth, source range, and water depth are denoted by z_s, x_s, and z_b, respectively. (b) Four shallow water SSP models used for parameter inversion. The results using these four models (represented by solid, chain-dotted, dashed, and dotted lines) are summarized in Table I. The thick dashed line denotes the true SSP. (c) The four estimated SSP's in the sediment corresponding respectively to the four SSP models in (b). The thick dashed line denotes the true SSP.

Let $i=1,...,7$ denote the bottom refracted ray, the head

TABLE I. Estimated results of a shallow water example using the four inaccurate SSP's shown in Fig. 1(b). These SSP's are fixed during the inversion process. A symbol * is put next to the worst estimate of each parameter, with which the maximum error is calculated.

	δ (ms)	x_s (m)	z_s (m)	α (degrees)	d (m)	z_b (m)	Δ (ms)
Initial		−550	41.0	1.75	8	165	>6.5
True		−650	51	0.6	5	155	0
Maximum error		45	1.5	0.76	3.0	5.3	
Solid	0	−649.6	50.50	0.6230	4.682	154.1	0.786
	0.5	−642.7	50.47	0.4797	4.170	153.4	0.826
	1	−631.5	50.37	0.2662	3.359	152.2	1.025
	2	−615.0	50.29	−0.0934	2.134	150.6	1.630
Chain-dotted	0	−640.4	52.11	0.8778	5.880	154.8	0.735
	0.5	−634.1	52.09	0.7512	5.409	154.1	0.790
	1	−623.2	52.00	0.5604	4.630	153.0	0.986
	2	−605*	51.77	0.3145	3.239	150.8	1.585
Dashed	0	−651.9	50.55	0.4448	4.439	155.5	0.716
	0.5	−644.3	50.51	0.3224	3.934	154.7	0.778
	1	−633.7	50.47	0.1392	3.208	153.5	0.986
	2	−615.5	50.38	−0.166*	1.982*	151.6	1.602
Dotted	0	−647.2	52.5*	0.9899	6.264	153.3	0.835
	0.5	−640.7	52.44	0.8806	5.778	152.6	0.865
	1	−630.2	52.36	0.7180	5.002	151.4	1.039
	2	−614.4	52.29	0.4452	3.822	149.7*	1.628

wave, the direct ray, the two once-reflected rays, and the two twice-reflected rays, respectively (see Fig. 2 in Ref. 5). These seven rays are the first seven ray arrivals. The ''measured'' travel times T_{ij} of the ith ray, $i=1,...,7$, at the jth receiver, $j=1,...,11$, are generated in the following way. At first, the true travel times t_{ij} of the ith rays arriving at the jth receiver are computed by a ray tracing code[5] using the true SSP, source location, and array parameters. Second, positive random numbers δ_{ij}, for every ij, with a fixed mean value denoted by δ, are generated. Finally, either δ_{ij} or $-\delta_{ij}$ (selected randomly) is added to the corresponding true travel times t_{ij}. The resulted travel times $\{T_{ij}=t_{ij}+\delta_{ij}$ or $t_{ij}-\delta_{ij}\}$ are considered as the measured data which will be used to search for system and environmental parameters. Note that the random numbers $\{\delta_{ij}\}$ simulate the measurement errors of the travel times due to noise, numerical errors, and other possible experimental errors.

In numerical simulations, four values of δ (0, 0.5, 1, 2 ms) and four inaccurate SSP models are employed for simulations. Figure 1(b) shows the true SSP (in thick-dashed curve) and the four inaccurate SSP's. As mentioned earlier, the true SSP is used to generate the measured ray travel times. The four inaccurate SSP's are arbitrarily chosen. They are somewhat different from the true SSP. They serve as the nominal models and will be employed for parameter inversion.

Consider first the inversion of five system parameters (x_s, z_s, α, d, and z_b) using measurement data of the direct ray, the two once-reflected rays, and the two twice-reflected rays. Their final estimated results for the above-mentioned four δ's and the four SSP's are summarized in Table I. For references, initial estimates, true values, and maximum estimated errors of the five parameters are listed in the second to the fourth rows, respectively. A symbol * is put next to the worst estimate of each parameter. This worst estimate is used to calculate the maximum error. The cost term Δ is the average mismatch between the measured data (T_{ij}) and the simulated data (τ_{ij}). In other words, Δ is the average of the difference, $|T_{ij}-\tau_{ij}|$, over all indexes ij. In each case, the simulated data (τ_{ij}) is calculated using the estimated parameter values and the corresponding inaccurate SSP and δ.

Using the initial inaccurate estimates in the second row of Table I, the cost Δ is larger than 6.5 ms for each case. It is greatly reduced after the inversion process converges. For $\delta=0$, the estimated result using the thin-dashed SSP model has the minimum Δ (0.716 ms) because, among the four estimated SSP's, the thin-dashed SSP is closest to the true SSP [see Fig. 1(b)]. The estimated result using the dotted SSP has the maximum Δ (0.835 ms) because the dotted SSP has the largest deviation from the true SSP. As δ increases, Δ increases. The Δ is around 1.6 ms when δ is 2 ms. Although a smaller Δ usually assumes a better estimation accuracy for most parameters (especially when the travel time error δ is small), it does not generally guarantee a better estimation accuracy for every parameter (for example, see the array tilt α in Table I). This phenomenon is quite common in multiparameter estimation problems where the best match for most parameters is not necessary the best match for a certain parameter. The primary source of the cost Δ in the inversion results is due to the mismatch of SSP when travel-time detection error δ is small. As δ increases beyond a threshold value (approximately equal to 0.9 ms in this example), the primary source of Δ is then dominated by the travel time detection error δ where the mismatch of SSP becomes less significant. It is interesting to see that Δ is smaller than δ when δ is large (see Table I with $\delta=2$ ms). In this case,

TABLE II. Estimated results of a shallow water example where the SSP and other system parameters are characterized simultaneously. In case 1, a piecewise linear model where the sound speeds at nodes with depths 30, 40 and 100 m are allowed to vary. In case 2, a piecewise linear model where the sound speeds at surface, depth 40 m, and bottom are allowed to vary. In case 3 and 4, an EOF model with three coefficients is employed, but the sound speeds are only specified at surface, depth 40 m, and bottom in case 4. The four estimated SSP's with $\delta=2$ ms of cases 1–4, respectively, are shown in Fig. 2. A symbol * is put next to the worst estimate of each parameter. The symbol # denotes the case with wrong results whose values are not used to calculate the maximum error.

	δ (ms)	x_s (m)	z_s (m)	α (degrees)	d (m)	z_b (m)	Δ (ms)
Initial		−550	41.0	1.75	8	165	>6.5
True		−650	51	0.6	5	155	0
Maximum error		46	2.2	0.44	1.9	4.5	
Case 1	0	−649.8	51.03	0.6129	5.018	155.0	0.666
	0.5	−644.3	51.10	0.5317	4.609	154.4	0.734
	1	−637.7	51.23	0.4161	4.060	153.6	0.931
	2	−629.2	51.31	0.158*	3.070*	152.5	1.585
Case 2	0	−631.0	51.01	0.6268	5.069	154.9	0.722
	0.5	−696*	51.46	0.5611	4.960	154.6	0.738
	1	−896#	52.10	0.4635	4.850	154.3	0.901
	2	−1091#	53.2*	0.2133	4.706	156.8	0.165
Case 3	0	−658.6	51.24	0.6001	5.040	154.4	0.094
	0.5	−652.9	51.39	0.5190	4.702	153.8	0.307
	1	−641.6	51.61	0.4191	4.177	152.7	0.738
	2	−610.0	52.05	0.2142	3.645	150.5*	1.255
Case 4	0	−632.8	50.83	0.6445	4.897	154.6	0.048
	0.5	−606.6	51.04	0.5715	4.654	154.0	0.292
	1	−552#	51.33	0.4169	4.266	152.9	0.698
	2	−631.2	51.70	0.1708	3.360	151.8	1.470

further reduction of Δ is meaningless. Generally speaking, the accuracy of the estimated parameters deteriorates as the travel time detection error δ increases, and better match on the SSP model yields better accuracy in the estimated results. However, from these numerical results, the algorithm seems rather insensitive to small SSP mismatches (less than 40 m/s). This observation will be further examined in the next section.

After determining the source and array parameters, head wave and bottom refracted wave are used to determine the SSP in sediment. The result is shown in Fig. 1(c). The thick-dashed cure is the true SSP in the bottom. The four estimated results are corresponding to the four SSP models in Fig. 1(b). The thin-dashed curve has the best estimation accuracy in the bottom since the thin-dashed SSP in the water is closer than others to the true one [see Fig. 1(b)]. Here, the measurement error $\delta=1$ ms.

II. INVERSION OF SSP IN SHALLOW WATER

Section I has shown that the ray travel-time inversion algorithm is insensitive to small SSP mismatches. It is good when one is not interested in estimating the SSP. However, it sounds very bad if one is interested in characterizing the SSP accurately using the ray travel-time approach. In this section, the SSP and relevant system parameters will be simultaneously characterized. Two piecewise linear models (cases 1 and 2) and two EOF models (cases 3 and 4) are employed in this simulation. Using the same shallow water example used in the previous section, Table II shows the estimated system parameter results for four δ values (0, 0.5, 1, 2 ms), and Fig. 2 shows the worst case results of the estimated SSP when $\delta=2$ ms.

As in Table I, the initial estimates, true values, and maximum estimated errors of unknown parameters are listed for references in the second to the fourth rows, respectively, of Table II. A symbol * is put next to the worst estimate of each parameter in Table II. For small measurement error δ's, one can achieve very small cost Δ's (e.g., 0.048 ms in case 4) by simultaneously characterizing the SSP and other system parameters. A smaller cost Δ usually represents a better set of parameter estimations. For large measurement error δ's (e.g., $\delta=2$ ms), a smaller cost Δ does not usually represents a better set of parameter estimations. Comparing the results listed in Tables I and II, one observes that simultaneous characterization of the SSP and system parameters (Table II) does not always yield a better set of system parameter estimates than characterization of system parameter with a fixed SSP (Table I). This observation is generally true if the SSP model employed in the latter process is reasonable close to the true SSP (say within an error of 40 m/s).

The worst estimated SSP results for the four cases with $\delta=2$ ms are shown in Fig. 2. The thick-dashed curve is the true SSP. The solid, thin-line dashed, chain-dotted, dotted, and chain-dashed are the SSP curves obtained from the zeroth through fourth iterations in the inversion process. For case 1, the true SSP is used as the initial estimate, and the sound speeds at depths 30, 40, and 100 m are allowed to vary during the inversion process. The SSP estimations are quite

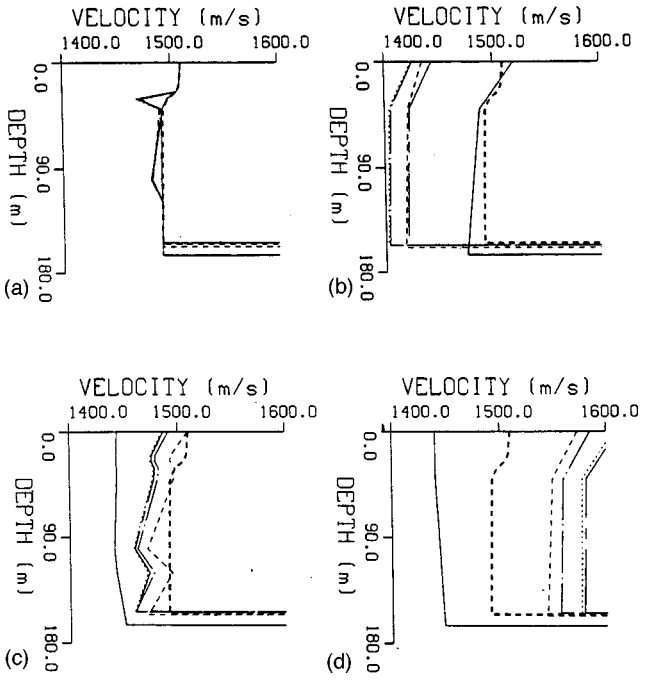

FIG. 2. The four estimated SSP's with $\delta=2$ ms for the four cases in Table II, respectively. The thick-line dashed curve is the true SSP. The solid, thin-line dashed, chain-dotted, dotted, and chain-dashed are the SSP curves obtained from the first through fifth iterations. (a) A piecewise linear model where the sound speeds at nodes with depths 30, 40, and 100 m are allowed to vary. (b) A piecewise linear model where the sound speeds at surface, depth 40 m, and bottom are allowed to vary. (c) An EOF model with three coefficients. (d) An EOF model with three coefficients, but the sound speeds are only specified at surface, depth 40 m, and bottom.

accurate for $\delta\leqslant 1$ ms using this model, which are not shown here. When $\delta=2$ ms, the estimated sound speeds at 30 and 100 m are 30 m/s lower than the true values [see Fig. 2(a)] disregarding that the initial estimate is the true SSP. This error is primarily induced from the travel-time measurement error. For case 2, the slopes of the initial SSP estimate are inaccurate, and sound speeds at the water surface, 40-m depth, and the bottom are allowed to vary during the inversion process. When $\delta=2$ ms, the slopes of the estimated SSP are recovered. However, the entire sound speed curve has a shift of approximately 100 m/s. The error (shift) in sound speed is ''compensated'' by the error of the estimated range x_s (see Table II; the values are denoted by #). This feature is also observed when $\delta=1$ ms. Note that the values denoted by # are not used to calculate the maximum error in Table II. For case 3, an EOF model is employed to describe the SSP. Note that the mean SSP of this EOF model [the solid line in Fig. 2(c)] is purposely chosen to be very different from the true SSP [the thick-dashed curve in Fig. 2(c)]. The estimated SSP with $\delta=2$ ms is shown in Fig. 2(c). It is interesting to see that the estimated curve is closer to the true one than the initial estimate. It is also remarkable that the estimated source and array parameters are still in good accuracy even when a poor initial estimate of SSP is used. For case 4, a combination of the EOF model and the piecewise linear approach is employed. The same EOF model as used in case 3 is employed during the inversion process to determine the sound speeds at the surface, the 40-m depth, and the bottom. A piecewise linear SSP model is then constructed using the

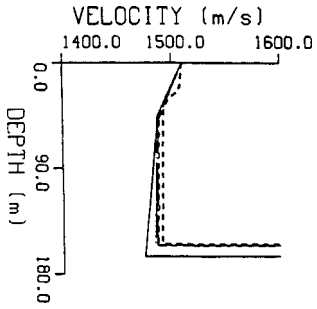

FIG. 3. Estimated SSP with $\delta=1$ ms and $\delta x_s=15$ m. Other estimated parameters are shown in Table III.

sound speeds at these three depths. The estimated SSP in Fig. 2(d) is similar to the result in Fig. 2(b). The slopes of the SSP curve at various depths are estimated properly, but the mean of SSP has a shift of approximately 100 m/s. The estimated system parameters seem more accurate than those for case 2 (but worse than those for case 1).

Intuitively, piecewise linear SSP models should be used in shallow waters for SSP characterization. However, it is difficult to get the break points accurately in inversion. Concluded from Fig. 2, we find that EOF models are usually more convenient than the piecewise linear models even in shallow waters. It is because, with the same number of unknowns, an EOF model allow variations of SSP at more depths and is able to adapt to random travel-time measurement errors better. For both piecewise linear and EOF models, the slopes of SSP can be estimated quite accurately (see cases 2 and 4) when the depth of the break point of the SSP (i.e., 40 m) is properly modeled. However, the mean value of SSP is off quite a bit when the travel time measurement error δ is large. In such situations, the estimated system parameters could become vary inaccurate. It is due to the fact that both SSP and x_s drift away from their true values in opposite directions, and their effects on the cost term Δ compensate each other. One way to prevent this drifting is to put some proper constraints on the SSP or x_s. The other way is to increase the number of break points of the SSP models (see cases 1 and 3). The perturbations of the resultant SSPs at break points in Fig. 2(a) and (c) are within the range of 40 m/s. They serve to compensate the travel-time measurement errors and prevent the drifting. When the general characteristics of SSP are roughly known and when the measurement error δ is small, relevant system parameters can be estimated with good accuracy. However, the accuracy of these system

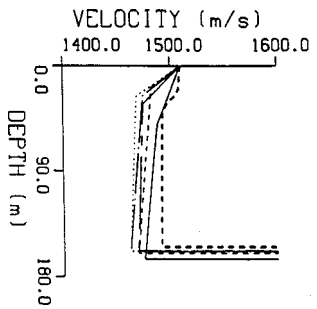

FIG. 4. Estimated SSP with $\delta=1$ ms and $\delta z_s=6$ m. Other estimated parameters are shown in Table IV.

TABLE III. Estimated results under various travel time measurement errors δ and various estimation errors δx_s of the separation distance between source and the receiving array. A symbol * is put next to the worst estimate of each parameter where the maximum error is calculated. The estimated SSP with $\delta=1$ ms and $\delta x_s=15$ m is shown in Fig. 3.

	x_s (m)	z_s (m)	α (degrees)	d (m)	z_b (m)	Δ (ms)
Initial		41.0	1.75	8	165	>6.5
True	−650	51	0.6	5	155	0
Maximum error		1.2	0.14	0.85	2.1	
$\delta=0$ ms	(−650)	51.02	0.6201	4.976	154.9	0.683
	(−645)	50.84	0.6108	4.713	154.4	0.684
	(−640)	50.65	0.6029	4.437	153.9	0.702
	(−635)	50.43	0.5964	4.147*	153.3	0.707
$\delta=0.5$ ms	(−650)	51.38	0.5488	4.875	154.4	0.771
	(−645)	51.39	0.5439	4.755	154.3	0.775
	(−640)	52.2*	0.5482	4.478	153.7	0.775
	(−635)	50.93	0.5501	4.171	153.1	0.777
$\delta=1$ ms	(−650)	52.14	0.460*	5.227	154.7	1.052
	(−645)	51.42	0.4922	4.410	153.7	0.991
	(−640)	51.76	0.4687	4.554	153.8	0.944
	(−635)	51.43	0.5069	4.218	152.9*	0.972

parameters does not always gain further improvements by allowing the SSP to be modified simultaneously during the inversion process. In fact, the accuracy of each parameter is limited by the travel time measurement error δ. For example, the minimum estimation error for x_s is approximately equal to 1.5δ m (1500 m/s times δ ms). Similarly, the minimum estimation error for SSP is approximately equal to 15δ m/s. The functional dependence of estimation errors of other system parameters on δ is more complicated (see Fig. 7 in Ref. 5).

III. SYSTEM PARAMETER MISMATCH

In this section, effects of system parameter mismatch on the accuracy of ray travel-time inversion approach are studied. Consider one parameter at a time. The parameter being considered is held at a fixed value while SSP and other system parameters are characterized simultaneously using the ray travel-time inversion approach. Table III shows the results under various travel time measurements error δ's and various estimation errors of the range x_s. The worst estimated SSP with $\delta=1$ ms and $\delta x_s=15$ m is shown in Fig. 3. Similarly, Table IV shows the results of source the depth z_s. The worst estimated SSP with $\delta=1$ ms and $\delta z_s=6$ m is shown in Fig. 4. Table V shows the results of the array tilt α. The worst estimated SSP with $\delta=1$ ms and $\delta\alpha=8.4$ degrees is shown in Fig. 5. Table VI shows the results of the array depth d. The worst estimated SSP with $\delta=1$ ms and $\delta d=3$ m is shown in Fig. 6. Table VII shows the results of the bottom depth z_b. The estimated SSP with $\delta=1$ ms and $\delta z_b=6$ m is shown in Fig. 7.

TABLE IV. Estimated results under various travel-time measurement errors δ and various estimation errors δz_s of the source depth. A symbol * is put next to the worst estimate of each parameter where the maximum error is calculated. The estimated SSP with $\delta=1$ ms and $\delta z_s=6$ m is shown in Fig. 4.

	x_s (m)	z_s (m)	α (degrees)	d (m)	z_b (m)	Δ (ms)
Initial	−550		1.75	8	165	>6.5
True	−650	51	0.6	5	155	0
Maximum error	45		0.74	5.9	4.5	
$\delta=0$ ms	−650.1	(51)	0.6167	4.961	154.9	0.683
	−663.6	(53)	0.8546	6.876	156.4	0.696
	−679.3	(55)	1.1101	8.879	157.9	0.698
	−695*	(57)	1.341*	10.91*	159.5*	0.739
$\delta=0.5$ ms	−647.5	(51)	0.5139	4.506	154.1	0.767
	−661.8	(53)	0.7513	6.448	155.7	0.767
	−668.4	(55)	0.9780	8.218	156.9	0.811
	−690.6	(57)	1.1151	10.36	157.8	0.882
$\delta=1$ ms	−631.1	(51)	0.4502	3.882	152.6	1.149
	−637.8	(53)	0.6993	5.682	153.5	1.020
	−651.0	(55)	0.8190	7.556	156.2	1.565
	−672.5	(57)	1.1740	9.824	157.2	0.979

TABLE V. Estimated results under various travel-time measurement errors δ and various estimation errors $\delta\alpha$ of the array tilt. A symbol * is put next to the worst estimate of each parameter where the maximum error is calculated. The symbol # denotes the case with wrong results whose values are not used to calculate the maximum error. The estimated SSP with $\delta=1$ ms and $\delta\alpha=8.4$ degrees is shown in Fig. 5.

	x_s (m)	z_s (m)	α (degrees)	d (m)	z_b (m)	Δ (ms)
Initial	−550	41.0		8	165	>6.5
True	−650	51	0.6	5	155	0
Maximum error	7.3	2.2		1.9	1.4	
$\delta=0$ ms	−650.2	51.00	(0)	4.950	154.9	0.683
	−652.0	51.58	(3)	5.579	154.7	0.686
	−651.9	52.20	(6)	6.232	154.3	1.118
	−655.3	52.28	(9)	6.898	154.4	0.697
$\delta=0.5$ ms	−642.7*	51.48	(0)	4.847	154.2	0.879
	−646.3	52.17	(3)	5.589	154.2	0.864
	−650.4	52.05	(6)	6.031	153.7	0.791
	−656.3	53.2*	(9)	6.918*	153.9	0.796
$\delta=1$ ms	−650.2	51.61	(0)	4.878	154.0	0.854
	−514#	52.5#	(3)	5.336#	152.6#	4.57#
	−654.4	52.92	(6)	6.221	153.6*	0.933
	−329#	121#	(9)	7.745#	246#	1.211

In Tables III–VII, the value of the selected parameter is shown in parentheses. This parameter is kept at this fixed value during each inversion process. As in Tables I and II, the initial estimates, true values, and maximum estimated errors of unknown parameters are listed in the second to the fourth rows, respectively, of each table. A symbol * is put next to the worst estimate of each parameter where the maximum error is calculated. It is obvious that the cases with a smaller δ and/or a smaller parameter mismatch yield better estimation accuracy of other system parameters. In Figs. 3–7, the thick-line dashed curve is the true SSP. The solid, thin-line dashed, chain-dotted, dotted, and chain-dashed are the SSP curves obtained from the zeroth through fourth interations, respectively. In the inversion process, both speed and depth of the node of the SSP are allowed to vary. All estimated SSP's fall in the neighborhood of the true SSP. Note that one obtains the best SSP estimate with fixed x_s values (see Fig. 3).

Consider first the situations with no travel-time measurement error ($\delta=0$) and no parameter mismatch (see the fifth rows of Tables III–VII). It is interesting to see that all parameters are estimated accurately even though the final cost function Δ's are not very small except that in Table VII. Next, consider the worst cases which are denoted by *. In most cases, the worst cases for different parameters happen at different occasions. From Table IV, it is interesting to see that the worst case happens at zero travel time measurement error but with the largest source depth mismatch. It implies

TABLE VI. Estimated results under various travel-time measurement errors δ and various estimation errors δd of the array depth. A symbol * is put next to the worst estimate of each parameter where the maximum error is calculated. The symbol # denotes the case with wrong results whose values are not used to calculate the maximum error. The estimated SSP with $\delta=1$ ms and $\delta d=3$ m is shown in Fig. 6.

	x_s (m)	z_s (m)	α (degrees)	d (m)	z_b (m)	Δ (ms)
Initial	−550	41.0	1.75		165	>6.5
True	−650	51	0.6	5	155	0
Maximum error	31	3.5	0.35		2.5	
$\delta=0$ ms	−647.0	51.14	0.6173	(5)	154.7	0.738
	−658.6	51.89	0.7293	(6)	155.8	0.680
	−667.1	52.73	0.8407	(7)	156.7	0.680
	−676.2	53.56	0.953*	(8)	157.5*	0.681
$\delta=0.5$ ms	−639.2	51.53	0.6301	(5)	152.9	0.801
	−654.2	52.46	0.6976	(6)	155.3	0.770
	−660.6	53.32	0.7820	(7)	156.2	0.794
	−668.9	54.19	0.8840	(8)	157.2	0.819
$\delta=1$ ms	−619*	52.18	0.5645	(5)	152.0	1.187
	−673.2	53.19	0.6105	(6)	154.0	1.367
	−1108#	54.4#	0.461#	(7)	154.9#	1.257
	−680.1	54.5*	0.8632	(8)	156.7	1.110

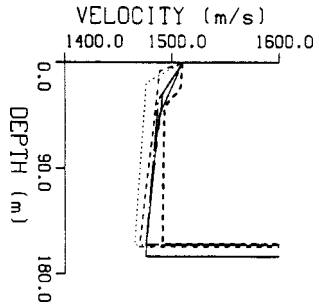

FIG. 5. Estimated SSP with $\delta=1$ ms and $\delta\alpha=8.4$ degrees. Other estimated parameters are shown in Table V.

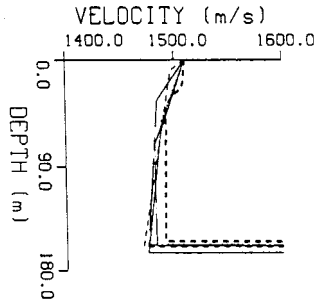

FIG. 6. Estimated SSP with $\delta=1$ ms and $\delta d=3$ m. Other estimated parameters are shown in Table VI.

that a system parameter mismatch can sometimes ruin the inversion accuracy badly, disregarding that other parameters are measured correctly. If one has a wrong presumption of a system parameter, it may be better to have a few measurement errors elsewhere to compensate for the presumption error. Finally, consider the cases which are not working properly (denoted by # in Tables V and VI). In these cases, both the system parameter errors and the travel-time measurement errors are too large. Thus, the array parameters are better to be treated as unknowns during the parameter inversion process if travel-time measurement errors are large. Generally speaking, if the mismatch of a parameter is small, the final estimated results obtained by keeping the parameter at a fixed (wrong) value is usually acceptable. However, a large system parameter mismatch may cause a large final estimation error. Therefore, if there are enough measured data, it is better to treat all important system parameters as unknowns and characterize them simultaneously as long as the system parameters are confined in appropriate ranges.

IV. INVERSION IN ARCTIC OCEAN USING SIMULATED DATA

Before analyzing the ICESHELF-89 data in the next section, simulation data of the Arctic ocean are employed to study the effect of different SSP models on the accuracy of the proposed inversion approach. Two examples are considered. Both are with an impulse source and a receiving array of 32 elements. In the first example (see Fig. 8 and Table VIII), the initial estimate of the SSP is not very different from the true SSP. In the second example (see Fig. 9 and Table IX) the initial estimate of the SSP differs from the true SSP more. In both Figs. 8 and 9, the true SSP and its initial estimate are shown as the thick dashed curve and the thin solid curve, respectively.

In the first example, two sets of inversion results are shown in Table VIII. The SSP is specified at 15 depths in case 1, but is specified at only four depths in case 2. For both cases, the EOF model with three coefficients are employed to describe the SSP. When there is no travel-time measurement error (i.e., $\delta=0$), very good estimates for all parameters and accurate SSP estimates are obtained from both cases. The cost Δ is within 0.1 ms which is very small. The estimated SSPs are very close to the true SSP and are therefore not shown here. When the travel-time measurement error δ increases to 1.5 ms, the cost Δ grows to 1.6 ms. However, the estimates of system parameters and SSP are still good. For example, the maximum error in range x_s is 32 m which is less than 2% error. The maximum sound speed error is less than 2 m/s for case 1, and is less than 5 m/s for case 2. When

TABLE VII. Estimated results under various travel-time measurement errors δ and various estimation errors δz_b of the bottom depth. A symbol * is put next to the worst estimate of each parameter where the maximum error is calculated. The estimated SSP with $\delta=1$ ms and $\delta z_b=6$ m is shown in Fig. 7.

	x_s (m)	z_s (m)	α (degrees)	d (m)	z_b (m)	Δ (ms)
Initial	−550	41.0	1.75	8		>6.5
True	−650	51	0.6	5	155	0
Maximum error	43	1.8	0.45	1.1		
$\delta=0$ ms	−651.2	51.07	0.6206	5.046	(155)	0.046
	−668.3	51.79	0.5799	5.986	(157)	0.103
	−678.4	51.76	0.4387	5.880	(159)	0.154
	−693*	51.81	0.3400	6.055*	(161)	0.212
$\delta=0.5$ ms	−652.8	51.60	0.5561	5.122	(155)	0.356
	−663.1	52.11	0.4371	5.570	(157)	0.395
	−677.2	52.20	0.3412	5.775	(159)	0.419
	−692.1	52.34	0.2544	6.045	(161)	0.459
$\delta=1$ ms	−653.2	52.18	0.4801	5.202	(155)	0.711
	−661.2	52.48	0.3370	5.381	(157)	0.755
	−676.3	52.65	0.2396	5.679	(159)	0.779
	−691.2	52.8*	0.148*	5.939	(161)	0.803

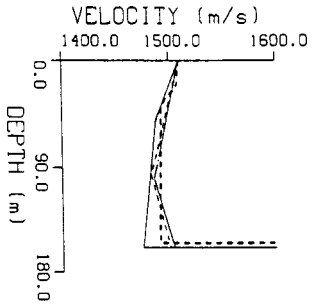

FIG. 7. Estimated SSP with $\delta=1$ ms and $\delta z_b=6$ m. Other estimated parameters are shown in Table VII.

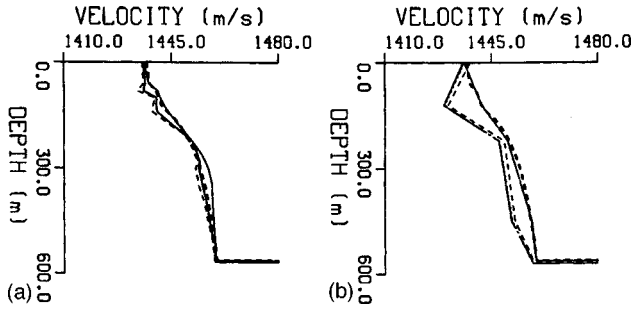

FIG. 8. The two estimated SSP's for the two cases, respectively, in Table VIII with $\delta=3.5$ ms. The thick-line dashed curve is the true SSP. The solid, thin-line dashed, chain-dotted, dotted, and chain-dashed are the SSP curves obtained from the first through fifth iterations. (a) The SSP is specified at 15 depths. (b) The SSP is specified at four depths.

the travel-time measurement error δ increases to 3.5 ms, the cost Δ grows to 3.1 ms. However, the estimates of both system parameters and SSP maintain in good shape. For example, the maximum error in range x_s is 62 m which is less than 5% error. The worst SSP estimates (with $\delta=3.5$ ms) are shown in Fig. 8(a) and (b) for cases 1 and 2, respectively. The maximum sound speed error is 4 m/s (at depth 100 m) for case 1, and is less than 12 m/s (at depth 125 m) for case 2. This example shows that good estimates can be obtained by using good SSP models disregarding large travel-time measurement errors. Moreover, insufficient sampling of SSP does not degrade the estimation accuracy significantly.

In the second example, a slope error is purposely introduced into the initial SSP estimate. Three cases of inversion results are shown in Table IX where two new columns are included. The symbols dC_0 and dC_b in Table IX denote the variations of the sound speeds at the water surface and water bottom, respectively. They are employed to correct the SSP slope error. For example, when velocity corrections at depths $z=0$ and $z=z_b$ are dC_0 and dC_b, respectively, the velocity correction dC_z at an arbitrary depth z is $[dC_0(z_b-z)+dC_bz]/z_b$. When the value (0) appears in the column of dC_0 or dC_b in Table IX, it denotes that no variation is allowed during the inversion for the corresponding variable. In case 1, the EOF model is employed to characterize the SSP, and no variation of sound speeds at the surface or the bottom is allowed. Piecewise linear models are employed for characterizing the SSP in cases 2 and 3. In case 2, the variations of sound speed at the surface and at the bottom are used to modify the SSP. In case 3, the variation of sound speed at the bottom is used to modify the SSP.

When there is no travel time measurement error, i.e., $\delta=0$, good estimates for all parameters and SSP are obtained from all three cases. The cost Δ is within 0.25 ms which is relatively small. When the travel-time measurement error δ increases to 1.5 ms, the cost Δ grows to 1.7 ms. However, the estimate of system parameters is still good. For example, the maximum error in range x_s is 64 m which is less than 4% error. When the travel-time measurement error δ increases to 3 ms, the cost Δ grows to 3.4 ms. However, the estimate of system parameters maintains in good shape. For example, the maximum error in range x_s is 81 m which is less than 5% error. The worst case SSP estimates (with $\delta=3$ ms) are shown in Fig. 9(a)–(c) for cases 1, 2, and 3, respectively. In case 3, the sound speed at the bottom (surface) is shifted such that the estimate SSP has approximately the same slopes as the true SSP in most depths. Similarly, the case 2, the sound speeds at both surface and bottom vary in such a manner that the estimated SSP has approximately the same slopes as the true SSP in most depths. Unfortunately, there exists a net shift (error) of 30 m/s from the true SSP to the estimated SSP. Using more depth samples of SSP, the EOF model in case 1 tends to provide small but irregular variations of SSP while searching for the optimum solution in inversion. These irregular variations serve to compensate the travel-time measurement error and do not reflect the true

TABLE VIII. Two sets of inversion results of an Arctic ocean example. In case 1, SSP is specified at 15 depths. In case 2, SSP is specified at four depths. A symbol * is put next to the worst estimate of each parameter where the maximum error is calculated. The two corresponding estimated SSPs with $\delta=3.5$ ms are shown in Fig. 8.

		x_s(m)	z_s(m)	α (degrees)	d (m)	z_b(m)	Δ(ms)
Initial values		−1628	259	−1.11	6	562	>5.64
True values		−1688	253	−1.49	8	562	0
Maximum error		62	1.5	0.06	2.3	7.6	
$\delta=0$ ms	case 1	−1688	253.2	−1.485	8.180	562.1	0.102
	case 2	−1689	252.7	−1.504	7.714	561.9	0.057
$\delta=1.5$ ms	case 1	−1710	253.8	−1.507	9.156	564.8	1.564
	case 2	−1720	253.8	−1.524	9.121	565.9	1.582
$\delta=3.5$ ms	case 1	−1729	254.5	−1.522	10.10	567.3	3.117
	case 2	−1750*	254.5*	−1.55*	10.26*	569.6*	3.144

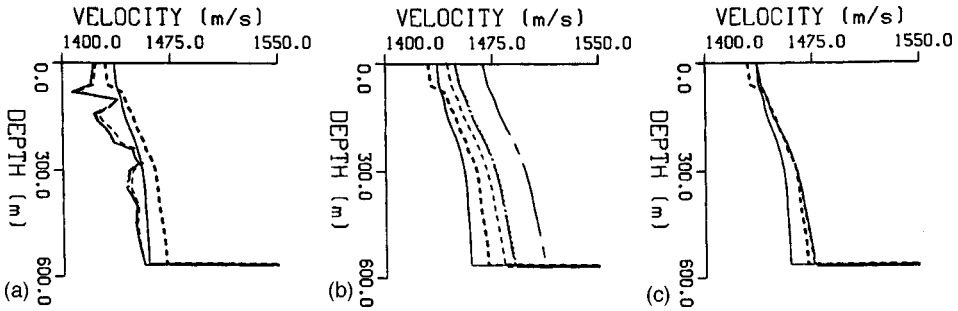

FIG. 9. The three estimated SSP's for the three cases, respectively, in Table IX with $\delta = 3$ ms. The thick-line dashed curve is the true SSP. The solid, thin-line dashed, chain-dotted, dotted, and chain-dashed are the SSP curves obtained from the first through fifth iterations. (a) The EOF model is employed. (b) Both dC_0 and dC_b are allowed to vary. (c) Only dC_b is allowed to vary.

SSP. These observations will be used in the next section to analyze the ICESHELF-89 data.

V. INVERSION IN ARCTIC OCEAN USING THE ICESHELF-89 EXPERIMENT DATA

A. First shot data

Since the travel-time measurement error δ of the ICESHELF experiment was unknown, we did not known the cost $\Delta = 1.3$ ms obtained previously in Ref. 5 for the first shot data was small enough or not. In order to further improve and quantify the accuracy, the first shot data are analyzed again in this section. In the previous estimation,[5] SSP is fixed during the inversion and the environment is considered range independent. Here, the SSP and other system parameters are simultaneously adjusted by the ray travel-time approach. Various SSP models in both range-independent and -dependent situations are employed. Travel-time measurement error δ and estimation accuracy of various parameters will be quantified.

In the first attempt, the SSP and system parameters obtained in Ref. 8 are used as the initial estimates. The environment is considered as range independent. There are five cases shown in Table X. The cost Δ is 7.87 ms for this initial parameter set. In case 1 of Table X, we basically repeat what we have done in Ref. 5. Here Δ is reduced to 1.3 ms by searching for a better set of system parameters where the SSP is not allowed to be modified in the inversion process. From cases 2–5, the SSP is modified during the inversion process. Piecewise linear models are employed in cases 2 and 3, and EOF models are employed in cases 4 and 5. (The sound speeds at nodes of depths 60, 80, 120, 240, and 400 m and bottom are allowed to vary in case 2; the sound speeds at nodes of depths 240 and 400 m and bottom are allowed to vary in case 3; three EOF coefficients are employed in case 4; and six EOF coefficients are used in case 5.) The estimated SSP's for cases 4 and 5 show irregular fluctuations as seen in Fig. 9(a). Based on the experience obtained from previous examples using simulation data, the irregular fluctuations in the SSP of case 5 are most likely spurious and, therefore, the cost function Δ's observed in cases 4 and 5 are not reliable. Comparing to the results in case 1, the results in cases 2 and 3 do not show much improvement on Δ.

In the second attempt, the waveguide is considered to be weakly range dependent by taking the bottom slope (dz/dx) into consideration. Eight estimated results obtained using eight SSP models are shown in Table XI. A fixed, but different, bottom slope is assumed for each of cases 1–5. As for cases 6–8, the bottom slope is treated as an unknown and will be obtained in the inversion process. In addition, dC_0 (the surface sound speed) and dC_b (the bottom sound speed) are employed to correct any possible SSP slope error of the initial SSP estimate. In cases 1–5 and case 7, dC_0 is set to zero, but dC_b is set to zero only in case 8. Different piecewise linear models are employed in cases 1–8, respectively. Since the EOF model tends to give irregular SSP variations, its results are discarded. For cases 1–8, the cost function Δ's are around 0.95 ms, which cannot be further reduced significantly. The difference between the initial and the final estimated sound speeds at any depth is within 5%. From these

TABLE IX. Three sets of inversion results of an Arctic ocean example. In case 1, an EOF model is employed. In case 2, both dC_0 and dC_b are allowed to vary. In case 3, only dC_b is allowed to vary. A symbol * is put next to the worst estimate of each parameter where the maximum error is calculated. The three corresponding estimated SSPs with $\delta = 3$ ms are shown in Fig. 9.

		x_s (m)	z_s (m)	α (degrees)	d (m)	z_b (m)	dc_0 (m/s)	dc_b (m/s)	Δ (ms)
Initial values		−1688	253	−1.49	8	562	0	0	>7.5
True values		−1628	259	−1.146	6	562			0
Maximum error		81	3.1	0.75	3.37	8.5			
δ=0 ms	case 1	−1662	260.0	−1.084	7.246	563.7	(0)	(0)	0.149
	case 2	−1648	260.4	−1.153	7.443	564.9	−4.419	10.83	0.209
	case 3	−1641	260.4	1.150	7.445	564.7	(0)	15.54	0.208
δ=1.5 ms	case 1	−1686	260.6	−1.92*	8.006	566.6	(0)	(0)	1.673
	case 2	−1623	260.9	−1.214	8.261	567.1	22.55	41.56	1.702
	case 3	−1661	261.1	−1.189	8.481	567.7	(0)	16.66	1.703
δ=3 ms	case 1	−1709*	261.2	−1.114	8.925	569.4	(0)	(0)	3.362
	case 2	−1668	262.*	−1.224	9.339	570.0	6.223	24.52	3.340
	case 3	−1680	261.7	1.242	9.37*	570.5*	(0)	18.10	3.342

TABLE X. Five estimated results of the first shot data of the ICESHELF-89 experiment. In case 1, the SSP is fixed in the inversion. In case 2, the sound speeds at nodes of depths 60, 80, 120, 240, and 400 m, and bottom are allowed to vary. In case 3, the sound speeds at nodes of depths 240 and 400 m, and bottom are allowed to vary, In case 4, an EOF model with three coefficients is employed. In case 5, an EOF model with six coefficients is employed.

	x_s (m)	z_s (m)	α (degrees)	d (m)	z_b(m)	Δ (ms)
Initial	−1688	253	−1.49	8	562	7.87
Case 1	−1617	252	1.49	9.23	551	1.30
Case 2	−1714	253	1.39	10.77	561	1.16
Case 3	−1645	251	1.37	8.85	556	1.19
Case 4	−1645	251	1.33	8.59	554	0.903
Case 5	−1727	253	1.35	9.90	560	0.766

results, we conclude that the environment is basically range independent. The correction of SSP slope is important. It can usually further reduce the cost function. In this example, the travel-time measurement error is estimated to be around 1 ms.

In many practical situations, the accuracy of estimated results in inverse problems cannot be obtained directly. However, it might be obtained indirectly if the inversion approach is very efficient and robust. Various nominal values of system parameters and SSP models are used to estimate the unknown parameters. The estimated results obtained from these inversions using different nominal parameter values are close to one another as shown in Table XI. The means of these estimated results are therefore used as the final estimated results, and their variances are used to quantify the errors. Summarized from Table XI, the bottom slope dz/dx is ± 0.002; the range $x_s = 1625 \pm 20$ m; the source depth $z_s = 250 \pm 3$ m; the array tilt $\alpha = 1.32 \pm 0.17$ degrees, the array depth $d = 8.5 \pm 1.5$ m, and the bottom depth $z_b = 552 \pm 3$ m. We essentially derive the same results as reported previously in Ref. 5. The bottom properties are given in Ref. 5 and are omitted here. The ray approach results in this paper are similar to the modal approach results in Ref. 8. However, our approach is two to three orders more efficient. Moreover, we obtain a better agreement between the simulated and the observed travel times, and the accuracy of the estimated parameters are quantified.

B. Second shot data

Consider the data set generated by the second SUS source received by a vertical array in the ICESHELF-89 experiment. The arrangement of source and receiver array is shown in Fig. 1(a). The nominal sound speed profile (SSP) is shown as the thick dashed curve in Fig. 9. The environment is range dependent. The normal modal approach becomes inconvenient, but the ray travel-time inversion approach can still be applied conveniently. The location of the source, the position of the array, the sound speed profile in water, and the bathymetry are obtained by the ray travel-time approach. The details of various estimation attempts are very similar to the first shot and are omitted. Except the SSP (which is close to the SSP estimate obtained from the first shot data), the estimated results are summarized in Fig. 10. The cost Δ of this estimation is within 1.5 ms. The sediment properties cannot be obtained because head waves and bottom penetration waves cannot be identified in this experimental data.

VI. DISCUSSIONS AND CONCLUSIONS

Effects of travel time measurement error δ, sound speed profile mismatch, and source/array parameters mismatch on the accuracy of the ray travel time inversion scheme have been studied. The first two shots of the Iceshelf-89 experiment have been analyzed where the second shot involves a range-dependent environment. Cases with smaller δ, SSP mismatch, or system parameter mismatch yield better estimation accuracy. The accuracy of the estimated parameters deteriorates as the travel time detection error δ increases. It is remarkable that good accuracy on parameter estimation is achieved in some situations with $\delta = 3$ ms when the nominal SSP model is accurate. A system parameter mismatch usually generates larger estimation error than the case where the particular parameter is also characterized simultaneously during the inversion process. If there are enough measured data, it is better to treat all important system parameters as unknowns and characterize them simultaneously. However, proper bounds have to be set for these unknown parameters,

TABLE XI. Eight more estimated results of the first shot data of the ICESHELF-89 experiment. From cases 1–5, the bottom slope is fixed of be −0.02, −0.01, 0, 0.01, and 0.02 respectively. In addition dC_b is allowed to vary. From cases 6–8, the bottom slope is allowed to vary. In case 6, both dC_0 are dC_b are allowed to vary. In case 7, only dC_b is allowed to vary. In case 8, only dC_0 is allowed to vary.

	x_s (m)	z_s (m)	α (degrees)	d (m)	z_b (m)	dz/dx	dc_0 (m/s)	dc_b (m/s)	Δ (ms)
Initial	−1688	253	−1.49	8	562	0	0	0	7.87
Case 1	−1635	253	1.37	9.39	552	(−0.002)	(0)	−1.04	0.937
Case 2	−1635	250	1.13	7.97	553	(−0.001)	(0)	4.95	0.947
Case 3	−1615	252	1.49	9.17	550	(0)	(0)	−2.03	0.978
Case 4	−1623	250	1.31	8.92	553	(0.001)	(0)	2.31	0.936
Case 5	−1623	250	1.46	10.0	553	(0.002)	(0)	0.328	0.950
Case 6	−1614	251	1.33	9.15	552	−0.000 18	8.89	10.45	0.956
Case 7	−1645	251	1.17	9.28	555	−0.000 27	(0)	3.38	0.978
Case 8	−1629	248	1.15	7.03	554	0.001 44	−6.63	(0)	0.963

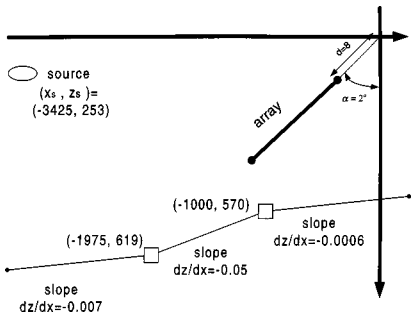

FIG. 10. Estimated results of the location of the source, the position of the array, and the bathymetry using the second shot data. The source depth is 253 m, the source range is -3245 m, the array tilt angle is 2 degrees, and the array depth is 8 m. The bottom bathymetry is modeled by three line segments joined at two locations: ($x=-1000$ m, $z=570$ m) and ($x=-1975$ m, $z=619$ m). The slopes of the three line segments are -0.0006, -0.05, and 0.007, respectively.

especially the range or the mean sound speed. If no bounds have been set, the estimated results could be totally wrong under certain situations.

In the ray travel time inversion approach, the travel time misfit Δ is employed as a cost function which is to be minimized. The primary source of the cost Δ in the inversion results is due to the mismatch of SSP when travel time detection error δ is small. For small measurement error δ, one can achieve very small cost functions Δ's by simultaneously characterizing the SSP and other system parameters. When δ increases, Δ also increases. As δ elevates beyond a certain threshold value, the primary source of the cost Δ is then dominated by the travel time detection error δ where the small mismatch of SSP becomes less significant. When $\delta > \Delta$, a further reduction of Δ is not meaningful. When $\delta < \Delta$, a smaller cost Δ usually yields a better set of parameter estimation. However, it does not always guarantee a better estimation accuracy for a certain parameter.

Although a better initial estimate of SSP usually derives a better estimated result, it seems that the estimation accuracy of system parameters is not very sensitive to the small mismatch (within 5% error) of the SSP. Therefore, it is difficult to estimate SSP with very good accuracy. An accurate SSP estimate can only be achieved when the source locations and array parameters are calibrated with great accuracy. Both the piecewise linear model and EOF model have been employed to characterized the SSP. In the piecewise linear model, the number of nodes and their corresponding depths are important parameters. Too many nodes will generate spurious fluctuations of SSP. Too few nodes will not be able to describe the SSP with sufficient resolution. The model is very sensitive to the depths of the nodes. Sometimes, the inversion does not converge when the depths of the nodes are allowed to vary. In the EOF model, the background SSP is very important. If the background SSP differs greatly from the true SSP, it is impossible to obtain an accurate estimate of the true SSP. A SSP slope correction scheme (using $dC_{0,b}$) has been developed to remedy this difficulty. When the travel time measurement error is large, the resolution of SSP is very poor. In fact, spurious fluctuations of SSP will occur. When the SSP and other system parameters are simultaneously characterized, better accuracy can usually be obtained. However, special cautions have to be paid to ensure the SSPs stay in the proper range because a big shift of the entire SSP may occur and will cause large estimation error.

ACKNOWLEDGMENT

The work is supported by ONR.

[1] B. Cornuelle, C. Wunsch, D. Behringer, T. Birdsall, R. Heinmiller, R. Knox, K. Metzger, W. Munk, J. Spiesberger, R. Spindel, D. Webb, and P. Worcester, ''Tomographic maps of the ocean mesoscale. Part I: Pure acoustics,'' J. Phys. Oceanogr. **15**, 133–152 (1985).
[2] T. M. Georges, D. R. Palmer, R. M. Jones, and J. P. Riley, ''A survey of acoustic techniques for monitoring EL NINO,'' NOAA Technical Memorandum ERL WPL-149 (1988).
[3] M. D. Collins and W. A. Kuperman, ''Focalization: Environmental focusing and source localization,'' J. Acoust. Soc. Am. **90**, 1410–1422 (1991).
[4] P. Gerstoft, ''Inversion of seismoacoustic data using genetic algorithms and a posteriori probability distributions,'' J. Acoust. Soc. Am. **95**, 770–782 (1994).
[5] I. T. Lu, ''Simultaneous characterization of source, array and environment using a ray travel-time inversion approach,'' J. Comput. Acoust. **5**(2), 193–218 (1997).
[6] P. Voltz and I. T. Lu, ''A back-propagating ray technique for source localization,'' J. Acoust. Soc. Am. **95**, 805–812 (1994).
[7] J. M. Zurada, R. J. Marks II, and C. J. Robinson, *Computational Intelligence Imitating Life*, IEEE, New York, Section III (1994).
[8] J. W. Wolf, ''Geoacoustic inversion in shallow water using broad band shot data,'' J. Acoust. Soc. Am. **94**, 1769 (1993).

Application of waveguide invariants to analysis of spectrograms from shallow water environments that vary in range and azimuth

G. L. D'Spain[a] and W. A. Kuperman
Marine Physical Laboratory, Scripps Institution of Oceanography, San Diego, California 92152

(Received 6 October 1998; revised 10 June 1999; accepted 12 July 1999)

The waveguide invariant summarizes in a single scalar parameter the dispersive propagation characteristics for a given environment. In this paper, an expression is derived for the invariant in shallow water environments where the bottom bathymetry varies with range and azimuth. It then is applied to the interpretation of broadband, single-element spectrograms collected during SWellEx-3, a shallow water acoustics experiment off the coast of San Diego. The unusual behavior of the interference patterns seen in the spectrograms from this experiment during the transmission of a 75–150-Hz pseudo-random noise sequence by a source towed over range-varying bottom bathymetry is well matched by the model predictions. © *1999 Acoustical Society of America.* [S0001-4966(99)00911-X]

PACS numbers: 43.30.Bp, 43.20.Mv, 43.30.Wi [SAC-B]

INTRODUCTION

Interference patterns, or striations, often are seen in underwater acoustic spectrograms from broadband sources with continuous source spectral levels. When the source is close to the receiver, the interference pattern is due to the well-known Lloyd's mirror effect.[1] A common example is the ''bathtub'' feature prevalent in spectrograms recorded during the closest point of approach (CPA) of a surface ship. However, for a source at sufficiently long range that a normal mode description of the acoustic field is valid, the striations arise from the mutual constructive/destructive interference between modes. Therefore, they are a direct measure of the mode wave number differences and so provide useful information for performing geoacoustic inversions of the ocean bottom and for ocean acoustic tomography.

A convenient framework for the analysis of these interference patterns is provided by the waveguide invariant approach.[2,3] The invariant, herein designated as β, summarizes in a single scalar parameter the dispersive characteristics of the field in a waveguide. The invariant formulation recently has been used to interpret the side-lobe behavior in broadband ambiguity surfaces in matched field processing[4] and to change the range of focusing in phase conjugation/time reversal experiments.[5]

The focus of this paper is on the interference patterns in spectrograms created by broadband sources at least several water depths in range from the receiver. At long range, the field interacts numerous times with the boundaries of the waveguide, resulting in a complicated multipath structure. In contrast, the Lloyd's mirror effect results from the interference between just a few multipath arrivals. In fact, only a single reflecting or refracting boundary is necessary to obtain the Lloyd's mirror effect, rather than the waveguide structure required for formation of the long range striation patterns studied here. To illustrate these differences, Figs. 1 and 2 present some numerical modeling results using a wave number integration program[6] that accounts for the near-field continuum. Plotted in both figures are the transmission loss versus range from 0 to 20 km for frequencies from 130 to 170 Hz in 1-Hz increments. The medium for both figures is composed of a 200-m-thick fluid layer overlying a highly absorbing (10 dB/λ) fluid half-space with a 1500-m/s sound speed. However, the sound speed profiles in the 200-m fluid layer differ in the two figures; in Fig. 1, it is constant at 1450 m/s, whereas in Fig. 2, it is such that the square of the index of refraction is linear with depth, starting at 1450 m/s at the surface and increasing to 1500 m/s at the 200-m deep bottom. The interference pattern over the smallest ranges is nearly identical in both figures, and represents the Lloyd's mirror effect. It is a near-field effect that is insensitive to the water column properties. At farther ranges, both plots show an evolution to a broader interference pattern. However, the direction and degree of the slope of the interference patterns is quite different; it is about three times greater in Fig. 2 than in Fig. 1 and is opposite in sign. The reason for the difference is that the mode group velocities increase with increasing mode number for the environment in Fig. 2 (because the energy in the higher-order modes penetrate to deeper parts of the water column where the medium sound speed is greater), whereas the mode group velocities decrease with increasing mode number in Fig. 1. The value of the waveguide invariant for the two cases summarizes the difference; for the environment in Fig. 1, it is approximately $+1$, as shown in the first part of Sec. III, whereas it is -3 in Fig. 2.[2] Therefore, the broadband interference pattern at the longer ranges contains useful information about the waveguide properties.

The purpose of this paper is to apply the waveguide invariant approach to the analysis of some puzzling broadband striation patterns seen in spectrograms recorded during SWellEx-3, a shallow water acoustics experiment off the coast of San Diego. The experiment and the strange striation patterns are discussed in Sec. I. Section II provides background development, followed by the derivation of the ex-

[a]Electronic mail: gld@mpl.ucsd.edu

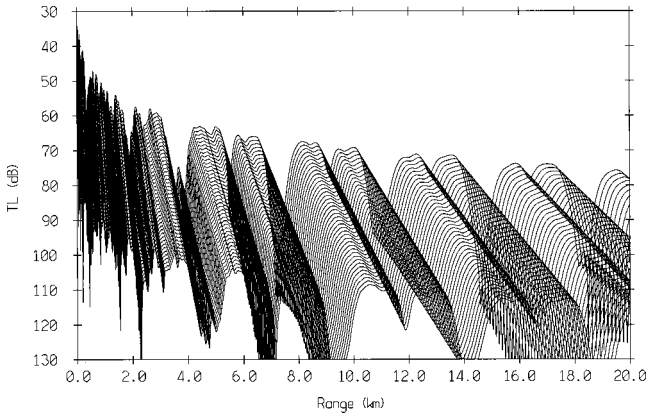

FIG. 1. Transmission loss versus range from 130 to 170 Hz calculated by OASES (Ref. 6) for an environment composed of a 200-m homogeneous fluid layer overlying a homogeneous, absorbing fluid half-space. The fluid layer has a 1450-m/s sound speed, whereas the bottom half-space has a sound speed of 1500 m/s and an attenuation of 10 dB/λ. The curves for increasing frequencies are progressively offset in 1-dB steps. The source and receiver depths are 20 and 100 m, respectively.

pression for the waveguide invariant, extended to environments that vary both in range and azimuth. This expression then is integrated to obtain predictions of the changes in frequency required for the striation patterns to maintain constant amplitude as a function of changes in source/receiver range and in environmental properties. In Sec. III, an expression is derived for the invariant in shallow water environments where the range and azimuth variation is due to the bottom bathymetry. Section IV presents the comparison of the predictions of the model, obtained from the combination of the results in Secs. II and III, with the actual spectrograms from SWellEx-3. Final remarks and implications of this work are contained in the Conclusions. In addition, two appendices are included in the paper. The first shows that the waveguide invariant, among other things, specifies the frequency dependence of the mode phase and group velocities. The second appendix presents a scheme for numerically evaluating one of the integrals in the paper.

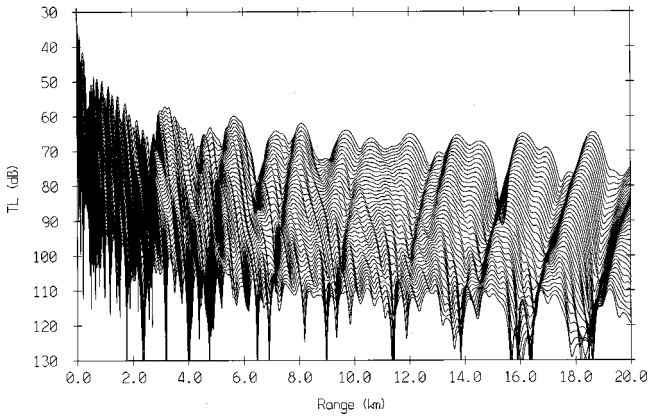

FIG. 2. Transmission loss versus range from 130 to 170 Hz calculated by OASES (Ref. 6) for an environment composed of a 200-m fluid layer with a linear-with-depth square index of refraction sound speed profile overlying a homogeneous, absorbing fluid half-space. The layer profile starts at 1450 m/s at the surface and increases to 1500 m/s at 200-m deep bottom. The half-space properties, as well as the source and receiver depths, are the same as those in Fig. 1.

I. DESCRIPTION OF THE EXPERIMENT AND DATA

Figure 3 shows a time-versus-frequency spectrogram estimated from data recorded by a single hydrophone. During the 10-min period of the plot, a towed acoustic projector steadily approached the receiver from a starting distance of 6.0 km. After 45 sec into the plot, the source started transmitting a pseudo-random-noise (PRN) sequence with a 150 dB $re\ 1\ \mu\mathrm{Pa}/\sqrt{\mathrm{Hz}}$ @ 1 m source level and a flat spectrum from 75 to 150 Hz. The most striking feature of the plot is the striations that run from the upper right to the lower left. (The final half-minute is contaminated by an interfering noise source, probably a transiting surface ship.) The three lines superimposed on the figure are the predictions of the temporal evolution of the frequency content of these striations from the model developed in this paper.

The data in Fig. 3, as well as the other data discussed herein, were collected during SWellEx-3, a shallow water experiment conducted 10–15 km west of San Diego in the summer of 1994. Prevailing ocean water properties were typical of mid-latitude Northeast Pacific, summer-time, shallow water environments, having a downward-refracting sound speed profile with a near-surface sound speed of 1525 m/s, a thermocline extending from near the surface to a depth of 50 to 60 m, and an isovelocity layer below that of 1490 m/s (see Fig. 11). The Marine Physical Lab's (MPL) FLoating Instrument Platform (FLIP) was used as the central data acquisition platform. R/P FLIP is a 100-m-long, manned spar buoy and was anchored to the ocean bottom with a three-point mooring configuration. A 64-element ''SRP'' array was deployed from FLIP in the vertical direction so that it covered the lower 120 m of the 200-m-deep water column at the site. These ''SRP'' arrays are large-dynamic-range, digital, hydrophone arrays designed and built at MPL. Details on the SRP array hardware are provided in Ref. 7. The array was cabled back to FLIP, where the data were recorded continuously throughout the 3-week duration of the experiment. A complete description of the experiment can be found in Ref. 8. Note that only the data from a single element of the array are displayed in Fig. 3.

Figure 4 presents a map of the experiment site showing contours of the ocean bottom bathymetry and the locations of FLIP with the vertical SRP array and the source tow tracks discussed in this paper. The data in Fig. 3 were recorded when the source followed the track in Fig. 4 labeled as track ''e.'' The underwater acoustic source was towed at a nominal depth of 50 m. The acoustic signal it transmitted consisted of a 5-min broadcast of a set of ten tones, from 53 to 197 Hz in 16-Hz intervals, followed by 10 min (in most cases) of the 75–150-Hz PRN sequence. Broadband matched field processing results and the effects of bottom bathymetry mismatch using data collected when the source continuously transmitted the ten-tone signal along approximately the same course as in Fig. 4 are discussed in Ref. 9. (See also Ref. 10.) Here, the focus is on the behavior of the single-element received signals during the PRN broadcasts and the interpretation of this behavior in terms of waveguide invariants.

All along track ''e,'' when the data in Fig. 3 were recorded, the conditions between source and receiver were

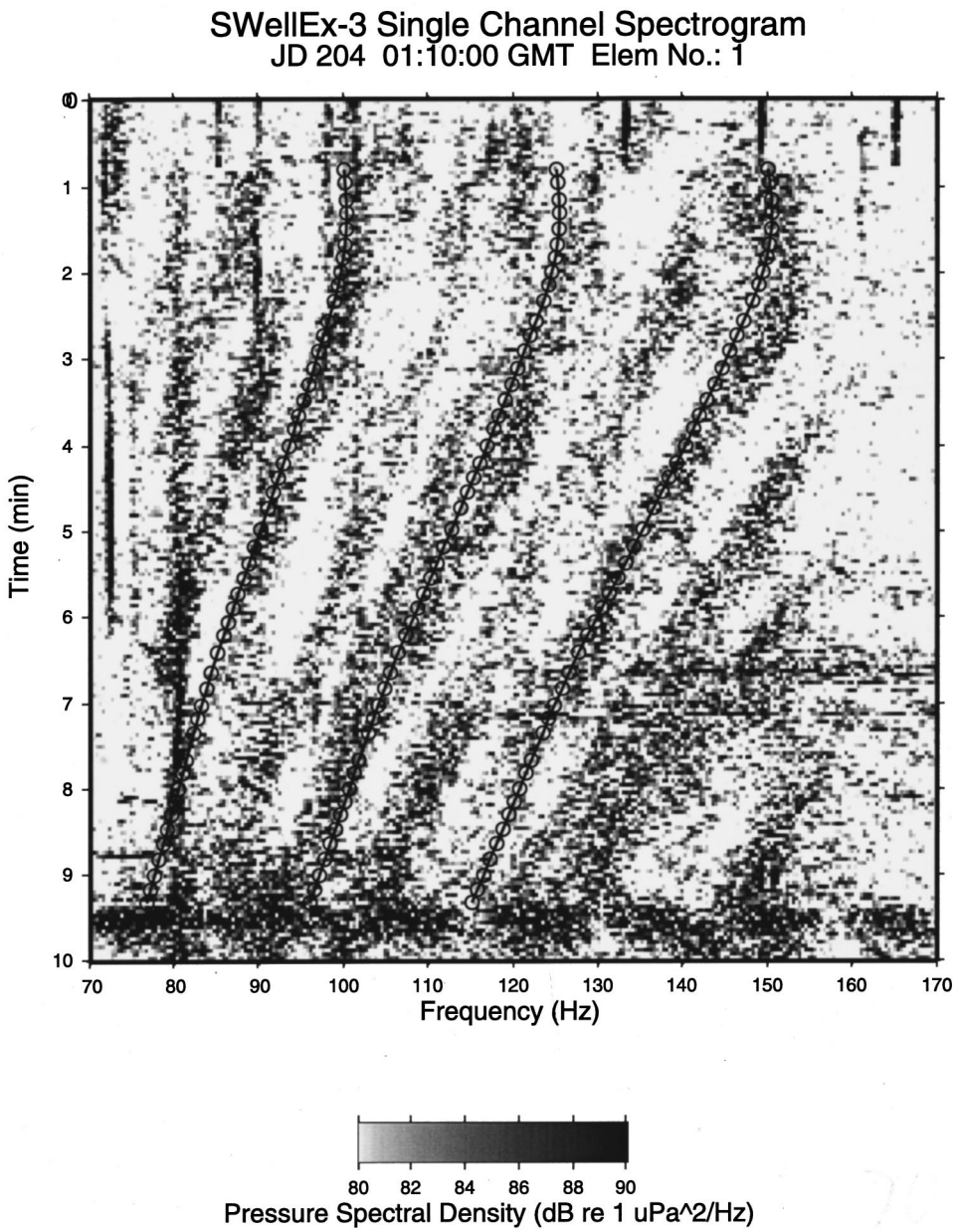

FIG. 3. Ten-minute pressure spectrogram over the 70–170-Hz band estimated from the data collected by the lowermost hydrophone in the vertical line array in SWellEx-3. A towed source, traveling along track ''e'' in Fig. 4, started about 45 s after the plot's beginning to transmit a pseudo-random-noise sequence with a 150 dB $re1\ \mu\mathrm{Pa}/\sqrt{\mathrm{Hz}}$ at 1-m source level and a flat spectrum from 75 to 150 Hz. The three lines of interconnected circles superimposed on the figure are the model predictions of the temporal evolution of the frequency content of the broadband interference patterns.

nearly range independent with a nominal water depth of 200 m. The range to the source steadily closed, leading to the slanted nature of the striation pattern in Fig. 3. This track was just one part of an event, herein referred to as ''ARCMFP2,'' in which the ship, starting to the east of FLIP in 80-m-deep water (at the southern end of track ''a''), proceeded to the north and west along an arc at approximately constant range from FLIP, passing along tracks ''a''–''d'' in sequence, into progressively deeper water. Over the course of the arc, the water depth changed by more than 150%. A turn to the south towards FLIP then was made to travel along tracks ''e'' and ''f.'' Tracks ''a''–''f'' were run during the time periods of the PRN broadcasts and are plotted as continuous open circles in Fig. 4. The thin lines connecting these tracks show the ship course during the ten-tone comb transmissions. Single-element spectrograms recorded during tracks ''a''–''d'' and ''f'' are shown in Figs. 5–9. Although each PRN signal transmission was scheduled to last for 10 min, in Fig. 5 it was on for only 8.5 min and only 5 min in Fig. 7. In any case, these figures show some puzzling features. That is, under range-independent conditions, the striation pattern would be expected to remain nearly constant over time as the course being run maintained a nearly constant source-receiver range. However, the broadband interference pattern clearly changes in a consistent and regular way as the water depth increases. These changes might be expected to be observed when the source traveled towards the receiver, as in Fig. 3. The goal of this paper is to account for these strange effects in the broadband striation pattern caused by changes in bottom bathymetry in terms of waveguide invariants.

II. DERIVATION AND INTERPRETATION OF WAVEGUIDE INVARIANT

The purpose of this section is to present a formulation that permits interpretation of many of the features of the spectrogram striations in Figs. 3 and 5–9. The derivation of the waveguide invariant, extended to environments that vary

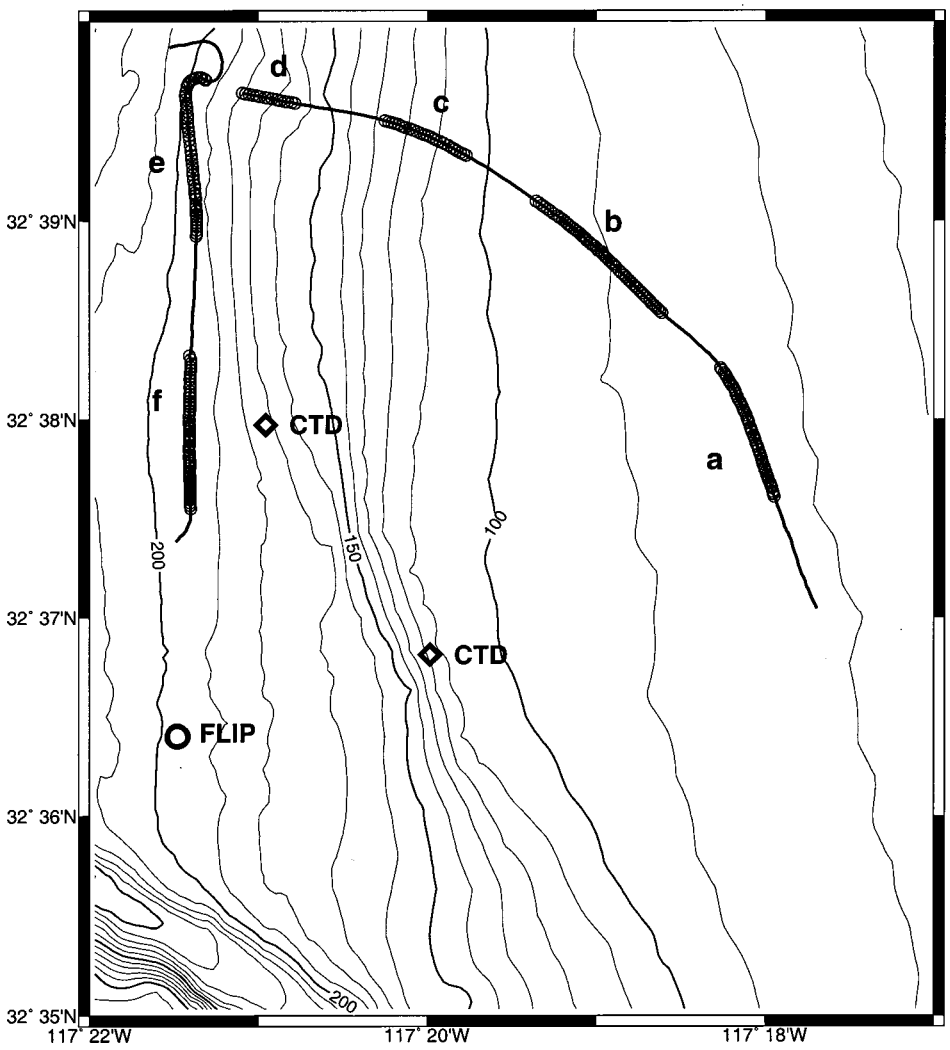

FIG. 4. A plan view of the SWellEx-3 experiment site showing the DGPS ship locations during the ARCMFP2 source tow event. The ship positions recorded during the transmission of the 75–150-Hz PRN sequence are plotted as open circles, defining the six tracks labeled ''a''–''f.'' (Note that a 7-min gap in the recording of the GPS position fixes occurred at the end of track ''d.'') Single-element spectrograms recorded during these transmissions are shown in Figs. 3 and 5–9. Bottom bathymetry contours are plotted at 10-m increments. The 120-m vertical aperture receiving array was deployed from R/P FLIP, whose location is plotted as a heavy, open circle. Also shown as heavy diamonds are the positions of two CTD casts taken near the time of the source tow event. The sound speed profiles derived from these CTD data are given in Fig. 11.

in range and azimuth, is given. Integration of the resulting expression provides a quantitative prediction of the behavior of the striations. The section also provides some physical insight into the nature of the invariant parameter.

A. Pressure spectrum using a mode formulation

At ranges greater than several water depths, the underwater acoustic pressure field from a single omnidirectional point source can be expressed as a finite sum of normal modes. Therefore, if the source generates a single tone with circular frequency, ω, and amplitude $A(\omega)$, at a depth, z_s, and range, r, from a omnidirectional point receiver at depth, z_r, then the complex pressure can be written as

$$p(r,z_r,z_s,\omega)=A(\omega)\sum_{n=0}^{N-1} B_n(z_s,z_r) \times \exp[-i(\omega t-\kappa_n r+\pi/4)], \quad (1)$$

where

$$B_n(z_s,z_r)\equiv\left(\frac{2\pi}{\kappa_n r}\right)^{1/2}\Psi_n(z_s)\Psi_n(z_r). \quad (2)$$

The mode eigenvalues (horizontal wave numbers) are κ_n and the eigenfunctions are $\Psi_n(z)$. The number of modes contributing to the field, N, is a function of frequency, $N(\omega)$. The received pressure spectrum, or mean square pressure, then is

$$I(r,z_r,z_s,\omega)\equiv\langle pp^*\rangle=P(\omega)\left(\sum_n B_n^2 + 2\sum_{n,m} B_nB_m\cos[\Delta\kappa_{mn}(\omega)r]\right). \quad (3)$$

The source spectal level is $P(\omega)$ and the difference in mode wave numbers is $\Delta\kappa_{mn}(\omega)\equiv\kappa_m(\omega)-\kappa_n(\omega)$, where $m\neq n$. The pressure spectrum is composed of the sum of two terms; the first one varies slowly with range and frequency (presuming that the mode amplitudes are not strong functions of frequency), whereas the second term oscillates due to mode interference. It is this oscillatory term that gives rise to the striation pattern in Figs. 3 and 5–9.

Equation (3) can be extended to gradually range- and azimuth-varying waveguides where mode propagation is adiabatic and horizontal refraction effects are negligible by making the following replacements:

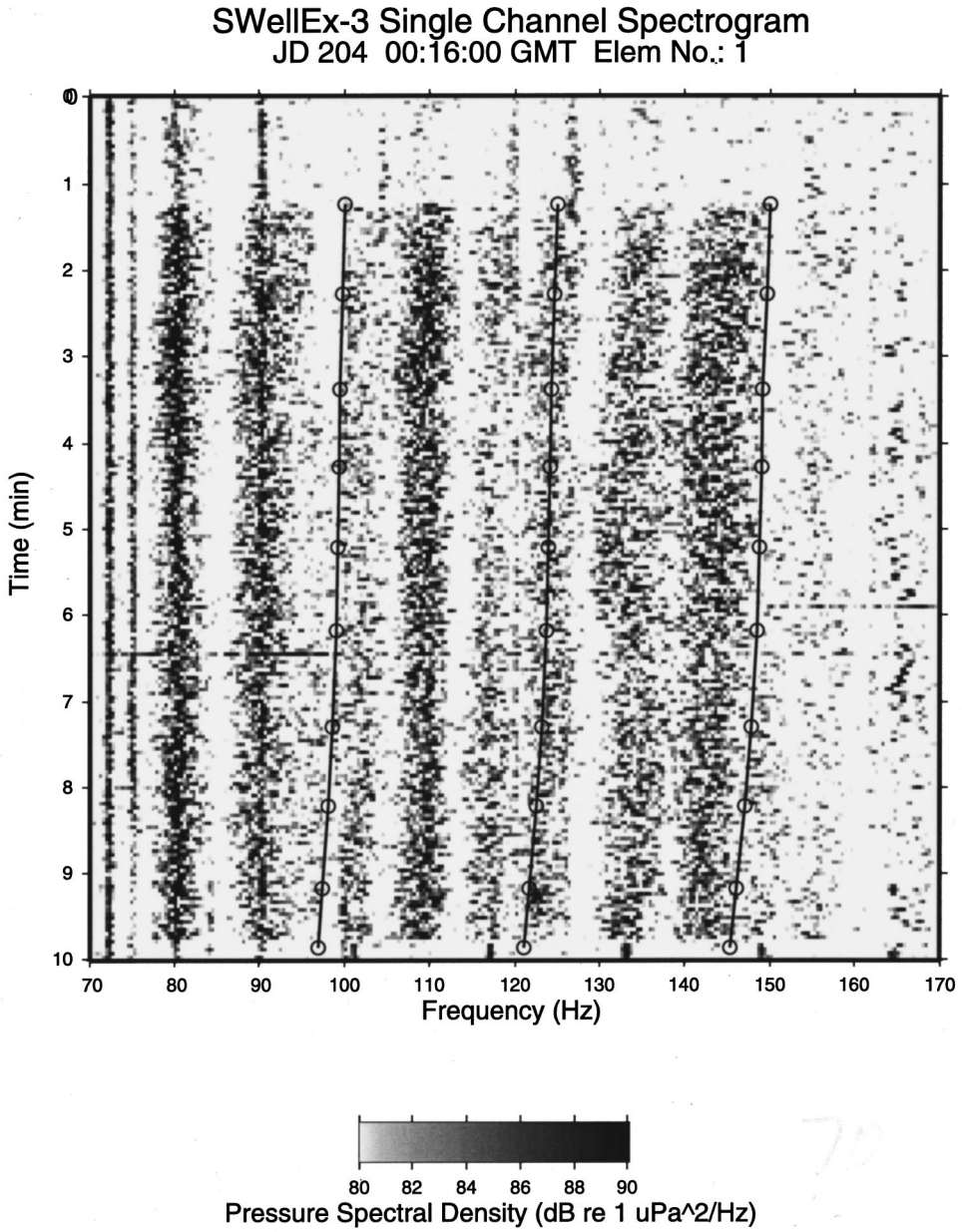

FIG. 5. Ten-minute single-element pressure spectrogram over the 70–170-Hz band along with the model predictions for track ''a'' (see Fig. 4).

$$\Delta\kappa_{mn}(\omega) \longrightarrow \frac{1}{r}\int_0^r \Delta\kappa_{mn}(r,\theta,\omega)\,dr,$$
$$B_n \longrightarrow B_n^{s,r} \equiv \left(\frac{2\pi}{\int \kappa_n dr}\right)^{1/2} \Psi_n^s(z_s)\Psi_n^r(z_r). \tag{4}$$

The quantities $\Psi_n^s(z)$ and $\Psi_n^r(z)$ are the mode n eigenfunctions at the source location and the receiver location, respectively. Both of these locations and the mode eigenfunctions and eigenvalues now are functions of azimuth, θ, as well as range. This ''N by 2D'' adiabatic approximation will be used to model the propagation effects of the range and azimuth variations in bottom bathymetry.

B. Oscillatory nature of the pressure spectrum

Information on the acoustic wave field can be obtained from examination of the oscillatory pattern of the pressure spectrum projected along either the time or frequency axis. For example, if the frequency is fixed at ω_0 and the range is varied, the pressure spectral pattern will vary (co)sinusoidally with a spatial frequency of $\Delta\kappa_{mn}(\omega_0)$. Since

$$\Delta\kappa_{mn}(\omega) = \omega[S_p^m(\omega) - S_p^n(\omega)] \equiv \omega\Delta S_p^{mn}(\omega), \tag{5}$$

where $S_p^m(\omega)$ and $S_p^n(\omega)$ are the mode phase slownesses (inverse phase velocities), then the spatial frequency at fixed ω_0 for variations in range is determined by the differences in mode phase slowness.

The spectrogram in Fig. 3 was estimated from data created by a source moving along a radial towards the receiver. Therefore, a change in time is equivalent to a change in range. At a fixed frequency, the oscillation in the pressure spectrum with range determines the mode *phase* slowness difference. If the range difference between two adjacent striations at a fixed frequency, ω_0, as measured on a spectrogram is ρ, then

$$2\pi = \omega_0 \Delta S_p^{mn}(\omega_0)\rho \tag{6a}$$

or

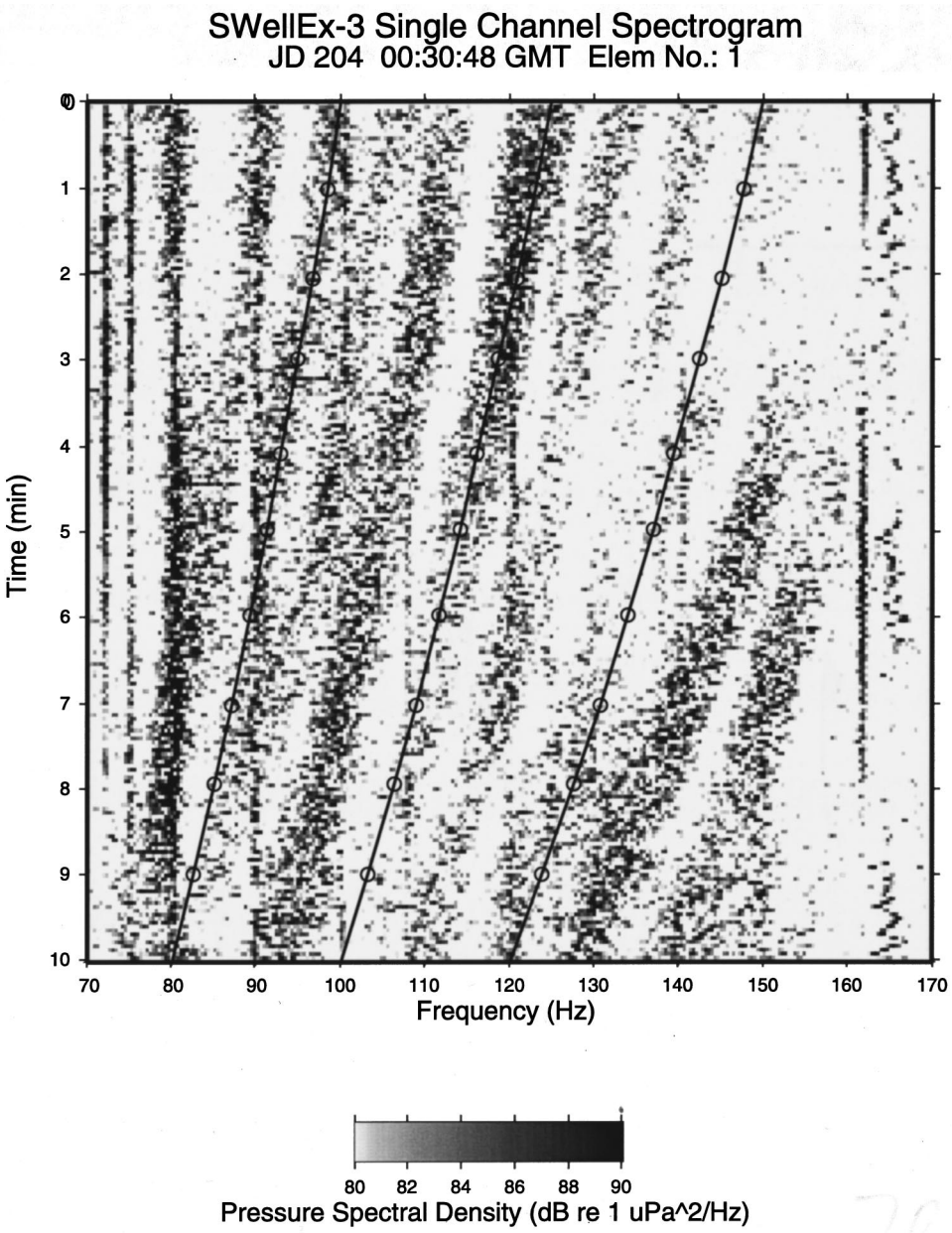

FIG. 6. Ten-minute single-element pressure spectrogram over the 70–170-Hz band along with the model predictions for track ''b'' (see Fig. 4).

$$\Delta S_p^{mn}(\omega_0) = \frac{1}{f_0 \rho}. \tag{6b}$$

In the orthogonal direction on the spectrogram, if the range is fixed at r_0 (corresponding to a given instant in time), then Eq. (3) shows that the spectral pattern also varies (co)sinusoidally. However, the rate of variation is not fixed, but rather is a function of frequency in most cases. The change with frequency is determined by the differences in *group* slowness, i.e.,

$$\frac{\partial \Delta \kappa_{mn}(\omega)}{\partial \omega} = S_g^m(\omega) - S_g^n(\omega) \equiv \Delta S_g^{mn}(\omega), \tag{7}$$

where $S_g^m(\omega)$ and $S_g^n(\omega)$ are the mth and nth modes' group slownesses (inverse group velocities). At fixed range, if the frequency difference between two striations that are located about a center frequency, ω_c, in the pressure spectrogram is Ω_c, then

$$2\pi = r_0 \Delta S_g^{mn}(\omega_c)(2\pi\Omega_c) \tag{8a}$$

or

$$\Delta S_g^{mn}(\omega_c) = \frac{1}{r_0 \Omega_c}. \tag{8b}$$

In summary, the distance between two striations at a fixed frequency gives the phase slowness difference [see Eq. (6)], whereas at a fixed range, the distance between two striations gives the group slowness difference [see Eq. (8)]. In addition, a sudden change in the striation pattern can occur with a small change in frequency. This change indicates the addition of a new, high-order mode whose cutoff frequency—the frequency at which the sudden change occurs—provides information on the geoacoustic properties of the waveguide.

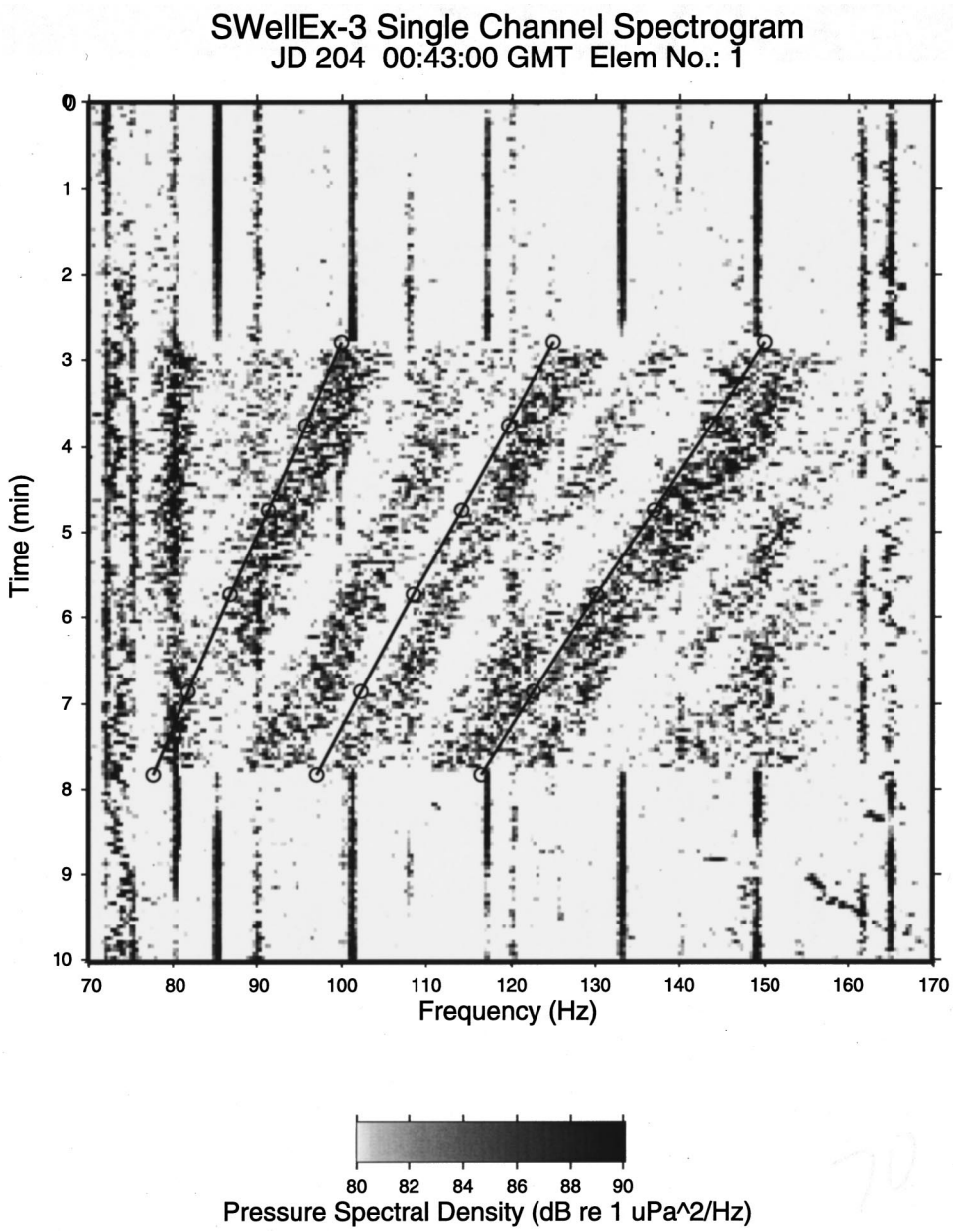

FIG. 7. Ten-minute single-element pressure spectrogram over the 70–170-Hz band encompassing the 5-min PRN transmission period for track ''c'' (see Fig. 4) along with the model predictions.

C. Derivation of the waveguide invariant

The presentation in this part of the section uses as a basis the approach given in Refs. 2 and 3. However, it is extended here to account for the range and azimuthal dependence of the environment. The resulting expression then is integrated in Sec. II D to obtain predictions of the changes in the frequencies of the striations with changes in environmental conditions and source/receiver range.

The condition along a line of constant spectral level is $dI=0$, so that

$$dI(r,\theta,\omega)=\frac{\partial I}{\partial \omega}\,\delta\omega+\frac{\partial I}{\partial r}\,\delta r+\frac{\partial I}{\partial \theta}\,\delta\theta=0. \tag{9}$$

Considering just two modes in Eq. (3), ignoring the range, azimuth, and frequency dependence of the mode amplitudes, and assuming that the source spectral level, $P(\omega)$, is approximately flat, then the partial derivatives are proportional to

$$\frac{\partial I(r,\theta,\omega)}{\partial \omega} \propto -\left(\int \frac{\partial \Delta\kappa_{mn}(\omega)}{\partial \omega}\,dr\right)\sin\left(\int \Delta\kappa_{mn}(\omega)\,dr\right), \tag{10a}$$

$$\frac{\partial I(r,\theta,\omega)}{\partial r} \propto -\Delta\kappa_{mn}(\omega,\mathrm{recr})\sin\left(\int \Delta\kappa_{mn}(\omega)\,dr\right), \tag{10b}$$

$$\frac{\partial I(r,\theta,\omega)}{\partial \theta} \propto -\frac{\partial}{\partial \theta}\left(\int \Delta\kappa_{mn}(\omega)dr\right)\sin\left(\int \Delta\kappa_{mn}(\omega)\,dr\right), \tag{10c}$$

where $\Delta\kappa_{mn}(\omega,\mathrm{recr})$ represents the wave number difference at the receiver location. Plugging these partial derivatives into Eq. (9) and rearranging gives the following:

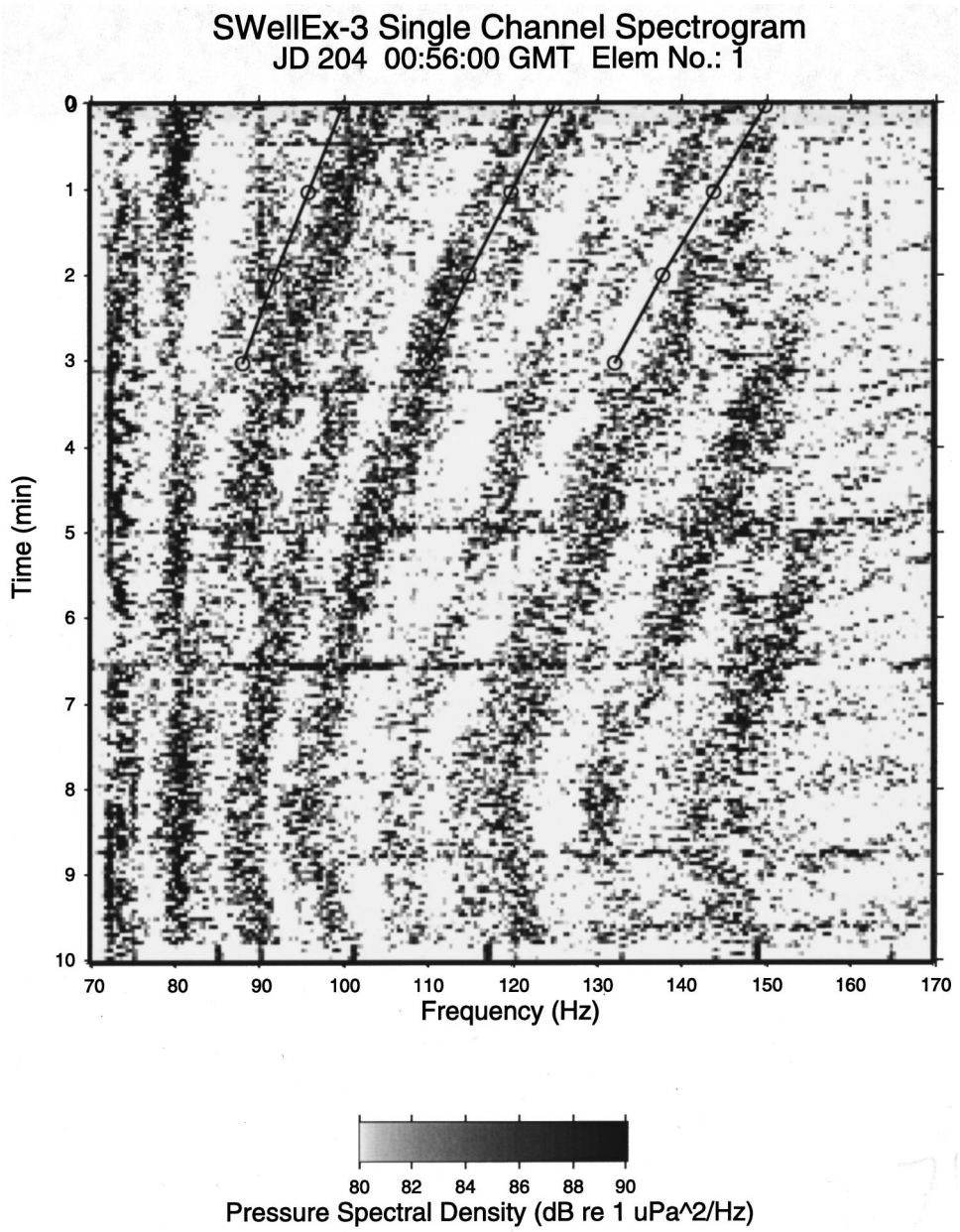

FIG. 8. Ten-minute single-element pressure spectrogram over the 70–170-Hz band along with the model predictions for track ''d'' (see Fig. 4). The model predictions are shown only for the first 3 min due to the loss of source ship DGPS recordings over the final 7 min of the track.

$$\frac{r}{\omega}\left(\frac{1}{r}\int \frac{\partial \Delta\kappa_{mn}}{\partial\omega}\,dr\right)\left(\frac{\Delta\kappa_{mn}(\omega,\mathrm{recr})}{\omega}\right)^{-1}\delta\omega+\delta r + \frac{1}{\Delta\kappa_{mn}(\omega,\mathrm{recr})}\frac{\partial}{\partial\theta}\left(\int \Delta\kappa\,dr\right)\delta\theta=0. \tag{11}$$

The expression for the waveguide invariant in Refs. 2 and 3 is given by the slope along a line of constant spectral level in range- and azimuth-independent environments. For this specific environment, Eq. (11) becomes

$$\frac{\delta r}{\delta\omega}=-\frac{r}{\omega}\frac{\partial\Delta\kappa_{mn}(\omega)/\partial\omega}{\Delta\kappa_{mn}(\omega)/\omega}=-\frac{r}{\omega}\frac{\partial S_g^{mn}(\omega)}{\partial S_p^{mn}(\omega)}. \tag{12}$$

The quantity $-\partial S_g^{mn}/\partial S_p^{mn}$ is approximately invariant for a group of closely spaced modes with respect to the range between source and receiver (in range-independent media), the depths of the source and receiver, the frequency, and the individual mode number within the mode group. It is denoted in Refs. 2 and 3 as

$$-\frac{\partial S_g}{\partial S_p}\equiv\frac{1}{\beta}. \tag{13}$$

In a weakly range-dependent waveguide where mode propagation is adiabatic, the expression for $\beta^{-1}(r)$ is given in Ref. 2 as

$$\frac{1}{\beta(r)}=-\left(\frac{1}{r}\int\frac{\partial\Delta\kappa_{mn}}{\partial\omega}\,dr\right)\left(\frac{\Delta\kappa_{mn}(\mathrm{recr})}{\omega}\right)^{-1}=-\frac{\partial\overline{S}_g(r)}{\partial S_p(\mathrm{recr})}, \tag{14}$$

where $\overline{S}_g(r)\equiv(1/r)\int_0^r S_g(x)\,dx$ is the average group slowness from the source to receiver, and $S_p(\mathrm{recr})$ and $\Delta\kappa_{mn}(\mathrm{recr})$ are the phase slowness and mode wave number difference at the receiver location, respectively.

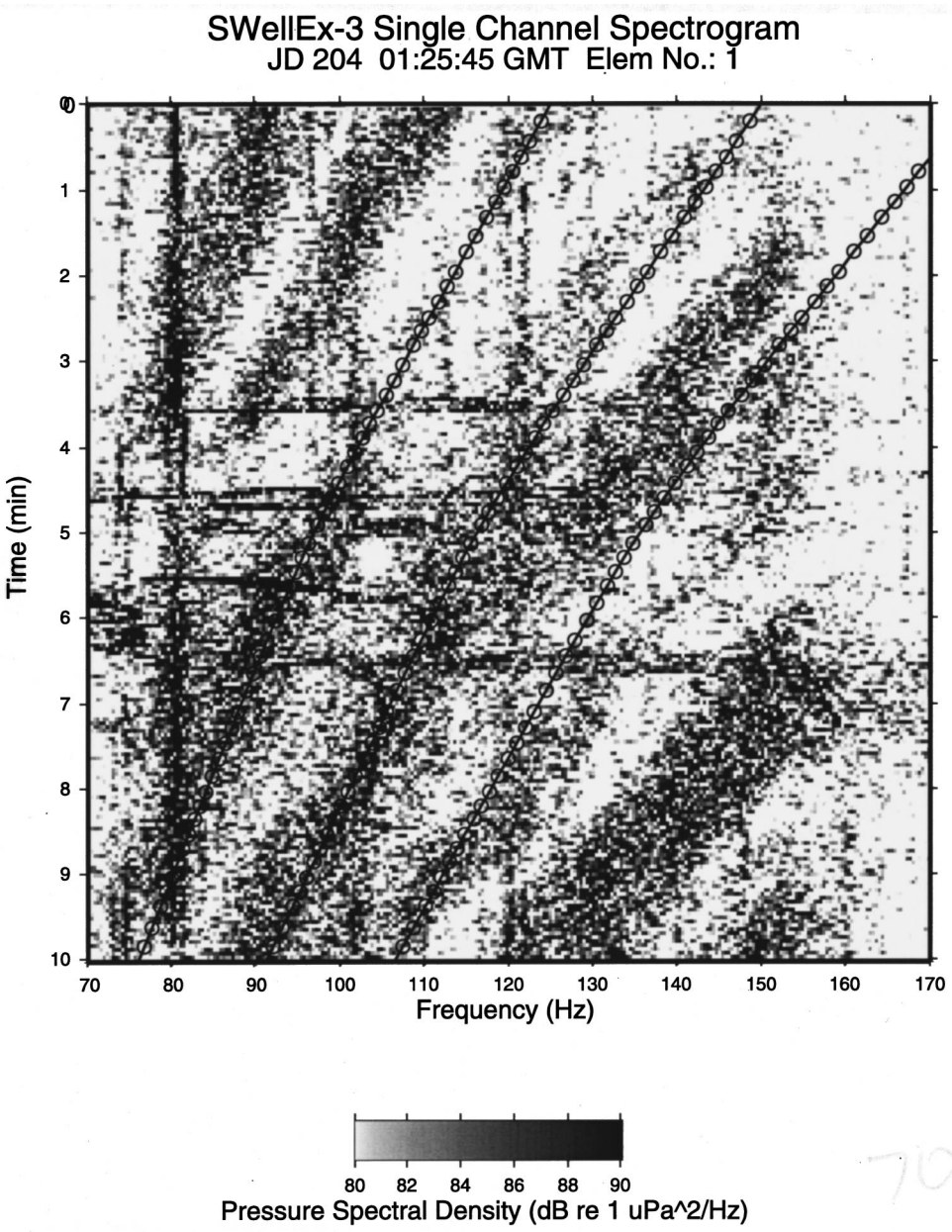

FIG. 9. Ten-minute single-element pressure spectrogram over the 70–170-Hz band along with the model predictions for track ''f'' (see Fig. 4).

Returning to Eq. (11), using the fact that $\Delta\kappa = \int (\partial \Delta\kappa/\partial\omega)\, d\omega$, and reversing the order of integration over range and frequency, then the third expression on the left-hand side can be written as

$$\frac{1}{\Delta\kappa(\mathrm{recr})}\frac{\partial}{\partial\theta}\left(\int \Delta\kappa\, dr\right)\delta\theta = \frac{r}{\Delta\kappa(\mathrm{recr})}\frac{\partial}{\partial\theta}\left\{\int\left[\frac{\Delta\kappa(\mathrm{recr})}{\omega}\left(\frac{1}{r}\int\frac{\partial\Delta\kappa}{\partial\omega}\, dr\right)\times\left(\frac{\Delta\kappa(\mathrm{recr})}{\omega}\right)^{-1}\right] d\omega\right\}\delta\theta. \quad (15)$$

Plugging in the expression for $\beta^{-1}(r)$ from Eq. (14), and recognizing that it is approximately independent of frequency and that $\Delta\kappa(\mathrm{recr})$ is independent of azimuth, then Eq. (15) becomes

$$\frac{1}{\Delta\kappa(\mathrm{recr})}\frac{\partial}{\partial\theta}\left(\int \Delta\kappa\, dr\right)\delta\theta = -\frac{r}{\Delta\kappa(\mathrm{recr})}\left\{\int\frac{\Delta\kappa(\mathrm{recr})}{\omega}\, d\omega\right\}\frac{\partial}{\partial\theta}\left\{\frac{1}{\beta(r,\theta)}\right\}\delta\theta. \quad (16)$$

The integral over frequency can be easily evaluated, using the results presented in Appendix A [see Eq. (A8)]; it equals $-\beta(\mathrm{recr})\Delta\kappa(\mathrm{recr})$. Substituting these results into Eq. (11), carrying out the differentiation with respect to θ on the right-hand side of Eq. (16), and rearranging terms yields

$$\frac{\delta\omega}{\omega} = \beta(r,\theta)\frac{\delta r}{r} - \frac{\beta(\mathrm{recr})}{\beta(r,\theta)}\frac{\partial}{\partial\theta}(\beta(r,\theta))\,\delta\theta. \quad (17)$$

This expression is integrated in the next part of this section to obtain predictions of the changes in the frequency of the striations as a broadband source moves through a range and azimuthally dependent environment.

D. Frequency dependence of the striation pattern

The condition along a line of constant spectral level in a broadband spectrogram is given by Eq. (17). Integrating this equation, specifying the variables as functions of time due to motion of the source, gives

$$\frac{\omega(t)}{\omega(t_0)} = \left(\frac{\beta(r(t),\theta(t))}{\beta(r(t),\theta(t_0))} \right)^{-\beta(\mathrm{recr})} \exp\left(\int_{r_0}^{r(t)} \frac{\beta(r,\theta)}{r}\, dr \right). \tag{18}$$

In general, the integral involving β over range must be done numerically. A straightforward approach is presented in Appendix B that can be used for this purpose. However, two special cases now will be considered that circumvent this integration. These special cases apply, to first approximation, to the environmental conditions along the SWellEx-3 tracks described in Sec. I.

For the first special case, the environment is assumed to be independent of range and azimuth. Equation (18) then becomes

$$\omega(t) = \omega_0 \left(\frac{r(t)}{r_0} \right)^{\beta}. \tag{19}$$

This equation is used to predict the behavior of the striation patterns in Figs. 3 and 9 as the towed source approached FLIP from the north along range independent tracks ''e'' and ''f.''

The second special case is where the source–receiver range remains constant. For this case, Eq. (18) is

$$\omega(t) = \omega_0 \left(\frac{\beta(t)}{\beta(t_0)} \right)^{-\beta(\mathrm{recr})}. \tag{20}$$

Equation (20) is used to predict the behavior of the striation patterns in Figs. 5–8 as the towed source traveled along the arc to the north and west of FLIP, along tracks ''a''–''d'' in Fig. 4. The expression for $\beta(t)$ in shallow water environments where the range dependence is due to variations in bottom bathymetry is derived in the next section.

III. RANGE-DEPENDENT INVARIANT IN SHALLOW WATER

This section presents the derivation of the waveguide invariant itself for shallow water environments with range-varying bottom bathymetry. The development holds in cases where the bottom of the waveguide is formed by reflection from the ocean/sediment interface rather than by refraction from within the bottom.

A. Range-independent, homogeneous waveguide

For a homogeneous, range-independent waveguide bounded by pressure-release surfaces, the vertical wave number, γ_n, is independent of frequency. It can easily be shown that

$$\frac{1}{\beta} = \frac{k^2}{\kappa_n^2} = \frac{1}{\cos^2(\phi_n)}, \tag{21}$$

where κ is the medium wave number. For the low-order modes, ϕ_n, the horizontal angle from the vertical, is small, giving the shallow water result of $\beta \approx 1$.

B. Range-dependent, homogeneous waveguide

The expression for $\beta^{-1}(r)$ in a range-dependent waveguide where mode propagation is adiabatic is given by Eq. (14). Applying this equation to a waveguide with constant sound speed but range-varying bottom bathymetry gives

$$\frac{1}{\beta(r)} = -\frac{\partial \overline{S_g^n}(r)/\partial\omega}{\partial S_p^n(\mathrm{recr})/\partial\omega} = \frac{(1-\gamma_n^2(\mathrm{recr})/k^2)^{1/2}}{\gamma_n^2(\mathrm{recr})} \frac{1}{r} \int_0^r \frac{\gamma_n^2(x)}{(1-\gamma_n^2(x)/k^2)^{3/2}}\, dx. \tag{22}$$

For the low-order modes where $\gamma_n^2/k^2 \ll 1$, then Eq. (22) becomes

$$\frac{1}{\beta(r)} \approx \frac{1}{\gamma_n^2(\mathrm{recr})} \left(1 - \frac{1}{2}\gamma_n^2(\mathrm{recr})/k^2 \right) \frac{1}{r} \int_0^r \gamma_n^2(x) \times (1 + \tfrac{3}{2}\gamma_n^2(x)/k^2)\, dx. \tag{23}$$

The first-order term in Eq. (23) yields

$$\frac{1}{\beta(r)} \approx \frac{1}{\gamma_n^2(\mathrm{recr})} \frac{1}{r} \int_0^r \gamma_n^2(x)\, dx = D^2(\mathrm{recr}) \frac{1}{r} \int_0^r \frac{1}{d^2(x)}\, dx, \tag{24}$$

where $\gamma_n(x) = n\pi/d(x)$ with $d(x)$ being the range dependent water depth and $D(\mathrm{recr})$ is the water depth at the receiver location. This expression can be used to provide the offset in estimated range in matched field source localization resulting from neglecting range dependence of the bottom bathymetry in a shallow water waveguide [see Eq. (27) of Ref. 9].

The integral in Eq. (24) can be evaluated easily if the bottom bathymetry between source and receiver is modeled by connected straight-line segments (see Ref. 9). The result is

$$\int \frac{1}{d^2(x)}\, dx = \sum_{i=1}^{M} \frac{x_i - x_{i-1}}{d_i d_{i-1}}. \tag{25}$$

The bottom bathymetry over the ith segment is $d(x) = d_{i-1} + \alpha_i(x - x_{i-1})$ for $x_{i-1} \leqslant x \leqslant x_i$, and the sum of the horizontal segment lengths over all M segments equals the range, i.e., $r = \Sigma_{i=1}^{M}(x_i - x_{i-1})$. If the actual bottom has approximately constant slope, so that it can be fit by a single straight-line segment, then

$$\frac{1}{\beta(r)} \approx \frac{D(\mathrm{recr})}{D(\mathrm{src})}, \tag{26}$$

where $D(\mathrm{src})$ is the water depth at the source location.

Equation (24) for the range-dependent invariant, along with Eq. (25), is used to obtain values for $\beta(t)$ in Eq. (20) to model the bottom bathymetry effects on the striation patterns, as discussed in the next section.

TABLE I. Equations used for figure predictions.

Figure No.	Track	Equation for predictions	
3	''e''	$\omega(t)=\omega_0(r(t)/r_0)^{\beta}$	(19)
5	''a''	$\omega(t)=\omega_0(\beta(t)/\beta(t_0))^{-\beta(\mathrm{recr})}$	(20)
6	''b''	$\omega(t)=\omega_0(\beta(t)/\beta(t_0))^{-\beta(\mathrm{recr})}$	(20)
7	''c''	$\omega(t)=\omega_0(\beta(t)/\beta(t_0))^{-\beta(\mathrm{recr})}$	(20)
8	''d''	$\omega(t)=\omega_0(\beta(t)/\beta(t_0))^{-\beta(\mathrm{recr})}$	(20)
9	''f''	$\omega(t)=\omega_0(r(t)/r_0)^{\beta}$	(19)

IV. COMPARISONS OF MODEL WITH DATA

Predictions of the frequency dependence of the striations from the analytical model in Secs. II D and III B are superimposed on the spectrograms in Figs. 3 and 5–9. Agreement between the model predictions and the data is excellent. The purpose of this section is to describe how these predictions were made and to discuss some of the aspects of the model/data comparison. As an aid to the reader, Table I summarizes which of the two equations in Sec. II D were used to make the predictions in each of the figures.

As a starting point, the receiving vertical array was taken to be motionless over the entire ARCMFP2 event. This assumption is valid since the bottom of the array was deployed on the ocean floor with the tension along the array being provided by positively buoyant floats above the uppermost array element. Although the top of the array was connected to R/P FLIP by the data cable, the differential global positioning system (DGPS)-derived motion of FLIP during ARCMFP2 was within the measurement accuracy of ± 3 m rms so that any tugging by FLIP on the top of the array was negligible. Also, the inclination from vertical measured by a tiltmeter at the top of the array never exceeded 1.4 degrees during the event. Therefore, the average of the DGPS position fixes recorded on FLIP over the entire ARCMFP2 event was used as the fixed array position, and the temporal dependence of the invariant was assumed to be due solely to the motion of the source.

The next step was to calculate the range-dependent values of β^{-1} at specific points along each of the six tracks. These points were chosen by selecting the DGPS position fixes recorded on the source tow ship at approximate 1-min intervals. These positions at 1-min increments (uncorrected for the horizontal offset between the ship DGPS antenna and the underwater source) and the fixed FLIP position were input into an algorithm that extracts the bottom bathymetry between source and receiver from a geoacoustic database for the SWellEx site.[11] Equations (24) and (25) then were used to calculate the value of β^{-1} for each bathymetry profile. The resulting values of β^{-1} along each of the six tracks are plotted in Fig. 10. As the figure shows, the invariant along tracks ''e'' and ''f'' is constant over time at the range-independent, shallow water value close to 1.0 (see Sec. III A). It is also nearly constant along track ''a,'' although at a significantly greater value of 3.3 due to the strong range-dependent bathymetry between source and receiver (see Fig. 4). However, for tracks ''b''–''d'', β^{-1} decreases appreciably over time because of the increasing water depth along these tracks. These invariant values were used in Eq. (20) to

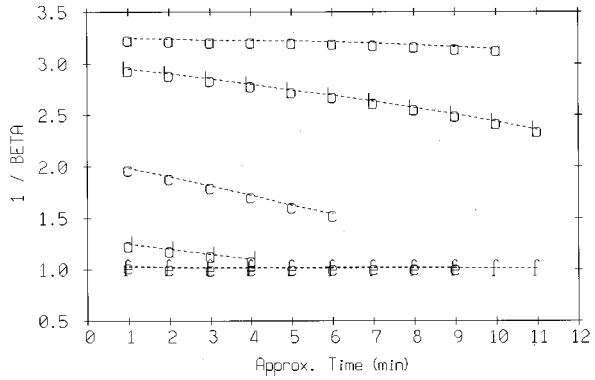

FIG. 10. Plots of β^{-1} as a function of time for each of the six tracks ''a''–''f,'' calculated from Eqs. (24) and (25) of the paper.

predict the striation pattern along tracks ''a''–''d'' where the source/receiver range was approximately constant, and in Eq. (19) to make predictions for tracks ''e'' and ''f'' where the bathymetry was range independent. In applying these equations, three values of ω_0 were arbitrarily chosen; 100, 125, and 150 Hz for tracks ''a''–''e'' and 125, 150, and 175 Hz for track ''f.'' In all cases, the temporal dependence of the striation frequencies are well matched by the model predictions.

The assumptions made in obtaining Eqs. (19) and (20) from Eq. (18) are only approximately true for the ARCMFP2 tracks. Another equation that is more generally applicable and that avoids the evaluation of the range integral can be obtained. That is, if the invariant is approximately range independent over the range interval from r_0 to $r(t)$ in Eq. (18), even if it is range dependent between source and receiver, then

$$\omega(t)=\omega_0\left[\frac{r(t)}{r_0}\right]^{\beta(t)}\left[\frac{\beta(t)}{\beta(t_0)}\right]^{-\beta(\mathrm{recr})}. \tag{27}$$

The result is, in effect, a combination of Eqs. (19) and (20). An example application of this equation is to the data from track ''a'' where the source increased slightly in range from FLIP, towards the end of the track, as can be seen in Fig. 4. This range increase tends to cancel the effects of increasing water depth along the source track and explains the small bias in the predictions towards more rapid decreases in frequency over the final 4 min of Fig. 5. The application of Eq. (27) eliminates this bias to a large extent. Clearly, then, if the source/receiver range along tracks ''a''–''d'' had increased at the appropriate rate, then it would have counteracted the effects of increasing water depth and the striation pattern would have remained constant over time. The appropriate rate of range increase can be obtained by setting the left-hand side of Eq. (18) to unity.

As mentioned previously, a gap in the recording of the DGPS position fixes on the source tow ship occurred over the last 7 min of track ''d.'' This gap is particularly unfortunate since the slope of the interference pattern in Fig. 8 changed over the course of this track, thereby presenting an interesting test of the analytical model. By connecting the end of track ''d'' to the next set of recorded DGPS fixes in Fig. 4, it appears that the ship continued to the west for 3–4 min and then executed a 180 degree turn to starboard. Over

the westbound portion, the water depth became progressively greater, leading to the continued decrease in striation frequency in Fig. 8. However, as the turn to the north was made, the source/receiver range began to increase following the bottom bathymetry contours. This range increase resulted in the change in slope of the striation pattern. The ''bathtub'' feature between the 8- and 9-min marks in Fig. 8 (i.e., the point where the striations change from sloping towards decreasing frequency with increasing time to that where they increase in frequency with increasing time) arises not from any Lloyd's mirror effect (the source/receiver range is about 30 water depths at this time), but from changing conditions of intermode interference.

To this point, all the changes in the striation patterns in Figs. 3 and 5–9 have been modeled as due either to changes in source/receiver range and/or in water depth. However, changes in water column sound speed also should have an impact on the striation pattern. A convenient way of including these effects into the analytical model is given by the generalized theory of waveguide invariants presented in Ref. 12. The main result there is that, for waveguide propagation in a range-independent medium, the mode wave number differences can be expressed in a power law relationship involving the frequency and the various waveguide parameters:

$$\Delta\kappa_{mn} = \alpha_{mn}\eta^{\gamma/\beta}\omega^{-1/\beta}, \tag{28}$$

where α_{mn} is a constant that depends upon mode order, η represents a waveguide parameter (e.g., sound speed, water depth, etc.), and γ is the corresponding invariant for the given waveguide parameter. For example, in a homogeneous, range-independent, ideal waveguide with constant sound speed, c,

$$\Delta\kappa_{mn} = \tfrac{1}{2}\pi^2(n^2-m^2)cD^{-2}\omega^{-1}. \tag{29}$$

Comparing this expression with Eq. (28) indicates that β equals 1 (as expected), the value of $\gamma(D)$ is -2, and that of $\gamma(c)$ is $+1$. Equation (28) is valid for range-independent waveguides. However, for adiabatic propagation, it can be extended in a straightforward way. Letting $\hat{\beta}$ and $\hat{\gamma}$ represent the invariants for the corresponding range-independent case, then making use of the definition for $\beta^{-1}(r)$ in Eq. (14), gives

$$\frac{1}{\beta(r)} = \frac{1}{\hat{\beta}}\left(\frac{1}{r}\int \eta(x)^{\hat{\gamma}/\hat{\beta}}\,dx\right)(\eta(\mathrm{recr})^{\hat{\gamma}/\hat{\beta}})^{-1}. \tag{30}$$

Note that Eq. (30) applied to a shallow water waveguide with range-independent sound speed but range-dependent bathymetry simplifies to Eq. (24). Including range dependence to the sound speed yields

$$\frac{1}{\beta(r)} = \frac{D^2(\mathrm{recr})}{c(\mathrm{recr})}\frac{1}{r}\int \frac{c(x)}{d^2(x)}\,dx. \tag{31}$$

Figure 11 presents plots of two sound speed profiles calculated from the two CTD (conductivity-temperature-depth) data taken nearest in time to the ARCMFP2 event. The locations of these two CTD casts are shown on the map in Fig. 4. The one just to the east of track ''f'' was collected in 175-m-deep water, whereas the other one to the southeast

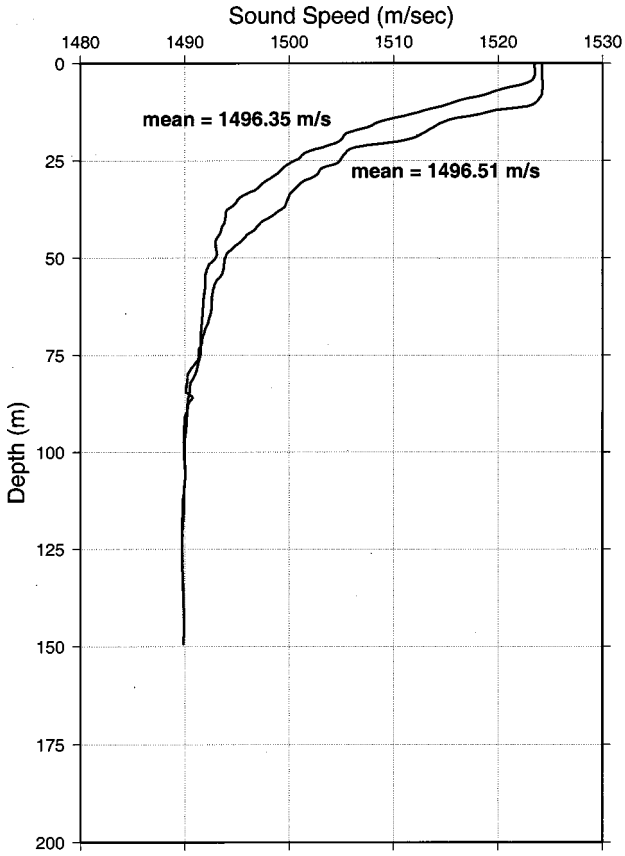

FIG. 11. Two sound speed profiles as a function of depth derived from the data taken during two CTD casts. The arithmetic mean over depth is given next to each profile. The locations of the two casts are shown in Fig. 4.

was taken in 120-m water. The arithmetic means of the two profiles also is given in Fig. 11. Because the sound speed profile in deeper water has a thicker mixed layer at the surface, but greater water column extent below the thermocline than the shallower profile, the two mean sound speeds are nearly identical. Therefore, changes in depth-average sound speed over the course of ARCMFP2 are negligible. In any case, the effect of changes of a few percent in average sound speed would be trivial in comparison to the effect of over 150% changes in water depth over the course of ARCMFP2.

Although the character of the broadband interference patterns is insensitive to water column sound speed changes in this shallow water environment, it clearly is a useful probe for determining changes in water depth. Therefore, Eq. (18), along with Eq. (24), provides a way of performing inversions for bottom bathymetry using moving sources of opportunity. For example, assume for simplicity that only source motion along radial tracks away from the receiver is considered. That is, for each track, the invariant is independent of azimuth. In this case, Eq. (18) becomes

$$\frac{\omega(t)}{\omega(t_0)} = \exp\left(\int_{r_0}^{r(t)} \frac{\beta(r,\theta)}{r}\,dr\right). \tag{32}$$

If the range of the broadband source, $r(t)$, is known as a function of time (e.g., radar tracking of a surface ship), then

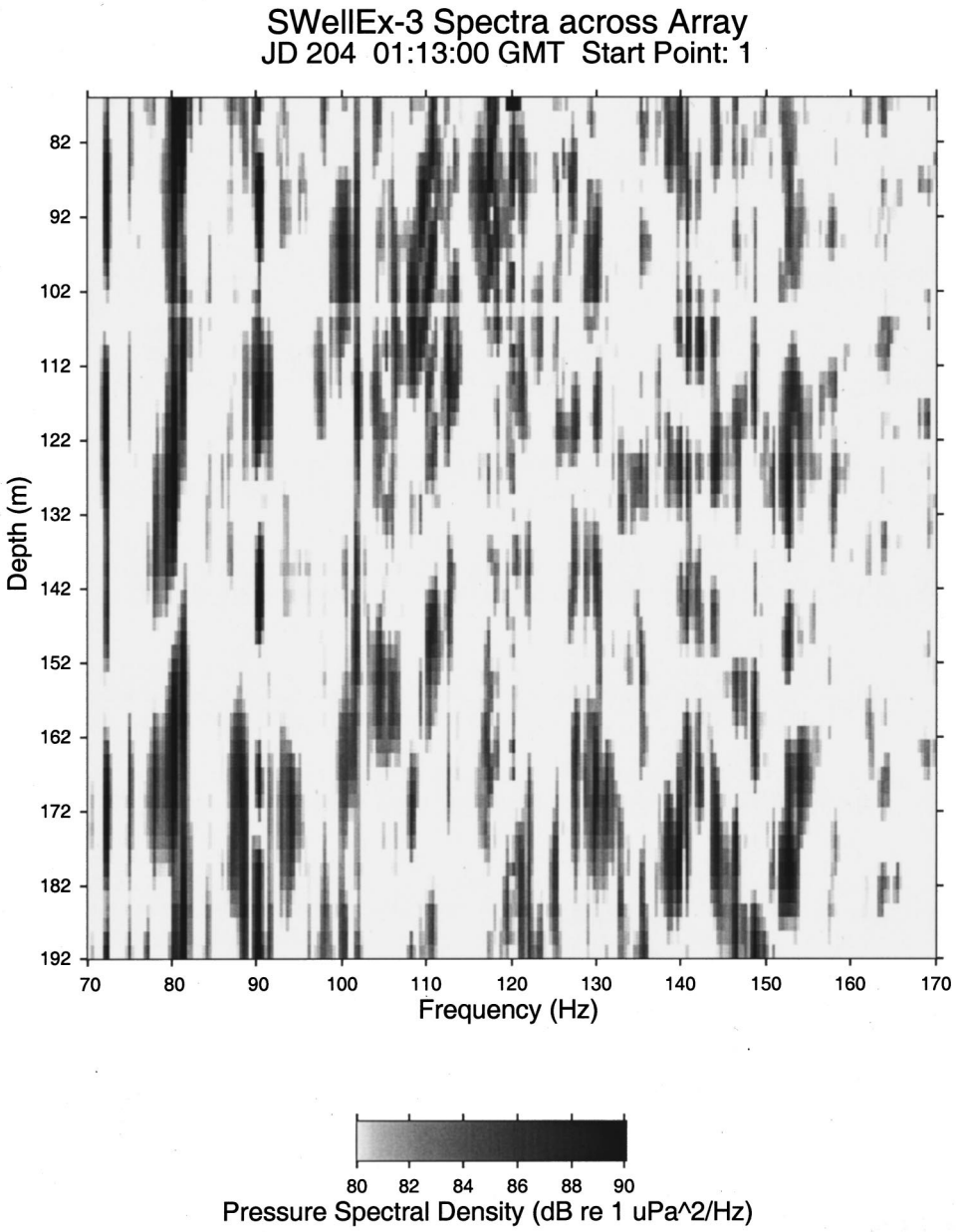

FIG. 12. The pressure spectral density as a function of depth over the receiving vertical array for a time period during track ''e.'' The spectra were estimated from 5.5 s of data starting 3 min after the beginning of the spectrogram in Fig. 3. Element 48 at 104-m depth had an abnormally low sensitivity.

the time-varying frequency content of the striations, $\omega(t)$, can be used as the data in a classical inversion approach for $\beta(r)$.

All of the underwater acoustic data presented so far were collected by the lowermost hydrophone of the 64-element vertical line array. To show how the interference pattern varies with array element, the pressure spectral density as a function of depth across the array for the range-independent track ''e'' is presented in Fig. 12. The patchy appearance is due to the oscillatory nature of the mode eigenfunctions with depth, with the highest-order dominant mode in the field giving rise to the smallest-spatial-scale fluctuations. For comparison, Fig. 13 shows the interference pattern with depth when the source was upslope from the receiving array running along track ''a.'' Here, the depth variations have longer spatial scales because of the smaller number of propagating modes imposed by the shallower water depth at the source location.

V. CONCLUSIONS

An analytical model based on the waveguide invariant approach has been developed to predict the frequency dependence of broadband interference patterns in shallow water, single-element spectrograms. The agreement between the model predictions and actual ocean acoustic data collected during the shallow water SWellEx-3 experiment off San Diego, as shown in Figs. 3 and 5–9, is quite good.

Equations (17) and (18) are applicable to any waveguide whose properties vary in range and azimuth. Their derivation assumes that the spectrum of the source signature is roughly flat across its band, and that the spatial variations in the environment are sufficiently weak that the adiabatic approximation can be used and that no azimuthal coupling occurs. The derivation of β makes the additional assumptions that the source is several waveguide depths in range from the receiver (the long-range approximation), that the mode

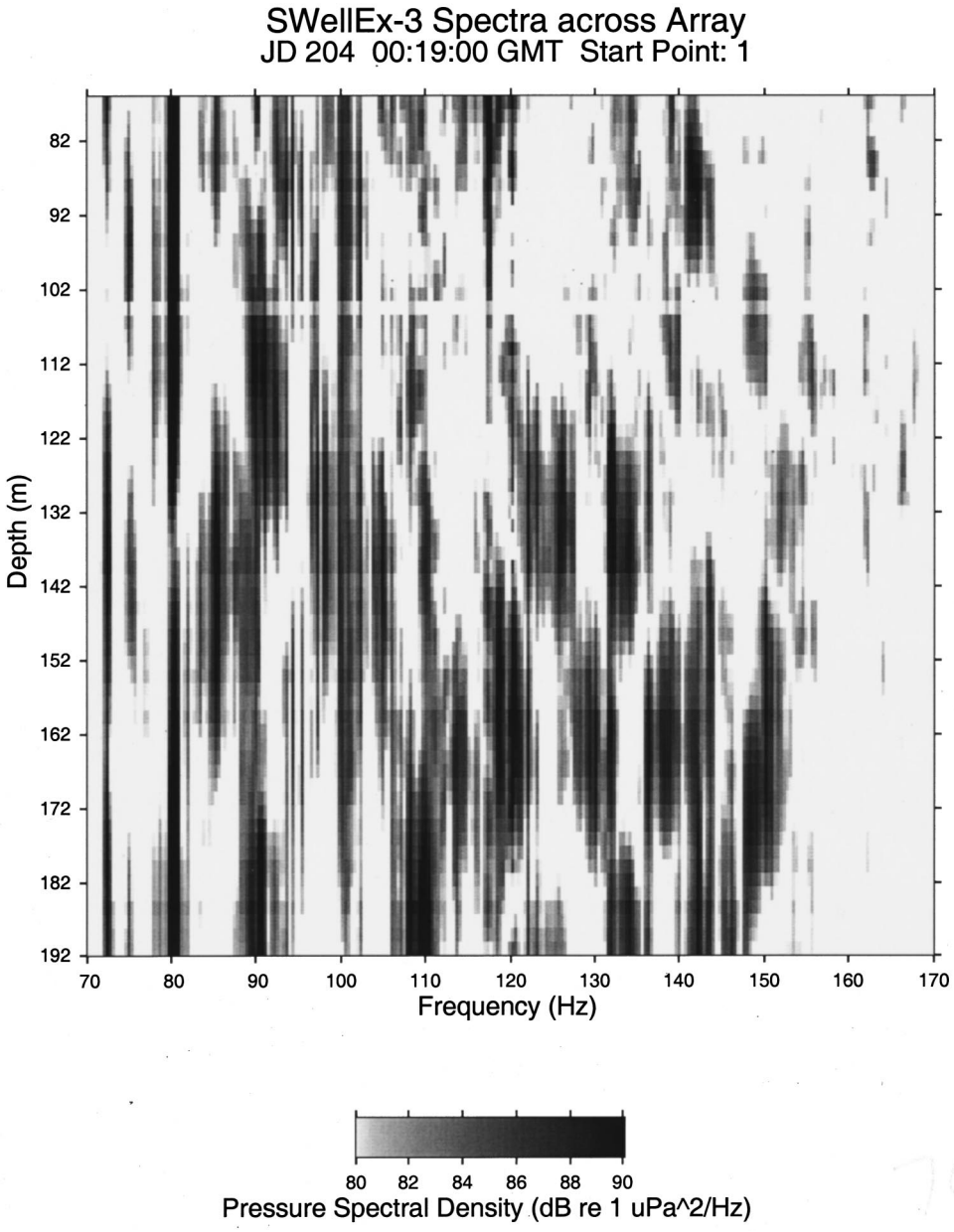

FIG. 13. The pressure spectral density estimates as a function of depth 3 min after the start of track ''a'' in Fig. 5. All other aspects of the plot are the same as in Fig. 12.

eigenfunctions are not strong functions of frequency, and that the Wentzel–Kramers–Brillovin (WKB) approximation applies. The expression for the range-dependent invariant in Eq. (30) also is generally applicable to spatially variable waveguides. However, Eq. (24) is specific to shallow water environments where bottom bathymetry changes are important. That is, it applies when the waveguide is formed by reflection from both the upper and lower boundaries. If one of the waveguide boundaries is formed by refraction, e.g., when bottom penetration is significant, then β no longer is approximately equal to one, and Eq. (24) must be modified accordingly. The close match between the model predictions and the data presented in this paper demonstrate the applicability of this expression to the SWellEx environment.

ACKNOWLEDGMENTS

Lewis Berger at MPL created most of the figures for this paper. Jim Murray, also at MPL, provided the database extraction programs for the range-dependent invariant calculations. Bill Hodgkiss and Bill Gaines of MPL, and Newell Booth and Joe Rice at SPAWAR Systems Center, San Diego, helped plan and conduct the SWellEx-3 experiment. Thanks also to the crew of R/P FLIP and the Acoustic Explorer for their at-sea support. Helpful suggestions were provided by Warren Denner of EOS Research Associates and Dale Barbour at the SACLANTCEN in La Spezia, Italy, after reading a first draft of this paper. This work was supported by the Office of Naval Research.

APPENDIX A: FREQUENCY DEPENDENCE OF WAVEGUIDE DISPERSION

One insight into the nature of the waveguide invariant, β, is that it specifies the frequency dependence of the dispersion characteristics of an acoustic field. This point can be demonstrated by starting with the definitions for phase and group slownesses, i.e., $S_p = \kappa/\omega$ and $S_g = \partial\kappa/\partial\omega$, giving

$$S_g = S_p + \omega \frac{\partial S_p}{\partial \omega}. \tag{A1}$$

Differentiating Eq. (A1) and plugging in the definition for β, recognizing that $-\partial S_g/\partial S_p = -(\partial S_g/\partial\omega)/(\partial S_p/\partial\omega)$, gives the following equation:

$$\omega \frac{\partial^2 S_p}{\partial \omega^2} + \left(2 + \frac{1}{\beta}\right)\frac{\partial S_p}{\partial \omega} = 0. \tag{A2}$$

This linear, second-order, differential equation can be solved by standard techniques, yielding

$$S_p(\omega) = C_1 \frac{1}{1+1/\beta} + C_2 \frac{1}{\omega^{(1+1/\beta)}}, \tag{A3}$$

where C_1 and C_2 are constants of integration independent of ω. Likewise, solving for the group slowness using Eq. (A1)

$$S_g(\omega) = C_1 \frac{1}{1+1/\beta} - C_2 \frac{1}{\beta}\frac{1}{\omega^{(1+1/\beta)}}. \tag{A4}$$

Therefore, the frequency dependence of the mode phase slowness is $+\omega^{-(1+1/\beta)}$, whereas for the mode group slowness, it is given by $-\omega^{-(1+1/\beta)}$.

The frequency dependence of the mode phase slownesses also can be derived analytically using the WKB approximation:

$$\begin{aligned} S_p^n(\omega) \equiv \frac{\kappa_n}{\omega} &= \frac{[k^2(z,\omega) - \gamma_n^2(z,\omega)]^{1/2}}{\omega} \\ &\approx \frac{k(z,\omega)}{\omega}\left(1 - \frac{1}{2}\frac{\gamma_n^2(z,\omega)}{k^2(z,\omega)}\right) \\ &= \frac{1}{c(z)} - \frac{1}{2}c(z)\gamma_n^2(z,\omega)\frac{1}{\omega^2}, \end{aligned} \tag{A5}$$

where $\gamma_n(z,\omega)$ is the mode vertical wave number. Comparing Eq. (A5) to Eq. (A3) provides expressions for the constants of integration in terms of β:

$$C_1 = \frac{1+1/\beta}{c(z)}, \tag{A6a}$$

$$C_2 = -\tfrac{1}{2}c(z)\gamma_n^2(z,\omega)\omega^{-(1-1/\beta)}. \tag{A6b}$$

By definition, C_2 is independent of frequency, so that

$$\gamma_n^2(\omega) \propto \omega^{(1-1/\beta)}. \tag{A7}$$

Also, given that C_1 is independent of mode number, then Eq. (A3) can be used to show that the mode wave number differences and the circular frequency have the following power law relationship:

$$\Delta\kappa_{mn}(\omega) = (C_2^n - C_2^m)\omega^{-1/\beta}. \tag{A8}$$

Therefore, the waveguide invariant, β, for a given environment provides the frequency dependence of the dispersion curves [Eqs. (A3) and (A4)] and the frequency dependence of the vertical and horizontal mode wave numbers under the WKB approximation. As an example, in a range-independent, shallow water waveguide where $\beta \approx 1$ (see Sec. III A), Eq. (A7) shows immediately that the mode vertical wave numbers are independent of frequency. This result helps justify the neglect of the frequency dependence of mode eigenfunctions in the derivation of the waveguide invariant in Sec. II C, at least for the case of shallow water waveguides.

The power law relationship between the mode wave number differences and the circular frequency in Eq. (A8) was obtained in Ref. 12 using a different approach. However, note that Eqs. (A3) and (A4) provide additional information on the dispersive characteristics of the waveguide.

APPENDIX B: EVALUATION OF WAVEGUIDE INVARIANT INTEGRAL

The integral of the waveguide invariant over range in Eq. (18) can be easily calculated. For example, dividing the range into consecutive segments within which β varies linearly with range, i.e., within the jth segment, $\beta(r) = \beta(r_{j-1}) + a_j r$, where $a_j = [\beta(r_j) - \beta(r_{j-1})]/[r_j - r_{j-1}]$, then

$$\int_{r_{j-1}}^{r_j} \frac{\beta(r_{j-1}) + a_j r}{r}\, dr = \ln\left(\frac{r_j}{r_{j-1}}\right)^{\beta(r_{j-1})} + \beta(r_j) - \beta(r_{j-1}). \tag{B1}$$

The factor on the right-hand side of Eq. (18) therefore is

$$\exp\left(\int_{r_0}^{r(t)} \frac{\beta(r,\theta)}{r}\, dr\right) = \prod_{j=1}^{L(t)} \left(\frac{r_j}{r_{j-1}}\right)^{\beta(r_{j-1})} \times \exp[\beta(r_j) - \beta(r_{j-1})] \tag{B2}$$

with $L(t)$ equal to the number of segments.

[1] R. J. Urick, *Principles of Underwater Sound*, 3rd ed. (McGraw-Hill, New York, 1983), pp. 131–133.

[2] S. D. Chuprov, ''Interference structure of a sound field in a layered ocean,'' in *Ocean Acoustics, Current State*, edited by L. M. Brekhovskikh and I. B. Andreevoi (Nauka, Moscow, 1982), pp. 71–91.

[3] L. M. Brekhovskikh and Y. P. Lysanov, *Fundamentals of Ocean Acoustics*, 2nd ed. (Springer-Verlag, New York, 1991), pp. 140–145.

[4] A. M. Thode, W. A. Kuperman, G. L. D'Spain, and W. S. Hodgkiss, ''Localization using Bartlett matched-field processor sidelobes,'' accepted for publ. in J. Acoust. Soc. Am. (1999).

[5] H. C. Song, W. A. Kuperman, and W. S. Hodgkiss, ''A time-reversal mirror with variable range focusing,'' J. Acoust. Soc. Am. **103**, 3234–3240 (1998).

[6] H. Schmidt, ''OASES—Ocean Acoustic and Seismic Exploration Synthesis,'' user's guide, Massachusetts Institute of Technology, Cambridge, MA (1990).

[7] W. S. Hodgkiss, J. C. Nickles, G. L. Edmonds, R. A. Harriss, and G. L. D'Spain, ''A large dynamic range vertical array of acoustic sensors,'' in *Full Field Inversion Methods in Ocean and Seismic Acoustics* (Kluwer Academic, Dordrecht, 1995), pp. 205–210.

[8] J. Rice and J. Determan, ''SWellEx-3 Data Report,'' Tech. Rept., NCCOSC RDT&E Division, Code 541 (1995).

[9] G. L. D'Spain, J. J. Murray, W. S. Hodgkiss, N. O. Booth, and P. W. Schey, ''Mirages in shallow water matched field processing,'' J. Acoust. Soc. Am. **105**, 3245–3265 (1999).

[10] N. O. Booth, P. A. Baxley, J. A. Rice, P. W. Schey, W. S. Hodgkiss, G. L. D'Spain, and J. J. Murray, ''Source localization with broad-band matched-field processing in shallow water,'' IEEE J. Ocean. Engin. **21**, 402–412 (1996).

[11] R. T. Bachman, P. W. Schey, N. O. Booth, and F. J. Ryan, ''Geoacoustic databases for matched-field processing: Preliminary results in shallow water off San Diego, California,'' J. Acoust. Soc. Am. **99**, 2077–2085 (1996).

[12] G. A. Grachev, ''Theory of acoustic field invariants in layered waveguides,'' Acoust. Phys. **39**(1), 67–71 (1993).

Analysis of high-frequency acoustic scattering data measured in the shallow waters of the Florida Strait

Andrew K. Rogers
Planning Systems Incorporated, METOC Technology Division, 7923 Jones Branch Drive, McLean, Virginia 22102-3304

Tokuo Yamamoto
University of Miami Rosenstiel School of Marine and Atmospheric Science, Department of Applied Marine Physics, 4600 Rickenbacker Causeway, Miami, Florida 33149

(Received 20 May 1998; accepted for publication 6 July 1999)

Experiments were conducted in the Florida Strait region of the United States in July 1995 to investigate the contribution of sediment volume scattering to measured acoustic backscatter levels at frequencies of 7.5 and 15 kHz. Five sites were analyzed for bottom backscattering level in the radial and azimuthal directions. Sediment geophysical parameters were established by a cross-well tomographic measurement and used as inputs for modeling. Both sediment volume and rough interface scattering models were utilized in analyzing the data. Comparison of model predictions with measured data showed that for grazing angles, at the water–sediment interface, from the critical angle to approximately 60 degrees, volume scattering dominated. For angles greater than approximately 60 degrees, surface roughness scattering consistently dominated. In geographic areas where the interface sound speed ratio exceeded one, roughness scattering controled the backscattered level for grazing angles less than the critical angle. Inversion of the measured acoustic backscatter data was performed using a genetic algorithm optimization developed for use with the volume scattering model. Inversion results were found to agree well with measured data and measured environmental parameters that describe the scattering volume. © *1999 Acoustical Society of America.* [S0001-4966(99)03011-8]

PACS numbers: 43.30.Ft, 43.30.Ky, 43.60.Pt, 43.30.Gv [DLB]

INTRODUCTION

For many sonar systems, sea bottom scattering has a detrimental and limiting effect; for others, the seafloor acoustic reverberation may be used as a tool for examining the physical properties of the seabed. In either case, a thorough knowledge of the effect of the sea bottom on acoustic propagation is needed to interpret propagation data.

A great deal of seafloor acoustic reverberation data has been collected in the past, much of which has been presented as bottom backscattering strength.[1–17] In general, the results have been described by the empirical value $10\log(\mu)$ taken from Lambert's rule: $\mathrm{BBS}=10\log(\mu\sin^2\theta)$. Here BBS is the bottom backscattering strength, θ is the grazing angle at the interface, and μ is the bottom scattering cross section.[18] Lambert's rule works well for many water–sediment interfaces, but neglects contributions from the sub-seafloor volume including sub-seafloor interfaces. This limitation is profound when the interface roughness is very small or when the impedance ratio between the water and sediment approaches unity. Under these conditions the volume and/or sub-water–sediment interface horizons become significant or even dominant scattering mechanisms and cannot be neglected.[19] The desire for a sound, physically realizable representation of the seafloor scattering mechanisms is a topic of significant interest in the acoustics community and has been the motivation for this study.

Recently, scattering models have been developed which consider the physics of acoustic interaction with distributions of scatterers.[4,6,8,9,20–34] By treating regions (i.e., surfaces or volumes) of scatterers with simple distributions this approach reduces the complexity of the problem while retaining the underlying physics. It has seen much success in recent efforts.[3–11]

In the case of a rough interface, scattering is controled by the relationship of the acoustic frequency, the distribution of roughness scales on the surface, and the composition of the interface material. For most operational sonar frequencies the material properties of the sediment at this interface may be considered uniform over a limited scattering region and are usually modeled as such. In very-high-frequency sonar cases, bioturbation and factors that disturb the fine structure of the surface and near surface sediments must be accounted for. At these very high frequencies sonar interacts on much finer scales with the sediment due to its shorter wavelength.[35–37] For sediment volumes, scattering is controled by the three-dimensional distribution of impedance fluctuations throughout the volume and the acoustic frequency. Rough interface and volume scattering are usually treated as separate scattering mechanisms and the individual model results combined to represent the total scattering strength of the bottom.

Obtaining an accurate description of the experimental region's environment is the most challenging task when trying to verify the scattering physics using model comparisons with data. Accurate measurements of the water column, the water–sediment-interface roughness, the sediment volume, and the sub-seafloor horizons are very difficult to obtain in

an ocean environment. A variety of instrumentation and methods have been developed to gather hydroacoustic and geoacoustic properties, including conductivity, temperature and depth sensors (CTDs), bathythermographs (BTs), stereo photography, sediment coring, chirp sonar, sidescan sonar, and cross-well tomography among others. Each has limitations upon its applicability that may include, for example, the acoustic frequency of the source, the depth of the water, or the sediment type. The Florida Strait experiments conducted for this study utilized diver observations and sediment samples to characterize the water–sediment interface and cross-well sediment tomography to measure the sediment volume properties. Due to the geometry of the experiment, the generally horizontal nature of the sound speed structure of the ocean, and the length of the acoustic propagation paths of the experiment (3–85 m one way), the experimental sound speed was approximated as a constant within the region. The value for sound speed was determined from a time-of-flight measurement along the direct path from the acoustic source to a receiver. Averaging of several time-of-flight measurements between the acoustic source and several receivers gave a statistically established sound speed value. The choice to use these methods was made based upon available technology and applicability within the experimental parameters.

Hardware availability dictated the frequency and source level of the experiment and defined the starting point for most other design decisions such as source output function, receiver characteristics, and source and receiver positions. It is known that multi-path propagation in the form of fathometer returns and hybrid acoustic paths may contaminate seafloor reverberation measurements.[38] The use of directional source and receiver pairs can help reduce or eliminate these fathometer and multipath effects. Although a directional source was not available for these experiments, a directional receiver was specifically designed to provide an excellent response function for the frequencies of interest. This alleviated much of the concern about fathometer and hybrid path contamination but did not completely eliminate the problem.

Because the ocean surface is time variant in comparison with the seafloor, the reverberation from the sea surface could be separated from the reverberation from the seafloor. By averaging a sufficient number of pings, the sea surface fathometer and multipath interference could be reduced below ambient noise levels in most cases, allowing discrimination of the seafloor reverberation (Fig. 1). One limitation of this method of averaging repeated received traces is that seemingly time-coherent seafloor reverberation is also smeared, leaving a net smoothing of the received levels as a function of time and angle.

Experimental equipment and measurements are discussed in Sec. II. In Sec. III we discuss the rough interface and sediment volume scattering models. In addition to the direct *in situ* cross-well tomographic measurement, sediment volume scattering properties were determined inversely using two methods. The first method used the measured acoustic scattering data and a genetic algorithm optimization of the scattering forward theory to invert for the model scattering parameters. The second method used an inversion of the two-dimensional spectrum of the compressional velocity

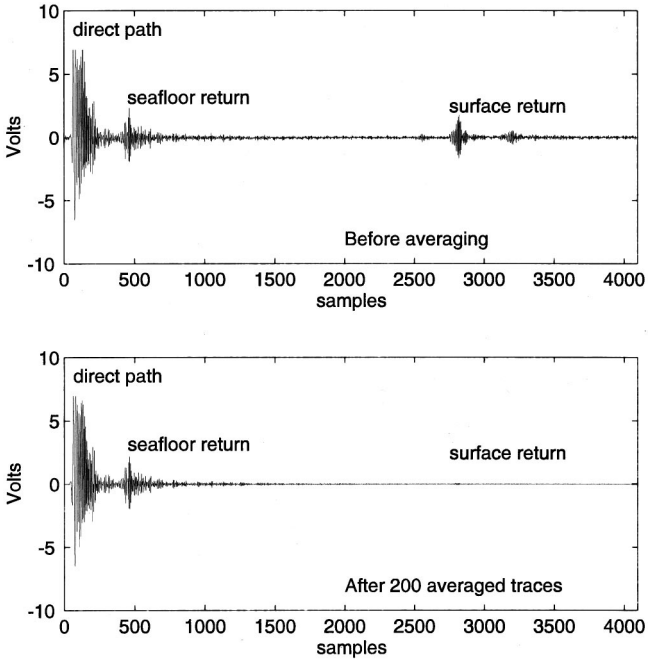

FIG. 1. An example of a received signal (a) before averaging and (b) after 200 averages.

field given by the cross-well tomographic measurement to achieve the model spectrum. The genetic algorithm optimized inversion method is discussed in Sec. III C. In Sec. IV we compare the results of data analysis using the scattering models and the volume scattering model inversion.

I. EXPERIMENT

The Florida Strait experiment included five acoustic backscatter sites and one cross-well tomographic experiment at site 1. The concentration of discussion within this paper is upon the 38-ft (11.6 m)-deep site 1. Figure 2 shows a map of the region of south central Florida where the experiments occurred. For both the acoustic backscatter and cross-well tomography measurements, center frequencies of 7.5 and 15 kHz were used. Cross-well tomography was used to measure acoustic properties of the sediment volume. Sediment acoustic property values are the geophysical input parameters needed for acoustic scatter modeling and as ground truth for inversion verification. During the boring of wells for cross-well tomography experiments divers noticed distinct layering. Layering was later confirmed by the cross-well tomography result. Based upon the cross-well tomography results and samples taken during the diving operation, the site has sediment volume structure consisting of sand and shell fragments embedded within layers of mud and silty clay. Gravity coring was attempted but proved unsuccessful due to equipment failure. The water–sediment interface was documented by divers to be sediment ripples with wavelengths measuring nominally 1.0 m and amplitudes of approximately 10 cm. The strike of the ripples was oriented perpendicular to 108 degrees magnetic, roughly parallel to the coast. The interface sediment was made up of shell fragments and medium sand. Sea state remained less than Beaufort two during the data collection.

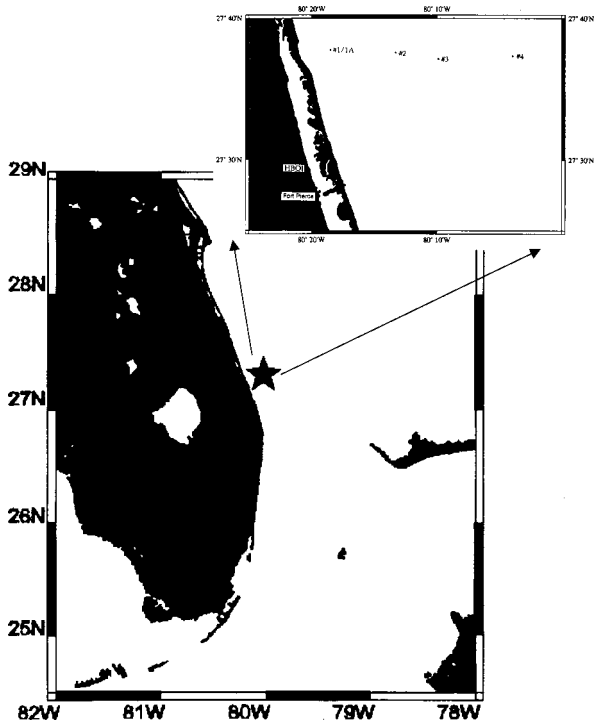

FIG. 2. The Florida Strait region with the experimental site indicated by a star. The inset shows a blown up region about the site indicating individually the offshore sites and their proximity to Ft. Pierce, FL, and Harbor Branch Oceanographic Institute.

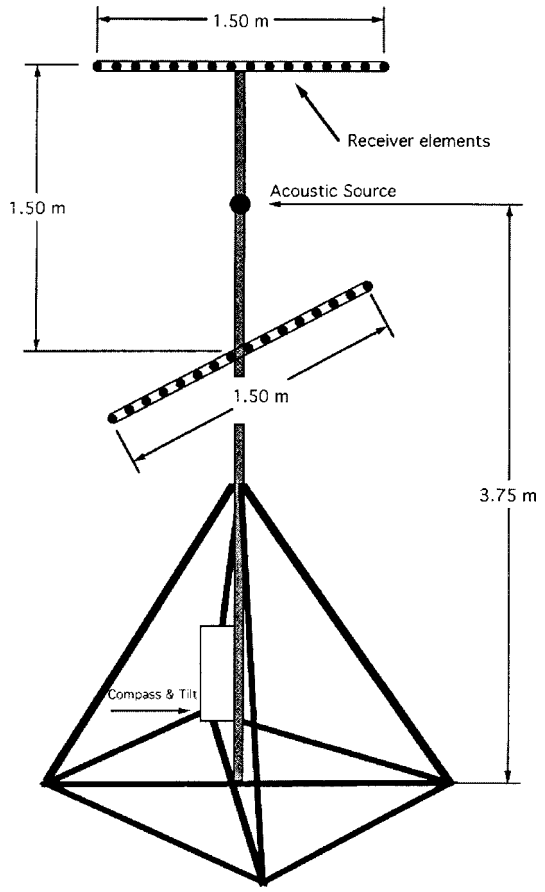

FIG. 3. A schematic diagram of the sparse volumetric array, acoustic source, and support structure.

A. Equipment

Traditional approaches to measuring acoustic backscatter from the seafloor use either a single fathometer style device which provides a reflection measurement (near grazing angle=90 degrees), a line array which has ambiguity about its axis when beamformed, or a seafloor-mounted tower with a directional source and receiver. The last of these three approaches is the most accurate and repeatable, but in its most common configuration requires that the directional source–receiver pair be steered to all angles of interest. This can make data collection a time-consuming endeavor. In an effort to minimize the experiment's duration and still examine all points on the bottom within the region around the measurement device, an array was chosen for which receivers could be recorded simultaneously and later beamformed to desired directions. The use of a broadband source signal with a sparse array yielded a high-resolution result for a minimal number of hydrophones.[39] The relative orientation between sensors was very important. After much simulation and evaluation, the sensors were arranged in a manner to give excellent broadband, beamformed response throughout all grazing and azimuthal angles for the frequencies of interest. The design, as shown in Fig. 3, is similar to a vertically expanded Mill's cross.

An omnidirectional source located at the geometric center of the array was activated repeatedly using Hanning-weighted linear-frequency-modulated (LFM) upswept signals, and the reverberation was recorded at each hydrophone. Averaging 200 repeated traces removed much of the incoherent noise, such as that associated with a moving sea surface.

B. Three-dimensional broadband array design

The standard approach to array design for signals that contain more than one octave of bandwidth has been to nest several subarrays, each cut for a different octave. Data from each subarray are bandpassed for the corresponding octave and beamformed conventionally. This method requires a significant number of sensor elements. An alternative method is to process the data over the entire frequency band using only the array cut for the lowest octave. Using this alternative method, with sufficient bandwidth, the many grating lobes which occur for spatially aliased frequencies (frequencies greater than the frequency for which the array was cut) tend to smear one another out, leaving the beam along the maximum response axis intact or even narrowed. This is illustrated in Appendix A.[40] Integration over the full bandwidth reveals a comparable directivity index while sharply reducing the number of sensors.[36,37] During processing, the backscattered data was examined every 2.5 degrees in azimuth and every 2 degrees of grazing angle.

The physical design of the volumetric broadband array consisted of two linear arrays of 16 hydrophones, each spaced 0.10 m and placed horizontally in orthogonal directions. A preamplifier providing 50 times gain accompanied each hydrophone. Vertical separation between the linear arrays was equivalent to a single linear segment's aperture of 1.5 m. Onboard compass and tilt sensors provided the array's relationship to the earth. Angles of inclination or declination

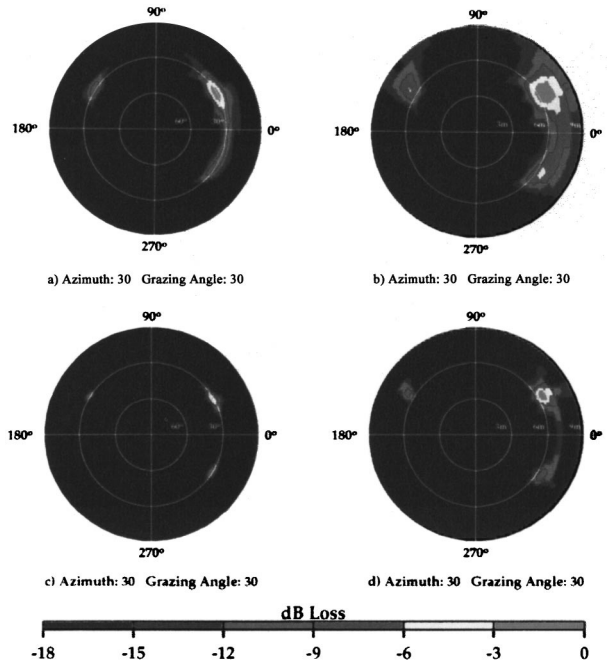

FIG. 4. Array response (a) 7.5 kHz versus grazing angle and azimuth, (b) 7.5 kHz versus range from the array and azimuth, (c) 15.0 kHz versus grazing angle, and azimuth (d) 15.0 kHz versus range from the array and azimuth.

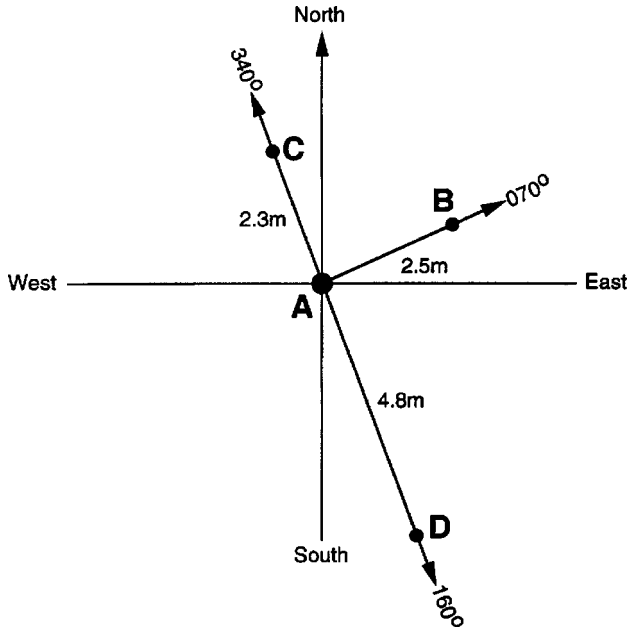

FIG. 5. Plan view of the cross well tomographic borehole layout. Boreholes are at positions A, B, C, and D.

were accounted for in the data processing. The array is illustrated in Fig. 3 with the acoustic source located at the geometric center of the receive array.

Examples of the array response when steered to a bearing of 30 degrees and a grazing angle of 30 degrees are shown in Fig. 4(a) and (b) for both 7.5- and 15-kHz center frequencies with bandwidth 15.0 kHz with 30 kHz, respectively. Figure 4(c) and (d) shows the associated beam patterns projected onto a plane surface 3.75 m below the geometric center of the array. This plane approximates the seafloor below the equipment tower for the experiments. As the array is symmetric, in all eight octants the response is equivalent.[41,42]

C. Acquisition of backscattering data

Source signals were Hanning-windowed linear-frequency-modulated (LFM) upsweeps of bandwidths 15 and 30 kHz centered at 7.5 and 15 kHz, respectively. Pulse length of the LFM varied with increased frequency from 0.002 to 0.001 s. These signals were chosen for their low sidelobe level upon correlation and superior correlation gain, i.e., high signal-to-noise ratio. Autocorrelation of the LFM-swept 7.51- and 15-kHz signals yielded gain factors of 23.6 and 13.1, respectively. These signals provided sufficient bandwidth for the broadband beamforming techniques employed in the processing.

Data acquisition took place via a cable connection to the research vessel. Traces were amplified 100 times and high-pass filtered using a -3-dB cutoff at 1 kHz. This ensured maximum amplitude would be recorded without clipping the A/D converter and that 60-Hz electronic noise would be suppressed without harming the data integrity. Data then passed through a 200-kHz throughput, 12-bit, 16-channel A/D converter and were recorded to the hard disk of a 486/66 personal computer. Experiment backup was made on Exabyte 8-mm magnetic tape. The control software recorded three channels simultaneously at 66 666 Hz for 0.2 s per shot. Two hundred shot points were recorded per station. This yielded a file size of 85.33 MB of data per experimental location and the duration of an experiment was just under 20 min. Data were later coherently averaged, correlated with the source function, and beamformed.

Radials from the array were considered every 2.5 degrees and processed for their direct path backscatter. This direct path processing is the norm for most reverberation data collected to date regardless of the source/receiver combination used. Obviously, the more directional the receiver, the greater the reduction of unwanted off-axis noise and the better this processing method approximates true direct paths. The Florida Strait sites were found to have no significant azimuthal variations in the acoustic backscatter at the source frequencies used, indicating a rather homogeneous acoustic scattering region for the purposes of this experiment. This was further verified by tomographic measurements of the sediment structure at site 1.

D. Cross-well tomography experiment

The tomography measurement was located at site 1. Four wells were bored into the seafloor approximately 2 m in depth. The orientation of these wells is shown in Fig. 5. Into well ''A'' an array of 16 acoustic sources spaced 0.10 m apart was deployed and into wells ''B, C, and D'' arrays of 16 receivers were deployed, also separated at 0.10 m. Multiple source shots were transmitted for all source locations and were recorded and averaged for each receiver. A shipboard display of successively averaged incoming traces was observed until it was determined that a sufficient signal-to-noise ratio was achieved and the first arrival of the signal

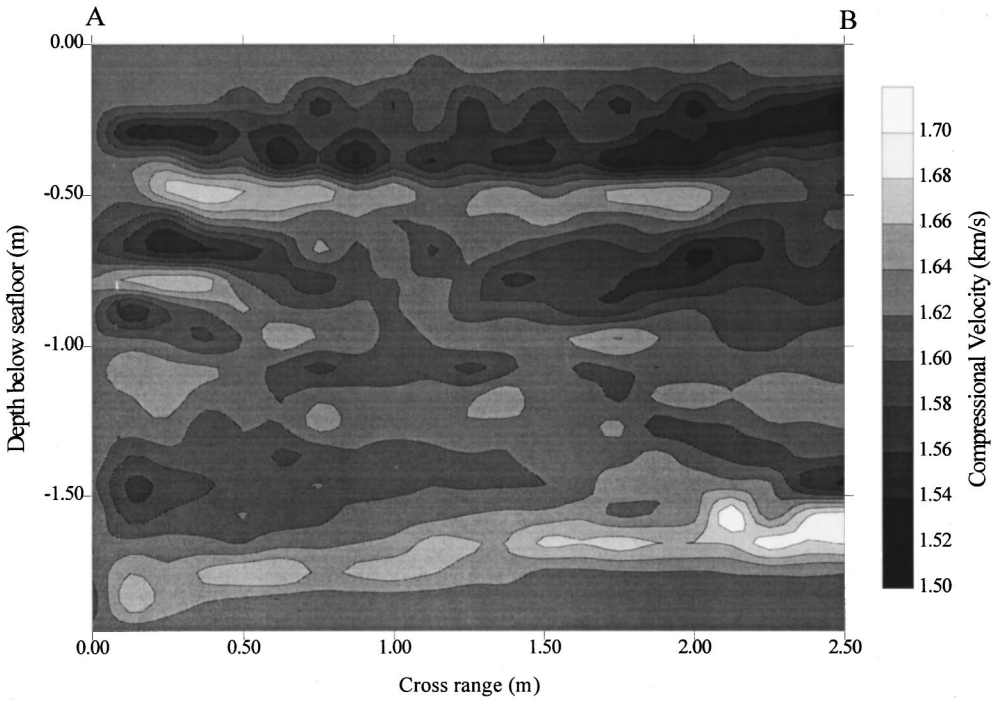

FIG. 6. The 7.5-kHz compressional velocity cross-well tomogram of section A–B at site 1 Florida Strait continental shelf acoustic experiments 1995.

could be determined. These data were archived and later used in the tomographic inversion that determined the compressional velocity structure of the sections between well ''A'' and the other wells. Information on tomographic inversion may be found in the papers by Bregman *et al.*,[43] Yamamoto *et al.*,[5,44,45] and Rapids *et al.*[46] The cross-well tomogram depicting compressional velocity in cross section A–B is shown in Fig. 6. Cross sections A–C and A–D showed similar sediment structure.

II. SCATTERING MODELS

Two acoustic scattering models, one developed for rough interface scattering and the other for volume scattering, were chosen for data analysis because of their physics-based approach to scattering. The Applied Physics Laboratory—University of Washington's (APL-UW) composite roughness model[6] and the Rosenstiel School of Marine and Atmospheric Science at the University of Miami's (RSMAS-UM) volume scattering model[9] are employed as theoretical representation of the physics of the scattering mechanisms.

A. The rough interface

The composite roughness model describes the rough interface using the Kirchhoff approximation for angles near the Snell's law direction and perturbation theory for all other directions. Interpolation combines the results of the two methods. Although the complete APL-UW model provides a formulation for volume scattering, it is disregarded in this work because of its empirical nature. The model result for interface backscatter (IBS) is as follows where $\sigma_r(\omega_2, \gamma_2)$ represents the rough interface scattering cross section per unit area:

$$\mathrm{IBS} = 10 \log (\sigma_r(\omega_2, \gamma_2)). \tag{1}$$

This model uses a power-law description of the spectrum of the interface roughness: ω_2 is the spectral strength and γ_2 is the spectral exponent. Other parameters required by the model are derivable from a standard geoacoustical description of the seafloor. A complete theoretical description is available in reports by APL-UW.[6]

B. The sediment volume

The RSMAS-UM[9] volume scattering model also uses perturbation theory and represents the scattering kernel with a power law to describe the fluctuations of compressional velocity within the volume. The general form of the volume scattering model is

$$\mathrm{VBS} = 10 \log (\sigma_v), \tag{2}$$

$$\sigma_v = k_0^4 \Gamma^2 \beta \Lambda^2 B (\Lambda^2 k_1^2 + \Lambda^2 k_2^2 + k_3^2)^{-(\beta+2)/2}, \tag{3}$$

where VBS is volume backscatter, σ_v is the differential backscattering cross section per unit volume, k is the wave number incident (subscript 0) and axial (subscripts 1, 2, 3), Γ is a magnification factor relating the density and compressional velocity fluctuations in the sediment, β is the spectral exponent factor, B is the spectral intensity factor, and Λ is the aspect ratio describing the anisotropy of the inhomogeneities in the sediment. A provision for dipped layering is included by Yamamoto in the definitions of the components of wavenumber.[5] For azimuthal directions, ϕ, and angles of dipped structure, δ, these components of wave number are

$$k_1 = k_x \cos\phi \cos\delta + k_y \sin\phi \cos\delta - k_z \sin\delta, \tag{4}$$

$$k_2 = -k_x \sin\phi + k_y \cos\phi, \tag{5}$$

$$k_3 = k_x \cos\phi \sin\delta + k_y \sin\phi \sin\delta + k_z \cos\delta. \tag{6}$$

Propagation effects are accounted for as direct-path spreading loss, attenuation, and transmissivity:

$$\sigma_a = \sigma_v \left(\frac{\sin \theta_s}{4\alpha} \right) T_{12}^2 T_{21}^2 \left(\frac{\cos^2 \theta_s}{\cos^2 \phi_w} \frac{\sin^2 \theta_w}{\sin^2 \theta_s} \right), \tag{7}$$

where θ_w and θ_s are the incident and transmitted (refracted) grazing angles at the water sediment interface, $T_{12}^2 T_{21}^2$ is the transmissivity across the interface, and $((\cos^2 \theta_s/\cos^2 \theta_w) \times (\sin^2 \theta_w/\sin^2 \theta_s))$ accounts for the spreading of incident wave energy at the interface. This result is expressed as an equivalent interface scattering strength and may be combined directly with the result from the composite roughness model. Total bottom backscatter (BBS) is computed as

$$\mathrm{BBS} = 10 \log (\sigma_r + \sigma_a). \tag{8}$$

Verification of the volume scattering model was the motivation behind much of the work done in the Florida Strait.

C. Inversion

Beyond its direct or forward application, the volume scattering model was inverted to find the sediment properties from the collected backscatter data. To do this, one of the first applications of genetic algorithm optimization techniques to underwater acoustics was implemented. This type of inversion was chosen for its robust nature and computational efficiency and provided a useful and unique tool for sediment classification.

Genetic algorithm optimization techniques are derived from the nature of genetic selection: survival of the fittest. The structure of the algorithm follows that analogy: From the set of all possible solutions, a population of solution sets is chosen. Each solution set is used to compute the model result. This result is measured for its fitness against the measured data. Through a process of structured evolutionary steps, the initial population evolves to better represent the data. The evolution selects the two most fit individual solution sets to be parents to a new generation. The parents are then operated upon using methods analogous to chromosomal exchange. First an exchange of part of the solutions is made, a crossover of chromosomal information, and then a random mutation of some parts of the newly generated children is made. These children, as well as their parents, are then introduced to a new population and the process is repeated until a solution is found that achieves a user-specified, optimum fit to the data.[47–51] A simple example illustrating the genetic algorithm concept is presented in Appendix B.

III. DATA ANALYSIS

A. Cross-well tomograms

The geoacoustic parameters in RSMAS-UM model by Yamamoto[9] described in Sec. III B are statistical properties. Therefore, the larger the total number of ensembles, the more reliable the average. The sound speed structure within the seabed at the test site imaged by cross-well tomography was utilized to maximize the number of ensembles. The one-dimensional parameters, the spectral intensity B and spectral exponent β, were determined from 30 vertical profiles taken from the three tomograms. The two-dimensional parameter, the aspect ratio Λ, was determined from an average of estimates from the three two-dimensional images. The three-dimensional parameters, the dip angles φ and δ, were determined from the only one 3-D image. Therefore, one must be cautioned that these model parameters determined from tomograms have different statistical significance. Further more, the RSMAS-UM model assumes that the fluctuations in the sound speed structure within the seabed sediments are random. Therefore, the diffused layers seen in the tomograms and felt by the divers are assumed to be random in this analysis. One may examine the effect of layered structure on acoustic scattering using the tomogram and acoustic scatter data presented in this paper.

To determine the properties needed for input to the acoustic models, the tomograms were analyzed using one- and two-dimensional Fourier analysis. Using virtual sediment cores, taken as one-dimensional sections through the tomogram depth, and analyzing the power spectral density of the compressional velocity fluctuations along each section, a first-order polynomial fit to the average spectrum exhibits power law behavior. This behavior, when associated with Eq. (3), provides spectral exponent and spectral intensity values, β and B, respectively. One-dimensional data cannot provide other information needed for modeling such as the aspect ratio or dipped structure. To find these we must look to higher-dimensional data.

From the two-dimensional power spectrum of the tomographic section, the aspect ratio of the anisotropy and any present dipped structure may be determined. A useful tool for finding all four of these parameters from the two-dimensional power spectrum was an inversion of the volume scattering model to fit the spectral data. A genetic algorithm as described in Sec. III C and exemplified in Appendix A was applied for this purpose. The algorithm optimized the fit between Eq. (3) and the two-dimensional power spectral density of the compressional velocity cross-well tomogram. An example of the two-dimensional power spectra of the compressional velocity cross section is shown in Fig. 7(a) and the result of the inversion in Fig. 7(b) for the 7.5-kHz analysis of section A–B.

Note the off-axis nature of the elliptical shape in Fig. 7(b). This indicates the existence of a preferential dipped structure at the site. Aspect ratio is determined as the ratio of the major $(k_z/\cos \delta)$ axis to minor $(k_x/\sin \delta)$ axis of the ellipse, where δ is the dip angle from the k_z axis. Table I lists the sediment parameters computed from both one- and two-dimensional techniques and inversion along with several estimates made for use with the scattering models where data were not available.

These statistical sediment model properties determined from the sound speed profiles computed using measurements by the cross-well tomography will be used in the forward modeling of bottom reverberation. These statistical properties will also be used for verification of the sediment model properties inverted from the bottom reverberation data. The resolution of the tomographic inversion is roughly 10 cm. This resolution may not be fine enough to model the acoustic scattering at 7.5 and 15 kHz, which requires the resolution of the sediment structure of the size of one-half the wavelength,

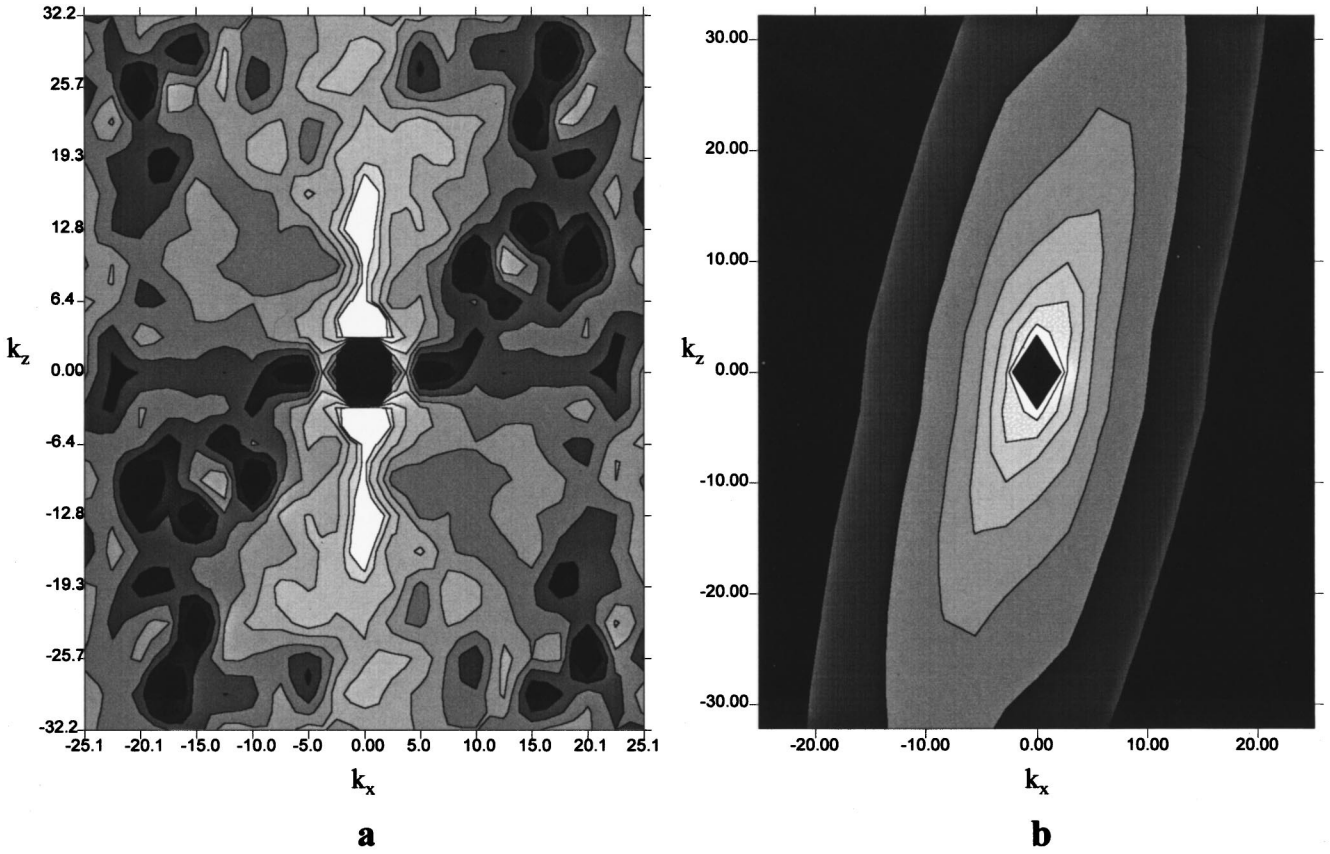

FIG. 7. (a) The power spectral density of compressional velocity cross well tomogram A–B from site 1. (b) The result of inversion using the RSMAS-UM volume scattering model fitted to the power spectral density computed directly from cross-well tomogram A–B. Axes are wave number ($1/m$).

or roughly 2.5–5 cm. However, the statistical sediment model properties are rather constant over a wide range of spatial scales according to the core analyses.[5,10] Therefore, the statistical sediment model properties measured using cross-well tomography having resolution of 10 cm are also expected to correctly represent the slightly finer sediment structures of 2.5–5 cm that interact with the acoustic waves of 7.5 and 15 kHz.

Interface properties at the site were estimated from diver observations and sediment samples with reference to previous work for similar sediment types by Jackson and Briggs.[8] Estimated parameters for interface properties and attenuation are underlined in Table I.

B. Backscatter

The beamformed acoustic scattering data were evaluated azimuthally and found to have only minor azimuthal variation at these sites. Emphasis was placed on the azimuthal data whose radials coincided with the directions of the measured cross well tomograms. From Fig. 5 it is seen that these lie along 70–250 degrees and 160–340 degrees magnetic. Along these azimuths, the measured and inverted sediment properties from Table I were input into the composite roughness and volume scattering models.

Figure 8(a) and (b) shows the measured data *versus* grazing angle at 7.5 and 15.0 kHz along with the forward model predictions based on the values from Table I. Note the effect of the dipped structure in the 070–250 degrees model result as the peak is offset to roughly 14 degrees. The volume scattering model at frequency 15 kHz shows a particularly good fit for this bearing at grazing angles greater than 123 degrees and less than 162 degrees. The choice of the interface scattering parameters is constant throughout these examples due to the lack of measured data, but gives some

TABLE I. Sediment parameters computed from one- and two-dimensional spectral techniques and inversion. Underlined values are estimated values for modeling purposes only.

	Volume values						Sediment			Surface values	
Line	Spectral B	Model β	Aspect ratio Λ	Dip from A δ (degree)	Vertical B	Cores β	Sound speed C_p/C_w	Attenuation α_a (dB/m/kHz)	Density ratio ρ	Spectral strength $\omega 2$	Spectral exponent γ
A–B	$4.98e-5$	0.312	4.556	−14.1	$1.16e-5$	0.500	1.039	0.15	1.79	0.0042	3.25
A–C	$1.27e-5$	0.214	4.442	1.36	$1.04e-5$	0.341	1.047	0.15	1.81	0.0042	3.25
A–D	$2.29e-5$	0.778	6.77	−1.39	$4.68e-5$	0.744	1.043	0.15	1.76	0.0042	3.35

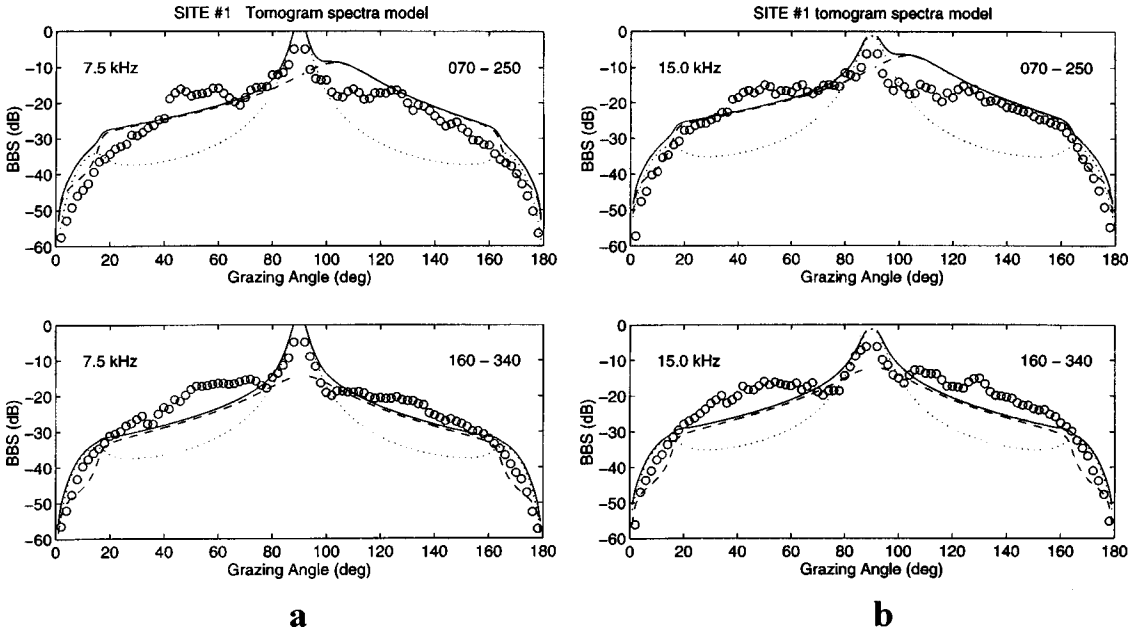

FIG. 8. Acoustic backscatter data and modeling results for the composite roughness model estimate (dotted line), the volume scattering model (dashed line), and their combination (solid line): (a) 7.5 kHz, 070–250 degrees and 7.5 kHz, 160–340 degrees; (b) 15.0 kHz, 070–250 degrees and 15.0 kHz, 160–340 degrees.

indication, under the assumption of similar sediment, of the roughness scattering effect. It shows that at very steep grazing angles (those near vertical incidence) and angles shallower than the critical angle, in this case the critical angle lies approximately 16 degrees from tangent, the rough interface scattering dominates. Through the mid-angle sections, volume scattering largely controls scattering behavior according to the model. The APL-UW roughness model[6] used in this paper is a statistical model. The roughness data from the diver observation are crude but give some quantitive values that are needed for the model calculations. The diver observation of long-crested ripples seems to conflict with the homogeneous acoustic scattering data for grazing angles smaller than the critical angle. This type of apparent contradiction is often reported by other investigators.[8]

Inversion of the volume scattering model was made for data at each of the azimuthal directions 70, 160, 250, and 340 degrees. The inversion predicted seven volume scattering model parameters: dip azimuth, dip grazing angle, spectral exponent, spectral intensity, aspect ratio, attenuation, and sound speed ratio at the water–sediment interface. Though sediment layering was identified at the site, for purposes of inversion of acoustic data, the sediment volume may be considered as a whole. In doing so, the physical scattering mechanisms associated with any layering are represented in the solution result as well as the model parameters that were inverted. Comparing model parameters inverted from acoustic backscatter with parameters derived from the spectra of compressional velocity tomograms is valid because the spectrum of a compressional velocity tomogram is a spectrum of the whole sediment structure and includes the layering. Table II shows the results for 7.5 and 15.0 kHz.

The best-fit inversion results for site 1 are shown in Fig. 9 using the previous estimates for inputs into the composite roughness model. It can be seen that at both frequencies there is excellent model-to-data agreement. The model-to-data error was less than 0.17 for all cases when measured as a ratio of the sum of the errors to the sum of the data: better than 83% agreement.

The inversion does not include the rough interface scattering model and therefore is limited in its ability to describing the total scattering. In the future, it is hoped that rough

TABLE II. Inversion results for experiments conducted in the Florida Strait at site 1.

Frequency (Hz)	Heading (degrees)	Dip azimuth (degrees)	Dip angle (degrees)	Spectral exponent	Spectral intensity	Aspect ratio	Attenuation (dB/m/kHz)	Sound speed ratio
7.5	070	12	−5.03	0.222	$5.02e-5$	6.53	0.35	1.061
7.5	160	263	19.8	0.379	$4.53e-5$	5.44	0.35	1.045
7.5	250	276	18.9	0.695	$5.77e-5$	2.85	0.29	1.040
7.5	340	193	3.4	0.746	$5.94e-5$	3.11	0.24	1.037
15.0	070	24	−15.7	0.318	$4.58E-5$	5.85	0.37	1.045
15.0	160	121	−12.6	0.382	$8.15E-5$	1.95	0.39	1.055
15.0	250	213	14.2	0.760	$1.0E-4$	1.97	0.20	1.041
15.0	340	2	2.54	0.633	$5.07E-5$	2.60	0.185	1.037

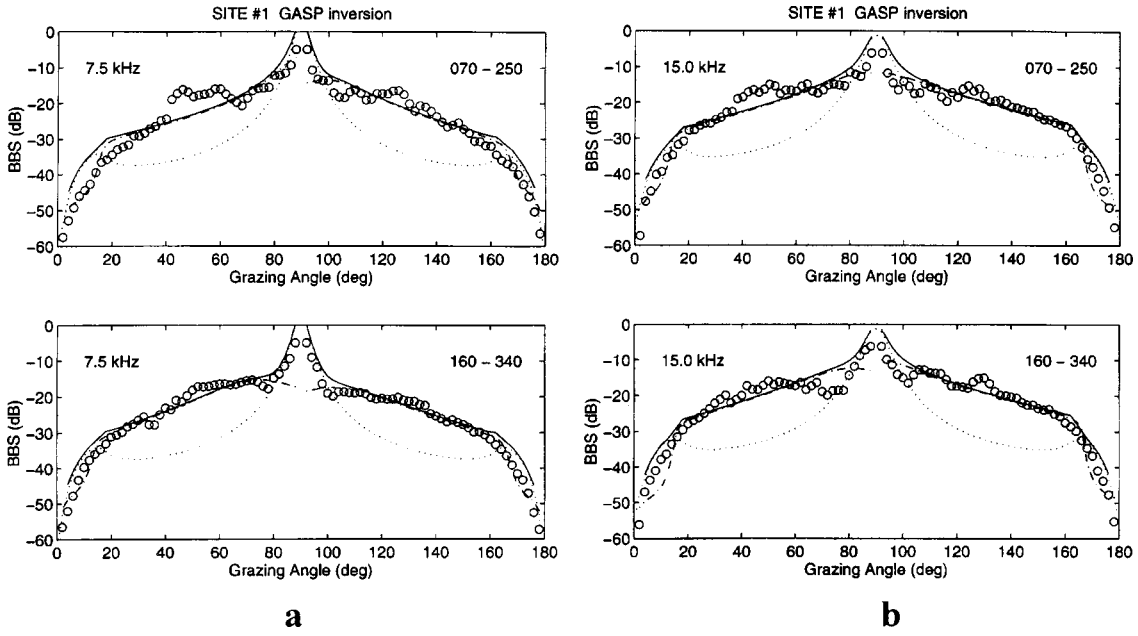

FIG. 9. Results of the volume scattering model inversion and composite roughness model estimates. The dash–dot, dotted, and solid lines indicate the volume model inversion, roughness model estimate, and combined inversion and roughness model estimate results respectively: (a) 7.5 kHz, 070–250 degrees and 7.5 kHz, 160–340 degrees; (b) 15.0 kHz, 070–250 degrees and 15.0 kHz, 160–340 degrees.

interface scattering will be included and the data reevaluated. The estimate made for this data evaluation of the rough interface backscatter level combined with the inversion result shows very good agreement to the data. Collocated interface and volume physical property measurements are needed and should be pursued. The volume/rough interface inverse model at that point could be evaluated and should prove a very useful tool for estimating the physical properties of the sediment via a single remote measurement.

IV. SUMMARY

The work performed for this study resulted in several interesting findings and capabilities being developed. Our experimental results, when compared with the scattering model results, showed that sediment volume scattering was the dominant scattering mechanism for mid-grazing angles: For example, those at site 1 between approximately 16 and 81 degrees or between approximately 95 and 164 degrees (Figs. 8 and 9). This was supported by the rough interface scattering model's inability to model this region given the sediment composition as measured. The rough interface model did, however, model the angular regions below the critical angle and at angles near normal incidence very well, indicating interface scattering to be the dominant mechanism in these regions. This is significant in that it is a result of *in situ* scattering data being compared with two modern scattering models. The relative contribution of the two scattering mechanisms represented by these models has been the subject of some controversy. Although the work done in this study is for an isolated sediment composition, the models and techniques used indicate a viable operational methodology for further study.

Both the APL-UW[6] and RSMAS-UM[9] models worked very well for this study. The use of their combination is appealing due to the similarity of the perturbation theory utilized in their development. A unified model should be a target for future work.

To make *in situ* measurements of acoustic backscatter, a unique receiver array configuration of 32 elements was found, built, and tested. The array can measure scattered acoustic wave energy with grazing and azimuthal resolution of approximately 2 degrees throughout ± 90-degree elevation and 360 degrees azimuth. This array configuration may find applicability in many areas of research where high-angular-resolution acoustic monitoring is needed.

This work developed a genetic algorithm-based optimization algorithm that was utilized to determine sediment properties based upon model comparisons with measured acoustic data. The sediment properties found were sound speed ratio, attenuation, spectral intensity parameter, spectral exponent, and dip angles. The sediment properties found using this inversion method agreed well with ground truth from cross-well tomography experiments.

ACKNOWLEDGMENTS

This work was supported by the United States Office of Naval Research Ocean Acoustics Program. Great appreciation is given to Murat Kuru, Brian Rapids, and Tom Nye from the University of Miami Geoacoustics Laboratory for their efforts. The experiments were conducted from the R/V Seward Johnson operated by the Harbor Branch Oceanographic Institute (HBOI).

APPENDIX A: BROADBAND ARRAY PROCESSING

An array designed to cover the frequency band 1000 to 16 000 Hz is shown in Fig. A1. To obtain a directivity index of approximately 11 dB at each octave requires that there be four nested arrays of 13 sensors each. Positioning some of

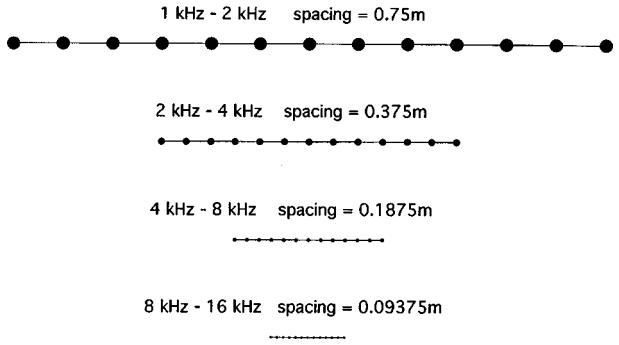

FIG. A1. Examples of linear arrays cut for increasing octave bands from 1 to 16 kHz.

the sensors so that they may be shared between nests, the minimum number of sensors in this linear array is 31.[39,40]

If we process over the entire frequency band using only the data from the array cut for the lowest octave, we find that the directivity index is retained at roughly 11 dB but we have reduced the required number of sensors to 13. The issue now becomes the beam pattern response for non-isotropic noise. Implementing the beamformer

$$s(t)=\frac{1}{N}\sum_{j=1}^{N}\frac{1}{2\pi}\int_{\omega_1}^{\omega_2}W_j(\omega)R_j(\omega)e^{i\omega(t-\tau_j)}\,d\omega, \qquad \text{(A1)}$$

where $W_j(\omega)$ is the receiver weighting function, $R_j(\omega)$ is the spectrum of the received signal, and the steering time delay $\tau_i=r_i\cos(\gamma-\theta)\sin\phi/f$, the array response is

$$A(\theta,\phi)=\int_{k_a}^{k_b}\left(\frac{1}{N}\sum_{j=1}^{N}e^{ikr_j\cos(\gamma-\theta)\sin\phi}\right)^2 dk, \qquad \text{(A2)}$$

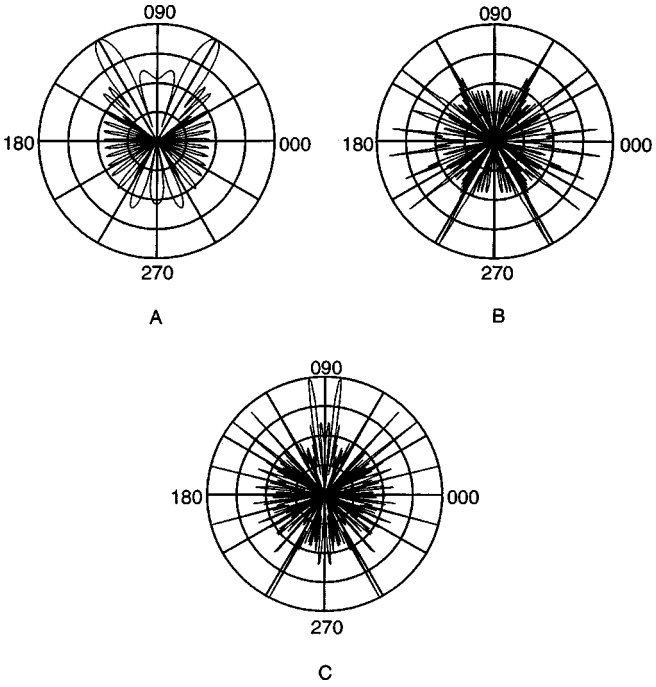

FIG. A2. Single frequency array response patterns for a 13-channel 0.75-m spaced linear array steered to 60 degrees from broadside for (a) 1 kHz, (b) 8 kHz, and (c) 16 kHz.

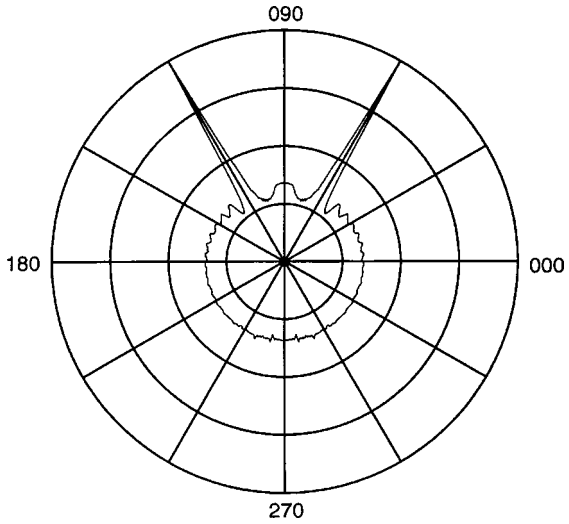

FIG. A3. Broadband 1–16 kHz beampattern computed using the full bandwidth for a 13-channel 0.75-m spaced linear array steered to 60 degrees from broadside.

where $k_a=\omega_a/c$ and $k_b=\omega_b/c$ are the lower (a) and upper (b) limits of the frequency band in question.[41,42]

It is seen in Fig. A2(a) that for a beam steered to 60 degrees at the lowest frequency of interest (1000 Hz), in a plane cut through the array, there is left–right ambiguity but low side lobe levels. For frequencies above that at which the array was cut, it is seen that there are several grating lobes [Fig. A2(b) and (c)]. The number and position of the grating lobes are determined by the frequency examined. These grating lobes would normally prohibit directional study, but when the entire bandwidth is utilized the effect is that the grating lobes tend to smear themselves out, leaving the primary lobe in the steered direction intact and, in fact, narrowed, yielding a higher directionality.[36–39] Figure A3 shows the broadband beamforming technique for the same array element spacing but with the full bandwidth 1000 to 16 000 Hz. The increased directional capability of the main lobe can be seen clearly as well as the smearing effect of the grating and side lobes.

APPENDIX B: A SIMPLE GENETIC ALGORITHM EXAMPLE

For example, a set of ten data points is collected. The data in question may be described by a theoretical model which has two variables A and B. It is known through some experience that A may vary from A^- to A^+ and B from B^- to B^+. We wish to find the values of A and B which, when used as input to the model, cause the model result to approximate the data. To test the ''fit'' of the model to the data we use the sum of the differences between the model, M_i, and data, D_i, divided by the sum of the data values as a measure of the percent error between the model and data:

$$\%=100-100*\left[\sum_{i=1}^{N}|M_i-D_i|\Big/\sum_{i=1}^{N}|D_i|\right], \qquad \text{(B1)}$$

where N is the number of data samples.

To begin the inversion process we start with a number of selections of A and B as solution sets. For this example we

TABLE BI. The binary complements for A and B parameter selections in a population of six solution sets. The percentage of fitness between the model result compared with the measured data is also shown.

Solution set	A	B	% fit
1	0101	0001	10%
2	1100	1011	65%
3	1001	0110	75%
4	1010	0110	36%
5	0000	1010	53%
6	1110	1000	18%

will use six. The values of A and B are randomly chosen between A^- and A^+ and B^- and B^+, respectively. The randomly chosen values are now mapped into base two. To do this we choose a representation for this example of 2^4. The mapping is done by

$$2^4 \times \left(\frac{A_x - A^-}{A^+ - A^-} \right), \tag{B2}$$

where x varies from 1 to 6 in this case, similarly for B. Let us assume that the output of this mapping is as shown in Table B1.

Each of these pairs, A and B, denotes a solution set. We now must test each solution set using Eq. (B1). For the purposes of the example, we have assigned some hypothetical values of fitness to each solution set.

If we now decide that we would be satisfied with a fitness of 75%, then we have found our answer in solution set #3. If we would rather the model better approximate the data, say to 85%, then we must search further. This is done by first selecting the best two fit solution sets. In this case, that turns out to be sets two and three. The genetic algorithm optimization terminology refers to these solution sets as *parents* because through manipulation of their individual traits, A and B, we will produce two new solution sets.

The first manipulation is a cross over of 1's and 0's between the two strings (a string consists of A and B back to front, i.e., in #2: 11001011). The point of crossover is chosen randomly:

11001011,

10010110.

Crossover is made between the underlined sections in this example, producing

11010110,

10001011.

The next step is a random mutation of one of the two new strings (*children*) which equates to a reversal of 1's to 0's or 0's to 1's at randomly chosen sites. If we mutate the second string at underlined randomly chosen sites,

10001011,

we obtain

10100111.

We now have four solution sets that are retained, the original *parents* and their *offspring* found by the genetic information exchange processes of crossover and mutation:

11001011,

10010110,

11010110,

10100111.

These four are introduced to a new population of randomly chosen solution sets, which in this example would be two new sets to make another full complement of six. Their fitness is analyzed and the process continues until a ''best'' fit (85%) is found at which point we are satisfied and the goal has been accomplished. These methods have been found robust and computationally efficient in comparison with other inversion algorithms available today.[49]

[1] C. W. Horton, ''A review of reverberation, scattering, and echo structure,'' J. Acoust. Soc. Am. **51**, 1049–1061 (1971).
[2] C. G. Fox and D. E. Hayes, ''Quantitative methods for analyzing the roughness of the seafloor,'' Rev. Geophys. **23**, 1–48 (1985).
[3] D. R. Jackson, D. P. Winebrenner, and A. Ishimaru, ''Application of the composite roughness model to high frequency bottom backscattering,'' J. Acoust. Soc. Am. **79**, 1410–1422 (1986).
[4] P. D. Mourad and D. R. Jackson, ''High frequency sonar equation models for bottom backscatter and forward loss,'' in *Proceedings of OCEANS '89* (IEEE, New York, 1989), pp. 1168–1175.
[5] T. Yamamoto, ''Velocity fluctuations and other physical properties of marine sediments measured by cross well acoustic tomography and cores,'' J. Acoust. Soc. Am. **98**, 2235–2248 (1995).
[6] APL-UW High Frequency Environmental Acoustic Models Handbook, APL-UW TR 9407, AEAS 9501 (1994).
[7] D. R. Jackson, A. M. Baird, J. J. Crisp, and P. A. G. Thompson, ''High frequency bottom backscattering measurements in shallow water,'' J. Acoust. Soc. Am. **80**, 1188–1199 (1986).
[8] D. R. Jackson and K. B. Briggs, ''High frequency bottom backscattering: roughness versus volume scattering,'' J. Acoust. Soc. Am. **92**, 962–977 (1992).
[9] T. Yamamoto, ''Acoustic scattering in the ocean from velocity and density fluctuation in the sediment,'' J. Acoust. Soc. Am. **99**, 866–879 (1996).
[10] T. Yamamoto, A. Turgut, M. Schulkin, and R. Bennett, ''Geoacoustic properties of the seabed sediment critical to acoustic reverberation at 50 to 500 Hz: a preliminary data set,'' RSMAS TR-91-001, GAL Report No. 1014, Univ. of Miami (1991).
[11] A. K. Rogers, ''An experimental investigation of the contribution of sediment volume scattering to acoustic backscatter measured in the shallow waters of the Florida Strait,'' in Proceedings High Frequency Acoustics in Shallow Water conference, SACLANTCEN CP-45, pp. 459–466 (1997).
[12] S. Stanic, K. B. Briggs, P. Fleischer, R. I. Ray, and W. B. Sawyer, ''Shallow water high-frequency bottom scattering off Panama City, Florida,'' J. Acoust. Soc. Am. **83**, 2134–2144 (1988).
[13] S. Stanic, K. B. Briggs, P. Fleischer, W. B. Sawyer, and R. I. Ray, ''High frequency acoustic backscattering from a coarse shell ocean bottom,'' J. Acoust. Soc. Am. **85**, 125–136 (1989).
[14] C. M. McKinney and C. D. Anderson, ''Measurements of backscattering of sound from the ocean bottom,'' J. Acoust. Soc. Am. **36**, 158–163 (1964).
[15] K. Briggs, ''High-frequency acoustic scattering from sediment interface roughness and volume inhomogeneities,'' Ph.D. thesis, Univ. of Miami, 1994.
[16] A. K. Rogers, T. Yamamoto, and W. Carey, ''Experimental investigation of sediment effect on acoustic wave propagation in the shallow ocean,'' J. Acoust. Soc. Am. **93**, 1747–1761 (1993).
[17] K. D. Flowers and B. G. Hurdle, ''Monostatic scattering from the ocean bottom,'' J. Acoust. Soc. Am. **51**, 1109–1111 (1971).
[18] R. J. Urick, *Principles of Underwater Sound* (McGraw–Hill, New York, 1983).
[19] P. C. Hines, ''Theoretical model of acoustic backscatter from a smooth seabed,'' J. Acoust. Soc. Am. **88**, 324 (1990).

[20] A. N. Ivakin and Y. P. Lysanov, ''Theory of underwater sound scattering by random inhomogeneities of the bottom,'' Sov. Phys. Acoust. **27**, 61–64 (1981).
[21] A. N. Ivakin, ''Sound scattering by random inhomogeneities of stratified ocean sediments,'' Sov. Phys. Acoust. **32**, 492–496 (1986).
[22] A. N. Ivakin and Y. P. Lysanov, ''Underwater sound scattering by volume inhomogeneities of a bottom bounded by a rough surface,'' Sov. Phys. Acoust. **27**, 212–215 (1981).
[23] J. H. Stockhausen, ''Scattering from the volume of an inhomogeneous half space,'' NRE report 63/9 (1963).
[24] L. A. Chernov, *Wave Propagation in a Random Medium* (McGraw–Hill, New York, 1975).
[25] A. N. Ivakin and Y. P. Lysanov, ''Backscattering of sound from an inhomogeneous bottom at small grazing angles,'' Sov. Phys. Acoust. **31**, 236–237 (1985).
[26] D. J. Tang, ''Acoustic wave scattering from a random ocean bottom,'' Ph.D. thesis, MIT/WHOI 1991.
[27] A. Ishimaru, ''Theory and application of wave propagation and scattering in random media,'' Proc. IEEE **65**, 1030–1061 (1977).
[28] W. Shi, ''Acoustic backscattering in the ocean due to density and sound velocity fluctuations in the sediment,'' M.S. thesis, Univ. of Miami, 1993.
[29] H. R. Carleton, ''Theoretical development of volume reverberation as a first-order scattering phenomenon,'' J. Acoust. Soc. Am. **33**, 317–323 (1961).
[30] H. Boehme and N. P. Chotiros, ''Acoustic backscattering at low grazing angles from the ocean bottom,'' J. Acoust. Soc. Am. **84**, 1018–1029 (1988).
[31] E. Y. Kuo, ''Wave scattering and transmission at irregular surfaces,'' J. Acoust. Soc. Am. **36**, 2135 (1964).
[32] K. L. William and D. R. Jackson, ''Bistatic bottom scattering: Model, experiments, and model/data comparison,'' J. Acoust. Soc. Am. **103**, 169–181 (1998).
[33] D. R. Jackson and A. N. Ivakin, ''Scattering from elastic sea beds: First-order theory,'' J. Acoust. Soc. Am. **103**, 336–345 (1998).
[34] A. N. Ivakin and D. R. Jackson, ''Effects of shear elasticity on sea bed scattering: Numerical examples,'' J. Acoust. Soc. Am. **103**, 346–354 (1998).
[35] M. D. Richardson, ''Spatial variability of surficial shallow water sediment geoacoustic properties,'' in *Ocean Seismo Acoustics: Low Frequency Underwater Acoustics*, edited by T. Akal and J. M. Berkson (Plenum, New York, 1986), pp. 527–536.
[36] M. D. Richardson and D. K. Young, ''Geoacoustic models and bioturbation,'' Mar. Geol. **38**, 205–218 (1980).
[37] M. D. Richardson, K. B. Briggs, R. I. Ray, and W. H. Jahn, ''Environmental support for high-frequency acoustic experiments conducted at the Quinault Range, April-May 1983,' NORDA Rep. 132, Naval Oceanographic and Atmospheric Research Laboratory,'' NSTL Station, MS (1986).
[38] D. D. Ellis and J. B. Franklin, ''The importance of hybrid ray paths, bottom loss, and facet reflection on ocean bottom reverberation,'' in Progress in Underwater Acoustics, ICA12 Proceedings (1986), pp. 75–84.
[39] M. E. Huster, D. W. Miklovik, and S. L. Schmidt, ''Broadband sparse array image processing for localization and classification in shallow water environments,'' Arete Associated Report AS-93-0012.0 (1993).
[40] S. O. McConnell and J. H. McCown, ''Time-angle spread of bottom reflection using broadband signals and a sparse array,'' Arete Associates Report ARS-239-010-TR (1993).
[41] W. S. Burdic, *Underwater Acoustic System Analysis* (Prentice–Hall, Englewood Cliffs, NJ, 1991).
[42] S. Haykin, J. H. Justice, N. L. Owsley, J. L. Yen, and A. C. Kak, *Array Signal Processing* (Prentice–Hall, Englewood Cliffs, NJ, 1985).
[43] N. D. Bregman, C. Bailey, and C. H. Chapman, ''Crosshole seismic tomography,'' Geophysics **54**, 200–215 (1989).
[44] T. Yamamoto, T. Nye, and M. Kuru, ''Porosity, permeability, shear strength: cross well tomography below an iron foundry,'' Geophysics **59**(10), 1530–1541 (1994).
[45] T. Yamamoto, T. Nye, and M. Kuru, ''Imaging the permeability structure of a limestone aquifer by cross well acoustic tomography,'' Geophysics **60**(6), 1634–1645 (1995).
[46] B. Rapids, T. Nye, and T. Yamamoto, ''Pilot experiment for the acquisition of marine sediment properties via small scale tomography system,'' J. Acoust. Soc. Am. **103**, 212–224 (1998).
[47] L. Davis, *Handbook of Genetic Algorithms* (Van Nostrand Reinhold, New York, 1991).
[48] S. Mangano, ''Fuzzy, neural and genetic methods to overcome complexity,'' *Computer Design Magazine*, Pennwell Pub., May 1995.
[49] P. Gerstoft, ''Inversion of seismoacoustic data using genetic algorithms and a posteriori probability distributions,'' J. Acoust. Soc. Am. **95**, 770–782 (1994).
[50] D. F. Gingras and P. Gerstoft, ''Inversion for geoacoustic parameters in shallow water: Experimental results,'' J. Acoust. Soc. Am. **97**, 3589–3598 (1995).
[51] P. Gerstoft, ''Global inversion by genetic algorithms for both source position and environmental parameters,'' J. Comput. Acoust. **2**, 251–266 (1994).

Intermediate range fish detection with a 12-kHz sidescan sonar

David M. Farmer[a] and Mark V. Trevorrow[b]
Acoustical Oceanography, Institute of Ocean Sciences, 9860 West Saanich Road, Sidney, British Columbia V8L 4B2, Canada

Bjarke Pedersen[c]
LIC Engineering A/S, Ehlersvej 24, DK-2900 Hellerup, Denmark

(Received 9 February 1999; revised 2 July 1999; accepted 12 July 1999)

The application of a prototype 12-kHz sidescan sonar suitable for horizontal imaging of fish distributions is described. The sonar consisted of a 40-element (20λ) array transmitting a 1600 Hz×0.2 s FM sweep with correlation processing of the received echoes. Observations are reported for two different implementations: (i) a configuration in which the sonar was towed at ~35 m in water of depth 60–220 m in the southern Strait of Georgia, British Columbia, where the primary target was sockeye salmon, and (ii) a bottom-mounted deployment in a shallow (10–14 m) channel near Copenhagen, Denmark, where herring were present. In the Strait of Georgia, discrete fish targets were detected with up to 25-dB signal-to-reverberation ratio at ranges from 1 to 7 km. In the shallow Danish waters, herring schools were detected at ranges up to 1.2 km. In each case an acoustic propagation analysis identifies the useful detection characteristics. In the Strait of Georgia the signal is confined to a subsurface sound channel, requiring additional knowledge of vertical distributions of salmon in order to make abundance estimates. In contrast, fish detectability is nearly depth independent in the shallow Danish waters. In the Danish deployment the sonar could be swept in azimuth, providing a sequence of sector images that reveals the changing shape and movement of herring schools. These preliminary results provide an indication of the potential value and limitations of intermediate range sidescan surveys for fish stock assessment. [S0001-4966(99)00811-5]

PACS numbers: 43.30.Gv, 43.30.Sf [DLB]

INTRODUCTION

A challenge to fishery surveys is the acquisition of data over an area sufficient to allow accurate abundance estimates. Vertical echo-sounders and echo-integration techniques are well established, but the usefulness of such measurements is often compromised by limited spatial coverage within a survey area and the consequent need for statistical compensation. Surveys of shallow-water or epipelagic stocks are further limited by a small sampling volume beneath the ship and avoidance behavior by the fish. In contrast, side-looking sonars have the potential for fish detection to horizontal ranges of order several kilometers, even in shallow waters, providing spatial coverage significantly greater than that achieved with conventional echo-sounders or net trawls.

Fish have been detected at ranges up to 65 km using high-power, low-frequency sonars (Weston and Revie, 1971, 1989; Rusby *et al.*, 1973; Revie *et al.*, 1990; Weston and Andrews, 1990). The powerful sonars used in these earlier studies might have restricted application given current concerns about effects of noise on marine mammals. Similar concerns are likely to limit the use of explosives with towed horizontal line arrays, which have successfully detected high-seas salmon at ranges to 4 km (Nero and Huster, 1996). More recently, fish detection has been demonstrated using higher frequency (⩾30 kHz) horizontally oriented sonars at ranges up to a few hundred meters (e.g., Hewitt *et al.*, 1976; Gaudet, 1990; Misund *et al.*, 1995; Tarbox and Thorne, 1996; Trevorrow, 1997; Trevorrow and Claytor, 1998). In this work we explore the feasibility of 12-kHz sidescan sonars for fish detection over ranges of 1–7 km, which we identify as of intermediate range, lying between ranges accessible to the high (~100 kHz) and low (~1 kHz) frequency systems described previously.

Complications arise with the side-looking geometry due to boundary scattering, refraction, and multiple reflections. In contrast to vertically oriented sonar applications, acoustic propagation effects become important, necessitating knowledge of the bathymetry and sound speed distribution, combined with appropriate propagation analysis. Furthermore, at frequencies significantly higher than the swim bladder resonance the back-scatter cross section of a fish at horizontal incidence is sensitive to fish orientation relative to the acoustic beam. Although these acoustic features complicate interpretations of data from horizontally oriented fisheries sonars, improved understanding appears likely to lead to techniques that can add significantly to the more established vertical sounding methods.

The goal of the present work is to demonstrate the feasibility of fish detection with an intermediate range fisheries sonar (IRFS) and identify some of the practical applications and constraints on its use. A prototype 12-kHz sidescan system was developed and tested during the spring and summer of 1997. In the first sea trials (August 1997) the transducer array was mounted within a streamlined body [Fig. 1(a)] and

[a]Electronic mail: farmerd@dfo-mpo.gc.ca
[b]Electronic mail: trevorrowm@dfo-mpo.gc.ca
[c]Electronic mail: bp@liceng.dk

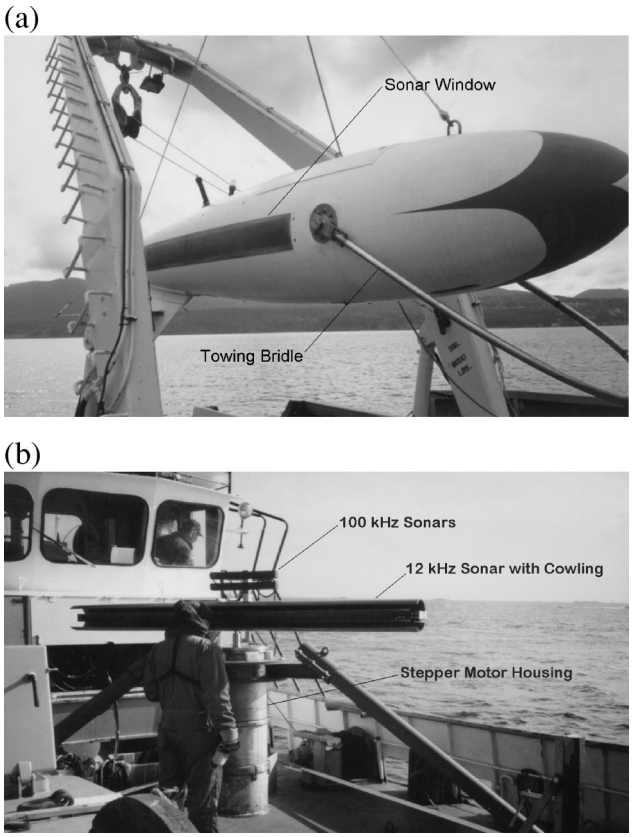

FIG. 1. Photographs of the 12-kHz array in two different deployment modes. (a) The sonar towed vehicle on deck prior to deployment. The 40-element transducer array is mounted behind the sonar window. (b) The sonar array mounted on a tripod with stepping motor, prior to deployment in Drogden Channel, Denmark.

towed at ~35-m depth in the southern Strait of Georgia, B.C. The timing was chosen to coincide with the large sockeye salmon (*Oncorhynchus nerka*) run known to enter the mouth of the Fraser River in late summer. During summer the southern Strait of Georgia has a sound channel at 20–60 m, formed beneath the warmer, fresher Fraser River outflow. In a second field trial we acquired time series measurements from a fixed location during the winter of 1997/98 in a shallow channel near Copenhagen, Denmark. The predominant acoustic target in this case was migratory herring (*Clupea harengus*). The sonar was mounted on a motor-driven assembly capable of scanning through 50 degrees in azimuth [see Fig. 1(b)]. The resulting measurements from both deployments provide some insight on the possibilities and limitations of fish detection at intermediate ranges.

I. DESCRIPTION OF 12-kHz SONAR AND FIELD OPERATIONS

Our prototype intermediate range fisheries sonar consisted of a 40-element (20λ) 12-kHz sidescan array connected to an EDO/Western model 248 Sonar Transceiver. The 12-kHz operating frequency was selected as a compromise between low acoustic absorption and a manageable transducer size which maintains directionality. The sonar utilized 40 model TR-229 Tonpilz piston elements assembled in a linear array and calibrated by EDO/Western. The array length was 2.49 m, yielding a one-way horizontal beam width of 2.8 degrees (to −3 dB), with a vertical beam-width of 122 degrees and front-to-back ratio of −6 dB. This front-to-back ratio was improved to approximately −20 dB (one-way) by installing a 75-mm-thick epoxy foam material behind the transducer. The transceiver was modified to accept an externally generated linear frequency modulated sweep from 11.2 to 12.8 kHz, of duration up to 200 ms, and was capable of delivering up to 2.0 kW (electrical) to the array, generating an on-axis acoustic source amplitude of 63.8 kPa/rms. (216 dB re 1 μPa) at 1 m. The EDO model 248 receiver was modified to provide fixed gain steps, and the array and transceiver were combined with a PC-based system for control, data acquisition, processing, display and data storage. The received signal is sampled with 16 bit resolution at 5333.3 Hz, or four samples every nine cycles of the 12-kHz center frequency. This undersampling scheme is equivalent to complex heterodyning the received signal to a ±1333.3-Hz bandwidth. Complex correlation with the transmit pulse template via fast Fourier transform (FFT) processing yields up to 24-dB processing gain. A time-varying gain (TVG) preamplifier was incorporated near the transducer, with 0-dB gain up to 200 ms, followed by a linear (in decibels) ramp to 40 dB over 6 s. Calibration of the transceiver and electronic components was carried out in the laboratory at the Institute of Ocean Sciences. Typical pulse repetition intervals were 10 s, allowing ranging up to 7400 m. The towed vehicle's heading, pitch-roll, and conductivity-temperature-depth (CTD) sensors were sampled at the end of each pulse cycle.

For the towed configuration, the sonar transducer array, TVG preamplifier, and environmental sensors were mounted within a streamlined fiberglass body of length 5.41 m and maximum diameter 0.89 m [Fig. 1(a)] with the transducers facing 5.5 degrees aft of starboard for alignment within the hull. A 250-m armored tow-cable was used with a 350-kg depressor weight attached 30 m ahead of this neutrally buoyant vehicle. While being towed at 4 knots and 35 m nominal depth, the tow-body maintained depth to ±0.5 m rms and heading to ±4 degrees rms, with the main source of disturbance arising from ship speed and heading changes.

Our initial test was in the southern Strait of Georgia (Fig. 2) during the period 4–15 August 1997 when sockeye salmon migrate through this area to the Fraser River. We followed a clockwise circuit: southbound along the shore and northbound in the center of the Strait. The southbound tracks were chosen to be close to shore while maintaining a minimum water depth of 80 m. Towing operations were conducted in daylight only, and began near 0800 h each day. Conductivity-temperature-depth (CTD) casts were taken at the beginning and end of each track and at turning points or other convenient times. The sonar was deployed at ~35-m depth and the ship directed to steam at a steady 3.5–4 knots relative to the water along a fixed heading. Ship position and velocity were continuously monitored with differential Global Positioning System (GPS).

Figure 3 shows a representative temperature, salinity, and sound speed profile from this area illustrating the characteristic mid-to late-summer sound channel centered at ~35 m. The surface waters (<10-m depth) were much warmer

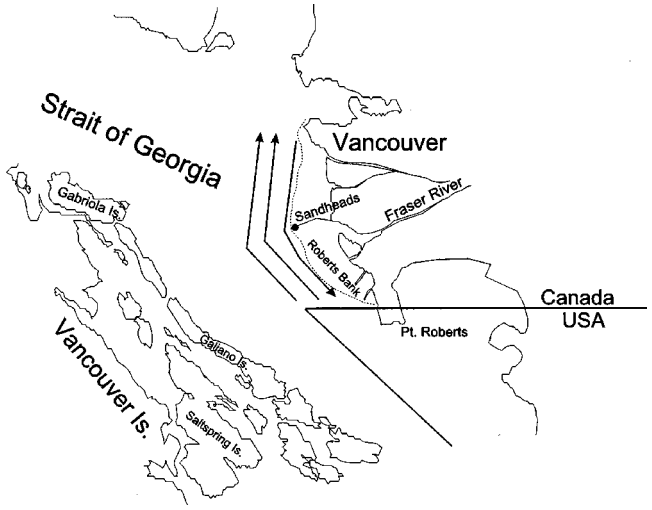

FIG. 2. Chart of the southern Strait of Georgia region, showing north- and southbound ship tracks.

and fresher as a result of the Fraser River outflow, forming strong vertical gradients as wind and tide mixed the surface layer with the deeper waters of the Strait of Georgia. The resulting sound channel possessed strong downward refraction near the surface layer and weaker upward refraction below. Prior studies indicate that salmon are generally restricted to the upper 40 m in this environment (Quinn and terHart, 1987). Near-surface refraction minimized scatter from surface wave and vessel wake backscatter, which is a common problem in other environments (Trevorrow, 1997; Trevorrow and Claytor, 1998). Although vessel wakes were

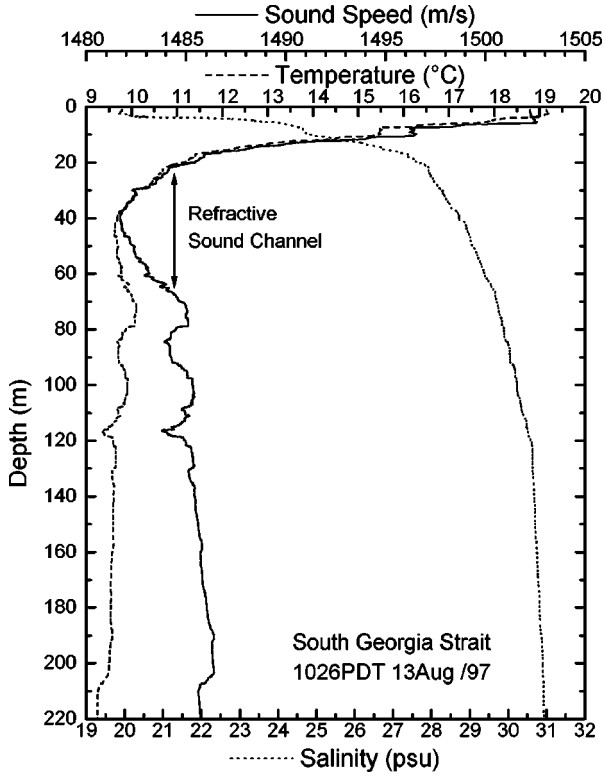

FIG. 3. Representative temperature, salinity, and sound speed profiles offshore of the Fraser River delta (see Fig. 2) 13 August 1997.

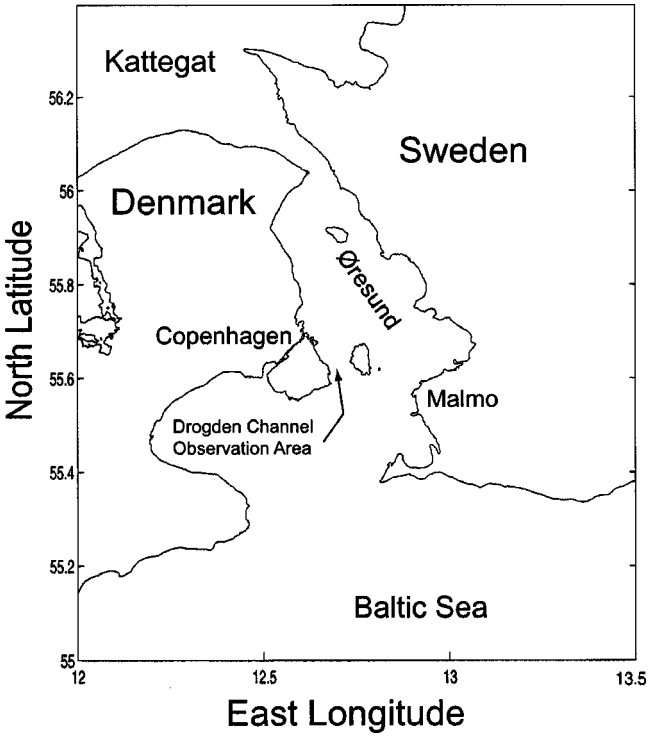

FIG. 4. Chart of the Øresund and Drogden Channel between Denmark and Sweden, showing the sonar deployment location.

not observed in this busy waterway, we did encounter occasional interference from ship propeller noise.

In contrast to our towed operations in the Strait of Georgia, the Danish tests were conducted from a fixed location. The sonar was deployed in Drogden Channel leading from the southern end of the Øresund between Denmark and Sweden (Fig. 4) in an area where herring migrate in the spring and fall (Staehr, 1997). These field trails were made alongside an ongoing 100-kHz sonar monitoring program started in the summer of 1996 (Pedersen and Trevorrow, 1999), which in turn was only a small part of an extensive environmental monitoring program conducted during a bridge and tunnel construction project. Water temperature, salinity, and current profiles were continuously monitored alongside the sonar installations.

The sonar was deployed at 8.4-m depth approximately 200 m northeast of the Nordre-Røse lighthouse, to which it was connected by underwater cable. This location was near the narrowest part of Drogden Channel, which was approximately 2 km wide and 11–14 m deep, with 2–5-m shallows of width 500 m on either side. The sonar installations were focused on the central 1 km of the channel because the herring were assumed to avoid the shallows. The transducer array was mounted on a tripod equipped with a stepper-motor steering assembly [Fig. 1(b)] that could scan a 50-degree sector oriented to the North across the channel. A 30-cm-diam cowling behind the array lined with 12-mm-thick cork-loaded rubber acoustic absorbing material provided improved forward directivity. The 50-degree sector was scanned in 2-degree steps to a range of 2.2 km, providing a measurement area in excess of $2\times10^6\,\mathrm{m}^2$ once every 150 s. The transceiver and data acquisition system were in

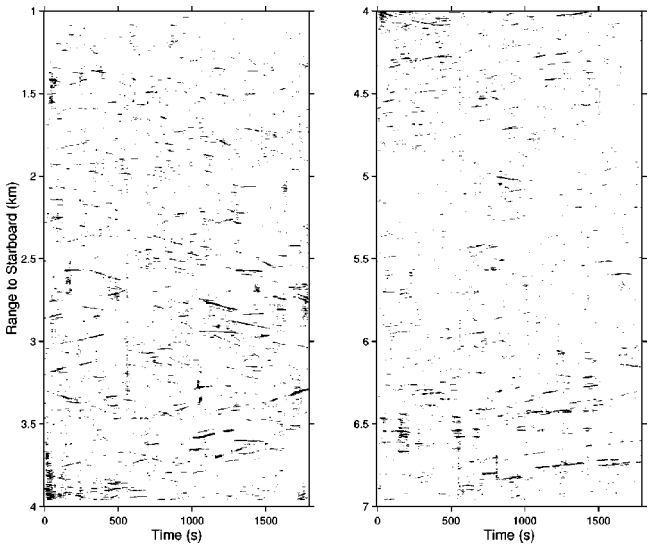

FIG. 5. Echo traces versus range and time image acquired during a southbound tow starting 0935 PDT, 9 August 1997 near Sturgeon Bank in the southern Strait of Georgia. Fish traces are shown only if their intensity is >6 dB relative to the time-averaged intensity versus range curve. Image has been enhanced with a two-dimensional high-pass frequency-wave number filter (see text).

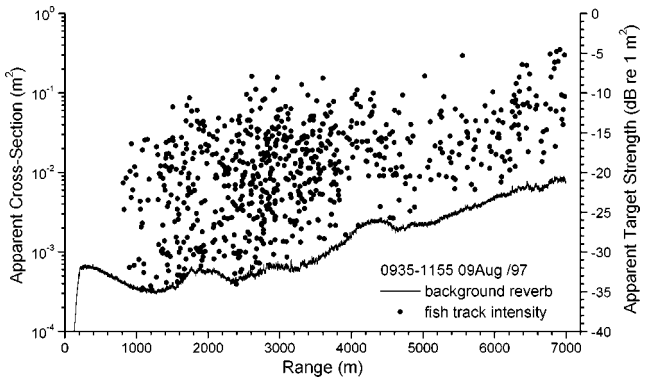

FIG. 6. Averaged background reverberation intensity versus range compared with fish target intensity for southbound tow shown in Fig. 5. Intensities have been converted to apparent cross section and TS, neglecting refraction and reflection effects. Background reverberation is averaged over 781 transmissions spanning 2 h and 10 min.

stalled inside the nearby lighthouse with access to electric power and telecommunications. The Drogden Channel waters were characterized by either a northward flow of relatively fresh (~10 psu) Baltic Sea water or a southward flow of more saline (~20 psu) water from the northern Øresund and Kattegat. Normally these waters were vertically mixed with little sound speed structure.

II. RESULTS AND DISCUSSIONS

A. Salmon detection in the Strait of Georgia, August 1997

Echogram traces attributable to fish were seen in data collected in the southern Strait of Georgia daily during the period 7–14 August 1997. Typically these traces occurred at ranges of 1000–7000 m, depending on conditions and fish abundance. Figure 5 shows a processed 30-min range versus time echogram during which the sonar transmitted at 10-s intervals or once every ~20 m along the ship track. The background reverberation has been suppressed by referencing the target intensities to the time-averaged intensity versus range curve, and is further enhanced with a 2-D high-pass frequency-wave-number filter which excludes signals having range and time scales exceeding 600 m and 180 s respectively. Only target traces with relative intensity >6 dB are shown. Fish echo traces thus appear as short linear streaks. At greater ranges each streak persisted 5–50 transmissions (1–8 min) and this persistence generally increased with range. Thus a stationary target at 2-km range would remain in this 2.8-degree beam for ~10 transmissions, whereas at 7 km the same target would be detectable for 34 transmissions. Targets at ranges <1 km lack persistence which makes identification difficult; a fish at 500-m range may remain in the beam for only one transmission. Of course, small variations in the beam orientation also affect persistence. Furthermore, fish movement in the same direction as, or opposite to, the ship track would increase or decrease the streak persistence, respectively. The streak slope indicates motion towards or away from the sonar.

Figure 6 compares the time-averaged background intensity with the intensity of individual fish target streaks for this same southbound run on 9 August. The target strength of individual streaks was determined by averaging over several transmissions near the center of each streak. As discussed above, fish targets closer than 1000 m cannot be reliably measured in this configuration because of their short duration in the narrow sonar beam. Using the system calibrations, the intensity data have been converted to *apparent* backscatter cross section, correcting only for spherical spreading and absorption losses (i.e., ignoring reflection and refraction effects which will be discussed later). The figure shows that fish targets can have signal-to-reverberation ratios (SRR) of up to 25 dB. The maximum range at which fish could be detected was limited by the travel time and pulse repetition rate, but fish echoes at 7 km had a SRR of up to 15 dB. In a separate run on 10 August with a transmission interval of 12.0 s, a few fish tracks were detected up to 8.4 km range. Model calculations discussed subsequently imply that in the absence of obscuring bathymetry, a fish with comparable target strength would be detectable to at least 10 km.

Individual fish target locations can be calculated from the measured position and heading of the ship together with the towed vehicle orientation. Figure 7 shows the spatial distribution of fish targets extracted from the southbound track sonar data of which Fig. 5 is a portion. The fact that fish targets were seen up to 7-km range during the first 40 min of the southbound run and then only at shorter ranges in the remainder can be attributed to a real spatial inhomogeneity in the fish targets and perhaps some change in the acoustic propagation conditions, although no differences in the background reverberation between the more northerly and southerly sections of the run were observed. Excluding the first kilometer in range, the total area covered during this 2.2-h run was approximately 8.4×10^7 m^2; however the actual insonified volume is constrained vertically by acoustic propagation conditions.

Lacking simultaneous net samples, unambiguous identi-

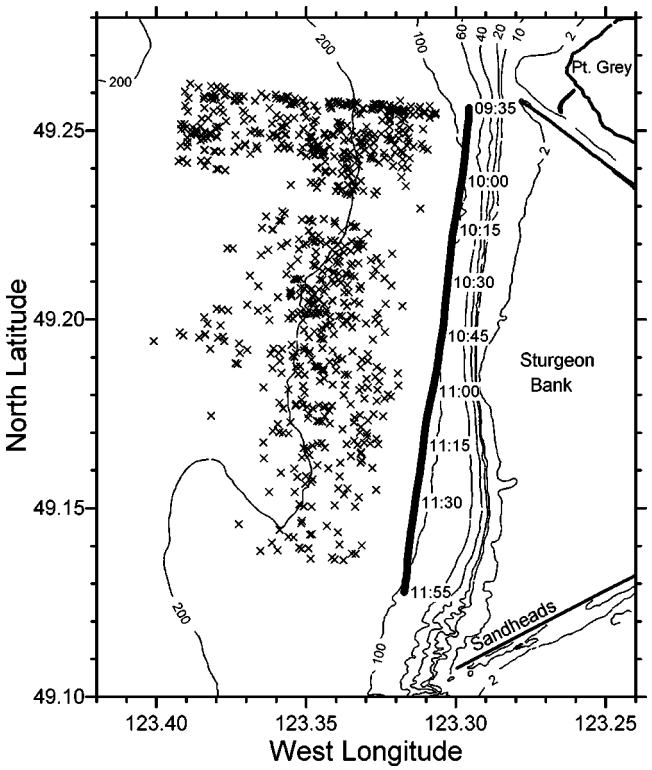

FIG. 7. Map showing ship track and observed fish target locations for the southbound tow corresponding to Figs. 5 and 6. Track length was 14.0 km over which 737 targets were detected. Depth contours are in meters.

fication of the targets was not possible. However, several aspects of salmon occurrence in this region in combination with the propagation characteristics point to sockeye salmon as by far the most likely targets. There was substantial evidence for high abundance of sockeye salmon in the southern Strait of Georgia during the measurement period. The IRFS surveys took place at the beginning of the summer sockeye run. Fish escapement in the Fraser River was continuously monitored at Mission, BC [approximately 80 km upriver, using hydroacoustic methods described in Banneheka *et al.* (1995)], and through daily test fisheries on the lower river. Sockeye escapement was 5.2 million at Mission during August, averaging 168 000 d^{-1} with a high of 466 000 d^{-1} on 21 August (J. Woodey, Pacific Salmon Commission, personal communication). Typical daily escapement during the IRFS sea trials was 60 000. Sockeye comprised 85%–99% of the daily catch on the Fraser River test fishery, and 990 000 sockeye were taken in commercial landings for the area. In particular, two gillnet fishery openings in the Sandheads area on 5 and 12 August netted an estimated 20 000 and 125 000 sockeye, respectively.

The nominal size of adult sockeye in the southern Strait of Georgia is 0.55 m in length with mean weight of 2.9 kg (Levy *et al.*, 1991, and confirmed by 1997 test fisheries). For salmonids of this size, Dahl and Mathisen (1983) reported a lateral-incidence backscatter cross section at 120 kHz of $2.0\times10^{-3}\,m^2$ (Target strength, (TS)$=-27$ dB *re* 1 m^2, using the definition TS$=10\log_{10}$[backscatter cross section in m^2]). Similarly, empirical relations due to Love (1977) predict a lateral-incidence backscatter cross section$=1.6\times10^{-3}\,m^2$ (TS$=-28$ dB) for 0.55-m fish at 12 kHz. Moreover, there is a strong azimuthal dependence to the cross section; for example the cross section at tail incidence is 25 times less than at lateral incidence (Love, 1977). If the salmon are randomly oriented relative to the sonar beam (we have no better information), a cross-section threshold of $6.3\times10^{-4}\,m^2$ (TS$=-32$ dB) selects only those fish oriented within ±30 degrees of lateral incidence, which comprise one-third of the population. This lateral-incidence cross section for sockeye is at least ten times higher than for other smaller fish species commonly found in the area such as hake and herring, with typical dorsal back-scatter cross sections of $1.3\times10^{-4}\,m^2$ and $5\times10^{-5}\,m^2$ (TS$=-39$ and -43 dB), respectively. Also, sockeye occur predominantly within 40 m of the surface in this area, with ~80% of the population above 20-m depth (Quinn and terHart, 1987; Levy *et al.*, 1991), whereas herring and hake are generally found at greater depths, especially during the day.

The acoustic propagation conditions determine the effectiveness of a horizontally oriented sonar. A ray-tracing code due to Bowlin *et al.* (1992) was used to calculate sound pressure level as a function of range and depth for a given source depth, bathymetry, sound speed profile, and reflection loss. Eigenrays connecting the source and a range-depth matrix of possible fish target locations were calculated for a launch angle interval within ±60 degrees of horizontal. The resulting intensities were summed incoherently on a grid with spacing 25-m range by 1.5-m depth. The sound speed profile from Fig. 3 was used, assuming as a first approximation no range dependence. Correction was made for the seawater absorption loss at 12 kHz ($0.0012\,dB\cdot m^{-1}$), a surface reflection loss of 1 dB per bounce, and a seabed forward reflection loss versus grazing angle calculated using classical two-layer interfacial theory (e.g., Medwin and Clay, 1998). Sediments in the Fraser River delta area are comprised of silty sands with assumed density and sound speed of $1900\,kg\cdot m^{-3}$ and $1600\,m\cdot s^{-1}$, respectively. Seabed reflections therefore have a 9.5-dB loss at normal incidence, decreasing with grazing angle.

Each boundary interaction contributes to the backscattered reverberation, which increases strongly with incident grazing angle and interfacial roughness. The sea surface was relatively calm during the measurement period and strong downward refraction in the surface layer ensured that seabed scatter dominated the backscatter. For silty sands the level of backscattered reverberation is relatively well known. McKinney and Anderson (1964) give

$$\mathrm{TS}_{\mathrm{bndry}}=-27-14.9\cdot\exp[-0.0837\cdot\phi]+10\cdot\log[\tfrac{1}{2}\cdot c\cdot\tau\cdot r\cdot\varphi\cdot\cos\phi]\,(\text{in dB}\,re\,1\,\mathrm{m}^2),$$

where ϕ is the grazing angle in degrees, c is the sound speed, τ is the effective pulse length after correlation (0.63 ms), and φ is the horizontal beam width (0.0489 rad). The measured reverberation level (e.g., Fig. 6) may be compared with predictions from the ray-tracing results using this model. Predicted and measured bottom reverberation agree in level and range dependence to within 1–2 dB up to 4000-m range, thus demonstrating consistency with calculations based on the sonar calibration.

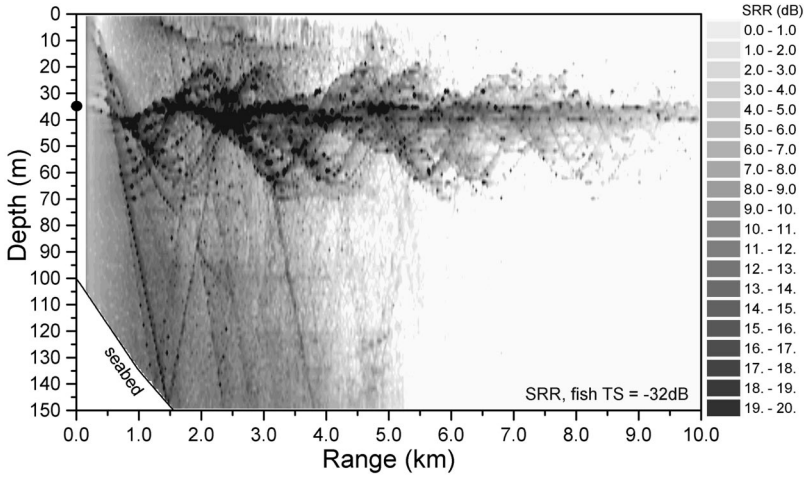

FIG. 8. Cross-sectional distribution of modeled fish echo signal to reverberation ratio (SRR), assuming fish cross-section threshold of $6.3\times10^{-4}\,\mathrm{m}^2$ (TS$=-32$ dB), sound speed profile as in Fig. 3, and background reverberation versus range profile as in Fig. 6. Source depth is 35 m.

Using the sonar calibration and a sockeye cross section of $6.3\times10^{-4}\,\mathrm{m}^2$ (TS$=-32$ dB) in the acoustic propagation model, the backscattered echo strength for salmon targets can be calculated as a function of range and depth. Comparing this with (dividing by) the measured background reverberation level allows identification of the minimum range-depth region within which fish can be detected (i.e., where SRR>3 dB). Detectability may be better than this because of the persistent nature of the target over several transmissions. Continuing with our example from 9 August, Fig. 8 shows the fish detection SRR cross section for this geometry. Acoustic energy is focused within the refractive sound channel from 20–60 m. Beyond 4-km range there is little sensitivity to salmon outside this 20–60-m depth interval. The typical enhancement in sound pressure level caused by refractive focusing within the sound channel (20 to 60 m) is 3–11 dB relative to spherical spreading for one-way propagation, which accounts for the overestimation of up to 22 dB in *apparent* fish cross section shown in Fig. 6. It should be emphasized that, although similar detection volumes are calculated for sonar source depths between 20 and 50 m, the salmon detectability field shown here is sensitive in its details to the sonar depth. In this calculation, the total cross-sectional area confined between the surface, seabed, 150-m depth, and from 1–10-km range was $1.34\times10^{6}\,\mathrm{m}^2$, of which salmon would be detectable (SRR>3 dB) within $6.13\times10^{5}\,\mathrm{m}^2$, or 45.7% of the total. Limiting our analysis to depths <40 m (where the salmon are located), the fish detection area is $1.90\times10^{5}\,\mathrm{m}^2$, or about 52.9% of the total available area from 1 to 10 km. Note that if the minimum detectable cross section was reduced to $6.3\times10^{-5}\,\mathrm{m}^2$ (TS$=-42$ dB), which includes all sockeye regardless of orientation, the fish detection area becomes too small to be useful. These calculations show that although the potential

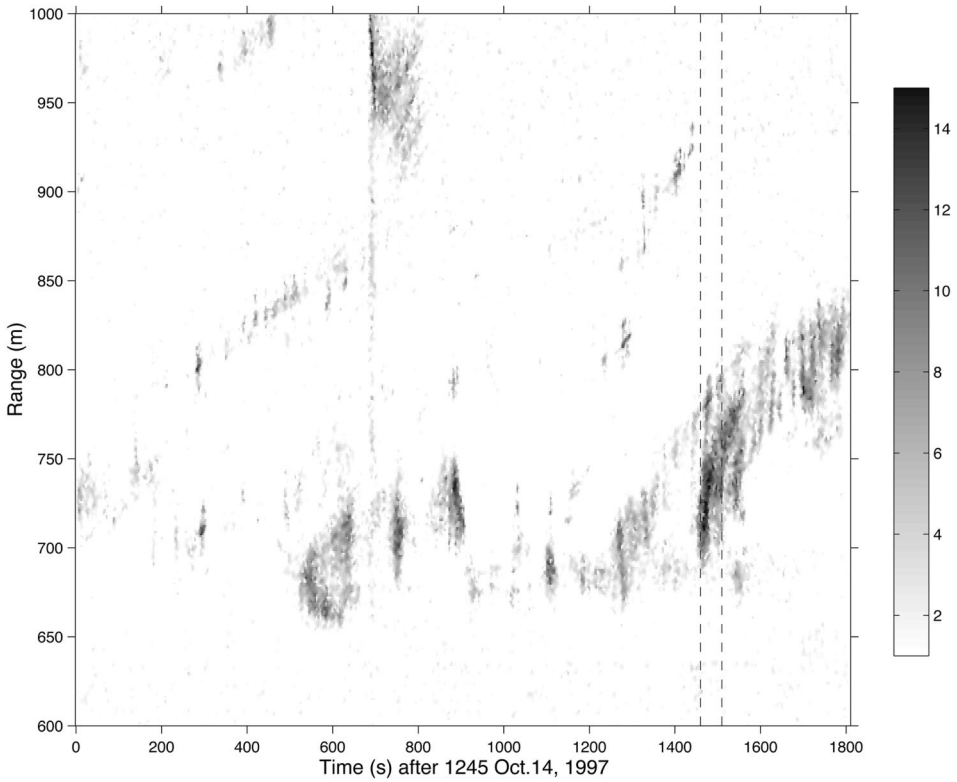

FIG. 9. Backscatter intensity versus range and time taken with sonar in fixed orientation, Drogden Channel, Denmark, 14 October 1997. Intensity is decibels referenced to time-averaged intensity versus range curve. Dashed line identifies measurement interval analyzed in Fig. 10.

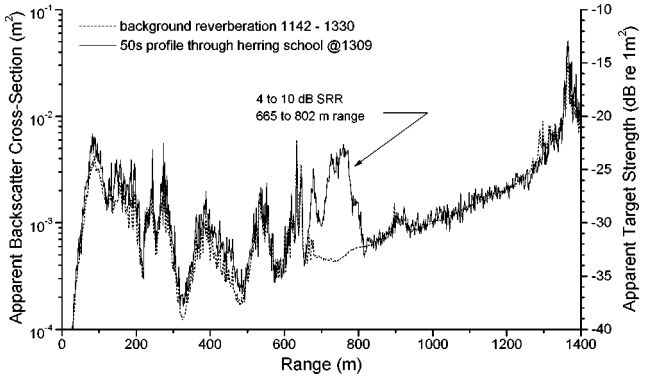

FIG. 10. Comparison between 50-s averaged intensity profile through herring school corresponding to Fig. 9, with background reverberation averaged over 1880 transmissions (spanning 1 h and 38 min).

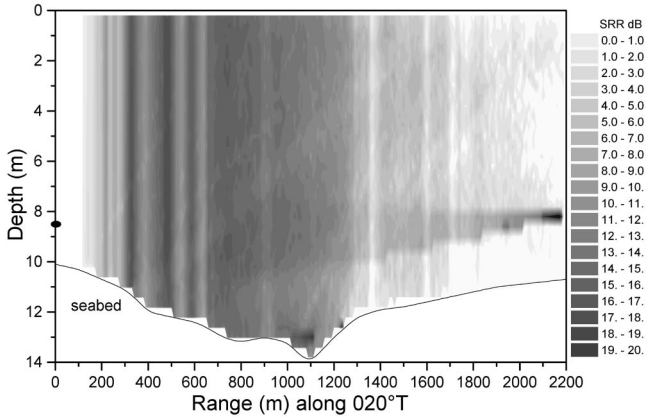

FIG. 11. Cross-sectional distribution of modeled fish echo strength versus reverberation ratio, assuming herring crosssection $=1.70\times10^{-5}\,\mathrm{m}^2$ (TS $=-47.7$ dB) with density of 1 per m^3, uniform sound velocity of 1472 m/s, and background reverberation profile as in Fig. 10.

detection volume is large, it is not inclusive and does not completely overlap the depths where salmon are located. Propagation analysis is essential to identify the effective sampling volume.

During the single 14-km southbound run discussed here, 737 fish targets were detected at ranges from 1 to 7 km. This corresponds to a biomass of 2140 kg (assuming the targets were sockeye salmon). For this 14-km run and using the calculation shown in Fig. 8, the total volume for fish detection from 1 to 7 km and shallower than 40 m was $2.36\times10^{9}\,\mathrm{m}^3$. Dividing the observed biomass by this detection volume yields an *apparent* sockeye biomass density of $9.07\times10^{-7}\,\mathrm{kg\cdot m}^{-3}$. Correcting for azimuthal dependence in detectability (i.e., only one-third are observable) implies an average biomass density of $2.7\times10^{-6}\,\mathrm{kg\cdot m}^{-3}$, which is similar to vertical echo-integration survey results from 20 to 40 m depth reported by Levy *et al.* (1991). Another result from the fish SRR calculation shown in Fig. 8 is that the sonar detects only 24.4% of total salmon present between 20- and 40-m depth and from 1- to 7-km range (i.e., 73.3% from acoustic propagation and one-third due to azimuthal orientation limits). Remembering that this represents only 20% of the overall sockeye population (from the salmon depth distribution), then the corrected number of sockeye over the $8.4\times10^{7}\,\mathrm{m}^2$ survey area should be 15 100, corresponding to an average areal density of $1.8\times10^{-4}\,\mathrm{fish\cdot m}^{-2}$.

B. Herring detection in Drogden Channel

The fixed-location deployments in Drogden Channel provided a quite different environment in which to evaluate the IRFS performance. The sonar was operated both in fixed orientation and scanning mode. For the period 9–14 October 1997 it was fixed at heading 020 degrees true, ~35 degrees from the channel axis (~345 degrees), with data collected up to 2200 m using a 50-ms FM sweep at 3.125-s intervals. In this geometry the seabed reverberation was nominally time invariant and moving targets such as herring schools were identifiable as transient events. The echogram in Fig. 9 reveals the passage of several typical herring schools. The time-invariant signal averaged over a long period isolates scatter from boulders and other targets on the seabed, which are subtracted from the image. Herring schools appear as cloudlike features with a range dimension of 20–200 m and persistence of 20–100 s; they generally move away from the sonar. At this time there was a northward Baltic outflow (approximately $50\,\mathrm{cm\cdot s}^{-1}$ at 345 degrees) with moderately well-mixed waters. Given the time of day (1300 h local) and shallow water conditions, schooling behavior can be expected. Figure 10 shows quantitatively the backscatter intensity during transit of the herring school identified by dashed lines in Fig. 9. The main part of the school passed through the beam in 16 transmissions (50 s) with a SRR of 4–10 dB spanning a range interval of 137 m. Again this calculation of *apparent* cross section assumes only spherical spreading and absorption losses, and ignores reflection and refraction effects. Other peaks in the 50-s averaged profile of Fig. 10 can be interpreted as time-invariant sea floor backscatter.

A similar acoustic propagation analysis was performed for Drogden Channel, with adjustment of parameters for the colder, fresher water conditions and harder, gravel sediments. In this case a calculation grid of 10-m range by 0.4-m depth was used, with a uniform sound speed profile. Lacking any direct measurements of herring cross section at 12 kHz, we must extrapolate from higher-frequency measurements. Using a well-known dorsal cross-section versus length relation for herring at 38 kHz (summarized by Foote, 1987) along with the mean length of autumn-migrating herring in the Øresund of 26 cm given by Staehr (1997), yields a dorsal-incidence backscatter cross section of $4.36\times10^{-5}\,\mathrm{m}^2$ (TS $=-43.6$ dB). This is 7.4 dB lower than predicted by Love's (1977) empirical result for generic fish of this size at 38 kHz. Love's model, which in this case is useful for quantifying the azimuthal variations in backscatter cross section, is valid where the ratio of fish length to acoustic wavelength is >1, which is satisfied for these 26-cm herring at 12 kHz. At 12 kHz Love's empirical model predicts lateral, head, and tail-incidence cross sections for a 26-cm fish of $3.70\times10^{-4}\,\mathrm{m}^2$, $2.12\times10^{-5}\,\mathrm{m}^2$, and $1.84\times10^{-5}\,\mathrm{m}^2$ (-34.3, -46.7, and -47.4 dB), respectively. We can adjust these values specifically for herring by subtracting 7.4 dB (the difference between Foote's and Love's results at 38 kHz). For herring of unknown, yet plausibly uniform azimuthal incidence relative to the sonar, the average value of 1.70

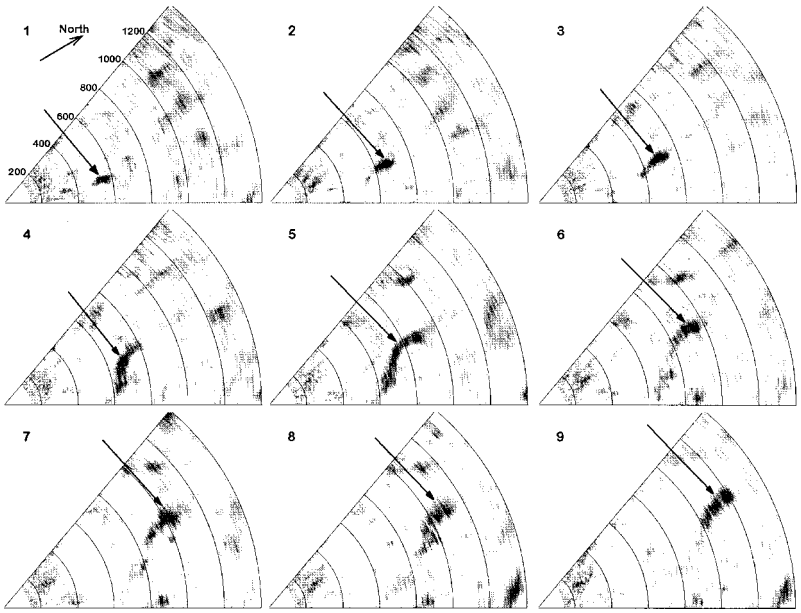

FIG. 12. Time sequence of backscattered intensity sector scans starting at 0140 local time 30 October 1997 illustrating movement of herring school. Arrow shows location of herring school. Range divisions are 200 m to a maximum range of 1400 m. Each scan is comprised of 25 transmissions spanning 150 s. Intensity scale is 0 to 12 dB referenced to matrix of time-averaged background intensity versus range and azimuthal angle.

$\times 10^{-5}\,\mathrm{m}^2$ (TS$=-47.7$ dB) is appropriate. If we assume a typical school density of $1\,\mathrm{fish}\cdot\mathrm{m}^{-3}$ (from Misund *et al.*, 1995) and include the linear increase in insonified volume with range, we may calculate the expected receive level for a herring school. Dividing this by the measured reverberation level versus range yields the fish detection SRR versus range and depth, shown in Fig. 11. Between 100- and 1300-m range the SRR was nearly uniform in depth, with values from 3 to 18 dB. The vertical stripes in SRR are created by peaks and nulls in the reverberation curve. Beyond ~1300 m the fish detection SRR diminishes, except for a reflection focusing region between 7- and 9-m depth. Quantitatively, 71.4% of the 25 500 m^2 total insonified cross section out to 2200 m is available (SRR>3 dB) for herring detection, with the bulk of it in the first 1300 m. In the first 1000 m the typical enhancement in sound pressure level relative to spherical spreading was 6.8 dB (one way), diminishing slightly with range due to seawater absorption and boundary reflection losses. Using the instrument calibration and modeled sound pressure level versus range, the average backscatter cross section of the herring school shown in Fig. 9 was $1.61\times 10^{-4}\,\mathrm{m}^2$ (TS$=-38.0$ dB), which when integrated in range for SRR>3 dB leads to an estimated 1310 herring in the school with average density of $0.11\,\mathrm{fish}\cdot\mathrm{m}^{-3}$. This implies that this school is somewhat smaller and less dense than typical, but still within reasonable limits for herring schools in the region.

In the sector-scanning mode, herring schools were again identifiable as transient objects relative to the time-invariant reverberation versus range and azimuthal angle. Figure 12 shows a sequence of sector scans from the early morning of 30 October. In this sequence the herring school (identified in the figure by an arrow) moved from 550- to 1200-m range over 22 mins. This implies an average northward speed of $0.5\,\mathrm{m}\cdot\mathrm{s}^{-1}$, consistent with the measured northward current, suggesting that the school was (on average) drifting rather than actively swimming. The school was observed to change in shape and size as it drifted northwards, increasing from ~100 m dimension in frame 1 to more than 400 m by frame 5. Generally, the school displayed a length to width ratio of 4. Applying the instrument calibration and modeled sound pressure levels to the school in Fig. 12, frame 9, the average *apparent* cross section was $3.55\times 10^{-4}\,\mathrm{m}^2$ (TS$=-34.5$ dB). Correcting for the insonified volume in the beam at 1000- to 1200-m range, the nominal density of herring was $0.14\,\mathrm{fish}\cdot\mathrm{m}^{-3}$. Multiplying by the planar area of the school (approximately 6460 m^2) and assuming a 6-m (half water depth) vertical dimension, this school was composed of roughly 5230 fish. Integrating over the same school in frames 1–8 of Fig. 12 yielded school size estimates from 2040 to 5500, with mean of 3820. This variation presumably represents the uncertainty in school size estimation by this method, however the average density of this school is similar to those estimated with the sonar in fixed orientation mode.

There are two additional comments that must be made for this shallow water herring detection problem. First, in addition to increasing the effective amplitude of the pulse, propagation through this shallow water environment will extend the effective pulse length due to reflected multi-paths. Ray-tracing calculations show that there are many possible multiply-reflected arrivals, but the intensities of the later arrivals are greatly attenuated relative to the direct path because of boundary reflection losses. If we limit our attention to arrivals with intensities within -10 dB of the direct path (for one-way propagation), then this reverberative pulse lengthening will reach a maximum of 8 ms near 600-m range, decreasing to 3.5 ms by 1200-m range. This pulse lengthening will increase the apparent size of the herring schools by only a few meters. The second comment pertains to biases in biomass estimation due to orientation of the herring relative to the sonar. We use a backscatter cross section that assumes the herring are uniformly distributed azimuthally. In both fixed and sweeping modes of operation, it is plausible that the herring could be aligned with the current flow, oriented between 0 and 35 degrees away from the sonar direction, and thus closer to tail incidence. At tail incidence,

the backscatter cross section for these herring decreases to $3.3\times10^{-6}\,m^2$ (-54.8 dB), increasing the estimated number of fish and density by a factor of 5.1. Biases of this sort need further investigation through combined sonar and net surveys, or possibly through the use of a second sonar imaging the same school from a different direction.

III. CONCLUDING COMMENTS

These results represent a preliminary demonstration of the potential for fish abundance measurement using a 12-kHz horizontally oriented sonar. Sidescan sonars acquire data that are qualitatively and quantitatively different from vertically oriented sonars. A limitation of this configuration is that the insonified volume is determined by the acoustic propagation environment, which can vary with respect to location and on both short time scales (e.g., tidal) and seasonally. Moreover, the interpretation of horizontal-incidence target strength is more variable and less well understood than vertical incidence data. Against these limitations must be balanced the potential for sampling much greater volumes and at distances where the fish behavior is unaffected by the presence of the ship or sonar installation. Although the modest power levels and intermediate frequency used here limit the range to a small fraction of that achieved in Weston's pioneering studies, the present results illustrate the flexibility of a smaller sonar which still achieves a useful sampling range.

Echo traces in the Strait of Georgia attributable to sockeye salmon were routinely acquired to ranges up to 7 km in water depths from 60–200 m. While the maximum range in this environment was not determined experimentally, calculations based on the observed SRR imply that detection should extend to at least 10 km. After correction for the insonified volume and expected fish depth distributions, the inferred areal and biomass densities were consistent with previous hydroacoustic surveys. Much more work is required to assess its performance in a variety of environments before the sonar's full potential can be assessed. We anticipate that an optimum application of the IRFS would be in combination with more traditional net and acoustic surveys. The merit of a towed horizontal imaging sonar would then be in developing improved estimates of the spatial distribution of the fish by illustrating the patterns and extent of fish distributions sampled by other means.

Implementation of the sonar in a very shallow channel in Denmark illustrates a quite different use. This application allows fish migration to be monitored over extended periods with real-time readout of the data ashore. The azimuthal scanning also allows observation of school behavior. In Drogden Channel, herring schools were detected to a range of 1200 m with a signal to reverberation ratio of 3–10 dB, somewhat less than in the Strait of Georgia sound channel, but still sufficient to provide a valuable long-term survey. Indeed, the remarkable aspect of these results is the distance at which fish can be detected in such seemingly adverse conditions. A positive conclusion from the acoustic analysis of the shallow Drogden Channel environment is the relative depth independence of fish detectability. This contrasts with effects of trapping within the sound channel in the Strait of Georgia and further illustrates the importance of planning such surveys with the aid of adequate propagation modeling.

The instrumentation discussed here could be improved in various ways, including the addition of a higher frequency, more vertically directional sonar with a higher transmission rate suitable for sampling the inner portion of the insonified volume. More robust mechanical tow-bodies would have to be developed before the sonar is appropriate for open ocean measurements in adverse weather. Electronic rather than mechanical steering would overcome the effects of orientation changes in the towed configuration as well as simplifying and improving the sector-scan approach in the moored configuration. Finally, greater confidence in the quantitative results of the measurement will come with more accurate horizontal backscattering models of fish in this frequency range. In summary, we conclude that an intermediate range sonar operating at 12 kHz has the potential for making a significant contribution to stock assessment, providing it is used with a proper understanding of the acoustic propagation environment.

ACKNOWLEDGMENTS

We are much indebted to Dr. David Weston for many helpful suggestions and to David Lemon of ASL Environmental Sciences Ltd. for assistance in the early stages of design. We also acknowledge insightful comments by our referees. This work was partially supported by grants from the National HydroAcoustics Program of Fisheries and Oceans Canada. The Danish herring monitoring program was funded by the Danish Environmental Protection Agency, Kontroll-och Styrgruppen for Øresundsforbindelsen (KSO Sweden) and Øresundskonsortiet A/S.

Banneheka, S., Routledge, R., Guthrie, I., and Woodey, J. (**1995**). ''Estimation of in-river fish passage using a combination of transect and stationary hydroacoustics sampling,'' Can. J. Fish. Aquat. Sci. **52**, 335–343.

Bowlin, J., Spiesberger, J., Duda, T., and Freitag, L. (**1992**). ''Ocean acoustical ray-tracing software RAY,'' Tech. Rep. WHOI-93-10, Woods Hole Oceanographic Institution, Woods Hole.

Dahl, P., and Mathisen, O. (**1983**). ''Measurement of fish target strength and associated directivity at high frequency,'' J. Acoust. Soc. Am. **73**, 1205–1211.

Foote, K. (**1987**). ''Fish target strengths for use in echo sounder surveys,'' J. Acoust. Soc. Am. **82**, 981–987.

Gaudet, D. (**1990**). ''Enumeration of migrating salmon populations using fixed-location sonar counters,'' Rapp. P.-V. Reun.-Cons. Int. Explor. Mer. **189**, 197–209.

Hewitt, R., Smith, P., and Brown, J. (**1976**). ''Development and use of sonar mapping for pelagic stock assessment in the California current area,'' Fish. Bull. **74**, 281–300.

Levy, D., Ransom, B., and Burczynski, J. (**1991**). ''Hydroacoustic estimation of sockeye salmon abundance and distribution in the Strait of Georgia, 1986,'' Pacific Salmon Commission Tech. Rep. No. 2.

Love, R. (**1977**). ''Target strength of an individual fish at any aspect,'' J. Acoust. Soc. Am. **62**, 1397–1403.

McKinney, C., and Anderson, C. (**1964**). ''Measurements of backscattering of sound from the ocean bottom,'' J. Acoust. Soc. Am. **36**, 158–163.

Medwin, H., and Clay, C. (**1998**). *Fundamentals of Acoustical Oceanography* (Academic, San Diego).

Misund, O., Aglen, A., and Fronaes, E. (**1995**). ''Mapping the shape, size, and density of fish schools by echo integration and a high-resolution sonar,'' ICES J. Mar. Sci. **52**, 11–20.

Nero, R., and Huster, M. (**1996**). ''Low-frequency acoustic imaging of Pacific salmon on the high seas,'' Can. J. Fish. Aquat. Sci. **53**, 2513–2523.

Pedersen, B., and Trevorrow, M. (**1999**). ''Continuous monitoring of fish in a shallow channel using a fixed horizontal sonar,'' J. Acoust. Soc. Am. **105**, 3126–3135.
Quinn, T., and terHart, B. (**1987**). ''Movements of adult sockeye salmon (*Oncorhynchus nerka*) in British Columbia coastal waters in relation to temperature and salinity stratification: ultrasonic telemetry results,'' Can. Spec. Publ. Fish. Aquat. Sci. **96**, 61–77.
Revie, J., Weston, D., Harden-Jones, F., and Fox, G. (**1990**). ''Identification of fish echoes located at 65 km range by shore-based sonar,'' J. Cons. Int. Explor. Mer **46**, 313–324.
Rusby, J., Somers, M., Revie, J., McCartney, B., and Stubbs, A. (**1973**). ''An experimental survey of a herring fishery by long-range sonar,'' Mar. Biol. **22**, 271–292.
Staehr, K.-J. (**1997**). ''Short summary of environmental impact monitoring on herring in the sound, autumn 1995 to spring 1997,'' Tech. Rep. Danish Institute For Fisheries Research, Copenhagen, DK.
Tarbox, K., and Thorne, R. (**1996**). ''Assessment of adult salmon in near-surface waters of Cook Inlet, Alaska,'' ICES J. Mar. Sci. **53**, 397–401.
Trevorrow, M. (**1997**). ''Detection of migratory salmon in the Fraser River using 100 kHz sidescan sonars,'' Can. J. Fish. Aquat. Sci. **54**, 1619–1629.
Trevorrow, M., and Claytor, R. (**1998**). ''Detection of herring schools in shallow waters using high-frequency sidescan sonars,'' Can. J. Fish. Aquat. Sci. **55**, 1419–1429.
Weston, D., and Andrews, H. (**1990**). ''Monthly estimates of fish numbers using a long-range sonar,'' J. Cons. Int. Explor. Mer **47**, 104–111.
Weston, D., and Revie, J. (**1971**). ''Fish echoes on a long-range sonar display,'' J. Sound Vib. **17**(1), 105–112.
Weston, D., and Revie, J. (**1989**). ''A 5-day long-range-sonar record of an extensive concentration of fish,'' J. Acoust. Soc. Am. **86**, 1608–1611.

The bi-azimuthal scattering distribution of an abyssal hill

Nicholas C. Makris[a] and Chin Swee Chia
Massachusetts Institute of Technology, Cambridge, Massachusetts 02139

Laurie T. Fialkowski
Naval Research Laboratory, Washington, DC 20375

(Received 16 September 1998; revised 15 June 1999; accepted 12 July 1999)

High-resolution bistatic images of a typical abyssal hill on the western flank of the Mid-Atlantic Ridge are made with a low-frequency towed-array system operating remotely at 1/2 convergence zone (~33.3 km) stand-off. Comparison with modeled images, generated from high-resolution supporting bathymetry sampled at 5-m intervals, roughly the wavelength scale, reveals that steep scarps return the strongest echoes because they project the largest area along the acoustic path from the source to receiver. Prominent returns deterministically image scarp morphology when the cross-range axis of the system's resolution footprint runs along the scarp axis. Statistical fluctuations inherent in the scattered field prevent the system from distinguishing smaller-scale anomalies on the scarps, such as canyons and gullies (~100–200 m scale), that would otherwise be resolvable in range, in certain bistatic geometries. The mean bi-azimuthal scattering distributions of the two major scarps on the abyssal hill are *identical* and have strengths equal to the *constant* $-17\,\mathrm{dB}\pm 8\,\mathrm{dB}$. This suggests that long-range reverberation from prominent geomorphological features of the world's mid-ocean ridges can be adequately modeled as Lambertian with albedo $\pi/10^{1.7}$, given supporting bathymetry sampled with sufficient frequency to resolve the projected area of these features. [S0001-4966(99)01911-6]

PACS numbers: 43.30.Hw, 43.30.Pc, 43.30.Gv [DLB]

INTRODUCTION

During the Office of Naval Research (ONR) Main Acoustics Experiment (MAE) of July 1993,[1,2] two research vessels equipped both with vertical source and horizontal receiving arrays made bistatic measurements of scattering from a typical, highly lineated, abyssal hill, referred to as B', on the western flank of the Mid-Atlantic Ridge (MAR).[2] These measurements were made for two primary reasons. The first was to investigate the extent to which an abyssal hill, one of the most commonly occurring bathymetric features of the world's oceans, can be deterministically resolved using a remotely operated bistatic towed-array imaging system. The second was to measure the bi-azimuthal scattering distribution of a typical abyssal hill.

In a previous paper, Ref. 2, it was shown that low-frequency towed-array systems can be used to generate wide-area images of prominent geological features in the deep ocean over hundreds of kilometers in near real-time. The brightest features in these images effectively resolve the shape of steep escarpments (~1 km wide) running along the axis of abyssal hills ($\sim 10\times 40$ km) and other bathymetric highs such as inside corner domes (~10 km diameter).[2] Because the resolution of these images greatly exceeds the roughly 10–20-km resolution of currently available bathymetric maps of the world's oceans, where individual abyssal hills remain indistinguishable, there is real promise that towed-array systems may provide a rapid means of charting previously undiscovered bathymetric highs in the deep ocean.

The first main objective of this work is to experimentally determine the effective resolving power of a towed-array system in remotely imaging deep-ocean bathymetry. To do so, an attempt is made to infer the detailed structure of the major scarps on the B' abyssal hill using MAE's bistatic system at 1/2 convergence zone (CZ) stand-off. Since the cross-range resolution of the system (~1.0 km @ 1/2 CZ) is insufficient for this task, its much higher range resolution (~40 m) is exploited.[2] The basic idea behind the analysis is that when the bistatic measurement geometry is such that the receiving array's cross-range direction is skew to the ridge axis, characteristic nonlinearities in scarp structure, such as canyons (~100–200 m wide) and gullies (~50 m wide) previously documented with high-resolution supporting bathymetry,[2,3] become potentially resolvable by the towed-array system in range. The analysis of a full suite of such bistatic measurements, spanning ±90° about ridge-axis broadside, could lead to a detailed accounting of the scarp's nonlinear structure. Experimental uncertainties in the orientation of the towed-array, sound-speed structure and source–receiver navigation as well as statistical fluctuations in the scattered returns are difficult to account for *a priori* and can severely degrade the system's theoretical resolution. The value of the present analysis lies in its *experimental* assessment of a towed-array imaging system's resolving power.

The second main objective is to experimentally determine the inherent bi-azimuthal scattering distribution of the primary scatterers on the B' abyssal hill, namely two primary scarps that run along its major axis, when waterborne propagation paths are effectively horizontal at the abyssal hill, as they are in remote sensing applications. The hope is that the bi-azimuthal scattering distributions measured for

[a]Electronic mail: makris@mit.edu

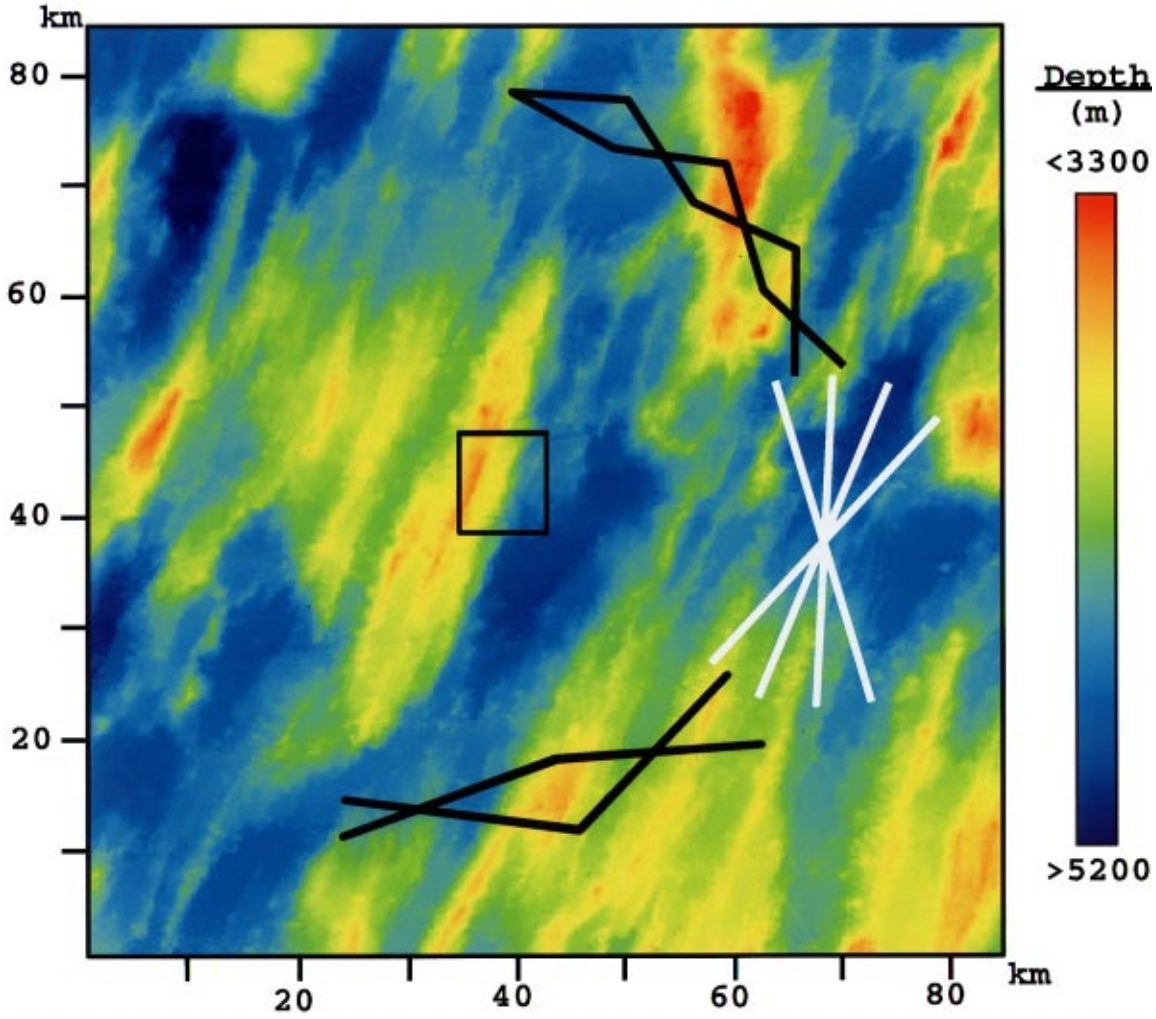

FIG. 1. The bistatic tow-ship tracks of the RV CORY CHOUEST (white lines) and RV ALLIANCE (black lines) during the B' experiment overlain on hydrosweep bathymetry (200-m sampling). The box indicates the region where high-resolution bathymetry (5-m sampling) is available. Conjugate depth with respect to the CORY source falls at 3800 m. Tracks for the entire $B'-C'$ experiment are shown in Ref. 2.

these may apply more generally to scarps found on abyssal hills throughout the MAR, many of which share the same highly lineated character. This type of knowledge about the scattering properties of abyssal hills is important because it enables one to (1) efficiently model bistatic scattering from abyssal hills, which often appears as clutter in active sonar systems operating in the deep ocean;[4] (2) ground-truth the output of seismo-acoustic scattering models with an empirical scattering function; and (3) classify bathymetric features according to their scattering properties so similar features may be identified in future towed-array surveys where there is no supporting bathymetric database.

To generalize the present bistatic scattering measurements, such effects as two-way transmission loss, the areal resolution of the measurement, and its foreshortening must be factored from them. In particular, high-resolution bathymetry, sampled at the scale of the acoustic wavelength, is used to determine surface orientation and foreshortening. The parabolic equation is used to compute two-way transmission, ray tracing to determine incident and scattered angles with respect to the seafloor surface, and a spatial convolution to account for the spatially varying areal resolution of the measurement system. Statistical fluctuations due to nonlinear speckle noise inherent in the measurements are reduced by stationary averaging and are stabilized by logarithmic transformation. Since all measurements of B' are at 1/2 CZ standoff, acoustic paths from the source and to the receiver are nearly horizontal when they intersect B'. This enables a relatively accurate calculation of the bi-azimuthal scattering distribution of the B' scarps which will be useful in the classification of similar scarps on mid-ocean abyssal hills by towed-array systems at $n+1/2$ CZ.

I. BISTATIC EXPERIMENTAL DESIGN, IMAGING RESOLUTION, AND THE GEOMORPHOLOGY OF THE B' ABYSSAL HILL

The geometry of the bistatic experimental survey of the B' abyssal hill is summarized here in Fig. 1, where the track design,[5,6] is overlain on hydrosweep bathymetry, sampled at 200-m intervals.[2,7] A more complete description of the $B'-C'$ corridor experiments, which comprised roughly 90% of MAE, can be found in Refs. 2, 5, and 6. The 8×9-km^2 box at the center of B' shows the region where high-

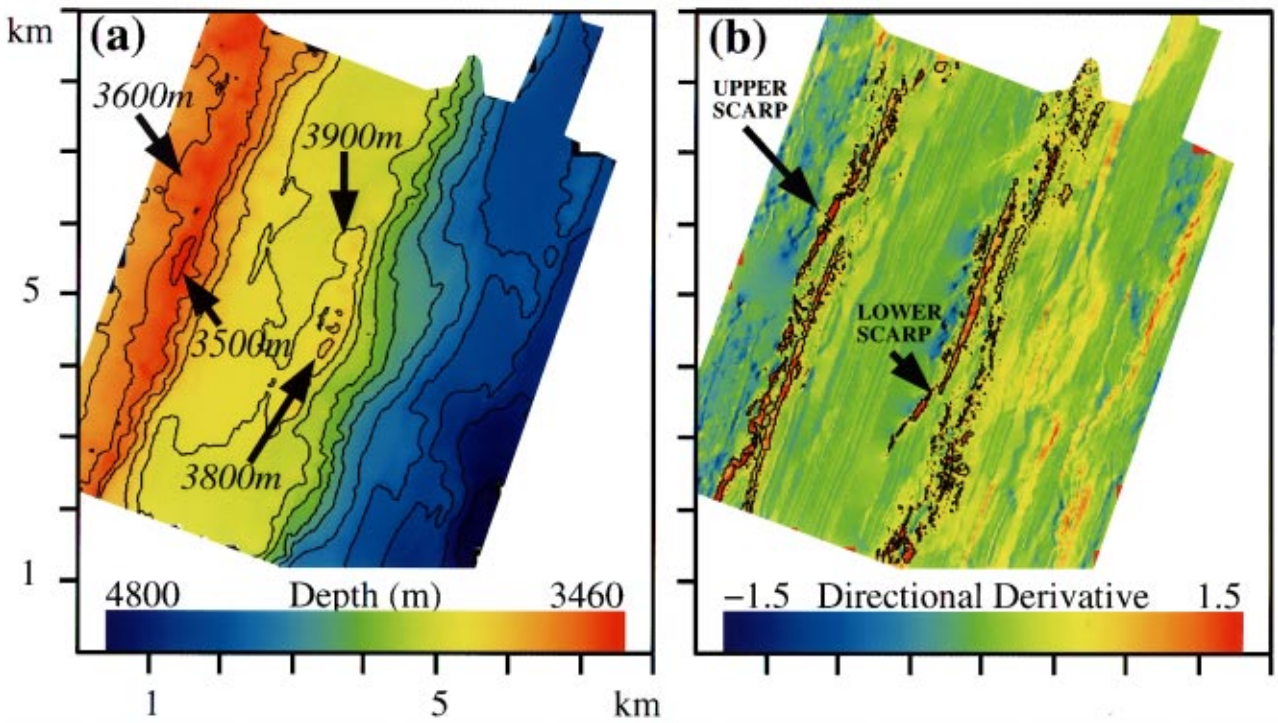

FIG. 2. (a) High-resolution bathymetry (5-m sampling) on the east-central face of B' as located in Fig. 1. Depth contours are at 100-m intervals. (b) The component of seafloor elevation gradient, or the directional derivative (DD), normal to the B' axis, computed from high-resolution bathymetry as in Fig. 22 of Ref. 2. Many steep cliffs (>60° slope) and smaller terraces (~45° slope) appear on both the upper and lower scarps that cannot be resolved by the hydrosweep bathymetry. Contours segment the upper and lower scarps as regions within which the DD exceeds 1/2. These same contours are used to identify the scarps throughout this paper.

resolution bathymetry, sampled at 5-m intervals, was collected in support of MAE.[2,3] The research vessel (RV) CORY CHOUEST traced the central star while the RV ALLIANCE followed the wings to the north and south. Each RV towed a horizontal receiving array with axis roughly coincident with the ship's straight-line course. To maximize cross-range resolution of B' and to minimize noise contamination from the other RV, the highest resolution beams at array broadside are directed towards the center of B', where high-resolution bathymetry is available, while the lowest resolution beams at array endfire are directed towards the other RV.[2,4,6] Only transmissions from the CORY CHOUEST source array are considered in this paper because of its significantly higher strength, 229 dB *re* 1 mPa @ 1 m, and directionality compared to that of the ALLIANCE.[2,8] The CORY's source array is steered to broadside for all transmissions studied in this paper.

Linear frequency modulated (LFM) waveforms of $\tau = 5$ s duration in the frequency band 200–255 Hz are exclusively analyzed here because they offer the highest available range resolution, which is given by $\Delta r = c/(2B) \sim 14$ m, where $c \sim 1510$ m/s is the mean sound speed and B is the bandwidth.[2] To reduce their standard deviation after pulse compression, instantaneous intensity measurements are averaged over time period $T = 0.0625$ s for CORY receptions and $T = 0.0533$ s for ALLIANCE receptions. This averaging leads to an effective range resolution of $\Delta r = cT/2 = 47$ m for the CORY and $\Delta r = 40$ m for the ALLIANCE.

With the assumption that the specific bathymetric features resolved by the towed-array system behave as Rayleigh targets,[9,10] due to their structural complexity with respect to the wavelength scale, the degrees-of-freedom $N \sim TB$ becomes roughly 3.4 for CORY and 2.9 for ALLIANCE LMF receptions. The further assumption of independence and stationarity among the roughly 3 range cells averaged leads to a standard deviation of 2.5 dB and a bias of 0.6 dB in the intensity level at any pixel of a towed-array image.[2,10] If, on the other hand, a particular range cell dominates the average, or if the range cells are correlated, μ may be as small as unity, which leads to a standard deviation of roughly 5.6 dB and a bias of 2.5 dB.[2,10]

The geomorphology of the B' abyssal hill is displayed in Fig. 2. Gross features are evident in the high-resolution bathymetry of Fig. 2(a). The central crest of B', for example, rises roughly 1400 m from the western segment valley floor at roughly 4900 m to nearly 400 m above the 3800-m conjugate depth[2] of the CORY source. Minute details of the high-resolution bathymetry are best cast in terms of the component of seafloor elevation gradient, or directional derivative, normal to the B' axis, shown in Fig. 2(b). This reveals two steep scarps separated by an extended plateau just below 3800 m. Both scarps run along the B' axis 21° from true North, and are characterized by steep unsedimented cliff faces that rise upwards for typically 100 m with characteristic slopes of 50°–90°. The scarps are segmented by a contour within which the directional derivative exceeds 1/2, corresponding to slope angles greater than ~26.6°. The contours, shown in Fig. 2(b), are used throughout the paper to designate the locations of the upper and lower scarps.

The bistatic locations of the two research vessels during

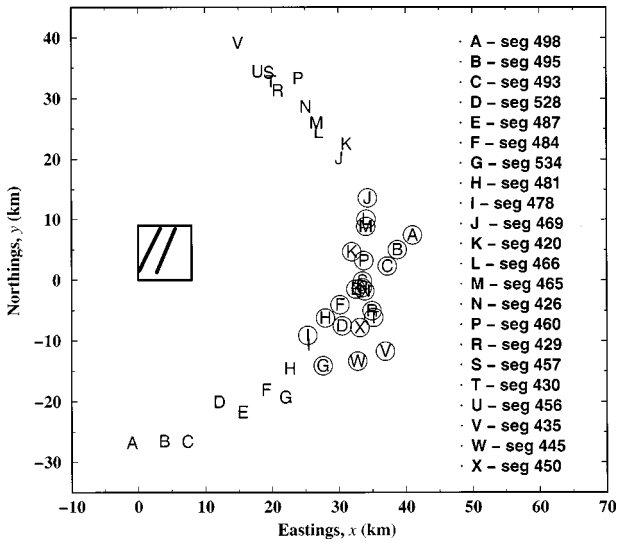

FIG. 3. The bistatic locations of the two research vessels during the LFM transmissions analyzed in this paper are given in eastings, *x*, and northings, *y*. These locations are distributed in a semicircle about the high-resolution region shown by the central box within which two diagonal lines indicate the upper and lower scarps. Circled letters indicate the location of the CORY while the same letters indicate the location of the ALLIANCE for the 20 bistatic segments given in the legend. Segments S430, S466, S481, and S495 are excluded from the monostatic analysis due to colocation with some of the other monostatic segments shown. Since ALLIANCE was at the apex of the northern wing and in the shadow of B' during S445 and S450, they are used as the only purely monostatic transmissions in this analysis, which then has a total of 18 monostatic segments.

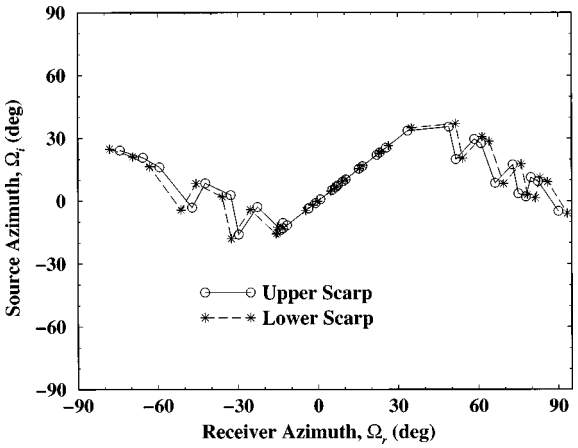

FIG. 4. The portion of bi-azimuthal space spanned by the source–receiver pairs. Azimuth is measured counterclockwise from a vector that originates from the center of the given scarp in the high-resolution region and points normal to its axis in a southeasterly direction. Source azimuths are denoted by Ω_i and receiver azimuths by Ω_r. The curves for the upper and lower scarps are nearly identical because their separation is small compared to the range to the respective RV. The portion of nonmonostatic space spanned is double that shown by acoustic reciprocity between source and receiver locations.

the LFM transmissions analyzed in this paper are given in eastings and northings in Fig. 3. These locations are distributed in a semicircle with bisecting diameter oriented along the B' axis and centered in the high-resolution region. A letter of the alphabet designates each transmission. Circled letters indicate the monostatic location of the CORY while unboxed letters indicate the bistatic location of the ALLIANCE for a given transmission. A *segment number* specifies each transmission, following the vernacular of the MAE.[1,2]

The portion of bi-azimuthal space spanned by the source–receiver pairs is shown in Fig. 4. Azimuth is measured counterclockwise from a vector that originates from the center of the given scarp in the high-resolution region and points normal to its axis in a southeasterly direction. The source azimuths Ω_i then fall within $|\Omega_i|<30°$, while the receiver azimuths Ω_r span the full 180° range. This bistatic geometry is appropriate because (1) the east-central face of B' is uniformly insonified with negligible shadowing, and (2) the receivers are never completely shadowed.

Expressions for the half-power or 3-dB beamwidth $\beta(\theta)$ of a narrow-band line array, steered to an angle θ from endfire, are given in Eqs. (1) and (2) of Ref. 11 as a function of aperture length and frequency. These expressions also approximate the azimuthal resolution of the MAE arrays for LFM reception when evaluated at the LFM center frequency of 227.5 Hz. Best resolution lies at broadside and is ~1.6° for the $L=318$ m receiving array of the CORY and ~2.0° for the $L=254$ m receiving array of the ALLIANCE. Cross-range resolution, defined as $r\beta(\theta)$ for a monostatic measurement at range r from the scattering patch, is then 0.9 km for the CORY and 1.1 km for the ALLIANCE at 1/2 CZ where $r=33.3$ km.

At 1/2 CZ, neither array has sufficient aperture to azimuthally resolve characteristic nonlinearities in scarp structure, such as canyons (~100–200 m wide) and gullies (~50 m wide) previously documented with high-resolution supporting bathymetry.[2,3] This is evident upon inspection of Fig. 5(a), where the resolution footprint of the towed-array system, a roughly 50 m by 1 km annular sector at 1/2 CZ, is superimposed on a bathymetric image of the B' upper scarp. These same features become potentially resolvable by the towed-array system in range when cross-range is skew to the ridge axis, as shown in Fig. 5(b), with the relatively safe assumption that the scarp, and not the plateaus above and below, cause the predominant reverberation. Analysis of a full suite of such bistatic measurements, spanning $|\Omega_r|<90°$, could provide a detailed accounting of the scarp's nonlinear structure, given sufficient charting accuracy and statistical stability of the measured reverberation.

The normalized autocorrelation function of upper scarp elevation, in Fig. 6, quantitatively reveals along and across-scarp correlation scales (*e*-folding lengths) of 150 and 50-m, respectively, consistent with a visual assessment of typical canyon and gully dimensions. The resolution footprint of the towed-array system integrates or blurs together scattered returns from roughly five major canyons when its cross-range range axis parallels the scarp's, as is characteristic of the monostatic measurements. This leads to a broad distribution of incident angles from a given source, or scattered angles to a given receiver, over the resolution footprint. This is shown in Fig. 7(a) for S435 where vertical refraction is taken into account via raytrace. Conversely, the resolution footprint typically blurs together scattered returns from the outer wall of a single canyon with those from plateaus above and below when its cross-range axis is skew to the scarp axis, as is characteristic of bistatic measurements with large $|\Omega_r|$. This

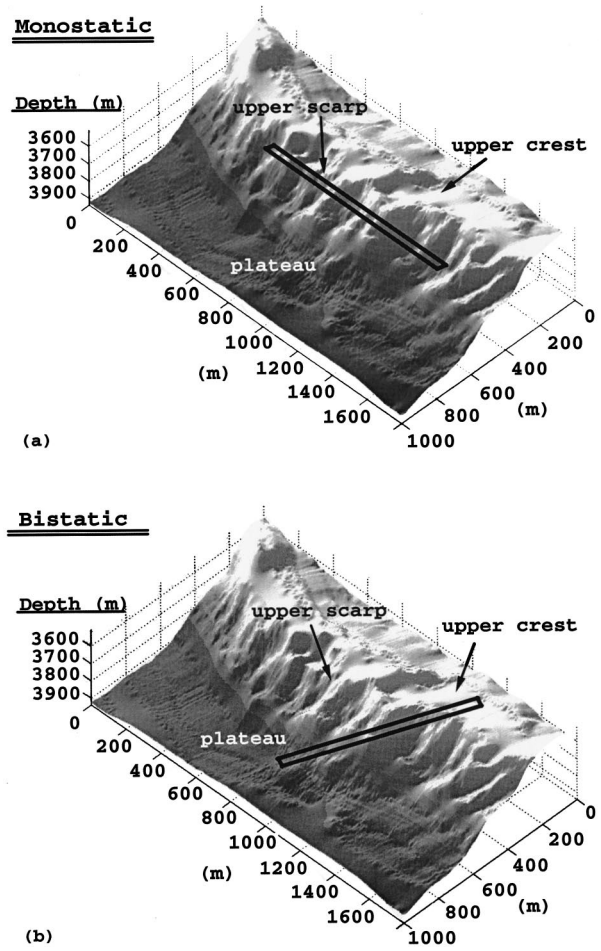

FIG. 5. Shaded relief of a portion of the B' upper scarp imaged with high-resolution bathymetry with the roughly 50-m by 1-km resolution footprint of the towed-array system overlain. (a) Monostatic geometry for S435. (b) Bistatic geometry for S435. In (a), the resolution footprint blurs together many characteristic nonlinearities in scarp structure, such as canyons and gullies. These features become potentially resolvable in range, as in (b), for some bistatic geometries of the present experiment.

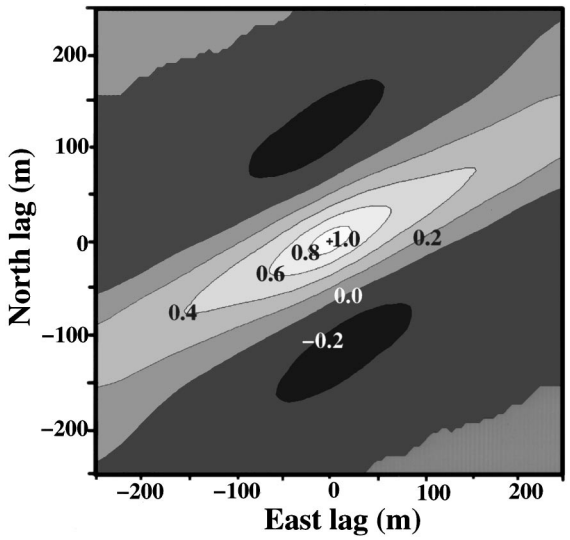

FIG. 6. The normalized 2-D autocorrelation of upper scarp elevation as a function of east and north spatial lag. The along-scarp and across-scarp *e*-folding lengths of ~150 and ~50 m, respectively, quantify the scale of typical nonlinearities along and across the scarp.

also leads to a broad distribution of incident angles or scattered angles over the resolution footprint, as shown in Fig. 7(b) and (c) for the same segment.

Since the surfaces resolved by the towed-array system on the B' scarps are not even approximately planar, there is no unique surface normal to characterize the bathymetry within the resolution footprint. Consequently, there is no unique incident or scattered angle. The *traditional surface scattering strength*, which depends upon the directions of incident and scattered waves defined relative to the local surface normal and *includes purely local foreshortening effects*, must then be reanalyzed to accommodate the reality of the present experiment, as will be discussed in later sections.

II. BISTATIC IMAGING OF THE B' ABYSSAL HILL FROM 1/2 CZ

A. Wide-area bistatic images

While a number of *monostatic*, reverberation charts of the B' abyssal hill have been presented and analyzed,[2,12–14] only two *bistatic* charts of B' have been previously studied in the literature.[2] These are for the 200–255-Hz LFMs of S478 and S487. Analysis of S478 is particularly significant because it characterizes all measurements for which the bistatic separation between the CORY and ALLIANCE is small relative to the range to B'. In these cases, bistatic and monostatic charts are similar with cross-range falling parallel to the B' axis. Prominent reverberation is then unambiguously charted to the steep escarpments, as demonstrated in Ref. 2. Monostatic and bistatic reverberation charts of the same transmission show great differences, however, when the bistatic separation is large. This is well illustrated here for S435 and S528, which are respectively at the northern extreme and midway to the southern extreme of the ALLIANCE

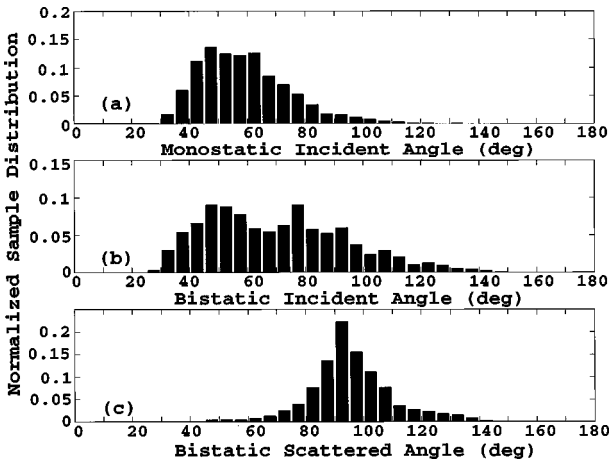

FIG. 7. The distribution of incident and scattered angles within the resolution footprints shown in Fig. 5 for S435. The incident angle is the inverse cosine of the inner product between the local surface normal and the vector pointing along the acoustic path to the source. The scattered angle is the inverse cosine of the inner product between the local surface normal and the vector pointing along the acoustic path to the receiver. Refraction is included. Angles greater than 90° indicate shadowing. (a) Monostatic case where incident and scattered angles are identical and axis of resolution footprint is along scarp axis. Bistatic case for (b) incident angles and (c) scattered angles, where axis of resolution footprint is skew to scarp axis.

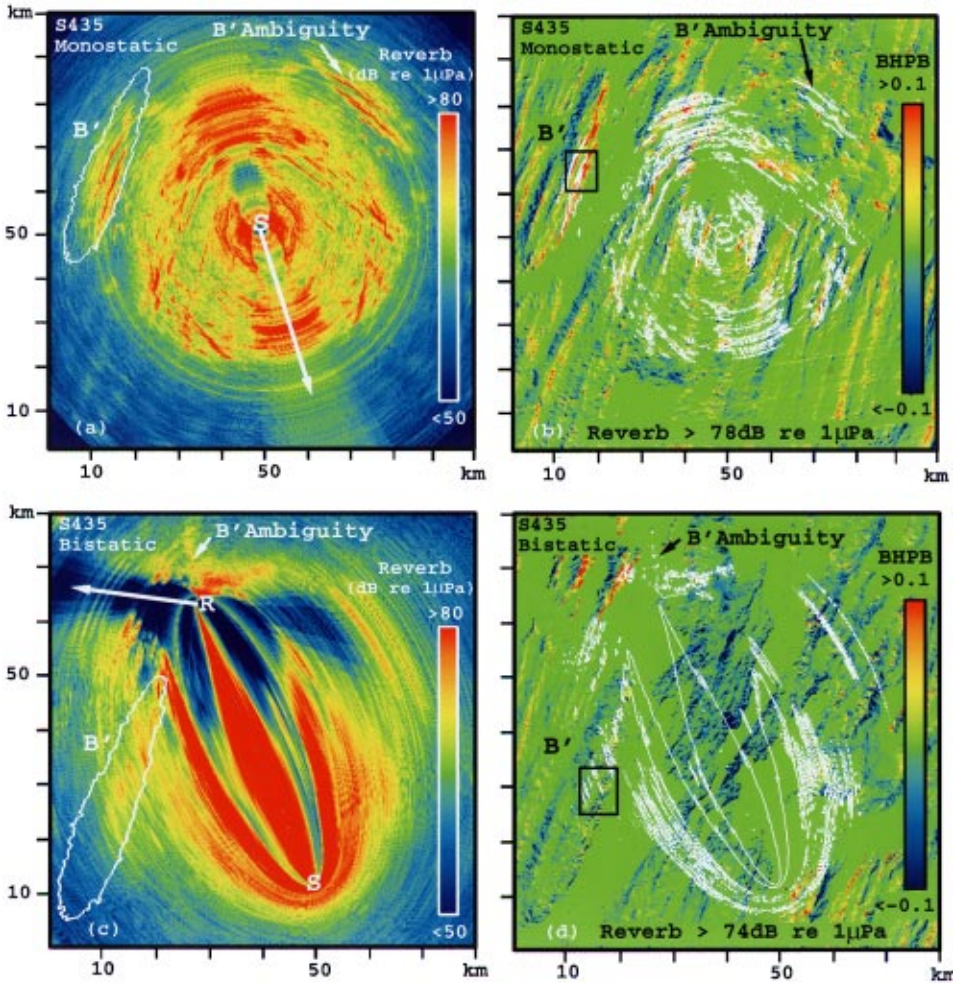

FIG. 8. Wide-area charts of monostatic and bistatic reverberation measured for the 200–255-Hz LFM S435, where ALLIANCE is near the apex of the northern wing. (a) Monostatic reverberation chart showing symmetry about the array axis for CORY heading 163°. (b) Contours of high-level backscatter, overlain on the bistatic horizontal projection of bathymetry (BHPB), coregister with major scarps on B' that have large areas projected towards the source–receiver. The false backscatter image of B' does not coregister with the BHPB. (c) Bistatic reverberation chart shows asymmetry about the array axis because this axis forms an oblique angle with the major axis of the bistatic ellipse. The ALLIANCE heading is 277°. (d) Contours of high-level backscatter, overlain on the BHPB, coregister with major scarps on B' that have large areas projected along the acoustic path from source to scatterer to receiver. Unlike the monostatic case, the cross-range axis of the resolution footprint forms an oblique angle with the scarp axis so that prominent returns are speckled across the scarp. The false backscatter image of B' does not coregister with the BHPB and exhibits severe spatial contraction. Source and receiver locations are indicated in (a) and (c). The product of a negative HPBR and a negative HBPS is always plotted as a negative HPBR to distinguish shadowed regions.

tracks. Specifically, $\Omega_i \sim -5°$ and $\Omega_r \sim 90°$ for S435 and $\Omega_i \sim -5°$ and $\Omega_r \sim -50°$ for S528, with respect to both upper and lower scarp reference centers.

To gain a broader perspective, consider first the wide-area charts of monostatic reverberation, in Figs. 8–10(a). These each have a character very similar to that found for short continuous wave (cw) transmissions in Figs. 8 and 9 of Ref. 2. When overlain on the bistatic horizontal projection of bathymetry (BHPB), prominent reverberation coregisters precisely with steep escarpments along the B' axis, as illustrated in Figs. 8–10(b). The bistatic horizontal projection of bathymetry is the product of the horizontal projection of bathymetry toward the source (HPBS) and the horizontal projection of bathymetry toward the receiver (HPBR). The former is inner product of the local seafloor normal and a unit vector pointing to the horizontal position of the source, while the latter is the inner product of the local seafloor normal and a unit vector pointing to the horizontal position of the receiver. To distinguish shadowed regions, the product of a negative HPBR and a negative HBPS is always plotted as a negative HPBR. In later sections, a far more precise computation of surface projection factors, accounting for refracted ray paths to and from the seafloor, is employed to analyze reverberation over the region of high-resolution bathymetry.

In the general limiting case of range-independent propagation and a flat bottom, range ambiguity of the bistatic towed-array system falls on elliptic arcs about foci coinciding with the source and receiver positions. The arcs are defined by conserving the two-way travel distance from source to scatterer to receiver as the sum of the radii. The arc length at 1/2 CZ, over the broadside resolution of the CORY or ALLIANCE receiving array, remains well approximated by the monostatic cross-range resolution $r\beta(\theta)$ for the entire suite of bistatic measurements taken at B', as shown in Appendix A. Here, r is range from the receiving array to the scattering site. For what we refer to here as ''monostatic'' measurements, the CORY's source and receiver arrays are not coincident but are in such close proximity (~1.12-km separation) that range ambiguity lies on nearly circular arcs at 1/2 CZ. When the bistatic separation between the CORY and ALLIANCE is not small compared to r, however, the arcs are far from circular. This accounts for some characteristic differences between monostatic and bistatic charts of the same transmission.

The right–left ambiguity of the receiving line array is also expressed differently in monostatic and bistatic charts. Prominent features are ambiguously charted in an almost symmetrical fashion about the receiving array's axis in monostatic geometries.[11,2] Only the incorporation of known bathymetry in the charting procedure leads to local breaks in symmetry.[2,14] Such extreme symmetry, however, is only

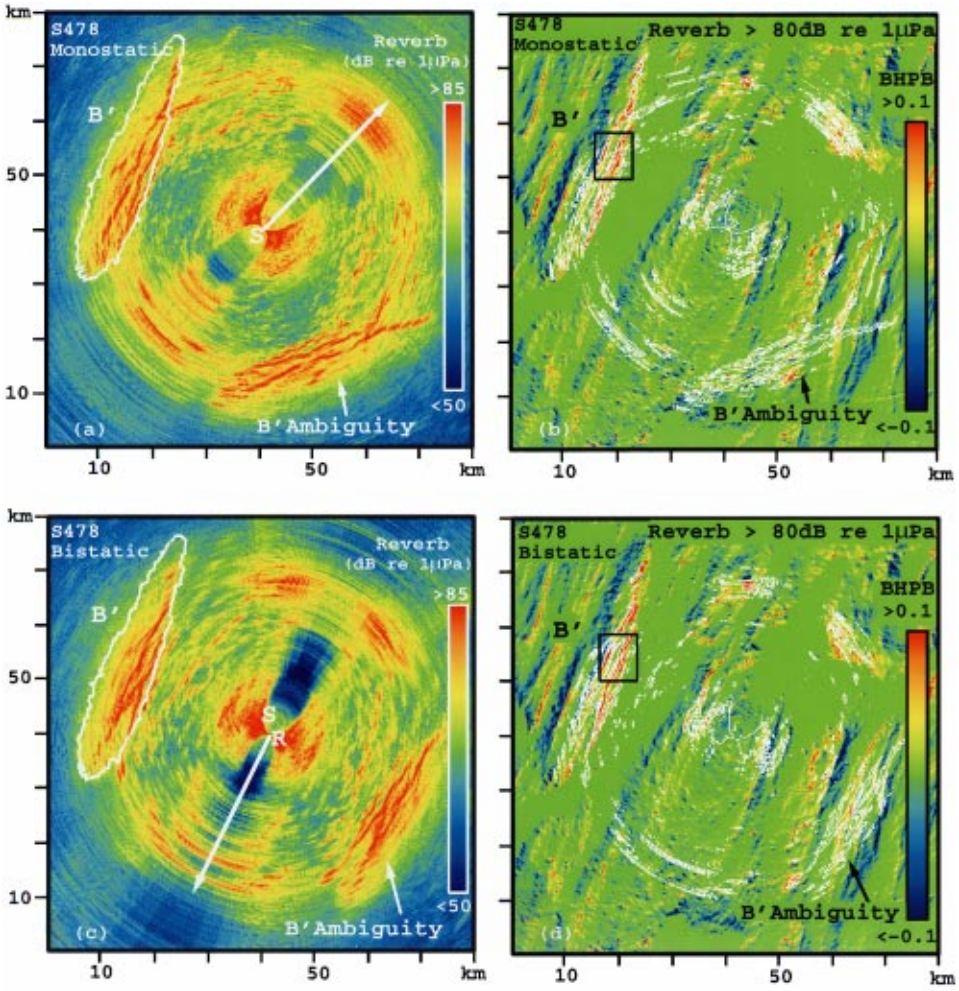

FIG. 9. Wide-area charts of monostatic and bistatic reverberation measured for the 200–255-Hz LFM S478. ALLIANCE and CORY are in close proximity. (a) Monostatic reverberation chart showing symmetry about the array axis for CORY heading 45°. (b) Contours of high-level backscatter, overlain on the BHPB, coregister with major scarps on B' that have large areas projected towards the source–receiver. (c) Bistatic reverberation chart shows symmetry about the array axis due to the close proximity of the CORY and ALLIANCE. The ALLIANCE heading is 207°. (d) Contours of high-level backscatter, overlain on the BHPB, coregister with major scarps on B' that have large areas projected along the acoustic path from source to scatterer to receiver.

available in bistatic scenarios when the receiving array axis parallels the line joining the source and receiver. This line defines the major axis of the bistatic ellipse. Otherwise, some distortion occurs. In the case of segment 435, the receiving array is at an oblique angle to the major axis of the bistatic ellipse. Prominent reverberation from the central scarps of B' correctly register at roughly 1/2 CZ (~33.3 km) from the receiving array. The corresponding ambiguous returns are mirrored about the array axis, and span the same annular sector as the true returns, but fall at a much shorter range to preserve the travel time. As a result, they are condensed to a much smaller spatial area than that spanned by the true returns. The converse is also true. True returns from this small area, where the right–left ambiguity of the receiving array intersects the elliptical range ambiguity of the bistatic system, may be falsely charted to a more extensive region on B'. The geometry of this type of ambiguity is given in Fig. A1. After a careful analysis of the registration between bathymetric directional derivatives and prominent reverberation, we find that the experimental design[5] was successful in exploiting the natural geomorphology of the region to avoid contamination from line-array ambiguity at B'.

Prominent bistatic returns are overlain on the bistatic horizontal projection of bathymetry (BHPB) in Figs. 8–10(d). In the limit of horizontal propagation to and from the bottom, which is a reasonable approximation for waterborne paths at $n+1/2$ CZ, the BHPB becomes a projection factor directly proportional to the incoherent intensity of the scattered field from an infinitesimal area of the seafloor, and so is useful for comparison with wide-area reverberation.

For large bistatic separations, as in S435 and S528, characteristic nonlinearities in scarp structure, such as canyons and gullies, lead to a speckled pattern of strong projections in the path connecting source, scatterer, and receiver. Over the same region, prominent bistatic reverberation displays analogous behavior as a speckled pattern of concentric arcs that obliquely cross the scarp axes. This phenomenon was previously observed in monostatic reverberation charts when the radial propagation path was parallel to or formed a shallow angle with the axis of a major bottom-limited ridge.[2] The effect is partially due to (1) anomalous surface projections, and (2) statistical fluctuations from random interference, as will be shown in the next sections.

B. High-resolution images of the east-central face of B'

The bending of acoustic paths from the source, to the scattering patch and back to the receiver, caused by naturally occurring depth-dependent variations in the ocean's refractive index, described in Ref. 2, must be taken into account for the charting accuracy of long-range echoes to be compa-

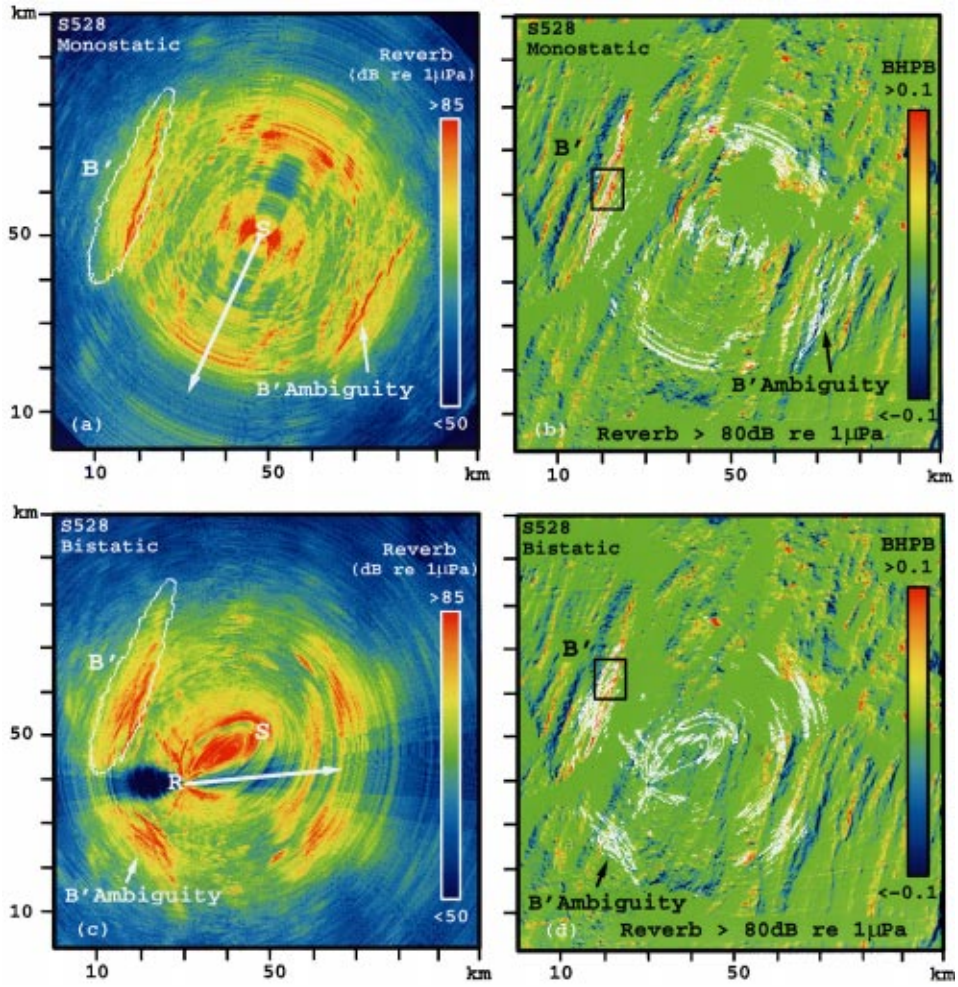

FIG. 10. Wide-area charts of monostatic and bistatic reverberation measured for the 200–255-Hz LFM S528. Alliance is midway along the southern wing. (a) Monostatic reverberation chart showing symmetry about the array axis for CORY heading 206°. (b) Contours of high-level backscatter, overlain on the BHPB, coregister with major scarps on B' that have large areas projected towards the source–receiver. The false backscatter image of B' does not coregister with the BHPB. (c) Bistatic reverberation chart shows asymmetry about the array axis due to the oblique angle it forms with the major axis of the bistatic ellipse. The ALLIANCE heading is 87°. (d) Contours of high-level backscatter, overlain on the BHPB, coregister with major scarps on B' that have large areas projected along the acoustic path from source to scatterer to receiver. The false backscatter image of B' does not coregister with the BHPB and exhibits severe spatial contraction.

rable to the 5-m sample interval of the high-resolution bathymetry shown in Fig. 2. A sophisticated, range-dependent ray-based propagation model known as RASP,[15] that includes the effects of multiple interactions between surface and bottom boundaries, was used to chart reverberation out to multiple CZ ranges in Ref. 2. A number of other methods have been developed and employed by other SRP researchers.[13,14,16]

For the purpose of the present analysis, where only waterborne insonification of the high-resolution area is considered, a somewhat simpler but more efficient raytrace model is used to obtain the two-way travel times. Rays are traced in a range-depth plane from a point source, located at the center of the respective source or receiving array, through a refractive ocean half-space with a pressure-release surface but no bottom boundary. Surface-reflected paths are accounted for, but the much slower and more attenuated bottom-reflected paths are neglected. Range-depth maps of minimum travel time are then generated. A range-depth map is then swept through the high resolution bathymetry of B' to determine minimum travel time to or from the bottom. This procedure is repeated for all source and receiver locations to obtain respective travel time maps in the horizontal plane over the high-resolution region. These maps are then used to chart the output of the beamformed and matched filtered reverberation data to the high-resolution region by the same bistatic mapping algorithm employed in Refs. 2, 11, and 12. Navigation data from the Global Positioning System (GPS)[17] of each RV are precisely converted to universal transverse Mercator (UTM)[18] coordinates, for long-range reverberation charting, by the United States Geological Survey (USGS) geodetic reference system[19] that is accurate to within roughly 1 m.

The error in computing travel time to the high-resolution region by slant-range, rather than raytrace, is illustrated in Fig. 11. Since the one-way errors shown are typically much greater than the roughly 0.003 s it takes to cross a 5-m sample interval of high-resolution bathymetry at the mean sound speed, the slant-range approach to charting reverberation is unacceptable.

High-resolution images of charted reverberation are illustrated in Figs. 12–14 for segments 435, 478 and 528, with contours overlain to specify locations of the upper and lower scarps. Both scarps tend to appear prominently and faithfully imaged in the monostatic charts, as in S478 and S435. This fidelity is possible because the cross-range axis of the resolution footprint lies along the scarp axes. In some segments, such as S528, however, the entire upper scarp vanishes amidst low-level background reverberation. This happens when the upper scarp falls in the shadow zone of the main beam's refractive path, due to its proximity to the source array's conjugate depth.[2] The lower scarp appears prominently in all monostatic charts because it lies below the

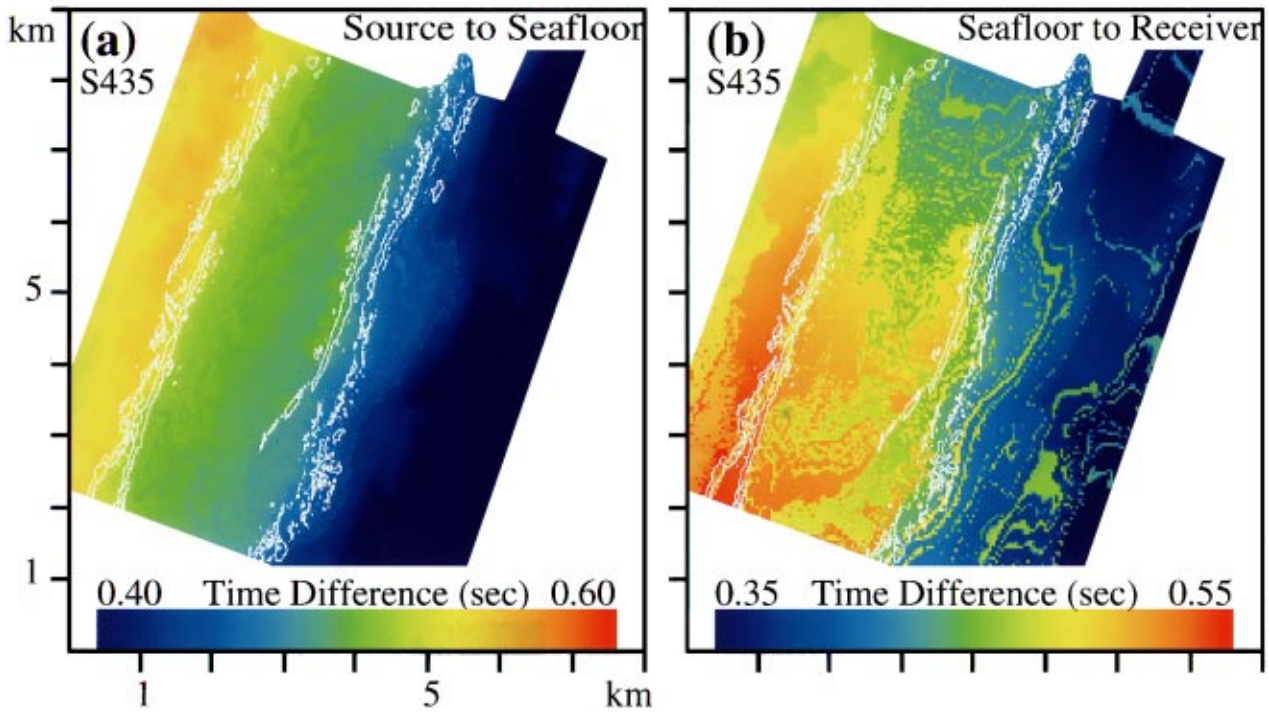

FIG. 11. (a) Slant-range travel time, using mean sound speed along the slant path, minus raytrace travel time from CORY source to seafloor for S435 using high-resolution bathymetry. (b) Same as (a) except from seafloor to ALLIANCE receiver for S435. These one-way errors are typically much greater than the 0.003-s travel time it takes to cross a 5-m sample interval of high-resolution bathymetry.

shadow zone, displayed in Fig. 15(a), and generally receives main-beam insonification.

The consistent coregistration between the locations of the strongest monostatic returns and the locations of the scarps carries much statistical weight. The upper 5% of reverberation within the high-resolution area is selected for each segment to demonstrate this. The frequency of overlap of these selected regions, over all 18 monostatic segments, is plotted in Fig. 16(a) together with overlays of the upper and lower scarps. This figure shows that the regions that most frequently return the strongest backscatter coincide with some of the steepest portions of the upper and lower scarps. The figure also shows that the frequency of strong backscatter rapidly decreases as the distance from the scarp increases in the cross-scarp direction. It is extremely unlikely, for example, to find even a single strong return charted to points lying at ranges beyond roughly 1.0 km of either scarp.

The bistatic charts for S435 and S528 are significantly different from the corresponding monostatic charts, as noted in the wide-area analysis of the previous section. The difference arises because the system's cross-range resolution is at an oblique angle to the scarp axes in the bistatic case, whereas it parallels it in the monostatic case. Prominent bistatic returns lie along nearly elliptical arcs centered across the scarp axes. This is seen in Figs. 12–14, which are typical of many of the bistatic segments studied. The strongest returns appear in a speckled fashion along the scarps axis. In extreme cases where cross-range is nearly normal to the scarps axes, as in S435, the towed-array system is sometimes unable to distinguish the upper from the lower scarp. This effect is apparently due to the relatively close proximity of the two scarps, roughly 2 km separation or twice the cross-range resolution of the receiver, and occasionally leads to strong returns continuously charted across both scarps in elliptic arcs centered through the plateau. This may lead one to the presumably *false* conclusion that the plateau contains geomorphological anomalies that may yield strong returns.

The spatial frequency distribution of the most prominent bistatic returns is shown in Fig. 16(c). As in the monostatic case, the upper 5% of reverberation over the high-resolution area is selected for each segment. The overlap frequency of these selected regions, across all 20 bistatic segments, is plotted together with overlays of the upper and lower scarps. While the global maxima appears on the steepest portion of the upper scarp, and local maxima often register with both the upper and lower scarps, the largest number of local maxima appear in the region between the scarps. Frequency tends to decrease as range increases from the region between and including both scarps. Single-frequency returns, however, remain densely spread with relative uniformity from the upper crest to the lower scarp, and only begin to disappear as the trench below the lower scarp is approached. While some cross-hatching of overlain returns is to be expected just above and below the upper and lower scarps, due to a combination of ridge morphology, track geometry, and cross-range blurring, the significantly higher concentration of high frequencies between the upper and lower scarps rules this combined effect out as the sole cause of off-scarp charting of prominent reverberation, as is shown in the next section. An explanation for the measured frequency distribution follows in Sec. II D.

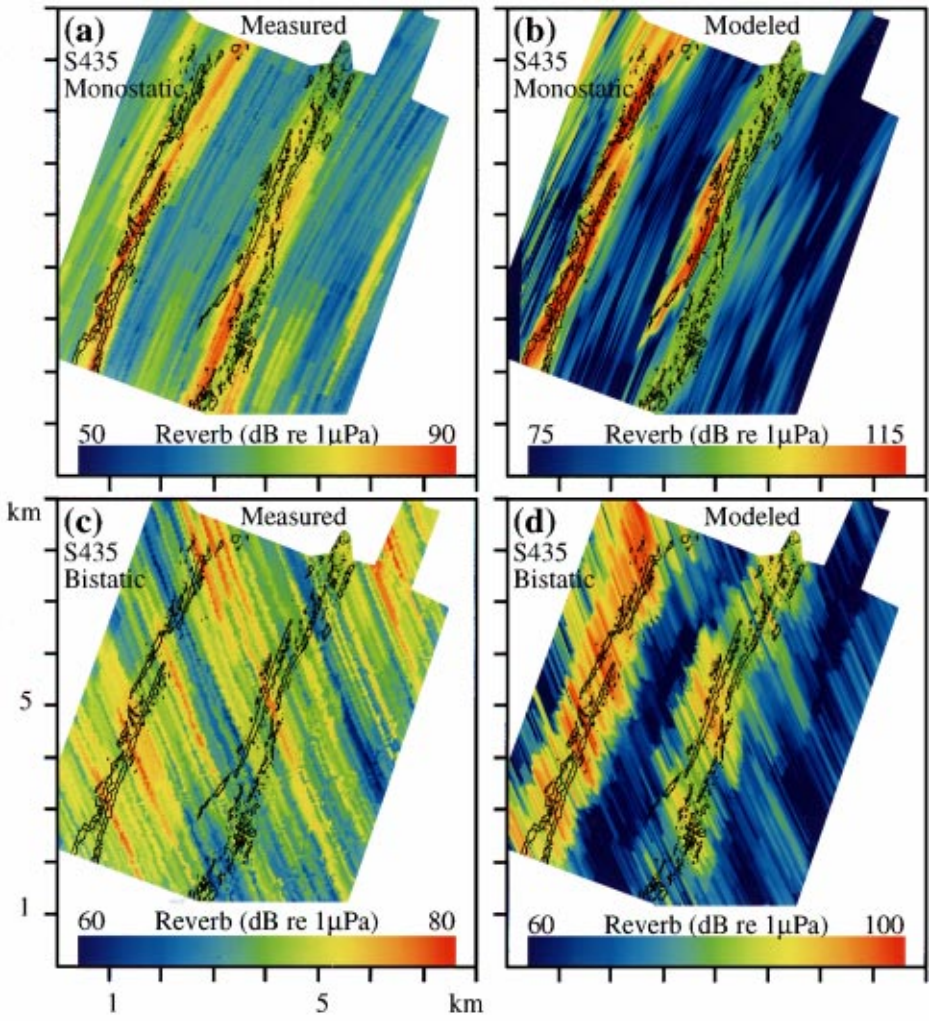

FIG. 12. High-resolution charts of monostatic and bistatic measured and modeled reverberation for S435 over the region shown in Fig. 2 with upper and lower scarp contours overlain. (a) Measured monostatic reverberation. (b) Modeled monostatic reverberation. (c) Measured bistatic reverberation. (d) Modeled bistatic reverberation.

C. Modeling high-resolution reverberation and estimating the scattering distribution

From an infinitesimal planar surface patch of area dA, in the far field of a source and receiver, the scattered intensity at the receiver can be written as

$$dI = f(\theta_i, \phi_i; \theta_r, \phi_r) w l_i l_r \cos\theta_i \cos\theta_r dA, \tag{1}$$

according to the basic principles of radiometry. Here, θ and ϕ denote polar and azimuth angles with respect to the local surface normal,[20] with incident and scattered angles identified by the subscripts i and r. The projected area of the surface patch in the direction of the scattered wave leaving the surface patch is $\cos\theta_r dA$. The other factors include the source power w, transmission coefficients l_i and l_r in inverse-square meters from the source to the surface patch and from the surface patch to the receiver, and the bidirectional scattering distribution function (BSDF) of the surface f,[20–22] which is a dimensionless parameter describing surface-scattering properties that are invariant in expected value to changes in transmission and projected area. It is noteworthy that $f\cos\theta_i\cos\theta_r$ is simply the antilog of the standard scattering strength of ocean acoustics[23] $S = 10\log(f\cos\theta_i\cos\theta_r)$, where f is essentially the quantity describing bidirectional surface ''reflectance'' properties that has become standard in radiometry after its introduction by the National Bureau of Standards in 1977.[21] A perfectly Lambertian surface, for example, has $f = 1/\pi$, whereas a perfectly specular surface has $f = \delta(\theta_i - \theta_r)\delta(\phi_i - \phi_r + \pi)/(\sin\theta_i \cos\theta_i)$. The latter singularity is necessary to escape the implicitly incoherent nature of a summation over dA in Eq. (1). When f is an angle-independent constant, it is related to the surface albedo[24] α by $f = \alpha/\pi$ and can be interpreted as becoming the constant μ associated with Mackenzie's formulation of seafloor scattering strength.[23]

It is practical to recast Eq. (1) in decibels, by dividing through by appropriate reference units and taking 10 log of both sides. This homomorphic transformation stabilizes the variance for optimal pattern recognition[10,25] and compresses the dynamic range. The result is

$$R_{dA} = F(\theta_i, \phi_i; \theta_r, \phi_r) + W - \mathrm{TL}_i - \mathrm{TL}_r + C_i + C_r + 10\log(dA/A_{\mathrm{ref}}), \tag{2}$$

where the reverberation level on the left in dB *re* 1 μPa is balanced by the scattering distribution's strength F, the source strength W in dB *re* 1 μPa @ 1 m, the transmission loss from the source to scattering patch TL_i, and from the scattering patch to the receiver TL_r, in dB *re* 1 m, the pro-

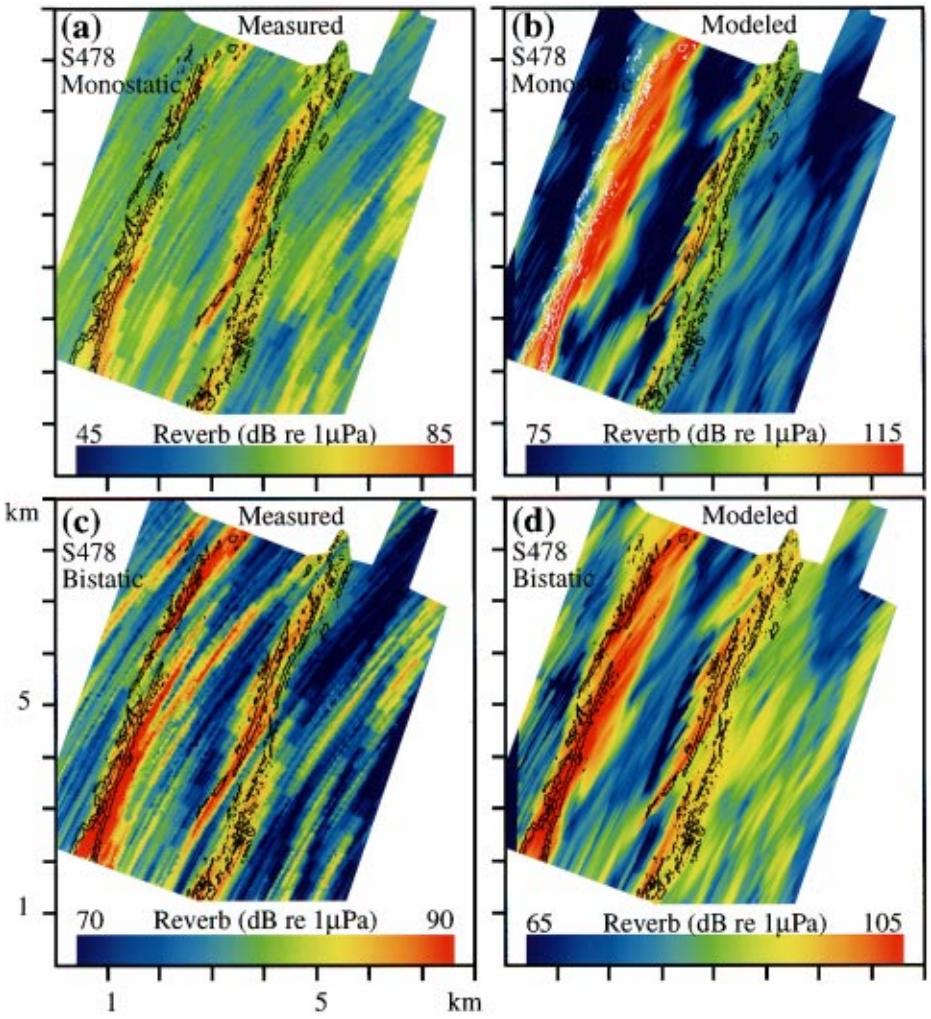

FIG. 13. High-resolution charts of monostatic and bistatic measured and modeled reverberation for S478 over the region shown in Fig. 2 with upper and lower scarp contours overlain. (a) Measured monostatic reverberation. (b) Modeled monostatic reverberation. (c) Measured bistatic reverberation. (d) Modeled bistatic reverberation.

jection terms $C_i = 10\log(\cos\theta_i)$, $C_r = 10\log(\cos\theta_r)$, and the area term, in dB *re* 1 m. With Cartesian coordinates for east and north specified by x and y, the differential area becomes $dA = dx\,dy$. In practice, the elements dx, dy represent the 5-m bathymetric sample interval of the high-resolution region of B', over which the seafloor can presumably be approximated as planar.

The strength of the bidirectional scattering distribution F then is *independent of the local seafloor foreshortening as seen from the perspectives of the source and receiver*, whereas the scattering strength S is not, so F is preferred over S as the parameter to empirically describe the inherent scattering properties of the MAR seafloor since there is no unique surface normal to characterize bathymetry within our system's resolution footprint.

To model reverberation, each of the spatially varying terms of Eq. (2), which excludes W and $10\log(dA/A_{\text{ref}})$, is charted in an x,y grid over the high-resolution region.

To compute the projection terms, range-depth maps of the propagation direction of minimum-travel-time rays spreading outward from a point source below a pressure-release surface are computed for a bottomless ocean, given the watercolumn sound-speed profile shown in Fig. 1 of Ref. 2. The point source is located (1) at the 181-m depth of the center of the CORY source array, for rays traveling to the virtual scattering surface, (2) at the 460-m depth of the ALLIANCE receiving array, by reciprocity, for rays traveling from the virtual scattering surface to the ALLIANCE receiver, and (3) at the 170-m depth of the CORY receiving array for rays traveling from the virtual scattering surface to the CORY receiver. The high-resolution bathymetry is then swept through the range-depth map to determine the incident and scattered angles at the bottom. The inner product of these angles with the local surface normal yields the cosine factors of Eq. (1), and log transformation yields the bathymetric projection terms of Eq. (2) that relate linearly to reverberation level.

Charts of transmission loss are computed in a similar fashion. Range-depth maps of the monochromatic field produced by a 10-element source array, computed using the parabolic equation,[26] are integrated across the 200–255-Hz frequency band of the LFM *incoherently*, to be consistent with actual rough surface scattering. The resulting incoherent broadband transmission loss, shown in Fig. 15(a), exhibits substantial structure with a well-defined main beam, the remnants of frequency-averaged Lloyd mirror interfering beams, and sidelobes. High-resolution bathymetry is then swept through this map to chart the incident transmission loss TL_i. A similar procedure is used to chart transmission loss to the receiver TL_r, except that a point source at the depth of the

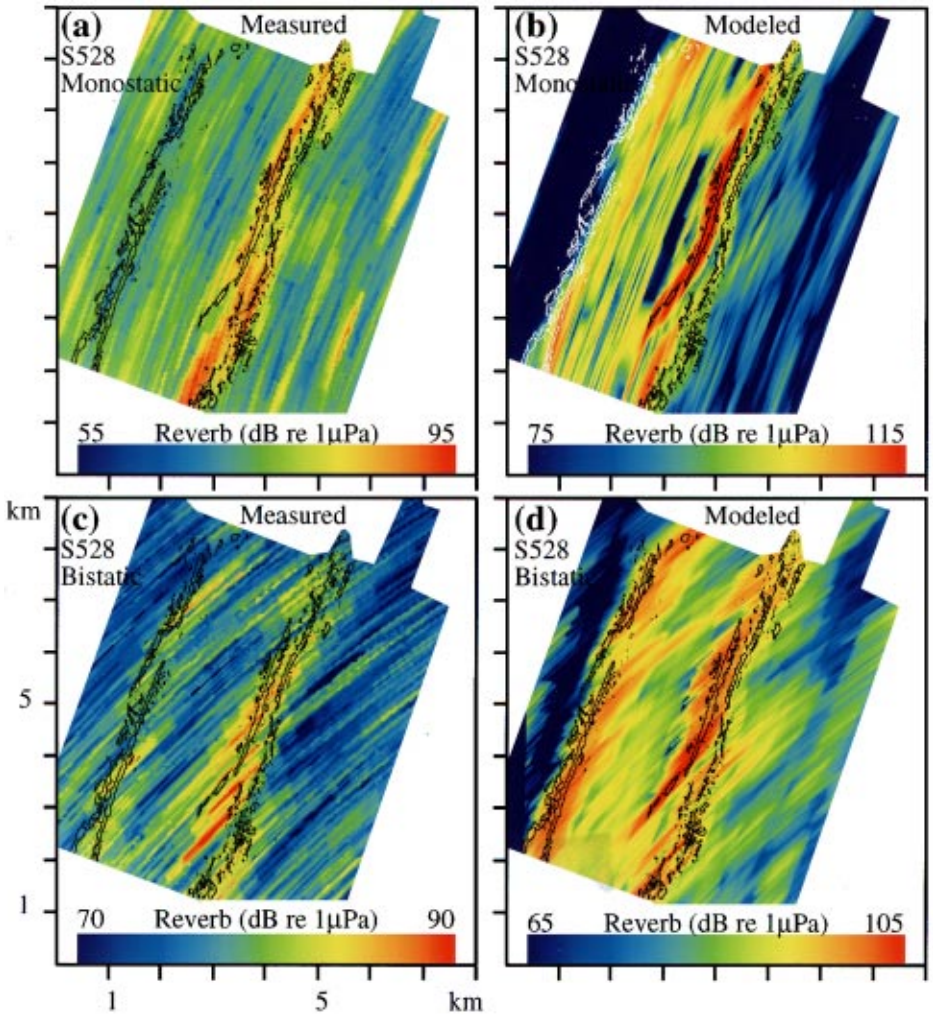

FIG. 14. High-resolution charts of monostatic and bistatic measured and modeled reverberation for S528 over the region shown in Fig. 2 with upper and lower scarp contours overlain. (a) Measured monostatic reverberation. (b) Modeled monostatic reverberation. (c) Measured bistatic reverberation. (d) Modeled bistatic reverberation.

given receiving array is used to exploit reciprocity from the scattering site. This follows the benign assumption that mean transmission loss will not vary significantly across the receiving array. The range-depth TL_r plotted in Fig. 15(b) and (c) shows less structure and leads to more uniform transmission loss back to the receiver across the region where high-resolution bathymetry is available, which lies at the 1/2 CZ vertex.

Charts of the various projection and transmission loss terms of Eq. (2), presented in Fig. 17 over the region of high-resolution bathymetry for S435, show substantial spatial structure that varies considerably from monostatic to bistatic geometries when the bistatic separation is large.

Since bathymetry within the resolution footprint of the MAE bistatic towed-array systems *cannot* be approximated as a planar surface, as demonstrated in Sec. I, Eqs. (1) and (2) cannot directly describe measured reverberation and its level. The complicated nature of bathymetry within the resolution footprint, however, leads to a simple *statistical* description of the *expected* intensity at the receiver that makes these expressions relevant. Specifically, the system resolution footprint covers an annular sector of roughly 50 m by 1000 m at 1/2 CZ, and so contains surface roughness of high complexity with respect to the mean acoustic wavelength of 6.7 m. The total field received from the footprint then behaves as the sum of a large number of statistically independent fields scattered from disjoint subregions of the resolved seafloor patch.[27] The *expected* intensity radiated from the resolution patch, proportional to the *variance* of the received field, can then be charted to the centroid of the patch by the convolution

$$\langle I(x,y|\mathbf{r}_i,\mathbf{r}_r)\rangle = \int\int_{-\infty}^{\infty} G(x-X,\ y-Y|\mathbf{r}_i,\mathbf{r}_r) \times f(\theta_i,\phi_i;\theta_r,\phi_r) \times w l_i l_r \cos\theta_i \cos\theta_r dX\, dY, \tag{3}$$

where $G(x,y|\mathbf{r}_i,\mathbf{r}_r)$ is a point-spread function[27] equal to the squared magnitude of the combined linear beam pattern and matched-filter functions that define the towed-array receiver. Here, all cosine, transmission loss, and BSDF factors are implicit functions of the spatial coordinates of the integral, and the expected intensity is a function of the source and receiver locations $\mathbf{r}_i$, $\mathbf{r}_r$, which may vary in 3-D.

The overwhelming contribution to the convolution integral typically comes from the resolution footprint $A_f(x,y|\mathbf{r}_i,\mathbf{r}_r)$ which is defined in Appendix A. This observation has been previously exploited in Refs. 28, 11, and 2, and leads to the relation

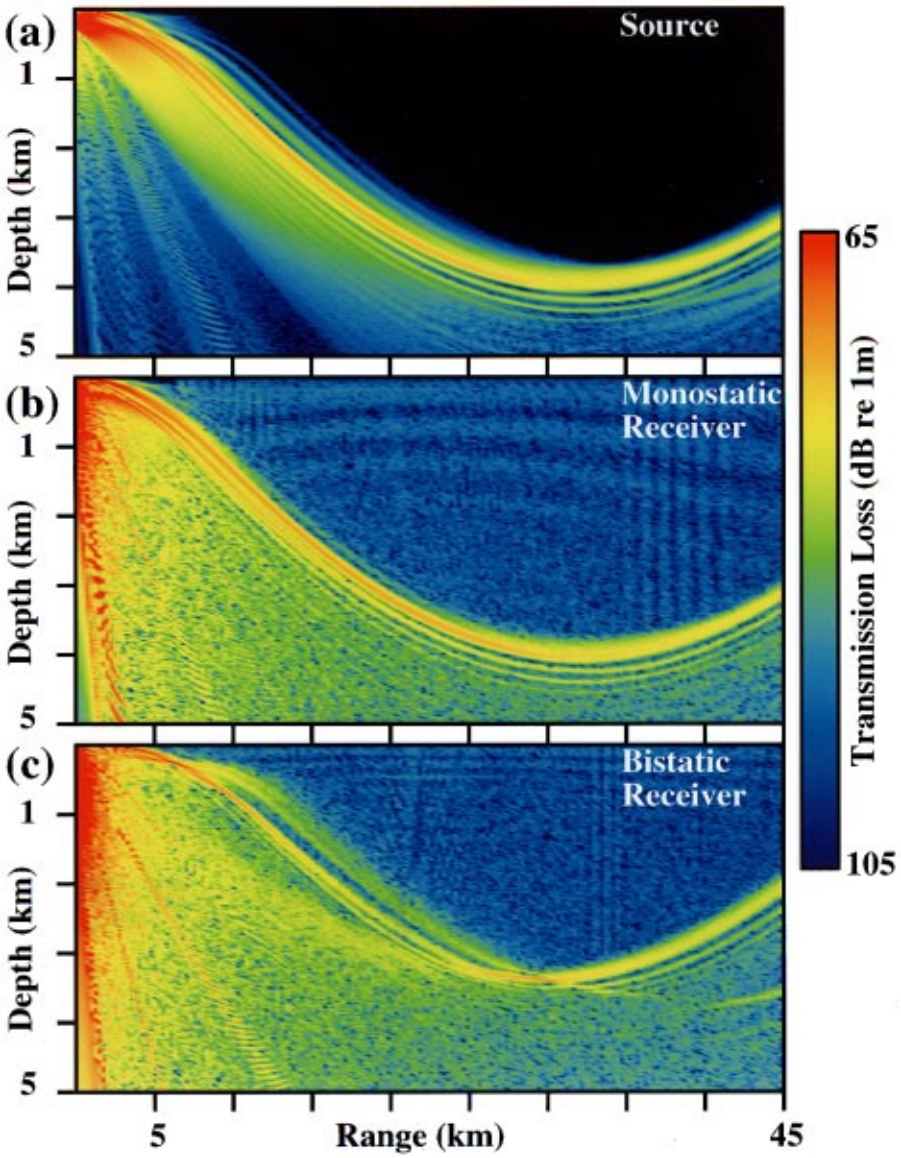

FIG. 15. (a) Range-depth slice of broadband transmission loss in the 200–255-Hz band modeled incoherently with the parabolic equation for the CORY 10-element source array, centered at 181 m depth with 2.5-m projector spacing and MAR vertical sound-speed structure (Ref. 2) in a bottomless ocean. (b) Same as (a) except source is now at a single point, at the 170-m depth of the CORY receiving array. (c) Same as (b) except source is a point at the 460-m depth of the ALLIANCE receiving array. The B' abyssal hill is typically 1/2 CZ (~33.3 km) from the source or receiver. Its peak lies at a depth of ~3500 m.

$$\langle I(x,y|\mathbf{r}_i,\mathbf{r}_r)\rangle \approx \int\int_{A_f(x,y|\mathbf{r}_i,\mathbf{r}_r)} f(\theta_i,\phi_i;\theta_r,\phi_r) w l_i l_r \cos\theta_i \cos\theta_r dX\, dY, \tag{4}$$

which is a very close approximation to Eq. (3) when sidelobe leakage is insignificant, as it is for prominent returns across a fixed travel-time ellipse. Recasting it in decibels yields

$$R_{\langle I\rangle}(x,y|\mathbf{r}_i,\mathbf{r}_r) \approx W + 10\log\left(\int\int_{A_f(x,y|\mathbf{r}_i,\mathbf{r}_r)} 10^{[F(\theta_i,\phi_i;\theta_r,\phi_r)-\mathrm{TL}_i-\mathrm{TL}_r+C_i+C_r]/10} dX\, dY\right). \tag{5}$$

The important issue here is that scattering distribution's strength F is not linearly proportional to the level of expected reverberation unless F is a constant over the resolution footprint. Constancy of F in A_f requires either it be independent of spatial position, incident, and scattered angle or the scattering surface be a plane over which F may vary with incident and scattered angle but not position. To obtain F from measured reverberation in any other case requires a deconvolution, of the kind worked out in Ref. 28 and implemented with wide-area MAE data in Ref. 2. A successful deconvolution, however, depends on a sufficient set of independent measurements[28] as well as charting error that is insignificant compared to the dimension of the seafloor patch to be resolved. While both of these conditions were satisfied in the wide-area analysis of Ref. 2, neither is met in the present analysis of high-resolution data.

Given these considerations, any estimate of seafloor scattering strength obtained in the present analysis will inevitably be blurred over the resolution footprint of the towed-array system. To describe this blurring, it is convenient to define

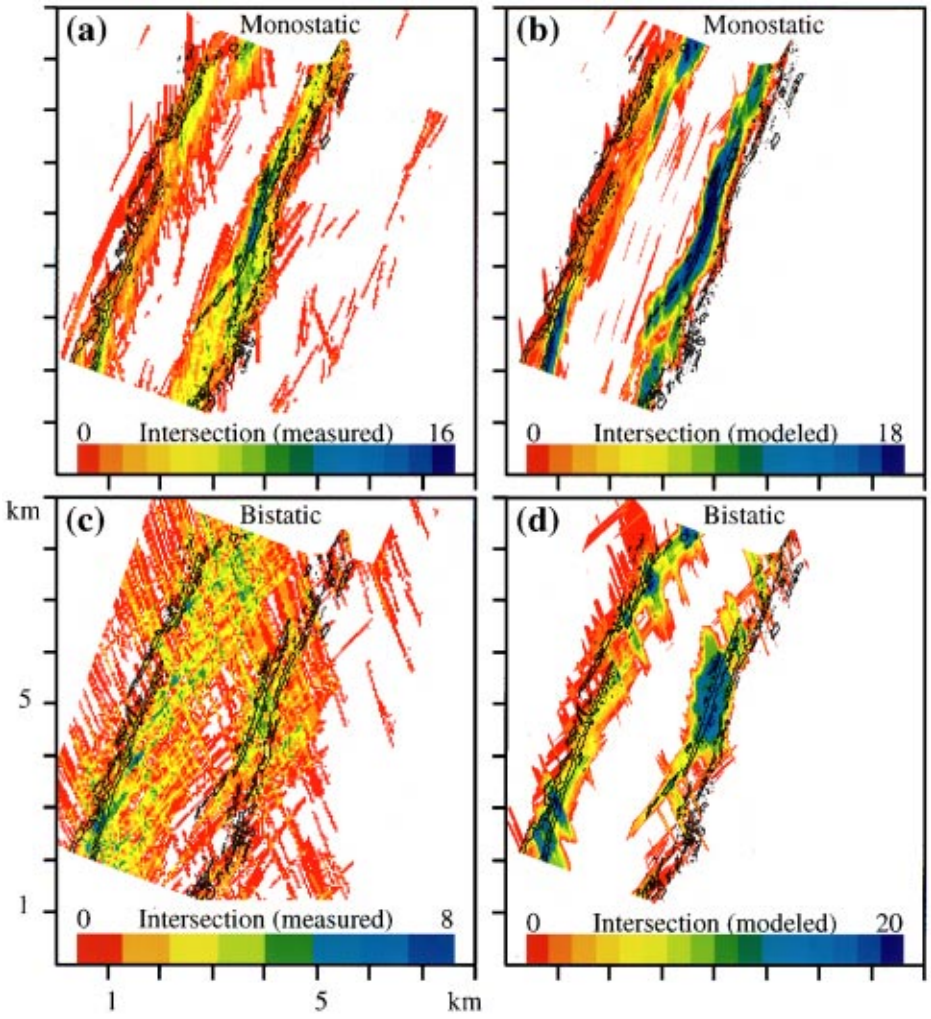

FIG. 16. Spatial distribution of the most prominent returns. The upper 5% of reverberation within the high-resolution region is selected for each segment. The overlap frequency of these selected regions is shown in (a) for monostatic measured reverberation, (b) monostatic modeled reverberation, (c) bistatic measured reverberation, and (d) bistatic modeled reverberation. Red indicates regions of zero intersection; that is, where reverberation is only in the upper 5% for a single segment. All 18 monostatic and 20 bistatic segments shown in Fig. 3 are used for this computation.

$$R_M(x,y|\mathbf{r}_i,\mathbf{r}_r)=W+10\log\left(\int\int_{A_f(x,y|\mathbf{r}_i,\mathbf{r}_r)} 10^{(-\mathrm{TL}_i-\mathrm{TL}_r+C_i+C_r)/10}dX\,dY\right), \tag{6}$$

as *modeled reverberation* from a seafloor that scatters equally in all directions. Variations in modeled reverberation then arise only as the integral of surface projection and transmission loss terms over A_f. This construction leads to a simple linear equation for the *mean* strength of the scattering distribution over the resolution footprint

$$\overline{F}(x,y|\mathbf{r}_i,\mathbf{r}_r)=R_{\langle I\rangle}(x,y|\mathbf{r}_i,\mathbf{r}_r)-R_M(x,y|\mathbf{r}_i,\mathbf{r}_r). \tag{7}$$

Note that both incident and scattered angles are integrated over the resolution footprint. Blurring is then considerable, since these angles have large standard deviations over the footprint, as shown in Sec. I.

From Eq. (7), the maximum likelihood estimate for $\overline{F}$ is

$$\hat{\overline{F}}(x,y|\mathbf{r}_i,\mathbf{r}_r)=R(x,y|\mathbf{r}_i,\mathbf{r}_r)-R_M(x,y|\mathbf{r}_i,\mathbf{r}_r), \tag{8}$$

namely, the difference between reverberation measured with MAE data $R(x,y|\mathbf{r}_i,\mathbf{r}_r)$ and $R_M(x,y|\mathbf{r}_i,\mathbf{r}_r)$ reverberation modeled with the diffuse scattering assumption $F=0$.

Under the assumption that the receiver measures a circular complex Gaussian random (CCGR) field,[2,27] reverberation measured from a given surface patch obeys the exponential-gamma distribution.[10] This follows from the central-limit theorem and the fact that the system resolution footprint is much larger than wavelength-scale surface roughness.[9,10,27] A bias-corrected estimate for $\overline{F}$ is then

$$\tilde{\overline{F}}(x,y|\mathbf{r}_i,\mathbf{r}_r)=R(x,y|\mathbf{r}_i,\mathbf{r}_r)-R_M(x,y|\mathbf{r}_i,\mathbf{r}_r)+(\psi(N)-\ln N)10\log e, \tag{9}$$

following Ref. 10 where $\psi(N)$ is Euler's psi function with measurement degrees of freedom N defined in Sec. I.

D. Comparison between measured and modeled charts of high-resolution reverberation

Charts of modeled reverberation R_M, obtained from transmission loss and surface projection maps by applying the spatial convolution described in Eq. (6), are presented in Figs. 12–14(b) and (d) for comparison with charts of measured reverberation R, in Figs. 12–14(a) and (c).

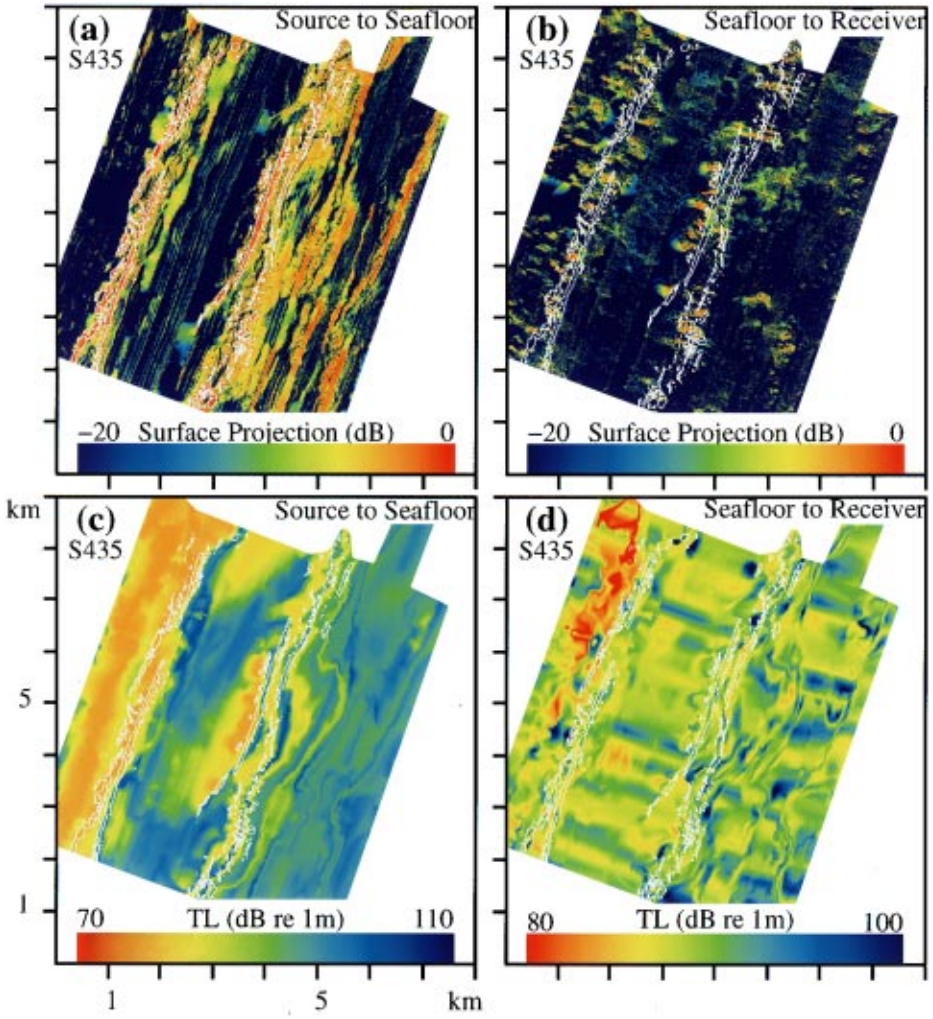

FIG. 17. Projection and transmission loss terms over the region of high-resolution bathymetry for S435 from Eq. (2). (a) Surface projection $C_i = 10\log(\cos\theta_i)$ of bathymetry from source to seafloor using raytrace. (b) Surface projection $C_r = 10\log(\cos\theta_r)$ of bathymetry from seafloor to ALLIANCE receiving array center point using raytrace. (c) Transmission loss TL_i from CORY 10-element source array to scattering patch using parabolic equation incoherently integrated from 200–255 Hz. (d) Transmission loss TL_r from seafloor to ALLIANCE receiving array center point using parabolic equation incoherently integrated from 200–255 Hz.

Measured and modeled reverberation show close qualitative agreement in all monostatic charts. The most prominent returns resolve the morphology of the upper and lower scarps with reasonable accuracy primarily because the cross-range axis of the resolution footprint typically lies along the scarp axis and so does not bleed into neighboring regions, such as the plateau and trench. Returns from these neighboring regions are typically about 20 to 30 decibels lower. Since this variation greatly exceeds the expected 2.5 to 5.6 dB standard deviation, the scarps emerge as deterministic features of the data. The measured and modeled reverberation charts also agree on when the upper scarp will fall in the shadow zone, as it does in S528.

The spatial frequency distribution of the upper 5% of modeled reverberation for the monostatic charts is shown in Fig. 16(b). The modeled distribution bears a close resemblance to the corresponding measured one, with the weight of prominent returns charted to the steepest portions of the upper and lower scarps. This result is consistent with the high visual correlation found between measured and modeled monostatic reverberation.

The situation is different for the bistatic data. While the general *character* of measured reverberation shows qualitative agreement with the modeled in all bistatic charts, the kind of high visual correlation found in the monostatic comparison only appears when the bistatic separation between source and receiver azimuths is small enough for prominent returns to faithfully image scarp morphology. More frequently, the bistatic separation is too large for this, and elliptic arcs of both measured and modeled reverberation, obliquely centered on the scarp axes, bleed into neighboring plateaus over lengths commensurate with the resolution footprint. As a result, the overall reverberation level in the vicinity of the scarps is much higher than in neighboring regions where no scarps are present, as is often more clearly seen in the wide-area charts of Sec. II A. This level fluctuates drastically along the scarp, in both measured and modeled charts, with an inner scale equaling the range resolution of the system. The most prominent *modeled* returns typically coincide with a characteristic nonlinearity of the scarp, such as a canyon wall, that projects area strongly along the acoustic path from source to scatterer to receiver for the given bistatic geometry. The separation between these large projections is typically much greater than the range resolution of the system, but shorter than the cross-range resolution. This is consistent with the greater uniformity in level found in monostatic reverberation images of the scarps, where many canyons are blurred together in cross-range.

The most prominent *measured* returns often do not coincide with the most prominent *modeled* returns when the bistatic separation is large, although they are all typically centered somewhere along the upper or lower scarp. To il-

lustrate this point, the expected spatial frequency distribution of the highest 5% of modeled bistatic reverberation is shown in Fig. 16(d). As in the monostatic case, prominent returns are most frequently charted to steep regions of the scarps in both the measured and modeled distributions. The measured distribution, however, differs significantly from the modeled one in that it shows a relatively high frequency of prominent returns charted to the plateau region between the two scarps, while a relatively small number are expected there according to the model. There are two plausible explanations for these inconsistencies. First, the model predicts variations in reverberation level along the scarp that are on the order of the 5.6-dB maximum standard deviation expected in the data. This type of signal-dependent noise, conventionally referred to as *speckle*,[10,25,27,28] is then sufficient to bury the pattern predicted by the model.[2] Second, there may be charting errors that exceed the range-resolution of the system. This is extremely plausible because fluctuations in receiver array heading in excess of 0.1° are sufficient to cause such errors at 1/2 CZ. Moreover, fluctuations of this order were often observed during reception of any given LFM by the ALLIANCE. The second explanation is consistent with an overall rotation of predicted reverberation and is consistent with off-scarp charting of prominent returns, but does not account for the apparent randomization bistatic returns along the scarp as does the presence of speckle noise.

III. BI-AZIMUTHAL SCATTERING FROM THE B' ABYSSAL HILL

A. Site-specific approach

The development of Sec. II C makes clear that it is typically not possible to estimate the BSDF of the B' abyssal hill directly from MAE data. Only the *mean* BSDF, or equivalently the strength of the mean scattering distribution over a resolution footprint, can be estimated. But, this central value is not necessarily independent of the method of measurement. To minimize the effects of the measurement and to make sense of the bidirectional scattering properties contained in reverberation charts, some further reduction of the data is necessary. The approach behind this reduction becomes clearer when the following four points are considered.

First, the seafloor within a resolution footprint of the towed-array imaging system cannot be approximated as a planar surface, except perhaps within the plateau region. Therefore, we find it senseless to plot estimates of scattering strength as a function of mean incident and scattered angle over the resolution footprint, and instead take another approach.

Second, the source and receiver locations for each transmission can be uniquely identified by the receiver azimuth which spans a full half-space about B', whereas the source azimuth is restricted to values near zero. It is both convenient and natural then to plot measured reverberation, modeled reverberation and estimated scattering strength as a function of receiver azimuth with respect to the B' axis, with the understanding that the full bi-azimuthal description can be easily regained by translation through Figs. 3 and 4. For example, an estimate of the mean strength of the scattering distribution $\hat{\hat{F}}(x,y|\mathbf{r}_i,\mathbf{r}_r)$ can be equivalently written as $\hat{\hat{F}}(x,y|\Omega_i,\Omega_r)$, for source and receiver azimuths Ω_i, Ω_r defined with respect to the upper or lower scarp since there is a unique Ω_i, Ω_r pair for every $\mathbf{r}_i$, $\mathbf{r}_r$ pair.

Third, the geomorphology of B' is not homogeneous, but may be naturally segmented into three distinct regions. These are the upper scarp, the lower scarp, and the plateau defined in Sec. I. The results of Secs. II B–D indicate that the upper and lower scarps return the strongest echoes[2] because they direct the largest projected areas along the acoustic path from source to receiver. The plateaus, on the other hand, scatter relatively weakly and uniformly since both incident and scattered waves intersect their surfaces at extremely shallow grazing in the present long-range experiment. This is evident in both the measured and modeled reverberation of Secs. II B–D when the cross-range axis of the system resolution footprint is along the scarp axis. When the bistatic separation is large enough that the cross-range axis of the resolution footprint runs across the scarp axis, however, returns from the scarps are often falsely charted to the plateau as described in Secs. I and II, and sidelobe leakage from the scarps often contaminates true returns from the plateau which are much weaker. These effects prevent accurate determination of the bi-azimuthal scattering properties of the *plateau* when the bistatic separation is large.

Fourth, measured reverberation, modeled reverberation, and the estimated strength of the scattering distribution undergo spatial fluctuations within these regions due to changes in geomorphology and the interference structure of the received field, as demonstrated in the reverberation charts of the previous section.

Our approach, in light of these points, is to arrive at a single mean strength for the bi-azimuthal scattering distribution across the upper scarp of the B' abyssal hill and a similar mean strength for the lower scarp. This is done by taking the average of $\hat{\hat{F}}(x,y|\Omega_i,\Omega_r)$ with respect to x,y over each scarp and plotting the result, along with its standard deviation, as a function of receiver azimuth Ω_r with the understanding that this also specifies the source azimuth. For example, the average of some function $\Psi(x,y)$ over area A is

$$\langle \Psi(x,y)\rangle_A = \frac{1}{A}\int\int_A \Psi(x,y)\,dx\,dy, \tag{10}$$

so that its standard deviation is

$$\sigma_A\{\Psi(x,y)\} = \mathrm{sqrt}(\langle \Psi(x,y)^2\rangle_A - \langle \Psi(x,y)\rangle_A^2). \tag{11}$$

Since the average value $\langle \hat{\hat{F}}(x,y|\Omega_i,\Omega_r)\rangle_A$ is over a large region A comprising either the upper or lower scarp, and F is independent of local seafloor foreshortening, its use (1) circumvents difficulties regarding the use of scattering strength to characterize nonplanar and poorly resolved scattering surfaces, (2) is consistent with a natural segmentation of seafloor geomorphology, (3) smooths over spatial fluctuations, and (4) remains highly relevant to long-range waterborne measurements since these generally entail the kind of near-

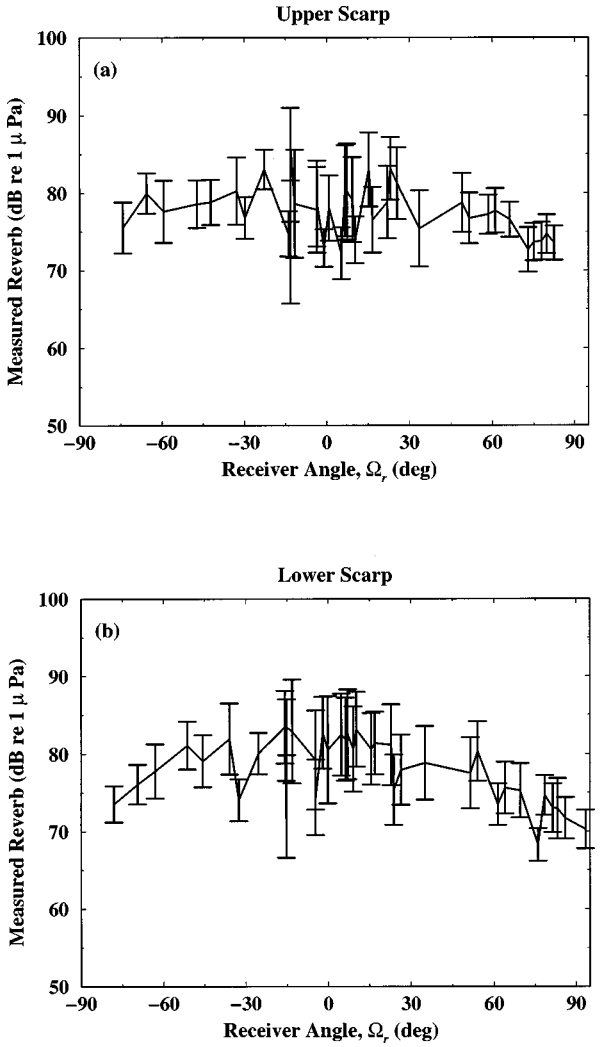

FIG. 18. The mean reverberation level measured over (a) the upper scarp $\langle R(x,y|\Omega_i,\Omega_r)\rangle_{A_{\rm up}}$ and (b) the lower scarp $\langle R(x,y|\Omega_i,\Omega_r)\rangle_{A_{\rm low}}$ as a function of receiver azimuth Ω_r with respective standard deviations $\sigma_{A_{\rm up}}\{R(x,y)\}$ and $\sigma_{A_{\rm low}}\{R(x,y)\}$.

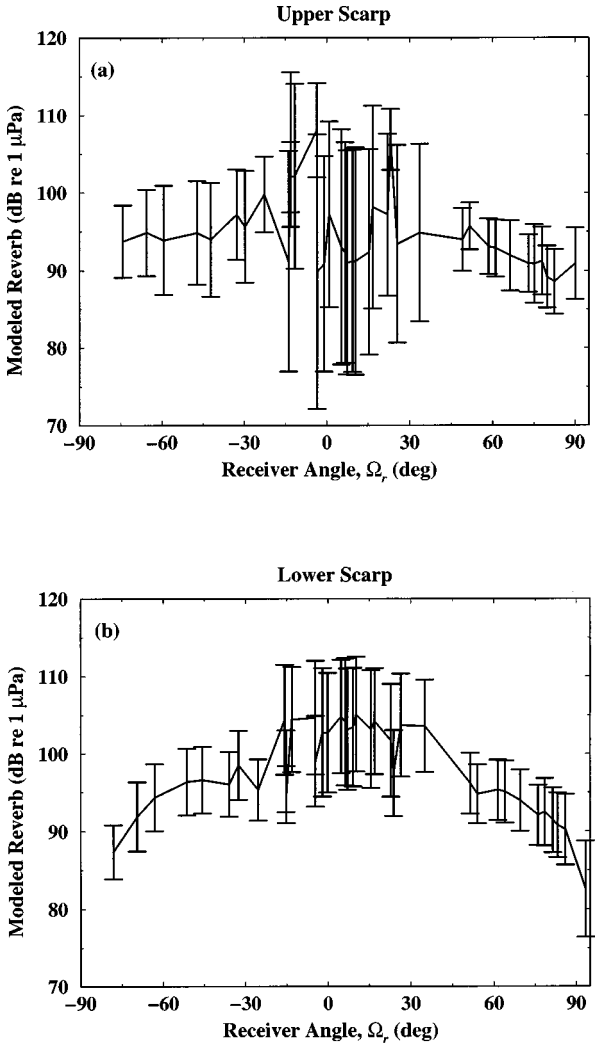

FIG. 19. The mean reverberation level modeled over (a) the upper scarp $\langle R_M(x,y|\Omega_i,\Omega_r)\rangle_{A_{\rm up}}$ and (b) the lower scarp $\langle R_M(x,y|\Omega_i,\Omega_r)\rangle_{A_{\rm low}}$ as a function of receiver azimuth Ω_r with respective standard deviations $\sigma_{A_{\rm up}}\{R_M(x,y)\}$ and $\sigma_{A_{\rm low}}\{R_M(x,y)\}$.

horizontal propagation to and from the seafloor inherent in MAE. An information-conserving alternative to the average that has all of these properties, but is far less wieldy, is presented in Appendix B.

B. Azimuthal dependence of measured and modeled reverberation from the upper and lower scarps

Curves of mean reverberation level, measured over the upper scarp $\langle R(x,y|\Omega_i,\Omega_r)\rangle_{A_{\rm up}}$ and lower scarp $\langle R(x,y|\Omega_i,\Omega_r)\rangle_{A_{\rm low}}$, are plotted as a function of Ω_r in Fig. 18(a) and (b) along with their corresponding standard deviations $\sigma_{A_{\rm up}}\{R(x,y)\}$, $\sigma_{A_{\rm low}}\{R(x,y)\}$. These summarize the azimuthal dependence of reverberation from geomorphological features on the B' abyssal hill that stand out in remote acoustic images.

The curve for the upper scarp is remarkably flat, while that for the lower scarp shows a gradual roll-off of at most 5 dB from the origin to extreme values of Ω_r. Fluctuations in the mean, however, are on the order of the standard deviation in both curves. The latter ranges from roughly 6 dB within $|\Omega_r|<30°$, to roughly 3 dB outside this range, so that the roll-off in the lower-scarp curve is barely significant.

The region of high standard deviation near the origin has a relatively straightforward explanation. This is where the monostatic data is concentrated and main beam propagation from the source to the narrow scarps is most sensitive to slight variations in range, since the cross-range axis of the resolution footprint is along the scarp axes. This same sensitivity partially explains the complete absence of a strong return from the upper scarp in S528 monostatic in Fig. 14(a) and (b). Conversely, the standard deviations decrease as $|\Omega_r|$ increases beyond 30° because the cross-range direction of the resolution footprint takes on such an oblique angle with the scarp axes that it becomes impossible for the main beam to miss either scarp. The observed standard deviations may also be partially explained by minor charting errors which would lead to much higher fluctuations for small $|\Omega_r|$, due to these same sensitivity issues.

For comparison, curves of the mean modeled reverberation level over the upper and lower scarps, $\langle R_M(x,y|\Omega_i,\Omega_r)\rangle_{A_{\rm up}}$ and $\langle R_M(x,y|\Omega_i,\Omega_r)\rangle_{A_{\rm low}}$, are plotted

as a function of receiver azimuth in Fig. 19(a) and (b) along with their corresponding standard deviations $\sigma_{A_{\rm up}}\{R_M(x,y)\}$, $\sigma_{A_{\rm low}}\{R_M(x,y)\}$. There are a number of important similarities and differences between the modeled and measured curves. For $|\Omega_r|>30°$, the standard deviations are again lower, typically near 5 dB. Within $|\Omega_r|<30°$, they increase more drastically on the upper scarp than the lower, at roughly 10 to 7 dB, primarily because the main beam of the source array is able to more consistently insonify the lower scarp for small $|\Omega_r|$. While the modeled mean across the upper scarp has a relatively flat dependence on receiver azimuth, in accord with the measured mean, the modeled mean across the lower scarp has an unambiguously convex dependence, peaking within $|\Omega_r|<30°$ and rolling off by roughly 10 dB as $|\Omega_r|$ approaches 90°.

An explanation for this behavior requires analysis of the projection and TL terms before convolution. The mean two-way transmission loss $\langle \mathrm{TL}_i(x,y|\Omega_i,\Omega_r)+\mathrm{TL}_r(x,y|\Omega_i,\Omega_r)\rangle_{A_{\rm up}}$, $\langle \mathrm{TL}_i(x,y|\Omega_i,\Omega_r)+\mathrm{TL}_r(x,y|\Omega_i,\Omega_r)\rangle_{A_{\rm low}}$ and mean surface projection $\langle C_i(x,y|\Omega_i,\Omega_r)+C_r(x,y|\Omega_i,\Omega_r)\rangle_{A_{\rm up}}$, $\langle C_i(x,y|\Omega_i,\Omega_r)+C_r(x,y|\Omega_i,\Omega_r)\rangle_{A_{\rm low}}$ over the upper and lower scarps are plotted as a function of receiver azimuth for this purpose in Figs. 20 and 21, along with their standard deviations.

The mean surface projection curves show very regular convex behavior with remarkably small standard deviation. At the extreme values of $|\Omega_r|$, however, levels are only about 5 dB down from the peak value which lies near the origin. Since this gradual roll-off falls within the standard deviation and mean fluctuations of the two-way transmission-loss curves, which typically exceed 10 dB, it is lost in the noise when the projection and TL terms are combined. As a result, mean modeled reverberation exhibits a relatively constant overall dependence on receiver azimuth, in accord with the measured mean. Extreme fluctuations in two-way TL arise because the upper scarp falls in the shadow zone of the main beam's refractive path, for some segments such as S528, due to its proximity to the source array's conjugate depth. Since the lower scarp lies much deeper, both the standard deviation and fluctuations in the mean are small enough that a clear convex dependence arises in the mean negative two-way transmission loss that reinforces the mean surface projection trend. This leads to an unambiguous central peak in mean modeled reverberation level across the lower scarp that may also be reflected in the measured curve. The central minimum in mean two-way transmission loss across the lower scarp arises because the main beam of the source array insonifies the lower scarp most uniformly when the propagation path runs across the scarp axes. The relatively small standard deviations found in curves of mean modeled and measured reverberation level, compared with those of two-way TL, follow from the smoothing effects of spatial convolution with the system resolution footprint.

The implication of this decomposition is that *spatial variations in transmission loss and projected area lead to the dominant spatial variations in measured reverberation at long range*. This finding for *high-resolution bistatic* data is entirely consistent with that of the previous *wide-area* analyses of *monostatic* data,[2,11] where the effect of projected surface area was incorporated implicitly in range-dependent propagation modeling via the parabolic equation.

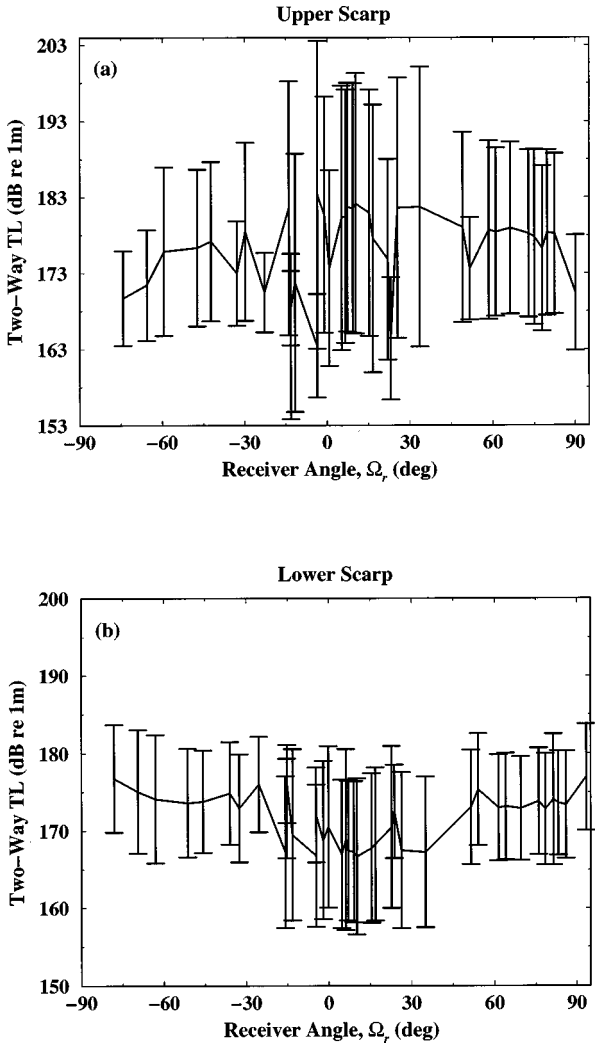

FIG. 20. The mean two-way transmission loss (a) over the upper scarp $\langle \mathrm{TL}_i(x,y|\Omega_i,\Omega_r)+\mathrm{TL}_r(x,y|\Omega_i,\Omega_r)\rangle_{A_{\rm up}}$ and (b) lower scarp $\langle \mathrm{TL}_i(x,y|\Omega_i,\Omega_r)+\mathrm{TL}_r(x,y|\Omega_i,\Omega_r)\rangle_{A_{\rm low}}$ as a function of receiver azimuth Ω_r along with standard deviations.

C. Bi-azimuthal scattering distribution of upper and lower scarps

Curves of the mean strength of the bi-azimuthal scattering distribution over the upper scarp $\langle \hat{\tilde{F}}(x,y|\Omega_i,\Omega_r)\rangle_{A_{\rm up}}$ and lower scarp $\langle \hat{\tilde{F}}(x,y|\Omega_i,\Omega_r)\rangle_{A_{\rm low}}$ are plotted as a function of receiver azimuth in Fig. 22, along with their corresponding standard deviations $\sigma_{A_{\rm up}}\{\hat{\tilde{F}}(x,y)\}$, $\sigma_{A_{\rm low}}\{\hat{\tilde{F}}(x,y)\}$. The mean strength over the upper scarp fluctuates about a constant value of roughly $-17\,\mathrm{dB}\pm 8\,\mathrm{dB}$. The larger standard deviation and fluctuations in the mean for small $|\Omega_r|$ are consistent with those found in both curves of measured and modeled reverberation level. While one may argue that a very mild concave trend is displayed in the mean scattering

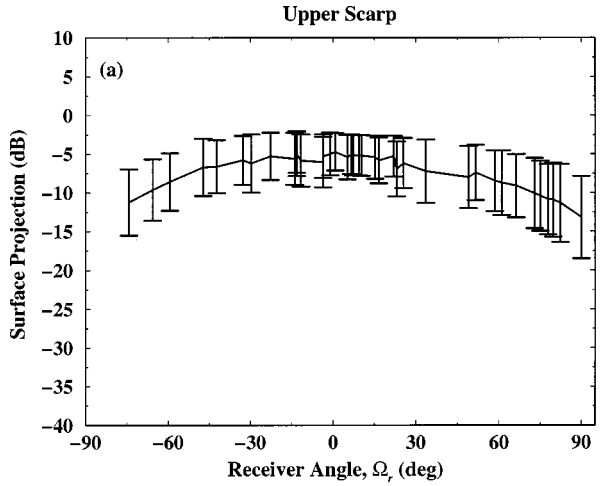

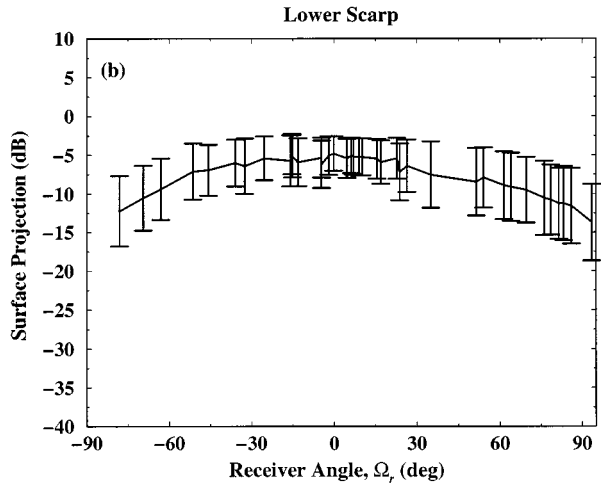

FIG. 21. The mean surface projection, in dB, (a) over the upper scarp $\langle C_i(x,y|\Omega_i,\Omega_r)+C_r(x,y|\Omega_i,\Omega_r)\rangle_{A_{\text{up}}}$ and (b) the lower scarp $\langle C_i(x,y|\Omega_i,\Omega_r)+C_r(x,y|\Omega_i,\Omega_r)\rangle_{A_{\text{low}}}$ as a function of receiver azimuth Ω_r along with standard deviations.

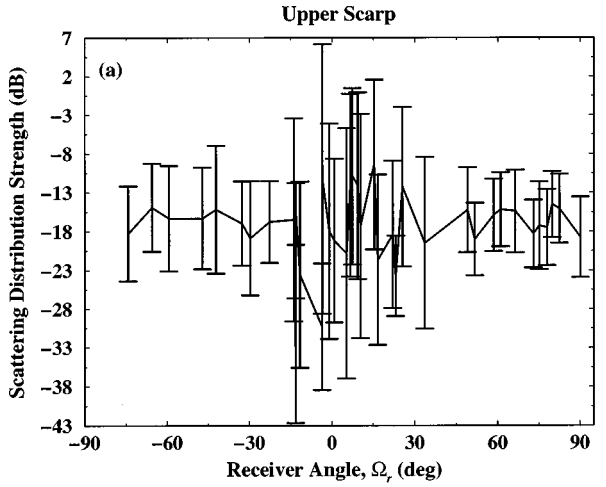

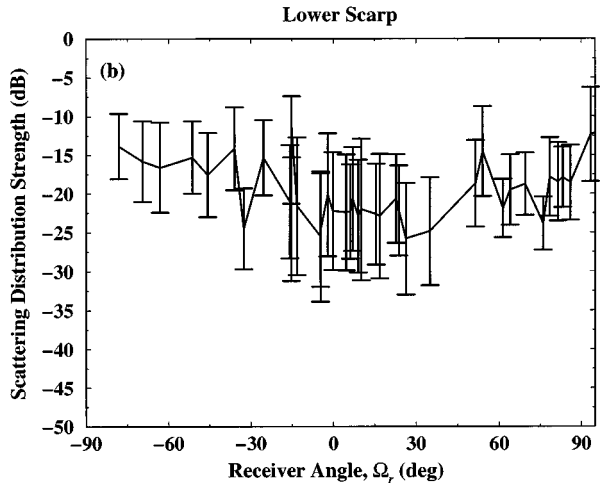

FIG. 22. The mean strength of the bi-azimuthal scattering distribution estimated over (a) the upper scarp $\langle \hat{\hat{F}}(x,y|\Omega_i,\Omega_r)\rangle_{A_{\text{up}}}$ and (b) the lower scarp $\langle \hat{\hat{F}}(x,y|\Omega_i,\Omega_r)\rangle_{A_{\text{low}}}$ as a function of receiver azimuth Ω_r along with the corresponding standard deviations $\sigma_{A_{\text{up}}}\{\hat{\hat{F}}(x,y)\}$, $\sigma_{A_{\text{low}}}\{\hat{\hat{F}}(x,y)\}$. The mean strength over the scarps fluctuates about a constant value of roughly -17 dB$\pm$8 dB.

strength curve for the lower scarp, this entire trend falls within the roughly 7-dB standard deviation shown. The far more important fact is that a constant line may be drawn across -17 dB that falls within all error bars. By reciprocity, these results remain the same if the source and receiver azimuths are interchanged.

In light of the data and our present analysis, we conclude that the *mean bi-azimuthal scattering distributions of the upper and lower scarps of the B′ abyssal hill are identical and have strengths roughly equal to the constant* -17 dB$\pm$8 dB. Whether the observed constancy is due to innate properties of the seafloor, or is a consequence of the large and nonplanar areas integrated by the resolution footprint of the towed-array system, is not particularly relevant to the type of remote sensing undertaken in the present study. The important issue is that the scarps *behave* as if their innate BSDF is spatially homogeneous and equal to the constant $10^{-1.7}$ when remotely imaged from waterborne paths at 1/2 CZ range or greater.

IV. CONCLUSIONS

High-resolution images of a typical mid-ocean abyssal hill, called B', are formed from acoustic measurements made remotely with a bistatic towed-array system at 1/2 convergence zone range. For comparison, modeled images are generated from high-resolution supporting bathymetry, sampled at the wavelength scale, with a combination of parabolic equation and ray approximations, under the assumption that the seafloor scatters uniformly in all directions. Narrow scarps, $\sim$100 m wide, that stretch along the ridge axis for kilometers, consistently produce the most prominent features in both measured and modeled images. Measured and modeled images show close agreement when the cross-range axis of the system resolution footprint is aligned with the scarp axis. In this case, prominent measured and modeled returns faithfully image scarp morphology while neighboring plateaus produce comparatively negligible returns. This is true

even though the scarps and plateaus typically share similar two-way transmission loss and exactly the same *modeled* scattering strength.

A primary conclusion can be drawn from this that could not be drawn in previous studies that relied upon lower resolution supporting bathymetry.[2,11–14] *Scarps return the strongest echoes because they project the largest area along the acoustic path from the source to receiver.* Scattering strength differences between the scarps and plateaus, arising from their differing material properties, are apparently of secondary importance in modeling long-range acoustic reverberation, which averages over large inhomogeneous seafloor areas, since a good first-order match between measured and modeled reverberation is obtained when these differences are neglected.

When the system's cross-range axis forms an oblique angle with the scarp axis, prominent returns are still centered on the scarps but also cross into neighboring plateaus over lengths commensurate with the resolution footprint's cross-range extent. Prominent *modeled* returns in this scenario typically coincide with characteristic anomalies on the scarps, such as canyon walls 100–200 m wide, that project area strongly along the acoustic path from source to receiver and lie at spatial minima in two-way transmission loss to the seafloor. While the *character* of prominent *measured* returns is similar to this, a one-to-one correspondence with *modeled* returns is absent at these oblique angles. The most likely explanation for this discrepancy is that the expected pattern along the scarp is lost in signal-dependent noise arising from statistical fluctuations of the scattered field. Specifically, the along-scarp variations in reverberation level predicted by the model are on the order of the 5.6-dB standard deviation expected in the scattered field by the central-limit theorem. While there is also some evidence of charting error, introduced by undersampled fluctuations in receiving-array orientation, this leads to rotational offsets in the images as opposed to the observed randomization.

This result can be cast in more general terms. *Signal-dependent noise, commonly referred to as speckle, is one of the primary factors limiting a towed-array imaging system's ability to remotely resolve seafloor geomorphology.* Degradation is most pronounced when the expected reverberation level has spatial variations that do not greatly exceed the 5.6-dB standard deviation of speckle noise, as is the case when the terrain to be imaged is relatively uniform, even if this means that it is uniformly rough as is the case along the B' scarps.

Both measured and modeled reverberation share the same nearly constant bi-azimuthal dependence, when averaged across either scarp of the B' abyssal hill. As a result, *the mean bi-azimuthal scattering distributions of the two major scarps on the B' abyssal hill are identical and have strengths roughly equal to the constant* $-17\,\mathrm{dB}\pm 8\,\mathrm{dB}$. Whether or not this constancy describes an innate property of the scarps that remains unchanged in more localized and high-resolution measurements is not relevant to the type of remote sensing undertaken in the present study. The important issue here is that the scarps *behave* as if their innate bi-azimuthal scattering distribution function is spatially homogeneous and equal to the constant $10^{-1.7}$ when remotely imaged from waterborne paths at $1/2+n$ CZ range. From these ranges, in other words, the scarps behave as Lambertian scatterers with albedo $\pi/10^{1.7}$.

This result for the B' abyssal hill leads to a more general hypothesis. *Spatial variations in transmission loss and seafloor projected area cause the dominant spatial variations in the expected value of long-range ocean-basin reverberation.* This hypothesis is appealing because it means that long-range reverberation from the ocean basin can be adequately modeled given two environmental inputs: (1) the refractive index of the water column, and (2) bathymetry. The latter must be of sufficient resolution to determine the projected area of primary seafloor scatterers. Research is presently directed to test this hypothesis by analyzing the bi-azimuthal scattering properties of an *inside corner*. The results of this research will be important because inside corners, and *outside corners* like the B' abyssal hill, comprise the two major geological classes of bathymetric highs in the world's mid-ocean ridges.[29]

APPENDIX A: THE RESOLUTION FOOTPRINT

The resolution footprint $A_f(x,y|\mathbf{r}_i,\mathbf{r}_r)$ can be described without loss of generality in a simple 2-D Cartesian coordinate system shown in Fig. A1, where the receiver $\mathbf{r}_r$ is at the origin and the source $\mathbf{r}_i$ on the y-axis at positive a. The travel-time radius from the source is $r_a=\sqrt{x^2+(y-a)^2}$ and that from the receiver is r. An ellipse of constant two-way travel time can be defined by holding $R=r_a+r$ fixed. Points on the ellipse are naturally described by polar coordinates with respect to the receiver location $x=r\cos\theta$ and y

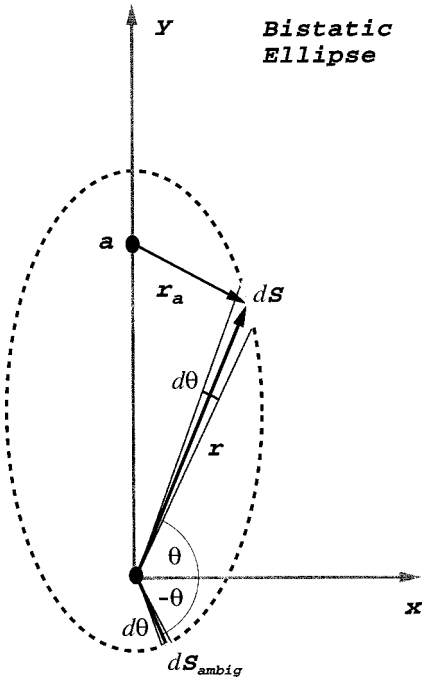

FIG. A1. Elliptical geometry of a bistatic measurement with a true feature at (r,θ). The receiving array lies along the x-axis and is centered at the origin so that the ambiguous azimuth is $-\theta$. If the receiving array has azimuthal resolution $b(\theta)=d\theta$, the system's cross-range resolution is dS, with an ambiguity of arc-length dS_{ambig} as shown.

$=r\sin\theta$ so that the azimuthal resolution of the receiving array is set to $\beta(\theta)=d\theta$, the range resolution to roughly dr, and the cross-range resolution to

$$ds=\sqrt{r^2+\left(\frac{\partial r}{\partial\theta}\right)^2}\,d\theta,$$

where

$$\frac{\partial r}{\partial\theta}=\frac{ra\cos\theta}{R-a\sin\theta}.$$

The resolution footprint in this coordinate system is then

$$A_f=dr\,ds=\sqrt{r^2+\left(\frac{ra\cos\theta}{R-a\sin\theta}\right)^2}\,dr\,d\theta.$$

The cross-range resolution ds then reduces to $rd\theta$ for monostatic geometries, while for general bistatic measurements in the present semicircular experimental geometry about B' it is roughly bounded by $\sqrt{3/2}rd\theta\approx 1.2rd\theta$ since the source–receiver separation a never exceeds r.

Minor perturbations in this elliptic geometry arise when travel time range is converted to actual spatial range, due to the combined effects of vertical refraction and bathymetric variation.

APPENDIX B: INFORMATION-CONSERVING SUMMARY OF THE BI-AZIMUTHAL SCATTERING DISTRIBUTION OF THE UPPER AND LOWER SCARPS

The mean reverberation and scattering distribution strength curves shown in Figs. 18, 19, and 22 only summarize the relevant data without loss of information[30] when the samples from which the means are extracted are Gaussian variates. This, however, is not the case with the present data, so an information-conserving summary of the azimuthal scattering distribution of the upper and lower scarps is presented in Figs. B1–B3. Here, histograms of measured reverberation, modeled reverberation, and scattering strength,

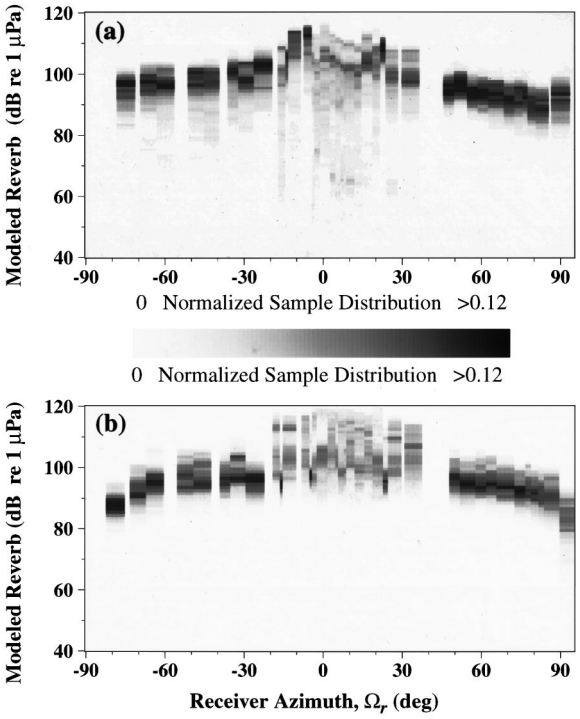

FIG. B2. Histogram of modeled reverberation level over (a) the upper scarp and (b) the lower scarp as a function of receiver azimuth Ω_r.

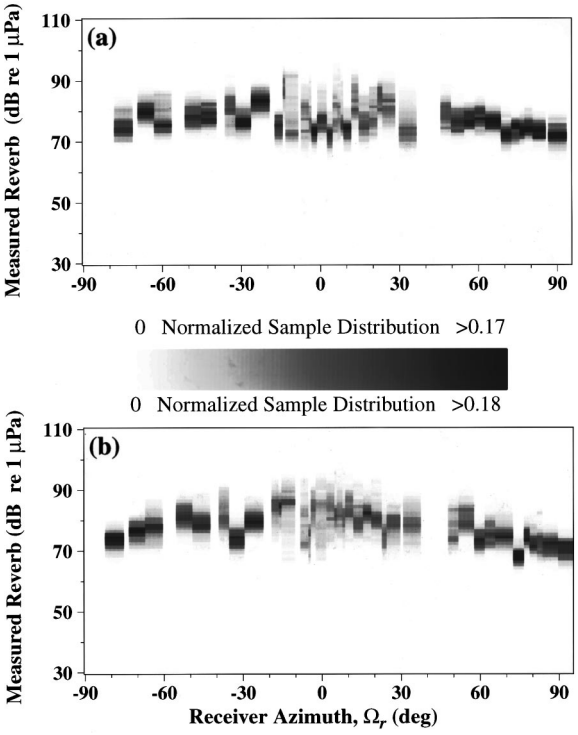

FIG. B1. Histogram of measured reverberation level over (a) the upper scarp and (b) the lower scarp as a function of receiver azimuth Ω_r.

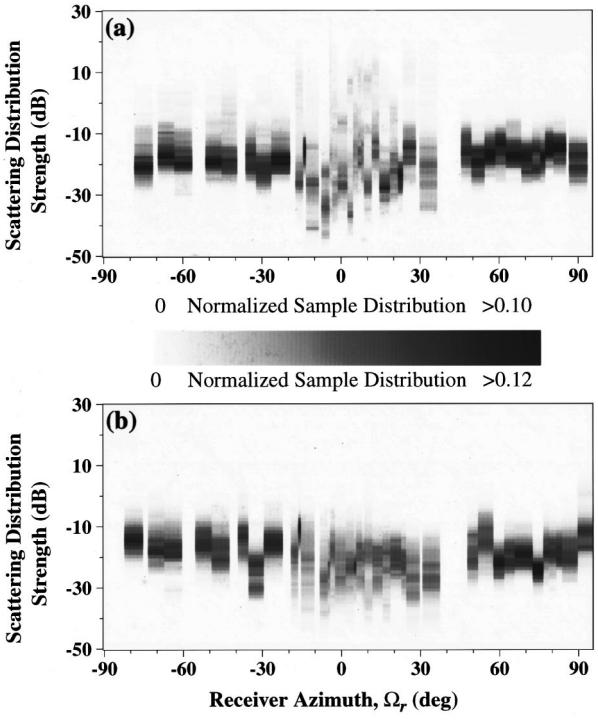

FIG. B3. Histogram of scattering distribution strength over (a) the upper scarp and (b) the lower scarp as a function of receiver azimuth Ω_r.

with samples taken over the upper and lower scarps, respectively, are given as a function of receiver azimuth.

[1] *Acoustic Reverberation Special Research Program Main Acoustics Experiment, Initial Report*, edited by J. Orcutt, Scripps Institution of Oceanography (1993).

[2] N. C. Makris, L. Z. Avelino, and R. Menis, ''Deterministic reverberation from ocean ridges,'' J. Acoust. Soc. Am. **97**, 3547–3574 (1995). [Bathymetry in Fig. 5 of this reference should be labeled <3600 m not <3200 m as shown. Also, the bistatic reverb for LFM/S478 should be labeled >87 dB *re* 1 μPa in Fig. 24, not >80 dB *re* 1 μPa as shown.]

[3] B. E. Tucholke, W. K. Stewart, and M. C. Kleinrock, ''Long-term denudation of ocean crust in the central North Atlantic Ocean,'' Geology **25**, 171–174 (1997).

[4] E. Gerjouy and A. Yaspan, ''Reverberation,'' in *The Physics of Sound in the Sea* (National Defense Research Committee, Washington, DC, 1946).

[5] N. C. Makris, ''Proposed experiment,'' in *Acoustic Reverberation Special Research Program Research Symposium*, Woods Hole Oceanographic Institution (1992).

[6] N. C. Makris and B. Gardner, ''Planned Tracks/Waypoints, Runs 3–9,'' in *Acoustic Reverberation Special Research Program Main Acoustics Experiment, Initial Report*, Scripps Institution of Oceanography (1993), pp. 65–80.

[7] B. E. Tucholke, J. Lin, M. C. Kleinrock, M. A. Tivey, T. B. Reed, J. Goff, and G. E. Jaroslow, ''Segmentation and crustal structure of the western Mid-Atlantic Ridge flank, 25° 25′–27°10′N and 0–29 m.y.,'' J. Geophys. Res. **102**, 10 (1997); **102**, 203–210 (1997); **102**, 223 (1997).

[8] J. R. Preston, E. Michelozzi, L. Troiano, and R. Hollet, ''Cruise report on RV ALLIANCE cruise MARE 5 July–1 August 1993 SACLANTCEN's joint experiment with ONR's ARSRP Group,'' SACLANT Undersea Research Centre, LaSpezia, Italy (1993).

[9] P. Swerling, ''Probability of detection for fluctuating targets,'' Rand Report RM 1217 (1954); reissued in Trans. IRE Prof. Group Inf. Theory **IT-6**, 269–308 (1960).

[10] N. C. Makris, ''The effect of saturated transmission scintillation on ocean acoustic intensity measurements,'' J. Acoust. Soc. Am. **100**, 769–783 (1996).

[11] N. C. Makris and J. M. Berkson, ''Long-range backscatter from the Mid-Atlantic Ridge,'' J. Acoust. Soc. Am. **95**, 1865–1881 (1994).

[12] N. C. Makris, L. Avelino, R. Menis, and J. M. Berkson, ''Preliminary results: Correlation between reverberation and geomorphology,'' in *Acoustic Reverberation Special Research Program Main Acoustics Experiment, Initial Report*, Scripps Institution of Oceanography (1993), pp. 336–355.

[13] K. B. Smith, W. S. Hodgkiss, and F. D. Tappert, ''Propagation and analytic issues in the prediction of long-range reverberation,'' J. Acoust. Soc. Am. **99**, 1387–1404 (1996).

[14] A. J. Harding, M. A. H. Hedlin, and J. A. Orcutt, ''Migration of backscatter data from the Mid-Atlantic Ridge,'' J. Acoust. Soc. Am. **103**, 1787–1803 (1998).

[15] D. M. Fromm, L. B. Palmer, and J. P. Crockett, ''Bi-RASP: The bistatic range-dependent active system prediction model,'' Technical Report NRL/FR/7140-95-9723 (Naval Research Laboratory, Washington D.C., 1996).

[16] V. Lupien, ''The importance of scale structure in scattering from random rough surfaces,'' Ph.D. thesis, Massachusetts Institute of Technology, Cambridge, MA, 1998.

[17] ''Positioning with GPS-1985,'' in *Proceedings First International Symposium on Precise Positioning with the Global Positioning System*, Vol. 1, C. C. Goad, Covenor, National Geodetic Information Center (NOAA, Rockville, Maryland, 1985).

[18] J. P. Snyder, ''Map projections—A working manual,'' USGS Professional Paper 1395 (1985).

[19] G. I. Evenden, ''Cartographic Projection Procedures for the Unix Environment—A user's manual,'' USGS Open-File Report 90-284 (1991).

[20] B. K. P. Horn and R. W. Sjoberg, ''Calculating the reflectance map,'' Appl. Opt. **18**, 1770–1779 (1979).

[21] F. E. Nicodemus, J. C. Richmond, J. J. Hsia, I. W. Ginsbrg, and T. Limperis, ''Geometrical considerations and nomenclature for reflectance,'' NBS Monograph 160 (National Bureau of Standards, Washington, D.C., October 1977).

[22] Readers must be warned that the Nicodemus *et al.* (Ref. 21) and Horn and Sjoberg references (Ref. 20) use the term *radiant intensity* to mean flux per unit solid angle, by a convention in modern radiometry. This differs from the term *intensity* used in field theory that means flux per unit area. Also, the BSDF here is equivalent to the bidirectional reflectance distribution function (BRDF) of modern radiometry, except inverse steradians units are stressed in the latter but not the former. The distinction, with no real difference, arises because the nondimensional steradian unit cannot be readily conserved in the relation $dA = r^2\, d\Omega$ between differential area dA and differential solid angle $d\Omega$. The term *scattering* is preferred here over *reflectance*, since the two are not equivalent in field theory.

[23] R. Urick, *Principles of Underwater Sound*, 3rd ed. (Peninsula, Los Altos, CA, 1983), pp. 274–278.

[24] S. Chandrasekhar, *Radiative Transfer* (Dover, New York, 1960).

[25] N. C. Makris, ''A foundation for logarithmic measures of fluctuating intensity in pattern recognition,'' Opt. Lett. **20**, 2012–2014 (1995).

[26] M. D. Collins, ''A self-starter for the parabolic equation method,'' J. Acoust. Soc. Am. **92**, 2069–2074 (1992).

[27] J. W. Goodman, *Statistical Optics* (Wiley, New York, 1985).

[28] N. C. Makris, ''Imaging ocean-basin reverberation via inversion,'' J. Acoust. Soc. Am. **94**, 983–993 (1993).

[29] B. E. Tucholke and J. Lin, ''A geological model for the structure of ridge segments in slow spreading ocean crust,'' J. Geophys. Res. **99**, 11937–11958 (1994).

[30] P. M. Woodward, *Probability and Information Theory with Applications to Radar* (Pergamon, Oxford, England, 1953).

Elimination of branch cuts from the normal-mode solution using gradient half spaces

Evan K. Westwood and Robert A. Koch
Applied Research Laboratories, The University of Texas at Austin, P. O. Box 8029, Austin, Texas 78713-8029

(Received 20 October 1998; revised 28 June 1999; accepted 14 July 1999)

A method for eliminating the branch cuts and branch line integrals from the normal-mode solution to the range-invariant acoustic wave equation has been developed and implemented. In the usual normal-mode formulation, evaluation of the vertical wave number in the ocean waveguide's lower half space involves a square root operation and gives rise to a branch point at the critical angle. When the Pekeris cut is chosen, energy steeper than the critical angle is represented by leaky modes, and lateral-wave energy near the critical angle is represented by the branch line integral. When a mode lies near the branch cut, the branch line integral can be significant at all ranges. Branch line integrals are cumbersome to compute, and, for range-dependent problems, cannot be included in adiabatic and coupled-mode algorithms. By inserting small attenuation and sound-speed gradients in the lower half space, the plane-wave solution is replaced by an Airy function solution, the branch point is eliminated, the Pekeris branch cut is replaced by a series of modes, and the leaky modes become bounded at infinite depth. Implementation of and example calculations using this approach using the normal-mode model ORCA are given. [S0001-4966(99)03611-5]

PACS numbers: 43.30.Bp, 43.20.Ks [DLB]

INTRODUCTION

Normal-mode theory is a useful and efficient approach for modeling and analyzing acoustic propagation in the ocean and other waveguides. For the simplest of ocean models, homogeneous water between a pressure-release surface and a rigid bottom, the normal-mode solution is analytic and exact. For more realistic representations of the ocean bottom, however, most normal-mode implementations are not exact because they ignore one or more components of the total field. The difficulties are associated with the treatment of energy that penetrates into the half spaces above and/or below the waveguide. (For typical underwater acoustics applications, propagation into the lower half space is the important phenomenon; in this paper we will therefore refer to the lower half space only, with the understanding that the upper half space may be treated in the same manner.)

The most important component of the total field is the modes that are evanescent in the lower half space. These ''trapped modes'' correspond to energy that propagates at angles for which total internal reflection occurs at (or above) the half-space boundary. Normal-mode implementations that include only the trapped modes are generally regarded as being accurate at ranges beyond a few waveguide depths; under certain circumstances, however, the trapped-mode solution can be inaccurate at all ranges.

The form of the non-trapped part of the modal solution depends on the choice of branch cut produced by the sound speed in the homogeneous lower half space. Figure 1 illustrates the two most common choices. When the Pekeris cut[1] is chosen [see Fig. 1(a)], the remainder of the field is made up of the Pekeris branch line integral (PBLI) and an infinite set of ''leaky'' modes. The PBLI represents energy that propagates near the half-space critical angle and is thus associated with lateral waves in the half space. The leaky modes represent steeper energy that is partially reflected at the half-space interface. Leaky modes decay exponentially with range and propagate in the lower half space. When the EJP cut (used by and named for the authors of Ref. 2) is chosen [see Fig. 1(b)], the remainder of the field is the EJP branch line integral (EBLI) alone. The total pressure field using the Pekeris and EJP cuts may therefore be written

$$p = \sum \mathrm{TM} + \mathrm{PBLI} + \sum \mathrm{LM} = \sum \mathrm{TM} + \mathrm{EBLI}, \tag{1}$$

where TM and LM stand for the trapped and leaky modes, respectively.

One approach to obtaining the exact field is to compute either of the branch line integrals numerically (see, for example, Ref. 3 for the EBLI and Refs. 4 and 5 for the PBLI). But such an approach is not desirable in a practical model for the following reasons: the integrand can be irregular; the integrals depend on source depth, receiver depth, and range; and branch line integrals are difficult to incorporate into coupled- or adiabatic-mode algorithms for range-dependent propagation. Other approaches include approximating the complex-valued leaky modes by virtual modes,[6,7] approximating the entire EBLI by a uniform asymptotic expansion,[8] and using the concept of ''radiation modes'' to account for the continuum.[9]

Although we prefer the Pekeris cut to the EJP cut because it allows more of the total field to be expressed in terms of modes, it is not uncommon for the TM+LM summation to be in error at all ranges. In particular, the PBLI can become important at all ranges and depths in the waveguide when a mode lies near the Pekeris branch cut. For a single-frequency calculation, the probability of this occurring is not

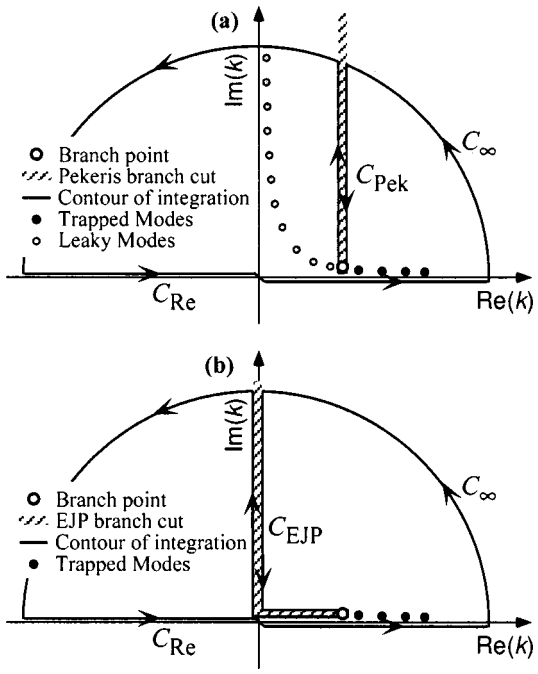

FIG. 1. Contours of integration and mode families in the complex horizontal wave number k plane for (a) the Pekeris branch cut and (b) the EJP branch cut.

great. For broadband calculations, however, the probability is high because modes move continuously past the branch point as a function of frequency. When the half-space attenuation does not force the branch point high in the complex k (horizontal wave number) plane, modes move past the branch point at regular frequency intervals and cause the field to be inaccurate there. A similar mode-cutoff phenomenon arises for single-frequency problems when the bathymetry varies.

The motivation for the work in this article lies not only in the desire to obtain an accurate answer using normal-mode theory under all conditions, but also in the desire to eliminate several unattractive features associated with the Pekeris branch cut and leaky modes. Searching for modes in the complex k plane is complicated by the need to keep track of the Riemann sheet on which the modes are found. When crossing a branch cut, the Riemann sheet of the associated branch point must be changed in order to keep the function continuous. (Changing sheets means evaluating the square root operator for the half-space vertical wave number with the opposite sign.) As frequency or water depth is varied, it is possible for a valid mode to cross the branch cut onto the incorrect Riemann sheet and to be replaced by a corresponding mode that emerges from the incorrect sheet, but at a location offset from the first crossing. An example of this phenomenon is shown in Sec. II B. It is in these regions that the PBLI is important and that the normal-mode field without the PBLI is incorrect and discontinuous in the parameter being varied. Elimination of the branch cut discontinuities simplifies numerical search routines and makes range-dependent adiabatic and coupled-mode algorithms more accurate.

The second unattractive feature of normal-mode theory using the Pekeris cut is that the leaky modes lie on the ''improper'' Riemann sheet and therefore increase exponentially in the lower half space.[10–12] Although the modes' behavior in the half space does not prevent them from being normalized, it does introduce serious difficulties in coupled-mode algorithms, where overlap integrals of the mode functions that extend to infinite depth are required to be computed.

In the present work the difficulties with the Pekeris branch cut are removed by introducing a small gradient in the lower half space. The gradient effectively removes the branch point and associated branch cut from the problem. A concomitant result of the gradient half-space approach is that the leaky modes eventually decay as a function of depth. They no longer lie on an ''improper'' sheet because no branch points, branch cuts, or sheets associated with the half space exist.

This approach is similar to the common approach of inserting a thick ''false bottom'' layer having the properties of the original half space (near the top of the layer) and making the new half space rigid (see, for example, Ref. 13). In the limit of giving the false bottom a slight sound speed and attenuation gradient and infinite thickness, the two approaches give the same results. The false bottom approach is somewhat less desirable from a computational standpoint because two additional layers are often required (one to mimic the homogeneous half space and one to absorb the energy before it reflects from the rigid bottom). In addition, choosing parameters for the false bottom approach tends to be less straightforward than for the gradient half-space approach.

Since the field represented by the PBLI is very complex and nonmodal in nature, it is not surprising that elimination of the branch cut generates a new and complex modal structure in the neighborhood of the former cut. The nature of that structure and its dependence on the choice of gradient is a major focus of this work. While we wish to develop the capability of introducing a half-space structure that reproduces as closely as possible a homogeneous bottom, we also wish to extend our normal-mode model to allow for a more general and perhaps more realistic type of half space.

Other works in which normal-mode theory has been applied to environments for which the half-space sound-speed profile is not uniform include Refs. 14–18. Brekhovskikh, in his classic textbook,[14] used a positive gradient half space below a pressure-release interface to represent a surface duct and solved for the modes and mode functions in terms of Airy functions. Pedersen and Gordon[15] considered a bilinear-gradient model of a surface channel, where the lower half space represented the (relatively large) negative sound-speed gradient below the surface duct. In Ref. 16, the authors found that two families of modes existed, the second of which appears to correspond to the ''branch line modes'' treated in this paper. Hall[18] summarized a number of half-space profiles for which solutions to the wave equation exist, analyzed the case of a vanishingly small negative gradient, and concluded that the resulting family of modes was equivalent to the PBLI of the isospeed half-space problem. The results herein are entirely consistent with the above-mentioned works; we have extended the basic approach of Ref. 15 to include half-space profiles with attenuation (as well as sound-speed) gradients and have adapted a recently devel-

oped mode-finding method to locate easily the branch line modes in the complex k plane.

We now summarize the organization of this article. Section I reviews the relevant theory behind the standard normal-mode formulation. Section II introduces our approach of inserting a gradient in the half space to eliminate the branch cut and considers two simple cases: a single gradient layer below a pressure-release interface and a Pekeris waveguide having a gradient half space. The effects of the half-space gradient on the modal eigenvalues, the mode functions, and their frequency dependence are examined in detail. Sections III and IV provide example calculations of transmission loss versus frequency and time series versus range, respectively, using the gradient half-space method. In Sec. V we summarize our conclusions.

I. THEORY

A. Standard derivation of normal-mode theory

Complete derivations of the normal-mode formulation for acoustic propagation in an ocean waveguide are given in Sec. 5.5 of Ref. 19 and in Chap. 3 of Ref. 13. Briefly summarized, the complex pressure field p at range r and depth z produced by a point source at depth z_s and range $r=0$ is

$$p(r,z)=\frac{1}{2}\int_{-\infty}^{\infty} G(z,z_s,k)kH_0^{(1)}(kr)dk, \tag{2}$$

where k is the horizontal wave number and $H_0^{(1)}$ is the zeroth-order Hankel function of the first kind. The Green's function G satisfies the ''forced'' depth-separated wave equation

$$\rho(G'/\rho)'+(K^2-k^2)G=-2\delta(z-z_s), \tag{3}$$

where $(\cdot)'=\partial(\cdot)/\partial z$ and the wave number $K(z)=\omega/c(z)$. The function G may be expressed as

$$G(z,z_s,k)=\frac{-2\phi s_-(z_-,k)\phi_+(z_+,k)}{W(z,k)}, \tag{4}$$

where ϕ_- and ϕ_+ satisfy the boundary conditions at the top and bottom of the waveguide, respectively, W is their Wronskian, $z_-=\min(z,z_s)$, and $z_+=\max(z,z_s)$. Substitution of Eq. (4) into Eq. (2) yields

$$p(r,z)=\int_{-\infty}^{\infty}\frac{-\phi_-(z_-,k)\phi_+(z_+,k)}{W(z_s,k)}kH_0^{(1)}(kr)dk. \tag{5}$$

We wish to solve Eq. (5) using Cauchy's Residue Theorem, for which we need a closed contour of integration. The contour for $p(r,z)$ in Eq. (5) corresponds to the real-axis section C_{Re} in Fig. 1 and is closed using a semicircle at infinite radius C_∞ in the upper half plane. At this point the branch cut becomes important. (We choose the Pekeris cut for the reasons stated in the Introduction; the origin of the branch point is discussed in Sec. I B.) Since the integrand is discontinuous across the branch cut, the contour must be made to circle around it, which gives rise to the PBLI denoted by $\int_{C_{\mathrm{Pek}}}$. Cauchy's Theorem applied to the closed contour yields

$$\int_{C_{\mathrm{Re}}}(\cdot)+\int_{C_\infty}(\cdot)+\int_{C_{\mathrm{Pek}}}(\cdot) =-2\pi i\sum_n \frac{\phi_n(z_s)\phi_n(z)}{[\partial W/\partial k]_{k=k_n}}k_nH_0^{(1)}(k_nr), \tag{6}$$

where $(\cdot)$ denotes the integrand in Eq. (5), and k_n are values of k inside the contour for which $W(z_s,k)=0$. Since the Wronskian of ϕ_- and ϕ_+ is zero at $k=k_n$, the solutions are identical (to within a multiplicative constant) for all z and are denoted $\phi_n(z)$. Finally, use of Eq. (5) and the fact that the C_∞ integral is zero results in

$$p(r,z)=2\pi i\sum_n \frac{\phi_n(z_s)\phi_n(z)}{-[\partial W/\partial k]_{k=k_n}}k_nH_0^{(1)}(k_nr)-\int_{C_{\mathrm{Pek}}}(\cdot). \tag{7}$$

In the ORCA normal-mode model,[20] the Wronskian W is written in terms of downward- and upward-looking reflection coefficients R_1 and R_2 at a reference depth z_{ref} [see Fig. 1 and Eq. (7) of Ref. 20],

$$W(k_n,z_{\mathrm{ref}})=2iA\gamma_{n\mathrm{ref}}(1-R_1R_2)=0, \tag{8}$$

where A is a constant that is chosen to be R_1, and $\gamma_{n\mathrm{ref}}$ is the vertical wave number at z_{ref}. The normal-mode criterion is then

$$R_1R_2=1, \tag{9}$$

and the derivative required for normalization of the mode functions is

$$[\partial W/\partial k]_{k_n}=-2iA\gamma_{n\mathrm{ref}}[\partial(R_1R_2)/\partial k]_{k_n}. \tag{10}$$

In ORCA, the reflection coefficients and their derivatives are computed analytically using exponential or Airy function solutions to the wave equation in layers in which $K^2(z)$ is constant or varies linearly.

B. Origin of branch cut in standard formulation

In the ORCA implemention of normal-mode theory, the branch cut arises from the computation of R_1, the downward-looking reflection coefficient at z_{ref}. For the simplest case where z_{ref} lies just above the lower half-space interface,

$$R_1=(m\gamma_{\mathrm{ref}}-\gamma_{\mathrm{HS}})/(m\gamma_{\mathrm{ref}}+\gamma_{\mathrm{HS}}), \tag{11}$$

where $m=\rho_{\mathrm{HS}}/\rho_{\mathrm{ref}}$, and the subscript HS indicates half-space values.[21] The half-space vertical wave number must be computed as

$$\gamma_{\mathrm{HS}}=\pm\sqrt{K_{\mathrm{HS}}^2-k^2}, \tag{12}$$

which generates a branch point at $k_{\mathrm{BP}}=K_{\mathrm{HS}}$ where the argument of the square root is zero. The branch cut is determined by the rule used to decide which of the two roots to take. Note that a branch point associated with γ_{ref} also exists. In the Appendix we show that the γ_{ref} branch cut neither affects the modes nor contributes to the total field.

The EJP cut is taken by requiring $\mathrm{Im}(\gamma)\geqslant 0$, which assures that the plane-wave $\exp(i\gamma z)$ does not grow exponentially with depth in the half space. The Pekeris cut is most

simply implemented by taking the usual FORTRAN square root [which results in $\mathrm{Re}(\gamma)\geqslant 0$] and changing its sign if $\mathrm{Im}(\gamma)<0$ and $\mathrm{Re}(k)>\mathrm{Re}(K_{\mathrm{HS}})$. The result (for the no-attenuation problem) is that, under the EJP and Pekeris cuts, γ_{HS} has the opposite sign in the region defined by $0<\mathrm{Re}(k)<\mathrm{Re}(K_{\mathrm{HS}})$ and $\mathrm{Im}(k)>0$. This region is where the leaky modes, having exponentially growing mode functions in the half space, are found when the Pekeris cut is taken (see Fig. 1).

II. ELIMINATION OF BRANCH CUT

The branch cut and branch line integrals are eliminated by simply introducing a small gradient in the sound-speed profile of the lower half space. In order to use Airy function solutions, we assume

$$K^2(z)=K_{\mathrm{HS}}^2+\eta^3(z-H) \quad \text{for } z\geqslant H, \tag{13}$$

where $K_{\mathrm{HS}}=\omega/c_{\mathrm{HS}}$ is now the wave number at the top of the half space $z=H^+$, and η^3 is a chosen gradient. By defining

$$\xi(z)=[k^2-K^2(z)]/\eta^2=(k^2-K_{\mathrm{HS}}^2)/\eta^2-\eta(z-H), \tag{14}$$

the Helmholtz equation may be transformed to the Airy differential equation,

$$d\phi^2/dz^2+\gamma^2(z)\phi=0 \Rightarrow d\phi^2/d\xi^2-\xi\phi=0. \tag{15}$$

The correct form of the solution for our problem is intimately tied to the cubic root taken to compute η in Eq. (14) from the gradient η^3 given in Eq. (13). We choose the solution

$$\phi(z)=A_1\,\mathrm{Ai}(\xi);\quad \phi'(z)=-\eta A_1\,\mathrm{Ai}'(\xi), \tag{16}$$

which is bounded as $|\xi|\to\infty$ only for $|\arg\xi|\leqslant\pi/3$ or $\arg\xi=\pi$. Since, as $z\to\infty$, $|\xi|\to\infty$ in the $-\eta$ direction [see Eq. (14)], we choose the cubic root of η^3 such that

$$|\arg(-\eta)|\leqslant\pi/3, \tag{17}$$

which is conveniently achieved in FORTRAN by $\eta=-(-\eta^3)^{1/3}$.

The half-space reflection coefficient R_{HS} referenced at $z=H^+$ is computed by inserting a vanishingly thin isospeed layer below the interface and matching ϕ and ϕ' at that depth. In the thin isospeed layer we have

$$\phi=e^{i\gamma_{\mathrm{HS}}(z-H)}+R_{\mathrm{HS}}e^{-i\gamma_{\mathrm{HS}}(z-H)}, \tag{18}$$

$$\phi'=i\gamma_{\mathrm{HS}}(e^{i\gamma_{\mathrm{HS}}(z-H)}-R_{\mathrm{HS}}e^{-i\gamma_{\mathrm{HS}}(z-H)}), \tag{19}$$

and in the half space we have Eqs. (16). After equating ϕ and ϕ' at $z=H^+$ and solving the two equations for the two unknowns R_{HS} and A_1, we obtain

$$R_{\mathrm{HS}}=(f+g)/(f-g), \tag{20}$$

where

$$f=i\gamma_{\mathrm{HS}}\mathrm{Ai}(\xi_{\mathrm{HS}})\ ;\ g=\eta Ai'(\xi_{\mathrm{HS}}). \tag{21}$$

In contrast, $R_{\mathrm{HS}}=0$ for a homogeneous half space.

A. Airy half space with pressure-release surface

Our objective in this section is to demonstrate how the structure of the mode eigenvalues in the complex k plane depends on the gradient for the simple case of a pressure-release surface above the gradient half space. In this case, $H=0$, $R_2=-1$, and the mode criterion of Eq. (9) becomes $R_{\mathrm{HS}}=-1$, which, by Eqs. (20) and (21), is satisfied when $\mathrm{Ai}(\xi_{\mathrm{HS}})=0$. The zeros of $\mathrm{Ai}(\xi)$, which we denote $\{\xi_n\}$, lie on the negative real ξ axis. Solving Eq. (14) for the eigenvalues, we obtain

$$k_n^2=K_{\mathrm{HS}}^2+\eta^2\xi_n. \tag{22}$$

Therefore, the eigenvalues in the k^2 plane lie on a radial at angle $\arg(-\eta^2)$ originating at the former branch point K_{HS}^2.

Since the location of the eigenvalues depends on η^2, which is related to the K^2-gradient η^3, we wish to explicitly relate η^3 to the sound speed and attenuation gradients. We define these gradients in terms of the following sound speed and attenuation differences: $\Delta c=c_{3\lambda}-c_{\mathrm{HS}}$ and $\Delta\alpha=\alpha_{3\lambda}-\alpha_{\mathrm{HS}}$, where the subscript 3λ indicates evaluation at a depth three wavelengths into the half space. For absorptive media, the complex wave number is computed as

$$K=(\omega/c)(1+i\alpha/\alpha_c), \tag{23}$$

where the attenuation α is in units of dB/λ and $\alpha_c=40\pi\log_{10}e\approx 54.575$. Assuming that $\Delta c/c_{\mathrm{HS}}\equiv\Delta\overline{c}\ll 1$ and $\Delta\alpha/\alpha_c\equiv\Delta\overline{\alpha}\ll 1$, we evaluate Eq. (13) at $z=H+3\lambda$ and solve for the gradient,

$$\eta^3\approx(1/3\pi)(\omega/c_{\mathrm{HS}})^3(-\Delta\overline{c}+i\Delta\overline{\alpha}). \tag{24}$$

When the cubic root is taken as prescribed in Eq. (17), we find that

$$\arg(-\eta)=(1/3)\arctan\left[\frac{\Delta\overline{\alpha}}{-\Delta\overline{c}}\right]. \tag{25}$$

Combining the condition that assures that $\lim_{z\to\infty}\phi(z)=0$ [see Eq. (17)] and the requirement that the attenuation gradient be non-negative, we find that

$$-\pi/3\leqslant\arg(-\eta)\leqslant 0. \tag{26}$$

Figure 2 illustrates the location of the first ten modes in the complex k plane for two values of $|-\Delta\overline{c}+i\Delta\overline{\alpha}|$ and five uniformly spaced values of $\arg(-\Delta\overline{c}+i\Delta\overline{\alpha})$ between π and 0. The frequency is $f=175$ Hz and $c_{\mathrm{HS}}=1650$ m/s. In representing the complex k plane graphically in Fig. 2 and in subsequent figures, the real part of k is normalized by a reference wave number (K_{HS} here), and the imaginary part of k, which represents the modal attenuation, is converted from units of nepers/m to units of dB/km. The axis lengths in Fig. 2 have been chosen such that angles in the k plane are preserved. It is clear that the magnitude of the gradient determines the mode spacing (smaller gradients produce finer spacing) and that the argument of the gradient determines the direction of the ''mode branch.''

Mathematical expressions for the initial and final directions of the mode branches illustrated in Fig. 2 may be obtained using binomial series expansions for k_n^2 in Eq. (22),

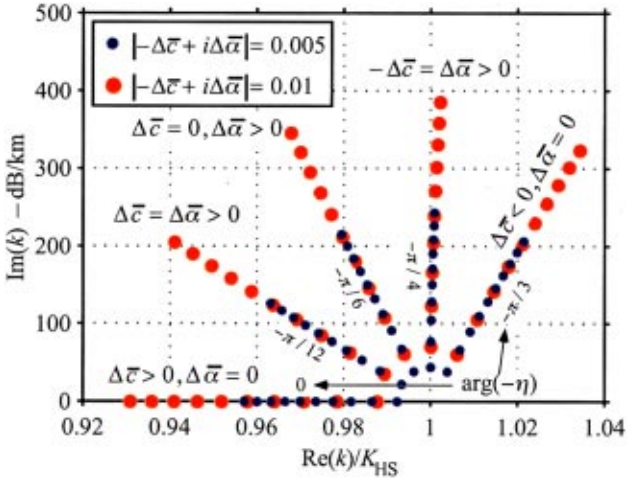

FIG. 2. Locations of first ten modes in complex k plane for a gradient half space with a pressure-release surface. Red and blue dots indicate $|-\Delta\bar{c}+i\Delta\bar{\alpha}|=0.01$ and 0.005, respectively, and the five lines correspond to arg$(-\Delta\bar{c}+i\Delta\bar{\alpha})$ uniformly spaced from π to 0.

$$k_1 \approx K_{\mathrm{HS}} + (1/2)\,\eta^2\xi_1/K_{\mathrm{HS}} \quad (|\eta^2\xi_1| \ll |K_{\mathrm{HS}}^2|), \tag{27}$$

$$k_{n\to\infty} \approx (1/2)K_{\mathrm{HS}}^2/\sqrt{\eta^2\xi_n} + \sqrt{\eta^2\xi_n} \quad (|\eta^2\xi_n| \gg |K_{\mathrm{HS}}^2|). \tag{28}$$

The initial and final directions in the k plane are thus arg$(-\eta^2)$ and (1/2)arg$(-\eta^2)$, respectively. We consider three of the cases illustrated in Fig. 2. For $\Delta\bar{c}>0$ and $\Delta\bar{\alpha}=0$, the mode branch leaves K_{HS} to the left, follows the real k axis to the origin, and finally moves up the positive imaginary k axis. In the limit of an infinitesimally small gradient, the modes represent the EJP branch cut. For $\Delta\bar{\alpha}>0$ and $\Delta\bar{c}=0$, the mode branch leaves K_{HS} at the angle arg$(-\eta^2)=2\pi/3$, eventually curves to the right, and asymptotically approaches $\pi/3$. Finally, for $\Delta\bar{c}<0$ and $\Delta\bar{\alpha}=0$ (the case of a duct at infinite depth), the modes leave K_{HS} at arg$(-\eta^2)=\pi/3$ and asymptotically approach $\pi/6$. Note that, despite the lack of attenuation in this case, all the modes are attenuated [Im$(k_n)>0$] because the downward-going energy is bent toward vertical by the negative sound-speed gradient and never returns. As the magnitude of the negative gradient increases, the mode attenuations increase, as does the rate at which the field decays with range.

The behavior of the mode functions $\phi_n(z)$ with depth is illustrated in Fig. 3. Recall that $\phi_n(z)\propto \mathrm{Ai}[\xi(k_n,z)]$ and $\xi(k_n,z)=\xi_n-\eta z$, where ξ_n is the nth zero of Ai [see Eqs. (16) and (14)]. Therefore, $\phi_n(z)$ is the Airy function evaluated along a line in the ξ plane beginning at the zero ξ_n and pointing in the arg$(-\eta)$ direction [see Eq. (25)]. ''Mode function lines'' in the ξ plane for the case where $\Delta\bar{\alpha}=0.01$ and $\Delta\bar{c}=0$ [arg$(-\eta)=-\pi/6$] are shown in Fig. 3 for $0\leqslant z\leqslant 10\lambda$. The filled circles correspond to the point $z=10\lambda$. For $\Delta\bar{c}>0$ and $\Delta\bar{\alpha}=0$, the lines would point toward the positive real ξ axis, and for $\Delta\bar{c}<0$ and $\Delta\bar{\alpha}=0$, the lines would point in the $-\pi/3$ direction.

An interesting characteristic of the mode functions in the Airy half space is that, except for the case where $\Delta\bar{c}>0$ and $\Delta\bar{\alpha}=0$, they increase in magnitude with depth before decaying. It is evident from Fig. 3 that the amount of increase is

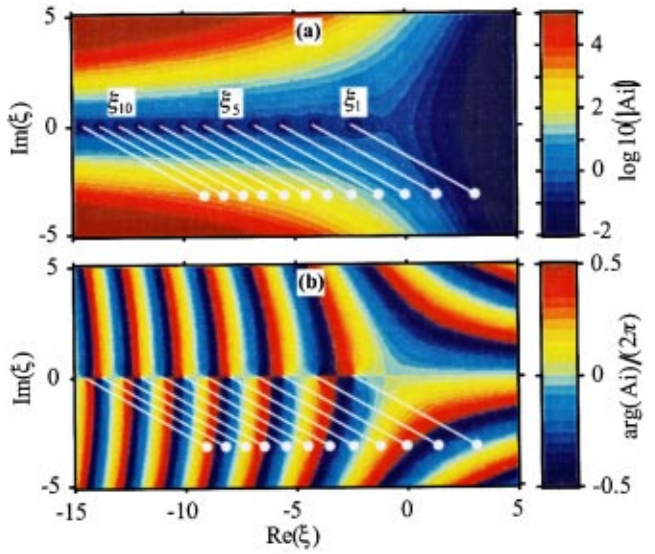

FIG. 3. (a) $|\mathrm{Ai}(\xi)|$ and (b) arg$[\mathrm{Ai}(\xi)]$ imaged in the complex ξ plane. Zeros of Ai lie on the negative real ξ axis and correspond to the mode set $\{\xi_n\}$. The white lines indicate the arguments of the mode functions $\phi_n(z)$ for $0\leqslant z\leqslant 10\lambda$ for the case where $\Delta\bar{\alpha}=0.01$ and $\Delta\bar{c}=0$ [arg$(-\eta)=-\pi/6$].

greater for the higher-order modes. But from Fig. 2 we also observe that the higher-order modes have higher attenuations and therefore decay more quickly with range. Except for the fact that $\lim_{z\to\infty}\phi_n(z)=0$, this behavior is similar to that of the leaky modes in a homogeneous half space. Another interesting point is that the (positive) sound-speed-only gradient produces the fastest depth decay but the slowest range decay, whereas the attenuation-only gradient produces the slowest depth decay but the fastest range decay. Therefore, to obtain a valid field deep in the half space and at short ranges, many modes would have to be used. Fortunately, the field in this region of space is typically not of interest.

B. Airy half space below isospeed waveguide

In this section we examine the behavior of the modes for the case of an isospeed ocean with a pressure-release interface above and an Airy half space below. We will observe how the branch cut for the homogeneous waveguide is replaced by the set of ''branch cut modes'' analyzed in Sec. II A and how these modes are influenced by the presence of the waveguide above. The parameters assumed for the Pekeris waveguide are $c_w=1500$ m/s, $c_{\mathrm{HS}}=1650$ m/s, $\rho_w=1$ g/cm^3, $\rho_{\mathrm{HS}}=1.5$ g/cm^3, and $\alpha_w=\alpha_{\mathrm{HS}}=0$, where the subscript w indicates values in the water. The waveguide depth is $H=40$ m, and the frequency is $f=175$ Hz. An attenuation-only gradient with $\Delta\bar{\alpha}=0.005$ is used.

In Fig. 4, the magnitude and argument of R_1R_2 are imaged in the complex k plane. Modes correspond to points where $\ln(|R_1R_2|)=0$ and arg$(R_1R_2)=0$. For a homogeneous half space [see Fig. 4(a) and (b)], the Pekeris branch cut extends upward from the branch point at Re$(k/k_w)=c_w/c_{\mathrm{HS}}=0.909$ and is manifested by a discontinuity in R_1R_2. The normal-mode model ORCA[20] finds four trapped modes to the right of the branch cut and the first leaky mode to the left by following the $|R_1R_2|=1$ contour. The difficulty of robustly following the contour as it crosses the cut and emerges from

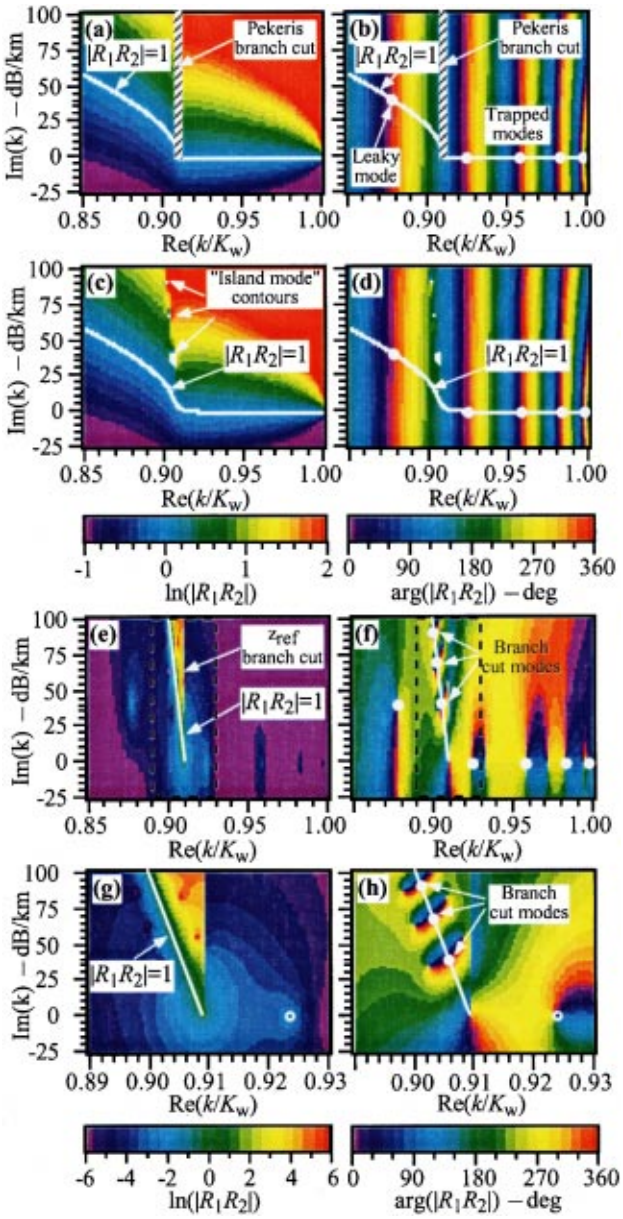

FIG. 4. ln($|R_1R_2|$) (left) and arg(R_1R_2) (right) imaged in the complex k plane for: (a), (b) a homogeneous half space; (c), (d) Airy half space with z_{ref} in the water; (e), (f) Airy half space with z_{ref} in the half space; and (g), (h) expanded views of dashed regions (e), (f). The Airy half space causes the branch cut in (b) to be replaced by the branch cut modes in (f) and (h).

the other sheet at a different location, especially for more complicated environments, is one of the factors that motivated the development and use of the Airy half space.

Figure 4(c) and (d) show R_1R_2 for the Airy half-space problem with z_{ref} in the water column. The images look very similar to the homogeneous half-space case except the branch cut has been replaced by a narrow strip in which R_1R_2 is rapidly changing (but continuous) and the $|R_1R_2|=1$ contour bends smoothly past the former branch point. For this choice of z_{ref}, the five modes found are very close to the ones found for the homogeneous half space [see dots in Fig. 4(b) and (d)].

Close examination of Fig. 4(c) and (d) reveals that three tiny circular $|R_1R_2|=1$ contours lie in the narrow strip of rapid change near the former branch cut. In Sec. II D of Ref. 20, the modes that lay on similar circles were called ''island modes'' due to the separation of their contours from the main $|R_1R_2|=1$ contour. Each of the circular contours in Fig. 4(c) and (d) contains an island mode associated with the branch cut. The ''branch cut modes'' are easily found when z_{ref} is moved to the top of the half space, as in Fig. 4(e) and (f). The change in z_{ref} causes the island modes of Fig. 4(e) and (f) to lie on the main $|R_1R_2|=1$ contour and the original five modes to become island modes.

The structure of the branch cut modes is very similar to the pressure-release case shown in Fig. 2. Expanded views of the dashed regions of Fig. 4(e) and (f) are shown in Fig. 4(g) and (h). We observe that $|R_1R_2|$ changes rapidly in the strip about the $|R_1R_2|=1$ contour and that sets of poles and zeros of R_1R_2 lie above and below the $|R_1R_2|=1$ contour with the same spacing as the modes [see points where all arg(R_1R_2) contours merge in Fig. 4(h)]. The reference depth branch cut discussed in Sec. I B is apparent in Fig. 4(e) and (g); as shown in Appendix A, however, it does not affect the field or the mode finding.

We now examine the behavior of the modes as the frequency changes. Figure 5(a) shows the mode trajectories in the complex k plane as the frequency decreases from 175 to 125 Hz. The modes are computed every 0.5 Hz, and a solid dot is placed every 5 Hz. Since the Re(k) axis is normalized by the water wave number, the location of the former branch point (red cross) does not change. The branch cut modes, as well as the first two modes, move relatively little as a function of frequency, whereas the higher-order trapped and leaky modes move more rapidly. The trapped modes remain on the real k axis until they get very close to K_{HS}/K_w, and the leaky modes follow very nearly the same path in the k plane.

Figure 5(b) shows an expanded view of the region near the former branch point K_{HS} [see dashed region in Fig. 5(a)]. Mode 4 passes below the branch cut modes, which follow rather erratic trajectories with frequency. The dots corresponding to modes 4–7 at 155 and 150 Hz have been made black to demonstrate that the branch cut modes become very sensitive to frequency as a regular mode passes through the transition region, especially those closest to the transisting mode.

The trajectories versus frequency of mode 4 for both an Airy and a homogeneous half space in an even smaller region near the former branch point are shown in Fig. 5(c). For the Airy case, no branch cut exists and the trajectory is smooth. For the homogeneous case, the trajectory disappears behind the branch cut and moves into the lower half plane between 158 and 157.5 Hz. Nearly simultaneously, a different mode 4 trajectory crosses the cut onto the positive sheet at a point displaced vertically along the branch cut. In fact, mode 4 at 157 Hz is on the negative sheet relative to the Pekeris cut. In order to obtain the correct, smooth field for the homogeneous case, the Pekeris branch line integral would have to be included.

The frequency and depth dependences of selected mode functions for this case are shown in Fig. 6. We image $20\log\phi_n^2$ because ϕ appears twice in the pressure field summation, and we examine down to 200 m in depth in order to

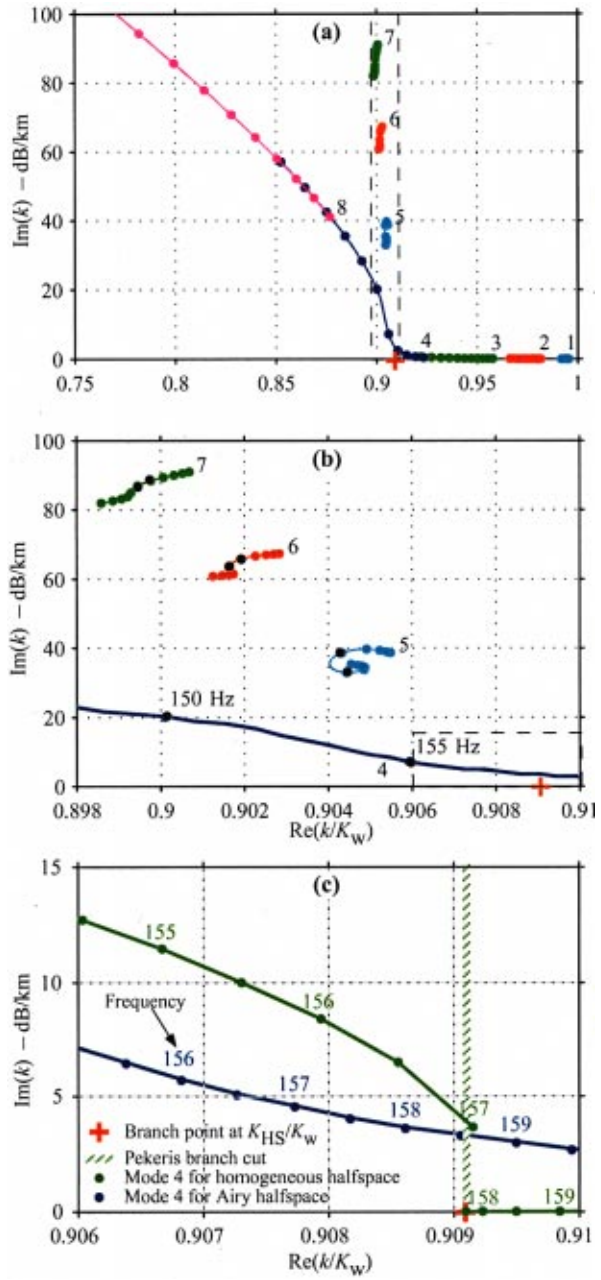

FIG. 5. (a) Mode trajectories as a function of frequency for the Airy half space below an isospeed waveguide. (b) Expanded view near former branch point (red cross) at K_{HS}. (c) Mode trajectories for homogeneous (green) and Airy (blue) half space near branch point.

ascertain the behavior of the mode functions for large depth. Figure 6(a)–(c) correspond to standard modes 3–5. As the frequency decreases, modes 3–5 change from trapped to leaky at frequencies of 107, 153, and 198 Hz, respectively. However, note that, unlike the leaky modes for a homogeneous half space, these modes eventually decay with depth. As the frequency decreases, their magnitude increases in the bottom, but their range attenuation [$\mathrm{Im}(k_n)$] also increases (see Fig. 5). (The blank region in the mode 5 image corresponds to frequencies for which the mode's high attenuation makes it unnecessary to compute.)

Figure 6(d)–(e) correspond to the first two branch line modes. We observe that, in the water column, they are relatively weak except at the frequencies where modes 3–5 become leaky. In terms of the frequency trajectories of the modes shown in Fig. 5, the amplitude of the branch line modes increases, particularly in the water column, when a standard mode passes just below the branch line mode. As this occurs, each branch line mode assumes the same depth structure in the water column as the standard mode that is passing below. In terms of rays, the branch line modes account for lateral wave energy, which resonates most strongly at the particular frequencies for which standard modes are near the critical angle also. We also observe that the branch line modes become weaker in the water column but stronger in the bottom as the mode number increases.

A final observation regarding Figs. 5 and 6 is that, using the standard mode ordering convention based on $\mathrm{Re}(k_n)$, the modes change order as the frequency (or, equivalently, the water depth) changes. The standard modes migrate to the left in the k plane diagrams of Fig. 5 as the frequency decreases, whereas the branch line modes remain relatively stationary. The change in order must be accounted for when performing range-dependent adiabatic-mode computations, for example. In this example case, separate orderings of the standard and branch line mode groups would solve this problem.

In Fig. 7 the modal dispersion curves are shown for Airy (red) and homogeneous (blue) half spaces. The standard modes have identical group velocities except in the region of the critical angle, where the Airy curves are smooth and the homogeneous curves are discontinuous. The Airy half space produces three additional modes (6–8) that represent the branch line integral and that have group velocities near $c_{\mathrm{HS}} = 1650$ m/s. The homogeneous modes briefly reach group velocities near c_{HS} just before cutoff.

III. TRANSMISSION LOSS CALCULATIONS

In this section we examine how the choice of half-space profile affects the transmission loss (TL) for the same 40-m-thick Pekeris waveguide described in Sec. II B. As discussed earlier, the Pekeris branch line integral can become important at all ranges when a mode passes near the branch point,

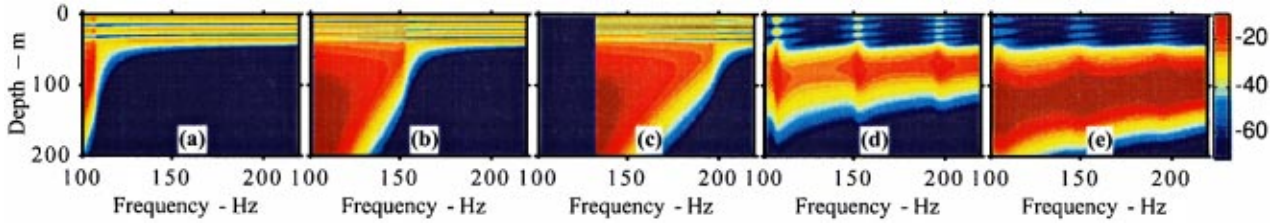

FIG. 6. Mode function magnitudes ($20 \log \phi_n^2$ in dB) imaged versus depth and frequency for a Pekeris waveguide with an Airy half space: (a)–(c) modes 3–5, (d)–(e) branch line modes 1 and 2.

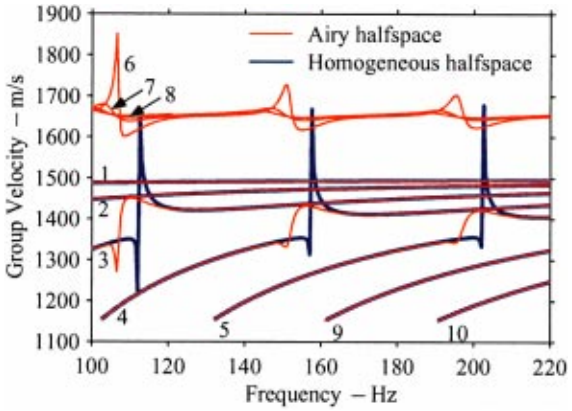

FIG. 7. Dispersion curves for Airy (red) and homogeneous (blue) half spaces.

an event that typically occurs at regular frequency intervals. We examine the frequency interval 105–125 Hz because mode 3 undergoes the trapped–leaky transition near 112 Hz [see Fig. 6(a)].

Figure 8(a) shows TL versus range at 112 Hz for a source at 20-m depth and a receiver on the bottom. The homogeneous half-space results are incorrect because mode 3 is very close to the branch point (its phase speed is 1649.1 m/s, compared to $c_{\mathrm{HS}}=1650$ m/s). The Airy half-space solution agrees closely with the reference OASES[22] solution, which uses a numerical approach to solve the homogeneous half-space problem. The mode solution uses three trapped and ten leaky modes (which correspond closely to those used in the homogeneous half-space solution), as well as eight branch line modes. The gradient for the Airy half space consists of $\Delta\overline{\alpha}=0.001$ [see Eq. (24)].

Figure 8(b) and (c) show images of TL versus range and frequency for the homogeneous half space and for OASES, respectively. (Airy half-space results are indistinguishable from the OASES results and are not shown.) These images illustrate the extent in frequency around the mode 3 transition frequency (112 Hz) where irregularities in the field occur for the homogeneous half space. Finally, a measure of the difference[23] between the OASES reference solution and the homogeneous and Airy half-space solutions are shown in Fig. 8(d) and (e), respectively. The black contour lines indicate the regions where the solutions differ by ± 0.5 dB, and the color map covers ± 3 dB. The differences at short range in Fig. 8(e) (as well as in Figs. 9 and 10 to follow) are apparently caused by OASES' use of the asymptotic expansion for the Hankel function, which breaks down at short range.[24]

From Fig. 8 one may deduce the consequences of ignoring the branch line integral in the case of the Pekeris waveguide being studied. The region of significant error in the homogeneous half-space mode solution is 3–5 Hz wide about 112 Hz, and such regions occur every 45 Hz or so. [Recall from Fig. 5(c) that mode 4 is cut off near 157 Hz.] If only a single continuous wave (cw) calculation in a range-invariant environment is of interest, the probability of encountering a problem with the PBLI is not high, but if a broadband and/or variable-bathymetry computation is of interest, the probability is quite high.

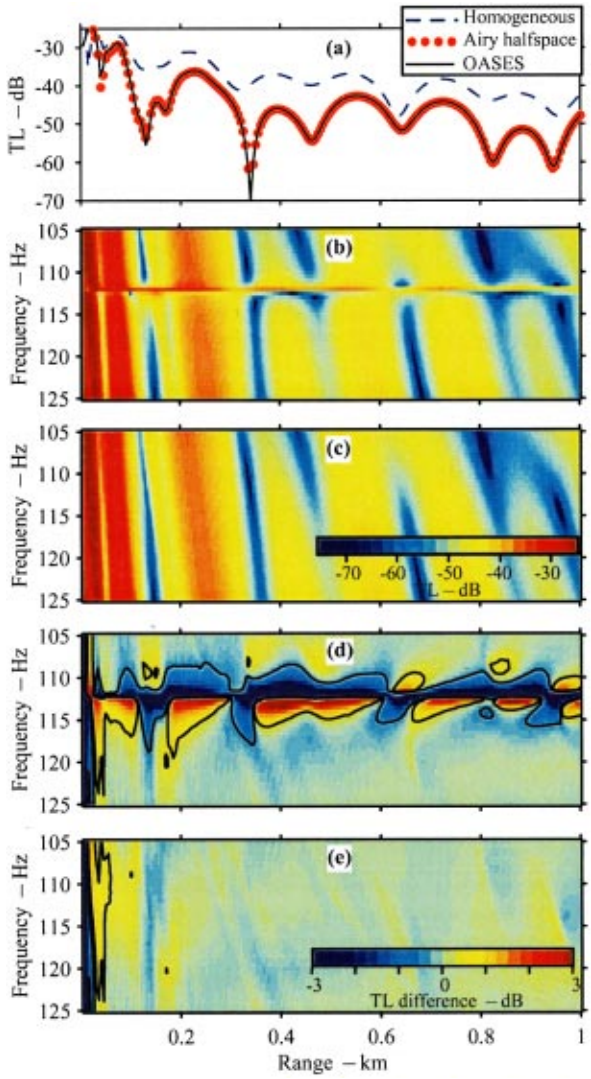

FIG. 8. Transmission loss comparisons for a Pekeris waveguide. (a) TL versus range at 112 Hz; TL versus range and frequency using the homogeneous half-space mode solution (b) and OASES (c); TL differences (Ref. 23) between the reference solution (OASES) and (d) the homogeneous half space mode solution and (e) the Airy half space mode solution.

Attenuation in the lower half space causes the Pekeris branch line integral to become less important. Mathematically, the reason is that the branch point moves farther off the real k axis. Physically, the reason is that the PBLI primarily represents the lateral wave, which, since it travels horizontally in the bottom becomes weaker as the bottom attenuation increases. Therefore, the homogeneous half-space TL errors in Fig. 8(d), which were for a lossless bottom, represent a worst-case scenario. In Fig. 9, results corresponding to Fig. 8(d) for half spaces with attenuations of 0.1, 0.25, and 0.5 dB/λ are shown. It is evident that the effects of the PBLI gradually become insignificant as the attenuation is raised to 0.5 dB/λ. Therefore, the need for introducing an Airy half space depends on environmental factors, one of which is the half-space attenuation.

Finally, a practical concern is the type and magnitude of gradient to insert in the half space. Figure 2 demonstrated how the branch line mode structure depends on gradient direction in the $\Delta\overline{c}-\Delta\overline{\alpha}$ plane. It is clear that a positive,

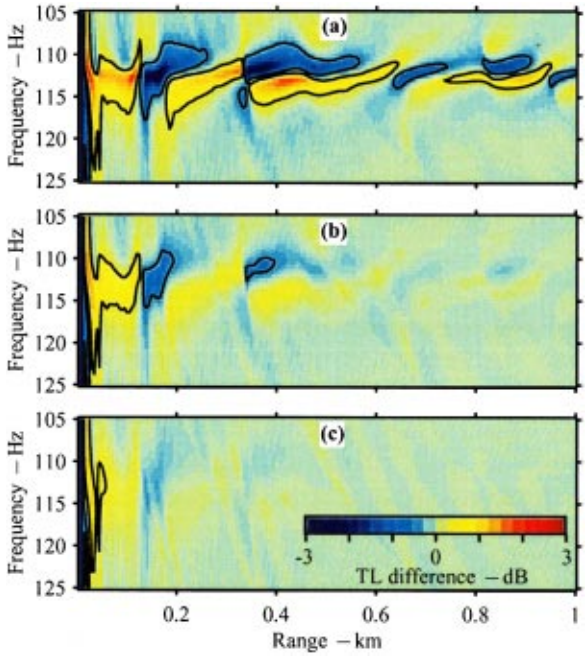

FIG. 9. Transmission loss differences between the homogeneous half-space mode solution and OASES for bottom attenuations of (a) 0.1, (b) 0.25, and (c) 0.5 dB/λ.

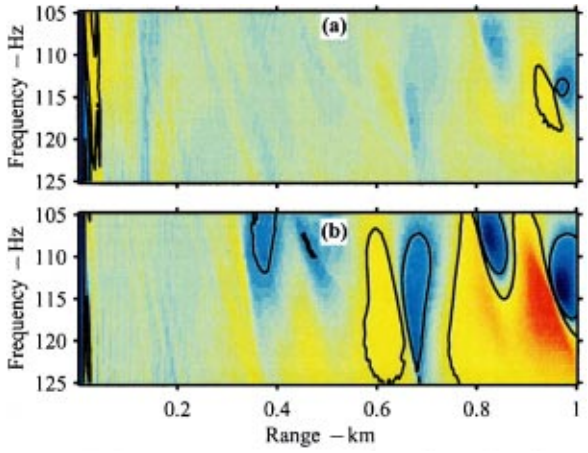

FIG. 10. Transmission loss differences between the OASES solution and Airy half-space mode solutions with gradients of (a) $\Delta\overline{\alpha}=0.002$ and (b) $\Delta\overline{\alpha}=0.010$. Compare with Fig. 8(e), which was for $\Delta\overline{\alpha}=0.001$. The attenuation gradients used here are too large to reproduce the homogeneous half-space model used by OASES.

sound-speed-only gradient is not a good choice because a large number of real-k-axis modes corresponding to the EJP branch cut must be computed. With the objectives of minimizing the number of modes having a given amount of attenuation and preventing the branch line modes from interfering with the trapped and leaky modes, we conclude that both $\Delta\overline{c}=0$, $\Delta\overline{\alpha}>0$ and $\Delta\overline{c}=-\Delta\overline{\alpha}>0$ are good choices. In terms of gradient magnitudes, Fig. 2 demonstrated that larger magnitudes result in fewer modes, but Fig. 10 shows that larger TL errors arise when the gradients are increased to $\Delta\overline{\alpha}=0.002$ and 0.010. [These may be compared to the $\Delta\overline{\alpha}=0.001$ case already shown in Fig. 8(e).] It is clear that the larger gradients produce errors that increase with range as the effect of the bottom becomes greater.

IV. TIME SERIES CALCULATIONS

In this section we illustrate the effect of introducing an Airy half space on a band-limited impulse response. For this purpose we choose the environment given in the inset of Fig. 11, which consists of 10 m of water, a 100-m lossy sand bottom, and a lossless lower half space [see inset to Fig. 11(a)]. We consider a pulse with a center frequency of 50 Hz and 20-dB-down points at 10 and 100 Hz. At 50 Hz no modes are trapped in the water column, and the modes trapped in the sand layer have large attenuations. Under these conditions, the best propagation mechanism at the longer ranges is the multiply reflected lateral wave, or head wave, in the lossless lower half space. (This type of situation could also arise in seismological applications, where a layer of lossy soil overlies a low-loss basement of limestone or basalt.)

Figure 11 shows the range-dependent pressure time series for a source and receiver on the bottom, where the time series have been (1) normalized to unit maximum amplitude at each range, and (2) shifted in time assuming a group speed of 1650 m/s. Figure 11(a) was produced using an Airy half space with a gradient corresponding to $\Delta\overline{\alpha}=0.001$, and Fig. 11(b) was produced using a homogeneous half space. The three primary propagation paths through the water, the sand layer, and the lower half space are labeled in (a), and the slopes corresponding to three propagation speeds are labeled in (b). Note that the water wave consists of the high-frequency portion of the source pulse because mode 1 is only trapped in the water layer at frequencies above 93 Hz. The sand wave, which would appear as vertical stripes because the speed used to shift the time series is 1650 m/s, is attenuated beyond 1 km.

The main difference between Fig. 11(a) and (b) is the appearance of the lateral wave arrivals. In Fig. 11(a), multiple orders of lateral waves in a quiescent background are clearly discernible, whereas in 11(b) a continuous set of ar-

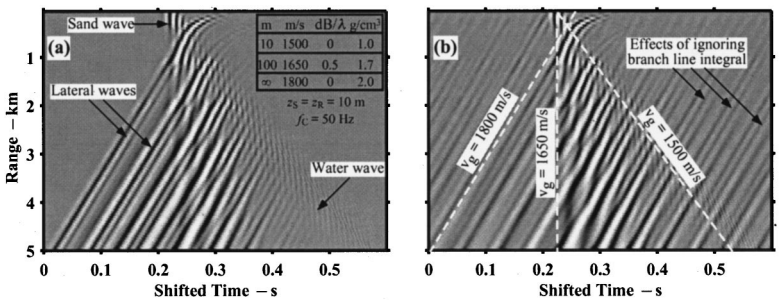

FIG. 11. Normalized pressure time series versus range for a 50-Hz pulse in 10 m of water with a 100-m lossy sand bottom layer and a lossless lower half space: (a) using an Airy half space with $\Delta\overline{\alpha}=0.001$, and (b) using a homogeneous half space. Use of the Airy half space correctly accounts for the multiply reflected lateral wave energy.

rivals, some of which are noncausal, overlies the others. Clearly, the inclusion of the branch line integral by way of the Airy half-space modes in (a) produces the correct lateral wave behavior. In (a) it is interesting to note that as the number of reflections through the attenuating sand layer increases, the frequency content of the lateral wave arrivals appears to shift downward.

V. SUMMARY

In this paper we have developed, analyzed, and implemented (in the normal-mode model ORCA) a method for eliminating the branch line integral in the normal-mode formulation for the pressure field in an oceanic waveguide. The homogeneous half space is replaced by one having a (complex) sound-speed gradient that is linear in wave number squared. The reflection coefficient is evaluated analytically in terms of Airy functions, and the branch line integral is replaced by a set of modes whose trajectory and spacing in the complex k plane depend on the magnitude and direction of the complex gradient. For a small, positive sound-speed gradient, the branch line modes correspond to the former EJP branch cut, which lies on the real k axis from K_{HS} to the origin and upward along the imaginary k axis. For a small, positive attenuation gradient, the branch line modes lie on a line that leaves the former branch point K_{HS} vertically and that corresponds approximately to the former Pekeris branch cut. The total number of modes is minimized by the latter choice of gradient, in which case the modal spectrum consists of a finite number of trapped modes and infinite numbers of leaky and branch line modes. Except when a mode lies near the former branch line, the trapped and leaky modes for a small-gradient Airy half space correspond closely with those for a homogeneous half space. Larger gradients result in fewer branch line modes, but errors in the pressure field can occur at long ranges if the gradient chosen is too large.

Modes for the Airy half-space problem are found using the same method as that used in the ORCA normal-mode model: the upward- and downward-looking reflection coefficients are computed at a reference depth, and the $|R_1R_2| = 1$ contour is followed in the complex k plane.[20] The usual trapped and leaky modes are found by placing the reference depth in the water column. The branch line modes, which appear as island modes for the usual choice of reference depth, are found on the main $|R_1R_2|=1$ contour when the reference depth is set to the top of the lower half space.

Characteristics of the branch line modes, such as the frequency dependence of their eigenvalues, depth functions, and group velocities, have been examined. The behavior is consistent with the notion that the branch line modes represent the resonant behavior of the lateral wave component of the field: the eigenvalues of the branch line modes correspond to energy near the critical angle; their mode functions are large in the half space and peak up in the water column only when a trapped mode passes below them in the complex k plane; and their group velocities lie near the half-space sound speed.

Broadband calculations using Airy half spaces were presented in both the frequency and time domains. Images of TL versus range and frequency demonstrated that the branch line modes become significant at frequencies where a mode is near the former branch point. For the Pekeris waveguide examined, the frequency interval over which the branch line modes were significant was 3–5 Hz, and these intervals occurred every 45 Hz. Introduction of attenuation in the lower half space reduced the importance of the branch line modes. Finally, images of time series versus range for an environment in which lateral waves were the primary mechanism of propagation showed that the Airy half space accurately accounted for the lateral waves. The effects of ignoring the branch line integral on a time series were also demonstrated.

The Airy half-space approach should also be useful for range-dependent normal-mode calculations based on adiabatic- or coupled-mode theory. Mode cutoff due to decreasing frequency is analogous to mode cutoff due to decreasing water depth, for example. Adiabatic treatment of the problem would be best achieved by keeping track of the branch line modes separately so that a trapped mode passing through cutoff transfers its energy to a leaky mode, rather than to a branch line mode. In reality, we would expect some degree of coupling at such a transition because the mode function of the trapped/leaky mode has a shape similar to those of the branch line modes. Another attractive aspect of the Airy half-space approach for coupled-mode calculations is that the leaky modes eventually decay with depth, making the overlap integrals well defined. If the integrals can be solved analytically using Airy function identities, then the coupling calculations would be very efficient.

Although the examples of the Airy half-space approach given in this article have involved fluid environments, the approach can also be applied to elastic layering. A small gradient in the shear wave profile of the lower half space would replace the shear wave BLI with a set of branch line modes. When the half-space shear speed is lower than the water sound speed, the modes would not be important to the water column field, but when it is higher they could be. ORCA currently finds the nonbranch line modes for elastic problems, but to find the branch line modes, the reference depth would have to be set inside an elastic layer. This would require the implementation of an eigenvalue criterion more complicated than the $R_1R_2=1$ criterion currently used for fluid reference depths.

Although the Airy half-space approach eliminates the discontinuity in R_1R_2 at the branch cut, some of the inconveniences of the branch cut can remain. For environments with lossy sediment layers over a low-loss homogeneous half space, for example, the $|R_1R_2|=1$ contour can intersect the branch cut from the right and emerge to the left at a point displaced vertically. Using the Airy half-space approach, the cut is replaced by a series of modes, and the $|R_1R_2|=1$ contour follows the former cut, picking up a (possibly large) set of branch line modes before emerging to the left. As a trapped mode moves to the left (as frequency or water depth is decreased, for example), it joins the branch line series. At nearly the same frequency or water depth, a mode farther up the branch line series suddenly emerges and becomes a leaky mode. This type of behavior makes interpolation of mode characteristics across frequency or bathymetry more difficult.

ACKNOWLEDGMENTS

This work was supported by ONR 321. The authors also thank M. Hall and the reviewers for bringing several pertinent references to their attention.

APPENDIX: BRANCH CUTS AT THE REFERENCE DEPTH

Note that in Eq. (11) for R_1, besides the branch point from γ_{HS}, a branch point also arises from the calculation of γ_{ref}. This fact is disconcerting because no interface waves should arise from the arbitrary choice of reference depth. Here we show that these cuts do not contribute to the field.

First we show that the choice of sheet for γ_{ref} does not affect the location of the modes or their normalization. From Eq. (11) it is clear that $R_{1-}(\gamma)=[R_{1+}(\gamma)]^{-1}$, where the $\pm$ subscript indicates the sheet on which γ_{ref} is evaluated. It follows that, for $I\equiv R_1R_2$, $I_-(\gamma)=[I_+(\gamma)]^{-1}$. Therefore, $I_+(\gamma)=1$ implies that $I_-(\gamma)=1$, which means that a mode on the $+$ sheet is also a mode on the $-$ sheet. In addition, it is straightforward to show that the term $[\partial W/\partial k]_{k_n}$ that appears in the normalization in Eq. (10) is the same on both sheets.

Next we show that the branch line integral around the γ_{ref} cut is zero. In Eqs. (3) and (5) of Ref. 20, it is shown that ϕ_- and ϕ_+ in the numerator of Eq. (5) of this paper are proportional to $1+R_2$ and $1+R_1$, respectively. From Eq. (8), W is proportional to $\gamma_{\mathrm{ref}}(1-R_1R_2)$. Using the fact that a change of sheet implies inverting R_1 and R_2 and negating γ_{ref}, the integrand of Eq. (5) for the two sheets, J_+ and J_-, may then be written

$$J_+=\frac{(1+R_1)(1+R_2)}{\gamma_{\mathrm{ref}}(1-R_1R_2)}, \tag{A1}$$

$$J_-=\frac{(1+1/R_1)(1+1/R_2)}{-\gamma_{\mathrm{ref}}[1-1/(R_1R_2)]}=J_+, \tag{A2}$$

where the final identity was obtained by multiplying numerator and denominator by R_1R_2. Since the BLI consists of a sum of line integrals on opposite sheets in opposite directions, the integrands being identical implies $C_{\mathrm{BLI}}=0$ for the γ_{ref} cut.

[1] C. L. Pekeris, ''Theory of propagation of explosive sound in shallow water,'' Geol. Soc. Am. Mem. **27** (1948).
[2] W. M. Ewing, W. S. Jardetzky, and F. Press, *Elastic Waves in Layered Media* (McGraw-Hill, New York, 1957), pp. 126–151.
[3] D. C. Stickler, ''Normal-mode program with both the discrete and branch line contributions,'' J. Acoust. Soc. Am. **57**, 856–861 (1975).
[4] C. L. Bartberger, ''Comparison of two normal-mode solutions based on different branch cuts,'' J. Acoust. Soc. Am. **61**, 1643 (1977).
[5] H. P. Bucker, ''Propagation in a liquid layer lying over a liquid half space (Pekeris cut),'' J. Acoust. Soc. Am. **65**, 906–908 (1979).
[6] C. T. Tindle, A. T. Stamp, and K. M. Guthrie, ''Virtual modes and the surface boundary condition in underwater acoustics,'' J. Sound Vib. **49**, 231–240 (1976).
[7] C. T. Tindle, A. T. Stamp, and K. M. Guthrie, ''Virtual modes and mode amplitudes near cutoff,'' J. Acoust. Soc. Am. **65**, 1423–1428 (1979).
[8] D. C. Stickler, ''Uniform asymptotic evaluation of the continuous spectrum contribution for the Pekeris model,'' J. Acoust. Soc. Am. **67**, 2018–2024 (1980).
[9] V. Maupin, ''The radiation modes of a vertically varying half-space: A new representation of the complete Green's function in terms of modes,'' Geophys. J. Int. **126**, 762–780 (1996).
[10] Despite the fact that leaky modes are unbounded in the lower half space, leaky modes are certainly useful because they are well-behaved inside the waveguide. Deep in the half space, where the total field must be small, the large field produced by the unbounded leaky modes is counteracted by a large field due to the PBLI. Haddon (Refs. 11 and 12) has developed a method for computing the pulse response of a waveguide using complex *frequencies*, as well as wave numbers, and has shown that the leaky modes become well-behaved.
[11] R. A. W. Haddon, ''Exact evaluation of the explosive response of a layered elastic medium to an explosive point source using leaking modes,'' Bull. Seismol. Soc. Am. **76**, 1755–1775 (1986).
[12] R. A. W. Haddon, ''Response of an oceanic waveguide to an explosive point source using leaking modes,'' Bull. Seismol. Soc. Am. **77**, 1804–1822 (1987).
[13] C. A. Boyles, *Acoustic Waveguides* (Wiley, New York, 1984).
[14] L. Brekhovskikh, *Waves in Layered Media*, 2nd ed. (Academic, New York, 1980).
[15] M. A. Pedersen and D. F. Gordon, ''Normal-mode theory applied to short-range propagation in an underwater acoustic surface duct,'' J. Acoust. Soc. Am. **37**, 105–118 (1965).
[16] M. A. Pedersen and D. F. Gordon, ''Theoretical investigation of a double family of normal modes in an underwater acoustic surface duct,'' J. Acoust. Soc. Am. **47**, 304–326 (1969).
[17] M. A. Pedersen and D. F. Gordon, ''Normal-mode and ray theory applied to underwater acoustic conditions of extreme downward refraction,'' J. Acoust. Soc. Am. **51**, 323–368 (1972).
[18] M. Hall, ''Normal mode theory: The role of the branch-line integral in Pederson–Gordon type models,'' J. Acoust. Soc. Am. **72**, 1978 (1988).
[19] F. B. Jensen, W. A. Kuperman, M. B. Porter, and H. Schmidt, *Computational Ocean Acoustics* (American Institute of Physics, New York, 1994).
[20] E. K. Westwood, C. T. Tindle, and N. R. Chapman, ''A normal mode model for acousto-elastic ocean environments,'' J. Acoust. Soc. Am. **100**, 3631–3645 (1996).
[21] For more complicated layering structures the branch cuts associated with the vertical wave numbers for the lower half space and reference depth remain in the functional behavior of R_1, but those in intermediate layers are cancelled out by intermediate operations.
[22] H. Schmidt and F. B. Jensen, ''A full wave solution for propagation in multilayered viscoelastic media with application to Gaussian beam reflection at fluid–solid interfaces,'' J. Acoust. Soc. Am. **77**, 813–825 (1985).
[23] TL differences in dB, defined as $20\log_{10}(p/p_{\mathrm{ref}})$, can be misleading when deep nulls exist. For example, a 3-dB difference at a null that is 20-dB below the surrounding values is less significant than a 3-dB difference at a relative peak. For this reason, the TL differences in Fig. 8 are defined as $\mathrm{TL}_{\mathrm{dif}}=20\log_{10}[(p-p_{\mathrm{ref}}+p_{\mathrm{avg}})/p_{\mathrm{avg}}]$, where p_{avg} is a range-averaged pressure. When $p\approx p_{\mathrm{ref}}\approx p_{\mathrm{avg}}$ the two definitions are the same. But for a 3-dB difference in a 20-dB null, the new definition results in a 0.35-dB difference.
[24] The option in OASES to refrain from using the asymptotic representation for the Bessel function is available in the broadband pulse module OASP, but not in the TL module OAST. Attempts by the authors to extract the correct single-frequency TL from the OASP module were not successful, apparently because of convergence problems. The validity of ORCA at short range was checked by placing the receiver 1 m from the source and verifying that the TL was approximately 0 dB, as was done for Fig. 5 of Ref. 20.

A self-consistent theory for seabed volume scattering

Brian H. Tracey[a] and Henrik Schmidt
Department of Ocean Engineering, Massachusetts Institute of Technology, Cambridge, Massachusetts 02139

(Received 20 April 1998; accepted for publication 8 July 1999)

A self-consistent perturbation method for three-dimensional acoustic scattering due to sound speed and density fluctuations is developed below. This method allows calculation of mean-field attenuation due to scattering, as well as second-moment statistics of the scattered field. Scattering from an inhomogeneous sediment bottom in shallow water is considered as an application. The power spectral density of the scattered field is calculated and used to study the effects of fluctuation statistics. Modal attenuation due to scattering is then calculated for several shallow-water scenarios. The scattering loss calculation is straightforward and is suitable for use with standard normal-mode codes. Numerical results show the influence of the statistical model used to represent bottom randomness and demonstrate the importance of scattering into the continuous spectrum. Scattering loss predictions are shown to agree well with a previous wave number-integration approach. [S0001-4966(99)04610-X]

PACS numbers: 43.30.Bp, 43.30.Ft, 43.30.Gv [DLB]

INTRODUCTION

Volume fluctuations in the ocean are known to strongly affect acoustic propagation. In deep water, the strongest effects come from oceanographic mixing and internal waves, while in shallow water, interaction with the inhomogeneous ocean bottom is generally more important. In seawater, density fluctuations are generally an order of magnitude smaller than sound-speed variations, and can be neglected.[1] As a result, a large amount of research has addressed scattering by sound-speed variations only, and has been applied to modeling the effects of internal waves.[2–4] When seabed scattering is considered, however, density fluctuations cannot be neglected and are often dominant.[5,6] Scattering from seabed sound-speed and density fluctuations has two main effects; first, energy is stripped from the coherent part of the acoustic field, and second, the scattered energy affects the acoustic field coherence. The theory developed here attempts to capture both effects.

Chernov[1] and Ishimaru[7] have published well-known treatments of propagation through an unbounded random media. Different approaches are appropriate depending on the scale of fluctuations in the medium. If variations in medium properties are small, a perturbation solution can be sought. This work has been extended to study sound incident from a water half-space on a sediment bottom containing random layers. The half-space problem neglects waveguide effects, which is justified for deep water or for high-frequency shallow-water scenarios. Volumetric scattering from within the bottom can be modeled by assuming the scattering sources are uncorrelated uniform spheres.[8,9] Several authors have developed perturbation approaches based on Chernov's work. Ivakin and Lysanov[10] used a plane wave approach which did not include contributions from lateral waves, while Hines[6] used the method of steepest descent to capture lateral as well as refracted wave contributions. Tang[11] developed a self-consistent perturbation theory to model scattering from sound-speed fluctuations in the sediment. Tang was able to calculate a coherent field-reflection coefficient which included loss due to scattering.[12]

More recently, attention has been focused on the role of bottom randomness in influencing propagation in shallow water waveguides. Tang has developed a modal treatment of reverberation due to both sound-speed and density fluctuations.[13] However, this work is based on the Born approximation and does not allow calculation of mean-field scattering loss.

In this paper, we develop a new, self-consistent theory for modeling volume scattering in the ocean. The methodology used is similar to the rough surface scattering approach of Kuperman and Schmidt.[14,15] In the first section, the basic theory for scattering from random sound-speed and density fluctuations in a three-dimensional ocean is presented. Sound-speed and density fluctuations are assumed to be fully correlated. This work allows calculation of the mean-field attenuation due to volume scattering, as well as the spatial statistics of the scattered field.

The approach presented below is a single-scattering theory. Since waveguide propagation is expected to involve multiple scattering events, a single-scatter theory is clearly not exact. However, Voronovich[16] and others[17,18] have argued that the single-scatter approximation is valid as long as the scatterer correlation length is small compared to ray cycle distances associated with propagating modes. In this case, which is typical for many ocean acoustic scenarios, previously scattered energy will be incoherent with both the mean and locally scattered fields when it returns to the inhomogeneous seabed. The scattering process can then be approximated as a series of uncorrelated interactions with the seabed, with single-scattering theory used to calculate secondary source terms for the reverberant field.

This argument is supported by Berman[19] with regard to calculation of the coherent field-reflection coefficient. Berman compared a full multiple-scattering formulation for

[a]Currently at Cambridge Collaborative, Inc., 689 Concord Ave., Cambridge, MA 02138. Electronic mail: btracey@ccinc.com

waveguides with results for a rough interface separating two half-spaces. Some dependence on roughness height was seen, but significant multiple-scattering effects were found only when the roughness correlation length was long compared to ray cycle distances. Because the coherent field-reflection coefficient can be used to calculate scattering loss, Berman's finding relates directly to the validity of the mode attenuations calculated below.

Recently, Berman has developed a multiple-scattering formulation to derive waveguide reverberation.[20] This work may provide a basis for numerically evaluating the single-scattering approximation for scattered field intensity.

The following sections concentrate on scattering of low-frequency sound from random layers in fluid sediment bottoms. First, we model the scattering from a plane wave incident on the ocean bottom, without taking waveguide effects or mean-field attenuation into account. Numerical examples are used to show the effects of sound-speed and density fluctuations over a range of parameter values. For short correlation lengths, the existence of density fluctuations can significantly enhance backscatter. The examples also show that out-of-plane scattering can be important.

Next, propagation of normal modes in a shallow-water waveguide is studied. A perturbation method is used to estimate mean-field normal mode attenuation coefficients due to scattering. Good agreement is demonstrated with mean-field losses calculated by Tang,[12] though results obtained from the modal approach are somewhat sensitive to the modeling of the continuous spectrum.

Finally, the theory developed here can be used to calculate the spatial correlation and cross-modal coherences for the scattered and total fields propagating in the ocean waveguide. A numerical implementation of the volume-scattering theory for a two-dimensional ocean is described elsewhere.[21,22] The close correspondence between the volume-scattering theory and Kuperman and Schmidt's rough-scattering theory facilitates comparison of the different scattering mechanisms.

I. THEORY

The wave equation for inhomogeneous medium has been derived by several authors, including Chernov.[1] Assuming harmonic time dependence, we write the inhomogeneous Helmholtz equation

$$[\nabla^2 + k^2(\mathbf{r},z)]p(\mathbf{r},z) - \frac{\nabla\rho(\mathbf{r},z)}{\rho(\mathbf{r},z)} \cdot \nabla p(\mathbf{r},z) = S_\omega \delta(\mathbf{x}-\mathbf{x}_s), \tag{1}$$

where a point source of strength S_ω located at $x_s=(0,0,z_s)$. We assume that there are small variations in both density and sound speed. In addition, we assume that variations in the sound speed and density are linked. Following Hines,[6] sound speed and density are then written as functions of the bottom *porosity* P.[6] If the background density is constant, we can write

$$c(\mathbf{r},z) = c_0(z) + \frac{\partial c}{\partial P}\,\delta P(\mathbf{r},z),$$

$$\rho(\mathbf{r},z) = \rho_0 + \frac{\partial \rho}{\partial P}\,\delta P(\mathbf{r},z), \tag{2}$$

where δP is the variation in the bottom porosity. Hines gives empirical values of the derivatives to be $\partial\rho/\partial P = -1.440\ \mathrm{g/cm^3}$ and $\partial c/\partial P = -570\ \mathrm{m/s}$. Next, we expand the pressure field in terms of a coherent mean field and an incoherent diffusely scattered field

$$p(\mathbf{r},z) = \langle p(\mathbf{r},z)\rangle + s(\mathbf{r},z). \tag{3}$$

Inserting this expansion in Eq. (1) above and averaging (remembering that sound-speed and density fluctuations are zero mean) gives an equation for the coherent field

$$[\nabla^2 + k_0^2(z)]\langle p(\mathbf{r},z)\rangle - \mu_c(z)\langle \delta P(\mathbf{r},z) s(\mathbf{r},z)\rangle - \mu_\rho \langle \nabla\,\delta P(\mathbf{r},z)\cdot\nabla s(\mathbf{r},z)\rangle = S_\omega \delta(\mathbf{x}-\mathbf{x}_s), \tag{4}$$

where the quantities

$$\mu_c(z) \equiv \frac{2k_0^2(z)\,\partial c/\partial P}{c_0(z)}, \quad \mu_\rho \equiv \frac{1}{\rho_0}\frac{\partial\rho}{\partial P}, \tag{5}$$

have been introduced to simplify the notation.

Subtracting this equation from the full unaveraged Helmholtz equation, we find an expression for the scattered field

$$[\nabla^2 + k_0^2(z)]s(\mathbf{r},z) = \mu_c(z)\,\delta P(\mathbf{r},z)\langle p(\mathbf{r},z)\rangle + \mu_\rho \nabla(\delta P(\mathbf{r},z))\cdot\nabla\langle p(\mathbf{r},z)\rangle. \tag{6}$$

In deriving this equation, we have made a single-scatter approximation by neglecting several terms involving products of the scattered field and the porosity fluctuations. This assumes that the scattered field produced during each scattering event is small. This equation is equivalent to Hines' Eq. (2). As discussed in the Introduction, single-scatter theory can be applied to waveguide propagation under the assumption that seabed inhomogeneity correlation lengths are much shorter than length scales over which scattered energy returns to the seabed (i.e., ray cycle distances).

The first term on the right-hand side above accounts for scattering generated by sound-speed fluctuations, and is monopole-like. The second term, which represents scattering from density fluctuations, will be shown below to enhance backscattering.

Our solution proceeds in a manner analogous to that of Kuperman and Schmidt. First, the equations above are Fourier transformed to yield expressions in the form of the depth-separated wave equation. We then find a solution for the transformed scattered field $\tilde{s}$ in terms of the coherent field. This solution is substituted into the transformed version of Eq. (4) to give a self-consistent equation for the coherent field. This equation takes into account the loss of coherent field energy due to scattering.

We begin by applying the 2-D wave number transform as defined in Ref. 15. Recognizing the right-hand side of Eq. (6) to be a source term distributed over depth, we can write the scattered field as (see Appendix A for details)

$$\tilde{s}(\mathbf{q},z) = -\int\int dz_0\, d\mathbf{k}'\, G_\omega(\mathbf{q},z,z_0)\Big[b_1(q,k') \times \widetilde{\delta P}(\mathbf{q}-\mathbf{k}',z)\langle \tilde{p}(\mathbf{k}',z_0)\rangle + \mu_\rho \frac{\partial \widetilde{\delta P}(\mathbf{q}-\mathbf{k}',z_0)}{\partial z_0}\frac{\partial\langle \tilde{p}(\mathbf{k}',z_0)\rangle}{\partial z_0}\Big], \tag{7}$$

where

$$b_1(q,k) = \mu_c(z_0) - \mu_\rho(\mathbf{q}-\mathbf{k})\cdot\mathbf{k}. \tag{8}$$

The horizontal derivatives in the density term have become algebraic factors of k and q.

Similarly, we can transform the mean-field equation, giving (see Appendix A)

$$[L(\mathbf{k}) + I(\mathbf{k},z)]\langle \tilde{p}(\mathbf{k},z)\rangle = S_\omega \delta(z-z_s), \tag{9}$$

where the operator

$$L(\mathbf{k}) = \frac{\partial^2}{\partial z^2} + k_0^2(z) - \mathbf{k}^2 \tag{10}$$

is the standard propagation operator for the depth-separated wave equation, and the scattering loss term

$$I(\mathbf{k},z) = -\frac{1}{2\pi}\int d^2\mathbf{q}\Big[a_1\langle \widetilde{\delta P}(\mathbf{k}-\mathbf{q},z)\tilde{s}(\mathbf{q},z)\rangle + \mu_\rho\Big\langle \frac{\partial \widetilde{\delta P}(\mathbf{k}-\mathbf{q},z)}{\partial z}\frac{\partial \tilde{s}(\mathbf{q},z)}{\partial z}\Big\rangle\Big] \tag{11}$$

describes scattering out of the mean-field wave number k into scattered-field wave numbers q as a function of depth. Equations (7) and (9) are combined to eliminate the scattered-field variable $\tilde{s}$, giving an equation involving only the coherent field $\langle\tilde{p}\rangle$. This substitution results in several second-moment expectations of the porosity fluctuations and their z-derivatives. We model the fluctuation statistics as being described by a correlation function which is separable into horizontal and vertical components

$$\langle \delta P(\mathbf{r},z)\,\delta P(\mathbf{r}+\boldsymbol{\rho},z_0)\rangle = \langle\sigma^2\rangle N(\mathbf{p}) M(z-z_0). \tag{12}$$

This is rewritten in the wave number domain as

$$\langle \widetilde{\delta P}(\mathbf{k},z)\widetilde{\delta P}(\mathbf{q},z_0)\rangle = 2\pi\langle\sigma^2\rangle P_H(\mathbf{q})\,\delta(\mathbf{k}+\mathbf{q})M(z-z_0), \tag{13}$$

where P_H is the power spectrum of horizontal fluctuations. Vertical derivatives of expectations involving δP translate into z-derivatives of M, which can be eliminated from the depth integrals using integration by parts. The detailed calculations are shown in Appendix B. The only restrictions placed on M are that $M(z-z_0)\to 0$ and and $\partial M(z-z_0)/\partial z \to 0$ as the depth separation $z-z_0$ becomes large. These conditions are satisfied by a number of physically reasonable correlation functions, for example Gaussian or decaying exponential forms of $M(z-z_0)$.

After the integrations by parts, the final form of the scattering loss correction term is

$$I(\mathbf{k},z) = \Big[F_1(\mathbf{q},\mathbf{k},z_0)\langle\tilde{p}(\mathbf{k},z_0)\rangle + F_2(\mathbf{q},\mathbf{k},z_0)\frac{\partial\langle\tilde{p}(\mathbf{k},z_0)\rangle}{\partial z_0}\Big]. \tag{14}$$

The quantities in the correction term are

$$F_1(\mathbf{q},\mathbf{k},z_0) = a_1 a_2 G_\omega(\mathbf{q},z,z_0) + \mu_\rho\Big[a_3\frac{\partial^2 G_\omega(\mathbf{q},z,z_0)}{\partial z\,\partial z_0} - a_4\frac{\partial G_\omega(\mathbf{q},z,z_0)}{\partial z}\Big], \tag{15}$$

and

$$F_2(\mathbf{q},\mathbf{k},z_0) = \mu_\rho(a_3-a_1)\frac{\partial G_\omega(\mathbf{q},z,z_0)}{\partial z_0}, \tag{16}$$

where

$$\begin{aligned} a_1 &= \mu_c(z_0) - \mu_\rho(\mathbf{k}-\mathbf{q})\cdot\mathbf{q},\\ a_2 &= \mu_c(z_0) + \mu_\rho(k_0^2 - \mathbf{q}\cdot\mathbf{k}),\\ a_3 &= \mu_c(z_0) + \mu_\rho(2k_0^2 - \mathbf{k}\cdot(\mathbf{k}+\mathbf{q})),\\ a_4 &= \frac{2\mu_\rho k_0^2(z_0) + 3\mu_c(z_0)}{c_0(z_0)}\frac{\partial c_0}{\partial z_0}. \end{aligned} \tag{17}$$

The algebraic terms multiplying the μ_ρ terms in a_1-a_3 result from horizontal and vertical derivatives. All terms including z-derivatives of the pressure field or Green's function also involve only the density fluctuations. These terms result from the spatial derivative term, $\Delta\rho(\mathbf{r},z)/\rho(\mathbf{r},z)$, in the inhomogeneous Helmholtz equation. The term a_4 takes account of any sound-speed gradient in the seabed.

This integro-differential equation is in general difficult to solve. However, experimental studies have shown that the vertical correlation lengths of fluctuations in sediment bottoms are usually quite short. For low frequencies, the vertical correlation length will be much smaller than an acoustic wavelength. It is then reasonable to approximate the vertical correlation function as a delta function[11]

$$M(z-z_0) \approx z_{\mathrm{CL}}\,\delta(z-z_0). \tag{18}$$

This delta function eliminates the depth integral in the mean-field equation. A perturbation solution can be used to estimate mean-field scattering loss, as detailed in Sec. III.

II. PLANE WAVE SCATTERING FROM SEDIMENT BOTTOMS: POWER SPECTRAL DENSITY

As a first application of the theory, we study plane wave scattering from a sediment bottom. A great deal of physical insight can be obtained by looking at the power spectral density $\langle\tilde{s}(\mathbf{q},z)\tilde{s}^*(\mathbf{q},z)\rangle$, the power scattered into each wave number q. This expectation includes cross-terms involving expectations of M and its z-derivatives, which can be simplified using integration by parts as above. The detailed calculations are discussed in Appendix A, with the final result

$$P_{\mathrm{Scat}}(\mathbf{q},z)=\langle \tilde{s}(\mathbf{q},z)\tilde{s}^{*}(\mathbf{q},z)\rangle$$
$$=2\pi\langle\sigma^{2}\rangle\int dz_{0}\int d\mathbf{k}P_{H}(\mathbf{q}-\mathbf{k})$$
$$\times\left|\Delta^{(1)}\frac{\partial G_{\omega}(\mathbf{q},z,z_{0})}{\partial z_{0}}+\Delta^{(2)}G_{\omega}(\mathbf{q},z,z_{0})\right|^{2}, \tag{19}$$

where

$$\Delta^{(1)}(\mathbf{k},z)=-\mu_{\rho}\frac{\partial\langle\tilde{p}(\mathbf{k},z)\rangle}{\partial z}$$
$$\Delta^{(2)}(\mathbf{q},\mathbf{k},z)=a_{2}(\mathbf{q},\mathbf{k},z)\frac{\partial\langle\tilde{p}(\mathbf{k},z)\rangle}{\partial z}. \tag{20}$$

We consider the case of a single plane wave incident on the sediment from the water column and scattering into plane waves in the sediment. As we are mainly concerned with angular distribution of the scattered energy, we will defer calculation of mean-field scattering loss until the next section. Ignoring scattering losses (the Born approximation), the coherent field is replaced by the unperturbed field: $\langle\tilde{p}(\mathbf{k},z)\rangle\approx\tilde{p}_{0}(\mathbf{k},z)$. The incident field in the bottom is then of the form

$$\tilde{p}_{0}(\mathbf{k},z_{0})=T_{12}(k)e^{-ik_{z2}z_{0}}, \tag{21}$$

where $T_{12}(k)$ is the transmission coefficient from the water into the sediment. We choose the Green's function to be the free-space Green's function. Thus, we can only evaluate the scattered field for receivers in the bottom medium. We will evaluate it at $z=0$, the water–sediment interface. The depth-dependent Green's function is given by

$$G_{\omega}(\mathbf{q},z,z_{0})=-\frac{e^{-iq_{z2}|z-z_{0}|}}{4\pi iq_{z2}}. \tag{22}$$

The square root singularity in the Green's function is not physically meaningful and can be removed by changing the variables of integration,[23] so it is not shown in the following plots.

The scattered field is strongly affected by the power spectrum chosen to represent the inhomogeneities. For these calculations, both two-dimensional Gaussian and Goff–Jordan[24] spectra are used

$$P_{\mathrm{Gauss}}(\mathbf{q})=\frac{L_{x}L_{y}}{2}e^{-[(L_{x}q_{x})^{2}+(L_{y}q_{y})^{2}]/4},$$
$$P_{\mathrm{Goff-Jordan}}(\mathbf{q})=\frac{L_{x}L_{y}}{[(L_{x}q_{x})^{2}+(L_{y}q_{y})^{2}+1]^{2}}, \tag{23}$$

where L_x and L_y are the correlation lengths in x and y, respectively. The Goff–Jordan spectrum is more peaked near its maximum and contains much more energy at higher wave numbers. This spectrum has been used in modeling rough-surface scattering,[18] and is chosen to reflect the idea that we expect variations in nature at many length scales. Also, it describes a power-law roll-off at high wave numbers like those measured by Yamamoto.[25]

Figures 1–5 show scattered-field power spectral density (PSD) for several scenarios. The spectra are plotted versus horizontal wave numbers in the x and y directions. A 100-Hz plane wave is assumed to be incident on the bottom along the x-axis ($q_y=0$), at a 10-deg vertical angle. The bottom properties are $\rho=1.9\ \mathrm{g/cm^3}$, $c_b=1650$ m/s, and $\delta c/c_0=0.1$. For this combination of incident angle and bottom type, the incident wave is evanescent in the bottom. Shown on the plot are the sediment wave number k_b (inner circle) and water wave number k_w (outer circle). Wave numbers inside the $|k|=k_b$ circle correspond to the continuous spectrum, wave numbers between the circles correspond to the discrete spectrum, and wave numbers outside the $|k|=k_w$ circle correspond to waves which are evanescent in both the water and sediment.

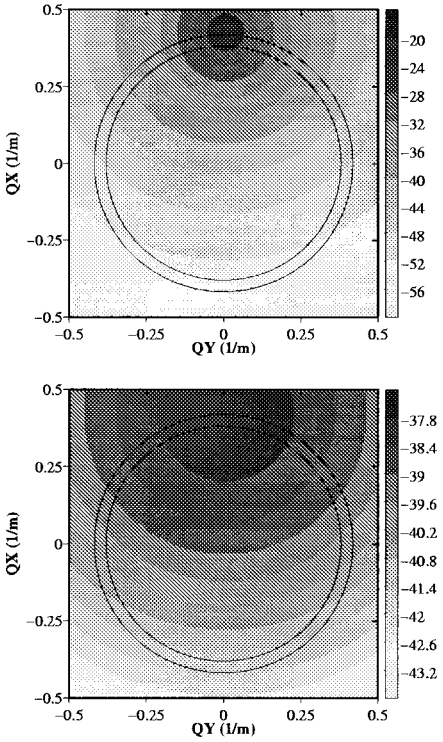

FIG. 1. Plane wave scattering from sound-speed fluctuations only. $f=100$ Hz; Goff–Jordan power spectrum, 10-deg incident wave; correlation lengths of 10 m (upper) and 1 m (lower).

Figures 1 and 2 compare the effect of the choice of power spectrum. Results for correlation lengths of 10 m and 1 m are shown. For these plots, scattering from sound-speed

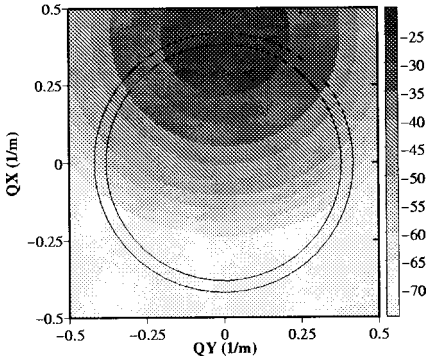

FIG. 2. Plane wave scattering from sound-speed fluctuations. $f=100$ Hz; Gaussian power spectrum, 10-deg incident wave; correlation length is 10 m. Note the Gaussian spectrum gives lower backscattering levels.

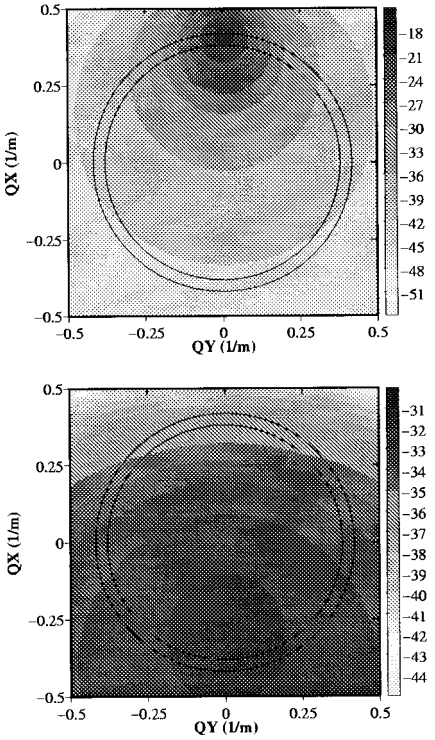

FIG. 3. Plane wave scattering from sound-speed and density fluctuations. $f=100$ Hz; Goff–Jordan power spectrum, 10-deg incident wave; correlation lengths of 10 m (upper) and 1 m (lower). For the shorter correlation length, density fluctuations greatly increase backscatter.

fluctuations alone is included. Comparing the plots for 10-m correlation lengths, the most striking difference is that the backscatter is greatly enhanced with the Goff–Jordan spectrum (Fig. 1) due to the longer tails of the power spectrum. Strong out-of-plane scattering is seen with both spectra, though a peak is observed at angles close to in-plane. In both cases the scattering is basically forward-directed, with the peak in scattered energy centered around the specular direction. Decreasing the correlation length to 1 m gives a much broader distribution of scattered energy. This is expected, since in the limit of small correlation length the inhomogeneities can be thought of as a random distribution of independent point scatterers. Each of these point scatterers radiates isotropically, so the overall scattering pattern is more diffuse. Decreasing the correlation length is also seen to reduce the peak scattered power considerably. This can be understood by remembering that sound will scatter most strongly from objects roughly the size of the wavelength or larger. Since the acoustic wavelength in this case is 16.5 m, most of the sound-speed fluctuations for the 1-m correlation length will have horizontal scales much less than a wavelength.

Figure 3 shows scattering from both sound-speed and density fluctuations in the sediment bottom. For the 10-m correlation length, the scattering intensity levels are only slightly higher than in the case without density fluctuations. Thus, we conclude that, for long horizontal correlation lengths, scattering from sound-speed fluctuations is dominant. When the correlation length is decreased to 1 m, the density scattering is dominant, as seen by comparing Figs. 1 and 3. Most importantly, the maximum is now in the *back-scattered* direction. This backscattering was predicted by Chernov for 1-D scattering, and can be seen in the $\mathbf{q}-\mathbf{k}$ term in Eq. (7), which shows the density-scattering contribution has a null in the forward direction. This preferential scattering in the backward direction can be understood by noting that spatial derivative operators in the density-scattering term have the effect of ''roughening'' the spectrum, emphasizing smaller-scale variability and increasing backscatter.

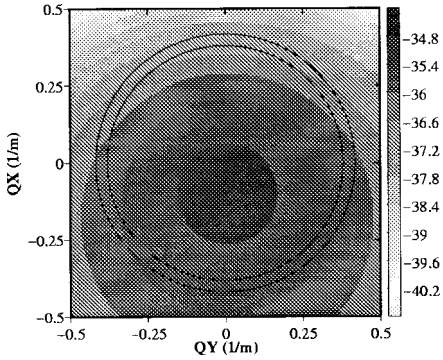

FIG. 4. Plane wave scattering from sound-speed and density fluctuations. $f=100$ Hz; Goff–Jordan power spectrum, 10-deg incident wave; normalized sound-speed and density fluctuations are adjusted to be equal.

The results so far have used Hines' empirically determined values of $\partial c/\partial P$ and $\partial \rho/\partial P$. These values were determined from a limited dataset, and can be expected to vary for different types of sediment bottom. Hines' values predict that the normalized density fluctuations $\delta\rho/\rho_0$ are about twice the normalized sound-speed fluctuations $\delta c/c_0$. In Fig. 4, results are shown in which $\delta\rho/\rho_0$ is adjusted so the normalized sound-speed and density fluctuations are equal. The effect of the density fluctuations is somewhat reduced, but still quite significant.

We can also study the effects of anisotropy in seabed property fluctuations. Figure 5 shows scattering of plane waves on a bottom with a correlation length of 2 m in x and 10 m in y. Increasing the correlation length in y gives a power spectrum with much less width in q_y. In Fig. 5 we let a plane wave be incident on the bottom at a vertical angle of 10 deg, and horizontal angles of 0 (along the x-axis), 45 deg, and 90 deg (along the y-axis). From observing the plots, we see that the anisotropy causes the scattered field to be skewed away from the incident angle for incident angles not aligned with the principal axes of the inhomogeneities. The anisotropy causes increased scattering into the continuous spectrum for the 0-deg incident wave, vs increased out-of-plane scattering for the 90-deg incident wave.

III. MODAL SCATTERING FROM RANDOM SEDIMENT BOTTOMS

For low-frequency shallow water propagation, the acoustic field is often well described as a sum of a reasonably small number of normal modes. This leads us to specialize the theory developed above to consider scattering of a modal sound field from inhomogeneities in fluid sediment bottoms. In doing so, we will make a number of simplifying assumptions. The most useful of these, discussed above, is that the vertical correlation function can be approximated as

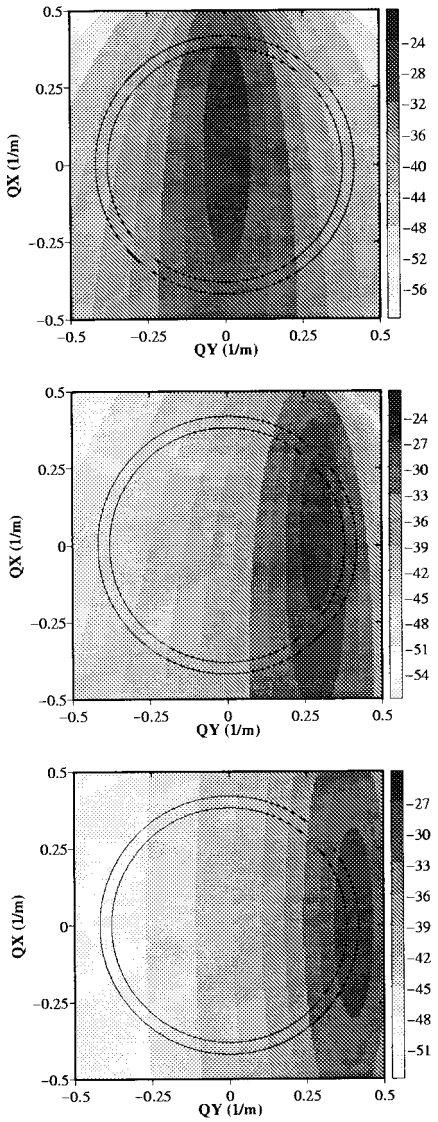

FIG. 5. Plane wave scattering from anisotropic sound-speed and density fluctuations, for incident angles of (from top) 0, 45, and 90 deg. $f = 100$ Hz; Goff–Jordan power spectrum; CL$x = 2$ m, CL$y = 10$ m.

a delta function. The second major simplification made is that the sound speed is constant in the layer where volume fluctuations are present. This assumption is limiting, but allows us to examine the basic scattering physics. For isovelocity layers, the field can be written in terms of up- and down-going plane waves, so depth integrals in the scattered-field expressions can be treated analytically. Depth integrals over the incident field modes and their derivatives must otherwise be performed numerically, making the calculations much slower and less accurate.

KRAKEN[26] or any other normal mode code can used to find the mode shapes and eigenvalues for the waveguide. The continuous spectrum contribution is included by introducing a false bottom deep in the sediment. The modal problem is then converted to a proper Sturm–Liouville problem and all modes are proper modes. Since there are both up- and down-going plane waves in the scattering layer, we write the mode shape as

$$\psi_n(z) = \begin{cases} \zeta_n(z), & z < z_1, \\ A_n e^{-ik_{zn}(z-z_1)} + B_n e^{ik_{zn}(z-z_1)}, & z > z_1, \end{cases} \tag{24}$$

where $\zeta_n(z)$ are the mode shapes found by the normal mode program and z_1 is the top of the volume-scattering layer. The plane wave coefficients A_n and B_n are found from the boundary conditions at the interface z_1, and sediment attenuation is included by introducing an imaginary part of the bottom wave number (Ref. 23, Chap. 2).

A. Mode attenuation coefficients

In this section, the mean-field equation is solved to find mean-field modal attenuations. This requires evaluating the scattering-loss correction term $I(k,z)$ from Eq. (9). The correction term is an $O(\sigma^2)$ perturbation to the mean field. Since the scattering theory retains terms only up to $O(\sigma^2)$, it is consistent to use the unperturbed eigenvalues and eigenfunctions when calculating $I(\mathbf{k},z)$; i.e., $I(\mathbf{k},z) \approx I(\mathbf{k}_0,z)$. This argument was made by Kuperman[27] in studying rough-surface scattering.

The scattering-loss correction contains terms proportional to both the mean field and its depth derivative [see Eq. (14)]. If we calculate attenuations for the propagating modes of the waveguide only, we can take advantage of the fact that these modes are exponentially decaying in the bottom to relate these terms by

$$\frac{\partial \langle \tilde{p}(\mathbf{k},z) \rangle}{\partial z} = -\alpha_b \langle \tilde{p}(\mathbf{k},z) \rangle, \tag{25}$$

where $\alpha_b = \sqrt{\mathbf{k}^2 - k_b^2}$. This lets us simplify the correction term and write the homogeneous mean-field equation in the form

$$[L(\mathbf{k}) + \langle \sigma^2 \rangle f(\mathbf{k},z)] \langle \tilde{p}(\mathbf{k},z) \rangle = 0, \tag{26}$$

where $f(\mathbf{k},z)$ is a combination of the F_1 and F_2 terms from Eq. (14).

We next substitute the modal forms of the Green's function (as a sum over modes m) into the mean-field equation, and switch to polar coordinates: $\int d^2\,\mathbf{q} = \int\int q\,dq\,d\theta$. Integrating over q exposes poles at $q = q_m$, leaving the integration over θ. Physically, this means that the scattered field will travel in the modes of the waveguide, but can be scattered into any horizontal angle. The correction term f becomes

$$\begin{aligned} f(\mathbf{k},z) = \frac{iz_{\mathrm{CL}}}{2\rho(z)} \int d\theta \sum_{m=1}^{M} P_H(\mathbf{q}_m - \mathbf{k}) [a_1 a_2 \psi_m^2(z) \\ + \mu_\rho a_3 (\psi_m'(z))^2 - \mu_\rho (a_4 - \alpha_b(z)(a_1 - a_2 \\ + \mu_\rho [q_m^2 - k_0^2(z)])) \psi_m(z) \psi_m'(z)]. \end{aligned} \tag{27}$$

Here, we have left implicit the dependence of the a_i terms

$$a_i = a_i(\mathbf{q}_m, \mathbf{k}, z), \tag{28}$$

where $\mathbf{q} = (q_m \cos\theta, q_m \sin\theta)$.

This equation can be rewritten in the form of an eigenvalue perturbation problem, giving

$$\left[\frac{\partial^2}{\partial z^2} + k_0^2(z) \right] \psi_n = k_n^2 \psi_n - \langle \sigma^2 \rangle f(\mathbf{k}_n, z) \psi_n. \tag{29}$$

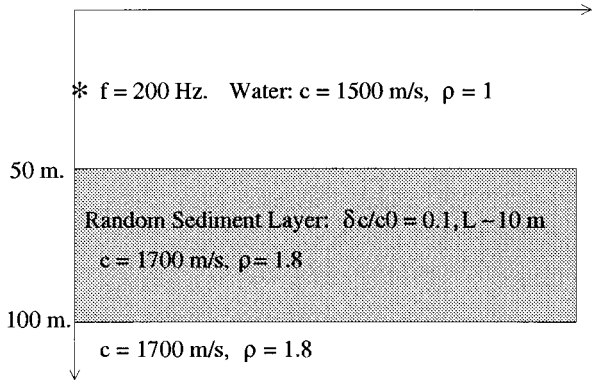

FIG. 6. Scenario for comparison with Tang's results. $f=200$ Hz; Gaussian spectrum, 10-m correlation length, $\delta c/c_0=0.1$.

The new eigenvalue can then be found using perturbation theory, as described by Bender and Orzag.[28] Appendix B shows that the first-order correction for the eigenvalue is

$$\Delta k_n=\frac{\langle\sigma^2\rangle}{2k_{n0}}\int_0^D\frac{f(\mathbf{k}_{n_0},z)\psi_n^2(z)}{\rho(z)}dz. \tag{30}$$

The imaginary part of Δk_n is the mode attenuation coefficient.

To validate our approach, we compare our method to results obtained by Tang[11] for a bottom containing sound-speed fluctuations only. Tang's code was used to calculate mean-field plane wave reflection coefficients for the sediment bottom. These reflection coefficients were used as a boundary condition for the normal mode code KRAKEN, which calculated the modified eigenvalues. The resulting change in the mode attenuation was taken to be Tang's prediction for scattering loss.

KRAKEN was then used to find the eigenvalues and mode shapes for the unperturbed scenario. These were used to find the mode attenuations from Eq. (30).

A simple scenario, shown in Fig. 6, was used for comparison. A 50-m-deep isovelocity water layer overlays a sediment half-space, the upper 50 m of which contains sound-speed inhomogeneities. The inhomogeneities are assumed to have a 2-D isotropic Gaussian correlation function in the horizontal and to be delta-correlated in the vertical. Attenuation in the water and sediment is neglected, so any loss is purely due to scattering.

Figure 7 shows the plane wave reflection coefficient for correlation function parameters which are used by Tang: $\delta c_{\rm rms}/c_0=0.1$, horizontal correlation length $l_0=10$ m, and vertical correlation length $z_{\rm CL}=1$ m.

The modal results are compared with Tang's attenuation coefficients in Fig. 8. Attenuation coefficients obtained using the modal approach are in reasonably good agreement with Tang's results, but are sensitive to the treatment of the continuous spectrum. However, the otherwise good agreement suggests that the approaches are compatible in describing the scattering physics.

Figure 8 shows modal attenuation coefficients for $f=200$ Hz, calculated from Tang's results and from the modal

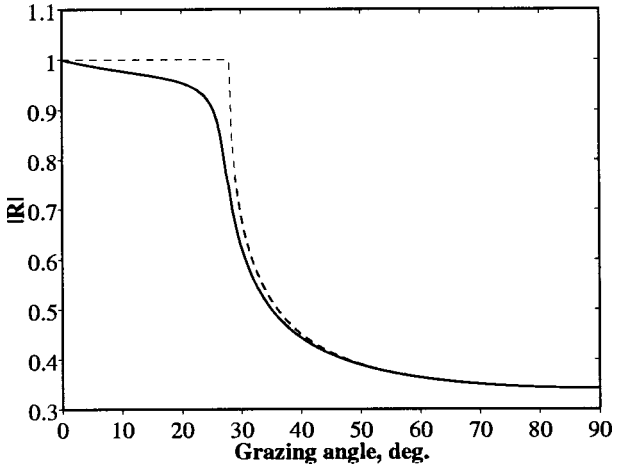

FIG. 7. Reflection coefficients for scenario. Dashed line is for nonrandom bottom; solid line is for bottom with random layer.

approach described above. When only scattering into proper modes is allowed, the modal calculation is seen to significantly underestimate the actual attenuation.

Scattering into the continuous spectrum is then approximated numerically by introducing a false bottom at 400-m depth (note we can allow a false bottom without any bottom attenuation only because we are interested here in scattering *into* the continuous spectrum; when calculating statistics of the scattered field, we must always include bottom attenuation so the continuous spectrum modes will decay quickly with range). When these extra modes are included, the agreement from the two methods is greatly improved. However, attenuations calculated using the modal approach are sensitive to the number of continuous spectrum modes included. As the number of modes included is increased, the results converge to the attenuations shown in Fig. 8, which includes 111 false-bottom modes in addition to the 6 proper modes. A calculation which includes 41 false-bottom modes shows nearly exact agreement with Tang's results for modes 1–4, but underestimates attenuation for modes 5 and 6.

This sensitivity is not surprising, as the normal mode

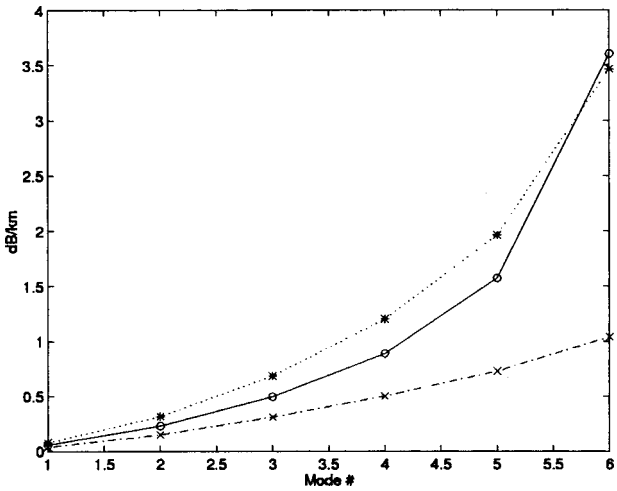

FIG. 8. Comparison with Tang's results. Open circles shows results from Tang; asterisk shows modal solution including continuous spectrum modes; ''×'' shows modal solution, proper modes only.

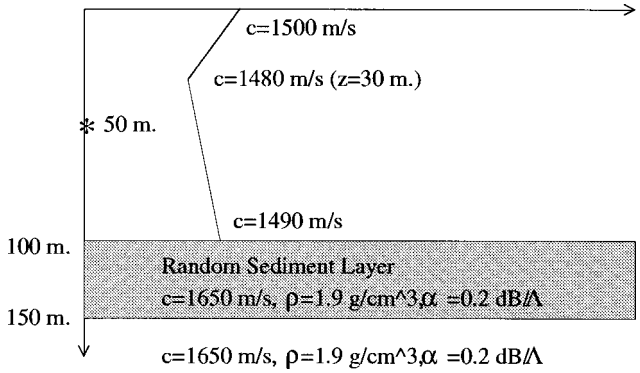

FIG. 9. Shallow water scattering scenario.

approach is known to have difficulty in modeling the continuous spectrum. The two main conclusions to be drawn from Fig. 8 are: first, that the current approach appears to agree with earlier work, and second, that scattering losses can be estimated fairly accurately with a modal approach. In many practical cases, uncertainty in environmental parameters will be larger than errors introduced by modeling of continuous spectrum modes.

Next, the fluid bottom, shallow water waveguide shown in Fig. 9 is considered. Both sound-speed and density fluctuations are included. For notational convenience, we define a parameter σ, which is set equal to the normalized sound-speed fluctuations $\delta c/c_0$. For a given σ, the density fluctuations are found from the relationship between density and sound-speed fluctuations given by Hines' constants.

We again examine horizontal correlation lengths of 1 and 10 m. The random scattering layer is assumed to be between 100- and 150-m depth. For the 10-m correlation length, seen in the upper plot of Fig. 10, including density scattering causes only a slight increase in mode attenuation. However, density fluctuations are the predominant cause of loss for the shorter 1-m correlation length case, shown in the lower plot of Fig. 10. This agrees with the trends seen above for plane wave scattering. The full scattering loss with the 1-m correlation length is of roughly the same order of magnitude as the loss caused by a bottom attenuation of 0.1 dB/λ. Whether or not attenuation due to volume scattering is a significant attenuation mechanism will depend on the environment considered. However, it has been demonstrated numerically[21] that the coherent field loss can significantly affect the correlation statistics of the total field.

IV. CONCLUSION

In this paper, a new self-consistent theory describing scattering from volume fluctuations in the ocean has been developed which includes scattering from both sound-speed and density fluctuations and allows calculation of coherent field attenuation due to scattering. Previous modeling including both sound-speed and density fluctuations has been based on the Born approximation, and does not give coherent field-scattering loss. The effects of including density fluctuations in a 3-D ocean were examined. When the horizontal correlation length of scatterers is small, scattering from density fluctuations significantly changes the backscattered energy.

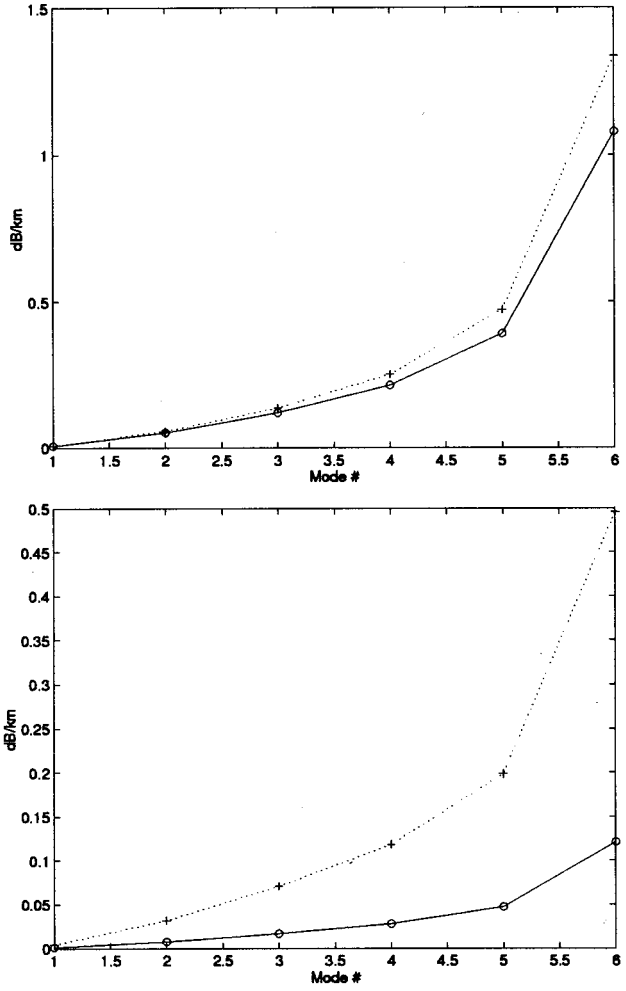

FIG. 10. Mode attenuations for shallow water example. $f=100$ Hz; Goff–Jordan spectrum, $\sigma=0.1$. Solid line includes effect of both sound-speed and density fluctuations, dotted line includes sound-speed fluctuations only. Correlation lengths of 10 m (upper plot) and 1 m (lower plot) are assumed.

The effects of out-of-plane scattering and anisotropic fluctuation statistics are also shown to be important. The theory was extended to find modal attenuations due to scattering, showing agreement with previous work which included sound-speed fluctuations only. For scenarios involving both sound-speed and density fluctuations, modal scattering losses can be comparable in magnitude to the effects of bottom attenuation.

ACKNOWLEDGMENTS

The authors gratefully acknowledge the support of the Office of Naval Research, under Contracts Nos. N00014-92-J-1282 and N00014-95-1-0307. Suggestions by Dr. Dajun Tang and Dr. Dan Li were very helpful.

APPENDIX A: SCATTERING INTEGRALS AND MEAN FIELD EQUATION

In this Appendix, the details of several calculations referred to above are shown. Before beginning we state several relationships which will be of use. From the definition of the wave number transform,

$$\delta P(\mathbf{r},z)=\frac{1}{2\pi}\int_{-\infty}^{\infty}d^2\,\mathbf{k}\widetilde{\delta P}(\mathbf{k},z)e^{-i\mathbf{k}\cdot\mathbf{r}}, \tag{A1}$$

$$\langle p(\mathbf{r},z)\rangle=\frac{1}{2\pi}\int_{-\infty}^{\infty}d^2\,\mathbf{k}\langle\tilde{p}(\mathbf{k},z)\rangle e^{-i\mathbf{k}\cdot\mathbf{r}}, \tag{A2}$$

$$s(\mathbf{r},z)=\frac{1}{2\pi}\int_{-\infty}^{\infty}d^2\,\mathbf{k}\tilde{s}(\mathbf{k},z)e^{-i\mathbf{k}\cdot\mathbf{z}}. \tag{A3}$$

Horizontal derivatives are transformed into algebraic factors; for example

$$\frac{\partial\delta P(\mathbf{r},z)}{\partial\mathbf{r}}=\frac{1}{2\pi}\int_{-\infty}^{\infty}d^2\,\mathbf{k}(-i\mathbf{k})\delta\tilde{P}(\mathbf{k},z)e^{-i\mathbf{k}\cdot\mathbf{r}}. \tag{A4}$$

We use also the following property of the delta function:

$$\frac{1}{(2\pi)^2}\int_{-\infty}^{\infty}d^2\,\mathbf{r}e^{i\mathbf{k}\cdot\mathbf{r}}=\delta(\mathbf{k}). \tag{A5}$$

First, we evaluate the wave number transform of the scattered-field equation. From the results in Sec. I, the transformed scattered field is given by

$$L(\mathbf{q})\tilde{s}(\mathbf{q},z)=\frac{1}{2\pi}\int d^2\,\mathbf{r}e^{i\mathbf{q}\cdot\mathbf{r}}[\mu_c(z)\delta P(\mathbf{r},z)\langle p(\mathbf{r},z)\rangle + \mu_\rho\nabla\delta P(\mathbf{r},z)\cdot\langle p(\mathbf{r},z)\rangle]. \tag{A6}$$

The work to be done is in evaluating the right-hand side (rhs). We begin by looking at the simpler first term, which involves only μ_c. Inserting the appropriate definitions from above gives

$$\text{rhs1}=\frac{\mu_c(z)}{(2\pi)^3}\int\int\int d^2\,\mathbf{k}_1d^2\,\mathbf{k}_2d^2\,\mathbf{r}\delta\tilde{P}(\mathbf{k}_1,z)\times\langle\tilde{p}(\mathbf{k}_2,z)\rangle e^{i[\mathbf{q}-(\mathbf{k}_1+\mathbf{k}_2)]\mathbf{r}}. \tag{A7}$$

Using the delta function property and integrating over $\mathbf{r}$

$$\text{rhs1}=\frac{1}{2\pi}\int\int d^2\,\mathbf{k}_1d^2\mathbf{k}_2\widetilde{\delta P}(\mathbf{k}_1,z)\langle\tilde{p}(\mathbf{k}_2,z)\rangle\times\delta[\mathbf{q}-(\mathbf{k}_1+\mathbf{k}_2)]. \tag{A8}$$

The delta function pulls out $\mathbf{k}_1=\mathbf{q}-\mathbf{k}_2$. Renaming $\mathbf{k}_2\equiv\mathbf{k}'$, we have

$$\text{rhs1}=\frac{\mu_c(z)}{2\pi}\int d^2\,\mathbf{k}'\,\delta\tilde{P}(\mathbf{q}-\mathbf{k}',z)\langle\tilde{p}(\mathbf{k}',z)\rangle. \tag{A9}$$

We next examine the second term, which involves spatial derivatives of $\rho(\mathbf{r},z)$. The derivative terms can be expanded into separate horizontal and vertical derivatives. Rewriting in terms of the transformed variables and integrating over $\mathbf{r}$ and $\mathbf{k}_1$ as above gives

$$\text{rhs2}=\frac{-\mu_\rho}{2\pi}\int d^2\,\mathbf{k}'\left[(\mathbf{q}-\mathbf{k}')\cdot\mathbf{k}'\widetilde{\delta P}(\mathbf{q}-\mathbf{k}',z)\times\langle\tilde{p}(\mathbf{k}',z)\rangle-\frac{\partial\widetilde{\delta P}(\mathbf{q}-\mathbf{k}')}{\partial z}\frac{\partial\langle\tilde{p}(\mathbf{k}',z)\rangle}{\partial z}\right]. \tag{A10}$$

Adding these results together gives the combined rhs for the scattered-field equation shown in Eq. (7).

The second result shown is the transformation of the mean-field equation, Eq. (4). Again, we break the equation into two terms, and look at the simpler one, multiplying μ_c first. This term is

$$I1=-\frac{\mu_c(z)}{2\pi}\int_{-\infty}^{\infty}\langle\delta P(\mathbf{r},z)s(\mathbf{r},z)\rangle e^{i\mathbf{k}\cdot\mathbf{z}}d^2\,\mathbf{r}. \tag{A11}$$

The calculation begins by substituting in the expressions for $s(\mathbf{r},z)$ and $\delta P(\mathbf{r},z)$

$$I1=-\frac{\mu_c(z)}{(2\pi)^3}\int\int\int d^2\,\mathbf{r}d^2\,\mathbf{k}_1d^2\,\mathbf{q}\times\langle\delta\tilde{P}(\mathbf{k}_1,z)\tilde{s}(\mathbf{q},z)\rangle e^{i(\mathbf{k}-(\mathbf{k}_1+\mathbf{q}))\mathbf{r}}d^2\,\mathbf{r}. \tag{A12}$$

Integrating over $\mathbf{r}$ again gives a delta function, which is satisfied when $\mathbf{k}_1=\mathbf{k}-\mathbf{q}$. This gives the result

$$I1=-\frac{\mu_c(z)}{2\pi}\int d\mathbf{q}\langle\delta\tilde{P}(\mathbf{k}-\mathbf{q},z)\tilde{s}(\mathbf{q},z)\rangle. \tag{A13}$$

Next, we look at the remaining terms, given by

$$I2=-\frac{\mu_\rho}{2\pi}\int d^2\,\mathbf{r}\left\langle\frac{\partial\delta P(\mathbf{r},z)}{\partial\mathbf{r}}\cdot\frac{\partial s(\mathbf{r},z)}{\partial\mathbf{r}}\right\rangle e^{i\mathbf{k}\cdot\mathbf{r}} - \frac{\mu_\rho}{2\pi}\int d^2\,\mathbf{r}\left\langle\frac{\partial\delta P(\mathbf{r},z)}{\partial z}\cdot\frac{\partial s(\mathbf{r},z)}{\partial z}\right\rangle e^{i\mathbf{k}\cdot\mathbf{r}}. \tag{A14}$$

Carrying out substitutions and integrations exactly as done above gives the result

$$I2=-\frac{\mu_\rho}{2\pi}\int d^2\,\mathbf{q}\left\{-(\mathbf{k}-\mathbf{q})\cdot\mathbf{q}\langle\widetilde{\delta P}(\mathbf{k}-\mathbf{q},z)\tilde{s}(\mathbf{q},z)\rangle + \left\langle\frac{\partial\widetilde{\delta P}(\mathbf{k}-\mathbf{q})}{\partial z}\frac{\partial\langle\mathbf{p}(\mathbf{q},z)\rangle}{\partial z}\right\rangle\right\}. \tag{A15}$$

These two terms are added to give the intermediate result shown in Eq. (11).

We proceed by evaluating the expectation terms above. This calculation is straightforward but long, so we will not show all details here. We first look at the first expectation in Eq. (A13)

$$E_1=\langle\delta\tilde{P}(\mathbf{k}-\mathbf{q},z)\tilde{s}(\mathbf{q},z)\rangle. \tag{A16}$$

Substituting in the expression for $\tilde{s}(q,z)$ from Eq. (7) gives one term involving a second-moment expectation of $\tilde{\delta}\tilde{P}$ and another term involving an expectation of $\tilde{\delta}\tilde{P}$ with its vertical derivative. From the definition of the power spectrum, vertical derivatives of porosity translate into derivatives of the vertical correlation function M. Assuming that the vertical correlation length $z_{\mathrm{CL}}\gg\lambda$ [Eq. (18)] lets us approximate M with a delta function. The first term resulting from Eq. (A16) gives

$$E_{11}=-2\pi\langle\sigma^2\rangle z_{\mathrm{CL}}P_H(\mathbf{q}-\mathbf{k})G_\omega(\mathbf{q},z,z_0)b1(\mathbf{q},\mathbf{k},z)\times\langle\tilde{p}(\mathbf{k},z)\rangle. \tag{A17}$$

The second integral, rewritten

$$E_{12} = -2\pi\langle\sigma^2\rangle P_H(\mathbf{q}-\mathbf{k}) \int z_0\, G_\omega(\mathbf{q},z,z_0) \times \frac{\partial M(z-z_0)}{\partial z_0}\, \frac{\partial\langle\tilde{p}(\mathbf{k},z_0)\rangle}{\partial z_0}, \tag{A18}$$

can be found using integration by parts, following Chernov.[1] Dropping the constants for a moment, we have

$$E_{12} \sim -G_\omega \frac{\partial\langle\tilde{p}\rangle}{\partial z_0} M\Big|_{-\infty}^{\infty} + \int dz_0\, M(z-z_0) \times \left[G_\omega(\mathbf{q},z,z_0)\, \frac{\partial^2\langle\tilde{p}(\mathbf{k},z_0)\rangle}{\partial z_0^2} + \frac{\partial G_\omega(\mathbf{q},z,z_0)}{\partial z_0}\, \frac{\partial\langle\tilde{p}(\mathbf{k},z_0)\rangle}{\partial z_0} \right]. \tag{A19}$$

The first term drops out as $M \to 0$ for large $(z-z_0)$, and Eq. (18) is used to eliminate the depth integral. The second derivative of $\langle\tilde{p}(\mathbf{k},z)\rangle$ is simplified using the Helmholtz equation. Finally, E_1 is found to be

$$E_1 = -2\pi z_{\mathrm{CL}} P_H(\mathbf{q}-\mathbf{k}) \left\{ a_2 G_\omega(\mathbf{q},z,z)\langle\tilde{p}(\mathbf{k},z_0)\rangle - \mu_\rho \frac{\partial G_\omega(\mathbf{q},z,z_0)}{\partial z_0}\Big|_z \frac{\partial\langle\tilde{p}(\mathbf{k},z_0)\rangle}{\partial z_0}\Big|_z \right\}, \tag{A20}$$

where a_2 is as defined in Sec. III A.

The calculation for the second expectation,

$$E_2 = \left\langle \frac{\partial\widetilde{\delta P}(\mathbf{k}-\mathbf{q},z)}{\partial z}\, \frac{\partial\tilde{s}(\mathbf{q},z)}{\partial z} \right\rangle \tag{A21}$$

is similar but more complicated. Substituting in the scattered-field expression again gives two expectations, one of which involves $\partial M(z-z_0)/\partial z$ and the other of which involves $\partial^2 M(z-z_0)/\partial z^2$. Using a change of variables argument, it is easy to show that $\partial M/\partial z = -\partial M/\partial z_0$, giving two integrals which involve derivatives with respect to z_0. We again use integration by parts, using the assumption that $\partial M(z-z_0)/\partial z_0 \to 0$ as $z-z_0$ becomes large to simplify the integral involving $\partial^2 M/\partial {z_0}^2$. Full details of the calculation are found in Ref. 21. Finally, E_1 and E_2 are combined to give the self-consistent equation for the mean field quoted in Eq. (14).

The power-spectral density, defined as $\langle\tilde{s}(\mathbf{q},z)\tilde{s}^*(\mathbf{q},z)\rangle$, measures the scattered energy in wave number $\mathbf{q}$ at depth z. The calculation involves cross-expectations of terms involving δP with terms involving $\partial\delta P/\partial z$, as seen from Eq. (7). These expectations are found using the definition of the power spectrum, Eq. (13), and integration by parts. The details of the calculations are very similar to those shown in the Appendix above and involve the same assumptions about the vertical correlation function M. The delta function resulting from the power spectrum is of the form $\delta(\mathbf{q}-\mathbf{k}_1-\mathbf{q}+\mathbf{k}_2)$, requiring $\mathbf{k}_1 = \mathbf{k}_2$. The resulting terms can be simplified through symmetry, giving the power-spectral density shown in Sec. II.

APPENDIX B: PERTURBATION THEORY FOR EIGENVALUE CORRECTION

Consider the form of the eigenvalue problem above:

$$\left[\frac{\partial^2}{\partial z^2} + k_0^2(z)\right]\psi_n = k_n^2\psi_n - \langle\sigma^2\rangle f(\mathbf{k}_{n_0},z)\,\psi_n. \tag{B1}$$

As this is the equation for the mean field, all quantities above are averaged, though this is not shown explicitly. The equation can be rewritten in the form

$$H\psi_n = E_n\psi_n - \langle\sigma^2\rangle f(\mathbf{k}_{n_0},z)\,\psi_n. \tag{B2}$$

Expanding the perturbed quantities to second order,

$$\begin{aligned} \psi_n &= \psi_n^{(0)} + \sigma\psi_n^{(1)} + \sigma^2\psi_n^{(2)} + \cdots, \\ E_n &= E_n^{(0)} + \sigma E_n^{(1)} + \sigma^2 E_n^{(2)} + \cdots. \end{aligned} \tag{B3}$$

Since we are interested in calculating the mean field, we average the equations above. Since σ is zero-mean, we find

$$\begin{aligned} \langle\psi_n\rangle &= \psi_n^{(0)} + \langle\sigma^2\rangle\psi_n^{(2)} + \cdots, \\ \langle E_n\rangle &= E_n^{(0)} + \langle\sigma^2\rangle E_n^{(2)} + \cdots, \end{aligned} \tag{B4}$$

where all quantities are averaged even if not explicitly written so. Substituting these above and equating terms of like order gives, for the first-order equation,

$$H^{(0)}\psi_n^{(0)} = E_n^{(0)}\psi_n^{(0)}. \tag{B5}$$

This is just the unperturbed equation. The $O(\sigma)$ terms are zero, by inspection. Finally, the second-order equation is

$$H^{(0)}\psi_n^{(2)} = E_n^{(0)}\psi_n^{(2)} + E_n^{(2)}\psi_n^{(0)} - \langle\sigma^2\rangle f(\mathbf{k}_{n_0},z)\,\psi_n^{(0)}. \tag{B6}$$

The first two terms are eliminated using the first-order solution. Operating on the remaining terms with

$$\int \frac{\psi_n^{(0)}}{\rho(z)}(\cdot)\,dz, \tag{B7}$$

and using the normalization condition, gives the result

$$E_n^{(2)} = \langle\sigma^2\rangle \int \frac{(\psi_n^{(0)})^2 f(\mathbf{k}_{n_0},z)}{\rho(z)}\,dz. \tag{B8}$$

We relate this to the eigenvalue perturbation Δk_n by noting that

$$k_n^2 = (k_{n0} + \Delta k_n)^2 = k_{n0}^2 + 2\Delta k_n k_{n0} + O(\sigma^4) + \cdots. \tag{B9}$$

Then, the final expression, quoted in Sec. III A, is

$$\Delta k_n = \frac{1}{2k_{n0}} E_n^{(2)} = \frac{\langle\sigma^2\rangle}{2k_{n0}} \int_0^D \frac{f(\mathbf{k}_{n_0},z)\,\psi_n^2(z)}{\rho(z)}\,dz. \tag{B10}$$

[1] L. A. Chernov, *Wave Propagation in a Random Medium* (McGraw-Hill, New York, 1960).

[2] L. B. Dozier and F. D. Tappert, ''Statistics of normal mode amplitudes in a random ocean: Theory,'' J. Acoust. Soc. Am. **63**, 352–365 (1977).

[3] Y. Desaubies, ''On the scattering of sound by internal waves in the ocean,'' J. Acoust. Soc. Am. **64**, 1460–1468 (1978).

[4] H. Essen, F. Schirmer, and S. Sirkes, ''Acoustic remote sensing of internal waves in shallow water,'' Int. J. Remote Sens. **4**(1), 33–47 (1983).

[5] T. Yamamoto, ''Acoustic scattering in the ocean from velocity and density fluctuations in the sediments,'' J. Acoust. Soc. Am. **99**, 866–879 (1996).

[6] P. Hines, ''Theoretical model of acoustic backscatter from a smooth seabed,'' J. Acoust. Soc. Am. **88**, 324–334 (1990).
[7] A. Ishimaru, *Wave Propagation and Scattering in Random Media* (Academic, New York, 1978).
[8] J. H. Stockhausen, ''Scattering from the volume of an inhomogeneous halfspace,'' NRE Report, 63/9 (1963).
[9] D. Jackson, D. Winebrenner, and A. Ishimaru, ''Application of the composite roughness model to high-frequency bottom backscattering,'' J. Acoust. Soc. Am. **79**, 1410–1422 (1986).
[10] A. N. Ivakin and Y. P. Lysanov, ''Theory of underwater sound scattering by volume inhomogeneities of the bottom,'' Sov. Phys. Acoust. **27**(1), 61–64 (1981).
[11] D. Tang, ''Acoustic Wave Scattering from a Random Ocean Bottom,'' Ph.D. thesis, Massachusetts Institute of Technology and Woods Hole Oceanographic Institute, June 1991.
[12] D. Tang and G. V. Frisk, ''Plane-wave reflection from a random fluid half-space,'' J. Acoust. Soc. Am. **90**, 2751–2756 (1991).
[13] D. Tang, ''Shallow water reverberation due to sediment volume inhomogeneities,'' J. Acoust. Soc. Am. **98**(A), 2988 (1995).
[14] W. A. Kuperman and H. Schmidt, ''Rough surface elastic wave scattering in a horizontally stratified ocean,'' J. Acoust. Soc. Am. **79**, 1767–1777 (1986).
[15] W. A. Kuperman and H. Schmidt, ''Self-consistent perturbation approach to rough surface scattering in stratified elastic media,'' J. Acoust. Soc. Am. **86**, 1511–1522 (1989).
[16] A. G. Voronovich, ''Approximation of uncorrelated reflections in the problem of sound propagation in a waveguide with a statistically rough boundary,'' Sov. Phys. Acoust. **33**(1), 11–17 (1987).
[17] H. Schmidt and W. A. Kuperman, ''Spectral representations of rough interface reverberation in stratified ocean waveguides,'' J. Acoust. Soc. Am. **97**, 2199–2209 (1995).
[18] K. D. LePage and H. Schmidt, ''Modeling of low frequency transmission loss in the central Arctic,'' J. Acoust. Soc. Am. **96**, 1783–1795 (1994).
[19] D. H. Berman, ''Computing effective reflection coefficients in layered media,'' J. Acoust. Soc. Am. **101**, 741–748 (1997).
[20] D. H. Berman, ''Reverberation in waveguides with rough surfaces,'' J. Acoust. Soc. Am. **105**, 672–686 (1999).
[21] B. Tracey, ''An integrated modal approach to surface and volume scattering in ocean acoustic waveguides,'' Ph.D. thesis, Massachusetts Institute of Technology and Woods Hole Oceanographic Institution, January 1995.
[22] B. Tracey and H. Schmidt, ''Seismo-acoustic field statistics in shallow water,'' IEEE J. Ocean Eng. **22**(2), 317–331 (1997).
[23] F. B. Jensen, W. A. Kuperman, M. B. Porter, and H. Schmidt, *Computational Ocean Acoustics* (American Institute of Physics, Woodbury, NY, 1994).
[24] J. Goff and T. Jordan, ''Stochastic modeling of seafloor morphology: Inversion of sea beam data for second order statistics,'' J. Geophys. Res. **93**, 13589–13608 (1993).
[25] T. Yamamoto, ''Velocity variabilities and other physical properties of marine sediments measured by crosswell acoustic tomography,'' J. Acoust. Soc. Am. **98**, 2235–2248 (1995).
[26] M. B. Porter, The KRAKEN normal mode program. Rep. SM-245 (SACLANT Undersea Research Centre, La Spezia, Italy), 1991.
[27] W. A. Kuperman, ''Coherent component of specular reflection and transmission at a randomly rough two-fluid interface,'' J. Acoust. Soc. Am. **58**, 365–370 (1975).
[28] C. Bender and S. Orszag, *Applied Mathematical Methods for Scientists and Engineers* (McGraw-Hill, New York, 1978).

Wave-number sampling at short range

Michael D. Collins
Naval Research Laboratory, Washington, DC 20375

(Received 23 March 1999; revised 12 July 1999; accepted 30 July 1999)

Spectral solutions can be obtained efficiently at long ranges by using a quadrature scheme that involves perturbing the integration contour off the real line [F. B. Jensen *et al.*, *Computational Ocean Acoustics* (American Institute of Physics, New York, 1994), pp. 231–240]. The efficiency of this implementation of the spectral solution is investigated for short-range problems. Examples are presented to illustrate that the self-starter [J. Acoust. Soc. Am. **92**, 2069–2074 (1992)] is about ten times faster at ranges on the order of ten wavelengths. The accuracy of the spectral solution and the self-starter are directly related to the accuracy of rational approximations. The rational function associated with the spectral solution is based on the numerical evaluation of the spectral integral. The rational function associated with the self-starter is based on the analytic evaluation of the spectral integral. The relationship between these approaches is analogous to the relationship between the finite-difference and split-step Padé [J. Acoust. Soc. Am. **93**, 1736–1742 (1993)] solutions of the parabolic equation. [S0001-4966(99)06211-6]

PACS numbers: 43.30.Bp [SAC-B]

INTRODUCTION

Recent trends in shallow-water problems and geoacoustic inverse problems have motivated interest in short-range propagation modeling. Since most research in ocean acoustics has focused on long-range problems, there are some issues in short-range problems that need to be addressed. Efficiency is an important issue for inverse problems because it is often necessary to solve the forward problem thousands of times. The spectral solution[1] is the most efficient separation of variables technique for short-range problems. Short-range solutions can also be obtained using the self-starter,[2] a parabolic equation technique for generating initial conditions that can be used to solve inverse problems efficiently.[3] With an implementation of the self-starter that is based on the method of undetermined coefficients,[4] it is possible to solve some inverse problems in a few seconds on the latest generation of desk-top computers.

In this paper, we investigate the number of samples that are required to accurately evaluate the wave-number integral of the spectral solution at short range. The self-starter and the discretized spectral solution both involve the evaluation of the spectrum at a finite set of wave numbers. At ranges on the order of ten wavelengths, accurate solutions can be obtained with the self-starter by using on the order of ten wave-number samples.[3] There have been unsubstantiated claims that the spectral solution provides similar efficiency.[5] We demonstrate that the basis for these claims, a sampling estimate that is valid for long ranges,[6] does not extrapolate to short ranges. In Sec. I, we show that the accuracy of the spectral solution and the self-starter depends on the accuracy of rational approximations. In Sec. II, we consider particular rational approximations. In Sec. III, we compare the efficiency of the spectral solution and the self-starter.

I. THE DISCRETIZED SPECTRAL SOLUTION AND THE SELF-STARTER

We consider a frequency-domain problem in two dimensions and work in Cartesian coordinates, where x is the range from a source and z is the depth below the surface. The factor $\exp(-i\omega t)$ is removed from the acoustic pressure p, which satisfies the Helmholtz equation,

$$\frac{\partial^2 p}{\partial x^2} + k_0^2(1+X)p = 2i\,\delta(x)\sigma(z), \tag{1}$$

$$X \equiv k_0^{-2}\left(\rho\,\frac{\partial}{\partial z}\,\frac{1}{\rho}\,\frac{\partial}{\partial z} + k^2 - k_0^2\right), \tag{2}$$

where ω is the circular frequency, t is time, $\sigma(z)$ is an arbitrary source condition, ρ is the density, $k=\omega/c$ is the wave number, c is the sound speed, $k_0=\omega/c_0$ is a representative wave number, c_0 is a representative sound speed, and $\lambda_0 = 2\pi/k_0$ is a representative wavelength. The sound speed is allowed to be complex to account for attenuation.

Taking the Fourier transform of Eq. (1), we obtain the spectral solution,

$$p(x,z) = \frac{1}{2\pi}\int_{-\infty}^{\infty} \exp(ihx)\hat{p}(h,z)\,dh, \tag{3}$$

$$(k_0^2(1+X) - h^2)\hat{p} = 2i\sigma(z), \tag{4}$$

where h is the horizontal wave number and $\hat{p}(h,z)$ is the wave-number spectrum. When the attenuation vanishes, it is necessary to perturb parts of the integration contour either above or below the singularities on the real line depending on the sign of x. We consider the case $x>0$. Substituting Eq. (4) into Eq. (3), we obtain

$$p(x,z) = f(X)\sigma(z), \tag{5}$$

$$f(X) \equiv \frac{i}{\pi}\int_{-\infty}^{\infty} \frac{\exp(ihx)}{k_0^2(1+X)-h^2}\,dh. \tag{6}$$

Evaluating the integral in Eq. (6) in terms of the residue at $h=k_0(1+X)^{1/2}$, we obtain

$$f(X)=k_0^{-1}(1+X)^{-1/2}\exp\,(ik_0x(1+X)^{1/2}). \tag{7}$$

The self-starter is based on replacing $f(X)$ in Eq. (5) by a rational approximation.[2]

The spectral solution is obtained by numerically evaluating the integral in Eq. (3). Estimating this integral by sampling the spectrum at N points, we obtain

$$p(x,z)\cong\sum_{j=1}^{N} A_j\exp\,(ih_jx)\hat{p}(h_j,z), \tag{8}$$

where the h_j are the wave-number samples and the A_j are the weights of the quadrature. From Eqs. (4) and (8) we obtain

$$p(x,z)\cong g(X)\sigma(z), \tag{9}$$

$$g(X)\equiv\sum_{j=1}^{N}\frac{2iA_j\exp\,(ih_jx)}{k_0^2(1+X)-h_j^2}. \tag{10}$$

Since $\sigma(z)$ is arbitrary, it follows from Eqs. (5) and (9) that the accuracy of the spectral solution is directly related to the accuracy of the approximation $f(X)\cong g(X)$. The self-starter is identical to the solution in Eq. (9), with the exception of the choices for the coefficients of the rational approximation. The rational approximation for the spectral solution is obtained indirectly by approximating an integral. The rational approximation for the self-starter is obtained directly by fitting $g(X)$ to $f(X)$. Both of the approximations break down near $X=-1$ since the branch point cannot be handled by a rational function.

II. RATIONAL APPROXIMATIONS

Rational approximations for parabolic equation techniques have been designed by performing least-squares fits,[3] matching derivatives,[7] mapping the real line to a circle,[8] applying accuracy and stability constraints,[9] and rotating branch cuts.[10] Rational approximations must be accurate for the modes that contribute significantly to the solution. For some applications, it is also necessary to prevent the solution from being corrupted by evanescent modes.[8–11] Rational approximations that satisfy these requirements can be obtained by enforcing accuracy constraints to ensure that the propagating modes are handled properly and stability constraints to ensure that the evanescent modes are annihilated.[3,9]

The requirements of rational approximations depend on range. To prevent the gradual accumulation of errors, long-range problems usually require accuracy to several decimal places over a relatively small range of wave numbers, which correspond to modes that are trapped in the water column. This can be achieved efficiently by matching derivatives at $X=0$. For short-range problems, accuracy to a few decimal places may be sufficient but is usually required over a relatively wide range of wave numbers, which correspond to trapped modes and leaky modes that interact with sediment layers. This can be achieved efficiently by performing a least-squares fit. Since damping effects accumulate with range, evanescent modes can often be annihilated by using just one stability constraint for long-range problems.[9] To annihilate evanescent modes at short ranges, we use a rational approximation of the form

$$f(X)\cong g(X)=\frac{\Sigma_{j=0}^{N-2}\gamma_jX^j}{1+\Sigma_{j=1}^{N}\delta_jX^j}=\sum_{j=1}^{N}\frac{\alpha_j}{1+\beta_jX}, \tag{11}$$

which is a generalization of the rational approximation of Ref. 3 and is applicable to the undetermined coefficients implementation of the self-starter.[4] The coefficients γ_j and δ_j can be obtained by performing a least-squares fit over points from an interval near $X=0$ for accuracy and an interval in the region $X<-1$ for stability. The coefficients α_j and β_j are then obtained by finding the roots of the polynomial in the denominator and expanding in partial fractions. Approximations of this form are efficient at annihilating the higher evanescent modes since $g(X)=O(|X|^{-2})$ for $|X|\gg1$.

The numerical evaluation of the spectral integral involves finite sampling along a segment of the contour that is comparable to k_0 in length. Efficiency can be improved by perturbing the contour below the singularities that are near the real line. A quadrature scheme that has proved to be useful for long-range problems[6] involves the sample spacing $\Delta h=\pi/x$ along a segment of the line $\mathrm{Im}(h)=-\varepsilon$, where

$$\varepsilon=\frac{3}{2x\log_{10}e}. \tag{12}$$

There have been claims that this quadrature scheme is also applicable at short ranges.[5] Assuming that this is correct and considering the case $x=10\lambda_0=20\pi/k_0$, we would obtain $\Delta h=\frac{1}{20}k_0$ and conclude that the approximation in Eq. (9) is accurate when N is on the order of ten. It would then follow that the spectral solution is about as efficient as the self-starter for ranges on the order of ten wavelengths.

Although the rational approximation associated with the quadrature scheme was not designed by explicitly fitting $g(X)$ to $f(X)$, it is very efficient for long-range problems because it is based on the sampling theorem,[12] which states that a relatively large Δh may be used under certain conditions, and it can be implemented with the fast Fourier transform,[13] which is very efficient when the solution is desired at many ranges. These advantages do not exist for some short-range problems. It follows from Eq. (12) that the quadrature scheme breaks down for sufficiently small x since it is based on the assumption that ε is small.[6] There is no advantage to the fast Fourier transform when the solution is desired at only one range.

III. COMPARISON OF THE SPECTRAL SOLUTION AND THE SELF-STARTER

The relationship between the spectral solution and the self-starter is analogous to the relationship between two approaches for solving the parabolic equation,

$$\frac{\partial p}{\partial x}=ik_0(1+X)^{1/2}p. \tag{13}$$

The finite-difference solution of Eq. (13) involves approximating the square root with a rational function and then ap-

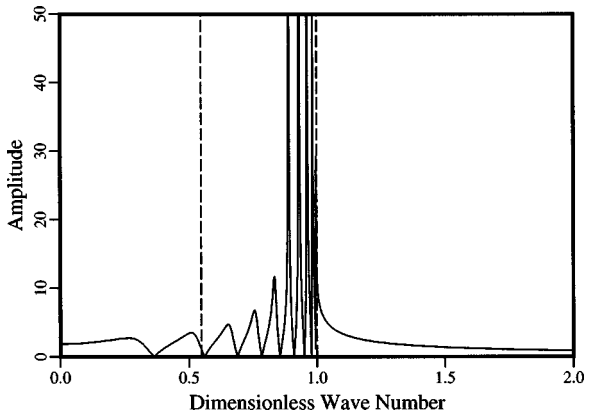

FIG. 1. The wave-number spectrum at $z=290$ m for a problem involving a 25-Hz source at $z=290$ m in an ocean of depth 300 m, where h/k_0 is the dimensionless wave number. The vertical dashed lines correspond to the end points of the interval $-0.7\leqslant X\leqslant 0$ over which the least-squares fit for the self-starter is applied. Since the source and receiver depths coincide, the spectrum decays relatively slowly as $h\rightarrow\infty$.

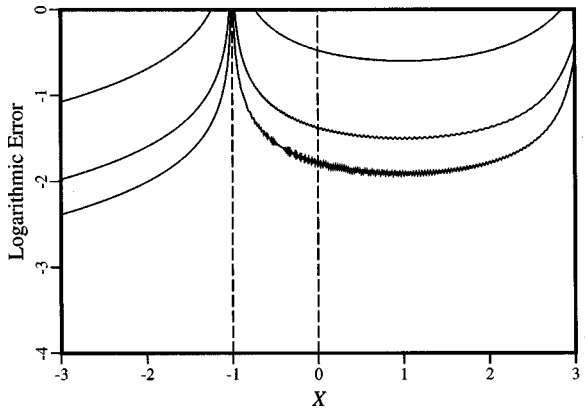

FIG. 2. The error $\log_{10} E(X)$ for rational approximations corresponding to the spectral solution for the case $x=10\lambda_0=600$ m. The region between the dashed lines corresponds to the propagating modes. The region $X<-1$ corresponds to the evanescent modes. The top curve corresponds to the quadrature scheme described in Ref. 6 for the case $N=40$. The other curves correspond to successive refinements of the quadrature scheme in which both Δh and ε are halved. The error is reduced but still relatively large in the middle curve, which corresponds to $N=80$. The error is on the order of 1% near $X=0$ in the lower curve, which corresponds to $N=160$.

plying standard numerical techniques to discretize in range and depth.[14] The split-step Padé solution[15] of Eq. (13) is based on the exact solution,

$$p(x+\Delta x,z)=\exp\left(ik_0\Delta x(1+X)^{1/2}\right)p(x,z). \tag{14}$$

The solution of Eq. (14) is obtained by approximating the exponential function with a rational function and then applying numerical techniques to discretize in depth. Higher-order rational functions can be used in the finite-difference and split-step Padé solutions to achieve higher-order accuracy in X. The finite-difference solution usually requires range steps that are a fraction of a wavelength. The split-step Padé solution provides higher-order in accuracy in $k_0\Delta x$ and permits range steps greater than ten wavelengths.[15] This gain in efficiency is achieved by integrating Eq. (13) analytically before applying a rational approximation. Similarly, the efficiency of the self-starter is based on integrating Eq. (6) analytically before applying a rational approximation. The spectral solution is based on integrating Eq. (6) numerically.

We consider a problem involving a 25-Hz source at $z=290$ m in an ocean of depth 300 m in which $c=c_0=1500$ m/s. In the sediment, $c=1700$ m/s, $\rho=1.5$ g/cm^3, and the attenuation is 0.5 dB/λ. The wave-number spectrum for this problem appears in Fig. 1. We assume that the rational approximation must be accurate for $-0.7\leqslant X\leqslant 0$, which corresponds to energy that propagates within about 56.8 degrees of horizontal in the water column and is appropriate for some geoacoustic inverse problems.[3] For this application, it is necessary to resolve arrivals that interact with sediment layers. Since these arrivals are often dominated by waterborne arrivals, the forward model must provide a relatively high level of accuracy. Errors on the order of 10% are too large. Errors on the order of 1% are probably acceptable in most cases.

We perform quadrature using the mid-point rule[16] over the interval $0<\mathrm{Re}(h)<2k_0$. We use this relatively wide interval to eliminate the truncation of the contour as a possible source of error. The length of the interval can be reduced in many cases to achieve efficiency gains up to about a factor of 2. As the spectrum in Fig. 1 illustrates, this must be done with care to avoid introducing errors near the source depth, especially at short ranges. For the wave-number sampling $\Delta h=\pi/x$, we obtain

$$N=\frac{2k_0}{\Delta h}=\frac{4x}{\lambda_0}. \tag{15}$$

We illustrate the accuracy of the rational approximation associated with the quadrature scheme for the case $x=10\lambda_0=600$ m, which corresponds to $N=40$. Appearing in Fig. 2 is the error,

$$E(X)=k_0|g(X)-f(X)|, \tag{16}$$

which is greater than 10% throughout the region between the dashed lines, where the propagating modes occur. The error is also large in the region $X<-1$, where evanescent modes occur. We performed convergence tests and found that the

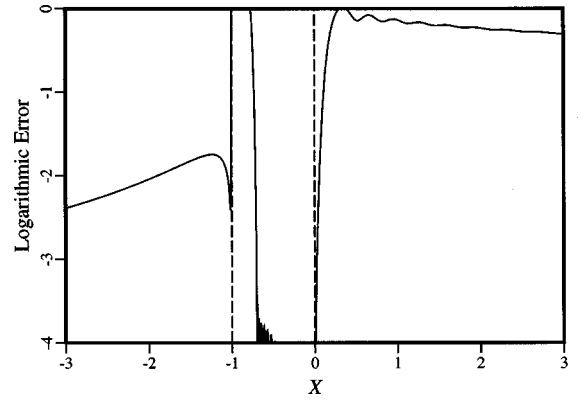

FIG. 3. The error $\log_{10} E(X)$ for a ten-term rational approximation corresponding to the self-starter for the case $x=10\lambda_0=600$ m. The region between the dashed lines corresponds to the propagating modes. The region $X<-1$ corresponds to the evanescent modes. The error is well under 1% within the interval $-0.7\leqslant X\leqslant 0$, where the rational function was fit by least squares. The error is also small in the evanescent region $X<-1$, which was handled by applying just one stability constraint.

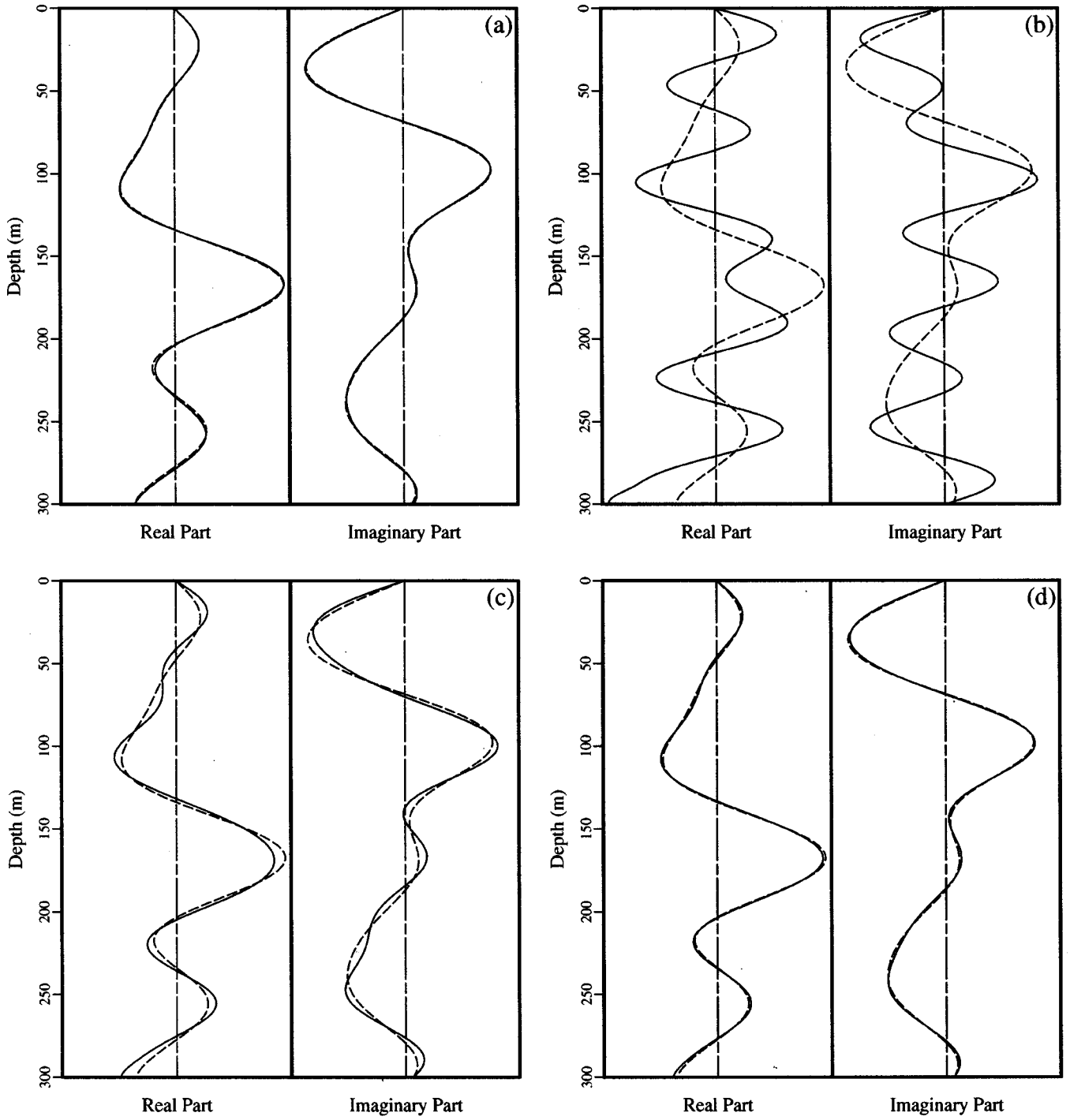

FIG. 4. The complex pressure at $x=10\lambda_0=600$ m generated with the spectral solution and the self-starter using the rational approximations illustrated in Figs. 2 and 3. The dashed curves correspond to a reference solution obtained by using small values of Δh and ε to evaluate the spectral integral. The solid curves correspond to (a) the self-starter for the case $N=10$ and the spectral solution for the cases (b) $N=40$, (c) $N=80$, and (d) $N=160$.

error does not reduce to an acceptable level when Δh is reduced and ε is fixed. Since it is necessary to reduce Δh when ε is reduced, we considered refinements of the quadrature scheme in which both of these parameters are halved. Appearing in Fig. 2 is the error corresponding to two refinements. The error is reduced but still relatively large after the first refinement, which corresponds to $N=80$. The error is on the order of 1% near $X=0$ after the second refinement, which corresponds to $N=160$.

We applied the self-starter to the test problem for the case $N=10$. We obtained the coefficients of the rational approximation in Eq. (11) using a least-squares fit over 80 equally spaced points selected from $-0.7\leqslant X\leqslant 0$. To annihilate the evanescent modes, we included the constraint $g(-1)=0$ in the least-squares fit. Appearing in Fig. 3 is the error in the rational approximation for the self-starter, which is well below 1% throughout the interval $-0.7\leqslant X\leqslant 0$. Due to the stability constraint and the built-in behavior for large X, the error is small in the region $X<-1$. Fields generated using the self-starter and the spectral solution appear in Fig.

4. The self-starter is accurate for $N=10$. The spectral solution breaks down for $N=40$, contains significant errors for $N=80$, and is accurate for $N=160$.

To analytically estimate the range at which the quadrature scheme of Ref. 1 begins to break down, we consider the quantity

$$I_\varepsilon(X)=\frac{i}{\pi}\int_0^{-i\varepsilon}\frac{\exp\,(ihx)}{k_0^2(1+X)-h^2}\,dh, \tag{17}$$

which is the integral along the vertical contour through $h=0$. Assuming that ε is small, we obtain

$$I_\varepsilon(X)\cong\frac{i}{\pi k_0^2(1+X)}\int_0^{-i\varepsilon}\exp\,(ihx)\,dh=\frac{\exp\,(\varepsilon x)-1}{\pi k_0^2 x(1+X)}. \tag{18}$$

For $x=M\lambda_0$, we obtain

$$I_\varepsilon(X)\cong\frac{\exp\,(\varepsilon x)-1}{2\pi^2 M k_0(1+X)}\cong\frac{1.55}{M k_0(1+X)}. \tag{19}$$

Comparing Eqs. (7) and (19), we conclude that the error is on the order of 1% when M is on the order of 100. We also conclude that large errors should occur when $M=10$, which is consistent with the numerical results.

IV. CONCLUSION

We have demonstrated that the self-starter is about an order of magnitude faster than the spectral solution described in Ref. 6 for a problem involving an array of receivers at a range of ten wavelengths from the source. This efficiency advantage should exist well beyond ten wavelengths since the number of terms required in the self-starter (which provides higher-order accuracy in k_0x) grows less than linearly with range. The discretized spectral solution is identical to the self starter, with the exception of the coefficients appearing in the rational approximations associated with these techniques. The self-starter may therefore be regarded as a quadrature scheme for the spectral solution that is specially designed for short-range problems. The rational approximation for the self-starter is based on evaluating the spectral integral analytically. The rational approximation for the spectral solution is based on evaluating the spectral integral numerically. It makes sense that an analytic approach designed for obtaining the solution at a specific range would be more efficient than a numerical approach designed for obtaining the solution at many ranges.

ACKNOWLEDGMENTS

This work was supported by the Office of Naval Research. The author thanks Dalcio K. Dacol, Joseph F. Lingevitch, and Nicholas C. Makris for useful technical discussions.

[1] F. B. Jensen, W. A. Kuperman, M. B. Porter, and H. Schmidt, *Computational Ocean Acoustics* (American Institute of Physics, New York, 1994), pp. 203–270.
[2] M. D. Collins, ''A self-starter for the parabolic equation method,'' J. Acoust. Soc. Am. **92**, 2069–2074 (1992).
[3] R. J. Cederberg and M. D. Collins, ''Application of an improved self-starter to geoacoustic inversion,'' IEEE J. Ocean Eng. **22**, 102–109 (1997).
[4] D. K. Dacol, M. D. Collins, and J. F. Lingevitch, ''An efficient parabolic equation solution based on the method of undetermined coefficients,'' J. Acoust. Soc. Am. **106**, 1727–1731 (1999).
[5] Personal communication by an anonymous reviewer and others. There seems to be a widespread misconception regarding this issue.
[6] Reference 1, pp. 231–240.
[7] A. Bamberger, B. Engquist, L. Halpern, and P. Joly, ''Higher order paraxial wave equation approximations in heterogeneous media,'' SIAM J. Appl. Math. **48**, 129–154 (1988).
[8] B. T. R. Wetton and G. H. Brooke, ''One-way wave equations for seismoacoustic propagation in elastic waveguides,'' J. Acoust. Soc. Am. **87**, 624–632 (1990).
[9] M. D. Collins, ''Higher-order parabolic approximations for accurate and stable elastic parabolic equations with application to interface wave propagation,'' J. Acoust. Soc. Am. **89**, 1050–1057 (1991).
[10] F. A. Milinazzo, C. A. Zala, and G. H. Brooke, ''Rational square-root approximations for parabolic equation algorithms,'' J. Acoust. Soc. Am. **101**, 760–766 (1997).
[11] M. D. Collins and E. K. Westwood, ''A higher-order energy-conserving parabolic equation for range-dependent ocean depth, sound speed, and density,'' J. Acoust. Soc. Am. **89**, 1068–1075 (1991).
[12] F. H. Press, S. A. Teukolsky, W. T. Vetterling, and B. P. Flannery, *Numerical Recipes in FORTRAN, Second Edition* (Cambridge U.P., Cambridge, 1992), pp. 494–495.
[13] Reference 12, pp. 498–502.
[14] M. D. Collins, ''Applications and time-domain solution of higher-order parabolic equations in underwater acoustics,'' J. Acoust. Soc. Am. **86**, 1097–1102 (1989).
[15] M. D. Collins, ''A split-step Padé solution for the parabolic equation method,'' J. Acoust. Soc. Am. **93**, 1736–1742 (1993).
[16] P. J. Davis and P. Rabinowitz, *Methods of Numerical Integration* (Academic, Orlando, 1984), p. 93.

Head wave data inversion for geoacoustic parameters of the ocean bottom off Vancouver Island

Oleg A. Godin,[a] N. Ross Chapman, Mark C. A. Laidlaw,[b] and David E. Hannay[c]
School of Earth and Ocean Sciences, University of Victoria, Victoria, British Columbia V8W 3P6, Canada

(Received 8 December 1998; revised 18 June 1999; accepted 2 July 1999)

Head wave signals from small explosive charges have been analyzed to determine a geoacoustic profile for a shallow water site off the West coast of Vancouver Island. The experimental design contained a vertical aperture, provided by a vertical line array, and a synthetic horizontal aperture from shots at different ranges from the vertical line array. The simultaneous use of travel time and amplitude data for both apertures provided improved accuracy and vertical resolution of the estimated geoacoustic profile. Travel time vs range data from head waves from three distinct sub-bottom interfaces were used to measure compressional speeds in the layers below the interfaces and estimate the layers' thicknesses. Spatial filtering of the vertical line array data was necessary to resolve the head wave arrival from the shallowest layers. Analysis of the interference structure of the head wave power spectra at the vertical line array provided the means to measure the travel time of the head wave from the deepest layer. In addition, the head wave power spectra were used to estimate the compressional wave attenuation, using a method based on the variation with range of the logarithmic derivative with respect to frequency of the head wave spectrum. © *1999 Acoustical Society of America.* [S0001-4966(99)04710-4]

PACS numbers: 43.30.Ma, 43.30.Pc [DLB]

INTRODUCTION

Acoustic head wave data from seismic refraction experiments are widely used in marine geophysics to determine sub-bottom sound speeds.[1,2] In these experiments, horizontal aperture is obtained using towed multichannel arrays or by deploying multiple sources at different ranges from a single sensor.[3–8] Seismologists generally have not made extensive use of vertical arrays, although Hunter[9] has described their advantages for resolving relatively low compressional speeds. On the other hand, vertical apertures are routinely used in ocean acoustics to take advantage of information in the vertical structure of the sound field in the water column. This geometry has proved to be very effective for matched-field inversion of acoustic field data to estimate geoacoustic profiles of the ocean bottom.[10,11]

This paper describes the analysis and interpretation of head wave (HW) data obtained with a vertical line array to determine a geoacoustic profile for a shallow water site on the continental shelf off Vancouver Island. A rich structure of precursor head waves was observed prior to the water wave signals from small explosive charges that were deployed in the experiment. Conventionally, HW data for single sensors are interpreted on the basis of travel time variation with range. However, the vertical aperture provides the capability to identify head waves and their sea surface reflections and resolve closely spaced HW arrivals by spatial filtering. Using travel time analysis of the beamformed data, compressional speeds were estimated for three sediment layers at the Vancouver Island site. In addition, spectral amplitude information was used to further resolve the compressional speeds as well as estimate compressional wave attenuation in the sediment column.

The Pacific Shelf experiment is described briefly in Sec. I, and a theoretical background for head waves is provided in Sec. II. The travel time and beamforming analysis is presented in Sec. III. The analysis of the power spectra for estimating sound speeds via position of spectral nulls is presented in Sec. IV, and for estimating attenuation in Sec. V. The geoacoustic profile determined from the HW data is discussed in Sec. VI. The results obtained are summarized in Sec. VII.

I. EXPERIMENTAL DETAILS

The Pacific Shelf experiments were carried out in September 1993 at a site on the continental shelf southwest of Vancouver Island (Fig. 1). The water depth was about 400 m. In the experiment reported here, 0.8-kg charges were deployed at nominal depths of 200 m by a ship (CSS W. E. RICKER) that opened range from a vertical line array (VLA) on a track along the 400-m contour. Shots were dropped at roughly 1-km intervals out to a range of 25 km. Data for the first ten shots are considered here. The VLA consisted of 16 hydrophones equispaced at 15-m intervals, with the top sensor at a depth of 80 m. This depth was monitored during the experiment by a pressure sensor. The hydrophones were suspended using a two-stage suspension system from a surface float that was anchored during the experiment. The acoustic data were high-pass filtered to suppress low-frequency am-

[a]Also affiliated with: Acoustic Wave Propagation Laboratory, P. P. Shirshov Oceanography Institute of the Russian Academy of Sciences, Moscow 117851, Russia.
[b]Current address: Department of Physics and Astronomy, University of British Columbia, Vancouver, B.C. V6T 1Z1, Canada.
[c]Also affiliated with: JASCO Research Ltd., Sidney, B.C. V8L 3S1, Canada.

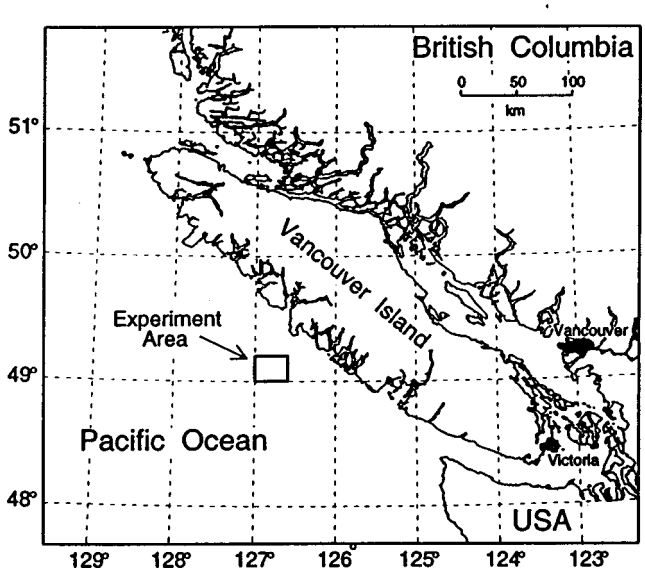

FIG. 1. The experimental area, outlined in black, is located on the continental shelf to the southwest of Vancouver Island.

bient noise, digitized at a sampling rate of 1500 Hz at an underwater electronics package, and the multiplexed data stream was transmitted from the surface float to a tending ship (CFAV ENDEAVOUR) over an rf link. The geometry of the experiment is illustrated in Fig. 2. The sound-speed profile in the water column was measured near the array site by CFAV ENDEAVOUR and at the end of the track by the shooting ship using expendable sound velocity probes (XSVs).

The ship track navigation was reconstructed using Global Positioning System (GPS) data that were recorded at 1-min intervals on the CSS W. E. RICKER and the array surface float. The uncertainty in source ranges from GPS was about ± 100 m. Since the ranges need to be known to a greater precision for the subsequent head wave analysis, the ranges were estimated by inverting the travel time differences of the waterborne signals.[12] The inversion used a simulated annealing search algorithm to optimize the model parameters that described the experimental geometry. Since the source depth and the array depth were known, the inversion estimated water depth, array tilt, and the range. Travel times were calculated by ray theory, using the measured sound-speed profile.

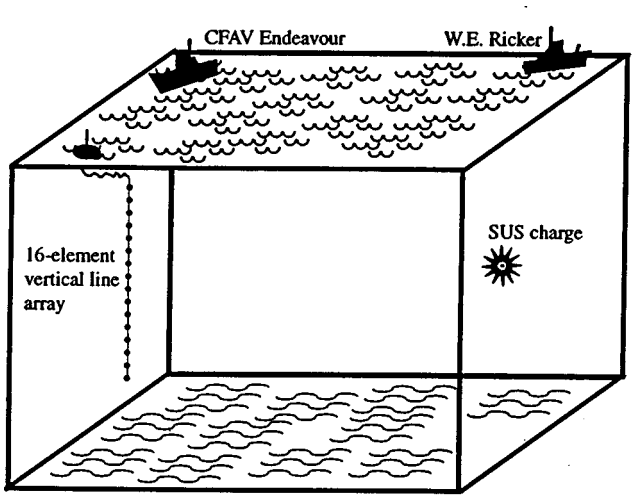

FIG. 2. The geometry of the experiment. The 16-element vertical hydrophone array was deployed and monitored by the CFAV ENDEAVOUR while the CSS W. E. RICKER opened range following the 400-m contour and released 0.82-kg SUS charges which exploded at a nominal depth of 200 m.

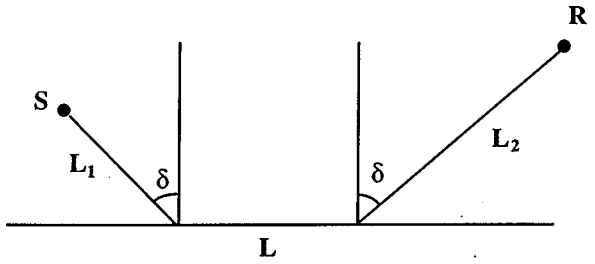

FIG. 3. Head wave trajectory in the problem of a spherical wave reflection from a plane interface of two homogeneous fluid half-spaces. *S*-sound source, *R*-receiver, $\delta = \arcsin n$ is critical angle of total reflection.

Although the environment was chosen as close to range independent as possible, there is a slight variation of bathymetry with range (<0.5 deg) and more significantly cross-range slope (1.5 deg). Likewise, the interfaces within the bottom may not be horizontally stratified, but there is very little constraint from ground truth data. Seismic profiles parallel to the track but taken in deeper water down the slope indicate horizons that are relatively flat.[13] Consequently (and also because the available acoustic data impose very limited constraint on the horizontal dependence of environmental parameters), we have assumed a layered earth model for the analysis of the head wave data that follows.

II. SOME THEORETICAL BACKGROUND

We interpret the observed acoustic signals arriving prior to the direct water wave, to be referred to as precursors, as *head waves*. The simplest problem that supports an acoustic head wave is the reflection of a spherical sound wave from a plane interface of a homogeneous fluid half-space of higher sound velocity. The acoustic pressure in the spectral component of the HW in the lower-speed ''upper'' medium is given by[14–16]

$$p = 2\,in\,S(\omega)[km(1-n^2)r^{1/2}L^{3/2}]^{-1} \times \exp[ik(L_1+L_2+nL)], \tag{1}$$

where $S(\omega)$ is the spectrum of the incident wave, ω is circular frequency, $k=\omega/c$ and c are, respectively, wave number and sound speed in the upper medium, $n<1$ is refraction index of the lower medium, m is ratio of lower and upper media densities, and r is source/receiver separation along the interface. The HW propagates along the interface as shown in Fig. 3, where L, L_1, and L_2 are the lengths of respective segments of the HW path in the lower and upper media.

Consider a more general environment where the sound speed and density are smooth, slowly varying functions $c(z)$ and $\rho(z)$ of depth z at $z>z_1$ and the half-space $z<z_1$ is occupied by a homogeneous fluid with parameters ρ_1 and c_1. We allow for attenuation of acoustic waves in the medium by attributing an imaginary part to the wave number: $k=\omega c^{-1}(1+i\beta/2\pi)$. Like the sound speed, the attenuation coefficient β is depth-dependent. For a given frequency, it

takes a constant value β_1 in the half-space $z<z_1$. Then, an omnidirectional point source at depth $z=z_s$ generates a HW[17] with acoustic pressure field

$$p=\frac{2i\rho(z_1)c_1S(\omega)}{\omega\rho_1 r^{1/2}L^{3/2}}\left(\frac{c_1^2}{c^2(z_1)}-1\right)^{-1/2}\times\left(\frac{c_1^2}{c^2(z)}-1\right)^{-1/4}\left(\frac{c_1^2}{c^2(z_s)}-1\right)^{-1/4}\times\exp\left[i\omega\tau-\frac{\omega\beta_1}{2\pi c_1}L-\frac{\omega}{2\pi}\left(\int_{z_1}^{z_s}+\int_{z_1}^{z}\right)\frac{\beta(z')dz'}{c(z')\sqrt{1-c^2(z')/c_1^2}}\right]. \quad (2)$$

The source spectrum here is normalized in such a way that in a homogeneous fluid the source would generate a spherical wave $S(\omega)\exp(ikR)/R$. In (2) $\rho(z_1)$ and $c(z_1)$ are the density and sound speed just above the interface $z=z_1$, L is the HW path length along the interface,

$$L=r-r_m, \quad r_m=\left(\int_{z_1}^{z_s}+\int_{z_1}^{z}\right)\left(\frac{c_1^2}{c^2(z')}-1\right)^{-1/2}dz', \quad (3)$$

and

$$\tau=\frac{r}{c_1}+\left(\int_{z_1}^{z_s}+\int_{z_1}^{z}\right)\sqrt{c^{-2}(z')-c_1^{-2}}dz' \quad (4)$$

is the travel time. The underlying assumption of a gradual depth-dependence of the fluid parameters in Eqs. (2)–(4) is required for ray considerations [or Wentzel–Kramers–Brillouin (WKB) solutions of 1-D wave equation] to be applicable in the analysis[17] of the wave field at $z>z_1$. We have also assumed, for simplicity, that attenuation per wavelength is small. Only linear terms in β are therefore retained in the exponent in (2); influence of the attenuation on the factor preceding the exponential in (2) is neglected. For the particular case when fluid is homogeneous at $z>z_1$ and attenuation is negligible, Eq. (2) reduces to Eq. (1).

When there exist interfaces between homogeneous or gradually inhomogeneous layers and, at the interfaces, the medium parameters vary over distances which are small compared to a wavelength or are discontinuous, a wave-theoretical analysis[17] and ray theory[2] give an expression for the HW[18] that differs from (2)–(4) in two respects. First, integrals over z in (2)–(4) are taken along the HW path, which may include several segments in any given layer other than the layer where the HW experiences critical reflection and propagates along the layer's interface. The number of segments in a layer is determined by the number of reflections that the HW experiences above and below it. In a horizontally stratified fluid, the HW path always has exactly one horizontal segment. Second, the expression for the complex HW amplitude in the right side of (2) should be multiplied by the product of respective transmission and reflection coefficients at the interfaces which a given HW penetrates or reflects from. The product of the reflection and transmission coefficients is exactly the same as as that for the complex amplitude of the usual ray that has the same grazing angle at the source and is reflected and transmitted at the same intermediate interfaces. However, unlike the HW, this ray is totally reflected at the interface where the HW is critically refracted (Fig. 4).

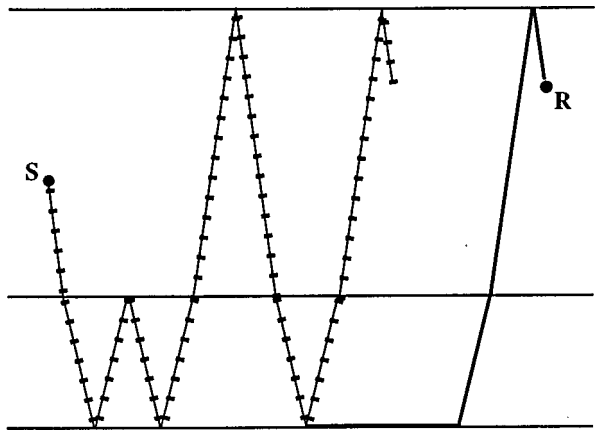

FIG. 4. Trajectory of a multiply reflected head wave in a layered medium (solid line) and associated conventional ray (dots).

Let us now note some characteristic properties of HWs in layered media that play an important role in the data analysis that follows. According to (4), HW travel time is a linear function of range and, within a layer of constant sound speed, of the receiver depth. For the point sound source, these features distinguish HW wavefronts from those of arrivals associated with bottom-reflected and refracted rays of geometric acoustics. Unlike normal modes, the group and phase velocities of HWs, according to (2) and (4), are nondispersive. In spite of differences in their trajectories, all HWs originating from a given layer have the same horizontal slowness, defined as the partial derivative of travel time with respect to range and equal to c_1^{-1} in Eq. (2). In the absence of absorption, the HW waveform is obtained by integration of that for the direct wave over time and, hence, the HW has a less sharp onset and a more broad ''tail.'' Absorption tends to strip high-frequency components of the wave and further slows the HW onset.

A stratified fluid with piece-wise continuous parameters supports a multitude of HW arrivals that differ, first, by the interface where they are critically refracted and, second, by their trajectory between the source and that interface. This is the environmental model we assume in interpreting experimental data. As discussed below, HW arrivals with the same horizontal slowness but different trajectories, and HW arrivals with different horizontal slownesses and coming from distinct interfaces within ocean bottom, have been observed in the experiment. In the case of an elastic bottom, the sound source may generate head waves that propagate as vertically polarized shear waves in some layers, further adding to the complexity of the precursor structure. However, we have not observed such HWs in the experimental data available and, therefore, do not discuss them in this paper.[19]

III. HEAD WAVE TRAVEL TIMES ANALYSIS

The acoustic data which form the basis of this study exhibit a rich structure of precursor head waves. The identification and classification of these waves was necessary in

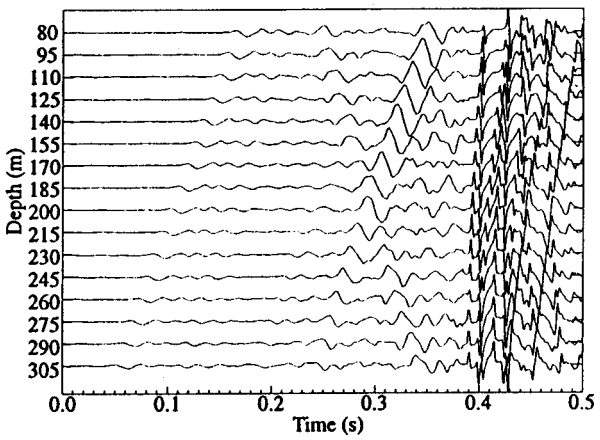

FIG. 5. Raw data. A 500-ms interval of data is shown. The trace for each hydrophone has been offset according to its position within the array. It is possible to clearly see the onset of the direct arrival at about 400 ms. The data prior to this have been multiplied by a factor of 10 so that they would be visible on the same scale as the direct arrival.

order to recover kinematic information, and also to determine other geoacoustic parameters of interest. When analyzing the arrivals which made up the data set, it was expected that the arrivals would fall into three distinct broad classes: conventional rays, head waves, and normal modes. For subsequent geoacoustic inversion, it was vital to discriminate between the arrivals which fell into these different classes. Several features facilitated the identification of conventional waterborne rays in contrast to either head waves or normal modes. The most striking of these was that at the source–receiver separations under consideration, the waterborne arrivals carried considerably more energy than the other arrivals. A second feature that assists in the identification of waterborne rays is that conventional rays exhibit curved wavefronts. The curvature of the wavefront can be identified by the vertical hydrophone array because the wavefront does not arrive at all the hydrophones simultaneously. This can be seen in a plot of arrival time against depth (Figs. 5 and 6), which is curved for these conventional rays.

The significance of distinguishing between head waves

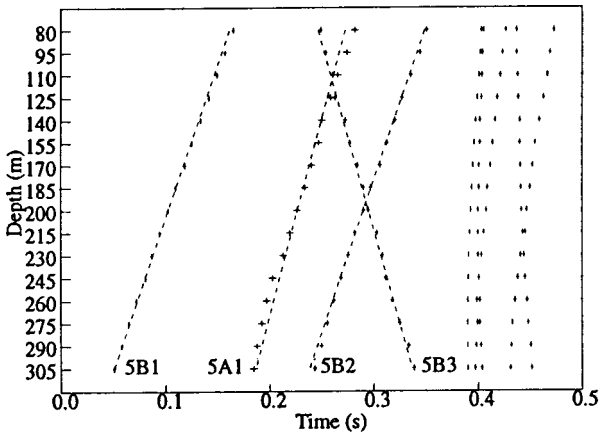

FIG. 6. Wavefronts of arrivals due to shot 5. The same 500-ms interval of data as in Fig. 5. The arrivals have been marked for both the precursors (5B1, 5A1, 5B2, and 5B3) and the waterborne waves. Note the linearity of the precursor arrivals' wavefronts as opposed to those of the water paths.

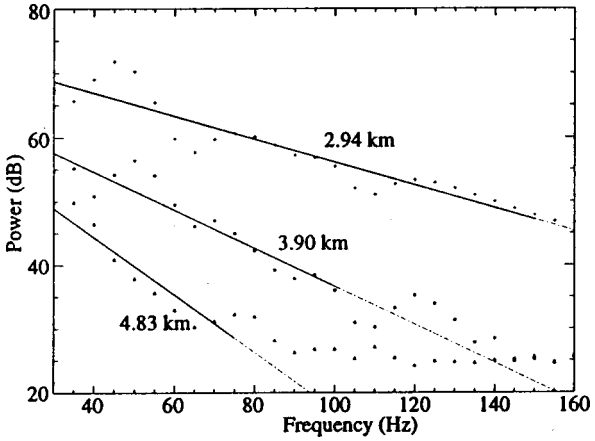

FIG. 7. Averaged power spectra. Depth-averaged power spectra for head waves from interface *B* and their linear approximation at three source–receiver separations: $r=2.94$ km (shot 4), 3.90 km (shot 5), and 4.83 km (shot 6).

and *normal modes* was discussed by Hall.[8] In contrast to conventional rays, both head waves and normal modes are predicted to have a linear dependence of arrival time on range. As will be seen in the subsequent analysis, frequency content of the precursor arrivals changed considerably from shot to shot due to sound absorption in the bottom (Fig. 7), but group velocity of the precursors remained unchanged. Hence, the precursors are not mode arrivals.

The arrivals for a source–receiver separation of 3.90 km are presented in Figs. 5 and 6. Figure 5 shows the raw data, with the precursor arrivals amplified by a factor of 10 so that they can be seen on the same scale as the waterborne arrivals. An initial precursor arrival, followed by a weaker precursor arrival that has a different but still linear dependence of arrival time on depth, are apparent in the data. In addition, the two later strong precursor arrivals exhibit similar dependence on depth to the initial precursor arrival. The linear dependence of the arrival time with receiver depth supports the hypothesis that these precursors represent head wave arrivals. For ease of identification, the arrivals were given labels which correspond to the interface from which they originate, and to the order in which they are detected by the deepest hydrophone of the vertical array. In this nomenclature, arrival B2 is the second arrival from interface *B* to be detected by the array. When arrivals from different shots need to be considered simultaneously, nomenclature like 5B2 is used where the first digit stands for the shot number. With this nomenclature in mind, the initial precursor arrival is seen to be arrival B1; it is followed by arrival A1, and then arrivals B2 and B3 intermesh. It is worth noting that since the reflection coefficient of the water surface is -1, the polarity of the arrivals B2 and B3 is consistent with each having been reflected once off the water surface. Figure 8 summarizes the paths that the waveforms take from source to receiver. The figure alludes to a third interface, designated *C*, which will be discussed at length below. The trajectories assigned are all in close agreement with ''zero intercepts,'' i.e., travel time projected back to zero range, for respective arrivals and with polarity of their waveforms.

The travel times for different HW arrivals are very ro-

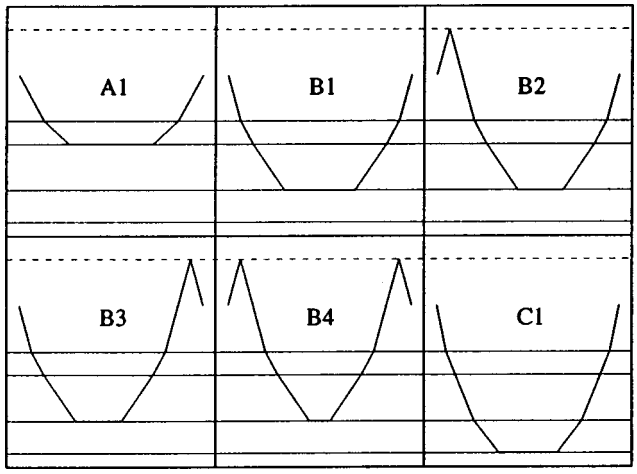

FIG. 8. Trajectories of identified head waves. This shows the interpreted trajectories of the precursor arrivals. All the trajectories are distinguished by having no reflections within the sediment layers.

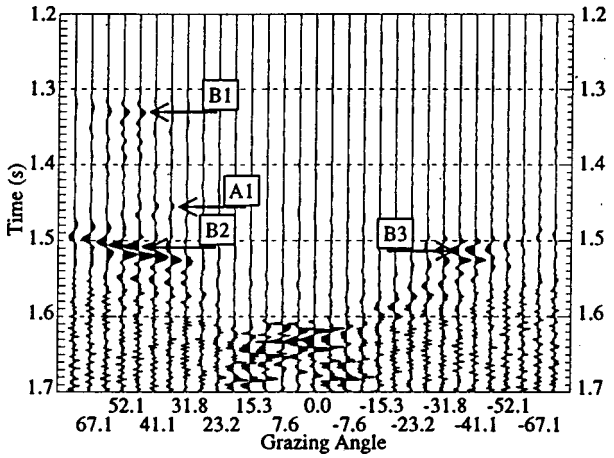

FIG. 9. Shot 5 data after beamforming. At a grazing angle about 0 deg the direct arrival can be seen. At an angle of 46 deg, arrivals 5B1 and 5B2 can be seen, while arrival 5B3 occurs at roughly the same time as 5B2, but at an angle of −41 deg. Between arrivals 5B1 and 5B2 we can see arrival 5A1 at an angle of 40 deg. The angles are given with respect to the VLA, which had an estimated tilt of 2.5 deg from the vertical in the case considered.

bust quantities whose accurate measurement provides a wealth of information about the structure of the sub-bottom layers. Since the shot instance was not measured in this experiment, the HW travel times were obtained by measuring the arrival time difference between the HW and the direct water path. The travel time for the direct path was then calculated based on the known source–receiver separation and the measured sound-speed profile of the water. This profile was constant at 1480 m/s ± 1 m/s over a depth range between 30-m depth and the sea floor, and in the upper 30 m the sound speed increased rapidly to 1494 m/s at a depth of 9 m. Since the uppermost hydrophone of the vertical array was within the isospeed water layer at a nominal depth of 80 m, the expected travel time of the direct water ray was calculated using a straight-line geometry approximation. To refine the travel time estimate, it was necessary to estimate the source depth using the bubble-pulse period of the waterborne arrival and the semiempirical formula for the depth of such sources developed in Ref. 20. In all cases, the depth of the sound source was found to be within 5 m of the nominal 200-m depth.

An additional technique that was used in the recovery of arrival time information for precursor waveforms was that of spatial filtering (time-delay beamforming).[21] This is carried out by adding the time series for each hydrophone with some offset. This operation transforms the time series from one for each hydrophone to a time series for each of a set of incidence angles at the vertical array. The process of offsetting the time series for the different hydrophones emphasizes the arrivals which occurred at the chosen angle and suppresses those at different incident angles. With each offset taken as an integer number of periods at the sampling frequency of 1500 Hz, the set of angles for which beamformer is evaluated is determined by hydrophone spacing in the array.

This technique proved particularly useful in distinguishing weaker head wave arrivals which were partially obscured by proximity in time with stronger arrivals. In Fig. 9 it is possible to distinguish arrivals which occur at different times with different incident angles. In particular, we can see three rising arrivals, two of which share a grazing angle of 46 deg, and separated by approximately 200 ms, and a weaker arrival, intermediate between these two, which has a grazing angle of 40 deg. These can be identified as the arrivals B1 and B2 with arrival A1 between them, as depicted in Figs. 5 and 6. In addition, arrival B3 can be seen at a different grazing angle, which clearly marks it as a surface reflected wave. From these considerations, it was possible to identify five separate sets of arrivals which represent two different propagation speeds.

Figure 10 shows the depth dependence of travel times of various arrivals overlaid by the theoretical depth dependence for the same arrivals. The first five profiles are from HWs identified as originating at interface *B*, the next two originate at interface *A*, and the final two profiles are those of the direct waterborne path for two different source–receiver separations. The horizontal error was assigned based on the difficulty of locating a maxima associated with the arrival, and the vertical error reflects the uncertainty in the array depth. The errors associated with arrivals from interface *A*

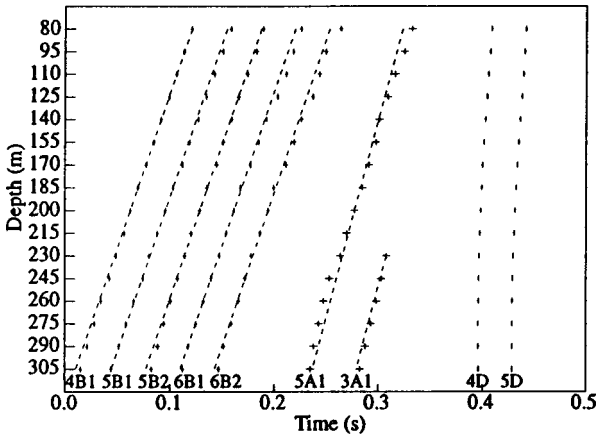

FIG. 10. Depth dependence of travel time for different arrivals. The vertical axis is the depth of the hydrophones within the array. The arrivals are marked with 4B1 indicating shot 4, arrival B1. The arrivals from interface *B* have a characteristic slope which is different from those from interface *A*.

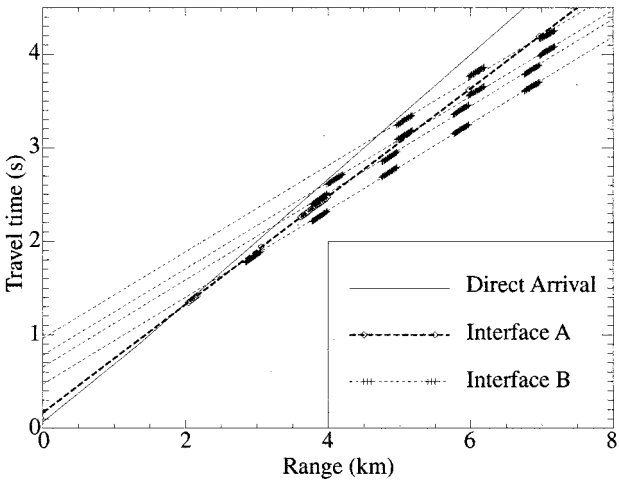

FIG. 11. Range dependence of travel times. Travel times of the direct water wave (solid line) and five distinct head waves (dashed lines) as a function of source–receiver separation. Symbols correspond to travel times measured at each hydrophone and recalculated to the lowest hydrophone depth.

are larger than those associated with interface *B* because the arrivals from interface *B* were stronger, and also the arrivals from interface *A* overlapped in time those from interface *B* which masked the signal from interface *A*. The deviation from the theoretical lines which can be observed near the top of the array results in part from the interference of an upgoing wave with a downgoing (surface reflected) wave. The arrival marked ''3A1'' contains only records for the lower hydrophones because for hydrophones above a depth of 230 m the direct water path arrival is the first recorded arrival, and the amplitude of the waterborne arrivals obscures the other arrivals. The direct water arrivals recorded in Fig. 10 have negligible error because the high-frequency content of the wave made it possible to determine the arrival time to within one sample at 1500 Hz. The contrast between the slopes of the first five arrivals pictured and the next two arrivals supports the inference that these are waveforms that propagate at different speeds. In addition, the profile of the direct arrivals is markedly different from the others, supporting the interpretation of them as a different type of arrival.

In Fig. 11 the travel time for the precursor waves is displayed as a function of range. The solid line represents the direct waterborne arrival. The arrivals at each hydrophone are recorded. These arrivals fall into several sets, each of which is characterized by a linear dependence of travel time on range, but these sets each appear to have one of two slopes. This pattern strongly suggests that all the arrivals which are depicted represent head waves which propagate along two separate interfaces with two distinct sound speeds. The set of arrivals which lie on the ''steeper'' slope corresponds to a sound speed of 1730 m/s$\pm$10 m/s, and the other sets of arrivals share a sound speed of 2149 m/s$\pm$5 m/s. From this, we inferred the existence of at least two sub-bottom layers. A linear fit to the arrivals with a sound speed of 1730 m/s indicates that these arrivals have a smaller ''zero intercept,'' which in turn suggests that the layer boundary that produced these head waves was the shallower of the two interfaces. The fact that the other sets of arrivals lie on lines corresponding to sound speeds which are identical to within the quoted errors suggests that these in fact are arrivals which have propagated along the same interface, but with different paths. In light of this, we designate the upper boundary of the shallower of the two sub-bottom layers interface *A*, and the upper boundary of the deeper of these layers interface *B*. In the upper corner of Fig. 11, there is a space between the reported arrivals and the calculated direct arrival. This does not indicate that there are no arrivals in this time window, but rather that the arrivals are intermingled in such a way that it is difficult to positively identify them.

For the purposes of further analysis (particularly, retrieving geoacoustic information from the precursors' power spectra), it was important to eliminate the possibility that the precursors were ''diving waves'' (Ref. 2, Chap. 6) which consist of refracted ray arrivals from a layer with positive sound-speed gradient. If the arrivals from interface *B* which are documented in Figs. 10 and 11 represented not true HWs but rather diving waves, it would be possible to observe in the time series an ''echo.'' This echo would be the result of the interaction between the principal diving ray and the ray which ''dived'' twice and reflected off the layer interface. In the approximation which is valid for small gradients, this difference in time would be given by $G^2L^3/(32c_s)$ (Ref. 2, Chap. 6) where the sound-speed profile is given by $c(z)=c_s(1+Gz)$ and L is the distance that the head wave would travel along the horizontal interface. For representative values: a sound-speed gradient of 1 s^{-1}, L of 2 km, and c_s of 2149 m/s, this corresponds to a time difference of 25 ms. In no case were arrivals with this structure observed, which argues against the hypothesis that these arrivals are produced by diving waves as opposed to true HWs. An additional and more stringent test that was performed compared the arrival times with those predicted by the expression for the travel time for diving waves. In the case of a small gradient, this is $\tau(r,z)=\tau_{\mathrm{HW}}(r,z)-G^2L^3/(24c_s)$ (Ref. 2, Chap. 6), where $\tau_{\mathrm{HW}}(r,z)$ is the linear range dependence of the head wave. Application of this formula yielded a gradient of 2.499 $\times10^{-2}$ s^{-1}. This gradient is negligible when compared with both the errors in the sound speed c, and with the observation, discussed in the next section, of an arrival from a layer with sound speed of 2349 m/s several hundred meters below interface *B*. These strongly indicate that the arrivals from interface *B* are true HWs rather than diving waves.

IV. NULLS OF THE POWER SPECTRUM

A salient feature of power spectra of the HWs is their complicated structure, including deep nulls at relatively low frequencies (Fig. 12). Positions of the nulls in the frequency domain depend on receiver range and depth. Thus, the nulls cannot be explained by deep minima in the source spectrum due to bubble pulses in the explosion waveform. Besides, for the explosion depths used in our experiment there are no such minima in the source spectrum at frequencies below 50 Hz.[20] Several conceivable propagation mechanisms were considered to explain the observed nulls, including (a) effect of the thickness of the homogeneous layer below interface *B* on the HW generation; (b) assumption that precursors associated with the interface *B* are diving waves (Ref. 2, Chap.

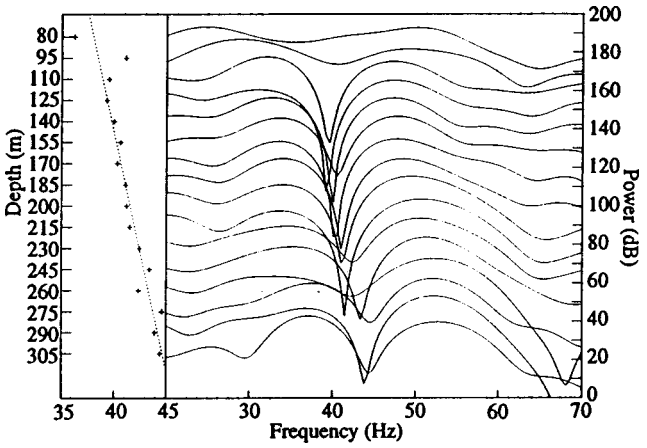

FIG. 12. Power spectrum of the precursor wave as a function of receiver depth for source–receiver separation of 3.90 km. The spectra corresponding to consecutive hydrophones are shifted by 12 dB for clarity. The position of the nulls of the power spectrum at about 40 Hz is shown to the left, as is a linear fit between this position and depth.

6), i.e., refracted ray arrivals from a layer with positive sound-speed gradient, rather than the HWs; (c) resonance attenuation[22] in a hypothetical thin sediment layer above the interface *B*, and (d) interference of arrivals with travel time difference less than the HW signal duration and, hence, less than the time-domain window used in calculating the power spectra. It has been found that only hypothesis (d) leads to properties of the spectrum nulls consistent with those observed in the experiment.

Consider the interference of two arrivals with travel times $\tau_1(r,z)$ and $\tau_2(r,z)$ (from the same sound source) recorded by a VLA. The travel time difference is assumed to be on the order of the signal duration or less, so that the arrivals are not separated in time. The condition for the destructive interference between the arrivals is given by

$$f_N(r,z)[\tau_1(r,z)-\tau_2(r,z)]=\mu+N, \quad N=0,\pm1,\pm2,\ldots. \tag{5}$$

Whether the power spectrum has a deep minimum (''null'') at given frequency f_N depends on the relative spectral amplitudes of the two interfering waves.

Note that $|N|$ in (5) is limited from above by the requirement that the travel time difference is smaller than the length of the time window used in the spectral analysis of the signal. The quantity μ in (5) is on the order of unity and depends on the type of interfering signals; μ is determined by the difference between the phase and the product $f\tau$ for each of the interfering waves. When their waveforms are similar (apart from a positive amplitude factor), $\mu=1/2$. When a wave interferes with a wave of the same type but has one extra surface reflection or when an HW interferes with a reflected wave that once touched a simple caustic (Ref. 16, Sec. 6.1), then $\mu=0$. If two ray arrivals interfere and their numbers of contact with caustics differ by 1, then $\mu=1/4$, etc.

The frequency minima are functions of range and depth, reflecting the similar dependence on range and depth for the travel time difference. Differentiating (5) with respect to depth, one obtains

$$\frac{1}{f_N}\frac{\partial f_N}{\partial z}=\frac{\cos\theta_1(r,z)-\cos\theta_2(r,z)}{c(r,z)[\tau_1(r,z)-\tau_2(r,z)]}, \tag{6}$$

where θ_1 and θ_2 are the angles of incidence of the respective arrivals. Unless the two waves have equal incidence angles, adjacent hydrophones in the array will record the spectral minima at slightly different frequencies. Note that f_N may increase or decrease with depth, depending on the order in which the two waves arrive and on their incidence angles. For instance, when both arrivals come to the array from below, f_N increases with depth when travel time of the steeper arrival is greater than that of the shallower arrival.

If spectral minima are recorded on a VLA and one of the two interfering waves is known, Eqs. (5) and (6) provide the means to determine travel time and incidence angle of the other wave to within an integer *N*.

Now, we apply the above considerations to the experimental data, and consider specifically the first precursor arrival for shot 5. The travel time analysis suggests that this part of the precursor is a HW of the type B1. The power spectra of the precursor (Fig. 12) clearly exhibit very deep nulls for all hydrophones except for two upper ones at frequencies from 39.2 to 44.6 Hz. A time window of 0.130-s length bracketing the arrival was used in the processing. For the two uppermost hydrophones, interference between HWs B1 and B2 distorts the spectrum. Note also interference-like maxima at frequencies smaller and greater than the deep nulls. The nulls at 39.2 to 44.6 Hz being much deeper than at other frequencies can be explained by noting that spectral amplitude variation is not exactly the same for the two waves. In other words, destructive interference occurs, according to (5), at a number of frequencies, but deep spectral nulls occur only when an additional condition of waves' amplitudes being close is met.

In the left panel of Fig. 12, the frequencies at which spectral nulls are observed are plotted vs hydrophone depth. For the lower 14 hydrophones in the array, a least-squares fit gives $\partial f_N/\partial z=(27.6\pm4.4)\times10^{-3}$ Hz/m for the slope of the null frequency depth dependence.

To verify the interpretation of the nulls as an interference phenomenon, spatial filtering was applied to the VLA data. The results are shown in Fig. 13, where the array response is plotted vs time. The angles correspond to directions from 80.7° to 0° (horizontal). The beamforming result reveals *two* arrivals with similar waveforms and travel time difference of about 60 ms. Within the accuracy of the spatial filtering,[23] the travel time and grazing angle of the stronger, earlier arrival coincides with those of HW B1, as expected. The travel time difference agrees with the value that follows from the destructive interference condition (5) with $\mu=1/2$ and $N=2$, while the difference in incidence angles of the two arrivals is consistent with that predicted by (6) from the measured $\partial f_N/\partial z$. Note that μ being equal to 1/2 in (5) suggests that the second (later and weaker) arrival is a HW like the first arrival. The similarity of the waveforms strongly supports this supposition.

Similar analysis was applied to precursors from shots 4 and 6 that show strong spectral nulls at frequencies 34.4–37.4 Hz and 21.2–23.4 Hz, respectively. All these data can

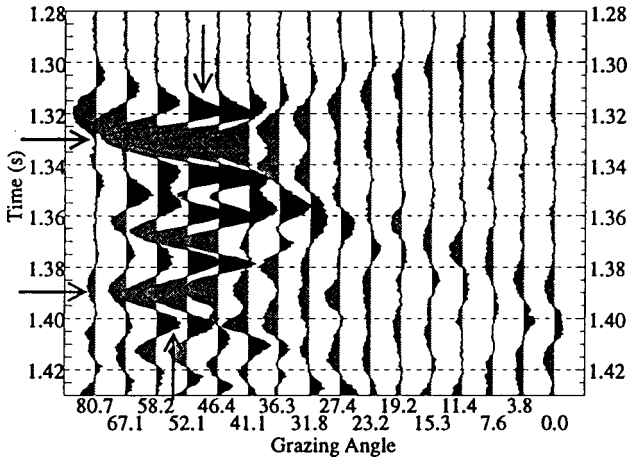

FIG. 13. A selected precursor arrival from shot 5 after beamforming. Arrival 5B1 can be seen at 1.33 s, at a grazing angle of 50 deg, and different arrival can be seen at 1.39 s at a grazing angle of 55 deg. This second arrival produces the deep nulls in the power spectrum seen in Fig. 12.

be explained, within experimental errors, by the hypothesis that the wave interfering with HW B1 is a HW C1 coming from some deeper interface *C*. Using Eqs. (5), (6), and the beamforming technique, the sound speed c_C below interface *C* can be determined in a variety of ways. In particular, one can find c_C from the incidence angle of the later arrival at Fig. 13, or from slope $\partial f_N/\partial z$, or from travel time variation from one shot to another. All the approaches lead to essentially the same value of c_C, albeit with rather different error margins. The quantitative estimates with the least uncertainty are derived from the travel time difference between shots 5 and 4 because travel times of HW C1 can be found very accurately from the null frequencies. In this way, the sound speed below interface *C* is 2349 ± 12 m/s. The ''zero intercept'' associated with the HW C1, that is, its travel time extrapolated to zero range, is estimated as 0.676 s. Note that accuracy of measuring c_C and the zero intercept from the spectral nulls is comparable to the accuracy of more direct measurements of analogous quantities for other HWs presented in Sec. III.

V. ESTIMATES OF ATTENUATION

The HW power spectra are characterized by three distinct frequency ranges. At low frequencies, power spectra are complicated because of interference of waves reflected from various interfaces within sediments. At intermediate frequencies, the spectra are more regular in terms of their depth and frequency dependence, with a monotone decrease in amplitude as frequency increases being the dominant trend. At high frequencies, the HW power spectrum flattens off when it reaches the ambient noise level.

The attenuation of acoustic waves in the ocean bottom accounts for most of the HW amplitude decrease in the intermediate frequency range. Comparison of the HW and source power spectra in this frequency range shows that, as long as signal-to-noise ratio (SNR) is positive, the rate of decrease for the HW spectra is large compared to decay rate for the source spectrum $S(\omega)$ (Ref. 20) of the explosive sources used in the experiment. The HW power spectral decay rate is also significantly more rapid than that of the function $S(\omega)/\omega^2$, which, according to (2), is proportional to the HW spectrum in the absence of attenuation. Naturally, the intermediate frequency range, where effects of absorption dominate over interference but signal-to-noise ratio remains sufficiently large, shifts towards lower frequencies for more distant sources (see Fig. 7) because attenuation accumulates with distance.

The attenuation coefficient in sediment layer *B* can be estimated from the spectral variation with range and frequency in the intermediate frequency band. For these frequencies (a) the spectra exhibit regular, predictable variation as functions of frequency and position, and (b) there exists a simple relation between the attenuation coefficient and certain parameters of the spectra.

It follows from the discussion in Sec. II [cf. Eq. (2)], that ratio of the HW amplitudes at ranges r_1 and r_2 from the source equals

$$|p(r_2,\omega)/p(r_1,\omega)| = \left[\frac{L^3(r_1)r_1}{L^3(r_2)r_2}\right]^{1/2} \exp\left(-\omega\beta_B(\omega)\frac{r_2-r_1}{c_B}\right). \quad (7)$$

We took into account that for any given HW type $L(r_2) - L(r_1) = r_2 - r_1$. Here, as before, *L* is the HW path length along interface *B*, and c_B and β_B are, respectively, the sound speed and the attenuation coefficient just below *B*. Note that the ratio of the amplitudes does not depend on (unknown) reflection and transmission coefficients at intermediate interfaces in the sediment that the HW intersects on its way from to the interface *B* and back to water. Moreover, the logarithmic derivative of the amplitude ratio with respect to frequency does not depend on $L(r)$. Hence, the attenuation coefficient β_B can be determined[17] without knowledge of the sound-speed variation above the interface *B*.[24]

The power spectra of HW B1 for three shot ranges are plotted on a logarithmic scale in Fig. 7. The power spectra have been averaged over hydrophone depth.[25] According to (7), the observed linear frequency dependence of the logarithm of the HW amplitude ratio for two shots corresponds to the frequency-independent attenuation coefficient expressed in dB per wavelength.

Using the spectral slopes of the spectra, i.e., $d(20\log|p|)/df$, determined for three shots, we have obtained the estimate $\beta_B = 0.32 \pm 0.05$ dB/λ for the attenuation coefficient. Previously determined values of c_B and ranges have been used in deriving the estimate. Three distinct methods of averaging HW amplitudes over depth have been used: averaging spectral amplitudes squared, averaging logarithms of power spectra calculated for individual hydrophones, and coherent averaging of HW time series prior to calculating spectra. Within the accuracy of the estimate, the three averaging methods have given the same average value of β_B but somewhat different deviations from the mean. For instance, the estimates of β_B are within 0.02 dB/λ for all the combinations of ranges when averaging of spectral amplitudes squared is used.

With source/receiver separation increasing beyond 5 km, the available data become less suitable for estimates of ab-

sorption because the frequency range where SNR is positive decreases. Nevertheless, when the analysis described above is applied to shot 7 at a distance of 5.84 km from the array, the experimentally measured slope of the HW power spectrum agrees within 3% with the value predicted using $\beta_B = 0.32\,\mathrm{dB}/\lambda$, and, hence, confirms the attenuation coefficient estimate derived from data for shots 4, 5, and 6. However, the absolute value of the HW amplitude is 5–6 dB stronger than expected from extrapolating the data for shots 4, 5, and 6. The reason for this increase in the amplitude is not clear. It is possible that the amplification is a three-dimensional effect resulting from HW rays focusing in the horizontal plane due to range dependence of sediment parameters and/or cross-range slope. Such an interpretation is consistent with the facts that the amplitude increase is uniform in frequency and that deviations from our HW model based on layered-medium approximation become more pronounced with range at longer ranges. Significant deviations from the range-independent model for shot 7 and more distant shots have also been noted in the analysis[12] of travel times of surface- and bottom-reflected arrivals.

So far, we assumed for simplicity that the power spectra of the precursors considered are those of HW B1. In fact, as discussed in Sec. IV, travel times of HWs B1 and C1 are very close for shots 4, 5, and 6, and the power spectra in Fig. 7 actually refer to a superposition of the two HWs. Interference of HWs may be responsible, in part, for the ''oscillations'' of the power spectra at Fig. 7 about their linear approximations. However, interference of the HWs essentially does not change the above estimates of the attenuation coefficient. This is for two reasons. First, in the intermediate frequency range used for the estimates, HW C1 is considerably weaker than HW B1. Second, after depth- and frequency-averaging, contributions of the HWs (even if these were of comparable amplitude) to the slopes of the power spectra are expected to be additive. Note also that variations from shot to shot in the length L of horizontal segment of their trajectory are the same for both HWs. Hence, the estimate of attenuation coefficient is, in fact, a weighted average of attenuation coefficients below interfaces *B* and *C*, with intensities of the HWs B1 and C1 being the weights. As we do not consider depth dependence of attenuation, the difference between the attenuation coefficient below interface *B* and the weighted average is of secondary importance.

Power spectra of HWs B2 and later HWs were too noisy to be used for estimates of β_B. Higher noise level for such HWs can be attributed to the presence of many waves scattered in the bottom that have close travel times. The HW B1 with the highest group velocity is obviously contaminated by such interference to a much lesser degree. Unfortunately, we do not have enough data for HWs A1 to apply the above analysis to estimate compressional wave attenuation in the vicinity of the interface *A*.

VI. DISCUSSION: A GEOACOUSTIC MODEL

As demonstrated in the previous sections, HW arrival times and power spectra have enabled us to establish existence of three distinct interfaces within ocean bottom, measure the associated compressional wave velocities, and estimate the compressional wave attenuation coefficient characteristic of the deeper sediment layers. The determination of the sound speed has been based on the *variation* of HW travel time with range. Additional information about the sound speed profile $c(z)$ in the ocean bottom is contained in the *absolute value* of the HW travel time at a given range or, equivalently, in the value of the travel time extrapolated to zero range. This value has been referred to as the zero intercept in Sec. III.

The zero intercepts have been reliably measured for HWs from all three interfaces, and can be used to determine parameters of the sound-speed profile in the sediment. HWs originating from the same interface but having different trajectories above it have different zero intercepts but, in a layered medium, do not provide independent information about $c(z)$. This is because these HWs have equal incidence angles at each depth. Therefore, the zero intercepts for HWs B1, B2, B3, and B4 cannot be used to obtain four integral equations on $c(z)$ but instead have been utilized to determine the zero intercept for HW B1 to a high accuracy.

In addition to travel time, constraints on the sound-speed profile occur from the very fact that the HW arrival is observed at a given point. Because the length L of the horizontal segment of HW path must be positive, the HW exists[26,27] only at ranges $r > r_m(z, z_s)$. The limiting range r_m as a function of source and receiver depths is defined in (3). The sound-speed profile should be such that $r_m(z, z_s)$ does not exceed the minimal range at which a HW arrival of a given type is received. Unlike data on the zero intercepts, this requirement does not provide an equation to determine a parameter of the sound-speed profile but rather a set of inequalities that limits the possible range of variations of the parameters determining the sound-speed profile on the bottom.

Although the HW data are insufficient to uniquely determine the geoacoustic profile of the stratified ocean bottom, it is possible to construct a set of *plausible* geoacoustic models that are consistent with the data. We will be interested in the simplest possible, low-parameter profile $c(z)$ consistent with the data. To keep the geoacoustic model simple, we assume monotone dependence of sound speed on depth and do not introduce any interfaces within the sediment other than the interfaces *A*, *B*, and *C*. We further assume that the sound speed is constant between the interfaces *A* and *B*, *B* and *C*, and below *C*. Then, the sound speeds in the three layers are known from the analysis in Secs. III and IV.

If one assumes that the sound speed is constant in the layer between the water/sediment interface and the interface *A*, then there are four unknown parameters (sound speed c_u in the upper layer and depths of the interfaces *A*, *B*, and *C*) and three algebraic equations relating these parameters to known zero intercepts for HWs from the three interfaces. Given the sound speed c_u, the other three parameters can be easily determined. It turns out, however, that for any c_u value greater than sound speed in water and smaller than the sound speed c_A in the next deepest layer, the limiting range r_m (3) for the HW C1 is greater than the range $r = 2.94$ km at which it was observed in the experiment. Hence, such an environmental model is not consistent with the data. Besides,

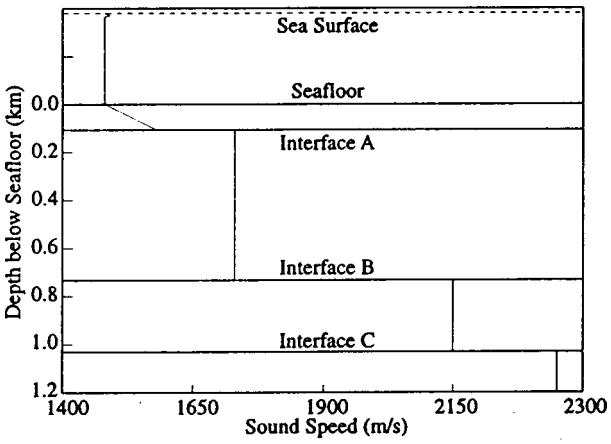

FIG. 14. The simplest geophysical model consistent with the experimental data. The sound-speed profile of a plausible geoacoustic model corresponds to a gradient of 1.0 s^{-1} in the top sediment layer. The interfaces discussed in the text are labeled.

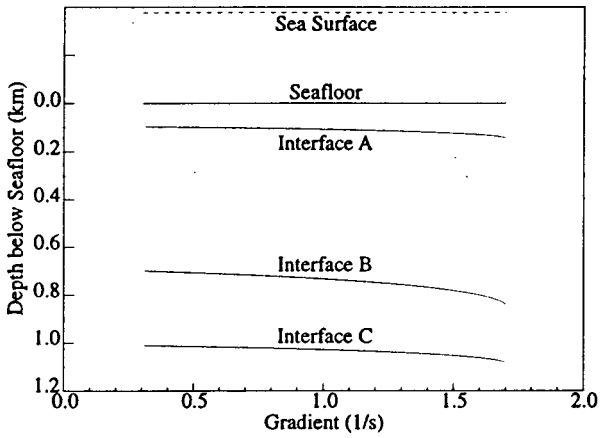

FIG. 15. Subsurface structure versus sound-speed gradient. The depth of the different interfaces is shown as a function of the gradient γ in the top sediment layer. No gradient below 0.3 s^{-1} is shown because these will not produce head wave C1 in the region in which it was observed. Similarly, gradients above 1.7 s^{-1} are not shown because they violate the assumption of monotone variation of sound speed with depth.

the assumption of a sound-speed discontinuity at the water/sediment interface is hard to reconcile with two other experimental facts, namely, lack of noticeable reflection of head waves from the water/sediment interface and absence of a HW originated at that interface.

As the next simplest model, we assume that the sound speed in the sediment layer above interface *A* is a linear function of depth, and continuous at the water/sediment interface for the reasons indicated above. (The latter assumption is also in agreement with the results of matched-field inversion[28] of an entirely different acoustic data set obtained at the same experimental site. The matched-field inversion gives surficial values of the bottom sound speed within several meters per second of the sound speed in water.) Note also that a linear increase in the sound speed with depth provides a more realistic model of the upper, unconsolidated portion of sediments than a homogeneous layer. The layers between the interfaces *A* and *B*, *B* and *C*, and below *C* are supposed to be homogeneous, as before. The depth dependence of the sound speed in the model is shown in Fig. 14. Again, there are three algebraic equations relating four unknown parameters. For any given value of the sound-speed gradient in the upper sediment layer, thickness of the layer (as well as that of two underlying layers) is calculated from the known values of the zero intercepts for the three HWs. Results of the inversion are presented in Fig. 15 as a function of the sound-speed gradient $\gamma = dc/dz$ in the top sediment layer. The admissible values of γ are bounded from above by $\gamma_U = 1.7\,s^{-1}$ due to the assumption of monotone $c(z)$ and from below by the requirement that the limiting range r_m is smaller than the actual source–receiver horizontal separation for all the HWs observed. HW C1 has the greatest limiting range and therefore determines the lower bound γ_L for γ. Taking the uncertainty in the range measurements into account, γ_L is estimated to be 0.3 s^{-1}.

Within the admissible range of variation for γ, with γ increasing, the thickness of the gradient layer above interface *A* increases from 95 to 142 m, the thickness of the layer between the interfaces *A* and *B* increases from 600 to 690 m, while the thickness of the layer between the interfaces *B* and *C* decreases from 310 to 245 m. Estimated depths of the interfaces from the sea floor increase with γ monotonically (Fig. 15), with depth of the interface *B* experiencing the strongest variation of 137 m.

VII. CONCLUSION

In this paper, we reported the analysis of precursor arrivals from small explosive charges deployed in a shallow water environment off Vancouver Island during the Pacific Shelf experiment of 1993. The analysis concentrated on arrivals recorded by a VLA from shots at ranges between 2 and 8 km. We demonstrated that the observed precursors were head waves originating from three distinct interfaces within the ocean bottom. Compressional wave velocities in three subbottom layers (the layers below interfaces *A*, *B*, and *C* in Fig. 14) were measured from HW travel times to be 1730 ± 10 m/s, 2149 ± 5 m/s, and 2349 ± 12 m/s. A plausible geoacoustic model consistent with the available HW data was constructed that describes the sound-speed variation in the upper 1100–1200 m of the ocean bottom (Fig. 15). The model consists of a top layer with linearly increasing sound speed overlying three homogeneous deeper layers.

In spite of considerable uncertainty in the properties of the sediments above the interface *B* that prevented us from calculating the absolute amplitude of the HWs, the estimation of the attenuation coefficient was made possible using a technique described in Ref. 17. The technique is based on the range variation of the logarithmic derivative of the HW power spectrum with respect to frequency. This quantity is determined by the attenuation in the layer where the HW propagates horizontally and, in stratified media, is affected by neither properties of the overburden nor uncertainties in the source spectrum.[17] For the layer between interfaces *B* and *C* in Fig. 14, we estimated the attenuation coefficient of compressional waves to be 0.32 ± 0.05 dB/λ. We conclude that, with explosive sound sources, this simple technique allows one to retrieve from HW data important additional informa-

tion on physical parameters of the sediments. To our knowledge, the technique has never been applied previously to experimental data.

A distinctive feature of the experimental design is the combination of a vertical aperture provided by a VLA and a synthesized horizontal aperture provided by shots at different ranges from the VLA. In shallow water, the structure of the precursors is relatively complex due to an overlap in the time domain of arrivals reflected at the ocean surface and/or interfaces within the bottom. Successful identification of most HW arrivals, as described in Sec. III above, relied on the VLA. In particular, HWs from interface *A* do not separate in time from other precursors and would not be found without spatial filtering of the VLA data. Similarly, the systematic pattern of interference nulls that led to the identification of a HW from interface *C* and a measurement of the HW travel time could not be observed without a VLA. Vertical dependence of travel times was used also to distinguish between HWs and conventional ray arrivals. In addition, the VLA was required to determine the attenuation coefficient because point measurements did not provide sufficient signal-to-noise ratio in the frequency range suitable for attenuation estimates. With single-hydrophone data, it would be possible to determine only the sound speed below interface *B* and a single constraint relating the depth of the interface to the average sound speed above it. There would be no vertical resolution in such an inversion. On the other hand, for the given experimental site, geometry, and sound sources, vertical data alone proved to be insufficient for accurate estimates of geoacoustic parameters. It is the simultaneous use of the data for both vertical and horizontal apertures that accounts for the accuracy and vertical resolution of the geoacoustic profile that was estimated in this inversion.

ACKNOWLEDGMENT

This work was supported by NSERC and the Department of National Defence, Canada.

[1] C. B. Officer, *Introduction to the Theory of Sound Transmission: with Application to the Ocean* (McGraw-Hill, New York, 1958).
[2] V. Červený and R. Ravindra, *Theory of Seismic Head Waves* (University of Toronto Press, Toronto, 1971).
[3] C. B. Officer and M. Ewing, ''Geophysical investigation in the emerged and submerged Atlantic coastal plain, Part VII,'' Bull. Geol. Soc. Am. **65**, 653 (1954).
[4] H. F. Weichart, ''Application of geophysical methods and equipment to explore the sea bottom,'' in *Bottom-Interacting Ocean Acoustics*, edited by W. A. Kuperman and F. B. Jensen (Plenum, New York, 1980), pp. 53–71.
[5] D. M. F. Chapman and D. D. Ellis, ''Propagation loss modelling on the Scotian shelf: The geo-acoustic model,'' in *Bottom-Interacting Ocean Acoustics*, edited by W. A. Kuperman and F. B. Jensen (Plenum, New York, 1980), pp. 525–539.
[6] A. G. McKay and P. M. McKay, ''Compressional-wave velocity measurement in seabed materials by use of equipment deployed near, but above the bottom,'' J. Acoust. Soc. Am. **71**, 871–877 (1982).
[7] A. G. McKay, J. A. Hunter, R. L. Good, and D. M. F. Chapman, ''A 12-channel marine eel for shallow refraction surveying of the seabottom in coastal waters,'' in *Ocean Seismo-Acoustics*, edited by T. Akal and J. M. Berkson (Plenum, New York, 1986), pp. 871–880.
[8] M. V. Hall, ''Measurement of seabed sound speeds from head waves in shallow water,'' IEEE J. Ocean Eng. **OE-21**, 413–422 (1996).
[9] J. A. Hunter and S. E. Pullan, ''A vertical array method for shallow seismic refraction surveying of the sea floor,'' Geophysics **55**, 92–96 (1990).
[10] D. F. Gingras and P. Gerstoft, ''Inversion for geometric and geoacoustic parameters in shallow water: Experimental results,'' J. Acoust. Soc. Am. **97**, 3589–3598 (1995).
[11] N. R. Chapman and C. E. Lindsay, ''Matched field inversion for geoacoustic model parameters in shallow water,'' IEEE J. Ocean Eng. **OE-21**, 347–354 (1996).
[12] D. E. Hannay, ''Broadband matched field processing for geoacoustic parameter estimation.'' Defense Research Establishment Pacific. Technical Report DREA\CR\96\402SPK, March, 1996.
[13] R. D. Hyndman, G. D. Spence, T. Yuan, and E. E. Davis, ''Regional geophysics and structural framework of the Vancouver Island margin accretionary prism,'' in Proceedings of the Ocean Drilling Program, Initial reports, Vol. 146 (part 1), pp. 399–419 (1994).
[14] L. M. Brekhovskikh, *Waves in Layered Media*, 2nd ed. (Academic, New York, 1980), Chap. 4, pp. 255–266.
[15] K. Aki and P. G. Richards, *Quantitative Seismology. Theory and Methods* (Freeman, San Francisco, 1980), Vol. 1, pp. 208–214.
[16] L. M. Brekhovskikh and O. A. Godin, *Acoustics of Layered Media. 2: Point Sources and Bounded Beams* (Springer, Berlin, 1992), Chap. 3, pp. 76–95.
[17] O. A. Godin, ''Low-frequency acoustic lateral waves in the ocean,'' Oceanology **26**, 442–445 (1986).
[18] In the narrow meaning of the word, the term *head* (or *lateral*) *wave* refers to the field component that is associated with a branch point in the plane-wave integral representation of wave field in a layered medium (Refs. 14–16). Then, a HW is necessarily related to propagation in a semi-infinite half-space along its boundary, as opposed to propagation along a boundary of two layers of finite thickness; and horizontal slowness of the HW equals the reciprocal of wave speed in the half-space. In this article, we use the term *head wave* more loosely. With impulse excitation and thickness of layers large enough, contributions to the field similar to the true HW can arise from finite layers as well. Such arrivals propagate, as a part of their trajectory, along the upper boundary of a layer with little interaction with its lower boundary. We refer to such waves as HWs as well. In the ray treatment of HWs (Ref. 2) such arrivals are predicted naturally because wave reflection at an interface is considered as a local process. In the wave-theoretical treatment of the problem (Ref. 16), HWs from an interface of finite layers can be analyzed much like true HWs if the field due to an incident plane wave is developed into a series in orders of reflection from the interface prior to reducing the original integral over plane waves into integrals along the steepest decent path and integrals around branch cuts that lead to HWs. (For more details, see Ref. 16, pp. 93–95, and references therein.)
[19] Lack of (identifiable) shear-related HWs in the data suggests that the shear wave velocity in upper sediments (above and immediately below interface *B*, see Sec. III) is smaller than the sound speed in water. Similar restriction on the shear velocity follows also from the estimated values of compressional velocity $c(z)$ (Secs. III and IV) in the sediment and the fact that shear velocity can not excede $2^{-1/2}c(z)$. This is a rather weak constraint on the shear velocity, though. Geological information available points toward shear velocities not exceeding one half of the water sound speed for the upper portion of the ocean bottom considered.
[20] N. R. Chapman, ''Source levels of shallow explosive charges,'' J. Acoust. Soc. Am. **84**, 697–702 (1988).
[21] W. S. Burdic, *Underwater Acoustic System Analysis* (Prentice-Hall, Englewood Cliffs, NJ, 1984), Chap. 11, pp. 322–360.
[22] N. R. Chapman and D. M. F. Chapman, ''A coherent ray model of plane-wave reflection from a thin sediment layer,'' J. Acoust. Soc. Am. **94**, 2731–2738 (1993).
[23] Numerical simulations performed under conditions mimicking those of the experiment enabled us to determine that, in spite of limited array length and number of hydrophones, the errors in determining HW and ray travel times using beamforming do not exceed a few milliseconds. The error in the incidence angle is more pronounced and depends on the incidence angle itself. For arrivals with incidence angle of about 45°, uncertainty may reach 5°–6°.
[24] It can be demonstrated that, as long as HWs of the same type are considered at two distinct ranges, the relation between the attenuation coefficient and the logarithmic derivative of the pressure amplitudes remains the same when shear modulus is nonzero in the sediments. This is because in layered media variation in the HW field with range is entirely due to variation in the length *L* of HW path along the interface *B*.

[25] In principle, the depth dependence of HW amplitudes can be used to determine attenuation coefficient, in a similar manner to using the range dependence. However, in our experiment variation in the path length L corresponding to the depth change between lowest and uppermost hydrophone in the array is about 20% of the L variation due to the range change from one shot to another. HW amplitude variation across the array aperture turned out to be too small for an accurate evaluation of the attenuation coefficient.

[26] When sound absorption in the bottom is taken into account, diffraction theory (Ref. 27; Ref. 16, pp. 85–90) predicts that the limiting range is somewhat greater than r_m (3).

[27] O. A. Godin, ''On the high-frequency theory of lateral waves,'' Wave Motion **6**, 105–117 (1984).

[28] M. Musil, ''Range-Dependent Matched-Field Inversion Using the Downhill Simplex Algorithm,'' M.S. thesis (University of Victoria, Victoria, 1998).

Anomalous absorption of bulk shear acoustic waves by an ultra-thin layer of a non-Newtonian fluid

Dmitri K. Gramotnev and Melissa L. Mather
Centre for Medical and Health Physics, School of Physical Sciences, Queensland University of Technology, GPO Box 2434, Brisbane, QLD 4001, Australia

(Received 24 April 1998; revised 14 June 1998; accepted 30 June 1999)

A strong maximum of absorptivity (as much as dozens of per cent) of bulk shear acoustic waves by an ultra-thin layer of a non-Newtonian fluid between two solid surfaces is shown to be achieved at an optimal layer thickness. This optimal thickness is demonstrated to be usually much smaller than the wavelength and the wave penetration depth in the fluid. The coefficients of reflection, transmission, and absorption of shear waves polarized perpendicular to the plane of incidence are determined as functions of incidence angle, layer thickness, fluid viscosity, relaxation time(s), frequency, and parameters of solids. A frictional contact approximation, in which the layer can be considered as a contact with friction is justified for non-Newtonian fluids. The anomalous absorption of bulk shear waves in thin nonuniform fluid layers with viscosity and/or relaxation time varying across the layer is analyzed in the frictional contact approximation. It is shown that unlike the anomalous absorption in Newtonian fluids, the anomalous absorption in non-Newtonian fluid layers is frequency dependent even in the frictional contact approximation. This dependence is analyzed analytically and numerically.
[S0001-4966(99)04010-2]

PACS numbers: 43.35.Bf [HEB]

INTRODUCTION

Acoustic waves in the vicinity of solid–fluid interfaces are intensively investigated theoretically and experimentally from the viewpoint of their application for design of highly sensitive viscosity sensors and methods for investigation and diagnostics of solid–fluid interfaces.[1–13] The main advantages of acoustic methods for fluid analysis are related with possible miniaturization of the acoustic devices, possibility of investigation of small amounts of fluids, high sensitivity of measurements (when using surface acoustic waves or plate modes[6–12]), small time of measurements, and possibility of investigation of high-frequency properties of fluids. In addition to this, very small penetration depth of shear waves, especially in low-viscosity fluids, makes it possible to use acoustic waves for analysis of regions of fluid in the immediate proximity to a solid–fluid interface, i.e., directly investigate these interfaces and their effect on fluid structure.

The anomalous absorption of acoustic waves by a thin layer of viscous fluid enclosed between elastic solid media[14–19] opens a new direction in development of acoustic methods for fluid diagnostics. This effect makes possible further substantial improvement of several important parameters of acoustic viscosity sensors and diagnostics techniques. For example, strongly increased absorptivity in a fluid layer, as compared with the semi-infinite fluid, will result in a substantial increase of sensor sensitivity. Methods based on the anomalous absorption will allow investigation of extremely small amounts of fluids (less than $10^{-5}\,\mathrm{cm}^3$). Due to the absorption taking place in a fluid layer, that is sometimes as thin as 10–100 nm, the anomalous absorption will enable investigation of fluid in extreme proximity to solid interfaces, thus enabling precise analysis of solid–fluid interfaces.

Use of high-frequency acoustic waves for fluid diagnostics is essential, because this may provide additional information about relaxation processes in fluids, microscopic structure of fluids, interactions at solid–fluid interfaces, etc. In addition, high-frequency acoustic waves are convenient for practical use since they can be easily generated and detected, and allow miniaturization of acoustic devices. At high frequencies almost all viscous fluids display non-Newtonian properties which can significantly affect the dissipation processes in fluids. However, the anomalous absorption of acoustic waves was analyzed previously only for Newtonian viscous fluids,[14–19] i.e., fluids at relatively low acoustic frequencies. Therefore, to correctly design new high-frequency devices and techniques for fluid diagnostics, based on the anomalous absorption, it is necessary to develop a consistent theory of anomalous absorption in thin layers of non-Newtonian fluids.

The aim of this paper is to analyze theoretically the anomalous absorption of bulk shear acoustic waves, polarized perpendicular to the plane of incidence, by a thin layer of a non-Newtonian fluid enclosed between two solid half-spaces. Non-Newtonian fluids with one or several relaxation times will be analyzed. The effect of the relaxation processes on the anomalous absorption (i.e., on the absorptivity maximum and optimal layer thickness) will be investigated. Frictional contact approximation (FCA) will be justified for a thin layer of a non-Newtonian fluid. As an example, the anomalous absorption of shear acoustic waves in a thin layer of poly-1-butene will be analyzed in the megahertz range of frequencies.

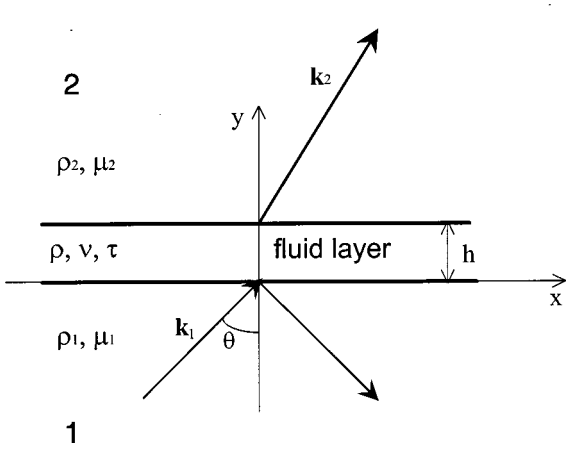

FIG. 1. A layered structure with the anomalous absorption of shear acoustic waves polarized normally to the plane of incidence; ρ_1, ρ_2 and μ_1, μ_2 are the densities and shear moduli of elastic media 1 and 2; ρ, ν, and τ are the density, kinematic viscosity, and relaxation time of the fluid; $\mathbf{k}_1$ and $\mathbf{k}_2$ are the wave vectors of shear waves in half-spaces 1 and 2, respectively.

I. ANOMALOUS ABSORPTION IN AN ARBITRARILY THICK LAYER

Let a bulk shear wave be incident on a layer of a non-Newtonian fluid enclosed between two solid half-spaces (Fig. 1). The displacements in the wave are perpendicular to the plane of incidence. The incident wave induces tangential displacements at the lower interface of the layer (Fig. 1). This results in generating shear acoustic waves in the layer, and causes a nonzero fluid velocity gradient. It was shown that if the angle of incidence is not too close to the angle of total internal reflection for the interface between elastic media 1 and 2, then the velocity gradient in the layer strongly increases with decreasing layer thickness h.[14,15] Therefore, the energy dissipation in a unit volume of the fluid layer, which is proportional to the square of the velocity gradient, must also increase substantially with decreasing layer thickness. On the other hand, the volume in which the dissipation takes place is decreased with decreasing layer thickness. This tends to decrease the overall dissipation in the fluid layer. Competition of these two opposing mechanisms results in an optimal layer thickness $h=h_m$ at which the absorptivity of the incident wave is maximal (often as good as 100%).[14,15] This qualitative consideration is equally applicable for both Newtonian[14,15] and non-Newtonian fluid layers.

A non-Newtonian fluid is a fluid in which shear displacements result not only in viscous but also elastic shear stresses.[1–4] The elastic stresses can only be noticeable if the displacements are sufficiently quick, i.e., for high acoustic frequencies: $\omega \geqslant 2\pi/\tau$, where τ is the time of relaxation of shear stresses in the fluid.[1–4] If $\omega \ll 2\pi/\tau$, the fluid behaves as a conventional Newtonian fluid that can be characterized by a density ρ and viscosity ν. If $\omega \gg 2\pi/\tau$, the fluid behaves as a solid with the density ρ and shear modulus $\mu_\infty = \rho\nu/\tau$.[1–4] If $\omega \sim 2\pi/\tau$, the fluid is called non-Newtonian and is characterized by the density, viscosity, and some residual shear modulus. In fact, almost all viscous fluids display non-Newtonian properties at sufficiently high frequencies.

Mathematical description of a non-Newtonian fluid is based on Maxwell's hypothesis which states that viscous and elastic stresses in a fluid are additive.[1–4] In this case the stress tensor component in the fluid is given by the equation:[3]

$$\sigma_{zy}^F = i\omega b\, \partial U_F/\partial y, \tag{1}$$

where

$$b = \rho\nu/(i\omega\tau - 1) = \mu_\infty \tau/(i\omega\tau - 1), \tag{2}$$

and U_F is the shear displacement in the fluid layer. If $\omega \gg 2\pi/\tau$, then Eq. (1) gives the equation for shear elastic stresses in a solid, while if $\omega \ll 2\pi/\tau$, Eq. (1) gives the equation for shear viscous stresses in a conventional Newtonian fluid.

Using Eq. (1), the boundary conditions at the layer boundaries can be written as

$$\begin{aligned} &\mu_1\, \partial U_1/\partial y|_{y=0} = i\omega b\, \partial U_F/\partial y|_{y=0}; \\ &\mu_2\, \partial U_2/\partial y|_{y=h} = i\omega b\, \partial U_F/\partial y|_{y=h}; \\ &U_1|_{y=0} = U_F|_{y=0}; \quad U_2|_{y=h} = U_F|_{y=h}, \end{aligned} \tag{3}$$

where $\mu_{1,2}$ are the shear moduli and $U_{1,2}$ are the displacements in the elastic media (Fig. 1).

Solving the wave equations for shear acoustic waves in solids and the fluid layer [with the stresses given by Eq. (1)], and satisfying boundary conditions Eqs. (3), gives the energy coefficients of reflection and transmission of the incident wave in the structure:

$$R = \left| \frac{(b^2\alpha^2 + c_1c_2)\tan(\alpha h) - b\alpha(c_1 - c_2)}{(b^2\alpha^2 - c_1c_2)\tan(\alpha h) + b\alpha(c_1 + c_2)} \right|^2, \tag{4}$$

$$T = 4c_1\, \mathrm{Re}(c_2) \left| \frac{b\alpha/\cos(\alpha h)}{(b^2\alpha^2 - c_1c_2)\tan(\alpha h) + b\alpha(c_1 + c_2)} \right|^2, \tag{5}$$

where $c_1 = (\mu_1\rho_1)^{1/2}\cos\theta$ and $c_2 = \mu_2 k_{2y}/\omega$ are the impedances of the surrounding solids, θ is the angle of incidence (Fig. 1),

$$k_{2y}^2 = k_2^2 - k_1^2 \sin^2\theta, \tag{6}$$

$$\alpha^2 = -i\omega\rho/b - k_1^2 \sin^2\theta, \tag{7}$$

$k_1 = \omega(\rho_1/\mu_1)^{1/2}$, $k_2 = \omega(\rho_2/\mu_2)^{1/2}$, signs of k_{2y} and α are chosen so, that $k_{2y} > 0$, or $\mathrm{Im}(k_{2y}) > 0$ if k_{2y} is imaginary, and $\mathrm{Re}(\alpha) < 0$ ($-\alpha$ is the complex reciprocal penetration depth of the shear wave into the fluid).

The energy absorption coefficient, M, can then be found using the equation:

$$M = 1 - R - T. \tag{8}$$

The above equations (4)–(8) determine the reflectivity, transmissivity, and absorptivity of an incident shear acoustic wave (polarized perpendicular to the plane of incidence) in a layer of a non-Newtonian fluid of arbitrary thickness. However, these equations are fairly complicated for explicit physical analysis. Moreover, the absorptivity is especially strong in fluid layers with small thickness. Therefore we will focus our attention on detailed analysis of the most important and interesting case of anomalous absorption of acoustic waves in thin fluid layers with thicknesses that are much less

than the wavelength and the penetration depth of shear acoustic waves in the fluid.

II. ANOMALOUS ABSORPTION IN THIN FLUID LAYERS

If the frequency and parameters of the fluid and solids are such that

$$|b\alpha|^2 \ll c_1 c_2, \tag{9}$$

and the layer thickness is much less than the complex penetration depth $-\alpha^{-1}$ of the wave into the fluid:

$$h|\alpha| \ll 1, \tag{10}$$

then general Eqs. (4), (5) can be noticeably simplified:

$$R = |c_1 c_2 - W(c_2 - c_1)|^2 / |c_1 c_2 + W(c_2 + c_1)|^2, \tag{11}$$

$$T = 4c_1 |W|^2 \,\mathrm{Re}(c_2) / |c_1 c_2 + W(c_2 + c_1)|^2, \tag{12}$$

where

$$W = \rho\nu / [h(1 - i\omega\tau)] = -b/h. \tag{13}$$

Note that condition Eq. (10) is required for replacing $\tan(\alpha h)$ in Eqs. (4) and (5) by αh. However, it can be seen that $\tan(\alpha h)$ differs from αh by less than 10% if

$$h|\alpha| < 0.5. \tag{10a}$$

Therefore inequality Eq. (10) seems to be excessively restrictive and can usually be replaced by inequality Eq. (10a).

The coefficient W can be considered as a coefficient of friction at the contact. This is because the same Eqs. (11) and (12) can be obtained when considering the wave reflection and transmission at an intermediate contact of the two solids with friction that is characterized by the coefficient W. In this case, instead of boundary conditions Eq. (3), we can use the conditions at the frictional contact:

$$\begin{aligned} &\mu_1 (\partial U_1/\partial y)_{y=0} = \mu_2 (\partial U_2/\partial y)_{y=0}, \\ &\mu_1 (\partial U_1/\partial y)_{y=0} = W(\partial U_2/\partial t - \partial U_1/\partial t)_{y=0}. \end{aligned} \tag{14}$$

These conditions can be derived from the general boundary conditions Eq. (3) if inequalities Eqs. (9) and (10) are satisfied. In this case,

$$\begin{aligned} -i\omega\, \partial U_F/\partial y|_{y=0} &\approx -i\omega\, \partial U_F/\partial y|_{y=h} \\ &\approx (\partial U_2/\partial t - \partial U_1/\partial t)/h, \end{aligned}$$

the stresses at the two solid interfaces must be approximately the same, and the mass of the layer together with its thickness can be neglected. Therefore, the first two equations of conditions Eqs. (3) are reduced to Eqs. (14), and the last two equations of conditions Eqs. (3) can be discarded.

Boundary conditions Eqs. (14) with the coefficient of friction Eq. (13) represent the frictional contact approximation for the anomalous absorption of shear acoustic waves by a layer of a non-Newtonian fluid. These conditions were used previously for analysis of the anomalous absorption of shear acoustic waves by a layer of a Newtonian fluid.[15] However, for Newtonian fluids (i.e., when $\omega\tau \ll 1$), the frictional coefficient is real and equal to $\rho\nu/h$, while for non-Newtonian fluids, the coefficient of friction W is complex and determined by Eq. (13). Equations (11) and (12) are also different from those for a Newtonian fluid layer[14,15] due to the different complex coefficient of friction Eq. (13).

Substituting Eqs. (11) and (12) into Eq. (8), and analyzing the resultant equation, we derive that the absorptivity of the incident shear wave is characterized by a strong (dozens of percent) maximum at an optimal layer thickness $h = h_m$, where

$$h_m = c_1^{-1} |b c_2^{-1}| \sqrt{|c_2|^2 + c_1^2 + 2c_1 a_1}, \tag{15}$$

and $a_1 \equiv \mathrm{Re}\{c_2\}$. This equation is correct for both the cases when $\theta > \theta_0$ and $\theta < \theta_0$, where $\theta_0 = \arcsin(k_2/k_1)$ is the angle of total internal reflection for an interface between the two solid media without the fluid layer (i.e., when $h = 0$). (If $\theta < \theta_0$, then $a_1 = c_2$, and if $\theta > \theta_0$, then $a_1 = 0$.) The absorptivity maximum corresponding to this optimal layer thickness is given by the equations:

$$M_m = 2b_1 [(1 + c_1/c_2)(b_1 - |b|)]^{-1}, \quad \text{if } \theta < \theta_0, \tag{16a}$$

$$M_m = 2a_2 b_1 [a_2 b_1 + b_2 c_1 - |b|(a_2^2 + c_1^2)^{1/2}]^{-1}, \quad \text{if } \theta > \theta_0, \tag{16b}$$

where $a_2 \equiv \mathrm{Im}\{c_2\}$, and $b \equiv b_1 + ib_2$.

The reflectivity and transmissivity of the shear wave at $h = h_m$ are determined as

$$R_m = \frac{|b|(c_1^2 + c_2^2) - b_1(c_1^2 - c_2^2)}{(|b| - b_1)(c_1 + c_2)^2}, \quad \text{if } \theta < \theta_0, \tag{17a}$$

$$R_m = \frac{|b|(a_2^2 + c_1^2)^{1/2} - b_2 c_1 + a_2 b_1}{|b|(a_2^2 + c_1^2)^{1/2} - b_2 c_1 - a_2 b_1}, \quad \text{if } \theta > \theta_0, \tag{17b}$$

$$T_m = \frac{2c_1 c_2}{(c_1 + c_2)^2 (1 - b_1/|b|)}, \quad \text{if } \theta < \theta_0, \tag{18a}$$

$$T_m = 0, \quad \text{if } \theta > \theta_0. \tag{18b}$$

Equations (15)–(18) demonstrate that, similar to the anomalous absorption of shear waves by a layer of a Newtonian fluid,[14,15] the anomalous absorption by a non-Newtonian fluid layer increases (i.e., the absorptivity maximum M_m increases) when the impedance of the first half-space c_1 is decreased. At the angle of total internal reflection, the impedance of the second half-space $c_2 = 0$, and the absorptivity maximum is zero [see Eqs. (16)]. This is again similar to the anomalous absorption by a Newtonian fluid layer.[14,15] However, unlike the case with the Newtonian fluid, the absorptivity maximum Eq. (16) does not reach 100% even if $c_1 \ll c_2$. In addition, reflectivity Eqs. (11) and (17), transmissivity Eqs. (12) and (18), absorptivity Eqs. (8) and (16), optimal layer thickness Eq. (15), and the coefficient of friction Eq. (13) for a non-Newtonian fluid layer are frequency-dependent even if conditions Eqs. (9) and (10) are satisfied.

The general tendency for non-Newtonian fluid layers is that the absorptivity maximum Eqs. (16) decreases with increase of frequency and/or relaxation time τ in the fluid. The optimal layer thickness Eq. (15) increases when at least one of the impedances c_1 or c_2 is reduced. However, if we reduce the impedance of the second half-space c_2, the absorptivity maximum Eq. (16a) becomes small (i.e., the anoma-

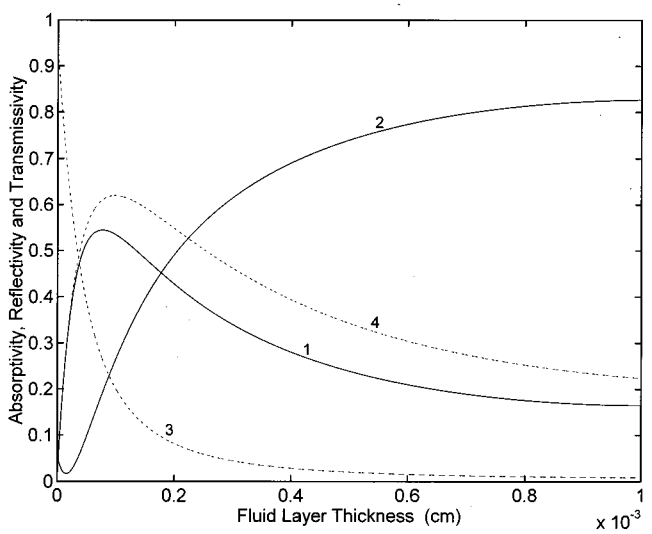

FIG. 2. The dependencies of the absorptivity M (curve 1), reflectivity R (curve 2), and transmissivity T (curve 3) for a shear acoustic wave ($\omega/2\pi = 20$ MHz, $\theta = 0$) on thickness h of a layer of poly-1-butene-16 in the structure SiO_2–fluid–Si. Curve 4 represents the absorptivity in the case of a Newtonian fluid layer with the same density $\rho \approx 0.88$ g/cm^3 and viscosity $\nu \approx 57$ cm^2/s, but zero relaxation time $\tau = 0$.

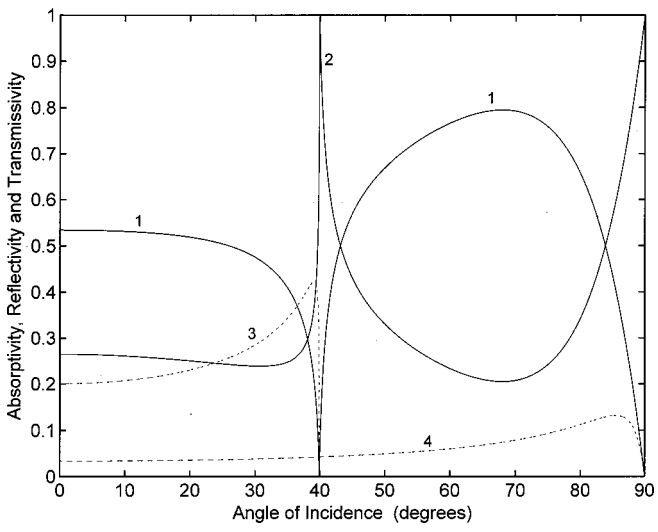

FIG. 3. The dependencies of the absorptivity M (curve 1), reflectivity R (curve 2), and transmissivity T (curve 3) of a shear wave ($\omega/2\pi = 20$ MHz) on the angle of incidence θ for a poly-1-butene-16 layer of thickness $h = 1$ μm between the SiO_2 and Si half-spaces. Curve 4 represents the absorptivity in the semi-infinite fluid within the area of 1 μm thickness near the SiO_2–fluid interface.

lous absorption is weak), while decreasing impedance c_1 results in increasing absorptivity maximum and optimal layer thickness. Increase of frequency and/or relaxation time results in decreasing optimal layer thickness Eq. (15) and the absorptivity maximum Eqs. (16).

III. NUMERICAL ANALYSIS

As an example, consider the structure with a thin layer of poly-1-butene of low molecular weight with 8 (average molecular weight is 448) and 16 (average molecular weight is 640) repeat units.[3] Fluid parameters were taken as $\rho \approx 0.86$ g/cm^3, $\nu \approx 6.42$ cm^2/s, $\tau \approx 1.16 \times 10^{-9}$ s for the fluid with 8 repeat units, and $\rho \approx 0.88$ g/cm^3, $\nu \approx 57$ cm^2/s, $\tau \approx 6.33 \times 10^{-9}$ s for the fluid with 16 repeat units.[3] The layer is placed between half-spaces made of fused quartz (half-space 1) and silicon (half-space 2) with the elastic parameters: $\rho_1 \approx 2.2$ g/cm^3, $\mu_1 \approx 3.11 \times 10^{11}$ dyne/cm^2, $\rho_2 \approx 2.3$ g/cm^3, $\mu_2 \approx 7.9 \times 10^{11}$ dyne/cm^2. Conditions of the frictional contact approximation Eqs. (9) and (10a) are satisfied for all numerical results and graphs below.

Figure 2 presents the dependencies of the absorptivity, reflectivity, and transmissivity (curves 1, 2, and 3, respectively) on thickness of a poly-1-butene-16 (i.e., with 16 repeat units) layer for the frequency 20 MHz. Curve 4 represents the dependence of the absorptivity for a layer of fluid with the same parameters as the poly-1-butene-16 layer, but with the zero relaxation time (i.e., for a Newtonian fluid layer with the same viscosity and density). Comparison of curves 1 and 4 confirms that the absorptivity decreases with increasing relaxation time and/or frequency (see also Sec. II). Thus non-Newtonian properties result in reduction of the anomalous absorption.

Figure 3 presents the angular dependencies of the absorptivity (curve 1), reflectivity (curve 2), and transmissivity (curve 3) on incidence angle θ at the frequency $\omega/2\pi = 20$ MHz and $h = 1$ μm (this thickness is approximately equal to the optimal thickness h_m at $\theta = 60°$). We can see that, similarly to the case of Newtonian fluid layer, the absorptivity is zero at the angle of total internal reflection $\theta_0 \approx 40°$. The explanation of this feature is exactly the same as for Newtonian fluid layers.[14,15]

Figure 4 presents the dependence of $M(\theta)$ (curve 1) for a layer with the same thickness, density, and viscosity, but with $\tau = 0$ (Newtonian fluid). It is obvious that this curve is higher than curve 1 in Fig. 3, i.e., the anomalous absorption

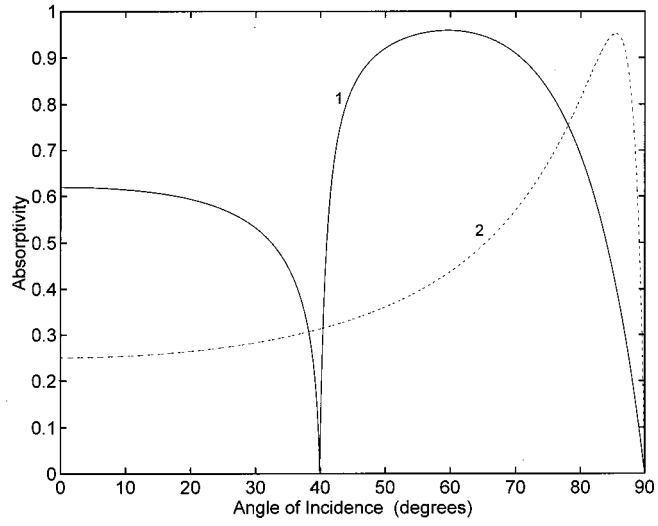

FIG. 4. The dependencies of the absorptivity M of a shear wave ($\omega/2\pi = 20$ MHz) on the angle of incidence θ. Curve 1 is for the SiO_2–fluid–Si structure with a Newtonian fluid layer of the thickness $h = 1$ μm, $\rho \approx 0.88$ g/cm^3, and $\nu \approx 57$ cm^2/s. Curve 2 gives the angular dependence of the absorptivity of the wave incident from the SiO_2 half-space onto the interface with the half-space of poly-1-butene-16.

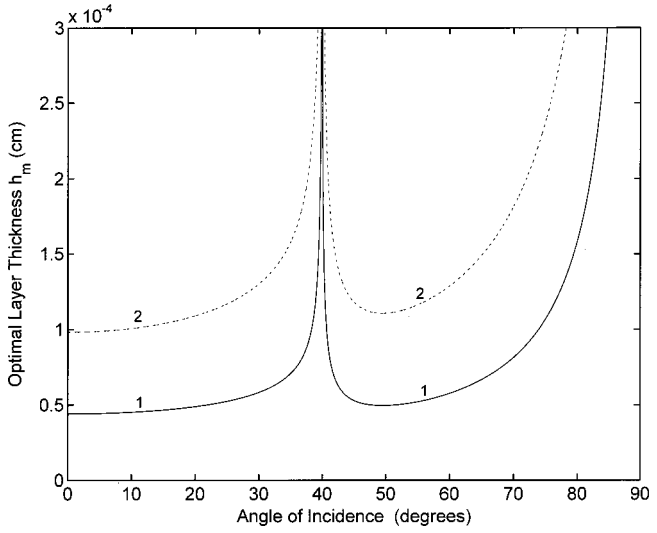

FIG. 5. The angular dependencies of optimal thickness h_m for a poly-1-butene-16 layer between SiO_2 (the first elastic half-space) and Si (the second elastic half-space) for the frequency $\omega/2\pi \approx 50$ MHz (curve 1), and optimal thickness h_m for a layer of a Newtonian fluid in the same structure and with the same density and viscosity as for the poly-1-butene-16 (curve 2).

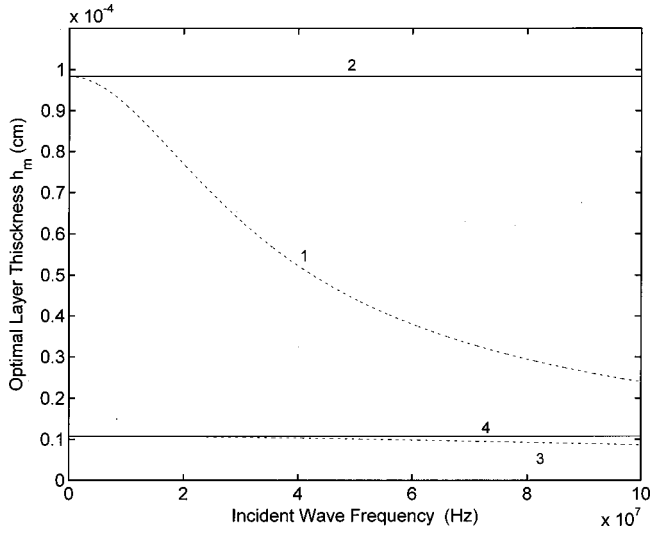

FIG. 6. The frequency dependencies of the optimal layer thicknesses h_m for poly-1-butene-16 (curve 1) and poly-1-butene-8 (curve 3) in the SiO_2–fluid–Si structure. Solid lines represent the frequency independent optimal layer thicknesses for Newtonian fluid layers with the same density and viscosity as for poly-1-butene-16 (line 2) and poly-1-butene-8 (line 4).

decreases with increasing frequency and/or relaxation time. Curve 2 in Fig. 4 represents the absorptivity in a poly-1-butene-16 half-space (non-Newtonian fluid), i.e., for $h = +\infty$. Comparing Fig. 3 and Fig. 4, one can see that for angles which are not too close to $\pi/2$ and θ_0, the absorptivity in a thin layer (the anomalous absorption) is noticeably larger than the absorptivity in the fluid half-space. Moreover, if $h = +\infty$ (curve 2 in Fig. 4), the dissipation takes place in the fluid region of the thickness $\sim -[\mathrm{Im}(\alpha)]^{-1}$ near the interface. At the same time, the anomalous absorption usually takes place in a layer of typical thickness $h \ll -[\mathrm{Im}(\alpha)]^{-1}$ [see conditions Eqs. (9) and (10)]. Therefore, to provide the absorptivity increase typical for the anomalous absorption, the energy dissipation in a unit volume of the layer must be much greater than in a unit volume near the interface between the solid and fluid half-spaces (i.e., at $h = +\infty$). This is demonstrated by curve 4 in Fig. 3, which represents the absorptivity of the incident wave in the fluid region of thickness $h = 1$ μm near the interface between the half-spaces of poly-1-butene-16 and SiO_2. Comparison of curves 1 and 4 in Fig. 3 demonstrates that, for example, at $\theta = 0$ the dissipation in a unit volume of the layer (the anomalous absorption) is about 18 times greater than the dissipation in a unit volume near the interface of the fluid and solid half-spaces. Only in the immediate proximity to the critical angle $\theta_0 \approx 40°$ the anomalous absorption gives weaker dissipation in a unit volume of the fluid (Fig. 3).

The dependence of optimal layer thickness h_m on angle of incidence for the SiO_2–fluid–Si structure with a poly-1-butene-16 layer is presented by curve 1 in Fig. 5 for the frequency $\omega/2\pi \approx 50$ MHz. A similar dependence for a layer of Newtonian fluid with the same viscosity and density ($\rho = 0.88\ \mathrm{g/cm^{-3}}$, $\nu = 57.01\ \mathrm{cm^2/s}$) is given by curve 2 in Fig. 5. Curves 1 and 2 seem to be similar in shape, but curve 1 corresponding to the non-Newtonian fluid is significantly lower than curve 2 corresponding to the Newtonian fluid layer. This figure does not show larger values of h_m for angles of incidence close to $\pi/2$ and θ_0, because these values do not satisfy conditions Eqs. (10) and (10a) for the considered frequency.

As we have mentioned, the anomalous absorption by a layer of a non-Newtonian fluid is frequency-dependent. For example, Fig. 6 presents the dependencies of optimal layer thickness h_m on frequency for $\theta = 0$ (normal incidence) for the structure SiO_2–fluid–Si for two different fluids: poly-1-butene with 16 repeat units (curve 1) and poly-1-butene with 8 repeat units (curve 3). Solid lines represent optimal layer thicknesses for layers of Newtonian fluids with viscosities and densities that are equal to those of poly-1-butene-16 (line 2) and poly-1-butene-8 (line 4). The figure demonstrates that the effect of increasing frequency on optimal layer thickness is significantly larger for larger relaxation times ($\tau \approx 6.33 \times 10^{-9}$ s for curve 1, and $\tau \approx 1.16 \times 10^{-9}$ s for curve 3). It can also be seen that at low frequencies the optimal layer thickness for the poly-1-butene-16 is about 10 times greater than for poly-1-butene-8. However, at larger frequencies this difference is quickly reduced to about 2.5 times for $\omega/2\pi = 10^8$ Hz (Fig. 6).

Figure 7 presents the dependencies of the absorptivity maximum M_m on frequency for two different angles of incidence $\theta = 0$ and $\theta = 60°$ in the SiO_2–fluid–Si structure. As predicted in Sec. II, the absorptivity maximum decreases with increasing frequency for non-Newtonian fluids (curves 1–4), whereas for Newtonian fluids it is independent of ω (curves 5 and 6). Increasing frequency from 10^7 Hz to 10^8 Hz results in more than 3 times decrease in the absorptivity maximum M_m for $\theta = 60°$ in a poly-1-butene-16 layer (curve 1), and in about 2.5 times decrease for the normal incidence (curve 4). As expected, the smaller the relaxation time in the fluid, the smaller the effect of increasing frequency on M_m. This is the reason for the difference between

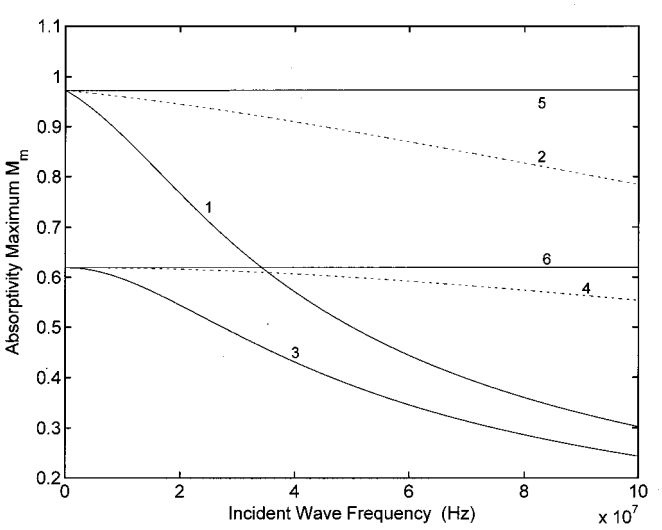

FIG. 7. The frequency dependencies of the absorptivity maximum M_m for layers of poly-1-butene-16 (curves 1 and 3), poly-1-butene-8 (curves 2 and 4), and Newtonian fluid with arbitrary parameters (lines 5 and 6) in the SiO_2–fluid–Si structure for the angles of incidence $\theta=60°$ (curves 1, 2 and 5) and $\theta=0$ (curves 3, 4 and 6).

curves 1 and 2, and 3 and 4 ($\tau=6.33\times10^{-9}$ s for curves 1 and 3, and $\tau=1.16\times10^{-9}$ s for curves 2 and 4).

IV. MULTIPLE RELAXATION TIMES

So far, we have considered only non-Newtonian fluids with one relaxation time τ, so that the stress tensor in the fluid is determined by Eq. (1) with the parameter b given by Eq. (2). It is not difficult to extend major obtained results to the case of two or more different relaxation times (relaxation processes) in the fluid. To do this, we must redefine the parameter b in Eq. (1) as follows[3]

$$b=\sum_m \frac{\mu_{\infty m}\tau_m}{i\omega\tau_m-1}, \tag{19}$$

where index m denotes different relaxation processes in the fluid layer, $\mu_{\infty m}$ are the contributions from each of these processes to the resultant shear modulus of the fluid at high frequencies (if $\omega\tau_m\gg1$ for all τ_m, then the fluid behaves as a solid with the shear modulus $\mu_\infty=\Sigma_m\mu_{\infty m}$).

Derivations of Eqs. (3)–(18) were implemented without use of Eq. (2), and thus b was considered as an arbitrary complex parameter. Therefore, Eqs. (3)–(18) with b defined by Eq. (19) describe the anomalous absorption of shear acoustic waves (polarized perpendicular to the plane of incidence) in a fluid layer with two or more different relaxation times τ_m. In particular, inequalities Eqs. (9), (10), and (10a) with b determined by Eq. (19) are the applicability conditions for the frictional contact approximation for a layer with several relaxation times.

V. NONUNIFORM LAYERS

Equation (15) suggests that layer thicknesses typical for the anomalous absorption can be very small, i.e., vary from tens of nanometers up to several micrometers, depending on the fluid viscosity. Therefore, solid surfaces may noticeably affect properties of the layer that can become nonuniform with viscosity, density, and relaxation time(s), being functions of distance from the layer interfaces. For example, long molecules in a fluid (such as molecules of poly-1-butene) can interact with the interfaces and form an ordered structure in the layer (similar to liquid crystals). The viscosity of such layer can be noticeably different from that of bulk fluids. The anomalous absorption in nonuniform layers will be especially important for development of techniques for diagnostics of biological and human fluids with large organic molecules, surface active substances, for analysis of solid–fluid interfaces, etc.

Theoretical analysis of the anomalous absorption in arbitrarily thick nonuniform layers is a very complicated problem. Fortunately, significant anomalous absorption normally takes place in very thin layers for which the frictional contact approximation is valid [see conditions Eqs. (9), (10), and (10a)]. In this approximation, fluid parameters are taken into account only through the frictional coefficient. If we are able to determine the frictional coefficient for a nonuniform layer, then Eqs. (8), (11), (12), (15)–(18) can immediately be used for determination of coefficients of reflection, transmission, and absorption in the layer.

Consider a nonuniform layer with viscosity $\nu(y)$, density $\rho(y)$, and relaxation time $\tau(y)$ being functions of the y-coordinate (Fig. 1). Conditions Eqs. (9) and (10a) are assumed to satisfy for all values of the fluid parameters in the layer. Then shear stresses in the fluid σ^F_{xy} are approximately constant across the layer. In accordance with Eqs. (14),

$$\sigma^F_{xy}=w(y)dv, \tag{20}$$

where $w(y)=-b(y)/dy$, dy is the distance between the planes y and $y+dy$ inside the layer, and $dv=v(y+dy)-v(y)$ is the relative velocity of these planes [$w(y)$ is the coefficient of friction between the planes]. Rearrangement and integration of Eq. (20) gives

$$\int_{v_1}^{v_2} dv=-\int_0^h(\sigma^E_{xy}b^{-1})dy, \tag{21}$$

where v_1 and v_2 are the velocities of the solid surfaces $y=0$ and $y=h$. Because in the frictional contact approximation the stresses σ^F_{xy} in the fluid are independent of the y coordinate, Eq. (21) gives

$$\sigma^F_{xy}=\frac{v_2-v_1}{-\int_0^h b^{-1}\,dy}. \tag{22}$$

On the other hand, the stresses at the interfaces (and thus in the fluid layer) are determined by the overall coefficient of friction W as $\sigma^F_{xy}=W(v_2-v_1)$. Comparing this equation with Eq. (22) gives

$$W=-\left(\int_0^h b^{-1}\,dy\right)^{-1}. \tag{23}$$

This equation is correct for Newtonian and non-Newtonian fluids with one or more relaxation times. For Newtonian fluids, $b=-\rho(y)\nu(y)$, while for non-Newtonian fluids b is given by Eq. (2) or (19) with ρ, ν, and τ (or τ_m and $\mu_{\infty m}$) being functions of the y coordinate.

Substituting the coefficient of friction Eq. (23) into Eqs. (11), (12), and (8), we immediately obtain the coefficients of reflection, transmission, and absorption in a nonuniform layer. Thus the frictional contact approximation appears to be a powerful tool for simple analysis of the anomalous absorption in thin nonuniform fluid layers.

Note that if a layer is strongly nonuniform with significantly different values of $|\alpha|$, then the requirement that inequality Eq. (10) [or Eq. (10a)] must be satisfied for all values of the fluid parameters in the layer is excessively restrictive. For example, if the layer is subdivided into several sub-layers, and the value of $|\alpha|$ in one of the sub-layers (of thickness $\Delta h \ll h$) is much larger than in the rest part of the nonuniform layer, then it would be unreasonable to require $[\max(|\alpha|)]^{-1}$ to be much less than the whole layer thickness h. In this case we must compare $[\max(|\alpha|)]^{-1}$ with Δh rather than with h. Therefore, for nonuniform layers, condition Eq. (10) should be replaced by the following more accurate inequality:

$$\int_0^h |\alpha| dx \ll 1. \tag{24}$$

However, if $|\alpha|$ does not vary strongly inside a nonuniform layer (this seems to be the most usual case), then we can still use inequality Eq. (10) that is noticeably simpler than Eq. (24).

VI. CONCLUSIONS

This paper has analyzed the anomalous absorption of bulk shear acoustic waves polarized perpendicular to the plane of incidence by an ultrathin layer of a non-Newtonian fluid between two semi-infinite elastic media. Angular and frequency dependencies of the coefficients of reflection, transmission, and absorption of the wave in the layer were determined for different parameters of the media in contact. The absorptivity was demonstrated to have a strong maximum (as much as dozens of percent) at an optimal layer thickness that is usually much smaller than the wavelength and wave penetration depth in the fluid. Maximal dissipation of incident wave energy in a unit volume of the layer was shown to be dozens of times greater than the dissipation in a unit volume near the interface of a semi-infinite fluid half-space.

The analysis has been carried out for non-Newtonian fluids with one or more relaxation times.

Frictional contact approximation was introduced and justified for thin fluid layers. Using this approximation, simple analytical equations for the coefficients of reflection, transmission, and absorption, as well as an equation for the optimal layer thickness were derived and analyzed in detail. Unlike the anomalous absorption in a layer of Newtonian fluid,[14–18] the anomalous absorption in a non-Newtonian fluid layer is frequency-dependent even in the frictional contact approximation. Moreover, the coefficient of friction Eq. (13) for a non-Newtonian fluid layer is also frequency-dependent. Increase of frequency of the incident acoustic wave [or/and increase of relaxation time(s)] was demonstrated to result in decreasing absorptivity maximum. Optimal layer thickness, at which the absorptivity maximum is achieved, was also shown to decrease significantly with increasing frequency of the incident wave.

The frictional contact approximation was demonstrated to be a powerful tool for substantial simplification of theoretical analysis of the anomalous absorption. This is not only because it allows the reduction of the number of boundary conditions by two, but also because the properties of the layer are taken into account only through the frictional coefficient. Therefore the frictional contact approximation allowed analytical analysis of the anomalous absorption in nonuniform non-Newtonian fluid layers.

One of the most feasible practical applications of the anomalous absorption of acoustic waves is related with new ultrasonic sensors and techniques for precise fluid diagnostics. For example, strongly increased absorptivity in the layer will result in a substantial increase in the sensitivity of viscosity sensors. Techniques based on the anomalous absorption will allow investigation of extremely small amounts of fluids (less than 10^{-5} cm^3). Due to the anomalous absorption taking place in a fluid layer of about tens or hundreds of nanometers, it will allow analysis of fluids in the extreme proximity to solid surfaces, thus enabling precise investigation of solid–fluid interfaces. Anomalous absorption can also be used for acoustic diagnostics and investigation of frictional contacts, lubricants, colloidal solutions, suspensions, biological and human fluids, etc. Use of high-frequency acoustic waves will give additional options for precise fluid analysis, including investigation of relaxation processes related with interaction of fluid (or solution) molecules with each other and with a solid–fluid interface(s).

ACKNOWLEDGMENT

This research was supported by a Queensland University of Technology Seeding Grant.

[1] A. J. Barlow, J. Lamb, A. J. Matheson, P. R. K. L. Padmini, and J. Richter, Proc. R. Soc. London, Ser. A **298**, 467–480 (1967).
[2] A. J. Barlow, A. Ervinsav, and J. Lamb, Proc. R. Soc. London, Ser. A **298**, 481 (1967).
[3] A. J. Barlow, R. A. Dickie, and J. Lamb, Proc. R. Soc. London, Ser. A **300**, 356–372 (1967).
[4] R. S. Moore and H. G. McSkimin, in *Physical Acoustics* (Academic, New York, 1970), Vol. 6, pp. 167–243.
[5] M. Schoenberg, J. Acoust. Soc. Am. **68**, 1516–1521 (1980).
[6] A. J. Ricco and S. J. Martin, Appl. Phys. Lett. **50**, 1474–1476 (1987).
[7] T. M. Niemczyk, S. J. Martin, G. C. Frye, and A. J. Ricco, J. Appl. Phys. **64**, 5002–5008 (1988).
[8] S. J. Martin, A. J. Ricco, T. M. Niemczyk, and G. C. Frye, Sens. Actuators **20**, 253–268 (1989).
[9] M. M. Vol'kenshtein and V. M. Levin, Pis'ma Zh. Tehk. Fiz. **12**, 1498–1503 (1986) [English transl.: Sov. Tech. Phys. Lett. **12**, 619–621 (1986)].
[10] P. Kielczynski and R. Plowiec, J. Acoust. Soc. Am. **86**, 818–827 (1989).
[11] T. Sato, H. Okajima, Y. Kashiwase, R. Motegi, and H. Nakajima, Jpn. J. Appl. Phys. **32**, 2392–2395 (1993).
[12] Hong-Tao Sun, Liang-Ying Zhang, Xi Yao, and W. Wlodarski, Sens. Actuators A **A43**, 208–212 (1994).
[13] V. Shah and K. Balasubramaniam, Ultrasonics **34**, 817–824 (1996).
[14] D. K. Gramotnev and S. N. Ermoshin, Pis'ma Zh. Tekh. Fiz. **15**, 62–66 (1989) [English transl.: Sov. Tech. Phys. Lett. **15**, 856–858 (1989)].
[15] D. K. Gramotnev, S. N. Ermoshin, and L. A. Chernozatonskii, Akust. Zh. **37**, 660–669 (1991) [English transl.: Sov. Phys. Acoust. **37**, 343–348 (1991)].
[16] M. L. Vyukov, D. K. Gramotnev, and L. A. Chernozatonskii, Akust. Zh.

37, 448–454 (1991) [English transl.: Sov. Phys. Acoust. **37**, 229–233 (1991)].
[17] L. A. Chernozatonskii, D. K. Gramotnev, and M. L. Vyukov, J. Phys. D **25**, 226–233 (1992).
[18] L. A. Chernozatonskii, D. K. Gramotnev, and M. L. Vyukov, Phys. Lett. A **164**, 126–132 (1992).
[19] D. K. Gramotnev and M. L. Vyukov, Int. J. Mod. Phys. B **8**, 1741–1764 (1994).

Determination of density and elastic constants of a thin phosphoric acid-anodized oxide film by acoustic microscopy

Pavel Zinin,[a] Odile Lefeuvre, and Andrew Briggs
Department of Materials, University of Oxford, Oxford OX1 3PH, United Kingdom

Brent D. Zeller, Peter Cawley, and Anthony Kinloch
Department of Mechanical Engineering, Imperial College, London SW7 2BX, United Kingdom

Xiaorong Zhou and George Thompson
Corrosion and Protection Centre, UMIST, Manchester M60 1QD, United Kingdom

(Received 8 October 1998; accepted for publication 22 July 1999)

Quantitative acoustic measurements have been carried out on phosphoric acid-anodized (PAA) aluminum. This process creates a porous oxide layer which varied from 1 to 22 μm thick in the different specimens used here. The elastic properties of the PAA oxide layer were determined by measurements of the dispersion curves in the complex plane [speed of the surface acoustic wave (SAW) and its attenuation] alone. This was possible because two modes were observed on samples with thicker oxide layers. It has also been shown that the dependence of the attenuation on the oxide layer thickness around the cutoff can be used for the determination of the density of the layer. The shape of the attenuation curve measured by the acoustic microscope near the cutoff was smoother than predicted by the theory, and this phenomenon has been discussed. © *1999 Acoustical Society of America.* [S0001-4966(99)04311-8]

PACS numbers: 43.35.Ns, 43.35.Pt, 43.35.Cg [HEB]

INTRODUCTION

Adhesive bonding of aluminum has many advantages over the traditional methods of construction in the aerospace industry.[1] In particular, it is a very flexible and cost-effective technique. One of the major factors which determines the strength and durability of this kind of joint is the nature of the interlayer between the adhesive and the adherend. This interlayer is a porous oxide layer created by anodization of the aluminum adherend. The pores tend to fill with adhesive (or primer), forming a ''microcomposite'' layer. The properties of this interlayer thus play a major role in the quality of the joint. However, the layer is generally only about 1 μm thick, making the measurement of these properties very difficult. The two most common anodization procedures, which are used in the aerospace industry, are phosphoric acid anodizing (PAA) and chromic acid anodizing (CAA). The first is used primarily in the United States and the second in Europe. For a more detailed description of the PAA and CAA procedures and the resulting oxide structures, see Ref. 1. The authors have recently studied the oxide layers formed by oxalic acid anodization (OAA).[2–4] OAA films can be grown to form very thick layers (of the order of 100 μm). This makes it possible to obtain some of the elastic constants from ultrasonic reflection coefficient measurements in the frequency range below 100 MHz.[5] In Ref. 3, the elastic constants and density of oxalic acid-anodized (OAA) films were determined by combining measurements of the surface acoustic wave (SAW) dispersion in an acoustic microscope in the frequency range 200–980 MHz with the lower frequency reflection coefficients. Unfortunately, this methodology could not be applied to PAA oxide films because it proved to be impossible to grow PAA films thicker than about 22 μm. This paper discusses an alternative approach using only measurements in the acoustic microscope.

I. MODEL

A. Specimens

Even an aluminum surface which has not been pretreated is coated by a thin layer consisting of a naturally forming oxide. The surface pretreatments remove this naturally occurring film and the anodization creates an oxide layer which is thicker and more uniform.[1] The substrates used here were all super pure aluminum (at least 99.99% pure). The films were grown in a 0.25-molar solution of phosphoric acid with a constant current density applied (25 milliamps per square centimeter). The solution was slowly stirred and immersed in a water bath to hold it at a constant temperature of 19 °C ($\pm$1 deg). Under these conditions, the phosphoric acid oxide film was expected to grow at a rate of about 1 μm in 1.2 min. The film thicknesses of the samples were checked by scanning electron microscope (SEM) measurements. For samples with predicted thicknesses below 15 μm, a worst-case error of 10% was found between the thickness measured in the SEM and that predicted by the expected growth rate and the anodization time. However, on a film of expected thickness 100 μm, SEM measurements showed that the oxide layer was only about 16 or 17 μm thick. This is probably because the phosphoric acid is so aggressive that it tends to dissolve the surface of the oxide as it is growing. The maximum thickness layer which was grown was 22 μm, so samples were available at thicknesses between 1 and 22 μm.

[a]Current address: 2525 Correa Road, SOEST, University of Hawaii, Honolulu, HI 96822. Electronic mail: zinin@soest.hawaii.edu

Figure 1 shows transmission electron micrographs (TEM) of a cross section and the top of a PAA film. The top view shows a fairly uniform distribution of pores, while the cross section indicates that the pores run roughly normal to the surface. This ''honeycomb'' structure is expected for this type of oxide.[1]

B. Experimental procedure

Measurements were carried out using an acoustic microscope and a line focus lens (LFM) at frequencies between 150 and 250 MHz. The SAW velocity, v_{saw}, was extracted from the $V(z)$ curves (see Fig. 2) as described by Kushibiki and Chubachi.[6] The SAW velocity was calculated using the well-known relationship[6,7]

$$v_{\mathrm{saw}}=\frac{v_w}{\sqrt{1-\left(1-\frac{v_w}{2f\Delta z}\right)^2}}, \tag{1}$$

where v_w is the speed of sound in water, f is the frequency, and Δz is the period of the oscillation of the $V(z)$ curve. The SAW attenuation, α, is related to δ, the exponential decay of the $V(z)$ curve due to energy leakage of the SAW into water, and the attenuation in water, α_w, by

$$\alpha=\frac{\delta}{2\tan\theta_R}+\frac{\alpha_w}{\sin\theta_R}, \tag{2}$$

where θ_R is the Rayleigh angle ($\sin\theta_R=v_w/v_{\mathrm{saw}}$). The geometry of the system is shown in Fig. 3, where the critical angle is θ_R. In our calculations, α_w has been determined from $\alpha_w/f^2=2.33\times10^{-15}\,\mathrm{s}^2/\mathrm{m}$.[8] The normalized attenuation factor, γ, is calculated by

$$\gamma=\alpha\frac{v_{\mathrm{saw}}}{2\pi f}. \tag{3}$$

Predictions of SAW propagation on a layered oxide/aluminum structure have been done using the DISPERSE software developed at Imperial College.[9,10] The predictions were intended to be illustrative only and modeled the oxide layer as a homogeneous, isotropic solid. The elastic properties used for the different layers are given in Table I. Book values of the aluminum and water properties were used, while the values for the oxide layer were obtained from the measurements discussed in Sec. III.

II. EXPERIMENTAL RESULTS

$V(z)$ curves measured on the PAA films are presented in Fig. 2. For small thicknesses of the oxide, only one mode was detected at 225 MHz. However, when the layer was 15 μm thick, a second, higher velocity [longer period in the $V(z)$ curve] mode was observed as shown in Fig 2(c). For the 22-μm thickness, the $V(z)$ curve at 225 MHz did not contain the ripples due to the SAW because of the high roughness of the surface (which was observed by scanning acoustic microscope, Fig. 4). In order to reduce the influence of the roughness and to detect a SAW for this specimen, the excitation frequency of the signal was decreased. The standard line-focus lens, with an opening semiangle of 60°, has a

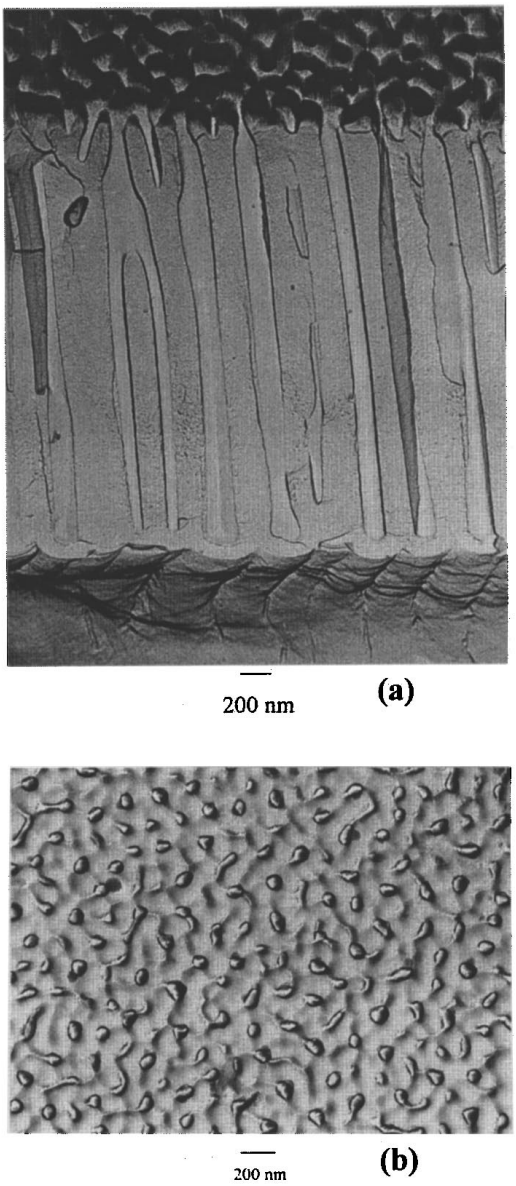

FIG. 1. TEM images of the PAA layer used in the experiments (a) cross section; (b) top view.

1-mm radius of curvature and a focal length of 1.15 mm when distilled water is used as the coupling medium. The water temperature was carefully controlled to allow measurements at increments of 1 °C between 19.5° and 22.5 °C.[11] The velocities measured do not show any obvious trend with water temperature, and the scatter within each set is very low, consistent with the best figure of 0.01% sometimes quoted.[12] Measurements of the z-stage movement used to produce the 225-MHz measurements showed that the error of SAW velocity measurement was limited to 0.14%.[13] The variation of the phase velocity due to roughness does not exceed 1%,[14] which is less than the variation of SAW velocity across the PAA films. Detailed description of the accuracy of SAW velocity measurements by LFM can be found elsewhere.[15,16] The lens was originally manufactured to work at a frequency of 225 MHz at which the accuracy of the SAW speed determination is the highest (about 0.1% according to Ref. 6) and a deviation from the working frequency of

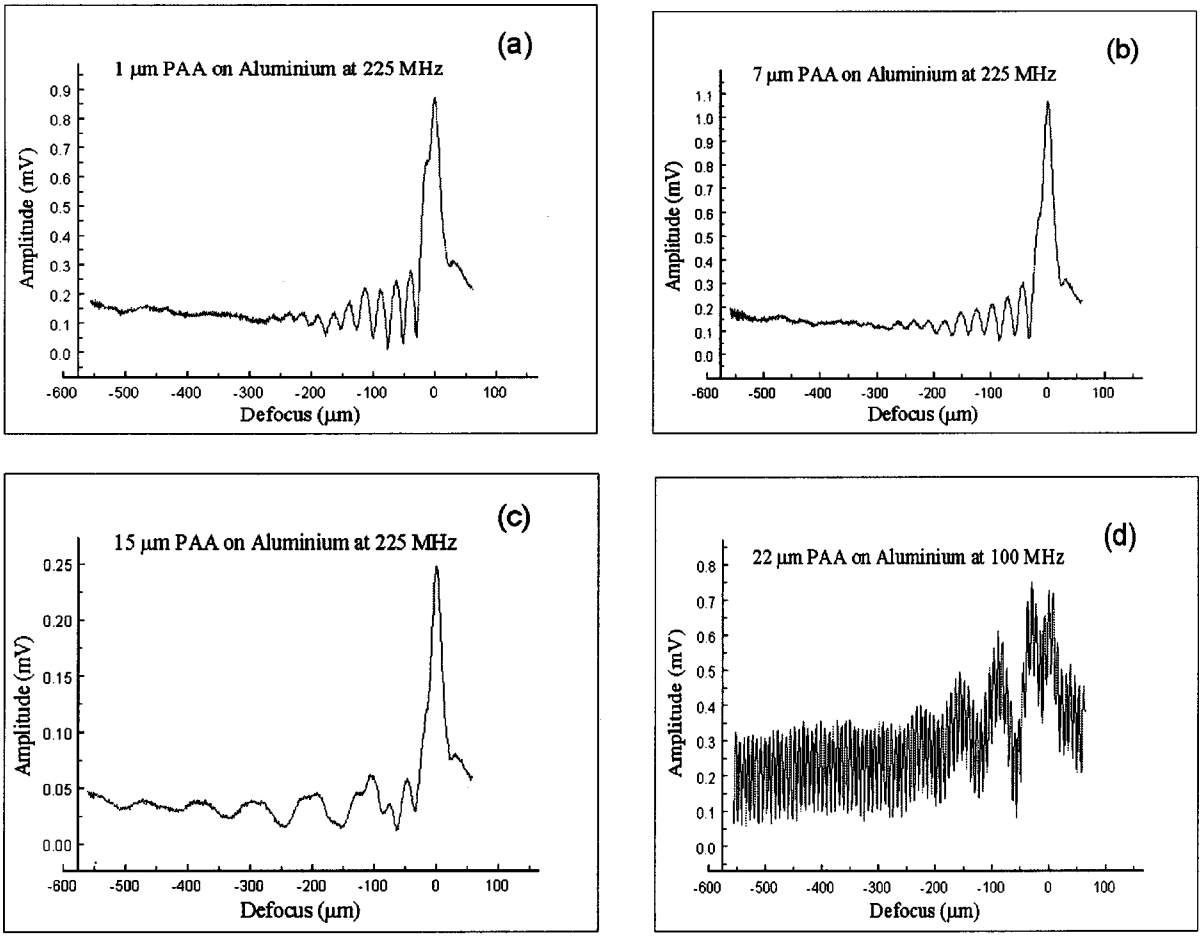

FIG. 2. $V(z)$ curves for different thicknesses of PAA film on aluminum (a) 1 μm, (b) 7 μm; (c) 15 μm; (d) 22 μm.

the lens causes a decrease in the accuracy of the measurements (up to 1%). However, it enabled us to investigate the thick films and, as will be shown later, the attenuation around the cutoff. The $V(z)$ curve for the 22-μm-thick specimen at a frequency of 100 MHz is shown in Fig. 2(d). The SAW mode is clearly detected (the high-frequency oscillations are due to water ripples;[15] they appear to be quite strong here because the signal from the sample was relatively weak). The SAW in this specimen was observed for frequencies up to 165 MHz. At 170 and 180 MHz, the high-speed mode was detected, but at higher frequencies, the signal was too weak for analysis.

The high-speed mode observed for the 15-μm layer across the full frequency range (Fig. 5) and the 22-μm layer at 170 and 180 MHz (Fig. 6) can be attributed to the longitudinal bulk wave in the PAA film propagating parallel to the surface.[17,18] The lateral wave appears as a branch point on the complex plate wave number (the x-component is the wave vector) plane. The plate wave number of the lateral wave is equal to the wave number of the bulk wave and the corresponding system matrix becomes singular (see the detailed description in Ref. 9, p. 539). Unlike poles, which represent solution of the dispersion equation for SAW, branch points are independent of the thickness of layer; this is in good agreement with the experimental data presented in Figs. 5 and 6. The observation of this mode in the $V(z)$ curve can be explained by the surface roughness of the PAA films. For a thin film, the level of roughness is small [see Fig. 4(a)] and therefore contributions of the specularly reflected ray and of the leaky SAW ray[19] to the output signal are dominant and the contribution of the lateral bulk wave to the $V(z)$ curve is small (Ref. 15, p. 124). Thus, the lateral wave is not

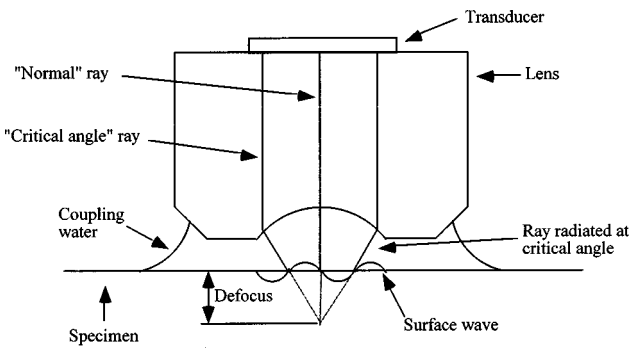

FIG. 3. Schematic diagram of the defocused acoustic lens.

TABLE I. Material properties used in calculations.

	ρ (kg/m^3)	v_l (km/s)	v_t (km/s)
Water	1000	1.483	10^{-5}
PAA	2600	5.503	3.54
Aluminum	2667	6.396	3.10

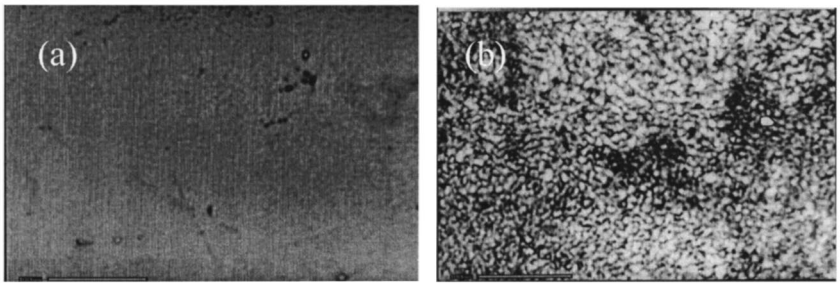

FIG. 4. Acoustic micrographs of PAA films; $f=300$ MHz, $z=0$ mm; (a) 15-μm-thick film; (b) 22-μm-thick film.

detected for thin films having a relatively smooth surface. The thicker oxide layers had rougher surfaces [see Fig. 4(b)] so the contribution of the leaky SAW became smaller due to scattering by the rough surface. The lateral bulk wave is not affected much by the roughness of the surface because, unlike a surface wave, its energy is not concentrated at the surface of the sample. Therefore, when the roughness is higher, the contributions of the leaky SAW wave and of the lateral wave to the output signal become comparable and the lateral wave can be observed in the $V(z)$ curves for the thicker samples. For the 22-μm-thick layer, the high-speed mode velocity decreased from 5.8 km/s at 150 MHz to 5.5 km/s at 250 MHz. The reasons for this change are not clear. This mode was attributed to the bulk longitudinal wave of the layer and thus for numerical simulations a velocity of 5.5 km/s measured at 225 MHz was chosen for the longitudinal velocity of the layer in the plane parallel to the surface, $\hat{v}_l$. The next step was to determine the shear velocity of the layer in the plane parallel to the surface, $\hat{v}_t$. In principle, this could be obtained from[20]

$$\frac{\hat{v}_R}{\hat{v}_t}=\frac{0.72-\left(\frac{\hat{v}_t}{\hat{v}_l}\right)^2}{0.75-\left(\frac{\hat{v}_t}{\hat{v}_l}\right)^2}. \tag{4}$$

However, the value of the Rayleigh velocity of the film, $\hat{v}_R$, cannot be obtained directly, because the film cannot be grown to a sufficient thickness for the energy of the SAW to be contained entirely in the film at the frequencies used. Consequently, the dispersion of the SAW at 225 MHz for different thicknesses of oxide was used to determine $\hat{v}_t$. Equation (4) is independent of the density of the layer, $\hat{\rho}$; it was therefore assumed that the influence of the layer density is small at high frequency thickness. At this stage in the calculations, a value 2500 kg/m^3 for the density of the layer was chosen arbitrarily (this was the density found for OAA films[2]). $\hat{v}_t$ could then be found by fitting to the experimental dispersion curves. The shear velocity thus obtained was 3.54 km/s. The dispersion curves calculated for different densities using this shear velocity are plotted in Fig. 7 and show that, as expected, the density has very little effect on the curves.

Although the density has only a very small effect on the velocity dispersion, it does affect the attenuation. The density of the layer can therefore be extracted using a procedure related to that proposed by Lee *et al.*[21] who obtained the density of solids by fitting predicted attenuation coefficients to measured data. However, it was not possible to measure the attenuation of a Rayleigh wave in the film alone because the films could not be grown sufficiently thick. Instead, we were able to use the fact that the attenuation around cutoff is very sensitive to the variation of the density of the layer.[2] The attenuation of the SAW measured for different thicknesses of oxide layer at a frequency of 225 MHz is presented in Fig. 8. The theoretical curves calculated for different values of density are plotted as continuous lines. The best least-squares fitting gives $\hat{\rho}=2600$ kg/m^3 for the density of the layer. The error bars on the measured values shown in Fig. 8 are relatively large. This reflects the difficulty of obtaining accurate attenuation measurements. Error bounds on the estimates of density and the elastic constants of the layer are discussed in Sec. IV.

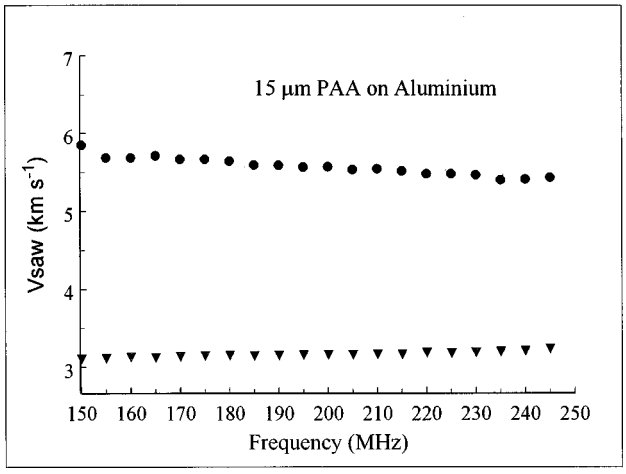

FIG. 5. Dispersion of leaky SAWs for 15-μm PAA film on aluminum.

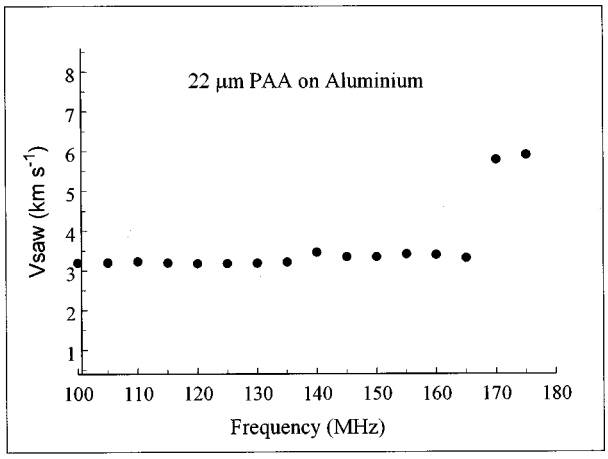

FIG. 6. Dispersion of leaky SAWs for 22-μm PAA film on aluminum.

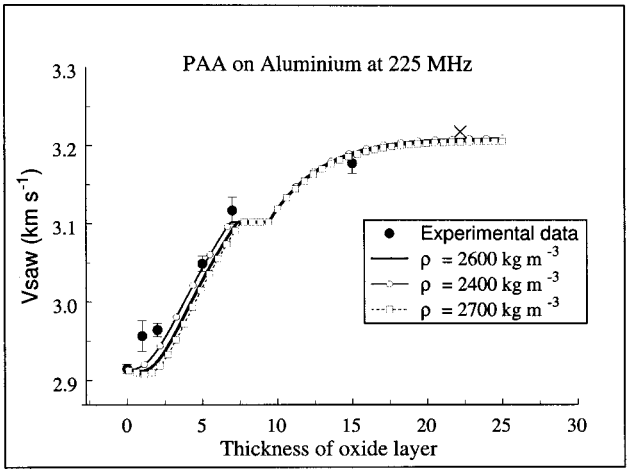

FIG. 7. Dispersion of leaky SAW for PAA film on aluminum at 225 MHz. Experimental data and theoretical lines are shown.

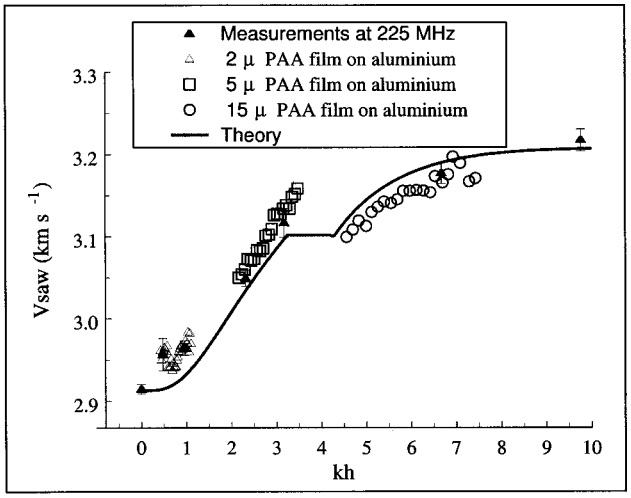

FIG. 9. Dispersion of leaky SAW for PAA film on aluminum measured at different frequencies.

III. ATTENUATION

The variation of attenuation with frequency thickness is an important aspect of the characterization of the films and is discussed further in this section. Since the behavior of the attenuation near cutoff is important for the determination of the oxide layer density, we examined it by changing the frequency of the SAW excitation. The measurements of the SAW speed and attenuation made at a single point on the 2-, 5-, and 15-μm PAA samples at different frequencies are presented in Figs. 9 and 10, respectively. The variation of attenuation and wave speed with frequency measured on the 2-μm-thick sample do not give significant information, since the range of kh covered (k is the wavenumber, h is the thickness of the layer) is small and the error bars are wide. For the thicker samples, clear frequency dependence can be seen. The attenuation (Fig. 10) has a minimum at kh $\approx$4.5 which is in line with the theoretical prediction, though the measured attenuation does not show the sudden step indicated by the theory. The reasons for this have been discussed by Zinin *et al.*[2] The theory of attenuation at cutoff and in particular the jump in attenuation caused by the onset of leakage into the substrate have been considered else-where.[2,13] The attenuation minimum occurs when the speed of the SAW equals the shear wave speed in aluminum (3.1 km/s). The identification of this point (the cutoff frequency, above which the surface wave leaks into the aluminum substrate) by the attenuation minimum could also be used as a way of measuring the shear velocity of the substrate.

The theoretical attenuation curve has an unusual shape. This occurs because the speed of the Rayleigh wave of the film (the asymptotic value reached at high kh or frequency-thickness product), 3.2 km/s, is slightly higher than the shear wave speed in the substrate. If the shear wave speed in the layer, $\hat{v}_t$, is reduced, the Rayleigh velocity in the layer is reduced, as shown in Eq. (4). Numerical simulations of the variation of SAW velocity with layer thickness at 225 MHz for different shear velocities of the layer ($\hat{v}_t$) are presented in Fig. 11. The dispersion curves become smoother with decreasing shear wave velocity of the layer. As the shear velocity of the layer becomes smaller, the speed of the Rayleigh velocity of the film at some stage becomes smaller than the speed of the shear wave in the substrate, and leakage of energy into the substrate cannot occur. In this case, the the-

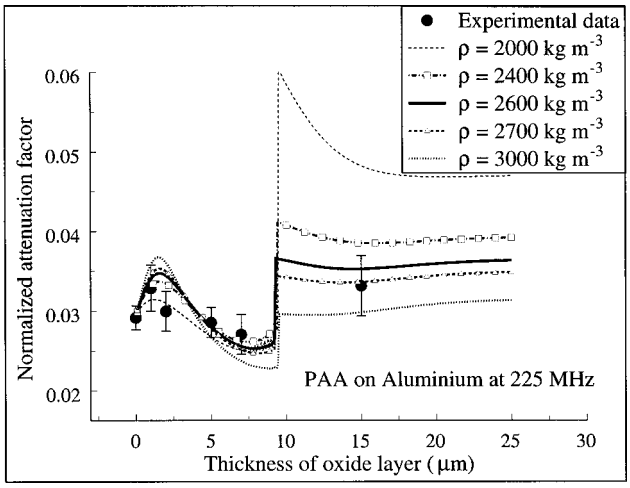

FIG. 8. Attenuation of leaky SAW for PAA film on aluminum at 225 MHz. Experimental data and theoretical lines are shown.

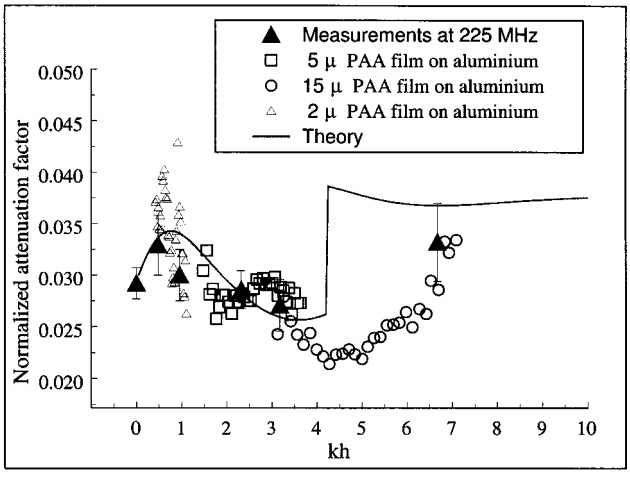

FIG. 10. Attenuation of leaky SAW for PAA film on aluminum measured at different frequencies.

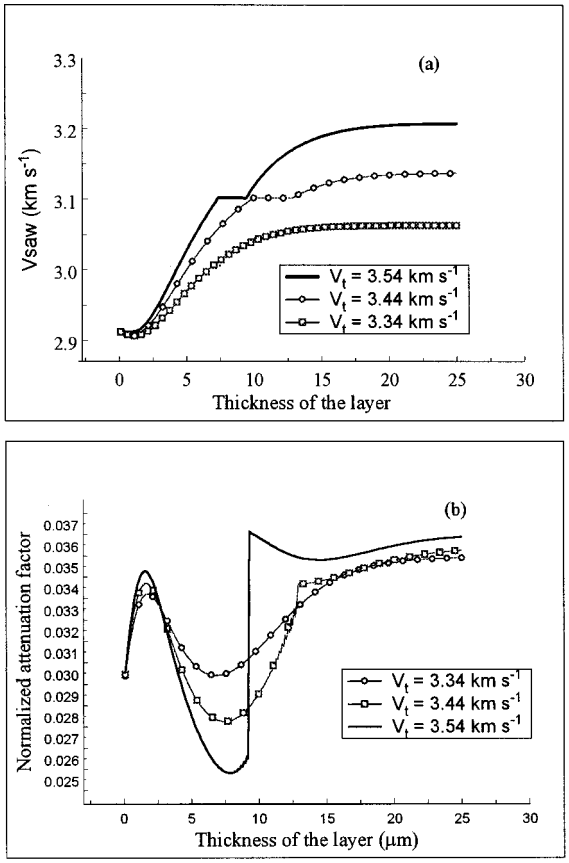

FIG. 11. Predicted influence of the shear velocity of the layer on the dispersion curves at 225 MHz (a) SAW velocity; (b) attenuation.

oretical velocity and attenuation dispersions are continuous. When the Rayleigh velocity in the layer is greater than the shear velocity in the substrate, there is a clear plateau in the velocity dispersion curves [Fig. 11(a)]. This means that there is a part of the dispersion curve for which the speed of the SAW is not changing with increasing thickness. However, Fig. 11(b) shows that the attenuation does vary over this region. When the speed of the SAW starts to increase again, the attenuation exhibits a sharp jump. When the speed of the Rayleigh wave in the layer is less than the shear wave speed in the substrate, the step in the velocity dispersion curves disappears [Fig. 11(a)] and the attenuation curve is smoother [Fig. 11(b)], as for the case of a slow-on-fast system. The determination of the density of the layer depended on a large variation of attenuation around its minimum value. This is only present if there is a cutoff frequency, i.e., the Rayleigh wave velocity of the film is greater than the shear velocity in the substrate. The method also requires the attenuation around the cutoff to be sufficiently small for measurements to be made with reasonable accuracy. Therefore, determination of the layer density from the variation in the attenuation around the cutoff requires the Rayleigh wave velocity of the layer to be higher than the shear velocity of the substrate; the attenuation must also be small enough to allow measurements to be made with reasonable accuracy.

IV. MODELING THE PAA OXIDE FILM

The PAA oxide film is porous in nature and has pores of an approximately constant cross-sectional area which extend through the oxide film, from the upper, free surface to the underlying, relatively thin, barrier layer[1,22] as shown previously in Fig. 1. The pores formed during steady-state anodizing conditions have relatively uniform size and their cross-sectional area is approximately constant through the thickness of the film. Further, the pores are parallel and are uniformly distributed and orientated normal to the plane of the film. Since the morphology is uniform in the 1–2 plane, but different in the direction of axis 3 (axis 3 is directed downwards and normal to the surface), the oxide film may be assumed to be transversely isotropic.

TABLE II. Properties of the porous PAA oxide film, with water in the pores.

Material property	Value
Density (kg/m^3)	2600
C_{11} (GPa)	75.8
C_{13} (GPa)	17.7
C_{33} (GPa)	113
C_{44} (GPa)	32.5

The above physical model is similar in form to a fiber-reinforced composite material where the cell walls may be considered to be the matrix, and the pores are the fibers. Nielsen[23] has developed a mathematical model for such a composite material, which predicts the properties of a two-phase composite from the properties of its isotropic constituent materials. Thus, for porous anodic oxide films of the type considered in this paper, we may use the Nielsen model where the solid oxide walls represent the matrix material and water represents the ''fibers'' contained in the pores. Indeed, the Nielsen model has been used successfully in previous studies on porous oxide films.[5,24] A transversely isotropic material has five independent elastic constants. In the coordinate system used in the present work, with axis 3 being the axis of symmetry, the constants extracted from the model using the experimental measurements as input were: $C_{11}(=C_{22})$, C_{33}, $C_{13}(=C_{23}=C_{31}=C_{32})$, and $C_{44}(=C_{55})$. The fifth independent constant, the in-plane shear modulus, C_{66}, does not affect the surface wave velocities, and so has not been considered.

In the present experimental studies, from examination of transmission electron micrographs of the PAA oxide film, such as those shown in Fig. 1, the average volume fraction of the pores has been determined to be 25%. From SAW measurements, the density of the water-filled oxide film is between 2500 and 2700 kg/m^{-3}, see Fig. 8. It was also found above that the bulk longitudinal wave velocity of the film parallel to the surface, measured at 225 MHz, was 5.5 km/s^{-1}, and this gives a value of C_{11} of 76 GPa assuming a density of 2600 kg/m^{-3}. Further, the shear wave velocity of the film parallel to the surface was 3.54 km/s^{-1}, and this gives a value of C_{44} of 32.5 GPa.

Using the above directly measured properties, together with the Nielsen model, the density and tensile and shear moduli of the cell-wall material (solid PAA oxide, assumed to be isotropic) and the constants C_{33} and C_{13} of the porous layer may be derived. The results from the best fit to the model are shown in Table II, for the PAA oxide containing

TABLE III. Properties of the solid PAA oxide (cell wall) and OAA oxide (Ref. 3).

Oxide	Density (kg/m^{-3})	Young's modulus (GPa)	Poisson ratio
PAA	3120	142	0.235
OAA	2850	195	0.226

water in its pores. The properties of the solid PAA oxide are given in Table III. They assume a Poisson's ratio of the cell-wall material of 0.235, which gave the best fit to the data. It should be noted that the experimental scatter in the values of the input parameters needed to determine the values for the PAA oxide film shown in Table III lead to coefficients of variation on the average density of $\pm 4\%$, and on the average moduli values of about $\pm 15\%$.

Finally, the differences between the values of the moduli for the present PAA oxide and the previously reported work on an oxide layer formed by anodizing in oxalic acid[3] are highlighted in Table III. Evidently, the solid PAA oxide has significantly lower values of moduli than the solid oxalic acid-anodized (OAA) oxide; although these values have experimental scatter associated with them, the corresponding average values appear to be well outside the limits of experimental scatter. The reasons for these differences may be ascribed to several causes. First, the films formed with oxalic acid were grown at an increased voltage compared with those formed in phosphoric acid. Hence, increased power is necessary for OAA oxide-film formation under similar conditions, leading to Joule heating within the oxide film, contributing possibly to increased sixfold coordination of aluminum with oxygen within the amorphous alumina which comprises the porous oxide film. Such symmetrical Al–O units may result in an increased modulus for the oxide film formed in oxalic acid. Second, the films formed in phosphoric acid are relatively heavily contaminated with electrolyte species [6% to 8% by weight of phosphate ions $(PO_4)^{3-}$]. On the other hand, the oxide films formed in oxalic acid are only associated with about 2% to 4% of $(COO)^{2-}$ species. The phosphate ions also have greater mobilities under the field applied during the formation of the oxide film than do $(COO)^{2-}$ species, giving rise to a more extensive incorporation of such species in the cell walls of the PAA oxide. Consequently, the oxide films formed in phosphoric acid have cell walls which consist of a reduced thickness of pure alumina. Thus, the PAA oxide film may be expected to possess lower values of moduli than the OAA oxide film on the basis of the presence of a reduced volume fraction of relatively pure alumina and an increased volume fraction of electrolyte anion.

V. CONCLUSIONS

A novel method for characterizing the elastic moduli and density of a thin, transversely isotropic layer on a substrate has been developed. The technique is based solely on surface acoustic wave measurements in an acoustic microscope. Full characterization depends on both the Rayleigh-type mode and the lateral bulk wave being measured. The density is obtained from measurements of the surface acoustic wave attenuation and is particularly applicable when the Rayleigh wave speed in the layer (i.e., the speed which would be measured if the layer were thick enough (or the frequency high enough) for the wave energy to be contained solely in the layer) is higher than the shear wave speed in the substrate. The method has been applied successfully to the oxide layers formed by phosphoric acid anodization of aluminum.

ACKNOWLEDGMENTS

We would like to thank Peter Sheasby of Alcan International Ltd., Jeff Sargeant of BAe, and Chris Scruby of AEA Technology for useful discussions. We are grateful to Professor J. Kushibiki for establishing the line-focus acoustic microscope at Oxford and for providing the 225-MHz lens. The research was supported by the Engineering and Physical Sciences Research Council (Grant Nos. GR/K48532 and GR/K23621), Alcan International Ltd., BAe, AEA Technology, and CEC (Grant No. MAT1-CT940045).

[1] A. J. Kinloch, *Durability of Structural Adhesives* (Applied Science, London, 1983).
[2] P. Zinin, O. Lefeuvre, G. A. D. Briggs, B. D. Zeller, P. Cawley, A. J. Kinloch, and G. E. Thompson, ''Anomalous behaviour of leaky surface waves for stiffening layer near cut-off,'' J. Appl. Phys. **82**(3), 1031–1035 (1997).
[3] B. D. Zeller, A. J. Kinloch, P. Cawley, P. Zinin, G. A. D. Briggs, G. E. Thompson, and X. Zhou, ''Adhesive/adherend interlayer property measurement by acoustic microscopy,'' in *Review of Progress in Quantitative Nondestructive Evaluation*, edited by D. O. Thompson and D. E. Chimenti (Plenum, New York, 1997), Vol. 16, pp. 1237–1244.
[4] P. Zinin, O. Lefeuvre, I. Goldfarb, G. A. D. Briggs, B. D. Zeller, A. J. Kinloch, P. Cawley, L. Robert, and G. E. Thompson, ''Cut-off properties of leaky surface-waves for the evaluation of adhesive–adherend interlayers by acoustic microscope,'' in *Proceeding of 1996 IEEE Ultrasonics Symposium*, edited by M. Levy, S. C. Schneider, and B. R. McAvoy (Institute of Electrical and Electronics Engineers, New York, 1996), Vol. 3, pp. 803–806.
[5] P. Cawley, T. Pialucha, and B. D. Zeller, ''The characterisation of oxide layer in adhesive joints using ultrasonic reflection measurements,'' Proc. R. Soc. London, Ser. A **452**, 1903–1926 (1996).
[6] J. Kushibiki and N. Chubachi, ''Material characterization by line-focus-beam acoustic microscope,'' IEEE Trans. Sonics Ultrason. **32**(2), 189–212 (1985).
[7] W. Parmon and H. L. Bertoni, ''Ray interpretation of the material signature in the acoustic microscope,'' Electron. Lett. **15**(12), 684–686 (1979).
[8] J. M. M. Pinkerton, ''The absorption of ultrasonic waves in liquids and its relation to molecular constitution,'' Proc. Phys. Soc. London, Sect. B **62**, 129–141 (1949).
[9] M. J. S. Lowe, ''Matrix techniques for modeling ultrasonic-waves in multilayered media,'' IEEE Trans. Ultrason. Ferroelectr. Freq. Control **42**(4), 525–542 (1995).
[10] B. Pavlakovic, M. J. S. Lowe, D. N. Alleyne, and P. Cawley, ''DISPERSE: a general purpose program for creating dispersion curves,'' in *Review of Progress in Quantitative Nondestructive Evaluation*, edited by D. O. Thompson and D. E. Chimenti (Plenum, New York, 1997), Vol. 16, pp. 185–192.
[11] Z. Sklar, ''Quantitative acoustic microscopy of coated materials,'' Ph.D. thesis, University of Oxford, Oxford, 1993.
[12] J. Kushibiki, A. Ohkubo, and N. Chubachi, ''Theoretical-analysis for $V(Z)$ curves obtained by acoustic microscope with line-focus beam,'' Electron. Lett. **18**(15), 663–664 (1982).
[13] O. Lefeuvre, ''Characterisation of stiffening layers by acoustic microscopy and Brillouin spectroscopy,'' Ph.D. thesis, University of Oxford, Oxford, 1998.

[14] C. Pecorari and G. A. D. Briggs, ''Acoustic microscopy and dispersion of leaky Rayleigh-waves on randomly rough surfaces—a theoretical study,'' IEEE Trans. Ultrason. Ferroelectr. Freq. Control **43**(3), 428–433 (1996).
[15] A. Briggs, *Acoustic Microscopy* (Clarendon, Oxford, 1992).
[16] G. A. D. Briggs, ''Quantitative Acoustic Microscopy,'' in *Materials Science and Technology*, edited by R. Cahn, P. Hassen, and E. J. Kramer (VCH Weinheim, 1994), Vol. 2B, pp. 241–279.
[17] W. Li and J. D. Achenbach, ''$V(Z)$ measurement of multiple leaky-wave velocities for elastic-constant determination,'' J. Acoust. Soc. Am. **100**, 1529–1537 (1996).
[18] Y. Tsukahara, Y. S. Liu, C. Neron, C. K. Jen, and J. Kushibiki, ''Longitudinal critical angle singularities and their effect on $V(Z)$ of the line-focus-beam acoustic microscope,'' IEEE Trans. Ultrason. Ferroelectr. Freq. Control **41**(4), 458–466 (1994).
[19] A. Atalar, H. Koymen, A. Bozkurt, and G. Yaralioglu, ''Lens Geometries for Quantitative Acoustic Microscopy,'' in *Advances in Acoustic Microscopy*, edited by A. Briggs (Plenum, New York, 1995), Vol. I, pp. 117–151.
[20] G. W. Farnell, ''Types and Properties of Surface Waves,'' in *Acoustic Surface Waves*, edited by A. A. Oliner (Springer, Berlin, 1978), pp. 15–60.
[21] Y. C. Lee, J. O. Kim, and J. D. Achenbach, ''Acoustic microscopy measurement of elastic-constants and mass density,'' IEEE Trans. Ultrason. Ferroelectr. Freq. Control **42**(2), 253–264 (1995).
[22] A. Bishop and G. E. Thompson, ''The role of the electron microscopy in the study of the adhesion to aluminium substrates,'' Surf. Interface Anal. **20**, 485–494 (1993).
[23] L. F. Nielsen, ''Elastic properties of two-phase materials,'' Mater. Sci. Eng. **52**, 39–62 (1982).
[24] S. I. Rokhlin and W. Wang, ''Measurements of elastic-constants of very thin anisotropic plates,'' J. Acoust. Soc. Am. **94**, 2721–2730 (1993).

Parallel projection and crosshole Lamb wave contact scanning tomography

James C. P. McKeon
Sonix, Inc., 8700 Morrissette Drive, Springfield, Virginia 22152

Mark K. Hinders
College of William and Mary, Department of Applied Science, Williamsburg, Virginia 23187

(Received 11 May 1998; revised 27 July 1999; accepted 3 August 1999)

Lamb waves are guided ultrasonic waves capable of propagating relatively long distances in thin plates and thin laminated structures, such as airframe skins, storage tanks, and pressure vessels. Their propagation properties in these media depend on the vibrational frequency as well as on the thickness and material properties of the structure. Structural flaws such as disbonds, corrosion, fatigue cracks, and voids represent changes in effective thickness and material properties, and therefore measurement of variations in Lamb wave propagation can be employed to assess the integrity of these structures. Lamb wave measurements can be made for a number of relative transducer positions (projections) and an image of the flawed region can be reconstructed tomographically. This paper presents a new technique in which two contact piezoelectric transducers are independently scanned along parallel lines in a fashion analogous to that commonly used in seismic crosshole tomography. These results are compared to those for parallel projection Lamb wave tomography data collected with an automated contact scanning apparatus. The advantages and drawbacks of these two methods in the development of automated tomographic Lamb wave scanners for quantitative mapping of thickness variation in platelike materials are discussed. [S0001-4966(99)05611-8]

PACS numbers: 43.35.Pt [HEB]

INTRODUCTION

The use of x-ray computerized tomography for medical noninvasive diagnostics is a mature technology, employing a set of projections around the body and a convolution-type of reconstruction to image cross sections through the body. Different tomographic techniques exist that are using seismic waves to image subsurface structures for development of oil and mineral deposits. We have borrowed the technology from these industries and recombined them in a new technique using ultrasonic Lamb waves as the probing energy for a cross-field geometry tomographic reconstruction. Previous ultrasonic work by Hutchins *et al.*,[1–5] Achenbach,[6] and Degertekin[7] used a parallel projection technique with the velocity and attenuation of Lamb waves as input for the tomographic reconstruction. For comparison to this earlier work, the results of a parallel projection technique for reconstruction using Lamb wave velocity data on an aluminum plate with a thinned region are presented here. This is followed by a ''crosshole'' tomographic reconstruction from Lamb wave data shown for the same sample. This preliminary work illustrates the technique for reconstructing the velocity over a planar structure using Lamb waves. The velocity can be used to back out the modulus parameter for the structure, providing rapid large-scale information on the quantitative health of the structure.

Lamb[8] developed the theoretical foundations for elastic waves in plates, and Worlton[9] provided experimental confirmation of Lamb waves at frequencies of interest to ultrasonic nondestructive evaluation (NDE). The details and background for elastic wave propagation, in general, and in plates and layered media, in particular, can be found in a number of texts.[10–19] In addition, there are many recent research papers describing specific advances in the application of Lamb waves to ultrasonic nondestructive evaluation. The use of lasers to generate and receive ultrasonic Lamb waves has received much attention,[20–37] as has the propagation of Lamb-type waves in multilayered and composite materials.[38–76] Characterization of bond strength, interfaces and coatings has been an active area of research.[77–94] Many other facets of Lamb waves have also been studied[95–118] including analogous guided wave modes in wires and pipes.[119–123] Finally, Lamb wave interactions with flaws and structural features have been investigated by a number of researchers.[124–141] The motivation for the present work is to find the best way to employ Lamb waves for the quantitative characterization of hidden defects in platelike structures.

In particular, we are interested in the detection of hidden corrosion in the skins of aging aircraft. Corrosion will alter the velocity of Lamb waves as they propagate through the thinned regions. We have found that by monitoring the change in arrival time of Lamb waves traveling between two contact transducers at known separation, we are able to detect areas of only a few percent thickness reduction. Although this has allowed us to locate areas of structural deterioration, it does not allow us to quantify the extent of the thinning. Tomographic reconstruction with Lamb waves allows accurate reconstruction of the variation of quantities of interest—such as thickness—throughout the region of interest.

There are two bodies of literature on tomographic reconstruction that are of interest to this work. The first is in medi-

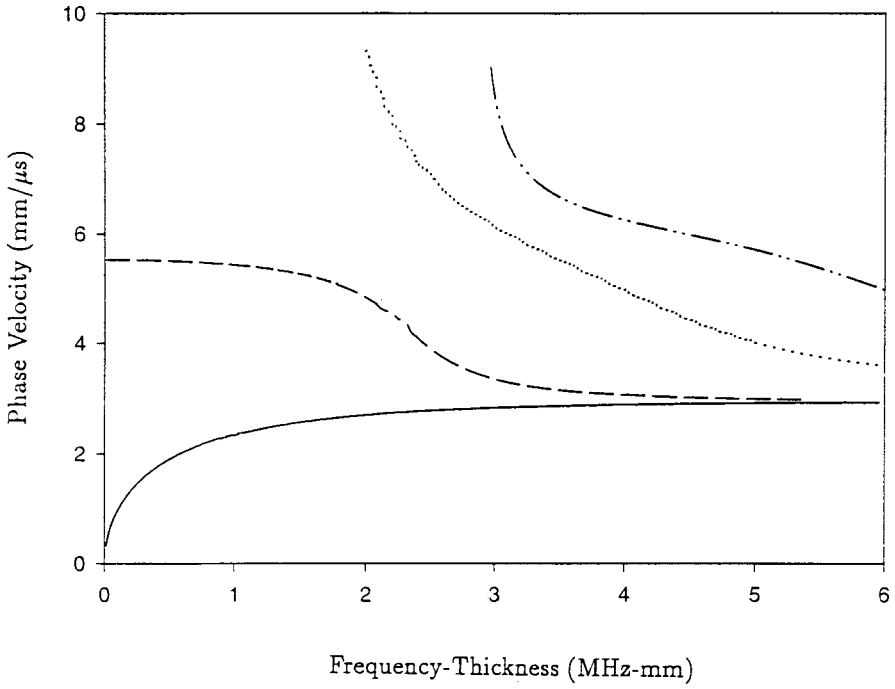

FIG. 1. Dispersion curves of the $S0$ (— — —), $A0$ (——–), $S1$ (·····), and $A1$ (— ·· —) Lamb wave modes in aluminum.

cal imaging, primarily for computed tomography (CT) scanning. These algorithms are summarized in the book by Kak and Slaney[142] and we have implemented them to reconstruct the data from our Lamb wave scanner. The second body of tomographic literature is in seismology,[143] where the cross-borehole tomography[144] is of interest because the geometry and physics are the same as those for Lamb wave scanning of, for example, an aircraft lap joint or doubler. In the seismic problem, the line of sources and the line of receivers are placed in boreholes on opposite sides of the region to be interrogated. In our problem, the sending and receiving contact transducers are scanned along opposite sides of the region of interest. Because of the many source–receiver combinations, there are a number of rays passing through each cell or subregion in between. One needs to pay particular attention to the density of rays because it is nonuniform and depends on the details of the scanning geometry. The quality of the reconstruction, of course, depends on the density of rays passing through each cell. The algorithms for cross-borehole tomography are well developed in seismology and we have implemented them to reconstruct the data from our Lamb wave scanner. We should note that these algebraic reconstruction algorithms are quite different from those used for parallel back projections, since they are not based on the Fourier slice theorem and the radon transformation, but are rather iterative algebraic reconstruction techniques.

This paper is organized as follows. In Sec. II we discuss those features of Lamb waves which are used in our measurements. In Sec. III we describe the experimental apparatus used in this work and outline the tomographic reconstruction algorithms appropriate for each. In Sec. IV we show tomographic reconstructions of simulated corrosion in an aluminum plate and discuss some of the challenges encountered in developing an automated Lamb wave tomographic scanning system.

I. LAMB WAVE MEASUREMENT SCHEME

Lamb waves are guided waves with an infinite number of modes, separated into two families: symmetric and antisymmetric. Dispersion curves for the four lowest modes in an aluminum plate are shown in Fig. 1. Note the separation of the lowest-order symmetric and antisymmetric modes for low frequencies. Our measurements are typically performed at $fd \approx 2$ MHz-mm, where only the $S0$ and $A0$ modes propagate appreciably. We use contact transducers excited by toneburst and then allow the Lamb wave modes to develop as the ultrasonic energy propagates. This is in contrast to other researchers who use angle-block transducers to select particular Lamb wave modes. We find that for automated scanning the careful coupling required to select particular waveguide modes via Snell's law is not practical. Instead we drive the transducers at a high enough frequency that the $S0$ mode has sufficient dispersion to give sensitivity to thickness variations, but low enough that all higher-order modes are cut off or negligible. Note from Fig. 1 that the $S0$ mode at $fd \approx 2$ MHz-mm is appreciably faster than the $A0$ mode, so that in our pitch-catch measurements the $S0$ signal will be distinct from the $A0$ signal. For corrosion detection we find it convenient to monitor changes in arrival time of the $S0$ signals, but depending on the flaws of interest we can monitor any combination of changes in arrival time or amplitude of the $S0$ and $A0$ modes. Although amplitude measurements are often most sensitive to the presence of flaws, the received signals are often more strongly affected by the variations in coupling inherent in automated scanning with contact transducers. Since tomographic reconstructions require many individual measurements to develop the projection data, we have concentrated our efforts on those measurement schemes which have the most promise for being fully automated.

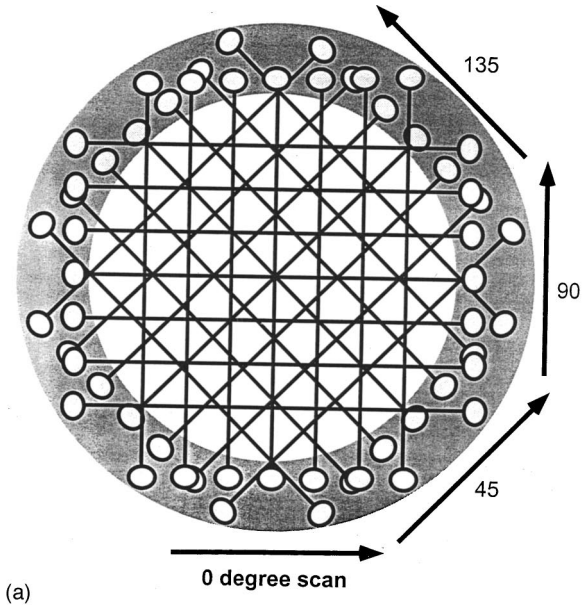

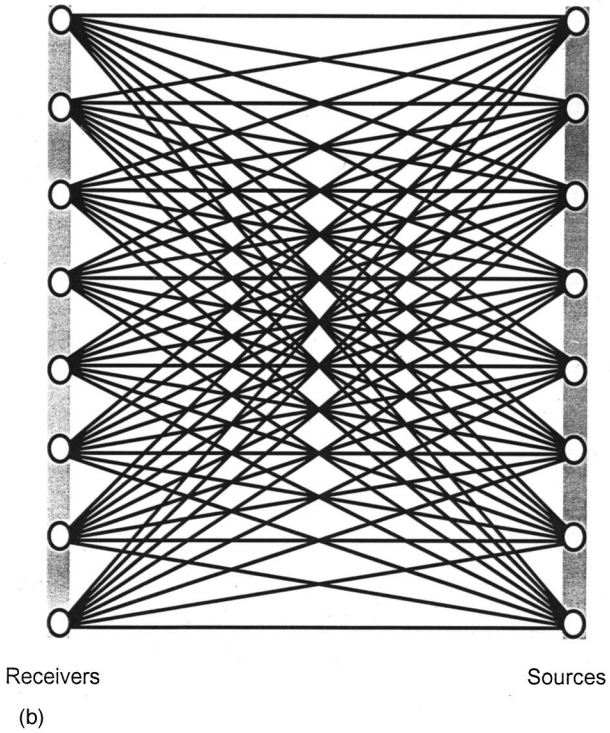

FIG. 2. (a) The geometry for parallel-projection tomography is shown here schematically for the case of seven parallel rays at four orientations. (b) The scanning geometry and ray paths for crosshole tomography are shown here schematically for the case of eight sources and eight receivers.

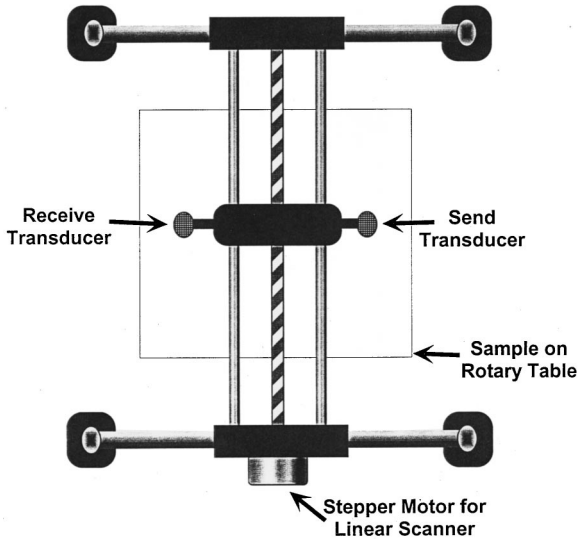

FIG. 3. The parallel projection scanning system is shown here schematically.

II. LAMB WAVE TOMOGRAPHIC SCANNING SYSTEM

Figure 2(a) shows schematically the geometry for parallel-projection tomography. The transducers are scanned along parallel lines with the Lamb waves propagating between them. At each position in the scan a measurement of some property of the Lamb waves, which are assumed to propagate along the straight rays shown, is recorded. Once the measurement has been done along each of the rays for that orientation, the sample is rotated by a fixed amount and the measurement is repeated. Projections consisting of seven parallel rays (transducer-pair positions) for four orientations (0, 45, 90 and 135 deg) are shown. The ''ray density'' is critical to the quality of reconstruction. Note that the ray density is uniform for parallel projection tomography; this will not be the case for crosshole tomography. Having the rays pass through the region of interest from many orientations is also important to the quality of the reconstruction. The rays for parallel projection tomography cover all angles since projections must be evenly spaced over 180 deg. This can be a disadvantage for contact scanning because a fairly large ring surrounding the region of interest [shown shaded in Fig. 2(a)] must be free of obstructions.

Figure 2(b) shows the scanning geometry and ray paths for crosshole tomography for eight combinations of sources and receivers. Note how the ray density varies and that the rays do not pass through the region of interest from all orientations. These drawbacks in the reconstruction quality are offset by the increased practicality of the measurement. Namely, only two narrow strips [shown shaded in Fig. 2(b)] need to be free of obstructions for contact scanning. This can be especially important in aircraft applications where one wants to scan a long line of rivets or a lap joint. Since a complete scan of any large structure will be done via a ''composite'' of many smaller scans, the rectangular scanning of the crosshole tomography is inherently superior to the circular scanning region of the parallel projection scheme.

In our laboratory we have assembled an ultrasonic system that allows us to perform Lamb wave scans in both parallel projection and crosshole geometries. Schematics of the parallel projection and crosshole scanners are shown in Figs. 3 and 4. Broadbanded contact piezoelectric transducers generate and receive the Lamb waves in a pitch-catch arrangement. For the parallel projection configuration, where the two transducers are always in the same relative orientation, shear contact transducers are automatically scanned in the direction perpendicular to the Lamb wave propagation. Two predominant signals, the lowest-order symmetric ($S0$

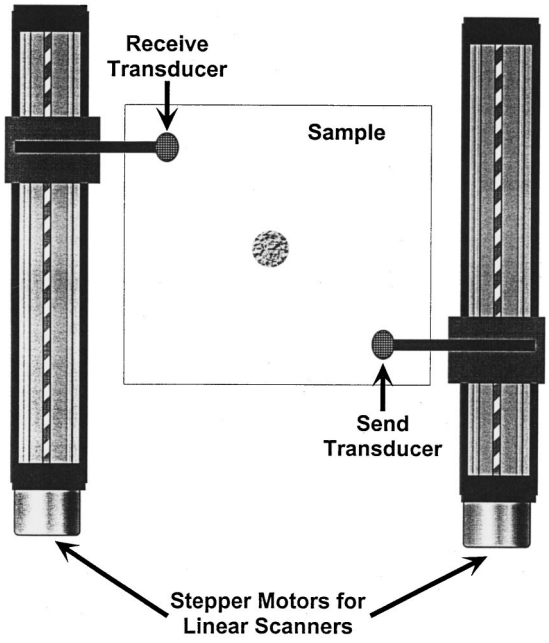

FIG. 4. The crosshole scanning system is shown here schematically.

mode is first arrival) and antisymmetric $A0$ is second arrival) can be observed at a frequency in the range 0.7 to 1.5 MHz. At each location of the transducer pair, the phase shift of the $S0$ mode is acquired through pulsed-phase-locked-loop (P2L2) circuitry. This instrument compares the phase of its pulsed output signal, which is sent to the transmitting transducer, with that of the amplified and low-pass filtered returned signal from the receiving transducer. A frequency counter is connected to the output of the P2L2, which gives information on the phase difference of the two signals in terms of frequency. The value of this reference frequency can be used to calculate both the time of flight and, because the distance between the two transducers is fixed, the integrated velocity of the Lamb waves. A normalized reference frequency provides the percentage change in these quantities, and allows us to detect changes in material properties. In our setup the sample is rotated by a fixed amount between each scan by a computer-controlled rotary table in order to obtain data from the different orientations necessary for tomographic measurements.

For the cross-borehole method, longitudinal contact transducers are scanned independently so that measurements are recorded at all of the necessary sender/receiver positions. Since the relative orientation of the transducers is constantly changing during the scan, the highly directional shear transducers cannot be used even though they give a better signal in contact scanning. Instead, longitudinal contact transducers are used so that signals could be received from any angle. The received signal is sent to a digital oscilloscope, and the digitized waveform is sent to a personal computer and saved for later analysis.

A. Parallel projection algorithm

For clarity, we include here some of the standard development[142] for recovering the image of a cross section of an object from projected data. We define the projection at some angle θ along some line $x\cos\theta+y\sin\theta=t$ as

$$P_\theta(t)=\int_{-\infty}^{\infty} f(t,s)ds, \tag{1}$$

where (t,s) is the coordinate system at an angle θ to the (x,y) system. Here $f(t,s)$ is called the object function. For example, if $f(t,s)$ is the two-dimensional distribution of slowness in the plate, then $P_\theta(t)$ is the travel time projection for the angle θ. The Fourier transform of $P_\theta(t)$ is

$$S_\theta(w)=\int_{-\infty}^{\infty} P_\theta(t)e^{-2\pi iwt}dt, \tag{2}$$

and substituting in our above definition for the projection gives

$$S_\theta(w)=\int_{-\infty}^{\infty}\int_{-\infty}^{\infty}[f(t,s)ds]e^{-2\pi iwt}dt. \tag{3}$$

(Note that w and t are not radian frequency and time, although the formulas do look like time-frequency Fourier transforms.) If we transform this back into the (x,y) coordinate system, we have

$$S_\theta(w)=\int_{-\infty}^{\infty}\int_{-\infty}^{\infty} f(x,y)e^{-2\pi iw(x\cos\theta+y\sin\theta)}dxdy, \tag{4}$$

and we see that the right-hand side is the two-dimensional Fourier transform of $f(x,y)$ at a spatial frequency of $(u=w\cos\theta,\ v=w\sin\theta)$, or

$$S_\theta(w)=F(w,\theta)=F(w\cos\theta,w\sin\theta)=F(u,v). \tag{5}$$

This equation indicates that the set of one-dimensional Fourier transforms of the individual projections of the object function, $S_\theta(w)$, at many angles, $\theta_1\ldots\theta_k$, corresponds to the two-dimensional spatial Fourier transform of the object function $F(u,v)$. Then the object function we want, $f(x,y)$, can be recovered by using the inverse transform,

$$f(x,y)=\int_{-\infty}^{\infty}\int_{-\infty}^{\infty} F(u,v)e^{2\pi i(ux+vy)}dudv. \tag{6}$$

Using polar coordinates we can write this as

$$f(x,y)=\int_{o}^{2\pi}\int_{0}^{\infty} F(w,\theta)e^{2\pi iw(x\cos\theta+y\sin\theta)}wdwd\theta, \tag{7}$$

and splitting the θ-integration into two parts and noting that $F(w,\theta+\pi)=F(-w,\theta)$, we have

$$f(x,y)=\int_{0}^{\infty}\int_{-\infty}^{\infty} F(w,\theta)|w|e^{2\pi iwt}dwd\theta, \tag{8}$$

where we have used $t=x\cos\theta+y\sin\theta$ for convenience. Finally, introducing

$$Q_\theta(t)=\int_{-\infty}^{\infty} S_\theta(w)|w|e^{2\pi iwt}dw, \tag{9}$$

we write

$$f(x,y)=\int_{0}^{\pi} Q_\theta(x\cos\theta+y\sin\theta)d\theta, \tag{10}$$

which gives the object function in terms of x, y, and the projection angle, θ_i. However, since we cannot take an infinite number of projections, these integrals need to be replaced with the appropriate summations. For example,

$$Q_\theta(k/2w) \approx \frac{2w}{N} \sum_{m=-N/2}^{N/2} S_\theta(m2w/N) \left| m \frac{2w}{N} \right| e^{2\pi i(mk/N)},$$
$$f(x,y) \approx \frac{\pi}{K} \sum_{i=1}^{K} Q_{\theta_i}(x \cos\theta_i + y \sin\theta_i). \tag{11}$$

Thus the scan is made for K angles θ_i and for N points along each of those scans. In Fig. 2(a) the full scan is made for 4 projection angles of 7 points each, and in our experiment we used 18 projection angles of 100 points each.

B. Cross borehole tomography

In this section the calculation for geophysical crosshole tomography is outlined for completeness. The geometry consists of a series of source and detector locations, and a ray projection exists for every combination. The intervening space is modeled as a rectangular grid space with a number of rays passing through each element in this space. The reconstruction of the value at each element, either the wave speed or attenuation, involves solving a large set of equations. We have chosen an algebraic reconstruction technique (ART) to study the method.[144]

In the Lamb wave measurements, I_{tot} is the number of source locations and J_{tot} is the number of columns between the sources and receivers. This means that the area between the source and receiver line is divided up into a rectangular area with ij number of cells. A ray connects every combination of source and receiver, and the corresponding line which goes through the cells is defined as

$$i = (i_d - i_s) j / J_{\text{tot}} + i_s, \tag{12}$$

where the source location is i_s and the detector location is i_d. To construct the data vector, we write

$$g_k = f_{ij} \Delta s_{ijk}, \tag{13}$$

where the summation over i and j is implied, Δs_{ijk} is the segment of the k-th ray passing through the cell ij, and f_{ij} corresponds to the value of the physical parameter of interest in the cell ij.

In order to determine the values of f_{ij} for the discretized space, we first calculate the Δs_{ijk}, estimate the f_{ij} components, and calculate g_k,

$$g_k = f_{ij}^q \Delta s_{ijk}. \tag{14}$$

Next, for each ray we use the difference between the g_k value and the corresponding data value, Ag_k, to calculate the update for the f_{ij}^q values for that ray.

$$\Delta f_{ijk}^q = (Ag_k - g_k)/L_k, \tag{15}$$

where L_k is the length of the k-th ray

$$L_k = \sqrt{(i_k - i_n)^2 + (J_{\text{tot}})^2}. \tag{16}$$

Then we add the update to the current f_{ij}^q values for that ray,

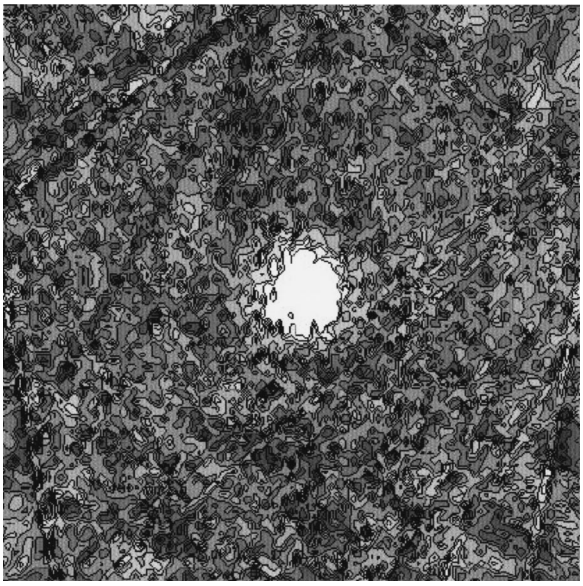

FIG. 5. Parallel projection tomographic reconstruction contour plot of Lamb wave contact scanning data taken on aluminum plate with flat-bottom hole.

$$f_{ij}^{q+1} = f_{ij}^q + \Delta f_{ijk}^q, \tag{17}$$

to obtain the next set of f_{ij} values, f_{ij}^{q+1}. A single iteration involves repeating this process for all of the rays, and iterations are repeated until a specified number has been reached or until the residual has approached some small number

$$r = \sum_k [g_k - Ag_k]^2. \tag{18}$$

In Fig. 2(b) we have 8 sources and 8 receivers, so a single iteration would involve 64 rays, while for our experiment we had 20 sources and 20 receivers, which gives 400 rays, and we performed 10 iterations.

III. RESULTS AND DISCUSSION

Tomographic reconstructions using Lamb waves allow us to map out the thickness variation of plates in an automated fashion. We discuss some of the details and subtleties involved below, as well as the relative advantages and disadvantages of the parallel projection to the crosshole tomography techniques.

Figure 5 shows a parallel projection tomographic reconstruction contour plot of Lamb wave contact scanning data taken on a 2.45-mm-thick aluminum plate with a 20-cm^2 circular region of 50% thickness reduction. The image covers 100×100 mm and was reconstructed from 18 projections of 100 rays each for a total of 1800 rays. The thinned region is shown clearly as the white region in the center of the image, although the actual extent of the flawed region is slightly larger than it appears in this image. Because we monitor the arrival time of the $S0$ mode for a known transducer pair separation, the tomographic reconstruction returns initially a velocity map of the scanned region. We have found that for automated contact scanning there is too much variability in coupling to make amplitude measurements reliable. For small changes in velocity, the $S0$ wave dispersion curve (see Fig. 1) is essentially linear and gives a simple

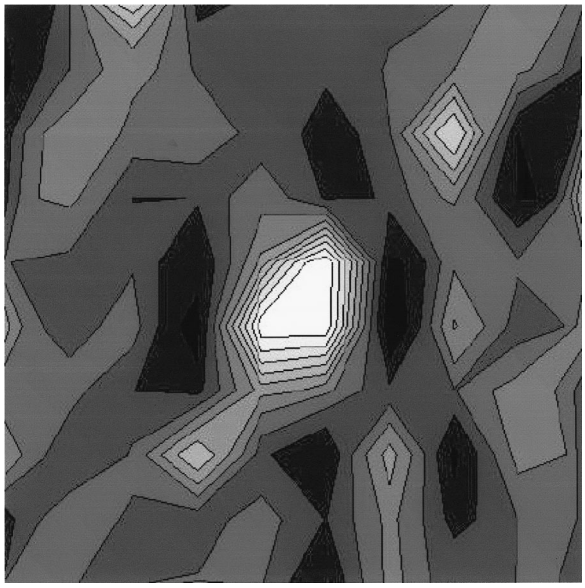

FIG. 6. Crosshole tomographic reconstruction of the same sample as Fig. 5.

relationship between velocity changes and thickness changes. Thus Fig. 5 represents a ''thickness contour map'' of the plate, with the darkest gray corresponding to the 2.45-mm plate thickness and white corresponding to half that value.

Figure 6 shows a crosshole tomographic reconstruction (thickness contour map on the same scale) of the same 100 $\times$100-mm region of the aluminum sample. This image was produced using the ART algorithm and 400 rays. Note that although the much lower ray density in the flaw region decreases the accuracy of the reconstruction, the location and size of the thinned region are fairly accurately reproduced. The crosshole image is inherently lower resolution because the number of pixels corresponds to a much coarser computational grid. The ray paths through the flawed region are also not from all angles, as they are in the parallel projection, which reduces the quality of the reconstruction.

The type of thickness maps represented by Figs. 5 and 6 can also be used directly to make quantitative measurements of corrosion loss, for example. The data file that generates these images contains the estimate of thickness at each location in the plate, and so the total volume of material loss or the minimum thickness throughout a region or various statistical measures of thickness variation can easily be calculated. Once a particular metric of interest is defined, then an appropriately accurate tomographic scanning geometry can be implemented.

One of the disadvantages of the parallel projection technique is, in fact, that it requires measurements to be made from all sides of the region of interest. This is clearly impractical in any number of materials testing situations. The crosshole technique requires access to only two sides of the region, although better reconstructions will be possible with transducers scanned along a third (or even fourth) side of the region of interest. This corresponds to having a line of receivers along the surface of the ground in addition to down the two boreholes in the seismic case. It increases the ray density and gives a larger number of ray directions through the region of interest. Both of these increase the accuracy of the reconstruction. In the development of a practical scanning technique we have opted for a two-leg system, but the algorithms and instrumentation developed here can easily be extended.

In the parallel projection tomographic scanner, the travel distance of the Lamb waves is fixed, so that we can use the P2L2 to detect very small changes in arrival time due to thickness changes. This is not possible for the crosshole tomography because the path length is different for each of the rays. Instead we digitized the entire received waveform for subsequent processing to extract the arrival times of the $S0$ modes needed for input to the ART code. In our initial studies we merely identified the peaks of interest manually, but with hundreds or even thousands of such waveforms required for input to the tomographic reconstruction algorithm, this was not practical. To automate this portion of the procedure, we have developed a rudimentary ''expert system'' which searches through the waveforms for a portion which corresponds to the characteristic $S0$ signal. It then records the time of arrival of that signal for each waveform and passes that to the tomographic code for the corresponding ray. The image shown in Fig. 6 used this automated procedure without other signal or image processing.

There are a number of issues yet to be addressed in this work. Many are practical issues associated with developing rapid and operator-independent tomographic Lamb wave images. Scanning with contact transducers is slow and prone to errors from variations in coupling of the ultrasonic energy in and out of the plate. The images shown here can be acquired by our contact scanner in several minutes, with tomographic reconstruction taking only a few seconds on a relatively modest PC. Neither of these are concerns in the laboratory, but are serious drawbacks in service. Both can be overcome by using arrays of transducers which are ''electronically'' scanned through all the various combinations. A ring of transducers could be used with standard fan-beam reconstructions and two or more linear arrays of transducers could be used with the crosshole algorithms. This would eliminate coupling problems, and would recover the speed inherent in Lamb wave techniques. The reconstruction algorithms run in near real time on modern PCs, so there appears to be no inherent limits on implementation of this technique in the field. Although the Lamb wave physics is fairly complicated, an expert system which automatically extracts the tomographic inputs from the received waveforms will make measurements possible by technicians who neither know or care about those subtleties. The inherent resolution of the technique is limited by the number of rays, with both measurement time and computational requirements increasing significantly as the number of rays increases.

The most serious limitation in the tomographic reconstruction algorithms that we have used in this work is that we have neglected diffraction and ray bending. We have assumed that the thinning only caused the Lamb wave velocity to change, but that there was no scattering of the Lamb waves. For slight changes in thickness this is a reasonable assumption, but for general flaws there will always be scattering. Reconstructions performed on highly scattering

samples, such as plates with deep flaws or through holes, have shown the expected tomographic artifacts increasing in severity with strength of scattering. Waveguide scattering is notoriously difficult, with coupling to other modes inherent. Incorporation of scattering effects into a Lamb wave diffraction tomography theory is the next step in our work. This will allow us to image cracks, disbonds, and other flaws. We also hope to be able to image flaws in the presence of strong scatterers such as lap joints and rivets in aircraft structures. We have also neglected anisotropy and associated ray bending in our analysis, assuming straight rays. For aluminum plates this is reasonable, but we have also found Lamb waves to be sensitive to impact, and thermal and fatigue damage in composites. For composites the anisotropy is significant because the effective stiffness is very different along the fibers vs across them. In graphite epoxy laminates we have found that the Lamb waves only propagate well along the fiber direction of one of the plys, making tomographic reconstructions which require propagation along many projection directions problematic. Incorporation of these effects into the crosshole tomographic algorithms is also important in future work.

[1] W. Wright, D. Hutchins, D. Jansen, and D. Schindel, ''Air- coupled Lamb wave tomography,'' IEEE Trans. Ultrason. Ferroelectr. Freq. Control **44**(1), 53 (1997).

[2] D. P. Jansen, D. A. Hutchins, and J. T. Mottram, ''Lamb wave tomography of advanced composite laminates containing damage,'' Ultrasonics **32** No. 2, 83 (1994).

[3] D. A. Hutchins, D. P. Jansen, and C. Edwards, ''Lamb wave tomography using non-contact transduction,'' Ultrasonics **31**, 97 (1993).

[4] D. P. Jansen and D. A. Hutchins, ''Immersion tomography using Rayleigh and Lamb Waves,'' Ultrasonics **30**(4), 245 (1992).

[5] D. P. Jansen and D. A. Hutchins, ''Lamb wave tomography,'' 1990 Ultrasonics Symposium (IEEE, New York), p. 1017.

[6] Y. Nagata, J. Huang, J. D. Achenbach, and S. Krishnaswamy, ''Lamb wave tomography using laser-based ultrasonics,'' in *Review of Progress in QNDE*, edited by D. O. Thompson and D. E. Chimenti (Plenum, New York, 1995), Vol 14, p. 561.

[7] F. L. Degertekin, J. Pei, B. T. Khuri-Yakub, and K. C. Saraswat, ''In situ acoustic temperature tomography of semiconductor wafers,'' Appl. Phys. Lett. **64**(11), 1338 (1994).

[8] H. Lamb, ''On waves in an elastic plate,'' Proc. R. Soc. London **XCIII**, 114 (1917).

[9] D. C. Worlton, ''Experimental confirmation of Lamb waves at megacycle frequencies,'' J. Appl. Phys. **32**, 967 (1961).

[10] J. D. Achenbach, *Wave Propagation in Elastic Solids* (North-Holland, New York, 1973).

[11] J. A. Hudson, *The Excitation and Propagation of Elastic Waves* (Cambridge University Press, Cambridge, 1980).

[12] L. M. Brekhovskikh, *Waves in Layered Media* (Academic, New York, 1960).

[13] J. Miklowitz, *Elastic Waves and Waveguides* (North-Holland, New York, 1978).

[14] K. F. Graff, *Wave Motion in Elastic Solids* (Dover, New York, 1980).

[15] H. Kolsky, *Stress Waves in Solids* (Dover, New York, 1963).

[16] B. A. Auld, *Acoustic Fields and Waves in Solids*, 2nd ed. (Robert E. Krieger, Malabar, FL, 1990).

[17] *Elastic Waves and Ultrasonic Nondestructive Evaluation*, edited by S. K. Datta, J. D. Achenbach, and Y. S. Rajapakse (North-Holland, New York, 1990).

[18] Y. H. Pao and C. C. Mow, *Diffraction of Elastic Waves and Dynamic Stress Concentrations* (Crane-Russak/Adam Hilger, New York, 1973).

[19] I. A. Viktorov, *Rayleigh and Lamb Waves* (Plenum, New York, 1967).

[20] S. G. Pierce, B. Culshaw, and Q. Shan, ''Laser generation of ultrasound using a modulated continuous wave laser diode,'' Appl. Phys. Lett. **72**(9), 1030 (1998).

[21] Z. Guo, J. D. Achenbach, and S. Krishnaswamy, ''EMAT generation and laser detection of single Lamb wave modes,'' Ultrasonics **35**, 423 (1997).

[22] Y. Nagata, J. Huang, J. D. Achenbach, and S. Krishnaswamy, ''Lamb wave tomography using laser-based ultrasonics,'' in *Review of Progress in Quantitative Nondestructive Evaluation*, edited by D. O. Thompson and D. E. Chimenti (Plenum, New York, 1995), Vol. 14, p. 561.

[23] R. C. Addison and A. D. W. McKie, ''Generation and detection of single mode Lamb waves using laser-based ultrasound,'' in *Review of Progress in Quantitative Nondestructive Evaluation*, edited by D. O. Thompson and D. E. Chimenti (Plenum, New York, 1995), Vol. 14, p. 521.

[24] W. M. D. Wright, D. A. Hutchins, A. Gachagan, and G. Hayward, ''Evaluation of fiber-reinforced composites using a non-contact laser/air-transducer system,'' in *Review of Progress in Quantitative Nondestructive Evaluation*, edited by D. O. Thompson and D. E. Chimenti (Plenum, New York, 1995), Vol. 14, p. 1333.

[25] M. Oksanen, J. Stor-Pellinen, and M. Luukkala, ''Determining mechanical properties of cardboard from photoacoustic Lamb wave transmission data'' in *Review of Progress in Quantitative Nondestructive Evaluation*, edited by D. O. Thompson and D. E. Chimenti (Plenum, New York, 1995), Vol. 14, p. 1649.

[26] N. A. Schumacher and C. P. Burger, ''Frequency based analysis methods for laser generated and detected Lamb Waves'' in *Review of Progress in Quantitative Nondestructive Evaluation*, edited by D. O. Thompson and D. E. Chimenti (Plenum, New York, 1994), Vol. 13, p. 157.

[27] R. D. Costley and Y. H. Berthelot, ''Dispersion curve analysis of laser-generated Lamb waves,'' Ultrasonics **32**(4), 249 (1994).

[28] L. Noui and R. J. Dewhurst, ''A laser beam deflection technique for the quantitative detection of ultrasonic Lamb waves,'' Ultrasonics **31**(6), 425 (1993).

[29] R. D. Costley and Y. H. Berthelot, ''Laser generation of Rayleigh and Lamb waves for ultrasonic nondestructive testing'' in *Review of Progress in Quantitative Nondestructive Evaluation*, edited by D. O. Thompson and D. E. Chimenti (Plenum, New York, 1993), Vol. 12, p. 579.

[30] C. Edwards, A. Al-Kassim, and S. B. Palmer, ''Laser ultrasound for the study of thin sheets,'' in *Review of Progress in Quantitative Nondestructive Evaluation*, edited by D. O. Thompson and D. E. Chimenti (Plenum, New York, 1993), Vol. 12, p. 539.

[31] S. E. Bobbin, J. W. Wagner, and R. C. Cammarata, ''Interpretation of laser-generated low-order Lamb waves for elastic modulus measurements in thin films,'' Ultrasonics **30**, 87 (1992).

[32] N. A. Schumacher, P. H. Gien, and C. P. Burger, ''Analysis of transient Lamb waves on metal plates, composite panels and curved members,'' in *Review of Progress in Quantitative Nondestructive Evaluation*, edited by D. O. Thompson and D. E. Chimenti (Plenum, New York, 1992), Vol. 11, p. 1569.

[33] K. Yamanaka and Y. Nagata, ''Generation of dispersive acoustic waves by the phase velocity scanning of a laser beam,'' in *Review of Progress in Quantitative Nondestructive Evaluation*, edited by D. O. Thompson and D. E. Chimenti (Plenum, New York, 1992), Vol. 11, p. 633.

[34] H. Nakano and S. Nagai, ''Laser generation of antisymmetric Lamb waves in thin plates,'' Ultrasonics **29**, 230 (1991).

[35] J. B. Spicer, A. D. W. McKie, and J. W. Wagner, ''Quantitative theory for laser ultrasonic wave in a thin plate,'' Appl. Phys. Lett. **57**, 1882 (1990).

[36] D. A. Hutchins, K. Lundgren, and S. B. Palmer, ''A laser study of transient Lamb waves in thin materials,'' J. Acoust. Soc. Am. **85**(4), 1441 (1989).

[37] R. J. Dewhurst, C. Edwards, A. D. W. McKie, and S. B. Palmer, ''Estimation of the thickness of thin metal sheets using laser generated ultrasound,'' Appl. Phys. Lett. **51**, 1066 (1987).

[38] E. Moreno and P. Acevedo, ''Thickness measurement in composite materials using Lamb waves,'' Ultrasonics **35**, 581 (1998).

[39] C. Bescond and M. Deschamps, ''Dynamical surface response of a semi-infinite anisotropic elastic medium to an impulsive force,'' J. Acoust. Soc. Am. **103**(1), 114 (1998).

[40] B. Zhang, W. Xiong, M. Yu, C. Q. Lan, and L. Li, ''Study of energy distribution of guided waves in multilayered media,'' J. Acoust. Soc. Am. **103**(1), 125 (1998).

[41] Y.-S. Wang and Z.-M. Zhang, ''Propagation of Love waves in a transversely isotropic fluid-saturated porous layered half-space,'' J. Acoust. Soc. Am. **103**(2), 695 (1998).

[42] A. N. Darinskii, ''Leaky waves and the elastic wave resonance reflection on a crystal-thin solid layer interface. II. Leaky waves given rise to by exceptional bulk waves,'' J. Acoust. Soc. Am. **103**(4), 1845 (1998).

[43] A. A. Mesquida, J. A. Otero, and R. R. Ramos, ''Wave propagation in layered piezoelectric structures,'' J. Appl. Phys. **83**(9), 4652 (1998).

[44] A. N. Darinskii, ''Leaky waves and the elastic wave resonance reflection on a crystal-thin solid layer interface,'' J. Acoust. Soc. Am. **102**(1), 283 (1997).
[45] X. Jia, ''Normal-mode theory of nonspecular phenomena for a finite-aperture ultrasonic beam reflected from layered media,'' Appl. Phys. Lett. **70**(3), 309 (1997).
[46] S. N. Makarov and A. L. Belkova, ''High velocity pseudosurface waves on $LiNbO_3$ with thin overlayers,'' Appl. Phys. Lett. **70**(16), 2100 (1997).
[47] E. Moulin, J. Assaad, C. Delebarre, H. Kaczmarek, and D. Balageas, ''Piezoelectric transducer embedded in a composite plate: Application to Lamb wave generation,'' J. Appl. Phys. **82**(5), 2049 (1997).
[48] J. Zhu, A. H. Shah, and S. K. Datta, ''Modal representation of wave propagation and scattering in an anisotropic plate,'' in *Review of Progress in Quantitative Nondestructive Evaluation*, edited by D. O. Thompson and D. E. Chimenti (Plenum, New York, 1995), Vol. 14, p. 569.
[49] S. P. Pelts and J. L. Rose, ''Acousto-ultrasonic source influence in an anisotropic layer,'' in *Review of Progress in Quantitative Nondestructive Evaluation*, edited by D. O. Thompson and D. E. Chimenti (Plenum, New York, 1995), Vol. 14, p. 1257.
[50] P. J. Shull, D. E. Chimenti, and S. K. Datta, ''Elastic guided waves and the Floquet concept in periodically layered plates,'' J. Acoust. Soc. Am. **95**, 99 (1994).
[51] P. J. Shull, D. E. Chimenti, S. K. Datta, and J. H. Ju, ''Considerations for elastic plate wave inspection of bilayered plates,'' in *Review of Progress in Quantitative Nondestructive Evaluation*, edited by D. O. Thompson and D. E. Chimenti (Plenum, New York, 1994), Vol. 13, p. 1407.
[52] M. D. Seale, B. T. Smith, W. H. Prosser, and J. E. Masters, ''Lamb wave response of fatigued composite samples,'' in *Review of Progress in Quantitative Nondestructive Evaluation*, edited by D. O. Thompson and D. E. Chimenti (Plenum, New York, 1994), Vol. 13, p. 1261.
[53] M. D. Seale and B. T. Smith, ''Lamb wave propagation in thermally damaged composites,'' in *Review of Progress in Quantitative Nondestructive Evaluation*, edited by D. O. Thompson and D. E. Chimenti (Plenum, New York, 1996), Vol. 15, p. 261.
[54] A. K. Mal, S.-S. Lih, and Y. Bar-Cohen, ''Characterization of the elastic constants of unidirectional laminates using oblique-incidence pulsed data,'' in *Review of Progress in Quantitative Nondestructive Evaluation*, edited by D. O. Thompson and D. E. Chimenti (Plenum, New York, 1994), Vol. 13, p. 1149.
[55] H.-T. Chien, S.-H. Sheen, and A. C. Raptis, ''Theoretical studies of wave propagation in multilayered piezoelectric media,'' in *Review of Progress in Quantitative Nondestructive Evaluation*, edited by D. O. Thompson and D. E. Chimenti (Plenum, New York, 1994), Vol. 13, p. 219.
[56] C. L. Yapura and V. K. Kinra, ''Lamb waves in an isotropic solid-fluid bilayer,'' in *Review of Progress in Quantitative Nondestructive Evaluation*, edited by D. O. Thompson and D. E. Chimenti (Plenum, New York, 1994), Vol. 13, p. 203.
[57] D. P. Jansen, D. A. Hutchins, and J. T. Mottram, ''Lamb wave tomography of advanced composite laminates containing damage,'' Ultrasonics **32**(2), 83 (1994).
[58] D. E. Chimenti, ''Lamb waves in microstructured plates,'' Ultrasonics **32**(4), 255 (1994).
[59] J. Laperre and W. Thys, ''Experimental and theoretical study of Lamb wave dispersion in aluminum/polymer bilayers,'' J. Acoust. Soc. Am. **94**, 268 (1993).
[60] P.-C. Xu, K.-E. Lindenschmidt, and S. A. Meguid, ''A new high-frequency analysis of coatings using leaky Lamb waves,'' J. Acoust. Soc. Am. **94**, 2954 (1993).
[61] H.-T. Chien, S.-H. Sheen and A. C. Raptis, ''An acousto-ultrasonic NDE technique for monitoring material anisotropy,'' in *Review of Progress in Quantitative Nondestructive Evaluation*, edited by D. O. Thompson and D. E. Chimenti (Plenum, New York, 1993), Vol. 12, p. 1225.
[62] A. H. Nayfeh and H.-T. Chien, ''The influence of piezoelectricity on free and reflected waves from fluid-loaded anisotropic plates,'' J. Acoust. Soc. Am. **91**, 1250 (1992).
[63] J. Laperre and W. Thys, ''Experimental and theoretical study of elastic wave dispersion in a liquid bilayer,'' J. Acoust. Soc. Am. **92**, 908 (1992).
[64] A. H. Nayfeh and H.-T. Chien, ''Wave propagation interaction with free and fluid-loaded piezoelectric substrates,'' J. Acoust. Soc. Am. **91**, 3126 (1992).
[65] N. Guo and P. Cawley, ''Lamb waves for the NDE of composite laminates,'' in *Review of Progress in Quantitative Nondestructive Evaluation*, edited by D. O. Thompson and D. E. Chimenti (Plenum, New York, 1992), Vol. 11, p. 1443.
[66] A. K. Mal and S.-S. Lih, ''Wave field produced in a composite laminate by a concentrated surface force,'' in *Review of Progress in Quantitative Nondestructive Evaluation*, edited by D. O. Thompson and D. E. Chimenti (Plenum, New York, 1992), Vol. 11, p. 137.
[67] V. Dayal and V. K. Kinra, ''Leaky Lamb waves in an anisotropic plate. II: Nondestructive evaluation of matrix cracks in fiber-reinforced composites,'' J. Acoust. Soc. Am. **89**, 1590 (1991).
[68] A. H. Nayfeh, ''The general problem of elastic wave propagation in multilayered anisotropic media,'' J. Acoust. Soc. Am. **89**, 1521 (1991).
[69] A. H. Nayfeh and D. E. Chimenti, ''Elastic wave propagation in fluid-loaded multiaxial anisotropic media,'' J. Acoust. Soc. Am. **89**, 542 (1991).
[70] D. E. Chimenti and R. W. Martin, ''Nondestructive evaluation of composite laminates by leaky Lamb waves,'' Ultrasonics **29**, 13 (1991).
[71] D. E. Chimenti and A. H. Nayfeh, ''Ultrasonic reflection and guided wave propagation in biaxially laminated composite plates,'' J. Acoust. Soc. Am. **87**, 1409 (1990).
[72] V. Dayal and V. K. Kinra, ''Leaky Lamb waves in an anisotropic plate. I: An exact solution and experiments,'' J. Acoust. Soc. Am. **85**, 2268 (1989).
[73] B. Tang and E. G. Henneke, ''Lamb-wave monitoring of axial stiffness reduction of laminated composite plates,'' Mater. Eval. **48**, 928 (1989).
[74] A. H. Nayfeh and D. E. Chimenti, ''Ultrasonic wave reflection from liquid-coupled orthotropic plates with application to fibrous composites,'' J. Appl. Mech. **55**, 863 (1988).
[75] D. E. Chimenti and A. H. Nayfeh, ''Anomalous ultrasonic dispersion in fluid-coupled, fibrous composite plates,'' Appl. Phys. Lett. **49**(9), 492 (1986).
[76] D. E. Chimenti and A. H. Nayfeh, ''Leaky Lamb waves in fibrous composite laminates,'' J. Appl. Phys. **58**(12), 4531 (1985).
[77] T. Kundu, A. Maji, T. Ghosh, and K. Maslov, ''Detection of kissing bonds by Lamb waves,'' Ultrasonics **35**, 573 (1998).
[78] D. W. Schindel, D. S. Forsyth, D. A. Hutchins, and A. Fahr, ''Air-coupled ultrasonic NDE of bonded aluminum lap joints,'' Ultrasonics **35**, 1 (1997).
[79] L. Singher, ''Bond strength measurement by ultrasonic guided waves,'' Ultrasonics **35**, 305 (1997).
[80] L. Singher, Y. Segal, and J. Shamir, ''Interaction of a guided wave with a nonuniform adhesion bond,'' Ultrasonics **35**, 385 (1997).
[81] D. A. Sotiropoulos, ''Guided elastic waves in pre-stressed solids for the ultrasonic characterization of interfacial zones,'' in *Review of Progress in Quantitative Nondestructive Evaluation*, edited by D. O. Thompson and D. E. Chimenti (Plenum, New York, 1995), Vol. 14, p. 195.
[82] J. L. Rose, A. Pilarski, and K. M. Rajana, ''Ultrasonic guided waves for lap splice joint inspection in aging aircraft,'' in *Review of Progress in Quantitative Nondestructive Evaluation*, edited by D. O. Thompson and D. E. Chimenti (Plenum, New York, 1995), Vol. 14, p. 1417.
[83] J. C. Johnson, R. B. Thompson, and E. E. Jamieson, ''Determination of Rayleigh and Lamb wave velocities in diamond films using an acoustic microscope,'' in *Review of Progress in Quantitative Nondestructive Evaluation*, edited by D. O. Thompson and D. E. Chimenti (Plenum, New York, 1995), Vol. 14, p. 1805.
[84] L. Singher, Y. Segal, and E. Segal, ''Considerations in bond strength evaluation by ultrasonic guided waves,'' J. Acoust. Soc. Am. **96**, 2497 (1994).
[85] J. L. Rose, A. Pilarski, K. Rajana, and J. J. Ditri, ''Coating influence on generation and reception of ultrasonic lamb type plate waves,'' in *Review of Progress in Quantitative Nondestructive Evaluation*, edited by D. O. Thompson and D. E. Chimenti (Plenum, New York, 1994), Vol. 13, p. 1903.
[86] K. J. Sun and P. H. Johnston, ''Disbond detection in bonded aluminum joints using Lamb wave amplitude and time-of-flight,'' in *Review of Progress in Quantitative Nondestructive Evaluation*, edited by D. O. Thompson and D. E. Chimenti (Plenum, New York, 1994), Vol. 13, p. 1507.
[87] A. Pilarski, J. L. Rose, J. Ditri, D. Jiao, and K. Rajana, ''Lamb wave mode selection for increased sensitivity to interfacial weakness of adhesive bonds,'' in *Review of Progress in Quantitative Nondestructive Evaluation*, edited by D. O. Thompson and D. E. Chimenti (Plenum, New York, 1993), Vol. 12, p. 1579.
[88] K. J. Sun and P. H. Johnston, ''Mode conversions of Lamb waves for inspection of disbonds,'' *Proceedings of the 1992 IEEE Ultrasonics Symposium* (IEEE, New York), p. 763.
[89] S. I. Rokhlin, ''Lamb wave interaction with lap-shear adhesive joints: Theory and experiment,'' J. Acoust. Soc. Am. **89**, 2758 (1991).
[90] S. I. Rokhlin and Y. J. Wang, ''Analysis of boundary conditions for elas-

tic wave interaction with an interface between two solids,'' J. Acoust. Soc. Am. **89**, 503 (1991).
[91] P.-C. Xu and S. K. Datta, ''Guided waves in a bonded plate: A parametric study,'' J. Appl. Phys. **67**, 6779 (1990).
[92] A. Pilarski, ''Ultrasonic evaluation of the adhesion degree in layered joints,'' Mater. Eval. **43**, 765 (1985).
[93] A. H. Nayfeh, D. E. Chimenti, L. Adler, and R. L. Crane, ''Ultrasonic leaky waves in the presence of a thin layer,'' J. Appl. Phys. **52**(8), 4985 (1981).
[94] S. Rokhlin, ''Diffraction of Lamb waves by a finite crack in an elastic layer,'' J. Acoust. Soc. Am. **67**, 1157 (1980).
[95] R. S. C. Monkhouse, P. D. Wilcox, and P. Cawley, ''Flexible interdigital PVDF transducers for the generation of Lamb waves in structures,'' Ultrasonics **35**, 489 (1997).
[96] N. A. Losin, ''Asymptotics of flexural waves in isotropic elastic plates,'' J. Appl. Mech. **64**, 337 (1997).
[97] M. de Billy, ''On the scattering of antisymmetric edge modes,'' J. Acoust. Soc. Am. **101**(6), 3261 (1997).
[98] O. Poncelet and M. Deschamps, ''Lamb waves generated by complex harmonic inhomogeneous plane waves,'' J. Acoust. Soc. Am. **102**(1), 292 (1997).
[99] P. Zinin, O. Lefeuvre, G. A. D. Briggs, B. D. Zeller, P. Cawley, J. Kinloch, and G. E. Thompson, ''Anomalous behaviour of leaky surface waves for stiffening layer near cutoff,'' J. Appl. Phys. **82**(3), 1031 (1997).
[100] P. Kielczynski, ''Attenuation of love waves in low- loss media,'' J. Appl. Phys. **82**(12), 5932 (1997).
[101] D. M. Benson, P. Karpur, T. E. Matikas, and T. Kundu, ''Experimental generation of Lamb wave dispersion using Fourier analysis of leaky modes,'' in *Review of Progress in Quantitative Nondestructive Evaluation*, edited by D. O. Thompson and D. E. Chimenti (Plenum, New York, 1995), Vol. 14, p. 187.
[102] B. Pavlakovic, J. L. Rose, and J. J. Ditri, ''Finite size and specimen thickness influence in acousto-ultrasonic nondestructive evaluation,'' in *Review of Progress in Quantitative Nondestructive Evaluation*, edited by D. O. Thompson and D. E. Chimenti (Plenum, New York, 1995), Vol. 14, p. 1037.
[103] V. Dayal, ''Automated Lamb wave measurements,'' in *Review of Progress in Quantitative Nondestructive Evaluation*, edited by D. O. Thompson and D. E. Chimenti (Plenum, New York, 1994), Vol. 13, p. 189.
[104] D. Alleyne and P. Cawley, ''The practical excitation and measurement of Lamb waves using piezoelectric transducers,'' in *Review of Progress in Quantitative Nondestructive Evaluation*, edited by D. O. Thompson and D. E. Chimenti (Plenum, New York, 1994), Vol. 13, p. 181.
[105] A. Pilarski, J. J. Ditri, K. Rajana, and J. L. Rose, ''Utilization of non-zero-order symmetric lamb wave modes at the first critical angle,'' in *Review of Progress in Quantitative Nondestructive Evaluation*, edited by D. O. Thompson and D. E. Chimenti (Plenum, New York, 1994), Vol. 13, p. 173.
[106] S. G. Joshi and Y. Jin, ''Electromechanical coupling coefficients of ultrasonic Lamb waves,'' J. Acoust. Soc. Am. **94**, 261 (1993).
[107] Q. Zhu and W. G. Mayer, ''On the crossing points of Lamb wave velocity dispersion curves,'' J. Acoust. Soc. Am. **93**, 1893 (1993).
[108] O. Lenoir, J. Duclos, J. M. Conoir, and J. L. Izbicki, ''Study of Lamb waves based on the frequency and angular derivatives of the phase of the reflection coefficient,'' J. Acoust. Soc. Am. **94**, 330 (1993).
[109] D. A. Hutchins, D. P. Jansen, and C. Edwards, ''Lamb-wave tomography using non-contact transduction,'' Ultrasonics **31**, 97 (1993).
[110] D. N. Alleyne, T. P. Pialucha, and P. Cawley, ''A signal regeneration technique for long-range propagation of dispersive Lamb waves,'' Ultrasonics **31**(3), 201 (1993).
[111] I.-T. Lu, H. L. Bertoni, and H.-Y. Chen, ''Coupling of plate waves at joints,'' J. Acoust. Soc. Am. **92**, 510 (1992).
[112] P. Pareige, F. Luppé, and J. Ripoche, ''Scattering of Lamb waves at the edge of a semi-infinite plate embedded in water,'' J. Acoust. Soc. Am. **92**, 1056 (1992).
[113] J. J. Ditri, J. L. Rose, and G. Chen, ''Mode selection criteria for defect detection optimization using Lamb waves,'' in *Review of Progress in Quantitative Nondestructive Evaluation*, edited by D. O. Thompson and D. E. Chimenti (Plenum, New York, 1992), Vol. 11, 2109.
[114] S. E. Bobbin, J. W. Wagner, and R. C. Cammarata, ''Determination of the flexural modulus of thin films from measurement of the first arrival of the symmetric Lamb wave,'' Appl. Phys. Lett. **59**, 1544 (1991).
[115] D. Alleyne and P. Cawley, ''A two-dimensional Fourier transform method for the measurement of propagating multimode signals,'' J. Acoust. Soc. Am. **89**, 1159 (1991).
[116] M. R. Karim, A. K. Mal, and Y. Bar-Cohen, ''Inversion of leaky-Lamb wave data by simplex algorithm,'' J. Acoust. Soc. Am. **88**, 482 (1990).
[117] M. de Billy and I. Molinero, ''On the nonobservance of nonspecular bounded beam reflection effects of Lamb waves,'' J. Acoust. Soc. Am. **83**, 1249 (1988).
[118] N. Vasudevan and A. K. Mal, ''Response of an elastic plate to localized transient sources,'' J. Appl. Mech. **52**, 356 (1985).
[119] M. K. T. Hansch, K. M. Rajana, and J. L. Rose, ''Flaw classification potential in tubing with guided waves,'' in *Review of Progress in Quantitative Nondestructive Evaluation*, edited by D. O. Thompson and D. E. Chimenti (Plenum, New York, 1995), Vol. 14, p. 803.
[120] D. Alleyne and P. Cawley, ''The long range detection of corrosion in pipes using Lamb waves,'' in *Review of Progress in Quantitative Nondestructive Evaluation*, edited by D. O. Thompson and D. E. Chimenti (Plenum, New York, 1995), Vol. 14, p. 2073.
[121] E. I. Madaras, T. Kohl, and W. P. Rogers, ''Material property characterization and pulse propagation in thin drawn wire waveguides,'' *Proceedings of the 1992 IEEE Ultrasonics Symposium* (IEEE, New York), p. 957.
[122] K. J. Sun and W. P. Winfree, ''Propagation of acoustic waves in a copper wire embedded in a curing epoxy,'' *Proceedings of the 1987 IEEE Ultrasonics Symposium* (IEEE, New York), p. 439.
[123] T. K. Lockett, ''Lamb and torsional waves and their use in flaw detection in tubes,'' Ultrasonics **11**, 31 (1973).
[124] C. Pecorari, ''Rayleigh wave dispersion due to a distribution of semi-elliptical surface-breaking cracks,'' J. Acoust. Soc. Am. **103**(3), 1383 (1998).
[125] L. Wang and J. Shen, ''Scattering of elastic waves by a crack in an isotropic plate,'' Ultrasonics **35**, 451 (1997).
[126] O. I. Lobkis and D. E. Chimenti, ''Elastic guided waves in plates with surface roughness. I. Model calculation,'' J. Acoust. Soc. Am. **102**(1), 143 (1997).
[127] O. I. Lobkis and D. E. Chimenti, ''Elastic guided waves in plates with surface roughness. II. Experiments,'' J. Acoust. Soc. Am. **102**(1), 150 (1997).
[128] T. K. Kapoor and H. Schmidt, ''Acoustic scattering from a three-dimensional protuberance on a thin, infinite, submerged elastic plate,'' J. Acoust. Soc. Am. **102**(1), 256 (1997).
[129] A. N. Norris and C. Vemula, ''Scattering of flexural waves on thin plates,'' J. Sound Vib. **181**, 115 (1995).
[130] A. Safaeinili and R. A. Roberts, ''An efficient approximate model for elastic wave scattering in plates,'' in *Review of Progress in Quantitative Nondestructive Evaluation*, edited by D. O. Thompson and D. E. Chimenti (Plenum, New York, 1995), Vol. 14, p. 147.
[131] K. J. Sun, D. Kishoni, and P. H. Johnston, ''Feasibility of using Lamb waves for corrosion detection in layered aluminum aircraft structures,'' in *Proceedings of the 1993 Ultrasonics Symposium* (IEEE, New York), p. 733 (1993).
[132] T.-T. Wu and J.-H. Gong, ''Application of transient elastic waves to the nondestructive evaluation of plate structure with cavity or inclusion,'' J. Acoust. Soc. Am. **94**, 1453 (1993).
[133] N. Guo and P. Cawley, ''The interaction of Lamb waves with delaminations in composite laminates,'' J. Acoust. Soc. Am. **94**, 2240 (1993).
[134] I. N. Komsky and J. D. Achenbach, ''Application of a self-calibrating ultrasonic technique to the detection of fatigue cracks by the use of Lamb waves,'' in *Review of Progress in Quantitative Nondestructive Evaluation*, edited by D. O. Thompson and D. E. Chimenti (Plenum, New York, 1993), Vol. 12, p. 2167.
[135] K. J. Sun, ''Application of guided acoustic waves to delamination detection,'' in *Review of Progress in Quantitative Nondestructive Evaluation*, edited by D. O. Thompson and D. E. Chimenti (Plenum, New York, 1992), Vol. 11, p. 1213.
[136] S. W. Liu, S. K. Datta, and A. H. Shah, ''Transient scattering of Rayleigh-Lamb waves by surface-breaking and buried cracks in a plate,'' in *Review of Progress in Quantitative Nondestructive Evaluation*, edited by D. O. Thompson and D. E. Chimenti (Plenum, New York, 1992), Vol. 11, p. 73.
[137] J. Wu and Z. Zhu, ''The interfacial mass detection with Lamb-wave sensors,'' in *Review of Progress in Quantitative Nondestructive Evaluation*, edited by D. O. Thompson and D. E. Chimenti (Plenum, New York, 1992), Vol. 11, p. 1051.
[138] G. S. Verdict, P. H. Gien, and C. P. Burger, ''Finite element study of

Lamb wave interactions with holes and through thickness defects in thin metal plates,'' in *Review of Progress in Quantitative Nondestructive Evaluation*, edited by D. O. Thompson and D. E. Chimenti (Plenum, New York, 1992), Vol. 11, p. 97.
[139] K. J. Sun and P. H. Johnston, ''Effect of rivet rows on propagation of Lamb waves in mechanically fastened two-layer aluminum plates,'' in *Review of Progress in Quantitative Nondestructive Evaluation*, edited by D. O. Thompson and D. E. Chimenti (Plenum, New York, 1995), Vol. 14, p. 1569.
[140] M. K. Hinders, ''Lamb wave scattering from rivets,'' in *Review of Progress in Quantitative Nondestructive Evaluation*, edited by D. O. Thompson and D. E. Chimenti (Plenum, New York, 1996), Vol. 15, p. 209.
[141] M. K. Hinders and J. C. P McKeon, ''Lamb wave scattering for aging aircraft NDT,'' in *Proceedings of the Fifth Annual Research Symposium* (ASNT, Columbus, 1996).
[142] A. C. Kak and M. Slaney, *Principles of Computerized Tomographic Imaging* (IEEE, New York, 1988).
[143] F. L. Paillet and C. H. Cheng, *Acoustic Waves in Boreholes* (CRC, Boca Raton, 1991).
[144] K. A. Dines and R. J. Lytle, ''Computerized geophysical tomography,'' Proc. IEEE **67**(7), 1065 (1979).

Direct imaging of traveling Lamb waves in plates using photorefractive dynamic holography

K. L. Telschow, V. A. Deason, R. S. Schley, and S. M. Watson
Idaho National Engineering and Environmental Laboratory, Lockheed Martin Idaho Technologies Co., P.O. Box 1625, Idaho Falls, Idaho 83415-2209

(Received 17 February 1999; accepted for publication 22 July 1999)

Anisotropic stiffness properties of sheet materials can be determined by measuring the propagation of Lamb waves in different directions, but this typically requires multiple positioning of a suitable transducer at several points or scanning over the area of the sample plate. A laser imaging approach is presented that utilizes the adaptive property of photorefractive materials to produce a real-time measurement of the antisymmetric Lamb traveling wave displacement and phase in all planar directions simultaneously without scanning. Continuous excitation and lock-in methodology is employed, enabling the data to be recorded and displayed by a video camera. Analysis of the image produces a direct quantitative determination of the phase velocity in all directions showing plate stiffness anisotropy in the plane. The method is applicable to materials that scatter light diffusely and provides quantitative imaging of the dynamic surface motion exhibited by traveling elastic waves. A description is given of this imaging process and, for the first time, its ability to perform lock-in measurement of elastic wave displacement amplitude and phase. © *1999 Acoustical Society of America.* [S0001-4966(99)05011-0]

PACS numbers: 43.35.Pt, 43.35.Cg, 43.35.Sx, 43.35.Yb [HEB]

INTRODUCTION

Many optical techniques for measuring ultrasonic motion at surfaces have been developed for use in applications such as vibration measurement and laser ultrasonics. Most of these methods have similar sensitivities and are based on time-domain processing using homodyne, heterodyne, Fabry-Perot,[1] and, more recently, photorefractive interferometry.[2] Generally, the methods described above do not allow measurement at more than one surface point simultaneously, requiring multiple beam movements or scanning in order to produce images of ultrasonic motion over an extended area. Electronic speckle interferometry and shearography do provide images of vibrational motion over large surface areas. This method has proven very durable in the field for large displacement amplitudes and a sensitivity of 1/3000 of the optical wavelength has been demonstrated under laboratory conditions.[3] Full-field imaging of traveling ultrasonic waves using digital shearography has been recently reported with sensitivity in the nanometer range.[4] With this method, optical interference occurs at the photodetector surface of the camera that records the speckle image from the sample surface. Multiple image frames are typically recorded and processed in a computer to produce an output proportional to sample surface displacement. This paper discusses a powerful alternative method that utilizes the photorefractive effect in optically nonlinear materials to perform adaptive optical interferometry in an imaging mode.[5,6] Optical interference occurs within the photorefractive material with this technique and the output is an optical image whose intensity distribution is directly proportional to the sample surface vibration amplitude for small ultrasonic displacements. Utilizing this approach, no post-processing of the data recorded by a video camera is required to produce images of the surface vibration amplitude over large areas. The application of this approach to imaging of standing wave resonant motion in plates has been previously described.[7–9] This paper describes results of an investigation into the fundamental operation and application of this technique to nonstationary wave forms through imaging of traveling Lamb waves in plates.[10] The ability to measure nonstationary wave forms not only at single points but also as an image over a surface comes from the inherent lock-in measurement process occurring. This recording mechanism is developed theoretically as well as experimentally here, for the first time, for imaging of flexural wave propagation in isotropic plates. Application to imaging flexural wave propagation in anisotropic plates is also presented. A benefit of the imaging approach is developed from the Fourier transform of the recorded wave front that produces a mapping of the propagation wave vector in all planar directions as a single image. This mapping yields information about the elastic symmetry of the wave propagation and, therefore, the material microstructure directly.

BACKGROUND

Photorefractivity[5] refers to that process where optical excitation and transport of electrically charged carriers within select nonlinear optical materials produces an optical diffraction grating from the interference pattern developed inside the material. A spatial and temporal charge distribution results in the photorefractive material that reflects the optical phase information impressed onto the optical signal beam by the vibrating sample surface. Several optical frequency domain measurement methods of vibration have been proposed using photorefractive two- and four-wave mixing in select materials.[11,12] These provide a time-averaged response that is a nonlinear function of the specimen vibration displacement amplitude. A method using an unconventional photorefractive process has been reported that provides out-

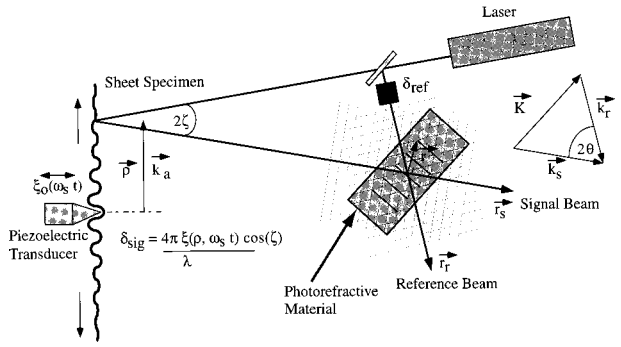

FIG. 1. Photorefractive two-wave mixing setup for optical vibration detection.

put linear with the vibration displacement amplitude, but it is limited to a select group of materials.[13] The method reported here utilizes the normal photorefractive effect to produce an optical grating at a fixed beat frequency between the phase-modulated signal and reference beams. It can be used in a manner that directly measures vibration amplitude and phase with a response proportional to the Bessel function of order one, providing a linear output for small amplitudes. The method accommodates rough surfaces, exhibits a flat frequency response above the photorefractive cutoff frequency, and can be used for detecting both standing and traveling waves. In this paper, the underlying physics of the optical detection process is developed and application of the method to full-field imaging of traveling Lamb waves in plates with isotropic and anisotropic stiffness properties is presented.

EXPERIMENTAL METHOD

The experimental setup for vibration detection is shown in Fig. 1. A solid-state laser source at 532 nm was split into two legs forming the signal and reference beams. The signal beam was reflected off traveling waves produced at the surface of a nickel plate driven at its center by a continuously excited piezoelectric transducer. The excited traveling waves occurring on the plate surface produced a phase modulation δ_{sig} of the signal beam. The reference beam was phase modulated by an electro-optic modulator at a fixed modulation depth δ_{ref}. The photorefractive material was from single-crystal bismuth silicon oxide (BSO) of size 10 by 10 by 2.25 mm and cut along the $\langle 001 \rangle$ and $\langle 011 \rangle$ directions. The measured time constant was 0.01 ms. The modulated beams were combined and interfered inside the BSO photorefractive crystal utilizing an external angle $2\theta = 55$ deg between the beams in order to produce a large response for operation in the diffusive charge transport regime. The refractive index grating produced within the photorefractive material can be read out by four-wave or two-wave mixing techniques.

In the four-wave mixing configuration, the reference beam was reflected back into the crystal along a counter-propagating path that matched the Bragg angle of the photorefractive grating in the medium. The vibration-induced optical phase grating was read out by the resulting diffracted reference beam, or conjugate signal beam, that propagated backward along the signal beam leg and was detected by deflecting it with a beamsplitter (not shown) toward a photodetector. Subsequently, when only one detection point was being interrogated, the photodetector signal was processed with conventional electrical lock-in methods to increase the measurement signal-to-noise ratio through utilizing a small detection bandwidth. A video charge-coupled device (CCD) camera was employed to record the demodulated optical phase grating and produce images of the elastic displacement wave front over the surface of the plate. Four-wave mixing isolated the signal beam phase information very effectively from the transmitted signal beam.

A significant drawback of the four-wave mixing approach is the low output intensity of the readout process. This was improved by employing a two-wave approach that recorded the forward diffracted beam enhanced by the gain of the two-wave mixing process. However, there was also a significant component of the directly transmitted signal beam that had to be discriminated against in order to achieve maximum sensitivity. Optically active photorefractive materials, in this case BSO, offer a means for providing the needed discrimination through optical activity and anisotropic self-diffraction, which produce a rotation in the linear polarization of the diffracted reference beam with respect to that of the transmitted signal beam. By using an appropriate thickness of the photorefractive crystal, it was possible to achieve a nearly 90° polarization shift between the two beams.[14] This allowed reduction of the directly transmitted signal beam through the use of high extinction ratio polarizers. The resulting intensity of the diffracted reference beam was dependent on the vibration displacement and temporally modulated at the frequency difference between the mixing waves in a manner analogous to the four-wave mixing case. As before, only the output intensity need be measured to obtain both the vibration amplitude and phase, thereby allowing direct imaging and ease of interpretation.

FLEXURAL WAVE DISPLACEMENT DISTRIBUTION

The mechanism that allows recording of traveling wave displacements can be illustrated by considering a traveling flexural wave in a plate. The classical differential equation of motion for the out-of-plane displacement of an isotropic homogeneous plate driven by a force per unit area of $f_p(\rho,t)$ is given by[15]

$$D\nabla^4\xi + \sigma\frac{\partial^2\xi}{\partial t^2} = f_p(\rho,t), \tag{1}$$

where $D \equiv Eh^3/12(1-s^2)$ is the bending stiffness of the plate, $\sigma \equiv \rho_m h$ the mass density per unit area, ρ_m = the mass density of the material, s = Poisson's ratio, E = Young's modulus, h = the plate thickness, ξ is the displacement normal to the plate surface, and ρ is the radial spatial coordinate. Equation (1) is valid at low frequencies where the elastic wavelength (λ_a) is much larger than the plate thickness, i.e., $k_a = 2\pi/\lambda_a$, for $k_a h \ll 1 \Rightarrow h \ll \lambda_a/2\pi$, and approximates the lowest antisymmetric Lamb or flexural wave mode. Consider a traveling flexural wave excited at a single point on the plate by a piezoelectric transducer undergoing continuous oscillation with frequency $\omega_s/2\pi$ and phase φ_s producing a point

force per unit area on the plate of $f_p(\rho,t) = \mathrm{Re}[F_0(\delta(\rho)/2\pi\rho)e^{-i(\omega_s t+\varphi_s)}]$, where the amplitude of the total force applied to the plate is F_0 and $\delta(x)$ is the Dirac delta function. Equation (1) can be rewritten utilizing $\xi(\rho,t)=\xi_\rho(\rho)e^{-i(\omega_s t+\varphi_s)}$, where $\xi_\rho(\rho)$ is the complex displacement amplitude, as follows:

$$(\nabla^2-k_a^2)(\nabla^2+k_a^2)\xi_\rho(\rho)=\frac{F_0}{2\pi D}\frac{\delta(\rho)}{\rho}, \tag{2}$$

where $k_a^4\equiv\sigma\omega^2/D$. Since Eq. (2) is a fourth-order differential equation, in addition to the two propagating wave modes, two nonpropagating heavily damped modes must also be included in order to form a complete solution satisfying the boundary conditions. The solution can be found by adopting the time dependence of the forcing function along with applying the two-dimensional spatial Fourier transform, which, for a circularly symmetric function, can be expressed in terms of the Hankel transform of order zero as[16]

$$\tilde{g}(k)=2\pi\int_0^\infty g(\rho)J_0(k\rho)\rho d\rho \Leftrightarrow$$

$$g(\rho)=\frac{1}{2\pi}\int_0^\infty \tilde{g}(k)J_0(k\rho)k dk, \tag{3}$$

with $\delta(\rho-\rho')/\rho=\int_0^\infty J_0(k\rho')J_0(k\rho)k dk$, and $\delta(k-k')/k=\int_0^\infty J_0(k'\rho)J_0(k\rho)\rho d\rho$. Applying the transform to Eq. (2) and using the orthogonality of the Bessel functions yields the radial solution in the Fourier domain as

$$\tilde{\xi}_\rho(k)=\frac{F_0}{D}\left[\frac{1}{(k^2-k_a^2)(k^2+k_a^2)}\right]. \tag{4}$$

The resultant wave form traveling outward from the excitation point in the spatial domain is obtained by the inverse transform according to

$$\xi_\rho(\rho)=\frac{F_0}{2\pi D}\int_0^\infty\left[\frac{J_0(k\rho)}{(k^2-k_a^2)(k^2+k_a^2)}\right]k dk, \tag{5}$$

which can be integrated using the relation $\int_0^\infty J_0(x\rho)x dx/(x^2+k^2)=K_0(k\rho)$,[17] where $K_0(x)$ is a modified Bessel function of the second kind. The resultant traveling wave solution is given by[18]

$$\xi(\rho,t)=\mathrm{Re}\{i\xi_0[H_0^1(k_a\rho)-H_0^1(ik_a\rho)]e^{-i(\omega_s t+\varphi_s)}\}, \tag{6}$$

where $\xi_0\equiv F_0/8\omega\sqrt{D\sigma}$, $k_a=2\pi/\lambda_a$, $\lambda_a=2\pi c_a/\omega_s$ is the antisymmetric traveling mode wavelength with phase velocity c_a and $H_0^1(x)=J_0(x)+iN_0(x)$ is the Hankel function of order zero representing a wave traveling outward from the origin. A central conclusion of this research is that the optical imaging approach described measures both the elastic wave amplitude and phase over the plate surface simultaneously in a manner similar to electrical signal lock-in detection. The explicit separation of the flexural wave displacement into terms depicting the elastic wave amplitude and phase is not readily apparent from Eq. (6). However, this separation can be achieved near the origin and far away by expanding the Hankel functions. Near the origin, the Bessel functions can be expanded as

$$J_0(x)\underset{x\to0}{\to}1-\frac{x^2}{4},$$

$$N_0(x)\underset{x\to0}{\to}\frac{2}{\pi}\left[\ln\left(\frac{x}{2}\right)+\gamma\right],\quad \gamma=0.5772\cdots,$$

to show that $\lim_{x\to0}[H_0^1(x)-H_0^1(ix)]=1$, designating ξ_0 as the displacement amplitude at the source point. Another way of writing the solution, using the relation $K_0(x)=(\pi i/2)H_0^1(ix)$, is

$$\xi(\rho,t)=\xi_0\left[J_0(k_a\rho)\sin(\omega_s t+\varphi_s)-\left[N_0(k_a\rho)+\frac{2}{\pi}K_0(k_a\rho)\right]\cos(\omega_s t+\varphi_s)\right], \tag{7}$$

which explicitly shows the traveling wave near-and far-field behavior as

$$\xi(\rho,t)\xrightarrow[k_a\rho\to0]{}\xi_0\sin(\omega_s t+\varphi_s),$$

$$\xi(\rho,t)\xrightarrow[k_a\rho\to\infty]{}\xi_0\sqrt{\frac{2}{\pi k_a\rho}}\sin\left(\omega_s t+\varphi_s-k_a\rho+\frac{\pi}{4}\right).$$

These expressions show that the displacement at the origin is ξ_0 and that as the elastic wave travels away from the origin, its phase increases linearly with radial distance. The normal lock-in method allows one to determine the flexural wave amplitude and phase separately and then reconstruct the displacement completely at any point. The next section shows this procedure explicitly for the photorefractive detection methodology.

PHOTOREFRACTIVE TRAVELING WAVE DETECTION

The method by which the photorefractive process demodulates the optical phase information can be illustrated by considering an approximation to the two-wave and four-wave mixing processes. The integral form of the Hankel function,[19]

$$H_0^1(x)=\sqrt{\frac{2}{\pi x}}e^{i(x-\pi/4)}\int_0^\infty\frac{e^{-u}}{\sqrt{\pi u}}\left(1+\frac{iu}{2x}\right)^{-1/2}du$$

$$=h_0(x)e^{i(x-\pi/4)},$$

can be used to write Eq. (6) for the traveling wave displacement as

$$\xi(\rho,t)=\mathrm{Re}[i\xi_0|h(k_a\rho)|e^{i\Phi_a}e^{i(k_a\rho-\pi/4-\omega_s t-\varphi_s)}], \tag{8}$$

where $|h(k_a\rho)|e^{i\Phi_a}\equiv h_0(k_a\rho)-h_0(ik_a\rho)e^{-k_a\rho(1+i)}$. The optical phase shift of the signal beam, referring to Fig. 1 and assuming normal incidence, $\zeta=0$, produced by the traveling wave, can be described using Eq. (8), with $\chi(\rho)=(k_a\rho-\pi/4+\Phi_a)$, as

$$\delta_{\mathrm{sig}}(\rho,t)=\frac{4\pi\xi(\rho,\omega_s t+\varphi_s-\chi(\rho))}{\lambda}$$

$$=\frac{4\pi\xi_0}{\lambda}|h(k_a\rho)|\sin(\omega_s t+\varphi_s-\chi(\rho)). \tag{9}$$

Using the relation $e^{ix\sin(\theta)}=\sum_{n=-\infty}^{n=\infty}J_n(x)e^{in\theta}$, the electric field amplitude of the optical signal beam can be represented, referring to Fig. 1, as

$$\begin{aligned}A_s(\mathbf{r},t)&=\sqrt{I_s}e^{i(\mathbf{k}_s\cdot\mathbf{R}_s-2\pi\nu t+\delta_{\mathrm{sig}}(\rho,t))}\\&=\sqrt{I_s}e^{i(\mathbf{k}_s\cdot\mathbf{R}_s-2\pi\nu t)}e^{i\delta_{\mathrm{sig0}}\sin(\omega_s t+\varphi_s-\chi(\rho))}\\&=\sqrt{I_s}e^{i(\mathbf{k}_s\cdot\mathbf{R}_s-2\pi\nu t)}\sum_{n=-\infty}^{n=\infty}J_n(\delta_{\mathrm{sig0}})e^{in(\omega_s t+\varphi_s-\chi(\rho))},\end{aligned}\tag{10}$$

where $\delta_{\mathrm{sig0}}=(4\pi\xi_0/\lambda)|h(k_a\rho)|$, $\mathbf{R}_s=\mathbf{r}+\mathbf{r}_s$, I_s is the optical signal beam intensity, $\mathbf{k}_s$ is the optical signal beam wave vector, and ν is the laser optical frequency. The reference beam is phase modulated with magnitude δ_{ref0}, at the frequency $\omega_r/2\pi$ and phase φ_r by an electro-optic modulator (EOM) according to $\delta_{\mathrm{ref}}=\delta_{\mathrm{ref0}}\sin(\omega_r t+\varphi_r)$, which produces a reference beam amplitude

$$\begin{aligned}A_r(r,t)&=\sqrt{I_r}e^{i(\mathbf{k}_r\cdot\mathbf{R}_r-2\pi\nu t+\delta_{\mathrm{ref}})}\\&=\sqrt{I_r}e^{i(\mathbf{k}_r\cdot\mathbf{R}_r-2\pi\nu t)}\sum_{m=\infty}^{m=-\infty}J_m(\delta_{\mathrm{ref0}})e^{im(\omega_r t+\varphi_r)},\end{aligned}\tag{11}$$

where $\mathbf{R}_r=\mathbf{r}+\mathbf{r}_r$, I_r is the optical reference beam intensity, and $\mathbf{k}_r$ is the optical reference beam wave vector.

Interference inside the crystal produces a spatially and temporally modulated intensity pattern, assuming the polarizations of the signal and reference beams are the same, as

$$I=I_0[1+M\cos(\mathbf{K}\cdot\mathbf{r}+\Sigma+\delta_{\mathrm{sig}}-\delta_{\mathrm{ref}})],$$

$$I_0=I_s+I_r,\quad M=\frac{2\sqrt{I_sI_r}}{I_0},\tag{12}$$

where $\mathbf{K}=\mathbf{k}_s-\mathbf{k}_r$ is the grating wave vector and $\Sigma=\mathbf{k}_s\cdot\mathbf{r}_s-\mathbf{k}_r\cdot\mathbf{r}_r$ accounts for path length differences between the two beams. The interference intensity distribution within the crystal generates a corresponding space-charge electric field distribution. The dynamic behavior of this field is controlled by the charge carrier mobility and trapping that produces, in the diffusive operation regime, a single relaxation time response given by[20]

$$\frac{\partial E_{sc}}{\partial t}+\frac{E_{sc}}{\tau}=\frac{iE_q}{\tau}\frac{2A_s\cdot A_r^*}{I_0},\tag{13}$$

where τ is the material response time. The maximum achievable space-charge field, $E_q=qN_A\Lambda/2\pi\varepsilon$, is controlled by the concentration of available charge trapping sites N_A, the fringe spacing $\Lambda=2\pi/K$, the carrier charge q, and the permittivity of the medium ε. Using Eqs. (10)–(12), the interference term in Eq. (13) becomes

$$\frac{2A_s\cdot A_r^*}{I_0}=M\sum_{n,m=-\infty}^{\infty}J_n(\delta_{\mathrm{sig0}})J_m(\delta_{\mathrm{ref0}})e^{i[\mathbf{K}\cdot\mathbf{r}+\Sigma+\omega_{nm}t+\varphi_{nm}-n\chi(\rho)]},\tag{14}$$

where $\omega_{nm}=n\omega_s-m\omega_r$, $\varphi_{nm}=n\varphi_s-m\varphi_r$.

Using the result of Eq. (14) and solving Eq. (13) for the space-charge field yields

$$E_{sc}(\mathbf{r},t)=E_qM\sum_{n,m=-\infty}^{\infty}J_n(\delta_{\mathrm{sig0}})J_m(\delta_{\mathrm{ref0}})\times\left[\frac{e^{i[\mathbf{K}\cdot\mathbf{r}+\Sigma+\pi/2+\omega_{nm}t+\varphi_{nm}-n\chi]}}{2(1+i\omega_{nm}\tau)}+\mathrm{c.c.}\right],\tag{15}$$

where c.c. stands for complex conjugate. Let

$$\tan(\psi_{nm})=\omega_{nm}\tau,$$

and

$$\Theta_{nm}=\mathbf{K}\cdot\mathbf{r}+\Sigma+\frac{\pi}{2}+\omega_{nm}t+\phi_{nm}-n\chi,$$

then

$$\begin{aligned}E_{sc}(\mathbf{r},t)&=E_qM\sum_{n,m=-\infty}^{\infty}J_n(\delta_{\mathrm{sig0}})J_m(\delta_{\mathrm{ref0}})\times\left[\frac{\cos[\Theta_{nm}]+\omega_{nm}\tau\sin[\Theta_{nm}]}{(1+\omega_{nm}^2\tau^2)}\right]\\&=-E_qM\sum_{n,m=-\infty}^{\infty}J_n(\delta_{\mathrm{sig0}})J_m(\delta_{\mathrm{ref0}})\times\left[\frac{\sin[\mathbf{K}\cdot\mathbf{r}+\Sigma+\omega_{nm}t+\varphi_{nm}-n\chi-\psi_{nm}]}{\sqrt{1+\omega_{nm}^2\tau^2}}\right].\end{aligned}\tag{16}$$

This can be expanded to

$$E_{sc}(\mathbf{r},t)=-E_qM\left[\begin{array}{l}\left(J_0(\delta_{\mathrm{sig0}})J_0(\delta_{\mathrm{ref0}})+\sum_{n=1}^{\infty}J_n(\delta_{\mathrm{sig0}})J_n(\delta_{\mathrm{ref0}})\frac{\cos(n[\Omega t+\Phi-\chi]-\psi_n)}{\sqrt{1+n^2\Omega^2\tau^2}}\right)\sin(\mathbf{K}\cdot\mathbf{r}+\Sigma)\\+\sum_{\substack{n,m=-\infty\\(n\neq m)}}^{\infty}J_n(\delta_{\mathrm{sig0}})J_m(\delta_{\mathrm{ref0}})\left(\frac{\sin[\mathbf{K}\cdot\mathbf{r}+\Sigma+(\omega_{nm}t+\varphi_{nm}-n\chi-\psi_{nm})]}{\sqrt{1+\omega_{nm}^2\tau^2}}\right)\end{array}\right],\tag{17}$$

where the frequency difference $\Omega=\omega_s-\omega_r$, the phase difference $\Phi=\varphi_s-\varphi_r$, J_n is the Bessel function of the first kind, and $\tan(\psi_n)=n\Omega\tau$. Equation (17) represents the electric space-charge field within the photorefractive crystal as a series of terms including a constant term, low-frequency terms at multiples of the difference frequency between the signal and reference beams, and higher frequency terms at multiples of the signal and reference frequencies. In the above configuration, the photorefractive crystal acts as a mixing and low-pass filtering element providing the benefits of lock-in detection. Therefore the

space-charge field responds to slowly varying phase modulations occurring within the material response time constant, allowing only the terms around the difference frequency Ω to be important, assuming that $\Omega \ll \omega_{s,r}$. Employing the low-pass filtering, Eq. (17) for the space-charge field becomes

$$E_{sc}(\mathbf{r},t) = -E_q M \Bigg[J_0(\delta_{\text{ref0}}) J_0(\delta_{\text{sig0}}(\rho)) + 2J_1(\delta_{\text{ref0}}) J_1(\delta_{\text{sig0}}(\rho)) \times \frac{\cos(\Omega t + \Phi - \chi(\rho) - \psi_1)}{\sqrt{1+\Omega^2\tau^2}} + \ldots \Bigg] \times \sin(\mathbf{K}\cdot\mathbf{r} + \Sigma), \tag{18}$$

which can be more compactly written as $E_{sc}(\mathbf{r},t) = E_q M f(\delta_{\text{sig0}}(\rho), \chi(\rho); t) \sin(\mathbf{K}\cdot\mathbf{r} + \Sigma)$.

The space-charge field modulates the local refractive index through the linear electro-optic effect. This effect creates a diffraction grating within the crystal that contains the low-frequency phase information desired. Several methods can be used to read out the space-charge field and diffraction grating, including (1) four-wave mixing, (2) two-wave mixing with polarization selection, and (3) electrical measurement through conduction of photoexcited carriers. The magnitude of the index of refraction grating produced is given by[5] $n_1 = -n_0^3 r_{41} E_{sc}/2$, where n_0 is the average refractive index of the medium, r_{41} is the effective, orientation-dependent electro-optic coefficient in BSO. The diffracted beam intensity is a direct measure of the grating established and its diffraction efficiency is determined by the wave coupling constant, according to the scattering theory developed by Kogelnik,[21]

$$\zeta \equiv \left[\frac{\pi n_1 L}{\lambda \cos\theta} \right] = \left[\frac{\pi n_0^3 r_{41} E_q L}{2\lambda \cos\theta} \right] M f(\delta_{\text{sig0}}(\rho), \chi(\rho); t) = \frac{\Gamma L}{2} M f(\delta_{\text{sig0}}(\rho), \chi(\rho); t), \tag{19}$$

where L is the interaction length, Γ is the two-wave mixing coupling constant,[5] and $\Gamma L = 0.16$ for the BSO crystal used with input beam polarizations along the $\langle 001 \rangle$ and perpendicular to the $\langle 110 \rangle$ directions, λ is the laser source wavelength, and 2θ is the angle between the mixing waves.

Operation in the four-wave mixing arrangement is described, as it provides a simpler analysis for demonstrating the mechanism whereby lock-in imaging occurs, since in this configuration there is no direct transmitted beam. The reference beam that passes through the crystal is reflected back into the crystal and diffracts from the photoinduced grating retracing the signal beam path, see Fig. 1. In the undepleted pump approximation, the diffracted (conjugate) beam intensity is[21]

$$I_4 = I_3 e^{-\alpha L/\cos\theta} |\sin\zeta|^2, \tag{20}$$

where I_3 is the back-propagated reference beam intensity and α is the material absorption coefficient. The refractive index modulation amplitude generated by the mixing process is generally small, so that $\zeta \ll 1$, and $\sin(\zeta) \approx \zeta$. The intensity of the diffracted conjugate beam is given by

$$\frac{I_4}{I_3 e^{-\alpha L/\cos\theta}} = \left(\frac{\Gamma L}{2} \right)^2 M^2 \Bigg[J_0^2(\delta_{\text{ref0}}) J_0^2(\delta_{\text{sig0}}) + \left[\frac{4 J_0(\delta_{\text{ref0}}) J_1(\delta_{\text{ref0}})}{\sqrt{1+\Omega^2\tau^2}} \right] J_0(\delta_{\text{sig0}}) \times J_1(\delta_{\text{sig0}}) \cos(\Omega t + \Phi - \chi(\rho) - \psi) + \ldots \Bigg], \tag{21}$$

where $\tan(\psi) = \Omega\tau$. Equation (21) shows that the magnitude and phase of the traveling wave have been placed as arguments of the Bessel functions for the magnitude and as the phase of a low-frequency alternating signal. The resultant measured intensity is then proportional to

$$I_{\text{AC}} \propto J_0(\delta_{\text{sig0}}) J_1(\delta_{\text{sig0}}) \cos(\Omega t + \Phi - \chi(\rho) - \psi), \tag{22}$$

which for small traveling wave displacement amplitudes becomes

$$I_{\text{AC}} \propto \frac{\delta_{\text{sig0}}}{2} \cos(\Omega t + \Phi - \chi(\rho) - \psi) \propto \left(\frac{1}{2} \right) \frac{4\pi\xi_0 |h(k_a\rho)|}{\lambda} \sin\left(\Omega t + \Phi - \chi(\rho) - \psi + \frac{\pi}{2} \right) \propto \frac{4\pi\xi(\rho, \Omega t + \vartheta - \chi(\rho))}{\lambda}, \quad \text{with} \quad \vartheta = \Phi - \psi + \frac{\pi}{2}. \tag{23}$$

Therefore, if Eq. (23) is compared with Eq. (9), the optical imaging approach can be seen to provide a true measure of the traveling wave amplitude and phase, for small amplitudes where $4\pi\xi(\rho,t)/\lambda \ll 1$. The maximum measured intensity of Eq. (22) occurs at a phase shift of 1.082 radians, which corresponds to a traveling wave amplitude of 45.8 nm for a probe wavelength of 532 nm. Comparison of the alternating and constant terms in Eq. (21), with knowledge of the reference beam modulation amplitude and the photorefractive crystal time constant, allows absolute calibration of the flexural wave displacement amplitude even when the maximum signal beam modulation amplitude cannot be realized.[22] Operation with the two-wave mixing method provides similar results whereby the diffraction process produces an output beam whose ac intensity component is proportional to the elastic wave displacement. This mode can be more efficient than the four-wave approach in that the output can be configured to be proportional to the two-wave mixing coupling constant Γ, rather than the square of this quantity. The analysis is complicated by the fact that a large directly transmitted beam is also present and does not further illustrate the lock-in measurement process under discussion; therefore, it is not presented here but will be the subject of future work.

SINGLE-POINT MEASUREMENTS

Single-point measurements were implemented with the two-wave mixing technique according to Fig. 1 by focusing

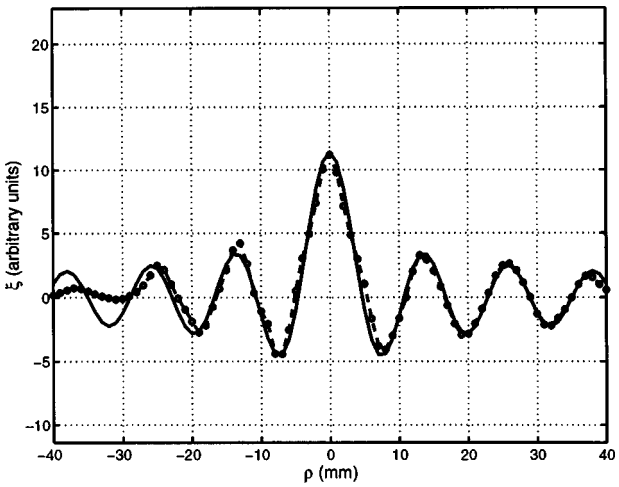

FIG. 2. Flexural mode traveling wave surface displacement on a 0.125-mm-thick nickel plate at 8.0 kHz.

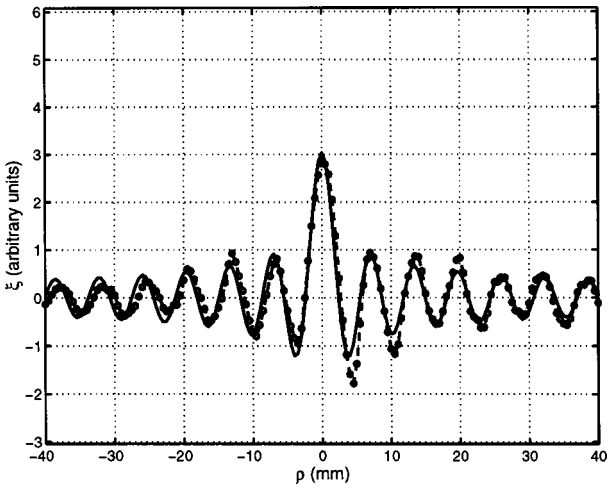

FIG. 4. Flexural mode traveling wave surface displacement on a 0.125-mm-thick nickel plate at 30.0 kHz.

the signal beam to a spot size of about 0.1 mm diameter onto a 0.125-mm-thick pure nickel plate. A piezoelectric transducer with a short length of metal rod ground to a point served as the source transducer. The tip of the rod was placed in contact with the plate surface by applying a small amount of pressure and its vibration generated flexural waves in the plate. The plate was clamped at the outer plate boundaries between two pieces of a viscoelastic damping material[23] that shows damping characteristics superior to natural rubber. Continuous excitation of the transducer then produced steady traveling waves emanating from the contact point at a prescribed signal frequency and wavelength according to Eq. (6). Although this method of excitation was suitable for the measurements here, difficulties were encountered due to the resonant behavior of the metal rod/transducer combination that allowed only discrete frequencies to be investigated. Figures 2–4 show the flexural wave amplitudes as a function of distance from the source for frequencies of 8.0, 15.0, and 30.0 kHz. The points are the result of direct measurement by translating the detection beam along a radius from the source point. The solid lines shown in the figures are the calculated results from Eq. (6). Good agreement is seen between the measurements and the calculation using only the displacement amplitude at the source point and the relative phase between the signal and reference beam modulations as adjustable parameters. Some deviation is seen in the 8-kHz data at the left of Fig. 2 that we attribute to insufficient damping of the wave reflected from the supporting clamp at the plate edge. Material elastic and physical constants of $E = 204\,\mathrm{GPa}$, $s = 0.31$, $\rho_m = 8.9\,\mathrm{g/cm^3}$, and $h = 0.125\,\mathrm{mm}$ were used for the nickel plate calculation. In each figure, both the traveling flexural wave displacement amplitude and phase were recorded by using ac lock-in measurement techniques. Figures 2–4 show the reconstructed wave forms taking into account the amplitudes and phases measured by the lock-in; the results are proportional to the out-of-plane displacement; no absolute calibration was performed. The sensitivity of the measurement was ultimately limited by optical phase noise produced by the detection laser and environmental vibrations which had previously been shown to correspond to a minimum detectability of about 0.002 nm for these point measurements.[9] At each frequency, the relative phase shift between the signal and reference beams was adjusted so that the maximum displacement amplitude occurred at the source point yielding the results shown. Each figure corresponds to a snapshot of the traveling wave displacement along the plate at a moment in time. The wavelength of the flexural wave can be obtained by Fourier transforming the data and employing Eq. (4). Measurements up to 1 MHz agreed well with the calculations, as shown in Fig. 5.

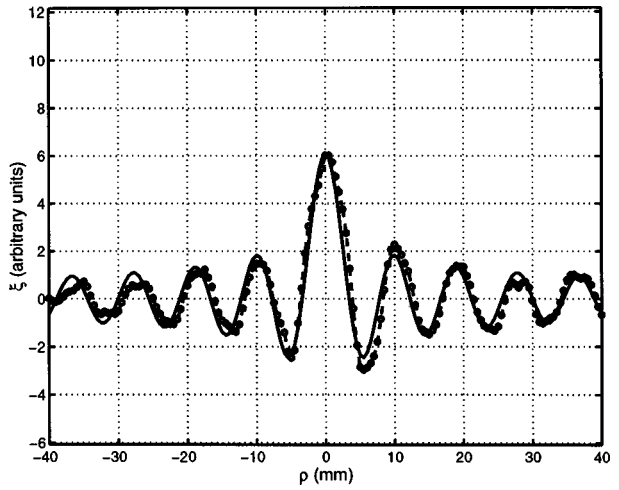

FIG. 3. Flexural mode traveling wave surface displacement on a 0.125-mm-thick nickel plate at 15.0 kHz.

PHOTOREFRACTIVE DYNAMIC HOLOGRAPHIC IMAGING

Since optical interference and the photorefractive effect occur throughout the photorefractive crystal, the point method described above can be generalized to that of an image of the vibration over the surface of the plate. The volume character of the photorefractive process creates a grating distribution that locally records the phase modulation measured from each point of the specimen surface as long as the surface is accurately represented within the photorefractive crystal. The output beam intensity can then be measured

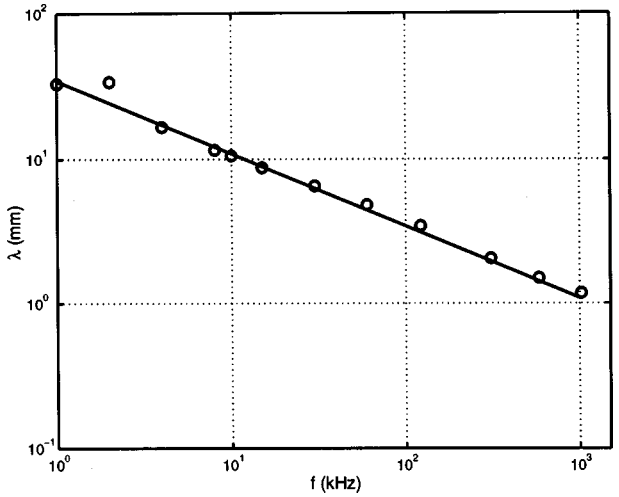

FIG. 5. Flexural wave wavelengths as a function of driving frequency for the 0.125-mm-thick nickel plate, calculated (line) using parameters described in the text and measured (circles).

by an array of detectors, or a highly pixelated device, such as a CCD camera. Each pixel records the local intensity from a point on the specimen producing an output proportional to that point's displacement. Even a diffusely reflecting surface can be measured if the surface is adequately imaged inside the photorefractive crystal by suitable optics.

The experimental setup for vibration imaging using polarization rotation through anisotropic self-diffraction is similar to that shown in Fig. 1 except that additional optical elements are used to illuminate and image the vibrating surface. A two-wave mixing configuration was used as the rough surface of the plate diffusely scattered the laser light, resulting in insufficient light approaching the video camera after diffracting from the grating in the four-wave method. Light from a solid-state laser source (532 nm, 1 W), was split into two legs forming the signal and reference beams. The signal beam was expanded and reflected off the surface of the plate undergoing continuous vibration. Traveling flexural waves in the plate were excited by a contact piezoelectric transducer in the same manner as with the point measurements. Light scattered from the plate was imaged in the photorefractive crystal by a collection lens. The modulated reference beam was also expanded and projected into the photorefractive crystal to produce the volume holographic grating. An input high extinction ratio polarizer selected one component of the signal beam from the plate. At the output of the crystal, the diffracted wave front was selected through use of another high extinction ratio polarizer.

Figure 6 shows images of the traveling flexural waves in the plate obtained with the two-wave mixing method at frequencies of 8, 15, and 30 kHz. The expected circular wave fronts due to the isotropic microstructure of the nickel plate are clearly defined and the relative vibration displacement phase is readily distinguishable. The figure shows single-frame image data at three different frequencies that have the background subtracted. For qualitative inspection of two-dimensional wave forms from the CCD output, the eye integrates over multiple video frames. If the difference frequency is held at zero or locked to the camera frame rate of

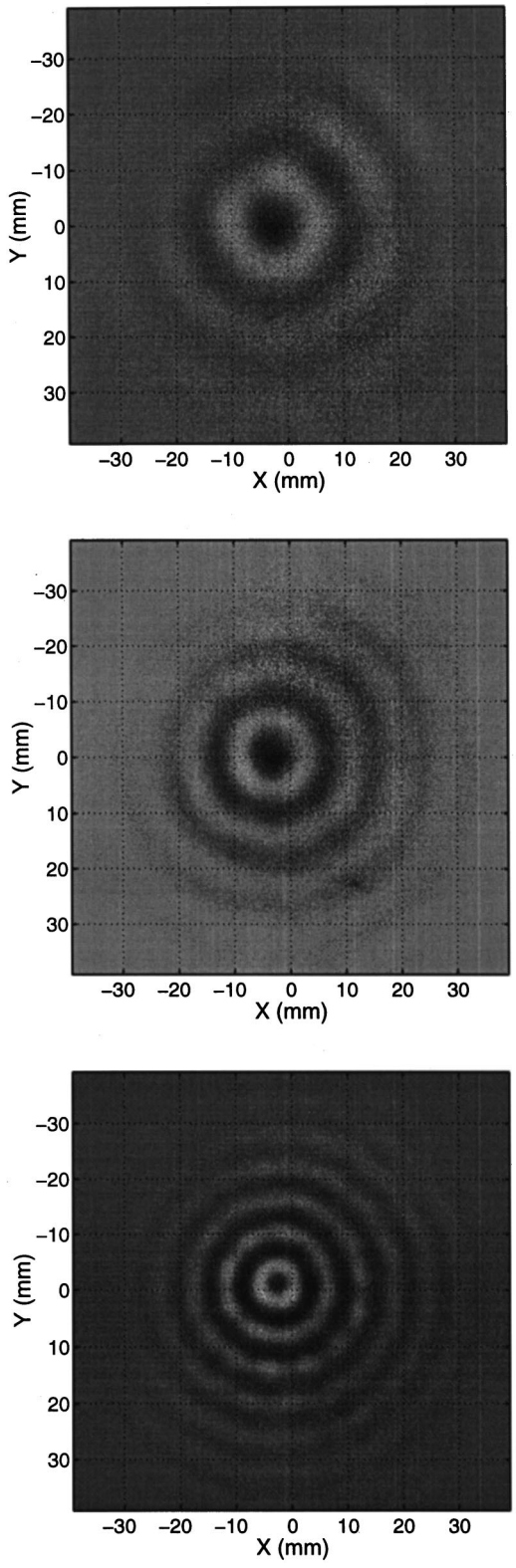

FIG. 6. Single-frame images of the traveling waves at (top) 8 kHz, (middle) 15 kHz, and (bottom) 30 kHz.

30 Hz, a stationary wave front pattern is observed. This signal averaging makes it possible to easily detect subtle patterns such as those brought about by the traveling waves. Also, the entire pattern can be made to change its phase continuously at the frequency, Ω, from 1–30 Hz, so that the appearance is that of waves emanating from the center and

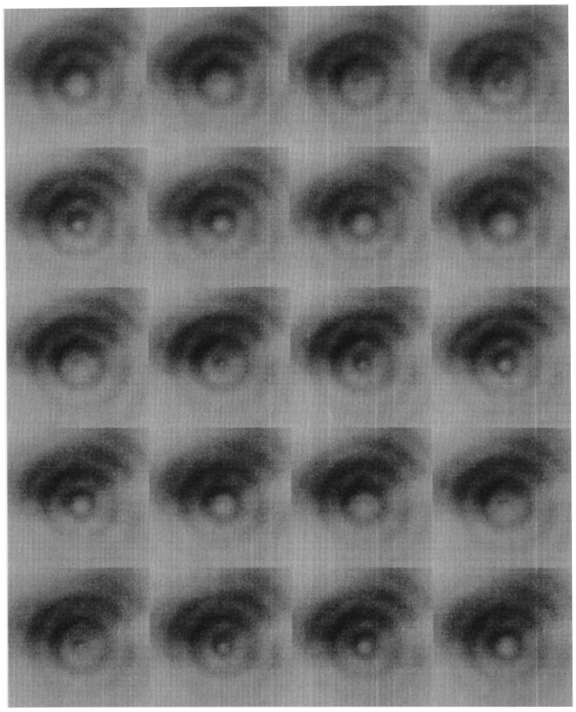

FIG. 7. Time-lapse picture of successive frames of the traveling wave images showing the emergence of the wave front from the center of the plate.

traveling outward. This is physically equivalent to the actual traveling wave motion except that viewing of the wave has been slowed to a much smaller observation frequency that is held constant and independent of the actual wave frequency. A sequence of successive frames is shown in Fig. 7. The frame rate is 30 Hz and the offset frequency is about 4 Hz, resulting in a continuous change in the relative phases between each image. The result is a time-lapse image that shows the viewer a wave emanating from the center and traveling outward and finally attenuated outside the field of view. This quasi-real-time imaging tells the viewer the wave front shape from which information about the plate material, such as the elastic constants or the locations of flaws along the wave path, can be determined. The photorefractive process yields a true picture of the actual wave out-of-plane displacement motion and does not require any additional processing to generate the images of Fig. 6. However, to obtain quantitative measurement of the flexural wave displacement at any point within the image, the intensity at that point must be compared with the background value. This background value is obtained from an average of several additional frames recorded at different phase shifts between the signal and reference images phase-locked so as to eliminate the flexural wave displacement when the average is taken. This procedure was previously illustrated in Ref. 9 concerning images of resonant vibrations in plates.

FREQUENCY ANALYSIS OF THE FLEXURAL WAVE IMAGES

The magnitude of the Fourier transform of the traveling wave displacement as a function of the radial propagation direction, Eq. (4), shows a real pole at the applied wave vector for the traveling wave and imaginary poles of the

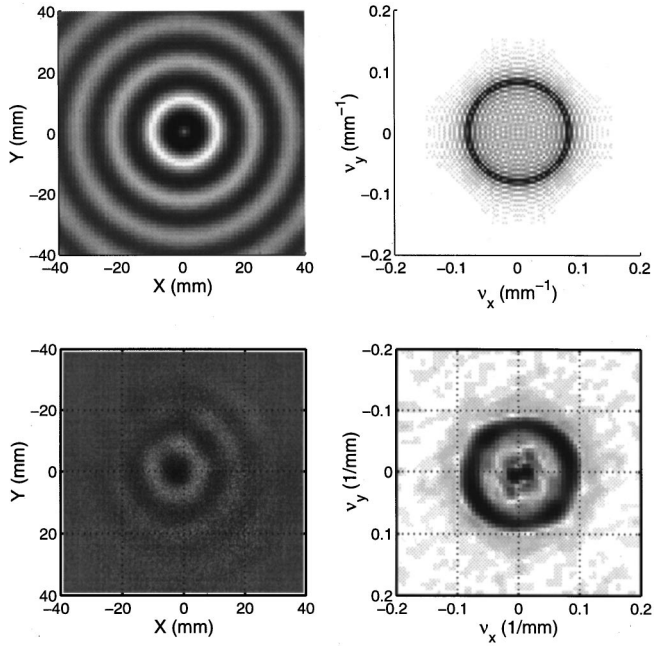

FIG. 8. Calculated (top) and measured (bottom) traveling wave displacements (left) and magnitude of the two-dimensional fast Fourier transform (FFT) (right) for the nickel plate at 8.0 kHz.

same value that contribute to satisfy the boundary conditions. Therefore, the Fourier-transform image of the traveling wave displacements should be a single ring at the applied wave vector delineating the propagating mode. Figures 8–10 show calculations and measurements of the traveling wave displacements as an image over the surface. The calculations are from Eq. (6) and the measurements those of Fig. 6. Beside the images are shown images of the magnitude of the Fourier transforms. A strong response is seen as a ring at the propagating wave vector, whose magnitude can be deter-

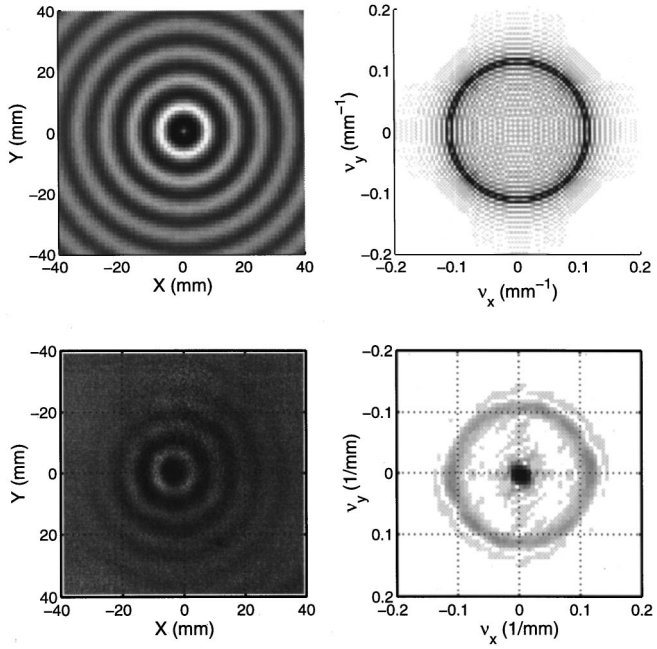

FIG. 9. Calculated (top) and measured (bottom) traveling wave displacements (left) and magnitude of the two-dimensional FFT (right) for the nickel plate at 15.0 kHz.

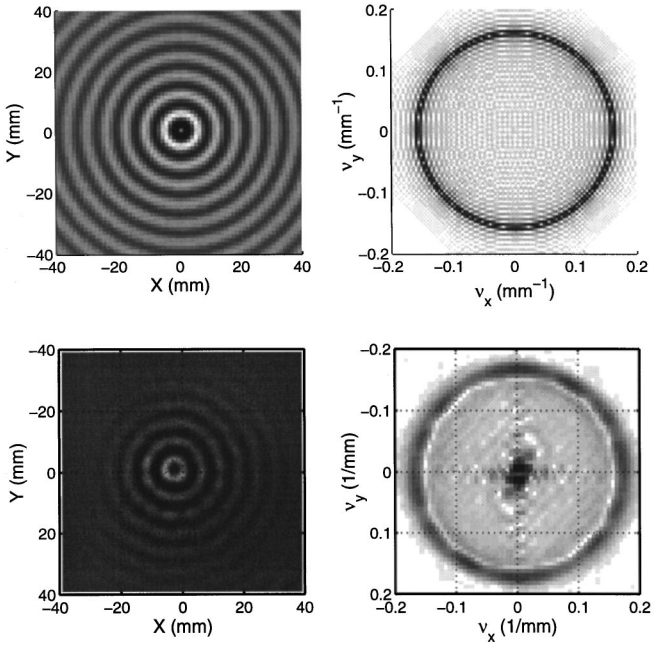

FIG. 10. Calculated (top) and measured (bottom) traveling wave displacements (left) and magnitude of the two-dimensional FFT (right) for the nickel plate at 30.0 kHz.

mined to allow calculation of the elastic stiffness of the plate, assuming the plate mass density per unit area is known. Both the wave front and the Fourier-transform images clearly show the isotropic character of the plate. Correspondingly, the figures also show the magnitude of the Fourier transforms of the measured image data. The large response is again seen as rings at the propagating wave vector values. This analysis procedure provides considerable information about the plate in one simple image.

ANISOTROPIC MATERIAL MEASUREMENTS

If the specimen is elastically anisotropic, then the wave speed varies with the propagation direction. Figure 11 shows this type of behavior for traveling waves in a sheet of carbon fiber composite. The carbon fiber sheet was approximately 0.18-mm thick with the fibers aligned in parallel along the vertical direction. The matrix is an isotropic resin material.

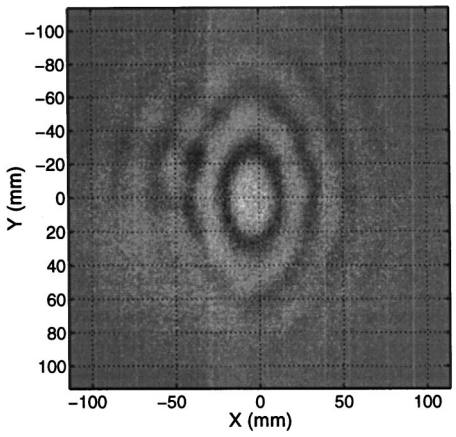

FIG. 11. Image of traveling wave in an anisotropic composite sheet at 37.8 kHz.

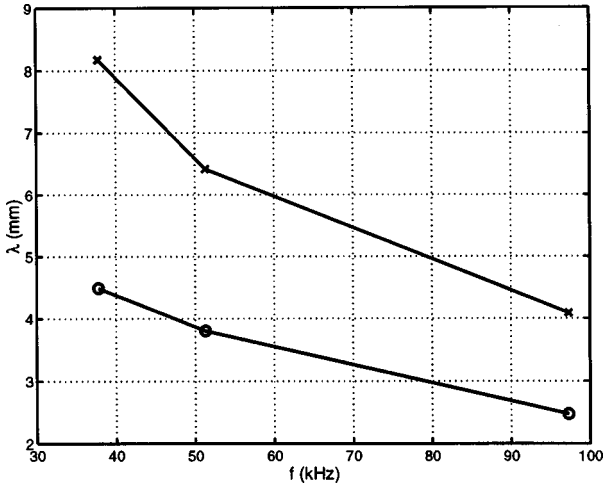

FIG. 12. Measurements of the wavelength in the vertical and horizontal directions in the anisotropic composite sheet.

The highly oblong wave front pattern seen in Fig. 11 shows the anisotropy clearly and immediately. Figure 12 shows the wavelengths measured for this composite sheet in the directions along (×'s) and perpendicular (○'s) to the fibers as a function of frequency. Clearly, a great deal of information about the anisotropic elastic properties of the sheet can be obtained directly from this image measurement technique.

CONCLUSIONS

An imaging photorefractive optical lock-in traveling wave measurement method has been described. Detailed operation of the imaging method for recording nonstationary wave fronts through the lock-in process has been presented. Four-wave and two-wave mixing were described for reading out the signal producing an output intensity directly proportional to the amplitude of the vibration being measured at a preset mechanical phase. Point measurements scanned along a propagation radius produced a spatial snapshot of the amplitude and phase of the traveling wave form. Direct two-dimensional surface images of the traveling wave were obtained by expanding the collection optics and imaging the output beam from the photorefractive material. These images showed the ultrasonic wavelength and wave front shape and provided a quantitative method for obtaining the elastic stiffness symmetry of sheet materials, as illustrated for an isotropic nickel plate and an anisotropic composite carbon sheet. The method is capable of flat frequency response over a wide range above the cutoff of the photorefractive effect and is applicable to imaging the ultrasonic motion of surfaces with rough diffusely reflecting finishes.

ACKNOWLEDGMENTS

This work was sponsored by the U.S. Department of Energy, Office of Science, Office of Basic Energy Sciences, Engineering Research Program and the INEEL Laboratory Directed Research & Development Program under DOE Idaho Operations Office Contract No. DE-AC07-94ID13223.

[1] J. W. Wagner, *Physical Acoustics*, edited by R. N. Thurston and A. D. Pierce (Academic, New York, 1990), Vol. XIX, Chap. 5.

[2] R. K. Ing and J.-P. Monchalin, Appl. Phys. Lett. **59**, 3233 (1991).
[3] S. Ellingsrud and G. O. Rosvold, J. Opt. Soc. Am. A **9**(2), 237–251 (1992).
[4] B. A. Bard, G. A. Gordon, and S. Wu, J. Acoust. Soc. Am. **103**(6), 3327–3335 (1998).
[5] P. Yeh, *Introduction to Photorefractive Nonlinear Optics* (Wiley, New York, 1993).
[6] S. I. Stepanov, *International Trends in Optics*, edited by J. W. Goodman (Academic, New York, 1991), Ch. 9.
[7] T. C. Chatters and K. L. Telschow, *Review of Progress in QNDE*, edited by D. O. Thompson and D. E. Chimenti (Plenum, New York, 1996), Vol. 15B, pp. 2165–2171.
[8] T. C. Hale and K. Telschow, Appl. Phys. Lett. **69**, 2632–2634 (1996).
[9] T. C. Hale, K. L. Telschow, and V. A. Deason, Appl. Opt. **36**, 8248–8258 (1997).
[10] K. L. Telschow, V. A. Deason, R. S. Schley, and S. M. Watson, *Review of Progress in QNDE*, edited by D. O. Thompson and D. E. Chimenti (Plenum, New York, 1999), Vol. 18A, pp. 999–1005.
[11] J. P. Huignard and A. Marrakchi, Opt. Lett. **6**(12), 622–624 (1981).
[12] H. Rohleder, P. M. Petersen, and A. Marrakchi, J. Appl. Phys. **76**(1), 81–84 (1994).
[13] H. R. Hofmeister and A. Yariv, Appl. Phys. Lett. **61**(20), 2395–2397 (1992).
[14] R. C. Troth and J. C. Dainty, Opt. Lett. **16**(1), 53–55 (1991).
[15] K. E. Graff, *Wave Motion in Elastic Solids* (Dover, New York, 1991), Chap. 4.
[16] P. M. Morse and H. Feshbach, *Methods of Theoretical Physics* (McGraw-Hill, New York, 1953), Part 1, Chap. 8.
[17] I. S. Gradshteyn and I. M. Ryzhik, *Table of Integrals, Series, and Products* (Academic, New York, 1965), p. 678.
[18] P. M. Morse and K. U. Ingard, *Theoretical Acoustics* (McGraw-Hill, New York, 1968), p. 219.
[19] I. S. Gradshteyn and I. M. Ryzhik, *Table of Integrals Series, and Products* (Academic, New York, 1965), p. 956.
[20] J. Khoury, V. Ryan, C. Woods, and M. Cronin-Golomb, Opt. Lett. **16**, 1442–1444 (1991).
[21] H. Kogelnik, ''Coupled wave theory for thick hologram gratings,'' Bell Syst. Tech. J. **48**, 2909–2947 (1969).
[22] K. L. Telschow, V. A. Deason, K. L. Ricks, and R. S. Schley, *Nondestructive Characterization of Materials VIII*, edited by R. E. Green, Jr. (Plenum, New York, 1998), pp. 79–84.
[23] Sorbothane, Inc., 2144 State Route 59, Kent, Ohio 44240.

Free vibration of a fluid-filled hollow sphere of a functionally graded material with spherical isotropy

W. Q. Chen[a)]
Department of Civil Engineering, Zhejiang University, Hangzhou, 310027, People's Republic of China

X. Wang
Department of Computer Science, Hangzhou Institute of Commerce, Hangzhou, 310012, People's Republic of China

H. J. Ding
Department of Civil Engineering, Zhejiang University, Hangzhou, 310027, People's Republic of China

(Received 6 March 1999; accepted for publication 23 June 1999)

An exact, three-dimensional method is developed in the paper to analyze the free vibration of a spherically isotropic hollow sphere made of a functionally graded material and filled with a compressible fluid medium. The material is assumed to be inhomogeneous along the radial direction. By introducing three displacement functions and employing the function expansion method, the governing equations are simplified to an uncoupled second-order ordinary differential equation, and a coupled system of two such equations. Solutions to these equations are given when the elastic constants and the mass density are power functions of the radial direction. To investigate the effect of material gradient on the natural frequencies, numerical calculations are finally performed. © *1999 Acoustical Society of America.* [S0001-4966(99)03010-6]'

PACS numbers: 43.40.Ey, 43.20.Ks [CBB]

INTRODUCTION

Functionally graded materials (FGMs) possess variations in constituent volume fractions that lead to continuous change in the composition, microstructure, porosity, etc. and this results in gradients in the mechanical and thermal properties.[1] FGMs have attracted much interest as heat-shielding materials and studies on FGMs associated with thermal stress and deformation analysis have been extensive.[2–5] Meanwhile, since the conventional piecewise homogeneous coatings are usually susceptible to cracking due to their low fracture toughness, FGM coatings have been developed. As a result, the fracture mechanics of FGMs have also been of intense research effort.[6–8] It is noted that though the dynamic parameters play an important role in the design of modern advanced structures, few dynamic investigations on FGM structures can be found in literature except the recent paper by Loy *et al.*,[9] who considered the free vibration problem of FGM cylindrical shells. They showed that by selecting the gradient parameter of FGM, it is possible for designer to obtain the desired dynamic properties of the shell. Their analysis is based on the classical Love-type shell theory and limited to isotropic elastic material. It is known that for thicker plates and shells, high mode approximate theories should be employed to give an accurate analysis, especially when the materials are anisotropic.

FGM is, in fact, a subset of inhomogeneous materials, of which the research history has been long. In regard to the vibration of inhomogeneous (hollow) sphere, Huston[10] studied the radial vibration of an isotropic sphere. Shulga *et al.*[11] presented a state equation by employing the separation technique as well as the spherical harmonic function expansion method for the nonaxisymmetric vibration of a radially inhomogeneous spherically isotropic hollow sphere. Numerical analysis has also been used for obtaining the vibration frequency of nonhomogeneous spheres.[12,13] It is also noted here that Puro[14] initiated the separation method for nonhomogeneous spherically isotropic elasticity to consider some static problems.

In many practical applications, plates and shells are working in acoustic environments. In such cases, the effect of ambient acoustic medium should be taken into consideration. It is necessary to develop exact methods based on three-dimensional elasticity to analyze the coupled free vibration problems of plates and shells. Such methods can serve as a benchmark for clarifying various two-dimensional approximate theories or numerical methods.[15–17]

In this paper, we follow the method proposed by Ding and Chen[15,16] to use three displacement functions to rewrite the components of displacement. The governing equations of motion of a spherically isotropic elastic body with radial inhomogeneity are then turned to an uncoupled partial differential equation and two coupled partial differential equations. For the general nonaxisymmetric free vibration problem, the resulting equations are further simplified to the corresponding ordinary differential ones by expanding the displacement functions in terms of spherical harmonics. For the case that the elastic constants and the mass density obey an identical power law in the radial direction, solutions to these equations are given in the paper. In particular, the matrix Frobenius power series method[18] is employed to solve the coupled set. Exact frequency equations are then derived for the coupled vibration of a FGM spherical shell filled with compressible fluid. Finally, numerical results are given to

[a)]Electronic mail: chenwq@rocketmail.com

show the effect of the material gradient on the natural frequencies.

I. THE THREE-DIMENSIONAL ELASTICITY METHOD

Assuming the center of anisotropy be identical to the origin of the spherical coordinates (r, θ, ϕ), the linear constitutive relations of a spherically isotropic elastic medium are

$$\begin{aligned}
&\sigma_{\theta\theta}=c_{11}s_{\theta\theta}+c_{12}s_{\phi\phi}+c_{13}s_{rr}, \quad \sigma_{r\theta}=2c_{44}s_{r\theta},\\
&\sigma_{\phi\phi}=c_{12}s_{\theta\theta}+c_{11}s_{\phi\phi}+c_{13}s_{rr}, \quad \sigma_{r\phi}=2c_{44}s_{r\phi},\\
&\sigma_{rr}=c_{13}s_{\theta\theta}+c_{13}s_{\phi\phi}+c_{33}s_{rr}, \quad \sigma_{\theta\phi}=(c_{11}-c_{12})s_{\theta\phi},
\end{aligned} \tag{1}$$

where σ_{ij} and s_{ij} are the stress and strain tensors, respectively. c_{ij} are elastic constants to be functions of the radial coordinate r. The strain-displacement relations and the equations of motion can be found in any textbook on elasticity.

Like the homogeneous spherically isotropic elasticity,[15,16] we rewrite the displacements in terms of three displacement functions w, G and ψ as follows:

$$u_\theta=-\frac{1}{\sin\theta}\frac{\partial\psi}{\partial\phi}-\frac{\partial G}{\partial\theta}, \quad u_\phi=\frac{\partial\psi}{\partial\theta}-\frac{1}{\sin\theta}\frac{\partial G}{\partial\phi}, \quad u_r=w. \tag{2}$$

The governing equations finally become

$$B+(\nabla_2 c_{44})(\nabla_2\psi-\psi)-r^2\rho_s\frac{\partial^2\psi}{\partial t^2}=0, \tag{3}$$

$$A+(\nabla_2 c_{44})w-(\nabla_2 c_{44})(\nabla_2 G-G)+r^2\rho_s\frac{\partial^2 G}{\partial t^2}=0, \tag{4}$$

$$\begin{aligned}
&[L_3+2(\nabla_2 c_{13})+(\nabla_2 c_{33})\nabla_2]w\\
&\quad-[L_4+(\nabla_2 c_{13})]\nabla_1^2 G-r^2\rho_s\frac{\partial^2 w}{\partial t^2}=0,
\end{aligned} \tag{5}$$

where ρ_s is the mass density, also a function of the radial coordinate r, and

$$\begin{aligned}
&A=L_1 w-L_2 G,\\
&B=[c_{44}\nabla_3^2-2c_{44}+c_{11}-c_{12}+\tfrac{1}{2}(c_{11}-c_{12})\nabla_1^2]\psi,\\
&L_1=(c_{13}+c_{44})\nabla_2+c_{11}+c_{12}+2c_{44},\\
&L_2=c_{44}\nabla_3^2-2c_{44}+c_{11}-c_{12}+c_{11}\nabla_1^2,\\
&L_3=c_{33}\nabla_3^2-2(c_{11}+c_{12}-c_{13})+c_{44}\nabla_1^2,\\
&L_4=(c_{13}+c_{44})\nabla_2-c_{44}-c_{11}-c_{12}+c_{13},\\
&\nabla_2=r\frac{\partial}{\partial r}, \quad \nabla_2^2=r\frac{\partial}{\partial r}r\frac{\partial}{\partial r},\\
&\nabla_3^2=\nabla_2^2+\nabla_2, \nabla_1^2=\frac{\partial^2}{\partial\theta^2}+\cot\theta\frac{\partial}{\partial\theta}+\frac{1}{\sin^2\theta}\frac{\partial^2}{\partial\phi^2}.
\end{aligned} \tag{6}$$

As shown above, Eq. (3) is a second-order, uncoupled partial differential equation in ψ; Eqs. (4) and (5) form a coupled partial differential equation set in w and G.

Considering the general nonaxisymmetric free vibration problem, one assumes

$$\begin{aligned}
&[\psi,G,w]\\
&\quad=R\sum_{n=0}^{\infty}[U_n(\xi),V_n(\xi),W_n(\xi)]S_n^m(\theta,\phi)\exp(i\omega t),
\end{aligned} \tag{7}$$

where $S_n^m(\theta,\phi)$ are spherical harmonics, ω is the circular frequency and $\xi=r/R$ is the nondimensional radial coordinate (R will be taken as the mean-radius of a spherical shell in the following). Substituting Eq. (7) into Eqs. (3)–(5), yields

$$\begin{aligned}
&\xi^2U_n''+(2+f_5)\xi U_n'\\
&\quad+\{\Omega^2\xi^2-[2+(n-1)(n+2)(f_1-f_2)/2+f_5]\}U_n=0,
\end{aligned} \tag{8}$$

$$\begin{aligned}
&\xi^2W_n''+(2+f_6)\xi W_n'+(\Omega^2\xi^2/f_4+p_1+2f_7)W_n\\
&\quad-p_2\xi V_n'-[p_3-n(n+1)f_7]V_n=0
\end{aligned} \tag{9}$$

$$\begin{aligned}
&\xi^2V_n''+(2+f_5)\xi V_n'+(\Omega^2\xi^2+p_4-f_5)V_n-p_5\xi W_n'\\
&\quad-(p_6+f_5)W_n=0,
\end{aligned} \tag{10}$$

where a prime denotes differentiation with respect to ξ, and

$$\begin{aligned}
&p_1=[2(f_3-f_1-f_2)-n(n+1)]/f_4,\\
&p_2=-n(n+1)(f_3+1)/f_4,\\
&p_3=n(n+1)(f_1+f_2+1-f_3)/f_4,\\
&p_4=f_1-f_2-n(n+1)f_1-2,\\
&p_5=f_3+1, \quad p_6=f_1+f_2+2, \quad \Omega=\omega R/v_2,\\
&f_1=c_{11}/c_{44}, \quad f_2=c_{12}/c_{44},\\
&f_3=c_{13}/c_{44}, \quad f_4=c_{33}/c_{44},\\
&f_5=(\nabla_2 c_{44})/c_{44}, \quad f_6=(\nabla_2 c_{33})/c_{33},\\
&f_7=(\nabla_2 c_{13})/c_{33},
\end{aligned} \tag{11}$$

in which $v_2=\sqrt{c_{44}/\rho_s}$ is the elastic wave velocity. Thus the governing equations have been turned to Eqs. (8)–(10) in a nondimensional form: Eq. (8) is an independent, second-order, ordinary differential equation in unknown U_n, while Eqs. (9) and (10) are coupled by two unknowns, V_n and W_n, and each equation involved is a second-order ordinary differential one. In the next section, we will give the solutions to these equations for a spherical shell having its material constants as power functions of radial distance with an identical power-law exponent.

II. SOLUTIONS TO EQS. (8)–(10)

Similar to the model employed by Loy *et al.*,[9] we here assume that all material constants have the same power function distribution along the radial direction, i.e., $c_{ij}=c_{ij}^0\xi^\alpha$ and $\rho_s=\rho_s^0\xi^\alpha$. Such a model is not only simple but also practical.[1,9] In this case, we have $f_5=f_6=\alpha$, $f_7=\alpha f_3/f_4$, and $f_1=c_{11}^0/c_{44}^0$, $f_2=c_{12}^0/c_{44}^0$, etc. The solution to Eq. (8) thus can be easily obtained as

$$U_n(\xi)=\xi^{-(1+\alpha)/2}[B_{n1}J_\eta(\Omega\xi)+B_{n2}Y_\eta(\Omega\xi)] \quad (n\geqslant 1), \tag{12}$$

where J_η and Y_η are the first and second kinds of Bessel functions, respectively; B_{n1} and B_{n2} are arbitrary constants, and $\eta^2=\frac{1}{4}[9+2(n^2+n-2)(f_1-f_2)+\alpha(6+\alpha)]>0$.

It is obvious that the mode $n=0$ corresponds to the purely radial vibration and function $V_n(\xi)$ contributes nothing to the elastic field. In this case, Eqs. (9) and (10) will degenerate to the following single equation:

$$\xi^2W_0''+(2+\alpha)\xi W_0'+(1/f_4)\times(\Omega^2\xi^2+2f_3-2f_1-2f_2+2\alpha f_3)W_0=0. \tag{13}$$

The solution of the foregoing equation is:

$$W_0(\xi)=\xi^{-(1+\alpha)/2}[C_{01}J_\zeta(\gamma\xi)+C_{02}Y_\zeta(\gamma\xi)] \quad (n=0), \tag{14}$$

where $\zeta^2=(1+\alpha)^2/4+2(f_1+f_2-f_3-\alpha f_3)/f_4>0$, C_{0i} are two arbitrary constants, and $\gamma=\Omega/\sqrt{f_4}$.

When $n\geqslant 1$, it is seen that $\xi=0$ is a regular singular point for the coupled system. To obtain the solution, the matrix Frobenius power series method developed in Ding *et al.*[18] is employed. Details are, however, omitted here for the sake of simplicity. The general solution finally is expressed as the linear combination of four independent solutions as follows:

$$W_n(\xi)=\sum_{j=1}^{4}C_{nj}W_{nj}(\xi), V_n(\xi)=\sum_{j=1}^{4}C_{nj}V_{nj}(\xi) \quad (n\geqslant 1), \tag{15}$$

where C_{nj} are arbitrary constants, W_{nj} and V_{nj} are convergent, infinite series in variable ξ.

III. COUPLED FREQUENCY EQUATIONS

It is now considered that a FGM spherical shell of inner radius a and outer radius b is filled with a compressible, inviscid fluid medium. For the coupled free vibration problem, it is assumed that the outer surface is free from tractions, i.e., $\sigma_r=\tau_{r\theta}=\tau_{r\phi}=0$, $(r=b)$. At the inner surface, besides the zero shear traction conditions $[\tau_{r\theta}=\tau_{r\phi}=0, (r=a)]$, the continuity conditions between the fluid and the shell demand[15]

$$\sigma_r=-\rho_f\omega c_f g_n(kr)w \quad (r=a), \tag{16}$$

where $g_n(x)=xj_n(x)/[nj_n(x)-xj_{n+1}(x)]$, j_n are spherical Bessel functions of the first kind; ρ_f and c_f are the density and sound velocity of the fluid, respectively; and $k=\omega/c_f$ is the wave number.

Using the results obtained above, one can find that the vibration is also separated into two independent classes, just like the homogeneous case.[15–17,19] The first class, which corresponds to an equivoluminal motion of the shell, is characterized by the absence of radial component of displacement while for the second class, the displacement has, in general, both transverse and radial components, but the rotation has no radial component. One then can derive two sets of linear homogeneous algebraic equations of undetermined constants B_{ni} and C_{ni}, respectively. For nontrivial solutions to exist, the coefficient determinants of the two systems should vanish so that the corresponding frequency equations are obtained.

A. Frequency equation of the first class ($n\geqslant 1$)

$$|E_{ij}^1|=0 \quad (i,j=1,2), \tag{17}$$

where

$$\begin{aligned}
E_{11}^1&=[\eta-(3+\alpha)/2]J_\eta(\Omega\xi_1)-\Omega\xi_1J_{\eta+1}(\Omega\xi_1),\\
E_{12}^1&=[\eta-(3+\alpha)/2]Y_\eta(\Omega\xi_1)-\Omega\xi_1Y_{\eta+1}(\Omega\xi_1),\\
E_{21}^1&=[\eta-(3+\alpha)/2]J_\eta(\Omega\xi_2)-\Omega\xi_2J_{\eta+1}(\Omega\xi_2),\\
E_{22}^1&=[\eta-(3+\alpha)/2]Y_\eta(\Omega\xi_2)-\Omega\xi_2Y_{\eta+1}(\Omega\xi_2),
\end{aligned} \tag{18}$$

and $\xi_1=a/R=1-t^*/2$, $\xi_2=b/R=1+t^*/2$, $R=(a+b)/2$; here $t^*=(b-a)/R$ is the thickness-to-mean radius ratio of the shell. Notice that when $n=1$, frequency Eq. (17) corresponds to a torsional or rotary mode of the shell. In particular, there exists a rigid body rotation, for which the frequency equals zero. It is seen that no fluid parameter is involved in the frequency Eq. (17). In fact, vibration of the first class of a fluid-filled inhomogeneous spherical shell is exactly the same as that of an empty one. This has also been observed in the homogeneous case.[15,16]

It is interesting to consider the case when $\Omega\xi_i$ $(i=1,2)$ are large (high frequency) and the spherical shell is thin, for which the asymptotic expansions of Bessel functions can be used. We thus can derive the following frequency equation:

$$\frac{\tan(\Omega t^*)}{\Omega t^*}=\frac{4\eta^2+15+4\alpha}{8\Omega^2\xi_1\xi_2-4\eta^2+33+16\alpha+2\alpha^2}, \tag{19}$$

Eq. (19) degenerates to that obtained by Cohen *et al.*[19] if the spherical shell is homogeneous $(\alpha=0)$.

B. Frequency equation of the second class ($n\geqslant 0$)

$$|E_{ij}^2|=0 \quad (i,j=1,2), \tag{20}$$

for $n=0$, where

$$\begin{aligned}
E_{11}^2&=\{2+f[\zeta-(1+\alpha)/2]\}J_\zeta(\gamma\xi_1)\\
&\quad -f\gamma\xi_1J_{\zeta+1}(\gamma\xi_1)+F_0(\xi_1)\xi_1J_\zeta(\gamma\xi_1)/f_3,\\
E_{12}^2&=\{2+f[\zeta-(1+\alpha)/2]\}Y_\zeta(\gamma\xi_1)\\
&\quad -f\gamma\xi_1Y_{\zeta+1}(\gamma\xi_1)+F_0(\xi_1)\xi_1Y_\zeta(\gamma\xi_1)/f_3,\\
E_{21}^2&=\{2+f[\zeta-(1+\alpha)/2]\}J_\zeta(\gamma\xi_2)-f\gamma\xi_2J_{\zeta+1}(\gamma\xi_2),\\
E_{22}^2&=\{2+f[\zeta-(1+\alpha)/2]\}Y_\zeta(\gamma\xi_2)-f\gamma\xi_2Y_{\zeta+1}(\gamma\xi_2),
\end{aligned} \tag{21}$$

where $f=f_4/f_3$, $F_n(x)=\rho_0c_0\Omega g_n(\Omega x/c_0)$, $\rho_0=\rho_f/\rho_s^0$ and $c_0=c_f/\nu_2$ are ratios of density and velocity between the fluid and shell, respectively. Obviously, frequency Eq. (20) corresponds to the purely radial vibration. When the fluid is absent, the asymptotic expansions of the Bessel functions can also be used to obtain the frequency equation of radial vibration in a simple form when $\Omega\xi_i(i=1,2)$ are large (high frequency) and the spherical shell is thin:

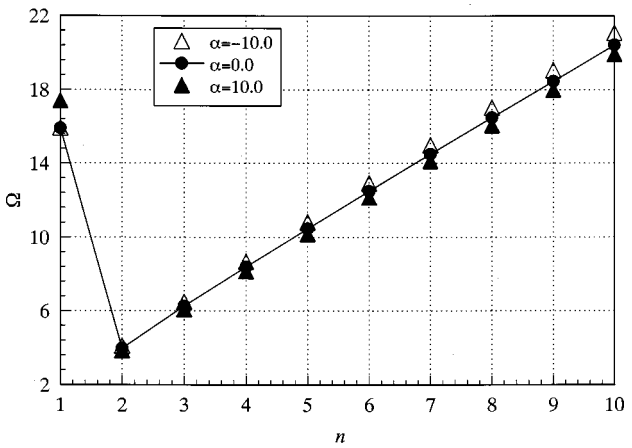

FIG. 1. The first class natural frequencies of a thin anisotropic FGM spherical shell (material II, $t^*=0.2$).

$$\frac{\tan(\Omega t^*)}{\Omega t^*} = \frac{-16f+(7+4\alpha+4\zeta^2)f^2}{32-16(2+\alpha)f+(9+8\alpha+2\alpha^2+8\Omega^2\xi_1\xi_2-4\zeta^2)f^2}. \tag{22}$$

When the fluid is present, however, a more complicated form will be obtained and is thus not given here.

$$|E_{ij}^3|=0 \quad (i,j=1,2,\ldots,4), \tag{23}$$

for $n\geqslant 1$, where

$$\begin{aligned}
E_{1i}^3 &= n(n+1)V_{ni}(\xi_1)/\xi_1+2W_{ni}(\xi_1)/\xi_1 \\
&\quad +(f_4/f_3)W'_{ni}(\xi_1)+F_n(\xi_1)W_{ni}(\xi_1)/f_3, \\
E_{2i}^3 &= W_{ni}(\xi_1)/\xi_1+V_{ni}(\xi_1)/\xi_1-V'_{ni}(\xi_1), \\
E_{3i}^3 &= W_{ni}(\xi_2)/\xi_2+V_{ni}(\xi_2)/\xi_2-V'_{ni}(\xi_2), \\
E_{4i}^3 &= n(n+1)V_{ni}(\xi_2)/\xi_2+2W_{ni}(\xi_2)/\xi_2+(f_4/f_3)W'_{ni}(\xi_2) \\
&\quad (i=1,2,\ldots,4).
\end{aligned} \tag{24}$$

It is noted here that for $n=1$, Eq. (23) has a trivial solution, i.e., $\Omega=0$. It corresponds to a rigid body translation of the coupled system. The existence of such a rigid body

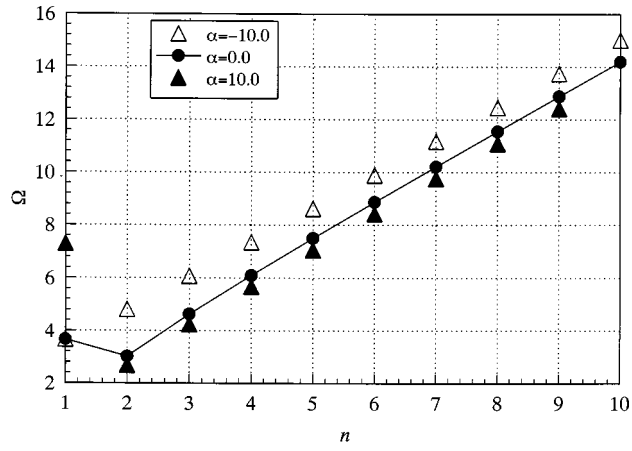

FIG. 2. The first class natural frequencies of a thick anisotropic FGM spherical shell (material II, $t^*=1.2$).

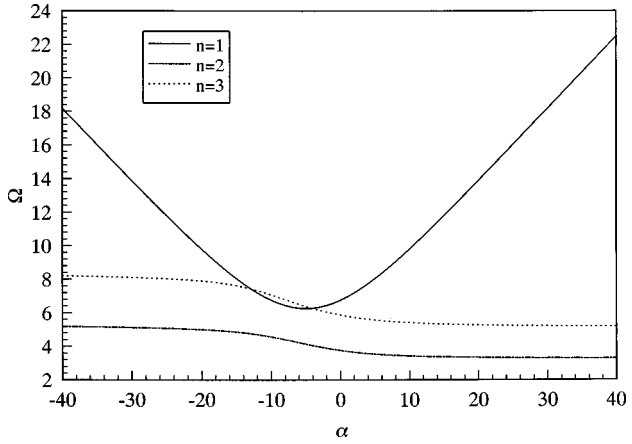

FIG. 3. Variation of the first class natural frequencies with the nonhomogeneous parameter α for a material II spherical shell ($t^*=0.5$).

movement also has been observed for the uncoupled vibration of a homogeneous spherical shell.[16] It is also the case for the vibration of a fluid-filled homogeneous hollow sphere.[15]

It is also seen that the integer m does not appear in the frequency equations as in the homogeneous case.[15–17,19] The reason given by Silbiger[20] to explain the same phenomenon for an empty, thin isotropic spherical shell is also valid here. In fact, the nonaxisymmetric modes of vibrations can be obtained by the superposition of the axisymmetric ones with respect to different oriented spherical coordinates of identical natural frequency.

IV. NUMERICAL EXAMPLES

Since the frequency equations are three dimensional, there is an infinite number of frequencies. In what follows, only the smallest positive natural frequency ($\Omega>0$) that is practically significant will be considered. Three types of materials will be used in numerical examples. Materials I and II are the inhomogeneous analogs of material I and material II that can be found in Cohen *et al.*[19] The nondimensional elastic constants f_i ($i=1,2,\ldots,4$) of these two materials are the same as the homogeneous case and have been given in Chen and Ding.[15] Material III is isotropic, for which Eq. (34) in

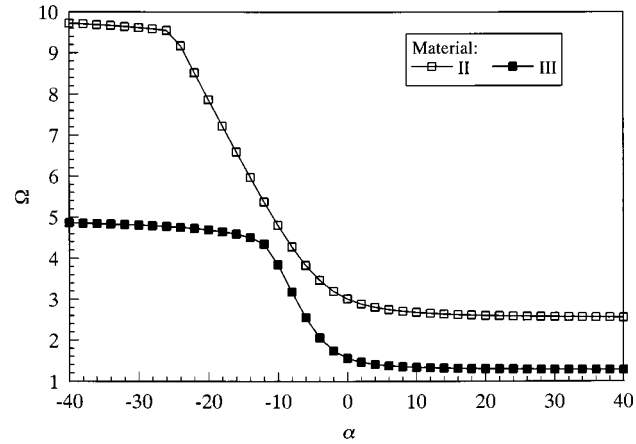

FIG. 4. Comparison of the first class natural frequencies between material II and III FGM spherical shells ($n=2$, $t^*=1.2$).

TABLE I. The breathing mode natural frequencies.[a,b]

α	Case[c]	t^*						
		0.01	0.05	0.1	0.3	0.5	0.8	1.0
0.0	I, filled	0.829 97	0.903 40	0.936 16	1.053 13	1.194 99	1.494 55	1.793 65
		(0.830 76)	(0.904 60)	(0.937 45)	(1.054 59)	(1.196 65)	(1.496 67)	(1.796 27)
		[0.841 56]	[0.907 32]	[0.938 61]	[1.054 72]	[1.196 65]	[1.496 70]	[1.796 33]
		{0.841 06}	{0.906 60}	{0.937 83}	{1.053 75}	{1.195 43}	{1.494 79}	{1.793 42}
	II, filled	0.890 30	0.918 80	0.944 28	1.056 14	1.197 03	1.496 29	1.795 55
		(0.890 79)	(0.919 34)	(0.944 84)	(1.056 81)	(1.197 86)	(1.497 47)	(1.797 06)
		[0.892 11]	[0.919 46]	[0.944 84]	[1.056 89]	[1.198 01]	[1.497 66]	[1.797 24]
		{0.892 00}	{0.919 34}	{0.944 72}	{1.056 75}	{1.197 83}	{1.497 40}	{1.796 89}
2.0	I, filled	0.830 53	0.904 25	0.937 07	1.054 16	1.196 15	1.495 99	1.795 39
	I, empty	2.934 96	2.934 32	2.932 31	2.910 33	2.864 00	2.743 99	2.633 43
	II, filled	0.890 42	0.918 94	0.944 42	1.056 32	1.197 23	1.496 55	1.795 86
	II, empty	7.483 41	7.748 563	7.492 34	7.539 56	7.497 41	6.987 71	6.542 33
−2.0	I, filled	0.829 41	0.902 52	0.935 19	1.051 90	1.193 47	1.492 48	1.791 08
	I, empty	2.935 06	2.936 77	2.942 11	2.999 45	3.116 12	3.405 38	3.655 77
	II, filled	0.890 17	0.918 66	0.944 12	1.055 94	1.196 79	1.496 00	1.795 20
	II, empty	7.483 66	7.491 87	7.517 33	7.768 72	8.143 97	8.080 77	7.595 22

[a]The nondimensional fluid parameters are selected as: $\rho_0 = c_0 = 0.2$.
[b]Data in parentheses, brackets, and braces are calculated by six-mode, five-mode and classical bending shell theories, respectively, for homogeneous spherical shell (Ref. 15).
[c]I, filled—Material I, filled with compressible fluid and so on.

Chen and Ding[15] should be employed to calculate the corresponding five elastic constants c_{ij}. It is shown that for isotropic materials, the power-law function assumption of elastic constants implies that Poisson's ratio is a constant rather than a function of the radial distance. The value of Poisson's ratio, ν, will be taken to be 0.3 in the following.

A. Vibration of the first class ($n \geqslant 1$)

Figures 1 and 2 display curves of the lowest natural frequency of the first class versus the mode number n of an anisotropic spherical shell (material II) for two values of the thickness-to-mean radius ratio t^*, respectively. By comparing these two figures, we find that the nonhomogeneous parameter α has a greater effect on the natural frequencies of a thick shell than on those of a thin shell. We also find that the lowest nondimensional frequencies $\Omega = \omega R \sqrt{\rho_s^0 / A_{44}^0}$ for the torsional mode ($n=1$) are the largest when the nonhomogeneous parameter α is the biggest ($\alpha = 10$) among the three values of α as indicated in Figs. 1 and 2. On the contrary, they become the smallest when $\alpha = 10$ for other nontorsional modes. However, it does not imply that for torsional mode greater α means greater Ω. The variation of Ω with the nonhomogeneous parameter α is shown in Fig. 3 for three lower mode numbers, $n=1$, 2, and 3. It is shown that for the torsional mode, Ω first decreases with the increase of α and then it increases from the point $\alpha \approx -5.0$. For the nontorsional modes, Ω decreases with the increase of α. The effect of α on the frequencies of shells made of anisotropic (material II) and isotropic (material III) materials is shown in Fig. 4 for the nontorsional mode $n=2$. It is noted here that when $n=1$, i.e., the torsional mode, the nondimensional frequency Ω is independent of material constants as we can see from the frequency Eq. (17). In fact, material constants only enter into the expression of η, which for $n=1$ is solely related to the nonhomogeneous parameter α.

B. Vibration of the second class ($n \geqslant 0$)

As mentioned earlier in this paper, the sphere vibrates only in radial direction when $n=0$. It is usually named as ''breathing mode'' in some textbooks. Table I gives the lowest breathing mode natural frequencies $\Omega = \omega R \sqrt{\rho_s^0 / A_{44}^0}$ for several different cases. The two nondimensional fluid parameters are selected to be $\rho_0 = c_0 = 0.2$ (As pointed out in Chen and Ding,[15] the spherical shell cannot vibrate at any frequency in the breathing mode if the filled fluid is incompressible.) Among the three values of α (−2.0, 0.0, and 2.0), it is shown that when $\alpha = 2.0$, the frequencies are the largest for the fluid-filled shell. However, they are the lowest for the empty shell. The natural frequencies of the homogeneous empty shell have been given in Table I of Chen and Ding[15] and hence are not repeated here. It is also noted that the frequencies of the fluid-filled homogeneous spherical shell

TABLE II. Effects of fluid parameters on the breathing mode frequencies of a fluid filled FGM spherical shell.

ρ_0, c_0	α	t^*			
		0.1	0.3	0.5	1.0
0.2, 0.2	−10.0	0.943 43	1.054 99	1.195 67	1.793 50
	0.0	0.944 28	1.056 14	1.197 03	1.795 55
	10.0	0.944 91	1.056 80	1.197 75	1.796 63
0.2, 0.4	−10.0	1.870 95	2.095 68	2.375 25	3.562 88
	0.0	1.877 85	2.105 20	2.386 46	3.579 79
	10.0	1.883 11	2.110 67	2.392 51	3.588 81
0.2, 0.6	−10.0	2.763 98	3.104 86	3.519 36	5.279 07
	0.0	2.787 62	3.138 36	3.558 98	5.338 91
	10.0	2.806 08	3.158 22	3.581 01	5.371 79
0.4, 0.2	−10.0	0.940 90	1.052 72	1.193 12	1.789 68
	0.0	0.942 58	1.055 02	1.195 81	1.793 74
	10.0	0.943 85	1.056 32	1.197 26	1.795 90
0.6, 0.2	−10.0	0.938 40	1.050 47	1.190 59	1.785 88
	0.0	0.940 90	1.053 89	1.194 61	1.791 94
	10.0	0.942 80	1.055 85	1.196 77	1.795 17

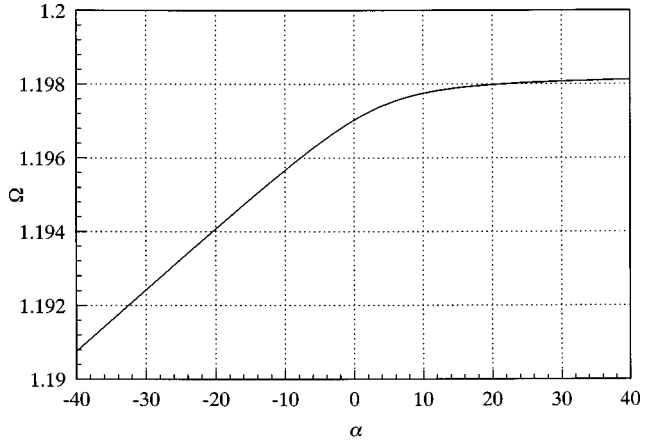

FIG. 5. Variation of the breathing mode natural frequencies with the nonhomogeneous parameter α for a material II spherical shell filled with compressible fluid medium ($t^*=0.5$, $\rho_0=c_0=0.2$).

obtained in Chen and Ding,[15] either by 3-D exact method or by three shell theories, are in fact not the lowest ones. These have been corrected in Table I of this paper. The numerical error comes from the fact that the frequency equations of the second class ($n\geqslant 0$) become violent when the sphere is filled with compressible fluid. Therefore, if a little large searching step is employed in the numerical program, one will possibly skip over some lowest roots of these equations, as we have met in the previous paper.[15] The same error is also found in Table II of Chen and Ding.[15] It is now corrected in Table II of this paper along with the results for a FGM spherical shell (material II). From Table II, we see that the compressibility of the fluid has an important effect on the natural frequencies of both homogeneous and inhomogeneous spherical shells.

The variation curve of the breathing mode frequency Ω versus the nonhomogeneous parameter α for a material II spherical shell is shown in Fig. 5. The relative parameters are as follows: $t^*=0.5$ and $\rho_0=c_0=0.2$. Figure 5 shows that, over a wide range of α, the breathing mode frequency Ω increases when α becomes larger.

Now let's turn our attention to the nonbreathing modes of the second class of vibration. At first, we would like to say

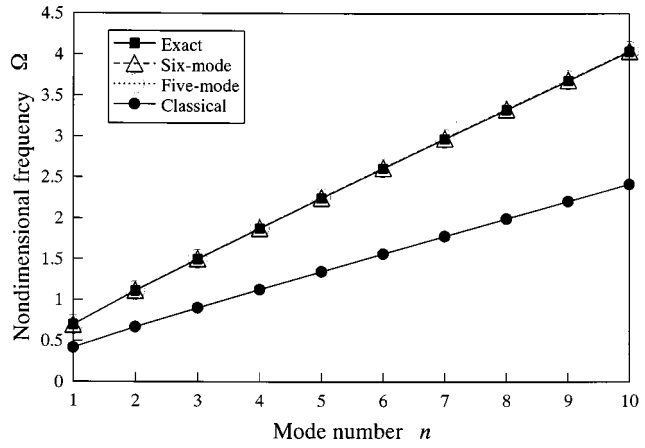

FIG. 6. The second class nonbreathing mode frequencies of a homogeneous spherical shell (material II) filled with compressible fluid ($\rho_0=c_0=0.2$) for $t^*=0.8$: ■ Exact; △ Six-mode; ○ Five-mode; ● Classical bending.

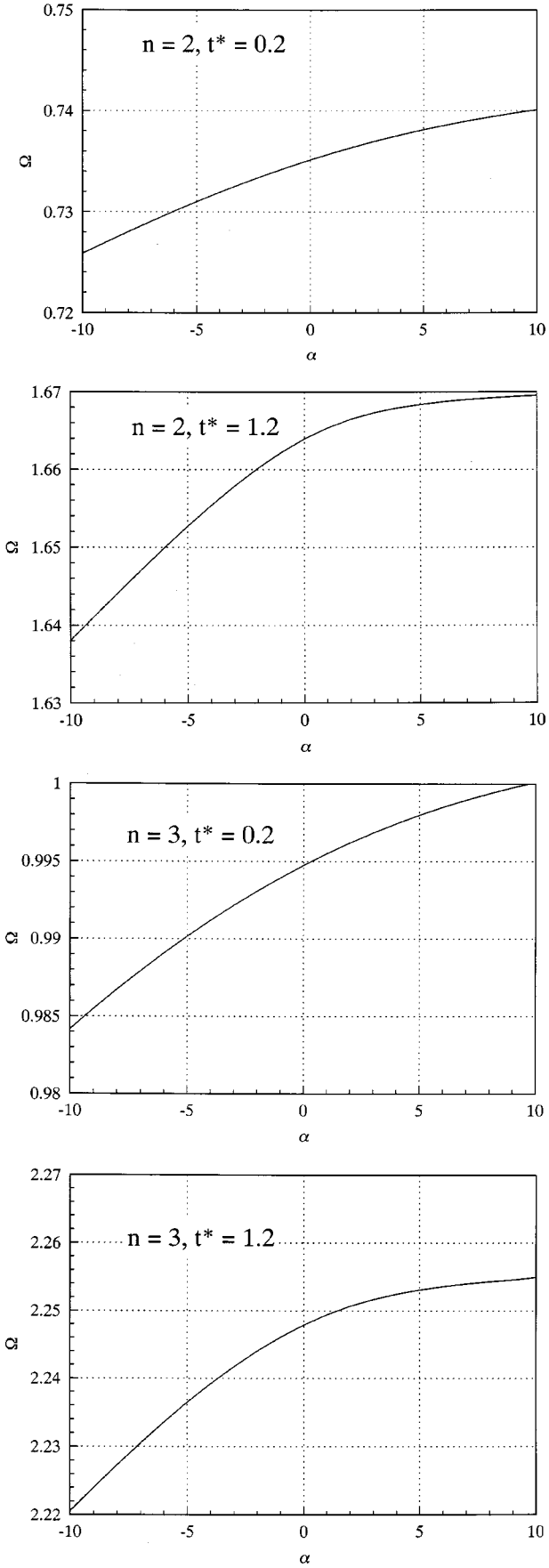

FIG. 7. Variation of the nonbreathing mode natural frequencies with the nonhomogeneous parameter α for a material II spherical shell filled with compressible fluid medium ($\rho_0=0.2$, $c_0=0.2$): (a) $n=2$, $t^*=0.2$; (b) $n=2$, $t^*=1.2$; (c) $n=3$, $t^*=0.2$; (d) $n=3$, $t^*=1.2$.

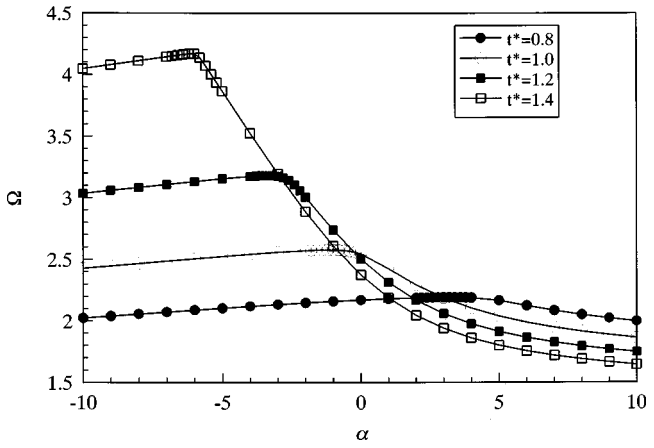

FIG. 8. Variation of the nonbreathing mode natural frequencies with the nonhomogeneous parameter α for a material II spherical shell filled with compressible fluid medium ($n=2$, $\rho_0=0.2$, $c_0=0.4$).

sorry that the corresponding frequencies obtained in our previous paper[15] are not all the lowest ones for homogeneous spherical shells filled with compressible fluid. The reason has been explained a little earlier. In particular, the irregularity characterized by curves in Figs. 2–7 and Fig. 10 of that paper suffers from numerical mistakes caused by using a searching step in the numerical program that was too large. Here to save the space, we just redisplay Fig. 6 of that paper also as Fig. 6 in this paper. From Fig. 6, one can see that the frequency spectra of all four theories are smooth and both the six-mode and five-mode shell theories agree well with the 3-D exact method, even for a thick shell.

To investigate the effect of material gradient on the nonbreathing mode frequency, we display four curves in Fig. 7 for four different cases, respectively. The filled-fluid parameters are as before, i.e., $\rho_0=c_0=0.2$. Two mode numbers $n=2$ and 3, and two values of thickness-to-mean radius ratio $t^*=0.2$ and 1.2 are considered. For all four cases, it is seen that with the increase of the nonhomogeneous parameter, α, the nondimensional frequency, Ω, increases. However, when different parameters are employed, the variation of Ω may become complicated, as it is shown in Fig. 8, for which the fluid parameters are $\rho_0=0.2$, $c_0=0.4$. Figure 8 also shows that the material gradient property has a more significant effect on the thick shell than on the thin one.

V. CONCLUSIONS

In this paper we generalize the displacement function method to simplify the basic equations of a spherically isotropic elastic medium with radial inhomogeneity. Based on such simplification, the free vibration problem of a fluid-filled spherical shell having its elastic constants as well as mass density ratio as power functions of the radial coordinate is exactly analyzed. Numerical results show that the nonhomogeneous parameter α (the index of the power function) has a great effect on the natural frequency. This indicates that through the selection of a proper value of the nonhomogeneous parameters or a certain way of arranging the nonhomogeneous scheme, engineers can obtain the desired dynamic parameters of structures and elements.

The method proposed in this paper is completely exact and thus can be used as a benchmark to check other approximate methods. It is also noted here that though single layered spherical shell is analyzed in this paper, it is not difficult to apply the method to the multi-layered case. Immediate practical application of the method can be found in geophysics.[21]

ACKNOWLEDGMENTS

The work was supported by the National Natural Science Foundation of China (No. 19872060) and the Zhejiang Provincial Natural Science Foundation. Part support of CWQ from the Ministry of Education, Science, Sports and Culture of Japanese Government is acknowledged. He also expresses sincere thanks here to Professor Tadashi Shioya for his kindness.

[1] M. Koizumi, ''The concept of FGM,'' Ceram. Trans. **34**, 3–10 (1993).
[2] R. C. Wetherhold, S. Seelman, and J. Z. Wang, ''Use of functionally graded materials to eliminate or control thermal deformation,'' Compos. Sci. Technol. **56**, 1099–1104 (1996).
[3] S. Takezono, K. Tao, E. Inamura, and M. Inoue, ''Thermal stress and deformation in functionally graded material shells of revolution under thermal loading due to fluid,'' JSME Int. J. Ser. A **39**, 573–581 (1996).
[4] X. D. Zhang, D. Q. Liu, and C. C. Ge, ''Thermal stress analysis of axial symmetry functionally gradient materials under steady temperature field,'' J. Funct. Mater. **25**, 452–455 (1994).
[5] Y. Obata and N. Noda, ''Steady thermal stresses in a hollow circular cylinder and a hollow sphere of a functionally gradient material,'' J. Thermal Stresses **17**, 471–487 (1994).
[6] F. Erdogan and M. Ozturk, ''Periodic cracking of functionally graded coatings,'' Int. J. Eng. Sci. **33**, 2179–2195 (1995).
[7] Z. H. Jin and R. C. Batra, ''Interface cracking between functionally graded coatings and a substrate under antiplane shear,'' Int. J. Eng. Sci. **34**, 1705–1716 (1996).
[8] F. Erdogan and B. H. Wu, ''The surface crack problem for a plate with functionally graded properties,'' J. Appl. Mech. **64**, 449–456 (1997).
[9] C. T. Loy, K. Y. Lam, and J. N. Reddy, ''Vibration of functionally graded cylindrical shells,'' Int. J. Mech. Sci. **41**, 309–324 (1999).
[10] R. L. Huston, ''On nonhomogeneous elastic spheres,'' Z. Angew. Math. Mech. **44**, 573–577 (1964).
[11] N. A. Shulga, A. Y. Grigorenko, and T. L. Efimova, ''Free nonaxisymmetric oscillations of a thick-walled, nonhomogeneous, transversely isotropic, hollow sphere,'' Sov. Appl. Mech. **24**, 439–444 (1988).
[12] M. W. Visser, A. Migliori, T. M. Bell, and R. A. Reinert, ''On the normal modes of free vibration of inhomogeneous and anisotropic elastic objects,'' J. Acoust. Soc. Am. **90**, 2154–2162 (1991).
[13] P. R. Heyliger and A. Jilani, ''The free vibrations of inhomogeneous elastic cylinders and spheres,'' Int. J. Solids Struct. **29**, 2689–2708 (1992).
[14] A. E. Puro, ''Variable separation in elasticity theory equations for spherically transversely isotropic inhomogeneous bodies,'' Sov. Appl. Mech. **16**, 117–121 (1980).
[15] W. Q. Chen and H. J. Ding, ''Natural frequencies of a fluid-filled anisotropic spherical shell,'' J. Acoust. Soc. Am. **105**, 174–182 (1999).
[16] H. J. Ding and W. Q. Chen, ''Nonaxisymmetric free vibrations of a spherically isotropic spherical shell embedded in an elastic medium,'' Int. J. Solids Struct. **33**, 2575–2590 (1996).
[17] W. Q. Chen and H. J. Ding, ''On free vibrations of an embedded anisotropic spherical shell,'' J. Pressure Vessel Technol. **119**, 481–487 (1997).
[18] H. J. Ding, W. Q. Chen, and Z. Liu, ''Solutions to equations of vibrations of spherical and cylindrical shells,'' Appl. Math. Mech. **16**, 1–15 (1995).
[19] H. Cohen, A. H. Shah, and C. V. Ramakrishnan, ''Free vibrations of a spherically isotropic hollow sphere,'' Acustica **26**, 329–333 (1972).
[20] A. Silbiger, ''Non-axisymmetric modes of vibrations of thin spherical shell,'' J. Acoust. Soc. Am. **34**, 862 (1962).
[21] J. P. Montagner and D. L. Anderson, ''Constrained reference mantle model,'' Phys. Earth Planet. Inter. **54**, 205–227 (1989).

Meridional ray contributions to scattering by tilted cylindrical shells above the coincidence frequency: ray theory and computations

Scot F. Morse[a] and Philip L. Marston
Department of Physics, Washington State University, Pullman, Washington 99164-2814

(Received 4 January 1999; accepted for publication 22 July 1999)

High-frequency scattering enhancements from a submerged infinite cylindrical shell are studied by means of partial wave series (PWS) calculations and a ray approximation. For certain oblique angles of incidence it is possible to launch a generalized leaky Lamb wave which propagates strictly in the axial direction on the shell. This meridional leaky wave radiates with a locally flat wavefront curvature and produces large far-field amplitudes over a range of tilt angles. When combined with a reflection from a discontinuity in the shell, this process can give rise to large backscattering enhancements at large tilt angles for thick finite cylindrical shells [S. F. Morse *et al.*, J. Acoust. Soc. Am. **103**, 785–794 (1998)] and is present in sonar images. A convolution formulation ray theory for the far-field meridional ray amplitude is compared with the exact PWS solution in the region where enhancements are observed for both the a_0 and s_0 Lamb waves. The ray theory correctly predicts both the peak enhancement amplitude and the general shape of the enhancement curve. © *1999 Acoustical Society of America.* [S0001-4966(99)04511-7]

PACS numbers: 43.40.Rj, 43.30.Gv, 43.20.Fn [CBB]

INTRODUCTION

When high-frequency sound is incident on a finite cylindrical shell submerged in water it is possible to have particularly large backscattered signals for certain tilt angles and frequencies.[1,2] Kaduchak[1] found that these returns greatly aided in identifying and localizing finite cylindrical shells in high-resolution sonar images. These returns are from leaky Lamb waves launched on the shell and reflected from the end so as to radiate strongly in the backscattering direction. The greatest backscattering occurs when the leaky wave is launched purely in the axial direction. This situation arises when the tilt angle of the shell nears a leaky wave coupling angle, given by $\gamma \approx \theta_l \equiv \sin^{-1}(c/c_l)$, where γ is the tilt angle of the cylinder measured from the normal to the axis of the shell, θ_l is the leaky wave coupling angle, c_l is the phase velocity ($c_l > c$) of the leaky wave of type l, and c is the speed of sound in the surrounding fluid. Figure 1 shows an appropriate ray diagram where this axial ray has been denoted a *meridional* ray[3,4] to distinguish it from the more general class of circumferential surface waves on a cylinder, e.g., the helical waves also shown in Fig. 1. This mechanism for backscattering does not principally involve the back side of the shell and therefore may be important in understanding the scattering from more complex objects. References 1 and 2 used a water-filled steel shell with $ka \approx 140$ (where $k = 2\pi f/c$ and a is the outer radius of the shell) and tilt angles near $\gamma \approx 18$ and 35 degrees. The enhancements were associated with generalizations of the a_0 and s_0 leaky Lamb waves. Morse *et al.*[4] extended the investigation to include thicker-walled hollow shells and broadband insonification over a large range of tilt angles to broadly characterize the meridional ray enhancement. For the shells studied, enhancements were observed for the a_0 meridional ray for tilt angles ranging continuously from $\gamma \approx 40$ degrees to $\gamma \approx 80$ degrees.

Ray analysis of these backscattering amplitudes may be useful for object detection and classification in sonar systems, for example, or in ultrasonic nondestructive evaluation of structures. The present research concerns meridional ray enhancement amplitudes for cylindrical shells. Marston's theory for the meridional ray amplitude on a solid rod[3,5] is extended here to shells. An extension of this ray theory was shown to agree with experimental results for backscattering by a finite solid cylinder near the Rayleigh wave coupling angle ($\gamma \approx 30$ degrees for steel in water).[6] The first step of benchmarking the ray theory for the case of an infinite cylindrical shell is given here; extension to the finite shell case is examined in Ref. 7.

It is worthwhile to place the present work on high-

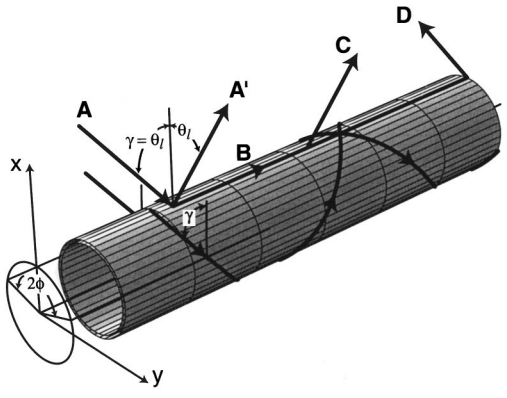

FIG. 1. Ray diagram for launching a meridional ray by trace velocity matching. When $\gamma = \theta_l = \sin^{-1}(c/c_l)$ the incident ray (**A**) launches a meridional ray (**B**) which travels along the cylinder meridian (in the x-z plane at $y = 0$). The meridional ray leaks radiation in the specular direction (**C**) as well as in the backscattering direction after reflection from the end (**D**). An example of counterpropagating helical waves is also shown.

[a]Present address: Naval Research Laboratory, Code 7136, 4555 Overlook Ave., SW, Washington, DC 20375. Electronic mail: morse@lpsa2.nrl.navy.mil

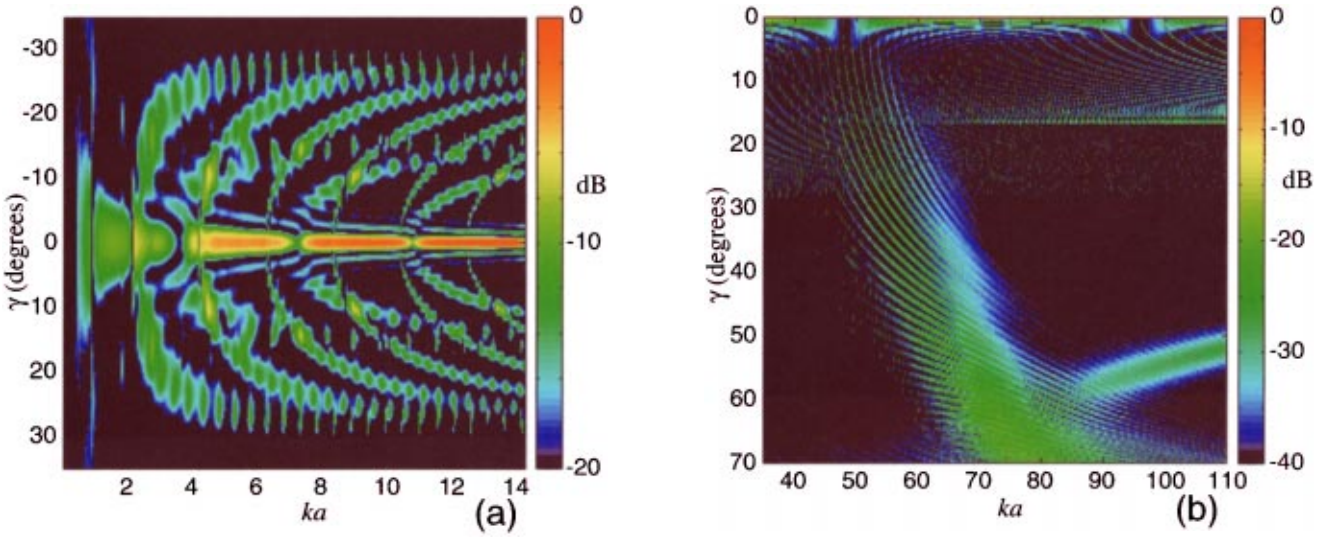

FIG. 2. (a) Calculated backscattering form function for a 1% thick hollow *finite* cylindrical shell showing membrane wave responses. The coincidence frequency is near $ka \approx 100$. (b) Same as (a) but for a 2% thick shell showing the coincidence frequency region $ka \approx 50$. Amplitudes are normalized with respect to the peak value at $\gamma = 0$ degrees in each figure.

frequency scattering by relatively thick-walled shells in the context of other research on scattering by submerged shells, which has often been limited to relatively low frequencies and thin-walled shells.[8–12] For thin-walled shells submerged in water the elastic mechanism by which acoustic energy is backscattered is usually the coupling to circumferential membrane waves, of which the quasi-compressional and quasi-shear are often the most important. (The quasi-flexural wave is often poorly coupled to the external fluid and not excited, except in cases where periodic structural constraints allow for coupling to flexural Bloch or Floquet waves.[12]) Figure 2(a) shows the typical low-*ka* pattern in frequency-angle space for the far-field backscattering spectrum of a *finite* hollow cylindrical shell. This example is calculated for a 1% thick (i.e., $a/h = 100$, where h is the shell wall thickness) hollow shell submerged in water using the approximate PWS solution of Ref. 4. This steel shell has a length (L) to radius ratio of $L/a = 12$; additionally, it is assumed to have

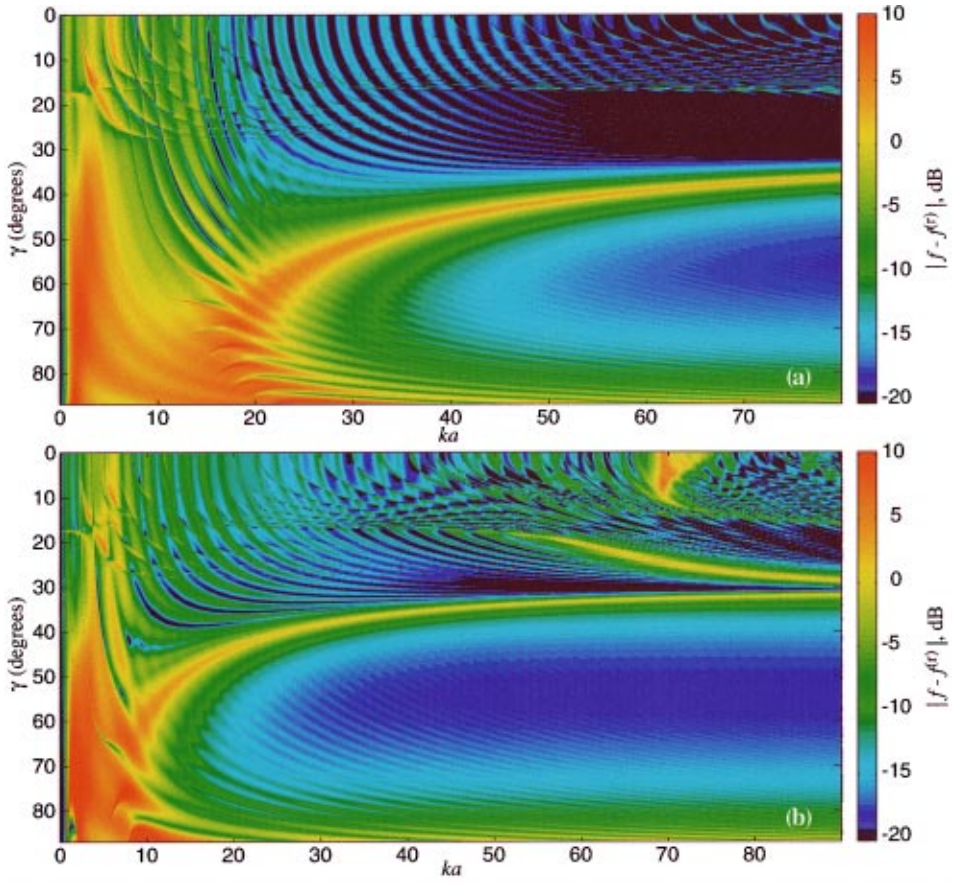

FIG. 3. (a) Form function modulus for scattering in the specular direction within the meridional plane calculated for an *infinite* cylindrical shell ($h/a = 0.076$) using the exact PWS solution. A rigid cylinder form function has been subtracted. The a_0 meridional ray enhancement is the large peak curving upwards to the right from near the coincidence frequency ($ka \approx 16$). (b) Same as (a) except the shell is considerably thicker ($h/a = 0.1625$). The coincidence frequency is near ($ka \approx 7$). The range of *ka* displayed here includes regions where coupling to the s_1, s_2, s_{2b}, and a_1 waves is possible. The amplitude scale in each figure is with respect to unity.

flat perpendicular ends and no endcaps. This figure may be compared with a similar calculation, which utilizes thin shell assumptions, found in Ref. 8; the reader is referred to that paper for a discussion of the scattering features.[13] The primary scattering features in the region 5 degrees$<\gamma<$28 degrees are due to the radiation of quasi-compressional (the lowest order of which is denoted here as the s_0) and quasi-shear (T_0) helical waves which have reflected from the end of the shell. If one were to examine considerably higher frequencies, near the shell's coincidence frequency (near $kh \approx 1$, for $ka \gg 1$; $ka \approx 100$),[4] one would expect to find backscattering contributions beyond $\gamma=30$ degrees from both the slightly subsonic (denoted by a_{0-}) and the supersonic (a_0) quasi-flexural waves just below and above the coincidence frequency, respectively. This is because near and above the coincidence frequency the flexural wave is well coupled to the external fluid. This behavior is indeed the case and is shown in Fig. 2(b), which was computed in the same manner as Fig. 2(a). Helical wave contributions from the a_{0-} wave are evident over the full range of tilt angles shown for $45 < ka < 85$, reminiscent of the coincidence frequency enhancement.[4,14] The smooth enhancement peak curving upward to the right toward higher frequencies from $ka \approx 85$ and $\gamma \approx 58$ degrees is primarily due to the meridional ray of the a_0 wave, which is slightly supersonic in this region. The location of this contribution in frequency-angle space can be determined with suitable values of the phase velocity of the a_0 on the shell.[4] For this case the fractional shell thickness has been increased to 2% ($a/h=50$) purely for computational convenience. This shifts the coincidence frequency to near $ka \approx 50$ and does not significantly alter the interpretation of the results. It should be noted that this continuation into the coincidence frequency region is permissible in this theory because the problem is treated within the framework of three-dimensional linearized elasticity theory. Solutions employing thin shell theory are generally not applicable in this region.[8–11] In the next two sections these enhancements are discussed for infinite shells and a ray theory is developed for the meridional feature.

I. SCATTERING IN THE MERIDIONAL PLANE FROM THE PWS SOLUTION

The scattering from an infinite cylindrical shell is given exactly by a partial-wave series,[15] in contrast to finite cylinders for which approximations are required. As illustrated in Fig. 1, in the specular direction within the meridional plane contributions arise from the specular reflection from the shell (ray $\mathbf{A}'$) and also from various elastic responses depending on the tilt angle and the excitation frequency. (The meridional plane is that plane defined by the axis of the cylinder and the incident wavevector.) Among these elastic responses are the meridional ray, labeled **B**, and various helical rays which have circumnavigated the shell in either direction. To isolate the elastic response when calculating the PWS solution it is possible to subtract a ''background'' response which corresponds to a rigid cylinder.[16]

Figure 3 shows calculations of the background subtracted form function for two relatively thick-walled shells, labeled A and B. These shells[4] are composed of stainless steel of type 304, for which $c_L=5.675$, $c_s=3.141$ (mm/μs), and $\rho_e=7.57$ g/cm^3, and have dimension: $h/a=0.076$ (shell A) and $h/a=0.1625$ (shell B). The surrounding fluid is water ($c=1.483$ mm/μs, $\rho=1.0$ g/cm^3) and the shells contain air ($c_{\text{air}}=0.330$ mm/μs, $\rho=1.2\times10^{-3}$ g/cm^3). The angle γ denotes both the incident angle as well as the scattering angle, in the forward sense, denoting the specular direction. In each figure one can immediately pick out the meridional ray feature of the a_0. It is the large peak originating at large γ near the coincidence frequency ($ka=16$, 7 for shell A and B, respectively; also, see the Appendix) and asymptoting at high frequency to the angle corresponding to the Rayleigh wave speed in the material,[3] i.e., $\gamma \approx 31$ degrees. The width of the peak appears to be broadest at low frequencies and fairly narrow at high frequencies. It is not the purpose of this paper to identify and discuss all the numerous contributions which are apparent in these figures; however, a brief discussion of the major features is given. Near the coincidence frequency the a_0 meridional feature is crossed, and modulated, by various curves (principally yellow as shown) which correspond to the individual helical waves of the a_0. These curves then turn upward to the left and approach $\gamma=0$ degrees. Helical waves of the a_0 can also be seen to originate at higher frequencies at $\gamma=0$ degrees and curve downwards to the right toward the a_0 meridional ray feature. These are shown as mostly blue in Fig. 3(a) and blue and green in Fig. 3(b). Also present for $\gamma<30$ degrees are the helical wave responses of the lowest order quasi-compressional (i.e., s_0) and quasi-shear (T_0) waves similar to those shown in Fig. 2(a). These are evident at low frequencies (below about $ka=15$) but are difficult to make out at higher frequencies due to the relative coarseness of the sampling in $ka-\gamma$ space in the plots ($\Delta ka=0.05$, $\Delta\gamma=0.2°$). Visible in Fig. 3(b) at high frequencies is the meridional ray feature of the s_0. This peak becomes appreciable in amplitude (yellow) near $ka=50$ and $\gamma=18$ degrees and asymptotes to the same high-frequency angle as the a_0 meridional ray feature. This onset of the s_0 meridional ray feature at $ka \approx 50$ is marked by a significant rise in that wave's radiation damping parameter [see Fig. A2(b)]. Finally, a large enhancement is present in Fig. 3(b) at $ka \approx 69$ between $\gamma=0$ and 12 degrees. This enhancement may be associated with the mode thresholds of the s_1 and ''backwards'' s_{2b} Lamb waves.[17] The identification of scattering features is made through the use of calculated dispersion curves for the corresponding guided waves. Some of these curves are shown in the Appendix while others, most notably for the helical waves, were calculated in Ref. 7. From the axial wavevector for propagation on the cylinder (k_z) the coupling angle (γ) may be computed simply by $(k_z)^{\text{inc}}=k \sin\gamma=k_z$.

II. RAY ANALYSIS OF MERIDIONAL PLANE SCATTERING AMPLITUDES

The approximate ray analysis of Ref. 3 provides an expression for the far-field form function for scattering in the meridional plane from an infinite solid rod when the tilt angle is near a leaky wave coupling angle. That result is applied here to infinite hollow cylindrical shells. The modulus of the far-field form function for the lth meridional ray is

TABLE I. Wave numbers used in the ray analysis.

	Shell A: a_0		Shell B: a_0, (s_0)	
ka	$(k_p a)_{\text{cylinder},n=0}$	$(k_p a)_{\text{plate}}$	$(k_p a)_{\text{cylinder},n=0}$	$(k_p a)_{\text{plate}}$
20			$13.7506+i0.2302$	$13.8658+i0.2184$
30	$23.2856+i0.5908$	$23.3423+i0.5780$	$18.5529+i0.2033$	$18.6222+i0.1930$
40	$28.2585+i0.4927$	$28.3065+i0.4821$	$23.2728+i0.1997$	$23.3219+i0.1890$
50	$33.0842+i0.4492$	$33.1208+i0.4394$	$27.9945+i0.2058$	$28.0324+i0.1935$
60	$37.8336+i0.4275$	$37.8629+i0.4180$	$32.7439+i0.2176$	$32.7749+i0.2031$
			$20.7627+i0.3681(s_0)$	$20.8253+i0.3735(s_0)$
70	$42.5476+i0.4172$	$42.5720+i0.4077$	$37.5283+i0.2341$	$37.5546+i0.2162$
			$29.2365+i0.4777(s_0)$	$29.3016+i0.4833(s_0)$
80	$47.2490+i0.4139$	$47.2698+i0.4040$		

given as a function of incidence angle by $|f_l(\gamma)| \approx 2^{3/2}|(\alpha/\nu)F(\mu'')|\{1+2\mu[(1/F(\mu))-1]\}^{-1/2}$, where the wave number associated with the meridional leaky ray is $k_p = k_l + i\alpha$, $\nu = \alpha + i(k\sin\gamma - k_l)$, $\mu = (\alpha a)\tan\theta_l$, $\mu'' = \mu(\nu/\alpha)(\cos\theta_l/\cos\gamma)$, and $F(\xi) = e^{\xi}\sqrt{\pi\xi}\,\text{erfc}(\sqrt{\xi})$. The term erfc is the complementary error function. The leaky wave coupling angle is given by $\theta_l = \sin^{-1}(k_l/k)$. The expression for the form function was derived for tilt angles near this angle. A noteworthy approximation used in the derivation is that the curvature of the radiated wavefront is approximated by using values derived for $\gamma = \theta_l$ even when $\gamma \neq \theta_l$. This is because the reduction in amplitude when $\gamma \neq \theta_l$ should be dominated by dephasing. This expression uses the complex meridional leaky wave number k_p. For a hollow cylindrical shell k_p may be approximated by the wave number of the axisymmetric mode of the cylinder (denoted by $n=0$) corresponding to that type of wave, e.g., flexural or compressional. This gives $k_p = (k_z)_{n=0}$. Alternatively k_p may be approximated with the wave number of the corresponding Lamb wave on a flat plate fluid loaded on one side only. Both approximations are examined here. The appropriate axisymmetric root of the characteristic equation for the submerged hollow cylindrical shell is calculated for the frequencies and wave types under consideration in a manner similar to Refs. 18 and 19. Specifically, the characteristic equation used is the determinant of the denominator found in Eq. (25) of Ref. 15. In the present case it is necessary to compute the complex $(k_z)_0$ root of the determinant for a given real frequency. The spatial radiation damping parameter, $\alpha = \text{Im}[(k_z)_0]$, is then found directly. Computed wave numbers are shown in Table I.

III. COMPARISON OF THE RAY THEORY WITH THE EXACT PWS SOLUTION

The approximate ray theory reviewed above will now be compared with the exact PWS solutions of Fig. 3. Figure 4 shows this comparison for six successive frequencies (ka) as a function of cylinder tilt angle for shell A. Figure 5 shows similar calculations for shell B. For the PWS calculations the solid curve in each of these figures corresponds to a vertical slice through Fig. 3(a) or (b). For shell A the prominent enhancement feature is, as discussed previously, due to the a_0 meridional ray. The open circles in Figs. 4 and 5 are computed with the ray theory using wave numbers calculated for the axisymmetric mode of a submerged hollow infinite cylindrical shell corresponding to the generalization of the a_0 leaky Lamb wave. The results for shell B are similar; however, in this case a significant enhancement from the s_0 meridional ray is also present above $ka \approx 50$ at a lesser tilt angle.

The agreement between the ray theory and exact PWS result is very good. For example, the average percent error $(\|f_{\text{pws}}| - |f_{\text{ray}}\|/|f_{\text{pws}}|)$ between the peak values predicted by the ray theory and the PWS solution is 0.36% for shell A and 1.96% for shell B, for the figures shown (a_0 peak only). The average percent error in the angular location of the peak enhancement is 0.06% and 0.09%, respectively. If the wave

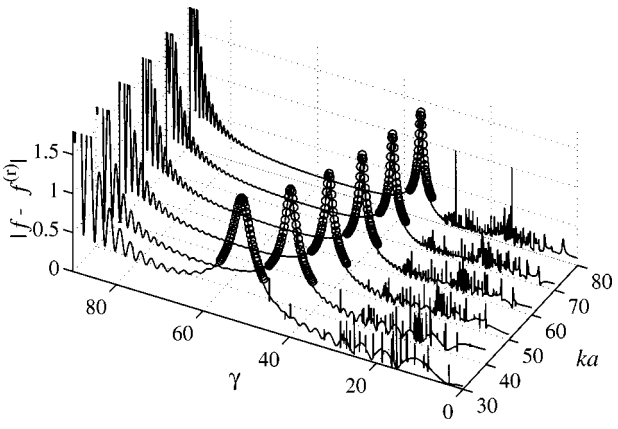

FIG. 4. Comparison of the ray theory (open circles) to the background subtracted PWS solution (solid curve) near the a_0 meridional ray feature (shell A).

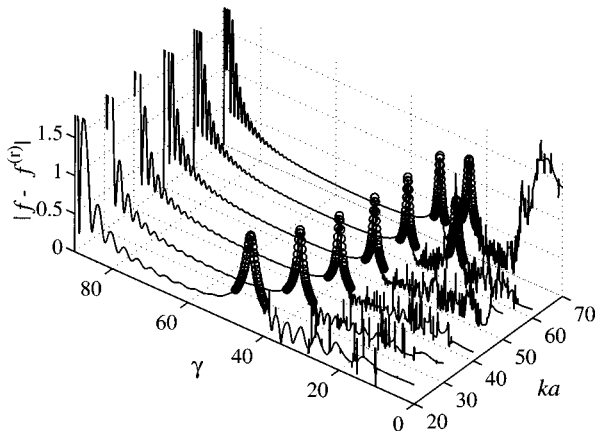

FIG. 5. Same as Fig. 4 but for shell B. This comparison also includes the s_0 meridional ray feature at the two highest frequencies shown.

numbers for the flat plate were used instead of the exact cylinder wave numbers, the average percent errors for the magnitude of the form function are 0.29% and 0.63%, respectively, with an average percent error in the angular location of the peak enhancement of 0.13% and 0.27%. Similar comparisons for the s_0 meridional ray peak in Fig. 5 are not nearly as good. This is because the s_0 meridional ray enhancement peak is found over a region where other helical wave responses (from the T_0) are present. These additional, narrow and smaller, responses interfere with the meridional ray feature and tend to confuse the comparison with the single meridional ray contribution. This illustrates why primarily the a_0 meridional ray was chosen for comparison with the ray theory.

The ray theory models the width of the enhancement peak for a range of angles. Generally, at low frequencies the peak is fairly broad and narrows as *ka* increases. The enhancement peak in the exact solution is slightly asymmetric; this characteristic is not recovered by the ray theory. Furthermore, the exact solution displays a number of smaller peaks at tilt angles less than the meridional ray peak. These are due to synchronous excitation of helical a_0 waves which circumnavigate the shell.

IV. DISCUSSION

From the agreement between the ray theory and the exact PWS solution a few conclusions can be made concerning scattering mechanisms. First, it can be seen that for the two wave types discussed (i.e., the a_0 and s_0), the wave parameters for the axisymmetric ($n=0$) solutions of an infinite cylindrical shell represent a good approximation of the actual meridional wave parameters. In the coupling diagram of Fig. 1 it is implied that the meridional ray travels down a meridian of the cylinder. The extent to which regions of the shell off the meridian play a role in the far-field scattered pressure may be inferred from the size of the Fresnel coupling patch.[3] The Fresnel patch for the meridional ray describes the surface area within which paths off the meridian have a phase defect of π or less compared to the Fermat path (ray **B** in Fig. 1) upon propagating to the radiation point on the meridian. Though the Fresnel patch is infinite in area for the meridional ray on an infinite cylinder, the coupling region may be limited to a finite area by considering only that region where the path amplitude is attenuated less than $1/e$. This corresponds to a distance on the shell of $1/\alpha$ which is typically small. It can be shown that the farthest point off the meridian still within the Fresnel patch is described by the angle $\phi_{\max}=\pm y'/a$ where y' is found by simultaneously satisfying the two equations: $k_l s+ka[1-\cos(y'/a)]\cos\gamma+k_l x'=\pi$ and $s=(1/\alpha)$, where $s=[(x')^2+(y')^2]^{1/2}$. When the cylinder is tilted at the leaky wave coupling angle (i.e., $\gamma=\theta_l$) this point on the shell ranges from $\phi_{\max}=\pm 25.2$ degrees at $ka=30$ to $\phi_{\max}=\pm 15.7$ degrees at $ka=80$ for shell A and similarly from $\phi_{\max}=\pm 34.6$ degrees at $ka=20$ to $\phi_{\max}=\pm 17.5$ degrees at $ka=70$ for shell B, considering only the a_0 wave. For the s_0 wave one finds $\phi_{\max}=\pm 18.0$ degrees at $ka=60$ to $\phi_{\max}=\pm 16.3$ degrees at $ka=70$ for shell B. The size of the Fresnel patch and the attenuation length affect the width of the meridional enhancement.[5] As the frequency is increased the significant portion of the Fresnel patch becomes more localized about the meridian. This has consequences for the case of a complex finite shell structure in that scattering from a small surface patch could lead to a large meridional ray enhancement even when the entire surface does not support the same enhancement due to variations in wall thickness.

ACKNOWLEDGMENTS

This work was supported by the Office of Naval Research. The authors acknowledge Greg Kaduchak for his contributions.

APPENDIX: COMPUTED DISPERSION CURVES FOR THE SHELL

This appendix presents the guided wave properties of the waves which contribute to the meridional ray scattering of Figs. 3–5. The properties of other wave types are included even though they do not appear to contribute significantly to the far-field scattering in the cases already discussed. These curves are useful for identifying the meridional ray features in Fig. 3 and in understanding why some wave types do not appear to have a strong meridional ray enhancement within this frequency range.

Figures A1 and A2 show the calculated dispersion curves for several types of waves propagating on thick cylindrical shells. For the wave types symmetric

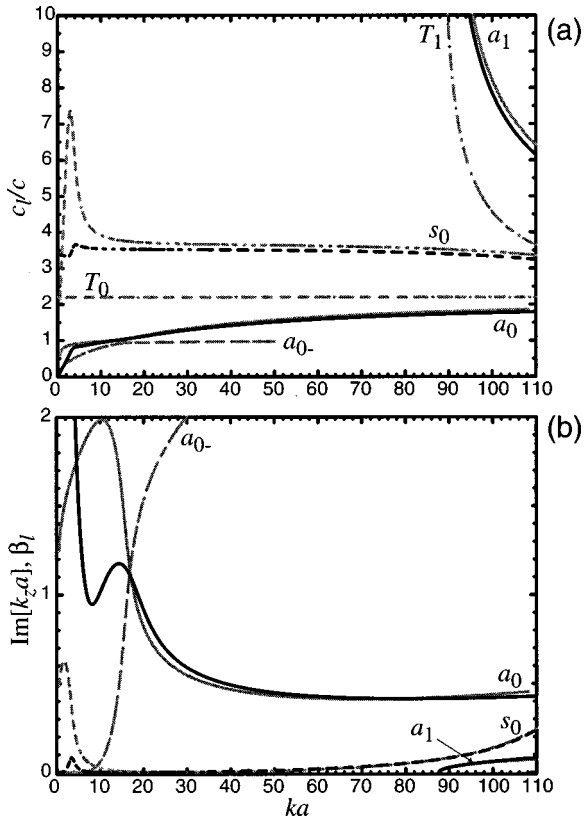

FIG. A1. Axisymmetric, $n=0$ (black curves), and purely circumferential, $k_z=0$ (gray curves), wave properties for a submerged hollow infinite cylindrical shell corresponding to shell A ($h/a=0.076$). (a) Normalized phase velocity and (b) damping.

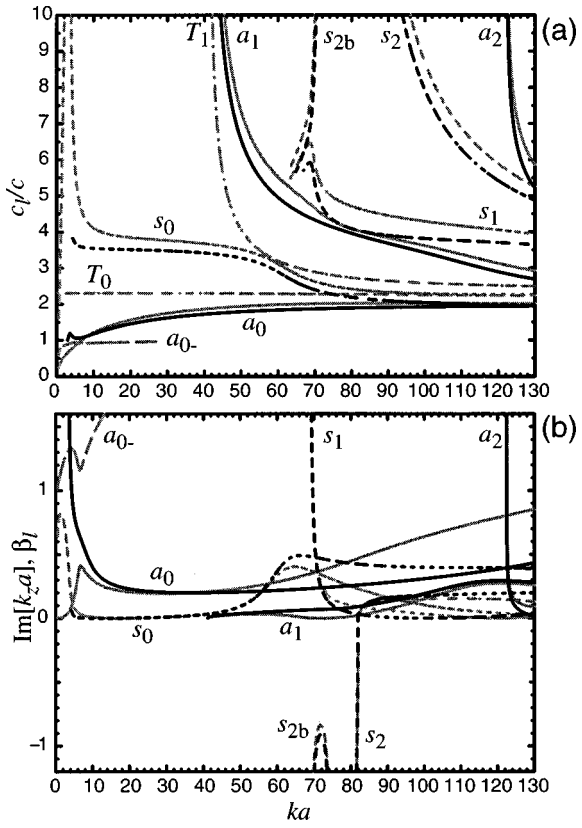

FIG. A2. Same as Fig. A1 but for shell B ($h/a=0.1625$).

(s_0, s_1, s_2, s_{2b}) and antisymmetric (a_0, a_1, a_2) Lamb waves, two dispersion curves are shown. The first set of curves is shown as black lines of various line styles and corresponds to the $n=0$ solutions of the infinite hollow cylindrical shell. These are axisymmetric solutions whereby the displacements in the shell are independent of azimuthal coordinate ϕ. These curves represent those values of axial wave number (k_z) and frequency (k), for which the determinant in the denominator of the PWS scattering solution for this problem (given in Ref. 15) vanishes, given that the azimuthal mode number (n) is equal to zero. Kargl's method[20] was extended to find these solutions. The second set of curves is shown as gray lines. These correspond to the same wave types but are solutions for strictly circumferential propagation on the shell. In this case $k_z=0$. These are calculated using the Watson methodology and the PWS scattering solution for a cylindrical shell at normal incidence.[21] For very high frequencies the propagation of these surface waves should become isotropic on the shell. With this in mind, the $n=0$ solutions are identified by their mimicking of circumferential solutions previously studied.[21]

Figures A1(a) and A2(a) show phase velocities normalized to the speed of sound in water. For the $n=0$ curves the phase velocity is simply $c_l/c=k/(\mathrm{Re}[k_z])$. Figures A1(b) and A2(b) show the radiation damping of these waves. For the $n=0$ curves this corresponds directly to the imaginary part of the azimuthal wave number while for the circumferential solutions it is given by β_l in Np/rad. For the purpose of comparison, the quantity $\mathrm{Im}[k_z a]$ is plotted since the form of the associated wave damping in the two cases is: $e^{-\mathrm{Im}[k_z]z}$ and $e^{-\beta_l \phi}$, where ϕ is the azimuthal coordinate. For propagation of the circumferential wave over an arc length $s=a\phi=z$ one finds that $\mathrm{Im}[k_z] \Leftrightarrow \beta_l/a$.

[1] G. Kaduchak, C. M. Wassmuth, and C. M. Loeffler, ''Elastic wave contributions in high resolution acoustic images of fluid-filled, finite cylindrical shells in water,'' J. Acoust. Soc. Am. **100**, 64–71 (1996).

[2] S. S. Dodd, ''Sonar Imaging of Elastic Fluid-Filled Cylindrical Shells,'' Ph.D. dissertation, University of Texas, Austin, Applied Research Laboratories, 1995.

[3] P. L. Marston, ''Approximate meridional leaky ray amplitudes for tilted cylinders: End-backscattering enhancements and comparisons with exact theory for infinite solid cylinders,'' J. Acoust. Soc. Am. **102**, 358–369 (1997); **103**, 2236 (1998).

[4] S. F. Morse, P. L. Marston, and G. Kaduchak, ''High-frequency backscattering enhancements by thick finite cylindrical shells in water at oblique incidence: Experiments, interpretation and calculations,'' J. Acoust. Soc. Am. **103**, 785–794 (1998).

[5] P. L. Marston, *Acoustical Imaging*, edited by S. Lees and L. A. Ferrari (Plenum, New York, 1997), Vol. 23, pp. 369–374.

[6] K. Gipson and P. L. Marston, ''Backscattering enhancements due to reflection of meridional leaky Rayleigh waves at the blunt truncation of a tilted solid cylinder in water: Observations and theory,'' J. Acoust. Soc. Am. **106**, 1673–1680 (1999).

[7] S. F. Morse, ''High Frequency Acoustic Backscattering Enhancements for Finite Cylindrical Shells in Water at Oblique Incidence,'' Ph.D. Dissertation, Washington State University, Department of Physics, 1998.

[8] M. L. Rumerman, ''Contribution of membrane wave reradiation to scattering from finite cylindrical steel shells in water,'' J. Acoust. Soc. Am. **93**, 55–65 (1993).

[9] A. N. Norris and D. A. Rebinsky, ''Acoustic coupling to membrane waves on elastic shells,'' J. Acoust. Soc. Am. **95**, 1809–1829 (1994).

[10] M. Tran-Van-Nhieu, ''Scattering from a finite cylindrical shell,'' J. Acoust. Soc. Am. **91**, 670–679 (1991).

[11] V. V. Muzychenko and S. A. Rybak, ''Low-frequency resonance scattering of sound by finite cylindrical shells (review),'' Sov. Phys. Acoust. **34**, 325–333 (1988).

[12] B. H. Houston, J. A. Bucaro, and D. M. Photiadis, ''Broadband acoustic scattering from a ribbed shell,'' J. Acoust. Soc. Am. **98**, 2851–2853 (1995).

[13] The material parameters for Fig. 2(a) are $c_L=5.74$, $c_s=3.07$, $c=1.483$ (mm/μs), $\rho_e=7.8$, $\rho_w=1.0$ (g/cm^3), $L/a=12$, and $b/a=0.99$. The shell in Fig. 2(b) is stainless type 304.

[14] G. Kaduchak and P. L. Marston, ''Obervation of the midfrequency enhancement of tone bursts backscattered by a thin spherical shell in water near the coincidence frequency,'' J. Acoust. Soc. Am. **93**, 224–230 (1993).

[15] F. Léon, F. Lecroq, D. Décultot, and G. Maze, ''Scattering of an obliquely incident acoustic wave by an infinite hollow cylindrical shell,'' J. Acoust. Soc. Am. **91**, 1388–1397 (1992).

[16] Specifically we subtract f_{rigid} from the complex PWS form function [Eq. (25) of Ref. 15] before taking the absolute magnitude, where f_{rigid} is given by Eq. (2) of Ref. 3 with $B_n=H_n^{(1)\prime}(k_r a), D_n=J_n(k_r a), k_r=k\sin\gamma$.

[17] G. Kaduchak, D. H. Hughes, and P. L. Marston, ''Enhancement of the backscattering of high-frequency tone bursts by thin spherical shells associated with a backwards wave: Observations and ray approximation,'' J. Acoust. Soc. Am. **96**, 3704–3714 (1994).

[18] D. C. Gazis, ''Three-dimensional investigation of the propagation of waves in hollow circular cylinders. I. Analytical foundation,'' J. Acoust. Soc. Am. **31**, 568–573 (1959); **31**, 573–578 (1959).

[19] B. K. Sinha, T. J. Plona, S. Kostek, and S-K. Chang, ''Axisymmetric wave propagation in fluid-loaded cylindrical shells. I: Theory,'' J. Acoust. Soc. Am. **92**, 1132–1143 (1992).

[20] S. G. Kargl and P. L. Marston, ''Observations and modeling of the backscattering of short tone bursts from a spherical shell: Lamb wave echoes, glory, and axial reverberations,'' J. Acoust. Soc. Am. **85**, 1014–1028 (1989); **89**, 2462 (1991).

[21] N. H. Sun and P. L. Marston, ''Ray synthesis of leaky Lamb wave contributions to backscattering from thick cylindrical shells,'' J. Acoust. Soc. Am. **91**, 1398–1402 (1992).

A high-resolution spectral estimation approach for evaluating the resonances of scattering returns from submerged targets

I-Tai Lu[a] and Fu-Po Wu
Polytechnic University, Route 110, Farmingdale, New York 11735

(Received 29 January 1998; revised 20 May 1999; accepted 1 July 1999)

The principal aim of this work is to estimate the complex resonant frequencies of scattering returns from the Mock-0 target. The experiments were conducted at the Naval Undersea Warfare Center. First, the singular value decomposition approach is employed for noise suppressing prefiltering where the initial estimate of the system order is obtained. Second, the eigen-matrix pencil method is employed to approximate the complex resonant frequencies. Finally, the system order and the complex resonances are determined by a systematic procedure in which the estimated results obtained from various system orders and aspect angles are compared. Echoes observed at the same aspect angle but excited by different incident pulses with overlapping frequency spectra can also be employed to obtain reliable estimations of resonant frequencies. The key feature of the proposed approach is robustness. © *1999 Acoustical Society of America.* [S0001-4966(99)03910-7]

PACS numbers: 43.40.Fz, 43.60.Gk, 43.40.Ey [CBB]

INTRODUCTION

There are two complementary descriptions of wave scattering from a target.[1–3] In the mode description, the wave phenomena are synthesized by resonances of the scatterer as a whole. These global resonances[4–6] take the form of damped sinusoidal responses which are characterized by complex resonant frequencies. These frequencies are totally independent of sources and sensors, but their excitation may be sensitive to the temporal and spatial spectra and the locations of sources. In the ray description,[7–9] the wave phenomena can be organized in terms of wavefronts that travel from the source to the scatterer, and then interact with the scatterer to generate new wavefronts which travel to the sensor. If the size of the scatterer is much larger than the acoustic wavelength, the interaction of the incident wave with the scatterer can be described in terms of multiple wavefront passes around the object and multiple diffractions from scattering centers in the scatterer. The ray description is relatively effective in representing the early time arrivals because of causality, and the mode description is relatively convenient for describing the late arrivals where the medium has fully responded to the excitation.

Generally speaking, a scattering return $s(t,\theta)$ can be approximated as a sum of early time response $r(t,\theta)$ and the late time response $o(t,\theta)$

$$s(t,\theta)\approx r(t,\theta)+o(t,\theta),\quad S(\omega,\theta)\approx R(\omega,\theta)+O(\omega,\theta). \tag{1}$$

Here, t and θ denote the time and the aspect angle, respectively. The progressing term $r(t,\theta)$ represents nonresonant single- and/or multiple-scattering returns characterized by their arriving times t_n. Its Fourier transform, $R(\omega,\theta)$, is analytic in the angular frequency ω domain. The oscillatory term $o(t,\theta)$ represents the resonant multiple-scattering returns. Its Fourier transform, $O(\omega,\theta)$, has pole singularities $\{\omega_m\}$ which are independent of θ.

In the mode description, wave phenomena are synthesized by resonances of the scatterer. These global resonances take the form of damped sinusoidal responses which are characterized by complex resonant frequencies s_m as below:

$$s(t,\theta)\approx o(t,\theta)\approx\sum_m A_m(\theta)e^{s_m t},\quad s_m=\alpha_m+j\omega_m. \tag{2}$$

In the ray description, wave phenomena can be organized in terms of wavefronts that travel from the source to the scatterer, and then interact with the scatterer to generate new wavefronts which travel to the sensor. These wavefronts are usually either nondispersive or weakly dispersive spectral objects and their frequency spectra can be expressed as

$$S(\omega,\theta)\approx R(\omega,\theta)=\sum_i B_i(\theta)e^{\tau_i(\theta)\omega},\quad \tau_i=\beta_i+jt_i, \tag{3}$$

where t_i and τ_i are the real and complex travel times, respectively. Note that Eqs. (2) and (3) are of exactly the same mathematical form. Therefore, the estimation of complex resonances or travel times is equivalent to the estimation of complex poles of a linear system.

The differences of arrival times dt_n give the information about target extent in the range direction, and the derivatives $dt_n/d\theta$ give the target extent in the aspect direction. The resonant poles ω_m gives the global information on target size and composition. Therefore, arrival times of wavefronts and resonant frequencies of oscillatory waves are good indicators of the target properties. If they are measurable, they can be employed to characterize the wave-scattering phenomena, determine the target range and orientation, or identify the target. From the Fourier theory, we know that the dominant resonances can be resolved in the frequency domain if the observation time interval is sufficiently large. In this case, the imaginary parts of the complex resonant frequencies may

[a]Electronic mail: itailu@rama.poly.edu

be obtained by a Fourier analysis. Similarly, for a short-time incident pulse (i.e., the signal bandwidth is very broad), the early time arrivals are separated in the time domain and their arrival times can be obtained easily.

When the time (or frequency) resolution is not sufficiently high, it becomes very challenging to extract the arrival times of wavefronts (or the complex frequencies of resonances) from experimental data which are usually contaminated by noise. Although there exist many conventional approaches,[10–14] none works satisfactorily. For examples, the spectral resolution of the fast Fourier transform (FFT)-based approaches is limited by the given system setup; high-resolution approaches such as MUltiple SIgnal Classification methods cannot provide the real parts of the complex exponents; Prony-based algorithms can only work in conditions with very high signal-to-noise ratios. The AutoRegressive and AutoRegressive Moving Average series usually have trouble in relating their estimated results directly to the physical unknowns. To remedy these difficulties, we apply a newly developed modified eigen-matrix pencil that was originally developed for identifying scattering centers for target identification,[15] and was used for wireless channel modeling,[16] and for complex wave number-spectrum estimation.[17] The validity of this new method is established in Refs. 16 and 17. The Cramer–Rao (CR) lower bound has been used as a benchmark for the variance and mean of the real and imaginary parts of the estimated complex parameters. Both mean and variance are very close to their CR bounds when signal-to-noise ratio (SNR) is larger than 15 dB (see Figs. 9 and 10 in Ref. 17). In fact, the new method yields very accurate estimated results (error $<0.05\%$) for travel times (see Table III in Ref. 16) or phases (see Table VII in Ref. 17) when SNR$\geqslant$15 dB if the unknown parameters do not cluster closely together. With large enough SNR (15 dB or larger), the system order can usually be estimated easily, and the method will provide a great enhancement of the system resolution. On the other hand, the system order cannot be obtained easily when SNR is small (SNR$<$15 dB). Typical spectral estimation methods will yield poor estimates of system parameters if the assumed system order is incorrect. However, if the system order is known, dominant parameters can be estimated fairly accurately (error $<5\%$) with a reasonable SNR (10 dB or higher).

Since resonances and wavefronts form a Fourier transform pair as shown in Eqs. (2) and (3) and Refs. 1 and 2, we will consider only the extraction of complex resonances in the rest of this paper. Here, we develop a systematic procedure to estimate the system order and the system poles simultaneously. Scattering data from the Mock-0 target collected at the Naval Undersea Warfare Center (NUWC) are analyzed where the complex resonances of the targets are extracted from the experimental data. Echoes observed at various aspect angles but excited by the same incident pulse or those observed at the same aspect angle but excited by different incident pulses (with overlapping frequency spectra) are employed to obtain reliable estimations of resonant frequencies. In the following, methodology, numerical results, and conclusions are presented in Secs. I, II, and III, respectively.

I. METHODOLOGY

Let $p[n]$ denote the oscillatory response $o(t)$ in Eq. (2) plus an undesired term $w(t)$ sampled at the nth time $t_n = t_0 + (n-N-1)\,\delta$, where δ is the time-sampling interval and $n = 1,2,...,2N+1$. Note that $w(t)$ consists of environmental and equipment noises and nonoscillatory scattering returns. In the following, for convenience, $w(t)$ will be referred to as noise. Here, we have assumed that the reference time t_0 is at the center of the observation time interval. Without loss of generality, the explicit aspect angle θ dependence shown in Eqs. (1)–(3) has been omitted here. Equation (2) may be written as

$$p[n] = \sum_{m=1}^{M} a_m z_m^{n-1} + w[n],$$

$$a_m = A_m e^{[t_0-(N+1)\delta]s_m},$$

$$z_m = e^{\delta s_m}, \quad n = 1,2,...,2N+1. \tag{4}$$

Our stable pole extraction algorithm consists of four steps. First, the initial estimate of the system order M is obtained by using the singular value decomposition (SVD) method[18] to filter out the white noise. Second, the eigen-matrix pencil method is used to identify the complex damped exponents. The eigen-matrix pencil method is similar to the matrix pencil by Hua and Sarkar,[19] because both methods use a matrix pencil to find the system poles in the transformed domain. However, the matrix pencil of the former is based on the principal eigenvectors of the Hermitian data matrix, while the matrix pencil of the latter is directly based on the data to be processed. Third, the complex amplitudes a_m can be obtained by a least-square approach. The final estimate of the system order and resonant frequencies is then determined.

A. Initial estimation of the system order *M*

Using $2N+1$ data samples, form the square Hankel matrix

$$\mathbf{P} = \begin{bmatrix} p[1] & p[2] & p[3] & \cdots & p[N+1] \\ p[2] & p[3] & p[4] & \cdots & p[N+2] \\ \cdot & \cdot & \cdot & & \cdot \\ \cdot & \cdot & \cdot & & \cdot \\ \cdot & \cdot & \cdot & & \cdot \\ p[N+1] & p[N+2] & p[N+3] & \cdots & p[2N+1] \end{bmatrix}, \tag{5}$$

which is of size $(N+1)\times(N+1)$ with $N\geqslant M$. The Hankel matrix $\mathbf{P}$ has equal elements along lines perpendicular to the principal diagonal.[20]

Define $\mathbf{W}$ as the Hankel noise matrix constructed from $w[n]$ in the same way as in (5). The Hankel data matrix $\mathbf{P}$ can then be decomposed as

$$\mathbf{P} = \mathbf{S_N A S_N^T} + \mathbf{W}, \tag{6}$$

where the $(N+1)\times M$ Vandermonde matrix $\mathbf{S}_N$ has the structure

$$\mathbf{S_N}=\begin{bmatrix} 1 & 1 & \cdots & 1 \\ z_1 & z_2 & \cdots & z_M \\ . & . & & . \\ . & . & & . \\ . & . & & . \\ z_1^N & z_2^N & \cdots & z_M^N \end{bmatrix}, \tag{7}$$

and $\mathbf{A}$ is an $M\times M$ diagonal matrix with the mth diagonal element given by a_m, $m=1,2,...,M$. Here, superscript ''T'' represents the matrix transpose. Both matrices $\mathbf{S}_N$ and $\mathbf{A}$ are of rank M. Thus, for the noiseless case, the $(N+1)\times(N+1)$ matrix $\mathbf{P}$ is also of rank M and has $(N+1-M)$ zero eigenvalues among the total $N+1$ eigenvalues.

With noise, the matrix $\mathbf{P}$ is of rank $N+1$ and the task of spectrum estimation becomes very difficult. Fortunately, we can employ the singular value decomposition algorithm to reduce noise strength in many practical occasions. The matrix $\mathbf{P}$ can be written as

$$\mathbf{P}=\sum_{n=1}^{N+1}\sigma_n\underline{\mathbf{u}}_n\underline{\mathbf{v}}_n^H, \tag{8}$$

where the superscript ''H'' denotes matrix Hermitian. Here, σ_n is the nth singular value and $\underline{\mathbf{u}}_n$ and $\underline{\mathbf{v}}_n$ are the corresponding singular vectors of the matrix $\mathbf{P}$, respectively. If $\mathbf{P}$ is Hermitian, $\underline{\mathbf{u}}_n=\underline{\mathbf{v}}_n$, and the SVD decomposition is reduced to the standard eigenvector expansion.

If the positive singular values σ_n $(n=1,2,...,N+1)$ are arranged with decreasing order and the signal strength is assumed to be sufficiently strong (SNR$>$15 dB; see Refs. 16 and 17), then, among the $N+1$ pairs of left and right eigenvectors, there are only M pairs (with M largest singular values) primarily spanning the M signal space. The other $N-M+1$ pairs primarily span the noise space. Thus, we can replace the matrix $\mathbf{P}$ through SVD with its rank-M approximation matrix $\mathbf{P}_0$

$$\mathbf{P}_0\equiv\sum_{m=1}^{M}\sigma_m\underline{\mathbf{u}}_m\underline{\mathbf{v}}_m^H\approx\mathbf{S_N}\mathbf{A}\mathbf{S_N^T}. \tag{9}$$

The rank-M approximation reduces the noise contribution to the data matrix and effectively enhances the SNR. The noise energy is given by the Frobenius norm of the difference matrix $\mathbf{P}-\mathbf{P}_0$ defined as $\|\mathbf{P}-\mathbf{P}_0\|_F=\Sigma\sigma_m^2$ where $m=M+1, M+2,...,N+1$.

B. The modified eigen-matrix pencil method

Let λ_n be the nth eigenvalue and $\mathbf{e}_n$ be the nth eigenvector of $\mathbf{P}_0$ where $n=1,2,...,N+1$. Since $\mathbf{P}_0$ is a $(N+1)\times(N+1)$ matrix but is with rank M, λ_n is 0 for $n=M+1$, $M+2,...,N+1$ and $\underline{\mathbf{e}}_n$ is an $(N+1)\times 1$ column vector. Construct an $(N+1)\times M$ matrix $\mathbf{E}=[\underline{\mathbf{e}}_1,\underline{\mathbf{e}}_2,\ldots,\underline{\mathbf{e}}_M]$ from the M principal eigenvectors. Then,

$$\mathbf{P}_0\mathbf{E}=\mathbf{E}\Lambda\approx\mathbf{S_N}\mathbf{A}\mathbf{S_N^T}\mathbf{E}, \tag{10}$$

where Λ is an $M\times M$ diagonal matrix with λ_n as its nth diagonal element. Therefore, we can express $\mathbf{E}$ as

$$\mathbf{E}\equiv\mathbf{S_N}\mathbf{D},\quad \mathbf{D}\approx\mathbf{A}\mathbf{S_N^T}\mathbf{E}\Lambda^{-1}, \tag{11}$$

where $\mathbf{D}$ is an $M\times M$ matrix with rank M.

Next, we form matrices $\mathbf{F}_1$ using the first row to the Lth row of $\mathbf{E}$, and $\mathbf{F}_2$ using the second row to the $(L+1)$th row of $\mathbf{E}$. Here, L can be any value larger than M. Then, $\mathbf{F}_1=\mathbf{S}_L\mathbf{D}$ and $\mathbf{F}_2=\mathbf{S}_L\mathbf{Z}\mathbf{D}$, where $\mathbf{S}_L$ is defined in Eq. (7) and $\mathbf{Z}$ is an M by M diagonal matrix with z_m as its mth element, $m=1,2,...,M$. The generalized eigenvalues of the matrix pencil $\{\mathbf{F}_1^H\mathbf{F}_1,\mathbf{F}_1^H\mathbf{F}_2\}$ are the complex roots of the characteristic polynomial

$$\det\{(\lambda\mathbf{F}_1^H\mathbf{F}_1)-(\mathbf{F}_1^H\mathbf{F}_2)\}=\det\{(\mathbf{F}_1^H\mathbf{S_L})(\lambda\mathbf{I_M}-\mathbf{Z})D\}$$
$$=\prod_{m=1}^{M}(\lambda-z_m)=0, \tag{12}$$

where $\mathbf{I}_M$ is an M-dimensional identity matrix and ''det'' denotes the determinant of the matrix. Solving Eq. (12) yields the desired complex spectral poles $s_m=(lnz_m)/\delta$ where $m=1,2,...,M$ and δ is the time-sampling interval. Note that z_m are assumed to be distinct.

C. Least-square approach

By defining vectors $\underline{\mathbf{a}}=[a_1,a_2,\ldots,a_M]^T$, $\underline{\mathbf{p}}=[p[1],p[2],\ldots,p[2N+1]]^T$, and $\mathbf{w}=[w[1],w[2],...,w[2N+1]]^T$, Eq. (4) can be expressed in matrix form

$$\underline{\mathbf{p}}=\mathbf{S_{2N}}\underline{\mathbf{a}}+\underline{\mathbf{w}}, \tag{13}$$

where the Vandermonde matrix $\mathbf{S}_{2N}$ is defined in Eq. (7). The least-square solution of Eq. (13) leads to the complex amplitudes $\underline{\mathbf{a}}$ as

$$\underline{\mathbf{a}}=(\mathbf{S_{2N}^H}\mathbf{S_{2N}})^{-1}\mathbf{S_{2N}^H}\underline{\mathbf{p}}. \tag{14}$$

D. Final estimate of the system order and resonant frequencies

The initial estimate of the system order M obtained by using the SVD method is accurate when the noise is small (SNR$>$15 dB; see Refs. 16 and 17). If the noise is not small, there usually exists an ambiguous interval of possible M's. Since the value of M cannot be uniquely determined, we have to use some additional procedures to determine the system order. When the scattering returns are measured at several (say, J) aspect angles, we can compare the estimated results from the scattering returns at different aspect angles for all possible system orders. Let s_{mj}, $m=1,2,...,M$, be the M estimated complex resonances using the scattering return obtained at the jth aspect angle θ_j, $j=1,2,...,J$. Let ''ω'' denote the imaginary part of a complex target resonance [s_m in Eq. (2)]. Then, the closest estimation of ω, corresponding to the system order M, in the jth aspect angle data set is $s_{m'j}$ if

$$\epsilon_j(\omega;M)\equiv|\mathrm{Im}(s_{m'j})-\omega|\leqslant|\mathrm{Im}(s_{mj})-\omega|,$$
$$\text{for every } m=1,...,M, \tag{15}$$

where $\epsilon_j(\omega;M)$ is considered as the estimation error. Note that m' is a function of ω, j, and M. Since the complex resonant frequencies are independent of the aspect angles, the average estimation error at a true resonant frequency should be small for some aspect angles in which the corre-

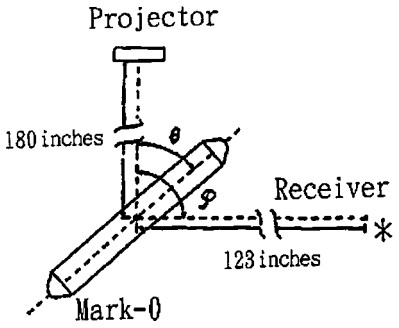

FIG. 1. Experimental setup.

sponding resonance is strongly excited. This is the clue we want to use to search for the resonant frequencies. The difficulty of this approach is that we cannot always include the estimates from *all* scattering returns in searching for the resonances because a particular resonance is not always observed in every aspect angle. Thus, the searching procedure has to be made on a trial-and-error basis. We define the average estimation error of n scattering returns as

$$\text{err\_}n(\omega;M) = \frac{1}{n}[\text{sum of } n \text{ smallest } \epsilon_j(\omega;M),\ \ j=\{1,...,J\}],\ \ n\leqslant J. \tag{16}$$

For a given system order M, we first compare the local minima of $\text{err\_}(\omega;M)$ in the frequency range of interests for some n's. If these local minima appear consistently in the same frequencies for most n's, they are the likely estimates of the resonant frequencies. We then compare the estimated resonant frequencies obtained for all possible system orders. By the same token, if the estimated frequencies are consistent for several system orders (M's), they are chosen to be the estimates of the resonant frequencies.

II. NUMERICAL RESULTS

We have studied various narrow-band and broadband data sets obtained from monostatic or bistatic measurements of the Mock-0 and Mock-3 models. The Mock-0 model consists of a cylindrical pipe with cone-shaped endcaps, a bulkhead, and an internal rib. The Mock-3 model is a copper scale model with seven external ribs distributed along the hull. The results obtained from these studies are very similar. Therefore, only selected narrow-band monostatic scattering data of the Mock-0 target collected at NUWC are presented in this section. Results of other data sets are briefly discussed in the next section.

A. Monostatic multiple-angle data

The measurement setup of Mock-0 is shown in Fig. 1. Two multiple-angle data sets are discussed in this subsection. For convenience, they are denoted as high-frequency and low-frequency data sets, respectively. Each data set consists of monostatic measurements from different aspect angles. The time records of all incident waves and echoes contain 2048 points. The sampling rate is 970 kHz. For the high-frequency data set, the time record and the frequency spectrum of the incident pulse are shown in Fig. 2(a) and (b), respectively. The pulse length is 0.25 ms, the center frequency is 23.7 kHz, and the bandwidth is around 2.4 kHz. Employed for analysis are the measured echoes taken at the following four aspect angles θ: 180, 196, 208, and 240 deg. The time record and the frequency spectrum of the scattering return of $\theta=180°$ are shown in Fig. 2(c) and (d), respectively. The amplitude and phase of the transfer function $H(\omega)$ of the scattering response at $\theta=180°$ between 18.4 and 28.0 kHz are shown in Fig. 3(a) and (b), respectively. Here, the transfer function is defined as the ratio between the echo spectrum and the incident spectrum. Let $h(t)$ be the

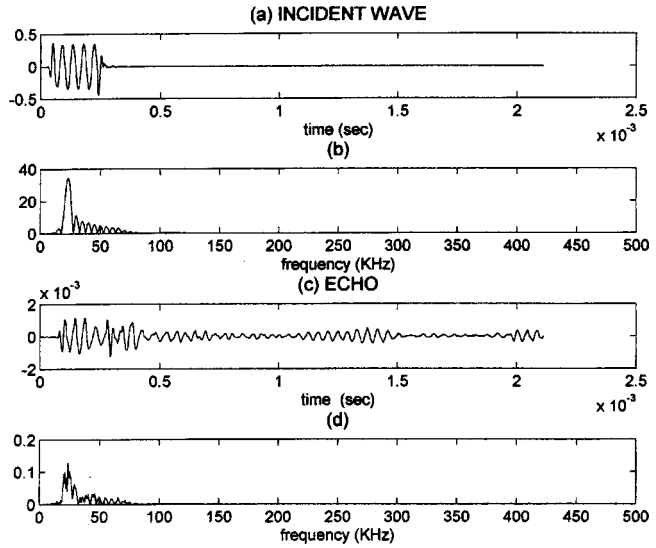

FIG. 2. A monostatic measurement ($\theta=\phi$ in Fig. 1) taken at the aspect angle response at $\theta=180°$ using Mock-0 as a target: (a) the time record of the incident pulse; (b) the frequency spectrum of the incident pulse; (c) the time record of the echo; (d) the frequency spectrum of the echo.

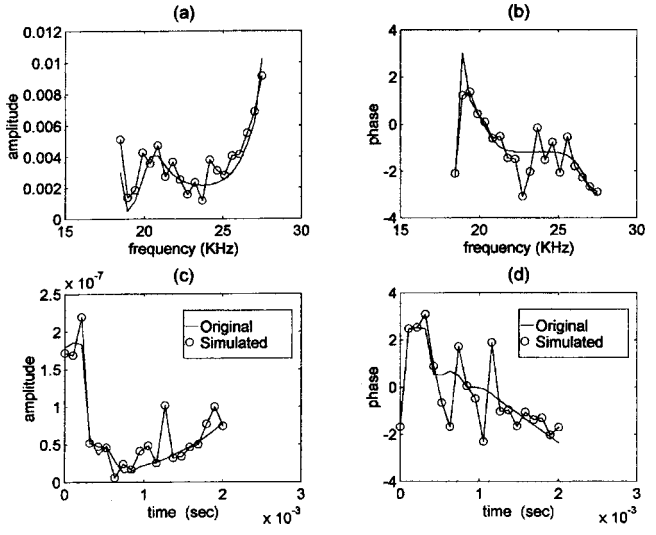

FIG. 3. The transfer function of the scattering response at $\theta=180°$ between 18.4 and 28.6 kHz and the corresponding impulse response: (a) amplitude of the transfer function; (b) phase of the transfer function; (c) amplitude of the corresponding impulse response; (d) phase of the corresponding impulse response. The curves with ° are obtained from the measurement data and the curves without ° are obtained from simulated results with $M=5$. The simulated results agree well with the measured results.

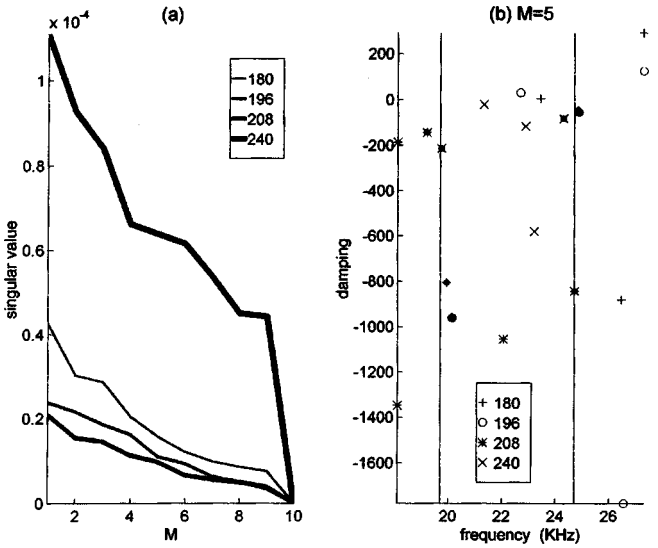

FIG. 4. Results from the high-frequency monostatic multiple-angle data set. The analyzed results of the ''impulse'' responses for the scattering returns observed at aspect angles $\theta = 180°$, 196°, 208°, and 240°: (a) the singular values; (b) the complex poles obtained with $M = 5$. The estimated complex resonant frequencies are marked by heavy dots and their average imaginary components are indicated by vertical lines.

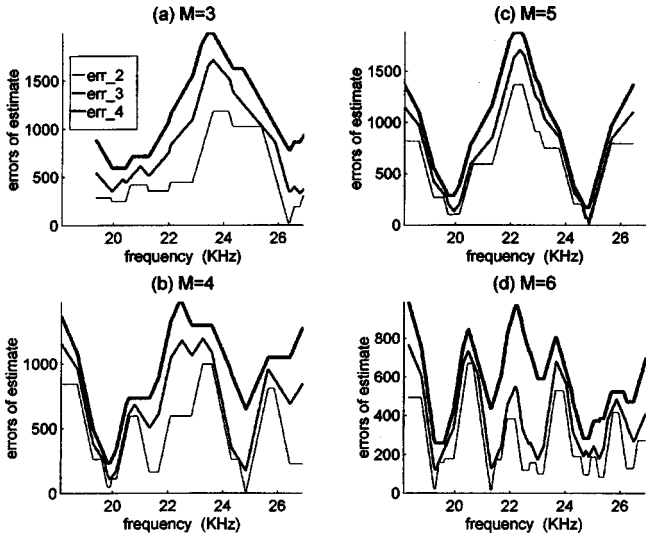

FIG. 5. Results from the high-frequency monostatic multiple-angle data set. The average error of the frequency estimate err_n for $n = 2,3$, and 4: (a) $M = 3$; (b) $M = 4$; (c) $M = 5$; (d) $M = 6$. The two local minima at $f = 19.7$ and 24.7 kHz happen at all n's and M's.

Fourier transform of $H(\omega - \omega_0)$ where $\omega_0 = 22.5$ kHz is the center frequency of $H(\omega)$. The amplitude and phase of the ''impulse response'' $h(t)$ are shown in Fig. 3(c) and (d), respectively.

We first used the SVD approach to estimate the system order. Figure 4(a) shows the singular values of the Hankel matrix in Eq. (5) for the scattering returns observed at various aspect angles. It is seen that the system order M is not clearly determined by the singular values alone. Since the system order M was unknown, we repeated the pole estimation process with various possible M. We chose M to be 3 to 6 and applied the eigen matrix pencil method to estimate the poles of the impulse response $h(t)$. The poles obtained with $M = 5$ for various scattering returns are shown in Fig. 4(b). After obtaining the poles, the model in Eq. (2) was employed to derive the simulated impulse response $h'(t)$ and its transfer function $H'(\omega)$. In most cases, the simulated $h'(t)$ and $H'(\omega)$ are in good agreement with the original measured $h(t)$ and $H(\omega)$ [see Fig. 3(a)–(d)]. The small discrepancy in Fig. 3 can be further reduced by increasing the system order M to provide better curve-fitting results. Since the noise here is usually significant because it includes not only environmental noise and measurement errors but also nonresonant scattering returns, further reduction of the discrepancy can be shown to be irrelevant.

Generally speaking, the poles obtained from various scattering returns for various aspect angles are not always consistent because of noise. [Note that the noise here includes environmental noise, measurement errors, and nonresonant scattering returns in Eq. (1).] The estimated poles may also vary as the system order M changes. Using the searching procedure discussed in the Sec. I D, the average error of the frequency estimate (err_n) is calculated, and is shown in Fig. 5 for $n = 2,3,4$ and $M = 3,4,5,6$. Note that n denotes the number of scattering returns used for searching for the complex resonances, and M is the estimated system order. It is obvious that smaller n's always correspond to smaller estimate errors. Fortunately, the final estimates of the complex resonances obtained using different system orders are very similar to one another. The two local minima of err_n, near $f = 19.7$ and 24.7 kHz, happen at all n's and M's. This is a strong indication of the existence of the target resonances. The final estimated resonant frequencies are marked by heavy dots and their average imaginary components are indicated by vertical lines in Fig. 4(b).

The low-frequency data set analyzed is also a monostatic measurement using Mock-0 as the target. The pulse length is 0.5 ms, the center frequency is 11.9 kHz, and the bandwidth is around 1.6 kHz. Employed for analysis are the measured echoes taken at the following eight aspect angles θ: 18, 34, 46, 58, 78, 90, 110, and 122 deg. The time records and the frequency spectra of the incident pulse and scattering returns are similar to those in Fig. 1 and are not shown here. Following the same procedure depicted previously, singular values of the Hankel matrix in Eq. (5) are computed for the scattering returns observed at various aspect angles. Since the system order M is not clearly determined by the singular values alone, we have to repeat the pole estimation process with various possible values of M. We choose M to be 2 to 5 and apply the eigen matrix pencil method to estimate the poles. The average error of the frequency estimate (err_n) is shown in Fig. 6 for $n = 4-8$ and $M = 2,3,4,5$. Note that ''n'' denotes the number of scattering returns used for searching for the complex resonances, and ''M'' is the estimated system order. The final estimates of the complex resonances obtained using different system orders are very similar to one another. The local minimum, near 13.4 kHz, happens at all n's and M's, and the local minimum near $f = 10.7$ kHz happens at all cases except $M = 2$. This is due to the fact that $M = 2$ is too small to represent the system response. It is remarkable that the resonant frequency 13.4 kHz is still predicted by the case with $M = 2$.

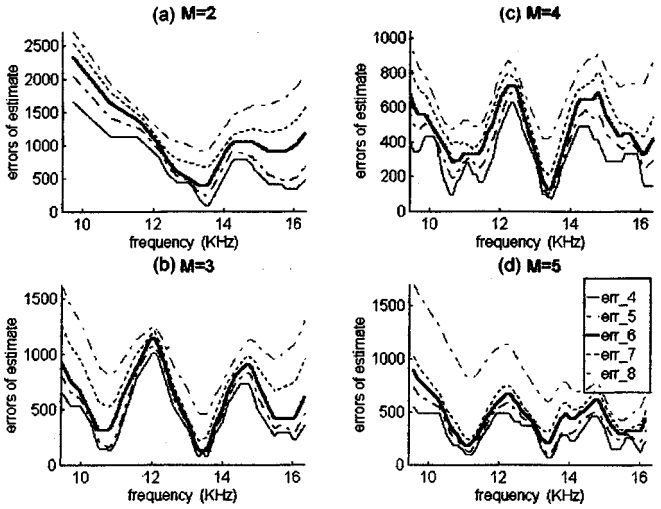

FIG. 6. Results from the low-frequency monostatic multiple-angle data set. The scattering returns were observed at aspect angles $\theta=18°$, 34°, 46°, 58°, 78°, 90°, 110°, and 122°. The average error of the frequency estimate err_n for $n=4$, 5, 6, 7, and 8: (a) $M=2$; (b) $M=3$; (c) $M=4$; (d) $M=5$. The two local minima at $f=10.7$ and 13.4 kHz happen at all n's and Ms.

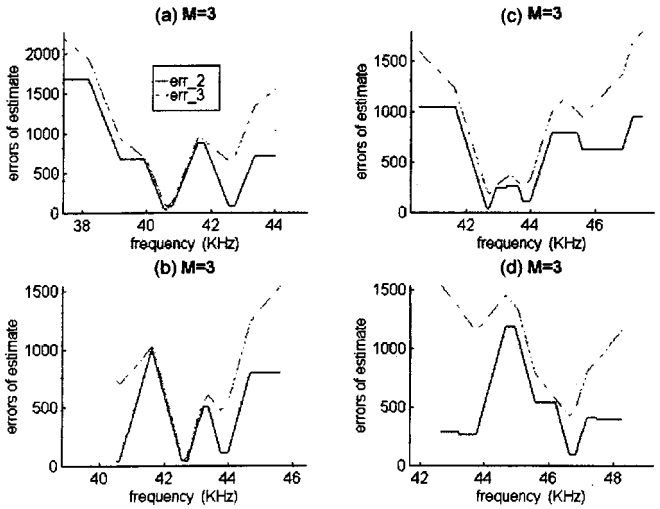

FIG. 8. Results from the monostatic multiple-frequency data set. The average error of the frequency estimate err_n for $n=2$ and 3 with $M=3$. Used for comparison are echoes at: (a) 39.3, 40.7, and 42.1 kHz; (b) 40.7, 42.1, and 43.5 kHz; (c) 42.1, 43.5, and 44.9 kHz; and (d) 43.5, 44.9, and 46.3 kHz.

B. Monostatic multiple-frequency data

The data set analyzed in this section was observed from monostatic measurements for various narrow bands at a single aspect angle. Data was taken from 39.3 to 120.5 kHz by 1.4-kHz increments. The aspect angle θ was 10 deg. The length of each pulse is 0.5 ms, resulting in a bandwidth of approximately 4.4 kHz. Figure 7(a) shows the singular values of the Hankel matrix in Eq. (5) for the scattering returns at the following frequencies: 39.3, 40.7, 42.1, 43.5, 44.9, and 46.3 kHz. Although all scattering returns were observed at the same aspect angle, the impulse responses of adjacent center frequencies have some overlapping frequency spectral bands. Therefore, we could still apply the search procedure described in Sec. I D to estimate the resonant frequencies. We chose the system order M to be 2 to 5 and applied the eigen matrix pencil method to estimate the system poles. The poles obtained with $M=3$ for the scattering returns at various frequencies are shown in Fig. 7(b). In this data set, the resonant frequencies obtained from various frequency spectra (not aspect angles) are available for comparison. Using a searching procedure similar to that discussed in Sec. I D, the average error of the frequency estimate (err_n) is shown in Fig. 8 for $n=2$ and 3 and $M=3$. Note that ''n'' denotes the number of scattering returns used for searching for the complex resonances, and ''M'' is the estimated system order. The estimated resonant frequencies obtained from different signals with some overlapping spectra are very close to one another. In other words, in the common frequency band, the minima of the err_n curves with fixed ''n'' derived from different pulses are nearly identical. The curves in Fig. 8(a), (b), and (c) have the same minimum at 42.6 kHz and the curves in Fig. 8(b), (c), and (d) have the same minimum at 43.9 kHz. This is a strong indication of the existence of these two target resonances.

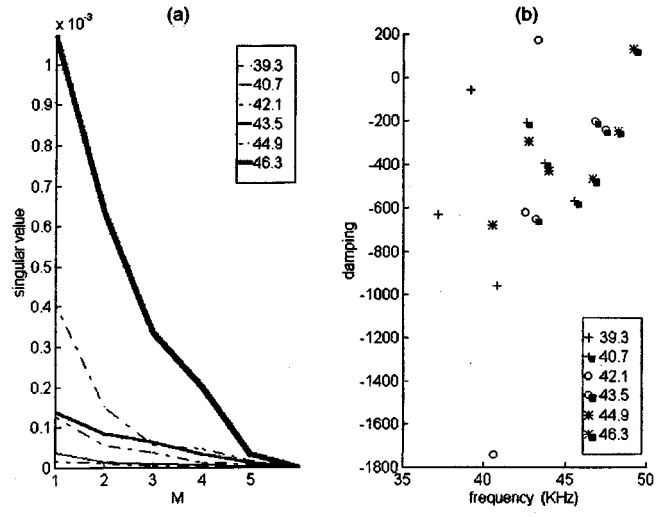

FIG. 7. Results from the monostatic multiple-frequency data set. The analyzed results of the impulse responses for the scattering returns of incident signals with various frequencies: (a) the singular values; (b) the complex poles obtained with $M=3$.

III. CONCLUSIONS

Arrival times of wavefronts and resonant frequencies of oscillatory waves can serve as good physical observables for characterizing wave-scattering phenomena. In this paper, experimental data are employed to derive the complex resonances of the Mock-0 target. The SVD approach is used to derive the initial estimate of the number of dominant resonances and the eigen matrix pencil method is used for estimating complex resonances. The final estimate of the resonance number is estimated by comparing the results using the scattering returns of different aspect angles or of different incident signals with overlapping spectra. A systematic procedure is employed for making such a comparison to obtain the final estimates of the complex resonances. In narrowband situations, the final estimates of the imaginary parts of the complex resonances obtained using different system or-

der M's are very similar to one another. This is a strong indication that these estimations are accurate assessments of the resonant frequencies of the targets. On the other hand, the damping components cannot be obtained easily because they are much more susceptible to noise contamination. In broadband situations, the estimated results show some inconsistency in system order estimation if the entire broadband impulse responses are used for estimating the target resonances. This is a fundamental issue of all spectral estimation approaches because they are based on curve fitting. The remedy is to subdivide the system responses into narrow-band components. The procedure discussed in the previous section can then be successfully employed to analyze each narrow-band component. The above conclusions hold for both monostatic and bistatic measurement setups of both Mock-0 and Mock-3 targets.

ACKNOWLEDGMENTS

Work is supported in parts by ONR and ARO. The Mock-0 data sets are provided by Theresa Baus and the Mock-3 data sets are provided by Russell Costa.

[1] L. B. Felsen, ''Progressing and oscillatory waves for hybrid synthesis of source excited propagation and diffraction,'' IRE Trans. Antennas Propag. **AP-32**, 775–796 (1984).
[2] I. T. Lu, ''A ray-mode (wavefront-resonance) approach for analyzing acoustic radiation and scattering by submerged structures,'' J. Acoust. Soc. Am. **99**, 114–132 (1996).
[3] I. T. Lu and Y. Q. Yao, ''Ray shooting, eigenray search, and complex resonances for submerged structures,'' J. Acoust. Soc. Am. **101**, 66–76 (1997).
[4] L. Flax, G. C. Gaunaurd, and H. Uberall, ''Theory of resonance scattering,'' in *Physical Acoustics*, edited by W. P. Mason and R. N. Thurston (Academic, New York, 1981), Vol. 10, pp. 1–60.
[5] G. C. Gaunard and M. F. Werby, ''Lamb and creeping waves around submerged spherical shells resonantly excited by sound scattering,'' J. Acoust. Soc. Am. **82**, 2021–2033 (1987).
[6] G. C. Gaunaurd and M. F. Werby, ''Acoustic resonance scattering by submerged elastic shells,'' Appl. Mech. Rev. **43**, 171–208 (1990).
[7] P. L. Marston, ''GTD for backscattering from elastic spheres and cylinders in water and the coupling of surface elastic waves with the acoustic field,'' J. Acoust. Soc. Am. **83**, 25–37 (1988).
[8] A. D. Pierce, ''Wave propagation on thin-walled elastic cylindrical shells,'' in *Elastic Wave Propagation*, edited by M. F. McCarthy and M. A. Hayes (Elsevier, New York, 1989), pp. 205–210.
[9] L. B. Felsen and I. T. Lu, ''Ray treatment of wave propagation on thin-walled curved elastic plates with truncations,'' J. Acoust. Soc. Am. **86**, 360–374 (1989).
[10] S. M. Kay, *Modern Spectral Estimation: Theory and Applications* (Prentice Hall, Englewood Cliffs, NJ, 1988).
[11] S. L. Marple, *Digital Spectral Analysis with Applications* (Prentice Hall, Englewood Cliffs, NJ, 1987).
[12] R. Roy, A. Paulraj, and T. Kailath, ''ESPRIT—A subspace rotation approach to estimation of parameters of cisoids in noise,'' IEEE Trans. Acoust., Speech, Signal Process. **34(10)**, 1340–1342 (1986).
[13] R. Kumaresan and D. W. Tufts, ''Estimating the parameters of exponentially damped sinusoids and pole-zero modeling in noise,'' IEEE Trans. Acoust., Speech, Signal Process. **30(6)**, 833–840 (1982).
[14] B. Porat and B. Friedlander, ''On the accuracy of the Kumeresan-Tufts method for estimating complex damped exponentials,'' IEEE Trans. Acoust., Speech, Signal Process. **35(2)**, 231–235 (1987).
[15] S. U. Pillai and H. S. Oh, ''Extraction of resonant modes from scattering noisy data,'' in *Ultra-Wideband Short-Pulse Electromagnetics II*, edited by L. Carin and L. B. Felsen (Plenum, New York, 1995), pp. 585–594.
[16] C. M. Qiu and I. T. Lu, ''Multipath resolving with frequency dependence for broadband wireless channel modeling,'' IEEE Trans. Veh. Techno. **48**(1), 273–285 (1999).
[17] I-T. Lu, Robert C. Qiu, and Jaeyoung Kwak, ''A high-resolution algorithm for complex-direction search,'' J. Acoust. Soc. Am. **104**, 288–299 (1998).
[18] G. H. Golub and C. F. Van Loan, *Matrix Computations* (Johns Hopkins University Press, Baltimore, 1993), pp. 1340–1342.
[19] Y. Hua and T. K. Sarkar, ''Matrix pencil method for estimating parameters of exponentially damped/undamped sinusoids in noise,'' IEEE Trans. Acoust., Speech, Signal Process. 814–824 (1990).
[20] A. K. Jain, *Fundamentals of Digital Image Processing* (Prentice Hall, Englewood Cliffs, NJ, 1989).

Influence of edge boundary conditions on the free vibrations of cross-ply laminated circular cylindrical panels

Arcangelo Messina
Università di Lecce, Facoltà di Ingegneria, 73100 Lecce, Italy

Kostas P. Soldatos
University of Nottingham, Pope Building, Nottingham NG7 2RD, England

(Received 28 September 1998; accepted for publication 28 June 1999)

This paper deals with the influence of different sets of edge boundary conditions on the dynamic characteristics of shear deformable, cross-ply laminated circular cylindrical panels. The analysis is based on the conjunction of the Ritz method with an appropriate, complete functional basis and its subsequent application on the energy functional of the Love-type version of a unified shear-deformable shell theory [T. Timarci and K. P. Soldatos, J. Sound Vib. **187**, 609–624 (1995); J. Eng. Math (to appear January 2000)]. As a result, two different kinds of shear deformable Love-type shell theories are employed and tested, including versions that either fulfill or violate the continuity of the interlaminar stresses along the shell thickness. Although the main theoretical model employed makes use of a certain type of continuous interlaminar stress, the results of the present analysis are initially tested and validated through appropriate comparisons with corresponding numerical results obtained in the relevant literature, mostly on the basis of discontinuous interlaminar plate and shell models. The present approach and analysis are then used for a more thorough investigation of the influence of the edge boundary conditions on the dynamic characteristics of circular cylindrical panels. © *1999 Acoustical Society of America.*
[S0001-4966(99)00311-2]

PACS numbers: 43.40.Ey [CBB]

INTRODUCTION

Due to the periodic nature of the displacements and stresses around the circumference of a complete circular cylindrical shell, the partial differential equations that govern the free vibration of such a shell can always be converted into a corresponding set of ordinary differential equations. This fact is independent of the type of the shell model employed and is therefore well documented in connection with either classical or refined shear deformable shell theories. Moreover, it is independent of the material properties of the cylindrical shell considered and has therefore been applied for the dynamic analysis of shells made of either a homogeneous (isotropic, orthotropic, monoclinic) or a layered material, the latter having any type of arbitrary, cross-ply or angle-ply, lay-up. Details and applications of this argument are discussed, for instance, in Refs. 1–15 as well as in other relevant publications that can be found through them. As a result of the described conversion, the free vibration problem of a complete circular cylindrical shell, subjected to any kind of edge boundary conditions, can mathematically be treated as a one-dimensional problem and can therefore be investigated by means of an analytical approach appropriate for the solution of ordinary differential equations. Such an analytical approach that has been used very frequently is based on the state space concept[5–7,10–12,15] or its earlier but mathematically equivalent versions.[2,4]

Other analytical approaches, which are mostly connected with error-minimization techniques, have however also been employed. The most important among them are associated with the application of the method of Galerkin[8] and the Ritz method.[9,13,14] It should be noted in this connection that, although these latter methods are usually regarded as approximate ones, they can asymptotically provide the exact solution of the problem considered, provided that they will be applied in association with an appropriate set of basis functions, which should be complete in the space of the functions that satisfy the edge boundary conditions assumed. Under these considerations, the proper application of such an error minimization approach may be regarded as superior to an approach based on the state space concept, in the sense that it can successfully yield the analytical solution of relevant problems in which the described ''one-dimensional,'' conversion of all the partial derivatives involved is not possible (e.g., dynamics of flat rectangular plates or curved open panels). It should be noted in this respect that, as is adequately documented in Refs. 13 and 14, the Ritz method has extensively and successfully been applied towards the analysis of such dynamical problems, but mostly on energy functionals which are consistent with the assumptions of the classical plate and shell theories.

References 13 and 14 dealt with the free vibrations of composite laminated complete cylindrical shells and open cylindrical panels, respectively, having all their edges free of external tractions. In both papers, the analysis was based on the conjunction of the Ritz method with an appropriate, complete functional basis and its subsequent application on the energy functional of the Love-type version of a unified shear-deformable shell theory.[11,16] As a result, several kinds of shear deformable Love-type shell theories were employed and tested, along with their classical counterpart, including versions that either fulfill[13] or violate[13,14] the continuity of

the interlaminar stresses along the shell thickness. Although the analytical approach employed[13,14] was outlined in a general manner, and could therefore be associated with any type of admissible basis functions, only bases of appropriate orthonormal polynomials suitable for free edges were used in both papers, for all the numerical results presented. The case of the free boundary conditions was particularly chosen and studied because completely free plates and shells constitute a privileged class of structural elements for laboratory tests. In this respect, some of the natural frequencies predicted analytically[13] were found to be in excellent agreement with corresponding results that were obtained experimentally.[17] Moreover, the efficiency of the analytical method was initially tested and exhibited in Ref. 13 by means of the excellent agreement of its numerical predictions with the very few existing relevant analytical results obtained, elsewhere,[7,11] on the basis of the state space concept. After these successful tests and comparisons,[13] the study was extended[14] towards the dynamic analysis of free edged plates and open cylindrical panels to which, as has already been mentioned, the state space concept cannot be applied directly.

This paper deals with the influence of different sets of edge boundary conditions on the dynamic characteristics of shear deformable, cross-ply laminated circular cylindrical panels and, in a sense, it may be considered as a natural, further extension of the studies presented in Refs. 13 and 14. This is still an open problem in the relevant literature, though certain of its aspects have already been addressed in some recent publications.[7,18–21] In more detail, Khdeir and Reddy[7] and Xavier *et al.*[18] dealt with cross-ply curved panels having both their straight edges and all four edges, respectively, simply supported, while Chen *et al.*[19] and Singh and Kumar[20,21] considered both cross-ply and angle-ply panels subjected to different sets of edge boundary conditions. Xavier *et al.*[18] employed a well-known, essentially trivial set of edge conditions that led to an exact solution of the governing equations by means of simple mathematical manipulations. They, however, made use of a higher-order shell theory, which accounts for the continuity of the transverse shear stresses at the shell material interfaces. Contrary to this, the more general and complicated approaches employed by Khdeir and Reddy,[7] Chen *et al.*[19] and Singh and Kumar[20,21] were applied on what is essentially the original version of the so-called parabolic shear deformable theory, which violates the continuity of the interlaminar stresses by erroneously assuming interlaminar continuity of the transverse shear strains. On the other hand, due to the simple support assumption that was imposed on both straight edges, Khdeir and Reddy[7] were able to convert the governing partial differential equations into corresponding ordinary differential equations (in the sense already described for complete cylindrical shells) and to subsequently solve those equations on the basis of the state space concept. Finally, Chen *et al.*[19] confined their study on flat plates only (zero curvature) and dealt with a large number of different sets of edge conditions while Singh and Kumar[20,21] applied their analysis to a variety of curved panels (cylindrical, conical and spherical) subjected, however, to a limited number of different edge conditions. It should be noted in this connection that the mathematical approach employed in Ref. 19 was based on the conjunction of the Ritz method with a complete polynomial basis and can therefore be clearly considered as analytical. The Ritz-type approach employed in Refs. 20 and 21 was applied in conjunction with Bezier surface patches and exhibited some good convergence features. It is, however, not known to the present authors whether the Bezier polynomials involved[20,21] form a complete functional basis for any given set of edge conditions, a fact that could characterize the approach as analytical rather than numerical.

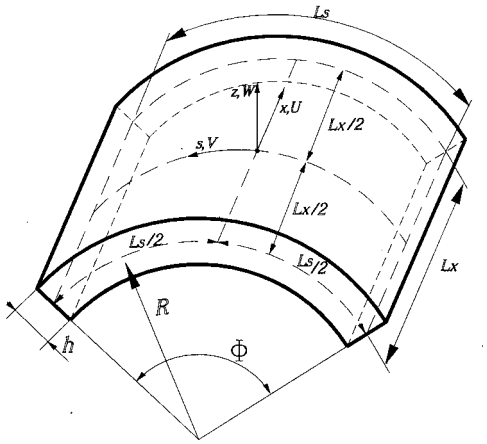

FIG. 1. Nomenclature for the cylindrical panel/flat plate.

Since the present study deals with cross-ply laminates only, its numerical results can only be related and are therefore initially compared with corresponding results presented either in Refs. 7 and 18 or in those parts of Refs. 19–21 that dealt with plates and cylindrical panels having a cross-ply lay-up. Since, on the other hand, the analysis is essentially based on the aforementioned unified shear deformable shell theory,[11,16] it naturally employs the parabolic shear deformable shell model in an intrinsic manner, in either its continuous[18] (PAR_{cs}) or its discontinuous[7,19–21] (PAR_{ds}) interlaminar stresses version. It will become clear in this connection that, upon nullifying the cylindrical panel curvature, the present PAR_{ds} analysis yields identical numerical results with those tabulated in Ref. 19, for cross-ply laminated plates, regardless of the edge boundary conditions employed. Moreover, further numerical comparisons, involving results based on both the (PAR_{cs}) and (PAR_{ds}) models, are performed with corresponding numerical results tabulated in Refs. 7, 18, 20, and 21. These validate further the excellent performance of the present approach and analysis, both of which are finally used for a more thorough investigation of the influence of the edge boundary conditions on the dynamic characteristics of circular cylindrical panels. It might be further noted, in this connection, that this is the first paper in the relevant literature that, for boundary conditions different than simply supported,[18] presents vibration frequencies for nonsymmetrically laminated cross-ply laminated panels obtained on the basis of a theory that accounts for continuity of the interlaminar stresses.

I. THEORY

Figure 1 shows the full nomenclature of the open cylindrical panel considered. This has a constant thickness *h*, an

axial length L_x, a middle surface circumferential length L_s and a middle surface radius R, so that its shallowness angle is given as $\phi = L_s/R$. The particular geometry of a plate is then obtained by setting $\phi = 0$ or, equivalently by allowing R to approach infinity. Figure 1 also shows the right-handed curvilinear coordinate system used, with x, s and z denoting the axial, circumferential and normal to the middle surface length parameters, respectively. U, V and W denote the corresponding displacement components. This cylindrical shell segment is assumed as made of an arbitrary number (L, say) of thin, specially orthotropic layers,[22] which are perfectly bonded together in the form of a cross-ply lay-up. Hence, the common assumption of negligible radial stress and strain, throughout the shell thickness, yields the following stress-strain relationship in the kth layer (starting counting from the inner layer):

$$\begin{bmatrix} \sigma_x^{(k)} \\ \sigma_s^{(k)} \\ \tau_{xs}^{(k)} \end{bmatrix} = \begin{bmatrix} Q_{11}^{(k)} & Q_{12}^{(k)} & 0 \\ Q_{12}^{(k)} & Q_{22}^{(k)} & 0 \\ 0 & 0 & Q_{66}^{(k)} \end{bmatrix} \begin{bmatrix} \varepsilon_x \\ \varepsilon_s \\ \gamma_{xs} \end{bmatrix},$$

$$(k = 1,2,\ldots,L), \tag{1}$$

$$\begin{bmatrix} \tau_{sz}^{(k)} \\ \tau_{xz}^{(k)} \end{bmatrix} = \begin{bmatrix} Q_{44}^{(k)} & 0 \\ 0 & Q_{55}^{(k)} \end{bmatrix} \begin{bmatrix} \gamma_{sz} \\ \gamma_{xz} \end{bmatrix},$$

where the Q's are the well-known reduced stiffnesses.[22,23]

The following global displacement field,

$$\begin{aligned} U(x,s,z;t) &= u(x,s;t) - z w_{,x} + \Phi_1(z) u_1(x,s;t), \\ V(x,s,z;t) &= (1 + z/R) v(x,s;t) - z w_{,s} \\ &\quad + \Phi_2(z) v_1(x,s;t), \\ W(x,s,z;t) &= w(x,s;t), \end{aligned} \tag{2}$$

which is consistent with the general Love-type shear deformable shell theory detailed in Refs. 11 and 16, yields the following kinematic relations,

$$\begin{aligned} \varepsilon_x &= u_{,x} - z w_{,xx} + \Phi_1(z) u_{1,x}, \\ \varepsilon_s &= (1 + z/R) v_{,s} - z w_{,ss} + \Phi_2(z) v_{1,s} + w/R, \\ \gamma_{sz} &= \Phi_2' v_1, \quad \gamma_{xz} = \Phi_1' u_1, \\ \gamma_{xs} &= u_{,s} + v_{,x} + z(-2 w_{,xs} + v_{,x}/R) + \Phi_1 u_{1,s} + \Phi_2 v_{1,x}. \end{aligned} \tag{3}$$

Here, u, v, w, u_1 and v_1 are the degrees of freedom of the theory,[11,16] $\Phi_1(z)$ and $\Phi_2(z)$ are the relevant shape functions, which will be specified *a posteriori*, and a prime denotes ordinary differentiation with respect to normal coordinate parameter, z. As has already been implied, the present theoretical developments hold for any choice of the shape functions, $\Phi_1(z)$ and $\Phi_2(z)$, regardless of whether that choice can guarantee the continuity of interlaminar stresses at the material interfaces of the composite structural component considered. As will be detailed in what follows, numerical applications in this paper involve model shape functions that either satisfy or violate this continuity condition.

The force and moment resultants of the theory are defined according to

$$\begin{aligned} (N_x, N_s, N_{xs}) &= \int_{-h/2}^{h/2} (\sigma_x, \sigma_s, \tau_{xs})\, dz, \\ (M_x, M_s, M_{xs}) &= \int_{-h/2}^{h/2} (\sigma_x, \sigma_s, \tau_{xs}) z\, dz, \\ (M_x^a, M_{xs}^a) &= \int_{-h/2}^{h/2} (\sigma_x, \tau_{xs}) \Phi_1(z)\, dz, \\ (M_s^a, M_{sx}^a) &= \int_{-h/2}^{h/2} (\sigma_s, \tau_{sx}) \Phi_2(z)\, dz, \\ Q_x^a &= \int_{-h/2}^{h/2} \tau_{xz} \Phi_1'\, dz, \quad Q_s^a = \int_{-h/2}^{h/2} \tau_{sz} \Phi_2' dz, \end{aligned} \tag{4}$$

and, after Eqs. (1), they yield the following constitutive equations:

$$\begin{bmatrix} N_x \\ N_s \\ N_{xs} \\ M_x \\ M_s \\ M_{xs} \\ M_x^a \\ M_s^a \\ M_{xs}^a \\ M_{sx}^a \end{bmatrix} = \begin{bmatrix} A_{11} & A_{12} & 0 & B_{11} & B_{12} & 0 & B_{111} & B_{122} & 0 & 0 \\ A_{12} & A_{22} & 0 & B_{12} & B_{22} & 0 & B_{121} & B_{222} & 0 & 0 \\ 0 & 0 & A_{66} & 0 & 0 & B_{66} & 0 & 0 & B_{661} & B_{662} \\ B_{11} & B_{12} & 0 & D_{11} & D_{12} & 0 & D_{111} & D_{122} & 0 & 0 \\ B_{12} & B_{22} & 0 & D_{12} & D_{22} & 0 & D_{121} & D_{222} & 0 & 0 \\ 0 & 0 & B_{66} & 0 & 0 & D_{66} & 0 & 0 & D_{661} & D_{662} \\ B_{111} & B_{121} & 0 & D_{111} & D_{121} & 0 & D_{1111} & D_{1212} & 0 & 0 \\ B_{122} & B_{222} & 0 & D_{122} & D_{222} & 0 & D_{1212} & D_{2222} & 0 & 0 \\ 0 & 0 & B_{661} & 0 & 0 & D_{661} & 0 & 0 & D_{6611} & D_{6612} \\ 0 & 0 & B_{662} & 0 & 0 & D_{662} & 0 & 0 & D_{6612} & D_{6622} \end{bmatrix} \begin{bmatrix} u_{,x} \\ v_{,s} + (w/R) \\ u_{,s} + v_{,x} \\ -w_{,xx} \\ -w_{,ss} + (v_{,s}/R) \\ -2w_{,xs} + (v_{,x}/R) \\ u_{1,x} \\ v_{1,s} \\ u_{1,s} \\ v_{1,x} \end{bmatrix},$$

$$\begin{bmatrix} Q_s^a \\ Q_x^a \end{bmatrix} = \begin{bmatrix} A_{4422} & 0 \\ 0 & A_{5511} \end{bmatrix} \begin{bmatrix} v_1 \\ u_1 \end{bmatrix}, \tag{5}$$

where the appearing rigidities are defined as follows:

$$A_{ij}=\int_{-h/2}^{h/2} Q_{ij}^{(k)}\,dz, \quad A_{jjll}=\int_{-h/2}^{h/2} Q_{jj}^{(k)}(\Phi_l')^2\,dz,$$
$$B_{ij}=\int_{-h/2}^{h/2} Q_{ij}^{(k)} z\,dz, \quad B_{ijl}=\int_{-h/2}^{h/2} Q_{ij}^{(k)}\Phi_l\,dz,$$
$$D_{ij}=\int_{-h/2}^{h/2} Q_{ij}^{(k)} z^2\,dz, \quad D_{ijl}=\int_{-h/2}^{h/2} Q_{ij}^{(k)}\Phi_l z\,dz, \tag{6}$$
$$D_{ijlm}=\int_{-h/2}^{h/2} Q_{ij}^{(k)}\Phi_l\Phi_m\,dz.$$

With the purpose to apply the Ritz method, the five unknown displacement functions are expressed as follows:

$$u(x,s;t)=\cos(\omega t) f_u(x) g_u(s)\sum_{m=0}^{M}\sum_{n=0}^{N} A_{mn} X_m^u(x) S_n^u(s),$$
$$v(x,s;t)=\cos(\omega t) f_v(x) g_v(s)\sum_{m=0}^{M}\sum_{n=0}^{N} B_{mn} X_m^v(x) S_n^v(s),$$
$$w(x,s;t)=\cos(\omega t) f_w(x) g_w(s)\sum_{m=0}^{M}\sum_{n=0}^{N} C_{mn} X_m^w(x) S_n^w(s), \tag{7}$$
$$u_1(x,s;t)$$
$$=\cos(\omega t) f_{u1}(x) g_{u1}(s)\sum_{m=0}^{M}\sum_{n=0}^{N} D_{mn} X_m^{u1}(x) S_n^{u1}(s),$$
$$v_1(x,s;t)$$
$$=\cos(\omega t) f_{v1}(x) g_{v1}(s)\sum_{m=0}^{M}\sum_{n=0}^{N} E_{mn} X_m^{v1}(x) S_n^{v1}(s).$$

Here, ω is an unknown natural frequency of vibration while the unknown constant coefficients A_{mn}, B_{mn}, C_{mn}, D_{mn} and E_{mn} will be determined by minimizing the energy functional of the shell theory employed. The appearing X and S basis functions can be chosen in any convenient way that ensures for the completeness of the resulting, two-dimensional, functional basis when both integers m and n approach infinity. The form of the appearing weighting functions, f and g, depends on the choice of the corresponding X and S functions and, particularly, on whether these latter functions can satisfy the displacement boundary conditions of the problem considered. If, for instance, all the appearing X and S functions are chosen to satisfy those edge boundary conditions (e.g., appropriate orthogonal polynomials[13,14]), then all the weighting functions should be set equal to unity. If, on the other hand, some or all of the appearing X and S functions do not satisfy those boundary conditions, the appropriate choice of the corresponding weighting functions should force them to do so. Such a simple but interesting choice of the X and S functions is as follows:

$$X_m(x)=(x/L_x)^m, \quad S_n(s)=(s/L_s)^n, \tag{8}$$

and produces a complete, two-dimensional, power series basis. This does not generally satisfy any particular set of displacement boundary conditions, but, for reasons that will be explained later, it will be used in the next section in conjunction with the simple weighting functions tabulated in Ref. 19. Here, it is only mentioned that, regardless of the particular choice of all the weighting and the basis functions appearing in expressions (7), an application of the Ritz method on the energy functional of the present shell theory yields an algebraic eigenvalue problem, which can generally be described as follows:

$$(\mathbf{K}-\omega^2\mathbf{M})\mathbf{X}=\mathbf{0}. \tag{9}$$

Since most general forms of the appearing stiffness and inertia matrices are given in Ref. 14, for laminated composite shells made of monoclinic layers, their elements will not be cited in this paper. These may be obtained by specializing the corresponding matrix elements presented in Ref. 14 for the particular case of a cross-ply lay-up.

II. NUMERICAL RESULTS AND DISCUSSION

The above discussion makes clear that, upon nullifying the cylindrical panel curvature ($\phi=0$), the analysis presented in the preceding section becomes suitable for the study of the corresponding flat plate problem. This problem has been considered and, for symmetric cross-ply laminated plates, has already been studied separately to a considerable extent.[19] As has already been mentioned, on the other hand, the analysis presented in Ref. 19 was applied only on the original version of the parabolic shear deformable plate model,[24,25] which violates the continuity of the interlaminar stresses ($\mathrm{PAR}_{\mathrm{ds}}$) at the material interfaces of the symmetrically laminated plate considered. That plate model can be obtained as a particular case of the present shell theory by merging the aforementioned zero-curvature restriction with the following shape functions,

$$(\mathrm{PAR}_{\mathrm{ds}}):\Phi_1(z)=\Phi_2(z)=z(1-4z^2/3h^2). \tag{10}$$

Hence, for verification purposes only, the present analysis was initially applied and validated in connection with the cross-ply laminated plate examples considered in Ref. 19, the analysis of which was also based on the Ritz method.

For any given set of edge boundary conditions, Ref. 19 applied the Ritz method in conjunction with the complete, two-dimensional, infinite power-series basis [see Eqs. (7) and (8)], which is, in principle, equivalent to the two-dimensional orthogonal polynomial bases considered in Ref. 14 (see also Refs. 26 and 27). For practical purposes, however, that approach[19] was applied by appropriately truncating the so-called Pascal triangle,[28] namely by keeping all the homogeneous, two-dimensional monomials involved up to a certain power (p, say), which made sure that the obtained numerical results converged, satisfactorily, to the required accuracy. This process yields $(p+1)(p+2)/2$ two-dimensional power terms in each truncated series, the number of which is approximately half the number, $(p+1)^2$, of the corresponding terms retained after a similar, conventional truncation of the equivalent two-dimensional orthogonal polynomial basis.[14,26] Under these considerations, the present authors decided to pursue the numerical validation of the present, general, Ritz-type analysis by applying it in con-

TABLE I. Frequency parameters $\bar{\omega}=\omega L_x^2\sqrt{\rho/E_2h^2}$ for different numbers of monomial terms and different boundary conditions; [0 degrees/90 degrees/0 degrees] ($Lx/h=10$, $Lx/Ls=1$, $E_1=25\ E_2$, $G_{12}=G_{13}=0.5\ E_2$, $G_{23}=0.2\ E_2$, $\nu_{12}=0.25$).

Monomial terms	SS	SC	CC	FF	FS	FC
			$R/Lx=5$			
6 ($p=2$)	12.140	14.501	16.878	4.5706	5.0281	6.6903
15 ($p=4$)	11.840	13.964	16.180	3.7700	4.3061	6.1315
28 ($p=6$)	11.839	13.881	16.051	3.7672	4.2996	6.1166
45 ($p=8$)	11.839	13.863	16.027	3.7672	4.2985	6.1140
66 ($p=10$)	11.839	13.860	16.023	3.7672	4.2983	6.1136
Ref. 7	11.846	13.866	16.028	3.783	4.312	6.123
			$R/Lx=20$			
6 ($p=2$)	11.852	14.257	16.655	3.8465	4.3874	6.1876
15 ($p=4$)	11.793	13.928	16.152	3.7888	4.3288	6.1038
28 ($p=6$)	11.793	13.846	16.027	3.7886	4.3245	6.0919
45 ($p=8$)	11.793	13.828	16.002	3.7886	4.3234	6.0893
66 ($p=10$)	11.793	13.825	15.999	3.7886	4.3232	6.0889
Ref. 7	11.793	13.825	15.999	3.789	4.322	6.089

junction with both of these functional bases. This process verified completely the effectiveness of the present approach, which, regardless of which functional basis was employed, always produced identical numerical results to those presented in Ref. 19. As is further detailed in Ref. 29, this validation process generally confirmed the superiority of the Pascal triangle truncation procedure,[19,28] but only with regard to the computational speed and the efficiency of the Ritz method. This conclusion was further confirmed with regard to the free vibration analysis of cylindrical shell panels (nonzero curvature) by comparing the numerical predictions obtained by means of both of the aforementioned functional bases for panels having all their four edges free of external tractions (see Ref. 14). Under these considerations, all results presented and discussed in what follows were obtained by applying the Ritz-type analysis, outlined in the preceding section, only in conjunction with the two-dimensional, simple power-series bases[19] (7) and (8). Moreover, flat plates and cylindrical panels having all their edges free of traction are excluded from the present investigation, since they have been studied separately in Ref. 14.

In dealing with the free vibration characteristics of open cylindrical shell panels, the numerical predictions of the present approach were initially compared with corresponding numerical results presented in Ref. 7 for panels having both their straight edges simply supported and their curved edges subjected to different sets of edge boundary conditions. The analysis presented in Ref. 7 was applied on the original version of the parabolic shear deformable shell model,[30] which violates the continuity of the interlaminar stresses ($\mathrm{PAR_{ds}}$) and can therefore be obtained as a particular case of the present shell theory (nonzero curvature) by employing the shape functions (10). Under these considerations, Tables I and II show only ($\mathrm{PAR_{ds}}$) results obtained for a three-layered

TABLE II. Frequency parameters $\bar{\omega}=\omega L_x^2\sqrt{\rho/E_2h^2}$ for different numbers of monomial terms and different boundary conditions; [0 degrees/90 degrees] ($Lx/h=10$, $Lx/Ls=1$, $E_1=25\ E_2$, $G_{12}=G_{13}=0.5\ E_2$, $G_{23}=0.2\ E_2$, $\nu_{12}=0.25$).

Monomial terms	SS	SC	CC	FF	FS	FC
			$R/Lx=5$			
6 ($p=2$)	9.9940	11.703	14.272	6.9236	7.1868	7.6525
15 ($p=4$)	8.9918	10.886	13.210	5.7450	6.0622	6.5723
28 ($p=6$)	8.9872	10.850	13.117	5.7413	6.0566	6.5592
45 ($p=8$)	8.9872	10.843	13.100	5.7413	6.0559	6.5578
66 ($p=10$)	8.9872	10.841	13.095	5.7413	6.0558	6.5575
Ref. 7	9.024	10.871	13.119	5.7	5.101	6.600
			$R/Lx=20$			
6 ($p=2$)	9.5417	11.272	13.762	6.3329	6.6359	7.0865
15 ($p=4$)	8.9693	10.857	13.169	5.8103	6.1371	6.5984
28 ($p=6$)	8.9668	10.827	13.092	5.8088	6.1336	6.5895
45 ($p=8$)	8.9668	10.820	13.075	5.8088	6.1330	6.5879
66 ($p=10$)	8.9668	10.817	13.070	5.8088	6.1329	6.5876
Ref. 7	8.973	10.882	12.07	5.8	6.139	6.594

symmetric and a two-layered regularly antisymmetric cross-ply lay-up, respectively. In more detail, both tables show the manner in which the fundamental frequency parameter,

$$\overline{\omega} = \omega L_x^2 \sqrt{\rho / E_2 h^2}, \tag{11}$$

converges with increasing the number of the monomial terms (or, equivalently, the value, p, of the highest power retained in the Pascal triangle) and compare their adequately convergent values with the corresponding results obtained in Ref. 7 on the basis of the state space concept.

It should be noted, in this connection, that the state space concept was applicable in Ref. 7 due to the assumption of simply supported straight edges. As is well known, these yield mode shapes that are circumferentially represented in the form of simple trigonometric functions and, as in the case of a complete cylinder, they allow the conversion of the governing partial differential equations into corresponding ordinary differential equations. After this conversion, the state space concept can treat with relative ease any set of variationally consistent boundary conditions[16] imposed on the curved edges of the panel. On the other hand, only the satisfaction of the geometric boundary conditions is required for the application of the Ritz method. Hence, as far as the present approach is concerned, the relevant notation shown in Tables I and II, as well as elsewhere in this section, implies that the following geometrical conditions were imposed on a curved edge of the panel:

(S) Simply supported curved edge: $v = w = v_1 = 0$,

(C) Clamped curved edge: $u = v = w = w_{,x} = u_1 = v_1 = 0$, (12)

while no geometric constraints were imposed for a free (F) edge.

Both Tables I and II show a very fast convergence of the present approach and, in most cases, a remarkable agreement with the corresponding numerical results obtained on the basis of the state space concept.[7] Apart from the case of the very short, three-layered, cylindrical panel (Table I, $R/L_x = 20$), the first 15 to 28 monomials in the Pascal triangle ($p = 4$ to $p = 6$) were always enough to produce results of the same accuracy to those presented in Ref. 7. More monomial terms were, however, needed in that exceptional case (Table I, $R/L_x = 20$). There were also a couple of cases (FS in the top and CC in the bottom of Table II) in which substantial discrepancies of the corresponding numerical results were observed. These can, however, be considered as two isolated cases only, which cannot alter the general excellent picture shown from the comparisons performed in both tables. Moreover, the nature of these discrepancies reveals that at least one (if not both) of them might be due to a typographical error in Ref. 7. Apart from the good convergence performance, the results produced and compared in Tables I and II have also revealed some excellent stability characteristics of the present numerical scheme. All results shown next were therefore obtained by using a rather large amount of monomials in the Pascal triangle ($p = 12$), which ensured that sufficient convergence was achieved up to the fourth significant figure.

For certain families of three-layered symmetric and two-layered antisymmetric cross-ply laminated cylindrical panels having all their edges simply supported, Tables III and IV, respectively, show the values of frequency parameter,

$$\hat{\omega} = \omega L_x^2 \sqrt{\rho / E_1 R h}, \tag{13}$$

TABLE III. Frequency parameters $\hat{\omega} = \omega L_x^2 \sqrt{\rho / E_1 R h}$ and modal indices (m,n) for simply supported shells; material with symmetric stacking sequence: [90 degrees/0 degrees/90 degrees] ($R = 5$, $Lx = 25$, $\phi = 60°$, $E_1 = 25\ E_2$, $G_{12} = G_{13} = 0.5\ E_2$, $G_{23} = 0.2\ E_2$, $\nu_{12} = 0.25$).

		Mode No.							
Model	R/h	1	2	3	4	5	6	7	8
Ref. 18	10	⋯	12.99	13.59	⋯	⋯	⋯	⋯	⋯
PAR_{ds}		7.025	13.33	13.94	14.05	15.04	16.58	18.55	20.91
PAR_{cs}		7.025	12.94	13.56	14.05	14.68	16.25	18.25	20.65
		(1,0)	(1,1)	(2,1)	(2,0)	(3,1)	(4,1)	(5,1)	(6,1)
Ref. 18	20	⋯	11.25	12.41	⋯	⋯	⋯	⋯	⋯
PAR_{ds}		9.935	11.37	12.54	14.49	16.92	19.69	19.87	22.70
PAR_{cs}		9.935	11.23	12.42	14.38	16.82	19.60	19.87	22.63
		(1,0)	(1,1)	(2,1)	(3,1)	(4,1)	(5,1)	(2,0)	(6,1)
Ref. 18	50	8.20	11.47	⋯	⋯	⋯	⋯	⋯	⋯
PAR_{ds}		8.223	11.52	15.71	15.92	20.61	25.40	30.21	31.42
PAR_{cs}		8.207	11.50	15.71	15.91	20.61	25.39	30.21	31.42
		(1,1)	(2,1)	(1,0)	(3,1)	(4,1)	(5,1)	(6,1)	(2,0)
Ref. 18	100	7.11	13.33	⋯	⋯	24.19	24.66	⋯	⋯
PAR_{ds}		7.120	13.38	20.43	22.21	24.24	24.72	25.84	27.46
PAR_{cs}		7.118	13.38	20.42	22.21	24.18	24.66	25.79	27.46
		(1,1)	(2,1)	(3,1)	(1,0)	(1,2)	(2,2)	(3,2)	(4,1)
Ref. 18	500	10.68	11.45	15.42	⋯	⋯	⋯	27.33	⋯
PAR_{ds}		10.71	11.45	15.44	22.48	25.26	25.84	27.45	27.54
PAR_{cs}		10.71	11.45	15.43	22.47	25.25	25.84	27.45	27.54
		(1,1)	(1,2)	(2,2)	(3,2)	(1,3)	(2,3)	(2,1)	(3,3)

TABLE IV. Frequency parameters $\hat{\omega}=\omega L_x^2\sqrt{\rho/E_1Rh}$ and modal indices (m,n) for simply supported shells; material with antisymmetric stacking sequence: [90 degrees/0 degrees] ($R=5$, $Lx=25$, $\phi=60°$, $E_1=25\ E_2$, $G_{12}=G_{13}=0.5\ E_2$, $G_{23}=0.2\ E_2$, $\nu_{12}=0.25$).

		Mode No.							
Model	R/h	1	2	3	4	5	6	7	8
Ref. 18	10	⋯	7.87	9.06	⋯	⋯	⋯	⋯	⋯
PAR_{ds}		7.025	7.702	8.932	10.94	13.57	14.05	16.74	20.40
PAR_{cs}		7.025	7.825	9.035	11.03	13.66	14.05	16.88	20.64
		(1,0)	(1,1)	(2,1)	(3,1)	(4,1)	(2,0)	(5,1)	(6,1)
Ref. 18	20	5.96	8.15	⋯	⋯	⋯	⋯	⋯	⋯
PAR_{ds}		5.932	8.153	9.935	11.12	14.45	18.03	19.87	21.87
PAR_{cs}		5.953	8.166	9.935	11.13	14.46	18.05	19.87	21.90
		(1,1)	(2,1)	(1,0)	(3,1)	(4,1)	(5,1)	(2,0)	(6,1)
Ref. 18	50	5.05	9.74	⋯	15.46	⋯	16.03	⋯	⋯
PAR_{ds}		5.049	9.774	14.84	15.40	15.71	15.98	17.13	18.77
PAR_{cs}		5.051	9.774	14.84	15.44	15.71	16.01	17.16	18.80
		(1,1)	(2,1)	(3,1)	(1,2)	(1,0)	(2,2)	(3,2)	(4,2)
Ref. 18	100	5.71	11.05	12.28	12.97	⋯	⋯	⋯	⋯
PAR_{ds}		5.724	11.03	12.27	13.03	14.62	17.61	20.31	20.95
PAR_{cs}		5.724	11.04	12.28	13.03	14.62	17.61	20.31	20.95
		(1,1)	(1,2)	(2,2)	(2,1)	(3,2)	(4,2)	(3,1)	(5,2)
Ref. 18	500	6.26	⋯	11.51	12.94	⋯	⋯	⋯	⋯
PAR_{ds}		6.261	11.35	11.54	12.98	12.99	16.63	20.03	20.50
PAR_{cs}		6.261	11.35	11.54	12.98	12.99	16.63	20.03	20.50
		(1,2)	(1,3)	(1,1)	(2,2)	(2,3)	(3,3)	(1,4)	(2,4)

obtained on the basis of the present approach and, where possible, they compare them with corresponding results presented in Ref. 18. As has already been mentioned, Xavier *et al.*[18] employed the well-known, essentially trivial set of simply supported edge boundary conditions, which leads to an exact solution of the governing equations by means of simple mathematical manipulations. They, however, made use of a higher-order shell theory, which accounts for the continuity of the transverse shear stresses at the shell material interfaces. For the results shown and compared in Tables III and IV the present approach was therefore applied in connection with the parabolic shear deformable shell theory that assumes either continuous (PAR_{cs}) or discontinuous (PAR_{ds}) interlaminar stresses. While the (PAR_{ds}) shell model is still obtained by employing the shape functions (10), the manner in which the shape functions that produce continuous interlaminar stresses are constructed is outlined in the Appendix. Each group of compared natural frequencies is also associated with its modal characteristic indices [(m, n), say], which, for the simply supported panels considered, represent the axial (m) and the circumferential (n) half-wave number of the corresponding mode shape. It should be noted in this connection that, although the simple mathematical approach employed in Ref. 18 uses these indices as input data (however, not clearly defined in Ref. 18), the present analysis enables their determination *a posteriori*, after the mode shape that corresponds to each one of the determined natural frequencies is carefully plotted and examined.

The comparisons made in both Tables III and IV show an excellent agreement between all frequencies obtained on the basis of the present (PAR_{cs}) shell model and the corresponding frequencies tabulated in Ref. 18. Moreover, for thin

TABLE V. Frequency parameters $\Omega=\omega R\sqrt{\rho/E_1}$ for a two layered cross-ply cantilevered panel; material with antisymmetric stacking sequence: [90 degrees/0 degrees] ($R/h=240$, $Lx/R=0.9167$, $\phi=1$ rad, $E_1=15.27\ E_2$, $G_{12}=G_{13}=0.645\ E_2$, $G_{23}=0.321\ E_2$, $\nu_{12}=0.313$).

	Par_{ds}					Refs. 20 and 21				
Mode	105×105 ($p=5$)	180×180 ($p=7$)	275×275 ($p=9$)	390×390 ($p=11$)	525×525 ($p=13$)	125×125	180×180	245×245	320×320	405×405
1	0.018 81	0.017 99	0.017 88	0.017 86	0.017 85	0.019 55	0.018 23	0.017 91	0.017 89	0.017 76
2	0.024 31	0.021 26	0.020 96	0.020 95	0.020 94	0.026 54	0.023 61	0.021 20	0.021 04	0.020 84
3	0.060 71	0.047 95	0.046 82	0.046 71	0.046 70	0.060 69	0.056 40	0.047 79	0.047 48	0.047 03
4	0.078 25	0.053 80	0.050 69	0.050 24	0.050 15	0.062 33	0.059 62	0.052 23	0.050 62	0.049 83
5	0.088 98	0.057 81	0.051 44	0.050 31	0.050 22	0.076 77	0.060 21	0.055 24	0.051 94	0.050 36
6	0.095 98	0.077 54	0.071 89	0.071 62	0.071 60	0.081 59	0.080 72	0.079 63	0.075 38	0.071 46
7	0.149 75	0.081 16	0.079 75	0.079 61	0.079 60	0.139 85	0.104 09	0.100 01	0.080 50	0.079 59
8	0.186 00	0.118 58	0.096 94	0.092 05	0.091 16	0.193 92	0.119 58	0.103 51	0.094 68	0.089 24
9	0.228 61	0.132 41	0.098 50	0.092 78	0.091 33	0.201 88	0.130 20	0.116 94	0.094 68	0.092 25
10	0.258 33	0.141 01	0.112 25	0.108 34	0.108 10	0.258 96	0.134 36	0.131 50	0.109 55	0.106 04

TABLE VI. Frequency parameters $\bar{\omega}=\omega L_x^2\sqrt{\rho/E_2h^2}$ with boundary conditions CFFF with symmetric stacking sequence: [0 degrees/90 degrees/0 degrees] ($Lx/h=20$); PAR_{cs} model.

Shallowness angle ϕ (degrees)	Modes 1	2	3	4	5	6	7	8
0	4.764	5.457	11.19	20.69	24.41	24.83	25.38	28.65
15	4.982	5.478	11.16	20.69	24.70	24.75	25.36	28.71
30	5.542	5.554	11.07	20.70	24.40	25.41	25.45	28.96
45	5.649	6.304	10.96	20.72	23.72	25.61	26.31	29.62
60	5.801	7.070	10.86	20.74	22.78	25.91	26.86	30.94
75	6.000	7.702	10.88	20.76	21.65	26.29	27.11	32.76
90	6.245	8.062	11.12	20.23	20.91	26.73	27.22	34.82

TABLE VIII. Frequency parameters $\bar{\omega}=\omega L_x^2\sqrt{\rho/E_2h^2}$ with boundary conditions SSFF with symmetric stacking sequence: [0 degrees/90 degrees/0 degrees] ($Lx/h=20$); PAR_{cs} model.

Shallowness angle ϕ (degrees)	Modes 1	2	3	4	5	6	7	8
0	12.71	13.30	17.36	29.18	41.40	41.88	41.90	44.23
15	12.97	13.33	17.39	29.05	41.67	41.90	41.93	44.30
30	13.44	13.64	17.52	28.69	41.93	42.09	42.36	43.92
45	13.63	14.47	17.86	28.11	41.97	42.36	42.99	43.30
60	13.88	15.11	18.64	27.34	42.03	42.43	42.70	43.31
75	14.20	15.41	19.89	26.43	41.32	42.10	42.79	43.11
90	14.58	15.49	21.40	25.44	40.00	40.46	42.19	43.55

shells ($R/h>50$), both the (PAR_{cs}) and (PAR_{ds}) shell models essentially produce identical numerical results. This is not a surprising result since the consideration of the transverse shear deformation was not expected to influence particularly the vibration frequencies of thin shells (thin shell frequencies may be predicted quite accurately even by using a classical shell theory). Upon increasing, however, the shell thickness, the (PAR_{cs}) and (PAR_{ds}) model predictions split gradually apart, the former expected to be more accurate than the latter. It is also of interest to note that although the fundamental vibration frequencies were always expected to be associated with the modal indices (1, 1), this was not found to be the case. In more detail, the strong bending–stretching coupling, due to both lamination and nonzero curvature, forces the frequency associated with the modal indices (1, 1) to appear as the third frequency of the thinnest, two-layered panel considered in Table IV. In that case ($R/h=500$), the fundamental vibration frequency appears as being associated with the modal indices (1, 2). For different reasons, in the case of a relatively thick symmetrically laminated panel ($R/h=10R/h=20$ in Table III), the frequency associated with the modal indices (1, 1) appears as being the second vibration frequency, the fundamental frequency being the one associated with the modal indices (1, 0). With $n=0$ (zero transverse and axial displacement components), this is an in-plane, purely circumferential, vibration frequency. This result indicates that such a long and moderately thick cylindrical panel is more sensitive to a torsional-type than to a flexural-type resonance.

The final check of the present analysis was against the Ritz-type approach employed in Refs. 20 and 21. As has already been mentioned, Singh and Kumar[20,21] associated their Ritz analysis with Bezier polynomials and applied it on the energy functional of the parabolic shear deformable shell theory that violates the continuity of the interlaminar stresses. Hence, for the numerical results presented in Table V, the present analysis was also applied on the energy functional of the same shell model (PAR_{ds}). In more detail, for a certain antisymmetric laminated cantilevered panel (one curved edge clamped and all the remaining edges free), Table V compares the convergence characteristics of the frequency parameters,

$$\Omega=\omega R\sqrt{\rho/E_1}, \tag{14}$$

obtained on the basis of both approaches. The results tabulated in each column were obtained by continuously increasing the degree, p, of the polynomial terms involved. The order of the corresponding eigenvalue problem, $[5(p+1)\times(p+2)/2]\times[5(p+1)(p+2)/2]$, is denoted on the top of each column. In all but a few cases, in which, however, a final convergence has not as yet been achieved, the present approach appears to converge in faster rates. On the other hand, for the first seven modes for which convergence was achieved to an acceptable degree, a very close agreement is observed between all the corresponding vibration frequencies. As has already been mentioned, it is, however, not known to the present authors whether the Bezier polynomials[20,21] form a complete functional basis for any given set of edge conditions. If their completeness was or has been shown, it could characterize the approach employed in Refs. 20 and 21 as analytical rather than numerical and, therefore, equivalent to the present approach.

TABLE VII. Frequency parameters $\bar{\omega}=\omega L_x^2\sqrt{\rho/E_2h^2}$ with boundary conditions CCCC with symmetric stacking sequence: [0 degrees/90 degrees/0 degrees] ($Lx/h=20$); PAR_{cs} model.

Shallowness angle ϕ (degrees)	Modes 1	2	3	4	5	6	7	8
0	24.51	32.96	49.69	51.76	56.84	68.54	72.77	85.00
15	27.72	32.92	49.83	53.39	56.93	68.64	72.39	86.03
30	32.81	34.69	50.76	57.22	57.50	69.26	71.28	86.18
45	32.65	40.23	54.59	57.68	61.57	69.47	71.80	84.82
60	32.46	41.70	58.29	62.14	63.13	67.03	77.46	83.01
75	32.28	41.15	59.03	63.15	64.06	69.85	80.84	83.93
90	32.15	39.88	59.84	60.66	62.68	74.09	78.44	88.08

After the success of all the numerical comparisons attempted, the analysis was applied for a study of the influence of the edge boundary on the natural frequency parameters, $\bar{\omega}$, of certain cylindrical panels having a square plan-form and a three-layered symmetric (Tables VI–X) or a regular antisymmetric lay-up (Tables XI–XIII). As far as the geometrical characteristics of these panels are concerned, their circumferential length is given, as a function of the shallowness angle ϕ, according to the following formula:

$$L_s=L_x\phi/2\sin(\phi/2). \tag{15}$$

Moreover, the material properties in each one of their layers

TABLE IX. Frequency parameters $\bar{\omega}=\omega L_x^2\sqrt{\rho/E_2h^2}$ with boundary conditions SSCC with symmetric stacking sequence: [0 degrees/90 degrees/0 degrees] ($Lx/h=20$); PAR_{cs} model.

Shallowness angle ϕ (degrees)	Modes 1	2	3	4	5	6	7	8
0	15.96	27.45	42.85	44.43	46.40	49.07	62.46	70.69
15	20.56	27.41	44.30	44.82	46.55	49.20	62.58	70.31
30	27.30	29.33	43.92	47.51	49.58	49.68	63.23	69.16
45	27.14	35.84	43.30	50.19	51.48	54.48	65.90	67.29
60	26.98	37.57	42.43	51.01	56.38	59.36	64.76	71.94
75	26.85	36.99	41.32	51.97	56.48	61.67	67.40	75.99
90	26.80	35.57	40.00	53.02	56.00	58.12	71.89	73.46

TABLE X. Frequency parameters $\bar{\omega}=\omega L_x^2\sqrt{\rho/E_2h^2}$ with boundary conditions CCCF with symmetric stacking sequence: [0 degrees/90 degrees/0 degrees] ($Lx/h=20$); PAR_{cs} model.

Shallowness angle ϕ (degrees)	Modes 1	2	3	4	5	6	7	8
0	22.78	24.84	33.55	50.63	50.77	52.24	57.64	69.73
15	22.94	25.10	33.50	50.39	50.99	52.62	57.70	69.60
30	23.25	25.95	33.37	49.69	51.33	53.88	57.93	69.23
45	23.50	27.25	33.22	48.57	51.59	55.52	58.66	68.68
60	23.70	28.56	33.17	47.09	51.85	56.54	60.35	68.08
75	23.88	29.47	33.45	45.34	52.10	57.04	62.22	65.21
90	24.06	29.80	34.12	43.42	52.34	57.45	61.74	63.05

are given as follows:

$$E_1/E_2=25, \quad G_{12}/E_2=G_{13}/E_2=0.5,$$
$$G_{23}/E_2=0.2, \quad \nu_{12}=0.25. \tag{16}$$

As far as the notation of the edge boundary conditions is concerned, the first two of the appearing four capital letters refer to the curved edges of the cylindrical panel considered while the remaining two refer to its straight edges. Hence, the relevant notation shown in Tables VI–XIII implies that the geometrical conditions imposed on a simply supported or a clamped curved edge of the panel are still given in accordance with Eqs. (12). Moreover, the corresponding conditions imposed on a straight edge are as follows:

$$\text{(C) Clamped straight edge: } u=v=w=w_{,s}=u_1=v_1=0, \tag{17}$$

while no geometric constraints were imposed on a free (F) edge.

In dealing with the natural vibration frequencies of the symmetrically laminated panels, no decisive or particular trends were observed for any of the particular sets of edge boundary conditions employed. Hence, the vibration frequencies tabulated in Tables VI–X were just arranged in an ascending order. It should be noted, however, that, as was expected, all the frequencies predicted for CCCC panels (Table VII) were always higher than the corresponding frequencies predicted of all the remaining sets of boundary conditions considered. These were followed by the frequencies of the less stiff CCCF (Table X) and the SSCC panels (Table IX), while the less rigidly supported cantilevered panels (Table VI) always vibrate with the lowest frequencies.

This reasonable trend of the natural vibration frequencies is also observed in Tables XI–XIII where, for the regular antisymmetric lay-up considered, the CCCC (Table XI) and the CFFF (Table IX) panels vibrate with the highest and the lowest natural frequencies, respectively. Since, for a nonsymmetric lay-up, this is the first paper in the literature that presents frequencies on the basis of a laminate model that accounts for continuity of interlaminar stresses, both curved panel ($\phi=60$ degrees) and corresponding flat plate results ($\phi=0$ degrees) are shown in Tables XI–XIII. Moreover, all the (PAR_{cs}) results are accompanied and compared with their corresponding (PAR_{ds}) counterparts. It is generally observed that, apart from a particularly small number of cases, the effect of the nonzero curvature is to increase the value of the natural frequencies from that of their flat plate counterpart. On the other hand, although in several cases the (PAR_{cs}) and (PAR_{ds}) models give practically identical results, there are also cases of considerable disagreement between the corresponding vibration frequencies. Most interestingly and regardless of the boundary conditions employed, the frequencies obtained on the basis of the (PAR_{cs}) model were always higher than their (PAR_{ds}) counterparts for two-layered panels, while the opposite was true when the number of layers increased. It is therefore concluded that this trend should be attributed to the well-known bending–stretching coupling due to lamination which exhibits its strongest effect on the two-layered lay-up, but dies out very rapidly upon increasing the layer number in an antisymmetric cross-ply lay-up.[22] The mechanism, however, that causes this trend does not appear to have an obvious explanation and its understanding is therefore left for future investigation.

TABLE XI. Frequency parameters $\bar{\omega}=\omega L_x^2\sqrt{\rho/E_2h^2}$ of panels having a square planform with boundary conditions CFFF with antisymmetric stacking sequence: [0 degrees/90 degrees] and different number of layers ($Lx/h=20$).

No. layers and theory	Modes ($\phi=60$ degrees) 1	2	3	4	Modes ($\phi=0$ degrees: plate) and theory 1	2	3	4
2; PAR_{cs}	3.927	5.662	13.25	16.37	2.189	3.512	13.33	14.78
PAR_{ds}	3.923	5.653	13.19	16.20	2.185	3.506	13.14	14.70
10; PAR_{cs}	4.816	6.422	19.98	20.43	3.525	4.464	19.44	20.43
PAR_{ds}	4.845	6.447	20.19	20.46	3.542	4.495	19.92	20.43
100; PAR_{cs}	4.852	6.454	20.27	20.44	3.570	4.499	19.66	20.43
PAR_{ds}	4.881	6.480	20.47	20.49	3.586	4.530	20.14	20.43

TABLE XII. Frequency parameters $\bar{\omega}=\omega L_x^2\sqrt{\rho/E_2h^2}$ of panels having a square planform with boundary conditions CCCC with antisymmetric stacking sequence: [0 degrees/90 degrees] and different number of layers ($Lx/h=20$).

No. layers and theory	Modes ($\phi=60$ degrees)				Modes ($\phi=0$ degrees: plate)			
	1	2	3	4	1	2	3	4
2; PAR_{cs}	35.59	50.45	52.09	61.90	19.44	38.45	38.45	51.72
PAR_{ds}	34.48	48.55	50.45	59.66	19.02	36.96	36.96	49.62
10; PAR_{cs}	44.19	56.81	61.71	69.92	26.45	47.33	47.33	61.87
PAR_{ds}	46.14	58.36	64.47	72.36	27.36	49.66	49.66	65.10
100; PAR_{cs}	44.68	57.21	62.28	70.42	26.73	47.77	47.77	62.41
PAR_{ds}	46.64	58.74	65.07	72.85	27.63	50.11	50.11	65.66

III. CONCLUSIONS

This paper studied the influence of different sets of edge boundary conditions on the dynamic characteristics of shear deformable, cross-ply laminated circular cylindrical panels. Certain aspects of this problem had been addressed in some recent publications, which were however based on inferior plate and shell models or confined into a limited number of different sets of boundary conditions. The present study was based on a unified shear-deformable shell model and, mainly, in one of its versions that accounts for the continuity of the interlaminar stresses (PAR_{cs}). The analysis was based on the application of the Ritz method, which was applied on the energy functional of the shell model employed in conjunction with the complete functional basis of simple, two-dimensional, infinite power series. The choice of such a complete functional basis made sure that the present approach is asymptotically exact. For practical purposes, however, it was applied by appropriately truncating the so-called Pascal triangle,[28] namely by keeping all the homogeneous, two-dimensional, monomials involved up to a certain power, which made sure that the obtained numerical results converged, satisfactorily, to the required accuracy. This truncation approach was found to be particularly effective in the sense that, in particular cases, it produced equivalent results to those produced elsewhere, while, at the same time, it reduced substantially the size of the stiffness and inertia matrices involved in the final algebraic eigenvalue problem.

In more detail, in the particular case of a flat plate (zero curvature), the present analysis was capable of producing identical results to those presented by Chen *et al.*,[19] who applied precisely the same approach on the energy functional of the parabolic shear deformable plate theory that violates the interlaminar stress continuity (PAR_{ds}). As far as the vibration of shell panels with free edges is concerned, the present analysis also produced identical results to those presented by Messina and Soldatos,[14] through the complete functional basis of the appropriate orthonormal polynomials. In dealing with cylindrical panels having their straight edges simply supported and their curved edges subjected to different sets of edge boundary conditions, a remarkable agreement was observed with the numerical results obtained by Khdeir and Reddy,[7] who applied the state space concept on the governing equations of the (PAR_{ds}) shell theory. In dealing with panels having all their edges simply supported, an excellent agreement was observed with the numerical results presented by Xavier *et al.*,[18] which were based on the alternative, simple exact solution of the governing equations of a refined (PAR_{cs}) shell model. Dealing finally with a certain antisymmetric laminated cantilevered panel, a very close agreement was observed with the corresponding vibration frequencies obtained by Singh and Kumar,[20] who associated their Ritz analysis with Bezier polynomials and applied it on the energy functional of the (PAR_{ds}) shell theory.

For a more thorough investigation of the influence of the edge conditions on the vibration characteristics of cross-ply laminated plates and cylindrical panels, several different combinations of simply supported (S), clamped (C) and free (F) boundaries were considered and tested. These confirmed the reasonable expectation that all the frequencies predicted for CCCC panels are higher than the corresponding frequencies predicted for the remaining sets of boundary conditions considered. Contrary to this, the lowest frequencies occurred for the cantilevered panels considered. It was also observed that, for two-layered antisymmetric panels and regardless of

TABLE XIII. Frequency parameters $\bar{\omega}=\omega L_x^2\sqrt{\rho/E_2h^2}$ of panels having a square planform with boundary conditions CCCF with antisymmetric stacking sequence: [0 degrees/90 degrees] and different number of layers ($Lx/h=20$).

No. layers and theory	Modes ($\phi=60$ degrees)				Modes ($\phi=0$ degrees: plate)			
	1	2	3	4	1	2	3	4
2; PAR_{cs}	16.12	24.88	36.66	37.86	13.82	20.15	35.53	39.57
PAR_{ds}	15.85	24.66	35.81	36.46	13.54	19.79	34.05	38.20
10; PAR_{cs}	21.04	29.92	45.47	47.20	19.01	27.45	43.46	48.33
PAR_{ds}	21.63	30.46	47.60	48.97	19.64	28.28	45.68	50.62
100; PAR_{cs}	21.24	30.18	45.86	47.73	19.21	27.73	43.86	48.77
PAR_{ds}	21.82	30.73	48.01	49.50	19.84	28.56	46.10	51.07

the boundary conditions employed, the (PAR_{cs}) model predicts higher vibration frequencies than the (PAR_{ds}) does, while the opposite is true when the number of layers increases. This trend was therefore attributed to the well-known bending–stretching coupling due to lamination, which is very strong in two-layered antisymmetric cross-ply laminates but dies out very rapidly upon increasing their number of layers. The mechanism, however, that causes this trend did not appear to have an obvious explanation and its understanding was therefore left as a matter for future investigation.

The mathematical analysis presented in this paper can easily be extended towards the study of the influence of the edge conditions on the vibration characteristics of shear deformable laminated plates and cylindrical panels having an arbitrary angle-ply lay-up. To a certain extent, this problem has already been considered in Refs. 18, 20, and 21 but only in association with the shear deformable model that violates the continuity of the interlaminar stresses (PAR_{ds}). On the other hand, as far as the theoretical modeling is concerned, the main purpose of the present study was to successfully employ and exhibit the performance of the version of the unified shear-deformable shell theory (PAR_{cs}) that accounts for the continuity of the interlaminar stresses. Hence, with this model being currently available only for the case of a cross-ply lay-up, angle-ply laminates were naturally excluded from the present investigation. Hence, as soon as the manner can be found that makes the (PAR_{cs}) model applicable to angle-ply laminates, the present analysis can be extended towards laminated plates and circular cylindrical panels having an arbitrary angle-ply lay-up.

ACKNOWLEDGMENTS

The work reported in this paper was supported by a European Joint Project Grant awarded to the authors by the Royal Society of London.

APPENDIX: CONTINUITY CONDITIONS

For the laminated cylindrical panel shown in Fig. 1, consider the cross-ply shown in Fig. A1. This is having a total number of layers (L), all of which have the same thickness ($h_u = h/L$). As shown in Fig. A1, the panel can be made either by an even number or by an odd number of layers, which is the typical stacking sequence of either a regular antisymmetric or regular symmetrical cross-ply lay-up, respectively. Denote further with R_k the middle-surface radius of the kth layer and with z_k the transverse coordinate of the kth material interface. Under these considerations, $k = 0, \pm 1, \pm 2, \ldots, \pm (L-1)/2$ for an odd number of layers, where $k=0$ is referred to the central layer. On the other hand, $k = 0^{\pm}, \pm 1, \pm 2, \ldots, \pm (L/2-1)$ for an even number of layers, in which case the couple the index 0^+ and 0^- is associated with the layer which is immediately above and immediately below the panel middle-surface, respectively. Under these considerations, the reference surface of the panel always coincides with its middle surface, which, although for an odd number of layers does not represent a material interface, is always located on $z = z_0 = 0$.

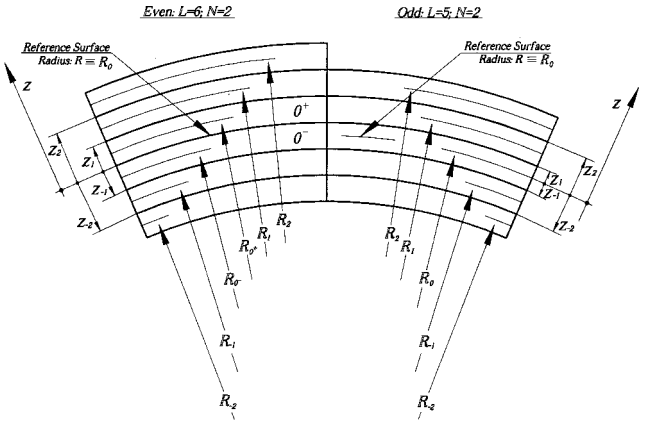

FIG. A1. Nomenclature of the antisymmetric and symmetric cross-ply lay-up.

The principal assumption to build a PAR_{cs} model[11] is to consider the kth layer as an independent cylindrical panel. In a close connection with the displacement model (2), it is therefore reasonable to approximate the displacement field of the kth layer as follows:

$$\begin{aligned} U^{(k)} &= u^{(k)} - z w_{,x} + \varphi_1^{(k)}(z) u_1^{(k)}, \\ V^{(k)} &= (1 + z/R_k + \delta_k) v^{(k)} - z w_{,s} + \varphi_2^{(k)}(z)_1^{(k)} v_1^{(k)}, \\ W^{(k)} &= w^{(k)} = w. \end{aligned} \tag{A1}$$

The term δ_k, which is missing in Ref. 11, is added for as a small correction in the circumferential displacement of the kth layer that accounts for the fact that the transverse coordinate parameter, z, represents the global transverse coordinate of the laminated shell panel considered and not the corresponding local coordinate within its kth layer. The correction term δ_k has therefore been added into the circumferential displacement of the kth layer in order to account for an appropriate shift of the origin of the global coordinate system and the subsequent translation of the reference surface on the middle-surface of the kth layer. For a panel with an even or an odd number of layers, this factor is respectively given as follows:

$$\begin{aligned} \delta_k &= \frac{-(k \pm 1/2) h_u}{R_k L}, \quad k = 0^{\pm}, \pm 1, \pm 2, \ldots, \pm (L/2-1), \\ \delta_k &= \frac{-k h_u}{R_k L}, \quad k = 0, \pm 1, \pm 2, \ldots, \pm (L-1)/2, \end{aligned} \tag{A2}$$

where the notation 0^+ or 0^- is considered when k is positive or negative, respectively.

Under these considerations, the continuity of the displacement and the transverse shear stresses is imposed in the manner described in Refs. 11 and 13. This yields the global shape functions appearing in Eqs. (2), in terms of the local shape functions appearing in Eq. (A1), as follows:

$$\begin{aligned} \Phi_1(z) &= A_k \varphi_1^{(k)}(z) + B_k, \\ \Phi_2(z) &= C_k \varphi_2^{(k)}(z) + (1 + z/R_k) E_k, \end{aligned} \tag{A3}$$

where

$$
\begin{aligned}
A_k &= \frac{Q_{55}^{(k\mp1)}}{Q_{55}^{(k)}}\,\frac{\varphi_1'^{(k\mp1)}(z_k)}{\varphi_1'^{(k)}(z_k)}A_{k\mp1}, \quad A_0=1,\\
B_k &= B_{k\mp1}+[\varphi_1^{(k\mp1)}(z_k)A_{k\mp1}-\varphi_1^{(k)}(z_k)A_k], \quad B_0=0,\\
C_k &= \frac{Q_{44}^{(k\mp1)}}{Q_{44}^{(k)}}C_{k\mp1}+\left(\frac{E_k}{R_k}-\frac{Q_{44}^{(k\mp1)}}{Q_{44}^{(k)}}\,\frac{E_{k\mp1}}{R_{k\mp1}}\right)\frac{1}{\varphi'^{(k)}(z_k)}, \quad C_0=1,\\
D_k &= \frac{1+z_k/R_{k\mp1}+\delta_{k\mp1}}{1+z_k/R_k+\delta_k}D_{k\mp1}, \quad D_0=1,\\
E_k &= \frac{\left[\dfrac{D_k}{D_{k\mp1}}-\dfrac{z_k/R_{k\mp1}}{1+z_k/R_k+\delta_k}+\dfrac{\varphi^{(k)}(z_k)}{\varphi'^{(k)}(z_k)}\,\dfrac{Q_{44}^{k\mp1}}{Q_{44}^{k}}\,\dfrac{1}{R_{k\mp1}}\right]E_{k\mp1}+C_{k\mp1}\left(1-\dfrac{Q_{44}^{k\mp1}}{Q_{44}^{k}}\right)\varphi^{(k)}(z_k)}{1+\dfrac{\varphi^{(k)}(z_k)}{\varphi'^{(k)}(z_k)}\,\dfrac{1}{R_k}+\delta_k}, \quad E_0=0,
\end{aligned}
\tag{A4}
$$

and a prime denotes ordinary differentiation. These equations were obtained by following the procedure outlined in Ref. 13, in connection with the following local shape functions:

$$
\begin{aligned}
\varphi_1^{(k)}(z) &= z(1-4z^2/3h^2),\\
\varphi_2^{(k)}(z) &= z(1-E_k/C_kR_k)-4z^3/3h^2,
\end{aligned}
\tag{A5}
$$

the choice of which is consistent with the ($\mathrm{PAR_{cs}}$) shell model considered in this paper and guarantees for the satisfaction of the zero shear traction boundary conditions imposed on both the lateral shell surfaces. It is recalled that, as far as a symmetric lay-up is concerned,[11,13] four of the five degrees of freedom of the central, zeroth layer ($u^{(0)}$, $u_1^{(0)}$, $v^{(0)}$ and $v_1^{(0)}$) should replace u, u_1, v and v_1, respectively, in Eqs. (2) and, together with the common transverse displacement component w, become the corresponding global degrees of freedom for the whole laminate. In the case of an antisymmetric lay-up, which has not been considered previously in the literature, the notation shown in Eqs. (A3) and (A4) still holds, provided that the displacement components u, u_1, v and v_1 are replaced in Eqs. (2) with the corresponding degrees of freedom of the 0^+-th layer.

[1] R. N. Arnold and G. B. Warburton, ''Flexural vibrations of the wall of thin cylindrical shells having freely supported ends,'' Proc. R. Soc. London Ser. A **197**, 238–256 (1949).

[2] K. Forsberg, ''Influence of boundary conditions on the modal characteristics of thin elastic shells,'' AIAA J. **2**, 2150–2157 (1964).

[3] A. W. Leissa, ''Vibration of Shells,'' NASA SP-228 (1973). Reprinted, 1994, by the Acoustical Society of America.

[4] M. E. Vanderpool and C. W. Bert, ''Vibration of a materially monoclinic, thick-wall circular cylindrical shell,'' AIAA J. **19**, 634–641 (1981).

[5] A. A. Khdeir, J. N. Reddy, and D. Frederick, ''A study of bending, vibration and buckling of cross-ply circular cylindrical shells with various shell theories,'' Int. J. Eng. Sci. **27**, 1337–1351 (1989).

[6] L. Librescu, A. A. Khdeir, and D. Frederick, ''A shear deformable theory of laminated composite shallow shell-type panels and their response analysis I: Free vibration and buckling,'' Acta Mech. **76**, 1–33 (1989).

[7] A. A. Khdeir and J. N. Reddy, ''Influence of edge conditions on the modal characteristics of cross-ply laminated shells,'' Comput. Struct. **34**, 817–826 (1990).

[8] K. P Soldatos, ''A refined laminated plate and shell theory with applications,'' J. Sound Vib. **144**, 109–129 (1991).

[9] Y. Narita, Y. Ohta, G. Yamada, and Y. Kobayashi, ''Analytical method for vibration of angle-ply cylindrical shells having arbitrary edges,'' AIAA J. **30**, 790–796 (1992).

[10] A. Nosier and J. N. Reddy, ''Vibration and stability analyses of cross-ply laminated circular cylindrical shells,'' J. Sound Vib. **157**, 139–159 (1992).

[11] T. Timarci and K. P. Soldatos, ''Comparative dynamic studies for symmetric cross-ply circular cylindrical shells on the basis of a unified shear deformable shell theory,'' J. Sound Vib. **187**, 609–624 (1995).

[12] T. Timarci, ''Vibrations of Composite Laminated Cylindrical Shells,'' Ph.D. Thesis, Department of Theoretical Mechanics, University of Nottingham, 1995.

[13] K. P. Soldatos and A. Messina, ''Vibration studies of cross-ply laminated shear deformable circular cylinders on the basis of orthogonal polynomials,'' J. Sound Vib. **218**(2), 219–243 (1998).

[14] A. Messina and K. P. Soldatos, ''Vibration of completely free composite plates and cylindrical shell panels by a higher-order theory,'' Int. J. Mech. Sci. **41**, 891–918 (1999).

[15] T. Timarci and K. P. Soldatos, ''Vibrations of angle-ply laminated circular cylindrical shells subjected to different sets of edge boundary conditions,'' J. Eng Math. (scheduled to appear in the January 2000 issue).

[16] K. P. Soldatos and T. Timarci, ''A unified formulation of laminated composite, shear deformable, five-degrees-of-freedom cylindrical shell theories,'' Comput. Struct. **25**, 165–171 (1993).

[17] I. A. Jones, E. J. Williams, and A. Messina, ''Theoretical, experimental and finite element modelling of laminated composite shells,'' Proc. 2nd Int. Conf. Struct. Dyn. Model., NAFEM, pp. 267–279, Cumbria (1996).

[18] P. B. Xavier, C. H. Chew, and K. H. Lee, ''Buckling and vibration of multilayer orthotropic composite shells using a simple higher-order layerwise theory,'' Int. J. Solids Struct. **32**(23), 3479–3497 (1995).

[19] C. C. Chen, K. M. Liew, C. W. Lim, and S. Kitipornchai, ''Vibration analysis of symmetrically laminated thick rectangular plates using the higher-order theory and p-Ritz method,'' J. Acoust. Soc. Am. **102**, 1600–1611 (1997).

[20] A. V. Singh and V. Kumar, ''On free vibrations of fiber reinforced doubly curved panels, Part 1: Formulation/Convergence study,'' Trans. ASME, J. Vib. Acoust. **120**, 287–294 (1998).

[21] A. V. Singh and V. Kumar, ''On free vibrations of fiber reinforced doubly curved panels, Part 2: Applications,'' Trans. ASME, J. Vib. Acoust. **120**, 295–300 (1998).

[22] R. M. Jones, *Mechanics of Composite Materials* (Hemisphere, New York, 1975).

[23] J. M. Whitney, *Structural Analysis of Laminated Anisotropic Plates* (Technomic, Lancaster, 1987).

[24] A. Bhimaraddi and L. K. Stevens, ''A higher order theory for free vibration of orthotropic, homogeneous and laminated rectangular plates,'' J. Appl. Mech. **51**, 195–198 (1984).

[25] J. N. Reddy, ''A simple higher-order theory for laminated composite plates,'' J. Appl. Mech. **51**, 745–752 (1984).
[26] P. S. Frederiksen, ''Single-layer plate theories applied to the flexural vibration of completely free thick laminates,'' J. Sound Vib. **186**, 743–759 (1995).
[27] R. B. Bhat, ''Natural frequencies of rectangular plates using characteristic orthogonal polynomials in Rayleigh-Ritz method,'' J. Sound Vib. **102**, 493–499 (1985).
[28] K.-J. Bathe, *Finite Element Procedures* (Prentice–Hall, London, 1996), pp. 244–246.
[29] A. Messina and K. P. Soldatos, ''Influence of edge boundary conditions on the vibration characteristics of symmetrically laminated rectangular plates,'' Proc. 2nd Int. Conf. Identif. Engng. Syst., University of Wales, Swansea, 29–31 March 1999, pp. 527–537.
[30] J. N. Reddy and C. F. Liu, ''A higher-order shear deformation theory of laminated elastic shells,'' Int. J. Eng. Sci. **23**, 319–330 (1985).

Feedback control of structurally radiated sound into enclosed spaces using structural sensing

Steven Griffin
Air Force Research Laboratory, 3550 Aberdeen Avenue, SE, Kirtland AFB, New Mexico 87117

Colin Hansen and Ben Cazzolato
Department of Mechanical Engineering, The University of Adelaide, Adelaide, South Australia 5001, Australia

(Received 11 August 1998; accepted for publication 20 July 1999)

A technique is developed that addresses sensor and actuator placement and feedback control of structural/acoustic problems that can be described as a flexible structure surrounding an acoustic cavity. Specifically, this work is directed at the space launch vehicle problem, where it is assumed that it is not possible to obtain, in advance of a required control output, a coherent measurement of the disturbance or to directly measure the quantity to be controlled. These assumptions necessitate the use of structural sensing to predict the sound pressure in the cavity and of feedback control to reduce the radiated sound. A method for selecting sensor and actuator positions based on a transformation of the problem into radiation modes is covered as well as an optimal feedback control approach which allows the control of radiated pressure into a defined subvolume of the cavity using only structural actuators and sensors. Finally, an example problem is completed which draws on all of the theoretical development to suppress radiated sound within a subvolume. [S0001-4966(99)02711-3]

PACS numbers: 43.40.Rj, 43.40.Vn [CBB]

INTRODUCTION

There are many aerospace structures that can be described as a flexible structure enclosing an acoustic cavity. Vibration of the structure due to an acoustic or structural disturbance causes an acoustic response in the cavity. In aircraft, this acoustic response can affect operator and passenger comfort and even pose health and safety risks. In space launch vehicles, sound and structurally induced vibrations can destroy or damage the payload. The vibration/acoustic launch environment has been blamed for between 30% and 60% of first day satellite failures.[1]

Feedforward active noise control solutions to problems falling into this category have met with considerable success when the disturbance is periodic or can be measured well in advance of the required control input, and the sound pressure to be controled can be measured directly with a microphone.[2] For systems in which a direct measure of the disturbance is not possible, it has been found that structural measurements can be used to predict sound pressure levels generated by baffled beams, plates, and shells radiating into free space.[3–8] Structural vibration measurements can also be used to predict the sound pressure distribution pressure into a cavity.[9] This technique has been used in conjunction with feedforward control to reduce transmitted pressure into a cavity.[3,10]

When the disturbance is broadband, a measurement of the disturbance is often not available in sufficient time for a useful control signal to be generated, and feedforward control is not applicable. In these cases, feedback control using structural sensing must be implemented. Structural sensing to predict transmitted pressure into the free field has been used in the past with feedback control to reduce radiated pressure by beams and plates.[11–13] Examples of broadband disturbances that have been controled include an impulse,[11] filtered white noise,[12] and turbulent boundary layers.[13]

The work reported here is directed at the space launch vehicle problem, where it is not possible to obtain, in advance of a required control output, a coherent measurement of the disturbance or to directly measure the quantity to be controlled. These constraints are imposed to minimize the impact of the solutions under investigation on launch vehicle operation. For instance, inclusion of an error microphone on or near the payload may have the potential to increase control performance but would also impose additional interface requirements that would complicate payload integration aspects of launch vehicle operations. Since the launch vehicle has a flexible shroud that encloses an acoustic cavity containing the payload, it is possible to use structural sensing to predict the sound pressure in the cavity and feedback control with structural actuators to reduce the radiated sound. Since power, space, and added weight are all at a premium in the launch vehicle, it is necessary to consider efficient sensor and actuator placement as well as the efficiency of the control algorithms. This paper will first discuss the modeling of a structural/acoustic system with all of the essential components to aid in understanding the physics of the launch vehicle problem. A LQG (linear-quadratic-Gaussian) feedback control approach will be discussed which allows the control of radiated pressure into a defined subvolume of the cavity using only structural actuators and sensors. A method for selecting sensor and actuator positions based on a transformation of the problem into radiation modes will also be covered. Finally, to provide further clarification, an example problem will be completed which draws on all of the theo-

retical development to suppress radiated sound within a subvolume.

I. MODELING OF THE STRUCTURAL/ACOUSTIC SYSTEM

The problem considered here is an acoustic cavity enclosed by a flexible structure. Movement of the structure, either by out-of-plane vibration control inputs or by external pressure fluctuations, results in an acoustic response inside the cavity. A modal-interaction approach for the prediction of the interior acoustic response to either type of disturbance is an alternative method to a fully coupled finite element (FEM) analysis.[14] This method is computationally less intensive than the fully coupled problem, requiring significantly shorter solution times.[15] This method also allows the reformulation of the problem into radiation modes that will be shown to greatly facilitate efficient sensor and actuator placement for active control design. The modal-interaction approach requires solution of both the *in vacuo* structural and rigid wall acoustic cavity problems. These results are then combined to give the solution to the coupled problem.

A. Acoustic response due to structural motion

In general, the sound pressure at frequency ω at any point $\vec{\mathbf{r}}$ in the cavity due to out-of-plane motion of the structure is given by Ref. 9 as

$$p_p(\vec{\mathbf{r}},\omega)=\phi(\vec{\mathbf{r}})^T\mathbf{Z}_a(\omega)\mathbf{v}_p(\omega), \tag{1}$$

where $\phi(\vec{\mathbf{r}})^T$ is the row vector of acoustic mode shape functions evaluated at location $\vec{\mathbf{r}}$ in the cavity. For simplicity in the formulation the frequency dependence of the above variables will be omitted from here onwards. The matrix $\mathbf{Z}_a$ is the structural to acoustic modal internal transfer function matrix at frequency ω whose terms are given by

$$Z_a(l,i)=\frac{j\rho_0 S\omega c_0^2}{\Lambda_l(\omega_l^2+j\xi_l\omega_l\omega-\omega^2)}B_{l,i}, \tag{2}$$

where ρ_0 is the density of the fluid in the cavity, c_0 is the speed of sound in the cavity, ξ_l is the modal loss factor of the lth cavity mode, ω_l is the resonance frequency of the lth cavity mode, S is the surface area of the structure, and Λ_l is the modal volume of the lth cavity mode defined by

$$\Lambda_l=\int_V \phi_l^2(\vec{\mathbf{r}})dV, \tag{3}$$

where $\phi_l(\vec{\mathbf{r}})$ is the mode shape function of the lth acoustic mode and V is the volume of the enclosed space. Here $B_{l,i}$ is the nondimensional coupling coefficient between the lth acoustic mode and the ith structural mode defined as

$$B_{l,i}=\frac{1}{S}\int_S \phi_l(\vec{\mathbf{r}})\psi_i(\vec{\mathbf{r}})dS, \tag{4}$$

where $\psi_i(\vec{\mathbf{r}})$ is the ith structural mode shape function evaluated at location $\vec{\mathbf{r}}$ on the structure with components normal to the structural surface. The vector $\mathbf{v}_p$ in Eq. (1) is the column vector of structural modal velocities that are due to the excitation.

If the FEM is used to obtain the acoustic and structural mode shapes and resonance frequencies, Eq. (1) becomes

$$\mathbf{P}=\phi^T\mathbf{Z}_a\mathbf{v}_p, \tag{5}$$

where $\mathbf{P}$ is the column vector of length b giving the pressure at each of the b nodes of the acoustic FEM model, ϕ^T is the $b\times n$ acoustic mode shape matrix for n unity normalized acoustic modes, $\mathbf{Z}_a$ is the $n\times m$ matrix of elements defined by Eq. (2) for m structural modes, and $\mathbf{v}_p$ is the $m\times 1$ column vector of modal out-of-plane structural velocities. An approximation for Eq. (3) using the FEM results is

$$\Lambda_l\approx\phi_l^T\mathbf{V}\phi_l, \tag{6}$$

where ϕ_l is the lth column vector making up ϕ and $\mathbf{V}$ is a $b\times b$ diagonal matrix where the lth diagonal element is the acoustic volume associated with the lth node. An approximation for Eq. (4) gives the $n\times m$ coupling matrix $\mathbf{B}$ as

$$\mathbf{B}\approx\phi'^T\mathbf{A}\psi, \tag{7}$$

where ψ is the $c\times m$ matrix of mass orthonormalized structural mode shapes for c structural nodes and ϕ' is the $c\times n$ acoustic mode shape matrix for the c acoustic nodes which are coincident with structural nodes. The matrix $\mathbf{A}$ is a $c\times c$ nondimensional diagonal matrix that gives the area associated with each structural node as a fraction of the total surface area.

B. The radiation transfer function matrix and MIMO state space model for an enclosed space

Recalling Eq. (5), the quantity $\phi^T\mathbf{Z}_a$ can be further defined as the radiation transfer function matrix between the modal structural velocities and the pressures at the acoustic FEM nodes in the cavity. To facilitate active control design and further modeling and simulation, $\phi^T\mathbf{Z}_a$ can be converted to a multi-input/multi-output (MIMO) state space model. The conversion from transfer function matrix to state space is not unique. Since $\phi^T\mathbf{Z}_a$ is, in general, a fully populated transfer function matrix, a direct conversion into a minimum realization state space model such as the technique suggested in Ref. 16 or arbitrary conversion followed by minimum realization conversion methods would be very sensitive to mathematical precision. In practice, this imposes a limit on the ultimate size of the $\phi^T\mathbf{Z}_a$ matrix, thus limiting the number of structural modes used and the number of pressure points.

Referring to Eqs. (1) and (2), the matrix $\mathbf{Z}_a$ can be factored as

$$\mathbf{Z}_a=\mathbf{FB}, \tag{8}$$

where $\mathbf{F}$ is an $n\times n$ diagonal matrix whose elements are given by

$$F_{l,l}=\frac{s\rho_0 Sc_0^2}{\Lambda_l(s^2+s\xi_l\omega_l+\omega_l^2)}, \tag{9}$$

where s has been substituted for $j\omega$. Thus the frequency-dependent part of the radiation transfer function matrix has been moved entirely to $\mathbf{F}$. Since $\mathbf{F}$ is diagonal, a minimal realization which is relatively insensitive to mathematical precision can be obtained directly by independently synthe-

sizing a state space model for each diagonal term in controler canonical form. The individual state space models may then be appended to form the state space model

$$\dot{\mathbf{r}}=\mathbf{A}'\mathbf{r}+\mathbf{B}'\mathbf{u}, \quad \mathbf{y}=\mathbf{C}'\mathbf{r}, \tag{10}$$

where the $\mathbf{A}'$ matrix is $2n\times 2n$ for n acoustic modes, and $\mathbf{r}$ is the state vector of the model. Since the model realization is not unique, $\mathbf{r}$ has no direct physical meaning. To represent the complete state space model for the radiation transfer matrix, $\phi^T\mathbf{Z}_a$, the $\mathbf{B}'$ and the $\mathbf{C}'$ matrices must be post- and premultiplied by the $\mathbf{B}$ and ϕ^T matrices, respectively. These products give the $\mathbf{B}''$ and the $\mathbf{C}''$ matrices of the radiation state space model

$$\dot{\mathbf{r}}=\mathbf{A}'\mathbf{r}+\mathbf{B}''\mathbf{w}, \quad \mathbf{P}=\mathbf{C}''\mathbf{r}. \tag{11}$$

It is convenient to define the structural state $\mathbf{w}$ as

$$\mathbf{w}=\begin{bmatrix}\mathbf{x}\\ \dot{\mathbf{x}}\end{bmatrix}, \tag{12}$$

where $\mathbf{x}$ are the modal out-of-plane structural displacements and $\dot{\mathbf{x}}$ are $\mathbf{v}_p$. The $\mathbf{B}''$ matrix has been padded with zeros in the first m columns so that $\mathbf{v}_p$ are the inputs to the model.

C. The coupled model

The structural state space model can be assembled from the *in vacuo* mass orthonormalized mode shapes and frequencies of the FEM model as

$$\dot{\mathbf{w}}=\mathbf{A}\mathbf{w}+\mathbf{B}\mathbf{u}, \quad \mathbf{y}=\mathbf{C}\mathbf{w}, \tag{13}$$

where the output $\mathbf{y}$ is a vector structural sensor outputs and $\mathbf{u}$ is a vector of structural actuator inputs.

The coupled model can now be assembled by combining Eqs. (11) and (13) as

$$\begin{aligned}\dot{\mathbf{z}}&=\begin{bmatrix}\mathbf{A} & \mathbf{0}\\ \mathbf{B}'' & \mathbf{A}'\end{bmatrix}\mathbf{z}+\begin{bmatrix}\mathbf{B}\\ \mathbf{0}\end{bmatrix}\mathbf{u}+\mathbf{H}\mathbf{v},\\ \mathbf{y}&=[\mathbf{C} \quad \mathbf{0}]\mathbf{z},\\ \mathbf{y}'&[\mathbf{0} \quad \mathbf{C}'']\mathbf{z},\end{aligned} \tag{14}$$

where

$$\mathbf{z}=\begin{bmatrix}\mathbf{w}\\ \mathbf{r}\end{bmatrix} \tag{15}$$

and $\mathbf{v}$ is a vector of white noise inputs whose transmission path into the system is determined by $\mathbf{H}$.

II. CONTROL FORMULATION

To show the feasibility of feedback control of transmitted pressure on the coupled model, a LQG optimal control method is used where the goal is to minimize

$$\int \{\mathbf{z}'\mathbf{Q}\mathbf{z}+\mathbf{u}'\mathbf{R}\mathbf{u}\}dt. \tag{16}$$

Since the $\mathbf{z}$ vector includes both the transmitted pressure states and the structural states, the control effort can be directed at any combination of these quantities. Assuming only structural sensors and actuators are available, the vector $\mathbf{u}$ in the integral only includes inputs at the structural actuator positions.

Since the pressure states are not being measured at all and the structural states are not being measured directly, it is necessary to formulate an optimal estimator or Kalman–Bucy filter[17] which is formed by minimizing

$$\lim_{l\to\infty} E\{\tilde{\mathbf{z}}^T\mathbf{C}^T\mathbf{C}\tilde{\mathbf{z}}\}, \tag{17}$$

where $\tilde{\mathbf{z}}$ is the estimation error and the estimator is optimal for any selected $\mathbf{C}$. The optimal estimator allows the reconstruction of the states, including the radiation states, from structural measurements. It is worth noting that a limitation of feedback control in acoustics when a microphone is used to directly sense acoustic pressure is the delay between the feedback microphone and the control speaker. This is one of the factors that makes it necessary to locate the microphone relatively close to the control speaker. The structural sensing technique allows a penalty to be placed on the pressure states without having to actually use the pressure output signal. This avoids the delay problem and lifts a major constraint to feedback control of sound. In practice, the implementation of the estimator in this problem would also constitute a hardware limitation since a complex structural/acoustic system would require many states to realize the estimator. A realistic hardware implementation would almost certainly involve an initial calibration to determine a minimal hardware realization of the estimator. After this initial calibration, the identified estimator could be combined with the control algorithm on DSP hardware to allow exclusive structural sensing.

III. SENSOR AND ACTUATOR PLACEMENT

Provided both the structural and acoustic modal densities are relatively low and modal damping is also relatively low, a spectrum of the measured acoustic response to broadband structural vibration will have large peaks corresponding to resonances of the coupled system for a given location within the cavity. Finding good structural locations to control these peaks can be accomplished by taking advantage of the physical insight gained by the solution method outlined. For a given subvolume within the cavity it is possible to get the modal expansion for the acoustic potential energy as[10]

$$E_p=\mathbf{v}_p^H\Pi\mathbf{v}_p, \tag{18}$$

where the matrix Π is given by

$$\Pi=\frac{\mathbf{Z}_a^H\phi''\mathbf{V}\phi''^T\mathbf{Z}_a}{4\rho_0 c_0}, \tag{19}$$

where the dimensions of $\mathbf{V}$ are now determined by the number of acoustic nodes in the defined subvolume, d, and ϕ'' is the $d\times n$ acoustic mode shape matrix.

Since Π is a Hermitian matrix,[18] it may be diagonalized as

$$\Pi=\mathbf{U}\mathbf{S}\mathbf{U}^H. \tag{20}$$

If Π is of rank n, the diagonal matrix $\mathbf{S}$ contains n real eigenvalues which can be considered as radiation efficiencies of each radiation mode at a given frequency. The magnitude of the elements of the corresponding eigenvectors which

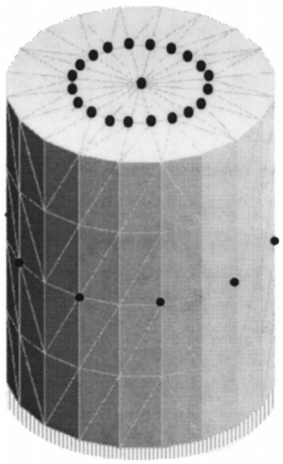

FIG. 1. Example problem with black dots designating colocated sensor and actuator positions.

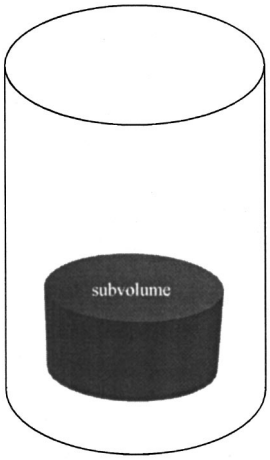

FIG. 2. Approximate location of the subvolume within the cylinder.

make up **U** give the level of participation of each structural mode in the radiation mode. The reason for such a transformation, similar to the case of radiation modes used in free space analysis,[5–8] is that the radiation modes contribute orthogonally to the acoustic potential energy within the subvolume, since **S** is diagonal. This means that suppression of radiation modes decreases the acoustic potential energy within the subvolume. This same argument cannot be made for suppression of structural modes since, in general, they do not contribute orthogonally to acoustic potential energy. Another compelling reason to carry out the diagonalization described by Eq. (20) is that, as with shells radiating into free space,[5–8] it is typically sufficient to consider only the first few radiation modes to account for the majority of sound power in the subvolume.[15]

The solution of Eq. (20) at the frequency of each of the peaks in the acoustic response gives a relative measure of the efficiency of each radiation mode at that frequency. For those radiation modes that dominate, the relative contribution of the structural modes can be obtained from the corresponding eigenvector. Structural sensor and actuator locations that couple well into these dominant structural modes are good structural sensor and actuator locations for the acoustic control problem. For out-of-plane sensors and actuators such as accelerometers, shakers, and proof mass actuators, these locations would be regions where there is an overlap of out-of-plane displacement for all of the dominant structural modes. For in-plane sensors and actuators like piezoceramic wafers, a region where there is an overlap of high in-plane strain for the dominant structural modes should be sought.

IV. EXAMPLE PROBLEM

In order to illustrate the ideas discussed in the previous sections, the example of a 2-m-high, 1.55-m-diam steel cylinder with end caps shown in Fig. 1 is considered. The steel is 2 mm thick and the fluid inside the cylinder is air. A 142-node FEM analysis of the structure and a 165-node FEM analysis of the acoustic cavity were done in UAI Nastran using three-noded triangular thin shell elements to model the structure and four-noded tetrahedron solid elements to model the air in the cavity. The number of acoustic and structural modes retained in the model place an upper limit on the frequency over which it is accurate. The relatively low number of modes considered in this example was considered adequate to model a relatively low-frequency range ($<$150 Hz). This is consistent with active control being more cost effective in reducing low-frequency rather than mid- or high-frequency acoustic radiation in the launch acoustic problem.[19] The first 5 acoustic modes and the first 25 structural modes were used to formulate a 60th-order MIMO state space model of the coupled system. A modal damping coefficient of 1.5% was applied to both the structural and acoustic modes. This state space model was then used to investigate an LQG feedback control method of suppressing the sound in a subvolume within the acoustic cavity in response to a broadband input.

A. Sensor and actuator placement on cylinder

A subvolume was defined where it was desirable to minimize sound pressure. Figure 2 shows the approximate location of the subvolume within the cylinder. There were three FEM acoustic nodes (not locations of zero displacement) within the defined subvolume. A 15 000 time point simulation with a spacing of 0.0025 s was run in Matlab to determine the acoustic response over time at the three acoustic nodes. This time spacing gives a 200-Hz upper limit in subsequent FFT-based (fast Fourier transform) analysis of the time data. The applied disturbance was random noise inputs at all of the structural nodes. The averaged power spectrum of the acoustic response data was then taken to identify dominant peaks. The power spectrums corresponding to one of the three acoustic nodes is shown in Fig. 3. In Fig. 3 and all of the following power spectrum results, the amplitude has been normalized to the amplitude of the first, dominant peak at around 8 Hz. The power spectrums at the other two nodes also show the same five dominant peaks.

Since the modal density is relatively low at low frequencies, it is possible to draw some conclusions as to the origins of each of the peaks based on their proximity to uncoupled structural and acoustic resonances in the frequency spectrum. Peaks 1 and 2 correspond to structural resonances with mo-

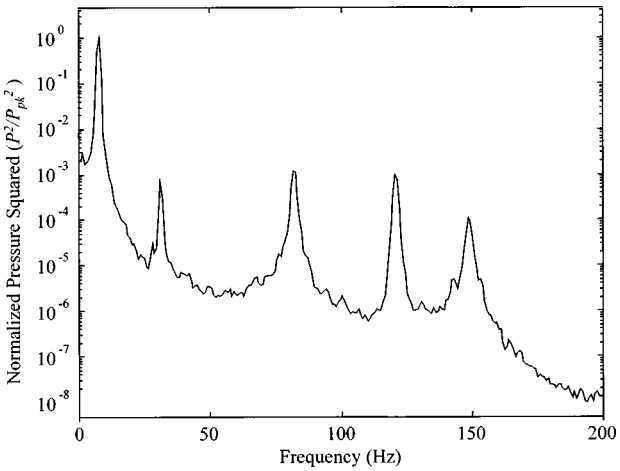

FIG. 3. Power spectrum at representative acoustic node within subvolume.

tion primarily in the top plate of the cylinder. Motion of the top plates associated with the structural mode shapes corresponding to these resonances is shown in Fig. 4. The movement of the top plate in the first structural mode shape is similar to the fundamental mode of a circular plate. This helps explain the relatively large amplitude of the first peak in the power spectrum, since the radiation efficiency of the fundamental mode of a panel is generally dominant.[14] Peak 3 corresponds to an acoustic mode. Peaks 4 and 5 have both uncoupled structural and acoustic resonances in close frequency proximity, so it is impossible to draw any conclusions without further analysis.

In order to determine the structural modes that dominate the primary radiation modes at each peak, the acoustic potential energy is computed within the subvolume at each of these peak frequencies. The acoustic nodes within the subvolume determine the **V** matrix in Eq. (6) which, in turn, determines the matrix Π. The four largest eigenvalues resulting from the transformation of Π at the frequency of each peak are given in Table I. At each frequency, the list of eigenvalues is unity normalized to facilitate comparison, and values below 0.000 000 1 have been set identically equal to zero. It is clear from Table I that for all but the fourth peak frequency, the first radiation mode is dominant. Table II gives the magnitudes of the first unity normalized eigenvector at each frequency along with the second for the fourth peak frequency. The data represent the relative contributions of each structural mode to each radiation mode. Values less than 0.01 in Table II have been set identically equal to zero.

For this example problem the structural modes used for sensor and actuator location were those with values in Table II were greater than 0.01. This decision was somewhat arbitrary, but a formal weighting procedure could be established using the data in Tables I and II. The structural modes selected were 1, 2, 3, 6, and 23. The magnitudes of the out-of-plane motion for each of these unity normalized mode shapes were then added together at each structural node. This summation was again unity normalized and is shown in Fig. 5. For each angular position theta, the data corresponding to structural nodes along the sides of the cylinder are displayed with respect to axial length on the lower plot, and the data corresponding to nodes of the top of the cylinder are displayed with respect to radial length on the upper plot. Based on Fig. 5, the points marked with black dots in Fig. 1 designate structural nodes that were selected as good sensor and actuator positions. Physically, these dots correspond to large, out-of-plane displacement locations for the structural mode shapes that were selected based on the results in Table II. Counting the five points along the middle of the cylinder which are obstructed from view, there are 31 selected nodes. For the control simulation, structural sensor and actuators were placed at each of the 31 nodes. These sensors and actuators were idealized in the sense that the actuators provided an out-of-plane force proportional to the control input and the sensors provided displacement without adding any dynamics to the system. The out-of-plane mode shape amplitudes at each of these nodes were used to form the **B** and **C** matrices in Eqs. (14). The **H** matrix for the example problem

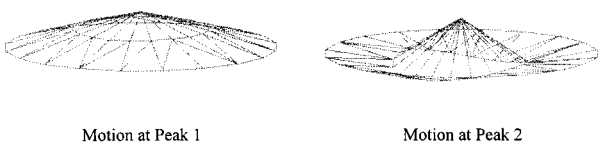

FIG. 4. Top plate motion of structural mode shapes corresponding to peaks 1 and 2.

TABLE I. Highest eigenvalues at each peak frequency.

Eigenvalue	Peak 1	Peak 2	Peak 3	Peak 4	Peak 5
1	1	1	1	1	1
2	0	0.0026	0	0.7409	0.0007
3	0	0.0008	0	0.011	0.0002
4	0	0.0001	0	0	0

TABLE II. Eigenvectors corresponding to dominant radiation modes.

Structural mode	Peak 1	Peak 2	Peak 3	Peak 4-1	Peak 4-2	Peak 5
1	1	1	1	0.1	0.1	1
2	0	0	0	1	0.7	0.6
3	0	0	0	0.7	1	0.2
4	0	0	0	0	0	0.1
5	0	0	0	0	0	0.1
6	0.2	0.2	0.2	0	0	0.2
7	0	0	0	0	0	0
8	0	0	0	0	0	0
9	0	0	0	0	0	0
10	0	0	0	0	0	0
11	0	0	0	0	0	0
12	0	0	0	0	0	0
13	0	0	0	0	0	0
14	0	0	0	0	0	0
15	0	0	0	0.1	0	0
16	0	0	0	0	0	0
17	0	0	0	0	0	0
18	0	0	0	0	0	0
19	0	0	0	0	0	0
20	0	0	0	0	0	0
21	0	0	0	0	0	0
22	0	0	0	0.1	0.1	0
23	0	0	0	0.1	0.2	0
24	0	0	0	0	0	0
25	0	0	0	0	0	0

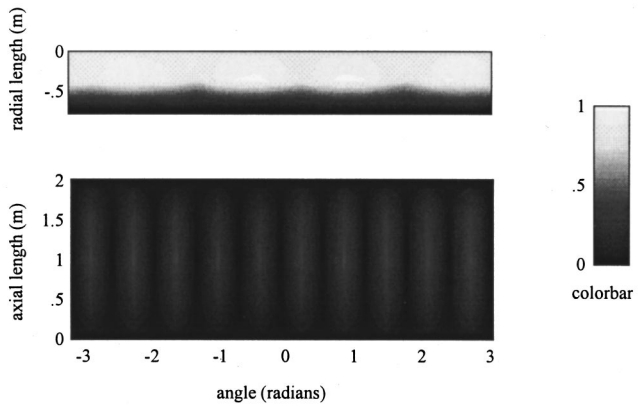

FIG. 5. Unity normalized summation of dominant mode shapes.

was selected so that random noise was input into the structure at every structural node, including the sensor and actuator positions.

To establish the comparative control authority of actuators placed at these 31 locations, an open-loop simulation was performed of the same time length and spacing as the previous simulation. Random disturbances were used as inputs at each of the selected actuator locations. The mean square amplitude over time at each of the three selected acoustic nodes was averaged and square rooted to give a spatially averaged rms value. Similarly, 100 time-based simulations were performed with the same disturbance and 31 randomly selected actuator locations. The mean spatially averaged rms value for the random actuator locations was less than half that of the same quantity for the actuator locations selected using the radiation mode approach. This result suggests that use of the radiation mode approach in selecting sensor and actuator locations for this problem will lead to more than twice the control authority than would a random selection of actuator locations.

B. Control results on cylinder

The first control objective was a uniform weighting on all the states, $\mathbf{Q}=\rho\mathbf{I}$. This means that the controler will try to suppress both structural vibration and acoustic radiation into the subvolume. The matrix $\mathbf{R}$ was also set equal to the identity matrix. The full-state feedback problem was then completed as a benchmark, varying ρ progressively until a reduction was noticeable between the closed- and open-loop transfer function behavior of a typical control input position and acoustic node in the selected subvolume. The parameters of the optimal estimator were then selected to give similar performance to the full-state feedback problem using output feedback. A simulation was then done on the closed-loop system using the same random inputs, time length, and time spacing as with the open-loop system. Figure 6 shows the closed-loop spectrum at the same acoustic node position shown in Fig. 3. The mean square amplitude over time at each of the three selected acoustic nodes was averaged and square rooted to give a spatially averaged rms value to compare between the open- and closed-loop cases. The first control objective resulted in a 16-dB reduction in the rms pressure response. The mean square amplitude over time for each of the control inputs, $\mathbf{U}$, was also averaged and square rooted to give a measure of control effort. Since the sensors and actuators are ideal and no attempt has been made to model their dynamics or efficiency, the control effort does not have a direct physical meaning. It is useful, however, to compare

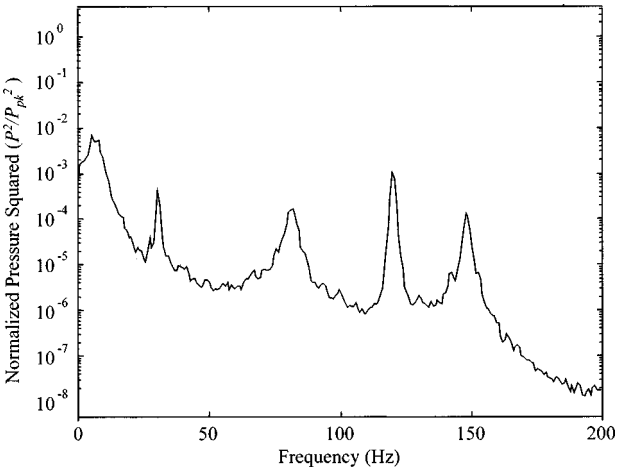

FIG. 7. Closed loop spectrum for control objective 2.

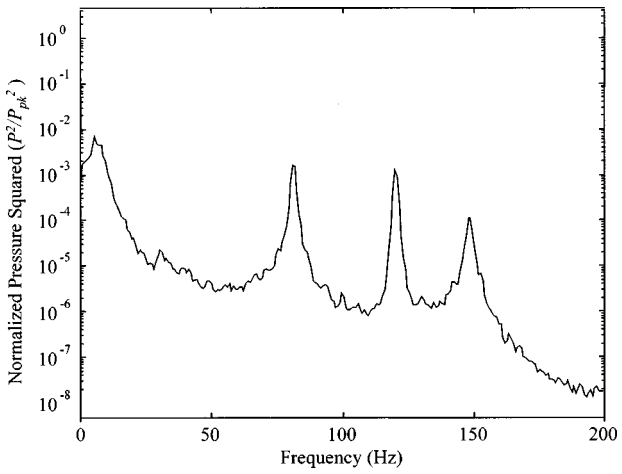

FIG. 6. Closed loop spectrum for control objective 1.

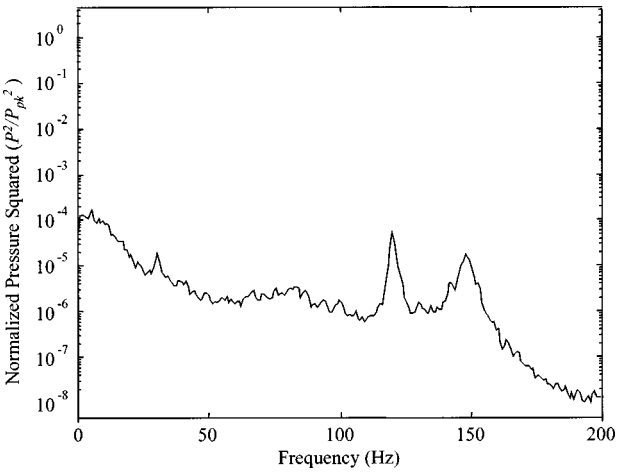

FIG. 8. Closed loop spectrum for control objective 3.

TABLE III. Example problem control results.

Control objective	rms pressure reduction (dB)	rms control effort
1	16 dB	0.036
2	16 dB	0.011
3	28 dB	0.036

the control cost associated with various control results. The control effort calculated in this manner for the first control objective was 0.036.

The second and third control objectives both had a uniform weighting on all of the pressure states but zero weighting on all of the structural states. This means that the controler should only try to suppress acoustic radiation into the subvolume. This was accomplished by setting $\mathbf{Q}=\rho\mathbf{J}$ where $\mathbf{J}$ is a diagonal matrix with ones corresponding to the pressure states $\mathbf{r}$ and zeros corresponding to the structural states $\mathbf{w}$. For the second control objective, ρ was varied and simulations were done until the same decibel reduction in the overall rms response was calculated as for the first control objective. The control effort to accomplish this reduction was 0.011. For the third control objective, ρ was varied and simulations were done until the same control effort was expended as for the first control objective. This same control effort resulted in a 28-dB reduction from the open-loop value. Figures 7 and 8 show the closed-loop spectrum at the same acoustic node position shown in Figs. 3 and 6. Table III summarizes the control results.

If the goal of feedback control is a reduction of acoustic response in the subvolume, the first control objective wastes control effort when compared to the second and third control objectives. This is because the nonzero weighting of all of the states causes control effort to be used to suppress structural vibration that does not necessarily contribute to the acoustic response.

V. CONCLUSIONS AND FUTURE RESEARCH

It has been shown that it is possible to actively suppress radiated sound in an acoustic cavity surrounded by a flexible structure that is subject to a broadband disturbance. Structural sensing and feedback control were used since it was assumed that a measure of the disturbance was not available and a direct measurement of the sound pressure to be reduced was also not available. This work presents all the essential components to explore the physics of the space launch vehicle noise problem. The use of the modal-interaction approach led to a MIMO radiation state-space model that relates the out-of-plane structural modal velocity inputs to the spatially varying pressure in the cavity. The modal-interaction approach also allowed the decomposition of the acoustic response into radiation modes, which proved essential for the efficient location of sensors and actuators. The control simulation showed that a weighting of the pressure states in the LQG control problem was a relatively efficient way to effect a reduction in acoustic response within a defined subvolume when compared to a uniform weighting of both the pressure and structural states.

One limitation of this method in the launch vehicle problem is the inability to accurately model a large number of structural modes in a very complex structure. This could be compensated for by experimentally obtaining the radiation transfer matrix and inclusion of structural measurements for model update of the structural model. A related limitation is the failure to include the effects of robustness in the presence of model uncertainties between the model of the system and the actual system in the control simulation. This also highlights the need to incorporate system identification or model update using measured data in any realistic implementation of the method. A limitation of the FEM-aided solution to the modal-interaction approach is that reorientation of structural and acoustic modes is not possible in response to control efforts. This limitation was allowed for the idealized symmetrical model discussed here since, in practice, both the launch vehicle structure and acoustic cavity have unsymmetric parts such as seams, vents, and payloads which will force the orientation of these modes to be fixed.

Future research will concentrate on updating the parameters of the structure and geometrical parameters of the problem to reflect the Air Force Minotaur space launch vehicle. This will include a detailed FEM model of both the structure and the acoustic cavity as well as an attempt to use an acoustic disturbance in the simulation that is representative of acoustic launch loads. The additional pressure loading on the interior of the structure due to acoustic radiation will also be added to the model to further refine structural/acoustic coupling. In addition, piezoceramic actuators will be investigated as both sensors and actuators, since these have been shown to have many potential advantages over out-of-plane sensors and actuators in the space launch vehicle problem.[19]

ACKNOWLEDGMENTS

The authors gratefully acknowledge the support of the Air Force Office of Scientific Research through both the Windows on Science program and the task ''Theoretical and Experimental Studies of Vibroacoustic Systems'' under the management of Major Brian Sanders. The first author would also like to acknowledge the hospitality of The University of Adelaide Mechanical Engineering Department who hosted him during the course of this research.

[1] A. Timmins and R. Heuser, ''A study of first-day malfunctions,'' NASA TN D-6474 (1971).
[2] S. Elliott and P. Nelson, *Active Control of Sound* (Academic, New York, 1992), pp. 350–356.
[3] S. Snyder and N. Tanaka, ''On feedforward active control of sound using error signals,'' J. Acoust. Soc. Am. **94**, 2181–2193 (1993).
[4] K. Cunefare and M. Currey, ''On exterior acoustic radiation modes of structures,'' J. Acoust. Soc. Am. **96**, 2302–2312 (1994).
[5] K. Burgemeister, ''Novel methods of transduction for active control of harmonic sound radiated by vibrating surfaces,'' Ph.D. dissertation, The University of Adelaide, 1996.
[6] S. Elliot and M. Johnson, ''Radiation modes and the active control of sound power,'' J. Acoust. Soc. Am. **94**, 2194–2204 (1993).
[7] G. Borgiotti, ''The power radiated by a vibrating body in an acoustic fluid and its determination from boundary measurements,'' J. Acoust. Soc. Am. **88**, 1884–1893 (1990).

[8] G. Borgiotti and K. Jones, ''Frequency independence property of radiation spatial filters,'' J. Acoust. Soc. Am. **96**, 3516–3524 (1994).
[9] S. Snyder and C. Hansen, ''The design of systems to actively control periodic sound transmission into enclosed spaces, part 1: Analytical models,'' J. Sound Vib. **170**, 433–449 (1994).
[10] B. Cazzolato and C. Hansen, ''Active control of sound transmission using structural error sensing,'' J. Acoust. Soc. Am. **104**, 2878–2889 (1998).
[11] W. Baumann, W. Saunders, and H. Robertshaw, ''Active suppression of acoustic radiation from impulsively excited structures,'' J. Acoust. Soc. Am. **90**, 3202–3208 (1991).
[12] W. Baumann, F-S. Ho, and H. Robertshaw, ''Active structural acoustic control of broadband disturbances,'' J. Acoust. Soc. Am. **92**, 1998–2005 (1992).
[13] D. Thomas and P. Nelson, ''Feedback control of sound radiation from a plate excited by a turbulent boundary layer,'' J. Acoust. Soc. Am. **98**, 2651–2662 (1995).
[14] F. Fahy, *Sound and Structural Vibration* (Academic, New York, 1985).
[15] B. Cazzolato, ''Novel transduction methods for active control of sound transmission into enclosures,'' Ph.D. dissertation, The University of Adelaide, 1998.
[16] C. Chen, *Linear System Theory and Design* (Holt, Rinehart and Winston, New York, 1970).
[17] H. Eves, *Elementary Matrix Theory* (Dover, New York, 1966).
[18] P. Dorato, A. Chaouki, and V. Cerone, *Linear-Quadratic Control* (Prentice–Hall, Englewood Cliffs, NJ, 1995).
[19] D. Leo and E. Anderson, ''Vibroacoustic modeling of a launch vehicle payload fairing for active acoustic control,'' presented at the 39th annual SDM conference in Long Beach, CA, AIAA-98-2086 (1998).

Auditory hazard from airbag noise exposure

G. Richard Price and Joel T. Kalb
U.S. Army Research Laboratory, Human Research and Engineering Directorate, Aberdeen Proving Ground, Maryland 21005-5425

(Received 10 July 1998; revised 30 July 1999; accepted 2 August 1999)

Airbag deployment includes very intense acoustic stimulation, yet almost no tests of auditory hazard have been done with real ears. Therefore 32 anesthetized cats, positioned at the driver and passenger locations in a pickup truck, were exposed in pairs to one airbag deployment (electrically initiated). Hearing was tested at 1, 2, 4, 8, and 16 kHz by evoked-response audiometry just before exposure, immediately after and at 1 month and 6 months. Exposure conditions included doors open, compartment closed, and closed compartment sealed with tape: seven exposures to passenger bag only and nine to driver and passenger bags. Peak pressures ranged from 167 to 173 dB with unweighted energies as high as 4000 J/m^2 (or 8 hr L_{EQA}=95.5 dB). The immediate threshold shift averaged 60 dB at 4.0 kHz that resolved to an average permanent shift of 37 dB. By extrapolation, these data from cats may indicate that susceptible human ears risk permanent hearing loss from airbag noise. [S0001-4966(99)05711-2]

PACS numbers: 43.50.Qp, 43.66.Ed, 43.64.Wn [MRS]

INTRODUCTION

Automotive airbags are proving to be a mixed blessing. They undoubtedly save lives in frontal impacts, but because their deployment is a highly energetic event, they can themselves cause injuries and even death through physical contact with vehicle occupants. Not surprisingly, they may be an auditory hazard as well. Peak pressures in the passenger compartment can exceed 170 dB and the total acoustic energy may equal that in the crew area of a howitzer (Price *et al.*, 1996). Tests run when airbags were first proposed for automotive use indicated negligible hazard (Nixon, 1969); however, as experience with airbags has grown, some evidence is accumulating which indicates that permanent changes in hearing can result in some individuals (Mattox and Price, 1995; Saunders *et al.*, 1998, 1995; Yaremchuk, 1998). Given the increasing numbers of automobiles with airbags, the growing number and new locations of airbags within individual automobiles, and their possible hazard to the ear, we undertook the present investigation to reexamine airbag noise exposures for hazard to hearing.

Part of the problem in assessing noise hazard from airbags stems from difficulties with existing-noise standards that might be used for such sounds. If airbag impulses (Nixon, 1969; Rouhana *et al.*, 1994; Price *et al.*, 1996) are plotted on the damage risk criterion for unprotected ears used in the United States (CHABA, 1968), the data are far above the acceptable level. On the other hand, tests run when airbags were first proposed for automotive use indicated negligible hazard (Nixon, 1969). Recent experience with airbags in automobiles has generally supported these data in that there appears to be no epidemic of large hearing losses associated with airbag deployments. Part of the explanation for the apparent discrepancy between the predicted and actual hazard may be that the damage–risk criterion in use in the United States (CHABA, 1968) may overestimate hazard for impulses with low spectral content (Dancer *et al.*, 1985; NATO RSG6/PANEL8, 1987; Price *et al.*, 1989). While this may be true, it means that there is no standard in the United States that can be used with certainty for guiding the design or rating the hazard of inflatable restraint systems. The situation at the international level is similar because no standard for impulse noise exposure at these peak pressures has been agreed upon by nations outside the United States. The combined lack of a valid noise standard and almost no database on auditory hazard from this type of impulse leaves both the automobile industry and regulatory agencies without guidance at a moment when airbag use is proliferating and design decisions need to be made.

Possibilities abound in the world of design, raising new issues with respect to airbag use. Protection from side impacts suggests smaller airbags much closer to the occupants' ears. In another setting, the question of the effect of venting the passenger compartment produces diametrically opposed possibilities. Venting the passenger compartment might make a difference in hazard by reducing peak pressure and shortening the duration (CHABA, 1968) or with reduced venting the higher peak pressures and longer durations might be more tolerable even if the number and size of bags increase (Price and Kalb, 1996a).

The existing tests of auditory hazard from airbag noise have not been definitive, leaving many possibilities to be examined. In the original test of airbag hazard, Nixon (1969) included only the closed compartment condition for a small sedan. The pressure history would change dramatically in a convertible or a car with open windows because there is little opportunity for a buildup of pressure. Nixon and Sommer (1973) demonstrated through a simulation of airbag noise that threshold shifts were *greater* if the low-frequency component were eliminated, leaving only the higher-frequency energy (hiss of bag filling). In principle, then, hazard in the vented compartment may be greater than in the closed compartment, even if peak pressures and energies are lower. In the Nixon (1969) experiment, the bag was inflated from a pressurized cylinder. Today, airbags are commonly inflated

by burning a propellant. Are the two acoustic signatures equally hazardous? In the original experiment, the subjects knew that the airbag was going to be deployed and in preparing for the impulse could have contracted their middle ear muscles in advance of the impulse's arrival. Had they been surprised, the middle ear muscles may have contracted only reflexively and hazard might have increased significantly.

From the foregoing considerations, it is apparent that many issues still need to be addressed before we can be confident about designing and using airbags; yet airbags are legally mandated in automobiles. It appears that adventitious experiments addressing these issues will be conducted on our highways.

The purpose of these experiments was to acquire pressure histories from airbags and hearing loss data from quiescent biological ears exposed to the airbag impulses under a variety of compartment venting conditions.

I. METHOD

A. Subjects

The subjects were 36 adult female cats, weighing 3–4 Kg. All procedures used in the conduct of this research were in compliance with provisions in the Guide for the Care and Use of Laboratory Animals established by the Institute of Animal Resources, Commission on Life Sciences, National Research Council. Because ears that have just been exposed to noise might reasonably be expected to be particularly susceptible to additional exposure (Ahroon and Hamernik, 1996), special precautions were taken in the colony to maintain quiet and avoid banging of cages or trays and as an additional precaution, animals wore foam ear plugs for approximately 24 hours after exposure.

B. Experimental procedures

1. General procedures

These experiments were conducted in a bay of a research building in which the test vehicle was parked next to a mobile audiometric facility. For reasons of economy, experiments were run on two animals at a time. The animals were anesthetized for the audiometric tests and hearing was tested binaurally. They were then wrapped in blankets to maintain body temperature and placed on resting platforms at the driver and passenger head positions in the test vehicle. The bags were deployed electrically, and immediately afterward the animals were returned to the audiometric trailer for testing. The noise exposure process took about 5 min and testing resumed in about 15 min. The left ear was always tested first, then the right ear, followed immediately by the second animal (driver and passenger locations alternated in testing order). Testing five frequencies in each ear took about 30 min per ear. Conceivably, ongoing recovery processes might have produced a tendency to measure smaller losses in ears tested later. There is experimental evidence that this is probably not a serious problem because for exposures to very intense sounds, post-exposure thresholds tend to change very slowly and losses may even grow slightly for a few hours (Hamernik *et al.*, 1988; Luz and Hodge, 1971). The animals were allowed to recover for 1 month and were retested. One month of recovery is commonly taken as sufficient to reach a stable state in the ear and hence measure a permanent threshold shift (PTS). As a test of this premise, half the exposed animals ($N=16$) were maintained an additional 5 months and retested.

2. Tests of hearing

Audiometric procedures required that the animals be anesthetized at the time of recording; therefore, they were premedicated with a subcutaneous injection of atropine (0.05 mg/kg) and anesthetized about 10 min later with an IP injection of sodium pentobarbital (28.6 mg/kg). Body temperature was monitored rectally and controlled by an indicating controller operating a hot water heating pad to maintain body temperature at 38.6 °C. The animals' heads were clipped closely and a depilatory applied before application of the surface electrodes on the vertex and frontal sinus.

Ears were routinely otoscoped before testing and swabbed if necessary. Hearing tests were conducted in a double-walled sound attenuating chamber. Hearing sensitivity was established by measuring brain-stem-evoked responses (BSER) to tone pips at 1, 2, 4, 8, and 16 kHz presented in 5-dB steps. Threshold was taken to be 2.5 dB below the lowest level at which Wave V of the BSER could be seen following an average of 1024 stimuli. The tone pips (two cycles on the rising, plateau, and falling phases) were delivered at 16 per second through an Etymotic™ ER-2 insert earphone positioned in the outer ear canal of the animal. Because of the distinctive anatomy of the cat ear canal it was easy to position the earphone tip repeatably. Given the tendency for negative pressures to develop in the unventilated middle ear and hence to block sound transmission (Guinan and Peake, 1967), a gentle tug on the animal's tongue encouraged swallowing and clearing the middle ear before tests and just before the noise exposure. With the Etymotic earphone, the interaural attenuation was adequate to allow the right and left ears to be tested independently. Electrode impedances were accepted if they were less than 5 kOhms and were most often near 1 kOhm. Potentials were amplified (10 000 times by a Princeton Applied Research™ PAR 113 amplifier), bandpass filtered (300–10 000 Hz), and averaged using Tucker-Davis™ modules and a locally developed program implemented in a PC.

With the stimulating system, the maximum sound pressure that could be produced was somewhat above 90 dB; hence the maximum threshold *shift* that could be measured was 70 or 80 dB. If a BSER could not be measured following an exposure, the threshold was arbitrarily recorded as >80 dB and for statistical purposes the shift was taken to be 80 dB. This procedure was required in 22% of the measures immediately after exposure and in 4% of the measures following recovery. The intent was to be statistically neutral; however, it may have been somewhat conservative (threshold shifts recorded may have been smaller than actual shifts).

3. Noise exposures

Animals were exposed to the sound of airbag inflations inside the cab of a midsized pick-up truck. Resting platforms

in the cab provided minimum acoustic obstruction between the animals' pinnas and the airbags and held the animals facing forward with their ear canals at the level normally occupied by the canals of a human passenger or driver. Their heads were supported in this position by a small chin rest formed from modeling clay.

Airbags are designed to fit the physical and crash requirements of specific vehicles, taking into account the space available for the module's storage as well as the space into which they must deploy. The airbags in our experiments were prototypes of those normally fitted in the test vehicle and the inflation mechanism was gas produced by a burning propellant (sodium azide). We intended to produce a generic airbag waveform that would be of applied interest and at the same time provide a challenge for our mathematical model of auditory hazard (Price and Kalb, 1991). In all, there were 16 exposures (32 animals) with the remaining 4 animals used as controls.

Three different passenger compartment venting conditions were tested: (1) the doors open, (2) the doors and windows closed, and (3) the doors and windows closed and seams sealed with duct tape. In conditions (1) and (2), both passenger and driver bags were deployed (four deployments for each venting condition) and in condition (3) the passenger bag only was deployed in seven cases, both bags in one case. In order to maintain a fairly realistic volume in the passenger compartment (compensating for the missing body volumes of human occupants), a wooden timber and bags of absorbent clay were placed on the seat and floor of the compartment.

4. Noise measurement

Airbag noise is a measurement challenge because of its combination of wide bandwidth and high sound-pressure levels. In a closed passenger compartment there is a low-frequency pressure rise and decay which has significant energy in the 1-Hz frequency region, which we believe needs to be measured accurately. While 1 Hz may be well below the nominal limit of hearing for the ear, the hazard model suggests that it may nevertheless be important because the low-frequency pressure may cause the stapes to displace and reach its limit of travel. This would stiffen the middle ear and modulate transmission of the frequencies that *are* in the normal range of hearing (Price and Kalb, 1991). An alternate basis for needing to measure low-frequency energy is the fact that some damage-risk criteria rate hazard based on peak pressure. Hence, this low-frequency pedestal needs to be reproduced accurately because it is a part of the true peak pressure. We conclude that the low-frequency cutoff of the measurement system has to be much lower than has normally been thought acceptable. Beyond the question of extended low-frequency sensitivity is the problem of measuring the high sound-pressure levels. Condenser microphones commonly begin to distort above 160 dB and airbags may produce pressures 10 dB higher than that. Piezo-resistive gauges suitable for higher pressures commonly have a higher noise floor and lose some high-frequency sensitivity. A thorough discussion of measurement techniques is beyond the scope of this article, but the problem of getting an accurate pressure history is real and is noted so that the reader may be aware of the problem.

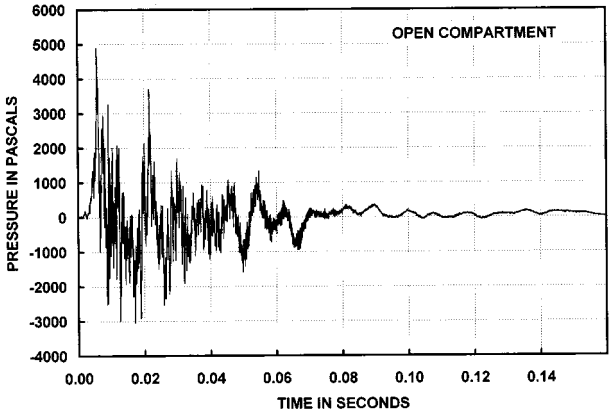

FIG. 1. Pressure history at the driver's right ear position for an airbag deployment with the doors to the passenger compartment open. Both driver and passenger airbags were deployed.

The measurement techniques used in the present study followed those of Rouhana *et al.* (1994). Pressure histories were transduced by Dytran™ 2013V pressure gauges mounted just inside the inboard ears of the animals (right ear of the ''driver,'' left ear of the ''passenger''), with the sensing surface at grazing incidence to the waveform from the nearer airbag. The waveforms were digitized at 50-kHz sampling rate with a 12-bit digitizer and were stored on disk for analysis off-line. The system had a frequency response from 1 Hz to 10 kHz (± 1 dB).

II. RESULTS

A. Acoustic data

Typical pressure histories recorded for the three venting conditions are shown in Figs. 1–3 and a numeric summary of the mean acoustic data is presented in Table I. In general, the acoustic data were highly similar for the two measurement locations (driver's right ear and passenger's left ear) and were consistent with previous studies (Nixon, 1969; Rouhana *et al.*, 1994). In that context, we note that because the acoustic measuring system used on the Nixon study had a 30-Hz low-frequency cutoff, their measured peak pressures were probably somewhat lower than they should have been.

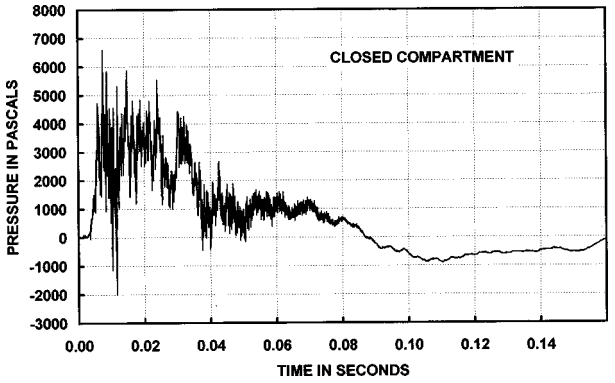

FIG. 2. Pressure history at the driver's right ear position for an airbag deployment when the passenger compartment doors were closed. Both driver and passenger airbags were deployed.

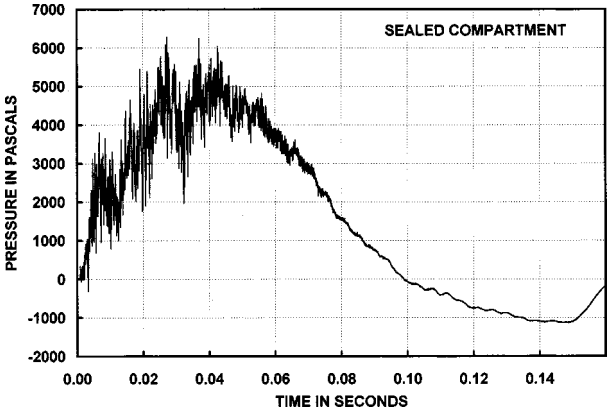

FIG. 3. Pressure history at the driver's right ear position for an airbag deployment when the passenger compartment doors were closed and sealed with tape. Only the passenger bag was deployed.

The airbag is in reality a complex set of acoustic sources and in addition, the deployments occurred in a small passenger compartment which meant that the sound field also included many reflected components. In any case, the patterns and pressures were generally repeatable, e.g., the standard deviations for peak pressure in Table I are between 0.9 and 1.9 dB. An analysis of the sources of airbag noise (Hickling and Posey, 1973; Posey and Hickling, 1973) suggests that the pressurization of the closed passenger compartment by the discharge of gas from the inflation system produces the highest pressure and has a spectral peak below 20 Hz. A second source is associated with the unfolding and movement of the bag surfaces (producing sounds largely in the 500- to 3500-Hz region). Finally, the third source is noise associated with gas production and flow into the bag (describable as a broadband jet noise with frequencies up to at least 10 kHz). Our examination of the present acoustic data is consistent with this analysis. The peak pressure from the fill (open compartment) was about 165 dB. The lower-frequency components (seen in the closed compartment) reached peak pressures about 2 to 4 dB higher and together produced peak pressures in the vicinity of 170 dB.

A pressure history for the open door condition is shown in Fig. 1. It was measured at the driver's right ear and includes the inflation of both the driver and passenger bags. The waveform reflects filling and expansion of the bags without a general pressure buildup in the passenger compartment. In Fig. 2 we see a pressure history at the driver's right ear for the closed compartment condition (both bags deployed). The initial positive portion of the waveform has returned to ambient pressure in about 35 msec while the filling noise is still present. In contrast, Fig. 3 shows that when the compartment has been sealed—and in spite of the fact that only the passenger bag was deployed—the positive phase of the pressure lasts much longer, returning to baseline pressure only after 100 msec, well after the filling noise has subsided.

TABLE I. Acoustic analysis of airbag waveforms. All numeric data are arithmetic means. For open and closed conditions, both passenger and driver airbags were deployed, but for the sealed condition only the passenger bag was deployed. Energies stated in this article were calculated by dividing the integral of the squared pressure (in pascals) by the impedance of air (taken to be 407 rayls).

Venting	Peak SPL	SD	Energy (unweighted)	Energy (A-weighted)
Open	168.2 dB	1.9 dB	191 J/m^2	56 J/m^2
Closed	171.4 dB	0.86 dB	1248 J/m^2	81 J/m^2
Sealed	170.1 dB	1.3 dB	2599 J/m^2	40 J/m^2

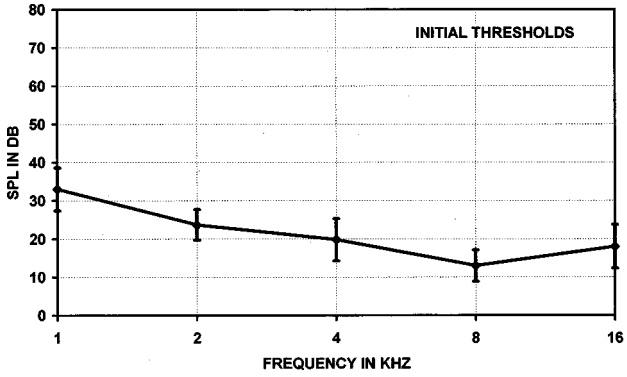

FIG. 4. Mean thresholds for all exposed animals ($N=32$) measured before exposure. The error bars represent ± 1 SD at each frequency.

The peak pressures are as expected from simple physical considerations. Given a passenger compartment with a volume of approximately 2 m^3 and passenger and driver airbags with volumes of about 0.08 and 0.06 m^3, respectively, then, ignoring the gas venting from the bags, leaks in the passenger compartment, the absorbency of the upholstery, etc., the change in effective volume of 0.14 m^3 would increase the pressure to a little over 170 dB, which is essentially what we measured when two bags were deployed.

The average unweighted energies in the impulses rose from about 200 J/m^2 for the open condition to more than 2500 J/m^2 for the sealed compartment. This increase was largely due to the addition of energy in the very low-frequency region. If the energy in the impulses is A-weighted (which cuts the very low frequencies severely), then energies are more nearly equal for all deployments. The average A-weighted energy for all deployments was 55 J/m^2, which in yet another frame of reference is an L_{AEQ8} of 93 dB.

B. Auditory data

1. Initial sensitivity

The mean thresholds for all the ears are presented in Fig. 4 along with error bars ($\pm$ one standard deviation) at each frequency. The sensitivities are those expected for the cat ear measured in this fashion (Price and Wansack, 1989). The average standard deviation was 5 dB, as would be expected in normal audiometry.

2. Threshold shift data

Hearing loss measured immediately after exposure is traditionally referred to as compound threshold shift (CTS) because it includes both temporary and permanent components. The CTSs were large and the distribution of loss followed the same pattern for all venting conditions. The mean CTSs are plotted in Figs. 5–7 for each condition. Permanent

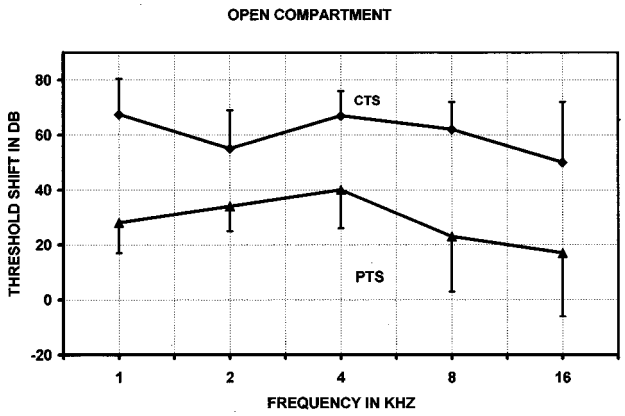

FIG. 5. Mean threshold shift measured immediately after exposure (CTS) and at one month post exposure (PTS) for the 8 animals (16 ears) exposed in the open passenger compartment.

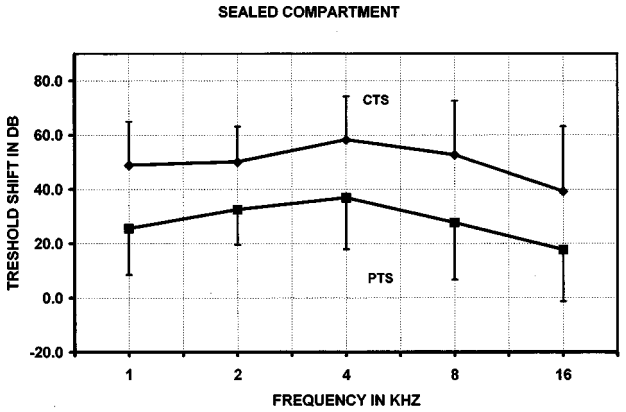

FIG. 7. Mean threshold shift measured immediately after exposure (CTS) and at one month post exposure (PTS) for the 16 animals (32 ears) exposed in the sealed passenger compartment.

threshold shifts (PTSs) are also plotted for comparison on the same graphs. The CTSs were approximately 60 dB at 4.0 kHz and slightly less at higher and lower frequencies. In general, the losses fell in a range that allowed interpretation, i.e., all ears showed some loss; yet enough residual hearing remained that the ears could be evaluated.

Clearly, airbag noise represents a significant hazard for the cat ear. Admittedly, the present experiments were designed to test ears in a maximally susceptible state. With anesthetized animals, there was no ongoing middle ear muscle activity and no likelihood of a protective contraction in advance of the impulse. While we are confident that the middle ear muscles were quiescent at the time the impulse arrived, there is still an open question as to whether or not the middle ear muscles could have contracted during the impulse. At least for the sound intensities reached in normal laboratory tests (typically a little over 100 dB), the anesthetic is thought to effectively prevent contractions. However, the sound field from the airbag is some 60 dB higher and in addition, at those pressures (near 1 pound per square inch, for those who still think in traditional units) the mechanical stimulation of the face by the waveform is perceptible and is also known to elicit a muscle response. Therefore, given the intense stimulation and the extremely short latency for the middle ear muscle reflex (4–10 msec) (Carmel and Starr, 1963; Djupesland, 1965; Eliasson and Gisselsson, 1955; Simmons, 1963), it is possible that an elicited middle ear muscle response could have acted in time to affect the latter portion of the airbag impulse. We conclude that while we are confident that the middle ear muscles were quiescent at the onset of the impulse, we cannot rule out the possibility that they may have been active in the latter part of the exposure and have provided the ear some protection.

The PTSs are also plotted in Figs. 5–7 and they parallel the CTSs. The maximum PTS remained at 4.0 kHz and there was slightly less loss at higher and lower frequencies. Visual inspection of PTS reveals somewhat smaller values for the open compartment condition as compared with the closed or sealed compartments, especially at the higher frequencies. This difference is not statistically significant (paired T-tests) and is largely due to the relatively small number of animals tested ($N=7$) and the fact that the initial thresholds for one animal may have been somewhat high (hence shifts were low).

3. CTS/PTS relationship

The scatter plot in Fig. 8 portrays the relationship between CTS and eventual PTS. In it, PTS at 4.0 kHz is plotted as a function of CTS at the same frequency and a least-squares regression line has been fitted to the data. The slope of the line is 0.86 (every dB of CTS is likely to become 0.86

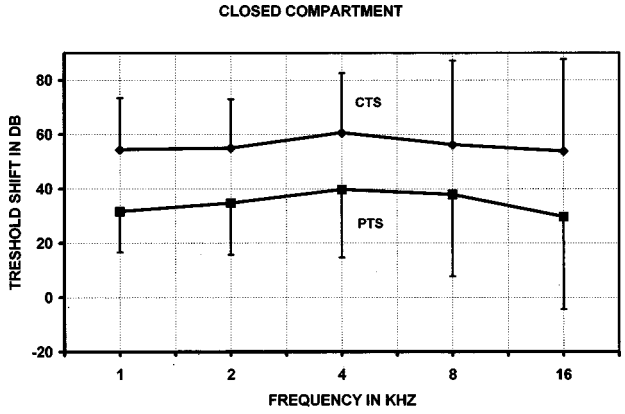

FIG. 6. Mean threshold shift measured immediately after exposure (CTS) and at one month post exposure (PTS) for the 8 animals (16 ears) exposed in the closed passenger compartment.

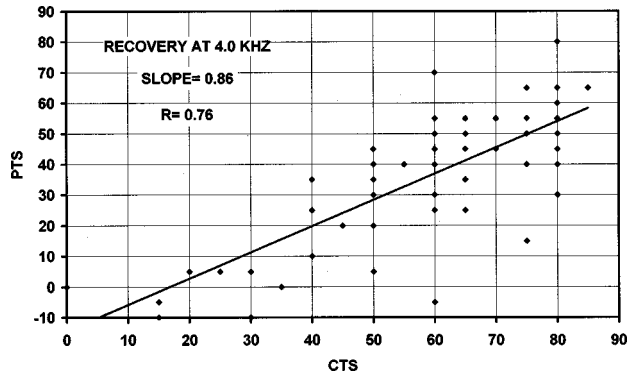

FIG. 8. Scatter plot of PTS as a function of CTS at 4.0 kHz for all 64 ears. A least-squares regression line has been fitted to the data.

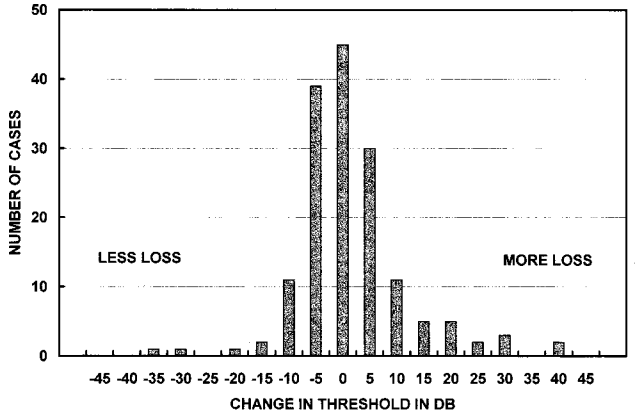

FIG. 9. Change in threshold between 1 month and 6 months for all five test frequencies, both ears of 16 animals. Size and direction of change on the *x*-axis and number of cases on the *y*-axis.

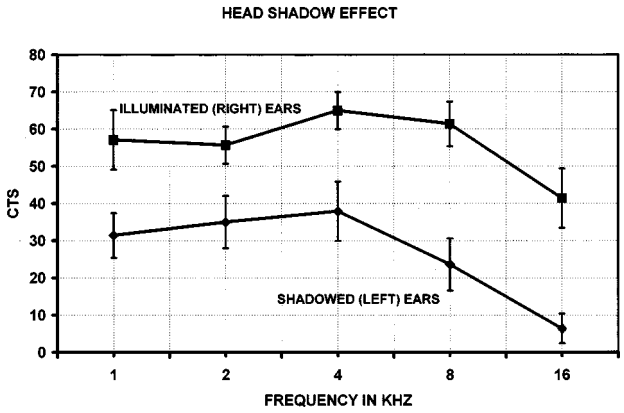

FIG. 10. Mean threshold shift measured immediately after exposure for the right ears (top curve) and left ears (lower curve) of the seven cats in the driver position, sealed passenger compartment, in which only the passenger-side airbag was deployed.

dB of PTS) and its X-intercept is 16.8 dB (a CTS that size is projected to give no PTS). Similar plots could have been included for all test frequencies. The mean slope for all five regression lines was 0.67, the mean X-intercept was 9.2 dB, and the mean correlation between CTS and PTS was 0.67. These data are very much like those previously reported for the cat ear exposed to primers, rifles, and howitzers (Price, 1986; Price and Wansack, 1989) and also for the chinchilla exposed to intense impulses from a speaker (Patterson *et al.*, 1986). When an ear has been exposed to very intense sounds (above a ''critical level'' for that ear) it appears that CTSs greater than 10 to 15 dB will resolve to about 7 dB of PTS for every 10 dB of CTS. This relatively limited recovery is consistent with the contention that at very high exposure levels, the ear has sustained serious mechanical injury.

4. Longer term recovery

Thresholds were measured at 1 month in all the animals and half were retested after an additional 5 months. To see whether the ears had indeed stabilized at 1 month, changes in threshold between the 1 month and 6 month measures were plotted on the abscissa of Fig. 9 and the number of thresholds showing that change on the ordinate. In all, there were 160 data points (16 animals$\times$2 ears$\times$5 frequencies). There is an obvious collection of data points around 0-dB change: 71% of the data were within $\pm$5 dB and 85% were within $\pm$10 dB. The location of the peak at 0-dB change suggests that no general process of recovery or deterioration is taking place after 1 month, and the general width of at least the central portion of the distribution suggests that the variability is about what would be expected from test–retest variability in good audiometry. On the other hand, 15 data points from 7 animals show more than 15 dB of change. One animal accounted for 6 of the data points (its hearing had grown worse), but if we isolate just the 15 data points and check the size of the initial CTS, an insight emerges. Namely, it appears that continued worsening of hearing was associated with initial losses that were 40 dB or greater and continuing improvement was associated with initial losses that were 30 dB or less. There are too few data to make much of this interpretation, but it does have the virtue of being reasonable. With respect to the question of whether or not recovery is complete at 1 month, while most of the changes may have run their course, nevertheless, some changes may still be occurring in the 1- to 6-month period.

5. Head shadow effect

There is one instance in which there was a real difference in the action of the airbag noise. If we take only those cases in which just a passenger-side airbag was deployed (seven in the sealed passenger compartment), then an interesting analytical possibility presents itself. For the driver position, the primary acoustic source was the passenger-side airbag located to the right front of the animal. The left ear was thus on the far side of the head from the impulse source and was potentially afforded the protection of the head's acoustic shadow. This contention is weakened by the fact that the cat's head is small (and can therefore be a significant shadow only for high frequencies) and the noise field was reverberant, in which case one cannot maintain that the sound field actually has a single angle of incidence. Nevertheless, the CTSs in the right and left ears of these animals are shown in Fig. 10. The difference between the two curves averages about 30 dB, which is highly significant statistically at all frequencies (paired T-test, $P<0.0003$). Furthermore, the difference was maintained following 1 month of recovery ($P<0.003$). We can conclude that the head shadow probably did offer significant protection to the left ears of the driver cats. The T-statistic was used in comparisons (rather than an ANOVA) because of the authors' concern that due to the mechanical nature of the loss process at very high intensities, threshold shifts for individual frequencies could not be considered independent.

The protection afforded the shadowed ears might have been the result of only a few dB of attenuation. Previous work (Patterson *et al.*, 1986; Price and Wansack, 1989) has shown that at least for the cat and chinchilla, once a loss threshold has been exceeded for very intense sounds, CTS grows very rapidly, i.e., for every dB of increase in SPL, the CTS grows by 7 dB. Thus an attenuation of only 3 to 5 dB could explain the differences between the two ears. The head-related transfer function data for the cat from Wiener

et al. (1965), while not measured at precisely the angle appropriate for the exposure in the present experiment, nevertheless indicate that differences between the ears of at least that magnitude do exist in the free field.

In passing, it might be noted that the reduced threshold shift in the shadowed ears does result in the plots of mean CTS and PTS in Fig. 7 (threshold shifts in the sealed compartment) being slightly lower. If just the nonshadowed ears are plotted, the curves match those in Figs. 5 and 6 much more closely.

III. DISCUSSION

A. General implications for methods of assessing hazard

The present experiments join others in offering insights with respect to the general question of damage mechanisms as a function of level. The question is often raised as to whether A-weighted energy, now commonly used for assessing occupational noise hazard, might be used for all noise exposures, even up to the very high sound-pressure levels characteristic of gunfire. If the middle ear is linear under all conditions and the loss mechanisms in the cochlea are in fact related in a simple way to the energy reaching it, then it is reasonable to suppose that an A-weighted energy measure could serve for hazard evaluations at all levels (Price, 1982). If not, then the data should reflect it.

The results of the present experiment join others in suggesting that an energy measure fails at very high intensities. For example, Miller *et al.* (1963) exposed the cat ear to continuous noise (peak pressure less than 115 dB, spectral peak in the midrange), with the result that an exposure of 2200 J/m^2 produced a 38-dB PTS. In contrast, the airbag impulses in the present study did essentially the same damage and involved only 40 to 81 J/m^2 (A-weighted) at peak pressures of 168 to 171 dB. Exposures of the cat ear to gunfire-type impulses at 140-dB peak pressure have produced essentially the same PTS, but with exposure energies of only 0.3 J/m^2 (Pierson *et al.*, 1995; Price *et al.*, 1996; Price and Wansack, 1989).

In this regard, there might be a question about the legitimacy of A-weighting energy with the cat ear. Although the cat ear is more sensitive in the midrange than the human, the low-frequency slope of its sensitivity is close to that of the human (about 12 dB/oct) (Rosowski, 1994). Hence, at least on a relative scale, we might argue that A-weighting could also be used in rating the susceptibility of the cat ear.

The airbag data join the gunfire-type impulses in suggesting that relatively little energy at high SPLs can produce large losses. With 14 to 17 dB less energy, airbags produced the same damage as the exposure of Miller *et al.* (1963). And the gunfire-type exposures were equally hazardous with 39-dB less energy. These data can be viewed as supporting the contention that there is a level, in this case between 115 and 140 dB, where the loss mechanism becomes fundamentally mechanical in nature and relatively little energy produces large losses (Price, 1981).

However, these data hold an additional complexity. Namely, gunfire at 140 dB produced 40-dB PTSs with 22- to 25-dB *less* energy than did the airbags at about 170 dB. This peculiar ''inversion'' of effect can be explained by a peak-clipping conductive nonlinearity in the middle ear that limits stapes displacements for the airbag impulses and offers considerable protection to the inner ear (Nixon and Sommer, 1973; Price and Kalb, 1991; Price, 1974). The complex response of the ear just outlined, i.e., increasing susceptibility at high SPLs yet reduced susceptibility when pressures are even higher, has been captured by a mathematical model of the ear which does predict the hazards at high levels (Price and Kalb, 1996b, 1991). Given the complexity of the ear's behavior, it is reasonable to conclude that something more than A-weighted energy will be needed to cover the full range of hazard assessment from ordinary occupational noises to airbags.

B. Application to human exposure

Even though airbag impulses can cause large losses in the cat ear, both the pioneering study of Nixon (1969) and a paucity of hearing loss currently reported from ''accidental'' exposures on the highway (Yaremchuk, 1998) appear to argue that there is little problem for the human ear. The answer to this conundrum is probably embedded in some combination of the following list of possibilities, which could form the basis for additional investigations.

First, it may be that the cat ear is simply much more susceptible than the human ear. As previously indicated, this is probably true, and given the fact that in the present experiments the animals were deprived from at least some of the protection offered by their middle ear muscles, they may have been in an especially susceptible state.

Second, hearing losses from adventitious exposures of human ears in accidents may be present but unrecognized. There are anecdotal reports of accident victims seeing people's mouths move but hearing no sound, which would indicate at least a serious temporary loss of hearing. The literature also includes a small number of cases of permanent hearing loss that can reasonably be connected to airbag noise exposure (Mattox and Price, 1995; Saunders *et al.*, 1995; Yaremchuk, 1998). The fact that relatively few cases of permanent hearing loss have been established may say little about the actual rate of incidence of hearing loss. A significant amount of hearing loss might actually be present but unreported. It is often observed in the clinic that adults may have a sizable hearing loss and be unaware of it. Of course, the same thing would be especially true for babies or young children who may be more susceptible than adults (Price, 1976). It is also possible that reduced hearing sensitivity may not be the only auditory effect. There are also some reports of tinnitus and hyperacusis associated with accidents in which airbags deployed (Tabachnick, 1996; Yaremchuk, 1998). Given the intrusive character of these conditions, it is interesting to speculate that they rather than hearing losses would be reported.

There are no definitive data relating susceptibility in the cat ear (or any other ear for that matter) to human susceptibility. However, the two ears are very similar and it is commonly assumed that the average cat is like a ''susceptible''

human. If that is indeed the case, then it is probable that some small percentage of human ears risk permanent hearing impairment from airbag noise exposure.

Third, the original experiment on airbag safety (Nixon, 1969), which essentially gave the airbag a clean bill of health, was well designed and executed; however, it should not be overinterpreted. With more than a quarter century of hindsight, a number of issues might now be raised. First, the use of young, adult, volunteers with good hearing may have inadvertently excluded the most susceptible individuals. Additionally, there was the understandable exclusion of babies and children. Second, the subjects knew approximately when the airbag was going to be deployed, and as a result, in bracing for the event they had involuntarily contracted their middle ear muscles and protected themselves. In practice, the same thing may be true for the individual who sees the accident coming. However, some passengers (or even drivers) may be asleep or otherwise unaware at the time of the accident and hence lack middle ear muscle protection at the start of the exposure (like the cats in our experiments). A final comment on the conclusions of the Nixon (1969) study can be no more than a word of caution. Analysis of the present airbag impulses with a human ear model suggests that for the human ear, a vented passenger compartment and middle ear muscles not already contracting at the start of the impulse could result in permanent hearing losses in a significant portion of those exposed (Price, 1997, 1998).

What then can we conclude with respect to human exposure? While it is true that there are only a few clinical reports of hearing loss from airbag noise exposure, the hearing loss seen in the cat ear clearly argues that it is premature to assume that there is no hazard to the human ear. At present, it would be prudent to assume that airbag noise represents a finite risk for a susceptible human ear.

C. Follow-on research

The foregoing discussion makes testable contentions with respect to noise hazard from airbags. First, in practice we might expect to find hearing loss associated with airbag noise exposure in a susceptible portion of the exposed population, especially if the persons were unaware that an accident was in progress and did not benefit from a middle ear muscle contraction in advance of airbag deployment. In the same vein, those who may have diminished middle ear muscle reflexes may be especially susceptible. A further prediction would be that if the head or other acoustic barrier were between the airbag and an ear, then the ''shadowed'' ear should be less affected.

Clearly, these possibilities should be explored and quantified. However, the problems associated with actually acquiring such evidence are legion. Emergency rooms are not normally equipped for audiometry and with the other trauma associated with accidents, audiometric tests surely don't have a high priority. If hearing were tested at some point, then with no preexposure audiogram, there would be no way to know whether a loss had actually occurred as a function of the accident. For that matter, is the noise of an accident hazardous even without an airbag? We have only unpublished data, but the peak pressure in a barrier crash probably exceeds 145 dB (Rouhana, 1997). A definitive study would need to demonstrate, with both pre- and post-exposure measures, that the incidence of hearing loss in accidents in which airbags deploy is different from that in accidents of equal severity but in which no airbags deployed. In addition, the study would correlate losses with the proposed susceptibility factors.

Finally, a valid theory of hearing loss to intense sounds would be an asset in ordering and interpreting any data that are developed. Such a theory could be used proactively to suggest designs that are both safe and effective (Price, 1997).

ACKNOWLEDGMENTS

The authors would like to recognize the expert technical assistance of Howard Bender, Jean Breitenbach, Joseph McCleary, Stephen Rouhana, and David Salva, who participated in the experimental phase of this research.

Ahroon, W. A., and Hamernik, R. P. (**1996**). ''The effects of noise during recovery from an acute acoustic trauma,'' J. Acoust. Soc. Am. **100**, 2627.

Carmel, P. W., and Starr, A. (**1963**). ''Acoustic and nonacoustic factors modifying middle-ear muscle activity in waking cats,'' J. Neurophysiol. **26**, 598–616.

CHABA (**1968**). ''Proposed damage-risk criterion for impulse noise (gunfire),'' Report of Working Group 57, NAS-NRC Committee on Hearing, Bioacoustics and Biomechanics, Washington, D.C.

Dancer, A., Buck, K., Vassout, P., and Lenoir, M. (**1985**). ''Influence du niveau de crete et de la duree d'ondes de choc (bruits d'armes) sur l'audition du cobaye,'' Acustica **59**, 21–29.

Djupesland, G. (**1965**). ''Electromyography of the tympanic muscles in man,'' Intern. Audiol. **4**, 34–41.

Eliasson, S., and Gisselsson, L. (**1955**). ''Electromyographic studies of the middle ear muscles of the cat,'' Electroencephalogr. Clin. Neurophysiol. **7**, 399–406.

Guinan, J. J., and Peake, W. T. (**1967**). ''Middle-ear characteristics of anesthetized cats,'' J. Acoust. Soc. Am. **41**, 1237–1261.

Hamernik, R. P., Ahroon, W. A., and Patterson, Jr., J. H. (**1988**). ''Threshold recovery functions following impulse noise trauma,'' J. Acoust. Soc. Am. **84**, 941–950.

Hickling, R., and Posey, J. W. (**1973**). ''Noise mechanisms in the inflation of automotive safety airbag,'' J. Acoust. Soc. Am. **54**, 331.

Luz, G. A., and Hodge, D. C. (**1971**). ''The recovery from impulse noise-induced TTS in monkeys and man: Descriptive model,'' J. Acoust. Soc. Am. **49**, 1770–1777.

Mattox, D. E., and Price, G. R. (**1995**). ''Acoustic properties of automobile airbag deployment,'' *Proceedings of 18th Midwinter Meeting of Assoc. for Research in Otolaryngol*, St. Petersburg, FL, p. 168.

Miller, J. D., Watson, C. S., and Covell, W. P. (**1963**). ''Deafening effects of noise on the cat,'' Acta Oto-Laryngol. Suppl. **176**, 91.

NATO RSG6/PANEL8 (**1987**). ''The effects of impulse noise,'' Document AO/243/(PANEL8/RSG.6)D/9, NATO, 1110 Brussels, p. 33.

Nixon, C. W. (**1969**). ''Human auditory response to an airbag inflation noise,'' Report for Contract No. P.O. #9-1-1151, U.S. Department of Transportation, Federal Highway Administration, National Highway Safety Bureau, Washington, D.C. 20591.

Nixon, C. W., and Sommer, H. C. (**1973**). ''Primary components of simulated airbag noise and their relative effects on human hearing,'' Report on DOT Interagency Agreement IA-o-1-2160, National Highway Traffic Safety Administration Research Institute, Office of Vehicle Structures Research, Biomechanics Div., Washington, D.C. 20024.

Patterson, J. H., Lomba-Gautier, I. M., Curd, D. L., Hamernik, R. P., Salvi, R. J., Hargett, Jr., C. E., and Turrentine, G. (**1986**). ''The role of peak pressure in determining the auditory hazard of impulse noise,'' U.S. Army Aeromedical Research Laboratory Rep. No. 86-7, USAARL, Ft. Rucker, AL 36362-5000.

Pierson, L. L., Price, G. R., Kalb, J. T., and Mundis, P. A. (**1995**). ''Comparison of impulse noise effects generated by two rifle muzzles,'' J. Acoust. Soc. Am. **97**, 3344.

Posey, J. W., and Hickling, R. (**1973**). ''Noise mechanisms in the inflation of the automotive safety airbag,'' GM Research Publication 1411.
Price, G. R. (**1998**). ''Airbag noise hazard: From theory toward validation,'' J. Acoust. Soc. Am. **104**, 1769.
Price, G. R. (**1997**). ''Airbag noise hazard examined with mathematical model of the human ear,'' J. Acoust. Soc. Am. **102**, 3201.
Price, G. R. (**1986**). ''Impulse noise hazard as a function of level and spectral distribution,'' in *Basic and Applied Aspects of Noise-Induced Hearing Loss*, edited by R. J. Salvi, D. Henderson, R. P. Hamernik, and V. Coletti (Plenum, New York), pp. 379–392.
Price, G. R. (**1982**). ''A-weighting and the rating of auditory hazard,'' J. Acoust. Soc. Am. **72**, S25.
Price, G. R. (**1981**). ''Implications of a critical level in the ear for the assessment of noise hazard at high intensities,'' J. Acoust. Soc. Am. **69**, 171–177.
Price, G. R. (**1976**). ''Age as a factor in susceptibility to hearing loss: Young versus adult ears,'' J. Acoust. Soc. Am. **60**, 886–892.
Price, G. R. (**1974**). ''Upper limit to Stapes displacement: Implications for hearing loss,'' J. Acoust. Soc. Am. **56**, 195–197.
Price, G. R., and Kalb, J. T. (**1996a**). ''Evaluation of hazard from intense sound with a mathematical model of the human ear,'' J. Acoust. Soc. Am. **100**, 2674.
Price, G. R., and Kalb, J. T. (**1996b**). ''Modeling auditory hazard from impulses with large low-frequency components,'' J. Acoust. Soc. Am. **99**, 2464.
Price, G. R., and Kalb, J. T. (**1991**). ''Insights into hazard from intense impulses from a mathematical model of the ear,'' J. Acoust. Soc. Am. **90**, 219–227.
Price, G. R., Kim, H. N., Lim, D. J., and Dunn, D. (**1989**). ''Hazard from weapons impulses: Histological and electrophysiological evidence,'' J. Acoust. Soc. Am. **85**, 1245–1254.
Price, G. R., Pierson, L. L., Kalb, J. T., and Mundis, P. (**1995**). ''Validating a mathematical model of noise hazard with varying numbers of rounds and peak pressures produced by a rifle,'' J. Acoust. Soc. Am. **97**, 3343.
Price, G. R., Rouhana, S. W., and Kalb, J. T. (**1996**). ''Hearing hazard from the noise of airbag deployment,'' J. Acoust. Soc. Am. **99**, 2464.
Price, G. R., and Wansack, S. (**1989**). ''Hazard from an intense mid-range impulse,'' J. Acoust. Soc. Am. **86**, 2185–2191.
Rosowski, J. J. (**1994**). ''Outer and middle ears,'' in *Comparative Hearing: Mammals*, edited by R. R. Fay and A. N. Popper (Springer-Verlag, New York), pp. 172–247.
Rouhana, S. W. (**1997**). Unpublished data.
Rouhana, S. W., Webb, S. R., Wooley, R. G., McCleary, J. D., Wood, F. D., and Salva, D. B. (**1994**). ''Investigation into the noise associated with airbag deployment: Part I—Measurement technique and parameter study,'' *Proceedings 38th Stapp Car Crash Conference*, pp. 191–212.
Saunders, J. E., Luxford, W. M., and Slattery III, W. H. (**1995**). ''Automobile airbag impulse noise: Otologic symptoms in five patients,'' in *Proceedings of Meeting of Otolaryngology-Head and Neck Surgery*, p. 60.
Saunders, J. E., Slatttery III, W. H., and Luxford, W. M. (**1998**). ''Automobile airbag impulse noise: Otologic symptoms in six patients,'' J. Acoust. Soc. Am. **104**, 1769.
Simmons, F. Blair (**1963**). ''An analysis of the middle-ear-muscle acoustic reflex of the cat,'' in *Middle Ear Function Seminar*, Report No. 576, U.S. Army Medical Research and Development Command, Ft. Knox, KY, pp. 32–62.
Tabachnick, B. (**1996**). ''Airbag safety—airbag risk,'' Tinnitus Today **21**, 9–12.
Wiener, F. M., Pfeiffer, R. R., and Backus, S. N. (**1965**). ''On the sound pressure transformation by the head and auditory meatus of the cat,'' Acta Oto-Laryngol. **61**, 255–269.
Yaremchuk, K. (**1998**). ''Otologic effects of airbag deployment,'' J. Acoust. Soc. Am. **104**, 1770.

Sound field modeling in streets with a diffusion equation

J. Picaut,[a] L. Simon, and J. Hardy
Institut d'Acoustique et de Mécanique, LAUM UMR CNRS 6613, Avenue O. Messiaen, 72085 Le Mans Cedex 9, France

(Received 3 December 1998; accepted for publication 18 July 1999)

By assuming that the surface irregularities of the building facades are adequate to produce diffusion in streets, a diffuse sound field model using the mathematical theory of diffusion is used to predict the sound propagation and its reverberation in rectangular streets. This model, developed to predict the sound field in rooms with diffusely reflecting boundaries, is applied in this paper to urban acoustics. A 3D diffusion equation is derived for the sound energy density and solved for time-varying sources and in steady state. A diffusion parameter is introduced to characterize the amount of diffusion in the street. An exchange coefficient depending on the absorption coefficient is also used to take into account the wall absorption. When the diffusion coefficient is rightly chosen, the predicted reverberation times and sound attenuations are in accordance with measurements in a scale model of a street. © *1999 Acoustical Society of America.* [S0001-4966(99)02511-4]

PACS numbers: 43.50.Vt, 43.20.Fn, 43.28.Fp, 43.50.Lj [MRS]

INTRODUCTION

Because of the high economical cost of noise impact in urban areas, and also since people look for a better way of life, the modeling of noise propagation in a city has attracted considerable attention.

Since Wiener's works,[1] many authors have modeled streets as long channels with absorbing walls and a reflecting pavement, in order to apply methods of virtual sources[2–4] and propagating modes.[5] However, differences were observed between models and measurements in streets. Lyon[6] suggested that the part of multiple reflections, diffraction and diffusion of sound by building facades, could be more significant than expected and could account for these discrepancies. Following this idea, Donavan[7] and Davies[8] proposed more accurate models based also on image sources and taking into account scattering and multiple diffuse reflections by facades. Nevertheless, there is no result in the literature showing in which frequency range this assumption of diffuse sound field holds in practice. There are indeed very little experimental data concerning the sound level and the reverberation in street, and most of these experimental works give only results in a full frequency range. However, considering the size of the building facade irregularities, like balconies, carpentries, etc., it may be assumed that scattering and diffuse reflections occur from 250–500 Hz.

Then, considering this assumption of diffuse sound field in streets, a new model of sound propagation in urban areas is developed here. This theory is based on a diffusion equation which was first proposed for the modeling of diffuse sound fields in rooms[9] and long enclosures.[10] By changing some boundary conditions and introducing the three dimensions of space, this diffuse model is here applied to the modeling of the sound propagation in streets.

The main interest of this model is that the multiple diffuse reflections in the streets are simply taken into account by introducing a new parameter which describes the ''sound diffusivity'' of the building facades. Moreover, analytical solutions for both time-varying and steady sources can be found for standard urban configurations. Lastly and, although the model is applied in this paper only to rectangular streets, this diffusion theory may be easily extended to other urban configurations.

The basic theory of the diffusion model is presented in the next section and applied to streets. A diffusion equation is then derived for the sound energy density and solved both in time-varying and steady states. Finally, comparisons with measurements in a scale model of a street are discussed in Sec. II, which show good agreement.

I. THEORY

A. Basic theory of the diffusion model

In room acoustics, the sound field is usually modeled by sound particles having the same constant energy, propagating along straight lines and hitting wall or scattering objects. Consequently, such a process may be easily compared with the movement of a single particle in a gas. A diffusion theory was then developed to model the sound field in rooms[9] with diffusely reflecting boundaries by the use of this analogy. It was shown that the energy flow $\mathbf{J}$ in rooms, by unit surface and unit time, follows a diffusion gradient equation

$$\mathbf{J} = -D \operatorname{grad} w, \tag{1}$$

where w is the sound energy density. Here $D = \lambda c/3$ is a diffusion coefficient, depending on the mean free path λ of the room and on the sound velocity c. This equation is important, since it allows for a nonuniform sound energy in rooms and therefore for a flow of energy inside absorbing boundaries. Experimental observations of this phenomenon have already been done for a long time, but no suitable mathematical justification was given until now. The fundamental

[a]New address: Laboratoire Central des Ponts et Chaussées, Centre de Nantes, Route de Bouaye, B.P. 4129, 44341 Bouguenais Cedex, France. Electronic mail: Judicael.Picaut@lcpc.fr

consequence of relation (1) is that the energy density in rooms is described by a simple diffusion equation

$$\frac{\partial w}{\partial t} - D\Delta w = 0, \tag{2}$$

which is a mathematical extension of the classic concept of diffuse sound field in rooms. The energy distribution and the sound decay in rooms are found by solving Eq. (2) with the initial and boundary conditions. For walls with low absorption, an additional parameter, called *exchange coefficient h*, can be introduced in the boundary conditions.[10] According to the definition of *h*, the energy flow on a wall has to satisfy the following condition:

$$-D\frac{\partial w}{\partial n} = hw, \tag{3}$$

where *n* is the normal to the wall (set positively to the outside of the wall) and where *h* is defined by the absorption coefficient α of the wall and the sound velocity *c* by

$$h = \frac{c\alpha}{4}. \tag{4}$$

B. Diffusion model in streets

In this paper, it is assumed that the surface irregularities of buildings assure the diffusion of sound, such that the diffusion model can be applied without fundamental changes for the modeling of diffuse sound field in streets.

In rooms, considering that walls are uniformly diffusing, the diffusion coefficient *D* is supposed to be constant in all directions of propagation. In streets, the sound diffusion by buildings facades and by the pavement are different. Moreover, there is no sound reflection at both extremities and at the open top of the street. Then, the diffusion is not uniform in the street but depends on the directions of propagation. As a consequence, the diffusion coefficient in streets cannot be expressed by a single term, but by a set of diffusion coefficients. These coefficients define a new term **D**, written in Cartesian coordinates, as

$$\mathbf{D} = \begin{pmatrix} D_{xx} & D_{xy} & D_{xz} \\ D_{yx} & D_{yy} & D_{yz} \\ D_{zx} & D_{zy} & D_{zz} \end{pmatrix}, \tag{5}$$

and the diffusion gradient equation (1) is now written

$$\mathbf{J} = -\mathbf{D}\,\mathrm{grad}\,w. \tag{6}$$

In this paper, only rectangular streets are considered, but the model can be generalized to other street configurations. Because of symmetries and by having the *x*, *y*, *z* axis parallel to the axis of the street (Fig. 1), the diffusion coefficient is reduced to its diagonal components D_{xx}, D_{yy}, and D_{zz}.

Let *S* be the surface around the volume *V* of the street. The energy flow, crossing *S* through the open top, both extremities, the pavement and the side walls, to the inside of the street (**n** designing the normal to the wall), is given by

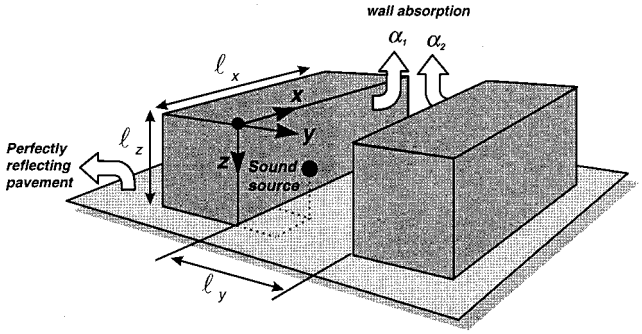

FIG. 1. Geometry of a rectangular street of size $l_x \times l_y \times l_z$. The pavement is assumed perfectly reflecting, while the side walls are characterized by their absorption coefficients α_1 and α_2. The origin is arbitrary set at a corner of a building. The volume *V* of propagation in the street is delimited by an imaginary surface *S* defined by the side walls, the pavement, the open top, and the two extremities.

$$\int\int_S \mathbf{n}\cdot\mathbf{J}\,dS = \int\int\int_V \nabla\cdot\mathbf{J}\,dV \tag{7}$$

and is opposed to the variation of sound energy by unit time in the street

$$\frac{\partial}{\partial t}\int\int\int_V w\,dV. \tag{8}$$

Without any internal sound source, the energy conservation in the street is obtained by summing Eqs. (7) and (8):

$$\int\int\int_V \left[\frac{\partial w}{\partial t} + \nabla\cdot\mathbf{J}\right] dV = 0. \tag{9}$$

Considering both relations (6) and (9), the diffusion equation for the sound energy $w(x,y,z,t)$ in the street is then written

$$\frac{\partial w}{\partial t} - \nabla\cdot(\mathbf{D}\cdot\mathrm{grad}\,w) = 0, \tag{10}$$

or, which is equivalent, in Cartesian coordinates

$$\frac{\partial w}{\partial t} - D_{xx}\frac{\partial^2 w}{\partial x^2} - D_{yy}\frac{\partial^2 w}{\partial y^2} - D_{zz}\frac{\partial^2 w}{\partial z^2} = 0. \tag{11}$$

C. Sound energy in rectangular streets

1. Initial conditions

Considering an impulsive sound source, at (x_0, y_0, z_0), the energy density at $t=0$ in the street has to satisfy

$$w(x,y,z,0) = w_0\,\delta(x-x_0)\,\delta(y-y_0)\,\delta(z-z_0), \tag{12}$$

where w_0 is the amplitude of the sound source and δ is the Dirac distribution.

2. Boundary conditions

The street is supposed to be rectangular of size $l_x \times l_y \times l_z$. The pavement is taken to be perfectly reflecting, since in practice it was shown that road and pavement are very good reflectors.[11] The side walls at $y=0$ and $y=l_y$ are char-

acterized respectively by the absorption coefficients α_1 and α_2, and by the exchange coefficients h_1 and h_2:

$$h_1=\frac{c\alpha_1}{4} \tag{13a}$$

and

$$h_2=\frac{c\alpha_2}{4}. \tag{13b}$$

At both extremities of the street ($x=0$ and $x=l_x$) and at the open top ($z=0$), the boundary condition (3) cannot be used since previous works[10] have shown that expression (4) is valid only for small absorption. Moreover, the relation (3) with (4) expresses a condition of reflection (with absorption) and not a condition of sound transmission or radiation. Nevertheless, if the sound source is inside the street and if the street is sufficiently long and buildings sufficiently high, the sound energy at the extremities is very weak with regards to the sound energy near the sound source. Then, the sound energy at the extremities may be neglected ($w=0$) in comparison with the sound field inside the street. Lastly, it is supposed there is no sound radiation at the extremities and the open top. These assumptions are introduced in order to simplify the model but should be revised in further developments.

As a consequence, the energy density in the street satisfies the following conditions, at the both extremities, on the side walls, at the pavement, and the open top:

$$w(0,y,z,t)=0, \tag{14a}$$

$$w(l_x,y,z,t)=0, \tag{14b}$$

$$-D_{yy}\frac{\partial w}{\partial y}(x,l_y,z,t)=h_2 w(x,l_y,z,t), \tag{15a}$$

$$D_{yy}\frac{\partial w}{\partial y}(x,0,z,t)=h_1 w(x,0,z,t), \tag{15b}$$

$$-D_{zz}\frac{\partial w}{\partial z}(x,y,l_z,t)=0, \tag{16a}$$

$$w(x,y,0,t)=0. \tag{16b}$$

3. Solution

A method is proposed in the Appendix to solve the equation of diffusion (11) with the initial and boundary conditions defined by Eqs. (12) and (14)–(16). According to Eqs. (A9), (A22), (A25) with (A26), and (A29) of the Appendix, the sound energy in a rectangular street is written in the following form:

$$\begin{aligned} w(x,y,z,t)=&\sum_{k,m,n=1}^{\infty} a_{kmn}\sin\left(\frac{k\pi x}{l_x}\right)\sin\left(-\frac{(2n-1)\pi z}{2l_z}\right)\\ &\times\left[u_m\cos\left(\frac{u_m y}{l_y}\right)+B_1\sin\left(\frac{u_m y}{l_y}\right)\right]\\ &\times\exp\left[-\frac{k^2\pi^2}{l_x^2}D_{xx}t-\frac{u_m^2}{l_y^2}D_{yy}t\right.\\ &\left.-\frac{(2n-1)^2\pi^2}{4l_z^2}D_{zz}t\right]. \end{aligned} \tag{17}$$

The first two lines of this equation expresses the spatial distribution of sound energy in the street, while the argument of the exponential describes the decay of sound with time.

The coefficients a_{kmn} are defined from the initial and boundary conditions by

$$a_{kmn}=\frac{8w_0}{l_x l_y l_z}\sin\left(\frac{k\pi x_0}{l_x}\right)\sin\left(-\frac{(2n-1)\pi z_0}{2l_z}\right)\frac{u_m\cos(u_m y_0/l_y)+B_1\sin(u_m y_0/l_y)}{u_m^2+B_1^2+2B_1+\cos^2 u_m(u_m^2+B_1^2)(B_2-B_1)/(u_m^2-B_1B_2)}. \tag{18}$$

Values of u_m are found by resolving the following equation which expresses the sound absorption by the two building facades:

$$(u_m^2-B_1B_2)\tan u_m=(B_1+B_2)u_m, \tag{19}$$

where B_1 and B_2 are respectively defined from the exchange coefficients h_1 and h_2 by

$$B_1=\frac{h_1 l_y}{D_{yy}} \tag{20a}$$

and

$$B_2=\frac{h_2 l_y}{D_{yy}}. \tag{20b}$$

Since Eq. (19) has no analytical solutions (excepted when $B_1=B_2=0$), values of u_m have to be calculated numerically. However, because the values of u_m tend quickly to $(m-1)\pi$ (Fig. 2), only the first terms have to be found with accuracy.

Since the sound source is impulsive, the steady state in the street is estimated simply by integrating Eq. (17) on the time t from 0 to $+\infty$:

$$\begin{aligned} W(x,y,z)=&\sum_{k,m,n=1}^{\infty} a_{kmn}\sin\left(\frac{k\pi x}{l_x}\right)\sin\left(-\frac{(2n-1)\pi z}{2l_z}\right)\\ &\times\left[u_m\cos\left(\frac{u_m y}{l_y}\right)+B_1\sin\left(\frac{u_m y}{l_y}\right)\right]\\ &\times\left[\frac{k^2\pi^2}{l_x^2}D_{xx}+\frac{u_m^2}{l_y^2}D_{yy}+\frac{(2n-1)^2\pi^2}{4l_z^2}D_{zz}\right]^{-1}. \end{aligned} \tag{21}$$

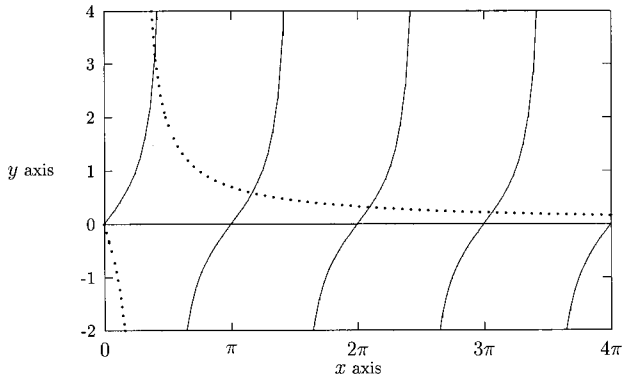

FIG. 2. Functions $y_1=\tan(x)$ (———) and $y_2=(B_1+B_2)x/(x^2-B_1B_2)$ (···), with $\alpha_1=0.3$, $\alpha_2=0.1$, $l_y=30$ m, and $D_{yy}=504\ \mathrm{ms}^{-2}$. The coefficients u_m are found numerically at the intersections between y_1 and y_2.

The main problem of the diffusion model in streets is the lack of knowledge about the values of the diffusion coefficients D_{xx}, D_{yy}, and D_{zz}. Indeed, the theoretical expression of the diffusion coefficient found in room acoustics has no sense in an urban acoustics framework, since it is difficult to define a finite mean-free path in a street. However, in order to overcome this problem, some observations resulting from previous developments of the diffusion model in rectangular rooms and in corridors[9,10] are considered here. First, it was noticed that the diffusion coefficient increases with the room size. Second, when one dimension of the room is greater than the other ones (i.e., in a corridor with $l_x \gg l_y, l_z$), a one-dimensional model (function of x) is sufficient to predict sound attenuation and reverberation. It means that the diffusion is more important in this direction (l_x) than in the other ones. It supposes that the dependency of the diffusion coefficient (D_{xx}) is larger for the room length in the corresponding direction (l_x) than for the other directions (l_y and l_z). As a first approximation, it is assumed that D_{xx} depends only on l_x (idem for D_{yy} and D_{zz}). As a consequence of these observations and hypotheses, the following relation for the diffusion coefficients in streets may be assumed:

$$\frac{D_{xx}}{l_x}=\frac{D_{yy}}{l_y}=\frac{D_{zz}}{l_z}=\mathbb{D}. \tag{22}$$

One of the interests of a such condition is that all the complexity of the sound diffusion by building facades is introduced by the knowledge of one single term, noted $\mathbb{D}$ (in m/s) and called *diffusion parameter*. Although the relation (22) is difficult to justify now, the next section shows it allows a good agreement with experimental data.

II. VALIDATION

A. Estimation of the diffusion parameter

The sound energy decay at a receiver $R(x_R, y_R, z_R)$ in the street is defined by relation (17), which can be developed as follows

$$w_R(t)=\sum_{k,m,n=1}^{\infty} a_{kmn}b_{kmn}\exp[-\tau_{kmn}\mathbb{D}t] \tag{23}$$

$$\begin{aligned}&=a_{111}b_{111}\exp[-\tau_{111}\mathbb{D}t]+a_{121}b_{121}\exp[-\tau_{121}\mathbb{D}t]\\&\quad+a_{112}b_{112}\exp[-\tau_{112}\mathbb{D}t]+a_{211}b_{211}\exp[-\tau_{211}\mathbb{D}t]\\&\quad+a_{222}b_{222}\exp[-\tau_{222}\mathbb{D}t]+\cdots,\end{aligned} \tag{24}$$

where b_{kmn} depends on the position R and τ_{kmn} is given by

$$\tau_{kmn}=\frac{k^2\pi^2}{l_x}+\frac{u_m^2}{l_y}+\frac{(2n-1)^2\pi^2}{4l_z}. \tag{25}$$

Since $\mathbb{D}t$ is large, only the first term (111) of the sum (24) is important, the other terms tending quickly to 0. As a consequence, the decay of sound energy at a position R is given approximately by

$$w_R(t)\approx a_{111}b_{111}\exp[-\tau_{111}\mathbb{D}t]. \tag{26}$$

The measurement of the sound decay at every location in the street allows us to estimate the value of $\mathbb{D}$ provided τ_{111} is known. However, this last quantity depends on u_{111}, and thus on B_2 and B_1, which belongs also to $\mathbb{D}$! A simple solution to overcome this problem is to suppose that the buildings are perfectly reflecting ($h_1=h_2=B_1=B_2=0$), which is quite well verified in practice. In this case, u_1 is equal to 0 and τ_{111} simply becomes

$$\tau_{111}\approx\frac{\pi^2}{l_x}+\frac{\pi^2}{4l_z}. \tag{27}$$

Real values of u_m are then calculated from the value of $\mathbb{D}$ which is estimated with the previous approximations (26) and (27).

B. Theory-measurement comparisons

In order to validate the diffusion model, Eqs. (17) and (21) have been compared to measurements of reverberation times and sound attenuations in a $\frac{1}{50}$ scale model of a street of size $96\times8\times12\ \mathrm{m}^3$. In this experiment, the facade irregularities of a real building can be statistically reproduced in the scale model, in order to simulate phenomena (i.e., multiple reflections and diffraction) which are responsible of the sound diffusion (see Fig. 3). Details of the experiment will be proposed in a future paper. Only results are given here.

Most authors assume values of wall absorption between 0 (perfectly reflecting) to 0.1,[7,8,12] which are well in accordance with typical facing brickwork for frequencies between 125 Hz and 2 kHz.[11] Because it is not easy in practice to find the exact values of absorption in streets, an average value for α_1 and α_2 of 0.05 is taken here for the wall absorption. Moreover, this value is well in accordance with the side wall absorption of the scale model.

FIG. 3. A $\frac{1}{50}$ scale model of a street. Irregularities of building façades are simulated by an arrangement of wooden cubes. This disposition allows us to reproduce statistically a real distribution of balconies, windows, etc. Details of the experiment will be published in a future paper.

Because the frequency dependence of the reverberation times and the sound attenuations measured in the scale model is weak between 400 Hz and 1.6 kHz, data which are analyzed later are averaged on this frequency range. It does not mean that $\mathbb{D}$ is not function of frequency. On the contrary, because the sound diffraction and the diffusion depend on the size of the facade irregularities and on the wave number, $\mathbb{D}$ should depend on frequency. However, since the frequency range of the scale model is limited by technical considerations, the frequency dependence of $\mathbb{D}$ was not observed in our experiment.

Since the expressions of the sound energy densities in streets, in time-varying state (17) and in steady state (21), are written as infinite crossed series, only the first terms can be taken into account in simulations. Figures 4 and 5 show that the stability of these solutions is quickly reached with orders $k=m=n=5$ for relation (17) and with $k=30$, $m=n=10$ for relation (21).

Following the method described in Sec. II and by measuring the time decay at several locations in the scale model

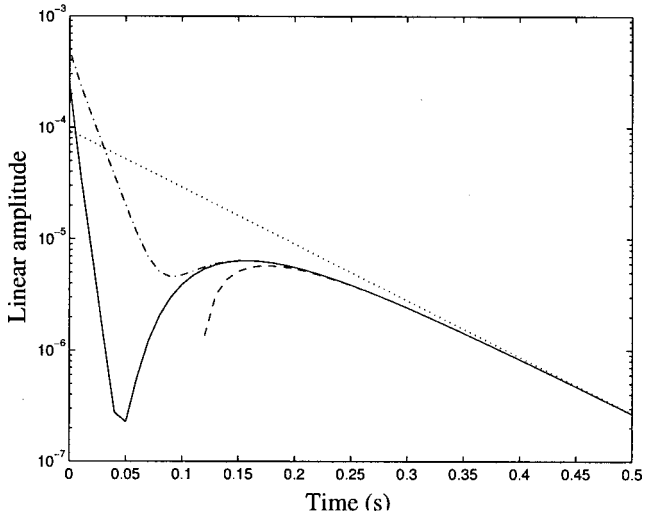

FIG. 4. Stability of Eq. (17): (···) $k=m=n=1$. (– – –) $k=m=n=2$. (–·–·) $k=m=n=3$. (———) $k=m=n=5$.

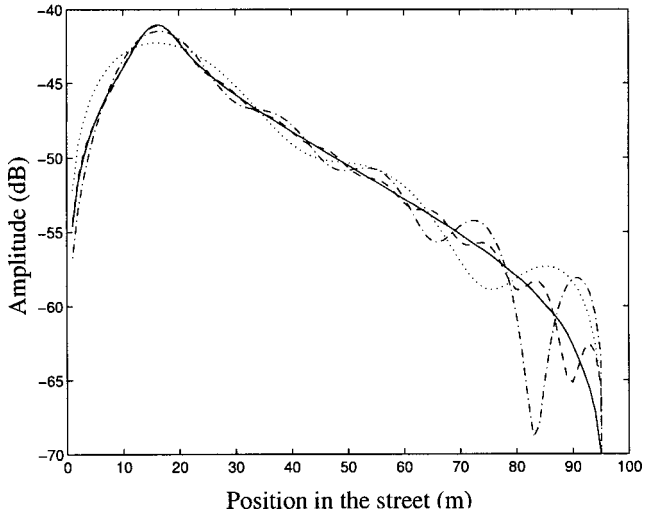

FIG. 5. Stability of Eq. (21): (···) $k=5$, $m=n=10$. (–·–·) $k=10$, $m=n=10$. (– – –) $k=20$, $m=n=10$. (———) $k=30$, $m=n=10$.

of the street, the diffusion parameter $\mathbb{D}$ was estimated to 35 m/s.

Figure 6 shows a comparison between the reverberation times measured in the scale model (averaged on the frequency range 400 Hz to 1.6 kHz) and the reverberation times estimated from the sound decay calculated by Eq. (17). Predicted values are quite in accordance with experimental data, especially at the end of the street, where the diffuse sound field is important in comparison with the early reflections.

Predicted sound attenuations in the street are also compared to the sound attenuation measured in the scale model for two positions of the sound source (Fig. 7). For practical reasons, because the direct field close to the sound source is always important, a simple model including both the direct field and the diffuse sound field is also proposed:

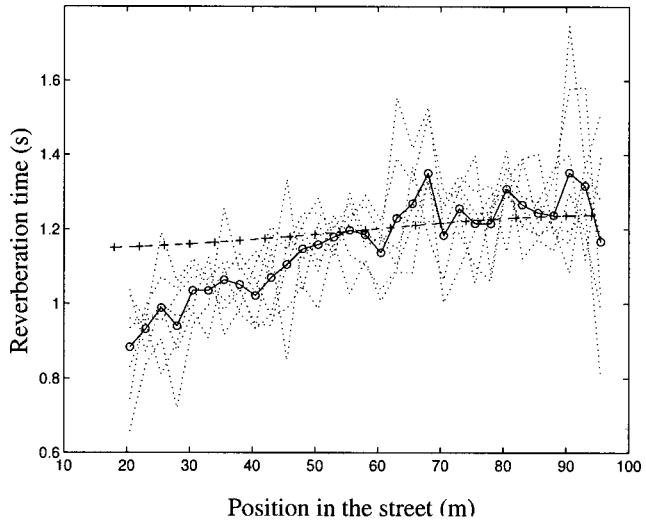

FIG. 6. Reverberation time (in s) in the street. Comparison between experimental data [(···) reverberation times for $\frac{1}{3}$ octave bands between 400 Hz and 1.6 kHz, (∘–∘) mean values] and predicted values (+–+) along the street at 2-m height with $\mathbb{D}=35$ m/s. Source at $x_0=16$ m, $y_0=4$ m and $z_0=10$ m. $\alpha_1=\alpha_2=0.05$.

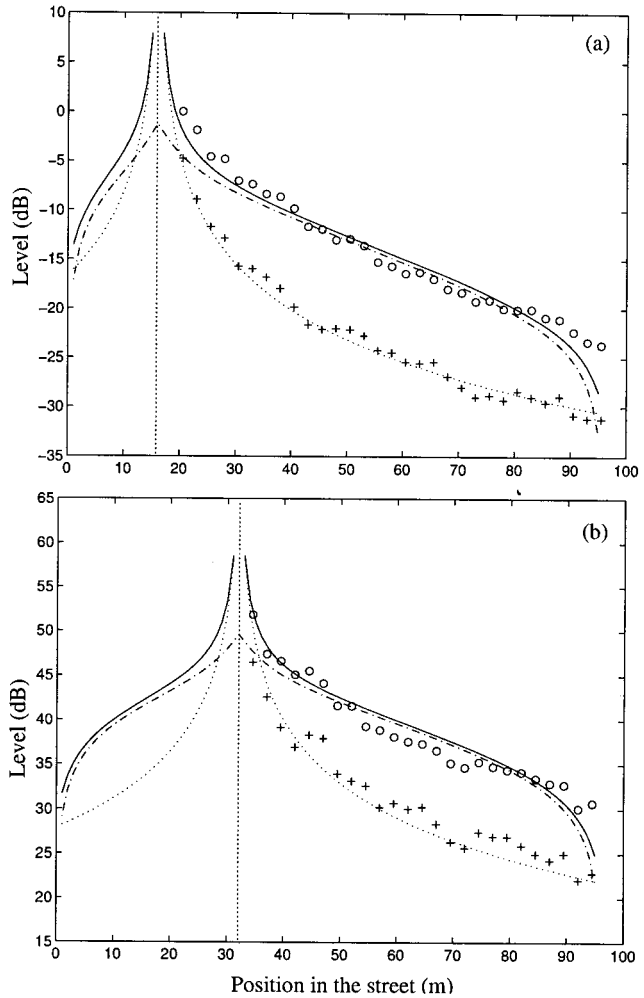

FIG. 7. Sound attenuation in the street. (a) Source at $x_0=16$ m, $y_0=4$ m and $z_0=10$ m. (b) Source at $x_0=32$ m, $y_0=4$ m and $z_0=10$ m. Comparison between experimental data and predicted values at 2-m height with $\mathbb{D}=35$ m/s. (○) Sound level measurement in the scale model. (+) Direct field estimation from measurements. (···) Sound attenuation of the direct field (estimation by a $1/r^2$ law). (·–·–) Diffusion model by Eq. (21). (———) Diffusion model with direct field by Eq. (28). $\alpha_1=\alpha_2=0.05$.

$$\Omega(x,y,z)=\frac{\mu}{4\pi d^2}+\epsilon W(x,y,z), \tag{28}$$

where d is the source–receiver distance. The ratio ϵ/μ expresses the influence of the diffuse sound field in comparison with the direct field. In the experiments, this ratio was estimated at 80, but it probably depends on the facade diffusivity and the street size. A very good agreement is observed between measurements and predicted values of the sound attenuation in street. At the end of the street, a small deviation with measurements is observed. It is explained partly by the fact that the sound energy at the extremities is assumed very weak [as written by the boundary conditions (14)] in regard to the sound energy closed to the source.

III. CONCLUSION

A diffusion model based on a diffusion equation was proposed to predict analytically the sound propagation in a rectangular street. Only one parameter, called the *diffusion parameter*, is introduced to take into account all complex phenomena playing a major part of the sound propagation in streets, like multiple reflections, diffraction, and diffusion by building facades. Simple boundary conditions are also given to model the sound absorption and reflection by the building facades, the pavement, and the opening.

When the *diffusion parameter* is correctly chosen, the predicted sound reverberation and attenuation are in accordance with measurements in a scale model of a street. At the present time, the main limitation of the diffusion model is that we have a very little knowledge of correlations between the *diffusion parameter*, the sound frequency, and the size and the disposition of the facades irregularities. New theoretical developments are now in progress to link the *diffusion parameter* to architectural morphological parameters, for example, using fractal indicators.[13] At the same time, an experimental study, based on scale model experiments, has also started to determine the sensitivity of the diffusion parameter with the dimensions of the streets and the architectural morphology of the buildings facades.

In this paper, the model was first applied to predict the sound attenuation and the reverberation in rectangular streets with a point source. Nevertheless, other urban configurations (i.e., a street with intersections, a street with a varying width) and other kinds of sound sources (i.e., a line source, a moving point source) can also be investigated: the diffusion equation does not change, but the boundary and the initial conditions have to be adapted. Last, if the urban configurations are too complicated to be solved theoretically (i.e., a set of streets), the use of numerical methods like finite element methods can be considered. Indeed, since the diffusion model is based on an analogy with the heat transfer problem, it is interesting to note that the adjustment of the current numerical code used to solve heat transfer problems could be a solution for complex acoustics problems. Before developing functional applications, like the modeling of sound propagation in city, it will be necessary to introduce also the atmospheric attenuation and the radiation by openings. Then, the diffusion model should be a simple solution to the prediction of noise impact in urban areas.

APPENDIX: SOLUTION OF THE DIFFUSION EQUATION

1. Method of resolution

In this Appendix, a method is proposed to solve the diffusion equation defined at Eq. (11) by

$$\frac{\partial w}{\partial t}-D_{xx}\frac{\partial^2 w}{\partial x^2}-D_{yy}\frac{\partial^2 w}{\partial y^2}-D_{zz}\frac{\partial^2 w}{\partial z^2}=0. \tag{A1}$$

Such a method was developed first to solve heat conduction problems and is applied here to the sound diffusion in the case of a rectangular street.

Let us consider three elemental functions $w_x(x,t)$, $w_y(y,t)$, and $w_z(z,t)$, respectively solutions of the following equations and boundary conditions.

For w_x,

$$D_{xx}\frac{\partial^2 w_x}{\partial x^2}-\frac{\partial w_x}{\partial t}=0 \tag{A2}$$

with

$$w_x(0,t)=0, \tag{A3a}$$

$$w_x(l_x,t)=0. \tag{A3b}$$

For w_y,

$$D_{yy}\frac{\partial^2 w_y}{\partial y^2}-\frac{\partial w_y}{\partial t}=0 \tag{A4}$$

with

$$-D_{yy}\frac{\partial w_y}{\partial y}(l_y,t)=h_2 w_y(l_y,t), \tag{A5a}$$

$$D_{yy}\frac{\partial w_y}{\partial y}(0,t)=h_1 w_y(0,t). \tag{A5b}$$

For w_z,

$$D_{zz}\frac{\partial^2 w_z}{\partial z^2}-\frac{\partial w_z}{\partial t}=0 \tag{A6}$$

with

$$-D_{zz}\frac{\partial w_z}{\partial z}(l_z,t)=0, \tag{A7a}$$

$$w_z(0,t)=0. \tag{A7b}$$

By multiplying each one of these diffusion equations, respectively, by $w_y w_z$, $w_x w_z$, and $w_x w_y$, and by summing all resulting relations, it gives

$$\begin{aligned} &D_{xx}w_y w_z\frac{\partial^2}{\partial x^2}w_x-w_y w_z\frac{\partial}{\partial t}w_x+D_{yy}w_x w_z\frac{\partial^2}{\partial y^2}w_y \\ &-w_x w_z\frac{\partial}{\partial t}w_y+D_{zz}w_x w_y\frac{\partial^2}{\partial z^2}w_z-w_x w_y\frac{\partial}{\partial t}w_z \\ &=\left[D_{xx}\frac{\partial^2}{\partial x^2}+D_{yy}\frac{\partial^2}{\partial y^2}+D_{zz}\frac{\partial^2}{\partial z^2}-\frac{\partial}{\partial t}\right]w_x w_y w_z=0. \end{aligned} \tag{A8}$$

The product $w_x w_y w_z$ is then the solution of Eq. (11) with respect of the boundary conditions (14)–(16). Since the initial condition (12) is also separable in three independent functions of space, the function defined by

$$w(x,y,z,t)=w_x(x,t)\times w_y(y,t)\times w_z(z,t) \tag{A9}$$

is the solution of the diffusion equation in streets. The three-dimensional problem is then changed into three one-dimensional problems.

2. Form of the one-dimensional solutions

Here, it is assumed that the previous solutions [noted $w_u(u,t)$ with $u=x,y,z$] of the diffusion equation

$$D_{uu}\frac{\partial^2 w_u}{\partial^2 u}-\frac{\partial w_u}{\partial t}=0 \tag{A10}$$

may be separated in two functions of the space u and the time t:

$$w_u(u,t)=f(u)\times g(t). \tag{A11}$$

It implies that $g(t)$ may be written

$$g(t)=\exp[-mt], \tag{A12}$$

and that the function $f(u)$ verifies

$$D_{uu}\Delta f+mf=0. \tag{A13}$$

Because of the boundary conditions (A3)–(A7) imply an infinity of possible values for m (noted m_k), there are also an infinite number of solutions $g_k(t)$ for $g(t)$ and then an infinite number of solutions $f_k(u)$ for f verifying Eq. (A13). Consequently, the general solution of the diffusion equation (A10) can be written as the sum

$$w_u(u,t)=\sum_{k=0}^{\infty} a_k f_k(u)\exp[-m_k t]. \tag{A14}$$

The initial condition is then

$$w_u(u,0)=w_u^0(u)=\sum_{k=0}^{\infty} a_k f_k(u). \tag{A15}$$

It is easy to show that the boundary conditions of the one-dimensional diffusion equation are verified if each function $f_k(u)$ expresses the same conditions for w_u.

Two kinds of conditions are considered in this paper:

$$-D\frac{\partial f_k}{\partial u}=\pm h f_k \tag{A16a}$$

and/or

$$f_k=0. \tag{A16b}$$

Since these boundary conditions are homogeneous, the functions f_k are orthogonal, which allows us to find easily the coefficient a_k from the initial condition (A15) by

$$a_k=\frac{\int w_u^0(u) f_k\,du}{\int f_k^2\,du}. \tag{A17}$$

According to the rectangular geometry of the street, the quantity $a_k f_k(u)$ may be replaced by the following form:

$$[a_k\cos(r_k u/l_u)+b_k\sin(r_k u/l_u)], \tag{A18}$$

which verifies well a normality condition. Equation (A13) implies also that

$$m_k=D_{uu}r_k^2. \tag{A19}$$

3. Elemental solutions

a. Function w_x

According to the boundary conditions (A3), it is easy to show that the coefficients a_k are equal to 0, and that $r_k=k\pi$. The solution of the diffusion equation (A2) is then

$$w_x(x,t)=\sum_{k=1}^{\infty} b_k\sin(k\pi x/l_x)\exp[(-k^2\pi^2 D_{xx}t/l_x], \tag{A20}$$

where the coefficients b_k are given with the help of relation (A17) (applied to b_k):

$$b_k=\frac{2}{l_x}\int_0^{l_x} w_x^0(x)\sin(k\pi x/l_x)dx. \tag{A21}$$

For an impulsive sound source such as $w_x^0(x)=\delta(x-x_0)$, we find finally

$$w_x(x,t)=\frac{2}{l_x}\sum_{k=1}^{\infty}\sin(k\pi x/l_x)\sin(k\pi x_0/l_x)\times\exp[-k^2\pi^2 D_{xx}t/l_x^2]. \quad \text{(A22)}$$

b. Function w_y

The boundary conditions (A5) applied to expression (A18) allow us to give two conditions for the coefficients a_k, b_k, and r_k:

$$\frac{b_k}{a_k}=\frac{h_1 l_y}{r_k D_{yy}}=\frac{B_1}{r_k} \quad \text{(A23)}$$

and

$$(r_k^2-B_1B_2)\tan r_k=(B_1+B_2)r_k, \quad \text{(A24)}$$

with $B_2=h_2 l_y/D_{yy}$. The solution of the diffusion equation (A4) is then of the following form:

$$w_y(y,t)=\sum_{k=1}^{\infty}\frac{a_k}{r_k}[r_k\cos(r_k y/l_y)+B_1\sin(r_k y/l_y)]\times\exp[-r_k^2 D_{yy}t/l_y^2], \quad \text{(A25)}$$

where the ratio a_k/r_k is given with the help of (A17) for an impulsive sound source defined by $w_y^0(y)=\delta(y-y_0)$:

$$\frac{a_k}{r_k}=\frac{2}{l_y}\frac{r_k\cos(r_k y_0/l_y)+B_1\sin(r_k y_0/l_y)}{r_k^2+B_1^2+2B_1+\cos^2 r_k(r_k^2+B_1^2)(B_2-B_1)/(r_k^2-B_1B_2)}. \quad \text{(A26)}$$

c. Function w_z

The boundary condition at $z=0$ gives simply $a_k=0$, while the condition at $z=l_z$ gives

$$r_k=(2k-1)\frac{\pi}{2}. \quad \text{(A27)}$$

According to (A17), the coefficients b_k are defined, for an impulsive source such as $w_z^0(z)=\delta(z-z_0)$, by the following relation:

$$b_k=\frac{2}{l_z}\sin\left((2k-1)\frac{\pi}{2}\frac{z_0}{l_z}\right). \quad \text{(A28)}$$

The final solution for w_z is then

$$w_z(z,t)=\sum_{k=1}^{\infty}\frac{2}{l_z}\sin\left((2k-1)\frac{\pi}{2}\frac{z_0}{l_z}\right)\times\sin\left((2k-1)\frac{\pi}{2}\frac{z}{l_z}\right)\exp\left[-(2k-1)^2\frac{\pi^2}{4}\frac{D_{zz}t}{l_z^2}\right]. \quad \text{(A29)}$$

[1] F. M. Wiener, C. I. Malme, and C. M. Gogos, ''Sound Propagation in Urban Areas,'' J. Acoust. Soc. Am. **37**, 738–747 (1965).
[2] W. R. Schlatter, ''Sound Power Measurement in a Semi-Confined Space,'' M.Sc. thesis, Massachusetts Institute of Technology, Cambridge, 1971.
[3] M. V. Sergeev, ''Scattered Sound and Reverberation on City and in Tunnels,'' Sov. Phys. Acoust. **25**, 248–252 (1979).
[4] R. Y. Vinokur, ''Propagation of Sound Generated by a Point Source in Certain Built-Up Urban Environments,'' Sov. Phys. Acoust. **25**, 377–379 (1979).
[5] H. G. Davies and R. H. Lyon, ''Noise Propagation in Cellular Urban and Industrial Spaces,'' J. Acoust. Soc. Am. **54**, 1565–1570 (1973).
[6] R. H. Lyon, ''Role of Multiple Reflections and Reverberation in Urban Noise Propagation,'' J. Acoust. Soc. Am. **55**, 493–503 (1974).
[7] P. R. Donavan, ''Sound Propagation in Urband Space,'' Ph.D. thesis, Massachusetts Institute of Technology, Cambridge, 1976.
[8] H. G. Davies, ''Multiple-Reflection Diffuse-Scattering Model for Noise Propagation in Streets,'' J. Acoust. Soc. Am. **64**, 517–521 (1978).
[9] J. Picaut, J.-D. Polack, and L. Simon, ''A Mathematical Model of Diffuse Sound Field Based on a Diffusion Equation,'' Acust. Acta Acust. **83**, 614–621 (1997).
[10] J. Picaut, L. Simon, and J.-D. Polack, ''Sound Field in Long Rooms with Diffusely Reflecting Boundaries,'' Appl. Acoust. **56**(4), 217–240 (1999).
[11] M. E. Delany, A. J. Rennie, and K. M. Collins, ''Scale Model Investigations of Traffic Noise Propagation,'' Acoustics Report Ac 58, National Physical Laboratory, Teddington, Middlesex, United Kingdom, 1972 (unpublished).
[12] K. Heutschi, ''A Simple Method to Evaluate the Increase of Traffic Noise Emission Level Due to Buildings, for a Long Straight Street,'' Appl. Acoust. **44**, 259–274 (1995).
[13] P. Woloszyn, F. Raymond, and J. Picaut, in *Proceedings of the Sixth Western Pacific Regional Acoustic Conference* (The Hong Kong Institute of Acoustics, Hong Kong, 1997).

A broadband passive–active sound absorption system

Jerome P. Smith, Brody D. Johnson, and Ricardo A. Burdisso
Vibration and Acoustics Laboratories, Mechanical Engineering Department,
Virginia Polytechnic Institute and State University, Blacksburg, Virginia 24061-0238

(Received 26 August 1998; accepted for publication 7 July 1999)

In recent years, hybrid absorption systems have been implemented which achieve high sound absorption over a broad frequency range. This work is an experimental study of a broadband hybrid absorption system which is comprised of a layer of sound-absorbing material (the passive component) positioned at a distance from a movable wall (the active component) inside an impedance tube. The movable wall is used to impose desired boundary conditions in the cavity behind the passive layer, thereby increasing the absorption of the system at frequencies where the passive material is not independently effective. Both pressure-release (i.e., minimizing the pressure at the back surface of the layer) and impedance-matching (i.e., minimizing the reflected wave from the layer) boundary conditions are studied. The performance of the hybrid system for these two boundary conditions is compared for broadband disturbances over a frequency range of 100–1000 Hz. The unmodified passive system showed absorption coefficients greater than 0.7 only above 500 Hz, while the impedance-matching condition yielded absorption coefficients of 0.8 to 1.0 over the 100–1000-Hz range. The impedance-matching condition provided significantly better absorption than that achieved with the pressure-release condition. The sensitivity of these control approaches to system parameters is also investigated.
[S0001-4966(99)00711-0]

PACS numbers: 43.55.Ev [PJR]

INTRODUCTION

Before discussing previous work on hybrid absorption systems, the advantages of such a system shall be discussed. Consider an entirely passive noise control approach relying on sound-absorbing materials. An increasing amount of material is required for effective noise reduction at low frequencies, making passive methods impractical for a given application below some low-frequency limit. On the other hand, an entirely active noise control approach becomes infeasible at high frequencies, due to the increased computational loads induced by the higher sample rate and longer filter lengths necessary. It is only natural, then, to combine the two approaches, utilizing a primarily passive effect at high frequencies and a primarily active effect at low frequencies, keeping each component relatively easy (inexpensive) to implement. Guicking and Lorenz[1] provide one of the earliest applications of a hybrid noise absorption system, in which a porous plate is placed in an impedance tube a small distance away from a control speaker located at the end of the tube. The signal sensed by a reference microphone in front of the panel was issued to the control speaker via a complex amplification factor so as to minimize the sound pressure sensed by a second microphone directly behind the plate. This pressure-release condition on the back surface of the panel led to nearly perfect absorption over a frequency range from 100 to 600 Hz.

Thenail *et al.*[2] also investigated a hybrid absorption system making use of a fiberglass absorbing layer backed by an air cavity terminated with an active surface. A pressure-release condition on the back surface of the fiberglass was generated, resulting in increased absorptivity over a frequency range from 200 to 800 Hz. Both numerical and experimental results were given which demonstrate sensitivity of the system to both the fiberglass thickness and porosity.

Furstoss *et al.*[3] more recently performed a theoretical study to determine the optimal impedance at the back face of a porous layer to result in no reflection at the front surface of the layer, for oblique and normal sound incidence. The optimal impedance was based on a model of the properties of the porous layer. An experimental study utilized an accelerometer placed on the control speaker in conjunction with a nearby microphone in an error-sensing strategy designed to result in the desired impedance behind the fiberglass, and results at a single frequency were shown to compare well with the model. Another experimental study where a pressure-release condition was imposed at the back of a fiberglass panel was shown to result in high absorption coefficients over the frequency range from 150 to 500 Hz. For oblique sound incidence, the pressure-release-imposed impedance differed significantly from the theoretical low-frequency optimal impedance condition, but still resulted in a significant increase in the sound absorption.

A theoretical study investigating the control effort and displacements required for introducing forces to the front layer of an absorptive foam material to result in increased absorption was performed by Bolton *et al.*[4] Partially reticulated foams with high flow resistivity were shown to have good properties for low required control effort at low frequencies.

Another twist on the active absorption approach was provided by Fuller *et al.*,[5] in which adaptive polyvinylidene fluoride foam (PVDF) was experimentally evaluated for application to radiation and reflection control. By positioning the active PVDF foam against the inside of a rigid end cap of

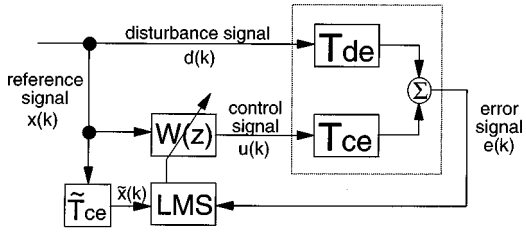

FIG. 1. Block diagram of the SISO adaptive feedforward filtered-X LMS control algorithm.

an impedance tube and minimizing the wave reflected by the foam via a wave deconvolver, an attenuation of up to 40 dB was achieved in the reflected wave for frequencies above 600 Hz. The results were reported for a frequency range from 100 to 1000 Hz. The absorption of the PVDF foam without active control was reported to be low.

Enhancing the absorption properties of passive materials, particularly in the low-frequency range, has potential applications toward improvement of anechoic facilities and in duct acoustics. Another application was demonstrated by Ver and Digman,[6] who showed the application of a control technique for foam absorption enhancement in an experimentally simulated augmentor exhaust silencer tube. A pressure-release condition introduced behind the surface of a section of resistive liner in the tube showed increases in low-frequency noise attenuation ranging from 4 to 12 dB beyond the reduction obtained with the passive material only.

Beyene and Burdisso[7] provide both numerical and experimental studies of a new impedance-matching approach as applied to the cavity absorption problem. Again, a layer of sound-absorbing material is mounted a short distance away from an active wall. The creation of a pressure-release condition at the back surface of the layer[1,2] is abandoned for the new impedance-matching condition, in which the reflected wave inside the cavity is to be minimized. The authors demonstrate the effectiveness of the approach both numerically and experimentally for normal incident waves of single frequency excitations. Numerical results showed absorption coefficients ranging from 0.8 to 1.0 could be achieved from 100 to 2000 Hz.

Further study of the impedance-matching boundary condition for use in a hybrid sound absorption system is presented here. Previous work has dealt primarily with single frequency excitations and has provided no direct comparison between the pressure-release and impedance-matching conditions in terms of performance and control effort. In this experimental work, the performance and control effort of the active portions for the pressure-release and impedance-matching boundary condition approaches will be compared in the 100- to 1000-Hz broadband frequency range. Additional results will be presented which demonstrate the relative sensitivities of the two approaches to both the thickness of the absorbing layer and the depth of the cavity backing this layer.

A brief explanation of the motivation behind impedance-matching shall be offered before continuing to a description of the experimental approach and associated results. The basis for the pressure-release condition stems from the desire to

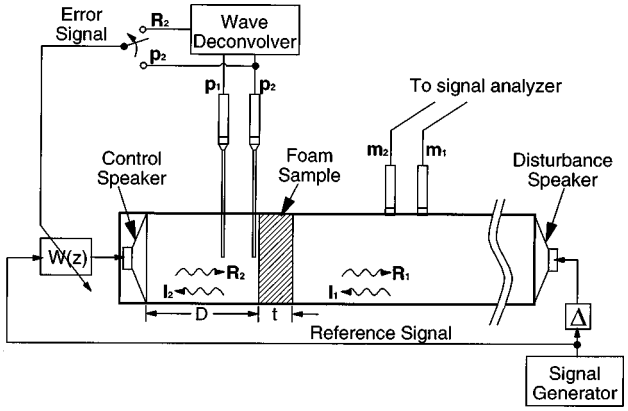

FIG. 2. Schematic of the hybrid absorption system inside a standing wave tube.

have maximum particle velocity occurring in the foam, thereby maximizing viscous losses in the incident pressure wave. This method is limited because it has only a local effect, observed at the location where the pressure is minimized. With impedance matching, however, the active component modifies the system so as to mimic the ambient acoustic impedance at the surface of the absorbing layer, preventing reflection of the incident wave. Hence, the main benefit of the impedance-matching boundary condition is that, unlike the pressure-release boundary condition, the impedance-matching condition induces more than a localized effect.

I. CONTROL ALGORITHM

The active portion of the hybrid absorption system relies upon the application of the filtered-X LMS (least mean square) feedforward algorithm in a single-input, single-output (SISO) configuration. Feedforward algorithms of this type have been successfully employed in various vibration and noise control scenarios including Active Structural Acoustic Control (ASAC) and Active Noise Control (ANC).[8,9]

A block diagram for the SISO control system is given as Fig. 1. Feedforward control relies heavily upon the determination of a reference signal, $x(k)$, which is coherent with the disturbance, $d(k)$, and independent of the control signal, $u(k)$. The subscript k indicates the kth time sample. In many applications it is possible to measure the reference signal directly, while in others electronic compensation is necessary to prevent feedback of the control signal into the measured reference signal. Once determined, the reference signal is filtered via an adaptive finite impulse response (FIR) filter, $W(z)$, to produce the control signal.

The adaptive filter, or compensator, consists of a finite number of coefficients that are updated with each time step of the algorithm so as to minimize a defined error signal. The sample rate and convergence parameter dictate the speed with which the filter coefficients converge. A FIR filter representation of the control path transfer function, T_{ce}, is required before the convergence process may be initiated. This model, $\tilde{T}_{ce}$, is either measured or computed, and is used to filter the reference signal to create the filtered-X signal, $\tilde{x}_k$.

The LMS algorithm then combines knowledge of the error signal and the filtered-X signal to compute the updated compensator coefficients at each time step. For a thorough explanation of the LMS algorithm in the context of a multiple channel control system the reader is referred to the work of Elliot *et al.*[10] In practice, the FIR filter modeling the control transfer function is determined by a system identification procedure that uses an algorithm similar to that of the control algorithm itself.[11]

A Texas Instruments TMS320C30 digital signal processing (DSP) board was used to implement the control algorithm. The board was resident in an Intel 80386 PC host computer and the controler codes were written in ''C'' language with embedded assembly code instructions. The code allows for user definition of the filter lengths, sample rate, and convergence parameter. Another feature of the control code is the ability to delay the disturbance signal by a number of time samples to ensure adequate response time for the controler and avoid causality issues.

II. EXPERIMENTAL SETUP

The tests were conducted inside a cylindrical standing wave (or impedance) tube having a diameter of 10 cm and a length of 1.2 m. The tube has lower and upper frequency limits of 90 and 2000 Hz, respectively. A depiction of the setup is given in Fig. 2. A white noise generator was used to create a broadband disturbance signal with uniform frequency content from 0 to 1600 Hz. This signal is issued first to the controler as a reference signal and second to the disturbance speaker with a variable delay. The disturbance speaker is mounted at one the end of the wave tube, while the control speaker is mounted at the opposite end, behind the absorbing layer and the air cavity. Inside the cavity, two microphones, labeled p_1 and p_2, are shown in Fig. 2. The p_2 microphone is used as the error sensor for configurations with the pressure-release boundary condition. For the impedance-matching boundary condition, the error signal to be minimized is the reflected wave in the cavity R_2, which is measured by means of an analog wave deconvolution circuit in conjunction with the two cavity microphones. The deconvolution circuit follows a pattern initially presented by Fahy.[12] The two microphones, labeled m_1 and m_2, outside the cavity are used for computation of the absorptivity using the ASTM two-microphone technique.[13]

TABLE I. Comparison of average absorption coefficient for impedance-matching and pressure-release boundary conditions for various system configurations (100 to 1000 Hz).

Cavity depth (mm)	Foam thickness (mm)				
	12.7	25.4	38.1	50.8	B.C.
60	0.96	0.95	0.90	0.87	I.M.
	0.79	0.89	0.85	0.85	P.R.
80	0.95	0.94	0.87	0.86	I.M.
	0.76	0.87	0.83	0.82	P.R.
100	0.91	0.91	0.85	0.83	I.M.
	0.72	0.82	0.80	0.81	P.R.
120	0.88	0.87	0.81	···	I.M.
	0.67	0.78	0.76	···	P.M.

The method used for computation of the absorption properties has frequency limitations on the low end dictated by the phase mismatch of the measurement microphones, and on the high end by the microphone spacing used. These limitations are well defined in Ref. 13 and resulted in a usable frequency range from approximately 100 to 1600 Hz in these experiments.

The sensitivity of the hybrid absorption system is to be studied relative to the cavity depth, D, and the thickness of the foam sample, t (see Fig. 2). Tests were performed for cavity depths of 60, 80, 100, and 120 mm and foam thicknesses of 12.7, 25.4, 38.1, and 50.8 mm. For each configuration, the controller ran the filtered-X LMS adaptive feedforward control algorithm with a sample rate of 3200 Hz, using a 140-coefficient FIR compensator and a 40-sample delay between the reference and disturbance signals. The 40-sample delay was introduced to remove any causality constraints from the experiment. The issue of causality in feedforward broadband applications has been addressed by Burdisso *et al.*[14] In practical applications, the need for a coherent, *a priori* reference signal may limit the implementation and will require some strategy based on the particular configuration.

III. EXPERIMENTAL RESULTS

Experiments using both the pressure-release and impedance-matching hybrid absorption systems shall be described in this section. Results contrasting the performance of the impedance-matching and pressure-release boundary conditions shall first be presented. Following this discussion, the sensitivity of the hybrid absorption system to change in the cavity depth and the foam thickness will be quantified for each boundary condition.

A. Performance comparison

For each boundary condition (pressure release and impedance matching), 15 cavity configurations were studied in this work, in which both the cavity depth and foam thickness were independently varied. A spectrum yielding the absorption coefficient as a function of frequency was measured for each configuration. The FIR compensator coefficients of the controller were also recorded for each case. From these coefficients the frequency response function of the controller may be obtained, providing a quantifier of the controller effort for direct comparison of any two configurations. Rather than attempting the cumbersome task of presenting all of this data, another means for comparing configurations shall be contrived. First, the absorption coefficient spectrum shall be replaced by the linear average of the absorption coefficient. Since our concern lies in the frequency range between 100 and 1000 Hz, the average reflects only this portion of the spectrum. As a reminder, it is noted that the wave tube has a lower frequency limit of 90 Hz, preventing comparison of the two approaches below roughly 100 Hz. Second, in place of the control compensator frequency response the average compensator gain over the 100- to 1000-Hz frequency range shall be presented. After considering this abbreviated format of the experimental data, the results for two configurations shall be described in detail.

TABLE II. Average control compensator gain (dB) for pressure-release and impedance-matching boundary conditions for various system configurations (100 to 1000 Hz).

Cavity depth (mm)	Foam thickness (mm)				
	12.7	25.4	38.1	50.8	B.C.
60	−6.62	−7.57	−9.33	−9.58	I.M.
	−2.54	−4.40	−6.11	−7.19	P.R.
80	−6.98	−8.18	−9.22	−11.09	I.M.
	−3.89	−5.42	−6.49	−7.91	P.R.
100	−7.70	−9.21	−9.90	−11.00	I.M.
	−3.65	−6.11	−6.71	−8.75	P.R.
120	−7.97	−9.48	−10.55	···	I.M.
	−4.62	−6.56	−7.80	···	P.R.

Tables I and II, respectively, reflect the performance and controller effort quantifiers described in the preceding paragraph. As shown in Table I, the average absorption coefficient over the 100- to 1000-Hz range is higher with impedance matching than with pressure release in each of the 15 cases. The average absorption coefficient was computed as a linear average of the absorption coefficients over the frequency range in order to give a single quantitative value for the absorption effects of each case. The results in Tables I and II are not to say that impedance-matching provides greater absorption over the entire frequency range in every case, but only that the average absorption is higher. In some instances the pressure-release condition provided better absorption coefficients over certain frequency ranges. From Table II, it is evident that the impedance-matching approach requires less control effort, in all instances yielding an average compensator gain more than 3 dB less than the corresponding pressure-release configuration. Note that a 3-dB difference in the compensator gain corresponds to approximately a factor of 2 in terms of power consumption.

Having in mind an overview of the results, a more thorough description of two specific configurations shall now be given. First, let us consider the upper-leftmost configuration presented in the tables, corresponding to a cavity depth of 60 mm and a foam thickness of 12.7 mm. The measured absorption coefficient is given as a function of frequency in Fig. 3. Again, note that below about 100 Hz the measurement of the absorption coefficient is no longer accurate. Nearly perfect absorption is achieved from 100 to 1000 Hz with the impedance-matching boundary configuration and throughout this range the impedance-matching approach improves the absorption relative to the passive system alone. The pressure-release approach, on the other hand, increases the absorption over the passive case for three considerably smaller frequency ranges and actually acts to lessen the absorption of the cavity for some frequencies. Table I indicates that the average absorption coefficient for this configuration is 0.17 greater with the impedance-matching condition. The magnitude of the compensator frequency response function is given in Fig. 4 for each boundary condition. It is apparent that the impedance-matching boundary condition requires less effort from the active component, especially between about 100 and 700 Hz. Based on the average compensator gain data in Table II the pressure-release approach requires 2.5 times the power of the corresponding impedance-

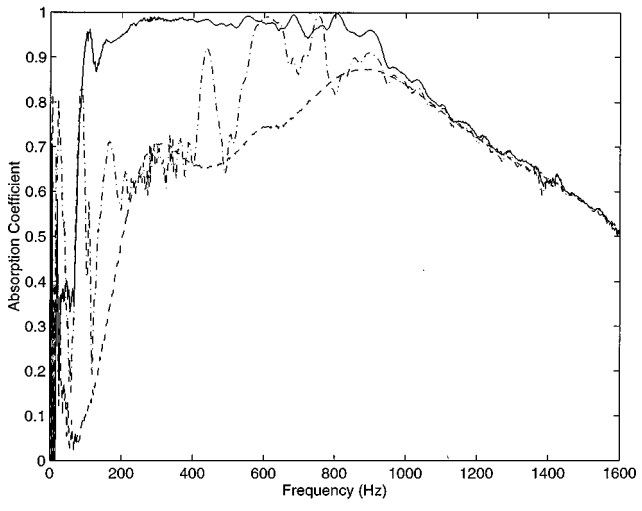

FIG. 3. Absorption coefficient frequency spectrum for $D=60$ mm and $t=12.7$ mm. Condition: ——— impedance matching, -·-·- pressure release, --- passive.

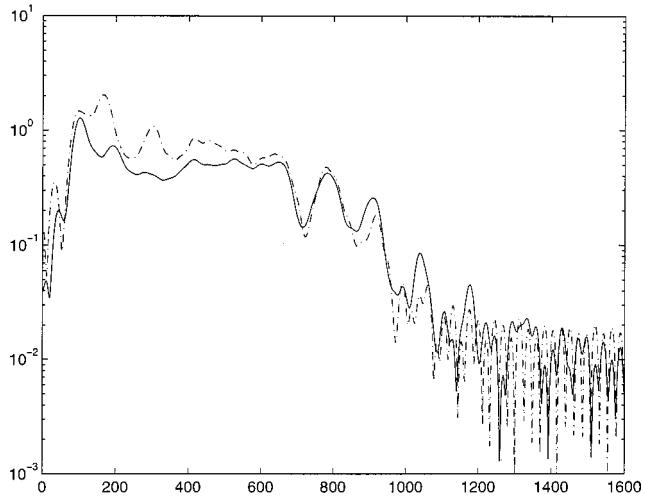

FIG. 4. Control compensator magnitude (V/V) for $D=60$ mm and $t=12.7$ mm. Condition: ——— impedance matching, -·-·- pressure release.

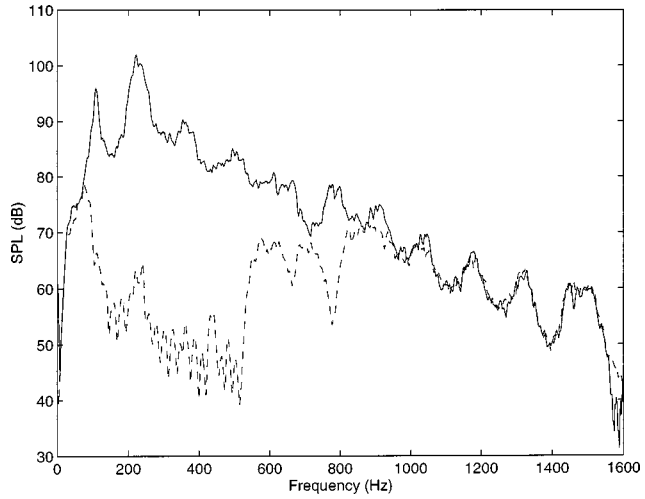

FIG. 5. Frequency spectrum of the impedance-matching error signal: ——— before control, --- after control.

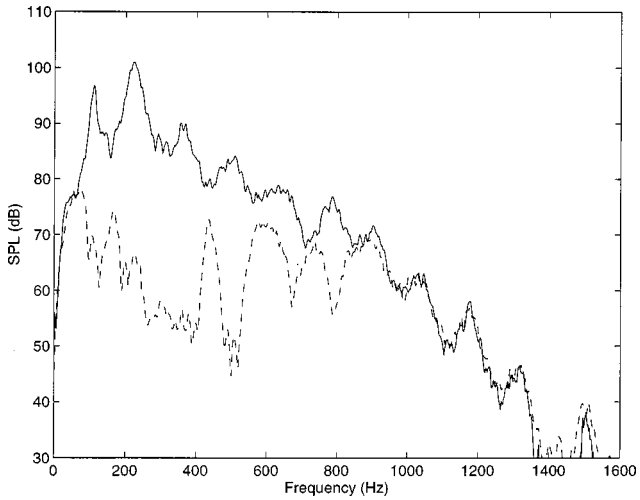

FIG. 6. Frequency spectrum of the pressure-release error signal: ——— before control, --- after control.

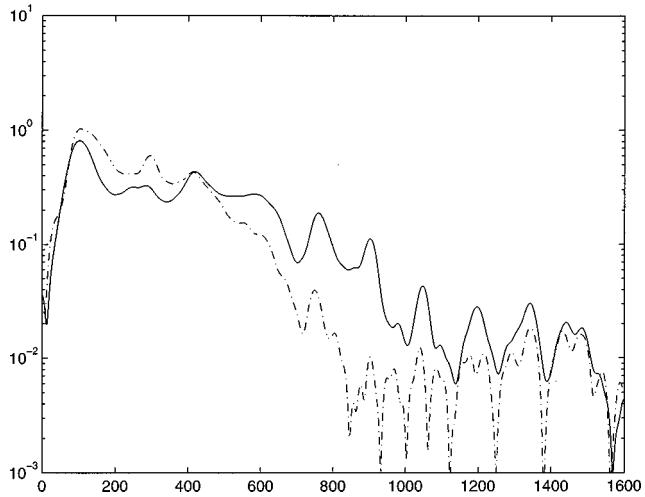

FIG. 8. Control compensator magnitude (V/V) for $D=100$ mm and $t=50.8$ mm. Condition: ——— impedance matching, -·-·- pressure release.

matching system. Finally, Figs. 5 and 6 depict the error signal frequency responses for the impedance-matching and pressure-release conditions, respectively. Over the 100- to 1000-Hz frequency range an overall reduction of 20.8 dB was observed for the impedance-matching case, while a 19.8-dB reduction was achieved for the pressure-release configuration. The similarity in overall reduction of the error signals assures independence of the hybrid absorption system relative to the controler, isolating the effects of each boundary condition on the performance.

As a second in-depth comparison of the two hybrid absorption approaches we shall consider a cavity depth of 100 mm and a foam thickness of 50.8 mm, corresponding to the lower right of the tables presented earlier in this work. In Fig. 7, the measured absorption coefficient as a function of frequency is given. Here we see that both boundary conditions result in a degradation of absorption between 300 and 700 Hz. While the impedance-matching condition provides better absorption in this range, the pressure-release condition yields greater absorption from 100 to 300 Hz. Referring to Table I, we find a difference of only 0.01 in the average absorption coefficient for these two configurations. As with the previous case, however, the required controller effort is significantly less for the impedance-matching case, as the pressure-release approach requires 50% more power. This is evidenced by Fig. 8, which contains the compensator magnitude frequency responses determined for each boundary condition with this cavity configuration.

B. Sensitivity analysis

In the preceding section the impedance-matching boundary condition was compared to the pressure-release boundary condition both in terms of absorption performance and control effort. Here we seek to demonstrate the sensitivity of each approach to changes in the cavity depth and the thickness of the absorbing foam layer. As a first indicator Tables I and II may again be consulted. First, let us consider the impedance-matching data. It is easily seen that as the foam layer is thickened, the average absorption coefficient and the average compensator gain each decrease. A similar trend is

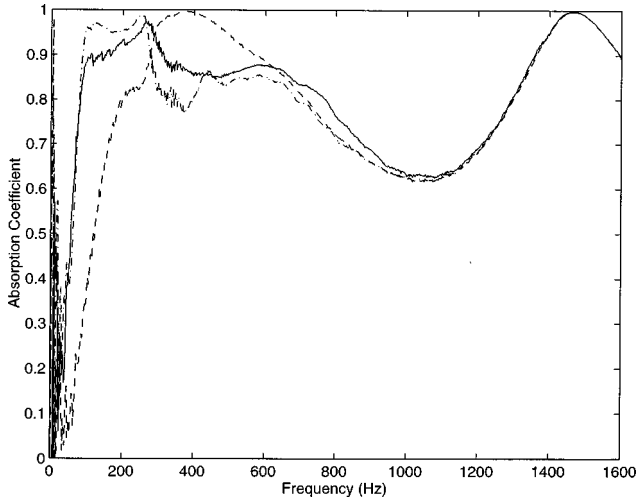

FIG. 7. Absorption coefficient frequency spectrum for $D=100$ mm and $t=50.8$ mm. Condition: ——— impedance matching, -·-·- pressure release, --- passive.

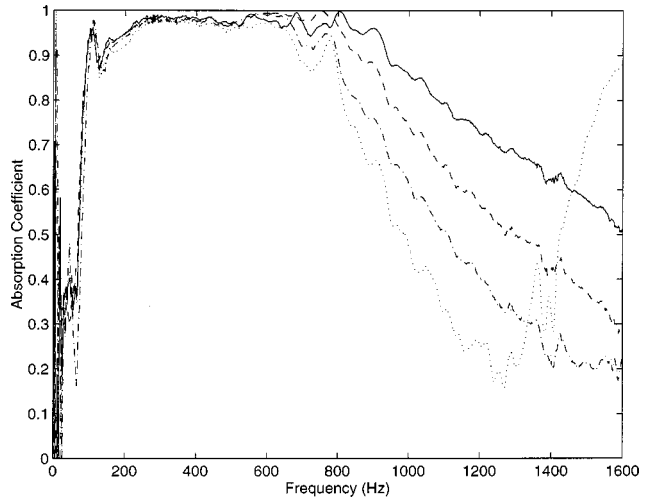

FIG. 9. Absorption coefficient frequency spectrum with impedance matching for $t=12.7$ mm. D: ——— 60 mm, -·-·- 80 mm, --- 100 mm, ··· 120 mm.

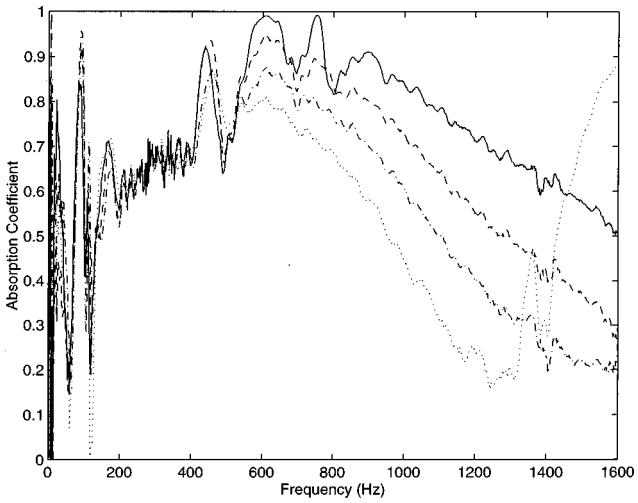

FIG. 10. Absorption coefficient frequency spectrum with pressure release for $t=12.7$ mm. D: ——— 60 mm, -·-·- 80 mm, --- 100 mm, ··· 120 mm.

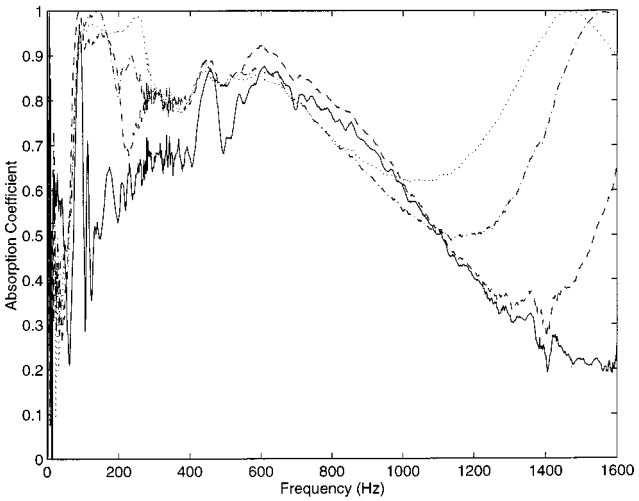

FIG. 12. Absorption coefficient frequency spectrum with pressure release for $D=100$ mm. t: ——— 12.7 mm, -·-·- 25.4 mm, --- 38.1 mm, ··· 50.8 mm.

observed as the cavity depth is increased. Second, we consider the results observed with the pressure-release boundary condition. With increasing foam thickness, a decrease is again observed in the average compensator gain; however, the average absorption coefficient is seen to increase and then decrease, suggesting the presence of an optimal thickness. This optimal thickness likely depends on the absorbing material, the cavity depth, and the frequency range of interest. As the cavity depth is increased, a general decline is observed in both the average absorption coefficient and the average compensator gain. The performance of the impedance-matching condition is seen to be less sensitive to the cavity depth than the pressure-release condition. Physical insight into these trends would require an analytical model which includes the physical properties of the absorption material.

The average absorption coefficient provides a useful glance at the sensitivity of the hybrid absorption system to the cavity geometry, but it does not offer a means by which to study this sensitivity. In order to understand better the effect of the cavity geometry on the system, the frequency dependence of the absorption coefficient for varied cavity geometries shall be considered. Figure 9 contains the absorption coefficient frequency spectra measured with the impedance-matching approach, a fixed foam thickness of 12.7 mm, and four cavity depths. A rolloff in the absorption coefficient is observed near 700 Hz, the grade of this decline becoming steeper with increasing cavity depths. This is likely a passive effect stemming from a change in the cavity resonance as the depth of the cavity is changed. Figure 10 represents the corresponding results for the pressure-release condition, depicting a nearly identical trend.

Lastly, the frequency dependence of the absorption coefficient shall be investigated under a fixed cavity depth and varied foam thickness for each boundary condition. The cavity depth used for this study was 100 mm. In Fig. 11 the sensitivity of the impedance-matching approach to a varied foam thickness is illustrated. Above about 1000 Hz the increasing foam thickness results in an increase in the absorptivity, which is again suspected to be caused by a shifting of the cavity resonance. Between 300 and 1000 Hz the increased foam thickness results in a deterioration of the absorption coefficient. The high-frequency absorption behavior observed with impedance matching is mirrored in the results obtained with pressure release, as depicted in Fig. 12. This similarity strengthens the conclusion that this phenomenon is a passive effect as it is independent of the chosen boundary condition. In the low-frequency range, between about 100 and 800 Hz, the pressure-release approach yields an irregular variation in the absorption coefficient with respect to the foam thickness. It is evident that the pressure-release approach is more sensitive to this change than the impedance-matching approach.

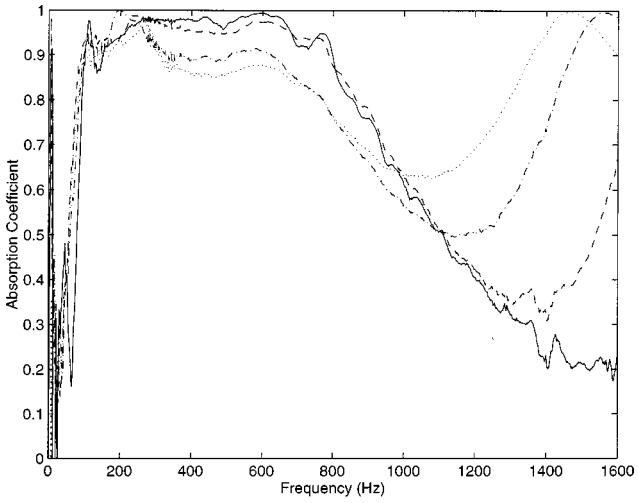

FIG. 11. Absorption coefficient frequency spectrum with impedance matching for $D=100$ mm. t: ——— 12.7 mm, -·-·- 25.4 mm, --- 38.1 mm, ··· 50.8 mm.

IV. CONCLUSIONS

An experimental study was conducted which demonstrates the superiority of the impedance-matching technique over that of the pressure-release approach for application to the active component of a broadband hybrid absorption

system comprised of an active wall positioned at the rear of an air cavity terminated by a sound-absorbing layer. Sensing and minimizing the reflected wave inside the cavity achieved greater absorption coefficients than by achieving a pressure-release condition at the back of the absorbing layer. Moreover, this increased performance was obtained with substantially less control effort, in many cases requiring half the power of the corresponding system based upon the pressure-release approach. Furthermore, with the impedance-matching approach absorption coefficients between 0.8 and 1.0 were generally attained over the 100–1000-Hz range, with specific geometries yielding absorption coefficients upwards of 0.9 throughout this frequency range. These results are expected to be applicable to other types of porous materials.

[1] D. Guicking and E. Lorenz, ''An Active Sound Absorber with Porous Plate,'' Journal of Vibration, Acoustics, Stress and Reliability in Design **106**, 389–392 (1984).

[2] D. Thenail, M. Galland, M. Sunyach, and M. Sunhack, ''Active Enhancement of the Absorbent Properties of a Porous Material,'' Smart Mater. Struct. **3**, 18–25 (1994).

[3] M. Furstoss, D. Thenail, and M. A. Galland, ''Surface Impedance Control for Sound Absorption: Direct and Hybrid Passive/Active Strategies,'' J. Sound Vib. **203**, 219–236 (1997).

[4] J. S. Bolton and E. R. Green, ''Smart foams for active absorption of sound,'' in *Second Conference on Recent Advances in Active Noise Control of Sound and Vibration*, Blacksburg, VA (1993), pp. 139–149.

[5] C. R. Fuller, M. J. Bronzel, C. H. Gentry, and D. E. Whittington, ''Control of Sound Radiation/Reflection with Adaptive Foams,'' in Proceedings of Noise-Con 1994 (1994), pp. 429–436.

[6] I. L. Ver and M. Digman, ''Active Liner System for Jet Engine Exhaust Silencers,'' Internoise 95, Newport Beach, CA (1995), pp. 481–484.

[7] S. Beyene and R. A. Burdisso, ''A New Hybrid Passive/Active Noise Absorption System,'' J. Acoust. Soc. Am. **101**, 1512–1515 (1997).

[8] J. P. Smith, C. R. Fuller, and R. A. Burdisso, ''Control of Broadband Radiated Sound with Adaptive Structures,'' Proc. SPIE Conf., Smart Structures and Intelligent Systems, **1917** (Pt. 1), 587–597 (February 1993).

[9] S. J. Elliott, P. A. Nelson, I. M. Stothers, and C. C. Boucher, ''In Flight Experiments on the Active Control of Propeller-Induced Cabin Noise,'' J. Sound Vib. **140**, 219–238 (1990).

[10] S. J. Elliott, I. M. Stothers, and P. A. Nelson, ''A Multiple Error LMS Algorithm and its application to the Active Control of Sound and Vibration,'' IEEE Trans. Acoust., Speech, Signal Process. **35**, 1423–1434 (1987).

[11] B. Widrow and S. D. Stearns, *Adaptive Signal Processing* (Prentice-Hall, Englewood Cliffs, NJ, 1985).

[12] F. J. Fahy, ''A Technique for Measuring Sound Intensity with a Sound Level Meter,'' Noise Control Eng. **9**, 155–162 (1977).

[13] ''Standard Test Method for Impedance and Absorption of Acoustical Materials by the Impedance Tube Method,'' ASTM C384, Philadelphia (1990).

[14] R. A. Burdisso, J. S. Vipperman, and C. R. Fuller, ''Causality analysis of feedforward-controlled systems with broadband inputs,'' J. Acoust Soc. Am. **94**, 234–242 (1993).

Iterative inverse scattering algorithms: Methods of computing Fréchet derivatives

Stephen J. Norton[a)]
Oak Ridge National Laboratory, Oak Ridge, Tennessee 37831-6200

(Received 22 July 1997; revised 21 January 1999; accepted 21 July 1999)

Iterative approaches to the nonlinear inverse scattering problem generally attempt to find the scattering distribution that best predicts the data by minimizing a global error norm (e.g., the mean-square error) which quantifies the misfit between a set of measured data and data predicted on the basis of a forward calculation. A crucial quantity in this minimization is the Fréchet derivative of the error norm which tells us how to update the current estimate of the scattering distribution to reduce the global error at each iteration. This paper demonstrates how to compute the Fréchet derivative using three different, but fundamentally equivalent, methods: the conventional adjoint method, the Lagrange multiplier method, and the integral equation method. The first two begin with the wave equation, while the latter method is based on a Lippmann–Schwinger integral equation. These techniques are not only far more efficient, but also numerically less error prone, than ''brute force'' methods for computing derivatives based, for example, on finite differences. For simplicity, a variational approach is employed in which the fields and scattering distribution are represented by continuous functions, but the finite-dimensional (discretized) problem is shown to follow directly from the continuous-space results.
[S0001-4966(99)03311-1]

PACS numbers: 43.60.Pt, 43.60.Rw, 43.30.Pc [JCB]

INTRODUCTION

The task of deriving the structure or shape of a remote object from acoustic scattering measurements, or the inverse-scattering problem, has potential applications in many diverse areas, including the ultrasonic characterization of materials, medical ultrasonic imaging, and seismology.

Here we consider the generic problem of reconstructing an unknown distribution of some acoustic scattering parameter (e.g., density, wave speed, etc.) from remote scattering measurements. For brevity, we refer to this unknown parameter distribution as the ''scattering potential.'' Our basic approach is to construct a hypothetical scattering potential that gives rise to scattering data in agreement with the measured data subject, perhaps, to some additional constraints. A variety of global error norms can be used as the measure of this agreement, but a convenient choice is the weighted mean-squared difference between the predicted and measured data. Because the problem is nonlinear, iterative descent algorithms are generally required to drive the global error to a minimum. A key requirement of any descent algorithm is a means of numerically calculating the functional gradient (or Fréchet derivative) of the error norm; this tells us in what ''direction'' to update the scattering potential to reduce the error norm at each iteration. A brute force approach to computing the gradient is to vary the potential in some systematic way and compute the resulting change in the error norm (i.e., a finite difference approach). Assuming the potential is parametrized in some fashion (e.g., expanded into basis functions or divided into pixels) and N is the number of parameters, a finite-difference approach would require at least N distinct forward scattering solutions to compute the N-component gradient per iteration. Here we show how this effort can be avoided by solving just two forward problems per iteration: the ordinary forward problem and its adjoint. The method is independent of the number of parameters, N, as well as the number of observation points (or receivers). The adjoint method is not only vastly more efficient, but less susceptible to round-off error since it is analytically exact, i.e., derived from an infinitesimal difference at a point rather than from a finite difference at two nearby points. We describe three formulations of the adjoint method. Although all three methods are shown to be fundamentally equivalent, the choice of method may have advantages depending upon the choice of algorithm employed for the numerical solution of the forward problem. The first two adjoint formulations, that is, the conventional adjoint method and the Lagrange multiplier method, both begin with the wave equation, while the third formulation is based on the Lippmann–Schwinger integral equation.

In this paper, we represent fields and the scattering potential as continuous functions for the benefit of clarity and economy of exposition. This distinguishes our approach from many others (particularly in the geophysical literature) which discretize first, after which manipulations are applied to matrices, rather than to the governing differential or integral equations. However, the continuous-space results are also applicable when the problem is ultimately discretized, or when the scattering potential is characterized *a priori* by a finite number of undetermined parameters (the finite-dimensional problem), as we show below.

A clear discussion of what we call the ''conventional adjoint method,'' with emphasis on geophysical inverse

[a)]Current address: Geophex, Ltd., 605 Mercury St., Raleigh, NC 27603. Electronic mail: norton@geophex.com

problems, is given by McGillivray and Oldenburg.[1] We emphasize that the adjoint method is quite general and can be applied to problems governed by other field equations. Other problems where it has been applied include the electrical potential inverse problem,[1] the electromagnetic induction inverse problem,[2,3] the inverse transport problem,[4] and the inverse heat-conduction problem.[5]

Our purpose here is to present some original material and to unify the results of several papers treating a variety of inverse problems using the adjoint concept (EM induction, EM resistivity, thermal diffusion, particle transport) using a variety of formulations (differential, integral, time-domain, frequency-domain, continuous space, discrete space) all in the context of an acoustical scattering problem. We also present an original approach to deriving the Fréchet derivative of the shape of a soft acoustical scattering object.

The paper is organized as follows. In Sec. I we define the global error functional to be minimized, and briefly discuss descent algorithms for performing this minimization. In the first several sections, we assume for simplicity that the fields obey a time-independent wave equation (the Helmholtz equation). In Sec. II we define the forward scattering problem. In Secs. III and IV we derive, respectively, the Fréchet derivative of the global error using the conventional adjoint method and the Lagrange multiplier method. In Sec. V we show how the Fréchet derivative is modified by adding a regularization term to the global error. In Sec. VI we treat the time-dependent wave equation using the adjoint method. In Sec. VII we show how the continuous-space results are applied to the finite-dimensional problem. In Sec. VIII we treat the problem of reconstructing the shape of a ''soft'' scatterer. Finally, in Sec. IX we derive the Fréchet derivative from an integral equation formulation of the scattering problem (the Lippmann–Schwinger equation).

I. THE ITERATIVE INVERSE SCATTERING PROBLEM

For simplicity, we illustrate with the scalar wave equation, but the generalization to vector or dyadic field equations is straightforward in principle. Consider a medium with a spatially varying sound speed, $c(\mathbf{r})$, confined to a finite region of space, D. Outside of D we assume $c(\mathbf{r})=c_0$ $=$const. Suppose the acoustic refractive index, $n(\mathbf{r})$ $=c_0/c(\mathbf{r})$ plays the role of our unknown scattering potential [we assume $n(\mathbf{r})$ is real for convenience]. Let $S(\mathbf{r})$ denote a source of an incident monochromatic wave that impinges upon D. Then the total field (incident plus scattered), $\psi(\mathbf{r})$, obeys the reduced wave equation

$$\nabla^2\psi(\mathbf{r})+k^2n(\mathbf{r})\psi(\mathbf{r})=-S(\mathbf{r}), \tag{1}$$

where $k=\omega/c_0$ is the wave number of the incident field outside D, and ω denotes frequency. As data, we assume that the field $\psi(\mathbf{r})$ is measured at M receiving points $\{\mathbf{r}_m,\ m=1,...,M\}$ outside of D. Our approach is to minimize the mean-square error functional

$$\mathcal{E}[n(\mathbf{r})]=\frac{1}{2}\sum_{m=1}^{M} w_m|\psi(\mathbf{r}_m)-\psi_{\mathrm{obs}}(\mathbf{r}_m)|^2 \tag{2}$$

with respect to $n(\mathbf{r})$. In (2), $\psi_{\mathrm{obs}}(\mathbf{r}_m)$ is the observed field at $\mathbf{r}_m$, and w_m is a positive weight that can be selected to provide different emphasis to different measurements if so desired.[6]

To find $n(\mathbf{r})$ that minimizes $\mathcal{E}$, we determine the variation in $\mathcal{E}$ due to an infinitesimal variation in $n(\mathbf{r})$. This process will lead to the functional gradient, or Fréchet derivative, of $\mathcal{E}$ with respect to $n(\mathbf{r})$, denoted by $\nabla_F\mathcal{E}(\mathbf{r})$, and defined by the relation

$$\delta\mathcal{E}[n(\mathbf{r})]\equiv\int\int\int \nabla_F\mathcal{E}(\mathbf{r})\,\delta n(\mathbf{r})\,d^3\mathbf{r}, \tag{3}$$

where $\delta\mathcal{E}$ is the variation in $\mathcal{E}$ due to an (arbitrary) variation $\delta n(\mathbf{r})$ in the function $n(\mathbf{r})$. The above relation can be viewed as the continuous-space analog of the discrete-space directional derivative; that is, $\delta\mathcal{E}$ is analogous to the dot product of the gradient $\nabla_F\mathcal{E}(\mathbf{r})$ with the infinite-dimensional ''vector'' $\delta n(\mathbf{r})$.

Once $\nabla_F\mathcal{E}(\mathbf{r})$ is known, we see from (3) that the global error $\mathcal{E}$ is guaranteed to decrease by selecting the ''direction'' $\delta n(r)=-\alpha\nabla_F\mathcal{E}(\mathbf{r})$, where α is a positive constant. Thus, if $n^{(j)}(\mathbf{r})$ is the current estimate of $n(\mathbf{r})$, then a better estimate is given by

$$n^{(j+1)}(\mathbf{r})=n^{(j)}(\mathbf{r})-\alpha_j\nabla_F\mathcal{E}^{(j)}(\mathbf{r}), \tag{4}$$

where the gradient $\nabla_F\mathcal{E}^{(j)}(\mathbf{r})$ is computed on the basis of the current estimate $n^{(j)}(\mathbf{r})$. This is the steepest-descent algorithm. In (4), α_j is a step-size parameter that tells us how far to advance in the ''direction'' $\nabla_F\mathcal{E}^{(j)}(\mathbf{r})$. A number of strategies can be employed in selecting α_j, the simplest being to perform a 1-D line search in the direction $\nabla_F\mathcal{E}^{(j)}(\mathbf{r})$ for the α that minimizes $\mathcal{E}$ in that direction. Other gradient descent algorithms that converge much more rapidly than (4) exist and are preferred, such as the conjugate-gradient or quasi-Newton methods.[7] For example, the conjugate-gradient algorithm has the form

$$\begin{aligned} s^{(j)}(\mathbf{r})&=-\nabla_F\mathcal{E}^{(j)}(\mathbf{r})+\beta_j s^{(j-1)}(\mathbf{r}),\\ n^{(j+1)}(\mathbf{r})&=n^{(j)}(\mathbf{r})+\alpha_j s^{(j)}(\mathbf{r}), \end{aligned} \tag{5}$$

where α_j and β_j are appropriate constants, and $s^{(0)}(\mathbf{r})\equiv 0$. Further discussion of these algorithms and the definitions of α_j and β_j can be found in any text on numerical optimization.[7] The point here is that any descent algorithm requires some means of computing the functional gradient, $\nabla_F\mathcal{E}(\mathbf{r})$.

II. A NOTE ON THE FORWARD PROBLEM

At each iteration of a descent algorithm, we require solutions to the forward problem computed on the basis of the current estimate of $n(\mathbf{r})$. The details of the forward algorithm are not relevant for our purposes, but accuracy and speed are obviously desirable traits. Suffice it to note that the differential equation (1) can be solved using a variety of numerical schemes, such as finite element or finite difference methods. Alternatively, (1) can be converted into an integral equation via Green's theorem and this solved numerically. That is, if the Green's function, $g(\mathbf{r}|\mathbf{r}')$, obeys

$$\nabla^2g(\mathbf{r}|\mathbf{r}')+k^2g(\mathbf{r}|\mathbf{r}')=-\delta(\mathbf{r}-\mathbf{r}'), \tag{6}$$

then (1) can be transformed with the aid of Green's theorem into

$$\psi(\mathbf{r}) = \psi_i(\mathbf{r}) + k^2 \int\int\int g(\mathbf{r}|\mathbf{r}')[n(\mathbf{r}')-1]\psi(\mathbf{r}')d^3\mathbf{r}', \tag{7}$$

where

$$\psi_i(\mathbf{r}) \equiv \int\int\int g(\mathbf{r}|\mathbf{r}')S(\mathbf{r}')d^3\mathbf{r}'. \tag{8}$$

Equation (7) is linear in the field $\psi(\mathbf{r})$ when $n(\mathbf{r})$ is given and can be solved for the field by a variety of linear inversion schemes.

We now turn to our main objective: computing the functional gradient, $\nabla_F \mathcal{E}(\mathbf{r})$, of the error functional, $\mathcal{E}$.

III. ADJOINT METHOD

Consider an infinitesimal variation, $\delta n(\mathbf{r})$, in the scattering potential, $n(\mathbf{r})$. This will result in a variation in the field, $\delta\psi(\mathbf{r})$, and hence in a variation in the error functional, $\delta\mathcal{E}$. Thus, taking the variation in the wave equation (1), and the variation in the functional (2), gives respectively

$$\nabla^2 \delta\psi(\mathbf{r}) + k^2 n(\mathbf{r})\delta\psi(\mathbf{r}) + k^2 \delta n(\mathbf{r})\psi(\mathbf{r}) = 0, \tag{9}$$

and

$$\delta\mathcal{E}[n(\mathbf{r})] = \mathrm{Re}\sum_{m=1}^{M} w_m[\psi(\mathbf{r}_m) - \psi_{\mathrm{obs}}(\mathbf{r}_m)]^* \delta\psi(\mathbf{r}_m), \tag{10}$$

where Re means real part and* denotes complex conjugate.

Our approach to deriving the functional gradient, $\nabla_F \mathcal{E}(\mathbf{r})$, is to seek an expression of the form (3), that is, an integral containing $\delta n(\mathbf{r})$; we can then identify the quantity in the integrand multiplying the (arbitrary) variation $\delta n(\mathbf{r})$ as the Fréchet derivative, $\nabla_F \mathcal{E}(\mathbf{r})$. To achieve this, we first need to eliminate the unknown field variation, $\delta\psi$, from (10); we will see that (9) is used to accomplish this.

Now, define the adjoint field, $\tilde{\psi}(\mathbf{r})$, as the solution to the wave equation

$$\nabla^2 \tilde{\psi}(\mathbf{r}) + k^2 n(\mathbf{r})\tilde{\psi}(\mathbf{r}) = -\tilde{S}(\mathbf{r}), \tag{11}$$

where the adjoint source is defined by

$$\tilde{S}(\mathbf{r}) = \sum_{m=1}^{M} w_m[\psi(\mathbf{r}_m) - \psi_{\mathrm{obs}}(\mathbf{r}_m)]^* \delta(\mathbf{r}-\mathbf{r}_m), \tag{12}$$

and $\delta(\mathbf{r}-\mathbf{r}_m)$ is the 3-D Dirac delta function. Then by comparing (12) and (10), we can write

$$\delta\mathcal{E}[n(\mathbf{r})] = \mathrm{Re}\int\int\int \tilde{S}(\mathbf{r})\delta\psi(\mathbf{r})d^3\mathbf{r}. \tag{13}$$

That is, putting (12) into (13) gives (10). Next, substituting the left-hand side of (11) into (13) gives

$$\delta\mathcal{E}[n(\mathbf{r})] = -\mathrm{Re}\int\int\int [\nabla^2\tilde{\psi}(\mathbf{r}) + k^2 n(\mathbf{r})\tilde{\psi}(\mathbf{r})]\delta\psi(\mathbf{r})d^3\mathbf{r}. \tag{14}$$

The first term in the above integral can be integrated by parts with the aid of the relation $\delta\psi\nabla^2\tilde{\psi} = -\tilde{\psi}\nabla^2\delta\psi + \nabla\cdot(\tilde{\psi}\nabla\delta\psi - \delta\psi\nabla\tilde{\psi})$. The integral of the latter term can be converted to a surface integral using the divergence theorem which then vanishes on allowing the domain of integration to expand to infinity.[8,9] Equation (14) then becomes

$$\delta\mathcal{E}[n(\mathbf{r})] = -\mathrm{Re}\int\int\int \tilde{\psi}(\mathbf{r})[\nabla^2\delta\psi(\mathbf{r}) + k^2 n(\mathbf{r})\delta\psi(\mathbf{r})]d^3\mathbf{r}. \tag{15}$$

Now substituting from (9), this becomes

$$\delta\mathcal{E}[n(\mathbf{r})] = k^2\,\mathrm{Re}\int\int\int \tilde{\psi}(\mathbf{r})\psi(\mathbf{r})\delta n(\mathbf{r})d^3\mathbf{r}, \tag{16}$$

which is in the form of (3). Finally, comparing (16) to (3), we find for the functional gradient

$$\nabla_F \mathcal{E}(\mathbf{r}) = k^2\,\mathrm{Re}[\tilde{\psi}(\mathbf{r})\psi(\mathbf{r})]. \tag{17}$$

This is the desired result. Thus, the functional gradient follows once we obtain numerical solutions to the forward problem (1) and its adjoint (11), with the adjoint source defined by (12). Observe from (12) that the adjoint source is a weighted summation of waves emitted at the M receiving points $\{\mathbf{r}_m,\ m=1,...,M\}$. It is important to note that, although we may have many receivers, only one adjoint solution is needed independent of the receiver number, N.

IV. LAGRANGE MULTIPLIER METHOD

In this approach, the adjoint field will be interpreted as a continuous Lagrange multiplier function. Here, we wish to minimize the error functional, $\mathcal{E}$, subject to the constraint that the field, $\psi(\mathbf{r})$, obey the wave equation (1). We thus consider (1) as a side condition and construct the augmented functional

$$\mathcal{E}_A[n(\mathbf{r})] = \mathcal{E}[n(\mathbf{r})] + \mathrm{Re}\int\int\int \lambda(\mathbf{r})[\nabla^2\psi(\mathbf{r}) + k^2 n(\mathbf{r})\psi(\mathbf{r}) + S(\mathbf{r})]d^3\mathbf{r}, \tag{18}$$

where $\mathcal{E}[n(\mathbf{r})]$ is again given by (2) and $\lambda(\mathbf{r})$ may be regarded as a continuous Lagrange multiplier. We also allow $\lambda(\mathbf{r})$ to be complex.[10] After substituting (2) for $\mathcal{E}[n(\mathbf{r})]$, we vary (18) to obtain[11]

$$\delta\mathcal{E}_A[n(\mathbf{r})] = \mathrm{Re}\sum_{m=1}^{M} w_m[\psi(\mathbf{r}_m) - \psi_{\mathrm{obs}}(\mathbf{r}_m)]^*\delta\psi(\mathbf{r}_m) + \mathrm{Re}\int\int\int \lambda(\mathbf{r})[\nabla^2\delta\psi(\mathbf{r}) + k^2 n(\mathbf{r})\delta\psi(\mathbf{r}) + \delta n(\mathbf{r})\psi(\mathbf{r})]d^3\mathbf{r}. \tag{19}$$

Using the definition of the adjoint source (12), the first term can be rewritten to give

$$\delta\mathcal{E}_A[n(\mathbf{r})] = \mathrm{Re}\int\int\int \tilde{S}(\mathbf{r})\delta\psi(\mathbf{r})d^3\mathbf{r} + \mathrm{Re}\int\int\int \lambda(\mathbf{r})[\nabla^2\delta\psi(\mathbf{r}) + k^2 n(\mathbf{r})\delta\psi(\mathbf{r}) + \delta n(\mathbf{r})\psi(\mathbf{r})]d^3\mathbf{r}. \tag{20}$$

Finally, integrating (20) by parts, employing the divergence theorem, and assuming the integrated part vanishes, we have

$$\delta\mathcal{E}_A[n(\mathbf{r})] = \mathrm{Re}\int\int\int \tilde{S}(\mathbf{r})\,\delta\psi(\mathbf{r})\,d^3\mathbf{r} + \mathrm{Re}\int\int\int \{[\nabla^2\lambda(\mathbf{r}) + k^2 n(\mathbf{r})\lambda(\mathbf{r})] \times \delta\psi(\mathbf{r}) + k^2\lambda(\mathbf{r})\psi(\mathbf{r})\,\delta n(\mathbf{r})\}\,d^3\mathbf{r}. \quad (21)$$

If we now demand that the Lagrange multiplier obey the following wave equation

$$\nabla^2\lambda(\mathbf{r}) + k^2 n(\mathbf{r})\lambda(\mathbf{r}) = -\tilde{S}(\mathbf{r}), \quad (22)$$

then terms in (21) multiplying the variation $\delta\psi(\mathbf{r})$ vanish and (21) reduces to

$$\delta\mathcal{E}_A[n(\mathbf{r})] = k^2\,\mathrm{Re}\int\int\int \lambda(\mathbf{r})\psi(\mathbf{r})\,\delta n(\mathbf{r})\,d^3\mathbf{r}. \quad (23)$$

Comparing this to (3), we obtain for the functional gradient

$$\nabla_F\mathcal{E}_A(\mathbf{r}) = k^2\,\mathrm{Re}[\lambda(\mathbf{r})\psi(\mathbf{r})]. \quad (24)$$

Note that (22) and (24) are identical to (11) and (17), respectively, when the Lagrange multiplier, $\lambda(\mathbf{r})$, is identified with the adjoint field, $\tilde{\psi}(\mathbf{r})$.

As noted, only a single adjoint equation needs to be computed when multiple receiving locations $\{\mathbf{r}_m,\ m = 1,...,M\}$ are employed. The adjoint source is constructed from a weighted summation of the receiver points, as seen from (12). We can also consider additional degrees of freedom in the measurement, such as distinct source locations and/or different frequencies. In this case, one adjoint problem will need to be solved for each of these additional measurement parameters. This is perhaps most easily exemplified using the Lagrange multiplier method. Suppose p represents an index that identifies a particular scattering experiment, where $p = 1,...,P$. For example, p could identify a new source location, or the angle of incidence of a plane wave, or a different frequency (in which case we change k to k_p). For our purposes, we need not be much more specific about the parameter p that distinguishes experiments. Let $\psi_p(\mathbf{r})$ represent the field identified by p and $S_p(\mathbf{r})$ the associated source. Then the augmented functional (18) generalizes to

$$\mathcal{E}_A[n(\mathbf{r})] = \frac{1}{2}\sum_{p=1}^{P}\sum_{m=1}^{M} |\psi_p(\mathbf{r}_m) - \psi_{\mathrm{obs},p}(\mathbf{r}_m)|^2 + \mathrm{Re}\sum_{p=1}^{P}\int\int\int \lambda_p(\mathbf{r})[\nabla^2\psi_p(\mathbf{r}) + k_p^2 n(\mathbf{r})\psi_p(\mathbf{r}) + S_p(\mathbf{r})]\,d^3\mathbf{r}. \quad (25)$$

To obtain the functional gradient, $\nabla_F\mathcal{E}_A(\mathbf{r})$, we need to solve the P forward problems defined by

$$\nabla^2\psi_p(\mathbf{r}) + k_p^2 n(\mathbf{r})\psi_p(\mathbf{r}) = -S_p(\mathbf{r}), \quad (26)$$

as well as P adjoint problems defined by

$$\nabla^2\lambda_p(\mathbf{r}) + k_p^2 n(\mathbf{r})\lambda_p(\mathbf{r}) = -\tilde{S}_p(\mathbf{r}), \quad (27)$$

where the adjoint source is now given by

$$\tilde{S}_p(\mathbf{r}) = \sum_{m=1}^{M} w_m[\psi_p(\mathbf{r}_m) - \psi_{\mathrm{obs},p}(\mathbf{r}_m)]^*\,\delta(\mathbf{r}-\mathbf{r}_m). \quad (28)$$

Then the functional gradient (24) generalizes to

$$\nabla_F\mathcal{E}_A(\mathbf{r}) = \sum_{p=1}^{P} k_p^2\,\mathrm{Re}[\lambda_p(\mathbf{r})\psi_p(\mathbf{r})]. \quad (29)$$

V. ADDING A REGULARIZATION TERM

If the inverse problem is ill conditioned, it may be beneficial to add a constraint term to the mean-square error functional (2) which could, for example, penalize large variations in $n(\mathbf{r})$ or emphasize smoother solutions. Regularization of this kind is designed to mitigate ill conditioning in the inversion and can also serve to force uniqueness in an underdetermined problem. Equation (2) is then modified to read

$$\mathcal{E}[n(\mathbf{r})] = \frac{1}{2}\sum_{m=1}^{M} w_m|\psi(\mathbf{r}_m) - \psi_{\mathrm{obs}}(\mathbf{r}_m)|^2 + \frac{1}{2}\beta\int\int\int C(n)\,d^3\mathbf{r}, \quad (30)$$

where $C(n)$ is a penalty function and β is a parameter which controls the relative importance of the two terms in (30). Reasonable choices for $C(n)$ might be

$$C(n) = n(\mathbf{r})^2 \quad (31)$$

or

$$C(n) = \nabla n(\mathbf{r})\cdot\nabla n(\mathbf{r}). \quad (32)$$

Working through the same derivation as that of Sec. III with the above modified mean-square error, we obtain, respectively, for the two choices of penalty functions (31) and (32):

$$\nabla_F\mathcal{E}(\mathbf{r}) = k^2\,\mathrm{Re}[\tilde{\psi}(\mathbf{r})\psi(\mathbf{r})] + \beta n(\mathbf{r}), \quad (33)$$

$$\nabla_F\mathcal{E}(\mathbf{r}) = k^2\,\mathrm{Re}[\tilde{\psi}(\mathbf{r})\psi(\mathbf{r})] - \beta\nabla^2 n(\mathbf{r}). \quad (34)$$

In deriving the latter result, we have used the fact that the variation of the penalty function (32) may be written $\delta C = 2\nabla n\cdot\nabla\,\delta n = 2\nabla\cdot(\delta n\nabla n) - 2\,\delta n\nabla^2 n$. On integrating this result, the first term vanishes by virtue of the divergence theorem, leaving the Laplacian-like term that appears in (34).

VI. THE ADJOINT METHOD FOR THE TIME-DEPENDENT WAVE EQUATION

Here we illustrate how the adjoint method is applied to time-dependent problems. In particular, we replace (1) with the following time-dependent wave equation:

$$\nabla^2\psi(\mathbf{r},t) - \frac{1}{c(\mathbf{r})^2}\frac{\partial^2\psi(\mathbf{r},t)}{\partial t^2} = -S(\mathbf{r},t), \quad (35)$$

where the spatially varying wave speed is $c(\mathbf{r})$, $S(\mathbf{r},t)$ is a general space- and time-dependent source, and now $\psi(\mathbf{r},t)$ is real. Letting $v(\mathbf{r}) \equiv (c_0/c(\mathbf{r}))^2$, this becomes

$$\nabla^2\psi(\mathbf{r},t) - \frac{v(\mathbf{r})}{c_0^2}\frac{\partial^2\psi(\mathbf{r},t)}{\partial t^2} = -S(\mathbf{r},t), \quad (36)$$

where we now let $v(\mathbf{r})$ play the role of our unknown scattering potential. We assume zero initial conditions at $t=0$ so that the solution to the homogeneous form of (36) vanishes:

$$\psi(\mathbf{r},0)=0 \quad \text{and} \quad \left.\frac{\partial\psi(\mathbf{r},t)}{\partial t}\right|_{t=0}=0. \tag{37}$$

As before, we assume that the field, $\psi(\mathbf{r},t)$, is measured at M receiving points $\{\mathbf{r}_m,\ m=1,...,M\}$, but now over a time interval $[0,T]$. The following mean-square error functional, which we wish to minimize, now replaces (2):

$$\mathcal{E}[v(\mathbf{r})]=\frac{1}{2}\sum_{m=1}^{M}\int_0^T dt\, w_m(t)[\psi(\mathbf{r}_m,t)-\psi_{\text{obs}}(\mathbf{r}_m,t)]^2, \tag{38}$$

where we now compute the weighted time-integrated error over the observation interval $[0,T]$. For generality, we will allow the positive weight, $w_m(t)$, to be time dependent. Finally, the time-domain fields, $\psi(\mathbf{r},t)$, are assumed to be real. The variation of (38) is then

$$\delta\mathcal{E}[v(\mathbf{r})]=\sum_{m=1}^{M}\int_0^T dt\, w_m(t)[\psi(\mathbf{r}_m,t) - \psi_{\text{obs}}(\mathbf{r}_m,t)]\delta\psi(\mathbf{r}_m,t). \tag{39}$$

Next define the adjoint wave equation given by

$$\nabla^2\tilde{\psi}(\mathbf{r},t)-\frac{v(\mathbf{r})}{c_0^2}\frac{\partial^2\tilde{\psi}(\mathbf{r},t)}{\partial t^2}=-\tilde{S}(\mathbf{r},t), \tag{40}$$

where the following ''terminal'' (as opposed to initial) conditions are imposed at time $t=T$:

$$\tilde{\psi}(\mathbf{r},T)=0 \quad \text{and} \quad \left.\frac{\partial\tilde{\psi}(\mathbf{r},t)}{\partial t}\right|_{t=T}=0. \tag{41}$$

Thus the adjoint field propagates backward in time from $t=T$. The reason for these terminal conditions will become apparent below. Bear in mind that, as before, the adjoint field need not be physically realizable; it merely needs to be computable. We now define as the time-dependent adjoint source

$$\tilde{S}(\mathbf{r},t)=\sum_{m=1}^{M} w_m(t)[\psi(\mathbf{r}_m,t)-\psi_{\text{obs}}(\mathbf{r}_m,t)]\delta(\mathbf{r}-\mathbf{r}_m) \tag{42}$$

over the interval $[0,T]$. As a result, (39) can be written

$$\delta\mathcal{E}[v(\mathbf{r})]=\int\int\int d^3\mathbf{r}\int_0^T dt\,\tilde{S}(\mathbf{r},t)\,\delta\psi(\mathbf{r},t). \tag{43}$$

Next, substituting the left-hand side of (40) into (43) gives

$$\delta\mathcal{E}[v(\mathbf{r})]=-\int\int\int d^3\mathbf{r}\int_0^T dt\left[\nabla^2\tilde{\psi}(\mathbf{r},t) - \frac{v(\mathbf{r})}{c_0^2}\frac{\partial^2\tilde{\psi}(\mathbf{r},t)}{\partial t^2}\right]\delta\psi(\mathbf{r},t). \tag{44}$$

Integrating by parts with respect to both space and time, this becomes

$$\delta\mathcal{E}[v(\mathbf{r})]=-\int\int\int d^3\mathbf{r}\int_0^T dt\left[\nabla^2\delta\psi(\mathbf{r},t) - \frac{v(\mathbf{r})}{c_0^2}\frac{\partial^2\delta\psi(\mathbf{r},t)}{\partial t^2}\right]\tilde{\psi}(\mathbf{r},t). \tag{45}$$

When integrating by parts with respect to time, the integrated terms vanish on account of the initial conditions (37) since the variation $\delta\psi(\mathbf{r},t)$ will also obey these initial conditions at $t=0$, and also on account of the terminal conditions (41) obeyed by $\tilde{\psi}(\mathbf{r},t)$ at $t=T$. This is the reason for the requirement of terminal conditions for the adjoint field, $\tilde{\psi}(\mathbf{r},t)$. Next, the variation of (36) is

$$\nabla^2\delta\psi(\mathbf{r},t)-\frac{v(\mathbf{r})}{c_0^2}\frac{\partial^2\delta\psi(\mathbf{r},t)}{\partial t^2}-\frac{\delta v(\mathbf{r})}{c_0^2}\frac{\partial^2\psi(\mathbf{r},t)}{\partial t^2}=0, \tag{46}$$

and on substituting for the first two terms in (46), we have

$$\delta\mathcal{E}[v(\mathbf{r})]=-\frac{1}{c_0^2}\int\int\int\left[\int_0^T\frac{\partial^2\psi(\mathbf{r},t)}{\partial t^2}\tilde{\psi}(\mathbf{r},t)dt\right]\delta v(\mathbf{r})d^3\mathbf{r} = \frac{1}{c_0^2}\int\int\int\left[\int_0^T\frac{\partial\psi(\mathbf{r},t)}{\partial t}\frac{\partial\tilde{\psi}(\mathbf{r},t)}{\partial t}dt\right]\delta v(\mathbf{r})d^3\mathbf{r}, \tag{47}$$

where the last step was obtained by integrating by parts with respect to t. Finally, comparing this to (3) with $v(\mathbf{r})$ substituted for $n(\mathbf{r})$, we find for the functional gradient

$$\nabla_F\mathcal{E}(\mathbf{r})=\frac{1}{c_0^2}\int_0^T\frac{\partial\psi(\mathbf{r},t)}{\partial t}\frac{\partial\tilde{\psi}(\mathbf{r},t)}{\partial t}dt, \tag{48}$$

which is the desired result. Thus, the functional gradient follows from numerical solutions to the wave equation (36), subject to the initial conditions (37), and the adjoint wave equation (40), subject to the terminal conditions (41) and using the adjoint source defined by (42). These solutions are then differentiated with respect to time and integrated over the interval $[0,T]$, as specified by (48). We point out that Bunks *et al.*[12] obtain an equation essentially identical to the first line of (47) in their treatment of a seismic inversion problem.[13]

VII. FINITE-DIMENSIONAL CASE

In this section, we consider the case where the scattering potential can be characterized by a finite number of parameters. For simplicity, we illustrate with the reduced wave equation (1), but the general approach is applicable to all problems. We thus write the potential as $n(\mathbf{r};\mathbf{p})$, where $\mathbf{p}$ is a vector of P (real) parameters, p_i, to be determined. We assume that the functional dependence of $n(\mathbf{r};\mathbf{p})$ on $\mathbf{p}$ is known. In this finite-dimensional problem, the Fréchet derivative of the mean-square error $\mathcal{E}$ reduces to an ordinary P component gradient, where the ith component is $\partial\mathcal{E}/\partial p_i$. Here we find an explicit expression for $\partial\mathcal{E}/\partial p_i$ in terms of the field, ψ, and its adjoint, $\tilde{\psi}$, as follows. First write the variation of $n(\mathbf{r};\mathbf{p})$ as

$$\delta n(\mathbf{r};\mathbf{p}) = \sum_{i=1}^{P} \frac{\partial n}{\partial p_i}\,\delta p_i . \tag{49}$$

Substituting (49) into (16) and interchanging orders of integration and summation gives

$$\delta\mathcal{E}[v(\mathbf{r})] = k^2\,\mathrm{Re}\sum_{i=1}^{P}\left[\int\int\int \tilde{\psi}(\mathbf{r})\psi(\mathbf{r})\frac{\partial n}{\partial p_i}d^3\mathbf{r}\right]\delta p_i . \tag{50}$$

Now note that

$$\delta\mathcal{E}[v(\mathbf{r})] = \sum_{i=1}^{P}\frac{\partial\mathcal{E}}{\partial p_i}\,\delta p_i . \tag{51}$$

Assuming arbitrary variations, δp_i, comparing (51) and (50) shows that

$$\frac{\partial\mathcal{E}}{\partial p_i} = k^2\,\mathrm{Re}\int\int\int \tilde{\psi}(\mathbf{r})\psi(\mathbf{r})\frac{\partial n(\mathbf{r},\mathbf{p})}{\partial p_i}d^3\mathbf{r}. \tag{52}$$

Thus, once again the finite-dimensional gradient can be obtained after forward solutions are numerically computed for the fields ψ and $\tilde{\psi}$. As a simple example, suppose that the parameters, p_i, are the coefficients of $n(\mathbf{r};\mathbf{p})$ expanded in a set of basis functions, $\phi_i(\mathbf{r})$:

$$n(\mathbf{r};\mathbf{p}) = \sum_{i=1}^{P} p_i\phi_i(\mathbf{r}). \tag{53}$$

Then $\partial n/\partial p_i = \phi_i(\mathbf{r})$, and (52) becomes

$$\frac{\partial\mathcal{E}}{\partial p_i} = k^2\,\mathrm{Re}\int\int\int \tilde{\psi}(\mathbf{r})\psi(\mathbf{r})\phi_i(\mathbf{r})d^3\mathbf{r}. \tag{54}$$

VIII. RECONSTRUCTING THE SHAPE OF AN OBJECT

Here we consider the problem of reconstructing the shape, or boundary, of a bounded and homogeneous scattering region Ω. We assume the scattering potential is a constant value $n(\mathbf{r}) = n_1$ inside Ω and the constant $n(\mathbf{r}) = n_0$ outside Ω. Let Γ denote the boundary of Ω. Our objective is to reconstruct the shape of the surface, Γ, from scattering data. In three-dimensional space, define the surface Γ by the functional relation

$$F(\mathbf{r};\mathbf{p}) = 0, \tag{55}$$

where $\mathbf{p}$ is any convenient set of variables that parametrizes Γ. A variety of surface parametrizations are possible, e.g., $\mathbf{p}$ could represent the coordinates of the nodes of a spline fit to the surface Γ, or the coefficients of a spherical harmonic expansion of the surface Γ. For our purposes, the details of the parametrization are not important.

Since the points $\mathbf{r}$ for which (55) is satisfied lie on the boundary Γ, we can write for the scattering potential

$$n(\mathbf{r};\mathbf{p}) = \begin{cases} n_0 & \text{for } F(\mathbf{r};\mathbf{p}) > 0, \\ n_1 & \text{for } F(\mathbf{r};\mathbf{p}) \leqslant 0. \end{cases} \tag{56}$$

This can be equivalently written

$$n(\mathbf{r};\mathbf{p}) = n_1 + (n_0 - n_1)\mathrm{H}[F(\mathbf{r};\mathbf{p})], \tag{57}$$

where $\mathrm{H}(x)$ is the Heaviside step function [$\mathrm{H}(x) = 1$ for $x > 0$ and $\mathrm{H}(x) = 0$ for $x \leqslant 0$]. Differentiating (57) with respect to the parameter p_i then gives

$$\frac{\partial n(\mathbf{r};\mathbf{p})}{\partial p_i} = (n_0 - n_1)\,\delta[F(\mathbf{r};\mathbf{p})]\frac{\partial F(\mathbf{r};\mathbf{p})}{\partial p_i}, \tag{58}$$

where $\delta(\cdot)$ is the one-dimensional Dirac delta function.

Suppose, for example, that the function $f(x,y;\mathbf{p})$ defines the surface in Cartesian coordinates. Then $F(\mathbf{r};\mathbf{p})$ can be written

$$F(\mathbf{r};\mathbf{p}) = F(x,y,z;\mathbf{p}) = z - f(x,y;\mathbf{p}) \tag{59}$$

for $z > 0$. For simplicity, we assume that the surface is constrained for $z < 0$, i.e., does not depend on $\mathbf{p}$ for $z < 0$, so that $\mathbf{p}$ only parametrizes the upper surface ($z > 0$). This simply avoids complications in representing a closed surface by a single-valued function in Cartesian coordinates. The lower ($z < 0$) surface can, of course, be treated, but with a little more effort. Substituting (59) into (58) results in

$$\frac{\partial n(\mathbf{r};\mathbf{p})}{\partial p_i} = -(n_0 - n_1)\,\delta[z - f(x,y;\mathbf{p})]\frac{\partial f(x,y;\mathbf{p})}{\partial p_i}, \tag{60}$$

and substituting this into (52) gives the derivative of the mean-square error with respect to p_i:

$$\frac{\partial\mathcal{E}}{\partial p_i} = -k^2(n_0 - n_1)\int\int\int \tilde{\psi}(x,y,z)\psi(x,y,z) \times \delta[z - f(x,y;\mathbf{p})]\frac{\partial f(x,y;\mathbf{p})}{\partial p_i}\,dx\,dy\,dz. \tag{61}$$

On integrating with respect to z,

$$\frac{\partial\mathcal{E}}{\partial p_i} = -k^2(n_0 - n_1)\int\int \tilde{\psi}[x,y,f(x,y;\mathbf{p})]\psi[x,y,f(x,y;\mathbf{p})] \times \frac{\partial f(x,y;\mathbf{p})}{\partial p_i}\,dx\,dy. \tag{62}$$

If $\hat{n}$ is the unit vector normal to the surface, we have $dx\,dy = \hat{n}\cdot\hat{z}\,d\Gamma$, where $\hat{z}$ is the z-directed unit vector and $d\Gamma$ is an element of surface area. Then (62) can be equivalently written as a surface integral over the boundary:

$$\frac{\partial\mathcal{E}}{\partial p_i} = -k^2(n_0 - n_1)\int_{\Gamma}\tilde{\psi}[x,y,f(x,y;\mathbf{p})]\psi[x,y,f(x,y;\mathbf{p})] \times \frac{\partial f(x,y;\mathbf{p})}{\partial p_i}\,\hat{n}\cdot\hat{z}\,d\Gamma. \tag{63}$$

As a very simple example, suppose Γ is the surface of a sphere and we have a single parameter, the unknown spherical radius a. Then (59) may be written

$$F(x,y,z;a) = z - \sqrt{a^2 - x^2 - y^2}, \tag{64}$$

with a similar expression for negative z (the lower hemisphere). Substituting this into (63) and converting to spherical coordinates [writing $\psi(x,y,z) = \psi(r,\theta,\phi)$] gives the derivative of the mean-square error with respect to the radius of the sphere as

$$\frac{\partial \mathcal{E}}{\partial a} = -(ka)^2(n_0 - n_1) \times \int_0^{2\pi} d\phi \int_0^{\pi} d\theta \sin\theta \cos\theta \tilde{\psi}(a,\theta,\phi)\psi(a,\theta,\phi). \tag{65}$$

We note that this analysis implicitly assumes continuity of the field quantities ψ and $\tilde{\psi}$ across the boundary Γ as well as their normal derivatives. This is always true when the jump in the scattering potential $n(\mathbf{r})$ at the boundary Γ is finite in magnitude, as can be shown by integrating the differential equation along a line normal to the boundary. For a hard scatterer, in which the field or its normal derivative vanishes at the boundary, a somewhat different treatment is needed.

IX. INTEGRAL EQUATION METHOD

Here we show how the same functional gradient relations can be obtained from an integral equation formulation of the scattering problem, that is, from Eq. (7). For brevity, define the new scattering potential

$$v(\mathbf{r}) \equiv k^2[n(\mathbf{r}) - 1], \tag{66}$$

so (7) reads

$$\psi(\mathbf{r}) = \psi_i(\mathbf{r}) + \int\int\int g(\mathbf{r}|\mathbf{r}')v(\mathbf{r}')\psi(\mathbf{r}')d^3\mathbf{r}'. \tag{67}$$

For a given $v(\mathbf{r})$, we can solve the forward problem and compute the predicted measurement at $\mathbf{r}_m$:

$$\psi(\mathbf{r}_m) = \psi_i(\mathbf{r}_m) + \int\int\int g(\mathbf{r}_m|\mathbf{r}')v(\mathbf{r}')\psi(\mathbf{r}')d^3\mathbf{r}'. \tag{68}$$

Now varying (67) and (68), respectively, gives

$$\delta\psi(\mathbf{r}) = \int\int\int g(\mathbf{r}|\mathbf{r}')\delta v(\mathbf{r}')\psi(\mathbf{r}')d^3\mathbf{r}' + \int\int\int g(\mathbf{r}|\mathbf{r}')v(\mathbf{r}')\delta\psi(\mathbf{r}')d^3\mathbf{r}', \tag{69}$$

and

$$\delta\psi(\mathbf{r}_m) = \int\int\int g(\mathbf{r}_m|\mathbf{r}')\delta v(\mathbf{r}')\psi(\mathbf{r}')d^3\mathbf{r}' + \int\int\int g(\mathbf{r}_m|\mathbf{r}')v(\mathbf{r}')\delta\psi(\mathbf{r}')d^3\mathbf{r}'. \tag{70}$$

Next define the adjoint field, $\tilde{\psi}(\mathbf{r})$, as the solution to the following integral equation:

$$\tilde{\psi}(\mathbf{r}') = \tilde{\psi}_i(\mathbf{r}') + \int\int\int \tilde{g}(\mathbf{r}'|\mathbf{r})v(\mathbf{r})\tilde{\psi}(\mathbf{r})d^3\mathbf{r}, \tag{71}$$

where the adjoint Green's function, $\tilde{g}(\mathbf{r}'|\mathbf{r})$, is defined by[14,15]

$$\tilde{g}(\mathbf{r}'|\mathbf{r}) = g(\mathbf{r}|\mathbf{r}'). \tag{72}$$

In (71), we define the adjoint ''incident field'' as

$$\tilde{\psi}_i(\mathbf{r}') = \sum_{m=1}^{M} [\psi(\mathbf{r}_m) - \psi_{\text{obs}}(\mathbf{r}_m)]^* g(\mathbf{r}_m|\mathbf{r}'). \tag{73}$$

Now substituting (70) into (10), interchanging orders of integration and summation, and using the definition (73), we obtain

$$\delta\mathcal{E} = \text{Re}\left\{ \int\int\int d^3\mathbf{r}' \tilde{\psi}_i(\mathbf{r}')\delta v(\mathbf{r}')\psi(\mathbf{r}') + \int\int\int d^3\mathbf{r}' \tilde{\psi}_i(\mathbf{r}')v(\mathbf{r}')\delta\psi(\mathbf{r}') \right\}. \tag{74}$$

Our objective is to remove the unknown field variation, $\delta\psi$, in (74), leaving only the variation δn in the scattering potential. To proceed, use (71) to eliminate $\tilde{\psi}_i$ in the second integral in (74). This gives

$$\delta\mathcal{E} = \text{Re}\int\int\int d^3\mathbf{r}' \tilde{\psi}_i(\mathbf{r}')\psi(\mathbf{r}')\delta v(\mathbf{r}') + \text{Re}\int\int\int d^3\mathbf{r}' \left\{ \tilde{\psi}(\mathbf{r}') - \int\int\int d^3\mathbf{r}\tilde{g}(\mathbf{r}'|\mathbf{r})v(\mathbf{r})\tilde{\psi}(\mathbf{r}) \right\} v(\mathbf{r}')\delta\psi(\mathbf{r}').$$

After interchanging orders of integration in $\mathbf{r}$ and $\mathbf{r}'$ in the second line and using $\tilde{g}(\mathbf{r}'|\mathbf{r}) = g(\mathbf{r}|\mathbf{r}')$, we obtain

$$\begin{aligned}\delta\mathcal{E} &= \text{Re}\int\int\int d^3\mathbf{r}' \tilde{\psi}_i(\mathbf{r}')\psi(\mathbf{r}')\delta v(\mathbf{r}') + \text{Re}\int\int\int d^3\mathbf{r} v(\mathbf{r})\tilde{\psi}(\mathbf{r}) \left\{ \delta\psi(\mathbf{r}) - \int\int\int d^3\mathbf{r}' g(\mathbf{r}|\mathbf{r}')v(\mathbf{r}')\delta\psi(\mathbf{r}') \right\} \\ &= \text{Re}\int\int\int d^3\mathbf{r}' \tilde{\psi}_i(\mathbf{r}')\psi(\mathbf{r}')\delta v(\mathbf{r}') + \text{Re}\int\int\int d^3\mathbf{r} v(\mathbf{r})\tilde{\psi}(\mathbf{r}) \int\int\int d^3\mathbf{r}' g(\mathbf{r}|\mathbf{r}') \times \delta v(\mathbf{r}')\psi(\mathbf{r}'),\end{aligned}$$

where the last line follows from (69). Interchanging orders of integration once again and using $\tilde{g}(\mathbf{r}'|\mathbf{r}) = g(\mathbf{r}|\mathbf{r}')$, we obtain

$$\delta\mathcal{E} = \text{Re}\int\int\int d^3\mathbf{r}' \delta v(\mathbf{r}')\psi(\mathbf{r}') \times \left\{ \tilde{\psi}_i(\mathbf{r}') + \int\int\int d^3\mathbf{r}\tilde{g}(\mathbf{r}'|\mathbf{r})v(\mathbf{r})\tilde{\psi}(\mathbf{r}) \right\}.$$

The quantity in curly brackets is seen to be $\tilde{\psi}(\mathbf{r}')$ from (71), so we finally obtain

$$\delta\mathcal{E} = \text{Re}\int\int\int d^3\mathbf{r}\psi(\mathbf{r})\tilde{\psi}(\mathbf{r})\delta v(\mathbf{r}), \tag{75}$$

which is identical to (16) on noting from (66) that $\delta v(\mathbf{r}) = k^2\delta n(\mathbf{r})$.

To verify that $\tilde{\psi}(\mathbf{r})$ defined by (71) is the same adjoint field that obeys the wave equation (11), first rewrite (11) as

follows:

$$\nabla^2\tilde{\psi}(\mathbf{r})+k^2\tilde{\psi}(\mathbf{r})=-\tilde{S}(\mathbf{r})-v(\mathbf{r})\tilde{\psi}(\mathbf{r}), \tag{76}$$

where the definition (66) of $v(\mathbf{r})$ was used. Now substitute $\tilde{\psi}(\mathbf{r})$ given by (71) into the left-hand side of (76). Note first that

$$[\nabla^2+k^2]\tilde{\psi}_i(\mathbf{r})=-\sum_{m=1}^{M}[\psi(\mathbf{r}_m)-\psi_{\text{obs}}(\mathbf{r}_m)]^*\delta(\mathbf{r}-\mathbf{r}_m)$$

$$=-\tilde{S}(\mathbf{r}), \tag{77}$$

in view of the definition (73) of $\tilde{\psi}_i(\mathbf{r})$ and the property (6). The last equality is merely the definition of the adjoint source given by (12). Finally, the integral in (71) contributes

$$[\nabla^2+k^2]\int\int\int\tilde{g}(\mathbf{r}'|\mathbf{r})v(\mathbf{r})\tilde{\psi}(\mathbf{r})d^3\mathbf{r}=-v(\mathbf{r}')\tilde{\psi}(\mathbf{r}'), \tag{78}$$

which follows on interchanging orders of differentiation and integration and using the property that

$$\nabla^2\tilde{g}(\mathbf{r}'|\mathbf{r})+k^2\tilde{g}(\mathbf{r}'|\mathbf{r})=-\delta(\mathbf{r}-\mathbf{r}'), \tag{79}$$

which in turn follows on substituting (72) into (6). Finally, after dropping the prime on $\mathbf{r}'$ on the right-hand side of (78) and adding (77), we obtain the right-hand side of (76), as desired.

X. DISCUSSION AND CONCLUSION

In this paper, three formulations of the adjoint method are presented for computing the Fréchet derivative of the error functional to be minimized. As emphasized, in performing this minimization, a truly practical algorithm will depend critically on our ability to compute this quantity with accuracy and efficiency. For the benefit of clarity, a variational approach using continuous functions was employed, but the finite-dimensional case was shown to follow directly from the continuous space results. We emphasize that the approach used here is very general and can be applied to a wide range of problems in which a global functional is to be minimized subject to the constraint that a field equation is obeyed. The concept of the adjoint field is closely related to the physical notion of reciprocity, in which sources and receivers are interchanged. For a time-dependent scattering problem, the adjoint solution corresponds to a terminal value problem (as opposed to an initial value problem) in which the adjoint field is emitted from the observation points and propagates backward in time. Although the adjoint field is generally nonphysical, it can be computed using numerical algorithms essentially identical to those used to solve the forward problem; in fact, for self-adjoint field equations, merely boundary and initial conditions change. It is interesting to note that the process of computing the adjoint solution is somewhat analogous to the back-propagation operation in diffraction tomography[16] since the adjoint field is ''emitted'' from the observation points. In fact, in the very first iteration of an iterative algorithm [when $\psi(\mathbf{r}_m)\equiv 0$], the adjoint source (12) back-propagates the complex conjugate of the measured field from the observation points. Thus the adjoint field is in a sense focused ''backwards'' into the medium. This process is reminiscent of phase conjugation for monochromatic fields and time reversal[17] for transient fields.

[1] P. R. McGillivray and D. W. Oldenburg, ''Methods for calculating Fréchet derivatives and sensitivities for the non-linear inverse problem: a comparative study,'' Geophys. Prospect. **38**, 499–524 (1990).

[2] S. J. Norton and J. R. Bowler, ''Theory of eddy-current inversion,'' J. Appl. Phys. **73**, 501–512 (1993).

[3] T. Wang, M. Oristaglio, A. Tripp, and G. Hohmann, ''Inversion of diffusive transient electromagnetic data by a conjugate-gradient method,'' Radio Sci. **29**, 1143–1156 (1994).

[4] S. J. Norton, ''A general nonlinear inverse transport algorithm using forward and adjoint flux computations,'' IEEE Trans. Nucl. Sci. **44**, 153–162 (1997).

[5] Y. Jarny, M. N. Ozisik, and J. P. Bardon, ''A general optimization method using adjoint equations for solving multidimensional inverse heat conduction,'' Int. J. Heat Mass Transf. **34**, 2911–2919 (1991).

[6] If desired, the analysis in this paper could be carried through with the most general form of the ''mean-square error'' given by $\Sigma_m\Sigma_n[\psi(\mathbf{r}_m)-\psi_{\text{obs}}(\mathbf{r}_m)]^*w_{mn}[\psi(\mathbf{r}_n)-\psi_{\text{obs}}(\mathbf{r}_n)]$, where w_{mn} are the elements of a Hermitian matrix ($w_{mn}=w_{nm}^*$). In a maximum likelihood formulation, for example, the w_{mn} would correspond to the matrix elements of the inverse of a measurement covariance matrix, which quantifies possible statistical correlations between measurement noise at distinct receiving sites.

[7] See, for example: D. G. Luenberger, *Linear and Nonlinear Programming*, 2nd ed. (Addison–Wesley, Reading, MA, 1984); P. E. Gill, W. Murray, and M. H. Wright, *Practical Optimization* (Academic, San Diego, 1981); or W. H. Press, S. A. Teukolsky, W. J. Vetterling, and B. P. Flannery, *Numerical Recipes in FORTRAN*, 2nd ed. (Cambridge U.P., Cambridge, UK, 1992).

[8] The assumption that the fields $\delta\psi$ and $\tilde{\psi}$ obey the usual Sommerfeld radiation condition (Ref. 9) is sufficient to guarantee that the surface integral vanishes as the integration volume expands to infinity.

[9] J. D. Jackson, *Classical Electrodynamics*, 2nd ed. (Wiley, New York, 1974), p. 429.

[10] Taking the real part only of the constraint term in (18) can be shown to be sufficient to enforce the constraint since the Lagrange multiplier is permitted to be complex, and thus is comprised of two functions: its real and imaginary parts. The following argument can be made. One could begin with two independent Lagrange multiplier functions, λ_1 and λ_2, one multiplying the wave equation, and the second multiplying the complex conjugate of the wave equation, where the field, ψ, and its complex conjugate, ψ^*, are regarded as independent. If we proceed as if the two Lagrange functions are also independent and perform the variations of ψ and ψ^*, we ultimately find that $\lambda_1=\lambda_2^*$, giving the result (18).

[11] When the variation is performed, there is an additional term containing the variation of the Lagrange multiplier, $\delta\lambda$, but this term vanishes because $\delta\lambda$ multiplies the constraint equation [i.e., the quantity in square brackets in (18)], which is zero by virtue of (1).

[12] C. Bunks, F. M. Saleck, and G. Chavent, ''Multiscale seismic waveform inversion,'' Geophysics **60**, 1457–1473 (1995).

[13] The author would like to thank an anonymous reviewer for pointing out this reference.

[14] Because the Helmholtz operator is self-adjoint, the Green's function, $g(\mathbf{r}|\mathbf{r}')$, can be shown to be symmetrical in its arguments, implying that the Green's function and its adjoint are identical: $\tilde{g}(\mathbf{r}'|\mathbf{r})\equiv g(\mathbf{r}|\mathbf{r}')=g(\mathbf{r}'|\mathbf{r})$. However, some field equations may not be self-adjoint (e.g., the diffusion equation or a lossy wave equation), so for the sake of generality we maintain this distinction. Also, when considering the time-dependent scattering problem with the Green's function, $g(\mathbf{r},t|\mathbf{r}',t')$, the adjoint Green's function (Ref. 15) is $\tilde{g}(\mathbf{r},t|\mathbf{r}',t')=g(\mathbf{r},-t|\mathbf{r}',-t')$. We finally note that, for vector field equations, the Green's function becomes a dyad, $\mathbf{g}(\mathbf{r}|\mathbf{r}')$, and (72) generalizes to $\tilde{\mathbf{g}}(\mathbf{r}'|\mathbf{r})=\mathbf{g}^T(\mathbf{r}|\mathbf{r}')$, where ^{T} means transpose.

[15] P. M. Morse and H. Feshbach, *Methods of Theoretical Physics* (McGraw-Hill, New York, 1953), p. 873.

[16] A. J. Devaney, ''A filtered backpropagation algorithm for diffraction tomography,'' Ultrason. Imaging **4**, 336–360 (1982).

[17] M. Fink, ''Time reversal of ultrasonic fields—Part I: Basic principles,'' IEEE Trans. Ultrason., Ferroelectr. Freq. Control **39**, 555–566 (1992).

Analysis of the f_2-f_1 and $2f_1-f_2$ distortion components generated by the hair cell mechanoelectrical transducer: Dependence on the amplitudes of the primaries and feedback gain

Andrei N. Lukashkin[a] and Ian J. Russell
School of Biological Sciences, University of Sussex, Falmer, Brighton BN1 9QG, United Kingdom

(Received 16 November 1998; revised 28 June 1999; accepted 21 July 1999)

This paper describes the pattern of f_2-f_1 and $2f_1-f_2$ components at the output of the nonlinear hair cell mechanoelectrical transducer when the input consists of two sinusoidal signals. The mechanoelectrical transducer was represented by a second-order Boltzmann function. It is shown that some experimental observations, which have been cited to prove the existence of two discrete sources of distortion product otoacoustic emissions in the cochlea, can be produced by a single nonlinearity. These observations include the pattern of magnitude and phase ''notches'' in the growth functions of the distortion product otoacoustic emissions when measured in the two-dimensional space of the amplitudes of the two primaries. A single saturating nonlinearity also explains the distinctive response of the distortion product otoacoustic emissions to the decreasing gain of the cochlear amplifier. A possible basis for the differences in distortion product otoacoustic emissions, which have been measured in humans and rodents, is discussed. © *1999 Acoustical Society of America.* [S0001-4966(99)03811-4]

PACS numbers: 43.64.Bt, 43.64.Jb, 43.64.Kc [RDF]

INTRODUCTION

The dependence of the amplitude and phase angle of the distortion product otoacoustic emission (DPOAE) on the frequency separation and levels of the two primary tones is complex but distinctive (Lonsbury-Martin *et al.*, 1987; Brown and Gaskill, 1990; Brown *et al.*, 1992; Whitehead *et al.*, 1992a, 1992b; He and Schmiedt, 1993; Mills and Rubel, 1994; Whitehead *et al.*, 1995; He and Schmiedt, 1997). In order to explain the phase changes and fine structure of DPOAEs measured in the ear canal, it has been suggested that two discrete places of DPOAE generation exist, each associated with a different latency (Brown *et al.*, 1996; Moulin and Kemp, 1996a, 1996b; Stover *et al.*, 1996; Wable *et al.*, 1996; Whitehead *et al.*, 1996; Fahey and Allen, 1997; He and Schmiedt, 1997; Heitmann *et al.*, 1998). Accordingly, differences in phase of DPOAEs from different origins would give rise to the experimentally observed complex pattern of summating DPOAEs in the ear canal. One of the DPOAE components is generated in the region of the basilar membrane (BM) peak displacement for the high frequency primary tone (f_2 place). The other component is reflected from the DPOAE peak region situated *apically* along the cochlear duct. More recently, Mills (1997) developed an elegant model, which assumes the existence of an alternative region of DPOAE generation that is located *basal* to the f_2 place. The model provides a good explanation for the dependence of the DPOAE amplitude and phase angle on the input amplitude of the primaries in the *two-dimensional space of the primaries amplitudes*. Notably, when the frequency ratio is fixed, a notch is observed for constant amplitude of either of the two primaries when the amplitude of the second primary is varied (Whitehead *et al.*, 1992a, 1992b; Mills and Rubel, 1994; Mills, 1997). The model also explains the changes in the distortion product (DP) amplitude, which are observed when the gain of the cochlear amplifier is changed (Mills *et al.*, 1993; Mills and Rubel, 1994; Mills, 1997). The essence of Mills' hypothesis is that the phase cancellation of DPOAEs from the f_2 or ''peak'' region of the cochlear partition, and the ''basal'' region, is due to a 180° phase difference between them. The vector summation of these two components produces the experimentally observed, nonmonotonic dependence of the DP amplitude on the amplitude of the primaries. This interaction is characterized by local minima or ''notches.'' However, the existence of notches in the DP amplitude does not necessarily involve phase cancellation as a consequence of the interaction of two processes. Weiss and Leong (1985) showed that notch-producing behavior could be observed for a single nonlinearity (e.g., nonlinearity of the mechanoelectrical transducer). Whereas Weiss and Leong (1985) limited their consideration only to harmonic distortion; it is apparent that the same nonmonotonic growth of the input–output functions could be observed for the spectral components of the intermodulation distortion arising from a two-tone input signal (Lukashkin and Russell, 1998). While it has been appreciated that the local minima of the distortion components depend on both the specific type of nonlinearity (e.g., the cochlear hair cell transducer conductance, Kros *et al.*, 1995) and combination of stimulus parameters, the physiological basis of the notches and the way they change with the stimulus parameters is poorly understood. Hence, the purpose of this paper is to simulate the specific experimental paradigms used for gener-

[a]Electronic mail: a.lukashkin@sussex.ac.uk

ating DPOAEs by varying the amplitudes of the primaries and changing the gain of the cochlear amplifier.

The DPOAE measurements (Brown *et al.*, 1996; Moulin and Kemp, 1996a, 1996b; Stover *et al.*, 1996; Wable *et al.*, 1996; Whitehead *et al.*, 1996; Fahey and Allen, 1997; He and Schmiedt, 1997; Heitmann *et al.*, 1998) support the possibility of phase cancellation between emission from the f_2 region and remission from the DPOAE peak region. However, in this paper we show that the experimental observations (Whitehead *et al.*, 1992a, 1992b; Mills and Rubel, 1994; Mills, 1997) which have been cited in support of the existence of phase cancellation between two origins of DPOAEs, one located at the f_2 ''peak'' and the other located ''basal'' to this, do not in actual fact support it. A similar pattern of DPs can be observed in the output of a *single* nonlinearity when driven by two, simultaneous, sinusoidal inputs. We have associated this nonlinearity with the nonlinear mechanoelectrical transducer of the hair cells. Two cases have been considered. The first is for transducer nonlinearity without feedback and the second is for nonlinearity with a positive feedback loop to mimic the existence of the active process in the cochlea (Kemp, 1979; Davis, 1983). As in Mills' (1997) model, we do not consider the dependence of the DPs on either the frequencies of the primaries or on their frequency separation. Instead, two stimuli of different frequencies but of equal amplitude produce identical hair bundle displacements. Therefore, the model reflects neither the frequency selectivity of the real cochlea (von Békésy, 1960) nor the dependence of the DP amplitude and phase on the filtering properties of the cochlea (Brown *et al.*, 1992; Allen and Fahey, 1993).

I. TRANSDUCER NONLINEARITY WITHOUT FEEDBACK

Let us consider a nonlinearity $N(x)$ in the form (Fig. 1),

$$N(x)=G_{\mathrm{tr}}-G_{\mathrm{tr}}(0), \tag{1}$$

where x is the displacement of the hair bundle from its resting position, $G_{\mathrm{tr}}(x)$ is the conductance of the hair cell mechanoelectrical transducer, and $G_{\mathrm{tr}}(0)$ is the transducer conductance when the displacement of the hair bundle is zero. Let us define the transducer operating point as the transducer conductance with zero displacement of the hair bundle, $G_{\mathrm{tr}}(0)$. Biasing of the transducer operating point may be introduced as a steady-state displacement x_{set} of the hair bundle and the biased transducer operating point is $G_{\mathrm{tr}}(x_{\mathrm{set}})$. Then the conductance of the transducer $G_{\mathrm{tr}}(x(t))$ is given by (Crawford *et al.*, 1989; Kros *et al.*, 1995)

$$G_{\mathrm{tr}}(x)=G_{\mathrm{tr\,max}}[1+\exp[a_2[x_2-x_{\mathrm{set}}-x]] \times[1+\exp[a_1[x_1-x_{\mathrm{set}}-x]]]]^{-1}, \tag{2}$$

where $G_{\mathrm{tr\,max}}$ is the maximal transducer conductance, x_{set} is the steady-state displacement of the hair bundle, and a_1, a_2, x_1, x_2 are constants.

The output of the nonlinearity $N(x)$ for the double sinusoidal input $x+y=L_1\cos\theta_1+L_2\cos\theta_2$, where $\theta_i=2\pi ft$, could be expressed as

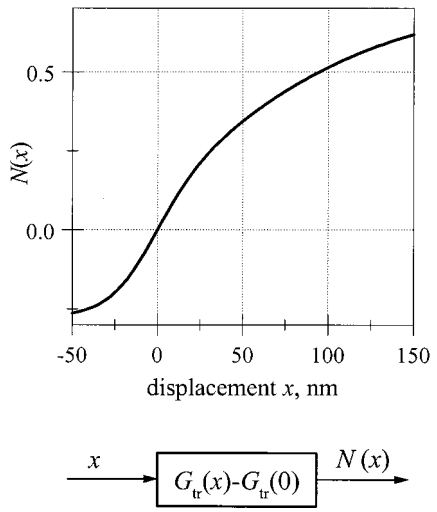

FIG. 1. Nonlinear input–output function, $N(x)$, of the hair cell mechanoelectrical transducer. x is the displacement of the hair bundle from its resting position, $G_{\mathrm{tr}}(x)$ is the conductance of the hair cell mechanoelectrical transducer, and $G_{\mathrm{tr}}(0)$ is the transducer conductance with zero displacement of the hair bundle. The function was normalized for maximum transducer conductance $G_{\mathrm{tr\,max}}=7$ nS (Kros *et al.*, 1995) and modified by moving the operating point into the point of inflection of the function. The function is given by Eq. (1) with $a_1=0.065$, $a_2=0.016\ \mathrm{nm}^{-1}$, $x_1=24$, $x_2=41$ nm, which are the parameters used by Kros *et al.* (1995) to fit their experimental data.

$$N(x,y)=\sum_{m,n=0}^{\infty} a_{m,n}\cos(m\theta_1\pm n\theta_2), \tag{3}$$

where $a_{m,n}$ are the amplitudes of the DPs of order $m+n$. We shall limit our analysis to terms at frequencies f_2-f_1 and $2f_1-f_2$ which are the DPOAEs most usually measured.

When measured in the $L_1\times L_2$ parameter space, the $2f_1-f_2$ DPOAE component shows notches which occur for constant amplitude of either primary with variable amplitude of the second primary (Whitehead *et al.*, 1992a, 1992b; Mills and Rubel, 1994; Mills, 1997). In Mills' (1997) model the notches appear as being due to phase cancellation between the emissions from two different regions of the BM. In order to explain the independence of the notches on the amplitude of the second primary, Mills (1997) argued that one of the primaries dominates the response of the other primary in the place of the DPOAE generation. However, one can prove (see Appendix) that the same pattern of DP should occur for small values of L_1 and L_2 at the output of a polynomial nonlinearity without assuming a phase cancellation. Figure 2 illustrates[1] this statement for the nonlinear function $N(x)$ (Fig. 1). Notably, the phase difference of the DPs in the regions below and above the notches is 180° as has been observed for DPOAEs in gerbils and rabbits (Whitehead *et al.*, 1992a; Mills and Rubel, 1994; Mills, 1997). As one might expect, the slope of the $2f_1-f_2$ DP as a function of L_2 is lower than as a function of L_1, a result which is in agreement with experimental observations.

In a comment on Mills' model, Whitehead (1998) pointed out a difference between DPOAEs recorded in humans and rodents. Namely, there are no consistent notches in human DPOAEs analogous to those observed in rodents. Notches in human DPOAEs are associated with the fine

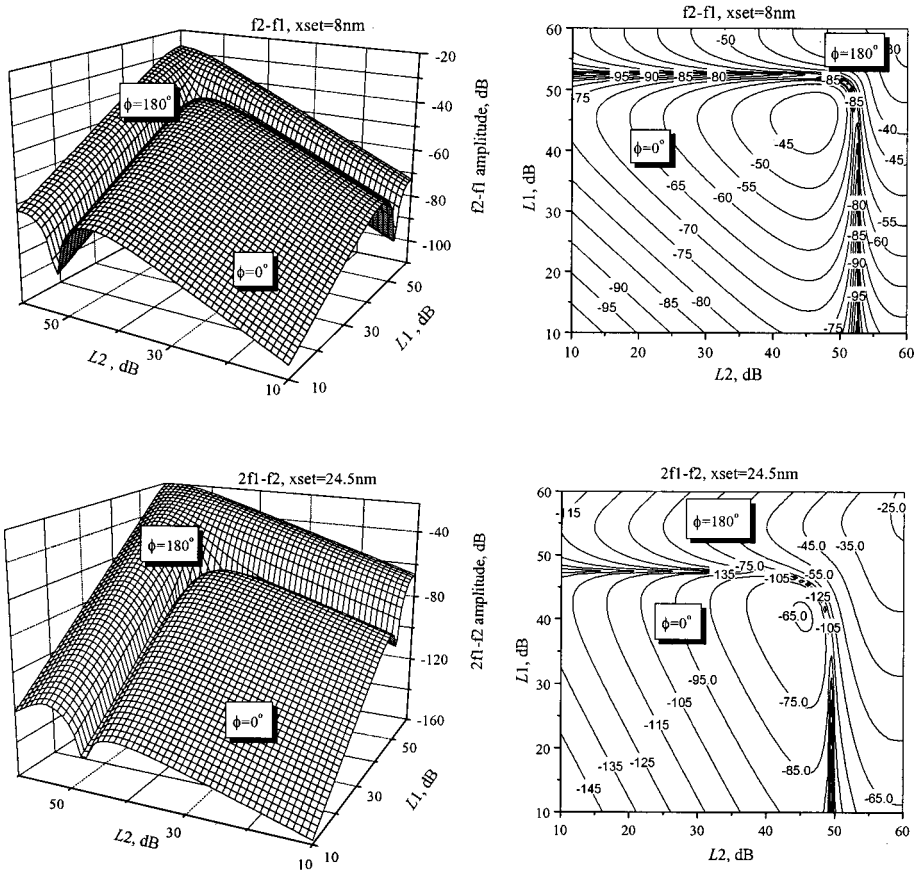

FIG. 2. Amplitude and phase angle of the DP at the output of the nonlinearity $N(x)$ as a function of the amplitudes of the primary tones, L_1 and L_2. DP at frequencies f_2-f_1 (upper row) and $2f_1-f_2$ (lower row) are shown. Two different styles of presentation, three-dimensional plots (left column) and contour plots (right column), were used to illustrate the same results. Relative phase angle, ϕ, is indicated by labels inside each region of the plots. The shift of the operating point, x_{set}, is shown above each panel. Amplitude of the DPs is expressed in decibels re $G_{\text{tr max}}$. 0 dB for the amplitudes of the primaries, L_1 and L_2, is equal to 0.1 nm.

structure of the DPOAE as a function of frequency (He and Schmiedt, 1993, 1997). However, the DPOAE fine structure is thought to be the result of phase cancellation between the emissions from the f_2 peak region and the DPOAE peak region, which is located apically to the f_2 place (Brown *et al.*, 1996; Moulin and Kemp, 1996a, 1996b; Stover *et al.*, 1996; Wable *et al.*, 1996; Whitehead *et al.*, 1996; Fahey and Allen, 1997; He and Schmiedt, 1997; Heitmann *et al.*, 1998).

Therefore, the origin of the notches in the human DPOAE seems to be different than that of rodents (Whitehead, 1998). Certainly, DPs generated by the nonlinear function $N(x)$ do not demonstrate the frequency dependence seen in human DPOAEs, but a lack of notches similar to those observed in rodents can be explained quite naturally. Figure 3 shows the DP growth functions at the output of the nonlinearity $N(x)$ for different positions of the operating point x_{set}. One can see that there are two distinctive regions of x_{set} with qualitatively different behavior of the growth functions: a range of x_{set} when the notch occurs for finite values of $L_1 \times L_2$ and a range of x_{set} when the notch never appears. For example, the growth functions of the f_2-f_1 component have no notch for negative x_{set} [Fig. 3(a)]. Figure 4(a) illustrates this in $L_1 \times L_2$ space. The notch appears for positive x_{set}, and the required values of L_1 and L_2, to meet the notch, grow when x_{set} moves farther away from zero in the positive direction [Fig. 3(a)]. The growth functions of the $2f_1-f_2$ DP have no notch for x_{set} within the range $-15 < x_{\text{set}} < +18$ nm [Fig. 3(b)]. The absence of a notch for a value of x_{set} within these limits (+12 nm) is illustrated in $L_1 \times L_2$ space in Fig. 4(b). For x_{set} outside of the range -15–$+18$ nm, the notch occurs at larger amplitudes of L_1 and L_2, when x_{set} is moved farther away from the region -15–$+18$ nm, in either the positive or negative directions [Fig. 3(b)]. The range of x_{set} for the condition when the notch is absent becomes smaller if a positive feedback is present in the system (see below).

II. TRANSDUCER NONLINEARITY WITH A POSITIVE FEEDBACK

In order to mimic the presence of the cochlear active process (Kemp, 1979), we introduced positive feedback as shown in Fig. 5. The nonlinear input–output function, $N'(x)$, is defined by the equation

$$\begin{aligned} N'(x) &= G_{\text{tr}}(x, N(x)) - G_{\text{tr}}(0) \\ &= G_{\text{tr max}}[1+\exp[a_2[x_2 - x - HN'(x)]] \\ &\quad \times [1+\exp[a_1[x_1 - x - HN'(x)]]]]^{-1} - G(0), \end{aligned} \tag{4}$$

where H is the feedback gain constant. The gains of the nonlinear functions $N(x)$ and $N'(x)$ near their operating point are

$$K = \left.\frac{dN(x)}{dx}\right|_{x=0} \quad \text{and} \quad K' = \left.\frac{dN'(x)}{dx}\right|_{x=0}, \tag{5}$$

where the derivatives are calculated at the operating point x_{set}. Then the relative gain achieved by the system due to the existence of the feedback is

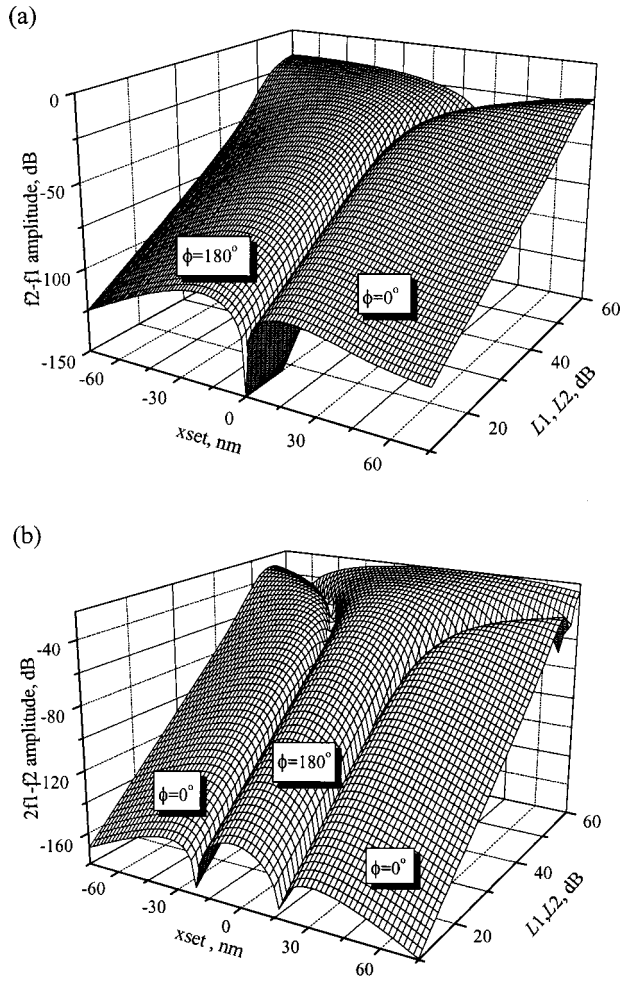

FIG. 3. Dependence of the DP growth functions at the output of the nonlinearity $N(x)$ on the position of the operating point. (a) DP at frequency f_2-f_1. (b) DP at frequency $2f_1-f_2$. Relative phase angle, ϕ, is indicated by labels inside each region of the plots. Amplitude of the DPs is expressed in decibels re $G_{\text{tr max}}$. 0 dB for the amplitudes of the primaries, L_1 and L_2, is equal to 0.1 nm.

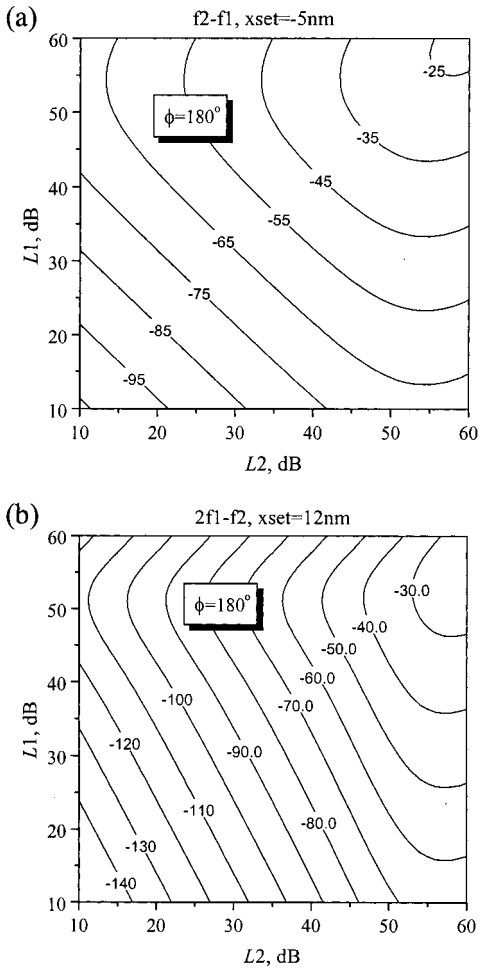

FIG. 4. Amplitude and phase angle of the DP at the output of the nonlinearity $N(x)$ as a function of the amplitudes of the primaries, L_1 and L_2, for positions of the transducer operating point when the notch never appears (see the text). (a) DP at the f_2-f_1 frequency. (b) DP at frequency $2f_1-f_2$. Relative phase angle, ϕ, is indicated by labels inside the plots. Amplitude of the DPs is expressed in decibels re $G_{\text{tr max}}$. 0 dB for the amplitudes of the primaries, L_1 and L_2, is equal to 0.1 nm.

$$K_r = K'/K = = \left.\frac{dN'(x)}{dN(x)}\right|_{x=0}. \tag{6}$$

Figure 5 gives examples of $N'(x)$ for a few values of K_r. In order to calculate the response for a given value of K_r at a particular x_{set}, the constant H can be found. For small x, i.e., linearizing the input–output function, one can write

$$dN'(x) = \frac{dN(x)/dx|_{x=0}}{1 - H dN(x)/dx|_{x=0}}\,dx, \tag{7}$$

and after rearranging,

$$H = \frac{1 - 1/K_r}{dN(x)/dx|_{x=0}}. \tag{8}$$

The DPs at the output of the nonlinearity $N'(x)$ demonstrate qualitatively the same pattern of behavior as described for the nonlinearity without feedback. Additionally, the position of the notches along the axis of x_{set} depends on the value of the gain, K_r (Fig. 6). This last observation provides the basis for explaining data that were obtained in experiments where the gain of the cochlear amplifier was manipulated (Mills *et al.*, 1993; Mills and Rubel, 1994; Mills, 1997). Namely, Mills and Rubel observed a notch and corresponding phase change in the response of the $2f_1-f_2$ DPOAE for moderate amplitudes of the primaries recorded in gerbils when the gain of the cochlear amplifier gradually declined following furosemide injection (e.g., see Fig. 10 from Mills, 1997). The notch is absent from emissions recorded during furosemide for large or low sound stimulus levels and the emissions generated by large and low stimulus levels are in opposite phase. Mills (1997) ascribed this level-dependent response as being due to phase cancellation between the ''peak'' and ''basal'' places of DPOAE generation. However, a direct comparison of Fig. 10(b) from Mills (1997) and Fig. 7 here permits us to conclude that it is possible to obtain the same amplitude and phase changes of the $2f_1-f_2$ DP at the output $N'(x)$, i.e., due to a single nonlinearity. One should take into account that the gain of the cochlear amplifier decreases gradually after initial furosemide injection (Ruggero and Rich, 1991b; Mills *et al.*, 1993). Therefore, the horizontal axes in Fig. 7 and, for example, in Fig. 10(b) from Mills (1997), are mirror images of each other. Again, the ampli-

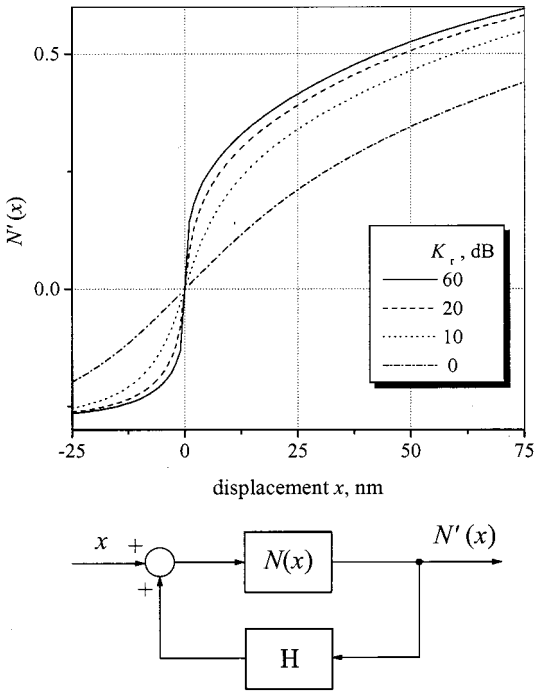

FIG. 5. Nonlinear input–output function, $N'(x)$, of the hair cell mechano-electrical transducer with positive feedback. The function was normalized for maximum transducer conductance $G_{\text{tr max}}=7$ nS (Kros *et al.*, 1995), $N(x)$ is the nonlinearity presented in Fig. 1. H is the feedback gain constant. Relative gain, K_r, for each curve is indicated in decibels re gain without feedback, K.

tude and phase changes are illustrated for one particular value of x_{set} and they vary with the shift of the operating point.

It is worth noting that the distance along the horizontal axis between the left and right notches of the $2f_1-f_2$ DP

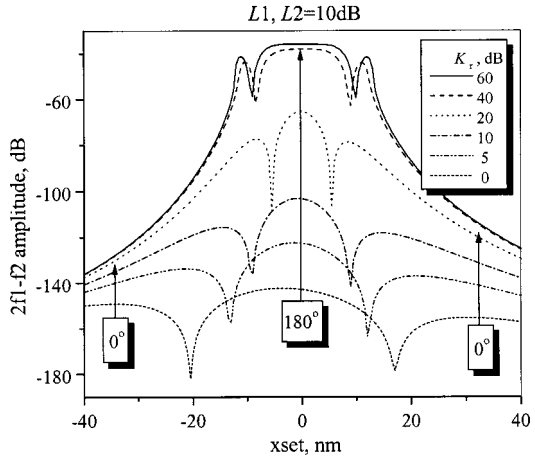

FIG. 6. Dependence of the $2f_1-f_2$ component at the output of the nonlinearity $N'(x)$ on bias, x_{set}, of the operating point for different values of the gain K_r. The curves are generated by direct numerical solution of Eq. (4). H was calculated according to Eq. (8) for $x_{\text{set}}=0$ and kept constant with varying x_{set}. K_r is shown for each curve inside the panel. Amplitudes of both primaries, L_1 and L_2, are equal to 10 dB re 0.1 nm. The phase angle is indicated by the labels, and arrows indicate each part of the curve limited by the notch. The absolute value of the DP amplitude approaches zero at the bottom of the notch. It has a finite value in the figure because of the discrete step of x_{set}, 0.5 nm, used for the numerical calculations. The amplitude of the DP is expressed in decibels re $G_{\text{tr max}}$.

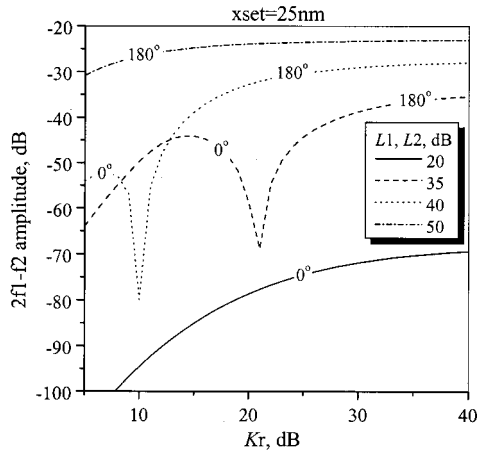

FIG. 7. Dependence of the $2f_1-f_2$ component at the output of nonlinearity $N'(x)$ on the value of the gain, K_r, for a single position of the operating point, $x_{\text{set}}=25$ nm. The curves are generated by direct numerical solution of Eq. (4). H was calculated according to Eq. (8) for $x_{\text{set}}=0$. L_1 and L_2 are shown for each curve inside the panel in decibels re 0.1 nm. The phase angle is indicated for each part of the curves limited by the notch. The absolute value of the DP amplitude approaches zero at the bottom of the notch. It has finite value in the figure because of the discrete 0.5-nm step of x_{set}, which was used for numerical calculations. The amplitude of the DP is expressed in decibels re $G_{\text{tr max}}$.

decreases with increasing gain (Fig. 6). Hence, the absolute values of the x_{set} bias, which are necessary to obtain either one or the other pattern of the DPs, become smaller with increasing gain. This conclusion is relevant not only to the responses of the DPs to changes in the feedback gain (Fig. 7) but also to the properties of DPs produced by the nonlinearity without feedback.

III. DISCUSSION

It is not within the scope of this paper to analyze all of the evidence for and against the existence of multiple sites of DPOAE generation. In fact, the data in support of DPOAE reemission from the DPOAE peak region are quite strong (Brown *et al.*, 1996; Moulin and Kemp, 1996a, 1996b; Stover *et al.*, 1996; Wable *et al.*, 1996; Whitehead *et al.*, 1996; Fahey and Allen, 1997; He and Schmiedt, 1997; Heitmann *et al.*, 1998). However, it has been shown in this paper that some of the experimental observations, which have been referred to as proving the existence of two discrete sources of DPOAE in the cochlea (Whitehead *et al.*, 1992a, 1992b; Mills and Rubel, 1994; Mills, 1997), can be produced by a single nonlinearity. These experimental observations are the particular patterns of the notch in the DPOAE level functions when measured in $L_1\times L_2$ parameter space and the distinctive response of the DPOAE to a decrease in the gain of the cochlear amplifier.

The notch-producing behavior analyzed in this paper is not specific to the intermodulation distortion observed with two-sinusoidal input signals. In 1985, Weiss and Leong provided a detailed description of the harmonic distortion produced by a sigmoidal transducer nonlinearity. According to these authors, minima in harmonic level functions are an intrinsic attribute of a system with a nonlinear input–output function. The harmonic distortion pattern depends on the

specific form of the transducer function as well as on the position of its operating point. It was shown that infinitely small shifts of the transducer operating point near certain positions lead to bifurcation of the output signal spectrum. Weiss and Leong (1985) demonstrated, on the basis of their analysis, that the presence of notches and corresponding phase changes, which had been observed in the harmonic components of cochlear responses, was not sufficient evidence to conclude that these phenomena were due to signal production and phase cancellation of signals from multiple sites. This conclusion can now be extended to the notches and phase jumps which have been observed in the intermodulation distortion produced when the cochlea is stimulated by two low-level tones (Lukashkin and Russell, 1998).

For the purpose of evaluating the model, we have taken the nonlinearity to be that of the cochlear hair cell's mechanoelectrical transducer conductance (Kros *et al.*, 1995). However, the precise nature of the nonlinearity producing the DPOAE is not important and the conclusions of this paper are valid for any system with a saturating input–output function. Moreover, we do not make any assumptions about the nature of the nonlinearity in our consideration of the appearance of notches in DPs generated by the combination of constant amplitude of either primary with variable amplitude of the second primary (see Appendix). Consequently, it would be possible to observe this type of notch-producing behavior with any nonlinear function differentiable at its operating point. Patuzzi *et al.* (1989) and Santos-Sacchi (1993) proposed that the mechanoelectrical transducer function is a dominant nonlinearity which could distort the cochlear response to sound *in vivo*. A shift of the transducer operating point underlies the responses of DPOAEs to electrical and acoustical biasing of the cochlear partitions (Frank and Kössl, 1996, 1997). A similar conclusion has been drawn by van Emst *et al.* (1997) to explain furosemide-induced changes in the DP in the cochlear electrical responses and by Lukashkin and Russell (1998) to explain the frequency and level-dependent bipolarity of the OHC DC receptor potential (Dallos *et al.*, 1982; Dallos, 1986; Dallos and Cheatham, 1989; Cody and Russell, 1987).

An interesting outcome of the model is the demonstration that the difference between DPOAEs measured in humans and rodents (Whitehead, 1998) could be explained in terms of different positions of the transducer operating point. If we can assume that the operating point of the nonlinearity in humans is situated near the point of maximum sensitivity of the input–output function, i.e., near its point of inflection, then it would not be possible to observe a notch in human DPOAE level functions (Figs. 3, 4) analogous to that observed in the DPOAEs from rodents. The existence of a similar mechanism for optimization of the OHC voltage response has been shown in the basal turn of the guinea pig cochlea (Kössl and Russell, 1992). It would appear that this mechanism is less effective in the lower frequency turns of the cochlea of rodents, and the operating point of the nonlinearity lies farther away from its point of inflection so that the notch is seen in the DPOAE level functions (Figs. 2, 3) (Cody and Russell, 1987; Cheatham and Dallos, 1997; Lukashkin and Russell, 1998). The magnitude of the bias of the operating point in either positive or negative direction from $x=0$ which is necessary to cause the observed differences in the level functions of humans and rodents is a matter of a few nanometers for a system with a positive feedback (Fig. 6). The frequency and level-dependent polarity of the OHC DC receptor potential recorded from both the low frequency (Dallos *et al.*, 1982; Dallos, 1986; Dallos and Cheatham, 1989) and the high frequency (Cody and Russell, 1987) regions of the cochlea might be expected if the operating point is situated above the point of inflection (Lukashkin and Russell, 1998). Frank and Kössl (1996, 1997) have drawn a similar conclusion about the position of the operating point on the basis of their experiments with electrical and acoustical biasing of the cochlear partitions. Frank and Kössl (1997) also observed a shift in the operating point of the cochlear amplifier with increasing sound intensity. Intense tones have been hypothesized to shift the operating point of the OHC transducer function (Cody and Russell, 1992, 1995). A similar explanation, a shift of the operating point with increasing the sound intensity away from a position close to the point of inflection, might account for the appearance of notches in the harmonics of OHC receptor potentials recorded in the basal turn of the guinea pig cochlea. The notches appear in response to low frequency tones when these are presented in combination with intense tones at frequencies a half octave below their characteristic frequency (16 kHz) (Cody and Russell, 1992).

ACKNOWLEDGMENTS

We thank Sergei Dolgobrodov and Manfred Kössl for valuable discussion and critical reading of an early version of this manuscript. This work was supported by grants from the Medical Research Council and Wellcome Trust.

APPENDIX

The output of the nonlinearity $N(x,y)$ for the double sinusoidal input $x+y=L_1\cos\theta_1+L_2\cos\theta_2$, where $\theta_i=2\pi ft$, could be expressed as (e.g., see Atherton, 1975)

$$N(x,y)=\sum_{m=0}^{\infty}\sum_{n=0}^{\infty}\varepsilon_m\varepsilon_n\alpha_{mn}\cos m\theta_1\cos n\theta_2, \tag{A1}$$

and $\varepsilon_n=1$ for $n=0$ and $\varepsilon_n=2$ for $n>0$, and α_{mn} is given by

$$\alpha_{mn}=\int_{-L1}^{L1}\int_{-L2}^{L2}N(x,y)T_m(x/L_1)T_n(y/L_2)\times p(x)p(y)dxdy, \tag{A2}$$

where $T_n(x/A)=\cos[n\arccos(x/A)]$ is the Chebyshev polynomial of the first kind and $p(x)=(A^2-x^2)^{-1/2}$. Let us expand $N(x)$ in a Taylor's series about $x=0$,

$$N(x,y)=\sum_{i+j=0}^{\infty}c_{ij}x^iy^j, \tag{A3}$$

where

$$c_{ij}=\frac{1}{i!j!}\left.\frac{\partial^i\partial^jN(x,y)}{\partial x\partial y}\right|_{x,y=0}. \tag{A4}$$

After substituting Eq. (A3) into Eq. (A2) and rearranging, we have

$$\alpha_{mn}=\sum_{i+j=0}^{\infty} c_{ij}\int_{-L1}^{L1} x^i T_m(x/L_1)p(x)dx \times\int_{-L2}^{L2} y^j T_n(y/L_2)p(y)dy. \quad \text{(A5)}$$

For frequency component $f_2\pm f_1$ and $2f_1\pm f_2$ we can write

$$\alpha_{11}=\frac{1}{L_1L_2}\sum_{i+j=0}^{\infty} c_{ij}\int_{-L1}^{L1} x^{i+1}p(x)dx \times\int_{-L2}^{L2} y(x_{\text{set}}-y)^{j+1}p(y)dy, \quad \text{(A6)}$$

$$\alpha_{21}=\frac{1}{L_1^2L_2}\sum_{i+j=0}^{\infty} c_{ij}\int_{-L1}^{L1} x^i(2x^2-L_1^2)p(x)dx \times\int_{-L2}^{L2} y^{j+1}p(y)dy. \quad \text{(A7)}$$

Both integrals in Eqs. (A6) and (A7) are functions of one variable only. Therefore, if one of the integrals in products is equal to zero for a particular value of L_2, then α_{ij} is equal to zero too for any L_1. The same is valid if one of the integrals is equal to zero for a particular value of L_1.

[1]To find the amplitude and phase angle of the DPs for all figures in this paper, equations for $N(x)$ [Eq. (1)] and $N'(x)$ [Eq. (4)] were solved numerically in the time domain and the fast Fourier transform (FFT) was applied to the generated time response of either nonlinearity. Either Eq. (1) or Eq. (4) has one real root for any given value of x. MATLAB algorithm (findzero), which was used to find the root, always converges and guarantees that the root is situated in the interval [$N(x)-$tolerance, $N(x)+$tolerance] (Brent, 1973). The tolerance was set to $2*10^{-16}$. The number of sampling points for FFT was increased until we were able to obtain six significant decimal places for the magnitude of the wave form spectrum.

Allen, J. B., and Fahey, P. F. (**1993**). ''A second cochlear frequency map that correlates distortion product and neural tuning measurement,'' J. Acoust. Soc. Am. **94**, 809–817.

Atherton, D. P. (**1975**). *Nonlinear Control Engineering* (Van Nostrand Reinhold, London).

Brent, R. P. (**1973**). *Algorithms for Minimization Without Derivatives* (Prentice-Hall, Englewood Cliffs, NJ).

Brown, A. M., and Gaskill, S. A. (**1990**). ''Measurement of acoustic distortion reveals underlying similarities between human and rodent mechanical responses,'' J. Acoust. Soc. Am. **88**, 840–849.

Brown, A. M., Harris, F. P., and Beveridge, H. A. (**1996**). ''Two sources of acoustic distortion products from the human cochlea,'' J. Acoust. Soc. Am. **100**, 3260–3267.

Brown, A. M., Gaskill, S. A., and Williams, D. M. (**1992**). ''Mechanical filtering of sound in the inner ear,'' Proc. R. Soc. London, Ser. B **250**, 29–34.

Cheatham, M. A., and Dallos, P. (**1997**). ''Intermodulation components in inner hair cells and organ of Corti responses,'' J. Acoust. Soc. Am. **102**, 1038–1048.

Cody, A. R., and Russell, I. J. (**1987**). ''The responses of hair cells in the basal turn of the guinea-pig cochlea to tones,'' J. Physiol. (London) **383**, 551–569.

Cody, A. R., and Russell, I. J. (**1992**). ''The effects of intense acoustic stimulation on the nonlinear properties of mammalian hair cells,'' in *Noise-Induced Hearing Loss*, edited by A. L. Dancer, D. Henderson, R. J. Salvi, and R. P. Hamernik (Mosby–Year Book, St. Louis), pp. 11–27.

Cody, A. R., and Russell, I. J. (**1995**). ''Time-varying voltage responses of mammalian hair cells to isoamplitude acoustic stimulation,'' Aud. Neurosci. **1**, 351–361.

Crawford, A. C., Evans, M. G., and Fettiplace, R. (**1989**). ''Activation and adaptation of transducer currents in turtle hair cells,'' J. Physiol. (London) **419**, 405–434.

Dallos, P. (**1986**). ''Neurobiology of cochlear inner and outer hair cells: Intracellular recordings,'' Hearing Res. **22**, 185–198.

Dallos, P., and Cheatham, M. A. (**1989**). ''Nonlinearities in cochlear receptor potentials and their origins,'' J. Acoust. Soc. Am. **86**, 1790–1796.

Dallos, P., Santos-Sacchi, J., and Flock, A. (**1982**). ''Intracellular recordings from cochlear outer hair cells,'' Science **218**, 582–584.

Davis, H. (**1983**). ''An active process in cochlear mechanics,'' Hearing Res. **9**, 79–90.

Fahey, P. F., and Allen, J. B. (**1997**). ''Measurement of distortion product phase in the ear canal of the cat,'' J. Acoust. Soc. Am. **102**, 2880–2891.

Frank, G., and Kössl, M. (**1996**). ''The acoustic two tone distortions $2f1-f2$ and $f2-f1$ and their possible relation to changes in the gain and the operating point of the cochlear amplifier,'' Hearing Res. **98**, 104–115.

Frank, G., and Kössl, M. (**1997**). ''Acoustical and electrical biasing of the cochlear partition. Effects on the acoustic two tone distortions f_2-f_1 and $2f_1-f_2$,'' Hearing Res. **113**, 57–68.

He, N., and Schmiedt, R. A. (**1993**). ''Fine structure of the $2f_1-f_2$ acoustic distortion product: Changes with primary level,'' J. Acoust. Soc. Am. **94**, 2659–2669.

He, N., and Schmiedt, R. A. (**1997**). ''Fine structure of the $2f_1-f_2$ acoustic distortion product: Effects of primary level and frequency ratios,'' J. Acoust. Soc. Am. **101**, 3554–3565.

Heitmann, J., Waldmann, B., Schnitzler, H. U., Plinkert, P. K., and Zenner, H. P. (**1998**). ''Suppression of distortion product otoacoustic emissions (DPOAE) near $2f_1-f_2$ removes DP-gram fine structure—Evidence for a secondary generator,'' J. Acoust. Soc. Am. **103**, 1527–1531.

Kemp, D. T. (**1979**). ''Evidence of mechanical nonlinearity and frequency selective wave amplification in the cochlea,'' Arch. Otorhinolaryngol. **224**, 37–45.

Kössl, M., and Russell, I. J. (**1992**). ''The phase and magnitude of hair cell receptor potentials and frequency tuning in the guinea pig cochlea,'' J. Neurosci. **12**, 1575–1586.

Kros, C. J., Lennan, G. W. T., and Richardson, G. P. (**1995**). ''Transducer currents and bundle movements in outer hair cells of neonatal mice,'' in *Active Hearing*, edited by A. Flock, D. Ottoson, and M. Ulfendahl (Elsevier Science, Amsterdam), pp. 113–125.

Lonsbury-Martin, B. L., Martin, G. K., Probst, R., and Coats, A. C. (**1987**). ''Acoustic distortion products in rabbit ear canal. I. Basic features and physiological vulnerability,'' Hearing Res. **28**, 173–189.

Lukashkin, A. N., and Russell, I. J. (**1998**). ''A descriptive model of the receptor potential nonlinearities generated by the hair cell mechanoelectrical transducer,'' J. Acoust. Soc. Am. **103**, 973–980.

Mills, D. M. (**1997**). ''Interpretation of distortion product otoacoustic emission measurements. I. Two stimulus tones,'' J. Acoust. Soc. Am. **102**, 413–429.

Mills, D. M., Norton, S. J., and Rubel, E. W. (**1993**). ''Vulnerability and adaptation of distortion product otoacoustic emissions to endocochlear potential variation,'' J. Acoust. Soc. Am. **94**, 2108–2122.

Mills, D. M., and Rubel, E. W. (**1994**). ''Variation of distortion product otoacoustic emission with furosemide injection,'' Hearing Res. **77**, 183–199.

Moulin, A., and Kemp, D. T. (**1996a**). ''Multicomponent acoustic distortion product otoacoustic phase in humans. I. General characteristics,'' J. Acoust. Soc. Am. **100**, 1617–1639.

Moulin, A., and Kemp, D. T. (**1996b**). ''Multicomponent acoustic distortion product otoacoustic phase in humans. II. Implications for distortion product otoacoustic emissions generation,'' J. Acoust. Soc. Am. **100**, 1640–1662.

Patuzzi, R. B., Yates, G. K., and Johnstone, B. M. (**1989**). ''Outer hair cell receptor current and sensorineural hearing loss,'' Hearing Res. **42**, 47–72.

Ruggero, M. A., and Rich, N. C. (**1991**). ''Furosemide alters organ of Corti mechanics: Evidence for feedback of outer hair cells upon the basilar membrane,'' J. Neurosci. **11**, 1057–1067.

Santos-Sacchi, J. (**1993**). ''Harmonics of outer hair cell motility,'' Biophys. J. **65**, 2217–2227.

Stover, L. J., Neely, S. T., and Gorga, M. P. (**1996**). ''Latency and multiple sources of distortion product otoacoustic emissions,'' J. Acoust. Soc. Am. **99**, 1016–1024.

van Emst, M. G., Klis, S. F. L., and Smoorenburg, G. F. (**1997**). ''Identification of the nonlinearity governing even-order distortion products in cochlear potentials,'' Hearing Res. **114**, 93–101.
von Békésy, G. (**1960**). *Experiments in Hearing* (McGraw-Hill, New York).
Wable, J., Collet, L., and Chèry-Croze, S. (**1996**). ''Phase delay measurements of distortion product otoacoustic emissions at $2f_1-f_2$ and $2f_2-f_1$ in human ears,'' J. Acoust. Soc. Am. **100**, 2228–2235.
Weiss, T. F., and Leong, R. (**1985**). ''A model for signal transmission in an ear having hair cells with free-standing stereocilia. IV. Mechanoelectric transduction stage,'' Hearing Res. **20**, 175–195.
Whitehead, M. L. (**1998**). ''Species differences of distortion-product otoacoustic emissions: Comment on Interpretation of distortion product otoacoustic emission measurements. I. Two stimulus tones [J. Acoust. Soc. Am. **102**, 413–429 (1997)],'' J. Acoust. Soc. Am. **103**, 2740–2742.
Whitehead, M. L., Lonsbury-Martin, B. L., and Martin, G. K. (**1992a**). ''Evidence for two discrete sources of $2f_1-f_2$ distortion—product otoacoustic emission in rabbit: I: Differential dependence on stimulus parameters,'' J. Acoust. Soc. Am. **91**, 1587–1607.
Whitehead, M. L., Lonsbury-Martin, B. L., and Martin, G. K. (**1992b**). ''Evidence for two discrete sources of $2f_1-f_2$ distortion—product otoacoustic emission in rabbit: II: Differential physiological vulnerability,'' J. Acoust. Soc. Am. **92**, 2662–2682.
Whitehead, M. L., Stagner, B. B., Martin, G. K., and Lonsbury-Martin, B. L. (**1996**). ''Visualization of the onset of distortion-product otoacoustic emissions, and measurement of their latency,'' J. Acoust. Soc. Am. **100**, 1663–1679.
Whitehead, M. L., Stagner, B. B., McCoy, M. J., Lonsbury-Martin, B. L., and Martin, G. K. (**1995**). ''Dependence of distortion-product otoacoustic emissions on primary levels in normal and impaired ears. II. Asymmetry in L_1,L_2 space,'' J. Acoust. Soc. Am. **97**, 2359–2377.

Cochlear generation of intermodulation distortion revealed by DPOAE frequency functions in normal and impaired ears

Lisa J. Stover,[a] Stephen T. Neely, and Michael P. Gorga
Boys Town National Research Hospital, 555 North 30th Street, Omaha, Nebraska 68131

(Received 29 January 1999; accepted for publication 22 July 1999)

Distortion product otoacoustic emission (DPOAE) frequency functions were measured in normal-hearing and hearing-impaired ears. A fixed-f_2/swept-f_1 paradigm was used with f_2 fixed at half-octave intervals from 1 to 8 kHz. L_1 was always 10 dB greater than L_2, and L_2 was varied from 65 to 10 dB SPL in 5-dB steps. The responses were quantified by the frequency and amplitude of the peak response. Peak responses were closer to f_2 in higher frequency regions and for lower intensity stimulation. Results from hearing-impaired subjects suggest that audiometric thresholds at the distortion product frequency, f_{dp}, in addition to hearing status at f_2, can affect DPOAE results. Results are discussed in terms of several manifestations of a second resonance model, as well as a dual source model for the generation of DPOAEs as measured in the ear canal of humans. It appears that a dual source model accounts for the data better than second filter models. © *1999 Acoustical Society of America.* [S0001-4966(99)03911-9]

PACS numbers: 43.64.Jb [BLM]

INTRODUCTION

It has long been known that the cochlea produces intermodulation distortion. It is most easily demonstrated when two sinusoids, or primaries, of slightly different frequency ($f_1, f_2; f_1 < f_2$) are presented to the ear. The psychophysical perception of this distortion, particularly the cubic distortion product ($2f_1 - f_2$), has been documented and studied for many years (e.g., Goldstein, 1967; Smoorenburg, 1972). Distortion has also been demonstrated in the responses of primary afferent nerve fibers (Goldstein and Kiang, 1968), in the basilar membrane response (Robles *et al.*, 1993), and in the cochlear microphonic (Dallos *et al.*, 1969). Kemp (1979) reported that this distortion could also be measured acoustically in the ear canal as a distortion product otoacoustic emission (DPOAE).

One characteristic of DPOAEs is that they exhibit a bandpass shape when the frequency of either primary is varied. If one holds f_2 constant and varies f_1, then the DPOAE will reach a maximum absolute amplitude when the distortion product (f_{dp}) occurs at a specific frequency below f_2, and decreases as f_{dp} either approaches or further separates from f_2 (Brown *et al.*, 1992). Similar bandpass shapes in DPOAE amplitude have been reported when f_1 is held constant and f_2 is swept (Gaskill and Brown, 1990; O'Mahoney and Kemp, 1995), and if f_{dp} is held constant and both primary frequencies are changed (Harris *et al.*, 1989).

There are two reasons why this bandpass characteristic is of interest. First, in trying to define clinical test parameters there is a need to determine the ''optimal'' frequency ratio, defined as that ratio which most often produces a response, or the f_2/f_1 ratio which produces the maximum amplitude DPOAE in normal-hearing ears (Harris *et al.*, 1989).[1] Although the frequency at which this maximum occurs depends on the overall and relative levels of the primaries, as well as the frequency region being tested, an f_2/f_1 ratio of approximately 1.2 generally yields a DPOAE amplitude within 3 dB of the maximum (Harris *et al.*, 1989; Gaskill and Brown, 1990), and has been generally adopted in clinical protocols (Nielson *et al.*, 1993).

The bandpass nature of DPOAEs is also important for the more theoretical study of basic cochlear mechanics. This feature has been investigated to better understand the cochlear mechanism(s) that might underly its generation. There is considerable empirical evidence that the primary source of distortion is closely linked to the f_2 cochlear place (Harris *et al.*, 1992; Martin *et al.*, 1987; Zwicker and Harris, 1990). Theoretically, the primary source generates distortion proportional to the displacement of the basilar membrane distributed around the point of maximal interaction between the two primaries. This means that at the f_2 place, distortion is generated that decreases in amplitude monotonically as the primaries are separated, as Fig. 1(b) would suggest and as has been corroborated by empirical data (Robles *et al.*, 1993). This distortion propagates to the f_{dp} place and generates a neural response which leads to the perceived distortion. Thus the psychophysical distortion monotonically decreases in amplitude as the primaries are separated. The question then becomes, ''How does a low pass characteristic at f_2 place become a bandpass characteristic in the ear canal?'' Three different hypotheses will be examined herein.

Several cochlear models have been developed which incorporate a second resonance (Neely and Stover, 1993; Allen and Fahey, 1993). It has been suggested that the second resonance may be found in the structure of the tectorial membrane (TM) (Allen and Fahey, 1993; Zwislocki and Kletsky, 1980). This TM theory and model, however, is not supported by the findings of Taschenberger *et al.* (1995), who found DPOAE frequency functions in owls and lizards that are similar to those seen in mammalian ears. In avian ears, the TM internal structure and its connection to the hair cells are significantly different from mammalian ears. Furthermore,

[a]Electronic mail: stover.59@osu.edu

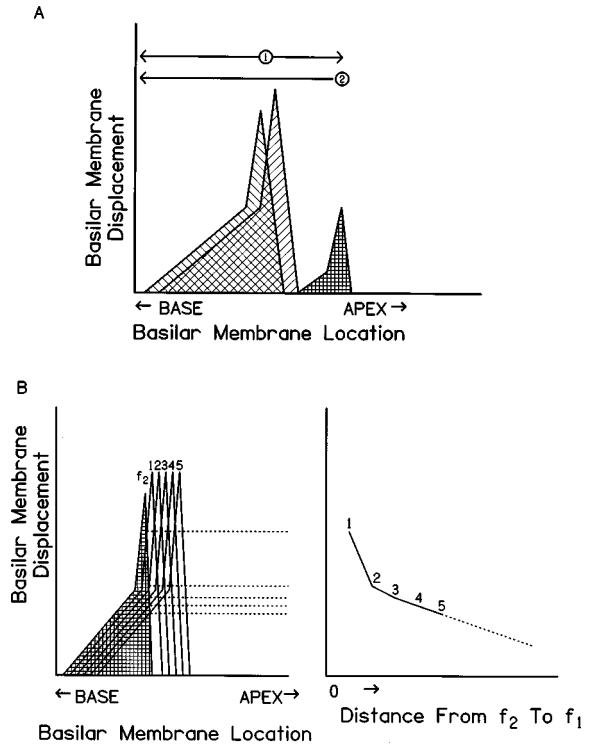

FIG. 1. (a) A schematic of the dual source model. Primary distortion generation occurs at the point of maximal interaction on the basilar membrane between the f_1 and f_2 stimuli. (1) That distortion then propagates basally to the stapes and apically to the f_{dp} place. (2) At the f_{dp} place a stimulus frequency emission is generated which propagates to the stapes. Those two signals combine at the stapes and for certain frequency (distance) relationships a cancellation of the primary distortion occurs. (b) A schematic of basilar membrane displacement in a fixed-f_2/swept-f_1 paradigm. The left panel shows a hypothetical displacement pattern for a single f_2 stimulus and several f_1 stimuli. The point of maximal interaction is indicated by the horizontal dashed lines. The right panel shows the amount of basilar membrane displacement as a function of the distance between f_1 and f_2. This displacement is assumed to be proportional to the amount of distortion generated.

reptilian ears lack a TM altogether over the higher frequency range. This makes it less likely that the TM is responsible for DPOAE tuning in mammalian ears for which the model was developed. In addition, the idea of a second resonance to explain DPOAE behavior is also questioned by the model of Matthews (1986), which produces typical DPOAE bandpass characteristics without the use of a second resonance.

Whatever the physiological manifestation of the second resonance may be, the models also differ in how the resonance affects the DPOAE response. One theory is that the resonance is associated with the frequency of the peak amplitude of the DPOAE bandpass (Allen and Fahey, 1993). In this model, which we will refer to as the second-filter enhancing model, the resonance enhances the response at its resonant frequency in the basalward traveling wave and thus increases the amplitude in the ear canal. The second theory associates the second resonance with the high-frequency side of the ''bandpass.'' In this model, which we will refer to as the second-filter canceling model, the resonance absorbs energy from the response. Thus the dip on the high-frequency side of DPOAE frequency functions is the result of energy removed from the high-pass nature of the distortion generator that is evident in the psychophysical and basilar membrane data.

An alternative explanation for this phenomenon that also accounts for psychophysical distortion product data is the idea that there are multiple sources for the distortion generated in the cochlea by two tones (Wilson, 1980; Furst *et al.*, 1988; Whitehead *et al.*, 1992). In this model, which is illustrated in Fig. 1(a), distortion is initially generated at or very near to the f_2 place and then propagates both basally toward the stapes and apically to the f_{dp} place, where it causes a psychophysical percept. At the f_{dp} place, however, a stimulus frequency emission is also generated which in turn propagates toward the stapes. (It should be noted here that stimulus frequency emission is also generated at the f_1 and f_2 places; however, the energy generated there does not contain DP frequencies. The primary stimulus frequency emission probably impacts on the relationship between the two primaries but not on the distortion product directly.) Thus the signal measured in the ear canal at the DP frequency represents some combination of inputs from the f_2 and f_{dp} places in the cochlea. Support for this hypothesis can be seen in the complex latency that has been observed when DPOAE ''filter'' functions are converted into ''impulse'' responses (Stover *et al.*, 1996). For certain distance/time/phase relationships between f_2 and f_{dp}, the primary distortion, generated very near the f_2 place, and the stimulus frequency emission, generated around the place where f_{dp} is represented, might partially cancel each other, thereby causing a decrease in amplitude of the acoustic distortion as f_{dp} approaches f_2. Although this multiple source model is as yet not established, empirical data demonstrating DPOAE bandpass characteristics would be consistent with its predictions.

A resonant tectorial membrane (RTM) model of cochlear mechanics was first proposed nearly two decades ago. However, the physiology of the tectorial membrane has not been well defined and the TM as a second resonance source remains controversial. RTM models of the cochlea have also been largely abandoned in favor of cochlear amplifier models to explain other phenomena such as spontaneous otoacoustic emissions or the fine structure observed in various otoacoustic emissions (Shera and Zweig, 1993). Nevertheless, the TM appears to be an important structure in the cochlea, and until its function is better understood, the idea of a RTM will remain. On the other hand, it is also well accepted that the source for DPOAEs is distributed across multiple places on the BM (Furst *et al.*, 1988; Harris *et al.*, 1989; Brown *et al.*, 1992). How these sources interact and whether that interaction may be responsible for the overall shape of DPOAE frequency responses or for the microstructure of those responses is still not well understood and completely satisfactory models remain to be developed. Both mechanisms could theoretically be operating simultaneously, either in concert or in opposition.

The present study was designed to further explore the bandpass characteristics of DPOAEs in humans in the hopes of providing additional insights into the underlying mechanisms responsible for this feature. Data from normal-hearing subjects are compared to those from subjects with well-defined cochlear hearing losses, which will be used to ''re-

TABLE I. Audiometric thresholds, age, and test ear for each of 15 hearing-impaired subjects. Thresholds in boldface indicate the f_2 frequencies for which data were collected.

			Audiometric thresholds (dBHL)								
Subject	Age	Ear	500	750	1000	1500	2000	3000	4000	6000	8000
100	62	R	35		**20**	15	**0**	**25**	**35**		**35**
107	74	R	35	25	**10**	**20**	**30**	**30**	**40**	55	**75**
113	64	R	5	10	**10**	10	**15**	**40**	**45**	45	**45**
131	67	L	45	30	**20**	**15**	**10**	15	**15**	25	**20**
133	79	L	5	5	**0**	0	**10**	**20**	**30**	**25**	**25**
134	39	R	10	5	**5**	0	**0**	0	**0**	**65**	**75**
138	54	L	15	15	**20**	25	**30**	**25**	**20**	**45**	**40**
139	47	L	5	5	**10**	5	**5**	5	**20**	35	**35**
141	46	L	30	40	**35**	**15**	**10**	10	**10**	10	**5**
143	36	R	45	50	**45**	45	**30**	**25**	**20**	**10**	**10**
145	18	L	45	45	**40**	**20**	**5**	10	**5**	**20**	**10**
146	55	R	20	10	5	10	**5**	**25**	**40**	**5**	**25**
153	57	L	15	30	**35**	**10**	**10**	**25**	**55**	65	**65**
200	12	L	0	0	20	25	45	**45**	**10**	**65**	**55**
203	14	R	35	30	40	40	35	**25**	**5**	**0**	**5**

strict'' the cochlear region(s) contributing to any measured response. These data should enable us to directly test the extent to which the multiple source hypothesis is correct.

I. METHODS

Fourteen young adults with normal hearing and 15 adolescents and adults with hearing impairment served as subjects. Normal hearing was defined as audiometric thresholds of 20 dB HL or better for half-octave frequencies from 500 to 8000 Hz. All hearing losses were cochlear in origin and stable. Both groups of subjects had normal middle ear function at the time of DPOAE data collection, determined by standard clinical acoustic immittance procedures. All subjects were seated in a comfortable recliner in a sound treated room. During data collection they were asked only to sit quietly and were allowed to read or sleep.

Considerable effort was made to include subjects with atypical audiometric configurations that were thought to possibly isolate DPOAE sources. (The audiometric thresholds for the 15 hearing-impaired subjects are given in Table I.) Subjects with steeply rising audiometric configurations were of particular interest because these subjects presumably could have normal cochlear function at the primary generation site for distortion (i.e., very near to f_2), while having abnormal cochlear function at the site where a stimulus frequency distortion product would be generated (i.e., the f_{dp} place). In contrast to data from subjects with normal cochlear function at both the f_2 and f_{dp} places, or data from subjects with more typical sloping configurations where f_{dp} would be less compromised than f_2, the DPOAEs from subjects with rising audiometric configurations should include distortion generated only at the f_2 place.

A fixed-f_2/swept-f_1 paradigm was used with f_2 fixed at one of seven frequencies in half-octave steps from 1000 to 8000 Hz. For each f_2 frequency, f_1 was moved from an f_2/f_1 ratio of 1.01 to 1.5 in 25-Hz steps. L_1 was always 10 dB greater than L_2, and L_2 was decreased in 5-dB steps from 65 dB SPL until no discernible response could be observed. Stimuli have been described in more detail elsewhere (Stover *et al.*, 1996). Stimulus generation and data acquisition were controlled by locally written software (EMAV, Neely and Liu, 1993). Stimuli were delivered to the ear canal via Etymotic ER-2 transducers and the ear canal sound pressure was measured using an Etymotic ER-10B microphone system. For each f_2/f_1 combination, the following data were obtained: L_1, L_2, and amplitude, phase, and noise floor at each of four DP frequencies ($2f_1-f_2$, $3f_1-2f_2$, $4f_1-3f_2$ and either $5f_1-4f_2$ or $2f_2-f_1$). These data were then used to construct DPOAE frequency functions, which are plots of DPOAE amplitude as a function of f_{dp} (see Fig. 2 for example). For each DPOAE frequency function, the following parameters were measured: the peak amplitude, DP frequency at which peak amplitude occurred, the low and high DP frequency edges of the complete response, and the average amplitude of the complete response. Although an attempt was made to analyze a 3-dB bandwidth, it was not possible to measure in all cases, especially when there was considerable microstructure in the response or if spontaneous otoacoustic emissions (SOAEs) were present. (While SOAEs were present in some ears, only two or three cases arose where SOAE frequencies were within the range being measured. In no case did SOAEs change the overall shape or interpretation of the data.)

Data collection required approximately 10 hours in normal-hearing subjects divided into 1–2-hour sessions and anywhere from 2 to 10 hours in hearing-impaired subjects, depending on amount of hearing loss and dynamic range of their DPOAE response. Further details of data collection have been reported previously (Stover *et al.*, 1996).

II. RESULTS

A. Normal-hearing subjects

Figure 2 displays mean data from all 14 subjects with normal hearing. Although the mean functions were smoother, lacking some of the fine structure of data from individual subjects, the relevant features remain consistently salient. Therefore, most of the results from the normal sub-

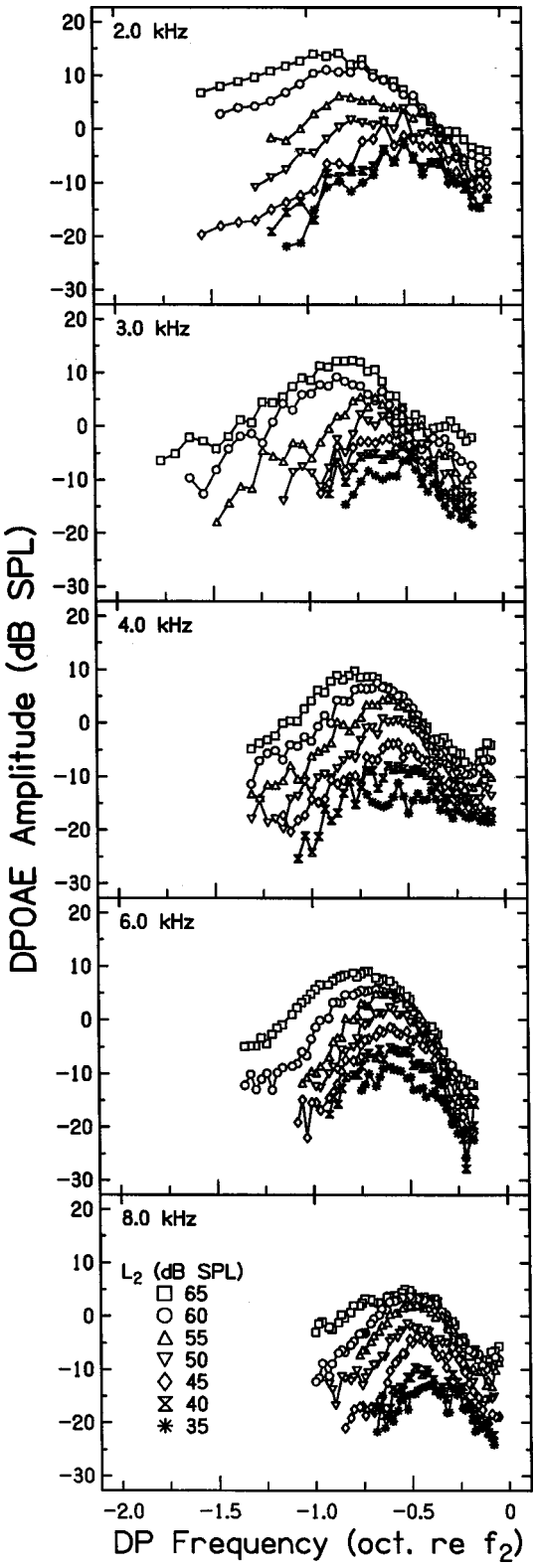

FIG. 2. Mean DPOAE frequency responses from all normal subjects for five different f_2 frequencies indicated at the top left of each panel. The amplitude of the DPOAE is plotted as a function of the DP frequency. The level of stimulation used to elicit the response is indicated by the symbol as described in the lower panel. Note the broadening of the response in lower frequency regions and higher levels of stimulation. Note also the relative stability of the high side of the function as opposed to either the low side or the peak. (Error bars are not included in this figure for the sake of clarity; however, a general idea of the variation in the individual data included in these mean data can be seen in Figs. 4–6.)

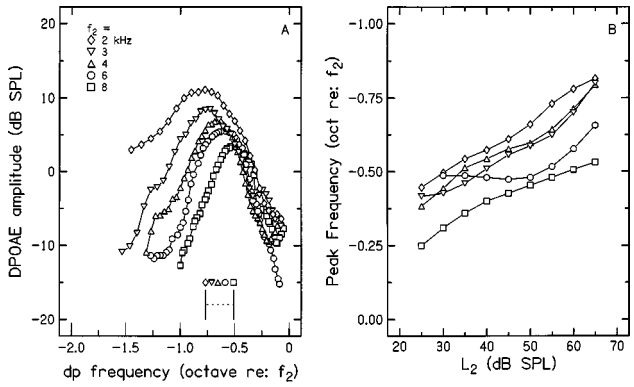

FIG. 3. (a) Mean DPOAE frequency functions with $L_1/L_2=65/55$ dB SPL for five f_2 frequencies from 2 to 8 kHz. The frequencies are indicated by the symbols as given in the top left of the figure. The bars and symbols at the bottom of the figure indicate the systematic shift of the frequencies of peak amplitudes toward f_2 as f_2 increases. Note also the similarity among frequency functions on the high-frequency side. (b) Mean peak frequencies as a function of L_2 for five f_2 frequencies indicated by the symbols as described in (a). There is a systematic shift away from f_2 as the level of stimulation is increased.

jects will be illustrated with mean data. In each panel, DPOAE amplitude is plotted as a function of f_{dp} on a logarithmic scale (i.e., in octaves relative to f_2) in order to allow comparison of data across the full range of f_2 frequencies.[2] The f_2 frequency is noted in the upper-left corner of each panel. Within each panel, individual functions represent data for different primary levels, ranging from $L_2=65$ to 35 dB SPL in 5-dB steps.

As Fig. 2 demonstrates, the peak of the DPOAE frequency function approaches f_2 and the bandwidth narrows as f_2 increases in frequency. For example, at 8 kHz with $L_1/L_2=65/55$ dB SPL, the peak occurred at a DP frequency 0.5 octaves below 8 kHz (i.e., approximately 5600 Hz). In contrast, the peak occurred at an f_{dp} about 0.75 octaves below f_2 when f_2 was fixed at 2 kHz for the same stimulus levels. The peak of the functions systematically became more distant (on a logarithmic scale) as f_2 decreased. This feature of the data is summarized in Fig. 3(a), which shows the mean frequency functions for each f_2 for stimulus intensities of 65/55 dB SPL. The symbols and bar at the bottom of the figure indicate the frequencies and range of amplitude maxima. These results are consistent with previous reports (Harris *et al.*, 1989) and with what is known about tuning of the peripheral auditory system. Specifically, psychophysical tuning curves, neural tuning curves, and basilar membrane motion studies all indicate that the auditory system is more broadly tuned, on a logarithmic frequency scale, as frequency decreases.

A second feature of the frequency functions in Fig. 2 is a shift in peak frequency as stimulus level was reduced. This pattern is summarized for all stimulus intensities and frequencies in Fig. 3(b), which plots the mean DP frequency at which the peak amplitude occurred as a function of stimulus level. The parameter is f_2 frequency. The peak occurs between 0.22 and 0.8 octaves below f_2; however, it migrates systematically toward f_2 as f_2 is increased or L_2 is decreased. As with the previously discussed frequency effect, this primary level effect might be expected based on psycho-

physical and physiological data. Specifically, masking patterns and the low-frequency shift of tuning curves both indicate a loss of tuning with increased intensity of stimulation.

Perhaps the most striking feature in Fig. 2 is the asymmetry of both the frequency and level effects. As intensity is increased in each panel, the peak shifts away from f_2, but this effect is primarily due to the broadening of the low-frequency side of the functions. While the high-frequency side remains relatively stable, particularly in terms of slope, the low-frequency side changes in both slope and amplitude. Although it is not as readily apparent in Fig. 2, the same statement can be made for the peak shift across f_2. It can be seen more easily in Fig. 3(a) that the broadening occurs only on the low-frequency side of the function, while the high-frequency slope remains relatively constant across f_2.

There are two possible explanations for this asymmetry. First, this pattern is very consistent with a dual source model. The two sources, distributed near the f_2 and f_{dp} places, do not change cochlear places with changes in level. Therefore, the frequency of cancellation would also remain constant, thus resulting in the ''dip'' occurring at the same frequency across level. The amount of cancellation might change with level because of the different saturation rates and amplitudes of the two sources. Specifically, the stimulus frequency generator saturates at input levels approximating 40 dB SPL (Kemp and Chum, 1980), while the primary generator (presumably very close to f_2) does not saturate, at least for the levels used in this study. Thus, at high levels of stimulation, the level of the ''interfering'' stimulus (from f_{dp} place) is reduced relative to the primary generation and the ''dip'' becomes less pronounced (see Fig. 2). Because frequency is mapped logarithmically along the cochlear partition, one would expect that the distance, in octaves, between f_2 and f_{dp}, for which cancellation would occur, would be similar regardless of f_2. The data shown in Fig. 3(a) are consistent with this idea.

The second explanation for this asymmetry in the data is that a second resonance exists, which would, however, be measured by the ''dip'' in the function rather than the peak. That is, the second resonance would change the high-pass characteristic of the primary generator by absorbing energy rather than adding energy. Such a second resonance would be located at the zero of the function rather than at the peak. This resonance also would have to be sharply tuned and relatively independent of both f_2 and stimulus intensity. No such model has, as yet, been proposed, perhaps because of such unusual requirements.

In summary, the normal cochlea produces distortion in response to two tones of slightly different frequency. DPOAE frequency functions, in which f_2 is held constant and f_1 is varied, reveal an amplitude peak whose frequency location is determined by both the frequency region being stimulated and the intensity of that stimulation. The high-frequency slopes of these functions, however, are relatively constant across both frequency and intensity. Because various arguments can be made for each of the models regarding these features, however, data from normal-hearing subjects cannot adequately differentiate between the three models under consideration.

III. HEARING-IMPAIRED SUBJECTS

Data from subjects with hearing loss provide a unique opportunity to evaluate different explanations for the shape of DPOAE frequency functions. For instance, one might expect a broadened ''filter'' response if these frequency functions reflect changes in frequency selectivity similar to the changes observed in other measures of auditory function (i.e., tuning curves, critical bands) following cochlear damage. On the other hand, if there are multiple sources, one might be able to isolate those sources through frequency specific hearing losses. Therefore, attempts were made to include hearing losses in the mild range (when some damage exists but not enough to completely eliminate DPOAE responses) and those with audiometric configurations in which DPOAEs might be eliminated from one source but not the other. (It should be noted that audiometric thresholds at half-octave frequencies do not supply the precision or accuracy needed to evaluate cochlear function for the purposes stated here. However, if the effects we predict can be seen with such a gross measure of cochlear status, then the argument is only strengthened further.) The nature of these data are such that it is not possible to collapse results across hearing-impaired subjects. We are constrained to illustrate response patterns by presenting data from individual subjects with hearing loss. These individual sets of data are compared with the overall response patterns that were seen in subjects with normal hearing. Subjects were selected to represent hearing losses whose underlying cochlear conditions might represent one of the following situations: (1) intact cochlea at both f_2 and f_{dp} regions with damage in other regions; (2) intact cochlea in f_{dp} region with damage at f_2; and (3) intact cochlea at f_2 with damage in f_{dp} regions.

The first situation was chosen to ensure that areas of the cochlea remote to the frequency regions of interest are not involved in the generation of DPOAEs. This can be seen in areas of normal hearing in subjects with high-frequency hearing loss (i.e., S100, S113, S133, S134, S139, and S146 for $f_2=2$ kHz; S131, S134, S139, and S141 for $f_2=4$ kHz, etc.) An example, shown in Fig. 4, demonstrates that, if the f_2 place and the f_{dp} region are intact, then the patterns of acoustic distortion are essentially normal. The panels on the left show the frequency functions for a subject with hearing loss, whose audiogram is shown on the right. Data from four primary levels are shown for illustration and are compared to the mean frequency functions for the 14 normal-hearing subjects (solid lines). The dotted lines represent $\pm$ one standard deviation based on the normative data set. The star in the audiogram represents f_2 and the short and long horizontal bars indicate the ranges of f_1 and f_{dp}, respectively. For this subject, hearing thresholds (and thus presumably cochlear status) are normal throughout the frequency range of all three parameters (f_2, f_1, f_{dp}). The DPOAE frequency functions also fall within the normal range in terms of peak amplitude, peak frequency, overall shape, and the dynamic range of the response. Thus, these data are consistent with the prediction that remote regions of the cochlea do not contribute to the DPOAE.

The second situation was chosen such that only the primary distortion generation site (f_2) had sustained some dam-

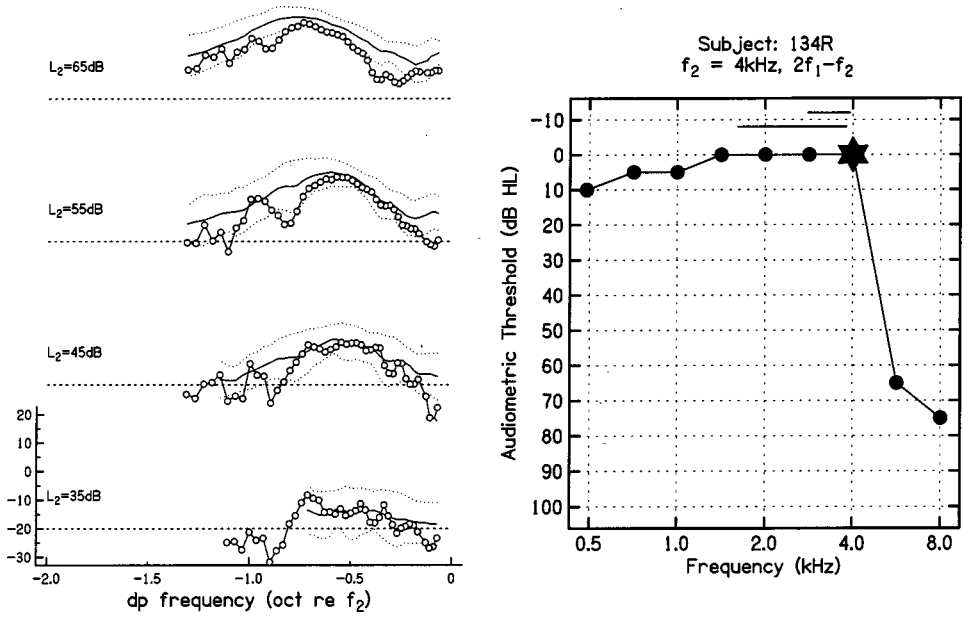

FIG. 4. Frequency responses from a hearing-impaired subject with normal hearing in the frequency range being measured. The subject's audiogram is given on the right with the frequency indicated by the large star symbol. The bars at the top of the audiogram indicate the frequency ranges of f_1 and f_{dp}. The left column shows the subject's DPOAE response by the symbols for a range of stimulus intensities (given to the left of each function). The amplitude range is given in the bottom panel and the horizontal dashed line in each panel indicates the −20-dB SPL noise floor reference. For comparison, the mean normal frequency function is given in each panel by the solid line, ± one standard deviation by the dotted lines. For this subject the response is essentially normal in shape and amplitude.

age. This situation is one in which predictions differ between the second resonance models and the dual source model. For all three models, primary generation must happen at the f_2 place. However, a second resonance model would predict a broadening of the frequency response similar to the changes that have been observed in other measures of frequency selectivity in damaged cochleae. Thus one might expect either a broadening of the peak (second-filter enhancing) or the dip (second-filter canceling), or a shifting of either peak or dip further away from f_2. In a dual source model, the relative contributions from the f_2 and f_{dp} places would change because the output of the f_2 generator would be reduced, while the output from the f_{dp} place would be reduced very little, if at all because of the assumed saturation of the stimulus frequency emission generator. Thus with greater relative contribution from the ''interfering'' stimulus (from f_{dp} place), one would predict that there would be more cancellation, which would manifest as a broader dip in the frequency function. Because the primary generator at f_2 is affected, all three models would predict reduced amplitude and smaller dynamic range.

This situation can be found in the typical sloping hearing loss (i.e., S107 at 2 kHz; S100 and S113 at 3 kHz; S133, S146, and S153 at 4 kHz S134, S138, and S139 at 6 kHz). It should be noted that when threshold was over 40 dB HL for f_2, either no response or only a weak response at the highest levels of stimulation could be measured, with the exception of one case (S200 at 3 kHz). In several cases, no response could be seen when threshold at f_2 was between 20 and 40 dB HL (S139 at 8 and S143 at 2 kHz). In all other cases of mild hearing loss, a response could be measured with sufficient dynamic range to evaluate the data.

Figure 5 shows audiometric and DPOAE data for a subject in whom the primary generation site was functionally abnormal but still capable of producing distortion. The representations follow the same conventions as were used in Fig. 4. The overall amplitude is, indeed, reduced compared to data from normal subjects, as is the dynamic range due to an elevated threshold of the DPOAE. The shape of the response, however, does not indicate any broadening of the peak, nor is it shifted in frequency, as would be expected from a model in which a second resonance is manifested in the peak of the response. The ''dip,'' however, is broader, as predicted by both the second resonance canceling model and the dual source model.

The final case was chosen to represent that the region of primary generation within the cochlea (f_2) was normal, but the regions where the secondary generation might occur (i.e., the regions where f_{dp} is represented) were damaged. This is the situation that will most clearly distinguish between the two explanations. Both second resonance models would predict normal DPOAE frequency functions as long as the cochlea was intact in the region of primary distortion generation (i.e., the f_2 place) because the second resonance is assumed to be located at, or near, the f_2 place. The dual source model, on the other hand, would predict a more high-pass characteristic to the DPOAE frequency function because the regions responsible for generating the secondary energy (i.e., the f_{dp} place) would not produce a response. Thus little or no cancellation might occur.

In this instance, a more atypical upward sloping audiogram is required, even one with a fairly steep slope in order to remove the lower frequency f_{dp} contributions. This criterion was met in several of the subjects (i.e., S141, S145, and S153 at 1500 Hz; S145 at 2 kHz; and S200 and S203 at 4 kHz). While there were several other instances of reverse sloping audiograms, the slopes were probably too shallow to remove the f_{dp} component. The results for this situation are demonstrated in Fig. 6 following the conventions of Figs. 4 and 5. There is clearly a difference between the shape of this response and that from normal-hearing subjects. The response has a high-pass characteristic, as a dual source model would predict. Note, however, that the peak amplitude (which in this case occurs at a frequency very close to f_2) and dynamic range are within the normal range of variabil-

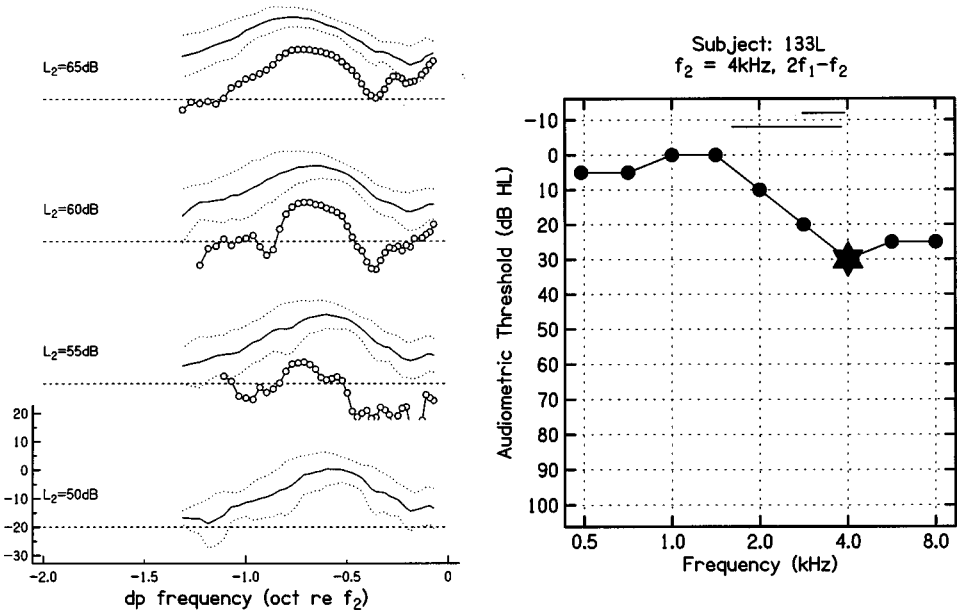

FIG. 5. As in Fig. 4. In this case the subject has a mild hearing loss at f_2 with improving thresholds in the range of f_{dp}. The DPOAE is reduced in amplitude but the peak is not systematically shifted from the normal response. However, the high-frequency side ''dip'' is broader than the normals.

ity, again consistent with the predicted pattern for a dual source model if the cochlea is intact at f_2.

In summary, the data from hearing-impaired subjects would appear to favor a dual source model of DPOAE generation. Specifically, it was observed that regions remote from f_2 and f_{dp} are not involved in distortion generation; that even if the f_2 region was damaged, the response does not broaden, as a ''filter'' model would predict; and that if the f_{dp} region is damaged, thus eliminating the ''interfering'' stimulus, the apparent bandpass characteristic is eliminated. If input from a second DP source is intact, relatively more cancellation occurs (seen as a broadening of the dip), and if the second DP source is removed, the frequency response changes, and reveals a high-pass characteristic of the primary f_2 source alone. Although the broadening of the dip could also be explained by a second resonance theory if the action of the resonance is energy absorption, the results from the upward sloping hearing losses cannot be explained by either of the second resonance hypotheses.

IV. DISCUSSION

We have considered three classes of models in attempts to account for DPOAE frequency functions: a second resonance filtering distortion which is bandpass in nature and defined by the peak of the function; a second resonance which is energy absorbing and defined by the ''dip'' of the function as the primaries approach each other; and a dual source model in which two sources of energy combine in such a way as to cancel the distortion as measured in the ear canal. While the present data do not disagree with previous data, our conclusions regarding underlying mechanisms involve different models. The underlying assumptions of each model can be assessed by evaluating the present data in dif-

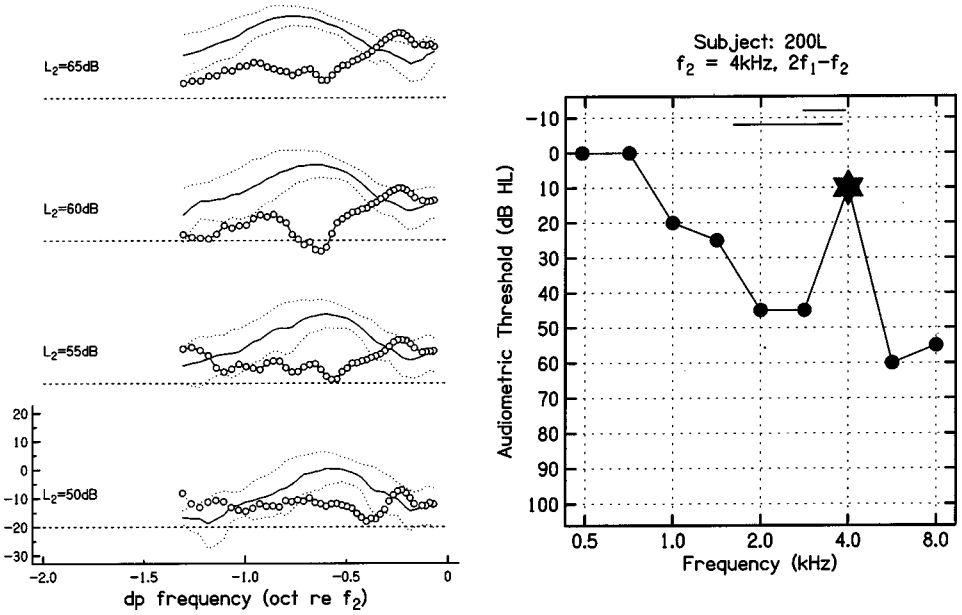

FIG. 6. As in Figs. 4 and 5. This subject has normal hearing at f_2 but reduced hearing in the f_{dp} region. Without the contribution from the f_{dp} region the response is characterized by a high-pass shape and is significantly different than the normal frequency functions. This is difficult to explain in terms of a second filter model but is predicted by a dual source model.

ferent ways. For instance, the peak is only relevant to the enhancing second resonance model, while the ''dip'' is intrinsically more important to the other two models. We should be able to determine which model is most consistent with these data by examining the underlying assumptions of each model and comparing all aspects of the data rather than simply the peak frequency and amplitude.

The concept of a second cochlear filter has been considered for some time. A second filter was hypothesized to account for the difference between broad basilar membrane tuning and sharp neural tuning (Evans and Wilson, 1973). The need for a second filter was eliminated as better measurement techniques for BM motion were developed and the difference between mechanical and neural tuning decreased. Most of the phenomena which were attributed to a second resonance are now believed to be due to the action of the motile outer hair cell system. Since many measures of cochlear response can now be accounted for without involving a second filter, perhaps such a ''filter'' is not needed to account for DPOAE data either.

Two arguments have been made for second resonance models. The original explanations for the DPOAE frequency functions involved either a suppression or a cancellation process between the two primary stimuli. The second filter idea was resurrected when higher-order distortion data refuted the primary interaction theory (Brown *et al.*, 1992; Brown and Williams, 1993). The argument was that if the results were not due to the two primaries interacting, then there may be a ''filter'' associated with the f_2 place which would act on all distortion products similarly. However, the original explanation could be altered such that the DPOAE frequency functions involve a cancellation process between f_2 and f_{dp}, rather than f_1. In that case, ''filter functions'' would be independent of DP order (at least in terms of the frequency of the peak or the ''dip'') but would depend on the frequency at which the DP occurs, be it $2f_1-f_2$, $3f_1-2f_2$, or any other DP. This is essentially the dual source model.

A second argument for a DPOAE filter revolved around the half-octave shift between the peak frequency and f_2. The half-octave difference is consistent with several well-studied psychophysical and physiological phenomena, such as noise-induced temporary threshold shift (TTS), contralateral efferent effects, and the tip/tail juncture in tuning curves. The first and third of these phenomena (TTS and the tip/tail juncture) have been explained by a second resonance hypothesis (Allen and Fahey, 1993); there are no current theories regarding efferent effects which involve a second cochlear resonance. Furthermore, the observation of effects at the ''half-octave'' may be an oversimplification of the data. The present data do not indicate an exact ''half-octave'' between f_2 and the peak, but rather a range from a quarter-octave to one full octave. There is a similar imprecision to the half-octave relationships in the other types of data as well.

At a first pass, it would seem that some features of DPOAE frequency functions are consistent with other frequency tuning characteristics. The changes in ''tuning'' of the second filter (both in terms of peak-to-f_2 and filter bandwidth) with frequency are similar to those seen in both psychophysical and physiological data. The primary resonance of the basilar membrane is indeed more sharply tuned at the base than the apex. If the bandwidth of a second resonance is also frequency dependent, then the two frequency maps will not be parallel but rather closer together at the base and increasingly more separated further toward the apex. Such a relationship has been reported in estimates of a second frequency map for cat (Allen and Fahey, 1993), although those calculations are subject to the argument, above, regarding the imprecision and subjectivity of tip/tail measurement.

Basilar membrane, neural, and psychophysical data also show that the auditory system loses some tuning as stimulus level increases. However, the high degree of tuning for low level stimuli results from the action of the outer hair cells (OHCs) when they are in their linear mode of operation. As stimulus level is increased, the relative input from the OHCs becomes less, due to their saturating nonlinearity. The basilar membrane remains broadly tuned across levels of stimulation. Thus the level effect is not intrinsic to the basilar membrane, but rather is due to the added energy of the OHCs. Invoking the same line of reasoning for a second resonance, in order for the same level effect to be seen, the mechanism of that second resonance (presumably the TM) will also probably be affected by the OHCs rather than intrinsically changing its tuning with level of stimulation. It is not clear whether the coupling of the stereocilia with the TM is strong enough to actually change its motion as would be required by this line of reasoning.

The fact that there is a high-pass characteristic seen in frequency functions of basilar membrane motion and in the psychophysical distortion product literature suggests a two-step process in DPOAE generation. The second ''filtering'' must occur either after the primary generation in time or basal to it in order for the high-pass stimulus to propagate to the DP place and generate the psychophysical percept. Given this constraint, the input to the second resonance is not the same as the input to the primary distortion generator (the representation of the two primary tones near f_2 place), but rather the output of the distortion generator which is characteristically high pass in nature. The TM is intrinsically involved in the primary generation of distortion as a consequence of its role in the shear displacement of the stereocilia of the OHCs. Thus for the TM to be the source of a second resonance it would have to be responsible for both a high-pass response and also a bandpass second resonance response at the same time.

The previous discussion applies to a second filter defined by the peak of DPOAE frequency functions. However, a second resonance might be more appropriately described by the ''dip'' of the frequency function. The second resonance must account for the difference between primary generation, distributed at the f_2 place, which has a high-pass characteristic (according to psychophysical and physiological data), and the acoustic distortion in the ear canal, which has a bandpass characteristic. The primary difference between the two ''filter responses'' is a removal of energy for f_{dp}'s approaching f_2. Even a peak-defined filter will have to include a ''zero'' to account for this feature. The second resonance would thus be absorbing energy rather than adding energy to the response.

A second filter of this type would be inherently different from one defined by the peak. First of all, such a filter would necessarily be highly tuned, as the often seen increase in DPOAE amplitude for very close f_2/f_{dp} relationships on the other side of the dip would suggest. Although the ''dip'' was not quantified in the present data (and would be more difficult to quantify than the peak), qualitative observation indicates that it is relatively independent of f_2, or cochlear location, a pattern that would be consistent with a second frequency map parallel to the BM frequency map. The frequency of the dip is also independent of stimulus intensity, although the depth of the dip seems to be less at higher intensities. These characteristics of a ''dip''-defined second filter allow it to be less intrinsically attached to the primary distortion generator, which avoids some of the difficulties just discussed. However, there are currently no second resonance models of this type.

The dual source model is consistent with the data from normal-hearing subjects. This model can account for the difference between psychophysical and acoustic distortion, because it is inherently a cancellation model and thus is manifested by the ''dip'' rather than the peak. The peak is simply a function of the juxtaposition of the high-pass primary distortion generator and the cancellation from the second source. Because frequency is logarithmically mapped, the frequency of the dip should be relatively independent of f_2 frequency, when plotted on an octave scale, as shown in Fig. 3. The frequency of the dip should also be independent of stimulus intensity. The model would, however, predict changes in the relative contributions from the two sources as stimulus intensity changed, because the stimulus frequency emission from the f_{dp} place would be expected to saturate more and to lower levels than the primary generator at f_2. Thus there would not be changes in the frequency of the effect but the amount of cancellation would be less for higher intensity stimulation. Although a general trend toward shallower dips at high intensities was observed, further study is needed prior to any conclusive statements.

The data from the hearing-impaired subjects present perhaps the strongest argument in favor of a dual source model. The fact that predicted high-pass frequency functions were obtained from subjects in which hearing loss was used to isolate the primary source (at f_2 place) is difficult for a second filter model to explain. If a second filter is associated with the generator at f_2 place, cochlear damage at f_{dp} place should not affect the output. Damage at the f_2 place may limit the output magnitude but the overall frequency function is unchanged as long as there remain two cochlear sources. This type of data requires further exploration, particularly with a more precise measure of hearing (cochlear) status, such as threshold microstructure with laboratory threshold procedures rather than half-octave thresholds with clinical threshold procedures. However, the preliminary results from these few subjects present a challenge for any second-filter model.

In summary, the arguments for a second resonance explanation for DPOAE frequency functions are not compelling. Furthermore, although it is not clear what effect such a second resonance would have on modeling cochlear processes other than DPOAEs, there are some inherent difficulties in modeling an underlying mechanism as a second filter. We do not argue, necessarily, that there is no second resonance in the cochlea, only that it is not a necessary, nor the most parsimonious, explanation for DPOAE frequency functions. A dual source model accounts for the data and does not have far-reaching implications in terms of other auditory processing.

This does not mean that DPOAE frequency functions are not worthy of further investigation. There are significant clinical implications in these findings. The I/O functions and the data from hearing-impaired subjects indicate that a standardized test with an f_2/f_1 ratio of 1.2 may require further examination, and that configuration of the hearing loss, not just cochlear status at f_2, can affect the measured DPOAE response (although if no distortion is generated at f_2, the status at the f_{dp} place is irrelevant). Furthermore, the source of the frequency microstructure in the response and its effect on clinical interpretation need to be addressed. These questions require further investigation.

ACKNOWLEDGMENTS

We wish to thank Doug Keefe for helpful comments on an earlier draft of this manuscript. Portions of this work were previously presented at the ARO Midwinter Meeting in 1996 and 1994. This work was supported by grants from the NIDCD (P60DC00982 and R01DC02251).

[1]Although defining the stimulus characteristics yielding the largest response in normal ears is useful, from a clinical perspective, optimal stimulus conditions are those that result in the greatest separation between the distribution of responses from ears with normal hearing and ears with hearing loss.
[2]The data for f_2 at 1000 and 1414 Hz were sparse and often contaminated with a high noise floor. While the same trends presented below were present in these data they are not specifically included in further discussion.

Allen, J. B., and Fahey, P. F. (**1993**). ''A second cochlear-frequency map that correlates distortion product and neural tuning measurements,'' J. Acoust. Soc. Am. **94**, 809–816.
Brown, A. M., and Williams, D. M. (**1993**). ''A second filter in the cochlea,'' in *Biophysics of Hair Cell Sensory Systems*, edited by H. Duifhuis, J. W. Horst, P. van Dijk, and S. M. van Netten (World Scientific, London), pp. 72–77.
Brown, A. M., Gaskill, S. A., and Williams, D. M. (**1992**). ''Mechanical filtering of sound in the inner ear,'' Proc. R. Soc. London, Ser. B **250**, 29–34.
Dallos, P., Schoeny, Z. G., Worthington, D. W., and Cheatham, M. A. (**1969**). ''Some problems in the measurement of cochlear distortion,'' J. Acoust. Soc. Am. **46**, 356–361.
Evans, E. F., and Wilson, J. P. (**1973**). ''The frequency selectivity of the cochlea,'' in *Basic Mechanisms of Hearing*, edited by A. R. Moller (Academic, New York), pp. 519–554.
Furst, M., Rabinowitz, W. M., and Zurek, P. M. (**1988**). ''Ear canal acoustic distortion at $2f_1-f_2$ from human ears: Relation to other emissions and perceived combination tones,'' J. Acoust. Soc. Am. **84**, 215–221.
Gaskill, S. A., and Brown, A. M. (**1990**). ''The behavior of the acoustic distortion product, $2f_1-f_2$, from the human ear and its relation to auditory sensitivity,'' J. Acoust. Soc. Am. **88**, 821–839.
Goldstein, J. L. (**1967**). ''Auditory nonlinearity,'' J. Acoust. Soc. Am. **41**, 676–689.
Goldstein, J. L., and Kiang, N. Y.-S. (**1968**). ''Neural correlates of the aural combination tone $2f_1-f_2$,'' Proc. IEEE **56**, 981–999.
Harris, F. P., Probst, R., and Xu, L. (**1992**). ''Suppression of the $2f_1-f_2$ otoacoustic emission in humans,'' Hear. Res. **64**, 133–141.

Harris, F. P., Lonsbury-Martin, B. L., Stagner, B. B., Coats, A. C., and Martin, G. K. (**1989**). ''Acoustic distortion products in humans: Systematic changes in amplitude as a function of f_2/f_1 ratio,'' J. Acoust. Soc. Am. **85**, 220–229.

Kemp, D. T. (**1979**). ''Evidence of mechanical nonlinearity and frequency selective wave amplification in the cochlea,'' Arch. Otorhinolaryngol. **224**, 37–45.

Kemp, D. T., and Chum, R. (**1980**). ''Observations on the generator mechanism of stimulus frequency acoustic emissions—two tone suppression'' in *Psychophysical, Physiological and Behavioural Studies in Hearing*, edited by G. van den Brink and F. A. Bilsen (Delft University Press, The Netherlands), pp. 34–42.

Martin, G. K., Lonsbury-Martin, B. L., Probst, R., Schinin, S. A., and Coats, A. C. (**1987**). ''Acoustic distortion products in rabbit ear canal. II. Sites of origin revealed by suppression contours and pure tone exposures,'' Hear. Res. **28**, 191–208.

Matthews, J. W. (**1986**). ''Modeling intracochlear and ear canal distortion produce $(2f_1-f_2)$,'' in *Peripheral Auditory Mechanisms*, edited by J. B. Allen, J. L. Hall, A. Hubbard, S. T. Neely, and A. Tubis (Springer, New York), pp. 258–265.

Neely, S. T., and Liu, Z. (**1993**). ''EMAV: Otoacoustic emission averager,'' Tech. Memo No. 17 (Boys Town National Research Hospital, Omaha).

Nielsen, L. H., Popelka, G. R., Rasmussen, A. N., and Osterhammel, P. A. (**1993**). ''Clinical significance of probe-tone frequency ratio on distortion product otoacoustic emissions,'' Scand. Audiol. **22**, 159–164

O'Mahoney, S., and Kemp, D. T. (**1995**). ''Distortion product otoacoustic emission delay measurement in human ears,'' J. Acoust. Soc. Am. **97**, 3721–3735.

Robles, L., Ruggero, M. A., and Rich, N. C. (**1993**). ''Distortion products at the basilar membrane of the cochlea: Dependence on stimulus frequency and intensity and effect of acoustic trauma,'' Neurosci. Abstracts **19**, 1421.

Shera, C. A., and Zweig, G. (**1993**). ''Noninvasive measurement of the cochlear traveling-wave ratio,'' J. Acoust. Soc. Am. **93**, 3333–3352.

Smoorenburg, G. F. (**1972**). ''Audibility region of combination tones,'' J. Acoust. Soc. Am. **52**, 603–614.

Stover, L. J., Neely, S. T., and Gorga, M. P. (**1996**). ''Latency and multiple sources of distortion product otoacoustic emissions,'' J. Acoust. Soc. Am. **99**, 1016–1024.

Taschenberger, G., Gallo, L., and Manley, G. A. (**1995**). ''Filtering of distortion-product otoacoustic emissions in the inner ear of birds and lizards,'' Hear. Res. **91**, 87–92.

Whitehead, M. L., Lonsbury-Martin, B. L., and Martin, G. D. (**1992**). ''Evidence for two discrete sources of $2f_1-f_2$ distortion-product otoacoustic emission in rabbit: I. Differential dependence on stimulus parameters,'' J. Acoust. Soc. Am. **91**, 1587–1607.

Wilson, J. P. (**1980**). ''The combination tone, $2f_1-f_2$, in psychophysics and ear-canal recording,'' in *Psychophysical, Physiological and Behavioural Studies in Hearing*, edited by G. van den Brink and F. A. Bilsen (Delft University Press, The Netherlands), pp. 43–52.

Zwiskocki, J. J., and Kletsky, E. J. (**1980**). ''Micromechanics in the theory of cochlear mechanics,'' Hear. Res. **2**, 205–212.

A possible neurophysiological basis of the octave enlargement effect

Martin F. McKinney[a)]
Speech and Hearing Sciences Program, Harvard University–Massachusetts Institute of Technology, Division of Health Sciences and Technology and Eaton-Peabody Laboratory, Massachusetts Eye and Ear Infirmary, 243 Charles Street, Boston, Massachusetts 02114

Bertrand Delgutte
Eaton-Peabody Laboratory, Massachusetts Eye and Ear Infirmary, 243 Charles Street, Boston, Massachusetts 02114 and Research Laboratory of Electronics, Massachusetts Institute of Technology and Speech and Hearing Sciences Program, Harvard University–Massachusetts Institute of Technology, Division of Health Sciences and Technology

(Received 24 August 1998; revised 14 July 1999; accepted 23 July 1999)

Although the physical octave is defined as a simple ratio of 2:1, listeners prefer slightly greater octave ratios. Ohgushi [J. Acoust. Soc. Am. **73**, 1694–1700 (1983)] suggested that a temporal model for octave matching would predict this *octave enlargement* effect because, in response to pure tones, auditory-nerve interspike intervals are slightly larger than the stimulus period. In an effort to test Ohgushi's hypothesis, auditory-nerve single-unit responses to pure-tone stimuli were collected from Dial-anesthetized cats. It was found that although interspike interval distributions show clear phase-locking to the stimulus, intervals systematically deviate from integer multiples of the stimulus period. Due to refractory effects, intervals smaller than 5 msec are slightly larger than the stimulus period and deviate most for small intervals. On the other hand, first-order intervals are smaller than the stimulus period for stimulus frequencies less than 500 Hz. It is shown that this deviation is the combined effect of phase-locking and multiple spikes within one stimulus period. A model for octave matching was implemented which compares frequency estimates of two tones based on their interspike interval distributions. The model quantitatively predicts the octave enlargement effect. These results are consistent with the idea that musical pitch is derived from auditory-nerve interspike interval distributions. © *1999 Acoustical Society of America.* [S0001-4966(99)05111-5]

PACS numbers: 43.64.Pg, 43.66.Ba, 43.66.Hg [RDF]

INTRODUCTION

The octave is the basis of most known tonal systems throughout the world (Dowling and Harwood, 1986).[1] Pitches that are an octave apart are deemed equivalent to some degree and can serve the same musical function within certain tonal contexts. The prevalence of the octave as the fundamental building block of tonal systems suggests that there may be a physiological basis for octave equivalence.

A physical octave is defined as a frequency ratio of 2:1. It is known, however, that listeners prefer octave ratios slightly greater than 2:1 (Ward, 1954; Walliser, 1969; Terhardt, 1971; Sundberg and Lindqvist, 1973). In a typical procedure to measure this *octave enlargement* effect, a subject listens to a lower standard tone alternating with an adjustable higher tone and is instructed to adjust the frequency of the higher tone until it sounds one octave above the lower tone. Results of three such experiments are shown in Fig. 1. The size of the preferred or subjective octave is close to 2:1 at low frequencies but increases with frequency and exceeds the physical octave by almost 3% at 2 kHz. It is difficult for listeners to make octave judgments for tones above about 2 kHz. This corresponds to an upper limit in musical pitch of about 4–5 kHz (Ward, 1954; Attneave and Olson, 1971). There is considerable variability in the octave enlargement effect across listeners but it is nonetheless a statistically significant effect in all the reported studies. The effect is also seen in a wide variety of stimulus conditions and in subjects with various musical backgrounds. It is seen when the two tones are presented simultaneously (Ward, 1954; Demany and Semal, 1990) and under the method of constant stimuli (Dobbins and Cuddy, 1982). The studies shown in Fig. 1 were all performed using pure-tone stimuli but Sundberg and Lindqvist (1973) reported the effect with complex tones as well as pure tones. Ward (1954) reported the presence of the effect in listeners without musical training and in listeners with musical training as well as in possessors of absolute pitch. Dowling and Harwood (1986, p. 103) reported the effect in a number of musical cultures.

The presence of the octave enlargement effect under a wide range of subject and stimulus conditions suggests that the effect may have a general physiological basis. Ohgushi (1983) proposed an octave matching scheme based on a temporal model for pitch that predicts the octave enlargement effect. In an earlier study, he noticed that, in response to pure tones, auditory-nerve interspike intervals are slightly longer than integer multiples of the stimulus period (Ohgushi, 1978). He then showed, using a temporal model for octave

a)Author to whom correspondence should be addressed.

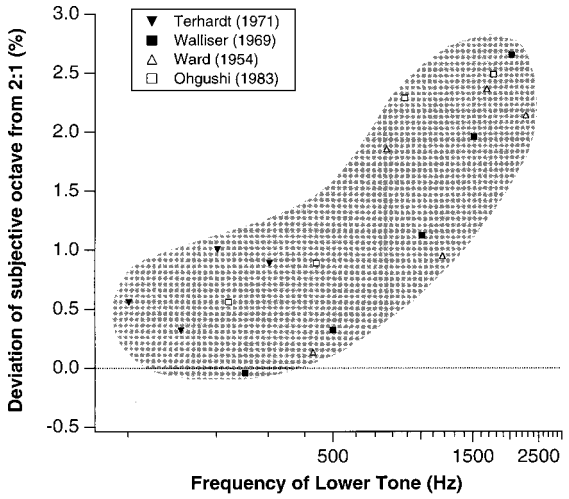

FIG. 1. Psychoacoustic measures of the octave enlargement. Adapted from Fig. 4 in Sundberg and Lindqvist (1973) and Fig. 9 in Ohgushi (1983). The subjective octave, obtained from octave matching experiments, is plotted as a deviation from the physical octave versus the frequency of the lower tone in the octave pair. The subjective octave is larger than the physical octave and the deviation grows with frequency.

matching, that these deviations lead to a prediction of the octave enlargement effect (Ohgushi, 1983).

Upon review of Ohgushi's (1983) model for octave matching, Hartmann (1993) pointed out an arbitrary factor of two. This scaling factor, which is not based on any physiological process, allows a model listener to theoretically set it, and thus the octave interval, to any value. Hartmann suggested a variation of the model that would not rely on such a scaling factor. He also suggested that if the model operated on all-order interspike intervals instead of first-order interspike intervals, it may better predict the psychoacoustic data.

The work presented here was motivated by the hypotheses presented by Ohgushi and Hartmann. Neither one of them could reliably test their predictions because the existing physiological data consisted of only a small number of coarse-resolution interspike-interval distributions. It was therefore difficult to measure the modes of the distributions, i.e., characterize the intervals, with high precision. Special methods were used in this study to ensure high-precision interval analyses so that predictions of temporal models for octave matching could be reliably evaluated. We combined spike data across fibers to form pooled interspike interval histograms which have been shown to reflect a wide variety of pitch phenomena (Cariani and Delgutte, 1996a, 1996b). In addition to characterizing interspike intervals, we have developed and evaluated models for octave matching, based on Ohgushi's and Hartmann's ideas, which operate on pooled interspike interval histograms.

I. METHOD

The methods used in this study differ from typical auditory-nerve (AN) studies in that specific efforts were taken to ensure accurate estimation of interspike intervals (ISIs): Unusually long recordings were made to ensure the inclusion of a high number of spikes in each record; very fine binwidths (1 μsec) were used when generating ISI histograms in order to accurately estimate the modes.

A. Experiment

Data were recorded from auditory-nerve fibers in six healthy, adult cats. Cat preparation and recording techniques were standard for our laboratory (Kiang *et al.*, 1965; Cariani and Delgutte, 1996a).

In each experiment, the cat was Dial-anesthetized with an initial dose of 75 mg per kg of body weight and subsequent doses of 7.5 mg per kg of body weight. A craniectomy was performed and the middle-ear and bulla cavities were opened to access the round window. The cerebellum was retracted to expose the AN. Injections of dexamethasone (0.26 mg/kg of body weight/day), to reduce brain swelling, and Ringer's saline (50 ml/day), to prevent dehydration, were given throughout the experiment.

The cat was placed on a vibration isolation table in an electrically shielded, temperature-controlled (38 °C) chamber. The AN compound action potential (CAP) in response to click stimuli was monitored with a metal electrode placed near the round window. The cat's hearing was assessed by monitoring the CAP threshold and single-unit thresholds.

Sound was delivered to the cat's ear through a closed acoustic assembly driven by a (Beyerdynamic DT 48A) headphone. The acoustic assembly was calibrated with respect to the voltage delivered to the headphone, allowing for accurate control over the sound-pressure level at the tympanic membrane. Stimuli were generated by a 16-bit, Concurrent (DA04H) digital-to-analog converter using a sampling rate of 100 kHz. The total harmonic distortion for pure tones between 110 and 3000 Hz was less than -55 dB re fundamental when measured at a stimulus level of 95 dB SPL.

AN action potentials (spikes) were recorded with glass micropipette electrodes filled with 2 M KCl. The electrodes were visually placed on the nerve and then mechanically stepped through the nerve using a micropositioner (Kopf 650). The electrode signal was band pass filtered and fed into a spike detector. The times of spike peaks were recorded with 1-μs precision.

Nerve fibers were sought using a click (near 55 dB SPL) as a search stimulus. Upon contact with a fiber, a threshold tuning curve was generated using the Moxon (Kiang *et al.*, 1970) algorithm with a criterion of 0. The spontaneous rate of the fiber was then measured by counting the number of spikes over a 20-sec period. Units with a characteristic-frequency (CF) threshold more than two standard deviations away from the mean threshold for normal AN fibers (as found by Liberman and Kiang, 1978) were not included in the analysis.

An estimate of the number of false triggers in the spike record was derived from examination of the ISIs. Because the absolute refractory period of AN fibers prohibits ISIs smaller than about 0.5 msec (Gaumond *et al.*, 1982, 1983), intervals shorter than 0.5 msec were assumed to be false triggers. Spike records containing more than 0.1% of these short intervals were not included in the analysis.

The experimental data were recorded using pure-tone

stimuli at frequencies of 110, 220, 440, 880, 1500, 1760, and 3000 Hz and at levels of 5, 10, 15, 20, 25, 40, and 60 dB re threshold. The stimulus was presented once per second (400 msec on, 600 msec off, 2.5 msec rise and fall times) for 180 sec or until 20 000 spikes had been recorded, whichever came first. In order to avoid the possible complex effects of onset transients and adaptation, spikes that occurred during the first 20 msec following the onset of each stimulus and during the stimulus off-time were excluded. Recordings containing fewer than 5000 spikes were not included in the analysis. This unusually high requirement on the minimum number of spikes in the record ensures a reliable estimate of the ISI distribution.

B. Analysis

Auditory-nerve responses to low-frequency stimuli tend to occur at a specific phase with respect to the stimulus (Rose *et al.*, 1967; Kiang *et al.*, 1965). Thus ISI distributions display modes at intervals corresponding, roughly, to integer multiples of the stimulus period. The main goal of the analysis in this study was to accurately estimate modes of AN ISI distributions in order to quantitatively verify Ohgushi's (1978) observation that the intervals deviate from the stimulus period.

There were three main steps to the analysis of the ISI distributions. First, a histogram of the intervals was produced. Second, the mean interval of each mode in the histogram was estimated by fitting, in the maximum likelihood sense, a Gaussian mixture density to the histogram. Third, deviation of the interval modes from stimulus periods was characterized.

1. Histogram generation

The first step in the analysis was to generate histograms of the ISIs. The histogram binwidths were 2 μsec for frequencies less than 300 Hz and 1 μsec for frequencies above 300 Hz. Both first-order and all-order ISI histograms were computed.

2. Mode estimation

The second step in the analysis was to estimate the modes of the interspike interval distribution. A maximum likelihood (ML) estimation approach was implemented in which the interval distributions were modeled as a mixture of Gaussian densities with each mode in the distribution corresponding to a single density. This *mixture density* was fit (in the ML sense) to the interval histograms and the means of the individual Gaussian densities were taken as the estimated modes in the histogram. Two forms of mixture density were used, one for estimating individual modes in the interval distributions and another for estimating the fundamental mode (i.e., stimulus period) in the distributions (and subsequently the stimulus frequency). In the first case, the individual Gaussian densities in the mixture had mutually independent means and variances. In the second case, they were assumed to have harmonically related means and a common variance.

Because obtaining the ML estimates of the parameters is not analytically straightforward, we used the expectation-maximization (EM) algorithm, an iterative technique which converges to the ML estimate (Redner and Walker, 1984; Moon, 1996). Mathematical details of our implementation are included in the Appendix.

3. Mode offset

The third step in the analysis was to calculate the mode offset (MO), the difference between the mode estimate (ME) and the corresponding multiple of the stimulus period,

$$\mathrm{MO}_n = \mathrm{ME}_n - \frac{n}{f}, \tag{1}$$

where f is the frequency of the stimulus and n is the mode number (e.g., mode 1 contains intervals that are roughly one stimulus period in length and mode 2 contains intervals that are roughly 2 stimulus periods in length). Figure 3(e) illustrates the above calculation for MO_1.

In an effort to represent the total AN population response to the stimuli, pooled histograms were generated by summing all of the individual ISI histograms for a specific stimulus frequency. Mode estimates of the pooled histograms were calculated as well.

II. RESULTS

From six experiments, a total of 399 spike records from 164 fibers were obtained that met our requirements in terms of the minimum number of spikes, normal thresholds, and small number of false triggers. The majority (79%) of the records were from high spontaneous rate fibers. CFs ranged from 150 to 17 000 Hz.

Figure 2(a) shows a schematic representation of a stimulus wave form and a hypothetical spike record. ISIs are roughly integer multiples of the stimulus period. First-order intervals are those between consecutive spikes, second-order intervals are those between every other spike, etc.

Figure 2(b) shows a histogram of first-order ISIs from a single-unit recording generated with an 880-Hz tone stimulus. The modal distribution of intervals clearly reflects the synchronization of the spike train to the stimulus and the position of the modes provides information about the stimulus frequency (Rose *et al.*, 1967).

Figure 2(c) displays first-, second-, and third-order histograms based on the same spike record as in (b). As one would expect, first-order intervals are, on average, shorter than second- and third-order intervals and thus fall into earlier modes. There is, however, a great deal of overlap in the distributions of the intervals of different orders and the intervals of a particular order are not confined to a single mode in the histogram.

The histogram shown in Fig. 2(d) contains ISIs of all orders, and is thus termed the all-order ISI histogram. This histogram is sometimes referred to as the autocorrelation or autocoincidence histogram (Perkel *et al.*, 1967; Rodieck, 1967; Ruggero, 1973; Evans, 1983).

An important difference between first-order and all-order ISI histograms is their general shape: the size of the modes in the first-order ISI histogram tends to decrease as the mode number increases; the size of the modes in the all-order ISI histogram is relatively constant. In other words,

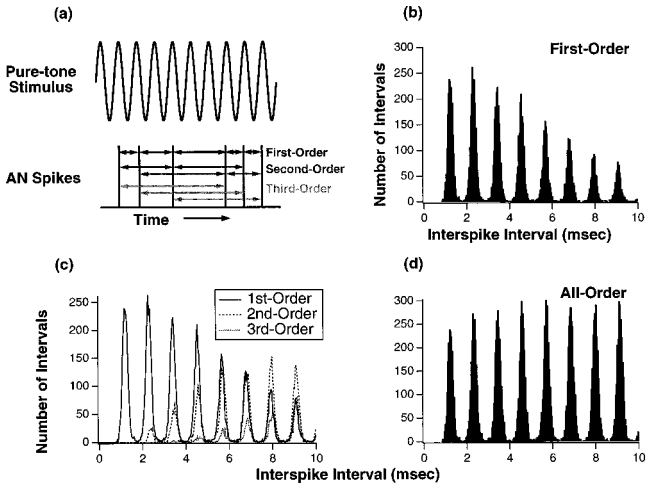

FIG. 2. Histogram generation. (a) is a schematized representation of a pure-tone stimulus and corresponding spike record from the auditory nerve. The order of the interspike interval is based on the number of spikes included in the interval: first-order intervals are those between consecutive spikes; second-order intervals are those between every other spike; third-order intervals are those between every third spike. (b) and (c) are histograms of the various types of interspike intervals. (d) is an interval histogram containing intervals of all orders, thus termed an all-order histogram. All of the histograms were generated from the same spike record. The stimulus was an 880-Hz pure tone at 84 dB SPL. The auditory-nerve fiber from which the recording was made had the following properties: CF: 2609 Hz; SR: 29 spikes/sec. The histograms have a binwidth of 40 μsec and the following number of total intervals: first-order: 10 305; second-order: 5696; third-order: 1643; all-order: 17 874.

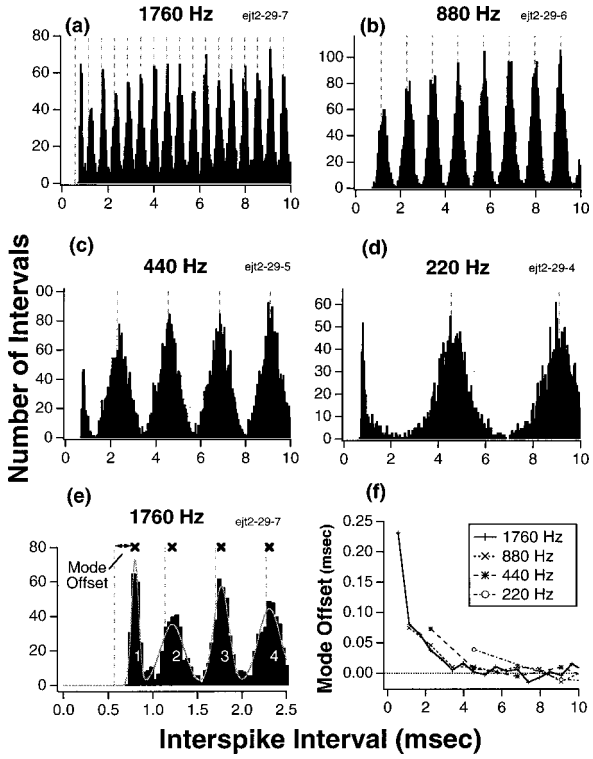

FIG. 3. Histogram mode offset. (a)–(d) are all-order ISI histograms of specified frequency with 40-μsec binwidths. Vertical dashed lines mark integer multiples of the stimulus period. (e) is a magnification of the first four modes of (a). The gray curve outlining the histogram is the ML estimate of the Gaussian mixture density corresponding to the histogram. The $\times$'s above the modes in (e) mark the ML estimate of the mode (the ML means of the individual Gaussian pdfs in the mixture density), obtained from Eq. (A7) operating on a histogram with 1-μsec binwidths. The mode offset is the deviation of the mode estimate from the corresponding integer multiple of the stimulus period. Each histogram was generated from a separate spike record but each spike record was obtained from the same auditory-nerve fiber. Fiber characteristics: CF=2602 Hz; SR=66 spikes/sec. The stimulus levels were all 10 dB re threshold, corresponding to the following levels for each spike record (in dB SPL): (a) 27; (b) 45; (c) 62; (d) 70. (f) displays the mode offsets from the histograms in (a)–(d). Mode offsets are primarily a decreasing function of interval, although, at corresponding intervals, lower frequency stimuli yield slightly larger mode offsets.

when one examines very long ISIs, few are first-order intervals. The all-order ISI histogram does not reflect the decaying trend because higher-order intervals are included and ''fill in'' the modes at long intervals.

In addition to the 399 spike records included in the analysis, 28 spike records that met our data requirements were excluded from the analysis because their histograms displayed peak-splitting. At moderate to high levels of pure-tone low-frequency stimulation, AN ISI histograms can exhibit two or sometimes three peaks per stimulus cycle instead of the normal one (Kiang and Moxon, 1972; Kiang, 1980; Liberman and Kiang, 1984; Kiang, 1990; Ruggero *et al.*, 1996). Most of the fibers from which we recorded did not exhibit this behavior within our stimulus-level range, but those records that did were excluded to simplify the analysis. In our data, peak splitting occurred primarily at stimulus frequencies below 440 Hz.

A. All-order interspike intervals

Figure 3(a)–(d) are all-order ISI histograms from one AN fiber for four different stimulus frequencies. Figure 3(e) is a magnification of the histogram in (a) with the mode estimates indicated by $\times$'s above each mode. As previously reported by Ohgushi (1978, 1983), the short intervals (early modes) are slightly longer than stimulus periods. This deviation is presumed to be at least partially due to the refractory period of the auditory-nerve fiber (Ohgushi, 1978). The mode offset for the first mode is labeled in the figure.

Mode offsets from the histograms in Fig. 3(a)–(d) are plotted in (f) as a function of ISI length. The mode offset decreases monotonically as the ISI increases [Fig. 3(f)] and for intervals greater than about 5 msec, mode offsets are insignificant. To a first approximation, the mode offsets depend primarily on ISI and not stimulus frequency. However, at any particular ISI $\lesssim$5 msec, lower frequency stimuli generally yield slightly larger mode offsets.

Figure 4(a)–(c) show how mode offsets vary with fiber CF, spontaneous rate (SR), and discharge rate (DR) for all-order histograms of 220 and 1760 Hz. The DR is typically a compressed function of stimulus level ranging from SR to saturation rate. The mode offsets in all-order ISI histograms do not obviously depend on the fiber CF, SR, or DR. Because of this, we decided to pool the ISI data (across fibers and stimulus levels) and use pooled histograms for testing the model presented in the next section. Because pooled histograms contain many more intervals than single-fiber histograms, they more accurately represent the underlying interval probability distributions. Figure 4(d) shows mode offsets grouped by the cat from which they were measured. There is a small, but statistically significant (see caption) variation across cats for the 1760-Hz data. Despite this trend, we de-

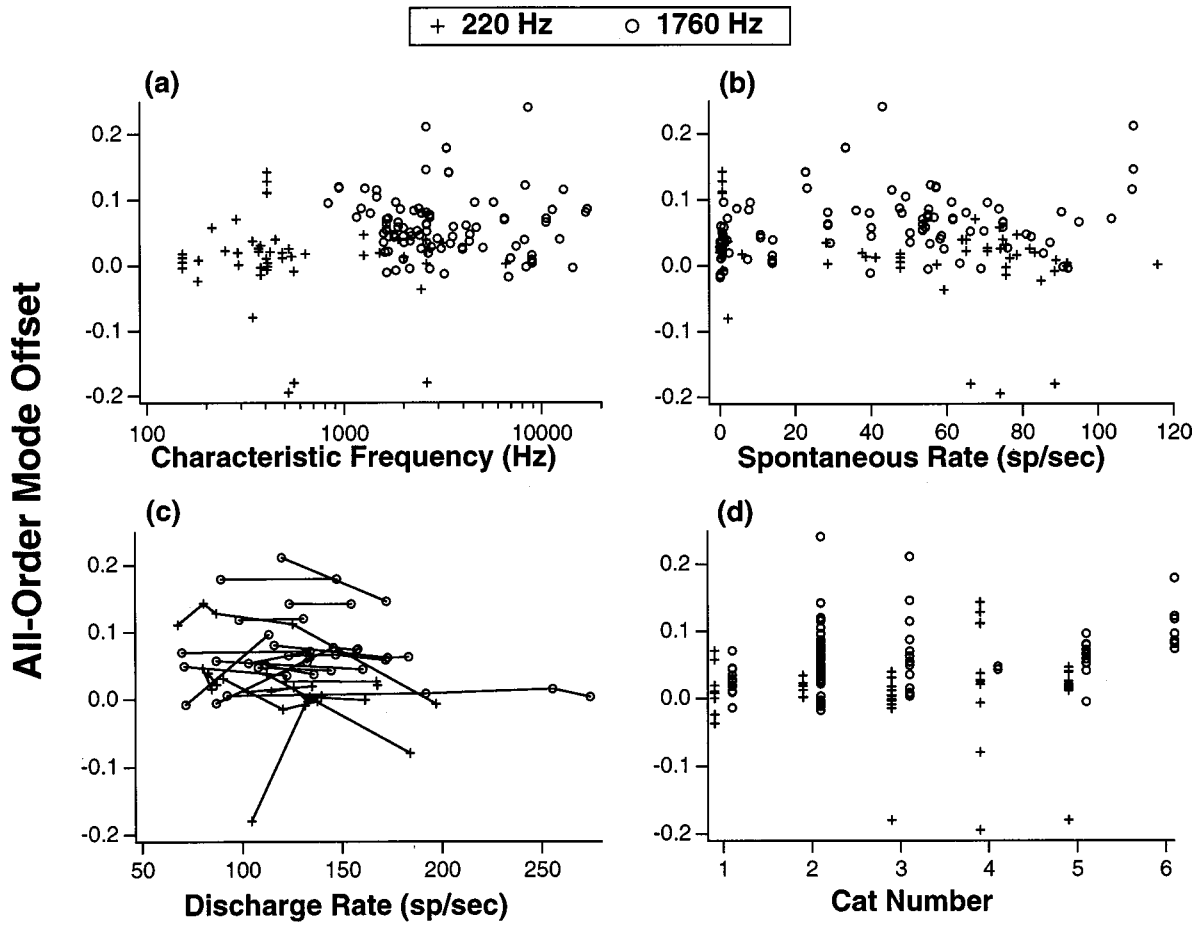

FIG. 4. Variation of mode offset across spontaneous rate, characteristic frequency, discharge rate, and cat. +'s mark the first mode offset of every individual 220-Hz data record and ○'s mark the second mode offset of every individual 1760-Hz data record. These frequencies and mode numbers were chosen as typical representatives of our low- and high-frequency data. In (c), lines connect mode offsets (plotted against DR) that were derived from the same fiber. (a), (b), and (c) show that there is no obvious dependence of mode offset on CF, SR, or DR. (d) shows how mode offset depends on the cat from which it was measured. One-way ANOVA on the data in (d), using the cat number as the individual factor, yielded the following p-values: $p=0.003$ for 1760 Hz and $p=0.139$ for 220 Hz. Although there were significant differences in mode offsets across cats, our decision to pool data across cats did not affect our general conclusions.

cided to also pool data across cats. Conclusions based on the analysis of data from individual cats were not different from those based on pooled data.

Figure 5 shows pooled histograms for six stimulus frequencies. The pooled histograms are much smoother than the single-fiber histograms due to the large number of intervals they contain. Mode offsets are clearly visible at intervals less than about 5 msec. Modes in the 110 and 220 Hz histograms show no offset because even the earliest modes occur at intervals greater than or near 5 msec.

Figure 6(a)–(e) show mode offsets as a function of interval length for pooled histograms as well as for single-fiber histograms. Figure 6(f) shows just the pooled histogram mode offsets for five stimulus frequencies. Although there is some variation across fibers in the size of mode offsets, the characteristics seen in the single-fiber data are evident in the pooled data: the mode offset is a monotonically decreasing function of ISI; mode offsets for intervals greater than about 5 msec are insignificant; and for a given ISI, lower frequency stimuli yield slightly larger mode offsets. Thus these characteristics seem to be general phenomena and not just particular to one type of auditory-nerve fiber or stimulus intensity.

B. First-order interspike intervals

The general shape of first-order histograms changes with fiber discharge rate while the shape of all-order histograms remains relatively constant (Cariani and Delgutte, 1996a). Figure 7 shows interval histograms from one AN fiber for a 220-Hz tone at three stimulus levels. As the SPL, and therefore discharge rate, increases, the average first-order interval gets shorter and the relative sizes of the histogram modes reflect this change: the later modes get smaller and the early modes get larger. In contrast, as the discharge rate increases, higher-order intervals fill in the modes that get depleted of first-order intervals so that the general shape of all-order histograms remains unchanged.

The main difference between mode offsets of first-order and all-order intervals is the presence of negative mode offsets for low stimulus frequencies in the first-order data. A negative mode offset means that a particular ISI mode is shorter than the corresponding stimulus-period multiple. This is illustrated in the first-order low-frequency histograms in Fig. 8(a) and (b): the modes occur slightly to the left of the stimulus period lines. Mode offset data for low-frequency

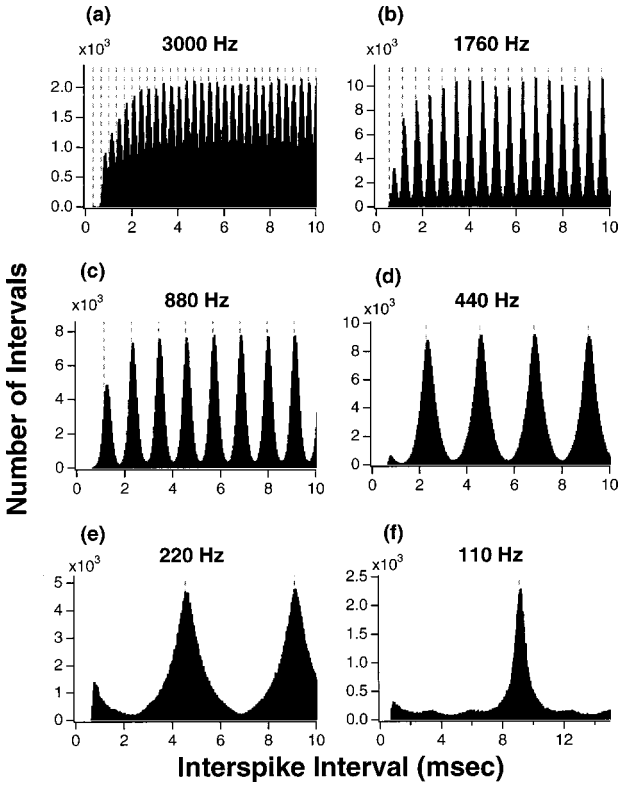

FIG. 5. Pooled histograms. (a)–(f) are pooled all-order ISI histograms of specified frequency. The histograms have the same format as Fig. 3(a)–(d). The intervals are pooled from the following number of fibers: (a) 26; (b) 75; (c) 58; (d) 47; (e) 33; (f) 10. Positive mode offsets are visible for intervals $\lesssim$5 msec (i.e., modes at intervals smaller than 5 msec are shifted slightly to the right of their corresponding stimulus-period multiple). Note that the scale of the abscissa in (f) is different than the other panels.

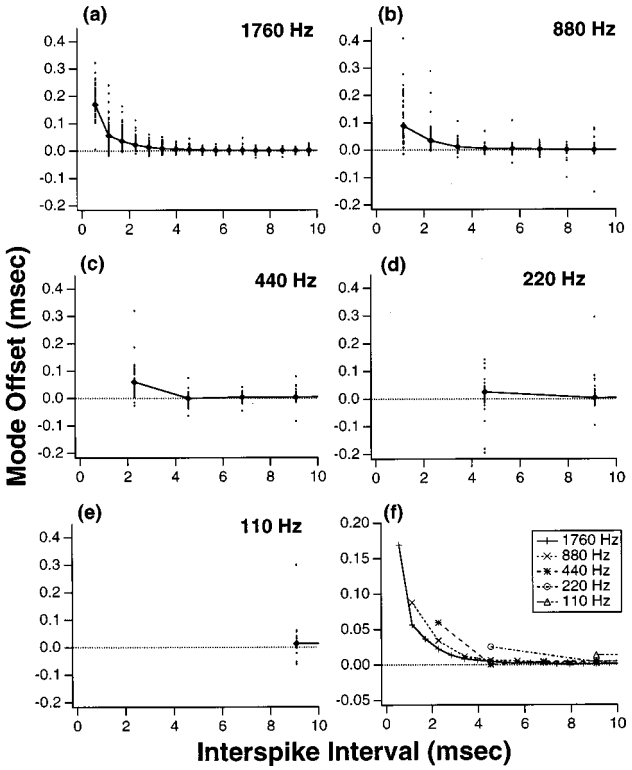

FIG. 6. Mode offsets of all-order ISI histograms. (a)–(e) display the mode offsets of pooled and individual histograms of specified frequency. Lines connect the mode offsets of pooled histograms and dots mark the mode offsets of individual histograms. (f) shows the pooled-histogram mode offsets for most of the experimental stimulus frequencies. Mode offsets in pooled histograms show the same trend with interval as those in individual histograms: mode offset is primarily a monotonically decreasing function of interval, although lower-frequency stimuli yield slightly larger mode offsets at corresponding intervals. Note that the scale of the ordinate in (f) is different than the other panels.

first-order ISI histograms are shown in panels (c)–(f). These mode offsets show a greater variability at low stimulus frequencies than those from all-order ISIs.

The negative mode offsets in low-frequency first-order ISI histograms are due to the presence of intervals in Mode *zero* (0). As Fig. 9(a) and (b) illustrate, an interval falls into Mode 0 if two spikes occur within the same half-period of the stimulus. Mode 0 is bounded on the left by the absolute refractory period and on the right by half the stimulus period. Due to the refractory period of the AN fiber, only low-frequency stimuli ($\lesssim$500 Hz) produce ISI histograms that contain a Mode 0. When an interval occurs in Mode 0, the preceding and following first-order intervals tend to be smaller than if just a single spike had occurred in that half-period. The relationship between consecutive intervals can be seen by examining a joint ISI histogram (Rodieck *et al.*, 1962), as shown in Fig. 9(c). The joint ISI histogram is a two-dimensional histogram which plots the ISI size against that of the previous ISI. It is displayed here as a gray scale image in which gray level indicates the number of interval pairs in a small square bin. As is the case for one-dimensional ISI histograms, the modal distribution of intervals is clearly evident in this plot: the intervals tend to cluster near integer multiples of the stimulus period. We will use the notation Mode(n,m) to refer to the mode in which the previous interval is in Mode n and the current interval is in Mode m. Examination of Mode(0,1), Mode(0,2), and Mode(0,3) shows that if the previous interval lies in Mode 0, the current interval tends to be shorter than the corresponding stimulus-period multiple. Also, examination of Mode(1,0), Mode(2,0), and Mode(3,0) shows a similar dependency on mode 0 for the current interval. Thus in a first-order ISI histogram, the presence of intervals in Mode 0 effectively biases the other modes toward smaller values.

Offsets of higher modes in all-order ISI histograms are not affected by the presence of intervals in Mode 0 because these histograms include higher-order intervals. For every first-order interval that is shortened by the presence of an interval in Mode 0, there is a second-order interval (which includes the one in Mode 0) that is lengthened. This can be seen schematically in Fig. 9(a). The lengthened second-order interval falls into the same mode as the shortened first-order interval and counteracts its effect on the mode offset.

The effect of Mode 0 on first-order ISI histograms can be quantified by selecting only those intervals that do not precede or follow intervals in Mode 0. This conditioning was performed on all of the 220-Hz stimulated spike records and then histograms of the conditioned intervals were generated. The distribution of the mode estimates for Mode 1 in these conditioned interval distributions is plotted in Fig. 9(d) along with similar unconditioned distributions from first-order and all-order ISI histograms. The alignment of the mode-estimate

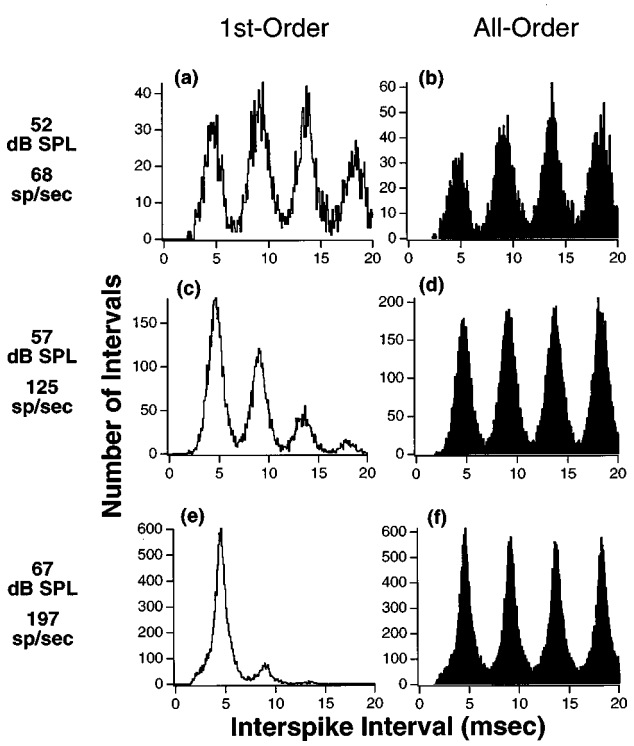

FIG. 7. A series of 220-Hz ISI histograms (from the same auditory-nerve fiber) over a range of discharge rates. Stimulus level and fiber discharge rate are indicated to the left of the plots. First-order ISI histograms are plotted in (a), (c), and (e). All-order ISI histograms are plotted in (b), (d), and (f). Fiber characteristics: CF: 409 Hz; SR: 0.7 spikes/sec; threshold at 220 Hz: 47 dB SPL. The histogram binwidths are 80 μsec.

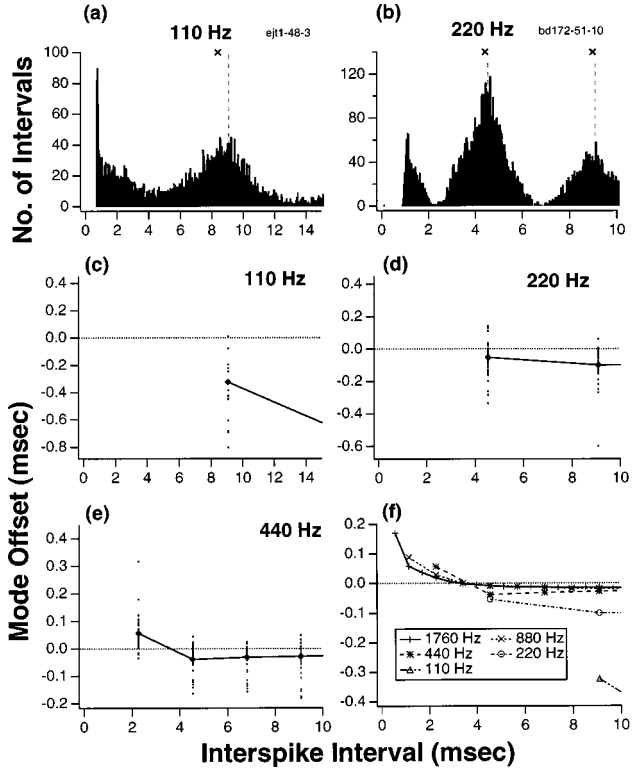

FIG. 8. Low-frequency first-order ISI histograms display negative mode offsets. (a) and (b) show first-order ISI histograms in the same format as those in Fig. 3. The $\times$'s above the modes mark the ML estimate of the mode. (c), (d), and (e) show mode offsets from first-order ISI histograms in the same format as Fig. 6. (f) shows the pooled-histogram mode offsets for most of the stimulus frequencies. Below $\sim$500 Hz, first-order ISI histograms display large negative mode offsets (i.e., modes are shifted slightly to the left of their corresponding stimulus-period multiple), in contrast to the insignificant mode offsets present in low-frequency all-order ISI histograms. Note that the scales of the axes vary across panels.

distributions for all-order and conditioned first-order ISIs indicates that the presence of intervals in Mode 0 accounts for nearly all of the difference between mode estimates in all-order and first-order ISI histograms.

The negative correlation between consecutive intervals is a characteristic of our data that is not well documented in the literature. The joint ISI histogram in Fig. 9(c) shows a clear dependence between the previous and current first-order ISI. All of the modes are oval with the long axis going diagonally from the top left to the bottom right of the figure. This means that if the previous interval was shorter than average, the current interval will tend to be longer than average and vice versa. This is a consequence of phase-locking: every interval longer than the stimulus period must be compensated for by a shorter interval if the spikes are to remain phase-locked.

III. MODEL

Our primary objective in formulating a (central) model for octave matching is to evaluate how physiological constraints in the auditory periphery, i.e., deviations in AN ISIs, affect the central processor. This is best accomplished with simple models that have few, if any, free parameters, so that the effect of the peripheral physiological behavior is not clouded. With this in mind, we developed a temporal model for pure-tone octave matching based on Ohgushi's (1983) model.

A. Model for estimating pure-tone frequency

The basic assumption of the model is that perceived pitch is equal to a biased estimate of the stimulus frequency derived from AN ISIs. The bias in the frequency estimate comes from the mode offsets in the ISI histograms. Frequency estimates were derived from interval histograms using the EM algorithm [Eqs. (A1) and (A2)], assuming a mixture density of Gaussians with harmonically related means [Eq. (A9)],

$$\hat{f} = \frac{1}{\hat{\mu}_{\mathrm{ML}}(N_{\max})}, \tag{2}$$

where $\hat{f}$ is the estimate of stimulus frequency f, $\hat{\mu}_{\mathrm{ML}}$ is the ML estimate of the fundamental mean in the mixture density [μ^+ in Eq. (A10)], and $N_{\max}$ is the number of modes included in the calculation [M in Eqs. (A10) and (A11)]. If the modes occur exactly at integer multiples of the stimulus period, $\hat{\mu}_{\mathrm{ML}}$ will equal the stimulus period and the frequency estimate will be equal to the stimulus frequency.

Estimates for each stimulus frequency were calculated using pooled ISI histograms and their deviations from the stimulus frequency were derived as follows:

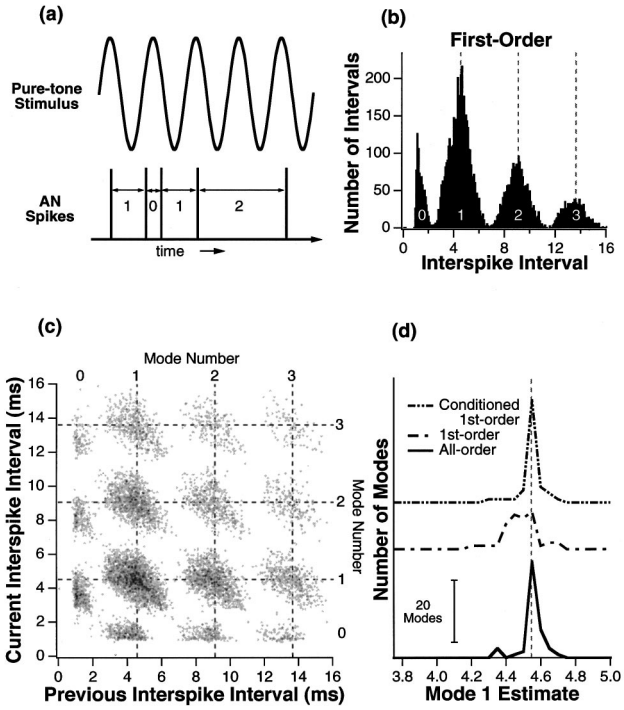

FIG. 9. Intervals in Mode 0. (a) is a schematic representation of a stimulus and a corresponding spike record. The number between the spikes in (a) indicates the mode of the histogram, shown in (b), to which the first-order interval belongs. (b) is a first-order ISI histogram and (c) is a joint first-order ISI histogram of the same auditory-nerve spike record. The joint ISI histogram is a two-dimensional histogram which plots ISI size against that of the previous ISI. It is displayed as a gray-scale image in which gray level indicates the number of interval pairs in a small square bin. The dashed lines in (b) and (c) mark integer multiples of the stimulus period. The stimulus was a 220-Hz pure tone at 61 dB SPL. The fiber characteristics are: CF: 379 Hz; SR: 76 spikes/sec; threshold at 220 Hz: 36 dB SPL. The histogram binwidth is 80 μsec in (b) and 64 μsec for both dimensions in (c). (d) shows the distribution of the estimates of Mode 1 in 50 individual 220 Hz histograms for all-order, first-order, and conditioned first-order ISIs. The condition in the third case is that the intervals do not follow or precede an interval in Mode 0. The traces are vertically offset for clarity and the vertical bar in the lower left denotes 20 modes. The binwidth of the mode estimate distribution is 50 μsec. The vertical dashed line marks the stimulus period. Negative mode offsets in low-frequency first-order ISI histograms are due to shortened intervals caused by intervals in Mode 0 (i.e., two spikes within the same half-period of the stimulus).

$$\hat{f}_{\mathrm{DEV}} = 100 \cdot \frac{\hat{f} - f}{f}, \tag{3}$$

where $\hat{f}_{\mathrm{DEV}}$ is the percent deviation of the frequency estimate and $\hat{f}$ is the frequency estimate.

$\hat{f}_{\mathrm{DEV}}$ is plotted versus stimulus frequency in Fig. 10 for three values of $N_{\max}$. For both all-order intervals and first-order intervals, $\hat{f}_{\mathrm{DEV}}$ is a decreasing function of stimulus frequency.[2] This trend is a direct result of the dependence of mode offset on interval size. As the stimulus frequency increases, the stimulus period decreases and the offset for any given mode number increases. This results in a larger estimate of the fundamental period, $\hat{\mu}_{\mathrm{ML}}$, and hence, a decrease in the frequency estimate. For all-order intervals, $\hat{f}_{\mathrm{DEV}}$ is always negative because mode offsets are always positive. On the other hand, first-order ISI intervals yield positive

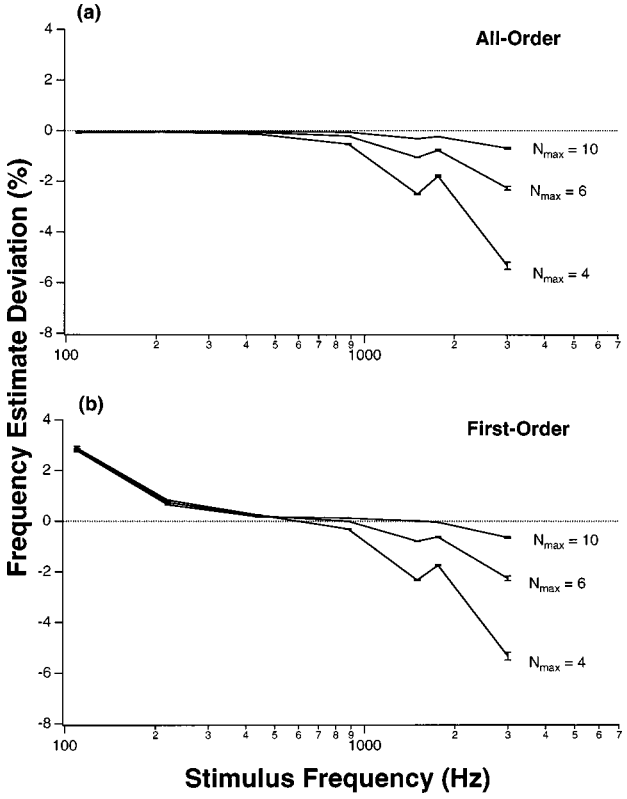

FIG. 10. Frequency estimate deviation ($\hat{f}_{\mathrm{DEV}}$) vs frequency. (a) displays $\hat{f}_{\mathrm{DEV}}$ calculated from pooled all-order ISI histograms for the values of $N_{\max}$ shown next to each trace. (b) displays $\hat{f}_{\mathrm{DEV}}$ calculated from pooled first-order ISI histograms. For frequencies $\gtrsim$500 Hz, $\hat{f}_{\mathrm{DEV}}$ is a decreasing function of both frequency and $N_{\max}$. Error bars show an estimate of the standard error of $\hat{f}_{\mathrm{DEV}}$. The estimate was calculated using the bootstrap technique (Efron and Tibshirani, 1993): 50 simulations of the frequency estimate were calculated [Eq. (2)] in which pooled histograms were generated by randomly choosing (with replacement) spike records of individual stimulus presentations. The standard deviation of the frequency estimates from these simulations is an estimate of the standard error of the mean.

$\hat{f}_{\mathrm{DEV}}$'s for low stimulus frequencies because the histograms contain negative mode offsets.

Figure 10 also shows that the free parameter $N_{\max}$ greatly influences the frequency estimate at high frequencies. For low values of $N_{\max}$, the frequency estimate has a relatively large bias from the mode offsets of the lower modes. Since the mode offset is minimal in the higher modes, the frequency estimate becomes less biased as $N_{\max}$ increases. On the other hand, $N_{\max}$ has little effect on the estimates at low frequencies because either the mode offsets are consistently small for all modes (all-order ISIs), or the higher modes contain few intervals and thus little weight in the calculation of $\hat{f}$ (first-order ISIs).

B. Model for octave matching

The model operates on two sets of pooled ISI histograms to predict the size of the pitch interval separating their respective stimuli. The pitch interval prediction is obtained by comparing the frequency estimate [Eq. (2)] of a low-frequency tone, f_1, with the frequency estimate of a high-frequency tone, f_2. The model predicts that f_1 and f_2 are separated by a subjective octave when,

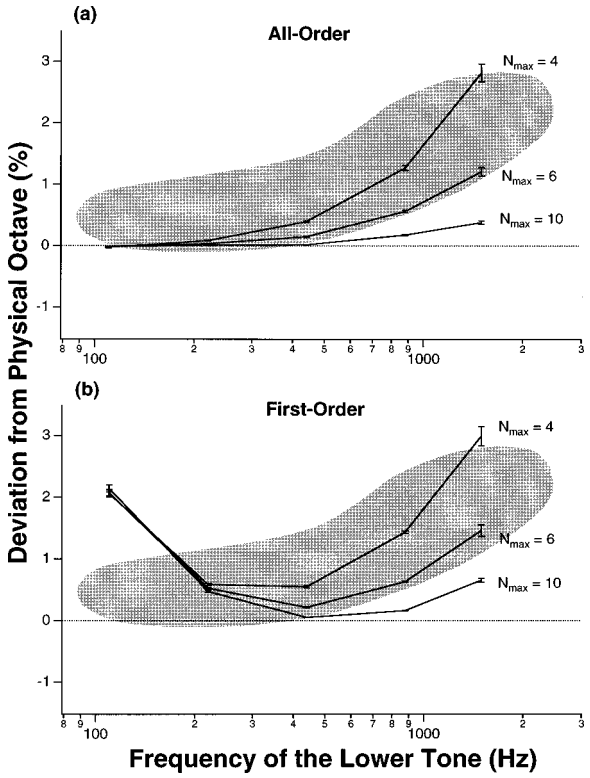

FIG. 11. Model predictions of the octave enlargement effect. The model predictions are based on pooled histograms for each stimulus frequency. Error bars show the estimated standard error of the subjective octave prediction and were calculated in a similar manner to those in Fig. 10. (a) shows the model predictions for all-order ISIs and several values of $N_{\max}$. (b) shows the same for first-order ISIs. Although low-frequency data are not well predicted by the model, the predictions based on all-order intervals are within the range of the psychoacoustic data with $N_{\max} \approx 4$–6.

$$\hat{f}_2 = 2 \cdot \hat{f}_1 . \tag{4}$$

The model algorithm can be interpreted graphically as attempting to align the modes of the scaled (by two) f_1 histogram with the modes of the f_2 histogram. An octave is predicted when the modes are best aligned.

The deviation of the model prediction (i.e., ''subjective octave'') from the physical octave, Δ_{SO}, is:

$$\Delta_{SO} = 100 \cdot \frac{2 \cdot \hat{f}_1 - \hat{f}_2}{f_1}, \tag{5}$$

for f_1 and f_2 separated by a physical octave.

Model predictions are shown in Fig. 11 for several values of $N_{\max}$. As in the frequency estimate (Fig. 10), variation in $N_{\max}$ results in large changes in model predictions at high frequencies. As $N_{\max}$ increases, more modes with little or no offset are included in the frequency estimates and the resulting deviation of the subjective octave decreases.

When all-order ISIs are used as model input, the model predicts an octave enlargement in general agreement with the psychoacoustic data [Fig. 11(a)] at most frequencies for $N_{\max} \approx 4$–6. At low frequencies, the model underestimates the psychoacoustic octave enlargement for all values of $N_{\max}$, but its predictions are still within the range of the psychoacoustic data. At 1500 Hz, the model predicts the range of psychoacoustic data simply by varying $N_{\max}$ from 4 to 6.

When operating on first-order ISIs, the model, with $N_{\max} = 4$, predicts an octave enlargement in general agreement with the psychoacoustic data, except at 100 Hz, where the model predicts a much larger deviation [Fig. 11(b)]. In addition, the model predicts a decrease in deviation as frequency increases (at low frequencies) but the psychoacoustic data show the opposite trend. The model's predicted octave enlargement at low frequencies is due to the negative mode offsets in the first-order ISI histograms. The frequency estimates of these low-frequency tones are higher than the true frequency [see Fig. 10(b)] and when they are matched to estimates of (upper) tone frequencies that produce little or no negative mode offsets, an octave enlargement is predicted.

In summary, the model, operating on first- or all-order ISIs with $N_{\max} \approx 4$–6, predicts the octave enlargement effect at mid- to high frequencies. At low frequencies, the model underestimates the effect when operating on all-order ISIs and overestimates it when operating on first-order ISIs.

IV. DISCUSSION

A. Auditory nerve physiology

We have shown that, in response to low-frequency pure tones, AN ISIs deviate systematically from integer multiples of the stimulus period. When quantitatively expressed as mode offsets in ISI histograms [Eq. (1)], the deviations are positive for ISIs less than 5 msec and decrease with increasing ISI until they become insignificant for ISIs greater than 5 msec. In addition, first-order intervals show negative mode offsets for stimulus frequencies less than 500 Hz. These robust phenomena exist for all CFs and SRs and over a wide range of stimulus levels. Our quantitative characterization of these physiological properties provides a solid basis to study how they can effect any temporally based estimate of the stimulus frequency.

Our data and analyses suggest that positive and negative mode offsets in ISI histograms arise from fundamentally different mechanisms. We showed in Fig. 9 that negative mode offsets, seen in first-order ISI distributions for low-frequency stimuli, are due to the occurrence of multiple spikes within the same half-period. In order to maintain phase-locking between the stimulus and AN response, the intervals before and after these multiple spikes tend to be slightly shorter, on average, than multiples of the stimulus period. Positive mode offsets, on the other hand, have been attributed to the refractory properties of the neurons (Ohgushi, 1983, 1978) and, specifically, to a reduction in conduction velocity during the relative refractory period (de Cheveigné, 1985). While these ideas are reasonable, it is important to note that the delays causing the offsets could arise at any point from the basilar membrane to the AN fiber.

A physiological characteristic that we saw in our data but ignored in the analysis is peak splitting. This phenomenon causes two or more modes of intervals to be present within a single stimulus period of an ISI histogram instead of the usual one mode per stimulus period. The multiple modes

are the result of the AN response going through a change in phase (as much as 180°) relative to the stimulus as the stimulus level is increased (Kiang and Moxon, 1972; Johnson, 1980; Kiang, 1980, 1990).

At first sight, peak splitting would seem to wreak havoc on temporal models for pitch. At stimulus intensities where peak splitting occurs, a model operating on the intervals would estimate multiple frequencies, depending on the degree of phase shift. However, because the stimulus intensity at which peak splitting occurs depends on both fiber CF and stimulus frequency, only a small fraction of AN fibers will exhibit peak splitting at the same stimulus intensity. So, in a temporal model for pitch that operates on intervals pooled from fibers across many CFs, peak splitting most likely has a small effect on the pooled interval distribution, leaving the overall frequency estimate relatively unchanged.

B. Temporal models for octave matching and pitch perception

Our model for octave matching makes pitch-interval judgments based on frequency estimates of two tones. Each frequency estimate is computed from a pooled AN ISI histogram by fitting it with a Gaussian mixture density with harmonically related means. An octave is predicted when the frequency estimate of one tone is twice that of another tone. The model predicts the octave enlargement effect except at very low frequencies, where it slightly underestimates the effect when operating on all-order ISIs and overestimates the effect when operating on first-order ISIs.

1. Comparison with Ohgushi's model

Our model is similar to Ohgushi's (1983) model for octave matching. The basic elements of the models are the same although there are three primary differences in his implementation: he uses first-order ISIs only; his frequency estimates were based on just the first two modes of the histogram while we used a variable number ($N_{\max}$) of modes; and he calculates frequency estimates from the modes with weights obtained by fitting the model predictions to the psychoacoustic data and adjusting two free variables. These differences lead to different predictions at low frequencies when operating on first-order ISIs. Ohgushi's model predictions are consistent with the psychoacoustic data on the octave enlargement for all frequencies while our model has difficulties at very low frequencies ($<$200 Hz). It should be pointed out that with two free parameters, Ohgushi had more flexibility with which to fit the data.

In addition, Ohgushi operated on rather coarse (100-μsec binwidth) single-fiber ISI histograms from only four AN fibers, published by Rose *et al.* (1967, 1968), while our model predictions were based on fine-resolution pooled histograms which represent a large number of fibers and spikes. Analysis of our data using Ohgushi's method yields results similar to his.

2. Interpretation of N_{max}

The one free parameter in our model is $N_{\max}$, the number of modes over which the frequency estimate is calculated. $N_{\max}$ can greatly affect the frequency estimate and resulting octave interval prediction. Rather than treating it as an arbitrary free parameter, it would be nice to give $N_{\max}$ a physiological or psychoacoustic interpretation. If one assumes that pure-tone pitch is based on the interspike interval distribution of AN spikes, $N_{\max}$ could be related to the minimum tone duration required to elicit a pitch.

A number of psychoacoustic studies have investigated the effect of tone duration (for very short tones) on pitch (Doughty and Garner, 1947, 1948; Pollack, 1967) and the ability to recognize musical melodies (Patterson *et al.*, 1983). A general result from these studies is that, for tones below about 1000 Hz, a minimum number of cycles (6 ± 3) is required to elicit a stable pitch or to achieve maximum performance in melody recognition. On the other hand, above 1000 Hz, a minimum tone duration ($\sim$10 msec) is required to elicit a stable pitch (Gulick *et al.*, 1989). If $N_{\max}$ is taken as the number of cycles required to elicit a pitch for low frequencies, our empirically derived range for $N_{\max}$ ($\sim$4–6) is consistent with this result. It should be noted that our analyses do not include the first 20 msec of the AN response. Verification of such a relationship between $N_{\max}$ and minimum duration for pitch would require a study which carefully addresses the effects of adaptation and ringing of the cochlear filter for short-duration tones. Nevertheless, our results suggest that there may be a link between the two ''integration times.''

Another consideration related to $N_{\max}$ is that the overall neural delay required to perform octave matches for low-frequency tones may be physiologically implausible. For example, with $N_{\max}=5$, the total delay required to obtain a frequency estimate for a 60-Hz tone is 83 msec. There is however, evidence for the existence of a lower limit to musical pitch around 90 Hz (Biasutti, 1997), which reduces the maximum required neural delay in our model to about 55 msec.

3. An alternative model for octave matching

We developed and implemented a second model for octave matching following a suggestion by Hartmann (1993). Noting that the scaling factor of two in Ohgushi's (1983) model for octave matching is arbitrary, Hartmann suggested that a more physiologically grounded model is one that attempts to correlate the ISIs without first scaling those from the low-frequency tone. The comparison is then made between two tones using only the intervals from the even modes in the ISI histogram for the high-frequency tone. This model can be interpreted graphically as attempting to align the modes of the f_1 histogram with the even modes of the f_2 histogram.

Despite the appeal of Hartmann's suggestion, we found that this model fails to predict the octave enlargement phenomenon and instead predicts a slight octave contraction. The cause of this prediction can be seen by examining the mode offsets at the same interval size in Fig. 6(f). In an octave comparison between two tones separated by a physical octave, the second mode in the ISI histogram for the high-frequency tone has a smaller mode offset than the first mode of the lower frequency tone. This causes the sub-octave estimate of the higher tone to be slightly higher than

the frequency estimate of the lower tone. In order to achieve a subjective octave match, the higher frequency tone needs to be slightly lower in frequency than the physical octave above the lower tone. This results in a predicted octave contraction rather than an octave enlargement.

4. Temporal models for pitch

Our model for octave matching is similar to existing models for frequency discrimination (Siebert, 1970; Goldstein and Srulovicz, 1977) in that they are based on the idea that pitch is a frequency estimate of a pure-tone stimulus based on temporal discharge patterns. Both Siebert (1970) and Goldstein and Srulovicz (1977) represent AN activity with nonhomogeneous Poisson processes. Siebert's main objective was to investigate the limitations in frequency discrimination of an optimal processor operating on spike times of modeled AN activity. He discovered that there is enough temporal information in the all-order intervals from a small number of auditory-nerve fibers to account for the psychoacoustic data on frequency discrimination. However, the slope of the predicted frequency discrimination limen versus stimulus duration far exceeded psychoacoustic performance. Goldstein and Srulovicz showed that a similar model operating on only first-order ISIs better predicts the dependence of the psychoacoustic frequency difference limen on stimulus duration.

The essential difference between these models and ours is that the optimal processor models give unbiased (ML) estimates of the stimulus frequency. The octave matching model relies on biased frequency estimates which result from the assumption that modes of the ISI distribution are harmonically related to the stimulus period. These biases were lacking in the Siebert and Goldstein models because refractory effects were not included in the Poisson processes.

An important distinction within the class of temporal models for pitch is between those that operate on first-order ISIs and those that operate on all-order ISIs. All-order intervals can be obtained from a spike train using delay lines and coincidence detectors as proposed by Licklider (1951). Analysis of first-order intervals, on the other hand, requires an extra stage of processing to eliminate the higher-order intervals. This makes a model based on first-order ISIs less appealing, physiologically, than one that operates on all-order intervals. A further advantage for a model operating on all-order intervals may be the fact that all-order interval distributions tend to be more stable across stimulus level than first-order interval distributions, as shown in Fig. 7.

We have seen in this study, as have Goldstein and Srulovicz (1977), that model predictions based on one or the other type of ISI can yield different results. Goldstein and Srulovicz show that in the context of frequency discrimination, operating on first-order ISIs results in a better fit to the psychoacoustic data than operating on all-order ISIs. Also, psychophysical experiments attempting to distinguish between the two kinds of ISI-based pitch models have favored first-order ISIs (Kaernbach and Demany, 1996). Kaernbach and Demany used random click train stimuli with specified first- and higher-order interclick distributions and found that discrimination between those stimuli and randomly distributed clicks was better for regular first-order interclick intervals. Results of our study do not strongly favor either first- or all-order intervals. Model predictions based on first-order ISIs overestimate the subjective octave at low frequencies and those based on all-order ISIs slightly underestimate the subjective octave. The trend with frequency, however, of those predictions based on all-order ISIs is more consistent with the psychoacoustic data. Nevertheless, we can not rule out models based on intermediate combinations of the two types of intervals or other more complex models, such as Ohgushi's, which predict the octave enlargement based on first-order ISIs. Also, it is conceivable that different physiological cues may be responsible for discriminating frequency than for matching octaves or for performing other tasks involving musical pitch.

Our model for octave matching is also analogous to the optimum processor introduced by Goldstein (1973). He uses a template of Gaussian density functions spaced harmonically along the spectral axis to fit, in the ML sense, the excitation pattern produced by a complex tone. Although his implementation operates on spectral excitation, there is nothing inherent to the model that precludes its operation on interval distributions. Our model is similar to his in that it fits harmonic templates to noisy and possibly inharmonic data. In Goldstein's case, the inharmonicity only arises if the stimulus contains inharmonically related partials. In our case, the inharmonicity is always present and comes from mode offsets in ISI distributions.

Although we have concentrated solely on temporal models, we should not forget that there exist alternative schemes for octave matching, namely rate/place models. Terhardt's (1971, 1974) model for virtual pitch theoretically predicts the octave enlargement effect and is discussed in that light by Hartmann (1993). Terhardt suggests that through pervasive listening to natural tone complexes we develop memory templates of tonotopic excitation patterns and that we make octave judgments based on the places of maximum excitation in these memory templates. He further postulates that these templates are stretched, i.e., the places of maximum excitation corresponding to the harmonics in the tone complex are shifted (upwards in frequency) due to masking effects caused by the presence of the lower harmonics. Thus the subjective octave, based on these stretched templates, is slightly larger than the physical octave. There is some evidence that lower-frequency masking stimuli can lower the CF of an AN fiber (Kiang and Moxon, 1974; Delgutte, 1990) but the effect of masking depends on the overall stimulus level and on the relative levels of the signal and masker. It is not known whether these effects are quantitatively adequate to validate Terhardt's theory.

V. CONCLUSION

We have shown that, in response to low-frequency pure tones, AN ISIs less than 5 msec are systematically larger than integer multiples of the stimulus period and, for frequencies less than 500 Hz, first-order ISIs are smaller than integer multiples of the stimulus period. These deviations result in biased estimates of frequency and can lead directly to a prediction of the octave enlargement effect by temporal-

based models. Thus computational models for pitch may have to incorporate detailed physiological properties of the auditory periphery, such as refractoriness, in order to predict effects such as octave enlargement.

Correlating psychoacoustic behavior in the context of pitch effects with physiological responses to the same set of stimulus conditions can lead to valuable insights into the neurophysiological basis of pitch. Here, we have examined models for octave matching operating on two forms of ISIs and, although no model is completely satisfactory, one of them, operating on all-order intervals, comes close to predicting the octave enlargement effect over its entire frequency range. This result is consistent with the notion that musical pitch is based on a temporal code.

ACKNOWLEDGMENTS

The authors would like to thank Drs. P. A. Cariani, J. J. Guinan, M. C. Liberman, and three anonymous reviewers for comments on previous revisions of this manuscript. Dr. L. D. Braida suggested the use of ML estimation for analyzing interval histograms and provided helpful guidance on the EM algorithm. This work was supported by Grant Nos. R01 DC02258 and T32 DC00038 from the NIDCD, NIH.

APPENDIX: THE EM ALGORITHM

In order to find the ML estimates of parameters in the Gaussian mixture densities described in Eqs. (A3), (A4), and (A9), we used the iterative EM algorithm (Redner and Walker, 1984; Moon, 1996). This Appendix briefly describes the EM algorithm and shows the mathematical details of our implementation.

The general idea of the EM algorithm is as follows: Ideally, one would like to obtain ML estimates for parameters, $\mathbf{\Phi}$, of a pdf, $f(\mathbf{y}|\mathbf{\Phi})$, over the complete sample space, $\mathbf{Y}$. At hand, however, is an incomplete data sample, $\mathbf{x}$, which is insufficient to compute and maximize the log-likelihood function over $\mathbf{Y}$. In our case, the vector $\mathbf{x}=\{x_k:k=1,N\}$ is the interspike interval distribution where x_k is a single interval and N is the number of intervals. The data sample is incomplete because the component density in the mixture from which a particular interval arises is not known. A complete data sample, $y_k=(x_k,i_k)$, would consist of the interspike interval, x_k, and an indicator, i_k, of the component density from which x_k originated. So, instead of maximizing the log-likelihood over $\mathbf{Y}$, the EM algorithm maximizes the expectation of $\log(f(\mathbf{y}))$ given the data, $\mathbf{x}$, and the current parameter estimates, $\mathbf{\Phi}'$. The two-step EM algorithm is,

$$\text{E-step: Determine: } Q(\mathbf{\Phi}|\mathbf{\Phi}')=E(\log(f(\mathbf{y}|\mathbf{\Phi}))|\mathbf{x},\mathbf{\Phi}'). \tag{A1}$$

$$\text{M-step: Choose: } \mathbf{\Phi}^+\in\arg\max_{\mathbf{\Phi}} Q(\mathbf{\Phi}|\mathbf{\Phi}'). \tag{A2}$$

With each iteration, the next parameter estimates, $\mathbf{\Phi}^+$, replace the current parameter estimates, $\mathbf{\Phi}'$, until convergence or until the difference between sequential sets of parameters is less than some designated ϵ. Our implementation of the EM algorithm follows directly from equations developed in Redner and Walker (1984), so we refer the reader to their paper for details on the preliminary derivations and focus here on details pertinent to our implementation.

1. Gaussians with independent means and variances

To characterize the individual modes of ISI histograms, we modeled each interval distribution as a mixture of M-weighted, univariate Gaussian probability density functions (PDF) with independent means and variances,

$$p(x|\mathbf{\Phi})=\sum_{i=1}^{M}\alpha_i p_i(x|\phi_i), \tag{A3}$$

where x is a single interval in the distribution, $\mathbf{\Phi}=(\alpha_1,\ldots,\alpha_M,\phi_1,\ldots,\phi_M)$, α_i is a non-negative weighting, $\Sigma_{i=1}^{M}\alpha_i=1$, and p_i is a univariate Gaussian pdf with parameters $\phi_i=(\mu_i,\sigma_i)$,

$$p_i(x|\phi_i)=\frac{1}{\sqrt{2\pi}\sigma_i}e^{(x-\mu_i)^2/2\sigma_i^2}. \tag{A4}$$

For a mixture of Gaussian densities in the form of Eqs. (A3) and (A4), Redner and Walker (1984) derive $Q(\mathbf{\Phi}|\mathbf{\Phi}')$ in their Eq. (4.1),

$$Q(\mathbf{\Phi}|\mathbf{\Phi}')=\sum_{i=1}^{M}\left[\sum_{k=1}^{N}\frac{\alpha_i' p_i(x_k|\phi_i')}{p(x_k|\mathbf{\Phi}')}\right]\log\alpha_i + \sum_{i=1}^{M}\sum_{k=1}^{N}\log p_i(x_k|\phi_i)\frac{\alpha_i' p_i(x_k|\phi_i')}{p(x_k|\mathbf{\Phi}')}, \tag{A5}$$

where N is the number of data samples (number of intervals in the histogram), and the other variables are as defined in Eq. (A3). Note that maximization of $Q(\mathbf{\Phi}|\mathbf{\Phi}')$ with respect to the weights, α_i, is independent of the parameters, ϕ_i, of the individual densities. Maximizing $Q(\mathbf{\Phi}|\mathbf{\Phi}')$ with respect to the individual parameters leads to the following relations, which are special cases of Eqs. (4.5), (4.8), and (4.9) in Redner and Walker (1984),

$$\alpha_i^+=\frac{\alpha_i'}{N}\sum_{k=1}^{N}\frac{p_i(x_k|\phi_i')}{p(x_k|\mathbf{\Phi}')}, \tag{A6}$$

$$\mu_i^+=\left\{\sum_{k=1}^{N}x_k\frac{\alpha_i' p_i(x_k|\phi_i')}{p(x_k|\mathbf{\Phi}')}\right\}\Bigg/\left\{\sum_{k=1}^{N}\frac{\alpha_i' p_i(x_k|\phi_i')}{p(x_k|\mathbf{\Phi}')}\right\}, \tag{A7}$$

$$\sigma_i^{+2}=\frac{\left\{\sum_{k=1}^{N}(x_k-\mu_i^+)^2\frac{\alpha_i' p_i(x_k|\phi_i')}{p(x_k|\mathbf{\Phi}')}\right\}}{\left\{\sum_{k=1}^{N}\frac{\alpha_i' p_i(x_k|\phi_i')}{p(x_k|\mathbf{\Phi}')}\right\}}, \tag{A8}$$

where α_i^+, μ_i^+, and σ_i^{+2} are the parameter values used in the subsequent iteration of the algorithm. In this form of mixture density, the weights, means, and variances of the individual densities in the mixture are mutually independent. This form was used to characterize the individual modes in the interval histograms. The ML estimate of μ_i was used as an estimate of the ith mode.

2. Gaussians with harmonically related means and a common variance

To estimate the fundamental mode, i.e., stimulus period, of ISI histograms, we modeled their distribution as a Gaussian mixture density with harmonically related means and a common variance,

$$p_i(x|\phi_i) = \frac{1}{\sqrt{2\pi}\sigma} e^{(x-i\cdot\mu)^2/2\sigma^2}. \tag{A9}$$

The ML estimate of μ was used as an estimate of the stimulus period.

A different set of iteration equations result when considering the mixture density described by Eqs. (A3) and (A9). In this case, maximizing $Q(\mathbf{\Phi}|\mathbf{\Phi}')$ with respect to the individual parameters leads to the following iteration equations, similar to Eqs. (A7) and (A8),

$$\mu^+ = \frac{\left\{\sum_{i=1}^{M}\sum_{k=1}^{N} x_k \cdot i \frac{\alpha_i' p_i(x_k|\phi_i')}{p(x_k|\mathbf{\Phi}')}\right\}}{\left\{\sum_{i=1}^{M}\sum_{k=1}^{N} i^2 \frac{\alpha_i' p_i(x_k|\phi_i')}{p(x_k|\mathbf{\Phi}')}\right\}}, \tag{A10}$$

$$\sigma^{+2} = \frac{\left\{\sum_{i=1}^{M}\sum_{k=1}^{N} (x_k - i\cdot\mu^+)^2 \frac{\alpha_i' p_i(x_k|\phi_i')}{p(x_k|\mathbf{\Phi}')}\right\}}{\left\{\sum_{i=1}^{M}\sum_{k=1}^{N} \frac{\alpha_i' p_i(x_k|\phi_i')}{p(x_k|\mathbf{\Phi}')}\right\}}. \tag{A11}$$

The weights of the individual densities, α_i^+, are the same as in Eq. (A6).

[1]Dowling and Harwood (1986) report (on p. 93) only one known tonal system, from an aboriginal culture in Australia, that is not based on the octave.

[2]The slight deviation from monotonicity near 1500 Hz is due to differences in mode offsets across cats and uneven sampling across cats. The data at 1500 and 3000 Hz are primarily from two cats which showed relatively large mode offsets in their AN responses [cats 5 and 6 in Fig. 4(d)].

Attneave, F., and Olson, R. (**1971**). ''Pitch as a medium: A new approach to psychophysical scaling,'' Am. J. Psychol. **84**, 147–166.

Biasutti, M. (**1997**). ''Sharp low- and high-frequency limits on musical chord recognition,'' Hear. Res. **105**, 77–84.

Cariani, P. A., and Delgutte, B. (**1996a**). ''Neural correlates of the pitch of complex tones. I. Pitch and pitch salience,'' J. Neurophysiol. **76**, 1698–1716.

Cariani, P. A., and Delgutte, B. (**1996b**). ''Neural correlates of the pitch of complex tones. II. Pitch shift, pitch ambiguity, phase invariance, pitch circularity, rate pitch, and the dominance region for pitch,'' J. Neurophysiol. **76**, 1717–1734.

de Cheveigné, A. (**1985**). ''A nerve fiber discharge model for the study of pitch,'' in *Transactions of the Committee on Speech Research/Hearing Research* (The Acoustical Society of Japan, Tokyo), S85-37, pp. 279–286.

Delgutte, B. (**1990**). ''Physiological mechanisms of psychophysical masking: Observations from auditory-nerve fibers,'' J. Acoust. Soc. Am. **87**, 791–809.

Demany, L., and Semal, C. (**1990**). ''Harmonic and melodic octave templates,'' J. Acoust. Soc. Am. **88**, 2126–2135.

Dobbins, P. A., and Cuddy, L. L. (**1982**). ''Octave discrimination: An experimental confirmation of the 'stretched' subjective octave,'' J. Acoust. Soc. Am. **72**, 411–415.

Doughty, J., and Garner, W. (**1947**). ''Pitch characteristics of short tones. I. Two kinds of pitch threshold,'' J. Exp. Psychol. **37**, 351–365.

Doughty, J., and Garner, W. (**1948**). ''Pitch characteristics of short tones. II. Pitch as a function of tonal duration,'' J. Exp. Psychol. **38**, 478–494.

Dowling, W. J., and Harwood, D. L. (**1986**). *Music Cognition* (Academic, San Diego), Series in Cognition and Perception.

Efron, B., and Tibshirani, R. (**1993**). *An Introduction to the Bootstrap* (Chapman & Hall, New York), Monographs on Statistics and Applied Probability.

Evans, E. (**1983**). ''Pitch and cochlear nerve fibre temporal discharge patterns,'' in *Hearing: Physiological Bases and Psychophysics*, edited by R. Klinke and R. Hartmann (Springer Verlag, Berlin), pp. 140–146.

Gaumond, R., Kim, D., and Molnar, C. (**1983**). ''Response of cochlear nerve fibers to brief acoustic stimuli: Role of discharge-history effects,'' J. Acoust. Soc. Am. **74**, 1392–1398.

Gaumond, R., Molnar, C., and Kim, D. (**1982**). ''Stimulus and recovery dependence of cat cochlear nerve fiber spike discharge probability,'' J. Neurophysiol. **48**, 856–873.

Goldstein, J. (**1973**). ''An optimum processor theory for the central formation of the pitch of complex tones,'' J. Acoust. Soc. Am. **54**, 1496–1516.

Goldstein, J., and Srulovicz, P. (**1977**). ''Auditory-nerve spike intervals as an adequate basis for aural frequency measurement,'' in *Psychophysics and Physiology of Hearing*, edited by E. Evans and J. Wilson (Academic, London), pp. 337–346.

Gulick, W., Gescheider, G., and Frisina, R. (**1989**). *Hearing: Physiological Acoustics, Neural Coding and Psychoacoustics* (Oxford University Press, New York).

Hartmann, W. (**1993**). ''On the origin of the enlarged melodic octave,'' J. Acoust. Soc. Am. **93**, 3400–3409.

Johnson, D. H. (**1980**). ''The relationship between spike rate and synchrony in responses of auditory-nerve fibers to single tones,'' J. Acoust. Soc. Am. **68**, 1115–1122.

Kaernbach, C., and Demany, L. (**1998**). ''Psychophysical evidence against the autocorrelation theory of auditory temporal processing,'' J. Acoust. Soc. Am. **104**, 2298–2306.

Kiang, N. (**1980**). ''Peripheral neural processing of auditory information,'' in *Handbook of Physiology*, edited by I. Darian-Smith (American Physiological Society, Bethesda, MD).

Kiang, N. (**1990**). ''Curious oddments of auditory-nerve studies,'' Hear. Res. **49**, 1–16.

Kiang, N., and Moxon, E. (**1972**). ''Physiological considerations in artificial stimulation of the inner ear,'' Ann. Otol. Rhinol. Laryngol. **81**, 714–730.

Kiang, N., and Moxon, E. (**1974**). ''Tails of tuning curves of auditory-nerve fibers,'' J. Acoust. Soc. Am. **55**, 620–630.

Kiang, N., Moxon, E., and Levine, R. (**1970**). ''Auditory-nerve activity in cats with normal and abnormal cochleas,'' in *Sensorineural Hearing Loss*, edited by G. Wolstenholme and J. Knight (J. & A. Churchill, London), pp. 241–273.

Kiang, N., Watanabe, T., Thomas, E., and Clark, L. (**1965**). *Discharge Patterns of Single Fibers in the Cat's Auditory Nerve* (The MIT Press, Cambridge, MA).

Liberman, M., and Kiang, N. (**1978**). ''Acoustic trauma in cats: Cochlear pathology and auditory-nerve activity,'' Acta Oto-Laryngol. Suppl. **358**, 1–63.

Liberman, M. C., and Kiang, N. Y. (**1984**). ''Single-neuron labeling and chronic cochlear pathology. IV. Stereocilia damage and alterations in rate- and phase-level functions,'' Hear. Res. **16**, 75–90.

Licklider, L. (**1951**). ''A duplex theory of pitch perception,'' Experientia **7**, 128–134.

Moon, T. (**1996**). ''The expectation-maximization algorithm,'' IEEE Signal Process. Mag. **13**(6), 47–60.

Ohgushi, K. (**1978**). ''On the role of spatial and temporal cues in the perception of the pitch of complex tones,'' J. Acoust. Soc. Am. **64**, 764–771.

Ohgushi, K. (**1983**). ''The origin of tonality and a possible explanation of the octave enlargement phenomenon,'' J. Acoust. Soc. Am. **73**, 1694–1700.

Patterson, R., Peters, R., and Milroy, R. (**1983**). ''Threshold duration for melodic pitch,'' in *Hearing: Physiological Bases and Psychophysics*, edited by R. Klinke and R. Hartmann (Springer-Verlag, Berlin), pp. 321–325.

Perkel, D., Gerstein, G., and Moore, G. (**1967**). ''Neuronal spike trains and stochastic point processes. I. The single spike train,'' Biophys. J. **7**, 391–418.

Pollack, I. (**1967**). ''Number of pulses required for minimal pitch,'' J. Acoust. Soc. Am. **42**, 895.

Redner, R., and Walker, H. (**1984**). ''Mixture densities, maximum likelihood and the EM algorithm,'' SIAM Rev. **26**, 195–239.

Rodieck, R. (**1967**). ''Maintained activity of cat retinal ganglion cells,'' J. Neurophysiol. **30**, 1043–1071.

Rodieck, R., Kiang, N., and Gerstein, G. (**1962**). ''Some quantitative methods for the study of spontaneous activity of single neurons,'' Biophys. J. **2**, 351–368.

Rose, J. E., Brugge, J. F., Anderson, D. J., and Hind, J. E. (**1967**). ''Phase-locked response to low-frequency tones in single auditory nerve fibers of the squirrel monkey,'' J. Neurophysiol. **30**, 769–793.

Rose, J. E., Brugge, J. F., Anderson, D. J., and Hind, J. E. (**1968**). ''Patterns of activity in single auditory nerve fibers of the squirrel monkey,'' in *Hearing Mechanisms in Vertebrates*, edited by A. V. S. de Reuck and J. Knight (Churchill, London), pp. 144–168.

Ruggero, M. (**1973**). ''Response to noise of auditory nerve fibers in the squirrel monkey,'' J. Neurophysiol. **36**, 569–587.

Ruggero, M. A., Rich, N. C., Shivapuja, B. G., and Temchin, A. N. (**1996**). ''Auditory-nerve responses to low-frequency tones: Intensity dependence,'' Aud. Neurosci. **2**, 159–185.

Siebert, W. M. (**1970**). ''Frequency discrimination in the auditory system: Place or periodicity mechanisms?,'' Proc. IEEE **58**, 723–730.

Sundberg, J., and Lindqvist, J. (**1973**). ''Musical octaves and pitch,'' J. Acoust. Soc. Am. **54**, 922–929.

Terhardt, E. (**1971**). ''Die tonhöhe harmonischer klänge und das oktavintervall,'' Acustica **24**, 126–136.

Terhardt, E. (**1974**). ''Pitch, consonance, and harmony,'' J. Acoust. Soc. Am. **55**, 1061–1069.

Walliser, V. (**1969**). ''Über die spreizung von empfundenen intervallen gegenüber mathematisch harmonishen intervallen bei sinustönen,'' Frequenz **23**, 139–143.

Ward, W. (**1954**). ''Subjective musical pitch,'' J. Acoust. Soc. Am. **26**, 369–380.

Contrast enhancement improves the representation of /ε/-like vowels in the hearing-impaired auditory nerve

Roger L. Miller[a)]
Hearing Research Laboratories, Division of Otolaryngology-Head and Neck Surgery, Box 3550, Duke University Medical Center, Durham, North Carolina 27710

Barbara M. Calhoun[b)] and Eric D. Young
Department of Biomedical Engineering and Center for Hearing Sciences, Johns Hopkins University, Baltimore, Maryland 21205

(Received 28 January 1999; revised 16 June 1999; accepted 28 July 1999)

This study examines the neural representation of the vowel /ε/ in the auditory nerve of acoustically traumatized cats and asks whether spectral modifications of the vowel can restore a normal neural representation. Four variants of /ε/, which differed primarily in the frequency of the second formant (*F*2), were used as stimuli. Normally, the rate-place code provides a robust representation of *F*2 for these vowels, in the sense that rate changes encode changes in *F*2 frequency [Conley and Keilson, J. Acoust. Soc. Am. **98**, 3223 (1995)]. This representation is lost after acoustic trauma [Miller *et al.*, J. Acoust. Soc. Am. **105**, 311 (1999)]. Here it is shown that an improved representation of the *F*2 frequency can be gained by a form of high-frequency emphasis that is determined by both the hearing-loss profile and the spectral envelope of the vowel. Essentially, the vowel was high-pass filtered so that the *F*2 and *F*3 peaks were amplified without amplifying frequencies in the trough between *F*1 and *F*2. This modification improved the quality of the rate and temporal tonotopic representations of the vowel and restored sensitivity to the *F*2 frequency. Although a completely normal representation was not restored, this method shows promise as an approach to hearing-aid signal processing. [S0001-4966(99)04011-4]

PACS numbers: 43.64.Sj, 43.64.Pg, 43.66.Ts [RDF]

INTRODUCTION

Acoustic trauma causes several changes in the properties of auditory nerve fibers, including an increase in threshold and a broadening of tuning (Kiang *et al.*, 1976; Liberman and Mulroy, 1982; Salvi *et al.*, 1982; Schmiedt *et al.*, 1980). As a result of these and other changes, the neural representation of a complex stimulus like speech is degraded (Palmer and Moorjani, 1993; Miller *et al.*, 1997, 1999; Schilling *et al.*, 1998). The effects of the broadened tuning are especially important in that the normal tonotopic separation of the responses to different frequency components in a complex stimulus is lost. Normally, fibers tuned to frequencies near the first formant (*F*1) frequency respond primarily or exclusively to the *F*1 component of the stimulus, and responses to the second and third formants (*F*2 and *F*3) are found among fibers tuned to the corresponding frequencies. Following acoustic trauma, these narrow-band responses are not observed. Instead, fibers in the damaged region of the cochlea respond to components of the stimulus over a broad frequency range (Miller *et al.*, 1997; Schilling *et al.*, 1998). This spread of response degrades the neural representation of the stimulus in three ways: (1) Strong responses to *F*1 are observed in fibers of all best frequencies (BFs) from the *F*1 place toward higher BFs, including the *F*2 and *F*3 places; (2) responses to *F*3 become very weak or disappear and are replaced by responses to *F*1, *F*2, and other stimulus components; and (3) fibers of all BFs, including *F*1 and *F*2, respond to a broad range of frequency components of the stimulus. The combination of these effects means that there is no place in the acoustically traumatized cochlea where fibers respond exclusively to any one formant component of the stimulus, as is observed in the normal ear for *F*1, *F*2, and, to a lesser extent, *F*3. This paper describes an approach that partially alleviates the degradation through hearing-aid signal processing.

The perceptual consequences of the degraded neural representation have been inferred by testing the sensitivity of the representation to changes in the *F*2 frequency for the vowel /ε/ (Miller *et al.*, 1999). In normal animals, there is a clear and robust tonotopic representation of *F*2 in the auditory nerve (Conley and Keilson, 1995); when the *F*2 frequency changes, there is a corresponding change in the location, or cochlear place, of fibers that respond to *F*2. This representation is expressed clearly by changes in the discharge rate of fibers with BFs near *F*2. Using signal detection theory, May and colleagues (1996) showed that the *F*2-dependent rate changes are sufficient to account for a cat's ability to discriminate changes in *F*2 frequency (Hienz *et al.*, 1996). However, after an acoustic trauma that produces a moderate sloping high-frequency hearing loss, this rate change cue disappears completely (Miller *et al.*, 1999).

One of the effects of acoustic trauma, the spread of responses to *F*1 into fibers of all BFs, can be alleviated by

[a)]Electronic mail: rlmiller@duke.edu
[b)]Present address: Scientific Learning Corporation, Berkeley, CA 94704-1074.

TABLE I. Noise exposure and test conditions for the four cats. The noise exposure was continued for 4 h; the free-field level at the position of the cat's head is given in column 2. Maximum vowel level is the maximum level for the CEFS stimuli. The last column gives the number of fibers included in the data sample from each cat.

Cat ID	Exposure level (dB SPL)	Recovery period (days)	Maximum vowel level (dB SPL)	Number of fibers isolated
201_155	108	90	103	158
201_183	103	82	102	96
201_199	103	65	103	113
201_231	103	69	102	94
Mean	104	77	103	Total 461

high-pass amplification of the *F*2/*F*3 portion of the stimulus (Schilling *et al.*, 1998) in a fashion similar to the half-gain rule of hearing-aid technology (Lybarger, 1978). In this system, the gain of the aid at a particular frequency is half the threshold shift at that frequency. With high-pass amplification, the response to *F*1 was confined to fibers with BFs near *F*1. However, high-pass amplification did not eliminate the broadband nature of the phase-locking in the vicinity of the *F*2 place. That is, there was still no place in the cochlea which responded exclusively to *F*2. In addition, with the particular combination of vowel and gain rule used, artifactual responses to frequency components between *F*1 and *F*2 were produced which might be confusing to the listener.

In this paper, we present results using an improved spectral modification paradigm in which the changes of the spectrum are specific to each vowel. The same high-frequency emphasis is applied to stimulus components near *F*2 and *F*3, but stimulus components in the trough between *F*1 and *F*2 are not amplified. With this spectral modification, which we have called *contrast-enhanced frequency shaping* (CEFS), the spread of *F*1 is prevented by amplifying the *F*2/*F*3 energy as before. In addition, because components in the trough between *F*1 and *F*2 are not amplified, the broadband phase-locking characteristic of earlier studies is not observed and the sensitivity to *F*2 frequency is restored.

I. METHODS

The results reported here were obtained in four healthy adult male cats, purchased from Liberty Labs; each cat weighed about 3.5 kg and showed no signs of middle or external ear pathology. The animal use protocol was approved by the Johns Hopkins Animal Care and Use Committee (protocol number CA96M302). The methods have been discussed in detail in previous publications (Miller *et al.*, 1997, 1999; Schilling *et al.*, 1998) and are described here only briefly.

A. Acoustic trauma

For the sound exposure, anesthetized cats (ketamine 200, acepromazine 2, and atropine 0.1 mg im) were exposed for 4 hr to a noise band of 50-Hz bandwidth, centered at 2 kHz at a free-field level of 103 or 108 dB (Table I). A period of 65–90 days was allowed for recovery from temporary threshold shift.

B. Single-fiber recording

Cats were anesthetized with xylazine (0.2 mg im) followed by ketamine (generally 150 mg im), and an areflexic state of anesthesia was maintained for the duration of the experiment with pentobarbital (≈12 mg/hr iv, to effect). Physiological saline (1–5 ml/hr iv) and lactated Ringer's (≈10 ml/24 hr iv) were given to prevent dehydration. Atropine (0.1 mg im) was given every 24 hours. A tracheotomy was performed and the bulla was vented. Body temperature was maintained near 38.5 °C with a feedback-controlled heating pad.

The cat was placed in a soundproofed room and single auditory nerve fibers were recorded using standard techniques. Experiments were terminated when fiber thresholds increased relative to previous fibers of similar BF or when single-fiber responses could no longer be isolated. Experiments usually lasted 2–3 days and were terminated by a lethal dose of barbiturate.

Isolated fibers were characterized by their tuning curves (Kiang *et al.*, 1970). Responses to the synthetic vowels described below were then obtained. If the fiber remained well-isolated, a 10-s sample of spontaneous activity was taken to determine the spontaneous firing rate (SR) and a tone was presented at the fiber's BF, 50 dB above threshold, to determine the maximum firing rate. If the SR data were not obtained, then SR was estimated from the interstimulus intervals of the trials in which the vowel was presented at the lowest level.

C. Stimuli

The original and modified (CEFS) vowel stimuli are shown in Fig. 1. The line spectra show the vowels' spectral features as originally synthesized; these are the same vowels that were used in previous studies (Conley and Keilson, 1995; Hienz *et al.*, 1996; Miller *et al.*, 1999). They were synthesized using a series-resonant synthesizer (Klatt, 1980) on a fundamental frequency of 100 Hz; all variants had first and third formants at 500 and 2500 Hz, respectively. The second formants were set at 1400 (V14), 1500 (V15), 1700 (V17), and 2000 Hz (V20) to generate four vowels with different *F*2s, but otherwise similar spectra. In earlier papers (Miller *et al.*, 1997 and Schilling *et al.*, 1998) the vowels were filtered with the human external ear transfer function (Wiener and Ross, 1946). That was not done for the vowels used here in order to keep the *F*2 levels fixed across vowels. External ear filtering was also not done by Conley and Keilson (1995) and Miller *et al.* (1999), although the Methods section of the latter paper mistakenly states that external ear filtering was done.

The spectral envelopes shown by lines in Fig. 1 are the vowel spectra after CEFS processing. The vowels were high-pass filtered using a digital filter with a transition slope of >160 dB/decade and <5 dB of passband ripple; the filter produced 30 dB of gain in its passband. The cutoff frequency of the filter varies with the vowel and is shown as f_c in Fig. 1. These cutoff frequencies were set at *F*2-50 Hz and were chosen to amplify the *F*2 and *F*3 energy in the signal without amplifying the harmonics in the trough between *F*1 and *F*2.

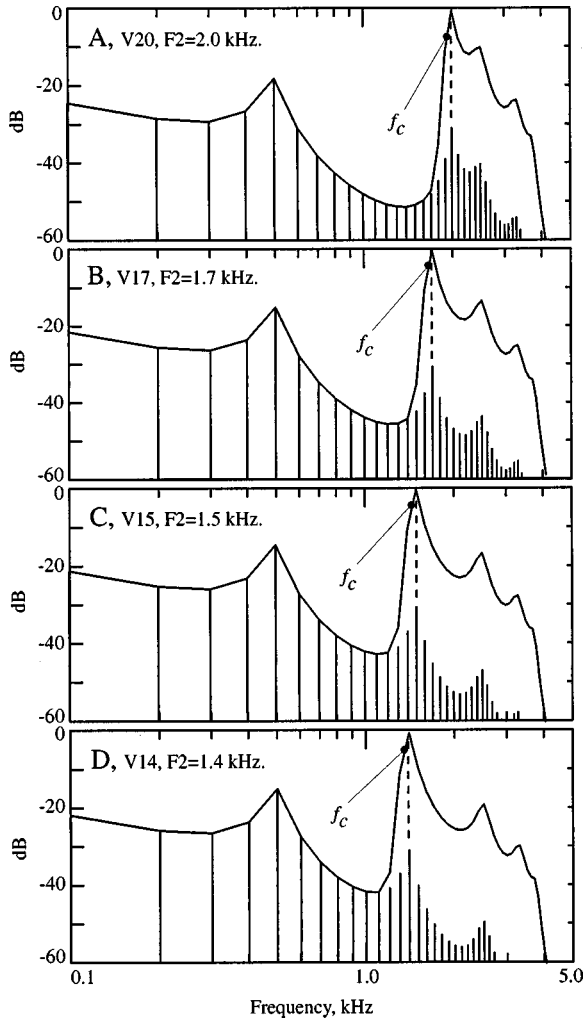

FIG. 1. The spectra of the unmodified and CEFS-modified vowels. *F*2 frequency during synthesis is indicated by the vowel name, e.g., V20 for 2000 V17 for 1700 Hz, etc. The line spectra show the unprocessed vowels' spectral shapes and the solid lines show the CEFS-modified spectra (see text). The two spectra converge at frequencies below the marker labeled f_c, which is the high-pass filter cutoff. This parameter was fit to each vowel so that the trough harmonics remained unamplified, but the harmonics at *F*2 and higher received 30 dB of gain. The vertical dashed lines show the *F*2 frequency.

Note the difference between the CEFS modification and the frequency shaping used previously (Schilling *et al.*, 1998). Previously the filter had a fixed cutoff frequency corresponding to the frequency at which the threshold shift began. This produced considerable amplification of the trough frequencies between *F*1 and *F*2, so that their level was only about 15 dB below the level of *F*2.

Acoustic stimuli were delivered to the ear through a hollow earbar from a dynamic speaker (Schilling, 1995). The spectrum was modified slightly by the acoustic system (for examples, see Miller *et al.*, 1999, Fig. 1), but the modifications did not significantly affect overall vowel shape. The vowels had a duration of 400 ms and were presented with an interstimulus interval of 600 ms. To facilitate comparison of responses to different vowels, they were presented together in alternating pairs (V14 with V20 and V15 with V17); usually 30–50 repetitions were obtained. CEFS-modified stimuli were presented first at 103 and 83 dB, followed by unmodified stimuli at 117 dB; these data were taken first for V14/V20, followed by the data for V15/V17. Finally, vowels were tested at lower sound levels, 63 dB for the CEFS-modified vowels and 97 and 77 dB for the unmodified vowels. Vowel levels are given in dB *re* 20 μPa for the energy in the first 50 harmonics of the vowel. There was a slight variation in the vowel levels from experiment to experiment (Table I, fourth column). The sound levels were chosen so that the levels of the *F*2 components of the two types of stimuli were approximately equal: that is, the *F*2 components of the CEFS stimuli at 103 (83 or 63) dB were approximately equal to the *F*2 components of the unmodified vowels at 117 (97 or 77) dB. Of course, when the *F*2 levels are equated, the *F*1 levels differ significantly (by 30 dB) because of the effects of the spectral modification.

Because the unmodified vowels were presented last, fibers were frequently lost before those data could be taken. [To improve the sample size, responses to the same unmodified vowels from a previous study (Miller *et al.*, 1999) are used in Figs. 3 and 4.]

D. Analysis

Average rate was computed over the final 380 of the 400-ms vowel response and averaged across 30 to 50 repetitions of the vowel; driven rate was computed by subtracting SR. Temporal responses were analyzed using synchronized rate, computed as the magnitude of the Fourier transform of the windowed peristimulus time histogram (PST) histogram of the response (see Miller *et al.*, 1997, 1999 for a complete description). The PST histogram was computed with 100-μs bins and the final 380 of the 400-ms response were used for the Fourier transform.

The difference between responses to different stimuli was characterized using a signed d' measure, defined as

$$d' = \frac{r_1 - r_2}{\sqrt{\sigma_{r_1}^2 + \sigma_{r_2}^2}}, \tag{1}$$

where r_1 and r_2 are the responses to two different vowels and the $\sigma_{r_i}^2$ are the corresponding variances of the responses. See Miller *et al.* (1999) for details of these calculations.

II. RESULTS

A. Characterization of the noise-induced hearing loss

Data were taken from 461 fibers in four noise-exposed cats; these data were pooled together in order to obtain a dense sampling of fibers at different BFs. The noise exposure and recovery period for each animal are given in Table I. The thresholds, Q_{10}s, and BF distribution of fibers included in the pool are shown in Fig. 2. Data from each fiber are plotted as a function of BF, which was chosen as the frequency of the local minimum threshold nearest the high-frequency slope portion of the tuning curve (see Miller *et al.*, 1997, Fig. 8 for examples). In cats with noise-induced trauma, this method gives a more reliable measure of the original BF (the point of innervation of the basilar membrane) than the frequency at which the threshold is actually at a minimum (Liberman and Dodds, 1984). Fibers are grouped into the

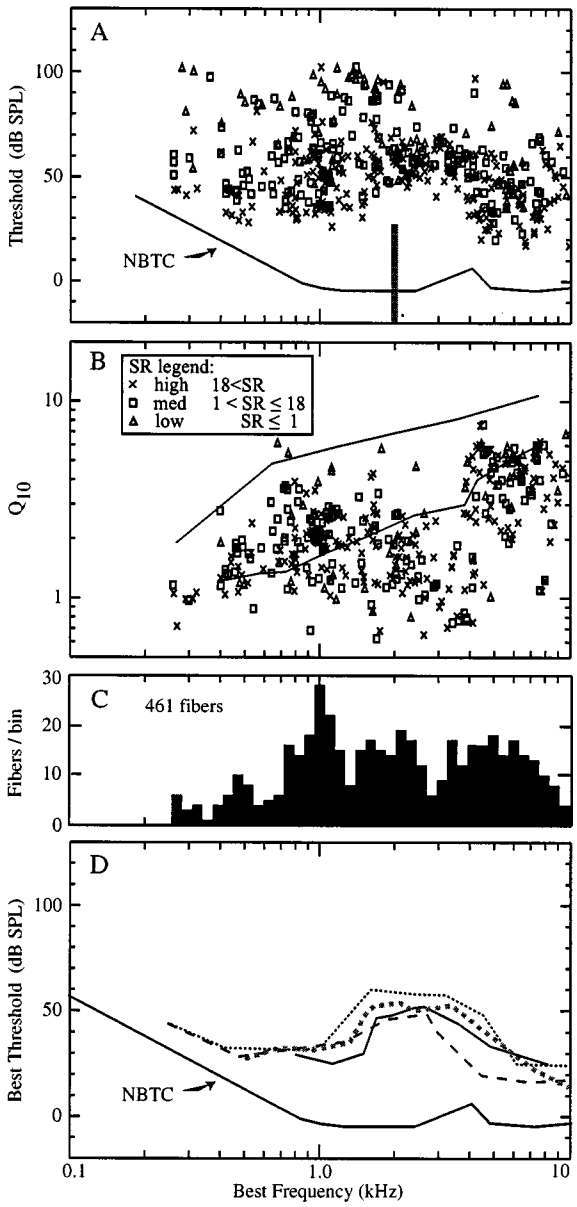

FIG. 2. (a) Threshold sound level at BF for all fibers in the four cats from which data were taken. Spontaneous firing rate (SR) is indicated by symbol shape, defined in the legend of (b). The line marked NBTC indicates the best thresholds in unexposed animals from the same supplier (Miller *et al.*, 1997). The vertical gray bar shows the frequency, but not the level, of the noise exposure. Note the threshold shift of up to 50 dB over the frequency range of 1–4 kHz. (b) Tuning curve widths for all fibers are plotted as Q_{10}, which is BF divided by tuning curve bandwidth 10 dB above threshold. Lines show the range of Q_{10}s in unexposed cats (Miller *et al.*, 1997). Fibers with BFs above 1 kHz were often broadly tuned, as indicated by the symbols falling below the normal range of values. (c) Histogram showing the distribution of BFs of the fibers in panels (a) and (b). (d) Best thresholds for each cat are shown in comparison to data taken from normal cats (NBTC). These lines indicate the minimum single-fiber thresholds at each BF.

usual SR groups, noted in the legend for Fig. 2, and this classification is indicated by symbol shape in this and subsequent plots.

Figure 2(a) shows single-fiber thresholds in comparison to the best thresholds obtained previously in unexposed cats from our supplier (the line marked NBTC, from Miller *et al.*, 1997). The threshold shift induced by the acoustic trauma was greatest for fibers with BFs in the range from 1 to 4 kHz. Figure 2(b) shows the Q_{10} measure of tuning curve sharpness; again, the lines show the range of data from normal animals. In the frequency region showing the greatest threshold shift, the Q_{10}s are below the lines, because tuning is broadened. Figure 2(c) shows a histogram of the distribution of BFs in the data sample. The majority of the fibers studied had BFs in the range from 0.7 to 7 kHz, which reflects our sampling bias in favor of fibers with BFs in the traumatized region.

Figure 2(d) shows a comparison of the best thresholds of the fibers studied in the four cats. These contours are defined by passing a line through the lowest thresholds measured at each BF. The contours are similar in shape across animals and typically vary by less than 20 dB at each frequency, with a maximum variation of 30 dB near 4.5 kHz. The threshold shifts shown in Fig. 2(d) are about equal to the smallest threshold shifts for the cats in our previous studies, including the most relevant study (Miller *et al.*, 1999), where we used the same set of stimuli without CEFS modification. However, the fact that the hearing losses were slightly greater in the previous study does not account for the improved representation reported in this paper. It will be shown below that the population studied here showed the same degraded representation of the unmodified stimulus as was reported in the previous paper. Consistent with this, the broadening of tuning indicated by the Q_{10} data in Fig. 2(b) is similar to the broadening of tuning observed in previous studies (Miller *et al.*, 1997, 1999).

B. Population representations of the vowel spectra based upon firing rate

Neural representations based upon average firing rate are considered first. Figure 3 shows the driven rate in response to the stimulus plotted as a function of fiber BF for the two vowels V20 [Fig. 3(a)–(d)] and V14 [Fig. 3(e)–(h)]. Figure 3(a) and (e) show responses to the unmodified vowels at the highest sound level and the remaining panels show responses to CEFS-modified stimuli. The vowels were tested at the levels indicated in each panel. The data points show responses of individual fibers, with the symbols indicating their SRs [as in Fig. 2(b)]. At the lowest level, 63 dB, the stimuli were below or just above threshold for most fibers and little response was seen. Significant responses were observed at the higher levels.

The lines in Fig. 3 show moving-window averages of the data points, computed as explained in the caption. The effects of CEFS processing can be seen by comparing the lines computed from the data (solid lines) to the dashed lines, which show moving-window averages for responses to the unmodified vowels from a previous study (Miller *et al.*, 1999). The average data were selected for each plot to match the levels of *F*2 in the unmodified and CEFS-modified stimuli. Data for the unmodified stimuli were taken from the previous study because the sample size was much larger for the unmodified stimuli in that study. In panels (a) and (e), responses to the unmodified stimuli at 117 dB are compared between this study (points and solid lines) and the previous study (dashed lines). The two sets of responses are similar

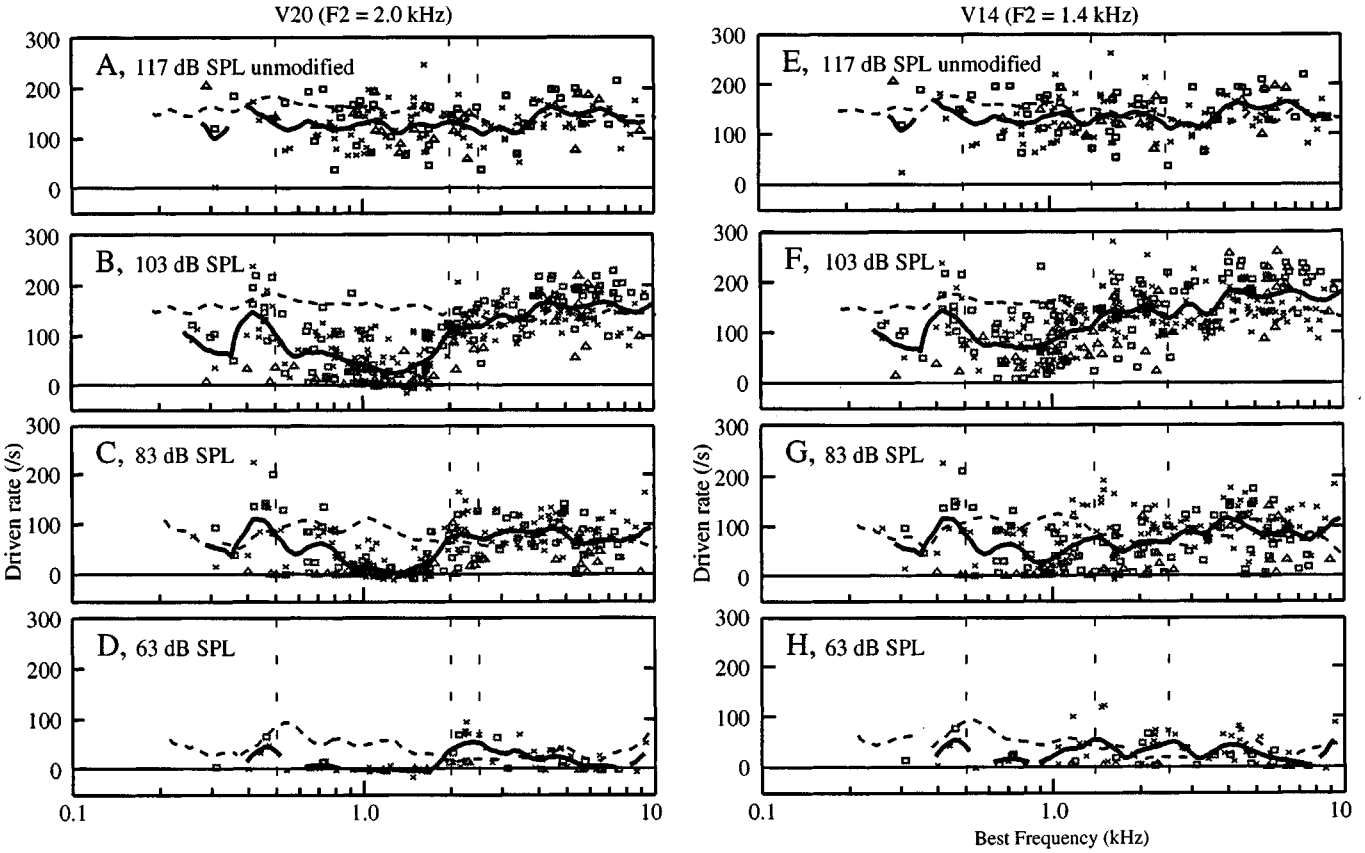

FIG. 3. Driven rate is plotted as a function of fiber BF for fibers from impaired ears responding to vowels V20 (a)–(d) and V14 (e)–(h). (a) and (e) show responses to the unmodified stimuli at 117 dB. The remaining figures show responses to CEFS-modified stimuli at three different sound levels, given in the legends. Points show the responses of individual fibers, with SR identified by the symbols, as defined in Fig. 2(b). The vertical dashed lines show the frequencies of the first three formants. Solid lines show a log-triangular weighted average of the data (each average value includes data from fibers with BFs within ± 0.25 octaves; the average point at frequency f weights the response of a fiber with BF b as $[1-|\log_2(b/f)/0.25|]$). Dashed lines show the average response to unmodified vowels of fibers in cats with similar hearing loss from a previous study (Miller *et al.*, 1999). The levels of the unmodified vowels were 117, 97, and 77 dB, respectively in parts (b), (c) and (d) and also (f), (g), and (h); they are superimposed on the CEFS data with approximately the same *F*2 component level. In (a) and (e), the data and solid lines show responses to the unmodified stimuli at 117 dB from this study and the dashed lines show responses from the previous study at the same level. In the previous study, more fibers with BFs near *F*1 were sampled, so the dashed lines are better estimates of the low-frequency behavior of these profiles than the solid lines. Note the improved representation of the trough between *F*1 and *F*2 with the CEFS-modified stimuli.

and differ mainly at low BFs where there are few data from this study. These data are typical of those at all three levels in that there are no clear features related to the formant frequencies at any sound level for the unmodified stimuli.

The major effect of the CEFS modification is to create a clear valley at BFs in the trough of the stimulus spectrum between *F*1 and *F*2. For both vowels, the moving-window averages of responses to the CEFS-modified stimuli [solid lines in panels (b)–(d) and (f)–(h)] show a peak in rate for BFs near *F*1 and a broad rate plateau at BFs near and above *F*2 and *F*3. These profiles are similar to rate profiles in normal animals (Conley and Keilson, 1995) in that there is a response peak at *F*1 and a trough between *F*1 and *F*2. They differ from the results in normal animals in that the rates at BFs above *F*2 and *F*3 do not decrease to zero, as they do in normals. The reason for this difference will be apparent later in the paper when phase-locking data are discussed. Despite this difference, the responses to the CEFS-modified stimuli clearly provide more information about the stimulus spectrum than do the responses to the unmodified stimuli.

C. CEFS processing improves the rate-difference representation

The quality of the *F*2 representation can be evaluated by analyzing the sensitivity of the responses to the *F*2 frequency. Figure 4 shows the rate changes produced by a change in *F*2 frequency. The vowels are identified in column A, where the dB differences in their spectra after CEFS processing are plotted versus frequency. Columns B and C show rate differences plotted versus BF for two sound levels, 83 and 103 dB. The data points show the rate change in each fiber when the stimulus was changed from one vowel to the other; the solid lines overlaid on the data points show a moving-window average of the data, computed in the same way as described for Fig. 3. The dashed lines, which are offset vertically for clarity, show similar moving-window averages from impaired-ear fibers tested with unmodified vowels, again from the previous study (Miller *et al.*, 1999). The levels are again chosen to match the amplitudes of the *F*2 components between the unmodified and CEFS processed stimuli (97 and 117 dB in columns B and C). Results with

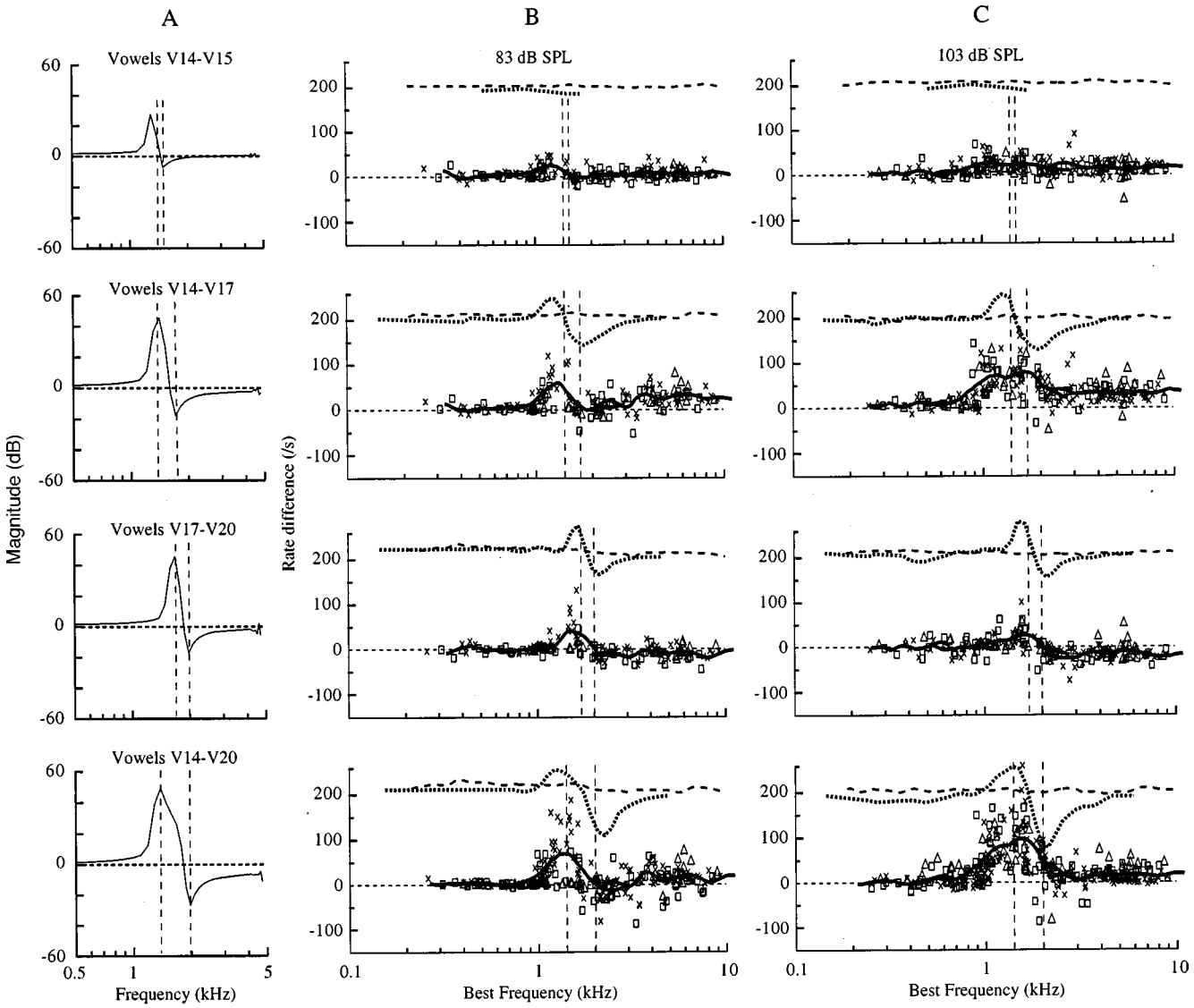

FIG. 4. Rate change versus BF for four vowel pairs. Column A shows the ratio of the magnitude spectra of four CEFS-modified vowel pairs, identified in the legends. Differences in discharge rate evoked by these pairs of vowels are plotted against BF for two sound levels, 83 dB (column B) and 103 dB (column C). Vertical dashed lines indicate the *F*2 frequencies of the two vowels of each pair. Data in the top row represent the vowel pair V14–V15, which has the weakest cue for discriminability, *F*2 differs by only 100 Hz, and data in the bottom row represent the vowel pair V14–V20 with the strongest cue tested, a 600-Hz change in *F*2. The heavy solid lines superimposed on the data are moving-window averages (see the caption of Fig. 3) of the data. Heavy dotted lines show moving-window averages of data taken from fibers in normal-hearing cats (Conley and Keilson, 1995). Dashed lines show responses to the unmodified vowels in cats with a similar hearing impairment at 97 and 117 dB, respectively, in the center and right columns (from Miller *et al.*, 1999). Comparison curves are displaced vertically to aid visualization. Note that the response obtained with CEFS-modified vowels shows rate changes where none were observed with unmodified vowels; the responses are not the same as in normal animals, however.

unmodified vowels in the cats used in this experiment (not shown) are identical to the dashed lines. The heavy dotted lines, also offset vertically, show results from normal animals (Conley and Keilson, 1995). Conley and Keilson computed moving-window averages separately for low/medium and high SR fibers; the lines in Fig. 4 are recomputed from their data for fibers of all SR.

Vowels presented with CEFS enhancement show a clear improvement over unmodified vowels. The vertical dashed lines in Fig. 4 show the *F*2 frequencies of the two vowels. The effect of CEFS is to produce a substantial spectral change (column A) and corresponding rate changes (columns B and C) near the lower of the two *F*2 frequencies. Both changes correspond to changing the upper frequency edge of the trough between the formants in Fig. 3. Recall that this trough is the main feature in the rate profiles.

Although the responses to the CEFS-modified vowels show a clear improvement over the representation in impaired animals with unmodified vowels, the CEFS processing does not produce the same representation as in the normal ear. Normally, there are two peaks, a negative one and a positive one, corresponding to the two *F*2 frequencies. With CEFS, only the peak at the lower *F*2 frequency is present, corresponding to moving the edge of the trough.

The single-fiber rate differences can serve as the basis for a signal-detection analysis of the discriminability of two vowels based upon firing rate alone (Conley and Keilson, 1995; May *et al.*, 1996). Figure 5 shows an analysis of dis-

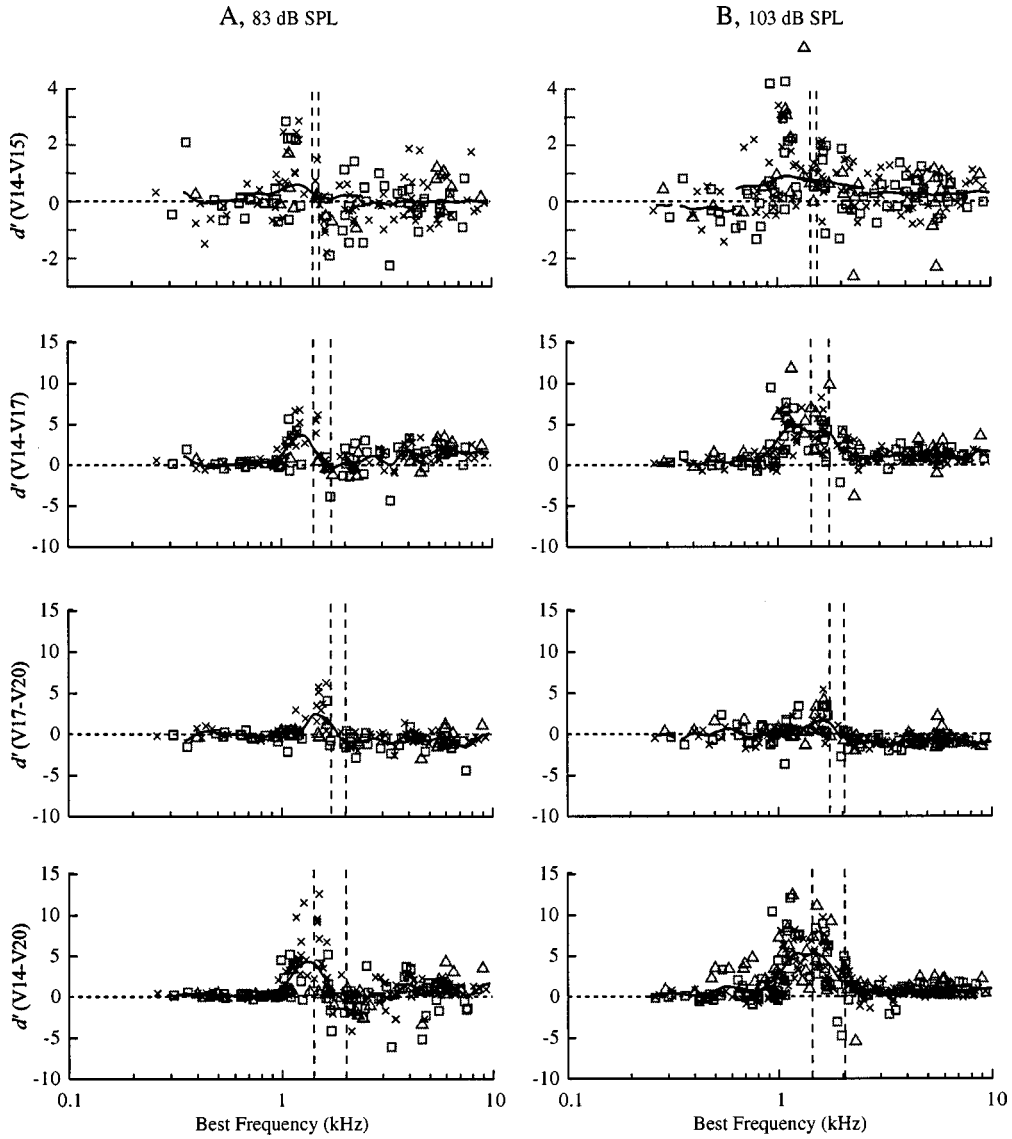

FIG. 5. The differences in average rate in Fig. 4 are replotted as signed d' [Eq. (1)]. The d' values for fibers with BFs near the $F2$ frequencies are greater than 1, which is the criterion for discriminability on the basis of average firing rate alone. Solid lines are moving-window averages of the data points.

criminability for the data shown in Fig. 4, calculated as the signed d' defined in Eq. (1), with rates and variances of rate as the variables. A d' of one for a fiber indicates that the two vowels should be just discriminable, based upon the firing rate of that one fiber to one 400-ms presentation of each of the two vowels. Note that in the region of the rate changes near the $F2$ frequencies, there are many fibers with d' values of one or more, showing that the neural representations of the CEFS-modified vowels should be discriminable on the basis of rate alone. With the unmodified vowels, there are d' values larger than 1 (not shown), but they are not systematically related to the $F2$ frequencies or to the change in $F2$ frequency (Miller *et al.*, 1999).

D. Temporal analysis of a fiber's responses to the second formant

Analysis of the temporal or phase-locked responses of fibers provides useful information for interpreting the rate responses described above. Figures 6 and 7 show examples of the phase-locked responses of two impaired fibers to the unmodified and CEFS-modified vowels. The tuning curves of the fibers are shown in Fig. 8(b), in comparison to a typical normal fiber of similar BF in Fig. 8(a). The vertical dashed lines in Fig. 8 show the $F2$ frequency range for the four vowels. Impaired fiber A has a lower BF that predicts a greater sensitivity for the vowels with lower $F2$s, i.e., V14 and V15, whereas impaired fiber B has relatively flat tuning across the $F2$ frequency range because of its higher BF.

The top four rows of Fig. 6 (panels A–H) show the responses of the two impaired fibers to the unmodified vowels at 97 dB; data from fibers A and B are shown in the left and right columns, respectively. These data are consistent with previous results (Miller *et al.*, 1999) in that they show a broadband response to many harmonics of the vowel, especially $F1$. By contrast, when $F2$ is within the tuning curve, normal fibers with similar BFs would show narrowband responses with synchrony primarily to $F2$ (Young and Sachs, 1979; Delgutte and Kiang, 1984; Miller *et al.*, 1997). A fiber like A should respond strongly to V14 and V15 with narrowband synchrony to the $F2$ component but respond only

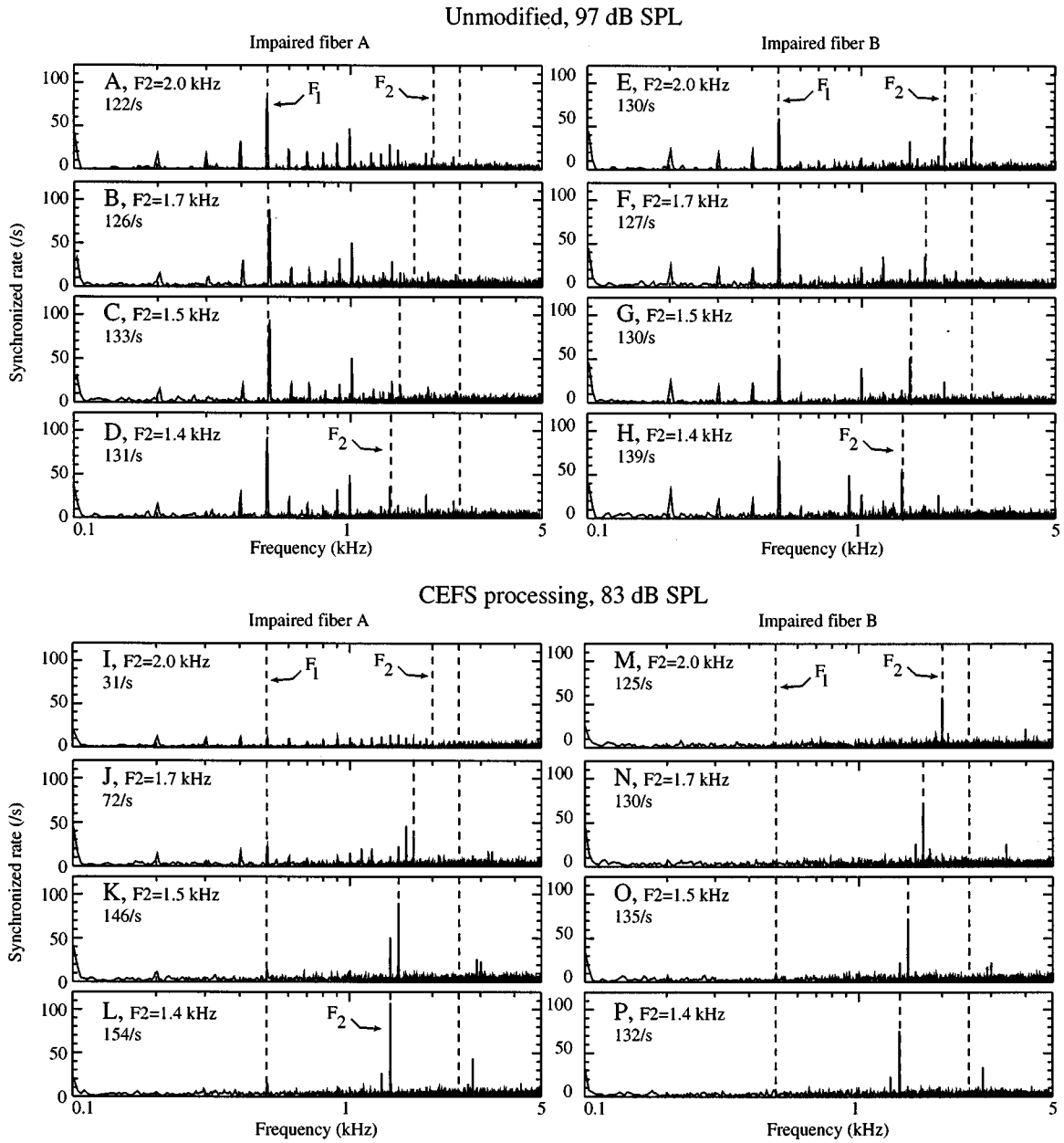

FIG. 6. Synchronized rates of the responses of the impaired fibers in Fig. 8 to the unmodified vowels (panels A–H, top four rows) and to the vowels with CEFS processing (panels I–P, bottom four rows). Synchronized rate is the magnitude of the Fourier transform of the PST histogram (for details, see Miller *et al.*, 1997, 1999). Peaks of synchronized rate are interpreted as the strength of the fiber's response at a particular frequency. For these vowel responses, peaks occur only at harmonics of the vowel's fundamental frequency (multiples of 100 Hz); small values at intermediate frequencies are noise. Data from impaired fibers A and B are shown in the left and right columns, respectively. The *F*2 frequencies of the vowels and the fibers' discharge rates are given in the legends; vertical dashed lines show the frequencies of *F*1, *F*2, and *F*3. The broadband responses driven by the unmodified stimuli (top four rows) are typical of those seen in impaired fibers; note especially the large response to *F*1 and the responses to multiple harmonics between *F*1 and *F*2. The responses to the CEFS-processed vowels (bottom four rows) are closer to the narrow-band synchrony to *F*2 that is typical for normal fibers. Note that the response rate for fiber A changes in response to the different vowels when tested with CEFS amplification (panels I–L), but not when tested with unmodified stimuli (panels A–D). The rate of fiber B does not change in either case. At these two sound levels, the amplitudes of the *F*2 harmonics of the two vowels are approximately equal; *F*1 is substantially louder (about 30 dB) for the unmodified stimuli.

weakly to V20. Instead, the fiber gives a broadband response to all vowels with a substantial *F*1 component and little or no *F*2 response. Similarly, fiber B responds mainly to *F*1 for all four vowels with relatively weak *F*2 responses. In a normal animal, fiber B would probably respond mainly to *F*3; after acoustic trauma, *F*3 responses are not observed (Miller *et al.*, 1997). Note that the firing rates, given in the legends, are nearly equal across all four vowels for both fibers. Presumably, the firing rates are determined primarily by the large *F*1 component of the responses.

The bottom four rows of Fig. 6 (panels I–P) show responses to the CEFS-modified vowels, again at a level that approximately matches the *F*2 component's amplitude to that of the unmodified vowels in Fig. 7(a)–(h). With these stimuli, reasonably narrowband responses to the *F*2 frequency component and its nearest neighbors are observed, without the responses to *F*1 and to frequency components in the trough between *F*1 and *F*2. Fiber A now shows a substantial rate change across the four vowels; its response is sensitive to *F*2 frequency because the *F*2 frequencies span

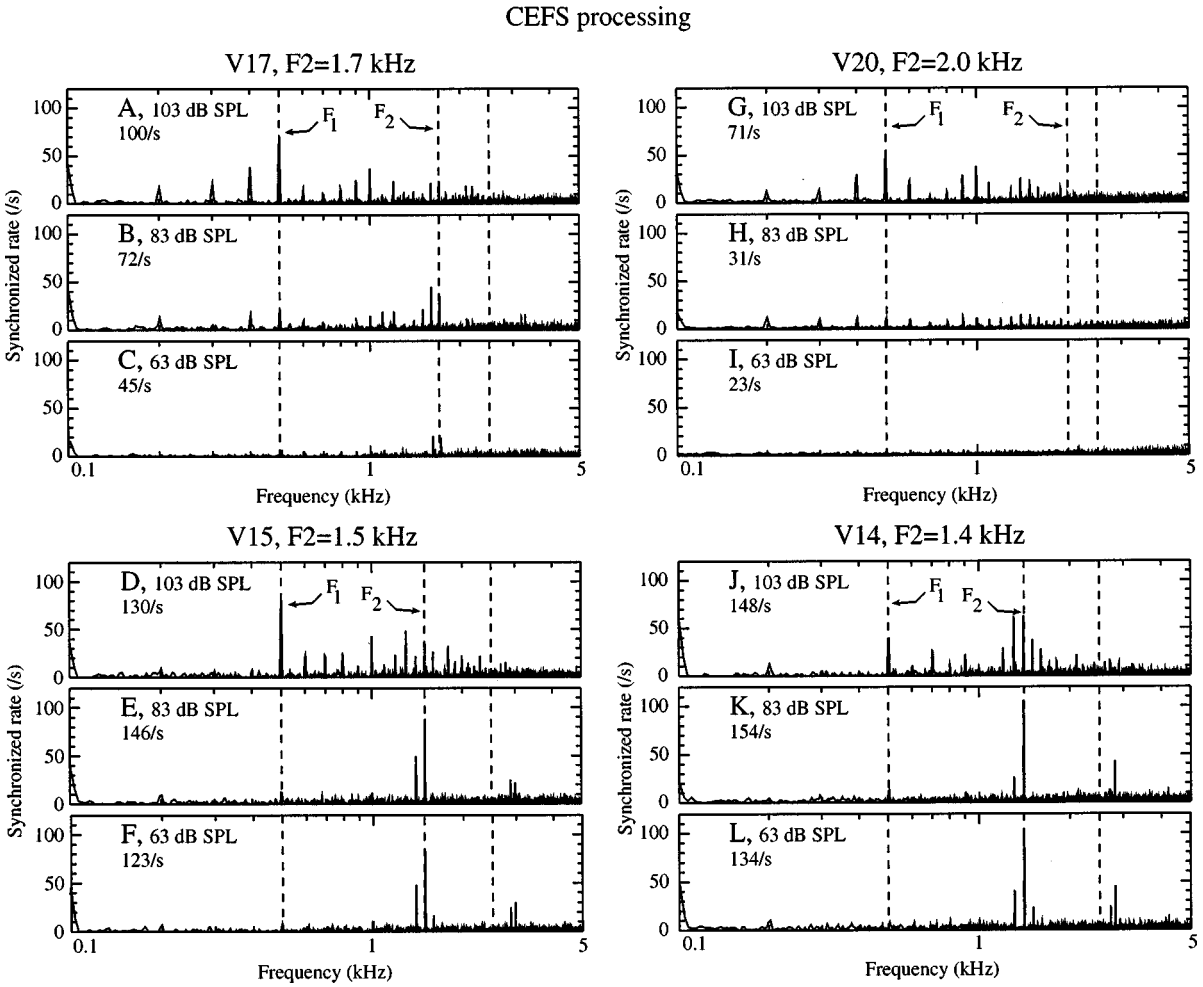

FIG. 7. The effects of sound level on the responses to the CEFS-modified vowels, illustrated by synchronized rate responses for impaired fiber A at three levels. Each triplet of plots shows the response to a particular CEFS-modified vowel at 63, 83, and 103 dB. The narrowband responses, which were seen at the lower two levels, became broadband responses when the vowels were presented at 103 dB SPL. The amplitude of the *F*1 response increased most, but significant responses are seen at many frequencies at 103 dB; a similar increase in *F*1 amplitude is seen at high levels in normal animals (Wong *et al.*, 1998).

the sharp upper frequency cutoff of its tuning curve. Fiber B still shows no rate change, because its sensitivities to the four *F*2 frequencies are roughly equal.

The different behavior of these two example fibers shows why the rate change data in Fig. 4 have only a positive peak, and not the negative peak seen in the normal fiber data. The CEFS processing is taking advantage of the sharply tuned high-frequency side of the tuning curve, which is the only sharp tuning remaining in the impaired ears. For fiber A, this separates V14 and V15 on one hand from V17 and V20 on the other. For fiber B, the high-frequency cutoff is too high to separate any of the vowels. The positive peak at the lower of the two *F*2 frequencies in Fig. 4 results from fibers like A and there is no negative peak because fibers like B are unable to produce it.

A major difference between the responses to unmodified and CEFS-processed vowels in Fig. 6 is the lack of a response to *F*1 with the CEFS processing. This difference is probably due to the large difference in the *F*1 component levels between the two stimuli (about 30 dB) and would be produced by any high-frequency emphasis scheme. However, the second difference, the smaller responses to stimulus components in the trough between *F*1 and *F*2 with CEFS processing, is probably due to the reduction in the amplitude of trough stimulus components due to the CEFS processing.

The narrow-band synchrony driven by CEFS processing is dependent upon presenting the stimuli at an appropriate sound level, as shown in Fig. 7. These responses were taken from impaired fiber A at levels from 63 to 103 dB. At the lowest level tested, 63 dB SPL (panels 9 C, F, I, L), the response is near or just above threshold and the average firing rate is low. The responses at both 63 and 83 dB are narrowband and are located near *F*2; at both levels good rate changes occur as *F*2 frequency changes. At 103 dB, the response becomes quite broadband, including a significant *F*1 response. At this level, *F*1 and the frequency components in the trough between *F*1 and *F*2 are above threshold and the advantages of the CEFS modification are smaller, although a significant change in *F*2 response from V14 to V20 leads to a net rate change. The responses at this level begin to resemble those seen at all levels with unmodified stimuli.

E. Population responses to CEFS-modified vowels

Figures 9, 10, and 11 show population representations of the phase-locked responses to unmodified (Fig. 9) and

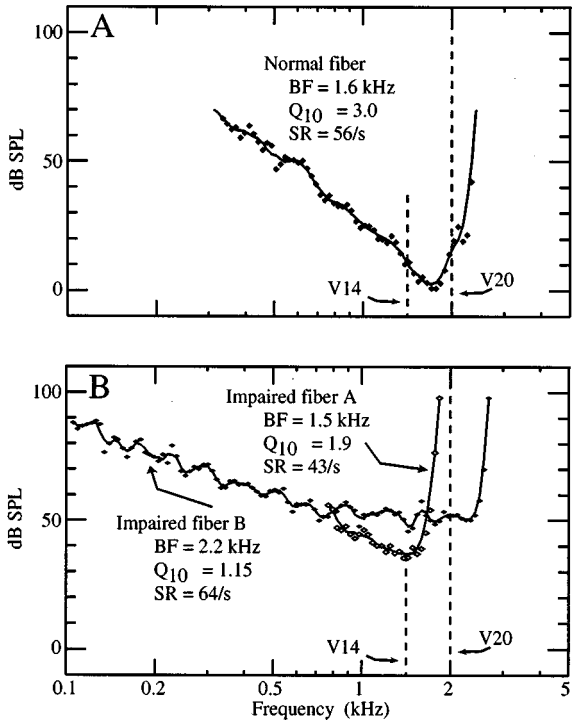

FIG. 8. Tuning curves for a normal fiber (a) and two impaired fibers (b) with BFs near the *F*2 frequencies of the vowels; the ordinate scales in (a) and (b) are the same. The lowest and highest *F*2 frequencies, 1.4 and 2.0 kHz, are indicated with vertical dashed lines. The BFs and other characteristics of these fibers are given in the legends. BFs were chosen as the local minimum nearest the high-frequency rolloff of the tuning curve.

CEFS-modified (Figs. 10 and 11) vowels. The responses to the unmodified vowels in Fig. 9 are shown for comparison; because the unmodified vowels were presented last, there is less data in Fig. 9 than in the other figures. More extensive data on all four unmodified vowels have been shown previously (Miller *et al.*, 1999), with exactly the same pattern of results. The plots in Figs. 9–11 show BF on the abscissa. Each column of boxes shows the averaged synchronized rates of the fibers with BFs within a bin of width 0.133 octaves. The scale for the boxes is given by the legend at upper left in panel A.

For the unmodified vowel (Fig. 9), the largest response is to *F*1, which appears as a strong horizontal band of synchronized rate at the *F*1 frequency in all four panels. Normally, the *F*1 response should be confined to the vicinity of its place in the cochlea, i.e., the area between the diagonal lines (Miller *et al.*, 1997). Relatively weak responses to *F*2 are seen, especially for V20, and there is no particular response to *F*3. In addition to the formant responses, there is significant phase-locking to a wide range of stimulus components, especially components in the trough between *F*1 and *F*2. This is in contrast to normal animals where the phase-locking by fibers with BFs near *F*1 and *F*2 should be exclusively to those two frequencies (Miller *et al.*, 1997; Schilling *et al.*, 1998).

CEFS processing substantially improves the phase-locked representation of the vowels. Figure 10 shows responses to all four CEFS-modified vowels at 83 dB. The response to *F*1 is now confined to the *F*1 place (between the diagonal lines) and a substantial response to *F*2 is seen among neurons at the *F*2 place and at higher BFs (up to the highest BF studied, 10 kHz in this case). Responses to *F*3 are still not evident and responses at the *F*3 place are dominated by *F*2. The most dramatic change from Fig. 9 is the great reduction in responses to frequencies other than *F*1 and *F*2. As shown in Fig. 9 and in Figs. 8 and 9 of a previous paper (Miller *et al.*, 1999), most of this response is to stimulus components in the trough between *F*1 and *F*2. By reducing the relative level of the trough, CEFS processing reduces responses to these components. Consistent with Fig. 6, the responses of fibers with BFs near *F*2 are narrow band, consisting almost entirely of phase-locking to the *F*2 frequency component. Such narrow-band phase-locking is typical of normal animals.

Presenting the vowels at 103 dB SPL (Fig. 11) increased the average synchronized rates in response to both *F*1 and *F*2, as indicated by the increased symbol sizes relative to those in Fig. 10. At the same time, fibers at the *F*2 place show a somewhat more broadband response than is seen at the lower level. There is an increase in response to stimulus harmonics other than the formants, consistent with the data in Fig. 6. Especially noticeable are the responses to the first harmonic (100 Hz) and to harmonics in the trough between *F*1 and *F*2. Even with these changes, the representation is still better than that seen with unmodified stimuli in Fig. 9, in that the spread of *F*1 response toward higher BFs is not seen and the broadband phase-locking to harmonics other than the formants is minimal.

Previously, we showed for unmodified vowels that the changes in phase-locking from one vowel to another provided a theoretically adequate cue to discriminate the vowels on the basis of temporal information, even if it did not allow discrimination on the basis of rate changes (Miller *et al.*, 1999, Fig. 10). In that paper, Eq. (1) was used to compute a d' value for the discriminability of synchronized rates at each frequency component of the stimulus. Discriminabilities up to $d'=1.5$ were observed at the *F*2 frequencies for the unmodified vowels. The phase-locking to *F*2 shown in Figs. 10 and 11 for the CEFS-modified vowels is stronger than that seen with unmodified vowels, suggesting that the temporal cues for discriminating these vowels should be stronger. That is in fact the case, since d' values computed from the data in Figs. 10 and 11 ranged up to $d'=2.5$ (not shown) for stimulus frequencies near *F*2.

III. DISCUSSION

A. Noise-induced loss, vowel discriminability, and CEFS modifications

Because the correlation between tuning-curve shape and hair cell damage has been established for acoustic trauma (Liberman and Dodds, 1984), tuning-curve data can be used to assay the damage caused by the trauma in our experiments. Based on Liberman and Dodds' results, the nature of the damage induced by our noise exposures, especially the large threshold shifts and broadening of tuning, can be interpreted as resulting from significant damage to outer-hair cells, with some additional damage to inner-hair cells. This

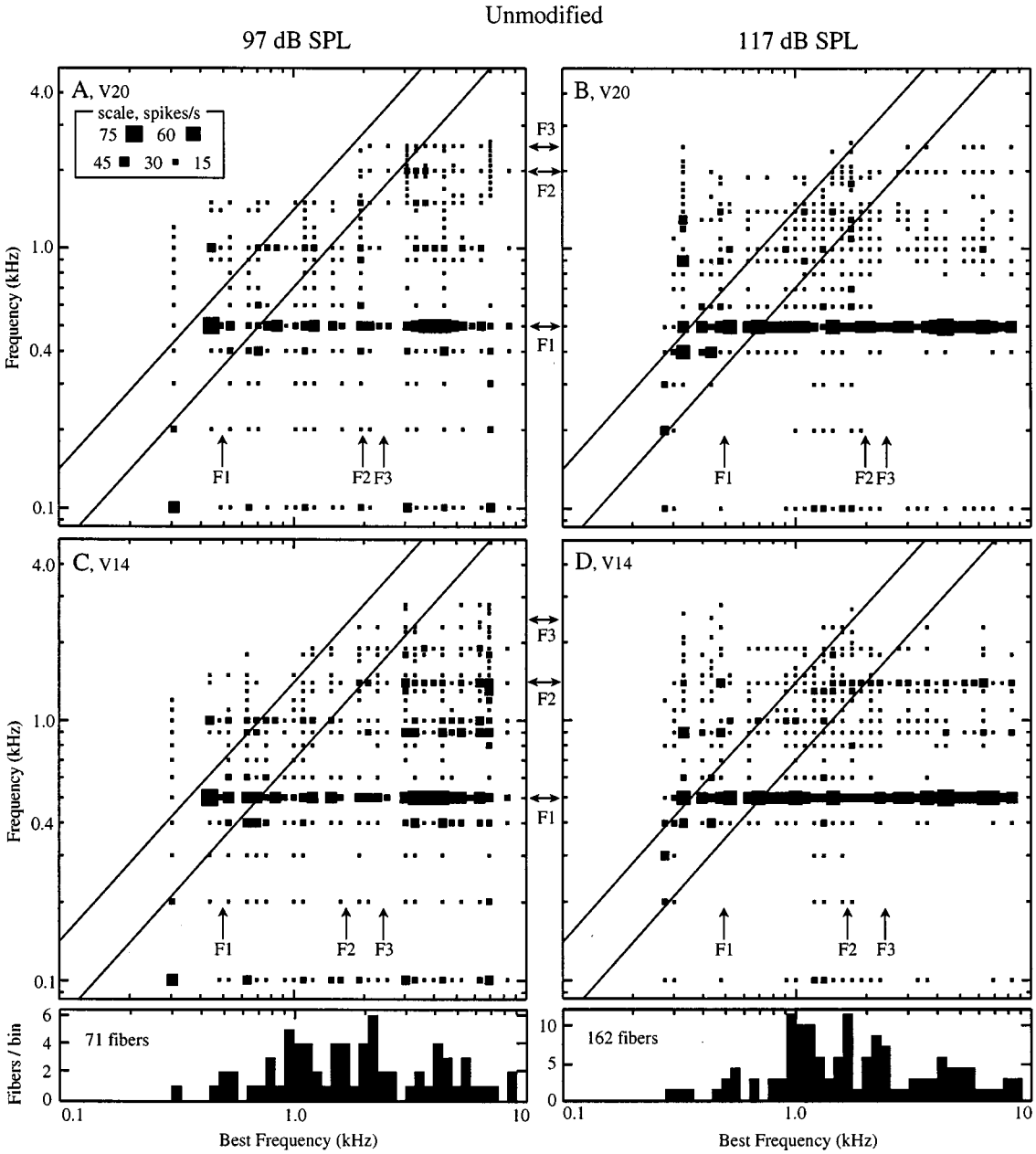

FIG. 9. Population distribution of synchronized rates in response to the unmodified vowels V20 (a) and (b) and V14 (c) and (d) at two sound levels, labeled at the top of the columns. The horizontal axis is fiber BF; the histograms at the bottom show the BF distribution of fibers in the plots above. Each column of squares shows the average synchronized rate for all fibers within a BF bin of width 0.133 octave. The size of each square represents the synchronized rate, as defined in the legend in panel (a); for example, the largest squares are synchronized rates between 60 and 75 spikes/s. Response components fewer than 15 spikes/s are not plotted. Formant frequency positions are marked with horizontal arrows at the center of the figure and points where BF equals formant frequency are shown by vertical arrows at the bottom of each panel. Boxes within the diagonal lines show phase-locking to frequencies within 0.5 octaves of BF. Note the heavy horizontal bands of boxes showing responses to *F*1 and the weak or nonexistent responses at *F*2 and *F*3. Note also the broad distribution of phase-locking across many harmonics of the stimulus in each column.

preparation can be considered to be a model for mild to moderate high-frequency hearing loss, typical of presbyacusis or some types of noise damage.

The loss of tuning evident in the tuning-curve data has direct implications for the responses to complex stimuli: broader tuning allows a wider range of stimulus frequencies to drive the response. An earlier modeling study has investigated the changes in discharge synchrony that would be expected from the broadened tuning of an impaired fiber as compared to the narrower tuning of a normal fiber (Geisler, 1989). This model did not incorporate two-tone suppression, so the frequency selectivity of the model's responses is primarily determined by a linear filter preceding the synaptic stage of the model. This is in contrast to the response of a normal fiber, in which the effects of two-tone suppression can be quite strong (Sachs and Young, 1979; LePrell *et al.*, 1996; Wong *et al.*, 1998). Although suppression is weakened with noise trauma in the preparation we use, it is not abolished (Miller *et al.*, 1997), so the Geisler model cannot be expected to fully capture the effects we observe. Nonetheless, the effects of broadening the filter in the model are qualitatively similar to the effects of acoustic trauma de-

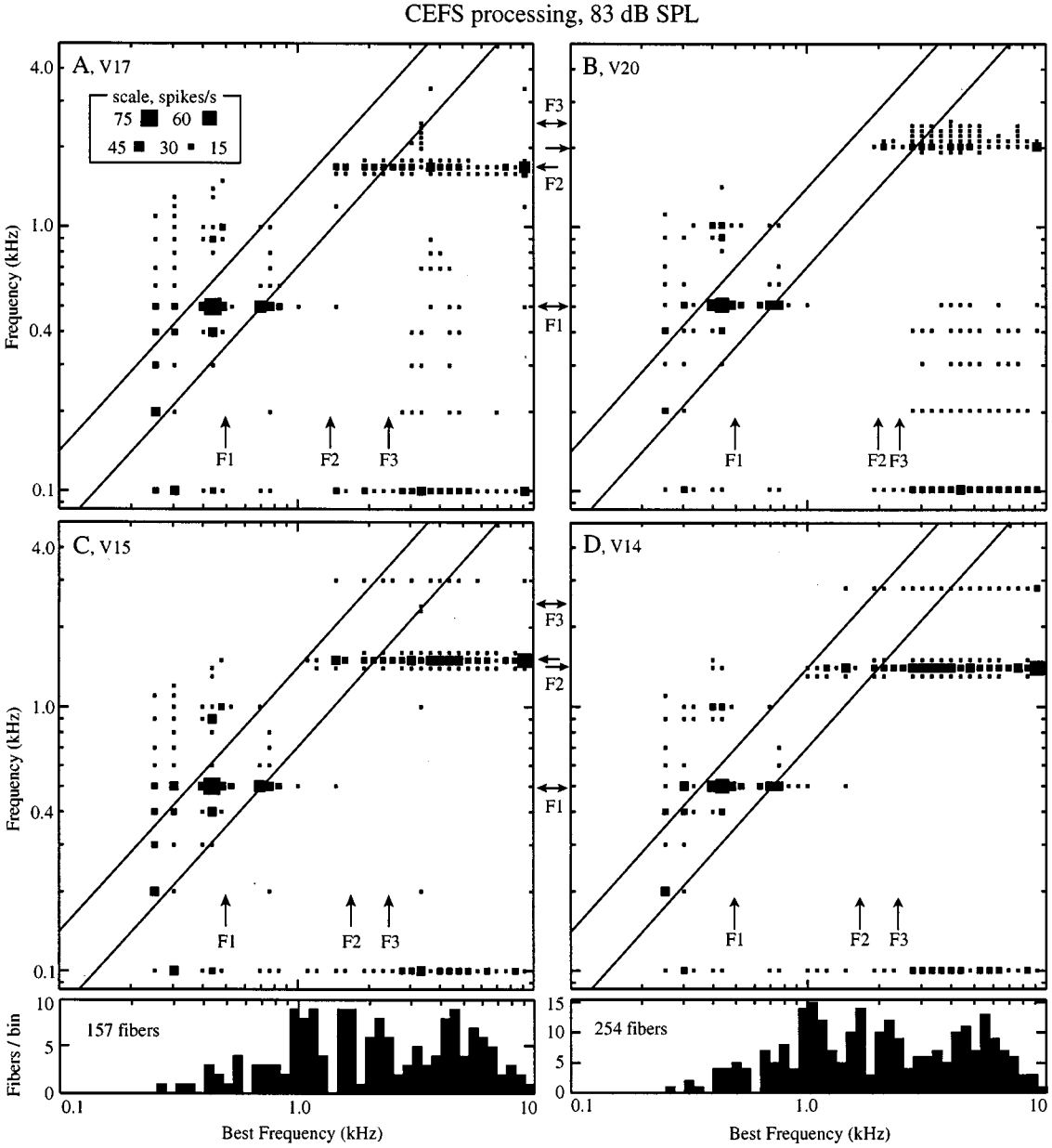

FIG. 10. Synchronized rate profiles for all four vowels presented with CEFS processing at 83 dB SPL. Each plot is the response to one vowel, labeled in the legend; the plots are in the same format as Fig. 9. Note that responses are seen mainly at the first two formants and that the response to *F*1 is confined to its tonotopically appropriate place (between the diagonal lines). Responses to *F*2 still spread to BFs above *F*2 and there is no response to *F*3.

scribed here in that the frequency-specificity of the response is lost. In both cases, significant responses to *F*1 are seen at higher frequency cochlear places. In addition, analysis of phase-locking data shows that neurons with BFs near *F*2 in the acoustically traumatized ears give broadband responses to a wide array of stimulus components, including *F*1 and most of the stimulus harmonics between *F*1 and *F*2. This is in contrast to the normal ear, where neurons with BFs near *F*2 respond essentially only to the *F*2 component of the stimulus, a behavior labeled synchrony capture.

In a previous paper, it was shown that the loss of synchrony capture results in a loss of sensitivity to the frequency of *F*2, in that rate changes normally produced by changes in *F*2 frequency do not occur following acoustic trauma (Miller *et al.*, 1999). In this paper, we show that appropriate modifications of the spectrum of the vowel can partially restore the rate representation of *F*2 frequency and can also improve other aspects of the damaged responses. The spectral modifications work by amplifying the *F*2 (and *F*3) energy in the stimulus, which prevents the spread of *F*1 to higher BF fibers (Schilling *et al.*, 1998), and by not amplifying the stimulus components in the trough between *F*1 and *F*2, which produces a response something like synchrony capture at the *F*2 place.

Not amplifying the trough harmonics between *F*1 and *F*2 is important to the success of the CEFS processing. If the trough harmonics are amplified along with *F*2, keeping the relative level of the trough harmonics and *F*2 fixed (Schilling *et al.*, 1998), synchrony capture is not observed at *F*2 or *F*1 and the quality of the representation of *F*2 is improved only by separating the phase-locking to *F*1 and *F*2 onto different BF regions; substantial responses to trough harmonics are

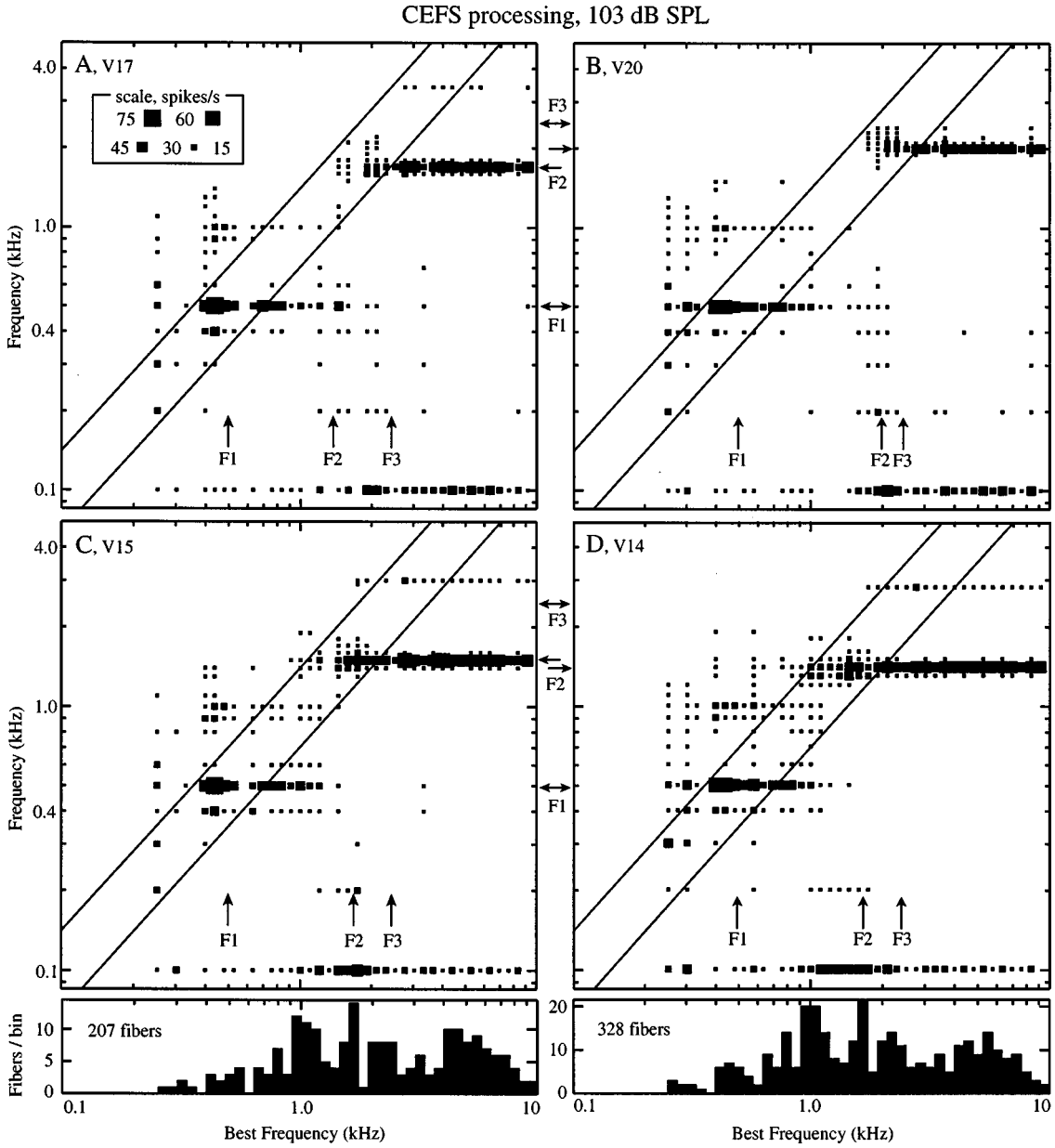

FIG. 11. Same as Fig. 10, except at 103-dB SPL. Synchrony to *F*1 and *F*2 is stronger than in Fig. 10 and there is some response to the harmonics between *F*1 and *F*2.

observed along with the responses to *F*1 and *F*2. The results in Figs. 10 and 11 show a noticeable improvement over those in Fig. 8 of Schilling *et al.* (1998), in that there is little or no response to trough harmonics with CEFS processing. This result emphasizes the necessity of the context-dependence of CEFS processing. The cutoff frequency of the amplification must track the changes in formant frequencies, so that *F*2 can be amplified relative to *F*1 to compensate for the high-frequency hearing loss, while not amplifying the trough harmonics. Implementing a system to track *F*2 changes in real time is, of course, very difficult and the question arises as to whether a high-pass filter with a sharp cutoff at a fixed frequency would suffice. Although we do not have data bearing directly on this question, it seems unlikely that a fixed cutoff system would work. *F*2 values for vowels range widely, from less than 1 to more than 3 kHz. Any fixed cutoff in this range would amplify the trough harmonics of those vowels with *F*2s above the cutoff and fail to amplify the *F*2s of other vowels with *F*2 frequency below the cutoff. In either case, a poor representation of *F*2 would be the result.

While the processing used here improves the neural representation of *F*2 considerably, it does not improve the situation at *F*3. For the /ɛ/-like vowels used here, there is essentially no representation of *F*3 in the traumatized ears. Fibers at the *F*3 place respond primarily to *F*2, with additional responses to *F*1 and to other components, depending on the degree of spectral modification applied to the stimulus. In fact, the *F*2 response spreads to higher-BF regions of the cochlea in a fashion similar to the spread of *F*1 for unmodified vowels. The spread of *F*2 was not helped by the processing used in this or previous papers. It is possible that *F*3 responses could be strengthened by further modifications of the stimulus spectrum, but this awaits further research.

B. Implications for hearing-aid signal processing

In this paper, we have used the theoretical discriminability of vowels as an index of the effects of hearing impairment and as a measure of the usefulness of a signal processing strategy. Although it is usually held to be the case that vowel perception is severely degraded only with profound hearing loss, it is still the case that consistent deficits in vowel discrimination and identification can be observed in subjects with moderate hearing losses, for similar vowels (Van Tasell *et al.*, 1987; Turner and Henn, 1989; Nabelek *et al.*, 1992; Coughlin *et al.*, 1998). Thus vowel discrimination can be a useful index of hearing impairment, even though performance approaches a ceiling.

In perceptual studies, the internal representation of the vowel's spectrum has been estimated from the vowel's masking patterns (Bacon and Brandt, 1982; Sidwell and Summerfield, 1985; Van Tasell *et al.*, 1987) or has been computed from the subject's auditory filters (Turner and Henn, 1989; Leek and Summers, 1996). Those studies show a flattening of the internal spectrum relative to the pattern in normal observers, wherein the spectral peaks associated with vowel formants are reduced in contrast or abolished. The flattening of the internal spectrum is generally assumed to arise from the broadening of auditory filters with hearing impairment. In a direct test of this idea using rippled spectra, Summers and Leek (1994) have shown that the reduced sensitivity of hearing-impaired listeners for spectral contrast can be accounted for by their broadened auditory filters. The implications of the flattened internal spectrum for vowel perception were analyzed by Turner and Henn (1989). They used a model for the perceptual phonetic difference between vowels that was developed by Klatt (1982). In this model, the difference is largely determined by the formant frequencies of the vowels. The difference between two vowels is calculated from their spectra, or their internal spectra, and depends heavily on the slopes of the spectra near formant peaks and on the amplitudes of the peaks. The calculated differences were smaller with the flattened internal spectra in hearing-impaired subjects and were found to predict the discriminability of vowels reasonably well.

The auditory nerve responses with unmodified stimuli are consistent with such a flattening of the internal representation. The fact that, with unmodified stimuli, the discharge rate does not vary along the basilar membrane (Fig. 3, dashed lines), and the fact that the response is dominated by the $F1$ component of the stimulus at every point with BF higher than $F1$ (Fig. 9), means that almost any neural model of the internal spectrum mentioned above will show no peak, or a reduced peak, at the second formant. Clearly the CEFS processing will improve the situation by producing differences in neural responses to the two vowels in the vicinity of $F2$. It should be pointed out that the difference metric used here (Figs. 4 and 5) is based on the absolute difference between the two spectra; this metric was shown by Klatt and Turner and Henn not to work as well as Klatt's slope metric in modeling human vowel discrimination. However, because there are no differences between the neural representations of the vowels with unmodified stimuli and significant differences with CEFS processing, either metric will show an improved performance with CEFS processing; for the purposes of this paper, it does not matter which metric is used.

The results presented here are consistent with previous literature in suggesting that high-frequency emphasis should be beneficial for hearing aids in persons with high-frequency hearing losses. First, such amplification is needed to make the high-frequency components of speech audible in these subjects. Audibility is clearly the first goal of a hearing aid; however, the question of whether audibility is sufficient has not been answered satisfactorily. In some studies in which the audibility of nonsense syllables was equated between normal and hearing-impaired listeners by using noise masking in the normal listeners, the performance of the two groups was essentially identical (Humes *et al.*, 1987; Zurek and Delhorne, 1987). However, our results show that making sounds audible is not, by itself, sufficient to restore a normal neural representation of the stimulus (Miller *et al.*, 1997; Schilling *et al.*, 1998). Similarly, other perceptual studies show that restoring audibility does not restore speech perception performance to the extent predicted by pure measures of audibility, like the articulation index (e.g., Ching *et al.*, 1998). Moreover, Hogan and Turner (1998) have shown that high-frequency speech information cannot always be used by listeners with high-frequency hearing loss, even when it is made audible; in extreme cases, high-frequency amplification can even be detrimental. Both the effects described by Ching *et al.* and by Hogan and Turner are worse as the degree of hearing loss increases. Studies like these provide evidence that there are suprathreshold deficits in the impaired ear which prevent efficient use of information in the speech wave form.

A common hypothesis about departures from the predictions of audibility theory in hearing-impaired listeners is that there is a degeneration in the internal representation of speech at the high sound levels needed to allow hearing-impaired listeners to hear the speech. Studies of the neural representation of speechlike stimuli at high sound levels support this hypothesis (Wong *et al.*, 1998). As discussed above, in normal animals, auditory nerve fibers with BFs near $F2$ show a narrowband response to the $F2$ component of the stimulus, meaning that they respond as if the stimulus consisted only of a tone at the frequency of $F2$. This gives a high-quality tonotopic representation of $F2$ which is sensitive to small changes in $F2$ frequency. At high sound levels (80–100 dB, depending on the BF), this narrowband response is replaced by a mixed response to $F1$ and $F2$. As sound level increases, the response to $F1$ becomes stronger and the response to $F2$ can disappear. This loss of response to $F2$ will clearly result in problems with speech perception and this effect may account for the need for high-level corrections to the articulation index (French and Steinberg, 1947).

High-frequency emphasis can be used in hearing aids to make high-frequency sound audible to listeners with high-frequency hearing losses. The results presented here and in a previous paper (Schilling *et al.*, 1998) show that high-frequency emphasis has additional benefits beyond making the sound audible. Most important, high-frequency emphasis controls the spread of response to $F1$ and thus improves the

frequency specificity of responses in the *F*2 region. The spread of the neural response to *F*1 toward fibers of higher BF corresponds to upward spread of masking in the perceptual literature (e.g., Danaher and Pickett, 1975; Summers and Leek, 1997). Hearing-impaired listeners, and normal listeners at high sound levels, show masking of *F*2 by *F*1 which is alleviated by attenuating *F*1. The masking effect is generally worse for hearing-impaired listeners and worsens as the degree of hearing loss increases (reviewed by Summers and Leek, 1997). The psychophysical interpretation of increased upward spread of masking in hearing-impaired listeners is that the perceptual auditory filters are broader, especially on the low-frequency side (Tyler *et al.*, 1984; Stelmachowicz *et al.*, 1985; Glasberg and Moore, 1986), which allows increased response to *F*1, and therefore masking, in the *F*2 filters. The obvious neural correlate is broadening of auditory nerve tuning curves, which also occurs primarily on the low-frequency side (Dallos and Harris, 1978; Schmiedt *et al.*, 1980; Liberman and Dodds, 1984). High-frequency emphasis in amplification counteracts the poor tuning on the low-frequency side of tuning curves in hearing-impaired subjects by boosting the level of *F*2 relative to *F*1 and decreasing the masking effect of *F*1 in the *F*2 fibers.

Even when the upward spread of *F*1 is controlled by high-frequency emphasis, differences between the hearing-impaired and normal ears remain. One problem is the broadband phase-locking in fibers with BFs near *F*2; these fibers show substantial responses to frequencies in the trough between *F*1 and *F*2. In normal animals, such phase-locking is not seen even at high sound levels (Wong *et al.*, 1998), whereas it is seen in acoustically traumatized animals with or without high-frequency emphasis (Schilling *et al.*, 1998). This phase-locking degrades the quality of the representation of *F*2 by making the responses of the *F*2 fibers depend on a large number of frequency components of the vowel, decreasing their sensitivity to *F*2.

A principal goal of CEFS processing is to eliminate the responses to trough frequencies by not amplifying them while still amplifying *F*2. The high-frequency emphasis used in perceptual studies is not of this type; typically, a fixed gain function is used which depends only on the degree of hearing loss. As a result, trough frequencies are amplified about as much as *F*2, for a vowel like /ε/. Thus responses to trough frequencies may provide an explanation for apparent suprathreshold deficits in hearing-impaired listeners, even when provided with the benefits of adequate high-frequency amplification.

CEFS processing resembles the signal processing done in spectral-enhancement hearing aids (Summerfield *et al.*, 1985; Simpson *et al.*, 1990; Stone and Moore, 1992; Baer *et al.*, 1993). The goal of these aids is to counteract the broadening of impaired auditory filters by sharpening the spectral shape of the stimulus. The sharpening has been done in a variety of ways, which include narrowing the formant bandwidths and increasing the contrast in the stimulus spectrum by filtering. The benefits obtained from these manipulations were small or nonexistent for speech intelligibility, although consistent improvements in perceived speech quality were reported. These results, then, seem to be in opposition to the suggestion that CEFS processing should improve hearing-aid performance. It is difficult to evaluate the reasons for the poor performance of the reported attempts at spectral enhancement. In the cases that are described best, it is apparent that high-frequency emphasis was not combined with the enhancement. In this case, upward spread of *F*1 would not be prevented. The deleterious effects of the upward spread of *F*1 on the responses of neurons with BFs near *F*2 are certainly larger than the effects of the trough harmonics; thus the omission of high-frequency emphasis is likely to have limited the improvement gained by spectral enhancement alone. It is also important to note that the spectral enhancement achieved by CEFS processing removes the power from a single band of frequencies in the trough between formants, regardless of the degree of hearing loss at the trough frequencies. In essence, the spectral enhancement is fit to both the hearing loss and the stimulus spectrum; this is unlike the spectral enhancement used in previous studies.

The particular form of spectral enhancement described here is promising in that it provides dramatic improvement in the neural representation of the stimulus. As mentioned above, further work is necessary to determine the feasibility of extending these benefits to *F*3. In addition, only one speech sound, the vowel /ε/, has been analyzed so far, and further research is needed to work out the dependence of the best processing algorithm on the particular speech spectrum and the particular hearing loss. Nevertheless, the data in this paper suggest that, through appropriate hearing-aid signal processing, it may be possible to achieve the goal of making normal the responses of auditory nerve fibers in acoustically traumatized ears.

ACKNOWLEDGMENTS

The comments of Kevin Davis, Brad May, David Smith, Leslie Collins, Chris Turner, and one anonymous reviewer were helpful in preparing this manuscript. Technical assistance of Ron Atkinson and Phyllis Taylor is appreciated. This work was supported by NIDCD Grant No. DC00109. Training support for R.L.M. was provided by Grant No. DC00979 and support for B.M.C. was provided by Fellowship DC00202.

Bacon, S., and Brandt, J. F. (**1982**). ''Auditory processing of vowels by normal-hearing and hearing-impaired listeners,'' J. Speech Hear. Res. **25**, 339–347.

Baer, T., Moore, B. C. J., and Gatehouse, S. (**1993**). ''Spectral contrast enhancement of speech in noise for listeners with sensorineural hearing impairment: Effects on intelligibility, quality, and response times,'' J. Rehabil. Res. Dev. **30**, 49–72.

Ching, T. Y. C., Dillon, H., and Byrne, D. (**1998**). ''Speech recognition of hearing-impaired listeners: Predictions from audibility and the limited role of high-frequency amplification,'' J. Acoust. Soc. Am. **103**, 1128–1140.

Conley, R. A., and Keilson, S. E. (**1995**). ''Rate representation and discriminability of second formant frequencies for /ε/-like steady-state vowels in cat auditory nerve,'' J. Acoust. Soc. Am. **98**, 3223–3234.

Coughlin, M., Kewley-Port, D., and Humes, L. E. (**1998**). ''The relation between identification and discrimination of vowels in young and elderly listeners,'' J. Acoust. Soc. Am. **104**, 3597–3607.

Dallos, P., and Harris, D. (**1978**). ''Properties of auditory nerve responses in absence of outer hair cells,'' J. Neurophysiol. **41**, 365–383.

Danaher, E. M., and Pickett, J. M. (**1975**). ''Some masking effects produced by low-frequency vowel formants in persons with sensorineural hearing loss,'' J. Speech Hear. Res. **18**, 261–271.

Delgutte, B., and Kiang, N. Y. S. (**1984**). ''Speech coding in the auditory nerve: I. Vowel-like sounds,'' J. Acoust. Soc. Am. **75**, 866–878.
French, N. R., and Steinberg, J. C. (**1947**). ''Factors governing the intelligibility of speech sounds,'' J. Acoust. Soc. Am. **19**, 90–119.
Geisler, C. D. (**1989**). ''The responses of models of ''high-spontaneous'' auditory-nerve fibers in a damaged cochlea to speech syllables in noise,'' J. Acoust. Soc. Am. **86**, 2192–2205.
Glasberg, B. R., and Moore, B. C. J. (**1986**). ''Auditory filter shapes in subjects with unilateral and bilateral cochlear impairments,'' J. Acoust. Soc. Am. **79**, 1020–1033.
Hienz, R. D., Aleszczyk, C. M., and May, B. J. (**1996**). ''Vowel discrimination in cats: Thresholds for the detection of second formant changes in the vowel /ε/,'' J. Acoust. Soc. Am. **100**, 1052–1058.
Hogan, C. A., and Turner, C. W. (**1998**). ''High-frequency audibility: Benefits for hearing-impaired listeners,'' J. Acoust. Soc. Am. **104**, 432–441.
Humes, L. E., Dirks, D. D., Bell, T. S., and Kincaid, G. E. (**1987**). ''Recognition of nonsense syllables by hearing-impaired listeners and by noise-masked normal hearers,'' J. Acoust. Soc. Am. **81**, 765–773.
Kiang, N. Y. S., Moxon, E. C., and Levine, R. A. **(1970)**. ''Auditory-nerve activity in cats with normal and abnormal cochleas,'' in *Sensorineural Hearing Loss*, edited by G. E. W. Wolstenholme and T. Knight (Churchill, London), pp. 241–268.
Kiang, N. Y. S., Liberman, M. C., and Levine, R. A. (**1976**). ''Auditory-nerve activity in cats exposed to ototoxic drugs and high-intensity sounds,'' Ann. Otol. Rhinol. Laryngol. **85**, 752–768.
Klatt, D. H. (**1980**). ''Software for a cascade/parallel formant synthesizer,'' J. Acoust. Soc. Am. **67**, 971–995.
Klatt, D. H. (**1982**). ''Prediction of perceived phonetic distance from critical-band spectra: A first step,'' Proc. IEEE Int. Congress Acoust. Speech, Signal Process. **129**, 1278–1281.
Leek, M. R., and Summers, V. (**1996**). ''Reduced frequency selectivity and the preservation of spectral contrast in noise,'' J. Acoust. Soc. Am. **100**, 1796–1806.
LePrell, G., Sachs, M. B., and May, B. J. (**1996**). ''Representation of vowel-like spectra by discharge rate responses of individual auditory-nerve fibers,'' Aud. Neurosci. **2**, 275–288.
Liberman, M. C., and Dodds, L. W. (**1984**). ''Single-neuron labeling and chronic cochlear pathology. III. Stereocilia damage and alterations of threshold tuning curves,'' Hearing Res. **16**, 55–74.
Liberman, M. C., and Mulroy, M. J. **(1982)**. ''Acute and chronic effects of acoustic trauma: Cochlear pathology and auditory nerve pathophysiology,'' in *New Perspectives on Noise-Induced Hearing Loss*, edited by R. P. Hamernik, D. Henderson, and R. Salvi (Raven, New York), pp. 105–135.
Lybarger, S. F. (**1978**). ''Selective amplification—a review and evaluation,'' J. Am. Audiol. Soc. **3**, 258–266.
May, B. J., Huang, A., LePrell, G., and Hienz, R. D. (**1996**). ''Vowel formant frequency discrimination in cats: Comparison of auditory nerve representations and psychophysical thresholds,'' Aud. Neurosci. **3**, 135–162.
Miller, R. L., Schilling, J. R., Franck, K. R., and Young, E. D. (**1997**). ''Effects of acoustic trauma on the representation of the vowel /ε/ in cat auditory nerve fibers'' J. Acoust. Soc. Am. **101**, 3602–3616.
Miller, R. L., Calhoun, B. M., and Young, E. D. (**1999**). ''Discriminability of vowel representations in cat auditory nerve fibers after acoustic trauma,'' J. Acoust. Soc. Am. **105**, 311–325.
Nabelek, A. K., Czyzewski, Z., and Krishnan, L. A. (**1992**). ''The influence of talker differences on vowel identification by normal-hearing and hearing-impaired listeners,'' J. Acoust. Soc. Am. **92**, 1228–1246.
Palmer, A. R., and Moorjani, P. A. (**1993**). ''Responses to speech signals in the normal and pathological peripheral auditory system,'' Prog. Brain Res. **97**, 107–115.
Sachs, M. B., and Young, E. D. (**1979**). ''Encoding of steady-state vowels in the auditory nerve: Representation in terms of discharge rate,'' J. Acoust. Soc. Am. **66**, 470–479.
Salvi, R., Perry, J., Hamernik, R. P., and Henderson, D. **(1982)**. ''Relationships between cochlear pathologies and auditory nerve and behavioral responses following acoustic trauma,'' in *New Perspectives on Noise-Induced Hearing Loss*, edited by R. P. Hamernik, D. Henderson, and R. Salvi (Raven, New York), pp. 165–188.
Schilling, J. R. **(1995)**. *The Effect of Acoustic Trauma and Hearing-Aid Processing on the Encoding of Vowels in the Auditory Nerve*, M.S.E. Thesis, Johns Hopkins University.
Schilling, J. R., Miller, R. L., Sachs, M. B., and Young, E. D. (**1998**). ''Frequency shaped amplification changes the neural representation of speech with noise-induced hearing loss,'' Hear. Res. **117**, 57–70.
Schmiedt, R. A., Zwislocki, J. J., and Hamernik, R. P. (**1980**). ''Effects of hair cell lesions on responses of cochlear nerve fibers. I. Lesions, tuning curves, two-tone inhibition, and responses to trapezoidal-wave patterns,'' J. Neurophysiol. **43**, 1367–1389.
Sidwell, A., and Summerfield, Q. (**1985**). ''The effect of enhanced spectral contrast on the internal representation of vowel-shaped noise,'' J. Acoust. Soc. Am. **78**, 495–506.
Simpson, A. M., Moore, B. C., and Glasberg, B. R. (**1990**). ''Spectral enhancement to improve the intelligibility of speech in noise for hearing-impaired listeners,'' Acta Oto-Laryngol. Suppl. **469**, 101–107.
Stelmachowicz, P. G., Jesteadt, W., Gorga, M. P., and Mott, J. (**1985**). ''Speech perception ability and psychophysical tuning curves in hearing-impaired listeners,'' J. Acoust. Soc. Am. **77**, 620–627.
Stone, M. A., and Moore, B. C. J. (**1992**). ''Spectral feature enhancement for people with sensorineural hearing impairment: Effects on speech intelligibility and quality,'' J. Rehabil. Res. Dev. **29**, 39–56.
Summerfield, A. Q., Foster, J., Tyler, R. S., and Bailey, P. J. (**1985**). ''Influences of formant narrowing and auditory frequency selectivity on identification of place of articulation in stop consonants,'' Speech Commun. **4**, 213–229.
Summers, V., and Leek, M. R. (**1994**). ''The internal representation of spectral contrast in hearing-impaired listeners,'' J. Acoust. Soc. Am. **95**, 3518–3528.
Summers, V., and Leek, M. R. (**1997**). ''Intraspeech spread of masking in normal-hearing and hearing-impaired listeners,'' J. Acoust. Soc. Am. **101**, 2866–2876.
Turner, C. W., and Henn, C. C. (**1989**). ''The relation between vowel recognition and measures of frequency resolution,'' J. Speech Hear. Res. **32**, 49–58.
Tyler, R. S., Hall, J. W., Glasberg, B. R., Moore, B. C., and Patterson, R. D. (**1984**). ''Auditory filter asymmetry in the hearing impaired,'' J. Acoust. Soc. Am. **76**, 1363–1368.
Van Tasell, D. J., Fabry, D. A., and Thibodeau, L. M. (**1987**). ''Vowel identification and vowel masking patterns of hearing-impaired subjects,'' J. Acoust. Soc. Am. **81**, 1586–1597.
Wiener, F. M., and Ross, D. A. (**1946**). ''The pressure distribution in the auditory canal in a progressive sound field,'' J. Acoust. Soc. Am. **18**, 401–408.
Wong, J. C., Miller, R. L., Calhoun, B. M., Sachs, M. B., and Young, E. D. (**1998**). ''Effects of high sound levels on responses to the vowel /ε/ in cat auditory nerve,'' Hear. Res. **123**, 61–77.
Young, E. D., and Sachs, M. B. (**1979**). ''Representation of steady-state vowels in the temporal aspects of the discharge patterns of populations of auditory-nerve fibers,'' J. Acoust. Soc. Am. **66**, 1381–1403.
Zurek, P. M., and Delhorne, L. A. (**1987**). ''Consonant reception in noise by listeners with mild and moderate sensorineural hearing impairment,'' J. Acoust. Soc. Am. **82**, 1548–1559.

Quantifying the distortion products generated by amplitude-modulated noise

Lutz Wiegrebe[a)]
Zoologisches Institut der Universität München, Luisenstrasse 14, 80333 München, Germany

Roy D. Patterson[b)]
Centre for the Neural Basis of Hearing, Physiology Department, Cambridge University, Downing Street, Cambridge CB2 3EG, United Kingdom

(Received 8 July 1998; revised 29 January 1999; accepted 15 July 1999)

When sinusoidal amplitude modulation (SAM) is applied to noise or tone carriers, the stimuli can generate audible distortion products in the region of the modulation frequency. As a result, when bandpass-filtered SAM noise is used to investigate temporal processing, a band of unmodulated noise is typically positioned at the modulation frequency to mask any distortion products. This study was designed to investigate the distortion products for bandpass noise carriers, and so reduce ambiguity about the form of this distortion and its role in perception. The distortion consists of two distortion-noise bands and a distortion tone at the modulation frequency. In the first two experiments, the level and phase of the distortion tone are measured using two different experimental paradigms. In the third experiment, modulation-frequency difference limens are measured for filtered SAM noise and it is shown that performance deteriorates markedly when the distortion tone is canceled. In a fourth experiment, masked threshold is measured at low frequencies for bands of high-frequency, unmodulated noise with the same levels and spectra as the SAM noises in the earlier experiments. The results confirm that unmodulated noise also produces quadratic distortion which may explain some aspects of earlier reports on remote masking. © *1999 Acoustical Society of America.* [S0001-4966(99)01411-3]

PACS numbers: 43.66.Ba, 43.66.Dc, 43.66.Hg, 43.66.Mk [JWH]

INTRODUCTION

Sinusoidally amplitude-modulated noise (SAM noise) has been used repeatedly to investigate temporal properties of auditory processing. In many cases, the noise is broadband, but several investigators have used filtered SAM noise and, typically, the noise is filtered after modulation. Strickland and Viemeister (1997) reported that in this case the bandpass-filtered SAM noise produces an audible distortion tone at the modulation frequency. Informal listening in our lab confirmed Strickland and Viemeister's (1997) report inasmuch as (a) the timbre of the distortion product was that of a sinusoid, (b) a sinusoid with a frequency 6 Hz above or below the modulation frequency produced 6-Hz beats, and (c) a sinusoid at the modulation frequency with the level that produced the strongest beats would enhance or greatly reduce the loudness of the distortion product depending on its phase. These observations indicate that there is, indeed, a sinusoidal distortion tone on the basilar membrane at the modulation frequency.

This distortion tone produces a potential confounding in experiments designed to investigate auditory temporal processing in the absence of spectral cues because it introduces a spectral cue at the modulation frequency. It is not immediately clear that bandpass SAM noise should produce distortion products that are different from those of unmodulated noise, because the long-term magnitude spectrum of SAM noise, which is first modulated and then filtered, is continuous and flat within the passband, like the spectrum of unmodulated bandpass noise. This may be the reason why many investigators using bandpass-filtered SAM noise did not explicitly consider these distortion products. Nevertheless, most psychoacoustic experiments involving filtered SAM noise have included an unmodulated-noise masker with a complementary spectral shape to the modulated noise, but the reasons for including the masker are often vague. Burns and Viemeister (1976, 1981) established that the pitch of SAM noise is a nonspectral pitch. When they used filtered SAM noise, they presented, in most conditions, an unmodulated background noise to ''mask possible distortion products.'' The recognition of filtered, SAM-noise melodies deteriorated markedly but was still above chance when the band-rejected unmodulated noise masker was introduced. Patterson *et al.* (1978) compared modulation threshold with the modulation depth required to detect a 325-cent change in modulation frequency, and showed that the rate change was detectable once the modulation depth was about double that required to detect modulation. They employed an unmodulated low-pass or band-stop masking noise together with the filtered SAM noise to ''restrict the listening region.'' Formby (1985) and Formby and Muir (1988) measured modulation-frequency detection and discrimination with filtered SAM noise. They also employed complementary unmodulated noise maskers for the same reasons as given in Patterson *et al.* (1978). There is one study with filtered SAM noise that did not include a masker at the modulation frequency (Hanna, 1992), but it used low presentation levels

[a)]Electronic mail: wiegrebe@zi.biologie.uni-muenchen.de
[b)]Electronic mail: roy.patterson@mrc-cbu.cam.ac.uk

and any distortion products would probably have been near or below absolute threshold. Eddins (1993) used a low-level broadband noise together with modulated or unmodulated bandpass noise to ''mask image frequencies'' after digital filtering. Although none of the above studies seems to be confounded by an audible distortion tone at the modulation frequency, the variety of reasons given for the use of unmodulated-noise maskers suggests that the distortion tone of bandpass-filtered SAM noise has not received appropriate attention so far.

Instead of masking the distortion tone, the current experiments are designed to quantify the distortion tone in terms of its phase and level, and its dependence on SAM noise parameters like bandwidth. In the first two experiments, we measure the level and phase of the distortion tone for two different modulation frequencies and three different bandwidths using a cancellation technique and two different psychophysical paradigms. In the third experiment, we investigate how modulation-frequency discrimination is influenced by adding cancellation tones to the modulated stimuli. We then present a more detailed version of Strickland and Viemeister's (1997) hypothesis that the distortion tone generated by SAM noise is a difference tone; it is the vector sum of the combination of all spectral components in the noise band with their corresponding sidebands, insofar as these are preserved after filtering. The fourth experiment relates the distortion tone of filtered SAM noise to the ''distortion noise bands'' produced by unmodulated, bandpass noise. These distortion noise bands were thoroughly investigated by Greenwood (1971, 1991) but with the emphasis on *cubic* distortion rather than the quadratic distortion responsible for the SAM-noise distortion tone.

I. EXPERIMENT I: QUANTIFYING THE DISTORTION TONE USING MODULATION DETECTION

The effective modulation depth of SAM noise is reduced when the noise is first modulated and then filtered, and the reduction increases as modulation frequency increases or as noise bandwidth decreases. Informal experiments indicated that the detection of a 250-Hz modulation on a 500-Hz-wide band of noise centered at 4.25 kHz decreased to chance levels when a low-pass noise masker was used to mask the 250-Hz region. This suggested that, when the noise bandwidth is only twice the modulation frequency, the filtering reduced the modulation depth to the point where it no longer supported modulation detection based on the temporal cue, that is, the modulation in the passband. At the same time, however, the modulation depth was still sufficient to produce a spectral cue in the form of a distortion tone. In experiment I, we use this combination of modulation frequency and bandwidth to enable us to measure the level and phase of the SAM distortion tone, using a cancellation procedure embedded in a modulation-detection experiment.

A. Method

To begin with, an adjustment experiment was performed to establish the approximate level and phase of the distortion tone: Listeners were presented with a bandpass SAM noise with cutoff frequencies of 4 and 4.5 kHz and a modulation frequency of 250 Hz (as in experiment Ia below), or a bandpass SAM noise with cutoff frequencies of 4 and 6 kHz and a modulation frequency of 1 kHz (as in experiment Ib below). Listeners were asked to adjust the level and phase of the simultaneous cancellation tone, whose frequency was the same as the modulation frequency, to minimize the pure-tone sensation in the perception of the filtered SAM noise. For reference, listeners could switch back and forth between the SAM bandpass noise plus the cancellation tone and an unmodulated bandpass noise. These preliminary adjustments established the appropriate range of cancellation-tone levels and phases for experiments I and II.

In the main experiment, listeners were asked to detect a 250-Hz modulation in a bandpass noise in the presence of a cancellation tone at the modulation frequency. The noise cutoffs were 4 and 4.5 kHz. The modulation detection is trivial for large noise bandwidths relative to the modulation frequency. But, when the modulation frequency is half the noise bandwidth, then the stimuli are indiscriminable when the distortion tone is masked (see above). When the distortion tone is not masked, the modulation-detection procedure can be used to titrate the level and phase of a pure tone that cancels the distortion tone.

1. Stimuli

The stimuli consisted of samples of Gaussian noise bandpass filtered between 4 and 4.5 kHz (experiment Ia) or between 4 and 6 kHz (experiment Ib). The stimulus duration was 327.7 ms including 20-ms raised-cosine gates. When the noise was amplitude modulated, the modulation was applied before the filtering to prevent the use of spectral sidebands for modulation detection. The modulation depth before filtering was always 100%; however, the filtering decreases the effective modulation depth. For the SAM-noise stimuli used in the current experiments, this was quantified by calculating the magnitude of the Fourier component of the waveform Hilbert envelope at the modulation frequency relative to the magnitude of this component in the unfiltered SAM-noise envelope. With a modulation frequency of 250 Hz and a passband from 4 to 4.5 kHz (experiment Ia), the effective modulation depth decreased to 50%. In experiment Ib (a 1-kHz modulation frequency and a 4 to 6-kHz passband) the effective modulation depth also decreased to 50% because the relation between modulation frequency and passband width is the same as in experiment Ia. The filtering was performed digitally by setting the magnitude spectrum outside the passband to zero. The noise stimuli for each trial were equalized in energy and presented at a spectrum level of 45 dB SPL/Hz to the left ear. When the noise was amplitude modulated, an equal-duration, cancellation tone of variable level and phase was presented simultaneously at the modulation frequency. The stimuli were presented via a Sennheiser 540 Reference headphone. The experimental setup was shown to generate negligible distortion (cf. Sec. IV A).

2. Procedure

Psychometric functions were measured for the detection of amplitude modulation as a function of either the level or phase of the cancellation tone. First, performance was mea-

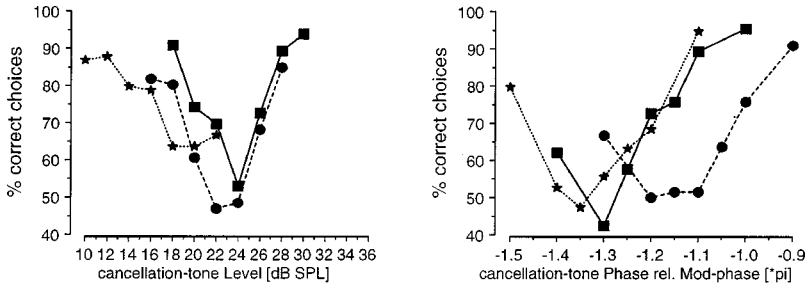

FIG. 1. Psychometric functions for modulation detection in bandpass noise with cutoff frequencies of 4 and 4.5 kHz, as a function of the level (left panel) and the phase (right panel) of a cancellation tone at the modulation frequency, 250 Hz. The modulation was applied before filtering with a depth of 100%. Different symbols and line styles show the functions for the different listeners. Performance drops to chance levels for an individual combination of level and phase for all listeners.

sured as a function of cancellation-tone level while the cancellation-tone phase was fixed at the value determined in the adjustment experiment. Then, the cancellation-tone level was fixed at the value which produced worst performance and modulation detection was measured as a function of cancellation-tone phase. In each trial, three stimuli were presented, separated by 500-ms silent pauses. The first stimulus was always unmodulated bandpass noise. Either the second or the third stimulus was the bandpass SAM noise plus the cancellation tone. Listeners were asked to choose the interval which differed from the first interval; they were provided with visual feedback. Each data point in the psychometric function is based on 99 trials.

3. Listeners

Three listeners aged between 23 and 40 took part in experiments I–III. One of these listeners was unable to take part in experiment IV and was replaced by another listener aged 18. One of the listeners was the first author. All listeners had absolute thresholds within 10 dB of the 1969 ANSI standard at all audiometric frequencies. Listeners were seated individually in a double-walled sound-attenuating booth.

B. Results and discussion

The modulation-detection performance for bandpass SAM noise with a modulation frequency of 250 Hz and cutoff frequencies of 4 and 4.5 kHz is shown in Fig. 1, as a function of cancellation-tone level (left panel) and cancellation-tone phase (right panel). For the results shown in the left panel, the cancellation-tone phase was set to the value obtained individually in the preliminary adjustment experiment; for the results shown in the right panel, the cancellation-tone level was set to that value where the performance shown in the left panel was worst. The different symbols and line styles show the data for the individual listeners.

The V-shapes of the psychometric functions are in agreement with the hypothesis that, in this condition, the detection of amplitude modulation is based exclusively on a distortion tone at the modulation frequency: when the cancellation-tone level is lower than that of the distortion tone, listeners can detect the modulated interval using the distortion tone; when the cancellation-tone level is greater than that of the distortion tone, listeners can identify the modulated interval using the cancellation tone itself. The psychometric functions fall below 70% correct in both conditions for all three listeners. For each listener, at least one of the two psychometric functions drops to chance performance. This means that there exists a specific level and phase of the cancellation tone for each listener where they are no longer able to detect the amplitude modulation. With these cancellation-tone parameters, the SAM-noise detection is at chance level like in the informal masking experiment described above.

The experiment was then repeated with noises whose passbands extended from 4 to 6 kHz, and with a modulation frequency of 1 kHz. All other parameters and aspects of the procedure were unchanged. The spectrum level was held constant and so the overall level of the SAM bandpass noise increased by 6 dB. The results are shown in Fig. 2 in the same format as in Fig. 1.

Again, the psychometric functions are V-shaped, showing that there is a specific level and phase of the cancellation tone where a 1-kHz amplitude modulation of a 2-kHz-wide noise is no longer detectable. In both experiments Ia and Ib, the modulation frequency was half the bandwidth of the bandpass SAM noise. When the bandwidth was four times the modulation frequency, the amplitude-modulated noise with cancellation tone was always discriminable from unmodulated noise. Listeners reported detecting a ''rattle'' in the filtered SAM noise which was not present in the unmodulated noise. This rattle appears to be the temporal cue associated with bandpass-filtered SAM noise. This temporal cue is more salient when the bandwidth is four times the modulation frequency because the modulation depth is re-

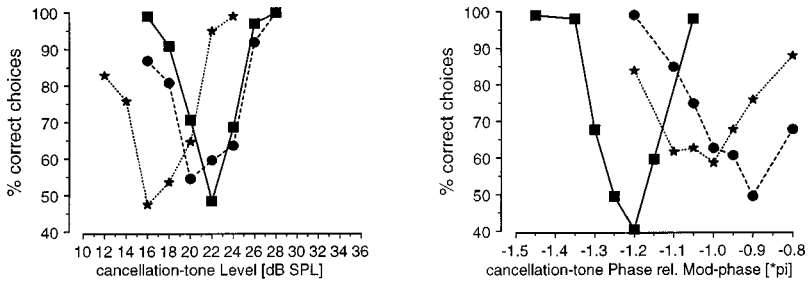

FIG. 2. Psychometric functions for modulation detection in bandpass noise as in Fig. 1 but for cutoff frequencies of 4 and 6 kHz, and a modulation/cancellation-tone frequency of 1 kHz. Again, performance drops to chance levels for a specific combination of level and phase for all listeners.

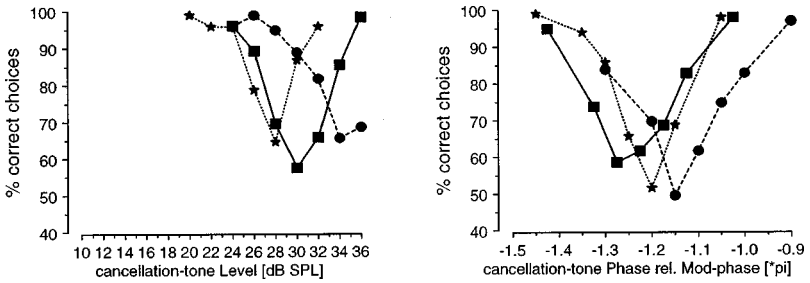

FIG. 3. Detection of a 6%-change of the modulation frequency of SAM bandpass noise with cutoff frequencies of 4 and 5 kHz. Detection performance is plotted against the level (left panel) and phase (right panel) of a cancellation tone at the modulation frequency, 250 Hz.

duced less than in the case where the bandwidth is twice the modulation frequency.

II. EXPERIMENT II: QUANTIFYING THE DISTORTION TONE USING MODULATION-FREQUENCY DISCRIMINATION

Burns and Viemeister (1981) and Hanna (1992) reported modulation-frequency difference limens of about 13% at a modulation frequency of 224 Hz for SAM noise filtered between 2900 and 4000 Hz. Burns and Viemeister (1976) also found that, for broadband SAM noise where the relevance of distortion tones can be neglected, listeners were not able to discriminate between two modulation frequencies that differed by a semitone (a 100-cent or 6% difference in modulation frequency). For pure tones, a 6% frequency difference leads to near-perfect discrimination. The distinction between the difference limens for pure tones and high-frequency filtered SAM noise without audible distortion tones can be used to reveal conditions in which the listener is using the distortion tone. Specifically, in a cancellation-tone paradigm, listeners are required to identify which of two intervals has the SAM noise with the higher modulation frequency, as a function of the level and phase of the cancellation tone. When the modulation-frequency difference between the two intervals is fixed at 6%, it is ample for discriminating pure tones, but not for discriminating the modulation frequency of SAM noise in the absence of audible distortion tones. So, when listeners can perform the task, the distortion tone is audible.

A. Method

1. Stimuli

The stimulus duration and spectrum level were the same as in the previous experiment. The standard modulation frequency was chosen randomly for each trial in the range between 235 and 265 Hz. The modulation frequencies for the two stimuli in one trial differed by 6% and they were centered around the standard modulation frequency. The frequencies of the cancellation tones in the two intervals were always the same as the modulation frequencies. The noise stimuli were first amplitude modulated with a depth of 100% and then digitally bandpass filtered between 4 and 5 kHz using rectangular filtering. Stimulus generation and presentation were identical to experiment I.

2. Procedure

Psychometric functions were obtained for the detection of a 6% difference in modulation frequency between two bandpass SAM noises as a function of the phase or level of a cancellation tone at the modulation frequency. The range of cancellation-tone levels and phases presented in this experiment was determined with a small adjustment experiment as in experiment I.

In a two-alternative, forced-choice paradigm, listeners had to indicate the stimulus with the higher modulation frequency. Visual feedback was provided. Having taken part in experiment I, listeners did not have additional training for this experiment. The data points show the average performance for 99 presentations of each stimulus condition. Performance was measured first as a function of cancellation-tone level with the phase fixed at the value individually determined in the adjustment experiment. Then, performance was measured as a function of cancellation-tone phase with the level fixed at that value where performance as a function of level was worst.

B. Results and discussion

Psychometric functions for the detection of a 6% difference in modulation frequency between the modulation frequencies of two SAM noises, bandpass filtered between 4 and 5 kHz, are shown in Fig. 3 as a function of the level (left panel) and the phase (right panel) of the cancellation tone. As in Figs. 1 and 2, different symbols present the data for different listeners.

As in the previous experiment, the psychometric functions are V-shaped. For every listener, there exists a specific level and phase of the cancellation tone where a 6% difference in modulation frequency is no longer detectable, presumably because the distortion tone of amplitude-modulated noise is canceled. In this case, a 6% difference of the modulation frequency does not produce a detectable change (Hanna, 1992; Burns and Viemeister, 1976). When the distortion tone is not completely canceled, the 6% change in the distortion tone provides a detection cue.

The cancellation-tone levels obtained in this experiment are higher than those obtained in experiment Ia for the same modulation frequency. The increase can be explained in terms of the effective modulation depth of the stimulus. When the bandwidth of the SAM noise is increased from double the modulation frequency to four times the modulation frequency, the effective modulation depth after bandpass filtering increases from 50% (cf. experiment I) to 70%. The strength of an even-order distortion product generated by the modulation of the stimulus would be expected to increase in this case.

TABLE I. Modulation-frequency DLs for filtered SAM noise with cutoff frequencies of 4 and 5 kHz. DLs were measured around a modulation frequency of 250 Hz. When a cancellation tone was included (condition II), its level and phase were set to the values determined individually for best cancellation of the distortion tone in experiment II.

Listener #	Fmod DL *without* cancellation tones (condition I) [% of 250 Hz]	Standard deviation	Fmod DL *with* cancellation tones (condition II) [% of 250 Hz]	Standard deviation
1	2.4	0.35	13.9	0.6
2	3.3	0.67	41.3	13
3	0.9	0.21	20.8	6.3

III. EXPERIMENT III: MODULATION-FREQUENCY DIFFERENCE LIMENS WITH AND WITHOUT CANCELLATION TONES

Experiment II showed that, when the distortion tone of bandpass SAM noise is canceled, a 6%-change of the modulation frequency is no longer detectable. In experiment III, we measure modulation-frequency difference limens (fmod DLs) for the stimuli in experiment II with and without the cancellation tone, to determine the extent to which modulation-frequency information is preserved after the distortion tone has been canceled.

A. Method

1. Stimuli

As in experiments I and II, the stimuli were bandpass-filtered SAM noise with 100% modulation before filtering, a signal duration of 327.7 ms, and a spectrum level of 45 dB SPL/Hz. Modulation frequency DLs were centered around a standard modulation frequency of 250 Hz. The stimuli were filtered between 4 and 5 kHz. The experiment was performed without cancellation tones (condition I) and with cancellation tones (condition II). The cancellation tone was presented at the modulation frequency and with the same duration as the SAM noise. The cancellation-tone level and phase were set to the values determined individually in experiment II for optimal cancellation. Stimulus generation and presentation was identical to the previous experiments.

2. Procedure

Modulation frequency DLs were measured with an adaptive two-alternative, forced-choice paradigm using the three-down, one-up rule which estimates the 79.4%-correct value on the psychometric function (Levitt, 1971). The modulation frequency difference was initially set to 30 Hz (12% of the reference modulation frequency) and changed in steps of 50% of the previous value for the first two reversals, in steps of 10% for reversals three to five, and in steps of 5% for reversals six to 11. The average of these last six reversals was taken as threshold for the run. The threshold data show the average and standard deviation of four runs obtained after a training session which consisted of five practice runs for each condition. Data were collected first for condition I (without cancellation tone) and then for condition II (with cancellation tone). Listeners were provided with visual feedback.

B. Results and discussion

Modulation-frequency DLs with and without cancellation tones at the modulation frequency are shown for the three listeners in Table I. Without added cancellation tones (condition I), the modulation-frequency DLs are between 0.9% and 3.3%. Wier *et al.* (1977) measured frequency DLs for pure tones as a function of their sensation level. The results of experiment II together with those of experiment IV (see below) show that the sensation level of the distortion tone in the current experiment is around 10 dB. At a standard frequency of 200 Hz and a similar sensation level, the results of Wier *et al.* (1977) are in good agreement with the current DLs measured in the presence of the distortion tone. When the distortion tone is canceled, (condition II), the modulation-frequency DLs increase markedly to between 14% and 41%. Moreover, DLs in condition II represent ''best-case'' values: The level and phase of the cancellation tone was determined for a modulation frequency of 250 Hz. With increasing frequency differences, the actual modulation frequencies deviated more and more from the modulation frequency for which cancellation was optimal. It may thus be the case, that the threshold values with cancellation tones represent values where cancellation is no longer complete. To avoid this problem, it would be necessary to repeat experiment II for every modulation frequency in the present experiment. The result would probably be a further increase in modulation-frequency DLs, and since a large increase in the DLs already occurs with the cancellation-tone parameters determined at 250 Hz, we felt there was little to be gained by measuring the cancellation-tone parameters for all of the modulation frequencies presented.

The modulation-frequency DLs with cancellation tones for Listeners 2 and 3 are poorer than those reported by Hanna (1992) or Formby (1985) for broadband noise. The reason for the discrepancy may just be the stimulus bandwidth. In the case of Hanna (1992), it is also possible that there was an audible distortion tone despite the low level of the stimuli. Bandpass filtering after amplitude modulation decreases the effective modulation depth and the decrease of modulation depth depends on the relationship between stimulus bandwidth and modulation frequency. Hanna (1992) measured discrimination thresholds around 40% when he limited the band to 1100 Hz (500–1600 Hz). When the listening band was shifted upwards (2900–4000 Hz), performance improved to about 14% at a modulation frequency of 224 Hz. Informal observations suggest that the level of the quadratic distortion tone is dependent on the frequency po-

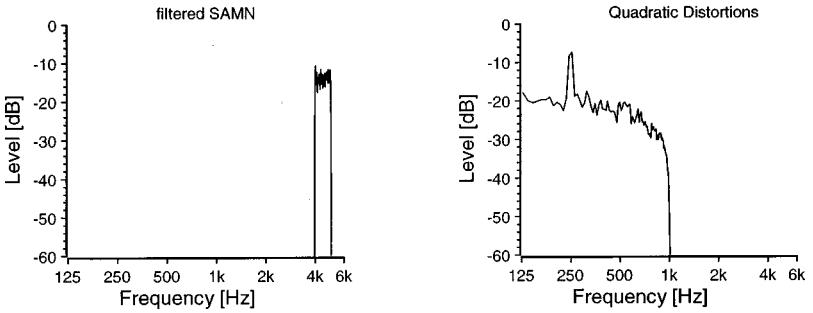

FIG. 4. Quadratic distortions (right panel) generated by a filtered SAM noise (left panel) with cutoff frequencies of 4 and 5 kHz and a modulation frequency of 250 Hz. The distortion spectrum is obtained by squaring the waveform. Quadratic distortions have a low-pass shape with a cutoff frequency corresponding to the noise bandwidth. The amplitude modulation of the primary noise leads to a peak in the distortion band at the modulation frequency.

sition of the bandpass SAM noise. It may thus be the case that in Hanna's experiments, with low presentation levels and no masking noise, the improvement in performance with increasing center frequency is due to an audible quadratic distortion tone in combination with a stronger temporal cue due to wider auditory filters.

IV. THE GENERATION OF A SAM NOISE DISTORTION TONE

Strickland and Viemeister (1997) argued that the distortion tone at the modulation frequency is a difference tone. How can a stimulus with a flat long-term spectrum generate a discrete difference tone? Spectral information about the modulation frequency in SAM noise has been investigated in, for example, Pierce *et al.* (1977) and Houtsma *et al.* (1980): In unmodulated noise, amplitudes are Rayleigh distributed and phases are distributed uniformly. For SAM noise, however, every frequency component, *f*, has two sideband components at $f \pm \text{fmod}$ with the same phase as the component at *f*. In the presence of quadratic nonlinearity, quadratic difference tones, $f2-f1$, are generated between each pair of frequency components in the noise. For unmodulated bandpass noise, these quadratic difference tones add up to a distortion noise band which has a low-pass characteristic due to the bandpass characteristic of the primary noise band (Greenwood, 1971). For bandpass-filtered SAM noise, the occurrence of the sideband components leads to an ''over-representation'' of spectral components with a frequency separation equal to fmod. Quadratic distortion components between each frequency component and its sidebands add up and, due to their over-representation, lead to a peak in the distortion noise band at the modulation frequency. The spectrum of a SAM noise modulated at 250 Hz and filtered between 4 and 5 kHz is plotted in the left panel of Fig. 4. The right panel shows the spectrum of the squared waveform which is the first-order quadratic distortion product. The distortion product consists of a low-pass distortion noise band with a cutoff frequency corresponding to the bandwidth of the stimulus. The distortion noise band has a distinct peak at the modulation frequency. Although not plotted, quadratic distortion also produces spectral components above the noise passband. However, these are not investigated in the current paper.

A. Quadratic distortion in the experimental equipment

To test for distortion in the equipment, SAM noise with a modulation frequency of 250 Hz and bandpass cutoffs of 4 and 4.5 kHz was recorded from the Sennheiser headphone used in the experiment with a B&K 4153 artificial ear. The signal level was the same as in experiment I. The average power spectrum, over ten samples, is presented in the left panel of Fig. 5 and it shows that there is no spectral peak at the modulation frequency of 250 Hz. The right panel shows the average spectrum for ten samples of the same modulated noise with the cancellation tone added in at 250 Hz. The level and phase of the cancellation tone are set to the optimal cancellation values for Listener 1, and it produces a peak in the spectrum, as would be expected. Note that the listener heard a pure tone at the modulation frequency when presented with the stimulus whose spectrum at the eardrum had no peak at that frequency (left panel). However, the listener did *not* hear a pure tone when presented with the stimulus whose spectrum contained a peak at the modulation frequency (right panel). Neither of these results would occur had the equipment generated the audible distortion tone.

B. Aural distortion

Traditionally, quadratic distortion has been attributed to the middle ear (Zwicker, 1955). However, Hall (1972) and Brown (1993) (among others) showed that the level of the quadratic distortion tone depends on the frequency separation between the primaries. This is difficult to explain in

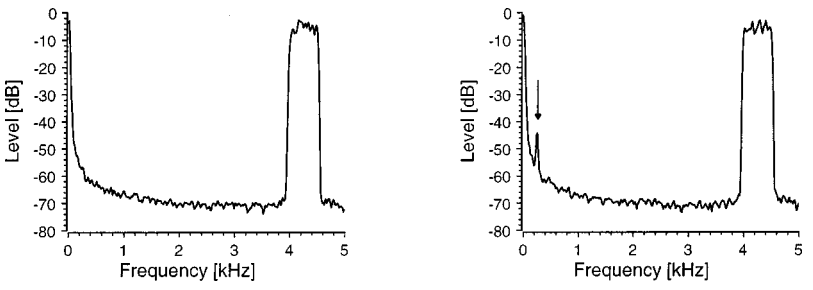

FIG. 5. Frequency response of the headphones used in the experiments with filtered SAM noise. The left panel shows the headset response to the modulated noise alone. This stimulus is easily discriminated from unmodulated bandpass noise. The right panel shows the headset response to the modulated noise with a cancellation tone added at the modulation frequency, 250 Hz. The level and phase of the cancellation tone were set to the values that produced cancellation for Listener 1 in experiment I. In contrast to the stimulus in the left panel, the stimulus in the right panel is no longer discriminable from unmodulated noise despite the peak at 250 Hz.

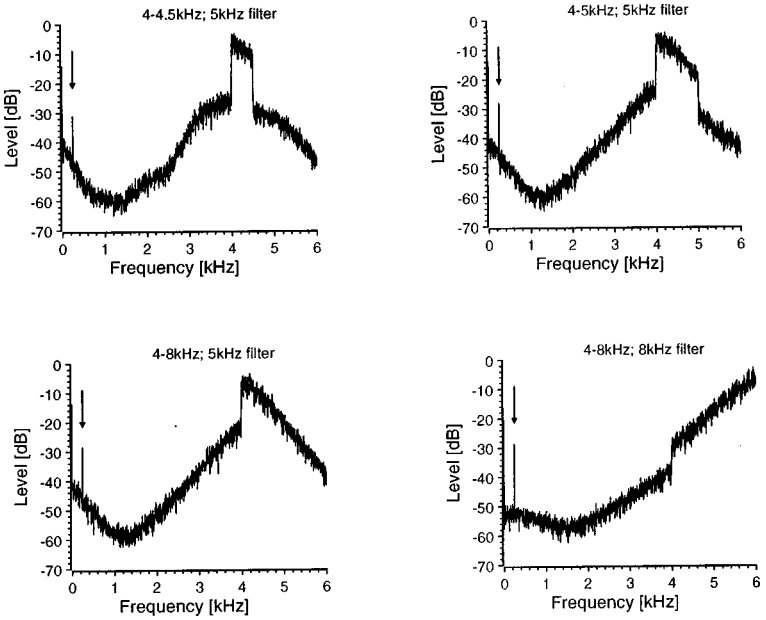

FIG. 6. Spectral analysis of the output of a simulated auditory filter suggested by Carney (1993) in response to filtered SAM noise with a modulation frequency of 250 Hz (arrows). The upper panels show the response of a 5-kHz filter to bandpass noise from 4 to 4.5 kHz (left panel) and from 4 to 5 kHz (right panel). The lower panels show the response of a 5-kHz (left) and an 8-kHz (right) filter when the noise passband is 4–8 kHz. Nonlinearity in the auditory filter causes the best frequency of the filter to shift downward with increasing stimulus level. See the text for a detailed discussion.

terms of middle-ear function and suggests a generation site in the cochlea. Recent refined models of cochlear filtering, for example Carney (1993), simulate active mechanisms using an asymmetrically saturating feedback loop, and this asymmetry produces quadratic distortion. We calculated the responses of Carney's auditory filter at center frequencies of 5 and 8 kHz to bandpass SAM noises with bandwidths of 500 Hz and 1 kHz. The spectra of the outputs of the 5-kHz filter are plotted in the upper two panels of Fig. 6; the noise extending from 4 to 4.5 kHz is in the left panel, and the noise extending from 4 to 5 kHz is in the right panel. The spectra show both low-pass and high-pass distortion-noise bands, and a peak at the 250-Hz modulation frequency. The low-pass distortion noise and the peak at the modulation frequency are produced in Carney's auditory-filter simulation by asymmetric compression in the mechanoelectrical transduction of the outer-hair cells. The low-pass cutoff frequency of the distortion-noise band increases with increasing stimulus bandwidth, and the strength of the component at the modulation frequency also increases. The latter would explain the difference in cancellation-tone level between experiments I and II, where the level required for optimal cancellation increased with increasing noise bandwidth.

The low-pass cutoff of this even-order distortion-noise band is also influenced by auditory filter width. This is illustrated in the lower two panels of Fig. 6, which show the responses of a 5-kHz filter (left panel) and an 8-kHz filter (right panel) to amplitude-modulated noise extending from 4 to 8 kHz. The 5-kHz filter still produces a low-pass distortion noise even though the stimulus is 4 kHz wide. In this case, the width of the distortion-noise band is limited by filter bandwidth. The 8-kHz auditory filter is wider and so the even-order distortion band and the odd-order distortion band overlap and produce a relatively flat distortion-noise spectrum. Thus, a nonlinear cochlear filter model with asymmetrically saturating feedback may provide a physiological basis for the distortion tone measured in the present study.

It is important to point out that the power spectra in Fig. 6 are not representations of the internal auditory spectra produced by these SAM noises; instead, they show the spectral distribution of the output of an isolated nonlinear filter without the interaction between filters that occurs in the cochlea. That is, in the cochlea, distortion components produced by compression would travel through the endocochlear fluid or over the basilar membrane to the place associated with the frequency of the distortion. The current model does not include the contributions produced by this propagation in the cochlea. There are cochlear simulations capable of producing and propagating combination tones. One example is the wave digital filter model constructed by Giguere and Woodland (1994) and used by Giguere *et al.* (1997) to model cubic distortion products. Unfortunately, the implementation does not include the asymmetric compression required to explain quadratic distortion, and the model is not easily modified.

The final experiment was designed to extend the distortion-tone research to the distortion-noise bands generated by bandpass-filtered noise. Greenwood (1971) made extensive measurements of the masking produced by distortion-noise bands, but he focused mainly on cubic distortion. Bandpass-filtered noise produces a band of cubic distortion noise with a high-pass filtered shape just below the band of primaries, and the band elevates masked threshold in this region. Quadratic distortion produces a low-pass distortion-noise band, and in the final experiment, we measured masked thresholds at low frequencies to reveal the effect of this distortion noise. The stimuli were bandpass noise maskers with the same levels and bandwidths used in the previous experiments.

V. EXPERIMENT V: REMOTE MASKING BY BANDPASS NOISE

A. Method

1. Stimuli

Bandpass noise maskers were generated with a lower cutoff frequency of 4 kHz and an upper cutoff of 4.5, 5, 6, or

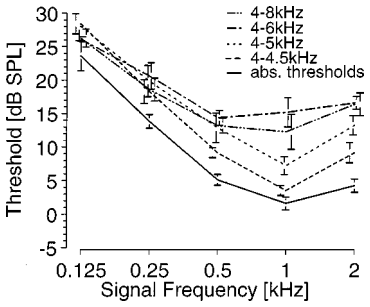

FIG. 7. Average thresholds for sinusoids masked by bandpass noise with a constant spectrum level of 45 dB SPL. The lower noise cutoff frequency is constant at 4 kHz, the upper noise cutoff frequency is 4.5 kHz (dashed line), 5 kHz (dotted line), 6 kHz (dash–dotted line), or 8 kHz (dash–dot–dotted line). Average absolute thresholds are presented by the solid line. The error bars show across-listener' standard errors. For signal frequencies of 125 and 250 Hz, threshold elevations are largely independent of noise bandwidth; for the higher-frequency signals, threshold elevations depend on masker bandwidth in a systematic way. See the text for an interpretation in terms of distortion-noise bands.

8 kHz. The spectrum level was fixed at 45 dB SPL/Hz. Thus, the overall stimulus level varied from 72 to 81 dB SPL. The signals were pure tones with frequencies ranging from 125 to 2000 Hz in octave steps. The masker and signal durations were 327.7 ms including 20-ms raised-cosine gates. Stimuli were presented monaurally to the left ear using the same experimental equipment as in the previous experiments.

2. Procedure

In an adaptive two-alternative, forced-choice paradigm, absolute and masked thresholds were measured using the ''three-down, one-up'' rule which estimates the 79.4%-correct point on the psychometric function (Levitt, 1971). Initially, the level of the sinusoidal signal was changed in steps of 10 dB; the step size was reduced to 5 dB after the second reversal, and to 2 dB after the fifth reversal. The average of reversals six to 11 was taken to be the threshold for that run. Individual threshold values show the average over three runs following a single practice run. The listeners were the same as for experiments I–III apart from Listener 3, who was replaced by another listener aged 18.

B. Results and discussion

Absolute and masked thresholds are plotted in Fig. 7. Absolute thresholds averaged over the three listeners are presented by the solid line with across-listener standard errors. The broken lines present averaged masked thresholds for maskers with different bandwidths (again, with across-listener standard errors). The dashed line presents thresholds for the masker-noise band extending from 4 to 4.5 kHz, the dotted line for the band from 4 to 5 kHz, the dash–dotted line for the band from 4 to 6 kHz, and the dash–dot–dotted line for the band from 4 to 8 kHz.

The presence of a masker noise above 4 kHz raises signal thresholds for all signal frequencies in the experiment, despite the fact that auditory excitation patterns (Moore and Glasberg, 1987) would not predict any masking below 2.5 kHz for maskers with a lower cutoff frequency of 4 kHz. For signal frequencies of 125 and 250 Hz, masked threshold is 3 to 5 dB above absolute threshold, and is largely independent of masker bandwidth. At 500 Hz, threshold is elevated by about 9 dB by all maskers except for the narrowest, 500 Hz, where the threshold elevation is 4 dB. At 1 kHz, the 500-Hz masker produces almost no masking, the 1-kHz masker produces 5 dB of masking, and the wider maskers produce about 10 dB of masking. At 2 kHz, threshold increases with bandwidth up to 2 kHz.

In the following, these remote masking data are interpreted in terms of both quadratic and cubic distortion noise. The masked thresholds are assumed to reflect the compound effect of both types of distortion. For signal frequencies of 125 and 250 Hz, threshold elevation appears to be largely produced be quadratic distortion, and evaluations are independent of masker bandwidth. At 500 Hz, however, threshold is lower for the 500-Hz-wide masker than for the broader maskers. This is presumably the case because the low-pass cutoff frequency of the quadratic distortion band depends on masker bandwidth. As the first-order quadratic distortion band for the 500-Hz masker ends at 500 Hz, it produces less masking at a signal frequency of 500 Hz than the broader maskers. At 1 kHz, the 500-Hz-wide masker produces virtually no masking, presumably because the signal frequency is above the quadratic distortion band and below the cubic distortion band. At 2 kHz, the 500-Hz-wide masker produces masking, which we assume is due to downward spreading cubic distortion. When the masker bandwidth is 1 kHz, it produces more masking at 500 Hz than the 500-Hz-wide masker due to the higher cutoff of the quadratic distortion band, and there may also be a contribution from the cubic distortion band. With increasing masker bandwidth, masking at 1 and 2 kHz increases rapidly because of the downward spread of the cubic distortion and the simultaneous upward spread of the quadratic distortion. In these conditions, the individual contributions of the two distortion bands cannot be dissociated.

When the masker bandwidth is increased from 2 to 4 kHz, masking at 2 kHz does not increase, and at 1 kHz it decreases slightly. This effect cannot readily be explained within the current framework. When the masker bandwidth is increased from 2 to 4 kHz, the overall masker level is increased from 78 to 81 dB SPL. It may be the case that this increase elicited the acoustic reflex which in turn may have changed the spectral shape and magnitude of the distortion noise bands.

Bilger (1958) measured what he referred to as remote masking as a function of masker noise bandwidth. The spectrum level of the noise was fixed at 76 dB SPL/Hz and the bandwidths were 500 Hz, 1, 2, and 4 kHz, corresponding to overall levels of 103, 106, 109, and 112 dB SPL, respectively. These presentation levels are much higher than those in the current experiment and they produced greater threshold elevations. It is probably the case that these high presentation levels produce not only first-order, quadratic, and cubic distortion noise, but also high-order distortion noise.

Greenwood (1971) investigated the effect of distortion noise bands on the shape of the masked audiogram with pure-tone and narrow-band maskers, in a band-widening experiment similar to experiment IV. He explained the results in terms of first-order and higher-order cubic distortion

which limited the rising slope of the masked audiogram. He did not use signal frequencies low enough to reveal the effects of quadratic distortion. The current results indicate that quadratic distortion does influence the masked audiogram in some cases, but to a much lesser extent than cubic distortion, and with no direct implications for measures of auditory frequency selectivity. The more interesting aspect of quadratic distortion is perhaps its influence on pitch and modulation perception with high-pass filtered stimuli.

VI. QUADRATIC DISTORTION AS AN AUDITORY REPRESENTATION OF THE STIMULUS MODULATION SPECTRUM

The even-order distortion products produced by a band of SAM noise are reminiscent of the spectrum of the stimulus envelope, commonly referred to as the modulation spectrum. The modulation spectrum is calculated by taking the Fourier transform of the Hilbert envelope, or the Fourier transform of the output of an auditory filter which has been half-wave rectified and low-pass filtered to extract a stimulus envelope as it may be represented in the auditory system. Dau *et al.* (1997) have recently demonstrated the value of the modulation spectrum in explaining modulation detection data. In their model, following cochlear filtering, neural transduction, and envelope extraction, a modulation filterbank is used to produce a modulation spectrum for each frequency channel. The set of modulation spectra for all of the frequency channels is proposed as an internal representation that the auditory system could use to analyze the modulation properties of sounds. The experiments in the current paper indicate that some of the information in the modulation spectrum may already be present in the cochlea as a result of quadratic distortion. For amplitude-modulated stimuli with moderate to high levels and modulation frequencies above, say 50 Hz, it appears that there is excitation on the basilar membrane at the modulation frequency. When no care is taken to mask or cancel quadratic distortion, it may confound experimental results intended to reveal aspects of temporal processing. Studies on the pitch of SAM noise (Burns and Viemeister, 1976, 1981; Patterson *et al.*, 1978) and modulation detection (Formby and Muir, 1988; Eddins, 1993) included unmodulated noise to mask possible distortion components, and Hanna (1992) used a low presentation level which made it unlikely that quadratic distortion products were audible. Blamey *et al.* (1984), however, measured modulation frequency discrimination for noise stimuli with smoothed rectangular modulators that were bandpass filtered at center frequencies between 1 and 10 kHz. For some listeners, they found modulation frequency difference limens as low as 2 to 3 percent even with filters centered at relatively high frequencies. They did not use a masking noise and so the interpretation of the results is complicated by potential distortion products, both at the modulation frequency and its integer multiples.

SAM tones, like SAM noise, will produce a distortion tone at the modulation frequency under some conditions, and SAM tones have frequently been used in physiological studies of temporal processing in the auditory system (for a review, see Langner, 1992). Schulze and Langner (1997) investigated modulation tuning in the primary auditory cortex of the Mongolian gerbil and found that units with low-frequency pure-tone response areas showed modulation tuning to SAM tones positioned well above their response area. In the discussion of the role of distortion tones in their experiments, the authors assumed that quadratic distortion is independent of the frequency range and spectral separation of the primaries. This has been contradicted by the studies of Brown (1993) and Hall (1972). Nevertheless, Schulze and Langner (1997) concluded that distortion products were not involved in their experiments. The current experimental findings emphasize the importance of quadratic distortion in the perception of amplitude modulation. Even if some of the results reported by Schulze and Langner (1997) do not reveal the influence of a quadratic distortion tone, this tone will certainly influence the response of a neuron tuned to the distortion-tone frequency as long as the distortion tone is not masked or canceled.

VII. SUMMARY AND CONCLUSIONS

The present study shows that bands of filtered SAM noise produce a quadratic distortion tone at the modulation frequency which can be canceled using a pure tone. When the distortion tone is canceled, the amplitude modulation of the noise band is no longer detectable, provided the bandwidth of the noise is equal to, or less than, double the modulation frequency. For wider bandwidths (relative to the modulation frequency), the amplitude modulation is detectable in the absence of the distortion tone, but discrimination of the modulation frequency is greatly reduced when compared to conditions without the cancellation tone. Thus, these experiments provide two different psychoacoustical paradigms for quantifying the quadratic distortion tone elicited by SAM noise.

The quadratic distortion tone can be explained in terms of summating difference tones generated by components within the passband of the SAM noise. While some functional simulations of peripheral auditory filtering include the asymmetric nonlinearity required to generate cochlear difference tones, a full simulation of the observed effects requires a model that can propagate distortion products to their frequency place.

Quadratic distortion may also be responsible for some aspects of the data on ''remote masking,'' that is, the elevation in the masked audiogram produced by high-frequency bands of noise.

The pronounced perceptual effects of quadratic distortion in the current psychoacoustical experiments stress the need to consider, and control, quadratic distortion in studies of temporal processing with amplitude-modulated stimuli. While psychophysical studies have typically masked quadratic distortion products, physiological studies of temporal processing with AM tones typically have not and so their results may be confounded with the spectral cues arising from quadratic distortion, especially when across-frequency processing of amplitude modulation is studied.

ACKNOWLEDGMENTS

The experiments were performed while the first author was a visiting scientist at the Centre for the Neural Basis of Hearing. The research was supported by the Medical Research Council, UK, Grant No. (G9703469) and by a research grant from the ''Deutsche Forschungsgemeinschaft'' to the first author. We would like to thank Manfred Kössl for very fruitful discussions and comments on earlier versions of this manuscript. We would like to thank Ed Burns and an unknown reviewer for their helpful comments and suggestions on earlier versions of this paper.

Bilger, R. C. (**1958**). ''Intensive determinants of remote masking,'' J. Acoust. Soc. Am. **30**, 817–824.

Blamey, P. J., Dowell, Y. C., Tong, Y. C., and Clark, G. M. (**1984**). ''An acoustic model of a multiple-channel cochlear implant,'' J. Acoust. Soc. Am. **76**, 97–103.

Brown, A. M. (**1993**). ''Distortion in the cochlea: Acoustic $f2-f1$ at low stimulus levels,'' Hear. Res. **70**, 160–166.

Burns, E. M., and Viemeister, N. F. (**1976**). ''Nonspectral pitch,'' J. Acoust. Soc. Am. **60**, 863–868.

Burns, E. M., and Viemeister, N. F. (**1981**). ''Played again SAM: Further observations on the pitch of amplitude-modulated noise,'' J. Acoust. Soc. Am. **70**, 1655–1660.

Carney, L. (**1993**). ''A model for the response of low-frequency auditory-nerve fibers in cat,'' J. Acoust. Soc. Am. **93**, 401–417.

Dau, T., Kollmeier, B., and Kohlrausch, A. (**1997**). ''Modeling auditory processing of amplitude modulation. I. Detection and masking with narrow-band carriers,'' J. Acoust. Soc. Am. **102**, 2892–2905.

Eddins, D. A. (**1993**). ''Amplitude modulation detection of narrow-band noise: Effects of absolute bandwidth and frequency region,'' J. Acoust. Soc. Am. **93**, 470–479.

Formby, C. (**1985**). ''Differential sensitivity to tonal frequency and to the rate of amplitude modulation of broadband noise by normally hearing listeners,'' J. Acoust. Soc. Am. **78**, 70–77.

Formby, C., and Muir, K. (**1988**). ''Modulation and gap detection for broadband and filtered noise signals,'' J. Acoust. Soc. Am. **84**, 545–550.

Giguere, C., and Woodland, P. C. (**1994**). ''A computational model of the auditory periphery for speech and hearing research. I. Ascending path,'' J. Acoust. Soc. Am. **95**, 331–342.

Giguere, C., Smoorenburg, G. F., and Kunov, H. (**1997**). ''The generation of psychoacoustic combination tones in relation to two-tone suppression effects in a computational model,'' J. Acoust. Soc. Am. **102**, 2821–2830.

Greenwood, D. D. (**1971**). ''Aural combination tones and auditory masking,'' J. Acoust. Soc. Am. **50**, 502–543.

Greenwood, D. D. (**1991**). ''Critical bandwidth and consonance in relation to cochlear frequency-position coordinates,'' Hear. Res. **54**, 164–208.

Hall, J. L. (**1972**). ''Auditory distortion products $f2-f1$ and $2f1-f2$,'' J. Acoust. Soc. Am. **51**, 1863–1871.

Hanna, T. E. (**1992**). ''Discrimination and identification of modulation rate using a noise carrier,'' J. Acoust. Soc. Am. **91**, 2122–2128.

Houtsma, A. J. M., Wicke, R. W., and Ordubadi, A. (**1980**). ''Pitch of amplitude-modulated low-pass noise and predictions by temporal and spectral theories,'' J. Acoust. Soc. Am. **67**, 1312–1322.

Langner, G. (**1992**). ''Periodicity coding in the auditory system,'' Hear. Res. **60**, 115–142.

Levitt, H. (**1971**). ''Transformed up–down methods in psychoacoustics,'' J. Acoust. Soc. Am. **49**, 467–477.

Moore, B. C. J., and Glasberg, B. R. (**1987**). ''Formulae describing frequency selectivity as a function of frequency and level and their use in calculating excitation patterns,'' Hear. Res. **28**, 209–225.

Patterson, R. D., Johnson-Davies, D., and Milroy, R. (**1978**). ''Amplitude modulated noise: The detection of modulation versus the detection of modulation rate,'' J. Acoust. Soc. Am. **63**, 1904–1911.

Pierce, J. R., Lipes, R., and Cheetham, C. (**1977**). ''Uncertainty concerning the direct use of time information in hearing: Place cues in white-spectra stimuli,'' J. Acoust. Soc. Am. **61**, 1609–1621.

Schulze, H., and Langner, G. (**1997**). ''Periodicity coding in the primary auditory cortex of the Mongolian gerbil (*Meriones unguiculatus*): Two different coding strategies for pitch and rhythm?'' J. Comp. Physiol. A **181**, 651–663.

Strickland, E. A., and Viemeister, N. F. (**1997**). ''The effects of frequency region and bandwidth on the temporal modulation transfer function,'' J. Acoust. Soc. Am. **102**, 1799–1810.

Wier, C. C., Jesteadt, W., and Green, D. M. (**1977**). ''Frequency discrimination as a function of frequency and sensation level,'' J. Acoust. Soc. Am. **61**, 178–184.

Zwicker, E. (**1955**). ''Der ungewoehnliche Amplitudengang der nichtlinearen Verzerrungen des Ohres,'' Acustica **5**, 67–74.

Spectro-temporal modulation transfer functions and speech intelligibility

Taishih Chi, Yujie Gao, Matthew C. Guyton, Powen Ru, and Shihab Shamma
Center for Auditory and Acoustics Research, Institute for Systems Research, Electrical Engineering Department, University of Maryland, College Park, Maryland 20742

(Received 14 December 1998; accepted for publication 21 June 1999)

Detection thresholds for spectral and temporal modulations are measured using broadband spectra with sinusoidally rippled profiles that drift up or down the log-frequency axis at constant velocities. Spectro-temporal modulation transfer functions (MTFs) are derived as a function of ripple peak density (Ω cycles/octave) and drifting velocity (ω Hz). The MTFs exhibit a low-pass function with respect to both dimensions, with 50% bandwidths of about 16 Hz and 2 cycles/octave. The data replicate (as special cases) previously measured purely temporal MTFs ($\Omega=0$) [Viemeister, J. Acoust. Soc. Am. **66**, 1364–1380 (1979)] and purely spectral MTFs ($\omega=0$) [Green, in *Auditory Frequency Selectivity* (Plenum, Cambridge, 1986), pp. 351–359]. A computational auditory model is presented that exhibits spectro-temporal MTFs consistent with the salient trends in the data. The model is used to demonstrate the potential relevance of these MTFs to the assessment of speech intelligibility in noise and reverberant conditions. © *1999 Acoustical Society of America.* [S0001-4966(99)02210-9]

PACS numbers: 43.66.Ba, 43.71.Gv [RVS]

INTRODUCTION

The most obvious feature of a speech spectrogram is the energy modulations, both in time in any given frequency channel, and along the spectral axis at any instant, due to formant peaks and their transitions, spectral edges, and rapid amplitude modulations at onsets/offsets. These modulations occur at relatively slow temporal rates (few Hz) reflecting the speed of the articulatory gestures, and hence the phonetic and syllabic rates of speech. Speech intelligibility is critically dependent on the clarity of these spectro-temporal modulations. Thus speech reconstructed from smoothed spectrograms along either dimension suffers from progressive loss of intelligibility (Shannon *et al.*, 1995; Arai *et al.*, 1996; Drullman *et al.*, 1994).

Human sensitivity to spectral and temporal modulations has been studied extensively in various experimental settings. In most cases, these two measurements are treated separately. For instance, sensitivity measurements to *purely temporal* modulations—usually referred to as a temporal ''modulation transfer function (**MTF**)''—are illustrated in Fig. 1(a). They employ either amplitude-modulated white noise (Viemeister, 1979) [Fig. 1(a), left panel] or temporally modulated harmonic-like spectra (Yost and Moore, 1987; van Zanten and Senten, 1983) [Fig. 1(a), right panel]. While both MTFs are low pass in character, they exhibit substantially different upper cutoff rates, with flat noise being detectable to much higher rates (exceeding 64 Hz compared to less than 10 Hz for the noise-delayed stimulus). Complementary tests of *purely spectral* sensitivity are shown in Fig. 1(b). They employ stationary (static) spectra with sinusoidal envelopes along the logarithmic frequency axis—also called *ripples* (Hillier, 1991; Green, 1986). This spectral MTF demonstrates that our ability to detect closely spaced ripple peaks deteriorates above about 4 cycles/octave.[1] Spectral MTFs in birds also exhibit similar trends and upper limits, although there is some variability across different species (Amagai *et al.*, 1999).

All MTFs described in Fig. 1 are essentially one-dimensional in that they are measured by varying either the spectral or temporal modulation rates while holding the other constant. This is the case even for the spectrally complex stimuli in Yost and Moore (1987) and van Zanten and Senten (1983) because such harmonic like spectra preserve their shape against the tonotopic (logarithmic frequency) axis of the auditory system regardless of the change in their frequency spacing. Consequently, MTFs are effectively always measured with the same spectral pattern (except for a translation to a different frequency region).[2]

Modulations in speech spectrograms are usually combined spectro-temporal modulations. Thus, speech is rarely a flat modulated spectrum nor is it a stationary peaked spectrum, but rather it is both—a spectrum with dynamic peaks. Therefore, sensitivity to these types of combined modulations relates directly to speech perception. But, are spectro-temporal MTFs separable? That is, can the combined spectro-temporal MTF be derived from a product of purely temporal and spectral MTFs?

A particularly useful and simple example of a combined spectro-temporal modulation is the spectral ripple that drifts upwards or downwards at a constant velocity, as illustrated in Fig. 2(a). By varying the density of the peaks along the spectral axis (Ω, cyc/oct), and the drifting speed (ω, Hz) and directions, it is possible to measure a full combined spectro-temporal MTF. These stimuli are also interesting from a theoretical perspective in that they form a complete set of orthonormal basis functions for the spectrogram. Thus, any arbitrary spectrogram can be decomposed (by a two-dimensional Fourier transform) into a linearly weighted sum

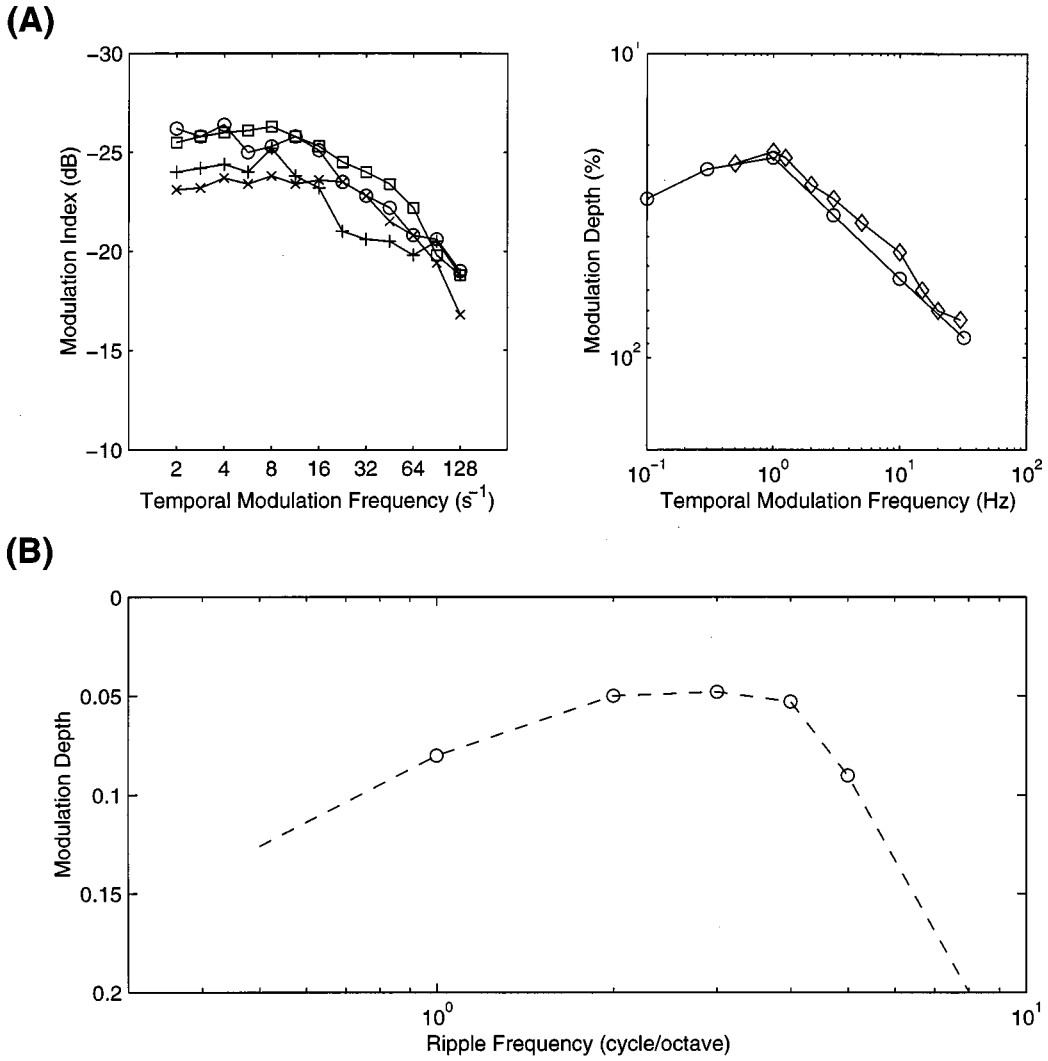

FIG. 1. Temporal and spectral modulation transfer functions (MTF). (a) Left panel—temporal MTFs measured using amplitude modulated white noise (Viemeister, 1979). Right panel—temporal MTFs measured using rippled noise with sinusoidally modulated delays (van Zanten and Senten, 1983). (b) Spectral modulation transfer functions measured using ripples (Green, 1986).

of such drifting ripples with different spectral densities, velocities and directions [Fig. 2(b)]. Because of this property, ripples have played a useful role in characterizing the linear aspects of the spectro-temporal response fields in the auditory cortex (Simon *et al.*, 1998). Moreover, there is neurophysiological evidence that these dynamically rippled spectra are especially effective in eliciting responses in the auditory cortex (Kowalski *et al.*, 1996; deCharms *et al.*, 1998).

In order to characterize the role of these modulations in the perception of speech and other complex sounds, we have measured the sensitivity of human subjects to spectro-temporal modulations over the perceptually important range of 0.25–8 cycles/octave and 1–128 Hz. The experimental methods and results are discussed in Sec. II. A simplified model of early and central auditory processing that accounts for the major trends in the data is presented in Sec. III. In Sec. IV, the utility of the model is demonstrated by a preliminary evaluation of the intelligibility of speech in different kinds of noise. Finally, we discuss the relevance of these results in the wider context of visual and other auditory tasks.

I. METHODS

Psychoacoustical MTFs were measured for four subjects who are graduate students familiar with this task. The results shown below followed a period of training after which subjects' performance stabilized with little further improvements.

A. Testing procedures

A ''two-alternative two-interval'' forced choice adaptive procedure was used to estimate thresholds. Each trial consisted of two 1-s long observation intervals separated by a 200-ms pause. After the listener's response, a short visual feedback was provided and a new trial started until all 50 trials that comprise one block were presented.

The discrimination task was to distinguish between a spectrally flat *standard*, which did not change over a block of

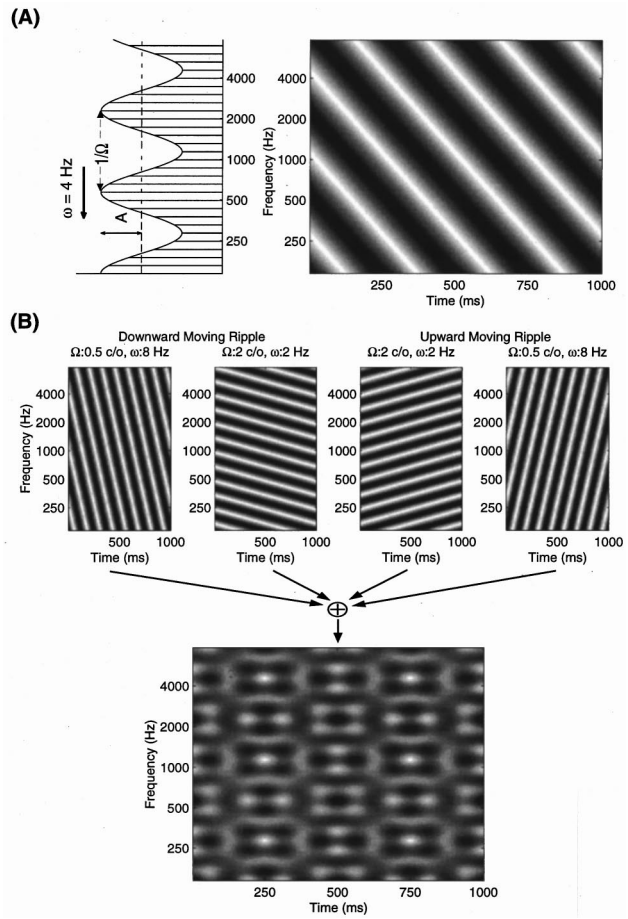

FIG. 2. Moving ripples: parameters and motivations. (a) Definition of moving ripple spectrum parameters. The left panel illustrates a ripple spectrum with an envelope of amplitude *A*, sinusoidally modulated along the spectral axis *x* with a density of $\Omega=0.5$ cyc/oct, and is moving at velocity $\omega=4$ Hz. The right panel displays the ripple spectrogram. (b) A weighted sum of ripples can be used to construct any arbitrary spectrogram. The top row illustrates spectrograms of four upward/downward moving ripples with different Ω, ω combinations. Adding these ripples produces a complex spectrogram.

trials, and the *signal*, which resembled the *standard* except for an added modulation on the profile whose amplitude changed in steps adaptively. On the first trial the signal was three step sizes away from the standard. On each subsequent trial the signal was changed according to the ''two-down–one-up'' procedure in order to estimate the level that produces 70.7% correct answers (Levitt 1971). The step size was halved after three reversals and the threshold was estimated as the average of the signal across the last even number of reversals, excluding the first three. Signal and standard occurred with equal *a priori* probability in one of the two intervals. The overall presentation level was randomized across trials and within a trial over a 20 dB range in 1-dB resolution, in order to ensure that listeners based their judgment on a change in spectral shape rather than on absolute level change in a particular frequency band (Green, 1986).

B. The moving ripple stimulus

In all tests, sounds were generated digitally with 16-bit resolution and 16-kHz sampling rate. They were low-pass filtered at 8 kHz. Before presentation to listeners, sounds were gated for a 1-s duration, including 10-ms rise and decay ramps. Sounds were delivered inside an acoustic chamber through a loudspeaker (ADS L470).

The broadband ripple spectra consisted of 92 tones equally spaced along the logarithmic frequency axis and spanning 5.75 octaves (0.14–7.34 kHz), as illustrated in Fig. 2(a). The *spectral envelope (or profile)* of the complex was modulated as a single sinusoid along the logarithmic frequency axis on a linear amplitude scale [Fig. 2(a)]. The amplitude of the ripple profile (A) is defined relative to the unit base or flat spectrum. Thus, $A=0$ to 1 corresponds to 0% to 100% modulation of the flat ripple profile. The ripple density Ω is in units of cycles/octave (cyc/oct). The ripple phase is given in radians or degrees relative to a sine wave starting at the low-frequency edge of the complex [Fig. 2(a)]. Therefore, the profile of a *stationary* ripple spectrum is given by

$$S(x)=A\cdot\sin(2\pi\cdot\Omega\cdot x+\Phi), \tag{1}$$

where x is the position on the logarithmic frequency axis (in octaves) defined as: $x=\log_2(f/f_0)$ with f_0 the lower edge of the spectrum (0.14 kHz), and f as frequency; Φ is the phase of the profile.

The stimuli of interest in this study, however, are also modulated in time by having the ripple profile move up or down the spectral axis at a constant velocity. Ripple velocity (ω) is defined as the number of ripple cycles-per-second (Hz) sweeping past the low-frequency edge of the spectrum. The resulting moving ripple profile is fully characterized by

$$S(x,t)=A\cdot\sin(2\pi\cdot(\omega\cdot t+\Omega\cdot x)+\Phi). \tag{2}$$

Therefore, a positive (negative) ω corresponds to a ripple envelope drifting downward (upward) in frequency.

Figure 2(b) illustrates spectrograms of moving ripple profiles with different (Ω, ω) combinations. Note that the spectrograms appear as two-dimensional gratings with orientations determined by the ratio of the spectral to temporal modulation rates (Ω/ω). A program to generate these stimuli interactively is available at *http://www.isr.umd.edu/CAAR/pubs.html*.

II. RESULTS

Threshold measurements can be conceptually inverted and interpreted as sensitivity measures to different spectro-temporal modulations, hence reflecting the gain of the system or its modulation transfer function, e.g., as in Viemeister (1979) and Yost and Moore (1987). The average thresholds for four subjects are presented in Fig. 3 as a function of Ω and ω for upward and downward drifting ripples.

The data generally exhibit a low-pass function in both dimensions. Sensitivity slightly peaks in a small region around 2–8 Hz. Subjects maintain high sensitivity to temporal modulations of low-Ω spectra up to 32 Hz; in fact, temporal MTFs at $\Omega=0.25$–2 cyc/oct are almost identical to those measured by Viemeister (1979) with flat spectra. The data also suggest that, apart from an overall decrease in sensitivity, the temporal transfer functions approximately preserve their low-pass shape at higher Ω. For instance, tempo-

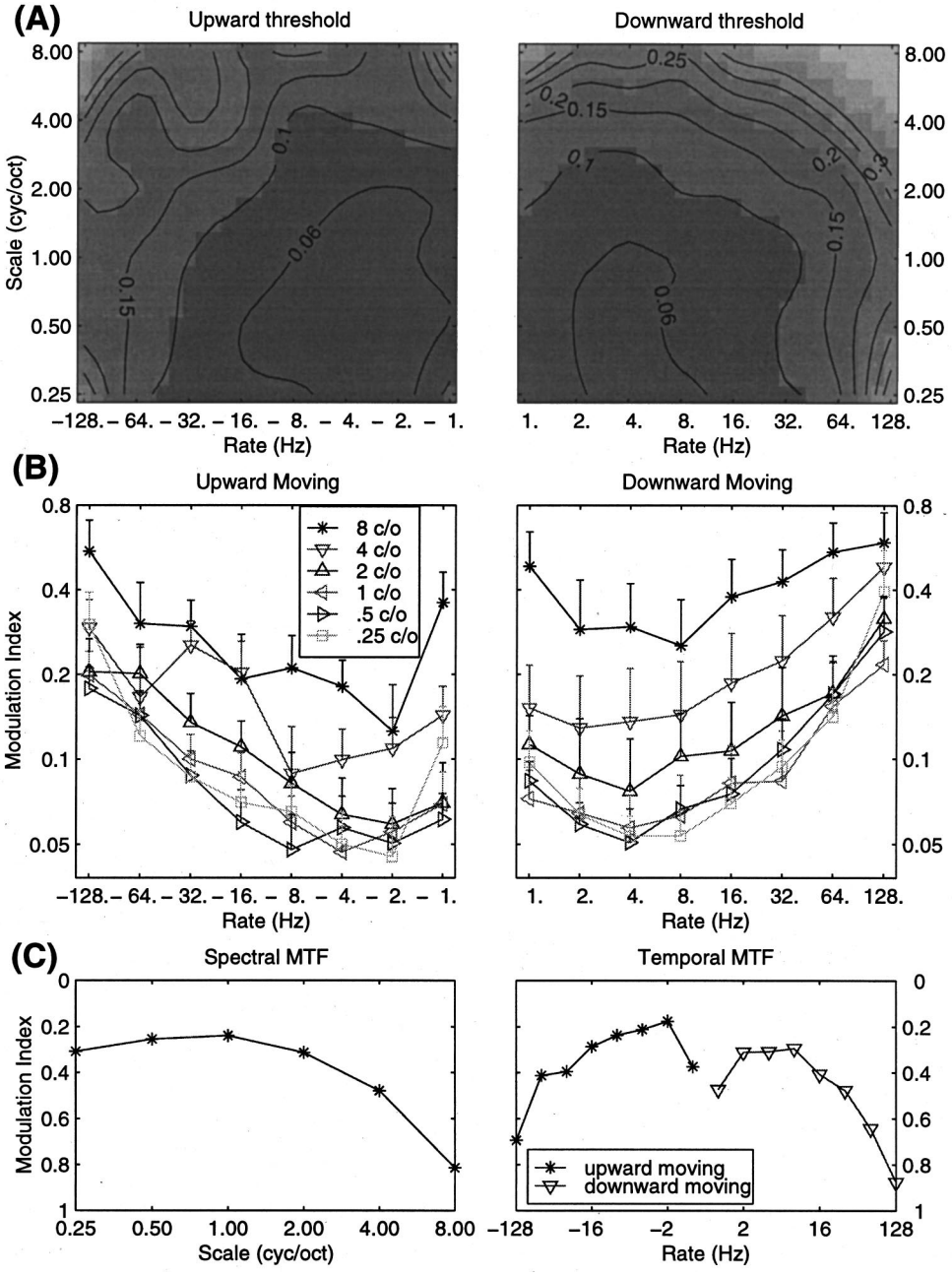

FIG. 3. Detection thresholds of moving ripples as a function of ripple density (Ω), velocity (ω), and direction. (a) Contour and gray scale interpolated representation of the ripple amplitudes at threshold. (b) Same thresholds as above plotted as a function of ripple velocity, with density as parameter. For display purpose, only the upper error bars with half the standard deviation error ranges are shown. (c) The one-dimensional temporal (left) and spectral (right) MTFs (or thresholds) derived by singular-value-decomposition procedure from the combined data in (b) above (see text for details).

ral MTFs at $\Omega=0.25$, 4, and 8 cyc/oct are approximately shifted upwards relative to each other reflecting the rising detection thresholds to high Ω (Fig. 3). This implies that the spectro-temporal MTF is approximately the product of purely temporal (Viemeister, 1979) and purely spectral (Green, 1986) MTFs, i.e., it is *separable*.

To confirm this impression, we have applied the singular value decomposition (SVD) method to analyze the data in Fig. 3(b). Specifically, the MTF is diagonalized as $\Lambda = U \cdot \mathrm{MTF} \cdot V$, where Λ is the eigenvalue matrix, and U, V are the corresponding eigenvectors (Haykin, 1996). If the MTF matrix is separable, i.e., expressible as the product of two vectors (a purely temporal and spectral MTF), then it should have only one nonzero eigenvalue; otherwise, relatively sizable secondary eigenvalues occur. Figure 3(c) illustrates the results of such an analysis on the MTFs shown in Fig. 3(a) and (b). Only one significant eigenvalue is found ($\lambda_i/\lambda_1 < 15\%$ for $i=2,...,6$). The corresponding purely temporal and spectral threshold functions (or MTFs) are shown in Fig. 3(c). The spectro-temporal MTF surface reconstructed by a pure product of these two functions produces a MTF that is to within 3.4% of the original data (in mean-square-error sense). This error is well within the bounds of the experimental errors indicated by the bars. These results strongly argue for the full separability of the MTFs in Fig. 3(a) and (b).

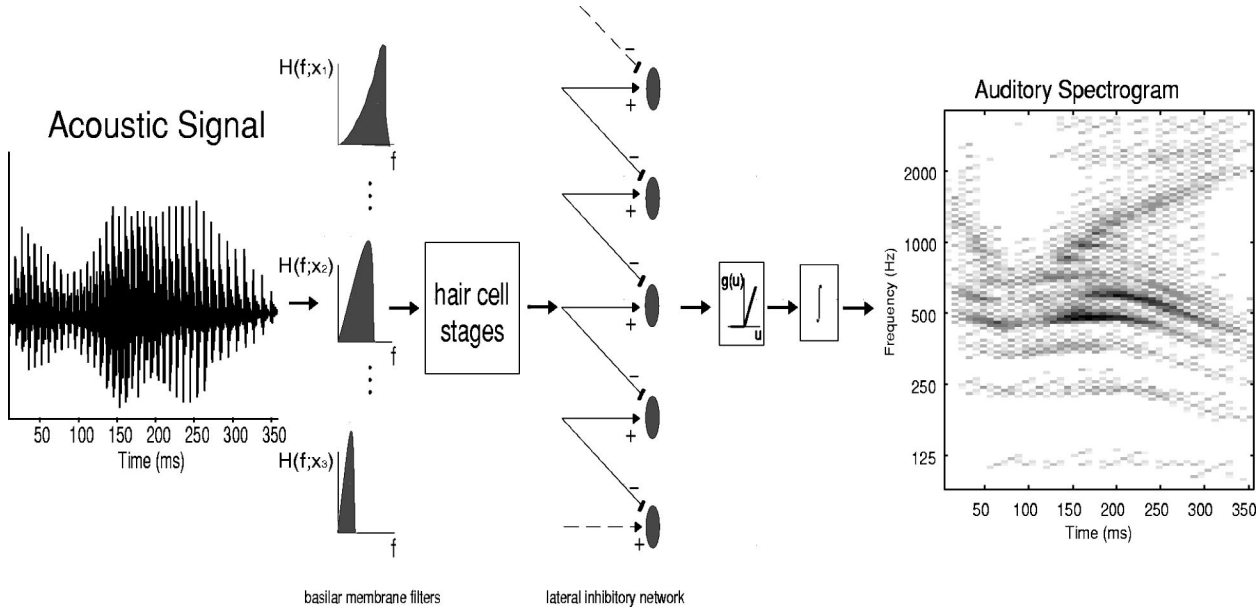

FIG. 4. Schematic of processing in the early auditory stages [details in Wang and Shamma (1995) and Yang *et al.* (1992)]. The acoustic signal is analyzed by a bank of constant-*Q* cochlearlike filters. The output of each filter is then processed by a hair cell model, and then by a lateral inhibitory network. The output at each point is then rectified and integrated to produce the *auditory spectrogram*.

III. MODEL

A model of spectro-temporal modulation sensitivity is developed here to explain the origin of the salient trends in the data, and to serve as a computational module in applications requiring analysis of the spectro-temporal modulations in sound spectrograms. The model is inspired and is consistent with known biophysics of the peripheral auditory system, and with single unit responses in the primary auditory cortex (Kowalski *et al.*, 1996). It consists conceptually of two parts: (1) an early auditory portion which models the transformation of the acoustic signal into an *auditory spectrogram*, and (2) a central portion which further analyzes the auditory pattern into a modulation *scale-rate* plot using a family of corticallike filters.

We first describe schematically these two stages. Next, a precise mathematical formulation is presented, followed by a brief illustration of the model overall MTF. All model stages are available as a MATLAB library on *http://www.isr.umd.edu/CAAR/pubs.html* (NSL Tools Package).

A. The early auditory spectrogram

The early stages of the auditory system transform sound into a pattern of neural activity that represents an enhanced and noise-robust version of the acoustic spectrum, henceforth called the *auditory spectrogram*. Extensive details of the biophysical basis, anatomical structures, and computational implementation of the model used here to generate the auditory spectral profiles are available in Yang *et al.* (1992) and Wang and Shamma (1994). Figure 4 illustrates the various stages of the model. Briefly, it consists of a bank of 120 asymmetric critical overlapping bandpass filters that are equally spaced over a 5 oct frequency range (24 filters/octave) [see Wang and Shamma (1994) for details of the filter parameters and implementations]. The output of each filter is processed by a hair cell stage which consists of a high-pass filter, followed by nonlinear compression (optional), and then a low-pass filter (Shamma *et al.*, 1986). The final stage mimics the action of a lateral inhibitory network (Shamma, 1988) which sharpens the filter outputs, and hence the filter bank frequency selectivity. It is implemented by a first-difference operation across the channel array, followed by a half-wave rectifier, and a short-term integration to estimate the final output (Yang *et al.*, 1992). Figure 5(a) shows the auditory spectrogram of a speech sentence ''*Come home right away*.'' Spectrograms of other sentences and moving ripples are illustrated in Figs. 5 and 6(b) and (c).

B. The modulation scale-rate plot

The auditory spectrum is relayed to the primary auditory cortex (AI) through several stages of processing (Clarey *et al.*, 1992). The AI responses integrate influences from preceding nuclei which likely are involved in a host of other perceptual tasks such as binaural localization and pitch estimation.

Neural responses in AI exhibit a complex and highly varied pattern of spectro-temporal selectivity. For instance, an AI unit is usually tuned to a range of frequencies around a ''best frequency'' (BF). Within this range, responses change from excitatory to inhibitory in a pattern that varies from one cell to another in its width and asymmetry around the BF (Kowalski *et al.*, 1996). AI units also exhibit a similar selectivity and variability in their *temporal* responses (Simon *et al.*, 1998). Some units are best responsive to fast changing spectra, while others are rather sluggish. In addition, AI units often respond selectively to the direction of movement of a spectral peak near their BF. These response properties are summarized by the so-called spectro-temporal response field (STRF), which is a generalization of the classic response areas in auditory physiology (Clarey *et al.*, 1992) or receptive fields in the retina and visual cortex (De-Valois and

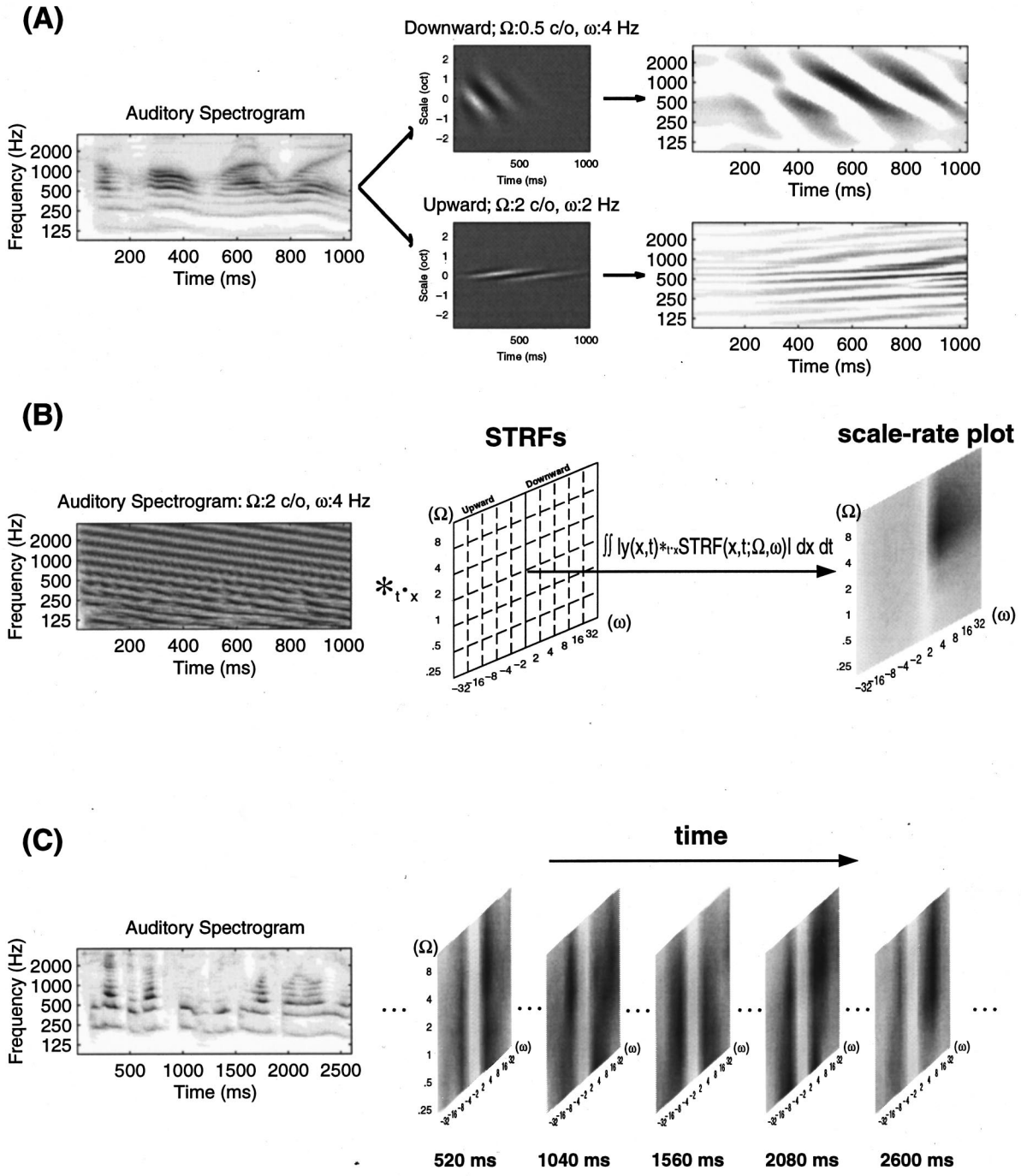

FIG. 5. Model of central auditory processing and the *scale-rate plot*. (a) Cortical analysis of the auditory spectrogram. The spectrogram of the sentence ''Come home right away'' is analyzed by a bank of cortical spectro-temporal response fields (STRFs). Two model STRFs are shown; in each, black (white) color represents excitatory (inhibitory) regions of the STRF. The panels on the right illustrate the results of processing the original auditory spectrogram through each of the STRFs. Only downward broad spectral transitions survive in the upper panel; the opposite spectro-temporal features are seen in the lower panel. (b) Measuring the output of cortical STRFs. The auditory spectrogram (left) is projected to a bank of STRFs with all Ω, ω parameters represented middle. The ripple spectrogram activates maximally the STRF that matches its outline best (i.e., the STRF at 2 cyc/oct and 4 Hz). The output from all STRF's is summarized in the scale-rate plot (right), which shows a peak at $\Omega=2$ cyc/oct and $\omega=4$ Hz. (c) The scale-rate plots vary as a function of time reflecting the changing ripple content of a speech spectrogram.

De-Valois, 1990). It represents the spectro-temporal pattern that best excites the cell. Figure 5(a) displays two model STRFs that are sensitive to very different spectro-temporal patterns. On top, the STRF is relatively broadly tuned (responds best to ripples of $\Omega=0.5$ cyc/oct), dynamically agile (responds best to ripples drifting at $\omega=4$ Hz), and exhibits a downward directional selectivity. In comparison, the STRF on the bottom is spectrally narrowly tuned (best $\Omega=2$ cyc/oct), temporally slow (best $\omega=2$ Hz), and is upwardly sensitive. The STRFs in AI vary along these multiple dimensions, exhibiting spectral bandwidths from 0.5 to 2 oct (in ferrets and cats), temporal selectivity that ranges from rapid (over 16 Hz) to very slow (under 2 Hz), and directional sensitivities to upwards, bidirectional, and downwards mov-

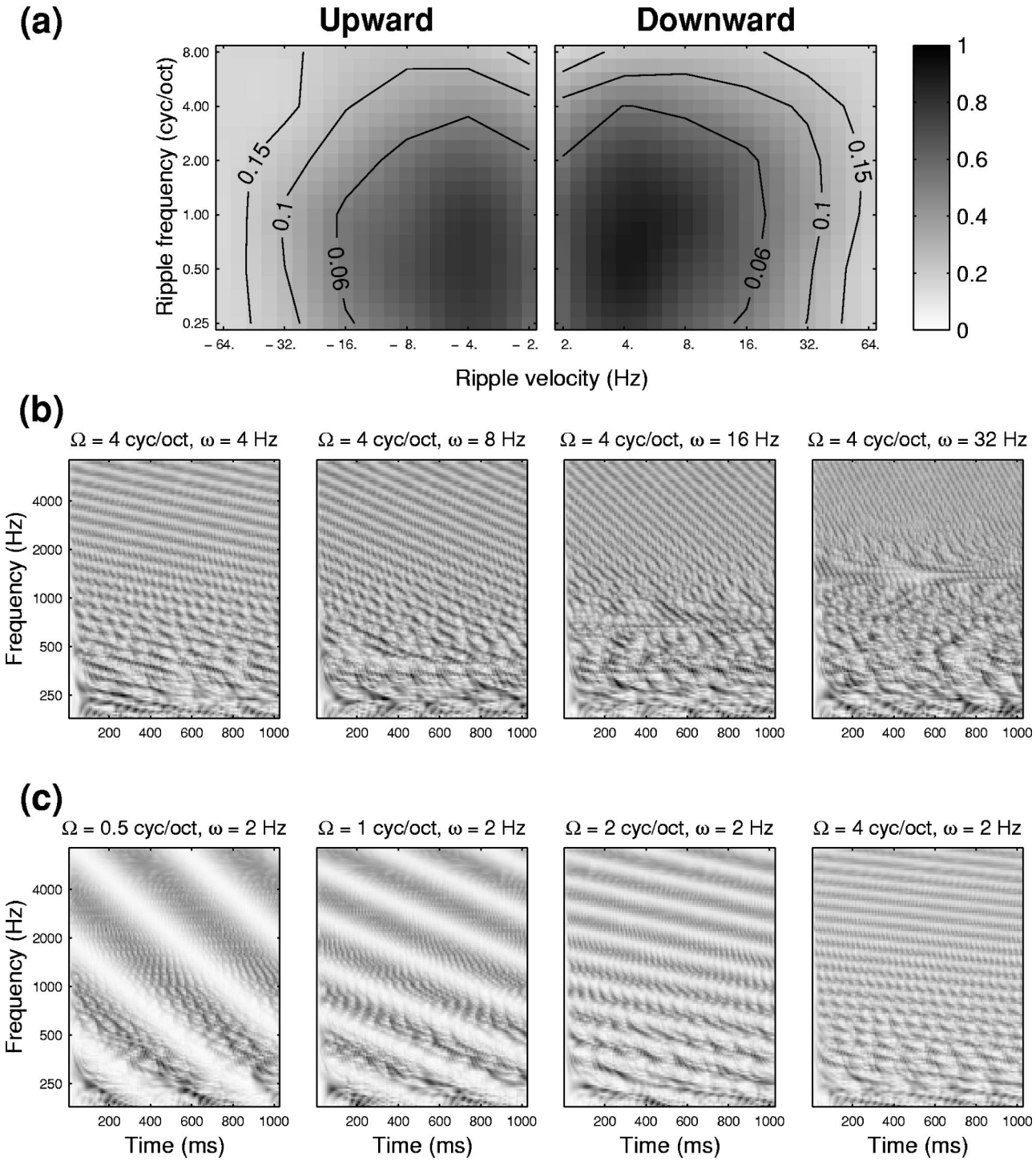

FIG. 6. Spectro-temporal MTFs of the full auditory model. (a) The model MTF shown in arbitrary linear gray scale (bar on the right). The contour surfaces depict thresholds predicted by the model. They are derived by normalizing the minimum perceptual threshold in Fig. 4 (=0.035) by the model MTF. (b) Origin of the temporal low-pass shape in the MTF. With increasing ripple velocity, the low BF regions fail to follow rapid modulations and hence become progressively more distorted, thus causing the decrease in the corresponding STRF outputs. (c) Origin of the spectral low-pass shape in the MTF. Cochlear filters gradually fail to resolve higher density ripples, causing a decrease in overall output.

ing spectral energy (deCharms *et al.*, 1998; Simon *et al.*, 1998; Kowalski *et al.*, 1996).

Therefore, from a functional and computational point of view, AI can be considered a bank of *modulation filters* which analyzes the spectro-temporal modulation rates of its input spectrogram. This view is illustrated in Fig. 5(b) where we construct the *scale-rate* plot to summarize the AI responses. The computations consist of two stages. First, the auditory spectrum is analyzed by a bank of STRFs with varying spectro-temporal (Ω-ω) selectivities. Then we estimate the total output power from the STRFs at each Ω-ω combination and plot the results in a *scale-rate* plot as shown in Fig. 5(b). For example, a downward moving ripple (Ω=2 cyc/oct, ω=4 Hz) evokes a fairly circumscribed pattern of

scale-rate activation centered around the corresponding Ω-ω location [Fig. 5(b)]. A nonstationary speech spectrogram evokes a series of short-time *scale-rate* plots reflecting the changing modulation content of the utterance [Fig. 5(c)].

C. Mathematical formulation of the cortical model

The cortical response (r) produced by the STRF analysis of the auditory spectrogram $y(x,t)$ is defined as

$$r(x,t;\Omega,\omega)=y(x,t)*_{t\cdot x}\mathrm{STRF}(x,t;\Omega,\omega), \tag{3}$$

where $*_{t\cdot x}$ denotes convolution with respect to t and multiplication with respect to x. Note that the $\mathrm{STRF}(x,t;\Omega,\omega)$ is parametrized by its most sensitive spectral and temporal modulations (Ω, ω), and these in turn reflect the bandwidth, dynamics, and orientation of its excitatory and inhibitory fields.

The *scale-rate* plot is derived from the cortical response by integrating the output over the whole spectrum x (5 oct):

$$\mathrm{SR}(t;\Omega,\omega)=\int_0^5 |r(x,t;\Omega,\omega)|\,dx. \tag{4}$$

An intuitive interpretation of the *scale-rate* plot (SR) is that it displays the total amount of modulation that $y(x,t)$ contains at each Ω, ω combination *regardless of its distribution along the spectral axis (x).*

We assume that each upward or downward STRF can be represented by the product of two separate spectral and temporal functions: a response field RF (x) along the frequency (tonotopic) axis and a temporal impulse response $h_{\mathrm{IR}}(t)$. Therefore,

$$\mathrm{STRF}(x,t;\Omega,\omega)=\mathrm{RF}(x;\Omega,\phi)\cdot h_{\mathrm{IR}}(t;\omega,\theta). \tag{5}$$

Here RF (x) is defined by a symmetric seed function $h_s(x;\Omega)$ and its Hilbert transform

$$\mathrm{RF}(x;x_c,\Omega,\phi)=h_s(x-x_c;\Omega)\cos\phi + \hat{h}(x-x_c;\Omega)\sin\phi,$$

where x_c, Ω, and ϕ are respectively the center frequency, density, and phase of the most sensitive ripple; its Hilbert transform is

$$\hat{h}_s(x)=\frac{1}{\pi}\int_{-\infty}^{\infty}\frac{h_s(x)}{z-x}\,dz.$$

Here we choose a Gabor-like function to approximate $h_s(\cdot)$:

$$h_s(x)=(1-x^2)e^{-x^2/2},\quad h_s(x;\Omega)=\Omega h_s(\Omega x).$$

Similarly, the temporal impulse response can be expressed as

$$h_{\mathrm{IR}}(t;\omega,\theta)=h_t(t;\omega)\cos\theta+\hat{h}_t(t;\omega)\sin\theta,$$

where ω is the most sensitive ripple velocity. $h_t(\cdot)$ is modeled by one gamma probability density function

$$h_t(t)=t^3e^{-4t}\cos(2\pi t),\quad h_t(t;\omega)=\omega h_t(\omega t).$$

In many instances, we will need to consider the *average* scale-rate plot of a sentence or even an entire corpus of speech. This is simply defined as

$$\mathrm{SR}_{\mathrm{avg}}(\Omega,\omega)=\frac{1}{T}\int_T|\mathrm{SR}(t;\Omega,\omega)|\,dt,$$

where T denotes the entire interval over which SR is averaged.

D. Spectro-temporal MTF of the auditory model

The MTF of the full auditory model is shown in Fig. 6(a). It is measured by presenting single ripples of all Ω, ω combinations and noting for each output at the corresponding SR(Ω, ω). The model responses capture the main trends seen in the threshold MTF illustrated earlier in Fig. 3. Specifically, the model exhibits low-pass MTFs with very similar spectral and temporal rate cutoffs. The origin of these response characteristics is the effectively narrow bandwidths used to compute the auditory spectrogram. The cochlear filters have a typical critical-band gammatone shape. However, the lateral inhibition stage in the model effectively narrows the filter bandwidths and slows down its dynamics [see Wang and Shamma (1995) for details].

The MTF loss of sensitivity at high ripple velocities is evident in the auditory spectrograms [Fig. 6(b)] of a 4-cyc/oct ripple at ω=4, 8, 16, and 32 Hz. In all panels, the temporal modulations are poorly represented at the lowest BFs where the auditory filters are narrowest and dynamically slowest. At higher modulation rates, the disruption spreads towards higher, hence reducing the corresponding SR outputs.

The decrease in output at high density ripples is due to the finite bandwidths of the cochlear filters. As ripple peaks become closely spaced, they are less resolved by the cochlear filters, and their amplitudes decrease as illustrated in Fig. 6(c). Based on these arguments, it is evident that the upper limits of the temporal and spectral modulation rates are inversely related through the effective bandwidths of the cochlear filters.

Finally, the model responses exhibit a slight symmetry with respect to ripple directions at high rates (e.g., responses at -32 Hz are smaller than at 32 Hz). Experimental data, however, do not replicate such a preference. The model asymmetry is due to the staggered cochlear filter group delays which give rise to a (basilar membrane) traveling wave towards the lower frequency channels, i.e., in the downward direction. These delays disrupt the flow of responses to upward ripple, but less so to downward ripples.

IV. APPLICATION TO SPEECH INTELLIGIBILITY

Auditory spectrograms of speech are rich in spectro-temporal modulations which are important in preserving its intelligibility. Numerous tests have estimated a critical range of temporal modulations in speech at between 2 and 8 Hz (Greenberg *et al.*, 1996). In fact, filtering out temporal

modulations outside of this range has proven to be an effective strategy for combating the deleterious effects of noise and reverberations in real world speech signals (Hermansky and Morgan, 1994; Greenberg and Kingsbury, 1997).

However, not all spectro-temporal modulations of speech (or other environmental sounds) are equally perceived by humans. To determine the most perceptually salient range of speech modulations, we computed the long-term average scale-rate plot of 380 spoken sentences. These sentences were extracted from a subset of TIMIT corpus[3] (the training portion of the New England dialect region) which contains a total of 24 male speakers (240 sentences) and 14 female speakers (140 sentences). Figure 7 illustrates that spectro-temporal ripples bounded by the range between 4–8 Hz and <4 cyc/oct are the critical perceptible modulations in speech. It is important to note that in marking this range, we consider *both* the spectral and temporal dimensions simultaneously. For instance, temporal modulations at 4–8 Hz are not important for densely rippled spectra (e.g., >4 cyc/oct).

Speech often suffers significant loss of intelligibility in noisy or reverberant environments. Presumably this is partly because these conditions disrupt the modulations of normal clean speech. Therefore, the scale-rate plot could serve as a useful indicator of this disruption by providing a sensitive spectro-temporal representation from which an ''intelligibility index'' could be derived. This is analogous to the way traditional critical-band spectra and single-tone temporal MTFs have been utilized to derive the classical *articulation index* (Kryter, 1962) and *speech transmission index* (Houtgast *et al.*, 1980).

Figure 7(b) and (c) illustrates the effects of noise and reverberations on the scale-rate plots of clean speech. Figure 7(b) shows a series of average scale-rate plots $[\mathrm{SR}_{\mathrm{avg}}(\Omega,\omega)]$ for a sentence contaminated with increasing levels of white noise (decreasing S/N). Another series of similar plots for speech with increasing reverberation delays is shown in Fig. 7(c).[4] In both cases, a suitably defined measure of the similarity between the clean and distorted plots could serve as an indicator of the noise perceived by the listener as described next.

A. Deriving an intelligibility measure from the scale-rate plots

Assume that the scale-rate plots of a clean speech utterance $\mathrm{SR}_c(t;\Omega,\omega)$ and its noisy version $\mathrm{SR}_n(t;\Omega,\omega)$ are available. Then the similarity (or correlation) between any corresponding $(\Omega,\ \omega)$ channels is defined as (Duda and Hart, 1973)

$$\rho_0(\Omega,\omega)=\frac{\langle \mathrm{SR}_c(t;\Omega,\omega)-\mu_{\mathrm{SR}_c(t;\Omega,\omega)},\mathrm{SR}_n(t;\Omega,\omega)-\mu_{\mathrm{SR}_c(t;\Omega,\omega)}\rangle}{\|\mathrm{SR}_c(t;\Omega,\omega)-\mu_{\mathrm{SR}_c(t;\Omega,\omega)}\|\cdot\|\mathrm{SR}_n(t;\Omega,\omega)-\mu_{\mathrm{SR}_c(t;\Omega,\omega)}\|},\tag{6}$$

where μ_{SR_c} is the mean of the random variable SR_c and the inner product and the induced norm are defined as (note that dependence on Ω, ω, and t in all quantities below is suppressed to simplify notation)

$$\langle \mathrm{SR}_c-\mu_{\mathrm{SR}_c},\mathrm{SR}_n-\mu_{\mathrm{SR}_c}\rangle=\int_T (SR_c(t)-\mu_{\mathrm{SR}_c})\cdot(\mathrm{SR}_n(t)-\mu_{\mathrm{SR}_c})\,dt$$

and

$$\|\mathrm{SR}-\mu\|=\sqrt{\langle \mathrm{SR}-\mu,\mathrm{SR}-\mu\rangle}.$$

This similarity measure ρ_0 compares the $\mathrm{SR}(\cdot)$ of the clean and noisy signals *frame-by-frame*, and not simply through the time-averaged plot $\mathrm{SR}_{\mathrm{avg}}$. Consequently, such a measure is only useful if *both* clean and noisy samples of the *same* sentence are available.

A slightly modified measure can be defined which requires only knowledge of the mean and variance of the clean speech scale-rate plot [SR_c in Fig. 7(a)]. It is used in situations where only noisy speech samples are provided, or if clean and noisy samples are of different utterances. We assume that the effect of added noise and reverberations at a given channel can be modeled as a change in the mean and variances of the random variables SR_c:

$$\mathrm{SR}_n(t;\Omega,\omega)=A_{\Omega\omega}\cdot\mathrm{SR}_c(t;\Omega,\omega)+C_{\Omega\omega},\tag{7}$$

where $A_{\Omega\omega}$ and $C_{\Omega\omega}$ are measurable from the long-term average scale-rate output of the clean and noisy speech samples as

$$\mu_{\mathrm{SR}_n}=A\cdot\mu_{\mathrm{SR}_c}+C,\tag{8}$$

$$\sigma_{\mathrm{SR}_n}=A\cdot\sigma_{\mathrm{SR}_c},\tag{9}$$

where μ_{SR} and σ_{SR} are the mean and standard deviation of the random variable SR at each channel $(\Omega,\ \omega)$.

For discrete time interpretation, substituting Eqs. (7)–(9) into Eq. (6) and noting that $\Sigma_n(\mathrm{SR}_c[n]-\mu_{\mathrm{SR}_c})=0$, the numerator of Eq. (6) can be written as

$$\sum_n (\mathrm{SR}_c[n]-\mu_{\mathrm{SR}_c})(\mathrm{SR}_n[n]-\mu_{\mathrm{SR}_c})$$

$$=\sum_n (\mathrm{SR}_c[n]-\mu_{\mathrm{SR}_c})(A\cdot\mathrm{SR}_c[n]-\mu_{\mathrm{SR}_c}+C)$$

$$=A\cdot\sum_n (\mathrm{SR}_c[n]-\mu_{\mathrm{SR}_c})^2,\tag{10}$$

and the denominator can be simplified to

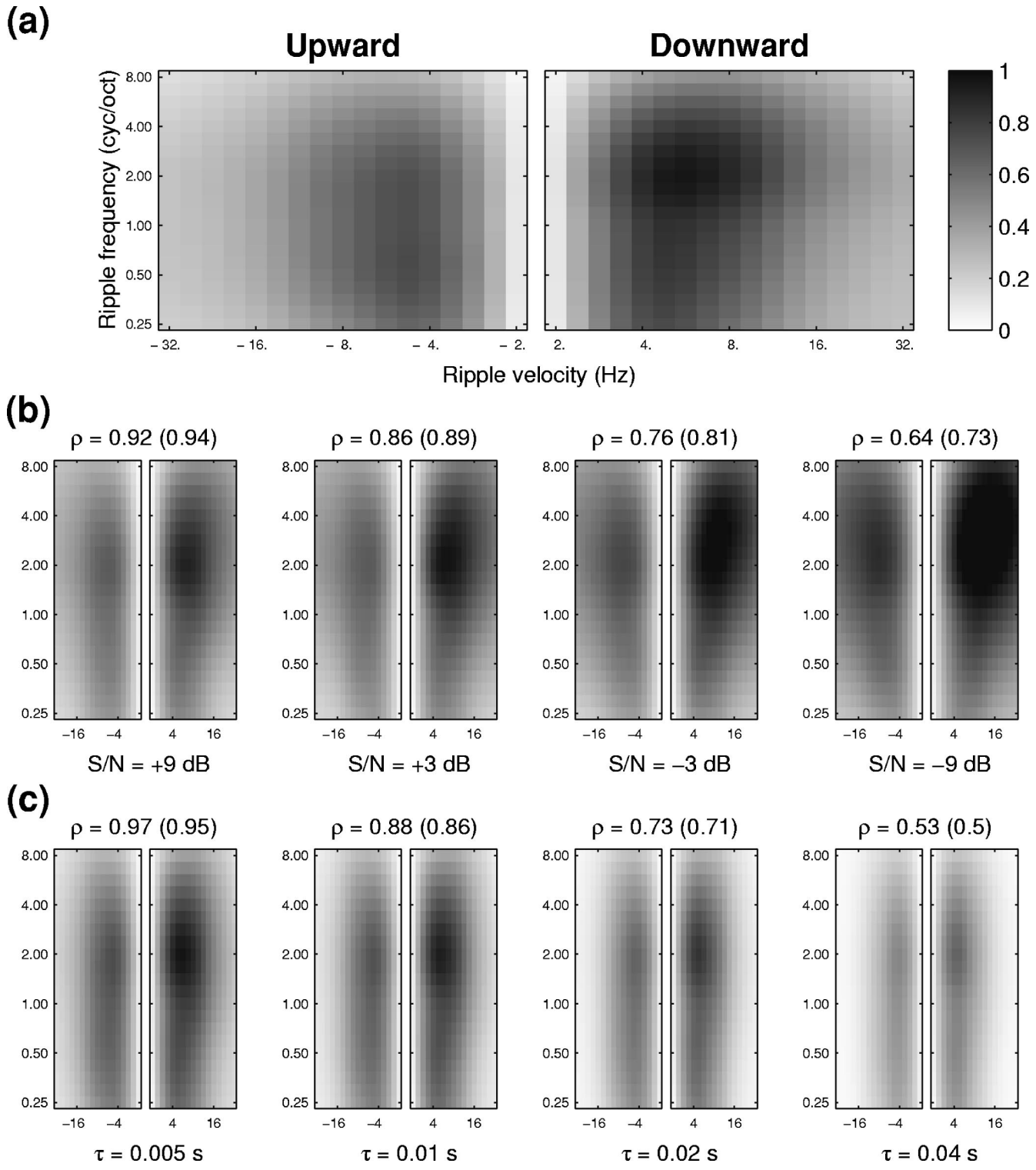

FIG. 7. Spectro-temporal modulations in speech. (a) The average (mean) scale-rate plot of modulations in speech (μ_{SR_c}). On average, the strongest modulations are downward, and in the 4–8-Hz range and under 4 cyc/oct. (b) Average scale-rate plots (SR_{avg}) of speech contaminated by stationary white noise at different S/N ratios. Above each panel is a measure of the similarity (ρ) between the *frame-by-frame* scale-rate plots of the clean and noisy speech signals. The number in the parenthesis is a simplified version of ρ that uses averaged SR only (see text for details on both measures). As the S/N ratio decreases, ρ values decrease, reflecting distortions due to the noise. (c) The effect of reverberation delays: ρ decreases gradually with increasing reverberation delays (τ).

$$\sqrt{\left(\sum_n (\mathrm{SR}_c[n]-\mu_{\mathrm{SR}_c})^2\right)\left(\sum_n (\mathrm{SR}_n[n]-\mu_{\mathrm{SR}_c})^2\right)}$$
$$=\sqrt{\left(\sum_n (\mathrm{SR}_c[n]-\mu_{\mathrm{SR}_c})^2\right)\left(\sum_n [A\cdot(\mathrm{SR}_c[n]-\mu_{\mathrm{SR}_c})+(A-1)\mu_{\mathrm{SR}_c}+C]^2\right)}$$
$$=\sqrt{\left(\sum_n (\mathrm{SR}_c[n]-\mu_{\mathrm{SR}_c})^2\right)\left(A^2\sum_n (\mathrm{SR}_c[n]-\mu_{\mathrm{SR}_c})^2+N[(A-1)\mu_{\mathrm{SR}_c}+C]^2\right)}, \quad (11)$$

where N is the total number of samples along n axis. Therefore, ρ_0 can be simplified to ρ_s:

$$\rho_s(\Omega,\omega)=\sqrt{\frac{1}{1+\left(\dfrac{(A_{\Omega\omega}-1)\cdot\mu_{\mathrm{SR}_c(\Omega,\omega)}+C_{\Omega\omega}}{A_{\Omega\omega}\cdot\sigma_{\mathrm{SR}_c(\Omega,\omega)}}\right)^2}}$$
$$=\sqrt{\frac{1}{1+\left(\dfrac{\mu_{\mathrm{SR}_n(\Omega,\omega)}-\mu_{\mathrm{SR}_c(\Omega,\omega)}}{\sigma_{\mathrm{SR}_n(\Omega,\omega)}}\right)^2}}. \quad (12)$$

A final indicator ρ of the total similarity between clean and noisy samples is derived as the average [over all Ω and ω of all $\rho_0(\Omega,\omega)$ or $\rho_s(\Omega,\omega)$]:

$$\rho=\frac{1}{N_\Omega\cdot N_\omega}\sum_\Omega\sum_\omega \rho_0(\Omega,\omega) \quad (13)$$

or

$$\rho=\frac{1}{N_\Omega\cdot N_\omega}\sum_\Omega\sum_\omega \rho_s(\Omega,\omega), \quad (14)$$

where N_Ω and N_ω are the number of channels along Ω and ω axes.

The validity of the assumptions leading to the derivation of the simplified ρ [Eq. (14)] is demonstrated by the approximate correspondence between the two ρ measures [Eqs. (13) and (14)] for the noisy speech samples shown in Fig. 7(b) and (c). It is important to note here that the proposed measures are defined and computed irrespective of the nature (or model) of the distorting process, i.e., ρ reflects the perceptual change the same way whether it is caused by broadband noise, reverberations, or any other process. Therefore, ρ serves as a *spectro-temporal modulation index (STMI)*, a measure of the total change in the modulations away from those of clean speech.

B. Assessing speech intelligibility with STMI (ρ)

We discuss the use of the STMI in two situations: (1) determining the quality of a transmission medium (e.g., a telephone channel or an auditorium) and (2) assessing the intelligibility of a given noisy speech sample.

In the first case, clean speech is transmitted through a noisy or reverberant channel (or recorded in an auditorium). The clean and transmitted versions of the *same* sentence are compared by computing ρ [Eq. (13)]. The resulting values predict the quality of the transmission medium. Informal experiments in our laboratory indicate that ρ values near 0.75 reflect marginally intelligible speech, corresponding to S/N ratios of about -3 dB [Fig. 7(b)] or reverberation delays of 20 ms [Fig. 7(c)].

In the second situation, the goal is to estimate the intelligibility of noisy speech samples recorded in different S/N conditions. No clean samples of the noisy speech are available. Instead, we rely on the long-term average of the clean speech in Fig. 7(a) to provide the reference against which to measure the effects of the noise. To illustrate this procedure, we have utilized data supplied to us by the Southwest Research Institute based on speech intelligibility tests in different S/N conditions conducted with five subjects. Each test consisted of the following conditions and test materials:

(1) a specific S/N condition,
(2) a total of eight nonsense sentences,
(3) each sentence consisted of five randomly chosen monosyllabic words, and
(4) each word consisted of three phonemes with approximately balanced presentation of vowels versus consonants (typically 40% versus 60% over the entire set of sentences). Examples of words used are: GAB, BAR, WHET, BUG, LOT.

In a given test, each subject was presented the five-word sentences and asked to enter the phonemes heard in each word, including the option of ''not certain'' at any position in a word. The subjects also had the option of hearing the sentences again before responding. Numerous measures of the responses were compiled including the correct percentage of responses for vowels and consonants combined and separately, total number of 100% correct words, and the average correct phonemes all subjects entered correctly. For the purposes of this paper, we focus on the correct percentage of phonemes perceived as a function of the S/N ratio of the test. A more elaborate analysis of the data is underway in which ρ is computed separately over specific phonemes (e.g., vowels, consonants, or restricted vowel types), and compared to the corresponding identification results in the tests.

Figure 8 illustrates the correspondence between the ρ [Eq. (14)] and the percentage of correct phonemes at each of the seven S/N conditions tested. The ρ evidently provides a fair average measure of the integrity of the phoneme percepts.

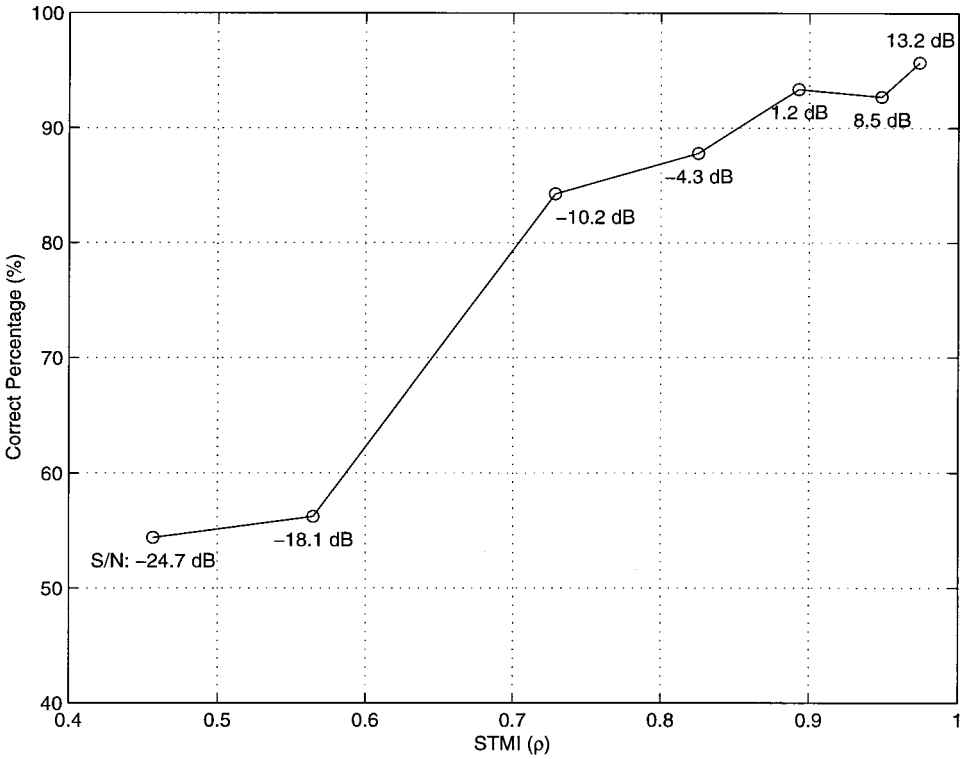

FIG. 8. The spectro-temporal modulation index ρ plotted against the percentage of correct phonemes (as reported by five subjects) in seven different S/N conditions.

V. DISCUSSION

We have reported new measurements of the spectro-temporal MTFs using moving ripple spectra. The MTFs exhibit a low-pass function with respect to both dimensions, with 50% bandwidths of about 16 Hz and 2 cyc/oct (Fig. 3). We have also formulated a computational auditory model that exhibits spectro-temporal MTFs consistent with the salient trends in the data. The model was used to demonstrate the potential relevance of these MTFs to the assessment of speech intelligibility.

A. Relation to psychoacoustic modulation transfer functions

Modulation transfer functions have been measured with different types of acoustic stimuli. For purely spectrally modulated spectra, two sets of largely comparable measurements are available (Green, 1986; Hillier, 1991), and both are in agreement with the spectral transfer functions in Fig. 3(a) at low temporal modulations ($<$32 Hz). For *temporal* modulation transfer functions, the data using modulated flat noise (Viemeister, 1979) or rippled noise (Yost and Moore, 1987; van Zanten and Senten, 1983) give quite different results. With flat noise, subjects detect modulation rates well over 64 Hz. By contrast, modulation of rippled noise is not detectable beyond about 10 Hz. Yost and Moore (1987) discussed and discounted several hypotheses that could account for this difference. More recently, Yost (personal communication) suggested that a possible reason for this disparity is that temporal modulations of a flat noise yield amplitude modulations that are in-phase over the whole spectrum. By comparison, modulations of the linear ripple produce out-of-phase amplitude modulations in different parts of the spectrum, and hence will cancel out if they are centrally integrated.

Our data indicate that Viemeister's temporal MTFs are valid not just for flat spectra, but for any spectra composed of ripples up to 2 cyc/oct. The data also suggest that the low-pass form of the MTFs persists at higher ripple densities ($>$2 cyc/oct) (Fig. 3), but with significant overall loss of sensitivity presumably due to the higher thresholds associated with high density ripples in general (Green, 1986; Hillier, 1991). This finding argues for the separability of the temporal and spectral dimensions of the MTFs, a conjecture that is strongly supported by the SVD analysis.

The stimuli of Yost and Moore (1987) and van Zanten and Senten (1983) are fundamentally different in that they are not pure ripples (on the tonotopic axis), but rather a collection of ripples of many densities. Consequently, to predict their detection thresholds, we need to specify further detection procedures for arbitrary spectra, which are beyond the scope of the present model formulation. However, it is intuitively possible to see that our results are at least consistent with the notion that ripple-noise thresholds are high because they contain high-density profiles ($\Omega>4$ cyc/oct) which are poorly perceived in the MTFs (Fig. 3). Our model further suggests that the locus of spectral integration that gives rise to this phenomenon is not necessarily central, but is instead the limited resolution of the cochlear filters.

B. Spectro-temporal modulations and speech intelligibility

The experiments reported in Sec. IV illustrate the potential utility of spectro-temporal MTFs in quantifying speech intelligibility. Their promise seems to derive from their integration of spectral and temporal factors into one measure. In this sense, they can be viewed as closely related to, or in fact combining two widely used intelligibility measures: *articu-*

lation index (Kryter, 1962) and *speech transmission index* (Houtgast *et al.*, 1980). These two measures represent in some sense extreme versions of the STMI. The *articulation index* captures effectively the distortions due to stationary broadband noise and hence is purely spectral. The *speech transmission index* was specifically designed to deal with problems arising from severe reverberations and is therefore mostly temporal. We have demonstrated in Fig. 7 that the *scale-rate* plot, and its associated measure ρ, are sensitive to both kinds of distortions, and that they seem to reflect sensibly the perceptual degradation of the speech signal (Fig. 8). Therefore, the STMI has potentially the advantage of being useful in a wide range of noisy environments and applications. Moreover, it can be used for *frame-by-frame* comparisons and with *long-term* averages as illustrated in Sec. IV. Clearly, much more experimental work is needed to ''calibrate'' the numerical values of STMI against human speech perception under controled noisy situations, and against accepted estimates of the *articulation index* and the *speech transmission index*.

C. Relation to vision spatio-temporal MTFs

Visual spatio-temporal MTFs are usually measured with sinusoidally modulated gratings, with various orientations and drifting velocities (Dong and Atick, 1995; Kelly, 1961). These measurements are analogous to our spectro-temporal MTFs if we consider the spatial axis of the retina as analogous to the tonotopic axis of the auditory system. Visual and auditory MTFs are generally similar in that they both exhibit an overall low-pass function in both dimensions. There are, however, three important details to note about the data:

(1) Both visual and auditory MTFs exhibit a small but consistent high-pass edge at the lowest modulation rates, giving the MTF more of a bandpass shape [see Fig. 3(c)].
(2) Temporal cutoff rates of visual and auditory MTFs are quite comparable, contrary to the common assumption that auditory processes are generally faster.
(3) Unlike auditory MTFs, visual MTFs seem to be inseparable, i.e., they cannot be reduced to a product of purely temporal and spatial MTFs (Dong and Atick, 1995). This conclusion may be revised based on the criteria and tests one accepts for separability. To first order, however, it is clear that our auditory spectro-temporal MTFs can be derived from a simple product of (Viemeister, 1979) temporal MTFs and (Green, 1986) spectral MTFs (assuming that the high-pass shape of the latter curve is ignored).

D. Further refinements and considerations of the auditory model

The auditory model described here (Sec. III) combines a simplified version of an early auditory model, and a computational module that captures the main features so far observed in auditory cortical responses. It is evident that most of the MTF features are due to the early auditory processing stages (e.g., bandwidths of cochlear filters, and the lateral inhibitory network). The primary purpose of the cortical module is to derive an estimate of the distribution of power in the spectrogram modulations. A major simplification in our analysis and displays is the integration of the spectrogram over the entire tonotopic axis x [Eq. (4)]. This allows us to generate the two-dimensional scale-rate plots, and to ignore the contribution of different frequency ranges to the final displays. Clearly, this variable must be considered in future work in ways that reflect the specific applications. For instance, the effect of noise should be weighted more heavily in the intermediate frequency ranges (near 1 kHz) where hearing thresholds are lowest and speech spectra are concentrated. Another useful addition to the model is a detection criteria that will enable us to predict sensitivity to changes in arbitrary spectrograms, and to derive MTFs for arbitrarily complex spectra and manipulations such as Yost's ripple noise.

ACKNOWLEDGMENTS

This work is supported by a contract with the Southwest Research Institute, and partially by the Office of Naval Research through a MURI grant (Center for Auditory and Acoustic Research). We are grateful to Dr. Brian Zook (at Southwest Research Institute) for supplying the speech intelligibility data.

[1]Sensitivity also decreases to very low ripples (below about 1 cyc/oct), although this is probably due to the design of the test which uses a flat spectrum as the standard.
[2]This is the case for one of two stimuli presented in Yost and Moore (1987). In the other, the spectrum is translated periodically at different rates along the linear frequency axis. Along the logarithmic frequency axis, the spectral pattern periodically changes shape in a complicated manner, but thresholds are measured only with respect to the change in temporal rates. Thus, strictly speaking, this stimulus does not fit neatly in the purely temporal versus spectral classification.
[3]A more extensive description of corpus design, collection, and transcription can be found in the printed documentation from National Institute of Standards and Technology (NIST No. PB91-100354).
[4]The reverberation model is an exponentially decaying function, $m(F) = [1 + (2\pi F\tau)^2]^{-1/2}$, applied to the envelope of each channel in the spectrogram, where F is the temporal modulation frequency of the envelope (Houtgast *et al.*, 1980).

Amagai, S., Dooling, R., Shamma, S., Kidd, T., and Lohr, B. (**1999**). ''Perception of rippled spectra in the parakeet and zebra finches,'' J. Acoust. Soc. Am. (in press).
Arai, T., Pavel, M., Hermansky, H., and Avendano, C. (**1996**). ''Intelligibility of speech with filtered time trajectories of spectral envelopes,'' Proc. ICSLP, pp. 2490–2492.
Clarey, J., Barone, P., and Imig, T. (**1992**). ''Physiology of thalamus and cortex,'' in *The Mammalian Auditory Pathway: Neurophysiology*, edited by D. Webster, A. Popper, and R. Fay (Springer Verlag, New York), pp. 232–334.
De-Valois, R., and De-Valois, K. (**1990**). *Spatial Vision* (Oxford U. P., New York).
deCharms, R., Blake, D., and Merzenich, M. (**1998**). ''Optimizing sound features for cortical neurons,'' Science **280**, 1439.
Dong, D., and Atick, J. (**1995**). ''Statistics of natural time-varying images,'' Network Comput. Neural Syst. **6**, 345–358.
Drullman, R., Festen, J., and Plomp, R. (**1994**). ''Effect of envelope smearing on speech reception,'' J. Acoust. Soc. Am. **95**, 1053–1064.
Duda, R., and Hart, P. (**1973**). *Pattern Classification* (Wiley–Interscience, New York).
Green, D. (**1986**). '''Frequency' and the detection of spectral shape change,'' in *Auditory Frequency Selectivity*, edited by B. C. J. Moore and R. Patterson (Plenum, Cambridge), pp. 351–359.

Greenberg, S., and Kingsbury, B. (**1997**). ''The modulation spectrogram: In pursuit of an invariant representation of speech,'' ICASSP-97, pp. 1647–1650.
Greenberg, S., Hollenback, J., and Ellis, D. (**1996**). ''Insights into spoken language gleaned from phonetic transcription of the switchboard corpus,'' in *ICSLP-96 Proc. 4th Int. Conf. Spoken Lang*. (IEEE, New York), pp. S32–S35.
Haykin, S. (**1996**). *Adaptive Filter Theory* (Prentice–Hall, Englewood Cliffs, NJ).
Hermansky, H., and Morgan, N. (**1994**). ''RASTA processing of speech,'' IEEE Trans. Speech Audio Process. **2**(4), 578–589.
Hillier, D. (**1991**). ''Auditory processing of sinusoidal spectral envelopes,'' Ph.D. thesis, The Washington University and Severn Institute.
Houtgast, T., Steeneken, H., and Plomp, R. (**1980**). ''Predicting speech intelligibility in rooms from the Modulation transfer function: General room acoustics,'' Acustica **46**, 60–72.
Kelly, D. H. (**1961**). ''Visual responses to time-dependent stimuli,'' J. Opt. Soc. Am. **51**, 422–429.
Kowalski, N., Depireux, D., and Shamma, S. (**1996**). ''Analysis of dynamic spectra in ferret primary auditory cortex: Characteristics of single unit responses to moving ripple spectra,'' J. Neurophysiol. **76**(5), 3503–3523.
Kryter, K. (**1962**). ''Methods for the calculation and Use of the articulation index,'' J. Acoust. Soc. Am. **34**(11), 1689–2147.
Levitt, W. (**1971**). ''T transformed up–down methods in psychoacoustics,'' J. Acoust. Soc. Am. **49**, 467–477.
Shamma, S. (**1988**). ''The acoustic features of speech sounds in a model of auditory processing: vowels and voiceless fricatives,'' J. Phonetics **16**, 77–91.
Shamma, S., Chadwick, R., Wilbur, J., Morrish, K., and Rinzel, J. (**1986**). ''A biophysical model of cochlear processing: Intensity dependence of pure tone responses,'' J. Acoust. Soc. Am. **80**, 133–145.
Shannon, R., Zeng, F.-G., Wygonski, J., Kamath, V., and Ekelid, M. (**1995**). ''Speech recognition with primarily temporal cues,'' Science **270**, 303–304.
Simon, J., Depireux, D. A., and Shamma, S. A. (**1998**). ''Representation of complex spectra in auditory cortex,'' in *Psychophysical and Physiological Advances in Hearing. Proceedings of the 11th International Symposium on Hearing*, edited by A. R. Palmer, A. Ress, A. Q. Summerfield, and R. Meddis (Whurr, London), pp. 513–520.
van Zanten, G., and Senten, C. (**1983**). ''Spectro-temporal modulation transfer functions (STMTF) for various types of temporal modulation and a peak distance of 200 Hz,'' J. Acoust. Soc. Am. **74**, 52–62.
Viemeister, N. (**1979**). ''Temporal modulation transfer functions based upon modulation thresholds,'' J. Acoust. Soc. Am. **66**, 1364–1380.
Wang, K., and Shamma, S. A. (**1994**). ''Self-normalization and noise-robustness in early auditory representations,'' IEEE Trans. Speech Audio Process. **2**, 421–435.
Wang, K., and Shamma, S. (**1995**). ''Representation of spectral profiles in primary auditory cortex,'' IEEE Trans. Speech Audio Process. **3**, 382–395.
Yang, X., Wang, K., and Shamma, S. A. (**1992**). ''Auditory representations of acoustic signals,'' IEEE Trans. Inf. Theory Special Issue on Wavelet Transforms and Multiresolution Signal Analysis) **38**, 824–839.
Yost, W., and Moore, M. (**1987**). ''Temporal changes in a complex spectral profile,'' J. Acoust. Soc. Am. **81**, 1896–1905.

Within-channel cues in comodulation masking release (CMR): Experiments and model predictions using a modulation-filterbank model

Jesko L. Verhey, Torsten Dau, and Birger Kollmeier
Graduiertenkolleg Psychoakustik, AG Medizinsche Physik, Carl-von-Ossietzky Universität Oldenburg, Postfach 2503, D-26129 Oldenburg, Germany

(Received 19 May 1998; revised 11 February 1999; accepted 2 July 1999)

Experiments and model calculations were performed to study the influence of within-channel cues versus across-channel cues in comodulation masking release (CMR). A class of CMR experiments is considered that are characterized by a single (unmodulated or modulated) bandpass noise masker with variable bandwidth centered at the signal frequency. A modulation-filterbank model suggested by Dau *et al.* [J. Acoust. Soc. Am. **102**, 2892–2905 (1997)] was employed to quantitatively predict the experimental data. Effects of varying masker bandwidth, center frequency, modulator bandwidth, modulator type, and signal duration on CMR were examined. In addition, the effect of band limiting the noise before or after modulation was shown to influence the CMR in the same way as a systematic variation of the modulation depth. It is demonstrated that a single-channel analysis, which analyzes only the information from one peripheral channel, quantitatively accounts for the CMR in most cases, indicating that an across-channel process is generally not necessary for simulating results from this class of CMR experiments. True across-channel processes may be found in another class of CMR experiments.
[S0001-4966(99)01611-2]

PACS numbers: 43.66.Ba, 43.66.Dc [JWH]

INTRODUCTION

Detection thresholds for a test signal presented in a noise masker can be markedly lower when the masker is modulated compared to the reference condition in which the masker is unmodulated. Hall *et al.* (1984) were some of the first investigators who examined this effect using several masker types. In one of their experiments they measured the detectability of a sinusoidal signal in the presence of a bandpass-noise masker which was spectrally centered at the signal frequency. They found that for masker bandwidths larger than the critical band, signal thresholds in the modulated-noise condition were up to 9 dB lower than in the reference condition where unmodulated bandpass noise was used as the masker. This difference between the modulated and unmodulated condition diminished when the masker bandwidth was smaller than the critical bandwidth. Based on these findings, Hall *et al.* suggested that the observers may have compared the envelope fluctuations between different auditory channels, i.e., they took advantage of the correlated masker envelope across frequency bands in the modulated condition. Hence, they called the difference in threshold between unmodulated and modulated conditions ''comodulation masking release'' (CMR).

In the literature the CMR experiments can be divided in two different classes according to their different masker types. In the first class of experiments the masker is a single bandpass noise centered at the signal frequency (as just described) (Hall *et al.*, 1984; Haggard *et al.*, 1990; Schooneveldt and Moore, 1989a; Carlyon *et al.*, 1989; Hall *et al.*, 1996). In the second class of experiments the masker consists of several masker bands, one at the signal frequency (on-frequency band) and one or more other bands (flanking bands) spectrally separated from the on-frequency band. It has been shown that adding one comodulated band to an on-frequency band can improve the detectability of the sinusoidal signal by up to 8 dB (e.g., Hall *et al.*, 1984, 1989; Schooneveldt and Moore, 1987, 1989b; Fantini *et al.*, 1993; Eddins and Wright, 1994; Hatch *et al.*, 1995). In contrast to the experiments of the first class, the difference between the reference condition (on-frequency band alone) and the comodulated condition is largest for a small spectral distance between the two masker bands (smaller than the critical bandwidth) and decreases with increasing spectral distance. It has been argued that some of the effect in the second class of experiments might result from beating between components of the two masker bands within one peripheral channel, i.e., it results from a within-channel cue (McFadden, 1986; Schooneveldt and Moore, 1987). For large spectral distances, however, the threshold difference between reference and comodulated condition (e.g., Moore, 1992) amounts to about 2–6 dB. It is assumed that this is a consequence of an across-channel process and is therefore called ''true'' or ''across-channel'' CMR.

Several authors have also discussed the most appropriate reference condition to define CMR in the second class of experiments. The CMR is normally obtained by subtracting the thresholds with no flanking band from thresholds with comodulated flanking band(s). However, in some studies another definition of CMR is proposed: CMR is defined as the difference between thresholds with comodulated flanking bands and thresholds with non-comodulated flanking bands.

This latter convention is more similar to the definition of CMR in the first class of experiments. In most cases it gives larger values for CMR because thresholds are generally higher in the presence of non-comodulated flanking bands than for the on-frequency band alone even for large spectral distances (e.g., Schooneveldt and Moore, 1987).

Concerning the first class of experiments, Carlyon *et al.* (1989) argued that the difference between the unmodulated and modulated conditions is not an accurate way to determine ''across-channel'' CMR, because in some cases a modulation of the masker produces a masking release even for subcritical masker bandwidths, where the role of across-channel processes is unclear (Carlyon *et al.*, 1989; Schooneveldt and Moore, 1989a). Hence Carlyon *et al.* (1989) suggested calling the threshold difference between the modulated and unmodulated condition ''MUD'' and only the masking release due to across-channel processes ''CMR.'' To get a measure of the ''across-channel'' CMR, the authors suggested subtracting the threshold difference for a subcritical condition from the threshold difference obtained for bandwidths larger than the critical bandwidth. This would be more or less equivalent to the definition of CMR in the second class of experiments where the on-frequency band-alone condition was proposed as the reference. However, as mentioned by Hall *et al.* (1996), this definition of CMR is somewhat problematic, because it assumes that there is a clear distinction between bandwidths where ''pure'' within-channel processes are the reason for the threshold difference and bandwidths where across-channel processes occur as well. Furthermore, the amount of ''across-channel'' CMR depends on the definition of the critical bandwidth, since most of the data in the literature show a continuous increase of masking release for subcritical bandwidths (e.g., Hall *et al.*, 1984; Schooneveldt and Moore, 1989a; Haggard *et al.*, 1990; Bacon *et al.*, 1997). Thus, although it may be more appropriate to reserve the term ''CMR'' for the masking release due to across-channel processes, in the present study CMR is used according to the definition by Hall *et al.* (1984) to mean the threshold difference between the unmodulated and modulated condition, since the exact amount of masking release due to across-channel processes is still not well defined. This definition of CMR is also used to indicate that in the literature these experiments are referred to as CMR experiments.

Schooneveldt and Moore (1989a) explained the amount of CMR in the first class of experiments in terms of envelope statistics within one critical band (within-channel process). They argued that changes in the statistical properties of the envelope produced by adding the signal to the noise can produce threshold reduction also for noise bandwidths smaller than the critical band. Because of this within-channel cue, which facilitates the detection of the signal in modulated noise, they stated that the magnitude of the ''across-channel'' CMR is overestimated, when it is defined as the difference in thresholds between modulated and unmodulated conditions.

Although several studies have qualitatively discussed the role of within-channel processes in CMR experiments, there is no study that quantifies the amount of masking release due to within-channel cues. Therefore, simulations with a (single-channel) model suggested by Dau *et al.* (1997a) were performed here and compared with experimental data. The model analyzes the envelope of the peripheral channel tuned to the signal frequency by a modulation filterbank. The model of Dau *et al.* has been previously tested and evaluated in modulation detection and masking conditions.

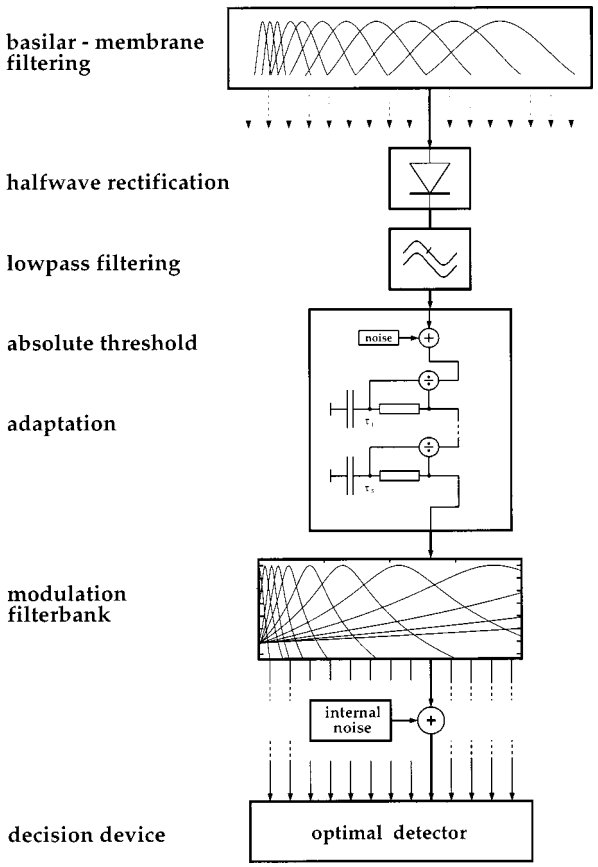

FIG. 1. Block diagram of the psychoacoustical model as described in Dau *et al.* (1997a). The signals are preprocessed, subjected to adaptation, filtered by a modulation filterbank, and finally added to internal noise. The decision device is realized as an optimal detector.

This paper is focused on the first class of experiments. Some experiments from the literature were repeated to ensure identical conditions in experiment and corresponding simulations (experiments 1, 2, 3, and 6). Two new experiments were performed to examine the effect of waveform generation of the modulated masker on CMR (experiments 4 and 5).

I. SINGLE-CHANNEL MODEL

Dau *et al.* (1997a) proposed a model to describe modulation detection and modulation masking. The model combines several preprocessing stages with an optimal detector as the decision device (see Fig. 1). The first stage of the model is the linear gammatone filterbank model of Patterson *et al.* (1987), which simulates the bandpass characteristic of the basilar membrane. To investigate within-channel cues in the present study, a single-channel version of the model is applied, i.e., only the output of the gammatone filter centered at the signal frequency was processed. The signal at the out-

put of the specific filter was half-wave rectified and low-pass filtered at 1000 Hz, i.e., for high center frequencies only the envelope of the signal was further processed. To simulate the adaptive properties of the auditory periphery, a chain of five consecutive nonlinear feedback loops was incorporated (Püschel, 1988). The feedback loops were initially developed to describe forward masking experiments. In addition to adaptation, this stage transforms stationary signals approximately to the logarithm of the input. In contrast, fast fluctuations are transformed nearly linearly. To further analyze the amplitude fluctuations of the envelope, a linear modulation filterbank was incorporated in the model. The frequency selectivity for modulation frequencies is based on physiological findings and psychoacoustical data from modulation masking and modulation detection studies. The center frequency of the highest modulation filter was set to a quarter of the center frequency of the peripheral filter. This slight modification of the model is motivated by physiological findings by Langner and Schreiner (1988). Apart from that, all parameters of the model are identical to those described by Dau *et al.* (1996a, b, 1997a, b). To model a limit of resolution, an internal noise with a constant variance was added to the output of each modulation filter. In the decision process, a stored temporal representation of the signal to be detected (the template) is compared with the actual activity pattern by calculating the unnormalized cross correlation between the two temporal patterns (Dau *et al.*, 1996a, 1997a). This is comparable to a ''matched filtering'' process. The template is derived once at a clearly supra-threshold signal value. The idea is that at the beginning of an experiment the signal is usually presented at a highly detectable level where the subject is assumed to be able to get an ''image'' of the signal.

In the simulations the stimuli were presented in the same way as in real psychoacoustical measurements, i.e., thresholds were determined with a three-interval forced-choice (3IFC) procedure with adaptive level tracking (two-down one-up). Thus, the model could be considered as ''imitating'' a human observer. Because stochastic stimuli were used in the experiments, thresholds can vary between different simulated runs of the experiment. Therefore, as the final simulated threshold, the mean (and standard deviation) of at least ten simulated experimental runs was used.

II. METHODS

A. Procedure

In all experimental conditions, a 3IFC procedure was used to measure the masked threshold of a sinusoidal signal in the presence of a noise masker. A trial contained three intervals separated by 500 ms of silence. Two intervals consisted of the masker alone, and one randomly chosen interval contained the masker plus signal. Subjects had to indicate the interval with the signal by pressing the corresponding key on a keyboard. Feedback was provided on a screen in front of the subjects as to whether the response was correct or not. The level of the signal was varied according to a one-up two-down procedure. This procedure estimates the 70.7% point on the psychometric function (Levitt, 1971). The step size was 8 dB at the beginning of the experiment. It was reduced to 4 dB after the first reversal and finally to 2 dB after the second reversal. Then the step size was held constant over the next ten reversals. The threshold was determined by calculating the median of the levels at the last ten reversals. The final threshold estimate was taken as the mean over three runs.

B. Apparatus and stimuli

The stimuli were generated digitally with a sampling rate of 32 kHz. Stimulus generation and presentation were controlled by a Silicon Graphics workstation (INDY), which also sampled the listener's responses and controled the procedure. The software package SI, developed at the Universität Göttingen, was used for signal generation and control of the experiments. The stimuli were D/A converted (16 bits), and then preamplified and low-pass filtered at 16 kHz with a computer-controled audiometric amplifier (Kollmeier, 1996). The subjects were situated in a sound-attenuating booth. The stimuli were presented diotically via a Sennheizer HDA 200 headphone without free-field equalization.

The masker was a band-limited noise centered at the signal frequency, i.e., at 1, 2, or 4 kHz. The masker bandwidth was 50, 100, 200, 400, 1000, or 2000 Hz. In general, two different noise generation processes were used. In the ''reference condition'' a digitally bandpass-filtered Gaussian noise was applied. In the ''comodulated condition'' a broadband noise (from 0 to 10 000 Hz) was first multiplied with a digitally filtered low-pass noise and finally restricted to the desired bandwidth. The cutoff frequency of the low-pass noise (modulator bandwidth) differed in the experiments. The spectrum level of the bandpass noise was 30 dB. In the experiments 4–6, a different ''comodulated noise'' was used (see below). The masker duration was 600 ms including 10 ms cosine-squared rise/fall time. This period was randomly cut out from a fixed noise waveform which was generated at the beginning of each experiment and had a periodicity of 3 s.

In all experiments the sinusoidal signal had a duration of 300 ms (except for the third experiment where the effect of varying signal duration was tested explicitly) including 50-ms cosine-squared rise/fall time. The signal onset was 150 ms after the masker onset.

C. Subjects

Five normal hearing subjects (two male, three female) ranging in age between 24 and 32 years participated voluntarily in the experiments. Two of them were the authors JV and TD. One subject participated in all experimental conditions. At least three subjects were used for each experiment. All subjects had prior experience in psychoacoustic experiments.

III. RESULTS

A. Experiment 1: CMR as a function of carrier frequency and masker bandwidth

In this experiment the dependence of CMR on the center frequency CF of the noise band was investigated. The signal

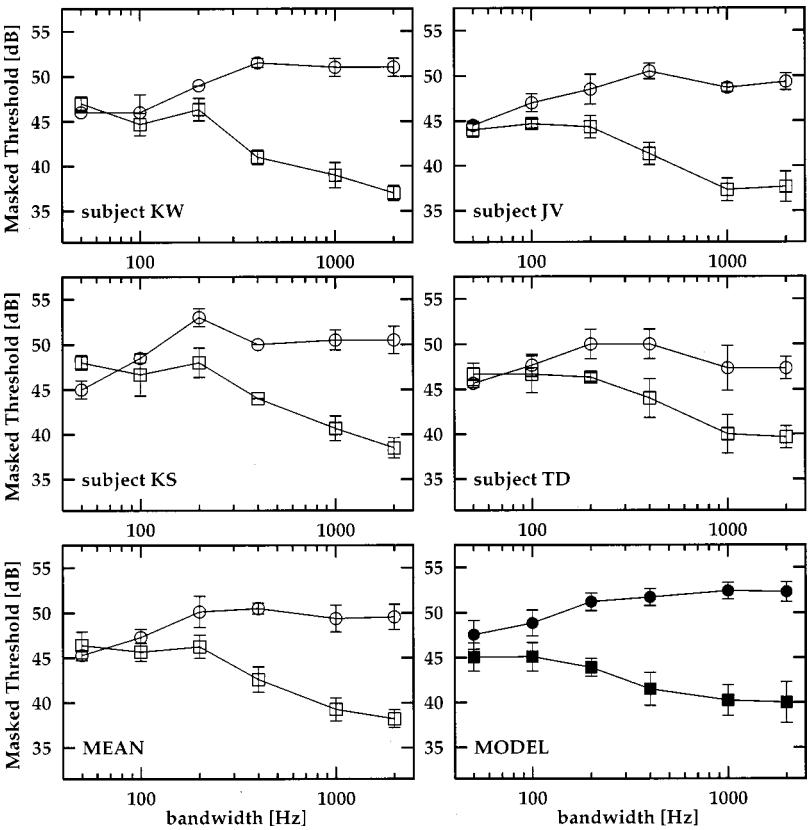

FIG. 2. Signal threshold as a function of the masker bandwidth in random noise (○) and modulated noise (□). The modulator bandwidth was 50 Hz, the signal frequency was 2 kHz. The upper four panels show individual data. The error bars represent plus and minus one intraindividual standard deviation calculated across three repetitions for each subject and condition. The lower left panel shows the average data across all subjects. In this panel, the vertical bars show the amount of variability across subjects, calculated as plus and minus one (interindividual) standard deviation of the means across subjects. The lower right panel shows simulated mean data and standard deviation across ten simulated threshold runs.

frequency was 1, 2, or 4 kHz. The modulator bandwidth Δf_{mod} was 50 Hz. The experiment is similar to that described by Haggard *et al.* (1990). It was replicated here with a slightly different threshold procedure and method of stimulus generation.

Figure 2 shows individual data for four subjects (upper and middle panels), mean data across subjects (lower left panel), and simulated data (lower right panel) for a signal frequency of CF=2 kHz. The figure shows masked thresholds of a sinusoidal signal as a function of the masker bandwidth. The circles represent thresholds for the reference condition whereas the squares represent thresholds for the comodulated condition. In the reference condition, thresholds first increase with increasing bandwidth and then reach a constant value for masker bandwidths $\Delta f \geqslant 200$ Hz. With the classical procedure of fitting two lines to the data (Fletcher, 1940), a critical bandwidth of 220 Hz is obtained on average which is larger than the bandwidth reported by Fletcher, but slightly smaller than the critical bandwidths of 240–310 Hz measured in more recent studies (Scharf, 1970; Moore and Glasberg, 1983; Schooneveldt and Moore, 1989a). In the comodulated condition, thresholds are independent of masker bandwidth for $\Delta f \leqslant 200$ Hz and decrease with increasing masker bandwidth for $\Delta f > 200$ Hz. The difference in threshold between the reference condition and the comodulated condition (CMR) increases with increasing bandwidth. For large bandwidths (≥1000 Hz) this CMR value converges at a value of 8–14 dB, depending on the subject.

The simulated thresholds (lower right panel) are in good agreement with experimental results. However, there is a constant threshold shift of about 2 dB towards higher thresholds. In the reference condition, thresholds increase with increasing masker bandwidth up to the critical bandwidth and then remain at a constant level (of 53 dB) whereas in the comodulated condition threshold decreases with increasing bandwidth. The model predicts a CMR effect of 11 dB for large masker bandwidths which is the same as in the experiment.

Figure 3 shows averaged experimental data of three subjects (open symbols) and simulated data (filled symbols) for three signal frequencies: 1 kHz (upper panels), 2 kHz (middle panels), and 4 kHz (lower panels).[1] The circles represent thresholds for the reference condition and squares show thresholds for the comodulated condition. The thresholds for a masker bandwidth of 50 Hz vary very little with center frequency and are more or less the same in both conditions. For all center frequencies the threshold in the reference condition first increases with increasing masker bandwidth up to the maximum threshold at about 48–53 dB depending on center frequency. In the ''comodulated condition'' the thresholds remain constant or slightly increase up to $\Delta f = 100$ Hz for CF=1 kHz and up to $\Delta f = 200$ Hz for CF=2 and 4 kHz. Beyond this masker bandwidth thresholds decrease with increasing masker bandwidth. The maximum threshold difference between reference and comodulated condition (CMR) for large masker bandwidths (≥1000 Hz) is 11 dB for CF=1 and 2 kHz and 13 dB for CF=4 kHz. The thresholds are 10 dB lower than in a comparable experiment by Hall *et al.* (1984). This shift is due to a different spectrum level in the two studies (40 dB in their experiment versus 30 dB in the present paper). In addition, the general shape of our data deviates slightly from the experimental results presented by Haggard *et al.* (1990). They found, that

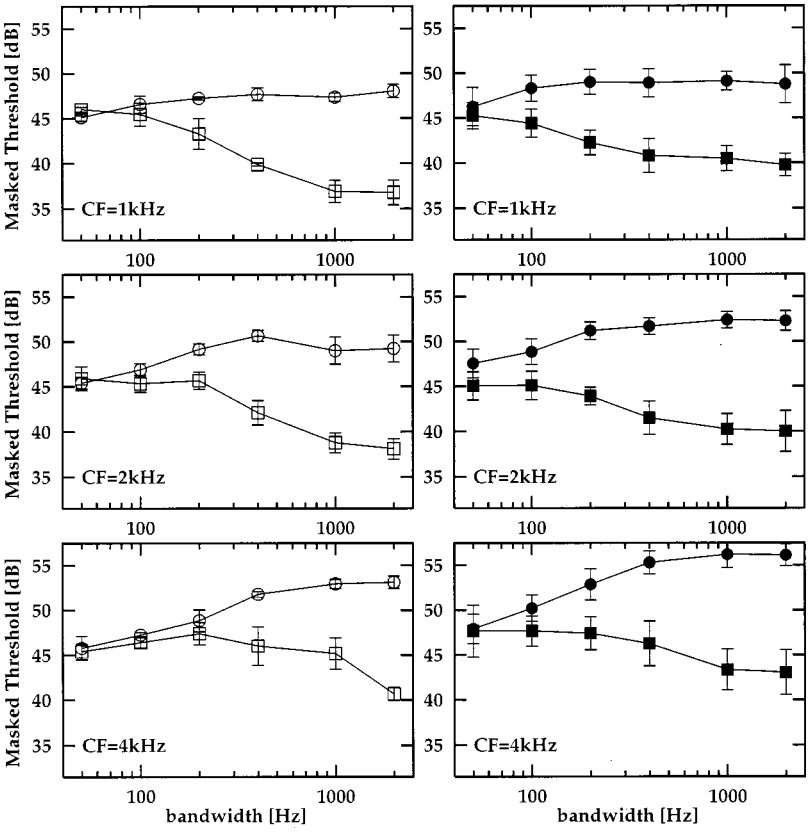

FIG. 3. Mean measured data over three subjects (left column of panels) and simulated thresholds (right column of panels) for a signal presented in random noise (○) and modulated noise (modulator bandwidth of 50 Hz, □) as a function of masker bandwidth. The signal frequency was 1 kHz (upper panels), 2 kHz (middle panels), and 4 kHz (lower panels).

the ''CMR existence region'' (all masker bandwidths with CMR greater than +3 dB) varies with center frequency in a way similar to the critical bandwidth. Our data do not show such a direct correlate. There is a negligible effect of center frequency on the ''CMR existence region.'' This difference might be due to a different way of generating the noise masker. Haggard *et al.* generated bandpass noise by multiplying low-pass noise with a sinusoid at the center frequency of the desired passband. The low-pass noise was either Gaussian (reference) or a multiplied noise (comodulated) and had a cutoff frequency of half the bandwidth. The procedure applied in the present study is the same as that described by Hall *et al.* (1984), where bandpass noise was generated by bandpass filtering a broadband Gaussian or multiplied noise.

In general, the simulated data (right column of Fig. 3) are in good agreement with the present experimental data. In particular the total amount of CMR is accounted for by the single-channel model at least for center frequencies of 2 and 4 kHz. However, for CF=1 kHz and for large masker bandwidths the model predicts a CMR effect of only 9 dB, which is 2 dB less than in the averaged data (11 dB). The predicted amount of CMR increases with increasing bandwidth for all center frequencies, which is in agreement with the measured data. However, the absolute value of the predicted threshold deviates in some cases from the observed thresholds. For example, for CF=4 kHz, the simulated thresholds are about 3 dB higher than the corresponding measured thresholds, whereas the difference is less than 1 dB for CF=1 kHz. On the basis of the critical band hypothesis (assuming peripheral filters with a constant *Q*-value) one would expect a 6 dB higher threshold for CF=4 kHz than for CF=1 kHz for the reference condition at large masker bandwidths. Indeed, such an effect can be observed in the simulated data, whereas in the measured data, the effect amounts 5 dB. This is in line with Green *et al.* (1959), who also reported about an increase in the critical ratio of about 5 dB. The small deviation might be due to interindividual variances in the bandwidth of peripheral auditory filters as a function of center frequency (e.g., Glasberg and Moore, 1986).[2]

B. Experiment 2: CMR as a function of modulator and masker bandwidth

Schooneveldt and Moore (1989a) and Carlyon *et al.* (1989) investigated how the amount of CMR depends on modulator bandwidth. Carlyon *et al.* (1989) found a slight increase in masking release of 2.7 dB (on average) as the modulator bandwidth decreases from 50 to 16 Hz. The effect is smaller in Schooneveldt and Moore's (1989a) data. They measured thresholds for a wider range of modulator bandwidths. They found that for modulator bandwidths larger than 50 Hz, CMR decreases with increasing modulator bandwidth whereas for modulator bandwidths smaller than 50 Hz there was no dependence of CMR (for large masker bandwidths) on the modulator bandwidth.

The experiment performed by Schooneveldt and Moore was replicated here for modulator bandwidths Δf_{mod} of 12.5, 50, and 200 Hz at CF=2 kHz. The signal parameters were the same as described in Sec. II. They slightly differ from those in Schooneveldt and Moore (1989a), but these differences are not expected to change the results (cf. Hall *et al.*, 1996).

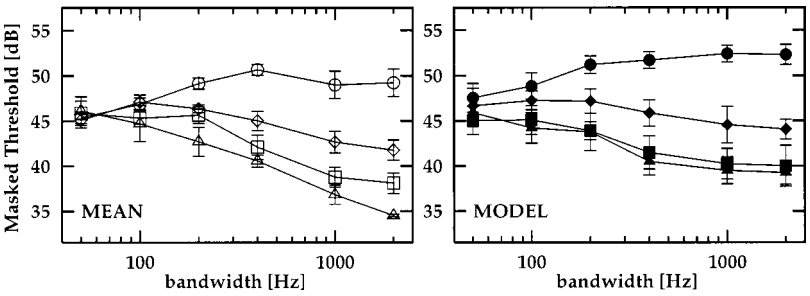

FIG. 4. Mean measured data over three subjects (left panel) and simulated thresholds (right panel) for a signal presented in random noise (○) and modulated noise as a function of the masker bandwidth. The modulator bandwidth was 12.5 Hz (△), 50 Hz (□), and 200 Hz (◇), respectively.

The left panel of Fig. 4 shows mean measured data of three subjects for modulator bandwidths $\Delta f_{\mathrm{mod}} = 12.5$ Hz (△), 50 Hz (□), and 200 Hz (◇), and for the reference condition (○). Except at the narrowest bandwidths (50 and 100 Hz), thresholds in the comodulated conditions are always lower than in the reference condition. In agreement with the data of Schooneveldt and Moore (1989), the measured CMR decreases with increasing modulator bandwidth. The largest amount of CMR is about 14 dB for $\Delta f_{\mathrm{mod}} = 12.5$ Hz whereas it is only 7 dB for $\Delta f_{\mathrm{mod}} = 200$ Hz.

The right panel of Fig. 4 shows simulated data. There is again a good agreement between simulated data and measured data. The model shows a reduction in CMR for a modulator bandwidth of 200 Hz which is the same as in the data, whereas the magnitude of the CMR varies little for the modulator bandwidths 12.5 and 50 Hz in agreement with the data. However, for the smallest masker bandwidth, the model still predicts a small masking release of up to 3 dB which in contrast to the measured data. This may indicate that the model slightly overestimates the masking release for small masker bandwidths. Note, however, that concerning this point, the present data are not consistent with the data in the literature, where a CMR effect of 4 dB was found for a modulator bandwidth $\Delta f_{\mathrm{mod}} = 12.5$ Hz and a masker bandwidth of 50 Hz (Schooneveldt and Moore, 1989a). The reason for this difference is unclear. It might be due to a different way of bandlimiting the noise. In the present study the modulator and the noise masker were filtered digitally whereas Schooneveldt and Moore used analog filters. Therefore, the difference may be caused by analog filtering, since the reduction of the modulation depth due to the filtering after modulation is less pronounced when the bandpass filter has a shallower slope (see Sec. IV).

C. Experiment 3: CMR as a function of signal duration and masker bandwidth

Schooneveldt and Moore (1989a) investigated the effect of signal duration on CMR. Their experiment was replicated here for three signal durations (25, 200, and 400 ms), a modulator bandwidth of 12.5 Hz, and a center frequency of 2 kHz. Both the masker and signal were gated with 10-ms raised cosine ramps.[3]

Mean measured data over three subjects are shown in the left three panels in Fig. 5. Thresholds in the reference condition (○) increase with decreasing signal duration for all masker bandwidths. In the case of wide noise maskers ($\Delta f \geqslant 1000$ Hz) and a signal duration of 25 ms, for example, thresholds are 9 dB higher than thresholds for a 200-ms signal. This decrease in threshold is in line with experiments on temporal integration (e.g., Florentine *et al.*, 1988), where doubling the signal duration results in a decrease in threshold of about 3 dB. For signal durations of 200 and 400 ms the general shape of the threshold function for the comodulated condition (□) is similar to that found before (Sec. III.A and B), e.g., for large masker bandwidths thresholds are always slightly lower than those in the reference condition whereas no CMR can be found for the smallest bandwidth (50 Hz). The largest difference in CMR between the two durations is about 3 dB at masker bandwidths of 400 and 1000 Hz. This finding corresponds to the data presented by Schooneveldt and Moore (1989a), where, for bandwidths of 400 and 800 Hz, CMR was found to increase by 2–3 dB with increasing duration from 200 to 400 ms. For a signal duration of 25 ms, thresholds in the comodulated conditions are about the same as the reference condition for almost all masker bandwidths. These findings do not agree with the results from Schooneveldt and Moore. The reason for the difference between the two studies is unclear. It may be due to the different experimental setups in the two studies and a slightly different definition of duration.[3]

The right column of Fig. 5 shows simulated data. The model accounts qualitatively for the threshold decrease in the reference condition with increasing signal duration. However, the difference between the highest threshold for a duration of 25 ms and the highest threshold for a duration of 400 ms amounts to only 5 dB. This contrasts with the measurements (10 dB). The inability of the model to describe temporal integration was already mentioned in Dau *et al.* (1996b). The authors explained the shortcoming by the unrealistic behavior of the feedback loops at the stimulus onset.

The model accounts for the observed CMR for signal durations of 200 and 400 ms. Nevertheless, the predicted maximum CMR for the large durations is smaller (7 dB for a duration of 200 ms and 11 dB for a duration of 400 ms) than the measured CMR (13 dB for a duration of 200 ms and 15 dB for a duration of 400 ms). The smaller amount of CMR in the simulated case in comparison to the simulations in the previous section is mainly a consequence of the shorter ramps of the signal (see Sec. IV). For a duration of 25 ms, the measured data show no CMR for all masker bandwidths except for the largest bandwidth, where a small masking release of about 4 dB is observed. The model does predict no CMR for all masker bandwidths. It is possible that this rest effect of about 4 dB is due to a ''true'' CMR resulting from across-channel processing.

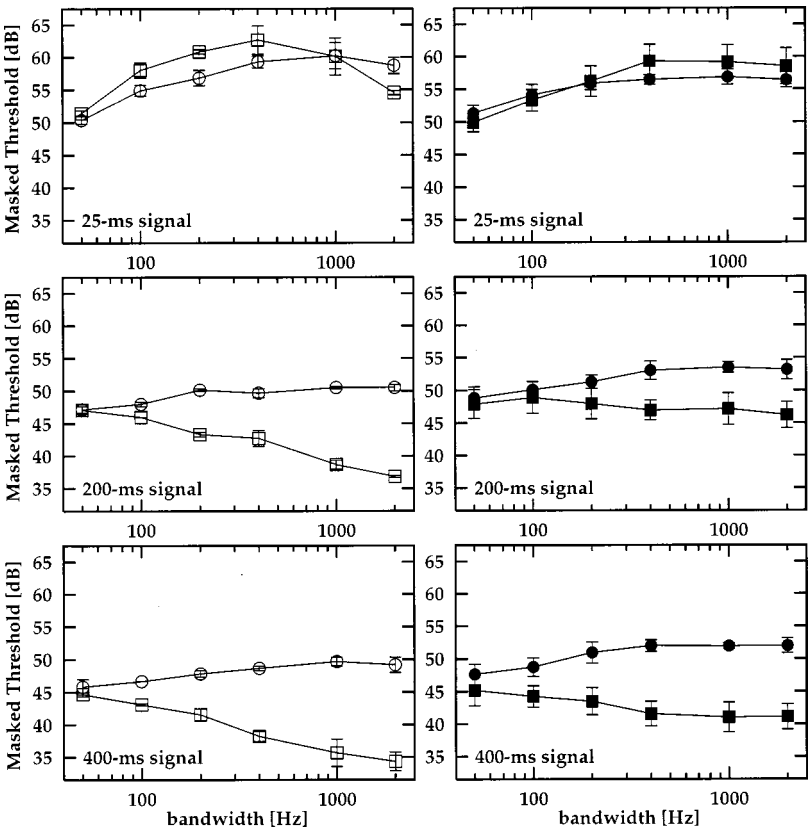

FIG. 5. Mean measured thresholds over three subjects (left column of panels) and simulated thresholds (right column of panels) for a signal presented in random noise (○) and modulated noise (modulator bandwidth of 12.5 Hz, □) as a function of the masker bandwidth. Signal duration was either 25 ms (upper panels), 200 ms (middle panels), or 400 ms (lower panels). The signal frequency was 2 kHz.

D. Experiment 4: Effects of bandlimiting the masker before or after modulation

This section analyzes which factors are responsible for the decrease in CMR with decreasing masker bandwidth Δf. A new experiment was performed where the comodulated masker was generated in a slightly different manner than before.[4] The experimental conditions were equivalent to the experiments of Secs. III A and B. The signal frequency was 4 kHz and a modulator bandwidth of 50 Hz was used.

In contrast to the classical generation of comodulated noise, a broadband Gaussian noise was first bandpass filtered and then modulated (e.g., multiplied with a low-pass noise). To obtain the same masker bandwidth Δf as in the previous experiments, the broadband noise was bandlimited to $\Delta f - 2 \cdot \Delta f_{\mathrm{mod}}$ prior to modulation, where Δf_{mod} is the modulator bandwidth. Hence, the smallest masker bandwidth that can be achieved is determined by twice the modulator bandwidth $\Delta f = 2 \cdot \Delta f_{\mathrm{mod}}$, provided that a sinusoid with random starting phase is used as carrier. The overall level of the masker in the comodulated condition (condition 2) was the same as in the classical comodulated condition (condition 1) with the same masker bandwidth.

Figure 6 shows mean measured data from three subjects (TD, KT, JV)[5] (left panel) and simulated data (right panel). Circles indicate thresholds in the reference condition, squares indicate thresholds in the ''classical'' comodulated condition (condition 1) and triangles indicate the thresholds obtained in the new experimental condition (condition 2). For almost all masker bandwidths, thresholds are markedly lower (up to 5 dB) in condition 2 than in condition 1. This difference diminishes for the largest masker bandwidth of 2000 Hz. Simulated thresholds are plotted in the right panel of Fig. 6. The model predicts lower thresholds for condition 2 than for condition 1 for masker bandwidths smaller than 1000 Hz, whereas thresholds are the same for both conditions for the largest masker bandwidths. However, some deviations between simulated and measured data occur at small masker bandwidths: In the experimental data, the threshold in the prefiltered comodulated condition (condition 2) tends to slightly increase with decreasing masker bandwidth

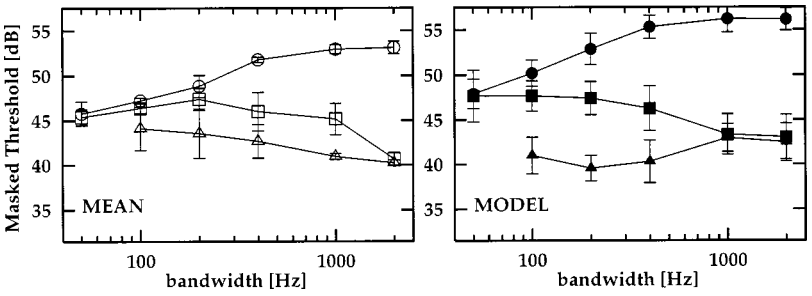

FIG. 6. Thresholds for a 4-kHz sinusoidal signal in random noise (○), and in two different modulated noises as a function of masker bandwidth. Squares indicate thresholds for the modulated condition, where the masker is first modulated and then bandlimited. This is the classical way to generate modulated noise. Triangles indicate thresholds for the condition where the masker is first band-pass filtered and then modulated. The left panel show mean measured data over three subjects and the right panel show simulated data.

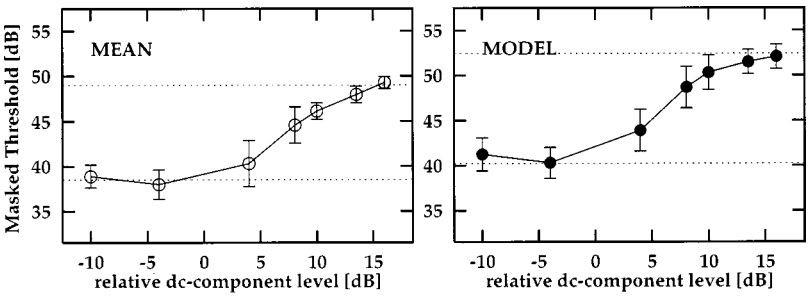

FIG. 7. Mean measured data (left panel) and simulated data (right panel) for a sinusoidal signal in the presence of a 1000-Hz-wide modulated noise masker as a function of the added dc component to the modulator. In addition thresholds for random noise (upper line) and modulated noise (lower line), where no dc value is added (experimental condition as in Fig. 1), are shown.

whereas the model predicts a threshold almost independent of the masker bandwidth. The slight increase in the measured data may reflect a true across-channel process. However, this effect is rather small (<4 dB).

E. Experiment 5: Effects of varying masker modulation depth

Moore (1992) reviewed the factors that influence the occurrence of CMR. He proposed that CMR is large for high modulation depths in the comodulated condition. This assumption is based on findings from Moore and Jorasz (1991) and Fantini and Moore (1992). In their studies the task was to detect a change in modulation depth between two spectrally separated carriers. Hence, these experiments belong to the second class of CMR experiments (see the Introduction). Concerning the first class of experiments, however, there is no comparable study on the effect of masker modulation depth on CMR.

In the present study the masker modulation depth is varied in the comodulated condition by adding a dc component to the low-pass noise modulator. The procedure to generate the comodulated-noise masker was the same as described in Sec. II. Figure 7 shows masked thresholds for a 2-kHz sinusoidal signal in the presence of a 1000-Hz-wide bandpass noise masker as a function of the amount of added dc component. The magnitude of the dc component is expressed as the difference in level (dB) between the dc component and the root-mean-square value of the low-pass noise modulator.[6] The left panel of Fig. 7 shows measured data averaged across four subjects (TD, KT, KS, JV). The right panel shows simulated data. The dotted lines show threshold for the reference condition (upper line) and the ''classical'' comodulated condition (lower line), where no dc component was added for a masker bandwidth of 1000 Hz. For dc values of -10 and -4 dB, thresholds remain the same as in the classical comodulated condition. For larger dc values, they increase to converge on the threshold for the reference condition at the largest dc values. Again the simulated data are in good agreement with experimental results.

F. Experiment 6: CMR for square-wave modulation

In most of the early studies on CMR in the first class of CMR experiments, low-pass noise modulators were used (Hall *et al.*, 1984; Schooneveldt and Moore, 1989a; Haggard *et al.*, 1990). Carlyon *et al.* (1989) investigated how CMR depends on the type of the modulator. They found a larger masking release for a square-wave modulator than for a low-pass noise modulator when the cutoff frequency of the low-pass modulator was equal to the frequency of the square-wave modulator. With decreasing modulator/cutoff frequency the difference increased from about 2–3 dB for 50 Hz up to about 7 dB for 16 Hz.[7]

In two recent studies (Peters and Hall, 1994; Hall *et al.*, 1996), the masking for square-wave modulators was found to be significantly larger than that found by Carlyon *et al.* (1989). For example, Hall *et al.*'s (1996) data for a 10-Hz square-wave modulation showed a CMR effect of 40 dB for large masker bandwidths compared to only about 18–24 dB (depending on the subject) in the study by Carlyon *et al.* (1989). Peters and Hall's (1994) data also showed a larger masking release of about 30 dB in this condition. For a frequency of 40 Hz, the difference between the results of Hall *et al.*'s study and Carlyon *et al.*'s data still amounts to 5–10 dB. Thus, the difference between the masking release for a square-wave modulator and for a low-pass modulator may still be larger than reported by Carlyon *et al.* (1989).

Certainly a direct comparison between the data of the different studies is difficult, because they did not use the same experimental setup. For example, Hall *et al.* used longer test signals, and, as shown previously in experiment 3, the duration affects the masking release. In addition, Hall *et al.* used a 30 dB higher spectrum level which also may affect the amount of CMR. We performed an experiment to directly relate both types of experiments to each other. The signal configuration was the same as in experiment 1 except for the modulating waveform, which consists of a square wave with a repetition rate of 50 Hz and a duty cycle of 50:50. The modulator was dc shifted, i.e., it only assumed the values of 0 and 1. The signal was again a sinusoid at 2 kHz with 300-ms duration. The experiment is an extension of the existing data set. Carlyon *et al.* (1989) measured the masking release only for two very extreme bandwidth conditions and within the other studies (e.g., Hall *et al.*, 1984, 1996; Peters and Hall, 1994) only one modulator type was used.

Figure 8 shows masked thresholds in the modulated condition with the square wave modulated masker (△). The left panel shows mean measured data of four subjects. The right panel shows simulated data. In addition, for comparison, the data for the low-pass noise modulator with cutoff frequency equal to the square-wave frequency (□) and the thresholds for the unmodulated condition (○) are replotted from Fig. 2. Square-wave modulators produce a masking release of up to about 18 dB. This is in contrast to the findings by Peters and Hall (1994) and Carlyon *et al.* (1989) which showed a masking release of 11–12 dB for a 50-Hz square-wave modulator.

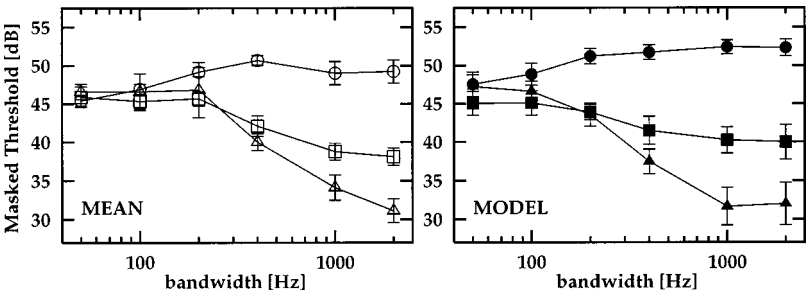

FIG. 8. Mean data over three subjects (left panel) and simulated data (right panel) showing thresholds for a signal presented in random noise (○), in modulated noise with a 50-Hz lowpass-noise modulator (□), and in modulated noise with a 50-Hz square-wave modulator (△) as a function masker bandwidth.

However, the result of the present study is in line with the data presented by Hall *et al.* (1996).

In contrast to the masking release of 18 dB for the square-wave modulator, the low-pass modulator with the same cutoff frequency produces a masking release of only about 11 dB. The difference between the conditions decreases with decreasing masker bandwidth. For the smallest masker bandwidths, the same masking release was found for the two different modulator types.

Apart from the fact that the simulated data are slightly shifted towards higher thresholds, they are in good agreement with the measured data. The model accounts for the increasing difference between the two conditions with increasing masker bandwidth. For large bandwidths ($\geqslant$1000 Hz) the simulated masking release for the square-wave modulator is 20 dB. Thus, the total amount of CMR is accounted for by the model.

IV. DISCUSSION

The role of within-channel cues in CMR experiments characterized by a single bandpass noise centered at the signal frequency has often been discussed. To quantify the role of within-channel cues, the present study performed simulations with a single-channel modulation filterbank model and compared the results to experimental data. The most important finding is that a large proportion of the masking release can be predicted by a single-channel analysis, provided that the temporal envelope is processed appropriately. In some conditions, the predicted CMR is slightly larger than in the experimental data, which indicates that the current model may overestimate the contribution of within-channel cues to CMR. However, in almost all experiments, the difference between simulated and measured data is smaller than 3 dB, demonstrating that in this class of CMR experiments the amount of CMR due to across-channel processes certainly is much smaller than expected from the traditional way of calculating ''across-channel'' CMR (Carlyon *et al.*, 1989).

A. Role of modulation processing

In the comodulated condition, the envelope of the masker shows distinct minima because the noise is overmodulated, i.e., the envelope spends a large proportion of time at values near zero. Adding a signal to the modulated noise will smooth out the sharp minima, as already mentioned by Schooneveldt and Moore (1989a). This yields a decrease in modulation depth, which is detected by the model in a manner presumed to be similar to that in human listeners. Since the minima are very distinct and mark only very short time intervals, high modulation rates must be processed by the model, i.e., a good temporal resolution is required (as already stated by Buus, 1985). The role of high modulation rates is shown in Fig. 9. The simulated CMR effect is shown for a masker bandwidth of 1000 Hz, a modulator bandwidth of 50 Hz, and a signal frequency of 2 kHz as a function of the highest modulation center frequency of the modulation filterbank used in the model. All previously presented simulations were performed with an upper cutoff frequency of a quarter of the signal frequency CF (center frequency of the peripheral filter), i.e., in this case 500 Hz for CF$=$2 kHz. The predicted CMR is independent of the highest modulation center frequency (CF_{mod}) for CF_{mod} $\geqslant$250 Hz. For $CF_{mod}<250$ Hz, the predicted CMR decreases with decreasing CF_{mod}. The CMR effect almost completely disappears when only a modulation low-pass filter is used (first data point in Fig. 9) as implemented in Dau *et al.* (1996a).

As mentioned in the literature (Moore, 1992; Moore and Jorasz, 1996), CMR occurs when the added signal produces an increase in level in the valleys of the masker. This is possible if the modulation depth of the masker is high. In experiment 5 the effect of modulation depth was tested explicitly (see Fig. 7). It was shown that if the modulation depth is decreased, the CMR is decreased and diminishes for large added dc components. This is consistent with the hypothesis that changes in modulation depth are the reason for the masking release in this kind of experiment. When a dc component is added, the signal level has to be higher to produce a decrease in modulation depth. When the dc component is very large, the change in overall energy produced by adding the signal will be the strongest cue, whereas changes in modulation depth will play a secondary role. This

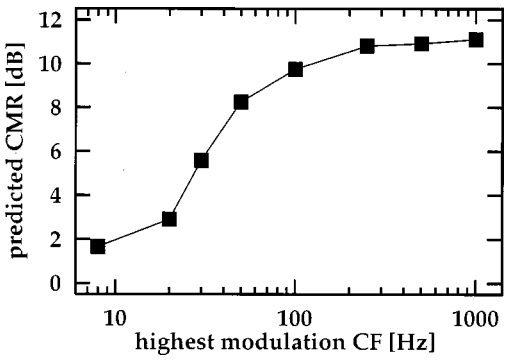

FIG. 9. Simulated CMR for a masker bandwidth of 1000 Hz, a modulator bandwidth of 50 Hz, and a signal frequency of 2 kHz. Parameter is the highest modulation center frequency of the modulation filters.

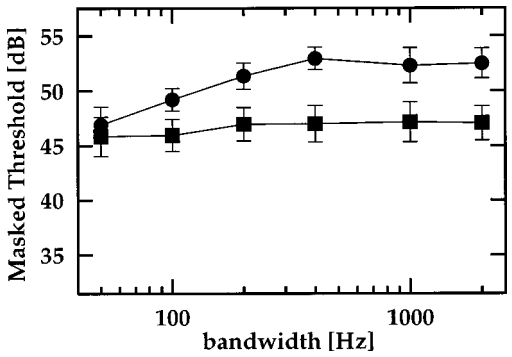

FIG. 10. Simulated data for a 2-kHz sinusoidal signal in random noise (circles) and comodulated noise (squares). In this simulation instead of a gammatone filter a rectangular filter with the same bandwidth was applied.

latter strategy is equivalent to the strategy used in the reference condition. As a consequence, no CMR will be observed, as shown in the experimental results.

If the comodulated masker consists of a square-wave modulated noise (see experiment 6 and Fig. 8), envelope amplitudes spend more time near zero than the classical comodulated condition that employs a low-pass modulator. As a consequence, and in agreement with the model predictions, the masking release is larger than in the classical CMR experiments. This point of view agrees with Zwicker and Schorn's (1982) assumption that the reduced masking in square-wave modulated noise compared to continuous noise (reference) can be interpreted in terms of temporal resolution. An across-channel process, as stated in the literature (Buus, 1985; Hall *et al.*, 1996), seems not to be necessary in the class of experiments considered here.

B. Role of the critical band filter

It was proposed in the literature (Carlyon *et al.*, 1989) that the across-frequency portion of the masking release could be estimated by subtracting out the masking release for a masker bandwidth equal to the auditory filter bandwidth at the signal frequency. However, as mentioned in the Introduction, this procedure is somewhat problematic because it postulates a clear distinction between within-channel and across-channel effects at the value of the critical bandwidth (Hall *et al.*, 1996). The present study shows that this approach is not able to predict ''across-channel'' CMR properly: Even a single-channel model operating on only one critical band predicts a decrease in thresholds for masker bandwidths larger than the critical bandwidth in the comodulated condition (see, e.g., Fig. 3). The predicted decrease in threshold beyond the critical bandwidth is a consequence of the auditory filters incorporated in the model. Although frequency components of the masker outside the critical bandwidth are strongly attenuated, they still contribute to the output of the auditory filter. To quantify this effect, simulations were performed with a model that employed a rectangular filter with the same bandwidth instead of the gammatone filter. Figure 10 shows simulated data on the basis of the modified model for CF=2 kHz. Circles represent thresholds in the reference condition whereas squares represent thresholds in the comodulated condition. In the reference condition thresholds increase with increasing masker bandwidth up to the critical bandwidth and then stay constant whereas in the comodulated condition thresholds are independent of masker bandwidth. As expected, there is no increase in CMR for masker bandwidths larger than the critical bandwidth. The predicted CMR of 6 dB for large masker bandwidths is 5 dB smaller than the simulated CMR effect with the original model (cf. Fig. 2).

C. Role of filtering the masker

In the classical comodulated condition the masker is bandlimited after modulation. As argued in the literature on modulation detection (Eddins, 1993; Strickland and Viemeister, 1997), spectral filtering after modulation decreases the modulation depth of the stimuli. Schooneveldt and Moore (1989a) discussed this effect with respect to cases when the modulator bandwidth is equal or greater than half the masker bandwidth. They argued that frequency components of the modulator greater than half the bandwidth are filtered out and no longer contribute to the modulation. They concluded that conditions where the modulator bandwidth was equal or greater than half the masker bandwidth are equivalent to the unmodulated condition.

However, for modulator bandwidths smaller than half the masker bandwidth, the modulation depth will still be reduced by filtering after modulation. The hypothesis in the present study is that the reduction in modulation depth due to filtering after modulation is the reason for the increase in threshold with decreasing masker bandwidth in the comodulated condition. It is based on the assumption that the reduced thresholds in the comodulated condition compared to those in the reference condition are a consequence of changes in modulation depth when the signal is added. To test our hypothesis, experiment 4 was performed (see Fig. 6) where the masker was first bandlimited and then modulated. The slope of the threshold curve is markedly reduced when the masker is modulated after filtering. This further demonstrates that thresholds in the comodulated condition strongly depend on the modulation depth of the masker.

D. Relation to modulation detection experiments

For large masker bandwidths ($\geqslant$800 Hz) CMR decreases for modulator bandwidth Δf_{mod} larger than 50 Hz whereas CMR is more or less independent of modulator bandwidth for $\Delta f_{\mathrm{mod}} \leqslant 50$ Hz (Sec. III B; Schooneveldt and Moore, 1989a). Schooneveldt and Moore compared this result with the data on amplitude modulation detection in noise (e.g., Viemeister, 1979). They argued that CMR is largest for modulator bandwidths $\leqslant$50 Hz because the auditory system is most sensitive to amplitude modulation in this modulation frequency region. However, a direct comparison of the data on modulation detection and results from CMR experiments is difficult for several reasons: First, Viemeister obtained modulation detection thresholds for sinusoidal modulation, whereas in CMR experiments generally noise modulators were used. Thus, the imposed modulator was deterministic in the modulation detection condition whereas it was random in the CMR conditions. Second, whereas in modulation detec-

tion experiments an imposed modulation is to be detected, in CMR experiments the sinusoidal signal effectively changes the modulation depth of the modulator. However, it is difficult to quantify the modulation depth of a carrier which is overmodulated with a noise modulator. A more appropriate description of the modulated noise may be given by the envelope distribution, a technique which was first proposed by Schooneveldt and Moore (1989a). They found that for a modulator bandwidth of 200 Hz the envelope spends a smaller proportion of time at values near 0 compared to a modulator bandwidth of 50 Hz. This means less minima are partially filled in by the signal. Thus, the reduction in overall modulation depth will be smaller than in the 50-Hz modulator condition. As a consequence, our model predicts a smaller CMR effect in agreement with the data.

E. Role of the signal duration

The CMR effect depends on the duration of the signal (Sec. III C; Schooneveldt and Moore, 1989a). With decreasing signal duration the CMR effect decreases. The current model predicts this effect because the time over which the modulation depth is reduced due to the presence of the signal is reduced. Schooneveldt and Moore (1989a) argued that the auditory system needs a reasonable length of time to sample the signal, if within-channel cues are exploited. They concluded that for durations greater than 100 ms within-channel processes might contribute to the masking release in CMR experiments. In contrast, for durations $\leqslant$100 ms they assumed that CMR is a consequence of a ''pure'' across-channel process where within-channel cues do not play any role. The present paper cannot rule out this hypothesis. However, for a signal duration of 25 ms, the CMR of about 5 dB for masker bandwidths larger than 400 Hz as measured by Schooneveldt and Moore was not found in the present experiments. The present data show no CMR for a signal duration of 25 ms for masker bandwidth up to 1000 Hz. However, for a 2000-Hz-wide masker there is a small CMR (4 dB) in the data which is not accounted for by the model.

The simulated CMR for signal durations of 200 and 400 ms is smaller than the measured CMR. The deviations of the simulated results from the experimentally derived results can be explained in the same way as was already done with respect to simulations of temporal integration by the model (Dau *et al.*, 1996b). Because the adaptation loops are very sensitive to fast changes in the input, the short signal ramps in the experiment (10 ms) will cause very strong oscillations at the output of this stage when the signal is switched on. As a consequence, the template for the simulated experimental runs are dominated by an overshoot in the first few milliseconds of the signal.[8] It is possible to reduce this unrealistic large overshoot within the model by choosing smaller time constants within the feedback loops. However, a change of the model parameters would affect the dynamic properties of the model, e.g., modulations would be transformed more compressively than in the original model. As a consequence, such a change would worsen the capabilities of the model to account for modulation detection data and forward masking data. Thus, there is no simple solution to the overshoot problem without changing the global structure of the model and losing the model's capability to predict other psychoacoustical data.

F. Modulation filterbank concept

The modulation filterbank model which was originally developed to describe modulation detection and modulation masking experiments was used in the present study. It was assumed that within-channel cues in CMR are based on the ability of the auditory system to detect changes in modulation depth. The modulation filterbank model (Dau *et al.*, 1997a, b) differs considerably in its structure from the model of modulation detection by Viemeister (1979). The model of Viemeister consists of a broad predetection filter (with a bandwidth $\Delta f = 2000$ Hz) which is followed by a half-wave rectification and a low-pass filter with a cutoff frequency of 64 Hz. As decision variable, Viemeister suggested the ac-coupled root-mean-square of the output of the low-pass filter. Based on the Viemeister model, Berg (1996) presented simulated data with a slightly modified model for the second class of CMR experiments. This model derives the calculations of the decision statistic from the amplitude spectrum of the output of the leaky integrator. Berg showed that (i) CMR can be predicted by a model based on the envelope amplitude spectrum, and (ii) the disruption of the CMR effect by adding a single tone to the stimuli can be simulated by the model. Unfortunately, the spectral separation of comodulation bands in his CMR experiment is in the range of the critical bandwidth of the peripheral filter at the signal frequency. Thus, it is generally assumed that within-channel processes might contribute to the masking release in the CMR experiment performed by Berg. In a recent paper, Buss *et al.* (1998) demonstrated that the model proposed by Berg is unable to predict the CMR in all experiments of the second class of CMR experiments.

The present study did not use the Viemeister model to describe modulation detection because of several reasons: (i) First, the Viemeister model is not adequate to simulate within-channel cues. The term ''within-channel cue'' assumes that the auditory system extracts envelope information from the temporal output of each peripheral filter, whereas in the Viemeister model the concept of peripheral filtering is not incorporated. (ii) Second, as a consequence, the Viemeister model would fail to predict the present data (first class of CMR experiments), because the thresholds in the reference condition are assumed to be a function of the energy in the peripheral filter at the signal frequency. In contrast to the Viemeister model, the modulation filterbank model is able to predict threshold curves both for the reference and comodulated condition because it assumes that the modulation analysis is performed in parallel on the output of each peripheral channel.

G. Across-channel processing in CMR

The simulations of the present study indicate that the traditional way of calculating the ''across-channel'' CMR (Carlyon *et al.*, 1989) clearly overestimates the across-

channel contribution to the masking release in this class of experiments. In fact, a large amount of the masking release in the first class of experiments can be predicted without assuming an across-channel process. In some experimental conditions, e.g., for short signal durations and large masker bandwidths, the predicted masking release is smaller than the measured release. In those conditions, an across-channel process may contribute to the CMR. However, the effect is smaller than 3 dB. Thus, a simple band-widening experiment probably is not appropriate to study across-channel processing.[9]

In contrast, the masking release found in experiments from the second class of experiments presumably reflect ''true'' across-channel processes, at least when the spectral distance between the masker band and the cueband(s) amounts to more than one octave (e.g., Cohen, 1991). For smaller spectral distances, it is generally assumed that some of the masking release results from within-channel cues (see the Introduction).

Apart from the monaural experiment, dichotic CMR experiments have been performed in several studies, where the cueband was presented to the nonsignal ear (e.g., Schooneveldt and Moore, 1989b; Cohen, 1991). In those conditions, within-channel cues cannot contribute to the masking release. However, in dichotic CMR experiments, binaural processes may influence the results in addition to across-channel cues.

V. CONCLUSION

A single-channel model accounts quantitatively for several aspects of CMR. Specifically, the effects of varying masker bandwidth, signal duration, modulator bandwidth, modulator type, and center frequency are predicted reasonably well with an appropriate single-channel analysis. Modulation filters with a center frequency up to at least 250 Hz are necessary to simulate the whole amount of CMR. In agreement with assumptions in the literature, large modulation depths of the masker are necessary to obtain large CMR effects. The decrease in threshold for masker bandwidths larger than the critical bandwidth can be predicted because the model does not use unrealistic rectangular filters. Hence, frequency components outside the critical band, although strongly attenuated by the peripheral filter, still affect the performance of the model. Filtering the masker after modulation reduces the modulation depth of the masker especially for masker bandwidths which are comparable to the modulator bandwidth. Thus, the decrease in threshold with increasing masker bandwidth in the comodulated condition strongly depends on the technique of generating the masker. In some conditions, the predicted CMR is slightly smaller than in the experimental results. This difference between measured and simulated results might be a consequence of a ''true'' across-channel process. However, this effect amounts to a maximum size of only about 3 dB. The present study does not rule out across-channel processes in CMR experiments. Presumably, a larger proportion of the masking release due to across-channel processes can be found in the second class of CMR experiments where the masker consists of a narrow-band noise at the signal frequency and one or more noise bands spectrally separated from the on-frequency band.

ACKNOWLEDGMENTS

We would like to thank all our colleagues of the ''Graduiertenkolleg Psychoakusik'' and the ''Arbeitsgruppe Medizinsche Physik'' at the University of Oldenburg for fruitful discussions on the content of this paper. We also thank Steven van de Par, Armin Kohlrausch for his comments and suggestions concerning this study, and Brian C. J. Moore and William S. Woods for their critical reading of earlier versions of this paper. The work was supported by the Graduiertenkolleg Psychoakustik, DFG KO 942/12.

[1]Subject KS only participated in the experimental condition with CF=2 kHz. Therefore, to compare the data across signal frequencies, for CF=2 kHz only the data for subjects KW, TD, and JV were averaged.

[2]Signal detection theory would predict that thresholds increase 1.5 dB per doubling of bandwidth, because the standard deviation of the noise energy increases as the square root of bandwidth. However, if performance is solely determined by the energy of the masker, thresholds increase by 3 dB per doubling the bandwidth. This is shown in the simulated data—at least for large masker bandwidth. The measured data are closer to the predictions of the current model than to the prediction of signal detection theory.

[3]Schooneveldt and Moore defined the duration at the 6-dB down points of the ramps, whereas in the present study the rise/fall time is included.

[4]This experiment was first presented in Verhey and van de Par (1997).

[5]KT did not participate in experiment 1. Therefore small deviations occur between mean thresholds in Fig. 3 and those in this section.

[6]The difference in level between the dc component and the root-mean-square of the low-pass noise-modulator was $20 * \log(\mathrm{dc}/\mathrm{rms}_{\mathrm{lp}})$, where $\mathrm{rms}_{\mathrm{lp}}$, the root-mean-square value of the low-pass noise, was 0.316 and the dc component was 0.1, 0.2, 0.5, 0.8, 1.0, 1.5, or 2.0.

[7]Carlyon *et al.* (1989) displayed their data as a function of the envelope frequency f_e defined as twice the cutoff frequency of the low-pass modulator and equal to the frequency of the square-wave modulation. At the same f_e, the masking release (MUD) for square-wave was similar to that for low-pass modulators. If one follows Carlyon *et al.*'s arguments, the data should be compared at the same zero crossings rate, which is equal to 1.12 times the cutoff frequency of the low-pass modulator and equal to the frequency of the square-wave modulation, not at the same f_e. Consequently, the comparison between the two modulator types is similar whether it is made at the same zero crossings rate or with the square-wave modulator frequency equal to the low-pass cutoff frequency. The present study uses the latter frequency scale.

[8]This unrealistic weighting of signal information over time can be reduced if longer signal ramps are used. In fact, as can be seen in Sec. III B, the whole CMR effect can be predicted by the model, if longer ramps (e.g., 50 ms) are used.

[9]An interesting alternative to the simple band-widening experiments was proposed by Carlyon *et al.* (1989). They compared the masking release for a subcritical bandwidth with that obtained in the condition where the masker consisted of a subcritical bandwidth at the signal frequency and an additional low-pass noise (cue-band condition). The cue-band condition is a combination of the classical conditions of the first and the second class of CMR experiments. If the spectral distance between the upper edge of the low-pass noise and the signal frequency is large (several critical bands), it is more likely that ''across-channel'' CMR is measured. The present study does not consider this experimental condition, since it does not belong directly to the first class of experiments. Moreover, the beating in peripheral filters with a center frequency between the cutoff frequencies of the two masker bands may provide additional information in the comodulated condition.

Bacon, S. P., Lee, J., Peterson, D. M., and Rainey, D. (**1997**). ''Masking by modulated and unmodulated noise: Effects of bandwidth, modulation rate, signal frequency, and masker level,'' J Acoust. Soc. Am. **100**, 1600–1610.

Berg, B. G. (**1996**). ''On the relation between comodulation masking release and temporal modulation transfer functions,'' J. Acoust. Soc. Am. **100**, 1013–1023.
Buus, S. (**1985**). ''Release from masking caused by envelope fluctuations,'' J. Acoust. Soc. Am. **78**, 1958–1965.
Buss, E., Hall, J. W., and Grose, J. H. (**1998**). ''Change in envelope beats as a possible cue in comodulation masking release (CMR),'' J. Acoust. Soc. Am. **103**, 1592–1597.
Carlyon, R. P., Buus, S., and Florentine, M. (**1989**). ''Comodulation Masking Release for three types of modulator as a function of modulation rate,'' Hear. Res. **42**, 37–46.
Cohen, M. F. (**1991**). ''Comodulation masking release over a three octave range,'' J. Acoust. Soc. Am. **90**, 1381–1384.
Dau, T., Püschel, D., and Kohlrausch, A. (**1996a**). ''A quantitative model of the 'effective' signal processing in the auditory system: I. Model structure,'' J. Acoust. Soc. Am. **99**, 3615–3622.
Dau, T., Püschel, D., and Kohlrausch, A. (**1996b**). ''A quantitative model of the 'effective' signal processing in the auditory system: II. Simulations and measurements,'' J. Acoust. Soc. Am. **99**, 3623–3631.
Dau, T., Kollmeier, B., and Kohlrausch, A. (**1997a**). ''Modeling auditory processing of amplitude modulation. I. Modulation detection and masking with narrowband carriers,'' J. Acoust. Soc. Am. **102**, 2892–2905.
Dau, T., Kollmeier, B., and Kohlrausch, A. (**1997b**). ''Modeling auditory processing of amplitude modulation. II. Spectral and temporal integration in modulation detection,'' J. Acoust. Soc. Am. **102**, 2906–2919.
Eddins, D. (**1993**). ''Amplitude modulation detection of narrow-band noise: Effects of absolute bandwidth and frequency region,'' J. Acoust. Soc. Am. **93**, 470–479.
Eddins, D. A. and Wright, B. A. (**1994**). ''Comodulation masking release for single and multiple rates of envelope fluctuation,'' J. Acoust. Soc. Am. **96**, 3432–3442.
Fantini, D. A., and Moore, B. C. J. (**1992**). ''Comodulation Masking Release (CMR) and Profile Analysis: the Effect of Varying Modulation Depth,'' Adv. Biosci. **83**, 479–485.
Fantini, D. A., Moore, B. C. J., and Schooneveldt, G. P. (**1993**). ''Comodulation masking release (CMR) as a function of type of signal, gated or continuous masking, monaural or dichotic presentation of flanking bands, and center frequency,'' J. Acoust. Soc. Am. **93**, 2106–2115.
Fletcher, H. (**1940**). ''Auditory patterns,'' Rev. Mod. Phys. **12**, 47–61.
Florentine, M., Fastl, H., and Buus, S. (**1988**). ''Temporal integration in normal hearing, cochlear impairment, and impairment simulated by masking,'' J. Acoust. Soc. Am. **84**, 195–203.
Glasberg, B. R., and Moore, B. C. J. (**1986**). ''Auditory filter shapes in subjects with unilateral and bilateral cochlear impairments,'' J. Acoust. Soc. Am. **79**, 1020–1033.
Green, D. M., McKey, M. J., and Licklider, J. C. R. (**1959**). ''Detection of a pulsed sinusoid in noise as a function of frequency,'' J. Acoust. Soc. Am. **31**, 1446–1452.
Haggard, M. P., Hall, J. W., and Grose, J. H. (**1990**). ''Comodulation masking release as a function of bandwidth and test frequency,'' J. Acoust. Soc. Am. **88**, 113–118.
Hall, J. W., Grose, J. H., and Haggard, M. P. (**1989**). ''Effects of flanking band proximity, number, and modulation pattern on comodulation masking release,'' J. Acoust. Soc. Am. **87**, 269–283.
Hall, J. W., Grose, J. H., and Hatch, D. R. (**1996**). ''Effects of gating for signal detection in unmodulated and modulated noise,'' J. Acoust. Soc. Am. **100**, 2365–2372.
Hall, J. W., Haggard, M. P., and Fernandes, M. A. (**1984**). ''Detection in noise by spectro-temporal pattern analysis,'' J. Acoust. Soc. Am. **76**, 50–56.
Hatch, D. R., Arne, B. C., and Hall, J. W. (**1995**). ''Comodulation masking release (CMR): Effects of gating as a function of number of flanking bands and masker bandwidth,'' J. Acoust. Soc. Am. **97**, 3768–3774.
Kollmeier, B. (**1996**). ''Computer-controlled speech audiometric techniques for the assessment of hearing loss and the evaluation of hearing aids,'' in *Psychoacoustics, Speech and Hearing Aids*, edited by B. Kollmeier (World Scientific, Singapore, 1996), pp. 57–68.
Langner, G., and Schreiner, C. (**1988**). ''Periodicity coding in the inferior colliculus of the cat. I. Neuronal mechanism,'' J. Neurophysiol. **60**, 1799–1822.
Levitt, H. (**1971**). ''Transformed up–down procedures in psychoacoustics,'' J. Acoust. Soc. Am. **49**, 467–477.
McFadden, D. (**1986**). ''Comodulation masking release: Effects of varying the level, duration, and time delay of the cue band,'' J. Acoust. Soc. Am. **80**, 1658–1667.
Moore, B. C. J. (**1992**). ''Across-channel processes in auditory masking,'' J. Acoust. Soc. Jpn. **13**, 25–37.
Moore, B. C. J., and Glasberg, B. R. (**1983**). ''Suggested formulae for calculating auditory-filter bandwidths and excitation patterns,'' J. Acoust. Soc. Am. **74**, 750–753.
Moore, B. C. J., and Jorasz, U. (**1991**). ''Detection of changes in modulation depth of a target sound in the presence of other modulated sounds,'' J. Acoust. Soc. Am. **91**, 1051–1061.
Moore, B. C. J., and Jorasz, U. (**1996**). ''Modulation discrimination interference and comodulation masking release as a function of the number and spectral placement of narrow-band noise modulators,'' J. Acoust. Soc. Am. **100**, 2373–2381.
Patterson, R., Nimmo-Smith, I., Holdsworth, J., and Rice, P. (**1987**). ''An efficient auditory filterbank based on the gammatone function,'' *Meeting of the IOC Speech group on Auditory Modeling at RSRE (December 1987)*, pp. 14–15.
Peters, R. W., and Hall, J. W. (**1994**). ''Comodulation masking release for elderly listeners with relatively normal audiograms,'' J. Acoust. Soc. Am. **96**, 2674–2682.
Püschel, D. (**1988**). ''Prinzipien der zeitlichen Analyse beim Hören,'' Ph.D. thesis, University of Göttingen.
Scharf, B. (**1970**). ''Critical bands,'' in *Foundation of Modern Auditory Theory*, edited by J.V. (Academic, New York), Vol. 1.
Schooneveldt, G. P., and Moore, B. C. J. (**1987**). ''Comodulation masking release (CMR): Effects of signal frequency, flanking-band frequency, masker bandwidth, flanking-band level, and monotic versus dichotic presentation of flanking band,'' J. Acoust. Soc. Am. **82**, 1944–1956.
Schooneveldt, G. P., and Moore, B. C. J. (**1989a**). ''Comodulation masking release (CMR) as a function of masker bandwidth, modulator bandwidth, and signal duration,'' J. Acoust. Soc. Am. **85**, 273–281.
Schooneveldt, G. P., and Moore, B. C. J. (**1989b**). ''Comodulation masking release for various monaural and binaural combinations of the signal, on-frequency, and flanking bands,'' J. Acoust. Soc. Am. **85**, 262–272.
Strickland, E. A., and Viemeister, N. F. (**1997**). ''The effect of frequency region and bandwidth on the temporal modulation transfer function,'' J. Acoust. Soc. Am. **102**, 1799–1810.
Verhey, J. L., and van de Par, S. (**1997**). ''Messungen und Modellrechnungen zu (CMR),'' Fortschritte der Akustik—DAGA'97, DEGA, Oldenburg.
Viemeister, N. F. (**1979**). ''Temporal modulation transfer functions based upon modulation thresholds,'' J. Acoust. Soc. Am. **66**, 1364–1380.
Zwicker, E., and Schorn, K. (**1982**). ''Temporal modulation transfer functions based upon modulation thresholds,'' Audiology **21**, 474–492.

Evidence against an effect of grouping by spectral regularity on the perception of virtual pitch

Valter Ciocca[a)]
Department of Speech and Hearing Sciences, University of Hong Kong, Hong Kong

(Received 13 January 1999; revised 21 June 1999; accepted 9 July 1999)

Two experiments investigated the role of the regularity of the frequency spacing of harmonics, as a separate factor from harmonicity, on the perception of the virtual pitch of a harmonic series. The first experiment compared the shifts produced by mistuning the 3rd, 4th, and 5th harmonics in the pitch of two harmonic series: the odd-H and the all-H tones. The odd-H tone contained odd harmonics 1 to 11, plus the 4th harmonic; the all-H tone contained harmonics 1 to 12. Both tones had a fundamental frequency of 155 Hz. Pitch shifts produced by mistuning the 3rd harmonic, but not the 4th and 5th harmonics, were found to be significantly larger for the odd-H tone than for the all-H tone. This finding was consistent with the idea that grouping by spectral regularity affects pitch perception since an odd harmonic made a larger contribution than an adjacent even harmonic to the pitch of the odd-H tone. However, an alternative explanation was that the 3rd mistuned harmonic produced larger pitch shifts within the odd-H tone than the 4th mistuned harmonic because of differences in the partial masking of these harmonics by adjacent harmonics. The second experiment tested these explanations by measuring pitch shifts for a modified all-H tone in which each mistuned odd harmonic was tested in the presence of the 4th harmonic, but in the absence of its other even-numbered neighbor. The results showed that, for all mistuned harmonics, pitch shifts for the modified all-H tone were not significantly different from those for the odd-H tone. These findings suggest that the harmonic relations among frequency components, rather than the regularity of their frequency spacing, is the primary factor for the perception of the virtual pitch of complex sounds. [S0001-4966(99)00611-6]

PACS numbers: 43.66.Ba, 43.66.Hg [SPB]

INTRODUCTION

In a series of studies, Roberts and his colleagues have demonstrated that the auditory grouping of a frequency component into a complex tone is affected by how well the component fits in with the spectral pattern of the complex tone (Roberts and Bregman, 1991; Roberts and Bailey, 1993a, b). Roberts and Bregman (1991) asked subjects to rate how clearly individual even- or odd-numbered harmonics could be ''heard out'' of a complex tone composed only of odd harmonics. Subjects gave higher perceived clarity ratings to even than odd harmonics, in spite of the fact that even- and odd-numbered harmonics had a common fundamental frequency ($F0$). The greater perceptual salience of even harmonics was surprising given that the partial masking of an even harmonic was greater than that of its odd-numbered neighbors in complex stimuli composed of odd harmonics. The authors suggested that even-numbered harmonics were more easily segregated than odd harmonics because the former violated the pattern of spectral regularity of the odd-harmonic series. Roberts and Bregman also found that the effect of spectral regularity was $F0$ dependent, since it was observed for $F0$'s of 100 and 200 Hz, but not 400 Hz. Roberts (1998) replicated earlier perceived clarity ratings results by using a two-internal forced choice (2IFC) procedure and by obtaining a difference in d' scores between even- and odd-numbered harmonics.

Roberts and Bailey (1996) demonstrated that the effects of spectral regularity were not restricted to frequency components that are harmonically related, but also occurred for inharmonic complex tones whose components were arranged in a regular spectral pattern. Roberts and Brunstrom (1998) provided further evidence for the role of spectral regularity as a grouping factor by investigating the perceptual integration of mistuned frequency components within complex tones (see Hartmann *et al.*, 1990). Roberts and Brunstrom found that the perceptual segregation and the perceived pitch shifts of individual mistuned components were similar for harmonic and inharmonic, but spectrally regular, complex tones. These results, which were interpreted as evidence for the role of spectral regularity as a grouping principle distinct from harmonicity (Roberts and Bailey, 1996; Roberts and Brunstrom, 1998), raise the interesting possibility that spectral regularity might also affect the integration of frequency components into a single ''virtual'' (or ''residue'') pitch (the term ''pitch'' will be used as synonymous of ''virtual pitch,'' hereafter).

Several models of virtual pitch perception are based on the assumption that the pitch of complex tones is determined by the frequencies of the resolved, low-numbered harmonics (see, e.g., Goldstein, 1973; Terhardt, 1974). In order to obtain an accurate estimate of the pitch of a complex sound in the presence of other simultaneous sounds, the auditory system must decide which frequency components should contribute to the pitch of the complex sound. This decision is likely to be made on the basis of several auditory scene

a)Electronic mail: vciocca@hkusua.hku.hk

analysis (or auditory grouping) principles (see, for example, Bregman, 1990; Darwin and Ciocca, 1992). Several studies demonstrated that the integration of frequency components into a single pitch is affected by grouping factors such as onset time and ear of presentation (Darwin and Ciocca, 1992; Ciocca and Darwin, 1993), frequency modulation (Darwin *et al.*, 1994), and sequential grouping by frequency proximity (Darwin *et al.*, 1995). For example, Darwin and Ciocca (1992) found that a mistuned component that starts 300 ms before the onset of the remainder of a harmonic series does not make a contribution to the pitch of the series. They also found that when the mistuned component and the harmonic series were presented to opposite ears the contribution of the mistuned component to the pitch of the harmonic series was reduced, albeit only slightly. One of the grouping principles that has been shown to affect pitch perception is the principle of harmonicity: frequency components that are harmonics of the same fundamental frequency would contribute to a single virtual pitch. The operation of this principle has been likened to a ''harmonic sieve'' whose ''slots'' are centered on the harmonic frequencies of a fundamental frequency (Duifhuis *et al.*, 1982). Moore *et al.* (1985) provided evidence for the existence of such a mechanism by showing that frequency components contribute to the pitch of a harmonic series as long as their frequency is not too far from one of the harmonic frequencies. Moore *et al.* showed that mistuned harmonics made the largest contribution to the pitch of a harmonic series for mistunings equal or smaller than $\pm 3\%$ of the harmonic frequencies. For mistunings larger than $\pm 3\%$, the contribution of the mistuned harmonics was gradually reduced and became very small for mistunings of $\pm 8\%$ (the largest mistuning used).

If spectral regularity is a grouping factor which is distinct from harmonicity, then it is possible that pitch perception processes might exploit the pattern of spectral regularity of frequency components to assign them to a single virtual pitch. This investigation attempted to find evidence for this hypothesis by using the ''pitch matching'' paradigm developed by Moore *et al.* (1985). In this paradigm, listeners are asked to match the pitch of two harmonic series, the target and the matching complexes. Across trials, a low-numbered harmonic of the target complex can be mistuned by various amounts; the amount of mistuning is fixed within each trial. Pitch matches are carried out by adjusting the $F0$ of the matching complex as many times as necessary for listeners to achieve a satisfactory match. Typical results show that when the frequency of the mistuned harmonic is higher than the harmonic frequency (''positive'' mistuning), the matched $F0$ of the target is also higher than the matched $F0$ of the same target complex whose harmonics are not mistuned. Pitch shifts of similar size but opposite direction occur for ''negative'' mistunings. Since it has been shown that changes in the matched $F0$ of the matching complex reflect changes in the virtual pitch of the target complex (Moore, 1987), this procedure is ideally suited for studying the conditions under which a frequency component is integrated into the pitch of a complex tone. The present study investigated the effects of spectral regularity on pitch perception by measuring the pitch shifts for the target complex as a function of the harmonic number of the mistuned harmonic, and of the spectral content of the target complex.

I. EXPERIMENT 1

If grouping by spectral regularity affects the perception of virtual pitch, then frequency components that do not fit in with the pattern of frequency spacing of a complex tone should make a relatively small contribution to the pitch of that tone. Therefore, odd-numbered mistuned harmonics should produce larger pitch shifts than adjacent even-numbered harmonics in the pitch of a harmonic series composed of primarily odd harmonics. Moreover, mistuned odd harmonics, but not even-numbered ones, should produce larger pitch shifts in an odd-harmonic series than in a series that contains both odd and even harmonics.

A. Method

On each trial, the subjects adjusted the $F0$ of a harmonic series (matching complex) so that the pitch of that series matched the pitch of a target complex. Two target complexes were used in the experiment, the ''odd-H'' tone and the ''all-H'' tone. The all-H tone contained 12 consecutive harmonics (1st to 12th) of a 155-Hz $F0$; this target complex was the same as the one used in previous studies by Darwin and his colleagues (see, e.g., Darwin and Ciocca, 1992). The odd-H tone had the same fundamental frequency as the all-H tone, but was composed of the odd harmonics 1 to 11, plus the 4th harmonic. A 155-Hz $F0$ was selected because the effect of spectral regularity was observed for fundamental frequencies of 100 and 200 Hz (Roberts and Bregman, 1991). Moore and his colleagues (1985) showed that the contribution of a mistuned harmonic to the pitch of a complex tone that contained both odd and even harmonics depended on the harmonic number of the mistuned component. They found that the largest pitch shifts were obtained when the 3rd and 4th harmonics were mistuned and that, for fundamental frequencies above 100 Hz, pitch shifts produced by mistuning the 5th and higher harmonics were very small for two out of three subjects. Following these findings, the present study tested the role of spectral regularity in pitch perception by comparing the relative size of the pitch shifts produced by mistuning the 3rd, 4th, and 5th harmonics in the two target complexes. These harmonics could be mistuned by $\pm 3\%$ of the harmonic frequency. This amount of mistuning was selected because it was found to produce the largest pitch shifts in a 155-Hz $F0$ harmonic series (Darwin and Ciocca, 1992). The mistuned 3rd harmonic had a frequency of 451 or 479 Hz ($-$ or $+3\%$ mistuning, respectively); the mistuned 4th harmonic had a frequency of 600 or 640 Hz, and the mistuned 5th harmonic had a frequency of 752 or 798 Hz. Within a trial, only one of the three harmonics was mistuned. The 4th harmonic was included in the odd-H tone when the 3rd and 5th harmonics were mistuned in order to ensure that pitch shifts for odd and even harmonics were measured with targets that contained the same frequency components, except for the mistuned harmonic. Two matching complexes were used in order to minimize timbre differences that might have affected the adjustment of the pitch of the matching complex to that of the target complex (see, for example, Moore and

Glasberg, 1990; Singh and Hirsh, 1992). When the target was the all-H tone, the matching complex consisted of harmonics 1 to 12; the matching complex employed with odd-H tone was composed of the 1st, 3rd, 4th, 5th, 7th, 9th, and 11th harmonics. None of the harmonics of the matching complexes was mistuned. Subjects could adjust the $F0$ of the matching complexes between 151 and 159 Hz (155 ± 4 Hz).

Within each trial, the matching complex followed the target complex after a 500-ms silent interval. At the beginning of each trial, the fundamental frequency of the matching complex was set to a random value selected from the permitted range (155 ± 4 Hz), and the cursor was displayed at the center of a computer screen. Subjects adjusted the frequency of the matching complex by moving a roller-ball up or down, which moved upward or downward the position of the cursor on the screen. The fundamental frequency of the matching complex varied in steps of 0.0066 Hz per pixel, which corresponded to a variation of 3.2 Hz for a complete excursion of the cursor from the top to the bottom of the screen (see Darwin and Ciocca, 1992). Subjects could make as many adjustments as needed to achieve a satisfactory match by clicking the mouse button after each adjustment. When the match was satisfactory, subjects pressed the ''return'' key and proceeded to the next trial. Since the mistuned harmonics could be heard out as individual pure tones, listeners were instructed to ignore any pure tones they might hear, and to focus their attention on the pitches of the two complex tones.

To summarize, the experiment consisted of 12 stimuli: two mistunings (-3%, $+3\%$ of the harmonic frequency) by three harmonic numbers (3rd, 4th, and 5th harmonic) by two types of target complex (all-H and odd-H). Five matches were obtained for each stimulus, thus giving a total of 60 trials (12 stimuli by 5 matches). The order of presentation was randomized within each block of 12 stimuli. The experiment was completed within either one or two sessions. Each session took from 1 to 2 h to complete, including rest breaks.

All components were presented to the left ear at the same amplitude (corresponding to 58 dB SPL, for a 1000-Hz tone). All components started at sine phase. The mistuned component, the target complex, and the matching complex had a total duration of 90 ms, including 5-ms rise/fall raised-cosine ramps. This duration was the same as that used in previous pitch matching experiments (Darwin and Ciocca, 1992; Ciocca and Darwin, 1993). Sounds were presented through Sennheiser HD250 Linear headphones in a single-walled sound-attenuating booth (Industrial Acoustics) that was located in a sound-treated room. Sounds were synthesized in real-time at 44.1 kHz using custom software (Russell and Darwin, 1991) written for the 56001 processor of the Digidesign Audiomedia II board, and output through that board's 16-bit DACs and anti-aliasing filters. The board was attached to a PowerMacintosh 7100/66 computer which controlled the experiment.

Seven subjects (four undergraduate students and three university staff, including the author) participated in the experiment. Two of the subjects had received musical training. All had participated in previous pitch matching experiments and had pure tone thresholds within 15 dB HL around the stimulus frequencies used in the experiment.

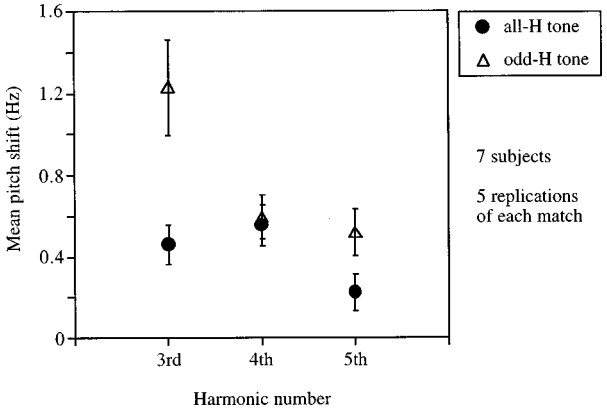

FIG. 1. Mean pitch shifts with standard error bars for the odd-H tone (open triangles) and the all-H tone (filled circles), as a function of the harmonic number of the mistuned component, in experiment 1.

B. Results and discussion

The effects of the mistuning of the three harmonics (3rd, 4th, and 5th) on the pitch of the target complex were measured by calculating the average of the difference between the pitch matches for positive and negative mistunings (mean pitch shifts) for each mistuned harmonic and each subject. The mean pitch shifts for each mistuned harmonic and target complex, averaged across the seven subjects, are displayed in Fig. 1.

A two-way ANOVA with repeated measures was applied to the mean pitch shifts. The factors were the ''harmonic number'' of the mistuned harmonic (3rd, 4th, or 5th) and the ''type of target'' (all-H or odd-H tone). The main effect of harmonic number was statistically significant, $F(2,12)=8.33$, $p<0.01$. Significantly larger mean pitch shifts were observed for the odd-H tone than for the all-H tone (main effect of ''target type,'' $F(1,6)=6.76$, $p<0.05$). The ''target type'' by ''harmonic number'' interaction shows that the pattern of pitch shifts for the two target complexes was significantly different, $F(2,12)=5.19$, $p<0.05$. The nature of this interaction can be illustrated by comparing the pitch shifts obtained with odd-H and all-H targets for each harmonic number. Pitch shifts were significantly larger for the odd-H than for the all-H tone for the 3rd harmonic (planned comparison, $p<0.001$). These results support the hypothesis that odd harmonics are more strongly integrated into the pitch of odd-H tones than even harmonics, and that grouping by spectral regularity affects virtual pitch perception. According to the same hypothesis, one would also have expected that pitch shifts produced by the 4th harmonic were significantly smaller for the odd-H than for the all-H tone. However, this comparison was not statistically significant (planned comparison, $p>0.05$). Although pitch shifts for the 5th harmonic were more than twice as large for the odd-H tone (0.52 Hz) than for the all-H tone (0.23 Hz), this difference failed to reach statistical significance (planned comparison, $p=0.093$). The failure to find a significant difference in the size of pitch shifts for the 5th harmonic in

odd-H and all-H tones was probably due to the fact that pitch shifts for this component were small with respect to the variance in the data (see also Moore *et al.*, 1985).

To conclude, the finding that pitch shifts produced by a mistuned 3rd harmonic were larger for the odd-H tone than for the all-H tone supports the idea that grouping by spectral regularity affects virtual pitch perception. The failure to observe a decrease in pitch shifts for a mistuned 4th harmonic within the odd-H tone, relative to the shifts produced by the same mistuned harmonic in the all-H, could be interpreted as evidence against a role of spectral regularity in pitch perception. However, the latter result could also be taken as evidence in favor of an effect of spectral regularity if one considers that the contribution of a mistuned component to the pitch of a harmonic series might be a function of the total number of partials in the harmonic series.[1] Moore and his colleagues demonstrated that harmonics 1 to 6 are dominant for the perception of the virtual pitch of harmonic series whose *F*0's are in the 100–200-Hz frequency region (Moore *et al.*, 1985; Moore and Glasberg, 1990). In this experiment, the odd-H tone contained four harmonics in the dominance region while the all-H tone contained six harmonics. For this reason, one might have expected that the pitch shifts produced by each mistuned component should have been larger for the odd-H than for the all-H tone. The failure to observe an increase in the pitch shifts produced by the 4th harmonic in the odd-H tone, relative to the all-H tone, could be interpreted as an effect of the perceptual segregation of the 4th harmonic from the remaining odd harmonics in the odd-H tone.

An alternative explanation for the difference in the pitch shifts produced by the 3rd and 4th harmonics within the odd-H tone is based on the fact that the 3rd harmonic was flanked by only one adjacent harmonic (i.e., the 4th harmonic). By contrast, the 4th harmonic was flanked by two adjacent harmonics (the 3rd and the 5th harmonics) both in the odd-H and the all-H tones.[2] Moore *et al.* (1985) showed that the contribution of the 2nd harmonic to the virtual pitch of a 200-Hz *F*0, all-H tone decreased as the level of the harmonic was reduced relative to the level of adjacent harmonics. Therefore, it is possible that the greater amount of masking of the 4th harmonic could explain its reduced contribution to the pitch of the odd-H tone, relative to the pitch shifts obtained with the 3rd harmonic. Moreover, because of the upward spread of masking, the partial masking of the 5th harmonic by the 4th harmonic should be greater than the partial masking of the 3rd harmonic by the 4th harmonic. This partial masking difference could also have contributed to the finding that pitch shifts for the 3rd mistuned harmonic were significantly larger for the odd-H than for the all-H tone while no difference was found for the 5th mistuned harmonic between the pitch shifts for the odd-H and the all-H tones.

II. EXPERIMENT 2

This experiment was conducted to test whether the results of experiment 1 were likely to be due to differences in masking rather than spectral regularity. To do this, the pitch shifts produced in an odd-H tone were compared with those obtained in a target complex which contained all the harmonics up to the 11th, except for the 2nd or the 6th harmonic (modified all-H tone). The 2nd harmonic was removed from the all-H tone when the 3rd harmonic was mistuned; the 6th harmonic was missing when the 5th harmonic was mistuned. These stimuli were used to compare pitch shifts in the two target complexes under the same amount of masking by adjacent harmonics. If spectral regularity does not affect pitch perception, then the pitch shifts in the two target complexes should be identical for each mistuned harmonic. By contrast, if the integration of harmonics into a single pitch is affected by spectral regularity, the pattern of pitch shifts observed in experiment 1 as a function of the harmonic number of the mistuned harmonic should be obtained with the odd-H, but not with the modified all-H tone.

A. Method

The harmonic numbers and the amounts of mistuning of the mistuned harmonics were identical to those of experiment 1, except that an in-tune condition (0% mistuning) was included. Two target complexes were used in the experiment: the odd-H tone and the ''modified all-H tone.'' The former was identical to the odd-H tone used in the first experiment. The latter contained harmonics 1 to 11 of a 155-Hz *F*0, except that one harmonic could be missing. The missing harmonic was harmonic 2 (when the 3rd harmonic was mistuned), or harmonic 6 (when the 5th harmonic was mistuned). No harmonic was missing when the 4th harmonic of the modified all-H tone was mistuned. When the modified all-H tone was presented in a trial, the matching complex consisted of the same harmonics as the modified all-H tone within that trial. For example, if the 3rd harmonic was mistuned within the modified all-H tone, the matching complex contained harmonic 1 and harmonics 3–11 (harmonic 2 was missing). The matching complex employed with the odd-H tone was composed of the 1st, 3rd, 4th, 5th, 7th, 9th, and 11th harmonics. The pitch matching procedure was identical to that employed in experiment 1.

To summarize, the experiment consisted of 18 stimuli: three mistunings (−3%, 0%, +3% of the harmonic frequency) by three harmonic numbers (3rd, 4th, and 5th harmonic) by two types of target complexes (modified all-H and odd-H tones). Subjects completed between five and eight matches for each stimulus; for each subject, all stimuli were matched an equal number of times. The order of presentation was randomized within each block of 18 stimuli. The experiment was completed within either one or two sessions. Each session took from 1 to 2 h to complete, including rest breaks.

The stimuli were presented at the same level and had the same duration as in the first experiment. The software/hardware experimental setup was the same as in the previous experiment.

Six listeners, including the author, took part in the experiment; three of the listeners were musically trained. All subjects had pure tone thresholds within 15 dB HL around the stimulus frequencies used in the experiment. Five listeners had participated in experiment 1.

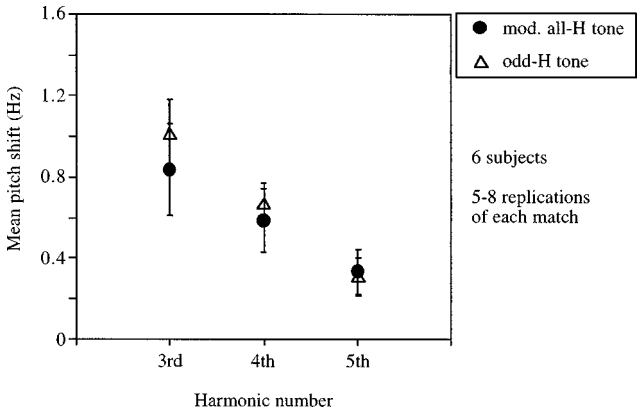

FIG. 2. Mean pitch shifts with standard error bars for the odd-H tone (open triangles) and the modified all-H tone (filled circles), as a function of the harmonic number of the mistuned component, in experiment 2.

B. Results

The mean pitch shifts for each mistuned harmonic and target complex, averaged across the six subjects, are displayed in Fig. 2. This figure shows that the pattern of pitch shifts for the odd-H and the all-H targets was very similar. A two-way ANOVA with repeated measures was applied to the mean pitch shifts. The factors were the ''harmonic number'' (3rd, 4th, or 5th) of the mistuned harmonic and the ''type of target'' (modified all-H or odd-H tone). The main effect of harmonic number was statistically significant, $F(2,10) = 6.04$, $p < 0.05$. This effect replicated the results of experiment 1. All other effects were not statistically significant. For all harmonics, the planned comparisons between the pitch shifts for the modified all-H and the odd-H target complexes failed to reach statistical significance. The fact that pitch shifts produced by the 3rd harmonic in the odd-H tone were slightly smaller in this experiment (1.02 Hz; see Fig. 2) than in the previous one (1.23 Hz; see Fig. 1) might have contributed in reducing the difference between pitch shifts produced by the 3rd harmonic in the present experiment. However, in both experiments pitch shifts in the odd-H tone were significantly larger for harmonic 3 than for harmonic 4 (Newman-Keuls *post hoc* test, $p < 0.05$). For this reason, it seems unlikely that a decrease in pitch shifts for the 3rd harmonic in the odd-H tone in the present experiment was the major reason for the failure to find a statistically significant difference between pitch shifts for the odd-H and the modified all-H tones.

As discussed previously (Sec. I B), the contribution of a mistuned harmonic to the pitch of the target complex might have been affected by the number of partials (up to the sixth) which were present in the target complexes. In this experiment, the odd-H tone still contained four partials, while the modified all-H tone contained either five or six of the harmonics (1–6) which were found to be dominant for pitch perception (Moore *et al.*, 1985; Moore and Glasberg, 1990). In spite of this difference, neither the main effect of the type of target nor the pairwise comparisons between pitch shifts in the two target complexes for each mistuned component were statistically significant. Therefore, it seems likely that the results of this experiment were not affected by differences in the number of harmonics which were present in the target complexes.

In conclusion, the results of this experiment support the hypothesis that the differences in the pattern of pitch shifts for odd-H and all-H tones observed in experiment 1 can be attributed to the effects of partial masking, not to the effects of grouping by spectral regularity.

III. GENERAL DISCUSSION

In the first experiment, pitch shifts produced by the 3rd harmonic in the odd-H tone were significantly larger than shifts produced by the same mistuned harmonic in the all-H tone. This difference was not statistically significant when the 4th harmonic was mistuned. These results could have been interpreted as evidence for the effect of spectral regularity on pitch perception. The second experiment showed that when the same adjacent harmonics flanked the mistuned harmonics, pitch shifts for the odd-H tone and for the modified all-H tone were similar for all mistuned harmonics. These findings demonstrated that the difference in the pitch shifts for odd and even harmonics found in experiment 1 was probably due to differences in partial masking, and not to effects of spectral regularity.

Roberts and Bailey (1996) suggested that grouping by harmonicity could be considered as a special case of grouping by spectral regularity, and that some of the grouping effects normally attributed to harmonicity could, in fact, be cases of grouping by spectral regularity. The results of the current study suggest that grouping by spectral regularity does not affect the integration of frequency components into a single virtual pitch. In the case of pitch perception, it is likely that the assignment of simultaneous frequency components to a single pitch is determined mainly on the basis of the harmonic relationships among components (''harmonic sieve'' mechanism; Duifhuis *et al.*, 1982; Moore *et al.*, 1985). Harmonics of the same fundamental frequency would pass through the sieve, and make a contribution to the pitch of a harmonic series, independently of whether they fit with the regularity of the spectral pattern of the series.

This conclusion is consistent with the idea that the perceptual segregation of individual frequency components and pitch perception processes operate on the basis of different grouping constraints. In fact, Moore and his colleagues found that frequency components can contribute to the pitch of a harmonic series for mistunings of up to 8% of the harmonic frequency (Moore *et al.*, 1985), even though they are perceptually segregated from the series when they are mistuned by about 1% or more (Moore *et al.*, 1986). Therefore, it appears that spectral regularity might affect the perceptual separation of a frequency component but not its integration into the pitch of a harmonic series. Although the current data argue against the effects of grouping by spectral regularity on pitch perception, it is possible that this grouping principle plays a role not only in the perceptual segregation of frequency components, but also in the processing of other characteristics of perceived sounds, such as timbre and perceived location. The effects of grouping by spectral regularity on these perceptual attributes of sounds have yet to be investigated.

ACKNOWLEDGMENTS

The author would like to thank Brian Roberts, Robert Carlyon, and Sid Bacon for providing helpful comments on the manuscript and Duncan Lam, Chloe Lam, and Ida Tsui for helping with data collection. The study was funded through grant H.K.R.G.C. HKU 362/94M awarded to the author.

[1]The author would like to thank Brian Roberts for suggesting this interpretation of the results of experiment 1.

[2]Within the odd-H tone the equivalent regular band width (ERB) separation between the 3rd harmonic and the 1st harmonic (the adjacent, lower-frequency harmonic), calculated using Glasberg and Moore's (1990) formulas, was 5.5 ERB units. Within the all-H tone, the 3rd harmonic and the adjacent, lower-frequency harmonic (harmonic 2) were separated by 2.39 ERB units. Therefore, within the all-H tone, the partial masking of the 3rd harmonic by adjacent harmonics was probably larger than within the odd-H tone. Moreover, the ERB separation between harmonics 3 and 4 was 1.87 ERB units. Therefore, the partial masking of the 4th harmonic was larger than that of the 3rd harmonic within an odd-H tone.

Bregman, A. S. (**1990**). *Auditory Scene Analysis: The Perceptual Organisation of Sound* (MIT, Cambridge, MA).

Ciocca, V., and Darwin, C. J. (**1993**). ''Effects of onset asynchrony on pitch perception: Adaptation or grouping?'' J. Acoust. Soc. Am. **93**, 2870–2878.

Darwin, C. J., and Ciocca, V. (**1992**). ''Grouping in pitch perception: Effects of onset asynchrony and ear of presentation of a mistuned component,'' J. Acoust. Soc. Am. **91**, 3381–3390.

Darwin, C. J., Ciocca, V., and Sandell, G. J. (**1994**). ''Effects of frequency and amplitude modulation on the pitch of a complex tone with a mistuned harmonic,'' J. Acoust. Soc. Am. **95**, 2631–2636.

Darwin, C. J., Hukin, R. W., and Al-Khatib, B. Y. (**1995**). ''Grouping in pitch perception: Evidence for sequential constraints,'' J. Acoust. Soc. Am. **98**, 880–885.

Duifhuis, H., Willems, L. F., and Sluyter, R. J. (**1982**). ''Measurement of pitch in speech: an implementation of Goldstein's theory of pitch perception,'' J. Acoust. Soc. Am. **71**, 1568–1580.

Glasberg, B. R., and Moore, B. C. J. (**1990**). ''Derivation of auditory filter shapes from notched-noise data,'' Hear. Res. **47**, 103–138.

Goldstein, J. L. (**1973**). ''An optimum processor theory for the central formation of the pitch of complex tones,'' J. Acoust. Soc. Am. **54**, 1496–1516.

Hartmann, W. M., McAdams, S., and Smith, B. K. (**1990**). ''Hearing a mistuned harmonic in an otherwise periodic complex tone,'' J. Acoust. Soc. Am. **88**, 1712–1724.

Moore, B. C. J. (**1987**). ''The perception of inharmonic complex tones,'' *Auditory Processing of Complex Sounds*, edited by W. A. Yost and C. S. Watson (Erlbaum, Hillsdale, NJ), pp. 180–189.

Moore, B. C. J., and Glasberg, B. R. (**1990**). ''Frequency discrimination of complex tones with overlapping and non-overlapping harmonics,'' J. Acoust. Soc. Am. **87**, 2163–2177.

Moore, B. C. J., Glasberg, B. R., and Peters, R. W. (**1985**). ''Relative dominance of individual partials in determining the pitch of complex tones,'' J. Acoust. Soc. Am. **77**, 1853–1860.

Moore, B. C. J., Glasberg, B. R., and Peters, R. W. (**1986**). ''Thresholds for hearing mistuned partials as separate tones in harmonic complexes,'' J. Acoust. Soc. Am. **80**, 479–483.

Roberts, B. (**1998**). ''Effects of spectral pattern on the perceptual salience of partials in harmonic and frequency-shifted complex tones: A performance measure,'' J. Acoust. Soc. Am. **103**, 3588–3596.

Roberts, B., and Bailey, P. J. (**1993a**). ''Spectral pattern and the perceptual fusion of harmonics: I. The role of temporal factors,'' J. Acoust. Soc. Am. **94**, 3153–3164.

Roberts, B., and Bailey, P. J. (**1993b**). ''Spectral pattern and the perceptual fusion of harmonics: II. A special status for added components?'' J. Acoust. Soc. Am. **94**, 3165–3177.

Roberts, B., and Bailey, P. J. (**1996**). ''Spectral regularity as a factor distinct from harmonic relations in auditory grouping,'' J. Exp. Psychol. **22**(3), 604–614.

Roberts, B., and Bregman, A. S. (**1991**). ''Effects of the pattern of spectral spacing on the perceptual fusion of harmonics,'' J. Acoust. Soc. Am. **90**, 3050–3060.

Roberts, B., and Brunstrom, J. M. (**1998**). ''Perceptual segregation and pitch shifts of mistuned components in harmonic complexes and in regular inharmonic complexes,'' J. Acoust. Soc. Am. **104**, 2326–2338.

Russell, P., and Darwin, C. J. (**1991**). ''Real-time synthesis of complex sounds on a Mac II with 56001 DSP chip,'' Br. J. Audiol. **25**, 59–60.

Singh, P. G., and Hirsh, I. J. (**1992**). ''Influence of spectral locus and *F*0 changes on the pitch and timbre of complex tones,'' J. Acoust. Soc. Am. **92**, 2650–2661.

Terhardt, E. (**1974**). ''Pitch, consonance, and harmony,'' J. Acoust. Soc. Am. **55**, 1061–1069.

Intrinsic envelope fluctuations and modulation-detection thresholds for narrow-band noise carriers[a)]

Torsten Dau[b)] and Jesko Verhey
Carl von Ossietzky Universität Oldenburg, AG Medizinische Physik, Graduiertenkolleg Psychoakustik, D-26111 Oldenburg, Germany

Armin Kohlrausch
IPO Center for Research on User-System Interaction, P.O. Box 513, 5600 MB Eindhoven, The Netherlands and Philips Research Laboratories Eindhoven, Prof. Holstlaan 4, 5656 AA Eindhoven, The Netherlands

(Received 12 May 1998; revised 11 February 1999; accepted 2 July 1999)

A model is presented which calculates the intrinsic envelope power of a bandpass noise carrier within the passband of a hypothetical modulation filter tuned to a specific modulation frequency. Model predictions are compared to experimentally obtained amplitude modulation (AM) detection thresholds. In experiment 1, thresholds for modulation rates of 5, 25, and 100 Hz imposed on a bandpass Gaussian noise carrier with a fixed upper cutoff frequency of 6 kHz and a bandwidth in the range from 1 to 6000 Hz were obtained. In experiment 2, three noises with different spectra of the intrinsic fluctuations served as the carrier: Gaussian noise, multiplied noise, and low-noise noise. In each case, the carrier was spectrally centered at 5 kHz and had a bandwidth of 50 Hz. The AM detection thresholds were obtained for modulation frequencies of 10, 20, 30, 50, 70, and 100 Hz. The intrinsic envelope power of the carrier at the output of the modulation filter tuned to the signal modulation frequency appears to provide a good estimate for AM detection threshold. The results are compared with predictions on the basis of the more complex auditory processing model by Dau *et al.* [J. Acoust. Soc. Am. **99**, 3615–3622 (1997)]. [S0001-4966(99)02611-9]

PACS numbers: 43.66.Ba, 43.66.Dc, 43.66.Mk [JWH]

INTRODUCTION

When discussing temporal variations of an auditory stimulus, it is necessary to distinguish between the fine structure of the sound, i.e., the variations in instantaneous pressure, and the envelope of the sound, i.e., the slower overall changes in the amplitude. In psychoacoustics, temporal resolution normally refers to the latter (e.g., Viemeister and Plack, 1993). It is commonly assumed that in the auditory system two general sources for limits of temporal resolution can be distinguished: those of ''peripheral'' and those of ''central'' origin. The term peripheral is associated with the first stages of auditory processing, up to and including the processing in the auditory nerve. These stages include the filtering of the basilar membrane which necessarily influences temporal resolution: Temporal fluctuations which occur with a higher rate than approximately half the bandwidth of the auditory filter will be attenuated by the transfer function of the filter.

Additional limitations of temporal resolution result from the processing of information at higher stages in the auditory pathway. When measuring thresholds for detecting fluctuations in the amplitude of a broadband noise as a function of the rate of fluctuation, it is observed that thresholds progressively increase with increasing modulation rate (e.g., Viemeister, 1979; Bacon and Viemeister, 1985; Forrest and Green, 1987). The auditory system seems to become less sensitive to amplitude modulations as the rate of modulation increases. Since, at least at high frequencies, the response of the peripheral stages is too fast to be the limiting factor, this has led to the idea that there is a process at a higher level which is ''sluggish'' in some way (e.g., Moore and Glasberg, 1986; Viemeister and Plack, 1993). Models of temporal resolution are especially concerned with this process.

There is a popular type of model described in the literature, which has been developed for describing temporal resolution (e.g., Rodenburg, 1977; Viemeister, 1977, 1979). This model consists of the following stages: (i) bandpass filtering, (ii) a rectifying nonlinearity, (iii) a low-pass filter, and (iv) a decision mechanism (for a review, see Viemeister and Plack, 1993). The bandpass filtering corresponds to peripheral filtering. The nonlinearity (e.g., half-wave rectification) introduces low-frequency components corresponding to the envelope of the signal. The next stage of low-pass filtering (or integration) is intended to simulate the temporal resolution limit by attenuating rapid changes in the envelope of the signal. The decision mechanism is intended to simulate how the subject uses the output of the integrator to make a discrimination in a specific task.

In a more recent study, a model was presented that differs considerably from the above modeling approach (Dau *et al.*, 1997a, b). The most substantial new part of signal processing in this model is a modulation filterbank which was introduced to analyze the envelope fluctuations of the

[a)]Part of this research was presented at the 131st and 133rd meetings of the Acoustical Society of America [Dau *et al.*, J. Acoust. Soc. Am. **99**, Pt. 2, S2564 (1996) and T. Dau, J. Acoust. Soc. Am. **101**, Pt. 2, S3061 (1997)].
[b)]Electronic mail: torsten.dau@medi.physik.uni-oldenburg.de

stimuli in each peripheral auditory filter. The inclusion of a modulation filterbank was motivated by results from several studies on modulation masking (Bacon and Grantham, 1989; Houtgast, 1989). The model accounts for modulation masking data which show bandpass-shaped masking patterns with maximum masking for a signal modulation frequency close to the masker frequency. The model also accounts for the shape of the temporal modulation transfer function (TMTF) for a broadband noise carrier which has usually been interpreted as reflecting a low-pass filtering process. Within the modulation filterbank model the ability to detect the imposed modulation is mainly limited by the intrinsic random fluctuations in the noise as they appear at the output of the modulation filter. It was assumed that the bandwidth of the modulation filters increases with increasing modulation center frequency. In this way, for a white noise carrier, the power of the random intrinsic fluctuations appearing at the output of a modulation filter increases with increasing modulation filter bandwidth. Thus, more random intrinsic amplitude fluctuations appear at the outputs of modulation filters tuned to higher frequencies, and this makes it progressively harder to detect an imposed modulation as the modulation frequency increases, resulting in the low-pass characteristic of the TMTF for noise carriers.

However, in this model, it is the *interaction* of peripheral filtering, a subsequent adaptation stage, the modulation filterbank, and a decision algorithm based on a pattern recognition scheme that determines threshold. The purpose of the present study is to examine the extent to which modulation detection data can be simply explained in terms of the intrinsic envelope power of the carrier itself. A model is presented which only contains envelope extraction and calculation of the power at the output of a specific modulation filter. The model does not include peripheral filtering and effects of adaptation. Model predictions will be compared with experimentally obtained modulation detection thresholds, and also with simulations derived with the more complex processing model by Dau *et al.* (1997a, b).

I. METHOD

A. Procedure and subjects

Modulation detection thresholds were measured and simulated using an adaptive three-interval forced-choice (3IFC) procedure. The carrier was presented in three consecutive intervals separated by silent intervals of 300 ms. In one randomly chosen interval the carrier was sinusoidally amplitude modulated. In the other intervals it was unmodulated. The subject's task was to specify the interval containing the modulation. During a threshold run, the modulation depth in dB ($20 \log m$) was adjusted using a two-down one-up rule (Levitt, 1971) which provides an estimate of the modulation depth necessary for 70.7% correct responses. The step size was 4 dB at the start of a run and was divided by 2 after every second reversal of the modulation depth until the step size reached a minimum of 1 dB, at which time it was fixed. Using this 1-dB step size, ten reversals were obtained and the median value of the modulation depths at these ten reversals was used as the threshold value. The subjects received visual feedback after each response. The procedure was repeated four times for each signal configuration and subject. All figures show the median and interquartile ranges based on four single measurements. All three subjects had experience in psychoacoustic measurements and had clinically normal hearing. They were between 23 and 29 years old and participated voluntarily in the study.

B. Apparatus

All acoustic stimuli were digitally generated at a sampling frequency of 32 kHz. The stimuli were transformed to analog signals with the aid of a two-channel 16-bit D/A converter, attenuated, low-pass filtered at 10 kHz, and diotically presented via headphones (HDA 200, Sennheiser) in a sound-attenuating booth. Signal generation and presentation were controled by a SUN-Workstation using a signal-processing software package developed at the Drittes Physikalisches Institut in Göttingen.

C. Stimuli

Modulation detection thresholds were obtained using bandpass noise as the carrier. An independent sample of noise randomly cut out of a 10-s-long realization was presented in each interval. The noise stimuli were digitally filtered before modulation by setting the magnitude of the Fourier coefficients to zero outside the desired passband. The subject's task was to detect a sinusoidal signal modulation that was imposed on the noise carrier. The level of the noise carrier was 65 dB SPL. The duration of the carrier and the modulator was 500 ms. The stimuli were shaped with 50-ms Hanning ramps. The sinusoidal modulation was applied with zero onset phase. To eliminate level cues when generating amplitude-modulated narrow-band stimuli the digital waveforms were adjusted to have equal power in each interval of the forced-choice trial.[1]

II. EXPERIMENT 1

A. Conditions

A modulation detection experiment was performed using Gaussian noise as the carrier. The subject's task was to detect the imposed signal modulation of 5, 25, or 100 Hz. The carrier had a fixed upper-cutoff frequency of 6 kHz. The parameter was the carrier bandwidth which was either 1, 5, 10, 25, 50, 100, 250, 500, 1000, 4000, or 6000 Hz.

B. Results

Figure 1 shows averaged experimental data for three subjects. Modulation depth at threshold is plotted as a function of modulation frequency. The parameter is the carrier bandwidth. The figure shows TMTFs with only three data points (modulation frequencies of 5, 25, and 100 Hz) per condition. There are considerable differences in the shape of the threshold functions for different carrier bandwidths. For the bandwidths $\Delta f = 1$, 5, 10, and 25 Hz, indicated by the solid curves, the threshold function has a high-pass characteristic, with a decrease in threshold with increasing modulation frequency. The dashed–dotted curves represent the

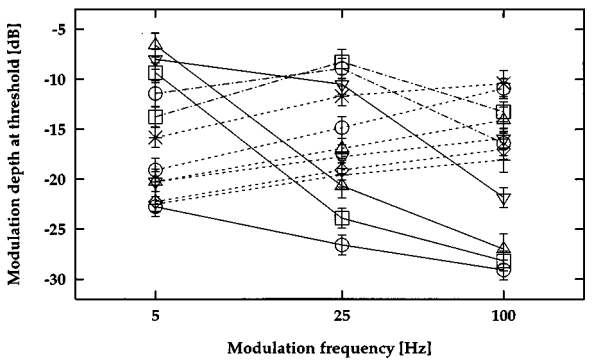

FIG. 1. Averaged modulation detection thresholds for modulation rates of 5, 25, and 100 Hz using a Gaussian-noise carrier. The parameter is the bandwidth Δf of the carrier: The solid lines indicate threshold functions for $\Delta f = 1$ Hz (○), 5 Hz (□), 10 Hz (△), and 25 Hz (▽). The dashed–dotted curves represent conditions for $\Delta f = 50$ Hz (○), and $\Delta f = 100$ Hz (□). The dashed lines show threshold functions for $\Delta f = 250$ Hz (×), $\Delta f = 500$ Hz (○), $\Delta f = 1000$ Hz (△), $\Delta f = 2000$ Hz (▽), $\Delta f = 4000$ Hz (◇), and $\Delta f = 6000$ Hz (+).

conditions $\Delta f = 50$ and 100 Hz, respectively, showing a bandpass characteristic, with the highest threshold for a modulation frequency of 25 Hz. Finally, for $\Delta f = 250$ Hz and higher (dashed curves), the threshold function has a low-pass characteristic, with an increase in threshold with increasing modulation frequency. The results are in line with those from previous studies (Fleischer, 1982a, b; Dau *et al.*, 1997a).

The data may also be illustrated in a different way when replotted as a function of the carrier bandwidth, with modulation frequency (f_{mod}) as the parameter. This was done in Fig. 2. This figure shows three threshold curves, for $f_{\mathrm{mod}} = 5$ Hz (○), $f_{\mathrm{mod}} = 25$ Hz (◇), and $f_{\mathrm{mod}} = 100$ Hz (△), respectively. Each curve has a maximum that occurs at a bandwidth equal to two to four times the imposed modulation frequency.

C. Model predictions

In the following, the experimental data are compared with model predictions. The analysis only contains envelope extraction of the noise carrier, modulation bandpass filtering, and calculation of the ac-coupled power at the output of a specific modulation filter. The parameters for the modulation filter are the same as in Dau *et al.* (1997a). The value for the

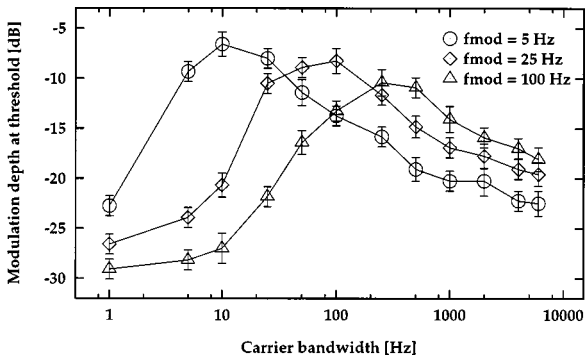

FIG. 2. Replot from Fig. 1. Thresholds are plotted as a function of the carrier bandwidth. Parameter is the signal modulation frequency: $f_{\mathrm{mod}} = 5$ Hz (○), $f_{\mathrm{mod}} = 25$ Hz (◇), and $f_{\mathrm{mod}} = 100$ Hz (△).

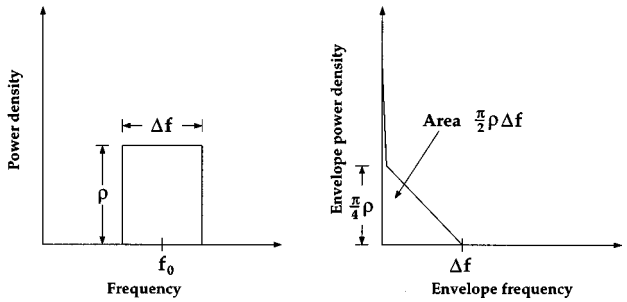

FIG. 3. Power spectrum (left panel) and envelope spectrum (right panel) of Gaussian bandpass noise. The right curve represents a close approximation of the exact shape of the (linear) envelope spectrum (for details, see Lawson and Uhlenbeck, 1950).

modulation power is given relative to the rms level of the carrier (in dB). In order to introduce a *lower* limit for the resulting envelope power in the model, a value corresponding to −30 dB is added. This value is intended to reflect the empirically found ''absolute'' detection threshold for a signal modulation imposed on a sinusoidal carrier at a medium level (e.g., Kohlrausch *et al.*, 1999; Viemeister, 1979).[2] The analysis excludes peripheral filtering and effects of adaptation.

Assuming a rectangular shape of the power spectrum of the Gaussian carrier, Lawson and Uhlenbeck (1950) have shown that the envelope spectrum, $N = N(f_{\mathrm{env}})$, i.e., the power spectrum of the envelope of the carrier, is given approximately by the formula

$$N_{\Delta f,\rho}(f_{\mathrm{env}}) \approx \pi \Delta f \rho \, \delta(f_{\mathrm{env}}) + \frac{\pi \rho}{4 \Delta f}(\Delta f - f_{\mathrm{env}}), \qquad (1)$$

where Δf is the carrier bandwidth, ρ is the power spectral density of the carrier, and f_{env} indicates the envelope frequency. Figure 3 shows the power spectrum (left panel) and envelope spectrum (right panel) according to Eq. (1). Besides the dc peak there is a triangular continuous spectrum. The following aspects of Fig. 3 are of particular relevance for modulation detection experiments using narrow-band noise carriers.

(i) For a constant overall level of a noise band, the total power of intrinsic envelope fluctuations, i.e., the total area under the triangle in the right panel of Fig. 3, remains constant. What changes with varying carrier bandwidth is the spectral region over which the envelope spectrum stretches.

(ii) With increasing noise bandwidth, the envelope spectrum becomes broader and flatter. This leads to a reduction in envelope power for low envelope frequencies while envelope power is increased for higher frequencies.

Figure 4 (upper panel) shows the idealized envelope spectra for a set of carrier bandwidths between 10 and 250 Hz. In the middle panel of Fig. 4, the transfer functions of three modulation filters tuned to the frequencies 5, 25, and 100 Hz are shown, as they are used for the calculations. The parameters for the modulation filters were the same as in Dau

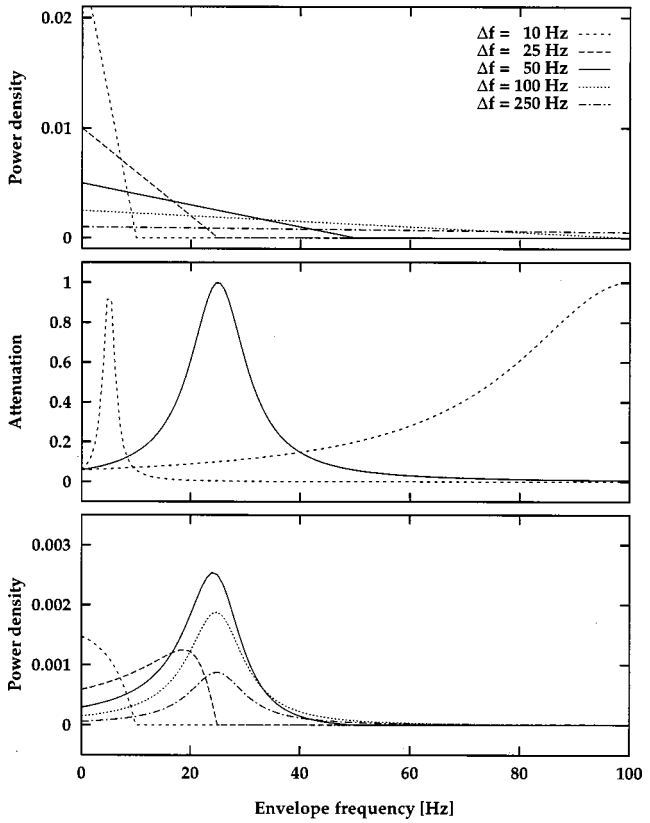

FIG. 4. Upper panel: Idealized envelope spectra for a set of Gaussian bandpass noises. The parameter is the noise bandwidth in the range from 10 to 250 Hz. Middle panel: Transfer functions of the modulation filters tuned to the modulation frequencies 5, 25, and 100 Hz based on Dau *et al.* (1997a). Lower panel: Spectral power density of the noises at the output of the modulation filter tuned to 25 Hz. The curves result from multiplication of the spectra in the upper panel and the transfer function of the 25-Hz modulation filter in the middle panel.

et al. (1997a) where they have been determined to account for modulation detection and modulation masking data within the framework of the more complex modulation filterbank model.

To calculate the spectral power density of the envelope of a specific noise within the pass band of a specific modulation filter with modulation center frequency MCF, the envelope spectrum of the carrier, $N_{\Delta f,\rho}$, was multiplied by the squared amplitude transfer function of the modulation filter, denoted as W_{MCF}. The lower panel of Fig. 4 shows, as an example, the spectral envelope power density as a function of envelope frequency at the output of the 25-Hz modulation filter. The parameter in this panel is the noise bandwidth Δf, which is indicated by the same line types as in the top panel.

To determine the total envelope power of the noise within the pass band of the specific modulation filter, the curves from the lower panel have to be integrated across envelope frequency. This integrated magnitude, P, is proportional to the area under each curve and is given by

$$P_{\Delta f,\rho,\mathrm{MCF}} = \int_0^\infty N_{\Delta f,\rho} \cdot W_{\mathrm{MCF}}\, df_{\mathrm{env}}. \tag{2}$$

Figure 5 shows this envelope power P as a function of the carrier bandwidth for three modulation filters tuned to

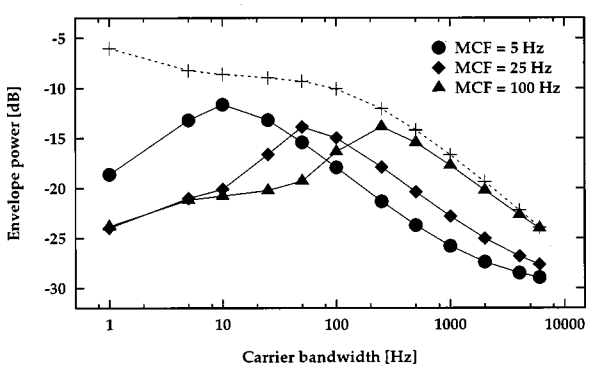

FIG. 5. Integrated envelope power as a function of the noise bandwidth in the passband of three modulation filters tuned to 5 Hz (●), 25 Hz (♦), and 100 Hz (▲). In addition, the envelope power resulting from integration within the passband of a modulation low-pass filter as proposed by Viemeister (1979) is included in the figure (+).

MCF=5 Hz (●), 25 Hz (♦), and 100 Hz (▲), respectively. In addition, for comparison, the envelope power resulting from integration within the passband of a modulation *low-pass* filter as proposed by Viemeister (1979) is plotted in the figure (+). The values at the ordinate represent overall envelope power relative to the rms level of the carrier, in dB. The three envelope power functions shown in Fig. 5 decrease at low and high carrier bandwidths, having a maximum at the bandwidths 10, 50, and 250 Hz for MCF=5, 25, and 100 Hz, respectively. The curve for the modulation low-pass filter decreases monotonically with increasing carrier bandwidth.

A straightforward way to relate these values to modulation detection thresholds would be to assume a certain fixed signal-to-noise ratio between *imposed* modulation and intrinsic fluctuations—as it is done for tone-in-noise detection. For such a derivation, the possible attenuation of the imposed modulation by the modulation filters has to be taken into account. For the modulation filterbank, the ''attenuation'' is the same for all three signal modulation frequencies, because the modulation filter tuned to the signal modulation is always used. The modulation low-pass filter, on the other hand, attenuates modulation frequencies according to its transfer characteristic. Viemeister suggested a cutoff frequency of 64 Hz. For such a characteristic, signal modulations of 5 and 25 Hz are transformed in the same way while a signal modulation of 100 Hz is somewhat attenuated. This would have to be considered when relating envelope power of the carrier noise to modulation detection threshold in case of the modulation low-pass filter.

The calculated pattern of the envelope power at the output of the specific modulation filters (Fig. 5) has a form similar to the threshold pattern from Fig. 2. In particular, the peak frequencies correspond to those in the measured data. In the calculated pattern, the envelope power values at the peak frequencies are the same for MCF=25 Hz and MCF=100 Hz. The ''form-invariant'' shape of the pattern for these two modulation center frequencies is due to the same Q-value of the corresponding modulation filters. For MCF=5 Hz (●), the envelope power at the peak frequency is increased since the corresponding modulation filter only has a lower Q-value of 1 according to Dau *et al.* (1997a). In

the data from Fig. 2, however, the thresholds at the peak frequencies continuously decrease with increasing modulation frequency. One systematic deviation between the model predictions and the data is that the slope of the patterns for carrier bandwidths above the corresponding peak frequency is steeper in the simulations than in the data while it is consistently shallower than in the data for bandwidths below the peak frequency. This discrepancy may be due to effects of adaptation which are not included in the model. This will be discussed in Sec. IV.

In summary, the interaction between the spectral distribution of envelope power of the applied noise carrier with the modulation filters generally accounts for the data.

III. EXPERIMENT 2

The analysis in the previous section has revealed that the intrinsic envelope power of the noise carrier integrated over the passband of the modulation filters is a good first predictor for modulation detection thresholds. So far, Gaussian noise was used as the carrier and modulation detection thresholds were derived as a function of the carrier bandwidth. A further test of the above hypothesis would be to consider the TMTF of noise carriers having the same bandwidth but a completely different shape of their envelope spectra. The TMTF is expected to change considerably in the different noise conditions. This is investigated in the present section for Gaussian noise, multiplied noise, and low-noise noise as the carrier.

A. Noise carrier characteristics

Gaussian noise was generated by digitally filtering broadband Gaussian noise (before modulation) by setting the magnitude of the Fourier coefficients to zero outside the desired passband of 50 Hz centered at 5 kHz. Multiplied noise was generated by multiplying a sinusoid at 5 kHz with a modulator. The modulator consisted of a low-pass Gaussian noise with a cutoff frequency of 25 Hz at a rms value of -10 dB (relative to amplitude 1) to which a dc component of value 1 was added.

This ensured that the 10-s-long realization of the noise waveform used in the experiments and the simulations was not overmodulated. Low-noise noise was generated in a way described by Kohlrausch *et al.* (1997). It represents an efficient way of generating a bandpass noise with a smoothed temporal envelope. The generation started with a Gaussian noise signal with a rectangular power spectrum. The following steps were iterated ten times: The envelope of the noise was calculated, representing the absolute value of the analytic signal, and the time waveform was divided by this envelope on a sample-by-sample basis and then restricted to its original bandwidth of 50 Hz by zeroing the corresponding components in the power spectrum. Iteration of the procedure leads to a decreasing amount of spectral splatter after each division by the envelope. The power spectrum within the passband is slightly different from that at the beginning of the iteration (for details, see Kohlrausch *et al.*, 1997). The method differs considerably from the original algorithm for generating low-noise noise described by Pumplin (1985) and Hartmann and Pumplin (1988, 1991) in which envelope fluctuations for a noise signal were minimized by optimizing the phase spectrum using a gradient search procedure while rigorously maintaining the power spectrum.

Their procedure for generating low-noise noise is, however, quite time consuming and not easily implemented.

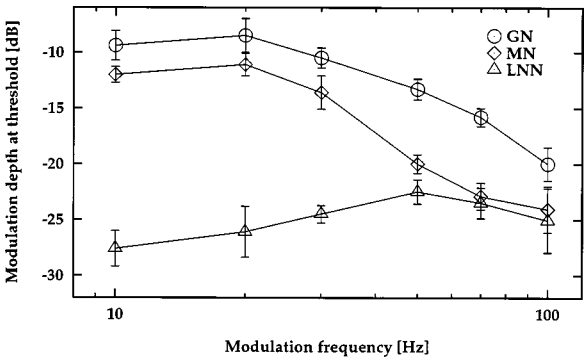

FIG. 6. Averaged thresholds for the modulation frequencies 10, 20, 30, 50, 70, and 100 Hz for a Gaussian noise (○), a multiplied noise (◇), and a low-noise noise (△). Carrier bandwidth: 50 Hz, center frequency: 5 kHz, level: 65 dB SPL.

B. Conditions

Modulation detection thresholds were obtained with Gaussian noise (GN), multiplied noise (MN), and low-noise noise (LNN) as the carrier. The center frequency of the carrier was 5 kHz and its bandwidth was 50 Hz. The subject's task was to detect a sinusoidal signal modulation of 10, 20, 30, 50, 70, and 100 Hz that was imposed on the noise carrier.

C. Results

Figure 6 shows modulation depth, m, at threshold as a function of modulation frequency. Data for GN are represented by the circles, thresholds for MN and LNN are indicated by diamonds and triangles, respectively. The three TMTFs are very different in shape. The highest thresholds were obtained for GN as the carrier. In this case, thresholds for modulation rates of 10 and 20 Hz have a level of about -8 to -9 dB and drop slowly and continuously for modulations rates above $\Delta f/2$. This is consistent with earlier results by Fleischer (1982a, b) and Dau *et al.* (1997a). For $f_{\mathrm{mod}}=100$ Hz threshold has reached a value of -20 dB. For multiplied noise (MN) as the carrier, thresholds are shifted towards lower values for all modulation rates, compared with the GN condition. The difference between both functions amounts to 3 dB at $f_{\mathrm{mod}}=10$ Hz and increases with increasing modulation rate to a maximum value of about 7 dB at $f_{\mathrm{mod}}=70$ Hz. The TMTF obtained with low-noise noise (LNN) as the carrier has a completely different shape than those obtained with GN and MN. At $f_{\mathrm{mod}}=10$ Hz threshold is at -27 dB, which is only about 3 dB higher than the threshold for a sinusoidal carrier at 5 kHz for the same subjects (not shown). With increasing modulation rate, threshold slightly increases and reaches a maximum value of $m=-23$ dB for $f_{\mathrm{mod}}=50$ Hz before it decreases again with further increasing modulation rate. At modulation rates of 70 and 100 Hz thresholds for LNN coincide with those obtained with MN.

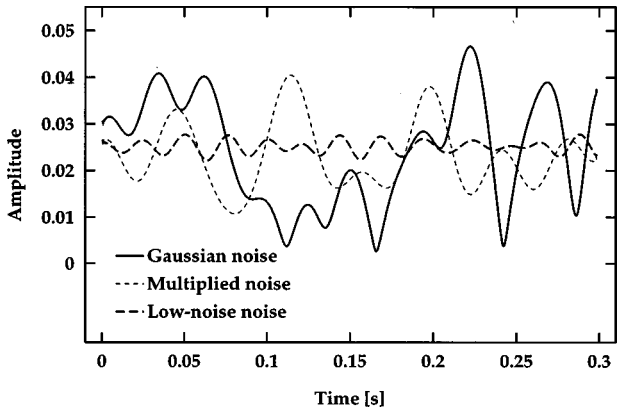

FIG. 7. Envelopes of 300-ms realizations of Gaussian noise (GN), multiplied noise (MN), and low-noise noise (LNN).

D. Model predictions

Figure 7 shows the envelopes of a 300-ms section of each noise type. The envelope of LNN (thick dashed curve) is very smooth compared to the envelope of GN and MN. In addition, it can be seen from the figure that for GN and LNN, the rate of changes in amplitude is considerably higher than for MN.

Figure 8 shows the envelope spectra for GN (upper panel), MN (middle panel), and LNN (lower panel). Power density is plotted on a logarithmic scale, relative to the power of the dc component of the noise envelopes. The solid curves represent averaged envelopes from 1000 single 1-s-long realizations which were randomly selected from a 10-s-long noise buffer. Hanning ramps with 50-ms rise and fall times were applied to the single realizations. The dashed curves represent idealized envelope spectra. In the case of GN, the curve reflects the solution according to Eq. (1) of the present study, based on Lawson and Uhlenbeck (1950). This function thus would have a triangular shape on a linear scale. In the case of MN and LNN, the idealized envelope spectra represent relatively simple fits of the averaged curves. The envelope spectrum for MN is fitted by a rectangle that stretches from 0 to 25 Hz, which is half the noise bandwidth. The envelope spectrum of LNN is fitted by a triangle, with the maximum value at 50 Hz. It has a much lower level than GN and MN. These fits were used for the simulations presented in the following.

The upper panel of Fig. 9 replots the idealized envelope spectra of GN (solid line), MN (dotted line), and LNN (dashed line). Envelope power density is plotted on a linear scale as a function of envelope frequency. The middle panel shows the transfer functions of the modulation filters tuned to the frequencies 10, 20, 30, 50, 70, and 100 Hz, respectively, as they are used in the simulations. The filter tuned to 30 Hz is emphasized by the solid line. The lower panel of Fig. 9 shows, as an example, the envelope power densities for the three noise maskers considering only the modulation filter tuned to 30 Hz.

To determine the total ac-coupled envelope power of the noise within the passband of the modulation filter the curves were integrated across envelope frequency (compare Sec. II B). Figure 10 shows the integrated envelope power for

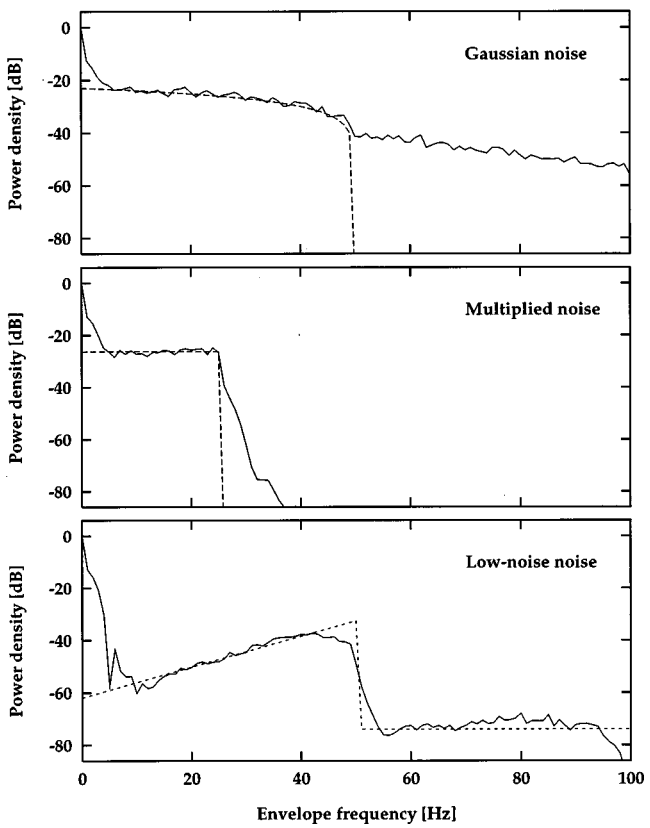

FIG. 8. Idealized envelope spectra (dashed curves) and averaged spectra of Hilbert envelopes (solid curves) of Gaussian noise (upper panel), multiplied noise (middle panel), and low-noise noise (lower panel). Each averaged curve results from 1000 1-s-long realizations which were randomly selected from a 10-s-long noise buffer and then windowed with 50-ms Hanning ramps. The idealized curve for Gaussian noise is according to Eq. (1) of the present study, based on Lawson and Uhlenbeck (1950). The idealized envelope spectra for multiplied and low-noise noise represent fits (see text). Note that the power density is plotted on a logarithmic scale.

GN, MN, and LNN as a function of the center frequency (MCF) of the modulation filter (compare Sec. II C). These frequencies are chosen to be equal to the imposed signal modulation frequency in the experiment from Fig. 6. As expected from the low level of the envelope spectrum of LNN, the values for the integrated envelope power for LNN are low compared to those obtained with GN and MN. For LNN, the envelope power slightly increases with increasing modulation center frequency (MCF) and then decreases for MCF >50 Hz. For GN and MN the integrated envelope power is considerably higher at low modulation center frequencies, and decreases for frequencies larger than 20 and 30 Hz, respectively. The values for GN are always higher than those for MN. In order to check the appropriateness of the approximation of the envelope spectra, the calculation was repeated for the Gaussian noise using the ''realistic'' (averaged) envelope spectrum from Fig. 8 (solid curve in the upper panel). The computed values differed less than 1 dB from the values for the idealized modulation spectrum shown in Fig. 10.

The predicted curves cover the shape of the three experimental TMTFs from Fig. 6. This indicates that the envelope power in the passband of a specific modulation bandpass filter is the primary cause for the shape of the TMTFs. However, there are again certain discrepancies between model

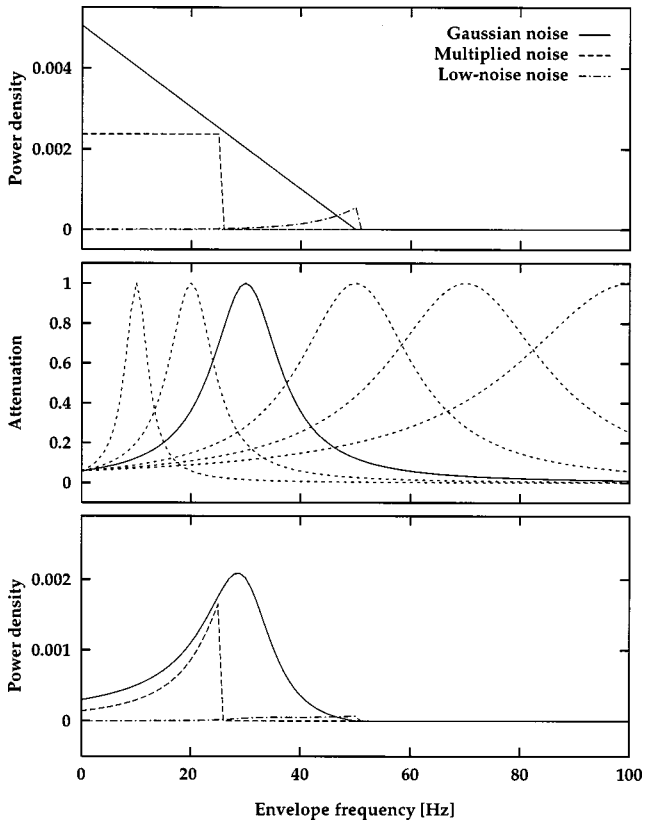

FIG. 9. Upper panel: Idealized envelope spectra of Gaussian noise (solid line), multiplied noise (dotted line), and low-noise noise (dashed line). Power density is plotted on a linear scale as a function of envelope frequency. Middle panel: Transfer functions of the modulation filters tuned to the modulation frequencies 10, 20, 30, 50, 70, and 100 Hz. Lower panel: Spectral power densities at the output of the modulation filter tuned to 30 Hz derived by multiplying the modulation filter transfer function from the middle panel with the envelope spectra of the noises in the upper panel.

predictions and data. Especially, at low frequencies predicted values are about 2–5 dB lower than the experimental values leading to a smaller dynamic range of only 5 dB for GN and 7 dB for MN in contrast to 12 and 13 dB in the data, respectively. In the case of LNN, the threshold pattern is shifted towards lower values compared with the data whereas the dynamic range is the same in both cases.

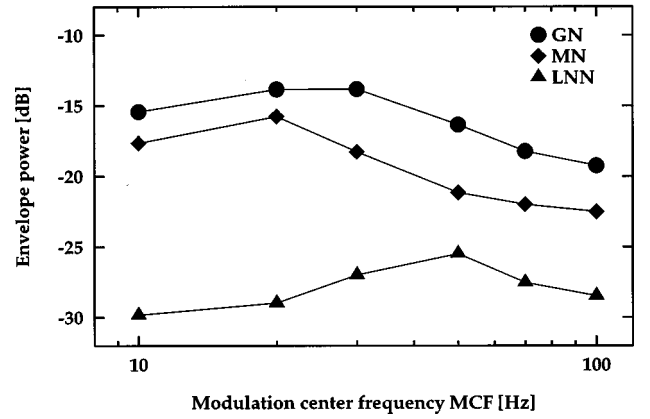

FIG. 10. Integrated envelope power for Gaussian noise (●), multiplied noise (♦), and low-noise noise (▲) as a function of the center frequency of the modulation filter (MCF).

IV. DISCUSSION

In this study, model predictions were presented which calculate the intrinsic envelope power of the noise carrier in the passband of a modulation bandpass filter. The modulation filter was tuned to the signal modulation frequency and its parameters were taken from Dau *et al.* (1997a). Amplitude modulation detection thresholds were estimated from the ac-coupled envelope power relative to the rms value of the carrier. In both experiments presented in the study, the principal shape of the threshold curves found in the experimental data as well accounted for by the model.

Effects of peripheral filtering, adaptation, and a more ''realistic'' decision algorithm were not taken into account. Concerning the effects of peripheral filtering on modulation detection, it has been suggested that combination of information about the signal modulation across carrier frequency probably occurs at a level higher than the periphery: the observer can combine information nearly optimally from widely spaced critical bands (e.g., Green and Swets, 1966; Dau *et al.*, 1997b).[3] This implies that peripheral filtering would have an influence on modulation detection in conditions in which the imposed signal modulation be attenuated below the ''absolute'' threshold for modulation in one or more peripheral filters. If a broadband noise is used and a relatively high-frequency signal modulation of, for example, several hundred Hertz is imposed, than this signal modulation (which is coherent across the critical bands) will be strongly attenuated by the transfer function of the peripheral filters tuned to low (carrier) frequencies. As long as the signal modulation is not attenuated below its absolute detection threshold within any of the stimulated peripheral filters, signal information will be recombined across frequency at the decision stage. However, if the signal modulation is attenuated below this threshold, the corresponding peripheral filter(s) will not contribute anymore to signal detection. In such a case, only the higher-frequency channels determine detection threshold. However, in the experiments of the present study, only modulation frequencies in the range of 5 to 100 Hz were used and, in addition, the carrier bandpass noise was applied in the high-frequency region in most cases. Therefore, the effect of peripheral filtering can be assumed to be negligible in the conditions considered here.

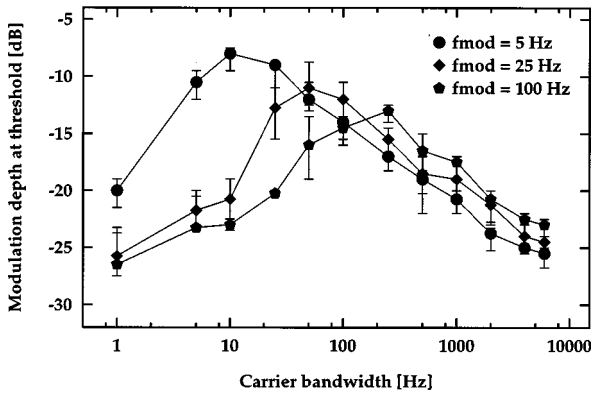

FIG. 11. Simulated thresholds using the modulation-filterbank model by Dau *et al.* (1997a). Experimental condition as in Fig. 2 (experiment 1).

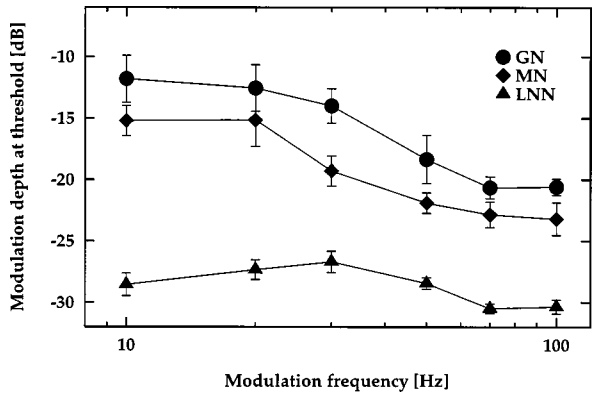

FIG. 12. Simulated thresholds using the modulation-filterbank model by Dau *et al.* (1997a). Experimental condition as in Fig. 6 (experiment 2).

The model also does not include effects of peripheral compression and adaptation. Peripheral compression has been found in a number of physiological studies (e.g., Rhode, 1971; Robles *et al.*, 1986; Yates, 1990) and has been found to have major effects on behavioral data (e.g., Oxenham and Moore, 1995; Oxenham and Plack, 1997; van de Par and Kohlrausch, 1998). However, a ''static'' compression probably would not alter the predicted results since it would act on each component in the envelope spectrum in the same way and would affect the carrier envelope in the same way as the imposed signal modulation. This is not the case for a dynamic compression stage that acts differently for different modulation rates, as realized in the adaptation stage within the auditory processing model by Dau *et al.* (1996a, 1997a).[4] This adaptation stage compresses low-frequency envelope components while it emphasizes high-frequency envelope fluctuations. Its transfer characteristic is more complex than that of a linear modulation high-pass filter which also would attenuate low-frequency components relative to higher frequencies.[5]

In order to show the influence of adaptation and dynamic compression, modulation detection thresholds were predicted using the processing model from Dau *et al.* (1997a). Figure 11 shows the corresponding simulated modulation detection thresholds for the condition described in experiment 1 of the present study. In agreement with the data, the threshold functions have a bandpass shape and the peaks of the three curves are lower the higher the imposed modulation frequency. The model predictions also agree better with the experimental data at very low and very high carrier bandwidths than do the predictions of the model from the present study (cf. Fig. 5). This is the case even though, especially for the modulation frequencies 25 and 100 Hz, the processing model overestimates human performance in conditions of $\Delta f > 1000$ Hz by about 5 dB. Figure 12 shows predictions of the processing model for the experimental conditions described in the second experiment of the present study. Again, the processing model allows a more accurate description of the experimental results than does the model from the present study. However, for the highest modulation frequencies, the processing model predicts too low thresholds for LNN, similar to the results of the predictions from the present study. The reason for this is unclear. Possibly, as was discussed by Kohlrausch *et al.* (1997), envelope fluctuations in *off-frequency* filters also play a role in the case of LNN (and not in the cases of GN and MN). Such an off-frequency effect is not included in the present on-frequency channel simulations (at 5 kHz).

V. CONCLUSIONS

(i) The intrinsic envelope power of the carrier at the output of a modulation filter tuned to the signal modulation frequency appears to yield a good estimate for AM detection threshold. It qualitatively accounts for the different slopes of the TMTF for different carrier bandwidths and carrier envelope statistics.

(ii) This finding further strengthens the hypothesis of frequency selectivity in the modulation domain. A modulation–low-pass approach clearly fails in these experiments.

(iii) To quantitatively account for modulation detection data, a more complex processing model as proposed by Dau *et al.* (1997a, b) may be used. Such a model includes, besides the assumption of frequency selectivity for modulation, effects of peripheral filtering and adaptation as well as a more realistic decision statistic.

ACKNOWLEDGMENTS

This work was supported by the Deutsche Forschungsgemeinschaft (DFG KO 942/12, ''Graduiertenkolleg Psychoakustik''). We thank Chris Plack and an anonymous reviewer for helpful discussions and comments on an earlier version of the paper.

[1]Recently, it has been shown that the loudness of a modulated carrier can differ from that of the unmodulated carrier, as a result of nonlinearities in the auditory periphery and possibly elsewhere (Zhang and Zeng, 1997; Moore *et al.*, 1999). If loudness is determined by the peak level (for low modulation rates), then the steady sound should have a higher rms level than the modulated sound at the same point of equal loudness. However, the effect of modulation on the perception of overall loudness was rather weak; equal rms level led to approximately equal loudness for steady and modulated stimuli (Moore *et al.*, 1999). Thus, level normalization as used in the present study appears to be adequate and decisions are most likely not based on loudness differences between the intervals of a trial.

[2]Sinusoidal carriers do not exhibit intrinsic fluctuations like noise carriers so that modulation detection must be limited by *internal* noise.

[3]In the processing model by Dau *et al.* (1996a, 1997a) an ''optimal detector'' is implemented which performs a kind of pattern recognition of the whole temporal course of the internal representation of the stimuli. Within the ''multi-channel'' version of the model (Dau *et al.*, 1997b), the internal representation of the stimuli has four dimensions, namely amplitude, time, modulation center frequency, and (audio) center frequency. The internal representations of the different peripheral channels are appended one after another in one large array. Decisions are based on the cross correlation between the actual internal representation of the actual stimulus and a normalized suprathreshold template representation.

[4]The adaptation stage simulates adaptive properties of the periphery and enables the model to account for forward masking data (Püschel, 1988; Dau *et al.*, 1996a, b). This strategy differs from the approach in which forward masking results from static peripheral compression followed by a certain temporal integrator (Penner, 1980; Oxenham and Moore, 1994, 1995; Plack and Oxenham, 1998).

[5]The shapes of the modulation filters have been derived in the framework of the processing model (Dau *et al.*, 1997a) assuming dynamic compression and adaptation. It is possible that if different filter shapes were used, the processing model might work equally well with just static compression or

no compression at all in conditions of modulation detection. Within the model, the ''asymmetric'' processing of low-frequency envelope components (including the dc-component which reflects the energy) and high-frequency envelope components, in combination with the ''linear'' decision criterion (optimal detector), allows the description of simultaneous and nonsimultaneous masking data (Dau *et al.*, 1996b) as well as of modulation detection and modulation masking data (Dau *et al.*, 1997a, b). Alternatively, one may also establish a model which processes all envelope components in the *same* way; in such a model, however, one would have to assume different (''asymmetric'') decision criteria to account for the different conditions.

Bacon, S. P., and Grantham, D. W. (**1989**). ''Modulation masking: Effects of modulation frequency, depth, and phase,'' J. Acoust. Soc. Am. **85**, 2575–2580.

Bacon, S. P., and Viemeister, N. F. (**1985**). ''Temporal modulation transfer functions in normal-hearing and hearing-impaired listeners,'' Audiology **24**, 117–134.

Dau, T., Kollmeier, B., and Kohlrausch, A. (**1997a**). ''Modeling auditory processing of amplitude modulation: I. Modulation detection and masking with narrow-band carriers,'' J. Acoust. Soc. Am. **102**, 2892–2905.

Dau, T., Kollmeier, B., and Kohlrausch, A. (**1997b**). ''Modeling auditory processing of amplitude modulation: II. Spectral and temporal integration in modulation detection,'' J. Acoust. Soc. Am. **102**, 2906–2919.

Dau, T., Püschel, D., and Kohlrausch, A. (**1996a**). ''A quantitative model of the 'effective' signal processing in the auditory system: I. Model structure,'' J. Acoust. Soc. Am. **99**, 3615–3622.

Dau, T., Püschel, D., and Kohlrausch, A. (**1996b**). ''A quantitative model of the 'effective' signal processing in the auditory system: II. Simulations and measurements,'' J. Acoust. Soc. Am. **99**, 3623–3631.

Fleischer, H. (**1982a**). ''Modulationsschwellen von Schmalbandrauschen,'' Acustica **51**, 154–161.

Fleischer, H. (**1982b**). ''Calculating psychoacoustic parameters of amplitude modulated narrow noise bands,'' Biol. Cybern. **44**, 177–184.

Forrest, T. G., and Green, D. M. (**1987**). ''Detection of partially filled gaps in noise and the temporal modulation transfer function,'' J. Acoust. Soc. Am. **82**, 1933–1943.

Green, D. M., and Swets, J. A. (**1966**). *Signal Detection Theory and Psychophysics* (Wiley, New York).

Hartmann, W. M., and Pumplin, J. (**1988**). ''Noise power fluctuation and the masking of sine signals,'' J. Acoust. Soc. Am. **83**, 2277–2289.

Hartmann, W. M., and Pumplin, J. (**1991**). ''Periodic signals with minimal power fluctuations,'' J. Acoust. Soc. Am. **90**, 1310–1317.

Houtgast, T. (**1989**). ''Frequency selectivity in amplitude-modulation detection,'' J. Acoust. Soc. Am. **85**, 1676–1680.

Kohlrausch, A., Fassel, R., and Dau, T. (**1999**). ''The influence of carrier level and frequency on modulation and beat-detection thresholds for sinusoidal carriers,'' submitted to J. Acoust. Soc. Am.

Kohlrausch, A., Fassel, R., van der Heijden, M., Kortekaas, R., van de Par, S., Oxenham, A., and Püschel, D. (**1997**). ''Detection of tones in low-noise noise: Further evidence for the role of envelope fluctuations,'' Acust. Acta Acust. **83**, 659–669.

Lawson, J. L., and Uhlenbeck, G. E. (**1950**). *Threshold Signals*, Vol. 24 of *Radiation Laboratory Series* (McGraw–Hill, New York).

Levitt, H. (**1971**). ''Transformed up–down procedures in psychoacoustics,'' J. Acoust. Soc. Am. **49**, 467–477.

Moore, B. C. J., and Glasberg, B. R. (**1986**). ''The role of frequency selectivity in the perception of loudness, pitch and time,'' in *Frequency Selectivity in Hearing*, edited by B. C. J. Moore (Academic, London), pp. 251–308.

Moore, B. C. J., Vickers, D. A., and Launer, S. (**1999**). ''Factors affecting the loudness of modulated sounds,'' J. Acoust. Soc. Am. **105**, 2757–2772.

Oxenham, A. J., and Moore, B. C. J. (**1994**). ''Modeling the additivity of nonsimultaneous masking,'' Hear. Res. **80**, 105–118.

Oxenham, A. J., and Moore, B. C. J. (**1995**). ''Additivity of masking in normally hearing and hearing-impaired listeners,'' J. Acoust. Soc. Am. **98**, 1921–1934.

Oxenham, A. J., and Plack, C. J. (**1997**). ''A behavioral measure of basilar-membrane nonlinearity in listeners with normal and impaired hearing,'' J. Acoust. Soc. Am. **101**, 3678–3687.

Penner, M. J. (**1980**). ''The coding of intensity and the interaction of forward and backward masking,'' J. Acoust. Soc. Am. **67**, 608–616.

Plack, C. J., and Oxenham, A. J. (**1998**). ''Basilar-membrane nonlinearity and the growth of forward masking,'' J. Acoust. Soc. Am. **103**, 1598–1608.

Pumplin, J. (**1985**). ''Low-noise noise,'' J. Acoust. Soc. Am. **78**, 100–104.

Püschel, D. (**1988**). ''Prinzipien der zeitlichen Analyse beim Hören,'' Doctoral Thesis, University of Göttingen.

Rhode, W. S. (**1971**). ''Observations of the vibration of the basilar membrane in squirrel monkeys using the Mössbauer technique,'' J. Acoust. Soc. Am. **49**, 1218–1231.

Robles, L., Ruggero, M. A., and Rich, N. C. (**1986**). ''Basilar membrane mechanics at the base of the chinchilla cochlea: I. Input–output functions, tuning curves, and response phases,'' J. Acoust. Soc. Am. **80**, 1364–1374.

Rodenburg, M. (**1977**). ''Investigation of temporal effects with amplitude modulated signals'' in *Psychophysics and Physiology of Hearing*, edited by E. F. Evans and J. P. Wilson (Academic, London), pp. 429–437.

van de Par, S., and Kohlrausch, A. (**1998**). ''Diotic and dichotic detection using multiplied-noise maskers,'' J. Acoust. Soc. Am. **103**, 2100–2110.

Viemeister, N. V. (**1977**). ''Temporal factors in audition: A systems analysis approach,'' in *Psychophysics and Physiology of Hearing*, edited by E. F. Evans and J. P. Wilson (Academic, London), pp. 419–427.

Viemeister, N. F. (**1979**). ''Temporal modulation transfer functions based upon modulation thresholds,'' J. Acoust. Soc. Am. **66**, 1364–1380.

Viemeister, N. F., and Plack, C. J. (**1993**). ''Time analysis,'' in *Human Psychophysics*, edited by W. A. Yost, A. N. Popper, and R. R. Fay (Springer, New York), pp. 116–154.

Yates, G. K. (**1990**). ''Basilar membrane nonlinearity and its influence on auditory nerve rate-intensity functions,'' Hear. Res. **50**, 145–162.

Zhang, C., and Zeng, F.-G. (**1997**). ''Loudness of dynamic stimuli in acoustic and electric hearing,'' J. Acoust. Soc. Am. **102**, 2925–2934.

Inter-relationship between different psychoacoustic measures assumed to be related to the cochlear active mechanism

Brian C. J. Moore[a] and Deborah A. Vickers
Department of Experimental Psychology, University of Cambridge, Downing Street, Cambridge CB2 3EB, England

Christopher J. Plack
Department of Psychology, University of Essex, Wivenhoe Park, Colchester CO4 3SQ, England

Andrew J. Oxenham
Research Laboratory of Electronics, Massachusetts Institute of Technology, Rm. 36-763, Cambridge, Massachusetts 02139

(Received 4 February 1999; accepted for publication 9 July 1999)

The active mechanism in the cochlea is thought to depend on the integrity of the outer hair cells (OHCs). Cochlear hearing loss is usually associated with damage to both inner hair cells (IHCs) and OHCs, with the latter resulting in a reduction in or complete loss of the function of the active mechanism. It is believed that the active mechanism contributes to the sharpness of tuning on the basilar membrane (BM) and is also responsible for compressive input–output functions on the BM. Hence, one would expect a close relationship between measures of sharpness of tuning and measures of compression. This idea was tested by comparing three different measures of the status of the active mechanism, at center frequencies of 2, 4, and 6 kHz, using subjects with normal hearing, with unilateral or highly asymmetric cochlear hearing loss, and with bilateral loss. The first measure, HL_{OHC}, was an indirect measure of the amount of the hearing loss attributable to OHC damage; this was based on loudness matches between the two ears of subjects with unilateral hearing loss and was derived using a loudness model. The second measure was the equivalent rectangular bandwidth (ERB) of the auditory filter, which was estimated using the notched-noise method. The third measure was based on the slopes of growth-of-masking functions obtained in forward masking. The ratio of slopes for a masker centered well below the signal frequency and a masker centered at the signal frequency gives a measure of BM compression at the place corresponding to the signal frequency; a ratio close to 1 indicates little or no compression, while ratios less than 1 indicate that compression is occurring at the signal place. Generally, the results showed the expected pattern. The ERB tended to increase with increasing HL_{OHC}. The ratio of the forward-masking slopes increased from about 0.3 to about 1 as HL_{OHC} increased from 0 to 55 dB. The ratio of the slopes was highly correlated with the ERB ($r=0.92$), indicating that the sharpness of the auditory filter decreases as the compression on the BM decreases. © *1999 Acoustical Society of America.* [S0001-4966(99)00211-8]

PACS numbers: 43.66.Dc, 43.66.Cb, 43.66.Sr [SPB]

INTRODUCTION

It is widely believed that the patterns of vibration on the basilar membrane in a normal ear are strongly influenced by an active mechanism that depends on the operation of the outer hair cells (OHCs); for a review, see Yates (1995). One consequence of this active mechanism is nonlinearity in the input–output functions of the basilar membrane. These functions show marked compression at medium input levels (40 to 80 dB SPL) and become more linear at very low and perhaps at very high levels (Rhode, 1971; Robles *et al.*, 1986; Yates, 1990; Ruggero *et al.*, 1997). The compression occurs only for tones that are reasonably close to the characteristic frequency (CF) for the place whose response is being measured. The response to tones with frequencies well below CF is approximately linear. When the OHCs are destroyed, or rendered inactive by drugs, the input–output functions of the basilar membrane become linear for all frequencies (Ruggero and Rich, 1991; Ruggero *et al.*, 1996).

A second consequence of the active mechanism is connected with the tuning of the basilar membrane. The normal sharp tuning of the basilar membrane at low sound levels is thought to depend on the active mechanism (Sellick *et al.*, 1982; Khanna and Leonard, 1982; Yates, 1995). The sharpness of tuning decreases progressively with increasing sound level, which probably reflects a progressively reducing contribution of the active mechanism. When the OHCs are damaged, or their functioning is impaired, the tuning on the basilar membrane (Sellick *et al.*, 1982; Khanna and Leonard, 1982) or in primary auditory neurons (Evans and Harrison, 1976) becomes broader.

There are many aspects of auditory perception that are thought to be affected by the active mechanism and by the loss of that mechanism when the OHCs are damaged; for

[a]Author to whom correspondence should be addressed. Electronic mail: bcjm@cus.cam.ac.uk

reviews, see Moore and Oxenham (1998) and Moore (1998). This paper is particularly concerned with three of these aspects. The first is frequency selectivity, as measured behaviorally in masking experiments and quantified in terms of the equivalent rectangular bandwidth (ERB) of the auditory filter (Glasberg and Moore, 1990). It is widely believed that the frequency selectivity revealed in masking experiments depends primarily on the filtering that takes place within the cochlea (Fletcher, 1940; Pickles, 1986; Moore, 1986; Evans *et al.*, 1989). People with cochlear hearing loss usually have ERBs that are markedly greater than normal (Leshowitz *et al.*, 1975; Pick *et al.*, 1977; Glasberg and Moore, 1986; Moore, 1998), and this is thought to reflect damage to the OHCs and the consequent disruption of the active mechanism.

The correlation between the ERB and the audiometric threshold at the test frequency is not high (Pick *et al.*, 1977; Glasberg and Moore, 1986; Laroche *et al.*, 1992; Moore, 1998), and the scatter of the ERB values for hearing losses in the range 50–70 dB can be considerable. This scatter may reflect the fact that elevation in absolute threshold can arise both from outer hair-cell damage and from inner hair-cell damage (Liberman and Dodds, 1984; Liberman *et al.*, 1986; Borg *et al.*, 1995; Moore, 1998); the former results in reduced basilar-membrane vibration for a given input sound level together with reduced sharpness of tuning, while the latter results in less efficient transduction of the basilar-membrane vibration into neural activity. In theory, the ERB of the auditory filter should be highly correlated with the amount of outer hair-cell damage, since the tuning on the basilar membrane appears to depend strongly on outer hair-cell function. However, IHC damage is thought not to affect the tuning on the basilar membrane (Liberman and Dodds, 1984; Liberman *et al.*, 1986). Therefore, the ERB should not necessarily be correlated with the amount of inner hair-cell damage, unless outer and inner hair-cell damage are themselves highly correlated. One aim of this paper is to assess the correlation between the ERB of the auditory filter and an estimate of outer hair-cell damage based on loudness measurements (see below for details). We also examine the correlation between the ERB and a more direct measure of basilar-membrane compression that has been described by Oxenham and Plack (1997).

The second psychoacoustic factor of interest for the present paper is the loudness recruitment that is usually associated with cochlear hearing loss (Fowler, 1936; Steinberg and Gardner, 1937). This may be described as follows. The absolute threshold is higher than normal. However, when a sound is increased in level above the absolute threshold, the rate of growth of loudness level with increasing sound level is greater than normal. When the level is sufficiently high, usually around 90 to 100 dB SPL, the loudness reaches its ''normal'' value; the sound appears as loud to the person with impaired hearing as it would to a normally hearing person. With further increases in sound level above 90–100 dB SPL, the loudness grows in an almost normal manner.

Two factors have been suggested to contribute to loudness recruitment. The first is a reduction in, or loss of, the compressive nonlinearity in the input–output function of the basilar membrane (Yates, 1990; Moore and Glasberg, 1997). In an ear where the damage is confined largely to the OHCs, with inner hair cells (IHCs) intact, the transformation from basilar-membrane velocity or amplitude to neural activity (spike rate) probably remains largely normal (Yates, 1990; Patuzzi, 1992). However, in an ear with damage to the IHCs as well, the transduction process may also be affected (Yates, 1990; Liberman *et al.*, 1986).

If the input–output function on the basilar membrane is steeper (less compressive) than normal in an ear with outer hair-cell damage, this would be expected to lead to an increased rate of growth of loudness level with increasing sound level. However, the magnitude of the basilar-membrane response at high sound levels can be roughly the same in a normal and an impaired ear (Ruggero and Rich, 1991; but see Ruggero *et al.*, 1997). This could explain why the loudness in an impaired ear usually ''catches up'' with that in a normal ear at sound levels around 90–100 dB SPL.

Another factor that may contribute to loudness recruitment is reduced frequency selectivity. For a sinusoidal stimulus, reduced frequency selectivity leads to an excitation pattern which is broader (spreads over a greater range of CFs) in an impaired than in a normal ear. Kiang *et al.* (1970) and Evans (1975) suggested that this might be the main factor contributing to loudness recruitment. They suggested that, once the level of a sound exceeds threshold, the excitation in an ear with cochlear damage spreads more rapidly than normal across the array of neurons, and this leads to the abnormally rapid growth of loudness with increasing level. However, experiments using filtered noise to mask signal-evoked excitation at CFs remote from the signal frequency indicate that reduced frequency selectivity is not a major contributor to loudness recruitment (Moore *et al.*, 1985; Hellman, 1978; Hellman and Meiselman, 1986); such noise has only a small effect on the perceived loudness of the signal. Although spread of excitation may play a small role, the loss of compressive nonlinearity on the basilar membrane seems to be a more dominant factor.

This conclusion is reinforced by a model of loudness perception applied to cochlear hearing loss, as proposed by Moore and Glasberg (1997). The model attempts to partition the overall hearing loss between the loss due to outer hair-cell damage, called HL_{OHC}, and the loss due to inner hair-cell damage, called HL_{IHC}; the sum of HL_{OHC} and HL_{IHC} is equal to the total hearing loss, HL_{TOTAL}. HL_{OHC} is associated with loss of compression and reduced frequency selectivity, while HL_{IHC} is associated simply with reduced sensitivity. The model accounts well for measures of loudness recruitment in people with unilateral cochlear hearing loss. It also accounts for the fact that changes in loudness with stimulus bandwidth (Zwicker *et al.*, 1957) are smaller in hearing-impaired than in normally hearing people (Florentine and Zwicker, 1979; Bonding, 1979; Bonding and Elberling, 1980; Moore *et al.*, 1999).

The model starts by calculation of an excitation pattern for the sound under consideration. Excitation patterns are calculated for a normal ear in a manner similar to that described by Glasberg and Moore (1990). The excitation patterns are made broader (but change less with level) as HL_{OHC}

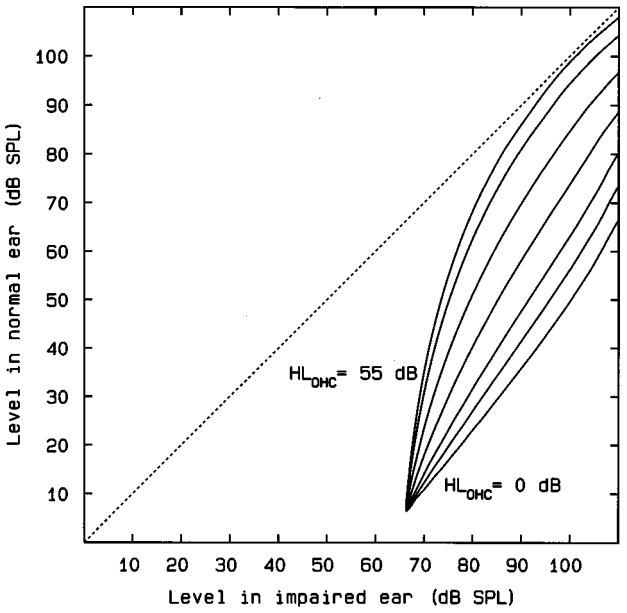

FIG. 1. The effect on loudness-matching functions of changing the value of the parameter HL_{OHC} for a hypothetical subject with a flat hearing loss of 60 dB in one ear and normal hearing in the other ear. The value of HL_{OHC} was 0, 10, 20, 30, 40, 50, or 55 dB.

increases, but they do not depend on the value of HL_{IHC}. The excitation pattern is then transformed to a specific loudness pattern. The total area under the specific loudness pattern gives the predicted overall loudness. The transformation from excitation to specific loudness at a given frequency is normally compressive, but it is made progressively less compressive as HL_{OHC} increases; again, it does not depend on HL_{IHC}. The effects of inner hair-cell loss are modeled simply by attenuating the excitation level at a given frequency by the value of HL_{IHC} at that frequency, prior to the transformation to specific loudness.

Figure 1 illustrates the effect of varying the parameter HL_{OHC} for a hypothetical subject with a flat hearing loss of 60 dB at all frequencies in one ear, with the other ear having completely normal audiometric thresholds. The figure shows the predicted sound levels required to match the loudness of a 1-kHz sinusoid between the two ears. To generate these predictions, the loudness was calculated as a function of level for each ear separately, and the loudness functions were used to calculate the levels giving equal loudness in the two ears. The slopes of the functions vary with HL_{OHC}. They have a downward curvature for large values of HL_{OHC}, but become almost straight for moderate values of HL_{OHC}, and even have a slight upward curvature for very small values of HL_{OHC}. Empirically measured loudness growth functions can vary markedly in slope and in curvature across subjects, even for subjects with similar absolute thresholds (Hellman and Meiselman, 1990, 1993; Kiessling *et al.*, 1993; Moore and Glasberg, 1997), and variations in the parameter HL_{OHC} allow the model to fit this observed range. The method of deriving the values of HL_{OHC} as a function of frequency for individual subjects is described later.

Moore and Glasberg (1997) obtained estimates of HL_{OHC} as a function of CF for several subjects with unilateral or highly asymmetric cochlear hearing loss. The estimates were based on loudness matches of tones presented alternately to the two ears. Some of those subjects were used in the present experiment, so that we could examine the relationship between the HL_{OHC} estimates and the estimates of the ERBs of their auditory filters obtained using notched-noise masking (Glasberg and Moore, 1990; Stone *et al.*, 1992). If both the HL_{OHC} values and the ERBs depend on the degree to which the active mechanism is operative, then the two should be highly correlated.

The third factor of interest for this paper is the magnitude of compression on the basilar membrane, estimated by measuring growth-of-masking functions in forward masking. Oxenham and Plack (1997) investigated forward masking for a 6-kHz sinusoidal signal and a masker of the same frequency or one octave lower. Forward masking was used to prevent interactions between the masker and the signal on the basilar membrane, which can lead to nonlinear effects such as suppression and combination tone generation. For the on-frequency case (signal frequency equal to masker frequency), they showed that under certain conditions, if the signal is made very brief and the time delay between the masker and signal is very short, the level of the signal at threshold is approximately equal to the masker level. Under these conditions, the growth-of-masking function (masker level as a function of signal level) has a slope of 1; each 10-dB increase in signal level requires a 10-dB increase in masker level. For the off-frequency case (masker frequency equal to 3 kHz instead of 6 kHz), the growth-of-masking function had a slope much less than 1; a 40-dB increase in signal level required only a 10-dB increase in signal level. This can be explained in the following way: the signal threshold depends on the response evoked by the masker at the signal CF. The growth of response on the basilar membrane for tones well below the CF is linear. Thus, the signal is subject to compression while the masker is not. This gives rise to the shallow growth-of-masking function. The slope value of around 0.25 corresponds to a compression of about 4 to 1, which is in good agreement with the estimates of Oxenham and Moore (1994, 1995). For midrange levels, Oxenham and Plack found even more compression, with a slope of about 0.16.

Even when the slope of the growth-of-masking function for the on-frequency case (signal frequency equals masker frequency) is not equal to 1, the compression on the basilar membrane can still be estimated from the ratio of slopes for the on-frequency case and the off-frequency case (Oxenham and Plack, 1997), and that is the approach taken in the present study. For brevity, in the remainder of this paper, we will refer to this quantity simply as the ''ratio of slopes.''

If the compression on the basilar membrane is lost as a consequence of cochlear hearing loss, then the growth-of-masking functions in forward masking (in dB per dB) should have slopes close to unity, except when the signal is very close to its absolute threshold (Oxenham and Moore, 1997; Moore and Oxenham, 1998). Furthermore, the slopes should remain close to unity, regardless of the relative frequencies of the masker and signal, as all frequencies should be processed linearly. Empirical data have confirmed these predictions (Oxenham and Moore, 1995, 1997; Oxenham and

TABLE I. Comparison of different compression-related measures at 2 kHz. The column headed HL gives the absolute threshold in dB HL. Values of HL_{OHC} were estimated from loudness matches between the two ears. Values of the ERB were estimated from notched-noise masking. The slope ratio is the slope of the growth-of-masking function in forward masking for a masker one octave below the signal frequency divided by the slope for a masker at the signal frequency. Parentheses indicate that at least one of the slope values was based on three or less points covering a small range of signal levels; there is a large possible error associated with these slope ratios.

Subject	Ear	HL	HL_{OHC}	ERB	Slope ratio
DF	Better	9	7	0.16	0.42
DF	Worse	60	30	0.75	0.73
AW	Better	26	21	0.16	0.38
AW	Worse	75	55	0.45	0.67
VF	Better	22	18	0.19	0.65
VF	Worse	60	50	>1	1.28
DT	Better	53		0.71	1.02
AR	Better	62		0.50	1.14
VW	Better	66		0.48	(>1)

Plack, 1997). In this paper, we consider several cases of hearing loss where there was probably some remaining outer hair-cell function, and hence some residual compression on the basilar membrane. Thus, we could examine the relationship between the estimated threshold elevation due to outer hair-cell damage (HL_{OHC}) and the amount of residual compression, as estimated from the ratio of slopes.

In summary, the aim of this study was to compare several psychoacoustic measures that are thought to be related to the functioning of the active mechanism in the cochlea. These measures were: the absolute threshold in dB HL; the estimated amount of the hearing loss attributable to outer hair-cell damage, HL_{OHC}; the ERB of the auditory filter as estimated from masking with notched noise; and the compression on the basilar membrane as estimated from the ratio of slopes. In addition, psychophysical tuning curves PTCs (Chistovich, 1957; Small, 1959; Moore, 1978) were obtained to check for the possibility of ''dead regions,'' i.e., regions in the cochlea where the IHCs or neurons are destroyed or nonfunctional. When the signal is presented at a frequency corresponding to a dead region, the tip of the PTC is shifted away from the signal frequency (Thornton and Abbas, 1980; Florentine and Houtsma, 1983; Moore, 1998).

I. METHOD

A. Subjects

Three groups of subjects were tested. The first was composed of six normally hearing subjects; all had thresholds

TABLE II. As Table I, but for a frequency of 4 kHz.

Subject	Ear	HL	HL_{OHC}	ERB	Slope ratio
DF	Better	14	11	0.16	0.55
DF	Worse	55	35	0.44	(0.67)
AW	Better	39	31	0.21	0.60
AW	Worse	66	55	0.48	0.74
VF	Better	10	8	0.14	0.34
VF	Worse	54	45	0.53	0.76
DT	Better	62		0.55	1.03
AR	Better	60		0.36	0.62
VW	Better	57		0.21	(1.07)

TABLE III. As Table I, but for a frequency of 6 kHz.

Subject	Ear	HL	HL_{OHC}	ERB	Slope ratio
DF	Better	35	28	0.16	0.55
DF	Worse	65	65	1.05	1.35
AW	Better	49	39	0.22	0.45
AW	Worse	75	55	1.07	1.41
VF	Better	18	14	0.165	0.28
VF	Worse	47	45	0.27	0.79
DT	Better	57		0.82	0.96
AR	Better	47		0.21	0.48
VW	Better	67		0.84	1.32

better than 15 dB HL at the standard audiometric frequencies from 250 to 8000 Hz. Their ages ranged from 19 to 48 years (mean 29). They were tested only in the experiment measuring the ratio of slopes in forward masking. The second group consisted of three subjects with unilateral or highly asymmetric hearing loss. The third group consisted of three subjects with bilateral hearing loss. The ages of the hearing-impaired subjects ranged from 48 to 85 years (mean 67). All losses were diagnosed as being of cochlear origin as indicated by: lack of an air-bone gap, signs of loudness recruitment; normal tympanograms, and normal acoustic reflex thresholds. The subjects with highly asymmetric losses were tested separately in each ear. When the worse ear was being tested, pink noise with a spectrum level of 25 dB at 1 kHz was presented to the better ear, to prevent ''cross hearing.'' Only the better ear was tested for the subjects with bilateral losses. The absolute thresholds of the ears tested are specified in dB HL at 2, 4, and 6 kHz (the test frequencies used in the experiments) in Tables I–III. The other quantities given in the tables will be described later.

All of the subjects (both hearing impaired and normally hearing) had previous experience in psychoacoustic tests, including masking experiments. They were given practice in each task until their performance appeared to be stable. This generally took 2–4 h per task.

B. Stimulus generation

Except for measurements of the ratio of slopes in forward masking, all stimuli were generated digitally using a Tucker-Davis Technologies (TDT) System II, controlled by a PC, using a sampling rate of 32 000 or 50 000 Hz. For generation of the notched-noise maskers used to estimate the ERB of the auditory filter, the stimuli were initially specified in the frequency domain, and were transformed into the time domain via an inverse Fourier transform, using a routine supplied by Tucker-Davis. The spectral values were specified at 1-Hz intervals up to approximately 16 000 Hz, and a 1-s noise buffer was generated. The three noise bursts for a given trial were taken as consecutive segments from that buffer. A new noise buffer was generated for every trial. The spectral slopes were essentially infinite. Stimuli were converted to analog form using two channels of a TDT DD1, one for the signal and one for the masker.

For measurements of the ratio of slopes in forward masking, the sinusoidal signal and masker were generated using two Farnell DSG1 signal generators, and were gated

using TDT SW2 gates. For all measurements, the levels of the signal and masker were controlled by TDT PA4 programmable attenuators, and signal and masker were mixed (TDT SM3) before being passed to a headphone buffer (TDT HB6), a final manual attenuator (Hatfield 2125), and one earpiece of a headphone. Most of the data were gathered using a Sennheiser HD414 earphone. However, the notched-noise masking data at 6 kHz were gathered using an Etymotic Research ER2 insert earphone, which gives a flatter response at the eardrum. Also, some of the psychophysical tuning curves for a signal frequency of 6 kHz were obtained using the ER2 earphone.

C. General procedure

Thresholds were measured using a two- or three-alternative forced-choice, three-down one-up procedure tracking the 79.4%-point on the psychometric function. A three-alternative procedure was used for measurements of notched-noise masking and PTCs. A two-alternative procedure was used for measurements of absolute threshold and forward masking (this was done for consistency with the previous work of Oxenham and Plack, 1997). Observation intervals were marked by lights on the response box and feedback was provided after each trial by a light indicating the correct interval. Twelve turnpoints were obtained in a given run, and the threshold estimate for that run was taken as the mean value of the levels at the last eight turnpoints. The step size was usually 5 dB up to the first four turnpoints, and 2 dB thereafter. At least two runs were obtained for each condition. When the thresholds for those two runs differed by more than 2 dB, at least one additional run was obtained.

D. Absolute thresholds

Absolute thresholds were initially measured using the above procedure, using sinusoidal stimuli with 200-ms steady-state and 10-ms raised-cosine rise/fall times. Sound levels were specified in dB SPL at the eardrum, using a previously obtained calibration of the HD414 earphones based on probe microphone measurements (Rastronics Portarem 2000 system) in ten ears. They were converted to thresholds in dB HL, using the values for the monaural absolute threshold at the eardrum specified in Moore *et al.* (1997).

E. Estimation of the values of HL_{OHC}

The estimates of the values of HL_{OHC} were taken from Moore and Glasberg (1997), who tested five subjects with highly asymmetric hearing loss, three of whom were tested in the present experiment. The HL_{OHC} estimates were based on loudness matches between the two ears of the subjects with highly asymmetric hearing loss, using sinusoidal stimuli covering a wide range of frequencies. The value of the parameter HL_{OHC} at each frequency was adjusted so that the loudness-matching functions predicted by the model fitted the data as closely as possible. In general, the steeper the loudness growth in a given ear at a given frequency, the greater the value of HL_{OHC} at that frequency. However, the loudness growth at a given frequency can be somewhat affected by the value of HL_{OHC} at other frequencies, as the model assumes that the overall loudness of a sound is related to the total area under the specific loudness pattern (Zwicker and Scharf, 1965). The values of HL_{OHC} were adjusted so as to give the best overall fit to the data, rather than to optimize the fit at any single frequency. To a first approximation, the value of HL_{OHC} at a given frequency can be regarded as a quantitative estimate of the amount of loudness recruitment at that frequency.

It should be noted that the values of HL_{OHC} could not be derived independently for the two ears of a given subject, as they were based on loudness matches between the two ears. Where there was a hearing loss in the better ear, it was assumed that the value of HL_{OHC} for that ear was 80% of the total hearing loss, which was argued by Moore and Glasberg (1997) to be a typical value for mild hearing losses (losses around 40 dB HL). The hearing losses in the better ear were usually small, and the value assumed for the better ear at a given frequency had only a small effect on the value fitted for the impaired ear of the same subject at that same frequency. The values of HL_{OHC} are given in Tables I–III. Estimates of HL_{OHC} were not available for the subjects with bilateral hearing loss (DT, AR, and VW).

F. Estimation of the ERB of the auditory filter using notched-noise masking

The ERB of the auditory filter was estimated using an abbreviated version of the notched-noise method (Patterson, 1976; Patterson and Nimmo-Smith, 1980; Glasberg and Moore, 1990) described by Stone *et al.* (1992). Thresholds for detecting a sinusoid with frequency f_c (2, 4, or 6 kHz) were measured in the presence of a masker with a spectral notch around f_c. The width of the notch was systematically varied. The notch was placed both symmetrically and asymmetrically about f_c. In practice, each masker actually consisted of two noise bands, one above and one below f_c, each with a bandwidth of $0.4f_c$. The deviation in frequency of the nearer edge of each noise band from f_c is expressed relative to f_c and denoted by Δ. Values of Δ for the lower and upper bands, respectively, were: 0 and 0; 0.2 and 0.2; 0.4 and 0.4; 0.2 and 0.4; 0.4 and 0.2. The spectrum level within the passband of each noise band was 50 dB (*re* 20 μPa).

On each trial, the noise was presented in three bursts, each with 10-ms raised-cosine rise/fall times and a 200-ms steady-state portion. The interval between bursts was 500 ms. The signal was presented synchronously with one of the noise bursts, chosen at random on each trial. The starting signal level was about 10 dB above the estimated masked threshold determined in pilot experiments.

The filter shapes were derived from the data using the method described by Patterson and Nimmo-Smith (1980) and later modified by Glasberg and Moore (1990). The auditory filter was assumed to have the form of the roex(p,r) filter described by Patterson *et al.* (1982)

$$W(g) = (1-r)(1+pg)\exp(-pg) + r, \tag{1}$$

where g is the normalized frequency deviation from the center of the filter (deviation from center frequency divided by center frequency), p is a parameter determining the slope of

the filter skirts, and r is a parameter that places a dynamic range limitation on the filter. The value of p was allowed to differ for the upper and lower halves of the filter. The upper and lower p values are called p_u and p_l, respectively. The value of r was assumed to be the same for the two sides of the filter. Thus, the filter shape was defined by three parameters. The fitting procedure works by finding the values of p_u, p_l, and r that give the best fit to the data; see Glasberg and Moore (1990) for details. These best-fitting values define the filter shape. The fitting procedure took into account the transfer function of the earphone (i.e., the sound level at the eardrum as a function of frequency for a fixed input voltage), and also the assumed transfer function through the middle ear; the middle-ear transfer function was as specified in Moore *et al.* (1997).

When the auditory filter is very broad, as it often is in hearing-impaired persons, the asymmetry of the auditory filter is not well defined by the data obtained using the abbreviated notched-noise method, although the bandwidth of the filter is reasonably well defined. Therefore, in the present paper we present only the ERBs of the auditory filters determined from the fitted values of the three parameters.

G. Estimation of the ratio of slopes

Growth-of-masking functions in forward masking were measured for three signal frequencies (2, 4, and 6 kHz), with a sinusoidal masker centered either at the signal frequency or one octave below it. Following Oxenham and Plack (1997), within a given run the signal level was fixed and the masker level was varied to determine the masked threshold. The fixed signal level ranged from about 10 dB above the absolute threshold to 90 or 95 dB SPL. The absolute threshold for the brief signal was initially measured using a two-alternative forced-choice procedure. The initial level of the masker was about 10 dB below the level needed to mask the signal, as estimated in pilot experiments. The masker was presented in two bursts with 100-ms steady-state portions, 2-ms raised-cosine rise/fall ramps, and 500-ms interburst interval. The signal was presented following one of the two bursts, selected randomly on each trial. Data were initially gathered using a signal with a raised-cosine envelope of total duration 4 ms, i.e., there were two 2-ms ramps, with no steady-state portion. The silent interval between the masker and signal was 2 ms. This signal duration was probably long enough to minimize audible spectral splatter at 4 and 6 kHz (Oxenham, 1997). However, we later became concerned that the results for the 2-kHz signal might have been influenced by spectral splatter. Hence, the conditions using the 2-kHz signal were rerun with a longer signal duration. The total signal duration was increased to 10 ms (two 5-ms ramps). The masker onset and offset ramps were also increased to 5 ms, and the masker–signal silent interval was decreased to 0 ms.

H. Psychophysical tuning curves

As mentioned earlier, psychophysical tuning curves (PTCs) were obtained mainly to check for the existence of ''dead regions'' where there are no functional IHCs or neurons. In such cases, the tip of the PTC should be shifted away from the signal frequency. The PTCs were determined in simultaneous masking, and the timing of the stimuli was exactly as described for the notched-noise masking experiment. The signal was a sinusoid presented 10 dB above the absolute threshold. The masker was an 80-Hz-wide noise band, generated using the same method as described for the notched-noise masker. A noise band was used as the masker rather than a sinusoid, to reduce the influence of beats on the results. The exact masker frequencies were chosen individually for each subject, so as to define the position of the tip of the tuning curve with reasonable accuracy. Owing to limitations in the availability of subject VF, it was not possible to obtain PTCs for her.

II. RESULTS

A. Psychophysical tuning curves

The results of the PTC measurements are described first, as the outcome of these affected the subsequent analyses. As mentioned above, the main point of the PTC measurements was to determine whether any of the subjects had dead regions corresponding to any of the signal frequencies. In the great majority of cases, the tips of the PTCs fell at or close to the signal frequency, providing no evidence for dead regions. However, there was one exception. For the worse ear of subject DF, the tuning curve for the signal frequency of 2000 Hz was rather flat, but showed a small minimum close to 4000 Hz. However, the results were also very variable, especially across sessions. It is likely that she had a dead region in the low to middle frequencies, although the exact boundary of this region was difficult to determine. In the figures and correlational analyses that follow, the results for the worse ear of DF for a signal frequency of 2000 Hz are excluded.

Generally, there was a reasonable correspondence between the sharpness of the PTCs and the ERBs of the auditory filters measured using notched-noise masking (see below). However, some of the PTCs showed irregularities around the tips, possibly reflecting cues based on temporal interactions of the signal and masker (Moore *et al.*, 1998). Hence, in the rest of this paper we concentrate on the ERB values, as we believe that these were less affected than the PTCs by factors such as off-frequency listening (Johnson-Davies and Patterson, 1979; O'Loughlin and Moore, 1981a, 1981b) and temporal interactions between the signal and masker.

B. ERB values

The ERB values are given in Tables I–III. They are expressed as a proportion of the center frequency. The ERB values are plotted as a function of the absolute thresholds in dB HL in Fig. 2. The solid symbols at the far left show the mean ERB values for normally hearing subjects as specified in Glasberg and Moore (1990); note that these were derived using a larger number of notch widths than for the present experiments. The ERB values for the ears tested in the present experiment are only slightly greater than normal for absolute thresholds up to 35 dB HL, but tend to increase above that. As has been found in earlier studies (Pick *et al.*,

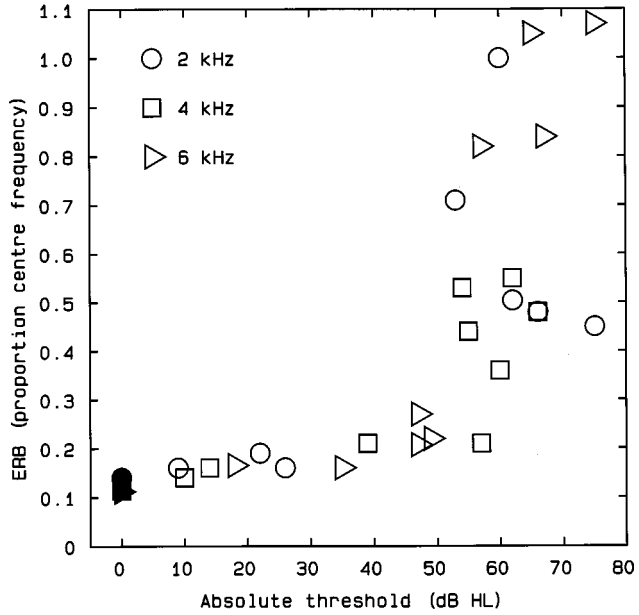

FIG. 2. The ERB of the auditory filter, expressed as a proportion of center frequency and plotted as a function of the absolute threshold in dB HL at the test frequency. Each symbol represents results for one frequency, as indicated in the figure. The solid symbols at the far left show mean ERBs for normally hearing subjects, given by Glasberg and Moore (1990).

1977; Glasberg and Moore, 1986; Laroche *et al.*, 1992; Moore, 1998), for absolute thresholds in the range 45–80 dB HL, the scatter in the ERB values is considerable. For example, in the range from 50 to 60 dB HL, the ERB values range from 0.21 to 1. Considering only cases where the absolute threshold was greater than 35 dB HL, roughly the hearing loss at which the ERB values start to increase, the (Pearson) correlation between the ERBs and the absolute thresholds is 0.58 ($n=19, p<0.01$).

Figure 3 shows the relationship between the ERBs and the values of HL_{OHC} (upper panel) or HL_{IHC} (lower panel). The former were estimated from the loudness-matching data of Moore and Glasberg (1997). The values of HL_{IHC} were obtained simply by subtracting the values of HL_{OHC} from the overall hearing loss at the same center frequency. For example, for a hearing loss of 55 dB at a specific frequency, if HL_{OHC} was 40 dB, then HL_{IHC} would be 15 dB. The ERB values tend to increase with increasing HL_{OHC}, as expected. Considering only cases where HL_{OHC} was greater than 25 dB HL, roughly the value at which the ERB values start to increase, the correlation between the ERBs and the values of HL_{OHC} is 0.75 ($n=11, p<0.01$). This correlation is higher than the correlation between the ERBs and the absolute thresholds, although the difference between the two correlations is not statistically significant according to the test described by Howell (1997); $z=0.72, p>0.05$. In contrast, the ERBs show no clear relationship to the values of HL_{IHC}. The correlation between these two quantities (excluding the mean results for the normal ears) is 0.38 ($n=18$, not significant). The correlation between the ERBs and the values of HL_{IHC} was not increased by excluding cases where HL_{IHC} was below a certain limit.

The results are consistent with our expectation that the ERB values would be more closely related to the values of

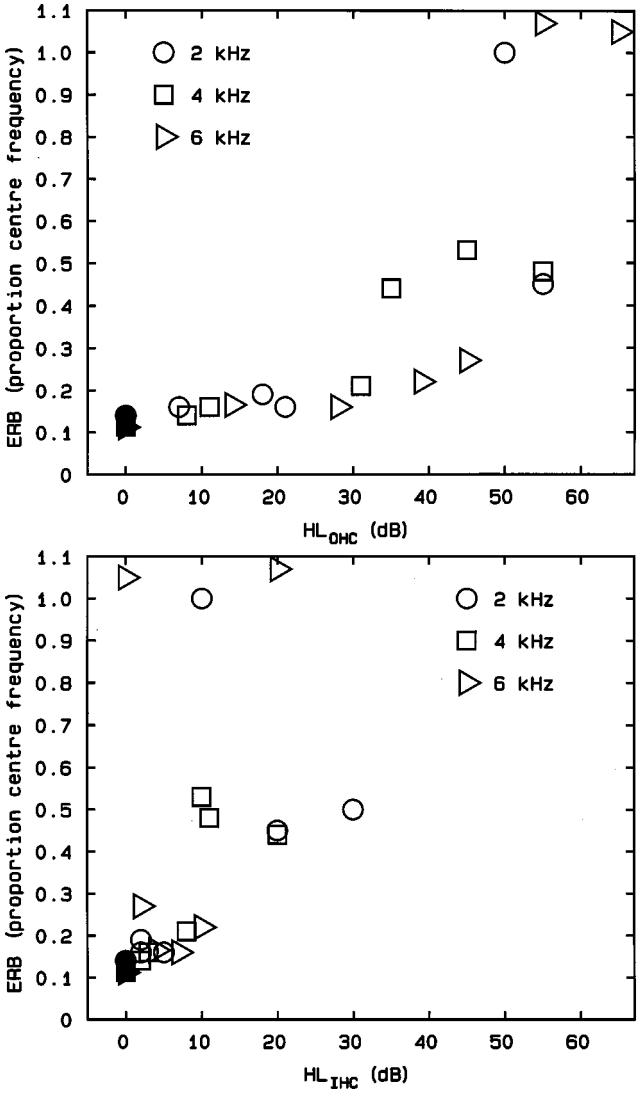

FIG. 3. The ERB of the auditory filter plotted as a function of HL_{OHC} (upper panel) or HL_{IHC} (lower panel).

HL_{OHC} than to the absolute thresholds, although the difference in correlation (ERB versus HL_{TOTAL} compared to ERB versus HL_{OHC}) failed to reach statistical significance. However, the ERB values plotted as a function of HL_{OHC} still show considerable scatter. This may reflect errors of measurement, especially in the estimates of HL_{OHC}. These were derived indirectly using the loudness model, based on loudness-matching data. Scatter in the original data was sometimes considerable, and this could easily have led to errors of 20% or so in the estimated values of HL_{OHC} ($\pm 20\%$ was the typical range of values of HL_{OHC} over which a reasonable fit to the data could be obtained).

C. Forward masking with on-frequency and off-frequency maskers

The individual results for the normally hearing subjects using the signal with 4-ms total duration are shown in Figs. 4 and 5. The masker level is plotted on the ordinate, because the masker level was varied to determine the threshold. For the on-frequency condition (masker frequency equals signal frequency—solid symbols), the masker level at threshold is

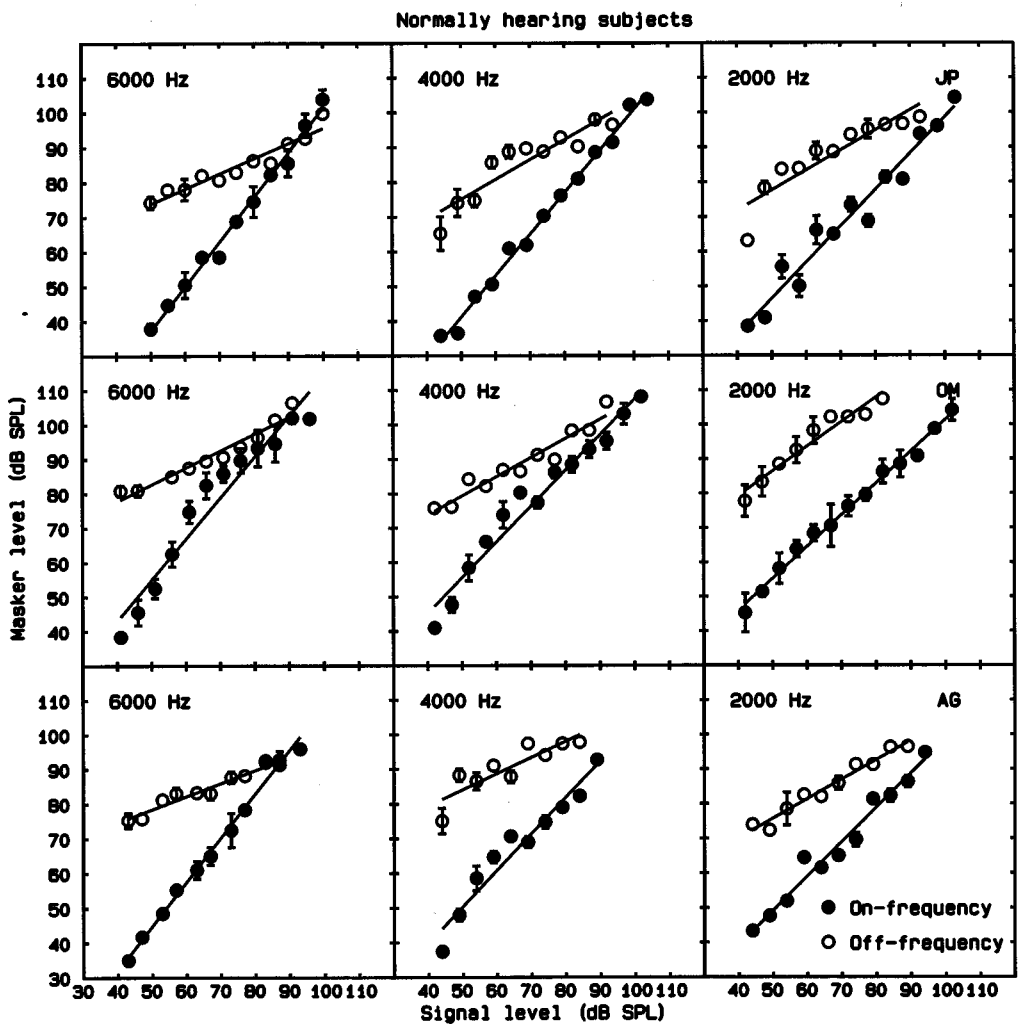

FIG. 4. Growth-of-masking functions in forward masking for normally hearing subjects JP, OM, and AG. The masker level required for threshold is plotted as a function of the signal level. Results for the on-frequency masker are shown by filled circles, and results for the off-frequency masker are shown by open circles. Each column shows results for one signal frequency and each row shows results for one subject. Error bars indicate ± one standard deviation across runs. Error bars are not shown where they would be smaller than the symbols.

usually roughly equal to the signal level, and the slopes of the fitted linear regression lines are close to unity. This is consistent with the data of Oxenham and Plack (Oxenham and Plack, 1997; Plack and Oxenham, 1998). Slopes close to unity have sometimes been taken as evidence for ''confusion'' of the signal with the masker (Moore and Glasberg, 1982, 1985; Neff, 1985, 1986). However, for our stimuli we believe it likely that the slopes close to unity reflect the short signal duration and brief masker–signal interval (which meant that the signal and masker levels were similar), rather than confusion. In fact, on average the slopes are slightly greater than unity, especially at 4000 and 6000 Hz; slope values are given later in Table IV. This means that the masker level required for threshold grows slightly more rapidly with increasing level than the signal level. For very low signal levels, approaching the absolute threshold, the functions sometimes become a little steeper, as expected. The lines were fitted to the data excluding the lowest data point (where the signal was only 10 dB above absolute threshold), but the slope values were almost the same when this point was included. The proportion of variance in the data accounted for by the fitted lines was between 0.79 and 0.996 (means 0.95, 0.90, and 0.95 at 2000, 4000, and 6000 Hz, respectively).

For the off-frequency maskers (one octave below the signal frequency—open circles), the functions have slopes markedly less than unity, especially for midrange levels. Again, this is consistent with the data of Oxenham and Plack (1997). However, for the 2000-Hz signal, the slopes are not always greatly different for the on-frequency and off-frequency maskers; see, for example, the results of subjects OM, DV, and RK. As mentioned earlier, we suspected that the results at 2000 Hz might have been influenced by spectral splatter. Splatter could affect the results in two ways. First, the spectrum of the 4-ms 2000-Hz signal contained energy at frequencies well above 2000 Hz. When the signal level was well above the absolute threshold, the level of the 1000-Hz masker needed to mask this splatter might have been greater than the level needed to mask the energy centered around 2000 Hz. Second, spectral splatter produced by the 2-ms offset ramp of the masker might have had a mask-

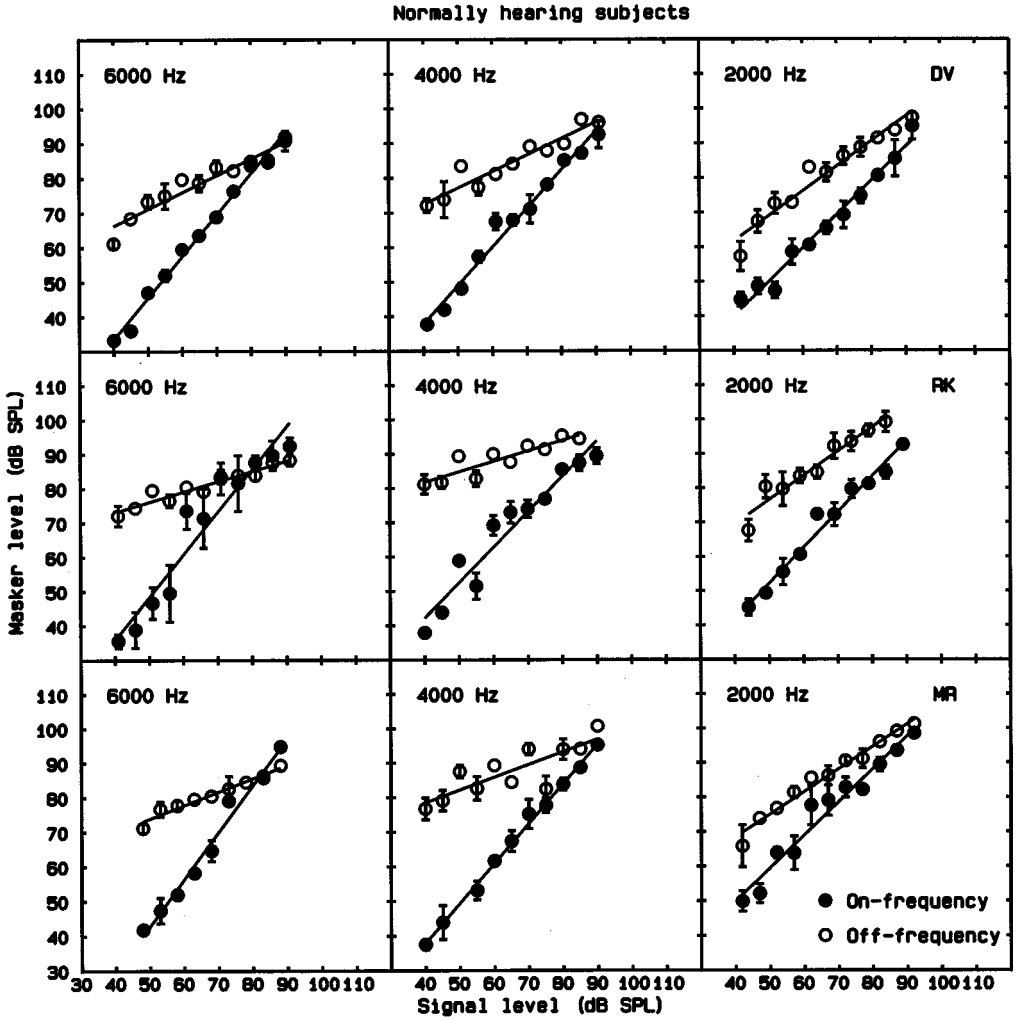

FIG. 5. As Fig. 4, but for normally hearing subjects DV, RK, and MR.

ing effect, reducing the masker level needed to mask the signal.

Figure 6 compares the results for the 2000-Hz signal with 4-ms total duration (2-ms ramps) and the 2000-Hz signal with 10-ms duration (5-ms ramps). Recall that the masker–signal interval was 2 ms for the former and 0 ms for the latter. Also, the offset ramp of the masker had a duration of 2 ms for the former and 5 ms for the latter. The proportion of variance in the data accounted for by the fitted lines for the longer signal duration was between 0.96 and 0.99 (mean 0.97). For the on-frequency masker, the masker level required at threshold was somewhat higher for the longer signal, as expected, but the slopes of the growth-of-masking functions were only slightly affected by the signal duration. The mean slope across the six subjects (standard deviation across subjects in parentheses) was 0.99 (0.047) for the 4-ms signal and 1.11 (0.084) for the 10-ms signal. The small increase is consistent with earlier work on the effect of signal duration or delay in forward masking, except that the earlier work usually measured signal threshold as a function of masker level, so the slope decreased with increasing duration or delay (Weber and Green, 1978; Jesteadt *et al.*, 1982; Moore, 1981; Moore and Glasberg, 1983).

For the off-frequency masker, the slope was sometimes markedly less for the 10-ms signal than for the 4-ms signal. This was especially true for subjects DV and RK. The main effect of the change in timing was that the masker level at threshold increased markedly for the longer signal. This is probably explicable in terms of two factors. The first is the normal ''decay of masking'' that occurs in forward masking as the signal duration is increased. The second is connected with the fact that the masker offset ramp had a longer duration for the longer signal. This longer offset ramp would have produced less spectral splatter, making it much less likely that the splatter produced at the masker offset would have a significant masking effect. As the masking would then have been determined by the on-frequency energy in the masker, the masker level at threshold had to be increased.

Since it seems likely that the results at 2000 Hz were affected by spectral splatter for the 4-ms signal but were not (or were affected much less) for the 10-ms signal, the results for the latter will be used in further analyses. Linear regression lines were fitted to the growth-of-masking functions for the off-frequency masker, excluding the lowest data point, for which the signal level would have been only 10 dB above the absolute threshold. The slopes and slope ratios of the

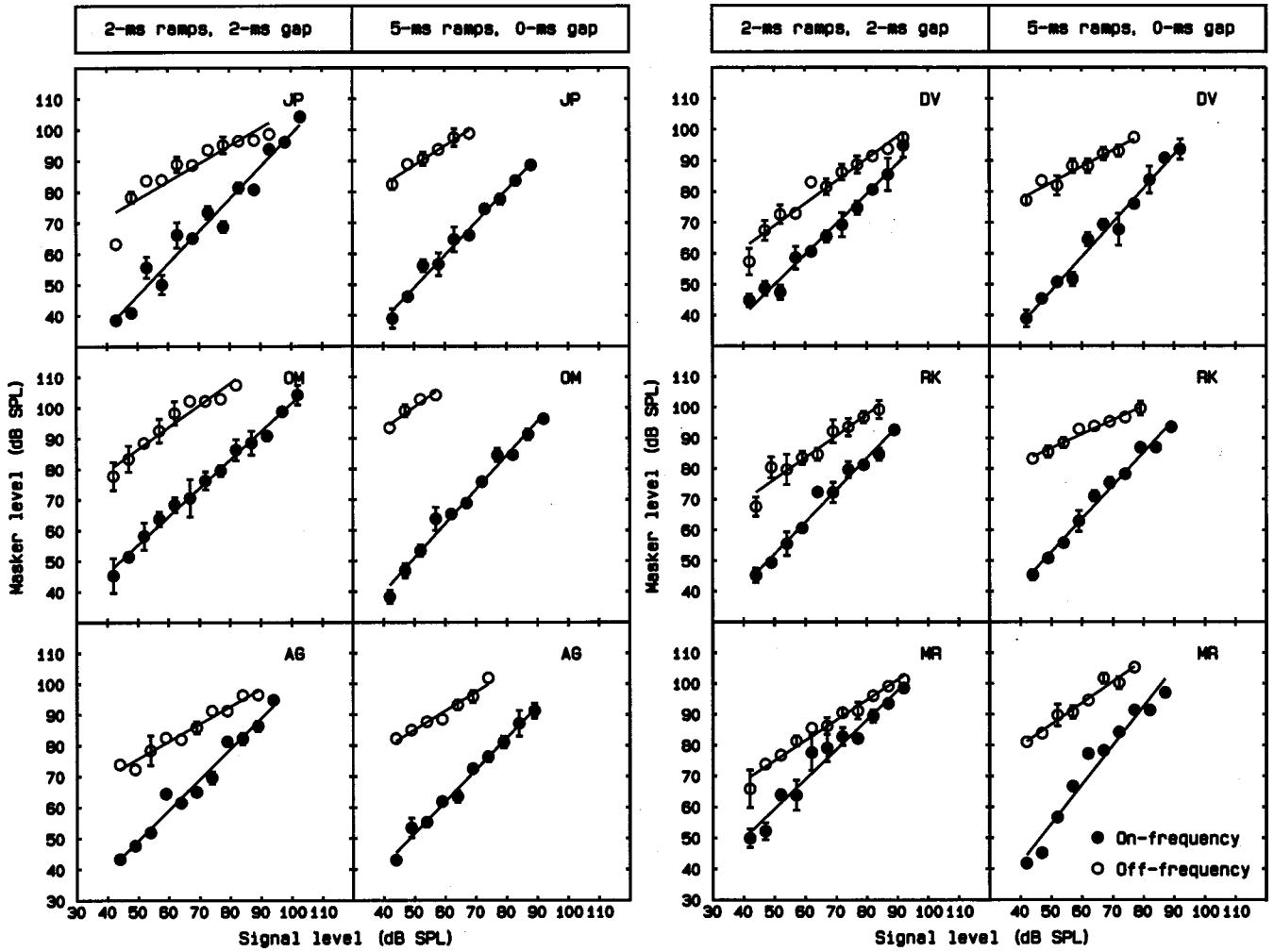

FIG. 6. Comparison of growth-of-masking functions in forward masking for two temporal configurations of the masker and signal; the configuration is indicated at the top of each column. Results are shown for six normally hearing subjects. The signal frequency was 2 kHz.

lines fitted to the growth-of-masking functions are shown in Table IV. Following the convention used by Oxenham and Plack (1997), the ratios are expressed as the slope for the off-frequency masker divided by the slope for the on-frequency masker. Thus, smaller numbers indicate more basilar-membrane compression. For example, a ratio of 0.3 means that the basilar-membrane response at CF grows by about 3 dB for each 10-dB increase in signal level.

The slope ratios at 6000 Hz are slightly larger than those found by Oxenham and Plack (1997). However, they estimated the slopes of the growth-of-masking functions only for signal levels between 50 and 80 dB SPL. Fitting our data in the same way resulted in slope ratios close to theirs. Their ratios may be regarded as estimates of the slope of the basilar membrane input–output function over the range where the compression is maximal. Our ratios indicate the slope of the input–output function averaged over a somewhat wider intensity range.

The slope ratios increase with decreasing frequency, which is consistent with physiological and psychoacoustical measurements indicating less basilar-membrane compression at lower frequencies (Yates, 1990, 1995; Neely, 1993; Rhode and Cooper, 1996; Hicks and Bacon, 1999). However, Oxenham and Plack (1997) also measured growth-of-masking functions for a 2000-Hz signal, but only for the off-frequency masker. They found somewhat shallower growth-of-masking functions than reported here, consistent with

TABLE IV. Slopes and slope ratios of the growth-of-masking functions in forward masking for the normally hearing subjects (first six rows), for the mean of the normally hearing subjects, and for the better ears of the subjects with asymmetric hearing loss.

	Frequency								
	6000 Hz			4000 Hz			2000 Hz		
Subject	On	Off	Ratio	On	Off	Ratio	On	Off	Ratio
JP	1.28	0.43	0.34	1.19	0.57	0.48	1.06	0.64	0.60
OM	1.18	0.49	0.41	1.12	0.60	0.53	1.12	0.72	0.64
AG	1.27	0.37	0.29	1.21	0.67	0.55	1.03	0.62	0.60
DV	1.19	0.48	0.40	1.11	0.47	0.42	1.10	0.52	0.47
RK	1.24	0.30	0.24	1.03	0.30	0.29	1.08	0.46	0.43
MR	1.36	0.39	0.29	1.15	0.37	0.32	1.27	0.69	0.54
Mean	1.25	0.41	0.33	1.14	0.50	0.42	1.11	0.61	0.55
AW	1.52	0.69	0.45	1.26	0.76	0.60	1.34	0.51	0.38
DF	1.07	0.60	0.55	1.28	0.70	0.55	1.18	0.50	0.42
VF	1.47	0.41	0.28	1.39	0.47	0.34	0.99	0.64	0.65

similar midlevel compression at 2000 and 6000 Hz. A possible factor contributing to the difference between the two studies was their use of a high-pass background noise. This was designed to prevent off-frequency listening. In our experiments, when the masker frequency was below the signal frequency, the signal might have been detected mainly using a region of the basilar membrane with CF somewhat above the signal frequency. The response of such a region would be less compressive than for the CF region. Also, as pointed out by Oxenham and Plack (1997), the results for the off-frequency masker when the signal frequency was 2000 Hz may have been influenced by the acoustic reflex. At high masker levels, the reflex was probably activated, and it would have attenuated the 1000-Hz masker more than the 2000-Hz signal. As a result, the masker level required for threshold would have increased. This effect would be absent for lower masker levels, so the overall effect would be a steeper growth-of-masking function. Thus, the slope ratios at 2000 Hz may underestimate the true amount of basilar-membrane compression.

For some subjects (e.g., JP, RK, and MR), the growth-of-masking functions for the on-frequency masker at 6000 Hz lay above those for the off-frequency masker, for masker levels above 90 dB SPL. In other words, the on-frequency masker had to be higher in level than the off-frequency masker to achieve a given amount of masking. It should be noted, however, that the levels plotted in Figs. 4–6 are nominal levels, assuming that the earphones produced equal eardrum sound levels at all frequencies for a given input voltage. This was not, in fact, the case. The Sennheiser HD414 earphones are designed to have a ''diffuse field'' response, and the frequency response measured at the eardrum shows a 10–12-dB peak for frequencies around 3000 Hz. Thus, the effective level of the off-frequency masker would have been about 10–12 dB higher than the nominal level plotted in the figures. Allowing for this, the growth-of-masking functions for the off-frequency and on-frequency maskers would not actually cross over, but they would converge at very high levels, consistent with an almost low-pass characteristic of basilar-membrane filtering at very high levels (Ruggero *et al.*, 1997).

Due to limited availability of the hearing-impaired subjects, it was not possible to test them at 2000 Hz with the longer signal duration. However, we feel that the results for the impaired ears were unlikely to be affected by spectral splatter, owing to the reduced frequency selectivity and reduced dynamic range associated with cochlear hearing loss. The results for the better ears of the subjects with unilateral or highly asymmetric hearing losses are shown in Fig. 7; slope values are given in Table IV. The proportion of variance in the data accounted for by the fitted lines was between 0.59 and 0.996 (means 0.92, 0.89, and 0.95 at 2000, 4000, and 6000 Hz, respectively). The results resemble those for the normally hearing subjects in general form. Even though the results at 2000 Hz were obtained with the shorter signal, there are still substantial slope differences between the on-frequency and off-frequency cases. The slope ratios are given in Tables I–IV. They mostly fall within the range of those for the normally hearing subjects (obtained with the longer signal at 2000 Hz), although, on average, the ratios are slightly larger, indicating less compression.

The results for the worse ears of the subjects with unilateral or highly asymmetric hearing losses are shown in Fig. 8. The proportion of variance in the data accounted for by the fitted lines was between 0.88 and 1.0 (means 0.95, 0.93, and 0.94 at 2000, 4000, and 6000 Hz, respectively). The results cover a much smaller range of levels than for the normal ears, as the subjects had only a limited dynamic range. The lowest signal level used was usually 10 dB above the absolute threshold for the signal, and the highest signal level was chosen so that the masker level did not exceed the uncomfortable loudness level. This limited range of levels made it more difficult to determine the slopes of the growth-of-masking functions accurately. Nevertheless, it is clear that the slopes for the off-frequency maskers are generally steeper than those found for the better ears of the same subjects or for the normally hearing subjects. The slopes for the on-frequency maskers, however, are close to unity, similar to those for the normally hearing subjects. Thus, the slope ratios, shown in Tables I–III, are markedly greater than for the better ears of the same subjects or for the normally hearing subjects. These results are consistent with those of Oxenham and Plack (1997).

The results for the bilaterally hearing-impaired subjects are shown in Fig. 9. The proportion of variance in the data accounted for by the fitted lines was between 0.91 and 1.0 (means 0.99, 0.97, and 0.99 at 2000, 4000, and 6000 Hz, respectively). Again, in some cases it was only possible to obtain results over a very limited range of signal levels, making it difficult to estimate the slopes of the growth-of-masking functions, especially for the off-frequency masker. But, the general pattern of results is similar to that for the worse ears of the unilaterally impaired subjects; the slopes for the off-frequency maskers are not generally markedly smaller than those for the on-frequency maskers. The slope ratios are given in Tables I–III. Mostly, they are close to unity, indicating little or no compression. But, there is evidence of residual compression for subject AR at 6000 and 4000 Hz.

Figure 10 shows the slope ratios plotted as a function of the absolute threshold at the test frequency. Filled symbols show the mean results for the normally hearing subjects, while open symbols show the results for the subjects with unilateral or bilateral hearing impairment. There is a clear trend for the slope ratios to increase with increasing hearing loss, for losses above about 35 dB. The correlation between the slope ratios and the absolute thresholds, excluding cases where the absolute threshold was below 35 dB HI, was 0.56 ($n=17, p<0.02$). The relatively low correlation reflects the large scatter in the slope ratios for a given hearing loss, especially around 60 dB HL. This might happen because the absolute threshold is affected by both IHC and OHC loss, but the slope ratio is related mainly to the latter.

Figure 11 shows the slope ratios plotted as a function of HL_{OHC} (upper panel) and HL_{IHC} (lower panel). The slope ratios tend to increase with increasing HL_{OHC}, as expected. Considering only cases where HL_{OHC} was greater than 25 dB HL, roughly the value at which the ratios start to increase,

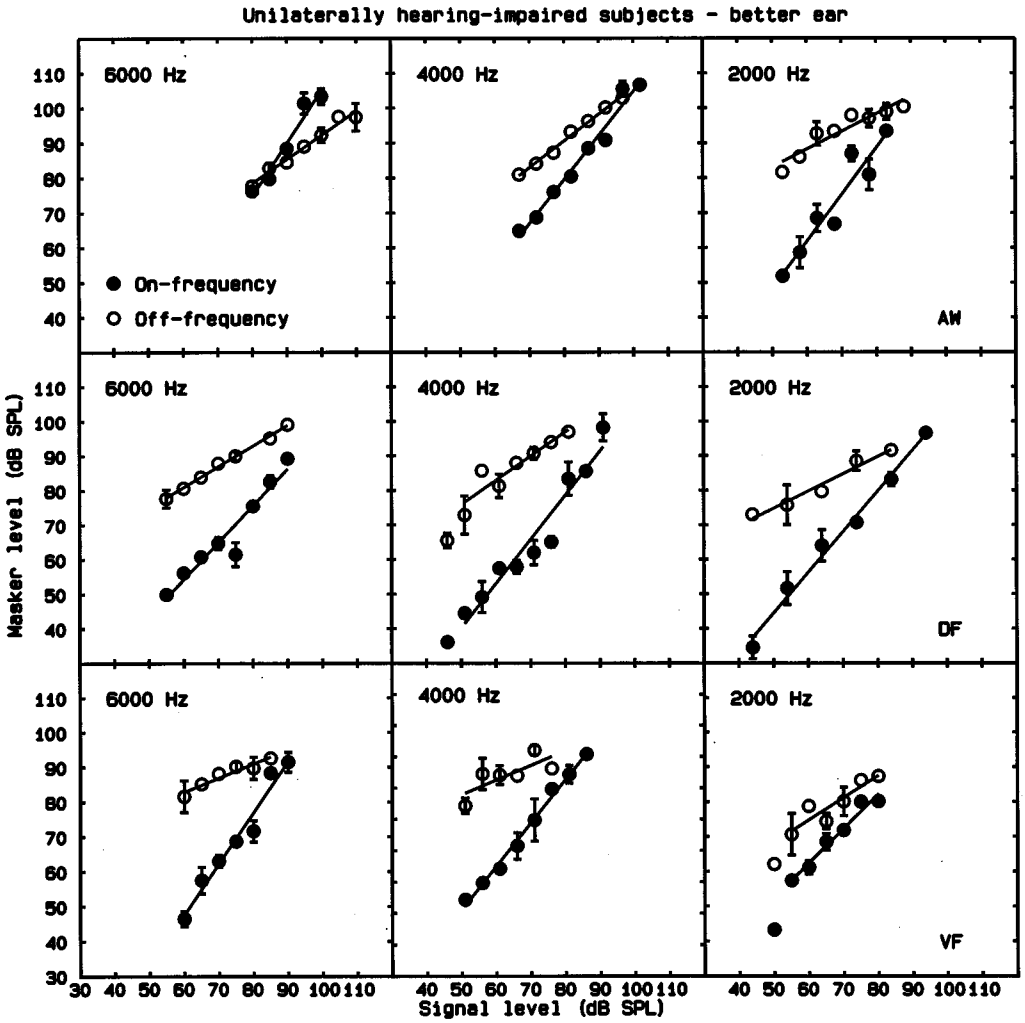

FIG. 7. As Fig. 4, but showing results for the better ears of three subjects with unilateral or highly asymmetric hearing loss.

the correlation between the slope ratios and the values of HL_{OHC} is 0.68 ($n=11, p=0.01$). This correlation is higher than the correlation between the HL_{OHC} values and the absolute thresholds, although the difference between the two correlations is not statistically significant according to the test described by Howell (1997); $z=0.46, p>0.05$. In contrast, the slope ratios show no clear relationship to the values of HL_{IHC}. The correlation between these two quantities (excluding the mean results for the normal ears) is 0.262 ($n=17$, not significant).

D. Relationship between the ERBs and the slope ratios

Figure 12 shows the relationship between the ERBs and the slope ratios. The solid symbols show the mean results for the normally hearing subjects, while open symbols show the results for the subjects with unilateral or bilateral hearing impairment. The two quantities are clearly closely related. The correlation (excluding the mean results for the normally hearing subjects) is 0.92 ($n=24, p<0.001$). It is interesting that the correlation between the ERBs and the slope ratios is higher than the correlation between the ERBs and the values of HL_{OHC}, although the difference between the two correlations fails to reach the 5% significance level, according to the test described by Howell (1997) ($z=1.54, p=0.1$). The correlation between the ERBs and the slope ratios is also higher than the correlation between the slope ratios and the values of HL_{OHC} and this difference is marginally significant ($z=1.88, p=0.06$). We also applied a test of the significance of the difference between two correlations described by Williams (1959). This test is applicable when comparing two correlations where one of the quantities is common to the two correlations. For example, when comparing the correlation of the slope ratio with the ERB and the correlation of HL_{OHC} with the ERB, the ERB values are common to the two. The test requires that equal numbers of samples contribute to each correlation, so we applied the test to the data for both ears of the unilaterally impaired subjects (the only ones for whom HL_{OHC} estimates were available), but excluding the data for the worse ear of DF at 2 kHz. The correlation of the slope ratio with the ERB, 0.952, was significantly higher than the correlation of the slope ratio with HL_{OHC}, 0.776 ($t=3.05, p<0.005$). In addition, the correlation of the slope ratio with the ERB was significantly higher than the correlation of the ERB with HL_{OHC}, 0.785 ($t=2.85, p<0.01$).

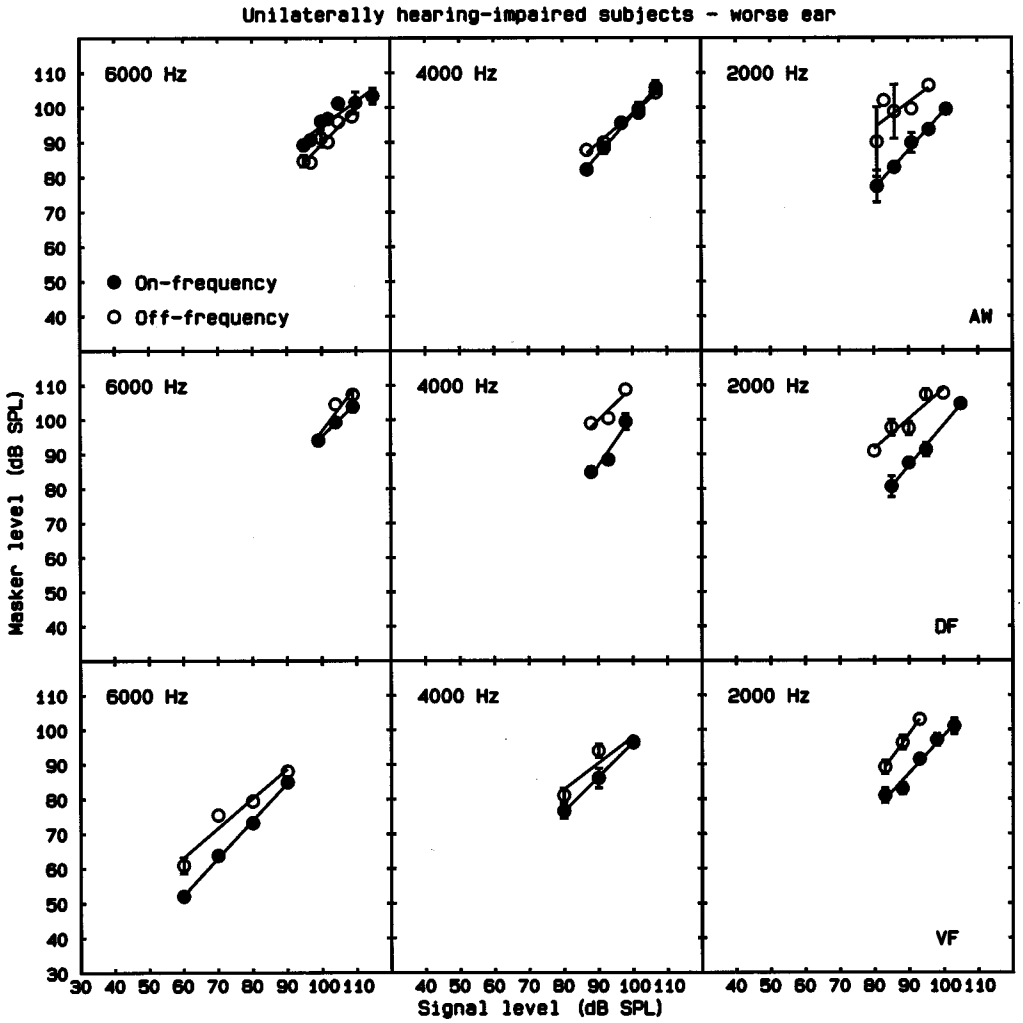

FIG. 8. As Fig. 4, but showing results for the worse ears of three subjects with unilateral or highly asymmetric hearing loss.

III. DISCUSSION

The experiments described in this study, together with the loudness-matching results of Moore and Glasberg (1997), provide three independently derived measures (the ERB, the value of HL_{OHC} and the slope ratio) that are significantly correlated with each other across different frequencies and hearing-impaired listeners. The correlation between the ERB and the slope ratio is particularly high (0.92). In contrast, the correlations between the absolute threshold and either the ERB (0.58) or the slope ratio (0.56) are considerably lower. These differences in correlation are significant, according to the test described by Howell (1997): for the former, $z=2.94$, $p<0.005$; for the latter, $z=2.85$, $p<0.005$. These findings are consistent with the ideas outlined in the Introduction, namely that cochlear hearing loss comprises at least two components, each with effects on hearing that are to a certain extent separable. The first component may be ascribed to the functioning of the cochlear active mechanism; damage to the OHCs reduces the level-dependent and frequency-selective gain of this mechanism. This would be expected to lead not only to elevated thresholds, but would also affect the ERB, the slope ratio, and loudness recruitment (estimated by parameter HL_{OHC}). The high correlation found between the ERB and the slope ratio is consistent with the idea that both reflect this first component. The second component may reflect damage to the IHCs, and hence a reduction in transduction efficiency. While this component could increase absolute thresholds, it would not be expected to affect frequency selectivity (as estimated by the ERB) or compression at CF (as estimated by the slope ratio). Thus, the lower correlation between overall hearing loss and either the ERB or the slope ratio may be due to the overall hearing loss being affected by both components, while the ERB and the slope ratio are only affected by the first component.

The correlations between the parameter HL_{OHC} and either the ERB (0.75) or the slope ratio (0.68) are both significant, but are nonetheless lower than the correlation between the ERB and slope ratio (0.92). As discussed above, this may be due to errors in estimating HL_{OHC}. In addition, HL_{OHC} is derived from loudness judgments. The function relating sound intensity to loudness is complex and may be determined by many factors beyond the initial acoustic to mechanical transduction in the cochlea. Moore and Glasberg (1997), following Launer (1995; Launer *et al.*, 1997), assumed that hearing loss due to inner hair-cell damage, represented by the quantity HL_{IHC}, could be modeled as a level-independent attenuation of the excitation level. This may be an oversimplification. For instance, damaged IHCs might re-

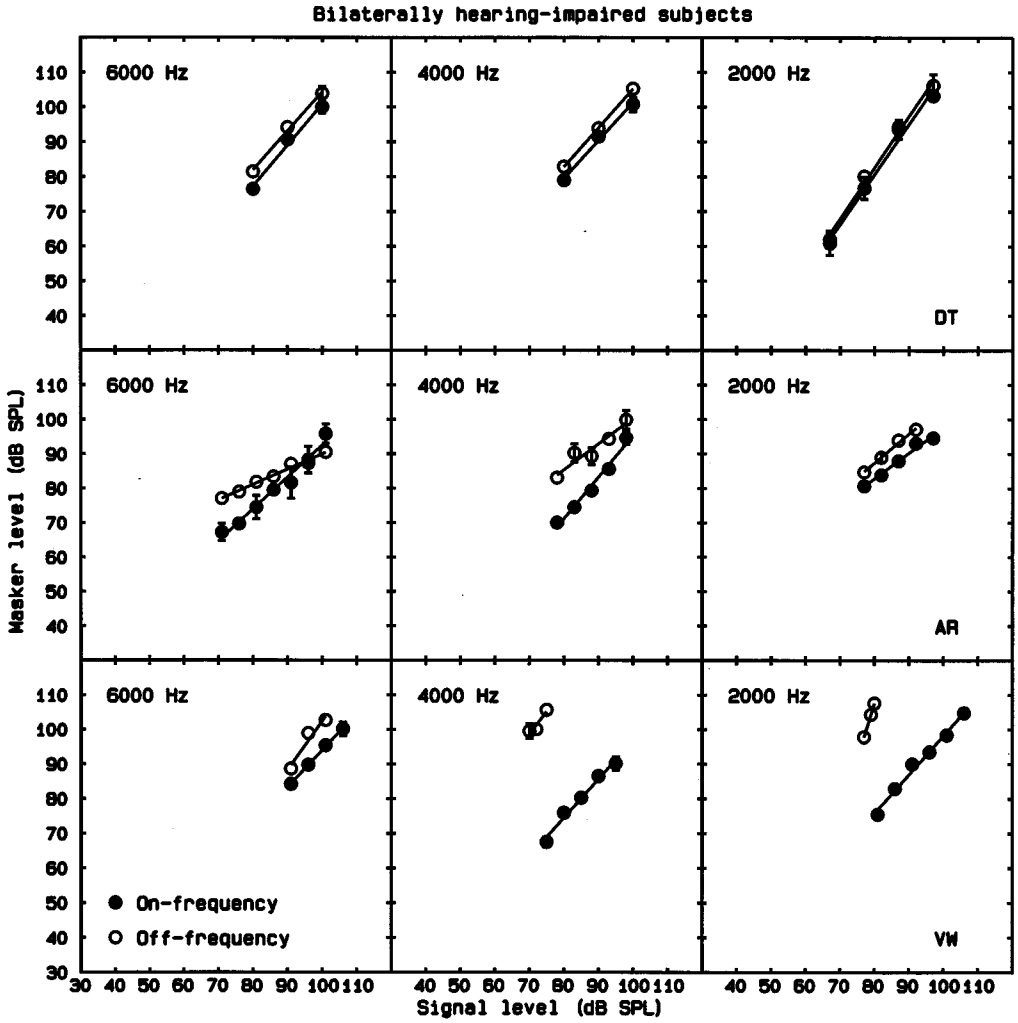

FIG. 9. As Fig. 4, but showing results for the better ears of three subjects with bilateral hearing loss.

spond very weakly to low-level stimulation, but respond nearly normally to high-level stimulation. This would elevate absolute thresholds, but might not affect loudness at high levels. The result would be something akin to loudness recruitment, but it would not be expected to lead to reduced frequency selectivity or reduced BM compression. Thus, there exists the possibility for a dissociation of the amount of loudness recruitment and the ERB or the slope ratio, which is not accounted for in the two-component model of cochlear hearing loss. In summary, while the ERB and the slope ratio should not be affected by IHC damage, it is at least conceivable that loudness recruitment may be, to some extent. This may explain the somewhat lower correlations associated with HL_{OHC}.

Psychoacoustic measures associated with basilar-membrane compression may well have clinical applications. For example, complete loss of basilar-membrane compression would probably be associated with strong loudness recruitment and a limited dynamic range, indicating the need for a hearing aid incorporating some form of automatic gain control or compression. While loudness recruitment can be measured clinically, using subjective loudness judgments (Pascoe, 1978; Hellbrück and Moser, 1985; Allen and Jeng, 1990; Kiessling *et al.*, 1993; Cox *et al.*, 1997), there is controversy about the validity and reliability of these procedures (Elberling, 1999). Estimates of loudness obtained by numerical ratings or categorical ratings can be strongly influenced by factors such as the range of stimuli used and the instructions given (Heller, 1991; Hellbrück, 1993; Hohmann, 1993). Often, listeners distribute their responses across the range of available categories whatever range of stimulus levels is used (Garner, 1954). Even for normal listeners, the variability of loudness judgments for a given sound level can be considerable (Elberling and Nielsen, 1993; Kiessling, 1997; Elberling, 1999). Given the uncertainty about the validity and reliability of loudness scaling procedures, it might be preferable to use a more objective measure of basilar-membrane compression, such as the ratio of slopes estimated in forward masking, or the ERB of the auditory filter estimated using notched-noise masking. In a clinical setting, it would not be necessary to measure the growth-of-masking functions using a large number of signal levels, as was done in the present experiment. Rather, reasonably accurate slope estimates could be obtained using just two signal levels, one 10 dB above and one 30 dB above the absolute threshold. In our experiments, it was always possible to use a signal at 30 dB above the absolute threshold without the masker becom-

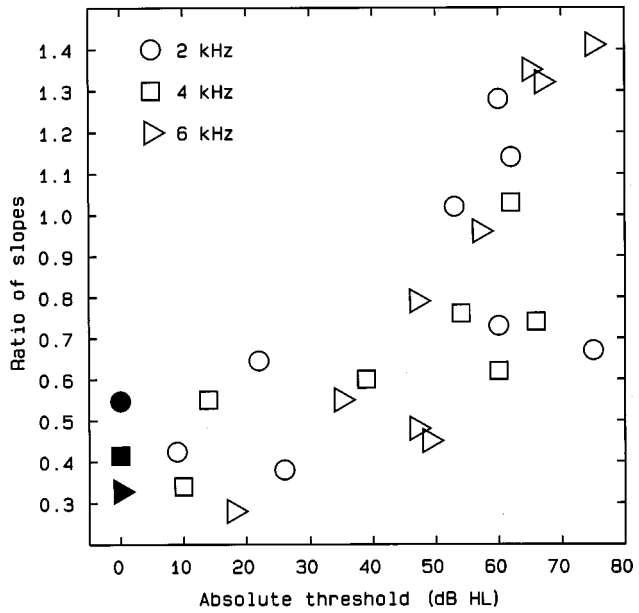

FIG. 10. Ratio of the slopes of the growth-of-masking functions in forward masking, plotted as a function of absolute threshold in dB HL at the test frequency. Each symbol represents results for one frequency, as indicated in the figure. The solid symbols at the far left show the mean ratios for the six normally hearing subjects. Small numbers indicate strong basilar-membrane compression, while numbers around 1 indicate little or no compression.

ing uncomfortably loud, although this might not be possible in cases of severe to profound hearing loss.

Another clinical application is in the estimation of inner hair-cell damage. There is evidence that inner hair-cell damage is associated with particular difficulty in understanding speech, especially when background noise is present (Killion, 1997; Hogan and Turner, 1998; Moore, 1998). Hearing-impaired persons with extensive inner hair-cell damage over a certain range of CFs may receive little or no benefit from amplification in that frequency range (Murray and Byrne, 1986; Hogan and Turner, 1998). Inner hair-cell damage could be estimated indirectly by estimating the hearing loss due to outer hair-cell damage from the ratio of slopes, and then subtracting that estimate from the overall loss. However, further work is needed to determine whether such an approach would be useful in clinical practice.

IV. SUMMARY AND CONCLUSIONS

We have examined the relationship between three different measures of the status of the cochlear active mechanism, at center frequencies of 2, 4, and 6 kHz, using subjects with normal hearing, with unilateral or highly asymmetric cochlear hearing loss, and with bilateral loss. The first measure, HL_{OHC}, was an indirect measure of the amount of the hearing loss attributable to OHC damage; this was based on loudness matches between the two ears of subjects with unilateral hearing loss and was derived using a loudness model. The steeper the rate of loudness growth in a given ear at a given frequency, the greater the estimate of HL_{OHC}. The second measure was the ERB of the auditory filter, which was estimated using the notched-noise method. The third measure was based on the ratios of the slopes of growth-of-masking functions obtained in forward masking for off-frequency and on-frequency maskers; small ratios indicate strong compression. The results show the following:

(1) For the hearing-impaired subjects, the ERB of the auditory filter was correlated with the absolute threshold at the test frequency ($r=0.58$ for hearing losses greater than 35 dB), but it was more highly correlated with HL_{OHC} ($r=0.75$ for values of HL_{OHC} greater than 25 dB). However, the difference between the two correlations failed to reach statistical significance. The ERB was not significantly correlated with HL_{IHC}, the estimated amount of the hearing loss attributable to inner hair-cell damage ($r=0.38$).

(2) For normally hearing subjects, the ratio of slopes in forward masking had mean values of 0.33, 0.42, and 0.55 at 6, 4, and 2 kHz, respectively. This may indicate that basilar-membrane compression decreases with decreasing frequency. However, the results at 2 kHz may have been affected by activation of the acoustic reflex which would tend to increase the ratio of slopes.

(3) For the subjects with hearing impairment, the ratio of

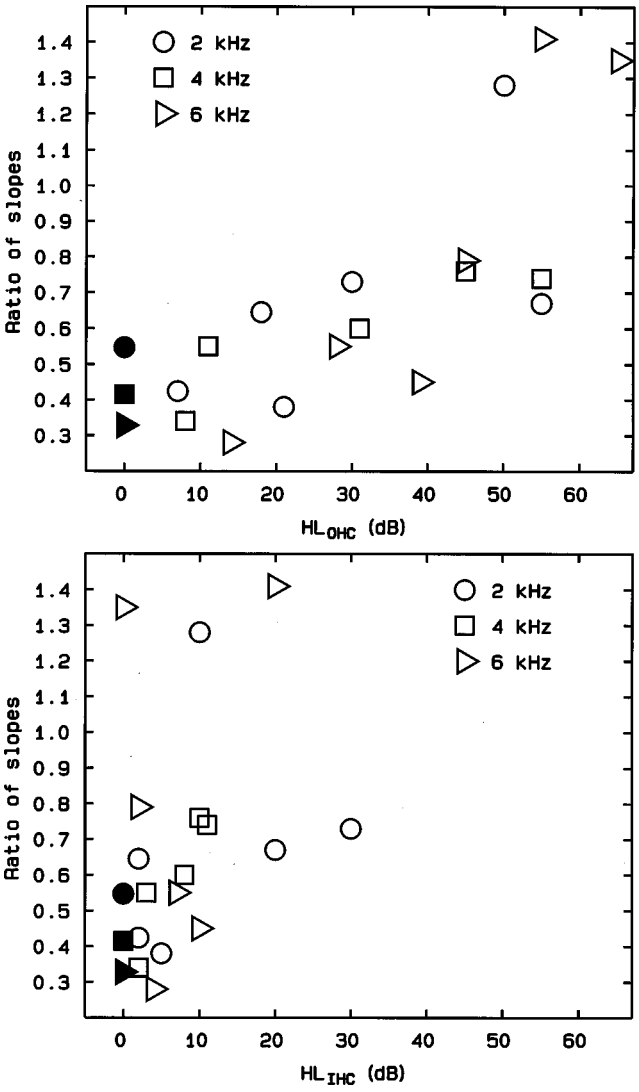

FIG. 11. Ratio of the slopes of the growth-of-masking functions in forward masking, plotted as a function of HL_{OHC} (upper panel) or HL_{IHC} (lower panel).

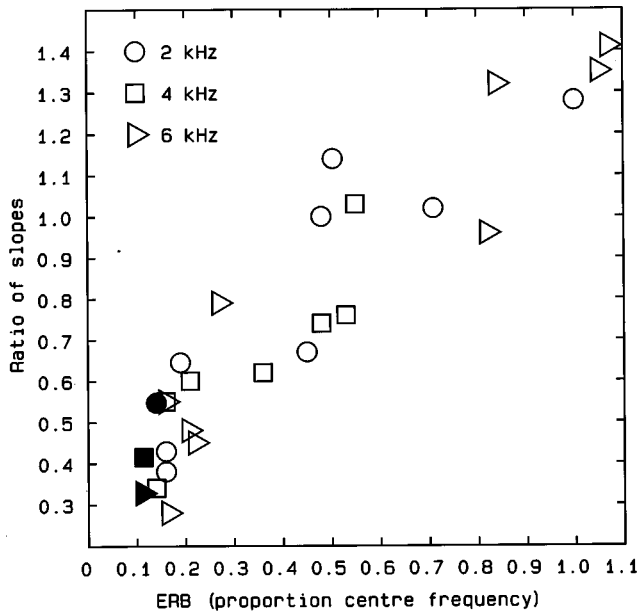

FIG. 12. Ratio of the slopes of the growth-of-masking functions in forward masking, plotted as a function of the ERB of the auditory filter. Each symbol represents results for one frequency, as indicated in the figure. The solid symbols at the far left show the mean ratios for the six normally hearing subjects, plotted as a function of the ERB values for normally hearing subjects given by Glasberg and Moore (1990).

slopes in forward masking was correlated with the absolute threshold at the test frequency ($r=0.56$ for hearing losses greater than 35 dB), but it was more highly correlated with HL_{OHC} ($r=0.68$ for values of HL_{OHC} greater than 25 dB). However, the difference between the two correlations failed to reach statistical significance. The ratio of slopes was not significantly correlated with HL_{IHC} ($r=0.26$).

(4) The ERB of the auditory filter was highly correlated with the ratio of slopes ($r=0.92$). This suggests that both of these measures give a reasonably direct measure of the status of the active mechanism at a given CF. The sharpness of tuning declines progressively as the amount of basilar-membrane compression decreases.

ACKNOWLEDGMENTS

This work was supported by the Medical Research Council (UK). Chris Plack is supported by the Royal Society and Andrew Oxenham is supported by the NIH (Grant Number R03 DC03628). We thank Brian Glasberg for assistance with several aspects of this work. We also thank Sid Bacon and two anonymous reviewers for helpful comments on an earlier version of this paper.

Allen, J. B., and Jeng, P. S. (**1990**). ''Loudness growth in 1/2-octave bands (LGOB); a procedure for the assessment of loudness,'' J. Acoust. Soc. Am. **88**, 745–753.

Bonding, P. (**1979**). ''Critical bandwidth in loudness summation in sensorineural hearing loss,'' Br. J. Audiol. **13**, 23–30.

Bonding, P., and Elberling, C. (**1980**). ''Loudness summation across frequency under masking and in sensorineural hearing loss,'' Audiology **19**, 57–74.

Borg, E., Canlon, B., and Engström, B. (**1995**). ''Noise-induced hearing loss—Literature review and experiments in rabbits,'' Scand. Audiol. **24**, Suppl. 40, 1–147.

Chistovich, L. A. (**1957**). ''Frequency characteristics of masking effect,'' Biophys. J. **2**, 743–755.

Cox, R. M., Alexander, G. C., Taylor, I. M., and Gray, G. A. (**1997**). ''The contour test of loudness perception,'' Ear Hear. **18**, 388–400.

Elberling, C. (**1999**). ''Loudness scaling revisited,'' J. Am. Acad. Audiol **10**, 248–260.

Elberling, C., and Nielsen, C. (**1993**). ''The dynamics of speech and the auditory dynamic range in sensorineural hearing impairment,'' in *Recent Developments in Hearing Instrument Technology*, edited by J. Beilin and G. R. Jensen (Stougaard Jensen, Copenhagen).

Evans, E. F. (**1975**). ''The sharpening of frequency selectivity in the normal and abnormal cochlea,'' Audiology **14**, 419–442.

Evans, E. F., and Harrison, R. V. (**1976**). ''Correlation between outer hair cell damage and deterioration of cochlear nerve tuning properties in the guinea pig,'' J. Physiol. (London) **252**, 43–44.

Evans, E. F., Pratt, S. R., and Cooper, N. P. (**1989**). ''Correspondence between behavioural and physiological frequency selectivity in the guinea pig,'' Br. J. Audiol. **23**, 151–152.

Fletcher, H. (**1940**). ''Auditory patterns,'' Rev. Mod. Phys. **12**, 47–65.

Florentine, M., and Houtsma, A. J. M. (**1983**). ''Tuning curves and pitch matches in a listener with a unilateral, low-frequency hearing loss,'' J. Acoust. Soc. Am. **73**, 961–965.

Florentine, M., and Zwicker, E. (**1979**). ''A model of loudness summation applied to noise-induced hearing loss,'' Hearing Res. **1**, 121–132.

Fowler, E. P. (**1936**). ''A method for the early detection of otosclerosis,'' Arch. Otolaryngol. **24**, 731–741.

Garner, W. R. (**1954**). ''Context effects and the validity of loudness scales,'' J. Exp. Psychol. **48**, 218–224.

Glasberg, B. R., and Moore, B. C. J. (**1986**). ''Auditory filter shapes in subjects with unilateral and bilateral cochlear impairments,'' J. Acoust. Soc. Am. **79**, 1020–1033.

Glasberg, B. R., and Moore, B. C. J. (**1990**). ''Derivation of auditory filter shapes from notched-noise data,'' Hearing Res. **47**, 103–138.

Hellbrück, J. (**1993**). *Hören* (Hogrefe Verlag, Göttingen).

Hellbrück, J., and Moser, L. M. (**1985**). ''Hörgeräte Audiometrie: Ein computer-unterstütztes psychologisches Verfahren zur Hörgeräteanpassung,'' Psychol. Beitr. **27**, 494–509.

Heller, O. (**1991**). ''Oriented category scaling of loudness and speech audiometric validation,'' in *Contributions to Psychological Acoustics*, edited by A. Schick (BIS, Oldenburg).

Hellman, R. P. (**1978**). ''Dependence of loudness growth on skirts of excitation patterns,'' J. Acoust. Soc. Am. **63**, 1114–1119.

Hellman, R. P., and Meiselman, C. H. (**1986**). ''Is high-frequency hearing necessary for normal loudness growth at low frequencies?,'' 12th ICA Paper B11-5.

Hellman, R. P., and Meiselman, C. H. (**1990**). ''Loudness relations for individual and groups in normal and impaired hearing,'' J. Acoust. Soc. Am. **88**, 2596–2606.

Hellman, R. P., and Meiselman, C. H. (**1993**). ''Rate of loudness growth for pure tones in normal and impaired hearing,'' J. Acoust. Soc. Am. **93**, 966–975.

Hicks, M. L., and Bacon, S. P. (**1999**). ''Psychophysical measures of auditory nonlinearities as a function of frequency in individuals with normal hearing,'' J. Acoust. Soc. Am. **105**, 326–338.

Hogan, C. A., and Turner, C. W. (**1998**). ''High-frequency audibility: Benefits for hearing-impaired listeners,'' J. Acoust. Soc. Am. **104**, 432–441.

Hohmann, V. (**1993**). *Dynamikkompression für Hörgeräte-Psychoakustische Grundlagen und Algorithmen* (VDI-Verlag, Düsseldorf).

Howell, D. C. (**1997**). *Statistical Methods for Psychology*, 4th ed. (Duxbury, Belmont, CA).

Jesteadt, W., Bacon, S. P., and Lehman, J. R. (**1982**). ''Forward masking as a function of frequency, masker level, and signal delay,'' J. Acoust. Soc. Am. **71**, 950–962.

Johnson-Davies, D., and Patterson, R. D. (**1979**). ''Psychophysical tuning curves: restricting the listening band to the signal region,'' J. Acoust. Soc. Am. **65**, 675–770.

Khanna, S. M., and Leonard, D. G. B. (**1982**). ''Basilar membrane tuning in the cat cochlea,'' Science **215**, 305–306.

Kiang, N. Y. S., Moxon, E. C., and Levine, R. A. (**1970**). ''Auditory nerve activity in cats with normal and abnormal cochleas,'' in *Sensorineural Hearing Loss*, edited by G. E. W. Wolstenholme and J. J. Knight (Churchill, London).

Kiessling, J. (**1997**). ''Scaling methods for the selection, fitting and evaluation of hearing aids,'' in *Psychoacoustics, Speech and Hearing Aids*, edited by B. Kollmeier (World Scientific, Singapore).
Kiessling, J., Steffens, T., and Wagner, I. (**1993**). ''Untersuchungen zur praktischen Anwendbarkeit der Lautheitsskalierung,'' Audi. Akust. **4/93**, 100–115.
Killion, M. C. (**1997**). ''Hearing aids: Past, present and future: Moving toward normal conversations in noise,'' Br. J. Audiol. **31**, 141–148.
Laroche, C., Hétu, R., Quoc, H. T., Josserand, B., and Glasberg, B. (**1992**). ''Frequency selectivity in workers with noise-induced hearing loss,'' Hearing Res. **64**, 61–72.
Launer, S. (**1995**). ''Loudness perception in listeners with sensorineural hearing impairment,'' Ph.D. thesis, Oldenburg, Germany.
Launer, S., Hohmann, V., and Kollmeier, B. (**1997**). ''Modeling loudness growth and loudness summation in hearing-impaired listeners,'' in *Modeling Sensorineural Hearing Loss*, edited by W. Jesteadt (Erlbaum, Mahwah, NJ).
Leshowitz, B., Linstrom, R., and Zurek, P. (**1975**). ''Psychophysical tuning curves in normal and impaired ears,'' J. Acoust. Soc. Am. **58**, S71.
Liberman, M. C., and Dodds, L. W. (**1984**). ''Single neuron labeling and chronic cochlea pathology. III. Stereocilia damage and alterations in threshold tuning curves,'' Hearing Res. **16**, 54–74.
Liberman, M. C., Dodds, L. W., and Learson, D. A. (**1986**). ''Structure-function correlation in noise-damaged ears: A light and electron-microscopic study,'' in *Basic and Applied Aspects of Noise-Induced Hearing Loss*, edited by R. J. Salvi, D. Henderson, R. P. Hamernik, and V. Colletti (Plenum, New York).
Moore, B. C. J. (**1978**). ''Psychophysical tuning curves measured in simultaneous and forward masking,'' J. Acoust. Soc. Am. **63**, 524–532.
Moore, B. C. J. (**1981**). ''Interactions of masker bandwidth with signal duration and delay in forward masking,'' J. Acoust. Soc. Am. **70**, 62–68.
Moore, B. C. J. (**1986**). ''Parallels between frequency selectivity measured psychophysically and in cochlear mechanics,'' Scand. Audiol. Suppl. **25**, 139–152.
Moore, B. C. J. (**1998**). *Cochlear Hearing Loss* (Whurr, London).
Moore, B. C. J., Alcántara, J. I., and Dau, T. (**1998**). ''Masking patterns for sinusoidal and narrowband noise maskers,'' J. Acoust. Soc. Am. **104**, 1023–1038.
Moore, B. C. J., and Glasberg, B. R. (**1982**). ''Contralateral and ipsilateral cueing in forward masking,'' J. Acoust. Soc. Am. **71**, 942–945.
Moore, B. C. J., and Glasberg, B. R. (**1983**). ''Growth of forward masking for sinusoidal and noise maskers as a function of signal delay: implications for suppression in noise,'' J. Acoust. Soc. Am. **73**, 1249–1259.
Moore, B. C. J., and Glasberg, B. R. (**1985**). ''The danger of using narrowband noise maskers to measure suppression,'' J. Acoust. Soc. Am. **77**, 2137–2141.
Moore, B. C. J., and Glasberg, B. R. (**1997**). ''A model of loudness perception applied to cochlear hearing loss,'' Aud. Neurosci. **3**, 289–311.
Moore, B. C. J., Glasberg, B. R., and Baer, T. (**1997**). ''A model for the prediction of thresholds, loudness and partial loudness,'' J. Audio Eng. Soc. **45**, 224–240.
Moore, B. C. J., Glasberg, B. R., Hess, R. F., and Birchall, J. P. (**1985**). ''Effects of flanking noise bands on the rate of growth of loudness of tones in normal and recruiting ears,'' J. Acoust. Soc. Am. **77**, 1505–1515.
Moore, B. C. J., Glasberg, B. R., and Vickers, D. A. (**1999**). ''Further evaluation of a model of loudness perception applied to cochlear hearing loss,'' J. Acoust. Soc. Am. **106**, 898–907.
Moore, B. C. J., and Oxenham, A. J. (**1998**). ''Psychoacoustic consequences of compression in the peripheral auditory system,'' Psychol. Rev. **105**, 108–124.
Murray, N., and Byrne, D. (**1986**). ''Performance of hearing-impaired and normal hearing listeners with various high-frequency cut-offs in hearing aids,'' Aust. J. Audiol. **8**, 21–28.
Neely, S. T. (**1993**). ''A model of cochlear mechanics with outer hair cell motility,'' J. Acoust. Soc. Am. **94**, 137–146.
Neff, D. L. (**1985**). ''Stimulus parameters governing confusion effects in forward masking,'' J. Acoust. Soc. Am. **78**, 1966–1976.
Neff, D. L. (**1986**). ''Confusion effects with sinusoidal and narrowband-noise forward maskers,'' J. Acoust. Soc. Am. **79**, 1519–1529.
O'Loughlin, B. J., and Moore, B. C. J. (**1981a**). ''Improving psychoacoustical tuning curves,'' Hearing Res. **5**, 343–346.
O'Loughlin, B. J., and Moore, B. C. J. (**1981b**). ''Off-frequency listening: effects on psychoacoustical tuning curves obtained in simultaneous and forward masking,'' J. Acoust. Soc. Am. **69**, 1119–1125.
Oxenham, A. J. (**1997**). ''Increment and decrement detection in sinusoids as a measure of temporal resolution,'' J. Acoust. Soc. Am. **102**, 1779–1790.
Oxenham, A. J., and Moore, B. C. J. (**1994**). ''Modeling the additivity of nonsimultaneous masking,'' Hearing Res. **80**, 105–118.
Oxenham, A. J., and Moore, B. C. J. (**1995**). ''Additivity of masking in normally hearing and hearing-impaired subjects,'' J. Acoust. Soc. Am. **98**, 1921–1935.
Oxenham, A. J., and Moore, B. C. J. (**1997**). ''Modeling the effects of peripheral nonlinearity in listeners with normal and impaired hearing,'' in *Modeling Sensorineural Hearing Loss*, edited by W. Jesteadt (Erlbaum, Mahwah, New Jersey).
Oxenham, A. J., and Plack, C. J. (**1997**). ''A behavioral measure of basilar-membrane nonlinearity in listeners with normal and impaired hearing,'' J. Acoust. Soc. Am. **101**, 3666–3675.
Pascoe, D. P. (**1978**). ''An approach to hearing aid selection,'' Hearing Inst. **29**, 12–16.
Patterson, R. D. (**1976**). ''Auditory filter shapes derived with noise stimuli,'' J. Acoust. Soc. Am. **59**, 640–654.
Patterson, R. D., and Nimmo-Smith, I. (**1980**). ''Off-frequency listening and auditory filter asymmetry,'' J. Acoust. Soc. Am. **67**, 229–245.
Patterson, R. D., Nimmo-Smith, I., Weber, D. L., and Milroy, R. (**1982**). ''The deterioration of hearing with age: frequency selectivity, the critical ratio, the audiogram, and speech threshold,'' J. Acoust. Soc. Am. **72**, 1788–1803.
Patuzzi, R. B. (**1992**). ''Effects of noise on auditory nerve fiber response,'' in *Noise Induced Hearing Loss*, edited by A. Dancer, D. Henderson, R. Salvi, and R. Hamernik (Mosby Year Book, St. Louis).
Pick, G., Evans, E. F., and Wilson, J. P. (**1977**). ''Frequency resolution in patients with hearing loss of cochlear origin,'' in *Psychophysics and Physiology of Hearing*, edited by E. F. Evans and J. P. Wilson (Academic, London).
Pickles, J. O. (**1986**). ''The neurophysiological basis of frequency selectivity,'' in *Frequency Selectivity in Hearing*, edited by B. C. J. Moore (Academic, London).
Plack, C. J., and Oxenham, A. J. (**1998**). ''Basilar-membrane nonlinearity and the growth of forward masking,'' J. Acoust. Soc. Am. **103**, 1598–1608.
Rhode, W. S. (**1971**). ''Observations of the vibration of the basilar membrane in squirrel monkeys using the Mössbauer technique,'' J. Acoust. Soc. Am. **49**, 1218–1231.
Rhode, W. S., and Cooper, N. P. (**1996**). ''Nonlinear mechanics in the apical turn of the chinchilla cochlea *in vivo*,'' Aud. Neurosci. **3**, 101–121.
Robles, L., Ruggero, M. A., and Rich, N. C. (**1986**). ''Basilar membrane mechanics at the base of the chinchilla cochlea. I. Input–output functions, tuning curves, and response phases,'' J. Acoust. Soc. Am. **80**, 1364–1374.
Ruggero, M. A., and Rich, N. C. (**1991**). ''Furosemide alters organ of Corti mechanics: Evidence for feedback of outer hair cells upon the basilar membrane,'' J. Neurosci. **11**, 1057–1067.
Ruggero, M. A., Rich, N. C., Recio, A., Narayan, S. S., and Robles, L. (**1997**). ''Basilar-membrane responses to tones at the base of the chinchilla cochlea,'' J. Acoust. Soc. Am. **101**, 2151–2163.
Ruggero, M. A., Rich, N. C., Robles, L., and Recio, A. (**1996**). ''The effects of acoustic trauma, other cochlea injury and death on basilar membrane responses to sound,'' in *Scientific Basis of Noise-Induced Hearing Loss*, edited by A. Axelsson, H. Borchgrevink, R. P. Hamernik, P. A. Hellstrom, D. Henderson, and R. J. Salvi (Thieme, Stockholm).
Sellick, P. M., Patuzzi, R., and Johnstone, B. M. (**1982**). ''Measurement of basilar membrane motion in the guinea pig using the Mössbauer technique,'' J. Acoust. Soc. Am. **72**, 131–141.
Small, A. M. (**1959**). ''Pure-tone masking,'' J. Acoust. Soc. Am. **31**, 1619–1625.
Steinberg, J. C., and Gardner, M. B. (**1937**). ''The dependency of hearing impairment on sound intensity,'' J. Acoust. Soc. Am. **9**, 11–23.
Stone, M. A., Glasberg, B. R., and Moore, B. C. J. (**1992**). ''Simplified measurement of impaired auditory filter shapes using the notched-noise method,'' Br. J. Audiol. **26**, 329–334.
Thornton, A. R., and Abbas, P. J. (**1980**). ''Low-frequency hearing loss: perception of filtered speech, psychophysical tuning curves, and masking,'' J. Acoust. Soc. Am. **67**, 638–643.
Weber, D. L., and Green, D. M. (**1978**). ''Temporal factors and suppression effects in backward and forward masking,'' J. Acoust. Soc. Am. **64**, 1392–1399.
Williams, E. J. (**1959**). ''The comparison of regression variables,'' J. Royal. Stat. Soc. (B) **21**, 396–399.

Yates, G. K. (**1990**). ''Basilar membrane nonlinearity and its influence on auditory nerve rate-intensity functions,'' Hearing Res. **50**, 145–162.
Yates, G. K. (**1995**). ''Cochlear structure and function,'' in *Hearing*, edited by B. C. J. Moore (Academic, San Diego).
Zwicker, E., Flottorp, G., and Stevens, S. S. (**1957**). ''Critical bandwidth in loudness summation,'' J. Acoust. Soc. Am. **29**, 548–557.
Zwicker, E., and Scharf, B. (**1965**). ''A model of loudness summation,'' Psychol. Rev. **72**, 3–26.

Different auditory filter bandwidth estimates based on profile analysis, notched noise, and hybrid tasks

Jennifer J. Lentz
Department of Bioengineering, 120 Hayden Hall, Walnut Street, University of Pennsylvania, Philadelphia, Pennsylvania 19104

Virginia M. Richards and Matthew R. Matiasek
Department of Psychology, 3815 Walnut Street, University of Pennsylvania, Philadelphia, Pennsylvania 19104

(Received 17 September 1998; revised 9 April 1999; accepted 2 July 1999)

Auditory filter bandwidths were estimated in three experiments. The first experiment was a profile-analysis experiment. The stimuli were composed of sinusoidal components ranging in frequency from 200 to 5000 Hz. The standard stimulus was the sum of equal-amplitude tones, and the signal stimulus had a power spectrum that varied up–down...up–down. The number of components ranged from four to 60. Interval-by-interval level randomization prevented the change in level of a single component from reliably indicating the change from standard to signal. The second experiment was a notched-noise experiment in which the 1000-Hz tone to be detected was added to a noise with a notch arithmetically centered at 1000 Hz. Detection thresholds were estimated both in the presence of and in the absence of level randomization. In the third, hybrid, experiment a 1000-Hz tone was to be detected, and the masker was composed of equal-amplitude sinusoidal components ranging in frequency from 200 to 5000 Hz. For this experiment, thresholds were estimated both in the presence and absence of level variation. For both the notched-noise and hybrid experiments, only modest effects of level randomization were obtained. A variant of Durlach *et al.*'s channel model [''Towards a model for discrimination of broadband signals,'' J. Acoust. Soc. Am. **80**, 63–72 (1986)] was used to estimate auditory filter bandwidths for all three experiments. When a two-parameter roex(p,r) filter weighting function was used to fit the data, bandwidth estimates were approximately two to three times as large for the two detection tasks than for the profile-analysis task. © *1999 Acoustical Society of America.* [S0001-4966(99)01311-9]

PACS numbers: 43.66.Dc, 43.66.Ba [JWH]

INTRODUCTION

The first step in many models of auditory processing describes the frequency selectivity associated with the auditory system, represented as a bank of auditory filters. In order to estimate the auditory filter characteristics, a typical psychophysical experiment is one in which observers detect a tone added to a masker with a low-energy notch surrounding the frequency of the signal tone. By measuring detection thresholds for different notch bandwidths and applying the power spectrum model of masking to the resulting thresholds, characteristics of the auditory filter can be derived (see Patterson and Moore, 1986, for a review). As applied to notched-noise experiments, the power spectrum model of masking assumes that detection depends on increased power at a single frequency locus, or the output of a single auditory filter. Other types of psychophysical tasks, however, require that observers compare filter outputs across the whole of the frequency spectrum. For example, when sensitivity to changes in spectral shape is of interest, as in profile-analysis experiments (cf. Green, 1988), the overall levels of the stimuli are randomly chosen on each presentation to ensure that the level at the output of a *single* auditory filter cannot cue the change to be detected. For tasks such as these, the power spectrum model of masking does not account for the results, as it inherently describes single-channel processes. The linear channel model developed by Durlach *et al.* (1986) expands the power spectrum model of masking by providing an optimal decision rule for across-frequency comparisons of level.

Some preliminary modeling work in our lab has applied a variant of the Durlach *et al.* (1986) channel model to estimate auditory filter bandwidths using both profile-analysis data and notched-noise data taken from the literature (Patterson, 1976; Bernstein and Green, 1987; Richards and Lentz, 1998). The channel model was applied to the output of a bank of roex(p) filters. The simulations indicated that the filter bandwidth estimate depended on the data set modeled (Lentz, 1998). When applied to notched-noise data, the channel model (Durlach *et al.*, 1986) led to the same auditory filter bandwidth estimates as the power spectrum model of masking. This is not surprising, as notched-noise experiments do not have presentation-by-presentation level randomization, and therefore the channel model essentially degenerates into the power spectrum model of masking when it is applied to notched-noise data.[1] However, when the channel model was applied to profile-analysis data, much narrower auditory filter bandwidth estimates resulted.

In an effort to extend these preliminary modeling results, three experiments were run. The first is a profile-analysis experiment and essentially replicates the Richards and Lentz (1998; see also Dai and Green, 1993) experiment considered

in our preliminary modeling efforts. The standard stimulus was the sum of N equal-amplitude tones equispaced on a logarithmic frequency scale ranging from 200 to 5000 Hz. The signal stimulus was also composed of N tones and had a power spectrum that varied up–down...up–down. Presentation-by-presentation level randomization prevented the level at the output of a single auditory filter from cueing the difference between the standard and signal stimuli.

The second experiment was a notched-noise masking experiment. Observers detected a 1000-Hz tone added to a notched-noise masker. The notch bandwidth was parametrically altered. In two conditions, presentation-by-presentation level randomization was either present or absent. In the presence of level randomization, the level at the output of a single auditory filter cannot support detection unless detection thresholds are very high. If level variation has a negligible or only modest effect on thresholds, then the detection of a tone added to a notched-noise masker cannot be characterized using a single-channel energy model. Indeed, such a result might suggest that observers are depending on across-frequency comparisons in order to detect the added tone—that is, a profile-analysis approach for the detection of a tone added to notched-noise maskers would be suggested. Additionally, to the degree that internal noise is highly correlated across frequency (cf. Dai and Green, 1992), it is advantageous to incorporate multichannel comparisons so as to remove the common noise.[2] If small effects of level variation are measured, however, there are no guarantees that across-channel processing is incorporated; envelope-based models of detection which depend on the output of a single auditory filter are invariant with respect to level variation (e.g., Kidd *et al.*, 1989; Richards and Nekrich, 1993).

Based on preliminary modeling efforts, our expectation was that experiments I and II would lead to different auditory filter bandwidth estimates. Unlike our initial modeling work, however, such differences could not be attributed to differences in procedures and observers (which can be sizable, cf. Wright, 1996) that inevitably are present when one models data sets available in the literature. Nonetheless, there are several differences that might contribute to differences in auditory filter bandwidths estimates. First, notched-noise stimuli are spectrally dense, whereas profile-analysis stimuli have relatively sparse spectra (e.g., when the single-channel power spectrum model of masking is used, the auditory filter bandwidth estimate depends on stimulus level; Glasberg and Moore, 1990; Rosen and Baker, 1994). Thus, the filter estimates might be wider for the notched-noise experiments due to changes in spectral density. Second, for the profile-analysis experiment described in experiment I, the signal to be detected is a change in level distributed across frequency, whereas notched-noise experiments used tonal signals. Finally, the task demands for the detection of a tone added to a notched-noise masker vs the detection of changes in power spectra across frequency may be different. Commonly, it is assumed that the detection of a tone added to a notched-noise masker depends on the output of a *single* auditory filter. On the other hand, it seems reasonable to assume that sensitivity to changes in spectral shape depends on comparisons of level across the output of *multiple* filters. It might be the case that the frequency selectivity associated with these two tasks is in fact different. For example, the two tasks may tap distinct levels of auditory processing.

In an effort to examine the degree to which the three factors described above contribute to differences in auditory filter bandwidth estimates, a third experiment was introduced. Experiment III is a hybrid of experiments I and II. Observers detected a 1000-Hz tone, as in experiment II, but the masker was identical to the standard stimulus in experiment I. Thus, in this experiment the change to be detected, the addition of a tone, reflects a change at just one frequency, and the 1000-Hz signal tone is at the geometric center of the masker. For the multitone masker used in experiment III, there is no component at 1000 Hz, but as more masker components are introduced (N increases), the ''notch'' surrounding 1000 Hz narrows. In contrast to the notched-noise experiment, however, the masker is spectrally sparse. As in experiment II, presentation-by-presentation level randomization was either present or absent so as to determine whether single-channel energy cues contribute to the detection of the tone.

For each of the three experiments, auditory filter estimates were derived using a variant of the channel model of Durlach *et al.* (1986) and a bank of roex(p,r) filters. In our version of the channel model, the incoming sound is passed through a bank of filters, a zero-mean encoding noise is added at the output of each filter (using a dB scale), and then the resulting corrupted level estimates are processed optimally in the maximum likelihood sense. The current model includes a constant-Q assumption and a total of 41 filters ranging in frequency from 125 to 8000 Hz. The constant-Q assumption imposes severe limitations on both the modeling technique and the interpretation of the results, and this assumption is a critical one. Based on our preliminary work, however, our expectation was that the experiments would lead to very different bandwidth estimates depending on the task. Thus, only gross comparisons of auditory filter bandwidth estimates seemed necessary, and under those conditions, the limitations of the constant-Q assumption are somewhat ameliorated.

The channel model of Durlach *et al.* was chosen because it has been successful in accounting for profile-analysis data (Farrar *et al.*, 1987; Green, 1992; Lentz and Richards, 1997). Moreover, the channel model automatically incorporates interchannel correlation that occurs due to external level randomization and correlation in the excitation pattern that may occur due to overlapping auditory filters. When the channels are independent, the channel model and the multichannel model used by Florentine and Buus (1981) to describe intensity discrimination are the same. However, the channel model differs from the nonoptimal weighting model proposed by Moore and Sek (1994). This is noteworthy because Glasberg and Moore (1994) found the simple nonoptimal averaging model of Moore and Sek (1994) provided better fits to their masked detection data than the Florentine and Buus (1981) model. The current model contrasts with the one used by van der Heijden and Kohlrausch (1994), who used the outputs of a Glasberg and Moore (1990) filter bank to predict performance for a number of different masking

experiments. Rather than applying a multichannel integration model, van der Heijden and Kohlrausch used a decision rule which selected the single filter with the maximum target-to-masker ratio. This single-channel approach was adopted because they modeled data associated with narrow-band stimuli, whereas the current experiments and modeling efforts primarily emphasize wideband stimuli.

Consistent with our preliminary work, the results of experiments I and II led to different filter bandwidth estimates. If the auditory filter bandwidths estimates derived in the hybrid experiment (experiment III) are similar to those derived in the profile-analysis experiment (experiment I), it would suggest that differences in spectral density underlie the difference in auditory filter bandwidth estimates. Should this result hold, one must consider effects of stimulus level at each auditory filter in order to determine whether the change in level passed by a single auditory filter drives a shift in auditory filter bandwidth estimates. Alternatively, if estimates of auditory filter bandwidths for the hybrid experiment (experiment III) are more similar to those derived in the notched-noise experiment (experiment II), differences in spectral density are unlikely to account for the difference in estimates of frequency selectivity.

I. GENERAL PROCEDURES

First, a brief summary of the stimuli used for each experiment is given. Then, the procedures common to all experiments are presented. Additional details concerning the stimuli are included in the introduction for each experiment.

The stimuli used in the three experiments were as follows. The stimuli used in experiment I (profile analysis) were the sum of tones, equally spaced on a logarithmic scale and ranging in frequency from 200–5000 Hz. The standard stimulus had a flat spectrum, and the signal stimulus had every other component incremented or decremented in level. In experiment II (notched-noise), the masker consisted of two bandlimited noises separated by a notch arithmetically centered at 1000 Hz. A 1000-Hz signal tone was to be detected. Experiment III (hybrid) again involved the detection of a 1000-Hz signal tone, as in experiment II, but the masker was identical to the standard stimulus in experiment I.

A. Psychophysical methods

The three experiments used similar methods. The stimuli were digitally generated and presented through two channels of a 16-bit DAC using a sampling rate of 20 000 sample/s, low-pass filtered at 7 kHz (KEMO VBF 8; attenuation skirts approx. 85 dB/oct), and presented diotically by way of two channels of Sennheiser HD410SL headphones. When level variation was applied, the overall level of each stimulus was chosen at random from a uniform distribution with a 30-dB range using a 0.1-dB gradation. Signal levels were adjusted and level variation was applied using programmable attenuators (TDT PA4). The stimulus durations were 100 ms, including 5-ms raised cosine onset/offset ramps. When a tonal signal was to be detected, the signal was gated on and off with the masker. The interstimulus interval was approximately 330 ms.

A two-interval forced choice (2IFC) procedure was used, with the signal interval being as likely to be the first as the second interval. Visual feedback indicated the correctness of each response. Thresholds were estimated using a 3-down, 1-up staircase procedure which estimated the 79-percent-correct performance level (Levitt, 1971). Initial signal levels were approximately 10 dB above the ultimate threshold estimates. The initial step size was 4 dB and reduced to 2 dB following three reversals. The last even number of reversals, excluding at least the first two, was used to estimate threshold. Each threshold estimate was generated using blocks of 50 trials. For each data point, at least 15 threshold estimates were obtained. If observers demonstrated practice effects in any condition, five or more additional threshold estimates were obtained. The last ten threshold estimates were averaged to form the final threshold estimate.

Two observers (Obs 1 and 2) first finished the conditions in which level variation was absent, and two observers (Obs 3 and 4) first finished the conditions in which level variation was present. This ordering was chosen to allow a comparison of effects of level variation for observers that either did or did not have past experience in conditions in which energy cues were unreliable. No long-term effects were noted. Within these constraints, the experiments were completed in quasirandom order such that no two observers completed the experiments in the same order. Observers practiced on a variety of the conditions for at least 5 h prior to starting the first condition tested. At that point, and when a new experiment was introduced, observers practiced at least 1–2 h on several of the conditions. In addition, prior to beginning the profile-analysis experiment, observers practiced a minimum of 5 h.

Absolute thresholds also were measured for each observer. The procedure was identical to the notched-noise experiment without level randomization, except that the masker was not presented. The results indicate that all masked thresholds measured in experiments II and III are at least 8 dB above absolute threshold.

Observers ranged in age from 18 to 28 years and had thresholds in quiet of 10 dB HL or better (for frequencies ranging from 250 to 8000 Hz). One of the four observers had prior experience in psychoacoustic tasks. Tests were conducted with the observer seated in a double-walled sound-attenuated booth.

B. Modeling methods

1. Multichannel model

The model consists of two components, a bank of auditory filters followed by the channel model (Durlach *et al.*, 1986). Here, the channel model is implemented as using only across-frequency comparisons of level. The channel model is essentially a pattern discrimination model—in this case, signal and standard excitation patterns are discriminated. The model takes into account the differences in level in each channel, the magnitude of the variance in each channel, the correlation across channels, and yields an estimate of d', the index of detectability.

The auditory filter weighting functions are those associated with the linearly symmetric rounded-exponential or

roex(p,r) function: $W(g)=(1-r)(1+pg)e^{-pg}+r$, where g is normalized frequency (e.g., $|frequency-f_c|/f_c$), p is the slope parameter associated with the filter, and r is an asymptote parameter. Larger values of p are associated with steeper filter skirts, and so filters with narrower bandwidths. Because a constant-Q assumption is used here, the parameter p provides an estimate of the auditory filter bandwidths at all filter center frequencies. The r also was fixed across all filters.

The channel model was applied by means of a partial grid search using the parameters $\langle p,r,\sigma\rangle$. The first two parameters, p and r, are associated with the filter bank. The experimental stimuli were passed through the bank of filters to generate the excitation patterns. When the level at a filter's output (in dB SPL) was below the threshold of audibility for the filter's center frequency, the output level was set to the corresponding audibility threshold (minimum audible pressure, MAP, curves reported by Glasberg and Moore, 1990). Then, the level in dB at the output of each filter was corrupted by a deviate drawn independently from a Gaussian distribution with a mean of zero and a variance σ^2, where σ^2 is the variance of the ''channel'' or ''encoding'' noise. The magnitude of σ is estimated simultaneously with p and r. One thousand different estimates of the noisy representations of the filtered standard and signal stimuli were generated using different draws of channel noise and randomly chosen overall stimulus levels, as appropriate for each experiment. This allowed an estimate of the covariance matrix and an average difference vector, Δ in dB (each element of the vector is the mean change in level, filtered signal minus filtered standard, ΔL in dB). The number of filters was fixed at 41, meaning that the covariance matrix was a 41×41 matrix, and the difference vector had 41 elements. Then, d' was estimated using the equation $d'^2=\Delta\mathbf{G}\Delta^T$, where $\mathbf{G}$ is the inverse of the covariance matrix, and T signifies transpose (e.g., van Trees, 1968).

For each $\langle p,r,\sigma\rangle$, nine signal levels that led to d' values ranging from approximately 0.5 to 2 were tested. A linear least-squares fit to the resulting predicted psychometric function was used to estimate threshold. The proportion of variance accounted for in the data (thresholds across number of tones, across notch bandwidths, etc.) was computed, and the $\langle p,r,\sigma\rangle$ that maximized the proportion of variance accounted for was determined.

This multichannel model employed 41 filters with center frequencies equally spaced on a logarithmic frequency axis ranging from 125–8000 Hz. Spot checks indicated that fewer than or more than 41 filters led to similar bandwidth estimates. Thus, the use of 41 filters appeared appropriate because the number is not so small that the filter bandwidth estimates depended on the density of filters, yet small enough that the simulations were completed in a timely manner. It should be noted that the number of filters and the magnitude of σ trade to some degree. That is, increases in the number of filters are offset by increases in σ. Thus, the value of σ has little meaning in absolute terms. For example, imagine that a model with 61 rather than 41 filters was used to model the data. For the two models to generate equal thresholds, the 61-filter model will require larger channel noise than the 41-filter model because the 61-filter model provides more information about the change from standard to signal.

When the maskers ranged in frequency from 200–5000 Hz, the largest range tested psychophysically, the filters centered at 125 and 8000 Hz did not provide significant differences depending on the standard vs signal stimuli (e.g., the values of Δ were near zero for the filters with the lowest and highest center frequencies). That is, for the filter bandwidths tested, lower- and higher-frequency filters generally did not contribute to the model decision variables, and so a wider range of filters was not required. Fits were reproduced using the single-parameter roex(p) filter. On occasion, these fits will be referenced.

2. Single-channel model

For the notched-noise and hybrid data (experiments II and III), both single-channel and multichannel models were evaluated. Two fitting methods were used to fit the single-channel model. For one, the methods follow those outlined above, except that the level at the output of a *single* filter was assumed to form the decision variable. Fifteen hundred different perturbed filter outputs (e.g., 1500 draws of the channel noise) were used to estimate the percent correct. As with the multichannel model, once p, r, and σ were estimated, thresholds were estimated using the resulting model and linear interpolations based on a model psychometric function. Again, changes in the values of p, r, and σ led to reasonably distinct minima, and good fits to the threshold data were achieved.

For the second method, a curve-fitting approach was used. The function minimized the squared error between the thresholds and the predicted signal level, $\hat{P}_s = K\int N(f)W(f)df$, where N is the noise spectrum, W is the filter weighting function, and K is a constant that dictates the signal-to-noise ratio at constant detectability. Both the mean signal levels for the data and predictions are in dB SPL. Compared to the simulation method, the magnitude of the added channel noise, σ, essentially is replaced by K for the curve-fitting method.

Curve-fitting methods represent the typical method present in the literature. By comparing results using the curve-fitting and simulation methods, the stability of the simulation method could be established. When the same weighting function was tested, the estimates of the parameters and the quality of the fit did not depend on the estimation procedure, simulation versus curve fitting. For all methods and models, MATLAB 5.0 (MathWorks, 1996) was used to estimate the variable parameters.

3. Modeling protocol

For the profile-analysis experiment (experiment I), the data were fitted using only the multichannel model. For the notched-noise and hybrid experiments (experiments II and III), the data obtained in the absence of level randomization were fitted using the single-channel model, and the data obtained in the presence of level randomization were fitted using the multichannel model. The logic of this protocol is as follows. When there is no level randomization, the multi-

channel model reduces to the single-channel model because no internal across-channel correlation is incorporated into the model (see Footnote 1). Moreover, the single-channel model is the model most frequently fitted to notched-noise detection data. Spot checks indicate that the single- and multichannel models provide similar parameter estimates when applied to the detection thresholds measured without level randomization.

Once the single-channel model was fitted to the no-randomization data, single-channel predictions for the effects of level randomization were generated. The parameters for the single-channel model were fixed, and then thresholds were predicted by introducing level randomization at the input to the model. Using 1500 2IFC trials for each signal level, psychometric functions were generated and the signal level required for threshold was estimated using linear interpolation.

Finally, it should be noted that for the notched-noise task, the simulations are based on ''noise'' spectra with flat magnitudes. In contrast, the experimental stimuli were based on Gaussian noise (i.e., the magnitudes of the spectral components were Rayleigh distributed). Spot checks indicated that using the true experimental stimuli had no impact on the parameter values estimated.

II. EXPERIMENT I: PROFILE-ANALYSIS EXPERIMENT

A. Methods

For the profile-analysis task, observers discriminated between a flat standard and an up–down signal. These stimuli are somewhat different from the more traditional profile-analysis stimuli, which are a flat standard and a signal stimulus which has an increment in a *single* component. We chose the up–down signal for two reasons. One is that the pattern of thresholds with increasing numbers of components varies greatly across listeners (Kidd, 1993). The second is that preliminary modeling showed that for a single-signal increment, the model fits are poorly constrained, making auditory filter bandwidth estimates difficult. Here, the flat standard was the sum of N equal-amplitude tones, which were equispaced on a logarithmic scale ranging in frequency from 200 to 5000 Hz. The up–down signal stimulus was generated by adding a ''signal'' to the standard. The signal was composed of tones with the same frequencies as the standard and phases that were either identical to the standard components (increase in level) or 180° phase-shifted relative to the standard components (decrease in level). The magnitude of the change in level is described as the ratio of the ''signal''-to-standard amplitudes (sig *re* standard), in dB. Ns of 4, 6, 10, 16, 20, 30, 40, 50, and 60 were tested.[3] Because thresholds could not be measured for all observers for an $N=60$, the model fits did not include this data point. On each stimulus presentation, the starting phase of the individual components of the standard were randomly drawn from a uniform distribution with a range of 2π rad. The mean stimulus level was 50 dB SPL/component. This experiment is nearly identical to the one reported by Richards and Lentz (1998).

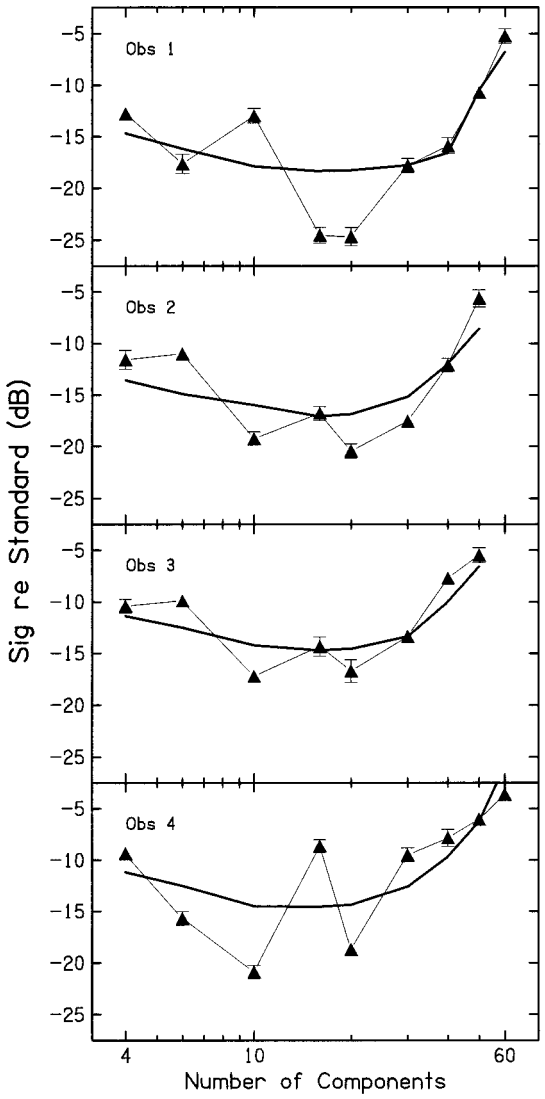

FIG. 1. Thresholds, as sig *re* standard in dB, are plotted as a function of the number of components (N) for experiment I, the profile-analysis experiment. The results for individual observers are shown in different panels. Error bars indicate the standard error of the means across 10 replicate threshold estimates ($n=10$).

B. Results of experiment I

Figure 1 shows the results of experiment I. For each observer, thresholds are plotted as a function of the number of components, N. Error bars indicate the standard error of the mean across ten threshold estimates. For Obs 2 and 3, thresholds for $N=60$ could not be measured (see Footnote 3). Figure 2 shows the results averaged across observers. In Fig. 2, error bars indicate the standard error of the mean across the four observers. The predictions of the channel model, presented below, are shown as the bold lines in Figs. 1 and 2. Both the averaged and individual data are plotted because the results are somewhat different across observers.

C. Auditory filter bandwidth estimates

For the averaged data, the function relating threshold and N is approximately U-shaped, consistent with the results reported by Richards and Lentz (1998). For small Ns, thresholds fall as N increases, presumably reflecting an increase in

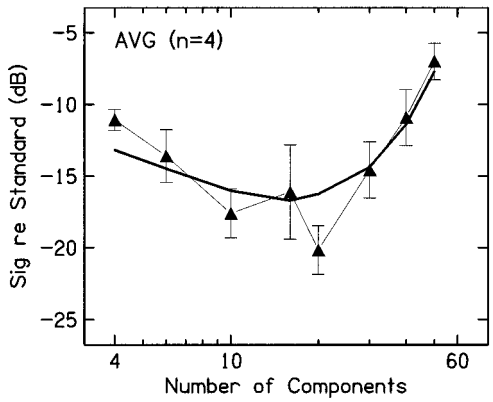

FIG. 2. Averaged thresholds, as sig *re* standard in dB, are plotted as a function of the number of components (N). Error bars indicate the standard error of the means across observers ($n=4$). The dark solid line shows the predictions of the channel model, using the parameters indicated in Table I.

the number of frequency regions conveying information concerning the presence of the signal. The minimum occurs at an N of 20, again consistent with the results of Richards and Lentz (1998). The increase in thresholds for Ns larger than 20 is taken to reflect the detrimental effects of limitations in frequency selectivity—as more and more components are crowded into the passbands of the auditory filters, the resulting excitation pattern cannot indicate the difference between the flat standard and the up–down signal (see also Dai and Green, 1993). Referring back to Fig. 1, note that Obs 4's data are distinct from the other observers in that the pattern of thresholds as a function of N are W-shaped. Her data are also markedly different from the other observers in the notched-noise experiment (experiment II, below). Compared to the Richards and Lentz (1998) study, the current thresholds are elevated somewhat at large N.

In terms of the channel model, the parameters of filter bandwidth and channel noise may be understood by evaluating changes in the parameters on the function relating threshold to N. Increases in channel noise lead to reductions in sensitivity, or higher thresholds. That is, referring to Fig. 2, increases in the magnitude of σ lead to upward translations along the ordinate. Changes in filter bandwidth are reflected in three ways. First, the point at which the minimum occurs depends on the filter bandwidth, with narrower filters leading to a shift in the minima to smaller Ns. Second, the slope of the falling portion of the function depends on bandwidth: wider filters lead to shallower slopes. Third, the slope of the rising portion of the function depends on bandwidth: wider bandwidths lead to steeper slopes.

Table I shows the results of the channel model applied to the thresholds estimated for the individual observers and the averaged data. For each observer, the equivalent rectangular bandwidth (ERB) for a filter centered at 1000 Hz (ERB_{1000}), the asymptote parameter in terms of $10\log(r)$, the standard deviation of the channel noise (σ), and the proportion of variance in the thresholds accounted for are shown (see Patterson and Moore, 1986 for a derivation of the ERB estimate from p). As the constant-Q assumption describes the filter bandwidth for all auditory filters, ERB_{1000} is chosen for ease in comparison with other auditory filter bandwidth estimates in the literature. The model is reasonably successful for Obs 1–3, but the fits to the data of Obs 4 are poorer. On average, the model does not predict sufficiently steep descending nor ascending slopes, a weakness that is also apparent in the fits to the averaged data (Fig. 2, bold line). For Obs 4, the W-shape is not in accord with the model. The final row of Table I shows the results for the average data. The ERB estimates of 80–85 Hz at 1000 Hz are much narrower than those estimated using the power spectrum model of masking and the notched-noise task. For the range of stimulus levels used in this experiment, Glasberg and Moore (1990) recommend auditory filter ERB_{1000}s ranging from 120–145 Hz for the 20-component standard and ranging from 124–153 Hz for the 60-component standard.

TABLE I. The modeling results for multichannel model applied to the results of experiment I are presented. For each observer, the ERBs for a filter centered at 1000 Hz (ERB_{1000} in Hz), rs [as $10\log(r)$], and σs (in dB) which lead to the best fits are shown. The percent of variance in the data accounted for by the resulting model is shown in the final column. Avg denotes results for the averaged data.

	ERB_{1000}	$10\log(r)$	σ	% Variance
Obs 1	83	−25.2	4.2	63
Obs 2	83	−25.2	5.0	68
Obs 3	80	−27.0	6.6	77
Obs 4	82	−30.0	7.2	53
Avg	85	−25.2	5.1	80

Because these estimates of filter bandwidth are much narrower than those recommended by Glasberg and Moore (1990), it should be noted that for this particular profile-analysis experiment, the rate at which thresholds increase with N may not reflect only limitations in frequency selectivity. Interactions within single auditory filters have a second potential impact on the data. When two or more components pass through a single auditory filter, the envelope at the filter output depends on the relative amplitudes of the components (where rates are sufficiently slow, i.e., for Ns of 20 or larger, cf. Viemeister, 1979). Even though the stimuli had phases that were randomly chosen on each stimulus presentation, the potential contribution of envelope cues should be examined. Because our version of the channel model used only level comparisons, the data set should be free from contributions of envelope cues. An auxiliary experiment was conducted to examine the potential contribution of single-channel envelope cues.

For the auxiliary experiment, observers discriminated between two sounds. Obs 1 in the current experiments was retested, along with two additional observers. One of the additional observers had prior experience in profile-analysis tasks, while the other had no prior experience in psychophysical tasks. It is our impression that the minimum 5 h of practice enforced prior to data collection in experiment I was not sufficient. Therefore, for the auxiliary experiment experienced observers received at least 6 h practice, and the naïve observer received 18 h of practice. Thresholds were measured in two conditions. For one, the spectrum of the signal stimulus varied up–down...up–down, and the spectrum of the standard stimulus varied down–up...down–up. For these two stimuli, single-channel comparisons of envelope are a

less reliable cue as the spectra are uneven for both the standard and signal stimuli. For the second condition, the stimuli were the same as in experiment I (up–down...up–down versus flat spectra).

The results may be summarized as follows. For the auxiliary experiment, and for large *N*s, thresholds measured in the up–down/down–up discrimination are elevated slightly relative to those measured in the up–down/flat discrimination. This indicates that envelope cues may have a modest impact on the data of experiment I. Then, the auxiliary data were fit using roex(p,r) filters. The results of the auxiliary experiment show that auditory filter bandwidth estimates derived using the up–down/down–up condition are slightly wider than the estimates derived using the up–down/flat condition. In addition, both data sets led to auditory filter bandwidth estimates narrower than those shown in Table I. Finally, the data of the auxiliary experiment were better fit by the channel model. For the individual observers, the percent of variance accounted for by the model ranged from 80%–94%.

Overall, even though the fits to the individual data are modest in experiment I, the fits from the auxiliary experiment in which observers had more practice are better. For both experiment I and the auxiliary experiment, the bandwidth estimates are very narrow relative to those provided by the power spectrum model of masking and notched-noise experiments.

III. EXPERIMENT II: NOTCHED-NOISE EXPERIMENT

In this experiment, observers detected a 1000-Hz tone added to a notched-noise masker. The signal was arithmetically centered in the notch, and notch bandwidths of 100, 200, 300, 400, and 800 Hz were tested. The mean spectrum level of the noise masker was 35 dB SPL. Level randomization was either present or absent. When present, the levels of the stimuli, either masker alone or signal+masker, were randomly chosen. Thus, thresholds are expressed as the *mean* signal level in dB SPL.

Four different maskers were tested. For three of them, two relatively narrow-band maskers were separated by the notch bandwidth. These three stimuli had bandwidths of 50, 100, and 300 Hz. For example, for the 50-Hz masker, a 50-Hz-wide noise band stood on each side of the notch. For the fourth, the stimulus ranged in frequency from 200 to 5000 Hz, save the region of the notch. Thus, the fourth, wideband masker had a frequency extent equal to that used in the profile-analysis and hybrid experiments (experiments I and III).

Because observers are sensitive to differences in power spectra, one might expect that when a wideband masker is used, the presence of energy at frequency regions distant from the signal frequency may provide a referent against which the level at the signal frequency may be compared (cf. Kidd *et al.*, 1989). Thus, if the detection of a tone added to a wideband notched masker depends on a profile-analysis detection strategy, one would expect little effect of level randomization. However, for narrow-band maskers, across-frequency comparisons of level may not be available. In all, if the detection decision depends on the *level* at the output of a *single* auditory filter, level variation should lead to increased thresholds for all masker bandwidths. In contrast, to the degree that observers incorporate across-frequency comparisons of level, increases in masker bandwidth should provide more stable comparisons, and thus, effects of level randomization would be reduced when wider masker bandwidths are used.

It should be noted that for the detection of a tone added to narrow-band Gaussian noise maskers (e.g., without a notch) effects of level randomization are modest (Kidd *et al.*, 1989). These data have been interpreted as reflecting, at least in part, the observers' reliance on changes in the envelope pattern associated with the addition of the tonal signal. It seems possible, then, that when a notched-noise masker with narrow flanking maskers is used (e.g., the masker's energy is restricted to a relatively narrow frequency range), envelope cues may also provide resilience to level randomization.

A. Methods

For each notch bandwidth and each masker bandwidth tested, 99 different maskers were digitally generated. The maskers were generated by summing tones with magnitudes independently drawn from a Rayleigh distribution and phases independently drawn from a uniform distribution with a range of 2π rad. The tones were separated by the inverse of the stimulus duration (including onset/offset ramps), approximately 10 Hz.

B. Results of experiment II

Figure 3 shows mean signal levels at threshold in dB SPL for the individual observers when the 50-Hz-wide masker was used, as individual differences were prominent. Figure 4 shows the average results when the 100-Hz, 300-Hz, and wideband maskers were tested (bottom to top panels, respectively). Unfilled symbols show the results obtained in the absence of level randomization, and filled symbols show the results obtained in the presence of a 30-dB presentation-by-presentation level randomization. In Fig. 3, error bars indicate the standard error of the mean across ten threshold estimates for each observer. In Fig. 4, error bars indicate the standard error of the mean across the four observers. Predictions of two models, which are presented below, are shown using bold lines.

First consider the empirical results for the 50-Hz-wide masker. For Obs 1–3, thresholds fall as the notch bandwidth increases. For Obs 4, however, the function relating threshold and notch bandwidth is nonmonotonic. Based on conversations with the observers, and to a large degree on our informal listening to the stimuli, it seems possible that a shift in strategy took place for a notch bandwidth of approximately 200–300 Hz. It might be the case that Obs 4 simply failed to incorporate multiple cues as one set of cues failed and another set emerged. Whatever the reasons for the individual differences, it is notable that for Obs 2 and 4 there is little effect of level randomization. For Obs 1 and 3 there is a small detrimental effect of level randomization. On average, randomly choosing the levels of the stimuli on a presentation-by-presentation basis leads to a 2.6-dB increase

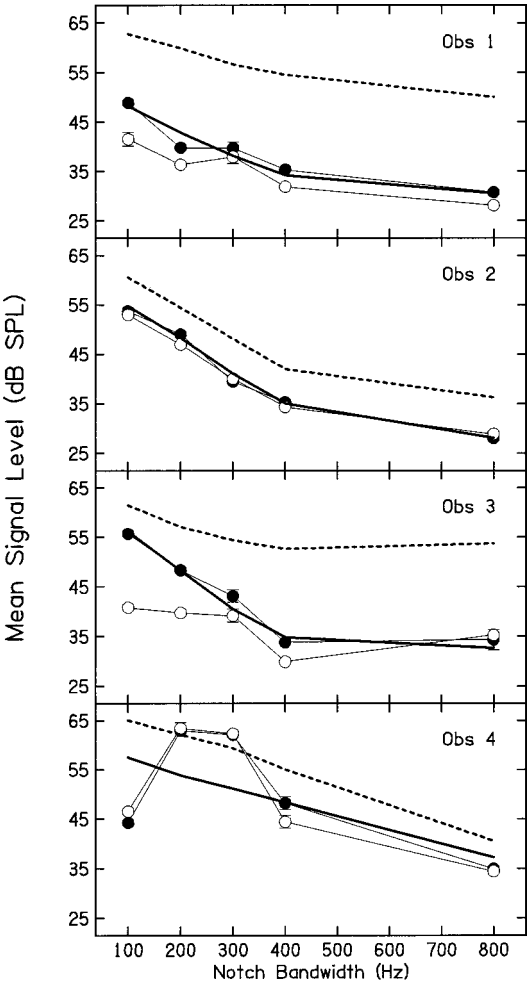

FIG. 3. Thresholds in dB SPL (mean signal level) are shown as a function of notch bandwidth for the 50-Hz masker. Thresholds are plotted as a function of the number of components, *N*. The results for the different observers are shown in different panels, and error bars indicate the standard errors of the mean for each threshold estimate ($n=10$). The dark solid line shows the predictions of the channel model, using the parameters indicated in Table II. The dark dashed line shows the predictions of the single-channel model (parameters indicated in Table III) when level randomization is applied.

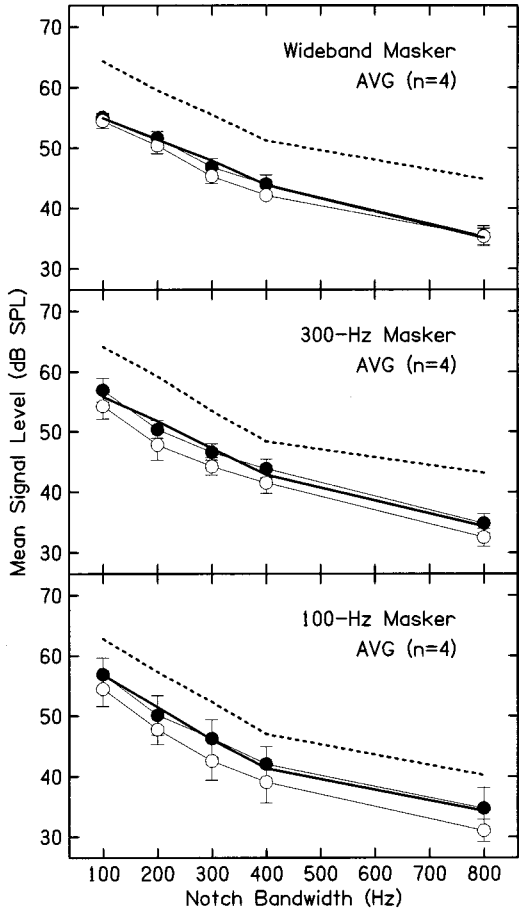

FIG. 4. Averaged thresholds as dB SPL (mean signal level) are shown as a function of notch bandwidth for the 100-Hz, 300-Hz, and wideband maskers (bottom to top). Error bars indicate the standard error of the mean across observers ($n=4$). The dark solid line shows the predictions of the channel model, using the parameters indicated in Table II. The dark dashed line shows the predictions of the single-channel model (parameters indicated in Table III) when level randomization is applied.

in thresholds relative to thresholds measured without level randomization.

Next, consider Fig. 4. For these maskers, thresholds fall with increases in notch bandwidth. An analysis of variance which treated observers as random variables revealed a significant effect of notch bandwidth [$F(4,12)=1558$, $p<0.0005$]. The average 2.2-dB effect of level randomization did not reach significance [$F(1,3)=142.7$, $p<0.08$]. The interaction terms did not approach significance.

C. Auditory filter bandwidth estimates

Tables II and III show the estimates of p (ERB_{1000}), $10\log(r)$, and σ in dB for the multichannel and single-channel models, respectively. Keep in mind that the single-channel model was fitted to the data collected in the absence of level randomization, and the multichannel model was fitted to data collected in the presence of level randomization. In both cases, a roex(p,r) weighting function was used. For the 50-Hz-wide maskers, the multichannel fits to the individual data are shown as solid lines in Fig. 3. For the other maskers, the multichannel fits to the averaged data are shown as solid lines in Fig. 4. As is apparent in Tables II and III, the single- and multichannel models lead to similar bandwidth estimates. For that reason, the single-channel fits are not plotted. However, note that the channel-noise estimates are different for both models. For wider notch bandwidths the multichannel model has more filters cueing the addition of the signal, leading to a larger channel-noise estimate to maintain the same threshold.

Both the single- and multichannel models are successful in fitting the data, save the fits for Obs 3 and 4 in the 50-Hz condition. This failure is largely due to the nonmonotonic shape of the function relating notch bandwidth and thresholds when there is no level randomization (unfilled symbols). For Obs 4, the function is also nonmonotonic when level randomization is present (filled circles), and thus, the fits to the channel model are also poor (Table II).

The dark, dashed lines in Figs. 3 and 4 indicate the predictions of the single-channel model for the case where level randomization is present. Except for Obs 4 and the 50-Hz masker bandwidth, predicted thresholds are considerably higher than the psychophysical thresholds. Given the

TABLE II. The modeling results for multichannel model applied to the portion of experiment II in which level randomization is present are shown. For each observer and the averaged data, ERBs for a filter centered at 1000 Hz (ERB_{1000} in Hz), rs [as $10\log(r)$], and σs (in dB) which lead to the best fits are shown. The percent of variance in the data accounted for by the resulting model is shown in the final column.

Masker BW		ERB_{1000}	$10\log(r)$	σ	% Variance
	Obs 1	138	−20.2	1.3	92
	Obs 2	108	−31.5	5.4	99
50 Hz	Obs 3	91	−30.0	7.5	97
	Obs 4	267	$\approx-\infty$	3.7	33
	Obs 1	154	−29.2	2.2	93
	Obs 2	121	−28.5	3.2	99
100 Hz	Obs 3	108	−22.3	6.9	99
	Obs 4	133	−32.2	11.4	99
	Avg	133	−27.2	4.9	99
	Obs 1	143	−33.0	3.4	97
	Obs 2	167	−28.5	2.2	99
300 Hz	Obs 3	154	−27.4	3.8	97
	Obs 4	143	−33.0	7.8	97
	Avg	154	−30.5	3.8	98
	Obs 1	127	−40.0	4.2	98
	Obs 2	200	−40.0	2.0	99
Wideband	Obs 3	200	−33.0	2.9	98
	Obs 4	163	−37.0	4.6	99
	Avg	170	−37.0	3.2	99

similarity of the bandwidth estimates and the relatively modest (not significant) effect of level randomization, it appears appropriate to conclude that single-channel level cues are probably not the sole determinant for detection when level randomization is absent.

Comparing the results in Tables I and II provides comparisons between ERB_{1000} estimates based on the profile-analysis data (experiment I) and the current notched-noise experiment. Restricting the comparison to the wideband notched-noise data, which had the same frequency extent as the profile-analysis experiment, the ERBs differ by approximately a factor of 2.

The current wideband condition is somewhat similar to an experiment completed by Patterson (1976). By comparison, Patterson's maskers were 600-Hz wide, and the spectrum level was 40 dB SPL. Comparing the data sets, the most obvious difference is that the current data exhibit higher thresholds at the largest notch bandwidth. Nonetheless, our ERB value is 170 Hz compared to Patterson's 160 Hz.

In summary, the data appear to provide the basis for rejecting single-channel, level-based models for the detection of a tone added to a notched-noise masker. The slight increase in thresholds associated with the introduction of level randomization suggests that more than one cue is incorporated into the decision when there is no level randomization. Neither the estimates of auditory filter bandwidths nor thresholds depend heavily upon whether level randomization was present or absent. Critically, the auditory filter bandwidth estimates based on the notched-noise experiment are wider than those based on the profile-analysis experiment. For the roex(p,r) filter, the difference is a factor of 2.

TABLE III. The modeling results for single-channel model applied to the portion of experiment II in which level randomization is absent are shown. For each observer and the averaged data, ERBs for a filter centered at 1000 Hz (ERB_{1000} in Hz), rs [as $10\log(r)$], and σs (in dB) that provided the best fits are shown. The percent of variance in the data accounted for by the resulting model is shown in the final column.

Masker (BW)		ERB_{1000}	$10\log(r)$	σ	% Variance
	Obs 1	200	−15.5	0.3	89
	Obs 2	108	−30.0	4.8	99
50 Hz	Obs 3	154	−11.9	0.4	55
	Obs 4	200	$\approx-\infty$	6.6	48
	Obs 1	160	−29.2	1.5	98
	Obs 2	114	−29.2	3.0	98
100 Hz	Obs 3	98	−28.0	3.8	96
	Obs 4	148	−33.0	8.3	98
	Avg	129	−29.2	3.6	99
	Obs 1	182	−28.9	1.0	95
	Obs 2	148	−29.6	1.5	99
300 Hz	Obs 3	160	−25.7	2.2	95
	Obs 4	133	−37.0	7.5	99
	Avg	154	−30.0	2.5	98
	Obs 1	148	−37.0	2.5	97
	Obs 2	167	−40.0	2.6	98
Wideband	Obs 3	167	−34.0	1.9	99
	Obs 4	129	−40.0	6.7	99
	Avg	148	−37.0	3.2	99

IV. EXPERIMENT III: HYBRID EXPERIMENT

Experiments I and II yield different estimates of auditory filter bandwidths, even though the same observers participated in both experiments and the same computational algorithm was applied in both experiments. There are three primary reasons that the differences might exist. First, the profile-analysis experiments employed tonal stimuli rather than spectrally dense Gaussian noise. In light of an experiment by Moore *et al.* (1995), this seems an unlikely explanation of the difference in bandwidth estimates. In their experiments, two types of maskers were tested. One masker is similar to the wideband condition of experiment II. In a second condition, the masker situated above the signal frequency was a tone instead of a band of noise. They found that the estimate of auditory filter bandwidths was only marginally influenced by the change in higher-frequency masker. Second, for the profile-analysis experiment the change to be detected is distributed in frequency while the signal in the notched-noise experiment is a single tone. Third, as a result of the difference in the frequency distribution of the signal, the processing demands in the two experiments may be quite different. In an effort to reduce the number of possible explanations of the differences in bandwidth estimates, a third, hybrid, experiment was run.

A. Methods

For the third, hybrid, experiment observers detected a 1000-Hz tone masked by a stimulus composed of N equal-amplitude tones. The masker stimulus was the same as the standard stimulus used in experiment I. Ns of 4, 6, 10, 16, 20, 30, 40, and 60 were tested. Because the tones were equispaced on a logarithmic frequency scale ranging from 200

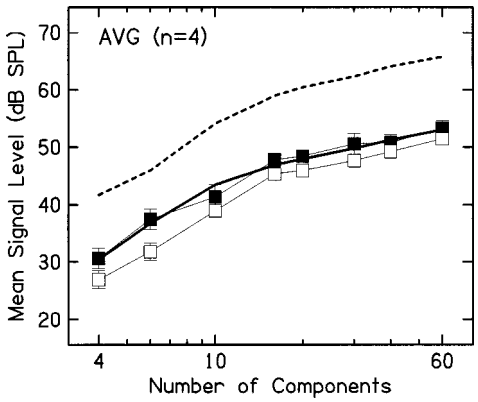

FIG. 5. Averaged thresholds are shown as a function of number of components (N) for the hybrid experiment (experiment III). Error bars indicate the standard errors of the mean across observers ($n=4$). The dark solid line shows the predictions of the channel model, using the parameters indicated in Table IV. The dark dashed line shows the predictions of the single-channel model (parameters indicated in Table V) when level randomization is applied.

to 5000 Hz, the masker did not have energy at 1000 Hz, but 1000 Hz was the geometric mean between the two central tones that made up the masker. On each stimulus presentation, the starting phases of the individual components of the masker, and when present, the signal, were randomly drawn from a uniform distribution with a range of 2π rad. Level randomization was either absent or present. When present, the overall level (masker alone or masker+signal) was drawn from a uniform distribution with a 30-dB range and a 0.1-dB gradation on each presentation. As in experiment II, thresholds are expressed as the *mean* signal level in dB SPL. Filter bandwidth estimates that rival those determined for experiment I would imply that differences in spectral density underlie the difference in auditory filter bandwidth estimates determined in experiments I and II. However, filter bandwidth estimates that rival those determined for experiment II would point to differences in processing strategies across these different tasks.

B. Results of experiment III

Because the trends in the data are similar across observers, Fig. 5 shows the average data. Mean signal levels at threshold in dB SPL are plotted as a function of the number of components, N. Error bars indicate the standard error of the mean across the four observers. Unfilled symbols indicate level randomization was absent, and filled symbols indicate that level randomization was present. Thresholds rise with increases in the number of components, or equivalently, with decreases in the notch bandwidth surrounding the signal frequency.

An analysis of variance which treated observers as a random variable revealed significant effects apparent in Fig. 5. The effect of number of components [$F(7,21)=551.4$, $p<0.0005$], and the average 2.9-dB effect of level randomization [$F(1,3)=12.3$, $p<0.04$] are significant. The N-by-level randomization interaction is also significant [$F(7,21)=4$, $p<0.007$]. The interaction is apparent in the slight reduction in the effect of level randomization concomitant with the increase in the number of components, N. It is difficult to know whether the interaction reflects ''energetic'' masking (frequency extent of the notch) vs the incorporation of energy at frequencies distant from the signal when there is level randomization.

TABLE IV. The modeling results for the multichannel model applied to the portion of experiment III in which level randomization is present are shown. For each observer and the averaged data, ERBs for a filter centered at 1000 Hz (ERB_{1000} in Hz), rs [as $10\log(r)$], and σs (in dB) that best fit the data are shown. The percent of variance in the data accounted for by the resulting model is shown in the final column.

	ERB_{1000}	$10\log(r)$	σ	% Variance
Obs 1	167	−22.3	1.1	95
Obs 2	235	−26.2	1.4	98
Obs 3	258	−21.1	2.3	95
Obs 4	235	−23.4	2.8	98
Avg	242	−23.3	1.7	98

C. Auditory filter bandwidth estimates

The parameter estimates for the multi- and single-channel models are shown in Tables IV and V, respectively, using a roex(p,r) weighting function. The fits are excellent, and the auditory filter bandwidth estimates are about the same for the two models. The dark line plotted in Fig. 5 shows the multichannel fits to the averaged data. The dark dashed line shows the predicted effects of level variation based on the single-channel model. A single-channel, level-based model cannot account for the thresholds measured in the presence of level variation.

The ERB_{1000}s for this experiment are consistently wider than the results for the wideband masker of experiment II and considerably wider than the ERB_{1000}s estimated in experiment I. Comparisons of these ERB_{1000}s values are considered below.

V. GENERAL DISCUSSION

The results of the experiments described above suggest two primary conclusions. First, when a tone added to a notched masker is to be detected, estimates of auditory filter bandwidth are wider than when the task is to detect differences in spectral profile. Thus, the channel model coupled with roex(p,r) weighting functions does not generalize from a single-channel to a multichannel model of processing. Second, consistent with previous reports, (e.g., Kidd *et al.*, 1989) changes in the level at the output of a single auditory

TABLE V. The modeling results for single-channel model applied to the portion of experiment III in which level randomization in absent are shown. For each observer and the averaged data, ERBs for a filter centered at 1000 Hz (ERB_{1000} in Hz), rs [as $10\log(r)$], and σs (in dB) for the best fits are shown. The percent of variance in the data accounted for by the resulting model is shown in the final column.

	ERB_{1000}	$10\log(r)$	σ	% Variance
Obs 1	174	−29.2	1.1	99
Obs 2	190	−24.9	1.1	99
Obs 3	211	−23.0	1.0	98
Obs 4	167	−24.0	1.8	99
Avg	186	−25.2	1.2	99

filter cannot account for the detection of a tone added to noise, even notched-noise maskers. In the following discussion, the differences in the auditory filter bandwidths are considered from two perspectives: the reliability of the measures and potential reasons that different bandwidths might be estimated.

A. A comparison of auditory filter bandwidth estimates

The estimated auditory filter bandwidth is widest for experiment III and narrowest for experiment I. However, the error functions associated with the fits to the different data sets are not the same, which makes the comparisons of bandwidth estimates difficult. To provide an example of the change in the error functions associated with the three sets of data, consider the change in percent of variance accounted for as a function of ERB_{1000}. In experiment III large changes in bandwidth barely impact on the quality of the model fit. For ERB_{1000}s ranging from 40 to 400 Hz, the percentage of variance accounted for ranges from 79% at 40 Hz to a maximum of 98% at 242 Hz, and falls only slightly to 94% when an ERB_{1000} of 400 Hz is tested. In the notched-noise experiment (experiment II) and for the wideband condition, the fits are more constrained: an ERB_{1000} of 40 Hz accounts for 10% of the variance, an ERB_{1000} of 170 Hz accounts for a maximal 99% of the variance, and the percent of variance accounted for falls to 78% for an ERB_{1000} of 400 Hz. In experiment I the error functions are less forgiving: an ERB_{1000} of 62 Hz accounts for 50% of the variance, an ERB_{1000} of 85 accounts for a maximal 80% of the variance, and the percent variance accounted for falls to 50% for an ERB_{1000} of 114 Hz.

Figure 6 demonstrates the impact of such differences in error functions for fits to experiments I and III. The top panel of Fig. 6 shows the profile-analysis data (triangles) and the bottom panel plots the hybrid data (squares) in the presence of level randomization. In the top panel, the solid lines show predictions for the filter bank derived using the profile-analysis data (parameters shown in the bottom row of Table I), and for the bottom panel the dotted lines show the predictions for the hybrid filter bank (bottom row of Table IV). Next, the profile-analysis filter bank was used to predict the hybrid experimental data by changing the standard deviation of the added channel noise, σ, in order to best fit the data. These predictions are shown as the solid line in the bottom panel. The profile-analysis filter bank does a reasonably good job in capturing the hybrid data, accounting for approximately 89 percent of the variance in the data. The hybrid filter bank was also used to predict the profile-analysis experimental data by varying the magnitude of σ. These model fits are shown as the dotted line in the top panel, and they greatly miss the profile-analysis data.

In general, the fits to the profile analysis data are most constrained and the fits to the hybrid data least constrained. For the hybrid experiment, the problem is associated with the r parameter. In the hybrid experiment, the increase in masking with increasing number of components is fairly well captured either by increasing the auditory filter bandwidth or increasing r, meaning bandwidth and r are not separable pa-

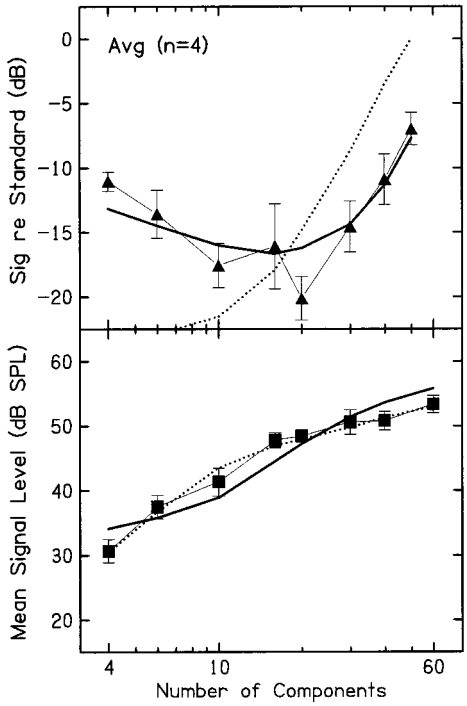

FIG. 6. Top panel: Data and roex(p,r) multichannel fits for the profile-analysis experiment. Bottom panel: Data and roex(p,r) multichannel fits for the hybrid experiment. The solid line shows best fits using the profile-analysis filter bank and the dotted line shows the best fits using the hybrid filter bank.

rameters for this data set. For that reason, we refit the data using a single-parameter roex(p) weighting function. Considering only the averaged data, the estimated ERB_{1000} for the profile-analysis experiment is 81 Hz, the ERB_{1000} for the wideband notched-noise experiment is 246 Hz, and the ERB_{1000} for the hybrid experiment is 308 Hz. For these fits, the percent of variances accounted for is 73, 94, and 97, respectively. Thus, compared to fits derived using the two-parameter roex(p,r) weighting shape, the bandwidth estimates are somewhat different. The roex(p) fits are more constrained (i.e., the proportion of variance accounted for changes more quickly as a function of bandwidth for narrow filter bandwidths), yet the hybrid and wideband notched-noise auditory filter estimates remain far wider than the estimates based on the profile-analysis experiment.

With regard to whether the differences in bandwidths across tasks are meaningful, several additional simulations were run. The first sequence of simulations was aimed at the difference in multichannel estimates derived from detection experiments, experiments II and III. The fits described above may be thought of as six-parameter fits to the aggregate data set (data collected in experiments II and III, p_n, p_c, r_n, r_c, σ_n, σ_c, where n refers to the notched-noise masker associated with experiment II and c refers to the complex multitone masker used in experiment III). Overall, the six-parameter fit accounts for 99% of the variance across experiments II and III. When a five-parameter model is fitted to the averaged data using a single p parameter (p, r_n, r_c, σ_n, σ_c, using newly determined values for p, r_n, r_c, σ_n, and σ_c), 99% of the variance is again accounted for by the model. Further restricting the model to a four-parameter fit using a single p

and a single r parameter for both data sets (p, r, σ_n, σ_c), 96% of the variance is accounted for.[4] Thus, there is little basis to claim that there are differences in the estimates of auditory filter bandwidths for experiments II and III. As a result, the estimates will be accepted as equivalent.

In a second sequence of simulations, a similar approach was used, except that the comparison was between the data of experiment III and experiment I. We were most interested in comparing these data sets because the standard stimulus is identical in the two tasks. Past estimates of auditory filter bandwidth indicate a nonlinear contribution of masker level (e.g., Patterson and Moore, 1986; Glasberg and Moore, 1990; Rosen and Baker, 1994); for higher stimulus levels, the bandwidth estimate is broader. By restricting comparisons to the results from experiments I and III, any error associated with the absence of a nonlinearity is minimized. As described above, six-parameter, five-parameter, and four-parameter models were fit to the aggregate data sets. For the four-through six-parameter models, 94%, 87%, and 87% of the variance in the data was accounted for, respectively.[5] Allowing two different values of p leads to a 7% increase in the percentage of the variance accounted for, suggesting that two p values better fit the data than just one. This 7% increase is small, and for the most part reflects the fact that large changes in the value of p lead to small changes in the percent of variance accounted for in experiment III.

To summarize, estimates of auditory filter bandwidths depend on the task. It is unlikely that the differences in the bandwidth estimates obtained for the two detection tasks, experiments II and III, are substantially different. It appears, however, that the estimated bandwidth associated with the profile-analysis task is considerably narrower than that associated with the detection tasks.

B. Evaluation of alternative explanations for the change in auditory filter bandwidth estimates

1. Modeling

There are at least three reasons why the ''wide'' (i.e., typical) auditory filters may fail to account for the profile-analysis data. First, only a few types of filter weighting functions were explored, one of which is reported here. It might be possible to design a weighting function that is consistent with all of the data sets. Second, the constant-Q assumption may be overly restrictive. Third, the current filters did not vary bandwidth with changes in stimulus energy.[6] In order to evaluate the latter two alternatives, the filters described by Glasberg and Moore (1990) were used to generate thresholds in the profile-analysis experiment. The channel model was used, and the standard deviation of the added channel noise, σ, was altered in order to generate the best fit to the data. For *large N*, the Glasberg and Moore (1990) filter bank can be made to account for the data by adjusting the magnitude of the channel noise. At small N, the predictions fail in the same way as the filters estimated in the hybrid experiment (Fig. 6, upper panel); they grossly overestimate the sensitivity seen in the data. This overestimate in sensitivity occurs because nearly *all* of the filters convey information about the spectral change in the stimuli; i.e., they are so wide that nearly all the filters pass significant energy, and therefore the output of nearly all the filters signals the spectral change in the stimuli. In short, the auditory filters are too wide to account for the trends seen in the data. To put it another way, it is the pattern of thresholds at *small N*s that leads to narrow filter bandwidth estimates in experiment I (Table I).

The proposition that a bank of *narrow-band* filters may be required for ''excitation pattern'' models to be successful depends upon the current choice of model, the optimal channel model. Nonoptimal processing schemes might provide a means by which wider filters could be used to account for both detection and profile-analysis data. For example, in Figs. 2 and 6 it is apparent that our version of the channel model does not completely capture the steepness of the change in thresholds for Ns increasing from 4 to 20. However, if one assumes that the number of filters is proportional to the number of components, the data are well captured (see also Green, 1992; i.e., thresholds expressed as ΔL in dB fall near a rate of $1/\sqrt{N}$). More interesting, if one assumes that the number of filters is proportional to the number of components for $N<20$ or so, simulations indicate that there is little basis for choosing narrow filters over wide filters. Under those circumstances, only the rising portion of the data (Fig. 1) impacts on the bandwidth estimate. Those data are largely consistent with wide auditory filters, although the fits are relatively unconstrained.

Past estimates of auditory filter bandwidths based on profile-analysis data (e.g., Bernstein and Green, 1987; Dai and Green, 1993) do not indicate narrow filter estimates relative to those found for notched-noise experiments. For the former study, rather stringent single-channel assumptions were used to estimate the filter bandwidths. Applying the current model to their experiment 2, filter bandwidths are consistent with those obtained in our experiment I (note these simulations compared results using roex(p) weighting functions). For Bernstein and Green's experiment 1, only the data for large Ns are consistent with the Durlach *et al.* (1986) model, and for that subset of the data, the data could not be fitted with certainty as only a few number of data points were obtained. For the Dai and Green (1993) experiment, there are interactions within single auditory filters, which is equivalent to the situation when N is large in our experiment. As described above, when there are interactions within auditory filters, filters wide relative to those determined in experiment I reasonably fit the data. These additional fits to existing data underscore the dependence of the relatively narrow filter estimates shown in Table I on the data collected at small Ns.

2. Auditory processing

The results indicate different auditory filter bandwidth estimates for profile-analysis versus notched-masker experiments. In contrast to our preliminary work, this cannot be due to differences in observers and/or procedures, as a single crew of observers and similar experimental procedures was used. A second explanation, differences in stimulus density, proved to be unimportant (comparing auditory filter bandwidth estimates in experiments II and III; see also Moore *et al.*, 1995).

Although it is far from certain, it might be the case that the processing demands associated with the different tasks drive the differences in the auditory filter bandwidth estimates. In order to explore this hypothesis, it is worth considering existing fits of linear models applied to profile-analysis and masking experiments. The available data indicate different patterns of combination weights. For example, Berg and Green (1990; Green and Berg, 1991) found that observers appear to depend on information across several octaves for profile-analysis tasks, whereas for tone-in-noise tasks observers appear to rely on frequencies neighboring the signal frequency (Richards and Buss, 1996; see also Ahumada and Lovell, 1971; Gilkey and Robinson, 1986). This difference in weighting patterns suggests different processing strategies. Finally, Berg and Green (1991) found that when observers discriminated between an eight-component up–down stimulus and a ''flat'' stimulus, observers emphasized information in a subset of the components. What is unclear is how different decision strategies affect estimates of frequency selectivity, and how changes in the number of components impact on decision strategies.

VI. SUMMARY AND CONCLUSIONS

Estimates of auditory filter bandwidths were derived in three experiments. The results indicate that the channel model (Durlach *et al.*, 1986) used in conjunction with a *single* bank of roex(p,r) auditory filters cannot account for the data of the three experiments. Filter bandwidths estimated in the profile-analysis experiment are narrow relative to those estimated for the detection tasks. The wider filters cannot account for profile-analysis data obtained when small Ns are tested. Notably, the profile-analysis data may be captured using wider filters if it is assumed that the number of filters contributing to the discrimination decision increases with increases in the number of components up to an N of 20 or so. Thus, there are two potential explanations of the data and modeling results. First, the substantial shift in bandwidth may hinge on differences in processing associated with single-tone detection vs profile analysis tasks. Second, it might be that the auditory system emphasizes peaks in the power spectra such that when sparse spectra are tested in profile-analysis tasks the decision process is nonoptimal. This amounts to monitoring only a subset of auditory filters. Such selective monitoring may be obligatory, or may reflect attentional mechanisms (even though those mechanisms are detrimental relative to an optimal detection mechanism).

The results also indicate that there is little effect of level randomization for the detection of a tone added to a notched masker. This suggests that changes in the level at the output of a single auditory filter poorly describes the detection of a tone added to a notched masker.

ACKNOWLEDGMENTS

This work was supported by Grant No. DC 02012 from the National Institutes of Health and a grant from the University of Pennsylvania Research Foundation. We are thankful to Jacob Nachmias, Gerald Kidd, Jr., and Chris R. Mason for their comments and suggestions on earlier versions of this paper. Two anonymous reviewers provided excellent suggestions as well.

[1]The assertion that the channel model degenerates to the power spectrum model of masking assumes no internal interchannel correlation. The current model assumes $d'^2 = \Delta \mathbf{G} \Delta^T$, where Δ is a vector that represents the mean difference in level, in dB, between two stimuli at the output of a bank of auditory filters (in the current formalization), $\mathbf{G}$ is the inverse of the interchannel covariance matrix, and T signifies the transpose (e.g., van Trees, 1968; Durlach *et al.*, 1986). When the signal to be detected is a single tone added to a notched masker, the Δ vector is expected to be zero except at the outputs of the auditory filters that pass significant signal energy. In the absence of interchannel correlation, the covariance matrix is zero-valued except along the diagonal. Thus, the index of detectability (d') is essentially the same as the one associated with the single-channel power spectrum model of masking. On the other hand, if interchannel covariance is present due to level variation or a noise source that covaries for neighboring auditory filters, the covariance matrix is not strictly zero on the nondiagonal entries. As a result, the inverse of the covariance matrix has nonzero values away from the diagonal. For that reason, in the presence of correlation across channels, the optimal decision rule is different from the single-channel power spectrum model of masking.

It should be noted that in the presence of level randomization, such as the 30-dB range used in the current experiments, the externally applied interchannel covariance is likely to swamp any internal interchannel covariance. Thus, when level randomization is applied, one may assume that the contribution of the internal interchannel covariance is negligible. We thank Dr. Huanping Dai for suggesting this simplifying assumption.

[2]This interesting observation was suggested by an anonymous reviewer.

[3]For large Ns, occasionally the tracking procedure led to signal levels of 0 dB. Because the signal level is defined as sig *re* standard in dB, signal levels of 0 dB indicate that only 1/2 the stimulus components were present. The rule applied was that in 500 trials a 0-dB value could be reached only eight times. Generally, the ceiling was reached infrequently for Ns of 50 and 60, and never for other Ns. For an N of 60, sensitivity of two of the observers did not meet this criterion.

[4]The comparisons of experiments II and III yielded the following parameters: For the six-parameter fit: $p_n = 23.5$, $p_c = 16.5$, $10\log(r_n) = -37$, $10\log(r_c) = -23.3$, $\sigma_n = 3.2$, $\sigma_c = 1.7$. For the five-parameter fit: $p = 21$, $10\log(r_n) = -35.2$, $10\log(r_c) = -22.4$, $\sigma_n = 2.4$, $\sigma_c = 2.1$. For the four-parameter fit: $p = 14$, $r = 0$, $\sigma_n = 1.2$, $\sigma_c = 1.7$.

[5]The comparisons of experiments I and III yielded the following parameters: Here, u denotes the up–down stimulus (experiment I). For the six-parameter fit: $p_u = 47$, $p_c = 16.5$, $10\log(r_u) = -25.2$, $10\log(r_c) = -23.2$, $\sigma_u = 5.1$, $\sigma_c = 1.7$. For the five-parameter fit: $p = 45$, $10\log(r_u) = -25.2$, $10\log(r_c) = -22.4$, $\sigma_u = 4.8$, $\sigma_c = 3.8$. For the four-parameter fit: $p = 45$, $10\log(r) = -22.2$, $\sigma_u = 4.5$, $\sigma_c = 3.5$.

[6]Spot checks indicate that incorporating filter bandwidths that vary with stimulus level in the current model did not lead to large increases in the goodness of fits for the profile-analysis data.

Ahumada, Jr., A., and Lovell, J. (**1971**). ''Stimulus features in signal detection,'' J. Acoust. Soc. Am. **49**, 1751–1756.

Berg, B. G., and Green, D. M. (**1990**). ''Spectral weights in profile listening,'' J. Acoust. Soc. Am. **88**, 758–766.

Berg, B. G., and Green, D. M. (**1991**). ''Discrimination of complex spectra: Spectral weights and performance efficiency,'' in *Auditory Physiology and Perception*, edited by Y. Cazals, L. Demany, and K. Horner (Pergamon, New York), pp. 373–379.

Bernstein, L. R., and Green, D. M. (**1987**). ''The profile-analysis bandwidth,'' J. Acoust. Soc. Am. **81**, 1888–1895.

Dai, H., and Green, D. M. (**1992**). ''Auditory intensity perception: Successive versus simultaneous, across-channel discriminations,'' J. Acoust. Soc. Am. **91**, 2845–2854.

Dai, H., and Green, D. M. (**1993**). ''Discrimination of spectral shape as a function of stimulus duration,'' J. Acoust. Soc. Am. **93**, 957–965.

Durlach, N. I., Braida, L. D., and Ito, Y. (**1986**). ''Towards a model for discrimination of broadband signals,'' J. Acoust. Soc. Am. **80**, 63–72.

Farrar, C. L., Reed, C. M., Ito, Y., Durlach, N. I., Delhorne, L. A., Zurek, P. M., and Braida, L. (**1987**). ''Spectral-shape discrimination I. Results from

normal-hearing listeners for stationary broadband noises'' J. Acoust. Soc. Am. **81**, 1085–1092.
Florentine, M., and Buus, S. (**1981**). ''An excitation-pattern model for intensity discrimination,'' J. Acoust. Soc. Am. **70**, 1646–1654.
Gilkey, R. H., and Robinson, D. (**1986**). ''Models of auditory masking: A molecular psychophysical approach,'' J. Acoust. Soc. Am. **79**, 1499–1510.
Glasberg, B. R., and Moore, B. C. J. (**1990**). ''Derivation of auditory filter shapes from notched-noise data,'' Hear. Res. **47**, 103–138.
Glasberg, B. R., and Moore, B. C. J. (**1994**). ''Growth-of-masking functions for several types of maskers,'' J. Acoust. Soc. Am. **96**, 134–144.
Green, D. M. (**1988**). *Profile Analysis: Auditory Intensity Discrimination* (Oxford University Press, New York).
Green, D. M. (**1992**). ''The number of components in profile analysis tasks,'' J. Acoust. Soc. Am. **91**, 1616–1623.
Green, D. M., and Berg, B. G. (**1991**). ''Spectral weights and the profile bowl,'' Q. J. Exp. Psychol. **43A**, 449–458.
Kidd, G., Jr. (**1993**). ''Individual differences in the improvement in spectral shape discrimination due to increasing number of nonsignal tones,'' J. Acoust. Soc. Am. **88**, 126–131.
Kidd, G., Mason, C. R., Brantley, M. A., and Owen, G. A. (**1989**). ''Roving-level tone-in-noise detection,'' J. Acoust. Soc. Am. **86**, 1310–1317.
Lentz, J. J., and Richards, V. M. (**1997**). ''Sensitivity to changes in overall level and spectral shape: An evaluation of a channel model,'' J. Acoust. Soc. Am. **101**, 3625–3635.
Lentz, J. J. (**1998**). ''A channel model applied to profile analysis,'' Doctoral dissertation, University of Pennsylvania, Philadelphia, PA.
Levitt, H. (**1971**). ''Transformed up–down methods in psychoacoustics,'' J. Acoust. Soc. Am. **49**, 167–177.
The MathWorks, Inc. (**1996**). MATLAB: *The Language of Technical Computing* (The MathWorks, Inc., Natick, MA).
Moore, B. C. J., Glasberg, B. R., van der Heijden, M., Houtsma, J. M., and Kohlrausch, A. (**1995**). ''Comparison of auditory filter shapes obtained with notched-noise and noise-tone maskers,'' J. Acoust. Soc. Am. **97**, 1175–1182.
Moore, B. C. J., and Sek, A. (**1994**). ''Effects of carrier frequency and background noise on the detection of mixed modulation,'' J. Acoust. Soc. Am. **96**, 741–751.
Patterson, R. D. (**1976**). ''Auditory filter shapes derived with noise stimuli,'' J. Acoust. Soc. Am. **59**, 640–654.
Patterson, R. D., and Moore, B. C. J. (**1986**). ''Auditory filters and excitation patterns as representations of frequency resolution,'' in *Frequency Selectivity in Hearing*, edited by B. C. J. Moore (Academic, London), pp. 123–177.
Richards, V. M., and Buss, E. (**1996**). ''Frequency correlation functions for the detection of a tone added to noise,'' J. Acoust. Soc. Am. **99**, 1645–1652.
Richards, V. M., and Lentz, J. J. (**1998**). ''Sensitivity to changes in level and envelope patterns across frequency,'' J. Acoust. Soc. Am. **104**, 3019–3029.
Richards, V. M., and Nekrich, R. D. (**1993**). ''The incorporation of level and level-invariant cues for the detection of a tone added to noise,'' J. Acoust. Soc. Am. **94**, 2560–2574.
Rosen, S., and Baker, R. J. (**1994**). ''Characterizing auditory filter nonlinearity,'' Hear. Res. **73**, 231–243.
van der Heijden, M., and Kohlrausch, A. (**1994**). ''Using an excitation-pattern model to predict auditory masking,'' Hear. Res. **80**, 38–52.
van Trees, H. L. (**1968**). *Detection, Estimation, and Modulation Theory* (Wiley, New York).
Viemeister, N. F. (**1979**). ''Temporal modulation transfer functions based upon modulation thresholds,'' J. Acoust. Soc. Am. **66**, 1364–1380.
Wright, B. A. (**1996**). ''Auditory filter asymmetry at 2000 Hz in 80 normal-hearing ears,'' J. Acoust. Soc. Am. **100**, 1717–1721.

Age differences in backward masking

Sara Elizabeth Gehr and Mitchell S. Sommers[a)]
Department of Psychology, Washington University, Campus Box 1125, St. Louis, Missouri 63130

(Received 17 February 1999; revised 2 August 1999; accepted 4 August 1999)

The present study was designed to assess the effects of age on the time course of backward masking. In experiment 1, thresholds for detecting a 10-ms, 500-Hz sinusoidal signal were measured as a function of the temporal separation between the signal and a 50-ms broadband masker. Subjects were younger (18–24) and older (over age 65) adults with normal hearing (thresholds less than 20 dB HL) for frequencies of 4 kHz and below. Younger subjects exhibited less overall masking and steeper recovery functions than did the older adults. Masked thresholds for younger participants approached unmasked thresholds for signal-masker delays greater than 6–8 ms. In contrast, older adults exhibited significant masking even at the longest delay tested (20 ms). In experiment 2, signal duration was decreased to 5 ms for a separate group of younger adults. Although overall thresholds were elevated for the shorter signal duration, the slope of the backward masking recovery function was not different from that observed for younger adults in experiment 1. The results suggest that age, independent of hearing loss, affects the temporal course of backward masking. © *1999 Acoustical Society of America.* [S0001-4966(99)05911-1]

PACS numbers: 43.66.Dc [SPB]

INTRODUCTION

Studies examining the time course of backward masking can provide important information about temporal processing in the auditory system. Previous studies (Newman and Spitzer, 1983; Raz *et al.*, 1990; Cobb *et al.*, 1993) have reported significant age differences in both the time course and overall level of backward masking. For example, Cobb *et al.* (1993) compared backward masking in younger and older adults using a broadband masker and signal frequencies of 500 and 4000 Hz. At the shortest signal-masker delay tested (2 ms), older adults exhibited approximately 28 dB more masking than younger adults. At the longest signal-masker delay (30 ms), older adults' thresholds exceeded those of younger adults by approximately 17 dB. These findings suggest that older adults exhibit greater overall masking and more prolonged recovery functions for backward masking and are consistent with other studies that have demonstrated age-related changes in temporal processing (see Fitzgibbons and Gordon-Salant, 1996 for review; but also see Moore *et al.*, 1992).

An important limitation on previous investigations of age-related changes in backward masking, however, is that most have confounded the effects of age and hearing impairment. For example, older subjects in the Cobb *et al.* (1993) investigation had significantly greater hearing loss than their younger counterparts.[1] Similarly, Newman and Spitzer (1983) compared backward recognition masking in normal-hearing younger adults and older subjects with age-adjusted normal hearing. In absolute terms, however, the older adults had significantly poorer sensitivity than the younger listeners. Consequently, it was not possible to dissociate the contributions of age and hearing loss to the observed differences in backward recognition masking.

A second difficulty with previous studies of age-related changes in backward masking is that the signal-masker delays that have been examined do not provide sufficiently detailed information about the function relating masked thresholds to signal-masker delays. Most previous investigations examining the time course of backward masking (Elliott, 1962a, b; Dolan and Small, 1984; Duifhuis, 1973; Oxenham and Moore, 1994, 1995) have reported functions that are relatively steep for signal-masker delays less than 15 ms and more gradual for intervals exceeding 20 ms. Thus, to obtain a sufficiently fine-grained analysis of backward masking recovery functions, it is necessary to sample a number of signal-masker delays less than 15 ms. Previous investigations of age-related changes in backward masking, however, have generally not included detailed sampling within the initial portion of the backward masking recovery function. For example, Cobb *et al.* (1993) sampled only two signal-masker delays less than 15 ms (2 and 8 ms). Newman and Spitzer (1983) tested a total of 12 delays ranging from 0 to 440 ms. All of the delays tested were separated by a minimum of 20 ms with a modal difference of 40 ms. The restricted range of signal-masker delays that has been tested in previous investigations, therefore, does not provide adequate details about age differences in backward masking at short signal-masker delays where most of the recovery occurs.

The present study was designed to provide a more fine-grained analysis of age differences in backward masking, independent of age-related hearing loss. The contribution of presbycusis was minimized by restricting participation to younger and older adults with audiologically normal hearing for frequencies of 4 kHz and below. In addition, a relatively low-frequency (500 Hz) signal was used because age differences in absolute sensitivity are generally small at this frequency (Gates and Cooper, 1991; Willott, 1991). Finally, the experiments used narrowly spaced signal-masker delays to obtain detailed characteristics of the time course of backward masking in the two age groups. On the basis of previous

[a)]Electronic mail: Msommers@artsci.wustl.edu

studies of age changes in temporal processing (Newman and Spitzer, 1983; Cobb *et al.*, 1993; Fitzgibbons and Gordon-Salant, 1996), the working hypothesis for the present investigation was that age would alter both the extent and time course of backward masking.

I. EXPERIMENT 1

A. Method

1. Subjects

Five older adults (age range 67–82) and ten younger adults (range 18–24) served as experimental subjects. Older adults were community-dwelling volunteers recruited from the subject pool maintained by the Aging and Development Program at Washington University. Younger adults were recruited by posted advertisements. All subjects were paid $10/hour for participating. As a group, older adults had greater experience with psychoacoustic tasks. Two of the older listeners had previously participated in an investigation of auditory filter shapes (approximately 15 h of testing) using both simultaneous and forward notched-noise maskers (Sommers and Gehr, 1998). In contrast, all of the younger adults were naive psychoacoustic observers. Pure-tone air-conduction thresholds for octave frequencies from 250–4000 Hz were less than 20 dB HL (ANSI, 1989) for all subjects. Mean thresholds for older and younger adults differed by less than 7 dB for all test frequencies except 250 Hz (thresholds 10 dB greater for older adults). Absolute sensitivity was measured using the same adaptive tracking procedure used to assess backward masking (see below) except that signal duration was 250 ms and no masker was presented.

2. Stimuli and equipment

The signal was a 10-ms, 500-Hz sinusoid gated with 2-ms raised-cosine ramps. The masker was a 50-ms sample of white noise gated with 2-ms raised-cosine ramps. A new sample of noise was generated for each interval of the adaptive tracking procedure. The signal and masker were digitally generated using a 20-kHz sampling rate (TDT AP2) and input to separate channels of a 16-Bit D/A converter (TDT DA1). The outputs of the D/A converter were low-pass filtered at 8.5 kHz (TDT FLT3), and the signal was attenuated (TDT PA3). The signal and masker were mixed (TDT SM3), input to a headphone driver (TDT HB6), and presented to one channel of Sony MDR-7506 headphones. The programmable attenuator controlled signal level. The level of the noise was 80 dB SPL ($N_0 = 41$ dB). Presentation levels were measured at the output of the transducer used for stimulus presentation in a NBS-9A 6-cc coupler with a Brüel and Kjaer sound level meter (model 2204) set on the linear weighting scale. The signals used for calibration had the same temporal and spectral characteristics as those used during testing. Signals were calibrated at maximum amplitude as computed on the array processor. Signal-masker delays (specified as the time interval between the 0 voltage points of the envelope of the electrical signals) of 1, 2, 4, 6, 8, 10, and 20 ms were tested.

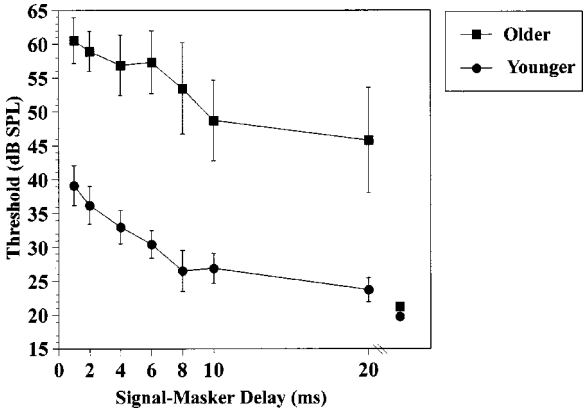

FIG. 1. Comparison of backward masking recovery functions for normal-hearing older and younger adults. The two single points show the mean unmasked thresholds for the two groups (older adults ■; younger adults ●). Error bars show standard deviations of the mean.

3. Procedure

Subjects were tested individually while seated in a double-walled sound attenuating booth (IAC). A two-interval forced-choice tracking procedure (two-down, one-up, Levitt, 1971) was used to determine signal threshold for each signal-masker delay. Each run consisted of 60 trials. For each trial, one interval contained the noise alone and the other contained noise plus signal. The interval containing the signal was selected randomly on each trial. There was a 700-ms delay between the two intervals in each trial and a 1-s delay between trials. For each threshold determination, the starting level of the signal was set at least 10 dB above the estimated threshold value. The initial step size was 10 dB. After the first three reversals, the step size was reduced to 2 dB. Feedback was provided after each trial. Threshold for each run was calculated as the average of the last even number of reversals (excluding the first 3). Unmasked thresholds for the 10-ms signal were obtained using the identical procedures and equipment without the masker.

Participants were asked to indicate which interval they thought contained the signal. Each signal-masker delay was run at least twice. Testing order for the different signal-masker delays was determined randomly for each participant with the exception that the same signal-masker delay could not be presented successively. If the difference between the two threshold estimates for a condition was greater than 5 dB, the condition was run again until two estimates met the 5-dB criterion. The final threshold was the average of the two trials that met the 5-dB criterion.

B. Results and discussion

Figure 1 displays mean signal thresholds as a function of signal-masker delay for older and younger adults. Unmasked thresholds are shown as unconnected points. As expected based on the similarity of their hearing profiles, unmasked thresholds were nearly identical for the two groups. Masked thresholds, however, were higher for older than for younger adults at all signal-masker delays. At the shortest delay (1 ms) younger adults exhibited approximately 19 dB of masking (masked threshold-unmasked threshold). Older adults, in

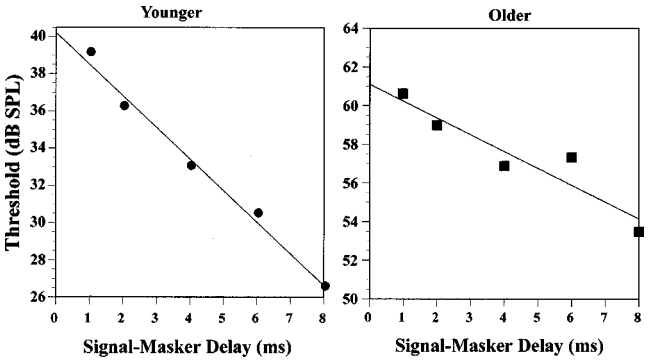

FIG. 2. Comparison of best fitting linear regressions for functions relating mean masked thresholds to signal-masker delay for younger and older subjects. Regressions were limited to signal-masker delays of 8 ms or less (see text). Both graphs have a range of 14 dB on the ordinate for ease of comparison.

contrast, exhibited approximately 40 dB of masking at the 1-ms signal-masker delay. Differences in masked thresholds for the two groups ranged from 22 to 25 dB across the set of delays tested. At the longest signal-masker delay (20 ms), masked thresholds for younger adults approached, but did not reach, values obtained for the unmasked condition. In contrast, older adults exhibited considerable masking (approximately 24 dB) even at the 20-ms signal-masker delay.

To examine age differences in the time course of backward masking, a mixed design analysis of variance was conducted on the masked threshold data from the two groups. Thresholds at each of the delay conditions were entered as repeated-measures variables. Age group served as an independent-measures variable. The analysis indicated a significant effect for delay condition [$F(7,91)=32.5$, $p<0.001$]; as expected, thresholds declined as a function of signal-masker delay. Thresholds were also significantly higher for older than for younger adults [$F(1,13)=31.43$, $p<0.001$].

To further examine the observed age differences, thresholds at each of the delays were compared to unmasked thresholds. *Post hoc* Tukey HSD pairwise comparisons indicated that, for younger adults, masked thresholds were not significantly different from unmasked thresholds for delays of 8 ms and above ($p<0.001$ for delays of 1, 2, and 4 ms; $p<0.01$ for 6-ms delay; and $p>0.4$ for delays exceeding 6 ms). This finding is consistent with previous studies of backward masking (Elliott, 1962a, b) indicating a relatively steep initial portion of the backward masking recovery function (i.e., signal-masker delays less than approximately 10–15 ms) in younger adults. Older adults, however, exhibited elevated thresholds for all signal-masker delays tested, including the longest of 20 ms ($p<0.001$ for all comparisons).

For both older and younger adults, best fitting linear regression lines were calculated for the function relating mean masked threshold to signal-masker delay. The results of these analyses are shown in Fig. 2. The regressions were limited to signal-masker delays between 1 and 8 ms because thresholds for younger adults had returned to baseline levels (i.e., were not significantly different from unmasked thresholds) by the 8-ms signal-masker delay. Overall, the linear regressions provided good fits to the obtained data (R^2 values were 0.99 and 0.88 for younger and older adults, respectively). For younger adults, the slope of the function relating signal threshold to signal-masker delay was -1.8 dB/ms (95% confidence intervals$=-1.9$ to -1.4). In comparison, the slope for the older listeners was -0.9 dB/ms^2 (95% confidence intervals$=-1.2$ to -0.3). These findings suggest that in addition to age-related increases in overall masking, older and younger adults differed with respect to the time course of backward masking.

One possible concern with this conclusion is that, although both groups had absolute sensitivity within normal limits (<20 dB HL), sensitivity was lower for the older than for the younger adults. To investigate whether this differential hearing loss contributed to age differences in backward masking, partial correlations (partialing out age) were computed between thresholds at 500 Hz and amount of backward masking at each of the signal-masker delays. No significant correlations were observed in the analyses, suggesting that age differences in backward masking were not simply a result of slightly elevated thresholds for older adults.

A second issue that was addressed is that, as shown in Fig. 1, both older and younger adults exhibited considerable individual variability in backward masking. One question raised by this finding is whether individual subjects varied with respect to the *relative* amount of masking they exhibited across delays. That is, did individuals who evidenced relatively high amounts of backward masking at one signal-masker delay also exhibit relatively high masking levels at other delays? To investigate this question, correlations were computed to determine the relationship between the amount of masking exhibited at each of the signal-masker delays. For young adults, the correlations were restricted to delays of 8 ms or less because, as noted, masked thresholds approached unmasked thresholds for delays of 8 ms and above. Correlation coefficients for this group were all positive and exceeded 0.5 (range 0.51 to 0.97). For older adults, the correlations were conducted across all signal-masker delays and ranged from 0.6 to 0.93. Taken together, these findings suggest that, although backward masking varies considerably across individuals, relative masking as a function of signal-masker delay was generally consistent across participants.

The findings from experiment 1 indicated that normal-hearing older adults exhibited a greater amount of, and slower recovery from, backward masking than younger adults. One issue that we wanted to investigate further was whether the observed age differences in the time course of backward masking were a consequence of the higher threshold values observed for older adults. Therefore, experiment 2 examined the time course of backward masking for younger adults when signal duration was reduced from 10 to 5 ms. Reducing signal duration shortens the window for temporal integration and was therefore expected to increase thresholds. Pilot testing with a group of participants not included in experiment 2 indicated that reducing stimulus duration from 10 to 5 ms increased thresholds 10–15 dB at the shortest signal-masker delay.[3] If the observed age-related changes in the time course of backward masking were a consequence of higher thresholds in older adults, then relative to experiment 1, younger listeners tested with a shorter duration signal

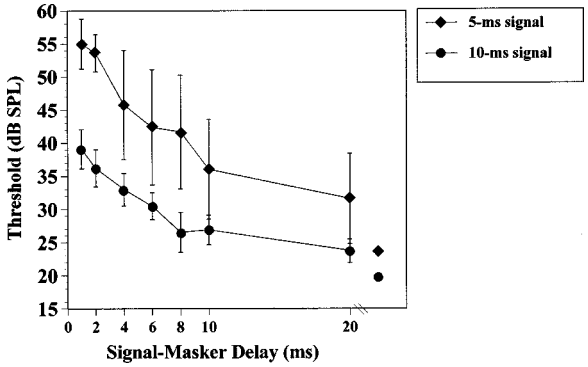

FIG. 3. Backward masking recovery functions for younger subjects for signal durations of 5 (♦) and 10 (●) ms. The two single points show mean unmasked thresholds for the two durations. The 10-ms data have been replotted from experiment 1. Error bars show standard deviations of the mean.

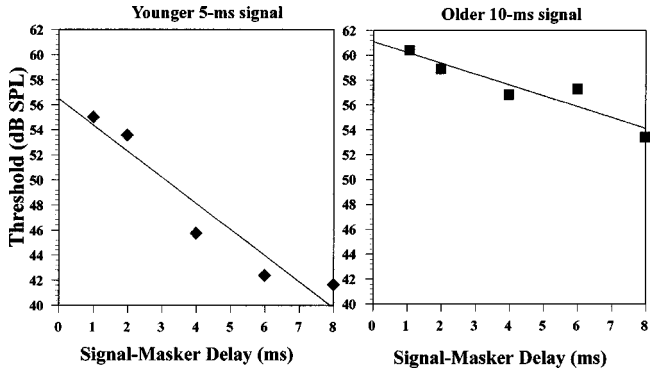

FIG. 4. Same as Fig. 2 except that the comparison is between younger subjects tested with a 5-ms signal and older subjects tested with a 10-ms signal. Ordinate values are identical for the two functions.

should exhibit higher thresholds and decreased slopes for the backward masking recovery function.

II. EXPERIMENT 2

A. Method

1. Subjects

Three younger adults with normal hearing (thresholds for octave frequencies from 250 to 4000 Hz $<$20 dB HL) were tested in experiment 2. Duration of testing and overall experience with the backward masking task were similar to younger adults tested in experiment 1. None of the subjects had participated in experiment 1. All subjects received course credit for their participation.

2. Stimuli, equipment, and procedures

The equipment and procedures were identical to experiment 1. The stimuli were also identical to experiment 1 except that signal duration was set to 5 rather than 10 ms.

B. Results and discussion

Figure 3 compares mean thresholds for younger adults tested with the 10-ms (experiment 1) and 5-ms (experiment 2) signal durations as a function of signal-masker delay. As expected, both masked and unmasked thresholds were elevated for the shorter signal duration. For the 1-ms signal-masker delay, masked thresholds for the 5-ms signal were elevated approximately 14 dB relative to the corresponding condition in experiment 1. At the longest signal-masker delay (20 ms), thresholds in experiment 2 were approximately 7 dB greater than unmasked thresholds (compared with a 4-dB difference between masked and unmasked thresholds at the 20-ms delay for experiment 1). Variability in thresholds was also greater in experiment 2 than in experiment 1 because of the smaller number of subjects. Overall, reducing signal duration increased thresholds at all signal-masker delays, but threshold values were still somewhat lower than was observed for older adults in experiment 1 (especially for the longer signal-masker delays).

Despite increased thresholds in experiment 2, the time course of backward masking for younger adults in experiments 1 and 2 was very similar. Figure 4 compares the slopes of backward masking recovery functions for younger adults tested with the 5-ms signal and older adults tested with the 10-ms signal duration. Note that masked thresholds for both groups were elevated considerably relative to younger adults tested with a 10-ms signal. In fact, at the 1-ms delay, masked thresholds for older adults tested with the 10-ms signal and younger adults tested with the 5-ms signal were within 5 dB. The figure shows best fitting linear regressions for the functions relating masked threshold to signal-masker delay for intervals less than or equal to 8 ms. The overall fit of the function for the 5-ms signal duration ($R^2=0.91$) was similar to that observed for younger adults in experiment 1 ($R^2=0.99$). The slope of the function was -2.0 dB/ms (95% confidence intervals$=-3.1$ to -1.1), which is similar to the slope observed for younger adults in experiment 1 (-1.7 dB/ms). These findings suggest that, despite significantly higher thresholds for younger adults in experiment 2 compared with experiment 1, the time course of backward masking was similar in the two experiments. Thus, the age differences in backward masking found in experiment 1 probably cannot be attributed to the higher thresholds observed in older listeners.

III. DISCUSSION

The results of the present study suggest that age, independent of hearing loss, can significantly affect both the extent and time course of backward masking. In experiment 1, masked thresholds for younger listeners approached unmasked thresholds for signal-masker delays exceeding approximately 6–8 ms. In contrast, masked thresholds for older adults were significantly elevated, relative to unmasked baselines, even for the longest signal-masker delay tested (20 ms). Experiment 2 demonstrated that reducing signal duration for younger adults increased masked thresholds but did not reduce the slope of the backward masking recovery function. This finding indicates that age differences in the time course of backward masking observed in experiment 1 were not simply a consequence of higher thresholds for older adults.

A number of findings from the present study are consistent with results of previous investigations of backward masking in older and younger adults (Elliott, 1962a, b; Duifhuis, 1973; Dolan and Small, 1984; Oxenham and Moore,

1994, 1995). First, as noted, prior studies of backward masking have generally reported that the function relating masked thresholds to signal-masker delay consists of two linear components—a steeper initial portion for signal-masker delays less than approximately 15 ms, followed by a more gradual approach to unmasked thresholds. Although these two components were not as distinct in the present experiment as in previous studies, the current findings are broadly consistent with these trends (especially for younger adults).

Also consistent with previous results (Cobb *et al.*, 1993), age differences in backward masking were not restricted to the initial portion of backward masking recovery functions. At the longest signal-masker delay (20 ms), older adults in experiment 1 exhibited approximately 25 dB of masking. In contrast, younger adults were within 5 dB of their unmasked thresholds for signal-masker delays greater than 6 ms. Cobb *et al.* (1993) also reported age differences in the effects of backward masking for long signal-masker delays. The mean threshold value for younger adults at a 30-ms signal-masker delay in their study did not differ significantly from unmasked thresholds. Older adults, in contrast, exhibited approximately 20 dB of masking for the 30-ms delay. Taken together, these findings support age-related declines in both the initial rate of recovery from backward masking and in the time required to eliminate backward masking effects.

The current findings also extend earlier results by providing a more detailed analysis of the initial portion of backward masking recovery functions. Examination of threshold functions for signal-masker delays of 8 ms or less indicated that the slopes of these functions were well fit by a straight line for both age groups but were approximately twice as high for younger than for older adults. Thus, even in the absence of significant age-related hearing loss, older adults exhibited poorer temporal processing than their younger counterparts.

At present, the mechanisms underlying backward masking are not well understood. Results from several investigations (Elliott, 1962a, b; Duifhuis, 1973; Dolan and Small, 1984) suggest that both central and peripheral factors may contribute to backward masking. Evidence that backward masking can be observed with dichotic as well as monotic presentations has been interpreted as indicating a central component of backward masking (Elliott, 1962a, b). However, several investigators (Duifhuis, 1973; Dolan and Small, 1984) have reported that backward masking varies inversely as a function of signal frequency, which would support a peripheral locus for the effect. The general shape of backward masking recovery functions has also been taken as evidence for both peripheral and central contributions (Dolan and Small, 1984). Specifically, Dolan and Small (1984) suggested that the steeply sloping initial portion of the function may be mediated by peripheral factors while the more gradually sloping later portion may reflect central factors.

Unfortunately, the proposal that the initial and final portions of backward masking recovery functions can be attributed to different mechanisms (peripheral and central, respectively) remains largely untested. To the extent that this hypothesis is correct, however, the present results suggest that both factors can contribute to age-related differences in backward masking. If the initial portion of backward masking recovery functions reflect the operation of peripheral factors, then the age-related slope differences observed for this portion of the function in experiment 1 would support peripheral declines as contributing to age differences in backward masking. Although older and younger adults in the present study had similar absolute sensitivity, Cobb *et al.* (1993) have argued that subclinical changes, such as age-related impairments in hair cell motility, may contribute to age differences in backward masking. Central factors would also be implicated in the current study because age differences were observed in the final as well as the initial portion of masking functions.

One peripheral factor that is unlikely to have contributed to the observed age differences is age-related changes in the width of auditory filters. Results from several studies (Duifhuis, 1973; Dolan and Small, 1984) suggest that the transient response time (ringing) of auditory filters can contribute to backward masking. Because wider auditory filters have reduced transient response times, age-related broadening of auditory filters could affect backward masking. However, a number of investigations (Peters and Moore, 1992; Sommers and Humes, 1993) have found similar auditory filter widths for normal-hearing older and younger adults. Furthermore, age-related broadening of auditory filters would tend to *reduce*, rather than increase, the effects of backward masking that result from ringing of auditory filters. Thus, it is unlikely that the increased backward masking for older adults in the present study was a result of differences in frequency selectivity.

Another factor that could have contributed to the observed age differences in backward masking is reduced masker sensation levels (SLs). Recall that, although absolute thresholds were within normal limits for both age groups, older adults had poorer absolute sensitivity for all test frequencies (octave frequencies from 250–4000 Hz). If the recovery function for backward masking is more gradual at lower masker SLs, the poorer absolute sensitivity of older adults may have contributed to the shallower slopes of their backward masking recovery functions. It is currently unclear how backward masking varies as a function of masker SL for broadband maskers, especially for relatively small differences in SL such as those for older and younger adults in the current study. One finding arguing against differences in masker SL as a primary contributor to age-related changes in backward masking is that the amount of backward masking was not correlated with absolute sensitivity at 500 Hz. Additional investigations examining slopes of backward masking recovery functions at different masker SLs for younger and older adults would nevertheless be a useful direction for future research trying to identify factors that may have contributed to the age differences observed in the present study.

A potential concern in studies of backward masking is the role of practice. Moore (1995) has suggested that estimates of backward masking are highly dependent upon the amount of practice that participants have with the task and that highly practiced subjects may fail to exhibit backward masking. In contrast, other investigators (Elliott, 1962a, b; Oxenham and Moore, 1994) have reported significant

amounts of backward masking even after extensive practice with the task. For example, Elliot (1962b) reported backward masking in both monotic and dichotic conditions for subjects who had been trained on the task for 12 h. Oxenham and Moore (1994, 1995) tested subjects in forward-only, backward-only, and combined forward and backward masking tasks. Significant amounts of backward masking were observed despite at least 8 h of practice for each subject (divided between the three different conditions). In fact, Oxenham and Moore (1994) reported that one of their subjects was trained for up to 4 h per day for 2 weeks and demonstrated little or no improvement for backward-only or forward-only masking.

In the present study, the order of signal-masker delays was randomized for each participant and the same signal-masker delay was never repeated on successive runs. Therefore, it was possible to examine practice effects by comparing threshold estimates obtained for the same signal-masker delay. Consistent with other reports (Elliott, 1962a, b; Oxenham and Moore, 1994), no systematic improvements in backward masking thresholds were observed for either age group even when the same signal-masker delay was separated by up to 3 h of testing. In addition, only a small percentage of the conditions for each subject failed to meet the stability criterion and this failure rate did not differ as a function of age. Failures to meet the stability criterion were also not related to the amount of practice between successive threshold determinations for either younger or older adults.

Despite these considerations, because backward masking exhibits greater individual variability and is more susceptible to training effects than most psychoacoustic tasks, it is important to note that a potential limitation of the current study is that older and younger adults may not have been performing at optimal levels. It is possible, for example, that older subjects require more extensive training than younger adults to obtain asymptotic performance. One finding arguing against this as a factor in the present experiment is that no age differences were observed in the number of conditions (intervals) that failed to meet the stability criterion. In addition, older adults were generally more experienced with psychoacoustic tasks than younger adults. This increased experience for older adults would serve to offset age differences that might arise from factors such as task novelty. Finally, despite considerable individual variability in backward masking, the slope estimates for two separate groups of young adults ($n=10$ for experiment 1 and $n=3$ for experiment 2) were quite similar (-1.7 and -2.0 dB/ms for experiments 1 and 2, respectively). In sum, the above considerations suggest that training alone would be unlikely to eliminate the observed age differences in backward masking but that additional practice might reduce the magnitude of such differences.

One clinical implication of the present findings is that they may partially explain why older adults exhibit poorer speech perception than younger listeners, even when audibility in the two groups is equated (CHABA, 1988). Specifically, age-related changes in backward masking may make it more difficult for older listeners to perceive earlier-occurring information in speech signals. In consonant–vowel–consonant (CVC) stimuli, for example, backward masking of the initial consonant by the more intense vowel may be greater for older adults. Consistent with this proposal, Sommers (1996) reported that the largest age differences in identifying monosyllabic CVC stimuli for normal-hearing older and younger adults was in recognition of initial consonants. Danaher *et al.* (1973) reported that backward masking significantly impaired listeners' ability to discriminate formant frequency transitions, which are important cues for phonetic discriminations. Thus, age differences in the extent and time course of backward masking may impair speech perception in older adults by increasing the difficulty of phonetic discriminations in earlier portions of the speech signal.

IV. SUMMARY AND CONCLUSIONS

(1) Older adults exhibited greater masking and slower recovery functions than younger adults in a backward masking task, despite similar absolute sensitivity for the two groups.
(2) Age differences in the time course of backward masking were probably not the result of age-related increases in masked thresholds.
(3) Although it is presently unclear what might account for the observed age differences in backward masking, there is some evidence to suggest that both peripheral and central factors may contribute to the changes.

ACKNOWLEDGMENTS

This research was supported by the Brookdale Foundation and NIDCD. The authors would like to thank Emily Buss and Peter Fitzgibbons for comments that substantially improved an earlier version of this manuscript. Lisa Marcus and Emily McCutcheon provided valuable help in conducting experimental sessions.

[1]Cobb (1995) acknowledged this problem and noted it as a limitation of the previous results.

[2]The regressions were limited to delays of 8 ms or less so that age comparisons could be made across an identical range of delays. The slope for the older adult function across all delays was -0.81 dB/ms ($R^2=0.90$; 95% confidence intervals$=-1.1$ to -0.4).

[3]We elected to elevate thresholds by changing signal duration, rather than increasing masker level, because pilot testing indicated that masker levels would need to exceed 95 dB SPL to increase thresholds for young adults to the point where they approximated those observed for older adults.

ANSI (**1989**). (ANSI S3.6, 1989). *Specification for audiometers* (American National Standards Institute, New York).

CHABA, Committee on Hearing and Biacoustics, Working Group on Speech Understanding and Aging. (**1988**). ''Speech understanding and aging,'' J. Acoust. Soc. Am. **83**, 859–895.

Cobb, F. E. (**1995**). ''Age-associated degeneration of backward masking task performance: Evidence of declining temporal resolution abilities in normal listeners: Commentary,'' Audiology **34**, 160.

Cobb, F. E., Jacobson, G. P., Newman, C. W., Kretschmer, L. W., and Donnelly, K. A. (**1993**). ''Age-associated degeneration of backward masking task performance: Evidence of declining temporal resolution abilities in normal listeners,'' Audiology **32**, 260–271.

Danaher, E. M., Osberger, M. J., and Pickett, J. M. (**1973**). ''Discrimination of formant frequency transitions in synthetic vowels,'' J. Speech Hear. Res. **16**, 439–451.

Dolan, T. G., and Small, Jr., A. M. (**1984**). ''Frequency effects in backward masking,'' J. Acoust. Soc. Am. **75**, 932–936.
Duifhuis, H. (**1973**). ''Consequences of peripheral frequency selectivity for nonsimultaneous masking,'' J. Acoust. Soc. Am. **54**, 1471–1488.
Elliott, L. L. (**1962a**). ''Backward masking: Monotic and dichotic conditions,'' J. Acoust. Soc. Am. **34**, 1108–1115.
Elliott, L. L. (**1962b**). ''Backward and forward masking of probe tones of different frequencies,'' J. Acoust. Soc. Am. **34**, 1116–1117.
Fitzgibbons, P. J., and Gordon-Salant, S. (**1996**). ''Auditory temporal processing in elderly listeners,'' J. Am. Acad. Audiol. **7**, 183–189.
Gates, G. A., and Cooper, J. C. (**1991**). ''Incidence of hearing decline in the elderly,'' Acta Oto-Laryngol. **111**, 240–248.
Levitt, H. (**1971**). ''Transformed up-down methods in psychoacoustics,'' J. Acoust. Soc. Am. **49**, 467–477.
Moore, B. C. (**1995**). ''Frequency analysis and masking,'' in *Hearing*, edited by Brian C. J. Moore (Academic, San Diego, CA), Chap. 5, pp. 194–195.
Moore, B. C., Peters, R. W., and Glasberg, B. R. (**1992**). ''Detection of temporal gaps in sinusoids by elderly subjects with and without hearing loss,'' J. Acoust. Soc. Am. **92**, 1923–1932.
Newman, C. W., and Spitzer, J. B. (**1983**). ''Prolonged auditory processing time in the elderly: evidence from a backward recognition-masking paradigm,'' Audiology **22**, 241–252.
Oxenham, A. J., and Moore, B. C. (**1994**). ''Modeling the additivity of nonsimultaneous masking,'' Hear. Res. **80**, 105–118.
Oxenham, A. J., and Moore, B. C. J. (**1995**). ''Additivity of masking in normally hearing and hearing-impaired subjects,'' J. Acoust. Soc. Am. **98**, 1921–1934.
Peters, R. W., and Moore, B. C. (**1992**). ''Auditory filter shapes at low center frequencies in young and elderly hearing-impaired subjects,'' J. Acoust. Soc. Am. **91**, 256–266.
Raz, N., Millman, D., and Moberg, P. J. (**1990**). ''Mechanism of age-related differences in frequency discrimination with backward masking: Speed of processing or stimulus persistence?'' Psychol. Aging **5**, 475–481.
Sommers, M. S. (**1996**). ''The structural organization of the mental lexicon and its contribution to age-related changes in spoken word recognition,'' Psychol. Aging **11**, 333–341.
Sommers, M. S., and Gehr, S. E. (**1998**). ''Auditory suppression and frequency selectivity in older and younger adults,'' J. Acoust. Soc. Am. **103**, 1067–1074.
Sommers, M. S., and Humes, L. E. (**1993**). ''Auditory filter shapes in normal-hearing, noise-masked normal, and elderly listeners,'' J. Acoust. Soc. Am. **93**, 2903–2914.
Willott, J. F. (**1991**). *Aging and the Auditory System: Anatomy, Physiology and Psychophysics* (Singular, San Diego).

Ripple depth and density resolution of rippled noise

A. Ya. Supin, V. V. Popov, O. N. Milekhina, and M. B. Tarakanov
Institute of Ecology and Evolution, Russian Academy of Sciences, 33 Leninsky Prosp., 117071 Moscow, Russia

(Received 13 August 1998; accepted for publication 22 July 1999)

Depth resolution of spectral ripples was measured in normal humans using a phase-reversal test. The principle of the test was to find the lowest ripple depth at which an interchange of peak and trough position (the phase reversal) in the rippled spectrum is detectable. Using this test, ripple-depth thresholds were measured as a function of ripple density of octave-band rippled noise at center frequencies from 0.5 to 8 kHz. The ripple-depth threshold in the power domain was around 0.2 at low ripple densities of 4–5 relative units (center-frequency-to-ripple-spacing ratio) or 3–3.5 ripples/oct. The threshold increased with the ripple density increase. It reached the highest possible level of 1.0 at ripple density from 7.5 relative units at 0.5 kHz center frequency to 14.3 relative units at 8 kHz (5.2 to 10.0 ripple/oct, respectively). The interrelation between the ripple depth threshold and ripple density can be satisfactorily described by transfer of the signal by frequency-tuned auditory filters. © *1999 Acoustical Society of America.* [S0001-4966(99)02011-1]

PACS numbers: 43.66.Fe, 43.66.Jh [RVS]

INTRODUCTION

Spectral shape resolution is of obvious importance for discriminating complex acoustic stimuli. It has been a subject of many psychophysical studies with the use of various signal types as complex sounds. A productive approach to study spectral shape discrimination is ''profile analysis'' when a signal is composed of a number of sinusoids; the adjustment of sinusoid amplitudes results in various spectral profiles (e.g., Green, 1983, 1988, 1992; Green *et al.*, 1984, 1987). Using this approach, various alterations of spectral shape were tested, in particular, increments to a single component, step functions, and sinusoidal ripples. Those studies used rather wide frequency spacing between adjacent components which made them addressing to different critical bands. Thus, the studies were addressed mainly to the question of how the auditory system compares intensity information in different frequency channels (Durlach *et al.*, 1986).

Another way was to use rippled spectra which imitate coarse or fine spectrum patterns depending on the ripple density. Many studies using rippled noise were directed to investigate pitch perception mechanisms (Yost *et al.*, 1977, 1996; Yost and Hill, 1979; Bilsen and Wieman, 1980; Yost, 1982; Patterson *et al.*, 1996). However, rippled noise can be considered as a model for complex sounds irrespective of the involved mechanisms. The resolvable ripple density (spacing) can be used as a measure of the spectrum pattern resolution (Supin *et al.*, 1994, 1997, 1998).

In those studies, major attention was paid for discrimination of spectral patterns with various ripple densities. For a better knowledge of spectral shape analysis, discrimination of both ripple density and ripple depth should be studied. For this purpose, a reliable model could be rippled spectra which vary both in ripple density and in ripple depth. In previous studies (Popov and Supin, 1984; Supin *et al.*, 1994) we have made preliminary measurements of ripple-depth thresholds as a function of ripple density. These measurements were made using only wideband rippled noise; thus, a question remained whether the ripple-depth threshold versus ripple density dependence is one and the same in any part of the frequency range of hearing.

Therefore, in the present study we investigated the ripple-depth threshold dependence versus ripple density using narrow-band rippled noises of different center frequencies. In order to make the results comparable with those obtained earlier, we used the same experimental paradigm as in our preceding studies (Supin *et al.*, 1994, 1997). Namely, to find the ripple depth discrimination limit, we used the phase reversal test. Its principle is depicted in Fig. 1. Rippled noise of a certain ripple depth and density is presented to a listener. At a certain instant, it is replaced by a noise of the same intensity, bandwidth, ripple depth, and density but with the opposite positions of spectral peaks and troughs at the frequency scale, i.e., ripple phase reversal occurs. This spectra pair is shown in Fig. 1 by open and filled areas. The listener can only detect this switch if he discriminates the rippled spectrum pattern. If the spectrum pattern is not resolvable since the ripple depth is too small, or the ripples are spaced too densely, or both, the switch cannot be detected because the noise before and after the switch is the same in all respects except for the peak and trough positions. Thus, the threshold ripple depth at a certain ripple density can be found. Immediate replacing of one spectral pattern by another makes the test addressing to sensory abilities without involving short-term memory, contrary to successive presentation of two compared stimuli with an interval between them. This approach is quite similar to one widely used to measure visual acuity: in both cases the phase reversal of a test grid is used to find the contrast threshold as a function of grid density.

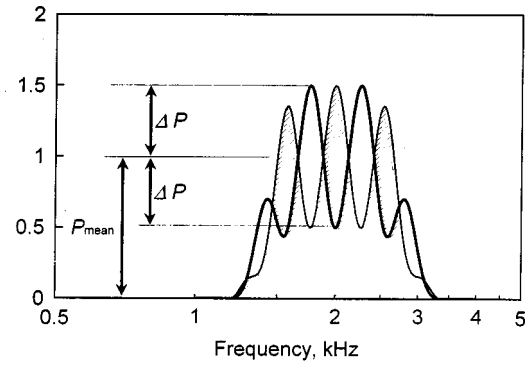

FIG. 1. Examples of rippled spectra with a center frequency of 2 kHz. Relative ripple density 4, ripple density 0.5. Filled and open areas—rippled spectra which replace one another at the phase-reversal test. Parameters P_{mean} and ΔP are indicated by arrows. Ripple spacing looks constant at the logarithmic frequency scale, i.e., ripple density is frequency proportional.

I. MATERIAL AND METHODS

A. Subjects

Five subjects (laboratory staff) were used. They were 25 to 38 years old and had no signs of hearing loss. All had praxis in psychoacoustic experiments. The experiments were performed in accordance with the guidelines of the Declaration of Helsinki.

B. Stimulus parameters

Rippled noise stimuli used in this study were of octave equivalent rectangular bandwidth (ERB). Their power spectra were enveloped by a function which was flat within ± 0.25 octave from the center frequency and bounded by two quarter-octave ramps which were cosine functions of frequency logarithm (Fig. 1). The shallow-ramped spectrum shape was chosen since sharp spectral edges result in edge effects increasing ripple resolution (Supin *et al.*, 1998). Within this envelope, spectra had ripples which were described by a cosine function (in the power domain) of frequency logarithm (frequency-proportional spaced).

To characterize a ripple pattern, two main parameters were used: ripple density and depth. The ripple density was defined as a ratio of the center frequency to ripple spacing (relative density):

$$D_{\text{rel}} = F_0 / \delta F, \tag{1}$$

where D_{rel} (relative units) is the density, F_0 (kHz) is the center frequency of a ripple cycle, and δF (kHz) is the ripple spacing. Since ripples were frequency proportional, the density D_{rel} was constant across the bandwidth. In this case, the ripple density can also be characterized as a number of ripples per octave (D_{oct}, cycles/oct). There is a constant ratio between these two metrics: $D_{\text{oct}} \approx D_{\text{rel}} \ln 2 \approx 0.7 D_{\text{rel}}$. Below we use both metrics to characterize the ripple density: the relative and octave density.

Ripple depth was defined as a relative deviation of peaks and troughs from the mean level:

$$m = \Delta P / P_{\text{mean}} = (P_{\max} - P_{\min}) / (P_{\max} + P_{\min}), \tag{2}$$

where m is the ripple depth, ΔP is the deviation from the mean power density P_{mean}, and $P_{\max}$ and $P_{\min}$ are the power densities at ripple peaks and troughs, respectively. With these definitions, Fig. 1 exemplifies spectra with a center frequency of 2 kHz, ripple density of $D_{\text{rel}} = 4$ ($D_{\text{oct}} = 2.8$), and ripple depth of 0.5. Note that the ripples seem equally spaced being presented at the logarithmic frequency scale.

The following stimulus parameters were used. Center frequencies were 0.5, 1, 2, 4, and 8 kHz. Ripple density D_{rel} varied by steps as follows: 4, 5, 6, 7, 8, 10, 12, 14, 16, 20, 24, 28, and 32 relative units (which corresponds to D_{oct} of 2.8 to 22.4 cycles/oct); densities lower than $D_{\text{rel}} = 4$ ($D_{\text{oct}} = 2.8$) were not tested because of an insufficient number of ripples (less than 3) within the noise bandwidth. Ripple depth defined according to Eq. (2) varied in steps: 0.05, 0.07, 0.1, 0.15, 0.2, 0.3, 0.5, 0.7, and 1.

C. Signal generation

The signals were digitally generated at sampling rates of 10, 14, 20, 28, or 40 kHz, keeping the sampling rate at least four times higher than the center frequency of the signal but not lower than 10 kHz and not higher than 40 kHz. The generation program simulated steps as follows. A wideband signal (random digital sequence with the sampling rate, uniformly distributed between ± 1) was filtered by one of the two digital filters. Frequency responses of the filters used are of the type shown in Fig. 1. The filters determined both the noise passband and ripple pattern (ripple density and depth). To perform filtering, a specified filter form was inversely Fourier transformed to obtain the temporal transfer function. Then the wideband signal (random digital sequence) was convoluted with the transfer function; the result was a filtered rippled noise.

To generate a signal with ripple phase-reversals, two filters were used which had equal passbands, levels, ripple densities, and depths but opposite ripple peak–trough positions (see Fig. 1). Phase reversals were performed by switching the wideband signal from one filter input to another; filter outputs were summed. If a noise burst without phase reversals was generated, the same procedure was used but both filters were identical.

Note that phase-reversal switches were made at the filter inputs, not outputs. Otherwise, clicks at phase reversals could arise. With phase reversals at the filter inputs, neither signal discontinuity nor transient spectrum splatter appeared at the filter outputs. Since both of the filters had equal rise–fall times (which was a direct consequence of their equal bandwidths), the signal level decay at one filter output was compensated by the signal level rise at another filter output, thus the switch did not result in any transient level shift exceeding fluctuations intrinsic in narrow-band noise. The generation procedure were described in more detail (Supin *et al.*, 1998).

Each noise burst (either with or without phase reversals) lasted 2 s. Phase reversals, if present, occurred every 333 ms, i.e., a burst with phase reversals contained three cycles of switching from one filter to another and back. These param-

eters were used since the phase-reversal rates higher than 1.5/s led to decreased ripple resolution (Supin *et al.*, 1997), and since the listeners reported that they needed at least a few seconds to listen to the signal and to decide whether the stimulus did or did not contain some alternations.

Pregenerated noise bursts were stored in computer memory. During experiments, they were played through a 14-bit D/A converter, amplified, attenuated, and presented diotically over TDS-7 earphones with the frequency response irregularity of no more than 10 dB within the range of 0.1–6 kHz and no more than 18 dB within the range of 0.1–16 kHz. A listener could choose a level which he considered to be the most comfortable and providing the easiest stimulus discrimination. A chosen level was constant for a given listener across all stimulation conditions. These levels were within a range of 70–80 dB SPL.

D. Procedure

A three-interval 2AFC procedure was used. Each trial consisted of three noise bursts, each of 2-s duration with 0.5-s intervals between them. Two trial types alternated randomly: either the first and third bursts contained phase reversals and the second did not contain them, or the second burst contained the phase reversals and the first and third did not. The listener knew that the first and third bursts were identical and different from the second one. The listener's task was to detect any modifications in the noise and to report whether they appeared in the first and third bursts or in the second one. The listener was informed of whether the response was true or false. Thus, the procedure was two-alternative and differed from a standard one in only the additional third signal which always duplicated the first one. This modification was used since the listeners reported that they were more confident to make a decision in the three-interval procedure rather than in the standard two-interval one: they could make a decision by comparing the first and second bursts and then verify it by comparing the second and third ones.

During a measurement run, ripple depth varied adaptively (one-up, two-down procedure) by steps indicated above (Sec. I B). This procedure causes stimuli to vary around a value providing 70.1% true responses which is close to the 75% threshold criterion (Levitt, 1971). Contrary to the standard Levitt's procedure, we used the adaptive stimulus presentation only to provide most of the signals to be just above and just below the threshold level. The threshold was calculated as in a constant-stimuli procedure, i.e., percentage of true responses was counted for presented values, and a ripple-depth value corresponding to 75% of true responses was found by interpolation between the nearest values. This threshold calculation provided better accuracy because of the use of the entire body of near-threshold data instead of a lesser number of extremes. On the other hand, because of the adaptive stimuli presentation, a majority of stimuli had one of two values (just above or just below the threshold) which were used for interpolation. This minimized the overall number of trials. Runs lasted until stimuli providing true response probability just above and just below the 75% level were presented 20 times each. It required 50 to 70, sometimes up to 100 trials. Except for a few cases, two runs were used to obtain a threshold estimate.

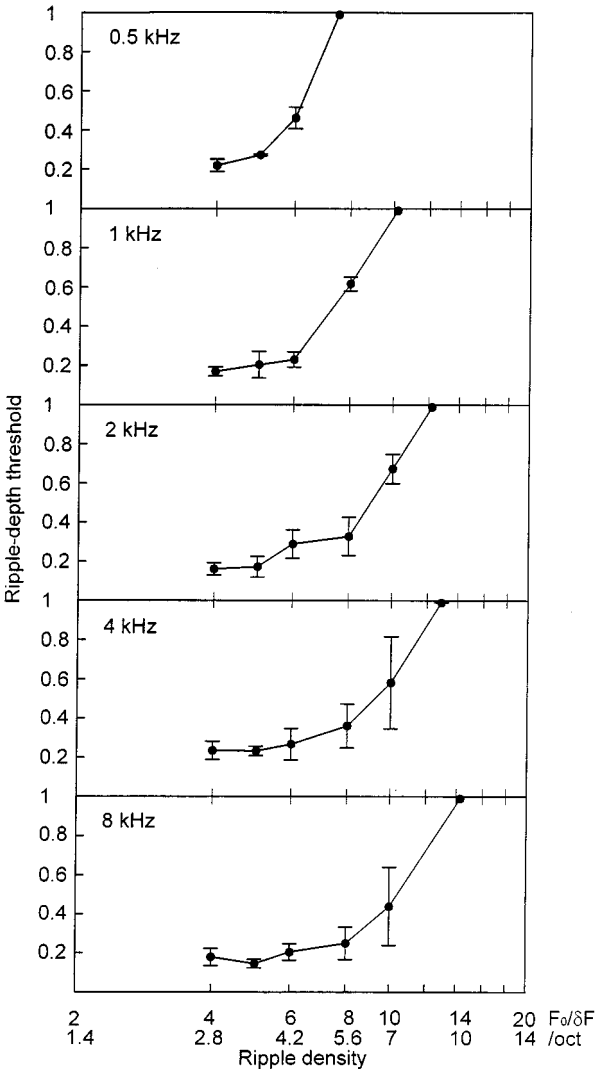

FIG. 2. Ripple depth threshold versus ripple density dependence for center frequencies from 0.5 to 8 kHz, as indicated. Interindividual averaging of data for five listeners (mean±s.d.). Ripple density is indicated in two measures: upper scale—relative density ($F_0/\delta F$), lower scale—octave density (number of ripples per octave).

The measurement runs were repeated at various ripple densities to obtain ripple-depth thresholds as a function of ripple density at a certain center frequency. The last point of the function was obtained by keeping the modulation depth at a constant level of 1.0 and varying ripple density. In these runs, the procedure was the same as described above, except that the ripple density was used as the varying parameter. Then all the measurement sets were repeated at different center frequencies.

II. RESULTS

The results of measurement are presented in Fig. 2 showing ripple-depth thresholds as functions of ripple density at various center frequencies, from 0.5 to 8 kHz. All the curves were characterized with low ripple-depth thresholds at low ripple densities and increased thresholds at higher

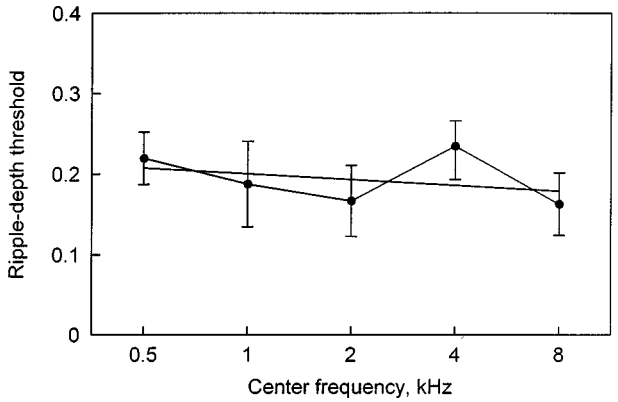

FIG. 3. Minimal ripple depth threshold versus center frequency dependence. Averaged data for five listeners at relative ripple densities of 4 and 5 (except a frequency of 0.5 kHz: data for ripple density 4 only) (mean±s.d.). The trend is shown by a straight line.

ripple densities. At low ripple densities (D_{rel} of 4 to 5, D_{oct} of 2.8 to 3.5), ripple-depth thresholds were from 0.15 to 0.27 at all center frequencies. Although some variation from one center frequency to another was observed, the trend was very little and insignificant (Fig. 3). So, it seemed reasonable to average the data across all the center frequencies to obtain a mean value of modulation depth threshold. This value was estimated as 0.19 ± 0.05 s.d.

At ripple densities higher than D_{rel} of 6 to 8 (D_{oct} of 4.2 to 5.6), ripple-depth thresholds rose steeply and reached the maximal value of 1.0 at ripple densities from $D_{\text{rel}}=7.5$ ($D_{\text{oct}}=5.2$) at 0.5-kHz center frequency to $D_{\text{rel}}=14.3$ ($D_{\text{oct}}=10.0$) at 8 kHz. These end points of the curves were found by varying the ripple density at a constant depth of 1.0; they represent ripple-density resolution limits at the used center frequencies.

III. DISCUSSION

A. Ripple-depth threshold

The ripple-depth threshold obtained herein (0.19) is close to the value (0.2) reported for wideband rippled noise (Supin *et al.*, 1994). In profile analysis experiments with the use of wideband signals composed of a number of sinusoids, a similar threshold for spectral contrast was found at low ripple densities (Green, 1983, 1987, 1988). Note, this value is for spectrum presentation in the power domain but not in the magnitude domain where the same value is around 0.1. Thus, the data presented herein show that the ripple-depth threshold does not depend significantly on frequency within a rather wide frequency range.

B. Interrelation between ripple depth and density

With increasing ripple density, ripple-depth threshold increases until it reaches the highest level of 1.0 at a ripple-density resolution limit. A simple model based on interaction between rippled spectra and frequency-tuned auditory filters may be proposed to explain this interrelation. It should be noted that both frequency-tuning processing [frequency-dependent masking studies by Houtgast (1974, 1977), Pick *et al.* (1977) and Pick (1980); ripple-density resolution studies by Wilson and Evans (1971) and Supin *et al.* (1994)] and temporal processing [pitch discrimination studies by Yost *et al.* (1996) and Patterson *et al.* (1996)] were suggested as mechanisms of rippled spectrum discrimination. Independent of the involved mechanisms, signal processing can be described in either temporal or frequency-spectrum domain. We use the spectral description as convenient for our purposes.

For definiteness sake, define the filter shape by a rounded exponential (roex) function (Patterson *et al.*, 1982):

$$W(g)=(1+pg)\exp(-pg), \tag{3}$$

where W is the output power, g is the relative deviation from the filter center frequency, and p is a parameter determining the filter tuning. For this filter form, the relative equivalent rectangular bandwidth E is equal to $4/p$, thus

$$W(g)=(1+4g/E)\exp(-4g/E). \tag{4}$$

Rippled power spectra of opposite peak–trough positions are defined as

$$P(g)=1\pm m\cos 2\pi Dg, \tag{5}$$

where D is the relative ripple density and m is the ripple depth. The power P_{peak} transmitted by the filter when a ripple peak is centered on the filter (spectrum $1+m\cos 2\pi Dg$) is

$$P_{\text{peak}}=2\int_0^\infty W(g)P(g)\,dg$$

$$=E[1+m/(1+\pi^2D^2E^2/4)^2]. \tag{6}$$

Similarly, for the ripple trough centered on the filter (spectrum $1-m\cos 2\pi Dg$), the transmitted power P_{tr} is

$$P_{\text{tr}}=E[1-m/(1+\pi^2D^2E^2/4)^2] \tag{7}$$

and the ratio of output signals at a ripple phase reversal is

$$\frac{P_{\text{peak}}}{P_{\text{tr}}}=\frac{(1+\pi^2D^2E^2/4)^2+m}{(1+\pi^2D^2E^2/4)^2-m}. \tag{8}$$

Suppose that a change in the transmitted power is detectable when this ratio exceeds a certain differential threshold R_{thr}. Substituting $P_{\text{peak}}/P_{\text{tr}}=R_{\text{thr}}$ to Eq. (8) gives the ripple depth threshold $m_{\text{thr}}(D)$:

$$m_{\text{thr}}(D)=(1+\pi^2D^2E^2/4)^2(R_{\text{thr}}-1)/(R_{\text{thr}}+1). \tag{9}$$

Equation (9) shows that the lowest ripple-depth threshold is $(R_{\text{thr}}-1)/(R_{\text{thr}}+1)$ at $D=0$, i.e., when the phase-reversal test reduces to a change of wideband noise level. In real experiments, $D>0$, thus the ripple-depth thresholds are higher than this lowest value.

Ripple-density resolution limit D_{lim} can be found from Eq. (9) taking $m=1$ (the highest possible value of m). It results in

$$D_{\text{lim}}=\frac{2}{\pi E}[(R_{\text{thr}}+1)^{1/2}(R_{\text{thr}}-1)^{-1/2}-1]^{1/2}. \tag{10}$$

To compare this model with experimental data, the data were normalized by presenting the ripple densities D in terms of equivalent rectangular bandwidth E according to

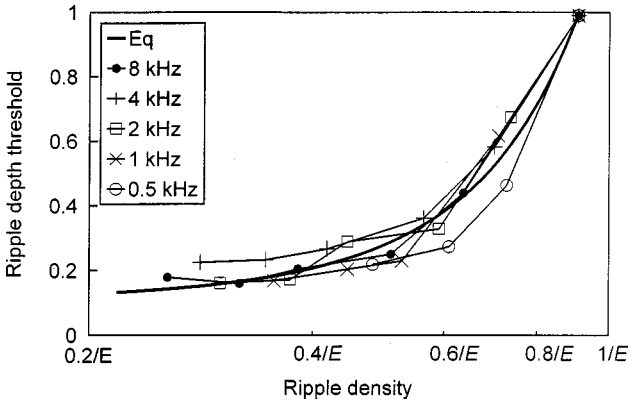

FIG. 4. Comparison of model predictions with experimental data. Eq—a function defined by Eq. (9); other curves—normalized experimental data for center frequencies from 0.5 to 8 kHz, as indicated.

Eq. (10) at a certain value of R_{thr}, and the parameter R_{thr} was adjusted to obtain the best fit of the function $m_{\text{thr}}(D)$ to the experimental data according to the least-mean-square criterion (Fig. 4). Being normalized, all the experimental curves grouped densely (by definition, they met a common point at $m_{\text{thr}}=1$). The best fit was found at $R_{\text{thr}}=1.24$ (i.e., about 1 dB); this is close to many estimations of the differential threshold in humans (e.g., Jestead *et al.*, 1977; also review Rabinowitz *et al.*, 1976; Kay, 1982; He *et al.*, 1998). At this R_{thr} value, Eq. (9) gives the lowest ripple-depth threshold (at $D=0$) of 0.11, and the ripple-depth thresholds at low but nonzero ripple densities ($0.3/E$ to $0.4/E$) of around 0.2. As for the ripple-density resolution, Eq. (10) gives a value of $D=0.91/E$. At found ripple-density resolution limits as high as 14.3 relative units, this results in relative E values of 0.06. This is a narrower bandwidth (better tuning) than that of peripheral auditory filters (around 0.1) found in a number of masking experiments (review Glasberg and Moore, 1990). Therefore the filter bandwidth E used in the model cannot be attributed to peripheral filters only and should be considered as an overall equivalent of all processes determining discrimination of spectral ripples. It seems that this simple model can be adopted as a first approximation of relationships between ripple depth and density resolutions.

ACKNOWLEDGMENT

The study was supported by the Russian Foundation for Basic Research, Grant No. 96-04-48036

Bilsen, F. A., and Wieman, J. L. (**1980**). ''Atonal periodicity sensation for comb filtered noise signals,'' in *Psychophysical and Behavioral Studies in Hearing*, edited by G. van der Brink and F. A. Bilsen (Delft U. P., Delft), pp. 379–382.

Durlach, N. I., Braida, D. L., and Ito, Y. (**1986**). ''Towards a model for discrimination of broadband signals,'' J. Acoust. Soc. Am. **80**, 63–72.

Glasberg, B. R., and Moore, B. C. J. (**1990**). ''Derivation of auditory filter shapes from notched-noise data,'' Hear. Res. **47**, 103–138.

Green, D. M. (**1983**). ''Profile analysis: A different view of auditory intensity discrimination,'' Am. Psychol. **38**, 133–142.

Green, D. M. (**1988**). *Profile Analysis: Auditory Intensity Discrimination* (Oxford U. P., New York).

Green, D. M. (**1992**). ''On the number of components in profile-analysis tasks,'' J. Acoust. Soc. Am. **91**, 1616–1623.

Green, D. M., Mason, C. R., and Kidd, Jr., G. (**1984**). ''Profile analysis: Critical band and duration,'' J. Acoust. Soc. Am. **75**, 1163–1167.

Green, D. M., Onsan, Z. A., and Forrest, T. G. (**1987**). ''Frequency effects in profile analysis,'' J. Acoust. Soc. Am. **81**, 692–699.

He, N., Dubno, J. R., and Mills, J. H. (**1998**). ''Frequency and intensity discrimination measured in a maximum-likelihood procedure from young and aged normal-hearing subjects,'' J. Acoust. Soc. Am. **103**, 553–565.

Houtgast, T. (**1974**). ''Masking patterns and lateral inhibition,'' in *Facts and Models in Hearing*, edited by E. Zwicker and E. Terhardt (Springer, Berlin), pp. 258–265.

Houtgast, T. (**1977**). ''Auditory-filter characteristics derived from direct-masking and pulsation-threshold data with a rippled-noise masker,'' J. Acoust. Soc. Am. **62**, 409–415.

Jesteadt, W., Wier, C. C., and Green, D. M. (**1977**). ''Intensity discrimination as a function of frequency and level,'' J. Acoust. Soc. Am. **61**, 169–177.

Kay, R. H. (**1982**). ''Hearing of modulation in sounds,'' Physiol. Rev. **62**, 894–975.

Levitt, H. (**1971**). ''Transformed up-down methods in psychoacoustics,'' J. Acoust. Soc. Am. **49**, 467–477.

Patterson, R. D., Nimmo-Smith, I., Weber, D. L., and Milroy, R. (**1982**). ''The deterioration of hearing with age: Frequency selectivity, the critical ratio, the audiogram, and speech threshold,'' J. Acoust. Soc. Am. **72**, 1788–1803.

Patterson, R. D., Handel, S., Yost, W. A., and Datta, A. J. (**1996**). ''The relative strength of the tone and noise components in iterated rippled noise,'' J. Acoust. Soc. Am. **100**, 3286–3294.

Pick, G. F. (**1980**). ''Level dependence of psychophysical frequency resolution and auditory filter shape,'' J. Acoust. Soc. Am. **68**, 1085–1095.

Pick, G. F., Evans, E. F., and Wilson, J. P. (**1977**). ''Frequency resolution in patients with hearing loss of cochlear origin,'' in *Psychophysics and Physiology of Hearing*, edited by E. F. Evans and J. P. Wilson (Academic, New York), pp. 273–282.

Popov, V. V., and Supin, A. Ya. (**1984**). ''Quantitative measurement of frequency resolving power of the human hearing,'' Dokl. Akad. Nauk SSSR (Proc. Acad. Sci. USSR) **278**, 1012–1016.

Rabinowitz, W. M., Lim, J. S., Braida, L. D., and Durlach, N. I. (**1976**). ''Intensity perception. VI. Summary of recent data on deviations from Weber's law for 1000-Hz tone pulses,'' J. Acoust. Soc. Am. **59**, 1506–1509.

Supin, A. Ya., Popov, V. V., Milekhina, O. N., and Tarakanov, M. B. (**1994**). ''Frequency resolving power measured by rippled noise,'' Hear. Res. **78**, 31–40.

Supin, A. Ya., Popov, V. V., Milekhina, O. N., and Tarakanov, M. B. (**1997**). ''Frequency-temporal resolution of hearing measured by rippled noise,'' Hear. Res. **108**, 17–27.

Supin, A. Ya., Popov, V. V., Milekhina, O. N., and Tarakanov, M. B. (**1998**). ''Ripple density resolution for various rippled-noise patterns,'' J. Acoust. Soc. Am. **103**, 2042–2050.

Wilson, J. P., and Evans, E. F. (**1971**). ''Grating acuity of the ear: psychophysical and neurophysiological measures of frequency resolving power,'' in *7th International Congress on Acoustics* (Akademiai Kiado, Budapest), Vol. 3, pp. 397–400.

Yost, W. A. (**1982**). ''The dominance region and ripple-noise pitch: A test of the peripheral weighting model,'' J. Acoust. Soc. Am. **72**, 416–425.

Yost, W. A., and Hill, R. (**1979**). ''Models of the pitch and pitch strength of ripple noise,'' J. Acoust. Soc. Am. **66**, 400–410.

Yost, W. A., Hill, R., and Perez-Falcon, T. (**1977**). ''Pitch discrimination of ripple noise,'' J. Acoust. Soc. Am. **63**, 1166–1173.

Yost, W. A., Patterson, R. D., and Sheft, S. (**1996**). ''A time domain description for the pitch strength of iterated rippled noise,'' J. Acoust. Soc. Am. **99**, 1066–1078.

Memory for pitch versus memory for loudness

Sylvain Clément, Laurent Demany, and Catherine Semal
Laboratoire de Neurophysiologie (UMR CNRS 5543), BP 63, Université Bordeaux 2, 146 rue Léo-Saignat, F-33076 Bordeaux Cedex, France

(Received 14 January 1999; revised 3 May 1999; accepted 28 June 1999)

The decays of pitch traces and loudness traces in short-term auditory memory were compared in forced-choice discrimination experiments. The two stimuli presented on each trial were separated by a variable delay (D); they consisted of pure tones, series of resolved harmonics, or series of unresolved harmonics mixed with lowpass noise. A roving procedure was employed in order to minimize the influence of context coding. During an initial phase of each experiment, frequency and intensity discrimination thresholds [$P(C)=0.80$] were measured with an adaptive staircase method while D was fixed at 0.5 s. The corresponding physical differences (in cents or dB) were then constantly presented at four values of D: 0.5, 2, 5, and 10 s. In the case of intensity discrimination, performance (d') markedly decreased when D increased from 0.5 to 2 s, but was not further reduced when D was longer. In the case of frequency discrimination, the decline of performance as a function of D was significantly less abrupt. This divergence suggests that pitch and loudness are processed in separate modules of auditory memory. © *1999 Acoustical Society of America.* [S0001-4966(99)03810-2]

PACS numbers: 43.66.Mk, 43.66.Fe, 43.66.Hg, 43.66.Cb [RVS]

INTRODUCTION

In order to compare two sounds separated by some delay (D), it is of course necessary to memorize the first sound during the delay. Two modes of memory operation were distinguished by Durlach and Braida (1969). In one mode, called the ''trace mode,'' the sensation produced by the second sound is compared to the sensory trace left by the first sound. This comparison may benefit from an overt or covert rehearsal of the trace by the listener (Keller *et al.*, 1995), but its accuracy will strongly depend on D. In the other memory mode, called the ''context-coding mode,'' the listener compares instead symbolic (e.g., verbal) representations of the two sounds; these representations result from a categorical evaluation of each sound's relation to a general context of sounds (for instance the set of sounds used in an experiment). This memory mode will be generally less efficient than the trace mode if D is short. However, given that categorical labels can be perfectly remembered for a long time, the context-coding mode can become the most efficient mode if D is long.

The present study was concerned with the organization of auditory memory in the trace mode. Should this memory be viewed as a single ''store'' or is it composed instead of several stores with different properties? Some authors suggested that it includes two stores operating on different time spans: a ''short'' store and a ''long'' store (Wickelgren, 1969; Cowan, 1984). Another hypothesis, on which we focused here, is that there is a set of stores or sub-stores which are specialized in the retention of different perceptual attributes of sound.

This hypothesis has already received some support from psychophysical studies of the interference effects produced by a sound on the sensory trace of a previous sound. In previous experiments from our laboratory (Semal and Demany, 1991, 1993; Semal *et al.*, 1996), listeners were required to make same/different judgments on two periodic test sounds separated by a delay during which other periodic sounds (to be ignored) were presented. The differences to be detected were always differences in period, and thus pitch (but the listeners were not informed of that). It was found that discrimination of the test sounds strongly depended on the pitches of the intervening sounds—as observed before by Deutsch (1972)—but was essentially independent of the intervening sounds' other perceptual attributes. Therefore, these data suggested there is a memory store specialized in the retention of pitch and deaf to any other auditory attribute. Starr and Pitt (1997) obtained analogous results from an experiment in which the differences between the test sounds were differences in timbre (spectral shape). In this case, performance strongly depended on the timbre of the intervening sounds, but not on their pitch, as though timbre (or at least a certain aspect of timbre) was memorized in a specialized store. Let us finally mention data from Botte *et al.* (1992) concerning memory for loudness. In this study, the test sounds and intervening sounds were pure tones at a constant frequency; only intensity was varied. It was found that intensity discrimination between the test tones was not determined by the intervening tones' intensity distance to the test tones, but simply worsened monotonically as the intervening tones' intensity increased. This is in marked contrast with the results of analogous experiments on pitch memory: Here, the crucial factor is the similarity in pitch between the test tones and intervening tones (Deutsch, 1972; Semal and Demany, 1991). The divergence suggests that pitch traces and loudness traces are maintained in separate stores.

Assume that pitch and loudness are indeed processed in separate memory stores. It could then be the case that, in the absence of any intervening stimulus, the trace of a pitch sensation does not fade away with time at the same rate as the trace of a loudness sensation. This would be strong evidence for a separation of stores. The decay of loudness traces (i.e.,

intensity discrimination) as a function of time was investigated by a number of authors (Kinchla and Smyzer, 1967; Berliner and Durlach, 1973; Berliner *et al.*, 1977; Green *et al.*, 1983; Botte *et al.*, 1992; Lü *et al.*, 1992). There are also some data about the temporal decay of pitch traces (i.e., frequency discrimination: Wolfe, 1886; Harris, 1952; Bachem, 1954; Rakowski, 1972). However, the methods used in these two sets of experiments were widely different. To the best of our knowledge, nobody has compared the decays of pitch and loudness traces using the same subjects and similar procedures. This was the aim of the present study.

Since we wished to investigate the trace mode of auditory memory, it was important to minimize the possible influence of context-coding processes. Several studies of intensity discrimination indicated that the efficiency of context coding decreases as the stimulus range increases (Berliner and Durlach, 1973; Braida and Durlach, 1988). This led us to incorporate a roving procedure in our 2I-2AFC framework: From trial to trial, the period and/or intensity of the first (standard) stimulus were varied randomly within wide ranges. Generally speaking, avoiding the use of fixed standards hindered the formation of precise long-term memories in the course of the experiments (Harris, 1952).

The discriminability of two stimuli separated by D s is determined in part by memory limitations but also depends, more basically, on the precision of their sensory encoding, i.e., on ''sensation noise'' (Durlach and Braida, 1969). For a fair comparison between pitch and loudness trace decays, it is desirable to keep constant the contribution of sensation noise to discrimination performance. We assumed that when D is as short as 0.5 s, the amount of trace decay is negligible and discrimination performance is determined only by sensation noise.[1] Therefore, the two experiments reported here included preliminary measurements intended to select frequency and intensity changes that were equally discriminable for $D=0.5$ s. We then varied D and measured its effect on the discrimination of the corresponding changes.

The temporal decay of a pitch trace may depend on the salience of the initial pitch sensation, or more generally on the spectral properties of the stimulus eliciting the pitch sensation. Salient pitches are evoked by pure tones and by complex tones with harmonics that the auditory system is able to resolve. The pitch of complex tones consisting of unresolvable harmonics is less salient and may be extracted by a specific mechanism (Houtsma and Smurzynski, 1990; Carlyon, 1998). We used these three types of stimuli in experiment 1. Another potentially important factor was stimulus duration: It could be hypothesized that the trace of a long-duration sound decays less rapidly than the trace of a shorter one, all other things being equal. This led us to use very different stimulus durations in experiments 1 and 2.

I. EXPERIMENT I

A. Method

1. Subjects

Four listeners without any known hearing deficit served as subjects. Two of them were authors SC and LD; they had a long previous experience with psychoacoustic experiments. The remaining two listeners (MM and MY) were students without such experience. None of the subjects possessed absolute pitch, but each of them had an interest in music and played a musical instrument.

2. Tasks and stimuli

On each trial, two periodic stimuli separated by a silent delay D were presented. Both stimuli (''$S1$'' and ''$S2$'') had a total duration of 500 ms and were gated on and off with 10-ms cosinusoidal amplitude ramps. There were four experimental conditions.

In condition INTENS, $S1$ and $S2$ were 1000-Hz pure tones differing in intensity. The direction of the intensity change was selected at random and the subject's task was to indicate which stimulus was louder. The SPL of $S1$ was randomly selected between 40 and 80 dB.

In the remaining three conditions (FREQ-PURE, FREQ-RES, and FREQ-UNRES), the two stimuli had a constant SPL of 60 dB but different periods. The direction of this change was also a random variable and the subject had to indicate which sound was higher in pitch. The frequency or fundamental frequency ($F0$) of $S1$ was randomly selected between limits specified below, frequency being in each case scaled logarithmically.

In condition FREQ-PURE, the stimuli were pure tones and the frequency of $S1$ varied between 500 Hz and 2000 Hz.

In condition FREQ-RES, the stimuli were complex tones consisting of the first five harmonics of some $F0$. The $F0$ of $S1$ varied between 100 and 400 Hz. Given their low ranks, the harmonics of each tone were resolvable by the auditory system (see, e.g., Plomp, 1976, Chap. 1). They were synthesized at equal amplitudes and added in sine phase.

In condition FREQ-UNRES, the stimuli were bandpass-filtered trains of 50-μs clicks, and the $F0$ of $S1$ varied between 40 and 200 Hz. The cutoff frequencies of the filters (Stanford Research SR640 and SR645; attenuation rate: about 100 dB/oct) were set at 2860 and 5000 Hz. In order to mask auditory distortion products (Plomp, 1976, Chap. 2), the stimuli were mixed with a white noise that was low-pass filtered at 2860 Hz and presented at 55 dB SPL. The amplitude of the clicks was systematically varied as a function of $F0$, in order to maintain the overall SPL of the stimuli at 60 dB. Given that $S1$ had a maximum $F0$ of 200 Hz and that all stimuli were high-pass filtered at 2860 Hz, the power spectrum of the stimuli consisted of equal-amplitude consecutive harmonics with ranks always exceeding 13. Such harmonics are not resolvable by the auditory system (see, e.g., Houtsma and Smurzynski, 1990).

Subjects were tested individually in a double-walled soundproof booth (Gisol, Bordeaux), using TDH39 earphones through which the stimuli were delivered diotically. Responses were given by pressing one of two buttons on a response box, and feedback was provided immediately: Following each correct response, an LED located just above the corresponding button was turned on for 300 ms; no LED was turned on if the response was wrong.

TABLE I. Thresholds measured in the preliminary phase of experiment 1.

Condition (unit)	INTENS (dB)	FREQ-PURE (cents)	FREQ-RES (cents)	FREQ-UNRES (cents)
Subject LD	1.8	8.2	5.9	108.9
SC	2.1	6.4	5.9	75.4
MM	1.7	6.9	5.3	84.6
MY	1.5	8.2	7.8	108.0
Mean	1.8	7.4	6.2	94.2

3. Preliminary measurements

In each of the four conditions defined above, we first determined the amount of stimulus change—in dB or in cents—for which the probability of a correct response was 0.80 when D was 0.5 s. These ''thresholds'' were measured with the adaptive procedure described by Kaernbach (1991). In a given daily session, four blocks of trials were run in each condition. At the outset of a block, the change from $S1$ to $S2$ (in dB or in cents) was large enough to make the task easy. Following each correct response, this change was divided by $1.5^{1/4}$. Following each incorrect response, it was multiplied by 1.5. This continued until 14 reversals had occurred in the variation of the change. The median of the changes used on all trials following the fourth reversal was taken as the threshold.

Subjects were trained until their performances appeared to be stable. This took five 1-h sessions for subjects LD and SC, and nine 1-h sessions for subjects MM and MY. For each condition and subject, the threshold value finally recorded was the median of the last 20 threshold measurements.

4. Assessment of memory decay

In this main part of the experiment, D was varied and the previously measured thresholds were used as constant changes from $S1$ to $S2$. (The changes had a constant size, but of course their direction was still a random variable.) In a given daily session, subjects were tested in only one of the four conditions. Each session began with a warm up consisting of 50 trials with $D=0.5$ s, and then comprised 16 blocks of 20 trials. From block to block, D varied in a sawtooth manner, taking four possible values: 0.5, 2, 5, and 10 s. When D was equal to 0.5 or 2 s, there was a pause of 1 s between each response and the onset of $S1$ in the next trial. When D was equal to 5 or 10 s, the pause had a duration of 5 s; 1 s before its end, a warning visual signal was produced by the LEDs of the response box.

From session to session, the four conditions were used alternately, four times each. Thus, for each subject, condition, and value of D, a total of 320 responses were collected. From these 320 responses, we computed four independent d' statistics—one d' per session—as well as the corresponding values of the response bias index β (Green and Swets, 1974).

B. Results

Table I displays the thresholds determined by the preliminary measurements and then used as constant stimulus changes.[2] Note that thresholds were much poorer in condition FREQ-UNRES than in conditions FREQ-PURE and FREQ-RES. This was predictable from the literature on frequency discrimination (e.g., Houtsma and Smurzynski, 1990).

Figure 1 shows the mean of the 16 d' statistics obtained for each condition and value of D in the main part of the experiment. For $D=0.5$ s, d' had an overall mean of 2.05. This d' value is not very different from 1.68, the value expected from the threshold measurements under the assumption that, in these preliminary measurements, responses were unbiased—i.e., not affected by ''time-order errors''—(Macmillan and Creelman, 1991). Moreover, as we wished, d' did not markedly vary with conditions for $D=0.5$ s. In condition INTENS, d' strongly decreased when D was increased from 0.5 to 2 s, but d' was not further reduced when D was longer. The decline of d' with D appeared to be more gradual in the FREQ conditions. For each subject, the decline of d' from $D=0.5$ s to $D=2$ s was smaller in each of the three FREQ conditions than in condition INTENS. An ANOVA in which sessions were used as the random factor

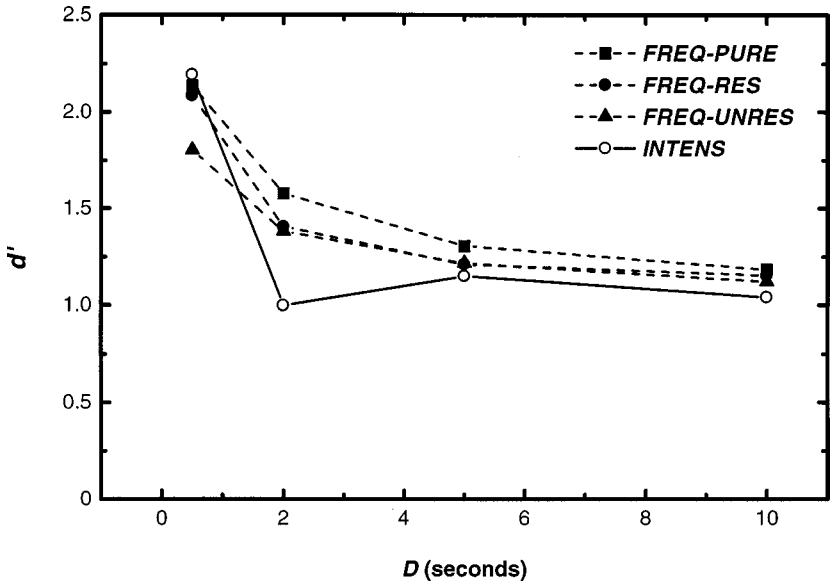

FIG. 1. d' as a function of D in the four conditions of experiment 1. Each data point represents the outcome of 1280 trials (4 sets of 80 trials for 4 subjects).

indicated that the effect of D on d' did not significantly differ across the three FREQ conditions [$F(6,18)<1$], but was reliably different in condition INTENS [$F(3,9)=7.15$, $P=0.009$]. There was no significant three-way interaction between subjects, conditions, and D [$F<1$ in each case]. Similar statistical tests were performed on the absolute values of $\log(\beta)$. Their outcomes were negative in each case. Thus the INTENS and FREQ conditions differed with regard to the effect of D on d' but not with regard to the effect of D on the magnitude of response bias.[3]

C. Discussion

In the three FREQ conditions, very different stimuli were used. For instance, whereas the tones used in condition FREQ-RES were quasi-vocal sounds, the tones of condition FREQ-PURE had pitches which were generally too high to be sung. More importantly, pitch was much less salient in condition FREQ-UNRES than in conditions FREQ-PURE and FREQ-RES. Yet, the three corresponding memory decays appeared to be similar. This suggests that the decay of a pitch memory trace is independent of the initial pitch sensation. However, this decay appears to differ from the decay of a loudness memory trace when one considers the results obtained in condition INTENS. Apparently, loudness traces decay more rapidly than pitch traces during the first two seconds following the stimulus.

In condition INTENS, d' took similar values, close to 1.0, for $D=2$, 5, and 10 s. A reasonable interpretation of this plateau is that, for $D\geqslant 2$ s, listeners memorized loudness in the ''context-coding'' mode, which is more resistant to the passage of time than the ''trace'' mode (Durlach and Braida, 1969). In intensity discrimination tasks, the context-coding mode can be more efficient than the trace mode if the interstimulus interval (D) is long and if the overall intensity range is small (Berliner and Durlach, 1973). Here, $S1$ varied within a 40-dB range. This is a wide range in so far as the total dynamic range of the auditory system is barely three times larger. Within 40 dB, however, there are only 22 steps of 1.8 dB (the average threshold for condition INTENS, cf. Table I). By contrast, the 2-oct ranges used in conditions FREQ-PURE and FREQ-RES included more than 300 steps of 7.4 or 6.2 cents (the average thresholds for these two conditions). On this basis, it is reasonable to think that context coding was more profitable in condition INTENS than in conditions FREQ-PURE or FREQ-RES. In condition FREQ-UNRES, on the other hand, the average threshold was only 30 times smaller than the range of $S1$; yet, the effect of D on d' was much more similar to the effect observed in the other two FREQ conditions than to the effect observed in condition INTENS. Hence, it is clear that the form of the decays was not determined *only* by the ''perceptual size'' of the stimulus ranges.

Nonetheless, the $S1$ stimuli used in condition INTENS had a variable SPL but a fixed frequency whereas the reverse was true for the FREQ conditions. One could imagine that this difference biased in some way the main outcome of experiment 1. In order to demonstrate quite convincingly that pitch traces do not decay in the same manner as loudness traces, it is of course desirable to compare these decays using identical sets of $S1$ stimuli. This is what we did in experiment 2. Another important novelty of experiment 2 was that its stimuli were ten times shorter than those of experiment 1.

TABLE II. Thresholds measured in the preliminary phase of experiment 2.

Condition (unit)	INTENS (dB)	FREQ (cents)
Subject LD	2.3	14.8
SC	3.2	10.0
VL	2.8	11.3
EB	2.1	16.3
Mean	2.6	13.1

II. EXPERIMENT 2

A. Method

Four listeners with normal audiograms participated in this experiment. Two of them were again authors SC and LD. The remaining two listeners (VL and EB) were students with no previous psychoacoustic experience but a strong interest in (popular) music.

The method was basically similar to that used in experiment 1. However, all stimuli were pure tones and had a total duration of 50 ms rather than 500 ms; they were gated on and off with 5-ms cosinusoidal amplitude ramps. Subjects were tested in only two conditions: $S1$ and $S2$ could differ from each other in SPL (condition INTENS) or in frequency (condition FREQ). On each trial, for *both* conditions, the frequency of $S1$ was randomly selected between 1000 and 2500 Hz (using again a logarithmic frequency scale), and its SPL was randomly selected between 42 and 88 dB.

Preliminary threshold measurements were performed as before, the two new conditions being presented alternately. In the main part of the experiment, again, we used the measured thresholds as constant changes from $S1$ to $S2$. Only one condition was presented throughout each experimental session, and the two conditions alternated from session to session. A total of 320 trials were run for each subject, condition, and value of D. The corresponding data were analyzed exactly like those of experiment 1.

B. Results and discussion

The measured thresholds are displayed in Table II. They were larger than those obtained in conditions INTENS and FREQ-PURE of experiment 1—an expected result since the stimuli were ten times shorter.

The four upper panels of Fig. 2 show the d's obtained in the main part of the experiment for each subject. The means across subjects are presented in the bottom panel. Clearly, the overall results are very similar to those obtained in experiment 1. For $D=0.5$ s, d' was close to 2.0 in both conditions. In condition INTENS, d' markedly decreased when D was increased to 2 s, but was approximately constant for $D=2$, 5, and 10 s. In condition FREQ, by contrast, d' declined continuously with D (or, in the case of subject LD, did not decline at all). From $D=0.5$ s to $D=2$ s, d' varied much more in condition INTENS than in condition FREQ for three

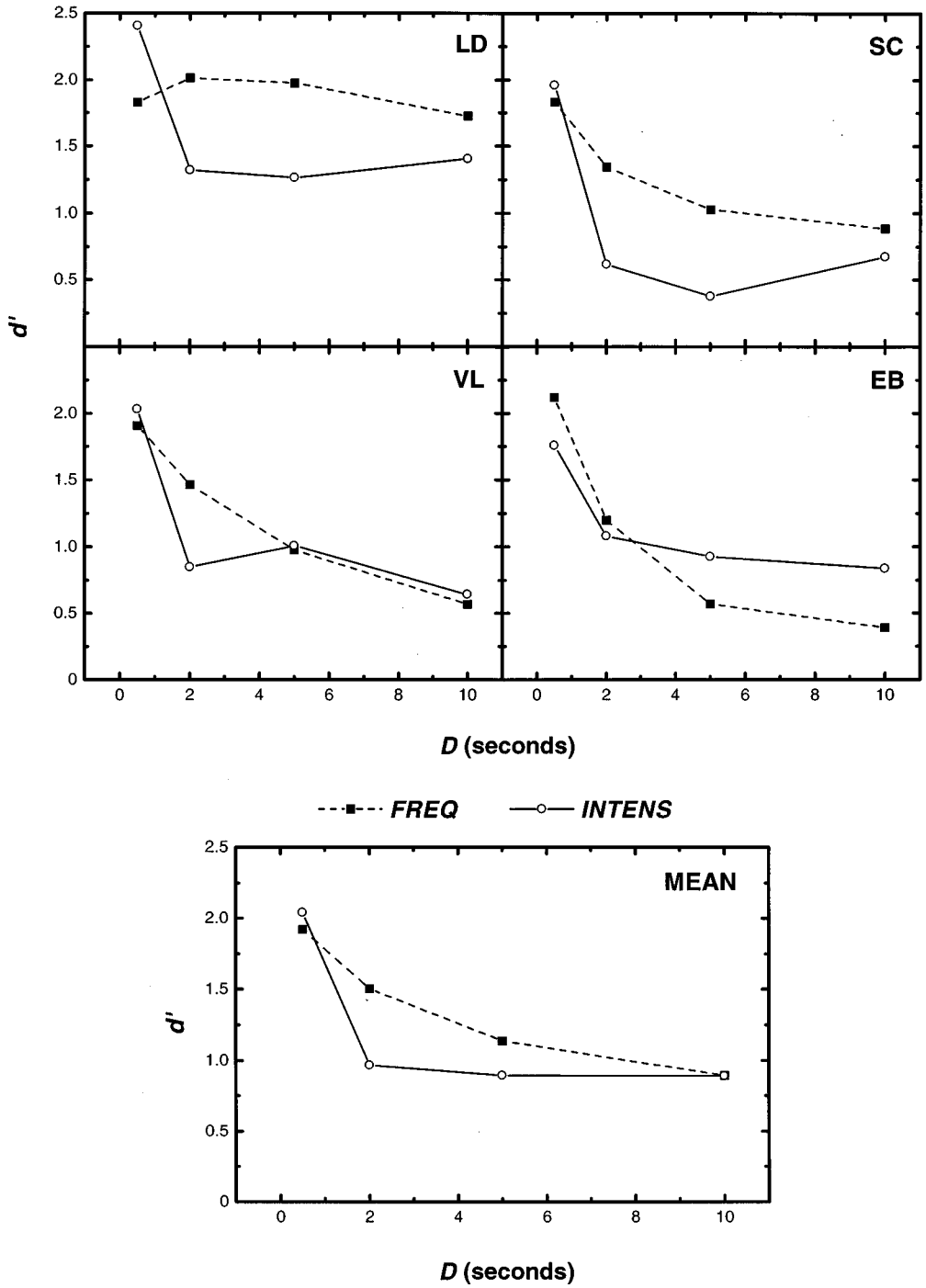

FIG. 2. d' as a function of D in the two conditions of experiment 2. Four upper panels: results obtained from each of the four subjects. Bottom panel: mean results.

subjects; however, this was not true for the fourth subject (EB). An ANOVA confirmed the existence of a significant interaction between D and the condition factor [$F(3,9) = 6.18$, $P = 0.014$]. A similar statistical test performed on $|\log(\beta)|$ rather than d' yielded a negative result [$F(3,9) = 1.10$, $P = 0.399$].

We undertook experiment 2 with the idea that, perhaps, the memory trace of a short tone decays more rapidly than the memory trace of a long tone. The results did not support this idea since they were very similar to those of experiment 1. Concerning the INTENS conditions of both experiments, one can argue that it was *a priori* impossible to observe a faster decay in experiment 2 if, as soon as D was equal to 2 s, performance reached a plateau determined by context-coding processes: To be able to demonstrate a difference in decay, we should have used at least one D value between 0.5 and 2 s. However, no such objection is possible concerning the FREQ conditions. It is important to note that because D was defined as the duration of the silence separating $S2$ from $S1$, differences in stimulus duration were associated with differences in onset-to-onset intervals. From experiment 1 to experiment 2, these intervals were reduced by 450 ms (500–50 ms). Thus they were almost halved when D was equal to 0.5 s. The fact that this big relative change did not

significantly modify the effects of D on d' suggests that the shortest value of D (0.5 s) was not short enough to truncate the *formation* [or ''acquisition'' (Wickelgren, 1969)] of an accurate memory trace of $S1$. If such truncatings had occurred for $D=0.5$ s, they should have been larger for the shorter stimulus duration. Hence, from $D=0.5$ s to $D=2$ s, the decrease of d' should have been smaller in experiment 2 than in experiment 1. There was a trend in this direction, for both the INTENS and the FREQ (or FREQ-PURE) conditions; but a comparison between Figs. 1 and 2 shows that these were very small trends.

III. GENERAL DISCUSSION

In both experiments, we found that the effect of D on d' was not the same in conditions FREQ and INTENS. The difference was largest when D varied from 0.5 to 2 s, and for these small values of D what the difference reveals is almost certainly a divergence in the memory decay of sensory traces: Apparently, the memory decay of a loudness trace is more rapid than the memory decay of a pitch trace. In the INTENS conditions, it is likely that context coding was operative as soon as D was equal to 2 s since d' did not decline when D was longer. But this would only mean that our results underestimated the rate of trace decay for loudness, and thus the divergence between loudness decay and pitch decay.

Three previous papers (Berliner and Durlach, 1973; Berliner *et al.*, 1977; Green *et al.*, 1983) reported experiments in which intensity discrimination (of pure tones) was measured as a function of inter-stimulus interval (i.e., D) with a roving procedure. Unfortunately, these three papers do not give a consistent picture of the memory decay of loudness traces. The results obtained by Berliner and his colleagues for wide roving ranges agree rather well with our data. They found that discrimination performance sharply decreases when D increases up to 2.5 s, and that for longer values of D an almost constant performance level is achieved thanks to context-coding processes (discrimination performance becomes similar to *identification* performance). By contrast, according to the results of Green *et al.*, performance does not decrease more between $D=0.5$ s and $D=2$ s than between $D=2$ s and $D=8$ s. Making sense of this discrepancy (ignored by Green *et al.*) is not easy. It may be significant that whereas Berliner and the present investigators measured d' as a function of D for fixed intensity changes, Green *et al.* measured instead, as a function of D, the values of intensity changes yielding a fixed d'.

Concerning frequency discrimination, the literature as a whole suggests that discrimination performance declines rather slowly with D. Harris (1952) performed on an enormous number of listeners an experiment which was analogous to that of Green *et al.* His stimuli were pure tones and the frequency of the first tone presented on each trial was roved between 950 and 1050 Hz. For $D=0.1$, 1, 3, and 7 s, the measured discrimination thresholds increased by only 29% (from 4.2 Hz to 5.4 Hz). In the experiment of Green *et al.*, on the other hand, the measured thresholds increased by as much as 250% (from 2.4 dB to 6 dB) when D varied from 0.5 s to 8 s. Therefore, our main finding does not come as a big surprise in the light of previous research. Note that a parallel can be drawn between this finding and the outcome of a recent study on *visual* short-term memory (Magnussen *et al.*, 1996). It was found by Magnussen *et al.* that the spatial frequency of a sinusoidal luminance grating was better memorized than its contrast. In the terminology proposed by Stevens (1966), loudness and perceived contrast are ''prothetic'' percepts whereas pitch and the perceptual correlate of spatial frequency are ''metathetic'' percepts. There might be a general law according to which the trace of a metathetic percept decays less rapidly than the trace of a prothetic percept.

From the fact that pitch traces and loudness traces do not decay at the same rate, it seems natural to infer that they are not retained in one and the same sensory store. We mentioned in the Introduction that previous psychophysical experiments already provided evidence for an autonomous processing of pitch (and of a certain aspect of timbre) in auditory memory. Let us point out here that there are also physiological data supporting the hypothesis of multiple and specialized auditory stores. When a listener is presented with a series of identical tones followed by a different tone, the different tone elicits an event-related brain potential called the ''mismatch negativity'' or MMN (Näätänen *et al.*, 1978). This brain potential is supposed to reflect a preattentive change detection based on a comparison between memory traces (see Schröger, 1997, for a recent review). According to Giard *et al.* (1995), the scalp topographies of the MMNs elicited by pure tones deviating from a repeated standard by either frequency, intensity, or duration vary with the type of stimulus deviance. Thus the corresponding MMNs originate from at least partly distinct neural populations (in the auditory cortex). Another remarkable fact is that the MMN obtained in response to a two-dimensional change in frequency and spatial location, or frequency and duration, or duration and intensity, is equal to the sum of the MMNs elicited by its one-dimensional components, exactly as if each of the combined one-dimensional components elicited its own MMN (see, e.g., Levänen *et al.*, 1993). Disappointingly, however, a similar summation does not seem to occur for combined changes in frequency and intensity (Wolff and Schröger, 1995).

Our main finding is consistent with the idea that the mnemonic processings of pitch and loudness are *completely* separate, but it is also consistent with a more subtle hypothesis. Assume that the architecture of auditory memory, in what Durlach and Braida (1969) called its ''trace'' mode, consists of: (1) an all-purpose ''short'' store retaining *global* ''echoic'' traces during a limited time; (2) a set of specialized stores permitting each a longer retention of a single auditory attribute. It could then be the case that only the short store is available for the retention of loudness, whereas one of the specialized stores is devoted to pitch. (Of course, some categorical information on loudness could nonetheless be kept for a long time by means of context-coding processes.) Lü *et al.* (1992) assessed psychophysically the decay of a loudness trace and found that it had the same lifetime—about 2 s—as the decay of the neural activation produced by the stimulus in the primary auditory cortex (this neural activation being assessed by magneto-encephalography). One

may speculate on this basis that the neural site of the short store is the primary auditory cortex while the specialized stores are located elsewhere.

Finally, let us come back on the fact that for one of the six listeners tested in the present study (subject EB, experiment 2), we found *no* evidence that pitch traces decay less rapidly than loudness traces. It is worthy to note that EB was probably the subject who ranked last in terms of musical practice. This suggests that a correlation might exist between pitch memory and musical experience—a suggestion already made by Pechmann and Mohr (1992). An interesting goal of future research would be to determine if indeed trace decay in auditory memory is correlated with musical experience, and more strongly for pitch traces than for loudness traces.

ACKNOWLEDGMENTS

This work is a part of the first author's doctoral dissertation. We thank the Conseil Régional d'Aquitaine for its support, as well as Ed Burns and an anonymous reviewer for comments on an earlier version of the manuscript.

[1]This assumption is consistent with the results of Harris (1952) concerning frequency discrimination, as well as those of Kinchla and Smyzer (1967) and Green *et al.* (1983) concerning intensity discrimination. It is not consistent, however, with data reported by Berliner and Durlach (1973) and Berliner *et al.* (1977): According to these authors, for relatively long tone bursts ($\geqslant$500 ms), intensity discrimination worsens significantly as soon as D exceeds 0. Berliner *et al.* (1977) mention that, ''for reasons unknown to [them]'' (p. 1579), their results for fixed standard tones are very different from those obtained by Kinchla and Smyzer (1967). In the present study, we thought that it was not desirable to set D below 0.5 s because two problems may arise if D is very small and the stimuli are rather short: (1) the first stimulus may have a deleterious ''forward-masking'' effect on the second one (Jaroszewski and Rakowski, 1976; Zeng and Turner, 1992); (2) the formation of an accurate memory trace of the first stimulus may not be complete when the second stimulus is presented (Wickelgren, 1969; Massaro, 1975).

[2]For subject MM, during the final experimental session run in each of the three FREQ conditions, the stimulus change was smaller than the threshold indicated in Table I; we respectively used changes of 5.7, 3.0, and 70.0 cents in conditions FREQ-PURE, FREQ-RES, and FREQ-UNRES. These deliberate decreases of the stimulus changes were intended to avoid ceiling effects for $D=0.5$ s: Apparently, MM had not reached her maximum level of performance in the preliminary experimental phase.

[3]The feedback provided on each trial allowed the subjects to reduce or eliminate their ''natural'' responses biases. For this reason, the obtained values of β were of little interest by themselves.

Bachem, A. (**1954**). ''Time factors in relative and absolute pitch determination,'' J. Acoust. Soc. Am. **26**, 751–753.

Berliner, J. E., and Durlach, N. I. (**1973**). ''Intensity perception. IV. Resolution in roving-level discrimination,'' J. Acoust. Soc. Am. **53**, 1270–2287.

Berliner, J. E., Braida, L. D., and Durlach, N. I. (**1977**). ''Intensity perception. VII. Further data on roving-level discrimination and the resolution and bias edge effects,'' J. Acoust. Soc. Am. **61**, 1256–1267.

Botte, M. C., Baruch, C., and Mönikheim, S. (**1991**). ''Memory for loudness: the role of loudness contour,'' in *Auditory Physiology and Perception*, edited by Y. Cazals, L. Demany, and K. Horner (Pergamon, Oxford), pp. 305–311.

Braida, L. D., and Durlach, N. I. (**1988**). ''Peripheral and central factors in intensity perception,'' in *Auditory Function*, edited by G. M. Edelman, W. E. Gall, and W. M. Cowan (Wiley, New York), pp. 559–584.

Carlyon, R. P. (**1998**). ''The effects of resolvability on the encoding of fundamental frequency by the auditory system,'' in *Psychophysical and Physiological Advances in Hearing*, edited by A. R. Palmer, A. Rees, A. Q. Summerfield, and R. Meddis (Whurr, London), pp. 246–254.

Cowan, N. (**1984**). ''On short and long auditory stores,'' Psychol. Bull. **96**, 341–370.

Deutsch, D. (**1972**). ''Mapping of interactions in the pitch memory store,'' Science **175**, 1020–1022.

Durlach, N. I., and Braida, L. D. (**1969**). ''Intensity perception. I. Preliminary theory of intensity resolution,'' J. Acoust. Soc. Am. **46**, 372–383.

Giard, M. H., Lavikainen, J., Reinakinen, K., Perrin, F., Bertrand, O., Pernier, J., and Näätänen, R. (**1995**). ''Separate representation of stimulus frequency, intensity and duration in auditory sensory memory: An event-related potential and dipole-model analysis,'' J. Cognit. Neurosci. **7**, 133–143.

Green, D. M., Kidd, G., and Picardi, M. C. (**1983**). ''Successive versus simultaneous comparison in auditory intensity discrimination,'' J. Acoust. Soc. Am. **73**, 639–643.

Green, D. M., and Swets, J. A. (**1974**). *Signal Detection Theory and Psychophysics* (Krieger, Huntington, NY).

Harris, J. D. (**1952**). ''The decline of pitch discrimination with time,'' J. Exp. Psychol. **43**, 96–99.

Houtsma, A. J. M., and Smurzynski, J. (**1990**). ''Pitch identification and discrimination for complex tones with many harmonics,'' J. Acoust. Soc. Am. **87**, 304–310.

Jaroszewski, A., and Rakowski, A. (**1976**). ''Pitch shifts in post-stimulatory masking,'' Acustica **34**, 220–223.

Kaernbach, C. (**1991**). ''Simple adaptative testing with the weighted up-down method,'' Percept. Psychophys. **49**, 227–229.

Keller, T. A., Cowan, N., and Saults, J. S. (**1995**). ''Can auditory memory for tone pitch be rehearsed?'' J. Exp. Psychol. (Learn., Mem. and Cogn.) **21**, 635–645.

Kinchla, R. A., and Smyzer, F. (**1967**). ''A diffusion model of perceptual memory,'' Percept. Psychophys. **2**, 219–229.

Levänen, S., Hari, R., McEvoy, L., and Sams, M. (**1993**). ''Responses of the human auditory cortex to changes in one versus two stimulus features,'' Exp. Brain Res. **97**, 177–183.

Lü, Z. L., Williamson, S. J., and Kaufman, L. (**1992**). ''Behavioral lifetime of human auditory sensory memory predicted by physiological measures,'' Science **258**, 1668–1670.

Macmillan, N. A., and Creelman, C. D. (**1991**). *Detection Theory: A User's Guide* (Cambridge University Press, Cambridge, U.K.).

Magnussen, S., Greenlee, M. W., and Thomas, J. P. (**1996**). ''Parallel processing in visual short-term memory,'' J. Exp. Psychol. (Hum. Percept. Perform.) **22**, 202–212.

Massaro, D. W. (**1975**). ''Backward recognition masking,'' J. Acoust. Soc. Am. **58**, 1059–1065.

Näätänen, R., Gaillard, A. W. K., and Mäntysalo, S. (**1978**). ''Early selective attention effect on evoked potential reinterpreted,'' Acta Psychol. **42**, 313–329.

Pechmann, T., and Mohr, G. (**1992**). ''Interference in memory for tonal pitch: Implications for a working-memory model,'' Mem. Cognition **20**, 314–320.

Plomp, R. (**1976**). *Aspects of Tone Sensation* (Academic, London).

Rakowski, A. (**1972**). ''Direct comparison of absolute and relative pitch,'' in *Proceedings of the Symposium on Hearing Theory* (Institut voor Perceptie Onderzoek, Eindhoven, Holland).

Schröger, E. (**1997**). ''On the detection of auditory deviations: a pre-attentive activation model,'' Psychophysiology **34**, 245–257.

Semal, C., and Demany, L. (**1991**). ''Dissociation of pitch from timbre in auditory short-term memory,'' J. Acoust. Soc. Am. **89**, 2404–2410.

Semal, C., and Demany, L. (**1993**). ''Further evidence for an autonomous processing of pitch in auditory short-term memory,'' J. Acoust. Soc. Am. **93**, 1315–1322.

Semal, C., Demany, L., Ueda, K., and Hallé, P. A. (**1996**). ''Speech versus nonspeech in pitch memory,'' J. Acoust. Soc. Am. **100**, 1132–1140.

Starr, G. E., and Pitt, M. A. (**1997**). ''Interference effects in short-term memory for timbre,'' J. Acoust. Soc. Am. **102**, 486–494.

Stevens, S. S. (**1966**). ''On the operation known as judgment,'' Am. Sci. **54**, 385–401.

Wickelgren, W. A. (**1969**). ''Associative strength theory of recognition memory for pitch,'' J. Math. Psychol. **6**, 13–61.

Wolfe, H. K. (**1886**). ''Untersuchungen über das Tongedächtniss,'' Philos. Stud. (Wundt) **3**, 534–571.

Wolff, C., and Schröger, E. (**1995**). ''MMN elicited by one-, two-, and three-dimensional deviants,'' J. Psychophysiol. **9**, 374.

Zeng, F. G., and Turner, C. W. (**1992**). ''Intensity discrimination in forward masking,'' J. Acoust. Soc. Am. **92**, 782–787.

Identification and localization of sound sources in the median sagittal plane

Brad Rakerd[a)]
Department of Audiology and Speech Sciences, Michigan State University, East Lansing, Michigan 48824

William M. Hartmann[b)] and Timothy L. McCaskey[c)]
Department of Physics and Astronomy, Michigan State University, East Lansing, Michigan 48824

(Received 7 December 1998; revised 16 June 1999; accepted 10 July 1999)

The ability of human listeners to identify broadband noises differing in spectral structure was studied for multiple sound-source locations in the median sagittal plane. The purpose of the study was to understand how sound identification is affected by spectral variations caused by directionally dependent head-related transfer functions. It was found that listeners could accurately identify noises with different spectral peaks and valleys when the source location was fixed. Listeners could also identify noises when the source location was roved in the median sagittal plane when the relevant spectral features were at low frequency. Listeners failed to identify noises with roved location when the spectral structure was at high frequency, presumably because the spectral structure was confused with the spectral variations caused by different locations. Parallel experiments on sound localization showed that listeners can localize noises that they cannot identify. The combination of identification and localization experiments leads to the conclusion that listeners cannot compensate for directionally dependent filtering by their own heads when they try to identify sounds. © *1999 Acoustical Society of America.* [S0001-4966(99)00111-3]

PACS numbers: 43.66.Qp, 43.66.Jh [DWG]

INTRODUCTION

The localization of sources of sound in the median sagittal plane (MSP) presents an unusual problem to a listener. The MSP includes the points directly in front, directly behind, and overhead. Therefore, it is symmetrical with respect to the two ears, and binaural differences—usually of paramount importance for sound localization—are minimal or absent. Nevertheless, most normally hearing individuals can successfully localize sounds in this plane. To do so, listeners use the fact that the external ears and head serve as an acoustical filter with a frequency response that depends on the direction of the sound source. Such a frequency response can be measured with probe microphones in the ear canals (Shaw, 1966; Hebrank and Wright, 1974; Wightman and Kistler, 1989a, b). The response to a source in front has a peak and valley structure that favors 4000 Hz compared to 1000 Hz. The response to a source in back has a response with the opposite peak and valley structure. A source overhead leads to a response curve with a peak near 8000 Hz. It is individual characteristic spectral features like these that are thought to enable listeners to localize in the absence of binaural difference cues (Butler and Belundiuk, 1977).

A logical problem with the process of localization on the basis of spectral features is that different real-world sources emit sounds with very different spectra. Spectral structure serves to identify sounds, for example to distinguish between different vowels. *A priori*, a listener does not know whether a particular spectral structure is caused by location-dependent filtering or whether it is intrinsic to the source itself (Durlach and Colburn, 1978). A sound with a spectral bump at 8000 Hz may not come from above; instead it may come from a source that happens to have considerable power at 8000 Hz. Confusions of this kind were dramatically demonstrated by Blauert (1969–70; also see Middlebrooks, 1992), who studied the perception of *narrow bands* of noise using loudspeakers that were in front, in back, and overhead. The perceived location of sources in the experiment was shown to be unrelated to the actual position of the loudspeakers. Instead, the perceived location of each noise band was determined by its frequency, whatever the true location of the source.

Blauert's experiment showed that for narrow-band signals in the MSP, the confusion between the spectral identity of a source and the location of the source is essentially complete. One can imagine that confusion would extend to broadband sounds as well, though the confusion might be less complete. Plenge and Brunschen (1971) conjectured that listeners would localize a broadband sound more successfully if they were familiar with it. With a familiar sound, the intrinsic spectrum might be regarded as known. Then, additional spectral structure could be interpreted unambiguously as a location cue. Plenge and Brunschen used speech fragments from known and unknown talkers. During a training phase, speech from the known talkers was presented from each of five loudspeakers in the upper-half MSP. In the test phase, speech from unknown talkers was sometimes substituted. Plenge and Brunschen found that in the test phase, correct localization dropped from near 90% for known talkers to much less than 50% for unknown talkers, thus supporting their conjecture.

The present article also studies the relationship between the identification of a sound and the localization of its source. It begins by asking the reverse of Plenge and Brun-

[a)]Electronic mail: rakerd@pilot.msu.edu
[b)]Electronic mail: hartmann@pa.msu.edu
[c)]Electronic mail: mccaskel@pilot.msu.edu

schen's question: Is it more difficult to identify a sound if its location in the MSP is uncertain?

I. EXPERIMENT 1—IDENTIFICATION IN THE MSP

Experiment 1 determined whether a listener could distinguish between two broadband noises having somewhat different spectra. Differences consisted of boosted or attenuated bands two-thirds of an octave in width. Two conditions were compared: a *fixed-location* condition, in which all of the sounds came from directly in front of the listener; and a *roved-location* condition, in which sounds randomly came from different locations in the MSP.

A. Environment

The listener was seated in an anechoic room (IAC 107840) with interior dimensions 3×4.3×2.4 m. There were five matched single-driver loudspeakers (Minimus 3.5) arrayed in the MSP.[1] The speakers were 122 cm from the listener's ears and equally spaced (45-deg increments) over the 180-deg span from directly in front to overhead, to directly behind. In order, they were called ''front,'' ''front–over,'' ''over,'' ''rear–over,'' and ''rear.''

B. Procedure

For each experimental run, there were two noises, called ''*A*'' and ''*B*,'' with different spectral structure. Each trial of a run consisted of a single presentation of a noise, either *A* or *B* selected randomly. The listener's task was to identify the noise as *A* or *B* and to indicate the choice by pressing a button on a response box. If the choice was correct, a lamp blinked on.

A run began with 15 training trials during which the listener learned to recognize the noises. On these trials, all stimuli came from the front speaker only. After training, the run continued with 50 data-collection trials. Data-collection trials were either fixed location or roved location. For fixed-location trials, the speaker in front was used exclusively; for roved-location trials, all five speakers were used with equal probability. Feedback was maintained throughout the data-collection trials.

Experimental runs were actually consecutive double runs, a fixed-location run followed by a roved-location run done with the same noise pair. The fixed-location run provided baseline data, as well as thorough training in the recognition of the noises prior to the rove. Each listener did three double runs for each *A*–*B* noise pair. The listener was always aware of whether a run was fixed location or roved location.

C. Noise spectra

Stimuli for the experiment were Gaussian noises, 0.5-s long (10-ms rise/fall time), presented at a level of 72 dBA. The noises were passed through a computer-controlled 1/3-octave band equalizer that was set to create boosted or attenuated bands, 2/3-octave wide. A boosted band, referred to here as a ''bump,'' was 10 dB high; an attenuated band, referred to as a ''dip,'' was 10 dB deep.[2] Six noises with bumps and six noises with dips were created. Table I (column 1) gives their center frequencies. (Center frequencies were the same for the bumps and the dips.)

TABLE I. Center frequencies of 2/3-octave bumps and dips used in experiment 1 are given in the first column. A neighboring pair of bumps/dips, used as an *A*–*B* pair in experiment 1, is characterized by a pair mean frequency, given in the second column.

Center frequency (kHz)	Pair mean frequency (kHz)
1.1	
	1.4
1.8	
	2.3
2.8	
	3.5
4.5	
	5.7
7.1	
	8.9
11.2	

The noises *A* and *B* presented on a run were either both bumps or both dips. *A* and *B* were always adjacent pairs from Table I, with their center frequencies separated by 2/3 of an octave. For example, noise *A* might be the 2/3-octave band centered on 4.5 kHz, and noise *B* the neighboring band centered on 7.1 kHz. Figure 1 shows how the equalizer was programed to create that pair of noises. A noise pair is referenced in this article by the geometric mean of its boosted (or attenuated) bands. The second column in Table I gives the mean frequency for each *A*–*B* pair. In all, there were ten *A*–*B* pairs (five with bumps and five with dips). The order of testing with these pairs was randomized differently for each listener.

D. Listeners

Four listeners were tested in this experiment and in the experiments that follow. Listener S1 was a male, age 19, with normal audiometric hearing in both ears and more than a year's experience in psychoacoustics experiments. Listener S2 was a female, age 21, with normal hearing in both ears and no prior experience. Listeners S3 and S4 were males, ages 45 and 59, respectively, with some bilateral high-

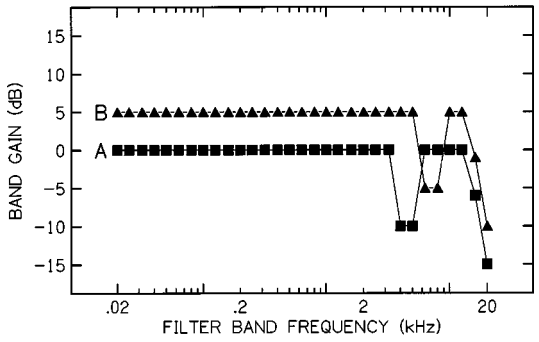

FIG. 1. A pair of noises used in experiment 1. Both noises have 2/3-octave dips as described in Table I. Noise *A* has a dip centered on 4.5 kHz, and noise *B* has a dip centered on 7.1 kHz. Noise *B* has been raised by 5 dB for clarity.

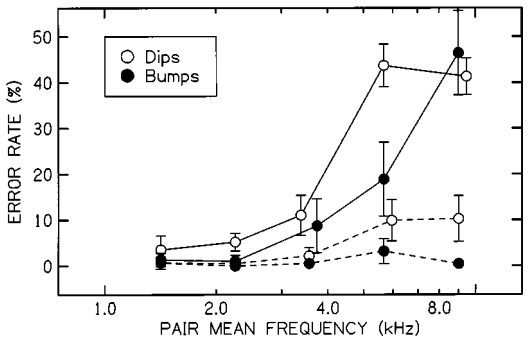

FIG. 2. Error rates for experiment 1. Roved-location runs are indicated by solid lines, fixed-location runs by dashed lines. The error bars show plus and minus one standard deviation for four listeners. (For the mean frequency near 9 kHz there were only three listeners.) Some data points have been shifted laterally for clarity.

frequency hearing loss. Both of these listeners had extensive listening experience. Listeners S1, S3, and S4 were the authors.

E. Results and discussion

The ten $A-B$ pairs and four listeners led to 40 combinations both for fixed-location and for roved-location runs. There were two combinations where a listener failed to establish a reliable baseline for the fixed location (error rate greater than 25%). In those two cases, the roved-location runs were omitted.

The four listeners had very similar results overall. Figure 2 shows their mean identification error rate (± 1 s.d.) for every noise pair, plotted as function of the pair mean frequency. Data are plotted separately for the bumps (filled symbols) and the dips (open symbols). Dashed lines connect results for fixed-location runs; solid lines connect results for roved-location runs.

The listeners generally found bumps easier to identify than dips [significantly lower overall error rate; $F(1,3) = 82.3$; $p < 0.001$], consistent with a previous report by Moore *et al.* (1989).

For bumps and dips, there was a significant interaction between the type of run—fixed location or roved location—and the mean frequency of a noise pair [$F(4,12) = 66.1$; $p < 0.001$]. When the spectral structure of the noises occurred at low frequency, near 1 or 2 kHz, identification was nearly perfect, no matter whether the location was fixed or roved. Listeners found the task easy to do. The spectral structure sometimes caused the noises to resemble vowel sounds, giving listeners an overlearned reference for identification. In other instances there was a pitch or timbre cue. As the frequency of the spectral structure increased, the error rate increased. Whereas the error rate for the fixed-location runs increased slightly, the error rate for the roved-location runs increased enormously, approaching the random guessing limit of 50% errors.

II. EXPERIMENT 2—ADDITIONAL SPECTRAL COMPARISONS

The frequency dependence found in experiment 1 was quite dramatic for all the listeners. Experiment 2 sought to determine whether a similar pattern would occur for a greater variety of stimuli. Otherwise, experiment 2 was the same as experiment 1.

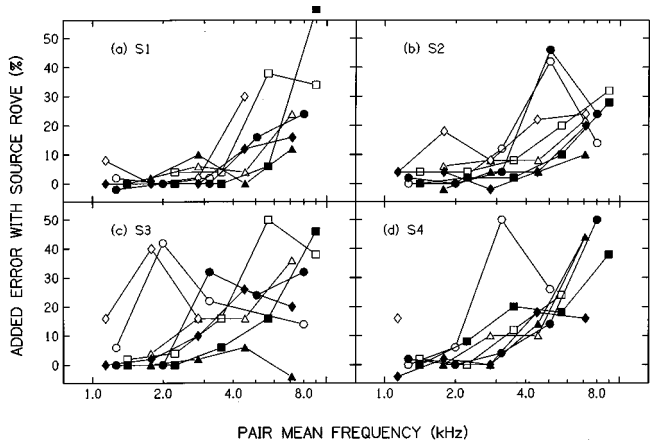

FIG. 3. Experiment 2 results. Added error is the increase in the percentage of errors in identification for pairs of noises when source location was roved compared to fixed-location presentation. Different panels show results for different listeners. Open symbols indicate pairs of spectral dips; filled symbols indicate pairs of spectral bumps. Different symbols represent different conditions, based on bandwidth and separation of the spectral structures as follows. Diamonds: one-third-octave bands separated by 2/3 octave; Circles: one-third-octave bands separated by 4/3 octave; Squares: two-thirds-octave bands separated by 2/3 octave; Triangles: two-thirds-octave bands separated by 4/3 octave.

A. Method

In addition to the 2/3-octave bumps and dips from the first experiment, experiment 2 included noises with bumps and dips that were only 1/3-octave wide. In addition to a 2/3-octave separation between the bumps (or dips) to be compared (as in experiment 1), experiment 2 included comparisons with 4/3-octave separation. Altogether, there were 38 $A-B$ noise pairs in experiment 2 (19 with bumps, and 19 with dips). Because of the large number, experiment 2 was limited to one double run per $A-B$ pair, a fixed-location run followed by a roved-location run.

B. Results

The results of experiment 2 are presented in Fig. 3. Each panel of the figure reports data for a different listener. In order to display the results for all $A-B$ noise pairs at once, the figure has a different format here than in experiment 1. Figure 3 reports the *difference* in error rates between a roved-location run and the corresponding fixed-location run. Therefore, the data indicate the additional error percentage caused by roving the source location. Data points connected by lines are from the same stimulus type.[3]

Figure 3 shows that the effect of frequency on identification is quite general. For all the conditions and all the listeners, there was a strong tendency for the error rate to increase with increasing mean frequency of the spectral structure. The error rate increased steeply in the high frequencies. For every listener, the added error due to source rove was significantly greater for the noises with spectral structure above 4 kHz than it was for the noises with struc-

ture below 4 kHz [subject S1: $t(6)=4.19$; $p=0.006$; S2: $t(7)=5.12$; $p=0.001$; S3: $t(6)=2.60$; $p=0.041$; S4: $t(6)=7.21$; $p<0.001$].

C. Discussion

Experiment 2 verified the effect of frequency range on the ability of listeners to distinguish between noises with different spectral structures. When the relevant structure occurred at low frequency, 1–3 kHz, it did not matter whether the source position was fixed or randomized in the MSP; listeners could identify the noise. When the relevant spectral structure occurred above 4 kHz, listeners had difficulty distinguishing between noises when the source position was roved, and the difficulty continued to increase as the frequency range of the structure increased. With structure near 8 kHz, it became effectively impossible to identify some noises well enough to distinguish them when the position was roved.

Almost certainly these results relate to the frequency dependence of the head-related transfer function (HRTF). Prominent HRTF pinna cues in particular are known to appear at high frequencies (Shaw, 1966, 1982; Shaw and Teranishi, 1968). Pinna cues seem to have had an especially disruptive influence on listeners' ability to maintain a sense of source identity. Just why this occurred is unclear. The finding is, in fact, surprising from at least two points of view.

One of these views is motivated by Blauert's (1969–70) narrow-band noise experiments. Blauert found perceptual and physical evidence indicating that MSP directional bands are present all across the spectrum. Given this, it might be expected that roving the source location would have disrupting influences all across it as well. That is, one might expect to see poor performance on roved-location identification at low and mid frequencies, as well as at high frequencies.

Another view—the view that motivated the present study—is that listeners have some ability to factor out spectral variations that accompany changes in source location, that is, to perceptually re-equalize the spectrum according to its location before making any decision about source identity. On this view, the expected outcome of roved-location experiments is that identification performance should be good all across the spectrum, so long as the listener can localize the source. Based on the results of experiments 1 and 2, we tentatively conclude that listeners cannot in fact perform such a re-equalization. There is, however, another possible explanation for the results. It is possible that our listeners could not identify noises with high-frequency spectral structure because they could not localize them. If they did not know where the sounds were coming from, then they could not compensate for directionally dependent filtering. Experiment 3 was done to test for the possibility that listeners could not identify because they could not localize.

III. EXPERIMENT 3—IDENTIFICATION AND LOCALIZATION

The purpose of experiment 3 was to directly compare the ability to identify with the ability to localize. The identification part of experiment 3 was the same as experiment 1—three double runs with the source fixed in front or roved over five locations. After subjects completed the identification test, they went through a localization test using the same stimuli. The format of a localization test was identical to that of a roved-location identification test except that listeners had to answer a different question. Instead of deciding whether a sound was noise *A* or noise *B*, they had to decide where the sound came from. Localization decisions were reported by pressing one of five buttons on a control box. There was no feedback on localization runs.

TABLE II. Experiment 3: Percentage of correct identification (ID) and correct localization (LOC) responses for roved sources. For each listener, S1–S4, there were pairs of noises that were easy to identify and pairs that were hard to identify. The identification scores show that large difference. The difference in localization scores is much smaller. Chance performance for ID is 50%; chance performance for localization is 20%.

	Easy identification		Hard Identification	
Listener	ID	LOC	ID	LOC
S1	99	86	52	84
S2	96	95	59	87
S3	99	95	56	74
S4	99	60	60	54

The $A-B$ noise pairs tested here were selected to include two pairs that were easy for a listener to identify and three pairs that were hard. Easy and hard pairs were selected on the basis of a listener's performance in experiment 2. Specifically, they were the $A-B$ pairs that had previously produced the smallest (easy) and largest (hard) values of added error for each listener, per Fig. 3.[4]

A. Results

Table II summarizes the results of experiment 3. The mean percent-correct scores on the roved-location identification and localization tasks are reported for the easy (300 trials per listener) and hard (450 trials per listener) identification noises. Table II shows a dramatic difference in identification scores when the easy condition is compared with the hard condition. That is not surprising; the experiment parameters were chosen to give this result.[5] What is interesting is the comparison in localization performance for the easy and hard conditions. Listener S1 shows hardly any difference at all, less than two percentage points in localization accuracy. Listeners S2 and S4 show a modest difference in localization, less than ten percentage points, and listener S3 shows a large difference.

B. Discussion

1. The re-equalization hypothesis

The central question addressed by this experiment is whether listeners can use their knowledge about the location of a source to help identify a sound. When sources have random locations in the MSP, there are random spectral shape changes that make it difficult for listeners to identify sounds on the basis of their spectra (experiments 1 and 2). In principle, this difficulty should be eliminated if listeners can re-equalize the received spectra based on their knowledge of

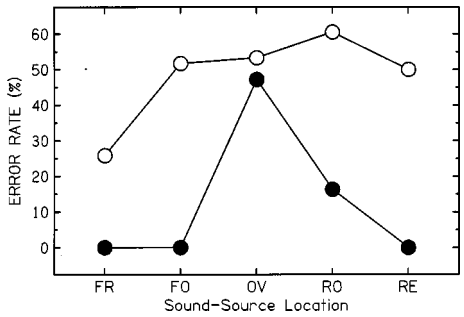

FIG. 4. Subject S1's error rates when localizing (filled symbols) and identifying (open symbols) the pair of 2/3-octave dips at 7.1 and 11.2 kHz. Errors rates are given for each of five sound-source locations in the MSP (FR=front, FO=front–over, OV=over, RO=rear–over, RE=rear).

source location. Such re-equalization could lead to a perceptual constancy whereby sounds can be identified regardless of their location in the MSP.

The results shown in Table II generally argue against the re-equalization hypothesis. The stimuli called ''hard'' are those for which the randomization of source location produced a large degradation in sound identification. Identification performance for those stimuli was poor indeed, quite near the 50 percent score expected for random guessing. However, the same stimuli were not poorly localized overall. To the contrary, Table II shows that localization performance was far better than the 20 percent score expected from random guessing and normally appreciably better than for identification. Therefore, the failure to identify cannot be attributed to a failure to localize.

Table II also reports a subject-specific difference that is relevant. Listener S4 was a poor sound localizer. His localization accuracy, although well above chance, was 30% below the mean accuracy for the others. Nevertheless, S4 identified sounds with an accuracy at or above the group mean for both the easy and hard identification runs. This result is additional evidence for a dissociation between localization and identification.

Still further evidence against the re-equalization hypothesis comes from a location-by-location comparison of identification and localization data. If re-equalization operates, then one might expect a listener to identify sounds accurately when they come from a location that is localized accurately and to identify sounds poorly when they come from a location that is mislocalized. In other words, identification performance should track localization performance, particularly for those locations where dramatic localization failure occurs. Three hard $A-B$ noise pairs for each of four listeners led to 12 opportunities to look for this. For each of those cases, we plotted the localization errors and identification errors at each location. Figure 4 shows an example.

Generally, localization errors showed sharp structure, with most of the errors occurring for only one or two sources, as in the example. For four cases, identification errors showed evidence of that same sharp structure. But for eight cases, including the example, identification errors were broadly distributed, occurring about equally often in each of the five loudspeaker locations, and so identification did not track localization. Therefore, most of the data argue against the concept of re-equalization.

TABLE III. A tally of the number of sound localization errors of different sizes that each subject made in experiment 3.

	Localization error size			
Listener	45 deg	90 deg	135 deg	180 deg
S1	108	0	2	1
S2	73	2	0	0
S3	130	3	0	0
S4	215	76	20	17

In sum, experiment 3 provided three kinds of evidence that sound identification and sound localization are largely dissociated, and hence three kinds of evidence against the re-equalization hypothesis. (i) There was evidence of dissociation across stimuli. For most listeners, localization accuracy was about the same for sounds that were easy to identify and sounds that were hard to identify. (ii) There was evidence of dissociation across listeners. Identification performance was more or less the same for all four listeners, despite the fact that one of them was decidedly poor at MSP sound localization, compared to the other three. (iii) There was evidence of dissociation across locations. Identification errors occurred about equally often for all five source locations, but localization errors occurred focally at one or two locations only.

2. Differences in sound localization ability

Table II shows some clear differences among the four subjects regarding their sound-localization abilities. Most especially, subject S4 was distinctly poorer than the others at sound localization. We wondered whether these subject differences were specific to the localization of bump/dip noises of the sort generated for the experiment, or more general. They proved to be more general. In a follow-up experiment, we presented white-noise stimuli randomly from the five loudspeaker locations and had the subjects make localization judgments, as in the main experiment. Listeners S1, S2, S3, and S4 correctly localized the white noise on 84%, 97%, 94%, and 51% of the trials, respectively. These results track the subject dependence seen in Table II and show that the differences among subjects in the localization part of experiment 3 are unrelated to the special spectral structures.

3. Localization error size

Table III shows an analysis of the localization errors made in experiment 3. Each subject's errors are broken out according to their size (in deg). The subjects differed substantially in terms of the total number of errors that they made, but they were in general agreement about error size. When errors occurred they were almost always 45-deg or 90-deg errors.

It is notable that front-to-back errors (180 deg) were few. For listeners S1, S2, S3, and S4, the numbers of front-to-back errors were: 1 in 289 (front or rear presentation) trials, 0 in 296 trials, 0 in 305 trials, and 17 in 298 trials, respectively. Thus, for listeners with normal localization

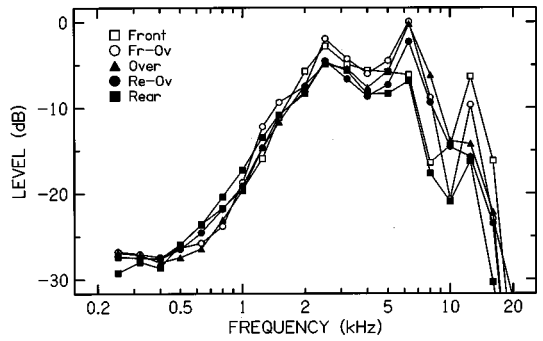

FIG. 5. Spectral density for a white noise presented from each of the five sources used in the identification and localization experiments. Measurements were made with the left ear of a KEMAR and are given in one-third-octave bands.

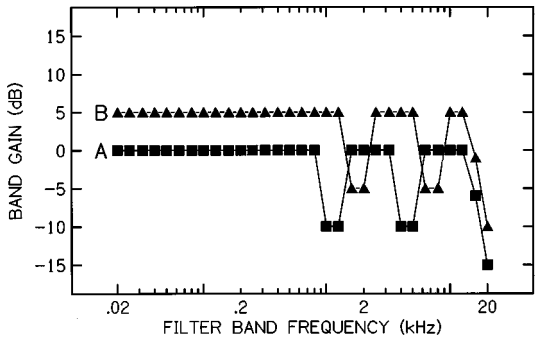

FIG. 6. A pair of noises used in experiment 4 with noise *B* raised by 5 dB for clarity. Each noise includes a high-frequency dip and a low-frequency dip.

abilities (S1–S3) there was only one front-to-back confusion in 890 trials with either the front or the rear speaker as the source. What seems remarkable about this result is that transfer functions measured in the ear canal or with a dummy head typically show that HRTFs are similar for sources at front and back locations. Therefore, front-to-back confusions are expected. The fact that our listeners made so few front-to-back errors seems paradoxical. Evidently, when presented with real-world sources, our listeners were able to make the fine distinctions necessary to avoid large localization errors. Further consideration of subjects' localization errors, and their relationship to HRTF features, is presented in the Appendix to this article.

4. Re-equalization again

Experiment 3 showed a number of instances in which listeners identified sounds poorly, but localized them accurately. We took these to be evidence against the re-equalization hypothesis. A counter argument would be that the spectral changes that mediate localization might be larger and more salient than the spectral differences between the sounds that listeners had to identify in our experiments. Therefore, an ability to localize might not necessarily imply an ability to identify. To get quantitative information on this point, we made recordings with a Knowles Electronics Manikin for Acoustic Research (KEMAR) placed at the listener's position in the anechoic room. Binaural recordings were made for white noise sent to each of the five loudspeakers.[6]

The left- and right-ear recordings were not ideal HRTFs; they included the response of the loud-speakers and stimulus roll-off above 12.5 kHz associated with the equalizer program (Fig. 1). The advantage of the recordings was that they were made in the conditions experienced by our listeners. Responses measured for the manikin's left ear are shown in Fig. 5. The right-ear response functions were similar, though not identical. (Left and right KEMAR ears are not exact mirror images.) The response functions for both ears showed a number of features that are expected for HRTFs. For example, there was a broad outer-ear resonance above 2 kHz. Sources overhead lead to a peak near 6 or 7 kHz. The response to a source in the rear was greater than the response to a source in front over a broad region around 1 kHz.

Figure 5 shows that the re-equalization counter argument is incorrect. Spectral differences between sources 45 deg apart (or, better, 90 deg apart) are not greater than the 10-dB bumps and dips that we introduced to try to make sounds distinguishable from one another. The fact that listeners can localize to within 90 deg with nearly 100-percent reliability means that they are sensitive to rather subtle spectral differences, smaller than the stimulus distortions of 10 dB in 1/3- or 2/3-octave bands. Therefore, there is no quantitative physical argument against the conclusion that listeners are unable to re-equalize.

IV. EXPERIMENT 4—COMPLEX STRUCTURE

Perceptual experiments 1 through 3 above asked listeners to identify noises characterized by spectral structure in a single frequency region and found evidence of substantial confusion when the structure was at high frequency and the source location was roved. Most ecologically significant sounds do not have their spectral structure confined to a single region. For example, speech has formant bands all across the spectrum. To learn more about sounds like speech, experiment 4 had listeners identify noises with complex structure.

A. Method

The experiment was done according to the protocol of experiment 1, with three double runs for each $A-B$ noise pair. Complex noises of two types were presented. There were *double-dip* noises that combined a 2/3-octave dip at low frequency with a 2/3-octave dip at high frequency, and there were *double-bump* noises that combined low- and high-frequency bumps. For each listener, we found a pair of low-frequency dips/bumps that was well identified in experiment 1, and a pair of high-frequency dips/bumps that was poorly identified. We then combined them in low–high pairs to make the complex noise stimuli for this experiment.[7]

Figure 6 shows an example. Noise *A* is a double-dip noise that marries dips at 1.1 and 4.5 kHz. Noise *B* is a double-dip noise that marries dips at 1.8 and 7.1 kHz. We always combined the lower-frequency member of a low-frequency pair with the lower-frequency member of a high-frequency pair to derive one double-dip/bump stimulus, and then combined the higher-frequency members of each pair to

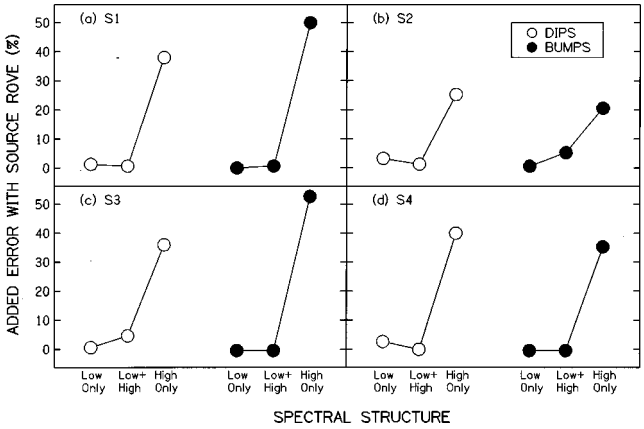

FIG. 7. Experiment 4 results for listeners S1–S4 in panels (a)–(d), respectively. As in Fig. 3, the ordinate shows added error when a source is roved.

derive the other stimulus, as in the example. Each listener heard one double-dip pair and one double-bump pair in the experiment.

B. Results and discussion

The results of experiment 4 are shown in Fig. 7. The added error due to source rove is plotted there for three kinds of spectral structure. There is a *low-only* data point from experiment 1 with an $A-B$ noise pair consisting of low-frequency bumps/dips. There is a *high-only* data point, also from experiment 1, with an $A-B$ noise pair consisting of high-frequency bumps/dips. Finally, there is a *low+high* data point from the present experiment using an $A-B$ pair of complex noises that combined the low-only and high-only spectral features.

For every listener (different figure panels) and for both bumps (filled symbols) and dips (open symbols), the outcome was the same. Roving location caused little or no added error for identification of complex noises with low +high spectral structure. They were identified as accurately under rove as were the low-only noises, and dramatically better than the high-only noises. We conclude that when source location varies, listeners can maintain constancy in their identification of complex sounds by latching onto low-frequency structure in the sound spectrum. Their grip on low-frequency structure appears to be firm, firm enough to anchor perception of what would be otherwise ambiguous high-frequency structural components.

V. CONCLUSIONS

Experiments 1 and 2 tested listeners' ability to identify broadband sounds with different spectral structures. The experiments showed that when the source location of the noises was fixed in space, listeners could usually identify the noises successfully. Listeners were somewhat more successful at identifying noises with low-frequency structure (1 to 3 kHz) than noises with high-frequency structure (above 4 kHz), possibly because low-frequency structure often led to vowel-like sounds. However, the difference between low and high frequencies was not great. By contrast, when source location was randomized among five locations in the median sagittal plane (MSP), listeners were still able to identify noises with low-frequency spectral structure, but their ability to identify high-frequency structure fell almost to the chance level.

Experiment 3 compared the listeners' ability to identify noises with their ability to localize them. It showed that the difference in identification between noises with low- and high-frequency structure cannot be explained by any corresponding differences in MSP sound localization. Three listeners localized all of the noises with a high accuracy, no matter what the spectral structure. A fourth listener localized less well than the others, but substantially better than chance, and at about the same level no matter whether the noises to be localized had low-frequency or high-frequency structure.

Overall, the pattern of localization and identification results for experiment 3 argued against a *re-equalization* hypothesis, which says that listeners can compensate for spectral distortions due to their HRTFs before deciding about the identity of incoming sounds. Because they can localize sounds on the basis of their spectral signatures, it must be presumed that listeners are aware, at some level, of the directionally dependent filtering that takes place. The information provided by a known source location could, in principle, be used to re-equalize the spectra to enable identification. Our results nevertheless showed that listeners cannot do that, even after substantial practice. The failure to distinguish among high-frequency spectral structures with roving location was dramatic and quite similar for all our listeners in experiments 1–3. The failure was also persistent. It persisted throughout a run, showing up equally at its beginning and end, and when there were multiple identification runs with a particular noise pair it persisted across the runs.

Macpherson (1995) also concluded that listeners cannot compensate for their location-dependent HRTFs. In a headphone profile analysis experiment, Macpherson caused a listener's identification task to be difficult by filtering the signals with assorted HRTFs. He found that identification performance was not best when the HRTFs were intended to provide a realistic representation of source location. Rather, it was best for certain mismatched left–right pairs of HRTFs that did not correspond to any location. Although his experiments did not measure perceived localization directly, the results are consistent with the dissociation between identification and localization found here.

Finally, experiment 4 showed that listeners can distinguish between complex noises that include spectral structure at both high and low frequencies. This is true whether the source location is fixed or roved in the MSP. The significance of this result is that although high-frequency structure may be perturbed to the point of confusion by the roving of location, listeners can ignore that confusion and identify complex sounds on the basis of the low-frequency structure alone.

ACKNOWLEDGMENTS

This project was supported by the National Institutes of Health through NIDCD Grant No. DC00181. Funds were also provided by the National Science Foundation Research Experience for Undergraduates (REU) Program in the Michigan State University Department of Physics and Astronomy.

We are grateful for the help of Melanie Koskamp, a participant in the REU program, and to Ewan Macpherson for useful discussions.

APPENDIX: MSP SOUND LOCALIZATION AND HRTFS

In experiment 3, three listeners (S1–S3) accurately localized noises with a variety of bump and dip structures most of the time, and when they did make mistakes their errors were almost always confusions with a nearest-neighbor location in the loudspeaker array (i.e., 45-deg errors; see Table III). A fourth listener (S4) made more localization errors than the others, but those errors too were predominantly confusions with a nearest neighbor or, to a lesser extent, a next-nearest neighbor.

A notable feature of the listeners' errors was that they were not at all uniformly distributed among the five sound-source locations. For listeners S1–S3, adding particular bumps or dips to the spectrum often caused the overhead location, or the rear–over location, or sometimes both, to be incorrectly localized. The failures for these one or two locations were dramatic and systematic. For example, putting a 10-dB dip in the two-thirds-octave band at 7.1 kHz caused listener S1 to miss 7 out of 14 overhead localizations, and every missed overhead was mislocalized as rear–over. The identical error was made by listener S2 on 6 out of 10 trials for this stimulus. For listener S3, this stimulus caused rear–over to be mislocalized as rear on 9 out of the 11 trials.

It is interesting to ask whether these highly systematic localization errors can be understood on the basis of deformations in the apparent HRTFs. Accordingly, we compared the errors with the KEMAR HRTF measurements that were made for experiment 3 (Fig. 5). The comparison is not ideal because KEMAR's HRTFs and those of an individual listener can differ, sometimes substantially. We nevertheless found several notable points of correspondence with the localization results. The failure of listeners S1 and S2 to correctly localize the overhead source in the presence of a 10-dB dip at 7.1 kHz seemed easy to understand. Figure 5 shows that the overhead position is most favored at 8 kHz. It also shows what Butler and Musicant (1993) have called a ''covert peak,'' a peak at the overhead position in a plot of intensity vs position for a given frequency of 8 kHz. Putting a dip in the 7.1-kHz band makes the overhead source look more like the other sources. It is less evident why this spectral change should cause the image of the overhead source always to appear at the rear–over position. This is probably caused by similarities between rear and rear–overhead at lower-frequency regions of the spectrum. For listener S3, the rear–over source reliably appeared at the rear position, and this result is also consistent with the change in the tall peak of an apparent HRTF.

Given the above results with a 10-dB spectral dip at 7.1 kHz, it might be predicted that its opposite, namely a 10-dB bump in that band, would lead to errors of the opposite kind. As it turned out, both listeners S1 and S2 had that bump on their menu, and both experienced the erroneous localizations as expected. For listener S1, the rear–over location was missed on 8 out of 15 trials and the incorrect localization always went to overhead. For listener S3, the rear location was missed on 10 of 15 trials and the incorrect localization always went to rear–over. Thus, for both S1 and S3, the spectral dip and the complementary spectral bump produced errors of exactly opposite kinds.

Other systematic errors are more difficult to explain in terms of the KEMAR data. Adding a spectral bump in the two-thirds-octave band at 11.2 kHz caused listener S1 to hear the overhead source at the rear–over position on 10 out of 14 trials. HRTFs measured with the KEMAR do not show any kind of peak for the rear–over location in this frequency region. One might understand the judgments of S1 by assuming that he uses the high-frequency region above 10 kHz as a reference against which other peaks may be judged in the manner of profile analysis (Green, 1988). Boosting this high-frequency region would make a peak near 8 kHz due to an overhead source seem relatively less prominent and possibly cause the overhead source to be incorrectly localized.

Although it is possible to explain certain systematic errors in localization in terms of HRTFs and the spectral distortions deliberately introduced in our experiments, an arguably larger issue is to explain why our listeners localized as well as they did. Despite large spectral distortions in frequency ranges known to be important for localization in the MSP, their localization performance was good overall. It seems likely that one key to understanding this behavior is that our spectral distortions occurred in isolated frequency regions. Our results suggest that listeners do not rely entirely on isolated spectral features, such as the frequencies of high-frequency peaks or valleys. Instead, they may use those features in combination with spectral details from a wide range of frequencies. Alternatively, it may be that localization depends on a rather coarse analysis of the HRTF, as proposed in several recent models (Fuzessery, 1986; Zakarauskas and Cynader, 1993; Macpherson, 1997). If this is the case, then local distortions, like the ones introduced here, could leave much of the spectral information intact.

[1]The five loudspeakers were selected from a batch of 79 on the basis of their best-matched frequency response, as determined by an automated comparison made at 76 frequencies from 125 to 11 000 Hz.

[2]The equalizer was a model IEQ made by Applied Research and Technology. This equalizer has a ''smart curve'' feature that makes the spectral shape of a bump or dip close to the rectangular ideal by automatically adjusting the gains of adjacent one-third-octave bands.

[3]The caption of Fig. 3 gives the different combinations of bump/dip bandwidths and separations between spectral features that were included in experiment 2. Error rates on the fixed-location runs provided a baseline for the ''added error due to source rove'' computation. The fixed-location rates for experiment 2 were similar to those observed in experiment 1 (see Fig. 1). For bumps, fixed-location error rates were generally less than 5% at all frequencies. For dips, rates were somewhat higher, 5%–10% at frequencies below 4 kHz, and 5%–15% above 4 kHz. As in experiment 1, if a listener had an error rate greater than 25% for a fixed-location run, the corresponding roved-location run was omitted. Only spectral dips led to such failures in experiment 2; bumps never did. Of 40 combinations of listener and one-third-octave dips, there were 11 failures. Of 36 combinations of listener and two-thirds-octave dips, there was one failure.

[4]The ''easy'' and ''hard'' $A-B$ pairs selected for each subject were as follows. S1-easy: 2/3-octave dips at 1.1 and 1.8 kHz, 2/3-octave bumps at 1.8 and 2.8 kHz. S1-hard: 2/3-octave bumps at 7.1 and 11.2 kHz, 2/3-octave dips at 4.5 and 7.1 kHz, 2/3-octave dips at 7.1 and 11.2 kHz. S2-easy: 2/3-octave dips at 1.8 and 2.8 kHz, 2/3-octave bumps at 1.1 and 1.8 kHz. S2-hard: 1/3-octave bumps at 4.0 and 6.3 kHz, 1/3-octave dips at 4.0 and 6.3 kHz, 2/3-octave dips at 7.1 and 11.2 kHz. S3-easy: 2/3-octave dips

at 1.1 and 1.8 kHz, 2/3-octave bumps at 1.8 and 2.8 kHz. S3-hard: 2/3-octave dips at 7.1 and 11.2 kHz, 2/3-octave dips at 4.5 and 7.1 kHz, 2/3-octave bumps at 7.1 and 11.2 kHz. S4-easy: 2/3-octave dips at 1.1 and 1.8 kHz, 2/3-octave bumps at 1.1 and 1.8 kHz. S4-hard: 1/3-octave bumps at 6.3 and 10.0 kHz, 1/3-octave dips at 2.5 and 4.0 kHz, 2/3-octave dips at 4.5 and 11.2 kHz.

[5]The difference between the easy identification and hard identification runs was equally dramatic when measured as added error due to source rove. The average added error was 1.1% for the easy runs and 36.1% for the hard ones.

[6]The KEMAR (Knowles Electronics Manikin for Acoustics Research) was fitted with two large ears, Knowles DB-065 and DB-066, and Zwislocki couplers. The couplers included Etymotic ER-11 half-inch microphones with accompanying preamplifiers set to a ''flat'' response. Output signals from KEMAR's left and right ears were analyzed in 30 one-third-octave bands by a Stanford Research Systems SR-760 FFT spectrum analyzer.

[7]S1 double-dips: 1.1 and 7.1 kHz, 1.8 and 11.2 kHz. S1 double-bumps: 1.8 and 7.1 kHz, 2.8 and 11.2 kHz. S2 double-dips: 1.8 and 7.1 kHz, 2.8 and 11.2 kHz. S2 double-bumps: 1.1 and 4.5 kHz, 1.8 and 7.1 kHz. S3 double-dips: 1.1 and 4.5 kHz, 1.8 and 7.1 kHz. S3 double-bumps: 1.8 and 7.1 kHz, 2.8 and 11.2 kHz. S4 double-dips: 1.1 and 4.5 kHz, 1.8 and 7.1 kHz. S4 double-bumps: 1.1 and 7.1 kHz, 1.8 and 11.2 kHz.

Blauert, J. (**1969–70**). ''Sound localization in the median plane,'' Acustica **22**, 205–213.

Butler, R. A., and Belundiuk, K. (**1977**). ''Spectral cues utilized in the location of sound in the median sagittal plane,'' J. Acoust. Soc. Am. **61**, 1264–1269.

Butler, R. A., and Musicant, A. M. (**1993**). ''Binaural localization: Influence of stimulus frequency and the linkage to covert peak areas,'' Hearing Res. **67**, 220–229.

Durlach, N. I., and Colburn, H. S. (**1978**). ''Binaural Phenomena,'' in *Handbook of Perception*, Vol. IV, edited by E. Carterette (Academic, New York).

Fuzessery, Z. M. (**1986**). ''Speculations on the role of frequency in sound localization,'' Brain Behav. Evol. **28**, 95–108.

Green, D. M. (**1988**). *Profile Analysis Auditory-Intensity Discrimination*, Oxford Psychology Series No. 13 (Oxford, New York).

Hebrank, J., and Wright, D. (**1974**). ''Spectral cues used in the localization of sound sources on the median plane,'' J. Acoust. Soc. Am. **56**, 1829–1834.

Macpherson, E. A. (**1995**). ''Source spectrum recovery at different spatial locations,'' J. Acoust. Soc. Am. **98**, 2946(A).

Macpherson, E. A. (**1997**). ''A comparison of spectral correlation and local feature-matching models of pinna cue processing,'' J. Acoust. Soc. Am. **101**, 3104(A).

Middlebrooks, J. C. (**1992**). ''Narrow-band sound localization related to external ear acoustics,'' J. Acoust. Soc. Am. **92**, 2607–2624.

Moore, B. C., Oldfield, S. R., and Dooley, G. J. (**1989**). ''Detection and discrimination of spectral peaks and notches at 1 and 8 kHz,'' J. Acoust. Soc. Am. **85**, 820–836.

Plenge, G., and Brunschen, G. (**1971**). ''*A priori* knowledge of the signal when determining the direction of speech in the median plane,'' Proceedings of the Seventh International Congress on Acoustics, 19, H10.

Shaw, E. A. G. (**1966**). ''Ear canal pressure generated by a free sound field,'' J. Acoust. Soc. Am. **39**, 465–470.

Shaw, E. A. G. (**1982**). ''External ear response and sound localization,'' in *Localization of Sound: Theory and Applications*, edited by R. W. Gatehouse (Amphora, Groton, CT).

Shaw, E. A. G., and Teranishi, R. (**1968**). ''Sound pressure generated in an external ear replica and real human ears by a nearby point source,'' J. Acoust. Soc. Am. **44**, 240–249.

Wightman, F. L., and Kistler, D. J. (**1989a**). ''Headphone simulation of free field listening I,'' J. Acoust. Soc. Am. **85**, 858–867.

Wightman, F. L., and Kistler, D. J. (**1989b**). ''Headphone simulation of free field listening II,'' J. Acoust. Soc. Am. **85**, 868–878.

Zakarauskas, P., and Cynader, M. S. (**1993**). ''A computational theory of spectral cue localization,'' J. Acoust. Soc. Am. **94**, 1323–1331.

Variations in the feedback of hearing aids

Johan Hellgren, Thomas Lunner, and Stig Arlinger
Department of Neuroscience and Locomotion, Division of Technical Audiology, Linköping University, 581 85 Linköping, Sweden

(Received 25 March 1999; revised 22 June 1999; accepted 3 August 1999)

Variations in the loop response of hearing aids caused by jaw movements, variations in acoustics outside the ear, and variations of vent size have been identified. Behind The Ear (BTE) and In The Ear Canal (ITEC) hearing aids were considered. The largest variations among the variations of the acoustics outside the ear, except when the hearing aid was partly removed, were found with the ITEC when a telephone set was placed by the ear. The variations of the loop response caused by changes in vent size were compared with the variations of a theoretical model of the feedback path. The theoretical model was also used to compare the feedback of different designs of the vent that gives the same acoustic impedance at low frequencies. The calculated feedback was less with the short vents (12 mm) than the long vents (24 mm). © *1999 Acoustical Society of America.* [S0001-4966(99)05811-7]

PACS numbers: 43.66.Ts, 43.64.Ha [SPB]

INTRODUCTION

Oscillation caused by feedback is a very common complaint by hearing aid users that in many cases limits the gain that can be provided by the hearing aid. For some users the hearing aid is stable most of the time but starts to oscillate in some situations, e.g., when a telephone set is placed at the ear. The feedback and the effect of it on different types of hearing aids have been studied by Grover and Martin (1974), Lybarger (1975), Johansen (1975), Lundh (1982), Dyrlund (1989), Gatehouse (1989), Erickson and van Tasell (1991), Kuk (1994), and Hellgren *et al.* (1999). All of these studies were performed with a static feedback path. No changes of the acoustics outside the ear or changes of the shape of the ear canal were used.

The loop response of a system with feedback is the transfer function of the opened loop, and is thus the transfer function of the forward path in series with the feedback path. The hearing aid will start to oscillate when the loop response is 0 dB at a frequency where the phase is a multiple of 360°. The feedback, and thus the loop response, depends on a number of factors. Behind The Ear (BTE), In The Ear (ITE), and In The Ear Canal (ITEC) hearing aids have different microphone positions and will thus have different feedback paths. The dimensions of the vent in the earmold affect the feedback. The diameter is often reduced during fitting of the hearing aid if there are feedback problems. The acoustics outside the ear will also affect the feedback. The palm of the hand or a telephone set close to the hearing aid often causes oscillation. A change of the shape of the ear canal will affect the fit of the earmold and thus also the feedback.

The hearing aid category (BTE, ITE, or ITEC) and the dimensions of the vent are examples of factors that will be constant once the fitting of the hearing aid is completed. The fit of the earmold and the acoustics outside the ear vary as the hearing aid is used. Jaw movements will produce changes in the shape of the ear canal with a time frame of seconds/minutes (Oliviera, 1997). Production and disposal of cerumen will cause changes with a time frame of weeks and months, while aging introduces changes with a time frame of years.

In the present study, variations of the loop response caused by the acoustics outside the ear, jaw movements, and vent size have been studied. The loop response will depend on the type of hearing aid used. However, the variations of the loop in the cases studied will be the same among hearing aids, under the assumption that the forward path of the hearing aids has the same variations. The results of the present study can thus be applied to any hearing aid under this assumption.

When the hearing aid is adjusted, some amount of margin to 0-dB loop response has to be used to allow for variations in the feedback path. It can be assumed that a larger margin will be used when a hearing aid without volume control is adjusted by the dispenser than when the user has access to a volume control. With the volume control, the user can reduce the gain if the hearing aid starts to howl. The results of the present study provide information about the amount of variations in the loop response and thus the margin to 0-dB loop response required in the normal situation to avoid oscillation when the feedback changes. The results also provide information of the reduction in loop response as the vent diameter is reduced.

A. Occlusion and feedback

The occlusion of the ear canal can cause annoyance and changes of the perception of one's own voice. Seventy-three percent of the hearing aid users investigated by Hansen (1997) experienced some occlusion effect on their own voice. Significantly fewer patients reported blocked-up feeling with a 2-mm vent than without in the study by MacKenzie *et al.* (1989). The input impedance of the vent and thus the occlusion effect can be reduced by increasing the diameter or decreasing the length of the vent. However, this will in general also increase the feedback. The dimensions of the vent can thus be used to control the compromise between feedback and occlusion. The problem with occlusion is primarily found at low frequencies while feedback problems are

primarily found at high frequencies. It would thus be desirable to have a vent with as low input impedance as possible at low frequencies to reduce the occlusion effect, but as high impedance as possible at high frequencies to reduce the feedback problem. The theoretical transfer function of the feedback for different designs of the vent that give approximately the same impedance at low frequencies has been identified and compared.

B. Feedback cancellation systems and variations of loop response

One way to avoid problems associated with feedback in hearing aids is to introduce feedback cancellation as proposed by Best (1985), Bustamante *et al.* (1989), Kates (1991), Bisgaard and Dyrlund (1991), Kuo and Voepel (1992), Engebretson and French-St. George (1993), and Joson *et al.* (1993). In such systems the feedback signal is predicted and cancelled from the microphone signal. The prediction is generated by filtering the output signal of the hearing aid through a filter. The filter has to have the same transfer function as the feedback. The filter has thus to be adaptive in order to follow the changes of the feedback. The changes that the adaptive filter has to adapt to are then the changes of the loop response. The results of the present study illustrate the flexibility required by such an adaptive filter.

I. MATERIAL AND METHODS

Two types of hearing aids were used: Oticon Personic 425 representing BTE hearing aids, and a specially designed ITEC hearing aid. The hearing aids were modified by opening the signal path between the microphone and the receiver. The microphone and the receiver were connected to the Analog to Digital converter (AD) and Digital to Analog converter (DA), respectively, of a Digital Signal Processor (DSP) board in a host PC. The DSP board was used to generate a broadband noise applied to the receiver and to record the signals of the microphone and the receiver on the hard disk for off-line analysis. Sixteen-bit AD and DA converters were used at a sampling frequency of 15.75 kHz. A signal conditioner was used to adjust the microphone signals to the DSP board. The bandwidth of the acquisition system was 7.1 kHz.

The measurements with BTE and ITEC were made on five human subjects, four male and one female. Measurements with BTE were also made on a Knowles Ear Manikin (KEMAR) equipped with a Brüel & Kjær ear simulator type 4157 (IEC 711, 1981). The mean length of the vents used on human subjects was 17.4 and 18.6 mm for the BTE and ITEC instruments, respectively. The length of the vent used with KEMAR was 15.5 mm. The distance between the center of the microphone inlet and the vent opening on the faceplate was 14.2 mm for ITEC instruments. The diameters of vents in the earmolds were 3.1, 2.1, and 2.2 mm for the ITEC, BTE on human subjects, and BTE on KEMAR, respectively. The human subjects used individual hearing aids. Five BTE hearing aids were used on KEMAR. The measurements were performed in an anechoic room.

The variations were calculated as the ratio between the loop response in the situations tested (e.g., telephone set by the ear) and in the normal situation. The loop responses were calculated by applying spectral analysis (Ljung and Glad, 1994) to the signals of the microphone and receiver. A Hanning window that was nonzero for 255 samples ($-8.1 < \tau < 8.1$ ms) was used in the spectral analysis.

The group delay in the loop was about 60 samples ($\sim$3.8 ms). The long delay was mainly caused by the DA and AD converters that together introduced a group delay of 54 samples. In the spectral analysis, the input signal (signal to receiver) was delayed by 64 samples, in order to get most of the correlation between input and output in the middle of the window. The phase of the results was then adjusted for the 64-sample delay.

A. Tested cases

A number of cases that could be expected to influence the feedback were tested.
The four cases of variations of the acoustics outside the ear were:

(a) A telephone set at the ear
(b) A wall at a distance of 10 cm from the head
(c) A hug
(d) Wearing a knitted cap

A sheet of particleboard covered with a plastic layer was used to simulate the wall. The board had the dimensions $400 \times 830 \times 19$ mm.
Four cases of variations of the shape of the ear canal were tested:

(1) Yawning
(2) Mouth shaped for saying [ɑ:]
(3) Mouth shaped for saying [i:]
(4) Biting

The case ''mouth shaped for saying [i:]'' is similar to smiling. Compare to ''say cheese!''
Two other cases of the fit of the earmold were tested:

(1) Earmold partly removed (only tested with ITEC).
(2) Earmold not placed correctly in Cymba conchae (only tested with BTE).

Only the first four cases with variations of the acoustics outside the ear (telephone, wall, hug, and knitted cap) were tested with KEMAR. The last case with misplaced earmold was realized by inserting the earmold in such a way that the helix of the earmold was placed over the crus of helix of the pinna. [See Alvord and Farmer (1997) for nomenclature.] This is fairly common when an earmold with a helix is misplaced.

A number of vent dimensions were also tested. The vent was reduced by inserting tubes called ''select a tube'' (SAT) with lengths of approximately 5 mm and various inner diameters. On the ITEC hearing aids that used vents with a diameter of 3.1 mm, SAT with inner diameter of 2.1, 1.2, and 0.8 mm were used. Two cases with blocked vent were also tested: one with the normal fit of the hearing aid and one

with some impression material around the hearing aid to reduce the leak. The BTE instruments used on human subjects were tested with SAT with inner diameter of 1.2 mm, the two cases with blocked vent, and with a separate earmold with a 3.1-mm vent. The earmold used for the reference had a vent with a diameter of 2.1 mm. The earmold with the 3.1-mm vent was produced from the same impression as the earmold with the 2.1-mm vent and was only used on one of the subjects. SAT with inner diameters of 1.2, 0.7, and 0 mm were used to reduce the 2.2-mm vent of the earmold on KEMAR.

All the measurements were static in the sense that the above parameters were held constant during each measurement. This means that the transition between two cases has not been investigated.

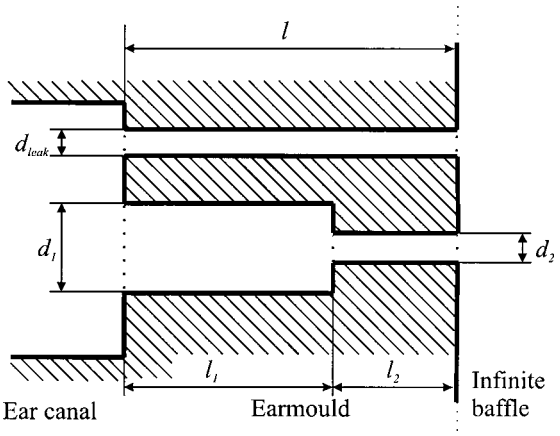

FIG. 1. Model of the feedback path.

B. Measures of the change

The sample mean and sample estimate of the standard deviation of the measured changes from the normal situation were calculated as a function of frequency. Changes both in amplitude and in phase were calculated. The choice to present data in this way was done to provide a reasonable amount of data. The mean and the standard deviation do not reveal all of the characteristics of the individual data, but they give a measure of the range where most of the individual data will be found. Sixty eight percent of the cases will be within the interval given by $(m-\sigma, m+\sigma)$, if it is assumed that the change is a normally distributed stochastic variable with an expected value m and a standard deviation σ. The 95% confidence interval for the expected value is $(x-1.24*SD, x+1.24*SD)$ when the sample size is five measurements. x is the sample mean and SD is the sample estimate of the standard deviation.

The maximum increase of the amplitude of the loop response in the 2–5 kHz frequency range was used as a scalar measure of the change. The 2–5 kHz frequency range was chosen since howling often occurs at these frequencies (Dyrlund and Lundh, 1990). This measure can be considered the worst-case gain margin required in the normal situation to avoid oscillation in the tested case. It should be noted that uncertainties in the analysis and variations of the normal situation will introduce a bias in this measure. This means that the expected value of this measure will not be zero if two measurements of the normal situation are compared. The frequency response of the hearing aid, which differs between hearing aids, will affect the loop response. It is thus not certain that the oscillation will occur at the frequency with the largest increase in the loop response. The mean value of the change in the 2–5-kHz frequency range was used as a more conservative and unbiased scalar measure of the change.

C. Theoretical model of the feedback path from ear canal to microphone

The variations of the loop response will be the same as the variations of the feedback path, under the assumption that the forward path of the system is constant. Varying the vent size will affect the load impedance of the hearing aid and thus the transfer function of the forward path. The transfer function will vary substantially for frequencies below the range of interest for feedback (2 to 5 kHz), while it will be close to unchanged within the range (Grover, 1976). Thus the changes of the feedback path can be used to predict the changes of the loop response at high frequencies.

A theoretical model of the feedback path was used to calculate the variations cased by the variations in vent size. The model was configured according to Fig. 1. The reference plane was the tip of the earmold. An infinite baffle was used to correspond to the pinnae and head. The point of interest (corresponding to the microphone position) was a point by the infinite baffle. The vent was modeled by two circular tubes corresponding to the original vent of the earmold and the SAT. The diameters of the two tubes were d_1 and d_2 and the lengths l_1 and l_2. The total length of the two tubes was l. The leak was modeled by a circular tube with length l and diameter d_{leak}.

The pressure transfer function across and the input impedance to a tube with loss, for a given load impedance, is given in the Appendix of Kates (1988). The use of these equations is subject to several assumptions made in the derivation by Iberall (1950), and summarized by Egolf (1977). The radiation impedance of a tube in an infinite baffle, also given by Kates (1988), was used as load impedance when the tube ended in the infinite baffle. The transfer function from the opening in the infinite baffle to the point of interest (position of the hearing aid microphone) is given by Egolf *et al.* (1985). The transfer function from the reference plane to the point of interest was calculated separately for each path (vent and leak) and then added to obtain an estimate of the transfer function of the model. This resulted in the effect on the pressure at the reference plane due to feedback of the signal radiating from the vent opening back to the ear canal via the leak (and vice versa) being ignored, as well as the impact of the tube modeling the leak on the radiation impedance at the vent opening (and vice versa). These simplifications were judged to have only minor effects on the results.

The point of interest was by the baffle and 40 mm from the vent opening with BTE and 14.2 mm with ITEC. The same values were used for the distance between leak and point of interest. The diameter of the tube corresponding to the original vent of the earmold was set to 2.1, 2.2, and 3.1

TABLE I. Change of loop response with BTE hearing aid on human subjects and KEMAR.

	Human subjects				KEMAR			
	Mean over frequency and subjects (dB)	Maximum increase in 2–5 kHz			Mean over frequency and measurements (dB)	Maximum increase in 2–5 kHz		
		Minimum (dB)	Mean (dB)	Maximum (dB)		Minimum (dB)	Mean (dB)	Maximum (dB)
Telephone	4.3	11.3	13.7	16.4	7.2	8.1	10.6	12.4
Hug	1.3	5.0	6.0	6.4	0.6	5.8	6.9	9.4
Wall	1.1	2.6	5.1	7.9	0.0	4.3	4.7	5.0
Knitted cap	0.4	1.2	3.4	5.7	0.2	2.5	3.8	4.9
Yawning	1.2	1.4	2.9	5.9				
Saying [ɑ:]	0.6	0.1	1.8	4.0				
Saying [i:]	−0.1	0.1	1.6	5.9				
Biting	−0.3	−0.2	0.8	1.9				
Earmold not placed correctly	2.7	0.1	5.7	9.3				
3-mm vent	9.2	10.9	10.9	10.9				
1.2-mm SAT	−4.3	−6.6	−1.5	2.6	−3.9	−4.9	−1.1	4.7
0.7-mm SAT					−11.7	−10.8	−7.1	−2.3
No vent	−8.6	−8.5	−4.3	−1.1	−16.2	−12.1	−11.6	−11.4
No vent and impression material around earmold	−14.1	−19.3	−9.7	−1.2				

mm for the BTE on human subjects, BTE on KEMAR, and ITEC, respectively. The diameter of the other tube was set to the values of the used SAT. The length of this tube was set to 5 mm. The diameter of the tube modeling the leak was adjusted so that the reduction of feedback when occluding the vent was the same as the mean measured reduction of loop response over the 2- to 5-kHz region.

1. Comparison of occlusion effect and feedback with different designs of the vent

It would be desirable to design a vent that provides low input impedance at low frequencies (to minimize the occlusion effect) and as little feedback as possible at higher frequencies (2 to 5 kHz). The theoretical model was used to compare the feedback of eight different configurations of the vent that gave approximately the same input impedance at 200 Hz. Four cases used a total length of the vent (l) of 12 and the other four 24 mm. One case with the SAT ''inserted'' from the opening in the infinite baffle, one with the SAT ''inserted'' from the earmold tip, one with increased diameter the last 5 mm, and one with homogenous diameter were used for each value of the length l. The case with increased diameter the last 5 mm was used as an approximation of a horn-shaped vent. These cases were chosen to compare short and narrow vents with long and wide, and vents with varying diameter.

In the cases of varying diameter, the diameter of the tube with smaller diameter was set to half the diameter of the other tube. Both tubes used the same diameter in the cases with homogenous diameter. The diameter of the tube modeling the leak (d_{leak}) was set to zero in all cases. Thus the leak was not incorporated in this comparison. The diameters were adjusted so that the absolute value of the input impedance at 200 Hz at the earmold tip was the same in the case with a 12-mm-long vent with a homogenous diameter of 1.2 mm.

II. RESULTS AND DISCUSSION

The scalar measures of the change of the loop response for the BTE and ITEC are presented in Tables I and II, respectively. The bias introduced when using the maximum increase was estimated by calculating the maximum increase of a number of measurements in the normal situation. Five measurements were performed on each subject. The earmold was removed and repositioned between each measurement. The mean of the maximum increase of each measurement relative to the individual mean was found to be 0.8 and 0.9 dB for the BTE and ITEC, respectively.

TABLE II. Change of loop response with ITEC.

	Mean over frequency and subjects (dB)	Maximum increase in 2–5 kHz		
		Minimum (dB)	Mean (dB)	Maximum (dB)
Telephone	5.7	10.6	17.4	25.1
Hug	−1.1	1.1	7.9	15.1
Wall	−0.5	0.7	1.7	3.2
Knitted cap	1.6	0.4	4.8	10.1
Yawning	1.1	1.2	2.8	3.8
Saying [ɑ:]	0.3	0.6	2.2	7.0
Saying [i:]	0.4	0.0	2.8	6.5
Biting	−0.2	−0.5	1.5	6.3
Earmold partly removed	10.3	2.5	21.4	36.9
2.1-mm SAT	−2.7	−2.9	3.3	12.6
1.2-mm SAT	−6.6	−5.9	0.8	3.7
0.8-mm SAT	−10.0	−6.9	−0.9	9.5
No vent	−16.0	−18.0	−8.0	−1.8
No vent and impression material around earmold	−19.6	−22.3	−12.9	−2.0

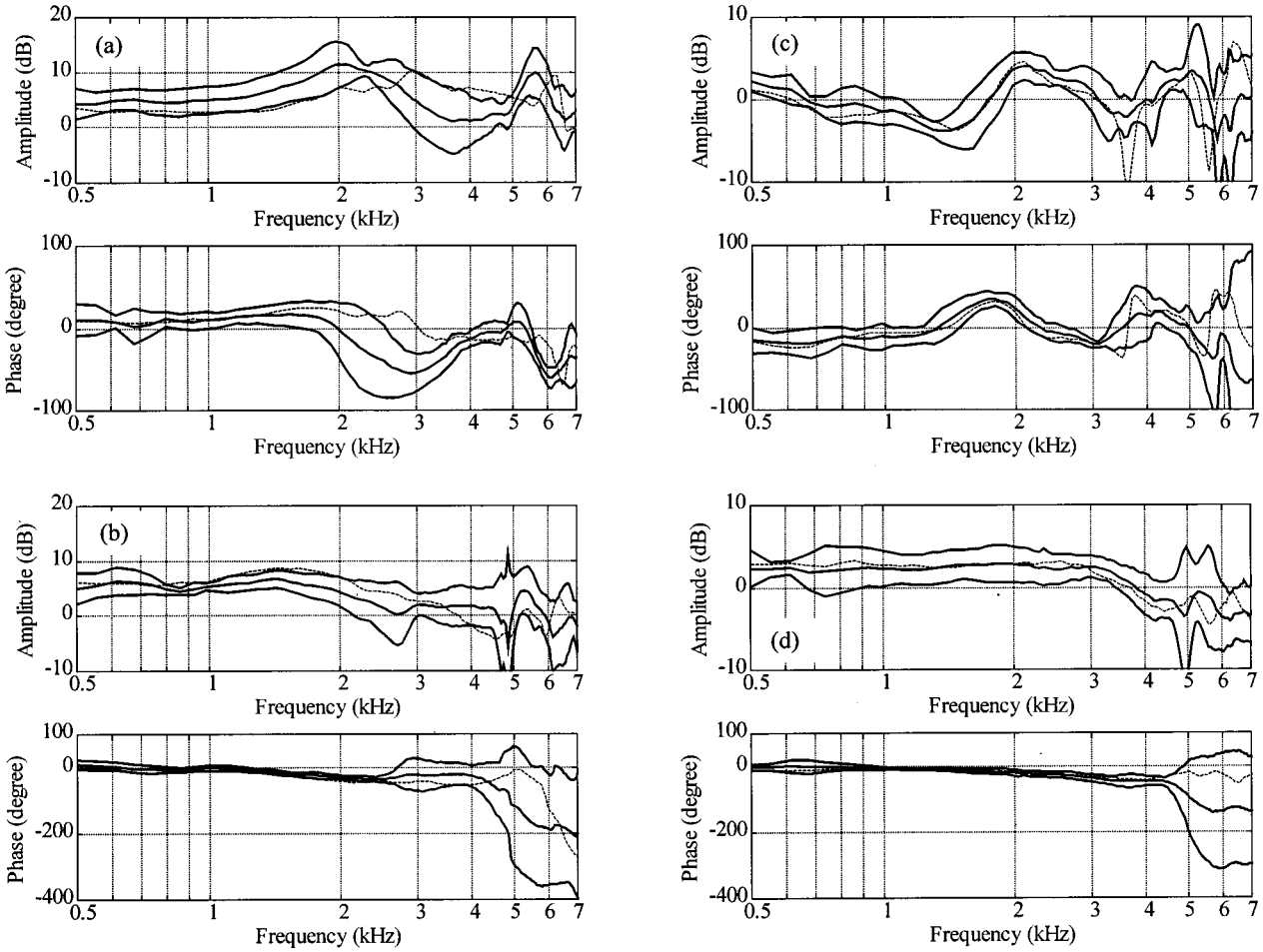

FIG. 2. Change of loop response of BTE from the normal acoustic situation when the acoustics outside the ear was altered. Solid lines are mean and mean ± 1 SD, $n=5$. The dashed lines are the mean of measurements on KEMAR, $n=5$. (a) Telephone set at the ear. (b) Hug. (c) Wall at 10-cm distance from ear. (d) Knitted cap.

A. Changes caused by acoustics outside the ear

Figures 2 and 3 show the mean and mean ± 1 standard deviation (SD), of the changes of loop response when the acoustics outside the ear was changed, measured with BTE and ITEC, respectively.

The telephone gives, with BTE and ITEC, peaks in the changes at approximately 2 and 5 kHz. The changes are somewhat larger with the ITEC with a mean at 2 kHz of 16.1 compared to 11.4 dB with the BTE on human subjects. The maximum increases found were 25.1 dB with ITEC and 16.4 dB with BTE. The change with BTE on KEMAR is about the same as on human subjects, but with the peaks at higher frequencies. The peaks are probably caused by reflections in the telephone set. The frequency of the peak will then depend on the distance between the hearing aid and the telephone set. The differences between the changes with BTE on human subjects and KEMAR could thus to some extent be caused by differences in how the telephone was held. The hug gave similar changes as the telephone, but with lower magnitude and somewhat lower frequencies of the peaks. With the ITEC the wall gave peaks at 2, 4, and 5.5 kHz. With the BTE on KEMAR peaks were found at approximately 2, 5, and 6.2 kHz. Well-defined notches were found between the peaks. The notches were less well defined in the mean curves of the human subjects, but the peaks at 2 and 5 kHz could be found. The mean of the maximum increase with BTE on human subjects was 5.1 compared to 1.7 dB with ITEC. The mean change over frequency was on average 1.1 and -0.5 dB for BTE and ITEC, respectively.

The knitted cap gave a low-pass function with about 3 dB higher mean loop response for frequencies below 3 kHz for both BTE and ITEC. For frequencies above 4 kHz the mean loop response was about 3 dB lower with the BTE, and relatively unchanged with ITEC. However, increases of 5.7 and 10.1 dB were recorded with the BTE and ITEC, respectively.

It can be hypothesized that the ITEC is less sensitive than the BTE to reflecting objects at a distance (>5 cm) from the ear. The ITEC has a shorter direct path from vent opening (and leak) to the microphone. Thus the relative distance of the path from the vent to the microphone via the reflecting object will be longer. It can then be assumed that the reflected signal will be of relatively lower amplitude than the direct signal and thus the relative change of the loop response smaller. With the BTE, the length of the reflected path is in the same order as the direct path. This would then explain the smaller changes found with the ITEC when the wall was placed at a distance of 10 cm from the skull.

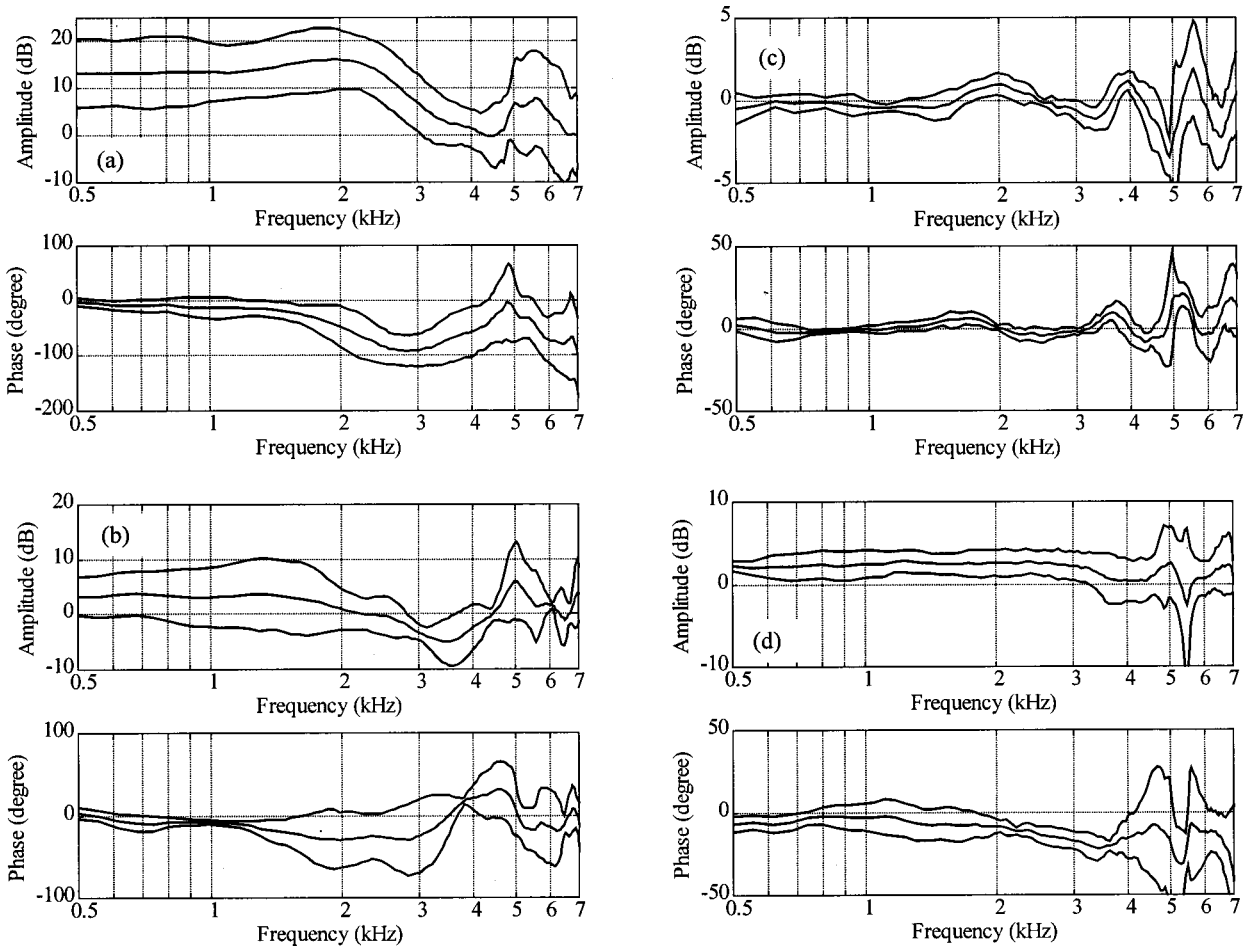

FIG. 3. Mean and mean ±1 SD of change of loop response with ITEC when the acoustic situation was changed from normal. $n=5$ except for (b) with $n=3$. (a) Telephone. (b) Hug. (c) Wall at 10-cm distance from ear. (d) Knitted cap.

The telephone can be held to form an obstacle in the path from the vent to the microphone with the BTE. With the ITEC, the telephone will more or less occlude the ear and thus give higher radiation impedance at the vent and higher SPL at the microphone. This can explain the larger changes found with the ITEC when a telephone set is placed by the ear.

The maximum increase in the 2–5 kHz range was used to analyze if there were differences between the BTE (on human subjects) and ITEC in the four cases with variations of the acoustics outside the ear. Tables I and II show that the telephone with ITEC gave the largest mean changes, and the wall with ITEC the smallest. A *t*-test for dependent samples was used for each case. The only case that showed a significant difference was the wall ($p<0.0065$), where the mean maximum value was 5.1 and 1.7 dB for BTE and ITEC, respectively.

Multiple analysis of variance (MANOVA) was performed on the data from human subjects to investigate if there was an interaction between hearing aid type and acoustic situation. If this is the case, the changes in the tested situations will differ between BTE and ITEC hearing aids. The MANOVA was also used to test if the changes were dependent on the hearing aid type and the acoustic situation separately. The interaction was not significant [$F(3,12)=3.12$; $p<0.066$]. The *t*-test showed significant differences with the wall and the MANOVA gave a low *p*-value, although not significant. This indicates that there might be an interaction effect between the acoustic situation and the hearing aid category that the MANOVA did not prove significant due to the limited sample size.

The general difference between ITEC and BTE was not significant [$F(1,4)=.53$; $p<0.50$]. A significant effect of the acoustic situation was found [$F(3,12)=31.73$; $p<0.0001$]. This implies that the cases tested gave rise to different changes of the loop response.

B. Changes caused by jaw movements

Figures 4 and 5 show the changes when the shape of the ear canal was altered with BTE and ITEC, respectively. The mean changes of the magnitude, as well as phase, were small in these cases for both BTE and ITEC. The standard deviation, however, exceeded 6 dB for both ITEC and BTE at some frequencies in some cases. Thus some individuals may have problems with the hearing aid starting to howl even if the mean changes are very small.

Oliviera (1997) investigated the impact of the jaw movements on the shape of the ear canal. Impressions of the ear canal were taken at different jaw positions. The largest changes were found between the first and second bend of the ear canal. The mean of the largest increase of the ear canal in

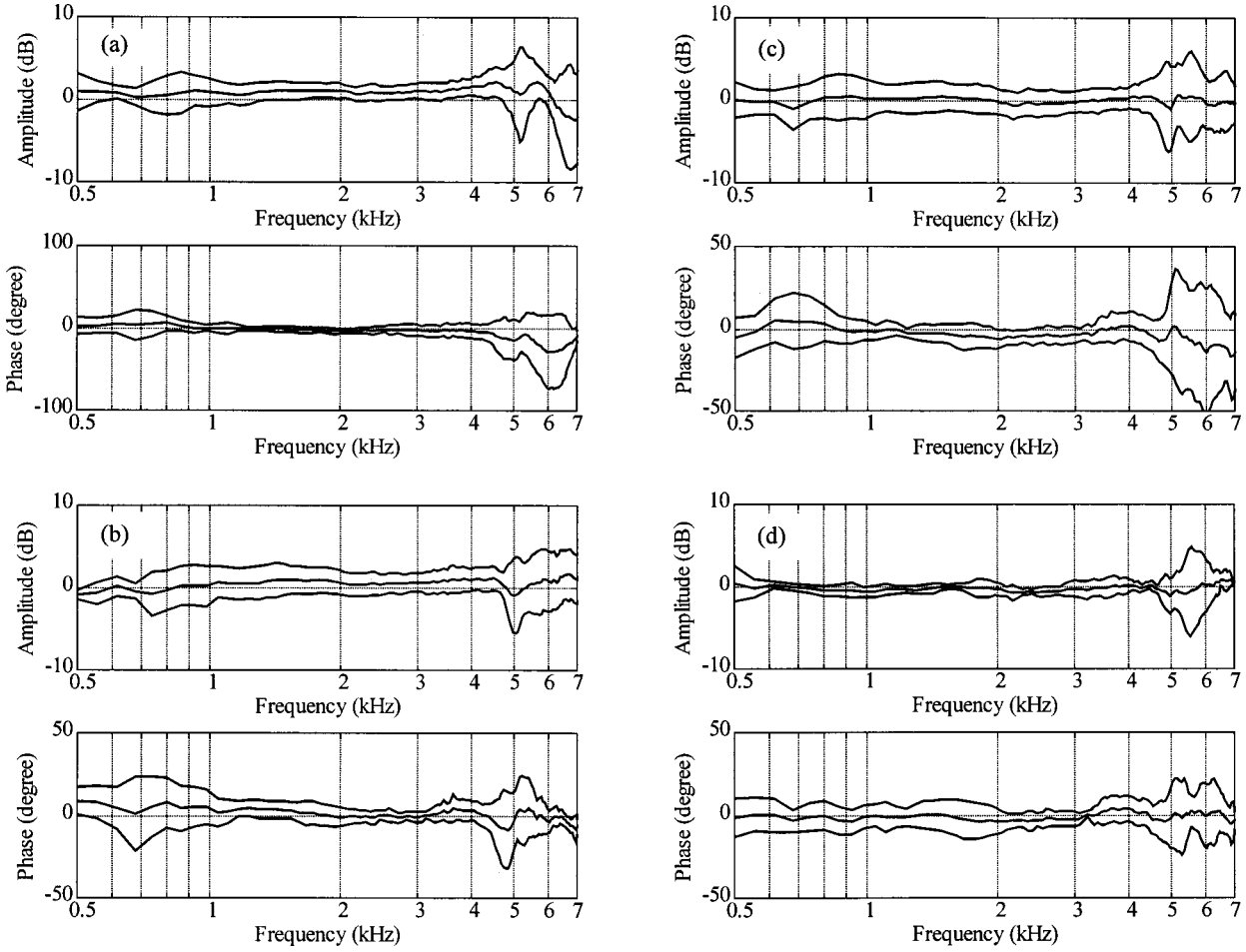

FIG. 4. Mean and mean ±1 SD of change of loop response with BTE when the fit of the earmold was altered. $n=5$ for all cases except for (d) where $n=4$ due to missing data. (a) Yawning. (b) Mouth shaped for saying [ɑ:]. (c) Mouth shaped for saying [i:]. (d) Bite.

the anterior–posterior dimension (width of ear canal) was 10% when a 32-mm depressor was placed between incisors compared to the closed-jaw position. This corresponds to a 0.7-mm change for a typical adult ear canal. In the superior–inferior dimension (height of ear canal) the ear canal was close to unchanged. This jaw position is approximately the same as when yawning. However, it is difficult to compare the results of Oliviera (1997) and the present study, as there is no simple relation between the maximum change of the dimensions of the ear canal and the leak of the earmold. It can also be argued that the ear canal might behave differently by with an earmold in place.

It can be assumed that the leak may occur anywhere around the earmold. The microphone of ITE and ITEC hearing aids and the vent is often separated as much as possible on the faceplate. Therefore, a leak is likely to be closer to the microphone than the vent opening. If it is assumed that attenuation increases with distance, the feedback caused by a leak will be attenuated less than the feedback via the vent. On BTE instruments, the paths from the vent opening and from the leak will be approximately the same. Thus it can be hypothesized that changes of the fit of the earmold give larger changes of loop response with ITE and ITEC instruments than with BTE instruments.

The vent size is another parameter that is likely to influence the sensitivity to the fit of the earmold. The absolute change of the loop response due to a change of the leak can be assumed to be independent of the vent. The relative change will then be smaller with a large vent than with a small vent. Thus it can be hypothesized that hearing aids with large vent diameters are less sensitive to jaw movements. According to the first hypothesis, the ITEC would give larger changes, but the larger vent of the ITEC would give smaller changes. The data of the measurements can thus not be used to test the two hypotheses. In order to do so, a test where only one of the parameters is varied at the time has to be used.

The mean of the maximum increase over the four cases of jaw movements and the five subjects is 1.8 and 2.3 dB for the BTE and ITEC, respectively. No significant differences between the results of BTE and ITEC were found when the *t*-test for dependent variables was used to test the different cases, nor when all cases were tested together with MANOVA.

C. Changes caused by misplaced and partly removed earmold

Figure 6 shows the change of the loop response, when the helix of the earmold used together with the BTE was not correctly placed in cymba conchae. The mean change shows the characteristics of a high-pass filter with a cutoff fre-

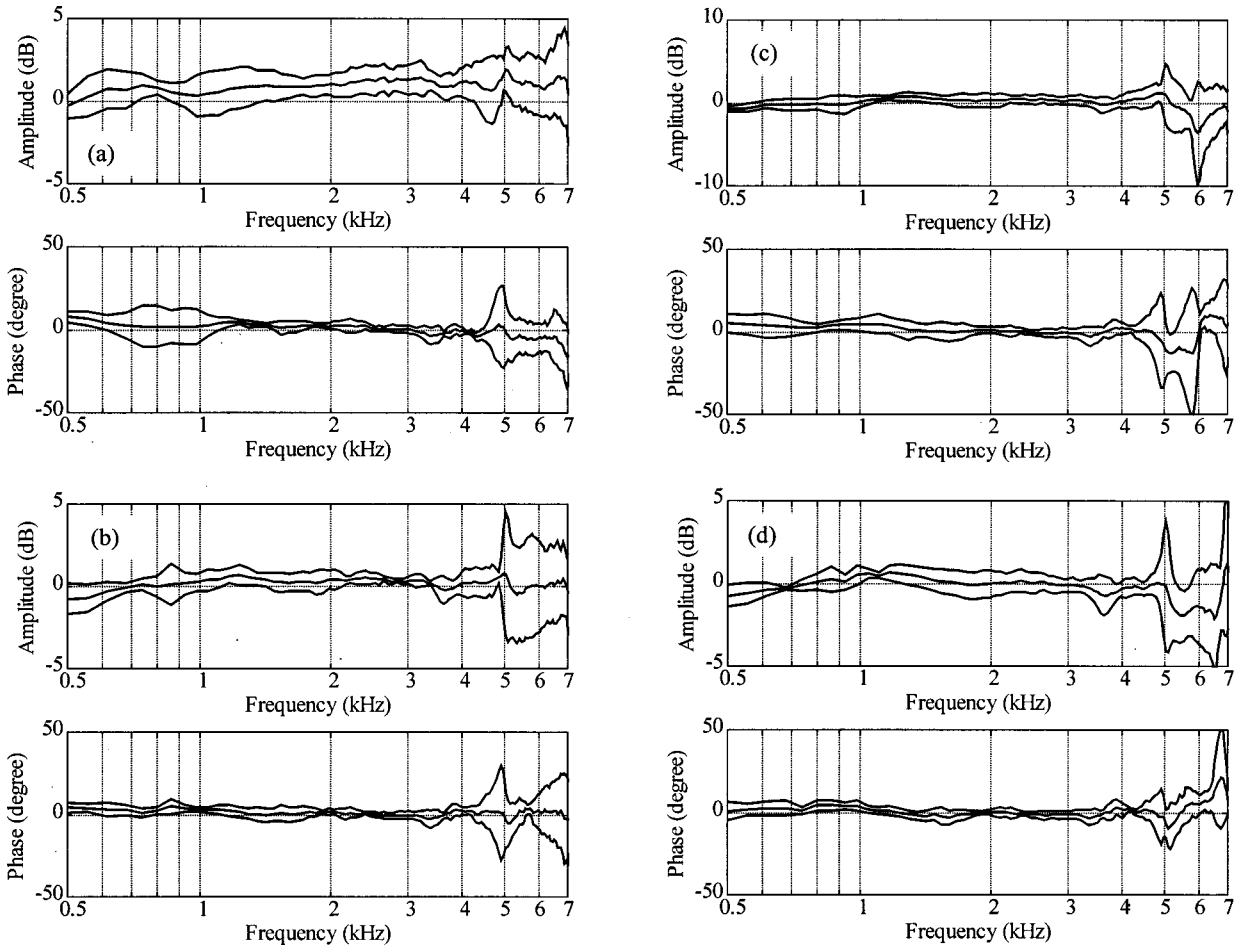

FIG. 5. Mean and mean ±1 SD of change of loop response with ITEC when the fit of the earmold is altered. $n=5$ except in (a) where $n=4$. (a) Open mouth. (b) Mouth shaped for saying [ɑ:]. (c) Mouth shaped for saying [i:]. (d) Bite.

quency of about 800 Hz. The reduction of the magnitude of the loop response at low frequencies originates from the reduction of the gain from the hearing aid to the ear canal, caused by the reduced impedance in the ear canal. This is the same effect as when the vent diameter is increased. The mean curve has a mean value of 2.7 dB for frequencies in the 2–5 kHz frequency range. The mean maximum value of the change was 5.7 dB.

The loop response increased by a mean of 10.3 dB in the 2–5-kHz frequency region when the ITEC was partly removed from the ear, as seen in Fig. 7. The mean magnitude of the loop response was reduced at frequencies below 1 kHz. The maximum increase was on average 21.4 dB. The large increase of the loop gain at high frequencies makes it very likely that the hearing aid starts to oscillate when it is removed/inserted. Some users find this useful as it shows that the hearing aid is working, while others consider it undesirable and uncomfortable.

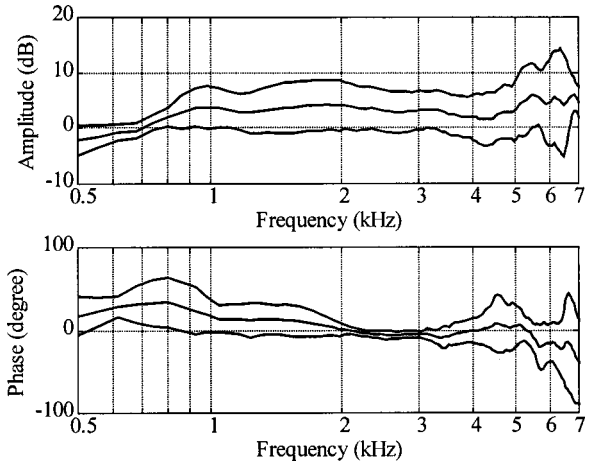

FIG. 6. Mean and mean ±1 SD of change of loop response with BTE when the earmold was not placed correctly in cymba conchae, $n=5$.

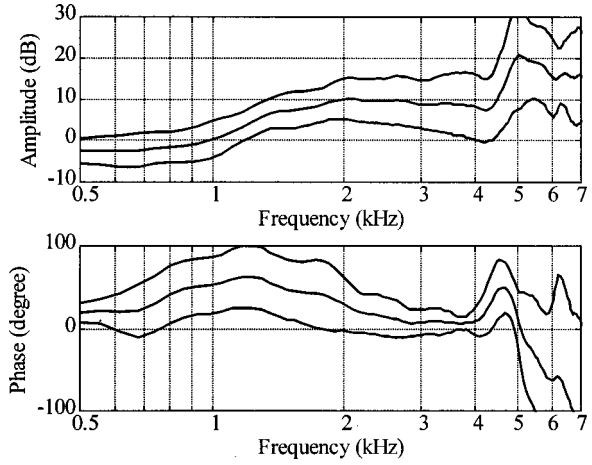

FIG. 7. Mean and mean ±1 SD of change of loop response with ITEC when it was partly removed from the ear canal, $n=5$.

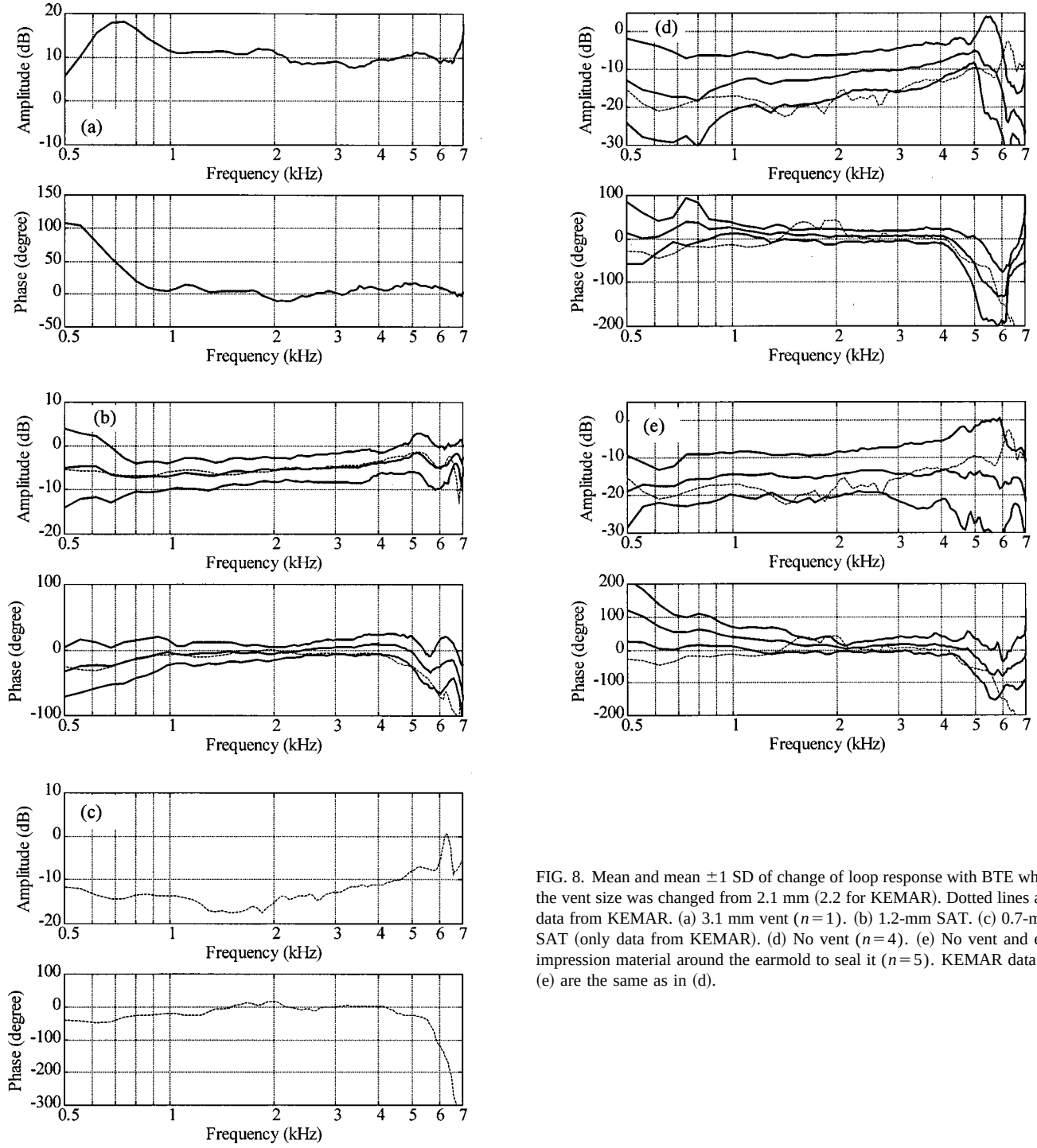

FIG. 8. Mean and mean ±1 SD of change of loop response with BTE when the vent size was changed from 2.1 mm (2.2 for KEMAR). Dotted lines are data from KEMAR. (a) 3.1 mm vent ($n=1$). (b) 1.2-mm SAT. (c) 0.7-mm SAT (only data from KEMAR). (d) No vent ($n=4$). (e) No vent and ear impression material around the earmold to seal it ($n=5$). KEMAR data in (e) are the same as in (d).

D. Variations caused by change of vent size

Figure 8(a) shows the increase of the loop response as the earmold with a 2.1-mm vent was replaced by an ear mold with a 3.1-mm vent. The increase is about 10 dB for frequencies above 1 kHz. This case was only measured on one subject. Figure 8(b)–(e) show the changes of the loop response with BTE when the vent was reduced with SAT of various diameters. The mean changes with the 1.2-mm SAT were about the same with the KEMAR and human subjects, with approximately 6-dB reduction at 1 kHz and 2-dB reduction at 5 kHz. Some individuals even had an increase in the feedback at 5 kHz. The maximum increase was 2.6 dB. The 0.7-mm SAT, which was only tested with KEMAR, gave a mean attenuation of 15 dB at 2 kHz, but a small increase of 0.5 dB at 6.3 kHz. Without vent, the mean reduction on human subjects was 13 dB at 1 kHz and 5 dB at 5 kHz. With KEMAR, the corresponding figures were 17 and 10 dB. When impression material was used around the ear mold the attenuation on human subjects increased to 14 dB at both 1 and 5 kHz.

The mean change of the magnitude over the 2- to 5-kHz range and over the human subjects was 9.2, −4.3, −8.6, and −14 dB for the cases with 3.1-mm vent, 1.2-mm SAT, no vent, and no vent and impression material, respectively. The

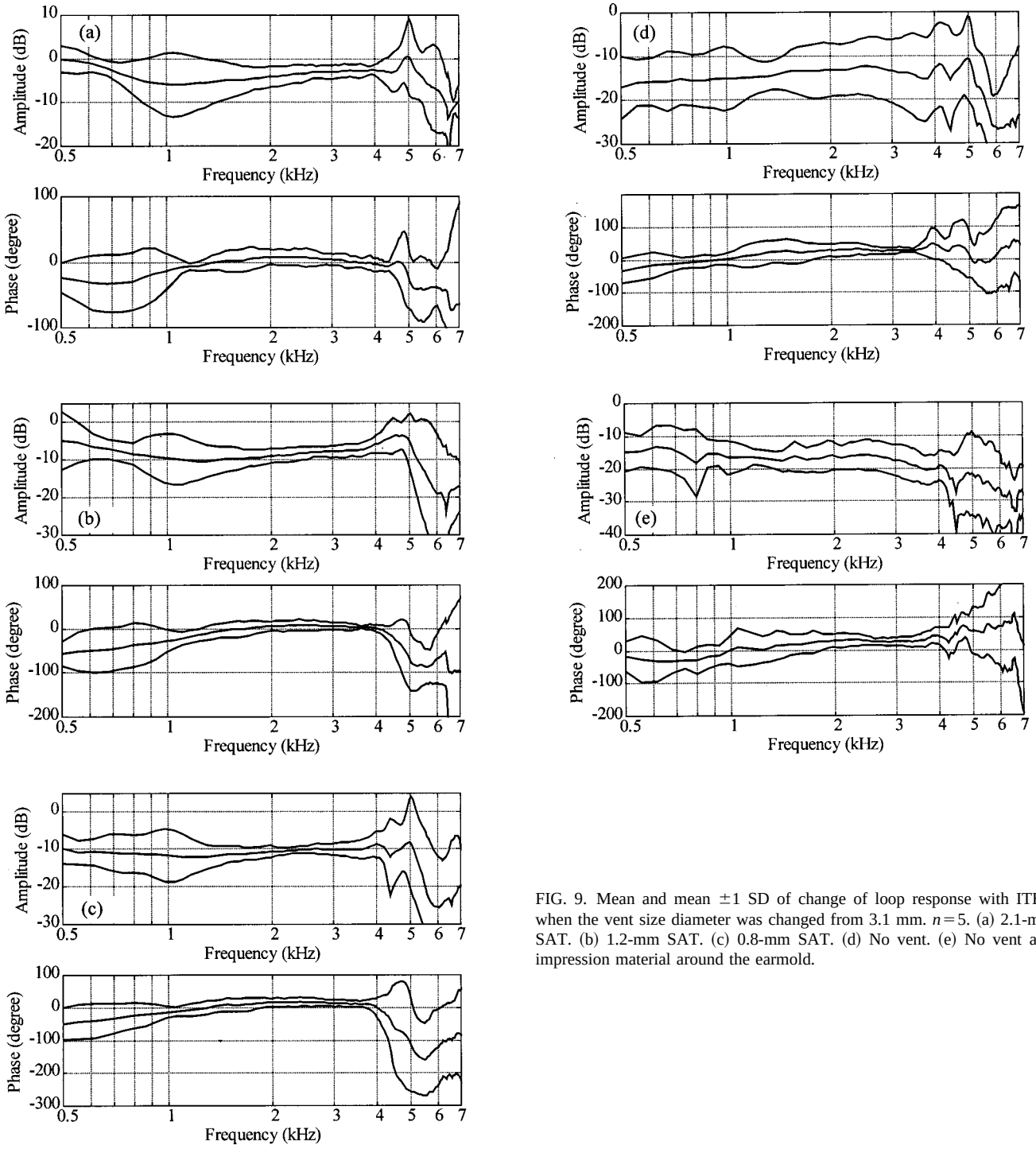

FIG. 9. Mean and mean ±1 SD of change of loop response with ITEC when the vent size diameter was changed from 3.1 mm. $n=5$. (a) 2.1-mm SAT. (b) 1.2-mm SAT. (c) 0.8-mm SAT. (d) No vent. (e) No vent and impression material around the earmold.

figures with KEMAR were −3.9, −11.7, and −16.2 dB for the cases with 1.2, 0.7 mm, and no vent, respectively. One measurement without vent on KEMAR was excluded, judged as an outlier, as it gave smaller changes than the 1.2- and 0.7-mm SAT.

Figure 9 shows the results of the five tested cases with the ITEC: SAT with inner diameter of 2.1, 1.2, 0.8, 0, and 0 mm with impression material around the earmold. The mean change of the magnitude over the 2- to 5-kHz range and over subjects was −2.7, −6.6, −10.0, −16.0, and −19.6 dB for the tested cases. One of the measurements with 0-mm SAT was excluded when the mean was calculated, as it only gave a change of −2 dB while the 1.2-mm SAT gave a change of −8 dB on the same subject. The trend found with BTE, with larger changes at 1 than at 5 kHz when using SAT, was also found with the ITEC. The only exception was the case without vent and with impression material around the earmold, where the attenuation was 17 and 22 dB at 1 and 5 kHz, respectively.

1. Changes with the theoretical model

The mean measured reduction of the loop response without vent was 8.6, 16.2, and 16.0 dB for the BTE on human

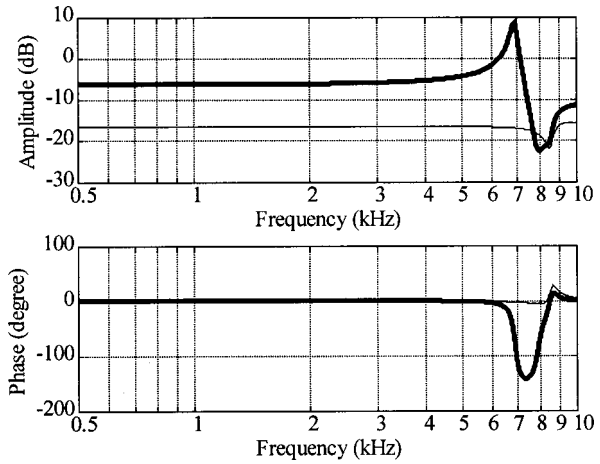

FIG. 10. Calculated change of feedback for the ITEC as the vent diameter is reduced from 3.1 mm. Thick line is the change with a 1.2-mm SAT. Thin line is the change when the diameter of the entire vent is reduced to 1.2 mm.

subjects, BTE on KEMAR, and ITEC on human subjects, respectively. The diameter of the tube modeling the leak in the theoretical model was adjusted to give the same mean reduction when occluding the vent. This gave a diameter of the leak of 1.62, 0.95, and 1.35 mm for the BTE on human subjects, BTE on KEMAR and ITEC on human subjects, respectively. The leak with BTE on human subjects was thus modeled by a tube with a diameter of 1.62 and a length of 17.6 mm. The corresponding values found by Johansen (1975) were 1.6 and 22 mm.

Figure 10 shows the calculated change in the feedback path when the vent is reduced by inserting a SAT with length (l_2) 5 mm and diameter (d_2) 1.2 mm, for the case of an ITEC. The calculated effect of reducing the diameter of the entire vent to 1.2 mm is also included. The SAT gave a smaller change. The change was close to constant over frequency when the diameter of the entire vent was reduced, while it varied with frequency when SAT was used. At frequencies around 7 kHz the feedback even increased as the SAT was inserted in the vent. The peak is caused by reflection due to the increased impedance of the SAT. The frequency of the peak with SAT was 6.8 kHz. This gives a quarter wavelength of 12.5 mm, which is close to the length of the vent from the ear canal to the SAT (13.6 mm). It can thus be assumed that the frequency of the peak will increase as the length of the SAT is increased. The calculated change of the feedback path represented by the thick line in Fig. 10 can be compared with the corresponding measured change of the loop response found in Fig. 9(b). The shape of the change is about the same with a dip at high frequencies and an accompanying peak at slightly lower frequency. The frequencies of the peak and dip are higher in the calculated change and the difference in magnitude of peak and dip is smaller in the mean of the measurements. The latter is to some extent caused by the averaging used in the measurements.

The mean change of the magnitude in dB in the frequency range from 2 to 5 kHz was used when the changes calculated with the model were compared with the corresponding measured data. Figure 11 shows the changes calculated with the theoretical model together with measured data from BTE on human subjects, BTE on KEMAR, and ITEC. The model gave changes that were within the range of the measured data in all cases where SAT was used except with 0.7-mm SAT with BTE on KEMAR. It can thus be concluded that the calculated changes for the use of SAT agreed fairly well with the measurements. The change when the diameter of the entire vent of a BTE on a human subject was increased to 3.1 mm was calculated to 4.7 dB. This can

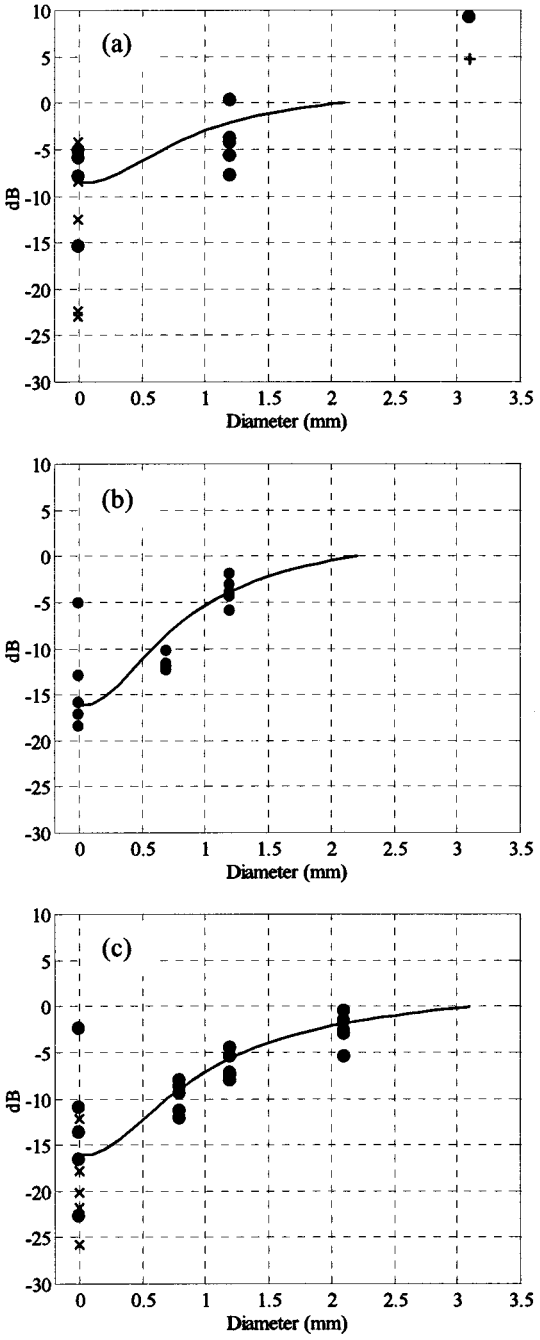

FIG. 11. Mean change of loop response in the 2- to 5-kHz frequency region for different diameters of SAT. Symbols ● are data from the measurements. Symbols × are data from measurements when impression material was used around the earmold. The line is the calculated change of the feedback path. Symbol + is the calculated change when the diameter of the entire vent is changed. (a) BTE on human subjects with 2.1-mm vent diameter. (b) BTE on KEMAR with 2.2-mm vent diameter. (c) ITEC on human subjects with 3.1-mm vent diameter.

TABLE III. Dimensions and results of the eight cases used to compare different vent designs.

Case	l (mm)	l_1 (mm)	d_1 (mm)	l_2 (mm)	d_2 (mm)	Absolute value of impedance at 200 Hz (Acoustic ohms)	Mean amplitude of feedback path in the 2–5 kHz range (dB)
Case 1 Short vent, homogeneous diameter	12	12	1.2000	0	···	188.5	−68.3
Case 2 Short vent, SAT inserted from exterior of earmold	12	7	1.8230	5	0.9115	188.6	−68.2
Case 3 Short vent, SAT inserted from earmold tip	12	5	0.9005	7	1.8010	188.5	−68.1
Case 4 Short vent, increased diameter at exterior of earmold	12	7	0.9928	5	1.9856	188.5	−68.3
Case 5 Long vent, homogeneous diameter	24	24	1.6645	0	···	188.5	−64.8
Case 6 Long vent, SAT inserted from exterior of earmold	24	19	2.1540	5	1.0770	188.6	−62.1
Case 7 Long vent, SAT inserted from earmold tip	24	5	2.1270	19	4.2540	188.6	−61.6
Case 8 Long vent, increased diameter at exterior of earmold	24	19	1.5220	5	3.0440	188.7	−65.6

be compared with the corresponding measurement of the change of loop response that gave 9.2 dB. This case was only measured on one of the subjects.

2. Impact of vent design on occlusion and feedback

The theoretical model with a length of the vent of 12 and a diameter of 1.2 mm gave an absolute value of the acoustic input impedance at the reference plane of 188.5 acoustic ohms at 200 Hz. The diameters of the other cases used to compare different vent designs were adjusted so that the absolute impedance was within 0.2 acoustic ohms of this value. The acoustic reactance that dominated the impedance ranged from 184.8 acoustic to 187.2 acoustic ohms. It can thus be assumed that the occlusion in the eight cases only marginally differed. Table III summarizes the eight tested cases.

Figure 12 shows the calculated transfer function of the feedback from the ear canal to the hearing aid microphone in the eight cases. The short vents gave less feedback than the cases with a long vent. The feedback with the short vent with constant diameter was 3.6 dB higher in the 2–5 kHz region than the corresponding long vent. The reason for the lesser feedback with the short vents is that these have higher resonance frequency. The feedback for frequencies below 1 kHz was about the same in all eight cases. The long vents had resonance frequencies between 5 and 8 kHz, while the shorter vents had peaks above 10 kHz. The use of vents with varying diameter gave only marginal effect on the feedback below 5 kHz when the vent was short. The differences were greater among the long vents, where the difference between the extremes in mean feedback in the 2–5 kHz region was 4.1 dB. The case with increased diameter at the exterior of the earmold gave the least amount of feedback in the region of interest while the two cases that modeled the use of SAT gave the most. This shows that it can be preferable to have a vent with increasing diameter at the vent opening on the exterior of the earmold, compared to a vent with constant diameter.

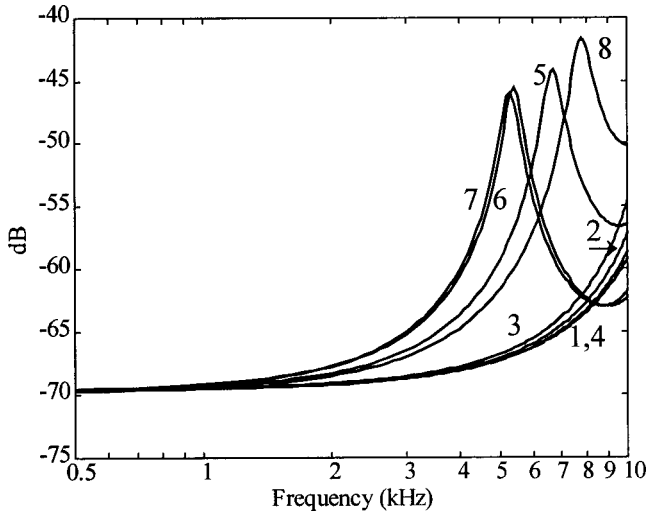

FIG. 12. Calculated transfer function from vent opening to position of BTE microphone for the cases described in Table III. The curves of case 1 and case 4 are almost identical.

It can thus be assumed that short vents will cause less feedback at the same amount of occlusion if all other parameters are kept constant. However, it will be hard to keep other parameters that affect the occlusion constant while shortening the vent. If the length of the tip of an earmold is shortened, the residual volume of the ear canal is changed. This will affect the occlusion (Pirzanski, 1998). It can also be argued that feedback caused by the leak around the earmold will increase as the tip of the earmold is shortened.

III. SUMMARY

The changes of the loop response with BTE and ITEC hearing aids have been measured. The largest changes (except when the ITEC hearing aid was partly removed) were found with the ITEC when a telephone set was placed by the ear. The magnitude of the loop response then increased on average by 16.1 dB at 2 kHz. The ITEC showed a significantly smaller change than the BTE when a wall was positioned close to the ear. The jaw movements gave small

changes both for ITEC and BTE. However, there was substantial variation in some cases at some frequencies, indicating that some test subjects could have problems with the hearing aid starting to oscillate when changing the position of the jaw. The ITEC, which has a short distance between vent and microphone, will have smaller relative changes of the loop response than the BTE, when objects are placed at some distance from the ear. In addition, the ITEC will have larger relative changes than the BTE when the leak is altered, since the distance between the leak and the microphone is shorter than the path from vent opening to microphone. The vent was altered by the use of SAT. This gave smaller changes of the loop response than if the diameter of the entire vent had been altered. The SAT reduced the feedback at 5 less than at 1 kHz. The feedback even increased at 5 kHz for some subjects. The mean changes of the theoretical model of the acoustic path from ear canal to the microphone agreed reasonably well with measured changes of the loop response. It was shown with the theoretical models that the feedback in the 2–5 kHz region differs among configurations of the vent even though the absolute impedance at low frequencies was the same. The lowest magnitude of the feedback among the tested cases was found with the short (12 mm) vent. The feedback below 5 kHz only varied marginally between the tested cases with short vent. The case with an increase of the vent diameter at the vent opening gave the lowest mean amplitude in the 2–5-kHz region, and the highest resonance frequency, among the cases with a vent length of 24 mm. The cases that were used to model a 24-mm-long vent with a SAT inserted from either vent opening gave the highest mean feedback in the 2–5-kHz region, and the lowest resonance frequency.

ACKNOWLEDGMENTS

The financial support from the Swedish Research Council for Engineering Sciences is gratefully acknowledged. Many thanks to Erica Billermark at Linköping University Hospital for performing measurements, to Mette Boel Pedersen, Peter Lundh, Kim Vejlby Hansen, and Leif Hansen at Oticon A/S for advice and sharing knowledge, and for production and modifications of hearing aids.

Alvord, L. S., and Farmer, B. L. (**1997**). ''Anatomy and orientation of the human external ear,'' J. Am. Acad. Audiol **8**, 383–390.

Best, L. C. (**1985**). ''Digital suppression of acoustic feedback in hearing aids'' (Department of Electrical Engineering, University of Wyoming).

Bisgaard, N., and Dyrlund, O. (**1991**). ''Acoustic feedback. Part 2: A digital system for feedback suppression of feedback,'' Hear. Instr. **42**, 44–45.

Bustamante, D. K., Worrall, T. L., and Williamson, M. J. (**1989**). ''Measurement and adaptive suppression of acoustic feedback in hearing aids,'' *Proceedings from International Conference on Acoustics, Speech, and Signal Processing*, pp. 2017–2020.

Dyrlund, O. (**1989**). ''Acoustical feedback associated with the use of post aural hearing aids for profoundly deaf children,'' Scand. Audiol. **18**, 237–241.

Dyrlund, O., and Lundh, P. (**1990**). ''Gain and feedback problems when fitting behind-the-ear hearing aids to profoundly hearing-impaired children,'' Scand. Audiol. **19**, 89–95.

Egolf, D. P. (**1977**). ''Mathematical model of a probe tube microphone,'' J. Acoust. Soc. Am. **61**, 200–205.

Egolf, D. P., Howell, H. C., Weawer, K. A., and Barker, D. S. (**1985**). ''The hearing aid feedback path: Mathematical simulations and experimental verification,'' J. Acoust. Soc. Am. **78**, 1578–1587.

Engebretson, A. M., and French-St. George, M. (**1993**). ''Properties of an adaptive feedback equalization algorithm,'' J. Rehabil. Res. Dev. **30**, 8–16.

Erickson, F. N., and van Tasell, D. J. (**1991**). ''Maximum real-ear gain of in-the-ear hearing aids,'' J. Speech Hear. Res. **34**, 351–359.

Gatehouse, S. (**1989**). ''Limitations on insertion gains with vented earmolds imposed by oscillatory feedback,'' Br. J. Audiol. **23**, 133–136.

Grover, B. C. (**1976**). ''Acoustic modifications to earmolds,'' Br. J. Audiol. **10**, 8–12.

Grover, B. C., and Martin, M. C. (**1974**). ''On the practical gain limit for post-aural hearing aids,'' Br. J. Audiol. **8**, 121–124.

Hansen, M. Ø. (**1997**). ''Occlusion effects, Part I, Hearing aid users experiences of the occlusion effect compared to the real ear sound level,'' Report No. 71 (Dept. of Technical Audiology, Technical University of Denmark).

Hellgren, J., Lunner, T., and Arlinger, S. (**1999**). ''System identification of feedback in hearing aids,'' J. Acoust. Soc. Am. **105**, 2999–3587.

Iberall, A. S. (**1950**). ''Attenuation of oscillary pressures in instrument lines,'' J. Res. Natl. Bur. Stand. **45**, 85–108.

IEC (**1981**). IEC 711, ''Occluded ear simulator for the measurement of earphones coupled to the ear by ear inserts'' (International Electrotechnical Commission, Geneva).

Johansen, P. A. (**1975**). ''An evaluation of the acoustic feedback damping for behind the ear hearing aids,'' Report No. 75.1 (Odense, Denmark, Research Laboratory for Technical Audiology, University Hospital).

Joson, H. A. L., Asano, F., Suzuki, Y., and Sone, T. (**1993**). ''Adaptive feedback cancellation with frequency compression for hearing aids,'' J. Acoust. Soc. Am. **94**, 3248–3254.

Kates, J. M. (**1988**). ''A computer simulation of hearing aid response and the effects of ear canal size,'' J. Acoust. Soc. Am. **83**, 1952–1963.

Kates, J. M. (**1991**). ''Feedback cancellation in hearing aids: Results from a computer simulation,'' IEEE Trans. Signal Process. **39**, 553–561.

Kuk, F. K. (**1994**). ''Maximum usable real-ear insertion gain with ten earmold designs,'' J. Am. Acad. Audiol. **5**, 44–51.

Kuo, S. M., and Voepel, S. (**1992**). ''Integrated frequency-domain digital hearing aid with the lapped transform,'' Electron. Lett. **28**, 2117–2118.

Ljung, L., and Glad, T. (**1994**). *Modeling of Dynamic Systems* (Prentice-Hall, Englewood Cliffs, NJ).

Lundh, P. (**1982**). ''Acoustical feedback problems associated with hearing aids,'' Otilcon internal report No. 19-8-6, Oticon A/S, Copenhagen, Denmark.

Lybarger, S. F. (**1975**). ''Sound leakage from vented earmolds,'' Scand. Audiol. Suppl. **5**, 260–270.

MacKenzie, K., Browning, G. G., and McClymont, L. G. (**1989**). ''Relationship between earmold venting, comfort and feedback,'' Br. J. Audiol. **23**, 335–337.

Oliviera, R. J. (**1997**). ''The active earcanal,'' J. Am. Acad. Audiol. **8**, 401–410.

Pirzanski, C. Z. (**1998**). ''Diminishing the occlusion effect: Clinician/manufacturer-related factors,'' Hear. J. **51**, 66–78.

A model of facial biomechanics for speech production

Jorge C. Lucero[a)]
Departamento de Matematica, Universidade de Brasilia, Brasilia DF 70910-900, Brazil

Kevin G. Munhall[b)]
Departments of Psychology & Otolaryngology, Queen's University, Kingston, Ontario K7L 3N6, Canada

(Received 10 September 1998; revised 18 June 1999; accepted 23 June 1999)

Modeling the peripheral speech motor system can advance the understanding of speech motor control and audiovisual speech perception. A 3-D physical model of the human face is presented. The model represents the soft tissue biomechanics with a multilayer deformable mesh. The mesh is controlled by a set of modeled facial muscles which uses a standard Hill-type representation of muscle dynamics. In a test of the model, recorded intramuscular electromyography (EMG) was used to activate the modeled muscles and the kinematics of the mesh was compared with 3-D kinematics recorded with OPTOTRAK. Overall, there was a good match between the recorded data and the model's movements. Animations of the model are provided as MPEG movies. © *1999 Acoustical Society of America.* [S0001-4966(99)02810-6]

PACS numbers: 43.70.Aj, 43.70.Bk, 43.70.Jt [AL]

INTRODUCTION

The human face provides visible information during speech (Summerfield, 1992) and influences the acoustics of speech by determining the shape and size of the opening of the acoustic tube produced by the vocal tract (Lindblom and Sundberg, 1971). In recent years, there has been considerable interest in simulations of facial motion for the purposes of understanding speech motor control (e.g., Muller, Milenkovic, and McCleod, 1984), for producing realistic facial animation (Terzopoulos and Waters, 1990; Parke and Waters, 1996), and for stimulus generation for audiovisual speech research (Cohen and Massaro, 1990). In the present paper, we describe work on a 3-D facial model that extends the work of Terzopoulos and Waters (1990) on facial animation and produces a facial model that can be useful for speech perception and production research. In Terzopoulos and Waters' facial model, the biomechanical parameters related to muscles and skin, as well as geometrical dimensions, were selected using a heuristic approach. Although they were based on the actual physiology of a face, they were treated as dimensionless parameters, and their orders of magnitude were chosen so as to produce a realistic simulation. This approach complicates comparisons with experimental data. Here, we have tuned the model with realistic parameters obtained from experimental measurements. Further, we have modified the muscle geometry and the muscle model, according to physiological data. In addition, we have modified the manner in which motion is simulated using this model. In the original Terzopoulos and Waters' model, the face motion was obtained as a sequence of equilibrium states of the model. That is, at each single step (frame) of the animation, muscle forces were manually adjusted and the model was allowed to reach an equilibrium state before going to the next step. Although this technique may be used to produce reasonable animations, it does not correspond to the actual dynamics of the face. In the present work, we have driven the model dynamically, using perioral electromyographic data and 3-D position data recorded during speech production.

The present work follows the pioneering work of Eric Muller (Muller *et al.*, 1984) on facial modeling for physiological research. Muller argued that detailed modeling of the peripheral motor system is essential to understand the neural control of speech. A realistic representation of tissue and muscle permits control processes to be examined with the transfer function of the biological plant taken into account. There is abundant evidence that the peripheral motor system is not simply a passive channel for the transmission of signals from the central nervous system. Rather, the nonlinear mechanics of tissue and muscle, the inertial forces of the moving articulators, and the complexities of force generation in muscles perform a transform on those signals. The final form of the speech motor output is, thus, an interaction of the biomechanics and physiology of the vocal tract and the neural control signals.

The present research also has a second rationale. In audiovisual speech perception research, the visual stimuli are usually not controlled in any systematic fashion (see Munhall and Vatikiotis-Bateson, 1998). In published work in this area, it is rare to be provided with stimulus parameters for the moving face beyond the gender of the talker. This lack of direct visual stimulus control leaves many audiovisual experiments confounding image displacement and velocity factors with phonetic manipulations. Our secondary aim is to provide a tool that can be used to produce realistic facial animation in which facial movements can be manipulated in a systematic way for perception experiments (cf. Cohen and Massaro, 1990).

For both of these goals, the physics-based animation begun by Keith Waters and Demetri Terzopoulos (Lee, Terzopoulos, and Waters, 1993, 1995; Parke and Waters, 1996; Terzopoulos and Waters, 1993; Waters and Terzopoulos,

a)Electronic mail: lucero@mat.unb.br
b)Electronic mail: munhallk@psyc.queensu.ca

1991, 1992) offers a suitable research framework. The graphics environment created by Waters and Terzopoulos and their students allows physiological parameters for skin and muscle to be specified and permits realistic equations of motion to be implemented. This approach is consistent with a growing body of physiological modeling in speech which has proceeded on an articulator-by-articulator basis. Considerable progress has been made in modeling of the biomechanics of the vocal folds (Titze and Talkin, 1979), tongue (Kakita, Fujimura, and Honda, 1985; Wilhelms-Tricarico, 1995), velum (Berry, Moon, and Kuehn, 1998), jaw (Laboissière, Ostry, and Feldman, 1996) and tongue/jaw system (Sanguinetti, Laboissière, and Ostry, 1998). In each of these models, the biophysics of passive tissue as well as active muscle has been represented in great detail.

In order to model the human face in detailed biomechanical and physiological terms, a vast array of muscle properties and passive tissue characteristics must be specified. Unfortunately, good estimates are not available for all of these parameters. In spite of a long history of research interest in facial anatomy (Lightoller, 1925), there is still some uncertainty about the gross anatomy of the perioral musculature (e.g., Vinkka-Puhakka, Kean, and Heap, 1989) and little statistical data reporting the distribution of muscle lengths, muscle cross-sectional areas, etc. in the population. All of the facial muscles, and the perioral muscles in particular, are highly interdigitated (Blair, 1986; Blair and Smith, 1986), thus complicating their anatomical description. There is even less information about the motor unit/fiber types in the perioral muscles (cf. Sufit *et al.*, 1984).

The biomechanical properties of skin and facial tissues are also difficult to characterize. The constitutive equations for skin vary widely in the literature and parameters differ for different sites of the body, age, degree of obesity, etc. (See Lanir, 1987, for a review of skin modeling.) Further, the skin's properties vary according to direction. For example, the resting tension of the skin follows reliable directional patterns called Langer's lines (Barbenel, 1989).

I. FACIAL MODEL

This complex facial physiology is represented in our model by separate skin and muscle elements. The muscles are modeled using a standard Hill-type formulation (Winters, 1990; Zajac, 1989) that contains force generation due to the contractile element (the dependence of force on muscle length and velocity) and the passive dependence of force on muscle length. For a first approximation, we have assumed simple lines of action of the muscles and standard skeletal muscle physiology. With the exception of the orbicularis oris superior (OOS) and the orbicularis oris inferior (OOI), the perioral muscles have origins in the bony surfaces of the mandible and maxilla (see Kennedy and Abbs, 1979, for an overview of speech muscle anatomy). Thus, we have represented these muscles as linear force vectors. For the skin and connective tissues we have made similar first approximations. While the stress/strain characteristics of the skin are nonlinear and anisotropic (e.g., Lanir, 1987; Ho *et al.*, 1982; Larrabee, 1986), we have adopted a linear, isotropic approximation to the skin's mechanical characteristics. The skin is represented by a multilayered mesh that is parametrized with linear or piecewise linear estimates of the biomechanical properties of the skin. Finally, the facial morphology is individualized to match subjects using data from a laser range finder. This step allows direct comparisons between model behavior and recorded kinematics. Below, we provide the details for each component of the model.

A. Facial mesh

The modeled face consists of a deformable multilayered mesh. The nodes in the mesh are point masses, and each segment connecting nodes in the mesh consists of a spring and a damper in a parallel configuration. The nodes are arranged in three layers representing the structure of facial tissues. The top layer represents the epidermis, the middle layer represents the fascia, and the bottom layer represents the skull surface. The elements between the top and middle layers represent the dermal-fatty tissues, and elements between the middle and bottom layer represent the muscle. The skull nodes are fixed in the three-dimensional space. The fascia nodes are connected to the skull layer except in the region around the upper and lower lips and the cheeks.

The mesh has a uniform thickness with a separation of 1.5 mm between the topmost and middle layers and 2.5 mm between the middle and bottom layers.[1] All the nodes in the mesh have the same mass. Taking a mean skin density of 1142 kg/m^3 (Duck, 1990), and estimating from the model a mean node density of 5 node/cm^3, we obtain a mass $m = 0.23$ g for each node.

All springs, except for the dermal-fatty springs, are linear at elongation. We consider a Young's modulus for the skin of 7350 dyne/cm (Larrabee, 1986), and estimate the number of springs working in parallel in 1 cm^2 of mesh surface. Thus, we obtain a mean stiffness coefficient of about 600 dyne/cm for a spring 1 cm long. The stiffness coefficients of springs in the topmost layer are made higher (1200 dyne/cm) to represent the stiffer characteristic of the epidermis. The stiffness coefficients of all other springs are set to 600 dyne/cm. Since in general, the spring lengths are different than 1 cm, the stiffness coefficients for the actual springs in the mesh are properly scaled according to their rest length.

For the dermal-fatty springs, a biphasic approximation for the force-elongation characteristics is used (Parke and Waters, 1996; Terzopoulos and Waters, 1990). In real dermal tissue, the stiffness of the dermis with small stretches is mainly determined by elastin fibers, hence, the stiffness is low. As the elongation increases, collagen fibers uncoil. Once the collagen fibers are fully stretched, the skin stiffness increases suddenly and resists further elongation. The biphasic characteristic responds to the expression

$$g = \begin{cases} k_1 \Delta l, & \text{if } \Delta l / l_0 \leqslant 0.2 \\ 0.2 k_1 l_0 + k_2 (\Delta l - 0.2 l_0), & \text{if } \Delta l / l_0 > 0.2, \end{cases} \quad (1)$$

where g is the spring force, l_0 is the rest length, Δl is the elongation, and k_1 and k_2 are the stiffness coefficients. We adopt the estimated value of 600 dyne/cm for k_1 and 6000 dyne/cm for k_2 (for a spring with a rest length $l_0 = 1$ cm). The value of k_2 was set at 10 times the value of k_1 to ap-

TABLE I. Biomechanical constants of the facial mesh.

Parameter	Value
Mass	0.23 g
Damping	30 dyne s/cm
Stiffness:	
epidermal layer	1200 dyne/cm
dermal-fatty layer	600 dyne/cm (low deformation)
	6000 dyne/cm (large deformation)
fascia layer	600 dyne/cm
muscle layer	600 dyne/cm

proximate the nonlinear function of the epidermal skin layer (Lanir, 1987).

At compression of the springs, we use the following nonlinear function to provide an infinite growth of the spring force as its length tends to zero (Lee *et al.*, 1995):

$$g = k \tan\left(\frac{\pi\sigma\Delta l}{2l_0}\right), \tag{2}$$

where k_1 is the same stiffness coefficient adopted for the elongation characteristics, and $\sigma = 0.98$ is a scaling factor.

The damping coefficient is $r = 30$ dyne s/cm for all the layers. This value was selected through visual evaluation of the animations. With a stiffness coefficient for the dermis $k = 600$ dyne/cm, the response time is $\tau = r/k = 50$ ms, which is in the order of experimental values (e.g., Muller *et al.*, 1984).

The above biomechanical constants for the skin are summarized in Table I.

B. Muscle models

The mesh is deformed by action of a set of modeled muscles of facial expression. The human face is controlled by dozens of anatomically distinct muscles, but a subset of 15 pairs of muscles is represented in the model. These modeled muscles can be divided into those muscles associated with upper face movement (corrugator, corrugator supercilli, major frontalis, lateral frontalis, inner frontalis) and the perioral muscles (depressor anguli oris, zygomatic major, zygomatic minor, levator labii superioris, levator labii nasi, depressor labii inferioris, risorius, mentalis, orbicularis oris superior, and orbicularis oris inferior). This subset of 15 muscles was chosen based on traditional analysis of emotional expression (Duchenne, 1990; Ekman and Friesen, 1975) and anatomical studies of the speech musculature (Kennedy and Abbs, 1979). Figure 1 shows the lines of action of these muscles.

All of the muscles, except the orbicularis oris superior and inferior, attach at one or more nodes of the fascia layer (middle layer). When activated, they exert a force on those nodes in the direction of the nodes of attachment to the skull layer [see Fig. 2(a)]. The orbicularis oris muscles attach to a path of fascia nodes along their length. When activated, they exert forces on the fascia nodes in the direction of that path [see Fig. 2(b)]. The nodes of attachment of the muscles were selected following anatomical descriptions in the literature (e.g., Kennedy and Abbs, 1979) and cadaver dissections carried out at Queen's University.

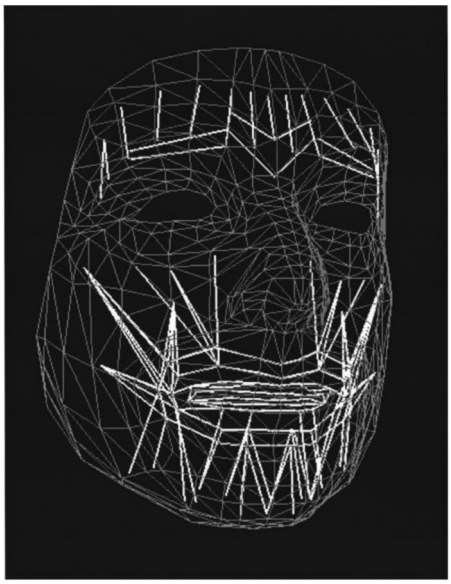

FIG. 1. Lines of action of facial muscles.

The generation of muscle force is computed by using integrated EMG as a measure of muscle activity, as follows.

The steady-state force $\bar{M}$ generated by the muscle is

$$\bar{M} = k_f SE, \tag{3}$$

where S is the muscle cross-sectional area, E is the integrated EMG level normalized to a range between 0 (mean of baseline muscle activity) and 1 (maximum activity recorded across the experiment, including a series of ''maximal'' facial gestures; cf. Zajac, 1989), and $k_f = 2500$ dyne/cm^2 is a

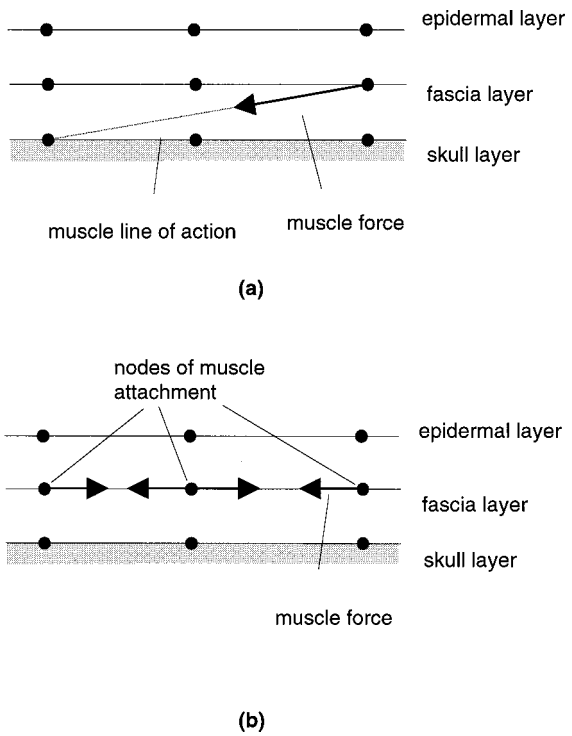

FIG. 2. Muscle force on the mesh. (a) Muscles attached to the skull, (b) orbicularis oris muscles.

TABLE II. Cross-sectional areas, stiffness, and number of fascia attachment for each muscle.

Muscle	Area (cm^2)	Stiffness (dyne/cm)
Zygomatic major	0.1	1730
Levator labii superioris	0.15	2595
Depressor anguli oris	0.4	6920
Depressor labii inferioris	0.11	1903
Mentalis	0.07	1211
Levator anguli oris	0.1	1730
Orbicularis oris superior	0.6	10 380
Orbicularis oris inferior	0.6	10 380

scaling coefficient (selected according to the results of the animations).

A graded force development of the muscle force M is simulated by the second-order, low-pass filtering of the steady-state force $\bar{M}$, according to the equation (Laboissière *et al.*, 1996)

$$\tau^2\ddot{M}+2\tau\dot{M}+M=\bar{M}, \tag{4}$$

where $\tau=15$ ms. A force-length characteristic is added using the equation (Otten, 1987; Brown, Scott, and Loeb, 1996)

$$M'=M\exp\left[-\left|\frac{(l/l_0)^{2.3}-1}{1.26}\right|^{1.62}\right], \tag{5}$$

where l is the actual muscle length and l_0 its rest length.

Finally, force-velocity and passive stiffness characteristics are added to compute the total muscle force F, according to the equation (Laboissière *et al.*, 1996)

$$F=M[f_1+f_2\arctan(f_3+f_4\dot{l})]+[k_m\Delta l]^+, \tag{6}$$

where $f_1=0.82$, $f_2=0.5$, $f_3=0.43$, $f_4=0.2$ s/cm, k_m is the passive muscle stiffness, and

$$[x]^+=\begin{cases}x, & \text{if } x>0\\ 0, & \text{if } x\leqslant 0.\end{cases} \tag{7}$$

The passive muscle stiffness for each muscle was computed by scaling a reference value according to the cross-sectional area of each muscle. As reference, we used a cross-sectional area of 1 cm^2 and passive stiffness of 17 300 dyne/cm for the hyoid depressor muscle (Laboissière *et al.*, 1996). The cross-sectional areas were taken from Kennedy and Abbs (1979) or estimated from experimental measurements on a dissected cadaver. Table II shows the cross-sectional areas and the passive stiffness used in the simulations. Only the perioral muscles shown in the table were considered for the present work.

The steady-state muscle force was also computed by scaling according to the cross-sectional area, as explained later in Sec. II C.

C. Equations of motion

The equation of motion for each node i of the model has the general expression (Lee *et al.*, 1995)

$$m\frac{d^2\mathbf{x}_i}{dt^2}+r\sum_j\left(\frac{d\mathbf{x}_i}{dt}-\frac{d\mathbf{x}_j}{dt}\right)+\sum_j\mathbf{g}_{ij}+\sum_e\mathbf{q}_i^e+\mathbf{s}_i+\mathbf{h}_i=\mathbf{F}_i. \tag{8}$$

In this equation, $\mathbf{x}_i$ is the current position of node i. The second term is the total damping force acting on the node, and the index j represents all the nodes that are neighbor to node i. The third term is the total spring force, and the force contribution $\mathbf{g}_{ij}$ of spring-connecting nodes i and j is calculated using Eqs. (1) and (2).

The fourth term models the incompressibility of human skin. $\mathbf{q}_i^e$ is the force at node i, produced by the preservation of volume of the triangular prism element e to which node i belongs. This force is calculated as

$$\mathbf{q}_i^e=k_{e1}(V^e-\tilde{V}^e)\mathbf{n}_i^e+k_{e2}(\mathbf{p}_i^e-\tilde{\mathbf{p}}_i^e), \tag{9}$$

where V^e and $\tilde{V}^e$ are, respectively, the current and rest volumes of element e, $\mathbf{n}_i^e$ is the epidermal normal at node i, $\mathbf{p}_i^e$ and $\tilde{p}_i^e$ are the current and rest nodal coordinates for node i with respect to the center of mass of element e, and $k_{e1}=1000$ dyne/cm^3, $k_{e2}=2000$ dyne/cm are scaling factors.

The fifth term $\mathbf{s}_i$ in Eq. (8) is a force to penalize fascia nodes penetrating the skull. This force cancels out the force component on the fascia node in the direction towards the skull, and is calculated as

$$\mathbf{s}_i=\begin{cases}-(\mathbf{f}_i^n\cdot\mathbf{n}_i)\mathbf{n}_i, & \text{if } \mathbf{f}_i^n\cdot\mathbf{n}_i<0\\ 0, & \text{otherwise}\end{cases}, \tag{10}$$

where $\mathbf{f}_i^n$ is the net force on fascia node i and n_i is the nodal normal.

The last term on the left side in Eq. (8), $\mathbf{h}_i$, is a nodal restoration force applied to the fascia nodes connected to the skull. It is calculated as

$$\mathbf{h}_i=k_h(\mathbf{x}_i-\tilde{\mathbf{x}}_i), \tag{11}$$

where $\tilde{\mathbf{x}}_i$ is the rest position of fascia node i and $k_h=200$ dyne/cm is a scaling factor. This equation acts as an extra force modeling the attachment to the skull of the skin, and compensates in part the cancellation of the force component between fascia nodes and the skull due to penalization of skull penetration. It is necessary to help bring the nodes back to the rest (initial) position when muscle forces are deactivated (without this force, the nodes tend to wander around the rest position).

Finally, $\mathbf{F}^i$ in Eq. (8) is the total muscle force applied to node i.

II. FACIAL ANIMATIONS

The model described above represents a first approximation of the peripheral biomechanics and physiology of the human face. To test the accuracy of this representation of the plant, electromyographic (EMG) data were collected from a set of seven perioral muscles. The aim was to test the transfer function between muscle activity and facial surface kinematics and to examine the model's capability to reproduce the dynamical behavior of the face during speech production. Specifically, we used the recorded EMG to drive the modeled muscles. We then compared the model kinematics to the observed subject kinematics. The model was individualized to the subject's morphology using data from a Cyberware laser scanner (Lee *et al.*, 1993, 1995). Thus, direct kinematic

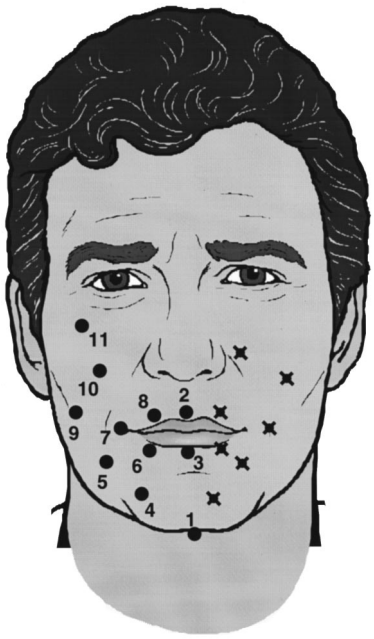

FIG. 3. Position of OPTOTRAK IREDs and electrode insertion points (crosses) for EMG collection.

comparisons were possible. The next sections will describe in detail the animation process and comparisons with recorded facial kinematics.

A. EMG and kinematic data

Intramuscular EMG data were collected from perioral muscles on the left side of a single subject's face, while the subject produced English sentence material [20 Central Institute of the Deaf (CID) everyday sentences].[2] The subject was a male, native speaker of American English. The EMG was recorded from the levator labii superioris, levator anguli oris/zygomatic major,[3] depressor anguli oris, depressor labii inferioris, mentalis, orbicularis oris superior, and orbicularis oris inferior using intramuscular hooked-wire, bipolar electrodes. Figure 3 shows the approximate electrode positions (crosses). Electrode insertions were determined with reference to Kennedy and Abbs (1979) and were verified using a series of nonspeech maneuvers. The acoustic signal was simultaneously recorded. The sampling frequency of the EMG and acoustic signal was 2500 Hz.

At the same time, we recorded the three-dimensional position of 11 markers (infrared emitting diodes (IRED)) on the right side of the face (see Fig. 3) using an OPTOTRAK (model 3010, Northern Digital, Inc.) system at a sampling frequency of 60 Hz. The position data were corrected for motion of the head, and transformed to a coordinate system in which the origin is the incisor cusp and the horizontal and protrusion axes lie along the bite surface (Ramsay *et al.*, 1996).

B. Data preprocessing

The EMG signals were first rectified and next integrated and downsampled to 60 Hz to match the sampling frequency of the position data, using a median filtering algorithm with a 17-ms trapezoidal window (Vatikiotis-Bateson and Yehia, 1996). Finally, the signals for each muscle were normalized to a range between 0 and 1 by dividing them by the maximum level of each muscle. As indicated above, each muscle's maximum was set to the highest level recorded in the speech material or during a set of extreme facial gestures (e.g., extreme lip protrusion).

The position data from the OPTOTRAK system were transformed to the coordinate system used in the face model. In the face model, the origin is at the node immediately below the highest node of the nose, and the *x*-axis is horizontal from left to right, the *y* is vertical to the top, and the *z*-axis is the protrusion axis.

Since the dynamics of the jaw were not yet implemented in the model, we rotated the jaw using position data of the subject's chin during the animations for the CID sentences. The rotation of jaw was computed using the OPTOTRAK data for marker 1. First, the vertical displacement of the marker was computed, in relation to its rest (initial) position. Then, we computed the rotation angle of the nodes in the jaw in the facial mesh that would produce the same vertical displacement of these nodes. In the case of the bite-block experiments, the jaw rotation was kept fixed at its initial value, computed from the OPTOTRAK data.

C. Animation

The face model was implemented as a set of programs written in C language and using OPENGL for the graphic interface, adapted from the original programs by Lee *et al.* (1995). It runs on an Ultra Sparc workstation, and an animation of 3 s took about 4 min to compute.

The animation was performed as follows. The equations of motion of the mesh nodes were solved with an Euler algorithm, and a time step of 0.33 ms. To obtain a final rate of 60 Hz, a frame with the animated face was saved every 50 iterations of the algorithm. Also, the positions of nodes closest to the positions of markers in the subject's face were saved every 50 iterations.

At the beginning of each series of 50 iterations, the computed rotation of the jaw was read, and all the jaw nodes in the mesh at the skull layer were rotated accordingly. To compensate for a time delay in the propagation of the jaw rotation from the skull layer to the epidermal layer (recall that jaw rotation was computed from a marker on the epidermis), we introduce an artificial time advance of two sampling points (33 ms) to the jaw rotation data. Next, the processed EMG was read, and the force exerted by each muscle was computed. The activity level of the zygomatic major was set equal to the levator anguli oris.

The equations of motion were then solved, considering the muscle force and the jaw rotation constants during the 50 iteration period. This process was repeated until the end of the EMG data files.

D. Results for CID sentences

Figures 4, 5, and 6 show the displacement (vertical and protrusion)[4] and acceleration of nodes corresponding to IREDs 3, 5, and 7, for the CID sentence ''Where are you going?'' The figures also show the measured displacement

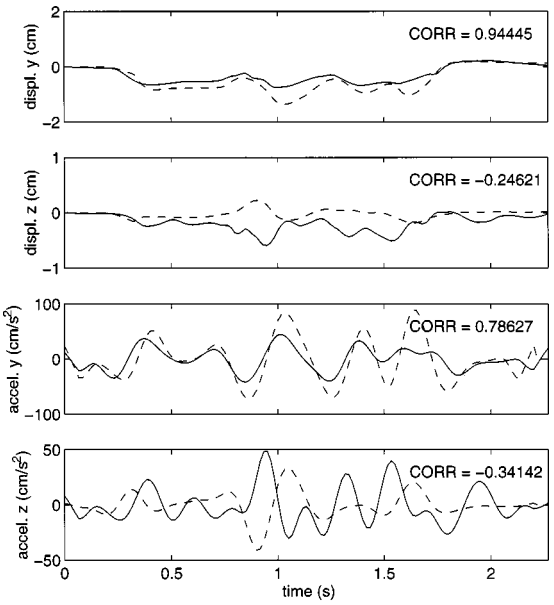

FIG. 4. Displacement and accelerations in the vertical (y) and protrusion (z) directions corresponding to IRED 3 for the CID sentence ''Where are you going?'' Full line: animation results; broken line: measured data. The cross-correlation between the animation and measured data is shown.

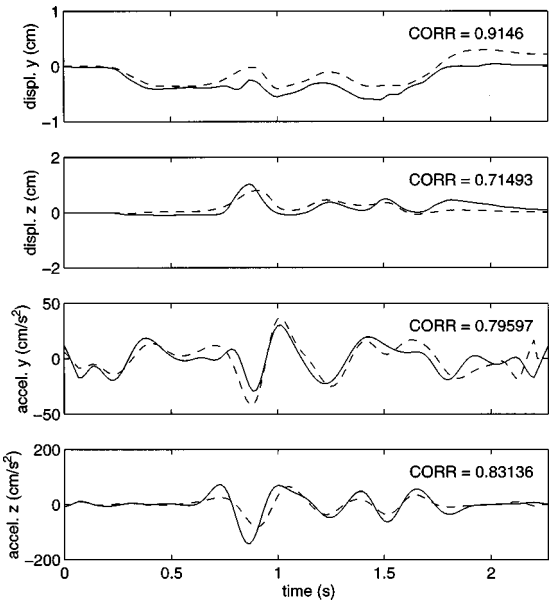

FIG. 6. Displacement and accelerations in the vertical (y) and protrusion (z) directions corresponding to IRED 7 for the CID sentence ''Where are you going?'' Full line: animation results; broken line: measured data. The cross-correlation between the animation and measured data is shown.

and acceleration of the IREDs, and the cross-correlation between the animated and measured kinematics.

In general, there is a good match between the animated and measured kinematics. Tables III and IV show mean, maximum, and minimum cross-correlation coefficients for all IREDs and corresponding model nodes for all of the sentences. As can be seen, the match tends to be better in the vertical (y) displacements and acceleration than the protrusion (z) records. There is also a difference in the degree of correlation across the various IRED positions. There is a tendency for the IREDs immediately surrounding the mouth to show lower cross-correlations.[5]

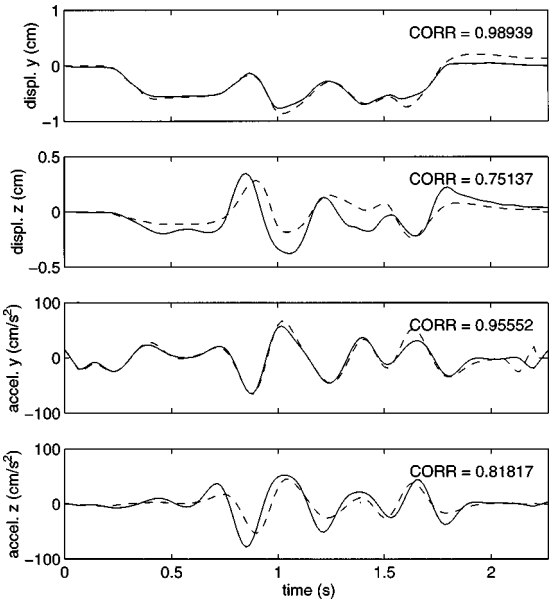

FIG. 5. Displacement and accelerations in the vertical (y) and protrusion (z) directions corresponding to IRED 5 for the CID sentence ''Where are you going?'' Full line: animation results; broken line: measured data. The cross-correlation between the animation and measured data is shown.

E. The movies

Research on the face allows a second type of measure of the success of modeling efforts. In addition to statistical measures of movement similarity between the model and real facial kinematics, the animations can be simply viewed to assess the degree of perceived realism of the motion. Two MPEG movies are available on our web page[6] for this purpose. The first shows the CID sentence ''Where are you going?'' The second shows repetition of the vowel–consonant–vowel (VCV) utterance /upæ/ with the subject using a bite block to immobilize the jaw. EMG was collected for the same muscle set and used to drive the model. Thus, for the bite-block movie all of the animation is produced by the muscle activation. The movies are produced at 60 frames per s and their viewing speed will depend on the processor

TABLE III. Cross-correlation coefficients between animated and measured displacements of markers for CID sentences.

	Vertical			Protrusion		
Marker #	Mean	Maximum	Minimum	Mean	Maximum	Minimum
1	0.986	0.996	0.969	0.840	0.932	0.578
2	0.344	0.645	0.072	−0.001	0.581	−0.617
3	0.896	0.954	0.775	0.369	0.772	−0.246
4	0.976	0.992	0.949	0.739	0.883	0.307
5	0.971	0.991	0.941	0.694	0.917	0.523
6	0.916	0.963	0.831	0.265	0.600	−0.428
7	0.886	0.958	0.728	0.469	0.770	0.087
8	0.508	0.883	−0.315	0.309	0.816	0.068
9	0.857	0.930	0.747	0.724	0.930	0.566
10	0.467	0.714	−0.063	0.371	0.785	−0.199
11	0.785	0.951	0.515	0.294	0.561	−0.104

TABLE IV. Cross-correlation coefficients between animated and measured accelerations of markers for CID sentences.

	Vertical			Protrusion		
Marker #	Mean	Maximum	Minimum	Mean	Maximum	Minimum
1	0.959	0.985	0.851	0.870	0.945	0.657
2	0.339	0.600	−0.086	−0.121	0.420	−0.674
3	0.848	0.933	0.601	0.263	0.625	−0.341
4	0.942	0.970	0.844	0.714	0.881	0.184
5	0.946	0.976	0.835	0.702	0.868	0.307
6	0.861	0.942	0.670	0.331	0.778	−0.071
7	0.867	0.957	0.662	0.505	0.831	0.112
8	0.408	0.765	−0.490	0.288	0.787	−0.267
9	0.773	0.926	0.375	0.661	0.873	0.336
10	0.365	0.768	−0.314	0.291	0.735	−0.300
11	0.737	0.851	0.539	0.410	0.690	−0.108

speed of the reader's computer. As can be seen, in both cases the model produces highly realistic speech movement and natural skin motion.

III. DISCUSSION

The model described here incorporates active muscle properties as well as passive muscle and tissue properties in a detailed 3-D simulation of facial dynamics. Realistic speech animation is produced by driving the physical model with recorded EMG data. Good cross-correlations between model kinematics and recorded data were observed and natural patterns of skin deformation can be observed in movies of the animation. This initial version of the model is quite promising, yet both the model and the test of the model involved significant simplifications. The tissue biomechanical properties are represented by linear approximations. While the muscle activation dynamics are represented in a sophisticated manner, the lines of action of the muscles are simplified. In addition, only a subset of the full set of facial muscles is modeled.

The test of the model's performance was shaped by a number of practical considerations. The EMG and kinematics were recorded from opposite sides of the face. This was done to avoid having electrical noise from the OPTOTRAK contaminate the muscle activity recordings. Thus, we have tacitly assumed symmetry in the structure and action of the face. This assumption ignores the known asymmetries in facial morphology and lip movement (Campbell, 1982) and thus adds error variance to our modeling. Our use of the EMG to drive the model allowed a direct test of the representation of the biomechanics of the face. However, the use of perioral EMG raises a set of separate issues. Intramuscular EMG recordings such as the ones we used are imperfect measures of the full muscle activation and force generation. The reasons for this include recording noise in the signals, interdigitation of the muscle fibers potentially leading to recordings from multiple muscles at any single recording site (Blair and Smith, 1986), possible compartmentalized muscles (Binder and Stuart, 1980) in which different motor units within a muscle have different functional roles, and nonlinearities between EMG and force generation.

In spite of these potential problems, the model's performance was surprisingly good. What accounts for the model performance? No single factor can explain this, but a combination of the following factors seems most likely. The primary determinant of facial motion is the movement of the jaw. When the jaw opens, the facial tissue and muscles are stretched and the skin deforms to accommodate the movement. In the simulations, we moved the jaw based on recorded kinematics and thus the modeled facial tissue responded well to this change. While the tissue changes in response to the jaw kinematics are realistic, it leaves the question of the extent to which the perioral muscles are accurately portrayed. The bite-block trial shown in the second movie indicates that realistic animation can be produced in the absence of jaw movement. However, we did not collect enough of the bite-block data to carry out statistical analyses. It is likely the cross-correlations would be lower in this case.

A second contribution to the good performance is the fact that the face in speech is controlled with few degrees of freedom (Ramsay *et al.*, 1996) and may be quite crudely controlled (Löfqvist and Gracco, 1997). Ramsay *et al.*'s principal component analysis of the lip motion indicates that the motion along a single dominant trajectory accounted for much of the variance in the data and that the motion of any single position marker on the lip was strongly one-dimensional. Löfqvist and Gracco have shown that the lips often make contact in bilabial stops at peak velocity and that contact forces are involved in deceleration. This would imply that there is considerable redundancy in the motor control of the lips and face for phonetic targets and that these targets are not specified with great precision. Thus, with tissue parameters in the biological ballpark and EMG patterns prescribing a time structure for the behavior, the facial animation looked realistic.

As noted above, the potential for problems in the EMG is great and its use is a bit of an experimental gamble. However, the performance of the model here and separate analyses on the same EMG and kinematic data (Vatikiotis-Bateson and Yehia, 1996) indicate that the recorded EMG signals were very good correlates of the muscle activity. Vatikiotis-Bateson and Yehia (1996) have shown, using a second-order autoregressive model, that the EMG can be used to estimate the facial motion with very high accuracy. One interpretation of this is that the facial muscle activity overdetermines the relatively simple facial speech gestures. Thus, in combination, a range of muscle recordings can provide good estimates of the time course of perioral force generation.

One final aspect of the model may contribute to its good performance. The model's overall performance may be dominated by the mesh viscoelastic properties. If this is the case, the response of the model will be determined mainly by the time constants of the mesh, and high accuracy in the time histories of the muscle activities would not be necessary. We are currently exploring this question with sensitivity analysis of the model.

Models of this kind provide an essential tool for understanding speech motor control. In the study of speech, we can measure only the end product of a complex chain of

planning and control processes. However, the kinematics of speech and the EMG are the result of an interaction between linguistic and motoric planning processes and the biomechanics of the speech articulators. To understand this complex sensorimotor process, we must be able to assign variance components in the data to different stages in the production process. At the very least, variance components due to the central commands and the biological plant must be separated. If models such as the one described here can provide a biologically plausible representation of the plant, then comparisons between different ideas about the central control of the speech motor system can be made.

This particular model also has another role in speech research. As indicated in the introduction, there is little visual stimulus control or visual stimulus specification in research on audiovisual speech perception. Some individuals are easier to lipread than others, and speaking style and phonetic context change the facial kinematics. The timing and velocities of speech movements, the magnitudes of facial motions, the visibility of the oral cavity, and the size and velocity of head motion all can vary from talker to talker and from context to context. Yet, visual stimulus characteristics are rarely reported (cf. Munhall *et al.*, 1996; Munhall and Tohkura, 1998). In acoustic speech perception, the field has developed on the basis of detailed synthesis and multivariate parameter specification. Audiovisual and visual speech perception research must follow similar standards of stimulus control, and models such as the one described in this paper will be important tools for creating factorial studies of visual cues (cf. Massaro, 1987, 1998).

ACKNOWLEDGMENTS

We are grateful to Eric Vatikiotis-Bateson and Vince Gracco for help collecting the EMG and OPTOTRAK data. The data were collected at ATR Human Information Processing Research Laboratories and the authors gratefully acknowledge their support. We thank Demetri Terzopoulos and Victor Lee for generously sharing their time and software. André Tan helped with the cadaver dissection. Michel Pitermann made helpful comments on an earlier draft. This work was funded by NIH Grant No. DC-00594 from the National Institute of Deafness and other Communication Disorders and NSERC.

[1]This is a simplification that we will explore in future research. The skin's layers are not uniform in thickness (e.g., Kennedy and Abbs, 1979) and the location of tissue thickness changes presumably contributes significantly to individual facial characteristics.

[2]Data for two of the sentences were lost due to recording errors.

[3]We could not reliably distinguish these muscles and thus we have driven both of these muscles in the model with the signal from this single recording site.

[4]Since there is little lateral motion in speech (Vatikiotis-Bateson and Ostry, 1995), we have focused on the vertical and protrusion movements only. However, note that this is a 3-D model of the face with motion in all planes.

[5]The poorer performance of the model at the lips is most likely due to an omission in the current model. The lips do not penetrate each other when they make contact because of a penetration penalty force, but we have not modeled the friction forces on the lip surfaces. As a result, the lips tend to slide upon contact rather than compress and deform. This results in inaccuracies in the detailed kinematics of lip shape. In our current work, we are exploring implementation of a skin surface friction.

[6]http://130.15.96.12/~munhallk/home.html

Barbenel, J. C. (**1989**). ''Biomechanics of Skin,'' in *Systems and Control Encyclopedia: Theory, Technology, Applications* (Pergamon, Oxford).

Berry, D. A., Moon, J. B., and Kuehn, D. P. (**1998**). A Histologically-based Finite Element Model of the Soft Palate, *National Center for Voice and Speech: Status and Progress Report* (Vol. 12, pp. 71–77).

Binder, M. D., and Stuart, D. G. (**1980**). ''Motor Unit-muscle Receptor Interactions: Design Features of the Neuromuscular Control System,'' in *Progress in Clinical Neurophysiology, Spinal and Supraspinal Mechanisms of Voluntary Motor Control and Locomotion*, edited by J. E. Desmedt (Karger, Basel, Switzerland).

Blair, C. (**1986**). ''Interdigitating Muscle Fibers Throughout Orbicularis Oris Inferior: Preliminary Observations,'' J. Speech Hear. Res. **29**, 266–269.

Blair, C., and Smith, A. (**1986**). ''EMG Recording in Human Lip Muscles: Can Single Muscles Be Isolated?'' J. Speech Hear. Res. **29**, 256–266.

Brown, I. E., Scott, S. H., and Loeb, G. E. (**1996**). ''Mechanics of Feline Soleus: II. Design and Validation of a Mathematical Model,'' J. Muscle Res. Cell Motil. **17**, 221–233.

Campbell, R. (**1982**). ''Asymmetries in Moving Faces,'' British J. Psychol. **73**, 95–103.

Cohen, M. M., and Massaro, D. W. (**1990**). ''Synthesis of Visible Speech,'' Behav. Res. Methods Instrum. Comput. **22**, 260–263.

Duchenne, G. B. (**1990**). *The Mechanism of Human Facial Expression* (Cambridge University Press, New York).

Duck, F. A. (**1990**). *Physical Properties of Tissue: A Comprehensive Reference Book* (Academic, London).

Ekman, P., and Friesen, W. V. (**1975**). *Unmasking the Face* (Consulting Psychologists, Palo Alto, CA).

Ho, S. P., Azar, K., Weinstein, S., and Bowley, W. W. (**1982**). ''Physical Properties of Human Lips: Experimental and Theoretical Analysis,'' J. Biomech. **15**(11), 859–866.

Kakita, Y., Fujimura, O., and Honda, K. (**1985**). ''Computation of Mapping from Muscular Contraction Patterns to Format Patterns in Vowel Space,'' in *Phonetic Linguistics: Essays in Honor of Peter Ladefoged*, edited by V. Fromkin (Academic, New York).

Kennedy, J. G., and Abbs, J. H. (**1979**). ''Anatomic Studies of the Perioral Motor System: Foundations for Studies in Speech Physiology,'' Speech Lang. Adv. Res. Pract. **1**, 211–270.

Laboissière, R., Ostry, D. J., and Feldman, A. G. (**1996**). ''The Control of Multimuscle Systems: Human Jaw and Hyoid Movements,'' Biol. Cybern. **74**, 373–384.

Lanir, Y. (**1987**). ''Skin Mechanics,'' in *Handbook of Bioengineering*, edited by R. Skalak and S. Chien (McGraw-Hill, New York).

Larabee, W. F. (**1986**). ''A Finite Element Model of Skin Deformation. I. Biomechanics of Skin and Soft Tissue: A Review,'' Laryngoscope **96**, 399–405.

Lee, Y., Terzopoulos, D., and Waters, K. (**1993**). Constructing Physics-based Facial Models of Individuals. Paper presented at the Proceedings of Graphics Interface '93.

Lee, Y., Terzopoulos, D., and Waters, K. (**1995**). ''Realistic Modeling for Facial Animation,'' Comput. Graph. **29**, 55–62.

Lightoller, G. H. S. (**1925**). ''Facial Muscles: The Modiolus and Muscles Surrounding the Rima Oris with Some Remarks About the Panniculus Adiposus,'' J. Anat. **LX** (Part 1), 1–85.

Lindblom, B., and Sundberg, J. (**1971**). ''Acoustical Consequences of Lip, Tongue, Jaw and Larynx Movement,'' J. Acoust. Soc. Am. **50**, 1166–1179.

Löfqvist, A., and Gracco, V. L. (**1997**). ''Bilabial Stop Consonant Production: Lip and Jaw Kinematics.'' J. Speech Hear. Res. **40**, 877–893.

Massaro, D. W. (**1987**). *Speech Perception by Ear and Eye* (Erlbaum, Hillsdale, NJ).

Massaro, D. W. (**1998**). *Perceiving Talking Faces* (Bradford, Cambridge, MA).

Muller, E. M., Milenkovic, P., and MacLeod, G. (**1984**). ''Perioral Tissue Mechanics During Speech Production,'' in *Proceedings of the Second IMAC International Symposium on Biomedical Systems Modeling*, edited by C. DeLisi and J. Eisendfeld (North Holland, Amsterdam).

Munhall, K. G., Gribble, P., Sacco, L., and Ward, M. (**1996**). ''Temporal Constraints on the McGurk Effect,'' Percept. Psychophys. **58**, 351–362.

Munhall, K. G., and Tohkura, Y. (**1998**). ''Audiovisual Gating and the Time Course of Speech Perception,'' J. Acoust. Soc. Am. **104**, 530–539.
Munhall, K. G., and Vatikiotis-Bateson, E. (**1998**). ''The Moving Face During Speech Communication,'' in *Hearing By Eye, Part 2: The Psychology of Speechreading and Audiovisual Speech*, edited by R. Campbell, B. Dodd, and D. Burnham (Taylor & Francis Psychology, London).
Otten, E. (**1987**). ''A Myocybernetic Model of the Jaw System of the Rat,'' J. Neurosci. Methods **21**, 287–302.
Parke, F., and Waters, K. (**1996**). *Computer Facial Animation* (AK Peters, Wellesley, MA).
Ramsay, J. O., Munhall, K. G., Gracco, V. L., and Ostry, D. J. (**1996**). ''Functional Data Analyses of Lip Motion,'' J. Acoust. Soc. Am. **99**, 3718–3728.
Sanguineti, V., Laboissière, R., and Ostry, D. J. (**1998**). ''An Integrated Model of the Biomechanics and Neural Control of the Tongue, Jaw, Hyoid and Larynx Systems,'' J. Acoust. Soc. Am. **103**, 1615–1627.
Sufit, R. L., Poulsen, G., Welt, C., and Abbs, J. H. (**1984**). ''Morphology and Histochemistry of the Facial Muscles and Fascicularis,'' Soc. Neurosci. Abs. **10**, 779.
Summerfield, Q. (**1992**). ''Lipreading and Audio-Visual Speech Perception,'' Philos. Trans. R. Soc. London, Ser. B **335**, 71–78.
Terzopoulos, D., and Waters, K. (**1990**). ''Physically-based Facial Modeling, Analysis, and Animation,'' Visual. Comput. Anim. **1**, 73–80.
Terzopoulos, D., and Waters, K. (**1993**). ''Analysis and Synthesis of Facial Image Sequences Using Physical and Anatomical Models,'' IEEE Trans. Pattern. Anal. Mach. Intell. **15**, 569–579.
Titze, I. R., and Talkin, D. T. (**1979**). ''A Theoretical Study of the Effects of Various Laryngeal Configurations on the Acoustics of Phonation,'' J. Acoust. Soc. Am. **66**, 60–74.
Vatikiotis-Bateson, E., and Ostry, D. (**1995**). ''An Analysis of the Dimensionality of Jaw Motion in Speech,'' J. Phonetics **23**, 101–117.
Vatikiotis-Bateson, E., and Yehia, H. (**1996**). ''Physiological Modeling of Facial Motion During Speech,'' Trans. Tech. Com. Psycho. Physio. Acoust., H-96 **65**, 1–8.
Vinkka-Puhakka, H., Kean, M. R., and Heap, S. W. (**1989**). ''Ultrasonic Investigation of the Circumoral Musculature,'' J. Anat. **166**, 121–133.
Waters, K., and Terzopoulos, D. (**1991**). ''Modeling and Animating Faces Using Scanned Data,'' J. Visualiz. Comput. Anim. **2**, 123–128.
Waters, K., and Terzopoulos, D. (**1992**). ''The Computer Synthesis of Expressive Faces,'' Philos. Trans. R. Soc. London, Ser. B **335**, 87–93.
Wilhelms-Tricarico, R. (**1995**). ''Physiological Modeling of Speech Production: Methods for Modeling of Soft-Tissue Articulators,'' J. Acoust. Soc. Am. **97**, 3085–3098.
Winters, J. M. (**1990**). ''Hill-based Muscle Models: A Systems Engineering Perspective,'' in *Multiple Muscle Systems: Biomechanics and Movement Organization*, edited by J. Winters and S. Woo (Springer, London), pp. 69–93.
Zajac, F. E. (**1989**). ''Muscle and Tendon: Properties, Models, Scaling and Application to Biomechanics and Motor Control,'' Crit. Rev. Biomed. Eng. **17**, 359–411.

The effect of partially restored hearing on speech production of postlingually deafened adults with multichannel cochlear implants

Liat Kishon-Rabin,[a] Riki Taitelbaum,[b] Yishai Tobin,[c] and Minka Hildesheimer
Department of Communication Disorders, Sackler Faculty of Medicine, Tel-Aviv University, Israel

(Received 16 December 1998; revised 24 May 1999; accepted 15 June 1999)

The effect of auditory feedback on speech production was investigated in five postlingually deafened adults implanted with the 22-channel Nucleus device. Changes in speech production were measured before implant and 1, 6, and 24 months postimplant. Acoustic measurements included: $F1$ and $F2$ of vowels in word-in-isolation and word-in-sentence context, voice-onset-time (VOT), spectral range of sibilants, fundamental frequency ($F0$) of word-in-isolation and word-in-sentence context, and word and sentence duration. Perceptual ratings of speech quality were done by ten listeners. The significant changes after cochlear implantation included: a decrease of $F0$, word and sentence duration, and $F1$ values, and an increase of voiced plosives' voicing lead (from positive to negative VOT values) and fricatives' spectral range. Significant changes occurred until 2 years postimplant when most measured values fell within Hebrew norms. Listeners were found to be sensitive to the acoustic changes in the speech from preimplant to 1, 6, and 24 months postimplant. Results suggest that when hearing is restored in postlingually deafened adults, calibration of speech is not immediate and occurs over time depending on the age-at-onset of deafness, years of deafness, and perception skills. The results also concur with hypothesis that the observed changes of some speech parameters are an indirect consequence of intentional changes in other articulatory parameters. [S0001-4966(99)04909-7]

PACS numbers: 43.70.Dn, 43.70.Fq, 43.64.Me [AL]

INTRODUCTION

The role of hearing in speech production has undergone lengthy debates. There is compelling evidence that the loss of hearing *prior to and during* language and speech acquisition greatly affects speech production (Osberger and McGarr, 1982; Tobey, 1993). Thus, consensus among researchers is that hearing plays a key role in the *acquisition* of speech production skills. More controversial, however, is the effect of hearing on speech production of individuals who became deaf *after* they acquired normal speech production skills. Some researchers argue that once normal speech production is established, the role of auditory feedback is minimal (Goehl and Kaufman, 1984; Sapir and Canter, 1991). Conversely, others have suggested that auditory feedback provides valuable information which helps to control finer speech movements which otherwise cannot be controled by feedback from the tactile and proprioceptive channels. Among this latter group of researchers are those who believe that auditory information is used in a close-loop system which provides moment-to-moment feedback for control of speech production. Their belief is based on studies that showed immediate voice changes of normal-hearing individuals when their auditory feedback had been altered. These voice changes included increased intensity when subjected to background noise (also known as the Lombard effect) (Lane and Tranel, 1971), decrease in speech rate when auditory feedback is artificially delayed (Davidson, 1959), and changes in fundamental frequency when auditory feedback frequencies have been altered (Elman, 1981). A more recent study reported changes in vowel production to compensate for feedback alterations in the first three formants of the vowel, changes that were large enough to change the vowel's perceived phonetic identity (Houde and Jordan, 1998).

The majority of the researchers believe that although the possibility of correction of ongoing gestures cannot be ruled out for suprasegmental parameters (Svirsky *et al.*, 1992), it is unlikely that immediate information provided by the auditory signal is used for correcting the production of the segmental features. These investigators argue that most of the relevant auditory information reaches the speaker after the articulatory movements have been completed (Cowie and Douglas-Cowie, 1983; Lane and Webster, 1991; Zimmerman and Retaliatta, 1981). The fact that individuals with profound postlingual hearing loss maintain highly intelligible speech suggests that mature phonemic motor patterns are quite robust, and do not depend heavily on auditory feedback. These researchers argue in favor of a predominantly open-loop speech motor control system, i.e., the speaker ''knows'' the relationship between motor commands and resulting sound output and uses this knowledge to compute the motor sequence for producing the desired speech output (Matthies *et al.*, 1996). It is further suggested that for individuals who acquired normal speech patterns, the auditory modality may serve as a calibrator of fine movements in order to produce

[a]Mailing address: Department of Communication Disorders, Sheba Medical Center, Tel-Hashomer, Israel 52621. Electronic mail: Irabin@post.tau.ac.il
[b]Also of the Speech and Hearing Center, Chaim Sheba Medical Center, Tel-Hashomer, Israel 52621.
[c]Also of the Department of Behavioral Sciences, Ben-Gurion University of the Negev, Israel.

articulatory precision. The slow and gradual deterioration of speech and its intelligibility in postlingual deaf adults supports this theory.

The effect of hearing loss on the speech production of postlingually deafened adults has been examined at both the segmental and suprasegmental levels. Changes at the segmental level include: (1) decreased vowel space due to ''centralization'' of the first two formants (Plant, 1984; Read, 1989; Waldstein, 1990); (2) inaccurate production of /s/ and /sh/ (Plant, 1993); (3) similar voice-onset time values of voiced and voiceless plosives (Waldstein, 1990); (4) substitution of affricates with fricatives, substitution of /r/ with /w/ (and vice versa) (Binnie *et al.*, 1982; Leder and Spitzer, 1990; Read, 1989); and (5) the tendency to eliminate consonants in final position (Binnie *et al.*, 1982; Leder and Spitzer, 1990; Plant, 1984). These results suggest that absence of auditory feedback affects the accuracy of the acoustic-phonetic pattern of some speech sounds of adults who had established normal speech production prior to their hearing loss.

Results of some studies investigating the suprasegmental changes of postlingually deafened adults showed changes in fundamental frequency and intonation patterns (Lane and Webster, 1991) while others did not (Waldstein, 1990). Other studies showed a significant increase in voice intensity (Leder and Spitzer, 1993; Leder *et al.*, 1987a) and lengthening of speech utterances (Lane and Webster, 1991; Leder *et al.*, 1987b; Waldstein, 1990). Furthermore, normal-hearing subjects judged rate, intonation, and quality of postlingually deafened individuals speech as inappropriate in comparison to that of normal-hearing speakers (Leder and Spitzer, 1990; Plant, 1984, 1993; Plant and Oster, 1986).

The changes in speech production observed in deafened adults appear to have little effect on speech intelligibility in cases where onset of deafness occurred in adulthood. The earlier the onset of deafness, the greater the effect of hearing loss on intelligibility (Binnie *et al.*, 1982; Cowie *et al.*, 1982; Plant, 1984).

Many of the studies investigating the effect of hearing loss on speech production of postlingually deafened adults focused primarily on the deviation of speech from normal production. The use of cochlear implants in the last couple of decades has facilitated testing of the reverse effect, i.e., that of partially restored hearing on speech production. Investigators have used two research designs to test this: longitudinal designs (Economou *et al.*, 1992; Langereis *et al.*, 1997; Perkell *et al.*, 1992; Smyth *et al.*, 1991; Tartter *et al.*, 1989) and short-term experiments where the auditory input was interrupted or altered temporarily (Matthies *et al.*, 1996; Richardson *et al.*, 1993; Svirsky *et al.*, 1992; Svirsky and Tobey, 1991). Both types of experiments offer some insights into the role that partially restored hearing plays in the speech production process. This article focuses on the changes in the production of speech after cochlear implantation. Thus, most of the studies cited below are longitudinally designed.

In general, restoration of hearing via a single-channel, intra- or extracochlear implant device resulted in a decrease in average fundamental frequency ($F0$); a shift in the range of $F0$ to values of normal-hearing individuals; close-to-normal vocal intensity, stress, and intonation patterns; ''decrease in the length of utterances,'' and improved voice quality (for extracochlear devices: Ball and Faulkner, 1989; Oster, 1987; Plant and Oster, 1986; for intracochlear: Leder *et al.*, 1986; Read, 1989).

Additional improvements were observed with the multichannel cochlear implant devices. These changes included mainly larger vowel ''space'' which is a result of greater frequency separations of first and second formants (Economou *et al.*, 1992; Langereis *et al.*, 1997; Perkell *et al.*, 1992; Smyth *et al.*, 1991), better voice-voiceless distinction (Economou *et al.*, 1992; Lane *et al.*, 1994, 1995; Tartter *et al.*, 1989), and increase in the distinctiveness of fricatives and affricales (Economou *et al.*, 1992; Tartter *et al.*, 1989) and between the fricatives /s/ and /sh/ (Matthies *et al.*, 1994). The variability in the magnitude of these changes between and within studies is large. This variability can be attributed to the small number of subjects in each study, evaluating techniques, test material, coding strategies of the implant device, speech training provided for some subjects, the use of auditory feedback for the adjustment of speech production, and the already reported differences that exist in the speech behavior of speakers including those that are normally hearing (Borden *et al.*, 1994). It is noteworthy that most studies measured the changes in acoustical parameters up to 1 year postimplant. It is not clear from the data reported thus far, whether, and for which, measured parameters changes continue after 1 year of implant use.

From the published data there are several issues that require further clarification. One issue is the relationship between acoustical analysis and speech quality ratings. Another relates to the longitudinal changes of segmental and suprasegmental speech features beyond 1 year of cochlear implant use. A third issue concerns the fact that all the studies have measured the effect of auditory information provided by the cochlear implant on speech production and the deviation of this speech from English norms. Would similar changes in speech production occur when the deaf individuals speak a different language of a different sound system?

Modern (General Israeli) Hebrew, for example, differs from the English language in many aspects. For the purpose of this paper, however, only very basic differences in the phonology of the two languages will be mentioned briefly. The basic phonemic inventory of Modern Hebrew is limited to five vowels /i, e, a, o, u/, which were primarily adapted from the Sephardic Jews from Arabic/Judezmo background, and 19 consonants /p, b, f, v, m, t, d, s, z, ts, n, j, l, ʃ, k, g, x, ɣ, h/ which were primarily adapted from Ashkenazi Jews of Central and Eastern Europe (Berman, 1997). In contrast, a simplified view of American English phonemic inventory includes 12 basic vowels (not including diphthongs) and 24 consonants (Boothroyd, 1986). A comparative table of the phonological systems of these two languages is shown in Table I. Some of the most notable differences between the systems may be summarized as follows: The Hebrew vowel system does not include the tense-lax distinction as a distinctive feature, nor does it have low front, low back, or central vowels. The two languages share 16 consonant phonemes /p, b, f, v, m, t, d, s, z, l, n, ʃ, j, k, g, h/ with slight differences

TABLE I. A comparison of the Israeli Hebrew and American English phonological systems (simplified).

	Israeli Hebrew	American English
Consonants:		
Labial	/b, p, f, v, m/	/b, p, f, v, m, w/
Apical	/t, d, s, z, ts, l, n/	/t, d, θ, x̟, s, z, tʃ, dʒ, l, n, r/
Palatal	/ʃ, j/	/ʃ, j, ʒ/
Velar	/k, g, x, ɣ/	/k, g, ng/
Glottis	/h/	/h/
Vowels (without diphtongs):		
	/i, e, a, o, u/	/i, ɪ, e, E, ae, ə, e, ʌ, ɜ, o, U, u/

in pronunciation: e.g., Hebrew apical consonants are usually apical-dental while English apical consonants are usually apical-alveolar (Harshav, 1993; Tobin, 1997). In addition, Hebrew has the consonants /ts, x, ɣ/ while English has the consonants /w, θ, x̟, tʃ, dʒ r, ʒ, ng/. It should be noted that although the consonants in Hebrew and American English differ, the same features classify them all.

In terms of the acoustics of the speech sounds, the only available data in Hebrew are for formants of the vowels and voice-onset-time of stop-plosives. In the most recent and extensive study on Hebrew vowels, Amir (1995) measured the first three formants of vowels in CVC monosyllabic words spoken by 30 young males, 30 young females, and 30 children who are native of Israel. When plotting the vowel space ($F2$ vs $F1$) in Hebrew compared to that of English (using formant values from Peterson and Barney study from 1952) he found the Hebrew vowel space to be much more centralized and more triangle in shape than the English one. The differences between the vowels of the two languages differed particularly in $F1$ values. When comparing the Hebrew vowel space to those of languages with the same number of vowels represented by the same phonetic symbols (Spanish and Shona), again the Hebrew vowel system was more centralized than the others with the major differences in $F1$ values. One of the implications of the reduced vowel space in Hebrew is the smaller acoustic difference that exists between the vowels in Hebrew compared to differences between vowels in other languages. There is data to show that these differences have an effect on the *perception* of vowels in Hebrew. Kishon-Rabin (1999) and Kishon-Rabin *et al.* (1998) showed that vowels that differ by their tongue height are perceived poorly by cochlear implant users. These results were explained by the fact that the $F1$ values of vowels that differed by tongue height fell within the frequency range of the same electrode or adjacent electrodes. It remains to be seen whether the difficulty in perceiving certain vowels has an effect on the production of these vowels compared to vowels that are perceived more easily.

Raphael *et al.* (1995) cite their own studies, as well as others, in which voice-onset-time (VOT) was measured for voiced and voiceless Hebrew stop-plosives. In general, Hebrew voiced plosives were found to have a considerable amount of voicing lead (approximately VOT of −90 ms), which is typical of those found in languages that use voicing lead for one phonological category of stops. The average VOT of Hebrew voiceless plosives, on the other hand, was found to be in the range of 28, 36, and 56 ms for /p/, /t/, and /k/, respectively. These data for the voiceless stop-plosives are generally intermediate to those found in languages, such as English, that contrast short-lag and long-lag stops. It is also not in keeping with the assertion that in languages employing a single phonological voicing opposition, such as Hebrew and English, speakers realize stops phonetically using VOTs from adjacent categories (i.e., from the voicing lead and zero onset/short-lag categories, or from the zero onset/short-lag and long-lag categories; cited in Raphael *et al.*, 1995). Thus, it appears that Hebrew speakers use the voicing lead category for the voiced stop-plosives, but use an in-between category (between the short-lag and long-lag) for the voiceless ones. In contrast, American English speakers typically use zero-onset/short lag (approximately 0 to +30 VOT) for voiced stop-plosives and long lag (approximately +50 ms or more VOT) for the voiceless ones (Borden *et al.*, 1994). To summarize, English and Hebrew speakers use different categories of VOT for the voice–voiceless distinction. Furthermore, Hebrew uses an intermediate category for the voiceless stops that its VOT values lie between the English voiced and voiceless stops. Auditory perception data show that 12 postlingually deafened adults with multichannel cochlear implants were able to perceive approximately 80% (after correction for guessing) of the items in the initial voicing subtest of the Hebrew Speech Pattern Contrast test (Kishon-Rabin *et al.*, 1998). It is not clear how (and if at all) the ability to perceive the voicing contrast in initial word position by the cochlear implant and the inherent differences in VOT values between the Hebrew and English languages may influence the effect that cochlear implants have on the production of Hebrew voiced and voiceless stop-plosives.

The following study was, therefore, designed to investigate the longitudinal changes of suprasegmental and segmental features in Hebrew speaking postlingually deafened adults who received a multichannel cochlear implant using acoustical analyses and speech quality ratings.

I. METHOD

A. Subjects

Five postlingually deafened adults (four males, one female), between 35 and 61 years of age (average 50.2 years) participated in the study. Table II depicts the personal information of the subjects. Also shown in Table II are the subjects' results on closed-set and open-set speech perception tests. All subjects had no known speech and/or voice disorders.

B. Implant and speech processor

All subjects were using the 22-channel Nucleus WSP-III cochlear implant. The electrode array contains 22 electrodes that are inserted in the scala tympani of the cochlea. Each electrode is preassigned an acoustic frequency band and those bands cover the frequency range of approximately 300–4000 Hz. The speech processor extracts a number of speech parameters from the ongoing acoustic signals including the fundamental frequency and estimates of amplitudes

TABLE II. Background information for the five postlingually deafened adults that participated in the present study.

	S1	S2	S3	S4	S5
Gender	Male	Male	Male	Male	Female
Onset of deafness (yrs)	16	48	36	54	41
Etiology	Cogan syndrome	Ototoxicity	Unknown	Acoustic trauma	Surgical Trauma
Duration of deafness	19	8	19	7	3
Thresholds of Better Ear preimplant[a]					
500 Hz	NR[b]	NR	NR	NR	NR
1000 Hz	NR	NR	NR	NR	NR
2000 Hz	NR	NR	NR	NR	NR
Aided thresholds of better ear preimplant					
500 Hz	NR	110	NR	85	95
1000 Hz	NR	105	NR	80	NR
2000 Hz	NR	NR	NR	NR	NR
Age of implant (yrs)	35	56	55	61	44
Mode of stimulation	Bipolar	Bipolar	Bipolar	Bipolar	Bipolar+1
No. of active electrodes	21	15	14	16	19
Speech perception Test[c] (in %) (at 2 years postimplant) Hebrew CID	96	35	0	11	21

[a]dB HL *re*: ANSI (S3.6, 1989).
[b]No response. Maximum output of audiometer was 110 dB HL.
[c]The test was recorded by a Hebrew speaker and presented by audition only. All Hebrew tests were developed using the same criteria and guidelines that were used to develop the original tests in English.

and frequencies of the highest energy bands in the regions 300–1000 and 800–4000 Hz. These regions correspond to probable locations of the two lowest formant frequencies when the input signal is speech. The formant frequency estimates determine the electrodes excited. Lower frequency peaks stimulate more apical channels and higher peaks stimulate more basal channels. Pulses stimulate, in rapid succession, two electrodes determined by formant estimates. Rate of stimulation per electrode is determined whether the sound is voiced or voiceless. For voiced sounds, the stimulation rate is equal to the fundamental frequency. For voiceless sounds, stimulation rate is random and is of approximately 100 Hz. Stimulation pulses are biphasic square waves. Amplitude estimates determine current levels.

C. Stimuli and procedure

Stimuli consisted of 50 monosyllabic, minimal-pair words which represented the 17 consonants and 5 vowels of the Hebrew language, 12 every-day sentences (7 declaratives, 3 questions, and 2 imperatives), and spontaneous speech. Each of the every-day sentences consisted of 4–5 words, and each word had 1–3 vowels. Note that in Hebrew words such as ''in,'' ''the,'' or ''to,'' for example, are added as a prefix to the subject or adjective of the sentence. Thus, an English sentence of 7–8 words can be translated into a shorter Hebrew sentence of 4–5 words only. For each subject, recordings of the stimuli were made on four separate occasions: premplant and 1 month, 6 months, and 24 months postimplant. Subjects were recorded individually in a sound-treated booth using a Sony TC K2A tape recorder and an international microphone, positioned 12 to 15 cm from the speaker's mouth. Order of recording was randomized between and within subjects.

D. Speech assessment

Speech production was assessed using acoustical analyses and subjective rating scales.

1. Acoustical analyses

Selected suprasegmental and segmental properties were measured for acoustical analyses. The suprasegmental properties included fundamental frequency ($F0$) and duration of words and sentences. The segmental properties included first and second formants ($F1$ and $F2$) of the five Hebrew vowels, voice onset time of plosives in initial position (/b,p,d,t,g,k/), and spectral distribution of fricatives /s/ and /sh/. Stimuli were low-pass filtered and digitized at 20 000 samples per second and 12-bit quantization levels, using a commercial speech analysis program SS1 (Sensimetric Speech Station Ver. 2.1, Ariel Corporation).

A fundamental frequency extraction algorithm, a built-in feature of the SS1 program, based on an autocorrelation function was used to estimate $F0$. Each $F0$ estimate was made over 512 samples of data. Values of $F0$ were obtained in the middle of the steady-state portion of all the vowels using spectrogram display of 128-point window. A total of 170 $F0$ measurements were obtained: 50 in monosyllabic words and 120 in sentences, for each subject and recording. Note that, on average, ten measurements of $F0$ were obtained for each sentence at relatively equal spacing throughout the duration of the sentence.

The duration of words and sentences were measured from the initiation of the ulterance's energy to its termination based on the waveform and spectrogram displays using a fast Fourier transform (FFT) with a 512-point window.

The first two formants were calculated using linear predictive coding (LPC) measured in the middle of the steady-state portion of each vowel (at the same location where $F0$ was determined). An order of 18 was used to estimate the locations of the resonances in the spectrum. These measurements were corroborated by overlaying a Fourier spectrum on the LPC spectrum and by visual inspection of the spectrogram display using a 128-point window. At least 30 measurements were obtained for each vowel, subject, and recording.

The voice-onset time of plosives in the initial position (/b,p,d,t,g,k/) was determined as time elapsed from start of the burst, signaling release of oral closure, to the first sign of periodicity, signaling onset of voicing. In tokens were there was voicing lead, measurements were made from the onset of periodicity to the start of the burst. Voice-onset time measurements were obtained for 11 voiced plosives and 11 voiceless plosives, in the monosyllabic words, for each subject at each recording.

The range of the frication noise of /s/ and /sh/ was measured using the Fourier spectrum display (512-point window). A horizontal line was drawn at 15 dB below the frequency with maximum energy. The range between the points where the horizontal line crossed the FFT spectrum display was taken as the spectral range of the fricative. This method is similar to the method used to measure frequency response of acoustical systems. Measurements of the spectral range were obtained at the midpoint of the fricative as determined from the waveform and spectrogram displays. Nine measurements were made for each of the two sibilants for each subject and recording.

2. Subjective rating scales

Ten speech therapists with at least 5 years of experience in the field, but inexperienced in deaf speech, served as judges for this part of the experiment. Each of the ten judges paid careful attention to the words, sentences, and spontaneous speech of each implantee. For every implantee, each of the judges listened to all four recordings (preimplant and 1 month, 6 months, and 2 years postimplant) in random order before proceeding to listen to the next for each implantee. After each recording, the general quality of the implantee's speech and voice was rated by the judges. In other words, each of the judges determined which recording was the best, acceptable, bad, and worst for each implantee. The five subjects were randomly presented to each of the judges. Each judge listened to the recordings in one 20-min session.

II. RESULTS

A. Acoustical analyses

1. Fundamental frequency (F0)

Tables III and IV depict the mean fundamental frequency and standard deviation for each of the subjects at each of the recording times as measured in words and in sentences, respectively. Also shown for comparison in Table III is the average $F0$ of 30 young male and 30 young female Hebrew-speaking adults as measured in vowels of CVC monosyllabic words (Amir, 1995). Tables III and IV show that $F0$ values have decreased from preimplant to 2 years postimplant by relatively small values (6–25 and 4–20 Hz in words and sentences, respectively). Nonetheless, a one-way repeated-measures analysis of variance (ANOVA) on the data of the male implantees revealed a significant effect of recording time for words in isolation and in sentences [$F(4,12)=47.6$, $p<0.01$) and $F(4,12)=44.9$, $p<0.01$, respectively]. Further analysis showed that for both words in isolation and words in sentences, the males average $F0$ values were significantly higher before implant, compared to values 1 month postimplant [$F(1,3)=39.06$, $p<0.01$) and $F(1,3)=25.55$, $p<0.01$, respectively]. Furthermore, for words, $F0$ continued to decrease significantly from 6 months to 2 years postimplant [$F(1,3)=30.9$, $p<0.01$], whereas for sentences, $F0$ decreased significantly from 1 to 6 months postimplant [$F(1,3)=36.5$, $p<0.01$], but not from 6 months to 2 years postimplant. (Note that analyses for the males

TABLE III. Mean fundamental frequency ($F0$), in Hz, measured in isolated word context only. (Note: s.d. in parentheses; M=male, F=female, and XM=mean of male speakers only.)

Subject	Sex	Preimplant	Postimplant 1 month	Postimplant 6 months	Postimplant 2 years	Hebrew norms (Amir, 1995)
1	M	170.6 (17.9)	153.9 (9.4)	166.6 (14.7)	145.3 (10.8)	
2	M	156.3 (9.4)	172.4 (15.6)	153.7 (10.9)	144.3 (6.4)	
3	M	142.2 (20.6)	121.4 (11.3)	131 (16.8)	123.1 (13.2)	
4	M	132.2 (11.9)	124.8 (5.9)	118.6 (8.5)	138.5 (7.3)	
5	F	230.0 (16.4)	209.7 (14.7)	229 (21)	218.4 (16.3)	212[a] (31)
	XM	151 (21.3)	144.5 (24)	143.8 (22.8)	138.2 (13.1)	140[b] (27)

[a]Average $F0$ of 30 young female Hebrew-speaking adults.
[b]Average $F0$ of 30 young male Hebrew-speaking adults.

TABLE IV. Mean fundamental frequency ($F0$), in Hz, measured in words in context. (Note: s.d. in parentheses; M=male, F=female, and XM=mean of male speakers only.)

Subject	Sex	Preimplant	Postimplant 1 month	Postimplant 6 months	Postimplant 2 years
1	M	149.5 (17.1)	144.3 (11.9)	156 (13.5)	133.8 (17.3)
2	M	152.0 (19.8)	145.0 (22.1)	141.0 (19.5)	133.0 (18.7)
3	M	118.1 (20.6)	121.4 (11.3)	114.9 (14.0)	114.8 (16.1)
4	M	139.8 (20.3)	134.5 (15.8)	117.5 (6.9)	144.0 (14.1)
5	F	201.2 (30.1)	186.3 (20.2)	194 (22.8)	191.9 (37.5)
	XM	139.7 (22.8)	136.1 (19.3)	132.4 (22.2)	131.3 (19.6)

TABLE V. Mean duration of words produced in isolation (in ms). (Note: s.d. in parentheses.)

Subject	Preimplant	Postimplant		
		1 month	6 months	2 years
1	586	525	568	538
	(86)	(91)	(97)	(74)
2	672	639	625	572
	(134)	(14)	(126)	(97)
3	476	616	516	510
	(150)	(163)	(115)	(112)
4	661	623	705	632
	(90)	(79)	(83)	(71)
5	558	524	517	542
	(80)	(73)	(73)	(94)
$\bar{x}$	592	585	585	559
	(131)	(127)	(122)	(99)

TABLE VI. Mean duration of sentences (in/s). (Note: s.d. in parantheses.)

Subject	Preimplant	Postimplant		
		1 month	6 months	2 years
1	2.18	2.49	2.21	2.08
	(0.4)	(0.54)	(0.43)	(0.39)
2	2.83	3.04	2.89	2.60
	(0.40)	(0.39)	(0.35)	(0.32)
3	2.82	3.02	2.64	2.50
	(0.32)	(0.36)	(0.31)	(0.41)
4	3.23	2.83	3.16	3.25
	(0.66)	(0.5)	(0.53)	(0.65)
5	2.31	2.42	2.23	2.19
	(0.41)	(0.42)	(0.4)	(0.36)
$\bar{x}$	2.67	2.76	2.63	2.53
	(0.58)	(0.50)	(0.54)	(0.59)

were separate from the female subject because of the significant difference between the $F0$ of men and women.)

The statistical analysis also revealed a significant main effect of subject for both words and sentences [$F(3,3) = 166.27$, $p < 0.01$ and $F(3,3) = 99.25$, $p < 0.01$], respectively). The subjects differed in both the absolute values of $F0$ and the course of change over time. Note that for most subjects, the changes of $F0$ over time were not monotonic. Subjects 1 and 5, for example, showed at 1 month postimplant a decrease in $F0$, after which it increased, only to decrease again at 2 years postimplant and reached Hebrew norms. Subject 2, on the other hand, showed an increase of $F0$ at 1 month postimplant after which it decreased monotonically until it reached normal values at 24 months. Subject 3 also showed a non-monotonic decrease in $F0$ over time. In his case, however, $F0$ was within normal values before implantation and it decreased below the norms with the implant. Nonetheless, the average male $F0$ values showed a monotonic and significant $F0$ decrease over time.

For the female subject $F0$ decreased significantly after implantation [$F(1,48) = 96.7$, $p < 0.01$ and $F(1,112) = 45$, $p < 0.01$, for words and sentences, respectively]. Further significant decrease was noted only for words in isolation between 6 months to 2 years postimplant [$F(1,48) = 22$, $p < 0.01$]. On average, $F0$ decreased postimplant for both male and female cochlear implant recipients and approached Hebrew norms after 2 years with the device.

2. Duration

The average duration of the monosyllabic words and sentences for each of the five subjects, their standard deviations, and the group means are shown in Tables V and VI, respectively. For both word and sentence length, the duration of the utterance decreased from preimplant to 2 years postimplant. This decrease was significant for word duration only ($r = 0.979$, $p < 0.05$). The average decrease in utterance duration from preimplant to 2 years postimplant conditions was 27 and 280 ms for words and sentences, respectively. These differences were found to be significant [$F(1,4) = 8.93$, $p < 0.01$ and $F(1,4) = 11.27$, $p < 0.01$, respectively]. Intersubject variability is seen for the duration measurements as well. For three of the five subjects, duration of sentences increased at 1 month postimplant after which it decreased at 6 months and continued to decrease at 2 years postimplant. For one subject (subject 4), duration of sentences did not change over time.

3. Vowel formants (F1 and F2)

The average values of the first and second formants ($F1$ and $F2$) for each vowel in word context and sentence context are shown in Tables VII and VIII, respectively, for the individual implantees and the group mean. Results of one-way repeated ANOVA are summarized in Table IX. These results suggest that most of the significant changes over time occurred for $F1$ only. In the preimplant condition, mean $F1$ of male adults was abnormally high. With the implant device, values of $F1$ decreased significantly at 1 month postimplant, compared to the preimplant condition for all vowels but /o/ and /u/ in sentences for which the first significant decrease in $F1$ values was at 6 months postimplant (compared to the preimplant condition). First formant ($F1$) values continued to decrease for most vowels and context from 1 to 6 months postimplant and from 6 months to 2 years postimplant. At 2 years postimplant, the group male $F1$ values were close to normal values reported by Amir (1995) for normal-hearing Hebrew speakers. These Hebrew norms are indicated in the left panels of Fig. 1. The group mean of $F2$, on the other hand, remained relatively unchanged with one exception: the vowel /i/. For the vowel /i/, $F2$ values in isolated words increased significantly from preimplant to 6 months postimplant, after which it remained relatively unchanged. In sentence context, $F2$ values of /i/ increased from preimplant to 2 years postimplant. These formant values are also in very good agreement with $F2$ values found by Amir (1995). Note that the values of the female were not included in the group mean. In contrast to the male findings, separate analyses of the woman's data revealed no significant change in formant values as a result of the implant.

Figure 1 illustrates the acoustic vowel spaces for each of the five implantees in two of the testing conditions: preimplant and 2 years postimplant. Each vowel space was obtained by plotting the mean first- and second-formant values for each individual. While some subject-to-subject variability is evident, it is clear that for each speaker, the vowels create a well-defined triangle formed by the vowels /i/, /u/, and /a/

TABLE VII. The means of $F1$ and $F2$ (in Hz) as measured in vowels in word-only context. (Note: Recording times: Pre=preimplant; 1-m=1 month postimplant; 6-m=6 months postimplant; 2-y=2 years postimplant.)

	/i/								/e/								/a/							
	Pre		1-m		6-m		2-y		Pre		1-m		6-m		2-y		Pre		1-m		6-m		2-y	
Subject	$F1$	$F2$	$F1$	$F2$	$F1$	$F2$	$F1$	$F2$	$F1$	$F2$	$F1$	$F2$	$F1$	$F2$	$F1$	$F2$	$F1$	$F2$	$F1$	$F2$	$F1$	$F2$	$F1$	$F2$
1	496	1680	420	1622	372	1902	364	1911	644	1566	522	1505	489	1676	486	1684	710	1326	613	1319	695	1363	651	1365
	(58)	(154)	(64)	(67)	(57)	(206)	(39)	(111)	(53)	(64)	(53)	(94)	(55)	(105)	(33)	(82)	(67)	(54)	(26)	(81)	(44)	(76)	(40)	(63)
2	479	2178	409	2341	403	2265	331	2239	676	1760	616	1892	573	1700	479	1836	820	1310	808	1365	690	1277	671	1360
	(46)	(142)	(59)	(157)	(48)	(117)	(35)	(171)	(46)	(75)	(59)	(91)	(48)	(83)	(33)	(90)	(55)	(76)	(32)	(40)	(39)	(49)	(24)	(60)
3	423	2175	426	2030	359	2108	373	2022	521	1855	501	1812	489	1819	477	1755	790	1409	737	1357	734	1359	684	1301
	(40)	(72)	(40)	(58)	(16)	(95)	(31)	(111)	(41)	(52)	(12)	(57)	(34)	(79)	(24)	(109)	(51)	(88)	(43)	(60)	(28)	(74)	(33)	(50)
4	367	2159	295	2259	300	2267	289	2276	585	1750	462	1984	452	1913	455	2029	719	1435	562	1507	630	1501	645	1470
	(56)	(197)	(38)	(86)	(32)	(115)	(18)	(122)	(41)	(68)	(23)	(98)	(42)	(145)	(39)	(72)	(25)	(68)	(60)	(94)	(43)	(48)	(54)	(71)
5	379	2438	421	2463	439	2392	434	2401	505	2261	551	2306	548	2186	516	2142	791	1634	889	1673	803	1655	831	1626
	(46)	(98)	(27)	(95)	(50)	(116)	(10)	(10)	(39)	(66)	(52)	(81)	(52)	(87)	(37)	(63)	(78)	(130)	(77)	(132)	(60)	(109)	(28)	(97)
$\bar{X}^a$	447	2033	391	2053	362	2129	340	2107	607	1729	527	1794	503	1770	475	1823	761	1366	684	1382	689	1369	663	1372
	(70)	(265)	(72)	(312)	(55)	(208)	(44)	(201)	(73)	(124)	(71)	(202)	(63)	(138)	(34)	(155)	(70)	(88)	(105)	(98)	(52)	(100)	(41)	(84)

	/o/								/u/							
1	510	940	493	1004	484	1043	466	1050	407	789	399	815	362	780	333	791
	(21)	(70)	(36)	(66)	(38)	(52)	(36)	(66)	(52)	(62)	(55)	(71)	(46)	(51)	(27)	(110)
2	699	1130	672	1117	583	1084	503	1098	546	1028	496	1015	427	1013	346	958
	(56)	(88)	(35)	(59)	(22)	(43)	(29)	(66)	(72)	(63)	(70)	(74)	(50)	(84)	(26)	(99)
3	539	943	509	989	519	1005	485	952	443	868	421	871	392	946	387	949
	(29)	(102)	(19)	(78)	(25)	(68)	(27)	(80)	(49)	(31)	(31)	(70)	(26)	(52)	(19)	(69)
4	536	934	406	802	398	841	407	820	443	786	343	722	324	719	324	734
	(28)	(48)	(27)	(65)	(42)	(90)	(27)	(37)	(40)	(99)	(43)	(76)	(48)	(80)	(32)	(97)
5	640	1325	692	1386	669	1318	617	1285	429	1017	461	1046	441	1005	463	1090
	(81)	(194)	(101)	(237)	(70)	(161)	(89)	(169)	(35)	(66)	(26)	(81)	(37)	(87)	(14)	(63)
$\bar{X}^a$	573	990	523	982	497	996	466	984	461	873	417	860	377	866	347	859
	(85)	(114)	(102)	(131)	(75)	(112)	(46)	(124)	(76)	(120)	(76)	(130)	(57)	(138)	(35)	(134)

[a]X=Group average of males only, i.e., participants 1–4.

located in the extreme left upper and lower corners, and right corner, respectively. A significant change can be seen between preimplant and 2 years postimplant in values of $F1$. For all vowels, when produced both in isolation and in sentences by the male speakers, values of $F1$ decreased significantly after 2 years with the implant. This is demonstrated by the shift to the left of individual vowel spaces. It can also be seen that in three of the subjects (S1, S2, and S4), space of vowels in monosyllabic words was somewhat more restricted in range in the preimplant condition than that of 2 years postimplant. No change in the range of the vowel space was observed for the remaining two subjects (S3 and S5). In general, the spaces of vowels produced in sentences appear to be more restricted in range than spaces of vowels produced in isolated words.

4. Voice onset time (VOT)

The average VOT and standard deviation for each subject and testing condition for the voiced plosives /b, d, g/ and the voiceless plosives /p, t, k/ are shown in Table X. (Note the VOT values were measured in the monosyllabic words only.) The group mean VOT is illustrated for each of the phonemes in Fig. 2. It is apparent from the figure that the implant had an affect on VOT for the voiced plosives only. Results of one-way repeated ANOVA revealed that for each of the voiced plosives, VOT values decreased significantly (i.e., became more negative) from preimplant to 1 month postimplant, and continued to decrease significantly from 1 to 6 months postimplant. These results are summarized in Table XI. Interestingly, a significant change in direction occurred from 6 months to 2 years postimplant. At 2 years postimplant, however, the VOT values for the voiced plosives increased (i.e., became less negative) and were similar to those of Hebrew norms (Raphael *et al.*, 1995). In contrast, the VOT of the voiceless plosives did not change over time and were similar to normal values in the preimplant condition.

5. Spectral range

The mean spectral range of /s/ and /sh/ of the male speakers are shown in Fig. 3. The spectral range of /s/ for male speakers increased from a mean group of 2390–8250 Hz preimplant to 3818–9265 at 2 years postimplant. The spectral range for /sh/ shifted from 2058–6025 Hz preimplant to 1990–6608 Hz 2 years postimplant. One-way repeated ANOVA revealed that for the /s/ the minimum frequency of the frication noise increased significantly from preimplant to 6 months postimplant $[F(1,4)=12,\ p<0.01]$ and continued to increase significantly from 6 months to 2 years postimplant $[F(1,4)=10.2,\ p<0.01]$. The mean maximum frequency of the /s/ noise increased significantly only from preimplant to 2 years postimplant $[F(1,4)=26.95,\ p<0.01]$. For the /sh/ sound, the minimum and maximum frequencies of the noise range did not change significantly as a result of the implant. Thus, it appears that the changes over time measured in the frequency distribution of /s/ and /sh/

TABLE VIII. The means of $F1$ and $F2$ (in Hz) as measured in vowels in word-in-sentence context. (Note: Recording times: Pre=preimplant; 1-m=1 month postimplant; 6-m=6 months postimplant; 2-y=2 years postimplant.)

	/i/								/e/								/a/							
	Pre		1-m		6-m		2-y		Pre		1-m		6-m		2-y		Pre		1-m		6-m		2-y	
Subject	$F1$	$F2$	$F1$	$F2$	$F1$	$F2$	$F1$	$F2$	$F1$	$F2$	$F1$	$F2$	$F1$	$F2$	$F1$	$F2$	$F1$	$F2$	$F1$	$F2$	$F1$	$F2$	$F1$	$F2$
1	425	1685	369	1607	321	1747	358	1714	552	1481	468	1407	424	1566	433	1502	703	1301	583	1251	579	1325	538	1282
	(99)	(104)	(51)	(110)	(39)	(199)	(42)	(122)	(73)	(122)	(57)	(129)	(60)	(146)	(40)	(147)	(90)	(119)	(58)	(94)	(81)	(123)	(67)	(142)
2	412	2029	414	2124	410	1999	342	2113	558	1725	568	1773	535	1681	446	1680	721	1374	730	1369	656	1314	603	1410
	(49)	(165)	(58)	(128)	(40)	(165)	(49)	(112)	(43)	(112)	(39)	(106)	(48)	(138)	(61)	(157)	(58)	(90)	(50)	(80)	(46)	(75)	(60)	(90)
3	416	1877	436	1819	389	1792	380	1799	502	1638	521	1564	469	1539	479	1541	637	1292	657	1307	611	1257	614	1222
	(45)	(116)	(46)	(58)	(35)	(90)	(40)	(147)	(34)	(114)	(32)	(113)	(26)	(130)	(36)	(128)	(59)	(108)	(60)	(60)	(78)	(94)	(52)	(102)
4	379	2002	321	2107	330	2024	294	2158	528	1636	429	1740	446	1716	395	1776	658	1387	527	1466	555	1445	467	1507
	(59)	(108)	(53)	(106)	(87)	(114)	(114)	(107)	(75)	(203)	(60)	(219)	(98)	(202)	(81)	(195)	(59)	(108)	(53)	(106)	(87)	(114)	(114)	(107)
5	367	2395	375	2447	376	2360	375	2374	467	2110	501	2190	487	2015	467	2034	690	1639	743	1686	694	1659	692	1654
	(57)	(141)	(52)	(124)	(55)	(97)	(52)	(132)	(63)	(240)	(74)	(233)	(70)	(229)	(74)	(250)	(148)	(191)	(109)	(198)	(128)	(167)	(141)	(189)
$\bar{X}^a$	408	1898	385	1908	362	1890	343	1945	534	1621	495	1623	468	1626	438	1627	680	1337	623	1345	600	1334	556	1353
	(64)	(201)	(68)	(240)	(57)	(193)	(53)	(233)	(62)	(167)	(72)	(208)	(62)	(172)	(65)	(192)	(76)	(114)	(94)	(120)	(77)	(123)	(96)	(157)

	/o/								/u/							
1	492	868	474	917	385	932	416	878	392	871	375	939	361	976	336	990
	(113)	(162)	(106)	(142)	(84)	(146)	(78)	(154)	(38)	(148)	(29)	(135)	(62)	(97)	(45)	(194)
2	585	1192	594	1130	515	1071	442	1099	448	1034	470	1059	404	1064	344	1059
	(63)	(109)	(64)	(135)	(52)	(115)	(68)	(142)	(56)	(163)	(59)	(103)	(46)	(122)	(31)	(75)
3	502	902	533	978	440	926	448	930	439	912	473	968	397	959	397	927
	(76)	(151)	(59)	(126)	(41)	(133)	(42)	(112)	(23)	(103)	(39)	(123)	(33)	(98)	(29)	(141)
4	518	1028	414	980	355	963	377	993	392	905	334	910	292	907	282	819
	(67)	(189)	(50)	(197)	(65)	(262)	(90)	(213)	(13)	(141)	(50)	(168)	(84)	(218)	(68)	(90)
5	503	1199	540	1139	455	1149	433	1119	397	1073	400	1112	414	1071	392	1220
	(76)	(170)	(95)	(197)	(82)	(157)	(79)	(145)	(63)	(184)	(52)	(166)	(88)	(145)	(58)	(120)
$\bar{X}^a$	524	998	504	1001	424	973	421	975	418	930	413	969	364	976	340	949
	(87)	(197)	(97)	(166)	(92)	(177)	(73)	(177)	(43)	(148)	(75)	(139)	(72)	(147)	(60)	(155)

[a]X=Group average of males only, i.e., participants 1–4.

increased the distinction between these two phonemes. There are no Hebrew norms available, however, to compare the data with.

B. Subjective rating scales

Figure 4 illustrates the results of normal-hearing judges who were asked to assess the general quality of voice and speech of each of the five implantees in the four different testing conditions presented at random. It can be seen that over 70% of the judges concluded that the preimplant recordings as ''worst,'' in comparison to only 3% who judged the 2-year postimplant recordings as ''worst.'' In contrast, 60% of the 2-year postimplant recordings were assessed as ''best,'' compared to 10% who judged the preimplant as ''best.'' Also, a larger percent of listeners judged the 6 month postimplant to be better than the 1 month postimplant. Thus, it appears that although stimuli were all highly intelligible (although not formally tested), listeners were able to detect changes in voice quality at the different recording times.

III. DISCUSSION

The results of this study demonstrate some changes in speech production of individuals who had acquired speech patterns prior to their hearing loss and have partially restored their hearing via the Nucleus cochlear implant. These changes included lower $F0$, shorter syllable duration, decrease in values of $F1$ for vowels /i, e, a/, increased voicing lead for the voiced stops, and increase in the separation of the spectral range for fricatives. The discussion will focus primarily on three issues that are related to the results: (1) changes that may be attributed to the speakers use of the partially restored auditory information to enhance phonemic contrast and the relevance to the unique acoustics of the Hebrew language; (2) changes in acoustical parameters that may be attributed to global changes in production as a result of postural adjustments; and (3) intersubject variability.

The finding that after years of deafness $F0$ may be higher than normal is in keeping with what is generally found in the production of postlingually deafened adults (Leder *et al.*, 1987a; Leder and Spitzer, 1993) but not in all studies (Waldstein, 1990). The intersubject variability in $F0$ values was demonstrated in the present study as well. Only one (subject 1) of the two subjects that were deaf for the longest period of time (19 years) had abnormally high $F0$ values in the preimplant condition. The other subject (subject 3) had preimplant $F0$ values that were within Hebrew norms (Amir, 1995). Interestingly, Subject 1 was also deafened at the youngest age (16 years of age). Subject 2, on the other hand, was deaf for 8 years from the age of 48 and his $F0$ values in preimplant condition were also abnormally high. Langereis *et al.* (1998) and Leder *et al.* (1987a), for example, did not find an effect of age of onset and duration of deafness. In contrast, Cowie *et al.* (1982) found that age at onset of deafness was an important factor. In another attempt to explain the intersubject variability, Perkell *et al.* (1992)

TABLE IX. Results of one-way repeated measures ANOVA testing the change in formants for consecutive time periods of male speakers only. [Note: For all analyses $df=(1,3)$. $^{**}p<0.01$.]

	Preimplant versus 1 month postimplant	1 month versus 6 months postimplant	6 months versus 2 years postimplant
/i/ in			
isolated words			
*F*1	24.1**	5.3**	ns
*F*2	ns[a]	ns	ns
words in sentences			
*F*1	12.04**	16.3**	9.1**
*F*2	ns[b]	ns	ns
/e/ in			
isolated words			
*F*1	147.85**	13.43**	16**
*F*2	23.12**	ns	ns
words in sentences			
*F*1	41.99**	29.3**	27.9**
*F*2	ns	ns	ns
/a/ in			
isolated words			
*F*1	109.8**	ns	11.7**
*F*2	ns	ns	ns
words in sentences			
*F*1	161.5**	28.4**	64.8**
*F*2	ns[c]	ns	ns
/o/ in			
isolated words			
*F*1	62.6**	16.8**	23.8**
*F*2	ns	ns	ns
words in sentences			
*F*1	ns[d]	23.7**	ns
*F*2	ns	ns	ns
/u/ in			
isolated words			
*F*1	18.9**	18.9**	16.1**
*F*2	ns	ns	ns
words in sentences			
*F*1	ns[e]	29.1**	5.7**
*F*2	ns	ns	ns

[a]Preimplant versus 6 months postimplant $F=8.5^{**}$.
[b]Preimplant versus 2 years postimplant $F=8.5^{**}$.
[c]Preimplant versus 2 years postimplant $F=6.0^{**}$.
[d]Preimplant versus 6 months postimplant $F=35.0^{**}$; preimplant versus 2 years postimplant $F=58.9^{**}$.
[e]Preimplant versus 6 months postimplant $F=18.6^{**}$; preimplant versus 2 years postimplant $F=53.6^{**}$.

hypothesized that acoustic parameter values of the phonemes are determined by two factors: posture and intrinsic properties of the phoneme itself. They argue that following the restoration of some hearing some of the changes in the values of acoustic parameters may indeed be a direct result of the speaker detecting a discrepancy, for a given speech sound, between phonemic intentions and the acoustic results and making, therefore, articulatory adjustments that would bring the abnormal values into line with the phonemic intentions. Other changes, however, including changes in sound pressure level, rate of speech, syllable duration, $F0$, $F1$, and VOT, may be the result of changes in posture. The underlying assumption is that when speech transmission conditions change, the speaker responds by changing postural settings in order to ensure that speech is, for example, loud enough and slow enough to be understood (Lane *et al.*, 1995). Because phonemic and postural speech parameters are often physically interdependent, it is often difficult to separate postural changes from phonemic resetting. Thus, one cannot rule out the possibility that measured changes in acoustic values are not necessarily the result of the restored hearing on phonemic resetting, but rather the effect of posture or both. Subjects may also differ, therefore, in their postural adjustments as a result of partial restoration of hearing and not only in their use of audition for specific articulatory-acoustic adjustments.

The first significant finding is that implant activation causes a decrease in $F0$ in some of the subjects and is in keeping with much of the published data (Ball and Faulkner, 1989; Langereis *et al.*, 1998; Lane *et al.*, 1995; Leder *et al.*, 1986; Oster, 1987). Langereis *et al.* (1998), for example, found that approximately a third of their group of postlingually deafened adult subjects (4 females and 2 males from a total of 20) had abnormally high $F0$ values in the preimplant condition which decreased significantly over a 12-month period with the implant device towards normative values. Perkell *et al.* (1992), on the other hand, found a significant decrease in $F0$ value in the postimplant condition in only one of three subjects who showed abnormally high $F0$ values in the preimplant condition. In our study, $F0$ values of two subjects (3 and 5) were within the norms in the preimplant condition but decreased significantly by a small amount (12–20 Hz) by 2 years postimplant. It is possible that the $F0$ changes were secondary, unintended consequence of changes in SPL (Perkell *et al.*, 1992). Because SPL measurements of speech were not included in this study, it is difficult to substantiate this theory.

The intersubject variability reported here for the longitudinal studies is also in keeping with the intersubject variability found in studies investigating the effect of short-term auditory deprivation on $F0$ of adult cochlear implant users. Svirsky *et al.* (1992), for example, reported that their three subjects had abnormally high $F0$ after 24-h auditory deprivation period when the processor was turned off. Specifically, average $F0$ values after this period of auditory deprivation were 14–23 Hz higher than postactivation values. The effect of turning the speech processor on was found to be the same for all three subjects: a drop in $F0$ that brought them close to their post activation values. Different results were reported by Langereis *et al.* (1998). They reported a significant $F0$ difference between implant-on and implant-off conditions in only 5 of their 20 subjects. The discrepancy in the results were explained by the much shorter duration of the implant off condition (30 min) in Langereis *et al.* study. Again, one cannot rule out the possibility that changes in $F0$ were secondary to changes in SPL.

The second significant finding, decrease in word duration in postimplant conditions, is also consistent with the published data (Lane *et al.*, 1998; Leder *et al.*, 1986; Oster, 1987; Perkell *et al.*, 1992; Plant and Oster, 1986; Tartter *et al.*, 1989; Waters, 1986). Investigators have observed that postlingually deafened adults have significantly longer sentence duration (Kirk and Edgerton, 1983; Lane and Webster, 1991; Lane *et al.*, 1998) which is a result of significantly longer syllables (Lane and Webster, 1991; Leder *et al.*,

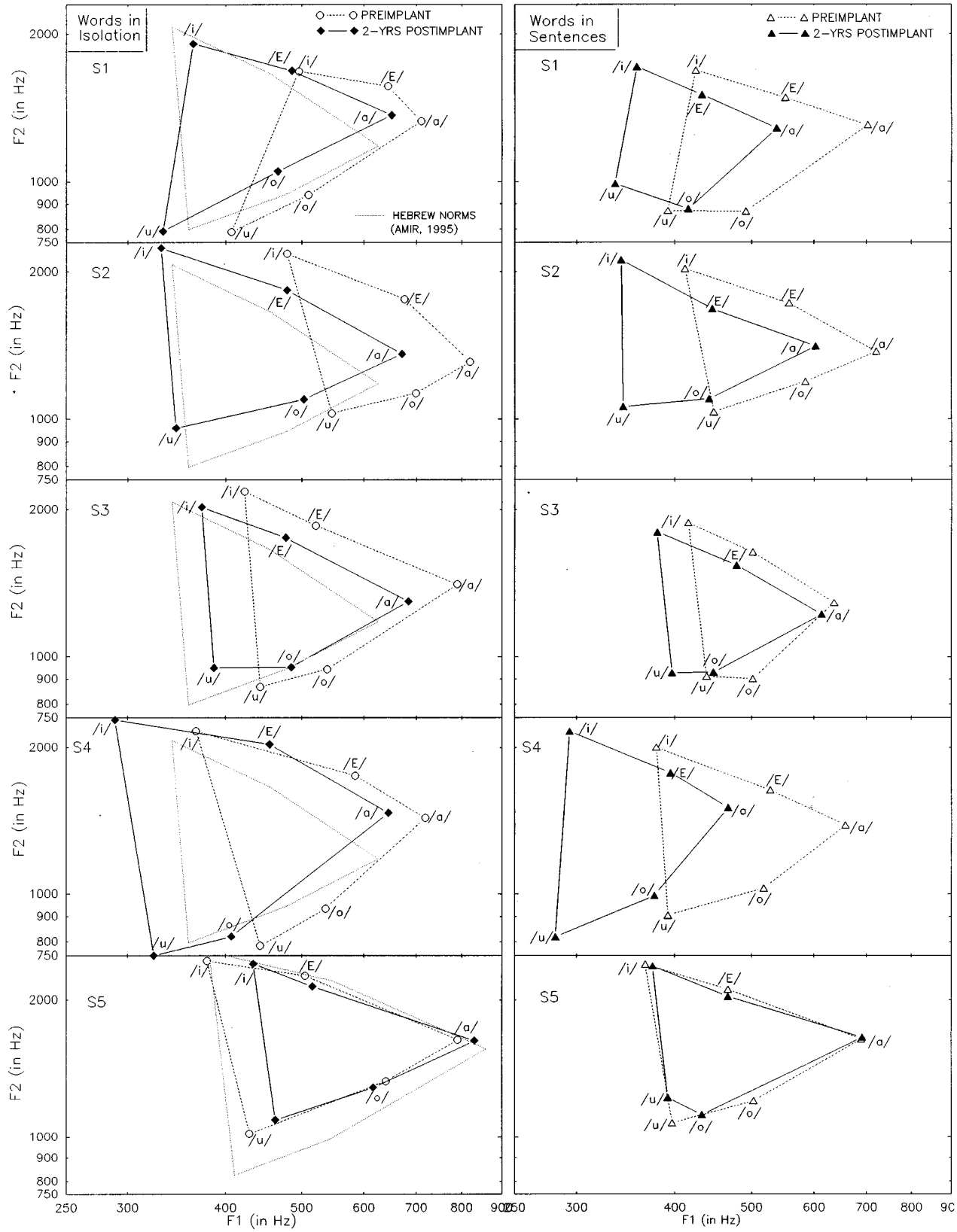

FIG. 1. Acoustic vowel space for each postingually deafened adult before implant and 2 years postimplant measured in word-only context (left side) and word-in-sentence context (right side). Also shown for each subject are the normative formant values in Hebrew (from Amir, 1995).

1987b), pause duration (Lane and Webster, 1991), and vowel duration (Waldstein, 1990). Lane *et al.* (1998) found that all of their seven postlingually deafened adults spoke at articulation rates below the normative range. After implant activation, five of the speakers increased articulation rate, one did not change, and one decreased. Lane *et al.* argued that slower reading rates are associated with ''clear speech'' and with greater intelligibility and are therefore used to achieve

TABLE X. Mean voice-onset-time (in ms) for (a) voiced stops and (b) voiceless stops, in initial word position.

(a)

	Preimplant			Postimplant								
				1 month			6 months			2 years		
Subject	/b/	/d/	/g/	/b/	/d/	/g/	/b/	/d/	/g/	/b/	/d/	/g/
1	11.3	8.6	33	3.3	27.6	−59	−161.6	−146.6	−112.8	−76.3	−141.6	−77.6
	(19.6)	(15)	(8.3)	(5.8)	(11)	(59.6)	(9.1)	(24.4)	(15.8)	(67.6)	(10.4)	(18.6)
2	0	37	58	−22.3	8.0	45.8	−205.6	−187	−152.4	−117.6	−88.3	−94.2
	(0)	(6.1)	(20.7)	(38.7)	(49.7)	(21.5)	(23.8)	(14.7)	(41.3)	(51.7)	(56.4)	(10.7)
3	12.3	18.7	33.4	13	25	36.6	−86.3	−2.3	−44.2	−11.6	16.6	−50.4
	(10.7)	(6.1)	(13.2)	(4.4)	(2.0)	(10.1)	(10.5)	(28.3)	(33.1)	(20.2)	(2.5)	(77.9)
4	−91.3	−87	−92.6	−119.3	−97.3	−61.4	−83.6	−155	−127.8	−107	−100.6	−106
	(24.8)	(33)	(15.5)	(10.5)	(26.7)	(54.1)	(53.2)	(24.5)	(37)	(59.6)	(9.0)	(20.5)
5	−66.3	−97	−14.2	−117.3	−112.6	−54.4	−88.0	−73.5	−67.2	−129	−87.3	−61.8
	(60.4)	(14.2)	(65.5)	(45.5)	(12.9)	(43.8)	(40.7)	(10.6)	(52.1)	(27.6)	(30.6)	(52.4)
Mean	−26.8	−24	3.4	−48.5	−29.8	−18.4	−125	−115.7	−100.8	−88.3	−80.2	−77.9
	(51.)	(60.3)	(61.9)	(64.4)	(67.8)	(63)	(58.4)	(73)	(53.1)	(60.1)	(59.6)	(45.2)

(b)

	Preimplant			Postimplant								
				1 month			6 months			2 years		
Subject	/p/	/t/	/k/	/p/	/t/	/k/	/p/	/t/	/k/	/p/	/t/	/k/
1	22.6	33.6	70.0	27.3	28.4	82.2	17.6	31.0	72.0	35.0	27.4	67.8
	(11.9)	(13.5)	(12.4)	(13.8)	(19.2)	(7.7)	(15.7)	(12.0)	(17.0)	(4.4)	(4.8)	(12.6)
2	19.8	35.0	85	13.0	32.4	50.2	16.5	36.8	62.8	16.3	49.2	68.0
	(14.7)	(7.7)	(36.5)	(1.8)	(11.5)	(9.0)	(11.0)	(12.6)	(27.6)	(10.6)	(10.6)	(6.2)
3	13.0	19.8	48.2	22	27.4	62.0	10.5	20.6	40.2	11.0	20.8	50.2
	(3.6)	(2.5)	(20.0)	(9.3)	(5.5)	(13.7)	(3.5)	(5.7)	(17.3)	(2.9)	(3.7)	(13.7)
4	23.0	22.2	64.2	25.5	30.3	57.8	14.0	25.8	53.6	31.0	23.0	59.4
	(6.5)	(8.0)	(34.7)	(12.1)	(3.3)	(19.0)	(3.7)	(5.2)	(7.4)	(4.4)	(2.4)	(11.3)
5	15.3	23.6	68.4	11.3	12.6	60.8	21.3	19.2	51.0	36.5	19.8	66.0
	(7.1)	(5.3)	(20.2)	(4.9)	(5.0)	(18.8)	(14.6)	(7.9)	(7.2)	14.5)	(2.2)	(14.3)
Mean	19.7	27.1	67.1	19.4	26.0	62.6	15.8	26.7	55.9	25.1	28.0	62.2
	(9.8)	(9.9)	(26.9)	(10.4)	(12.2)	(17.0)	(10.0)	(10.9)	(19.0)	(13.4)	(12.2)	(22.1)

better transmission conditions. Once hearing is partially restored and transmission conditions are improved, the speaker increases his rate of articulation. Lane *et al.* concluded their findings in that some changes are the result of postural adjustments. The reduced word and sentence duration after implant activation found in the present study are also in keeping with Perkell *et al.* (1992) model. These results, together with our finding that $F1$ decreases significantly after hearing is partially restored, provide further support to the model and its hypothesis that $F1$ and speech rate covary. The argument, however, that led Perkell and colleagues to hypothesize the relationship between $F1$ and duration is not convincing in relation to our results. They argued that increase in speech rate should induce decrease vowel duration which in turn should ''allow less time for tongue body lowering for low vowels, leading to an average increase in their tongue height and a decrease in their values of $F1$'' (Perkell *et al.*, 1992; p 2973). One would assume, however, that reduced duration would presumably result in less time for both lowering and

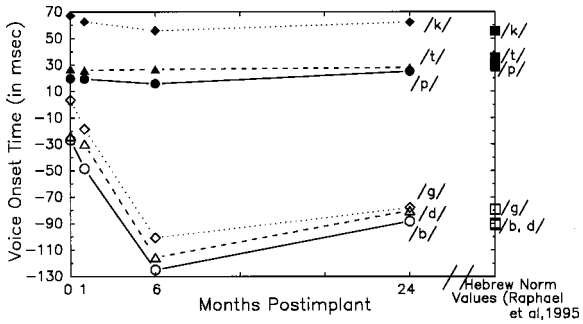

FIG. 2. Mean group VOT for voiced and voiceless stops before and 1 month, 6 months, and 2 years postimplant. Also shown are the normative VOT in Hebrew (from Raphael *et al.*, 1995).

TABLE XI. Results of one-way repeated measures ANOVA testing the change in VOT for voiced plosives between consecutive time periods. [Note: For all analyses $df=(1,4)$. $p<0.05$, $^{**}p<0.01$.]

	Preimplant versus 1 month postimplant	1 month versus 6 months postimplant	6 months versus 2 years postimplant
/b/	5.6*	85.2**	6.6*
/d/	ns[a]	78.7**	10.8**
/g/	5.2*	71**	6.8*

[a]Preimplant versus 6 months postimplant $F=107.7^{**}$; preimplant versus 2 years postimplant $F=47.5^{**}$.

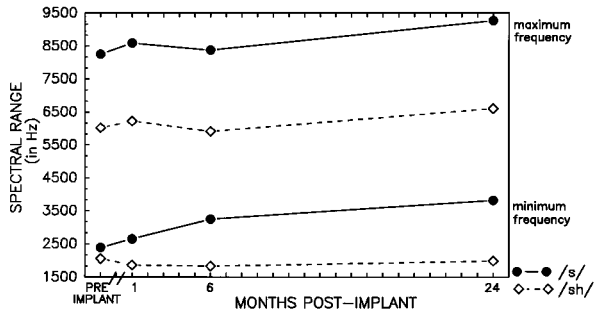

FIG. 3. Group mean range of spectral distribution for the /s/ and /sh/ sibilants before and 1 month, 6 months, and 2 years postimplant.

raising the tongue body. If that were the case, then we would expect reduced $F1$ for the low vowels and increased $F1$ for the high vowels. The data, however, show that $F1$ decreased for all vowels and all subjects. In terms of perception, all subjects were not able to perceive the vowels based on differences in tongue height. Results of the vowel height subtest of the SPAC test originally developed by Boothroyd (1984) and adapted into Hebrew (Kishon-Rabin, 1999) showed that all subjects scored between 0% and 58% (after correcting for guessing). As explained previously, the implant may fail to provide information on vowel height because $F1$ values of different vowels may ''fall'' within the same channel or adjacent channels. The finding that subjects decreased $F1$ even though they were not able to discriminate between vowels that differ by tongue height may support the idea of some global speech changes that may have a secondary effect on $F1$.

In contrast to published data (Langereis *et al.*, 1997; Perkell *et al.*, 1992), our third finding is that $F2$ values were almost unaffected by the hearing loss with the exception of /i/ and /a/, and, for these vowels, only slight changes were noted and not for all subjects. The biggest change was a 231-Hz $F2$ increase for subject 1 who was, as noted, deafened at the youngest age and for the longest period of time. Although statistically significant increases were measured for the vowel /a/, they mounted to 40–50 Hz only. The fact that the Hebrew vowel system includes only five vowels /a, e, i, o, u/, with most of them being (extreme) point vowels, may explain why no vowel space reduction was observed in contrast to reports of others (Economou *et al.*, 1992; Langereis *et al.*, 1997; Smyth *et al.*, 1991). The effect of implant activation on the vowels of postlingually deafened adults needs to be further investigated in languages with few vowels like Spanish, for example. Also, studies that would compare the change of intelligibility of the vowels (after implant activation) with their acoustics may provide insight as to whether the changes are a result of a need to enhance phonemic contrast.

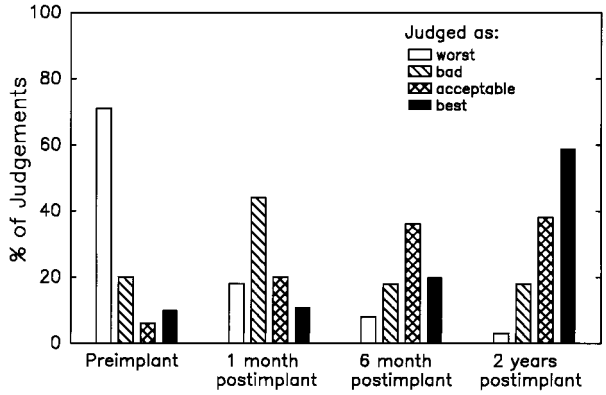

FIG. 4. Subjective rating of judges before and 1 month, 6 months, and 2 years postimplant.

The fourth important finding of this study is the significant change in VOT, a change towards Hebrew norms, for the voiced stops after hearing was partially restored. In the preimplant recording, the Hebrew speakers maintained a bimodal VOT distribution, although separation between the categories was small. Specifically, for three of the speakers, short voice lags were produced for the voiced plosives which is abnormal compared to the large voicing lead reported by Raphael *et al.* (1995) for VOT of Hebrew voiced stops. One speaker (subject 4) had VOT values that were within normal values of normally hearing Hebrew speakers and the female speaker (subject 5) had short voicing lead only for /g/. Waldstein (1990) reported that all but one of her postlingually deafened speakers produced voiceless plosives with shorter than normal VOT and showed less than normal differences in VOT between the voiced and voiceless cognates, although differences between the voice/voiceless plosives were evident. The one exception to her results was a speaker deafened at age 40 whose productions were within the range of normally hearing speakers. In contrast, the two subjects who showed the most abnormal VOT values where deafened at childhood. Lane *et al.* (1994) reported that their four postlingually deafened adults had VOT values that were shorter than normal or close to normal before implantation. Nonetheless, their subjects also maintained a distinct difference in the VOT of their voiced and voiceless plosives before receiving their implants. This finding is consistent with the idea that postlingually deafened adults have a robust internal model of the relation between articulatory commands and the desired acoustic-phonetic result, a model that continued to serve them when hearing was lost (Lane *et al.*, 1994). Interestingly, the most vulnerable sounds are those with greater absolute values of VOT (voiceless plosives in English, voiced ones in Hebrew). Insight into this issue can be obtained by further investigating the effect of deafness in postlingually deafened adults in languages that have voicing lead and intermediate or short lags (like Hebrew) compared to languages with short and long lags (like English).

With activation of the implant processors, exaggerated voicing lead was observed for four of the speakers at various points in time. After 2 years with the implant, VOT values were within normal ranges. The exception was subject 3, who failed to show significant voicing lead for /d/ even after 2 years postimplant and values of VOT for /g/ and /b/ that approached Hebrew norms. These results can be partially explained by the abilities of these subjects to perceive the voicing contrast. The results of the initial voicing subtest of the Hebrew SPAC test (Kishon-Rabin, 1999) show that after

2 years of implant use, subject 3 scored 0% (after correcting for guessing) whereas subjects 1, 4, and 5 scored 100%, 66.67%, and 91.67% (after correcting for guessing), respectively. (No voicing data are available for subject 2 because he died shortly after the last recording.) Lane *et al.* (1994) argued that the ability to perceive and produce the voicing contrast provides support to the hypothesis that temporal envelope cues of initial voicing are readily available to the implant users. For all their speakers changes were apparent in both the production of the voiced plosives and in the ability to perceive the voice/voiceless contrast in the initial position. Lane *et al.*'s subjects, however, used the Ineraid cochlear implant that is designed to provide temporal cues. The subjects in the present study are using the Nucleus WSP-III implant device processor that extracts $F0$, $F1$, and $F2$. It is assumed that these subjects were able to perceive the relative timing of $F0$ and the release of the stop, thus not necessarily relying on information from the envelope. In this study, reasonably accurate perception of plosive voicing in initial position yielded accurate production after 2 years of implant use. Inability to perceive voicing (subject 3) yielded inaccurate production. These findings are not entirely in keeping with Lane *et al.* (1994), whose subjects had reasonable voicing perception but inaccurate production although gradual changes in VOT towards English normative values were reported in three of the four speakers when some hearing was restored. The findings reported here also do not support the hypothesis that duration was decreased due to increase of speech rate. Lane *et al.* (1995) found an inverse relationship between speech rate and VOT: the faster the speech then the shorter the VOT. The results reported here show both increase in VOT and decrease in duration after implant activation. This issue needs to be further explored. In general, however, the findings reported here are consistent with the hypothesis that timing relationship, such as the one involved in the production of voiced stops, is vulnerable in postlingually deafened adults. Furthermore, most subjects were able to perceive and utilize voicing information from their implant device. Finally, it should be noted that the effect of place of articulation is evident in the present data for both voiced and voiceless stops in the pre- and postimplant conditions. Prevoicing became less pronounced as place of articulation moved further back in the vocal tract, i.e., labial to alveolar to velar. Similarly, voice lag was greater as place of articulation moved from /p/ to /k/. These results are in keeping with published data (Waldstein, 1990).

The fifth significant finding is the shift of the lower and upper frequency boundaries of the spectral range for the sibilant /s/. These results support previous findings that fricatives are vulnerable to deterioration following deafening (Lane and Webster, 1991; Tartter *et al.*, 1989). They also are in keeping with the general finding that postlingually deafened adults continue to differentiate between the two fricatives, regardless of their hearing status (Lane and Webster, 1991). Once hearing was restored, the absolute frequency values of the spectral range of /s/ increased significantly, whereas the spectrum of /sh/ remained relatively unchanged. This frequency shift resulted in a more distinct separation in the spectral ranges of the two sibilants, as reported by Economou *et al.* (1992) on one subject and by Matthies *et al.* (1996). The acoustic cues for the sibilants are mediated by the spectral distribution of the noise. When no auditory feedback was provided, the postlingually deafened adults seemed to maintain an intelligible /s/ and /sh/, although the frequencies of /s/ were lowered. With the implant, the spectral range of the frication noise shifted towards the higher frequencies. This occurred despite the fact that the information provided by the implant is limited to $F0$ and formant information up to 4000 Hz. It appears that the implant users were able to utilize some information and increase the lower end of the spectral range. By doing so, an automatic increase in the upper frequency of the range occurred, thus maintaining a fixed spectral range.

The sixth significant finding is that the listeners judged the general voice and speech quality of the preimplant recordings as the worst, the 2-year postimplant recordings as best, and the 1- and 6-months postimplant recordings in between. These results, in keeping with most published data (Economou *et al.*, 1992; Read, 1989; Tartter *et al.*, 1989; Waters, 1986), suggest that although the speech of the postlingual deafened adults was highly intelligible, the effect of the hearing loss and implant on speech was pronounced enough not only to be measured in different acoustic parameters, but to be perceived by normal-hearing listeners. It is possible that the suprasegmental characteristics contributed the most to the subjective judgment of voice quality. However, one cannot rule out the effect of the segmental characteristics on these judgments as well. Future studies should include speech intelligibility tests in order to quantify the ''normalcy'' of the subjects' speech production.

IV. SUMMARY AND CONCLUSIONS

In summary, the results of the present study demonstrate that speech of adults with acquired deafness may degrade in subtle ways as a result of the hearing loss, even though the phonemically distinct productions of speech sounds seem to be maintained. This last issue was not formally evaluated and needs to be in future studies. Furthermore, once hearing is partially restored via the cochlear implant, some of these individuals appear immediately to utilize the new auditory-electro feedback to calibrate their speech. With the implant device, changes were observed in suprasegmental features, such as decrease in $F0$ and utterance duration, as well as in segmental features such as decrease in $F1$ and improved phonetic distinctiveness between voiced and voiceless sounds, and between the /s/ and /sh/ sounds, although large intersubject variability was noted. The continued contribution of partially restored hearing to the production of these speech parameters was evident until the final recording at 2 years postimplant suggesting that calibration is not immediate, but occurs over time. How much time is actually needed may depend on individual characteristics, such as age at onset of deafness, years of deafness, use of auditory feedback or alternative feedback systems for speech production, and auditory perception skills. In order to be able to determine the exact course of change, recordings should be obtained in more discrete intervals. The findings of a decrease in $F0$, syllable duration, and $F1$ are in keeping with the model pro-

posed by Perkell *et al.* (1992) in that the observed changes of certain speech parameters are an indirect consequence of intentional changes in other articulatory parameters. This theory has been supported by empirical data which showed that many of the changes in acoustic parameter values with the partial restoration of hearing were found to be correlated (Lane *et al.*, 1994, 1995; Perkell *et al.*, 1992). The present study, however, was not designed to separate the possible factors that may be contributing to the measured acoustical changes. The results of the present study are specific to the WSP-III processor. One would expect that with newer speech coding strategies, different information would be available to the implant user that would improve speech perception, and as a result this information could be used to restore the distinctiveness between certain speech sounds. Finally, this study showed results of the effect of deafness and partial restoration of hearing in postlingually deafened adults in Hebrew, a language that differs phonemically and acoustically from English. The suprasegmental changes that occurred are similar to English and appear to be not language related, possibly related to postural adjustments. Other changes such as decrease in $F1$ and changes in VOT need to be further investigated in languages that are more similar to Hebrew and, alternatively, in other languages that are more similar in their vowel system and voicing categories to English.

ACKNOWLEDGMENTS

The authors gratefully acknowledge Emma Sachratov for her technical support and Esther Shabtai for assistance in data analyses.

Amir, O. (**1995**). ''The Hebrew vowel system—An acoustical study,'' unpublished master's thesis. Tel-Aviv University, Israel.

ANSI (**1989**). Specifications for Audiometers (ANSI, New York).

Ball, G., and Faulkner, A. (**1989**). ''Speech production of postlingually deafened adults using electrical and acoustic speech pattern prostheses,'' Speech, Hearing, and Language: Work in Progress (U.C.L.) **3**, 13–32.

Berman, R. (**1997**). ''Modern Hebrew,'' in *Semetic Languages*, edited by R. Hetzron (University Publishing Projects, Tel-Aviv).

Binnie, C., Daniloff, R., and Buckingham, H. (**1982**). ''Phonetic disintegration in a five-year old following sudden hearing loss,'' J. Speech Hear. Disord. **47**, 181–189.

Boothroyd, A. (**1984**). ''Auditory perception of speech contrasts by subjects with sensorineural hearing loss,'' J. Speech Hear. Res. **27**, 134–144.

Boothroyd, A. (**1986**). *Speech Acoustics and Perception* (Pro-Ed, Austin).

Borden, G. J., Harris, K. S., and Raphael, L. J. (**1994**). *Speech Science Primer* (Williams and Wilkins, Baltimore).

Cowie, R., and Douglas-Cowie, E. (**1983**). ''Speech production in profound postlingual deafness,'' in *Hearing Science and Hearing Disorders*, edited by M. Lutman and M. Haggard (Academic, New York).

Cowie, R., Douglas-Cowie, E., Phil, D., and Kerr, A. G. (**1982**). ''A study of speech deterioration in post-lingually deafened adults,'' J. Laryngol. Otol. **96**, 101–112.

Davidson, I. (**1959**). ''Sidetone delay, reading rate, articulation and pitch,'' J. Speech Hear. Res. **2**, 266–270.

Economou, A., Tartter, V. C., Chute, P. M., and Hellman, S. A. (**1992**). ''Speech changes following reimplantation from a single-channel to a multichannel cochlear implant,'' J. Acoust. Soc. Am. **92**, 1310–1323.

Elman, J. (**1981**). ''Effects of frequency-shifted feedback on the pitch of vocal productions,'' J. Acoust. Soc. Am. **70**, 45–50.

Goehl, H., and Kaufman, D. (**1984**). ''Do the effects of adventitious deafness include disordered speech.'' J. Speech Hear. Disord. **13**, 397–418.

Harshav, B. (**1993**). *Language in Time of Revolution* (Univ. of California, Berkeley).

Houde, J. F., and Jordan, M. I. (**1998**). ''Sensorimotor adaptation in speech production,'' Science **279**, 1213–1216.

Kirk, K., and Edgerton, B. J. (**1983**). ''The effects of cochlear implant use on voice parameters,'' Otolaryngol. Clin North Am. **16**, 281–292.

Kishon-Rabin, L. (**1999**). ''Assessment of speech perception in hearing impaired children,'' J. Israeli Speech Lang. Hear. **21**, 99–110.

Kishon-Rabin, L., Tatelbaum, R., Segal, O., Henkin, Y., Tene, S., Muchnik, C., Kronnenberg, J., and Hildesheimer, M. (**1998**). ''Long-term use of cochlear implants in prelingually deaf children: Sensory evidence and the use of context,'' presented at the 4th European Symposium on Pediatric Cochlear Implantation, s'Hetrogenbosch, The Netherlands.

Lane, H. L., and Tranel, B. (**1971**). ''The Lombard sign and the role of hearing in speech,'' J. Speech Hear. Res. **14**, 677–709.

Lane, H. L., and Webster, J. (**1991**). ''Speech deterioration in postlingually deafened adults,'' J. Acoust. Soc. Am. **89**, 859–866.

Lane, H. L., Wozniak, J., and Perkell, J. (**1994**). ''Changes in voice-onset time in speakers with cochlear implants,'' J. Acoust. Soc. Am. **96**, 56–64.

Lane, H. L., Wozniak, J., Matthies, M., Svirsky, M., and Perkell, J. (**1995**). ''Phonemic resetting versus postural adjustments in the speech of cochlear implant users: An exploration of voice-onset time,'' J. Acoust. Soc. Am. **98**, 3096–3106.

Lane, H. L., Perkell, J., Wozniak, J., Manzella, J., Guiod, P., Matthies, M., MacCollin, M., and Vick, J. (**1998**). ''The effect of changes in hearing status on speech sound level and speech breathing: A study conducted with cochlear implant users and NF-2 patients,'' J. Acoust. Soc. Am. **104**, 3059–3069.

Langereis, M. C., Bosman, A. J., van Olphen, A. F., and Smoorenburg, G. F. (**1997**). ''Changes in vowel quality in post-lingually deafened cochlear implant users,'' Audiology **36**, 279–297.

Langereis, M. C., Bosman, A. J., van Olphen, A. F., and Smoorenburg, G. F. (**1998**). ''Effect of cochlear implantation on voice fundamental frequency in post-lingually deafened adults,'' Audiology **37**, 219–230.

Leder, S. B., and Spitzer, J. B. (**1990**). ''Longitudinal effects of single-channel cochlear implantation on voice quality,'' Laryngoscope **100**, 395–398.

Leder, S. B., and Spitzer, J. B. (**1993**). ''Speaking fundamental frequency, intensity, and rate of adventitiously profoundly hearing-impaired adult women,'' J. Acoust. Soc. Am. **93**, 2146–2151.

Leder, S. B., Spitzer, J. B., Kirchner, J., Phillips, C., Milner, P., and Richardson, F. (**1987a**). ''Voice intensity of prospective cochlear implant candidates and normal hearing males,'' Laryngoscope **97**, 224–227.

Leder, S. B., Spitzer, J. B., Milner, P., Phillips, C., Richardson, F., and Kirchner, J. (**1986**). ''Reacquisition of contrastive stress in an adventitiously deaf speaker using a single channel cochlear implant,'' J. Acoust. Soc. Am. **79**, 1967–1974.

Leder, S. B., Spitzer, J. B., Phillips, C., Milner, P., Kirchner, J., and Richardson, F. (**1987b**). ''Speaking rate of adventitiously deaf male cochlear implant candidates,'' J. Acoust. Soc. Am. **82**, 843–846.

Matthies, M. L., Svirsky, M. A., Lane, H. L., and Perkell, J. S. (**1994**). ''A preliminary study of the effects of cochlear implants on the production of sibilants,'' J. Acoust. Soc. Am. **96**, 1367–1373.

Matthies, M. L., Svirsky, M. A., Perkell, J. S., and Lane, H. L. (**1996**). ''Acoustic and articulatory measures of sibilant production with and without auditory feedback from a cochlear implant,'' J. Speech Hear. Res. **39**, 936–946.

Osberger, M., and McGarr, N. (**1982**). ''Speech production characteristics of the hearing impaired,'' in *Speech and Language: Advances in Basic Research and Practice*, edited by N. Lass (Academic, New York).

Oster, A. M. (**1987**). ''Some effects of cochlear implantation on speech production,'' Speech Transmission Lab. Q. Prog. Stat. Rep. **1**, 81–89.

Peterson, G. E., and Barney, H. L. (**1952**). ''Control methods used in a study of vowels,'' J. Acoust. Soc. Am. **24**, 175–184.

Perkell, J. S., Lane, H. L., Svirsky, M. A., and Webster, J. (**1992**). ''Speech of cochlear implant patients: A longitudinal study of vowel production,'' J. Acoust. Soc. Am. **91**, 2961–2978.

Plant, G. (**1984**). ''The effects of an acquired profound hearing loss on speech production,'' Br. J. Audiol. **18**, 39–48.

Plant, G. (**1993**). ''The speech of adults with acquired profound hearing losses: I. A perceptual evaluation,'' Eur. J. Disord. Commun. **28**, 273–288.

Plant, G., and Oster, A. (**1986**). ''The effects of cochlear implantation on speech production. A case study,'' Speech Transmission Lab. Q. Prog. Stat. Rep. **1**, 65–84.

Raphael, L. G., Tobin, Y., Faber, A., Most, T., Kollia, B. H., and Milstein,

D. (**1995**). ''Intermediate Values of voice onset time,'' in *Producing Speech: Contemporary Issues for Katherine Safford Harris*, edited by F. Bell-Berti and L. J. Raphael (AIP, New York).
Read, T. (**1989**). ''Improvement in speech production following use of the UCH/RNID cochlear implant,'' J. Laryngol. Otol. Suppl. **18**, 45–49.
Richardson, L. M., Busby, P. A., Blamey, P. J., Dowell, R. C., and Clark, G. M. (**1993**). ''The effects of auditory feedback from the Nucleus cochlear implant on the vowel formant frequencies produced by children and adults,'' Ear Hear. **14**, 339–349.
Sapir, S., and Canter, G. J. (**1991**). ''Postlingual deaf speech and the role of audition in speech production: Comments on Waldstein's paper,'' J. Acoust. Soc. Am. **90**, 1672–2978.
Smyth, V., Murdoch, B. E., McCormack, P., and Marshall, I. (**1991**). ''Objective and subjective evaluation of subjects fitted with the cochlear multichannel cochlear prostheses: 3 studies,'' Austral. J. Human Comm. Disord. **19**, 32–52.
Svirsky, M. A., and Tobey, E. A. (**1991**). ''Effect of different types of auditory stimulation on vowel formant frequencies in multichannel cochlear implant users,'' J. Acoust. Soc. Am. **89**, 2895–2904.
Svirsky, M. A., Lane, H. L., Perkell, J. S., and Wozniak, J. (**1992**). ''Effects of short-term auditory deprivation on speech production in adult cochlear implant users,'' J. Acoust. Soc. Am. **92**, 1284–1300.
Tartter, V. C., Chute, P. M., and Hellman, S. A. (**1989**). ''The speech of a postlingually deafened teenager during the first year use of a multichannel cochlear implant,'' J. Acoust. Soc. Am. **86**, 2113–2121.
Tobey, E. A. (**1993**). ''Speech production,'' in *Cochlear Implants: Audiological Foundations*, edited by R. S. Tyler (Singular, San Diego).
Tobin, Y. (**1997**). *Phonology as Human Behavior: Theoretical Implications and Clinical Applications* (Duke U. P., Durham).
Waldstein, R. S. (**1990**). ''Effects of postlingual deafness on speech production: Implications for the role of auditory feedback,'' J. Acoust. Soc. Am. **88**, 2099–2114.
Waters, T. (**1986**). ''Speech therapy with cochlear implant wearers,'' Br. J. Audiol. **20**, 35–43.
Zimmermann, G., and Rettaliata, P. (**1981**). ''Articulatory patterns of an adventitiously deaf speaker: Implications for the role of auditory information in speech production,'' J. Speech Hear. Res. **24**, 169–178.

Three-dimensional tongue surface reconstruction: Practical considerations for ultrasound data

Andrew J. Lundberg[a)]
Department of Computer Science, Johns Hopkins University, 3400 North Charles Street, Baltimore, Maryland 21218

Maureen Stone
Division of Otolaryngology, University of Maryland Medical School, 16 South Eutaw Street, Suite 500, Baltimore, Maryland 21201

(Received 8 September 1998; revised 10 June 1999; accepted 29 June 1999)

This paper discusses methods for reconstructing the tongue from sparse data sets. Sixty ultrasound slices already have been used to reconstruct three-dimensional (3D) tongue surface shapes [Stone and Lundberg, J. Acoust. Soc. Am. **99**, 3728–3737 (1996)]. To reconstruct 3D surfaces, particularly in motion, collecting 60 slices would be impractical, and possibly unnecessary. The goal of this study was to select a sparse set of slices that would best reconstruct the 18 measured speech sounds. First a coronal sparse set was calculated from 3D surface reconstructions. Selection of contours was globally optimized using coarse to fine search. Sparse and dense reconstructions were compared using maximum error, standard deviation error, and surface coverage. For all speech sounds, maximum error was less than 1.5 mm, standard deviation error was less than 0.32 mm, and average reconstruction coverage was 80%. To generalize the method across subjects, optimal slice locations were calculated from only the midsagittal contour. Six midsagittal points were optimized to reconstruct the midsagittal contour. Corresponding coronal slices were then used to reconstruct 3D surfaces. For data collection planning, a midsagittal sample can be collected first and optimal coronal slices can be determined from it. Errors and reconstruction coverage from the midsagittal source set were comparable to the optimized coronal sparse set. These sparse surfaces reconstructed static 3D surfaces, and should be usable for motion sequences as well. [S0001-4966(99)03610-3]

PACS numbers: 43.70.Jt [AL]

INTRODUCTION

Ultrasound imaging has been used to represent tongue positions for over 15 years (Sonies *et al.*, 1981; Keller and Ostry, 1983; Stone *et al.*, 1983). Like other imaging systems, it provides a 2D measurement of the tongue surface contour in a single plane (such as midsagittal, coronal, or oblique). One strength of ultrasound is that it images tongue contour movement using a fairly rapid frame rate (30 Hz). Another is that contours from several spatial planes can be reconstructed into 3D surfaces (Stone and Lundberg, 1996). However, as ultrasound collects 2D slices, the subject must repeat the speech corpus once for each desired slice. Also, both contours and surfaces are represented by many points. Thus, compact quantification of movement is difficult in the case of contours and even more difficult in the case of surfaces. Two improvements of the ultrasound technique would radically increase its usefulness: reduced dimensionality of a tongue contour or surface, and accurate representation of surface motion. Prior research has accurately represented static 3D tongue surface shapes from dense data sets of ultrasound images (Stone and Lundberg, 1996). The present paper presents methodology to accurately represent static 3D tongue surface shapes and motion from sparse data sets of ultrasound images. The method also reduces the dimensionality of tongue surface representation and maintains highly accurate reproduction of local deformation features. This modification is an essential step if multi-plane tongue movements are to be reconstructed practically into tongue surface movements. Ultrasound has been shown to be a useful tool for collecting 3D tongue surface data. It is noninvasive, has no exposure limits, and is relatively inexpensive ($20 000 USD).

In previous research, a series of 2D images was used for reconstructing a detailed 3D view of the tongue surface (Stone and Lundberg, 1996). This required a special transducer, however, which collected 60 slices in a polar sweep of 60 degrees in 10 s. While this was feasible for a 3D static speech sample, this method is too slow for 4D data collection (3D surfaces moving in time). As there are not yet any 3D ultrasound devices that simultaneously collect multiple 2D slices in motion, any 4D sample would need to be repeated N times (where N is the number of slices to be used in the reconstruction).

The motion of three-dimensional tongue surfaces is of interest because the tongue is a complex system that is critical in speaking, swallowing, and breathing. The tongue is a volume preserving, deformable object. That is, tongue shape is systematically related to tongue position, because tongue volume can be redistributed, but not increased or decreased. Complicated tongue surface shapes can be produced in 2D and 3D due to the complex distribution of the tongue's

a)Electronic mail: lundberg@cs.jhu.edu

muscles and its lack of bony tissue (Kier and Smith, 1985). The intrinsic muscles originate and insert on soft tissue; the extrinsic muscles also insert on soft tissue, thus insuring deformation with every movement. Contracting various muscles and contacting the palate allows complicated shapes to be made. Subtle changes in these shapes reflect difference due to coarticulation (Stone and Lele, 1992), dialect and language (Stone and Yeni-Komshian, 1991), and speech disorders (Stone, 1995). In order to capture subtle shape changes due to these factors, especially over time, accurate tongue surface representation is essential.

The present study used the database acquired in Stone and Lundberg (1996) to determine a minimal number, or sparse set, of coronal slices needed for reasonable reconstructions. The specific coronal slices to collect must be specified, as well as what error tolerances define a reasonable reconstruction. Earlier work (Miyawaki *et al.*, 1975; Stone, 1990) suggested that 3D tongue surface shape could be adequately specified using five lengthwise segments. Therefore, although many sparse sets of coronal slices were tested, five slices were hypothesized to be optimal. In fact, six slices were determined to give the most accurate compact representation, as discussed below.

While real-time 3D ultrasound devices do not yet exist, there are experimental ultrasound systems that simplify the data collection of multiple static 2D slices. These approaches use a 2D ultrasound transducer with an automated 3D spatial positioning system. One system is the scanning 3D transducer used in Stone and Lundberg (1996), which internally moves a 2D transducer through a radial space (Acoustic Imaging Inc., Phoenix, AZ). The second is a holder that externally rotates a traditional 2D transducer (Tomtec Inc., Denver, CO). The first is static; the second allows time-varying data to be collected independently at several slices and then reconstructed. Both systems collect up to 60 planes of data and use computer control to position the transducer, but the commercial reconstruction algorithms are quite poor, and slices in planes, other than the original, are very unrealistic. Moreover, measurement of 60 tongue planes at 30 frames per second is unrealistically time consuming and unnecessarily dense spatially.

An alternative method, data-driven slice selection, calculates from subject data an optimal sparse source set of coronal slices from which reasonable 3D surfaces can be constructed. For this method, an externally rotated transducer, or even a manually positioned system, would be sufficient for 4D data collection. Thus, to collect data for 4D reconstructions, one would do multiple data collections of coronal tongue image sequences at a few specific orientations. The separate image sequences would then be aligned in 3D space from their respective collection orientations. In this paper, data-driven slice selection is simulated by selecting a sparse set of slices from the already existing dense set of coronal slices described in Stone and Lundberg (1996).

I. METHODS

A. Subject and speech materials

The subject was a 26-year-old white female with a Baltimore Maryland accent. Nineteen English speech sounds were studied: /i/, /ɪ/, /e/, /ɛ/ /æ/, /ɑ/, /ʌ/, /ɔ/, /o/, /ʊ/, /u/, /ɝ/, /ɜ/, /θ/, /ʃ/, /s/, /l/, /n/, /ŋ/. The subject sustained each phoneme for 10 s while 60 slices were collected. The data was collected with the subject lying on her back because the 3D transducer required a non-upright position for clear images (due to a fluid bubble within the transducer head that would obscure ultrasound when the transducer was in an upright position). Complete recording procedures and subject information can be found in Stone and Lundberg (1996). In addition, for this experiment, several additional tongue surfaces were collected. For validation of the reconstruction procedures the vowel /æ/ was collected twice using sagittal and coronal slices. To study variability the sound /l/ was collected twice, once with a normal articulation, and once pushing the tongue tip into the palate to induce variability.

B. Validation of dense data set

Prior to determining an optimal sparse source set for the 3D reconstructions, validation of the dense data sets was performed to guarantee the accuracy of the original (dense) data reconstructions. Further validation was performed on the reconstruction method beyond the original phantom reconstruction of a known surface done in Stone and Lundberg (1996). Data collection and reconstructions of the tongue surface were done from the coronal and sagittal dense data sets for /æ/. The first collection was done with the 60 slices oriented in the coronal direction. For the second data set, the transducer was rotated 90 degrees so that the 60 slices were oriented in the sagittal direction. Surface reconstruction was performed on each data set, and they were overlaid in 3D space to find the best fit in terms of overlap and minimal error (measured as the 3D distance between surface points on the data sets). It should be noted that this error would include the normal variability between repeated tokens of the same phoneme. For the coronal and sagittal /æ/ data, the maximum error achieved was 2.6 mm, with a standard deviation error of 1.16 mm, and 86% overlap of the two data sets (see Fig. 1). Figure 1 shows the reconstructed /æ/ surfaces from coronal (left) and sagittal (right) slice sets and a set of distance vectors (bottom) comparing the two surfaces. The distance vector image is a set of vectors from the first (left) reconstructed surface to the second (right) surface. The length of any vector corresponds to the 3D distance between the surfaces at that point (the orientation of the vectors is not necessarily in the direction of the shortest 3D distance between the surfaces).

These intersurface differences were largely due to differences in measurement errors that occur in coronal and sagittal tongue contours when using ultrasound. Tissue edges become difficult to measure whenever the surface is oblique to the ultrasound beam. This is most problematic for sagittal images when the tongue surface is grooved, and a sagittal contour may lie entirely along the descending slope of the groove. In the coronal plane, this is most problematic in the tongue root, where the entire contour may be oblique to the ultrasound beam. In general, one can recover a groove more easily from a coronal scan, and one can measure more of the tongue root on sagittal scans.

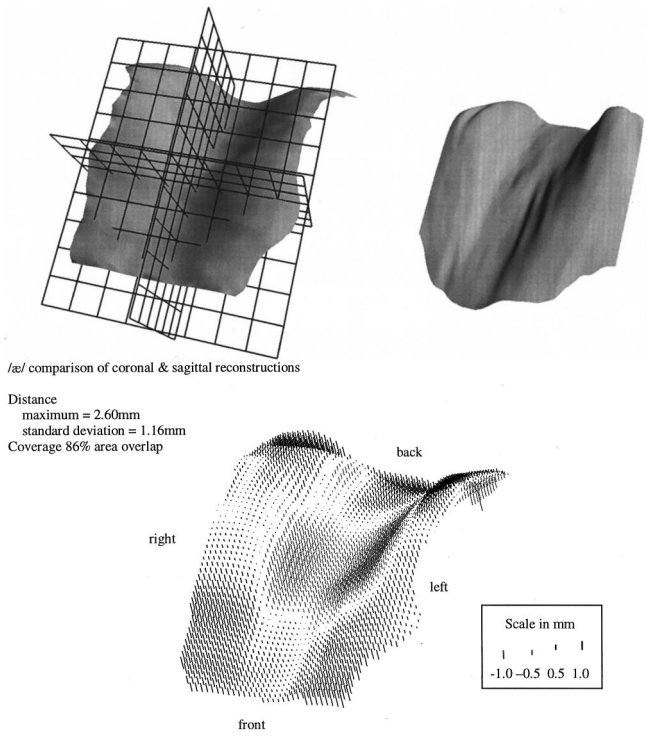

FIG. 1. Reconstructions of coronal /æ/ surface (left) and sagittal /æ/ surface (right) and distance vectors showing the distances between them.

For comparison, and to test measurement repeatability, the same judge twice measured the /ɑ/ surface of a single coronal ultrasound image (see Fig. 2). A year had passed between the two measurements of the images. The error distance between the two reconstructed surfaces had a maximum error of 1.84 mm, standard deviation error of 0.32 mm, and 96% overlap. The maximum error was greater than the error induced by using sparse reconstructions.

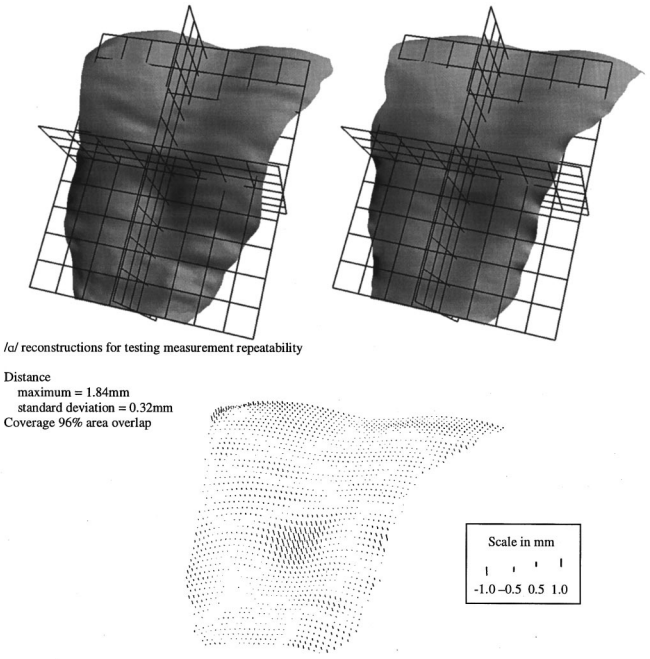

FIG. 2. Two reconstructions of an /ɑ/ measured twice from the coronal images to test measurement repeatability and the distance vector surface between them.

C. Determining an optimal sparse source set

For the dense data sets, tongue surfaces were reconstructed as a b-spline surface that interpolated the dense set of coronal tongue surface contours (Stone and Lundberg, 1996). As tongue surfaces are fairly smooth, particularly between the measured contours of the dense data set, a b-spline surface is a sufficient model. For the sparse data sets, tongue surfaces were similarly reconstructed by defining the b-spline surface that most smoothly interpolated the few coronal tongue surface contours (measured from ultrasound slice images). Tongue surfaces are simple enough to be reconstructed by a small set of coronal contours by this method, but the position of these coronal slices becomes important. For example, for an arched surface the coronal slices must be selected near the point of maximal curvature and displacement. If inappropriate coronal contours are used to reconstruct the tongue, the resulting surface may (at worst) intersect the true surface only along those contours, and may be of a significantly different shape. Selection of a reasonable set of coronal contours is critical to sparse reconstruction of the tongue.

A sparse reconstruction contains just a few coronal slices from the dense set of 60 coronal slices, so there are many possible sparse sets one could collect. In fact, the dense data set can be considered to be 56 slices, as none of the speech sounds had measurable data beyond the 55th slice and slice numbering starts at 0 (see Fig. 3). We considered selecting six slices because this was in fact determined to be the most appropriate choice for balancing data collection constraints and reconstruction accuracy (see Fig. 4). There were then 56 choose 6 [6 selected from 56 without regard to selection order$=56!/(6!(56-6)!)$], or about 32 million possible sets of six coronal slices. The optimal slice set had to be defined globally for all 19 speech sounds, even though each sound had a different optimal set, because the transducer is fixed during actual speech production. There were two desirable properties used in defining an optimal sparse reconstruction. The first was maximal reconstruction coverage, i.e., the ratio of the tongue surface measured in the dense set of tongue slices that was covered by the sparse set. The second was minimizing error.

1. Reconstruction coverage

As the tongue moved forward and back in the mouth during speech, the first and last measurable coronal images (for a fixed dense set of radial images) varied widely (see Fig. 3). Loss of the front slice(s) occurred when the tongue was pulled back and up, creating a sublingual air cavity. In the back, limits on measurable slices were not from tongue position, but from reduced image clarity caused by the increasingly oblique orientation of the tongue surface to the ultrasound beam (which varied in different tongue surfaces and speech sounds). The sound /i/ exemplifies both these problems, as /i/ is the highest of the front raised vowels, and is also very oblique and difficult to measure in the back.

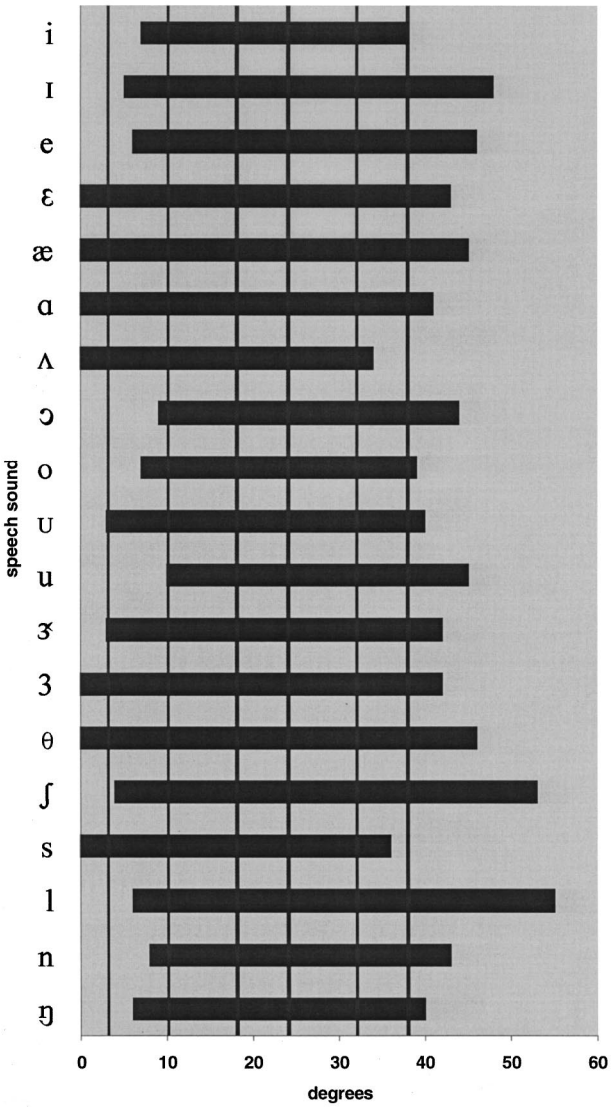

FIG. 3. The range of measurable slices for each of the data sets and vertical lines showing the locations of the six-point optimal sparse source set of coronal slices.

Each of the speech sounds had a specific range of measurable surface contours within the 60-degree 3D sector. For any speech sound, if the extremes of that measurable range are in the sparse data set, the sparse reconstruction of that speech sound will cover the full 3D sector range that a dense data set covered. If the extreme measurable slices are not part of the sparse set, the sparse reconstruction will be truncated at the most extreme slice that does lie within its measurable range. Reconstruction coverage is the area ratio of the sparse reconstruction over the dense reconstruction. As the coronal slices were collected in a polar sweep, the reconstruction coverage can be estimated by the degree range covered by the measurable slices of the sparse set divided by the range covered by all measurable slices for any specific sound. For example, for /i/ only four of the six slices fell within the measurable surface (see Fig. 3), so its reconstruction coverage is 25 degrees/31 degrees.

In order for a 3D reconstruction to be useful it should cover as much of the tongue as possible. Therefore, sparse sets containing from two to nine-slices were optimized for maximum coverage (see Fig. 4). The benefit gained from increasing the number of slices diminished beyond six slices. A second consideration was the practical limitations of real speech data collection. Using current ultrasound instruments, the subject must repeat the speech corpus once for each slice, as they are collected independently. Therefore, fewer slices are preferred. The third consideration was a prior indication that a large reduction in the number of slices was feasible (Stone, 1990). Based on these three considerations and the data in Fig. 4, six-slice sets were optimized.

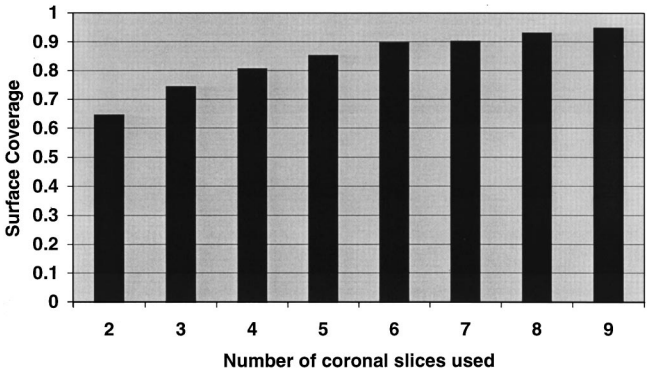

FIG. 4. Coverage of reconstructions for sparse data sets with different numbers of coronal slices.

2. Error analysis of the six-slice set

The second property desired in an optimal reconstruction was minimal error. Sparse sets of six slices were optimized for minimum error. Reconstruction of the tongue surface from a sparse set of slices was identical to the method for reconstructing from a dense data set. An interpolating b-spline surface was fit to the set of surface data points. For the sparse data set from six coronal slices, this had the effect of simplifying the reconstructed surfaces along the sagittal axis. The resulting tongue surfaces were smoother, and might lose detail. To measure the errors induced by this data reduction, the dense reconstruction was compared to the sparse one. To do this, a regularly spaced 2D grid of vertical lines (about one 1-mm spacing) was intersected with the tongue surface. A large enough grid was selected so that all the tongue surfaces in the data set were covered. These intersections gave a regularly spaced set of tongue surface points from the dense reconstructions. For each grid point in the dense data set reconstruction, the closest surface point was found for the sparse reconstruction. The 3D distances between these point sets over all points gave a set of errors. From these, maximum and standard deviation errors measured in millimeters were determined for each of 19 tongue surfaces (corresponding to 19 different static speech sounds). The 3D distances were used as a distance measure, as purely vertical error measures would exaggerate the distances for oblique areas of the surface. In contrast, 3D error distances are measured in a direction normal to the surfaces in all areas.

TABLE I. Reconstruction errors resulting from sparse reconstructions based on different optimizations. No optimization (None) refers to simply taking an equidistant spacing of slices over the full range of the data. Errors reported are for 3D error measured over the surfaces of the 19 speech sounds, except for the six-point set.

Optimization	Selected slices	Average error	Maximum error	Standard deviation error	Coverage	Error cost=max+s.d. +[2×(1-coverage)^3]
None	(0 11 22 33 44 55)	0.37	2.66	0.53	0.79	4.21
Six-slice set	(0 8 16 24 33 38)	0.23	1.42	0.32	0.82	2.63
Six-point set	(3 10 18 24 32 38)	0.21	1.40	0.29	0.80	2.67
Six-point set[a]	(3 10 18 24 32 38)	0.20[a]	0.81[a]	0.27[a]	0.80[a]	2.06[a]

[a]Errors measured for the midsagittal contour only.

3. Optimization of global error cost

To select a set of optimal sparse coronal slices, optimality was defined as minimizing the error cost function:

$$\text{error cost} = \text{maximum error} + \text{s.d. error} + [2 \times (1 - \text{reconstruction coverage})^3]. \quad (1)$$

In addition to this cost function, sparse sets covering an average of less than 0.66 of the 19 speech sound set were eliminated from consideration to prevent the optimization from being skewed by outlying maximum errors. The constant 2 in the error cost equation balances the optimization between the goals of minimizing error and maximizing coverage. Some balance is necessary because simply maximizing coverage results in high surface errors (larger errors than the default equidistant errors in Table I), and optimizing for error only would result in shrinking the sparse surface to consecutive slices one degree apart. For all subjects presented in this paper, the value 2 worked well for both sagittal contour and 3D surface optimizations. Evaluation of the error cost for any slice set required a sparse reconstruction for each of the speech sounds. A brute force search of the 32 million possible sets would require roughly a year of processing time. Thus, a search was needed that could give a fast approximation to the global optimum. A coarse to fine method was used to first get a rough estimation of the global optimum, and then refine that estimation. To do this, the method tests all possible six-slice sets with the restriction that only every fourth possible slice from the dense set is considered. This is equivalent to finding the best sparse reconstruction from a set of coronal slices space 4 degrees apart. So, at this most coarse level, there are only $56/4=14$ possible slices. Since 14 choose 6 is only 3003, all these possibilities can be tested. After determining this coarse step optimum, six-slice sets at a finer level are tested. Now restricted to every second slice, all possible six-slice sets within a single size 2-degree step are considered. In other words, at each slice position, consider the slice 2 degrees before, the current slice, and the slice 2 degrees after, and choose the best permutation across all six slices. Thus, selecting from three slices at six positions gives $3^6=729$ permutations to consider. The best of these permutations is then refined by the same process, using a step size of 1 degree, to give a global optimum approximation. This coarse to fine method is much faster than considering the full range of permutations. It considers $3003+729+729=4461$ rather than 32 million possibilities. The possibilities it does not consider are those where multiple slices are within 4 degrees of one another. For creating sparse data sets, it is highly unlikely that such data sets will be optimal (over the total range of 50+ degrees), so the use of the coarse to fine method should be very reasonable.

The optimal sparse coronal set, for all 19 sounds, resulted in an average error of 0.25 mm, a standard deviation of 0.33 mm, a maximum error of 1.47 mm, and 84% coverage of the dense data sets. Due to the variability in length of tongue surfaces the maximal reconstruction coverage possible for any six-slice set would be 90% (see Fig. 4). As ultrasound has a measurement error around 0.5 mm, the sparse data set was a very good approximation. This indicated that accurate reconstructions could be made from time-varying ultrasound with as few as six slices (at the appropriate positions).

D. Optimizing source sets for individual subjects

These data sets and analyses were based on a single subject, so there is legitimate concern that any subject's optimal sparse source set will vary based on factors of speech production, subject size, or the surrounding vocal tract shape. It would be foolish and impractical to do a dense 3D reconstruction of each subject simply to find the best sparse slices. For this reason, a simpler method for estimating optimal sparse source sets was sought. Instead of measuring the error in the entire 3D surface reconstruction from a sparse coronal slice set, error was measured only in the 2D midsagittal contour reconstruction from a sparse midsagittal point data set. In effect, this would concentrate on the midsagittal slice, and perform the same analysis as finding the best set of slices but in only two dimensions. This was simulated on the dense data set by extracting the midsagittal profiles for the 19 speech sounds, and determining the optimal set of points needed to best reconstruct the global set of profiles. The coronal slices corresponding to the optimal midsagittal points were remarkably close to those selected by the 3D analysis. Using them as the sparse set resulted in slightly reduced surface coverage, but also gave improved error measurements particularly at midline.

II. RESULTS

The goal of this study was to reduce the representation of the tongue surface to a few key slices (i.e., optimal sparse source slices). These slices had to reconstruct 3D tongue surfaces with the highest accuracy possible. If this step was accomplished adequately, the procedure could be developed further to collect time varying data at each slice for use in 4D

TABLE II. Errors in 3D reconstructions based on the optimizations of six coronal slices and six midsaggital points.

	6 slices				6 points			
Sound	Average error	Maximum error	Standard deviation error	Coverage	Average error	Maximum error	Standard deviation error	Coverage
i	0.37	1.42	0.48	0.97	0.32	1.37	0.44	0.90
ɪ	0.17	0.88	0.22	0.70	0.17	1.03	0.23	0.65
e	0.16	0.82	0.21	0.75	0.15	0.51	0.20	0.70
ɛ	0.23	1.34	0.31	0.88	0.26	1.40	0.32	0.81
æ	0.26	0.77	0.28	0.94	0.19	0.72	0.25	0.83
ɑ	0.19	0.79	0.25	0.93	0.21	1.06	0.28	0.85
ʌ	0.42	1.42	0.52	0.97	0.31	1.18	0.40	0.85
ɔ	0.32	1.20	0.41	0.73	0.28	1.29	0.36	0.93
o	0.16	0.74	0.21	0.83	0.18	0.70	0.24	0.73
ʊ	0.20	0.89	0.29	0.81	0.12	0.49	0.15	0.95
u	0.21	0.86	0.27	0.63	0.17	1.14	0.24	0.80
ɝ	0.38	1.38	0.50	0.80	0.20	1.06	0.27	0.90
ɜ	0.14	0.53	0.17	0.91	0.21	0.79	0.28	0.83
θ	0.15	0.83	0.20	0.83	0.15	0.60	0.19	0.76
ʃ	0.32	1.24	0.42	0.73	0.29	0.99	0.36	0.68
s	0.18	0.64	0.22	0.92	0.16	0.52	0.20	0.81
l	0.22	1.07	0.30	0.61	0.24	0.90	0.30	0.57
n	0.20	1.38	0.30	0.86	0.19	1.14	0.27	0.80
ŋ	0.22	0.86	0.29	0.88	0.27	0.84	0.34	0.82
Range	0.14–0.42	0.64–1.42	0.17–0.52	0.61–0.97	0.12–0.31	0.49–1.40	0.12–0.44	0.57–0.95

reconstructions (x,y,z,t). Two sparse source sets were considered. The first was the set of six coronal slices optimized from all the coronal slices of the 56-slice dense set (hereafter called the six-slice set). The second set was the six coronal slices corresponding to the midsagittal points optimized for reconstructing the midsagittal profile (hereafter called the six-point set).

A. Global characteristics of the reconstructions

For each of the sparse sets, global measures of reconstruction accuracy were calculated. Table I shows the optimal six-point and six-slice sets with their global reconstruction errors. Maximum error, standard deviation error, surface coverage, and the resulting cost function were calculated for the entire set of surfaces. The results indicated that the best optimal sparse source was the six-point set. Surface coverage was degraded from the six-slice set optimum and error was improved. Use of midsagittal points as a source set tended to produce better reconstructed surfaces than the coronal set, in many cases, because midsagittal points focused the optimization algorithm on midsagittal features. Thus local depressions, or ''dimples,'' as seen in /l/ and /ɑ/, and steep slopes, as seen in /i/ and /ɝ/, were better captured using the midsagittal source sets. Larger error was seen instead at the surfaces' extreme edges (the least important areas) and also in areas of left-to-right asymmetry, as midsagittal optimization ignores and thus may diminish asymmetries. Errors for individual sounds are shown in Table II. The six-point reconstructions had smaller average errors than the six-slice reconstructions for 11 of the 19 sounds; maximum error was smaller for 13 of the sounds, including all the consonants. Coverage was improved in only four cases. The sparse reconstructions were also more accurate than repeated measurements of a frame (Fig. 2) or comparing sagittal versus coronal dense data sets (Fig. 1). This would indicate that human error in edge detection would be the primary source of error in sparse reconstructions. Concurrent with the present study, a new and automated edge detection system is being developed that should improve measurement reliability.

B. Preservation of local features

In addition to global statistical error measurement, four ''local'' features were considered: left-to-right asymmetry, abrupt changes in slope, local surface depressions, and the constriction location in fricatives. Visual inspection of the dense reconstructions indicate that depressions and abrupt changes in slope were most evident in the midsagittal plane (Stone and Lundberg, 1996; Figs. 4–6). Preservation of these two features in the sparse reconstructions was enhanced by optimizing slice selection in the midsagittal plane. A source set determined by midsagittal points cannot account for left/right differences in shape or motion. In these data sets asymmetry was least well represented. If the selected slices passed through maximally asymmetric regions, the length of the asymmetry would be overestimated. If the slices missed the areas of maximal asymmetry, the degree of asymmetry would be underestimated. The most asymmetrical tongue shape in the data set was /i/ where the maximum error was 1.37 mm.

The second and most easily resolved local feature was the local dimple seen in low back vowels and /l/ (Stone and Lundberg, 1996; Figs. 5 and 6). The use of the five- and six-point sparse sets instead of the coronal sparse set greatly improved resolution of centrally occurring depressions in the 3D surfaces, as they were key features in the midsagittal profile as well. Figure 5 compares the dimple in the dense and sparse surfaces for /l/.

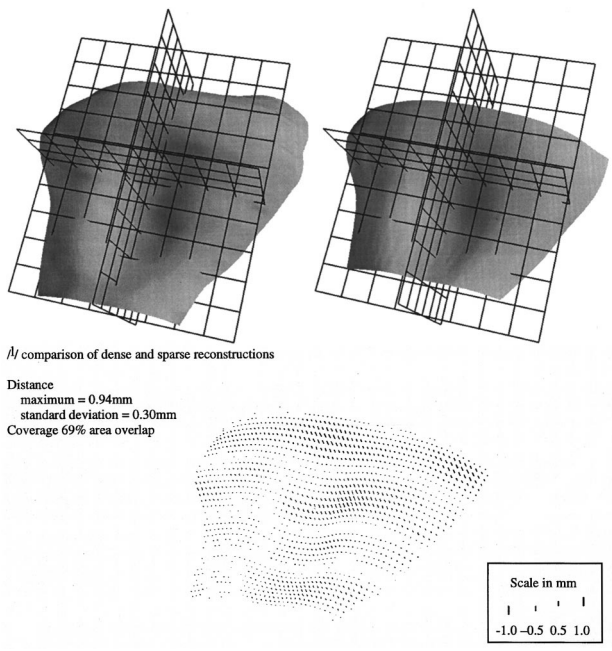

FIG. 5. Reconstructions from a dense set of slices (left), and from a six-slice set (right) for /l/ and the distance vector surface between them.

The third local feature was abrupt change in slope. This feature was particularly evident for /i/ which had an arched tongue in the front, and abruptly became grooved in the back. In addition, the measurable tongue surface was very short. The six-point set resulted in four measurable slices for even the shortest tongue surfaces, and captured the grooves very accurately. Figure 6 shows good representation of abrupt slope changes and deep groove in /i/.

The fourth local feature was the location of fricative constrictions. Fricative constructions in English often occur slightly off midline. Moreover, they may not be marked by

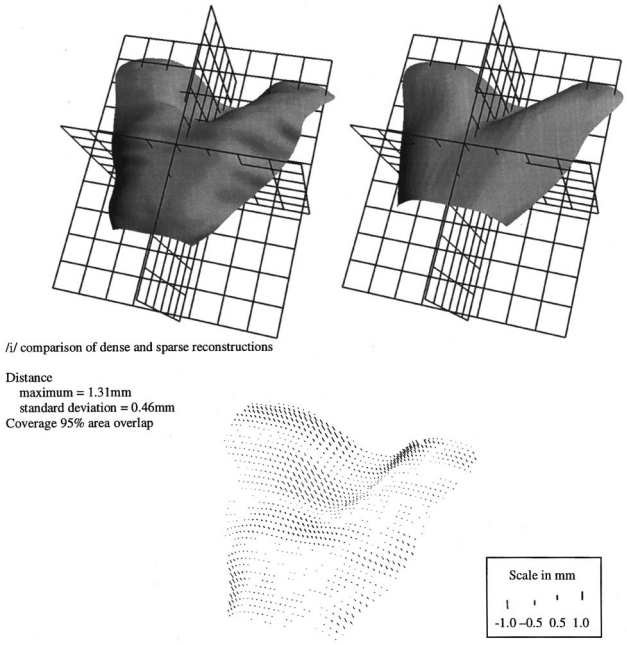

FIG. 6. Reconstructions from a dense set of slices (left), and from a six-slice set (right) for /i/ and the distance vector surface between them.

midline tongue features. Therefore, particular attention was paid to the error in the three fricatives /θ/, /s/, and /ʃ/. Table II shows the maximum error for each sound. For /θ/ the maximum error 0.60 occurred laterally, though not at the edges. Maximum error was 0.2 mm at the constriction. Electropalatography (EPG) data confirmed the subjects constriction locations (see Stone and Lundberg, 1996). For the /s/ the largest error was 0.5 mm and occurred at the edge. At the constriction, the largest error was 0.3 mm. The /θ/ and /s/ shapes were actually fairly easy to predict from a sparse set because the tongue shape did not change dramatically from front to back. The /ʃ/ had a more changeable surface shape and had larger average and maximum errors. The largest error, 0.99 mm, occurred laterally. Several errors of 0.7 mm did appear in the constriction region slightly off the midsagittal plane. In the constriction region, the sparse data set was below the dense data set, which overestimated the channel size.

C. Variability

Intrasubject variation occurs because humans do not say an utterance exactly the same way every time. Phoneme production varies slightly from repetition to repetition. Intrasubject variation could not be seen in these single utterances. One example of variation was contrived, however. The phoneme /l/ was repeated twice by the subject with the goal of creating two different shapes. The first, /l_1/, was produced normally. The second, /l_2/, was produced with a forceful apical contact. Both were sustained about 10 s. The two tongue surfaces were measured and reconstructed using the same procedure as in Figs. 5 and 6. In the /l/ comparison, however, the two surfaces were dense reconstructions of different repetitions (see Fig. 7). We were interested in what causes the midsagittal depression often seen just behind the tongue blade in /l/. It was hypothesized that the more forceful apical contact would create a larger deformation for /l_2/, the more extreme or ''tense'' production. Therefore, the /l_2/ would have a deeper depression than /l_1/. This was found to be true. The lower left portion of Fig. 7 shows the two tongues spatially aligned and superimposed. The /l_2/ tongue is higher than /l_1/ in back and on the sides, and lower in the depression region. The depression depths were 2 mm for /l_1/ and 4 mm for /l_2/, at the deepest point relative to the highest point in the same coronal slice. The important features, the dimples, differed across the repetitions by 2 mm, larger than the maximal error for sparse reconstructions. This number should be accurate since it occurred in the midsagittal region where we generally expect smaller reconstruction errors.

Intersubject variation occurs because humans have slightly different oral morphologies and use different strategies for creating speech gestures. Table III presents midsagittal optimization data from 17 additional subjects. Four speech sounds were collected for each of these subjects: /æ/, /ɑ/, /i/, and /u/. The best six-point sparse set (optimal selections) is compared to the equidistant six-point sparse set (default selections). The optimized selections column presents the optimized range of slices. This makes it clear that across subjects there existed a variety of tongue lengths and feature locations. Smaller ranges were caused by two things: tongues that had incomplete data at one end or the other; and little

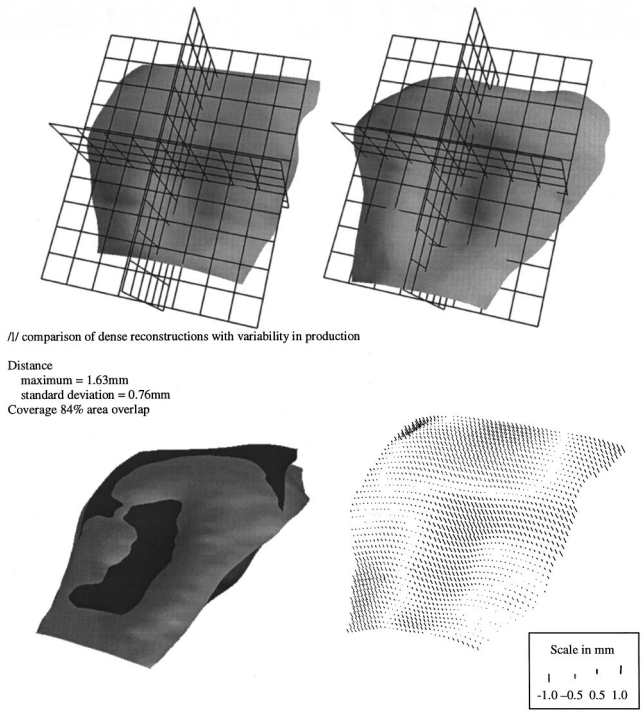

FIG. 7. Reconstructions of dense sets from two distinct productions of /l/ (normal and tense) to show intrasubject variability, the distance vectors between them, and, on the lower left, the two surfaces superimposed in their best alignment. The black surface is for normal production, $/l_1/$, and the gray surface is for tense production, $/l_2/$.

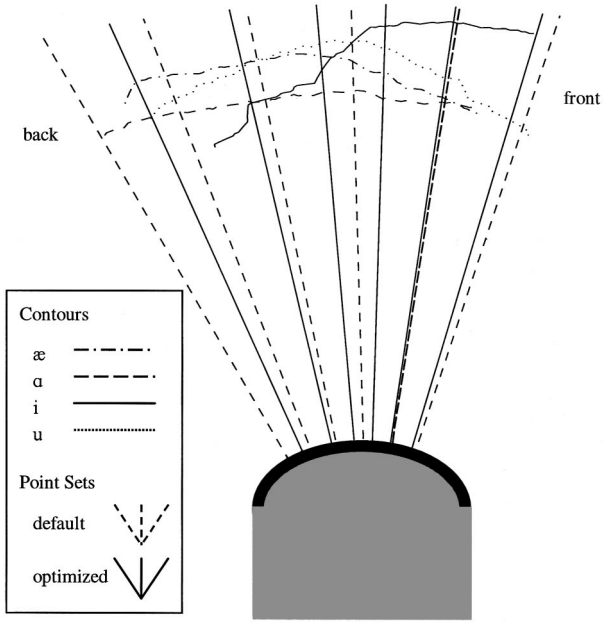

FIG. 8. Sagittal contours of the tongue for subject 7 showing radial lines indicating the default (dashed) and optimal (solid) point sets and their intersections with the four speech sounds.

anterior-to-posterior differences among sounds. Different starting and ending slices among subjects, e.g., subject 3 versus subject 16, reflect rotational differences in positioning the transducer, not true position differences. The primary subject is the subject used in the rest of the paper.

Table III shows that for 11 of the 17 subjects the optimization reduced the maximum error by at least 0.8 mm and for 13 subjects it increased the surface coverage. Subject 7 benefited the most from the optimization. Her default equidistant point set selected points 6 degrees apart with an overall tongue length of 30 degrees. After optimization, her tongue length was 25 degrees, and her interpoint distances were 5, 4, 4, 5, and 8 degrees apart, indicating a greater representation in the anterior tongue. Figure 8 shows the four vowel contours and the optimized points for subject 7 as radial trajectories. With these modifications in point location for this subject, the average error decreased from 0.52 to 0.28, the maximum error decreased from 2.42 to 1.04 mm, and the standard deviation decreased from 0.68 to 0.37. The least improvement was seen for subject 10 whose errors improved only slightly. For some subjects, the optimization was essential, for without it some sounds only had two of the

TABLE III. Midsagittal optimization for the primary and additional subjects based on four speech sounds. The default selections and results (in parentheses) use simple equidistantly spaced points. Values of (---) are displayed for selections that captured only two points for at least one sound, so that no spline estimation can be done for that sound. Errors reported here are measured only on the midsagittal contour.

Subject	Optimal selections	Default selections	Average error	Maximum error	Standard deviation	Coverage
Primary	[00 10 18 23 31 35]	(00 09 18 27 36 45)	0.15 (0.27)	0.45 (1.40)	0.19 (0.38)	0.84 (0.82)
1. A. C.	[10 13 21 29 38 43]	(09 16 24 31 39 46)	0.50 (0.54)	1.49 (1.86)	0.63 (0.70)	0.90 (0.87)
2. C. S.	[12 17 21 29 35 42]	(09 16 22 29 35 42)	0.32 (0.43)	0.94 (2.15)	0.41 (0.56)	0.88 (0.93)
3. E. B.	[04 12 17 21 26 29]	(02 09 16 22 29 36)	0.21 (0.36)	0.71 (1.59)	0.28 (0.48)	0.79 (0.82)
4. E. D.	[08 14 18 23 27 32]	(02 09 16 22 29 36)	0.37 (0.50)	1.16 (2.01)	0.49 (0.65)	0.84 (0.76)
5. E. L.	[05 10 19 27 35 42]	(00 08 17 25 34 42)	0.41 (---)	1.30 (---)	0.52 (---)	0.88 (0.69)
6. E. S.	[07 12 16 21 26 31]	(01 08 14 21 27 34)	0.35 (---)	0.99 (---)	0.44 (---)	0.84 (0.62)
7. F. S.	[10 15 19 23 28 35]	(09 15 21 27 33 39)	0.28 (0.52)	1.04 (2.42)	0.37 (0.68)	0.86 (0.80)
8. J. M.	[06 10 16 23 31 45]	(05 13 21 29 37 45)	0.43 (0.46)	1.40 (2.27)	0.55 (0.65)	0.83 (0.78)
9. J. U.	[03 07 13 19 25 30]	(00 08 16 24 32 40)	0.27 (0.42)	1.02 (2.40)	0.36 (0.57)	0.81 (0.81)
10. K. L.	[02 06 15 22 30 42]	(01 10 18 27 35 44)	0.47 (0.53)	1.65 (1.68)	0.58 (0.68)	0.90 (0.79)
11. K. R.	[16 21 24 28 33 38]	(13 18 23 29 34 39)	0.31 (0.50)	0.99 (2.07)	0.42 (0.69)	0.87 (0.83)
12. M. B.	[17 21 25 29 32 35]	(14 19 24 28 33 38)	0.23 (0.36)	0.71 (1.42)	0.32 (0.51)	0.84 (0.77)
13. R. S.	[15 19 22 24 29 34]	(12 17 23 28 34 39)	0.28 (0.40)	0.98 (1.40)	0.39 (0.56)	0.85 (0.86)
14. S. F.	[07 10 15 17 23 31]	(03 10 17 24 31 38)	0.39 (0.44)	1.44 (1.50)	0.50 (0.53)	0.79 (0.82)
15. S. G.	[01 08 16 24 32 45]	(00 10 20 31 41 51)	0.39 (---)	1.16 (---)	0.48 (---)	0.84 (0.66)
16. T. M.	[19 23 27 32 37 40]	(16 22 27 33 38 44)	0.38 (0.45)	1.33 (1.54)	0.50 (0.63)	0.84 (0.83)
17. V. S.	[18 23 28 31 34 38]	(17 22 26 31 35 40)	0.34 (0.49)	1.18 (1.45)	0.46 (0.62)	0.93 (0.78)

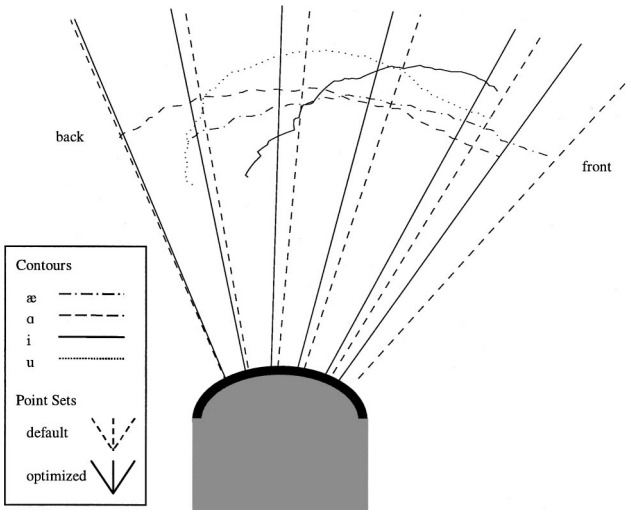

FIG. 9. Sagittal contours of the tongue for subject 5 showing that the default set (dashed) fails to measure the contours for one sound at three (the solid or more points, while the optimal set does intersect each contour at three or more points.

six equidistant points fall on the tongue surface, as marked by (---). This occurred when the subject had great anterior–posterior differences in tongue position across sounds. Figure 9 presents an example of this positional difference for subject 5. The contour for /i/ went from a two-point to a three-point representation after the optimization.

III. DISCUSSION

This study was able to reconstruct 3D tongue surface shapes using as few as six coronal slices. The best slice selection used an optimized set of midsagittal points.

Three important issues are involved in choosing a sparse data set for 3D reconstruction. The first and most important issue is finding the best six-point source set for each subject. Without this, results cannot be generalized across subjects and validity of the method is breached. The optimal sparse source sets determined here will certainly not be optimal for all subjects. Therefore, prior to data collection, a midsagittal data set needs to be collected for each subject. From this data set an optimal source point set is determined for reconstruction of the midsagittal profile. Coronal images would then be collected at each point and reconstructed as described earlier. This procedure can be used to collect time-varying speech samples at each coronal slice angle for use in 3D time–motion reconstructions of the tongue surface during speech. The midsagittal data can be used in the reconstructions as well.

Second, the transducer must be positioned in an accurate and precise manner. A positional error of a few degrees in one slice will reduce significantly the capture of local shape features such as dimples and degree of grooving. Although not addressed in this paper, a 3D automated head and transducer support system (AHATS) based on the currently used 2D head and transducer support (HATS) system (Stone and Davis, 1995) is under construction. This system uses computer (or manually) controled positioning of the transducer at predetermined angles for collection of real-time sagittal and coronal motion. Manual transducer positioning is acceptable if predetermined slice positions are calculated accurately, and precision of transducer placement is assured.

The third issue of importance is reconstruction accuracy of 3D shape and motion. Global reconstruction was optimized by minimizing the maximum and standard deviation errors. As a result, the average errors were below the measurement error for ultrasound. The largest maximum error for all 19 sounds was 1.40 mm, which occurred in /ɛ/ one time on an extreme edge. The greatest standard deviation error was 0.44 mm, which occurred for /i/. Errors above 1.2 mm occurred exclusively at the most lateral edge, and errors above 1.0 tended to occur in the posterior most row.

Optimized reconstructions also need to represent local features well, such as asymmetry, local depressions, and steep slopes. Optimization improved representation of local features compared to equidistant slices. Midsagittal optimization further improved midsagittal features. The first feature, tongue asymmetry, is more prevalent in tongue motion than in static data and so will be even more important for future studies. Left-to-right rotation and a ''leading edge'' are seen fairly often in coronal ultrasound images of speech. These asymmetries do not vary systematically with palatal shape, or handedness (Hamlet, 1987); they are more prevalent in some subjects and some tasks, however. When the slice selection is based on midsagittal points, asymmetries cannot be taken into account, since no lateral information is available. However, leading edges and left-to-right rotations extend across a fairly long region of the lengthwise tongue and, therefore, should be captured by one or more sparse slices. Future research will continue to carefully assess error in representation of asymmetry using the current method.

The second feature, local tongue depressions or dimples, was visible in this data set for nonhigh back vowels and /l/. They have been observed fairly often in other ultrasound data sets (Davis, 1996; Fig. 1) and can be inferred from some point tracking data [Stone, 1990 (Table I)] and MRI data (Kumada *et al.*, 1992; Niitsu *et al.*, 1992) as well. They tend to appear in the ''middle'' segment of the tongue (approximately 2.5–4 cm back from the protruded tip) (cf. Stone, 1990). The present 3D reconstructions captured dimples very accurately because dimples occur at midline and the six-point sparse set optimized their representations.

Accurate representation of steep slopes was the third feature examined in the reconstructions. Front raised sounds (e.g., high front vowels) have a very advanced tongue root. This is due to genioglossus posterior (GGP) contraction, which causes a deep posterior groove defined by a steep slope midsagittally and laterally. Anteriorly, the tongue surface is high and flat, or even arched. Therefore, a sharp inflection point in the midsagittal profile separates the anterior arch from the posterior groove. Choosing a point too far from the inflection point will cause a serious underestimation in the slope magnitude and origin point. Moreover, during changes from front raising to other shape categories, such as back raising, 3D motion reconstructions from inappropriately selected slices will misrepresent and reduce the accuracy of the deformation.

One type of ''error'' is utterance-to-utterance variation,

or free variation. Humans do not produce repeated speech sounds identically. We expect that the induced variation in shape between the /l_1/ and /l_2/ (1.63-mm maximum difference) is the same size or larger than would occur in free variation and is consistent with systematic differences due to morphological constraints. If so, such differences would be larger than the maximum measurement error (1.40 mm) caused by using the sparse data set and should be well represented, especially if the important features occur at midline.

The current sparse set criteria minimize the problem of accurate 3D tongue reconstruction from a sparse slice set, as can be seen from the maximum and standard deviation errors in Table II. The standard deviation errors seen in the data were no worse than typical measurement error. The maximum errors (above 1.3 mm) were seen on the edges. Our expectation is that the selection of fairly equidistant slices, and the optimization across all the lingual sounds in English, will continue to provide as reasonable a 3D coverage as is possible.

ACKNOWLEDGMENT

This work was supported by a research grant from the National Institute of Deafness and Other Communication Disorders (NIH-R01DC01758).

Davis, E., Douglas, A., and Stone, M. (**1996**). ''A Continuum Mechanics Representation of Tongue Motion in Speech,'' Proceedings of the 4th International Conference on Spoken Language Processing, Vol. 2, pp. 788–792.

Hamlet, S. (**1987**). ''Handedness and articulatory asymmetries on /s/ and /l/,'' J. Phonetics **15**, 191–195.

Keller, E., and Ostry, D. (**1983**). ''Computerized measurement of tongue dorsum movements with pulsed echo ultrasound,'' J. Acoust. Soc. Am. **73**, 1309–1315.

Kier, W. M., and Smith, K. (**1985**). ''Tongues, tentacles and trunks: the biomechanics of movement in muscular-hydrostats,'' Zoo. J. Linnean Soc. **83**, 307–324.

Kumada, M., Niitsu, M., Niimi, S., and Hirose, H. (**1992**). ''A Study on the Inner Structure of the Tongue in the Production of the 5 Japanese Vowels by Tagging Snapshot MRI,'' Research Institute of Logopedics and Phoniatrics, University of Tokyo, Annual Bulletin, Vol. 26, pp. 1–13.

Miyawaki, K., Hirose, H., Ushijima, T., and Sawashima, M. (**1975**). ''A preliminary report on the electromyographic study of the activity of lingual muscles,'' Research Institute of Logopedics and Phoniatrics, University of Tokyo, Annual Bulletin, Vol. 9, pp. 91–106.

Niitsu, Kumada, M., Niimi, S., and Itai, Y. (**1992**). ''Tongue Movement during Phonation: A Rapid Quantitative Visualization Using Tagging Snapshot MRI Imaging,'' Research Institute of Logopedics and Phoniatrics, University of Tokyo, Annual Bulletin, Vol. 26, pp. 149–156.

Sonies, B., Shawker, T., Hall, T., Gerber, L., and Leighton, S. (**1981**). ''Ultrasonic Visualization of Tongue Motion During Speech,'' J. Acoust. Soc. Am. **70**, 683–686.

Stone, M. (**1990**). ''A three-dimensional model of tongue movement based on ultrasound and x-ray microbeam data,'' J. Acoust. Soc. Am. **87**, 2207–2217.

Stone, M. (**1995**). ''How the tongue takes advantage of the palate during speech,'' in *Producing Speech: Contemporary Issues: A Festschrift for Katherine Safford Harris*, edited by F. Bell-Berti and L. J. Raphael (American Institute of Physics, New York), Chap. 10, pp. 143–153.

Stone, M., and Davis, E. P. (**1995**). ''A head and transducer support system for making ultrasound images of tongue/jaw movement,'' J. Acoust. Soc. Am. **98**, 3107–3112.

Stone, M., and Lele, S. (**1992**). ''Representing the Tongue Surface With Curve Fits,'' Proceedings of the International Conference on Spoken Language Processing, Vol. 2, pp. 875–878.

Stone, M., and Lundberg, A. (**1996**). ''Three-dimensional tongue surface shapes of English consonants and vowels,'' J. Acoust. Soc. Am. **99**, 3728–3737.

Stone, M., and Yeni-Komshian, G. (**1991**). ''Some effects of pharyngealization on tongue shape as seen on ultrasound,'' J. Acoust. Soc. Am. **89**, S1979 (A).

Stone, M., Sonies, B., Shawker, T., Weiss, G., and Nadel, L. (**1983**). ''Analysis of real-time ultrasound images of tongue configuration using a grid-digitizing system,'' J. Acoust. Soc. Am. **11**, 207–218.

Perception of coarticulatory nasalization by speakers of English and Thai: Evidence for partial compensation

Patrice Speeter Beddor[a)]
Program in Linguistics, University of Michigan, Ann Arbor, Michigan 48109

Rena Arens Krakow[b)]
Department of Communication Sciences, Temple University, Philadelphia, Pennsylvania 19122 and Haskins Laboratories, New Haven, Connecticut 06511

(Received 12 January 1999; revised 18 June 1999; accepted 21 June 1999)

The conditions under which listeners do and do not compensate for coarticulatory vowel nasalization were examined through a series of experiments of listeners' perception of naturally produced American English oral and nasal vowels spliced into three contexts: oral (C_C), nasal (N_N), and isolation. Two perceptual paradigms, a rating task in which listeners judged the relative nasality of stimulus pairs and a 4IAX discrimination task in which listeners judged vowel similarity, were used with two listener groups, native English speakers and native Thai speakers. Thai and English speakers were chosen because their languages differ in the temporal extent of anticipatory vowel nasalization. Listeners' responses were highly context dependent. For both perceptual paradigms and both language groups, listeners were less accurate at judging vowels in nasal than in non-nasal (oral or isolation) contexts; nasal vowels in nasal contexts were the most difficult to judge. Response patterns were generally consistent with the hypothesis that, given an appropriate and detectable nasal consonant context, listeners compensate for contextual vowel nasalization and attribute the acoustic effects of the nasal context to their coarticulatory source. However, the results also indicated that listeners do not hear nasal vowels in nasal contexts as oral; listeners retained some sensitivity to vowel nasalization in all contexts, indicating partial compensation for coarticulatory vowel nasalization. Moreover, there were small but systematic differences between the native Thai- and native English-speaking groups. These differences are as expected if perceptual compensation is partial and the extent of compensation is linked to patterns of coarticulatory nasalization in the listeners' native language.
[S0001-4966(99)03310-X]

PACS numbers: 43.71.An, 43.71.Hw, 43.71.Es [JMH]

INTRODUCTION

Considerable evidence, spanning some 40 years of research, indicates that perception of speech sounds is influenced by the phonetic context in which sounds occur (for reviews of selected aspects of context effects, see Repp, 1982; Repp and Liberman, 1987; Nearey, 1992; Miller and Eimas, 1994; McQueen, 1996). Response patterns in which listeners appear to be compensating for a sound's coarticulatory context have held particular interest both for theories of speech perception, and for theories of the factors that shape sound systems.

''Compensation'' refers to listener responses consistent with perceptual reduction or perceptual elimination of the acoustic effects of a coarticulatory context on a target sound (Mann, 1980; Fowler, 1984). For example, Mann and Repp (1980) found that synthetic fricative noises ranging from [ʃ] to [s] were more often identified by English listeners as /s/ when followed by [u] than by [a]. That is, listeners accepted lower noise frequencies as /s/ in a rounded vowel context—a context that would, in natural coarticulated speech, be expected to lower the frequency of the fricative noise. [For similar findings, see also Whalen (1981, 1989), for English, and Kunisaki and Fujisaki (1977), for Japanese.] As another example, three studies testing a single set of stimuli found that adult English speakers (Mann, 1980), adult Japanese speakers (Mann, 1986) and 4-month-old infants in an English-speaking environment (Fowler *et al.*, 1990) showed a category boundary shift for a /da–ga/ continuum depending on whether the stop was preceded by /l/ or /ɹ/. The shift resulted in more /g/ (i.e., more back) responses following /l/ than /ɹ/, suggesting perceptual reduction of the coarticulatory fronting effects of /l/ on a following velar consonant. Compensation for prosodic properties, including fundamental frequency (Petersen, 1986; Silverman, 1987), duration (Whalen, 1989), and tone (Yu, 1994), has also been reported.

Compensatory perceptual responses are not limited to identification tasks. Kawasaki (1986) used a rating task in which English speakers were asked to rank the nasality of natural vowels originally produced in a nasal consonant context ([m_m]). She found that listeners heard contextually nasalized vowels in a clearly audible nasal consonant context as relatively oral; the same vowels sounded increasingly nasal as the amplitude of flanking nasal consonants was attenuated. As with category boundary shifts, listeners in Kawasaki's study perceptually reduced the acoustic effects (here, vowel nasalization) of the coarticulatory context.

a)Electronic mail: beddor@umich.edu
b)Electronic mail: rkrakow@unix.temple.edu

Fowler (1981, 1984; Fowler and Smith, 1986) investigated listeners' use of coarticulatory information using a 4IAX discrimination procedure in which trials compared acoustically *different* target sounds in coarticulatorily *appropriate* contexts with acoustically *identical* targets, one of which was spliced into a coarticulatorily *inappropriate* context. For example, [g]s from different vowel contexts were cross spliced, creating trials such as [g_ii]–[g_iu], with acoustically identical [g]s, paired with [g_ii]–[g_uu], with coarticulatorily appropriate [g]s (where [g_i] and [g_u] are from original [gi] and [gu], respectively). Overall, Fowler's results showed that listeners often based their similarity judgments on coarticulatory appropriateness rather than on acoustic similarity, in keeping with the notion that listeners use contextual information to perceptually reduce acoustic variation (thereby facilitating segmentation of the acoustic stream).

Not surprisingly, different theoretical approaches offer differing accounts of these compensatory context effects. Auditory theories (e.g., Diehl and Kluender, 1989; Kingston, 1992; Kingston and Diehl, 1995; Lotto and Kluender, 1998) do not predict that listeners will use contextual information to separate perceptually the acoustic effects of coarticulation. Instead, such theories attribute context-induced shifts in category boundaries to general auditory processes such as frequency contrast or spectral contrast. Recent evidence offered in support of a general auditory account comes from further exploration of the effects of preceding /l/ and /ɹ/ on the /da–ga/ boundary, originally investigated by Mann. This work showed context effects when the listeners were nonhuman (Lotto *et al.*, 1997) and for human listeners when the liquid context was a nonspeech sine wave analog of /l/ and /ɹ/ (Lotto and Kluender, 1998).

Explanations of compensatory context effects that attribute these effects to a source other than general auditory processes cover a range of theoretical perspectives. The account offered by articulatory/gestural theorists is that listeners parse the acoustic signal in terms of its articulatory/gestural sources, hearing the acoustic properties of a target sound that are due to coarticulatory overlap as belonging to the coarticulatory context rather than to the target (e.g., Fowler, 1996).[1] Albeit from a nongestural theoretical perspective, Ohala (1981, 1986, 1993) also interpreted context effects of the type just described as evidence that listeners typically ''factor out'' predictable acoustic properties, effectively adjusting for contextual variation. Offering a theory of the listener's role in sound change and sound systems, Ohala proposed that contextual variation can lead to sound change when listeners either fail to adjust, or overadjust, for acoustic effects of coarticulation. Nearey (1992, 1997) offered an account of such perceptual hypo- and hypercorrections for coarticulatory overlap within his double-weak theory of speech perception.

Theoretical perspective notwithstanding, aspects of compensatory effects remain poorly understood. For example, under what conditions might listeners fail to compensate for contextual variation? Ohala (1993 and elsewhere) has suggested (correctly, in our view) that listeners will fail to compensate if they do not detect the coarticulatory source, or conditioning environment, for the variation. But assuming detection of the context, will listeners necessarily compensate for its acoustic effects? And if they do, is the compensation ''correct,'' that is to say, complete? And if not complete, which types of contexts trigger more versus less compensation? Existing data are far from clear on these issues.

As an illustration, consider the findings of previous studies of the perceptual consequences of nasal coarticulation. The results of several studies are consistent with the interpretation that listeners attribute the acoustic effects of contextual nasalization to its coarticulatory source. As noted above, Kawasaki (1986) found that nasalized vowels sound more nasal when embedded between acoustically weakened nasal consonants. Lahiri and Marslen-Wilson (1991) conducted a gating study in which listeners gave complete word responses when presented with fragments of CVC and CVN words. Listeners responded with CVN as well as CVC words when presented with oral [CV] fragments (from original CVC words), suggesting that they did not perceive oral vowels as incompatible with a following nasal consonant. Focusing on the perceived height rather than on the nasality of nasal vowels, Krakow *et al.* (1988) found that listeners misjudged the height of synthetic nasal vowels in an oral consonant context ([b_d]), but correctly judged the height of the same nasal vowels in a nasal consonant context ([b_nd]).[2] In this case, English-speaking listeners attributed the low-frequency effects of nasalization on perceived height to the nasal consonant context rather than to the vowel itself. Results reported by Manuel (1995) suggest that listeners also attribute coarticulatory nasalization of consonants (specifically, carryover nasalization on /ð/ in /nð/ sequences) to the flanking nasal context.

However, not all of the available evidence indicates that listeners are so successful in attributing contextual variation to its coarticulatory source. In a study that was a precursor to the present set of experiments, Krakow and Beddor (1991) edited and spliced natural bed and men tokens to create stimuli in which oral and nasal vowels each occurred in oral and nasal contexts and isolation. English-speaking listeners judged vowel similarity in an ABX matching task (e.g., AB [mɛn]–[mɛ̃n]; X=[ɛ] or [ɛ̃]); listeners also judged the relative vowel nasality in a rating task (where pairings included [mɛ̃n]–[bɛd] and [mɛ̃n]–[ɛ]). Listeners compensating for vowel nasality in a nasal context should perform poorly on trials involving this context, because nasal vowels in an [m_n] context should sound relatively oral. Although this general pattern was upheld, listeners made fewer errors than we might expect on the basis of Kawasaki's findings. In addition, other findings suggest that listeners do not adjust for perceived nasal vowel height in nasal consonant contexts under some testing conditions. In a series of vowel classification experiments using the Garner paradigm, in which listeners judged both height and nasality of synthetic vowel stimuli, Kingston and Macmillan (1995) found that height perception was influenced by vowel nasality in both oral and nasal contexts, contrary to the findings of Krakow *et al.* (1988) which indicated that listeners separated these parameters when given an appropriate coarticulatory (i.e., nasal) context.[3]

The present set of experiments further explores the effect of coarticulatory context on speech perception, with particular focus on the types of contextual conditions that are particularly likely or unlikely to lead to compensatory responses. We chose to investigate coarticulatory vowel nasalization primarily because previous studies on nasalization have shown that listeners are able to make judgments about vowel nasality under a variety of testing conditions and that, under certain testing conditions, (American English) listeners do compensate for contextual nasalization. Hence, there is reason to expect that systematic manipulation of the contexts of vowel nasalization will allow us to tease apart some of the factors relevant to compensation. We also selected vowel nasalization because languages differ in the spatial and temporal extent of coarticulatory vowel nasalization (e.g., Clumeck, 1976; Henderson, 1984; Cohn, 1990; Rochet and Rochet, 1991; Solé, 1992, 1995), and speakers of languages that differ in this respect prefer different amounts and temporal patterns of nasalization when judging stimulus naturalness (Stevens *et al.*, 1987). Study of whether listeners' perceptual responses to nasalization in different phonetic contexts depend on their native language's coarticulatory organization will further delineate the conditions relevant to compensation.[4]

We designed a series of experiments to investigate the extent to which listeners' perception of vowel nasalization was dependent on the context—oral context, nasal context, or isolation—in which the vowels occurred. Oral and nasal vowels were placed into each of these contextual conditions by applying excising and cross-splicing techniques to natural productions of a native American English speaker. To test for the generality of any context effects, we incorporated three experimental manipulations. First, all experiments were conducted with two vowel qualities, front unrounded /ɛ/ and back rounded /o/. Second, two types of perceptual paradigms were used, a rating task in which listeners heard pairs of stimuli and judged the relative vowel nasality of pair members (experiments 1 and 3), and a 41AX task in which listeners judged vowel similarity (experiments 2 and 4). The former task requires listeners to make metalinguistic judgments concerning vowel nasality and is similar to tasks used by Kawasaki (1986) and Krakow and Beddor (1991). The latter task was included as a measure of listeners' discriminatory abilities and thus as a potentially more sensitive perceptual measure. (The same listeners participated in both tasks, but the discrimination task always preceded the rating task.)

As a third manipulation, tasks were presented to two groups of listeners, native American English speakers and native Thai speakers. Both languages are typically viewed as having nondistinctive vowel nasalization.[5] American English shows extensive anticipatory vowel nasalization (Clumeck, 1976; Krakow, 1989, 1999; Solé, 1992, 1995). Tanowitz and Beddor's (1997) acoustic analysis of temporal patterns of anticipatory nasalization in CVN(C) syllables showed that, in the speech of four English speakers from Michigan (the dialect of nearly all participants in experiments 1 and 2), on average 80% of a vowel followed by a nasal consonant was nasalized. This percentage held regardless of vowel length (i.e., for long tense vowels as well as shorter lax vowels). In comparison, an ongoing analysis of the productions of native Thai speakers showed that, on average, only 45% of the vowel in a Thai CVN syllable was nasalized. In addition, nonlow (contrastively) long vowels in Thai were proportionately less nasalized than their short counterparts (Beddor *et al.*, in preparation). That Thai listeners might be sensitive to these temporal differences is suggested by native Thai speaker Onsuwan's (1997) observation that English vowels in nasal contexts sound heavily nasalized, whereas those of Thai in comparable contexts do not.

What predictions would a hypothesis that listeners compensate for the acoustic effects of coarticulation make concerning listeners' responses to these experiments? Broadly speaking, listeners should do well judging vowel nasality (rating task) or determining vowel similarity (4IAX discrimination task) when presented with vowels in an oral context or isolation; that is, when there is no coarticulatory context to which to attribute vowel nasalization, the acoustic effects of nasalization should be heard as part of the vowel itself, and perception should be accurate. For example, when presented with rating pairs such as $\tilde{V}$–V, C$\tilde{V}$C–CVC, C$\tilde{V}$C–V or $\tilde{V}$–CVC (where C and V are oral and $\tilde{V}$ is nasal), the vowel in the first stimulus in each of these pairs should (correctly) sound more nasal than that in the second. However, listeners are predicted to perform poorly when judging nasal vowels in a nasal consonant context because, under a coarticulatory compensation hypothesis, vowel nasalization should be attributed to the context; a nasal vowel would therefore be heard as (relatively) oral. For example, listeners should incorrectly rate the vowels in pairs such as N$\tilde{V}$N–V or N$\tilde{V}$N–CVC (where N is a nasal consonant) as equally nasal; in N$\tilde{V}$N–$\tilde{V}$ or N$\tilde{V}$N–C$\tilde{V}$C pairs, the vowel of the first pair member should, again incorrectly, sound less nasal. (*A priori*, the hypothesis does not make clear predictions about listener performance on *oral* vowels in a nasal consonant context, although listeners should do relatively poorly if they attempt to compensate for the *expected* effects of a nasal context.)

Whether English- and Thai-speaking listeners are predicted to differ in their performance depends on the theoretical framework within which context effects are couched. The language-general interpretation offered by Mann (1986) and Fowler *et al.* (1990) predicts similar performance for the two language groups, because listeners are expected to compensate for coarticulatory influences to the extent they are specified in the signal. Of course, theories that attribute context effects to general auditory processes would also predict similar response patterns for the two language groups. Alternatively, we might predict that Thai listeners would perform differently than English listeners if native language experience influences perceptual compensation (see Beddor *et al.*, 1986, for general discussion along these lines). Under this approach, because Thai speakers have native language experience with less extensive coarticulatory nasalization than English speakers, their responses to English stimuli would be expected to be less fully compensatory than those of native English speakers.

I. EXPERIMENT 1: ENGLISH RATING

A. Methods

1. Stimulus materials

The original stimuli were produced by an adult male native speaker of American English who read a randomized word list containing five tokens each of bed, men, bode, and moan, as well as other monosyllabic words with the vowels /ɛ/ and /o/ to be used in a separate study. The recording was digitized at 10 kHz and two tokens of each of the four words were selected for subsequent manipulation. Because the manipulations involved cross splicing of vowels of a given type (/ɛ/ or /o/) from one consonantal context into another, tokens were selected on the basis of similarity of vocalic pitch, loudness, and duration. (Durations were acoustically determined whereas pitch and loudness judgments were perceptual.) For each of the eight selected stimuli, vowel onset and offset were located using a combination of waveform and spectrographic displays.

For each stimulus, the signal between vowel onset and offset was excised from its original context at the zero crossing in the acoustic waveform. The excised vowels were (a) spliced into the consonantal context of the alternate token of that word type (e.g., ɛ of bed_1 was spliced into b_d of bed_2), (b) spliced into the consonantal context of the ''opposite'' (oral→nasal, nasal→oral) word type (e.g., ɛ of bed_1 was spliced into m_n of men_1), or (c) left excised from context (e.g., isolated ɛ). Condition (a) was included so that excising/splicing techniques would be applied to all stimuli; no original stimulus remained intact. This resulted in six syllable types: [bVd], [bṼd], [mVn], [mṼn], [V], and [Ṽ] (where V=oral vowel from an original b_d context and Ṽ=nasal vowel from an original m_n context). The two vowels, /ɛ/ and /o/, both with and without nasalization, each spliced or excised into the three contexts as well as into the alternate token, yielded 24 manipulated test stimuli. The manipulated stimuli contained no audible discontinuities; also, excising and splicing had no noticeable effect on flanking consonants (i.e., [mon] and [mɛn] stimuli contained clear [m_n] despite the absence of vowel nasalization; [bõd] and [bɛ̃d] stimuli contained clear [b_d] despite the presence of vowel nasalization). In what follows, sequences with /ɛ/ and /o/ (whether oral or nasal) are referred to as /ɛ/ and /o/ sets, respectively.

For each vowel set, 21 types of test pairings were created; pair types are illustrated in Table I for the /o/ set. The pair types fall into three basic categories according to vowel nasality and consonantal context. First, for six pair types, paired vowels had the same nasality and occurred in the same context (Table Ia). These control pairs consisted of two different tokens of each syllable type (e.g., $[õ_1]$–$[õ_2]$; $[bo_1d]$–$[bo_2d]$). Second, for six pair types, paired vowels also had the same nasality, but occurred in different contexts (Table Ib). Vowels in these test pairs were acoustically identical (e.g., $[bõ_1d]$–$[õ_1]$; $[bo_2d]$–$[mo_2n]$). Third, nine types of test pairs had vowels that differed in nasality; vowel contexts included all possible pairings of the three contexts (Table Ic). For these cross-nasality pair types, a particular pairing of oral and nasal vowels was consistently used (i.e., possible pairs were $[o_1]$–$[õ_1]$ and $[o_2]$–$[õ_2]$, but not $[o_1]$–$[õ_2]$ or $[o_2]$–$[õ_1]$).

TABLE I. Rating pair types for the /o/ set.

a. Same vowel nasality, same context (control pairs).

Vowel Context	Vowel Nasality: Oral	Vowel Nasality: Nasal
Isolation	[o]–[o]	[õ]–[õ]
Oral	[bod]–[bod]	[bõd]–[bõd]
Nasal	[mon]–[mon]	[mõn]–[mõn]

b. Same vowel nasality, different contexts.

Vowel Context	Vowel Nasality: Oral	Vowel Nasality: Nasal
Oral Context – Isolation	[bod]–[o]	[bõd]–[õ]
Nasal Context – Isolation	[mon]–[o]	[mõn]–[õ]
Oral – Nasal Context	[bod]–[mon]	[bõd]–[mõn]

c. Different vowel nasality.

Nasal Vowel Context	Oral Vowel Context: Isolation	Oral	Nasal
Isolation	[o]–[õ]	[bod]–[õ]	[mon]–[õ]
Oral	[o]–[bõd]	[bod]–[bõd]	[mon]–[bõd]
Nasal	[o]–[mõn]	[bod]–[mõn]	[mon]–[mõn]

One limitation of this experimental design is that, despite our efforts to select stimuli whose vowels were relatively similar in characteristics other than nasality, the duration of vowels in oral and nasal contexts systematically differed: Vowels in nasal contexts were shorter than vowels in oral contexts, as seen in Table II. Consequently, nasal vowels spliced into oral contexts, and oral vowels spliced into nasal contexts, would be inappropriate in both nasality and duration. Also, because isolated vowels tend to be relatively long, excised nasal vowels would be temporally more inappropriate than excised oral vowels. Although we wanted to retain the original durations in order to compare identical vowels in cross-context comparisons (e.g., [Ṽ] vs [mṼn] vs [bṼd]), additionally we wanted to make the same comparisons with vowels of contextually appropriate duration. Therefore, we added a vowel duration manipulation to the /ɛ/ set (chosen because, on average, this set had the greater oral–nasal duration difference). Nasal [ɛ̃]s were lengthened by iterating pitch pulses to the duration of their oral vowel counterparts (e.g., $[ɛ̃_1]$ was lengthened to match $[ɛ_1]$ duration); oral [ɛ]s were shortened by deleting pitch pulses to the duration of their nasal vowel counterparts (e.g., $[ɛ_1]$ was shortened to match $[ɛ̃_1]$ duration). Full pitch pulses were manipulated, hence ''matched'' durations were not identical, but always fell within 3 ms of each other. All pairings are shown in Table III (where $_L$=lengthened, $_S$=shortened, and

TABLE II. Duration of vocalic portions of the eight original stimuli.

	Duration (ms)	
	Token 1	Token 2
bɛd	289	285
mɛ̃n	230	234
bod	364	366
mõn	328	313

TABLE III. Rating pair types for the /ɛ/ set. Because the original vowels were longer in oral than in nasal contexts, vowel duration was manipulated in selected pairs ($_L$=lengthened; $_S$=shortened; see text for explanation). Only the pairs with context-appropriate vowel durations (top pair type in cells with two pairs) were included in the primary ANOVAs. The Appendix gives the ANOVA results for the matched-duration vowels (bottom pair type in two-pair cells).

a. Same vowel nasality, same context (control pairs).

Vowel Context	Vowel Nasality: Oral	Vowel Nasality: Nasal
Isolation	[ɛ]–[ɛ]	[ɛ̃$_L$]–[ɛ̃$_L$] [ɛ̃]–[ɛ̃]
Oral	[bɛd]–[bɛd]	[bɛ̃$_L$d]–[bɛ̃$_L$d]
Nasal	[mɛ$_S$n]–[mɛ$_S$n]	[mɛ̃n]–[mɛ̃n]

b. Same vowel nasality, different contexts.

Vowel Context	Vowel Nasality: Oral	Vowel Nasality: Nasal
Oral Context - Isolation	[bɛd]–[ɛ]	[bɛ̃$_L$d]–[ɛ̃$_L$]
Nasal Context - Isolation	[mɛ$_S$n]–[ɛ] [mɛn]–[ɛ]	[mɛ̃n]–[ɛ̃$_L$] [mɛ̃n]–[ɛ̃]
Oral - Nasal Context	[bɛd]–[mɛ$_S$n] [bɛd]–[mɛn]	[bɛ̃$_L$d]–[mɛ̃n] [bɛ̃d]–[mɛ̃n]

c. Different vowel nasality.

Nasal Vowel Context	Oral Vowel Context: Isolation	Oral Vowel Context: Oral	Oral Vowel Context: Nasal
Isolation	[ɛ]–[ɛ̃$_L$]	[bɛd]–[ɛ̃$_L$]	[mɛ$_S$n]–[ɛ̃$_L$] [mɛ$_S$n]–[ɛ̃]
Oral	[ɛ]–[bɛ̃$_L$d]	[bɛd]–[bɛ̃$_L$d]	[mɛ$_S$n]–[bɛ̃$_L$d] [mɛ$_S$n]–[bɛ̃d]
Nasal	[ɛ]–[mɛ̃n] [ɛ$_S$]–[mɛ̃n]	[bɛd]–[mɛ̃n]	[mɛ$_S$n]–[mɛ̃n]

no subscript=original duration). Cells with only one pair type have vowels with contextually appropriate, matched durations; the one exception is [bɛd]–[mɛ̃n] (Table IIIc) with different (original) vowel durations. For cells with two pair types, the vowels of the top pair have context-appropriate but unmatched durations, and those of the bottom pair have matched durations with that duration being contextually inappropriate for one pair member. The isolated vowel pairings in Table IIIa are exceptions to this general pattern.

Each vowel set had two tokens for each noncontrol pair type and one token for each control pair type, yielding 36 pairs for the /o/ set [6 controls+(2×15) noncontrols; Table I] and 51 pairs for the /ɛ/ set [7 controls+(2×22) noncontrols; Table III]. The within-trial ISI was 1 s and across-trial interval was 4 s. A ten-item practice sequence was also created for each of the /o/ and /ɛ/ sets.

2. Listeners

Listeners were 16 native English-speaking undergraduate students recruited from introductory linguistics classes at the University of Michigan (age range was 19–24 years; mean age: 20.3 years). No listener had more than rudimentary training in phonetics or phonology and none reported hearing or speaking deficiencies. Listeners were paid for their participation.

Fourteen of the 16 listeners had studied a second language; of these languages, only French (studied by 5 listeners) has contrastive nasalization. Two listeners were bilingual in English and Chinese, although, like the other listeners, they were born and raised in the U.S. (Thirteen listeners had lived most of their lives in Michigan.) All listeners' results are pooled below.

3. Procedure

Test sequences contained two repetitions of each of the two orders of each pair, for a total of 144 (2×2×36) randomized /o/ trials and 204 (2×2×51) randomized /ɛ/ trials. The rating tests for the two vowel sets were output to digital audio tape and presented over headphones to small groups of up to four listeners in a sound-attenuated room in the Phonetics Laboratory at the University of Michigan. Listeners were told that they would hear computer-manipulated syllables from English. They were instructed to focus on the vowel sounds in the syllables and to decide, for each pair of syllables, whether the vowel in the first or second syllable sounded more nasal, or whether they sounded equally nasal (or equally non-nasal). The experimenter provided the following explanation of ''nasal:'' ''You probably already have an intuitive notion of what it means for a vowel to sound nasal. If any of you have studied a language such as French, Portuguese, or Hindi, you know that in these languages nasalization on a vowel changes the meaning of a word. In French, for example, the word [bo] means ''handsome,'' but [bõ] (with a nasal ''o'') means ''good.'' In English, vowels also can be nasalized next to certain consonants. For example, the ''ah'' sound in mom is usually quite nasal.''

The response sheets indicated the type of trial in English orthography. For example, for [bõd]–[mon] the options were *bode moan same*; for [mon]–[o]: *moan o same*; for [o]–[õ]: *o o same*; and so on. Listeners were told to circle one option per trial. The order of presentation of the two tests, /ɛ/ and /o/, was counterbalanced across listener groups. For each set, listeners first heard the corresponding practice series, without feedback, to familiarize them with the task. Total rating test time was less than 1 h.

B. Results

The results for the three basic types of comparisons according to vowel nasality and vowel context (Tables Ia–c and IIIa–c) were separately analyzed using repeated measures ANOVAs. *Post hoc* Tukey tests investigated significant main effects of factors having more than two levels or significant interactions. For each of the three data sets, the results entered into the primary ANOVA were the mean percent correct responses of each listener to each pair type from the /o/ set, and from the /ɛ/ set with context-appropriate vowel durations (in Table III, the top pair in cells with two members). All discussion in the results sections of this paper refer to those items. Separate ANOVAs were also conducted on the results for the matched-duration /ɛ/ set (the bottom pair in cells with two members in Table III); the results of these latter ANOVAs, which largely serve to reinforce the findings of the primary analyses, are presented in the Appendix. The two different duration conditions were not directly compared because we were not interested in duration *per se*,

but rather in whether the same pattern of results would hold when only vowel nasality varied as when vowel duration and nasality covaried.

In reporting the results, the oral [b_d] context is referred to as C_C, the nasal [m_n] context as N_N, and isolation as #_#.

1. Control comparisons

Listeners were expected to perform relatively well on the control comparisons, in which paired vowels had the same nasality and occurred in the same context (Tables Ia and IIIa). Summing across /ɛ/ and /o/, mean rating accuracy ranged from 74% to 91% correct, with accuracy at or above 85% correct on the pairs V–V, $\tilde{V}$–$\tilde{V}$, and CVC–CVC, and dropping below 80% correct on N$\tilde{V}$N–N$\tilde{V}$N, NVN–NVN, and C$\tilde{V}$C–C$\tilde{V}$C. A three-way ANOVA testing for the effects of vowel nasality (V, $\tilde{V}$), vowel context (C_C, N_N, #_#), and vowel quality (/ɛ/, /o/) showed that vowel context was significant [$F(1,30)=3.44$, $p<0.05$], as was its interaction with vowel nasality [$F(2,30)=3.58$, $p<0.05$]. No other main effect or interaction was significant.

Two types of *post hoc* Tukey analyses explored the interaction between vowel context and vowel nasality. *Post hoc* tests for an effect of vowel context for oral and nasal vowels showed that, for nasal vowels, listeners were more accurate on $\tilde{V}$ trials than on N$\tilde{V}$N and C$\tilde{V}$C trials [$t(30)=2.36$, $p<0.05$ for the $\tilde{V}$–N$\tilde{V}$N comparison and 2.88, $p<0.01$ for $\tilde{V}$–C$\tilde{V}$C]; for oral vowels, none of the differences between contexts was significant. *Post hoc* tests for an effect of vowel nasality in each of the context pairings showed no significant differences between oral and nasal vowels. That listeners judged the relative nasality of nasal vowels as accurately as that of oral vowels in this control condition is encouraging, as it indicates that rating the nasality of nasal vowels was not inherently difficult for these listeners.

2. Comparisons with same vowel nasality and different vowel contexts

We turn to pairings in which context varied but vowel nasality was held constant (Tables IIb and IIIb). Of main interest is whether overall accuracy is affected by context and, in particular, whether context influences judgments of nasal vowels more than those of oral vowels. Under a coarticulatory compensation hypothesis, listeners are predicted to perform poorly when rating the nasality of a nasal vowel in the N_N context relative to that of the same vowel in a non-nasal (#_# or C_C) context.

Figure 1 shows listeners' pooled percent correct ratings (i.e., percent ''same'' nasality judgments) of oral and nasal vowels, collapsed across vowel quality, for the three types of pairings of vowel contexts. Listeners' performance was, on average, better on pairs with oral vowels (73%) than nasal ones (49%), and better on vowels in C_C–#_# pairs (84%) than on pairings with N_N (50%). A three-way ANOVA tested for the effects of vowel nasality (V, $\tilde{V}$), vowel contexts (C_C–#_#; N_N–#_#; C_C–N_N), and vowel quality (/ɛ/, /o/). There were significant main effects of vowel

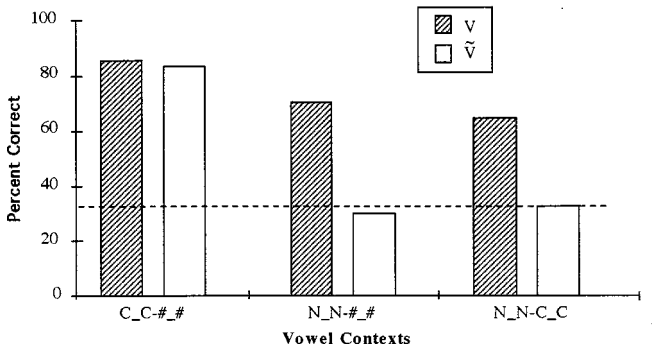

FIG. 1. Experiment 1: Pooled percent correct responses of English listeners to rating pairs with different vowel contexts and same vowel nasality, according to contexts (abscissa) and nasality (bar type: Striped=oral vowel; unfilled=nasal vowel). (For example, the left-most bar represents the pair CVC-V.) The dashed horizontal line indicates chance performance.

nasality [$F(1,15)=11.22$, $p<0.01$] and vowel contexts [$F(2,30)=36.64$, $p<0.001$], and a significant interaction between the two [$F(2,165)=11.27$, $p<0.001$]. No other main effect or interaction was significant.

Post hoc Tukey tests for the effect of vowel nasality in each of the three context pairings showed that accuracy was higher for oral vowels than for nasal vowels in comparisons involving the N_N context [$t(30)=4.47$ and 3.59, $p<0.001$ and 0.01, for N_N–#_# (middle pairs in Fig. 1) and N_N–C_C (right) pairs, respectively]. The difference was not significant for C_C–#_# pairs (left), where accuracy for both oral and nasal vowels was in the range of control-comparison performance. The relative difficulty of the three comparison types held for individual listeners as well, with all but one listener rating oral vowels more accurately than nasal vowels for the N_N–#_# comparisons and all but two listeners doing the same for the N_N–C_C comparisons.

The statistical tests, taken together with the means, indicate that cross-context comparisons are most difficult when such comparisons involve, as one member, a nasal vowel in a nasal consonant context. Performance on oral vowel pairings is also poorer when one of the vowels occurs in a nasal consonant context; however, performance is still far better for such oral vowel comparisons than for the corresponding nasal vowel comparisons. The same pattern of results was obtained for the matched-duration /ɛ/ set, reported in the Appendix.

Because the comparisons with different vowel contexts revealed significant differences in performance as a function of the combination of contexts and vowel nasality, it seemed appropriate to look in more detail at the error patterns for each comparison pair. Collapsing across the /o/ and /ɛ/ sets, Fig. 2 shows the three-way response breakdown: The vowel in the first stimulus is ''more nasal,'' the vowel in the second stimulus is ''more nasal,'' or the vowels have the ''same'' nasality. Figure 2(a), oral vowels, reinforces what we already know about oral vowel pairings: Listeners are highly accurate judging such pairs when no nasal context is involved (CVC–V); performance falls off but is well above chance when one oral vowel is embedded in the N_N context (NVN–V and NVN–CVC). Interestingly, in the N_N–C_C comparison, the most common error is the identification of

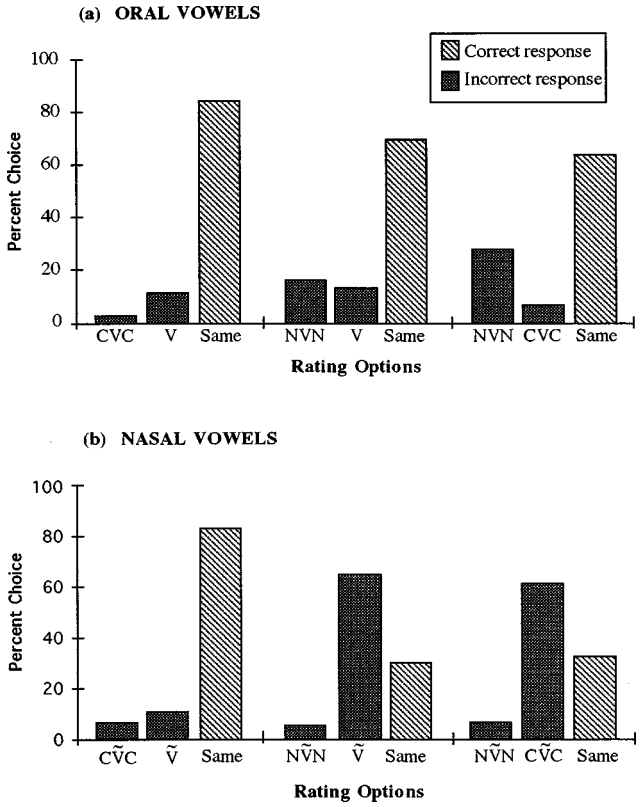

FIG. 2. Experiment 1: Pooled percent choice responses of English listeners to C_C–#_# (left), N_N–#_# (middle), and N_N–C_C (right) pairs with same vowel nasality: Frequency of listeners' choice of each of the three rating options for oral vowels [panel (a)] and nasal vowels [panel (b)].

the oral vowel in the N_N context as ''more nasal.'' (The same is marginally true in the N_N–#_# comparison.) For pairings of nasal vowels [Fig. 2(b)], rating of pairs that do not include the N_N context is again highly accurate, but in this case rating accuracy for pairs that include the N_N context is at chance level. The single most common response for NṼN–Ṽ and NṼN–CṼC pairs was a compensatory response: The nasal vowel in the non-nasal context (CṼC, Ṽ) was heard as ''more nasal'' than the same vowel in the nasal NṼN context.

3. Comparisons with different vowel nasality

This set of analyses examines all comparisons that paired an oral vowel with a nasal vowel, whether or not the vowel contexts were identical (Tables Ic and IIIc). If listeners compensate for coarticulatory nasalization, Ṽ should be rated as more nasal than V when Ṽ is in a non-nasal context, but Ṽ and V should be rated as (roughly) equally nasal when Ṽ is in a nasal context.

Figure 3 presents the combined /ɛ/–/o/ data, where nasal vowel context is shown along the abscissa and oral vowel context is shown by different bar types. In each case, the correct response was to select the nasal vowel as ''more nasal.'' The most obvious outcome seen in Fig. 3 is the especially poor performance on pairs involving NṼN (right set of bars)—a pattern already observed in the preceding section (and a pattern that held for the individual results of

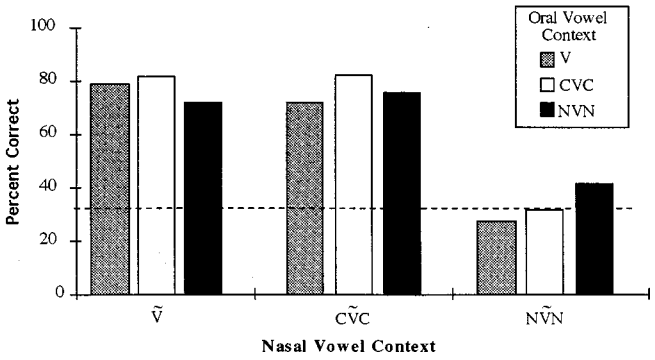

FIG. 3. Experiment 1: Percent correct responses of English listeners to rating pairs with different vowel nasality. Grouping of bars indicates nasal vowel context. Bar type indicates oral vowel context. (For example, the left-most bar represents the pair V–Ṽ).

15 of the 16 listeners). A three-way ANOVA on the effects of oral vowel context (CVC, NVN, V), nasal vowel context (CṼC, NṼN, Ṽ), and vowel quality (/ɛ/, /o/) showed that the only significant main effect was that of nasal vowel context [$F(2,30)=37.15$, $p<0.001$]. The significant interactions were a two-way interaction between nasal and oral vowel contexts [$F(4,60)=6.03$, $p<0.001$] and a three-way interaction among all factors [$F(4,60)=3.70$, $p<0.01$].

The interaction between nasal and oral vowel contexts was due to improved rating accuracy when paired oral and nasal vowels occurred in the same consonant context. Although listeners did poorly on pairings with a nasal vowel in the N_N context, accuracy improved when the oral vowel of the pair also occurred in that context (i.e., NṼN–NVN; right-most bar in Fig. 3). Similarly, for pairings with a nasal vowel in the C_C context (middle set of bars), listeners performed best when the paired oral vowel was in the same context (CṼC–CVC). However, the facilitatory effect of the same context was more consistent for the /ɛ/s than the /o/s, hence the interaction of nasal and oral vowel contexts with vowel quality. Tests for the simple main effect of oral vowel context in each of the nasal vowel contexts, conducted separately for the /ɛ/ and /o/ sets, showed that oral vowel context was not significant for either set when the nasal vowel was in isolation (left set of bars). When the nasal vowel was in the N_N context, oral vowel context was significant only for the /ɛ/s [$F(2,30)=5.91$, $p<0.01$], with *post hoc* tests showing better performance when the oral vowel context was NVN (i.e., the matched context) than when it was V or CVC [$t(30)=2.81$ and 3.13 for V and CVC, respectively, $p<0.01$]. Similarly, when the nasal vowel was in the C_C context, oral vowel context was again significant only for the /ɛ/s [$F(2,30)=4.02$, $p<0.05$], with accuracy higher when CṼC was paired with CVC than when paired with V or NVN [$t(30)=2.15$ and 2.68 for V and NVN, respectively, $p<0.05$]. The matched-duration /ɛ/ set also showed the pattern of more accurate rating when paired vowel contexts are the same (see the Appendix).

Because pairings with NṼN were so problematic for listeners, we again examined the three-way pattern of responses to these pair types, shown in Fig. 4. Only for the NṼN–NVN

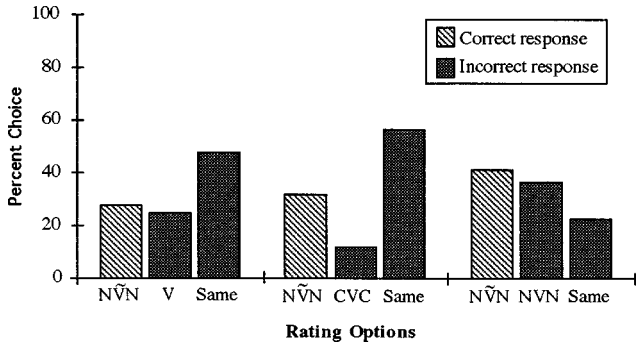

FIG. 4. Experiment 1: Pooled percent choice responses of English listeners to rating comparisons involving NṼN paired with an oral vowel in the #_# (left), C_C (middle), and N_N (right) contexts: Frequency of listeners' choice of each of the three rating options.

pairings (i.e., same context; right set of bars) was listeners' single most common response the correct response. For NṼN–V pairings (left) and NṼN–CVC pairings (middle), ''same'' nasality was the single most common response and the correct NṼN choice was the second most common (although only marginally so for NṼN–V). Thus, for different-context pairings, listeners were most likely to judge the vowels as equally nasal (52%)—i.e., the compensatory judgment—but when they chose one vowel as more nasal than the other, they were more likely to make the correct (30%) than the incorrect (18%) choice.

C. Discussion

As predicted by the compensation hypothesis, native English listeners showed consistent difficulties in judging the nasality of nasal vowels in an appropriate, NṼN, context. Importantly, nasal vowels were not inherently difficult to rate: Listeners were much more accurate on nasal vowels in isolation and in an oral C_C context. Even the comparison of nasal vowels occurring in different contexts was not problematic for listeners, as long as the contexts were non-nasal. Indeed, listener ratings of nasal CṼC–Ṽ pairs were as accurate as those of oral CVC–V pairs (around 80% correct)—and ratings of both of these pair types were nearly as accurate as ratings of the control (same vowel context and nasality) comparisons. In contrast, the most common response to pairings of a nasal vowel in the N_N context with an oral vowel in a non-nasal context (C_C or #_#) was that the two vowels sounded ''equally nasal,'' indicating that listeners attribute vowel nasality to a nasal consonant context, when present. Still, in more than 25% of these cases, listeners correctly reported that NṼN was the most nasal member of the pair. Hence, compensation, although clearly evident for NṼN sequences, cannot be said to be complete. Finally, we note that performance on oral vowels in N_N contexts was neither as poor as that on nasal vowels in this context nor as accurate as that on oral vowels in the other two contexts.

The generality of the patterns described here is supported by the vowel quality and the vowel duration manipulations. Most findings held for both the /o/ and /ɛ/ sets. Findings also held for both the contextually appropriate and matched durations of the /ɛ/ set (see the Appendix), indicating that the difficulty of judging vowel nasality in the N_N context was not due to contextually inappropriate vowel duration.

II. EXPERIMENT 2: ENGLISH DISCRIMINATION

As noted in the Introduction, the rating task requires listeners to make metalinguistic judgments concerning vowel nasality. It is possible that listeners might be more sensitive to the nasality of vowels in a nasal context in a task which required them not to rate nasality *per se*, but rather to discriminate vowels (or vowel pairs) differing in nasality. Experiment 2 was conducted to explore this possibility.

A. Methods

1. Stimulus materials

The same stimuli used in the rating task were arranged into a 4IAX discrimination paradigm. Each trial consisted of two stimulus pairs, one with vowels differing in nasality and one with vowels having the same nasality. The control trials, designed to verify listeners' ability to discriminate nasality differences using this paradigm, held vowel context constant and varied only vowel nasality. The test trials explored listeners' ability to discriminate vowel nasality differences across different contexts. We were particularly interested in performance when listener options were (a) two vowels differing in nasality (henceforth, ''mismatched'' nasality) but both in coarticulatorily appropriate contexts (e.g., [bod]–[mõn]) versus (b) two vowels with the same (''matched'') nasality but one in a coarticulatorily inappropriate context (e.g., [bõd]–[mõn] or [bod]–[mon]). Consequently, not all possible test trials were included; for trials with vowels in consonantal contexts, all trials had one stimulus pair in which vowel nasality was coarticulatorily appropriate.

The 14 types of discrimination trials for the /o/ set are given in Table IV. Selection of the test stimuli for each trial type was similar to the conditions established for the rating task. For the four same-context control trials (Table IVa), the pair whose vowels had the same nasality consisted of two different tokens of that syllable type (e.g., $[o_1]$–$[o_2]$). For the eight context-to-isolation trials (Table IVb) and the two oral-to-nasal context trials (Table IVc), the vowels in the pairs with the same nasality were acoustically identical (e.g., $[bo_1d]$–$[o_1]$; $[b\tilde{o}_2d]$–$[m\tilde{o}_2n]$).

Recall from experiment 1 that, because this speaker's nasal vowels were shorter than his oral vowels, the vowels in [bVd] and [mṼn] would differ in both nasality and duration if no adjustments were made. As in experiment 1, experiment 2 controlled for this temporal difference for the /ɛ/ set. The discrimination trials for the /ɛ/ set are given in Table V. As for the /o/ set, pairs whose vowels had the same nasality used two different tokens of that syllable type for same-context trials, but used acoustically identical vowels for the other trial types. However, for the /ɛ/ set, all vowels within a trial were equalized for duration, except for the oral-to-nasal context trials. For trials with equalized vowel duration (Table Va and Vb), the selected duration was appropriate for that

TABLE IV. Discrimination trials for the /o/ set. For each trial, the vowels in one pair had the same nasality (''matched'' nasality) and the vowels in the other pair differed in nasality (''mismatched'' nasality). In Table IVb, vowel nasality is (arbitrarily) coded by the nasality of the vowel in isolation.

a. Same-context (control trials).

		Vowel context		
		Isolation	Oral	Nasal
Matched vowel nasality	Oral	[o]–[o] / [o]–[õ]	[bod]–[bod] / [bod]–[bõd]	
	Nasal	[õ]–[õ] / [o]–[õ]		[mõn]–[mõn] / [mon]–[mõn]

b. Context-to-isolation.

			Vowel contexts	
	Matched	Mismatched	Oral - Isolation	Nasal - Isolation
Nasality of isolated vowel	Oral	Oral	[bod]–[o] / [bõd]–[o]	[mon]–[o] / [mõn]–[o]
		Nasal	[bod]–[o] / [bod]–[õ]	[mon]–[o] / [mon]–[õ]
	Nasal	Oral	[bõd]–[õ] / [bõd]–[o]	[mõn]–[õ] / [mõn]–[o]
		Nasal	[bõd]–[õ] / [bod]–[õ]	[mõn]–[õ] / [mon]–[õ]

c. Oral-to-nasal context.

Matched vowel nasality	Oral	[bod]–[mon] / [bod]–[mõn]
	Nasal	[bõd]–[mõn] / [bod]–[mõn]

TABLE V. Discrimination trials for the /ɛ/ set ($_L$=lengthened; $_S$=shortened). For cells with two trials (Vc), the vowels in the top trial have context-appropriate durations and the vowels in the bottom have the original durations. In b, vowel nasality is (arbitrarily) coded by the nasality of the vowel in isolation.

a. Same-context (control trials).

		Vowel context		
		Isolation	Oral	Nasal
Matched vowel nasality	Oral	[ɛ]–[ɛ] / [ɛ]–[ɛ̃$_L$]	[bɛd]–[bɛd] / [bɛd]–[bɛ̃$_L$d]	
	Nasal	[ɛ̃$_L$]–[ɛ̃$_L$] / [ɛ]–[ɛ̃$_L$]		[mɛ̃n]–[mɛ̃n] / [mɛ$_S$n]–[mɛ̃n]

b. Context-to-isolation.

			Vowel contexts	
	Matched	Mismatched	Oral - Isolation	Nasal - Isolation
Nasality of isolated vowel	Oral	Oral	[bɛd]–[ɛ] / [bɛ̃$_L$d]–[ɛ]	[mɛ$_S$n]–[ɛ$_S$] / [mɛ̃n]–[ɛ]
		Nasal	[bɛd]–[ɛ] / [bɛd]–[ɛ̃$_L$]	[mɛ$_S$n]–[ɛ$_S$] / [mɛn]–[ɛ̃]
	Nasal	Oral	[bɛ̃$_L$d]–[ɛ̃$_L$] / [bɛ̃$_L$d]–[ɛ]	[mɛ̃n]–[ɛ̃] / [mɛ̃n]–[ɛ$_S$]
		Nasal	[bɛ̃$_L$d]–[ɛ̃$_L$] / [bɛd]–[ɛ̃$_L$]	[mɛ̃n]–[ɛ̃] / [mɛ$_S$n]–[ɛ̃]

c. Oral-to-nasal context.

Matched vowel nasality	Oral	[bɛd]–[mɛ$_S$n] / [bɛd]–[mɛ̃n] [bɛd]–[mɛn] / [bɛd]–[mɛ̃n]
	Nasal	[bɛ̃$_L$d]–[mɛ̃n] / [bɛd]–[mɛ̃n] [bɛ̃d]–[mɛ̃n] / [bɛd]–[mɛ̃n]

context: Long for vowels in the #_# and [b_d] contexts; short for vowels in the [m_n] context, as well as vowels in [m_n]–#_# pairings. For the oral-to-nasal context trials (Table Vc), two types of duration pairings were selected: One pairing had context-appropriate durations (top trial in each cell) and the other retained the original vowel durations (bottom trial).

For each trial type, there were two versions of the comparison. Also, four stimulus orders were possible for each 4IAX comparison (i.e., substituting the numbers 1–2/3–4 for the stimuli in a comparison such as [bɛd]–[mɛ̃n]/[bɛd]–[mɛn], the possible orders are 1–2/3–4, 2–1/4–3, 3–4/1–2, and 4–3/2–1). For all discrimination trials, the within-pair interval was 0.4 s, the across-pair interval was 0.8 s, and the across-trial interval was 3 s.

2. Listeners

The 16 listeners who participated in experiment 1 also participated in experiment 2.

3. Procedure

Three separate randomized test sequences were constructed for each vowel set. The control sequence consisted of all same-context trials (4 trial types×2 tokens ×4 orders×2 repetitions=64 trials per vowel set). A second sequence had context-to-isolation trials (8 trial types×2 tokens×4 orders=64 trials per vowel set). A third sequence had oral-to-nasal context comparisons (2 trial types×2 tokens×4 orders×3 repetitions=48 /o/ trials; 4 trial types×2 tokens×4 orders×3 repetitions =96 /ɛ/ trials). (Different numbers of repetitions in the three sequences were used both to make sequence lengths more comparable and to reduce discrimination test time.) Half of the listeners heard all three /o/ sequences followed by all three /ɛ/ sequences; the other half heard the reverse order. Within each vowel set, the control sequence was always heard first; the order of the other two sequences was counterbalanced across listeners. Prior to each test sequence, listeners heard a 12-item practice sequence.

As in experiment 1, test sequences were output to digital audio tape and presented to small groups of listeners over headphones. Importantly, as noted above, listeners participated in experiment 2 *before* experiment 1 because we did not want listeners' metalinguistic assessment of nasality in experiment 1 to influence listeners' discrimination judgments in experiment 2. The two experiments were conducted in separate 1-h sessions within a few days of each other. In the discrimination test, as in the rating test, listeners were told to focus on the vowel sounds in the syllables. The listeners' task was to select, for each 4IAX trial, the pair in which the vowels sounded more different from each other. Response sheets indicated the trial type in English orthography.

B. Results

Listeners' responses to the discrimination test were analyzed according to the three test sequences presented to listeners: Same-context (#_#, C_C, N_N), context-to-isolation (C_C–#_# or N_N–#_#), and oral-to-nasal context (C_C–

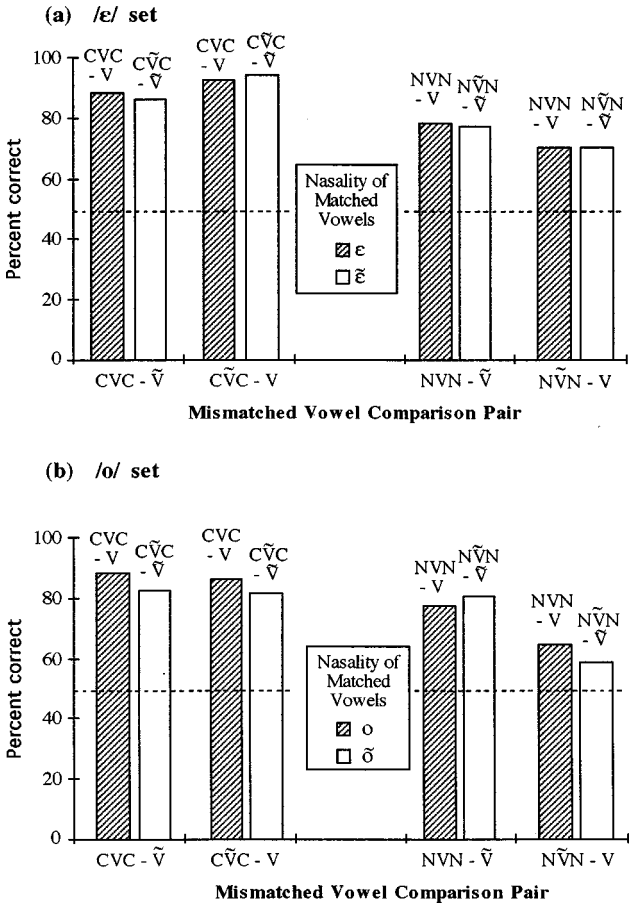

FIG. 5. Experiment 2: Pooled percent correct responses of English listeners to context-to-isolation 4IAX comparisons for the /ɛ/ [panel (a)] and /o/ [panel (b)] sets. Nasality of matched vowels is shown by bar type: Striped =oral and unfilled=nasal. (For clarity, the matched vowel pair is listed at the top of each pair.) Nasality and context of mismatched vowels are shown on the abscissa.

N_N) comparisons of oral and nasal vowels. As in experiment 1, a repeated measures ANOVA and *post hoc* Tukey comparisons were conducted on mean percent correct responses of each listener to each pair type in that test sequence. (However, unlike experiment 1, listeners were given only two response options per discrimination trial, hence chance performance in experiment 2 was at the 50% rather than the 33% level.) Because only the oral-to-nasal context comparisons had two /ɛ/ durations (see Table Vc), only this comparison set required a separate ANOVA for the matched-duration condition, reported in the Appendix.

1. Control (same-context) comparisons

When context is held constant, native English listeners can reliably discriminate vowel nasality within the 4IAX paradigm. Mean performance on the same-context comparisons ranged narrowly from 95% to 98% correct across the four comparison types (see Tables IVa and Va). Individual performance of most (12 of the 16) listeners also averaged 95% or better for these comparisons.

Accurate discrimination of all same-context discrimination trials, including NVN–NṼN/NṼN–NṼN, differs sharply from listeners' near-chance performance on the same-context NVN–NṼN *rating* pairs, suggesting that, as expected, the different tests assess different perceptual abili-

ties. At least for these same-context trials, listeners were able to discriminate oral and nasal vowel pairs whose relative nasality they found difficult to rate.

2. Context-to-isolation comparisons

Listeners are expected to be less accurate discriminators of the context-to-isolation trials than the same-context trials because of the added difficulty of the variable vowel context within each comparison pair. The central question is whether any effects of context are uniform across conditions, or whether discrimination of vowel nasality differences is consistently poorer when the paired vowel contexts are N_N–#_# (especially when the vowel in the N_N context is nasal) than when they are C_C–#_#.

Percent correct responses to the context-to-isolation comparisons for the /ɛ/ and /o/ sets, pooled across listeners, are given in Fig. 5. Oral C_C context pairs are represented by the four bars on the left of each panel and nasal N_N context pairs by the four bars on the right. Bar type shows the nasality of the matched vowels (both oral or both nasal) in each comparison; the abscissa indicates the mismatched pair (one oral vowel and one nasal vowel).

As expected, performance on the context-to-isolation comparisons is less accurate than on the control comparisons (above), a group difference which also held for the results of all individual listeners. However, the degree of difficulty is not uniform across all comparison pairs. To assess performance on these comparisons, a four-way ANOVA was conducted with the factors vowel context (C_C, N_N), matched vowel nasality (V, $\tilde{V}$), mismatched vowel nasality (whether the isolated vowel was V or $\tilde{V}$), and vowel quality (/ɛ/, /o/). Consistent with the rating results, vowel context was significant [$F(1,15)=41.25$, $p<0.001$], with trials involving the N_N context being more difficult than those with C_C [right versus left sides of Fig. 5(a) and (b)]. Vowel context also interacted significantly with mismatched vowel nasality [$F(1,15)=17.29$, $p<0.001$]. No other main effect or interaction was significant.

Post hoc comparisons to explore the interaction showed that, for the mismatched vowels, performance was better on comparisons with NVN–$\tilde{V}$ than on those with N$\tilde{V}$N–V [$t(15)=3.00$, $p<0.01$; third versus fourth pairs of bars in Fig. 5(a) and 5(b)]. However, the difference between comparisons with CVC–$\tilde{V}$ and C$\tilde{V}$C-V was not significant [first versus second pairs of bars in Fig. 5(a) and 5(b)]. Thus, although listeners made the correct choice more often than not in this task, they were most likely—as expected—to make the incorrect choice (i.e., to select the vowels of the mismatched oral-nasal vowel pair as more similar) when the nasal vowel was in the N_N context [two right-most bars in Fig. 5(a) and (b)].

3. Oral-to-nasal context comparisons

Like all discrimination trials, the oral-to-nasal context comparisons involved a mismatched oral–nasal vowel pair compared with a matched oral–oral or nasal–nasal vowel pair with spectrally identical vowels. However, in these comparisons, vowel identity and context appropriateness were in conflict. The members of the *mismatched* vowel pair were in coarticulatorily *appropriate* contexts (CVC–N$\tilde{V}$N) while one of the two members of the *matched* vowel pair (CVC-NVN or C$\tilde{V}$C–N$\tilde{V}$N) was in a coarticulatorily *inappropriate* context (see Tables IVc and Vc). Under a compensation hypothesis, we would expect context appropriateness to win out, with listeners incorrectly perceiving the mismatched vowel pair as more similar.

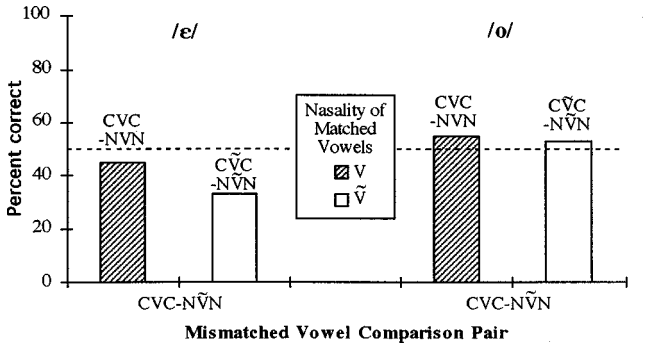

FIG. 6. Experiment 2: Pooled percent correct responses of English listeners to oral-to-nasal context 4IAX comparisons for the /ɛ/ (left) and /o/ (right) sets. Striped=matched oral vowels; unfilled=matched nasal vowels. The mismatched vowel pair was always CVC–N$\tilde{V}$N.

Figure 6 gives the results for the /ɛ/ and /o/ sets. Listeners' mean performance was near or below chance for all comparisons, indicating that listeners were not able to discriminate differences in vowel nasality when all vowels were embedded in consonantal contexts. Although performance was poorer on /ɛ/s than /o/s, and on comparisons in which the matched vowel pair was nasal than those in which it was oral, a two-way ANOVA assessing matched vowel nasality (V, $\tilde{V}$) and vowel quality (/ɛ/, /o/), showed that neither factor was significant. (Unlike the context-to-isolation comparisons, there is no mismatched vowel nasality factor; all comparisons had CVC–N$\tilde{V}$N as the mismatched pair.)

The near-chance level of the group responses in Fig. 6 is representative of the data of 8 of the 16 individual listeners. The other eight listeners showed more consistent patterns in their responses, but they fell into two categories: three poor discriminators, whose accuracy was below 10% on these comparisons, and five good discriminators, whose accuracy was above 65%. There was no obvious link between good discrimination and language background (e.g., only two of the five listeners who had studied French fell into this group).

C. Discussion

Overall performance on the discrimination controls was better than on the rating controls, indicating that the discrimination task was, as expected, a more sensitive measure of listeners' judgments of oral and nasal vowels. Nonetheless, the conclusions from the rating study find further support in the patterns obtained here. That is, despite their relatively strong performance on the discrimination controls, listeners' responses to test comparisons (an isolated vowel paired with a vowel in a consonantal context, or a vowel in the C_C context paired with a vowel in the N_N context)

revealed a pattern consistent with the notion that there is some compensation for vowel nasalization when it occurs in an appropriate coarticulatory context. Thus, when errors occurred in isolation-to-context comparisons, they were most likely to occur in conditions in which the mismatched pair included a nasal vowel in a nasal consonant context (i.e., N$\tilde{V}$N–V). For these errors, acoustically identical vowels (in NVN–V or N$\tilde{V}$N–$\tilde{V}$) were heard as more dissimilar than acoustically different, but contextually appropriate, vowels (in N$\tilde{V}$N–V). Still, listeners were accurate in their judgments of these pairings more often than not. Further support for partial compensation was obtained on the oral-to-nasal context pairings. Listeners displayed consistently poor performance on these trials by often selecting the acoustically matched vowel pair (CVC–NVN or C$\tilde{V}$C–N$\tilde{V}$N) as being more different in nasality than the mismatched pair (CVC–N$\tilde{V}$N). Despite the difficulty of this task for listeners (accuracy plummeted relative to both control and context-to-isolation trials, hovering around or below chance), correct responses were also obtained on a considerable number of trials.

Overall, the effects of the context in which a vowel occurs on the perception of vowel nasality are robust across different vowel qualities and durations, and generally similar across the two experimental tasks. One issue that cannot be addressed by the results of experiments 1 and 2 is the extent to which these contextual effects are a consequence of the linguistic background of native English-speaking listeners. As a first step in investigating this question, in experiments 3 and 4 we presented the tests used in experiments 1 and 2 to native speakers of Thai. As discussed in the Introduction, Thai-speaking listeners were chosen because their native language has been shown to differ from English in terms of patterns of coarticulatory nasalization, with Thai showing temporally less extensive anticipatory nasalization than English.

III. EXPERIMENT 3: THAI RATING

A. Methods

1. Stimulus materials and procedure

The rating test that was presented to native English speakers in experiment 1 was presented to native Thai speakers in experiment 3. Exactly the same testing procedure was used, except that the experimenter was a native Thai speaker and all instructions were given in Thai. Consent forms and questionnaires were in Thai script, but response forms were in English (i.e., identical to the forms used in experiment 1).

2. Listeners

Listeners were 15 native Thai speakers ranging in age from 19–32 years (mean age: 24.2 years). Fourteen speakers were (nonlinguistics) graduate students at the University of Michigan; the remaining speaker was studying English at the Michigan Language Center in Ann Arbor. As with the native English speakers, none of the Thai listeners was phonetically trained and none reported hearing or speaking deficiencies. Listeners were paid for their participation.

All Thai speakers also spoke English as a second language, although no Thai participant had lived in the U.S. for more than 2 years (length of time in U.S. ranged from 5 months to 2 years; mean stay: 12 months). Only two Thai speakers reported experience with a language other than English, both of whom were exposed to Chinese, in addition to Thai, at home as children.

B. Results

As non-native speakers of English, and as native speakers of a language in which vowels are nasalized to some extent in a nasal consonant context, Thai listeners' responses are expected to show some evidence of compensation for coarticulatory vowel nasalization. The main question under investigation is whether Thai listeners' native experience with a language that shows less extensive nasalization than English influences their responses to English vowels in ways that are consistent with the coarticulatory differences between the two languages. Specifically, Thai listeners' responses to nasal vowels are expected to be less consistently compensatory than those of native English listeners.

To assess the responses of Thai listeners to the rating test, we used the same statistical design in experiment 3 that was used for analyzing the native English listeners' responses in experiment 1. The statistical analyses do not directly compare Thai and native English listeners' performance because the relative accuracy of the two language groups is not our focus. For example, Thai listeners' responses to these non-native stimuli might be overall less accurate, but the relative difficulty of pair types could still parallel the native English response patterns. As with the native English data, the Thai data presented in the text are for the /o/ set and the /ɛ/ set with contextually appropriate durations; the results for the matched-duration /ɛ/ set are given in the Appendix.

1. Control comparisons

Rating accuracy of the Thai-speaking listeners on the control comparisons (i.e., same vowel nasality and same vowel context; Tables Ia and IIIa) ranged from 81% to 92% correct. Similar to native English listeners' results, Thai listeners were somewhat less accurate on the pairs N$\tilde{V}$N–N$\tilde{V}$N, NVN–NVN, and C$\tilde{V}$C–C$\tilde{V}$C than on the remaining comparisons, but the drop in accuracy was not as great for Thai listeners. A three-way ANOVA [vowel nasality (V, $\tilde{V}$), vowel context (C_C, N_N, #_#), and vowel quality (/ɛ/, /o/)] conducted on the Thai control data showed no significant main effects or interactions. In contrast, vowel context and its interaction with vowel nasality were significant for the English data. Therefore, for these control comparisons, the effect of nasal vowel context was not as great for Thai listeners as for English listeners.

2. Comparisons with same vowel nasality and different vowel contexts

Turning to rating pairs in which vowel context varied but vowel nasality did not, the hypothesis of coarticulatory compensation would predict that Thai speakers, like native

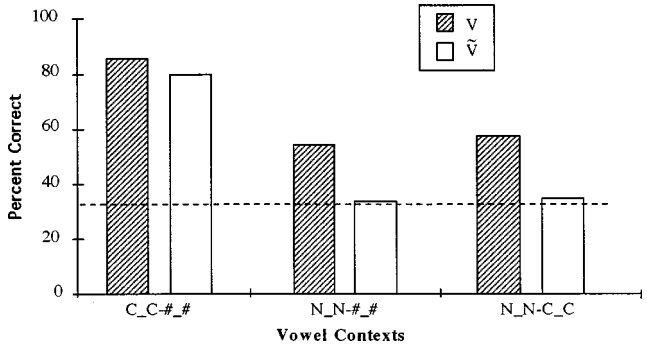

FIG. 7. Experiment 3: Pooled percent correct responses of Thai listeners to rating pairs with different vowel contexts and same vowel nasality, according to contexts (abscissa) and nasality (bar type).

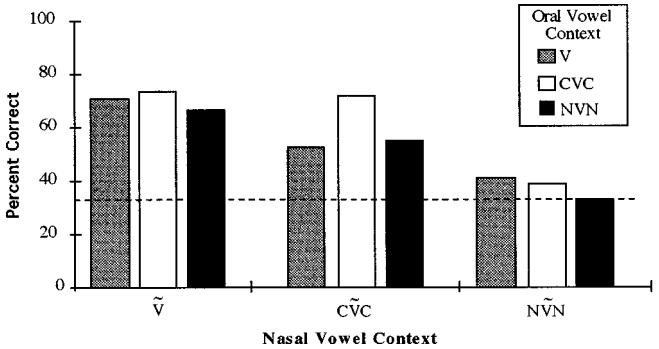

FIG. 9. Experiment 3: Pooled percent correct responses of Thai listeners to rating pairs with different vowel nasality. Grouping of bars indicates nasal vowel context. Bar type indicates oral vowel context.

English speakers, should perform relatively poorly on pairs in which one member involves a nasal vowel in a nasal context. At the same time, if compensation is linked to native-language experience, Thai speakers' responses might be less compensatory than English listeners' and hence show less of an effect of the nasal context.

Figure 7 shows the means obtained on the three types of context pairings, pooled across the /o/ and /ɛ/ sets. Overall on these comparison pairs, Thai listeners performed similarly to native English listeners. As in the English data (see Fig. 1), Thai listeners performed better on pairs with oral than nasal vowels (striped versus unfilled bars), and on pairs with non-nasal contexts (C_C–#_#; left bars in Fig. 7) than on pairs with a vowel in the N_N context (middle and right bars). Both of these findings held for the individual Thai listeners as well: All but two of the listeners showed the vowel nasality pattern and all but one showed the vowel context pattern.

A three-way ANOVA testing for the effects of vowel nasality (V,Ṽ), vowel contexts (C_C–#_#; N_N–#_#; C_C–N_N), and vowel quality (/ɛ/, /o/) showed that the same main effects, vowel nasality and vowel contexts, were significant for the Thai data as for the native English data [vowel nasality: $F(1,14)=8.74$, $p<0.01$; vowel contexts: $F(2,28)=29.57$, $p<0.001$]. Also as found for the English data, the interaction between these two factors was significant, with *post hoc* tests yielding the same pattern of relatively poor performance on pairs involving NṼN. Pairwise comparisons for the effect of vowel nasality in each of the three context pairings showed that rating accuracy was higher for oral vowels than for nasal vowels for N_N–#_# pairs [$t(28)=2.95$, $p<0.01$; middle comparison in Fig. 7] and for N_N–C_C pairs [$t(28)=3.26$, $p<0.01$; right-most comparison in Fig. 7], but the difference between oral and nasal vowels was not significant for C_C–#_# pairs (left).

We wondered whether the Thai listeners' responses would also show the same pattern of results as that of the native English listeners when the more detailed three-way response breakdown was taken into account. Focusing on nasal vowels, where both listener groups were most likely to give incorrect ratings, Fig. 8 gives the Thai results. Comparison with the corresponding English results in Fig. 2(b) shows that the relative percentages of the three response options for each of the three comparison types were the same for the two listener groups. At the same time, Thai listeners were 11% less likely than English listeners to rate Ṽ as ''more nasal'' than NṼN (middle bar of middle group of bars), and 10% less likely to rate CṼC as ''more nasal'' than NṼN (middle bar of right-most group). Thus, for these comparisons with NṼN, Thai listeners were less likely than English listeners to make compensatory responses.

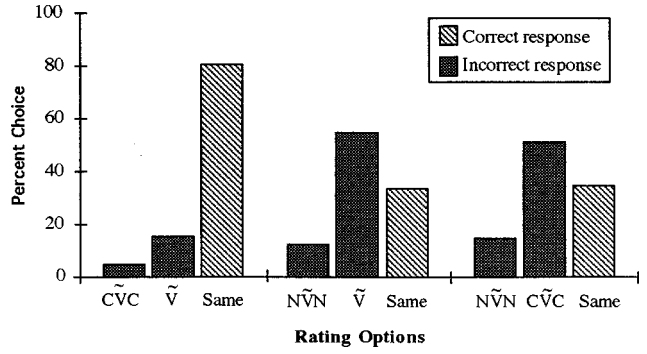

FIG. 8. Experiment 3: Pooled percent choice responses of Thai listeners to CṼC–Ṽ (left), NṼN–Ṽ (middle), and NṼN–CṼC (right) pairs: Frequency of listeners' choice of each of the three rating options.

3. Comparisons with different vowel nasality

Figure 9 shows Thai listeners' percent correct responses to comparisons in which one stimulus had a nasal vowel and the other, an oral vowel. Results are pooled across /ɛ/s and /o/s to facilitate comparison with the corresponding results for the native English listeners in Fig. 3. The most robust pattern in the English data in Fig. 3—poor performance when the nasal vowel is in the N_N context—is also seen in the Thai data in Fig. 9. A three-way ANOVA [oral vowel context (CVC, NVN, V), nasal vowel context (CṼC, NṼN, Ṽ), and vowel quality (/ɛ/, /o/)] revealed significant main effects of all three factors. The vowel quality effect [$F(1,14)=6.52$, $p<0.05$] was due to better performance on /o/ pairs (mean 62% correct) than on /ɛ/ pairs (50%). (English listeners showed no such effect.)

The effects of oral vowel context [$F(2,28)=3.64$, $p<0.05$] and nasal vowel context [$F(2,28)=6.93$, $p<0.01$] are best understood when their significant interaction [$F(4,56)=2.93$, $p<0.05$] is explored. One-way ANOVAs

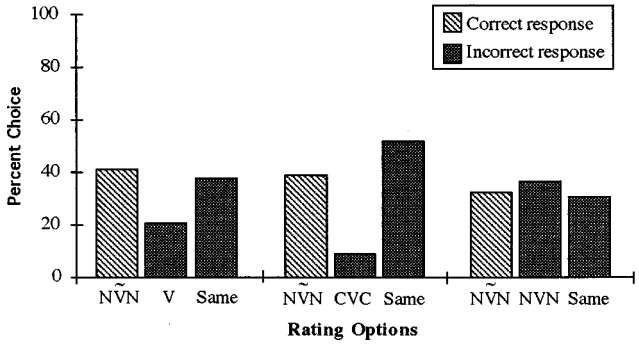

FIG. 10. Experiment 3: Pooled percent choice responses of Thai listeners to rating comparisons involving NṼN paired with an oral vowel in the #_# (left), C_C (middle), and N_N (right) contexts: Frequency of listeners' choice of each of the three rating options.

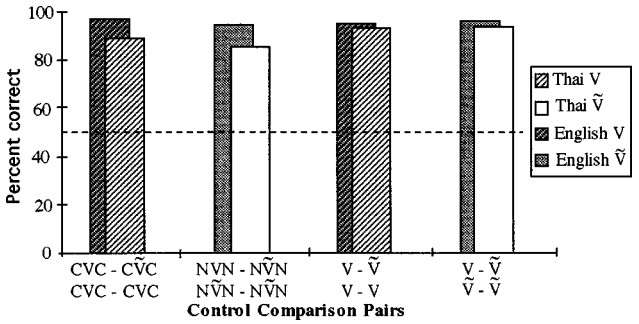

FIG. 11. Experiment 4: Pooled percent correct responses of Thai listeners to control (same-context) 4IAX comparisons. Striped=matched oral vowels; unfilled= matched nasal vowels. English results are shadowed for comparison.

testing for the simple main effect of oral vowel context in each of the nasal vowel contexts showed that oral vowel context (i.e., the three different bar types in Fig. 9) was significant only for comparisons in which the nasal vowel was in the oral C_C context [$F(2,73)=6.22$, $p<0.01$; middle set of bars]. *Post hoc* comparisons showed that Thai listeners performed best when the oral vowel was also in the C_C context [$t(73)=3.24$ and 2.82, $p<0.01$, for CṼC–CVC compared with CṼC–V and CṼC–NVN, respectively]. Native English listeners showed a similar facilitatory effect of same context. On the other hand, whereas English listeners also showed this facilitatory effect for the N_N context, Thai listeners did not (right-most bar). When the nasal vowel was in the N_N context, Thai listeners performed best when the oral vowel was in isolation (NṼN–V). However, as noted, performance remained poor on all pairs with NṼN. This group pattern held for individual listeners as well: 12 of the 15 Thai listeners were less accurate at rating vowel nasality when the nasal vowel was in the N_N context than when it was the non-nasal (#_#, C_C) contexts.

To examine further the pairs that pose the greatest difficulty to listeners, Fig. 10 plots the three-way response patterns of the Thai listeners to the three comparisons that included NṼN. Overall accuracy of Thai listeners on these comparisons (38% correct) is only slightly better than that of English listeners (34%) and, for the three comparison types, both language groups' responses are more often incorrect than correct (NṼN is the correct choice). However, some differences are noteworthy (compare Figs. 4 and 10). On both the NṼN–V and the NṼN–CVC pairs, Thai listeners were more accurate than native English listeners (14% for NṼN–V and 7% for NṼN–CVC) and were less likely to select the compensatory response ''same'' (10% and 4%, respectively). On the NṼN–NVN pairs (right), Thai listeners were less accurate than native English listeners, presumably because the non-native listeners did not benefit from the same-context comparison.

C. Discussion

On the rating task, the performance of the Thai speakers, like that of the native English speakers, indicated that it is difficult to judge accurately the nasality of a nasal vowel when it occurs in a contextually appropriate nasal consonant context. No other stimulus type elicited as poor performance (near chance), whether we consider test pairs with same vowel nasality or different vowel nasality. On pairs with same vowel nasality, but different contexts, Thai rating of the pairing with nasal vowels in non-nasal contexts (CṼC–Ṽ) was almost as accurate as that of the corresponding pairing with oral vowels (CVC–V) and close to native accuracy of around 80%. On pairs with different vowel nasality, rating of pairs with nasal vowels in non-nasal contexts dropped somewhat, suggesting that the oral-nasal vowel comparison (or at least these non-native comparisons) may be inherently more difficult for Thai than for native English listeners, but accuracy remained well above chance. As with English listeners, it appears that the main difficulty for Thai listeners is not vowel nasality *per se*, but rather that there is perceptual compensation when the nasal vowel is heard in a nasalizing environment.

Also consistent with the native English listeners' data, it is clear that the Thai listeners' compensation is not complete. However, the pattern of partial compensation exhibited by Thai listeners' responses differs in systematic ways from that of the English listeners. As predicted by the hypothesis that compensation is linked to native-language coarticulatory experience, Thai listeners were less likely than native English listeners to choose the compensatory response to pairs involving NṼN. This was seen for same-nasality NṼN–Ṽ and NṼN–CṼC pairs, where Thai listeners were less likely than native English listeners to identify the inappropriately nasalized vowel (Ṽ or CṼC) as the more nasal one. It was also seen for different-nasality NṼN–V and NṼN–CVC pairs, where Thai listeners less frequently identified the vowels as having the same nasality. Even for the control pairs (same vowel nasality, same context), the negative effect of nasal vowel context on rating accuracy was not as great for Thai as for native English listeners.

IV. EXPERIMENT 4: THAI DISCRIMINATION

A. Methods

The discrimination test from experiment 2 was presented to native Thai listeners in experiment 4. The identical testing

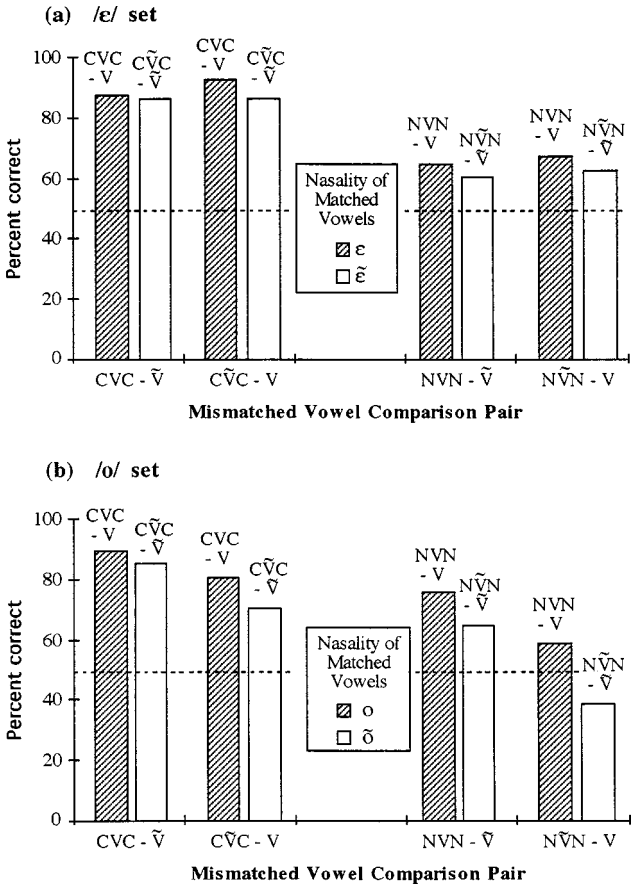

FIG. 12. Experiment 4: Pooled percent correct responses of Thai listeners to context-to-isolation 4IAX comparisons for the /ɛ/ [panel (a)] and /o/ [panel (b)] sets. Nasality of matched vowels is shown by bar type: Striped=oral and unfilled=nasal. (For clarity, the matched vowel pair is listed at the top of each pair.) Nasality and context of mismatched vowels are shown on the abscissa.

procedure was used except that the testing session was conducted in Thai. Listeners were the 15 listeners who had participated in experiment 3.

B. Results

1. Control (same-context) comparisons

Thai listeners' pooled responses to the same-context discrimination comparisons are given in Fig. 11; native English listeners' results are included for comparison. Overall, Thai listeners were less accurate than native English listeners in discriminating these stimulus pairs, but most of the discrepancy between the two language groups occurred in the comparison pairs involving vowels in a consonantal context (two left-most pairs of bars). Unlike English listeners who discriminated all control comparisons at essentially the same level of accuracy, Thai listeners were poorer at discriminating vowels in a consonantal context than those in isolation. A three-way ANOVA [vowel context (consonantal context, isolation), matched vowel nasality (V, $\tilde{\text{V}}$), and vowel quality (/ɛ/, /o/)] showed only the effect of vowel context to be significant [$F(1,14)=12.73$, $p<0.01$].

2. Context-to-isolation comparisons

Figure 12 gives the Thai pooled discrimination results for context-to-isolation trials. The most obvious outcome is that Thai listeners, like native English listeners (Fig. 5), were less accurate on trials involving the nasal N_N context than those with the oral C_C context.

A four-way ANOVA [vowel context (C_C, N_N), matched vowel nasality (V,$\tilde{\text{V}}$), mismatched vowel nasality (V,$\tilde{\text{V}}$), and vowel quality (/ɛ/, /o/)] conducted on the Thai responses to these comparisons showed significant main effects of vowel context and matched and mismatched vowel nasality. (Only vowel context, which interacted with mismatched vowel nasality, was significant for the native English data.) As just noted, Thai listeners were better at discriminating context-to-isolation comparisons when the context was C_C than when it was N_N [vowel context: $F(1,14)=40.66$, $p<0.001$]. Unlike English listeners, Thai listeners were also better at discriminating comparisons when the matched vowels were oral than when they were nasal [matched vowel nasality: $F(1,14)=6.79$, $p<0.05$]. This can be seen in Fig. 12 by comparing the corresponding striped (oral vowel) bars and unfilled (nasal vowel) bars for each of the eight matched vowel groupings: In all cases, performance was poorer when the matched vowels were nasal. These patterns also generally held for individual Thai listeners' responses. All Thai listeners showed better discrimination of trials with C_C than N_N; better discrimination of matched oral than nasal vowels was less systematic, but held for a majority of the listeners.

The effect of mismatched vowel nasality [$F(1,14)=6.70$, $p<0.05$] must be interpreted in terms of its significant interaction with vowel quality [$F(1,14)=15.34$, $p<0.01$]. Tukey paired comparisons indicated that the /o/, but not the /ɛ/, data showed poorer discrimination when the nasal vowels in the mismatched pairs were in a consonantal context (62%; second and fourth pairs) than when they were in isolation (79% correct; first and third pairs of bars) [$t(28)=4.53$, $p<0.001$]. The remaining interactions were not significant.

Contrary to expectations, Thai listeners were no less likely than native English listeners to give compensatory (i.e., incorrect) responses to context-to-isolation trials involving NṼN. Indeed, comparison of the Thai results in Fig. 12 with the English results in Fig. 5 seems to indicate that Thai listeners were even more likely than English listeners to give compensatory responses to these trials. However, the nature of the significant main effects indicates that a more accurate characterization of the Thai results is that Thai listeners are poorer at discriminating nasal vowels than oral ones, poorer yet when the nasal vowels are in a consonantal context, and poorest when this context is N_N. Thus Thai discrimination results for trials with NṼN is apparently due not only to compensation for a nasalizing context, but also to Thai listeners' more general difficulty discriminating nasal vowels—a difficulty not observed for the native English results.

3. Oral-to-nasal context comparisons

Results for the oral-to-nasal context comparisons for the /ɛ/ and /o/ sets are given in Fig. 13. Performance on all conditions was at chance level. A two-way ANOVA,

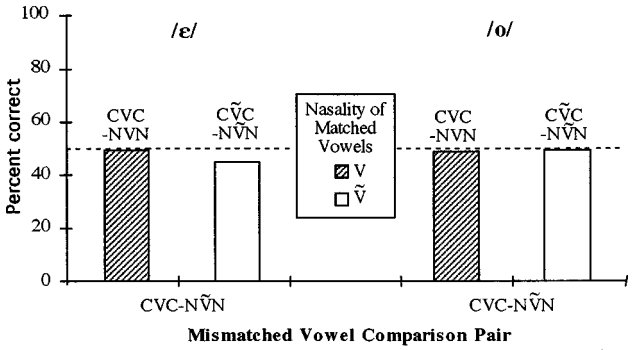

FIG. 13. Experiment 4: Pooled percent correct responses of Thai listeners to oral-to-nasal context 4IAX comparisons for the /ɛ/ (left) and /o/ (right) sets. Striped=matched oral vowels; unfilled=matched nasal vowels. The mismatched vowel pair was always CVC–NṼN.

matched vowel nasality (V,Ṽ) and vowel quality (/ɛ/, /o/), showed that neither factor was significant. Thus Thai listeners were similar to native English listeners in their overall poor discrimination of these comparisons.

The performance of individual Thai listeners on the oral-to-nasal context comparisons parallels the three types of native English listeners described above for these comparisons. Eight Thai listeners discriminated close to the chance level of the group responses, four listeners discriminated well above chance (above 65% correct), and three listeners discriminated well below chance (below 25% correct).

C. Discussion

The Thai listeners, like the native English listeners, were accurate discriminators of the control comparisons involving vowels in the same contexts. Also like the English listeners, Thai listeners were (near-)chance discriminators of different-context comparisons involving CVC–NṼN, which means that, on average, acoustically distinct oral and nasal vowels in coarticulatorily appropriate contexts sounded no more different than acoustically identical vowels (both oral or both nasal), one of which was in an inappropriate context (NVN or CṼC). Thai performance on most context-to-isolation pairings involving NṼN fell in between, with accuracy averaging 60%. Thus we see again the now-familiar pattern of partial compensation for vowel nasality in a coarticulatory nasal context: Thai listeners often, but not systematically, chose the coarticulatorily appropriate, compensatory response over the noncompensatory one.

Unlike the rating data, overall the discrimination data do not show that Thai listeners were less likely than native English listeners to provide compensatory responses to comparisons involving NṼN. The unexpectedly high percentage of Thai compensatory responses to these comparisons appears to be due in part to the general difficulty that Thai listeners, but not English listeners, had judging nasal vowels. The general difficulty was most apparent in the Thai responses to context-to-isolation discrimination trials, where matched oral vowels, even in non-nasal contexts, were consistently better discriminated than matched nasal vowels (i.e., when three of the four vowels in matched–mismatched 4IAX trials were oral as opposed to when three of the four vowels were nasal). Thai listeners' difficulty in judging oral-nasal vowel differences also emerged, but was less robust, for the different-nasality rating pairs in experiment 3.

Why might nasal vowels pose a general perceptual difficulty for Thai, but not English, listeners? The motivation for selecting Thai in comparison to English was that Thai has less coarticulatory vowel nasalization than English, at least in temporal extent. However, additionally, there is evidence that vowel nasalization has a different *phonological* status in Thai than in English. Although neither language has contrastively nasalized vowels in non-nasal contexts (but see footnote 4), the extensive and constant proportional nature of English vowel nasalization indicates that nasalization has become ''phonologized'' in this language (Solé, 1992, 1995; Ohala, 1993; Hajek, 1997). Thus at the allophonic level, and arguably at the phonological level, Thai listeners have less native language experience than English listeners with vowel nasalization, and this experiential difference might be responsible for the perceptual difference.

V. GENERAL DISCUSSION

In exploring the perceptual effects of coarticulatory context, we have investigated the influence of different contextual conditions on listeners' judgments of vowel nasality. We first consider the results in terms of an approach which attributes the contextual effects to listener compensation for coarticulatory nasalization. We then consider the extent to which the results might be accounted for in terms of more general auditory capabilities.

We begin by revisiting the predictions of a coarticulatory compensation hypothesis, as outlined in the Introduction. Error rates were expected to be low for nasal vowels in non-nasal contexts (C_C and isolation) because, in the absence of a coarticulatory context responsible for the nasalization, listeners should hear the acoustic effects of nasalization as part of the vowel itself. In contrast, error rates were predicted to be high for nasal vowels in the nasal N_N context: Listeners should attribute vowel nasalization to the context rather than the vowel and should judge the vowel of NṼN as less nasal than that of CṼC or isolated Ṽ. Importantly, we note that predictions of high error rates for NṼN are for laboratory conditions in which listeners are asked to rate or discriminate nasality. In natural communicative settings, we do not view such a pattern as error. On the contrary, assigning the vocalic variation introduced by coarticulatory nasalization to the nasal context is argued to facilitate perception.

The experimental predictions were largely upheld. The four experiments showed English and Thai listeners to be poor judges of nasal vowels in the nasal context. Nasality rating (experiments 1 and 3) was at or near chance level for *all* test pairings with NṼN. Similarly, discrimination (experiments 2 and 4) was poorest on comparisons involving NṼN, with performance plummeting to chance level or below on oral-to-nasal context (NṼN–CVC) comparisons. Also as predicted, listeners were comparatively accurate judges of

nasal vowels in non-nasal contexts (i.e., C$\tilde{V}$C and $\tilde{V}$ when not paired with an N_N stimulus). In fact, native English listeners rated and discriminated C$\tilde{V}$C and $\tilde{V}$ as accurately as their oral counterparts; Thai listeners performed less well on C$\tilde{V}$C and $\tilde{V}$ than on CVC and V, but better than on comparisons with N$\tilde{V}$N. That native English listeners judged nasal vowels in non-nasal contexts as accurately as oral vowels in those contexts is consistent with the findings of Kingston and Macmillan (1995). In addition, the finding that listeners are most inaccurate on vowel nasality or similarity judgments involving nasal vowels in a nasal context is compatible with earlier findings reported by Kawasaki (1986) and Krakow and Beddor (1991). However, this pattern conflicts with findings recently reported by Macmillan *et al.* (1999). Using classification and identification paradigms, Macmillan *et al.* investigated English listeners' perception of vowel nasalization (and vowel height) in oral C_C and nasal C_N contexts and found that, in the classification study, the nasality of the final consonant had little effect on vowel nasality judgments. Even more surprising relative to our findings is that their identification data showed that listeners were somewhat *more* likely to identify vowels as nasal when followed by a nasal consonant than when followed by an oral one. Clearly, listeners' nasality judgments were more consistently influenced by coarticulatory context in the current set of experiments than in theirs; this could be due to methodological differences between the two studies, although the precise source of the discrepancy is uncertain.

How do the present results fare against an even stronger version of the perceptual compensation hypothesis? As described in the Introduction, Fowler (e.g., 1996; Fowler and Smith, 1986), Ohala (e.g., 1993), and ourselves (Krakow *et al.*, 1988), among others, have analyzed context effects within frameworks which state that, given an appropriate and detectable context, listeners attribute the acoustic effects of the context to their coarticulatory source. It seems reasonable to interpret such approaches as predicting that listeners should succeed in attributing *all* of the contextually induced variation to the context. For example, nasal vowels embedded in N_N should not just sound less nasal than nasal vowels in non-nasal contexts, they should be systematically treated like *oral* vowels.

The rating and discrimination data provide counterevidence, indicating that native English and Thai listeners do *not* hear the vowel of N$\tilde{V}$N as oral. Listeners did not consistently rate the vowels of N$\tilde{V}$N and CVC or V as equally nasal, nor did they consistently rate the vowel of N$\tilde{V}$N as more nasal than that of C$\tilde{V}$C or $\tilde{V}$; instead, these incorrect choices averaged only 53% (38%–65% across conditions) of the total responses. Similarly, listeners did not systematically hear the (identical) vowels in N$\tilde{V}$N–$\tilde{V}$ or N$\tilde{V}$N–C$\tilde{V}$C pairs as more different than the (nonidentical) vowels in N$\tilde{V}$N–V or N$\tilde{V}$N–CVC pairs; in these cases, incorrect (i.e., compensatory) responses averaged 42% of the total responses for the context-to-isolation comparisons and 55% for the oral-to-nasal context comparisons.

One interpretation of this pattern, in which the vowel of N$\tilde{V}$N sounds less nasal than that of C$\tilde{V}$C or $\tilde{V}$ but still not oral, might seem to be that listeners are simply uncertain of the nasality of contextually nasalized vowels. Important aspects of the data argue against this interpretation. First, the three-way breakdown of listeners' nasality ratings (i.e., percent choice rather than percent correct) consistently show that, although English and Thai listeners usually selected the compensatory response more often than either noncompensatory one, their next most common choice was the *correct* response (e.g., the vowels of N$\tilde{V}$N and C$\tilde{V}$C or $\tilde{V}$ are equally nasal, or the vowel of N$\tilde{V}$N is more nasal than that of CVC or V). Second, contrary to an ''uncertainty'' interpretation, discrimination accuracy for the comparisons with N$\tilde{V}$N–V was consistently above chance level [with one exception for Thai listeners; Fig. 12(b)].

In our view, the overall results are more compatible with the interpretation that these listeners were *partially* compensating for contextual nasalization, that is, that listeners were attributing some, but not all, of coarticulatory vowel nasalization to the nasal consonant context. If listeners hear contextual nasal vowels as intermediate in nasality, the response patterns described under the two points immediately above are expected. In fact, for the discrimination results, we should expect that, like N$\tilde{V}$N–V, comparisons with N$\tilde{V}$N–CVC would also be discriminated above chance level; clearly the increased difficulty of the latter task (where the target sound is embedded in a context) affected listeners' performance level [see also Krakow and Beddor (1991) for a similar pattern of results using a different paradigm].

The cross-language differences in the perceptual results also are as expected if perceptual compensation is partial *and* the extent of compensation is linked to patterns of coarticulatory and ''phonologized'' vowel nasalization in the listeners' native language. In the rating task, Thai listeners were systematically less likely than English listeners to give compensatory nasality ratings for comparisons involving N$\tilde{V}$N, suggesting that Thai listeners attributed less of the nasality of the vowel in N$\tilde{V}$N to the coarticulatory context. This is in keeping with the finding that Thai speakers' productions exhibit less coarticulatory nasalization than that of many English speakers, at least for C$\tilde{V}$N sequences. The Thai discrimination data did not provide systematic evidence of less compensation for pairs with N$\tilde{V}$N. We have argued that possible compensatory differences may be hidden by the overall greater difficulty of nasal vowels for Thai listeners seen in C_C as well as N_N contexts, a difficulty we have in turn attributed to phonological factors.

Partial perceptual compensation that may be linked to coarticulatory and phonological patterns in the listeners' native language is consistent with an approach to perception in which contextual information is but one of many factors that enter into perceptual decisions about what the speaker has said [see Hawkins (1995); it is also generally consistent with Nearey's model (1992, 1997), which allows speakers of different languages to assign different weights to perceptual cues]. While contextual information facilitates perceptual decisions, it need not provide all the information a listener

needs to arrive at the speaker's intended utterance. Moreover, the discrepancy between the perceived and intended utterances might be particularly large when listeners' decisions involve phonetic properties whose realization depends on a wide range of factors. It is well known that coarticulatory nasalization is highly subject to such influences (e.g., syllable position, stress, speaking rate, vowel height; Schourup, 1973; Kent *et al.*, 1974; Clumeck, 1976; Bell-Berti and Krakow, 1991; Bell-Berti, 1993; Krakow, 1993, 1999).

The aim of these experiments was to delineate the contextual conditions that lead—or do not lead—to compensatory responses for vowel nasalization. We have argued that listeners' responses reveal a pattern of partial compensation in which listeners are least sensitive to vowel nasality in a nasal consonant context, but still retain some sensitivity. (See Beddor and Krakow, 1998, for discussion of the ways in which partial compensation might have influenced sound changes involving nasal vowels.) In concluding, we consider the extent to which these results are also compatible with a purely auditory account which attributes these patterns of responses to general contrast effects. Many aspects of these findings are entirely compatible with this interpretation, most notably that listeners perform most poorly on comparisons with N$\tilde{V}$N is precisely what would be expected on the basis of spectral contrast: Sensitivity to the nasal resonances of [$\tilde{\varepsilon}$] or [$\tilde{o}$] was lowered due to the nasal resonances of flanking N_N. However, at least two aspects of these findings are problematic for an interpretation along these lines. First, although performance was poorest on N$\tilde{V}$N comparisons, judging *oral* vowels in the N_N context (NVN) was also relatively difficult for listeners, with some discrimination conditions showing little or no difference in performance on comparisons with N$\tilde{V}$N versus NVN. Frequency contrast does not predict poor performance in the latter case. On the other hand, if listeners perceptually accommodate the dynamics of nasal coupling, they might be expected to attempt to compensate for the expected effects of a nasal context even in the absence of those effects. As Lotto and Kluender (1998) pointed out (in evaluating context effects on identification), an important test case for contrast as opposed to coarticulatory accounts would be a dissimilatory rather than assimilatory effect of coarticulation. Although coarticulatory vowel nasalization is assimilatory, these findings suggest that absence of coarticulatory vowel nasalization in a nasal context can lead to dissimilatory response patterns (i.e., hearing identical vowels in NVN–V or NVN–CVC pairings as different).

A second aspect of these results that is not consistent with spectral contrast, nor more generally with a purely auditory account, is the finding of cross-language differences. Thai listeners, unlike English listeners, had greater overall difficulty judging nasal vowels than oral vowels; Thai listeners also were less likely to provide compensatory responses to N$\tilde{V}$N stimuli in the rating task. Auditory mechanisms alone cannot explain these language group differences. In contrast, that these differences reflect coarticulatory compensation is suggested by the correspondence between listeners' perceptual responses and the languages' coarticulatory structures (Thai exhibiting less extensive vowel nasalization than many of the dialects of English that have been studied). While additional cross-language perceptual data would be needed to make strong claims concerning the relation between perceptual compensation and language-specific coarticulatory organization, the overall convergence among the patterns of partial perceptual compensation, nasal coarticulation, and nasal vowel phonology indicates that listeners perceptually adjust, albeit imperfectly, for the acoustic effects of nasalization under appropriate coarticulatory conditions.

ACKNOWLEDGMENTS

The research reported here was supported in part by NSF Grant No. SBR 9319597 to Patrice Beddor and NIH Grant No. NS-131617 to Haskins Laboratories. A subset of these data was presented at the Twenty-Fourth Annual Meeting of the Berkeley Linguistics Society and appears in the proceedings of that conference. We thank James Harnsberger for assistance in data collection and statistical analysis and Chutamanee Onsuwan for data collection assistance. We also thank the University of Michigan phonetics-phonology discussion group and participants at BLS 24 for comments on oral presentations, and Suzanne Boyce, Sharon Manuel, an anonymous reviewer, and Associate Editor James Hillenbrand for helpful advice on an earlier draft.

APPENDIX: MATCHED-DURATION /ɛ/ SET

As shown in Tables III and V, and as described in the main text, the duration of the /ɛ/ stimuli was manipulated to create two duration conditions for many of the /ɛ/ trials. In one condition, paired vowels had contextually appropriate (and, except for the control trials, different) durations; in the other condition, paired vowels had the same durations. This appendix presents the results of the latter, matched-duration set. Overall, the results support the findings for the larger (/o/s and /ɛ/s with context-appropriate durations) data set.

1. Experiment 1: English rating

For the control comparisons in experiment 1, only the [$\tilde{\varepsilon}$]–[$\tilde{\varepsilon}$] comparison had two duration conditions (Table IIIa). Mean accuracy on the two conditions differed by less than 2%.

For test comparisons in which paired /ɛ/s had the same nasality, but occurred in different contexts (Table IIIb), the results of the ANOVA for the matched-duration /ɛ/ set paralleled those of primary ANOVA (Sec. I B 2). A two-way ANOVA showed significant main effects of context [$F(2,30)=20.73$, $p<0.001$] and vowel nasality [$F(1,15)=7.70$, $p<0.05$], as well as a significant interaction between the two [$F(2,30)=17.31$, $p<0.001$]. *Post hoc* analyses showed that performance was significantly better on oral than nasal vowels in N_N–#_# pairs and N_N–C_C pairs [$t(30)=3.20$, $p<0.01$ and 4.29, $p<0.001$, respectively], but not in C_C–#_# pairs.

For test comparisons in which paired /ɛ/s differed in nasality, the results of a two-way ANOVA (nasal vowel context, oral vowel context) for the matched-duration /ɛ/s again paralleled those of the corresponding primary ANOVA (Sec.

I B 3): Nasal vowel context was significant [$F(2,30) = 12.51$, $p < .001$], as was the nasal and oral vowel contexts interaction [$F(4,60) = 9.08$, $p < 0.001$]. Testing for the simple main effect of oral vowel context in each of the nasal vowel contexts, we obtained the same results as for the larger data set. For trials involving N$\tilde{V}$N, oral vowel context was significant [$F(2,30) = 5.47$, $p < 0.01$], with *post hocs* showing more accurate rating when the oral vowel context was the matched NVN context than when it was V or CVC [$t(30) = 2.75$ and 2.97 for V and CVC, respectively, $p < 0.01$]. For trials involving C$\tilde{V}$C, oral vowel context was also significant [$F(2,30) = 4.60$, $p < 0.05$], with better performance when C$\tilde{V}$C was paired with CVC than when paired V or NVN [$t(30) = 2.19$ and 2.91 for V and NVN, $p < 0.05$ and 0.01, respectively]. Thus, judgments of the relative nasality of paired nasal and oral vowels were enhanced when the vowels occurred in the same consonant context.

2. Experiment 2: English discrimination

For the discrimination trials, only the oral-to-nasal context trial types had two durations for the /ɛ/ set. Listeners were somewhat more accurate on matched-(original) duration trials (47% correct) than on context-appropriate duration trials (40% correct). [We note that listeners were also more accurate on the matched- or original-duration /o/ trials (55% correct).] However, a one-way ANOVA of the matched-duration /ɛ/ results showed that, as for the larger data set, matched vowel nasality was not significant.

3. Experiment 3: Thai rating

For rating trials in which paired /ɛ/s had the same nasality, but occurred in different contexts, a two-way ANOVA (vowel nasality and vowel context) on the matched-duration /ɛ/ set showed a significant main effect of vowel context [$F(2,28) = 19.86$, $p < 0.001$]. *Post hoc* tests indicated that Thai listeners were more accurate rating pairs with non-nasal contexts than pairs with the N_N context: Performance was significantly better on C_C–#_# than on N_N–#_# [$t(28) = 5.95$, $p < 0.001$] or N_N–C_C [$t(28) = 4.77$, $p < 0.001$]. In the analysis of the larger data set (Sec. III B 2), vowel nasality was also significant, but that main effect only approached significance [$F(1,14) = 3.64$, $p < 0.077$] in this smaller data set.

For trials in which paired /ɛ/s differed in nasality, a two-way ANOVA (nasal vowel context, oral vowel context) run on the matched-duration /ɛ/s showed, consistent with the combined /ɛ/ and /o/ sets (Sec. III B 3), a significant main effect of nasal vowel context [$F(2,28) = 4.78$, $p < 0.05$]. *Post hoc* tests revealed that only the comparison between pairs with N$\tilde{V}$N and those with isolated $\tilde{V}$ was significant [$t(28) = 3.01$, $p < 0.05$]. The effect of oral vowel context, significant for the larger data set, approached significance here [$F(2,42) = 2.94$, $p < 0.064$].

4. Experiment 4: Thai discrimination

Recall that the only discrimination trials with two durations for the /ɛ/ set are the oral-to-nasal context trial types. As for the larger data set, a one-way ANOVA on the original-duration /ɛ/ set for these trials showed no effect of matched vowel nasality.

[1]For the interested reader, some arguments against purely auditory explanations for compensatory perceptual responses offered by articulatory/gestural theorists may be found in Mann and Liberman (1983), Repp and Liberman (1987), Fowler *et al.* (1990), and Fowler (1996). Arguments against articulatory/gestural accounts of such responses are presented in Lotto *et al.* (1997) and Lotto and Kluender (1998).

[2]Vowel height and vowel nasality interact in the vowel systems of many of the world's languages as well as in experimental studies of the perception of nasal vowel height (e.g., Beddor *et al.*, 1986; Wright, 1986; Beddor and Hawkins, 1990; Kingston, 1991; Kingston and Macmillan, 1995). The interaction is due to the effect of nasal coupling on the low-frequency region of the vowel spectrum, which broadens, flattens and often shifts the frequency of the lowest spectral prominence. Correctness of nasal vowel height judgments in Krakow *et al.*'s study was determined relative to listeners' judgments of otherwise identical *oral* vowels in the oral consonant context (i.e., listeners judged the height of the vowels of [bVd] and [b$\tilde{V}$nd] as the same, but the vowels of [b$\tilde{V}$d] were heard as lower).

[3]A likely factor in these cross-study differences, discussed in detail by Kingston and Macmillan (1995), was the difference in listeners' task. Another issue fundamental to compensation approaches is whether Kingston and Macmillan's findings were partially due to their synthetic stimuli: [b] and especially [d] were not always heard as oral by listeners; [n] and especially [m] were not always heard as nasal. If listeners do not hear a clear nasal context, then they would not be expected to compensate on the basis of that context. However, in a more recent study with more convincing stimuli (and a perceptual task similar to that used by Krakow *et al.*, 1988), Macmillan *et al.* (1999) obtained a pattern of results in keeping with that of the 1995 study (see also the General Discussion).

[4]The literature reports almost no cross-linguistic study of phonetic context effects. Mann's (1986) study of the effects of /l/ and /ɹ/ on Japanese listeners' phonetic boundaries, cited above, indicates that linguistically relevant experience—in this case, native language experience with the /l-ɹ/ contrast—is apparently not necessary for phonetic context effects. However, listeners whose native language provides experience with a particular sound or property may well adjust for its coarticulatory effects in ways that are dependent on the coarticulatory organization of that language.

[5]Although this is the usual analysis for both languages, in English nasal consonants before voiceless stops are short (Malécot, 1960; Fujimura, 1977; Tanowitz and Beddor, 1997), leaving the possibility of words differing only in vowel nasality, such as [k^hæt] cat and [$k^h\tilde{æ}$t] can't. Thai phonotactics do not permit syllable-final VNC sequences.

Beddor, P. S., and Hawkins, S. (**1990**). ''The influence of spectral prominence on perceived vowel quality,'' J. Acoust. Soc. Am. **87**, 2684–2704.

Beddor, P. S., and Krakow, R. A. (**1998**). ''Perceptual confusions and phonological change: How confused is the listener?'' in *Proceedings of the Twenty-Fourth Annual Meeting of the Berkeley Linguistics Society*, edited by B. K. Bergen, M. C. Plauché, and A. C. Bailey (Berkeley Linguistics Society, Berkeley, CA), pp. 320–334.

Beddor, P. S., Krakow, R. A., and Goldstein, L. M. (**1986**). ''Perceptual constraints and phonological change: A study of nasal vowel height,'' Phonology Yearbook **3**, 197–217.

Beddor, P. S., Onsuwan, C., and Diakoumakou, E. (**in preparation**). ''Temporal characteristics of nasal vowels and consonants in English, Hindi, and Thai.''

Bell-Berti, F. (**1993**). ''Understanding velic motor control: studies of segmental context,'' in *Nasals, Nasalization, and the Velum*, edited by M. K. Huffman and R. A. Krakow (Academic, New York, NY), pp. 63–85.

Bell-Berti, F., and Krakow, R. A. (**1991**). ''Anticipatory velar lowering: A coproduction account,'' J. Acoust. Soc. Am. **90**, 113–123.

Clumeck, H. (**1976**). ''Patterns of soft palate movements in six languages,'' J. Phonetics **4**, 337–351.

Cohn, A. C. (**1990**). ''Phonetic and phonological rules of nasalization,'' UCLA Working Papers in Phonetics **76**, 1–224.

Diehl, R. L., and Kluender, K. (**1989**). ''On the objects of speech perception,'' Ecological Psychology **1**, 121–144.

Fowler, C. A. (**1981**). ''Production and perception of coarticulation among stressed and unstressed vowels,'' J. Speech Hear. Res. **46**, 127–139.

Fowler, C. A. (**1984**). ''Segmentation of coarticulated speech in perception,'' Percept. Psychophys. **36**, 359–368.
Fowler, C. A. (**1996**). ''Listeners do hear sounds, not tongues,'' J. Acoust. Soc. Am. **99**, 1730–1741.
Fowler, C. A., and Smith, M. R. (**1986**). ''Speech perception as vector analysis: An approach to the problems of segmentation and invariance,'' in *Invariance and Variability of Speech Processes*, edited by J. Perkell and D. Klatt (Erlbaum, Hillsdale, NJ), pp. 123–139.
Fowler, C. A., Best, C. T., and McRoberts, G. W. (**1990**). ''Young infants' perception of liquid coarticulatory influences on following stop consonants,'' Percept. Psychophys. **48**, 559–570.
Fujimura, O. (**1977**). ''Recent findings on articulatory processes—velum and tongue movement as syllable features,'' Paper presented at the Symposium on Articulatory Modeling, Grenoble, France.
Hajek, J. (**1997**). *Universals of Sound Change in Nasalization* (Blackwell, Boston, MA).
Hawkins, S. (**1995**). ''Arguments for a non-segmental view of speech perception,'' in *Proceedings of the 13th International Congress of Phonetic Sciences*, edited by K. Elenius and P. Branderud (KTH and Stockholm University, Stockholm, Sweden), Vol. 3, pp. 18–25.
Henderson, J. B. (**1984**). ''Velopharyngeal function in oral and nasal vowels: A cross-language study,'' Doctoral dissertation, University of Connecticut, Storrs.
Kawasaki, H. (**1986**). ''Phonetic explanation for phonological universals: the case of distinctive vowel nasalization,'' in *Experimental Phonology*, edited by J. J. Ohala and J. J. Jaeger (Academic, Orlando, FL), pp. 81–103.
Kent, R. D., Carney, P. J., and Severeid, L. R. (**1974**). ''Velar movement and timing: Evaluation of a model of binary control,'' J. Speech Hear. Res. **17**, 470–488.
Kingston, J. (**1991**). ''Integrating articulations in the perception of vowel height,'' Phonetica **48**, 149–179.
Kingston, J. (**1992**). ''The phonetics and phonology of perceptually motivated articulatory covariation,'' Lang. Speech **35**, 99–113.
Kingston, J., and Diehl, R. L. (**1995**). ''Intermediate properties in the perception of distinctive feature values,'' in *Phonology and Phonetic Evidence: Papers in Laboratory Phonology IV*, edited by B. Connell and A. Arvaniti (Cambridge U.P., Cambridge, UK), pp. 7–27.
Kingston, J., and Macmillan, N. A. (**1995**). ''Integrality of nasalization and *F*1 in vowels in isolation and before oral and nasal consonants: A detection-theoretic application of the Garner paradigm,'' J. Acoust. Soc. Am. **97**, 1261–1285.
Krakow, R. A. (**1989**). ''The articulatory organization of syllables: A kinematic analysis of labial and velar gestures,'' Doctoral dissertation, Yale University, New Haven, CT.
Krakow, R. A. (**1993**). ''Nonsegmental influences on velum movement patterns: Syllables, sentences, stress, and speaking rate,'' in *Nasals, Nasalization, and the Velum*, edited by M. K. Huffman and R. A. Krakow (Academic, New York, NY), pp. 87–113.
Krakow, R. A. (**1999**). ''Articulatory organization of syllables: A review,'' J. Phonetics **27**, 23–54.
Krakow, R. A., and Beddor, P. S. (**1991**). ''Coarticulation and the perception of nasality,'' in *Proceedings of the 12th International Congress of Phonetic Sciences* (Université de Provence, Aix-en-Provence, France), Vol. 5, pp. 38–41.
Krakow, R. A., Beddor, P. S., Goldstein, L. M., and Fowler, C. A. (**1988**). ''Coarticulatory influences on the perceived height of nasal vowels,'' J. Acoust. Soc. Am. **83**, 1146–1158.
Kunisaki, O., and Fujisaki, H. (**1977**). ''On the influence of context upon the perception of fricative consonants,'' Research Institute of Logopedics and Phoniatrics Annual Bulletin (University of Tokyo, Japan), Vol. 11, pp. 85–91.
Lahiri, A., and Marslen-Wilson, W. (**1991**). ''The mental representation of lexical form: A phonological approach to the recognition lexicon,'' Cognition **38**, 256–294.
Lotto, A. J., and Kluender, K. R. (**1998**). ''General contrast effects in speech perception: Effect of preceding liquid on stop consonant identification,'' Percept. Psychophys. **60**, 602–619.
Lotto, A. J., Kluender, K. R., and Holt, L. L. (**1997**). ''Perceptual compensation for coarticulation by Japanese quail,'' J. Acoust. Soc. Am. **102**, 1134–1140.
Macmillan, N. A., Kingston, J., Thorburn, R., Dickey, L. W., and Bartels, C. (**1999**). ''Integrality of nasalization and *F*1. II. Basic sensitivity and phonetic labeling.'' Manuscript.
Malécot, A. (**1960**). ''Vowel nasality as a distinctive feature in American English,'' Language **36**, 222–229.
Mann, V. A. (**1980**). ''Influence of preceding liquid on stop-consonant perception,'' Percept. Psychophys. **28**, 407–412.
Mann, V. A. (**1986**). ''Distinguishing universal and language-dependent levels of speech perception: Evidence from Japanese listeners' perception of l and r,'' Cognition **24**, 169–196.
Mann, V. A., and Liberman, A. M. (**1983**). ''Some differences between phonetic and auditory modes of perception,'' Cognition **14**, 211–235.
Mann, V. A., and Repp, B. H. (**1980**). ''Influence of vocalic context on perception of the [ʃ]-[s] distinction,'' Percept. Psychophys. **28**, 213–228.
Manuel, S. Y. (**1995**). ''Speakers nasalize /ð/ after /n/, but listeners still hear /ð/,'' J. Phonetics **23**, 453–476.
McQueen, J. (**1996**). ''Phonetic categorization,'' Language and Cognitive Processes **11**, 655–664.
Miller, J. L., and Eimas, P. D. (**1994**). ''Observations on speech perception, its development, and the search for mechanism,'' in *The Development of Speech Perception: The Transition from Speech Sounds to Spoken Words*, edited by J. C. Goodman and H. C. Nusbaum (MIT, Cambridge, MA), pp. 37–55.
Nearey, T. (**1992**). ''Context effects in a double-weak theory of speech perception,'' Lang. Speech **35**, 153–171.
Nearey, T. (**1997**). ''Speech perception as pattern recognition,'' J. Acoust. Soc. Am. **101**, 3241–3254.
Ohala, J. J. (**1981**). ''The listener as a source of sound change,'' in *Papers from the Parasession on Language and Behavior*, edited by C. S. Masek, R. A. Hendrick, and M. F. Miller (Chicago Linguistic Society, Chicago, IL), pp. 178–203.
Ohala, J. J. (**1986**). ''Phonological evidence for top-down processing in speech perception,'' in *Invariance and Variability of Speech Processes*, edited by J. S. Perkell and D. H. Klatt (Erlbaum, Hillsdale, NJ), pp. 386–401.
Ohala, J. J. (**1993**). ''Coarticulation and phonology,'' Lang. Speech **36**, 155–170.
Onsuwan, C. (**1997**). Personal communication.
Petersen, N. R. (**1986**). ''Perceptual compensation for segmentally conditioned fundamental frequency perturbation,'' Phonetica **43**, 31–42.
Repp, B. H. (**1982**). ''Phonetic trading relations and context effects: New experimental evidence for a speech mode of perception,'' Psychol. Bull. **2**, 81–110.
Repp, B. H., and Liberman, A. M. (**1987**). ''Phonetic category boundaries are flexible,'' in *Categorical Perception*, edited by S. Harnad (Cambridge U.P., Cambridge, UK), pp. 89–112.
Rochet, A. P., and Rochet, B. L. (**1991**). ''The effect of vowel height on patterns of assimilation nasality in French and English,'' in *Proceedings of the 12th International Congress of Phonetic Sciences* (Université de Provence, Aix-en-Provence, France), Vol. 3, pp. 54–57.
Schourup, L. (**1973**). ''A cross-language study of vowel nasalization,'' Ohio State Working Papers in Linguistics **15**, 190–221.
Silverman, K. (**1987**). ''The structure and processing of fundamental frequency contours,'' Doctoral dissertation, Cambridge University, UK.
Solé, M.-J. (**1992**). ''Phonetic and phonological processes: The case of nasalization,'' Lang. Speech **35**, 29–43.
Solé, M.-J. (**1995**). ''Spatio-temporal patterns of velopharyngeal action in phonetic and phonological nasalization,'' Lang. Speech **38**, 1–23.
Stevens, K. N., Andrade, A., and Viana, M. C. (**1987**). ''Perception of vowel nasalization in VC contexts: A cross-language study,'' J. Acoust. Soc. Am. **82**, S119(A).
Tanowitz, J., and Beddor, P. S. (**1997**). ''Temporal characteristics of coarticulatory vowel nasalization in English,'' J. Acoust. Soc. Am. **101**, 3194(A).
Whalen, D. H. (**1981**). ''Effects of vocalic formant transitions and vowel quality on the English [s]–[ʃ] boundary,'' J. Acoust. Soc. Am. **69**, 275–282.
Whalen, D. H. (**1989**). ''Vowel and consonant judgments are not independent when cued by the same information,'' Percept. Psychophys. **46**, 284–292.
Wright, J. T. (**1986**). ''The behavior of nasalized vowels in the perceptual vowel space,'' in *Experimental Phonology*, edited by J. J. Ohala and J. J. Jaeger (Academic, Orlando, FL), pp. 45–67.
Yu, X. (**1994**). ''Production and perception of coarticulated tones,'' J. Acoust. Soc. Am. **95**, 2240–2253.

Continuous assessment of time-varying speech quality

Martin Hansen[a] and Birger Kollmeier[b]
AG Medizinische Physik, Universität Oldenburg, D-26111 Oldenburg, Germany

(Received 6 October 1998; revised 23 June 1999; accepted 6 July 1999)

This paper addresses the question of whether subjects are able to assess the perceived time-varying quality of speech material continuously. A method is introduced which is characterized by a subjective continuous rating of the perceived speech quality by moving a slider along a graphical scale. The usability of this method is illustrated with an experiment in which different sequences of sentences were degraded in quality with a Modulated Noise Reference Unit. The modulation depth was varied with time and the subject's task was to assess the perceived quality. The results indicate that subjects can monitor speech quality variations very accurately with a delay of approximately 1 s. An objective speech quality measure based on an auditory processing model was applied to predict the subjective speech quality results. The speech quality measure q_C was modified to allow for time-dependent objective measurement of the speech quality. The averaged subjective response data could be modeled by the scale transformed and low-pass filtered measure $q_C(t)$ with a high degree of accuracy. © *1999 Acoustical Society of America.* [S0001-4966(99)04810-9]

PACS numbers: 43.71.An, 43.71.Cq, 43.71.Gv, 43.72.Kb [DOS]

INTRODUCTION

In the development and optimization of speech codecs in mobile telephone networks, it is essential to assess the perceived speech transmission quality of the system under test. A number of methods are currently available to assess the (subjective) quality of a speech transmission channel. For more recent reviews on several aspects of speech quality assessment see, e.g., Quackenbush *et al.* (1988), Kitawaki (1990), Sotscheck (1992), Dimolitsas (1993), Jekosch (1993), and Kroon (1995). The ITU-recommendations P.800 and P.830 (ITU-T, 1996a,c) describe assessment methods that are applicable for the quality assessment of digital nonlinear speech transmission systems. The most common methods present subjects with short sequences of speech material and ask the subject about their quality impression on a given rating scale. In these measurements, *one* rating is requested from the subject for one typical test signal. It consists of two short sentences separated by speech pauses.

This limitation to relatively short test stimuli in these methods hinders their applicability for the assessment of realistic time-varying systems. In these systems, time-dependent transmission conditions are commonly experienced, e.g., due to fading radio transmission or due to variable rate speech coding caused by changing load of DCME (Digital Circuit Multiplication Equipment) devices. Under these conditions, several questions arise: If the phenomenon of a short-time instantaneous quality percept exists, how is it rated by subjects? How is the overall quality impression related to the time-varying course of the short-time instantaneous quality?

In order to overcome the short test stimulus limitation, the first necessary step to answer these questions is to investigate if and to which degree subjects are able to assess the time-varying speech quality instantaneously. Experiments on image quality assessment have successfully shown this ability in the visual sensory domain (Hamberg and de Ridder, 1995; de Ridder and Hamberg, 1997). Although their results seem promising, it is not clear if subjects show the same ability in the auditory modality for the case of speech quality perception. It is known that the auditory system is ''faster'' than the visual system in the sense that we are able to perceive temporal changes in the range of a few milliseconds. In the visual system temporal intensity variations above 60 Hz are unnoticeable. On the other hand, speech quality perception might be associated with much more central and probably ''slower'' cognitive processes. In addition, the motor action of a response task might limit the applicability of corresponding auditory quality experiments. Experiments on continuous loudness judgment have been performed by Namba *et al.* (1988), Kuwano and Fastl (1989), Fastl (1991), Weber (1991), and others. In these studies, an experimental setup similar to the one described in this study was used for loudness judgment of sound stimuli with a length of up to 17 min. These studies were aimed to find a relation between the averaged instantaneous loudness and overall loudness judgment. However, this relation is still subject to investigations (Gottschling and Fastl, 1998).

The current paper introduces a method for continuously assessing time-varying speech quality perception. The validity of the method is shown with an experiment that makes it possible to relate subjective time-varying quality results to a given controlled time-varying target quality (Hansen and Kollmeier, 1998a,b; Hansen, 1998). Second, the subjective results are related to model predictions obtained from a modified objective speech quality measure (Hansen, 1998; Hansen and Kollmeier, 1998c) based on a perception model (Dau *et al.*, 1996a,b).

The current method is motivated by similar experiments by Hamberg and de Ridder (1995), de Ridder and Hamberg (1997), Hamberg and de Ridder (1997) in the field of video

[a]Current address: Tøpholm & Westermann ApS, AUDLAB, Ny Vestergårdsvej 25, DK-3500 Værløse, Denmark.
[b]Corresponding author.

image quality assessment and partly by similar experiments on continuous loudness judgment. In this study, the emphasis is put on the general design and demonstration of the feasibility of the continuous assessment method for speech quality assessment purposes. One important prerequisite for the continuous assessment method is the subjects' ability to reliably assess the quality of instantaneous events in speech transmission. Only then can the continuous rating in response to ongoing speech be understood in a causal manner. Therefore, in the first experiment short isolated speech elements (i.e., segmented words taken from complete sentences) were presented to subjects with the task to rate the perceived short-time speech quality. In the second experiment the subjects were presented with a long sequence of sentences and their task was to continuously rate the perceived instantaneous quality as closely as possible.

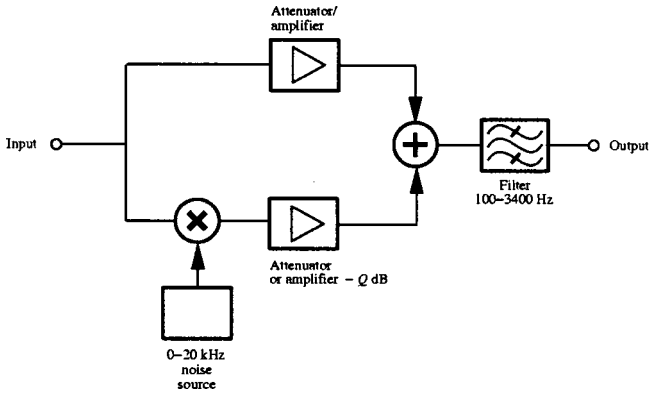

FIG. 1. Block diagram of the Modulated Noise Reference Unit (MNRU). The speech input signal is modulated by a wide-band white noise. The modulation depth m and the MNRU-parameter Q are related by $Q = -20 \log_{10} m$.

I. EXPERIMENTAL SETUP

A. Speech stimulus material

The speech material was selected from the reference material of the German language ETSI Halfrate Selection Test (ETSI, 1991, 1992). These sentences are part of the corpus ''Sätze für Sprachgütemessungen mit deutscher Sprache'' (Sotscheck, 1984), recorded by the Deutsche Telekom AG. The material was digitized with 16 bit resolution and sampled at 16 kHz and subsequently telephone-band-pass filtered by the modified Intermediate Reference System (IRS)-filter (ITU-T, 1996b,c). This filter is especially designed and standardized to have an average spectral telephone transmission characteristic. All sentences were calibrated to an equal Active Speech Level (ASL) (ITU-T, 1996b) of -30 dBov.[1] From the reference material, five sentences of each of the two male (m1, m2) and two female speakers (f1, f2) were chosen randomly. The speech stimuli were diotically presented to the subjects via Sennheiser HDA 200 headphones in a sound-insulated chamber. The listening level was adjusted to an ASL of 75 dB SPL.

B. Generation of quality degradation

A controlled speech quality degradation was generated by means of a Modulated Noise Reference Unit (MNRU) (CCITT, 1989). This device was developed to simulate fixed-rate PCM and ADPCM speech coding over error-free transmission channels. It is commonly used as a reference system for speech quality assessment. The principle of the MNRU is shown in Fig. 1. The MNRU modulates the input speech signal $s(t)$ according to

$$x(t) = s(t) \cdot (1 + m \cdot n(t)),$$

where $n(t)$ is a white noise with unity variance and m is the modulation depth. For the narrow-band MNRU, the modulated signal $x(t)$ is subsequently band-pass filtered to telephone bandwidth from 100 to 3400 Hz.

The MNRU was chosen as a starting point in this experiment because it is easy to use. The quality degradation can be controlled by a single parameter, i.e., the modulation depth. However, it should be noted that the MNRU is mostly suited to simulate ADPCM-like signal distortions but is not well-suited to simulate effects of variable rate speech coding and dynamic radio channel situations, which are most likely to produce time-varying speech transmission quality. On the other hand, the feasibility of the assessment technique (see below) can still be demonstrated by using the modified MNRU system.

C. Experiment 1: Quality assessment of isolated words

The 20 sentences uttered by the different speakers were (hand-)segmented into their single word constituents. This led to a total number of 102 words, i.e., 26 words for speaker f1, 27 for f2, 23 for m1, and 26 for m2. The duration of the words varied from 0.135 s for the very short monosyllabic word ''die'' to 0.911 s for the four-syllabic word ''gearbeitet.'' Despite the big variance in the duration of the word stimuli, it was decided not to partition the sentences into segments of equal length, e.g., syllables. This would have lead to partly unintelligible segments at least if the overall quality was poor. Such a percept of a degraded intelligibility would dominate the assessment of transmission quality. This dominance effect was observed by Preminger and Van Tasell (1995) during the comparison of the subjective quality and intelligibility of speech processed by different hearing aid algorithms. There, speech quality was highly correlated with speech intelligibility as long as the intelligibility of different test stimuli was not high and constant.

For the generation of stimuli with degraded quality, the Modulated Noise Reference Unit (MNRU) was applied. Each word of each speaker was processed by the MNRU at seven different levels of the (negative, logarithmic) modulation depth parameter $Q = (-1) \cdot 20 \log_{10} m = 0,5,10,15,20,25,35$ dB. Note that the standardized MNRU-parameter Q is positive for modulation depths $m < 1$. The procedure yielded 714 words in total at various levels of speech quality degradation which were expected to range from near reference quality ($Q = 35$ dB) to very poor quality ($Q = 0$ dB).

All words that belonged to one of the four speakers were arranged into a separate list of words. In one run, all words from one list were presented to the subject in random order.

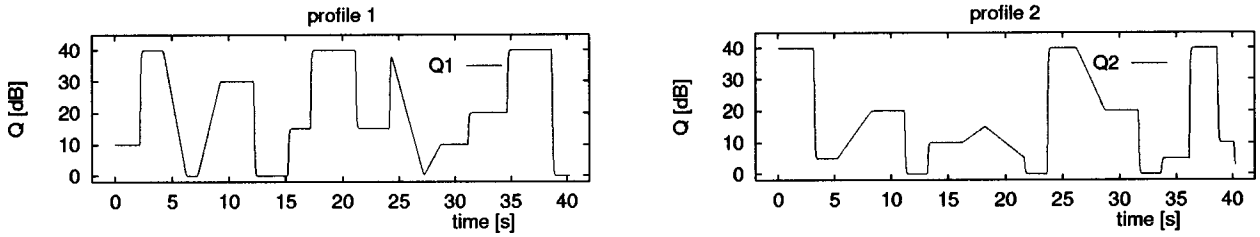

FIG. 2. Target quality profiles $Q_1(t)$ and $Q_2(t)$ that were used to control the time-varying quality introduced by the modified MNRU. Increasing Q indicates increasing speech quality.

The task was to give a rating on a five point Absolute Category Rating (ACR) scale, which is recommended by the ITU (ITU-T, 1996c). The categorical adjectives were ''ausgezeichnet,'' ''gut,'' ''ordentlich,'' ''mäßig,'' ''schlecht.''[2] The subjects had to select one of these categories that were presented on a monitor in front of them.

All subjects were familiarized with the setup and had read a written explanation. Subsequently they performed one run with each of the four lists. All runs of one subject took place on the same day, with pauses between different runs. The whole experiment was computer-controlled and self-paced by the subjects.

D. Experiment 2: Continuous assessment of time-varying speech quality

The same 20 sentences as used in experiment 1 were concatenated into one long utterance. This resulted in a long speech flow with short pauses in between. The durations of the pauses ranged from 0.1 s to 0.39 s. The different sentences did not relate to each other with respect to their linguistic contents. Two different orders of concatenation were used to produce the source stimuli named ''A'' and ''B.'' For source stimulus A the order of the speakers was f1-f2-m1-m2, while for B it was m1-m2-f1-f2.

A time-varying speech quality was generated by means of a MNRU which was modified to allow for a time-varying modulation-depth parameter Q. Two different target quality profiles, $Q_1(t)$ and $Q_2(t)$, were generated by defining the MNRU-parameter Q over time. The target profiles Q_1 and Q_2 are shown in Fig. 2.

The target quality profiles were designed according to the results from experiment 1 and from results of preinvestigations that showed that untrained subjects had difficulties in assessing a constantly changing quality. Therefore, $Q_i(t)$ were chosen to have constant sections, considerable instantaneous changes, and also linear decreases or increases over time intervals of 2–3 s. The target values for the different sections of constant Q were chosen at approximately equally spaced levels on the expected perceptual quality scale. Four different test stimuli were generated from the combination of two source stimuli and two modulation-depth profiles.

In one run, two repetitions of each of the four test stimuli were presented to the subjects in random order. Subjects were instructed to assess the perceived instantaneous speech quality by positioning a slider as closely as possible on a continuous linear scale. The scale was labeled into the same five categories as in experiment 1, i.e., with the German equivalents of ''excellent,'' ''good,'' ''fair,'' ''poor,'' and ''bad.'' The slider is depicted in Fig. 3. The length of the scale was $l=100$ mm. In the lowest position, the marker on the mid-point of the slider points to the lowest of the horizontal lines, and correspondingly for the highest slider position. The slider position $r=10$ mm points to the category name ''schlecht.'' The position $r(t)$ of the slider was sampled at a rate of 8 kHz and subsequently downsampled to 8 Hz. These downsampled data are denoted by $r_j(t)$ for subject j, or by $r_{ij}=r_j(i\Delta t)$.

E. Test subjects

All test subjects in the experiments were volunteers from the laboratory. They were not paid for their participation. They had normal hearing as defined by a hearing loss <15 dB at all audiological standard frequencies and no history of hearing problems. Five male subjects[3] aged between 25 and 42 years participated in experiment 1. Two were German native speakers and three were nonnative German speakers. All subjects were experts in speech processing technology, but were not familiar with this kind of experiment nor with the test stimuli. One female and ten male subjects[3] aged between 25 and 30 years participated in experiment 2. Two were nonnative German speakers and nine were native speakers. All these subjects had experience in

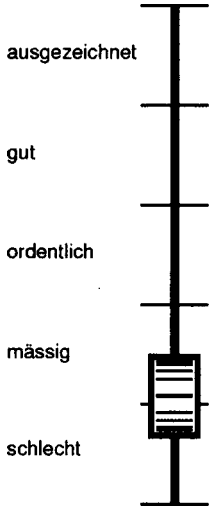

FIG. 3. Pictorial representations of the slider used to record the subjective continuous quality rating.

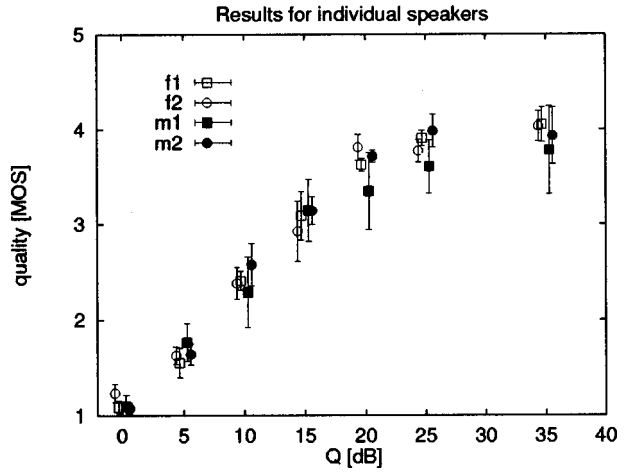

FIG. 4. Mean quality ratings obtained for isolated words as a function of the MNRU-parameter Q. Each symbol shows the average rating across all words and all subjects for the test stimuli of one speaker (mean value and standard deviation).

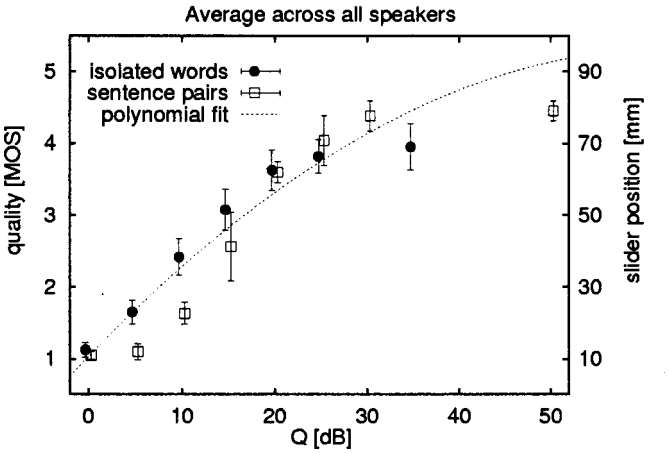

FIG. 5. Average quality rating for isolated words averaged across all speakers. For comparison, the MOS obtained with standard sentence pairs are shown, taken from the ETSI Halfrate Selection Test data base (ETSI, 1992). The dashed line shows the second order polynomial fit used to transform Q to the slider position in the subsequent experiment.

psychoacoustic listening tests, but only two were experts in speech processing technology. Two of the subjects also participated in experiment 1.

II. RESULTS

A. Experiment 1: Quality assessment of isolated words

Most subjects reported that they could not fully understand a few of the very short test words in conditions of severely degraded quality. In these cases the worst category was assigned by them. These data were not excluded from further analysis, although intelligibility was obviously assessed rather than speech quality because the response behavior could be regarded as consistent.

The inter-subject variability proved to be very small in comparison to the variability across words. For each of the four lists of words of one speaker, the quality ratings given to the test stimuli processed at the same level of Q were therefore averaged across subjects and across all words in the list. In addition, the average across all speakers, all words, and all subjects was calculated. The medians and interquartile ranges are shown in Fig. 4 for the individual speakers and in Fig. 5 for the overall average (filled symbols). Figure 5 also shows the subjective data for the assessment with the standard MOS method with sentence pairs (open squares) taken from the ETSI Halfrate Selection Test data base (ETSI, 1992). They result from 24 subjects and 4 different speakers for each level of Q.

The data for isolated words differ slightly between the four speakers. For speaker m1, the standard deviations are somewhat larger than for the other three speakers. For speaker f2, a nonmonotonic result is observed due to a higher quality rating at $Q=20$ dB than at $Q=25$ dB. For speaker m1, a somewhat lower rating is observed at $Q=20$ dB and $Q=25$ dB compared to the other three speakers. However, the MOS data for the stimuli uttered by the different speakers do not show any systematic dependency on the speaker. It is therefore reasonable to average across the different speakers. The standard deviations of the overall MOS data for isolated words range from 0.11 to 0.32 MOS units. This is in the same range as the standard deviation of the MOS in the ETSI Halfrate Selection Test result for standard sentence pairs, that ranges from 0.06 to 0.35 MOS units for the data given in Fig. 5.

B. Experiment 2: Continuous assessment of time-varying speech quality

The subjects had no difficulties with the continuous quality rating task except for their reported inability to reduce a certain delay between the auditory percept and their slider movement. In order to quantify this delay and to correlate the recorded slider position $r(t)$ with the corresponding time-varying ''target''-quality profile function $Q_i(t)$, a transformation of $Q_i(t)$ to a ''target''-slider profile function $R_i(t)$ was used. To do so, the first step was to transform Q to MOS via the curve shown in Fig. 5. This curve resulted from a second-order polynomial fit to the Q-MOS data gained in experiment 1 with isolated words. The MOS data were then linearly transformed to the slider position R by defining $R=(-10+20\cdot\mathrm{MOS})$ mm, which mapped the MOS interval [1,5] onto the interval [10,90] mm. The values 10 mm and 90 mm represented the categories ''bad'' and ''excellent,'' even though the slider had a length of 100 mm. The resulting relation was $R(Q)=(-0.002\cdot Q^2+0.16\cdot Q+0.93)$ mm.

For each individual subject, the sliding response data to *all stimuli* that were MNRU-processed with the *same target profile* were averaged and cross correlated with each of the two transformed ''target'' slider profile functions $R_i(t)$. The cross correlation functions are shown in Fig. 6 for profile R_1 and Fig. 7 for profile R_2. The position of the maximum was found at times ranging from 0.78 s to 1.09 s for profile R_1 and from 0.90 s to 1.22 s for R_2.

The small spread of the maxima of the cross correlation functions across subjects justifies averaging the response data from all subjects. Two different averaging methods were used: In the direct averaging method, all data in re-

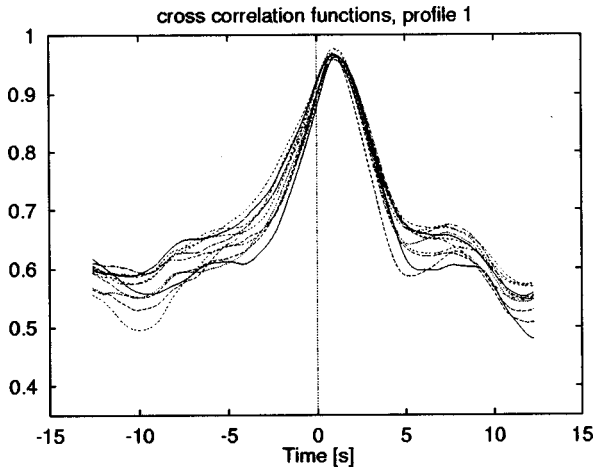

FIG. 6. Cross correlation function between averaged response data and the corresponding ''target'' slider position $R_1(t)$ [derived by transforming the target quality profile $Q_1(t)$], for the 11 different subjects.

sponse to the same test stimulus were averaged without any correction for different use of the response scale by the subject. To account for this possible difference in the response data, in the second averaging method the data of individual subjects were linearly transformed prior to averaging. The linear transformation (*z*-score-transformation) was performed in order to equalize the mean and standard deviation of the recorded response data across subjects.[4]

The results for the *z*-score-transformation averaging are shown in Fig. 8. In the four panels, $r(t)$ averaged across different subjects and repetitions is displayed with a thin-dotted line for the four combinations of input stimulus and target quality profile. The gray-shaded area surrounding the average data indicates the standard deviation. The target slider profiles $R_1(t)$ and $R_2(t)$ are depicted with a solid continuous line. The averaged subjective response data follow the target quality very closely with a delay of about 1 s. The subjects are obviously able to distinguish the different constant quality levels within the target profiles.

Note that the first four samples of the response data, beginning at $t=0$ s, have values close to $r\approx 0$ mm. This is an artifact of the interpolation in the downsampling process

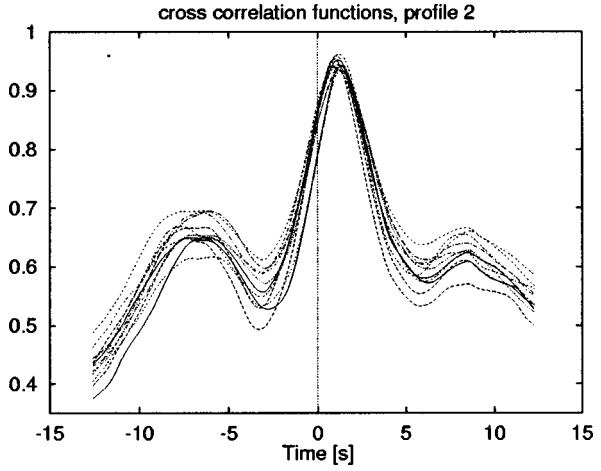

FIG. 7. Cross correlation function between averaged response data and the corresponding ''target'' slider position $R_2(t)$, for 11 different subjects.

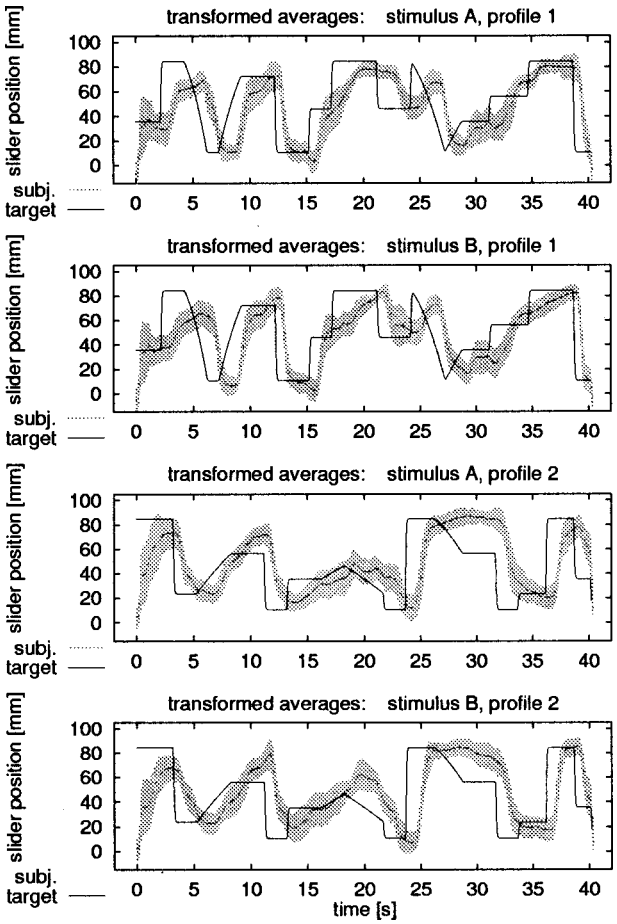

FIG. 8. Averaged transformed response data from 11 subjects for the four different test stimuli. The thin-dotted line shows the mean and the gray-shaded area indicates the standard deviation of the subjective responses.

from 8 kHz to 8 Hz sampling frequency. Consequently, the initial standard deviation is smaller than expected. Additionally, a larger standard deviation in the response data is observed in the beginning than at the end of the stimulus. For profile 2, a deviation of the mean response from the target slider position $R_2(t)$ is also observed at the beginning of the stimulus. Both of these observations can be explained by the fact that the subjects were not instructed to move the slider back to a specified starting position before the presentation of the next stimulus began.

A small difference in the data is encountered between source stimuli A and B when processed with the same target profile quality (cf. Fig. 9). One reason for this deviation might be the fact that at one point in time a female speaker was present in stimulus A while a male speaker was present in stimulus B, and vice versa. This deviation, however, is negligible in comparison to the intra-subject and inter-subject variability of the subjects' responses (shaded area in Fig. 8). A similar result as shown for the direct averaging method in Fig. 9 is obtained for the transformation averaging method.

Figure 10 gives the standard deviations resulting from the two averaging methods (direct averaging and *z*-score-transformed averaging of the subjects' responses). The standard deviation of the response data is smaller or at most equal for the transformation averaging compared to direct

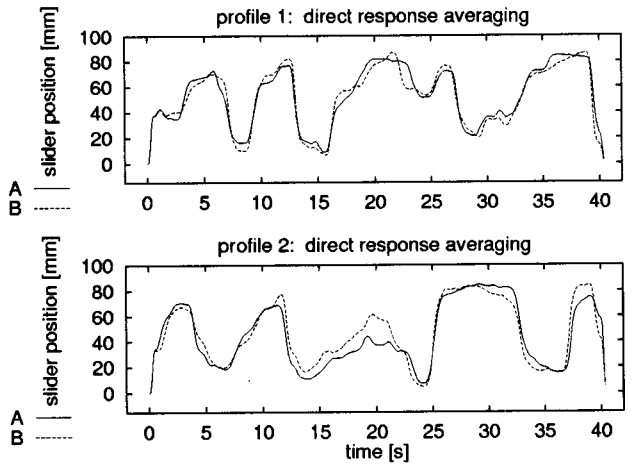

FIG. 9. Responses to source stimuli A (solid line) versus B (dashed line), directly averaged across subjects for each of the two target profiles.

averaging. This rank order inverts only occasionally and only for very short intervals. The relative difference of the standard deviations is on average in the range of 25%–50%. An F-test was performed on the data across all subjects, repetitions, and across time for each of the four conditions (stimulus A–profile 1, B–1, A–2, and B–2). The difference in the standard deviation is not significant for the data in response

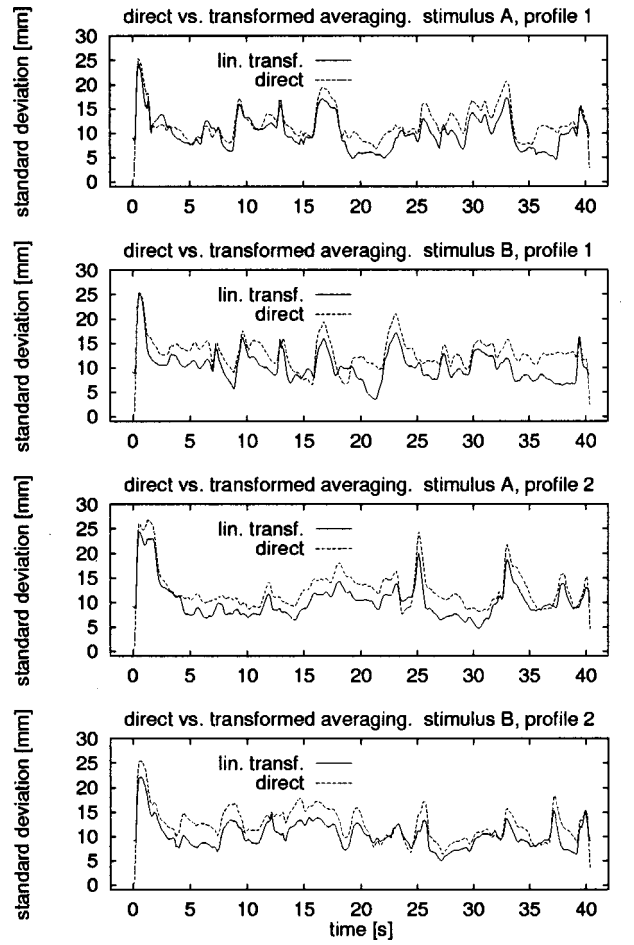

FIG. 10. Standard deviations across 11 subjects resulting from the direct averaging (dashed line) and transformation averaging (solid line) of the response data.

to the combination of stimulus A and target profile 1, while for the other three combinations, the difference is highly significant.[5] If the response data are additionally averaged across the two stimuli, the difference of the standard deviation between direct averaging and transformation averaging is highly significant for both target profiles.

III. DISCUSSION

A. Quality scores based on isolated words

Experiment 1 was designed to investigate whether subjects are in principle able to assess an instantaneous speech quality on the basis of short time intervals. This step was necessary in order to understand the response behavior of the subjects in experiment 2 where the time-varying speech quality assessment method was investigated.

Hamberg and de Ridder (1995) introduced the continuous assessment method to video quality assessment. They degraded the quality of an image over time by blurring the picture with a time-varying filter, i.e., the scene of the picture remained the same, while the perceived quality changed with time. They found that subjects were able to monitor the perceived quality almost instantaneously (with respect to the data sampling rate at 1 Hz).

Due to the different nature and dimensionality of visual versus auditory stimuli it is sometimes but not always possible to find equivalent paradigms for visual versus auditory stimulation. Experiment 1 was designed in order to investigate a comparable ability of subjects in the auditory domain: The concept of a still-picture was transferred to the presentation of isolated short words. It was decided not to repeat the same word periodically. In analogy to the time-varying image quality of a nonmoving image, the isolated, short words were presented at different quality levels during one run of the experiment. The consistent results of experiment 1 indicate that subjects are indeed able to form a short-time quality percept on the basis of short isolated word stimuli. The instantaneous quality was found to be independent of the gender of the speaker and of word length. However, there was a tendency for very short words at the very low quality end to be primarily assessed on the basis of speech intelligibility, which in this case was consistent with poor speech quality.

It is noteworthy that the MOS results for isolated words were somewhat higher than the MOS obtained with the standard sentences as test stimuli for $Q<20\,\mathrm{dB}$. For $Q>20\,\mathrm{dB}$ this tendency was reversed: With isolated short words the highest quality was rated at about 4 MOS units, while for sentences, the highest subjective quality rating reached 4.5 MOS (cf. Fig. 5). For both the isolated words and sentences, the transition from monotonically increasing MOS with increasing Q to the asymptotic MOS was found at a value of Q of about 30 dB. Both experiments showed the same standard deviation across subjects at different levels of Q. This deviation in slope between single speech elements (e.g., words) and sentences is also found for the discrimination function in speech intelligibility tests at a less favorable SNR than the one employed here. The steeper transition of the sentences is probably due to a higher number of independent speech ele-

ments and the redundancy that reduces the variability connected to the quality assessment of a single word.

In summary, the results of experiment 1 support the hypothesis that subjects can reliably assess the short-term quality impression connected to brief auditory speech events. The results are in line with equivalent findings in the visual domain and a high correspondence to MOS for sentence test material is found.

B. Continuous scaling method

Experiment 2 was a straightforward extension of experiment 1: It investigated continuous time-varying speech quality perception instead of short-time quality. It corresponded closely to the video quality experiments by de Ridder and Hamberg (1997), and Hamberg and de Ridder (1997).

The subjects' task of assessing 40 s of ongoing speech resembled much more a realistic situation than in standard sentence pair listening-only tests usually employed for speech quality assessment. The 40 s speech signals were of course still artificial, in that four different talkers were contained, each uttering five sentences. Also, the sentences were unrelated to each other (as is the case in standard sentence pair tests). This clearly differs from more realistic tests for telecommunication purposes where subjective conversation tests are employed as well as tests where subjects listen to one or two sides of a conversation. However, the 40 s samples of ongoing speech employed here already appear to be a sufficient average representation of running speech since all subjects developed a stable criterion to perform the task in the experiment. The quality degradation introduced in the experiment was chosen in order to provide parts with constant quality, abrupt changes, and linear decrease and increase of the MNRU quality parameter Q over time. The amount of quality variation over time was probably unrealistic, i.e., an exaggerated amount of change in a relatively short duration of 40 s. However, the results of Hamberg and de Ridder provide evidence that subjects might be able to assess time-varying speech quality also when less variability in quality is employed over a much longer duration of the stimulus material. In one experiment (de Ridder and Hamberg, 1997) they used a 50 s video section with a comparable amount of quality variability to that in experiment 2, while in another experiment (Hamberg and de Ridder, 1997) they presented material with a lower degree of variability in quality for a 300 s stimulus duration. Subjects were equally able to assess the time-varying quality in the two experiments. The delay between target slider position and subjective response found here corresponds very well to the results of de Ridder and Hamberg (1997) who also observed a delay of approximately 1 s with only small a deviation across subjects. However, in continuous loudness judgement experiments, e.g., Weber (1991) found a larger spread of this delay across subjects, ranging from 0.5 s to 1.5 s, although a delay of up to 3 s was observed in some subjects.

The results of experiment 2 show that subjects can assess time-varying speech quality continuously with a high degree of reliability and reproduceability. It is remarkable that all subjects seem to make use of the response scale in a reproduceable way. This is indicated by the low intra-subject and inter-subject deviation observed in the directly averaged data as shown in Fig. 9. This figure shows that subjects respond to different source stimuli processed with the same time-varying quality profile in an almost indistinguishable manner. The deviation of the directly averaged responses to stimulus A and B is much smaller than the standard deviation across subjects for either of the stimuli. The fact that this result is already found without any individual linear response scale transformation strongly confirms the applicability of the new method for time-varying speech quality assessment. Figure 9 shows that the averaged responses have an upper bound at about 80 mm on the quality scale. Subjects seem to take this 80 mm position as an anchor point corresponding to the highest perceived quality. It is interesting to note that exactly the same observation was made by Hamberg and de Ridder (1995, 1997) in several of their experiments. This may indicate a common strategy involved in the continuous assessment of visual or auditory quality perception. The value of 80 mm also corresponds well to the linearly transformed quality of 4.5 on the MOS scale, which is the highest rating typically found in standard quality assessment experiments with sentence pairs.

Despite the observation of the highly reproduceable use of the response scale by the subjects, even without any linear correction, the transformation averaging method should be applied. As can be expected, the individual linear scale transformation prior to averaging should reduce any individual bias or incomplete usage of the response scale. It can limit the potential influence of malperforming subjects.

IV. MODELING CONTINUOUS SCALING RESPONSES BY AN OBJECTIVE SPEECH QUALITY MEASURE

The results so far indicate that the continuous assessment of time-varying speech transmission quality appears to be a well-defined psychoacoustical task. Therefore, an attempt was made to model the subject's performance in this task based on a psychoacoustical processing model.

A. Speech quality based on the model of the ''effective'' auditory signal processing

In previous studies (Hansen, 1998; Hansen and Kollmeier, 1997, 1998c,d) an objective speech quality measure based on a model of the ''effective'' auditory signal processing was introduced and tested. Its application to speech quality prediction closely follows the design of the underlying experiments:

The speech quality measure q_C for stationary transmission conditions (Hansen and Kollmeier, 1997, 1998c) is based on either the cross correlation or the mean squared difference of the calculated ''internal representations'' of the test signal and the reference signal, averaged across the whole utterance of two sentences. In the case that speech material of different speakers was available in a test database, the averaging or cross correlation was performed across all sentences that were processed under the same coding condition. However, for the application to objective speech quality measurement, the internal representation was sampled with a period of 20 ms. These samples can be considered as corresponding to the temporal states of excitation

in response to an input signal. It is therefore straightforward to employ this auditory processing to model the continuous speech quality as assessed by the subjects in the experiment described in the previous sections.

Note that, in doing so, we did not aim to model the behavioral aspect of the transformation of the quality percept to a motor action, or the delay that is connected with it. Only a transformation of the objective quality measure to the rating scale is considered here. It can simply be modeled by a fitted (nonlinear) scale transformation. Hence, the subjective averaged response data will show a certain delay relative to the modeled objective instantaneous speech quality measure. This delay should be of the same order as that observed between the target slider profile and the subjective sliding response, i.e., approximately 1 s.

For the objective modeling of the continuous speech quality the procedure is the same as described in Hansen and Kollmeier (1997, 1998c). The source stimuli A and B were taken as reference signals; the MNRU-processed signals with time-varying speech quality according to the target profiles Q_1 and Q_2 were taken as test signal. Reference and test signal were transformed to their internal representations up to and including the last stage where downsampling of the internal representation takes place by averaging consecutive nonoverlapping frames across a duration $\tau = 20$ ms. In order to investigate the influence of this parameter τ on the performance of the continuous speech quality measure, the internal representation was averaged over frames of 20 ms duration (as before), and, additionally, over 100 ms.

The formal description of the resulting time-dependent speech quality measures $q_C(t)$ (correlation measure) and $q_S(t)$ (distance measure) is given in the Appendix. Both time-dependent measures, $q_S(t)$ and $q_C(t)$, were mapped to the $r(t)$ scale by means of a simple exponential transformation (see the Appendix) and subsequently low-pass filtered at 0.5 Hz. These transformed speech quality measures are denoted by $r_{q_C}(t)$ and $r_{q_S}(t)$, respectively.

The results of the time-dependent quality prediction by the objective measures $r_{q_C}(t)$ and $r_{q_S}(t)$ for the frame duration $\tau = 20$ ms are shown in Fig. 11. The directly averaged subjective response data (solid line), the model prediction by $r_{q_C}(t)$ (dashed line), and the target slider profile (thin dashed gray line) are plotted for each of the four different stimulus conditions. The delay in the subjective response data of approximately 1 s relative to the target profile has been compensated for in the this figure in order to facilitate a comparison. The results for $r_{q_S}(t)$ for frame duration $\tau = 20$ ms are shown in Fig. 12 in the same style. No significant difference between the 20 ms and the 100 ms option was found for the performance of either $r_{q_C}(t)$ or $r_{q_S}(t)$ in the prediction of the subjective speech quality data.

A general comparison of Figs. 11 and 12 shows that the speech quality prediction by $r_{q_C}(t)$ and $r_{q_S}(t)$ coincides highly with the subjective response data and the target slider profile. After shifting the subjective response data by the average delay of 1 s, the model predictions, the target slider profile, and the averaged subjective response data match each other accurately especially at temporal positions of

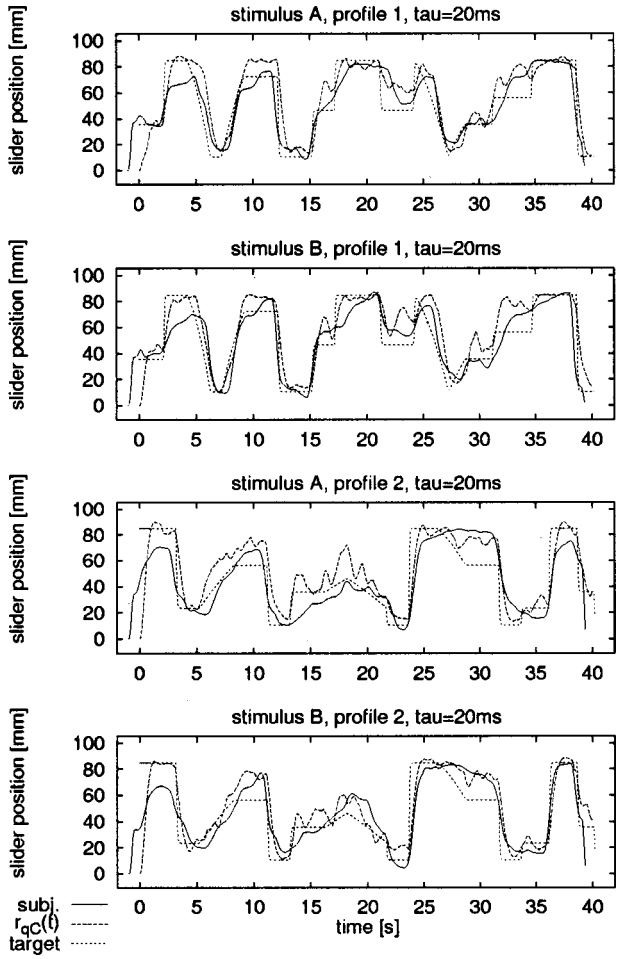

FIG. 11. Continuous-time speech quality prediction by the correlation speech quality measure $r_{q_C}(t)$ (dashed line) for a frame duration of 20 ms. The averaged subjective data (solid line, temporally shifted by 1 s) and the target slider profile (thin dotted line) are plotted for comparison.

large jumps of the speech quality, e.g., at $t \approx 2$, 5, 8, 12, 15, 26, and 38 s for profile 1 and at $t \approx 3$, 11, 24, 32, 36, and 38 s for profile 2. A further inspection of the data shows that the deviation of the different model predictions from the subjective response data is smaller than the inter-subject standard deviation across subjects for all stimulus conditions most of the time.

The rippled structure observed in the $r_{q_C}(t)$ and $r_{q_S}(t)$ data does not result from the frame length τ used for temporal averaging. The MNRU that was used for the generation of the test stimuli introduces speech quality degradations that are comodulated with the input signals' energy. The signal degradations that are detected by the objective measures are therefore also comodulated with the speech energy. This is reflected in the fluctuations of $r_{q_C}(t)$ and $r_{q_S}(t)$.

At intervals of low speech quality [i.e., $r(t) < 20$ mm] within a target profile, the absolute values of the model prediction, target profile, and the averaged subjective response match very closely. During intervals of high speech quality [i.e., $r(t) > 60$ mm] a slight deviation sometimes occurs between the predicted speech quality and either the averaged subjective speech quality or the target profile. This effect depends on the choice of the transformation from $q_C(t)$ or

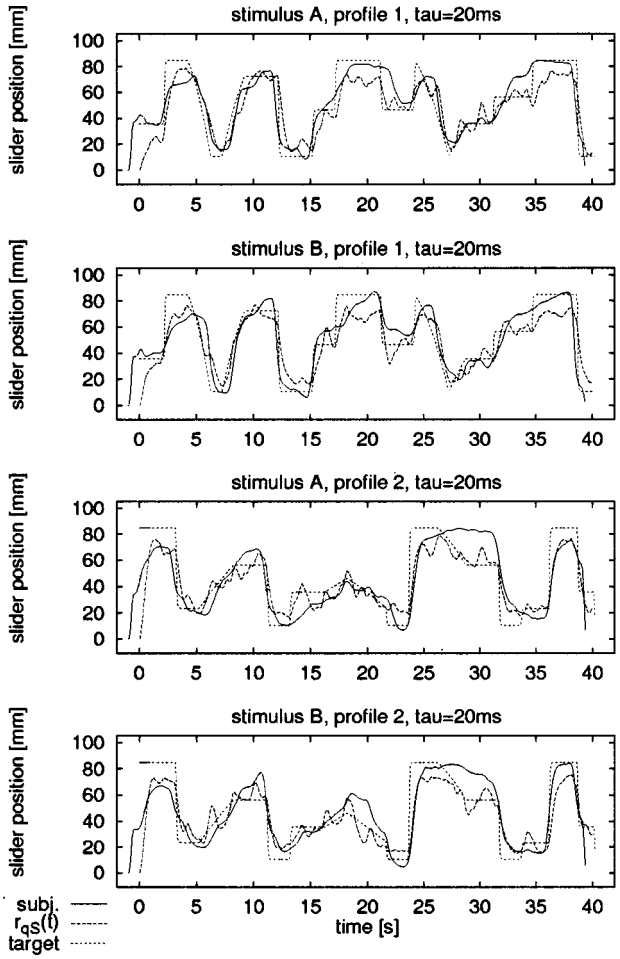

FIG. 12. Continuous-time speech quality prediction by the mean squared difference speech quality measure $r_{q_S}(t)$ (dashed line) for a frame duration of 20 ms. The averaged subjective data (solid line, temporally shifted by 1 s) and the target slider profile (thin dotted line) are plotted for comparison.

$q_S(t)$ to the mm scale of $r(t)$. The simple exponential transformation employed here (cf. the Appendix) might not be optimal for the purpose of transforming the complete range of q_C (or q_S) into the corresponding target slider positions. A two-parameter exponential fit results in smaller deviations between the transformed objective speech quality measure and the target value of the slider position (not shown here).

For profile 2 a larger deviation of up to 20 mm between the correlation speech quality measure $r_{q_C}(t)$ and the target profile $R_2(t)$ is observed in the intervals $8\,\mathrm{s} \leqslant t \leqslant 11\,\mathrm{s}$ and $27\,\mathrm{s} \leqslant t \leqslant 32\,\mathrm{s}$. However, it is interesting to note that the averaged subjective response data deviate from the target profile at the same time, so that $r_{q_C}(t)$ matches the subjective data very accurately. On the other hand, intervals are also observed where $r_{q_C}(t)$ matches the target profile very accurately but deviates from the subjective response, e.g., at $2\,\mathrm{s} \leqslant t \leqslant 5\,\mathrm{s}$ for profile 1 and $1\,\mathrm{s} \leqslant t \leqslant 3\,\mathrm{s}$ for profile 2. In this case, the deviation occurs shortly after the beginning of the stimulus which might be due to an uncertainty of the subjects' responses. The opposite is found for the mean squared difference measure $r_{q_S}(t)$ in the above mentioned intervals. $r_{q_S}(t)$ matches the subjective response at the beginning of both profiles, and it matches the target profile rather than subjective response in the interval $27\,\mathrm{s} \leqslant t \leqslant 32\,\mathrm{s}$ of profile 2. This effect may partly be explained by the nonlinear transformation of the two measures to the slider scale which might not be optimal (see above).

In summary, a highly satisfactory prediction of the time-varying speech quality is obtained from either of the measures $r_{q_C}(t)$ and $r_{q_S}(t)$. This supports the claim that the model can predict perceivable differences between the original and degraded signal that vary in time, based on their ''internal representations.'' The measure $r_{q_C}(t)$ has thus been shown to be sufficient to track the time-varying speech quality.

B. Time-varying speech quality modeling by segmental SNR

As the quality degradation in our experiments was generated by the relatively simple system of the modified MNRU, it would also be possible to objectively measure the resulting speech quality by a segmental Signal-to-Noise Ratio (SNRseg). The complexity of the SNRseg is much smaller than that of $r_{q_C}(t)$ and the SNRseg will be outperformed by $r_{q_C}(t)$ in the majority of applications for speech quality prediction.

However, to demonstrate the applicability of the SNRseg and in order to compare it with q_C, similar calculations as given above were performed with this measure. The SNRseg was calculated for signal segments of the same duration $\tau = 20\,\mathrm{ms}$, equal to the sampling period of $r_{q_C}(t)$ and $r_{q_S}(t)$, and subsequently low-pass filtered at 0.5 Hz. The formal description of the time-dependent SNRseg speech quality measure is given in the Appendix.

The SNRseg will be minimal (close to zero) when the parameter Q of the MNRU is minimal ($Q=0$), i.e., where the speech quality is at its lowest value. It will also be very small in speech pauses.

The results of the time-varying speech quality prediction by SNRseg are shown in Fig. 13. In the four panels, the SNRseg is shown for the four different stimulus conditions. The thick dash-dotted line shows SNRseg after low-pass filtering at 0.5 Hz. The subjective data with compensated delay are shown by the solid line. For comparison, also the prediction by $r_{q_C}(t)$ as shown in Fig. 11 is plotted into the same graph with the thin dashed line. In all four graphs $r_{\mathrm{SNRseg}}(t)$ exhibits regular strong dips toward low values that occur at the temporal positions of the regular speech pauses between adjacent sentences. This leads to more fluctuations of $r_{\mathrm{SEGsnr}}(t)$ and deviations from the target curve than observed for $r_{q_C}(t)$.

This difference may be explained by the fact that SNRseg does not account for any adaptive effects like temporal masking as modeled in q_C. The decay of temporal masking may last up to 500 ms which exceeds both the frame length τ and the duration of speech pauses in this example. Apart from the regular dips of $r_{\mathrm{SEGsnr}}(t)$, a reasonable prediction of the subjective data is achieved and no trend of a better performance of either $r_{q_C}(t)$ or $r_{\mathrm{SNRseg}}(t)$ can be observed. If the dips of $r_{\mathrm{SNRseg}}(t)$ are neglected, i.e., at times in the

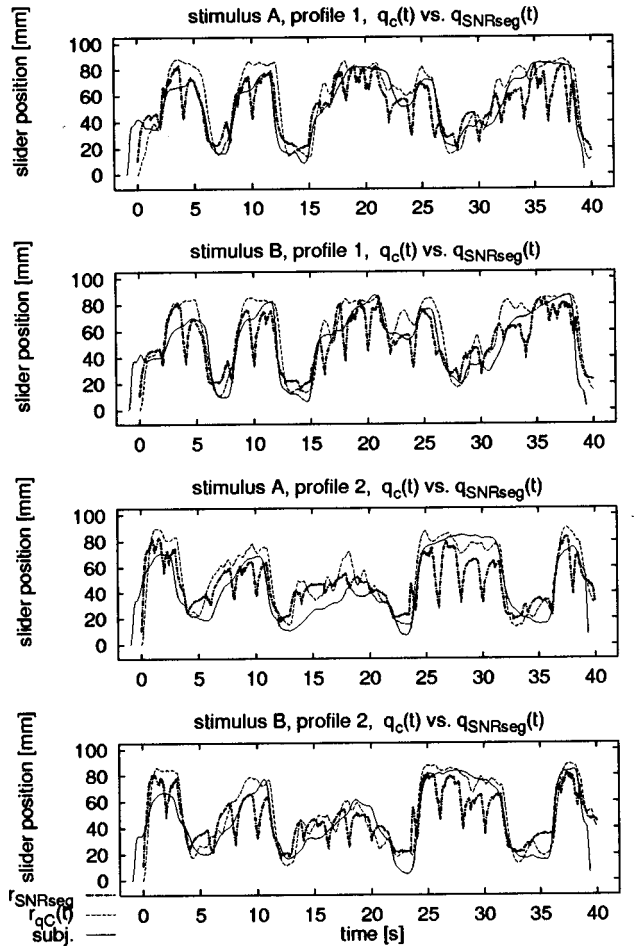

FIG. 13. Continuous-time speech quality prediction by the segmental SNR measure (thick dash-dotted line) for a frame duration of 20 ms. The prediction by $r_{q_C}(t)$ (thin dashed line) and the averaged subjective data (solid line, temporally shifted by 1 s) are plotted for comparison.

middle of corresponding test sentences, both measures perform equally well in discriminating different ranges of speech quality values.

V. SUMMARY AND CONCLUSION

In this study, a method for continuously assessing time-varying speech quality was described and tested. One experiment was concerned with the assessment of speech quality of isolated short speech elements and the other with the continuous assessment of time-varying speech quality of ongoing speech stimuli. The results of the first experiment showed that subjects are able to consistently assess the speech quality of short speech elements, i.e., words, in isolation. The subjective quality rating found for words in this experiment was compared with one set of results from the literature on the quality of sentence pairs as test stimuli and a good agreement was observed. The second experiment showed that subjects are able to accurately and reproducibly assess the time-varying quality of continuous speech stimuli. The subjective results showed a delay of approximately 1 s relative to the expected target quality profile. This observed delay was constant within $+/-0.15$ s across all subjects and for all four different stimulus conditions which demonstrates the consistency in the subject's results regarding their temporal behavior.

An objective speech quality measure based on a psychoacoustic processing model was used to predict the subjective speech quality results. The speech quality measures q_C and q_S (cf. Hansen and Kollmeier, 1997, 1998c; Hansen, 1998) were modified to allow for time-dependent objective measurement of the speech quality. The frame duration $\tau = 20$ ms and $\tau = 100$ ms used for temporal averaging of $q_C(t)$ and $q_S(t)$ did not result in a significant difference in the performance of $q_C(t)$ in predicting the subjective data. The averaged subjective response data could be modeled by the scale transformed measure $q_C(t)$ or $q_S(t)$ with a high degree of accuracy. This provides indirect support for the hypothesis that the psychoacoustic processing model extracts the relevant information about the perceived transmission quality of speech.

The feasibility of the new continuous assessment method was demonstrated using speech material that was processed with a modified MNRU with time-varying parameter Q. As stated before, this system served as a starting point for the current experiment, but it is not suited to simulate realistic variable rate speech coding and dynamic radio channel situations. The results using the MNRU-processed speech seem promising in that the new assessment technique is useful in realistic environments as well. As the MNRU distortions are relatively easy to measure, it may be expected that the performance of the objective speech quality measure $q_C(t)$ to predict the subjective results in the real-life environment is decreased. However, simple segmental SNR measures are very likely to fail to predict the subjective time-varying speech quality of realistic transmission systems. In follow-on experiments, the time-varying quality assessment of more realistic impairments, e.g., injection of bit errors into the GSM codec, should be investigated.

The new continuous assessment method provides the system developer with much more information about the performance/misperformance of an individual combination of coding and transmission devices. With continuous assessment it is possible to identify the point in time when a perceptually relevant instantaneous quality degradation occurs. This makes it possible to track its source. Also, the threshold for the strength or for the duration of a certain degradation might be measured more easily in this way than with standard MOS test methods. The continuous method can be expected to be much more sensitive to degradations that are of short duration.

In further studies on the continuous assessment method another aspect of quality assessment should be studied: It is often the case that the evaluator does not try to gain as much detailed information as possible but rather wants an answer to the question ''Which system has the better performance with respect to a planned application?'' This question leads to the investigation of the relation of continuous scaling response $r(t)$ to the ''overall quality,'' R, of the whole sequence. In recent studies on continuous video quality assessment, Hamberg and de Ridder (1997) investigated the relationship between these two entities. They found that the

perceived instantaneous quality degradations should be summed up by raising the degradations to the power $p=3$ (instead of the typical $p=2$ in squared difference measures), in combination with a decaying exponential weighting over time. In experiments on continuous loudness judgment a similar effect was observed by, e.g., Fastl (1991) and Weber (1991). The average overall loudness was found to be systematically larger than the arithmetic mean of the instantaneous loudness judgments which meant that the loud parts of a noise were more strongly weighted in determining the overall loudness than the soft parts. A similar study should be carried out for the case of continuous speech quality assessment.

ACKNOWLEDGMENTS

We thank Roelof Hamberg and Armin Kohlrausch for fruitful discussion on the design of the two experiments during a stay of the first author at the IPO-Center for Research on User-Systems Interaction, Eindhoven. Also Reinier Kortekaas provided helpful suggestions. Experiment 1 was in part carried out at the IPO. The authors thank and acknowledge the members of the Medical Physics Group and the ''Graduiertenkolleg Psychoakustik'' at Oldenburg University for constructive comments and discussions. We also thank Brian Moore for his critical reading of an earlier version of this paper. This study was supported by a grant from the Deutsche Forschungsgemeinschaft (DFG, Ko 942/12).

Part of this work has been presented at the 135th meeting of the American Society of Acoustics, the 16th International Conference on Acoustics in June 1998: Hansen and Kollmeier: ''Continuous Assessment and Modeling of Speech Transmission Quality.''

APPENDIX: CALCULATION OF THE TIME-DEPENDENT SPEECH QUALITY MEASURES

This Appendix gives a formal description of how the time-dependent speech quality measures $q_C(t)$ (based on the correlation coefficient), $q_S(t)$ (based on the mean squared difference), and SNRseg were calculated. q_C and q_S were calculated from the internal representations of the reference signal and test signal, while SNRseg was calculated directly from the waveform of the two signals.

Prior to the downsampling, the internal representation $X_{i,j}$ is sampled at times $t=i\Delta t$, $i=1,...,N$ and frequencies $f=(f_0+j\Delta f)$, $j=1,...,M$. By averaging across frames of duration $\tau=L\Delta t$, $X_{i,j}$ is transformed to $X'_{l,j}$ according to

$$X'_{l,j}=\frac{1}{L}\sum_{i=1}^{L} X_{(l-1)\cdot L+i,j}, \quad l=1,...,N/L. \tag{A1}$$

From the representations $X'_{l,j}$ and $Y'_{l,j}$ of the reference and test signal, respectively, the continuous-time speech quality measure was calculated in two different ways that correspond to the two definitions of the mean squared difference measure q_S and the correlation q_C (cf. Hansen, 1998; Hansen and Kollmeier, 1998c). However, *no* bandweighting was applied to the representations for the continuous-time speech quality measure.

At times $t=l\tau$, the mean squared difference measure $q_S(t)$ is defined as

$$q_S(t)=\frac{1}{M}\sum_{j=1}^{M} (X'_{l,j}-Y'_{l,j})^2 \tag{A2}$$

and the correlation measure $q_C(t)$ by

$$q_C(t)=\frac{\Sigma_{j=1}^{M}(X'_{l,j}-\overline{X'_l})\cdot(Y'_{l,j}-\overline{Y'_l})}{\sqrt{\Sigma_j(X'_{l,j}-\overline{X'_l})^2}\sqrt{\Sigma_j(Y'_{l,j}-\overline{Y'_l})^2}}, \tag{A3}$$

where $\overline{X'_l}$ and $\overline{Y'_l}$ denote the means of $X'_{l,j}$ and $Y'_{l,j}$ across the frequency index j. The above equations are similar to the original definitions of q_S and q_C given in Hansen (1998), and Hansen and Kollmeier (1998c). The difference lies in a missing summation along the time-index i. Note, that both the mean square summation and the correlation operation are performed across the two corresponding sets of $M=19$ spectral values at one point of time.

Both time-dependent distance measures were mapped to the $r(t)$ scale by means of a simple transformation and subsequently low-pass filtered at 0.5 Hz. For $q_S(t)$ an exponential transformation to the $r(t)$ quality scale of the form

$$r_S(q_S(t))=r_0 e^{\lambda_S\cdot q_S(t)} \tag{A4}$$

was fitted.

For $q_C(t)$ an exponential transformation of the form

$$r_C(q_C(t))=10+80\cdot e^{\lambda_C\cdot(q_C(t)-q_0)} \tag{A5}$$

was fitted. The parameters resulting from a Nelder–Mead type simplex search optimization (Press *et al.*, 1992) were $r_0=100$ and $\lambda_S=-0.078$, and $q_0=1$ and $\lambda_C=16.30$, in the case of $\tau=20$ ms.

The time-varying segmental Signal-to-Noise ratio SNRseg was defined in the following way. Let x_i denote the waveform of the original signal and y_i the processed signal, sampled at times $t=i\Delta t$. SNRseg_n was defined as (Quackenbush *et al.*, 1988)

$$\mathrm{SNRseg}_n=10\cdot\log\left(\frac{\Sigma_{i=n}^{n+N}x_i^2}{\Sigma_{i=n}^{n+N}(y_i-x_i)^2}\right), \tag{A6}$$

at times $t=n(N\Delta t)$ where $N\Delta t=20$ ms. Note that this definition does not consider a calculation of the SNR in different frequency bands but simply for the broadband signal. The transformation from SNRseg_n to the predicted slider position $r(t)$ was performed by using the same second-order polynomial $R(Q)$ that was previously used to transform the MNRU-parameter Q to the slider positions R (cf. Sec. II B), assuming that $Q=c\cdot\mathrm{SNRseg}$:

$$r_{\mathrm{SNRseg}}(t)=R(c\cdot\mathrm{SEGsnr}_n) \tag{A7}$$

with a constant c fitted to match the subjective data.

[1]dBov is defined as the level relative to that of a full range (digitized) dc signal. A full range sinusoid has a level of −3 dBov.

[2]These adjectives have been standardized for many different languages and are recommended by the ITU. The equivalent English translations are ''excellent,'' ''good,'' ''fair,'' ''poor,'' and ''bad.''

[3]Note that the majority of the subjects were male. However, there was no reason to expect that the gender of the subjects would have any influence on the task of speech quality assessment. No systematic difference in per-

formance was found between the female and the male listeners. The gender of the talkers uttering the test stimuli was of course equally balanced between male and female talkers (cf. Sec. II A).

[4]Let r_{ij} denote the sampled response data of subject and/or repetition j, $j=1...M$ at time $t=i\Delta t$, $i=1...N$. For all subjects and repetitions the mean across time $\mu_{r_j}=(1/N)\Sigma_{i=1}^{N} r_{ij}$ and the standard deviations $\sigma_{r_j}=\sqrt{(1/N-1)\Sigma_{i=1}^{N}(r_{ij}-\mu_{r_j})^2}$ are calculated. From the μ_{r_j} and σ_{r_j} the pooled mean and standard deviation $\mu_y=(1/M)\Sigma_{j=1}^{M}\mu_{r_j}$ and $\sigma_y=(1/M)\Sigma_{j=1}^{M}\sigma_{r_j}$ are calculated and finally the transformations are performed individually for each subject/repetition according to $y_{ij}=(\sigma_y/\sigma_{r_j})(r_{ij}-\mu_{r_j})+\mu_y$. In the literature this transformation is known under the name ''z-score-transformation'' (Chatfield, 1983). The term should not be confused with the z-transformation from signal processing.

[5]F-test: A-1: $F=1.021$, $P(F<f)=0.196$; B-1: $F=1.098$, $P=4\times10^{-5}$; A-2: $F=1.152$, $P<10^{-6}$; B-2: $F=1.111$, $P<10^{-6}$.

CCITT (**1989**). *Modulated Noise Reference Unit (MNRU)*, Blue Book Vol. V Rec. P.81.

Chatfield, C. (**1983**). *Statistics for Technology*, 3rd ed. (Chapman and Hall, London).

Dau, T., Püschel, D., and Kohlrausch, A. (**1996a**). ''A quantitative model of the 'effective' signal processing in the auditory system: I. Model structure,'' J. Acoust. Soc. Am. **99**, 3615–3622.

Dau, T., Püschel, D., and Kohlrausch, A. (**1996b**). ''A quantitative model of the 'effective' signal processing in the auditory system: II. Simulations and measurements,'' J. Acoust. Soc. Am. **99**, 3623–3631.

de Ridder, H., and Hamberg, R. (**1997**). ''Continuous assessment of image quality,'' SMPTE J. **106**, 123–128.

Dimolitsas, S. (**1993**). ''Subjective assessment methods for the measurement of digital speech quality,'' in *Speech and Audio Coding for Wireless and Network Applications*, edited by B. Atal, V. Cuperman, and A. Gersho (Kluwer Academic, Boston), pp. 43–54.

ETSI, TM/TM5/TCH-HS. (**1991**). *Global analysis of selection tests: Basic data*, Technical Report 91/74, ETSI.

ETSI, TM/TM5/TCH-HS. (**1992**). *Selection Test Phase II: Listening test results with German speech samples*, Technical Report 92/35, FI/DBP-Telekom. Experiment 1, IM 4.

Fastl, H. (**1991**). ''Evaluation and measurement of perceived average loudness,'' in *Contributions to Psychological Acoustics*, Vol. V, edited by A. Schick, J. Hellbrück, and R. Weber (Oldenburg, BIS), pp. 205–216.

Gottschling, G., and Fastl, H. (**1998**). ''Prognose der globalen Lautheit von Geräuschimmisionen anhand der Lautheit von Einzelereignissen,'' in *Fortschritte der Akustik DAGA '98* (Zürich, Dega).

Hamberg, R., and de Ridder, H. (**1995**). ''Continuous assessment of perceptual image quality,'' J. Opt. Soc. Am. A **12**, 2573–2577.

Hamberg, R., and de Ridder, H. (**1999**). ''Time-varying image quality: Modeling the relation between instantaneous and overall quality,'' SMPTE J. (submitted). Current version: IPO manuscript no. 1234.

Hansen, M. (**1998**). ''Assessment and prediction of speech transmission quality with an auditory processing model,'' Ph.D. thesis, Universität Oldenburg. Available through http://www.bis.uni-oldenburg.de/dissertation/hanass98/hanass98.html.

Hansen, M., and Kollmeier, B. (**1997**). ''Using a quantitative psychoacoustical signal representation for objective speech quality measurement,'' in Proc. ICASSP '97 (IEEE, Munich), pp. 1387–1390.

Hansen, M., and Kollmeier, B. (**1998a**). ''Continuous assessment and modeling of speech transmission quality,'' in Proc. 16th ICA/135th meeting ASA, pp. 229–230, Seattle.

Hansen, M., and Kollmeier, B. (**1998b**). ''Kontinuierliche Beurteilung von Sprachqualität: Messung und Modellierung,'' in *Fortschritte der Akustik DAGA '98* (Zürich, Dega).

Hansen, M., and Kollmeier, B. (**1998c**). ''Objective modeling of speech quality with a psychoacoustically validated auditory model,'' J. Audio Eng. Soc. (submitted).

Hansen, M., and Kollmeier, B. (**1998d**). ''Perception of band-specific speech quality distortions: Detection and pairwise comparison,'' Acta Acust. (submitted).

ITU-T (**1996a**). ''Methods for subjective determination of transmission quality,'' Series P: Telephone Transmission Quality, Recommendation P.800, ITU, Geneva.

ITU-T (**1996b**). ''Software tools for speech and audio coding standardization,'' Series G: Transmission systems and media, Recommendation G.191, ITU, Geneva.

ITU-T (**1996c**). ''Subjective performance assessment of telephone-band and wideband digital codes,'' Series P: Telephone Transmission Quality, Recommendation P.830, ITU, Geneva.

Jekosch, U. (**1993**). ''Speech quality assessment and evaluation,'' in Proc. Eurospeech (ESCA, Berlin), pp. 1387–1394.

Kitawaki, N. (**1990**). ''Quality assessment of coded speech,'' in *Advances in Speech Signal Processing*, edited by S. Furui and M. Sondhi (Marcel Dekker, New York), pp. 357–386.

Kroon, P. (**1995**). ''Evaluation of speech coders,'' in *Speech Coding and Synthesis*, edited by W. B. Kleijn and K. K. Paliwal (Elsevier Science B.V., Amsterdam), pp. 467–494.

Kuwano, S., and Fastl, H. (**1989**). ''Loudness evaluation of various kinds of nonsteady state sounds using the method of continuous judgment by category,'' in Proc. 13th ICA (Belgrade), Vol. 3, pp. 365–368.

Namba, S., Kuwano, S., and Fastl, H. (**1988**). ''Loudness of road traffic noise using the method of continuous judgment by category,'' in *Noise as a Public Health Problem*, Vol. 3, edited by B. Berglund, U. Berglund, I. Karlson, and T. Lindvall (Swedish Council for Building Research, Stockholm), pp. 241–246.

Preminger, J. E., and Van Tasell, D. J. (**1995**). ''Quantifying the relation between speech quality and speech intelligibility,'' J. Speech Hear. Res. **38**, 714–725.

Press, W., Tenholsky, S., Vetterhing, W., and Flaunery, B. (**1992**). *Numerical Recipes in C—The Art of Scientific Computing*, 2nd ed. (Cambridge University Press, Cambridge).

Quackenbush, S. R., Barnwell, T. P., and Clements, M. A. (**1988**). *Objective Measures for Speech Quality* (Prentice Hall, Englewood Cliffs).

Sotscheck, J. (**1984**). ''Sätze für Sprachgütemessungen und ihre phonologische Anpassung an die deutsche Sprache,'' in *Fortschritte der Akustik-DAGA '84* (DPG Verlag, Bad Honnef), pp. 873–876.

Sotscheck, J. (**1992**). ''Sprachqualitätstests aus der Nachrichtentechnik,'' in *Moderne Verfahren der Sprachaudiometrie, Buchreihe Audiologische Akustik*, edited by B. Kollmeier (Median-Verlag, Heidelberg).

Weber, R. (**1991**). ''The continuous loudness judgment of temporally variable sounds with an ''Analog'' category procedure,'' in *Contributions to Psychological Acoustics*, Vol. V, edited by A. Schick, J. Hellbrück, and R. Weber (Oldenburg, BIS), pp. 267–294.

Effects of categorization and discrimination training on auditory perceptual space

Frank H. Guenther[a)]
Department of Cognitive and Neural Systems, Boston University, 677 Beacon Street, Boston, Massachusetts 02215 and Research Laboratory of Electronics, Massachusetts Institute of Technology, Cambridge, Massachusetts 02139

Fatima T. Husain, Michael A. Cohen, and Barbara G. Shinn-Cunningham
Department of Cognitive and Neural Systems, Boston University, 677 Beacon Street, Boston, Massachusetts 02215

(Received 19 March 1999; revised 15 July 1999; accepted 16 July 1999)

Psychophysical phenomena such as categorical perception and the perceptual magnet effect indicate that our auditory perceptual spaces are warped for some stimuli. This paper investigates the effects of two different kinds of training on auditory perceptual space. It is first shown that categorization training using nonspeech stimuli, in which subjects learn to identify stimuli within a particular frequency range as members of the same category, can lead to a decrease in sensitivity to stimuli in that category. This phenomenon is an example of acquired similarity and apparently has not been previously demonstrated for a category-relevant dimension. Discrimination training with the same set of stimuli was shown to have the opposite effect: subjects became more sensitive to differences in the stimuli presented during training. Further experiments investigated some of the conditions that are necessary to generate the acquired similarity found in the first experiment. The results of these experiments are used to evaluate two neural network models of the perceptual magnet effect. These models, in combination with our experimental results, are used to generate an experimentally testable prediction concerning changes in the brain's auditory maps under different training conditions. © *1999 Acoustical Society of America.* [S0001-4966(99)00411-7]

PACS numbers: 43.71.An, 43.66.Ba [JMH]

INTRODUCTION

It is well-known that our perceptual spaces for some auditory stimuli, such as phonemes, are warped. That is, the perceptual distance between two stimuli, as evidenced by a subject's ability to discriminate them, is not always a straightforward function of their distance as measured along physical dimensions such as frequency or time.[1] English stop consonants, for example, have long been known to exhibit categorical perception (see Jusczyk, 1986; Liberman, 1996; Lieberman and Blumstein, 1988; and Repp, 1984 for reviews). For example, if subjects are presented with synthetic speech stimuli created by varying the second formant transition in small steps through a range corresponding to the phonemes /b/, /d/, and /g/, they show very poor discriminability when two stimuli both fall within one of the categories and very good discriminability for stimuli that straddle category boundaries, even though the stimulus pairs in these two cases are equidistant in frequency space (Liberman *et al.*, 1957; Eimas, 1963). Other experiments have shown similar categorical effects for voice onset time (VOT) distinctions between /d/ and /t/ (Liberman *et al.*, 1961b) and between /b/ and /p/ (Liberman *et al.*, 1961a). Similar effects have also been reported for a variety of nonspeech stimuli, including melodic musical intervals (Burns and Ward, 1978), simple visual shapes (Lane, 1965; Goldstone, 1994), and morphed faces along an intriguing ''John F. Kennedy to Bill Clinton'' continuum (Beale and Keil, 1995).

Researchers have also shown, relatively recently, that the perceptual space for some synthetic vowels and semivowels appears to be warped (e.g., Aaltonen *et al.*, 1997; Iverson *et al.*, 1994; Iverson and Kuhl, 1994, 1995; Kuhl, 1991, 1995; Kuhl *et al.*, 1992; Sussman and Lauckner-Morano, 1995). Kuhl (1991) referred to this warping as a ''perceptual magnet effect,'' thus distinguishing it from categorical perception. Roughly speaking, the effect is characterized by a warping of perceptual space such that acoustic patterns near phonemic category prototypes are perceived as closer together than equally spaced acoustic patterns that are further away from phonemic category prototypes. According to the Kuhl *et al.* account, the magnet effect differs from categorical perception in that it is characterized by differences in discriminability for prototypical vs nonprototypical stimuli that fall within the *same* phonemic category. Specifically, better discrimination is found near nonprototypical members of a category than near prototypical members. However, other researchers have claimed that categorical perception and the perceptual magnet effect are essentially the same. For example, Lotto, Kluender, and Holt (1998) conclude from their study that the magnet effect ''may be nothing more than further demonstration that general discriminability is greater for cross-category stimulus pairs than for within-category pairs'' (p. 3648). By either account, though, the perceptual space for vowels and semivowels ap-

a)Electronic mail: guenther@cns.bu.edu

pears to be warped, although apparently not as dramatically as for consonants.

It is very likely that some of the warping of auditory space is ''built in'' to the auditory nervous system. Evidence for this comes from studies of auditory perception in animals and newborn infants. For example, the discriminability by chinchillas of changes in VOT for stimuli varying between [dɑ] and [tɑ] is nonuniform and peaks at a VOT of about 30 ms, which is near the voiced/voiceless boundary in English (Kuhl and Miller, 1975, 1978; Kuhl, 1981). A similar result was also reported for macaque monkeys (Kuhl and Padden, 1982). Increased discriminability was also found at the /b/–/d/ and /d/–/g/ phonetic boundaries of a continuum of $F2$ transition onset frequencies in the macaque monkey (Kuhl and Padden, 1983). Eimas *et al.* (1971) showed that human infants 1–4 months old produced evidence of categorical perception for the voiced/voiceless distinction, further suggesting that this effect is a consequence of auditory mechanisms that are present at birth.

A. Experience-based warping of auditory space

Other aspects of the warping of auditory space appear to arise from learning, rather than from built-in properties of the auditory system. Evidence for this view comes from cross-language studies, since differences in the locations of warping in auditory space across languages are presumably the result of learning driven by linguistic experience. One example of such a difference is the small but systematic difference in the VOT boundary for the voiced/voiceless distinction across languages (e.g., Lisker and Abramson, 1970). Another example is the language specificity of the warping of auditory space for vowels as measured in studies of the perceptual magnet effect. In a study of 6-month-old English and Swedish infants presented with English and Swedish vowel stimuli, Kuhl *et al.* (1992) found that infants had more difficulty discriminating between stimuli falling near a prototypical vowel from their native language than stimuli falling near a prototypical vowel in the non-native language.

The experiments described in the current article were designed to investigate learned warpings of auditory perceptual space. Because the experiments were designed in part to test neural network models of the perceptual magnet effect (as described in the next section), and because the magnet effect is one of the most heavily studied examples of a learned warping of auditory space, we will frequently refer to it when discussing our experimental results. We do not mean to imply by this that the perceptual magnet effect should be considered as a separate phenomenon from learned instances of categorical perception.

Liberman (1957) identified two possible learning processes that might underlie categorical perception. The first, *acquired distinctiveness*, is defined as an increase in perceptual sensitivity for items that are repeatedly categorized differently in a learning situation. Liberman (1957) reported evidence for acquired distinctiveness in detecting duration differences for speech sounds versus nonspeech sounds, and later studies provided further examples of acquired distinctiveness for nonspeech stimulus sets (e.g., Lane, 1965; Goldstone, 1994). The second possible learning process identified by Liberman (1957) was *acquired similarity*, also referred to by some authors as *acquired equivalence*. In acquired similarity, sounds that were originally distinguishable from each other become less distinguishable after repeatedly being categorized together. It has been noted that very young infants are capable of making some acoustic distinctions that become more difficult to make later in life if those distinctions are not used to differentiate phonemes in the infant's native language (e.g., Eimas, 1975; Goto, 1971; Miyawaki *et al.*, 1975; Werker and Tees, 1984). These results appear to be examples of acquired similarity for a category-irrelevant stimulus dimension, i.e., a physical dimension which does not provide any information about category membership.

Goldstone (1994) reported another example of acquired similarity for a category-irrelevant dimension in adults performing a categorization learning task utilizing visual stimuli. Participants were trained to categorize visual stimuli that differed along two dimensions (brightness and size). For some subject groups, only one stimulus dimension was relevant for the categorization task. Goldstone (1994) found one case of acquired similarity for a category-irrelevant dimension, but no instances of acquired similarity were found for category-relevant dimensions.

However, if acquired similarity is playing a role in learned instances of categorical perception and the perceptual magnet effect, it must involve category-*relevant* dimensions. The very notion of ''nearer to the category boundary'' that is commonly used to describe these phenomena implies that we are talking about category-relevant dimensions, such as formant frequencies for vowels. Although attempts have been made (e.g., Goldstone, 1994), acquired similarity for a category-relevant dimension has apparently not been shown experimentally (Liberman, 1996, pp. 18–19).

B. Considerations from experimental and theoretical neuroscience

It seems reasonable to assume that infants are more commonly exposed to prototypical examples of a speech sound than nonprototypical examples during the learning process that leads to the perceptual magnet effect.[2] Perhaps relatedly, many neurophysiological studies of sensory maps have shown that disproportionately large exposure to a particular type of stimulus typically leads to a larger cortical representation for that stimulus. For example, kittens reared in a visual environment consisting only of vertical stripes have more visual cortex cells tuned to vertical contours than kittens reared in a normal environment (e.g., Rauschecker and Singer, 1981). Analogous results have been found in other sensory modalities. Preferential stimulation of a digit in monkeys leads to a larger cortical representation for that digit in somatosensory cortex (Jenkins, Merzenich, and Ochs, 1984; Jenkins *et al.*, 1990). In the auditory realm, Recanzone, Schreiner, and Merzenich (1993) found that repeatedly exposing monkeys to tones in a particular frequency range during learning of a tone discrimination task resulted in an increase in the area of auditory cortex preferentially activated by sounds in the trained frequency range and a concomitant increase in the discriminability of the training tones.

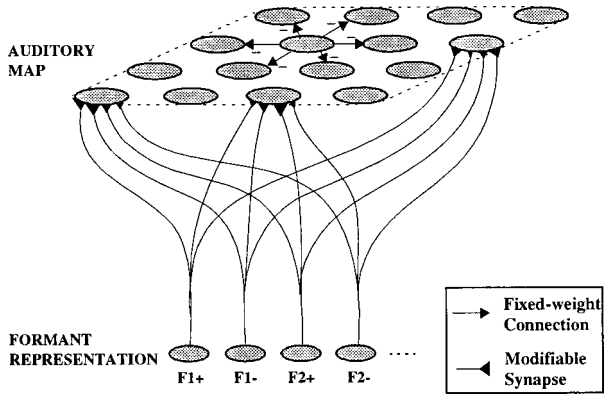

FIG. 1. Schematic of the Guenther and Gjaja (1996) neural network model of the perceptual magnet effect. See the text for details.

It is also commonly believed that, all else being equal, stimuli that have a larger cortical representation are more easily discriminated from one another than stimuli that have a smaller cortical representation. For example, the cortical representation of the fingers in human somatosensory cortex is disproportionately large when compared to the representation of the back, and, correspondingly, humans are typically much better at discriminating tactile stimuli with their fingers than with their backs (e.g., Kandel, 1985). Similarly, the primary visual cortex representation of the high-resolution foveal area of our retinas is much larger than the representation of the low-resolution visual periphery.

If one assumes that frequent exposure to a stimulus leads to a larger cortical representation, and that larger cortical representations lead to better discriminability, then one sees a paradoxical aspect of the perceptual magnet effect: in the magnet effect, discriminability of more frequently encountered stimuli (prototypical vowels) is *worse* than discriminability of less frequently encountered stimuli (nonprototypical vowels). Two recent neural network models posit explanations for the perceptual magnet effect in terms of experience-based formation of neural maps in the auditory system (Bauer, Der, and Herrmann, 1996; Guenther and Gjaja, 1996). These models are of interest because they make clear predictions about the organization of the brain that can be tested using recently available imaging techniques such as functional magnetic resonance imaging (FMRI) or positron emission tomography (PET).

A schematic of the Guenther and Gjaja (1996) model is provided in Fig. 1. The model uses two layers of neurons, referred to as the formant representation and the auditory map, connected by a set of modifiable synapses. When presented with a vowel input, the formant frequencies of the vowel are represented by the formant representation cells. Signals projecting from these cells to the auditory map through modifiable synapses lead to the activation of a subset of the cells in the auditory map. The strengths of the synapses determine which cells become active in the auditory map. The strengths of the synapses are then modified in a manner that depends on the pre- and post-synaptic cell activities, thus changing the ''firing preferences'' of the cells (i.e., the vowel stimuli that maximally activate the cells) in the auditory map. This process is carried out repeatedly with new vowel stimuli during a training period. The Bauer *et al.* (1996) model has a similar structure and function, differing primarily in the equations governing changes in the synaptic weights projecting to cells in the auditory map.

Though developed independently, the basic idea behind the Guenther and Gjaja (1996) and Bauer *et al.* (1996) models is the same. Exposure to vowel sounds in the early months of life causes changes in the distribution of firing preferences of neurons in an infant's auditory map. For example, in the Guenther and Gjaja (1996) model, more cells in the auditory map become tuned to the vowel sounds that the infant hears most often. It is these changes in the auditory map that underlie the perceptual magnet effect in both models.

Although the Guenther and Gjaja (1996) and Bauer *et al.* (1996) models are similar in many respects, they differ in how they account for the apparent paradox described above. In the Guenther and Gjaja (1996) model, the paradox is accounted for by differences in the training distributions for categorical stimuli as compared to noncategorical stimuli, where categorical stimuli are those that are typically perceived as members of a discrete set of categories (e.g., speech sounds) and noncategorical stimuli are those that are not typically perceived in this way (e.g., pure tones). Specifically, it is suggested that the training distribution of categorical stimuli has relatively sharp peaks near the category prototypes (i.e., infants hear many more examples of vowel-like sounds that fall near prototypical vowels than near nonprototypical vowels), as compared to the typically flatter distributions of noncategorical stimuli. This sharply peaked training distribution leads to a similarly peaked distribution of cell firing preferences in the neural map, and this in turn leads to a warping of perception toward the more prototypical exemplars due to population coding in the nervous system. The details of this process are presented in Guenther and Gjaja (1996); for current purposes, it suffices to note that this model predicts that it is the distribution of training stimuli, not the type of training, that leads to the perceptual magnet effect.

In the Bauer *et al.* (1996) model, it is assumed that, for some stimuli, the neural map formation process leads to *smaller* cortical representations for the most frequently encountered stimuli, rather than the larger cortical representations reported in the neurophysiological studies described above. Although not treated by Bauer *et al.*, we infer here that differences in the learning situation for categorical stimuli as compared to noncategorical stimuli lead to this difference in how the cortical representation changes size for these stimuli. In other words, whereas discrimination training leads to a larger cortical representation for the most frequently encountered stimuli, categorization training leads to a smaller cortical representation for the most frequently encountered stimuli. Although the differential effects of different types of training in the Bauer *et al.* model may seem more intuitive from a learning perspective, the Guenther and Gjaja model is more in line with the traditional view of neural map formation in the computational neuroscience literature.

C. Goals of the current experiments

The first purpose of the current studies was to observe whether it is possible to induce acquired similarity for a category-relevant dimension of nonspeech stimuli (auditory noise stimuli) using a categorization training task. This type of induced ''perceptual magnet effect'' is predicted by the Guenther and Gjaja (1996) model since this model attributes the reduced discriminability near a category prototype to neural map formation principles that are not specific to speech. Although this sort of acquired similarity had been identified as a possible learning mechanism underlying categorical perception several decades ago (e.g., Liberman, 1957; Lane, 1965), it apparently has not been demonstrated experimentally (Goldstone, 1994; Liberman, 1996). A second purpose of the current study was to investigate some of the learning conditions that are necessary to reduce sensitivity for frequently encountered stimuli, if it is indeed possible to induce such an effect. A final purpose of this study was to test between the Guenther and Gjaja (1996) and Bauer *et al.* (1996) neural models of the perceptual magnet effect in order to form a clear and testable hypothesis concerning the properties of the nervous system that lead to this effect. Most of the experimental results reported herein have been presented in preliminary form in conference publications (e.g., Husain and Guenther, 1998a,b).

I. EXPERIMENTS

Four experiments were performed. All experiments consisted of four phases: a calibration phase in which a subject's detection threshold for auditory stimuli like those used in later phases of the experiment was determined, a pretest phase to determine baseline sensitivity, a training phase, and a post-test phase to measure any change in sensitivity that may have resulted from training. Experiments I, II, and III used the same testing procedure; these experiments differed only in the type of training the subjects underwent during the training phase. The pre- and post-tests for experiment IV were modified slightly from the others. The common aspects of the experimental design are treated in the following paragraphs.

A. Participants

Subjects were male and female adults between the ages of 18 and 50 with no history of speech, language, or hearing disorders. Subjects were compensated at the rate of $8 an hour. Each subject participated in a single experimental session, consisting of a calibration phase lasting approximately 15 min, a pretest lasting approximately 15 min, a training session lasting approximately 45 min, and a post-test lasting approximately 15 min, for a total session length of approximately 1.5 h. No subjects were used in more than one experiment. A subject's results were excluded from analysis if the subject did not perform within a previously determined criterion on the training task, as described below. Subjects had no prior knowledge regarding the purpose of the experiment.

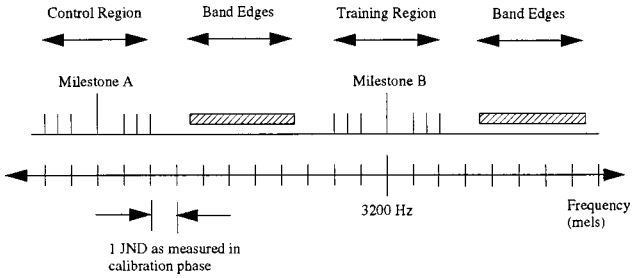

FIG. 2. The range of frequency space within which different types of stimuli were generated. Milestone A and its neighbors form the control region and milestone B and its neighbors form the training region. Regions spanning 4 jnds on either side of the training region are called ''band edges.'' See the text for details.

B. Apparatus and stimuli

The stimuli for all experiments were narrow-band filtered samples of white noise with different center frequencies. The center frequencies of the passband ranged between 1000 and 3500 Hz. The bandwidths of the stimuli were chosen to be equal in mel space, with the stimulus at 2500 Hz having a bandwidth of 100 Hz and the bandwidths of all stimuli falling within the range of 90–130 Hz. The stimuli were generated at a sampling rate of 16 kHz using Entropic's ESPS/WAVES software on a Sun SPARCstation 10 by filtering white noise through a bandpass filter (a linear phase finite-impulse response filter created using a weighted mean-square error criterion) with a falloff of approximately 20 dB per 100 Hz.

The sound files were sent through an Ariel D/A converter to both speakers of a set of headphones worn by the subject while sitting in a quiet room. The sounds were played at a level the subjects deemed most comfortable,[3] typically around 75 dB. Subjects' responses were entered using the mouse and keyboard of the computer that controlled the presentation of stimuli.

C. Calibration phase

Each individual subject's threshold for discriminating the stimuli was established at the beginning of the experiment. This was done to account for rather large intersubject differences in the ability to discriminate between the stimuli.[4] An adaptive up–down staircase method (AX same–different paradigm) was used to determine the discrimination threshold. Stimuli for this procedure consisted of narrow-band white noise centered at different frequencies around 2500 Hz with a bandwidth of 100 Hz. The step size that shifted the center frequency of the noise stimuli was fixed at 5 Hz. Thresholds were determined both for frequencies lower than and greater than 2500 Hz. The final threshold was the average of these two thresholds. This threshold, specified in mel units, was used as an estimate of the just noticeable difference (jnd) for that particular subject throughout the range of frequencies used in the experiment.

The stimuli for the remainder of the experiment were generated based on this jnd measure, as shown in Fig. 2. The hashmarks on the *x*-axis of this figure are spaced 1 jnd apart. First, a reference stimulus, labeled ''milestone B'' in Fig. 2, was located at 3200 Hz. This stimulus and six additional

stimuli spaced ±1, 1.5, and 2 jnd from it constitute the ''training region'' of frequency space. Next, a second reference stimulus, milestone A, was located at a frequency 11 jnd's less than milestone B. Milestone A and stimuli spaced ±1, 1.5, and 2 jnd from it constitute the ''control region'' of frequency space. (The spacing used for the stimuli in experiment IV was slightly different; this will be addressed in the description of that experiment.) In the pre- and post-tests, the subject's sensitivity to stimuli in both the control region and the training region was measured by estimating d' between the milestones A and B and their neighboring stimuli. Stimuli in the training region were involved in the training phase in a manner specific to the particular experiment; stimuli in the control region were not encountered during training. Comparison of the difference between pre- and post-test results for the training and control regions provides information about the effects of training on the listener's sensitivity to the training region stimuli. This design partially controls for shifts in response bias which may occur over the roughly 45-min training period separating the pretest and post-test.

The training regimes used in the experiments required the use of stimuli from outside of the training region but not in the control region. These additional stimuli were chosen from a uniform distribution over two regions of frequency space labeled ''band edges'' in Fig. 2: a 4-jnd-wide region between the training region and the control region, and a 4-jnd-wide region located above the training region in frequency space. There was a separation of 1.5 jnd's between the band edges and both the training and control regions.

D. Pre- and post-test phases

Tests were conducted to measure subjects' sensitivities to differences in the auditory stimuli for both the control and training regions before and after training. The pre- and post-test sessions for the same experiment were identical. The tests measured discriminability around milestone A and milestone B (see Fig. 2). Tests were conducted in two blocks of 64 trials each, using an AX same–different paradigm. One block of trials measured sensitivity in the control region, while the other block measured sensitivity in the training region. The order of presentation of the blocks was varied for different subjects, with roughly half the subjects performing tests with the control block first and the other half performing tests with the training block first. Subjects were not provided feedback concerning the correctness of their responses in the pre- and post-tests.

Each trial within a block was composed of a pair of stimuli. The first stimulus of the pair was always the milestone. The second stimulus of the trial was either the milestone again or any of its neighbors in the corresponding region, as shown in Table I. A total of 7 distinct pairs of stimuli was generated for each block, with 6 being ''different'' and 1 being ''same.'' There were 8 repetitions of each different pair and 16 repetitions of the same pair, for a total of 64 trials per block. The length of each of the stimuli in a trial was 500 ms, as shown in Fig. 3. In the first three experiments, the interstimulus interval (ISI) was 750 ms long with a brief burst of white noise, 250 ms long, in the middle.

TABLE I. Generation of pairs of stimuli for the AX same–different discrimination tests. *M* stands for milestone, and subscripts denote the distance from the milestone in jnd units.

A	X	Type of trial	Number
M	M	Same	16
M	M_{-1}	Different	8
M	$M_{-1.5}$	Different	8
M	M_{-2}	Different	8
M	M_{+1}	Different	8
M	$M_{+1.5}$	Different	8
M	M_{+2}	Different	8
		Total	64

In the fourth experiment, the ISI was 250 ms and there was no white noise between the two stimuli. The noise burst was added in the first three experiments to favor a categorical mode of sensory processing; this topic is discussed further in the description of the fourth experiment (Sec. I E 4).

Trials were presented in random order. Subjects indicated whether they thought the tones they heard were the same or different by pressing the ''*s*'' or ''*d*'' key on the keyboard. Subjects generally completed a test in 15 min.

The change in sensitivity between pre- and post-tests was analyzed for the group of subjects. Analysis of each subject's sensitivity (d') was performed using both hit and false-alarm rates. Group d' scores were then calculated from these individual measures to produce a collapsed d' measure (Macmillan and Creelman, 1991; Macmillan and Kaplan, 1985). This measure has been used by researchers such as Sussman and Lauckner-Morano (1995) to investigate the perceptual magnet effect. Pairwise *t*-tests (Howell, 1992) compared pre- and post-training d' scores to test for significant change in both the training region and the control region (whose sounds did not occur during the training session). Changes in sensitivity for the training region were then compared to changes in sensitivity for the control region.

Discriminability was compared across groups of subjects using the *G* statistic (Gourevitch and Galanter, 1967, p. 27) which allows for comparison of group d' measures. The *G* statistic tests the significance of the difference of the pre- and post-training d' scores by considering the number of observations per data point (10 subjects×8 trials=80 observations per data point).

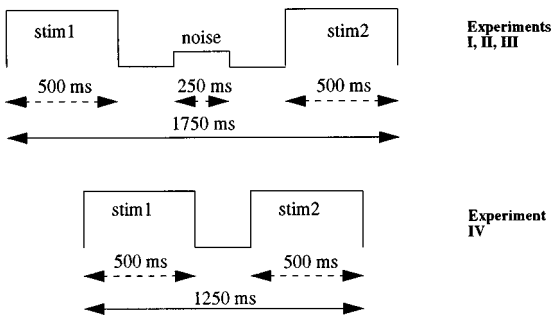

FIG. 3. Time course of a test trial. In experiments I, II, and III, the ISI was 750 ms long with a distractor noise of 250 ms. In experiment IV, the ISI was 250 ms long with no distractor noise.

E. Training phase

The type of training varied for each experiment, and the different training paradigms are explained along with the relevant experiments below. All experiments shared the following criterion for inclusion of a subject's results in the analysis: the subject must have responded correctly on half the trials of each of the ten training subsessions which comprised the training phase. If the subject did not meet this criterion, it was assumed that he/she did not succeed in learning the training task, and his/her results were thus excluded from the statistical analyses.

1. Experiment I

The main goal of the first experiment was to investigate whether it is possible to induce a decrease in discriminability along a category-relevant dimension of a set of nonspeech stimuli that was repeatedly encountered during a training session. This would constitute a demonstration of acquired similarity along a category-relevant dimension, and it would also be in keeping with models of the perceptual magnet effect that attribute the effect to neural map formation properties that are not specific to speech (Guenther and Gjaja, 1996).

a. Training. In the training phase of experiment I, subjects were trained to choose sounds that belonged to the training region (i.e., milestone B and its neighbors) from a list of sounds. Specifically, subjects were told that they were to learn to identify sounds from a category, referred to as the ''prototype category'' and corresponding to the training region of frequency space in Fig. 2, and that during training they would have to choose the prototype category sound from a list of sounds that included only one member of the prototype category. Since the subjects were taught to treat the training region sounds as members of the same category, we will refer to this type of training as *categorization training*. The subjects underwent two types of training trials: (1) listening trials in which they heard example sounds from the training region and did not have to make any response, and (2) identification trials in which they identified one sound from a list of sounds as belonging to the training region. During a listening trial, subjects heard four sounds randomly chosen from a set of nine sounds which were evenly spaced in 0.5-jnd increments within the training region. These included the milestone B and its six neighbors used in the testing procedure, plus the two stimuli falling ± 0.5 jnd from the milestone. During an identification trial, subjects heard a short list of sounds, only one of which came from the training region. The other sounds that comprised the identification trial were generated from the ''band edges'' regions flanking the training region (see Fig. 2). These sounds were randomly chosen from a set of 18 sounds: nine sounds spaced 0.5 jnd apart from within the band edge region lower in frequency than the training region, and nine sounds spaced 0.5 jnd apart from the band edge region higher in frequency than the training region. As noted earlier, the band edge regions did not overlap with either the training or control regions, and no sounds from the control region were presented during training.

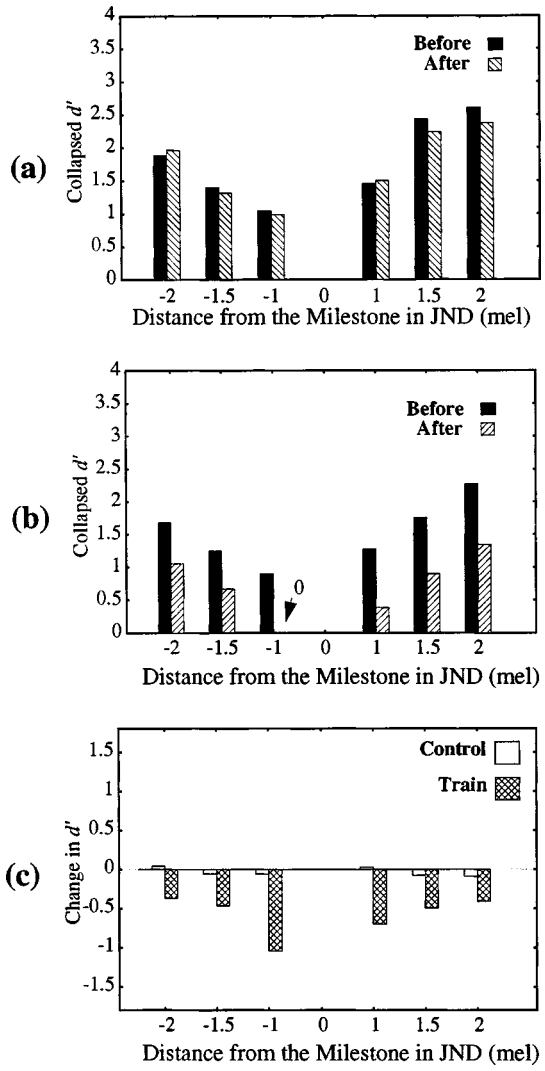

FIG. 4. (a) The *collapsed* d' score for the control region of experiment I, before and after training, as a function of distance from the milestone. (b) The *collapsed* d' score for the training region of experiment I, before and after training, as a function of distance from the milestone. (c) Change in sensitivity after training for the control and training regions in experiment I. Subjects showed a significant decrease in sensitivity for the stimuli in the training region but not in the control region.

Subjects could choose whether to perform a listening or an identification task for any given trial, with the stipulation that no more than 15 listening trials could be performed in any subsession. The subsession ended when 30 identification trials were completed. Each subject performed ten such subsessions, and subjects received feedback about the correctness of their responses. Task difficulty was increased over the ten subsessions by increasing the length of the list of sounds from which the subject had to identify the training region sound: a two-sound list was used in the first three subsessions, a three-sound list was used in the next three subsessions, and a four-sound list was used in the last four subsessions. Subjects generally completed the entire training phase in 45 min. Two of the 12 subjects who participated in the experiment performed below the established criterion during the training session and their data were thus excluded from subsequent analysis.

b. Results. Figure 4(a) shows the collapsed d' values for

TABLE II. *G* statistic comparison for experiment I. Asterisks denote statistically significant ($p<0.05$) changes in sensitivity.

Stimulus (jnd)	Control *G* score	Training *G* score
−2	0.27	−2.37*
−1.5	−0.29	−2.25*
−1	−0.20	−3.54*
1	0.15	−3.46*
1.5	−0.63	−3.28*
2	−0.73	−3.20*

sounds in the control region before and after training, and Fig. 4(b) shows the same results for the training region. Subjects were significantly worse ($p<0.05$) at discriminating stimuli in the training region after training compared to before training [$t(5)=-12.4$; $p<0.05$], but not in the control region [$t(5)=-1.48$; $p>0.05$]. Figure 4(c) compares the change in d' for the control and training regions. The change in d' was calculated as the percentage increase or decrease in d' from pretest to post-test. This figure indicates that the change in sensitivity for the training set of stimuli was significantly more negative [$t(5)=-5.14; p<0.05$] than the change in sensitivity for the control region. All ten subjects showed a decrease in sensitivity for the training region, and eight of the ten showed a larger sensitivity decrease in the training region than in the control region.

Discriminability before and after training was also compared across groups using Gourevitch and Galanter's (1967) *G* statistic. Overall, as seen in Table II, there was a general pattern for sensitivity to worsen (indicated by the negative values) for the training region. On the other hand, sensitivity for the control region, across all the comparison steps, did not change significantly.

c. Discussion. The results of the first experiment indicate that it is possible to induce acquired similarity along a category-relevant dimension if an appropriate training regime is utilized. Although the training region stimuli were encountered more frequently than the control region stimuli during the experiment, subjects showed a reduction in their ability to discriminate stimuli in the training region as compared to the control region. As mentioned in the Introduction, the perceptual magnet effect also appears to be a case of acquired similarity along category-relevant dimensions (formant frequencies) for more heavily experienced stimuli. The main result of experiment I might thus be interpreted as a case of inducing a ''perceptual magnet-like'' effect in a nonspeech modality, as predicted by the Guenther and Gjaja (1996) neural model of the perceptual magnet effect. Although Bauer *et al.* (1996) do not address the issue of whether the conditions leading to the magnet effect in their model are speech-specific, the results of experiment I are not inconsistent with the Bauer *et al.* model if one assumes that a reduced cortical representation with heavy exposure can occur for nonspeech stimuli as well as speech stimuli (see the General Discussion, Sec. II).

2. Experiment II

The second experiment tested whether a training regimen different from that used in experiment I could result in a different effect on the subjects' sensitivity to the training stimuli even though a similar distribution of sounds is presented during training. In this experiment, a discrimination training paradigm was used in which subjects were repeatedly asked to report whether they thought two sounds were the same or different. Subjects were given feedback concerning the correctness of their responses. One might expect that this sort of training would lead to an increase in the ability to discriminate the sounds encountered during training, as opposed to the decrease in discriminability seen in experiment I for approximately the same distribution of training sounds. As discussed further below, such a result would be inconsistent with the Guenther and Gjaja (1996) model of the perceptual magnet effect, since that model suggests that it is the shape of the distribution of vowel-like stimuli encountered by an infant that leads to the magnet effect, not the type of training.

Twelve adults with normal hearing participated in the second experiment. Two subjects performed below the established criterion during the training session, and their data were thus excluded from subsequent analysis.

a. Training. The set of training stimuli for experiment II was generated in an identical fashion to the training set for experiment I, consisting of sounds from the training region and band edge regions but not the control region. Care was taken to insure that the number of times each subject heard each training sound was approximately the same as in experiment I.[5] During the training session, subjects listened to pairs of stimuli and indicated whether they thought the two stimuli in the pair were the same or different by pressing the *s* or *d* key of the computer keyboard. Each training trial was of the same form as the pre- and post-test trials as described at the beginning of Sec. I (see top half of Fig. 3), except that subjects were provided with feedback about the correctness of their response. Each subsession consisted of 45 trials, 15 of which involved pairs of stimuli that were the same and 30 of which involved pairs of stimuli that differed. There were ten such subsessions within the training session, and the task difficulty of the subsessions increased as follows: the initial three subsessions required subjects to discriminate stimuli that were 2 jnd's apart, the next three subsessions involved stimuli spaced 1.5 jnd's apart, and the final four subsessions involved stimuli that were 1 jnd apart. Subjects generally completed the training session in about 45 min.

b. Results. Figure 5 shows the main results for experiment II. Figure 5(a) shows the results of the pre- and post-tests for the control region. Subjects became significantly worse at discriminating stimuli within the control region [$t(5)=-2.54$, $p<0.05$]. This differs from the effects of training on the control region in experiment I, where no significant change in d' was measured, though there was a very small negative change in sensitivity for the control region in that experiment. Although it is unclear why there are relatively small negative changes in d' for the control region in all four experiments (though not statistically significant in experiment I), we suspect that this may be due to subject fatigue toward the end of the approximately 1.5-h experimental session. Of course, fatigue would be expected to affect the training region as well, but the larger changes in-

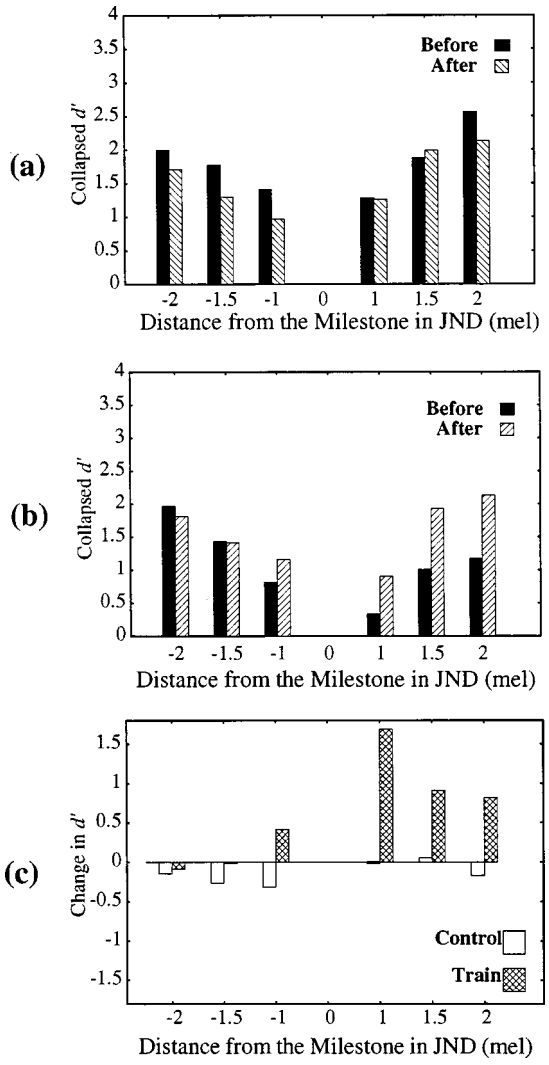

FIG. 5. (a) The *collapsed* d' scores for the control region of experiment II, before and after training. (b) The *collapsed* d' score for the training region of experiment II, before and after training. (c) Change in sensitivity after training for the control and training regions in experiment II.

duced by training would make this small fatigue effect difficult to detect. Because we are primarily interested in the relative effects of training on one region of frequency space (the training region) as compared to another (the control region), the source of the small negative changes in d' for the control region was not investigated further in this paper.

Figure 5(b) shows the results of the pre- and post-tests for the training region. Subjects showed a significant increase in d' [$t(5)=2.29$, $p<0.05$] after training. The increase in d' was significantly greater for the training region as compared to the control region [$t(5)=3.23$, $p<0.05$; see Fig. 5(c)].

The general pattern for sensitivity to improve for the training region, but not the control region, is also indicated by the *G* scores listed in Table III. Note that for the training region, the most positive change in sensitivity occurred to the right of the prototype of the training region. In fact, the sensitivity for the -2 and -1.5 jnd stimuli did not change significantly. Perhaps relatedly, subjects as a group showed far fewer errors for the -2 and -1.5 jnd stimuli during the pretest than they showed for the other four stimuli, with only

TABLE III. *G* statistic comparison for experiment II. Asterisks denote statistically significant ($p<0.05$) changes in sensitivity.

Stimulus (jnd)	Control *G* score	Training *G* score
−2	−0.48	−0.01
−1.5	−1.21	0.45
−1	−1.15	1.87*
1	0.46	2.74*
1.5	0.89	3.83*
2	−0.80	3.81*

nine total errors for the -2 jnd stimulus and 20 total errors for -1.5 jnd stimulus as compared to 38, 53, 32, and 27 errors, respectively, for the -1, 1, 1.5, and 2 jnd stimuli. We thus suspect that the lack of an increase in d' for the -2 and -1.5 jnd stimuli was a ceiling effect due to the very high level of sensitivity for these stimuli even before training, which was in turn apparently due to inaccuracies in calibrating the jnds for a subject across the entire range of frequencies used in the study.

c. Discussion. The results of this experiment indicate that the same distribution of training stimuli that led to a *decrease* in sensitivity for the training region in experiment I can lead to an *increase* in sensitivity if the training regime is changed to a discrimination training task. This is a case of acquired distinctiveness along a category-relevant dimension (see also Goldstone, 1994). Possible implications of this result for neural models of the perceptual magnet effect are treated in the General Discussion (Sec. II).

3. Experiment III

The third experiment was designed to elaborate on the training conditions required to induce the acquired similarity along a category-relevant dimension that was demonstrated in experiment I. The specific question this experiment sought to answer was whether training with only a single exemplar from a category is sufficient to induce decreased sensitivity in its immediate region of acoustic space. It is possible that a listener must experience many exemplars from the same category in order to induce acquired similarity. This scenario makes sense if one takes the view that acquired similarity is a case of learning to ignore differences between exemplars of the same category; if subjects hear only one exemplar of a category, there are no differences between category exemplars to learn to ignore.

Eleven adults participated in the third experiment. One subject's performance did not meet the established criterion, and this subject's results were thus not included in the analysis.

a. Training. This experiment involved a categorization training regime that differed from that of experiment I in only one respect: instead of hearing different exemplars from the training region when performing either a listening or identification trial, subjects always heard the same exemplar, milestone B (see Fig. 2).

b. Results. Figure 6 shows the main results for experiment III. Figure 6(a) shows pre- and post-test results for the control region. As in experiment II, subjects became signifi-

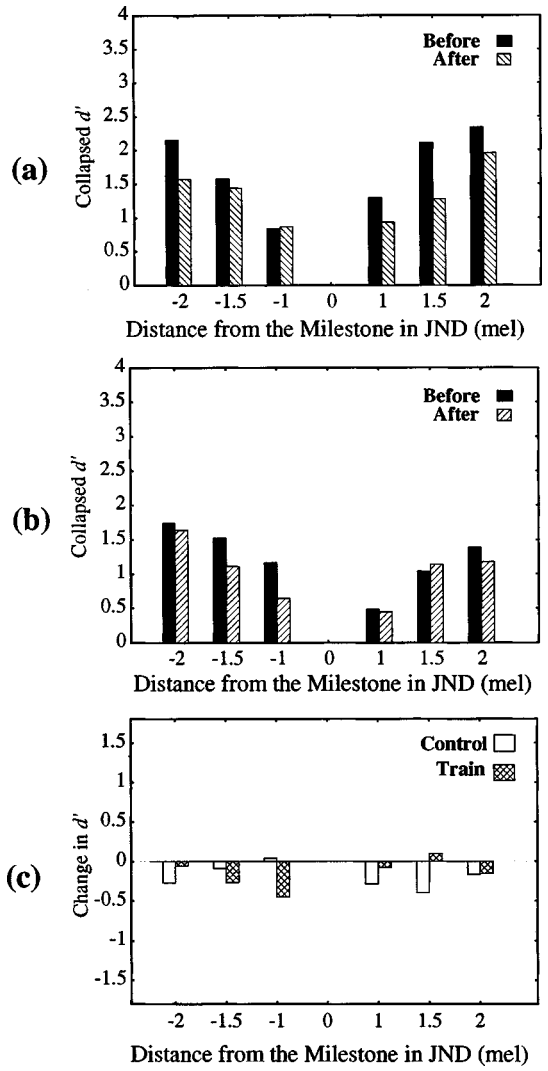

FIG. 6. (a) The *collapsed d′* scores for the control region of experiment III, before and after training. (b) The *collapsed d′* scores for the training region of experiment III, before and after training. (c) Change in sensitivity after training for the control and training regions in experiment III.

cantly worse at discriminating stimuli within the control region [$t(5)=-2.98$, $p<0.05$]. Again, general fatigue may have been a factor in this decrease in sensitivity. Subjects also became significantly worse at discriminating stimuli in the training region [Fig. 6(b); $t(5)=-2.04$, $p<0.05$]. More importantly, the change in sensitivity for the training region was not significantly different from the change in sensitivity for the control region [$t(5)=0.30$, $p>0.05$; see Fig. 6(c)]. In other words, using only a single exemplar from the training region during training did not lead to a significant decrease in discrimination performance for the training region as compared to the control region.

The *G* scores are shown in Table IV. The change across most of the testing distances after training was not significant for either the training or the control region, except in the case of the 1.5-jnd step to the right of the control milestone. The decrease for the training region was not significantly larger than the decrease for the control region. This indicates that training with only one exemplar of a category does not lead to significant acquired similarity in the immediate region of that exemplar.

TABLE IV. *G* statistic comparison for experiment III. Asterisk denotes statistically significant ($p<0.05$) changes in sensitivity.

Stimulus (jnd)	Control *G* score	Training *G* score
−2	1.51	−0.16
−1.5	−0.02	1.05
−1	−0.65	1.50
1	0.8	−0.38
1.5	2.44*	−0.92
2	0.75	0.29

c. Discussion. In both experiments I and III, the overall change for the control and the training regions was in the negative direction. However, the decrease in sensitivity for the training region in experiment I was highly significant when compared to the change in the control region, while the analogous comparison in experiment III was not significant. This suggests that a single category exemplar is not sufficient to induce acquired similiarity in the neighborhood of the category exemplar, or at minimum that a single exemplar does not induce as much acquired similarity as multiple exemplars. Perhaps relatedly, Goldstone (1994) was not successful in using two exemplars to induce acquired similarity of a category-relevant dimension for visual stimuli differing along two dimensions. A possible explanation for the success in inducing acquired similarity in experiment I and the failure to do so in experiment III and Goldstone (1994) is that many exemplars of a category, not just one or two, are needed to noticeably decrease sensitivity along a category-relevant dimension.

4. Experiment IV

Several investigators have suggested that the brain's representation of sounds can be broken into two different memory modes: a continuous auditory memory mode that consists of a reasonably accurate representation of a sound that decays relatively rapidly after the stimulus goes away or is interrupted by a new auditory stimulus, and a more ''discretized'' or ''categorical'' mode that can be maintained in memory for a longer period of time, e.g., for comparison to a second stimulus in a discrimination task with a relatively large interstimulus interval (ISI). When investigating speech sounds, Pisoni (1973) referred to the different memory forms as *auditory mode* and *phonetic mode*. In a model of sound-intensity discrimination, Durlach and Braida (1969) delineated two memory modes that they termed *sensory-trace mode* and *context-coding mode*; these modes are roughly analogous to Pisoni's auditory mode and phonetic mode, respectively. Macmillan, Goldberg, and Braida (1988) extended the Durlach and Braida (1969) model to explain experimental results involving speech stimuli. Since we are not dealing with speech stimuli directly in this experiment, we will use the terms *sensory-trace mode* and *context-coding mode* here.

The purpose of experiment IV was to determine whether the acquired similarity induced in experiment I could be bet-

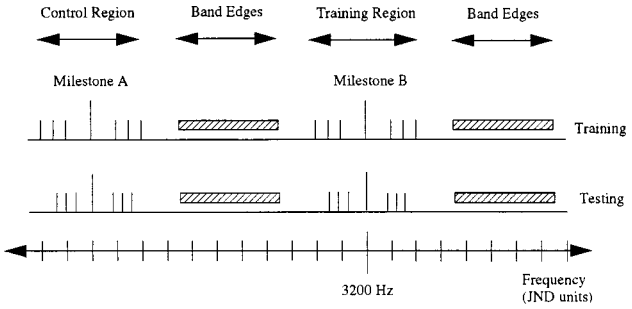

FIG. 7. The training and testing stimuli for experiment IV. Training stimuli were generated in exactly the same manner used in experiment I. Testing stimuli were more closely spaced than in experiments I–III to compensate for increased discriminability of the test sounds due to the shorter ISI and removal of the interstimulus noise burst. See the text for details.

ter characterized as a result of changes in the sensory-trace mode or the context-coding mode of auditory memory. It is usually assumed that increasing the ISI and/or adding a brief noise burst between two stimuli interferes with the sensory-trace mode of memory more than context-coding mode (e.g., Repp, 1984; Werker and Pegg, 1982). Given the relatively long ISI of experiment I and the use of a noise burst between the two stimuli in a discrimination trial, one might reasonably conclude that the effect measured in that experiment primarily involved the context-coding mode of auditory memory. In experiment IV, the ISI during discrimination training was reduced and the interstimulus noise was removed in order to better gauge whether the acquired similarity demonstrated in experiment I is also manifested in the sensory-trace mode of auditory memory.

a. Training and testing. The training and testing stimuli used in experiment IV are shown in Fig. 7. The training regime for experiment IV was identical to that of experiment I, and the training stimuli were generated in the exact same fashion as in that experiment. The testing procedure for experiment IV involved an ISI of 250 ms and there was no distractor noise between the two stimuli (see Fig. 3). In a pilot experiment, it was determined that these manipulations allowed subjects to discriminate the test stimuli almost perfectly. This invalidated the d' measures, since they are only accurate if a significant number of errors are made during testing. In order to obtain an accurate d' measure with the shorter ISI, the stimuli used in the testing sessions of experiment IV had to be more closely spaced than they were in the earlier experiments. Test stimuli for experiment IV were located at 0.75, 1.125, and 1.5 jnd units[6] above and below the milestones in the control and training regions, as compared to a spacing of 1, 1.5, and 2 jnd units in experiment I. The placement of the milestones and the positioning of the band edges regions were not affected by this change.

b. Results. Figure 8 shows the collapsed d' scores for the control region [Fig. 8(a)] and training region [Fig. 8(b)] before and after training. A significant decrease in sensitivity occurred for both the control region [$t(5)=-5$, $p<0.05$] and the training region [$t(5)=-3.8$, $p<0.05$]. The change in the training region was not significantly different from the change in the control region [$t(5)=-0.63$, $p>0.05$; see Fig. 8(c)]. The G scores for experiment IV are presented in Table V, with the group change in d' reaching significance

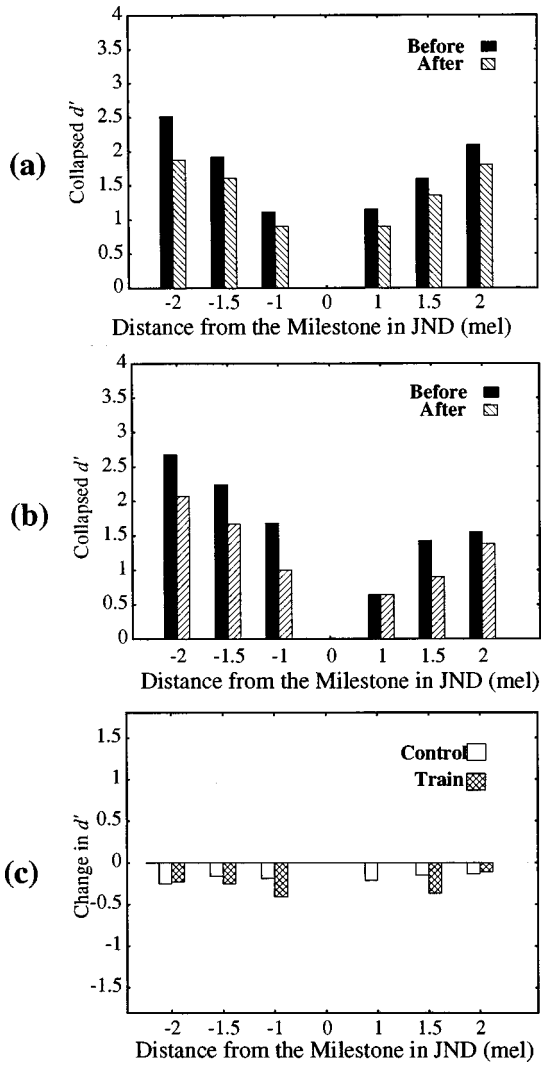

FIG. 8. (a) The *collapsed* d' scores for the control region of experiment IV, before and after training. (b) The *collapsed* d' scores for the training region of experiment III, before and after training. (c) Change in sensitivity after training for the control and training regions in experiment IV.

for only one test stimulus (-1 jnd in the training region).

c. Discussion. The results of this experiment indicate that the use of a shorter ISI and no noise burst between the two stimuli in the sensitivity testing trials essentially eradicates the acquired similarity found in experiment I despite the use of the same training regime as in that experiment. Since decreasing the ISI and removing the noise burst presumably favors a sensory-trace memory mode over a context-coding memory mode, this result suggests that the

TABLE V. G statistic comparison for experiment IV. Asterisk denotes statistically significant ($p<0.05$) changes in sensitivity.

Stimulus (jnd)	Control G score	Training G score
−2	1.56	1.39
−1.5	0.54	1.42
−1	0.23	1.90*
1	0.32	−0.53
1.5	0.31	1.35
2	0.45	0.10

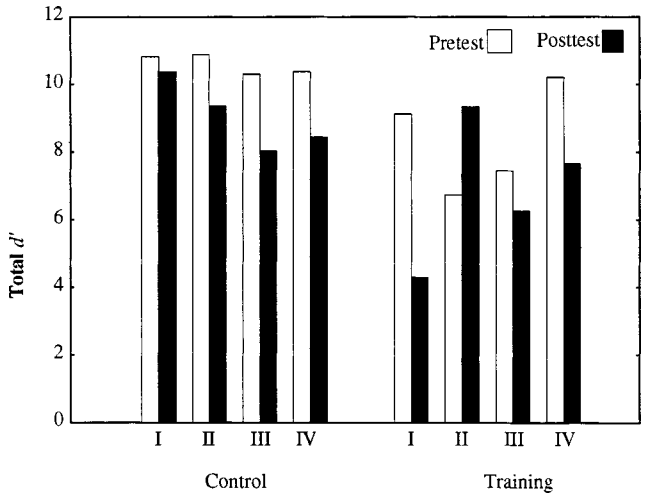

FIG. 9. Total d' in the control and training regions before and after training for experiments I through IV.

acquired similarity seen in experiment I was primarily associated with the context-coding mode of auditory short-term memory. This result is consistent with the hypotheses of Macmillan *et al.* (1988), Pisoni (1973), Repp (1984), and Werker and Pegg (1992) that a shorter ISI can diminish the categorical nature of the responses made by an observer.

II. GENERAL DISCUSSION

Figure 9 is a composite plot of the total d' measures collapsed across subjects before and after training in all four experiments. The left side of this figure illustrates that the change in sensitivity in the control region due to training in all four experiments was negative, though this change was relatively small and did not reach statistical significance in experiment I. Because the control region stimuli were not presented during training, we suspect that these small negative changes in d' were the result of generally poorer performance in the post-test as compared to the pretest, perhaps due to subject fatigue near the end of the roughly 1.5-h-long experimental session (see Sec. I E *2 b*).

The right half of Fig. 9 illustrates the d' measures for the training region before and after training. The results of the first two experiments indicate that, depending on the training regime, it is possible to induce either an increase or a decrease in the discriminability of a set of auditory stimuli. The first experiment indicated that categorization training, in which subjects were asked to identify sounds belonging to a small region of frequency space as members of the same category, led to a decrease in the discriminability of stimuli within this small range. That is, subjects exhibited acquired similarity along the category-relevant dimension of center frequency of the narrow-band noise stimuli. The third and fourth experiments helped elucidate some of the necessary conditions for attaining this acquired similarity. In experiment III, the small range of frequencies corresponding to the learned category in experiment I was shrunk down to a single exemplar during training. This eliminated the acquired similarity seen in experiment I, suggesting that a listener needs to be exposed to different examples of a category during training, not just a single exemplar, in order to decrease the listener's ability to discriminate between stimuli falling near the center of the category. In experiment IV, it was shown that a testing regime that favors a hypothesized sensory-trace mode of auditory memory over a context-coding mode (e.g., Durlach and Braida, 1969; Pisoni, 1973; Macmillan, Goldberg, and Braida, 1988) weakens the acquired similarity effect of training, suggesting that categorization training primarily affects the context mode of memory processing.

If we are to fully understand the neural processes that lead to experience-based warpings of auditory space such as the perceptual magnet effect, it is important to formulate and test hypotheses regarding the neural mechanisms underlying these phenomena. The Guenther and Gjaja (1996) and Bauer *et al.* (1996) models of the perceptual magnet effect attribute it to neural map formation properties in auditory brain areas such as the primary auditory cortex. According to both of these models, the learning process during which infants develop phonemic categories involves a change in the distribution of firing preferences of cells in auditory cortex. This change in the auditory neural map for vowel-like sounds is hypothesized to underlie the perceptual magnet effect.

Because the Guenther and Gjaja (1996) model posits that the magnet effect results from neural map formation properties that are not specific to speech stimuli, it predicts that exposing a listener to new, nonspeech auditory stimuli within a training regime that appropriately mimics the learning of phonemic categories by an infant should lead to a similar change in the distribution of firing preferences of cells coding these stimuli in auditory cortex. This change in the auditory neural map should in turn result in a measurable ''perceptual magnet-like'' effect for these auditory stimuli. That is, we should see a decreased ability for subjects to discriminate the training stimuli. The results of experiment I supported the prediction of decreased discrimination in the heavily experienced training region due to categorization training. Though not predicted by Bauer *et al.* (1996), the results of experiment I are not inconsistent with the their model if one assumes that the reduced cortical representation for heavily experienced sounds that underlies the magnet effect in the model results from a particular kind of training, rather than from speech-specific neural mechanisms, as we hypothesize below.

The results of experiment II indicated that the decrease in sensitivity was related to the categorical nature of the training task used in experiment I, since a discrimination training task led to an *increase* in the ability to discriminate training stimuli in experiment II. This result conflicts with the Guenther and Gjaja (1996) model, since this model posits that it is the distribution of training stimuli, not the type of training, that leads to the magnet effect. Bauer *et al.* (1996) do not speculate on what training conditions might be required to induce a perceptual magnet-like effect, but their model allows for different training conditions to have different effects on the size of the representation of training stimuli in the neural map. Based on the results of the current experiments, we propose that discrimination training and categorization training have opposite effects on the size of the neural representation of the training stimuli. This hypothesis,

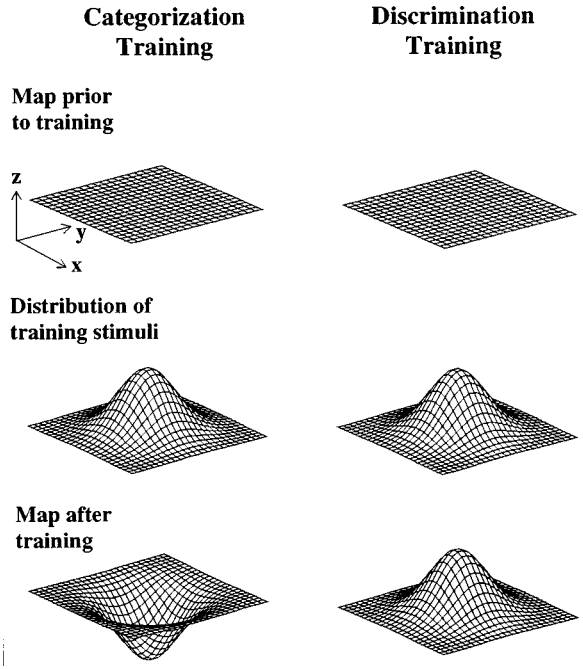

FIG. 10. Hypothesized changes in the neural map in auditory cortex as a result of categorization training (left; experiment I) and discrimination training (right; experiment II). The *x*- and *y*-axes of all plots correspond to two acoustic dimensions, such as the first two formant frequencies. The *z*-axis corresponds to the number of cells in the map devoted to each region of frequency space (top and bottom plots) or the number of training stimuli from that region of frequency space (middle plots). Categorization training leads to a decrease in the number of cells coding the most frequently encountered stimuli, whereas discrimination training leads to an increase in the number of cells coding the most frequently encountered stimuli.

in combination with the neural map model of Bauer *et al.* (1996), is schematized in Fig. 10. The left side of the figure corresponds to a categorization training situation, as in experiment I. The top and bottom panels schematize the auditory map as a function of acoustic space before and after training, and the middle panel schematizes the distribution of training stimuli in acoustic space. In categorization training, heavy exposure to a set of training sounds leads to fewer cells coding these sounds in the auditory map, and the resulting smaller cortical representation diminishes a listener's ability to differentiate sounds in this region of acoustic space. This is how the Bauer *et al.* (1996) model, with an appropriate parameter choice that leads to a negative magnification factor for the cortical representation, accounts for the perceptual magnet effect. The right side of Fig. 10 corresponds to a discrimination training situation, as in experiment II. Here, more cells in the map become tuned to the most frequently encountered training stimuli, and the resulting larger cortical representation increases the listener's ability to differentiate sounds in this region of acoustic space. This learning situation corresponds to the ''classical'' formulation of a self-organizing feature map in the computational neuroscience literature, in which increased exposure to a set of stimuli leads to a larger cortical representation for those stimuli (e.g., von der Malsburg, 1973; Grossberg, 1976; Kohonen, 1982), and can also be accounted for by using a positive magnification factor in the Bauer *et al.* (1996) model. We are currently testing predictions of the hypothesis illustrated in Fig. 10 using functional magnetic resonance imaging techniques.

ACKNOWLEDGMENTS

Frank Guenther is supported in part by the Alfred P. Sloan Foundation and the National Institute on Deafness and other Communication Disorders (NIDCD Grant No. R29 02852). Fatima Husain is supported by NIDCD Grant No. R29 02852. Barbara Shinn-Cunningham is supported in part by AFOSR Grant No. F49620-98-1-0108. The authors would like to thank Harlan Lane, David Pisoni, Jacob Beck, James Beale, Peter Chiu, and Kenneth Stevens for helpful discussions regarding this work.

[1]The term ''warping'' in this article refers to nonuniformities above and beyond the roughly logarithmic relationship between perceptual space and frequency in Hertz, as estimated by the bark and mel scales.

[2]It is difficult to ascertain the typical distribution of speech sounds heard by an infant during the first years of life, particularly given that most infants are exposed to ''motherese'' in which phonemes are often spoken in an exaggerated fashion as compared to casual speech. If one simply counts the number of occurrences in the Peterson and Barney vowel formant frequency database of /i/ sounds falling within a 120-mel radius of the prototypical and nonprototypical /i/ sounds used by Kuhl (1991), one finds that there are indeed more /i/ examples near the protypical /i/ than near the nonprototypical /i/. This evidence should be viewed as weak, however, as no female or child utterances of /i/ in the database fall within the 120-mel radius of either the prototypical or nonprototypical /i/ of Kuhl (1991).

[3]Steps were taken to ensure that stimuli differing in center frequency were played at the same absolute intensity level (dB SPL).

[4]Typical jnd measures determined in the calibration phase ranged between 10 and 50 Hz for the different subjects.

[5]Because subjects in experiment I could choose to perform fewer than 15 listening trials during each training subsession, the total number of times that each sample was heard during training varied from subject to subject. However, subjects usually used all 15 listening trials per subsession. The training stimulus distribution for experiment II was thus chosen to match the training distribution for experiment I under the assumption that all listening trials were used.

[6]Because the jnd was estimated in the calibration phase using a longer ISI and an interstimulus noise burst, it is expected to be larger than the jnd for the stimuli as presented during the pre- and post-tests, which had a shorter ISI and no interstimulus noise burst.

Aaltonen, O., Eerola, O., Hellström, Å., Uusipaikka, E., and Lang, A. H. (**1997**). ''Perceptual magnet effect in the light of behavioral and psychophysiological data,'' J. Acoust. Soc. Am. **101**, 1090–1105.

Bauer, H.-U., Der, R., and Herrmann, M. (**1996**). ''Controlling the magnification factor of self-organizing feature maps,'' Neural Comput. **8**, 757–771.

Beale, J. M., and Keil, F. C. (**1995**). ''Categorical effects in the perception of faces,'' Cognition **57**, 217–239.

Burns, E. M., and Ward, W. D. (**1978**). ''Categorical perception—phonemenon or epiphenomenon: Evidence from experiments in the perception of melodic musical intervals,'' J. Acoust. Soc. Am. **63**, 456–468.

Durlach, N. I., and Braida, L. D. (**1969**). ''Intensity perception. I. Preliminary theory of intensity resolution,'' J. Acoust. Soc. Am. **46**, Pt. 2, 372–383.

Eimas, P. D. (**1963**). ''The relation between identification and discrimination along speech and non-speech continua,'' Lang. Speech **6**, 206–217.

Eimas, P. D. (**1975**). ''Auditory and phonetic coding of the cues for speech: Discrimination of the (r-l) distinction by young infants,'' Percept. Psychophys. **18**, 341–347.

Eimas, P. D., Siqueland, E. R., Jusczyk, P., and Vigorito, J. (**1971**). ''Speech perception in infants,'' Science **171**, 303–306.

Goldstone, R. (**1994**). ''Influences of categorization on perceptual discrimination,'' J. Exp. Psychol. **123**, 178–200.

Goto, H. (**1971**). ''Auditory perception by normal Japanese adults of the sounds ''l'' and ''r'','' Neuropsychologia **9**, 317–323.

Gourevitch, V., and Galanter, E. (**1967**). ''A significance test for one-parameter isosensitivity functions,'' Psychometrika **32**, 25–33.
Grossberg, S. (**1976**). ''Adaptive pattern classification and universal recoding: I. Parallel development and coding of neural feature detectors,'' Biol. Cybern. **23**, 121–134.
Guenther, F. H., and Gjaja, M. N. (**1996**). ''The perceptual magnet effect as an emergent property of neural map formation,'' J. Acoust. Soc. Am. **100**, 1111–1121.
Howell, D. (**1992**). *Statistical Methods for Psychology* (Duxbury, Belmont, CA).
Husain, F. T., and Guenther, F. H. (**1998a**). ''Inducing a 'perceptual magnet'-like effect in a non-speech modality,'' Program of the 16th International Congress on Acoustics and the 135th meeting of the Acoustical Society of America, J. Acoust. Soc. Am. **103**, Pt. 2, 2982.
Husain, F. T., and Guenther, F. H. (**1998b**). ''Experimental tests of the neural models of the perceptual magnet effect,'' *Proceedings of the Second International Conference on Cognitive and Neural Systems* (Boston University, 28–30 May 1998, Boston).
Iverson, P., Diesch, E., Siebert, C., and Kuhl, P. K. (**1994**). ''Cross-language tests of the perceptual magnet effect for /ɪ/ and /l/,'' J. Acoust. Soc. Am. **96**, Pt. 2, 3228.
Iverson, P., and Kuhl, P. K. (**1994**). ''Tests of the perceptual magnet effect for American English /r/ and /l/,'' J. Acoust. Soc. Am. **95**, Pt. 2, 2976.
Iverson, P., and Kuhl, P. K. (**1995**). ''Mapping the perceptual magnet effect for speech using signal detection theory and multidimensional scaling,'' J. Acoust. Soc. Am. **97**, 553–562.
Jenkins, W. M., Merzenich, M. M., and Ochs, M. T. (**1984**). ''Behaviorally controlled differential use of restricted hand surfaces induce changes in the cortical representation of the hand in area 3*b* of adult owl monkeys,'' Soc. Neurosci. Abs. **10**, 665.
Jenkins, W. M., Merzenich, M. M., Ochs, M. T., Allard, T., and Guíc-Robles, E. (**1990**). ''Functional reorganization of primary somatosensory cortex in adult owl monkeys after behaviorally controlled tactile stimulation,'' J. Neurophysiol. **63**, 82–104.
Jusczyk, P. (**1986**). ''Speech perception,'' in *Handbook of Perception and Human Performance*, edited by K. R. Boff, L. Kaufman, and J. P. Thomas (Wiley, New York), Chap. 27.
Kandel, E. R. (**1985**). ''The central representation of touch,'' in *Principles of Neural Science*, edited by E. R. Kandel and J. H. Schwartz (Elsevier, New York), pp. 316–330.
Kohonen, T. (**1982**). ''Self-organized formation of topologically correct feature maps,'' Biol. Cybern. **43**, 59–69.
Kuhl, P. K. (**1981**). ''Discrimination of speech by nonhuman animals: Basic auditory sensitivities conductive to the perception of speech-sound categories,'' J. Acoust. Soc. Am. **70**, 340–349.
Kuhl, P. K. (**1991**). ''Human adults and human infants show a 'perceptual magnet effect' for the prototypes of speech categories, monkeys do not,'' Percept. Psychophys. **50**, 93–107.
Kuhl, P. K. (**1995**). ''Mechanisms of developmental change in speech and language,'' in *Proceedings of the XIIIth International Congress of Phonetic Sciences*, edited by K. Elenius and F. Branderud (KTH and Stockholm University, Stockholm), Vol. 2, pp. 132–139.
Kuhl, P. K., and Miller, J. D. (**1975**). ''Speech perception by the chinchilla: Voiced–voiceless distinction in alveolar plosive consonants,'' Science **190**, 69–72.
Kuhl, P. K., and Miller, J. D. (**1978**). ''Speech perception by the chinchilla: Identification functions for synthetic VOT stimuli,'' J. Acoust. Soc. Am. **63**, 905–917.
Kuhl, P. K., and Padden, D. M. (**1982**). ''Enhanced discriminability at the phonetic boundaries for the voicing feature in macaques,'' Percept. Psychophys. **32**, 542–550.
Kuhl, P. K., and Padden, D. M. (**1983**). ''Enhanced discriminability at the phonetic boundaries for the place feature in macaques,'' J. Acoust. Soc. Am. **73**, 1003–1010.
Kuhl, P. K., Williams, K. A., Lacerda, F., Stevens, K. N., and Lindblom, B. (**1992**). ''Linguistic experience alters phonetic perception in infants by 6 months of age,'' Science **255**, 606–608.
Lane, H. (**1965**). ''The motor theory of speech perception: A critical review,'' Psychol. Rev. **72**, 275–309.
Liberman, A. M. (**1957**). ''Some results of research on speech perception,'' J. Acoust. Soc. Am. **29**, 117–123.
Liberman, A. M. (**1996**). *Speech: A Special Code* (MIT Press, Cambridge, MA).
Liberman, A. M., Harris, K. S., Eimas, P., Lisker, L., and Bastian, J. (**1961a**). ''An effect of learning on speech perception: The discrimination of durations of silence with and without phonemic significance,'' Lang. Speech **4**, 175–195.
Liberman, A. M., Harris, K. S., Hoffman, H. S., and Griffith, B. C. (**1957**). ''The discrimination of speech sounds within and across phoneme boundaries,'' J. Exp. Psychol. **54**, 358–368.
Liberman, A. M., Harris, K. S., Kinney, J. A., and Lane, H. (**1961b**). ''The discrimination of relative onset time of the components of certain speech and nonspeech patterns,'' J. Exp. Psychol. **61**, 379–388.
Lieberman, P., and Blumstein, S. E. (**1988**). *Speech Physiology, Speech Perception, and Acoustic Phonetics* (Cambridge University Press, Cambridge, England).
Lisker, L., and Abramson, A. S. (**1970**). ''The voicing dimension: Some experiments in comparative phonetics,'' *Proceedings of the Sixth International Congress of Phonetic Sciences, Prague, 1967* (Academia, Prague), pp. 563–567.
Lotto, A. J., Kluender, K. R., and Holt, L. L. (**1998**). ''Depolarizing the perceptual magnet effect,'' J. Acoust. Soc. Am. **103**, 3648–3655.
Macmillan, N., and Creelman, C. (**1991**). *Detection Theory: A User's Guide* (Cambridge University Press, Cambridge).
MacMillan, N. A., Goldberg, R. F., and Braida, L. D. (**1988**). ''Resolution for speech sounds: Basic sensitivity and context memory on vowel and consonant continua,'' J. Acoust. Soc. Am. **84**, 1262–1280.
Macmillan, N., and Kaplan, H. (**1985**). ''Detection theory analysis of group data: Estimating sensitivity from average hit and false alarm rates,'' Psychol. Bull. **98**, 185–199.
Miyawaki, K., Strange, W., Verbrugge, R., Liberman, A. M., Jenkins, J. J., and Fujimura, O. (**1975**). ''An effect of linguistic experience: the discrimination of /r/ and /l/ by native speakers of Japanese and English,'' Percept. Psychophys. **18**, 331–340.
Pisoni, D. B. (**1973**). ''Auditory and phonetic memory codes in the discrimination of consonants and vowels,'' Percept. Psychophys. **13**, 253–260.
Rauschecker, J. P., and Singer, W. (**1981**). ''The effects of early visual experience on the cat's visual cortex and their possible explanation by Hebb synapses,'' J. Physiol. (London) **310**, 215–239.
Recanzone, G. H., Schreiner, C. E., and Merzenich, M. M. (**1993**). ''Plasticity in the frequency representation of primary auditory cortex following discrimination training in adult owl monkeys,'' J. Neurosci. **13**, 87–103.
Repp, B. (**1984**). ''Categorical perception: Issues, methods, and findings,'' in *Speech and Language: Advances in Basic Research and Practice*, Vol. 10, edited by N. J. Lass (Academic, New York).
Sussman, J. E., and Lauckner-Morano, V. J. (**1995**). ''Further tests of the 'perceptual magnet effect,' in the perception of [i]: Identification and change/no-change discrimination,'' J. Acoust. Soc. Am. **97**, 539–552.
von der Malsburg, C. (**1973**). ''Self-organization of orientation sensitive cells in the striata cortex,'' Kybernetik **14**, 85–100.
Werker, J. F., and Pegg, J. E. (**1992**). ''Infant speech perception and phonological acquisition,'' in *Phonological Development: Models, Research, Implications*, edited by C. A. Ferguson, L. Menn, and C. Stoel-Gammon (York, Parkton, MD).
Werker, J. F., and Tees, R. C. (**1984**). ''Cross-language speech perception: Evidence for perceptual reorganization during the first year of life,'' Infant Behav. Devel. **7**, 49–63.

Integrality of nasalization and F_1. II. Basic sensitivity and phonetic labeling measure distinct sensory and decision–rule interactions

Neil A. Macmillan[a)]
Psychology Department, Brooklyn College, City University of New York, Brooklyn, New York 11210

John Kingston, Rachel Thorburn, Laura Walsh Dickey,[b)] and Christine Bartels
Linguistics Department, South College, University of Massachusetts, Amherst, Massachusetts 01003

(Received 23 November 1998; revised 28 June 1999; accepted 16 July 1999)

In vowel perception, nasalization and height (the inverse of the first formant, F_1) interact. This paper asks whether the interaction results from a sensory process, decision mechanism, or both. Two experiments used vowels varying in height, degree of nasalization, and three other stimulus parameters: the frequency region of F_1, the location of the nasal pole/zero complex relative to F_1, and whether a consonant following the vowel was oral or nasal. A fixed-classification experiment, designed to estimate basic sensitivity between stimuli, measured accuracy for discriminating stimuli differing in F_1, in nasalization, and on both dimensions. A configuration derived by a multidimensional scaling analysis revealed a perceptual interaction that was stronger for stimuli in which the nasal pole/zero complex was below rather than above the oral pole, and that was present before both nasal and oral consonants. Phonetic identification experiments, designed to measure trading relations between the two dimensions, required listeners to identify height and nasalization in vowels varying in both. Judgments of nasalization depended on F_1 as well as on nasalization, whereas judgments of height depended primarily on F_1, and on nasalization more when the nasal complex was below than above the oral pole. This pattern was interpreted as a decision–rule interaction that is distinct from the interaction in basic sensitivity. Final consonant nasality had little effect in the classification experiment; in the identification experiment, nasal judgments were more likely when the following consonant was nasal. [S0001-4966(99)00511-1]

PACS numbers: 43.71.An, 43.71.Es [JMH]

INTRODUCTION

A. The psychophysics of perceptual interaction

Different physical dimensions of speech sounds can contribute to the same perceptual product. In Repp's classic characterization, these physical dimensions serve as multiple cues to phonetic contrasts, and ''a change in the setting of one cue...can be offset by an opposed change in the setting of another cue so as to maintain the original phonetic percept'' (Repp, 1982, p. 87). Such changes are often described as one cue ''trading'' with the other. In this paper we consider a well-established interaction of this sort, between the height and nasalization of vowels, and ask whether it arises at a basic, sensory level, or is located instead in the listener's decision-making process. The question, and our method for reaching an answer, have implications for all trading-relation results.

To make the sensory/decision distinction explicit, consider a 2×2 stimulus set constructed by combining two values on each of two dimensions. The elements of such a stimulus set can be represented as the four corners of a rectangle in a stimulus space. If each physical dimension is transduced into an independent perceptual one, then the representation of the stimulus set can be described as a rectangle in a *perceptual space*, as in Fig. 1(a). In our application, the dimensions are the perceptual correlates of the first formant (the *Cx* stimuli are higher, with smaller values of F_1), and nasalization (the *y0* stimuli have zero nasalization, the *yM* stimuli moderate nasalization). Each point may be thought of as the mean of a bivariate distribution of perceptual effects along these dimensions, and every point in the space corresponds to a percept that may arise on a particular trial. The circles around each mean connect points of equal likelihood, and indicate the spread of the distribution.

Now suppose that a listener in a trading-relations task must sort observations arising from these stimuli into categories such as ''high'' (an appropriate response for the *Cx* stimuli) or ''mid'' for the *Dx* stimuli). Any single point may arise from more than one stimulus, and the listener does best by establishing a *decision boundary* that divides the perceptual space into regions corresponding to each response. The solid line in Fig. 1(a) shows a boundary that is perpendicular to the dimension of judgment. Applying this boundary to the rectangular representation leads to the lack of a trading relation: the value of dimension 1 (perceived nasalization) has no effect on judgment of dimension 2 (perceived F_1, or inverse vowel height).

One way in which a trading relation can arise is by use of a nonorthogonal decision boundary like the dashed line in Fig. 1(a). Using this boundary, the ''high'' versus ''low''

[a)]Electronic mail: nmacmillan@gc.cuny.edu
[b)]Now at the Max Planck Institut für Psycholinguistik, PB 130, Nijmegen, NL 6500 AH, The Netherlands.

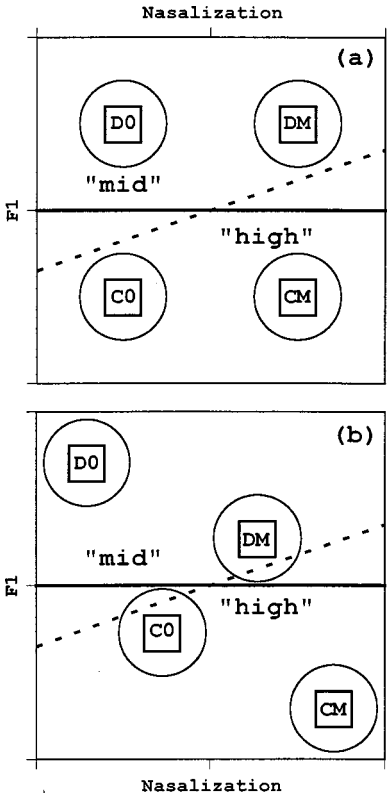

FIG. 1. Possible representations of four two-dimensional stimuli in a perceptual space. Squares represent the means of bivariate distributions. In (a), the representation is perceptually separable, because the squares form a rectangle, whereas in (b) it is perceptually integral. Solid and dashed lines are decision boundaries that might be used in phonetic identification of the vertical (F_1) dimension, the solid lines being perpendicular to perceived F_1 and the dashed ones not. Boundary shifts—discrepant positions of the boundary on the *D0-C0* and *DM-CM* segments—occur if either the boundary is nonorthogonal or the representation is perceptually integral.

decision is different for the *y0* column and the *yM* column: the *yM* stimuli are identified as ''high'' more often than the corresponding *y0* stimuli. The two stimulus dimensions provide independent information, but the listener's decision is based on a linear combination of them instead of just the relevant one; this is a trading relation whose source is *decisional*.

In Fig. 1(b), the representation itself leads to a trading relation, because the two independent stimulus dimensions map onto two nonindependent perceptual ones. To put it differently, the two stimulus dimensions contribute to a common perceptual variable that runs roughly from *D0* to *CM*. If the decision depends only on the vertical dimension, the solid-line decision boundary is used, but the result is still that the *yM* (nasalized) stimuli are identified as ''high'' more often than the corresponding *y0* (unnasalized) stimuli. This is a trading relation whose source is *sensory*. Finally, the dashed line in Fig. 1(b) shows a nonorthogonal boundary used in a non-independent space; in this case, the trading relation results from the combined sensory and decisional effects.

We report here two experiments designed to tease apart these sensory and decisional components. In experiment I, a replication and expansion of Kingston and Macmillan (1995), listeners classified stimuli from a large number of minimal, two-stimulus sets. The data allowed us to determine a sensory representation for vowels differing in F_1 and nasalization and to examine the stimulus characteristics that correspond to perceived height and nasalization. In experiment II, listeners judged F_1 while nasalization was varied irrelevantly (as in Krakow *et al.*, 1988), and in a separate condition judged nasalization while F_1 varied irrelevantly. The data provided information about both sensory and decisional aspects.

B. The trading-relations paradigm

In the trading-relations paradigm (Repp, 1982), observers provide phonetic labels for sounds drawn from a two-dimensional stimulus set. In a typical application, the data are summarized by *identification functions* that give the percentage of trials on which each value of a dimension leads to a particular response. The value of dimension 1 that is assigned on 50% of trials to each of two categories is termed a *boundary*, and the extent of trading is measured by the *boundary shift* on the stimulus axis when the value of dimension 2 is changed.

Krakow *et al.* (1988) used the trading-relations paradigm to study the interaction between the height and nasalization of vowels produced with an articulatory synthesizer. Their listeners classified vowels on continua between [æ] (a low vowel, with high F_1) and [ɛ] (a mid vowel, with lower F_1), and displayed a trading relation: The boundary between ''ɛ'' and ''æ'' shifted closer to [ɛ] with greater nasalization. Because lowering the soft palate (increasing nasal coupling) had the same perceptual effect as lowering the tongue, soft palate and tongue height can be said to integrate ''positively'' in Krakow *et al.*'s data. The same description can be applied to the acoustic consequences of these articulations, for F_1 and nasalization are inversely related to tongue and soft palate height, respectively. Krakow *et al.* obtained the boundary shift when the following consonant was oral (in context [bVd]), but not when it was nasal (in context [bVnd]). Krakow *et al.* argued that this last result occurred because listeners attributed the vowel's nasalization to coarticulation with the consonant, thereby hearing out the effect of tongue height alone.

As the comparison of Fig. 1(a) and (b) shows, such a shift in the decision boundary could arise either because the two stimulus dimensions do not map into independent perceptual dimensions, or because the decision criterion depends on the value of the orthogonal variable, or because both effects occur. The necessary independent means of determining the mapping from stimulus to perceptual dimensions is provided by fixed classification tasks.

C. The fixed-classification paradigm

In the fixed-classification paradigm, listeners' ability to distinguish between two incompletely discriminable stimuli is directly measured by asking them to assign different responses to the two stimuli. Performance is converted to an index with distance properties, such as the d' of detection theory. A geometric model of the data is constructed using data from many possible stimulus pairs.

Kingston and Macmillan (1995) examined the nasalization–F_1 interaction using this method. Stimuli were drawn from sets constructed by combining two values of F_1 with two of nasalization. Six pairs of stimuli can be drawn from each 2×2 array, a single pair differing in F_1, nasalization, or both. In any block of trials, only elements of one such pair were presented. Ability to distinguish a pair was indexed by d', and the six d' estimates were interpreted as the sides and diagonals of a parallelogram in perceptual space. Kingston and Macmillan (as well as Kingston, 1991) found that vowel pairs in which nasalization varied directly with F_1 (*DM* and *C0*) were consistently more difficult to classify than those in which they varied inversely (*D0* and *CM*), so that F_1 and nasalization integrated negatively, as in Fig. 1(b), a result that can be described as *mean-integrality*[1] (see Maddox, 1992). The effect was obtained whether the following consonant was nasal or oral.

Kingston and Macmillan's (1995) conclusions may appear to be in conflict with those reached by Krakow *et al.* (1988) using the trading-relations paradigm, but Fig. 1 makes it clear that the presence of a boundary effect and the finding of mean-integrality are, in fact, unrelated phenomena. As we have seen, a trading relation can occur whether or not dimensions are mean-integral, and vice versa. One way to understand the unrelatedness of the two measures is to see that integrality is a function of sensitivity values, whereas a boundary shift can be just a measure of response bias.

However, information about sensitivity is available from the phonetic identification task: The ability to distinguish two stimuli (differing in, say, F_1) can be estimated by subtracting the *z*-transformed proportions of ''high'' responses to them. This statistic can be interpreted as a d' value, and is related to the *slope* of the identification function. In a fixed classification study, sensitivity is measured directly as d', proportion correct $[p(c)]$, or a related variable. The major point of contact between the fixed classification and trading relations data is a comparison of their sensitivity estimates.

I. ACOUSTIC AND PSYCHOACOUSTIC DIMENSIONS CORRESPONDING TO VOWEL HEIGHT AND NASALIZATION

The dimensions of the presumed perceptual space, and their interrelation, are the consequence of a mapping from acoustic dimensions, which are themselves determined by the speaker's articulations. Both transformations are complex. Increasing the height of the tongue extends the pharyngeal cavity and narrows the vocal tract at the palate, thereby lowering F_1 and increasing perceived vowel height. Vowel nasalization is produced by lowering the soft palate, opening the velopharyngeal port and thereby acoustically coupling the nasal to the pharyngeal cavity. The two principal acoustic effects of nasal–pharyngeal coupling are adding a pole/zero pair in the low-frequency part of the spectrum, and raising F_1. Furthermore, nasalized vowels differ in the positions of the nasal pole/zero complex relative to the oral pole as a function of height: The complex lies above the low oral pole of high vowels, below the high oral pole of low vowels, and either above or below the mid-frequency oral pole of mid vowels. These effects are jointly produced in articulatorily synthesized vowels (e.g., Rubin *et al.*, 1981; Krakow *et al.*, 1988) but can also be obtained with a terminal analog synthesizer (Klatt and Klatt, 1990) by independently controlling the frequency difference between the nasal pole (N_1) and the nasal zero (N_0), and setting F_1 appropriately.

The frequency of the nasal pole/zero complex relative to F_1, and the frequency separation between the nasal pole and zero, affect both the center-of-gravity and bandwidth of the low-frequency region. The complex may consequently alter perception of the vowel's height as well as its nasalization. Perception of vowel height as well as nasalization is also altered by the F_1 raising caused by nasal–pharyngeal coupling. Finally, the listener may be uncertain about which peak to attribute to nasal–pharyngeal coupling and which to attribute to tongue height. It is not surprising, therefore, that perceptual interactions are found between height and nasalization, and that these occur whether nasalization is contrastive or not (as in English).

In this study, we factorially manipulated three stimulus variables that have been found to play a role in the perception of nasalization: consonantal context, the location of the nasal pole/zero complex relative to the oral pole, and F_1. Because of the high-dimensional nature of speech, we did not expect this design to uncover a single stimulus correlate of vowel nasalization or height, and it did not. However, the results do limit models of psychoacoustic processing, and we did not want our psychophysical conclusions to be specific to an idiosyncratic choice of stimuli.

A. Consonantal context

Our vowels were placed in CVC syllables, and the final consonant was either nasal or oral. In Kingston and Macmillan (1995) a similar manipulation had no effect on fixed classification, but in the trading relation study of Krakow *et al.* (1988) nasalized vowels were judged lower in an oral than in a nasal context. Other data also show that listeners are less likely to attribute vowel nasalization to a vowel if they perceive nasality in an adjacent, potentially coarticulating consonant. Kawasaki (1986) presented listeners with nasalized vowels between nasal consonants, and found that judged nasalization increased as the consonant's intensity was reduced. Krakow and Beddor (1991) asked listeners to match naturally produced vowels for nasalization and to judge how nasal they were. Their stimuli were oral vowels produced between oral consonants [b_d], nasalized vowels produced between nasal consonants [m_n], oral vowels cross-spliced into nasal [m_n] contexts, nasalized vowels cross-spliced into oral [b_d] contexts, and isolated oral and nasalized vowels spliced out of these contexts. Their listeners matched nasalized vowels most accurately when the vowels were in isolation, and more accurately when the nasalized vowels occurred in an oral than a nasal context. These listeners also judged a vowel to be more nasal in isolation and between oral consonants than between nasal consonants.

B. Frequencies of the nasal pole/zero and first formant

The nasal pole/zero complex may be located either above or below the oral pole: For low vowels, F_1 is high and

the complex falls below it, whereas for high vowels, F_1 is low and the complex falls above it. For mid vowels, Stevens *et al.* (1987) suggest a placement below F_1, and that is what Kingston and Macmillan (1995) used. However, Beddor and Hawkins (1990) and even more directly Maeda (1993) prescribe a placement above F_1 for such vowels. The mean F_1 frequency in Kingston and Macmillan's vowels was about 400 Hz, on the cusp between the above and below cases, according to Maeda (1993). In the present experiments, both placements were used, in separate conditions. We independently manipulated the F_1 range, a supposed determinant of the proper location of the pole/zero complex, by using two sets of vowels, with F_1 centered at 480 Hz for the higher range and at 380 Hz for the lower range.

II. EXPERIMENT I: ONE-DIMENSION AND TWO-DIMENSION (CORRELATED) CLASSIFICATION

A. Methods

1. Stimuli

Both experiments used stimulus sets in which F_1 and the nasal zero-pole difference N_0-N_1 (henceforth denoted N) varied orthogonally, using the Klatt and Klatt (1990) synthesizer. The ranges of all parameters but N were identical in the two experiments, and the difference in the range of N values in experiments I and II was only 3 Hz.

Stimuli for experiment I were of the form [CVC], the initial consonant being one of [b,d] and the final consonant one of [b,d,m,n]. The values of the formants in the vowel were appropriate for a high or mid, back, rounded quality (as in our previous experiments). There were two stimulus sets, Above and Below, named for the location of the nasal pole/zero complex *re* F_1. In each set, four values of F_1 and three values of N were combined independently. There were 8 variants (2 initial consonants×4 final consonants) of each the 12 combinations, for a total of 96 distinct stimuli in the Above and in the Below conditions.

In both the Above and Below sets, F_1 could be Low (360 or 400 Hz) or High (460 or 500 Hz), straddling the frequency at which Maeda (1993) predicts that the nasal pole/zero complex crosses over from above to below F_1. The Low-F_1 stimuli are closer to those used by Kingston and Macmillan (1995) (415–430 Hz) and Kingston (1991) (400–430 Hz). The larger 40-Hz interval was used here to increase listeners' success in classifying the vowels for F_1 differences. The degree of nasalization was Zero ($N=0$ Hz), Moderate (43 Hz), or Heavy (87 Hz).

Figure 2 shows values of F_1, N_1, and N_0 for some of the stimuli. The nasal pole N_1 was always separated from F_1 by 175 Hz. When the nasal complex was above F_1 [Fig. 2(a)], the frequencies F_1,N_1,N_0 were in that order; when the nasal complex was below F_1 [Fig. 2(b)], the frequencies N_1, N_0, F_1 were in ascending order. In this paper, we refer to each stimulus by a letter–number pair, as shown in Table I; for example *D0* is the stimulus with $F_1=500$ Hz and $N=0$ Hz, *CM* is the stimulus with $F_1=460$ Hz and $N=43$ Hz, etc. Other stimulus details are in Appendix A.

We used the VIIIth nerve response model of Moore and Glasberg (1987; Glasberg and Moore, 1990) to calculate,

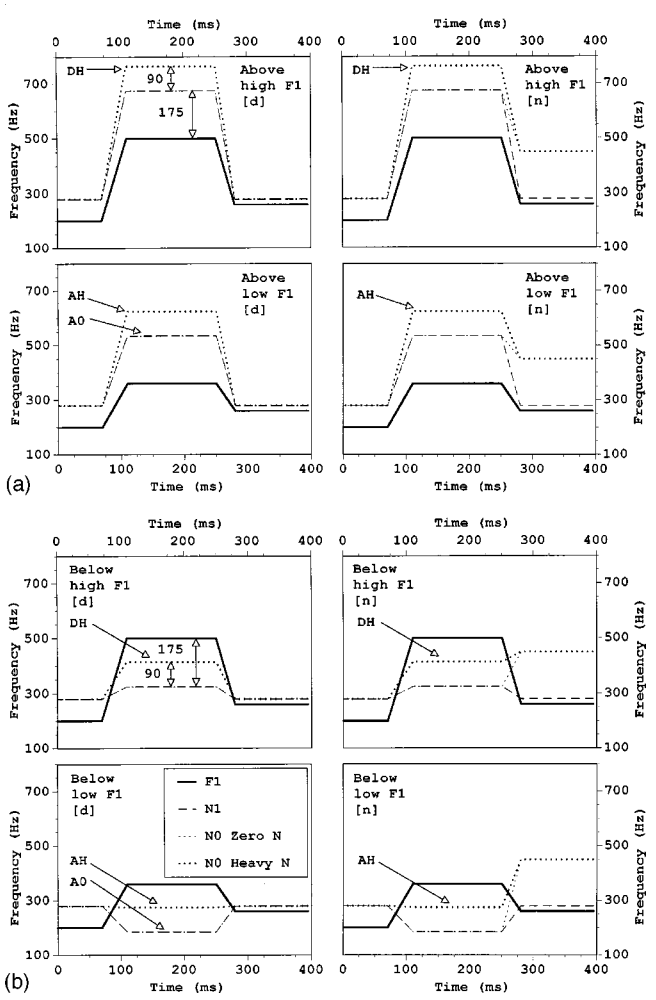

FIG. 2. Time course of oral pole, nasal pole, and nasal zero for (a) Below and (b) Above stimuli. Stimuli with the highest and lowest F_1 and highest and lowest N values and shown.

from 1024-point fast Fourier transform (FFT) spectra centered in the vowel, the sensory (equivalent rectangular bandwidth, or ERB rate) spectra of our vowels. These spectra are shown in Fig. 3. The *center of gravity* (COG) for each stimulus between 0 and 2 kHz, plotted in Fig. 4, drops with increasing nasalization and increases with F_1 both above and below.

2. Procedures

Experiment I used eight listeners, paid volunteers recruited by advertisement from the undergraduate student body at the University of Massachusetts, Amherst. All spoke

TABLE I. Nomenclature for vowel stimuli in experiment I.

	First formant (F_1) in Hz	Nasalization ($N=N_0-N_1$) in Hz		
		0 (Zero)	43 (Moderate)	87 (High)
High F_1	500	*D0*	*DM*	*DH*
	460	*C0*	*CM*	*CH*
Low F_1	400	*B0*	*BM*	*BH*
	360	*A0*	*AM*	*AH*

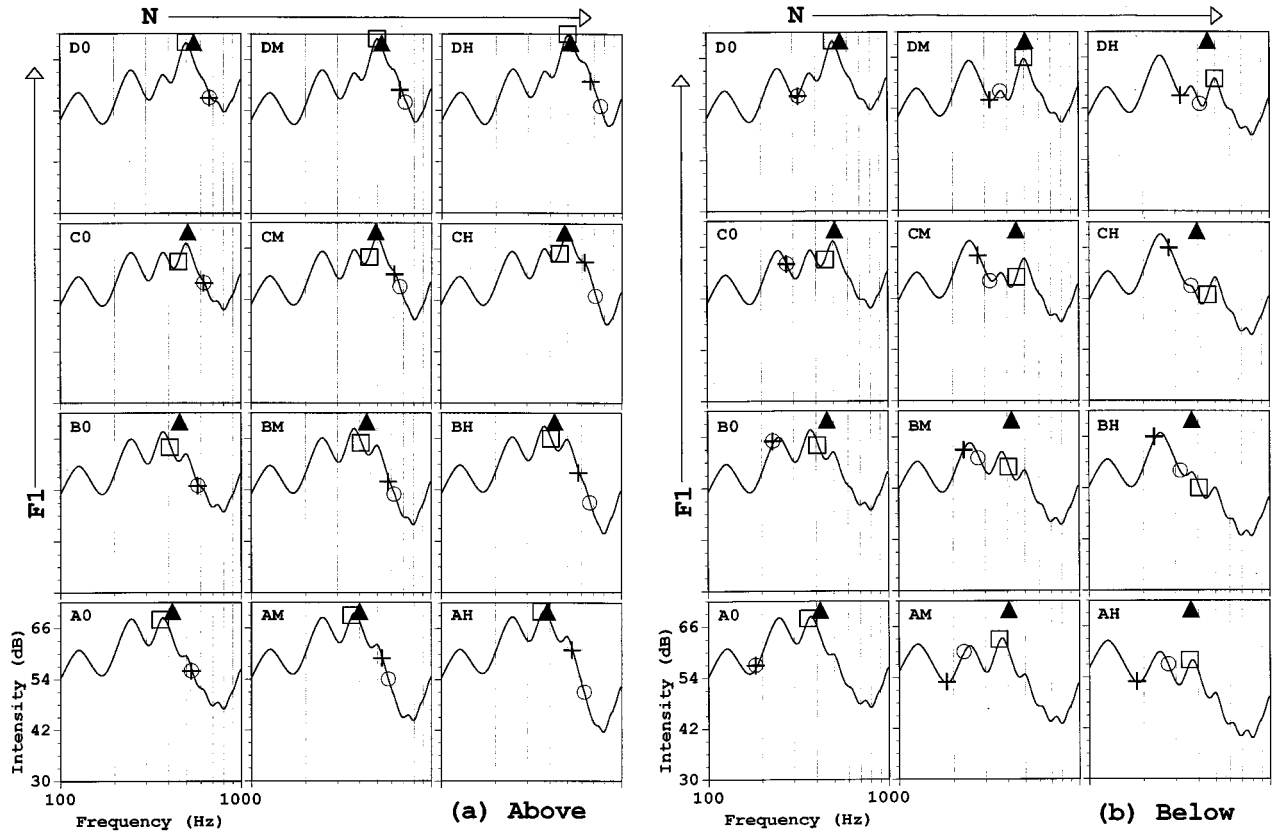

FIG. 3. The ERB-rate spectra from 0.1 to 1 kHz for selected stimuli in the (a) Above and (b) Below sets. Columns are Zero, Moderate, and Heavy nasalization; rows are $F_1 = 360$, 400, 460, and 500 Hz. Squares indicate F_1, plus signs indicate N_1, and circles indicate N_0; the triangles indicate the center-of-gravity (COG) of the 0.1- to 2-kHz interval.

English natively and none reported any speech or hearing pathology. Four were assigned to the Above condition and four to the Below condition.

Listeners heard the stimuli binaurally at self-selected comfortable listening levels over TDH-49 headphones, while sitting in semi-isolation in a sound-treated room. They performed all 18 possible one-dimension and all 12 possible two-dimension classification tasks with stimuli drawn from within the High-F_1 (stimuli *Dx* and *Cx* in Table I) and Low-F_1 (*Bx* and *Ax*) arrays. These tasks correspond to the sides (for example, *D0* vs *DM* or *B0* vs *A0*) and diagonals (for example, *D0* vs *CM* or *A0* vs *BM*) of all possible 2×2 stimulus subarrays. Listeners gave one of two responses to classify the stimulus, followed by a confidence rating on a 1–4 scale. For example, in the *D0* vs *DH* task, one button indicated that the stimulus was a ''*D0*,'' the other that it was a ''*DH*.'' The confidence judgment was prompted by a rapid tone triplet occurring 750 ms after the listener responded, and was entered, like the response, by a button press. The listener had 2000 ms to make the initial response and 1500 ms to make the confidence judgment. A 500-ms feedback light then came on over the button corresponding to the correct response, and there was an additional 1000 ms before the next trial began.

Each block consisted of 16 orientation trials in which the stimuli alternated between the two classes and between oral and nasal following consonants, and 80 randomized test trials in which the contrasting vowels occurred equally often

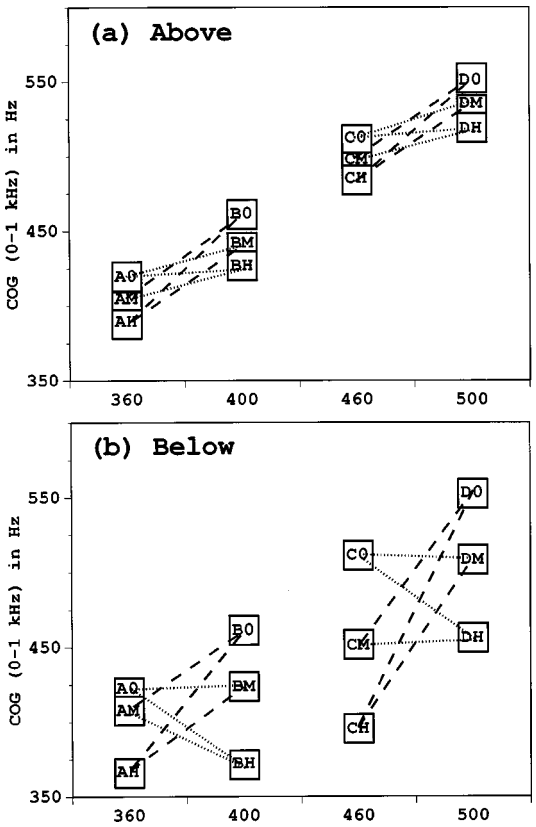

FIG. 4. Center-of-gravity for the 0- to 1-kHz region of the stimuli used in experiment I. Dashed lines connect stimuli in which F_1 and *N* are negatively related, dotted lines those in which they are positively related.

before oral and nasal following consonants. The listeners were taught which button to press for a particular stimulus by the orientation trials and by feedback; no other instructions were given.

Type of task alternated from day to day between single-dimension and two-dimension classification. Within a day, single-dimension tasks alternated in groups of three between the F_1 and N dimensions, and two-dimension tasks alternated from block to block between those in which the dimensions were correlated positively (for example, *C0* vs *DM*) and negatively (for example, *D0* vs *CM*). Tasks were drawn in a pseudo-randomized fashion from both the Low- and High-F_1 arrays within each day. The entire series of tasks was run twice, once early in the string of days and then again later, with the order of tasks reversed between the two runs. Task order during a day in the Above condition reversed that used in the Below condition. Between 9 and 12 blocks of trials were run each day in sessions lasting 90 min. As there were 6 different classifications for F_1, 12 different classifications for N, and 12 different combinations of F_1 and N, completing two passes through the 30 classification tasks plus the consonant identification blocks took 7–9 days, which were spread over 3–4 weeks.

To check that the final consonants were heard with the intended nasality, we asked listeners to identify the final consonants in the stimuli (as ''b,'' ''d,'' ''m,'' or ''n'') several times during the running of the experiment. Trials were presented in blocks that began with 16 orientation trials in which the stimuli cycled in a fixed pattern through the four final consonants, and continued with 96 randomized test trials in which each stimulus was presented once. All other procedures were identical to those used to collect the vowel judgments. Feedback was provided to train listeners in hearing the consonants with the intended nasality, but their success (see below) suggests that this was unnecessary. Three of the listeners in the Below condition heard four such blocks, the fourth listener five. All listeners in the Above condition heard eight blocks. As there were 24 stimuli for each final consonant, pooling responses across listeners yields 408 responses per consonant in the Below condition and 768 responses per consonant in the Above condition.

B. Results

1. Consonant identification

The overall error rate in consonant identification was 4.2%. This number is much lower than the 25.8% found by

TABLE II. Mean d_a values (standard errors) across listeners, pooled across replication and final consonant place of articulation. Stimulus parameters are F_1 (in Hz) and N [Z(ero), M(oderate), and H(eavy)]. The code for the stimuli is given in Table I.

a. Nasal complex Above F_1, vowel precedes Oral consonant

Stimulus	F_1,N	500,M	500,H	460,Z	460,M	460,H	Stimulus	F_1,N	400,M	400,H	360,Z	360,M	360,H
F_1, N	Code	*DM*	*DH*	*C0*	*CM*	*CH*	F_1, N	Code	*BM*	*BH*	*A0*	*AM*	*AH*
500, Z	*D0*	.62 (.21)	1.70 (.39)	1.23 (.38)	2.51 (.63)	3.62 (.65)	400, Z	*B0*	.96 (.42)	1.93 (.53)	2.30 (.50)	2.70 (.59)	3.49 (.25)
500, M	*DM*		.71 (.36)	.43 (.07)	.76 (.36)	1.63 (.21)	400, M	*BM*		.49 (.15)	1.93 (.35)	2.01 (.50)	3.31 (.41)
500, H	*DH*			1.63 (.21)	1.31 (.28)	.26 (.17)	400, H	*BH*			2.08 (.32)	1.90 (.26)	1.58 (.23)
460, Z	*C0*				.73 (.24)	1.47 (.52)	360, Z	*A0*				1.00 (.32)	1.79 (.47)
460, M	*CM*					1.00 (.23)	360, M	*AM*					1.18 (.27)

b. Nasal complex Above F_1, vowel precedes Nasal consonant

Stimulus	F_1,N	500,M	500,H	460,Z	460,M	460,H	Stimulus	F_1,N	400,M	400,H	360,Z	360,M	360,H
F_1, N	Code	*DM*	*DH*	*C0*	*CM*	*CH*	F_1, N	Code	*BM*	*BH*	*A0*	*AM*	*AH*
500, Z	*D0*	1.21 (.36)	1.95 (.68)	1.52 (.42)	2.66 (.56)	3.56 (.53)	400, Z	*B0*	1.14 (.36)	2.63 (.70)	1.13 (.29)	2.59 (.31)	3.84 (.14)
500, M	*DM*		.75 (.22)	.64 (.04)	.94 (.27)	2.05 (.32)	400, M	*BM*		.80 (.11)	1.45 (.44)	1.50 (.39)	2.74 (.29)
500, H	*DH*			1.60 (.43)	.59 (.13)	.54 (.31)	400, H	*BH*			1.54 (.11)	1.37 (.22)	.94 (.25)
460, Z	*C0*				1.14 (.25)	2.13 (.64)	360, Z	*A0*				1.32 (.39)	2.04 (.30)
460, M	*CM*					1.01 (.40)	360, M	*AM*					.82 (.16)

TABLE II. (*Continued.*)

c. Nasal complex Below F_1, vowel precedes Oral consonant

Stimulus	F_1,N	500,M	500,H	460,Z	460,M	460,H	Stimulus	F_1,N	400,M	400,H	360,Z	360,M	360,H
F_1, N	Code	*DM*	*DH*	*C0*	*CM*	*CH*	F_1, N	Code	*BM*	*BH*	*A0*	*AM*	*AH*
500, Z	*D0*	.43 (.26)	2.00 (.24)	1.10 (.06)	2.18 (.14)	3.81 (.39)	400, Z	*B0*	1.54 (.11)	3.78 (.30)	2.14 (.42)	3.27 (.45)	3.96 (.40)
500, M	*DM*		.67 (.16)	.62 (.24)	.87 (.15)	3.52 (.31)	400, M	*BM*		2.08 (.37)	.67 (.08)	2.32 (.17)	2.75 (.31)
500, H	*DH*			.74 (.26)	.68 (.18)	1.64 (.33)	400, H	*BH*			.35 (.23)	.17 (.14)	1.23 (.18)
460, Z	*C0*				.52 (.19)	3.17 (.47)	360, Z	*A0*				.69 (.19)	2.66 (.45)
460, M	*CM*					2.54 (.23)	360, M	*AM*					2.35 (.14)

d. Nasal complex Below F_1, vowel precedes Nasal consonant

Stimulus	F_1,N	500,M	500,H	460,Z	460,M	460,H	Stimulus	F_1,N	400,M	400,H	360,Z	360,M	360,H
F_1, N	Code	*DM*	*DH*	*C0*	*CM*	*CH*	F_1, N	Code	*BM*	*BH*	*A0*	*AM*	*AH*
500, Z	*D0*	.26 (.30)	1.75 (.15)	.89 (.10)	2.25 (.07)	3.75 (.53)	400, Z	*B0*	1.05 (.15)	3.21 (.25)	2.06 (.28)	3.51 (.40)	3.73 (.12)
500, M	*DM*		.37 (.15)	.73 (.31)	.62 (.11)	4.05 (.17)	400, M	*BM*		1.78 (.33)	.86 (.23)	2.34 (.13)	2.64 (.38)
500, H	*DH*			.15 (.28)	.28 (.17)	1.57 (.44)	400, H	*BH*			.45 (.15)	.48 (.06)	1.45 (.31)
460, Z	*C0*				.60 (.14)	3.18 (.30)	360, Z	*A0*				.68 (.17)	2.14 (.30)
460, M	*CM*					2.53 (.39)	360, M	*AM*					2.27 (.27)

Kingston and Macmillan (1995), a result of careful resynthesis of the stimuli. The largest errors were mistaking final [m] for [b] on 12.7% of trials in the Above condition, and mistaking [d] for [n] on 6.7% of trials in the Below condition. Oral:nasal confusions are thus few enough that the listeners can be considered to be hearing the vowels in consonantal contexts that are distinct on the oral:nasal dimension.

2. Vowel classification accuracy

For each pair of stimuli and subject, the data were pooled across place of articulation of the initial consonant and repetition of the task to produce a matrix in which each combination of response and confidence rating to each stimulus was separately represented. Using the method of Dorfman and Alf (1969), receiver operating characteristic (ROC) curves were fitted to the multiple estimates of hit and false-alarm proportions obtained from these matrices. A natural index of sensitivity is the area under the ROC curve, which equals optimal proportion correct in a two-alternative forced-choice task (Green and Swets, 1966; Macmillan and Creelman, 1991). We transformed this statistic to d_a, a distance measure that generalizes the better-known d' to models of unequal underlying variance (Swets and Pickett, 1982; Macmillan and Creelman, 1991). Values of d_a, averaged across subjects, with standard errors, are given in Table II. Four separate subtables are provided to describe the Above versus Below position of the nasal complex and the Oral versus Nasal feature of the following consonant.[2]

The most striking feature of the data is that the negatively correlated two-dimensional comparisons (e.g., *D0* vs *CM*) yield in every case greater accuracy than the corresponding positively correlated ones (e.g., *C0* vs *DM*). The discrepancy is quite large, averaging 2.39 d_a units. This indicates a perceptual interaction: Stimulus *C0* is hard to discriminate from *DM* because it is lower in both F_1 and *N*, and the effects of these differences cancel each other. Stimulus *CM* is easy to discriminate from *D0* because it is lower in F_1 but higher in *N*, and the effects of these differences augment each other. Lower *N* may cancel lower F_1 by undoing the lowering of COG, whereas higher *N* adds to the lowering of COG (see Figs. 3 and 4).

Geometric models of perceptual interaction (like those used in Kingston and Macmillan, 1995) take advantage of the status of d_a as a distance measure. The data allow us to test a critical distance axiom, the triangle inequality. Three sets of conditions can be examined. First, consider stimulus triples, like $\{D0,DM,DH\}$, that differ only on *N*. If these stimuli are represented as points on the same perceptual dimension, then we expect $d_a(D0,DM)+d_a(DM,DH)$

$= d_a(D0,DH)$; if not, we expect $d_a(D0,DM) + d_a(DM,DH) > d_a(D0,DH)$. Examining the 16 such triples in the table, the sum of the smaller values is 0.14 d_a units *less* than the larger one, a small violation of the triangle inequality. Second, none of the 48 triples involving the positively correlated comparisons, e.g., $\{D0,DM,C0\}$ and $\{DM,C0,CM\}$, violate the triangle inequality because d_a values for the positively correlated tasks, such as *DM* vs *C0*, are consistently small. The third relevant stimulus set is all triples, such as $\{D0,DM,CM\}$ and $\{D0,C0,CM\}$, that include a negatively correlated comparison (*D0* vs *CM*). Of 48 such comparisons, 36 fail to satisfy the triangle inequality, the average discrepancy being 0.34 d_a units.

The violation of the axiom is relatively small in magnitude (equivalent to about 4 or 5 percentage points for a d_a values of 2.0), and could be interpreted as a case of ''more-than-complete'' integrality, but the effect is too systematic to be entirely due to chance. One possible culprit is the implicit assumption of our detection-theoretic analysis that all distributions have the same covariance matrix; unfortunately, the experimental design does not allow for a test. We adopt instead a data-analysis strategy that adjusts the perceptual distances between stimuli so that they *do* satisfy the axioms: multidimensional scaling.

3. Multidimensional scaling (MDS) analysis of perceptual interaction

We performed multidimensional scaling (INDSCAL) on the values of d_a; because this statistic is a distance measure, we constrained the program to fit the actual data in Table II, not an arbitrary monotonic transformation of them. We expected that two perceptual dimensions, roughly corresponding to the two stimulus dimensions, would describe the data, and considered only two-dimensional outcomes. Each section of Table II contains all pairwise d_a values for both the High-F_1 and the Low-F_1 subset (but no comparisons between these subsets), so there are eight resulting configurations, shown in Fig. 5. Stress values range from 0.12 to 0.19, averaging 0.17 (Kruskal's stress formula 1). The proportion of variance in the data that is accounted for by distances in the configurations ranges from 0.63 to 0.91, averaging 0.77. These moderately low stress values and moderately high squared correlations imply, for metric scaling, that distances in the representation are approximately proportional to the input data, and thus justify the use of d_a as a distance measure.[3]

How is the nature of perceptual interaction captured by these representations? Let us first consider the Above/Nasal/High data [upper right panel of Fig. 5(a)]. A ''centroid'' (represented by a dot) is shown for each pair of stimuli sharing the same value of *N* (for example, *D0* and *C0*), and line segments are drawn in Fig. 5 between pairs of corresponding centroids (for example, those of $\{D0,C0\}$ and $\{DM,CM\}$). Three such segments, for Zero versus Medium *N*, Zero versus Heavy, and Medium versus Heavy, indicate the contours of perceptual change as *N* is increased, keeping F_1 constant. Three analogous line segments (for example, between the centers of gravity of $\{D0,DM\}$ and $\{C0,CM\}$) show the

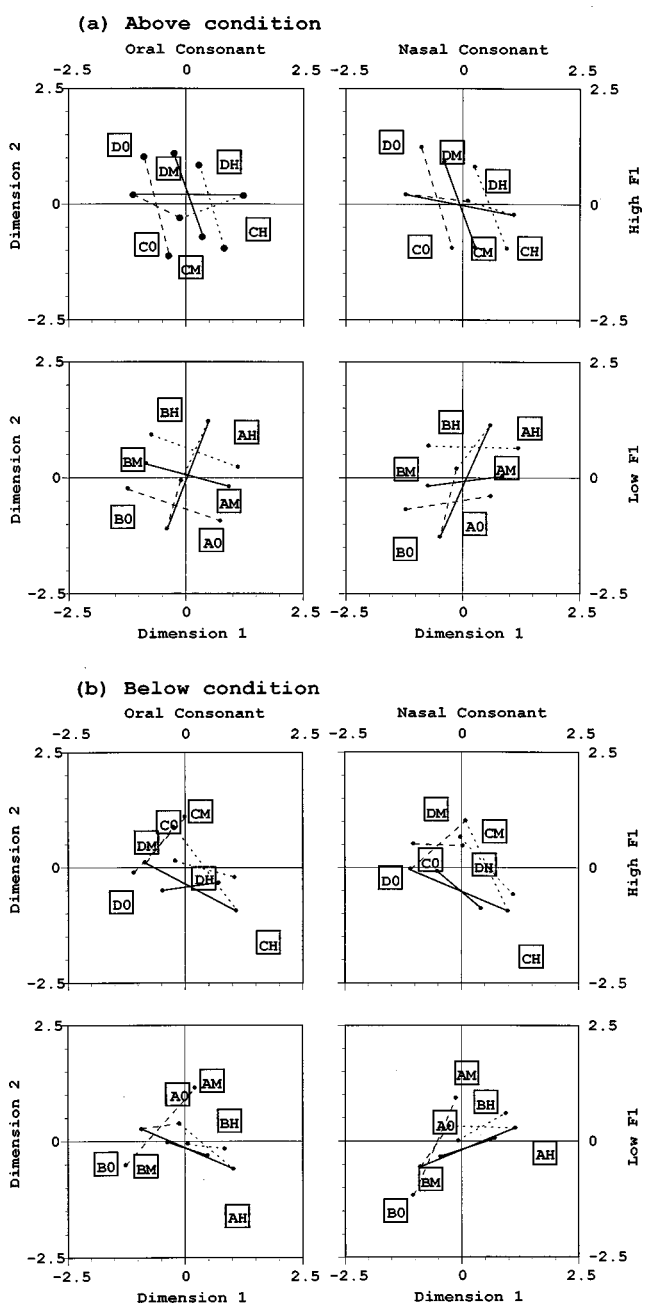

FIG. 5. The MDS configurations for all sets of six stimuli, based on the classification data of experiment I. In (a) the nasal complex is Above F_1 and in (b) it is Below. In each panel, the top row is for High-F_1 sets (stimuli *Dx* and *Cx*), the bottom row for Low-F_1 sets (stimuli *Bx* and *Ax*), the left column for vowels preceding an Oral consonant, and the right column for vowels preceding a Nasal consonant. Line segments connect midpoints of the sides of the implied quadrilateral for each pair of *N* values: solid lines for Zero: Heavy *N* (quadrilaterals $\{D0,DH,C0,CH\}$ for High F_1 and $\{B0,BH,A0,AH\}$ for Low F_1), dashed lines for Zero:Moderate *N* ($\{D0,DM,C0,CM\}$, $\{B0,BM,A0,AM\}$), and dotted lines for Moderate: Heavy *N* ($\{DM,DH,CM,CH\}$, $\{BM,BH,AM,AH\}$).

contours of perceptual change as F_1 decreases, keeping *N* constant.

Degree of interaction can be measured by the angle θ at which an *N* contour and an F_1 contour intersect. An angle of 90 degrees would reflect orthogonality (noninteraction), angles of 0 or 180 degrees complete (negative or positive) interaction. For the $\{D0,DM,C0,CM\}$ stimulus subset, these

TABLE III. Values of θ (in degrees) averaged across listeners (standard errors), representing extent of perceptual interaction between F_1 and N in various stimulus sets. All angles are less than 90 degrees, indicating a negative interaction; angles greater than 90 degrees would indicate a positive one. (Standard errors for row and column average are based on the number of measurements contributing to the mean, not the number of listeners.)

Stimulus set			Nasalization comparison			
N-complex location	Final consonant	F_1 region	Zero versus Moderate	Moderate versus Heavy	Zero versus Heavy	Average
Above F_1	Oral	High	29 (9)	87 (6)	56 (11)	57 (9)
		Low	63 (20)	74 (4)	69 (7)	68 (7)
	Nasal	High	35 (8)	51 (9)	44 (8)	43 (5)
		Low	46 (18)	48 (16)	37 (10)	44 (3)
	Average		43 (8)	65 (6)	51 (5)	53 (13)
Below F_1	Oral	High	29 (10)	32 (6)	24 (5)	28 (4)
		Low	34 (11)	28 (10)	16 (5)	26 (5)
	Nasal	High	30 (14)	20 (6)	26 (8)	25 (5)
		Low	30 (8)	35 (8)	10 (5)	25 (5)
	Average		30 (5)	28 (6)	18 (5)	26 (2)

contours intersect at an angle θ of 56 degrees, indicating that F_1 and N interact moderately in this region of the stimulus space. We used the angle θ to assess the degree of interaction in all conditions, with the results shown in Table III.

4. Effects of stimulus manipulations

Using θ as a measure, we now summarize the effects of stimulus variables on the degree of perceptual interaction.[4] To evaluate reliability, we applied the method described above to each listener's data in each condition,[5] and subjected the resulting θ values to a repeated-measures ANOVA. The independent within-subjects variables were F_1 range, N difference, and following consonant nasality; the independent between-subjects variable was the position of the nasal pole/zero complex with respect to the oral pole. There are three major results.

First, F_1 and N interacted in our listeners' perceptions: θ averaged 40 degrees (95% confidence interval $=\pm 6$ degrees), and all the values in Table III reflect negative interactions ($\theta < 90$ degrees), so that an increase in N and a decrease in F_1 had similar perceptual effects (as in Kingston and Macmillan, 1995). This conclusion paraphrases the earlier observation that highest discriminability is obtained with stimuli in which N and F_1 covary negatively.

Second, F_1 and N integrate more when the nasal pole/zero complex is below the oral pole ($\theta = 26$ degrees, ± 7 degrees) than when it is above [$\theta = 53$ degrees, ± 7 degrees; $F(1,6) = 40.6$, $p = 0.001$]. The effect in the Below condition is qualitatively different from that in the Above condition. The configurations of the Above-condition stimulus subsets are approximately parallelograms, and increases in N produce approximately linear paths through the space; whereas in the Below condition points in the perceptual space often do not form parallelograms, and increases in N produce nonlinear paths. In particular, stimuli *CH* and *AH* (heavy N and the lower value of F_1) differ from the other stimuli in a direction approximately orthogonal to the dimension along which the other stimuli vary.

Third, F_1 and N were more integral before nasal consonants ($\theta = 34$ degrees, ± 7) than oral ones [$\theta = 45$ degrees, ± 7; $F(1,6) = 6.68$, $p = 0.041$]. The difference in θ values before nasal and oral consonants was much smaller when the nasal pole/zero complex was below the oral pole (25 degrees, ± 8, versus 27 degrees, ± 10) than above (43 degrees, ± 8, versus 63 degrees, ± 10), but the interaction between these variables did not achieve significance [$F(1,6) = 4.34$, $p = 0.082$)].[6]

C. Discussion

Experiment I yielded strong evidence of mean-integrality. We first summarize this evidence and compare our MDS-psychological space assessment of interaction with our previous approach. We then examine psychoacoustic mechanisms that might be responsible for the effect.

1. Evidence of integrality

a. Perceptual-space analysis. Kingston and Macmillan's (1995) conclusion that F_1 and N integrate negatively is confirmed in these experiments. Using the MDS approach to assessing interaction, the present data display $\theta = 40$ degrees, the earlier data (when reanalyzed with MDS), $\theta = 47$ degrees (± 11). A better comparison may be with only the Below data ($\theta = 26$ degrees) or only the Below, Zero versus Heavy comparisons ($\theta = 19$ degrees), as the stimuli used to obtain the earlier data had the nasal pole/zero complex below the oral pole and a nasalization difference similar to that between Zero versus Heavy. Either comparison clearly supports the major conclusion about the direction of interaction. Under the reanalysis, the two studies also agree that the extent of integrality is greater for vowels followed by a nasal rather than oral consonant. In the present data, a nasal consonant decreases θ from 45 to 34 degrees overall, 63 to 43 degrees in the Above conditions, 27 to 25 degrees in the Below conditions; for the Kingston and Macmillan data, under the revised analysis, the shift is from 69 degrees (± 8) to 25 degrees (± 14).

The form of the interaction in the Above and Below sets is qualitatively different. For the Above data, it is clear that one dimension is related to perceived height, and perceived nasalization contributes a separate effect. As noted earlier,

the second dimension for the Below data seems primarily to distinguish stimuli *CH* and *AH* from the other five stimuli in each set.

There was no interaction between High versus Low range of F_1 and the location of the nasal complex. According to Maeda's (1993) model, listeners expect a shift in the frequency of the nasal complex relative to F_1 in the range 360–500 Hz, but we obtained no evidence for such a shift.

b. Parallelogram models. In our past work we used a different method to assess degree of interaction from similar data. Kingston and Macmillan (1995) and Kingston *et al.* (1997), using only 2×2 arrays, averaged d' values for opposite sides and fit a parallelogram to points corresponding to the four stimuli. The degree of interaction was estimated as an interior angle of this figure. For noiseless data that actually *do* form a parallelogram (or a trapezoid), this method is equivalent to the one used here, so the present method can be viewed as an extension and generalization of the previous one. To compare the two techniques for real data, we applied both to data from experiment I, and data from Kingston and Macmillan (1995).

For the present data, the correlation between the two values of θ was 0.80, but values of θ obtained from parallelogram analysis were lower than those obtained from MDS by an average of 32 degrees. For the Kingston and Macmillan (1995) data, values of d' representing single-dimension and correlated task performance by each of the eight listeners were submitted to INDSCAL, and θ values were calculated from the group solutions according to the method described earlier. The values are: 8 degrees (±3) before [n], 42 degrees (±22) before [m], 79 degrees (±13) before [d], and 60 degrees (±10) before [b]. On average, these figures are 24 degrees higher than those found with the parallelogram method [10 degrees (±16), 28 degrees (±18), 32 degrees (±30), and 22 degrees (±30), respectively], although the figure for [n] context is lower. Analyzed this way, the data show that integrality is stronger before nasal ($\theta=25$ degrees) than oral ($\theta=69$ degrees) consonants, as in the present experiment.

The discrepancy between the two methods probably arises because the parallelogram model gives too much weight to fitting large d' values accurately. The MDS assumes no specific geometric arrangement, and is thus more general. In any case, the positive relation between values of θ obtained by the two methods means that most qualitative conclusions are unaffected by the choice of technique.[7]

2. Psychoacoustic analysis

The major psychoacoustic questions raised by this experiment are: What aspects of the stimuli are used by the listeners in making their classifications? What type of processing led to the patterns of perceptual interaction displayed in Fig. 5 and the θ values calculated from them? We consider the related but different question of the physical correlates of speech *categories* in the discussion following Experiment II.

a. Center-of-gravity. For each pair of vowels that was discriminated in the experiment, we computed differences in the COGs of the ERB rate spectra (taken from Fig. 4). The correlations between COG differences and d_a, for the Above and Below stimulus sets and for the [d] and [n] contexts, averaged 0.72. About half the variance in d_a values is thus accounted for COG differences, suggesting that listeners rely heavily on this stimulus characteristic in classifying these vowels.

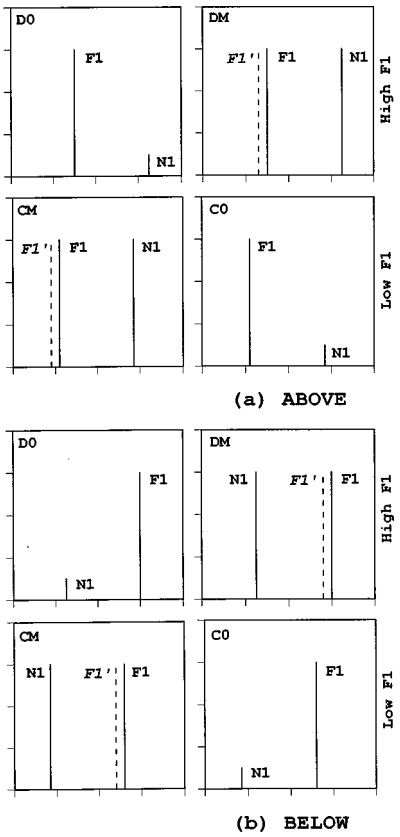

FIG. 6. Schematic spectra of stimuli *D0*, *DM*, *C0*, and *CM*. Solid lines represent the frequency and amplitude of F_1 and N_1, the dashed line the frequency and amplitude of perceived $F_1(F_1')$, which is lowered to compensate for the raising produced by nasalization.

Although previous work on nasalization has suggested that COG over the low-frequency region plays an important role in phonetic labeling (see the discussion following Experiment II), we are aware of no previous work investigating its role in fixed classification. The COG of our stimuli increases with F_1 and decreases with *N*, so that COG differences are greater for negatively than for positively correlated-stimulus pairs. The effect is visible in Fig. 4, where the negatively correlated stimuli in each 2×2 subset are connected by dashed lines and the corresponding positively correlated stimuli by dotted lines. The difference in COG (the vertical discrepancy, not the length of the line) is uniformly greater for the negatively correlated pairs.

To see that these two effects predict the negative integrality found in our data, focus on the stimulus subarray $\{D0, DM, C0, CM\}$. The COG values for these four stimuli are 552, 531, 511, and 493 Hz in the Above condition and 552, 508, 511, and 452 Hz in the Below condition. The difference between *DM* and *C0* (20 Hz Above and 3 Hz Below) is much less than that between *D0* and *CM* (59 Hz Above and 100 Hz Below), and the discriminabilities follow the same pattern: For the Above stimuli, $d'=2.51$ vs 0.43 before [d] and 2.66 vs 0.64 before [n]; for the Below stimuli, d_a

$=2.18$ vs 0.62 before [d] and 2.25 vs 0.73 before [n]. This asymmetry is captured, in the data analysis, by the statistic θ.

Thus there is evidence that COG is important in vowel classification. However, if decisions were based entirely on COG, the MDS representations in Fig. 5 would be one-dimensional, which they are not.

b. Perceived F_1. Diehl *et al.* (1990) suggested that judgments of both height and nasalization depend on perceived F_1, and that nasalization modifies this perception. In natural speech, the presence of nasalization increases F_1. If, as in our stimulus set, perceptible nasalization is added and F_1 stays the same, the listener may lower the perceived value of F_1 in compensation. That such a process could account for the integrality we observed is illustrated in Fig. 6, which displays schematic spectra (cf. Fig. 3) for stimuli *D0*, *DM*, *C0*, and *CM*. (The four spectra have been rearranged to highlight the key comparisons, *D0* vs *CM* and *DM* vs *C0*.) The dashed lines labeled F_1' represent the perceived location of the first formant after compensation for the raising effects of nasalization. The compensation process increases the *D0-CM* difference and reduces the *DM-C0* difference, and this effect occurs for both the Above and the Below stimuli. Baseline differences (horizontal and diagonal comparisons, in the figure) are unaffected.

The Diehl *et al.* hypothesis also makes a prediction about pairs of stimuli in which the covariation of F_1 and N does conform to listeners' expectations. With such a stimulus set, performance on the two correlated tasks should be more equal and the two stimulus dimensions should integrate less. Kingston and Macmillan (1995) used such a stimulus set. In their experiment II, stimuli were ''rotated'' 45 degrees in the stimulus space so that the A_{45}–D_{45} stimulus pair differed in F_1 but not N and the B_{45}–C_{45} stimulus pair differed in N but not F_1. Compensation for the expected effects of nasalization should have lowered perceived F_1 for B_{45} considerably relative to C_{45} because B_{45} was so heavily nasalized. On the other hand, the perceptual distance between A_{45} and D_{45} should not have been affected by compensation, as they were both equally nasalized. These effects should at least have equalized (and perhaps reversed) the differences in performance on the correlated tasks, compared to those obtained with the original unrotated stimulus array. Our MDS reanalysis of the degree of interaction in those experiments confirms these expectations: $\theta = 100$ degrees (95% confidence interval ± 18) overall for the rotated data, 92 degrees (± 20) before nasal consonants and 108 degrees ($\pm$ 18) before oral consonants. These values are all close to 90 degrees, indicating that performance was nearly equal on the two correlated tasks.

Compensating for the expected raising of F_1 by nasalization is a top-down process that depends on separating nasalization from F_1 perceptually. Comparing the COG values of two stimuli, on the other hand, is an entirely bottom-up process. We reconsider the effects of COG and perceived F_1 after describing experiment II, and argue that these factors are also implicated in vowel identification.

III. EXPERIMENT II: TRADING RELATIONS

In this trading-relations experiment, listeners judged a vowel height continuum while vowel nasalization was varied (as in Krakow *et al.*, 1988), and a nasalization continuum while F_1 was varied. Both judgments were made on stimuli in which the following consonant's nasality was varied orthogonally. Two sets of results are reported here, one obtained from the same listeners who had earlier participated in experiment I and another from naive listeners. The two groups are compared to determine the effects of this prior experience.

A. Methods

1. Stimuli

The vowel array was a finer subdivision of that used in experiment I. Seven equally spaced values spanned the total ranges of F_1 and of N (see Table I). Thus, the range of F_1 was 360–500 Hz, with 23–24-Hz intervals between adjacent F_1 values, and the range of N was 0–90 Hz, with 15-Hz intervals. Otherwise, the stimuli were constructed in exactly the same way as in the previous experiment, except that the initial consonant was always [b]. Four 7×7 $F_1\times N$ arrays were constructed by varying the final consonant ([d] or [n]) and the location of the nasal complex (Above or Below F_1).

2. Subjects

Listeners who participated in experiment I remained in the same condition, Above or Below. Six additional listeners heard the Above stimuli, and six more the Below stimuli. The listeners who had participated in experiment I will be referred to henceforth as ''trained'' listeners, those who did not as ''untrained.''

3. Procedures

For the trained listeners, experimental blocks of trials began with 28 ordered orientation trials, which stepped through the relevant dimension, alternating between the lowest and highest values of the orthogonal dimension and between Oral and Nasal following consonants (7 stimulus values$\times$2 following consonants$\times$2 endpoints). The orientation trials were followed by 98 randomized test trials, one for each stimulus in the $2\times7\times7$ array. Listeners gave one of two responses: ''U'' versus ''O'' (henceforth ''high'' versus ''mid'') if the relevant dimension was F_1, and ''oral'' versus ''nasal'' if the relevant dimension was N. They had 2000 ms to give their response after hearing the stimulus and 1500 ms before the next trial began. Blocks alternated between F_1 and N judgments, a total of 15 blocks for each dimension in the Above condition and 17 in the Below condition. Two 2-h sessions over two days were needed. Other procedural details were as in experiment I.

A slightly different orientation procedure was used for the untrained listeners. Before having to categorize the full stimulus continua, they were presented with one or two blocks of trials in which the 28 endpoint stimuli were presented in random order. The listeners responded ''high'' versus ''mid'' or ''oral'' versus ''nasal'' and were given trial-by-trial feedback. One orientation block of this kind was

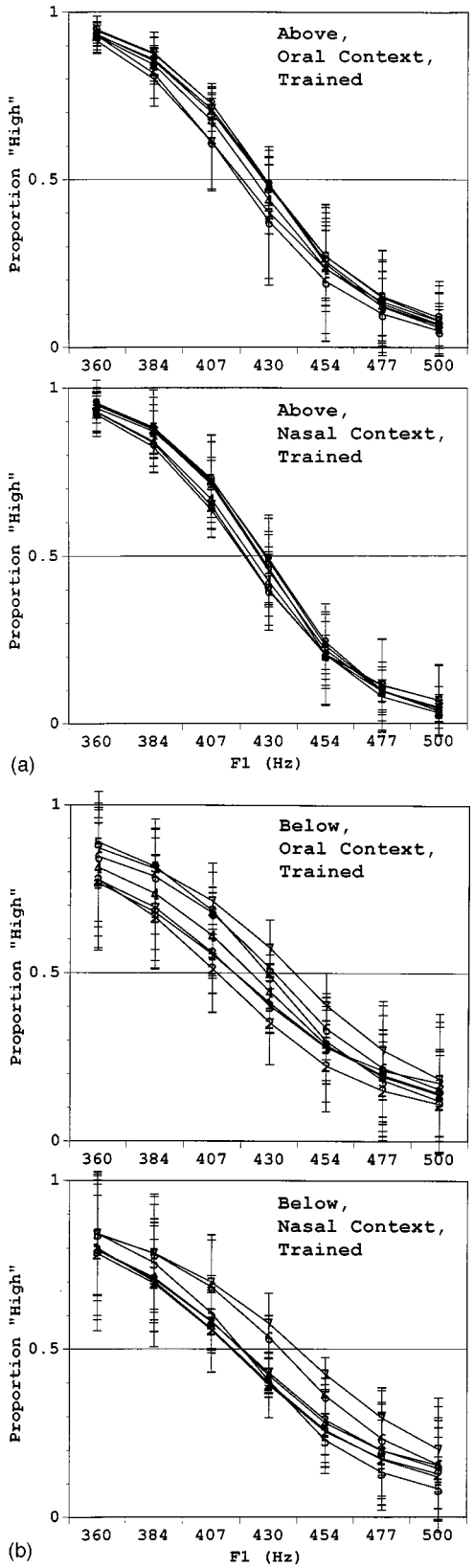

FIG. 7. Identification functions for trained listeners responding ''high'' as F_1 varies (experiment II). In (a), the nasal complex is Above F_1, in (b) Below. The parameter is N; the symbol 1 indicates 0 Hz, 7 is 90 Hz, and the other numerals are spaced at 15-Hz intervals between these values. In each panel, responses to vowels preceding an Oral consonant are displayed at the top, responses to vowels preceding a Nasal consonant at the bottom.

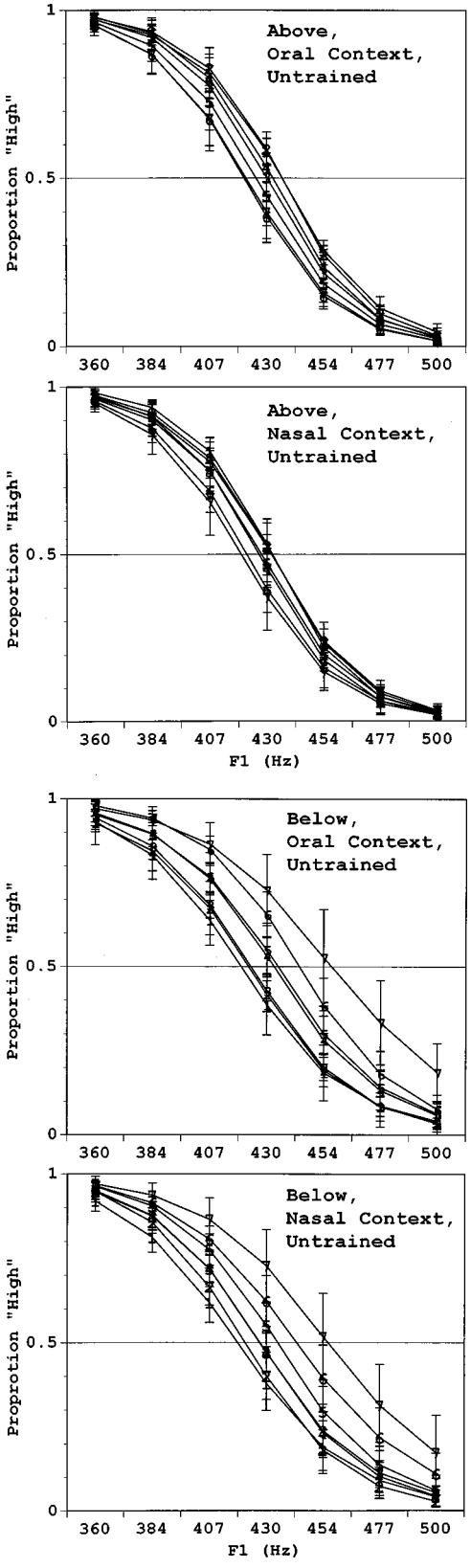

FIG. 8. Identification functions for untrained listeners responding ''high'' as F_1 varies (experiment II). See Fig. 7.

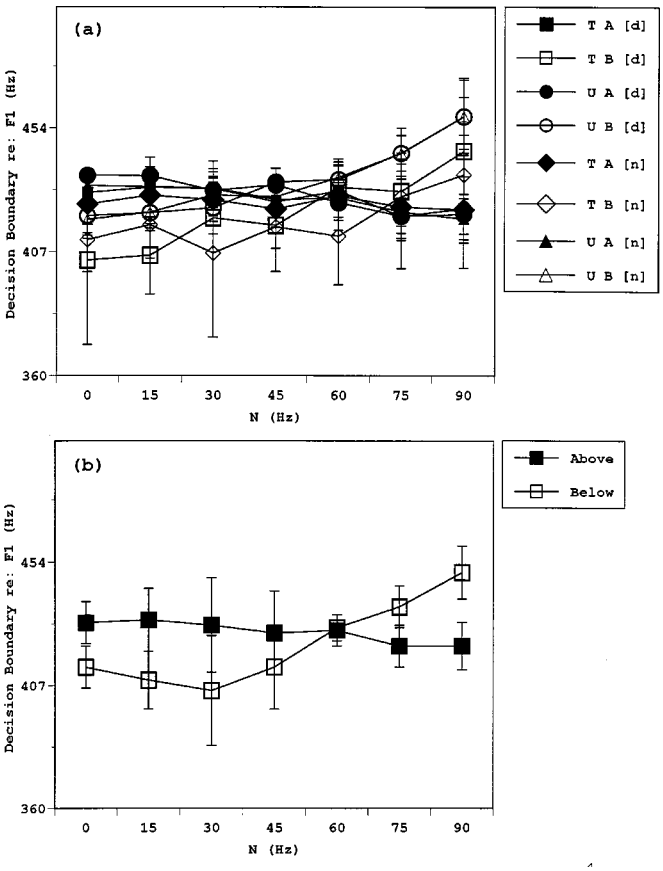

FIG. 9. Crossover (50% responding points) for ''high'': ''mid'' judgments, from the F_1 identification functions in Figs. 7 and 8. (a) Separate lines and plotting figures are used for each combination of Trained (T) and Untrained (U) listeners, Above (A) and Below (B) placement of the nasal complex, and Oral ([d]) and Nasal ([n]) consonant conditions. (b) The average result for Above and Below. Bars are 95% confidence intervals.

sufficient for ''high'' versus ''mid'' categorization, two for ''oral'' versus ''nasal'' categorization. The procedure was thus the same as for trained listeners, except that untrained listeners categorized the stimuli for ''high'' versus ''mid'' or ''oral'' versus ''nasal'' in three successive blocks before switching to the other categorization. Between 13 and 16 such blocks were run for both categorizations in 2-h time periods on different days.

Because of occasional failure to respond in the allotted time, the results reported here for trained listeners are based on an average of 14 out of the possible 15 judgments per stimulus per listener for each dimension in the Above condition and an average of 15–16 of the possible 17 judgments in the Below condition. Results for untrained listeners are based on an average of 13–16 responses in the Above condition and an average of 15 responses in the Below condition.

B. Results

1. ''High'' judgments

The average proportion of ''high'' judgments is plotted against F_1 in Fig. 7 for trained listeners and in Fig. 8 for untrained listeners. The multiple panels reflect the Above/Below distinction and Oral versus Nasal context, and the separate functions in each panel are for the seven possible values of nasalization. Logistic psychometric functions fitted to the response frequencies were used to estimate a crossover point, or category boundary—the stimulus value judged 50% of the time in each category—and a slope.

Category boundaries for ''high'' judgments are plotted in Fig. 9(a). In the Below condition, the F_1 crossover point increases as a function of N by 35–40 Hz, but in the Above condition it instead decreases by about 10 Hz. A repeated measure ANOVA was run in which Trained versus Untrained and Above versus Below were between-subjects variables and N and following consonant were within-subjects variables. The only significant main effect was N [$F(6,96) = 3.28$, $p = 0.006$] and the only significant interaction was $N \times$ Above/Below [$F(6,96) = 6.84$, $p < 0.001$]. Crossover points decrease slightly and then increase noticeably in the Below condition as a function of N, whereas they decrease steadily in the Above condition [Fig. 9(b)].

To abstract sensitivity measures for ''high'' judgments, we examined the slopes of the psychometric functions in Figs. 7 and 8; these are plotted in Fig. 10(a). The slopes are steeper for the Untrained than the Trained listeners, and in the Above than the Below condition. In a repeated measures ANOVA using the same independent variables as in the analysis of crossover points, only the main effects of the between-subjects variables, Trained versus Untrained and Above versus Below, reached significance [Trained versus Untrained: $F(1,16) = 5.07$, $p = 0.039$; Above versus Below: $F(1,16) = 5.30$, $p = 0.035$]; see Fig. 10(b). The interaction between following consonant and Above versus Below approached significance [$F(1,16) = 3.66$, $p = 0.074$], reflecting steeper slopes before nasal [n] Above but before oral [d] Below.

2. ''Oral'' judgments

The average proportion of ''oral'' judgments for trained and untrained listeners is plotted against N in Figs. 11 and 12. The multiple panels reflect the Above/Below distinction and Oral versus Nasal context, and the separate functions in each panel are for the seven possible values of F_1. Logistic psychometric functions could not always be fit reliably to the response frequencies, because in many instances (especially for the untrained listeners) the psychometric functions changed little as a function of N. Analysis of the ''oral'' judgments is based instead on the average proportions of ''oral'' responses across all seven N values for each value of F_1 and final consonant.

Mean proportions of ''oral'' judgments across N values for each F_1 value and following Consonant are plotted in Fig. 13(a).[8] ''Oral'' responses increase with F_1 generally, but this effect is relatively small for the untrained listeners in the Above condition. In a repeated measures ANOVA using the same independent variables as in the previous analyses, the only significant main effect was for F_1 [$F(6,96) = 63.82$, $p < 0.001$]. F_1 also interacted significantly with Above versus Below [$F(6,96) = 3.28$, $p = 0.006$] and with the interaction between Above versus Below and Trained versus Untrained [$F(6,96) = 4.27$, $p < 0.001$]; see Fig. 13(b).

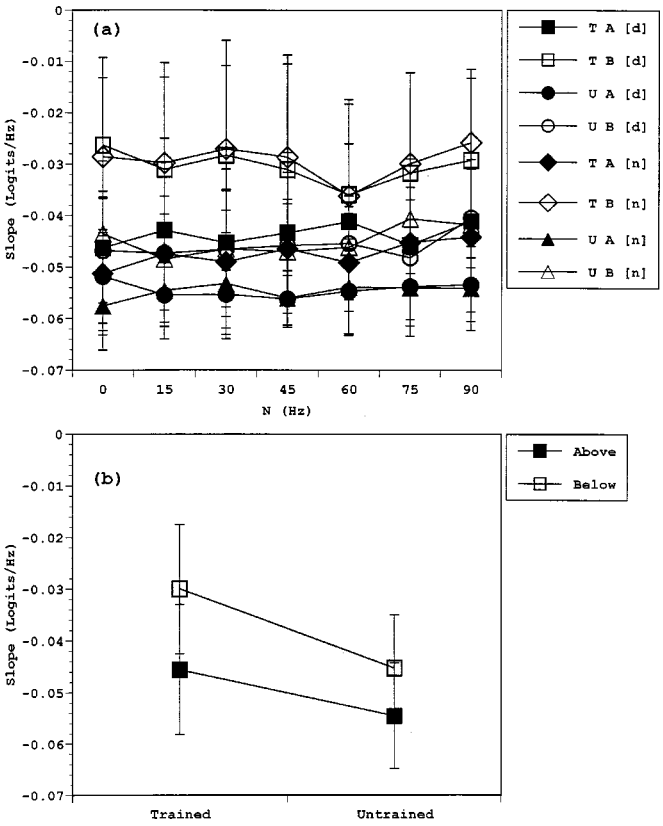

FIG. 10. Slopes for ''high'':''mid'' judgments, from the F_1 identification functions in Figs. 7 and 8. (a) Separate lines and plotting figures are used for each combination of Trained (T) and Untrained (U) listeners, Above (A) and Below (B) placement of the nasal complex, and Oral ([d]) and Nasal ([n]) consonant conditions. (b) The average result for Trained and Untrained listeners. Bars are 95% confidence intervals.

C. Discussion

The primary interest in these results is in the trading relations they display between F_1 and *N*, and in the effect of following-consonant nasality on these relations. A preliminary question concerns the ways in which experience in fixed classification and consonant identification (experiment I) affected these results. Comparison of the trained and untrained listeners shows two effects: (1) For ''high'' judgments, untrained listeners were *more* sensitive to F_1 differences than trained listeners, and sensitivity in the Above condition exceeded that in the Below condition more for the trained than the untrained listeners. (2) For ''oral'' judgments, untrained listeners were relatively insensitive to *N* differences in the Above (but not in the Below) condition. The overall pattern of results was otherwise very similar.

1. Height judgments

The likelihood of a ''high'' judgment depends on *N* in the Below condition, with more nasalized vowels more likely to be judged ''high'' [Figs. 7(b) and 8(b)]. On the other hand, more nasalized vowels are less likely to be judged ''high'' in the Above condition [Figs. 7(a) and 8(a)]. Increases in *N* produce decreases in COG (see Fig. 4) for both the Above and Below stimuli and, according to the hypothesis that COG is the mediating variable, more ''high'' judgments. The COG hypothesis is thus consistent with the Below but not the Above data.

A different hypothesis can account for the discrepancy between the Above and Below data. Suppose height judgments depend on the intensity of the harmonics on the upper skirt of the lowest spectral prominence, as well as on its COG. [This hypothesis is consistent with Assmann's (1985) finding that height judgments vary much more with the intensity of harmonics just Above F_1 than those just Below it.] These harmonics will become more intense as *N* increases for the Above but not the Below stimuli, because N_1 is Above rather Below F_1. This increase on the upper skirt can easily be seen by comparing panels within a row in Fig. 3(a). Above, this effect will oppose that of decreasing COG and may even lead listeners to mistake N_1 for F_1, thus reducing ''high'' responses as *N* increases. In the Below condition, on the other hand, decreasing COG and mistaking N_1 for F_1 cooperate, markedly increasing ''high'' responses as *N* increases.

Krakow and her colleagues have conducted extensive research on the nasalization–height interaction using the trading relations paradigm, but their use of an articulatory synthesizer renders their studies hard to compare with ours. For example, Krakow *et al.* (1988) used a continuum from ''mid'' [ɛ] to ''low'' [æ], and found that height judgments shifted towards ''low'' when vowels were nasalized. This is superficially the opposite of our result, but because F_1 increased in concert with *N* for their stimuli, the two results are quite consistent.

2. Nasalization judgments

The likelihood of an ''oral'' judgment depends strongly on F_1 in both the Above and Below conditions, with stimuli judged ''high'' more likely also to be judged ''nasal'' and stimuli judged ''mid'' more likely to be judged ''oral'' (Figs. 11 and 12). Further, sensitivity to *N* differences in making ''oral'' versus ''nasal'' judgments depends nonmonotonically on F_1. As a comparison with Figs. 7 and 8 shows, the effect of F_1 on ''oral'' judgments was much stronger than the effect of *N* on ''high'' judgments. The F_1 range is a little over 1.5 times as large as the *N* range, but changes response proportions by eight to nine times as much. Across the 140-Hz F_1 range, ''oral'' responses shift from 0.23 to 0.73 on average, whereas across the 90-Hz *N* range, ''high'' responses shift only from 0.45 to 0.50. Also unlike the effect of *N* on height, this interaction was equally large in the Above and Below conditions, at least for the trained listeners.

All of these asymmetries may follow from the fact that height but not nasalization is phonologically contrastive for American English vowels. In making nasalization judgments, our listeners were likely to have been judging the stimuli as much if not more in terms of their perceived vowel height as their perceived nasalization, but in making vowel height judgments, little if any mirror image effect was likely.

Speakers of Indic languages, in which nasalization is contrastive, respond more categorically to this feature than American English listeners (Beddor and Strange, 1982, for Hindi; Hawkins and Stevens, 1985, for Hindi, Gujerati, and Bangali). Hawkins and Stevens also report that Gujerati speakers showed the greatest degree of categoricalness, fol-

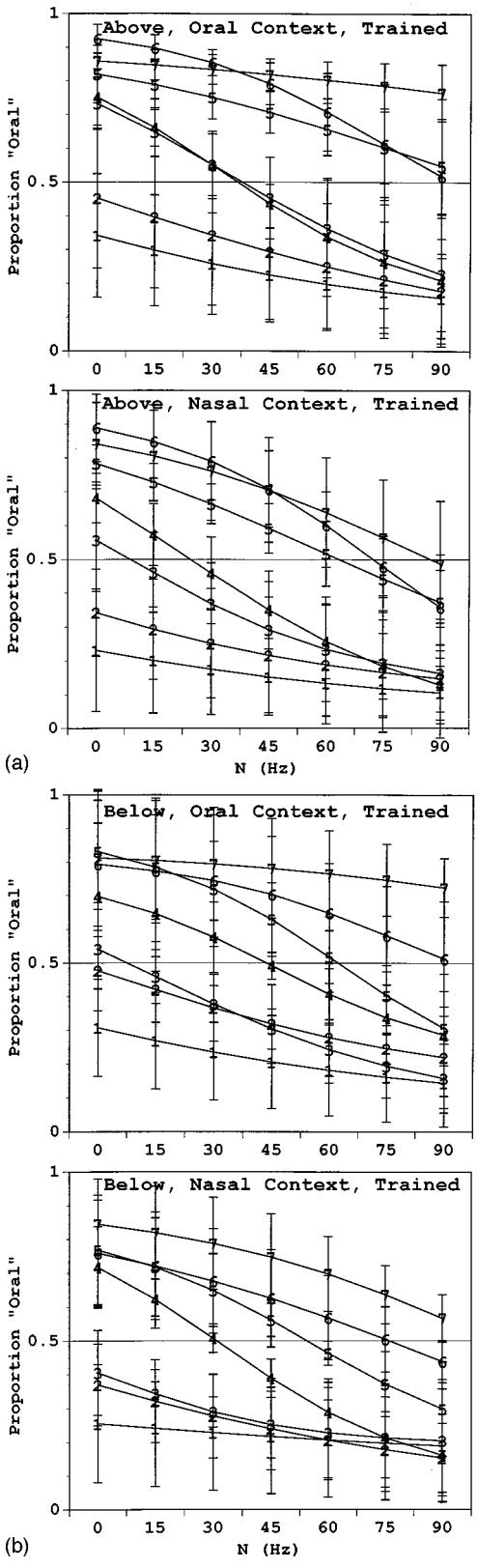

FIG. 11. Identification functions for trained listeners responding ''oral'' as N varies (experiment II). In (a), the nasal complex is Above F_1, in (b) Below. The parameter is F_1; the symbol 1 indicates 360 Hz, 7 is 500 Hz, and the other numerals are spaced at 23- to 24-Hz intervals between these values. In each panel, responses to vowels preceding an Oral consonant are displayed at the top, responses to vowels preceding a Nasal consonant at the bottom.

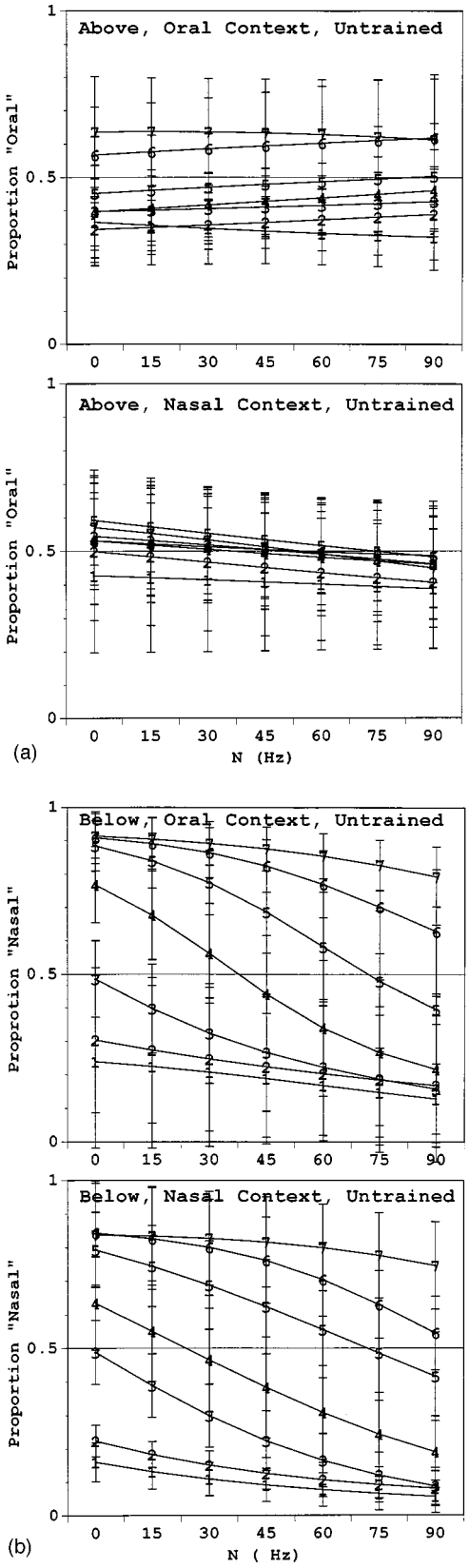

FIG. 12. Identification functions for untrained listeners responding ''oral'' as N varies (experiment II). See Fig. 11.

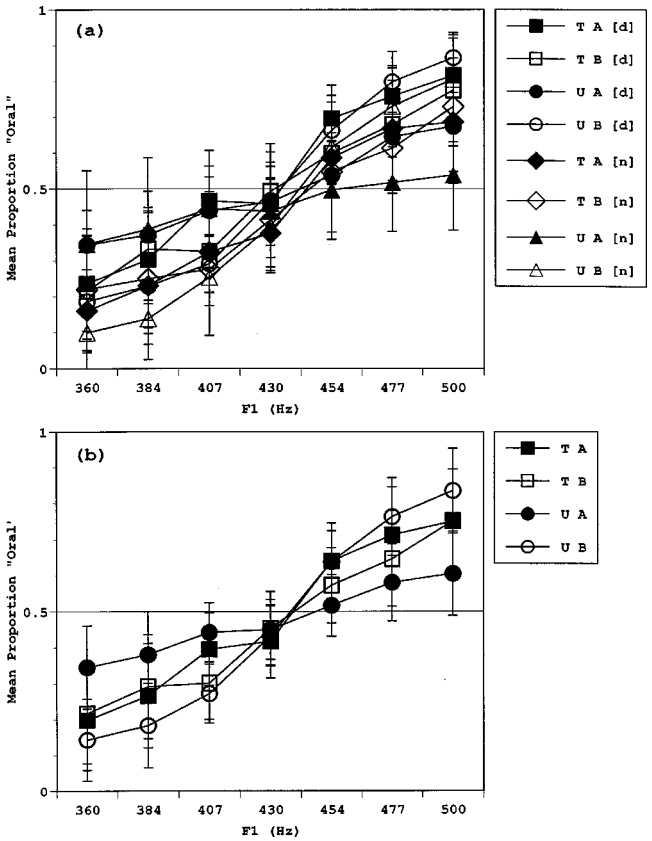

FIG. 13. Proportion of ''oral'' judgments, from the *N* identification functions in Figs. 11 and 12. (a) Separate lines and plotting figures are used for each combination of Trained (T) and Untrained (U) listeners, Above (A) and Below (B) placement of the nasal complex, and Oral ([d]) and Nasal ([n]) consonant conditions. (b) The average result for each combination of training and nasal complex placement. Bars are 95% confidence intervals.

lowed by Hindi and Bengali. Hindi and Gujerati listeners discriminated the intermediate nasalization values better than the extremes for all of [i, u, ɑ, e, o]. For American English listeners, Hawkins and Stevens found that vowels were discriminated equally well across the nasalization continuum when the vowel was [i, u, ɑ] but best with intermediate nasalization values when the vowel was [e, o]. A mid-range peak in nasalization discrimination has thus been consistently observed for mid vowels, both in our experiments (F_1 values of 360–500 Hz) and those of Hawkins and Stevens (400 Hz for [e], 430 Hz for [o]), suggesting that our listeners and theirs responded in terms of the same perceptual effects.

Hawkins and Stevens also observed that whereas the high and low vowels [i, u, ɑ] showed a discrimination peak near the crossover point for categorizing these vowels as oral versus nasal, the mid vowels [e,o] showed a peak at the point where N_1 separates from F_1 spectrally. They suggested that this separation causes listeners to hear a different vowel quality, an interpretation compatible with the conjecture that our listeners used vowel height percepts as much or more than nasalization percepts in identifying vowels as ''oral'' versus ''nasal.'' In Hawkins and Stevens's high and low vowel stimuli, [i, u, ɑ], the nasal pole/zero complex was always well separated from the oral pole, so increasing nasalization would not bring about a change in vowel quality. Further evidence that nasalization is perceived differently in mid than high or low vowels can be found in Beddor and Hawkins (1990). These authors report that in matching nasalized to oral vowels, American English listeners gave greater weight to F_1 than COG for high and low vowels, [i, u, æ, ɑ], but more or less equal weight to both F_1 and COG for mid vowels, [e, o].

3. Consonantal context

Contrary to past findings, our data do *not* reveal an interaction between perceived vowel height and the nasality of the following consonant. In Krakow *et al.* (1988), the boundary shift in height judgments with *N* did not occur when the following consonant was nasal, whereas in our data, the shift was equally strong before a nasal as an oral consonant. According to Kingston and Macmillan's (1995) reanalysis, Krakow *et al.* also found greater sensitivity when the vowel and consonant agreed in nasality: F_1 functions were steeper with higher *N* for vowels followed by a nasal consonant, but steeper with lower *N* for those followed by a oral consonant. No such slope differences are found in vowel height judgments reported here; instead, the Above data show consistently greater sensitivity to F_1 differences for all *N* values before both oral and nasal following consonants than the Below data, and this difference is greater for trained than untrained listeners [Fig. 12(a) and (b)].

There is a weak interaction between the following consonant's nasality and the nasal pole/zero complex's position relative to the oral pole: Sensitivity to F_1 is greater before [n] Above, but before [d] Below. Experiment I showed that F_1 integrates less with nasalization Above than Below. If lesser integration means that a vowel is more likely to sound nasalized for a given *N* value Above than Below, then in this respect our results correspond to those of Krakow *et al.* in showing greater sensitivity to F_1 when the vowel and consonant agree in nasality. Two caveats are, however, in order: (1) the effect observed in our data is at best marginally significant, and (2) the interaction is not between *N* and consonant nasality, but between the separability of the two dimensions and consonant nasality.

In experiments using a matching paradigm to study vowel nasalization judgments, Krakow and Beddor (1991) showed that naturally produced vowels are more reliably identified as nasalized in isolation and between oral consonants, rather than between nasal consonants, a context in which their nasalization could be coarticulatory. The psychometric functions for nasalization judgments in our data, on the other hand, do not differ between oral and nasal contexts in either the Above or Below conditions. Instead, sensitivity to *N* differences is greater for intermediate than extreme F_1 values before both oral and nasal consonants, both Above and Below (Figs. 11 and 12). Differences in how the consonant nasality contrast was implemented may account for these disparate effects of context. Krakow and Beddor compared m_n and b_d contexts, Krakow *et al.* (1988) b_nd and b_d contexts, and our experiments C_n and C_d. Again, however, the discrepancy may involve COG and perceived F_1: when F_1 was high it raised COG and perceived F_1 enough nearly to overwhelm the contrary influence of increasing *N* on these percepts, and vice versa. As a result,

responses crossed over more sharply when the orthogonal variable, here F_1, had intermediate values.

IV. GENERAL DISCUSSION: SENSORY AND DECISION PROCESSES IN PHONETIC IDENTIFICATION

Fixed classification and identification provide, we have argued, rather different information about vowel perception. In particular, the mean-integrality found in experiment I is logically unrelated to the boundary shifts observed in experiment II. However, the two tasks must ultimately tap the same information. In this section we attempt to describe the primary identification results (boundary shifts and sensitivity pattern) in terms of a common perceptual space, of the sort that was derived from fixed classification data.

To start, we return to Fig. 1, which offered some alternative interpretations of Repp's (1982) concept of cue trading in perceptual-space terms. The results of experiment I showed that most 2×2 stimulus subsets were represented by quadrilaterals that were not rectangular ($\theta=90$ degrees), but rather displayed a negative correlation between perceived F_1 and perceived N (θ averaged 53 degrees in the Above condition, 28 degrees Below). Of the possibilities outlined in the Introduction, this arrangement most resembles that of Fig. 1(c), an elaborated version of which is shown in Fig. 14 for the $\{C0,D0,CM,DM\}$ corner of the perceptual space.

The implications of this pattern for identification (experiment II) depend on the listener's decision boundary. Suppose this boundary is orthogonal to the perceived F_1 axis, as in Fig. 14(a). The boundary shift is the difference in proportion of ''high'' judgments for the nasalized and unnasalized stimuli, the vertical difference between two identification functions in graphs like Fig. 7. Expressed in z-units,

$$\text{boundary shift} = z[P(\text{``high''}|CM)] - z[P(\text{``high''}|C0)]. \quad (1)$$

For the trained observers, we calculated the average boundary shift by this method, with the results shown in Table IV. For F_1 judgments with the Above stimuli, the negative value indicates *a reduced* tendency to say ''high'' as N increases; the positive values in the other cases indicate positive interactions between these variables.

From the geometry of Fig. 14(a), the magnitude of shift predicted from fixed classification can be expressed[9] in terms of d'_N (sensitivity to N), and θ:

$$\text{boundary shift} = d'_N \cos(\theta). \quad (2)$$

These values are also given in Table IV, and it is clear that the observed boundary shifts are smaller than predicted for both F_1 and N judgments.

The assumption of an orthogonal decision rule also makes a prediction about sensitivity in the identification task. The observer's ability to discriminate two stimuli in this condition can be estimated, for F_1 judgments, by comparing the proportion of ''high'' responses to the stimuli:

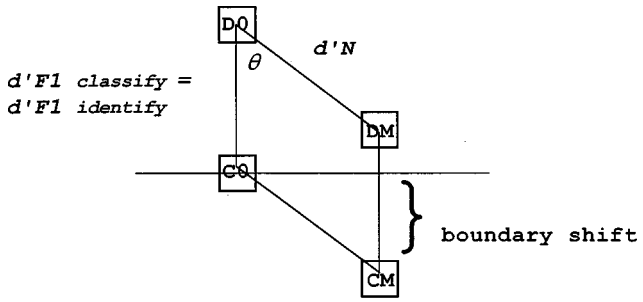

(a) Orthogonal decision boundary

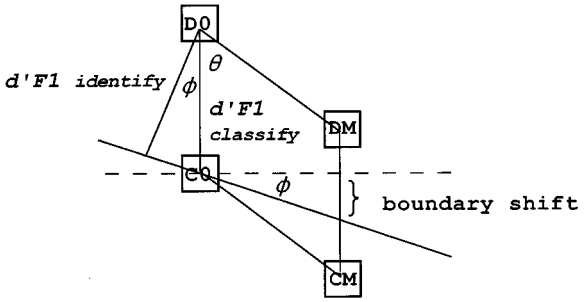

(b) Diagonal decision boundary

FIG. 14. A corner of a perceptual space that displays perceptual integrality. The vertical line from *D0* to *C0* is the optimal decision axis for a listener identifying stimuli by their F_1 values. The listener in (a) adopts a decision boundary orthogonal to this axis, obtains a sensitivity $d'(F_1)$ for discriminating these stimuli equal to that obtained in a fixed classification task, and displays a boundary shift, that is, will respond unequally to stimuli *C0* and *CM*. The listener in (b) adopts a nonorthogonal decision boundary shifted by an angle ϕ from the orthogonal one, obtains a lower sensitivity $d'(F_1)\cos(\phi)$ for discriminating *D0* and *C0*, and displays a smaller boundary shift.

$$d'_{F_1}(\text{identify}) = z[P(\text{``high''}|D0)] - z[P(\text{``high''}|C0)]. \quad (3)$$

Because the decision boundary is perpendicular to the perceived height dimension, this d' should be equal to that obtained in fixed discrimination. In fact, as Table IV shows, d' values estimated from experiment II are about half as large as the corresponding estimates from experiment I.

Both of these discrepancies between the two experiments, the prediction of too large a boundary shift and lower sensitivity in experiment II than in experiment I, can be addressed by modifying a single assumption. As shown in Fig. 14(b), let us allow the decision boundary to be a straight line that intersects the optimal boundary at a nonzero angle ϕ. The decision boundary now depends on *both* variables, a natural geometric interpretation of ''cue trading.'' Values Below the boundary are greater in both F_1 and N than corresponding values Above it. As Fig. 14(b) shows, the use of this diagonal decision rule produces a smaller boundary shift than did the orthogonal rule, namely,

TABLE IV. Observed sensitivity (experiments I and II) and boundary shifts (experiment II), together with predictions of orthogonal and nonorthogonal decision boundaries.

Dimension judged	Stimulus set	Fixed d_a	Identification d_a	θ (degrees)	Boundary shift (z-units)		ϕ (degrees)	Identification d_a predicted by Eq. (5)
					Observed	Predicted by Eq. (2)		
F_1	Above	1.23	0.92	53	−0.15	0.56	44	1.08
	Below	1.52	0.64	28	0.30	1.12	54	0.89
N	Above	0.93	0.46	53	0.46	0.74	16	0.89
	Below	1.27	0.48	28	0.45	1.34	51	0.79

$$\text{boundary shift}_1 = d'_N[\cos(\theta) - \sin(\theta)\tan(\phi)]. \quad (4)$$

This reduces to Eq. (2) when $\phi = 0$ degrees.

Perceptual distances between stimuli are now measured between points projected onto the new decision axis, which is perpendicular to the decision boundary. Under the diagonal strategy for judging F_1, sensitivity in identification drops from d'_{F_1} to

$$d'_{F_1}(\text{identify}) = d'_{F_1}\cos(\phi). \quad (5)$$

The diagonal rule model, then, predicts that boundary shifts in identification will be accompanied by lower sensitivity than in fixed classification, and thus accounts qualitatively for the important aspects of the data.

Because the model requires just one parameter to describe both results, it can be quantitatively evaluated. The parameter ϕ, estimated from Eq. (4), is given in Table IV. As Fig. 14(b) illustrates (for F_1 judgments, but the result is true for N judgments as well), the values obtained mean that listeners employ a decision boundary that depends on both F_1 and N. The last column of Table IV recalculates the predicted sensitivity in identification assuming the new decision boundary [Eq. (5)]. The average d' of 0.63 is still overpredicted—the model calculates 0.91—but the discrepancy is much less than for the orthogonal model, which predicts the same performance as in fixed classification, $d' = 1.24$. This remaining discrepancy is not entirely unexpected in view of the well-known observation that sensitivity is lower in tasks with large ranges of stimuli, like experiment II, than in fixed-classification tasks like experiment I (Braida and Durlach, 1972; Durlach *et al.*, 1989).

Let us summarize the conclusions to which these calculations have brought us. Identification functions obtained in trading-relations experiments provide two key pieces of information: a slope, which reflects sensitivity, and an intercept. If judgments of one variable actually depend on each of two variables, as is often postulated, slopes will decrease and intercepts will shift. That slopes have decreased can be determined by a converging task, fixed classification. Our data, which display this phenomenon, provide support for a psychophysical model of trading-relations effects. More generally, they show how multiple tasks, together with a model of the processes they require, can be used to explore a single perceptual model in a way that no single task can.

V. SUMMARY, CONCLUSIONS, AND A PROMISSORY NOTE

In this article, we asked whether there was a perceptual interaction between N and F_1 in vowel perception, and if so how it could be characterized. The tentative answer we have reached is that there are two distinct interactions in our data. A fixed classification experiment showed perceptual integrality of N and F_1: Increasing N or decreasing F_1 led to correlated changes in an underlying perceptual space. This is an interaction in sensitivity. A trading-relations experiment showed that judgments of N depend on both N and on F_1, and judgments of F_1 depend on largely on F_1 but to a lesser degree on N. This is an interaction in the decision process used by our observers.

We have presented a psychophysical analysis that accounts for some aspects of the data, particularly the relation between the fixed classification and identification data, and have also provided an entry point to a psychoacoustic analysis of the stimulus correlates of these perceptual outcomes. A companion paper (Kingston *et al.*, in preparation) describes yet another experiment on the interaction of N and F_1 that greatly expands the psychoacoustic analysis, and relates those results to the present ones.

ACKNOWLEDGMENTS

This work was supported by NSF Grant No. DBS 92-12043 and a grant from the PSC-CUNY award program to the first author, and NIH Grant Nos. RR07048-26 and DCO1708 to the second author. We thank our colleagues in the University of Massachusetts Phonetics Laboratory, Cecilia Kirk and Elliott Moreton, for their helpful comments on earlier drafts. Patrice Beddor, Paul Iverson, James Sawusch, and an anonymous reviewer played their roles well.

APPENDIX: STIMULUS DETAILS

In Tables AI–AIII are listed the values of the synthesis parameters (in the form of time-value pairs) other than F_1 and N in the vowel: Table AI lists source parameters, Table AII formant frequencies, and Table AIII format bandwidths and the frequencies of the nasal pole and zero in final nasal consonants. All parameters are linearly interpolated between the target values listed in theses tables.

TABLE AI. Source parameters for synthesis.

Time (ms)	F_0 (Hz)	Time (ms)	AV		Time (ms)	OQ (%)		TL (−dB at 3 kHz)	
0	100	0	45		0	75		40	
80	100	80	45		70	75		40	
					Vowel				
100	125	90	60		80	50		0	
200	125	270	60		250	50		0	
	Final consonant		b,d	m,n		b,d	m,n	b,d	m,n
280	100	280	45	54	280	75	50	40	14
355	100	355	45	54	355	75	50	40	14
390	100	390	0	0	390	75	50	40	14

TABLE AII. Formant frequencies for synthesis.

Time (ms)	F_1 (Hz)				F_2 (Hz)				F_3 (Hz)				F_4 (Hz)	
0	200				900				2100				3250	
70	200				900				2100				3250	
					Vowel									
110	Target				1025				2395				3250	
250	Target				1025				2395				3250	
Final consonant	b	d	m	n	b	d	m	n	b	d	m	n	b,m	d,n
280	260	260	220	240	840	1600	840	1240	2300	2795	2300	2590	3250	3750
285	260	260	220	240	840	1600	995	1140	2300	2795	2425	2590	3250	3750
390	260	260	220	240	840	1600	995	1140	2300	2795	2425	2590	3250	3750

TABLE AIII. Formant bandwidths and N_1 and N_0 values for synthesis. Other parameters were held constant throughout the stimuli: the bandwidths of N_1 and N_0 both = 90 Hz, $F_5 = 4200$ Hz, and $B_5 = 1500$ Hz.

Time (ms)	B_1 (Hz)			B_2 (Hz)			B_3 (Hz)			B_4 (Hz)			N_1		N_0	
0	1000			1000			1000			1000			280		280	
70	1000			1000			1000			1000			280		280	
							Vowel									
110	100			70			90			200			Target		Target	
250	100			70			90			200			Target		Target	
Final consonant	b,d	m	n	b,d	m	m	b,d	m	n	b,d	m,n	b,d	m,n	b,d	m,n	b,d	m,n
280	1000	230	120	1000	150	250	1000	250	150	1000	200	280	310	280	450		
390	1000	125	120	1000	150	250	1000	250	150	1000	200	280	310	280	450		

[1]Generalized Recognition Theory has introduced the terms *perceptual separability* and *perceptual integrality* (Ashby and Townsend, 1986) for (non)interactions inferred from a perceptual space, reserving unmodified *separability* and *integrality* to be used in Garner's (1974) operational sense. Perceptual integrality includes changes in variance and correlation as well as mean, so *mean-shift* (or just *mean-*) *integrality* (Maddox, 1992) is a more precise term for the kind of interaction shown in Fig. 1(b).

[2]Values of d_a did not differ significantly with place of articulation of the following consonant, but were sometimes reliably smaller in the second than the first repetition. All cases involved *N* differences in the Below condition: for Zero versus Moderate *N*, d_a was 1.58 (±0.28) in the first repetition and 1.36 (±0.19) in the second; for Moderate versus Heavy *N*, the values were 1.92 (±0.29) and 1.60(±0.24). Neither place of articulation nor repetition interacted significantly with any other variable in any 2×2 subset.

[3]INDSCAL provides a group solution to the collected individual listeners' distance matrices, which are composed of the d_a values for all stimulus pairs in the High- and Low-F_1 ranges. Weights are also provided for each dimension of the group solution for each listener. The stress values for our representations are higher than those often reported in the literature, but comparison is difficult because most applications use (a) more than six stimuli, and (b) nonmetric algorithms. Several aspects of the data reassure us. First, within the Above and Below stimulus conditions, the plots for High- and Low-F_1 ranges are very similar. Second, plots for the individual listeners are very similar to plots based on averages. Third, we also conducted nonmetric analyses. Nonmetric representations are very similar to metric ones (justifying the treatment of d_a as a distance measure) and have similar stress values (which may therefore be high due to the small number of stimuli).

[4]This rather ''processed'' statistic is a natural one for our geometric representations. It directly reflects the most important qualitative aspect of the data, the discrepancy between accuracy in classifying positively and negatively correlated pairs. For parallelogram-shaped integrality [as, for example, in Fig. 1(b)], it is equivalent to the measure, also called θ, used by Kingston and Macmillan (1995).

[5]Individual data were derived by applying each listener's weights for each

dimension to the group solution produced by INDSCAL.

[6]A final finding is peripheral to the major questions being investigated: The degree to which integrality was stronger in the Below condition was larger for comparisons involving the stimuli with Heavy *N* values. The interaction between *N* difference and Above:Below was not significant, but a planned comparison of the contrast between the different pairings of *N* values was: F_1 and *N* integrated more when Zero *N* was paired with Heavy *N*($\theta = 35$ degrees, ± 5) than when moderate *N* was paired with heavy *N* [$\theta = 47$ degrees, ± 8; $F(1,6) = 6.36$, $p = 0.045$]. The θ value for the pairing of Zero with Moderate *N*, 37 degrees (± 13), is similar to that of Zero versus Heavy *N*, but does not contrast significantly with that obtained for the Moderate versus Heavy pairing.

[7]Experiment I employed a paradigm that is often used to distinguish syndromes of interaction, integrality and separability (Garner, 1974). We did not use the complete Garner paradigm, which includes selective and divided attention, and our dependent measure was accuracy rather than the more common response time. Still, the data could be used to label the type of interaction as one of a small number of previously identified categories of perceptual interaction. The most direct approach, with our data, is to compare baseline d_a for one-step *N* and F_1 comparisons with the one-step correlated values. The result is that correlated d_a averages 0.59 units larger, 1.83 to 1.24. This ''correlated gain'' is larger for the Above conditions (0.78) than the Below (0.40), but occurs for both, and for both consonantal contexts, a pattern that marks the dimensions F_1 and *N* as ''integral.'' Examination of Fig. 5, however, makes clear that focusing on a ''correlated gain'' reverses the conclusion about the conditions in which F_1 and *N* integrate most, for θ values deviate more from 90 degrees in the Below than in the Above condition. There is no real conflict here: The traditional analysis is operational, whereas ours depends on characteristics of an inferred perceptual space. Another essential, but less easily quantified finding in this experiment is that the perceptual spacing in the two cases follows a different pattern; the traditional taxonomy does not distinguish among interactions that differ in this way.

[8]Mean proportions across the relevant stimulus continuum estimate response variability as a function of the orthogonal stimulus variables in much the same way as category boundaries. In a repeated measure ANOVA on mean ''high'' response proportions, a significant main effect of *N* [$F(6,90) = 5.02$, $p < 0.001$] and a significant interaction between *N* and Above versus Below [$F(6,90) = 25.51$, $p < 0.001$] were obtained, as in the comparable analysis of category boundaries. In addition, a significant interaction was obtained between *N*, Above versus Below, and Trained versus Untrained [$F(6,90) = 2.93$, $p = 0.012$], reflecting the fact that Above and Below conditions differ more as a function of *N* in the responses of the Untrained than the Trained listeners.

[9]The formulas are slightly different for the positive integration case (height judgments in the Above condition).

Ashby, F. G., and Townsend, J. T. (**1986**). ''Varieties of perceptual independence,'' Psychol. Rev. **93**, 154–179.

Assmann, P. F. (**1985**). ''The role of harmonics and formants in the perception of vowel quality,'' Ph.D. dissertation, University of Alberta.

Beddor, P. S., and Hawkins, S. (**1990**). ''The influence of spectral prominence on perceived vowel quality,'' J. Acoust. Soc. Am. **87**, 2684–2704.

Beddor, P. S., and Strange, W. (**1982**). ''Cross-language study of perception of the oral-nasal distinction,'' J. Acoust. Soc. Am. **71**, 1551–1561.

Braida, L. D., and Durlach, N. I. (**1972**). ''Intensity perception. II. Resolution in one-interval paradigms,'' J. Acoust. Soc. Am. **51**, 483–502.

Diehl, R. L., Kluender, K. R., and Walsh, M. A. (**1990**). ''Some auditory bases of speech perception and production,'' in *Advances in Speech, Hearing, and Language Processing*, edited by W. A. Ainsworth (JAI, London), Vol. 1, pp. 243–267.

Dorfman, D. D., and Alf, Jr., E. (**1969**). ''Maximum likelihood estimation of parameters of signal detection theory and determination of confidence intervals–Rating method data,'' J. Math. Psychol. **6**, 487–496.

Durlach, N. I., Tan, H. Z., Macmillan, N. A., Rabinowitz, W. R., and Braida, L. D. (**1989**). ''Resolution in one dimension with random variations in background dimensions,'' Percept. Psychophys. **46**, 293–296.

Garner, W. R. (**1974**). *The Processing of Information and Structure* (Erlbaum Associates, Potomac, MD).

Glasberg, B. R., and Moore, B. C. J. (**1990**). ''Derivation of auditory filter shapes from notched-noise data,'' Hearing Res. **47**, 103–138.

Green, D. M., and Swets, J. A. (**1966**). *Signal Detection Theory and Psychophysics* (Wiley, New York).

Hawkins, S., and Stevens, K. N. (**1985**). ''Acoustic and perceptual correlates of the nonnasal-nasal distinction for vowels,'' J. Acoust. Soc. Am. **77**, 1560–1575.

Kawasaki, H. (**1986**). ''Phonetic explanation for phonological universals: The case of distinctive vowel nasalization,'' in *Experimental Phonology*, edited by J. J. Ohala and J. J. Jaeger (Academic, Orlando, FL), Vol. 88, pp. 81–103.

Kingston, J. (**1991**). ''Integrating articulations in the perception of vowel height,'' Phonetica **48**, 149–179.

Kingston, J., and Macmillan, N. A. (**1995**). ''Integrality of nasalization and F_1 in vowels in isolation and before oral and nasal consonants: A detection-theoretic application of the Garner paradigm,'' J. Acoust. Soc. Am. **97**, 1261–1285.

Kingston, J., Macmillan, N. A., Dickey, L. W., Thorburn, R., and Bartels, C. (**1997**). ''Integrality in the perception of tongue root position and voice quality in vowels,'' J. Acoust. Soc. Am. **101**, 1696–1709.

Kingston, J., Macmillan, N. A., Dickey, L. W., Thorburn, R., and Bartels, C. (**in preparation**). ''Integrality of nasalization and F_1. III. Multinomial modeling of two-response identification.''

Klatt, D. H., and Klatt, L. (**1990**). ''Analysis, synthesis, and perception of voice quality variations among female and male talkers,'' J. Acoust. Soc. Am. **87**, 820–857.

Krakow, R. A., and Beddor, P. S. (**1991**). ''Coarticulation and the perception of nasality,'' in *Proceedings of the XII International Congress of Phonetic Sciences* (Publications de L'Universite de Provence, Aix-en-Provence), Vol. 5, pp. 38–41.

Krakow, R. A., Beddor, P. S., Goldstein, L. M., and Fowler, C. A. (**1988**). ''Coarticulatory influences on the perceived height of nasal vowels,'' J. Acoust. Soc. Am. **83**, 1146–1158.

Macmillan, N. A., and Creelman, C. D. (**1991**). *Detection Theory: A User's Guide* (Cambridge U. P., New York).

Maddox, W. T. (**1992**). ''Perceptual and decisional separability,'' in *Multidimensional Models of Perception and Cognition*, edited by F. G. Ashby (Erlbaum, Hillsdale, NJ), pp. 147–180.

Maeda, S. (**1993**). ''Acoustics of vowel nasalization and articulatory shifts in French nasal vowels,'' in *Nasals, Nasalization, and the Velum*, edited by M. K. Huffman and R. A. Krakow (Academic, San Diego), Vol. 5, pp. 147–167.

Moore, B. C. J., and Glasberg, B. R. (**1987**). ''Formulae describing frequency selectivity as a function of frequency and level, and their use in calculating excitation patterns,'' Hearing Res. **28**, 209–225.

Repp, B. H. (**1982**). ''Phonetic trading relations and context effects: New experimental evidence for a speech mode of perception,'' Psychol. Bull. **92**, 81–110.

Rubin, P., Baer, T., and Mermelstein, P. (**1981**). ''An articulatory synthesizer for perceptual research,'' J. Acoust. Soc. Am. **70**, 321–328.

Stevens, K. N., Fant, G., and Hawkins, S. (**1987**). ''Some acoustical and perceptual correlates of nasal vowels,'' in *Festschrift for Ilse Lehiste*, edited by R. Channon and L. Shockey (Foris, Dordrecht, The Netherlands), pp. 241–254.

Swets, J. A., and Pickett, R. M. (**1982**). *Evaluation of Diagnostic Systems: Methods from Signal Detection Theory* (Academic, New York).

The influence of early reflections on the identification and lateralization of vowels

Anthony J. Watkins[a)]
Department of Psychology, The University of Reading, Reading RG6 6AL, United Kingdom

(Received 19 March 1999; revised 22 July 1999; accepted 27 July 1999)

Sound coming directly from a source is often accompanied by reflections arriving from different directions. However, the ''precedence effect'' occurs when listeners judge such a source's direction: information in the direct, first-arriving sound tends to govern the direction heard for the overall sound. This paper asks whether the spectral envelope of the direct sound has a similar, dominant influence on the spectral envelope perceived for the whole sound. A continuum between two vowels was produced and then a ''two-part'' filter distorted each step. The beginning of this filter's unit-sample response simulated a direct sound with no distortion of the spectral envelope. The second part simulated a reflection pattern that distorted the spectral envelope. The reflections' frequency response was designed to give the spectral envelope of one of the continuum's end-points to the other end-point. Listeners' identifications showed that the reflections in two-part filters had a substantial influence because sounds tended to be identified as the positive vowel of the reflection pattern. This effect was not reduced when the interaural delays of the reflections and the direct sound were substantially different. Also, when the reflections were caused to precede the direct sound, the effects were much the same. By contrast, in measurements of lateralization the precedence effect was obtained. Here, the lateral position of the whole sound was largely governed by the interaural delay of the direct sound, and was hardly affected by the interaural delay of the reflections. [S0001-4966(99)04111-9]

PACS numbers: 43.71.An, 43.66.Pn, 43.66.Ba [JMH]

INTRODUCTION

When sounds are played in a room, the direct sound is often accompanied by reflections from the room's surfaces which arrive at the listener's ears from various directions. However, early reflections, arriving up to 50 ms after the direct sound, are not generally heard separately. They seem to become perceptually integrated with the direct sound. Haas (1951) observed that such reflections do contribute to the apparent level and intelligibility of speech, but the listener hears only a single overall sound. This is known as the Haas effect. In addition, the perceived direction of the overall sound is largely determined by the direction of its first arriving part. This is the precedence effect that Wallach, Newman, and Rosenzweig (1949) observed in the lateralization of binaural pairs of clicks. These two effects can often occur together in various sounds, and they have sometimes been considered as different aspects of the same basic phenomenon. However, it has been argued that the effects should be distinguished because of the way that they vary with the reflections' latency, which is the delay between the direct sound and the onset of the reflections. Both the effects described here become less prominent at longer reflection latencies, but the Haas effect can occur at longer latencies than the precedence effect (McFadden, 1973; Hartmann, 1997).

It has been suggested that the directional information in early reflections is suppressed when the precedence effect occurs (Zurek, 1987). However, in the lateralization of click stimuli it can be shown that reflections do influence the lateral position of the overall sound when they arrive within 2 or 3 ms of the first click (Tollin and Henning, 1998, 1999). In these experiments, the reflections' influence seems to come about through their contribution to the spectral characteristics of the overall sound. For longer reflection latencies, the directional information in the leading click dominates judgments of the sound's lateral position, although directional information in a reflection does remain accessible to a small extent in these circumstances (Stellmack, Dye, and Guzman, 1999).

Early reflections can have a substantial influence on the apparent level of the overall sound when the precedence effect occurs, as Haas (1951) had noticed with speech signals. Similar effects can be observed with simpler sounds, such as the brief noise bursts studied by Freyman, McCall, and Clifton (1998). They found that listeners could detect intensity changes in an early reflection as easily as they could detect intensity changes in a direct sound. This ability was attributed to the detection of loudness changes in the overall sound. It indicates that the early reflections had an influence on loudness that was just as great as the influence from the direct part of the sound.

Early reflections can also give rise to filtering effects, which alter the spectral envelope of sounds. The frequency characteristics of this filtering can be found with a sound that is a single impulse, by taking the Fourier transform of the direct sound along with its time-delayed reflections. The effects of these reflections on other sounds' spectral characteristics can then be readily obtained (e.g., by multiplying the magnitude values at corresponding frequencies in the spectra

a)Electronic mail: syswatkn@reading.ac.uk

of the impulse response and the sound in question). The perceptual consequences of this might be a change or ''coloration'' of the perceived tonal balance of a sound, so that its timbre is affected (Barron, 1971; Berkley, 1987). In some circumstances such coloration effects can appear to be suppressed when the precedence effect occurs, as was shown by Zurek (1979). He considered the dichotic situation that arises when a flat-spectrum noise source, which is located straight ahead of the listener, contains a single reflection that comes from one side. The reflection considered was specular, which means that all frequencies are reflected by an equal amount. Adding such a reflection brings about spectral-envelope perturbations in the signals at each ear. These ''combfilter'' patterns have a peak at a frequency that is the inverse of the reflection's latency as well as peaks at integer multiples of this frequency. The valley floors (tips of the comb's teeth) are at frequencies halfway between the peaks (on a linear frequency scale). The reflection's latency will be different at each ear because its angle of arrival adds an interaural delay to the reflection's latency at one ear. This reduces the interaural correlation of the sound's spectral envelopes in a way that depends on the reflection's latency and its angle of arrival. Zurek (1979) suggested that this might give rise to suppression of coloration if the monaural representations of spectral magnitude are summed binaurally. When such a summation is applied to combfilter patterns that arise from reflection latencies that differ by an interaural delay, it will give rise to a smoother spectral envelope than that of either monaural pattern alone. This idea was supported by Zurek's (1979) experiments where the reflection's amplitude was varied, and listeners were required to detect its presence. The reflection was much harder to detect in dichotic conditions than it was in diotic control conditions where each ear received the same combfilter pattern. This was true for reflection latencies shorter than about 5 or 10 ms when the interaural delay was 0.5 ms.

In other circumstances the coloration effects of reflections appear to persist when the precedence effect occurs. This can be used to improve the quality of sound in various ways, as reviewed by Gardner (1968, 1969). These applications include lecture and concert-hall design, where the effect is particularly useful when a ''sound re-enforcement'' system is provided. Such systems amplify the signal from a microphone close to the speaker or performer, and deliver the sound from a loudspeaker that is closer to the listeners. A suitable delay is added to the amplified signal to give the precedence effect, so that listeners get the impression that the overall sound comes from the person producing it. The overall sound is louder under these conditions, but the overall spectral envelope of the delayed sound seems also to be incorporated. This was shown in a lecture-room demonstration referred to by Gardner (1969). The demonstrator mingled with the audience holding a miniature speaker which had a narrow-band frequency response and which would normally give a tinny sound. However, this loudspeaker played the same signal as a broadband loudspeaker in a fixed position at the front of the lecture room. The apparent sound source was located at the tinny speaker when it was closer to listeners, but its sound seemed to have the rich and full qualities of the more distant broadband speaker. When the broadband speaker was switched off, the tinny quality of the miniature speaker was now much more evident.

The setup described by Gardner is like room conditions where reflections from surfaces are nonspecular, as they often are. When this is the case the sound's frequencies are reflected by different amounts, and in a pattern that will arrive at both of the listener's ears. In this way, nonspecular reflections can give rise to interaurally correlated alterations of spectral envelopes. Such alterations would therefore persist when there is the binaural summation described by Zurek (1979). This might serve to provide information about the acoustic properties of the environment (Benade, 1976; Clifton and Freyman, 1997). Conversely, there may be distorting effects that are detrimental when the sound's spectral envelope contains characteristics that are important for identification. This coloration might affect characteristics of musical instruments (Risset and Wessel, 1972) as well as characteristics of vowel and consonant sounds in speech (Haggard, 1974; Watkins and Makin, 1996).

In the binaural conditions of everyday listening situations, it can seem that coloration is less apparent than it is when listening monaurally. Some authors have therefore suggested that there is some binaural suppression of coloration, or ''decoloration,'' that occurs even when the reflection patterns give rise to interaurally correlated distortions of the spectral envelope (Blauert, 1997; Hartmann, 1997). This type of suppression might therefore happen when the precedence effect occurs (Moore, 1997). Another possibility is that decoloration goes hand-in-hand with the Haas effect, so that it happens when there is perceptual integration of early reflections with the direct sound. The present experiments were designed to test these two ideas.

Coloration effects are measured here by listeners' identifications of a vowel continuum between ''itch'' and ''etch.'' These sounds are played through ''two-part'' filters that simulate a direct sound that is followed by a reflection pattern. The direct, first-arriving sound is simulated here with a single unit sample at the beginning of the unit-sample response of a two-part filter. (A filter's unit sample response being the digital equivalent of its impulse response.) The direct sound's spectral envelope is thus not altered. The second part of the two-part filter's unit-sample response is one of two ''reflection-pattern'' filters. These patterns are designed to resemble a reflection from a room's surface, with a sharp onset and smoother decay. The frequency responses of these reflection patterns are the difference between the spectral envelopes of the vowels at each end of the continuum. Thus, there are two of these filters. They have opposing effects on the spectral envelopes of the continuum's members, making them more like one or another end-point vowel.

Listeners' identifications are used to calculate the continuum's phoneme boundary, which is conventionally defined as the continuum step or point between steps that listeners identify as ''itch'' on 50% of trials and as ''etch'' on the rest. This boundary can be calculated from the total number of itch responses to the full continuum, which is the method that is used here. Coloration effects may thus be judged by comparing phoneme boundaries for continua that

have been played through two-part filters containing the different reflection patterns. The difference between these phoneme boundaries is an indicator of the amount of coloration from the reflection patterns. When coloration from early reflections is suppressed, there will be less of a difference between the phoneme boundaries for the two types of reflection pattern.

Experiment 2 asks whether there is more suppression of coloration when the reflections' interaural delay is substantially different from that of the direct sound. These conditions are compared with conditions where the reflections and direct sound have the same interaural delay. Experiment 3 asks whether the reflection patterns can give more coloration when the temporal order of the direct sound and reflections is reversed. If the perceptual integration of early reflections is accompanied by some decoloration, then there will be more coloration when the ''reflections'' are caused to precede the direct part of the sound.

Experiments 1a and 1b check that the precedence effect happens with these stimuli. Lateralization of the continuum's mid-point is measured for the conditions of experiment 2. This is done with a paired-comparison procedure (Woodworth and Schlosbeg, 1954) where listeners decide whether the second of two successive sounds is to the right or to the left of the first. This experiment also checks the directional information in the part of the sound that emerges from the reflection-pattern filter. This part is played without the direct sound, and its lateralization is measured with the paired-comparisons method.

It has been found that the strength of the precedence effect decreases at very short reflection latencies as well as at long latencies. At short latencies there can be ''summing localization,'' whereby the reflections' direction has a strong influence on the overall sound's direction (Blauert, 1997). The reflections' latency was therefore varied in all three experiments here, to check for changes in the strength of the precedence effect and of any associated coloration-suppression effects.

I. EXPERIMENT 1

A. Test-word continuum between itch and etch

A continuum was formed between itch /ɪtʃ/ and etch /ɛtʃ/. Recordings of tokens of these end-point words and of /ʌtʃ/ were obtained from a male speaker (A.J.W.). Recordings were made in an IAC 1201 booth using a Sennheiser MKH 40 P48 microphone. These signals were amplified (Revox A77), low-pass filtered at 9 kHz with a 48-dB per octave cutoff slope (Kemo VBF8), digitized with 16-bit resolution at a sampling frequency of 20 kHz (Data Translation DT2823), and stored with the Interactive Laboratory System (ILS) program RDA (Signal Technology, 1989) running on a Victor PC386 computer. The recording of /ʌtʃ/ was divided into a 170-ms vowel, and a closure with affricate /tʃ/ lasting 340 ms. Digital waveforms of these sounds and the tokens of end-point vowels were transferred to a Sun Sparcstation computer for processing.

Signal-processing methods used to form the continuum were similar to those described in Watkins (1991) except that unless otherwise stated the filtering operations used the zero-phase methods described in Watkins and Makin (1994) to preserve the time-alignment of a filter's input and output.

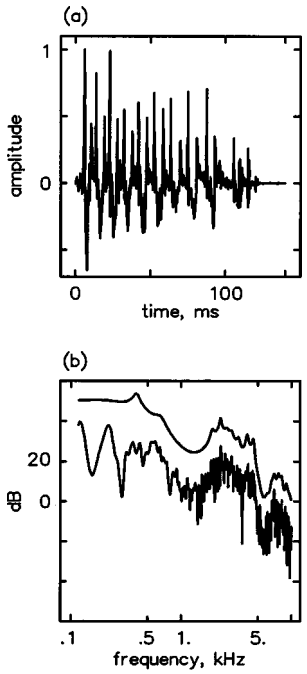

FIG. 1. Waveform (a) and spectrum (b) of the vowel from the test-word continuum's mid-point. The upper trace is an FFT of the filter function used to shape the spectral envelope of this vowel, calculated as described in the text. The lower trace is an FFT of the first 51.2 ms of the vowel, using a Hanning window. The zero of the spectrum's dB ordinate is arbitrary.

Spectral envelopes of the end-point vowels were obtained from a linear prediction (LP) lattice analysis of 16-ms segments of the recorded vowels, with segments centered at 28 ms from the vowels' nominal onset. The vowels of the continuum were derived from the recording of /ʌ/ in /ʌtʃ/. This sound was spectrally flattened using a linear prediction method (Watkins, 1991) before being passed through a reshaping filter. To generate the vowel for the itch end-point, the reshaping filter's frequency response was the spectral envelope from /ɪ/. Similarly, the spectral envelope from /ɛ/ was used to generate the vowel for the etch end-point. Intermediate steps were generated with filter responses that were found by interpolating between the end-point spectral envelopes. Interpolation values between 0.1 and 0.9 in steps of 0.1 were used along with the end-points (interpolations=0.0 and 1.0) to give an 11-step continuum. The /tʃ/ from /ʌtʃ/ was appended to each of these sounds to form the words of the continuum. Other details of this method are the same as in Watkins (1991).

Experiment 1 uses only the mid-point of this continuum, where the interpolation is 0.5. The waveform and spectrum of this sound's vowel are shown in Fig. 1.

B. Two-part filters that give a direct sound and a reflection pattern

These filters aim to bring about effects that are similar to those when a sound passes through a room. Accordingly, filtering is performed by way of a single, linear convolution with the filter's unit-sample response. The unit-sample re-

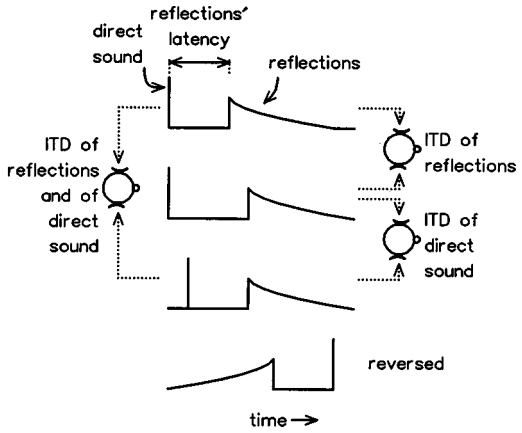

FIG. 2. Cartoons representing the temporal responses of the two-part filters that are used to simulate a direct sound followed by a pattern of early reflections. The upper three rows represent the relationships among onset times used for the direct sound and the reflections. Playing a test word through two filters separately produces binaural signals. Different combinations of the onset times in these filters give the various interaural time delays (ITDs) for the direct sound and reflections that are used in different experimental conditions. The bottom row represents a reversed two-part filter that was used in experiment 3.

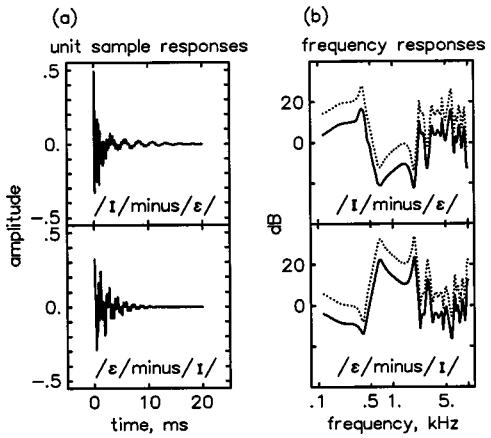

FIG. 3. The two reflection patterns. These are the unit-sample responses (a) and frequency responses (b) of filters used to simulate a reflection from a surface. The lower (solid line) traces of the frequency responses are FFTs (rectangular window) of the unit-sample responses after they were extended with samples set to zero to 51.2 ms. The upper (dotted line) traces of the frequency responses are the ''target'' spectra for these filters, as explained in the text. The zero of the dB ordinate for the frequency-response traces is arbitrary.

sponses are in two parts, as shown in Fig. 2. The first part simulates the sound that arrives directly from a source. It is a single unit sample, followed by a delay (samples set to zero). Thus, if sounds were played through only the first part of the filter, their spectral envelopes would not be altered. The second part of two-part filters is a reflection-pattern filter, designed to resemble a pattern of early reflections from a room's surface. It therefore has a fairly sharp onset and smoother decay. As nonspecular reflections are considered, the reflection pattern must extend over some brief period of time so that it alters the sound's spectral envelope. This time period was restricted to 20 ms for the reflection patterns that were used here.

There is a delay between the direct sound and the onset of the reflection pattern, which simulates travel-time differences between the direct sound's route and the reflections' route from the source to the receiver. Values used for this ''reflection latency'' were 0.5, 1, or 2 ms. These were selected with the aim of finding a region where the precedence and Haas effects would both occur, while bearing in mind the 20-ms duration of the reflection pattern. Results from experiments with specular reflections (Blauert, 1997) were used as a rough guide, while the final values were selected after some pilot listening.

The reflection patterns used are the unit sample responses of ''spectral difference filters'' (Watkins, 1991). Such filters' frequency responses are designed to change the spectral envelope of the vowel at one end of the continuum to give it the spectral envelope of the vowel at the other end of the continuum. Their frequency responses therefore aim to be the difference between the spectral envelopes of the vowels /ɪ/ and /ɛ/. Hence, there are two reflection-pattern filters, ''/ɪ/ minus /ɛ/'' and ''/ɛ/ minus /ɪ/,'' and their frequency responses are shown in Fig. 3.

In designing the reflection-pattern filters, there was a ''target'' frequency response. This response was the difference of spectral envelopes obtained from the recordings of the vowels /ɪ/ and /ɛ/ and used in a zero-phase filter, as described previously (e.g., Watkins and Makin, 1994). A signal that was a unit sample followed by 1023 samples set to zero was then played through this zero-phase filter. The resulting ''obtained'' signal's fast fourier transform (FFT) is only a crude approximation to the target frequency response. To improve the approximation an iterative technique was used. The FFT of the obtained signal (in dB) was subtracted from the target's FFT (also in dB) and this difference was used to zero-phase filter the obtained signal. The result then becomes the obtained signal for the next iteration, and so on. After 200 iterations the resulting unit-sample response was truncated to 20 ms (400 samples) and the final 10 ms was multiplied by the right-hand half of a Hanning window. The resulting filters' frequency responses were close to those of their targets, as shown in Fig. 3. Figure 3 also shows that the temporal responses of these filters have the desired characteristics, in that they have similarities to reflections from a surface.

The unit-sample responses of the reflection-pattern filters were scaled to give them both the same root-mean-squared level. This level was that of an equivalent specular reflection (a unit sample followed by 399 samples set to zero).

In order to generate interaurally delayed reflections, there were versions of the two-part filters with 0.6 ms added to the reflections' latency, as shown in Fig. 2. To generate an interaural delay of the direct sound, there were versions of the two-part filters where the onset of the direct sound was delayed by 0.6 ms, also as shown in Fig. 2.

The frequency responses when first and second parts of filters are combined are shown in Fig. 4. They differ from responses of reflection-pattern filters alone in that their contrast, i.e., the difference in dB between peaks and valleys, is generally lower. There is also a combfiltering effect associated with the reflections' latency (Zurek, 1979). Neverthe-

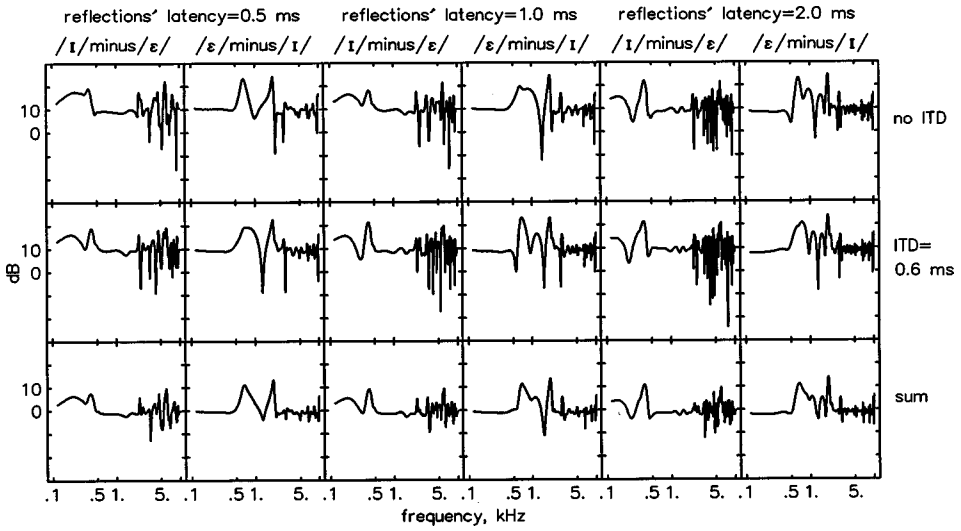

FIG. 4. Frequency responses of the two-part filters used to simulate a direct sound followed by reflections, with the two reflection patterns in different columns as indicated. The traces are FFTs (rectangular window) of unit-sample responses that were extended with samples set to zero to 51.2 ms. The top row shows the responses for the reflection latencies indicated, and for a direct sound onset at zero. The middle row shows the responses when a delay (ITD) of 0.6 ms is added to the reflections' latency. These two rows of panels show the responses of all the filters used here because filters with the same time interval between the direct sound and reflections have the same frequency response. The lower traces of the bottom panels show binaural summation of spectral power when one monaural channel has the response in the column's top panel and the other has the response in the column's middle panel. The zero of the dB ordinate is arbitrary.

less, features of the reflection-pattern filter's response, shown in Fig. 3, are still evident in the response of both parts together.

Test words were played through binaural versions of these filters in which the signals for each channel were filtered separately. Using appropriate combinations, the direct sound could be given one of three interaural delays. Similarly, the reflections' and direct sound's interaural delay could be made the same, or the reflections' interaural delay could be 0.6 ms larger or smaller than that of the direct sound. The values used for the direct sound's interaural delay were −0.575, 0.025, and 0.625 ms. (These values arise because the digital-to-analog conversion of the DT2823 alternates between channels with a period of 0.025 ms when the sampling frequency is 20 kHz on each of 2 channels, as it is here.)

Figure 4 also shows the effects that binaural summation of the monaural representation of spectral power (Zurek, 1979) has on these filters' frequency responses. The bottom panels show this summation for the response of two binaural filters that contain the reflection-pattern filters of the column. The frequency responses of the two channels are those shown in the top and middle panels of the column. The summed frequency responses still contain features of the individual reflection-pattern filters, despite the interaural delay. Thus, there is an interaurally correlated component to the spectral-envelope distortion that is generated by these filters. On the other hand, some of the combfiltering effect does seem to have been reduced by the summation as the interaural delay has decorrelated this aspect of the frequency response pattern.

Informal listening tests indicated that the Haas effect was reasonably strong with these sounds. When test words were played through both parts of the filters, there was generally the impression of an overall sound with a single identity coming from a particular spatial location. This was true for all the binaural configurations and for both reflection-pattern filters. Nevertheless, it was possible to identify the presence of some ''echo'' in these sounds, especially when they were compared with a test word that had not been played through a two-part filter.

C. Design

Experiment 1a asks whether the interaural delays in the different parts of the two-part filters are sufficient to bring about appropriate spatial effects in headphone listening. It measures lateralization of sounds filtered only by the direct-sound part of the filter, as well as lateralization of sounds filtered only by the reflection pattern. Experiment 1b measures lateralization of sounds filtered by both parts of the two-part filters to establish whether the precedence effect occurs with these stimuli. It measures the effect of interaural delays in the reflection pattern on the direction heard for the whole sound.

Lateralization was measured using a paired-comparisons procedure (Woodworth and Schlosberg, 1954). In each experimental condition there was a set of eight sounds that had different types of interaural delay. On each trial, subjects heard two sounds from this set that were played successively and separated by a silent gap of 500 ms. Subjects selected their response from two buttons labeled ''second sound is to the left of the first'' and ''second sound is to the right of the first.'' In this way, each sound in a set of eight was compared with every other sound in the set, and each comparison was presented in both orders. Therefore, each sound appeared in 14 of the 56 trials. From these data, the number of times that each sound was judged to be to the right was obtained. This was the number of ''to the left'' responses when the sound

was the first in a pair, added to the number of ''to the right'' responses when the sound was second in a pair.

Right was the ''positive side'' for half of the subjects in a condition, meaning that interaural delays leading to the right ear were designated as positive, while delays leading to the left ear were designated negative. For these subjects, the proportion of positive-side responses for a sound was the number of times it was judged to the right, divided by 14. For the other subjects left was the positive side, and their headphones were worn the other way around. Thus, the interaural delay in a sound that led to the right ear for right-positive subjects was caused to lead to the left ear for left-positive subjects. For left-positive subjects, the proportion of positive-side responses for a sound was the number of times it was judged to the left, divided by 14.

In experiment 1a, the paired-comparison set comprised test sounds filtered only by the direct-sound part of two-part filters, along with test sounds filtered only by one of the reflection patterns. Each subject judged a set of eight that contained four sounds with one of the reflection patterns, then, after a short break they judged a set of eight that contained four sounds with the other reflection pattern. The other sounds in the two sets were the direct sound only, and they were the same four in each set. Two of the four subjects judged the set with sounds that had the /ɪ/ minus /ɛ/ reflection pattern, and then judged the other set. The other two subjects judged the two paired-comparison sets in the opposite order. The direct sound and the reflection pattern had one of the three interaural delays, giving six of the sounds in the paired-comparison set. The two other sounds in the set were duplicates of the two with an interaural delay of 0.025 ms. This was done in order to achieve comparability with experiment 1b, which requires there to be eight sounds in the set. Proportions of positive-side responses to duplicates were averaged within the pairs for each subject before any subsequent analysis.

In experiment 1b, the test sound was played through both parts of two-part filters. The direct sound had one of the three interaural delays. The reflection pattern had either the same interaural delay as the direct sound, or an interaural delay that differed by 0.6 ms. This was done using appropriate combinations of delays in the filters at each ear, as illustrated in Fig. 2, giving eight types of interaural delay. For four of these types, the interaural delays of the direct sound and reflection pattern are different. For the other four types, the interaural delays of the direct sound and reflections are the same. There are two sounds where the direct sound and the reflections both have an interaural delay of 0.025 ms; one of these has 0.6 ms added to the reflections' latency while the other does not. The reflections' latency was 0.5 ms for one group of four subjects, 1 ms for a second group of four subjects, and 2 ms for a third group of four subjects. Each subject judged a set of eight sounds that had one of the reflection patterns; then, after a short break they judged a set of eight sounds that had the other reflection pattern. The order of the two sets was counterbalanced across subjects along with positive side, as in experiment 1a.

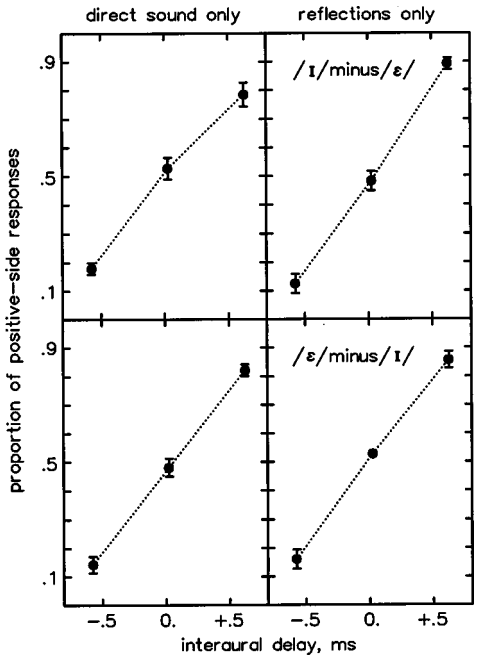

FIG. 5. Data from experiment 1a where the test word was filtered by only the direct sound or by only the reflection pattern. Plots are means of the proportion of positive-side responses across the four subjects as a function of interaural delay. Bars are one standard error on each side of the mean, and are only shown when they extend outside the data point. Data from the two paired comparison sets are shown in the rows, and the reflection pattern used in each set is indicated in the row's right-side panel.

D. Procedure

Sounds were delivered binaurally to subjects on-line under the control of the PC386 computer. Analog signals were generated from the digital waveforms with 16-bit resolution at a conversion rate of 20 kHz per channel (Data Translation DT2823) using the ILS program LDA. These signals were low-pass filtered at 9 kHz with a 48-dB per octave cutoff slope (Kemo VBF8) and presented to subjects with Sennheiser HD480 headphones at 53-dB sound-pressure level in an IAC 1201 booth.

There were 16 subjects in the four groups who were untrained and who reported no hearing problems. They were run one at time, and they took between 6 and 7 min each to judge one paired-comparison set. A different random order of trials was obtained before administering a paired-comparison set to a subject. The task was briefly explained but there were no practice trials. A pair of sounds was presented on each trial and the subject responded by pressing one of the two buttons. Visual prompts to listen or to respond were conveyed by messages on the computer's screen. The computer waited for the subject's button-press before recording the response and presenting the next trial, so that a response was necessary for progress from trial to trial. No feedback was provided, and a minimum intertrial interval of 4 s was enforced.

E. Results of experiment 1a

Results of experiment 1a are shown in Fig. 5. An analysis of variance was performed on the proportions of positive-side responses. The three factors were all within-subject, as

follows; direct sound versus reflection pattern (two levels), interaural delay (three levels), and type of reflection pattern in the paired-comparison set, i.e., /ɪ/ minus /ɛ/, or /ɛ/ minus /ɪ/ (two levels). There was a significant main effect of interaural delay [$F(2,6)=1046.5$, Huynh–Feldt epsilon$=0.82$, $p<0.0001$], indicating that clear spatial effects were heard. There were no other significant F-ratios. These data indicate that the sounds are heard to have distinct lateral positions relative to one another, and these positions correspond to the sounds' interaural delays. The spatial influences of interaural delays in the reflection patterns are substantial when there is no direct sound, and these effects are similar to those of interaural delays of the direct sound alone.

F. Results of experiment 1b

A three-way analysis of variance was performed on the proportions of positive-side responses. There was one between-subject factor, which was the reflections' latency (three levels). The two within-subject factors were the type of interaural delay (eight levels), and the type of reflection pattern in the paired-comparison set, i.e., /ɪ/ minus /ɛ/, or /ɛ/ minus /ɪ/ (two levels). This analysis revealed only one significant F-ratio, which was a main effect of type of interaural delay [$F(7,63)=163.5$, Huynh–Feldt epsilon$=0.86$, $p<0.0001$].

Mean proportions of positive-side responses are plotted in Fig. 6, pooled across the paired-comparison sets with the two different types of reflection pattern. Data are shown for each of the reflection latencies, and are plotted against interaural delay in two ways. In the left-side panels, the direct sound's interaural delay is the abscissa value. The same data are plotted in the right-side panels, but here the reflection pattern's interaural delay is the abscissa value. A precedence effect should lead to better correspondence of the data in the left-side panels, with data from sounds where the interaural delays of the direct sound and reflection pattern are different aligning with data from sounds where these interaural delays are the same. A substantial precedence effect is apparent.

To test for a precedence effect statistically, correlations were performed for the two types of pairing used in Fig. 6. The data were the proportions of positive-side responses from each subject and from each condition. Data from sounds where the interaural delays of direct sound and reflections were different were each paired with data from a corresponding sound where these delays were the same. The correspondence was either between the interaural delays of the direct-sound parts, or between the interaural delays of the reflection patterns. For the purposes of this part of the analysis, the data from the two interaural delays where the direct sound and reflections were both 0.025 ms were pooled by taking their average for each subject and for each condition. Each of these averages therefore appears in two of the pairs in both types of pairing. Pairing by interaural delay of the direct sound gives an overall correlation that is high and positive (Pearson's $r=0.893$, $n=96$, $p<0.001$), whereas pairing by interaural delay of reflections gives a correlation that is weak (Pearson's $r=0.029$, $n=96$, $p>0.05$). The difference between these correlation coefficients is significant using Hotelling's test of the difference between two Pearson's r's that are nonindependent [$t(93)=13.63$, $p<0.0005$]. Thus, over all conditions there is a reliable and substantial precedence effect.

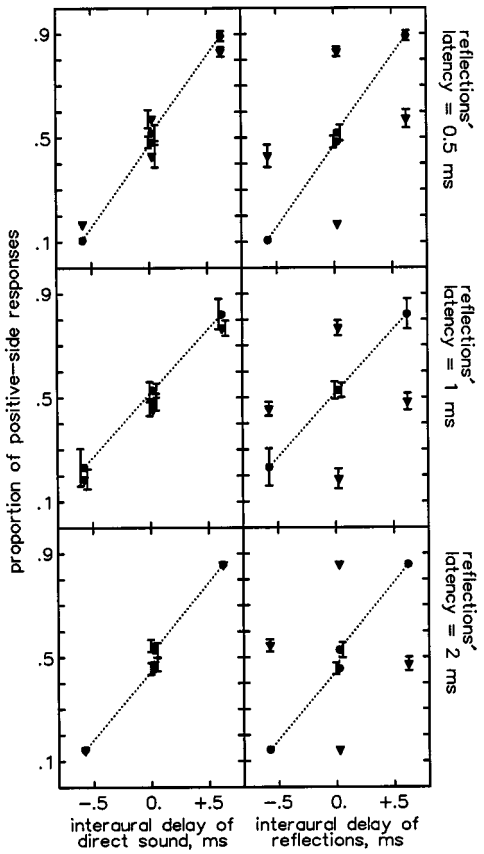

FIG. 6. Data from experiment 1b where the test word was filtered by both the direct sound and the reflection pattern using two-part filters. The filter's reflection latency varies from row to row as indicated. Plots are means of the proportion of positive-side responses across the four subjects in each reflection-latency group. The data is plotted in two ways to determine whether the direct sound's interaural delay has more influence on sounds' directions than the reflection pattern's interaural delay. Accordingly, the experiment's data are plotted against the direct sound's interaural delay in the left-side panels, and the same data are plotted against the reflections' interaural delay in the right-side panels. The circles connected by a dotted line are for conditions where the direct sound and reflections have the same interaural delay, so these data points do not change their alignment on the two abscissas. The triangles are for conditions where the interaural delays of the direct sound and the reflections differ by 0.6 ms. Bars are one standard error on each side of the mean, and are only shown when they extend outside the data point.

Correlations for the two types of pairing were also obtained for each of the three reflection latencies separately. Values of Pearson's r for pairing by interaural delay of the direct sound are all high and positive. They are 0.882, 0.859, and 0.955 for the latencies 0.5, 1.0, and 2.0 ms, respectively ($n=32$, $p<0.0001$, in each case). For these same latencies, values of Pearson's r for pairing by reflections' interaural delay are all weak, being 0.196, −0.025, and −0.099, for the latencies 0.5, 1.0, and 2.0 ms, respectively ($n=32$, $p>0.05$ for each of the three). The differences between the correlation coefficients at each latency are all significant [$t(29)=9.51$, $p<0.0005$; $t(29)=6.53$, $p<0.0005$; and $t(29)=14.7$, $p<0.0005$ for the latencies 0.5, 1.0, and 2.0 ms, respectively].

These analyses indicate that the influence of the reflections' interaural delay on the sounds' lateral positions is generally negligible. Hence, with the present stimuli there is little or no summing localization (Blauert, 1997). By contrast, there is clearly a substantial precedence effect at each of the reflection latencies.

II. EXPERIMENT 2

A. Rationale

Experiments 1a and 1b have shown that the directional information in the simulated reflection patterns has little influence on the direction heard for the overall sound, so that there is a precedence effect. Experiment 2 asks whether this effect is accompanied by a binaural suppression of coloration. If this is the case, then a difference between the interaural delays of the direct sound and the reflection pattern might bring about a reduction in the coloration from the reflection pattern.

Coloration effects are measured here by identifications of all the members of the itch to etch continuum. These sounds are played through two-part filters with the different reflection patterns to see if they give different phoneme boundaries. Binaural suppression of coloration should lead to a smaller difference between these phoneme boundaries in conditions where the interaural delays of the direct sound and the reflection pattern are different.

B. Method

A word from a continuum was presented on each trial and subjects identified the word by pressing either a button labeled itch or one labeled etch. Visual prompts to listen or to respond were conveyed by messages on the computer's screen.

Each subject heard the test words from 16 continua: eight of these continua were played through two-part filters containing one of the reflection patterns, while the other eight continua were played through two-part filters containing the other reflection pattern. For each type of reflection pattern there were four continua where the two-part filter's direct sound and its reflection pattern had the same interaural delay, along with four continua where these interaural delays differed by 0.6 ms. Different interaural delay conditions had reflections that were either leading by 0.6 ms in one or the other channel, or they were the same in each channel. Each of these sounds was presented to each subject once, giving 8 interaural delay conditions$\times$2 reflection-pattern filters$\times$11 continuum steps$=$176 trials for each of the subjects. The reflections' latency was varied among three subject groups; being 0.5, 1.0, or 2.0 ms. The four subjects in each group were untrained and reported no hearing problems.

Trials were administered in one 25-min session without feedback or practice, and different random orders of trials were used for each subject. Headphone orientation was again counterbalanced across subjects so that interaural delays designated as positive were leading to the right ear of half of the subjects in a group, and leading to the left ear of the rest. Other aspects of the method were the same as experiments 1a and 1b.

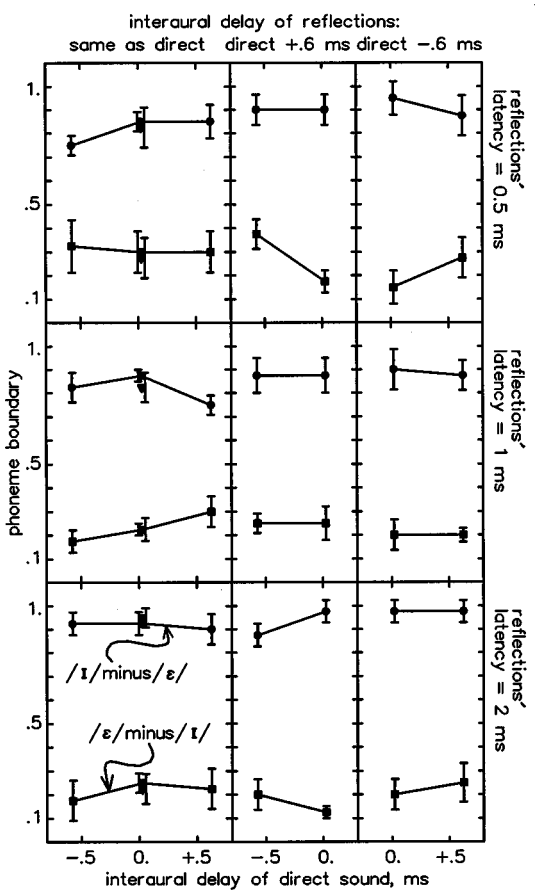

FIG. 7. Results of experiment 2 where listeners identified sounds from the entire test-word continuum, and where the test words were played through two-part filters. The data are means of phoneme boundaries across the four subjects in the three reflection-latency groups that are indicated for each row of panels. Results are for the two reflection patterns in all of the panels, using the symbols indicated in the lower-left panel. The left-side panels show results for the conditions where the direct sound and the reflections had the same interaural delay, while the middle and right-side panels show conditions where the interaural delays of the direct sound and reflections differed by 0.6 ms. The triangles in the left-side panels are for the conditions where both channels had the same two-part filter and where 0.6 ms was added to the reflections' latency. Bars are one standard error on each side of the mean.

Phoneme boundaries for each listener were calculated from the total number of itch responses to members of the continuum, using the method described in Watkins (1991). Here, this total is between 0 and 11, and it is converted to a phoneme boundary by subtracting 0.5 before dividing by 10. These boundaries therefore lie between -0.05 (etch response on all trials) and 1.05 (itch response on all trials).

C. Results

Figure 7 shows the phoneme boundaries averaged across the four subjects in each of the three groups. A three-way analysis of variance was performed on the phoneme boundaries, with one between-subject factor (reflection latency, three levels) and two within-subject factors (reflection-pattern filter, two levels, and interaural delay, eight levels). There is a main effect of reflection-pattern filter [$F(1,9) = 1643.98$, $p < 0.0001$]. This indicates that all the two-part filters influence the vowel that is played through them. More

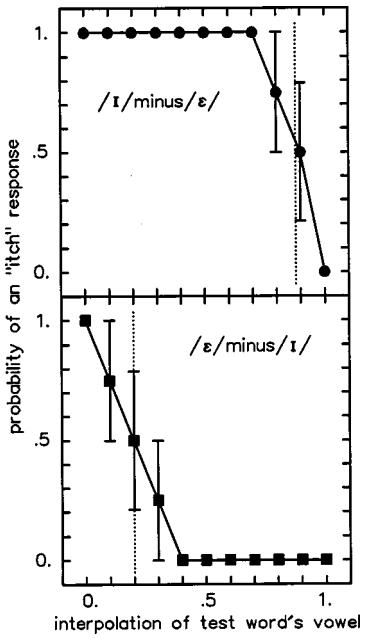

FIG. 8. Two examples of the identification functions from experiment 2, showing the mean number of itch responses for each step of the continuum. Bars are one standard error on each side of the mean. The dotted line is at the mean phoneme boundary. In this example the reflections' latency was 2 ms, the interaural delay of the direct sound was −0.575 ms, and the interaural delay of the reflections was 0.025 ms. The reflection patterns in the two-part filters are as indicated.

itch sounds are reported for one reflection-pattern filter, giving a relatively high phoneme boundary that lies towards the etch end of the continuum. The other filter gives much lower phoneme boundaries. This difference indicates that there is substantial coloration from these reflection patterns, with the vowels in the test words heard to be more like the positive vowel of the reflection-pattern filter that is applied to them. This effect tends to becomes more pronounced at the longer reflection-pattern latencies, as indicated by the interaction between reflection-latency and reflection-pattern filter [$F(2,9)=7.12$, $p<0.02$].

The interaction between interaural delay and reflection-pattern filter is also significant [$F(7,63)=6.30$, Huynh–Feldt epsilon>1, $p<0.0001$]. This seems primarily to reflect the increased effectiveness of the /ɪ/ minus /ɛ/ filter when the interaural delay of its reflection pattern differs from that of the direct-sound part of the filter. This effect tends to be more pronounced at the longer reflection-pattern latencies, as indicated by the three-way interaction of interaural delay, reflection latency, and reflection-pattern filter [$F(14,63)=2.26$, Huynh–Feldt epsilon>1, $p<0.02$]. There were no other significant F-ratios.

Identification functions were inspected to check that listeners did not hear two vowel sounds when test words were presented. This could happen if the Haas effect was not strong enough to prevent the perception of a separate sound from the reflection pattern. Identification functions in two of the conditions are shown in Fig. 8. These are typical in that there is little sign of disagreement among subjects about test-words' identities, except of course near phoneme boundaries. It can therefore be concluded that only one vowel sound was heard on each trial.

These results show that the coloration effects of early reflections are not reduced by binaural mechanisms if the coloration pattern is interaurally correlated. The spectral-envelope distortion introduced by the binaural filters gives a substantial difference between the phoneme boundaries for the different reflection patterns, and this effect is not reduced when the reflections and the direct sound have different interaural delays. If anything, the effects of the reflection patterns are more pronounced when they arrive with a different interaural delay to that of the direct sound.

The filtering effects of the reflection patterns are reduced when they are combined with the direct sound. This may be deduced from the fact that the reflection patterns are designed so that they give the spectral envelope of the vowel at one end of the continuum to the vowel at the other end. Thus, these filters would shift the phoneme boundaries beyond the ends of the continuum if the direct sound were not present. The phoneme boundaries obtained here when the direct sound is present are not shifted to such an extent, as they are found to lie within the continuum's end-point limits. However, this outcome seems largely to be a straightforward consequence of the reduction in spectral contrast that comes about when the direct sound is added, as can be seen by comparing corresponding spectra in Figs. 3 and 4.

The combfiltering effect, associated with the reflections' latency, might also reduce differences between phoneme boundaries for filters with the different reflection patterns. Such an effect would not be as pronounced when binaural summation smoothes the combfilter patterns (Zurek, 1979), and this would happen here in conditions where the interaural delays of the direct sound and the reflections are different (Fig. 4). Such a smoothing effect could account for the slight increase in differences between phoneme boundaries that is seen in these conditions.

There could also be some compensation for filtering due to monaural mechanisms. This might arise because filtering was applied to the /tʃ/ as well as to the vowel of test words. This sort of compensation, effected by later arriving sounds, is much smaller than that from preceding sounds, and it seems unlikely that it would affect the phoneme boundaries here by more than about 0.1 (Watkins and Makin, 1996).

III. EXPERIMENT 3

A. Rationale

Experiment 2 has shown that suppression of coloration from reflections or ''decoloration'' does not accompany the dominance of the direct sound's directional information when the precedence effect occurs. However, there might still be some decoloration when early reflections are perceptually integrated with the direct sound, i.e., when the Haas effect occurs. The present experiment was designed to test this idea. It asks whether there is more coloration when the reflections are caused to precede the direct sound instead of following it. For this purpose, conditions were run where the entire impulse response of the two-part filters was reversed, as shown in Fig. 2, before convolution with the test words. If the perceptual integration of early reflections is accompanied

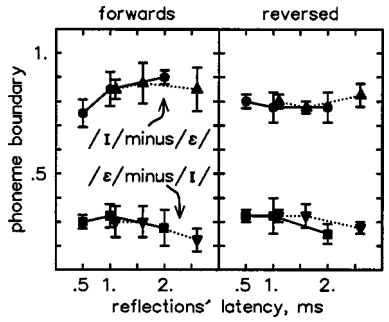

FIG. 9. Results of experiment 3 where the test words were played through the forward or the reversed two-part filters, as indicated. The data are means of phoneme boundaries across the four subjects and bars are one standard error on each side of the mean. Results are for the two reflection patterns in both the panels, using the symbols indicated in the left panel. Data points connected by dotted lines are for filters with a ''latency increment'' of 0.6 ms, as implied by their alignment along the abscissa.

by some decoloration, then there will be more coloration in reversed conditions than in conditions where the reflection pattern arrives after the direct sound.

When attempting to run reversed conditions, it was found that interaural delays did not shift sounds away from the middle of the head. This is probably because the abruptness of sounds' onsets was lost. Therefore, in this experiment, only the 0.025-ms interaural delay was used for all the sounds. It was possible to test for an effect of adding the 0.6-ms delay to the reflections' latency, but only when this ''latency increment'' was applied to both channels.

B. Method

There were 12 untrained listeners who reported no hearing problems. For one group of four listeners the reflections' latency was 0.5 or 1.1 ms, i.e., latencies with and without the 0.6-ms increment. For the second group of four listeners the latencies were 1.0 or 1.6 ms, and for the third group they were 2.0 or 2.6 ms. Each listener heard the test words from eight continua, with four played through two-part filters having the /ɪ/ minus /ɛ/ reflection pattern and four with the /ɛ/ minus /ɪ/ reflection pattern. In reversed conditions, the entire impulse response of the two-part filter was time reversed before the convolution. Each sound was presented once giving 2 filter directions (forward or reversed)$\times$2 reflection patterns$\times$2 latency increments$\times$11 continuum steps$=$88 trials for each of the listeners. Other aspects of the method were the same as for experiment 2.

C. Results

Mean phoneme boundaries are shown in Fig. 9. A four-way analysis of variance was performed on the phoneme boundaries. There is one between-subject factor (reflection latency, three levels) and three within-subject factors (reflection-pattern filter, two levels; forward versus reversed, two levels; latency increment, two levels). This analysis revealed a main effect of reflection-pattern filter, $F(1,9) = 1080.02$, $p < 0.0001$. This indicates that the vowels in the test words are heard to be more like the positive vowel of the reflection-pattern filter that is applied to them. There was also an interaction between reflection-pattern filter and forward versus reversed, $F(1,9) = 12.21$, $p < 0.007$. Inspection of Fig. 9 shows that the differences between phoneme boundaries for the different types of reflection pattern are a little smaller in the reversed condition. This indicates that there is actually less coloration in the reversed condition, the opposite of the result to be expected if coloration is reduced in the forward condition.

These results show that there is substantial coloration from the reflection patterns in both forward and reversed conditions. There is no sign of any suppression of coloration that is greater in the forward condition. Indeed, coloration is reduced a little when the reflections are caused to precede the direct sound. It is concluded that coloration from early reflections is not perceptually suppressed when the reflections follow after an ''uncolored'' direct sound.

IV. DISCUSSION

The results of experiment 1 show that the precedence effect occurs with the stimuli used here. The lateral position of the whole sound is primarily governed by the interaural delay of the first part of the two-part filter, i.e., the direct sound, which is a unit sample. The early reflections that are simulated by the second part of the filter have little influence on the sound's lateral position when their interaural delay differs from that of the direct part. Nevertheless, when these reflections are presented without the direct part, their interaural delay has a substantial influence on a sound's lateral position. This influence is about the same as that produced by interaural delays of the direct part when it is presented without early reflections. These results are consistent with other observations of the dominance of directional information from the direct sound in binaural processing (e.g., Zurek, 1987).

The results of experiment 2 show that coloration from early reflections is substantial, and is not reduced when the reflections' interaural delay differs from the direct sound's interaural delay. Thus, coloration from these reflections persists when their directional information is not influential. This indicates a dissociation of the directional and coloration effects of early reflections.

These findings are actually consistent with Zurek's (1979) ideas about how coloration effects of early reflections might sometimes be reduced in binaural listening. That model proposes a binaural summation of the monaural representations spectral magnitudes, so coloration effects are only reduced if the monaural spectra are decorrelated. When the early reflections used here have different interaural delays, features of the spectral difference filters remain prominent after summation of their monaural spectral magnitudes (Fig. 4). Thus, the filters give spectral envelope distortion that is correlated at each ear, and under these conditions there appears to be no other binaural mechanism that compensates for this distortion.

The precedence effect might be taken as an indication that binaural mechanisms are good at compensating for the spatial distortion that arises from early reflections. At the same time, binaural mechanisms appear to be limited in their ability to compensate for the spectral envelope distortion that arises from these reflections. The present experiments show

that there is no binaural compensation for distortions that are interaurally correlated. Even when there is a decorrelation of the spectra at each ear, the effect of spectral smoothing by binaural summation that Zurek (1979) points to can never completely eliminate the spectral-envelope distortion. Perfect smoothing would arise if the spectra at each ear were the inverse of each other, but interaural decorrelation of spectra that arises through the introduction of an interaural delay is very unlikely to have this effect. Furthermore, the decorrelation that interaural delays do introduce depends on the angle of the reflections' arrival, while the distortion itself is brought about by the reflections' delay pattern. As these two factors are largely independent in everyday reverberation patterns, it follows that there will commonly be combinations of angle of arrival and reflection pattern that give little or no reduction in spectral-envelope distortion after binaural summation.

The dissociation between coloration effects and spatial effects seen here would seem to arise because of the way that different parts of the signal are processed by the different perceptual mechanisms that are involved. Perception of the vowel's quality involves processing relatively long portions of the signal, and this type of processing is characterized by binaural summation across different interaural delays. Thus, early reflections contribute to this attribute of the sound. On the other hand, the lateral position of these sounds seems largely to be governed by their onsets' characteristics, as long as these are sufficiently sharp. Indeed, in the pilot work for experiment 3 it was found that manipulations that smoothed these sounds' onsets eliminated the spatial influences of interaural delay. Thus, the sort of processing involved here uses only short parts of the signal, and this processing is characterized by dominance of the onset's interaural delay over the subsequent interaural delays in early reflections (Zurek, 1987).

The experiments here indicate that early reflections, arriving with a spread of different interaural delays, will all be perceptually incorporated with the direct sound for the purpose of determining the sound's spectral envelope. This is consistent with studies using simultaneous sounds where it is found that interaural delay fails to segregate them. For example, pairs of simultaneous vowels are no better identified when played with different interaural delays than they are when they are both played with the same interaural delay (Shackleton and Meddis, 1992; Culling and Summerfield, 1995). However, in these experiments the spatial information in both sounds is available to listeners, as the different interaural delays did give the impression of different lateral positions for the two vowels.

It might be considered advantageous for binaural hearing to behave in the way described here. Early reflections contain misleading information about the sound's direction, so it makes sense for the system to suppress this information, while favoring the generally accurate directional information in the sound's direct part. On the other hand, early reflections do contain other information about the sound source. Indeed, without the reflected sound in rooms, many sound sources would be completely inaudible. Thus, it makes some sense to incorporate nonspatial information from reflected sound (Freyman, McCall, and Clifton, 1998). A disadvantage of this kind of incorporation is that it introduces spectral-envelope distortion, which arises from filtering effects of nonspecular reflections. We have seen that this distortion is not overcome by binaural mechanisms, and experiment 3 has shown that it is not overcome by mechanisms that bring about the perceptual integration of early reflections. However, there do appear to be other kinds of perceptual mechanism that can compensate for spectral-envelope distortion. These mechanisms extract information about the distortion from neighboring sounds to compensate for its effects on the spectral envelopes of subsequent and preceding sounds. Earlier arriving sounds seem to be particularly influential in this respect (Watkins, 1991; Watkins and Makin, 1996).

ACKNOWLEDGMENTS

Nigel Holt made numerous critical and constructive comments on an earlier draft of this paper. This version has benefited from the editorial comments of James Hillenbrand and from reviews including that of Tom Carrell.

Barron, M. (**1971**). ''The subjective effects of first reflections in concert halls-the need for lateral reflections,'' J. Sound Vib. **15**, 475–494.

Benade, A. H. (**1976**). *Fundamentals of Musical Acoustics* (Oxford, New York).

Berkley, D. (**1987**). ''Hearing in rooms,'' in *Directional Hearing*, edited by W. A. Yost and G. Gourevitch (Springer, New York), pp. 249–260.

Blauert, J. (**1997**). *Spatial Hearing*, Revised ed. (MIT, Cambridge, MA).

Clifton, R. K., and Freyman, R. L. (**1997**). ''The precedence effect: Beyond echo suppression,'' in *Binaural and Spatial Hearing in Real and Virtual Environments*, edited by R. H. Gilkey and T. A. Anderson (Erlbaum, Hillsdale, NJ), pp. 233–255.

Culling, J. F., and Summerfield, Q. (**1995**). ''Perceptual separation of concurrent speech sounds: Absence of across-frequency grouping by common interaural delay,'' J. Acoust. Soc. Am. **98**, 785–797.

Freyman, R. L., McCall, D. D., and Clifton, R. K. (**1998**). ''Intensity discrimination for precedence effect stimuli,'' J. Acoust. Soc. Am. **103**, 2031–2041.

Gardner, M. B. (**1968**). ''Historical background of the Haas and/or precedence effect,'' J. Acoust. Soc. Am. **43**, 1243–1248.

Gardner, M. B. (**1969**). ''Image fusion, broadening and displacement in sound localization,'' J. Acoust. Soc. Am. **46**, 339–349.

Haas, H. (**1951**). ''Über den einfluss des einfachechoes auf die hörsamkeit von sprache,'' Acustica **1**, 49–58.

Haggard, M. P. (**1974**). ''Selectivity for distortions and words in speech perception,'' Br. J. Psychol. **65**, 69–83.

Hartmann, W. M. (**1997**). ''Listening in a room and the precedence effect,'' in *Binaural and Spatial Hearing in Real and Virtual Environments*, edited by R. H. Gilkey and T. A. Anderson (Erlbaum, Hillsdale, NJ), pp. 191–210.

McFadden, D. (**1973**). ''Precedence effects and auditory cells with long characteristic delays,'' J. Acoust. Soc. Am. **56**, 1216–1220.

Moore, B. C. J. (**1997**). *An Introduction to the Psychology of Hearing*, 4th ed. (Academic, London).

Risset, J.-C., and Wessel, D. L. (**1972**). ''Exploration of timbre by analysis and synthesis,'' in *The Psychology of Music*, edited by D. Deutsch (Academic, New York), pp. 26–58.

Shackleton, T. M., and Meddis, R. (**1992**). ''The role of interaural time difference and fundamental frequency difference in the identification of concurrent vowel pairs,'' J. Acoust. Soc. Am. **91**, 3579–3581.

Signal Technology (**1989**). ILS-PC *Version 6.1* (Signal Technology, Inc., Goleta, CA).

Stellmack, M. A., Dye, R. H., and Guzman, S. J. (**1999**). ''Observer weighting of interaural delays in source and echo clicks,'' J. Acoust. Soc. Am. **105**, 377–387.

Tollin, D. J., and Henning, G. B. (**1998**). ''Some aspects of the lateralization of echoed sound in man. I. The classical interaural-delay based precedence effect,'' J. Acoust. Soc. Am. **104**, 3030–3038.

Tollin, D. J., and Henning, G. B. (**1999**). ''Some aspects of the lateralization of echoed sound in man. II. The role of stimulus spectrum,'' J. Acoust. Soc. Am. **105**, 838–849.
Wallach, H., Newman, E. B., and Rosenzweig, M. R. (**1949**). ''The precedence effect in sound localization,'' Am. J. Psychol. **62**, 315–337.
Watkins, A. J. (**1991**). ''Central, auditory mechanisms of perceptual compensation for spectral-envelope distortion,'' J. Acoust. Soc. Am. **90**, 2942–2955.
Watkins, A. J., and Makin, S. J. (**1994**). ''Perceptual compensation for speaker differences and for spectral-envelope distortion,'' J. Acoust. Soc. Am. **96**, 1263–1282.
Watkins, A. J., and Makin, S. J. (**1996**). ''Some effects of filtered contexts on the perception of vowels and fricatives,'' J. Acoust. Soc. Am. **99**, 588–594.
Woodworth, R. S., and Schlosberg, H. (**1954**). *Experimental Psychology* (Holt, New York).
Zurek, P. (**1979**). ''Measurements of echo suppression,'' J. Acoust. Soc. Am. **66**, 1750–1757.
Zurek, P. (**1987**). ''The precedence effect,'' in *Directional Hearing*, edited by W. A. Yost and G. Gourevitch (Springer, New York), pp. 85–105.

Vowel formant discrimination: Towards more ordinary listening conditions

Diane Kewley-Port[a] and Yijian Zheng[b]
Department of Speech and Hearing Sciences, Indiana University, Bloomington, Indiana 47405

(Received 11 May 1998; accepted for publication 6 July 1999)

Thresholds for formant frequency discrimination have been established using optimal listening conditions. In normal conversation, the ability to discriminate formant frequency is probably substantially degraded. The purpose of the present study was to change the listening procedures in several substantial ways from optimal towards more ordinary listening conditions, including a higher level of stimulus uncertainty, increased levels of phonetic context, and with the addition of a sentence identification task. Four vowels synthesized from a female talker were presented in isolation, or in the phonetic context of /bVd/ syllables, three-word phrases, or nine-word sentences. In the first experiment, formant resolution was estimated under medium stimulus uncertainty for three levels of phonetic context. Some undesirable training effects were obtained and led to the design of a new protocol for the second experiment to reduce this problem and to manipulate both length of phonetic context and level of difficulty in the simultaneous sentence identification task. Similar results were obtained in both experiments. The effect of phonetic context on formant discrimination is reduced as context lengthens such that no difference was found between vowels embedded in the phrase or sentence contexts. The addition of a challenging sentence identification task to the discrimination task did not degrade performance further and a stable pattern for formant discrimination in sentences emerged. This norm for the resolution of vowel formants under these more ordinary listening conditions was shown to be nearly a constant at 0.28 barks. Analysis of vowel spaces from 16 American English talkers determined that the closest vowels, on average, were 0.56 barks apart, that is, a factor of 2 larger than the norm obtained in these vowel formant discrimination tasks. [S0001-4966(99)01111-X]

PACS numbers: 43.71.Es, 43.66.Fe, 43.71.An [WS]

INTRODUCTION

Several recent studies have established the thresholds for formant frequency discrimination under optimal listening conditions (Kewley-Port and Watson, 1994; Hawks, 1994; Kewley-Port *et al.*, 1996a; Sommers and Kewley-Port, 1996). Optimal listening conditions to obtain the most accurate resolution of formant frequency use highly trained subjects listening in quiet under minimal stimulus uncertainty testing. In everyday speech perception, it is likely that formant resolution is degraded by large amounts relative to optimal listening conditions. In spite of this, our resolution for formant frequency appears to be good enough in everyday speech to support not only rapid vowel categorization, but also fine resolution that can specify distinctive dialectal variants of the same vowel category. The question that motivated this experiment was how substantial changes in experimental procedure from optimal listening conditions towards more ordinary listening conditions, as simulated in the laboratory, would affect formant discrimination.

In this study, vowel discrimination in more ordinary listening conditions measured a range of performance abilities that may occur in normal conversation for very predictable to somewhat unpredictable messages of moderate length. If the observed performance were stable and quantifiable, then a definition for a norm of the ability to discriminate formant differences under some ordinary listening conditions could be realized. This norm for ordinary formant discrimination would be useful in several ways, for example estimating the possible effects of hearing impairment on speech perception, or determining a perceptual basis for the structure of the vowel space in English.

In this research, the vowel properties investigated were spectral, namely the first and second formants ($F1$ and $F2$). While vowel research has clearly established that two other acoustic properties contribute to vowel identity in English, formant movement and vowel duration, the primary acoustic properties are spectral (Nearey, 1989; Jenkins *et al.*, 1994; Hillenbrand *et al.*, 1995; Kewley-Port and Neel, 1998). The focus of our research is on spectral cues in relation to vowel perception. However, there is a strong link between perception and production because vowels must be produced such that they are easily identified in normal conversation. The literature contains numerous reports of measurements of English vowels (Peterson and Barney, 1952; Hillenbrand *et al.*, 1995; Bradlow, 1995). The structure of the vowel space is usually described on the basis of primarily $F1$ and $F2$. In English, the $F1\times F2$ vowel space is very crowded, with many vowels clustered close together. A comparison of the ordinary ability to discriminate vowel formants to the distribution of vowels in English should reveal how the structure of vowel spaces relates to auditory processing constraints. While others have approached this question from very dif-

[a]Electronic mail: kewley@indiana.edu
[b]Electronic mail: yizheng@indiana.edu

ferent points of view [e.g., perceptual magnet theory by Kuhl and Iverson (1995) or vowel dispersion by Lindblom (1986)], the present approach offers new data concerning this question.

An overall goal of our series of studies on formant discrimination is first to establish optimal performance, and then to understand how processing abilities are degraded by systematically manipulating the stimuli and experimental task variables. The measurement of formant discrimination is reported as ΔF, the difference between the formant frequency of a standard vowel and a statistic representing the formant frequency that is just discriminable from the standard. Some terms used to relate ΔF to human performance include threshold, jnd (just noticeable difference), and DL (difference limen). For convenience, we will consistently use *thresholds* to refer to discrimination under optimal listening conditions, and *difference limens or DLs* for performance measured under other listening conditions.

Discrimination among sounds under more ordinary listening conditions occurs when listeners interpret sentences for meaning. Compared to optimal listening conditions, this may be simulated when three experimental variables are changed, specifically to higher levels of stimulus uncertainty, to longer amounts of phonetic context, and to increased levels of linguistic complexity. The present investigation manipulated two of these variables, phonetic context and linguistic complexity, while stimulus uncertainty was set to medium. The choice of experimental conditions and their rationale follows.

The basic vowel discrimination task was the same as for previous experiments (Kewley-Port and Watson, 1994). The test acoustic variable was either $F1$ or $F2$ of a vowel and was presented in a modified two-alternative forced-choice task. Discrimination ΔFs were obtained from well-trained listeners in quiet. The experimental variable of phonetic context was changed from isolated vowels, to vowels embedded in a syllable (/bVd/), in a three-word phrase, or in a nine-vowel sentence. Unfortunately, the specific choice of experimental conditions for the variable linguistic complexity received little guidance from previous research. The goal was to introduce an experimental factor of ''linguistic meaning'' into a series of studies on formant discrimination. In normal conversation, information about the incoming acoustic waveform must first be extracted by low-level auditory processes, and then at higher, cognitive levels categorized linguistically and associated with a meaningful interpretation. In terms of the psychophysical structure of this experiment, discrimination is ascribed to peripheral auditory processing, and the remainder of the processing is allocated to more cognitive levels to obtain linguistic meaning. In this experiment, we chose to manipulate linguistic meaning through the identification of words distributed across a nine-word sentence. The level of difficulty of the variable linguistic identification was varied by permitting between two and 16 possible identification responses. In the easiest condition, only the final word in the sentence had two possible alternatives, while in the hardest condition word alternatives in three sentence positions permitted 16 possible unique sentences. The usual way to remember linguistic information presented in a sentence is to store and rehearse it in short-term memory as a single meaningful sentence, as opposed to a list of nine dissociated words. Thus, in this experiment ordinary listening conditions are simulated in the laboratory by adding the factor of linguistic meaning, i.e., the identification of words in sentences, to the discrimination task.

Although level of stimulus uncertainty varies across sentences in normal communication, it was decided to fix the level as ''medium'' in this experiment, and investigate it directly in a companion study. From previous research on sound discrimination, we know that changes in stimulus uncertainty from minimal, to medium, to high, significantly degrade performance for complex tonal patterns (Watson, 1987) and analogous vowel sequences (Kewley-Port, 1990). The perception of words in sentences is partially predictable such that the level of stimulus uncertainty generally ranges from medium (more than four possibilities) to high (more than 30 possibilities). Thus, for the purposes of this study the level of medium uncertainty with eight possible discrimination stimuli was selected under the assumption that it is representative of the predictability of words occurring in short sentences.

Another issue in the experimental design was subject training because a pilot study of consonant–vowel–consonant syllables (CVCs) under medium uncertainty (Kewley-Port, 1992) yielded variable results in which training effects were observed in the data even after fairly lengthy exposure. Therefore, a subgoal of this experiment was to examine directly the training effects on formant discrimination in phonetic context. Thus, two experiments were planned. The first experiment was an initial study to examine the effects of phonetic context on formant thresholds. Experiment 1 also included a training component and a pilot study of the word identification task. Based on the results of experiment 1, the design of the second experiment refined the phonetic context study and included procedures to manipulate the effects of linguistic meaning. Results of these two experiments appear to establish a norm for performance for vowel discrimination under more ordinary listening conditions.

I. EXPERIMENT 1

The primary purpose of the first experiment was to establish a protocol to estimate the effects of phonetic context on the discrimination of formant frequency under medium stimulus uncertainty. Phonetic context was selected to be either the syllable /bVd/, or the three-word phrase ''say /bVd/ again,'' or the nine-word sentence ''Tell Sam to say /bVd/ again on the tape'' (the standard sentence). The four selected vowels yielded the words ''bid,'' ''bed,'' ''bad,'' or ''bud.'' In a previous pilot, experiments for vowels in syllable context under medium uncertainty (Kewley-Port, 1992) indicated that it was difficult to obtain uniform performance from listeners when both consonants and vowel varied in the CVC stimuli. In that pilot, we attempted to run four subjects under medium levels of stimulus uncertainty (four or eight formants tested per block) until they approached asymptotic performance. Even with extensive training (more than 15 h), the data had rather large variability across vowel conditions and subjects. For some CVCs in the eight-formant task, the

TABLE I. Frequencies in Hz for formants $F1$, $F2$, and $F3$ used in synthesizing the four vowels. The last two columns give the range of formant values for the 1st and 14th test stimuli in the test sets for $F1$ and $F2$.

	Standard vowels (Hz)			Ranges in test set (Hz)	
Vowel	$F1$	$F2$	$F3$	$F1$	$F2$
/ɪ/	450	2300	3000	455–522	2315–2513
/ɛ/	600	2200	3000	605–671	2210–2341
/ʌ/	700	1400	2600	705–771	1410–1542
/æ/	1000	1950	3000	1007–1107	1960–2091

TABLE II. Onset and offset frequencies in Hz and durations in milliseconds for the formant transitions of the /bVd/ stimuli.

Formant	Onset /b/ (Hz)	Formant transition time (ms)	Offset /d/ (Hz)	Formant transition time (ms)
$F1$	475	15	300	15
$F2$	1900	55	2050	55
$F3$	2750	35	3600	35

DLs obtained were identical to thresholds under minimal uncertainty. But for other CVCs, performance across subjects was less stable and varied by factors of 3 to 5.

To address the problem of stable performance, the protocol for experiment 1 included two features. First, subjects participated in a brief screening task in order to select a group with more uniform performance. By excluding the best and worst performers in the screening task, presumably variability would be reduced in the final medium uncertainty data. In addition, subjects were well trained on the minimal uncertainty task before testing began. During testing, ΔFs were obtained primarily based on the number of blocks per condition, rather than on a performance-based stopping rule. To maximize performance, phonetic context tasks were ordered in terms of difficulty, from syllable to phrase to sentence. Since this sequential presentation of tasks could introduce a ''training'' effect due to accumulated experience, the effects of training were measured by retesting two of the phonetic context tasks.

The second purpose of experiment 1 was to pilot an identification task in which linguistic meaning was added to the discrimination task. The nine-word sentence was modified such that the final word was ''tape'' or ''tip.'' Stimulus delivery and discrimination responses for $F1$ or $F2$ in the /bVd/ syllable were under computer control. The identification response was collected by the subject writing down the final word, tape or tip, on paper before typing the discrimination judgment on each trial. This written response added cognitive load to the overall task that presumably made it somewhat more linguistic. The experimenters found this sentence task with discrimination and written word identification to be extremely challenging.

A. Method

1. Stimuli

The vowels investigated were the English vowels /ɪ, ɛ, æ, ʌ/, modeled after a female talker, that have been used in several other discrimination studies in this series (Kewley-Port and Watson, 1994). These four vowels were selected because the range from the lowest $F1$ to the highest $F2$ covers reasonably the vowel space for this talker. The Klatt (1980) synthesizer was configured in the cascade/parallel configuration and used a 10 000-Hz sample rate. The vowels were synthesized in the syllable /bVd/ context. The formant values for the steady-state portion of the syllables are shown in Table I. The bandwidths for BW1, BW2, and BW3 were 70, 90, and 170 Hz, respectively. The values for $F4$ and BW4 were 4000 and 200 Hz and were kept constant. Length for the syllables alone (including formant transitions) was 250 ms and for the syllables in phrases and sentences was 220 ms. The transition parameters for the /bVd/ syllables are shown in Table II.

Synthesis parameters for the rest of the sentence were modeled after a female talker saying ''Tell Sam to say /bVd/ again on the tape'' using the CSRE analysis and synthesis package. A spectrogram of this sentence including the word /bæd/ is shown in Fig. 1. The sentence was synthesized in three parts, ''Tell Sam to,'' ''say /bVd/ again,'' and ''on the tape,'' where the parameters for /bVd/ were as described above. For the three-word phrase, only the middle part of the sentence was played. For the nine-word sentence, waveforms for all three parts were loaded into an output buffer and then

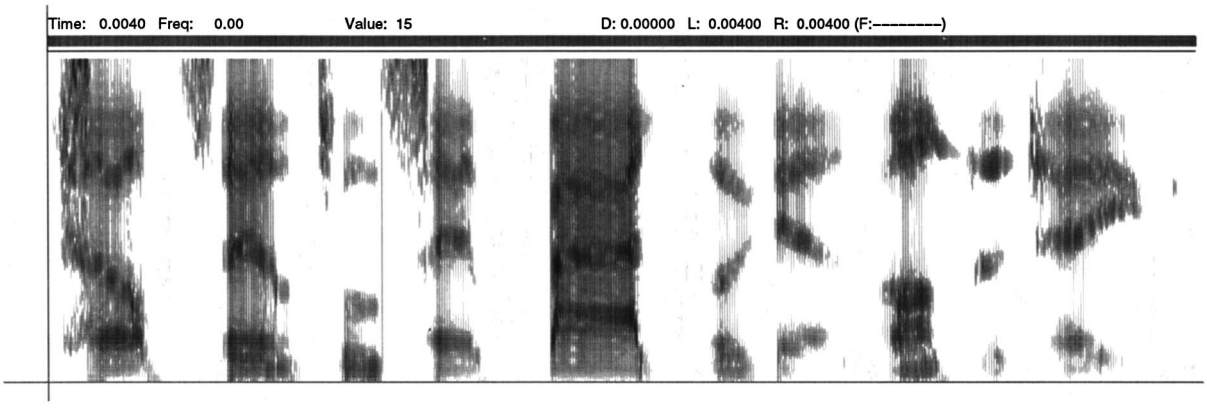

FIG. 1. Spectrogram of the synthesized sentence, ''Tell Sam to say bad again on the tape.''

played. A variant for the third part of the sentence, ''on the tip,'' was also synthesized and used in the pilot identification task. The fundamental frequency ($F0$) contour was the same for the target syllable in all phonetic contexts, falling linearly from 220 to 180 Hz. The amplitude contour also fell over the syllable. The $F0$ and amplitude contours over the rest of the sentence were modeled broadly after the female talker, who had a slight Texas accent. The syllables synthesized with these parameters are referred to as the *standard* vowels.

The test syllables to be discriminated from the standard syllables were synthesized in sets of 14, similarly to those in Kewley-Port and Watson (1994) and Kewley-Port (1995). The test formant was always incremented from the standard for 14 steps using log ratios. The range of the test formants is shown in Table I. For the /bVd/ syllables, changes in formant frequency were made first for the center, steady-state portion of the syllable, and then the formant transitions were linearly interpolated from the onset and offset frequencies shown in Table II to the center frequencies.

2. Subjects

Subjects were college students who were paid for their participation. The four subjects had pure-tone thresholds of 15 dB HL or better at octave intervals from 250 through 8000 Hz.

3. Procedures

Stimuli were presented over calibrated TDH-39 earphones to the right ears of subjects seated in a sound-treated, IAC booth. Each subject was run independently on one of four 486 computers. Sound presentation was controlled by TDT equipment including an array processor, a 16-bit D/A converter, a programmable filter and a headphone buffer. The programmable filter was configured as a low-pass filter with a cutoff frequency of 4300 Hz, and an attenuation level set by the calibration procedure. A synthetic /e/ vowel (3 s in length) was used as the calibration vowel. Output gain was set such that the sound-pressure level measured in the NBS-9A 6-c^3 coupler with a Larson-Davis sound-level meter was 77 dB SPL.

Test procedures followed those of Kewley-Port and Watson (1994). An adaptive-tracking task was used to measure the DLs at 71% correct following Levitt (1971). In each trial, stimuli were presented in a modified, two-alternative, forced-choice (2AFC) task with feedback. The standard was presented in the first interval, and subjects indicated on a keyboard which of the next two intervals contained the ''different'' (test) stimulus. In the sentence task with identification, the third part of the sentence was selected randomly as ''on the tape'' or ''on the tip,'' and was played once only during the standard. The phrase ''on the tape'' was played for each test interval. Testing was conducted in 80-trial blocks. Under medium stimulus uncertainty, each of the eight standard formants was played ten times per block in a random sequence.

An experimental protocol designed for 1.5-h testing sessions is shown in Table III. The 1-h screening task included a pure-tone audiogram and 1/2-h of testing the vowel /e/, $F1$ and $F2$, in the tracking task. The vowel /e/ was not used in the experimental tasks, but was synthesized using the parameters from Kewley-Port and Watson (1994). To measure training effects, two tasks were repeated in the protocol, the sentence and the syllable tasks. To provide a measure of performance under the most difficult conditions, the sentence task was presented for four blocks before any training and is called the untrained sentence task. Listeners next participated in the training phase of this study. An easy discrimination condition, the $F1$ for /ɪ/ in /bId/ was selected and presented under minimal stimulus uncertainty for three sessions with the expectation that performance should approach the asymptotic performance of previous subject groups. In the testing phase of the experiment, levels of phonetic context were ordered from easiest (syllable) to hardest (sentence). Following testing, a pilot of the sentence with the word identification task was conducted. Finally, the syllable task was retested to assess training effects.

TABLE III. Protocol for the tasks in experiment 1.

	Task	Data	Level of uncertainty	Duration (h)
(1)	Screening	Audiogram /e/ $F1$ & $F2$	Medium	0.5
(2)	Untrained sentence	8 formant DLs	Medium	1.5
(3)	Training	Threshold for /ɪ/ $F1$ in /bId/	Minimum	2.5
(4)	Syllable	8 formant DLs	Medium	3.5
(5)	Phrase-1	8 formant DLs	Medium	3.0
(6)	Sentence-1	8 formant DLs	Medium	3.0
(7)	Sentence+ID	8 formant DLs +2 AFC	Medium	1.5
(8)	Syllable-retest	8 formant DLs	Medium	1.5

For each block, a value of ΔF was calculated as the difference in the formant frequency between the standard and the test vowels using the average of the formant frequencies of the reversals. A formant-frequency ΔF for each subject was estimated from the last four blocks. Group means were calculated as the mean of the ΔF estimates across subjects. In this report, group means obtained under minimal stimulus uncertainty are called thresholds, whereas those collected under medium stimulus uncertainty are called DLs (difference limens).

B. Results

1. Screening

The screening procedure was included to select four subjects from a larger group of subjects. Unfortunately, due to timing of the experiment within the semester, only four subjects volunteered for the study. They participated in a discrimination task for $F1$ and $F2$ for /e/ for four blocks. The tracks for ΔF over the four blocks were examined. On the fourth block, three subjects already performed near the thresholds obtained in Kewley-Port and Watson (1994). The fourth subject improved enormously over the four blocks and ΔF for $F1$ was nearing threshold. Thus, the experiment proceeded with these four subjects.

TABLE IV. DLs are shown for the syllable and sentence tasks in experiment 1 obtained on different days during the test protocol. The time for the number of experimental hours before test data was obtained is relative to 0 h, the beginning of the experimental tasks.

	Syllable		Sentence	
Experimental hours before test data (h)	7.0	12.5	0.5	15.5
Average (Hz)	63.6	45.4	91.9	55.8
Standard deviation (Hz)	31.3	19.4	36.0	26.9

2. Reliability

A comparison of performance by subjects in experiment 1 with thresholds from previous reports was made for the first formant of /ɪ/ for the minimal uncertainty training task. Subjects participated for 12–14 blocks, or about 1000 trials. Threshold of ΔF estimated from the last four blocks in the present group was 12.9 Hz, with a standard deviation of 2.1, while thresholds for a group from the original formant threshold study (Kewley-Port and Watson, 1994), and a group in the consonantal context study (Kewley-Port, 1995) were 12.9 and 12.8 Hz, with standard deviations of 1.7 and 1.9, respectively. The average performance of the present subjects under minimal stimulus uncertainty appears comparable to those in previous experiments.

3. Training effects

Results from the syllable task were used to determine if there was improvement due to the accumulated experience over the medium uncertainty discrimination tasks. The hope was that the protocol had provided sufficient training time (7 h) before syllable testing such that the retest of the syllable task (after 15.5 h) would not be significantly different from the initial observation. Unfortunately, as shown in Table IV, the average retest DL was significantly lower than that of the first test [$t(7)=4.0$, $p<0.003$] using a paired t-test for each formant. This result indicated that comparisons between the different phonetic context conditions were somewhat contaminated with test experience. The retest DL was selected as the most representative of discrimination performance in syllables (called syllable-1) for further analysis. However, a new protocol was designed for experiment 2 to neutralize this training effect.

The results for the sentence task, untrained and trained, are also presented in Table IV. Because it was obvious that ΔF was improving over the first four blocks of the untrained sentence task for three of the four subjects, the estimated DL for the untrained sentence task was averaged over only the first two blocks. This average DL, as expected, improved significantly and was 65% lower after training [$t(7)=5.6$, $p<0.0001$].

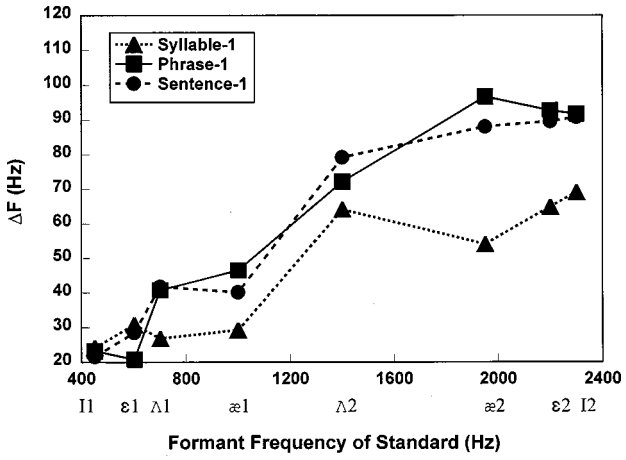

FIG. 2. Average DLs for eight formants in different phonetic contexts in experiment 1.

4. Phonetic context

The DLs obtained for each formant tested at different levels of phonetic context are shown in Table V and Fig. 2. Lines are used to connect the DLs on all figures to help visualize the differences between the experimental factors. Differences in discrimination performance were evaluated by a two-way analysis of variance (ANOVA), within subjects, for the factors of phonetic context and formant frequency. The main effects and interactions were all significant [context: $F(2,30)=27.0$, $p<0.0001$; formant: $F(7,105)=63.1$, $p<0.0001$; interaction: $F(14,210)=5.5$, $p<0.0001$]. As expected from previous research, DLs increased as formant frequency increased. The effect of phonetic context on discrimination was not simple. Rather, there was an interaction such that DLs for $F2$ in the syllable task were clearly lower than those for the phrase and sentence tasks, and little difference was observed for $F1$ DLs for phonetic context. To explore this further, a three-way ANOVA for the factors of formant ($F1$ or $F2$), context and vowel (/ɪ, ε, æ, ʌ/) was calculated. No difference was obtained for vowel [$F(3,45)=0.9$, $p=0.43$], but both formant [$F(1,15)=253.3$, $p<0.0001$] and context [$F(2,30)=27.0$, $p<0.0001$] were highly significantly different. Specific comparisons between phonetic context by each formant were examined by averaging over vowels using *post hoc* analysis (the Tukey honest significant difference test (HSD)

TABLE V. DLs in Hz for formant discrimination tasks in experiment 1.

	ɪ-$F1$	ε-$F1$	ʌ-$F1$	æ-$F1$	ʌ-$F2$	æ-$F2$	ε-$F2$	ɪ-$F2$
Format frequency	450	600	700	1000	1400	1950	2200	2300
Syllable-1	24.2	30.9	26.9	29.3	64.2	54.1	64.9	69.1
Phrase-1	23.2	20.8	40.8	46.5	72.2	96.7	92.7	91.7
Sentence-1	21.6	28.5	41.8	40.2	79.2	88.0	89.6	90.8
Untrained sentence	55.3	51.2	57.4	83.1	134.4	121.2	131.4	100.5
Sentence-1+2AFC	24.0	34.6	45.2	42.2	56.4	91.4	99.9	88.6

was used for the *post hoc* tests). All $F1$ comparisons were not significantly different ($p>0.05$). For $F2$, syllable DLs were better than those for the phrase or sentence tasks, and those DLs were almost equivalent.

In summary, under medium stimulus uncertainty, the ability to discriminate formants degrades as phonetic context is increased from syllables to sentences. However, it appears that discrimination of $F1$ is not affected by the length of phonetic context. For $F2$ with higher frequencies, discrimination is significantly better in syllables than in phrases or sentences. Further detailed analysis of the data from experiment 1 is not warranted since the ordered presentation of phonetic context tasks introduced training effects and awaits the improved protocol used in experiment 2.

5. Pilot sentence identification

In the pilot experiment, to estimate discrimination performance under more ordinary listening conditions, subjects identified the last word (tip or tape) in the sentence and wrote it down. DLs estimated from the last four blocks, called ''sentence-1+2AFC'' may be compared to the ''sentence-1'' DLs in Table V. The surprising outcome revealed essentially no reduced ability to discriminate formants when the identification task was added. A two-way ANOVA for the factors of task and formant showed no significant effects for task [$F(1,7)=1.45$, $p>0.25$], while there was an effect of formant frequency as expected [$F(7,49)=32.8$, $p<0.0001$]. The interaction observed was not interesting [$F(7,49)=2.6$, $p<0.02$] and appeared to reflect crossover of the functions. Because sentence DLs with and without identification were nearly equivalent, a comparison was made with DLs from the untrained sentence task to determine how close the sentence DLs were to this upper limit of poor performance. The untrained sentence average DL, 91.9 Hz, was clearly much poorer than the average DL of 60.3 Hz for sentence-1 with or without identification. Thus, there was clearly room to obtain an effect of linguistic identification task on formant discrimination. Therefore, in experiment 2, the sentence identification task was made substantially more challenging until a total of 16 unique sentences could be constructed using word choices distributed over the initial, middle, and end of the sentence.

C. Discussion of experiment 1

Results of the present study of the effects of phonetic context and subject training can be compared to those of Mermelstein (1978) and Kewley-Port (1995). Mermelstein estimated DLs for formants for the vowels /ɪ/ and /æ/ in isolation and in CVCs with consonants /b/ and /g/. In Mermelstein's study, DLs were obtained under medium uncertainty with eight formants judged within each block for subjects with little training. In Kewley-Port's (1995) study, thresholds were obtained from well-trained subjects under minimal stimulus uncertainty in CVC context for only the vowel /ɪ/, but in six consonantal contexts. Comparing DLs between the two studies, Kewley-Port's were a factor of 4–5 smaller than Mermelstein's (see her Fig. 5). In the present study, the syllable task had the same level of medium uncertainty (eight stimuli) as Mermelstein's, but subjects were well trained. To compare these two studies that differed primarily in subject training, the ratios of the average DLs in the two studies to the average DL (for the /ɪ/ and /æ/) in the syllable task in the present study were calculated and are shown in Fig. 3. The ratio for DLs in Mermelstein's results is more than a factor of 2 times poorer than ours. Further comparison was made to our untrained sentence task where subjects' time completing the task was more similar to Mermelstein's. As shown in Fig. 3, the ratio 1.64 of the untrained sentence to our syllable task is smaller than the ratio for Mermelstein's data. From the above comparisons, two claims about training in relation to our simulated ordinary listening conditions are supported. Adult listeners are already highly trained to discriminate within vowel differences in normal conversation. Thus, we believe that laboratory procedures require considerable training before stable performance can be achieved primarily because of the use of synthetic stimuli. The second claim is that the untrained sentence DLs provide a benchmark of poor discrimination performance in these phonetic context tasks. Although there is a very large space of ordinary listening conditions, it is useful to establish expectations of formant discrimination performance from optimal thresholds to some upper limit of poor performance for normal-hearing subjects listening to novel stimuli in novel sentences. The present analysis showed that similar poor performance was obtained for untrained subjects across two different experiments with different phonetic contexts. Thus, the claim that our untrained sentence task is a benchmark for poor formant discrimination in sentences appears reasonable.

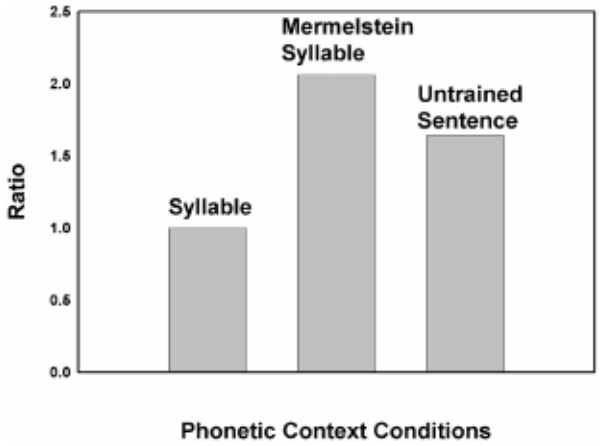

FIG. 3. Ratios of the average ΔF for formant discrimination data from three experiments are displayed. Data from experiment 1, labeled syllable, are for the syllables /bɪt/ and /bæt/ and the average serves as the reference with a ratio of 1. Data from Mermelstein (1978) are for the syllables /bɪb/, /bæb/, /gɪg/, and /gæg/. Data from the untrained sentence task in experiment 1 are for syllables /bɪt/ and /bæt/ in sentence context.

II. EXPERIMENT 2

Based on the results from experiment 1, a protocol for the second experiment was designed to meet the overall experimental objective of estimating formant discrimination under more ordinary listening conditions. In this protocol, the effects of phonetic context and linguistic meaning of a sentence were measured separately for one listener group.

TABLE VI. Word choices in the sentence task that specify the possible sentences, either with two, eight, or 16 alternatives. The discrimination task was always for a vowel formant in the /bVd/ word.

[sentence]	Tell Sam to say	bVd	again on the tape.
[2AFC]			tape, tip
[8AFC]		bid, bed, bad, bud	tape, tip
[16AFC]	Sam, Sim	bid, bed, bad, bud	tape, tip

These results can then be compared with other formant discrimination outcomes representing a range from optimal to poor performance in order to establish formant discrimination abilities under more ordinary listening conditions.

Several problems identified in experiment 1 were addressed in the experimental design. The first was to rigorously screen a group of subjects in order to obtain a set of subjects who would perform more uniformly. The second was to neutralize the training effects by including more training under medium uncertainty before test data were collected and by randomizing the levels of difficulty across subjects and trial blocks. To improve comparisons for phonetic context, the design also added a lower level of difficulty, vowels in isolation.

Given that adding a sentence identification task to the formant discrimination task in experiment 1 did not degrade discrimination performance, an effort was made to design an extremely challenging identification task for experiment 2. The experiment 1 task involved only a choice between two words in final sentence position. Examining the content of the nine-word sentence (Table VI), two other positions offered word choices. The first was the test word itself, the four choices of vowel in /bVd/ in sentence medial position. Also, the name ''Sam'' in the initial part of the sentence could be changed. Because this was a vowel discrimination task, it might be more challenging to have all substitutions involve only vowels. Thus, the name ''Sim'' was selected to alternate with ''Sam.''

Three levels of difficulty of the sentence identification task were selected by varying the number of unique sentences that could be constructed with the word choices shown in Table VI. In experiment 1, two choices in final word position is a two-alternative, forced-choice (2AFC) task for identification of the target sentences. Combining that task with four medial choices for /bVd/ allows for eight possible sentences (8AFC). Finally, adding a choice of the name yields 16 sentences (16AFC). The 16AFC condition seemed to meet our goal of providing a linguistically meaningful task in addition to the formant discrimination task. The target sentence was presented only on the first of three presentations of the sentence, in the ''standard,'' ''test 1,'' ''test 2'' trial structure. Thus, a listener first identified the words and then presumably rehearsed the sentence as a whole (not as a list of three word choices) during the time that the discrimination judgment was made during the ''test 1'' and ''test 2'' sentence presentations in each trial. The written response for the sentence consisted of circling word choices on a page, prior to entering the discrimination response via computer keyboard. The experimenters, neither novices to the task nor well trained, found the 16AFC sentence task extremely difficult.

TABLE VII. Protocol for the tasks in experiment 2.

	Task	Data	Level of uncertainty	Duration (h)
(1)	Screening 1	Audiogram /ɪ/ $F1$	Minimum	0.75
	Screening 2 (vowel)	8 formant DLs	Medium	1.0
(2)	Vowel training	8 formant DLs	Medium until stable	3.0
(3)	Context training	8 formant DLs Vowel, syllable, phrase, sentence	Medium, tasks ordered	2.0
(4)	Context testing	8 formant DLs Vowel, syllable-2, phrase-2, sentence-2	Medium, tasks randomized	4.0
(5)	Sentence+ID training	8 formant DLs+ 2, 8, 16 AFC	Medium, tasks ordered	3.0
(6)	Sentence+ID testing	8 formant DLs+ 2, 8, 16 AFC and sentence-3	Medium, tasks randomized	11.0

A. Method

1. Stimuli

The stimuli were nearly the same as in experiment 1 except for modifications to the sentence and the addition of isolated vowels. A second variant for the first part of the sentence was synthesized as ''Tell Sim to'' (see Table VI) following synthesis procedures described in experiment 1. The isolated vowels were synthesized with the vowel parameters shown in Table I for the /bVd/ syllables, except for a minor error that caused /e/ vowel formants to be substituted for /ɛ/ formants. Because the formant values were similar ($F1=550$ instead of 600 Hz and $F2=2500$ instead of 2200 Hz), and the thresholds obtained in Kewley-Port and Watson (1994) were quite similar to those obtained here (17.5 vs 14.0 Hz and 38.9 vs 36.8 Hz), DLs for the /e/ formants were used in the comparisons with the /ɛ/ formants implemented in all other experimental conditions. The length of the isolated vowels was 160 ms. $F0$ fell linearly from 220 to 180 Hz over the 160 ms similar to the /bVd/ syllables.

2. Subjects

Nine additional college students were recruited and paid for their participation. All subjects had pure-tone thresholds of 15 dB HL or better at octave intervals from 250 through 8000 Hz.

3. Procedures

The procedures for presenting the stimuli under computer control were essentially the same as in experiment 1. The DLs in ΔF were calculated the same way. The protocol, however, was different and is presented in Table VII. The screening was expanded to include a few trial blocks under both minimal and medium stimulus uncertainty. Subjects selected for the experiment ran in 1-h sessions daily. Training used the medium uncertainty task to provide extensive experience (5 h) before test data were obtained.

The testing phase to collect DLs across different conditions was redesigned to reduce training effects. After sub-

jects were familiar with each of the four tasks during training, tasks were randomized during testing. Specifically, each subject received a different random order of the four tasks on each testing day. This was true for first the four phonetic context tasks, and then for the four sentence plus identification tasks. The sentence task with discrimination only was repeated twice; ''sentence-2'' was part of the phonetic context testing; ''sentence-3'' was presented with the sentence plus identification task.

B. Results

1. Screening

Nine subjects volunteered to participate in the screening task. The adaptive tracks were compared visually across subjects for both the minimal uncertainty task with /ɪ/ $F1$ and the vowel-only medium uncertainty task. One subject stood out as a potential ''star,'' and three others performed more poorly than the rest of the group. Out of the five remaining subjects, only three volunteered to participate in the 5-week-long task. While participation of four subjects was preferable to three, in order to meet the criteria of the experimental protocol, the study proceeded with just the three subjects who met screening criteria for uniform performance.

2. Reliability

Given that subjects in experiment 2 participated in medium stimulus uncertainty tasks, reliability for this group of listeners could not be compared with thresholds from previous reports. However, reliability of DLs between experiment 1 and experiment 2 could be directly compared for the syllable, phrase, and sentence conditions that overlapped. Averages of DLs over all three conditions for each subject revealed somewhat higher DLs in experiment 2 than experiment 1. The primary difference across subjects was for one subject in experiment 1, S4, whose average DLs were about one-half of most other subjects. Although subject screening procedures were intended to eliminate such differences, in experiment 1 they were not rigorously followed; S4 was clearly a star out of the seven subjects.

To evaluate the reliability of the DLs between experiment 1 and experiment 2 in more detail, a two-way ANOVA for each individual condition of syllable, phrase, and sentence was calculated with one between-factor for experiment, and one within-factor for formant. Generally, DLs for all formants in experiment 2 for each phonetic context condition were significantly elevated compared to experiment 1 (at significance levels better than $p<0.02$). In addition, the sentence task in experiment 2 was repeated twice, once after 12 h of experience (sentence-2) and later after 25 h (sentence-3) and a significant improvement [$F(1,11)=10.5$, $p<0.01$] in thresholds was found after additional training for the experiment 2 listeners. Thus, long-term effects of training under medium uncertainty conditions were once again confirmed. However, across experiments, when listeners in experiment 2 had only a somewhat longer exposure than in experiment 1 (25 vs 17.5 h), no difference in DLs for the sentence task was obtained (two-way ANOVA, $p<0.78$). These results are open to two interpretations. First, the reliability of estimates of DLs under medium uncertainty, and therefore more generally in these simulated ordinary listening tasks, is not as good as the reliability demonstrated for thresholds. However, for the purposes of this study, estimates of DLs for experiment 1 and experiment 2 are sufficiently similar that they may be judiciously combined and/or compared in later analyses.

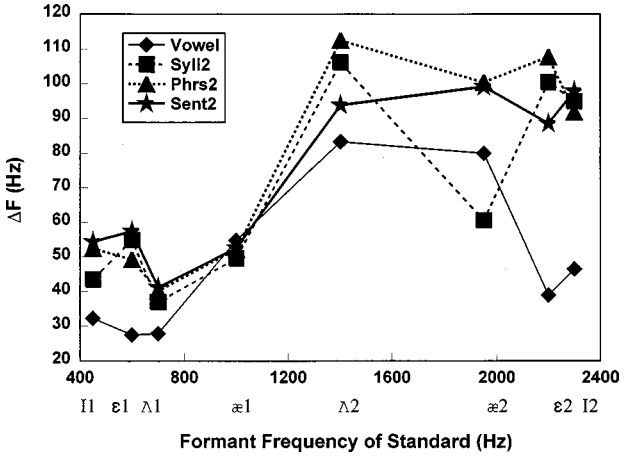

FIG. 4. Average DLs for eight formants in different phonetic contexts in experiment 2.

3. Phonetic context

The DLs for the four conditions in the phonetic context task are shown in Fig. 4 and in Table VIII and are labeled with ''2'' to indicate experiment 2 results. Differences in discrimination performance were evaluated by a two-way ANOVA for the factors of phonetic context and formant. The main effects and interactions were all significant [context: $F(3,33)=32.7$, $p<0.0001$; formant: $F(7,77)=44.4$, $p<0.0001$; interaction: $F(21,231)=6.1$, $p<0.0001$]. As expected, DLs increased with increases in formant fre-

TABLE VIII. DLs in Hz for formant discrimination tasks in different phonetic contexts in experiment 2 and for thresholds from Kewley-Port and Watson (1994).

	ɪ-$F1$	ɛ-$F1$	ʌ-$F1$	æ-$F1$	ʌ-$F2$	æ-$F2$	ɛ-$F2$	ɪ-$F2$
Format frequency	450	600	700	1000	1400	1950	2200	2300
Threshold (K-P and Watson, 1994)	12.6	17.5	12.4	22.0	27.3	23.4	36.7	28.5
Vowel	32.3	27.5	27.9	54.8	83.4	80.0	38.9	46.5
Syllable-2	43.5	54.9	37.0	49.6	106.2	60.6	100.5	95.0
Phrase-2	52.5	49.3	40.2	52.2	112.6	100.5	107.8	91.9
Sentence-2	54.4	57.5	41.2	52.6	93.9	99.2	88.6	97.9

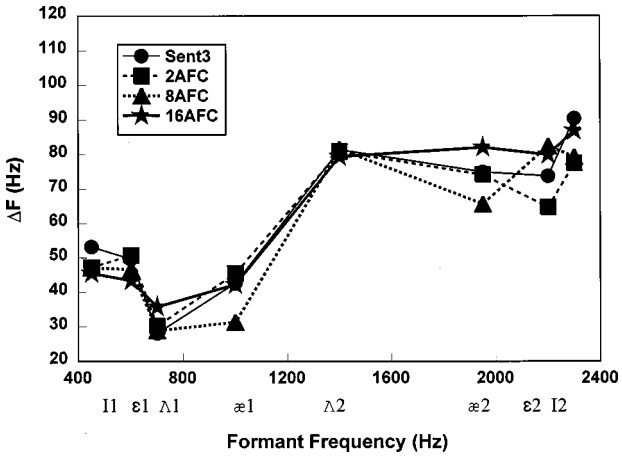

FIG. 5. Average DLs for eight formants in the sentence context, with and without identification, in experiment 2.

quency. However, the rather large decrease in DLs for the highest two formants for isolated vowels was unexpected although quite consistent for all three subjects. The obvious difference due to phonetic context was that the DLs for the isolated vowel condition were lower than for other phonetic contexts. *Post hoc* tests (Tukey HSD) confirmed that the average vowel DL (48.9 Hz) was significantly lower than for the syllable (68.4 Hz), phrase (75.8 Hz), or sentence (73.1 Hz) averages. Other results for phonetic contexts replicated those of experiment 1. Average syllable DLs were significantly lower than DLs for either phrase or sentence, but phrase and sentence DLs were not significantly different. In contrast to experiment 1 results, in experiment 2 when training effects were eliminated, DLs for the syllable were lower than for phrase and sentence DLs more generally across both $F1$ and $F2$.

4. Sentence identification

The sentence identification task consisted of a replication of the sentence task either with discrimination only (sentence-3) or with the addition of the identification tasks with three levels of difficulty, e.g., identification of two, eight, or 16 target sentences. Results shown in Fig. 5 and in Table IX did not appear to show any effect of adding sentence identification to the discrimination task. This was confirmed by a two-way ANOVA, for identification level and formant. The main effect for identification level and the interaction were not significant [identification: $F(3,33) = 0.94$, $p = 0.4$; interaction: $F(21,231) = 1.5$, $p = 0.08$], although DLs increased with increasing formant frequency as expected [formant: $F(7,77) = 44.4$, $p < 0.0001$]. To ascertain if subjects attended to the identification task as instructed, the average correct identification of words in the sentences was calculated for a subset of 48 trial blocks. Block averages across all sentence locations and subjects were either 99% or 100% correct. Clearly, subjects had no difficulty in identifying the sentences and remembering them while simultaneously required to make fine vowel discrimination judgments. Thus, efforts to design very challenging tasks involving both discrimination of within-vowel differences and meaningful sentence identification did not produce results that differed from those in the simpler, discrimination-only task.

Consider the various comparisons of discrimination abilities measured in sentence context in both experiment 1 and experiment 2. DLs for vowels in sentences were shown to be equivalent under several different experimental conditions for two groups of subjects. No significant differences were observed for DLs between the sentence-1 and sentence-3 results, the sentence-1 and sentence-1+2AFC task, or all four conditions in the experiment 2 sentence identification task. This equivalence in results across subject groups and tasks leads to the conclusion that the reliability of discrimination DLs in the sentence task, with and without addition of meaningful identification, appears to be unusually high. The significantly elevated DLs found between the sentence-2 and either sentence-1 or sentence-3 conditions is easily explained as a training effect because subjects had considerably less experimental time before the sentence-2 data were obtained compared to the other two data sets (Tables III and VII). Thus, formant discrimination in five out of the six tasks using sentences, with and without meaningful identification, was nearly the same. Therefore, a reasonable estimate of DLs under more ordinary listening conditions can be established as the average of comparable data in experiment 1 and experiment 2. In order to have an equal number of samples from each of the seven total subjects, an average was calculated from the overlapping conditions in experiment 1 and experiment 2, i.e., the sentence with discrimination only and the sentence plus two-alternative, forced-choice identification. This average for each formant, labeled ''Ordinary,'' is shown at the bottom of Table IX.

C. Discussion of experiment 2

1. A norm for discrimination in more ordinary listening

As part of the goal for this series of experiments, the level of difficulty of tasks in this experiment was varied sys-

TABLE IX. DLs in Hz for formant discrimination tasks in experiment 2 and the DLs calculated as a norm for ordinary listening conditions averaged over sentence-1, sentence-1+2AFC, sentence-3, and sentence-3+2AFC.

	ɪ-$F1$	ɛ-$F1$	ʌ-$F1$	æ-$F1$	ʌ-$F2$	æ-$F2$	ɛ-$F2$	ɪ-$F2$
Format frequency	450	600	700	1000	1400	1950	2200	2300
Sentence-3	53.2	49.6	28.1	42.6	81.4	75.0	73.8	90.5
Sentence+2AFC	47.2	50.8	30.2	45.5	80.9	74.2	64.7	77.5
Sentence+8AFC	47.2	46.7	28.9	31.4	81.6	65.7	82.5	79.3
Sentence+16AFC	45.5	43.4	35.8	42.3	79.4	82.1	79.9	86.9
Ordinary	36.5	40.8	36.4	42.6	74.5	82.1	82.0	86.8

tematically from easiest, for isolated vowels, to hardest, for vowels in sentences in a complex cognitive task. Presumably there exist some listening conditions, for example, very poor signal-to-noise conditions, under which the cognitive load of the task would make it impossible to do anything but discriminate gross differences between, say, /i/ and /ɑ/. However, the goal of this experiment was to target listening conditions that reflect more normal situations of communication in quiet. The experimental design under laboratory conditions simulated many characteristics of an ordinary communication task in which vowels must be discriminated from one another in order to extract the meaning of words in a sentence. Therefore, different levels of phonetic context were explored, as well as the difficulty level of extracting the meaningful identification of words in sentences. In the most challenging condition, vowel discrimination was required to identify words at three different locations in a nine-word sentence, initial, medial, and final, in order to identify the meaning of the sentence. While the conditions investigated here are few in relation to the large space of everyday communication, the conditions represent substantial changes from optimal ones towards more ordinary communication.

A clear outcome of this experiment is that within a sentence, DLs were equally good whether or not linguistic meaning was extracted from the sentence in addition to the discrimination judgement. This result surprised not only the investigators, but the listeners who reported being highly challenged by the task and who despaired during training for the identification task that they could maintain DLs at the level achieved for discrimination only. Nonetheless, a consistent level of discrimination ability was achieved by two groups of subjects tested in slightly different experimental conditions 8 months apart. Our results appear to provide a stable estimate, or norm, of discrimination ability under some ordinary listening conditions.

2. Measuring the effect of phonetic context

A primary goal of this experiment was to measure the effect of lengthening phonetic context on the ability to resolve small differences in vowel formants. The results of experiment 2 allow direct comparison between isolated vowels and vowels embedded in syllables, phrases, or sentences. As shown in Fig. 4, DLs for isolated vowels were significantly better than those for vowels embedded in any length of phonetic context. However, as phonetic context lengthened, the resulting effects were compressed. That is, the effects of phonetic context are greatest between isolated vowels and syllables, whereas DLs for three-word phrases and nine-word sentences were almost equivalent. In order to measure quantitatively the effect of phonetic context, it is preferable to remove the significant variability in DLs associated with the changes of formant frequency in order to provide one measure for both $F1$ and $F2$. This appears possible based on a recent report by Kewley-Port and Zheng (1998), who examined models of the variability in formant thresholds for two factors, $F0$ and formant frequency. The models examined involved detailed analysis of the spectral energy in the vowels, followed by subsequent transformations into excitation levels or specific loudness within a bank of auditory filters. They demonstrated that variability was best accounted for by a model that calculated the specific loudness within auditory filters. The outcome of that effort was that the better models flattened the effect of changes in formant frequency such that thresholds were a constant valued function across formant frequency.

TABLE X. Effect of phonetic context compared across experiments using bark ratios relative to individual vowel thresholds.

Type of discrimination	Average DL (barks)	Average ratio To threshold
Threshold	0.109	1
Vowel-2	0.242	2.2
Syllable-2	0.330	3.0
Avg. Phrs2 and Sent2	0.357	3.3
Ordinary	0.284	2.6
Untrained sentence	0.434	4.0

Recently, we have examined whether it was possible to emulate this explicit modeling of the auditory processing of vowel formants with a simple auditory scale. In other words, could the flattening effect observed in the models be simulated by transforming Hz into units appropriate for auditory scaling of frequency? Several auditory scales were applied to the data in Kewley-Port and Zheng (1998) to determine if the flattening of the ΔF functions would be observed. Auditory scales investigated included log frequency, several versions of Moore's equivalent rectangular bandwidth rate (ERB-rate) scales (Moore and Glasberg, 1987; Glasberg and Moore, 1990), and Zwicker's (1961) critical-band rate scale (z). Visual examination of the scaled threshold data indicated that the z-scale had flatter functions and was more effective in removing formant frequency effects than other scales. The primary difference between the ERB-rate scales (E) and the z-scale for vowel thresholds was that in the ΔF functions in the E-scale were not flat over $F1$, but clearly rose for small values of E. This outcome was also supported by Traunmüller (1990, 1998) who pointed out that the critical-band rate scale, z in barks, is derived from loudness summation. Therefore, the z-scale with units of barks was selected to compare results across both phonetic contexts and experiments.

Specifically, to compare the effects of phonetic context after variability due to formant frequency is removed, Eq. (6) in Traunmüller (1990), was applied. The formant frequencies in Hz for the standard vowel and standard frequency plus the DL were converted to the z-scale, and then subtracted to get a DL in barks. A useful way to compare the effects of phonetic context is to use vowel thresholds (in barks) as the reference of optimal performance. Thresholds for isolated vowels from Kewley-Port and Watson (1994) are shown in Table VIII for the vowel formants used in this experiment. The thresholds and DLs for each vowel formant in Table VIII were also converted to barks. Averages over discrimination conditions are shown in Table X. Since the DLs for the phrase-2 and sentence-2 conditions were not significantly different, they were averaged together as a single estimate for DLs in longer phonetic context.

To compare discrimination ability across experiments, the ratio of the DL for each vowel formant in phonetic context to the corresponding threshold was calculated, where the ratio of the average vowel threshold to itself is 1.0. These ratios were averaged across formants and are shown in Table X. Relative to the optimal ratio of 1, DLs for discrimination of vowels under medium vs minimal uncertainty conditions were degraded by a factor of 2.2. As vowels were discriminated in longer phonetic context under medium uncertainty, DLs increase, but not by large amounts. Vowel DLs in syllables degraded by a factor of 3.0 compared to thresholds, and in phrases and sentences by a factor of 3.3. This analysis clearly demonstrates that the effect of longer phonetic context is compressed as length approaches that of modest sentences. That is, an increase in length from isolated vowels to syllables resulted in a 36% reduction in resolution of formant frequency, while from syllables to phrases or sentences there was only an 8% reduction. The overall decrease in ability to discriminate formants for vowels in phrases and sentences compared to vowels in isolation under medium stimulus uncertainty was 50%.

III. GENERAL DISCUSSION

A. Range of formant discrimination abilities

A general goal of the present experiments is to establish a range of abilities to discriminate formants from optimal to more adverse listening conditions. Given that reports of reliable thresholds for isolated vowels are now well established (Kewley-Port and Watson, 1994; Kewley-Port *et al.*, 1996a; Hawks, 1994), the thresholds used in our previous reports may be used as representative of optimal performance. To estimate an upper range of poor discrimination in simulated ordinary listening conditions, it was argued above that DLs for the ''untrained sentence'' condition in experiment 1 can provide such a limit, where the adverse circumstance is lack of subject training rather than noise or lengthy phonetic context.

In experiment 2, we argued that results supported a norm for formant discrimination in more ordinary listening conditions as shown in Table VIII. These ordinary DLs can be compared in more detail with optimal and poor performance by converting the DLs to barks to eliminate the effect of formant frequency. A display of the range of performance from threshold, to a norm for ordinary listening to the untrained sentence for the eight formants, is shown in Fig. 6, and the bark averages are in Table X. The function for the ordinary DLs is flat and reasonably parallel to that for formant thresholds. The untrained sentence function in barks is flatter than its representation in Hz, but the observed variability is considerable and probably reflects that listeners could focus their attention through feedback on some easier formants to discriminate within the first half hour of the experiment.

Consider whether the estimated ordinary DLs shown in Fig. 6 are representative of various DLs reported for different phonetic context and across groups in this experiment. The average over seven listeners for the norm for ordinary DLs in barks was 0.28. This ratio was somewhat less than 3.3 for phrases and sentences in phonetic context data for just the three subjects in experiment 2. We noted that DLs were higher in phonetic context for experiment 2 than experiment 1, and that DLs for these three subjects improved in the subsequent sentence identification task. Calculating a ratio for each of the seven estimates in the sentence context, with and without identification, yields a range of ratios from 2.4 to 3.3. While this is a wide range, all ratios do fall clearly between 1.0 for thresholds and 4.0 for the untrained sentence task. Overall, the proposed norm for more ordinary discrimination, taken as an average over seven subjects in analogous conditions of sentence and sentence plus two-choice identification, appears to be the most representative estimate of discrimination abilities in simulated ordinary listening conditions.

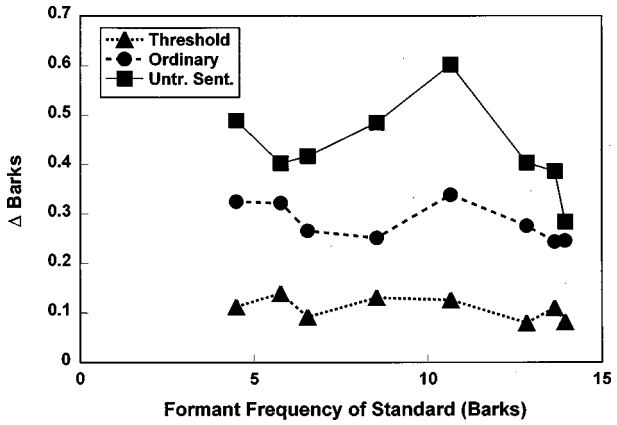

FIG. 6. Average DLs for eight formants in barks for three experimental conditions, for thresholds (Kewley-Port and Watson, 1994), for the norm for ordinary listening conditions, and for the sentence task with untrained subjects.

B. Discrimination and distances in the vowel space

The distribution of vowels in the $F1 \times F2$ space is quite different across the world's languages (Bradlow, 1995; Disner, 1983; Ladefoged and Maddieson, 1996; Lindblom, 1986). While many languages have only five vowels distributed widely over the $F1 \times F2$ space, other languages such as English have very crowded vowel spaces with overlapping vowel areas. In English, this overlap is observed in data measuring $F1$ and $F2$ across different talkers (men, women, and children: Peterson and Barney, 1952; Hillenbrand *et al.*, 1995), or for one talker within a variety of consonantal contexts (Broad and Fertig, 1970). Several explanations have been offered for how vowels are rapidly and accurately identified given the overlap of the two primary acoustic characteristics, $F1$ and $F2$, between vowels. Some have suggested normalization schemes (Nearey, 1989; Miller, 1989). Others have suggested that vowels are distinguished by the presence of features such as vowel length and dynamic formant transitions in addition to the spectral characteristics of $F1$ and $F2$ (Lehiste and Peterson, 1961; Nearey and Assmann, 1986; Neel and Kewley-Port, 1996; Neel, 1997). Even though length distinctions are well documented in some languages (Swedish long and short vowels), and formant transitions are

essential properties of the diphthongal nature of some vowels, spectral cues appear to take precedence (Kewley-Port *et al.*, 1996b).

Discrimination of differences in the spectral cues of vowels must be accurate enough to support the reliable identification of vowels. That is, vowels have been subject to evolutionary constraints such that a match between the capabilities of the production and perception of vowels for robust communication has developed (Liberman and Mattingly, 1989; Studdert-Kennedy, 1998). The relationship between the ability to discriminate vowel formants and the distribution of vowels in the $F1\times F2$ space is an interesting one when vowels are crowded, such as in English, because presumably even when vowels have close neighbors, they must still be rapidly categorized. The ordinary DL for formants was measured as 0.28 barks, meaning that listeners could discriminate between formants at the 0.28-bark distance 70% of the time. A modest investigation of English vowels from many talkers examined how the ordinary DL related to $F1$ and $F2$ differences for the most closely spaced vowels.

Several studies have measured vowel formants from many talkers at the steady-state part of a /CVC/ syllable. In the present analysis of closely spaced vowels, it was decided to select eight male and female talkers from three studies of speakers from different dialects. The first was Bradlow's (1993) study of talkers in upstate New York, the second was Hillenbrand *et al.*'s study (1995) of talkers from southern Michigan, and the third was a study of talkers in our laboratory from central Indiana. Reported formant values are averages of five measured tokens per talker except for Hillenbrand, who reported a single token.

To determine $F1$ and $F2$ differences for the closest vowels, a two-step analysis was developed. For each speaker, the Euclidean distance between all pairs of vowels in an $F1\times F2$ vowel space in bark units was calculated. A criterion of 1.5 barks for ''close'' vowel pairs was then selected after examining the distance matrices for all vowel pairs. For each talker, all pairs with distances less than 1.5 barks were noted. The number of close pairs over the eight talkers ranged from 3 to 17, with a mean of 8 pairs per talker, and would not have changed substantially for a criterion set between 1.0 and 2.0 barks. Twenty-eight different vowel pairs out of 45 possible were identified as close by the 1.5-bark criterion.

To compare the formant distances of these close pairs to the ordinary norm of 0.28 barks, Euclidean distances were not appropriate since $F1$ and $F2$ were combined. In order to get only $F1$ and $F2$ differences for the closest vowel pairs, the second step in the analysis selected the most frequently observed close pairs. The number of times each of the 28 pairs was found for the speakers was tallied. The most frequent pairs were /e–ɪ/ (all 16 talkers) and /æ–ɛ/ (12 talkers). Since the next most frequently observed pairs occurred for seven to nine of the talkers, it was decided to select a back vowel pair, /u–o/, which together with the other two pairs covered the high, mid, and back vowel space. For all 36 of these vowel pairs, the absolute differences were calculated separately for $F1$ and $F2$ in barks, and then averaged. The grand average of the formant distances between the closest vowel pairs was 0.56 barks.

The value of 0.56 barks is an average for formant distances of the closest vowel pairs observed in a database of 16 speakers with different dialects. In comparison, the norm DL for discriminating formants under more ordinary listening conditions is 0.28 barks. Therefore, the closest vowels in English are typically produced with formants two times further apart than the DLs for resolving formants, namely 0.56 to 0.28 barks. On face value, the ratio of 2:1 obtained between perception abilities and the spacing of closest vowels indicates a good match between production and perception. Consider the average DL for the untrained sentence of 0.43 barks in relation to 0.56 barks. These values are perhaps too similar, suggesting that identification of closest vowels would be based on the information that was just barely discriminable, not an ideal situation for robust communication. Given that the untrained sentence task is the only one here that involved adverse listening conditions, it remains for future research to see if noise or hearing impairment degrades formant discrimination performance sufficiently such that closely spaced vowels might be easily confused. On the other hand, we note that these close vowel pairs involve the vowel glides /e/ and /o/ that are generally produced with large amounts of formant movement. Thus, it is possible that the addition of formant dynamics is a necessary property of English vowel spaces given that closely spaced vowels approach the psychophysical limits of discriminating formants in normal communication. Verification of this hypothesis would rest on cross-language comparisons of vowel systems with particularly dense vowel spaces such as Danish or Austrian German (Ladefoged and Maddieson, 1996).

IV. CONCLUSIONS

Our series of experiments on vowel discrimination has sought to establish the range of abilities of listeners to process vowel information from optimal to more ordinary listening conditions. Optimal formant discrimination (Kewley-Port *et al.*, 1996a), has established thresholds over $F1$ as uniform in ΔF at 14 Hz, and over $F2$ as uniform in $\Delta F/F$ at 1.5%. The purpose of this study was to explore performance for vowel discrimination under more ordinary listening conditions. Ordinary listening conditions, as simulated in the laboratory, were defined as listening to moderate length sentences, extracting information both across linguistic categories to identify words and within categories to discriminate vowels. Two experimental factors were manipulated, the length of the phonetic context of the vowel and the difficulty of the sentence identification task. An important fixed factor was the level of stimulus uncertainty, and that was set to medium as somewhat representative of the predictability of words in sentences. Lengthening phonetic context from isolated vowels, to syllables, to phrases, and sentences degraded formant frequency resolution. However, the effect of phonetic context was compressed such that resolution was degraded by 35% between isolated vowels and vowels in syl-

lable context, by 8% between syllables and three-word phrases, and no difference was found for discrimination between phrases and sentences.

The second factor was the addition of sentence identification tasks to the formant discrimination task. Levels of difficulty increased from no identification response to that for 16 target sentences. No difference in discrimination ability was found across these tasks. Thus, a reliable, stable measure of performance was obtained such that a norm for discrimination of formant frequency under more ordinary listening conditions could be proposed. This norm, when calculated in bark differences, is 0.28 barks and is nearly constant across $F1$ and $F2$. It is important to note that this study did not set out to establish a ''norm'' for ordinary performance. Our assumption was that variability associated with the experimental factors would be measured, setting the stage for additional experiments. Instead, we obtained stable performance for formant discrimination across two groups of subjects, over phrases and sentences, with and without the identification of linguistic meaning. Thus, this experiment has discovered a norm for ordinary listening conditions of 0.28 barks for discriminating formants over a wide range of formant frequencies.

Analyses examined the relation between the norm for ordinary discrimination and the spectral structure of vowel spaces. English has a crowded vowel space, with several vowels close together in the $F1\times F2$ space. To determine the relation between the perceptual constraint provided by the norm for formant discrimination, and the production of vowels, the average difference between $F1$ or $F2$ for the closest pairs of English vowels was calculated. A value of 0.56 barks was obtained for the closest vowel pairs from 16 talkers. Thus, talkers produce vowels with formant differences twice that of the just discriminable difference under more ordinary listening conditions. This ratio of 2-to-1 appears to allow both for reliable identification of vowel categories, as well as room for variability within the categories to specify dialectal and other talker attributes. Presumably the norm for ordinary formant discrimination can be applied to other areas, in particular to predict speech perception capabilities under adverse conditions, including hearing impairment.

ACKNOWLEDGMENTS

This research was supported by the National Institutes of Health Grant No. DC-02229 to Indiana University. Discussions with Charles S. Watson in designing the experiment were very helpful. The assistance of Katherine Hucker in running the second experiment is gratefully acknowledged.

Bradlow, A. R. (**1993**). ''Language-specific and universal aspects of vowel production and perception: A cross-linguistic study of vowel inventories,'' Unpublished Ph.D. dissertation, Cornell University, Ithaca, NY.

Bradlow, A. R. (**1995**). ''A comparative acoustic study of English and Spanish vowels,'' J. Acoust. Soc. Am. **97**, 1916–1924.

Broad, D. J., and Fertig, R. H. (**1970**). ''Formant-frequency trajectories in selected CVC utterances,'' J. Acoust. Soc. Am. **47**, 1572–1582.

Disner, S. (**1983**). Vowel quality: The relation between universal and language-specific factors. UCLA Working Pap. Phon., 58.

Glasberg, B., and Moore, B. C. J. (**1990**). ''Derivation of auditory filter shapes from notched-noise data,'' Hear. Res. **47**, 103–138.

Hawks, J. W. (**1994**). ''Difference limens for formant patterns of vowel sounds,'' J. Acoust. Soc. Am. **95**, 1074–1084.

Hillenbrand, J., Getty, L. J., Clark, M. J., and Wheeler, K. (**1995**). ''Acoustic characteristics of American English vowels,'' J. Acoust. Soc. Am. **97**, 3099–3111.

Jenkins, J. J., Strange, W., and Miranda, S. (**1994**). ''Vowel identification in mixed-speaker silent-center syllables,'' J. Acoust. Soc. Am. **95**, 1030–1043.

Kewley-Port, D. (**1990**). ''Thresholds for formant-frequency discrimination in isolated vowels,'' J. Acoust. Soc. Am. Suppl. 1 **87**, S159.

Kewley-Port, D. (**1992**). ''Effect of levels of stimulus uncertainty and consonantal context on formant frequency discrimination,'' J. Acoust. Soc. Am. Suppl. 1 **91**, S2338.

Kewley-Port, D. (**1995**). ''Thresholds for formant-frequency discrimination of vowels in consonantal context,'' J. Acoust. Soc. Am. **97**, 3139–3146.

Kewley-Port, D., and Neel, A. T. (**1999**). ''Perception of the dynamic properties of speech: Peripheral and central processes,'' to appear in *Listening to Speech*, edited by W. A. Ainsworth and S. Greenberg (Oxford University Press, New York).

Kewley-Port, D., and Zheng, Y. (**1998**). ''Modeling formant frequency discrimination for isolated vowels,'' J. Acoust. Soc. Am. **103**, 1654–1666.

Kewley-Port, D., and Watson, C. S. (**1994**). ''Formant-frequency discrimination for isolated English vowels,'' J. Acoust. Soc. Am. **95**, 485–496.

Kewley-Port, D., Li, X., Zheng, Y., and Beardsley, A. (**1996a**). ''Fundamental frequency effects on thresholds for vowel formant discrimination,'' J. Acoust. Soc. Am. **100**, 2462–2470.

Kewley-Port, D., Akahane-Yamada, R., and Aikawa, K. (**1996b**). ''Intelligibility and acoustic correlates of Japanese-accented English vowels,'' Proceedings of ICSLP 96, pp. 450–453.

Klatt, D. H. (**1980**). ''Software for cascade/parallel formant synthesizer,'' J. Acoust. Soc. Am. **67**, 971–995.

Kuhl, P. K., and Iverson, P. (**1995**). ''Linguistic experience and the 'perceptual magnet effect,' '' in *Speech Perception and Linguistic Experience*, edited by W. Strange (York Press, Baltimore).

Ladefoged, P., and Maddieson, I. (**1996**). *The Sounds of the World's Languages* (Blackwell, Cambridge, MA).

Lehiste, I., and Peterson, G. E. (**1961**). ''Transitions, glides, and diphthongs,'' J. Acoust. Soc. Am. **33**, 268–277.

Levitt, H. (**1971**). ''Transformed up–down methods in psychoacoustics,'' J. Acoust. Soc. Am. **49**, 467–477.

Liberman, A. M., and Mattingly, I. G. (**1989**). ''A specialization for speech perception,'' Science **243**, 489–494.

Lindblom, B. (**1986**). ''Phonetic universals in vowel systems,'' in *Experimental Phonology*, edited by J. Ohala and J. Jaeger (Academic, New York), pp. 13–44.

Mermelstein, P. (**1978**). ''Difference limens for formant frequencies of steady-state and consonant-bound formants,'' J. Acoust. Soc. Am. **63**, 572–580.

Miller, J. D. (**1989**). ''Auditory-perceptual interpretation of the vowel,'' J. Acoust. Soc. Am. **85**, 2114–2134.

Moore, B. C. J., and Glasberg, B. (**1987**). ''Formulae describing frequency selectivity as a function of frequency and level, and their use in calculating excitation patterns,'' Hear. Res. **28**, 209–225.

Nearey, T. M. (**1989**). ''Static, dynamic, and relational properties in vowel perception,'' J. Acoust. Soc. Am. **85**, 2088–2113.

Nearey, T., and Assmann, P. (**1986**). ''Modeling the role of inherent spectral change in vowel identification,'' J. Acoust. Soc. Am. **80**, 1297–1308.

Neel, A. T., and Kewley-Port, D. (**1996**). ''Dynamic cues in vowel identification: A training study,'' J. Acoust. Soc. Am. **99**, 2593(A).

Neel, A. T. (**1997**). ''Factors affecting vowel identification in hearing-impaired listeners,'' J. Acoust. Soc. Am. **102**, 3095–3096(A).

Peterson, G. E., and Barney, H. L. (**1952**). ''Control methods used in a study of the vowels,'' J. Acoust. Soc. Am. **24**, 175–184.

Sommers, M., and Kewley-Port, D. (**1996**). ''Modeling formant frequency discrimination of female vowels,'' J. Acoust. Soc. Am. **99**, 3770–3781.

Studdert-Kennedy, M. (**1998**). ''The particulate origins of language generativity: From syllable to gesture,'' in *Approaches to the Evolution of Language: Social and Cognitive Base*, edited by J. Hurford, M. Studdert-Kennedy, and C. Knight (Cambridge University Press, Cambridge).

Traunmüller, H. (**1998**). Auditory scales of frequency representation. ⟨http://www.ling.su.se/staff/hartmut/bark.htm⟩ (Accessed 2/17/98).
Traunmüller, H. (**1990**). ''Analytical expressions for the tonotopic sensory scale,'' J. Acoust. Soc. Am. **88**, 97–100.
Watson, C. S. (**1987**). ''Uncertainty, informational masking, and the capacity of immediate auditory memory,'' in *Auditory Processing of Complex Sounds*, edited by W. Yost and C. S. Watson (Erlbaum, Hillsdale, NJ), pp. 267–277.
Zwicker, E. (**1961**). ''Subdivision of the audible frequency range into critical bands (*Frequenzgruppen*),'' J. Acoust. Soc. Am. **33**, 248.

Waveform interactions and the segregation of concurrent vowels

Alain de Cheveigné
Laboratoire de Linguistique Formelle, CNRS/Université Paris 7, 2 place Jussieu, case 7003, 75251, Paris, France and ATR Human Information Processing Research Laboratories, 2-2 Hikaridai, Seika-cho, Soraku-gun, Kyoto 619-02, Japan

(Received 2 April 1999; revised 12 July 1999; accepted 16 July 1999)

Two experiments investigated the effects of small values of fundamental frequency difference (ΔF_0) on the identification of concurrent vowels. As ΔF_0's get smaller, mechanisms that exploit them must necessarily fail, and the pattern of breakdown may tell which mechanisms are used by the auditory system. Small ΔF_0's also present a methodological difficulty. If the stimulus is shorter than the beat period, its spectrum depends on which part of the beat pattern is sampled. A different starting phase might produce a different experimental outcome, and the experiment may lack generality. The first experiment explored the effects of ΔF_0's as small as 0.4%. The smallest ΔF_0 conditions were synthesized with several starting phases obtained by gating successive segments of the beat pattern. An improvement in identification was demonstrated for ΔF_0's as small as 0.4% for all segments. Differences between segments (or starting phase) were also observed, but when averaged over vowel pairs they were of small magnitude compared to ΔF_0 effects. The nature of ΔF_0-induced waveform interactions and the factors that affect them are discussed in detail in a tutorial section, and the hypothesis that the improvement in identification is the result of such interactions (beat hypothesis) is examined. It is unlikely that this hypothesis can account for the effects observed. The reduced benefit of ΔF_0 for identification at smaller ΔF_0's more likely reflects the breakdown of the same F_0-guided segregation mechanism that operates at larger ΔF_0's. [S0001-4966(99)01811-1]

PACS numbers: 43.71.Es, 43.71.Pc, 43.66.Hg, 43.66.Ba [JH]

INTRODUCTION

A number of cues are useful when one tries to hear speech in a noisy environment (Cherry, 1953; Brokx and Nooteboom, 1982; Darwin and Carlyon, 1995). When both target and competitor are harmonic (for example, both voiced), a difference in fundamental frequency (F_0) is beneficial. This effect has been studied by many authors using pairs of synthetic vowels (see de Cheveigné *et al.*, 1997a for a review). When a ΔF_0 is introduced between vowels, identification generally improves up to about one semitone (6%), after which it remains constant before deteriorating again at the octave. The largest jump in identification rate usually occurs between $\Delta F_0 = 0\%$ and the smallest nonzero value used in the study (typically 6%, 3%, or 1.5%). However, the region below 1.5% where most of the improvement occurs has not been explored in detail.

Small ΔF_0's present a methodological difficulty. The shape of the compound stimulus fluctuates at a rate equal to ΔF_0. If the stimulus is shorter than the beat period $1/\Delta F_0$, both its long-term spectrum, and the set of short-term spectra that can be sampled within it, depend on which part of the beat pattern it spans, which in turn depends on the starting phase spectra. A different starting phase might produce a different experimental outcome, and so the generality of the experiment may be in question. What appears like a ΔF_0 effect might be the chance result of some particularly unfavorable phase spectrum at $\Delta F_0 = 0$, and/or a particularly favorable segment of the beat pattern at $\Delta F_0 \neq 0$.

A first aim of this study was to verify the generality of improvement of identification with ΔF_0 by assessing the effects of starting phase. It is impossible to test all possible phase spectra, but useful conclusions can be drawn by sampling several phase conditions. Differences among them tell us about the approximate size of phase effects, and comparisons of ΔF_0 effects across phase conditions tell us of their generality. In experiment 1 of this paper, at the smallest nonzero ΔF_0, the stimulus set included 4 consecutive portions of a double-vowel waveform, each shorter than the beat pattern. In experiment 2 it included two particular phase conditions: same-phase and antiphase. A second aim of this study was to test the hypothesis that beats contribute to the segregation of concurrent sounds. Beat-induced fluctuations might be sampled by the auditory system to enhance identification of a vowel pair. This so-called ''beat hypothesis'' has been proposed to explain the effects of small ΔF_0's (Culling and Darwin, 1993, 1994; Assmann and Summerfield, 1994). The experiments allow the effects of such fluctuations to be measured, so one can decide whether or not they are capable of explaining the ΔF_0 effects.

A major obstacle in dealing with waveform interactions on the basilar membrane is their complexity. The simplest beats (those between two partials) have dimensions of rate, phase, depth, and carrier frequency, which vary among channels of the peripheral filter. In response to the sum of two vowels, the shape of the waveform in each channel depends on channel characteristics (selectivity, phase distortion) as well as stimulus characteristics (amplitude and phase spectra of both vowels). It is also affected by demodulation or trans-

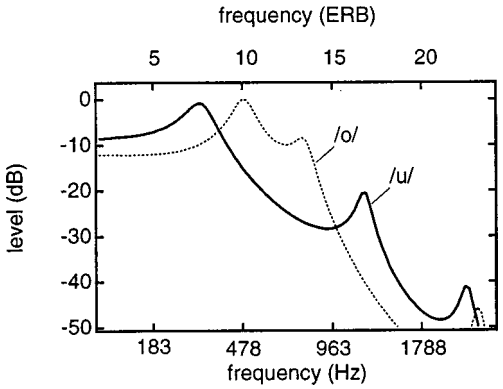

FIG. 1. Spectral envelopes of Japanese vowels /o/ and /u/. The abscissa represents frequency, warped to an ERB scale [uniform density in terms of equivalent rectangular bandwidth, Moore and Glasberg (1983)].

duction characteristics: nonlinearity, temporal integration, etc. To facilitate understanding of these phenomena, the next section offers a tutorial on ΔF_0-induced waveform interactions on the basilar membrane. It is followed by a section on models of how the auditory system might exploit beats to enhance identification. Next comes the description of two experiments that probe the effects of small ΔF_0's while controling for phase-dependent effects of waveform interactions. Finally, in Sec. V we weigh evidence for and against several models of segregation.

I. A TUTORIAL ON ΔF_0-INDUCED WAVEFORM INTERACTIONS

Beats are a temporal phenomenon, but the conditions that they depend upon are best described in the frequency domain. Actually, two frequency axes must be considered: the frequency axis of the *spectrum* of the stimulus (or of the vibration waveform at some point in the cochlea), and the *tonotopic axis* of the basilar membrane. If peripheral filters were infinitely narrow, each would select a single partial and these two axes could be merged. Unfortunately, waveform interactions occur precisely because filters allow several partials to pass through. In the following graphs the nature of the axis can be determined by checking whether it is labeled *frequency* or *filter CF*.

Figure 1 shows the spectral envelopes of the Japanese vowels /o/ and /u/. The abscissa here is frequency. For uniformity with following figures, it is warped so that frequencies are uniformly distributed on a scale of equivalent rectangular bandwidth (ERB) (Moore and Glasberg, 1983). The spectral envelope is not the spectrum of a waveform, but rather a function that determines the amplitude of each partial according to its frequency. It is a complex function that defines both level and phase, but the figure shows only the level. The phase spectrum usually has little effect on the sound of the vowel. When the vowel is produced, the spectral envelope is sampled at multiples of F_0 to obtain the actual spectrum of the vowel: densely if F_0 is low, or sparsely if it is high.

Figure 2 shows the magnitude of the short-term spectrum of the vowel /u/ synthesized at $F_0 = 132$ Hz. The frequency axis is again warped to an ERB scale. The spectrum

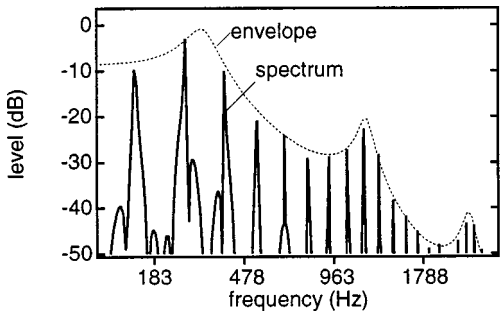

FIG. 2. Short-term spectrum of vowel /u/, calculated over a 250-ms stimulus. The abscissa represents frequency, warped to an ERB scale.

consists of a series of peaks. Their shape and width depend on the shape and width of the analysis window, itself constrained by the duration of the stimulus (in this case 250 ms including 20 ms raised cosine onset and offset). The vowel spectrum can be seen as the product of the line spectrum of a wideband periodic pulse train by the previous spectral envelope.

The spectrum of the waveform at any point of the basilar membrane also consists of peaks at harmonics of F_0. Each filter responds to several partials, but most of them are of low amplitude. Figure 3 shows their rms levels as a function of the filter's characteristic frequency (CF). Each line is for a different partial, the first few of which are labeled. The thin dotted line represents the total rms output in response to all partials together (excitation pattern). The figure uses the same warped scale as the preceding plots, but here it represents filter CF (or position along the basilar membrane) instead of the frequency axis of a spectrum. Basilar membrane filtering was simulated using the Auditory Toolbox software of Slaney (1993).

The number of partials in the filter output differs according to its CF. In the low-CF region, filters tuned near an individual partial respond mainly to that partial and exclude all others. Filters tuned between two partials respond to both, but weakly. In the high-CF region, all filters respond to several partials. The distance between the full line belonging to a given partial, and the dotted line, represents the proportion (in dB) of other partials in the total response. In the time domain, the waveform at the output of a low-CF filter tuned to a partial is approximately a sine-wave. That of other filters is a composite waveform that beats at the fundamental period. Such fast fluctuations at the pitch period are *not* what is meant by beats in the context of this paper.

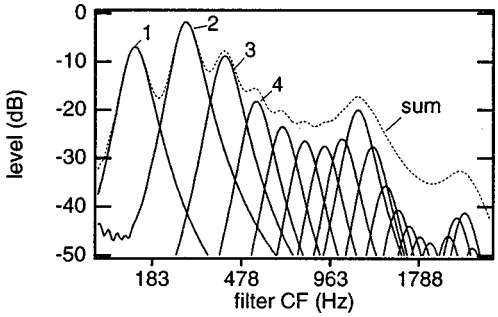

FIG. 3. Full lines: rms output of a cochlear filter bank as a function of characteristic frequency (CF), for each of the partials of vowel /u/. Dotted line: rms output in response to the entire vowel.

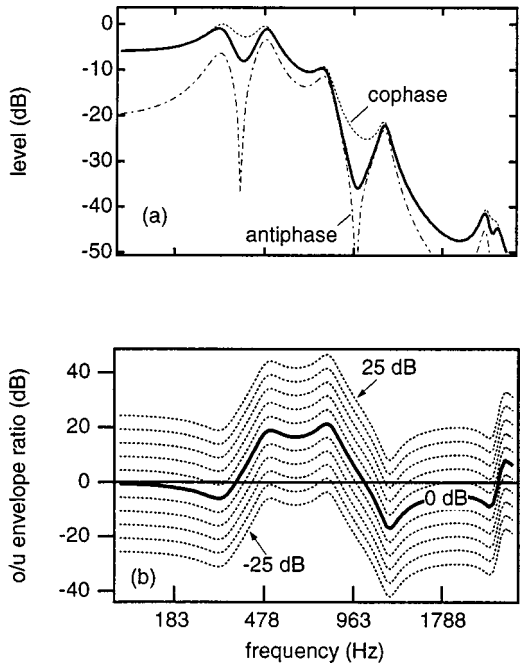

FIG. 4. (a) Vector sum of spectral envelopes of /o/ and /u/. Dotted line: both vowels have same phase spectra. Dot–dash: opposite phase spectra. Full line: both vowels are in Klatt phase [produced by the synthesizer of Klatt (1980) that approximates the phase spectrum of naturally produced vowels]. (b) Relative level in dB between magnitude spectral envelopes of /o/ and /u/ for values of the overall o/u rms relative level ranging from −25 to 25 dB in 5-dB steps. Note that for o/u ratio=20 and 25 dB the spectrum is entirely dominated by /o/, and at o/u ratio=−25 dB it is dominated by /u/.

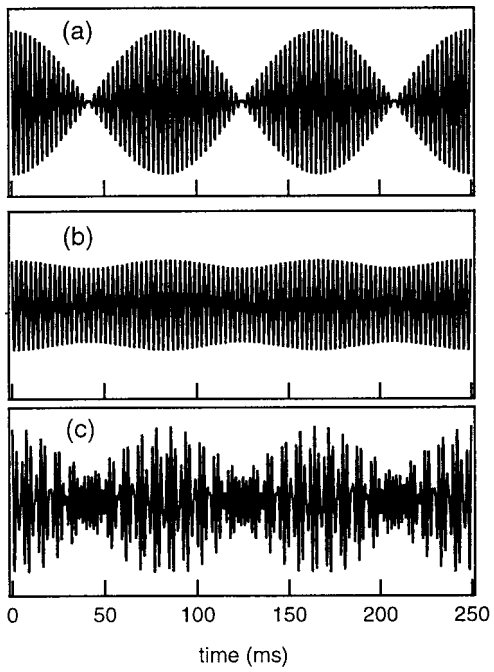

FIG. 5. (a) Beats between equal-amplitude partials of frequencies 390 and 402 Hz. The beat rate is 12 Hz. (b) Same, but the partials differ in level by 20 dB. (c) Same as (a) with the addition of a third partial of frequency 520 Hz.

When two vowels are added, the previous analysis can still be applied as long as they have the same F_0. The compound waveform consists of partials of that common F_0, with levels determined by a spectral envelope that can be calculated by *vector summation* of the complex envelopes of both vowels. The sum depends not only on the levels of both, but also on their relative *phases*. This is illustrated in Fig. 4(a), for vowels /o/ and /u/ with equal rms levels. The dotted line represents the sum supposing the vowels' phase spectra are identical (an unlikely occurrence), and the dot–dash line represents the difference if they are opposite (equally unlikely). For arbitrary phase spectra the envelope is somewhere between the two. The full line represents the sum if both vowels are in ''Klatt phase'' [the phase spectrum produced by the Klatt synthesizer (Klatt, 1980) that approximates the phase of natural vowels].

The experiments reported in this paper used pairs of vowels of unequal amplitude. Figure 4(b) shows the *relative level*, at each frequency, between envelopes of vowels /o/ and /u/, scaled with an overall rms relative level that was varied between −25 and +25 dB in 5-dB steps. The effect of phase on summation is largest where the vowel envelopes are of similar amplitudes, that is, where the plot crosses or approaches the 0-dB line. These plots are interesting also in that they show which parts of the spectrum are ''dominated'' by either vowel at a given overall relative level. At extreme levels the spectrum is entirely dominated by one vowel or the other (/o/ at +20 or +25 dB, /u/ at −25 dB). At intermediate levels it is ''partitioned'' between the two vowels (the plots cut the 0-dB line). We will see presently how this dominance pattern might be modified locally by cochlear filtering.

So far, the F_0's of both vowels were the same. If they are different but close, the previous analysis can be extended by interpreting partials of equal rank as having the same frequency but a progressively increasing (or decreasing) phase shift. The level of the sum varies between the limits described above [Fig. 4(a)], at a rate equal to $n\Delta F_0$ (where n is the rank of the partial). Partials of all ranks beat in this way, but with differences in *rate* (proportional to rank), *depth* (depending on the relative level between partials), and *phase* (depending on the difference between their starting phases).

Figure 5(a) gives an example of a beat between two partials of equal amplitude. Figure 5(b) illustrates the shallower beats that occur when their levels differ by 20 dB. The waveform of the stimulus (double vowel) is the superposition of various such beat patterns. In the context of the ''beat model,'' we are not directly interested in fluctuations of the acoustic waveform. Nor are we interested in the beats of individual partials, as they might occur if the partials were somehow isolated from the rest. Rather we are interested in the waveform fluctuations that actually occur on the *basilar membrane*, as a result of filtering the stimulus waveform. It is those fluctuations that would be exploited by a mechanism sensitive to beats.

The effects of filtering must thus be taken into account. First, filtering alters the relative amplitudes of partials of a pair, some channels favoring one partial and others the other. The depth of their beats may thus vary somewhat among channels. Second, the dispersive properties of the basilar membrane affect their relative phase. This effect is channel dependent, so beats may occur with different phases in different channels. Third and most importantly, filtering reduces

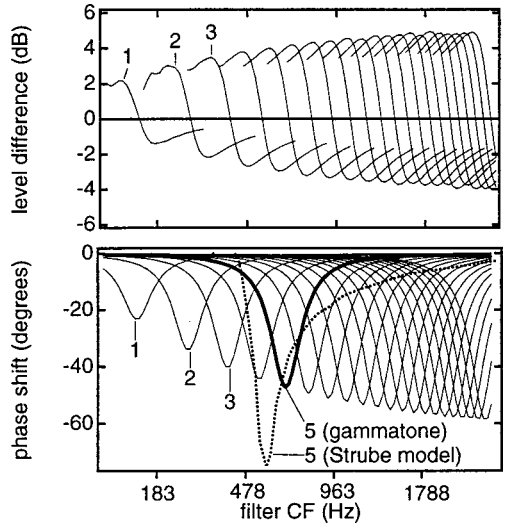

FIG. 6. Top: relative level between partials of same rank belonging to two equal-amplitude harmonic series of frequencies 128 and 132 Hz ($\Delta F_0 = 3\%$) filtered by a basilar membrane model, as a function of CF. Each curve is for a different rank, and is limited to CFs for which both partials are attenuated by less than 40 dB. Bottom: phase shift between partials of same rank belonging to two harmonic series of frequencies 128 and 132 Hz as a function of CF. Each curve is for a different rank.

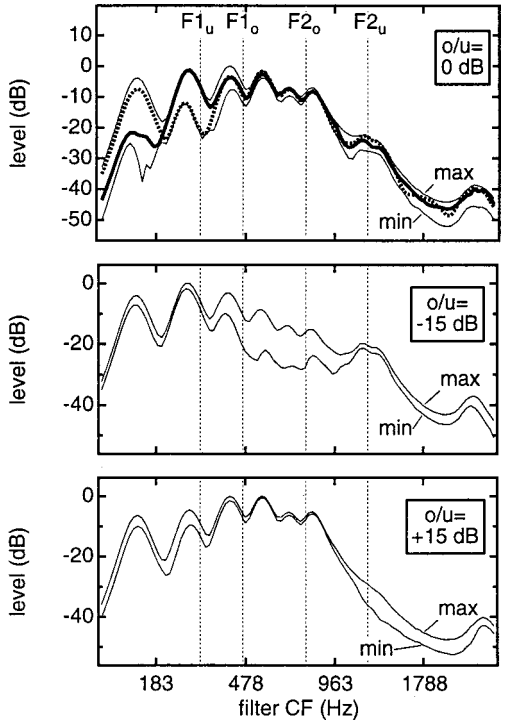

FIG. 7. Top, thin lines: limits of beat-induced variations of the rms output of a gammatone filter bank in response to the sum of vowels /o/ and /u/ for o/u relative level=0 dB, as a function of CF. Thick lines: profile of output at two instants (chosen for their dissimilarity). Middle and bottom: same, for o/u ratio= -15 and $+15$ dB. The simulation was performed with very slow beats, to avoid smoothing by temporal integration in the rms calculation stage. Vertical dotted lines indicate the positions of formants $F1$ and $F2$ of both vowels.

the number of partials that interact, with the result that the fluctuations of a filter output are simpler (and usually deeper) than those of the acoustic waveform. Some channels isolate individual partial pairs. The beat pattern at their output is similar to that shown in Fig. 5 (a or b). Other channels allow several partial pairs to interact together. The waveform at their output, which is more complex, can be understood as the superposition of two or more beat patterns.

The first two factors may be quantified. Figure 6 (top) shows the relative level, as a function of position along the basilar membrane, between partials of same rank from two harmonic series. The series had equal amplitudes, and F_0's $=128$ and 132 Hz ($\Delta F_0 = 3\%$). Each line is for a different rank, and each is limited to CFs for which both partials are attenuated by less than 40 dB by the filter. The shift (in dB) is positive for channels with CFs below the partial's frequency, and negative above. The result of this shift is to modify, within each channel, the pattern of dominance of Fig. 4(b). Within each channel, the ratio of partials of same rank differs from that specified in Fig. 4(b) by the amount specified in Fig. 6 (top). This plot is for $\Delta F_0 = 3\%$, for other values the magnitude of the shift would be in proportion. The simulation used a software implementation of the gammatone filterbank (Slaney, 1993; Patterson *et al.*, 1992).

A similar analysis can be made for phase. Figure 6(b) shows the *phase shift* introduced between two partials of same rank ($\Delta F_0 = 3\%$) as the result of the dispersive properties of the basilar membrane. The shift is proportional to the *slope* of the phase characteristic, which for the gammatone is steepest for the channel tuned to the frequency of the partial. A word of warning: this simulation depends critically on the choice of the *gammatone filter* to model peripheral selectivity. If cochlear filters have different dispersive properties, the magnitude and pattern of phase shifts must be different. For example, the dotted line shows similar data obtained with a software implementation of the model of Strube (1985), which according to Kohlrausch (1995) better matches the phase characteristics of the basilar membrane than the gammatone. The phase shift is greatest within channels tuned slightly below the partials.

The third factor (isolation of individual partial pairs) is crucial for the existence of deep beats in the waveform at the output of a filter. The reason is easy to grasp. Beat patterns of partial pairs have rates and phases that vary according to their rank. The minimum of one pattern is unlikely to coincide with a minimum of the others, with the result that the peak-to-valley ratio is reduced when the patterns are superposed. Figure 5(c) shows the same two partials as Fig. 5(a), together with a neighboring partial. The depth of the valley is reduced. Based on this reasoning, we expect that deep beats are most likely to occur in channels that are dominated by a single beating pair. Going back to Fig. 3, we see that this may be the case in low-CF channels tuned to a partial. Low-CF channels intermediate between two partials respond to the superposition of two beat patterns, and high-CF channels respond to even greater numbers of beating partials, and this is likely to produce limited peak-to-valley ratios.

Figure 7 (thin lines) shows the minimum and maximum levels in each channel in response to the mixture of /o/ and /u/ at relative levels of 0, -15, and $+15$ dB as a function of filter CF. Also shown (at 0 dB, top) are two samples of the instantaneous excitation pattern chosen for their dissimilarity (thick lines). At 0 dB, beats are deepest within channels with

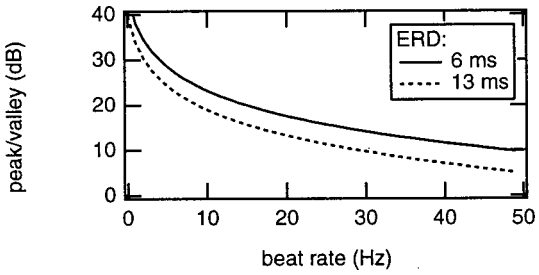

FIG. 8. The effect of temporal smoothing on beat amplitude. Peak/valley ratio of a maximally deep beat [e.g., Fig. 5(a)] after smoothing by a window of equivalent rectangular duration (ERD) 6 or 13 ms, as a function of beat rate. The peak/valley ratio of faster beats is reduced.

CFs below the first formants ($F1$) of /u/ and /o/. At an o/u ratio of -15 dB, beats are deepest in the vicinity of $F1$ and $F2$ of /o/ (middle plot). At $+15$ dB they are relatively shallow over all channels (bottom).

An important issue is the rate of beats. The overall beat pattern repeats itself at a rate equal to ΔF_0. In the experiment of Sec. III, at the smallest ΔF_0 (0.4%) the beat period was 2 s, or eight times the stimulus duration. At the largest ΔF_0 (6%) it was 125 ms, or one-half the stimulus duration. Beats between partial pairs of rank n (supposing they can be isolated) occur at a faster rate: $n\Delta F_0$. Restricted parts of the pattern of channel outputs may thus appear to pulsate faster than the overall pattern. In the vowel set used in the experiments, partials closest to $F1$ had ranks ranging from 2 to 6, and those closest to $F2$ ranks from 6 to 17. The fastest beats in the $F1-F2$ range thus occurred at 8.5 Hz for $\Delta F_0 = 0.4\%$, and 136 Hz for $\Delta F_0 = 8\%$ (at this spacing it makes little sense to distinguish beats between partials of same rank from those between partials of different rank).

A final consideration is that beats might be smoothed by temporal integration in the auditory system. Figure 8 shows the peak/valley ratio of a maximally deep beat pattern [such as that of Fig. 5(a)] after smoothing by a temporal window with an equivalent rectangular duration of 6 or 13 ms. These values are estimates obtained by Plack and Moore (1990). The former (6 ms) was obtained at frequencies of 900, 2700, and 8100 Hz, the latter (13 ms) was obtained at 300 Hz. Beat amplitude is reduced progressively with increasing beat rate. Note, however, that the detection of AM may not be limited by such low-pass filtering (Dau *et al.*, 1997). This question is discussed again later on.

II. BEATS AND SEGREGATION

It has been suggested that beats that arise in response to concurrent vowels with different F_0's might promote their identification, particularly at ΔF_0's too small to support other F_0-guided mechanisms (Culling and Darwin, 1993, 1994; Assmann and Summerfield, 1990, 1994). This section examines the various forms that can be given to this hypothesis, and discusses them critically in the light of the previous section.

A. The ''glimpsing'' model of Culling and Darwin

Culling and Darwin (1994) suggested that beats might cause the excitation pattern to momentarily assume a shape favorable for identification. Selected samples or ''glimpses'' of this pattern would benefit identification. Their model involved a perceptron pattern-recognizer, of which there were two variants. The first (''one-at-a-time'' strategy) used two sampling points, one for each vowel, chosen to give the highest and second-highest activation scores of the perceptron. The second (''both-at-once'' strategy) sampled the excitation pattern at a single point in time, chosen to give the highest value of a pairwise compound measure derived from the perceptron outputs. The process that produces the excitation pattern (filtering, transduction, and smoothing) involves integration over time, so each sample is actually derived from a windowed portion of the stimulus.

The both-at-once strategy was the more successful. The single sample was more often classified as the correct vowel pair than the constant pattern evoked at $\Delta F_0 = 0$. Another way to put it is that beat-induced fluctuations produced a cloud of points in feature space (instead of the single point at $\Delta F_0 = 0$), with an extent that was fortunately greatest in a direction that led to correct classification. The model exploited this favorable aspect of beat-induced variability. However, it is not clear that it would be as successful in the presence of intraclass variability of natural speech sounds, or variability induced by noise. Temporal sampling is antithetical to smoothing schemes used to deal with noise.

B. Serial differences between excitation patterns

An alternative hypothesis is that identification might benefit from dynamic cues, such as the *difference* between successive excitation patterns (ΔEP). It is well known that dynamic cues are important for vowel identification (e.g., Strange *et al.*, 1998). Kuwabara *et al.* (1983) found that a vowellike stimulus (''*X*'') with a spectrum intermediate between two vowels (''*A*'' and ''*B*'') was identified as vowel ''*A*'' when it appeared as the central portion of dynamic vowellike spectrum of shape ''*BXB*,'' and as vowel ''*B*'' when it appeared in an ''*AXA*'' pattern. Summerfield *et al.* (1984) found that subjects could perceive a vowel from a flat-spectrum complex if it were preceded by the ''complement'' of a vowel spectrum in which formant peaks were replaced by valleys. Summerfield *et al.* (1987) found further that a uniform-spectrum precursor enhanced the identification of vowellike stimuli with shallow envelopes. In both cases the auditory system seemed to exploit the difference (latter minus former) between two spectral shapes. The result was extended by Summerfield and Assmann (1987) to the case where the precursor was shaped like a first vowel, to which was later added a second vowel. Steps in spectral shape as small as 2 dB were effective. One might imagine that ΔEPs produced by beats are exploited in a similar fashion.

There are several difficulties with this proposition. First, Summerfield *et al.* (1984) found that transitions *toward* the target vowel's spectrum alone were effective. With beats, the auditory system would need to select transitions in the right direction and ignore the (possibly confusing) opposite transitions. Second, they also found that a transition had to be preceded by a precursor of at least 125 ms. Beat-induced valleys of modulation are often shorter than that, particularly

the sharp dips that occur within deep beats [Fig. 5(a)]. Finally, beats occur with different rates (and phases) in different channels, implying a rather disorderly succession of ΔEPs.

C. Modulation profile

A third proposition is that the profile of beat-induced pulsations across the basilar membrane supports identification, according to a mechanism similar to that which produces the sensation of roughness. Contrary to the previous proposals, the relative phases of beats between channels, or the sign of transitions, are indifferent. The auditory system must, however, be able to detect the pulsations and keep track of their distribution across the channels.

The detection threshold of sinusoidal modulation of an isolated high-frequency pure-tone carrier corresponds to a modulation ratio (ratio of peak excursion to average) $m = -30$ dB or a peak/valley ratio of 0.55 dB (Dau *et al.*, 1997). However, detection sensitivity for harmonics in vowels might be reduced by at least two factors. A first factor is the reduction of sensitivity to modulations at high rate. This is classically described as following a low-pass characteristic, but Dau *et al.* (1997) argue that modulation detection is best understood as involving a bank of *bandpass* filters tuned to modulation rates extending from 0 to at least 200 Hz. These filters are wide ($Q=2$), and therefore presumably liable to leakage from modulation at F_0, implying a low-pass characteristic similar to low-pass filtering in the modulation domain. In any case, sensitivity is likely to be reduced for the faster modulations that occur between partials of high rank or at large ΔF_0's. A second factor is modulation detection interference (MDI) (Yost and Sheft, 1989), by which modulation in one part of the spectrum interferes with the detection of modulation in other parts. Detection of a cue to identification might be hindered by beats that occur in other parts of the mixed-vowel spectrum.

Supposing that modulation is detected, it must be ''localized,'' that is, assigned to the right part of the spectrum. Marin and McAdams (1996) measured modulation thresholds for the detection and correct assignment of the center frequency (375, 750, or 1250 Hz) of a ''formant'' defined by the amplitude modulation of two or three consecutive partials. The modulation waveform was complex and comprised 13 harmonics of 5 Hz with amplitudes following a $1/f$ law. The threshold rms modulation index m_{rms} was in the range -19 to -13 dB (for sinusoidal modulation this would have corresponded to a modulation ratio m in the range -16 to -10 dB, or a peak/valley ratio of 2.8 to 5.7 dB). Overall, Marin and McAdams estimated that thresholds for correct ''localization'' of modulation were about three times higher than for its mere detection. Figure 9 shows the peak/valley ratio of beats as a function of CF for a mixture of vowels /o/ and /u/, for different o/u relative levels. The largest beat ratios are observed in low-frequency channels at relative levels near 0 dB. They correspond to beats with envelopes shaped as rectified cosines [as in Fig. 5(a)].[1] At other relative levels modulations are strongest in other channels. For example, at -15 dB there are beats near $F2$ of /o/, and at 0 dB near $F1$ and $F2$ of /u/. Assuming they can be detected and properly localized, ΔF_0-induced modulations might assist identification.

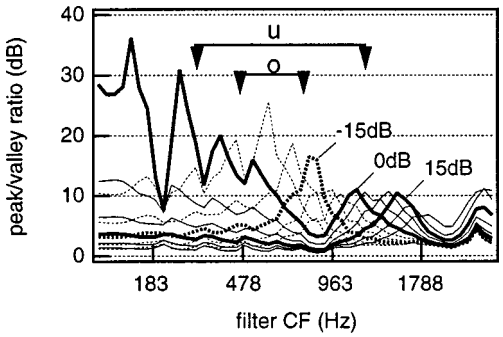

FIG. 9. Modulation profile: peak/valley ratio as a function of filter CF, for o/u relative levels ranging from -25 to $+25$ dB in 5-dB steps. Arrows indicate formant frequencies $F1$ and $F2$ of both vowels.

There are several difficulties with this proposition. First, the position of maximum beats is not the same at different relative levels, and does not always correspond to a formant of either vowel. This might confuse a vowel identification mechanism. Second, strong ΔF_0 effects are found in conditions for which beat amplitudes are small in all channels. Third, beats depend on the difference between partial frequencies, and should thus affect both vowels symmetrically. Yet a previous study found that if one vowel was harmonic and the other inharmonic, the inharmonic vowel was identified better (de Cheveigné *et al.*, 1995, 1997b). The same argument can be used against the other two schemes (glimpsing and ΔEP). A final argument against the modulation profile hypothesis comes from an experiment of Moore and Alcántara (1995). Subjects could identify ''vowels'' that were defined by amplitude modulation, in the region of their formants, of an otherwise flat-spectrum complex, but only if components started in cosine phase. For random starting phase they could not identify the vowels.

D. The generality of ΔF_0 experiments

The choice of starting phase spectra in concurrent vowel experiments is largely arbitrary. It is common to use the phase spectra produced by the synthesizer of Klatt (1980) that approximates natural vowels, and to give both vowels the particular starting phase produced by default by the software. This choice is not necessarily typical of natural situations, as different sources need not start out in synchrony, different path lengths from sources to ear(s) add to the phase shift of one source with respect to the other, and room acoustics may further scramble the phase spectra of both voices.

Manipulation of the phase spectrum is known to have little effect on the quality of isolated vowels. For concurrent vowels it could affect identification in three ways. Starting phase determines (a) the *set* of excitation patterns that may occur during a beat period, (b) the *order* in which they appear, and (c) the *subset* of these patterns that are available within a stimulus shorter than the beat period. A previous study (de Cheveigné *et al.*, 1997b) found that (a) and (b) had negligible effects: identification of concurrent vowels with durations twice the beat period was the same for all the

TABLE I. Formant frequencies and bandwidths of vowels.

	/a/	/i/	/u/	/e/	/o/	BW
*F*1	750	281	312	469	468	90
*F*2	1187	2281	1219	2031	781	110
*F*3	2595	3187	2469	2687	2656	170
*F*4	3781	3781	3406	3375	3281	250
*F*5	4200	4200	4200	4200	4200	300

starting-phase spectra investigated (both sine, both ''random'' with the same pattern, both random with different patterns, one sine and the other random). On the other hand (c) is likely to have a strong effect at small ΔF_0's for stimuli shorter than the beat period. As a related concern, starting phase determines the spectrum of the stimulus in the $\Delta F_0 = 0$ condition against which $\Delta F_0 \neq 0$ conditions are compared. Improvements observed with nonzero ΔF_0 might be specific to a particularly unfavorable starting phase spectrum at $\Delta F_0 = 0$.

The experiments reported in the next two sections explore the parameter region of small ΔF_0's, using various starting phase conditions to test the generality of the effects observed. They also challenge segregation models based on waveform interactions, insofar as those models lead us to expect phase and ΔF_0 effects to be of similar magnitude and to covary in an orderly fashion.

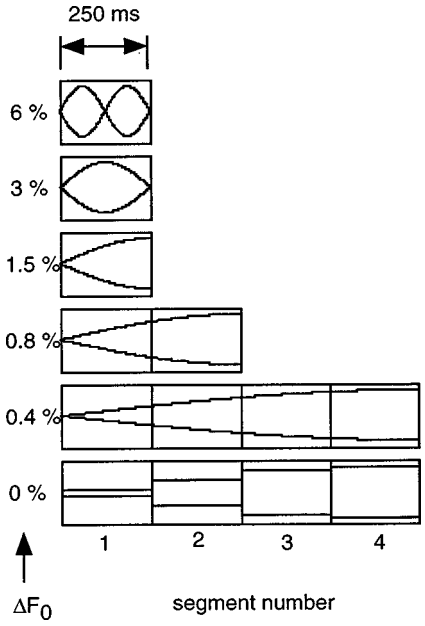

FIG. 10. Schematized beat patterns for each ΔF_0 and segment. Stimuli contain two beat periods at $\Delta F_0 = 6\%$ (top), one at 3%, and one half at 1.5%. The 0.8% condition is realized with two consecutive segments, and the 0.4% condition with four segments. The $\Delta F_0 = 0\%$ condition is realized in four versions, with phases equal to the ongoing phase at the centers of the 0.4% segments. The shape of real beat patterns is, of course, more complex than schematized here.

III. EXPERIMENT 1: SMALL ΔF_0's

A. Methods

Methods were similar to those of de Cheveigné *et al.* (1997a, b). Stimuli were constructed from synthetic tokens of Japanese vowels /a/, /e/, /i/, /o/, /u/ (formant frequencies and bandwidths are listed in Table I). Stimuli were 270 ms in duration, with 20-ms raised-cosine ramps at onset and offset (250-ms ''effective duration'' between −6-dB points). Vowels were synthesized at a 20-kHz sampling rate using a frequency-domain additive synthesizer (Culling, 1996) that emulates Klatt's cascade synthesizer (Klatt, 1980), and scaled to a standard rms value. To obtain double vowels, single-vowel tokens were paired, one vowel was scaled by an amplitude factor, both were summed, and their sum was scaled to a standard rms value. The result was output diotically to earphones from the NeXT computer. The sound pressure levels ranged from 63 to 70 dB (A) depending on the vowel pair, as measured by a Bruel and Kjaer artificial ear.

Fundamental frequencies (F_0) were chosen by pairs centered on 132 Hz, to obtain ΔF_0's of approximately 6% (128, 136 Hz), 3% (130, 134 Hz), 1.5% (131, 133 Hz), 0.75% (131.5, 132.5 Hz), and 0.375% (131.75, 132.25 Hz). For convenience, the latter ΔF_0 values are rounded to 0.8% and 0.4%, respectively, in the rest of the text. Both vowels were given a ''random'' phase spectrum that was the same for both vowels and all conditions. Partials of same rank thus had the same starting phase, allowing beat patterns to be more easily predicted. ''Random'' phase was preferred over alternatives such as sine or cosine, because it produces less peaky waveforms. ''Klatt'' phase (produced by default by the Klatt synthesizer) was not used because it differs between vowels.

The ΔF_0 results in a progressive phase shift between partials of same rank, with magnitude proportional to rank, ΔF_0, and time. Collectively, the beats produce a pattern that repeats with a period of $1/\Delta F_0$, as represented schematically in Fig. 10. To control for phase effects in stimuli shorter than the beat period, stimuli for the smallest ΔF_0 conditions were synthesized by windowing successive parts of a longer waveform. For the $\Delta F_0 = 0.4\%$ condition, a 1020-ms stimulus was synthesized from which four segments were windowed, each of 250-ms ''effective duration.'' The stimulus set also contained four stimuli at $\Delta F_0 = 0\%$, each with a starting phase spectrum equal to the phase spectrum of a $\Delta F_0 = 0.4\%$ segment, sampled at its center. These were obtained by synthesizing single vowel waveforms at $F_0 = 132$ Hz and time shifting them by $(0.5 \pm n)T_0/16$, $n = 0,1,2,3$, where T_0 is the fundamental period, before adding. Corresponding double-vowel segments at 0% and 0.4% therefore had similar long-term spectra, and differed from each other by ΔF_0 only. Segments at 0% and 0.4% were numbered 1, 2, 3, 4. In a similar fashion, two segments were prepared at $\Delta F_0 = 0.8\%$ by windowing consecutive 250-ms portions of a beat pattern.

To summarize, there was *one* segment each for $\Delta F_0 = 6\%$, 3%, and 1.5%, *two* segments for $\Delta F_0 = 0.8\%$, and *four* segments each for $\Delta F_0 = 0.4\%$ and 0%, a total of 13 ΔF_0-segment conditions. The stimuli cover two beat periods at 6%, one at 3%, and one-half of a beat period at 1.5%, 0.8%, and 0.4%. When designing the experiment, it was incorrectly assumed that beat patterns were symmetric in time,

and that covering half a period was equivalent to covering it all. Our sample is thus less complete than intended, but nevertheless sufficient to reveal any strong phase effects. When paired, vowels had either the same level (0 dB), or one vowel was weaker or stronger than the other by 15 dB. Strong ΔF_0 effects are expected for weak targets (-15 dB), but beats might be stronger at 0 dB and this condition was included to allow comparisons with other studies. Vowels within a pair were always different. There were a total of 780 double-vowel stimuli (vowel pair=/ae/,/ai/,/ao/,/au/,/ei/,/eo/,/eu/,/io/,/iu/,/ou/)$\times$(relative level$=-15,0,15$ dB)$\times(2F_0$orders)$\times(13\Delta F_0$-segment conditions). Ideally, the stimulus set should also have contained single vowels to make it consistent with the description made to the subjects (see below). However, the set was already very large, and so single-vowel conditions were not included.

Subjects were 15 Japanese students (seven male and eight female, aged 18 to 22 years) recruited for a series of ten experiments on concurrent vowel identification and paid for their services. Experiments 1 and 2 described in this paper were respectively the fourth and eighth of that series. Each stimulus was presented once. The subjects were told that it could be either a single vowel or two simultaneous different vowels. They were instructed to choose either one or two vowels as a response according to what they heard. If the response was inappropriate (more than two vowels, two identical vowels, a nonvowel, etc.), a message reminded them of the options and requested a new answer. They could pause at will, in which case the last stimulus presented before the pause was repeated after the pause (subjects paused on average five times per session). There was no feedback.

The response for each double-vowel stimulus was scored twice: each vowel in turn was nominated the ''target,'' the other being a ''competitor.'' A target was deemed identified if its name was among the one or two vowels reported by the subject. The *proportion of targets correctly identified* (constituent-correct or target-correct identification rate) was calculated for each target/competitor condition. The *average number of vowels reported* per stimulus was also recorded.

B. Results

Two overlapping subsets of the conditions are considered separately. The first subset consists of ($\Delta F_0=0\%,0.4\%$)$\times$(segment$=1,2,3,4$). The second subset consists of conditions ($\Delta F_0=0\%,0.4\%,0.8\%,1.5\%,3\%,6\%$), the first two of which are the ($\Delta F_0=0\%,0.4\%$) conditions of the first subset averaged over phase conditions. Segment conditions at $\Delta F_0=0.8\%$ showed no interesting differences and are not discussed in detail. Results are considered at target-to-competitor ratios of -15 and 0 dB. Identification rates at $+15$ dB were essentially perfect and are not discussed.

1. Segment effects at 0% and 0.4%

Target-correct identification rates for the subset ($\Delta F_0=0\%,0.4\%$)$\times$(segment$=1,2,3,4$) were submitted to a repeated-measures ANOVA with factors ΔF_0 and segment. This analysis was performed for target/competitor ratio $=-15$ and 0 dB.

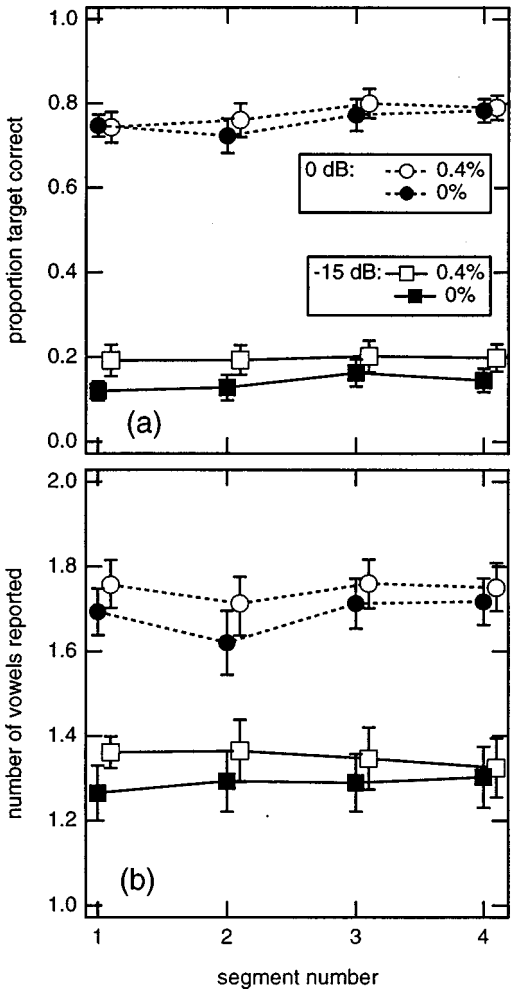

FIG. 11. Experiment 1. Target-correct identification rate (a) and number of vowels reported per stimulus (b) as a function of segment number, for $\Delta F_0=0\%$ (filled symbols) and 0.4% (open symbols), at 0 dB (circles) and -15 dB (squares). Error bars represent $\pm$ one standard error of the mean.

At -15 dB, the main effect of ΔF_0 was significant [$F(1,14)=17.42$, $p=0.0009$], as was that of segment [$F(3,42)=3.59$, $p=0.044$, GG$=0.63$] [Probabilities reflect, where necessary, a correction factor applied to the degrees of freedom to compensate for the correlation of repeated measures (Geisser and Greenhouse, 1958)]. Their interaction was not significant. Identification rates are plotted in Fig. 11(a) (square symbols). Identification was better at $\Delta F_0=0.4\%$ than at 0%. The average number of vowels reported per stimulus was also submitted to an ANOVA with factors ΔF_0 and segment. The main effect of ΔF_0 was again significant [$F(1,14)=14.65$, $p=0.0018$], that of segment was not, and their interaction was significant [$F(3,42)=4.78$, $p=0.0079$, GG$=0.90$]. The number of vowels reported per stimulus is plotted in Fig. 11(b) (square symbols).

At 0 dB, neither the main effect of ΔF_0 nor that of segment, nor their interaction were significant. The lack of segment effect or interaction was somewhat unexpected, as the similarity in amplitudes of partials of both vowels was expected to result in strong waveform interactions. In the

study of Assmann and Summerfield (1994), in which segment effects were found, vowels in a pair were excited by the same source (equal ''vocal effort'') and their rms levels were almost the same. The number of vowels reported was significantly affected by both ΔF_0 [$F(1,14)=9.43$, $p=0.008$] and the segment factor [$F(3,42)=3.78$, $p=0.04$, GG$=0.62$]. Their interaction was not significant. The identification rate and number of vowels reported are plotted in Fig. 11(a) and (b) (round symbols). An explanation for the rather small segment effects at 0 dB may be found in the pairwise response data described further on.

2. ΔF_0 effects

At target/competitor relative level$=-15$ dB, differences between segments were significant but not large, so one can reasonably average scores over segments for the lowest ΔF_0's. Target-correct identification rates for conditions ($\Delta F_0=0\%,0.4\%,0.8\%,1.5\%,3\%,6\%$) were submitted to a repeated-measures ANOVA with the single factor ΔF_0. The effect of ΔF_0 was significant [$F(5,14)=79.97$, $p<0.0001$, GG$=0.36$]. Identification rate is plotted with squares in Fig. 12(a). The average number of vowels reported per stimulus is plotted with squares in Fig. 12(b). There is a gradual increase of both measures with increasing ΔF_0. The question of the significance of the step between $\Delta F_0=0\%$ and 0.4% is discussed in Sec. III B. At target/competitor ratio$=0$ dB, effects were smaller than at -15 dB, as observed in previous experiments (de Cheveigné *et al.*, 1997a, b). Identification rates and number of vowels reported are plotted as circles in Fig. 12(a) and (b).

3. Segment effects for individual vowel pairs

Waveform interactions are expected to favor the identification of certain segments over others, but there is no reason why the pattern across segments should be the same for all vowel pairs. Data were reanalyzed with vowel pair as a factor (20 levels). Four separate analyses were performed, one on each of the subsets: $(0,-15\,\text{dB})\times(0\%,0.4\%)$. For each, an ANOVA was performed with factors (segment$=1,2,3,4)\times$(vowel pair).

At 0 dB and $\Delta F_0=0\%$, the main factors of segment and vowel pair were significant [$F(3,42)=5.57$, $p=0.0084$, GG $=0.69$, and $F(19,266)=9.21$, $p<0.0001$, GG$=0.27$ respectively]. The segment$\times$pair interaction was also significant [$F(57,798)=2.71$, $p=0.005$, GG$=0.17$]. Identification rates are plotted in Fig. 13 as a function of segment number for all pairs, six of which are labeled. For u/a and u/e, identification dropped between the first and second segments, and increased thereafter. For o/u and e/i, it instead increased and then leveled off or dropped, while for o/a the greatest change was between the second and third segment. Patterns are indeed different for different vowel pairs.

At 0 dB and $\Delta F_0=0.4\%$, the pair effect was significant [$F(19,266)=6.46$, $p<0.0001$, GG$=0.27$]. The segment effect was also significant [$F(3,42)=3.2$, $p=0.044$, GG $=0.825$] but small and the interaction with pair was not significant. Thus, the large pair-specific segment effects observed at $\Delta F_0=0\%$ were not found at $\Delta F_0=0.4\%$. At -15

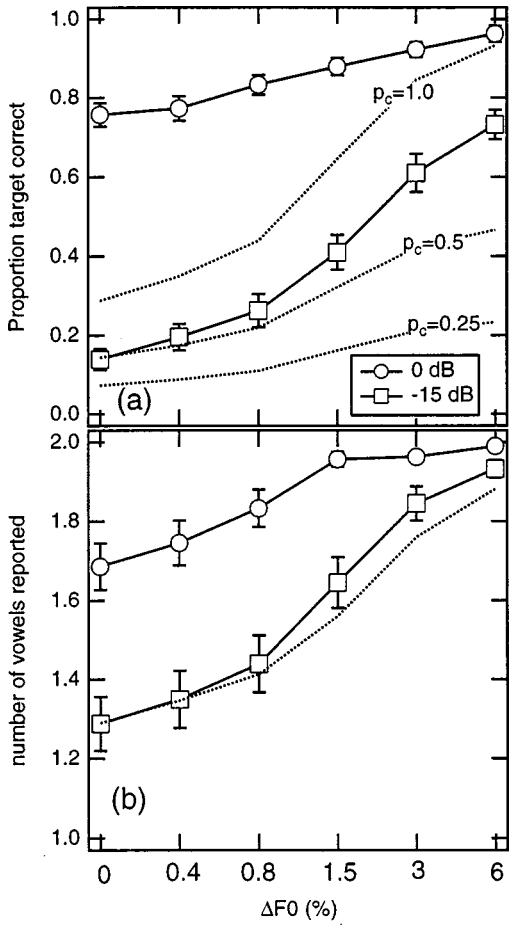

FIG. 12. Experiment 1. Target-correct identification rate (a) and number of vowels reported per stimulus (b) as a function of ΔF_0, at 0 dB (circles) and -15 dB (squares). Data points at the lowest three ΔF_0's are averaged over segment conditions. The dotted lines are predictions of one measure based on the other. The dotted lines in (a) show the identification rate expected supposing that the probability of the second vowel being correct is constant and equal to 1.0 (top), 0.5 (middle), or 0.25 (chance, bottom), and that responses are determined entirely by the subjects' tendency to report two vowels. The dotted line in (b) supposes instead that the number of vowels reported is determined by the identifiability of the second vowel as measured by the identification rate (see text).

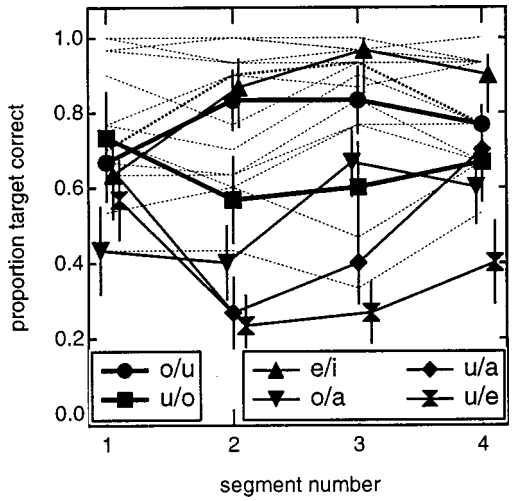

FIG. 13. Experiment 1. Identification rate as a function of segment number for individual vowel pairs, for $\Delta F_0=0\%$ and target/competitor ratio$=0$ dB.

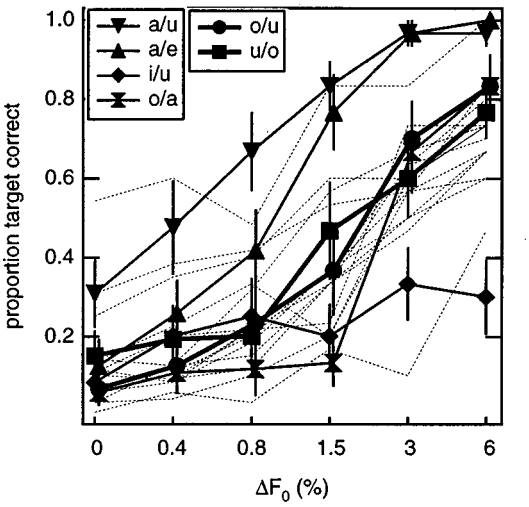

FIG. 14. Experiment 1. Identification rate as a function of ΔF_0 for individual vowel pairs, at target/competitor ratio $=-15$ dB (averaged where appropriate over segment).

dB, at both ΔF_0's, the main factors of segment and vowel pair were both significant but their interaction was not. The pair-specific segment effects observed at 0 dB and $\Delta F_0 = 0\%$ did not generalize to the case where the target vowel was weaker than its competitor. To summarize, strong pair-specific segment effects were found, but only at 0 dB and only for $\Delta F_0 = 0$.

4. ΔF_0 effects for individual vowel pairs

It is likewise interesting to know whether ΔF_0 effects were different between vowel pairs. The data for -15-dB targets were submitted to a repeated-measures ANOVA with factors $(\Delta F_0 = 0\%, 0.4\%, 0.8\%, 1.5\%, 3\%, 6\%) \times$ (vowel pair). The main effect of ΔF_0 was highly significant as found before, as was the main effect of pair. Their interaction was also significant [$F(95,1330) = 2.84$, $p = 0.0018$, GG $= 0.12$], indicating differences between pairs in the pattern of dependency of identification on ΔF_0. Data are plotted in Fig. 14 for all 20 pairs, 6 of which are labeled. Pairs o/u and u/o are typical of most. The ΔF_0 effect was largest for pair a/e and smallest for pair i/u. For o/a, identification hardly improved with ΔF_0 until 1.5%, after which it jumped sharply. The increment between 0% and 0.4% was positive for 18 out of 20 pairs. In summary, the average rates plotted in Fig. 12 are representative of most of the pair-specific trends.

IV. EXPERIMENT 2: VERY SMALL ΔF_0's

Experiment 1 found significant effects at the lowest ΔF_0 (0.4%), suggesting that measurable effects might be found at still lower values. Experiment 2 introduced ΔF_0's of 0.2% and 0.1%. Experiment 1 found segment effects that were either small or inconsistent across vowel pairs, but the segment conditions represented only a small sample of possible starting phases. Experiment 2 introduced two phase conditions likely to produce more radical waveform interaction effects: same and opposite phase. In Experiment 1, all F_0's were clustered around 132 Hz, and it is conceivable that many repetitions might have allowed the auditory system to ''tune in'' to this frequency, and perform segregation with an unnatural degree of accuracy. In experiment 2, F_0's were roved between three regions (124, 128, and 132 Hz) to discourage any such hypothetical fine tuning. The 0-dB inter-vowel relative level of experiment 1 was replaced by 5 dB, in the hope that identification rates at $+5$ dB would not be so high as to be at a ceiling, and thus possibly informative.

A. Methods

Methods were as in experiment 1. Single vowels were synthesized at F_0's of 124, 128, and 132 Hz, and at F_0's higher by 0.125, 0.25, 0.5, and 1 Hz. Single vowels were paired and added with a relative level of 5 or 15 dB, to form double vowels with ΔF_0's of approximately 0%, 0.1%, 0.2%, 0.4%, and 0.8% (the precise percentage depends on the baseline F_0). The 0.4% and 0.8% conditions at 15 dB were identical to conditions of experiment 1, apart from their starting phases and F_0's. Vowels were added in phase, denoted ''0,'' or else the polarity of one vowel was reversed before summation, denoted ''π.'' There were a total of 800 double vowel stimuli (vowel pair=/ae/,/ai/,/ao/,/au/,/ei/,/eo/, /eu/,/io/,/iu/,/ou/)$\times$(relative level$=-15,-5,5,15$ dB)$\times$(phase $=$''0,''''π'')$\times(5\Delta F_0$'s)$\times(2F0$orders). Absolute F_0 was assigned randomly from trial to trial. Again, the stimulus set lacked single vowels.

Note that the in-phase condition of experiment 2 is not quite the same as the segment 1 condition of experiment 1. The first segment at $\Delta F_0 = 0\%$ in experiment 1 was the sum of two vowels out of phase by $0.5 \pm T_0/16$, rather than perfectly in phase as in experiment 2. At $\Delta F_0 = 0.4\%$ and 0.8% the in-phase conditions of experiment 2 are the same as the segment 1 conditions of experiment 1.

B. Results

At target/competitor ratio $=-15$ dB, identification scores were submitted to a repeated-measures ANOVA with factors ΔF_0 and phase. The main effect of ΔF_0 was significant [$F(4,56) = 10.73$, $p = 0.0002$, GG $= 0.56$], as were those of phase [$F(1,14) = 18.44$, $p = 0.0007$] and their interaction [$F(4,56) = 7.46$, $p = 0.0015$, GG $= 0.57$]. Identification rates are plotted as full symbols in Fig. 15 as a function of ΔF_0 for the same-phase condition (downward pointing triangles) and the antiphase condition (upward pointing triangles). Also plotted are rates obtained in experiment 1 averaged over segment (dotted line).

Because of the difference in identification rate between phases at $\Delta F_0 = 0\%$, patterns of variation with ΔF_0 are not the same for both phase conditions. They cannot meaningfully be averaged, and one cannot speak of a ''ΔF_0 effect'' on the basis of these data. Nevertheless, given that phase effects were small for $\Delta F_0 = 0.4\%$ and 0.8%, one can compare corresponding data points of experiments 1 and 2 and conclude that roving the F_0 did not affect identification for ΔF_0's that size. At $\Delta F_0 = 0\%$, identification was better for same- than for antiphase, possibly because formants of the weaker vowel tended to produce ''bumps'' in the compound spectrum in the first case, and ''dips'' in the second. Spectral peaks are known to be perceptually more prominent than

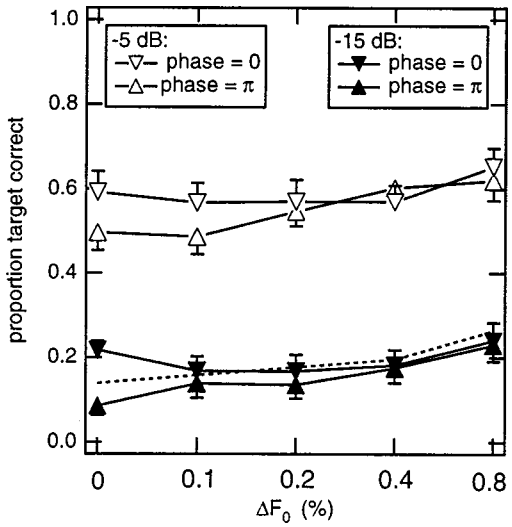

FIG. 15. Experiment 2. Identification rate a function of ΔF_0, at target/competitor ratios of -5 dB (open symbols) and -15 dB, for the same phase (downward pointing triangles) and opposite phase (upward pointing triangle) conditions. To avoid overlap, only half error bars are plotted. The dotted line represents scores from experiment 1 averaged over segment conditions.

valleys. Experiment 1 gave identification rates intermediate between these two, possibly because the phases used in experiment 1 produced spectra that were less radically favorable or unfavorable. For nonzero ΔF_0's, the differences between phase conditions were smaller, presumably because ongoing phase shifts quickly disrupted the favorable or unfavorable spectral summation that occurred at $\Delta F_0 = 0$.

For -5 dB targets, identification rates for the weaker vowel were submitted to a repeated-measures ANOVA with factors ΔF_0 and phase. The main effect of ΔF_0 was significant [$F(4,56) = 13.55$, $p < 0.0001$, GG$= 0.71$], as were those of phase [$F(1,14) = 9.01$, $p = 0.0095$] and their interaction [$F(4,56) = 4.92$, $p = 0.0035$, GG$= 0.84$]. Identification rates are plotted as open symbols in Fig. 15 as a function of ΔF_0 for the same-phase condition (downward pointing triangles) and the opposite-phase condition (upward pointing triangles). As observed at -15 dB, at 0 dB and $\Delta F_0 = 0\%$ the opposite-phase condition was unfavorable for identification compared to the same-phase condition. For $+5$ dB targets, contrary to what was hoped, identification rates were at a ceiling and no interesting effects were observed.

V. DISCUSSION

A. ΔF_0 effects

The ΔF_0 effects generally agree with other studies. At 6% they reproduce effects found previously with the same task and similar stimuli (de Cheveigné *et al.*, 1997a, b). At 1.5% and 3% they agree (allowing for differences in experimental procedure) with the observations of Assmann and Summerfield (1990, 1994) and Culling and Darwin (1993, 1994), and show that those observations were not particular to the starting phases they used. Effects found at 0.8% and 0.4% extend those studies and show that identification of concurrent vowels can benefit from F_0 differences that are very small indeed. For weak targets (-15 dB), effects did not differ radically within the set of starting phases we sampled, nor among different vowel pairs. The step in identification rate between $\Delta F_0 = 0$ and 0.4% was positive for 18 pairs out of 20, and 6 phase conditions out of 6.

On casual listening, stimuli at small ΔF_0's did not seem to have two pitches, and did not even sound strikingly inharmonic. In natural speech F_0's are unlikely to remain in such close proximity for any period of time. If they did, the imperfect periodicity of real speech would probably prevent such small ΔF_0's from being exploited. The ecological value of F_0-guided segregation mechanisms is no doubt limited to larger ΔF_0's. Nevertheless, the limit of small ΔF_0's is of theoretical interest as it reveals the pattern of breakdown of segregation mechanisms as ΔF_0 cues vanish. The gradual decrease of effect size suggests the gradual degradation of a single mechanism rather than a transition to a different mechanism.

B. Segment and phase effects

Segment effects in experiment 1 were either nonsignificant or small when averaged over vowel pairs. Individual pairs showed relatively strong effects, but only at $\Delta F_0 = 0$ and target/competitor ratio$= 0$ dB. However, these pair-specific effects were not significant at $\Delta F_0 = 0.4\%$, nor at any ΔF_0 at -15 dB. Overall, segment effects were small in comparison to ΔF_0 effects.

The segment conditions of experiment 1 represent one particular sample of starting phase spectra (various degrees of uniform delay applied to all partials of both vowels). Experiment 2 used another sample (in phase and antiphase) and found larger effects at both 0 and -15 dB. In-phase was favorable and antiphase unfavorable, but this effect was strong only at $\Delta F_0 = 0\%$ and decreased rapidly with ΔF_0's as small as 0.1% or 0.2%. At its largest, it was of the same order as the ΔF_0 effect observed between 0% and 0.4%, that is, small.

C. Evidence for a beat model

Given the small size of segment effects in some conditions, or inconsistency across vowel pairs in others, it is unlikely that the waveform interactions that produced them also produced the large and consistent ΔF_0 effects. An interesting comparison can be made between identification rates at $\Delta F_0 = 0.4\%$ and 1.5%. Beat patterns at different ΔF_0's differ by a mere stretching factor. For example, the patterns found within a 62.5-ms portion of a stimulus with $\Delta F_0 = 1.5\%$ are also found within a 250-ms portion of a stimulus with $\Delta F_0 = 0.375\%$ (nominally: 0.4%). Neglecting onset effects, the four $\Delta F_0 = 0.4\%$ stimuli thus collectively contain the same set of patterns as the single stimulus used at $\Delta F_0 = 1.5\%$. Supposing that a ''best'' pattern exists somewhere within the latter stimulus, it also appears within one of the former. Based on this reasoning, the best rate over segments at 0.4% should be similar to that obtained at 1.5%. This prediction was tested by means of a repeated-measures ANOVA with factors ($\Delta F_0 = 0.4\%, 1.5\%$) $\times$ (pair), using for each pair in the $\Delta F_0 = 0.4\%$ condition the segment that gave

the best scores for that pair (on average over subjects). Identification at $\Delta F_0 = 1.5\%$ was significantly better (0.41) than the best score over 0.4% segments (0.26) [$F(1,14) = 25.7$, $p = 0.0002$]. This was despite the fact that the segment selection process biased the 0.4% scores positively, and that the slower fluctuations at that ΔF_0 should have made spectral samples easier to exploit.

Another difficulty for the ''glimpsing'' hypothesis is that strong ΔF_0 effects occur in conditions for which beat-induced variations of the excitation pattern are small. An example is the sum of /o/ and /u/ at an o/u relative level of 15 dB (Fig. 7, bottom). Beat amplitudes are small, and yet ΔF_0's produce a strong increase in identification rate for the weaker vowel (/u/) of this pair (Fig. 14). A previous study (de Cheveigné *et al.*, 1997a) found no tendency for ΔF_0 effects to be largest at relative levels that favor strong beats near a target vowel's formants.

It remains to account for the evidence that Assmann and Summerfield (1994) found in favor of the ''glimpsing'' hypothesis. They presented subjects with four consecutive 50-ms segments gated from a 200-ms double vowel. ΔF_0's ranged from $\frac{1}{4}$ to 4 semitones (approximately 1.5, 3, 6, 12.5, and 26 Hz given the baseline F_0 of 100 Hz), and therefore the ''effective duration'' of the windowed stimulus (38.6 ms between -6-dB points) was in most cases shorter than the beat period (667, 333, 167, 80, and 38.5 ms, respectively). Identification varied between segments, except at $\Delta F_0 = 0$, where the four segments were identical, and at four semitones where the beat period was equal to the effective stimulus duration. The identification rate of the 200-ms stimulus could be predicted from that of the best 50-ms segment that it contained. This prediction failed to generalize to the present study, where segment effects were observed in some conditions, but were inconsistent across vowel pairs and vanished when averaged. However, one cannot exclude that such effects might have survived averaging with a different vowel set, for example, that used by Assmann and Summerfield. A factor that may have enhanced segment effects in their study was that their stimuli were short (38.6 ms between -6-dB points) in relation to the pitch period (about 10 ms). They were also synthesized with Klatt phase, which produces relatively peaky waveforms, so that differences in alignment of the small number of peaks (three to four) relative to segment boundaries might have led to stronger effects than observable with the longer stimuli (250 ms), shorter periods (7.6 ms), and random phase spectra of the present study.

D. Evidence for a ''multiplicity cue''

The task allowed subjects to report one or two vowels at will. One can speculate whether their choice was the result of the second vowel becoming more identifiable, or the result of a mere ''multiplicity'' cue that signaled that more than one vowel was present.

Suppose that subjects reported a second vowel entirely on the basis of a ''multiplicity cue,'' and that the probability of the second vowel being correct was unaffected by ΔF_0. The identification rate should follow a linear function of the proportion of two-vowel responses. The lowest dotted line in Fig. 12(a) shows the rate expected if identification of the second vowel were at chance ($p_c = 0.25$). The middle dotted line shows the rate for $p_c = 0.5$, and the uppermost for $p_c = 1.0$ (identification limited only by the reluctance of subjects to report two vowels). The match is not particularly good, indicating that subjects' responses are unlikely to result entirely from a ''multiplicity'' cue. ΔF_0 evidently also improved the identifiability of the second vowel.

At the other extreme is the hypothesis that subjects reported a second vowel when it was correctly identifiable, possibly in addition to a fixed number of incorrect answers. The dotted line in Fig. 12(b) predicts the response count as an affine function of the identification rate with slope one, supposing 15% of incorrect responses. Given the similarity to the measured data this hypothesis is tenable, but it is of course not the only possible account for the data. It is likely that ΔF_0 enhances *both* identifiability *and* a general perception of multiple sources, and that both of these aspects determined responses.

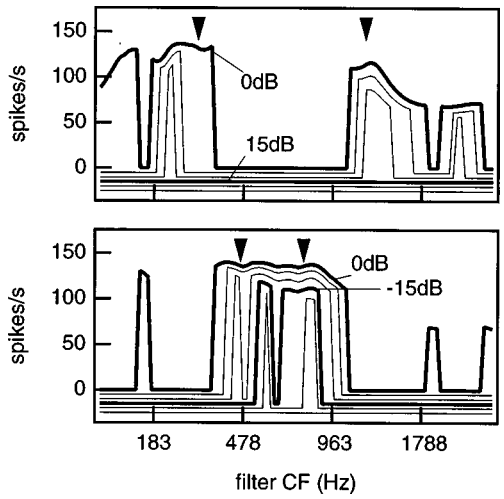

FIG. 16. Channel selection model of Meddis and Hewitt (1992). Top: output of channels *not* dominated by the periodicity of /o/ for o/u ratios of 0 to 25 dB in 5 dB steps. Nonselected channels are set to zero, and curves are offset vertically for clarity. Note that for o/u ratios$\geqslant$15 dB *all* channels are dominated by /o/, and the output is everywhere 0. Bottom: same for channels not dominated by /u/, for o/u ratios of -25 to 0 dB in 5-dB steps. In this case the model succeeds in partitioning channels at all ratios except at o/u$=-25$ dB. Arrows indicate formants $F1$ and $F2$ of /u/ (top) and /o/ (bottom).

E. Evidence for a channel-selection model

The concurrent vowel identification model of Meddis and Hewitt (1992) partitions the set of peripheral channels into two sets, dominated by one vowel or the other, on the basis of their periodicity as measured from the position of the ''period peak'' of the autocorrelation function (ACF). The partition is illustrated in Fig. 16. The top panel shows the output of channels left over after eliminating channels dominated by the periodicity of /o/ (channels dominated by /o/ are set to zero). Only data for positive o/u relative levels are shown. The lower panel similarly shows channels selected because they were not dominated by /u/, for negative o/u relative levels. Such partitions do not depend on the size of the ΔF_0, so *in principle* the model is effective for arbi-

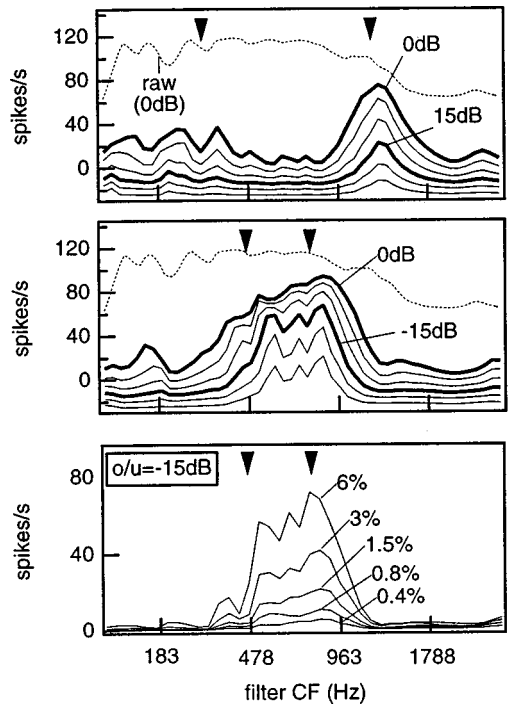

FIG. 17. Within-channel cancellation model of de Cheveigné (1997b). Top: output (full lines) of the harmonic cancellation filter as a function of CF, for o/u ratios of 0 to 25 dB in 5-dB steps, at $\Delta F_0 = 6\%$. The thin dotted line represents the input at 0 dB. The filter was tuned to cancel the period of /o/ (stronger vowel). Curves are offset vertically for clarity. Middle: same for o/u ratios of -25 to 0 dB. In this case the filter was tuned to cancel the period of /u/. Bottom: output of the cancellation filter tuned to cancel /u/, for o/u ratio $= -15$ dB and various values of ΔF_0. Arrows indicate formants $F1$ and $F2$ of /u/ (top) and /o/ (middle and bottom).

trarily small ΔF_0's. In practice, of course, smaller ΔF_0's strain the temporal resolution of the model. For example, discrimination between channels when F_0's differ by 0.4% (at 132 Hz) requires that ACF peak positions be determined with a time resolution of about 30 μs.

The pattern of selected channels characterizes the weaker vowel in a straightforward way, and it should be easy to exploit (Meddis and Hewitt's model used the low-lag portion of the summary autocorrelation function, but other schemes are possible). The main weakness of the scheme is that it breaks down if there is a level mismatch and all channels are dominated by the same vowel. Such is the case for o/u ratios of -25, 15, 20, and 25 dB (Fig. 16). Meddis and Hewitt's model cannot explain the ΔF_0 effects for u/o plotted in Fig. 14.

F. Evidence for a within-channel cancellation model

The author recently proposed a concurrent vowel identification model based on within-channel filtering to suppress responses at the period of the stronger vowel (de Cheveigné, 1997b). The top panel of Fig. 17 shows the output across channels of an array of cancellation filters tuned to the period of the vowel /o/ (data are restricted to positive o/u relative levels). The thin dotted line shows the profile before filtering (for o/u ratio $= 0$ dB). The middle panel shows the same for a filter tuned to suppress instead the period of /u/ (for negative o/u relative levels). As in Meddis and Hewitt's model, the weaker vowel is represented in a straightforward fashion. The advantage, over their model, is that the representation does not break down at extreme relative levels. It can thus explain ΔF_0 effects observed for very weak targets (de Cheveigné, 1997a, 1999).

Like Meddis and Hewitt's model, this model can work *in principle* for ΔF_0's however small. The lower panel of Fig. 17 shows the output of the filter array for various values of ΔF_0. The magnitude of the output decreases approximately linearly with ΔF_0, but in terms of ratio the pattern remains as prominent. In practice, of course, the implementation requires fine temporal resolution (as Meddis and Hewitt's model), and the neural representation must be sufficiently precise to allow the output of the cancellation filter to emerge from noise.

Like Meddis and Hewitt's model, this model assumes that the competitor is harmonic. It could possibly be extended to explain the results of Culling and Darwin (1993) (F_0's swapped between first and second formant regions) by assuming that cancellation filters are tuned differently in different channels. However, it is difficult to explain the results of Culling and Darwin (1994) with interleaved harmonics (every other partial swapped between vowels). Those results remain a mystery as far as this model is concerned.

VI. CONCLUSIONS

The F_0 differences between concurrent vowels result in complex patterns of beats and waveform interactions on the basilar membrane. These can affect identification in a phase-dependent way, but it is unlikely that they account entirely for improvements in identification with ΔF_0, even at small ΔF_0's. Effects of ΔF_0 decrease as this parameter tends to zero, but values as small as 0.4% ($\frac{1}{16}$ of a semitone) still produce a measurable benefit in terms of identification rate. To summarize, we have the following.

(1) For weak targets (target/competitor ratio $= -15$ dB), identification was improved by the presence of ΔF_0's as small as 0.4%. The effect was observed for six different phase conditions, and is unlikely to be specific to a particular choice of starting phase.
(2) Identification was in some cases affected by the choice of starting phase, confirming earlier observations by Assmann and Summerfield (1994). Effects were, however, small. In one condition (target/competitor ratio $= 0$ dB, $\Delta F_0 = 0$), strong segment effects were observed for certain pairs. However, these pair-specific effects did not generalize to $\Delta F_0 \neq 0$, or to target/competitor ratio $= 0$ dB.
(3) Given the small size of starting phase effects, it is unlikely that improvements in identification with ΔF_0 are the result of a mechanism exploiting waveform interactions or beats, at least for weak targets (-15 dB).
(4) Effects of small ΔF_0's can, in principle, be explained by the channel-selection model of Meddis and Hewitt (1992), except at extreme relative levels for which the model breaks down. The model requires high temporal resolution (on the order of 30 μs).

(5) They can also, in principle, be explained by the within-channel cancellation model of de Cheveigné (1997b). That model works, in principle, at all relative levels. In addition to high temporal resolution, it requires good linearity and a wide dynamic range.

ACKNOWLEDGMENTS

The experiments were carried out at ATR Human Information Processing Research Laboratories, within a research agreement between ATR and the Centre National de la Recherche Scientifique and University of Paris 7. The author thanks ATR for its kind hospitality, and the CNRS for leave of absence. Hideki Kawahara participated in the preparation, and Rieko Kubo supervised the experiments. Thanks to John Culling for providing the software for stimulus synthesis, and to him, Quentin Summerfield, Ray Meddis, and Sébastien Dupuis for comments. Thanks to Brian Moore, an anonymous reviewer, and the editor for their criticism. A previous version of this paper benefited from useful criticism of Winifred Strange, Chris Darwin, and one anonymous reviewer.

[1]According to Hartmann (1997, p. 462), beats between two partials are as detectable as if their envelope were reduced to its dc and fundamental component. For the deepest beats, the effective modulation percentage is thus $m=\frac{2}{3}$, implying a peak/valley ratio of 12 dB rather than infinite. For beats that are less deep, the envelope shape is closer to sinusoidal, and therefore two-partial beats are approximately equivalent to sinusoidal beats of similar peak/valley ratio.

Assmann, P. F., and Summerfield, Q. (**1990**). ''Modeling the perception of concurrent vowels: Vowels with different fundamental frequencies,'' J. Acoust. Soc. Am. **88**, 680–697.

Assmann, P. F., and Summerfield, Q. (**1994**). ''The contribution of waveform interactions to the perception of concurrent vowels,'' J. Acoust. Soc. Am. **95**, 471–484.

Brokx, J. P. L., and Nooteboom, S. G. (**1982**). ''Intonation and the perceptual separation of simultaneous voices,'' J. Phonetics **10**, 23–36.

Cherry, E. C. (**1953**). ''Some experiments on the recognition of speech with one, and with two ears,'' J. Acoust. Soc. Am. **25**, 975–979.

Culling, J. F. (**1996**). ''Signal processing software for teaching and research in psycholinguistics under UNIX and X-windows,'' Behav. Res. Methods Instrum. Comput. **28**, 376–382.

Culling, J. F., and Darwin, C. J. (**1993**). ''Perceptual separation of simultaneous vowels: Within and across-formant grouping by *F*0,'' J. Acoust. Soc. Am. **93**, 3454–3467.

Culling, J. F., and Darwin, C. J. (**1994**). ''Perceptual and computational separation of simultaneous vowels: Cues arising from low frequency beating,'' J. Acoust. Soc. Am. **95**, 1559–1569.

Darwin, C. J., and Carlyon, R. P. (**1995**). ''Auditory grouping,'' in *Handbook of Perception and Cognition: Hearing*, edited by B. C. J. Moore (Academic, New York), pp. 387–424.

Dau, T., Kollmeier, B., and Kohlrausch, A. (**1997**). ''Modeling auditory processing of amplitude modulation. I. Detection and masking with narrow-band carriers,'' J. Acoust. Soc. Am. **102**, 2892–2905.

de Cheveigné, A. (**1997a**). ''Ten experiments in concurrent vowel segregation,'' ATR Human Information Processing Research Labs technical report, TR-H-217.

de Cheveigné, A. (**1997b**). ''Concurrent vowel segregation III: A neural model of harmonic interference cancellation,'' J. Acoust. Soc. Am. **101**, 2857–2865.

de Cheveigné, A. (**1999**). ''Vowel-specific effects in concurrent vowel segregation,'' J. Acoust. Soc. Am. **106**, 327–340.

de Cheveigné, A., Kawahara, H., Tsuzaki, M., and Aikawa, K. (**1997a**). ''Concurrent vowel identification. I: Effects of relative level and *F*0 difference,'' J. Acoust. Soc. Am. **101**, 2839–2847.

de Cheveigné, A., McAdams, S., and Marin, C. (**1997b**). ''Concurrent vowel identification. II: Effects of phase, harmonicity and task,'' J. Acoust. Soc. Am. **101**, 2848–2856.

de Cheveigné, A., McAdams, S., Laroche, J., and Rosenberg, M. (**1995**). ''Identification of concurrent harmonic and inharmonic vowels: A test of the theory of harmonic cancellation and enhancement,'' J. Acoust. Soc. Am. **97**, 3736–3748.

Geisser, S., and Greenhouse, S. W. (**1958**). ''An extension of Box's results on the use of the F distribution in multivariate analysis,'' Ann. Math. Stat. **29**, 885–889.

Hartmann, W. H. (**1997**). *Signals, Sound, and Sensation* (AIP, Woodbury, NY).

Klatt, D. H. (**1980**). ''Software for a cascade/parallel formant synthesizer,'' J. Acoust. Soc. Am. **67**, 838–844.

Kohlrausch, A., and Sander, A. (**1995**). ''Phase effects in masking related to dispersion in the inner ear. II: Masking period patterns of short targets,'' J. Acoust. Soc. Am. **97**, 1817–1829.

Kuwabara, H. (**1983**). ''Vowel identification and dichotic fusion of time-varying synthetic speech sounds,'' Acustica **53**, 143–151.

Marin, C., and McAdams, S. (**1996**). ''The role of auditory beats induced by frequency modulation and polyperiodicity in the perception of spectrally embedded target sounds,'' J. Acoust. Soc. Am. **100**, 1736–1753.

Meddis, R., and Hewitt, M. J. (**1992**). ''Modeling the identification of concurrent vowels with different fundamental frequencies,'' J. Acoust. Soc. Am. **91**, 233–245.

Moore, B. C. J., and Alcántara, J. I. (**1995**). ''Identification of flat-spectrum vowels on the basis of amplitude modulation,'' J. Acoust. Soc. Am. **97**, 3274.

Moore, B. C. J., and Glasberg, B. R. (**1983**). ''Suggested formulae for calculating auditory-filter bandwidths and excitation patterns,'' J. Acoust. Soc. Am. **74**, 750–753.

Patterson, R. D., Robinson, K., Holdsworth, J., McKeown, D., Zhang, C., and Allerhand, M. (**1992**). ''Complex sounds and auditory images,'' in *Auditory Physiology and Perception*, edited by Y. Cazals, K. Horner, and L. Demany (Pergamon, Oxford), pp. 429–446.

Plack, C. J., and Moore, B. C. J. (**1990**). ''Temporal window shape as a function of frequency and level,'' J. Acoust. Soc. Am. **87**, 2178–2187.

Slaney, M. (**1993**). ''An efficient implementation of the Patterson-Holdsworth auditory filter bank,'' Apple Computer technical report, 35.

Strange, W., and Bohn, O.-S. (**1998**). ''Dynamic specification of coarticulated German vowels: Perceptual and acoustical studies,'' J. Acoust. Soc. Am. **104**, 488–504.

Strube, H. W. (**1985**). ''A computationally efficient basilar-membrane model,'' Acustica **58**, 207–214.

Summerfield, Q., and Assmann, P. A. (**1987**). ''Auditory enhancement and the perception of concurrent vowels,'' Percept. Psychophys. **45**, 529–536.

Summerfield, Q., Sidwell, A., and Nelson, T. (**1987**). ''Auditory enhancement of changes in spectral amplitude,'' J. Acoust. Soc. Am. **81**, 700–708.

Summerfield, Q., Haggard, M., Foster, J., and Gray, S. (**1984**). ''Perceiving vowels from uniform spectra: phonetic exploration of an auditory aftereffect,'' Percept. Psychophys. **35**, 203–213.

Yost, W. A., and Sheft, S. (**1989**). ''Across-critical-band processing of amplitude-modulated tones,'' J. Acoust. Soc. Am. **85**, 848–857.

Native Italian speakers' perception and production of English vowels

James Emil Flege[a)]
Department of Rehabilitation Sciences, University of Alabama at Birmingham, Birmingham, Alabama 35294

Ian R. A. MacKay
Department of Linguistics, University of Ottawa, Ottawa, Ontario K1S 5JS, Canada

Diane Meador
Speech and Language Sciences Research Laboratory, Juneau, Alaska

(Received 10 May 1999; revised 26 July 1999; accepted 29 July 1999)

This study examined the production and perception of English vowels by highly experienced native Italian speakers of English. The subjects were selected on the basis of the age at which they arrived in Canada and began to learn English, and how much they continued to use Italian. Vowel production accuracy was assessed through an intelligibility test in which native English-speaking listeners attempted to identify vowels spoken by the native Italian subjects. Vowel perception was assessed using a categorial discrimination test. The later in life the native Italian subjects began to learn English, the less accurately they produced and perceived English vowels. Neither of two groups of early Italian/English bilinguals differed significantly from native speakers of English either for production or perception. This finding is consistent with the hypothesis of the speech learning model [Flege, in *Speech Perception and Linguistic Experience: Theoretical and Methodological Issues* (York, Timonium, MD, 1995)] that early bilinguals establish new categories for vowels found in the second language (L2). The significant correlation observed to exist between the measures of L2 vowel production and perception is consistent with another hypothesis of the speech learning model, viz., that the accuracy with which L2 vowels are produced is limited by how accurately they are perceived. © *1999 Acoustical Society of America.* [S0001-4966(99)04711-6]

PACS numbers: 43.71.Hw [JMH]

INTRODUCTION

This study examined the production and perception of English vowels by groups of native Italian speakers who differed according to their age of arrival (AOA) in Canada and amount of self-reported continued use of Italian. The study addressed three questions. The first was whether the subjects' accuracy producing and perceiving English vowels would diminish as AOA increased. The second was whether the subjects who began to learn English as young children (''early'' bilinguals) would perform more like subjects in a native English comparison group than would the subjects who began to learn English as young adults (''late'' bilinguals). The final question was whether differences in amount of native language (L1) use would affect the native Italian subjects' production or perception of English vowels.

A. Previous research

Research has shown that late bilinguals often produce vowels in a second language (L2) differently than do monolingual native speakers (e.g., Major, 1987; Flege, 1992a, b; Busà, 1992, 1995; Munro, 1993; Jun and Cowie, 1994; Flege *et al.*, 1997a). Early bilinguals may produce L2 vowels more accurately than late bilinguals, although they may not produce the full range of L2 vowels exactly like monolingual native speakers.

In a study by Flege (1992a), native English-speaking listeners attempted to identify native Spanish speakers' productions of four English vowels (/i ɪ ɛ æ/). The intelligibility scores obtained for late bilinguals' vowels, but not those obtained for the early bilinguals, differed from the native English speakers' intelligibility scores. Both the early and late bilinguals produced large temporal differences between /i/–/ɪ/ and /ɛ/–/æ/. However, there was more spectral overlap between pairs of vowels produced by the late bilinguals than by the early bilinguals or the English monolinguals. In a study by Munro *et al.* (1996), native English-speaking listeners used a scale ranging from 1 (''wrong vowel or very strong foreign accent'') to 5 (''correctly produced English vowel, no foreign accent'') to rate vowels spoken by 240 native Italian subjects with AOAs ranging from 2 to 22 years. The production of an English vowel was accepted as ''nativelike'' if it received a rating that fell within two standard deviations of the mean rating obtained for native English speakers. The later the native Italian subjects began to learn English, the less likely they were to be credited with nativelike productions of English vowels.

Although early bilinguals appear to produce L2 vowels accurately overall, their production of certain vowels may differ from those of native speakers. Flege (1998) reexamined the ratings obtained by Munro *et al.* (1996) for 72 early bilinguals having AOAs of 2–8 years and 72 late bilinguals having AOAs of 16–22 years. A mean rating was calculated for each subject's production of English /i ɛ ɑ/

a)Electronic mail: jeflege@uab.edu

(which each differ slightly from a vowel found in Italian) and /ɪ ʊ ɚ/. The second set of English vowels might be considered ''new'' in the sense that no such vowels occur contrastively in Standard Italian. The results of the reanalysis were consistent with two hypotheses of the speech learning model, or SLM (Flege, 1995). As predicted, the late bilinguals' vowels received lower ratings (i.e., were more foreign accented) than the early bilinguals' vowels. This supported the hypothesis that the later L2 learning begins, the less likely L2 learners are to establish new categories for vowels in the L2. The early bilinguals' productions of /i ɛ ɑ/ but not /ɪ ʊ ɚ/ received significantly lower ratings than native English speakers' vowels. The presence of a detectable foreign accent in the early bilinguals' productions of /i ɛ ɑ/ was attributed to the blockage of category formation for these English vowels by the presence of phonetically similar Italian vowels. This finding was consistent with another hypothesis of the SLM, namely that the likelihood of category formation for L2 vowels is directly related to degree of perceived cross-language phonetic similarity.

Previous findings for vowel perception broadly parallel those just reported for vowel production. Research examining vowel perception has shown that late bilinguals often differ from monolingual native speakers. However, the magnitude of native versus non-native differences seems to depend on the degree of perceived similarity between L2 vowels and the closest L1 vowel (Polka, 1995; Best *et al.*, 1996; Flege *et al.*, 1997a, 1998; see also Best and Strange, 1992). The relation between AOA and the perception of L2 vowels and consonants (or ''sounds,'' for short) is as yet uncertain. MacKay *et al.* (under review) found that the frequency with which native Italian subjects erred in identifying word-initial English consonants increased as AOA increased. Yamada (1995) found that the earlier native speakers of Japanese had arrived in the United States (US), and the longer they had lived in the US, the more accurately they perceived synthetic English /ɹ/ and /l/ tokens.

To our knowledge, no previous study has assessed the effect of AOA on L2 vowel perception (see Strange, 1995). However, the results of several studies suggest that early bilinguals may not perceive all L2 vowels in a nativelike fashion. Mack (1989) examined the identification and discrimination of the members of a synthetic English /i/–/ɪ/ continuum by English monolinguals and early bilinguals who had learned both of their languages (English and French) as young children. The two groups' vowel discrimination did not differ, but the location of their phoneme boundaries did differ. This led Mack to conclude that the early bilinguals' perception of English vowels ''approximated but did not match'' that of monolinguals (p. 187).

More recently, Pallier *et al.* (1997) examined native speakers of Spanish who had begun to learn Catalan by the age of 6 years, had lived in Barcelona since birth, used both Catalan and Spanish frequently, and were highly proficient in both languages. The task was to identify and discriminate the members of a synthetic Catalan /e/–/ɛ/ continuum. (Catalan and Spanish both have an /e/, whereas Catalan but not Spanish has an /ɛ/.) The grouped identification function obtained for native speakers of Catalan revealed a clear crossover from /e/ to /ɛ/, and a discrimination peak near the phoneme boundary. However, the identification function obtained for the Spanish/Catalan bilingual group was flat, and this group's discrimination function revealed no peak. The authors concluded from these findings that ''even early exposure... is not sufficient'' for many individuals to learn ''two new phonetic categories which overlap'' a single L1 vowel category (1997, B14).

Finally, Sebastián-Gallés and Soto-Faraco (in press) used a modified version of the gating procedure to examine the identification of vowels in naturally produced disyllabic Catalan nonwords. The subjects' task was to identify the first vowel in CVC(C)V words as /e/ or /ɛ/ (or as /o/ or /ɔ/ in another condition). Spanish/Catalan bilinguals needed to hear significantly longer portions of the stimuli than did native speakers of Catalan in order to identify the Catalan vowels correctly. The authors concluded that the malleability of phonemic categories is severely limited, and that even early and extensive exposure to an L2 may be insufficient to ''overcome the influence of L1 phonemic categories in the formation of new non-native categories.''

B. The present study

The present study examined the production and perception of English vowels by four groups of Italian/English bilinguals. The subjects in three of the groups were selected on the basis of AOA. AOA averaged 7 years for the group designated ''early,'' 14 years for the group designated ''mid,'' and 19 years for subjects in the ''late'' group. The subjects in these three groups reported using Italian 31% of the time, on the average. The native Italian subjects in a fourth group, designated ''early-low,'' consisted of individuals who were matched to the subjects in the early group for AOA but reported using Italian less ($M=8\%$).

Experiment 1 of the present study assessed the production of ten English vowels (/i ɪ eˡ ɛ æ u ʊ o ʌ ɒ/). An intelligibility score was obtained for each vowel token by determining the percentage of times it was heard as intended by a panel of native English-speaking listeners. Research has shown that foreign accents in an L2 become progressively stronger as AOA increases (e.g., Flege *et al.*, 1995). Other research has shown that the more bilinguals continue to use their L1, the stronger their foreign accent in the L2 will be (Flege *et al.*, 1997a; Piske and MacKay, 1999; Guion *et al.*, under review). Still other research has shown that a strong correlation exists between overall degree of perceived foreign accent and the accuracy with which specific L2 vowels are produced (see Flege, 1998, for review). These findings led to two predictions concerning the vowel production results that might be obtained in experiment 1. The first was that the native Italian subjects' intelligibility scores would decrease as AOA increased. The second prediction was that the early bilinguals who used Italian often would produce English vowels less accurately than would the early bilinguals who used Italian seldom (i.e., subjects in the early-low group).

Vowel perception was assessed in experiment 2 using a categorial discrimination test. This test assessed phonetic sensitivity to contrasts between two English vowels (/i/–/ɪ/,

/u/–/ʊ/, /æ/–/ʌ/, and /ɒ/–/ʌ/), between an English vowel and an Italian vowel (/æ/–/a/, /ʌ/–/a/, /ʊ/–/o/, and /eᴵ/–/e/), and between two Italian vowels (/u/–/o/, /e/–/a/, /u/–/i/). Standard Italian contains the vowels /i e ɛ a ɔ o u/ (Agard and DiPietro, 1964). The vowel systems acquired as children by the native Italian subjects examined here were likely to vary (e.g., Trumper, 1995). We can nevertheless be sure that all of them contained fewer vowels than English. This being the case, both vowels in some of the ''English–English'' and ''English–Italian,'' contrasts were likely to have been identified as instances of one Italian category, at least at early stages of L2 acquisition.

It was more difficult to generate predictions concerning the discrimination scores than for the intelligibility scores obtained in experiment 1. For one thing, no previous study has examined the effect of AOA on vowel perception. Moreover, two existing theoretical models led to differing expectations. The spectral and temporal properties which define any L1 vowel category vary idiolectally and dialectally, and according to factors such as speaking rate and degree of stress. Thus, over time, the likelihood that typical realizations of an L2 vowel will fall within the range of tokens previously identified as being instances of an L1 category is likely to increase (Flege, 1992b). Also, as L1 categories become better defined during L1 development, they might ''assimilate'' L2 tokens more strongly (e.g., Best *et al.*, 1996; see also Kuhl, 1993).

According to the SLM, the formation of new phonetic categories (or functional equivalence classes; see, Kluender *et al.*, 1998) for L2 vowels becomes less likely with increasing age. By hypothesis, L2 vowels of a given degree of phonetic similarity to the closest L1 vowel will, with increasing age, become more likely to be heard as instances of an existing L1 category (i.e., to be functionally ''equated''). If this hypothesis is correct, then one would expect the early bilinguals examined here to discriminate L2 vowels—both from one another and from neighboring L1 vowels—more accurately than the late bilinguals. (This prediction assumes, of course, that instances of the two vowel categories being discriminated would, in early stages of exposure to the L2, be identified as instances of a single L1 category.)

The perceptual assimilation model (PAM) developed by Best and her colleagues (e.g., Best, 1995, 1999; Best *et al.*, 1996) does not predict an effect of AOA on L2 vowel discrimination. According to the PAM, the discriminability of any pair of vowels in an L2 will depend on the degree of perceived similarity of the L2 vowels to vowels in the L1. (As for the SLM, the perceived relation of phones drawn from two languages is assessed through listeners' classifications and ratings of goodness of fit to categories in the L1.) The PAM attributes ''malleability'' to the perceptual systems of adult L2 learners, and predicts that L2 vowel discriminability may improve as a function of L2 experience (Best and Strange, 1992). However, the PAM does not predict age-related differences in the perceived similarity of L2 vowels to the closest L1 vowel(s). Thus, the PAM leads to the expectation that AOA will not affect the discrimination of contrasts between two L2 vowels whose realizations are likely to be identified as instances of a single L1 category.

The data obtained in experiments 1 and 2 are relevant to the issue of how L2 segmental production and perception are related. This topic has generated considerable discussion over the years (see, e.g., Strange, 1995; Flege, 1999a, b). According to some (e.g., Rochet, 1995), the accuracy with which L2 phonetic segments are produced is limited by how accurately they are perceived. However, Bever (1981) hypothesized that a ''critical'' period for L2 speech learning ends when the phonological system of the L1 is fully established because there is no longer a need to align speech production and perception. On this view, L2 production accuracy will not be constrained by perceptual accuracy. In support of this, native Japanese speakers of English have been observed to produce /ɹ/ and /l/ accurately, yet to differ from native speakers in perceiving English liquids (e.g., Goto, 1971; Sheldon and Strange, 1982). Were such a finding to generalize to the production and perception of English vowels by highly experienced speakers of an L2, it would undermine the SLM. According to the SLM, learners of all ages retain the capacity to align their production of L2 phonetic segments to long-term memory representations for vowels and consonants in the L2. On this view, many segmental production errors observed for experienced speakers of an L2 are likely to have a perceptual basis. This hypothesis leads to a final prediction, namely that if early bilinguals are found to produce L2 vowels accurately, then they will also perceive L2 vowels accurately.

The present article is organized as follows. The vowel production experiment will be presented first, then the vowel discrimination experiment. The relation between the intelligibility scores obtained in experiment 1 and the discrimination scores obtained in experiment 2 will then be assessed in the third section. This will be done through regression analyses, and by comparing the vowel perception accuracy of subgroups of native Italian subjects who differed in L2 vowel production accuracy.

I. GENERAL METHOD

A. Subjects

Seventy-two of the subjects were born in Italy and began to learn English when they immigrated to Canada. All but two of the native Italian subjects were from working-class backgrounds (as indicated by parental occupation). They had lived in Canada for an average of 35 years at the time of testing, the minimum being 18 years. Most of the native Italian subjects were members of, or socially connected to, a predominantly Italian Roman Catholic parish in Ottawa where testing was carried out. The 18 monolingual native English speakers (or ''native English,'' for short) who were tested were also long time residents of Ottawa. The mean age of the 90 subjects was 48 years (s.d.=6). Subjects in the five groups did not differ in age [$F(4,85)=0.05$, $p>0.10$]. All 90 subjects passed a pure tone hearing screening (defined using a 35 dB HL criterion at 500, 1000, 2000, and 4000 Hz in the best ear) prior to participating; none of them reported a history of auditory disorder.

TABLE I. Characteristics of the five groups of subjects. ''Age'' indicates mean chronological age, in years. ''AOA'' and ''LOR'' indicate the native Italian subjects' mean age of arrival and length of residence in Canada, in years, and ''%Italian'' their mean self-estimated percentage use of Italian. Standard deviations are in parenthesis.

	Gender	Age	AOA	LOR	% Italian
Native	9m,9f	48 (7)	···	···	···
Early-low	9m,9f	48 (5)	7 (3)	40 (5)	8 (6)
Early	8m,10f	47 (6)	7 (2)	40 (6)	32 (16)
Mid	8m,10f	48 (6)	14 (1)	34 (7)	20 (11)
Late	8m,10f	48 (6)	19 (1)	28 (5)	41 (23)
M	···	48 (6)	12 (6)	35 (7)	25 (19)

As summarized in Table I, three groups of native Italian subjects differed primarily according to AOA (early—7, mid—14, late—19 years). Subjects in the early-low group were matched to those in the early group for AOA, but reported using Italian less (8% vs 32%). As summarized by MacKay *et al.* (under review), subjects in the early-low group seldom used Italian except when visiting relatives. They were less likely than were subjects in the early group to report using Italian at home, at work, on the telephone, or at social gatherings. There are reasons to think that the self-reports of Italian use were valid and reliable. There was a strong inverse correlation between the native Italian subjects' self-reported use of English and Italian ($r=-0.96$, $df=70$, $p<0.01$). There was also a strong correlation between the Italian use self-reports given by 62 subjects in this study and those given by these same subjects when they participated in the Flege *et al.* (1995) study [$r(60)=0.84$, $p<0.01$]. Also, as reported by MacKay *et al.* (under review), subjects in the early-low group made more grammatical and lexical errors when speaking Italian extemporaneously than did subjects in the early group.

As expected from previous research (e.g., Flege *et al.*, 1995; Yamada, 1995), the native Italian subjects' AOAs were correlated inversely with length of residence (LOR) ($r=-0.62$, $df=70$, $p<0.01$), leading to a significant effect of group on LOR [$F(3,68)=16.1$, $p<0.01$]. Also, the earlier the native Italian subjects had arrived in Canada, the less schooling they had received in Italy. The difference between groups (early-low: 1.8 years, early: 1.9 years, mid: 6.6 years, late: 8.5 years) was significant [$F(3,68)=46.3$, $p<0.01$].

All but 3 of the 72 native Italian subjects came from southern Italy. As discussed later, the vowel systems of southern Italian dialects differ in terms of the number and phonetic quality of contrastive vowels. Differences in the native vowel systems might have influenced the results obtained here, either for production or perception. However, the place of birth—and therefore by extension the native dialect—of the native Italian subjects did not appear to vary systematically across the four groups.

B. Procedure

The subjects participated in several experiments in addition to those reported here during two 1-h sessions. The other experiments involved repeating meaningful English sentences; speaking extemporaneously in English and Italian; identifying English consonants presented in noise (MacKay *et al.*, under review); and repeating semantically unpredictable English sentences (Meador *et al.*, under review). Also, as reported by MacKay *et al.*, the subjects repeated nonwords that were formed by splicing together 2–5 Italian CV syllables. This was done to assess phonological short-term memory. The dependent measure was the number of nonwords that were repeated correctly.

II. EXPERIMENT 1

The purpose of this experiment was to evaluate the native Italian subjects' productions of ten English vowels, /i ɪ eᴵ ɛ æ ɒ ʌ ɒ ʊ u/. This was done by determining the percentage of times that native English-speaking listeners heard the target vowels as intended.

A least some of the English vowels were likely to differ from vowels found in the native dialect of the native Italian subjects. Standard Italian is usually described as having seven vowels, /i e ɛ a o ɔ u/ (e.g., Agard and DiPietro, 1964). However, the number and nature of vowels in southern Italian dialects differ. For example, Romito and Trumper (1989) described a southern Italian dialect having eight vowels (/i y e ɛ æ ʌ ɔ u/) and another with five vowels (/i ɛ a o u/). Trumper (1995) observed that /a/ can be implemented with variants ranging from [æ] to [ɑ] in southern Italy. Further, southern Italians living in North America may speak a ''central-southern standard'' form of Italian in addition to their native dialect (Milani, 1996, p. 480). Although we cannot be certain what vowels the native Italian subjects' possessed when they arrived in Canada, we can be confident that considerable phonetic learning would be required for them to produce all 10 of the English vowels accurately.

A. Method

The technique used here to elicit the production of English words was similar to that employed by Bradlow *et al.* (1997). The subjects were provided with both visual and auditory prompts. The visual prompts consisted of a written list of four-word sequences, each of which contained one of the 10 target vowels of interest (e.g., *read, deed, heed, bead* for the vowel /i/). The auditory prompts, which were presented via a loudspeaker, consisted of digitized versions of the four-word sequences that had been spoken by an adult male native speaker of English. The sequences were presented in the same order in which they appeared on the written list. The subjects were told to say the four words in each sequence after hearing the entire sequence. Auditory prompts were used in addition to orthography to reduce the likelihood of spelling pronunciations (e.g., production of the /ɪ/ in ''bid'' as [i] because ''i'' in written Italian is pronounced [i]). However, the availability of native-produced models might conceivably have led to an overestimation of the native Italian subjects' accuracy in producing certain English vowels.

The subjects' production of the English words was recorded using a head-mounted microphone (Shure SM10A) and a portable DAT tape recorder. The final word in each sequence (viz., *bead, bid, bade, bed, bad, booed, bode, bud, god, hood*) was digitized at 22.05 kHz, then normalized for peak intensity. Not all of the words began with /b/, and some of the words were likely to differ in familiarity to the listeners who later evaluated them (compare, e.g., *bed* to *bade*). Either or both factors might have led to biases. Therefore, the 900 words (90 subjects×10) were edited to obscure the identity of the initial and final consonants (and, thus, lexical identity) while leaving intact cues to vowel identity insofar as possible. All portions of the waveform following the complete constriction of the final /d/ (defined on the basis of changes in waveform amplitude and/or shape) were removed. Any prevoicing present in words beginning with a stop consonant (/b/ or /g/) was removed, as was the /h/ in *hood*. A weighting function was then applied to an interval at the beginning of the remaining signal.[1]

The stimuli prepared in this way were presented for identification to six young adult native speakers of English who had been born and raised in the Ottawa, Ontario region. Some of the listeners knew French, but none of them was proficient in that or any language other than English. All passed a pure-tone hearing screening before participating. The listeners were tested one at a time at the Phonetics Laboratory of the University of Ottawa. The stimuli were presented via a loudspeaker at a self-selected comfortable level using a notebook computer. The interval between each response and presentation of the next stimulus was fixed at 1.0 s.

The listeners used keywords to identify the vowel in each stimulus. The vowels were randomly presented in two counterbalanced sets to restrict the number of keywords needed to represent the English vowels that were likely to be heard. The keywords offered for /i ɪ eᴵ ɛ æ/ were *heed, hid, hayed, head, had, hot,* and *hut*. The keywords offered for /u ʊ o ʌ ɒ/ were *who'd, hood, hoed, hut, hot, head,* and *had.* The listeners were told to identify each vowel by clicking one of seven keywords shown on the screen. Pilot work had been undertaken to identify the vowels most likely to be heard. However, given the possibility that listeners might hear some other English vowel, they were given a list of additional keywords that represented all of the English vowels not represented by a keyword shown on the screen. A supplementary keyword was used just 17 times.[2]

B. Results

Vowels spoken by the native English speakers were identified as intended at a higher average rate ($M=94\%$ correct) than were vowels spoken by subjects in the early group ($M=92\%$), mid group ($M=87\%$), or late group ($M=67\%$). Averaged across these four groups, the rates at which individual vowels were correctly identified ranged from 83% (for /ɪ ɛ ɒ/) to 94% (for /i/).

The vowels heard instead of the target vowels were tabulated. When vowels spoken by native speakers of Italian were not heard as intended, they were most frequently heard as a vowel that was slightly lower in vowel space than the target vowel (/eᴵ/-for-/i/, /ɛ/-for-/ɪ/, /ɛ/-for-/eᴵ/, /æ/-for-/ɛ/, /ɒ/-for-/ʌ/, /ɒ/-for-/o/, /o/-for-/ʊ/, and /ʊ/-for-/u/). Exceptions to this general rule were the two low target vowels (/æ/, /ɒ/) which were most frequently heard as slightly higher vowel (/ɛ/-for-/æ/ and /ʌ/-for-/ɒ/).

A total of 720 percent correct scores (72 subjects×10 vowels) were computed. Each score was based on the identification responses of six native English listeners. Following arcsine transformation (Kirk, 1968), the intelligibility scores were submitted to a (4) group by (10) vowel ANOVA. The ANOVA yielded significant main effects of group [$F(3,68)=23.9$, $p<0.01$] and vowel [$F(9,612)=9.6$, $p<0.01$] and a significant two-way interaction [$F(27,612)=1.7$, $p=0.018$].

As summarized in Table II, the simple effect of group was significant for all vowels except /eᴵ/, /ɛ/, and /ɒ/. Turkey's tests were used to determine which pairwise differences between groups were significant for the seven vowels showing a significant group effect. Six vowels spoken by subjects in the late group (viz., /i ɪ u ʊ o ʌ/) received intelligibility scores that were significantly lower than the native English groups' scores, and one vowel spoken by subjects in the mid group (/ʌ/) received significantly lower scores ($p<0.05$). No vowel spoken by the early group received significantly lower scores than those of the native English speakers ($p>0.10$).

The 540 scores obtained for the native English speakers and the two groups of early bilinguals were submitted to a 3 (group)×10 (vowel) ANOVA. The aims of this analysis were to determine if the early bilinguals who seldom spoke Italian (early-low) produced English vowels more accurately than did the early bilinguals who spoke Italian relatively often (early), and if either group differed from the native English group. The main effect of vowel was significant [$F(9,459)=8.7$, $p<0.01$], but not the main effect of group [$F(2,51)=1.6$, $p>0.10$] or the two-way interaction [$F(18,459)=1.2$, $p>0.10$].

C. Discussion

In agreement with Munro *et al.* (1996), the later the native Italian speakers arrived in Canada, the less accurately they produced English vowels. Six vowels produced by subjects in the late group (/i ɪ u ʊ o ʌ/) received significantly lower intelligibility scores than did the native English subjects' productions of these vowels. (A seventh vowel, /æ/, received scores that were lower than those obtained for vowels spoken by subjects in the early and mid groups.) Just one vowel spoken by subjects in the mid group was significantly less intelligible than the native English speakers' vowels. However, none of the English vowels spoken by either group of early bilinguals received a significantly lower intelligibility score than did vowels spoken by the native English group. In agreement with the results of Flege (1992b), this suggests that early bilinguals who are highly experienced in their L2 may produce L2 vowels in a nativelike fashion.

III. EXPERIMENT 2

As discussed in the Introduction, the results of several recent studies suggested that early bilinguals may perceive

TABLE II. The mean intelligibility scores obtained for ten English vowels spoken by a group of native English (''NE'') subjects and three group of native Italian subjects differing in age of arrival to Canada (''early,'' ''mid,'' ''late''). Standard deviations are in parentheses. Superscript a and b indicate significance at the 0.01 and 0.001 levels; respectively. An 0.05 level was used for the Tukey's *post hoc* tests.

	Group					
	NE	Early	Mid	Late	$F(3,68)$	Tukey's test
/i/	99	95	99	84	4.03[a]	late<NE, mid
	(4)	(13)	(4)	(28)		
/ɪ/	95	97	81	57	9.26[b]	late<NE, early, mid
	(16)	(6)	(34)	(41)		
/eᴵ/	95	99	89	81	2.26	
	(20)	(4)	(24)	(36)		
/ɛ/	91	86	83	70	2.46	
	(19)	(20)	(29)	(32)		
/æ/	84	89	95	62	4.29[a]	late<early, mid
	(31)	(22)	(14)	(40)		
/ɒ/	94	83	86	72	1.75	
	(10)	(32)	(29)	(32)		
/ʌ/	86	80	48	48	6.39[b]	mid, late<NE, early
	(12)	(23)	(41)	(44)		
/o/	99	100	95	72	6.55[b]	late<NE, early, mid
	(4)	(0)	(11)	(41)		
/ʊ/	97	94	97	56	14.51[b]	late<NE, early, mid
	(6)	(10)	(6)	(40)		
/u/	94	98	91	68	7.37[b]	late<NE, early, mid
	(13)	(5)	(17)	(36)		

L2 vowels differently than monolingual native speakers do (Mack, 1989; Pallier *et al.*, 1997; Sebastián-Gallés and Soto-Faraco, in press). However, when taken together with the production results obtained in experiment 1, the speech learning model (Flege, 1995) predicts that the early bilinguals examined here would perceive English vowels in a nativelike fashion. This was tested by assessing the native Italian subjects' phonetic sensitivity to differences between pairs of English and/or Italian vowels.

Four of the 11 vowel contrasts examined in this experiment involved two English vowels (/æ/–/ʌ/, /ʌ/–/ɒ/, /i/–/ɪ/, /u/–/ʊ/). Four others involved one English and one Italian vowel (/æ/–/a/, /ʌ/–/a/, /ʊ/–/o/, /eᴵ/–/e/), and the remaining three involved two Italian vowels (/u/–/o/, /e/–/a/, /u/–/i/). Five different individuals with different-sounding voices produced tokens of each vowel category. The average frequency of the first and second formants ($F1$,$F2$) at the acoustic midpoint of the five tokens of each category are shown in Fig. 1.[3]

The vowel stimuli were examined in a categorial discrimination test using a modified oddity format. The three stimuli presented on each trial were always spoken by different talkers, and so were physically different. Half of the trials (called ''different'' trials) contained an odd item out, and the remaining half (called ''catch'' trials) contained three instances of a single category.

The subjects were offered four response alternatives rather than the two alternatives offered in ABX and AXB tests (e.g., Gottfried, 1984; Best *et al.*, 1996). They were told to identify the serial position of an odd item out, if they judged one vowel to different from the other two, by clicking a button marked ''1,'' ''2,'' or ''3.'' They were told to click a button marked ''none'' if they heard three different examples of one vowel (i.e., for the catch trials). The presence of both different trials (where one vowel differed from the remaining two) and catch trials permitted the calculation of an unbiased measure of sensitivity (A') to the phonetic difference between the vowel contrasts examined here. To obtain a high score, the subjects had to respond to relevant phonetic differences while ignoring auditorily accessible differences (e.g., in voice quality) that were not phonetically relevant.

As mentioned earlier, the vowel systems of southern Italian dialects may vary considerably. For example, Trumper (1995) observed that /a/ can be implemented with variants ranging from [æ] to [ɑ] in southern Italy.

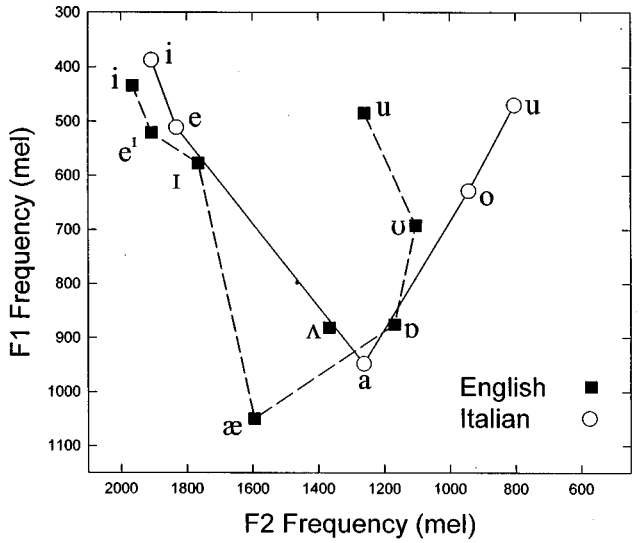

FIG. 1. The mean frequency of the first and second formants ($F1$,$F2$) in five naturally produced tokens each of English and Italian vowels, measured at the acoustic midpoint. All of the vowels shown except Italian /i/ were used as stimuli in a vowel discrimination experiment.

Given this, and the lack of empirical data pertaining to the perceived similarity of vowels in southern Italian dialects and Canadian English, it was not possible to make *a priori* predictions concerning the relative degree of discriminability of the 11 vowel contrasts examined here. However, several expectations could be derived from the acoustic values presented in Fig. 1. Among these was that the native Italian subjects would tend to identify the English /i/ and /eᴵ/ stimuli as instances of Italian /i/ and /e/, but they might not identify the fronted English /u/ stimuli as instances of Italian /u/. Other expectations were that the native Italian subjects would tend to identify the English /ɒ/ and /ʌ/ stimuli as instances of Italian /a/, and thus have difficulty with the /ʌ/–/ɒ/ contrast.

Cross-language comparisons of English and Italian (Agard and DiPietro, 1964) led us to expect that at least some native Italian subjects would have difficulty discriminating the English–English pairs /i/–/ɪ/ and /u/–/ʊ/ owing to the absence of lax vowels in Italian. The observation by Munro *et al.* (1996) that certain Italian subjects' productions of English /ʊ/ were heard as /o/, plus the acoustic data in Fig. 1, led us to expect difficulty for the English /ʊ/–Italian /o/ contrast. However, whether any of these predictions would actually be fulfilled was likely to depend on the nature of vowels in the subjects' native dialect of Italian, and also how (or if) the perceived relation between L1 and L2 vowels changes over time.

We had some general expectations concerning the three subsets of vowel contrasts examined here. We expected lower discrimination scores for the E–I (English versus Italian) contrasts than for the E–E (English versus English) contrasts. This was based on the assumption that the native Italian subjects would be more likely to identify both members of E–I contrasts as being instances of a single L1 category than to do so for both members of E–E contrasts.

We were less certain, however, how the native Italian subjects would respond to the I–I (Italian versus Italian) contrasts. The native Italian subjects might obtain near-perfect discrimination scores for the I–I contrasts because they involved two different L1 vowels. However, the SLM (Flege, 1995) leads to a different expectation, namely, that some native Italian subjects—especially those in the late group—might not obtain high scores for the I–I contrasts. According to the SLM, the subjects in the late group should be less likely than the early group subjects to form categories for English vowels. The SLM posits that when a category is not established for an L2 vowel, then the L1 category used to process tokens of the L2 vowel will change over time as the result of a process called ''assimilation.'' For example, if a category was not established for English /ʌ/, and if tokens of this vowel were judged to be instances of Italian /a/, then the extent of the Italian /a/ category might broaden so as to encompass instances of both English /ʌ/ and Italian /a/. If the late groups' Italian vowels were affected in this way more often than the early groups' Italian vowels, then the late groups' scores for the I–I contrasts might be lower than the early groups' scores.

A. Method

1. Stimuli

The English vowel stimuli were derived from words spoken by five female native speakers of English from Ottawa in a previous study (Munro *et al.*, 1996). The words (*bait, boot, back, but, bock, beat, bit, book*) were spoken at the end of a carrier phrase (*Now I say_*). A native speaker of Canadian English identified as intended all of the English vowels used as stimuli.

The Italian stimuli were derived from nonwords spoken by five female speakers of Italian living in Padua, Italy, who could be considered speakers of Standard Italian. Vowels spoken by these speakers were used as stimuli, rather than speakers of a southern Italian dialect, due to the lack of a cogent rationale for choosing one southern Italian dialect over another. The Italian nonword stimuli, which were formed by inserting /i e a o u/ into a /b_do/ frame, were produced immediately following the auditory presentation of four real words containing the vowel of interest (e.g., ''*rido, fido, lido, nido*'' for /i/). The identifiability of the Italian vowels could not be verified in a relevant fashion, as was done for the English stimuli. This is because the Italian vowels were representative of a northern Italian dialect, whereas the subjects tested here spoke varieties of southern Italian.

The English words and Italian nonwords were digitized at 22.05 kHz. Prevoicing, if any, was removed from the initial /b/ tokens, as was everything following the complete constriction of the postvocalic consonants. The edited signals were then linearly ramped off over the final 30 ms of the remaining signal. The 15 Italian stimuli were longer ($M = 243$ ms) than the 40 English stimuli were ($M = 180$ ms). Bohn (1995) hypothesized that non-native listeners may respond to differences in duration if they fail to perceive a spectral difference. The temporal difference between the Italian and English stimuli was reduced to prevent subjects from discriminating E–I contrasts on the basis of duration only. This was done by deleting ten nonsuccessive glottal pulses (mean duration = 49 ms) from the middle of the Italian vowel stimuli. The 55 stimuli were then normalized for peak intensity.

2. Procedure

The interstimulus interval between the three stimuli presented on each trial was 1.2 s. Each vowel contrast was tested by eight different trials. The odd item out in these trials occurred with equal frequency in all three possible serial positions. All 13 vowel categories were tested by four catch trials ($N = 52$) consisting of three physically different realizations of a single vowel category.

The stimuli were presented using a notebook computer. As mentioned, the subjects were told to click a button marked ''1,'' ''2,'' or ''3'' if they heard one vowel that differed from the other two vowels, or ''no'' if they heard three instances of a single vowel. The subjects were familiarized with the task before the experiment began through visually presented arrays of geometric figures (e.g., two circles and a square to illustrate the concept of oddity; three triangles differing in size to illustrate a configuration that

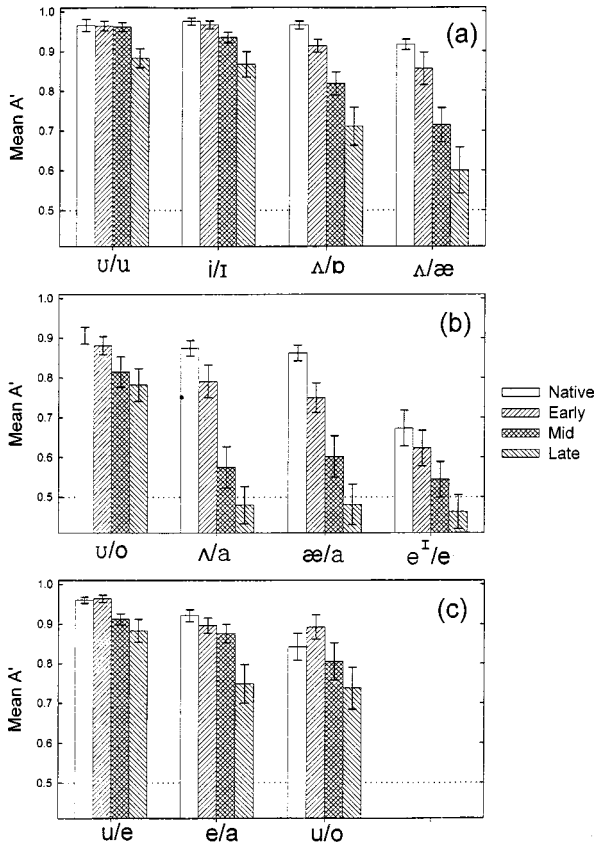

FIG. 2. The mean sensitivity (A′) of the subjects in four groups to phonetic differences between two English vowels (a), between English vowels and neighboring Italian vowels (b), or between two Italian vowels (c). The subjects were native speakers of English, and three groups of Italian/English bilinguals who differed according to the age of first extensive exposure to English (see text). The error bars bracket ∓ one SE.

required a response of ''no''). They received feedback during a practice session with I–E vowel contrasts not included in the test (/æ/–/u/, /i/–/a/). Feedback was not provided during the experiment, however.

An unbiased measure of phonetic sensitivity, A', was calculated for each of the 11 vowel contrasts based on the proportions of hits and false alarms (see Snodgrass *et al.*, 1985).[4] There was a maximum of eight possible hits for each contrast (i.e., eight opportunities to correctly select an odd item out in different trials), and a maximum of eight possible false alarms. (For the /i/–/ɪ/ contrast, for example, there were four catch trials for /i/ and four catch trials for /ɪ/.) An A' score of 1.0 indicated perfect sensitivity (i.e., correct responses to all eight catch trials and to all eight different trials). An A' score of 0.5, on the other hand, indicated a lack of phonetic sensitivity.

B. Results

1. The Effect of AOA

As shown in Fig. 2(a), the native English subjects obtained higher A' scores for all four English–English (E–E) contrasts than did the three groups of native Italian subjects differing in AOA. However, the size of native versus nonnative differences was larger for certain contrasts (/ʌ/–/ɒ/, /ʌ/–/æ/) than for others (/u/–/ʊ/, /i/–/ɪ/). The native Italian subjects' scores decreased as AOA increased. Subjects in the late group obtained lower scores than did subjects in the mid group who, in turn, obtained lower scores than did subjects in the early group.

The A' scores obtained for the E–E vowel contrasts were submitted to a mixed-design (4) group by (4) contrast ANOVA. The significant interaction it yielded [$F(9,204) = 4.84$, $p < 0.01$] was explored through simple effects tests. The effect of group was found to be significant for all four vowel contrasts ($p < 0.01$). Tukey's *post hoc* tests revealed that the late group obtained lower scores for all four E–E contrasts than the native English and Early group did ($p < 0.05$). Also, the late group obtained lower scores than the mid group for /u/–/ʊ/, and the mid group obtained lower scores than the native English group did for /ʌ/–/ɒ/ and /ʌ/–/æ/ ($p < 0.05$).

The scores obtained for the English–Italian (E–I) contrasts are shown in Fig. 2(b). Once again, the native English group obtained higher scores than the early, mid, and late groups, whose scores decreased as AOA increased. The size of between-group differences was larger for /ʌ/–/a/ and /æ/–/a/ than for /ʊ/–/o/ and /eɪ/–/e/, yielding a group by vowel contrast interaction [$F(9,204) = 3.07$, $p < 0.01$]. The simple effect of group was significant for all four E–I contrasts ($p < 0.01$). The late group obtained lower scores than the native English group for /ʌ–/a/, /æ/–/a/, and /eɪ/–/e/; the late group obtained lower scores than the early group for /ʌ/–/a/ and /æ/–/a/; and the mid group obtained lower scores than the native English group for /ʌ/–/a/ and /æ/–/a/ ($p < 0.05$ by Tukey's test).

Scores for the three Italian–Italian (I–I) contrasts are shown in Fig. 2(c). The average scores for the native English, early, and mid groups (means = 0.92, 0.91, and 0.86, respectively) were higher than those obtained for the late group ($M = 0.79$). An ANOVA examining the I–I scores yielded a significant main effect of group [$F(3,68) = 7.2$, $p < 0.01$] and a significant main effect of vowel contrast [$F(2,136) = 16.2$, $p < 0.01$], but not a significant two-way interaction [$F(6,136) = 0.97$, $p > 0.10$]. A Tukey's test examining the average scores obtained for the I–I contrasts revealed that the late group obtained significantly lower scores than the native English and early groups did ($p < 0.05$).

2. L1 use

The scores obtained for the E–E contrasts by the subjects in the native English, early-low, and early groups differed little (*means* = 0.96, 0.95 and 0.93, respectively). The E–E scores were submitted to a (3)group × (4)vowel contrast ANOVA. It yielded a nonsignificant main effect of group [$F(2,51) = 3.15$, $p = 0.051$] and a nonsignificant two-way interaction [$F(6,153) = 1.02$, $p > 0.10$]. The main effect of vowel contrast was significant [$F(3,153) = 16.3$, $p < 0.01$] because the scores for /ʌ/–/æ/ were lower than those for /i/–/ɪ/, /u/–/ʊ/, and /ʌ/–/ɒ/ ($p < 0.05$ by Tukey's test).

The mean scores obtained for the E–I contrasts by the native English, early-low, and early groups differed little (*means* = 0.83, 0.79, and 0.76, respectively). The ANOVA examining the E–I scores yielded a nonsignificant main effect of group [$F(2,51) = 2.52$, $p = 0.09$] and a nonsignificant

two-way interaction [$F(6,153)=1.45$, $p>0.10$]. The main effect of vowel contrast was significant [$F(3,153)=35.7$, $p<0.01$] because the scores for /eɪ/–/e/ were lower than those for /æ/–/a/, /ʌ/–/a/, and /ʊ/–/o/, and the scores for /æ/–/a/ were lower than those for /ʊ/–/o/ ($p<0.05$ by Tukey's test).

Finally, an ANOVA examining the I–I scores yielded a nonsignificant main effect of group [$F(2,51)=0.12$, $p>0.10$] and a nonsignificant two-way interaction [$F(4,102)=1.19$, $p>0.10$]. The main effect of vowel contrast was significant, however [$F(2,102)=22.1$, $p<0.01$], because the scores for /e/–/a/ and /u/–/o/ were lower than those for /u/–/e/ ($p<0.05$).

3. Comparison across contrast types

The analyses just presented examined the scores obtained for the E–E, E–I, and I–I contrasts separately. Here, average scores for the three contrast types were submitted to a (5) group by (3) contrast type ANOVA, which yielded a significant two-way interaction [$F(8,170)=215.0$, $p<0.01$]. The simple main effect of group was significant for all three contrast types, and the simple main effect of contrast type was significant for each group ($p<0.01$).

Tukey's tests revealed that the interaction had two sources. First, a different pattern of between-group differences was obtained for the three contrast types. Subjects in the late group obtained significantly lower scores for E–E contrasts than did subjects in the native English, early, early-low, and mid groups, and the mid group obtained lower scores than the native English group ($p<0.01$). The mid and late groups obtained significantly lower E–I scores than did the native English, early-low, and early groups ($p<0.01$). Finally, subjects in the late group, but not those in the mid group, obtained significantly lower I–I scores than did the native English, early, and early-low groups ($p<0.01$).

A second source of the two-way interaction was a differing pattern of between-contrast-type differences for the native English and native Italian subjects. All five groups obtained significantly lower scores for the E–I contrasts than for the E–E and I–I contrasts ($p<0.01$). However, only the native English group obtained lower scores for the I–I than E–E contrasts (0.91 vs 0.96, $p<0.01$).

4. Results for English /eɪ/ and Italian /e/

It is unlikely that new phonetic categories will be established for L2 vowels that are highly similar to an L1 vowel (Flege, 1995). The results of this study shed light on the magnitude of cross-language vowel differences needed to trigger category formation.

The English /eɪ/ and Italian /e/ stimuli were located in roughly the same portion of vowel space and, after editing (see above), differed little in duration (/e/ = 168 ms, /eɪ/ = 150 ms). However, the English /eɪ/ tokens showed more formant movement from the beginning to the end of the vowel (*mean F*1: 466 to 375 Hz, *mean F*2: 2429 to 2642 Hz) than did the Italian /e/ tokens (*mean F*1: 424 to 404 Hz, *mean F*2: 2434 to 2525 Hz).[5] The A′ scores obtained for the /eɪ/–/e/ contrast were submitted to a series of independent *t*-tests to determine if such small cross-language phonetic differences were discriminable. The aim was to determine if the A′ score obtained for any group was significantly greater than 0.50 (a score which, theoretically, represents a complete lack of sensitivity).

The scores obtained for the native English and early-low groups (*means* = 0.67 and 0.69, respectively) significantly exceeded the chance level (Bonferroni $p<0.01$), whereas the scores obtained for the early, mid, and late groups (0.62, 0.54, 0.46) did not. The early-low group's above-chance discrimination might be interpreted to mean that some subjects established a phonetic category for /eɪ/. However, such an interpretation is clearly not reasonable for the native English subjects, who did not speak Italian. Their above-chance discrimination of /eɪ/–/e/ might instead be attributed to the identification of the Italian /e/ tokens as /ɛ/ (see Gottfried, 1984).

C. Discussion

The perception results obtained here parallel those obtained earlier for vowel production. The later the native Italian subjects arrived in Canada, the less accurately they perceived English vowels. Eight contrasts involving an English vowel or vowels were examined. Subjects in the late group (mean AOA = 19 years) received significantly lower discrimination scores than the native English subjects did for all eight. Subjects in the mid group (mean AOA = 14 years) discriminated four contrasts less accurately than the native English subjects did. These differences are notable in that subjects in the mid and late groups had lived in Canada for an average of 31 years. It thus appears that certain native versus non-native differences in vowel perception persist.

None of the eight contrasts involving an English vowel were discriminated less accurately by either of two early bilingual groups (mean AOAs = 7 years) than by the native English group. This finding, which suggests that early bilinguals who are highly experienced in their L2 may perceive L2 vowels in a nativelike fashion, diverges from the results of several recent studies (Mack, 1989; Pallier *et al.*, 1997; Sebastián-Gallés and Soto-Faraco, in press). The success of the early bilinguals examined here might be attributed to the establishment of long-term memory representations (or ''phonetic categories'') for certain L2 vowels (Flege, 1995). Neither /ɪ/ nor /ʊ/ occur systematically in Italian. The fact that subjects in the late group, but not those in the early and mid groups, differed from the native English speakers in discriminating English /i/–/ɪ/ and /u/–/ʊ/ suggests that at least some subjects in the early and mid groups established phonetic categories for /ɪ/ and /ʊ/.

Other findings obtained here suggest indirectly that subjects in the Early group may have established a phonetic category for a low and/or a mid-central English vowel. Busà (1995) found that, in speech production, Italian late learners of English tended to neutralize differences between low and mid-central English vowels. This is probably because (Standard) Italian has an /a/ but no /æ/, /ɒ/ or /ʌ/. Subjects in the mid and late groups, but not those in the early group, obtained significantly lower discrimination scores than the native English group for /æ/–/a/, /ʌ/–/a/, /ʌ/–/ɒ/ and /ʌ/–/æ/.

The results obtained for the Italian–Italian (I–I) contrasts pose an interpretative challenge. The first issue to consider is why the native English subjects obtained scores that were well above chance ($M=0.91$). We suspect that the native English subjects identified Italian vowels in the /u/–/e/, /e/–/a/, and /u/–/o/ contrasts in terms of two different English vowels, but that the Italian vowels did not represent a good ''fit'' to their long-term memory representations (see, e.g., Best, 1995; Best *et al.*, 1996). This might explain why, of the five groups examined, only the native English group obtained significantly lower scores for the I–I than the E–E contrasts.

The second issue to consider is why the late group obtained lower scores for the I–I contrasts ($M=0.79$) than did the native English and early groups. Perhaps shortening the Italian vowel stimuli (see Sec. I) lessened the identifiability of these stimuli, or reduced their perceived goodness of fit to vowels in the L1 system of members of the late group. Another possibility is that the Italian vowel stimuli represented a poor fit to the late group's long-term memory representations because they were produced by speakers of a northern rather than a southern variety of Italian. A problem exists with both potential explanations, however. There is no reason to think that the effect of editing, or of cross-dialect differences, should have been greater for the late group than for the early group. This is because, as mentioned in Sec. I, the place of origin in Italy of subjects in the four groups seemed to be evenly distributed.

The categorial discrimination test used here placed a heavy load on working memory. Thus, another possible explanation is that some members of the late group had a deficient working memory. This possibility can probably be ruled out, however. As reported by MacKay *et al.* (under review), the subjects were asked to repeat nonwords that were formed by splicing together 2–5 Italian CV syllables. This was done to assess phonological short-term memory. The dependent variable was the number of nonwords repeated correctly. The late group's repetition scores did not differ from the scores obtained for any other group. In fact, the late groups' scores were nonsignificantly higher than those obtained for the native English and early groups. Moreover, when the nonword repetition scores were used as covariates in ANCOVAs, the same results as those reported earlier were obtained.

As mentioned in the Introduction, still another explanation for why the late group obtained relatively low scores for the I–I contrasts is that their long-term memory representations for Italian vowels changed as the result of learning English. More specifically, some of their Italian categories may have changed by assimilating a neighboring English vowel. Assimilation of this kind is predicted to occur only in the absence of category formation for an L2 vowel (which is predicted to occur more often for late than early bilinguals; Flege, 1995). This hypothesis will need to be tested by comparing the discrimination of I–I contrasts by Italian monolinguals and by early and late bilinguals who are highly experienced in English. If the hypothesis is correct, then late but not early bilinguals should obtain lower I–I discrimination scores than Italian monolinguals. If such a finding were obtained, it would provide a perceptual analog to the observation that production of an L1 consonant may become less accurate as the production of a corresponding L2 consonant improves (Flege, 1987).

TABLE III. Simple correlations between the intelligibility scores (a measure of vowel production accuracy) and the discrimination scores obtained for the 72 native Italian subjects. E-E, I-I, and E-I indicate contrasts between two English vowels, two Italian vowels, or between one English and one Italian vowel. ''L1 use'' refers to the percentage of self-reported use of Italian; ''AOA'' and ''LOR'' indicate age of arrival and length of residence in Canada, in years. Superscript a and b indicate significance at the 0.01 and 0.001 levels, respectively.

	E–E	E–I	I–I
Simple correlation	0.64^{b}	0.62^{b}	0.40^{b}
L1 use partialled out	0.59^{b}	0.57^{b}	0.41^{b}
AOA partialled out	0.37^{b}	0.30^{a}	0.17
LOR partialled out	0.48^{b}	0.46^{b}	0.28

IV. THE RELATION BETWEEN PRODUCTION AND PERCEPTION

According to the speech learning model (Flege, 1995), phonetic segments in an L2 can be produced in a nativelike fashion only if they are perceived in a nativelike fashion. The results presented in Sec. II indicated that the early Italian/English bilinguals produced English vowels in a nativelike fashion. This finding thus led to the prediction that, contrary to the findings of several vowel perception studies (Mack, 1989; Pallier *et al.*, 1997; Sebastian-Gallés and Soto-Faraco, in press), the early bilinguals examined here would also perceive English vowels accurately. This prediction was confirmed in Sec. III. The aim of the analyses presented here was to further explore the relation between L2 vowel production and perception.

The first specific question addressed here was whether a significant correlation existed between the intelligibility scores assessing the 72 native Italian subjects' English vowel production accuracy and the average discrimination scores they obtained for English–English (E–E), English–Italian (E–I), and Italian–Italian (I–I) contrasts. As shown in Table III, there was a significant correlation between the intelligibility scores and all three sets of vowel discrimination scores. However, the correlation between the intelligibility scores and the E–E discrimination scores was significantly stronger than was the correlation between the intelligibility scores and the I–I discrimination scores [$X(1)=11.8$, $p<0.01$]. There was also a stronger correlation between the intelligibility scores and the E–I discrimination scores than between the intelligibility and I–I discrimination scores [$X(1)=8.5$, $p<0.01$]. This last finding suggests that degree of L2 vowel production accuracy is related more closely to how L2 vowels are perceived than to how vowels in the L1 are perceived.

Partial correlations were also computed. As shown in Table III, the correlations between the intelligibility scores, on the one hand, and the E–E and E–I discrimination scores, on the other hand, remained significant when variation in L1 use, AOA, and length of residence in Canada were partialled out. However, the correlations between the intelligibility

TABLE IV. The discrimination (A′) scores obtained for three contrasts involving the English vowel /ʌ/ for the native English subjects ($n=18$) and for native Italian subjects who produced /ʌ/ relatively well ($n=41$) or poorly ($n=29$; see text). Standard deviations are in parentheses.

Vowel contrast	Native English	Good producers	Poor producers
/ʌ/ vs English /æ/	0.92 (0.06)	0.80 (0.20)	0.73 (0.23)
/ʌ/ vs Italian /a/	0.87 (0.08)	0.73 (0.21)	0.57 (0.24)
/ʌ/ vs English /ɒ/	0.97 (0.04)	0.87 (0.15)	0.82 (0.16)

scores and the I–I discrimination scores became nonsignificant when AOA and length of residence were partialled out.

A multiple regression analysis was able to account for just 57% of the variance in the intelligibility scores ($p<0.01$). AOA accounted for 48% of the variance at step 1, the E–E discrimination scores accounted for 5% of the variance at step 2, and years of residence in Canada accounted for 4% of the variance at step 3. It is possible that an imprecise measurement of L2 vowel production accuracy was responsible for the small amount of variance accounted for. More likely, perhaps, ceiling effects limited how much variance was accounted for. Of the 720 vowel tokens spoken by the native Italian subjects, 81% were heard as intended by at least five of the six listeners. The vowel most often misidentified was /ʌ/. Five or more listeners correctly identified the /ʌ/ productions of 41 native Italian subjects, whereas four or fewer listeners identified the /ʌ/ productions of the remaining 31 (10 each in the mid and late groups, 6 in the early group, and 5 in the early-low group).

If L2 vowel production is limited by L2 vowel perception accuracy, then the 41 subjects who produced /ʌ/ relatively well should also have perceived /ʌ/ relatively well. Difficulty perceiving /ʌ/ would most likely manifest itself in the discrimination of English /ʌ/ from Italian /a/, for this is likely to be the Italian vowel that is perceptually closest to English /ʌ/. (Unfortunately, no objective assessment of this inference exists at present.)

As summarized in Table IV, a series of ANOVAs examined the discrimination scores obtained for the native Italian subjects who produced /ʌ/ poorly ($N=31$), those who produced /ʌ/ relatively well ($N=41$), and the native English speakers ($N=18$). The effect of group on the /ʌ/–/a/ discrimination scores was significant [$F(2,87)=12.0$, $p<0.01$]. A Tukey's test revealed that the native English group obtained significantly higher /ʌ/–/a/ discrimination scores than did the poor but not the good producers of /ʌ/. Also, the good producers obtained significantly higher /ʌ/–/a/ discrimination scores than did the poor producers of /ʌ/ ($p<0.01$). The effect of group was also significant for the /ʌ/–/æ/ and /ʌ/–/ɒ/ contrasts [$F(2,87)=5.5$ and 6.2, $p<0.01$], but the good and poor producers' discrimination of these two English–English contrasts did not differ significantly.

V. GENERAL DISCUSSION

One experiment reported here examined the accuracy with which native speakers of Italian produced English vowels. The dependent variable was the percentage of correct identifications by native English-speaking listeners of the target English vowels. The later the native Italian subjects arrived in Canada, the less often their English vowels were heard as intended. The intelligibility scores obtained for the late group (mean age of arrival in Canada = 19 years) were significantly lower than were the intelligibility scores obtained for a group of native English speakers for six of the 10 vowels examined (/i ɪ u ʊ o ʌ/). The intelligibility scores obtained for the mid group (mean AOA = 14 years) were lower than the native English groups' scores for just one vowel (/ʌ/). Two groups of early Italian/English bilinguals matched for AOA ($M=7$ years) but differing in L1 use (early-low = 8%, early = 32%) were also examined. No vowel produced by either of these groups was significantly less intelligible than vowels spoken by the native English group. Nor, contrary to prediction (see the Introduction), did the two groups of early bilinguals differ significantly from one another.

Parallel perception results were obtained in a second experiment. A categorial discrimination test was used to assess the native Italian subjects' phonetic sensitivity to differences between four pairs of English vowels, and four English versus Italian vowel contrasts. Subjects in the late group received significantly lower discrimination scores for all eight vowel contrasts than did the native English subjects. Subjects in the mid group received significantly lower scores than did the native English subjects for four vowel contrasts. However, neither group of early bilinguals differed significantly from the native English group for any vowel contrast.

Not surprisingly, the vowel intelligibility scores and the discrimination scores obtained for the 72 Italian/English bilinguals were correlated, even when effects of the variables used to select them (age of arrival in Canada, percent use of Italian) were partialled out. These results are consistent with, but do not in themselves prove, the claim that accuracy in producing phonetic segments in an L2 is limited by how accurately the phonetic segments are perceived (e.g., Flege, 1999a,b).

Bradlow *et al.* (1997) also obtained evidence of a link between production and perception. These authors administered identification training to native Japanese adults using naturally produced English /ɹ/ and /l/ tokens. The subjects' perception improved as the result of the training and so too did their production of English liquids in the absence of any explicit production training. However, the size of gains in perception and production were uncorrelated, and one subject who showed a perceptual gain showed little evidence of improved production. This led Bradlow *et al.* (1997) to conclude that perceptual learning is not a ''necessary or sufficient condition'' for improved production (p. 2307), which may lag behind perceptual changes (see Flege, 1995, for a similar suggestion). If some perceptual changes are never ''transported'' to production (Bever, 1981), this might explain the lack of perfect correlation between production and perception observed in the present study. Another possible explanation for the modest production–perception correlations observed here was that errors were made in measuring

the subjects' vowel production accuracy, their vowel perception accuracy, or both (see Flege, 1999b).

The AOA effect on speech production observed here replicates the findings of Munro *et al.* (1996) for Italian/English bilinguals living in Ottawa. However, this is apparently the first time that an effect of AOA has been observed for the perception of vowels in an L2 (see Strange, 1995, for discussion). The effects of AOA on both vowel production and perception are notable because the native Italian subjects had been living in Canada for an average of 36 years (range: 18–48 years) when tested, and most of them used English more than Italian. Given that AOA indexed the age at which the native Italian subjects were first exposed extensively to English, these findings might be taken as support for the existence of a critical period for L2 speech learning (e.g., Scovel, 1988, 1969; Patkowski, 1989). However, an alternate account of these findings can be derived from the SLM (Flege, 1995, 1998). According to the SLM, age-related effects on L2 speech production and perception arise primarily from changes in how the L1 and L2 phonetic systems interact, not from a neurologically triggered loss in the ability to learn speech. The nature of L1–L2 interactions, according to the SLM, varies as a function of the state of development of the L1 phonetic system when L2 learning begins.

The lack of a vowel production difference between the early bilinguals and the native English speakers diverges from a previous finding. As mentioned in the Introduction, Flege (1998) found that mean ratings obtained for early Italian/English bilinguals' productions of English /i ɛ ɑ/, but not their productions of English /ɪ ʊ ɚ/, were significantly lower than the ratings obtained for native English speakers' productions of the same vowels. The difference between the early bilinguals' productions of /ɪ ʊ ɚ/ and /i ɛ ɑ/ was attributed to the formation of phonetic categories by the early bilinguals for /ɪ ʊ ɚ/ (which lack phonetic counterparts in Italian), but the lack of category formation for /i ɛ ɑ/ due to the presence of phonetically similar vowels in Italian. The intelligibility scores obtained here were sufficiently sensitive to reveal differences between the native English group and the mid and late groups. Still, the Flege (1998) results suggest the possibility that the early bilinguals might have been found to differ from the native English speakers, at least for certain English vowels, had a more sensitive technique been used to assess their production of English vowels.

The lack of a vowel perception difference between the early bilinguals and the native English speakers also appears to diverge from previous findings. As mentioned in the Introduction, several studies identified differences between early bilinguals and monolingual native speakers (Mack, 1989; Pallier *et al.*, 1997; Sebastián-Gallés and Soto-Faraco, in press). The apparent difference between studies may be due to the use of different testing procedures and/or stimuli. The present study employed a categorial discrimination test and made use of multiple natural tokens of each vowel category of interest. Mack's (1989) study, on the other hand, examined the identification and discrimination of the members of a synthetic English /i–ɪ/ continuum. Pallier *et al.* (1997) examined the identification and discrimination of the members of a synthetic Catalan /e/–/ɛ/ continuum. Finally, Sebastián-Gallés and Soto-Faraco (in press) examined the identification of increasingly longer portions of naturally produced vowels using a modified version of the gating task.

Another possible source of the apparent difference between perceptual studies examining early bilinguals is a difference in the subjects examined. All of the early bilinguals examined by Mack (1989) had learned their L2 (either French or English) by the age of 8 years. It is likely that all of them used English more than French, for all of these individuals were living in Providence, RI, at the time of testing. The Spanish/Catalan bilinguals examined by Pallier *et al.* (1997) began to learn Catalan in Barcelona, Spain by the age of 6 years. These subjects used both Catalan and Spanish frequently, had always lived in Barcelona, and were said to be highly proficient in both of their languages. Sebastián-Gallés and Soto-Faraco (in press) also examined Spanish/Catalan bilinguals. The subjects in the present study appear to have been older (mean age=48 years) than the predominantly college-aged subjects examined in the studies just cited, and were likely to have used their L2 for a longer period of time. Their use of the L1 (Italian) appears to have been restricted because the Italian-speaking community in Ottawa is small.

The subjects tested in Barcelona by Pallier *et al.* and by Sebastián-Gallés and Soto-Faraco may have had more opportunity and need to use their L1 (Spanish) than the early bilinguals examined here. If so, then the L1 system of the Spanish/Catalan bilinguals may have exerted a stronger influence on long-term memory representations developed for L2 (Catalan) vowels than the L1 system of the Italian/English bilinguals exerted on their representations for L2 (English) vowels. Support for this inference was provided by a recent study (Flege and MacKay, under review) which examined the categorial discrimination of nine pairs of English vowels. Early Italian/English bilinguals who used Italian relatively often were found to perceive English vowels significantly less accurately than did AOA-matched group of early Italian/English bilinguals who seldom used Italian.

Even if the SLM is correct in its claim that early bilinguals often establish new categories for certain L2 sounds, it is important to note that their L2 categories may differ from monolinguals.' Grosjean (1989) suggested that bilinguals can not function exactly like ''two monolinguals in one person'' because they use two languages systems, not one. According to the SLM (Flege, 1995), the L1 and L2 phonetic systems exist in a ''common phonological space.'' The SLM proposes two mechanisms that might lead to differences between monolinguals' and bilinguals' phonetic categories. One mechanism is an age-related restriction on the use of features, or feature combinations, that are exploited in the L2 but not the L1. A multi-dimensional scaling (MDS) study by Fox *et al.* (1995) revealed that native Spanish speakers of English used fewer dimensions when perceiving vowels than did native speakers of English. McAllister *et al.* (1999) examined the perception of distinctions between phonologically long versus short Swedish vowels by native speakers of an L1 that possesses phonological length distinctions (viz., Estonian) and of L1s that do not (English and Spanish). The native Estonian subjects performed much like native speak-

ers of Swedish. However, many of the native English subjects, and even more of the native Spanish subjects, were unable to differentiate familiar Swedish words based on their phonological length specification. Flege *et al.* (1996) found that highly experienced Japanese speakers of English identified /ɹ/ tokens at nativelike rates. However, their identification of English liquids, unlike that of native English subjects, was affected by lexical familiarity. This suggested that the native Japanese subjects' representations for English /ɹ/ may have differed from the native English speakers,' perhaps because it was based on a different array of features (see Yamada, 1995, Fig. 3).

Another mechanism proposed by the SLM that might lead to differences in early bilinguals' L2 vowel is categories dissimilation. By hypothesis, a category established for an L2 vowel in the same portion of vowel space occupied by an L1 vowel may ''deflect away'' from the existing L1 category to preserve phonetic contrast within a common L1–L2 phonological space. Such a process, if confirmed, would be analogous to aspects of historical sound change (e.g., Martinet, 1955) and to between-dialect differences. For example, Moulton (1945) observed that in Swiss German dialects without an /æ/ category, /a/ is produced with central or even fronted variants. However, in dialects having an /æ/, /a/ has been deflected backward in vowel space. A case study by Mack (1990) illustrates the effect predicted for L2 speech. Voice onset time (VOT) was measured in stop consonants produced by a 10-year-old who spoke French at home and English elsewhere. The child produced /b d g/ with short-lag VOT values in both French and English, but he produced /p t k/ with much longer average VOT values in English than in French (108 vs 66 ms). The child may have increased VOT in English /p t k/ beyond values typical for English to distinguish these stops from French /p t k/. He may have increased VOT in French /p t k/ beyond values typical for French in order to distinguish these stops from the short-lag productions of /b d g/ that are found in English but not French.

The findings obtained in the present study are consistent with the hypothesis that early bilinguals establish long-term memory representations (or ''phonetic categories'') for certain L2 vowels. This conclusion has implications for another model that deals with cross-language perception, the perceptual assimilation model (PAM) of Best and colleagues (e.g., Best, 1995, 1999; Best *et al.*, 1996). The PAM generates predictions concerning the relative degree of discriminability of pairs of foreign-language phones. The subjects are typically infants, or adults who do not speak the languages(s) from which the foreign phones have been drawn. Predictions are derived from measures of the degree of perceived similarity of the foreign phones under examination to sounds in the L1. The PAM was extended to L2 learning in a study which examined the perception of English liquids and glides by adult native speakers of Japanese (Best and Strange, 1992). Subjects who had a great deal of conversational experience in English were found to perceive English/ɹ/ and /l/ tokens more like native speakers of English than did Japanese adults with less such experience. The authors concluded that English-language experience led to a ''reorganization of perceptual assimilation of non-native phones'' (p. 327).

Importantly, the PAM differs from the SLM in the predicted effect of variations in perceived similarity on the likelihood of category formation. According to the SLM, the likelihood of category formation increases linearly as perceived cross-language similarity decreases. The PAM, on the other hand, predicts a U-shaped function. That is, category formation is predicted to be more likely for L2 sounds judged to be moderately similar to an L1 category than for L2 sounds that are highly similar, or else so dissimilar as to not be classified as an instance of an L1 category (Best and Strange, 1992, p. 327). Also, the PAM makes no predictions regarding the effect of age of L2 learning on the discrimination of L2 vowels. However, if interpreted within the PAM framework, the AOA effect obtained here would seem to suggest one of two things. One is that the perceived relation between sounds in the L1 and L2 differs as a function of the age of first exposure to an L2. The other possibility is that the age of L2 learning later affects the extent to which cross-language assimilation patterns can be reorganized.

In summary, the age at which Italian/English bilinguals were first exposed to English influenced the accuracy with which they produced and perceived English vowels, even though they were all highly experienced in English. The study provided no evidence that early Italian/English bilinguals differed from monolingual native speakers of English in producing or perceiving English vowels. The early bilinguals' performance in both domains was nativelike, at least as assessed in the present study. The results obtained here are consistent with the hypothesis that early bilinguals establish new phonetic categories for certain L2 vowels. However, additional research using more sensitive procedures is needed to further examine early bilinguals' vowel production and perception in order to determine how, or if, their phonetic categories differ from those established by monolinguals.

ACKNOWLEDGMENTS

This study was supported by Grant No. DC00257 from the National Institute for Deafness and Other Communicative Disorders. The authors thank J. Prosperine and M. Pearse for their help recruiting subjects, St. Anthony's parish in Ottawa, and all of the subjects. The authors also thank G. Busà, S. Guion, T. Piske, W. Strange, T. Gottfried, and an anonymous reviewer for their helpful comments on earlier versions of this article.

[1]The first half of the weighting function attenuated the signal to zero, and the second half linearly ramped the signal from 0% to 100% of amplitude. Pilot work indicated that the shortest interval that would yield unidentifiable initial consonants, once the weighting function had been applied, varied as a function of word duration. A 30-ms interval was used for 29 stimuli that were shorter than 140 ms. A 46-ms weighting function was applied to the 737 stimuli having a duration of 140–300 ms; and a 60-ms weighting function was applied to the 224 stimuli that were longer than 300 ms. Auditory assessment by two of the authors revealed that none of the initial or final consonants was clearly identifiable.

[2]When the same four-word sequences were presented a second time, the subjects were required to insert the target vowel (e.g., /i/ in *read, deed, heed, bead*) into a /b_do/.frame, thereby forming a nonword. These pro-

ductions will not be assessed here. The listeners who identified the vowels, plus four others, also rated the vowels using a six-point scale prior to the identification experiment. Thus, they were highly familiar with the range of vowels to be identified. The goodness ratings will be presented in a separate study together with an analysis of vowels spoken in extemporaneous speech (Piske *et al.*, 1999).

[3]The mean values shown in Fig. 1 were obtained using the linear predictive coding analysis function (autocorrelation method) of Multispeech (Kay Elemetrics, Inc.). A 25-ms Hamming window was placed at the acoustic midpoint of each vowel token; 14 or 16 coefficients were calculated.

[4]If the proportion of hits (H) equaled the proportion of false alarms (FA), then A′ was set to 0.5. If H exceeded FA, then $A' = 0.5 + ((H-FA)*(1+H-FA))/((4*H)*(1-FA))$. If FA exceeded H, then $A' = 0.5 - ((FA-H)*(1+FA-H))/((4*FA)*(1-H))$.

[5]The frequencies just reported were obtained by placing a 25-ms Hamming window at points located 20% and 80% into the periodic portion of the edited stimuli.

Agard F., and DiPietro R. (**1964**). *The Sounds of English and Italian* (Univ. of Chicago, Chicago).

Best, C. (**1995**). ''A direct realist perspective on cross-language speech perception,'' in *Speech Perception and Linguistic Experience: Theoretical and Methodological Issues*, edited by W. Strange (York, Timonium, MD).

Best, C. (**1999**). ''Development of language-specific influences on speech perception and production in pre-verbal infancy,'' in *Proceedings of the 14th International Congress of Phonetic Sciences*, edited by J. J. Ohala, Y. Hasegawa, M. Ohala, D. Granville, and A. Bailey (Department of Linguistics, University of California at Berkeley), August 1999, pp. 1261–1263.

Best, C., and Strange, W. (**1992**). ''Effects of phonological and phonetic factors on cross-language perception of approximants,'' J. Phonetics **20**, 305–330.

Best, C., Faber, A., and Levitt, A. (**1996**). ''Perceptual assimilation of nonnative vowel contrasts to the American English vowel system,'' J. Acoust. Soc. Am. **99**, 2602(A).

Bever, T. (**1981**). ''Normal acquisition processes explain the critical period for language learning,'' in *Individual Differences in Language Learning Aptitude*, edited by K. Diller (Newbury House, Rowley, MA), pp. 176–198.

Bohn, O.-S. (**1995**). ''Cross-language speech perception in adults: First language transfer doesn't tell it all,'' in *Speech Perception and Linguistic Experience, Issues in Cross-Language Research*, edited by W. Strange (York, Timonium, MD), pp. 273–304.

Bradlow, A., Pisoni, D., Akahane-Yamada, R., and Tohkura, Y. (**1997**). ''Training Japanese listeners to identify English /r/ and /l/: IV. Some effects of perceptual learning on speech production,'' J. Acoust. Soc. Am. **101**, 2299–2310.

Busà, M. G. (**1992**). ''On the production of English vowels by Italian speakers with different degrees of accent,'' in *New Sounds 92, Proceedings of the 1992 Amsterdam Symposium on the Acquisition of Second-language Speech*, edited by J. Leather and A. James (Dept. of English, Univ. of Amsterdam), pp. 47–63.

Busà, M. G. (**1995**). *L'inglese Degli Italiani* (Unipress, Padua, Italy).

Flege, J. E. (**1987**). ''The production of 'new' and 'similar' phones in a foreign language: Evidence for the effect of equivalence classification,'' J. Phonetics **15**, 47–65.

Flege, J. E. (**1992a**). ''Speech learning in a second language,'' in *Phonological Development: Models, Research, and Implications*, edited by C. Ferguson, L. Menn, and C. Stoel-Gammon (York, Timonium, MD), pp. 565–604.

Flege, J. E. (**1992b**). ''The intelligibility of English vowels spoken by British and Dutch talkers,'' in *Intelligibility in Speech Disorders*, edited by R. Kent (Benjamins, Amsterdam), pp. 157–232.

Flege, J. E. (**1995**). ''Second-language speech learning: Theory, findings, and problems,'' in *Speech Perception and Linguistic Experience: Theoretical and Methodological Issues*, edited by W. Strange (York, Timonium, MD), pp. 233–272.

Flege, J. E. (**1998**). ''The role of subject and phonetic variables,'' in *Papers From the 34th Annual Meeting of the Chicago Linguistic Society, II*, edited by K. Gruber, D. Higgins, K. Olsen, and T. Wysocki (Chicago Linguistic Society, Chicago).

Flege, J. E. (**1999a**). ''Age of learning and second-language speech,'' in *New Perspectives on the Critical Period Hypothesis for Second Language Acquisition*, edited by D. P. Birdsong (Lawrence Erlbaum, Hillsdale, MD) (to appear).

Flege, J. E. (**1999b**). ''The relation between L2 production and perception,'' in *Proceedings of the 14th International Congress of Phonetic Sciences*, edited by J. J. Ohala, Y. Hasegawa, M. Ohala, D. Granville, and A. Bailey (Department of Linguistics, University of California at Berkeley), pp. 1273–1276.

Flege, J. E., and Mackay I. R. A. (in preparation).

Flege, J. E., Bohn, O.-S., and Jang, S. (**1997a**). ''Effects of experience on nonnative subjects' production and perception of English vowels,'' J. Phonetics **25**, 437–470.

Flege, J. E., Frieda, E. M., and Nozawa, T. (**1997b**). ''Amount of native-language (L1) use affects the pronunciation of an L2,'' J. Phonetics **25**, 169–186.

Flege, J. E., Guion, S. G., Akahane-Yamada, R., and Downs-Pruitt, J. (**1998**). ''Categorial discrimination of English and Japanese vowels and consonants by native Japanese and English subjects,'' in *Proceedings of the 135th Meeting of the Acoustical Society of America, IV*, edited by P. Kuhl and L. Crum (Acoustical Society of America, New York), pp. 2973–2974.

Flege, J. E., Munro, M. J., and MacKay, I. R. A. (**1995**). ''Factors affecting degree of perceived foreign accent in a second language,'' J. Acoust. Soc. Am. **97**, 3125–3134.

Flege, J. E., Takagi, N., and Mann, V. (**1996**). ''Lexical familiarity and English-language experience affect Japanese adults' perception of /ɹ/ and /l/,'' J. Acoust. Soc. Am. **99**, 1161–1173.

Fox, R. A., Flege, J. E., and Munro, M. J. (**1995**). ''The perception of English and Spanish vowels by native English and Spanish listeners: A multidimensional scaling analysis,'' J. Acoust. Soc. Am. **97**, 2540–2551.

Goto, H. (**1971**). ''Auditory perception by normal Japanese adults of the sounds 'l' and 'r,' '' Neuropsychologia **9**, 317–323.

Gottfried, T. L. (**1984**). ''Effect of consonant context on the perception of French vowels,'' J. Phonetics **12**, 91–114.

Grosjean, F. (**1989**). ''Neurolinguists, Beware! The bilingual is not two monolinguals in one person,'' Brain Lang **36**, 3–15.

Guion, S. G., Flege, J. E., and Loftin, J. D. (under review). ''The effect of L1 use on pronunciation in Quichua-Spanish bilinguals,'' to appear in J. Phonetics.

Jun, S.-A., and Cowie, I. (**1994**). ''Interference for 'new' and 'similar' vowels in Korean speakers of English,'' Ohio State Univ. Working Papers, Vol. 43, pp. 117–130.

Kirk, R. (**1968**). *Experimental Design: Procedures for the Behavioral Sciences* (Brooks/Cole, Belmont, CA).

Kluender, K., Lotto, A., Holt, L., and Bloedel, S. (**1998**). ''Role of experience for language-specific functional mappings of vowel sounds,'' J. Acoust. Soc. Am. **104**, 3568–3582.

Kuhl, P. (**1993**). ''Innate predispositions and the effects of experience in speech perception: The Native Language Magnet Theory,'' in *Developmental Neurocognition: Speech and Face Processing in the First Year of Life*, edited by D. de Boysson-Bardies, S. deSchonen, P. Jusczyk, P. MacNeilage, and J. Morton (Kluwer Academic, The Hague), pp. 259–274.

Mack, M. (**1989**). ''Consonant and vowel perception and production: Early English-French bilinguals and English monolinguals,'' Percept. Psychophys. **46**, 187–200.

Mack, M. (**1990**). ''Phonetic transfer in a French-English bilingual child,'' in *Language Attitudes and Language Conflict*, edited by P. H. Nelde (Dümmler, Bonn, Germany).

MacKay, I. R. A., Meador, D., and Flege, J. E. (under review). ''Factors affecting the identification of consonants in a second language.''

Major, R. (**1987**). ''Phonological similarity, markedness, and rate of L2 acquisition,'' Studies Sec. Lang. Acquis. **9**, 63–82.

Martinet, A. (**1955**). *Economie des Changements Phonétiques* (Franke, Berne).

McAllister, R., Flege, J. E., and Piske, T. (**1999**). ''The Acquisition of Swedish long vs short vowel contrasts by native speakers of English and Spanish,'' in *Proceedings of the 14th International Congress of Phonetic Sciences*, edited by J. J. Ohala, Y. Hasegawa, M. Ohala, D. Granville, and A. Bailey (Department of Linguistics, University of California at Berkeley), pp. 751–754.

Meador, D., Flege, J. E., and MacKay, I. R. A. (under review). ''Nonnative processing of English sentences presented in noise.''

Milani, C. (**1996**). ''Language contact among North American people of Italian origin,'' in *Language Contact Across the North Atlantic*, edited by P. Sture Ureland and I. Clarkson (Max Niemeyer, Tubingen), pp. 479–501.

Moulton, W. (**1945**). ''Dialect geography and the concept of phonological

space,'' Word **18**, 23–32.
Munro, M. J. (**1993**). ''Production of English vowels by native speakers' of Arabic: Acoustic measurements and accentedness ratings,'' Lang. Speech **36**, 39–66.
Munro, M. J., Flege, J. E., and MacKay, I. R. A. (**1996**). ''The effects of age of second-language learning on the production of English vowels,'' Appl. Psycholing. **17**, 313–334.
Pallier, C., Bosch, L., and Sebastián-Gallés, N. (**1997**). ''A limit on behavioral plasticity in speech perception,'' Cognition **64**, B9–B17.
Patkowski, M. (**1989**). ''Age and accent in a second language: A reply to James Emil Flege,'' Appl. Ling. **11**, 73–89.
Piske, T., and MacKay, I. A. R. (**1999**). ''Age and L1 Use effects on degree of foreign accent in English,'' in *Proceedings of the 14th International Congress of Phonetic Sciences*, edited by J. J. Ohala, Y. Hasegawa, M. Ohala, D. Granville, and A. Bailey (Department of Linguistics, University of California at Berkeley), pp. 1433–1436.
Piske, T., Flege, J. E., and MacKay, I. A. R. (**1999**). ''Non-natives' production of vowels in conversational speech,'' J. Acoust. Soc. Am. **105**, 1033(A).
Polka, L. (**1995**). ''Linguistic influences in adult perception of non-native vowel contrasts,'' J. Acoust. Soc. Am. **97**, 1286–1296.
Rochet, B. (**1995**). ''Perception and production of second-language speech sounds by adults,'' in *Speech Perception and Linguistic Experience*, edited by W. Strange (York, Timonium, MD).
Romito, L., and Trumper, J. (**1989**). ''Un problema della coarticulazione: L'isocronia rivistata,'' Acts of the 27th National Conference of the Italian Acoustical Association, pp. 449–455.
Scovel, T. (**1969**). ''Foreign accents, language acquisition, and cerebral dominance,'' Lang. Learning **19**, 245–253.
Scovel, T. (**1988**). *A Time to Speak. A Psycholinguistic Inquiry Into the Critical Period for Human Speech* (Newbury House, Cambridge, MA).
Sebastián-Gallés, N., and Soto-Faraco, S. (in press). ''On-line processing of native and non-native phonemic contrasts in early bilinguals,'' Cognition.
Sheldon, A., and Strange, W. (**1982**). ''The acquisition of /r/ and /l/ by Japanese learners of English: Evidence that speech production can precede speech perception,'' Appl. Pycholing. **3**, 243–261.
Snodgrass, J., Levy-Berger, G., and Haydon, M. (**1985**). *Human Experimental Psychology* (Oxford U. P., Oxford).
Strange, W. (**1995**). ''Phonetics of second-language acquisition: Past, present, future,'' in *Proceedings of the ICPhS 95*, edited by K. Elenius and P. Branderud (Arne Stombergs, Stockholm), pp. 77–83.
Trumper, J. (**1995**). ''L'influenza di eventi macrosismici su alcune discontinuità linguistiche (Calabria),'' in *Saggi Dialettologici in Area Italo-Romanza*, edited by G. B. Pellegrini (CNR, Padova), pp. 89–103.
Yamada, R. (**1995**). ''Age and acquisition of second language speech sounds: Perception of American English /ɹ/ and /l/ by native speakers of Japanese,'' in *Speech Perception and Linguistic Experience, Issues in Cross-Language Research*, edited by W. Strange (York, Timonium, MD), pp. 305–320.

A vowel synthesizer based on formant sinusoids modulated by fundamental frequency

Ingo Hertrich[a] and Hermann Ackermann
Department of Neurology, University of Tübingen, Hoppe-Seyler-Str. 3, D-72076 Tübingen, Germany

(Received 24 November 1998; accepted for publication 15 July 1999)

A vowel synthesis algorithm was developed resembling parallel formant synthesizers. However, the formants are computed as amplitude-and phase-modulated sinusoids instead of being represented by recursive filters or resonators. The fundamental frequency is imposed on the signal in the following way: Each pitch period exhibits an initial rise of a duration of $\pi/2$ of the first formant frequency; at the end of this ramp period all formants start as sinusoids at predefined phase angles and amplitudes, and successively undergo linear attenuation toward zero amplitude at the end of each pitch period. Adjacent pitch periods, thus, do not influence each other. In principle, the signals produced by this algorithm are similar to the output of parallel formant synthesizers [e.g., D. H. Klatt, J. Acoust. Soc. Am. **67**, 971–995 (1980)]. However, by incremental sample-by-sample computation of the formants' phase angles, formant frequencies are allowed to continuously change within single pitch periods. This new algorithm creates vowels as well as formant transitions signaling stop consonant–vowel syllables such as /ba/. The output signals exhibit a homogeneous, stereotypic voice quality. Because of its additive procedure, this method might allow us to implement a variety of further acoustic aspects of the human speaking voice in a well-controled manner. © *1999 Acoustical Society of America.* [S0001-4966(99)03211-7]

PACS numbers: 43.72.Ja, 43.70.Bk [DOS]

INTRODUCTION

Studies on speech perception often use synthetic stimuli in order to control for the various components of the acoustic signal. As concerns recent speech synthesizers, the technique of linear predictive coding (LPC) seems to be the most widespread procedure, in spite of some disadvantages with respect to the control of overall spectral energy distribution and voice quality across changes in formant structure. As an alternative, parallel formant synthesizers (Holmes, 1983; Klatt, 1980; Rabiner, 1968) might be considered for the generation of well-controled acoustic stimuli because of the possibility they provide to explicitly adjust a number of parameters such as formant amplitudes. In the present paper, a vowel synthesis algorithm is introduced that in some respects resembles a formant synthesizer, but is based on a different computational principle.

The source-filter model of speech production (Fant, 1973) suggests laryngeal excitation to be more or less independent of vocal tract resonances. Thus, speech synthesizers use to combine a glottal ''source'' (e.g., a series of impulse-like events) with a filter shaping the spectrum toward the desired formant structure. As a rule, the signal is synthesized in frames (e.g., one frame per pitch period), using invariant vocal tract filter characteristics within each period. Formant transitions, therefore, are modeled in a steplike manner rather than as continuous trajectories. Although the source-filter method simulates the actual physical processes during speaking, the technical implementation of speech synthesis might use different mechanisms. The present approach is based on fundamental frequency-driven modulations of formant sinusoids, allowing, first, for continuous formant changes within single pitch periods and, second, for a ''reset'' of the formants' phase relations within each pitch frame.

I. THE ALGORITHM

The phonetic characteristics of the signal to be synthesized are specified in an ASCII input file that can be written by any text editor. Each line of this text file contains a set of parameters referring to segment duration, signal amplitude, fundamental frequency ($F0$), and five formant frequencies ($F1$ to $F5$). Segment duration represents a time interval of linear changes with respect to the amplitude, $F0$, and formant values from the current input line to the respective parameter values of the following line (the duration parameter of the final line is not evaluated). For example, a vowel consisting of an initial formant transition, a more or less stationary nucleus, and a terminal transition phase is represented by four lines specifying the four edges of its seven-parameter time history.

As a first computational step the synthesis algorithm determines the length of all pitch frames by linear interpolation. For each pitch period the signal amplitude as well as the onset and offset frequencies of the five formants are then computed using linear interpolation. The signal within each frame starts with an initial rise followed by a decay period approaching zero intensity at the end of the pitch period. The duration of the initial rise amounts to a fourth of the period duration of the first formant, starting at zero amplitude and ending with the amplitude value (ampl) of the respective frame at the first formant's phase angle $\varphi_{F1}=\pi/2$. In order to avoid an abrupt transition at the onset of each pitch frame, the rise function was modeled as a linear increase multiplied by a sine function:

[a]Electronic mail: ingo.hertrich@uni-tuebingen.de

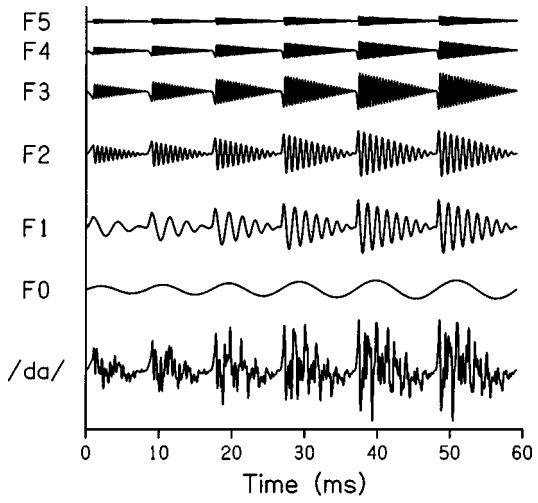

FIG. 1. Synthesis of the acoustic signal of the syllable /da/ (initial transition of about 35 ms followed by the stationary vowel phase). The bottom curve shows the final signal being the sum of the fundamental frequency ($F0$) and the five formants ($F1$ to $F5$) displayed above. During the transition period, signal intensity increases, $F0$ changes from 120 to 90 Hz, $F1$ from 250 to 750 Hz, $F2$ from 1700 to 1200 Hz, and $F3$ from 2800 to 2500 Hz. The fourth and fifth formants are characterized by a constant frequency of 3500 and 4500 Hz, respectively.

$$y(t) = \text{ampl} \cdot (2\varphi_{F1}(t)/\pi) \cdot \sin[\varphi_{F1}(t)],$$

where the local phase angle of the first formant

$$\varphi_{F1}(t) = \varphi_{F1}(t - dt) + [2\pi \cdot F1(t) \cdot dt]$$

is computed incrementally $[\varphi_{F1}(t_0) = 0]$ for each sample using the local frequency $F1(t)$ of the first formant (dt is the duration between two successive signal samples):

$$F1(t) = F1(t_0) + \{[(t - t_0)/(t_e - t_0)] \cdot [F1(t_e) - F1(t_0)]\};$$

$F1(t_0)$ and $F1(t_e)$ are the initial and final $F1$ frequencies of the current pitch period, respectively.

At the end of this frame-initial rise, all formants start with their relative amplitudes (see below) at predefined phase angles. If all formants start at $\pi/2$, the end of the initial rise represents the highest possible amplitude value of the respective pitch frame. In order to avoid excessive peakedness, the present implementation selected the following start angles for the five formants: $\pi/2$ for $F1$ and $F2$, $3\pi/2$ for $F3$ and $F4$, and zero for $F5$. The amplitude of the initial rise was adjusted to these phase angles. In order to achieve continuous change of the formant frequencies during the decay phase of a pitch period, the phase angles of the formants are similarly computed sample by sample as described in the above formula for $\varphi_{F1}(t)$:

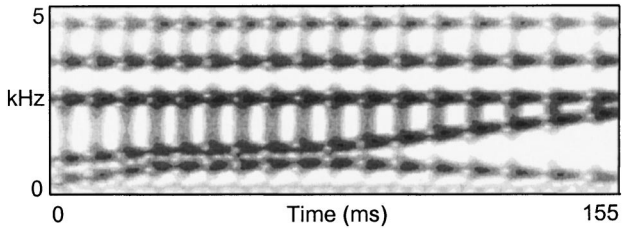

FIG. 2. Example of a spectrogram of the syllable /bai/ synthesized by using the parameter specifications given in Table I (CSL 4300, KAY Elemetrics, Lincoln Park, NJ, sampling rate=20 kHz, frame length=200 samples).

$$\varphi_{Fi}(t) = \varphi_{Fi}(t - dt) + [2\pi \cdot Fi(t) \cdot dt],$$

where $Fi(t)$ represents the local frequency of the ith formant. For each signal sample, the local amplitude values of the five formants are added together:

$$y(t) = a(t) \cdot \{a_{F1} \cdot \sin[\varphi_{F1}(t)] + a_{F2} \cdot \sin[\varphi_{F2}(t)] + \cdots + a_{F5} \cdot \sin[\varphi_{F5}(t)]\};$$

a_{F1} to a_{F5} refer to the relative amplitudes of the five formants specified as global parameters of the algorithm. They should approximately reflect the spectral slope that is observed in natural speech signals. However, they might be modified in order to model changes in vocal effort. The local signal amplitude $a(t)$ starts with ampl at the onset of the decay phase and is linearly decreased toward zero at the end of the respective pitch period.

In order to achieve a softer voice quality, the fundamental frequency, in terms of a sinusoid wave, may be mixed into the output signal with a relative amplitude a_{F0}. As an example, Fig. 1 displays a synthesized consonant–vowel transition and its various additive components.

II. COMMENTS

Preliminary listening experiments revealed reliable identification of synthesized vowels as well as homogeneous voice quality across variations of pitch and formant structure. Furthermore, intelligible stop consonant–vowel syllables may be produced by designing the respective vowel-initial formant transitions (see, e.g., Liberman, 1996), although no particular consonant features such as bursts, friction noise, and aspiration have been modeled yet. An example spectro-

TABLE I. Input parameters used for synthesis of the signal displayed in Fig. 2.

Amp1[a]	$F0$[b] (Hz)	Duration (ms)	Formant Frequency (Hz)				
			$F1$	$F2$	$F3$	$F4$	$F5$ [c]
15 000	120	35	250	800	2500	3500	4500
25 000	140	50	700	1100	2500	3500	4500
25 000	120	80	800	1200	2500	3500	4500
15 000	80	0	300	2200	2500	3500	4500

[a]ampl: signal amplitude (in units corresponding to a dynamic range of 32 bit).
[b]$F0$: fundamental frequency.
[c]$F1$–$F5$: formant frequencies.

gram of the algorithm's output is presented in Fig. 2, corresponding to the input values given in Table I.

Besides phonetic information, natural speech conveys indexical information on, for example, the identity, age, and sex of a speaker (e.g., Johnson and Mullennix, 1997). By further adjustments of the synthesis algorithm, various aspects of these nonverbal aspects of speech could be implemented. For example, dampening effects due to glottal opening might be accounted for by a specific modification of the decay function toward the end of each pitch frame. Furthermore, formant bandwidths can be introduced in a well-controled manner by imposing a sample-by-sample stochastic component on the phase velocity of the formants. Thus, the additive working principle of this algorithm represents a feasible alternative to conventional source-filter mechanisms for a variety of speech synthesis applications.

Pertinent audio files are available at http: /www.ims.uni-stuttgart.de/phonentik/tuesyn/.

Fant, G. (**1973**). *Speech Sounds and Features* (MIT, Cambridge, MA).

Holmes, J. N. (**1983**). ''Formant synthesizers: Cascade or parallel?'' Speech Commun. **2**, 251–273.

Johnson, K., and Mullenix, J. W. (eds.) (**1977**). *Talker Variability in Speech Processing* (Academic, San Diego, CA).

Klatt, D. H. (**1980**). ''Software for a cascade/parallel formant synthesizer,'' J. Acoust. Soc. Am. **67**, 971–995.

Liberman, A. M. (**1996**). *Speech: A Special Code* (MIT, Cambridge, MA).

Rabiner, L. R. (**1968**). ''Digital-formant synthesizer for speech-synthesis studies,'' J. Acoust. Soc. Am. **43**, 822–828.

Normal modes of a radially braced guitar determined by electronic TV holography

Thomas D. Rossing[a)]
Physics Department, Northern Illinois University, DeKalb, Illinois 60115

Gila Eban
22 Licata Terrace, Cos Cob, Connecticut 06807

(Received 8 February 1999; revised 27 June 1999; accepted 3 August 1999)

Electronic TV holography has been used to determine normal modes of vibration of a classical guitar having an innovative bracing design. The modes observed at frequencies up to 800 Hz are quite similar to those reported in other classical guitars. Observing modes of the air cavity with stationary plates and ribs helps to understand the normal modes of the guitar. Sound spectra indicate the relative sound radiation by the top and back plates at each modal frequency. © *1999 Acoustical Society of America.* [S0001-4966(99)06011-7]

PACS numbers: 43.75.Gh [WJS]

INTRODUCTION

Plucking a guitar string causes the instrument to vibrate and radiate sound. The complex vibrations of the guitar body are conveniently described in terms of normal modes of vibration. Each *normal mode* or *eigenmode* can be described in terms of the coupled motion of the component parts, mainly the top plate, back plate, ribs, and air cavity. To understand the acoustical behavior of the instrument, it is desirable to obtain as accurate a description of the normal modes as possible. Unfortunately, it is sometimes difficult to determine the normal modes of vibration of a complex vibrating structure such as a guitar.

When an external force is applied to a guitar body, the amplitude distribution is called an *operating deflection shape* (ODS). This shape is dependent on where and in what direction the force is applied and how the guitar is supported. A normal mode or eigenmode, on the other hand, is an intrinsic property of the guitar. When the guitar is excited at a resonance frequency, the ODS will be determined mainly by one normal mode, but away from a resonance several normal modes will contribute.

In this paper, we describe the use of electronic TV holography to determine the operating deflection shapes, and from these, the normal modes, of a classical guitar having an asymmetric radial bracing design.

I. EXPERIMENTAL METHOD

The TV holography system has already been described (Roberts and Rossing, 1997). The optical system is shown in Fig. 1. A beam splitter BS divides the light from a Nd:YAG laser to produce a reference beam and an object beam. The reference beam illuminates the CCD camera via a phase-stepping mirror PS and an optical fiber, while the object beam is reflected by mirror PM so that it illuminates the object to be studied. Reflected light from the object reaches the CCD camera, where it interferes with the reference beam to produce the holographic image. The speckle-averaging mechanism SAM in the object beam alters the illumination angle in small steps in order to reduce laser speckle noise in the interferograms. Holographic interferograms are displayed on a TV monitor and recorded on a digital printer.

A driving force was applied to the guitar by attaching a small (0.8-g) NdFeB magnet and passing the current from an audio amplifier through a small coil facing the magnet. The guitar was successively driven at the bass end of the bridge (next to the first string), the treble end of the bridge, and at a point just below the center of the bridge. In addition, the guitar was excited acoustically by the sound field from a loudspeaker.

The guitar was supported in a vertical orientation by lightly clamping the neck and letting the tail rest on the air-supported optical table used for holography. Air currents in the room added noise to the holograms of the modes of lowest frequency, but minimal support was preferred in order to minimize distortion of the normal mode shapes. The strings were damped.

''Room-averaged'' sound spectra were recorded on a FFT (fast Fourier transform) analyzer by placing a sound level meter 1 m in front of the center of the guitar while it was driven with band-limited random noise. While room-averaged spectra give only an approximate measure of total radiated sound power, they give a fairly accurate indication of which modes radiate effectively from the front and back of the guitar, and the difference in radiated sound between driving on the treble and the bass sides of the bridge.

In order to understand the normal modes of the guitar, we measured the air-cavity modes with the top and back plates and ribs made stationary by means of carefully fitted sand bags. A hose leading from a horn driver through the sound hole provided a sinusoidally varying pressure to drive the cavity. A microphone was moved around the cavity to locate the nodes and antinodes for the cavity modes.

a)Electronic mail: rossing@physics.niu.edu

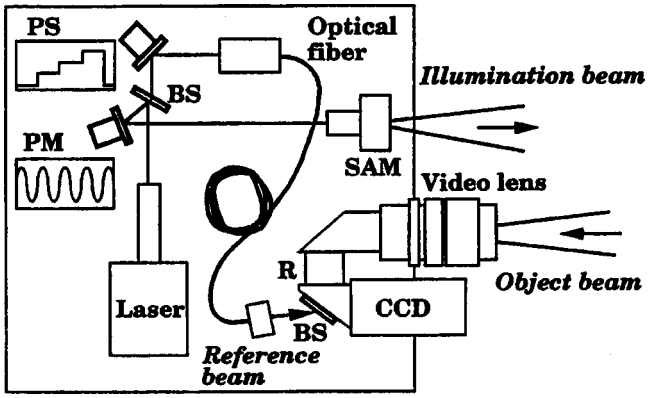

FIG. 1. Optical system for electronic TV holography.

II. THE GUITAR

The classical guitar used in these studies, constructed by Gila Eban and demonstrated at ISMA98 (Eban, 1998), received favorable comments by those who played it and heard it. The top plate is braced asymmetrically, as shown in Fig. 2. The bars radiate out from the bridge, which is wider on the bass side than the treble side. The back plate combines two transverse bars with radial braces in the lower bout.

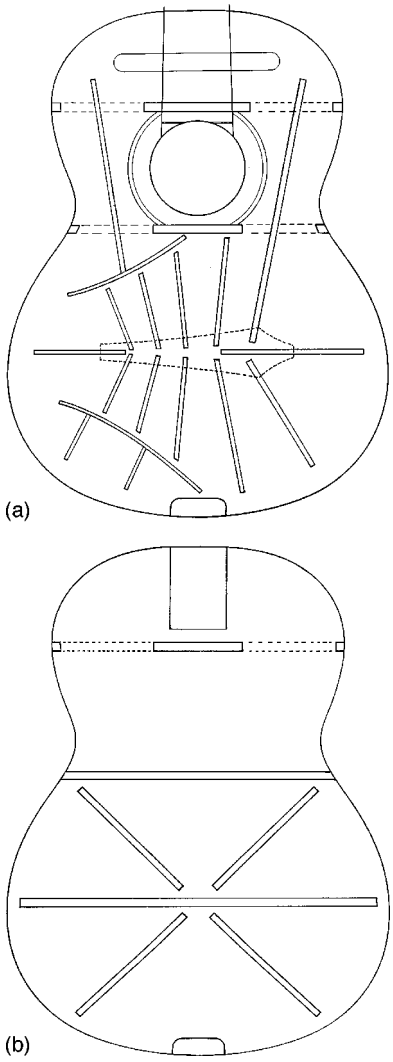

FIG. 2. Bracing patterns in the top and back plates of the guitar.

The spruce top plate varied in thickness from 3.1 mm in the upper bout and and the bass side of the lower bout to 2.9 mm on the treble side. The back, ribs, and bridge were Brazilian rosewood.

III. RESULTS

A. Cavity modes with fixed walls

The lowest cavity mode, the so-called Helmholtz or sound-hole resonance, was found at 124 Hz. This compares closely to the sound-hole resonance frequencies found in two classical guitars and also to those found in three folk guitars of the ''dreadnaught'' design (Rossing *et al.*, 1985). It may seem a little surprising that the sound-hole resonance frequencies would be the same in the larger folk guitars, but the sound holes in these larger bodies were proportionately larger as well. Unfortunately, some investigators have confused the true Helmholtz or sound-hole resonance, which requires stationary plates, with the first normal mode of the guitar, which occurs about 25% lower in frequency.

The next cavity mode, the longitudinal (0,1) mode, which has pressure maxima at the two ends of the guitar as well as in a plane halfway between them, occurs at 417 Hz. The transverse (1,0) mode, having pressure maximum at the ribs as well as halfway between them, occurs at 571 Hz. These are comparable to those found in other classical guitars, but are somewhat higher than those in the larger dreadnaught-style folk guitars (Rossing *et al.*, 1985). They are lower than those calculated by Roberts (1986) for a guitar-shaped cavity with a zero-pressure boundary condition at the soundhole, however.

The longitudinal (0,2) cavity mode was found at 785 Hz, and the transverse (2,0) mode was found at 1043 Hz, again at higher frequencies than measured in folk guitars and close to those calculated by Roberts (1986) using finite element methods. Finally, the (1,1) mode, having both a longitudinal and a transverse plane at which the sound pressure is maximum, was found at 792 Hz.

B. Normal modes of vibration

In most guitars, the frequency response in the range of 100 to 220 Hz is dominated by three normal modes which result from strong coupling between the (0,0) Helmholtz or sound-hole resonance with the so-called (0,0) modes in the top and back plates (Fletcher and Rossing, 1998). This guitar is no exception. In the first mode at 101 Hz, shown in Fig. 3(a), the lower parts of the top and back plate move in opposite directions so that the guitar ''breathes'' through the sound hole. It should be mentioned that the force amplitudes used to make the interferograms of the top, back, and ribs were not the same.

In the second mode at 155 Hz, shown in Fig. 3(b), the top and back plates move in the same direction and the ribs move in the opposite direction. When the guitar rests on its side so that one of the ribs is constrained, this mode becomes slightly asymmetrical and its frequency increases to 184 Hz. In the third mode at 210 Hz, the top and back plates again move in opposite directions, but the air flow in the sound hole is opposite in phase to that observed in the mode an

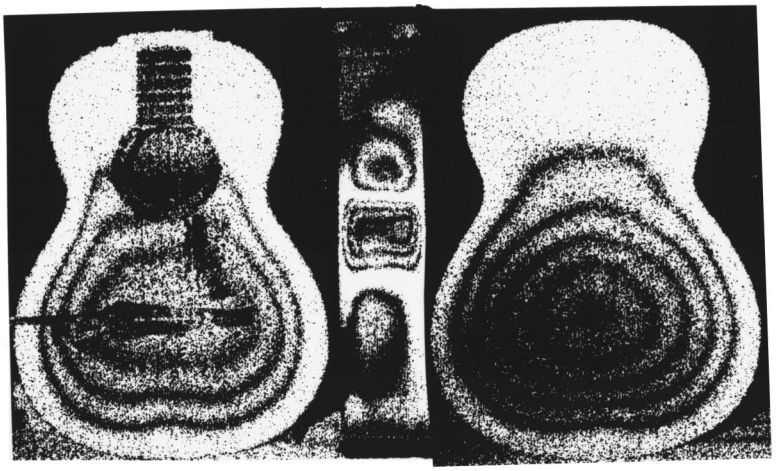

(a)

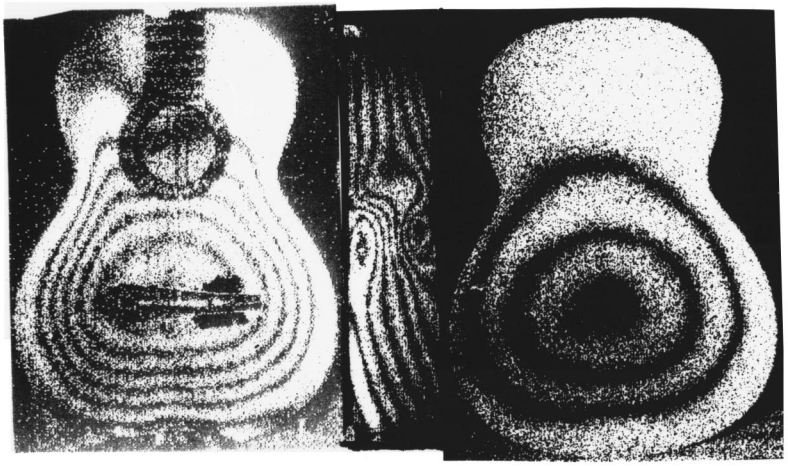

(b)

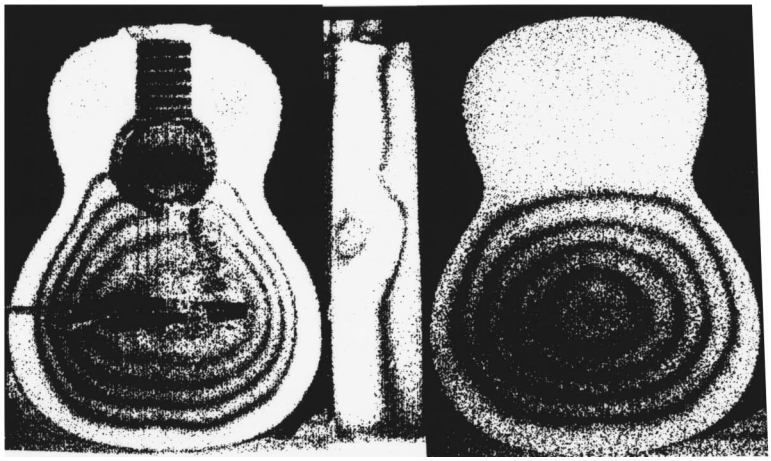

(c)

FIG. 3. Three normal modes that result from strong coupling between the (0,0) modes in the air cavity, the top plate, and the back plate: (a) 101 Hz; (b) 155 Hz; and (c) 210 Hz. Force amplitudes are not the same in the various interferograms.

octave lower at 101 Hz. These three modes, which result from coupled motion of top plate, back plate, and cavity modes having similar shapes, have been shown to be consistent with a ''three-mass'' model (Christensen, 1982).

In the next mode at 304 Hz, shown in Fig. 4, a longitudinal nodal line appears in both the top and back plates. Air ''sloshes'' from side to side inside the cavity, although the frequency of this mode is well below the (1,0) cavity resonance. This mode was observed at 303 Hz in a Kohno 30 classical guitar (Rossing *et al.*, 1985), at 275, 295, and 296 Hz in three Ramirez guitars (Caldersmith, 1989), and at 268 Hz in a classical guitar by Richardson (Richardson and Roberts, 1985), who points out its importance to the tonal characteristics of classical guitars. This mode generally occurs at somewhat higher frequencies in folk guitars having a stiffer top plate (e.g., at 377 Hz in a Martin D-28; see Rossing *et al.*, 1985).

The mode at 407 Hz, shown in Fig. 5, features longitudinal bending of the top and back plates, although the nodal patterns are different in the two plates. The nodes in the back plate appear to be located at the transverse braces, while the node in the top plate appears just above the bridge. Meyer

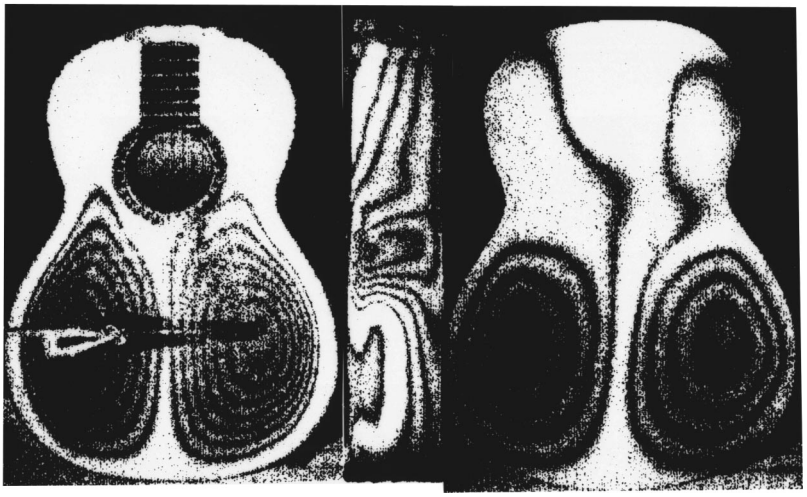

FIG. 4. Mode at 304 Hz characterized by ''see-saw'' motion of the top and back plates while air ''sloshes'' back and forth internally.

(1983) found the strength of the radiation from this mode to be the most important single factor in determining guitar quality. In a Kohno 30 classical guitar, a similar longitudinal mode was found at 427 Hz, although the back had a single transverse node, while in three Ramirez guitars it was observed at frequencies of 420, 424, and 428 Hz (Caldersmith, 1989). In a Martin D28 folk guitar, a similar mode was observed at 404 Hz (Rossing *et al.*, 1985). The longitudinal cavity mode occurs at 383 Hz in the Martin D28 compared to 417 Hz in the guitar described in this paper.

Two longitudinal nodes appear in the mode at 613 Hz, shown in Fig. 6. Modes with similar patterns of vibration in the top plate have been observed in classical guitars at 553 Hz (Richardson and Roberts, 1985) and 590 Hz (Rossing *et al.*, 1985), although the back plate patterns are different. Caldersmith (1989) observed this mode at 585, 586, and 600 Hz in three guitars by Ramirez and at 420 to 662 Hz in other classical guitars. It is generally weak or missing altogether in folk guitars.

Above 700 Hz, the effective coupling between the top and back plates is quite weak and modes appear independently in the top and back plates. Figure 7 shows a back plate mode at 774 Hz, excited by the sound field of a loudspeaker, in which the vibrational pattern correlates well with the bracing pattern used in the back plate. A rather similar modal pattern was observed at 760 Hz in a radially braced top plate by Marty *et al.* (1987).

C. Radiated sound

Room-averaged sound pressure levels 1 m from the top plate and from the back plate are shown in Fig. 8. The lowest mode at 102 Hz radiates primarily from the sound hole, so it shows up more strongly in front of the top plate. The modes at 155 and 210 Hz appear to be radiated equally well by the top and back plates, however.

The ''see-saw'' mode at 304 also radiates strongly from both the top and back plates even though the microphone is close to the center plane where the radiation should be weak if the mode were exactly symmetrical. Apparently a small asymmetry leads to a monopole component in the sound radiation field. The longitudinal mode at 407 Hz leads to stronger radiation from the back plate than from the top plate, it appears. This is a little surprising in light of the important role Meyer (1983) apparently found for this mode in determining the quality of classical guitars.

The mode at 613 Hz, having two longitudinal nodes in both the top and back plates, appears to radiate slightly more sound from the top plate, as does the (1,1)-type mode (not

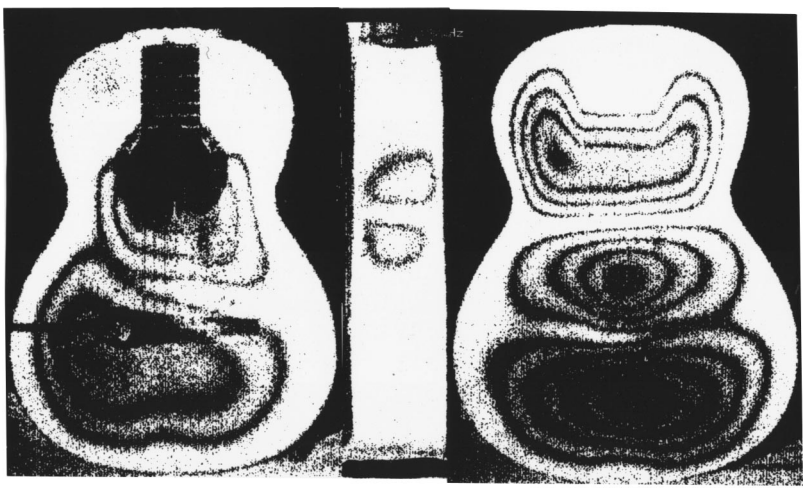

FIG. 5. Mode at 407 Hz features longitudinal bending of the top and back plates.

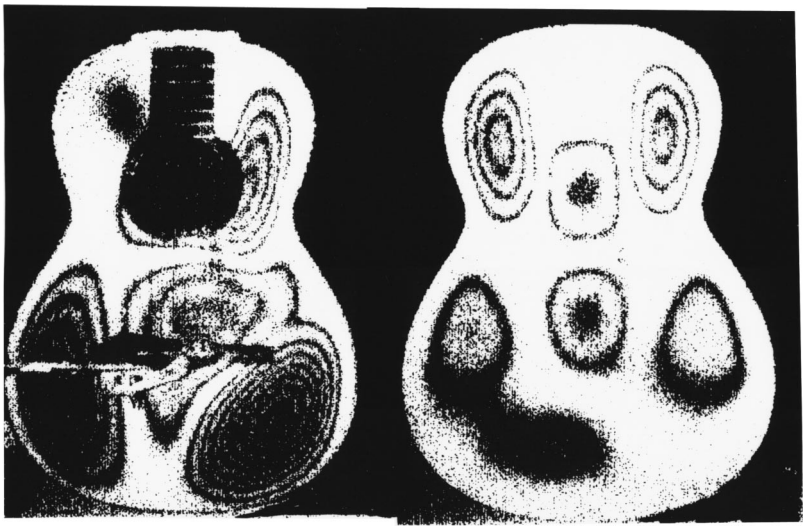

FIG. 6. Transverse bending mode at 613 Hz with two nodes.

shown) at 588 Hz. The mode at 810 Hz, however, radiates more strongly from the back.

IV. DISCUSSION

Compared to violins, which have reached a state of maturity, guitars are still evolving. Exciting experiments are taking place in acoustics laboratories, as well as luthiers' workshops, around the world. These experiments have ranged from the use of new materials and new systems for bracing the body to developing whole new families of instruments (Caldersmith, 1989).

The bracing pattern in the classical guitar described in this paper is substantially, though not radically, different from that used in traditional classical guitars. Some of the design philosophy is discussed in a recent paper given at ISMA98 (Eban, 1998). Radial bracing in the top plate appears to offer some advantages over the more traditional fan bracing. It allows the luthier to vary the effective mass of the low-order modes in the top plate, a desirable goal (Richardson, 1998), and yet keep the normal mode frequencies at the desired locations. This is one of the first guitars in which radial bracing has been used in the back plate as well, and it apparently encourages the back plate to vibrate in modes such as the one shown in Fig. 7. Further studies are needed to document the acoustical advantages or disadvantages.

An earlier model was constructed with a divided bridge, which is believed to have resulted in the absence of a (2,0) mode such as the one found in this guitar at 613 Hz (Eban,

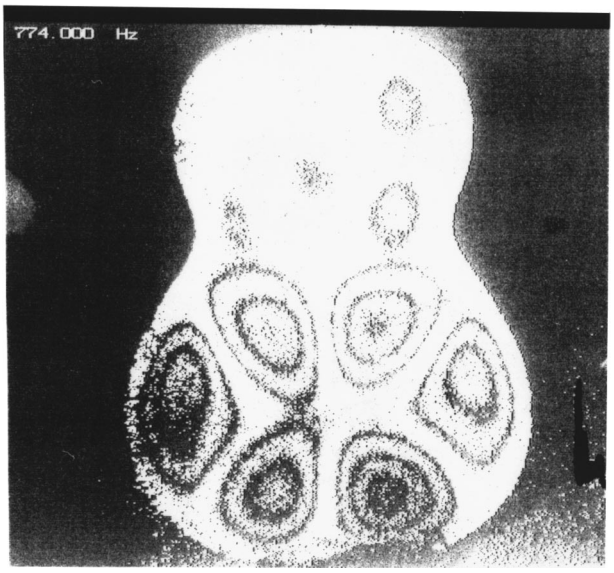

FIG. 7. Back plate mode at 774 Hz in which the vibrational pattern correlates well with the bracing pattern in the back plate [Fig. 2(b)].

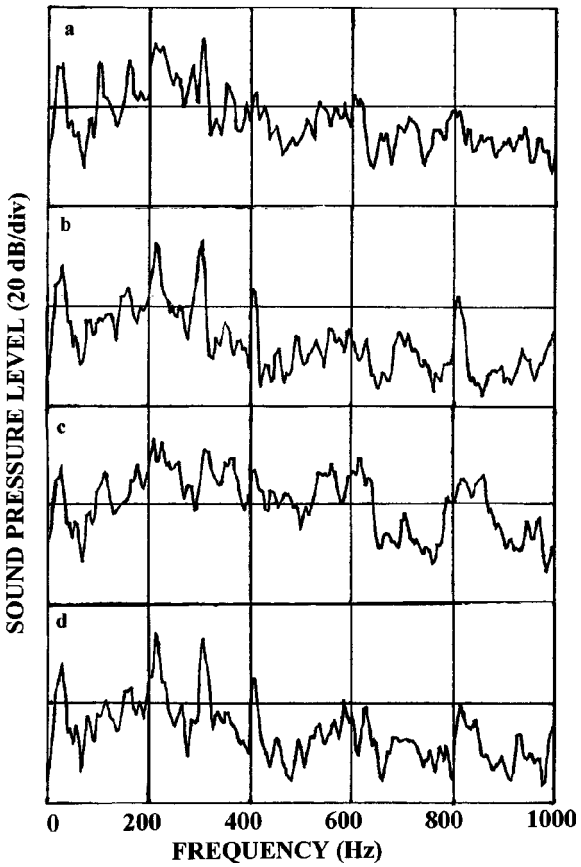

FIG. 8. Room-averaged sound levels recorded at 1 m. (a) Front: driven on the bass side of the bridge; (b) back: driven on the bass side; (c) front: driven on the treble side; and (d) back: driven on the treble side. A linear frequency scale is used.

1998). Substituting an undivided bridge made such a mode observable.

Other luthiers have experimented with bracing techniques that result in a top plate with low effective mass. Australian luthier Greg Smallman has pioneered the use of thin top plates with a lattice of light-weight braces of synthetic material such as carbon fiber and epoxy. Combining the low-mass top with a strong bridge, heavy ribs, and back has led to approval of his guitars by performers such as John Williams (Caldersmith and Williams, 1986). Frequencies of the (1,0), (0,1), and (2,0) modes in Smallman's guitars tend to be lower than in most classical guitars, however (Caldersmith, 1989).

Holographic interferometry provides the best spatial resolution of any method used to observe operating deflection shapes of vibrating structures from which the normal modes can be deduced. Recording the interferograms on photographic film is a time-consuming process, however. Electronic TV holography, in which the interferograms are displayed on a TV monitor each $\frac{1}{30}$ of a second, offers one the opportunity to view the patterns of vibration nearly in real time. Phase modulation allows one to determine the deflection phase in order to determine how well the normal modes are approximated by the operating deflection shapes observed (Engström and Rossing, 1998), although that feature was not employed in the studies reported here.

Although this investigation focused mainly on determining the normal modes of a guitar with radially braced top and back plates, it also revealed some interesting features of the radiated sound field which deserve further investigation. One is the rather large difference in the front and back sound levels at 101 Hz, especially when the guitar is excited on the bass side of the bridge, as compared with the small difference in the front and back sound levels at 210 Hz. Since the front and back plates show comparable amplitudes at both frequencies, the difference is apparently due to greater soundhole radiation at 101 Hz.

V. CONCLUSION

Electronic TV holography is an accurate and convenient way to study the normal modes of vibration of musical instruments, such as a classical guitar. Understanding the normal modes of vibration allows the luthier to adjust their frequencies and thus sculpt the tonal design of the guitar. The guitar is a comparatively young instrument, and its design is still evolving.

The normal modes of vibration at low frequencies observed in a classical guitar with radially braced top and back plates appear quite similar to those of traditional guitars with fan bracing. In the mid-frequency range, where modal shapes are more dependent on bracing configuration, radial bracing appears to enhance some modes that radiate efficiently. Radial bracing offers the luthier a desirable option for experimentation and possible improvement of sound quality.

ACKNOWLEDGMENTS

The authors thank their many colleagues, especially Graham Caldersmith, Bernard Richardson, John Popp, and the late James D'Aquisto for their helpful conversations over the years.

Caldersmith, G. W. (**1989**). ''Toward a classic guitar family,'' Am. Lutherie #18, 20–25.

Caldersmith, G. W., and Williams, J. (**1986**). ''Meet Greg Smallman,'' Am. Lutherie #8, 30–34.

Christensen, O. (**1982**). ''Quantitative models for low frequency guitar function,'' J. Guitar Acoustics **6**, 10–25.

Eban, G. (**1998**). ''The relation of musical acoustics research to guitar design and building,'' in Proc. Intl. Symp. Musical Acoustics 1998, Leavenworth, WA, pp. 97–102.

Engström, F., and Rossing, T. D. (**1998**). ''Using TV holography with phase modulation to determine the deflection phase in a baritone guitar,'' in Proc. Intl. Symp. Musical Acoustics 1998, Leavenworth, WA, pp. 103–108.

Fletcher, N. H., and Rossing, T. D. (**1998**). *Physics of Musical Instruments* (Springer-Verlag, New York), Chap. 9.

Marty, S. M., Oreb, B. F., and Hariharan, P. (**1987**). ''Assessment of innovations in the construction of the classical guitar: Part II. New developments in guitar construction,'' J. Catgut Acoust. Soc. **47**, 30–33.

Meyer, J. (**1983**). ''Quality aspects of the guitar tone,'' in *Function, Construction and Quality of the Guitar*, edited by E. V. Jansson (Royal Swedish Academy of Music, Stockholm), pp. 51–75.

Richardson, B. E. (**1998**). ''The classical guitar: Tone by design,'' in Proc. Intl. Symp. Musical Acoustics 1998, Leavenworth, WA, pp. 115–120.

Richardson, B. E., and Roberts, G. W. (**1985**). ''The adjustment of mode frequencies in guitars: A study by means of holographic interferometry and finite element analysis,'' in *Proceedings of SMAC 83* (Royal Swedish Academy of Music, Stockholm), pp. 285–302.

Roberts, G. W. (**1986**). ''Vibrations of shells and their relevance to musical instruments,'' Ph.D. dissertation, University College, Cardiff, UK.

Roberts, M., and Rossing, T. D. (**1997**). ''Normal modes of vibration in violins,'' Proc. Inst. of Acoustics **19**(5), 29–35.

Rossing, T. D., Popp, J., and Polstein, D. (**1985**). ''Acoustical response of guitars,'' in *Proceedings of SMAC 83* (Royal Swedish Academy of Music, Stockholm), pp. 311–332.

Electrical resonance in the cuticle of hornets (*Hymenoptera, Vespinae*)

Jacob S. Ishay
Department of Physiology and Pharmacology, Sackler Faculty of Medicine, Tel-Aviv University, Ramat-Aviv 69978, Israel

(Received 4 March 1999; revised 14 July 1999; accepted 20 July 1999)

Evidence of electrical resonance in the abdominal cuticle was investigated in 16 dead hornets, eight juvenile and eight adult. Electrical measurements were consistent with high-impedance (low current, wide bandwidth) series resonance in the 500-Hz region with some significant differences between juveniles and adults. These findings cannot be explained on a solely electrical basis, but rather suggest a combination of piezoelectric effects and a mechanically resonant system, both of which are known to exist in insect cuticle. It is tempting to contemplate a hypothetical sensor role for these sounds and vibrations in hornets and their colonies, but the data do not yet support such a conclusion. © *1999 Acoustical Society of America.* [S0001-4966(99)03711-X]

PACS numbers: 43.80.Gx [WWLA]

INTRODUCTION

Hornets and wasps (*Vespinae*) are social insects (Wilson, 1971; Edwards, 1980), mostly annual, which usually find a nest in a dark place. The adult population of the colony is initially comprised of one fertile queen and workers numbering from tens to thousands, but by the end of the season, also of young queens and males. The brood population is equally abundant and consists of open brood, namely eggs and larvae at different instars, as well as of sealed brood-prepupae and pupae. The adults are vividly tinted, their integument varying from dark brown–black (owing to the pigment melanin) to intensely bright shades of green, yellow, or red, where the predominant pigments are usually purines and pteridines (Ziegler and Harmsen, 1969).

Colonies of the predominant hornet in Israel (*Vespa orientalis*) have provided clear evidence of collaborative behavior insofar as feeding (Ishay and Ikan, 1968) or acoustic communication (Schaudinischky and Ishay, 1968), whether between the larvae and the adults or between the adults only (Ishay, 1967, 1976). A particularly outstanding example of interadult collaboration in the nest pertains to ventilation—an activity wherein the hornets stand on the brood comb along the burrow leading to the nest as well as on its outer periphery and all of them beat their wings in unison (Sadeh *et al.*, 1977). Interestingly, when one of these living ''ventilators'' ceases this strenuous activity, a ''fresh'' hornet approaches from behind and continues the ventilatory wing-beating at *precisely the same rhythm* (Ishay and Sadeh, 1982), even in the dark. Such synchronous behavior of so many individual hornets is quite amazing.

In past years we have investigated the electric properties of the integument of social hornets (and wasps), evincing the occurrence of the following phenomena: electric conductivity (Ishay and Shimony, 1980), electric capacitance (Shimony and Ishay, 1984), thermoconductivity (Ishay *et al.*, 1982; Seebeck effect), thermoelectricity (Shimony and Ishay, 1981), photoconductivity (Croitoru *et al.*, 1978), irradiation effects (Kristianpoller *et al.*, 1997), piezoelectricity and ferroelectric-like properties (Ishay and Litinetsky, 1998), and a hypothesis of a natural radar navigation system guiding hornet flight was recently suggested (Ishay and Gavan, 1999).

Owing to the mentioned properties, barring capacitance one could say that the integument of social wasps behaves like an organic semiconductor with traps, in which the conduction is accomplished by charge carriers activated at an optimal temperature. The presence of an electric capacitance in the hornet integument indicates that apart from electric properties, the vespan cuticle also houses a special, multilayered *structure* whose individual layers are of opposing electric charge (Ishay *et al.*, 1997, 1998). The capacitance is frequency dependent—at 100 Hz invariably higher than at 1000 Hz and significantly higher in juvenile cuticle than in that of older ones.

In preliminary experiments exposing living hornets to uniform mechanical frequencies, we were surprised to find that there was a special frequency to which each hornet responded by either marked beating of the wings or quivering of the antennae. This finding led us to conjecture that there was probably a *resonant receptor* in hornets geared to react to a specific frequency.

As is known, in every resonant electric circuit, capacitance is a mandatory component, and since we found in the vespan integument an electric capacitance, we commenced experimentation aimed at ascertaining the presence of an electric resonance in hornet cuticle. Since the various electric properties previously investigated by us in hornet integument were found to correlate with various biological factors such as age, pigment, or caste, as well as physical properties such as light, we deemed it important here, too, to ascertain the possible influence of such factors on the resonant frequency in hornets. As part of this investigation, complex electrical impedance of the abdominal cuticle was examined in a few individuals and evidence of resonance was found.

Resonance can occur in many systems including electrical, mechanical, and acoustic, whenever elements are present which can store and release kinetic and potential energy. Dissipative elements are inevitably also present in such systems, which are common in inorganic materials, in living organisms including humans, and in technology. Zon (1979)

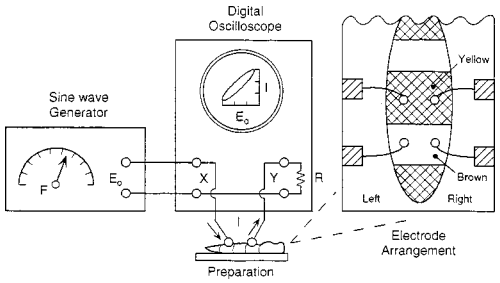

FIG. 1. Arrangement used for measurement of electrical impedance of hornet cuticle. An electronic function generator whose frequency could be varied from 100 to 10 000 Hz was adjusted to produce sine waves. Its constant output voltage E_0 at 50 ohms impedance, adjustable from zero to 22 volts peak to peak, was applied to the *X*-axis of an oscilloscope and to a selected electrode of the preparation under study while the second electrode was connected to ground through *R*, 10^6 ohms. Current through the preparation *I*, was in series with *R*, which was also connected across the oscilloscope's vertical axis. Voltage developed across the resistor, $E=I\times R$, produced a vertical deflection on the display while voltage applied to the preparation produced horizontal deflections. The resulting displays are described in the text and Fig. 2. Four colloidal silver electrodes 1–2 mm in diameter were placed on the hornet's abdomen as shown 5 mm apart. Electrodes were connected by tungsten leads to silver connectors on the acrylic base plate. Two electrodes were placed on an unpigmented brown segment and two on an adjacent pigmented yellow segment. This arrangement allowed study of six regions of the cuticle: transversely across yellow and brown segments, longitudinally between yellow and brown segments on left and right sides, and diagonally between yellow–brown segments. These regions are identified by six numbers in that order.

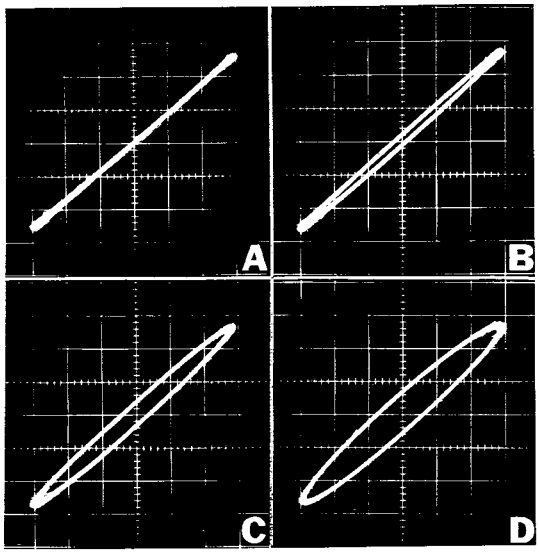

FIG. 2. Photographs of oscilloscope displays. Lissajou's figures produced by a resonant cuticle using the arrangement in Fig. 1 are shown. Voltage applied to the circuit is displayed on the horizontal scale and resulting current on the vertical scale. (A) shows a cuticle at resonance with no phase shift between current and voltage. (B), (C), and (D) show the specimen's response to frequencies increasingly further from resonance with increasing phase shift.

promotes the idea that organic semiconductors may have resonant effects similar to these produced in solid-state plasma.

Since resonance was detected electrically in hornet cuticle, electrical techniques were used in the present investigation. If a constant voltage of varying frequency is applied to an electrically resonant system, a point will be reached where impedance is minimum and current is maximum in a series resonant circuit, or current is minimum and impedance is maximum in a parallel resonant circuit. Parameters which characterize such circuits include:

(i) Resonant frequency,
(ii) Impedance (resistance) at resonance,
(iii) Bandwidth or rate of increase and decrease of current with frequency as one approaches and exceeds resonant frequency.

The above parameters were measured in the present examination of the resonant behavior of hornet cuticle.

Our paper describes the experiments carried out and the preliminary results obtained, which indeed point to the occurrence of a resonant frequency in vespan integument. However, electric phenomena alone are insufficient to explain such behavior in the cuticle, as will be discussed in some detail.

I. MATERIALS AND METHODS

Eight juvenile (1 day old) and eight adult (6–7 days old) hornets were killed by ether vapor and attached to 12 $\times$25-mm glass slides in supine position. Four 1–2-mm. colloidal Ag electrodes[1] were placed in the arrangement shown in Fig. 1. Electrode separation was typically 5 mm. Tungsten leads of 0.127-mm diameter electrically coupled these electrodes to Ag connectors on the slides.

Preparations were stored at (minus) $-20\,^{\circ}$C for 10 to 20 days and on the day of study, preparations were removed from the freezer and allowed 30 min to equilibrate with room temperature, which was controlled throughout the study (27–28 °C). Illumination was constant from standard incandescent lamps with a bench level of approximately 700 lux.

A sinusoidal oscillator,[2] with variable frequency *F* and constant but adjustable output voltage *E*, was connected to the horizontal or *X*-axis of an oscilloscope[3] and also across the hornet preparation in series with a 10^6 ohm resistor (Fig. 1). Voltage developed across this resistor by the current in the hornet cuticle was placed across the vertical or *Y*-input of the oscilloscope. A constant sinusoidal voltage *E* from the oscillator, at either 15 or 20 volts peak to peak, was varied in frequency from 100 to 1500 Hz and this voltage and the resulting current through the preparation were recorded from the oscilloscope.

In series resonance, current reaches a maximum and is in phase with the applied voltage. This produced a straight but tilted line [Fig. 2(A)] on the oscilloscope, whose slope $(\Delta Y/\Delta X)$ is the conductance $(\Delta I/\Delta E)$ of the cuticle plus the measuring circuit. Resistance of the cuticle alone was obtained by first substituting a series of known resistances for the specimens and then plotting the resulting *Y*-deflections as a function of the known resistance. Cuticle resistance at resonance was then read from this graph as a function of *Y*-deflection.

Resonant frequency was determined directly from the indicated frequency of the calibrated oscillator when current and *Y*-deflection were maximum and the phase shift zero as indicated by a display line [Fig. 2(A)]. This required no cor-

rection for resistance since resonant frequency in series circuits is unaffected by circuit resistance.

At frequencies other than resonance, like ''off resonance''—the current will be reduced and its phase angle shifted with respect to the driving voltage. This produces an ellipse on the oscilloscope display whose geometry is determined by how far the driving frequency is off resonance and by characteristics of the circuit [Fig. 2(B), (C), (D)]. By measuring frequencies above and below resonance which produce known amounts of current decrement and phase shift, a third important characteristic of a resonant circuit, namely, its ''bandwidth'' of current variation with frequency, may be determined.

The following measurements were made at each of the six cuticular regions on each hornet from the four electrodes and repeated at least once:

(i) Resonant frequency,
(ii) Impedance (resistance) at resonance,
(iii) Frequencies above and below resonance at three current levels—90%, 80%, and 70% of the current at resonance.

Voltage across the preparation ranged from 2 to 10 V.P.P., producing resonant currents on the order of 10^{-5} A.[4]

II. DATA ANALYSIS

The manually recorded data were transferred to spread sheets on a Compaq Presario PC using Microsoft statistical software. Means, medians, and s.d's were calculated. For each of the six selected cuticle regions in the young and adult hornet populations means, medians at s.d.'s were calculated as per:

(i) Resonant frequency,
(ii) Resistance at resonance,
(iii) Bandwidth at three amplitudes of current.

The means were examined for significant differences between the following categories (Figs. 1 and 2):

(i) Resonant frequencies for each cuticle region within and between young and adult,
(ii) Resistance for each cuticle region within and between young and adult.

The means and s.d.'s of resonant frequencies and resistance at resonance of all six cuticle regions in each hornet preparation were also calculated.

Relative or normalized[5] bandwidths for each cuticle region were calculated for each of the three current levels by dividing the bandwidth by resonant frequency, and means of the values obtained were examined for significant differences between regions in each population and between populations (Table I).

III. RESULTS

Resonant frequency measurements were made on the cuticle of six juvenile and eight adult hornets, while resistance values at resonance were obtained from six juvenile and five adults. Unstable or high electrode impedance appeared to be the cause of some erratic measurements, but even in these cases resonance phenomenon was evident.

Mean and s.d. for resonant frequencies of the six cuticle regions are shown Figs. 1, 2, and 3 for juvenile and adult populations together with means of each population.

Mean frequency in the adult population was 526 Hz, versus 654 Hz in the juvenile population, which is signifi-

TABLE I. Mean, s.d. and differences in normalized bandwidths for each cuticle region in juvenile and adult hornets.

Region	% of peak current	Juvenile mean±s.d.	Adult mean±s.d.	Difference probability juvenile vs adult
1	90	0.32±0.11	0.15±0.03	0.002[a]
	80	1.22±0.55	0.57±0.1	0.01[a]
	70	···	1.18±0.13	···
2	90	0.17±0.05	0.21±0.05	0.03[a]
	80	0.6±0.18	0.8±0.3	0.18
	70	1.36±0.026	1.46±0.64	0.73
3	90	0.2±0.07	0.16±0.03	0.23
	80	0.88±0.38	0.54±0.12	0.19
	70	1.35±0.3	1.26±0.22	0.15
4	90	0.25±0.06	0.17±0.05	0.03[a]
	80	1.08±0.42	0.66±0.15	0.03[a]
	70	1.75±0.27	1.25±0.32	0.05[a]
5	90	0.18±0.04	0.18±0.08	0.91
	80	0.82±0.22	0.71±0.14	0.32
	70	1.53±0.19	1.29±0.26	0.24
6	90	0.21±0.13	0.14±0.04	0.19
	80	0.97±0.42	0.62±0.11	0.06
	70	1.42±0.17	1.18±0.17	0.08

[a]Significant to $p \leqslant 0.05$.

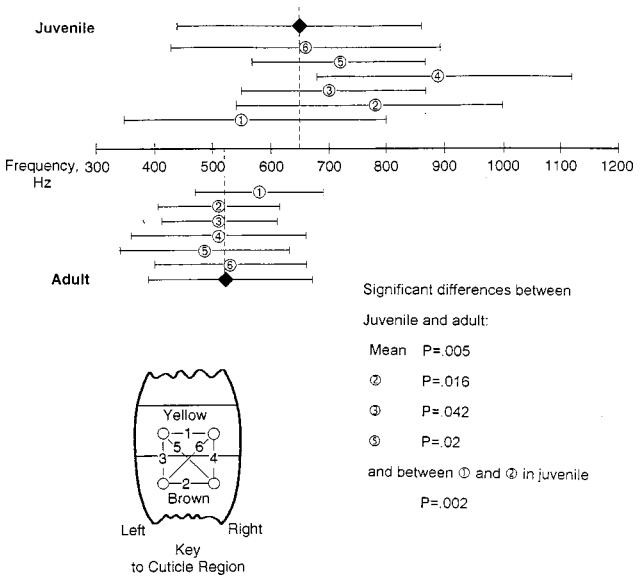

FIG. 3. Means and s.d.'s of resonant frequencies of six cuticle regions in juvenile and adult hornet populations and significant differences between regions in each population. Also shown is the electrode arrangement corresponding to the cuticular region. A significant difference was found in the mean resonant frequencies of combined regions in the two populations. There was a wide dispersion of values from individual regions, especially in the juvenile population. Other differences are also shown.

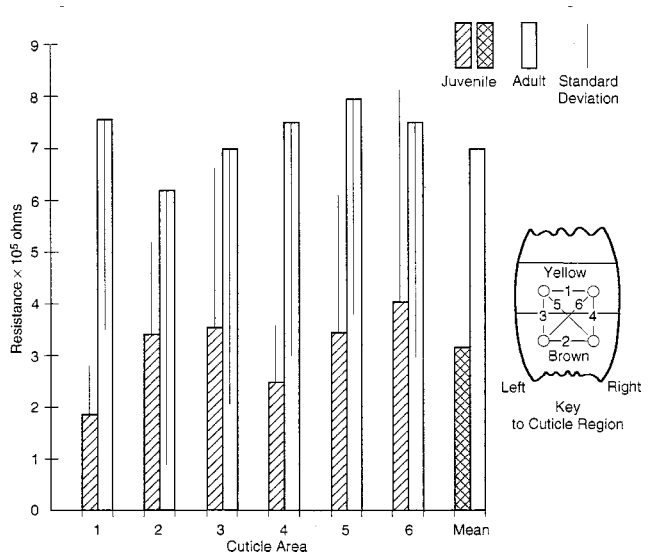

FIG. 4. Means and s.d.'s of resistance at resonance in the six cuticular regions of juvenile and adult hornets. A key to the regions is also shown. The mean resistance of all areas in the adult population was more than twice that in the juvenile population.

cantly higher ($p<0.005$). There is a very large spread of individual resonant frequencies in the six cuticle regions in the juvenile and somewhat less of a spread in the adults, as evident from the s.d.'s. Also, there is much less dispersion of the mean resonant frequencies in the cuticle regions of the adult as compared to the juvenile. There was a significant difference ($p=0.002$) between the yellow and other regions measured in the juvenile population, and also a significant difference between brown areas of the adult and juvenile ($p=0.016$).

Mean and s.d. of resistance at resonance of the individual and combined cuticle regions are shown graphically in Fig. 4. While there is a wide range of resistance within most of the cuticle regions, there is much less dispersion of mean values within the two populations. There is an obvious difference between populations, with the mean of adult values more than twice that of the juvenile.

Table I is a summary of normalized bandwidths and values for differences between cuticular regions in the two populations. These data were not plotted, for reasons to be explained later. The yellow region in juvenile hornets again showed a significant difference from brown regions.

IV. DISCUSSION

If the cuticle resonance was solely electrical, the characteristics that we measured could be fully explained in terms of the series circuit shown on the left side of Fig. 5. As will be argued shortly, this electric circuit *per se* cannot explain the recorded resonance but it does provide a good starting point for our proposal of a more complex system.

When a constant amplitude sinusoidal voltage is applied to a circuit with inductance L, capacitance C, and resistance R in series as in Fig. 5, and the frequency F is increased, mathematical values of negative capacitive reactance diminish while positive inductive reactance increases. At resonance R_0, capacitive and inductive reactances are equal, but

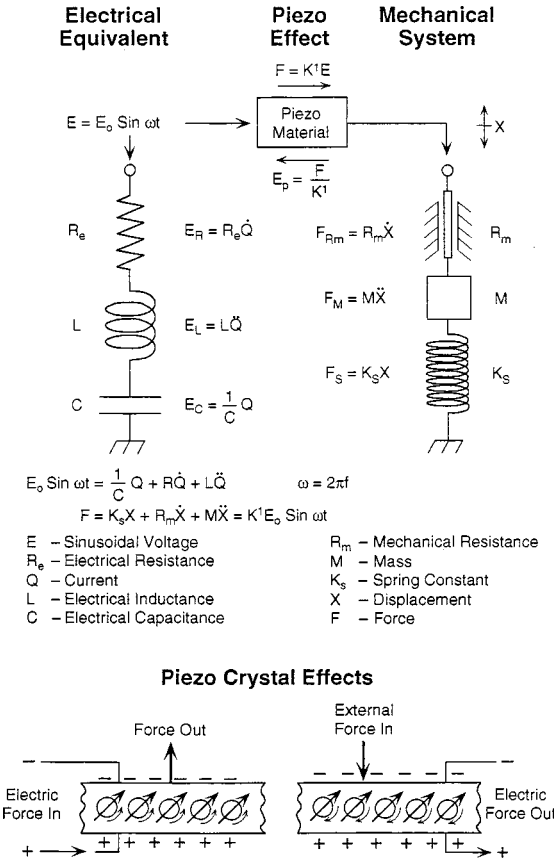

FIG. 5. Schematics of an electrical system and the postulated electromechanical systems showing the analogy of systems, components, and descriptive equations. A sketch of piezoelectric effects is also shown and described mathematically. Electrical measurements of the cuticle could be simulated by the circuit but known physical features of the chitin required the more complex electromechanical combination of piezoelectric transducers with a mechanical system. Both systems will display the same measured electrical response to the applied sinusoidal voltage E. Although the driving voltage will produce mechanical effects in the system on the right, it will be electrically sensed as the equivalent electrical circuit on the left. Simplistic sketches of piezoelectric effects are shown at the bottom of the page, with molecules represented by circles with vector arrows representing positive charges. With application of an electric field as on the left, mechanical force and displacement will result from torque on the charged molecules, while on the right an external force mechanically torques the molecules, producing an electric charge on the surface.

opposite and self-canceling, thus leaving resistance to limit current flow, which rises to a maximum at this point. Frequency at which this occurs is determined by the values of L and C.[6] At frequencies above resonance, impedance rises and current falls with increasing inductive reactance and decreasing capacitive reactance (Fig. 6).

The rate at which current rises and falls with frequencies below and above resonance is determined by the ratio of resistance to inductive reactance at resonance. This important ratio Z_0/R_0 has been designated q (capital Q is the usual designation, but that is used for charge in this paper) in electrical work. ($Z_0=2F_0\times L$, $R_0=$resistance at resonance). Figure 6 illustrates this with three normalized response curves of a series resonant circuit, such as Fig. 5, in which L and C are fixed and R is varied by orders of magnitude producing ratios or q's of 1, 10, and 100. Note that when the R is reduced, current and q are increased, and the bandwidth is reduced, and vice versa.

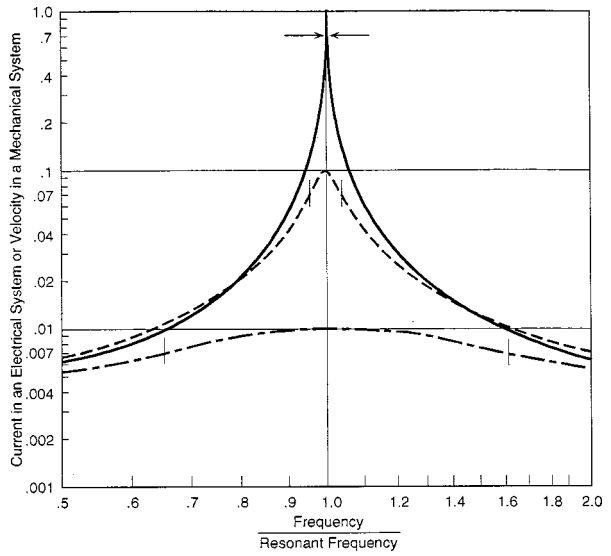

FIG. 6. Series resonance curves for an electric system (as shown on the left side of Fig. 5) or a mechanical system (as shown on the right side of Fig. 5). The value of the kinetic energy components, inductance in the electric circuit, or mass in the mechanical system remained the same, but the resistive element was increased in steps of 10 from q of 1 in the lowest curve to 100 in the upper curve. Note that peak current or velocity and bandwidth (at 70% of peak) increases as an inverse function of resistance. Resonances in the hornet corresponded to a region between the two curves of $q=1$ and $q=10$, $q=$reactance of mass or inductance at resonance/resistance, electrical or mechanical.

From the results obtained, we find that properties of a resonant electric circuit are present in the hornet cuticle (Fig. 7). Frequencies are relatively low and resistance is high at resonance, so that very large values of L would be required to achieve resonance.

Bandwidth is large and much, if not, most of this bandwidth is the result of the large value of the series current-sensing resistor, 10^6 ohms, added to the circuit for measurement purposes.[7] This resistance did not affect resonant frequency, but it decreased and distorted the response curve. While circuit resistance was measured and, in theory, the response curves could be corrected for the added resistance, in practice several factors including unknown electrode resistance made this problematical and such a general correction was not done. A first-order estimation of corrected response curves for two regions is shown in Fig. 7. What can be said with assurance is that the actual resonance peak, i.e., maximum response, would be larger than measured here by at least 2 to 6 times, bandwidths would be correspondingly reduced, and the significant differences found in the uncorrected data in Table I would be even more pronounced.

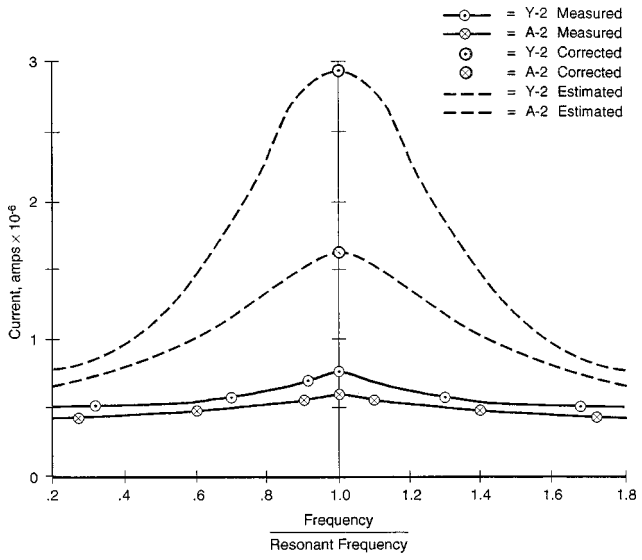

FIG. 7. Measured and corrected resonance curves from the mean values of region 2 in juvenile and adult populations. The two lower curves were plotted from raw data which were distorted by the large current sending resistor (R in Fig. 1). Currents at resonance were then calculated from measured circuit resistance at resonance (upper points). Estimated response curves were added to these points. The measured points included electrode resistance and the actual response at resonance was sometimes much greater with increased peak current and more narrow curves.

With such low frequencies we find two insurmountable problems in trying to explain the situation on a purely electrical basis, to wit: (1) a lack of physical evidence for electrical inductance in this case, and (2) the inductance values required would be impossibly high for this small insect.

Conversely, vespan cuticle has both mass and elasticity, the two elements essential for mechanical resonance, and mechanically resonant systems, like the one shown schematically on the right side of Fig. 5 are ubiquitous in living animals. Moreover, if one allows voltage E to become analogous to force F and displacement X becomes analogous to charge Q, then the differential equation of motion is exactly analogous to that of the electrical circuit, and solutions of the systems equations provide common descriptions of the behavior of both systems. Such analog techniques are well-known and were the basis for the once widely used electronic analog computer (Sze, 1981). For example, Fig. 6 is also an exact response of an analogous mechanical system.

If we had a means of physically converting electrical potential into force and charge into displacement, and this were connected as in Fig. 5, we would then have an electromechanical system that electrically responds exactly as the purely electrical system. The piezoelectric phenomenon, described by the Curie brothers in 1880, does just that by converting electrical potential into force, and vice versa (Anan'eva, 1965). Piezoelectricity is present in ten of 32 classes of natural crystal and in many synthetic crystals,[8] both types essential to modern technology (Cady, 1964; Johnson and Katz, 1987). It is also found in many plant and animal tissues, living and dead, including insects (Simhony and Athenstaedt, 1980). For our purposes, this phenomenon is simplistically illustrated in Fig. 5. Piezoelectric materials have regular arrays of polarized molecules shown by the vector arrows. When an electric field is applied, the molecules are torqued by their charges and produce a force and displacement proportional to the field strength and orientation and to the piezo constant of the crystal; thus $F=K^1E$ where K^1 is the piezo constant, F is force, and E is the applied electromotive-force (emf). It is significant to our discussion that this is a reciprocal phenomenon such that when a force is applied to the crystal a voltage is generated. The piezoelectric effect thus transforms electrical into mechanical effects, and vice versa. Provided this effect is present in the hornets' cuticle, it should allow the electrical phenomenon

normally associated with vespan electric circuitry to be translated into mechanical phenomena actually extant in this circumstance.

A simple equivalent circuit that would fully explain the cuticles' electrical behavior is the combination of a piezoelectric transducer driving a mechanical spring-mass system as shown in Fig. 5. Transducer and mechanical properties are apparently inherent to hornets' cuticle and, with the proposed model, the obtained results can be realistically extended to the actual situation so that cuticle displacement and motion will be detected and measured in terms of electric current, etc.

It is remarkable that these effects were found with such a simple test arrangement as used here, for typically electric fields have to be oriented to specific planes and axes relative to the lattice orientation in piezoelectric substances, and the field must be applied over a large area to excite them. The small electrode area may account for the large driving voltages required and the low currents/velocities produced. An alternative explanation is a low piezo coefficient, K^1. A few similarly configured adult preparations were placed in sound fields of 120–130 dB (0 dB=20 micro Pa SPL) and reciprocal resonant behavior was found in the 500-Hz region but voltage was very low, approximately 10^{-5}, again possibly indicating a low piezo constant.

In our statistically small sample, we found little difference in resonant frequency or resistance as a function of orientation except for the yellow pigmented band in the juvenile. Actual area and volume of the preparation which was set into motion by the exciting voltage is unknown.

Another remarkable feature is the low resonant frequency in such a small package as vespan abdominal cuticle. While the piezo crystals that produce audible signals in watches are also tiny, frequencies there are much higher. Although overall cuticle shape and mass loading by abdominal contents might play a role in reducing frequencies, it seems more likely to be an inherent property of the chitin, which micrographs have shown to consist of many layers, unlike the usually monolayered homogeneous crystal (Ishay *et al.*, 1998). Currently, virtually nothing is known on the mass or elastic properties or on the piezoelectric constant of hornet cuticle, but knowledge of such properties is essential for an adequate interpretation of the observed resonance phenomenon.

We obtained evidence of significant differences between the yellow and brown cuticular regions in the juvenile hornets including lower resonant frequency, and lower resistance at resonance but broader bandwidth, which would suggest larger mechanical compliance or reduced mass. Again, in the absence of knowledge of the physical characteristics of the chitin and proteins in hornet cuticle, this must remain speculation. However, we already know that the pigment in the brown areas is melanin, while in the yellow strips the yellow color is induced by a *layer* of symbiotic bacteria deposited horizontally over the basement membrane and under the many lamellae of the endocuticle (Ishay *et al.*, 1999). The daily needs of bacteria for solar irradiation (Caddick *et al.*, 1998) or their possible influence on the semiconducting properties of vespan yellow cuticle are not yet known.

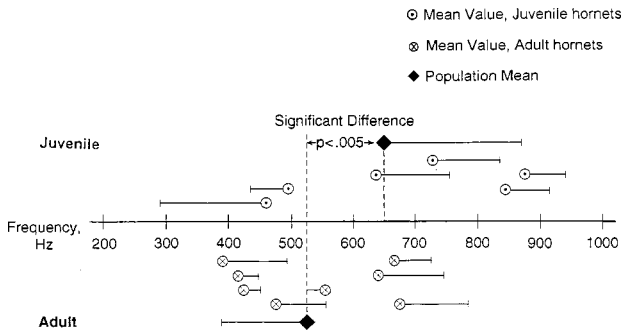

FIG. 8. Resonant frequencies of all regions for individual hornet preparations. Note the generally smaller s.d.'s for areas within an insect as compared to the differences within an area from all insects (Fig. 3). There were large individual differences in mean resonant frequencies.

There are apparently significant differences between ''juvenile'' and ''adult'' chitin in our preparations, with the latter showing a lower frequency, which might be caused by increased mass. At the same time, mean resistance at resonance was doubled in the adults. While this may be a characteristic of chitin, electrode impedance was not measured and differences from this source cannot be discounted. There are also striking individual differences in frequencies and resistance (Fig. 8), and this might be associated with size, mass, and exact age of these preparations.

The potential role of the discovered resonant phenomenon in nature merits at least theoretical consideration. At this stage we have assumed that a similar phenomenon will also be present in living hornets, but this remains to be proven. The reciprocal nature of piezoelectric effects (Popp *et al.*, 1979) renders two functions theoretically possible: (1) conversion of electrical energy into mechanical effects, and (2) conversion of mechanical energy into electric effects. Our finding of resonance insures that piezo effects would be most efficient over a limited range of frequencies.

The first possibility, conversion of electric into mechanical force, seems unlikely in the absence of known electric fields in this insect, especially fields intense enough to excite significant motion. The second possibility, conversion of vibrations or sound into a sensible electric field, seems more promising, especially since hornets are known to generate and respond to vibration and sound near the found frequency range (Ishay and Sadeh, 1982). While some investigators have postulated a sensory role for the piezo effect, there are presently many arguments contravening such a role in hornet cuticle, to wit:

(i) Conversion efficiency, at least in dead cuticle, is very low,
(ii) In hornets there is no reported evidence for neurological sensors that could connect the nervous system to either the electric or mechanical aspects of this system,
(iii) Resonant frequencies are not coherent within either population examined here.

Based on available information, the observed resonance appears to be an epiphenomenon associated with the nature

and structure of chitin, and could play a useful role in delineating the nature of this material.

For further investigation of the phenomenon, the following procedures are deemed beneficial:

(i) Confirm the finding of resonance in dead cuticle preparations using modern techniques including electrical and mechanical methodology,
(ii) Extend the study to living material,
(iii) Physically and chemically characterize the cuticle,
(iv) Look for potential connections to the nervous system.

Also, the electrical properties previously described in hornets should be reassessed and correlated with the new findings. For example, capacitance in the cuticle was found to be frequency dependent (Shimony and Ishay, 1984), which is consistent with the present findings, but the large values of capacitance previously reported (Benshalom-Shimony and Ishay, 1990) are inconsistent with the frequencies and other electrical behavior presently encountered.

Hornets and similar insects are likely to possess many as yet unknown features that could aid and greatly expand our understanding of living organisms.

ACKNOWLEDGMENTS

I would like to thank Professor W. E. Thornton for valuable help in preparing this manuscript, Dr. Joseph Kustanovitch for valuable measurements, Dr. Ed Mosely for statistical analysis, Sidney Jones for aid in the graphics, and Professor Jacob Gavan for critical review of the manuscript.

[1]Alfa Products, Danvers, MA.
[2]Neutronics function generator model 11200 TPC.
[3]Kenwood model CS 8010.
[4]This level of current and power was well below the level that would produce heating effects (9).
[5]$BW_{norm}=(F_2-F_1)/F_0$, where F_0=resonant frequency and F_1 and F_2 are frequencies below and above resonance which produce a stated fraction of the resonant current. See Fig. 7.
[6]$F_0=1/2\Pi(LC)$ (F_0=frequency, Hz; L=inductance, henry; C=capacitance, farad.
[7]The large value was a compromise between adequate resolution and sensitivity of the oscilloscope available.
[8]Piezo- and pyroelectric effects can occur in particular lattices of polarized molecules. Ferroelectricity is a subclass of piezoelectricity in which internal polarization may be altered by a strong external field (Pierce, 1943; Jona and Shirane, 1962; Xu, 1991).

Anan'eva, A. A. (**1965**). *Ceramic Acoustic Detectors* (Consultants Bureau, New York), p. 116.
Benshalom-Shimony, T., and Ishay, J. S. (**1990**). ''Electrical capacitance and current in the Oriental hornet silk cocoon cap,'' Comp. Biochem. Physiol. **97**, 555–563.
Cady, W. G. (**1964**). *Piezoelectricity* (Dover, New York), Vol. I, pp. 1–9.
Caddick, M. X., Baumberg, S., Hodgson, D. A., and Phillips-Jones, M. K. (**1998**). *Microbial Responses to Light and Time*, Published for the Society for General Microbiology (Cambridge University Press, Cambridge), p. 320.
Croitoru, N., Ishay, J., Arcan, L., and Perna, B. (**1978**). ''Electrical resistance of the yellow strips of social wasps under illumination,'' Photochem. Photobiol. **28**(2), 265–270.
Edwards, R. (**1980**). *Social Wasps. Their Biology and Control* (Rentokil Limited, East Grinstead), p. 398.
Ishay, J. (**1967**). ''Observations on the behavior of the different members of a colony of the Oriental hornet *Vespa orientalis*,'' Ph.D. thesis submitted to the Senat of the Hebrew University, Jerusalem, p. 112.
Ishay, J. S., and Gavan, J. (**1999**). ''Hypothesis stipulating that a natural RADAR navigational system guides hornet flight,'' J. Electromagn. Waves Appl. **13**, 1611–1625.
Ishay, J., and Ikan, R. (**1968**). ''Food exchange between adults and larvae in *Vespa orientalis*,'' Anim. Behav. **16**(2–3), 298–303.
Ishay, J. (**1976**). ''Acoustical communication in wasp colonies (*Vespinae*),'' in Proceedings of the XVth international Congress Entomol., Washington, D.C., pp. 406–435.
Ishay, J. S., and Litinetsky, L. (**1998**). ''Ferroelectric-like properties in hornet structures and construction,'' Phys. Chem. Phys. Med. NMR **30**(2), 185–201.
Ishay, J. S., and Sadeh, D. (**1982**). ''The sounds of honey bees and social wasps are always composed of a uniform frequency,'' J. Acoust. Soc. Am. **72**, 671–675.
Ishay, J. S., and Shimony, T. B. (**1980**). ''Changes in the cuticular pigments of hornets induced by Xanthine feeding and light exposure (*Hymenoptera: Vespinae*),'' Entomol. General. **6**(1), 25–38.
Ishay, J. S., Shimony, T. (Benshalom), Lereah, Y., and Duby, T. (**1982**). ''Temperature dependence of electrical resistance of hornet and ant cuticles in low temperature: Direct current measurements,'' Phys. Chem. Phys. Med. NMR **14**, 343–361.
Ishay, J. S., Goldstein, O., Rosenzweig, E., Kalicharan, D., and Jongebloed, W. L. (**1997**). ''Hornet yellow cuticle microstructure: A photovoltaic system,'' Phys. Chem. Phys. Med. NMR **29**(1), 71–93.
Ishay, J. S. Kirshboim, S., Steinberg, D., Kalicharan, D., and Jongeboled, W. L. (**1998**). ''Hornet cuticle: A composite structure comprised of a series of duplex lamellae attenuating toward the interior of the body,'' Comp. Biochem. Physiol. A **120**, 661–670.
Ishay, J. S., Kirshboim, S., Shabtai, Y., Kalicharan, D., and Jongebloed, W. L. (**1999**). ''Biodegradable organic polymers produced by hornets in cocoon or comb building,'' Physiol. Chem. Phys. Med. NMR **31** (in press).
Johnson, M. W., and Katz, J. L. (**1987**). ''Electromechanical Effects in Bone,'' in *Handbook of Bioengineering*, Chap. 3.
Jona, F., and Shirane, G. (**1962**). *Ferroelectric Crystals* (Pergamon, Oxford), p. 400.
Kristianpoller, N., Weiss, D., and Ishay, J. S. (**1997**). ''Irradiation effects in the Oriental hornet,'' J. Lumin. **74**(6), 591–592.
Pierce, G. W. (**1943**). ''The songs of insects,'' J. Franklin Inst. **236**, 141–146.
Popp, F. A., Becker, G., König, H. L., and Peschka, W. (**1979**). *Electromagnetic Bio-Information. Proc. Symp., Marburg., Sept. 1977* (Urban and Schwarzenberg, Munchen), p. 79.
Sadeh, D., Ishay, J., and Yotam, R. (**1977**). ''Hornet ventilation noise: Rhythm and energy content,'' Experientia **33**(3), 335–377.
Schaudinischky, L., and Ishay, J. (**1968**). ''On the nature of the sounds produced within the nest of the Oriental hornet *Vespa orientalis* (*Hymenoptera*),'' J. Acoust. Soc. Am. **44**, 1290–1301.
Shimony, T. B., and Ishay, J. S. (**1981**). ''Thermoelectric (Seebeck) effect on the cuticle of social wasps,'' J. Theor. Biol. **92**, 497–503.
Shimony, T. (Benshalom), and Ishay, J. (**1984**). ''Electrical capacitance in hornet integument: Frequency, light and temperature dependence; possible P–N junction effects,'' Phys. Chem. Phys. Med. NMR **16**(4), 333–349.
Simhony, M., and Athenstaedt, H. (**1980**). ''Measurement of the pyroelectric coefficient and permittivity on *Rhododendron* and *Encephalartor* leaves and on the insect *Periplaneta americana*,'' Biophys. J. **29**, 331–338.
Sze, S. M. (**1981**). *Physics of Semiconductor Devices*, 2nd ed. (Wiley, New York), p. 837.
Wilson, E. O. (**1971**). *The Insect Societies* (The Belknap Press, Harvard, Cambridge, MA).
Xu, Y. (**1991**). *Ferroelectric Materials and Their Applications* (North-Holland, Amsterdam), p. 391.
Ziegler, J., and Harmsen, R. (**1969**). ''The biology of pteridines in insects,'' J. Insect Physiol. **6**, 193–203.
Zon, J. R. (**1979**). ''Physical plasma in biological solids: a possible mechanism for resonant interactions between low intensity microwaves and biological systems,'' Physiol. Chem. Phys. **11**(6), 501–506.

Environmental constraints on sound transmission by humpback whales

Eduardo Mercado III[a)]
Gluck Lab, Center for Molecular and Behavioral Neuroscience, Rutgers University, 197 University Avenue, Newark, New Jersey 07102

L. Neil Frazer
Department of Geology and Geophysics, School of Ocean and Earth Sciences (SOEST), University of Hawaii at Manoa, Honolulu, Hawaii 96822

(Received 10 December 1998; accepted for publication 9 July 1999)

Singing humpback whales in Hawaii produce a variety of sounds at high source levels (ca. 185 dB *re*: 1 μPa), in coastal waters 15–500 m deep. These sounds are attenuated and distorted as they propagate away from a singer, limiting the utilizable range of the sounds. In the current study, simulations based on normal-mode theory were used to investigate how the effects of shallow-water propagation constrain humpback whales' use of sound. It is shown that humpbacks can greatly affect transmission range by adjusting their positions and sounds in response to environmental factors. Source depth, in particular, is shown to be a major determinant of which frequencies propagate the farthest. A preliminary analysis of range-dependent distortion suggests that spectral cues can potentially provide listening whales with information about how far a sound has traveled.
 [S0001-4966(99)01211-4]

PACS numbers: 43.80.Ka, 43.30.Bp, 43.30.Re [WA]

INTRODUCTION

An animal's ability to use sound is strongly constrained by environmental factors. In particular, the medium(s) through which sounds propagate determine not only where the sounds will travel, but also to what extent they will be transformed (e.g., through distortion) as they travel. Such constraints are clearly reflected in the sound repertoires used by various species. For example, animals that use acoustic signals to communicate over short distances tend to use graded repertoires, composed of sounds that vary continuously along one or more dimensions; graded vocal signals are often supported by concurrent visual signals. In contrast, animals that communicate over long distances typically use discrete repertoires, consisting of highly stereotyped sounds that differ along many dimensions;[1] such signals remain discriminable even after significant distortion. Echolocating species must contend with huge environmental constraints. Bats vary their sonar signals continuously as a function of their environment when they are searching for and capturing prey.[2–4] When foraging in open spaces, bats tend to produce stereotyped sequences of constant-frequency sonar signals.[5–8] By narrowing the frequency bandwidth and lengthening the duration of their sonar signals, bats are able to put more energy into each frequency band, allowing them to overcome the relatively high attenuation of sound in air and to optimize their long-range detection of targets.[8,9] When bats are echolocating in more cluttered spaces, or are closing in on a target, they tend to shift to shorter duration, broadband signals that are more limited in range. Because environmental properties play such a critical role in shaping how animals use sound, it is important to carefully consider such factors when examining the vocal behaviors of a particular species. This is especially true for species that vocalize in shallow-water environments.

Shallow-water sound propagation has received much attention from ocean acousticians in the last 50 years, both theoretically and experimentally (for reviews, see Refs. 10–14). The problem is highly complex because it involves multiple reflections from the surface and bottom. Propagation in shallow water depends on signal frequency, source and receiver depth, sound-speed profiles (SSPs) in the water and in the bottom, water depth, biomass, bottom variability as a function of range, surface roughness, and so on. The large number of interacting variables makes predicting how sounds will propagate in shallow water extremely difficult. This high level of complexity may explain why so few researchers have incorporated analyses of propagation effects into their investigations of the vocal behaviors of shallow-water species. Shallow-water environments place unique constraints on sound transmission. These constraints have undoubtedly affected the ways in which vocal marine species (e.g., cetaceans) use sound.

Although investigators recognized early on that the transmission properties of underwater environments played an important role in shaping the acoustic abilities of cetaceans,[15,16] few studies attempted to rigorously account for these factors. The few analyses of propagation that were attempted were primarily theoretical and based on highly simplified models.[17] Initially, studies of the range and directionality of delphinid echolocation signals[18–21] provided the only data with which to address questions related to propagation. The complexities of propagation in real-world environments inhabited by cetaceans have only recently begun to be examined more closely.[22–29] Similarly, the constraints on cetacean sound use resulting from environmental factors

[a)]Electronic mail: mercado@pavlov.rutgers.edu

(e.g., ambient noise levels) are only now being broadly considered.[12]

Effects of propagation become most relevant when sounds are transmitted over long distances. No animals transmit sounds over longer distances than baleen whales (the mysticetes). Empirical research on the propagation of blue and fin whale sounds has shown that they can be detected from as far away as 1600 km.[30,31] Although it is doubtful that whales actually use sounds over such long ranges, it is clear that the sounds are produced to travel. For whales producing sounds in shallow water (e.g., less than 200 m deep), effective long-range transmission cannot be efficiently achieved simply by increasing the intensity of sounds. In such an environment, the spectral and temporal features of sounds critically determine how far the sounds will propagate and their discriminability after distortion. The current study uses computational methods to examine how shallow-water environments constrain sound transmission by a notably vociferous whale, the humpback (*Megaptera novaeangliae*).

I. SOUND TRANSMISSION BY HUMPBACK WHALES

A. Characteristics of sounds

In terms of sound production, humpback whales have few rivals. Their vocalizations can be extremely loud (up to 190 dB *re* 1 μPa,[12,32,33]) and are detectable from long distances (as far away as 160 km[30]). When ''singing,'' humpbacks may produce sounds for as long as 10–20 h nonstop,[34,35] and can be heard day and night for several months.[36,37] Additionally, humpback whales' sound repertoire is subjectively more variable than that of any other baleen whale. The sound-producing behaviors of humpback whales have been observed to vary as a function of gender, season, year, social context, geographic location, and individual.[22,38–42] Humpback whale sounds have typically been classified based on context and production mode.[41,43–46] For example, distinctions are made between songs (produced rhythmically, typically by lone males), social sounds (produced sporadically in competitive groups/pods of whales), and feeding sounds (produced in groups of foraging whales).

Humpback whale sounds can generally be divided into two main types: vocal and nonvocal sounds.[45,47] Nonvocal sounds include sounds produced by breaching, slapping body parts on the surface of the water, and blowing. Humpback whales produce vocal sounds internally using mechanisms that are poorly understood. Most of the spectral energy in humpback whale vocalizations falls between 50–4000 Hz,[41,48,49] with peak energy typically lying below 1500 Hz. Sounds range in duration from 0.1 to 10 s.[48,49] The majority of vocalizations is pulsed sounds. Many are constant in pitch with only brief periods of modulation; higher-pitched sounds tend to be modulated more extensively. Gradual or rapid frequency upsweeps are prevalent, with downsweeps being much less common.[48,49] The sound repertoire used by humpback whales is not fixed, but gradually changes over time.[41,49–51] This is most clearly evident for sounds produced within songs. Subjectively, specific sound types used within songs tend to be comparable between consecutive years, but less so over longer periods of time. Sound types may also be continuously modulated along one or more dimensions within a song.[41] Thus, the repertoire of sounds used by humpbacks appears to be graded rather than discrete. Although the sounds used by humpbacks are continuously and progressively changing, they appear to modulate within the boundaries of strict constraints that are stable across years.[49,51] For example, distributions of many sound characteristics (e.g., duration) were found to be highly stable over a 14-year span.[49] Interestingly, the distribution that varied the most across years was that of the frequency with peak energy (i.e., bandwidths appeared to be used differentially across years). It is important to note, however, that many other factors other than time may account for this variability, including variability in recording locations across years.

B. Acoustic environment

Humpback whales are globally distributed, inhabiting relatively shallow waters. During the summer, humpbacks can be found in high latitudes near continental shelves[52,53] where they spend much of their time feeding. In late fall and early winter, whales begin migrating towards lower-latitude subtropical areas where they spend the winter in shallow coastal waters. Most mating activities are believed to occur in the winter. During late winter and early spring, the whales begin migrating back to the summer feeding areas. Whales have been observed vocalizing during all stages of this annual cycle. The majority of humpback whale vocalizations, however, has been recorded in the wintering grounds.

Vocalizing humpbacks have been studied most extensively in the Hawaiian Islands and the West Indies. Whitehead[53] reported that most vocalizing (i.e., singing) whales located on Silver, Navidad, and Mouchoir Banks were in water between 15 to 60 m deep. Singers acoustically located along the coast of Hawaii were found in waters 19 to 558 m deep; mean water depth was 230 m.[22,23] Whales in the Penguin Bank region were located in areas with a mean water depth of 94 m.[54] Major concentrations of humpback whales are known to occur in the coastal waters near Maui, Lanai, and Molokai, and around Penguin Bank. Water depth between Maui and Lanai ranges between about 30 to 80 m deep, and water depth over Penguin Bank ranges between 50 to 200 m deep.[52] The bathymetry in Hawaiian coastal waters has not been extensively studied. Recent reports indicate that the bottom consists primarily of silty sand and clay, with occasional outcrops of coral, limestone, and rocks.[22,52]

Sound speed in the ocean environment determines not only how rapidly sounds can be transmitted, but also how sounds will propagate. The speed of sound in water increases with increasing temperature, salinity, and pressure (which typically vary with depth). Numerous techniques have been developed to estimate sound speed using these three variables (for a review, see Ref. 10). In Hawaiian coastal waters, temperatures range between 21 and 29 °C and salinity ranges between 34.2 to 35.5 ppt.[52,55,56] A similar temperature range (24–28 °C) has been reported in the Caribbean.[53] In oceans, water near the surface is constantly mixed by wind and waves. This mixing stabilizes the temperature and salinity of near-surface water at a relatively constant value. Sound speed in this ''mixed layer'' of water slowly increases as a

function of depth due to increasing pressure. The depth of the mixed layer in Hawaii varies between 50 to 140 m.[52] Below the mixed layer is a layer of water in which temperature changes with depth; this layer is called the thermocline. Temperature decreases with depth in the thermocline, leading to a decrease in sound speed. The thermocline in Hawaii extends to depths of 275 to 365 m.[52] Detailed analyses of variations in sound speed as a function of depth have not been performed for shallow-water coastal environments in Hawaii or the Carribean. Recently, Frankel *et al.*[57] reported sound speeds between 1530 and 1535 m/s in the coastal waters off the island of Hawaii. They noted little change in sound speed down to 60 m, where a moderate thermocline began (−3 m/s gradient). Measurements taken at Silver Bank showed that the water was at a constant temperature from the surface to the seafloor.[53] The seafloor acts as a lower boundary on sound propagation. Bottom features (e.g., composition and smoothness) affect how sound propagates in the water above.[11] For example, soft bottom sediments such as mud are penetrable and remove significant fractions of energy; sandy bottoms tend to be much more reflective. Whitehead[53] found that singers were concentrated over regions with smooth bottoms. In such environments, the interaction between propagating sounds and the bottom depends primarily upon the materials that make up the bottom.

How well sounds propagate underwater is primarily determined by the properties of the environment (e.g., water temperature, salinity, and depth, bottom type, surface roughness) within which they are produced. A final feature of humpback whales' acoustic environment that constrains their use of sound, but that is somewhat independent of propagation effects, is ambient noise. Ambient noise in shallow-water coastal environments is quite variable depending on season, location, time of day, wind speed, bottom conditions, and the extent of biological and manmade sound production in the area; noise levels can vary by 10–20 dB from one day to the next.[12] In general, levels of ambient noise are influenced by the same factors that control transmission loss. Thus, regions of high transmission loss tend to have lower noise levels, and vice versa. Measurements of ambient noise levels in the humpback whale wintering grounds in Hawaii range from 58–95 dB *re* $1\mu Pa^2/Hz$ in the 100- to 4000-Hz band.[24,58–62] These values are comparable with those reported from other shallow-water environments.[10,16,63–65] When whales are present in an area, their vocalizations contribute significantly to ambient noise levels.[53,60,66,67] Large boats also generate considerable noise.[12,62] Although ambient noise levels do not physically constrain sound transmission, they may mask sounds produced by humpback whales, limiting the range at which they can be detected.

C. Sound-field control

Humpbacks have some control over the factors that affect how well their sounds will propagate. First, and probably most importantly, they can control when and where they produce sounds. Thus, they could choose an area or time period within which to vocalize based on its ''acoustic potential'' (e.g., propagation characteristics and noise levels). Note that knowledge of the relative propagation potential of different locales need not be explicit. Whales could implicitly learn what locales are effective based on experience and/or could be genetically predisposed to favor sites that are effective. Evidence suggestive of such site selection is provided by observations of increased singer densities in areas with smooth bottoms.[53]

Other important factors affecting maximum range, that are more physiologically constrained, include the source level, beam pattern, and frequency range used by humpbacks. Source level refers to the relative intensity of sound radiated by a projector (in this case, the whale), at a standard distance from the source. The term beam pattern refers to the directional variability of projected sounds. Of these three factors, only the frequency range of produced sounds is known with any certainty for humpbacks. Individual sounds within songs can vary greatly in intensity.[41,48,68–70] Source levels of between 144 and 190 dB *re* 1 μPa at 1 m have been reported.[12,22,32,60,66,71,72] These source levels have generally been derived using estimated ranges, theoretical models of propagation based on geometrical spreading, and a relatively small number of measurements of received levels. Because of the many potential sources of error, current estimates of humpback whale source levels should be taken as points within the range of possible values (see Ref. 73 for a detailed discussion of this issue). Consider that estimates of *average* source levels have ranged from 155 to 185 dB over the last 20 years (30 dB corresponds to a 1000% increase in estimated average intensity).

Even less information is available regarding humpback whale beam patterns. Levenson[71] reported greater differences in received levels at different positions along a linear array than would be expected if humpback whales projected sounds omnidirectionally, and Clark[47] noted similar differences in levels received from vocalizing bowheads based on their relative orientation. These observations may reflect fluctuations in transmission loss resulting from varying source–receiver configurations (i.e., their depths relative to the surface and distances between one another) or other parameters. It is more likely, however, that they are due to directional properties associated with whales' beam patterns. Although low-frequency sounds will generally be less directional than higher-frequency sounds,[74] the common assumption that humpback whales project sounds omnidirectionally[17,22,69] seems unlikely given that most vocal mammals produce sounds directionally, and that omnidirectional sound production would be highly inefficient in a sound channel bounded by the bottom, surface, and shoreline.

II. ASSESSING ENVIRONMENTAL CONSTRAINTS

A. Models of shallow-water propagation

Early models of shallow-water propagation focused on characterizing transmission loss (a parameter describing how a sound weakens as a function of distance from the source). These techniques integrated models of geometrical spreading with measurements of transmission loss (TL) in shallow water. For example, Marsh[75] developed three equations for modeling transmission loss in terms of different spreading

conditions. Sound energy was modeled as spherical spreading near the source ($TL = 20 \log r$, where r is range in m), spreading between spherical and cylindrical at ''medium'' ranges ($TL = 15 \log r$), and cylindrical spreading at longer ranges from the source ($TL = 10 \log r$). Such formulas work reasonably well when the bottom is uniform. Frankel *et al.*[59] reported a close correspondence between measured transmission losses and the losses predicted by the Marsh equations in environments frequented by humpback whales. These equations do not, however, account for variables such as source and receiver depth or complex bottom interactions. This may explain why empirically based estimates of transmission loss in Hawaiian coastal waters (derived using spreading loss models) have ranged from $TL = 10 \log r$[57] to $TL = 17 \pm 2.38 \log r$.[22,24]

More recent models of sound transmission in shallow water are based on solutions of the wave equation (for reviews, see Refs. 10, 11, 13, and 14). The wave equation is a partial differential equation that relates acoustic pressure to spatiotemporal coordinates. The acoustic field emitted from a point source can be calculated by solving the wave equation, given a set of initial conditions or boundary values corresponding to environmental parameters; such calculations are typically performed using a computer. Several theoretical approaches have been developed for solving the wave equation including ray theory, normal-mode theory, spectral methods, and the parabolic equation model.[11,13] The choice of theoretical approach depends on the propagation ranges of interest, computational power, and sound channel variability. Normal-mode theory is well suited for modeling sound propagation in the environments frequented by humpback whales because bottom properties are only moderately variable and the propagation ranges of interest are between 0.1 and 60 km.[11] Additionally, previous studies have found good agreement between measurements and predicted values based on normal-mode theory.[11,76–79] Normal-mode solutions have the advantage that once they are solved for a particular environment, the solution can be used for all possible source and receiver configurations.

The computations in this paper used Westwood *et al.*'s normal-mode model, ORCA.[80–82] ORCA calculates the field parameters for an acoustoelastic environment with a multilayered bottom. As ORCA is a plane-layered range-independent model, the effects of scattering due to variable bathymetry or a rough ocean surface are not included in the computation. The main effect of scattering is to increase transmission loss, whereas bathymetric changes with scale length much greater than a wavelength cause more fundamental changes in the signal. In general, the problem of determining optimal frequencies for environments with variable bathymetry must be considered on a case-by-case basis, and is beyond the scope of this paper.

B. Optimum frequencies

By optimum frequency, we mean the frequency that achieves the maximum propagation range, given a particular environment and source depth. In any real shallow-water environment, there is likely to be an optimum frequency.[11,13,83] This follows from the fact that different features of the environment affect transmission loss differently at different frequencies. For example, at low frequencies fewer modes propagate, and so transmission loss may be dominated by the effects of water depth. At higher frequencies, on the other hand, transmission loss may be dominated by intrinsic absorption of energy in seafloor sediments. Ignoring temporarily the effects of other variables, which can be equally important, one sees that there is likely to be an intermediate frequency at which neither effect dominates and transmission loss is minimized. However, the number of variables affecting transmission loss is so large that one cannot predict their relative effects without actual numerical simulations of the propagation process.

In addition to optimum frequency, there is also a cutoff frequency below which sound will not propagate at all in shallow water.[10,11,14] The cutoff frequency (f_c) for a shallow-water environment can be approximated by

$$f_c = \frac{c_w/4h}{\sqrt{1 - c_w^2/c_s^2}},$$

where c_w is the sound speed in water, c_s is the sound speed in the bottom, and h is the water depth.[14] For the water depths and bottom types encountered by vocalizing humpback whales, f_c ranges between about 1 to 100 Hz (estimated from Ref. 14, Fig. 5.8). The optimum frequency (f_o) depends on several variables including SSPs for the water and the bottom, and the depths of the water, source, and receiver.[11] Optimum frequencies can be calculated theoretically, using normal-mode methods, or empirically. Jensen and Kuperman[11] compared these two approaches and found that they produced similar results. They found that water depth was a primary determinant of f_o, and that f_o decreased with increasing water depth. Optimum frequency increased when either the source or receiver was not halfway between the bottom and the surface. They also noted that the effects of bottom properties on transmission led to different maximum propagation ranges at different water depths. The results of Jensen and Kuperman suggest that for humpbacks to maximize their propagation range in shallow water, they would need to produce sounds (1) with frequencies between 50 to 800 Hz, (2) at mid-depth in water between 30 to 300 m deep, and (3) over bottoms consisting primarily of sand and silt. These criteria correspond closely to the scenario that has been described for singing humpback whales.

Previous studies of humpback whale vocalizations have often suggested that lower-frequency vocalizations will propagate longer distances than higher-frequency vocalizations and that vocalizing humpbacks should therefore produce low frequencies to achieve the maximum propagation range.[69,84] It has also been suggested that low-frequency sounds might be used for long-distance communication, while higher-frequency sounds would be more appropriate for short-range communication.[41,69] Such suggestions appear to be based on (1) the fact that attenuation of sound by seawater increases with increasing frequency, (2) the assumption that lower-frequency signals are produced at levels equal to or greater than higher-frequency signals, and (3) the assumption that attenuation in the water channel is the primary

TABLE I. ORCA input files for full geoacoustic models: (a) 60-m water depth, without a thermocline; (b) 200-m water depth, with a thermocline starting at a depth of 70 m. Row 1 defines the physical properties of the upper boundary (air) for each environment, and row 4 defines the lower boundary (a basalt basement). The remaining rows define the physical properties of the channels through which sound propagates (i.e., the water and the bottom). cp=compressional speed in m/s, cs=shear speed in m/s, rho=density in g/cm^3, ap=compressional wave attenuation, as=shear wave attenuation, z=depth in m, nsvp=number of sound-speed profile points in the ocean, ctol=tolerance used in fitting SSP to eliminate layers (ctol=0 keeps all layers), nbot=number of layers in ocean bottom, ii=type of compressional speed profile (ii=1 is linear), h=layer thickness, cs1=compressional speed at the top of layer 1, cs2=compressional speed at the bottom of layer 1 (similarly for rho1 and rho2, ap1 and ap2, as1 and as2). Note that all environmental parameters are fixed across simulations except for nsvp, *z*, and cp in the ocean profile, and cp1 in the bottom profile; changes in these parameters reflect changes in SSPs. For further details, see Refs. 70 and 116 and Fig. 1.

(a) Hawaiian humpback whale environmental model without thermocline

(1) For upper halfspace: cp=350, cs=0.0, rho=0.001 21, ap=0.0, as=0.0
(2) Ocean profile: nsvp=2, ctol=0, z=0, cp=1534.3, rho=1.05, ap=0; z=60, cp=1535.2
(3) Bottom profile: nbot=1, ii=1, *h*=50, cp1=1565.9, cp2=1600, cs1=100, cs2=400, rho1=1.7, rho2=1.7, ap1=−0.5, ap2=−0.5, as1=0, as2=0
(4) For lower halfspace: cp=5250, cs=2500, rho=2.6, ap=−0.04, as=0

(b) Hawaiian humpback whale environmental model with thermocline

(1) For upper halfspace: cp=350, cs=0.0, rho=0.001 21, ap=0.0, as=0.0
(2) Ocean profile: nsvp=3, ctol=0, z=0, cp=1534.3, rho=1.05, ap=0; z=70, cp=1535.4, z=200, cp=1519.6
(3) Bottom profile: nbot=1, ii=1, *h*=50, cp1=1550, cp2=1600, cs1=100, cs2=400, rho1=1.7, rho2=1.7, ap1=−0.5, ap2=−0.5, as1=0, as2=0
(4) For lower halfspace: cp=5250, cs=2500, rho=2.6, ap=−0.04, as=0

determinant of how far different frequencies will propagate in shallow water. Effects of water depth, source depth, receiver depth, bottom type, and SSPs do not appear to have been considered in these previous analyses. The results of Jensen and Kuperman indicate that such factors can strongly affect which frequencies propagate best, and that in some environments higher-frequency vocalizations should propagate longer distances than lower frequency vocalizations of equal energy. The following simulations examine this possibility in greater detail.

III. ENVIRONMENTAL EFFECTS ON PROPAGATION

To investigate how shallow-water propagation effects might constrain how humpback whales use sound, simulations were run to calculate optimum frequencies in environments similar to those frequented by singing whales in Hawaii, and to assess whether there might be predictable, range-dependent, spectral distortion effects in these environments. To a certain extent, a subset of these analyses can be viewed as a replication of the analyses performed by Jensen and Kuperman.[11] It is thus useful to review the nature of their simulations, and how they compare with the ones performed in the current study.

Jensen and Kuperman looked at the effects of three main environmental parameters in their study: water depth, bottom type, and sound-speed profiles in the water channel. To simplify the analysis, they used a single, homogeneous bottom layer, always placed the source at mid-depth, and averaged the propagation loss over the water column for each receiver range. Jensen and Kuperman calculated optimum frequencies for (1) water depths between 25 to 400 m, (2) bottom types ranging from clay–silt to chalk–limestone; representative values obtained from the literature were used for porosity, relative density, relative speed, compressional speed, shear speed, compressional attenuation, and shear attenuation for each bottom type, and (3) two sound-speed profiles; one corresponding to typical winter profiles, with a surface speed of 1490 m/s and a constant gradient of 1.8 m/s, and the other corresponding to typical summer profiles, with a surface speed of 1535 m/s, a surface channel of 20 m, followed by a drop in sound speed to 1500 m/s, and then a constant gradient identical to the winter profile. The source depths they simulated ranged from 12.5 to 200 m, depending on the water depth, and transmission loss was calculated out to a range of about 85 km.

In the current study, environmental parameters for Hawaiian coastal waters (in particular, shallow-water regions near Maui) were estimated based primarily on measurements reported in previous studies or in computer databases maintained at the University of Hawaii. Effects of the following parameters on optimum frequency were investigated: water depth, source depth, receiver depth, and sound-speed profiles in the water channel. Water depths of 20, 40, 60, 100, 200, and 350 m were simulated. Because humpbacks only sing in Hawaii during the winter, and because previous reports indicate that a surface channel is not present, the ocean was modeled as a mixed layer over a thermocline. The mixed layer was modeled as being either 70 or 120 m deep. For water depths of 60 m or less, a thermocline layer was not included (see Table I and Fig. 1). SSPs were calculated using an empirically derived formula,[85] based on water temperature, salinity, and depth. A constant salinity of 35 ppt was used for all simulations. Temperature was constant at 25° above the thermocline and decreased at −0.052°/m within the thermocline (based on slopes from data presented in Ref. 55). Sound velocities calculated using this formula were consistent with measurements (e.g., $c=1534$ m/s near the surface). The bottom was modeled as a 50-m layer of sand and silt over basalt. Sound speed at the water-bottom boundary was set at 1.02*c* (after Ref. 11). Bottom SSP estimates were chosen to emulate the bottom properties particular to waters in Maui coastal regions. Source depths of 5, 15, and 30 m were chosen based on past reports of singer depths.[86] Sample ORCA input files for typical environments used in simulations

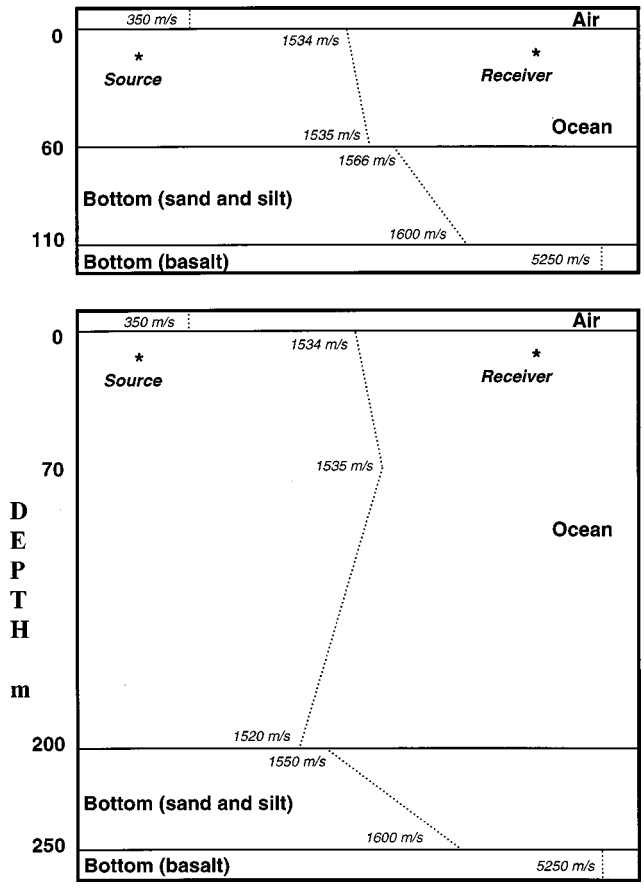

FIG. 1. Example environmental models used for ORCA simulations. The top figure corresponds to a 60-m water depth with no thermocline [see (a) in Table I], and the bottom figure corresponds to a 200-m water depth with a thermocline starting at 70 m [see (b) in Table I]. Solid lines show boundaries between channels, and dotted lines show how sound speed changes as a function of depth and material (where sound speed increases from left to right). Ocean sound-speed profiles varied as a function of water depth and thermocline depth. Bottom sound speed changed as a function of the sound speed in water at the interface. There are discrete jumps in sound speed at the air interface, bottom interface, and where the bottom changes to basalt. Only SSPs for the ocean channel and the first bottom layer were varied across simulations. Note that the figures are to scale vertically, but not horizontally. In a typical scenario (e.g., with a singer in 60-m deep water, and a receiver 6 km away), the range to depth ratio is about 100 (i.e., the ocean channel is a very thin disc).

are given in Table I; Fig. 1 illustrates these environments.

It is important to note from the outset that the results of these simulations should not be interpreted as precise estimates of the optimum frequencies in environments frequented by humpback whales. Jensen and Kuperman[11] had to manipulate shear-speed and compressional attenuation parameters in order to closely match theoretical results with measurements (these parameters are held constant in the current analysis; see Table I). Their calculated optimum frequencies were, however, roughly comparable to measured optimum frequencies even before such manipulations. The important data gained from the current simulations are the relative effects of changes in environmental parameters, rather than the absolute values of calculated optimum frequencies *per se*. Field measurements are needed to assess how accurately the model predicts actual optimum frequencies.

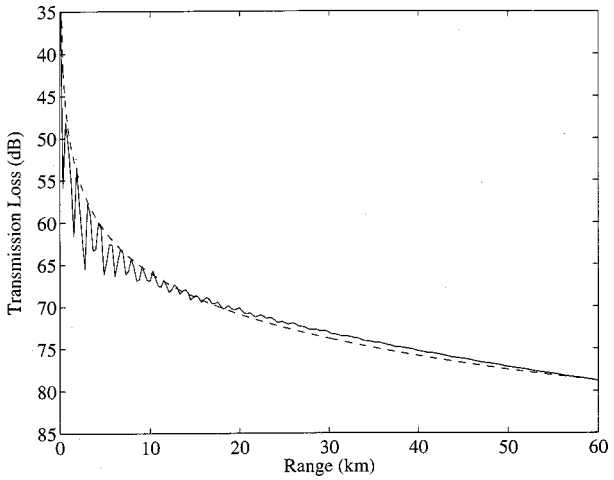

FIG. 2. Fitted transmission loss curve. The solid line is an example TL curve calculated by ORCA, and the dotted line is a logarithmic fitted curve calculated using MATLAB. Note that this estimation of transmission loss is conservative in that a listening whale exposed to varying received levels will detect the maximum received level in a given region (assuming it is above some perceptual threshold), as opposed to the average received level. Additionally, horizontally smoothed curves are more biologically relevant than averages calculated across vertical water columns (as in Ref. 11), because listening whales are more likely to be moving approximately parallel to the surface than to be bobbing up and down at a fixed range.

A. Dependence of optimum frequency on source depth, water depth, and thermocline depth

For the current analyses, optimum frequencies were calculated for a number of different scenarios using continuous-wave techniques. Simulations were initially run for 20 frequencies evenly spaced between 20 to 4000 Hz. Each simulation calculated the transmission loss (TL) at 200 distances from the source, evenly spaced between 50 to 60 000 m, and at 50 receiver depths evenly spaced between the surface and the bottom (resulting in a 50×200 matrix of TL values). A logarithmic curve of the form $\mathrm{TL}=a\log r$, was fit to each row of the matrix to provide an estimated transmission loss curve for each depth (see Fig. 2). The receiver depth corresponding to the minimum value of a for a single simulation was taken to be the ''optimal receiver depth'' (r_o) for that simulation. The optimum frequency (f_o) for a given scenario was found by comparing values of a across simulations (i.e., the frequency that led to the minimum overall value of a, thereby minimizing TL, was taken to be the optimum frequency). Table II summarizes the results of these analyses for the different scenarios considered.

Some of the data presented in Table II can be compared with the results reported by Jensen and Kuperman.[11] For example, for a water depth of 60 m and a source depth of 30 m, they report an optimum frequency between 400 and 800 Hz. The current simulations yielded an optimum frequency of 650 Hz. For simulations with a water depth of 40 m and a source depth of 20 m, Jensen and Kuperman report an optimum frequency of about 1600 Hz. The current analysis found an optimum frequency of 1700 Hz when the source was 15 m deep in 40-m-deep water. The current simulations showed that optimum frequencies increased as the source moved away from the mid-depth position, as noted in Ref. 11. Interestingly, water depth did not appear to strongly af-

TABLE II. Optimum frequencies for humpback environments in Hawaii, d_w = water depth, d_t = thermocline depth, d_s = source depth, f_o = optimum frequency, r_o = optimal receiver depth, $a_m = \min_i[a_i]\log r$, and $\overline{a}$ and σ_a are the mean and standard deviation over all a_i.

d_w (m)	d_t (m)	d_s (m)	f_o (Hz)	r_o (m)	a_m	$\overline{a}$	σ_a
20	NA	5	4000+	7.6	15.7	21.1	10.1
	NA	15	2740	8.4	16.5	21.2	9.6
40	NA	5	4000+	6.6	15.7	17.6	3.0
	NA	15	1700	13.7	15.7	16.9	2.5
	NA	30	3370	28.1	16.4	17.4	2.2
60	NA	5	4000+	8.2	15.7	17.4	2.9
	NA	15	1700	13.0	15.8	16.7	2.4
	NA	30	650	22.7	16.1	16.9	2.0
100	NA	5	4000+	7.1	15.7	17.2	2.3
	NA	15	1700	13.1	15.7	16.5	1.7
	NA	30	650	25.2	16.1	16.7	1.5
	70	5	4000+	7.1	15.7	17.4	2.5
	70	15	1700	13.1	15.7	16.7	1.9
	70	30	650	25.2	16.2	16.9	1.6
200	70	5	4000+	9.1	15.7	17.2	1.9
	70	15	1700	13.2	15.7	16.6	1.6
	70	30	1910	29.4	16.3	16.8	1.9
	120	5	4000+	9.1	15.7	17.1	1.3
	120	15	1910	13.2	15.7	16.4	0.8
	120	30	650	25.4	16.1	16.6	2.1
350	70	5	4000+	8.1	15.7	17.4	2.1
	70	15	1490	15.2	15.7	16.7	1.5
	70	30	1910	29.5	16.3	16.9	1.0
	120	5	4000+	8.1	15.6	17.0	1.6
	120	15	1490	15.2	15.8	16.4	0.9
	120	30	650	22.4	16.1	16.6	0.6

fect optimum frequencies ($r=-0.12$; where r is the correlation coefficient between the two variables), in contrast to previous reports. Rather, source depth appeared to be the main factor determining the optimum frequency ($r=-0.80$). This apparent discrepancy may be explained by the fact that Jensen and Kuperman always positioned the source at mid-depth, such that water depth and source depth were always covarying.

The mean optimum frequency across all simulations was 2400 Hz ($\sigma=1300$ Hz), somewhat higher than what might be expected given the data presented in Ref. 11 and the frequencies used by humpback whales. The optimum receiver depth was closely correlated with the source depth ($r=0.96$) and with transmission loss (as represented by a, $r=0.79$). The variability of transmission loss as a function of frequency (estimated by σ_a) appeared to decrease with increasing water depth ($r=-0.51$). Variability also seemed to decrease with increasing source depth ($r=-0.33$). The presence of a thermocline and its position led to some subtle changes in optimum frequencies and estimated transmission loss curves. For example, simulations where the source was 30 m deep and a thermocline was present at 120 m (vs 70 m) yielded lower optimum frequencies, shallower optimum receiver depths, and slightly lower a values.

Propagation contour maps provide a clearer picture of how transmission loss changes as a function of source depth and frequency. Figure 3 shows contour plots for simulations in 60-m-deep water. When the source is 5 m deep [Fig. 3(a)], there is no evidence of an optimum frequency. When the source is 15 m deep [Fig. 3(b)], the 74-dB contour shows a clear bulge near the optimum frequency of 1700 Hz. This indicates that signals near 1700 Hz will travel a longer distance before decreasing by 74 dB. When the source is 30 m deep [Fig. 3(c)], the 74-dB contour shows evidence of alternating near-optimum and suboptimum frequencies. The lowest bulge extends the farthest along the range axis and is centered on the optimum frequency of 650 Hz. Note that the optimum frequency for the source 30 m deep does not propagate as well as the optimum frequency for the source 15 m deep. In general, Fig. 3 looks the way it does because the depth of the source determines which normal modes are excited. Optimal propagation occurs for those normal modes that interact least with the lossy bottom, which typically are the lowest-order modes. Similarly, optimal propagation oc-

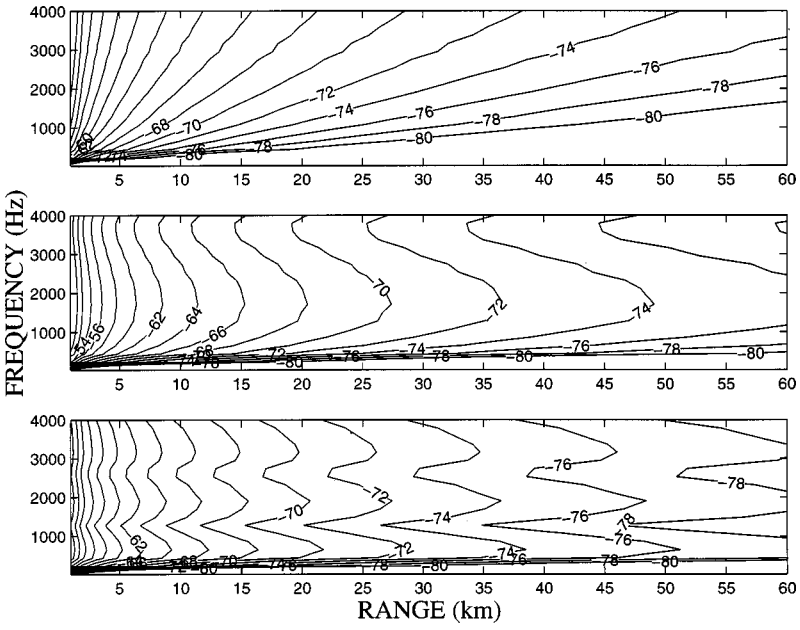

FIG. 3. Contour plots of transmission loss. Plots are based on fitted TL curves with the receiver at the optimal depth. Simulated scenario is for 60-m deep water (as described in Fig. 1 and Table I), with a source at (a) 5-m deep (top plot), (b) 15-m deep (middle plot), and (c) 30-m deep (bottom plot). The numbers on the contours indicate a particular transmission loss value, and the shapes of the contours show the range where signals at different frequencies will have decreased by this amount. The contours graphically illustrate how source depth and signal frequency can dramatically affect propagation. The high optimum frequencies computed for a 5-m deep source may in part reflect surface decoupling.[117] In real environments, scattering would likely attenuate higher frequencies preferentially, shifting the optimum to some mid frequency below 4000 Hz.

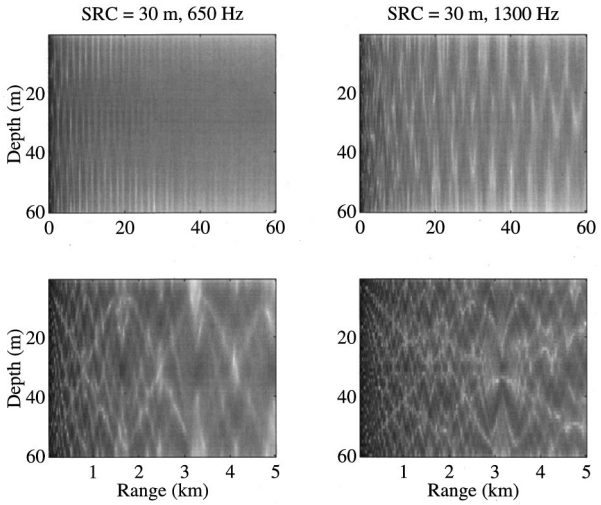

FIG. 4. Plots of transmission loss before smoothing. Simulated scenario is again for 60-m deep water (as described in Fig. 1 and Table I), with a 30-m deep source (the smoothed contour plot for this simulation is shown in Fig. 3). Bottom plots show a zoomed portion (the first 5 km) of the plots above them. Lighter coloration indicates greater losses. Note the complex range and depth-dependent variations in loss and how they vary with frequency. Also note the periodic interference patterns over longer distances. The optimum frequency for this scenario was found to be 650 Hz. At shorter distances, however, regions of high loss are larger for 650 Hz than for 1300 Hz.

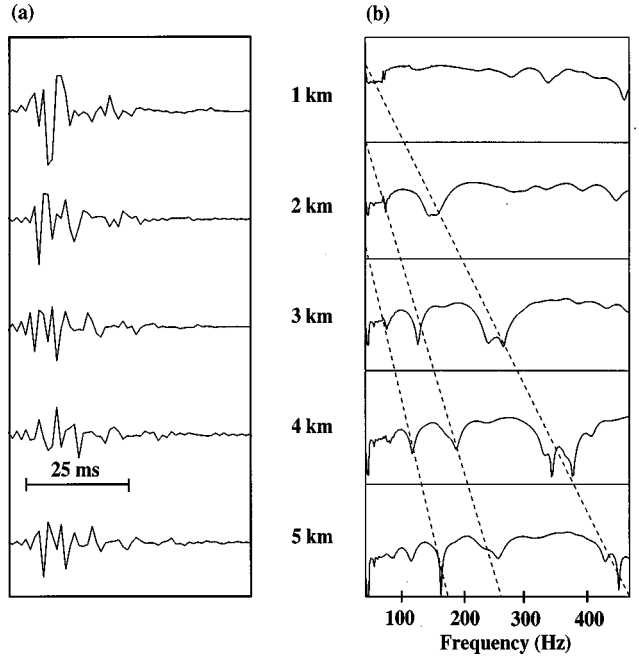

FIG. 5. Green's functions for a humpback's environment (60-m water depth, 15-m source and receiver depth). Waveforms in (a) show from top to bottom, Green's functions at ranges of 1, 2, 3, 4, and 5 km; peaks in these waveforms correspond to various ray paths. Spectra in (b) are of these waveforms. These spectra can be interpreted as the frequency responses of channel filters; i.e., the effects of propagation on a signal can be simulated by passing the signal through a filter with bandpass/stop features matching these spectra. Note the systematic, range-dependent spread of spectral peaks and troughs. It can be seen that the behavior of the Green's function becomes increasingly complex as the ratio of range to water depth increases. Dotted lines indicate trends in spectral distortion that appear to be correlated with range.

curs when the source and receiver are at the same depth because then the receiver is optimally positioned to receive those normal modes most effectively excited by the source.

It should be kept in mind that the data displayed in Table II and Fig. 3 are based on simplifications of the data generated by the ORCA simulations. Propagation loss varies greatly as a function of range and depth from the source. Figure 4 shows visual representations of the original 50×200 matrices for simulations with $d_w=60\,\mathrm{m}$, $d_s=30\,\mathrm{m}$, for two frequencies (650 and 1300 Hz); lighter areas indicate a larger transmission loss. Although overall propagation losses are clearly reduced for the optimum frequency (650 Hz) at long ranges, there appear to be larger regions of high loss at shorter ranges than for the suboptimum frequency (1300 Hz). Clearly, optimum frequencies are not optimal for all points within the sound channel, but rather are optimal for achieving the maximum range ''on the average.'' There is no frequency that will propagate optimally to every point in the sound channel.

B. Range-dependent spectral damping

Although knowledge of transmission loss is important for determining how far sounds will travel, such knowledge is only moderately useful for predicting how features of a signal other than amplitude will change as a signal propagates. One way to address this problem is to model the ocean channel using linear systems theory.[27,87] Propagation through an ocean channel can then be modeled as transmission of a signal through a set of linear, spatiotemporal-varying filters. The effect of propagation on any signal, for every source–receiver configuration, can be described in terms of a set of filter characteristics (specifically, a set of impulse response functions, also known as Green's functions). Once this set of filter characteristics is known (either through measurements or theoretical calculations), the signal properties that will be received at any point in the channel can be determined for arbitrary signals. In practice, it is extremely difficult to precisely determine the Green's functions across a wide band of frequencies for real-world environments. Reasonable approximations to these functions can, however, be obtained based on solutions of the wave equation (e.g., using wideband normal-mode techniques).

Preliminary calculations of Green's functions for a prototypical humpback whale environment were performed using ORCA's wideband analysis capabilities. Environmental parameters were identical to those used in the previous simulations. Water depth was fixed at 60 m. The source and receiver were both 15 m deep and at ranges between 1 to 5 km from one another. The bandwidth considered in the analyses was between 50 to 475 Hz (i.e., the Green's functions are valid for signals with spectral components limited to this range of frequencies). Figure 5 shows the Green's functions at ranges of 1, 2, 3, 4, and 5 km along with their spectra. These spectra, denoted as $G(w)$, reveal how signal features will likely be affected by transmission. For example, at 2 km, a clear trough is evident in $G(w)$ near 180 Hz. This indicates that, for this source–receiver configuration, the channel acts as a band-stop filter, significantly damping spectral energy near 180 Hz. At 3 km, two troughs are evident, one near 150 Hz and one near 280 Hz (with two minima). At 4 km, three

troughs can be seen. Visually, these separate troughs can be correlated across spectra. The single trough in $G(w)$ at 2 km appears to move to the right (increase in frequency) and develops two deep minima with increasing distance from the source. The 150-Hz trough at 3 km moves to the right and becomes shallower, and a smaller 90-Hz trough (at 3 km) moves to the right and becomes deeper. It appears that in this scenario, the distance a sound has traveled can be determined based on the spectral content of the received signal (independent of source amplitude), assuming the source signal is relatively broadband. Note that this result is not an artifact of the simplifying assumptions (e.g., flat bottom and surface) used in the simulations. A more complex environment would provide even more potential cues for determining the distance a sound has traveled.[88,89] The specific effects of the channel on a particular signal can be derived either by convolving the source waveform with the Green's function (for a particular range) or, equivalently, by multiplying the source spectrum times $G(w)$.[27]

IV. CONCLUSIONS

The simulations of sound propagation described in this paper have revealed several intrinsic constraints on humpback whales' use of sound that have not been previously noted. First, the results strongly suggest that humpback whales cannot increase the distances their sounds travel in shallow water simply by using lower frequencies. In contrast, all of the simulations indicate that maximum propagation ranges would actually be decreased for lower frequencies (below 200 Hz) and that humpback whales should typically produce higher frequencies rather than lower frequencies if they want their sounds to go farther. Second, source depth was found to be a critical determinant of the optimum frequency, optimum receiver depth, and maximum propagation range. Other factors such as water depth appear to be more relevant in determining the bandwidth of near-optimal frequencies. For example, transmission loss appears to vary less as a function of frequency in deeper water, whereas very shallow-water environments (20 m deep) strongly constrain long-range propagation to higher frequencies. Third, the large spatial variability in transmission loss as a function of range and receiver depth (see Fig. 4) suggests that propagation models based on geometrical spreading give a misleading impression of how sounds attenuate as they propagate away from a whale vocalizing in shallow water. It is possible (and even likely) that a whale 2 km from a singer would, at certain times and positions, experience higher received levels than a whale 1 km away from the same singer. Finally, the results seem to suggest that most humpback whale sounds are not acoustically optimal for long-range propagation. Although humpbacks do produce sounds within the range of optimum frequencies, most of their sounds are below this range. Possible reasons for this discrepancy are discussed below in more detail.

The current model is limited in that it does not account for the effects of scattering by the ocean surface or bottom, or the effects of bottom gradients (e.g., the model assumes a constant water depth and sound-speed field). Such factors undoubtedly affect transmission loss. For example, measurements and theoretical analyses of transmission loss in Hawaiian shallow-water environments, that take into account basic slope profiles (e.g., up-slope versus down-slope versus cross-slope), suggest that transmission loss is greatest for sounds propagating up-slope[24] (see also Ref. 90). Transmission loss in down-slope and cross-slope conditions was found to be significantly reduced in comparison to the up-slope condition; loss in the down-slope and cross-slope conditions was comparable. Past studies (e.g., Refs. 11, 76–79) have shown a close correspondence between transmission loss values predicted by simulations based on normal-mode theory and measured values, despite the simplifying assumptions made regarding the ''flatness'' of surface and bottom features. In some cases, the effects of a sloping bottom may be balanced by other factors. For example, sound traveling from shallow water to deeper water spreads out, but suffers less reflection loss, so that transmission loss may actually be decreased relative to an environment with a flat bottom.[12]

Although more advanced environmental models, which can simulate range-dependent water depths and bottom properties (e.g., parabolic equation models), can potentially allow more realistic scenarios to be investigated, it is not clear that this would clarify the constraints faced by humpback whales given the dearth of relevant data. Many of the critical environmental variables needed to develop more veridical models have yet to be measured, including the bathymetry, bottom composition, and sound-speed fields of areas frequented by vocalizing whales. Other important factors that are currently unknown are source directivity, the relative intensities of different frequencies produced by humpbacks, and the ranges at which humpbacks make use of sounds. Future studies can provide important tests of the current results as well as better estimates of environmental parameters. For example, recordings could be made simultaneously at multiple distances and depths from a vocalizing humpback, and the spectra of these recordings compared to look for predictable propagation effects and average transmission loss values. Alternatively, manmade sources could be placed in environments frequented by humpback whales (projecting broadband signals at various depths) to assess how different frequencies propagate and which frequencies propagate the farthest. As more precise measurements of environmental conditions are reported, the accuracy with which propagation effects can be predicted will obviously improve. Despite its limitations, the current model represents a significant advance over the purely geometric models that have been used in the past to assess environmental constraints on sound transmission by humpback whales. Previous computational studies of sound transmission by fin[27] and blue whales[28,29,91] indicate that consideration of such constraints is a crucial prerequisite for analyses of mysticete sounds.

The preliminary calculations of Green's functions described in this paper illustrate how the distorting effects of propagation through particular environments can be quantitatively predicted (see also Ref. 27). Empirically measured Green's functions can also be used for this purpose.[28,29,91–93] Currently, recorded vocalizations are often analyzed as if they were the ''true'' signals produced by whales, even though this is essentially never the case. If the Green's func-

tions for an environment are known, then features attributable to propagation effects can be more readily identified. Knowledge of the Green's functions associated with a particular sound channel can also allow information that otherwise might not be available (such as distance from the source) to be extracted from recorded signals. In theory, such knowledge allows the exact position of the source to be determined from a recording made with a single receiver (assuming the channel is sufficiently complex[88,94]). Knowledge of Green's functions for a particular environment can also be used to enhance signal processing.[28] Propagation effects can cause identical signals to appear to have different features depending on where they are received. Studies that attempt to analyze the variability of sounds across individuals thus need to consider the variability due to propagation effects. This can be accomplished either by making sure recordings from individuals are made from various locations, or by finding the Green's functions for the channel of interest.

The natural history of humpback whales suggests that they should have highly developed acoustic abilities. It would be surprising to find that they use sounds that are not well suited for their intended purpose. The mismatch between calculated optimum frequencies and those actually produced by humpbacks suggests that (1) the environmental model may not accurately simulate the environmental constraints encountered by vocalizing humpbacks, (2) factors other than maximum propagation potential may constrain the frequencies used by humpback whales, and/or (3) humpbacks may only use a subset of the frequencies they produce for long-range transmission. As noted previously, the optimum frequencies computed in the current analysis are only an initial estimate, so possibility (1) alone may account for this discrepancy. There have been previous reports, however, indicating that blue whales[91] and other mammalian species[95,96] do not always produce frequencies that propagate optimally over long ranges. Possibilities (2) and (3) should thus be considered more closely.

Anatomical and functional constraints undoubtedly limit the frequencies used by humpback whales. If the function of a sound does not require long-range propagation, then sounds with optimum frequencies for propagation may not be functionally optimal. Wiley and Richards[96] suggest that maximum range of detection is probably not the primary selection pressure on most animals' vocal repertoires, and that features that degrade predictably with range are more important. Physical properties of production mechanisms also limit the frequencies a whale can optimally produce (however, the wide range of frequencies produced by humpbacks seems to suggest that this is not a strong constraint). Finally, the spectrum of environmental noise will constrain the range of frequencies that will be maximally discriminable over long ranges. For example, in shallow water, low-frequency noise levels may be lower than in deeper water.[12] Consider also that if many animals in a localized region are producing similar sounds that propagate optimally, then the signals may begin to ''optimally'' interfere with one another. Consequently, the effective utilizable range of a sound may not be reflected by its maximum propagation range;[97] maximum range only provides an upper bound on utilizable range.

Whereas environmental constraints may not account for why humpbacks produce energy at lower frequencies, they may explain why they are capable of producing such a wide band of frequencies. Humpbacks produce frequencies that are much higher than many other smaller mammals. For example, professional sopranos seldom produce frequencies above 1200 Hz, and then only at relatively low intensities, for short periods of time.[98] In contrast, male humpbacks may produce frequencies between 1000–4000 Hz, at high intensities, hundreds of times a day. Other mysticetes have not demonstrated such abilities. It is also important to note that when humpback whales produce lower frequencies, they typically also produce a large number of harmonically related higher-frequency bands that can extend up to 8000 Hz. In some cases, the energy in these higher-frequency harmonics can be more intense than the energy in the low-frequency fundamental.[99] Such tone complexes likely include frequencies that are optimum or near optimum.

We noted earlier that vocalizing humpback whales can potentially reduce the limitations on propagation imposed by environmental constraints by properly positioning themselves. For example, to maximize their range and the predictability of propagation effects, singers could select an acoustic channel based mainly on water depth, bottom properties, and the presence or absence of a thermocline. Given known environmental conditions, they could then dive to an ''optimum'' depth and produce optimum frequencies. Humpback whales could also attempt to match their depth to that of potential receivers (assuming this information is known or can be predicted). To maximize propagation through positioning, whales would need feedback on how far their signals are traveling. If the utility of sounds is a function of how far they travel, then this ''feedback'' could be provided by natural selection. For example, individuals that frequently vocalized in environments/positions with good propagation characteristics would gain a selective advantage. A second potential source of feedback is echoes from structures in the environment. It is well-known that humpback song sounds generate strong echoes off the ocean floor, as well as banks and pinnacles, that are clearly detectable in recordings.[69,100] Other potential sources of echoes include schools of fish or other whales.[32,69,70,101–105] Such echoes provide information about how sounds are propagating in particular contexts. Whether humpback whales use this information to maximize propagation ranges is currently unknown. It is known that various other species do position themselves such that long-range propagation is enhanced.[96,106–109]

Humpback whales could also affect propagation range by modulating the spectral and energetic properties of the sounds they produce. Although there is currently little evidence suggesting that humpbacks or other whales change sound features to accommodate different nonbiological environmental features (e.g., topology, water depth), this lack of evidence may simply reflect the limited attention given to the issue. Au *et al.*[110] found that belugas used different echolocation signals when faced with different ambient noise lev-

els; differences between signals were highly correlated with signal amplitude. Singing humpback whales have also been observed to change their signals in response to changes in noise levels.[62] Humpbacks sang at a faster rate when noise levels increased moderately. When larger increases occurred (e.g., when large ships passed nearby), they sang faster and shifted to higher frequencies. Norris[62] suggested that these changes reflected increased stress levels rather than attempts by the whales to optimize their signals with respect to noise levels. Other species have been shown to dynamically manipulate the sounds they produce to match a particular environment or situation. Most notably, bats use different echolocation signals depending on the environment, target range, and sounds of other bats in the area.[2–4,111] Given the complexities of shallow-water propagation, it would be to a humpback whale's advantage to attend to the acoustically relevant physical features of the environment, and to modify his signals accordingly.

It has been shown previously that some birds can use the degradation of spectral features of known songs to determine the proximity of other vocalizing birds, and that such cues are more salient than intensity differences.[112,113] The results of the current analysis suggest that humpback whales could also potentially extract range information from the vocalizations of conspecifics. Although the sound-localization abilities of humpback whales are essentially unknown, the fact that singers space themselves apart[22,23] shows that they can at least roughly determine their distance from a source. Singing humpback whales appear to mimic the songs of other humpbacks,[114,115] suggesting that they are attending closely to the properties of sounds produced by other whales. Experimental playback studies analogous to those used with birds may clarify whether singers are relying more on spectral cues or intensity cues to maintain spacing. Given the variability of transmission loss in shallow water (as illustrated in Fig. 4), we expect that spectral cues will be found to be much more salient.

In summary, simulations based on normal-mode theory predict (1) that how far a singing humpback whale's sounds will propagate will be a function of the frequencies produced, the depth of the singer, and several environmental features such as water depth and bottom type, (2) that the optimal receiving depth (on average) will be approximately equal to the source depth, (3) that the bandwidth of near-optimum frequencies will increase with increasing water depth, and (4) that distortions caused by propagation can potentially provide useful information about the position of the source. Given the long evolutionary history of humpback whales, it seems likely that such factors are ''taken into account'' by vocalizing humpbacks, through genetic predispositions and/or behavioral adaptability. Computational models, such as the one used in this study, provide powerful tools for investigating the physical limits on cetaceans' use of sound and for assessing how propagation effects influence the sounds they produce.

ACKNOWLEDGMENTS

This study was conducted as part of a Ph.D. program at the University of Hawaii. The authors thank Alexandra Tolstoy for many helpful conversations and Whitlow Au for his thought-provoking questions. Roy Wilkens (University of Hawaii, Department of Geophysics) provided information regarding the bottom properties particular to waters in Maui coastal regions. Louis Herman and three anonymous reviewers provided useful comments on previous versions of this manuscript. We especially thank Evan Westwood for making the ORCA software freely available. Support of the National Science Foundation (Grant No. EAR95-26786) is gratefully acknowledged.

[1] S. Green and P. Marler, ''The analysis of animal communication,'' in *Handbook of Behavioral Neurobiology, Vol. 3: Social Behavior and Communication*, edited by P. Marler and J. G. Vandenbergh (Plenum, New York, 1979), pp. 73–157.
[2] M. K. Obrist, ''Flexible bat echolocation: The influence of individual, habitat and conspecifics on sonar signal design,'' Behav. Ecol. Sociobiol. **36**, 207–219 (1995).
[3] M. C. de Oliveira, ''Towards standardized descriptions of the echolocation calls of microchiropteran bats: Pulse design terminology for seventeen species from Queensland,'' Aust. J. Zool. **30**, 405–411 (1998).
[4] G. Neuweiler, ''Echolocation and adaptivity to ecological constraints,'' in *Neuroethology and Behavioral Physiology*, edited by F. Huber and H. Markl (Springer, Berlin, 1983), pp. 280–302.
[5] M. B. Fenton and G. P. Bell, ''Recognition of species of insectivorous bats by their echolocation calls,'' J. Mammal. **62**, 233–243 (1981).
[6] J. D. Pye, ''Echolocation signals and echoes in air,'' in *Animal Sonar Systems*, edited by R. G. Busnel and J. Fish (Plenum, New York, 1980), pp. 309–354.
[7] J. A. Simmons, W. A. Lavender, B. A. Lavender, J. E. Childs, K. Hulebak, M. R. Rigden, J. Sherman, and B. Woolman, ''Echolocation by free-tailed bats (*Tadarida*),'' J. Comp. Physiol. A **125**, 291–299 (1978).
[8] K. Zbinden and P. E. Zingg, ''Search and hunting signals of echolocating free-tailed bats, *Tadarida teniotis* in southern Switzerland,'' Mammalia **50**, 9–25 (1985).
[9] J. A. Simmons, ''A view of the world from the bat's ear: The formation of acoustic images in echolocation,'' Cognition **33**, 155–199 (1989).
[10] R. J. Urick, *Principles of Underwater Sound*, 3rd ed. (McGraw-Hill, New York, 1983).
[11] F. B. Jensen and W. A. Kuperman, ''Optimum frequency of propagation in shallow water environments,'' J. Acoust. Soc. Am. **73**, 813–819 (1983).
[12] W. J. Richardson, C. R. Greene, Jr., C. I. Malme, and D. H. Thomson, *Marine Mammals and Noise* (Academic, San Diego, 1995).
[13] W. A. Kuperman, ''Propagation of sound in the ocean,'' in *Encyclopedia of Acoustics*, edited by M. J. Crocker (Wiley, New York, 1997), pp. 391–500.
[14] P. H. Rogers and M. Cox, ''Underwater sound as a biological stimulus,'' in *Sensory Biology of Aquatic Animals*, edited by J. Atema, R. R. Fay, A. N. Popper, and W. N. Tavolga (Springer, New York, 1988), pp. 131–149.
[15] A. Parvulescu, ''Problems of propagation and processing,'' in *Marine Bioacoustics*, edited by W. N. Tavolga (Pergamon, New York, 1964), pp. 87–100.
[16] G. M. Wenz, ''Acoustic ambient noise in the ocean,'' J. Acoust. Soc. Am. **34**, 1936–1956 (1962).
[17] R. Payne and D. Webb, ''Orientation by means of long range acoustic signaling in baleen whales,'' Ann. (N.Y.) Acad. Sci. **188**, 110–141 (1971).
[18] W. W. L. Au, W. R. Floyd, and J. E. Haun, ''Propagation of Atlantic bottlenose dolphin echolocation signals,'' J. Acoust. Soc. Am. **64**, 411–422 (1978).
[19] W. E. Evans, W. W. Sutherland, and R. G. Beil, ''The directional characteristics of delphinid sounds,'' in *Marine Bioacoustics*, edited by W. N. Tavolga (Pergamon, New York, 1964), pp. 353–372.
[20] W. E. Schevill and W. A. Watkins, ''Sound structure and directionality in *Orcinus* (killer whale),'' Zoologica **51**, 71–76 (1966).
[21] K. S. Norris and W. E. Evans, ''Directionality of echolocation clicks in the rough-tooth porpoise, *Steno bredanensis* (Lesson),'' in *Marine Bioacoustics*, Vol. 2, edited by W. N. Tavolga (Pergamon, Oxford, U. K., 1967), pp. 305–316.

[22] A. S. Frankel, ''Acoustic and visual tracking reveals distribution, song variability and social roles of humpback whales in Hawaiian waters,'' Unpublished doctoral dissertation, University of Hawaii, Honolulu, 1994.
[23] A. S. Frankel, C. W. Clark, L. M. Herman, and C. M. Gabriele, ''Spatial distribution, habitat utilization, and social interactions of humpback whales, *Megaptera novaeangliae*, off Hawaii, determined using acoustic and visual techniques,'' Can. J. Zool. **73**, 1134–1146 (1995).
[24] A. S. Frankel and C. W. Clark, ''Results of low-frequency playback of *m*-sequence noise to humpback whales, *Megaptera novaeangliae*, in Hawai'i,'' Can. J. Zool. **76**, 521–535 (1998).
[25] K. M. Fristrup and J. L. Spiesberger, ''Passive localization of calling animals and sensing of their acoustic environment using acoustic tomography,'' Am. Natural. **135**, 107–156 (1990).
[26] J. A. Mossbridge and J. A. Thomas, ''Frequency partitioning of Antarctic killer whale and leopard seal sounds,'' Paper presented at the World Marine Mammal Conference, Monaco, 1998.
[27] V. Premus and J. L. Spiesberger, ''Can acoustic multipath explain finback (*B. physalus*) 20-Hz doublets in shallow water?'' J. Acoust. Soc. Am. **101**, 1127–1138 (1997).
[28] A. M. Thode, G. L. D'Spain, W. A. Kuperman, and W. S. Hodgkiss, ''Removal of environmental effects from whale calls using coherent beamforming methods,'' J. Acoust. Soc. Am. **100**, 2611 (1996).
[29] A. M. Thode, G. L. D'Spain, and W. A. Kuperman, ''Matched-field processing of baleen whale vocalizations using calibrated environmental models,'' J. Acoust. Soc. Am. **103**, 2909 (1998).
[30] C. W. Clark, ''Application of U.S. Navy underwater hydrophone arrays for scientific research on whales,'' Sci. Rep. Int. Whal. Comm. **44**, 1–12 (1994).
[31] C. W. Clark, ''Acoustic behaviors of blue and fin whales,'' Paper presented at the 24th International Ethology Conference, Honolulu, HI, 1995.
[32] N. C. Makris and D. H. Cato, ''Using singing whales to track nonsingers,'' J. Acoust. Soc. Am. **96**, 3270 (1994).
[33] P. O. Thompson, W. C. Cummings, and S. J. Ha, ''Sounds, source levels, and associated behaviors of humpback whales, southeast Alaska,'' J. Acoust. Soc. Am. **80**, 735–740 (1986).
[34] P. Tyack, ''Humpback whales respond to sounds of their neighbors,'' Unpublished doctoral dissertation, Rockefeller University, New York, 1982.
[35] L. K. Winn and H. E. Winn, *Wings in the Sea: The Humpback Whale* (University Press of New England, Hanover, NH, 1985).
[36] D. A. Helweg and L. M. Herman, ''Diurnal patterns of behavior and group structure of humpback whales (*Megaptera novaeangliae*) in Hawaiian waters,'' Ethology **98**, 298–311 (1994).
[37] P. O. Thompson and W. A. Friedl, ''A long term study of low frequency sounds from several species of whales off Oahu, Hawaii,'' Cetology **45**, 1–19 (1982).
[38] D. Chabot, ''Sound production of the humpback whale (*Megaptera novaeangliae*, Borowski) in Newfoundland waters,'' Unpublished masters thesis, Memorial University of Newfoundland, St. Johns, 1984.
[39] D. Chabot, ''A quantitative technique to compare and classify humpback whale (*Megaptera novaeangliae*) sounds,'' Ethology **77**, 89–102 (1988).
[40] A. S. Frankel, ''Interindividual variation in the songs of humpback whales,'' J. Acoust. Soc. Am. **99**, 2556 (1995).
[41] K. Payne and R. S. Payne, ''Large scale changes over 19 years in songs of humpback whales in Bermuda,'' Z. Tierpsychol. **68**, 89–114 (1985).
[42] H. E. Winn, T. J. Thompson, W. C. Cummings, J. Hain, J. Hudnall, H. Hays, and W. Steiner, ''Song of the humpback whale: Population comparisons,'' Behav. Ecol. Sociobiol. **8**, 41–46 (1981).
[43] C. W. Clark, ''The acoustic repertoire of the southern right whale: A quantitative analysis,'' Anim. Behav. **30**, 1060–1071 (1982).
[44] D. A. Helweg, A. S. Frankel, J. R. Mobley, Jr., and L. M. Herman, ''Humpback whale song: Our current understanding,'' in *Marine Mammal Sensory Systems*, edited by J. A. Thomas, R. A. Kastelein, and A. Y. Supin (Plenum, New York, 1992), pp. 459–483.
[45] L. M. Herman and W. N. Tavolga, ''The communication systems of cetaceans,'' in *Cetacean Behavior: Mechanisms and Functions*, edited by L. M. Herman (Interscience, New York, 1980), pp. 149–209.
[46] G. K. Silber, ''The relationship of social vocalizations to surface behavior and aggression in the Hawaiian humpback whale (*Megaptera novaeangliae*),'' Can. J. Zool. **64**, 2075–2080 (1986).
[47] C. W. Clark, ''Acoustic behavior of mysticete whales,'' in *Sensory Abilities of Cetaceans: Laboratory and Field Evidence*, edited by J. Thomas and R. Kastelein (Plenum, New York, 1990), pp. 571–583.
[48] A. Mednis, ''An acoustic analysis of the 1988 song of the humpback whale, *Megaptera novaeangliae*, off eastern Australia,'' Mem. Queens. Mus. **30**, 323–332 (1991).
[49] E. Mercado III, ''An acoustic analysis of humpback whale (*Megaptera novaeangliae*) song units,'' Unpublished masters thesis, University of Hawaii, Honolulu, 1995.
[50] P. Tyack, ''Interactions between singing Hawaiian humpback whales and conspecifics nearby,'' Behav. Ecol. Sociobiol. **8**, 105–116 (1981).
[51] D. H. Cato, ''Songs of humpback whales: The Australian perspective,'' Mem. Queens. Mus. **30**, 277–290 (1991).
[52] ''National Marine Sanctuaries. Hawaiian islands humpback whale national marine sanctuary,'' Final environmental impact statement/management plan, State of Hawaii, Honolulu, HI, 1997.
[53] H. P. Whitehead, ''The behavior and ecology of the humpback whale in the northwest Atlantic,'' Unpublished doctoral dissertation, University of Cambridge, Cambridge, UK, 1981.
[54] N. Forsyth, J. R. Mobley, Jr., and G. B. Bauer, ''Depth preferences in Hawaiian humpbacks,'' Paper presented at the 9th Biennial Conference on the Biology of Marine Mammals, Chicago, IL, 1991.
[55] Hawaii Ocean Time Series Database. HOT CTD data. Unpublished data, available at http://www.soest.hawaii.edu/HOT_WOCE/ctd.html, Honolulu, HI, 1997.
[56] K. Wyrtki, J. B. Burks, R. C. Latham, and W. M. Patzert, ''Oceanographic observations during 1965–1967 in the Hawaiian archipelago,'' Office of Naval Research HIG-67-15, Hawaii Institute of Geophysics, University of Hawaii, 1967.
[57] A. S. Frankel, C. W. Clark, and C. M. Gabriele, ''Preliminary results of the 1996 Hawaii MMRP playback experiments,'' MMRP/ATOC bimonthly Report No. 3, Cornell Laboratory of Ornithology, Ithaca, NY, 1996.
[58] A. S. Frankel, ''Effects of scaled ATOC playbacks on the behavior of humpback whales in Hawaii,'' J. Acoust. Soc. Am. **100**, 2611 (1995).
[59] A. S. Frankel, J. R. Mobley, Jr., and L. M. Herman, ''Estimation of auditory response thresholds in humpback whales using biologically meaningful sounds,'' in *Sensory Systems of Aquatic Mammals*, edited by R. Kastelein, J. Thomas, and P. Nachtigall (De Spil, Woerden, The Netherlands, 1995), pp. 55–70.
[60] W. A. Friedl and P. O. Thompson, ''Measuring acoustic noise around Kahoolawe island,'' NOSC Technical Report 732, Naval Ocean Systems Center, San Diego, CA, 1981.
[61] H. L. Maybaum, ''Effects of a 3.3-kHz sonar system on humpback whales, *Megaptera novaeangliae*, in Hawaiian waters,'' Unpublished masters thesis, University of Hawaii, Honolulu, 1989.
[62] T. F. Norris, ''Effects of boat noise on the singing behavior of humpback whales (*Megaptera novaeangliae*),'' Unpublished masters thesis, San Jose State University, San Jose, CA, 1995.
[63] D. H. Cato, ''Review of ambient noise in the ocean: Nonbiological sources,'' Bull. Austral. Acoust. Soc. **6**, 31–36 (1978).
[64] A. A. Myrberg, Jr, ''Ocean noise and the behavior of marine animals: Relationships and implications,'' in *Effects of Noise on Wildlife*, edited by J. L. Fletcher and R. G. Busnel (Academic, New York, 1978), pp. 169–208.
[65] G. M. Wenz, ''Curious noises and the sonic environment in the ocean,'' in *Marine Bioacoustics*, edited by W. N. Tavolga (Pergamon, New York, 1964), pp. 101–119.
[66] D. H. Cato, ''The biological contribution to the ambient noise in waters near Australia,'' Acoust. Austral. **20**, 76–80 (1992).
[67] A. C. Kibblewhite, R. N. Denham, and D. J. Barnes, ''Unusual low-frequency signals observed in New Zealand waters,'' J. Acoust. Soc. Am. **41**, 644–655 (1967).
[68] D. H. Cato, ''Sounds of humpback whales migrating along the Australian coastlines,'' 15th Int. Congress Acoust. **1**, 219–222 (1995).
[69] H. E. Winn and L. K. Winn, ''The song of the humpback whale *Megaptera novaeangliae* in the West Indies,'' Mar. Biol. (Berlin) **47**, 97–114 (1978).
[70] E. Mercado III, ''Humpback whale bioacoustics: From form to function,'' Unpublished doctoral dissertation, University of Hawaii, Honolulu, 1998.
[71] C. Levenson, ''Characteristics of sound produced by humpback whales (*Megaptera novaeangliae*),'' NAV-OCEANO Technical Note 7700-6-72, Naval Oceanographic Office, Washington, DC, 1972.
[72] H. E. Winn, P. J. Perkins, and T. C. Poulter, ''Sounds of the humpback whale,'' in Proceedings of the 7th Annual Conference on Biological Sonar and Diving Mammals, 1970, pp. 39–52.

[73] D. H. Cato, ''Simple methods of estimating source levels and locations of marine animal sounds,'' J. Acoust. Soc. Am. **104**, 1667–1678 (1998).
[74] P. E. Purves and G. E. Pilleri, *Echolocation of Whales and Dolphins* (Academic, New York, 1983).
[75] H. W. Marsh and M. Schulkin, ''Shallow water transmission,'' J. Acoust. Soc. Am. **34**, 863–864 (1962).
[76] R. H. Ferris, ''Comparison of measured and calculated normal-mode amplitude functions for acoustic waves in shallow water,'' J. Acoust. Soc. Am. **52**, 981–988 (1972).
[77] Z.-H. Michalopoulou and M. B. Porter, ''Matched-field processing for broad-band source localization,'' IEEE J. Ocean Eng. **21**, 384–392 (1996).
[78] J. M. Ozard, M. L. Yeremy, N. R. Chapman, and M. J. Wilmut, ''Matched-field processing in a range-dependent shallow water environment in the northeast Pacific Ocean,'' IEEE J. Ocean Eng. **21**, 377–383 (1996).
[79] C. T. Tindle, K. M. Guthrie, G. E. J. Bold, M. D. Johns, D. Jones, K. O. Dixon, and T. G. Birdsall, ''Measurements of the frequency dependence of normal modes,'' J. Acoust. Soc. Am. **64**, 1178–1185 (1978).
[80] E. K. Westwood, C. T. Tindle, and N. R. Chapman, ''A normal mode model for acoustoelastic ocean environments,'' J. Acoust. Soc. Am. **100**, 3631–3645 (1996).
[81] E. K. Westwood, C. T. Tindle, and N. R. Chapman, ''A normal mode model for multilayered acoustoelastic ocean environments based on an analytic reflection coefficient method,'' J. Acoust. Soc. Am. **95**, 2908 (1994).
[82] E. K. Westwood, ''An efficient broadband normal-mode model for acoustoelastic ocean environments,'' J. Acoust. Soc. Am. **96**, 3352 (1994).
[83] F. B. Jensen, W. A. Kuperman, M. B. Porter, and H. Schmidt, *Computational Ocean Acoustics* (American Institute of Physics, New York, 1994).
[84] C. W. Clark and W. T. Ellison, ''Low-frequency signaling behavior in mysticete whales,'' J. Acoust. Soc. Am. **101**, 3163 (1997).
[85] K. V. Mackenzie, ''Nine-term equation for sound speed in the oceans,'' J. Acoust. Soc. Am. **705**, 807–812 (1981).
[86] J. D. Darling, ''Migration, abundance and behavior of Hawaiian humpback whales (*Megaptera novaeangliae*),'' Unpublished doctoral dissertation, University of California, Santa Cruz, 1983.
[87] L. J. Ziomek, *Underwater Acoustics: A Linear Systems Theory Approach* (Academic, Orlando, 1985).
[88] L. N. Frazer and P. I. Pecholcs, ''Single hydrophone localization,'' J. Acoust. Soc. Am. **88**, 995–1002 (1990).
[89] J. S. Perkins and A. Kuperman, ''Environmental signal processing: Three-dimensional matched-field processing with a vertical array,'' J. Acoust. Soc. Am. **87**, 1553–1556 (1990).
[90] S. E. Dosso and N. R. Chapman, ''Measurements and modeling of downslope acoustic propagation loss over a continental slope,'' J. Acoust. Soc. Am. **81**, 258–268 (1987).
[91] A. M. Thode, G. L. D'Spain, and W. A. Kuperman, ''Physical constraints on blue whale sound production mechanisms derived from matched-field processing,'' J. Acoust. Soc. Am. **105**, 993 (1999).
[92] G. L. D'Spain, W. A. Kuperman, W. S. Hodgkiss, and L. F. Berger, ''Three-dimensional localization of a blue whale using broadband matched-field processing for range and depth and plane-wave adaptive beamforming for azimuth,'' J. Acoust. Soc. Am. **97**, 3353 (1995).
[93] G. L. D'Spain and W. A. Kuperman, ''Simultaneous source panging and bottom geoacoustic inversion using shallow water, broadband dispersion of fin whale calls,'' J. Acoust. Soc. Am. **97**, 3353 (1995).
[94] J. S. Perkins, W. A. Kuperman, and R. B. Evans, ''Three-dimensional oceanographic acoustics: Propagation, noise and array processing,'' in *Oceanography and Acoustics: Prediction and Propagation models*, edited by A. R. Robinson and D. Lee (American Institute of Physics, New York, 1994), pp. 161–178.
[95] H. C. Gerhardt, ''Communication and the environment,'' in *Animal Behavior: Vol. 2, Communication*, edited by T. R. Halliday and P. J. B. Slater (W. H. Freeman, New York, 1983), pp. 82–113.
[96] R. H. Wiley and D. G. Richards, ''Physical constraints on acoustic communication in the atmosphere: Implications for the evolution of animal vocalizations,'' Behav. Ecol. Sociobiol. **3**, 69–94 (1978).
[97] A. D. Hawkins and A. A. Myrberg, Jr., ''Hearing and sound communication underwater,'' in *Bioacoustics: A Comparative Perspective*, edited by B. Lewis (Academic, London, 1983), pp. 347–405.
[98] J. Sundberg, ''Human singing voice,'' in *Encyclopedia of Acoustics*, edited by M. J. Crocker (Wiley, New York, 1997), pp. 1687–1695.
[99] E. Mercado III, ''Computational models of sound production and reception in the humpback whale,'' unpublished masters thesis, University of Hawaii, Honolulu, 1998.
[100] R. S. Payne and S. McVay, ''Songs of humpback whales,'' Science **173**, 585–597 (1971).
[101] H. E. Winn and P. J. Perkins, ''Distribution and sounds of the minke whale, with a review of mysticete sounds,'' Cetology **19**, 1–12 (1976).
[102] R. H. Love, ''Target strengths of humpback whales, *Megaptera novaeangliae*,'' J. Acoust. Soc. Am. **54**, 1312–1315 (1973).
[103] L. N. Frazer, E. Mercado III, and A. Tolstoy, ''Understanding humpback whale sonar: A physicist's view,'' J. Acoust. Soc. Am. **100**, 2644 (1996).
[104] L. N. Frazer and E. Mercado III, ''A sonar model for humpback whale song,'' IEEE J. Ocean Eng. (in press).
[105] E. Mercado III, L. Frazer, and L. M. Herman, ''Humpback whale sonar,'' J. Acoust. Soc. Am. **100**, 2644 (1996).
[106] J. D. Crawford, P. Jacob, and V. Benech, ''Sound production and reproductive ecology of strongly acoustic fish in Africa: *Pollimyrus isidori, Mormyridae*,'' Behaviour **134**, 677–725 (1997).
[107] T. G. Forrest, G. L. Miller, and J. R. Zagar, ''Sound propagation in shallow water: Implications for acoustic communication by aquatic animals,'' Bioacoustics **4**, 259–270 (1993).
[108] V. M. Janik and P. J. B. Slater, ''Vocal learning in mammals,'' Adv. Study Behav. **26**, 59–94 (1997).
[109] P. M. Waser and R. H. Wiley, ''Mechanisms and evolution of spacing in animals,'' in *Handbook of Behavioral Neurobiology, Vol. 3: Social Behavior and Communication*, edited by P. Marler and T. G. Vandenbergh (Plenum, New York, 1979), pp. 159–223.
[110] W. W. L. Au, D. A. Carder, R. H. Penner, and B. L. Scronce, ''Demonstration of adaptation in beluga echolocation signals,'' J. Acoust. Soc. Am. **80**, 688–691 (1985).
[111] N. Suga, ''Processing of auditory information carried by species-specific complex sounds,'' in *The Cognitive Neurosciences*, edited by M. S. Gazzaniga (MIT Press, Cambridge, MA, 1995), pp. 295–313.
[112] E. S. Morton, ''Predictions from the ranging hypothesis for the evolution of long distance signals in birds,'' Behaviour **99**, 65–86 (1986).
[113] E. S. Morton, ''Degradation and signal ranging in birds: Memory matters,'' Behav. Ecol. Sociobiol. **42**, 135–137 (1998).
[114] L. N. Guinee, K. Chu, and E. M. Dorsey, ''Changes over time in the songs of known individual humpback whales (*Megaptera novaeangliae*),'' in *Communication and Behavior of Whales*, edited by R. Payne (Westview, Boulder, 1983), pp. 59–80.
[115] K. Payne, P. Tyack, and R. Payne, ''Progressive changes in the songs of humpback whales (*Megaptera novaeangliae*): A detailed analysis of two seasons in Hawaii,'' in *Communication and Behavior of Whales*, edited by R. Payne (Westview, Boulder, 1983), pp. 9–57.
[116] E. K. Westwood. ORCA ver1.6b User's Guide. Technical Report at ftp.arlut.utexas.edu; pub/westwood, Applied Research Laboratories, University of Texas, 1997.
[117] R. W. Bannister and M. A. Pedersen, ''Low-frequency surface interference effects in long-range sound propagation,'' J. Acoust. Soc. Am. **69**, 76–83 (1981).

Free-field audiogram of the Japanese macaque (*Macaca fuscata*)

Laura L. Jackson,[a] Rickye S. Heffner, and Henry E. Heffner[b]
Department of Psychology, University of Toledo, Toledo, Ohio 43606

(Received 9 March 1999; revised 23 July 1999; accepted 2 August 1999)

The audiograms of three Japanese macaques and seven humans were determined in a free-field environment using loudspeakers. The monkeys and humans were tested using tones ranging from 8 Hz to 40 kHz and 4 Hz to 22.4 kHz, respectively. At a level of 60 dB sound pressure level the monkeys were able to hear tones extending from 28 Hz to 37 kHz with their best sensitivity of 1 dB occurring at 4 kHz. The human 60-dB hearing range extended from 31 Hz to 17.6 kHz with a best sensitivity of −10 dB at 2 and 4 kHz. These results indicate that the Japanese macaque has low-frequency hearing equal to that of humans and better than that indicated by previous audiograms obtained using headphones. © *1999 Acoustical Society of America.* [S0001-4966(99)06511-X]

PACS numbers: 43.80.Lb, 43.66.Gf [WA]

INTRODUCTION

The audiogram as a basic measure of hearing has proven useful to the comparative study of hearing. Specifically, comparison of the audiograms of various species has revealed the existence of important variation in the hearing abilities of animals, especially in their ability to hear high- and low-frequency sounds. In the case of mammals, analysis of these differences has yielded clues regarding the selective pressures involved in the evolution of hearing (e.g., Koay *et al.*, 1997; Masterton *et al.*, 1969).

In order for the audiograms of different species to be comparable, they must be obtained under similar conditions. One consideration is that the behavioral methods used to test the animals must be capable of eliciting the best performance of the animal under test. Fortunately, this problem has largely been solved by the development of techniques for training animals to respond to sound (see Klump *et al.*, 1995). Another important concern is that the sound be presented in such a way that it can be accurately measured; there are two ways of doing this.

The most common way of presenting sounds to behaving animals is to play them through a loudspeaker, which is usually located directly in front of the animal being tested. In this procedure, care is taken to minimize acoustic reflections so that the sound reaching the animal is coming from only one direction, thereby approximating a free-field sound field that can be accurately measured. Thus, by generating a uniform sound field and using behavioral procedures that keep an animal's head fixed within that field, it has been possible to produce reliable audiograms that can be replicated on different individuals of the same species in different laboratories and years apart (cf. H. Heffner *et al.*, 1994; Kelly and Masterton, 1977).

Another way to present tones is through headphones, a method that is generally practicable only on larger animals. This method is often used with monkeys, especially macaques, which can be restrained in primate chairs to allow careful placement of the headphones. In this case, the sound field is considered to be a closed system in which a tight seal is made between the transducer and the animal's ear. Because sound-measuring microphones can be calibrated for either free-field or closed systems, it has generally been considered that the only differences between free-field and headphone audiograms would be due to the effect of the head and pinnae on the sound reaching the eardrum in the free-field test. Thus, a free-field audiogram could be considered to measure the sensitivity of an animal, whereas a headphone audiogram measures the sensitivity of the animal's ear.

Recently, we have had the opportunity to determine the free-field audiogram of Japanese macaques (*Macaca fuscata*), an animal commonly used in auditory research. When we compared it with thresholds determined in other laboratories using headphones (Owren *et al.*, 1988; Smith and Olszyk, 1997), we found significant differences between the audiograms at the low frequencies that could not be explained by the effect of the animal's head and pinnae. Nor could these differences be accounted for in terms of individual variation. The purpose of this paper, then, is to present the free-field audiogram of the Japanese macaque and to suggest reasons for the discrepancy in thresholds between the free-field and headphone audiograms. For comparison, the audiogram of humans was determined in the same free-field environment.

I. METHOD

The monkeys were tested using a conditioned avoidance procedure with a water reward (Heffner and Heffner, 1995). This involved training the animals to maintain steady contact with a water spout in order to obtain water and to break contact whenever they detected a tone in order to avoid a mild shock delivered through the water spout. The animals were tested in a specially constructed cage designed to minimize sound reflection and their heads were fixed within the sound field by requiring them to maintain contact with the water spout.

[a]Deceased.
[b]Correspondence and requests for materials should be addressed to H.E.H.; electronic mail: hheffne@pop3.utoledo.edu

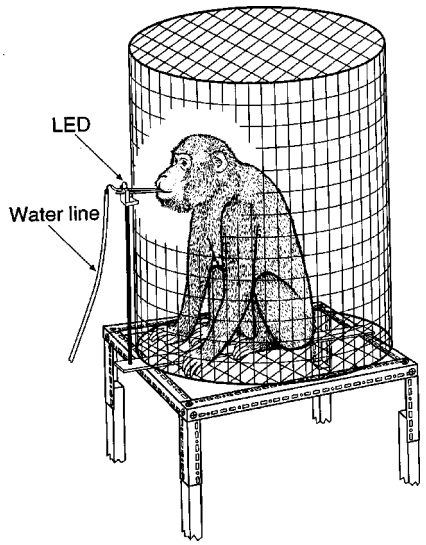

FIG. 1. Diagram illustrating the cage used in testing. The cage was specially constructed to minimize sound reflection.

A. Subjects

Three male Japanese Macaques (*Macaca fuscata*) were used in this study. Monkey 286 was 17 years old and monkeys 605 and 638 were 13 years old at the time of testing. The animals were housed individually in primate cages with free access to food. Water was used as a reward and was available only during testing, although additional water was given an animal in its home cage if needed. Each monkey's weight was checked daily to monitor its health and deprivational state.

Complete audiograms were obtained for six human subjects who had no known auditory disorders: CC (20-year-old male), HH (44-year-old male), JM (20-year-old female), PH (15-year-old male), RH (43-year-old female), and SM (23-year-old female). Low-frequency thresholds were obtained for an additional subject, LH (21-year-old female).

B. Behavioral apparatus

Testing was conducted in a double-walled acoustic chamber IAC model 1204 ($2.55\times2.75\times2.05$ m). The chamber floor was carpeted, and the walls and ceiling were lined with eggcrate foam to reduce sound reflections. The electronic equipment and microcomputer used for behavioral and stimulus control were located outside the chamber. The animals were monitored with two closed-circuit television systems. One camera was mounted on the wall in front of the animal and was directed toward the monkey's face; the second camera, mounted above and behind the animal, was directed at the back of the monkey's head. The cameras were used to verify that the monkey's head was facing directly toward the loudspeaker located in front of the cage.

The monkeys were tested in a cylindrical cage (66 cm diam, 76 cm high, mounted on 58-cm-high legs) constructed of 1×2-in. (2.54×5.08-cm) welded wire (Fig. 1). A double water spout was mounted horizontally on the front of the cage 42 cm above the cage floor (see Fig. 1), a height that allowed the animals to hold their heads in a normal posture while drinking. The spout consisted of two standard sipper tubes mounted parallel to each other and 1 cm apart to permit comfortable placement of a monkey's mouth on both sipper tubes. The degree to which the water spout protruded into the cage was adjusted so that the animals had to face the front of the cage and could not turn their heads sideways while drinking from the water spout; that they maintained a constant, frontal orientation was verified by daily observing the monkey's head positions on the closed-circuit monitors.

The two sipper tubes were electrically isolated from each other so that they could be attached to an electronic ''contact'' switch that detected when an animal had placed its mouth on them. A constant pressure water reservoir (a bottle with an air inlet tube that ended well below the water level, i.e., a Marriotte bottle) was connected to one spout via plastic tubing with an electrically operated water valve placed in line to control the flow of water. The water was trickled into the spout through a copper tube that fit loosely into the rear of one of the sipper tubes so that an animal could not increase water flow by sucking on the spout. The monkeys typically received 200–500 cc of water in a session lasting approximately 1 h.

A mild electric shock was provided by a constant-current shock generator (Grason-Stadler model 700) connected to the two spouts. Shock levels ranged from 1.6 mA at 350 V to 16 mA at 680 V. A light-emitting diode (LED) mounted just above the spout was turned on whenever the shock was on and turning the LED off signaled that the shock was over and that the animal could return to the spout.

The human subjects were tested by removing the cage and having them sit on a chair in the sound chamber in front of the loudspeaker. The sound field in the area occupied by a subject's head was carefully measured and the chair, which was small, did not protrude into the sound field. A subject was given a hand-held button and instructed to press it whenever he or she heard a tone.

C. Acoustical apparatus

Sine waves were generated by a signal generator (Krohn–Hite model 2400 AM/FM phase lock generator) that was calibrated daily with a frequency counter (Fluke 1900 A). The electrical signal was gated on and off with a rise/fall gate (Coulbourn S84-04), bandpass filtered at 1/3 octave above and below the test frequency (Krohn–Hite 3550 filter), attenuated (Hewlett–Packard 350D attenuator), amplified (Crown D75), and connected to a loudspeaker. The electrical signal to the loudspeaker was monitored with an oscilloscope for signs of distortion. In addition, the linearity of the attenuator was verified over the range of attenuation used for threshold testing at each frequency by measuring its output voltage and the resulting sound pressure level.

For frequencies 32 Hz and higher, a loudspeaker was placed approximately 1.0 m in front of the cage and oriented toward the position occupied by the animal's head when it was drinking from the water spout. The distance of the loudspeaker was varied by as much as 0.5 m as needed to achieve an even sound field of sufficient intensity around the monkey's head. The loudspeakers used were a 15-in. (38-cm) woofer for frequencies below 2000 Hz and a Foster ribbon tweeter for frequencies of 2000 Hz and higher.

For frequencies below 32 Hz, the 15-in. woofer was oriented toward one corner of the chamber while the subject was placed in the opposite corner where standing waves occurred. This was done to obtain intensities to over 100 dB SPL as attempting to produce such high intensities by increasing the gain of the amplifier resulted in measurable distortion of the signal. Although this situation was not a free field (i.e., the sound was coming from more than one direction), it was still possible to accurately calibrate the sound field as the sound-measuring microphones are omnidirectional at these very low frequencies and no correction for the orientation of the microphone to the sound sources is needed. That the orientation of the microphone to the direction of the sound was not critical was demonstrated by showing that the same sound-level reading was obtained regardless of the orientation of the microphone. Thus, by taking advantage of the standing waves, it was possible to obtain undistorted tones at high intensities. However, because placement of the monkey cage was limited by its size, it was not always possible to place it in the most intense portion of the sound field as was the case with the human subjects.

Pure tone thresholds for monkeys and/or humans were obtained at octave intervals from 4 Hz to 32 000 Hz with additional thresholds at 12.5, 25, 18 000, 20 000, 22 400, 26 000, and 40 000 Hz. Tones were a 3.0-s pulse, gated on at zero crossing, with rise/fall times of 50 ms for 8 Hz–1 kHz, and 10 ms for 2 kHz–40 kHz.

The sound pressure level (SPL re 20 μPa) was measured daily with a Bruel & Kjaer (B&K) 1/4-in. (0.64-cm) microphone (B&K 4135), preamplifier (B&K 2618), microphone amplifier (B&K 2608), and filter (Krohn–Hite 3550) set to pass one octave above and below the test frequency. The measuring system was calibrated with a pistonphone (B&K 4230). Sound measurements were taken by placing the microphone in the position occupied by the animal's head and pointing it directly toward the loudspeaker (0° incidence). Care was taken to produce a homogeneous sound field (± 1 dB) in the area occupied by the animal's head and ears while it was drinking from the waterspout. As a precaution against transmission of low-frequency substrate vibrations to the animals through the floor, 8-cm-thick foam pads were placed under the 15-in. (38-cm) woofer used for low-frequency testing and under the legs of the animal's testing cage. Furthermore, each frequency was examined for the presence of overtones using a spectrum analyzer (Zonic 3535) connected to the output of the microphone amplifier during sound calibration with the microphone amplifier filter setting on linear (i.e., unfiltered signal). Care was taken to ensure that any overtones present were at least 40 dB below the fundamental frequency and at least 20 dB below an animal's threshold. This procedure was of particular importance when testing low frequencies at high intensities.

D. Psychophysical procedure

A thirsty animal entered the test cage and drank from the waterspout. Tones were presented for 3 s at random intervals and followed at their offset by mild electric shock delivered through the spout. The animal quickly learned to avoid the shock by breaking contact with the spout whenever it heard a tone. The shock was adjusted for each individual to the lowest level that would reliably produce an avoidance response. The mildness of the shock was attested by the fact that none of the animals developed a fear of the spout as they returned to it without hesitation after the shock had been delivered.

Test sessions were divided into 3.0-s trials separated by 2.0-s intertrial intervals. Each trial contained either a continuous tone (''warning'' signal) or silence (''safe'' signal) with 22% of the trials containing a tone. A response was recorded if an animal broke contact for more than half of the last 150 ms of a trial (as determined by the microcomputer). The response was classified as a ''hit'' if the trial contained a tone and as a ''false alarm'' if no tone had been presented. Both the hit and false alarm rates were determined for each block of 5–7 warning trials (which also included approximately 25 safe trials) for each stimulus condition. The hit rate was corrected for false alarms according to the formula: performance = hit rate − (false alarm rate × hit rate), with the hit and false alarm rate expressed as percentages. This measure proportionately reduces the hit rate by the false alarm rate observed under each stimulus condition and varies from 0 (no hits) to 1 (100% hit rate and 0% false alarm rate).

Three additional steps were taken to reward the animals for correct performance. First, the duration of the shock, which determined the time the animal had to pause before it could return to the spout after a warning trial, was 0.25 s following a hit (i.e., the animal correctly broke contact when a tone was presented), but was increased to 4.0 s following a miss (i.e., the animal failed to break contact when a tone was presented). Second, an extra amount of water was delivered to the spout when the animal returned to it following a hit in order to reward the animal for correctly breaking contact with the spout and to make up for the water it lost by responding. Finally, the water flow was shut off for 2 s following a false alarm (i.e., when the animal broke contact with the spout when no tone was present) to discourage false positives.

Absolute thresholds were determined by reducing the intensity of a tone in successive blocks of 5–7 warning trials until the animal no longer responded to the signal above the 0.01 chance level (binomial distribution). Once a preliminary threshold had been obtained, final threshold determination was conducted by presenting tones varying in intensity in 5-dB increments extending from 10 dB below to at least 10 dB above the estimated threshold. Threshold was defined as the intensity corresponding to a performance of 0.50. Threshold testing for a particular frequency was considered complete when the thresholds obtained in at least two different sessions were within 3 dB of each other. Once a complete audiogram had been determined, each threshold was rechecked and further testing was given if the new threshold differed from the previous one by more than 3 dB.

Human subjects were tested by instructing them to hold down the button and release it whenever they heard a tone. Feedback was given on each tone trial by turning on a light at the end of each warning trial. Thus, the trials were presented in the same manner as with the monkeys except that shock was not used.

TABLE I. Free-field pure-tone thresholds of three Japanese macaques in decibels with respect to 20 μPa.

Frequency (in kHz)	Monkey 286	605	638	Average
0.008	>85	>85	83	···
0.0125	81	77	76	78
0.016	71	73	72	72
0.025	63	66	60	63
0.032	56	57	57	57
0.063	37	35	37	36
0.125	18	19	19	19
0.250	13	15	17	15
0.500	7	2	10	6
1.0	4	5	3	4
2.0	7	0	9	5
4.0	4	−2	1	1
8.0	8	0	6	5
16.0	9	1	0	3
32.0	41	37	38	39
36.0	77	64	72	71
40.0	92	85	89	89

TABLE II. Free-field pure-tone thresholds of seven humans in decibels with respect to 20 μPa.

Frequency (in kHz)	Subject CC	HH	JM	LH	PH	RH	SM	Average
0.004	101	100	101	101	100	100	101	101
0.008	95	92	95	95	95	92	92	94
0.016	88	78	83	87	87	86	68	82
0.032	63	58	62	65	62	56	42	58
0.063	38	39	39	34	38	29	34	36
0.125	20	12	17	···	21	12	21	17
0.250	14	13	7	···	11	7	8	10
0.500	11	14	8	···	10	10	7	10
1.0	−11	−8	−2	···	−4	1	2	−4
2.0	−10	−14	9	···	−14	−20	−10	−10
4.0	−11	−2	−4	···	−13	−12	−19	−10
8.0	14	17	4	···	2	4	13	9
16.0	14	41	28	···	17	49	4	26
18.0	67	81	77	···	66	85	51	71
20.0	91	>91	92	···	>91	>91	91	91+
22.4	>91	>91	>91	···	>91	>91	>91	>91

II. RESULTS

The three monkeys used in this study had been previously trained using the conditioned avoidance procedure and had prior experience on a variety of auditory tasks including sound localization and the discrimination of Japanese macaque vocalizations. Thus, the animals already knew how to perform the avoidance task and were experienced auditory observers.

The individual and average thresholds for the three Japanese macaques are given in Table I. Only one of the animals (monkey C) was able to hear 8 Hz at an intensity of 85 dB or less, the highest intensity that could be used without producing overtones in the acoustic signal that could be detected with the spectrum analyzer. However, all three animals were able to hear 12.5 Hz with an average threshold of 78 dB SPL with sensitivity improving as frequency was increased. The animals showed a broad range of good sensitivity extending from 125 Hz to 16 kHz with their best threshold of 1 dB at 4 kHz. Above 16 kHz their sensitivity decreased rapidly, with the monkeys able to hear 40 kHz with an average threshold of 89 dB. At an intensity of 60 dB, the average hearing range for the three monkeys extended from 28 Hz to 37 kHz, a range of over 10 octaves.

The individual and average thresholds for the seven human subjects are given in Table II. All of the subjects were able to hear down to 4 Hz, with an average threshold of 101 dB. The audiograms showed a broad range of good sensitivity extending from 125 Hz to 8 kHz, with a best average threshold of -10 dB at 2 and 4 kHz. Above 8 kHz, sensitivity decreased rapidly, with only three of the six subjects tested able to hear 20 kHz at a level of 91 dB (subject JM's performance on 20 kHz at 91 dB was slightly below 0.50 resulting in an extrapolated threshold of 92 dB). None of the human subjects were able to hear 22.4 kHz at a level of 91 dB. At an intensity of 60 dB, the average hearing range for the human subjects extended from 31 Hz to 17.6 kHz.

III. DISCUSSION

A. Japanese macaque and human free-field audiograms

Figure 2 compares the Japanese macaque and human audiograms generated by this study with the International Organization for Standardization free-field audiogram (ISO, 1961). In comparing these audiograms, three points can be made.

First, the human free-field audiogram obtained here is in good agreement with the ISO free-field audiogram especially at low frequencies (500 Hz and below), where the greatest difference is 3 dB. Similar close agreement is also found at high frequencies (above 4 kHz). Interestingly, the two audiograms differ most in the midrange where they reach a maximum difference of 12 dB at 2 kHz. Although this difference suggests that individual audiograms may vary most in the region of best sensitivity, and, indeed, our subjects varied by up to 29 dB at 2 kHz, we also had large variation at 32 Hz and 16 kHz, frequencies at which our average audiogram

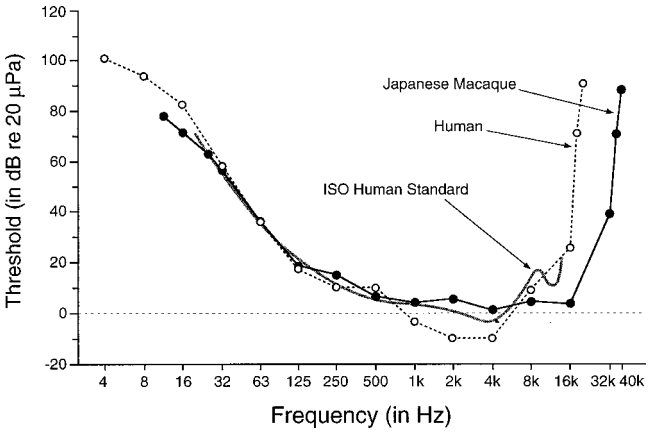

FIG. 2. Average free-field audiogram of three Japanese macaques and seven humans compared with the ISO free-field threshold curve (ISO, 1961). Note the similarity in low-frequency hearing between humans and Japanese macaques.

agreed well with the ISO standard (Table II and Fig. 1). However, it is the low- and high-frequency portions of mammalian audiograms that are of particular theoretical interest and the close agreement of the two human audiograms at these frequencies suggests that there was nothing unusual about either our sound field or our acoustic measurements that would affect our estimates of low- and high-frequency hearing.

Second, the free-field audiograms of both humans and Japanese macaques show very good low-frequency hearing, and the audiograms are virtually identical for frequencies below 1 kHz. Indeed, the similarity between the low-frequency hearing of humans and Japanese macaques has been noted in audiograms obtained using headphones (cf. Owren *et al.*, 1988). However, good low-frequency hearing is not universal as many mammals, such as the Norway rat, are not sensitive to low frequencies (H. Heffner *et al.*, 1994; R. Heffner *et al.*, 1994).

Finally, Japanese macaques have better high-frequency hearing than humans: We found the highest frequency audible to humans at a level of 60 dB SPL to be 17.6 kHz whereas the Japanese macaque can hear 37 kHz at that level. Because humans and macaques have similar low-frequency hearing, it is tempting to conclude that the human audiogram is truncated at the high-frequency end, perhaps as part of a specialization for the reception of speech. However, when viewed from the larger perspective of mammalian hearing as a whole, neither the low-frequency, nor the high-frequency portion of the human audiogram is unusual.

With regard to high-frequency hearing, mammals with small heads and pinnae need to hear higher frequencies than larger mammals in order to make adequate use of binaural spectral differences and pinna cues to localize sound. As illustrated in Fig. 3(a), there is a robust correlation between head size and high-frequency hearing such that small mammals hear higher frequencies than larger mammals (e.g., Koay *et al.*, 1997; Masterton *et al.*, 1969). Thus, the difference in high-frequency hearing between humans and macaques is explained by the difference in head size and, indeed, animals with larger heads, such as the Indian elephant, have even poorer high-frequency hearing than humans (Heffner and Heffner, 1982).

Low-frequency hearing, on the other hand, is correlated with high-frequency hearing such that animals with good high-frequency hearing usually have poor low-frequency hearing and vice versa [Fig. 3(b)]. However, there appears to be a floor effect such that the correlation differs between mammals depending on whether or not they hear well at low frequencies (e.g., Heffner and Heffner, 1985; Koay *et al.*, 1997, 1998). That is, among mammals with relatively poor low-frequency hearing (e.g., those that do not hear below 60 Hz), high- and low-frequency hearing are strongly correlated ($r=0.90, p<0.0001$) with low-frequency hearing shifting on average by 4.6 octaves for each octave change in high-frequency hearing. On the other hand, for mammals with good low-frequency hearing (e.g., those that do hear below 60 Hz), not only are high- and low-frequency hearing less strongly correlated ($r=0.67, p<0.0014$), but low-frequency hearing now shifts by only 0.44 octaves for each octave change in high-frequency hearing (see Koay *et al.*, 1997, 1998).

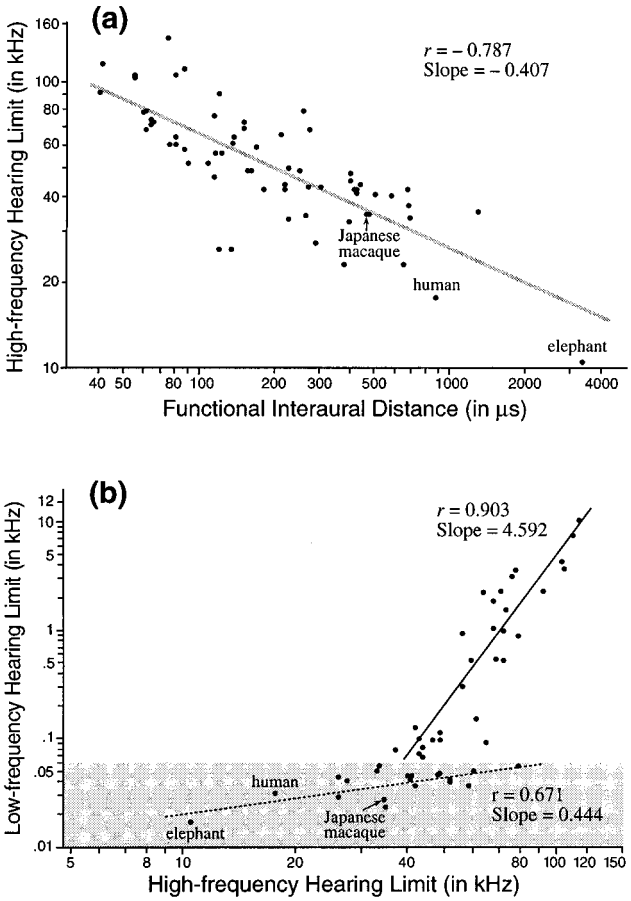

FIG. 3. (a) High-frequency hearing limit (highest frequency audible at 60 dB SPL) as a function of functional interaural distance (the number of microseconds required for a sound to travel from one auditory meatus to the other). This relationship is explained by the fact that mammals with small heads and pinnae require better high-frequency hearing than larger mammals in order to use binaural spectral and pinnae cues to localize sound. (b) Relation between the highest and lowest frequencies audible at 60 dB SPL. Although low-frequency hearing is highly correlated with high-frequency hearing, the slope of this relationship is much shallower among species with good low-frequency hearing, suggesting that there is a floor effect that limits improvement in low-frequency hearing. (Both figures modified from Koay *et al.*, 1998.)

Because both humans and Japanese macaques have good low-frequency hearing, they fall within the group for which changes in high-frequency hearing result in relatively small changes in low-frequency hearing. As a result, although their high-frequency limits are an octave apart, their predicted low-frequency limits are only 6 Hz apart—26 Hz for humans and 32 Hz for Japanese macaques. Moreover, the actual low-frequency limits of 31 Hz for humans and 28 Hz for the Japanese macaque are not significantly different from the predicted values. Thus, the human hearing range is not unusual when compared with those of other mammals.

B. Free-field versus headphone audiograms

The free-field audiogram of Japanese macaques is compared in Fig. 4 with two previous audiograms that were obtained using headphones, one using circumaural headphones (Owren *et al.*, 1988), the other using insert earphones (Smith

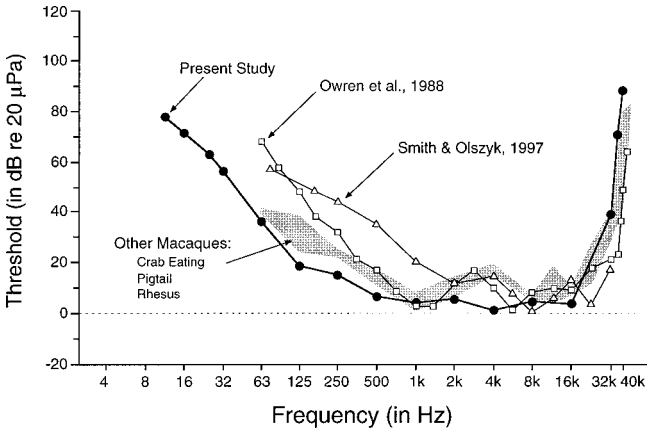

FIG. 4. Free-field audiogram of the Japanese macaque (present study) compared to previous Japanese macaque audiograms using headphones (Owren *et al.*, 1988, and Smith and Olszyk, 1997). Also shown is the range of thresholds for three other species of macaques (shaded area): rhesus macaque *M. mulatta* (Pfingst *et al.*, 1978), Philippine or crab-eating macaque, *M. irus*, and pigtail macaque, *M. nemistrina* (Stebbins *et al.*, 1966).

and Olszyk, 1997). Our free-field audiogram is in good agreement with the headphone audiograms at the mid and high frequencies. For example, the highest frequency audible at 60 dB SPL in the study by Owren *et al.* is 41.5 kHz, which is within 0.20 octaves of the 37-kHz 60-dB limit of our free-field audiogram. Such a difference is minor in a comparative analysis of mammals as their high-frequency hearing spans a range of more than 4 octaves (Koay *et al.*, 1997, 1998).

In contrast, at frequencies below 1 kHz, our free-field audiogram shows the hearing of Japanese macaques to be more sensitive than either of the two headphone audiograms. For example, the lowest frequency audible at 60 dB SPL in these two audiograms is approximately 80 Hz, which is 1.5 octaves higher than the 28-Hz limit of the free-field audiogram. Even though mammalian low-frequency hearing varies by more than 9 octaves (Koay *et al.*, 1997), this difference is too large to be ignored.

The difference between the headphone and free-field audiograms is most likely due to the difficulty in calibrating headphones. Whereas a free field is calibrated by placing a microphone in the sound field and pointing it at the loudspeaker, there is more than one way to calibrate headphones. One method is to insert a probe microphone underneath the cushion of a headphone or into the tube of an insertion earphone. Another way is to place the headphone or earphone on a coupler or artificial ear that simulates the volume of the ear canal. However, as Phingst and his colleagues have pointed out, these calibration procedures can result in estimates of threshold that vary by up to 20 dB, especially at low frequencies (Pfingst *et al.*, 1975). This uncertainty in calibration may account for not only the difference between the headphone and free-field audiograms, but also for the observation that audiograms conducted on the same species in different laboratories may show large differences when headphones are used (cf. the low-frequency portion of the two headphone audiograms shown in Fig. 4).

Although headphones are appropriate for studies involving pre- and post-treatment tests on the same animals, especially when the ears must be tested independently, carefully conducted free-field audiograms are known to result in audiograms that can be replicated across time and laboratories (cf. H. Heffner *et al.*, 1994; Kelly and Masterton, 1977). This reliability is essential when making cross-species comparisons in order to ensure that any differences between species are true species differences and not the result of procedural differences, acoustic or otherwise. An additional advantage is that the free-field audiogram tests the ability of the whole animal. That is, by placing an animal into a calibrated sound field, the resulting audiogram also reflects the effects of the animal's head and pinnae on its sensitivity to sound. However, should it be of interest to determine the sensitivity of the ear alone, it is possible to place a sedated animal into a calibrated sound field and then measure the intensity of the sound at the eardrum.

C. Hearing in macaques

Audiograms are available for three other species of macaques: the rhesus macaque *M. mulatta* (Pfingst *et al.*, 1978), Philippine or crab-eating macaque, *M. irus*, and pigtail macaque *M. nemistrina* (Stebbins *et al.*, 1966), all of which were determined using headphones. As can be seen in Fig. 4, the audiograms of these three species are quite similar to the Japanese macaque audiograms at the mid and high frequencies. At low frequencies, they more closely resemble the Japanese macaque free-field audiogram, even though they were determined with headphones themselves. Because all four species of macaques are closely related and are of similar size, it might be expected that their audiograms would likewise be quite similar. Thus, the differences between the audiograms at low frequencies may be due more to uncertainties inherent in calibrating headphones than to species differences.

ACKNOWLEDGMENTS

We thank G. Koay for his help with the illustrations and his comments on the manuscript. This work was supported by NIH Grant No. NS 30539 to H.E.H. and NIH postdoctoral fellowship DC 00305 to L.L.J.

Heffner, H. E., and Heffner, R. S. (**1995**). ''Conditioned avoidance,'' in *Methods in Comparative Psychoacoustics*, edited by G. M. Klump, R. J. Dooling, R. R. Fay, and W. C. Stebbins (Birkhäuser, Basel), pp. 73–87.

Heffner, H. E., Heffner, R. S., Contos, C., and Ott, T. (**1994**). ''Audiogram of the hooded Norway rat,'' Hear. Res. **73**, 244–247.

Heffner, R. S., and Heffner, H. E. (**1982**). ''Hearing in the elephant (*Elephas maximus*): Absolute sensitivity, frequency discrimination, and sound localization,'' J. Comp. Physiol. Psychol. **96**, 926–944.

Heffner, R. S., and Heffner, H. E. (**1985**). ''Hearing in mammals: The least weasel,'' J. Mammal. **66**, 745–755.

Heffner, R. S., Heffner, H. E., Contos, C., and Kearns, D. (**1994**). ''Hearing in prairie dogs: Transition between surface and subterranean rodents,'' Hear. Res. **73**, 185–189.

ISO (**1961**). ISO R. 226. ''Normal equal-loudness level contours'' (International Organization for Standardization, Switzerland).

Kelly, J. B., and Masterton, B. (**1977**). ''Auditory sensitivity of the albino rat,'' J. Comp. Physiol. Psychol. **91**, 930–936.

Klump, G. M., Dooling, R. J., Fay, R. R., and Stebbins, W. C., editors (**1995**). *Methods in Comparative Psychoacoustics* (Birkhäuser, Basel).

Koay, G., Heffner, H. E., and Heffner, R. S. (**1997**). ''Audiogram of the big brown bat (*Eptesicus fuscus*),'' Hear. Res. **105**, 202–210.
Koay, G., Heffner, R. S., and Heffner, H. E. (**1998**). ''Hearing in a megachiropteran fruit bat (*Rousettus aegyptiacus*),'' J. Comp. Psych. **112**, 371–382.
Masterton, B., Heffner, H., and Ravizza, R. (**1969**). ''The evolution of human hearing,'' J. Acoust. Soc. Am. **45**, 966–985.
Owren, M. J., Hopp, S. L., Sinnott, J. M., and Petersen, M. R. (**1988**). ''Absolute auditory thresholds in three old world monkey species (*Cercopithecus aethiops, C. neglectus, Macaca fuscata*) and Humans (*Homo sapiens*),'' J. Comp. Psych. **102**, 99–107.
Pfingst, B. E., Hienz, R., and Miller, J. (**1975**). ''Reaction-time procedure for measurement of hearing. II. Threshold functions,'' J. Acoust. Soc. Am. **57**, 431–436.
Pfingst, B. E., Laycock, J., Flammino, F., and Lonsbury-Martin, B. (**1978**). ''Pure tone thresholds for the rhesus monkey,'' Hear. Res. **1**, 43–47.
Smith, D. W., and Olszyk, V. B. (**1997**). ''Auditory behavioral thresholds for Japanese macaques using insert earphones,'' Am. J. Primatol **41**, 323–329.
Stebbins, W. C., Green, S., and Miller, F. L. (**1966**). ''Auditory sensitivity of the monkey,'' Science **153**, 1646–1647.

Shock wave–inertial microbubble interaction: A theoretical study based on the Gilmore formulation for bubble dynamics

Songlin Zhu and Pei Zhong[a)]
Department of Mechanical Engineering and Materials Science, Duke University, Durham, North Carolina 27708

(Received 20 April 1999; accepted for publication 13 July 1999)

The Gilmore formulation for bubble dynamics coupled with zeroth-order gas diffusion were used to investigate theoretically the cavitation activity produced by a modified XL-1 lithotripter [J. Acoust. Soc. Am. **105**, 1997–2009 (1999)]. The model calculation confirms many of the basic features in bubble dynamics observed experimentally, in particular the strong secondary shock wave emission generated by *in situ* lithotripter shock wave–inertial microbubble interaction. In addition, shock wave–inertial microbubble interaction produced by a Dornier HM-3, the most commonly used clinical lithotripter, was evaluated. It was shown that the forced collapse of inertial microbubbles with strong secondary shock wave emission could be produced consistently, provided that an appropriate preceding shock wave and interpulse delay were used. Further, it was demonstrated that truncation of the tensile stress of the lithotripter shock wave could significantly reduce the large expansion of the bubble following shock wave-inertial microbubble interaction, which may alleviate the risk for vascular injury during shock wave exposure.
[S0001-4966(99)01511-8]

PACS numbers: 43.80.Sh, 43.25.Yw [FD]

INTRODUCTION

To improve the efficiency of cavitation-mediated membrane permeabilization by lithotripter shock waves, we have recently developed a method of producing *in situ* shock wave–inertial microbubble interaction using a modified Dornier XL-1 lithotripter.[1] Briefly, inertial microbubbles are induced acoustically in an aqueous medium by a weak shock wave preceding the regular lithotripter pulse by a few microseconds. These microbubbles expand to a size of a few hundred microns before being collapsed *in situ* by the ensuing lithotripter pulse. This forced collapse of inertial microbubbles generates strong secondary shock wave emission and formation of microjets immediately behind the propagating lithotripter shock front. These unique features are absent from the dynamics of cavitation bubbles induced by standard lithotripter shock waves. With optimal combination of the preceding and lithotripter shock waves, membrane permeabilization of mouse lymphoid cells was found to be significantly enhanced at low exposure (50 shocks at 25 kV) while cell injury (defined as lysis and functional impairment of the cells) was substantially increased at high exposure ($>$100 shocks at 25 kV), compared to the standard lithotripter pulses.[1] Apparently, appropriate modification of the lithotripter waveform could dramatically alter the biological effect it produces.

To provide a theoretical perspective on the physical processes that may lead to a significantly altered bioeffect, we have studied the shock wave–inertial microbubble interaction using the Gilmore formulation for bubble dynamics coupled with zeroth-order gas diffusion, as originally described by Church.[2] First, we compared the dynamics of bubble oscillations produced by the various shock wave sequences investigated in our previous study.[1] The model calculations have confirmed qualitatively many of the characteristic features in bubble dynamics (except for microjet formation) produced by the modified XL-1 lithotripter. In particular, strong secondary shock wave emission due to the forced collapse of inertial microbubbles (70–250 μm in diameter at the moment of shock wave impingement) was predicted, which was found to be comparable to the shock wave emission generated by the inertial collapse of a much larger, millimeter-size bubble. Second, to identify the optimal preceding-lithotripter shock wave combination, we evaluated the effects of interpulse delay and the pressure amplitude of the preceding pulse on shock wave–inertial microbubble interaction. To ensure generality, the model calculation was carried out using a hypothetical modification of a Dornier HM-3 lithotripter, which is the most commonly used clinical lithotripter. It should be noted that two previous studies have examined the shock wave-inertial bubble interaction produced by two shock waves of similar pressure amplitudes with various phase combination and interpulse delay.[3,4] However, in both studies gas diffusion across the bubble wall was not included in the model calculation. Furthermore, in this study modification of the tensile component of the lithotripter shock wave was explored theoretically to assess the possibility of minimizing vascular injury by reducing the large expansion of the rebound bubbles following shock wave–inertial microbubble interaction. Finally, bubble dynamics in response to inverted lithotripter shock waveforms were calculated and contrasted with that produced by the preceding-lithotripter shock wave combination.

I. METHODS

A. Gilmore formulation for bubble dynamics

The Gilmore formulation for bubble dynamics, coupled with zeroth-order gas diffusion, has been used previously by

[a)]Electronic mail: pzl@me1.egr.duke.edu

TABLE I. Representative pulse parameters of the shock waves produced by the standard and modified Dornier XL-1 lithotripter at an output voltage of 25 kV.[a]

Reflector configuration	Preceding shock wave			Lithotripter shock wave				
	P^+ (MPa)	P^- (MPa)	t^- (μs)	P^+ (MPa)	P^- (MPa)	t^- (μs)	α (s^{-1})	I_{index}[c]
Standard				72.09	−19.81	4.32	0.878×10^6	3391
D2	3.36	−1.48	1.11	66.73	−22.76	1.83	1.868×10^6	1896
D3	3.33	−1.62[b]	1.54	64.33	−17.91	3.70	1.061×10^6	2374
D6	6.03	−2.14	2.19	59.77	−12.38	3.36	1.412×10^6	1030

[a]Maximum values (mean+s.d.) taken from previous measurements in Ref. 1.
[b]Value interpolated linearly based on the corresponding values of D2 and D6 reflector configurations.
[c]I_{index} is the mechanical index defined as $[P^-/\text{MPa}]^2*[2\ t^-/\mu\text{s}]$, which is roughly proportional to the mechanical work done to the bubble during the negative cycle of the lithotripter shock wave (see Ref. 18).

several groups to simulate the dynamics of cavitation bubbles in a lithotripter field.[2,5] For conciseness, a detailed description of the theory is omitted here, but instead summarized in the Appendix. Two primary assumptions of the Gilmore formulation are that the bubble remains spherical in shape throughout the oscillation and the initial radius of the bubble is much smaller than the wavelength of the driving acoustic pulse. In our previous study,[1] it was observed via high-speed shadowgraph imaging that the forced collapse of the majority of the inertial microbubbles by the lithotripter pulse leads to strong secondary shock wave emission and spherically rebounded bubbles, features that are characteristic of symmetric collapse of the bubbles. However, the collapse of a few microbubbles of larger size appeared to be asymmetric, as indicated by the formation of microjets in the rebound bubbles. It was observed that the tendency of asymmetric collapse of the bubble during shock wave-inertial microbubble interaction increases with the size of the microbubble, although the threshold for such a transition from symmetric to asymmetric collapse was not established.[1] In addition, the estimated diameter of the inertial microbubble at the instance of lithotripter shock wave impingement is less than 250 μm [to be shown later in Fig. 5(b)], which is about an order of magnitude smaller than the lithotripter pulse length. Hence, a uniform pressure distribution around the microbubble, as assumed by the Gilmore formulation, is reasonably satisfied. Overall, on a qualitative basis, the Gilmore formulation appears to be appropriate to simulate the dynamics of an inertial microbubble impinged by a lithotripter shock wave.

B. Lithotripter fields

In this work, three different lithotripter fields were considered, namely, the modified XL-1 that was used in our previous study, the Dornier HM-3, which is the most commonly used clinical lithotripter, and an experimental electrohydraulic lithotripter with pressure-release reflector (to produce inverted lithotripter shock wave). As shown by Church,[2] the typical lithotripter shock wave (LSW) can be modeled by

$$P_s(t)=2P^+e^{-\alpha t}\cos(2\pi ft+\pi/3), \tag{1}$$

where $P_s(t)$ is the time history of the LSW, and we set $P_s(t)=0$ for $t<0$, P^+ is the peak positive pressure of the shock wave, α is the decay constant, and f is the frequency determined by the negative pulse duration of the LSW, t^-, with $f=1/(2t^-)$. Notice that the rise time of the shock front is not included in Eq. (1) since it has a minimal effect on the dynamics of LSW-induced bubble oscillations.[5] In practice, it is usually convenient to substitute the values of P^+ and t^- measured experimentally into Eq. (1) and to adjust the value of α so that the best fit for the peak negative pressure, P^-, and the temporal profile of the LSW could be obtained.

As shown in Fig. 8 of Ref. 1, the modified XL-1 lithotripter produces, within 10 μs in front of the LSW, a preceding shock wave (PSW) and an intermediate shock wave (ISW). The PSW and ISW are generated, respectively, by wave diffraction and transmission through an annular ring reflector mounted on the aperture rim of the XL-1 reflector.[1] Using Eq. (1), the shock wave sequence produced by the modified XL-1 lithotripter in general can be described as

$$P_s=P_{\text{PSW}}(t)+P_{\text{ISW}}(t-\Delta t_{\text{PI}})+P_{\text{LSW}}(t-\Delta t_{\text{PL}}), \tag{2}$$

where $P_{\text{PSW}}(t)$, $P_{\text{ISW}}(t)$ and $P_{\text{LSW}}(t)$ are the time history of the PSW, ISW, and LSW, whereas Δt_{PI} and Δt_{PL} are the interpulse delay between PSW and ISW, and between PSW and LSW, respectively. Based on previous measurements,[1] we chose $P^+_{\text{ISW}}=P^+_{\text{PSW}}/4$, $\Delta t_{\text{PI}}=4$ μs, and $\Delta t_{\text{PL}}=9$ μs. In our previous study,[1] four different (standard and three modified, axisymmetric—D2, D3, and D6) reflector configurations were examined. The representative values of the P^+, P^-, and t^- for the PSW and LSW, generated by the XL-1 lithotripter at 25 kV, as well as the α value for the best fit of LSW are summarized in Table I. Notice that the maximum values (defined as mean+s.d.) from the experimentally measured data were chosen. The reasons are twofold: (1) polyvinylidene difluoride (PVDF) membrane hydrophone tends to underestimate the tensile pressure of the LSW,[6] and (2) enlargement of the electrode gap during shock wave lithotripsy (SWL) will increase the strength of the shock wave. Hence, a modeled shock wave based on the maximum values of the waveform parameters may be a better representative of the acoustic field used in the experiment, in which up to 250 shocks were delivered to a single sample,[1] and each electrode was used to produce a maximum of 1500 sparks at 25 kV. Figure 1 shows the modeled pressure waveforms of the shock wave sequences generated by the XL-1 lithotripter using the standard and the three modified reflector configurations, respectively. To facilitate comparison, each $P_s(t)$ curve was offset vertically except the bottom one, and, sub-

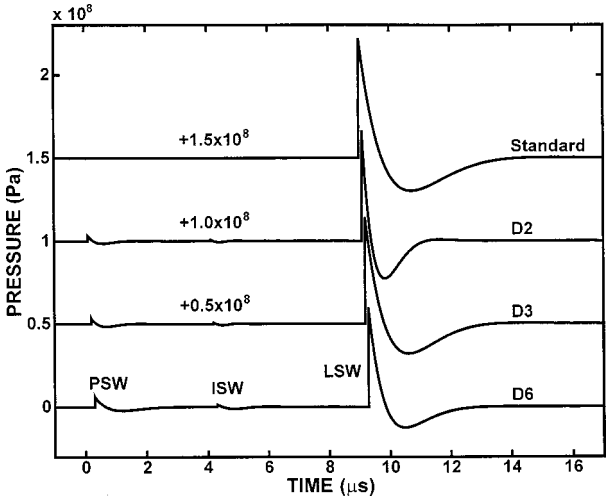

FIG. 1. Representative shock wave sequences generated by the original (or standard) and the modified Dornier XL-1 lithotripter with three different reflector configurations (D2, D3, and D6), modeled by Eq. (1) using pulse parameters listed in Table I.

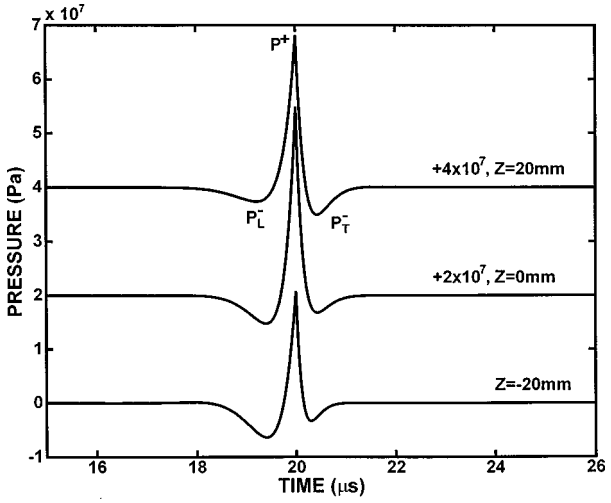

FIG. 3. Pressure waveforms of inverted lithotripter shock waves modeled using a combination of Eqs. (1) and (3), based on PVDF membrane hydrophone measurements taken at $z=-20$, 0, and 20 mm, respectively, along the major axis of an experimental electrohydraulic lithotripter (see Ref. 4).

sequently, this style of presentation was used throughout the paper.

For the shock wave produced by a standard HM-3 lithotripter,[7] the typical pressure waveform is modeled by Eq. (1) with $P^+=40$ MPa, $P^-=-10$ MPa, and $t^-=-12\,\mu$s, using a best fit α of $7.03\times10^5\,\mathrm{s}^{-1}$. In order to reduce the large expansion of the rebound bubbles, we assume that an acoustic diode[8] could be used to truncate the tensile pressure of the LSW below a threshold level, P_t^-. Such a modified pressure waveform can be described by Eq. (1) under the condition that $P_s(t)$ is set to equal to P_t^- when $P_s(t)<P_t^-$. Figure 2 illustrates a modeled pressure waveform generated by a HM-3 lithotripter with its tensile component truncated at $P_t^-=-5$ MPa.

To describe the shock waves generated by pressure-release reflectors, a time inverse lithotripter pressure waveform (a tensile wave followed by a compressive wave) is introduced as

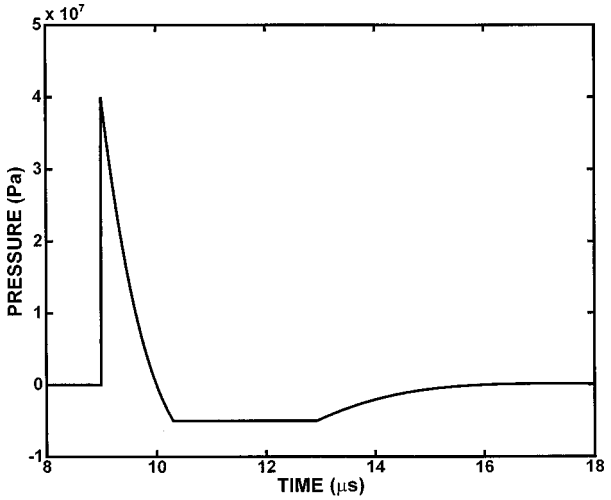

FIG. 2. Modeled pressure waveform of the shock wave generated by a Dornier HM-3 lithotripter with its tensile component truncated at -5 MPa.

$$P_s(t)=\begin{cases}2P^+e^{-\alpha(t_0-t)}\cos(2\pi f(t_0-t)+\pi/3), & 0<t<t_0\\ 0, \quad t<0,\ t<t_0,\end{cases} \tag{3}$$

where t_0 denotes the time instance from which the waveform is horizontally inverted, and t_0 is larger than the total pulse duration of the LSW. Using a combination of Eqs. (1) and (3), an inverted LSW can be constructed with a leading tensile component, P_L^-, followed by a compressive component and a trailing tensile component, P_T^-. Figure 3 shows the modeled pressure waveforms of the inverted LSW, based on PVDF membrane hydrophone measurements taken at $z=-20$, 0 (F_2—the external focus of the ellipsoidal reflector), and 20 mm along the major axis of an experimental electrohydraulic lithotripter equipped with a pressure-release reflector.[4]

C. Numerical algorithm and implementation

Notice that in response to a lithotripter pulse, the size of a bubble during its oscillation varies by several orders of magnitude.[2] Therefore, in order to reduce the numerical error in model computation, we have introduced the following dimensionless variables:

$$R'=\frac{R}{R_0},\quad t'=\frac{t}{T_0},\quad U'=\frac{dR'}{dt'}=\frac{dR}{dt}\frac{T_0}{R_0},$$
$$C'=C\frac{T_0}{R_0},\quad H'=H\frac{T_0^2}{R_0^2}, \tag{4}$$

and nondimensionalized the original Gilmore formulation [Eq. (A1)] to

$$R'\left(1-\frac{U'}{C'}\right)\frac{dU'}{dt'}+\frac{3}{2}\left(1-\frac{U'}{3C'}\right)U'^2$$
$$=\left(1+\frac{U'}{C'}\right)H'+\frac{1}{C'}\left(1-\frac{U'}{C'}\right)R'\frac{dH'}{dt'}, \tag{5}$$

where R_0 is the original bubble radius and T_0 is the reference time-scale for bubble oscillation. For convenience, T_0 is set to be 1 μs.

The nondimensionalized Gilmore formulation (5) was then solved by using the fifth-order Runge–Kutta–Fehlberg method with a step-size control algorithm.[9] To couple with gas diffusion [Eq. (A6)], an iterative method was used by first solving Eq. (5) with the initial number of moles of gas n_0 inside the bubble. The computed bubble response, $R(t)$, was then substituted into Eqs. (A6)–(A9) to determine a new number of moles of gas n inside the bubble, which, subsequently, was used to recalculate the bubble response curve. This computational process was repeated until the solution of n converges. The source code, written in MatLab Version 5 (The Mathworks Inc., Natick, MA), takes about 10 min to run a single simulation of the bubble response to lithotripter pulses on a Micron 166-MHz PC with Pentium processor and 32 MB RAM. The code was benchmarked against the calculations in Church's original paper[2] and excellent agreement was obtained.

Considering bubble oscillations in water, the values of the physical constants (see the Appendix for their definitions) used in the numerical calculations are $\rho_0=998$ kg/m^3, $\mu=1.046\times10^{-3}$ kg/m·s, $\sigma=72.583\times10^{-3}$ N/m, $C_l=1500$ m/s, $D=2.42\times10^{-9}$ m^2/s, $P_0=1.01\times10^5$ Pa, $C_0=0.7899$ mol/m^3, $C_i/C_0=0.9$, $B=3.039\times10^8$ Pa, $\eta=1.4$, and $n_0=6.9\times10^{-15}$ moles (for $R_0=3$ μm). In this study, the initial radius of the bubble nucleus, R_0, is set to be 3 μm for all cases.

II. RESULTS AND DISCUSSION

A. Modified XL-1 lithotripter

1. General characteristics

The response of a 3-μm cavitation nucleus, $R(t)$, to various XL-1 lithotripter-generated shock waves is shown in Fig. 4(a), in which R_{bi} denotes the radius of the bubble at the instance of shock wave–inertial microbubble (IMB) interaction. The typical response of the cavitation nucleus to a single shock wave (i.e., PSW or LSW) is an initial compression, a quick rebound and ensuing large expansion of the bubble, followed by an inertial collapse of the bubble and subsequent ringing. The maximum radius, $R_{\max}$, and the collapse time, t_c, of the bubble increases with the peak value and duration of the tensile pressure of the incident shock wave (see, for example, the results of PSW versus LSW). Compared to the response to the LSW, the most significant difference in the response of the cavitation nucleus to the modified XL-1 shock waves, i.e., PSW+LSW or PSW+ISW+LSW, is the forced collapse of the inertial microbubbles (induced by PSW or PSW+ISW) by the LSW. Figure 4(b) shows the corresponding secondary shock wave emission in water at a radial distance of 5 mm from the bubble center, calculated by using Eq. (A10). The first peak pressure in water, P_{w1}, produced by the forced collapse of the microbubble in the case of PSW+(ISW+) LSW is significantly stronger than the corresponding value produced by the compression of the nucleus by the LSW. Also, two distinct subpeaks could be observed in the region of P_{w1}. We will refer the first peak P_{w1} to the higher of the two subpeaks, which correspond to the initial collapse and the subsequent rebound of the bubble, respectively. The second peak pressure in water, P_{w2} is produced by the inertial collapse of the bubble after its maximum expansion. Similar

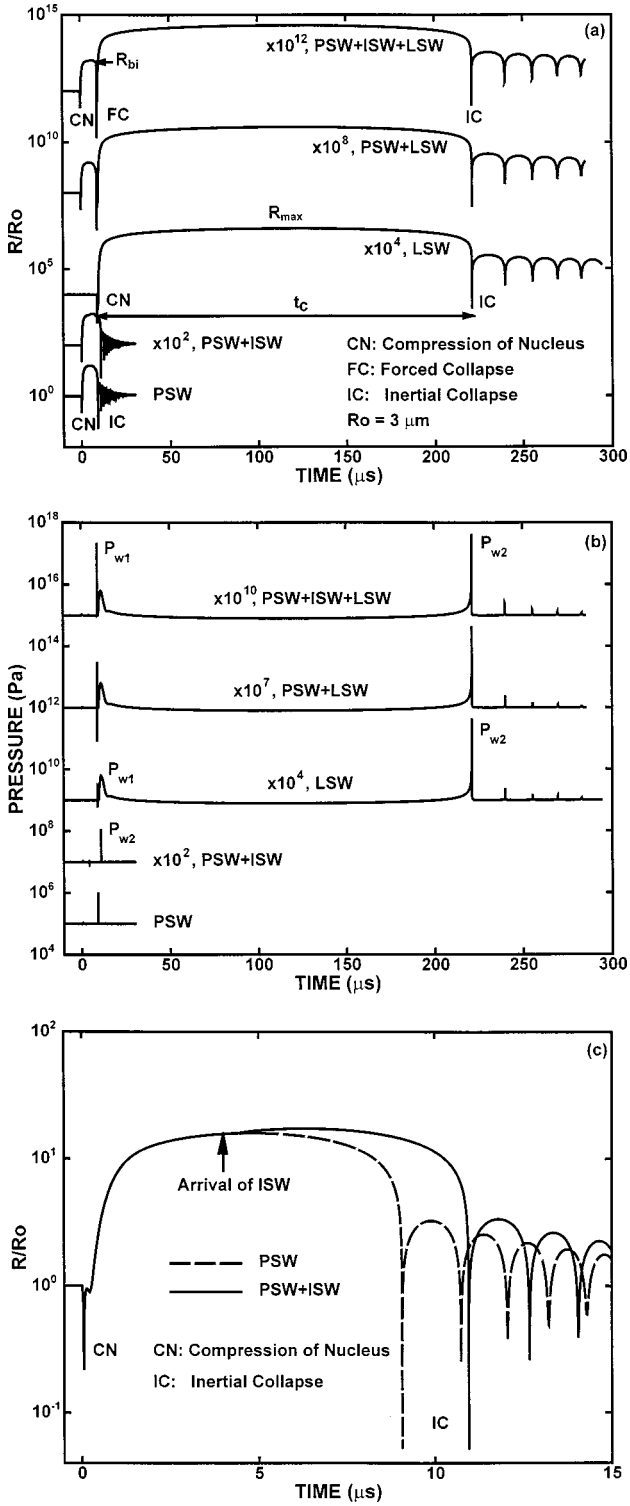

FIG. 4. Responses of a 3-μm cavitation nucleus to various combinations of shock waves produced by the modified Dornier XL-1 lithotripter with D3 reflector configuration. (a) Bubble radius normalized by the initial nucleus radius. (b) Corresponding secondary shock wave emission in water calculated at a radial distance of 5 mm from the bubble center. (c) Comparison of bubble response to PSW and PSW+ISW.

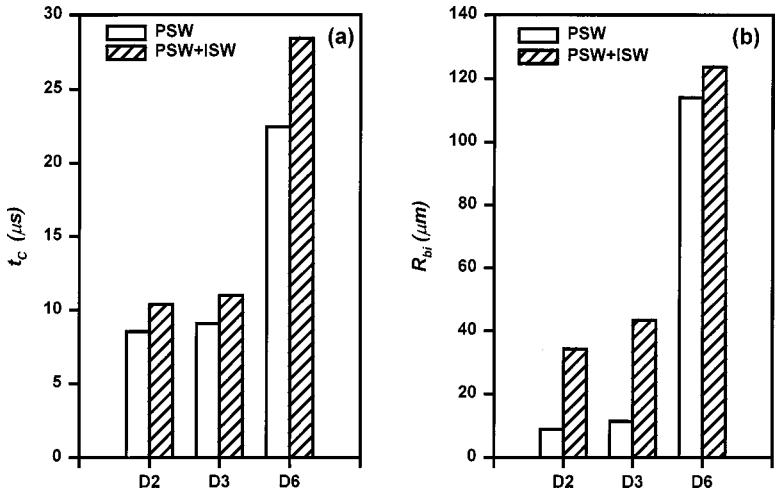

FIG. 5. The collapse time, t_c, shown in (a) and the size of the IMB at the instance of LSW impingement, R_b, shown in (b) produced by PSW and PSW+ISW (bubble size at $t=9$ μs) with different reflector configurations. $R_0=3$ μm.

values of P_{w2} were obtained for both cases of LSW and PSW+(ISW+) LSW. This result suggests that P_{w2} is determined primarily by the tensile stress of the LSW,[2] and is minimally influenced by the bubble size at the instance of shock wave–IMB interaction, which is determined by PSW (+ISW). It is also worth noting that the interaction of ISW with the PSW-induced IMB does not produce a forced collapse of the microbubble, due to the relative weakness of the P^+ of the ISW [Fig. 4(c)]. Instead, the microbubble is only slightly compressed by the compressive stress, and subsequently further expanded by the tensile stress of the ISW to a larger size before the inertial collapse. The net effect of ISW, therefore, is to enlarge the size of the microbubble, and subsequently increases the momentum transfer during the LSW–IMB interaction.

2. Comparison of different reflector configurations

As shown in Fig. 5, when the pressure amplitude(s) of the PSW(+ISW) increases from D2 to D6 reflector configurations, the values of t_c and R_{bi} of the microbubbles increase accordingly. As noted earlier, the time delay between the PSW and LSW produced by the modified XL-1 lithotripter is about 9 μs. Comparison of this interpulse time delay with the predicted value of t_c indicates that the LSW–IMB interaction is likely to occur in the collapsing phase of the IMB for the D2 and D3 reflector configurations, but in the expansion phase of the IMB for the D6 reflector configuration. Further, it can be seen that the addition of ISW significantly increases the value of R_{bi} from that produced by PSW alone, in particular for the D2 and D3 reflector configurations. The predicted value of R_{bi} induced by PSW+ISW varies from 35 to 125 μm, which is within the range ($<$200 μm) measured directly from high-speed photographic images in our previous study.[1]

The predicted value of P_{w1} from the forced collapse of the microbubbles using the modified reflector is also much higher than the value produced by the initial compression of the cavitation nuclei by the standard LSW [Fig. 6(a)]. In addition, P_{w1} also increases from the D2 to the D6 reflector configuration, although the positive peak pressure of the corresponding LSW is decreasing in this order (see Table I). This result suggests that R_{bi} is the primary determinant for P_{w1}, provided that LSW is sufficiently strong. The fact that P_{w1} increases significantly from PSW+LSW to PSW+ISW+LSW for the D2 and D3, but not for the D6 reflector configuration further supports this conclusion. In addition, the predicted values of P_{w2} for the modified reflectors are almost identical between LSW and PSW(+ISW)+LSW [Fig. 6(b)], indicating again that P_{w2} is determined primarily by the tensile strength of the LSW, or,

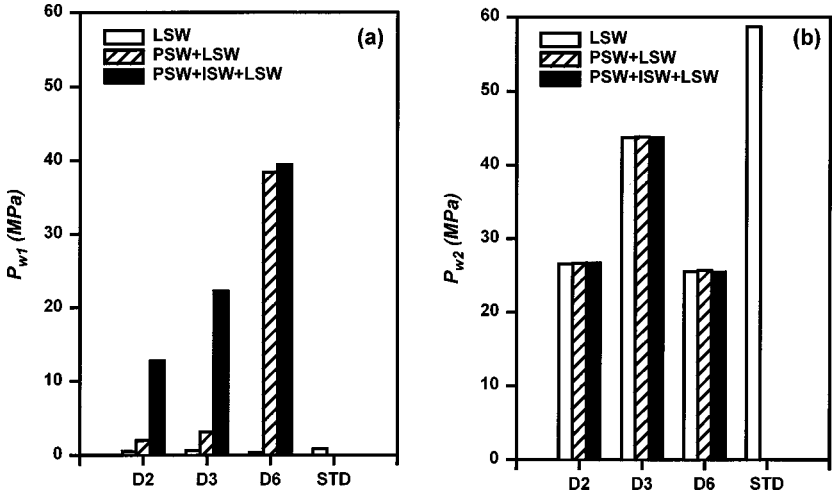

FIG. 6. Comparison of peak pressure produced in water by different reflector configurations and shock wave sequences. (a) P_{w1} and (b) P_{w2}. $R_0=3$ μm.

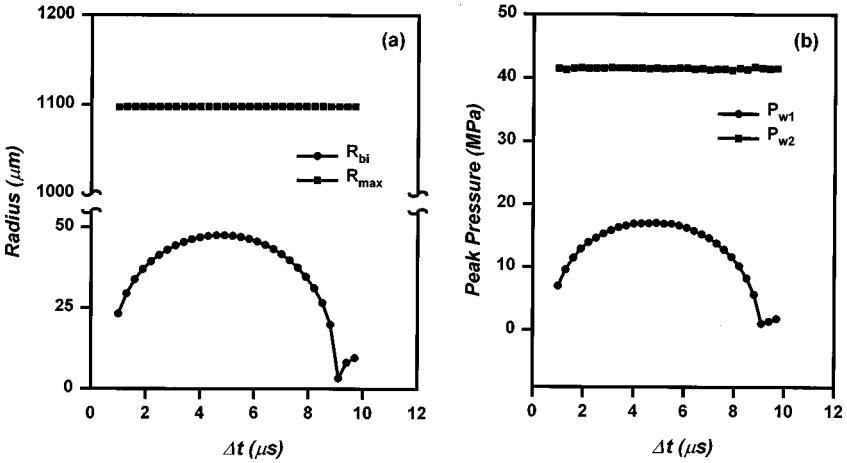

FIG. 7. Effect of interpulse delay, Δt, on (a) bubble radii and (b) secondary shock wave emissions produced by a modified HM-3 lithotripter. $R_0 = 3\ \mu$m.

more precisely, the mechanical work done on the bubble by the tensile stress of the LSW. The prediction that P_{w2} is larger for the D3 than for the D2 and D6 reflector configurations, and the largest value is produced by the standard reflector configuration further corroborates theoretically with this speculation (see Table I for the values of the mechanical index of the LSWs). It is also interesting to note that the predicted value of P_{w1} is smaller than P_{w2} for the D2, D3, and standard reflector configurations, but larger than P_{w2} for the D6 reflector configuration, which induces the largest microbubbles (Figs. 5 and 6). This prediction is consistent with the results of acoustic emission measurements from the modified XL-1 lithotripter.[1]

B. HM-3 lithotripter

To assess the optimal condition for producing desirable shock wave–IMB interaction, we have considered a hypothetical modification of the most widely used clinical lithotripter, the Dornier HM-3. We assume that the criterion for optimal combination of PSW and LSW is to produce the strongest forced collapse of IMB, which could be associated with the mechanical stresses that generate bioeffects. Further, we assume that following the concept described and tested in our previous study,[1] a similar modification of the ellipsoidal reflector of a HM-3 lithotripter could be made. For simplicity, we considered the addition of a PSW in front of the standard LSW produced by the HM-3. The ISW was omitted to simplify the model calculation, and, physically, it can be eliminated by acoustic masking. Three factors that may influence LSW–IMB interaction and the resultant bubble dynamics were considered, as described in the following.

1. Effect of interpulse delay between PSW and LSW

First, we evaluated the effect of interpulse delay between PSW and LSW, Δt, on the resultant bubble radii (R_{bi} and $R_{\max}$) and the secondary shock wave emissions (P_{w1} and P_{w2}) generated by the collapse of the bubble. In the following, PSW was assumed to be the one produced by the XL-1 lithotripter at 25 kV using the D3 reflector configuration (see Table I), unless otherwise specified. The LSW was modeled by Eq. (1) with $P^+/P^- = 40/-10$ MPa, and $t^- = -12\ \mu$s, as described previously. For a given combination of PSW and LSW, it was predicted that there is an optimal Δt at which maximum values of R_{bi} and P_{w1} could be obtained (Fig. 7). This optimal interpulse delay corresponds to the time needed for the inertial microbubble induced by the PSW to expand to its maximum size before being collapsed by the ensuing LSW, a condition that would ensure maximum momentum transfer during the LSW–IMB interaction. Similar results were also obtained in previous studies using two shock waves of different phase combination and interpulse delay.[3,4] On the other hand, the interpulse delay has no effect on $R_{\max}$ and P_{w2}, which are determined solely by the tensile strength of the LSW. It can also be noted that near the optimal value of Δt, the variations of R_{bi} and P_{w1} with respect to Δt are almost symmetric. Moreover, it should be pointed out that the forced collapse of the inertial microbubble could be produced within a range around the optimal Δt, despite the fact that under those conditions the interaction would occur at a smaller bubble size. As shown in Fig. 7, even with 50% variation of Δt around its optimal value, the corresponding decrease in P_{w1} (from 17.0 to 13.8 MPa) is less than 19%, and these pressure peaks are an order of magnitude higher than that (0.42 MPa) produced by the initial compression of the cavitation nuclei by LSW alone. This result indicates that with appropriate Δt, LSW–IMB interaction could produce forced collapse of inertial microbubbles in a volume around the lithotripter focus, as observed experimentally in our previous study.[1]

2. Effect of PSW

Second, we evaluated the effect of PSW on LSW–IMB interaction. While maintaining a constant ratio of $P^+/P^- = 2.06$, we varied the peak positive pressure of the PSW, P^+_{PSW}, and calculated the corresponding bubble dynamics and resultant acoustic emission. For each case, we used the optimal Δt between the PSW and LSW so that maximum values of R_{bi} and P_{w1} were obtained. The results show that R_{bi} and P_{w1} increase almost linearly with P^+_{PSW} while the corresponding values of $R_{\max}$ and P_{w2} remain unchanged (Fig. 8). Most interestingly, the calculations predict that when P^+_{PSW} exceeds 9.7 MPa, P_{w1} will become greater than P_{w2}, despite the fact that the corresponding value of R_{bi} (which leads to P_{w1} due to forced collapse) is an order of magnitude smaller than $R_{\max}$ (which leads to P_{w2} due to

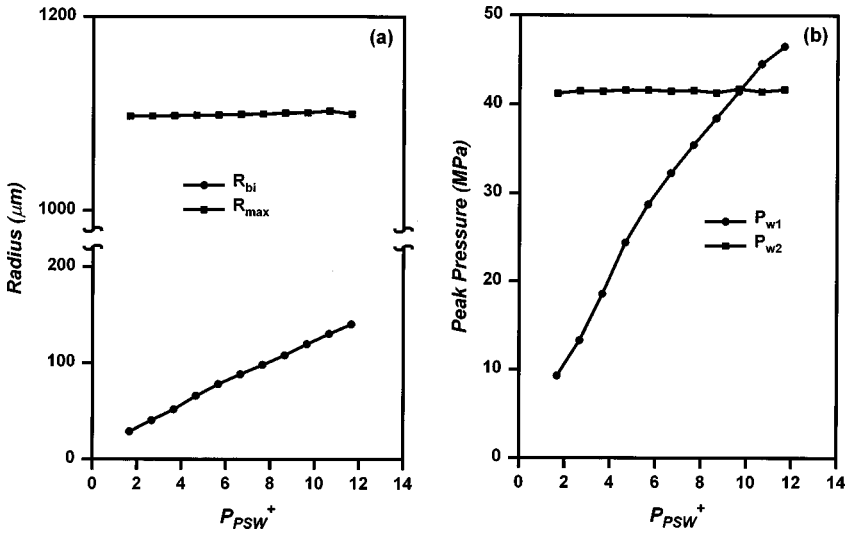

FIG. 8. Effect of preceding shock wave on (a) bubble radii and (b) secondary shock wave emissions produced by a modified HM-3 lithotripter. The interpulse delay, Δt, is set at the optimal value. $R_0 = 3\ \mu$m.

inertial collapse). This result clearly demonstrates the potential of using forced collapse of inertial microbubbles to produce strong bubble collapse *in vivo*, such as in blood vessels where the fluid-filled space is quite limited. In contrast to the model prediction of bubble dynamics *in vitro*, the expansion of LSW-induced cavitation bubbles *in vivo* could be severely hindered by surrounding tissue structure, resulting in nonspherical bubble deformation. Consequently, the violence of the subsequent inertial collapse of the bubble and the corresponding P_{w2} *in vivo* would be greatly reduced. This could be a primary reason for the general observation that the bioeffect produced by standard LSW *in vivo* is much less significant than that produced *in vitro*.[10] In contrast, the forced collapse of microbubbles capable of generating strong shock wave emission (and associated mechanical stresses) in limited fluid-filled space could have unique advantages for producing desirable biological effects *in vivo*. Further *in vivo* studies are needed to explore this unique property of the shock wave–IMB interaction.

3. Effect of truncated P^-_{LSW}

In vivo, the large expansion of LSW-induced cavitation bubbles is not only constrained by the surrounding tissue structure, it may also cause rupture of capillary and small blood vessels.[11] Thus, we further hypothesize that the optimal preceding-lithotripter shock wave sequence for effective and safe macromolecule delivery *in vivo* would be the one in which the LSW has a significantly reduced tensile component. To achieve this, an acoustic filter that can selectively reduce the tensile stress of the LSW, P^-_{LSW}, without significantly affecting the compressive pressure of the LSW is needed. Such an acoustic filter (or diode) was proposed by Riedlinger in 1989,[8] although its application to lithotripsy has not been reported. If we assume such an acoustic diode could be constructed for an HM-3 lithotripter, the impact on LSW-induced bubble expansion would be quite significant based on our model calculation. As shown in Fig. 9, theoretically when P^-_{LSW} is truncated from -10 to -0.5 MPa, the corresponding value of $R_{\max}$ and P_{w2} would drop monotonically from 1100 to 120 μm and from 41 to 4 MPa, respectively. This significant reduction in the maximum expansion of LSW-induced bubbles would greatly reduce the potential for vascular injury *in vivo* due to intraluminal bubble expansion.[11] Further experiments should be carried out to test this hypothesis.

C. Electrohydraulic lithotripter with pressure-release reflectors

Shock wave–IMB interaction may also be induced by inverted lithotripter shock waves (ILSW), which has a leading tensile component followed by a compressive wave.[12] Michael Bailey has described a method of using pressure-release reflector inserts inside an electrohydraulic lithotripter for the generation of ILSW.[4] Except for the inversion of the waveform, the ILSW has similar peak pressures, pulse duration, and acoustic energy compared to the standard LSW. However, because of the waveform inversion, cavitation activity is significantly suppressed, and minimal injury is produced in cells and renal tissue exposed to ILSW.[13,14] In the following, we will examine the basic features in bubble dy-

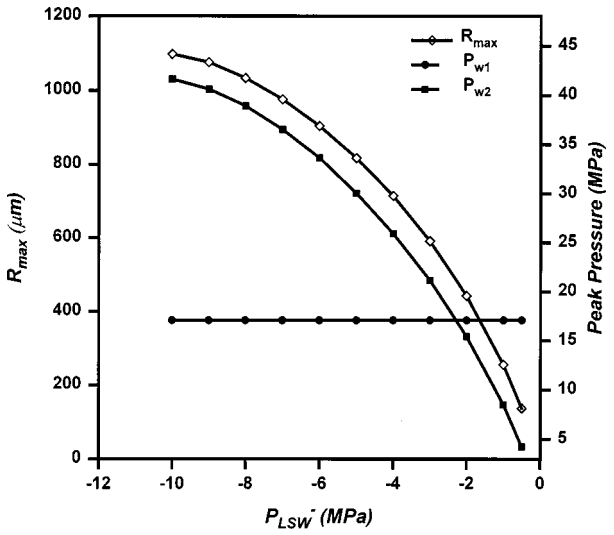

FIG. 9. Effect of truncation of the tensile pressure of LSW on maximum bubble radius and secondary shock wave emissions produced by a modified HM-3 lithotripter. $R_0 = 3\ \mu$m.

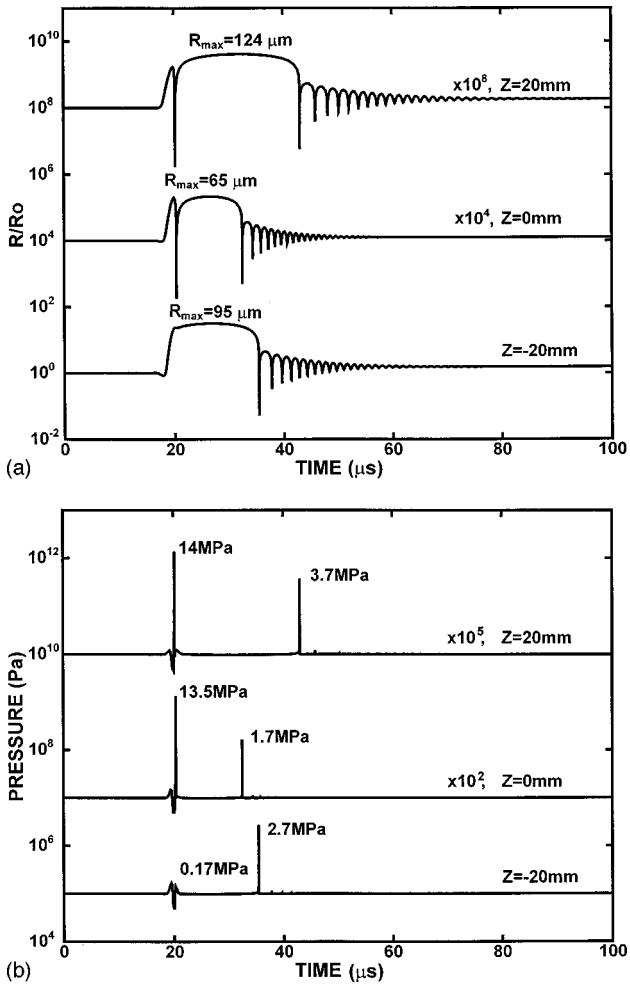

FIG. 10. Responses of a 3-μm cavitation nucleus to inverted lithotripter shock waves at three different positions along the axis of an experimental electrohydraulic lithotripter with pressure-release reflector (see Ref. 4). (a) Bubble radius normalized by the initial nucleus radius. (b) Corresponding secondary shock wave emissions in water calculated at a radial distance of 5 mm from the bubble center.

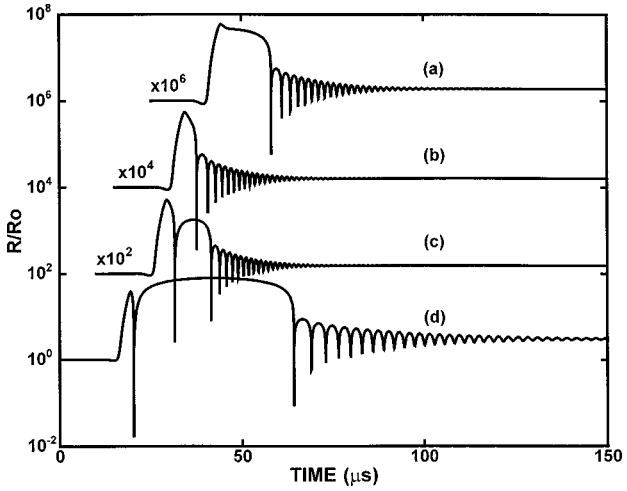

FIG. 11. Effect of the leading tensile pressure of ILSW, P_L^-, on bubble dynamics. The corresponding values of P_L^- are (a) -10 MPa, (b) -9 MPa, (c) -8.5 MPa, and (d) -6 MPa, respectively. In all four cases, $P^+/P_T^- = 40/-3.85$ MPa were used. Notice the transition from forced to nonforced collapse of the bubble at $P_L^- = -9$ MPa [see curve (b)]. $R_0 = 3$ μm.

namics produced by ILSW and compare them with that produced by preceding-lithotripter shock wave combination.

Figure 10(a) shows the predicted bubble response of a 3-μm nucleus to the three different ILSWs (see Fig. 3) measured at $z = -20$, 0 (F_2), and 20 mm along the major axis of an experimental electrohydraulic lithotripter equipped with a pressure-release reflector.[4] It can be seen that the bubble response is quite sensitive to the ratio of the leading peak negative pressure, P_L^-, to the ensuing peak compressive pressure P^+ of the wave (see also Fig. 3). When the ratio of P_L^-/P^+ is high, such as in the case of pressure waveform at $z = -20$ mm, the nuclei is first expanded by a strong leading tensile wave, and then the outward motion of the bubble is quickly slowed down by the ensuing compressive wave. However, because the initial expansion of the bubble is so strong, the compressive wave could only slightly reverse the motion of the bubble, but cannot force the bubble to collapse completely before the trailing tensile wave (P_T^-) reexpands the bubble again. On the other hand, for the pressure waveforms at $z = 0$ and 20 mm where the ratio of P_L^-/P^+ is low, the initial expansion of the bubble is not so strong that the ensuing compressive wave is sufficient to reverse the outward motion of the bubble, leading to a forced collapse of the bubble before its reexpansion by P_T^-. Correspondingly, the calculated shock wave emission (P_{w1}) in water is much higher for the bubble(s) with forced collapse than that without forced collapse [Fig. 10(b)]. The transition from forced collapse to nonforced collapse is clearly illustrated in Fig. 11 where P_L^- is hypothetically increased from -6 to -10 MPa while P^+ and P_T^- are kept unchanged. Initially, when P_L^- is relatively small, a forced collapse of the bubble is produced, followed immediately by a large reexpansion and then an inertial collapse of the bubble with subsequent ringing. As P_L^- becomes stronger, the forced collapse of the bubble becomes weaker, and the duration of the bubble reexpansion decreases. Eventually, when P_L^- approaches a critical value of -9 MPa, the forced collapse disappears, and only the inertial collapse is predicted after a time delay. Further increase of P_L^- will lengthen the time delay to the inertial collapse.

In comparison to the bubble dynamics generated by optimal preceding-lithotripter shock wave combination whereby forced collapse of an IMB is always produced, the bubble dynamics from ILSW is less consistent, and forced collapse of IMBs may not always occur. More importantly, the shock wave–IMB interaction produced by ILSW does not occur at the optimal phase of the IMB oscillation, as discussed previously.[1] This can be seen clearly by comparing the results in Fig. 10(b) (produced by ILSW) with those in Fig. 8(b) (from preceding-lithotripter shock wave combination). For a comparable preceding tensile wave, if the appropriate time delay were allowed for the IMB to grow to its maximum size before the LSW–IMB interaction, a significantly stronger P_{w1} would be generated. On the other hand, in general the maximum expansion of the bubble induced by ILSW is significantly reduced compared to that produced by a standard LSW. This feature, combined with the observation that minimal vascular injury is produced by ILSW in renal tissue, seems to corroborate the theory that intraluminal

bubble expansion is a primary mechanism for vascular injury during lithotripsy.[11]

III. CONCLUSIONS

The Gilmore model coupled with zeroth-order gas diffusion was used to simulate the bubble dynamics generated by various shock wave sequences of a modified XL-1 lithotripter. The results show that LSW–IMB interaction can generate strong secondary shock wave emission comparable to that produced by the inertial collapse of a much larger, millimeter-size bubble. The model prediction also confirms many of the features of bubble dynamics observed experimentally, in particular for bubble dynamics produced by different reflector configurations. This method was then extended to identify the optimal combination of preceding and lithotripter shock waves for producing the most desirable LSW–IMB interaction using a Dornier HM-3 lithotripter. The model calculation suggests that with appropriate PSW and interpulse delay between the PSW and LSW, the forced collapse of IMBs with strong secondary shock wave emission can be produced within a volume around the lithotripter focus. Further, it was demonstrated that truncation of the tensile stress of LSW could significantly reduce the large expansion of the bubble following LSW–IMB interaction, which may lessen the risk for vascular injury during shock wave exposure.

ACKNOWLEDGMENTS

This work was supported in part by NIH through Grant Nos. R21-HL60327, RO1-DK52985, and PO1-DK20543.

APPENDIX: THE GILMORE FORMULATION FOR BUBBLE DYNAMICS[2]

Considering the compressibility of the liquid, the radial oscillation of a single spherical bubble can be described by the original Gilmore formation:[15]

$$R\left(1-\frac{U}{C}\right)\frac{dU}{dt}+\frac{3}{2}\left(1-\frac{U}{3C}\right)U^2 = \left(1+\frac{U}{C}\right)H+\frac{1}{C}\left(1-\frac{U}{C}\right)R\frac{dH}{dt}, \tag{A1}$$

where R is the bubble radius, $U(=dR/dt)$ is the velocity of the bubble wall, and C and H are the speed of sound in the liquid at the bubble wall and the enthalpy difference between the liquid at pressure $P(R)$ and pressure P_∞, respectively, which are determined by

$$H=\int_{P_\infty}^{P(R)}\frac{dP}{\rho}, \tag{A2}$$

$$C=[C_l^2+(m-1)H]^{1/2}, \tag{A3}$$

where P and ρ are the time-varying pressure and density of liquid, P_∞ is the pressure at infinity, C_l is the infinitesimal speed of sound in the liquid, and m is a constant. When a lithotripter shock wave P_S is produced in the liquid far away from the bubble, we have $P_\infty=P_0+P_S$ where P_0 is the ambient pressure of the surrounding liquid. To determine H and C, the equation of state for a compressible fluid (Tait equation) and the pressure at the bubble wall, $P(R)$, in relation to the gas pressure inside the bubble (P_g), liquid viscosity (μ), and surface tension (σ) in the liquid are considered and given in the following,

$$P=A(\rho/\rho_0)^m-B, \tag{A4}$$

$$P(R)=P_g-\frac{2\sigma}{R}-\frac{4\mu}{R}U, \tag{A5}$$

where ρ_0 is the equilibrium liquid density, and $A=C_l^2\rho/P_0m$ with $m=7$ and $B=A-1$.

The instantaneous number of moles of gas n in a bubble may be calculated from the zeroth-order solution to the diffusion equation given by Eller and Flynn:[16]

$$n=n_0-4(\pi D)^{1/2}\int_0^\tau F(\tau')(\tau-\tau')^{-1/2}\,d\tau', \tag{A6}$$

where D is the diffusion constant of the gas in the liquid, n_0 is the number of moles of gas initially present in the bubble, and

$$\tau=\int_0^t R^4(t')\,dt', \tag{A7}$$

$$F(\tau)=C_0(P_g/P_0)-C_i, \tag{A8}$$

where

$$P_g=\left(P_0+\frac{2\sigma}{R_0}\right)\frac{n}{n_0}\left(\frac{R_0}{R}\right)^{3\eta}\left(\frac{R_{0n}}{R_0}\right)^{3(\eta-1)}, \tag{A9}$$

R_0 is the initial equilibrium radius of the bubble, $R_{0n}(t)$ is the time-varying equilibrium bubble radius, η is the polytropic exponent of the gas, C_0 is the saturation concentration of the gas in the liquid, and C_i is the initial concentration of the gas in the liquid far from the bubble.

As described by Akulichev,[17] the pressure distribution in the liquid at a distance r from the bubble center is given by

$$P_r(t)=A\left[\frac{2}{m+1}+\frac{m-1}{m+1}\left(1+\frac{m+1}{rC_l^2}G\right)^{1/2}\right]^{2m/(m-1)}-B, \tag{A10}$$

where G is an invariant of the bubble motion that may be specified at the bubble surface by

$$G=R(H+U^2/2). \tag{A11}$$

[1] P. Zhong, H. F. Lin, X. F. Xi, S. L. Zhu, and E. S. Bhogte, ''Shock wave-inertial microbubble interaction: Methodology, physical characterization, and bioeffect study,'' J. Acoust. Soc. Am. **105**, 1997–2009 (1999).

[2] C. C. Church, ''A theoretical study of cavitation generated by an extracorporeal shock wave lithotripter,'' J. Acoust. Soc. Am. **86**, 215–227 (1989).

[3] Z. Ding and S. M. Gracewski, ''Response of constrained and unconstrained bubbles to lithotripter shock wave pulses,'' J. Acoust. Soc. Am. **96**, 3636–3644 (1994).

[4] M. R. Bailey, ''Control of acoustic cavitation with application to lithotripsy,'' Ph.D. dissertation, Univ. of Texas at Austin, May 1997.

[5] M. J. Choi, A. J. Coleman, and J. E. Saunders, ''The influence of fluid properties and pulse amplitude on bubble dynamics in the field of a shock wave lithotripter,'' Phys. Med. Biol. **38**, 1561–1573 (1993).

[6] J. Staudenraus and W. Eisenmenger, ''Fiber-optic probe hydrophone for

ultrasonic and shock-wave measurements in water,'' Ultrasonics **31**, 267–273 (1993).
[7] A. J. Coleman and J. E. Saunders, ''A survey of the acoustic output of commercial extracorporeal shock wave lithotripters,'' Ultrasound Med. Biol. **15**, 213–227 (1989).
[8] R. Riedlinger, ''Acoustic diode,'' U.S. Patent 4618796 (1989).
[9] J. R. Rice, *Numerical Methods, Software, and Analysis* (Academic, San Diego, 1993), pp. 421–426.
[10] M. Delius, ''Medical applications and bioeffects of extracorporeal shock waves,'' Shock Waves **4**, 55–72 (1994).
[11] P. Zhong, I. Cioanta, S. L. Zhu, F. H. Cocks, and G. M. Preminger, ''Effects of tissue constraint on shock wave-induced bubble expansion *in vivo*,'' J. Acoust. Soc. Am. **104**, 3126–3129 (1998).
[12] M. Mueller, ''Experimental investigations on focusing of weak spherical shock waves in water by shallow ellipsoidal reflectors,'' Acustica **64**, 85–93 (1987).
[13] B. Jordan, M. R. Bailey, R. O. Cleveland, and L. A. Crum, ''Detection and control of lithotripsy-induced cavitation in blood,'' *Proceedings of the 16th International Congress on Acoustics and 135th meeting of the Acoustical Society of America*, Vol. 4, pp. 2809–2810 (1998).
[14] A. P. Evan, L. R. Willis, B. A. Connors, J. A. McAteer, J. E. Lingeman, R. O. Cleveland, M. R. Bailey, and L. A. Crum, ''Separation of cavitation and renal injury induced by shock wave lithotripsy (SWL) from SWL-induced impairment of renal hemodynamics,'' *Proceedings of the 16th International Congress on Acoustics and 135th meeting of the Acoustical Society of America*, Vol. 4, pp. 2487–2488 (1998).
[15] F. R. Gilmore, *The Growth or Collapse of a Spherical Bubble in a Viscous Compressible Liquid* (California Institute of Technology, Pasadena, CA, 1952), Report No. 26-4, pp. 1–40.
[16] A. Eller and H. G. Flynn, ''Rectified diffusion during nonlinear pulsations of cavitation bubbles,'' J. Acoust. Soc. Am. **37**, 493–501 (1965).
[17] V. A. Akulichev, in *High-Intensity Ultrasonic Fields*, edited by L. D. Rozenberg (Plenum, New York, 1971), pp. 203–259.
[18] T. G. Leighton, *The Acoustic Bubble* (Academic, London, 1994), pp. 329–332.

LETTERS TO THE EDITOR

This Letters section is for publishing (a) brief acoustical research or applied acoustical reports, (b) comments on articles or letters previously published in this Journal, and (c) a reply by the article author to criticism by the Letter author in (b). Extensive reports should be submitted as articles, not in a letter series. Letters are peer-reviewed on the same basis as articles, but usually require less review time before acceptance. Letters cannot exceed four printed pages (approximately 3000–4000 words) including figures, tables, references, and a required abstract of about 100 words.

Comments on "Ultrasonic interferences in polymer plates" [J. Acoust. Soc. Am. 104, 1232–1241 (1998)]

Michael A. Ainslie
CORDA Ltd., Apex Tower, 7 High Street, New Malden, Surrey KT3 4LH, England

(Received 15 December 1998; revised 24 June 1999; accepted 19 July 1999)

General formulas for reflection and transmission coefficients are quoted for a plane wave incident on a solid plate. The result used in the subject article is derived as a special case of the general solution. © *1999 Acoustical Society of America.* [S0001-4966(99)02411-X]

PACS numbers: 43.20.Gp, 43.30.Ma, 43.35.Mr, 43.35.Zc [AN]

In the subject article Juliac, Arman, and Harran (hereafter JAH)[1] consider nondestructive evaluation of a thin plate by comparing theoretical predictions of plane wave reflection and transmission coefficients with ultrasonic measurements. The theoretical coefficients are computed by coherent addition of pressure contributions from a finite number of reflected or transmitted ray multipaths. This procedure enables identification of specific ray paths responsible for observed interference features in the measurements, and this insight then allows important physical parameters of the plate to be deduced. JAH contrast this with Brekhovskikh's global matrix solution,[2] (extended by Glegg[3] to allow for a solid substrate) which, while providing a complete solution, does not provide the necessary insight to facilitate the deductive inversion.

JAH consider ray paths which are reflected up to a maximum of two times from the lower interface and state that a complete solution including all possible multipaths has (to their knowledge) never been achieved. The purpose of this letter is to point out that the complete sum has indeed been evaluated by at least three different research groups[4–6] and to derive the JAH result as a special case of the general solution.

References 4–6 use different methods to arrive at the same basic equations for reflection and transmission coefficients. In matrix form these are [see for example, Eqs. (22) from Ref. 6]

$$\mathbf{r}=\mathbf{r}_{12}+\mathbf{t}_{12}(\mathbf{1}-\mathbf{r}_{23}\mathbf{r}_{21})^{-1}\mathbf{r}_{23}\mathbf{t}_{21}, \tag{1a}$$

$$\mathbf{t}=\mathbf{t}_{12}(\mathbf{1}-\mathbf{r}_{23}\mathbf{r}_{21})^{-1}\mathbf{t}_{23}, \tag{1b}$$

where

$$\mathbf{r}_{ij}=\begin{pmatrix} r_{ij}^{pp} & r_{ij}^{ps} \\ r_{ij}^{sp} & r_{ij}^{ss} \end{pmatrix} \tag{2a}$$

and

$$\mathbf{t}_{ij}=\begin{pmatrix} t_{ij}^{pp} & t_{ij}^{ps} \\ t_{ij}^{sp} & t_{ij}^{ss} \end{pmatrix}. \tag{2b}$$

The partial coefficients $r_{ij}^{\alpha\beta}$ and $t_{ij}^{\alpha\beta}$ are defined as in Fig. 1. The resulting matrices in Eqs. (1a) and (1b) are the overall reflection coefficients **r** and **t** given by

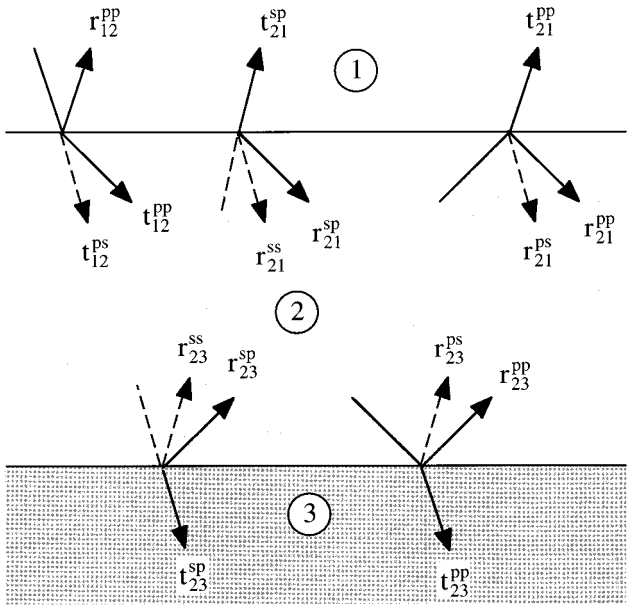

FIG. 1. Diagrammatic representation of partial reflection and transmission coefficients at the upper and lower boundaries. Compressional waves are represented by solid lines and shear waves by dashed lines.

TABLE I. Comparison between Eq. (4) and JAH expansions.

	Order	Equation (4) expansion	JAH equivalent
r^{pp}	ε^0	r_{12}^{pp}	R1
	ε^2	$t_{12}^{p\lambda} r_{23}^{\lambda\mu} t_{21}^{\mu p}$	R2–R5
	ε^4	$t_{12}^{p\lambda} r_{23}^{\lambda\mu} r_{21}^{\mu\nu} r_{23}^{\nu\sigma} t_{21}^{\sigma p}$	R6–R9
	ε^{2n+2}	$t_{12}^{p\lambda}[(\mathbf{r}_{23}\mathbf{r}_{21})^n]^{\lambda\mu} r_{23}^{\mu\nu} t_{21}^{\nu p}$ $(n \geqslant 0)$	N/A
t^{pp}	ε^1	$t_{12}^{p\lambda} t_{23}^{\lambda p}$	T1,T2
	ε^3	$t_{12}^{p\lambda} r_{23}^{\lambda\mu} r_{21}^{\mu\nu} t_{23}^{\nu p}$	T3–T6
	ε^{2n+1}	$t_{12}^{p\lambda}[(\mathbf{r}_{23}\mathbf{r}_{21})^n]^{\lambda\mu} t_{23}^{\mu p}$ $(n \geqslant 0)$	N/A

$$\mathbf{r} = \begin{pmatrix} r^{pp} & r^{ps} \\ r^{sp} & r^{ss} \end{pmatrix} \tag{3a}$$

and

$$\mathbf{t} = \begin{pmatrix} t^{pp} & t^{ps} \\ t^{sp} & t^{ss} \end{pmatrix}. \tag{3b}$$

Written in this form it is immediately apparent that Eqs. (1) are straightforward generalizations of the usual geometric series expressions for a fluid layer.[7] Notice that two-way phase and attenuation terms are included implicitly in $r_{23}^{\alpha\beta}$ (one-way in $t_{23}^{\alpha\beta}$).

The above equations are valid for a solid plate of arbitrary thickness sandwiched between two *solid* media.[5,6] As quoted here they apply to isotropic solids but can be generalized to anisotropic media as well.[5] The present use is for an isotropic solid plate immersed in a *fluid* so our interest is restricted to the top left elements r^{pp} and t^{pp}.

JAH consider the special case for which the partial reflection coefficients at the lower interface $r_{23}^{\alpha\beta}$ (that is, r_{23}^{pp}, r_{23}^{ps}, r_{23}^{sp}, and r_{23}^{ss}) are small, but not negligible, so that all waves are heavily attenuated each time they pass through the layer. If we let $\varepsilon_p(\varepsilon_s)$ be a ratio between 0 and 1 representing the decay in amplitude of a compressional (shear) wave during a single (i.e., one-way) traverse of the plate, it follows that $r_{23}^{\alpha\beta} \propto \varepsilon_\alpha \varepsilon_\beta$ and $t_{23}^{\alpha p} \propto \varepsilon_\alpha$. Defining ε to be the larger of ε_p and ε_s, it then makes sense to expand Eqs. (1) in powers of ε. The result is

$$r^{pp} \approx r_{12}^{pp} + t_{12}^{p\lambda} r_{23}^{\lambda\mu} (t_{21}^{\mu p} + r_{21}^{\mu\nu} r_{23}^{\nu\sigma} t_{21}^{\sigma p}) + O(\varepsilon^6), \tag{4a}$$

$$t^{pp} \approx t_{12}^{p\lambda} (t_{23}^{\lambda p} + r_{23}^{\lambda\mu} r_{21}^{\mu\nu} t_{23}^{\nu p}) + O(\varepsilon^5), \tag{4b}$$

where the use of repeated Greek indices λ, μ, ν, and σ implies summation over p and s, so that, for example,

$$r_{23}^{s\lambda} t_{21}^{\lambda p} \equiv r_{23}^{sp} t_{21}^{pp} + r_{23}^{ss} t_{21}^{sp}. \tag{5}$$

A term-by-term comparison shows that these expansions are equivalent to R1–R9 and T1–T6 respectively from JAH; this comparison is made easier by grouping terms of the same order in ε as in Table I. The two solutions are therefore equivalent to order ε^4. Although the general solution does not immediately provide the insight afforded by the JAH ray expansion and needed for their inversion, it permits a straightforward expansion to arbitrary order in ε; the insight is then provided by studying the effects of selectively discarding individual ray paths or groups of paths.

As a further example, consider an application from underwater acoustics where the role of the thin plate is played by a veneer of sand sandwiched between the ocean (above) and a solid rock substrate (below). Even though the sand layer may support shear waves, *p-s* mode conversion tends to be restricted to the sand–rock interface because of the good impedance match between water and water-saturated sand.[8] The effect of restricting mode conversion in this way is investigated in Ref. 6.

ACKNOWLEDGMENT

Constructive comments by Dr. A. J. Robins are gratefully acknowledged.

[1] E. Juliac, J. Arman, and D. Harran, ''Ultrasonic interferences in polymer plates,'' J. Acoust. Soc. Am. **104**, 1232–1241 (1998).
[2] L. M. Brekhovskikh, *Waves in Layered Media* (Academic, New York, 1980), p. 70.
[3] S. A. L. Glegg, ''The effective depth approximation for sound propagation in shallow water over a sediment layer and a hard rock basement,'' J. Acoust. Soc. Am. **94**, 3302–3311 (1993).
[4] M. Deschamps and C. Cao, ''Reflection/refraction of a solid layer by Debye's series expansion,'' Ultrasonics **29**, 288–293 (1991).
[5] S. I. Rokhlin and W. Huang, ''Ultrasonic wave interaction with a thin anisotropic layer between two anisotropic solids: Exact and asymptotic-boundary-condition methods,'' J. Acoust. Soc. Am. **92**, 1729–1742 (1992).
[6] M. A. Ainslie, ''Plane-wave reflection and transmission coefficients for a three-layered elastic medium,'' J. Acoust. Soc. Am. **97**, 954–961 (1995) [erratum: *ibid.* **105**, 2053 (1999)].
[7] C. S. Clay and H. Medwin, *Acoustical Oceanography: Principles and Applications* (Wiley, New York, 1977), p. 67.
[8] P. J. Vidmar, ''Ray path analysis of sediment shear wave effects on bottom reflection loss,'' J. Acoust. Soc. Am. **68**, 639–648 (1980).

Erratum: "Caustic diffraction fields in a downward refracting atmosphere" [J. Acoust. Soc. Am. 104, 3259–3272 (1998)]

Erik M. Salomons
TNO Institute of Applied Physics, P.O. Box 155, 2600 AD Delft, The Netherlands

[S0001-4966(99)06611-4]

PACS numbers: 43.28.Fp, 43.20.Dk, 43.50.Vt, 99.10.+g [LCS]

A typographical error has been found in Eq. (13) of the subject paper. The correct expression is

$$f_m = \left(\frac{r^2 + (z_1 - z_2)^2}{r^2} \right)^{1/2} \left(\frac{\cos \gamma_1 |\delta \gamma_1|}{|\sin \gamma_2| \rho} \right)^{1/2}, \tag{13}$$

where γ_2 is the elevation angle of the original ray at the receiver.

 0001-4966/99/106(5)/3036/1/$15.00